



IN THE UNITED STATES PATENT AND TRADEMARK OFFICE

In re Patent Application of

Applicants: Bednorz et al.

Serial No.: 08/479,810

Filed: June 7, 1995

For: NEW SUPERCONDUCTIVE COMPOUNDS HAVING HIGH TRANSITION
TEMPERATURE, METHODS FOR THEIR USE AND PREPARATION

Date: November 27, 2006

Docket: YO987-074BZ

Group Art Unit: 1751

Examiner: M. Kopec

Commissioner for Patents
United States Patent and Trademark Office
P.O. Box 1450
Alexandria, VA 22313-1450

APPEAL BRIEF

PART IX

CFR 37 § 41.37(c) (1) (ix)

SECTION 1

BRIEF ATTACHMENTS A TO Z

VOLUME 4

Respectfully submitted,

Dr. Daniel P. Morris, Esq.

Reg. No. 32,053

(914) 945-3217

IBM CORPORATION
Intellectual Property Law Dept.
P.O. Box 218
Yorktown Heights, New York 10598

BEST AVAILABLE COPY

BRIEF ATTACHMENT A



IN THE UNITED STATES PATENT AND TRADEMARK OFFICE

In re Patent Application of

Applicants: Bednorz et al.

Serial No.: 08/479,810

Filed: June 7, 1995

Date: March 1, 2005

Docket: YO987-074BZ

Group Art Unit: 1751

Examiner: M. Kopec

For: **NEW SUPERCONDUCTIVE COMPOUNDS HAVING HIGH TRANSITION
TEMPERATURE, METHODS FOR THEIR USE AND PREPARATION**

Commissioner for Patents
P.O. Box 1450
Alexandria, VA 22313-1450

FIRST SUPPLEMENTAL AMENDMENT

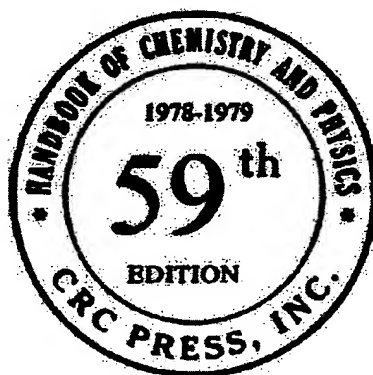
Sir:

In response to the Office Action dated July 28, 2004, please consider the
following:

ATTACHMENT A

CRC Handbook OF Chemistry and Physics

A Ready-Reference Book of Chemical and Physical Data



EDITOR

ROBERT C. WEAST, Ph.D.

*Vice President, Research, Consolidated Natural Gas Service Company, Inc.
Formerly Professor of Chemistry at Case Institute of Technology*

ASSOCIATE EDITOR

MELVIN J. ASTLE, Ph.D.

*Formerly Professor of Organic Chemistry at Case Institute of Technology
and
Manager of Research at Glidden-Durkee Division of SCM Corporation*

In collaboration with a large number of professional chemists and physicists
whose assistance is acknowledged in the list of general collaborators and in
connection with the particular tables or sections involved.



CRC PRESS, Inc.
2255 Palm Beach Lakes Blvd., West Palm Beach, Florida 33409

BEST AVAILABLE COPY

PROPERTIES OF RARE EARTH METALS

PROPERTIES OF RARE EARTH METALS

F. H. Spedding

Symbol	Crystal Structure at Room Temperature 25°C	Alloy Form Transition Temperatures Expressed in °C
Sc	Hex. (to 1335°)	bcc (above 1335°)
Y	Hex. (to 1478°)	bcc (above 1478°)
La	Hex. (to 310°) (usually contains fcc alloy)	fcc (310°-865°) bcc (above 865°)
Ce	fcc (~ 0° to 726°)	fcc (below 157° on cooling) (up to 24° on heating) Hex. (below 23° on cooling) (up to 168° on heating) bcc (above 795°) bcc (above 863°) bcc (above 926°)
Pr	Hex. (to 795°)	bcc (above 1235°)
Nd	Hex. (to 863°)	bcc (above 1289°)
Sm	* Rhomb. (to 926°)	bcc (above 1381°)
Eu	bcc	Not present pure metals
Gd	Hex. (to 1235°)	Not present pure metals
Tb	Hex. (to 1289°)	Not present pure metals
Dy	Hex. (to 1381°)	bcc (above 795°)
Ho	Hex.	Not present pure metals
Er	Hex.	Not present pure metals
Tm	Hex.	bcc (above 795°)
Yb	Hex. (to 795°)	Not present pure metals
Lu	Hex.	Not present pure metals

† Extrapolated from magnesium alloy studies. Hex. refers to close packed hexagonal. La, Ce, Pr, and Nd have a stacking order ABAC, the other rare earths ABAB. fcc refers to close packed face centered cubic with a stacking order ABC, bcc refers to body centered cubic. These high temperature forms are very soft and deform very easily.

* The rhombic Sm cell can be expressed as hexagonal with $a=3.6290\text{\AA}$, $c=2.6207$ and possess a stacking order ABABCBAC.

PERIODIC TABLE OF THE ELEMENTS

PERIODIC TABLE OF THE ELEMENTS

1a	2a	3a	4a	5a	6a	7a	0	Orbit										
1 H 1.0079 1							2 He 4.00260 2	K										
3 Li 6.94 2-1	4 Be 9.01218 2-2																	
11 Na 22.98977 2-8-1	12 Mg 24.305 2-8-2																	
19 K 39.0983 -8-8-1	20 Ca 40.08 -8-8-2	21 Sc 44.9559 -8-9-2	22 Ti 47.90 -8-10-2	23 V 50.9415 -8-11-2	24 Cr 51.996 -8-13-1	25 Mn 54.938 -8-13-2	26 Fe 55.847 -8-14-2	27 Co 58.9332 -8-15-2	28 Ni 58.71 -8-16-2	29 Cu 63.546 -8-18-1	30 Zn 65.38 -8-18-2	31 Ga 69.7235 -8-18-3	32 Ge 72.59 -8-18-4	33 As 74.9216 -8-18-5	34 Se 78.96 -8-18-6	35 Br 79.904 -8-18-7	36 Kr 83.80 -8-18-8	
37 Rb 85.467 -18-8-1	38 Sr 87.62 -18-8-2	39 Y 88.9059 -18-9-2	40 Zr 91.22 -18-10-2	41 Nb 92.9064 -18-12-1	42 Mo 95.94 -18-13-1	43 Tc 98.9062 -18-13-2	44 Ru 101.07 -18-13-3	45 Rh 102.9055 -18-16-1	46 Pd 106.4 -18-16-2	47 Ag 107.868 -18-18-1	48 Cd 112.41 -18-18-2	49 In 114.82 -18-18-3	50 Sn 118.69 -18-18-4	51 Sb 121.75 -18-18-5	52 Te 127.60 -18-18-6	53 I 126.9045 -18-18-7	54 Xe 131.30 -18-18-8	M-N-O
55 Cs 132.9054 -18-8-1	56 Ba 137.33 -18-8-2	57 La 138.9055 -18-9-2	58 Ce 140.12 -20-8-2	59 Pr 140.9077 -21-8-2	60 Nd 144.24 -22-8-2	61 Pm 144.9127 -23-8-2	62 Sm 150.4 -24-8-2	63 Eu 151.96 -25-8-2	64 Gd 157.25 -26-8-2	65 Tb 158.9254 -27-8-2	66 Dy 162.50 -28-8-2	67 Ho 164.9304 -29-8-2	68 Er 167.26 -30-8-2	69 Tm 168.9342 -31-8-2	70 Yb 173.04 -32-8-2	71 Lu 174.967 ± 0.003 -32-9-2		
87 Fr (223) -18-8-1	88 Ra 226.0254 -18-8-2	89 Ac (227) -18-9-2	90 Th 232.0381 -18-10-2	91 Pa 231.0359 -20-9-2	92 U 238.029 -21-9-2	93 Np 237.0482 -22-9-2	94 Pu 244.0642 -24-8-2	95 Am (243) -25-8-2	96 Cm (247) -26-8-2	97 Bk (247) -27-8-2	98 Cf (251) -28-8-2	99 Es (254) -29-8-2	100 Fm (257) -30-8-2	101 Md (258) -31-8-2	102 No (259) -32-8-2	103 Lr (260) -32-9-2		O-P-Q

KEY TO CHART

Atomic Number — 50 +2
Symbol — Sn +4
Atomic Weight — 118.69
18 18 4

— Oxidation States
— Electron Configuration

Transition Elements

Group 8

Transition Elements

*Lanthanides	58 Ce 140.12 -20-8-2	59 Pr 140.9077 -21-8-2	60 Nd 144.24 -22-8-2	61 Pm 144.9127 -23-8-2	62 Sm 150.4 -24-8-2	63 Eu 151.96 -25-8-2	64 Gd 157.25 -26-8-2	65 Tb 158.9254 -27-8-2	66 Dy 162.50 -28-8-2	67 Ho 164.9304 -29-8-2	68 Er 167.26 -30-8-2	69 Tm 168.9342 -31-8-2	70 Yb 173.04 -32-8-2	71 Lu 174.967 ± 0.003 -32-9-2
**Actinides	90 Th 232.0381 -18-10-2	91 Pa 231.0359 -20-9-2	92 U 238.029 -21-9-2	93 Np 237.0482 -22-9-2	94 Pu 244.0642 -24-8-2	95 Am (243) -25-8-2	96 Cm (247) -26-8-2	97 Bk (247) -27-8-2	98 Cf (251) -28-8-2	99 Es (254) -29-8-2	100 Fm (257) -30-8-2	101 Md (258) -31-8-2	102 No (259) -32-8-2	103 Lr (260) -32-9-2

Numbers in parentheses are mass numbers of most stable isotope of that element.

BRIEF ATTACHMENT B

IN THE UNITED STATES PATENT AND TRADEMARK OFFICE

In re Patent Application of

Applicants: Bednorz et al.

Serial No.: 08/479,810

Filed: June 7, 1995

For: **NEW SUPERCONDUCTIVE COMPOUNDS HAVING HIGH TRANSITION
TEMPERATURE, METHODS FOR THEIR USE AND PREPARATION**

Date: March 1, 2005

Docket: YO987-074BZ

Group Art Unit: 1751

Examiner: M. Kopec

Commissioner for Patents
P.O. Box 1450
Alexandria, VA 22313-1450

FIRST SUPPLEMENTAL AMENDMENT

Sir:

In response to the Office Action dated July 28, 2004, please consider the
following:

ATTACHMENT B

Introduction to Ceramics

Second Edition

W. D. Kingery

PROFESSOR OF CERAMICS
MASSACHUSETTS INSTITUTE OF TECHNOLOGY

H. K. Bowen

ASSOCIATE PROFESSOR OF CERAMICS
MASSACHUSETTS INSTITUTE OF TECHNOLOGY

D. R. Uhlmann

PROFESSOR OF CERAMICS AND POLYMERS
MASSACHUSETTS INSTITUTE OF TECHNOLOGY

A Wiley-Interscience Publication

JOHN WILEY & SONS, New York • Chichester • Brisbane • Toronto

The necessary
the recent avail
turing methods [
(1970); F. H. No
Norton, *Elemen*
(1974); F. V. T
Ogden Publ. C

or prepare fine particles, shape them, and then stick them back together by heating. The second basic process is to melt the material to form a liquid and then shape it during cooling and solidification; this is most widely practiced in forming glasses. For completeness, we should also mention forming shapes in a mold or by dipping a form with a slurry containing a ceramic binder such as portland cement or ethyl silicate.

Raw Materials. The types of minerals found in nature are controlled mainly by the abundance of the elements and their geochemical characteristics. Since oxygen, silicon, and aluminum together account for 90% of the elements in the earth's crust, as shown in Fig. 1.1, it is not surprising that the dominant minerals are silicates and aluminum silicates. These, together with other mineral compounds of oxygen, constitute the great bulk of naturally occurring ceramic raw materials.

The mineral raw materials used in the ceramic industry are mainly

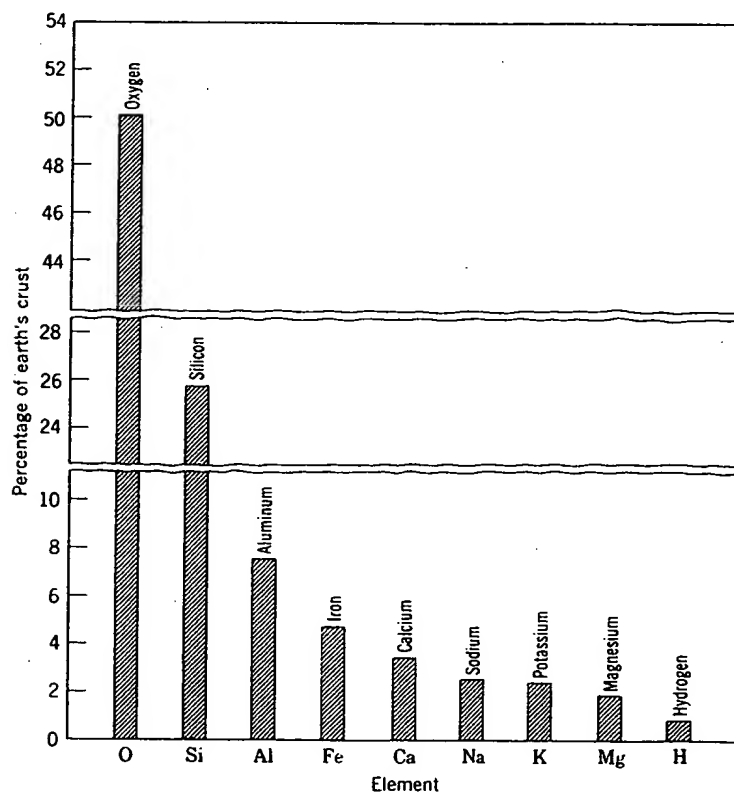


Fig. 1.1 Abundance of common elements in the earth's crust.

inorganic nonmetallic crystalline solids formed by complex geologic processes. Their ceramic properties are largely determined by the crystal structure and the chemical composition of their essential constituents and the nature and amounts of accessory minerals present. The mineralogic characteristics of such materials and therefore their ceramic properties are subject to wide variation among different occurrences or even within the same occurrence, depending on the geological environment in which the mineral deposit was formed as well as the physical and chemical modifications that have taken place during subsequent geological history.

Since silicate and aluminum silicate materials are widely distributed, they are also inexpensive and thus provide the backbone of high-tonnage products of the ceramic industry and determine to a considerable extent its form. Low-grade clays are available almost everywhere; as a result, the manufacture of building brick and tile not requiring exceptional properties is a localized industry for which extensive beneficiation of the raw material is not appropriate. In contrast, for fine ceramics requiring the use of better-controlled raw materials, the raw materials are normally beneficiated by mechanical concentration, froth floatation, and other relatively inexpensive processes. For materials in which the value added during manufacture is high, such as magnetic ceramics, nuclear-fuel materials, electronic ceramics, and specialized refractories, chemical purification and even chemical preparation of raw materials may be necessary and appropriate.

The raw materials of widest application are the clay minerals—fine-particle hydrous aluminum silicates which develop plasticity when mixed with water. They vary over wide limits in chemical, mineralogical, and physical characteristics, but a common characteristic is their crystalline layer structure, consisting of electrically neutral aluminosilicate layers, which leads to a fine particle size and platelike morphology and allows the particles to move readily over one another, giving rise to physical properties such as softness, soapy feel, and easy cleavage. Clays perform two important functions in ceramic bodies. First, their characteristic plasticity is basic to many of the forming processes commonly used; the ability of clay-water compositions to be formed and to maintain their shape and strength during drying and firing is unique. Second, they fuse over a temperature range, depending on composition, in such a way as to become dense and strong without losing their shape at temperatures which can be economically attained.

The most common clay minerals and those of primary interest to ceramists, since they are the major component of high-grade clays, are based on the kaolinite structure, $\text{Al}_2(\text{Si}_2\text{O}_5)(\text{OH})_4$. Other compositions often encountered are shown in Table 1.1.

st
M
of
m
st

an
in
ab
in
ab
oc
as
ma
bo
br
th
by

sti
(o
cal
gla
fel
Na
ma
ro
we
gro
ref

Table 1.1. Ideal Chemical Formulas of the Clay Minerals

Kaolinite	$\text{Al}_2(\text{Si}_2\text{O}_5)(\text{OH})_4$
Halloysite	$\text{Al}_2(\text{Si}_2\text{O}_5)(\text{OH})_4 \cdot 2\text{H}_2\text{O}$
Pyrophyllite	$\text{Al}_2(\text{Si}_2\text{O}_5)_2(\text{OH})_2$
Montmorillonite	$\left(\text{Al}_{1.67} \text{Na}_{0.33} \text{Mg}_{0.33} \right) (\text{Si}_2\text{O}_5)_2 (\text{OH})_2$
Mica	$\text{Al}_2\text{K}(\text{Si}_{1.5}\text{Al}_{0.5}\text{O}_5)_2 (\text{OH})_2$
Illite	$\text{Al}_{2-x}\text{Mg}_x\text{K}_{1-y}(\text{Si}_{1.5-y}\text{Al}_{0.5+y}\text{O}_5)_2 (\text{OH})_2$

A related material is talc, a hydrous magnesium silicate with a layer structure similar to the clay minerals and having the ideal formula $\text{Mg}_3(\text{Si}_2\text{O}_5)_2(\text{OH})_2$. Talc is an important raw material for the manufacture of electrical and electronic components and for making tile. Asbestos minerals are a group of hydrous magnesium silicates which have a fibrous structure. The principal variety is chrysotile, $\text{Mg}_3\text{Si}_2\text{O}_5(\text{OH})_4$.

In addition to the hydrous silicates already discussed, anhydrous silica and silicate materials are basic raw materials for much of the ceramic industry. SiO_2 is a major ingredient in glass, glazes, enamels, refractories, abrasives, and whiteware compositions. It is widely used because it is inexpensive, hard, chemically stable, and relatively infusible and has the ability to form glasses. There is a variety of mineral forms in which silica occurs, but by far the most important as a raw material is quartz. It is used as quartzite rock, as quartz sand, and as finely ground *potter's flint*. The major source of this material is sandstone, which consists of lightly bonded quartz grains. A denser quartzite, *gannister*, is used for refractory brick. Quartz is also used in the form of large, nearly perfect crystals, but these have been mostly supplanted by synthetic crystals, manufactured by a hydrothermal process.

Together with quartz, which serves as a refractory backbone constituent, and clay, which provides plasticity, traditional triaxial porcelains (originally invented in China) include feldspar, an anhydrous aluminosilicate containing K^+ , Na^+ , or Ca^{2+} as a flux which aids in the formation of a glass phase. The major materials of commercial interest are potash feldspar (microcline or orthoclase), $\text{K}(\text{AlSi}_3)\text{O}_8$, soda feldspar (albite), $\text{Na}(\text{AlSi}_3)\text{O}_8$, and lime feldspar (anorthite), $\text{Ca}(\text{Al}_2\text{Si}_2)\text{O}_8$. Other related materials sometimes used are nepheline syenite, a quartzfree igneous rock composed of nephelite, $\text{Na}_2(\text{Al}_2\text{Si}_2)\text{O}_8$, albite, and microcline; also wollastonite, CaSiO_3 . One group of silicate minerals, the sillimanite group, having the composition Al_2SiO_5 , is used for the manufacture of refractories.

Most of the naturally occurring nonsilicate materials are used primarily as refractories. Aluminum oxide is mostly prepared from the mineral bauxite by the Bayer process, which involves the selective leaching of the alumina by caustic soda, followed by the precipitation of aluminum hydroxide. Some bauxite is used directly in the electric-furnace production of alumina, but most is first purified. Magnesium oxide is produced both from natural magnesite, MgCO_3 , and from magnesium hydroxide, Mg(OH)_2 , obtained from seawater or brines. Dolomite, a solid solution of calcium and magnesium carbonates with the formula $\text{CaMg(CO}_3)_2$, is used to make basic brick for use in the steel industry. Another refractory widely used for metallurgical purposes is chrome ore, which consists primarily of a complex solid solution of spinels, $(\text{Mg,Fe})(\text{Al,Cr})_2\text{O}_4$, which make up most of the material; the remainder consists of various magnesium silicates.

Other mineral-based materials which are widely used include soda ash, Na_2CO_3 , mostly manufactured from sodium chloride; borate materials including kernite, $\text{Na}_2\text{B}_4\text{O}_7 \cdot 4\text{H}_2\text{O}$, and borax, $\text{Na}_2\text{B}_4\text{O}_7 \cdot 10\text{H}_2\text{O}$, used as fluxing agents; fluorspar, CaF_2 , used as a powerful flux for some glazes and glasses; and phosphate materials mostly derived from apatite, $\text{Ca}_5(\text{OH,F})(\text{PO}_4)_3$.

Although most traditional ceramic formulations are based on the use of natural mineral materials which are inexpensive and readily available, an increasing fraction of specialized ceramic ware depends on the availability of chemically processed materials which may or may not start directly from mined products and in which the particle-size characteristics and chemical purity are closely controlled. Silicon carbide for abrasives is manufactured by electrically heating mixtures of sand and coke to a temperature of about 2200°C where they react to form SiC and carbon monoxide. Already mentioned, seawater magnesia, Bayer alumina, and soda ash are widely used chemical products. In the manufacture of barium titanate capacitors, chemically purified titania and barium carbonate are used as raw materials. A wide range of magnetic ceramics is manufactured from chemically precipitated iron oxide. Nuclear-fuel elements are manufactured from chemically prepared UO_2 . Single crystals of sapphire and ruby and also porefree polycrystalline aluminum oxide are prepared from aluminum oxide made by precipitating and carefully calcining alum in order to maintain good control of both chemistry and particle size. Special techniques of material preparation such as freeze-drying droplets of solution to form homogeneous particles of small size and high purity are receiving increasing attention, as is the vapor deposition of thin-film materials in a carefully controlled chemical and physical form. In general, raw-material preparation is clearly headed

towa
tion
partic
on m

For
firing
conce
the ra
which
prepa
have
micro
beles
suspe
depen
stable
propo
coher
of the
partic
size, i
Mixing
the co
achiev
partic
result
numb
with a
during

In a
intima
within
firing
usual
ball m
impro
tion o
either
which
mainta
gates,
formin

toward the increasing use of mechanical, physical, and chemical purification and upgrading of raw materials together with special control of particle size and particle-size distribution and away from the sole reliance on materials in the form found in nature.

Forming and Firing. The most critical factors affecting forming and firing processes are the raw materials and their preparation. We have to be concerned with both the particle size and the particle-size distribution of the raw materials. Typical clay materials have a particle-size distribution which ranges from 0.1 to 50 microns for the individual particles. For the preparation of porcelain compositions the flint and feldspar constituents have a substantially larger particle size ranging between 10 and 200 microns. The fine-particle constituents, which for special ceramics may be less than 1 micron, are essential for the forming process, since colloidal suspensions, plastic mixes with a liquid-phase binder, and dry pressing all depend on very small particles flowing over one another or remaining in a stable suspension. For suspensions, the settling tendency is directly proportional to the density and particle size. For plastic forming the coherence of the mass and its yield point are determined by the capillarity of the liquid between particles; this force is inversely proportional to the particle size. However, if all the material were of a uniformly fine particle size, it would not be feasible to form a high concentration of solids. Mixing in a coarser material allows the fines to fill the interstices between the coarse particles such that a maximum particle-packing density is achieved at a ratio of about 70% coarse and 30% fine material when two particle sizes are used. In addition, during the drying process, shrinkage results from the removal of water films between particles. Since the number of films increases as the particle size decreases, bodies prepared with a liquid binder and all fine-particle materials have a high shrinkage during drying and the resultant problems of warping and distortion.

In addition to a desired particle size and particle-size distribution, intimate mixing of material is necessary for uniformity of properties within a body and for the reaction of individual constituents during the firing process. For preparing slurries or a fine-grain plastic mass, it is the usual practice to use wet mixing, with the raw materials placed together in ball mills or a blunger. Shearing stresses developed in the mixing process improve the properties of a plastic mix and ensure the uniform distribution of the fine-grain constituent. For dewatering the wet-milled mix, either a filter press may be used, or more commonly spray-drying, in which droplets of the slurry are dried with a countercurrent of warm air to maintain their uniform composition during drying. The resulting aggregates, normally 1 mm or so in size, flow and deform readily in subsequent forming.

Since the firing process also depends on the capillary forces resulting from surface energy to consolidate and densify the material and since these forces are inversely proportional to particle size, a substantial percentage of fine-particle material is necessary for successful firing. The clay minerals are unique in that their fine particle size provides both the capability for plastic forming and also sufficiently large capillary forces for successful firing. Other raw materials have to be prepared by chemical precipitation or by milling into the micron particle range for equivalent results to be obtained.

Perhaps the simplest method of compacting a ceramic shape consists of forming a dry or slightly damp powder, usually with an organic binder, in a metal die at sufficiently high pressures to form a dense, strong piece. This method is used extensively for refractories, tiles, special electrical and magnetic ceramics, spark-plug insulators and other technical ceramics, nuclear-fuel pellets, and a variety of products for which large numbers of simple shapes are required. It is relatively inexpensive and can form shapes to close tolerances. Pressures in the range of 3000 to 30,000 psi are commonly used, the higher pressures for the harder materials such as pure oxides and carbides. Automatic dry pressing at high rates of speed has been developed to a high state of effectiveness. One limitation is that for a shape with a high length-to-diameter ratio the frictional forces of the powder, particularly against the die wall, lead to pressure gradients and a resulting variation of density within the piece. During firing these density variations are eliminated by material flow during sintering; it necessarily follows that there is a variation in shrinkage and a loss of the original tolerances. One modification of the dry-pressing method which leads to a more uniform density is to enclose the sample in a rubber mold inserted in a hydrostatic chamber to make pieces by hydrostatic molding, in which the pressure is more uniformly applied. Variations in sample density and shrinkage are less objectionable. This method is widely used for the manufacture of spark-plug insulators and for special electrical components in which a high degree of uniformity and high level of product quality are required.

A quite different method of forming is to extrude a stiff plastic mix through a die orifice, a method commonly used for brick, sewer pipe, hollow tile, technical ceramics, electrical insulators, and other materials having an axis normal to a fixed cross section. The most widely practiced method is to use a vacuum auger to eliminate air bubbles, thoroughly mix the body with 12 to 20% water, and force it through a hardened steel or carbide die. Hydraulic piston extruders are also widely used.

The earliest method of forming clay ware, one still widely used, is to add enough water so that the ware can readily be formed at low pressures.

This may be done under hand pressure such as building ware with coils, free-forming ware, or hand throwing on a potter's wheel. The process can be mechanized by soft-plastic pressing between porous plaster molds and also by automatic *jigging*, which consists of placing a lump of soft plastic clay on the surface of a plaster-of-paris mold and rotating it at about 400 rpm while pulling a profile tool down on the surface to spread the clay and form the upper surface.

When a larger amount of water is added, the clay remains sticky plastic until a substantial amount has been added. Under a microscope it is seen that individual clay particles are gathered in aggregates or flocs. However, if a small quantity of sodium silicate is added to the system, there is a remarkable change, with a substantial increase in fluidity resulting from the individual particles being separated or *deflocculated*. With proper controls a fluid suspension can be formed with as little as 20% liquid, and a small change in the liquid content markedly affects the fluidity. When a suspension such as this is cast into a porous plaster-of-paris mold, the mold sucks liquid from the contact area, and a hard layer is built on the surface. This process can be continued until the entire interior of the mold is filled (solid casting) or the mold can be inverted and the excess liquid poured out after a suitable wall thickness is built up (drain casting).

In each of the processes which require the addition of some water content, the drying step in which the liquid is removed must be carefully controlled for satisfactory results, more so for the methods using a higher liquid content. During drying, the initial drying rate is independent of the water content, since in this period there is a continuous film of water at the surface. As the liquid evaporates, the particles become pressed more closely together and shrinkage occurs until they are in contact in a solid structure free from water film. During the shrinkage period, stresses, warping, and possibly cracks may develop because of local variations in the liquid content; during this period rates must be carefully controlled. Once the particles are in contact, drying can be continued at a more rapid rate without difficulty. For the dry-pressing or hydrostatic molding process, the difficulties associated with drying are avoided, an advantage for these methods.

After drying, ceramic ware is normally fired to temperatures ranging from 700 to 1800°C, depending on the composition and properties desired. Ware which is to be glazed or decorated may be fired in different ways. The most common procedure is to fire the ware without a glaze to a sufficiently high temperature to mature the body; then a glaze is applied and fired at a low temperature. Another method is to fire the ware initially to a low temperature, a *bisque* fire; then apply the glaze and mature the body and glaze together at a higher temperature. A third method is to

apply the glaze to the unfired ware and heat them together in a one-fire process.

During the firing process, either a viscous liquid or sufficient atomic mobility in the solid is developed to permit chemical reactions, grain growth, and sintering; the last consists of allowing the forces of surface tension to consolidate the ware and reduce the porosity. The volume shrinkage which occurs is just equal to the porosity decrease and varies from a few to 30 or 40 vol%, depending on the forming process and the ultimate density of the fired ware. For some special applications, complete density and freedom from all porosity are required, but for other applications some residual porosity is desirable. If shrinkage proceeds at an uneven rate during firing or if part of the ware is restrained from shrinking by friction with the material on which it is set, stresses, warping, and cracking can develop. Consequently, care is required in setting the ware to avoid friction. The rate of temperature rise and the temperature uniformity must be controlled to avoid variations in porosity and shrinkage. The nature of the processes taking place is discussed in detail in Chapters 11 and 12.

Several different types of kilns are used for firing ware. The simplest is a skove kiln in which a benchwork of brick is set up inside a surface coating with combustion chambers under the material to be fired. Chamber kilns of either the up-draft or down-draft type are widely used for batch firing in which temperature control and uniformity need not be too precise. In order to achieve uniform temperatures and maximum use of fuel, chamber kilns in which the air for combustion is preheated by the cooling ware in an adjacent chamber, the method used in ancient China, is employed. The general availability of more precise temperature controls for gas, oil, and electric heating and the demands for ware uniformity have led to the increased use of tunnel kilns in which a temperature profile is maintained constant and the ware is pushed through the kiln to provide a precise firing schedule under conditions such that effective control can be obtained.

Melting and Solidification. For most ceramic materials the high volume change occurring during solidification, the low thermal conductivity, and the brittle nature of the solid phase have made melting and solidification processes comparable with metal casting and foundry practice inappropriate. Recently, techniques have been developed for unidirectional solidification in which many of these difficulties can be substantially avoided. This process has mainly been applied to forming controlled structures of metal alloys which are particularly attractive for applications such as turbine blades for high-temperature gas turbines. So far as we are aware, there is no large scale manufacture of ceramics in this way,

but we anticipate that the development of techniques for the unidirectional solidification of ceramics will be an area of active research during the next decade.

Another case in which these limitations do not apply is that of glass-forming materials in which the viscosity increases over a broad temperature range so that there is no sharp volume discontinuity during solidification and the forming processes can be adjusted to the fluidity of the glass. Glass products are formed in a high-temperature viscous state by five general methods: (1) blowing, (2) pressing, (3) drawing, (4) rolling, and (5) casting. The ability to use these processes depends to a large extent on the viscous flow characteristics of the glass and its dependence on temperature. Often surface chilling permits the formation of a stable shape while the interior remains sufficiently fluid to avoid the buildup of dangerous stresses. Stresses generated during cooling are relieved by annealing at temperatures at which the force of gravity is insufficient to cause deformation. This is usually done in an annealing oven or lehr which, for many silicate glasses, operates at temperatures in the range of 400 to 500°C.

The characteristics most impressive about commercial glass-forming operations are the rapidity of forming and the wide extent of automation. Indeed, this development is typical of the way in which technical progress affects an industry. Before the advent of glass-forming machinery, a major part of the container industry was based on ceramic stoneware. Large numbers of relatively small stoneware potters existed solely for the manufacture of containers. The development of automatic glass-forming machinery allowing the rapid and effective production of containers on a continuous basis has eliminated stoneware containers from common use.

Special Processes. In addition to the broadly applicable and widely used processes discussed thus far, there is a variety of special processes which augment, modify, extend, or replace these forming methods. These include the application of glazes, enamels, and coatings, hot-pressing materials with the combined application of pressure and temperature, methods of joining metals to ceramics, glass crystallization, finishing and machining operations, preparation of single crystals, and vapor-deposition processes.

Much ceramic ware is coated with a glaze, and porcelain enamels are commonly applied on a base of sheet steel or cast iron as well as for special jewelry applications. Glazes and enamels are normally prepared in a wet process by milling together the ingredients and then applying the coating by brushing, spraying, or dipping. For continuous operation, spray coating is most frequently used, but for some applications more satisfactory coverage can be obtained by dipping or painting. For

porcelain enamels on cast iron, large castings heated in a furnace are coated with a dry enamel powder which must be distributed uniformly over the surface, where it fuses and sticks. In addition to these widely used processes, special coatings for technical ware have been applied by flame spraying to obtain a refractory dense layer; vacuum-deposited coatings have been formed by evaporation or cathodic sputtering; coatings have been applied by chemical vapor deposition; electrophoretic deposition has been applied; and other specialized techniques have had some limited applications.

To obtain a high density together with fine particle size, particularly for materials such as carbides and borides, the combination of pressure with high temperature is an effective technique mostly used for small samples of a simple configuration. At lower temperatures, glass-bonded mica is formed in this way for use as an inexpensive insulation. One of the main advantages of the hot-pressing method is that material preparation is less critical than for the sintering processes, which require a high degree of material uniformity for successful applications of the highest-quality products. The main difficulties with hot-pressing techniques are applying the method to large shapes and the time required for heating the mold and sample, which makes the method slow and expensive.

For many applications, joining processes are necessary to form fabricated units. In manufacturing teacups, for example, the handle is normally molded separately, dipped in a slip, and stuck on the body of the cup. Sanitary fixtures of complex design are similarly built up from separately formed parts. For many electronic applications requiring pressure-tight seals, it is necessary to form a bond between metals and ceramics. For glass-metal seals, the main problem is matching the expansion coefficient of the glass to that of the metal and designing the seal so that large stresses do not develop in use; special metal alloys and sealing glasses have been designed for this purpose. For crystalline ceramics, the most widely applied method has been to use a molybdenum-manganese layer which, when fired under partially oxidizing conditions, forms an oxide that reacts with the ceramic to give an adhesive bonding layer. In some cases, reactive metal brazes containing titanium or zirconium have been used.

One of the most important developments in ceramic forming has been to use a composition which can be formed as a glass and then transformed subsequent to forming into a product containing crystals of controlled size and amount. Classic examples of this are the striking gold-ruby glasses, in which the color results from the formation of colloidal gold particles. During rapid initial cooling, nucleation of the metal particles

occurs; subsequent reheating into the growth region develops proper crystallite sizes for the colloidal ruby color. In the past 10 years there has been extensive development of glasses in which the volume of crystals formed is much larger than the volume of the residual glass. By controlled nucleation and growth, glass-ceramics are made in which the advantage of automatic glass-forming processes is combined with some of the desirable properties of a highly crystalline body.

For most forming operations, some degree of finishing or machining is required which may range from fettling the mold lines from a slip-cast shape to diamond-grinding the final contour of a hard ceramic. For hard materials such as aluminum oxide, as much machining as feasible is done in the unfired state or the presintered state, with final finishing only done on the hard, dense ceramic where required.

A number of processes have been developed for the formation of ceramics directly from the vapor phase. Silica is formed by the oxidation of silicon tetrachloride. Boron and silicon carbide fibers are made by introducing a volatile chloride with a reducing agent into a hot zone, where deposition occurs on a fine tungsten filament. Pyrolytic graphite is prepared by the high-temperature deposition of graphite layers on a substrate surface by the pyrolytic decomposition of a carbon-containing gas. Many carbides, nitrides, and oxides have been formed by similar processes. For electronic applications, the development of single-crystal films by these techniques appears to have many potential applications.

Thin-wafer substrates are formed by several techniques, mostly from alumina. A widely used development is the technique in which a fluid body is prepared with an organic binder and uniformly spread on a moving nonporous belt by a doctor blade to form thin, tough films which can subsequently be cut to shape; holes can be introduced in a high-speed punch press.

There is an increasing number of applications in which it is necessary or desirable to have single-crystal ceramics because of special optical, electrical, magnetic, or strength requirements. The most widespread method of forming these is the Czochralski process, in which the crystal is slowly pulled from a molten melt, a process used for aluminum oxide, ruby, garnet, and other materials. In the Verneuil process a liquid cap is maintained on a growing boule by the constant-rate addition of powdered material at the liquid surface. For magnetic and optical applications thin single-crystal films are desirable which have been prepared by epitaxial growth from the vapor phase. Hydrothermal growth from solution is widely used for the preparation of quartz crystals, largely replacing the use of natural mineral crystals for device applications.

1.3 Ceramic Products

The diversity of ceramic products, which range from microscopic single-crystal whiskers, tiny magnets, and substrate chips to multiton refractory furnace blocks, from single-phase closely controlled compositions to multiphase multicomponent brick, and from porefree transparent crystals and glasses to lightweight insulating foams is such that no simple classification is appropriate. From the point of view of historical development and tonnage produced, it is convenient to consider the mineral-raw-material products, mostly silicates, separately from newer nonsilicate formulations.

Traditional Ceramics. We can define traditional ceramics as those comprising the silicate industries—primarily clay products, cement, and silicate glasses.

The art of making pottery by forming and burning clay has been practiced from the earliest civilizations. Indeed, the examination of pottery fragments has been one of the best tools of the archeologist. Burnt clayware has been found dating from about 6500 B.C. and was well developed as a commercial product by about 4000 B.C.

Similarly, the manufacture of silicate glasses is an ancient art. Naturally occurring glasses (obsidian) were used during the Stone Age, and there was a stable industry in Egypt by about 1500 B.C.

In contrast, the manufacture of portland cement has only been practiced for about 100 years. The Romans combined burned lime with volcanic ash to make a natural hydraulic cement; the art seems then to have disappeared, but the hydraulic properties of lightly burned clayey limes were rediscovered in England about 1750, and in the next 100 years the manufacturing process, essentially the same as that used now, was developed.

By far the largest segment of the silicate ceramic industry is the manufacture of various glass products. These are manufactured mostly as sodium-calcium-silicate glasses. The next largest segment of the ceramic industry is lime and cement products. In this category the largest group of materials is hydraulic cements such as those used for building construction. A much more diverse group of products is included in the classification of whitewares. This group includes pottery, porcelain, and similar fine-grained porcelainlike compositions which comprise a wide variety of specific products and uses. The next classification of traditional ceramics is porcelain enamels, which are mainly silicate glasslike coatings on metals. Another distinct group is the structural clay products, which consist mainly of brick and tile but include a variety of similar products such as sewer pipe. A particularly important group of the traditional

ceramics industry is refractories. About 40% of the refractory industry consists of fired-clay products, and another 40% consists of heavy nonclay refractories such as magnesite, chromite, and similar compositions. In addition there is a sizable demand for various special refractory compositions. The abrasives industry produce mainly silicon carbide and aluminum oxide abrasives. Finally, a segment of the ceramic industry which does not produce ceramic products as such is concerned with the mineral preparation of ceramic and related raw materials.

Most of these traditional ceramics could be adequately defined as the silicate industries, which indeed was the description originally proposed for the American Ceramic Society in 1899. The silicate industries still compose by far the largest part of the whole ceramic industry, and from this point of view they can be considered the backbone of the field.

New Ceramics. In spite of its antiquity, the ceramic industry is not stagnant. Although traditional ceramics, or silicate ceramics, account for the large bulk of material produced, both in tonnage and in dollar volume, a variety of new ceramics has been developed in the last 20 years. These are of particular interest because they have either unique or outstanding properties. Either they have been developed in order to fulfill a particular need in greater temperature resistance, superior mechanical properties, special electrical properties, and greater chemical resistivity, or they have been discovered more or less accidentally and have become an important part of the industry. In order to indicate the active state of development, it may be helpful to describe briefly a few of these new ceramics.

Pure oxide ceramics have been developed to a high state of uniformity and with outstanding properties for use as special electrical and refractory components. The oxides most often used are alumina (Al_2O_3), zirconia (ZrO_2), thoria (ThO_2), beryllia (BeO), magnesia (MgO), spinel (MgAl_2O_4), and forsterite (Mg_2SiO_4).

Nuclear fuels based on uranium dioxide (UO_2) are widely used. This material has the unique ability to maintain its good properties after long use as a fuel material in nuclear reactors.

Electrooptic ceramics such as lithium niobate (LiNbO_3) and lanthanum-modified lead zirconate titanate (PLZT) provide a medium by which electrical information can be transformed to optical information or by which optical functions can be performed on command of an electrical signal.

Magnetic ceramics with a variety of compositions and uses have been developed. They form the basis of magnetic memory units in large computers. Their unique electrical properties are particularly useful in high-frequency microwave electronic applications.

Single crystals of a variety of materials are now being manufactured,

either to replace natural crystals which are unavailable or for their own unique properties. Ruby and garnet laser crystals and sapphire tubes and substrates are grown from a melt; large quartz crystals are grown by a hydrothermal process.

Ceramic nitrides with unusually good properties for special applications have been developed. These include aluminum nitride, a laboratory refractory for melting aluminum; silicon nitrides and SiAlON, commercially important new refractories and potential gas turbine components; and boron nitride, which is useful as a refractory.

Enamels for aluminum have been developed and have become an important part of the architectural industry.

Metal-ceramic composites have been developed and are now an important part of the machine-tool industry and have important uses as refractories. The most important members of this group are various carbides bonded with metals and mixtures of a chromium alloy with aluminum oxide.

Ceramic carbides with unique properties have been developed. Silicon carbide and boron carbide in particular are important as abrasive materials.

Ceramic borides have been developed which have unique properties of high-temperature strength and oxidation resistance.

Ferroelectric ceramics such as barium titanate have been developed which have extremely high dielectric constants and are particularly important as electronic components.

Nonsilicate glasses have been developed and are particularly useful for infrared transmission, special optical properties, and semiconducting devices.

Molecular sieves which are similar to, but are more controlled than, natural zeolite compositions are being made with controlled structures so that the lattice spacing, which is quite large in these compounds, can be used as a means of separating compounds of different molecular sizes.

Glass-ceramics are a whole new family of materials based on fabricating ceramics by forming as a glass and then nucleating and crystallizing to form a highly crystalline ceramic material. Since the original introduction of Pyroceram by the Corning Glass Works the concept has been extended to dozens of compositions and applications.

Porefree polycrystalline oxides have been made based on alumina, yttria, spinel, magnesia, ferrites, and other compositions.

Literally dozens of other new ceramic materials, unknown 10 or 20 years ago are now being manufactured and used. From this point of view the ceramic industry is one of our most rapidly changing industries, with new products having new and useful properties constantly being de-

veloped. These ceramics are being developed because there is a real need for new materials to transform presently available designs into practical, serviceable products. By far the major hindrance to the development of many new technologically feasible structures and systems is the lack of satisfactory materials. New ceramics are constantly filling this need.

New Uses for Ceramics. In the same way that the demand for new and better properties has led to the development of new materials, the availability of new materials had led to new uses based on their unique properties. This cycle of new ceramics—new uses—new ceramics has accelerated with the attainment of a better understanding of ceramics and their properties.

One example of the development of new uses for ceramics has occurred in the field of magnetic ceramic materials. These materials have hysteresis loops which are typical for ferromagnetic materials. Some have very nearly the square loop that is most desirable for electronic computer memory circuits. This new use for ceramics has led to extensive studies and development of materials and processes.

Another example is the development of nuclear power, which requires uranium-containing fuels having large fractions of uranium (or sometimes thorium), stability against corrosion, and the ability to withstand the fissioning of a large part of the uranium atoms without deterioration. For many applications UO_2 is an outstanding material for this fuel. Urania ceramics have become an important part of reactor technology.

In rocketry and missile development two critical parts which must withstand extreme temperatures and have good erosion resistance are the nose cone and the rocket throat. Ceramic materials are used for both.

For machining metals at high speeds it has long been known that oxide ceramics are superior in many respects as cutting tools. However, their relatively low and irregular strength makes their regular use impossible. The development of alumina ceramics with high and uniform strength levels has made them practicable for machining metals and has opened up a new field for ceramics.

In 1946 it was discovered that barium titanate had a dielectric constant 100 times larger than that of other insulators. A whole new group of these ferroelectric materials has since been discovered. They allow the manufacture of capacitors which are smaller in size but have a larger capacity than other constructions, thus improving electronic circuitry and developing a new use for ceramic materials.

In jet aircraft and other applications metal parts have had to be formed from expensive, and in wartime unobtainable, alloys to withstand the moderately high temperatures encountered. When a protective ceramic coating is applied, the temperature limit is increased, and either higher

temperatures can be reached or less expensive and less critical alloys can be substituted.

Many further applications of ceramics which did not even exist a few years ago can be cited, and we may expect new uses to develop that we cannot now anticipate.

Suggested Reading

1. F. H. Norton, *Elements of Ceramics*, 2d ed., Addison Wesley Publishing Company, Inc., Reading, Mass., 1974.
2. F. H. Norton, *Fine Ceramics*, McGraw-Hill Book Company, New York, 1970.
3. F. H. Norton, *Refractories*, 4th ed., McGraw-Hill Book Company, New York, 1968.
4. Institute of Ceramics Textbook Series:
 - (a) W. E. Worrall, *Raw Materials*, Maclaren & Sons, Ltd., London, 1964.
 - (b) F. Moore, *Rheology of Ceramic Systems*, Maclaren & Sons, Ltd., London, 1965.
 - (c) R. W. Ford, *Drying*, Maclaren & Sons, Ltd., London, 1964.
 - (d) W. F. Ford, *The Effect of Heat on Ceramics*, Maclaren & Sons, Ltd., London, 1967.
5. "Fabrication Science," *Proc. Brit. Ceram. Soc.*, No. 3 (September, 1965).
6. "Fabrication Science: 2," *Proc. Brit. Ceram. Soc.*, No. 12 (March, 1969).
7. J. E. Burke, Ed., *Progress in Ceramic Science*, Vols. 1-4, Pergamon Press, Inc., New York, 1962-1966.
8. W. D. Kingery, Ed., *Ceramic Fabrication Processes*, John Wiley & Sons, Inc., New York, 1958.
9. F. V. Tooley, Ed., *Handbook of Glass Manufacture*, 2 Vols., Ogden Publishing Company, New York, 1961.
10. A. Davidson, Ed., *Fabrication of Non-metals: Handbook of Precision Engineering*, Vol. 3, McGraw-Hill Book Company, New York, 1971.

Ceramic Phase-Equilibrium Diagrams

At equilibrium a system is in its lowest free energy state for the composition, temperature, pressure, and other imposed conditions. When a given set of system parameters is fixed, there is only one mixture of phases that can be present, and the composition of each of these phases is determined. Phase-equilibrium diagrams provide a clear and concise method of graphically representing this equilibrium situation and are an invaluable tool for characterizing ceramic systems. They record the composition of each phase present, the number of phases present, and the amounts of each phase present at equilibrium.

The time that it takes to reach this equilibrium state from any arbitrary starting point is highly variable and depends on factors other than the final equilibrium state. Particularly for systems rich in silica the high viscosity of the liquid phase leads to slow reaction rates and very long times before equilibrium is established; equilibrium is rarely achieved. For these systems and for others, metastable equilibrium, in which the system tends to a lower but not the lowest free energy state, becomes particularly important.

It is obvious that the phases present and their composition are an essential element in analysing, controlling, improving, and developing ceramic materials. Phase diagrams are used for determining phase and composition change occurring when the partial pressure of oxygen or other gases is changed, for evaluating the effects of heat treatments on crystallization and precipitation processes, for planning new compositions, and for many other purposes. We have already seen the importance of thermodynamic equilibrium in our discussions of single-phase systems: crystalline solid solutions (Chapter 2), crystalline imperfections (Chapter 4), structure of glasses (Chapter 3), and surfaces and interfaces (Chapter 5). In this chapter we concentrate our attention on equilibria involving two or more phases.

7.1 Gibbs's Phase Rule

When a system is in equilibrium, it is necessary that the temperature and pressure be uniform throughout and that the chemical potential or vapor pressure of each constituent be the same in every phase. Otherwise there would be a tendency for heat or material to be transferred from one part of the system to some other part. In 1874 J. Willard Gibbs* showed that these equilibrium conditions can occur only if the relationship

$$P + V = C + 2 \quad (7.1)$$

is satisfied. This is known as the *phase rule*, with P being the number of phases present at equilibrium, V the variance or number of degrees of freedom, and C the number of components. This relationship is the basis for preparing and using phase-equilibrium diagrams.

A phase is defined as any part of the system which is physically homogeneous and bounded by a surface so that it is mechanically separable from other parts of the system. It need not be continuous; that is, two ice cubes in a drink are one phase. The number of degrees of freedom or the variance is the number of intensive variables (pressure, temperature, composition) that can be altered independently and arbitrarily without bringing about the disappearance of a phase or the appearance of a new phase. The number of components is the smallest number of independently variable chemical constituents necessary and sufficient to express the composition of each phase present. The meaning of these terms will become clearer as they are applied to specific systems in the following sections.

Deduction of the phase rule follows directly from the requirement that the chemical potential μ_i of each constituent i be the same in every phase present at equilibrium. The chemical potential is equal to the partial molar free energy \bar{G}_i ,

$$\bar{G}_i = \left(\frac{\partial G}{\partial n_i} \right)_{T, P, n_1, n_2, \dots}$$

which is the change in free energy of a system at constant temperature and pressure resulting from the addition of one mole of constituent i to such a large quantity of the system that there is no appreciable change in the concentration. In a system with C components we have an independent equation for each component representing the equality of chemical potentials. For a system containing P phases, we have

$$\mu_1^a = \mu_1^b = \mu_1^c = \dots = \mu_1^P \quad (7.2)$$

*Collected Works, Vol. 1, Longmans, Green & Co., Ltd., London, 1928.

which
C(P -
C - 1)
phases
impose

V

which i
The
equilibr
and het
equilibr
that equ
conform

7.2 Or

In a
liquid,
differen
graphic
reviewe
The ind
phases:
it boils;
water v
changes
present
Since
and diff
practice
usually
7.2d. Al
one as
pressure

381-518

$$\mu_2^a = \mu_2^b = \mu_2^c = \dots = \mu_2^P \quad (7.3)$$

etc.

which constitute $C(P - 1)$ independent equations which serve to fix $C(P - 1)$ variables. Since the composition of each phase is defined by $C - 1$ concentration terms, completely defining the composition of P phases requires $P(C - 1)$ concentration terms, which together with the imposed conditions of temperature and pressure give

$$\text{Total number of variables} = P(C - 1) + 2 \quad (7.4)$$

$$\text{Variables fixed by equality of chemical potentials} = C(P - 1) \quad (7.5)$$

$$\text{Variables remaining to be fixed} = P(C - 1) + 2 - C(P - 1) \quad (7.6)$$

$$V = C - P + 2 \quad (7.7)$$

which is Gibbs's phase rule (Eq. 7.1).

The main limitation on the phase rule is that it applies only to equilibrium states, requiring homogeneous equilibrium within each phase and heterogeneous equilibrium between phases. Although a system in equilibrium always obeys the phase rule (and nonconformance proves that equilibrium does not exist), the reverse is not always true. That is, conformance with the phase rule is not a demonstration of equilibrium.

7.2 One-Component Phase Diagrams

In a single-component system the phases that can occur are vapor, liquid, and various polymorphic forms of the solid. (The energy of different polymorphic forms as related to temperature and crystallographic structure has been discussed in Section 2.10, and might well be reviewed by the reader, since it is closely related to the present section.) The independent variables that cause appearance or disappearance of phases are temperature and pressure. For example, when we heat water, it boils; if we cool it, it freezes. If we put it in an evacuated chamber, the water vapor pressure quickly reaches some equilibrium value. These changes can be diagrammatically represented by showing the phases present at different temperatures and pressures (Fig. 7.1).

Since this is a one-component system, even the air phase is eliminated, and different phase distributions correspond to Fig. 7.2a to c. In actual practice measurements in which the vapor phase is unimportant are usually made at constant atmospheric pressure in a way similar to Fig. 7.2d. Although this is not an ideal closed system, it closely approximates one as long as the vapor pressure is low compared with atmospheric pressure (so that we can ignore the insignificant vapor phase which would

erature
ntial or
erwise
om one
howed
up

(7.1)

iber of
rees of
e basis

sically
nically
s; that
rees of
ssure,
bitrar-
ance
ber of
ient to
these
in the

nt that
phase
molar

erature
it i to
nge in
epen-
mical

(7.2)

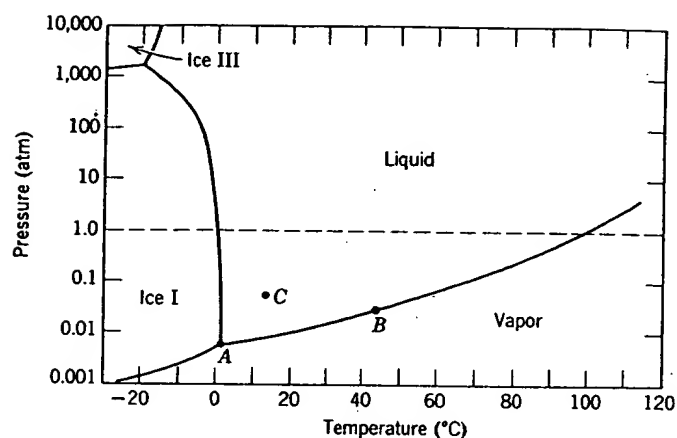
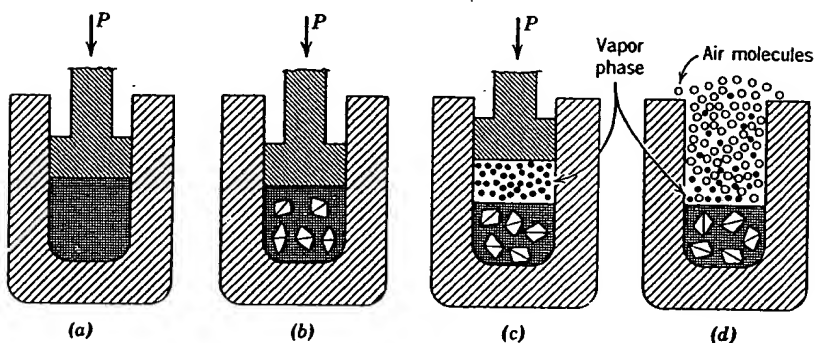
Fig. 7.1. Pressure-temperature diagram for H_2O .

Fig. 7.2. Experimental conditions for a single-component system with (a) one phase, (b) two phases, (c) three phases, and (d) common conditions, with the condensed phase exposed to a gas atmosphere.

not exist at all in a closed system) or is equal to or greater than atmospheric pressure (so that the vapor phase has the partial pressure predicted by the phase diagram). For many condensed systems of interest, the first criterion is satisfied.

In a one-component system the largest number of phases that can occur at equilibrium is given when the variance is zero: $P + V = C + 2$, $P + 0 = 1 + 2$, $P = 3$. When three phases are present at equilibrium (ice, water, vapor), as at point A in Fig. 7.1, any change in pressure or temperature causes the disappearance of a phase. The lines on the diagram represent conditions for two phases to exist together at equilibrium; for example, when liquid and vapor are present, as at point B, $P + V = C + 2$,

381-515

$2 + V = 1 + 2$, $V = 1$, and the variance is one. This means that either pressure or temperature, but not both, can be changed arbitrarily without the disappearance of a phase. If we change T_1 to T_2 , P_1 must also change to P_2 if both phases are to remain present. If only one phase is present, as at C,

$$P + V = C + 2, 1 + V = 1 + 2, V = 2,$$

and both pressure and temperature can be arbitrarily changed without the appearance of a new phase.

At 1 atm pressure, as shown in Fig. 7.1, equilibrium between the solid and liquid occurs at 0°C , the freezing point. Equilibrium coexistence of liquid and vapor occurs at 100°C , the boiling point. The slope of these phase-boundary curves is at any point determined by the Clausius-Clapeyron equation

$$\frac{dp}{dT} = \frac{\Delta H}{T \Delta V} \quad (7.8)$$

where ΔH is the molar heat of fusion, vaporization, or transformation, ΔV is the molar volume change, and T is the temperature. Since ΔH is always positive and ΔV is usually positive on going from a low-temperature to a high-temperature form, the slopes of these curves are usually positive. Since ΔV is usually small for condensed-phase transformations, lines between solid phases are often almost vertical.

There are a number of applications of one-component phase diagrams in ceramics. Perhaps the most spectacular of these is the development of the commercial production of synthetic diamonds from graphite. High temperatures and high pressures are necessary, as shown in Fig. 7.3. In addition, the presence of a liquid metal catalyst or mineralizer such as nickel is required for the reaction to proceed at a useful rate. Another system which has been extensively studied at high pressure and temperature is SiO_2 . At pressures above 30 to 40 kilobars a new phase, *coesite*, appears which has been found to occur in nature as a result of meteorite impacts. At even higher pressures, above 100 kilobars, another new phase, *stishovite*, has been found.

Of greater interest for ceramic applications are the low-pressure phases of silica, still subject to some dispute as to the role of minor impurities, but illustrated schematically in Fig. 7.4. There are five condensed phases which occur at equilibrium— α -quartz, β -quartz, β_2 -tridymite, β -cristobalite, and liquid silica. At 1 atm pressure the transition temperatures are as shown. As discussed in Section 2.10, the α -quartz- β -quartz transition at 573° is rapid and reversible. The other transformations shown are sluggish, so that long periods of time are required to reach equilib-

ecules

phase,
d phasethan
ssure
ns ofoccur
+ 0 =
water,
ature
esent
mple,
C + 2,

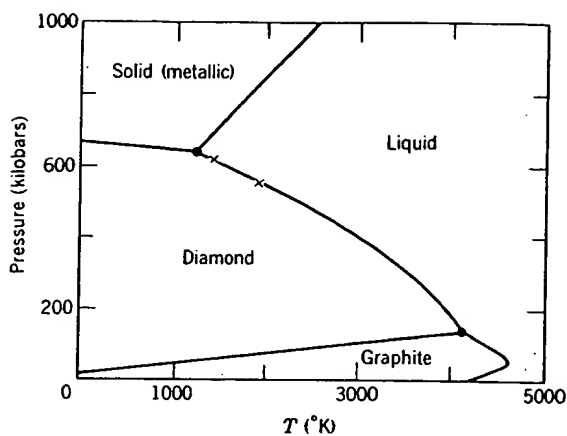


Fig. 7.3. High-pressure, high-temperature phase equilibrium diagram for carbon. From C. G. Suits, *Am. Sci.*, 52, 395 (1964).

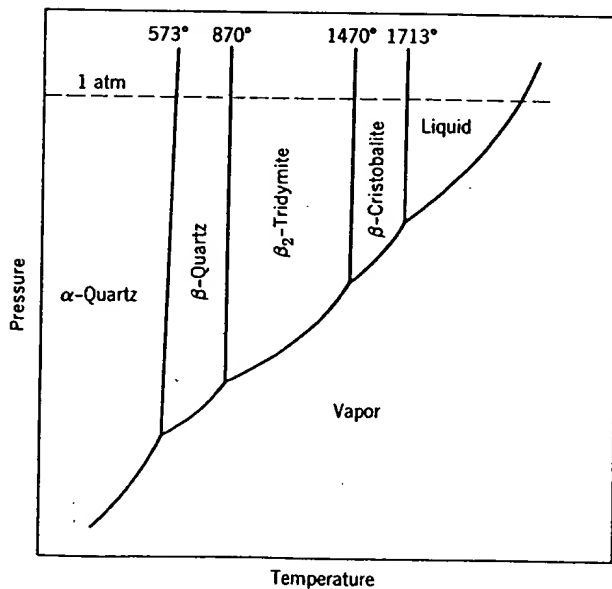


Fig. 7.4. Equilibrium diagram for SiO_2 .

rium. The chemical diagram may occur lines in the phase. For quartz is into α -cr and β -tr the form when cool this state

At any into another reverse transition however at 1100° β -tr-tridym

381-515

rium. The vapor pressure shown in the diagram is a measure of the chemical potential of silica in the different phases, and this same kind of diagram can be extended to include the metastable forms of silica which may occur (Fig. 7.5). The phase with the lowest vapor pressure (the heavy lines in the diagram) is the most stable at any temperature, the equilibrium phase. However, once formed, the transition between cristobalite and quartz is so sluggish that β -cristobalite commonly transforms on cooling into α -cristobalite. Similarly, β_2 -tridymite commonly transforms into α - and β -tridymite rather than into the equilibrium quartz forms. These are the forms present in the refractory silica brick, for example. Similarly, when cooled, the liquid forms silica glass, which can remain indefinitely in this state at room temperature.

At any constant temperature there is always a tendency to transform into another phase of lower free energy (lower vapor pressure), and the reverse transition is thermodynamically impossible. It is not necessary, however, to transform into the lowest energy form shown. For example, at 1100° silica glass could transform into β -cristobalite, β -quartz, or β_2 -tridymite. Which of these transformations actually takes place is

on. From C.

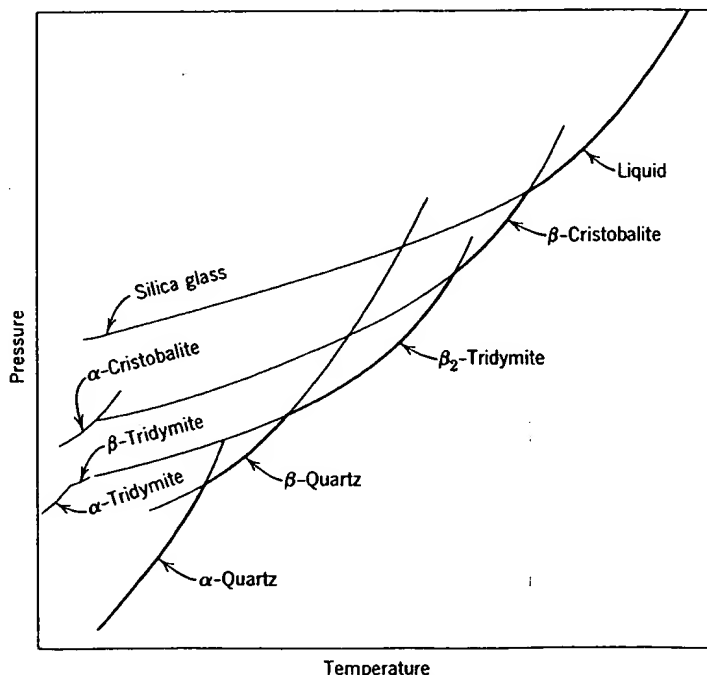


Fig. 7.5. Diagram including metastable phases occurring in the system SiO₂.

determined by the kinetics of these changes. In practice, when silica glass is heated for a long time at this temperature, it crystallizes, or devitrifies, to form cristobalite, which is not the lowest energy form but is structurally the most similar to silica glass. On cooling, β -cristobalite transforms into α -cristobalite.

The silica system illustrates that the phase-equilibrium diagram graphically represents the conditions for minimum free energy in a system; extension to include metastable forms also allows certain deductions about possible nonequilibrium behavior. Almost always, however, a number of alternative nonequilibrium courses are possible, but there is only one equilibrium possibility.

7.3 Techniques for Determining Phase-Equilibrium Diagrams

The phase-equilibrium diagrams discussed in the last section and in the rest of this chapter are the product of experimental studies of the phases present under various conditions of temperature and pressure. In using phase-equilibrium diagrams it is important to remember this experimental basis. In critical cases, for example, diagrams should not be used without referring directly to the original experimenter's description of exactly how the diagram was determined and with what detail the measurements were made. As additional measurements are carried out, diagrams are subject to constant revision.

There is a large body of literature describing methods of determining phase equilibrium. In general, any physical or chemical difference between phases or effect occurring on the appearance or disappearance of a phase can be used in determining phase equilibrium. Two general methods are used: dynamic methods use the change in properties of a system when phases appear or disappear, and static methods use a sample held under constant conditions until equilibrium is reached, when the number and composition of the phases present are determined.

Dynamic Methods. The most common dynamic method is thermal analysis, in which the temperature of a phase change is determined from changes in the rate of cooling or heating brought about by the heat of reaction. Other properties such as electrical conductivity, thermal expansion, and viscosity have also been used. Under the experimental conditions used, the phase change must take place rapidly and reversibly at the equilibrium temperature without undercooling, segregation, or other nonequilibrium effects. In silicate systems the rate of approach toward equilibrium is slow; as a result thermal-analysis methods are less useful for silicates than they are for metals, for example.

381-518

Dynamic methods are suitable for determining the temperature of phase changes but give no information about the exact reactions taking place. In addition to the measurements of temperature changes then, phase identification before and after any phase change is required. This analysis is usually carried out by chemical determination of composition, determination of optical characteristics, X-ray determination of crystal structure, and microscopic examination of phase amounts and phase distribution.

Static Methods. In contrast to dynamic measurements, static measurements often consist of three steps. Equilibrium conditions are held at elevated temperatures or pressures, the sample is quenched to room temperature sufficiently rapidly to prevent phase changes during cooling, and then the specimen is examined to determine the phases present. By carrying out these steps at a number of different temperatures, pressures, and compositions, the entire phase diagram can be determined. Sometimes high-temperature X-ray and high-temperature microscopic examinations can determine the phases present at high temperatures, making quenching unnecessary.

For silicate systems the major problem encountered in determining phase-equilibrium diagrams is the slow approach toward equilibrium and the difficulty in ensuring that equilibrium has actually been reached. For most systems this means that static measurements are necessary. A common technique is to mix together carefully constituents in the correct ratio to give the final composition desired. These are held at a constant temperature in platinum foil; after rapid cooling, the mixture is reground in a mortar and pestle and then heated for a second time and quenched. The phases present are examined, the sample mixture remixed, reheated, and quenched again. The resulting material is then reexamined to ensure that the phase composition has not changed.

This process requires much time and effort; since several thousand individual experiments, such as those just described, may be necessary for one ternary diagram, we can understand why only a few systems have been completely and exhaustively studied.

Reliability of Individual Diagrams. In general, the original experimenter investigating a particular phase diagram is usually concerned with some limited region of composition, temperature, and pressure. His effort is concentrated in that area, and the other parts of the phase diagram are determined with much less precision and detail. As reported in summarizing descriptions (such as those given in this chapter), the diagram is not evaluated as to which parts are most reliable. As a result, although the general configuration of diagrams given can be relied on, the exact temperatures and compositions of individual lines or points on the

diagram should only be accepted with caution. They represent the results of difficult experimental techniques and analysis.

These cautions are particularly applicable to regions of limited crystalline solution at high temperatures, since for many systems exsolution occurs rapidly on cooling and for many systems this was not a feature of the experimenters' interest. Similarly, phase separation at moderate and low temperatures often results in submicroscopic phases which are not recognized without the use of electron microscopy and electron diffraction, which have not as yet been widely applied to crystalline solid solutions.

7.4 Two-Component Systems

In two-component systems one additional variable, the composition, is introduced so that if only one phase is present, the variance is three: $P + V = C + 2$, $1 + V = 2 + 2$, $V = 3$. In order to represent the pressure, temperature, and composition region of the stability of a single phase, a three-dimensional diagram must be used. However, the effect of pressure is small for many condensed-phase systems, and we are most often concerned with the systems at or near atmospheric pressure. Consequently, diagrams at constant pressure can be drawn with temperature and composition as variables. A diagram of this kind is shown in Fig. 7.6.

If one phase is present, both temperature and composition can be arbitrarily varied, as illustrated for point A. In the areas in which two phases are present at equilibrium, the composition of each phase is

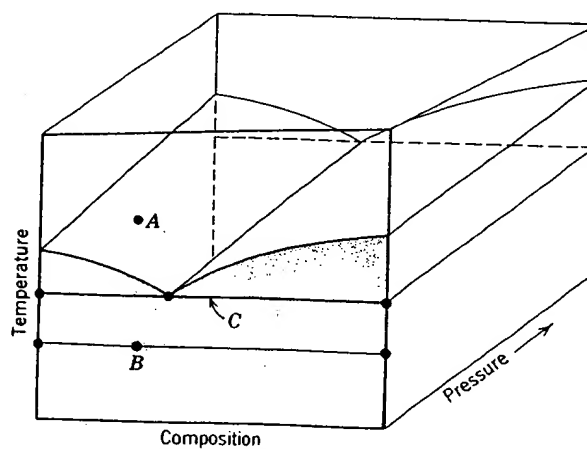


Fig. 7.6. Simple binary diagram.

381-515

indicated by lines on the diagram. (In binary diagrams two-phase regions will often be shaded, single-phase regions not.) The intersection of a constant-temperature "tie line" with the phase boundaries gives the compositions of the phases in equilibrium at temperature T . With two phases present, $P + V = C + 2$, $2 + V = 2 + 2$, $V = 2$. At an arbitrarily fixed pressure, any arbitrary change in either temperature or composition of one of the phases present requires a corresponding change in the other variable. The maximum number of phases that can be present where pressure is arbitrarily fixed ($V = 1$) is

$$P + V = C + 2, P + 1 = 2 + 2, P = 3.$$

When three phases are present, the composition of each phase and the temperature are fixed, as indicated by the solid horizontal line at C .

Systems in Which a Gas Phase Is Not Important. Systems containing only stable oxides in which the valence of the cations is fixed comprise a large fraction of the systems of interest for ceramics and can adequately be represented at a constant total pressure of 1 atm. At equilibrium the chemical potential of each constituent must be equal in each phase present. As a result the variation of chemical potential with composition is the underlying thermodynamic consideration which determines phase stability. If we consider a simple mechanical mixture of two pure components, the free energy of the mixture G^M is

$$G^M = X_A G_A + X_B G_B \quad (7.9)$$

For the simplest case, an ideal solution in which the heat of mixing and changes in vibrational entropy terms are zero, random mixing gives rise to a configurational entropy of mixing ΔS_m which has been derived in Eq. 4.14; the free energy of the solution is

$$G^{id,S} = G^M - T \Delta S_m \quad (7.10)$$

and under all conditions the free energy of the solution is less than that of a mechanical mixture; the free energy curves for the solid and liquid solutions and the resulting phase-equilibrium diagram are similar to those already illustrated in Fig. 4.2. Since very dilute solutions approach ideal behavior, Eq. 7.10 requires that there is always at least some minute solubility on the addition of any solute to any pure substance.

Most concentrated solutions are not ideal, but many can be well represented as *regular* solutions in which the excess entropy of the solution is negligible, but the excess enthalpy or heat of mixing ΔH^{xs} is significant. In this case the free energy of the regular solution is

$$G^{r,S} = G^M + \Delta H^{xs} - T \Delta S_m \quad (7.11)$$

The resulting forms of typical free-energy-composition curves for an ideal solution and for regular solutions with positive or negative excess enthalpies are shown in Fig. 7.7. In Fig. 7.7c the minimum free energy for the system at compositions intermediate between α and β consists of a mixture of α and β in which these two solution compositions have the same chemical potential for each component and a lower free energy than intermediate single-phase compositions; that is, phase separation occurs. When differences of crystal structure occur (as discussed in Chapter 2), a complete series of solid solutions between two components is not possible, and the free energy of the solution increases sharply after an initial decrease required by the configurational entropy of mixing. This

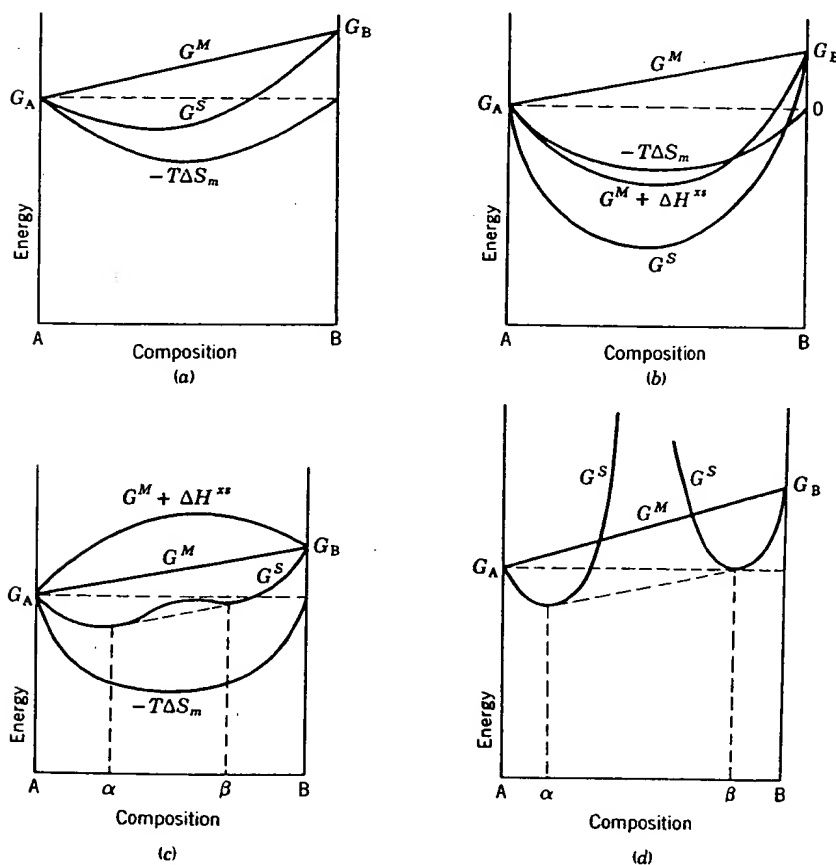


Fig. 7.7. Free-energy-composition diagrams for (a) ideal solution, (b) and (c) regular solutions, and (d) incomplete solid solution.

381-515

situation is illustrated in Fig. 7.7d, in which the minimum system free energy again consists of a mixture of the two solutions α and β .

When, for any temperature and composition, free-energy curves such as shown in Fig. 7.7 are known for each phase which may exist, these phases actually occur at equilibrium which give the lowest system free energy consistent with equal chemical potentials for the components in each phase. This has been illustrated for an ideal solution in Fig. 4.2, compound formation in Fig. 4.3, and phase separation in Fig. 3.10 and is illustrated for a series of temperatures in a eutectic system in Fig. 7.8.

Systems in Which a Gas Phase Is Important. In adjusting the oxygen pressure in an experimental system, it is often convenient to use the equilibria



In this case, with no condensed phase present, $P + V = C + 2$, $1 + V = 2 + 2$, $V = 3$, and it is necessary to fix the temperature, system total pressure, and the gas composition, that is, CO_2/CO or $\text{H}_2/\text{H}_2\text{O}$ ratio, in order to fix the oxygen partial pressure. If a condensed phase, that is, graphite, is in equilibrium with an oxygen-containing vapor phase, $P + V = C + 2$, $2 + V = 2 + 2$, $V = 2$, and fixing any two independent variables completely defines the system.

The most extensive experimental data available for a two-component system in which the gas phase is important is the Fe-O system, in which a number of condensed phases may be in equilibrium with the vapor phase. A useful diagram is shown in Fig. 7.9, in which the heavy lines are boundary curves separating the stability regions of the condensed phases and the dash-dot curves are oxygen isobars. In a single condensed-phase region (such as wüstite) $P + V = C + 2$, $2 + V = 2 + 2$, $V = 2$, and both the temperature and oxygen pressure have to be fixed in order to define the composition of the condensed phase. In a region of two condensed phases (such as wüstite plus magnetite) $P + V = C + 2$, $3 + V = 2 + 2$, $V = 1$, and fixing either the temperature or oxygen pressure fully defines the system. For this reason, the oxygen partial-pressure isobars are horizontal, that is, isothermal, in these regions, whereas they run diagonally across single condensed-phase regions.

An alternative method of representing the phases present at particular oxygen pressures is shown in Fig. 7.9b. In this representation we do not show the O/Fe ratio, that is, the composition of the condensed phases, but only the pressure-temperature ranges for each stable phase.

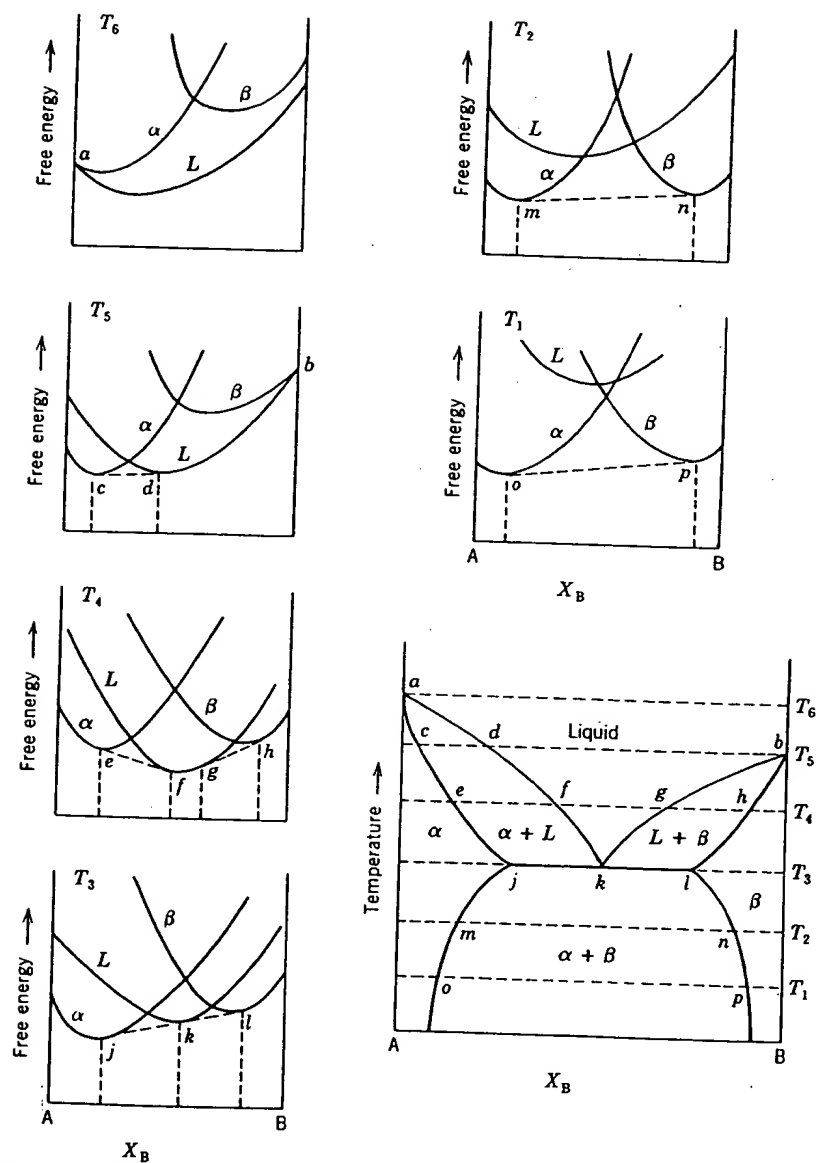


Fig. 7.8. Free-energy-composition curves and the temperature-composition equilibrium diagram for a eutectic system. From P. Gordon, *Principles of Phase Diagrams in Materials Systems*, McGraw-Hill Book Company, New York, 1968.

381-513

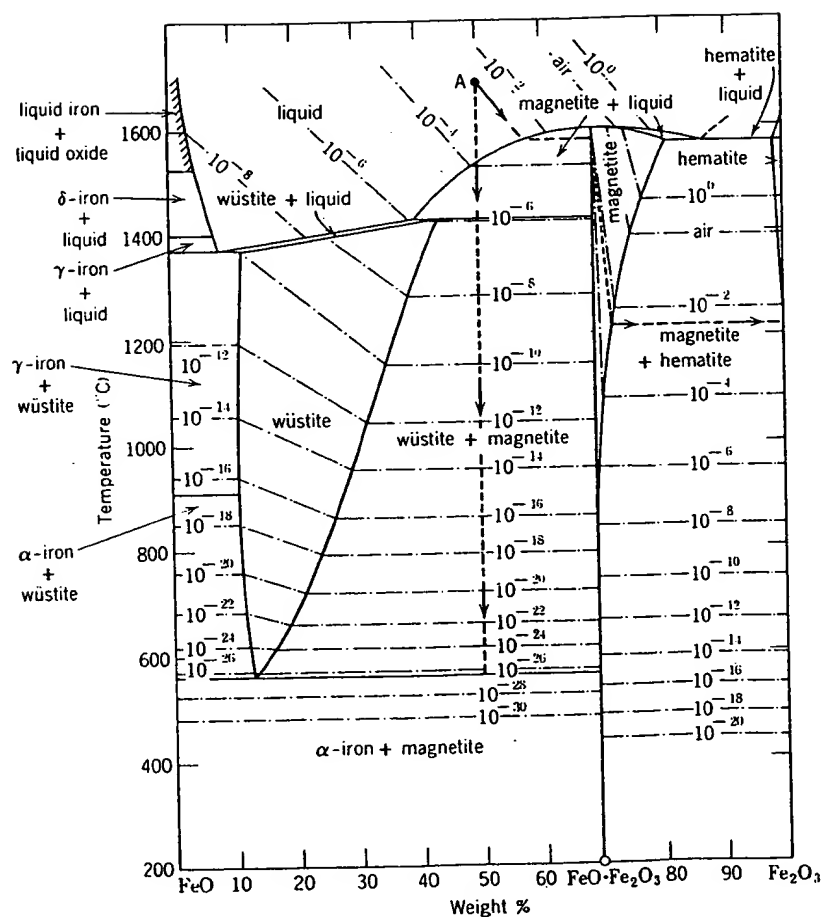


Fig. 7.9. (a) Phase relations in the FeO-Fe₂O₃ system. Dash-dot lines are oxygen isobars. Alternate solidification paths for composition A are discussed in text. From A. Muan and E. F. Osborn, *Phase Equilibria among Oxides in Steelmaking*, Addison-Wesley Publishing Company, Inc., Reading, Mass., 1965.

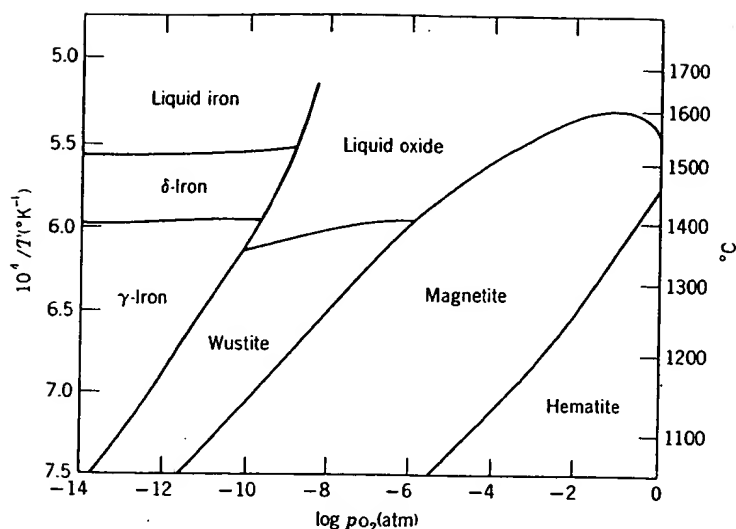


Fig. 7.9 (continued). (b) Temperature-oxygen pressure diagram for the Fe-Fe₂O₃ system. From J. B. Wagner, *Bull. Am. Cer. Soc.*, 53, 224 (1974).

7.5 Two-Component Phase Diagrams

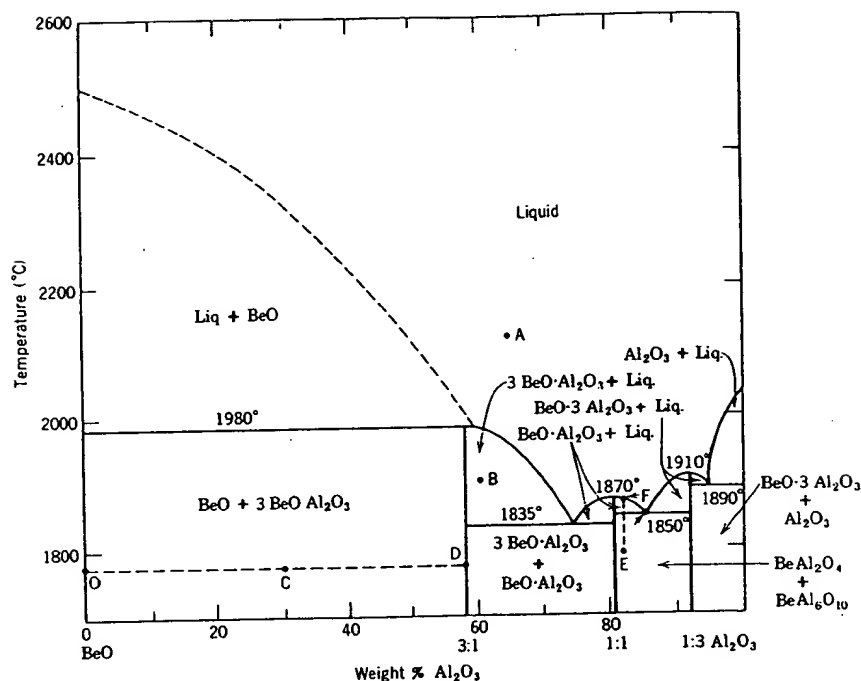
Phase-equilibrium diagrams are graphical representations of experimental observations. The most extensive collection of diagrams useful in ceramics is that published by the American Ceramic Society in two large volumes, which are an important working tool of every ceramist.* Phase diagrams can be classified into several general types.

Eutectic Diagrams. When a second component is added to a pure material, the freezing point is often lowered. A complete binary system consists of lowered liquidus curves for both end members, as illustrated in Fig. 7.8. The *eutectic temperature* is the temperature at which the liquidus curves intersect and is the lowest temperature at which liquid occurs. The eutectic composition is the composition of the liquid at this temperature, the liquid coexisting with two solid phases. At the eutectic temperature three phases are present, so the variance is one. Since pressure is fixed, the temperature cannot change unless one phase disappears.

In the binary system BeO-Al₂O₃ (Fig. 7.10) the regions of solid solution that are necessarily present have not been determined and are presumed

*E. M. Levin, C. R. Robbins, and H. F. McMurdie, *Phase Diagrams for Ceramists*, American Ceramic Society, Columbus, 1964; *Supplement*, 1969.

381-515

Fig. 7.10. The binary system BeO-Al₂O₃.

to be of limited extent, although this is uncertain, and are not shown in the diagram. The system can be divided into three simpler two-component systems (BeO-BeAl₂O₄, BeAl₂O₄-BeAl₆O₁₀, and BeAl₆O₁₀-Al₂O₃) in each of which the freezing point of the pure material is lowered by addition of the second component. The BeO-BeAl₂O₄ subsystem contains a compound, Be₃Al₂O₆, which melts incongruently, as discussed in the next section. In the single-phase regions there is only one phase present, its composition is obviously that of the entire system, and it comprises 100% of the system (point A in Fig. 7.10). In two-phase regions the phases present are indicated in the diagram (point B in Fig. 7.10); the composition of each phase is represented by the intersection of a constant temperature tie line and the phase-boundary lines. The amounts of each phase can also be determined from the fact that the sum of the composition times the amount of each phase present must equal the composition of the entire system. For example, at point C in Fig. 7.10 the entire system is composed of 29% Al₂O₃ and consists of two phases, BeO (containing no Al₂O₃) and 3BeO·Al₂O₃ (which contains 58% Al₂O₃). There

must be 50% of each phase present for a mass balance to give the correct overall composition. This can be represented graphically in the diagram by the *lever principle*, in which the distance from one phase boundary to the overall system composition, divided by the distance from that boundary to the second phase boundary, is the fraction of the second phase present. That is, in Fig. 7.10,

$$\frac{OC}{OD} (100) = \text{Per cent } 3\text{BeO} \cdot \text{Al}_2\text{O}_3$$

A little consideration indicates that the ratio of phases is given as

$$\frac{DC}{OC} = \frac{\text{BeO}}{3\text{BeO} \cdot \text{Al}_2\text{O}_3}$$

This same method can be used for determining the amounts of phases present at any point in the diagram.

Consider the changes that occur in the phases present on heating a composition such as *E*, which is a mixture of BeAl_2O_4 and $\text{BeAl}_6\text{O}_{10}$. These phases remain the only ones present until a temperature of 1850°C is reached; at this eutectic temperature there is a reaction, $\text{BeAl}_2\text{O}_4 + \text{BeAl}_6\text{O}_{10} = \text{Liquid (85\% Al}_2\text{O}_3)$, which continues at constant temperature to form the eutectic liquid until all the $\text{BeAl}_6\text{O}_{10}$ is consumed. On further heating more of the BeAl_2O_4 dissolves in the liquid, so that the liquid composition changes along *GF* until at about 1875°C all the BeAl_2O_4 has disappeared and the system is entirely liquid. On cooling this liquid, exactly the reverse occurs during equilibrium solidification.

As an exercise students should calculate the fraction of each phase present for different temperatures and different system compositions.

One of the main features of eutectic systems is the lowering of the temperature at which liquid is formed. In the $\text{BeO}-\text{Al}_2\text{O}_3$ system, for example, the pure end members melt at temperatures of 2500°C and 2040°C , respectively. In contrast, in the two-component system a liquid is formed at temperatures as low as 1835°C . This may be an advantage or disadvantage for different applications. For maximum temperature use as a refractory we want no liquid to be formed. Addition of even a small amount of BeO to Al_2O_3 results in the formation of a substantial amount of a fluid liquid at 1890°C and makes it useless as a refractory above this temperature. However, if high-temperature applications are not of major importance, it may be desirable to form the liquid as an aid to firing at lower temperatures, since liquid increases the ease of densification. This is true, for example, in the system TiO_2-UO_2 , in which addition of 1% TiO_2 forms a eutectic liquid, which is a great aid in obtaining high densities at low temperatures. The structure of this system, shown in Fig.

381-515

7.11, consists of large grains of UO_2 surrounded by the eutectic composition.

The effectiveness of eutectic systems in lowering the melting point is made use of in the $\text{Na}_2\text{O}-\text{SiO}_2$ system, in which glass compositions can be melted at low temperatures (Fig. 7.12). The liquidus is lowered from 1710°C in pure SiO_2 to about 790° for the eutectic composition at approximately 75% SiO_2 -25% Na_2O .

Formation of low-melting eutectics also leads to some severe limitations on the use of refractories. In the system $\text{CaO}-\text{Al}_2\text{O}_3$, the liquidus is strongly lowered by a series of eutectics. In general, strongly basic oxides such as CaO form low-melting eutectics with amphoteric or basic oxides, and these classes of materials cannot be used adjacent to each other, even though they are individually highly refractive.

Incongruent Melting. Sometimes a solid compound does not melt to form a liquid of its own composition but instead dissociates to form a new solid phase and a liquid. This is true of enstatite (MgSiO_3) at 1557°C (Fig. 7.13); this compound forms solid Mg_2SiO_4 , plus a liquid containing about 61% SiO_2 . At this *incongruent melting point* or *peritectic temperature* there

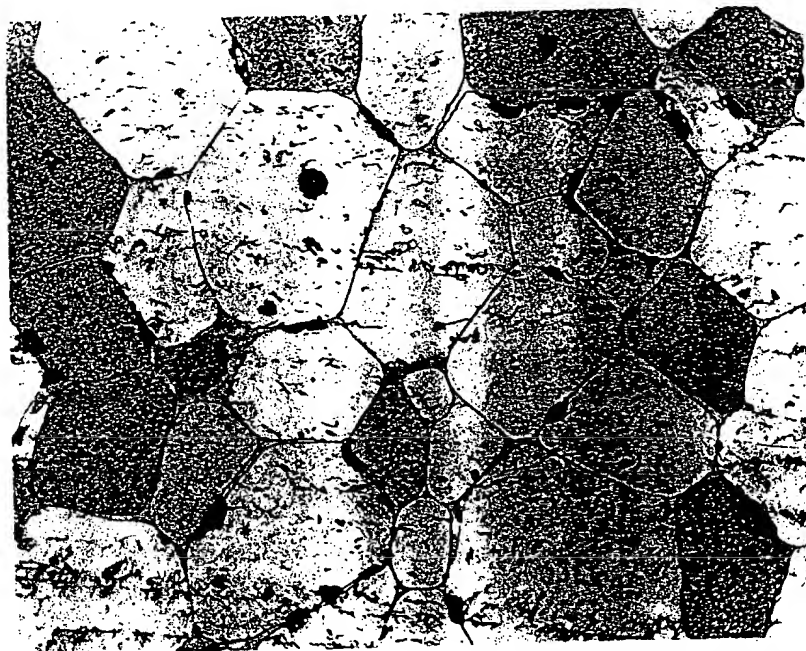


Fig. 7.11. Structure of 99% UO_2 -1% TiO_2 ceramic (228X, HNO_3 etch). UO_2 is the primary phase, bonded by eutectic composition. Courtesy G. Ploetz.

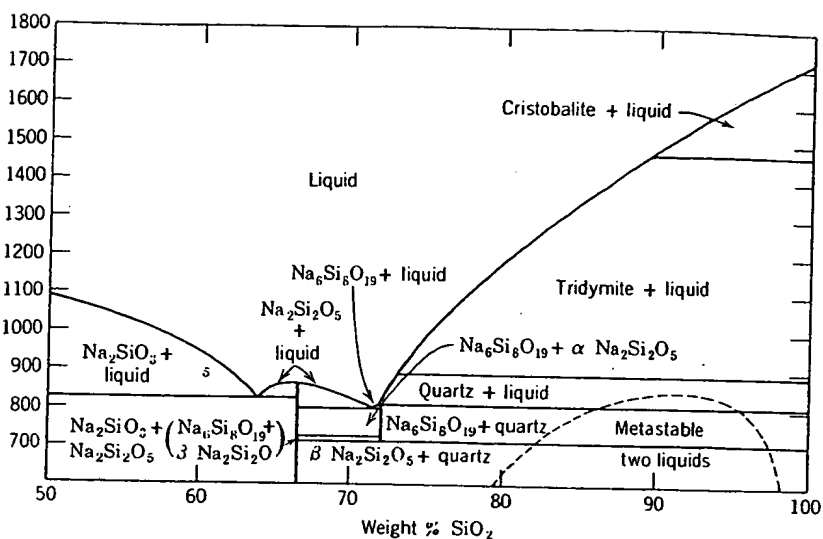


Fig. 7.12. The binary system Na_2SiO_3 - SiO_2 . The dashed line shows metastable liquid-liquid phase separation.

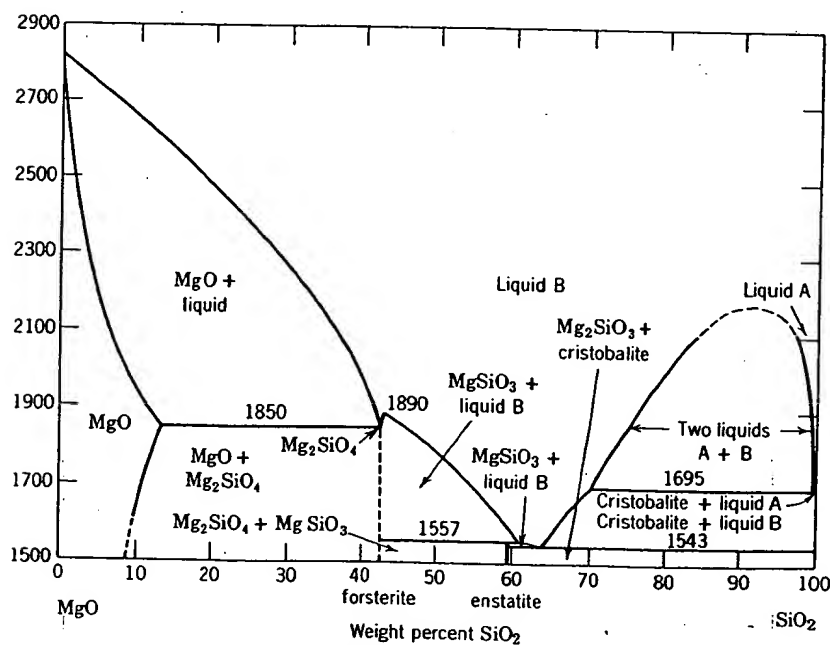


Fig. 7.13. The binary system MgO - SiO_2 .

381-518

are three phases present (two solids and a liquid), so that the temperature remains fixed until the reaction is completed. Potash feldspar (Fig. 7.14) also melts in this way.

Phase Separation. When a liquid or crystalline solution is cooled, it separates into two separate phases at the *consolute temperature* as long as the excess enthalpy is positive (see Fig. 7.7). This phenomenon is particularly important relative to the development of substructure in glasses, as discussed in Chapter 3 (Figs. 3.11, 3.12, 3.14 to 3.19). Although it has been less fully investigated for crystalline oxide solid solutions, it is probably equally important for these systems when they are exposed to moderate temperatures for long periods of time. The system CoO-NiO is shown in Fig. 7.15.

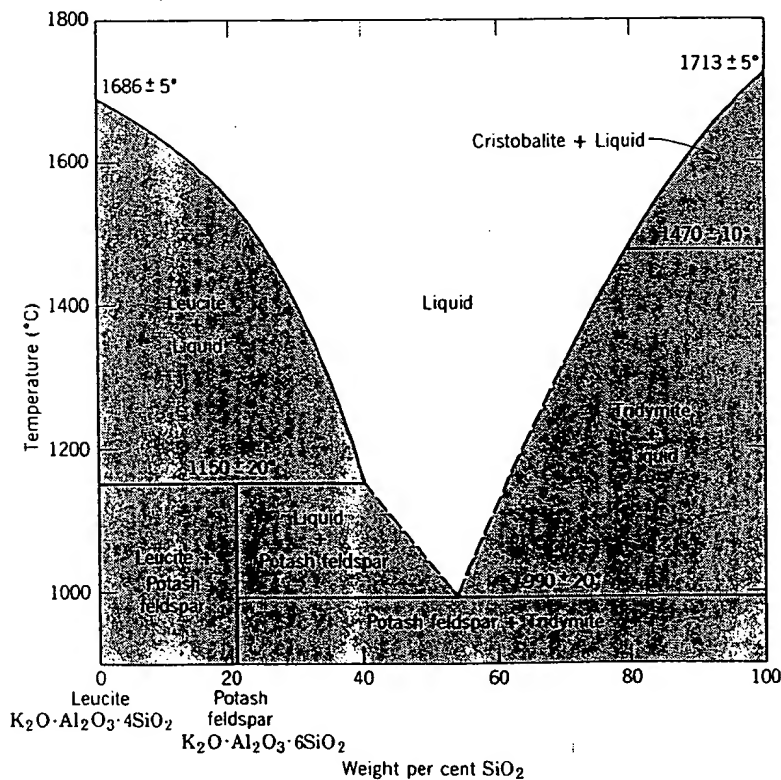


Fig. 7.14. The binary system $K_2O \cdot Al_2O_3 \cdot 4SiO_2$ (leucite)- SiO_2 . From J. F. Schairer and N. L. Bowen, *Bull. Soc. Geol. Finl.*, 20, 74 (1947). Two-phase regions are shown shaded in this diagram.

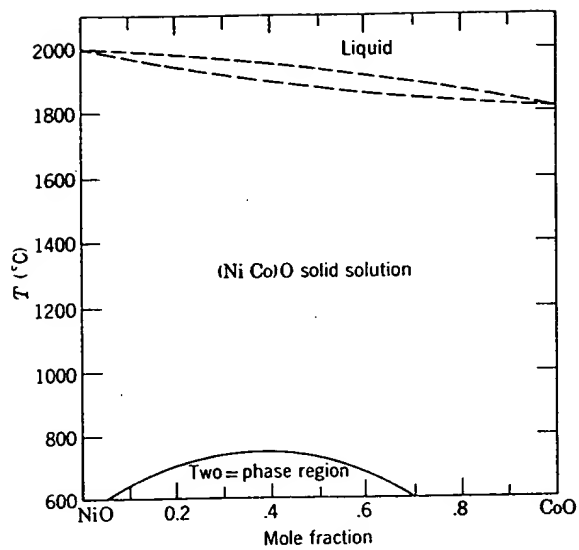


Fig. 7.15. The binary system NiO-CoO.

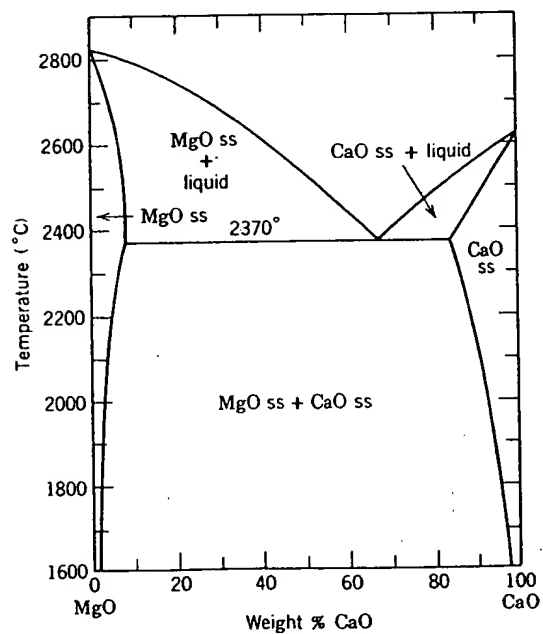


Fig. 7.16. The binary system MgO-CaO.

381-518

Solid Solutions. As discussed in Chapter 4 and in Section 7.4, a complete series of solid solutions occurs for some systems such as illustrated in Fig. 4.2 and Fig. 7.15, and some minute or significant limited solid solution occurs for all systems, as shown in Figs. 4.3, 7.13, and 7.15.

It has only been in the last decade or so that careful experimentation has revealed the wide extent of solid solubility, reaching several percent at high temperatures in many systems, as shown in Figs. 4.3, 7.13, and 7.15 and for the MgO–CaO system in Fig. 7.16 and the MgO–Cr₂O₃ system in Fig. 7.17. For steel-plant refractories directly bonded magnesia–chromite brick is formed when these materials are heated together at temperatures above 1600°C as a result of the partial solubility of the constituents; exsolution occurs on cooling. Almost all open-hearth roofs are formed of either direct-bonded, rebonded fine-grain, or fusion-cast magnesia–chromite refractories. In the basic oxygen-furnace process for steel making MgO–CaO refractories bonded with pitch are widely used, and the solid solubility at high temperatures forms a high-temperature bond. In magnesia refractories the lower solid solubility of SiO₂ as compared

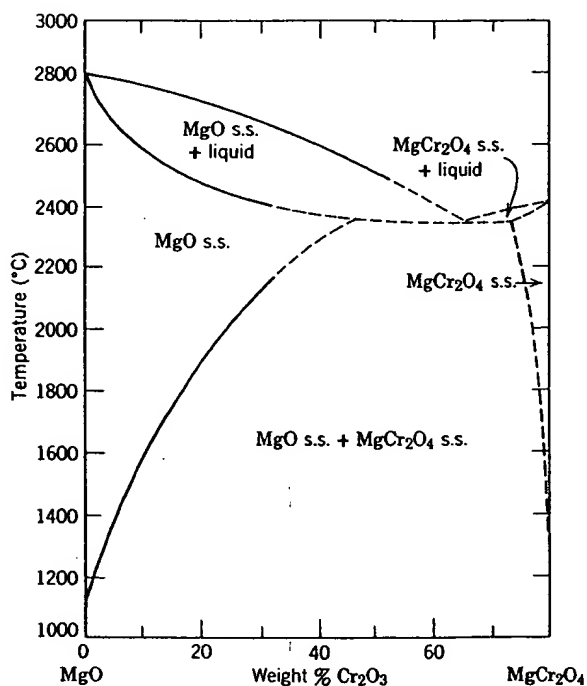


Fig. 7.17. The binary system MgO–MgCr₂O₄.

with CaO in MgO requires that excess CaO be added to prevent the formation of low-melting intergranular silicates.

In the MgO-Al₂O₃ system (Fig. 4.3) there is extensive solubility of MgO and of Al₂O₃ in spinel. As spinel in this composition range is cooled, the solubility decreases, and corundum precipitates as a separate solid phase (Fig. 7.18).

This same sort of limited solid solution is observed in the CaO-ZrO₂ system (Fig. 7.19); in this system there are three different fields of solid solution, the tetragonal form, the cubic form, and the monoclinic form. Pure ZrO₂ exhibits a monoclinic tetragonal phase transition at 1000°C, which involves a large volume change and makes the use of pure zirconia impossible as a ceramic material. Addition of lime to form the cubic solid solution, which has no phase transition, is one basis for *stabilized zirconia*, a valuable refractory.

Complex Diagrams. All the basic parts of binary phase-equilibrium diagrams have been illustrated; readers should be able to identify the number of phases, composition of phases, and amounts of phases present at any composition and temperature from any of these diagrams with ease and confidence. If they cannot, they should consult one of the more extensive treatments listed in the references.



Fig. 7.18. Precipitation of Al₂O₃ from spinel solid solution on cooling (400× H₂SO₄ etch). Courtesy R. L. Coble.

Fig. 7.1
J. Am.

Co:
fright
interj
find t
form:
alrea
Ge:
with
inter
partia

381-513

CERAMIC PHASE-EQUILIBRIUM DIAGRAMS

293

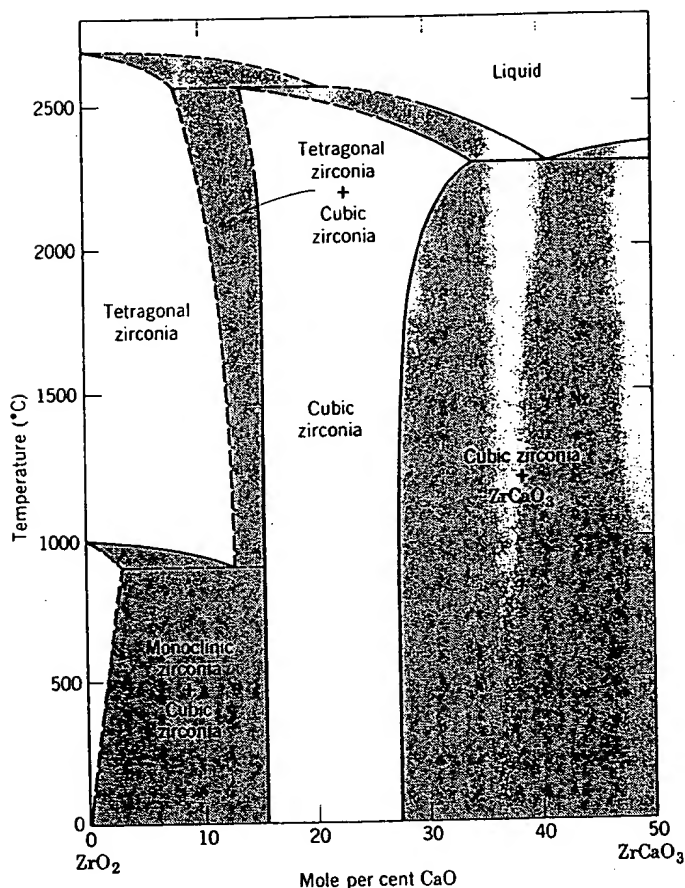


Fig. 7.19. The binary system CaO-ZrO₂. From P. Duwez, F. Odell, and F. H. Brown, Jr., *J. Am. Ceram. Soc.*, 35, 109 (1952). Two-phase regions are shown shaded in this figure.

Combinations of simple elements in one system sometimes appear frightening in their complexity but actually offer no new problems in interpretation. In the system Ba₂TiO₄-TiO₂ (Fig. 7.20), for example, we find two eutectics, three incongruently melting compounds, polymorphic forms of BaTiO₃, and an area of limited solid solution. All of these have already been discussed.

Generally phase diagrams are constructed at a total pressure of 1 atm with temperature and composition as independent variables. Since the interesting equilibrium conditions for many ceramics involve low oxygen partial pressures, phase diagrams at a fixed temperature but with oxygen

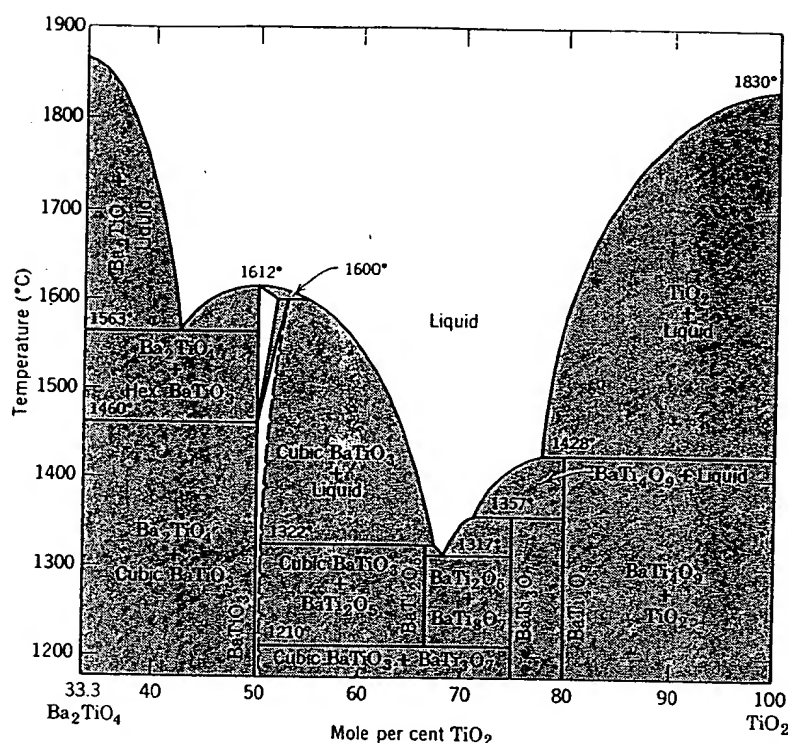


Fig. 7.20. The binary system $\text{Ba}_2\text{TiO}_4\text{-TiO}_2$. From D. E. Rase and R. Roy, *J. Am. Ceram. Soc.* **38**, 111 (1955). Two-phase regions are shown shaded in this figure.

pressure and composition as variables become a useful alternative for describing phase equilibria, for example, Fig. 7.9b. Figure 7.21(a-1) shows such a diagram for Co-Ni-O at 1600°K. The lens-shaped two-phase region between (Co,Ni)O and the NiCo alloy is similar to that between the liquid oxides and (Co,Ni)O in a temperature-composition plot (Fig. 7.15). Figure 7.21(a-2) shows the oxygen isobar tie lines between the metal alloy and the oxide solid solution; for example, the dotted line represents the equilibrium at $P_{\text{O}_2} = 1.5 \times 10^{-7}$ atm between $\text{Ni}_{0.62}\text{Co}_{0.38}\text{O}$ and $\text{Ni}_{0.9}\text{Co}_{0.1}$. (A tie line connects phases in equilibrium and designates the composition of each phase. For example, a constant temperature tie line in Fig. 7.17 at 2600°C specifies the composition of the solid solution, 10 w/o Cr_2O_3 , in equilibrium with the liquid, which contains 40 w/o Cr_2O_3 .) A plot of the nickel activity as a function of P_{O_2} is shown in Fig. 7.21(a-3). In systems which form intermediate compounds, such as spinels, the diagrams become more complex. The Fe-Cr-O ternary

syst
 P_{O_2}
 (Fe,
 chro
 betw

7.6

TI
 com
 pres
 fix t
 give
 tern
 tion:
 a ve
 two-
 equi

Fig. 7
 (2) o
 nicke

381-515

system at 1573°K is shown in Fig. 7.21b. At an oxygen pressure of $P_{O_2} = 10^{-10}$ atm, the stable phases may be FeO, FeO + (Fe,Cr)₂O₃, (Fe,Cr)₂O₃ + (Fe,Cr)₂O₃, or (Fe,Cr)₂O₃, depending on the concentration of chromium. The oxygen isobars shown in Fig. 7.21(b-2) are tie lines between the compositions in equilibrium at 1573°K.

7.6 Three-Component Phase Diagrams

Three-component systems are fundamentally no different from two-component systems, except that there are four independent variables—pressure, temperature, and the concentrations of two components (which fix the third). If pressure is arbitrarily fixed, the presence of four phases gives rise to an invariant system. A complete graphical representation of ternary systems is difficult, but if the pressure is held constant, compositions can be represented on an equilateral triangle and the temperature on a vertical ordinate to give a phase diagram such as Fig. 7.22. For two-dimensional representation the temperatures can be projected on an equilateral triangle, with the liquidus temperatures represented by

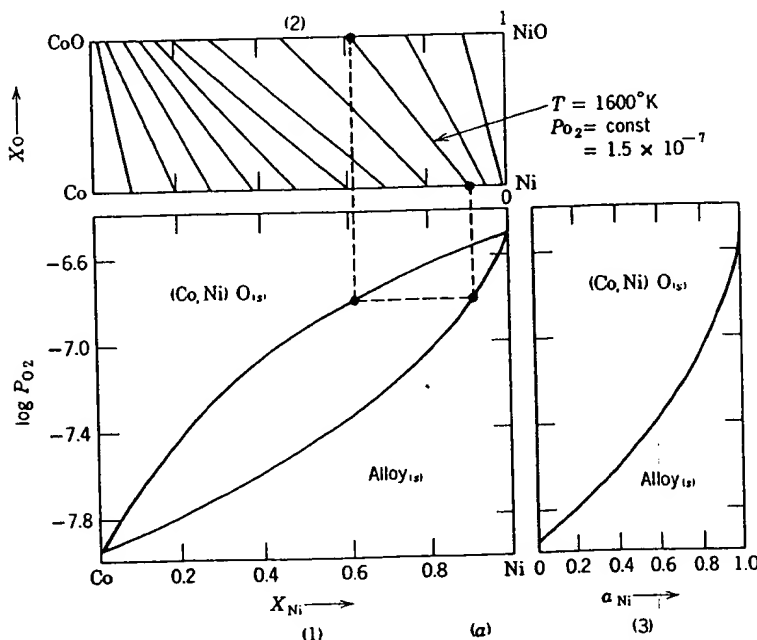


Fig. 7.21. (a) Co-Ni-O system. (1) Composition of condensed phases as a function of P_{O_2} ; (2) oxygen isobars for equilibrium between the oxide solid solution and the alloy solution; (3) nickel activity as a function of P_{O_2} .



100
TiO₂

Am. Ceram.

relative for
7.21(a-1)
oped two-
r to that
mposition
tie lines
mple, the
between
rium and
constant
ion of the
contains
shown in
s, such as
ternary

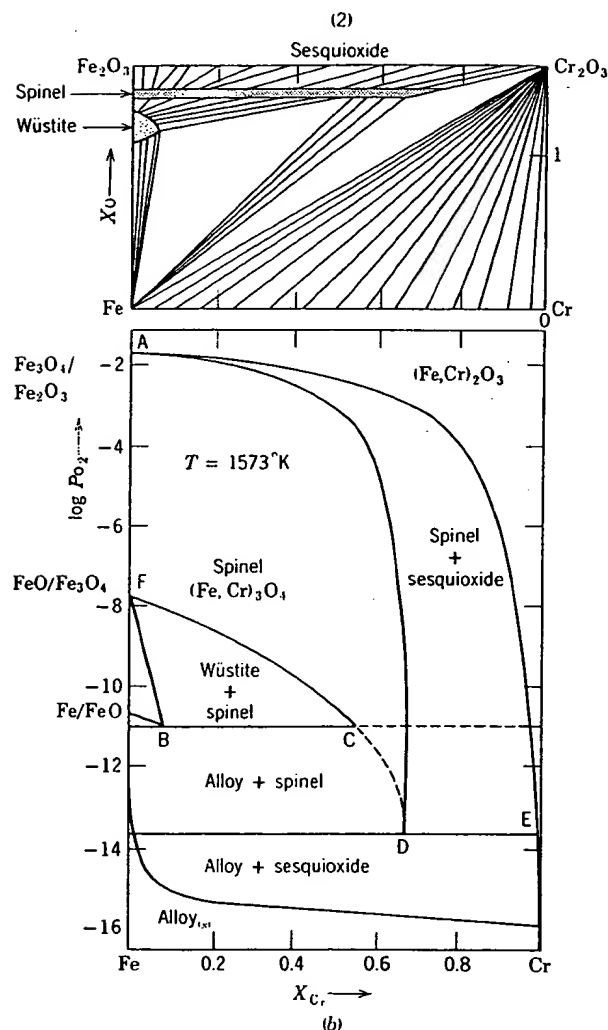


Fig. 7.21 (continued). (b) Fe-Cr-O system. (1) Composition- P_{O_2} diagram and (2) oxygen isobars for equilibrium between two phases. From A. Pelton and H. Schmalzried, *Met. Trans.*, 4, 1395 (1973).

isotherms. The diagram is divided into areas representing equilibrium between the liquid and a solid phase. Boundary curves represent equilibrium between two solids and the liquid, and intersections of three boundary curves represent points of four phases in equilibrium (invariant points in the constant-pressure system). Another method of two-

Fig. 7.22.

dimensional diagram.

Interpretation of the composition- P_{O_2} diagram. The diagram is divided into areas representing equilibrium between the liquid and a solid phase. Boundary curves represent equilibrium between two solids and the liquid, and intersections of three boundary curves represent points of four phases in equilibrium (invariant points in the constant-pressure system). Another method of two-

381-518

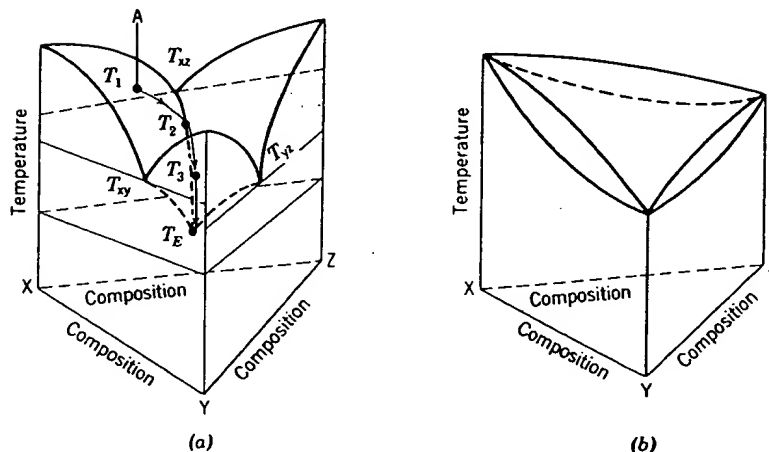


Fig. 7.22. Space diagram of (a) ternary eutectic and (b) complete series of solid solutions.

dimensional representation is to take a constant-temperature cut through the diagram, indicating the phases at equilibrium at some fixed temperature.

Interpretation of ternary diagrams is not fundamentally different from that of binary diagrams. The phases in equilibrium at any temperature and composition are shown; the composition of each phase is given by the phase-boundary surfaces or intersections; the relative amounts of each phase are determined by the principle that the sum of the individual phase compositions must equal the total composition of the entire system. In Fig. 7.22 and Fig. 7.23, for example, the composition A falls in the primary field of X. If we cool the liquid A, X begins to crystallize from the melt when the temperature reaches T_1 . The composition of the liquid changes along AB because of the loss of X. Along this line the lever principle applies, so that at any point the percentage of X present is given by $100(BA/XB)$. When the temperature reaches T_2 and the crystallization path reaches the boundary representing equilibrium between the liquid and two solid phases X and Z, Z begins to crystallize also, and the liquid changes in composition along the path CD. At L, the phases in equilibrium are a liquid of composition L and the solids X and Z, whereas the overall composition of the entire system is A. As shown in Fig. 7.23b, the only mixture of L, X, and Z that gives a total corresponding to A is $x_A/x_X (100) = \text{Per cent X}$, $z_A/z_Z (100) = \text{Per cent Z}$, $l_A/l_L (100) = \text{Per cent L}$. That is, the smaller triangle XZL is a ternary system in which the composition of A can be represented in terms of its three constituents.

gen
ns.,

im
ib-
ee
nt
o-

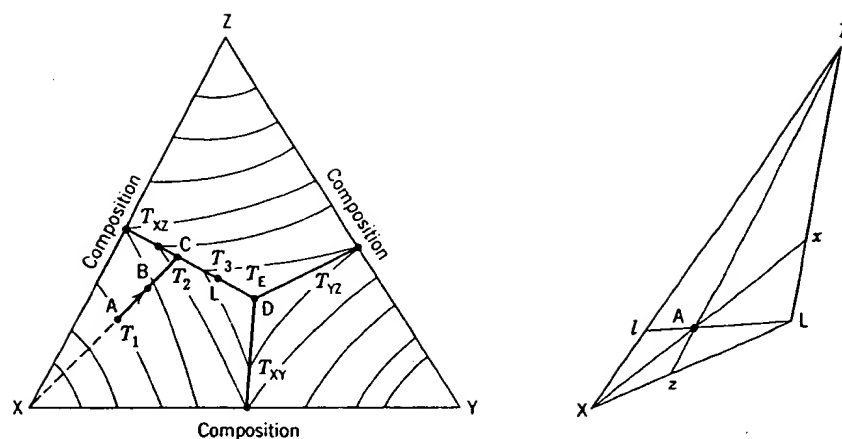


Fig. 7.23. (a) Crystallization path illustrated in Fig. 7.22a and (b) application of center of gravity principle to a ternary system.

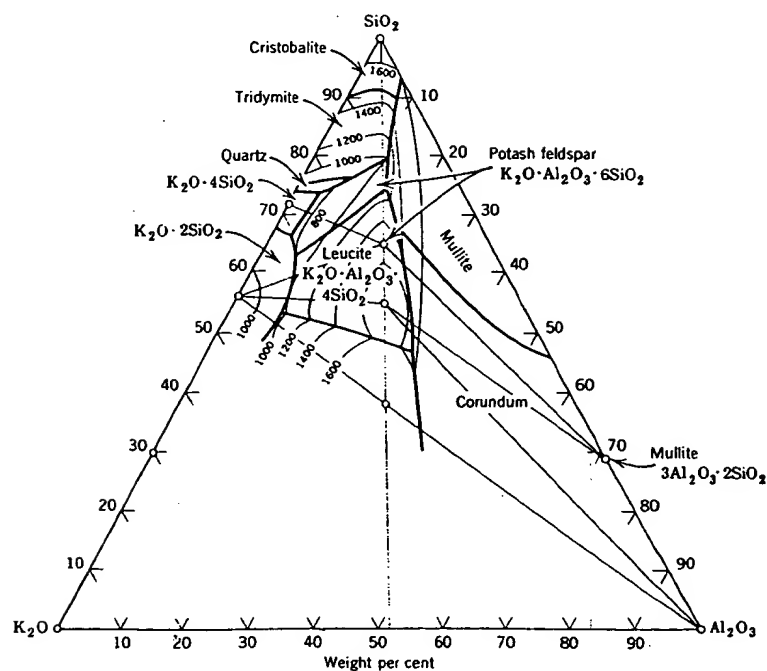


Fig. 7.24. The ternary system $K_2O-Al_2O_3-SiO_2$. From J. F. Schairer and N. L. Bowen, *Am. J. Sci.*, 245, 199 (1947).

Many t
ogy. Two
system, a
the MgC
 $K_2O-Al_2O_3$
compositi
silica-mu
discussed
the basis
systems
provides
 SiO_2 syst
tions fall
 $Na_2O \cdot 3C$

2N:
 $2Na_2O$
N
To Na

Fig. 7.25
Glass T

381-518

Many ternary systems are of interest in ceramic science and technology. Two of these, the $K_2O-Al_2O_3-SiO_2$ system and the $Na_2O-CaO-SiO_2$ system, are illustrated in Figs. 7.24 and 7.25. Another important system, the $MgO-Al_2O_3-SiO_2$ system, is discussed in Section 7.8. The $K_2O-Al_2O_3-SiO_2$ system is important as the basis for many porcelain compositions. The eutectic in the subsystem potash-feldspar-silica-mullite determines the firing behavior in many compositions. As discussed in Chapter 10, porcelain compositions are adjusted mainly on the basis of (a) ease in forming and (b) firing behavior. Although real systems are usually somewhat more complex, this ternary diagram provides a good description of the compositions used. The $Na_2O-CaO-SiO_2$ system forms the basis for much glass technology. Most compositions fall along the border between the primary phase of devitrite, $Na_2O \cdot 3CaO \cdot 6SiO_2$, and silica; the liquidus temperature is 900 to 1050°C.

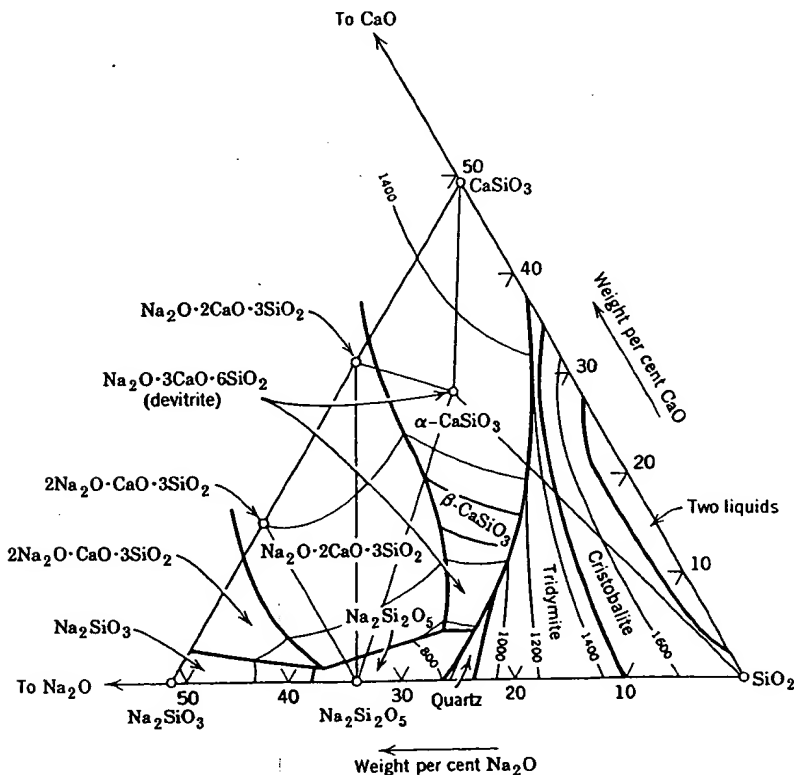


Fig. 7.25. The $Na_2O-O-CaO-SiO_2$ system. From G. W. Morey and N. L. Bowen, *J. Soc. Glass Technol.*, 9, 232 (1925).

This is a compositional area of low melting temperature, but the glasses formed contain sufficient calcium oxide for reasonable resistance to chemical attack. When glasses are heated for extended times above the transition range, devitrite or cristobalite is the crystalline phase formed as the devitrification product.

Very often constant-temperature diagrams are useful. These are illustrated for subsolidus temperatures in Figs. 7.24 and 7.25 by lines between the forms that exist at equilibrium. These lines form composition triangles in which three phases are present at equilibrium, sometimes called compatibility triangles. Constant-temperature diagrams at higher temperatures are useful, as illustrated in Fig. 7.26, in which the 1200° isothermal

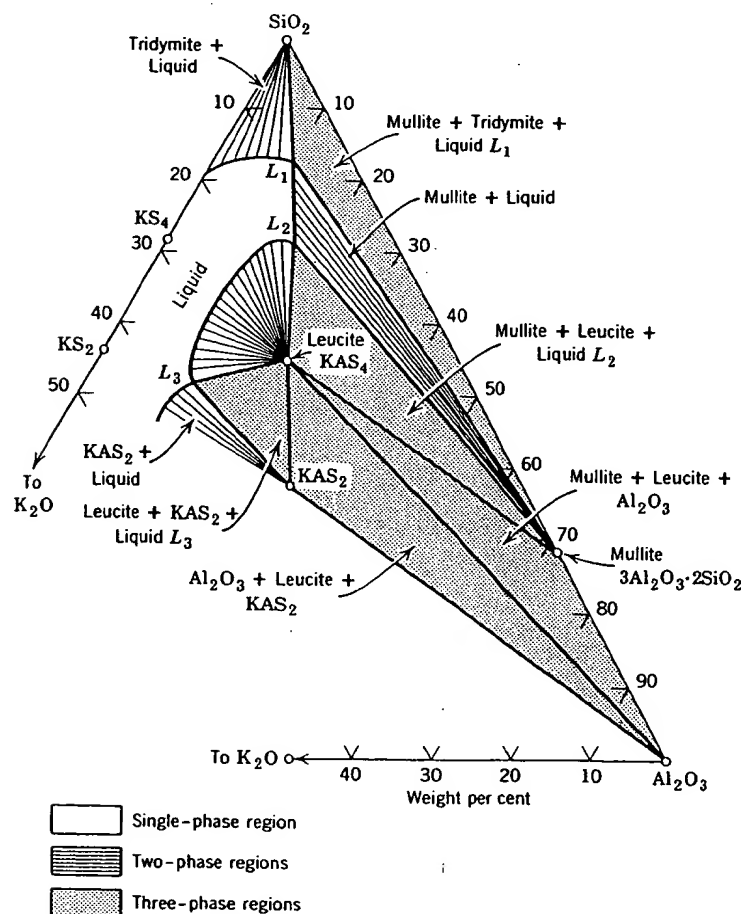


Fig. 7.26. Isothermal cut in the $K_2O-Al_2O_3-SiO_2$ diagram at 1200°C.

plane is shown. This system are amount of liquid isothermal diagram different compositions selected. Frequency rather than an

Although our and we do not component system familiar with the

7.7 Phase Con

One of the ceramic system temperatures. The amount of

Consider, for instance, the formation of 50 wt% forsterite at 1557°C. A composition of about 40% silica, the heating the amount at some temperature composition the phase, MgO. No composition be eutectic compositions and

Several things: the large difference in small change in 42% silica, the temperatures. liquid is formed chromite refractory 3MgO·2SiO2·2 sufficient MgO has a deleterious temperatures.

Another app

381-518

plane is shown for the $K_2O-Al_2O_3-SiO_2$ diagram. The liquids formed in this system are viscous; in order to obtain vitrification, a substantial amount of liquid must be present at the firing temperature. From isothermal diagrams the composition of liquid and amount of liquid for different compositions can be easily determined at the temperature selected. Frequently it is sufficient to determine an isothermal plane rather than an entire diagram, and obviously it is much easier.

Although our discussion of three-component diagrams has been brief and we do not discuss phase-equilibrium behavior for four or more component systems at all, students would be well advised to become familiar with these as an extra project.

7.7 Phase Composition versus Temperature

One of the useful applications for phase equilibrium diagrams in ceramic systems is the determination of the phases present at different temperatures. This information is most readily used in the form of plots of the amount of phases present versus temperature.

Consider, for example, the system $MgO-SiO_2$ (Fig. 7.13). For a composition of 50 wt% MgO -50 wt% SiO_2 , the solid phases present at equilibrium are forsterite and enstatite. As they are heated, no new phases are formed until 1557°C. At this temperature the enstatite disappears and a composition of about 40% liquid containing 61% SiO_2 is formed. On further heating the amount of liquid present increases until the liquidus is reached at some temperature near 1800°C. In contrast, for a 60% MgO -40% SiO_2 composition the solid phases present are forsterite, Mg_2SiO_4 , and periclase, MgO . No new phase is found on heating until 1850°C, when the composition becomes nearly all liquid, since this temperature is near the eutectic composition. The changes in phase occurring for these two compositions are illustrated in Fig. 7.27.

Several things are apparent from this graphical representation. One is the large difference in liquid content versus temperature for a relatively small change in composition. For compositions containing greater than 42% silica, the forsterite composition, liquids are formed at relatively low temperatures. For compositions with silica contents less than 42% no liquid is formed until 1850°C. This fact is used in the treatment of chromite refractories. The most common impurity present is serpentine, $3MgO \cdot 2SiO_2 \cdot 2H_2O$, having a composition of about 50 wt% SiO_2 . If sufficient MgO is added to put this in the MgO -forsterite field, it no longer has a deleterious effect. Without this addition a liquid is formed at low temperatures.

Another application of this diagram is in the selection of compositions

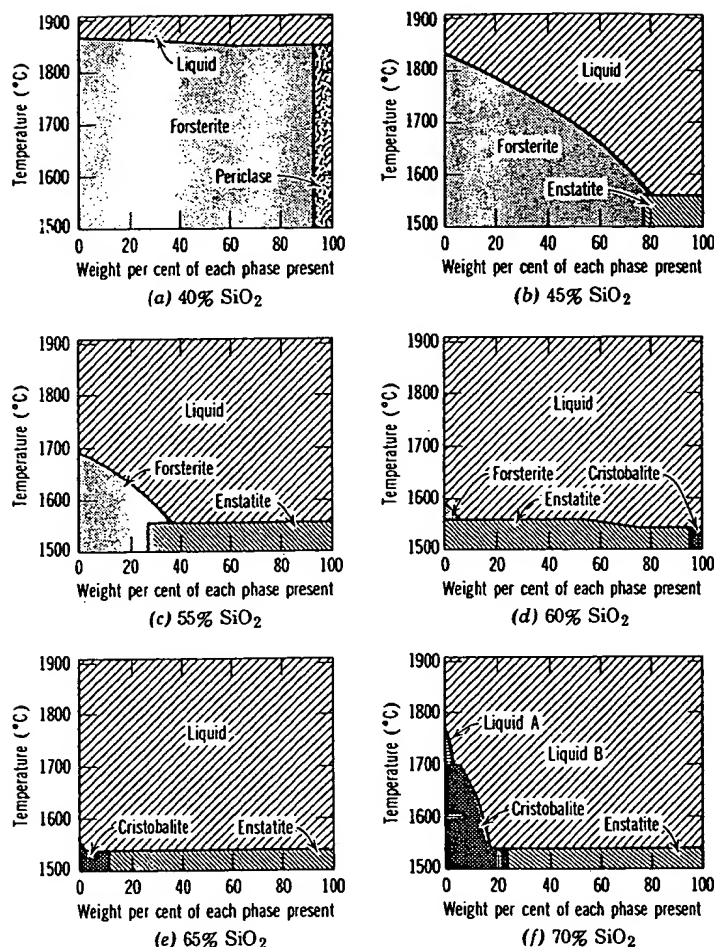


Fig. 7.27. Phase composition versus temperature for samples in the MgO-SiO₂ system.

that have desirable firing characteristics. It is necessary to form a sufficient amount of liquid for vitrification, but not so much that ware slumps or warps during firing. The limits of liquid required vary with the properties of the liquid but are in the range of 20 to 50 wt%. To have a sufficient range of firing temperature, it is desirable that the liquid content not change much with temperature. Forsterite compositions cannot be fired until very high temperatures if the composition is exactly 42% SiO₂, since no liquid is formed below 1850°C. Compositions in the forsterite-enstatite field which are mainly forsterite form a liquid at 1557°C, and

381-515

since the liquidus curve is steep, the amount of liquid present changes but slightly with temperature, as shown in Fig. 7.27. Consequently, these compositions have a good firing range and are easy to vitrify. In contrast, compositions that are mostly enstatite (55, 60, 65% SiO_2) form large amounts of liquid at low temperature, and the amount of liquid present changes rapidly with temperature. These materials have a limited firing range and pose difficult control problems for economic production.

For systems in which the gas phase is important the way in which condensed phases appear and their compositional changes on cooling depend on the conditions imposed. Referring back to the Fe-O system illustrated in Fig. 7.9, if the total condensed-phase composition remains constant, as occurs in a closed nonreactive container with only a negligible amount of gas phase present, the composition A solidifies along the dotted line with a corresponding decrease in the system oxygen pressure. In contrast, if the system is cooled at constant oxygen pressure, the solidification path is along the dashed line. In one case the resulting product at room temperature is a mixture of iron and magnetite; in the second case the resulting product is hematite. Obviously in such systems the control of oxygen pressure during cooling is essential for the control of the products formed.

For detailed discussions of crystallization paths in ternary systems the references should be consulted. The following summary* can serve as a review.

1. When a liquid is cooled, the first phase to appear is the primary phase for that part of the system in which the composition of the melt is represented.
2. The crystallization curve follows to the nearest boundary the extension of the straight line connecting the composition of the original liquid with that of the primary phase of that field. The composition of the liquid within the primary fields is represented by points on the crystallization curve. This curve is the intersection of a plane (perpendicular to the base triangle and passing through the compositions of original melt and the primary phase) with the liquidus surface.
3. At the boundary line a new phase appears which is the primary phase of the adjacent field. The two phases separate together along this boundary as the temperature is lowered.
4. The ratio of the two solids crystallizing is given by the intersection of the tangent to the boundary curve with a line connecting the composi-

*After E. M. Levin, H. F. McMurdie, and F. P. Hall, *Phase Diagrams for Ceramists*, American Ceramic Society, Cleveland, Ohio, 1956.

stem.

rm a
ware
h the
ave a
ntent
ot be
 SiO_2 ,
erite-
, and

tions of the two solid phases. Two things can occur. If this tangent line runs between the compositions of the two solid phases, the amount of each of these phases present increases. If the tangent line intersects an extension of the line between solid compositions, the first phase decreases in amount (is resorbed; Reaction $A + \text{Liquid} = B$) as crystallization proceeds. In some systems the crystallization curve leaves the boundary curve if the first phase is completely resorbed, leaving only the second phase. Systems in which this occurs may be inferred from a study of the mean composition of the solid separating between successive points on the crystallization path.

5. The crystallization curve always ends at the invariant point which represents equilibrium of liquid with the three solid phases of the three components within whose composition triangle the original liquid composition was found.

6. The mean composition of the solid which is crystallizing at any point on a boundary line is shown by the intersection at that point of the tangent with a line joining the composition of the two solid phases which are crystallizing.

7. The mean composition of the total solid that has crystallized up to any point on the crystallization curve is found by extending the line connecting the given point with the original liquid composition to the line connecting the compositions of the phases that have been separating.

8. The mean composition of the solid that has separated between two points on a boundary is found at the intersection of a line passing through these two points with a line connecting the compositions of the two solid phases separating along this boundary.

7.8 The System $\text{Al}_2\text{O}_3\text{-SiO}_2$

As an example of the usefulness of phase diagrams for considering high-temperature phenomena in ceramic systems, the $\text{Al}_2\text{O}_3\text{-SiO}_2$ system illustrates many of the features and problems encountered. In this system (Fig. 7.28), there is one compound present, mullite, which is shown as melting incongruently. (The melting behavior of mullite has been controversial; we show the metastable extensions of the phase boundaries in Fig. 7.28. For our purposes this is most important as indicative of the fact that experimental techniques are difficult and time consuming; the diagrams included here and in standard references are summaries of experimental data. They usually include many interpolations and extrapolations and have been compiled with greater or lesser care, depending on the needs of the original investigator.) The eutectic between mullite and

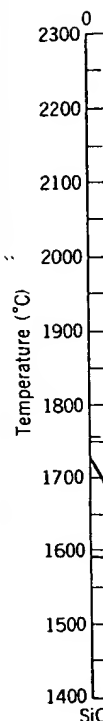


Fig. 7.28.

cristob
 SiO_2 . T

Fact
 can be
 1.0 wt%
 to 90 %
 sintered

At c
 furnac
 tempe
 furnac
 this te
 develo
 alumin

381-513

CERAMIC PHASE-EQUILIBRIUM DIAGRAMS

305

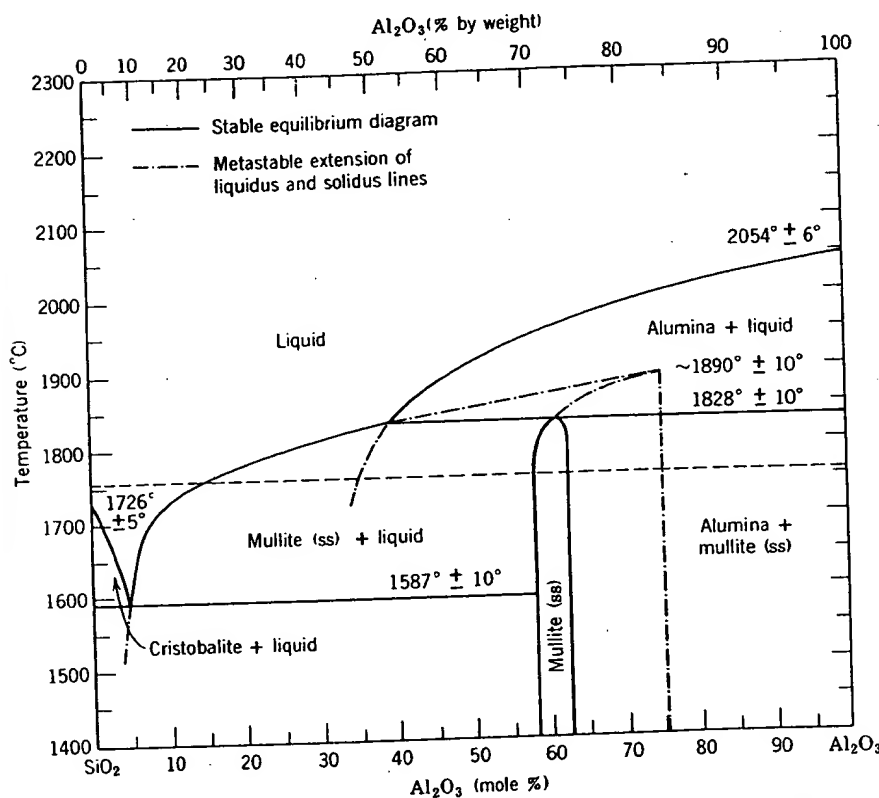


Fig. 7.28. The binary system Al_2O_3 - SiO_2 . From Aksay and Pask, *Science*, 183, 69 (1974).

cristobalite occurs at 1587°C to form a liquid containing about 95 mole% SiO_2 . The solidus temperature between mullite and alumina is at 1828°C .

Factors affecting the fabrication and use of several refractory products can be related to this diagram. They include refractory silica brick (0.2 to 1.0 wt% Al_2O_3), clay products (35 to 50 wt% Al_2O_3), high-alumina brick (60 to 90 wt% Al_2O_3), pure fused mullite (72 wt% Al_2O_3), and pure fused or sintered alumina (>90 wt% Al_2O_3).

At one end of the composition range are silica bricks widely used for furnace roofs and similar structures requiring high strength at high temperatures. A major application was as roof brick for open-hearth furnaces in which temperatures of 1625 to 1650°C are commonly used. At this temperature a part of the brick is actually in the liquid state. In the development of silica brick it has been found that small amounts of aluminum oxide are particularly deleterious to brick properties because

the eutectic composition is close to the silica end of the diagram. Consequently, even small additions of aluminum oxide mean that substantial amounts of liquid phase are present at temperatures above 1600°C. For this reason *supersilica* brick, which has a lower alumina content through special raw-material selection or treatment, is used in structures that will be heated to high temperatures.

Fire-clay bricks have a composition ranging from 35 to 55% aluminum oxide. For compositions without impurities the equilibrium phases present at temperatures below 1587°C are mullite and silica (Fig. 7.29). The relative amounts of these phases present change with composition, and there are corresponding changes in the properties of the brick. At temperatures above 1600°C the amount of liquid phase present is sensitive to the alumina-silica ratio, and for these high-temperature applications the higher-alumina brick is preferred.

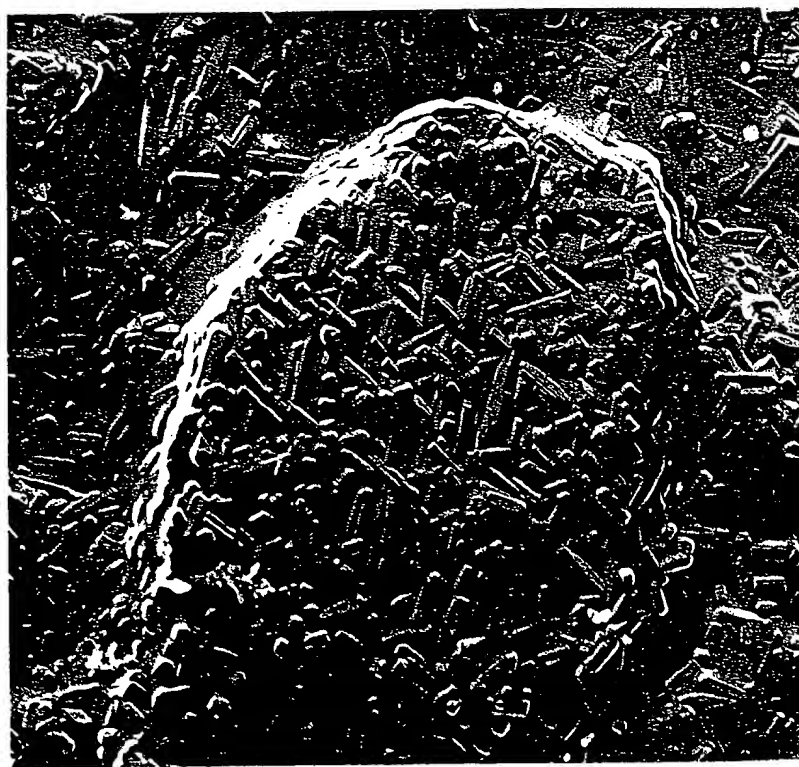


Fig. 7.29. Mullite crystals in silica matrix formed by heating kaolinite (37,000 \times). Courtesy J. J. Comer.

Refr.
cient a
greater
mullite
temper
mullite
deform
with p
fusion-

7.9 T

A te
of cera
Fig. 7.

d
Mg
2800

Fig. 7.3
Geol., 6

381-518

Refractory properties of brick can be substantially improved if sufficient alumina is added to increase the fraction of mullite present until at greater than 72 wt% alumina the brick is entirely mullite or a mixture of mullite plus alumina. Under these conditions no liquid is present until temperatures above 1828°C are reached. For some applications fused mullite brick is used; it has superior ability to resist corrosion and deformation at high temperatures. The highest refractoriness is obtained with pure alumina. Sintered Al_2O_3 is used for laboratory ware, and fusion-cast Al_2O_3 is used as a glass tank refractory.

7.9 The System $\text{MgO}-\text{Al}_2\text{O}_3-\text{SiO}_2$

A ternary system important in understanding the behavior of a number of ceramic compositions is the $\text{MgO}-\text{Al}_2\text{O}_3-\text{SiO}_2$ system, illustrated in Fig. 7.30. This system is composed of several binary compounds which

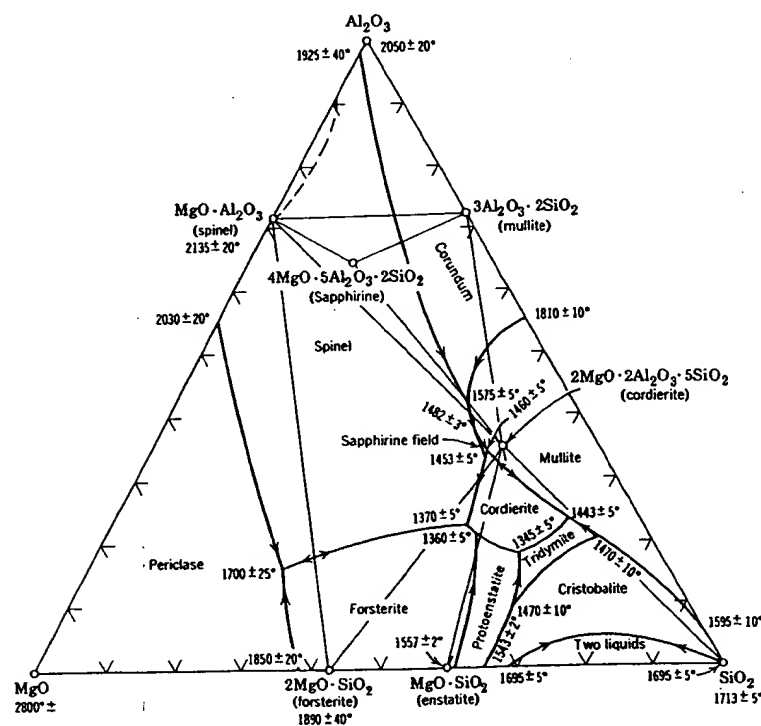


Fig. 7.30. The ternary system $\text{MgO}-\text{Al}_2\text{O}_3-\text{SiO}_2$. From M. L. Keith and J. F. Schairer, *J. Geol.*, 60, 182 (1952). Regions of solid solution are not shown; see Figs. 4.3 and 7.13.

have already been described, together with two ternary compounds, cordierite, $2\text{MgO} \cdot 2\text{Al}_2\text{O}_3 \cdot 5\text{SiO}_2$, and sapphirine, $4\text{MgO} \cdot 5\text{Al}_2\text{O}_3 \cdot 2\text{SiO}_2$, both of which melt incongruently. The lowest liquidus temperature is at the tridymite–protoenstatite–cordierite eutectic at 1345°C , but the cordierite–enstatite–forsterite eutectic at 1360°C is almost as low-melting.

Ceramic compositions that in large part appear on this diagram include magnesite refractories, forsterite ceramics, steatite ceramics, special low-loss steatites, and cordierite ceramics. The general composition areas of these products on the ternary diagram are illustrated in Fig. 7.31. In all but magnesite refractories, the use of clay and talc as raw materials is the basis for the compositional developments. These materials are valuable in large part because of their ease in forming; they are fine-grained and platy and are consequently plastic, nonabrasive, and easy to form. In addition, the fine-grained nature of these materials is essential for the

firing process. Clay decomposes to talc on heating, and the crystallization of the eutectic liquid promotes the growth of talc. At this temperature, SiO_2 is 33.4% $\text{MgO} \cdot \text{SiO}_2$.

The main reason for the firing range is fusion. In general, up to 35% of talc is indicated in the composition of the clay mixture, which is 90% talc. At the liquidus temperature, with temperature necessary,

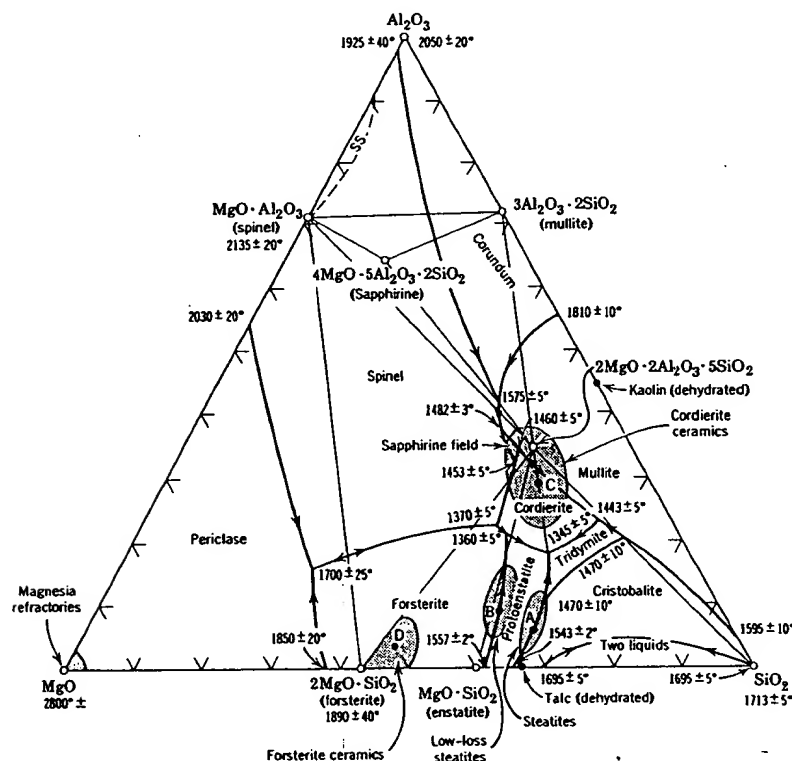


Fig. 7.31. Common compositions in the ternary system $\text{MgO}-\text{Al}_2\text{O}_3-\text{SiO}_2$. See text for other additives.

Fig. 7.32. A in Fig. 7.31.

381-518

firing process, which is described in more detail in Chapter 12. On heating, clay decomposes at 980°C to form fine-grained mullite in a silica matrix. Talc decomposes and gives rise to a similar mixture of fine-grained protoenstatite crystals, MgSiO_3 , in a silica matrix at about 1000°C. Further heating of clay gives rise to increased growth of mullite crystals, crystallization of the silica matrix as cristobalite, and formation of a eutectic liquid at 1595°C. Further heating of pure talc leads to crystal growth of the enstatite, and liquid is formed at a temperature of 1547°C. At this temperature almost all the composition melts, since talc (66.6% SiO_2 , 33.4% MgO) is not far from the eutectic composition in the MgO-SiO_2 system (Fig. 7.13).

The main feature which characterizes the melting behavior of cordierite, steatite porcelain, and low-loss steatite compositions is the limited firing range which results when pure materials are carried to partial fusion. In general, for firing to form a vitreous densified ceramic about 20 to 35% of a viscous silicate liquid is required. For pure talc, however, as indicated in Fig. 7.32, no liquid is formed until 1547°C, when the entire composition liquifies. This can be substantially improved by using talc-clay mixtures. For example, consider the composition A in Fig. 7.31 which is 90% talc-10% clay, similar to many commercial steatite compositions. At this composition about 30% liquid is formed abruptly at the liquidus temperature, 1345°C; the amount of liquid increases quite rapidly with temperature (Fig. 7.32), making close control of firing temperature necessary, since the firing range is short for obtaining a dense vitreous

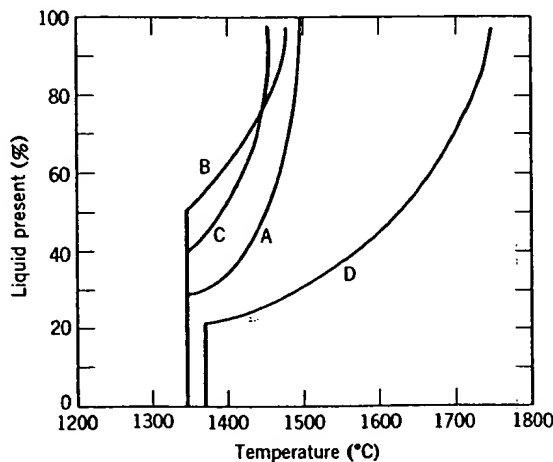


Fig. 7.32. Amount of liquid present at different temperatures for compositions illustrated in Fig. 7.31.

body (this composition would be fired at 1350 to 1370°C). In actual fact, however, the raw materials used contain Na_2O , K_2O , CaO , BaO , Fe_2O_3 , and TiO_2 as minor impurities which both lower and widen the fusion range. Additions of more than 10% clay again so shorten the firing range that they are not feasible, and only limited compositions are practicable. The addition of feldspar greatly increases the firing range and the ease of firing and has been used in the past for compositions intended as low-temperature insulators. However, the electrical properties are not good.

For low-loss steatites, additional magnesia is added to combine with the free silica to bring the composition nearer the composition triangle for forsterite-cordierite-enstatite. This changes the melting behavior so that a composition such as B in Fig. 7.31 forms about 50% liquid over a temperature range of a few degrees, and control in firing is very difficult (Fig. 7.32). In order to fire these compositions in practice to form vitreous bodies, added flux is essential. Barium oxide, added as the carbonate, is the most widely used.

Cordierite ceramics are particularly useful, since they have a very low coefficient of thermal expansion and consequently good resistance to thermal shock. As far as firing behavior is concerned, compositions show a short firing range corresponding to a flat liquidus surface which leads to the development of large amounts of liquid over a short temperature interval. If a mixture consisting of talc and clay, with alumina added to bring it closer to the cordierite composition, is heated, an initial liquidus is formed at 1345°C, as for composition C in Fig. 7.31. The amount of liquid rapidly increases; because of this it is difficult to form vitreous bodies. Frequently when these compositions are not intended for electrical applications, feldspar (3 to 10%) is added as a fluxing medium to increase the firing range.

Magnesia and forsterite compositions are different in that a eutectic liquid is formed of a composition widely different from the major phase with a steep liquidus curve so that a broad firing range is easy to obtain. This is illustrated for the forsterite composition D in Fig. 7.31 and the corresponding curve in Fig. 7.32. The initial liquid is formed at the 1360°C eutectic, and the amount of liquid depends mainly on composition and does not change markedly with temperature. Consequently, in contrast to the steatite and cordierite bodies, forsterite ceramics present few problems in firing.

In all these compositions there is normally present at the firing temperature an equilibrium mixture of crystalline and liquid phases. This is illustrated for a forsterite composition in Fig. 7.33. Forsterite crystals are present in a matrix of liquid silicate corresponding to the liquidus

composi
phase at
and the
liquid ph
(or a part
for fixin
deduced

7.10 No

The ki
in the ne
in Chapt
lowest e
systems.
free ene
illustrate
phases t
equilibri
solution
liquid an
phases in
the com
slowness

381-518

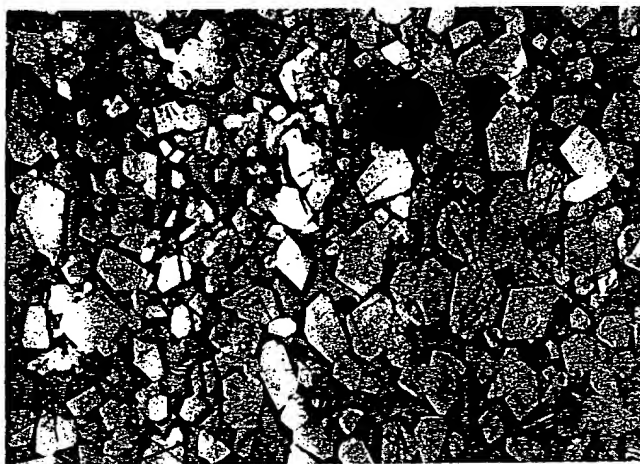


Fig. 7.33. Crystal-liquid structure of a forsterite composition (150 \times).

composition at the firing temperature. For other systems the crystalline phase at the firing temperature is protoenstatite, periclase, or cordierite, and the crystal size and morphology are usually different as well. The liquid phase frequently does not crystallize on cooling but forms a glass (or a partly glass mixture) so that the compatibility triangle cannot be used for fixing the phases present at room temperature, but they must be deduced instead from the firing conditions and subsequent heat treatment.

7.10 Nonequilibrium Phases

The kinetics of phase transitions and solid-state reactions is considered in the next two chapters; however, from our discussion of glass structure in Chapter 3 and atom mobility in Chapter 6 it is already apparent that the lowest energy state of phase equilibria is not achieved in many practical systems. For any change to take place in a system it is necessary that the free energy be lowered. As a result the sort of free-energy curves illustrated in Figs. 3.10, 4.2, 4.3, 7.7, and 7.8 for each of the possible phases that might be present remain an important guide to metastable equilibrium. In Fig. 7.8, for example, if at temperature T_2 the solid solution α were absent for any reason, the common tangent between the liquid and solid solution β would determine the composition of those phases in which the constituents have the same chemical potential. One of the common types of nonequilibrium behavior in silicate systems is the slowness of crystallization such that the liquid is supercooled. When this

happens, metastable phase separation of the liquid is quite common, discussed in Chapter 3.

Glasses. One of the most common departures from equilibrium behavior in ceramic systems is the ease with which many silicates are cooled from the liquid state to form noncrystalline products. This requires that the driving force for the liquid-crystal transformation be low and that the activation energy for the process be high. Both of these conditions are fulfilled for many silicate systems.

The rate of nucleation for a crystalline phase forming from the liquid is proportional to the product of the energy difference between the crystal and liquid and the mobility of the constituents that form a crystal, as discussed in Chapter 8. In silicate systems, both of these factors change so as to favor the formation of glasses as the silica content increases. Although data for the diffusion coefficient are not generally available, the limiting mobility is that of the large network-forming anions and is inversely proportional to the viscosity. Thus, the product of $\Delta H_f/T_{mp}$ and $1/\eta$ can be used as one index for the tendency to form glasses on cooling, as shown in Table 7.1.

Table 7.1. Factors Affecting Glass-Forming Ability

Compo- sition	$T_{mp}(^{\circ}\text{C})$	$\Delta H_f/T_{mp}$ (cal/mole/ $^{\circ}\text{K}$)	$(1/\eta)_{mp}$ (poise $^{-1}$)	$(\Delta H_f/T_{mp}) \times$ $(1/\eta)_{mp}$	Comments
B_2O_3	450	7.3	2×10^{-5}	1.5×10^{-4}	Good glass former
SiO_2	1713	1.1	1×10^{-6}	1.1×10^{-6}	Good glass former
$\text{Na}_2\text{Si}_2\text{O}_5$	874	7.4	5×10^{-4}	3.7×10^{-3}	Good glass former
Na_2SiO_3	1088	9.2	5×10^{-3}	4.5×10^{-2}	Poor glass former
CaSiO_3	1544	7.4	10^{-1}	0.74	Very difficult to form as glass
NaCl	800.5	6.9	50	345	Not a glass former

Metastable Crystalline Phases. Frequently in ceramic systems crystalline phases are present that are not the equilibrium phases for the conditions of temperature, pressure, and composition of the system. These remain present in a metastable state because the high activation

energ
rate
same
one
more
energ

Th
Fig.
energ
been
whic
into
into
preci
exam
phas
prese

Th
going
porc
of 12
quar
raw
trans
The
elim

381-515

ite common,

uilibrium be-
es are cooled
requires that
' and that the
onditions are

i the liquid is
n the crystal
a crystal, as
ctors change
nt increases.
available, the
ions and is
 $\Delta H_f/T_{mp}$ and
s on cooling,

Comments

Good glass
former
Good glass
former
Good glass
former
Poor glass
former
Very diffi-
cult to
form as
glass
Not a glass
former

ms crystal-
ses for the
he system.
i activation

energies required for their conversion into more stable phases cause a low rate of transition. The energy relationships among three phases of the same composition might be represented as given in Fig. 7.34. Once any one of these phases is formed, its rate of transformation into another more stable phase is slow. In particular, the rate of transition to the lowest energy state is specially slow for this system.

The kinetics of transformation in systems such as those illustrated in Fig. 7.34 are discussed in Chapter 9 in terms of the driving force and energy barrier. Structural aspects of transformations of this kind have been discussed in Chapter 2. In general, there are two common ways in which metastable crystals are formed. First, if a stable crystal is brought into the more stable form, metastable crystals are formed. Second, a precipitate or transformation may form a new metastable phase. For example, if phase 1 in Fig. 7.34 is cooled into the region of stability of phase 3, it may transform into the intermediate phase 2, which remains present as a metastable crystal.

The most commonly observed metastable crystalline phases not undergoing transformation are the various forms of silica (Fig. 7.5). When a porcelain body containing quartz as an ingredient is fired at a temperature of 1200 to 1400°C, tridymite is the stable form but it never is observed; the quartz always remains as such. In refractory silica brick, quartz used as a raw material must have about 2% calcium oxide added to it in order to be transformed into the tridymite and cristobalite forms which are desirable. The lime provides a solution-precipitation mechanism which essentially eliminates the activation energy barrier, shown in Fig. 7.34, and allows

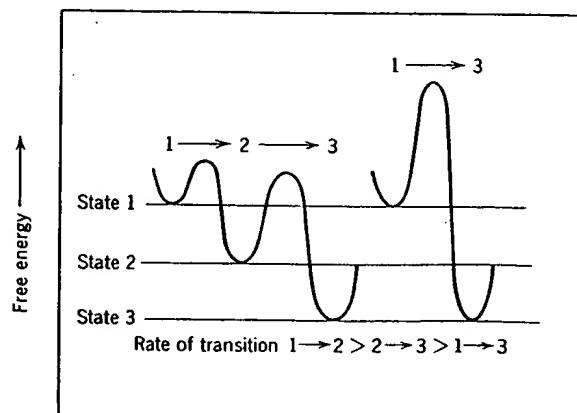


Fig. 7.34. Illustration of energy barriers between three different states of a system.

the stable phase to be formed. This is, in general, the effect of mineralizers such as fluorides, water, and alkalis in silicate systems. They provide a fluid phase through which reactions can proceed without the activation energy barrier present for the solid-state process.

Frequently, when high-temperature crystalline forms develop during firing of a ceramic body, they do not revert to the more stable forms on cooling. This is particularly true for tridymite and cristobalite, which never revert to the more stable quartz form. Similarly, in steatite bodies the main crystalline phase at the firing temperature is the protoenstatite form of MgSiO_3 . In fine-grained samples this phase remains as a metastable phase dispersed in a glassy matrix after cooling. In large-grain samples or on grinding at low temperature, protoenstatite reverts to the equilibrium form, clinoenstatite.

A common type of nonequilibrium behavior is the formation of a metastable phase which has a lower energy than the mother phase but is not the lowest-energy equilibrium phase. This corresponds to the situation illustrated in Fig. 7.34 in which the transition from the highest-energy phase to an intermediate energy state occurs with a much lower activation energy than the transition to the most stable state. It is exemplified by the devitrification of silica glass, which occurs in the temperature range of 1200 to 1400°C, to form cristobalite as the crystalline product instead of the more stable form, tridymite. The reasons for this are usually found in the structural relationships between the starting material and the final product. In general, high-temperature forms have a more open structure than low-temperature crystalline forms and consequently are more nearly like the structure of a glassy starting material. These factors tend to favor crystallization of the high-temperature form from a supercooled liquid or glass, even in the temperature range of stability of a lower-temperature modification.

This phenomenon has been observed in a number of systems. For example, J. B. Ferguson and H. E. Merwin* observed that when calcium-silicate glasses are cooled to temperatures below 1125°C, at which wollastonite (CaSiO_3) is the stable crystalline form, the high-temperature modification, pseudowollastonite, is found to crystallize first and then slowly transform into the more stable wollastonite. Similarly, on cooling compositions corresponding to $\text{Na}_2\text{O} \cdot \text{Al}_2\text{O}_3 \cdot 2\text{SiO}_2$, the high-temperature crystalline form (carnegieite) is observed to form as the reaction product, even in the range in which nephelite is the stable phase; transformation of carnegieite into nephelite occurs slowly.

In order for any new phase to form, it must be lower in free energy than the starting material but need not be the lowest of all possible new phases.

* *Am. J. Science, Series 4*, 48, 165 (1919).

This requires the phase diagram to show other phase precipitates. Fig. 7.35. difficulty frequently potassium eutectic temperature which both the liquid and this system cristobalite equilibrium quartz by the double

Extension

Temperature (°C)

Fig. 7.35. E system.

381-518

This requirement means that when a phase does not form as indicated on the phase equilibrium diagram, the liquidus curves of other phases on the diagram must be extended to determine the conditions under which some other phase becomes more stable than the starting solution and a possible precipitate. This is illustrated for the potassium disilicate-silica system in Fig. 7.35. Here, the compound $K_2O \cdot 4SiO_2$ crystallizes only with great difficulty so that the eutectic corresponding to this precipitation is frequently not observed. Instead, the liquidus curves for silica and for potassium disilicate intersect at a temperature about 200° below the true eutectic temperature. This nonequilibrium eutectic is the temperature at which both potassium disilicate and silica have a lower free energy than the liquid composition corresponding to the false eutectic. Actually, for this system the situation is complicated somewhat more by the fact that cristobalite commonly crystallizes from the melt in place of the equilibrium quartz phase. This gives additional possible behaviors, as indicated by the dotted line in Fig. 7.35.

Extension of equilibrium curves on phase diagrams, such as has been

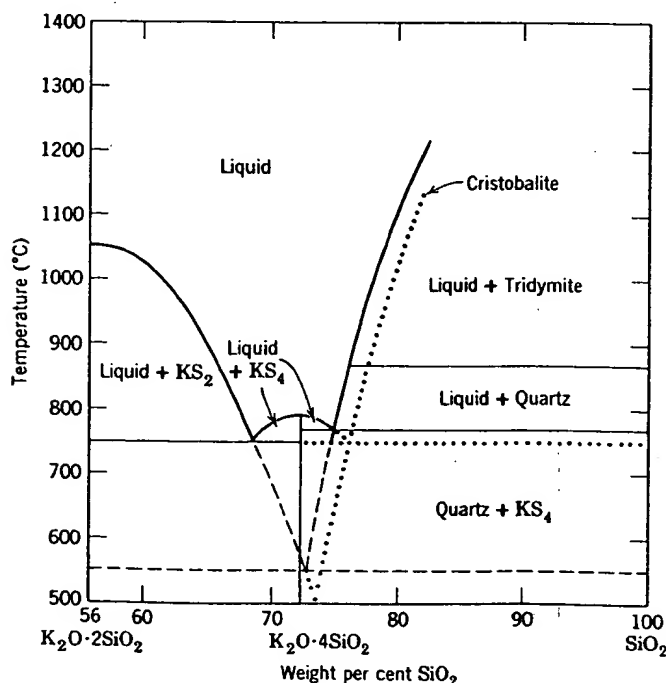


Fig. 7.35. Equilibrium and nonequilibrium liquidus curves in the potassium disilicate-silica system.

shown in Fig. 7.35 and also in Fig. 7.5, provides a general method of using equilibrium data to determine possible nonequilibrium behavior. It provides a highly useful guide to experimental observations. The actual behavior in any system may follow any one of several possible courses, so that an analysis of the kinetics of these processes (or more commonly experimental observations) is also required.

Incomplete Reactions. Probably the most common source of nonequilibrium phases in ceramic systems are reactions that are not completed in the time available during firing or heat treatment. Reaction rates in condensed phases are discussed in Chapter 9. The main kinds of incomplete reactions observed are incomplete solution, incomplete solid-state reactions, and incomplete resorption or solid-liquid reactions. All of these arise from the presence of reaction products which act as barrier layers and prevent further reaction. Perhaps the most striking example of incomplete reactions is the entire metallurgical industry, since almost all metals are thermodynamically unstable in the atmosphere but oxidize and corrode only slowly.

A particular example of incomplete solution is the existence of quartz grains which are undissolved in a porcelain body, even after firing at temperatures of 1200 to 1400°C. For the highly siliceous liquid in contact with the quartz grain, the diffusion coefficient is low, and there is no fluid flow to remove the boundary layer mechanically. The situation is similar to diffusion into an infinite medium, illustrated in Fig. 6.5. To a first approximation, the diffusion coefficient for SiO_2 at the highly siliceous boundary may be of the order of 10^{-8} to 10^{-9} cm^2/sec at 1400°C. With these data it is left as an exercise to estimate the thickness of the diffusion layer after 1 hr of firing at this temperature.

The way in which incomplete solid reactions can lead to residual starting material being present as nonequilibrium phases will be clear from the discussion in Chapter 9. However, new products that are not the final equilibrium composition can also be formed. For example, in heating equimolar mixtures of CaCO_3 and SiO_2 to form CaSiO_3 , the first product formed and the one that remains the major phase through most of the reaction is the orthosilicate, Ca_2SiO_4 . Similarly, when BaCO_3 and TiO_2 are reacted to form BaTiO_3 , substantial amounts of Ba_2TiO_4 , BaTi_2O_7 , and $\text{BaTi}_4\text{O}_{13}$ are formed during the reaction process, as might be expected from the phase-equilibrium diagram (Fig. 7.20). When a series of intermediate compounds is formed in a solid reaction, the rate at which each grows depends on the effective diffusion coefficient through it. Those layers for which the diffusion rate is high form most rapidly. For the CaO-SiO_2 system this is the orthosilicate. For the BaO-TiO_2 system the most rapidly forming compound is again the orthotitanate, Ba_2TiO_4 .

381-515

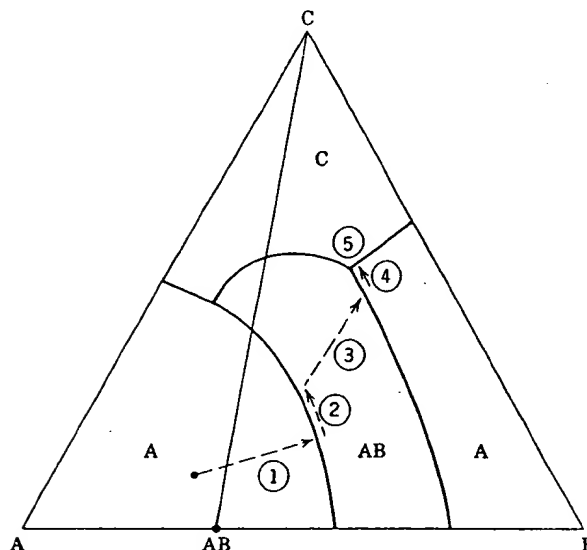


Fig. 7.36. Nonequilibrium crystallization path with (1) Liquid \rightarrow A, (2) A + liquid \rightarrow AB, (3) Liquid \rightarrow AB, (4) Liquid \rightarrow AB + B, (5) Liquid \rightarrow AB + B + C.

A final example of nonequilibrium conditions important in interpreting phase-equilibrium diagrams is the incomplete resorption that may occur whenever a reaction, $A + \text{Liquid} = AB$, takes place during crystallization. This is the case, for example, when a primary phase reacts with a liquid to form a new compound during cooling. A layer tends to build up on the surface of the original particle, forming a barrier to further reaction. As the temperature is lowered, the final products are not those anticipated from the equilibrium diagram. A nonequilibrium crystallization path for incomplete resorption is schematically illustrated in Fig. 7.36.

Suggested Reading

1. E. M. Levin, C. R. Robbins, and H. F. McMurdie, *Phase Diagrams for Ceramists*, American Ceramic Society, Columbus, Ohio, 1964.
2. E. M. Levin, C. R. Robbins, H. F. McMurdie, *Phase Diagrams for Ceramists, 1969 Supplement*, American Ceramic Society, Columbus, Ohio, 1969.
3. A. M. Alper, Ed., *Phase Diagrams: Materials Science and Technology*, Vol. I, "Theory, Principles, and Techniques of Phase Diagrams," Academic Press, Inc., New York, 1970; Vol. II, "The Use of Phase Diagrams in Metal, Refractory, Ceramic, and Cement Technology," Academic Press, Inc., New

thod of using
avior. It pro-
The actual
sible courses,
re commonly

urce of non-
are not com-
eaction rates
ain kinds of
mplete solid-
ctions. All of
act as barrier
g example of
ice almost all
it oxidize and

nce of quartz
after firing at
id in contact
ere is no fluid
ion is similar
5. To a first
hly siliceous
C. With these
diffusion layer

l to residual
will be clear
at are not the
le, in heating
first product
most of the
and TiO_2 are
 BaTi_3O_7 , and
be expected
ries of inter-
t which each
gh it. Those
idly. For the
 O_2 -system the
 Ba_2TiO_4 .

- York, 1970; Vol. III, "The Use of Phase Diagrams in Electronic Materials and Glass Technology," Academic Press, Inc., New York, 1970.
4. A. Muan and E. F. Osborn, *Phase Equilibria among Oxides in Steelmaking*, Addison-Wesley, Publishing Company, Inc., Reading, Mass., 1965.
 5. A. Reisman, *Phase Equilibria*, Academic Press, Inc., New York, 1970.
 6. P. Gordon, *Principles of Phase Diagrams in Materials Systems*, McGraw Hill Book Company, New York, 1968.
 7. A. M. Alper, Ed., *High Temperature Oxides*, Part I, "Magnesia, Lime and Chrome Refractories," Academic Press, Inc., New York, 1970; Part II, "Oxides of Rare Earth, Titanium, Zirconium, Hafnium, Niobium, and Tantalum," Academic Press, Inc., New York, 1970; Part III, "Magnesia, Alumina, and Beryllia Ceramics: Fabrication, Characterization and Properties," Academic Press, Inc., New York; Part IV, "Refractory Glasses, Glass-Ceramics, Ceramics," Academic Press, New York, Inc., 1971.
 8. J. E. Ricci, *The Phase Rule and Heterogeneous Equilibrium*, Dover Books, New York, 1966.

Problems

- 7.1. A power failure allowed a furnace used by a graduate student working in the K_2O - CaO - SiO_2 system to cool down over night. For the fun of it, the student analyzed the composition he was studying by X-ray diffraction. To his horror, he found β - $CaSiO_3$, $2K_2O \cdot CaO \cdot 3SiO_2$, $2K_2O \cdot CaO \cdot 6SiO_2$, $K_2O \cdot 3CaO \cdot 6SiO_2$, and $K_2O \cdot 2CaO \cdot 6SiO_2$ in his sample.
 - (a) How could he get more than three phases?
 - (b) Can you tell him in which composition triangle his original composition was?
 - (c) Can you predict the minimum temperature above which his furnace was operating before power failure?
 - (d) He thought at first he also had some questionable X-ray diffraction evidence for $K_2O \cdot CaO \cdot SiO_2$, but after thinking it over he decided $K_2O \cdot CaO \cdot SiO_2$ should not crystallize out of his sample. Why did he reach this conclusion?
- 7.2. According to Alper, McNally, Ribbe, and Doman,* the maximum solubility of Al_2O_3 in MgO is 18 wt% at 1995°C and of MgO in $MgAl_2O_4$ is 39% MgO , 51% Al_2O_3 . Assuming the NiO - Al_2O_3 binary is similar to the MgO - Al_2O_3 binary, construct a ternary. Make isothermal plots of this ternary at 2200°C, 1900°C, and 1700°C.
- 7.3. You have been assigned to study the electrical properties of calcium metasilicate by the director of the laboratory in which you work. If you were to make the material synthetically, give a batch composition of materials commonly obtainable in high purity. From a production standpoint, 10% liquid would increase the rate of sintering and reaction. Adjust your composition accordingly. What would be the expected firing temperature? Should the boss ask you to explore the possibility of lowering the firing temperature and maintain a white body, suggest the direction to procede. What polymorphic transformations would you be conscious of in working with the above systems?

*J. Am. Ceram. Soc. 45(6), 263-268 (1962).

7.4. Di
rel
on
an
im
7.5. A
ox

Al
7.6. Tr
ter
(m
ar
fo
ph
7.7. Fe
in
fo
tic
rit
sti
7.8. If
to
th
7.9. Th
Al
ter
th
fo

381-518

CERAMIC PHASE-EQUILIBRIUM DIAGRAMS

319

terials and

melmaking,

1970.

Graw Hill

Lime and

; Part II,

and Tan-

Alumina,

operties,"

s, Glass-

er Books,

the K_2O -
alyzed the
 β - $CaSiO_3$,
 SiO_2 in his

tion was?
nace was

idence for
should not

of Al_2O_3 in
Assuming
ary. Make

etasilicate
make the
ainable in
ie rate of
ld be the
sibility of
rection to
working

- 7.4. Discuss the importance of liquid-phase formation in the production and utilization of refractory bodies. Considering the phase diagram for the $MgO-SiO_2$ system, comment on the relative desirability in use of compositions containing 50 MgO -50 SiO_2 by weight and 60 MgO -40 SiO_2 by weight. What other characteristics of refractory bodies are important in their use?
- 7.5. A binary silicate of specified composition is melted from powders of the separate oxides and cooled in different ways, and the following observations are made:

Condition	Observations
(a) Cooled rapidly	Single phase, no evidence of crystallization
(b) Melted for 1 hr, held 80°C below liquidus for 2 hr	Crystallized from surface with primary phases SiO_2 plus glass
(c) Melted for 3 hr, held 80°C below liquidus for 2 hr	Crystallized from surface with primary phases compound $AO \cdot SiO_2$ plus glass
(d) Melted for 2 hr, cooled rapidly to 200°C below liquidus, held for 1 hr, and then cooled rapidly	No evidence of crystallization but resulting glass is cloudy

Are all these observations self consistent? How do you explain them?

- 7.6. Triaxial porcelains (flint-feldspar-clay) in which the equilibrium phases at the firing temperature are mullite and a silicate liquid have a long firing range; steatite porcelains (mixtures of talc plus kaolin) in which the equilibrium phases at the firing temperature are enstatite and a silicate liquid have a short firing range. Give plausible explanations for this difference in terms of phases present, properties of phases, and changes in phase composition and properties with temperature.
- 7.7. For the composition 40 MgO -55 SiO_2 -5 Al_2O_3 , trace the equilibrium crystallization path in Fig. 7.30. Also, determine the crystallization path if incomplete resorption of forsterite occurs along the forsterite-protoenstatite boundary. How do the compositions and temperatures of the eutectics compare for the equilibrium and nonequilibrium crystallization paths? What are the compositions and amounts of each constituent in the final product for the two cases?
- 7.8. If a homogeneous glass having the composition 13 Na_2O -13 CaO -74 SiO_2 were heated to 1050°C, 1000°C, 900°C, and 800°C, what would be the possible crystalline products that might form? Explain.
- 7.9. The clay mineral kaolinite, $Al_2Si_2O_5(OH)_4$, when heated above 600°C decomposes to $Al_2Si_2O_7$ and water vapor. If this composition is heated to 1600°C and left at that temperature until equilibrium is established, what phase(s) will be present. If more than one is present, what will be their weight percentages. Make the same calculations for 1585°C.

Reactions with and between Solids

In heterogeneous reactions there is a reaction interface between the reacting phases, such as nucleus and matrix or crystal and melt. In order for the reaction to proceed, three steps must take place in series—material transport to the interface, reaction at the phase boundary, and sometimes transport of reaction products away from the interface. In addition, reactions at the phase boundary liberate or absorb heat, changing the boundary temperature and limiting the rate of the process. Any of these steps may determine the overall rate at which a heterogeneous reaction takes place, since the overall reaction rate is determined by the slowest of these series steps.

In this chapter we consider these rate-determining steps as applied to changes taking place in ceramic systems. Decomposition of hydrates and carbonates, solid-state reactions, oxidation, corrosion, and many other phenomena must be considered on the basis of limitations imposed by the rates of phase-boundary reactions, material transport, and heat flow.

9.1 Kinetics of Heterogeneous Reactions

Reaction Order. Classical chemical-reaction kinetics has been mainly concerned with homogeneous reactions and cannot be directly applied to many phenomena of particular interest in ceramics, but it provides the basis for understanding rate phenomena. Reaction rates are frequently classified as to molecularity—the number of molecules or atoms formally taking part in the reaction. Overall reactions are also commonly classified as to reaction order—the sum of the powers to which concentrations c_1 , c_2 , and so on, must be raised to give empirical agreement with a rate equation of the form

$$\frac{-dc}{dt} = Kc_1^a c_2^b c_3^c \dots \quad (9.1)$$

In a first-order reaction, for example,

$$\frac{-dc}{dt} = Kc \quad (9.2)$$

On integration this gives

$$\ln \frac{c}{c_0} = K(t - t_0) \quad (9.3)$$

where K is a constant and c_0 is the initial concentration at time t_0 . For the simplest overall reactions which involve but one elementary step, the order and molecularity are the same. For more complex reactions which consist of several consecutive elementary steps involving different species and for heterogeneous reactions in general, the molecularity and order are quite different, and characterization by reaction order is a purely formal empirical method. In fact, zero and fractional reaction orders are sometimes found. Although the reaction-order concept is useful as a means of representing data for heterogeneous reactions, these cannot usually be interpreted simply in terms of molecular interactions.

Activation Energy and Reaction Rate. The effect of temperature on the rate of processes taking place is frequently great. The historical basis for its understanding is the Arrhenius equation, in which it was found that for many processes the specific reaction-rate constant could be related to temperature by the relation $\log K \sim 1/T$ or, alternatively, $K = A \exp(-Q/RT)$, where Q is the experimental activation energy. The basis of this relationship in a general theory of rate processes has been discussed in Chapter 6 in connection with diffusion as an activated process. In general, an activation energy is required for each of the steps involved in an overall rate process (Fig. 9.1).

Two general considerations are the basis for interpreting most kinetic data. The first of these is that each individual step in a rate process must be relatively simple and that the reaction path of each step, such as an individual atom jump in diffusion, a molecular decomposition, or a new chemical bond being formed, involves an *activated complex* or *transition state* of maximum energy along the reaction path. Of all possible parallel paths of reaction, the one with the lowest energy barrier is the most rapid and the major contributor to the overall process. This activated-complex theory has provided a general form of equation for rate processes and a model that allows semiempirical calculations for simple processes. The second general consideration has been that the overall rate of a complex process involving a series of consecutive steps is fixed by the rate of the slowest individual step.

If we plot energy along a distance coordinate corresponding to the

Fig. 9.1. Several steps each has a step.

(9.2)

(9.3)

For the ep, the which different ity and er is a eaction cept is , these ons.

on the isis for hat for ited to $K =$ y. The s been tivated e steps

kinetic s must as an a new nsition arallel t rapid mplex and a s. The mplex of the

to the

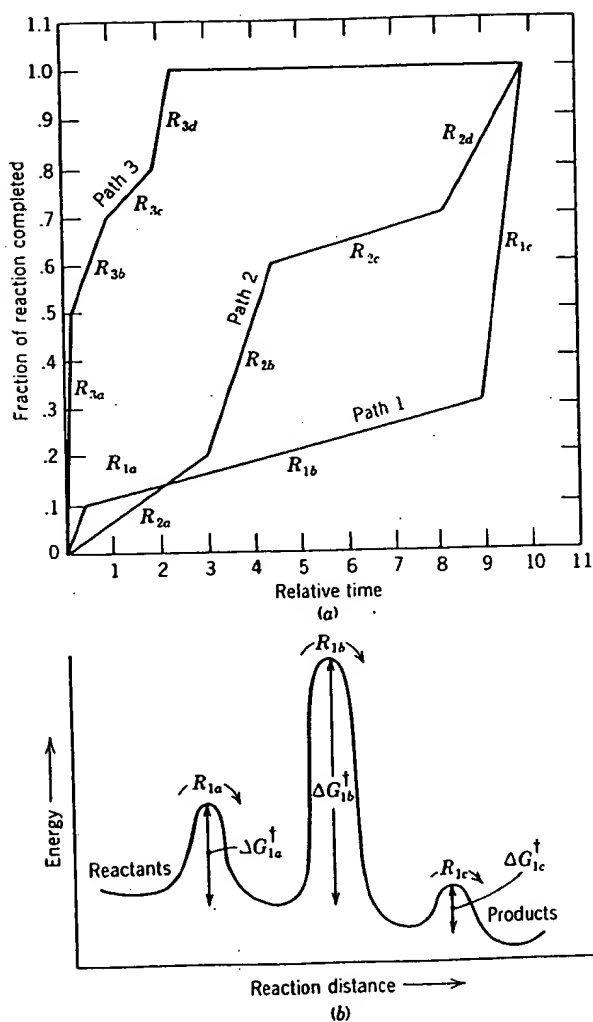


Fig. 9.1. Schematic representation of (a) multipath process in which each path contains several steps; the process is dominated by the fastest path (path 3). (b) Multistep path in which each step has an activation energy; the overall rate along this path is determined by the slowest step.

reaction path of lowest energy between the reactant and product, there is an energy maximum, actually a saddle point, corresponding to the activated complex or transition state, such as discussed for diffusion in Chapter 6. This concept of an activated complex has been generally accepted as the basis for reaction-rate studies and, as discussed in Chapter 6, leads to a specific reaction-rate constant given by

$$k = \frac{kT}{h} \exp\left(-\frac{\Delta H^\ddagger}{RT}\right) \exp \frac{\Delta S^\ddagger}{R} \quad (9.4)$$

where k is the Boltzmann constant, h the Planck constant, and ΔH^\ddagger and ΔS^\ddagger the enthalpy and entropy of activation, respectively. Individual reaction steps in an overall reaction process are usually simple and may be designated as monomolecular or bimolecular. Semiempirical treatments of the unit steps on the basis of activated-complex theory allow a rational theoretical approach to reaction processes.

Complex Processes. Overall processes are frequently complex and require a series of individual separate unit steps. In such a sequence the rate of any individual step depends on the specific reaction-rate constant and the concentration of the reactants for this step. For a series of consecutive steps,

$$A_1 = A_2 = \dots A_i = A_{i+1} = \dots A_n \quad (9.5)$$

We can define a *virtual maximum rate* for each step as the rate that would be found if equilibria were established for all previous and following steps. Under these conditions the reaction with the lowest virtual maximum rate controls the overall rate if it is much lower than the rates of other steps. Under these conditions equilibrium will have been virtually established for all previous steps but will not necessarily be established for the following steps. As shown schematically in Fig. 9.1, the reaction rate for path 1 is determined by step 1b of the process; it has the slowest rate and the largest activation energy barrier and accounts for 85% of the reaction time; steps 1a and 1c occur more rapidly. Reaction step R_{1a} will be slowed to a rate giving a virtual equilibrium concentration of products; reaction R_{1c} will be slowed because R_{1b} is producing few reactants for step R_{1c} .

We have already noted that most condensed-phase processes of interest in ceramics involve heterogeneous systems; changes take place at a phase boundary. The overall process involves (1) transport of reactants to the phase boundary, (2) reaction at the phase boundary, (3) transport of products away from the phase boundary. This series of reaction steps has relatively simple kinetics, provided the virtual maximum rate of one step is much slower than that of any of the other steps. If we assume this to be

the case, we have two general classes of heterogeneous reactions: (1) those controlled by transport rate and (2) those controlled by phase-boundary reaction rate. In general, both the transport process and the phase-boundary process involve a number of individual steps, one of which has the lowest virtual maximum rate. In going from reactants to products, there may be several possible reaction paths for transport processes and for phase-boundary reactions. There are three different possible reaction paths shown in Fig. 9-1a.

9.2 Reactant Transport through a Planar Boundary Layer

Slip Casting. As an example of the usefulness of determining the rate-limiting step for deriving kinetic equations, we begin with the ceramic processing technique of slip casting, in which a slurry containing clay particles dispersed in water is poured into a plaster of paris (gypsum) mold which contains fine capillaries (see Fig. 11.36) that absorb water from the slip. This causes a compact layer of clay particles to form at the mold-slip interface (Fig. 9.2). The rate of the process is determined by the

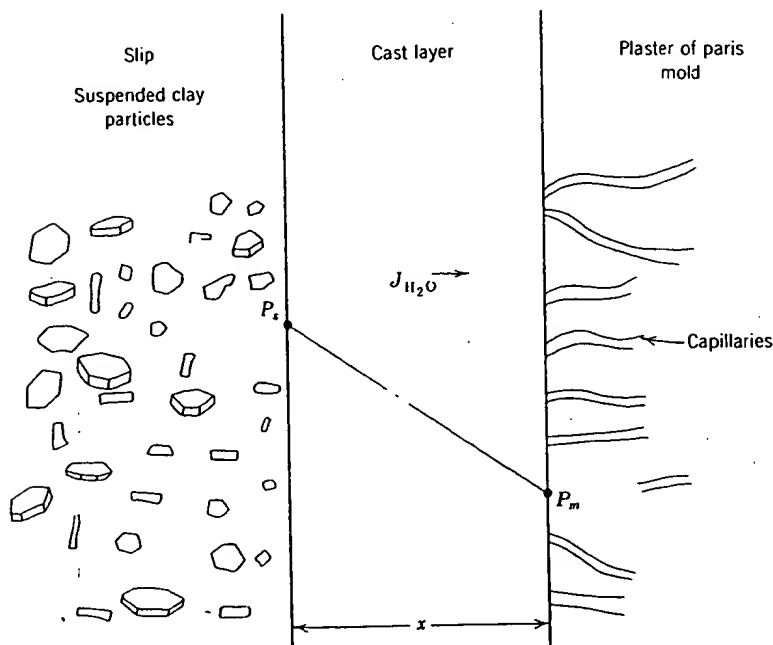


Fig. 9.2. Schematic representation of the formation of a slip-cast layer formed by the extraction of water by capillary action of a plaster of paris mold.

transport of water out of the slip and into the capillaries; the rate-limiting step is the flow of water through the compact clay layer. As the layer thickness increases, the overall rate of material transport decreases because of the increased permeation distance (similar to gas permeation through glasses, discussed in Chapter 6).

We begin by writing the flux equation for water,

$$J = -K \frac{dP}{dx} \quad (9.6)$$

where we assume a planar deposit (unidirectional flow) and that the water flux J_{H_2O} is proportional to the pressure gradient resulting from the capillaries of the plaster mold. The permeation coefficient K depends on the clay particle size, particle packing, and the viscosity of water and is temperature-sensitive. The water pressure in the slip, P_s , is 1 atm; in the mold, P_m , it is determined by capillarity, $\Delta P = P_s - P_m \approx 2\gamma/r$ (Chapter 5). The surface tension is a function of the deflocculating agents used. Until the capillaries become filled with water, ΔP is approximately constant, and the flux can be related to the change of the layer thickness dx/dt ,

$$J = \left(\frac{1}{\kappa\rho}\right) \frac{dx}{dt} = -K \frac{dP}{dx} = -K \frac{\Delta P}{x} \approx -K \frac{2\gamma}{rx} \quad (9.7)$$

where ρ is the density of the cast layer and κ is a factor for converting the volume of water removed to the volume of clay particles deposited. Integration of Eq. 9.7 gives

$$x = \left(2K\rho\kappa \frac{2\gamma}{r}\right)^{1/2} t^{1/2}$$

or in the general parabolic form

$$x = (K' t)^{1/2} \quad (9.8)$$

That is, the wall thickness of a planar casting should increase with the square root of time (Fig. 9.3).

This parabolic rate law is commonly observed for kinetic processes in which the limiting step is mass transport through a reaction layer.

Interdiffusion between Solids. In Section 6.3, we discussed the chemical diffusion coefficient and its formulation in terms of the tracer diffusion coefficients for the case of interdiffusion. If we measure the rate at which two ceramics interdiffuse, this too can be considered the formation of a reaction product which is a solid solution rather than a distinct or separate phase. Let us consider the interdiffusion between crystals of NiO and CoO at a high temperature. The solid solution that forms is nearly ideal;

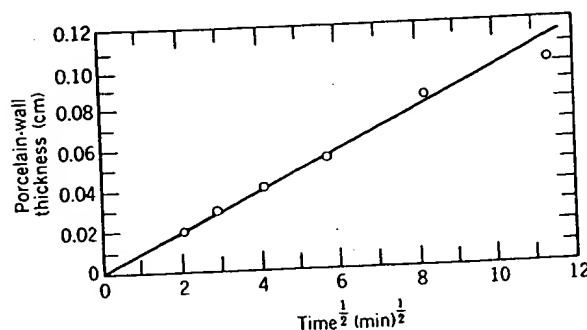


Fig. 9.3. Parabolic dependence of the slip-casting rate of a porcelain slip in a plaster of paris mold.

thus the chemical potential is related directly to the composition (concentration) by $\mu_i = \mu_i^\circ + RT \ln \gamma c_i$ where the activity coefficient γ is equal to one. Thus Eq. 6.41 becomes

$$\bar{D} = [D_1^T X_2 + D_2^T X_1] \left(1 + \frac{d \ln \gamma_1}{d \ln X_1} \right) = D_{Co}^T X_{Co} + D_{Ni}^T (1 - X_{Co}) \quad (9.9)$$

This is the familiar Darken equation and assumes local equilibrium everywhere in the interdiffusion zone and is not strictly valid in ceramics. As will be seen later, ambipolar coupling will decrease the value of \bar{D} through electrochemical fields which arise if one charged specie moves faster than another.

The measured interdiffusion data for the CoO-NiO system are shown in Fig. 9.4a. The curves on the plot were calculated from the tracer diffusivities (Fig. 9.4b) and Eq. 9.9, assuming ideal solution behavior. In the case of interdiffusion of NiO-MgO, Eq. 9.9 is not directly applicable because the tracer diffusivities are a function of the nickel concentration. The experimental interdiffusion coefficient (Fig. 9.5a) has an exponential dependence on the concentration of nickel. Trivalent nickel ions and cation vacancies become associated (see Sections 4.7 and 6.4) and increase the transport rate of nickel into MgO. The measurements were made in air, so that there is sufficient trivalent nickel to dominate the cation vacancy formation process. That is, most of the vacancies arise from the presence of Ni_{Ni}^{3+} . As discussed in Sections 4.7 and 6.4, a significant fraction of the trivalent nickel ions and cation vacancies are coupled by association. Data for some other systems are shown in Fig. 9.5b.

Next let us consider a reaction in which a compound is formed as the reaction layer, for example, the formation of nickel aluminate spinel ($NiAl_2O_4$) from NiO and Al_2O_3 . There are many possible reaction paths; five are shown schematically in Fig. 9.6. The rate of spinel formation

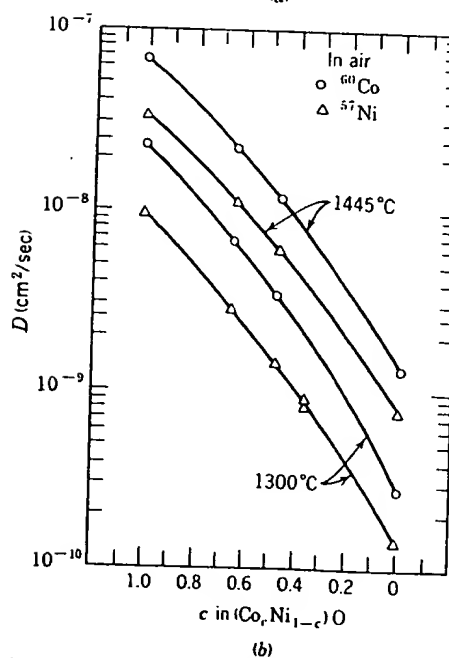
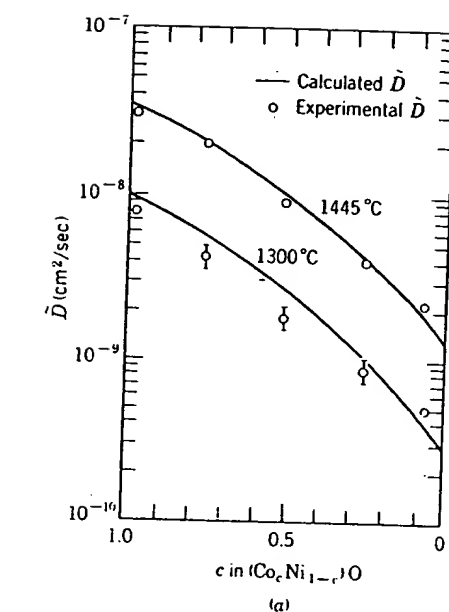


Fig. 9.4. (a) Comparison of the calculated interdiffusion coefficients \bar{D} and experimental values at 1445 and 1300°C in air. (b) Tracer diffusion coefficients of ^{60}Co and ^{57}Ni in $(\text{Co}_x\text{Ni}_{1-x})\text{O}$ crystals at 1445 and 1300°C in air. Plotted as $\log D$ versus c . From W. K. Chen and N. L. Petersen, *J. Phys. Chem. Soc.*, 34, 1093 (1973).

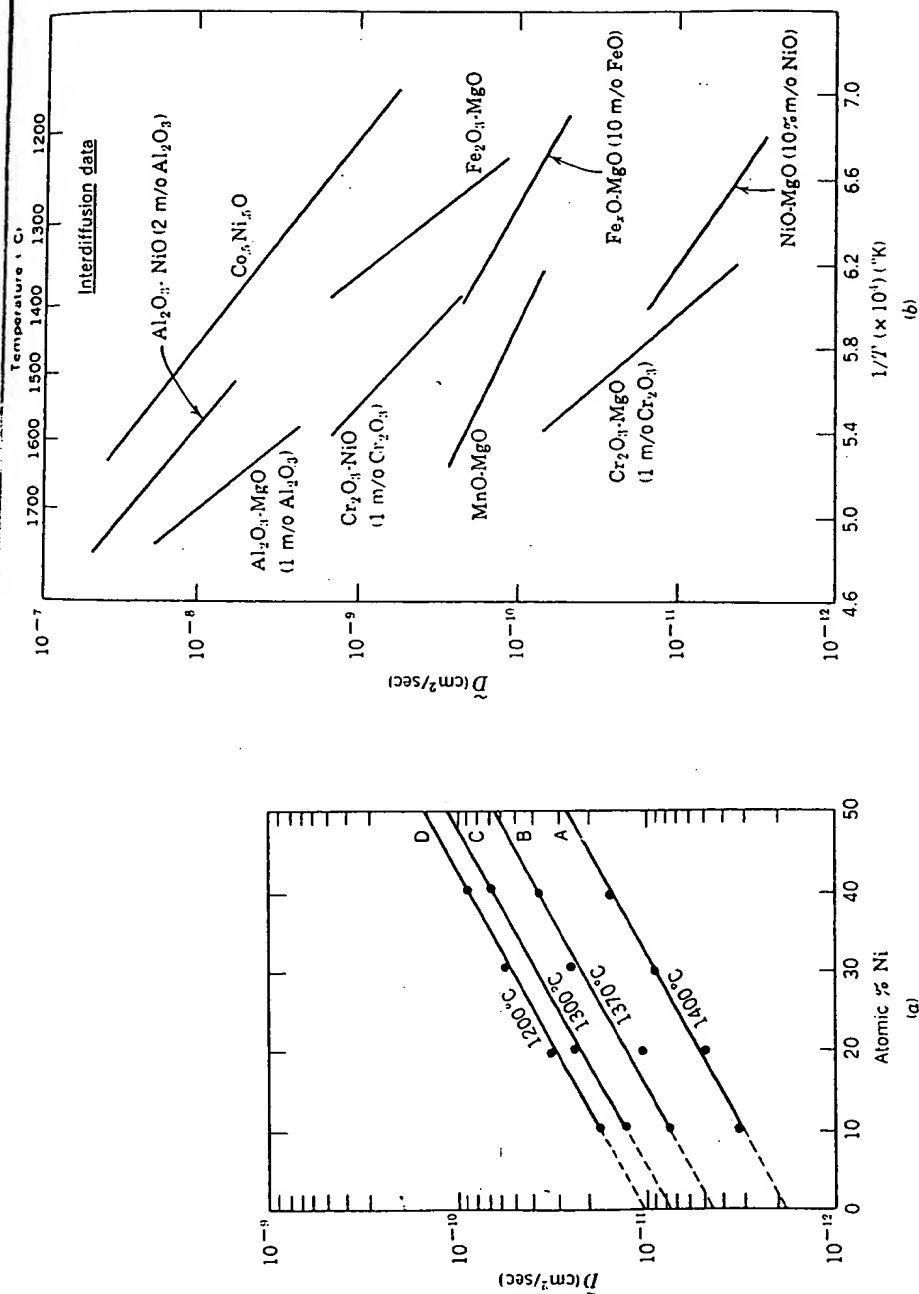
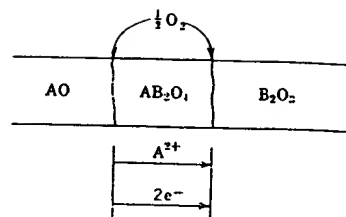
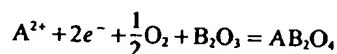
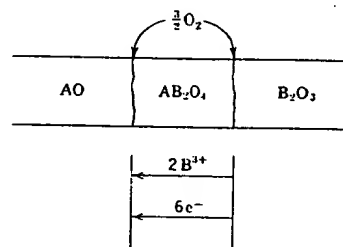
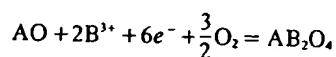


Fig. 9.5. (a) Diffusivity versus nickel concentration at several temperatures in the NiO-MgO system in air. From S. L. Blank and J. A. Pask, *J. Am. Ceram. Soc.*, 52, 669 (1969). (b) Interdiffusion coefficients in several oxides for specific compositions.

Reaction occurs at $AB_2O_4-B_2O_3$ interface:
oxygen gas phase transport with A^{2+} ion and
electron transport through AB_2O_4 :



Reaction occurs at $AO-AB_2O_4$ interface:
oxygen gas phase transport with B^{3+} ion and
electron transport through AB_2O_4 :

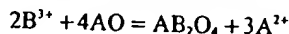


Oxygen and cation transport through AB_2O_4 :

- (1) Both cations diffuse ($J_{B^{3+}} = \frac{2}{3}J_{A^{2+}}$).

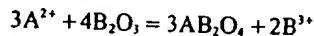
Reactions occur at

$AO-AB_2O_4$ interface



and at

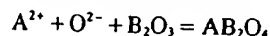
$AB_2O_4-B_2O_3$ interface



- (2) A^{2+} and O^{2-} diffuse.

Reaction at

$AB_2O_4-B_2O_3$ interface



- (3) B^{3+} and O^{2-} diffuse.

Reaction at

$AO-AB_2O_4$ interface

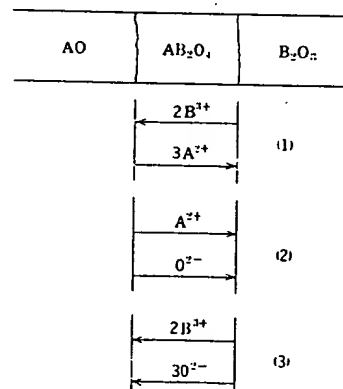
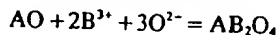


Fig. 9.6. Schematic representation of several mechanisms which may control the rate of AB_2O_4 (e.g., spinel) formation. From Ref. 1.

might
the tr
interf:
Wh
throu:
9.8), i
Figur
two c
plana
when
sed in

might be controlled by the diffusion of A^{2+} ions; B^{3+} ions or O^{2-} ions, by the transport of electrons (holes), by the transport of O_2 gas, or by the interface reactions at $AO-AB_2O_4$ or $AB_2O_4-B_2O_3$.

When the rate of reaction-product formation is controlled by diffusion through the planar product layer, the parabolic rate law is observed (Eq. 9.8), in which the diffusion coefficient is that for the rate-limiting process. Figure 9.7 shows the parabolic time dependence for $NiAl_2O_4$ formation at two different temperatures, and Fig. 9.8 is a photomicrograph of the planar spinel reaction product on Al_2O_3 . (More complex situations arise when several phases are formed as reaction products. These are discussed in reference 1 and by C. Wagner.*)

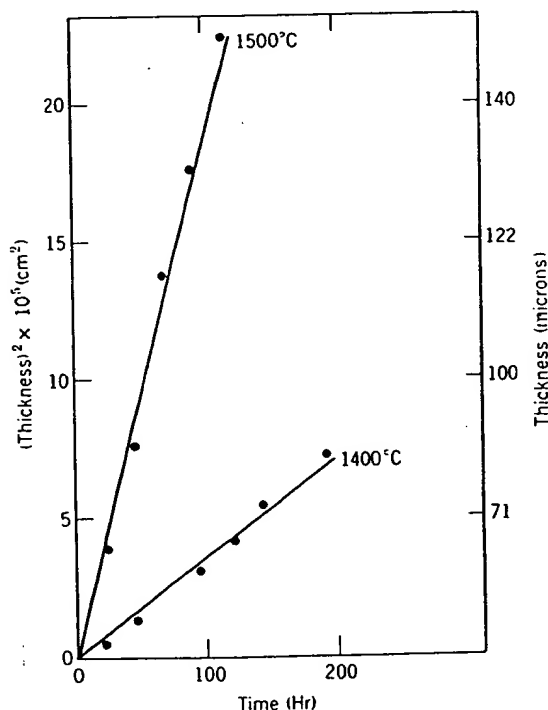


Fig. 9.7. Thickness of $NiAl_2O_4$ formed in $NiO-Al_2O_3$ couples as a function of time for couples heated in argon at 1400 and 1500°C. From F. S. Pettit et al., *J. Am. Ceram. Soc.*, **49**, 199 (1966).

The Electrochemical Potential in Ionic Solids. When considering point defects (Chapter 4) and atom mobility (Chapter 6), we noted that a

Acta Met.*, **17, 99 (1969).

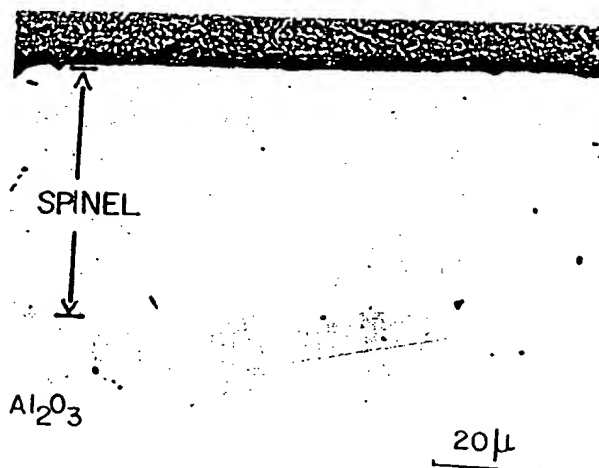


Fig. 9.8. Cross-sectional view of a typical NiAl_2O_4 layer formed in an $\text{NiO}-\text{Al}_2\text{O}_3$ couple after 73 hr at 1400°C . From F. S. Pettit, et al., *J. Am. Ceram. Soc.*, 49, 199 (1966).

distinguishing feature of ionic crystals is the effective charge that an atomic specie may have within the crystal lattice. When there is mass transport in a ceramic, the transport of one charged specie is usually coupled to the transport of an ion or defect of the opposite charge. We must therefore consider the electrochemical potential as the motivating force for mass transport rather than just the chemical potential or concentration gradient. The electrochemical potential of the i th specie η_i is the sum of the chemical potential μ_i and the electrical potential ϕ acting on it:

$$\eta_i = \mu_i + Z_i F \phi \quad (9.10)$$

where Z_i is the effective charge and F is the Faraday constant. We have already noted in Table 6.1 the interrelationship between the mobilities expressed in terms of electrical and chemical driving forces. The flux due to an electrochemical potential gradient is thus given by

$$j_i = c_i v_i = -c_i B_i \frac{\partial \eta_i}{\partial x} = -c_i B_i \left[\frac{\partial \mu_i}{\partial x} + Z_i F \frac{\partial \phi}{\partial x} \right] \quad (9.11)$$

Examination of the two gradient terms in this equation shows the importance of the ionic nature of ceramics. For example, a concentration gradient (chemical-potential gradient) in one direction may be offset by an electrical-field gradient that motivates the ion in the opposite direction. Another kind of effect results from the local electrical field between oppositely charged species. For example, the cations in most close-

packed oxide
 $\text{NiO}-\text{CoO}$
 case in which
 coefficient
 ions in alumina
 motion of
 (9.11) are

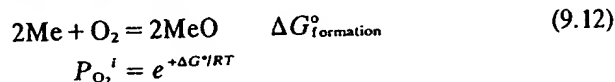
Oxidation
 law in which
 reaction products
 metals. They
 begin with
 results extending
 coherent oxide
 P_{O_2} and then
 determined
 of the oxide

The oxygen
 layer (Fig. 9.8)
 the metal-oxide
 metal ion is
 the oxygen
 also a net
 determines
 cations and
 and then
 determining

The flux
 changed to

packed oxides diffuse more rapidly than oxygen, as for the NiO-MgO and NiO-CoO interdiffusion already discussed. If this begins to happen in the case in which there is a net mass flow (not for the case of diffusion coefficient measurements using radioactive tracers), for example, Al^{3+} ions in alumina, a net electrical field results and thereby couples the motion of Al^{3+} ions and O^{2-} ions. Several solid reactions based on Eq. (9.11) are now considered.

Oxidation of a Metal. The most extensive studies of the parabolic rate law in which the process is controlled by diffusive transport through the reaction product are investigations into the formation of oxide layers on metals. The analysis techniques were developed by Carl Wagner which begin with Eq. (9.11). They are described here in some detail because the results extend to many ceramic problems. Consider the formation of a coherent oxide layer on a metal where the ambient oxygen pressure is $P_{\text{O}_2}^*$ and the effective oxygen pressure at the oxide-metal interface $P_{\text{O}_2}^i$ is determined by the temperature and the standard free energy of formation of the oxidation reaction (see Fig. 9.9):



The oxygen concentration gradient (chemical potential) across the oxide layer (Fig. 9.10) provides the driving force for oxygen diffusion towards the metal-oxide interface. A gradient of the chemical potential of the metal ion in the opposite direction produces metal-ion diffusion toward the oxygen atmosphere. If one atomic flux is larger than the other, there is also a net flux of electrons or electron holes. The net transport, which determines the rate of oxide growth, is the sum of flux of anions and cations and electrons or holes. First we must consider each of these fluxes and then we shall look for circumstances when one specie is rate-determining and the complex relationships reduce to more simple forms.

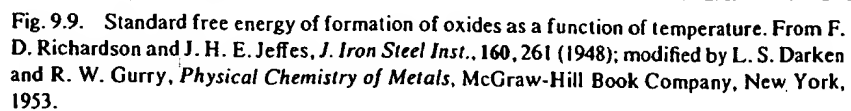
The flux of the atomic and electronic species given by Eq. 9.11 can be changed to the flux of charged particles by multiplying by the valence:

$$J_{\text{O}} = -|Z_{\text{O}}|c_{\text{O}}B_{\text{O}}\frac{\partial\eta_{\text{O}}}{\partial x} = |Z_{\text{O}}|j_{\text{O}}$$

$$J_{\text{Me}} = -|Z_{\text{Me}}|c_{\text{Me}}B_{\text{Me}}\frac{\partial\eta_{\text{Me}}}{\partial x} = |Z_{\text{Me}}|j_{\text{Me}} \quad (9.13)$$

$$J_{\text{e}} = -nB_{\text{e}}\frac{\partial\eta_{\text{e}}}{\partial x} = |-1|j_{\text{e}}$$

$$J_{\text{h}} = -pB_{\text{h}}\frac{\partial\eta_{\text{h}}}{\partial x} = |+1|j_{\text{h}}$$



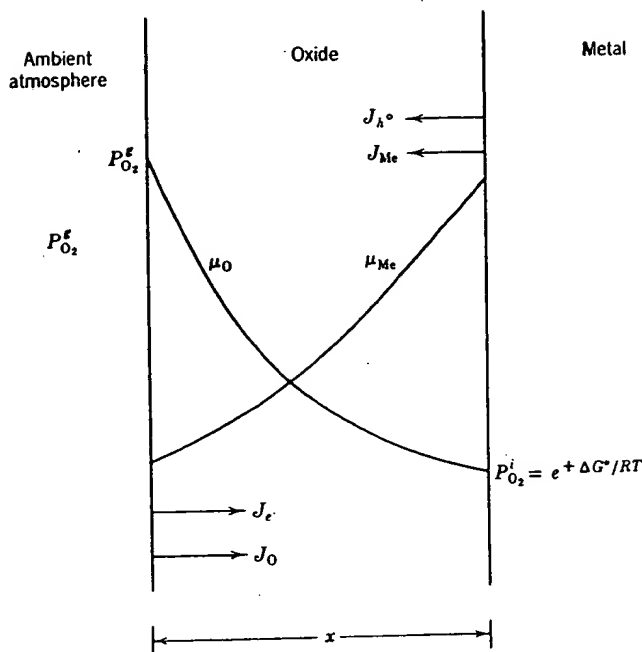


Fig. 9.10. Chemical-potential gradients across an oxide layer on a metal.

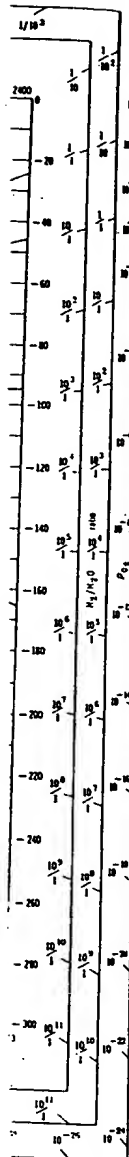
For a given oxide layer, either electrons or holes are predominant, so that only one of the last two equations is necessary. The constraint on the net flux is electrical neutrality. If we assume electrons to be the important electronic defect, this constraint requires that

$$J_0 + J_e = J_{Me} \quad (9.14)$$

The net flux and therefore the rate of oxidation is the sum $J_{ox} = |J_0| + |J_{Me}|$. The general result can be expressed in terms of the conductivity σ and the transference number t_i (see also Chapter 17), which represents the fraction of the total charge flux carried by a particular specie;

$$\begin{aligned} J_{ox} &= \frac{\sigma t_{e'}}{|Z_{Me}|F^2} (t_0 + t_{Me}) \left| \frac{\partial \mu_{Me}}{\partial x} \right| \\ &= \frac{\sigma t_{e'}}{|Z_0|F^2} (t_0 + t_{Me}) \left| \frac{\partial \mu_0}{\partial x} \right| \end{aligned} \quad (9.15)$$

Although the composition varies through the layer, average values can be assumed for t_i and σ to simplify the result, which yields a form of the



from F.
Darken
York,

parabolic rate law;

$$\frac{dx}{dt} = \frac{1}{x} \left[\frac{\bar{\sigma} \bar{t}_e}{|Z_{Mc}| F^2} (\bar{t}_0 + \bar{t}_{Mc}) |\Delta \mu_{Mc}| \right] = \frac{K}{x} \quad (9.16)$$

Recalling that,

$$t_i \sigma = \sigma_i = e Z_i c_i \mu_i = \frac{c_i Z_i^2 e^2 F^2}{RT} D_i \quad (9.17)$$

we can see that the oxidation rate is governed by the atomic mobilities or diffusivities. Let us now consider specific rate limiting cases:

1. The electrical current is carried primarily by electronic defects, $t_e \approx 1$ or $t_h \approx 1$:

a. If $D_0 \gg D_{Mc}$, then

$$K = \frac{\bar{\sigma} \bar{t}_0}{|Z_{Mc}| F^2} |\Delta \mu_{Mc}| \quad (9.18)$$

which for an oxide for predominant $V_o^{\cdot\cdot}$ defects reduces to the approximation

$$K \approx \frac{c_0}{2|Z_{Mc}|} \int_{\mu_0}^{\mu_0^*} D_0 d\mu_0 \quad (9.19)$$

since $\mu_0 = 1/2 \mu_{O_2} = 1/2 (\mu_{O_2}^0 + RT \ln P_{O_2})$. If we assume that $[V_o^{\cdot\cdot}] \propto P_{O_2}^{-1/6}$, as discussed in Chapter 6, and that the diffusion coefficient varies similarly;

$$D_0 = [V_o^{\cdot\cdot}] D_{V_o^{\cdot\cdot}} = \frac{(K_{V_o^{\cdot\cdot}})^{1/3}}{4^{1/3}} D_{V_o^{\cdot\cdot}} P_{O_2}^{-1/6} \quad (9.20)$$

and the rate constant becomes

$$K \approx \frac{3c_0}{4^{1/3}|Z_{Mc}|} (K_{V_o^{\cdot\cdot}})^{1/3} D_{V_o^{\cdot\cdot}} \{ (P_{O_2}^*)^{-1/6} - (P_{O_2}^i)^{-1/6} \} \quad (9.21)$$

b. If $D_{Mc} \gg D_0$ and we assume singly charged metal vacancies V'_{Mc} , the rate constant is

$$K \approx 2(K_{V'_{Mc}})^{1/2} D_{V'_{Mc}} \{ (P_{O_2}^*)^{1/4} - (P_{O_2}^i)^{1/4} \} c_{Mc} \quad (9.22)$$

note that $D_{V'_{Mc}} [V'_{Mc}] = D_{Mc}$.

2. If the electrical current is carried primarily by the ions, $(t_0 + t_{Mc}) \approx 1$, the rate constant from Eq. 9.16 becomes

$$K \approx \frac{kT}{8|Z_{Mc}| e^2} \int_{P_{O_2}^i}^{P_{O_2}^*} \sigma_{e,i} d \ln P_{O_2} \quad (9.23)$$

where $\sigma_{e,i}$ is the conduction due to electrons and holes which have mobilities μ_e and μ_h , respectively (see Table 6.1 $\mu_i = B_i''$).

$$\sigma_{e1} = en\mu_e + ep\mu_h \quad (9.24)$$

If we assume that the defect concentration does not have a large variation over the oxide layer

$$K \approx \frac{\sigma_{e1} kT}{8|Z_{Mc}|e^2} [\ln P_{O_2^s} - \ln P_{O_2^i}] \quad (9.25)$$

An example of the applicability of this relationship is the diffusive transport of oxygen through calcia-stabilized zirconia. The oxygen diffusion coefficient plotted in Fig. 6.11 is very large and accounts for $t_0 \approx 1$. Thus, the slower-moving specie, the electron hole, becomes rate-limiting for oxygen permeation (Eq. 9.25), as shown in Fig. 9.11.

3. If the metal undergoing oxidation has an impurity with a different oxidation state, for example, Li in Ni, the defect concentration in the oxide may be determined by the impurity concentration. As an example, consider the analogous case to Eq. 9.22 for which $D_{Mc} \gg D_0$ but where $[V'_{Mc}] = [F'_{Mc}]$. The thickness of this extrinsic layer is again determined by the parabolic rate law, Eq. 9.16, but with the reaction constant,

$$K_{ex} = 2D_{V'_{Mc}} [V'_{Mc}] [\ln P_{O_2^s} - \ln P_{O_2^i}] c_{Mc} \quad (9.26)$$

If the impurity concentration and oxygen pressure are such that the defect concentrations are in an intermediate range, an intrinsic layer may

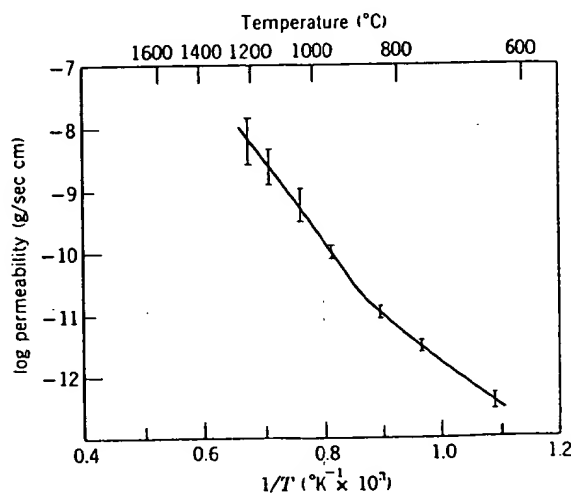


Fig. 9.11. Oxygen permeation through calcia-stabilized zirconia as a function of temperature. The oxygen transport is controlled by the concentration and mobility of electron holes, Eq. 9.25. From K. Kitazawa, Ph.D. thesis, MIT, 1972.

form on the oxygen-rich side (external) and an extrinsic oxide layer on the metal-rich side (at the oxide-metal interface).

Short-Circuit Diffusion Paths. In each of the examples of metal oxidation, lattice diffusion D_l was assumed to be the rate-determining transport process. In Section 6.6 the importance of other more rapid diffusion paths was discussed. The effects of short-circuit paths can be incorporated into the parabolic rate equations. For example, an apparent diffusivity D_a from Eq. 6.67 can be used in Eq. 9.16 to include the contributions from lattice D_l and boundary diffusion D_b ;

$$D_a = D_l(1 - f) + fD_b$$

$$\frac{dx}{dt} = \frac{K'D_a}{x} \quad (9.27)$$

where the diffusion coefficient has been extracted from the rate constant to give another constant K' . Low-temperature oxidation and oxide layers with fine grain sizes are expected to form by boundary diffusion.

Chemical Diffusion in Nonstoichiometric Oxides. The chemical diffusion coefficient for the counter diffusion of cations and anions can also be determined from the Wagner analysis. If we assume that electrical conduction is mainly electronic ($t_{el} \approx 1$) that is, movement of electrical charge is not the rate-limiting step for mass transport (ions), the chemical diffusion coefficient \bar{D} can be determined. In terms of diffusion coefficients rather than transference numbers Eq. 9.15 becomes

$$J_{ox} = \frac{c_o}{|Z_{Me}|} (|Z_{Me}|D_o + |Z_o|D_{Me}) \frac{1}{kT} \frac{d\mu_o}{dx} \quad (9.28)$$

In terms of Fick's first law this can be rewritten

$$J_{ox} = \left[(|Z_{Me}|D_o + |Z_o|D_{Me}) \frac{c_o}{|Z_{Me}|} \left(\frac{1}{kT} \frac{d\mu_o}{d\bar{c}} \right) \right] \frac{d\bar{c}}{dx} = \bar{D} \frac{d\bar{c}}{dx} \quad (9.29)$$

where \bar{c} represents the excess (or deficit) of the metal or oxygen in the nonstoichiometric compound. The chemical diffusion coefficient is the bracketed term. Consider, for example, the transition metal monoxides ($\text{Fe}_{1-\delta}\text{O}$, $\text{Ni}_{1-\delta}\text{O}$, $\text{Co}_{1-\delta}\text{O} \dots$) for which $\bar{c} \propto [V_{Me}^{\bullet}]$, where α is the effective charge on the vacancy and where $D_{Me} \gg D_o$. The chemical diffusion coefficient can be written from Eq. 9.29 in the form

$$\bar{D} = \frac{1}{2} \frac{c_{Me}}{[V_{Me}^{\bullet}]} D_{Me} \frac{d \ln P_{O_2}}{d \ln [V_{Me}^{\bullet}]} \quad (9.30)$$

for which the substitution $d\mu_o = 1/2 kT d \ln P_{O_2}$ has been made. From the defect equilibrium reaction, the mass action law gives

$$[h^{\bullet}]^{\alpha} [V_{Me}^{\bullet}] = K_{V_{Me}^{\bullet}} \cdot P_{O_2}^{1/2} \quad (9.31)$$

The

Sub:
cherThu
vac:If
O/M
oxic
type
the
in F
conFig
sev
(19)

The derivative in Eq. 9.30 can now be determined;

$$\frac{d \ln P_{O_2}}{d \ln [V_{Me}^{\alpha}]} = 2(\alpha + 1) \quad (9.32)$$

Substituting this into Eq. 9.30 and recalling that $c_{Me}D_{Me} = c_V D_V$, the chemical diffusion coefficient is given by

$$\tilde{D} = (\alpha + 1)D_{V_{Me}} \quad (9.33)$$

Thus for singly charged vacancies, $\tilde{D} = 2D_{V_{Me}}$, and for doubly charged vacancies, $\tilde{D} = D_{V_{Me}}$.

If the oxygen pressure is changed from one value to another, a new O/Me value is established in a nonstoichiometric oxide, and the oxidation-reduction rate is determined by a diffusion coefficient of the type in Eq. 9.33. This value is larger than the diffusivity of the cation or the anion. Figure 9.12 shows the chemical diffusion coefficient determined in $Fe_{1-x}O$ by step changes in the oxygen pressure which cause diffusion-controlled changes in the composition. The value of the chemical diffu-

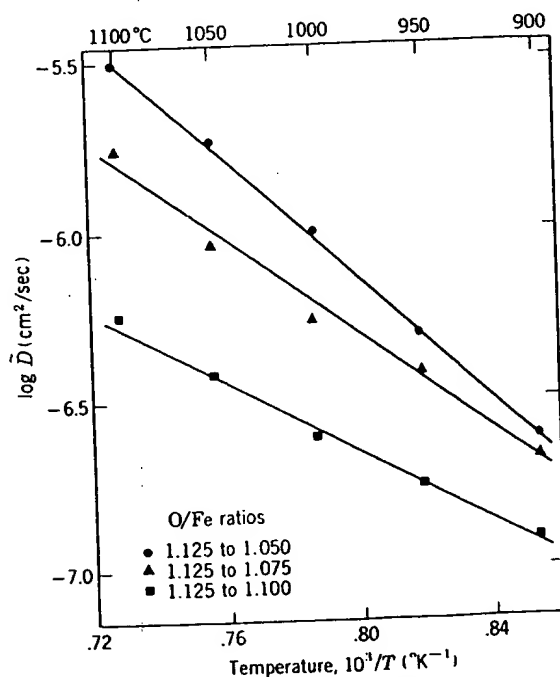


Fig. 9.12. Temperature dependence of the chemical-diffusion coefficient of wustite for several composition increments. From R. L. Levin and J. B. Wagner, *Trans. AIME*, 233, 159 (1965).

sion coefficient correlates with the tracer value (Eq. 9.30) when the defect equilibrium relationships are known.

Ambipolar Diffusion. The formality used to derive Eqs. 9.11 and 9.13 also allows us to determine the effective diffusion constants when cations and anions are flowing in the same direction. Referred to as ambipolar diffusion, a description of the atomistic process must again consider the coupling between the oppositely charged species when the transport of electrons and holes is slower than ion transport. If the flux of cations becomes excessive, a local internal electric field builds up to "drag" along the anions. This behavior is important in processes involving reactions which cause product formation, in processes which are in response to an applied electric field, and in processes which result in a shape change due to mechanical or surface tension forces such as sintering and creep.

As an example, consider a pure oxide for which $t_{el} \approx 0$. Equation 9.11 can be written for anion and cation transport as in Eq. 9.13. Since the transport of each ion is in the same direction, electrical neutrality is maintained when

$$J_T = \frac{J_o}{|Z_{Mc}|} = \frac{J_{Mc}}{|Z_o|} \quad (9.34)$$

where J_T refers to the total molecular flux. Equating the anion and cation charge flux allows for the solution of the internal electric field, $\partial\phi/\partial x$,

$$|Z_o|c_oB_o \left[\frac{\partial\mu_o}{\partial x} + Z_oF \frac{\partial\phi}{\partial x} \right] = |Z_{Mc}|c_{Mc}B_{Mc} \left[\frac{\partial\mu_{Mc}}{\partial x} + Z_{Mc}F \frac{\partial\phi}{\partial x} \right] \quad (9.35)$$

in terms of the chemical potential of the oxide, $\mu(\text{Me}_{Z_o}\text{O}_{Z_{Mc}})$. The chemical potential of the oxide is the sum of the chemical potentials of cations and anions,

$$d\mu(\text{Me}_{Z_o}\text{O}_{Z_{Mc}}) = Z_{Mc} d\mu_o + Z_o d\mu_{Mc} \quad (9.36)$$

which yields the coupling field in terms of mobilities, concentrations, and the chemical potential,

$$\frac{\partial\phi}{\partial x} = \frac{[|Z_o|c_oB_o - |Z_{Mc}|c_{Mc}B_{Mc}]}{F[|Z_{Mc}|c_{Mc}B_{Mc} - |Z_o|c_oB_o]} \frac{\partial\mu_{Mc}}{\partial x} \quad (9.37)$$

where we have assumed local equilibrium, $|Z_{Mc}| dc_{Mc} = |Z_o| dc_o$. Substitution of Eq. 9.37 into Eqs. 9.34 and 9.13 yields

$$J_T = \frac{-c_{Mc}B_{Mc}c_oB_o}{Z_{Mc}|Z_{Mc}|c_{Mc}B_{Mc} - |Z_o|c_oB_o} \frac{\partial\mu(\text{Me}_{Z_o}\text{O}_{Z_{Mc}})}{\partial x} \quad (9.38)$$

This term is the correction due to ambipolar effects to the diffusion transport resulting from a chemical potential gradient. Consider as an

example of the applicability of Eq. 9.38 to sintering of pure MgO for which the values of $Z_{Mg} = |Z_0| = 2$ and $c_{Mg} = c_0 = c$:

$$J_T = -\frac{cB_{Mg}B_0}{[B_{Mg} + B_0]} \frac{\partial \mu_{MgO}}{\partial x} \quad (9.39)$$

Since $\mu_{Mg} = \mu_{Mg}^0 + RT \ln a \approx \mu_{Mg}^0 + RT \ln c$, Eq. (9.39) can be expressed as

$$J_T = -\frac{c_{MgO}B_{Mg}B_0RT}{[B_{Mg} + B_0]} \frac{d \ln c_{MgO}}{dx} = -\frac{B_{Mg}B_0RT}{[B_{Mg} + B_0]} \frac{dc_{MgO}}{dx} \quad (9.40)$$

where $\frac{dc_{MgO}}{dx}$ is the concentration gradient due to curvature (Chapter 10).

Recalling that the tracer diffusion coefficient and mobility are related by Eq. (6.11),

$$J_T \approx -\frac{D_{Mg}^T D_0^T}{[D_{Mg}^T + D_0^T]} \frac{dc_{MgO}}{dx} \quad (9.41)$$

Thus the total molecular transport may be governed by the slowest-moving specie if there is a large difference in diffusivities (e.g., $D_{Mg} \gg D_0$; $J_T \propto D_0$) or by an intermediate value when they are not too dissimilar (e.g., $D_{Mg} = 3D_0$; $J_T \propto D_{Mg}/4$).

Since some ions transport more rapidly in boundaries or along dislocations, a relationship for ambipolar diffusion can be derived when paths other than the lattice are assumed. A simple case has been derived for steady-state grain boundary and lattice transport.* The effective area of transport in the lattice A^l and boundary A^b must be incorporated in the equation for total mass flow. For the case of a pure material MO the effective diffusion coefficient is similar in form to Eq. 9.41 and given by

$$D_{\text{effective}} \approx \frac{(A^l D_{Mc}^l + A^b D_{Mc}^b)(A^l D_0^l + A^b D_0^b)}{(A^l D_{Mc}^l + A^b D_{Mc}^b) + (A^l D_0^l + A^b D_0^b)} \quad (9.42)$$

where D^l refers to lattice diffusion and D^b refers to boundary diffusion. In many oxides, it has been observed that $A^b D_0^b \gg A^l D_0^l$ and that $A^l D_{Mc}^l > A^b D_{Mc}^b$; thus Eq. 9.42 reduces to

$$D_{\text{effective}} \approx \frac{A^l D_{Mc}^l A^b D_0^b}{A^l D_{Mc}^l + A^b D_0^b} \quad (9.43)$$

Diffusive transport in real materials is more complex, owing to impurities and imperfections, but relationships like these can be derived to include more complex situations.†

*R. S. Gordon, *J. Am. Ceram. Soc.*, 56, 147 (1973).

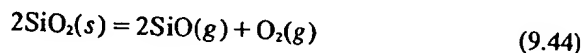
†D. W. Readey, *J. Am. Ceram. Soc.*, 49, 366 (1966).

9.3 Reactant Transport through a Fluid Phase

As discussed in Section 9.1, heterogeneous reactions at high temperatures require, first, material transfer to the reaction interface, second, reaction at the phase boundary, and in some cases diffusion of products away from the reaction site. Any of these steps can have the lowest virtual reaction rate and be rate-controlling for the overall process. Generally, once a reaction is initiated, material-transfer phenomena determine the overall rate in the high-temperature systems of importance in ceramics. As discussed in the previous section, the diffusion of ions and electrons through a stable oxide film on the surface of a metal determines the reaction rate. If, however, the film forms with cracks and fissures, the rate may be determined by gaseous diffusion through these channels. In this section we wish to consider several important examples of the way ceramic materials interact with gases and liquids and to determine the rate-limiting kinetic equations.

Gas-Solid Reactions: Vaporization. The simplest kind of solid-gas reactions are those related to vaporization or thermal decomposition of the solid. Section 9.4 contains a discussion of the decomposition of a solid to a gas and another solid; in this section we are primarily concerned with reactions in which the solid forms only gaseous products. The rate of decomposition is dependent on the thermodynamic driving forces, on the surface-reaction kinetics, on the condition of the reaction surface, and on the ambient atmosphere; for example, at high temperatures oxides volatilize much more rapidly in a vacuum than in air.

The loss of silica from glass and refractories in reducing atmospheres is an important factor which limits the usefulness of these ceramic products. Consider the following reaction which can cause the volatilization of SiO_2 :



At 1320°C , the equilibrium constant is

$$K_{eq} = \frac{P_{\text{SiO}}^2 P_{\text{O}_2}}{a_{\text{SiO}_2}^2} = 10^{-25} \quad (9.45)$$

Assuming unit activity for the silica, it is apparent that the ambient oxygen partial pressure controls the pressure of $\text{SiO}(g)$ and therefore the rate of vaporization. Under reducing conditions (inert atmosphere, H_2 or CO atmosphere) of $P_{\text{O}_2} = 10^{-18}$ atm, the SiO pressure is 3×10^{-4} atm (0.23 torr).

The rate of evaporation near equilibrium is given by the Knudsen

equation:*

where $\frac{dn_i}{dt}$ is sample area, weight of i , a gas flow rate sample is no evaporation, be in equilib, total pressure

where A is
When the
mixtures P_{O_2}

where P_{O_2} is
tion reaction

For the va
rate of abou
actual SiO_2 k
in hydrogen.

The effect of
from Fig. 9.
decreased by

Chemical
active transp
vapor-phase
film electron
controlling tl
rate of depos
the temperat

*M. Knudsen

equation:*

$$\frac{dn_i}{dt} = \frac{AP_i\alpha_i}{\sqrt{2\pi M_i RT}} \quad (9.46)$$

where $\frac{dn_i}{dt}$ is the loss of component i in moles per unit time, A is the sample area, α_i is the evaporation coefficient ($\alpha_i \leq 1$), M_i is the molecular weight of i , and P_i is the pressure of i above the sample. If there is a high gas flow rate over the sample or if the evaporation is into a vacuum, the sample is not able to maintain its equilibrium vapor pressure P_i , and the evaporation rate is controlled by the interface reaction rate. For the gas to be in equilibrium with the solid, the gas flow rate S (moles/sec) and the total pressure P^T (atm) must satisfy the inequality

$$\frac{A\alpha_i P^T}{S(M_i T)^{1/2}} \gg 2.3 \times 10^{-9} \quad (9.47)$$

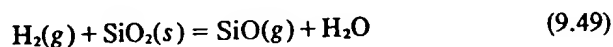
where A is in square centimeters and T in degrees Kelvin.

When the oxygen partial pressure in the gas phase is controlled by gas mixtures $P_{O_2}^{ext}$, the equation (9.46) becomes

$$J_{O_2} = \frac{(P_{O_2} - P_{O_2}^{ext})\alpha_{O_2}}{(2\pi M_{O_2} RT)^{1/2}} \quad (9.48)$$

where P_{O_2} is calculated from the standard free energy of the decomposition reaction (e.g. Eq. 9.45).

For the vaporization of SiO_2 by reaction (9.44), Eq. 9.46 predicts a loss rate of about 5×10^{-5} moles SiO_2/cm^2 sec at $1320^\circ C$. Figure 9.13 shows actual SiO_2 loss rates from various silica-containing refractories annealed in hydrogen. The overall decomposition reaction in this case is



The effect of a few mole percent water vapor in the gas stream is evident from Fig. 9.14. As predicted from Eq. 9.49, the $SiO(g)$ pressure is decreased by an increase in the $H_2O(g)$ pressure.

Chemical Vapor Transport. Next let us consider the reaction of an active transport gas with a ceramic. The net effect is to increase the vapor-phase transport. Some high-temperature ceramics and many thin-film electronic devices are prepared by chemical vapor deposition. By controlling the chemical potential (concentration) of reaction gases, the rate of deposition can be controlled. Generally the rate of deposition and the temperature of deposition determine the reaction kinetics and rates at

*M. Knudsen, *Ann. Phys.*, 47, 697 (1915).

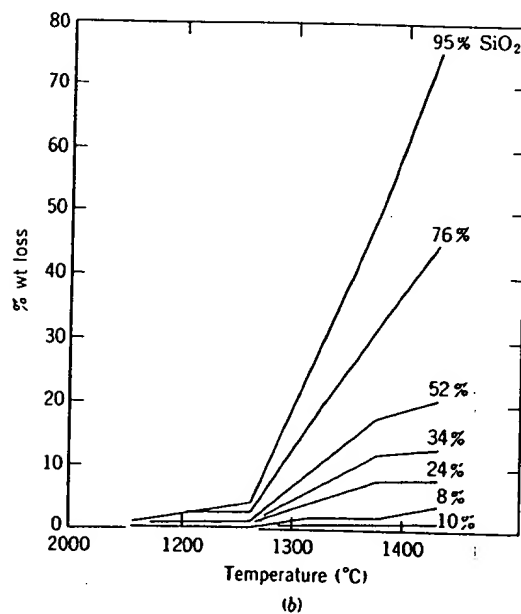
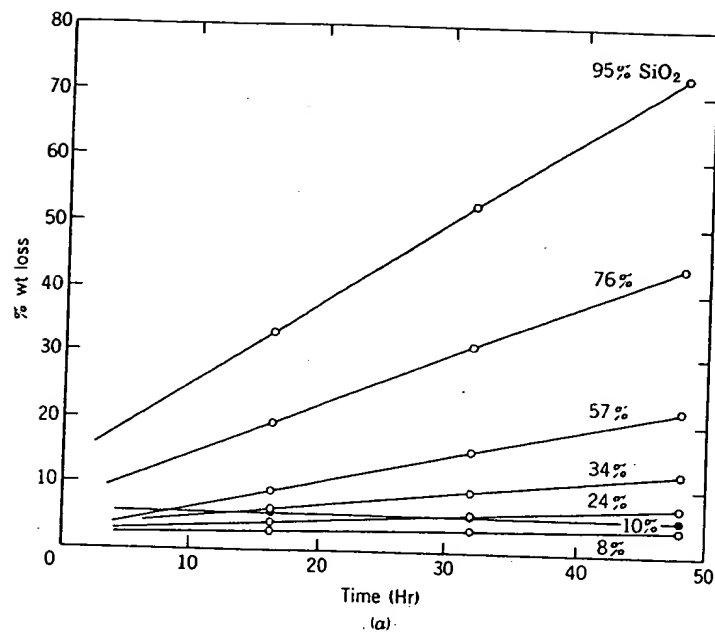


Fig. 9.13. (a) Weight loss of brick at 1425°C in 100% hydrogen. (b) Weight loss of brick after 50 hr in 100% hydrogen. From M. S. Crowley, *Bull. Am. Ceram. Soc.*, 46, 679 (1967).

Fig. 9.14
vapor wa

which
surface
tion oc
supers
a poly
porosit
material
temper
single-c
epitaxi
orienta

To u
a know
respect
reactan
nations
of the s
system
Consider
held at
chambe

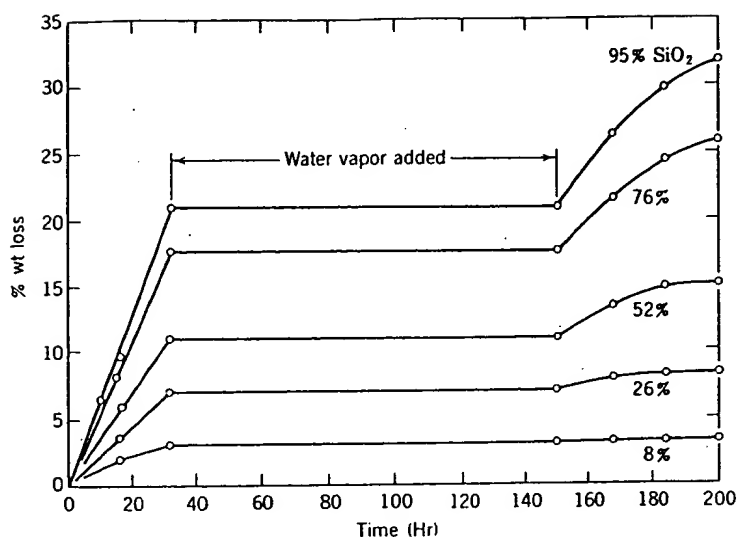


Fig. 9.14. Weight loss of brick at 1370°C in 75% H₂-25% N₂ atmosphere. After 32 hr water vapor was added for 150 hr. From M. S. Crowley, *Bull. Am. Ceram. Soc.*, 46, 679 (1967).

which the decomposition products can "crystallize" on the reaction surface. If the supersaturation is large, homogeneous gas-phase nucleation occurs; that is, a heterogeneous surface is not needed. As the supersaturation is reduced, the gases react in the vicinity of a surface, and a polycrystalline deposit is formed. The perfection of the deposit, porosity, preferred grain orientation, and so on, depend on the particular material and the rate of deposition; usually slower deposition and higher temperatures result in a more perfect reaction product. Finally, when a single-crystal substrate is used as the heterogeneous reaction surface, epitaxial deposition occurs. In the latter case, a single crystal with an orientation determined by the substrate is formed.

To understand the kinetics of chemical vapor deposition fully requires a knowledge of all of the thermodynamic equilibria involved and the respective kinetic processes for the generation of reactants, mixing of reactant gases, diffusion through the boundary layers, molecular combinations at the interface, exsolution of gaseous products, surface diffusion of the solid products, and so on. We have chosen, as an example, a simple system for which the rate-determining step is diffusion in the gas phase. Consider the closed system shown in Fig. 9.15 in which two chambers are held at thermal equilibrium. Assume that the chemical reactions in each chamber reach thermodynamic equilibrium such that the diffusion flux of

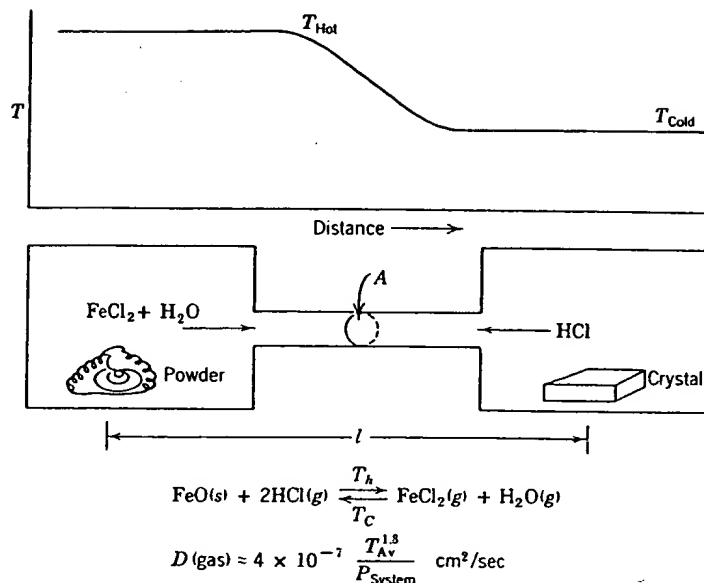


Fig. 9.15. Schematic diagram of chemical vapor transport of iron oxide in a temperature gradient.

matter is from the hot chamber to the cooler chamber because of the concentration gradient (the direction of transport is determined by the sign of the enthalpy of the reaction).

The kinetics of mass transport as determined by the diffusion of the rate-limiting specie—for example, diffusion of $\text{FeCl}_2(g)$ —is given by Fick's law:

$$\frac{dn}{dt} = -AD \frac{\partial c}{\partial x} = -AD \frac{\Delta c}{l} = -AD \frac{(c_h - c_c)}{l} \quad (9.50)$$

where n is the number of moles transported, A the cross-sectional area of the connecting tube (cm^2), D the diffusion coefficient of the rate-limiting specie, and c the concentrations in the respective isothermal chambers. For an ideal gas

$$c_h = \frac{n_h}{V_i} = \frac{P_h}{RT_h} \quad (9.51)$$

and the composition difference is

$$(c_h - c_c) \approx \frac{(P_h - P_c)}{RT_{av}} \quad (9.52)$$

Thus, the t

The equilib
of formatic

In a clos
B atm re
formation
(9.54) redu

which car
prediction

In gener
total pres
gas-phase
line-of-sig
diffusion-l
pressures
convection
boundary

Liquid-
of the kin
in liquids,
by molter
componen
ceramic t
required f
rate of th
fixed by t
crystal gr
leads to a
away from
material
the liquid
natural c
For a s

Thus, the transport rate is determined by

$$\frac{dn}{dt} = -\frac{AD}{lRT_{av}}(P_h - P_c) \quad (9.53)$$

The equilibrium pressures can be determined by the standard free energy of formation at each temperature; for example, at the higher temperature

$$\Delta G_h^\circ = -RT_h \ln \frac{P_{\text{FeCl}_2} P_{\text{H}_2\text{O}}}{P_{\text{HCl}}^2 a_{\text{FeO}}} \quad (9.54)$$

In a closed system such as a quartz ampoule an initial HCl pressure of B atm results in the adjustment of the formation reaction by the formation of equivalent numbers of moles FeCl_2 and H_2O . The expression (9.54) reduces to

$$\Delta G_h^\circ = -RT_h \ln \frac{P_{\text{FeCl}_2}^2}{(B - 2P_{\text{FeCl}_2})^2} \quad (9.55)$$

which can be solved for each temperature and therefore leads to a prediction of the transport rate from Eq. 9.53.

In general, the rate-limiting gas-phase transport step is a function of the total pressure of the system. At very low pressures ($P_{\text{total}} < 10^{-4}$ atm) gas-phase molecular collisions are infrequent and thus transport becomes line-of-sight. At intermediate pressures ($10^{-4} < P_{\text{total}} < 10^{-1}$ atm), the diffusion-limited case discussed above becomes important. At higher pressures ($P_{\text{total}} > 10^{-1}$ atm) convective mass transport is more rapid. If convection or forced flow becomes rapid, gas-phase diffusion through the boundary layer may become the rate-determining process.

Liquid-Solid Reactions: Refractory Corrosion. An important example of the kinetics of liquid-solid reactions is the rate of dissolution of solids in liquids, particularly important in connection with refractory corrosion by molten slags and glasses, with the rate of conversion of solid batch components to glass in the glass-making process, and with the firing of a ceramic body in which a liquid phase develops. No nucleation step is required for the dissolution of a solid. One process that can determine the rate of the overall reaction is the phase-boundary reaction rate which is fixed by the movement of ions across the interface in a way equivalent to crystal growth (Section 8.4). However, reaction at the phase boundary leads to an increased concentration at the interface. Material must diffuse away from the interface in order for the reaction to continue. The rate of material transfer, the dissolution rate, is controlled by mass transport in the liquid which may fall into three regimes: (1) molecular diffusion, (2) natural convection, and (3) forced convection.

For a stationary specimen in an unstirred liquid or in a liquid with no

fluid flow produced by hydrodynamic instabilities, the rate of dissolution is governed by molecular diffusion. The kinetics are similar to those discussed in Chapter 6 on diffusion. The effective diffusion length over which mass is transported is proportional to \sqrt{Dt} , and therefore the change in thickness of the specimen, which is proportional to the mass dissolved, varies with $t^{1/2}$. Even in a system which may undergo convection due to hydrodynamic instabilities from density gradients which arise from thermal gradients or from concentration gradients (due to dissolution), the initial dissolution kinetics should be governed by molecular diffusion.

The diffusion coefficient for dissolution kinetics must be considered in the same light as in Section 9.2; the electrical and chemical effects of the various possible species must be accounted for. For example, the dissolution of Al_2O_3 in a silicate slag may be controlled by any of the cations or anions in the Al_2O_3 or slag or more probably a combination (e.g., Eq. 9.41). An example of dissolution controlled by molecular diffusion is shown in Fig. 9.16 for the dissolution of sapphire in a $\text{CaO-Al}_2\text{O}_3\text{-SiO}_2$ melt containing 21 wt% Al_2O_3 .

Natural or free convection occurs, owing to hydrodynamic instabilities in the liquid which give rise to fluid flow over the solid. This enhances the dissolution kinetics. It has often been observed in metals processing that the amount of dissolution is dependent on whether or not the ceramic is totally immersed in the liquid. Generally, a partially submerged sample undergoes more extensive dissolution near the liquid-gas interface, called

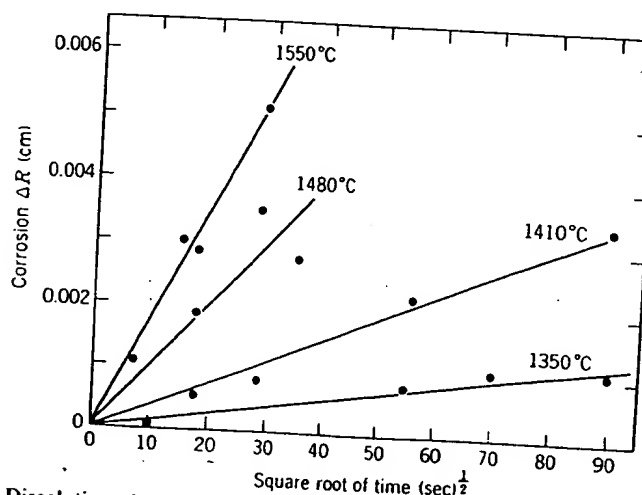


Fig. 9.16. Dissolution of sapphire cylinder in $\text{CaO-Al}_2\text{O}_3\text{-SiO}_2$ with 21 wt % Al_2O_3 , versus square root of time. From Ref. 6.

the metal line from free convection peak of dissolution for mass

where j is removed, c_∞ at the interface thickness, L layer, and \bar{V} Fig. 9.17 and

where (dc/dx) boundary layer of fluid flow slower material layers and present in glasses a combine to boundary layer aqueous solution. Also the

Fig. 9.17. Co

the metal line. Below this interface the corrosion kinetics can be analyzed from free convection principles. It is clear that after a relatively short induction period during which molecular diffusion kinetics prevail the rate of dissolution becomes nearly independent of time. The general expression for mass transport during convection is

$$j = \frac{dn/dt}{A} = \frac{D(c_i - c_\infty)}{\delta(1 - c_i \bar{V})} \quad (9.56)$$

where j is the number of moles per second per square centimeter removed, c_∞ is the concentration in the bulk liquid, c_i is the concentration at the interface (saturation concentration), δ is the boundary layer thickness, D is the effective diffusion coefficient through the boundary layer, and \bar{V} is the partial molar volume. The boundary layer is shown in Fig. 9.17 and defined by

$$\delta = \frac{c_i - c_\infty}{(dc/dy)} \quad (9.57)$$

where (dc/dy) is the concentration gradient at the interface. The boundary-layer thickness is determined by the hydrodynamic conditions of fluid flow. Viscous liquids form thicker boundary layers and cause slower material transfer. Higher liquid velocities form thinner boundary layers and permit more rapid material transfer. For refractory dissolution in glasses and silicate slags, the high viscosity and slow fluid velocity combine to give relatively thick boundary layers. The thickness of the boundary layer may be a centimeter. In comparison, for rapidly stirred aqueous solutions the boundary-layer thickness is a fraction of a millimeter. Also the diffusion rate is much slower in viscous silicate liquids than

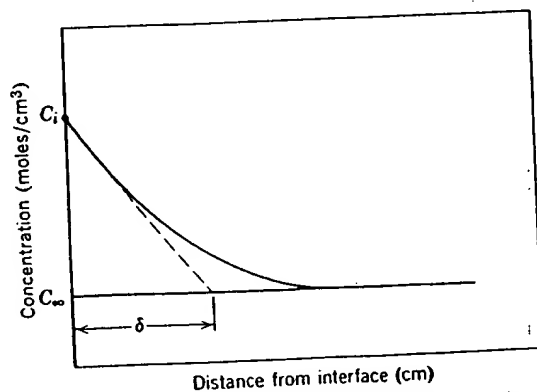


Fig. 9.17. Concentration gradient through diffusion layer at a solution interface.

in aqueous solutions, so that there is more of a tendency for the reaction process to be controlled by material-transfer phenomena rather than interface reactions.

Values for the boundary-layer thickness have been derived for special cases in fluid flow. The boundary-layer thickness for mass transport from a vertical slab with natural convection caused by density-difference driving forces is

$$\delta = 1.835 \times \left[\frac{D\nu\rho_{\infty}}{gx^3(\rho_i - \rho_{\infty})} \right]^{1/4} \quad (9.58)$$

where x is the distance from the leading edge of the plate, ν is the kinematic viscosity η/ρ , g is the gravitational constant, ρ_{∞} is the density of the bulk liquid, and ρ_i is the density of the saturated liquid (the liquid at the interface). Thus the average dissolution rate for a plate of height h is given by

$$J = \frac{dn/dt}{A} = 0.726D \left(\frac{g(\rho_i - \rho_{\infty})}{\nu Dh\rho_{\infty}} \right)^{1/4} (c_i - c_{\infty}) \quad (9.59)$$

The boundary-layer thickness for mass transport from a rotating disc is

$$\delta = 1.611 \left(\frac{D}{\nu} \right)^{1/3} \left(\frac{\nu}{\omega} \right)^{1/2} \quad (9.60)$$

where ω is the angular velocity (rad/sec). The mass transfer for a rotating disc is proportional to the square root of the angular velocity:

$$j = \frac{dn/dt}{A} = 0.62 D^{2/3} \nu^{-1/6} \omega^{1/2} \frac{(c_i - c_{\infty})}{(1 - c_i \bar{V})} \quad (9.61)$$

Figure 9.18 shows the dissolution kinetics of sapphire into $\text{CaO-Al}_2\text{O}_3\text{-SiO}_2$ for the free convection kinetics and in Fig. 9.19 for forced flow. In each case the kinetics are time-independent, as predicted by Eqs. 9.59 and 9.61.

Comparison of the data for sapphire dissolution at 1550°C for kinetics limited by molecular diffusion, free convection, and forced convection (126 rad/sec) show the dimensional change ΔR (cm) to be related to time as

$$\begin{aligned} \Delta R \text{ (molecular diffusion)} &= (1.77 \times 10^{-4} \text{ cm/sec}^{1/2}) t^{1/2} \\ \Delta R \text{ (free convection)} &= (3.15 \times 10^{-6} \text{ cm/sec}) t \\ \Delta R \text{ (forced convection)} &= (9.2 \times 10^{-5} \text{ cm/sec}) t \end{aligned} \quad (9.62)$$

The important parameters for convective dissolution are fluid velocity, kinematic viscosity, the diffusivity, and the composition gradient.

0.06
0.05
0.04
0.03
0.02
0.01
0

Corrosion ΔR (cm)

Fig. 9.18. Dissolution kinetics of 21 wt % Al_2O_3 in $\text{CaO-Al}_2\text{O}_3\text{-SiO}_2$.

It is clear from the data that the kinetics are extremely time-independent, limited kinetic dependence of the rate of dissolution is shown in Fig. 9.20.

Fig. 9.19. (a) Dissolution kinetics vs. angular velocity.

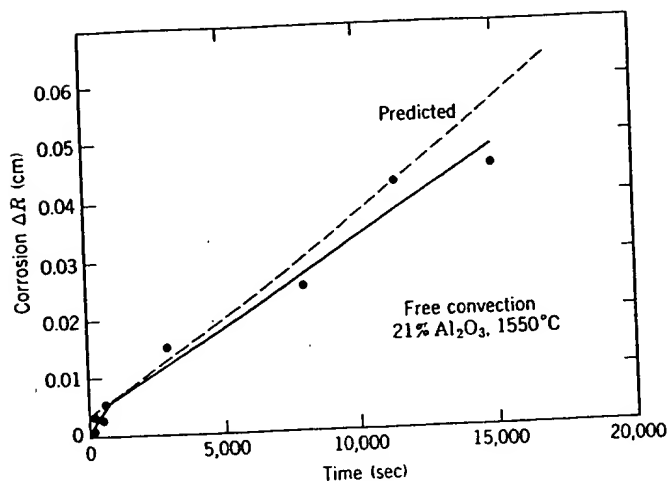


Fig. 9.18. Dissolution at relatively long times of sapphire cylinders in $\text{CaO-Al}_2\text{O}_3\text{-SiO}_2$ with 21 wt % Al_2O_3 versus time. From Ref. 6.

It is clear from the data in Figs. 9.16 and 9.19 that the dissolution rate is extremely temperature-sensitive. Since we have assumed transport-limited kinetics, the temperature dependence is largely determined by the exponential temperature dependence of diffusion (Eq. 6.39). The dependence of the corrosion rate of several ceramics on temperature is shown in Fig. 9.20.

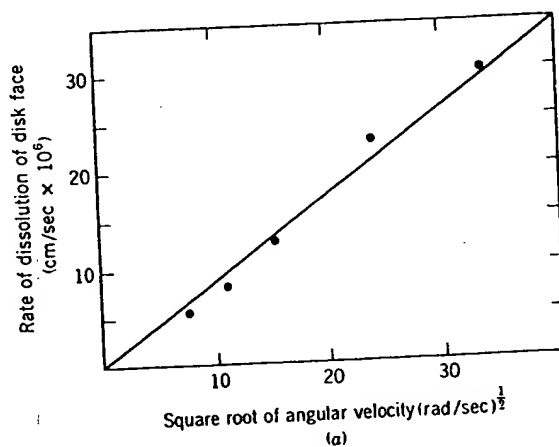


Fig. 9.19. (a) Dependence of rate of dissolution of face of sapphire disk on square root of angular velocity.

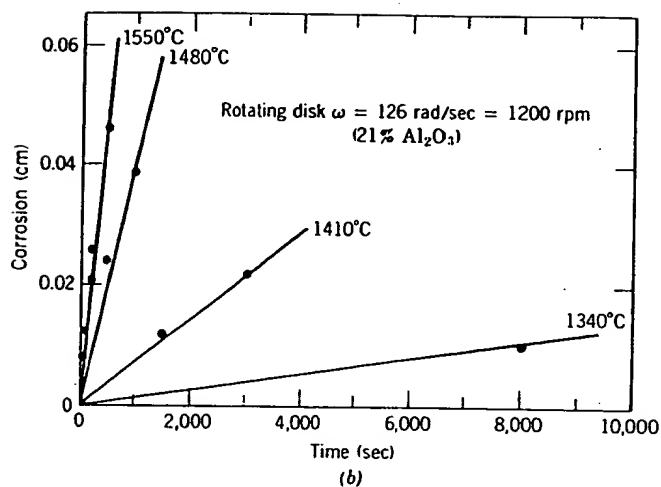


Fig. 9.19 (continued). (b) Rate of dissolution of face of sapphire disk rotating at 126 rad/sec on $\text{CaO-Al}_2\text{O}_3\text{-SiO}_2$ with 21 wt% Al_2O_3 . From Ref. 6.

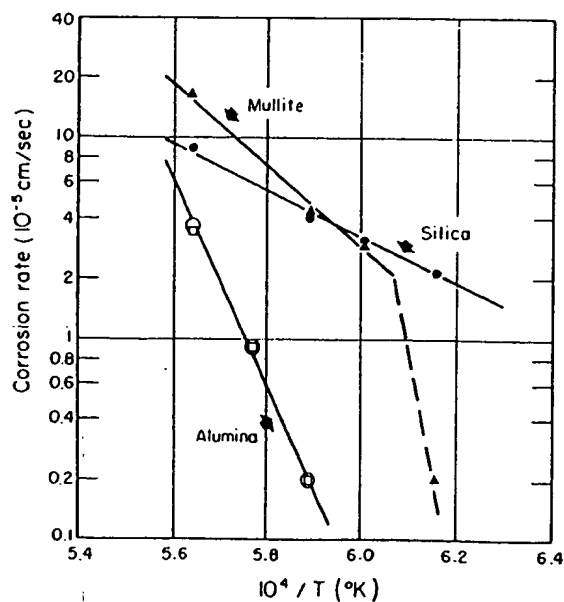


Fig. 9.20. Temperature dependence of forced convection corrosion in the $40\text{CaO-}20\text{Al}_2\text{O}_3\text{-}40\text{SiO}_2$ slag of alumina, mullite, and fused silica. From Ref. 6.

Fig. 9.21. Corrosion of indicate
From Ref. 6.

Refractor
ities in the
ideal surfac
bodies and
corrosion,
ceramics, c
from the da
is about 40

9.4 React

Of partic
tions which
the dehydr
polymorph
products in
of these re

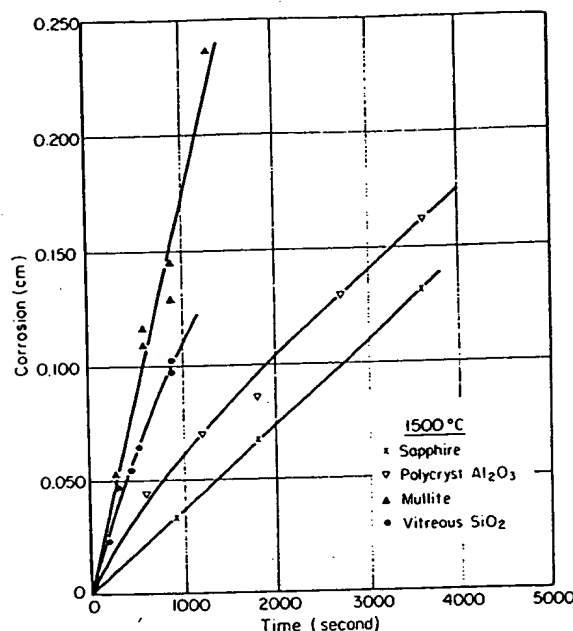


Fig. 9.21. Corrosion rate under forced convection conditions in the $40CaO-20Al_2O_3-40SiO_2$ slag of indicated specimens of sapphire, polycrystalline alumina, mullite, and vitreous silica. From Ref. 6.

Refractory corrosion is often much more complex. Besides complexities in the hydrodynamics of a molten bath, refractories seldom have ideal surfaces and are usually not of uniform composition. Multiphase bodies and brick with extensive porosity provide centers for accelerated corrosion, spalling, and penetration by the liquid. In dense single-phase ceramics, corrosion may be greatest at grain boundaries. This can be seen from the data in Fig. 9.21, in which the corrosion of polycrystalline Al_2O_3 is about 40% greater than sapphire after 2500 sec.

9.4 Reactant Transport in Particulate Systems

Of particular interest to ceramists is the large number of transformations which occur with granular or powdered raw materials; for example, the dehydration of minerals, decarbonization of carbonates, and polymorphic transformations. In general, the minerals and reaction products involved are used in large volumes; thus even though the nature of these reactions is complex, study of a few examples is important and

elucidates the important kinetic parameters and illustrates the concept of the rate-limiting step.

Calcination and Dehydration Reactions. Calcination reactions are common for the production of many oxides from carbonates, hydroxides, sulfates, nitrates, acetates, oxalates, alkoxides, and so on. In general the reactions produce an oxide and a volatile reaction product (e.g., CO_2 , SO_2 , H_2O , ...). The most extensively studied reactions are the decomposition of $\text{Mg}(\text{OH})_2$, MgCO_3 , and CaCO_3 . Depending on the particular conditions of temperature, time, ambient pressure, particle size, and so on, the process may be controlled (1) by the reaction rate at the reaction surface, (2) by gas diffusion or permeation through the oxide product layer, or (3) by heat transfer. The kinetics of each of these rate-limiting steps is considered.

Let us first consider the thermodynamics of decomposition, for example, the calcination of CaCO_3 :



The standard heat of reaction is 44.3 kcal/mole, that is, strongly endothermic, which is typical for most decomposable salts of interest. This means that heat must be supplied to the decomposing salt.

The standard free energy for the decomposition of CaCO_3 , MgCO_3 , and $\text{Mg}(\text{OH})_2$ is plotted in Fig. 9.22. The equilibrium partial pressure of the gas for each of the reactions is also plotted in Fig. 9.22. Note, for example, that when ΔG° becomes zero, P_{CO_2} above MgCO_3 and CaCO_3 and $P_{\text{H}_2\text{O}}$ above $\text{Mg}(\text{OH})_2$ have become 1 atm. The temperatures at which this occurs are 1156°K (CaCO_3), 672°K (MgCO_3), and 550°K ($\text{Mg}(\text{OH})_2$). The P_{CO_2} normally in the atmosphere and the range of $P_{\text{H}_2\text{O}}$ (humidity) in air are also shown in Fig. 9.22. From these values we can determine the temperature at which the salt becomes unstable when fired in air. For example, CaCO_3 becomes unstable over 810°K, MgCO_3 above 480°K. Depending on the relative humidity, $\text{Mg}(\text{OH})_2$ becomes unstable above 445 to 465°K. Because acetates, sulfates, oxalates, and nitrates have essentially zero partial pressure of product gases in the ambient atmosphere, it is clear that they are unstable at room temperature. That they exist as salts to a decomposition temperature of about 450°K indicates that their decomposition is governed by atomistic kinetic factors and not by thermodynamics.

The kinetics, as noted above, may be limited by the reaction at the surface, the flow of heat from the furnace to the reaction surface, or the diffusion (permeation) of the product gas from the reaction surface to the ambient furnace atmosphere. This is shown schematically in Fig. 9.23, which also includes the appropriate heat and mass flow equations. The

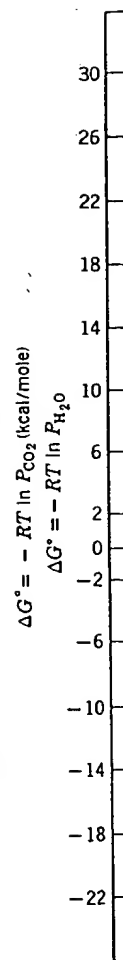


Fig. 9.22. the equilibri

rate-limit
decompo
atures th
tures su
atomistic

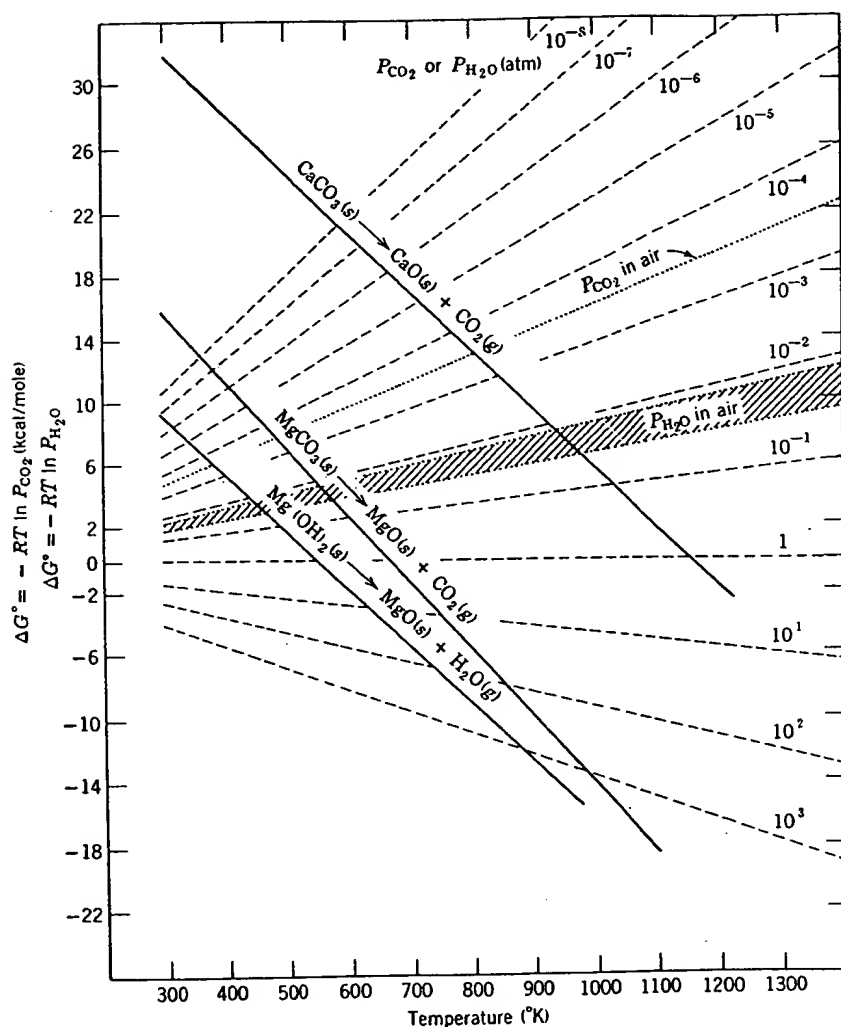
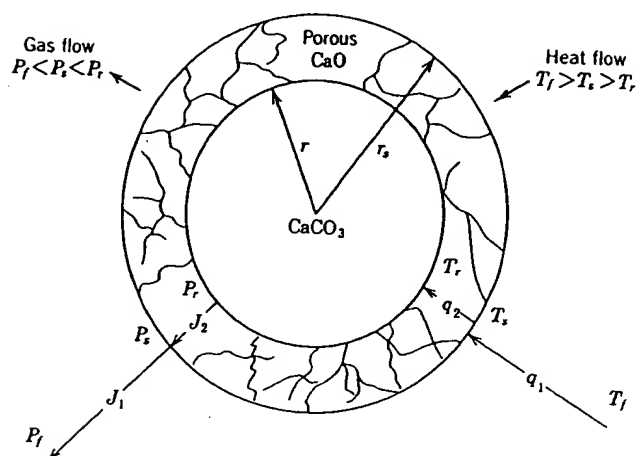


Fig. 9.22. Standard free energy of reaction as a function of temperature. The dashed lines are the equilibrium gas pressure above the oxide and carbonate (hydroxide).

rate-limiting step depends on the particular substance which is undergoing decomposition and the relative temperature. For example, at low temperatures the existence of unstable salts which decompose at higher temperatures suggests that the initial decomposition must be controlled by atomistic processes because there is no reaction-product interference in

CO₂ flow to furnace

$$J_{\text{interface}} = k_r 4\pi r^2 (P_r - P_r)$$

$$J_2 = 4\pi \frac{D_{\text{CO}_2}^{\text{eff}} (P_r - P_s) r r_s}{r_s - r}$$

$$J_1 = 4\pi r_s^2 \frac{D_{\text{CO}_2}^{\text{eff}}}{\delta} (P_s - P_f)$$

$$P_r = e^{-\Delta G^{\circ}/RT_i}$$

 δ = boundary-layer thickness

Heat flow to reaction interface

$$q_{\text{interface}} = \frac{4\pi r^2 \rho}{M} \Delta H^{\circ} \frac{dr}{dt}$$

$$q_1 = h_s 4\pi r_s^2 (T_f - T_s)$$

$$q_2 = \frac{4\pi k (T_s - T_r) r r_s}{r_s - r}$$

 ρ = density of CaCO₃ M = molecular weight h_s = heat-transfer coefficient k = thermal conductivity of CaO

Fig. 9.23. Schematic representation of the decomposition of a spherical particle (e.g., CaCO₃) of a salt which yields a porous oxide product (e.g., CaO) and a gas (CO₂). The reaction is endothermic, requiring heat transfer. The driving forces for heat and mass transport for steady-state decomposition are expressed as temperatures and pressures in the furnace (T_f, P_f), at the particle surface (T_r, P_r), and at the reaction interface (T_s, P_s).

the transport of heat to the reaction interface or gaseous product away from the interface.

The reaction shown schematically in Fig. 9.23 is heterogeneous; that is, the reaction occurs at a sharply defined reaction interface. Figure 9.24 shows this interfacial area for MgCO₃, for which the reaction proceeds from nucleation sites on the surface of the MgCO₃ platelets. The

Fig. 9.24. of basic n approachi crystallite: Ceram. Sc

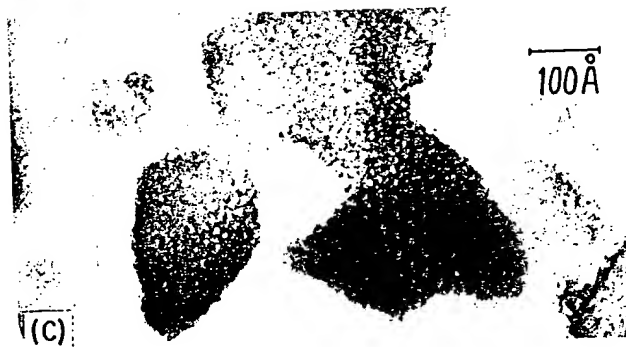
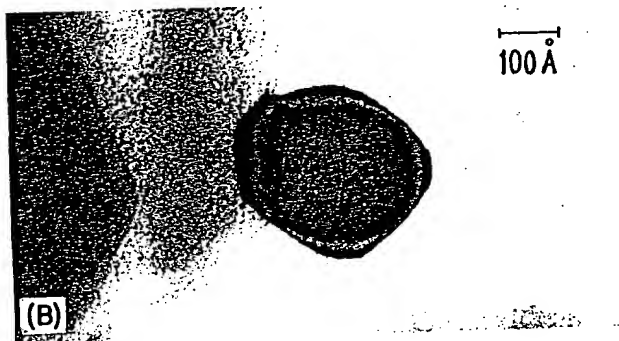
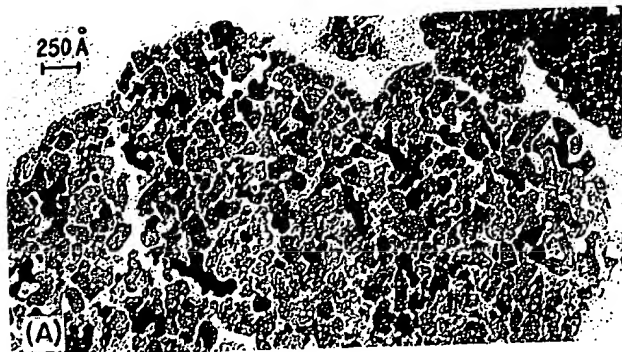


Fig. 9.24. Transmission electron micrographs of MgO prepared by thermal decomposition of basic magnesium carbonate. (a) Pseudomorphed MgO (550°C calcine); (b) crystallite approaching cube form (900°C calcine); (c) two-dimensional moiré pattern from overlapped crystallites (550°C calcine). From A. F. Moodie, C. E. Warble, and L. S. Williams, *J. Am. Ceram. Soc.*, 49, 676 (1966).

decomposition kinetics for cylindrical geometry is

$$(1 - \alpha)^{1/2} = 1 - kt/r_0 \quad (9.64)$$

where α is the fraction decomposed, k is the thermally activated kinetic constant, t is the time (assumed constant temperature), and r_0 is the initial particle radius. The first-order kinetics (Eq. 9.2) for this reaction at several temperatures is shown in Fig. 9.25 for decomposition of $\text{Mg}(\text{OH})_2$.

The importance of the surface on the decomposition rate is indicated by the time to decompose (700°C) a cleaved calcite crystal (CaCO_3), 60 hr, compared with an equivalent mass of the same material in powder form, 4 hr.

At low temperatures the crystallite size strongly affects the decomposition rate; however, at higher temperatures, as the chemical driving force increases and as the thermal energy to motivate diffusional processes and reaction kinetics increases, other steps may become rate-controlling, for example the rate of heat transfer. Figure 9.26 shows the center-line temperature of a cylindrical sample of pressed CaCO_3 powder which was thrust into a hot furnace. The sample temperature increases to a maximum, at which nucleation of CaO finally occurs. The decrease in temperature represents the endothermic heat absorbed by the reaction. The effect of varying the ambient CO_2 pressure is illustrated in Fig.

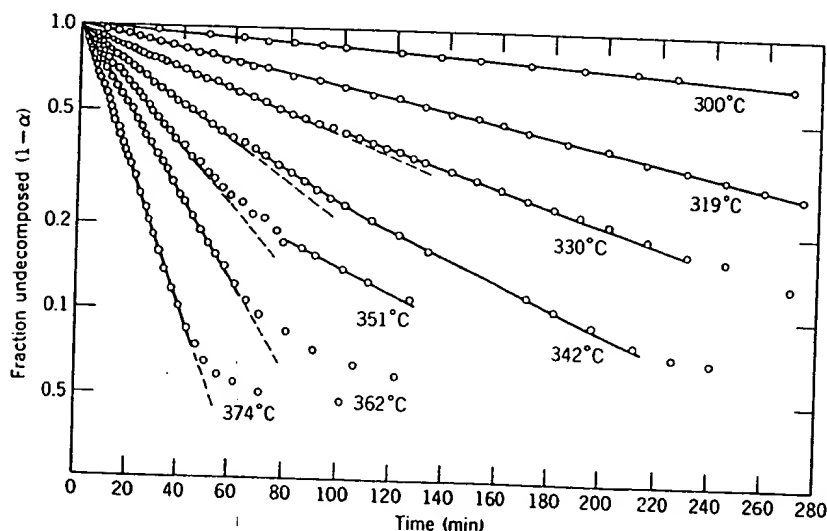


Fig. 9.25. Decomposition of $\text{Mg}(\text{OH})_2$ showing first-order kinetics. From R. S. Gordon and W. D. Kingery, *J. Am. Ceram. Soc.*, 50, 8 (1967).

Fig. 9.26.
sample of
A.I.C.H.E.J

9.27. As
decrease
Some
manner

Fig. 9.2
(1 - P_{CO_2})
 $R_0 = \text{dec}$
E. Wads

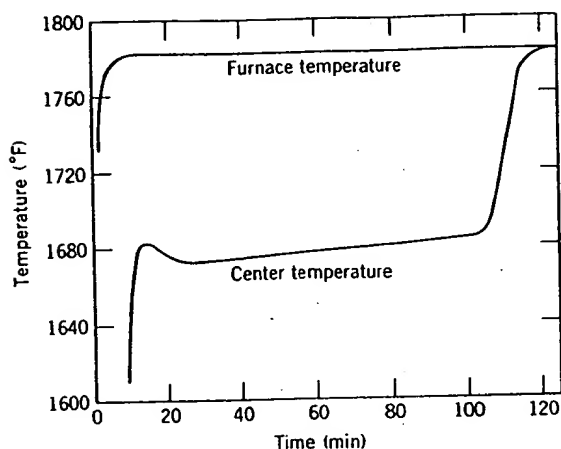


Fig. 9.26. Comparison of the furnace temperature to center-line temperature of a cylindrical sample of CaCO_3 thrust into a preheated furnace. From C. N. Satterfield and F. Feales, *A.I.C.H.E.J.*, 5, 1 (1959).

9.27. As the P_{CO_2} is increased, the driving potential for the reaction decreases, and thus the reaction rate is decreased.

Some of the clay minerals, kaolin in particular, do not decompose in the manner shown in Fig. 9.23; that is, they do not have a heterogeneous

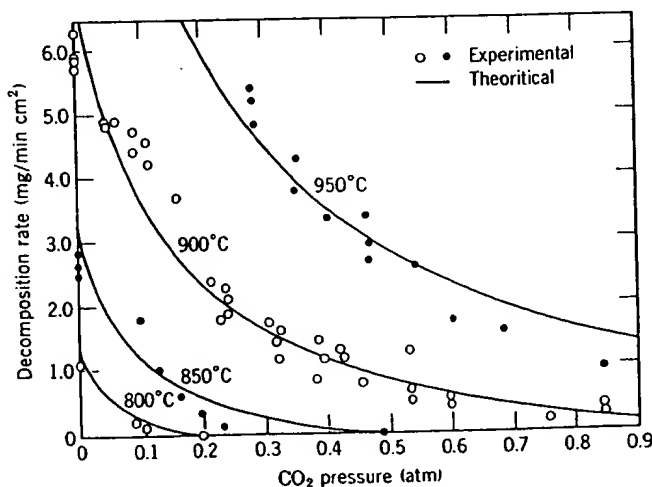


Fig. 9.27. Rate of decomposition of CaCO_3 in CO_2 atmosphere; $R_{\text{theor}} = (1 - P_{\text{CO}_2}/P_{\text{CO}_2^*})(BP_{\text{CO}_2^*} + 1/R_0)$, where $P_{\text{CO}_2^*}$ = equilibrium CO_2 pressure, B = constant, and R_0 = decomposition rate in a pure neutral atmosphere. From E. P. Hyatt, I. B. Cutler, and M. E. Wadsworth, *J. Am. Ceram. Soc.*, 41, 70 (1958).

reaction interface or a reaction product which breaks up into small crystallites. Above 500°C the water of crystallization is evolved, and a pseudomorphic structure remains until 980°C. The pseudomorph is a matrix of the original crystal structure containing large concentrations of vacant anion sites. Above 980°C the structure collapses irreversibly into crystalline mullite and silica, which releases heat (see Fig. 9.28).

The reaction kinetics is controlled by the diffusion of hydroxyl ions in the bulk rather than the heterogeneous surface decomposition illustrated in Fig. 9.23. The kinetics is thus homogeneous and controlled by diffusion in the solid, which gives a parabolic rate law. The dehydration kinetics of kaolinite is given (1) in Fig. 9.29 for size fractions. A similar situation is observed for the decomposition of $\text{Al}(\text{OH})_3$.

Powder Reactions. In most processes of interest in ceramic technology, solid-state reactions are carried out by intimately mixing fine powders. This changes the geometry from that considered in Fig. 9.6, and the actual reaction is more like that illustrated in Fig. 9.30.

If the reaction is carried out isothermally, the rate of formation of the reaction zone depends on the rate of diffusion. For the initial parts of the reaction the rate of growth of the interface layer is given to a good

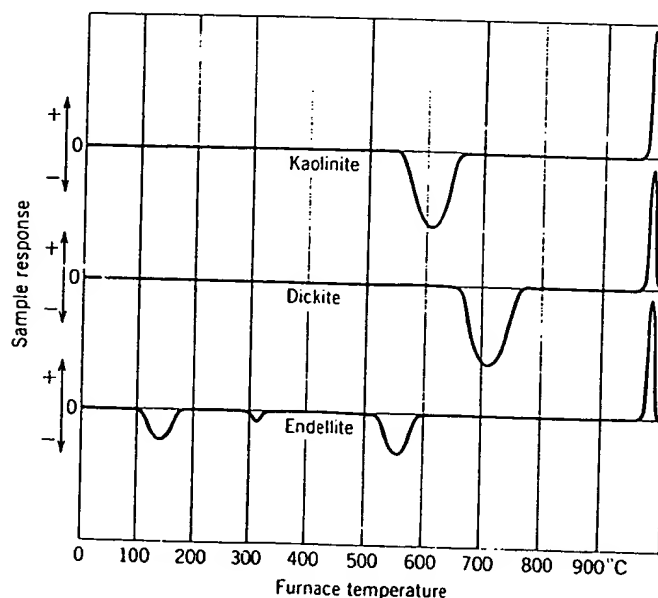


Fig. 9.28. Differential thermal analysis curves of kaolin clays. The sample temperature leads (+) or lags (-) the furnace temperature at levels at which heat is evolved or absorbed by chemical changes.

Fig. 9.2
Holt, I.

Fig. 9.
partic

small
and a
h is a
ons of
ly into

ions in
ated in
ision in
etics of
ation is

ech nol-
ng fine
9.6, and

a of the
s of the
a good

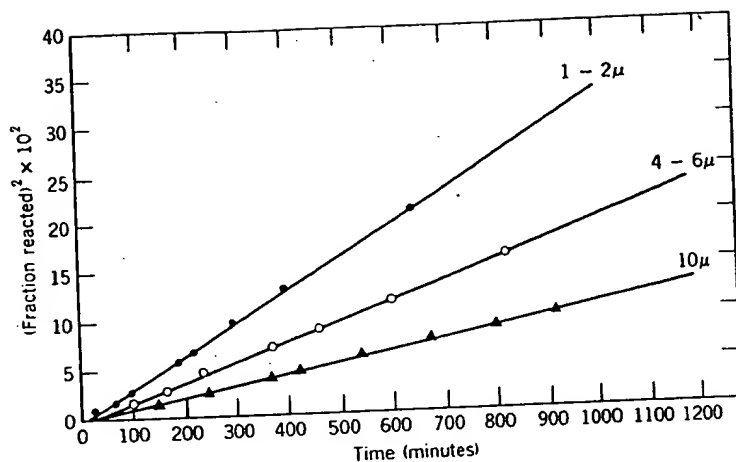


Fig. 9.29. Parabolic plots for three size fractions of kaolinite at 400°C in vacuum. From J. B. Holt, I. B. Cutler, and M. E. Wadsworth, *J. Am. Ceram. Soc.*, 45, 133 (1962).

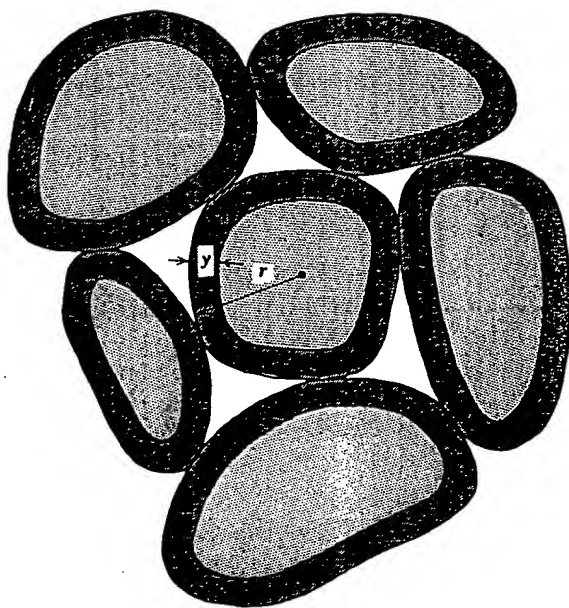


Fig. 9.30. Schematic representation of reaction-product layers forming on surface of particles in powder mixture.

ature leads
sorbed by

approximation by the parabolic relationship in Eq. 9.8. If V is the volume of material still unreacted at time t , then

$$V = \frac{4}{3} \pi (r - y)^3 \quad (9.65)$$

The volume of unreacted material is also given by

$$V = \frac{4}{3} \pi r^3 (1 - \alpha) \quad (9.66)$$

where α is the fraction of the volume that has already reacted. Combining Eqs. 9.65 and 9.66,

$$y = r(1 - \sqrt[3]{1 - \alpha}) \quad (9.67)$$

Combining this with Eq. 9.8 gives for the rate of reaction

$$(1 - \sqrt[3]{1 - \alpha})^2 = \left(\frac{KD}{r^2} \right) t \quad (9.68)$$

Note that this is for spherical geometry where Eq. 9.64 is for cylindrical geometry. By plotting $(1 - \sqrt[3]{1 - \alpha})^2$ against time, a reaction-rate constant equivalent to KD/r^2 can be obtained which is characteristic of the reaction conditions. The constant K is determined by the chemical-potential difference for the species diffusing across the reaction layer and by details of the geometry.

The relationship given in Eq. 9.68 has been found to hold for many solid-state reactions, including silicate systems, the formation of ferrites, reactions to form titanates, and other processes of interest in ceramics. The dependence on different variables is illustrated for the reaction between silica and barium carbonate in Fig. 9.31. In Fig. 9.31a it is observed that there is a linear dependence of the function $(1 - \sqrt[3]{1 - \alpha})^2$ on time. The dependence on particle size illustrated in Fig. 9.31b shows that the rate of the reaction is directly proportional to $1/r^2$ in agreement with Eq. 9.68: in 9.31c it is shown that the temperature dependence of the reaction-rate constant follows an Arrhenius equation, $K' = K_0 \exp(-Q/RT)$, as expected from its major dependence on diffusion coefficient.

There are two oversimplifications in Eq. 9.68 which limit its applicability and the range over which it adequately predicts reaction rates. First, Eq. 9.68 is valid only for a small reaction thickness, Δy ; and second, there was no consideration of a change in molar volume between the reactants and the product layer. The time dependence of the fraction reacted

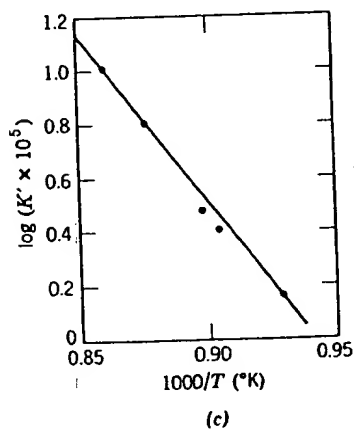
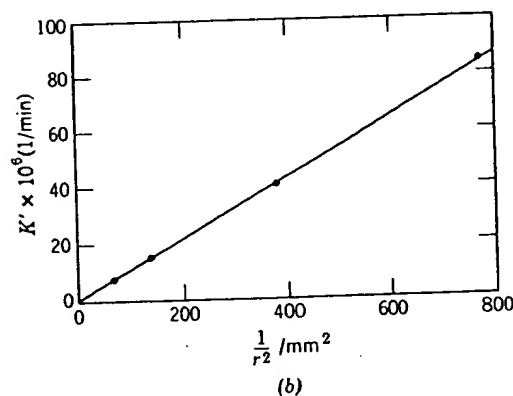
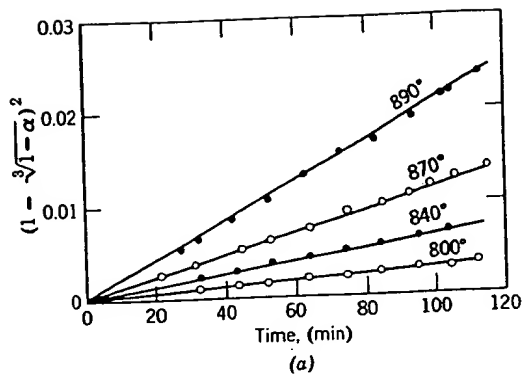


Fig. 9.31. Solid reaction between silica and barium carbonate showing (a) time dependence, (b) particle-size dependence, and (c) temperature dependence of reaction rate. From W. Jander, *Z. Anorg. Allg. Chem.*, 163, 1 (1927).

corrected for these two constraints is given as*

$$[1 + (Z - 1)\alpha]^{2/3} + (Z - 1)(1 - \alpha)^{2/3} = Z + (1 - Z) \left(\frac{KD}{r^2} \right) t \quad (9.69)$$

where Z is the volume of particle formed per unit volume of the spherical particle which is consumed, that is, the ratio of equivalent volumes. A demonstration that Eq. 9.69 is valid even to 100% reaction is shown in Fig. 9.32 for the reaction $\text{ZnO} + \text{Al}_2\text{O}_3 = \text{ZnAl}_2\text{O}_4$.

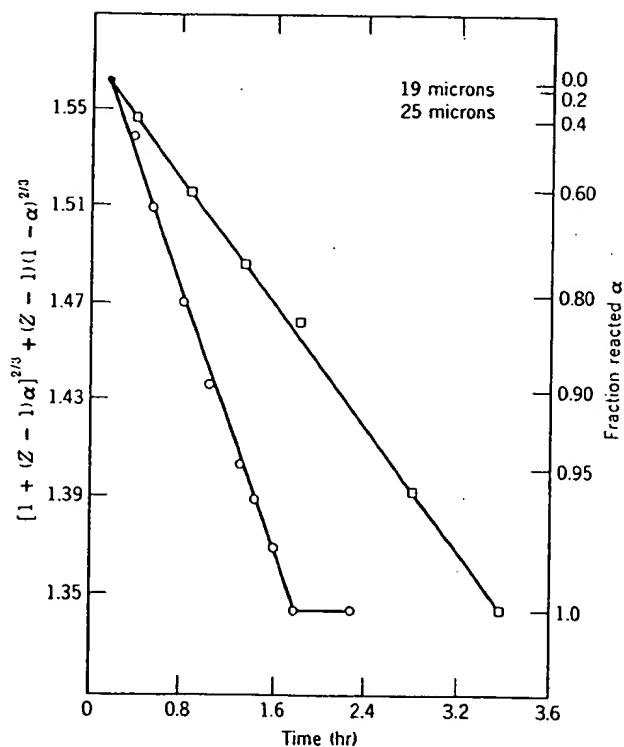


Fig. 9.32. Reaction between ZnO and Al_2O_3 to form ZnAl_2O_4 at 1400°C in air (two spherical particle sizes). See reference 1, p. 102.

Calculating the reaction rate given in Eqs. 9.68 and 9.69 on an absolute basis requires knowledge of the diffusion coefficient for all the ionic species together with a knowledge of the system's geometry and the chemical potential for each species as related to their position in the reaction-product layer. The diffusing species which control the reaction

*R. E. Carter, *J. Chem. Phys.*, 34, 2010 (1961); 35, 1137 (1961).

rate are the most arriving at a phase Section 9.2 must

Another difficulty dependence of α in many cases the coherent with the with many defects tunity for surface indicated in Eq. through a single lower limit for rate. When new temperatures, there be some nonequilibrium structure with α and growth in nonequilibrium product. For example observed at a α This effect is α changes at the extensively in α Also, at the transformation tends to which increase transfer. At present a quantitative

Coarsening α may undergo α represents a α Generally termed dispersed in α varying size in α ones dissolve α of the interface (ter 5) relates to α a relative to α

where γ is the

rate are the most rapidly moving ions, or ions plus electrons, capable of arriving at a phase-boundary interface. All the constraints discussed in Section 9.2 must be considered.

Another difficulty in detailed quantitative calculations is the strong dependence of reaction rates on the structure of the reaction product. In many cases the reaction product is formed in such a way that it is not coherent with the reactants. Because of volume changes it may be formed with many defects and fissures. Consequently, there is extensive opportunity for surface and boundary diffusion, and the diffusion coefficient indicated in Eqs. 9.68 and 9.69 is not necessarily identical with diffusion through a single-crystal or dense polycrystalline body; these values set a lower limit for the actual diffusion coefficient and the possible reaction rate. When new phases are formed, as by carbonate decomposition at low temperatures, there is a strong tendency for the initial lattice parameter to be some nonequilibrium value corresponding to a coherent interface and structure with the reactant, as discussed in connection with nucleation and growth in Sections 8.3 and 8.4. Diffusion coefficients for this nonequilibrium lattice are normally larger than for the final equilibrium product. For example, an increase in solid-state reaction rate is frequently observed at a polymorphic transition temperature (the Hedvall effect). This effect is related to lattice strains and fissures formed by volume changes at the transition point; these lattice strains and fissures occur extensively in quartz, for example, in which the volume change is large. Also, at the transition temperature equilibrium between two polymorphic forms tends to occur with a coherent interface giving rise to lattice strains which increase the diffusion coefficients and the opportunity for material transfer. At present there are no data available for putting these effects on a quantitative basis.

Coarsening of Particles. After a solid has precipitated, the particles may undergo a coarsening effect because the variation in particle size represents a variation in the chemical activity from particle to particle. Generally termed Ostwald ripening, the principles apply to precipitates dispersed in solids or liquids. For the system of dispersed particles of varying size in a medium in which they have some solubility, the smaller ones dissolve and the larger ones grow. The driving force is the reduction of the interfacial free energy. The Thompson-Freundlich equation (Chapter 5) relates the increased solubility of the precipitate c_a to the curvature a relative to that for a planar interface $c_{p.i.}$:

$$RT \ln \frac{c_a}{c_{p.i.}} = \frac{2\gamma M}{a \rho} \quad (9.70)$$

where γ is the interfacial energy (ergs/cm²), M the molecular weight, and

ρ the density of the precipitate particle. This relation also assumes that the activity is given by the concentration. If $\frac{2\gamma M}{RT\rho a_p} < 1$, the increased solubility is given by

$$c_a = c_{p.i.} \left(1 + \frac{2\gamma M}{RT\rho a_p} + \dots \right) = c_{p.i.} + \frac{2\gamma M c_{p.i.}}{RT\rho} \quad (9.71)$$

For simplicity, consider a system of two particle sizes a_1 and a_2 where $a_1 > a_2$. The a_2 particles are more soluble in the matrix and thus tend to dissolve because of the concentration driving force:

$$c_{a_1} - c_{a_2} = \frac{2\gamma M c_{p.i.}}{RT\rho} \left(\frac{1}{a_1} - \frac{1}{a_2} \right) \quad (9.72)$$

From Fick's law we can determine the rate of growth of these particles if we assume the rate is controlled by diffusion in the matrix, that is, solvent (see Fig. 9.33a). The rate of mass gain by a_1 is

$$\frac{dQ}{dt} = -D \left(\frac{A}{x} \right) (c_{a_1} - c_{a_2}) \quad (9.73)$$

where A/x is a representative area-to-length ratio for diffusion between two dissimilar particles. Substitution of Eq. 9.72 into 9.73 yields

$$\frac{dQ}{dt} = -D \left(\frac{A}{x} \right) \frac{2\gamma M c_{p.i.}}{RT\rho} \left(\frac{1}{a_1} - \frac{1}{a_2} \right) \quad (9.74a)$$

As we have assumed spherical particles and must conserve mass,

$$-\frac{dQ}{dt} = \rho 4\pi a_2^2 \frac{da_2}{dt} = -\rho 4\pi a_1^2 \frac{da_1}{dt} \quad (9.74b)$$

the growth of a_1 is

$$\rho 4\pi a_1^2 \frac{da_1}{dt} = -D \left(\frac{A}{x} \right) \frac{2\gamma M c_{p.i.}}{RT\rho} \left(\frac{1}{a_1} - \frac{1}{a_2} \right) \quad (9.75)$$

Equation 9.75 can be integrated under various approximations, however, the same solution results by considering the following approximate solution. If we assume that the small particles contribute solute to the matrix faster than the solute is precipitated onto the large particles, the growth of large particles can be treated as a diffusion-limited-growth problem. The rate-limiting step is assumed to be diffusion of matter to the large particle from the matrix. Assume a diffusion field of r ($r \gg a_1$)

Fig. 9.33. (a) C in a diffusion field

around the gr symmetry is

where

Recalling tha

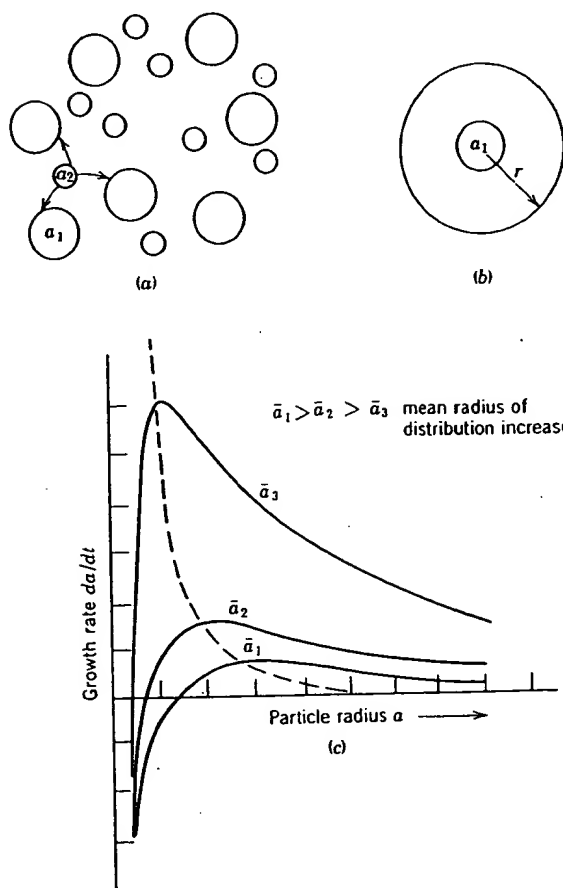


Fig. 9.33. (a) Coarsening of particles in a two-size particle system; (b) growth of particle a_1 in a diffusion field of radius r ; (c) variation in the particle growth rate with particle radius.

around the growing particle (Fig. 9.33b); thus Fick's first law of spherical symmetry is

$$J = 4\pi D \Delta c \left(\frac{a_1 r}{r - a_1} \right) \quad (9.76)$$

where

$$\Delta c = \frac{2M\gamma c_{p,i}}{RT\rho a_1}$$

Recalling that for dispersed particles $r \gg a_1$, the flux is given by

$$J = \frac{4\pi D 2M\gamma c_{p,i}}{RT\rho a_1} \left(\frac{a_1 r}{r - a_1} \right) \approx \frac{4\pi D c_{p,i} 2M\gamma}{RT\rho} = \text{const} \quad (9.77)$$

The flux is a constant, independent of the growing particle radius,

$$J = \text{constant} = \rho \frac{dV}{dt} = \rho 4\pi a_i^2 \frac{da_i}{dt} = \frac{4\pi Dc_{p,i} 2M\gamma}{\rho RT} \quad (9.78)$$

which after integration becomes

$$a_f^3 - a_i^3 = \frac{6Dc_{p,i}M\gamma}{\rho^2 RT} \quad (9.79)$$

or

$$\left(\frac{a(t)}{a_i}\right)^3 = 1 + \frac{t}{\tau}$$

where

$$\tau = \frac{6Dc_{p,i}M\gamma}{\rho^2 RTa_i^3} \quad (9.80)$$

More rigorous analyses give essentially the same result for a distribution of precipitates.* The variation in the growth rate for varying particle size and for increases in the mean radius is illustrated in Fig. 9.33c. The diffusion-limited growth of precipitates and of grains during liquid-phase sintering have been observed to have this cubic time dependence (Figs. 9.34 and 9.35).

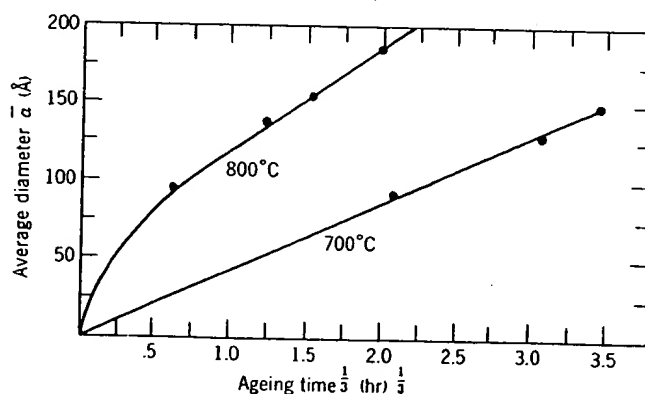


Fig. 9.34. Coarsening of $Mg_{1.2}Fe_{1.8}O_3$ precipitates in MgO. From G. P. Wirtz and M. E. Fine, *J. Am. Ceram. Soc.*, 51, 402 (1968).

The coarsening relationships discussed above assumed spherical particles. The following discussion demonstrates that faceted particles and even those with different surface energies can be included in the growth expressions by properly defining Δc , the concentration difference.

*C. Wagner, *Z. Electrochem.*, 65, 581-591 (1961); G. W. Greenwood, *Acta Met.*, 4, 243-248 (1956).

R
5.4
5.0
4.6
4.2
3.8
3.4
 $\log |(\bar{G}S)^3 - (\bar{G}S_0)^3|$

Fig. 9.35. Isotherm
microns, t = time in
Publishing Corpor:

Consider a si
to-volume ratio

The chemical
the planar inte

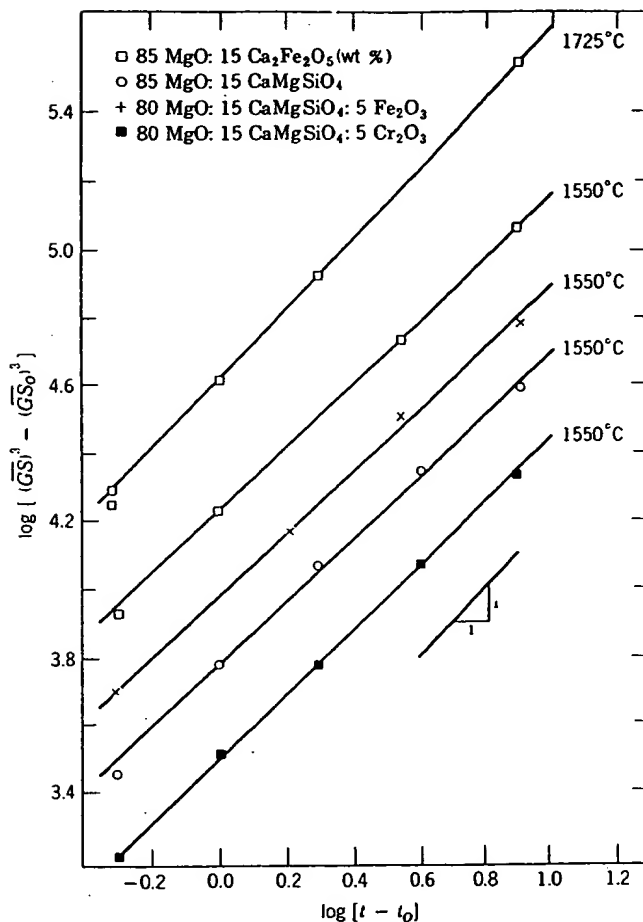


Fig. 9.35. Isothermal grain growth in systems containing MgO and liquid (GS = grain size in microns, t = time in hours) $(GS)^3$ at. From J. White in *Materials Sci. Research*, Vol. 6, Plenum Publishing Corporation, New York, 1973, p. 81.

Consider a size class of particles of constant shape but with a surface-to-volume ratio $S_v = S/V$. The surface contribution to the free energy is

$$G - G_{p.l.} = \gamma S = \gamma S_v V \quad (9.81)$$

The chemical potential difference between the faceted particle (μ) and the planar interface ($\mu_{p.l.}$) is

$$\mu - \mu_{p.l.} = \frac{d}{dn} (G - G_{p.l.}) = \gamma \bar{V} \left(\frac{dS}{dV} \right)_{S_v} \quad (9.82)$$

for phase separation mobility (Chap)

For nucleatic volume between free-energy change replaced by

— 10 —

where the strain ϵ , and b is the interfacial energy per unit area. The expression for ΔG^* , which contains ϵ and β structural parameters of the crystalline phase, is the energy of stable nuclei at the dislocation sites. The strain energy E_s is zero when a decomposition of precipitates occurs at the minimum increment of spherical particle size. The energy is proportional to the volume fraction of the precipitates. Strain energy of the interface E_i is the energy of the interface which phase separates into lamellae in pre-

The energy structure and general kinds of planes of atom second coordination boundary. In planes of atom giving rise to described in Cl order of magnitude formation of mother matrix commonly the formation in which

for phase separation occurs (Chapter 7); growth rates are limited by atom mobility (Chapter 6).

For nucleation in solids, strain energy resulting from differences in volume between precipitate and matrix must be included in evaluating the free-energy change on forming a nucleus. In these cases, Eq. 8.19 is replaced by

$$\Delta G_r = 4\pi r^2\gamma + \frac{4}{3}\pi r^3(\Delta G_v + \Delta G_e) \quad (9.87)$$

where the strain energy per unit volume is given by $\Delta G_e = b\epsilon^2$, ϵ is the strain, and b is a constant which depends on the shape of the nucleus and can be calculated from elasticity theory. The presence of ΔG_e in the expression for ΔG_r results in a free energy on forming the critical nucleus, ΔG^* , which corresponds to a definite crystallographic relation of the α and β structures and the boundary between them when both are crystalline phases. Inclusion of ΔG_e can affect greatly the morphology of stable nuclei and increase the tendency for nucleation at heterogeneous sites. The strain energy typically causes the formation of parallel platelets when a decomposition (precipitation) reaction occurs. The configuration of precipitates as parallel platelets allows growth to take place with the minimum increase in strain energy. In general, the formation of thick or spherical particles produces large values of strain; since the strain energy is proportional to ϵ^2 , precipitates with a platelike habit are preferred when the volume change on precipitation is appreciable, as is often the case. Strain energy also effects spinodal decomposition by increasing the energy of the inhomogeneous solution and depressing the temperature at which phase separation occurs and by causing separation to occur as lamellae in preferred crystallographic directions.

The energy for nucleation of a new phase depends on the interface structure and orientation, as discussed in Chapter 5. We can define two general kinds of precipitate. In a *coherent* precipitate, as in Fig. 9.36, planes of atoms are continuous across the interface so that only the second coordination of individual atoms is changed, similar to a twin boundary. In contrast, a *noncoherent* precipitate is one in which the planes of atoms, or some of them, are discontinuous across the interface, giving rise to dislocations or a random structure in the boundary layer, as described in Chapter 5. The interface energy of a coherent boundary is an order of magnitude less than that of an incoherent boundary, so that formation of new phases with definite structural relationships to the mother matrix is strongly preferred. In addition, the oxygen ions are commonly the more slowly moving in oxide structures, so that a transformation in which these ions must migrate to new positions is bound to be

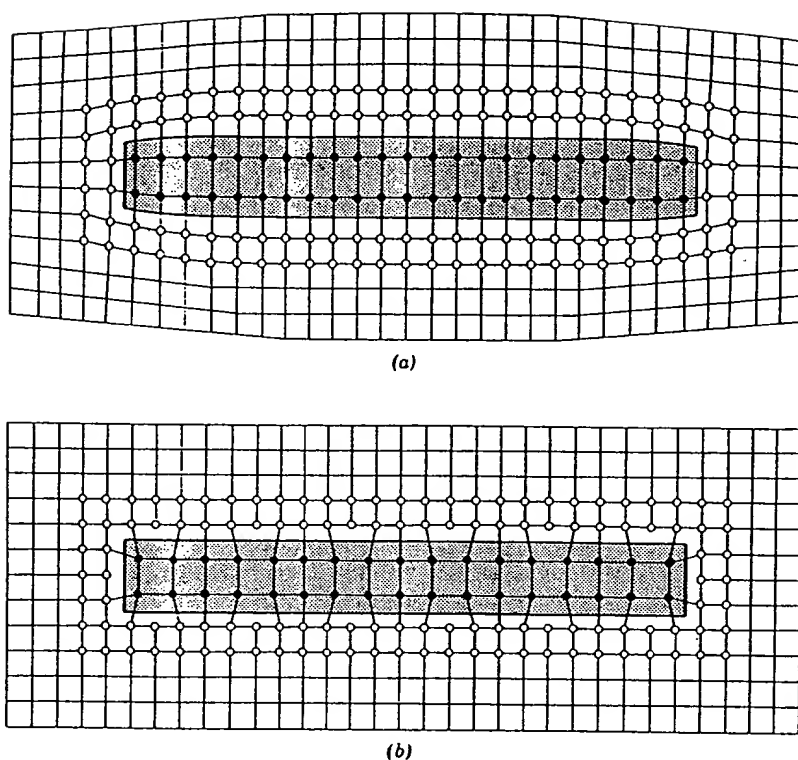


Fig. 9.36. (a) Coherent precipitate with continuous planes of atoms across the interface; (b) noncoherent precipitate with discontinuous planes of atoms across the interface.

relatively slow. Therefore, coherency of the oxygen ion lattice is favorable both for the driving force of nucleation and for the rate of nucleation and crystal growth.

Precipitation Kinetics. The kinetics of precipitation in a crystalline solid depend on both the rate of initiation or nucleation of the process and the rate of crystal growth, as discussed in Chapter 8. When the precipitation process consists of a combination of nucleation and growth, the sigmoidal curve characteristic of the Johnson-Mehl or Arrami relations (Chapter 8) results in an apparent incubation time period, as illustrated in Fig. 9.37. For precipitation processes far from an equilibrium phase boundary, which is the most usual case, both the nucleation rate and the growth rate increase with temperature, as illustrated in Fig. 9.38 such that the incubation time is decreased and the transformation time for formation of the new phase is decreased at higher temperatures, such as occurs for the process illustrated in Fig. 9.37. In many cases, however, the

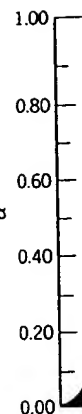


Fig. 9.37. Effect of temperature on the precipitation process for ZrO_2 -20 mole % Y_2O_3 at 1000°C; B, 1075°C; Viechnicki, J. A.

nucleation rate is high, the number of nucleation sites which heterogeneously nucleate matrix crystals is high. The rate of precipitation is increased by the existing nucleation sites. The precipitation of magnesium oxide in a paramagnetic matrix having an apparent incubation period is in accordance with the above.

Precipitation Interfaces. The precipitation of many oxide ions describes a process containing energy and

*G. P. Wirtz

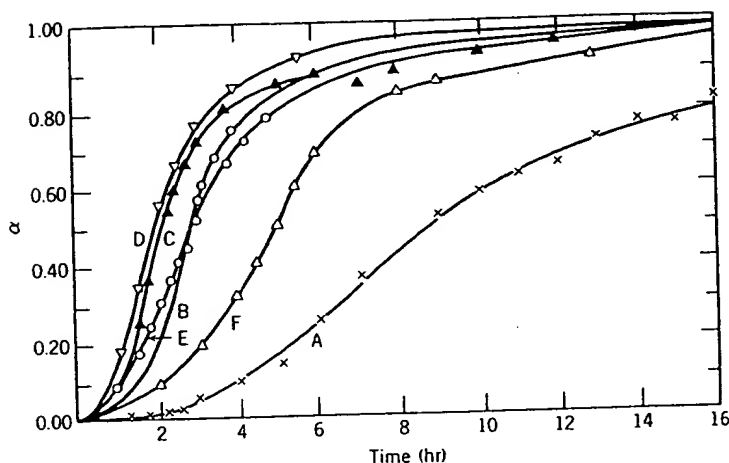


Fig. 9.37. Effect of temperature on the decomposition of solid solutions of 80 mole % ZrO_2 -20 mole % MgO . Solid solutions prepared at 1520°C for 1 hr and then decomposed at A, 1000°C ; B, 1075°C ; C, 1150°C ; D, 1250°C ; E, 1350°C ; F, 1375°C . From V. S. Stubican and D. J. Viechnicki, *J. Appl. Phys.*, 37, 2751 (1966).

nucleation process occurs rapidly during cooling, such that a large number of nuclei are available for growth. This is particularly the case in which heterogeneous nucleation sites are available in a not very perfect matrix crystal or in which the interface energy term is low for a coherent precipitate. When this occurs the overall precipitation process, as measured by the fraction of material transformed, corresponds to growth of existing nuclei and no incubation period is observed, as illustrated for precipitation of MgAl_2O_4 spinel from MgO in Fig. 9.39. For precipitation of magnesium ferrite, MgFe_2O_4 , from MgO , application of superparamagnetic measurements capable of identifying newly formed crystals having an average diameter of about 15 \AA has shown no indication of an incubation period; that is, the critical nucleus size is very very small in accordance with a low energy for the coherent interface.*

Precipitate Orientation. The influence of strain energy and coherent interfaces leads to a high degree of precipitate orientation for many oxide precipitation processes. These relationships are particularly strong for the many oxide structures based on close-packed arrangements of oxygen ions described in Chapter 2. In the case of magnesium aluminate spinel containing excess aluminum oxide in solid solution, the influence of strain energy and coherency relationships leads to precipitation of a metastable

*G. P. Wirtz and M. E. Fine, *J. Am. Ceram. Soc.*, 51, 402 (1968).

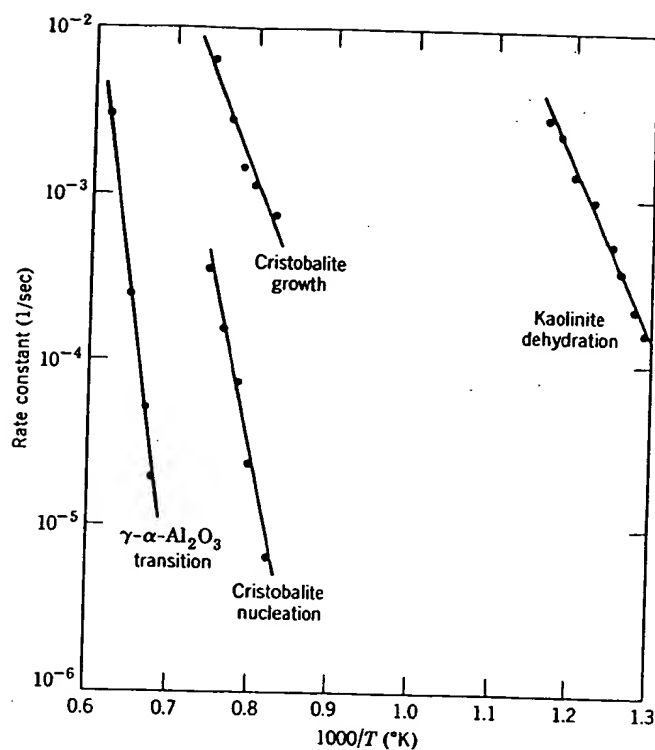


Fig. 9.38. Temperature dependence of rate of (a) nucleation, (b) growth of cristobalite from silica gel, (c) formation of α - Al_2O_3 , and (d) dehydration of kaolinite.

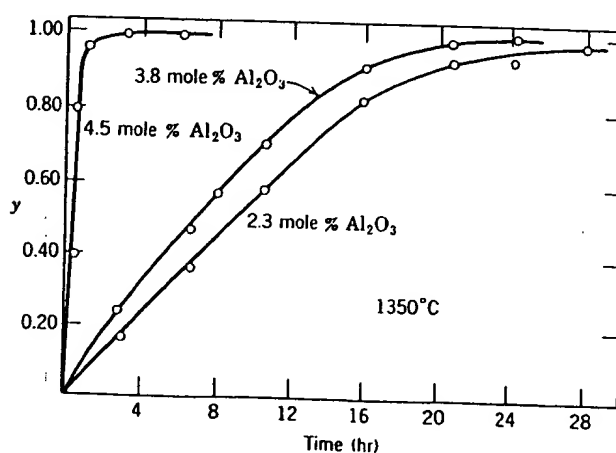


Fig. 9.39. The fractional precipitation y of spinel as a function of time at 1350°C . Specimens prepared at 1950°C . From V. S. Stubican and D. J. Viechnicki, *J. Appl. Phys.*, 37, 2751 (1966).

intermediate with product* which product, α -alumina metastable prealumina. After 1 expense of the

Synthetic statitaniferous pre 0.3% TiO_2 . Whence causes the times for precipitation 1500°C . The latter as for precipitation equilibrium phase

Strong orientation believed to exhibit SnO_2 - TiO_2 system 5-min anneal at corner of Fig. 9 to the 001 direction formed by spinel Al_2O_3 - Cr_2O_3 and this manner. As spinel phase from large metal deficiency (Chapter 4) is by agglomerates in forming the spinel the resulting high in this and relative 300°C . On cooling defect clusters,

When growth change, the rate the morphology dissipated or more inverse radius of dendritic forms remaining small

* H. Jagodzinski (1962).

intermediate with a structure similar to spinel as the first precipitation product* which is more easily nucleated than the stable equilibrium product, α -alumina. In fact, as shown in Fig. 9.40, two different types of metastable precipitates initially form, plus a smaller amount of α -alumina. After long annealing at 850°C the α -alumina particles grow at the expense of the metastable intermediate precipitates.

Synthetic star sapphires are produced by precipitating an alumina-rich titaniferous precipitate from single crystals of sapphire containing 0.1 to 0.3% TiO_2 . When viewed in the direction of the c -axis stellate opalescence causes the reflected light to form a well-defined six-ray star. Aging times for precipitation range from approximately 72 hr at 1100°C to 2 hr at 1500°C. The lath-shaped precipitates formed are illustrated in Fig. 9.41. As for precipitation from spinel, the precipitate particle formed is not the equilibrium phase (Al_2TiO_5) but a metastable product.

Strong orientation effects are also observed in systems which are believed to exhibit spinodal decomposition, shown in Fig. 9.42, for the SnO_2 - TiO_2 system in which a lamellar microstructure is formed after a 5-min anneal at 1000°C. The electron diffraction pattern at the lower corner of Fig. 9.42 shows streaking of the diffraction spots perpendicular to the 001 direction, which is to be expected for the periodic structure formed by spinodal decomposition. Other crystalline systems such as Al_2O_3 - Cr_2O_3 and CoFe_2O_4 - Co_3O_4 are also believed to phase separate in this manner. A similar structure, Fig. 9.43, is found for precipitation of the spinel phase from an FeO - MnO solid solution at low temperature. The large metal deficit in this highly nonstoichiometric system (discussed in Chapter 4) is believed to result in defect association on cooling; defect agglomerates may serve as nucleation sites for the precipitation reaction forming the spinel phase. Because of the high defect concentration and the resulting high diffusivity of the cations, precipitation processes occur in this and related systems at quite low temperatures, in this case about 300°C. On cooling a sample, it is not possible to prevent the formation of defect clusters, even with the most rapid quench.

When growth is rapid or occurs at low temperatures with a composition change, the rate of flow of heat or material limits the growth rate and fixes the morphology. Under these conditions the rate at which heat is dissipated or material added to a growing precipitate is proportional to the inverse radius of curvature of the growing tip of the crystal. As a result, dendritic forms result, with the radius of curvature of the growing tip remaining small and side arms developing to form a treelike structure.

* H. Jagodzinski, *Z. Krist.*, **109**, 388 (1957), and H. Saalfeld, *Ber. Deut. Keram. Ges.*, **39**, 52 (1962).

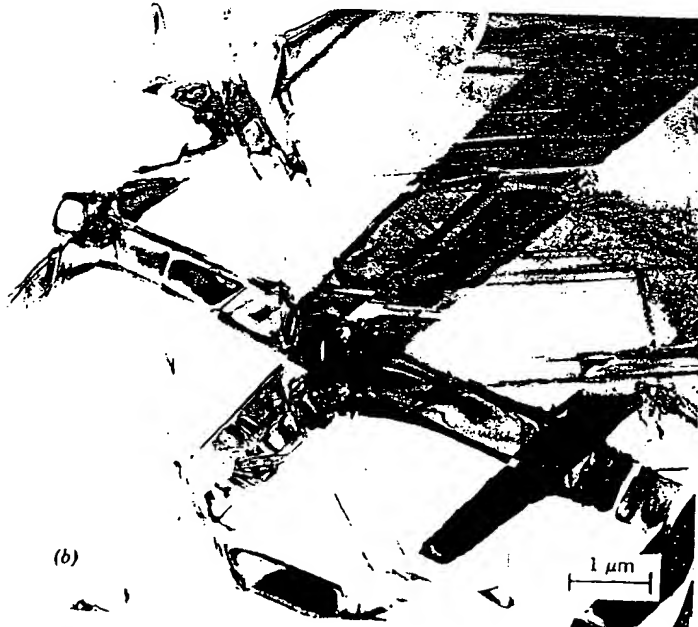


Fig. 9.40. (a) Metastable precipitates I and II first form along with $\alpha\text{-Al}_2\text{O}_3$ (A) on annealing spinel at 850°C; (b) after long times the $\alpha\text{-Al}_2\text{O}_3$ particles coarsen at the expense of the intermediate precipitates. Courtesy G. K. Bansal and A. Heuer.

Fig. 9.4
Courtes

Deper
illustr
basic
tion c
along
long p
rate-d
graph
limite
period
spher
minin
Het
that p
when
may s
precip
grain
wüsti

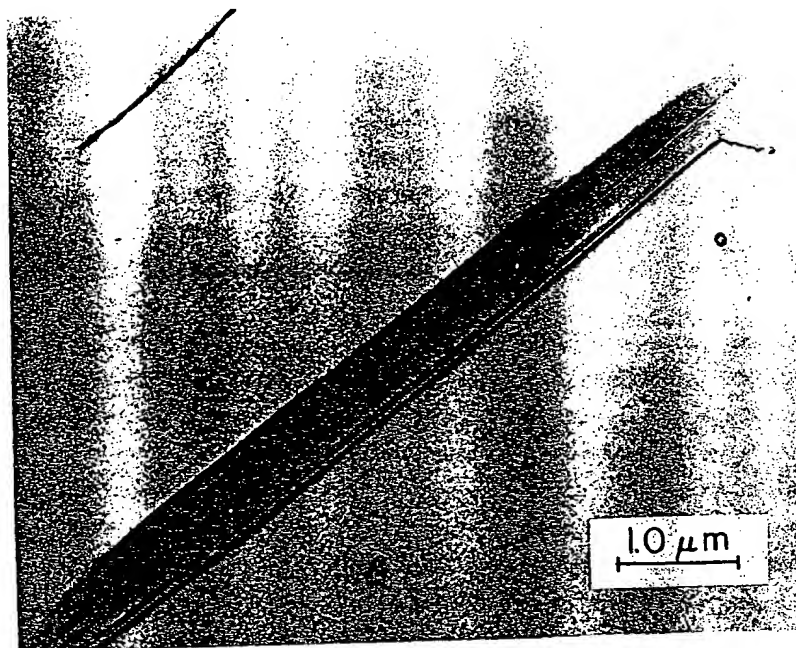


Fig. 9.41. Lath-shaped crystallographically oriented precipitate particles in star sapphire. Courtesy B. J. Pletka and A. Heuer.

Depending on the conditions of formation, different structures arise, as illustrated for the precipitation of magnesioferrite from magnesia in a basic refractory brick (Fig. 9.44). Sometimes a crystallographic orientation of the precipitate occurs in which the platelets of MgFe_2O_4 form along (100) planes in the parent magnesia phase. On precipitation during long periods of time at a lower temperature at which diffusion is probably rate-determining, dendritic precipitates form which still have crystallographic orientations with the matrix but in which the rate of growth is limited, so that starlike crystals result (Fig. 9.45b); finally, after long periods at the higher temperature levels, there is a tendency for a spheroidal precipitate to develop in which the total surface energy is a minimum and the strain energy may be relieved by plastic flow.

Heterogeneous Precipitation. It is frequently observed (Fig. 9.45a) that precipitation of a new phase occurs primarily along grain boundaries; when more extensive precipitation occurs (Fig. 9.45b) grain boundaries may show precipitates surrounded by an area of material which is nearly precipitation free. This can result from heterogeneous nucleation at the grain boundary, although in the case of precipitation of Fe_3O_4 from wüstite the microstructure observed at low magnifications results primar-

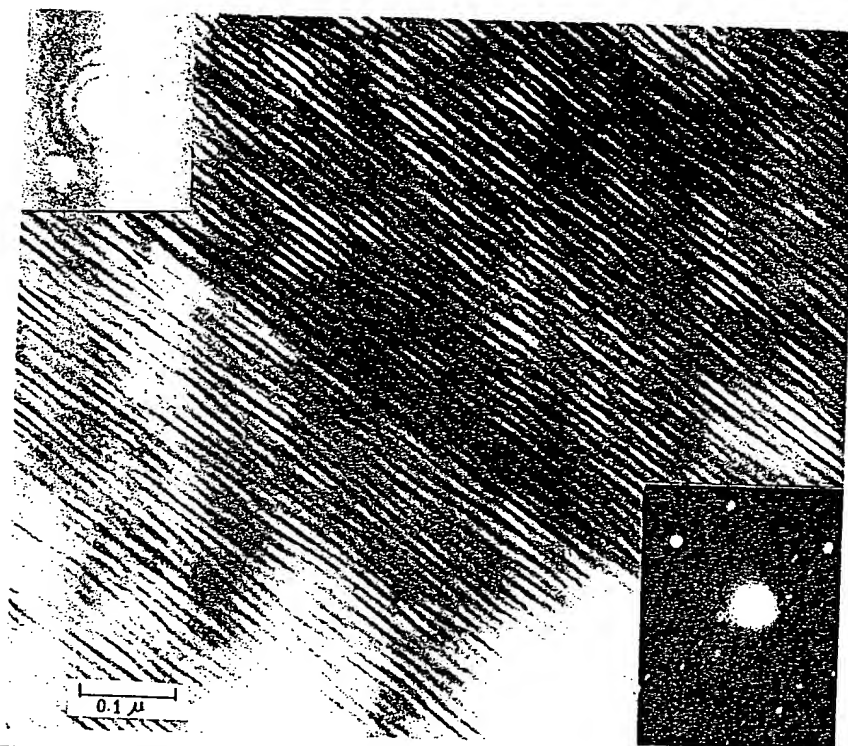


Fig. 9.42. Equimolar $\text{TiO}_2\text{-SnO}_2$ crystal homogenized at 1600°C and annealed 5 min at 1000°C . Electron diffraction pattern in lower right; optical diffraction pattern in upper left. Courtesy M. Park and A. Heuer.

ily from differences in the growth rate adjacent to grain boundaries rather than from a nucleation process. In this system the grain boundaries act as high diffusivity paths, discussed in Chapter 6, which allow nuclei at the grain boundary to grow initially at a faster rate than nuclei in the bulk, which tends to denude the area adjacent to the grain boundary of solute; at later stages in the precipitation process (Fig. 9.45b) there is an area adjacent to the grain boundaries which tends to be precipitate free. In this system, as for many of those previously described, the precipitate particles are coherent with the matrix crystal, and all have the same orientation in each grain of wüstite.

For samples in which solubility is small, direct observation of grain boundaries and dislocations indicates that second-phase precipitation at these sites is very common indeed. Particularly for many systems containing silicates as minor impurities, coherency is not to be expected;

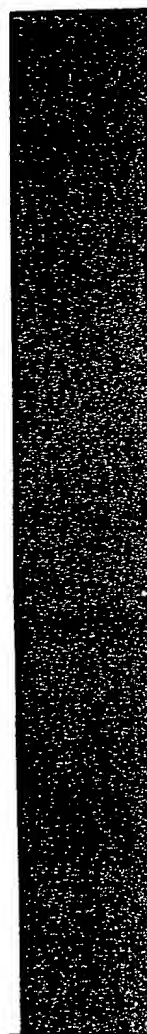


Fig. 9.43. L...
Courtesy C. J.



led 5 min at
n upper left.

ries rather
ries act as
clei at the
the bulk,
of solute;
is an area
ee. In this
recipitate
the same

1 of grain
itation at
systems
expected;

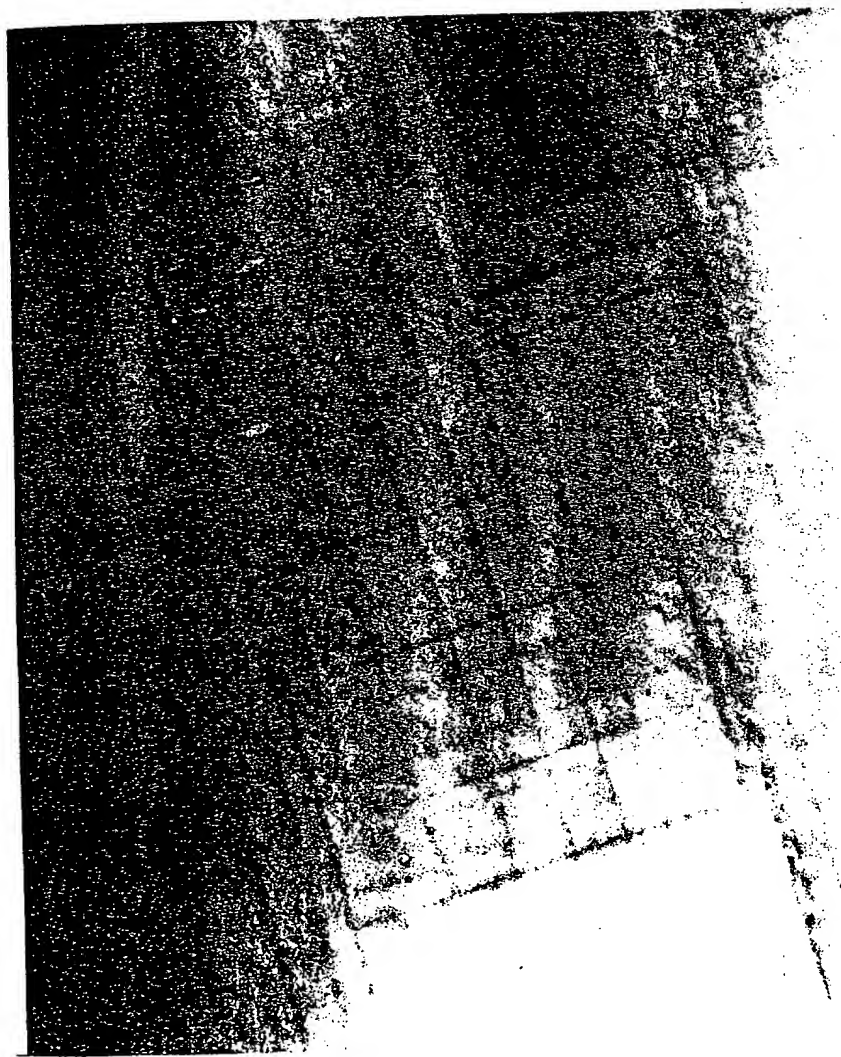


Fig. 9.43. Low-temperature precipitate of spinel phase from FeO-MnO solid solution.
Courtesy C. A. Goodwin, Ph.D. Thesis, MIT, 1973.

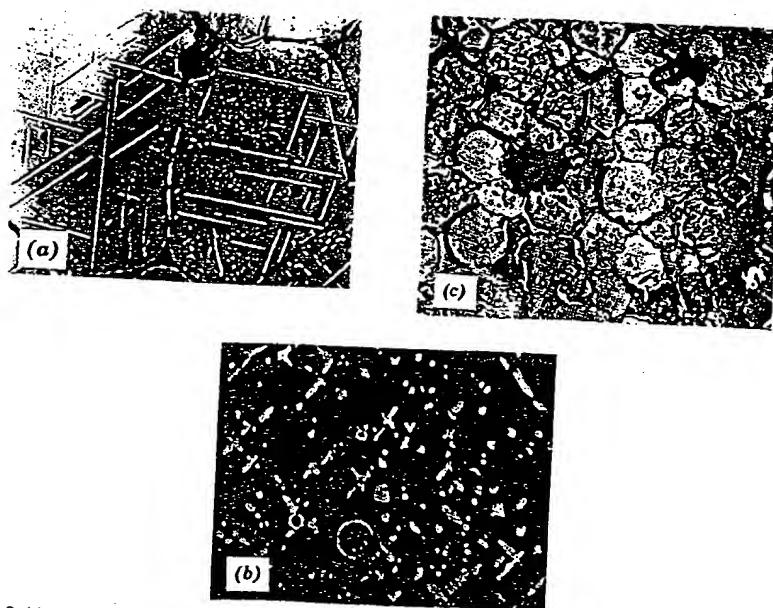


Fig. 9.44. Precipitation of MgFe_2O_4 from MgO in basic refractory brick as (a) platelets parallel to (100) planes in MgO (500 \times); (b) dendritic precipitate (975 \times); (c) spheroidal morphology (232 \times). Courtesy F. Trojer and K. Konopicky, *Radex Rdsch.*, 7, 8, 149 (1948), and B. Tavasci, *Radex Rdsch.*, 7, 245 (1949).

the smaller driving force and larger energy barrier to nucleation enhances the importance of heterogeneous nucleation and growth at dislocations and grain boundaries, as illustrated in Fig. 9.46.

9.6 Nonisothermal Processes

We have considered diffusional processes as they occur under isothermal conditions; however, many ceramic processing procedures include substantial nonisothermal periods. One important example of the effect of nonisothermal kinetic processes is the segregation and precipitation of impurities at grain boundaries while a specimen cools from a high temperature.*

If we assume that over the temperature range of interest, the diffusion coefficient is given by

$$D = D_0 e^{-Q/RT}$$

*See W. D. Kingery, *J. Am. Ceram. Soc.*, 57, 1 (1974).

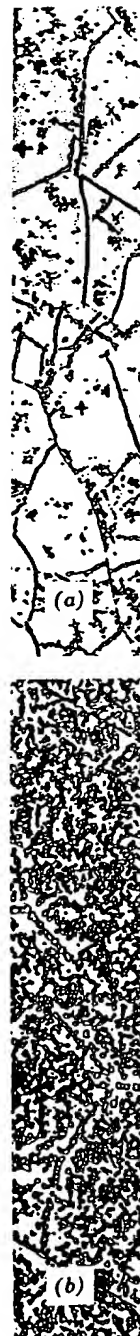


Fig. 9.45. Precipitation of MgFe_2O_4 from MgO in basic refractory brick as (a) platelets parallel to (100) planes in MgO (500 \times); (b) dendritic precipitate (975 \times). Courtesy F. Trojer and K. Konopicky, *Radex Rdsch.*, 7, 8, 149 (1948), and B. Tavasci, *Radex Rdsch.*, 7, 245 (1949).



ck as (a) platelets
×); (c) spheroidal
7, 8, 149 (1948), and

tion enhances
at dislocations

under isother-
dures include
of the effect of
ecipitation of
from a high

. the diffusion

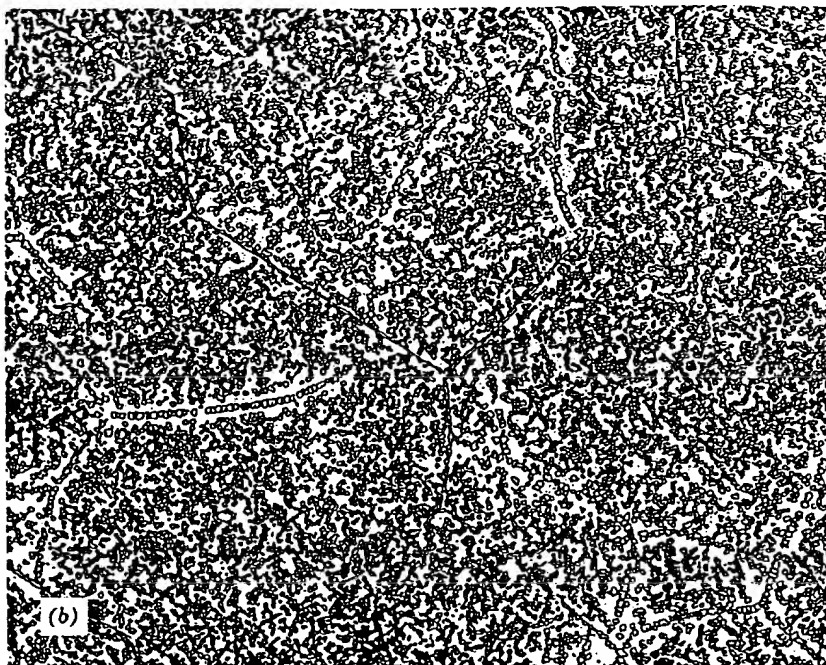


Fig. 9.45. Precipitate of Fe_3O_4 from wustite (Fe_xO) containing (a) 52.67 and (b) 53.10 atom % oxygen (95×). Courtesy L. Himmel.

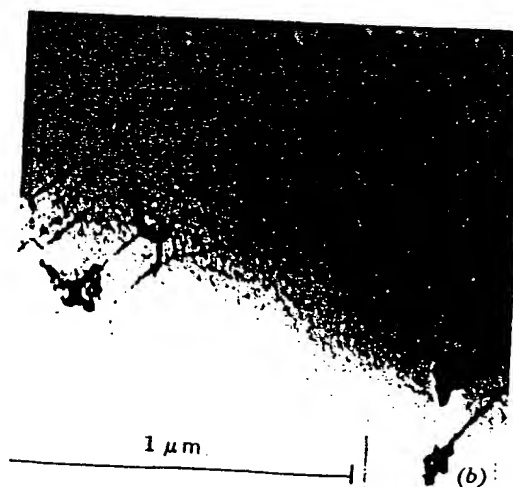
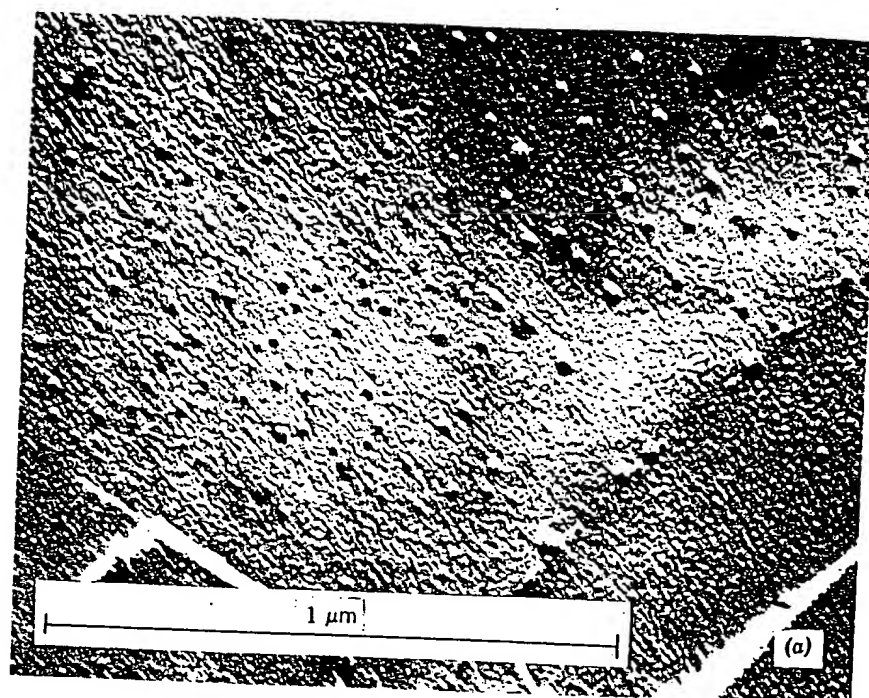


Fig. 9.46. (a) Manganese zinc ferrite containing 0.042% SiO_2 , heated 4 hr at 1200°C in $\text{N}_2 + 1\% \text{O}_2$, showing SiO_2 inclusions at grain-boundary fracture. Courtesy M. Paulus. (b) Precipitate particles at dislocations in MgO . Courtesy N. J. Tighe.

and we
the tim

An apj

Let us
 MgO .
to the g
becaus
6.4). Fr
to 75 l
diffusio
contain
limit at
assume
yields :
calcula
 $D \approx 5 :$

Ther
during
sed in
granula
finally
describ
tions.

First
9.63) in
determ
The re:
 CaCO_3

and we assume the temperature to vary from T_1 to T_2 at a linear rate of α , the time-dependent diffusion coefficient is

$$D = D_0 \exp \left[\frac{Q/R}{T_1 - \alpha t} \right] \quad (9.88)$$

An approximate diffusion length l may be estimated from the integral;

$$l^2 = D_0 \int_0^t \exp \left(\frac{-Q/R}{T_1 - \alpha t} \right) dt \quad (9.89)$$

$$l^2 \approx \frac{D_0 R}{\alpha Q} (T_1^2 e^{-Q/RT_1} - T_2^2 e^{-Q/RT_2}) \quad (9.90)$$

$$l^2 \approx \frac{R}{\alpha Q} [D_1 T_1^2 - D_2 T_2^2]$$

Let us consider, as an example of the use of Eq. 9.89, Al_2O_3 impurities in MgO . The diffusion of supersaturated aluminum ions from within a grain to the grain boundary is essentially that for the defect diffusion (vacancy) because of the impurity-vacancy pair which tends to form (see Section 6.4). From the data of impurity diffusion into MgO a value of 2 to 3 eV (50 to 75 kcal/mole) seems a reasonable activation energy for vacancy diffusion. Assume a sample of MgO annealed at high temperature contains 100 ppm Al_2O_3 . If the sample is cooled at $0.1^\circ\text{C}/\text{sec}$, the solubility limit at 1300°C produces the onset of grain-boundary precipitation. For an assumed diffusivity of $10^{-8} \text{ cm}^2/\text{sec}$ at 1300°C and $Q = 2 \text{ eV}$, Eq. 9.89 yields a value of 30 microns for the effective diffusion distance. A similar calculation for 100 ppm MgO in Al_2O_3 ($T_1 = 1530^\circ\text{C}$, $Q \approx 3 \text{ eV}$, and $D \approx 5 \times 10^{-8} \text{ cm}^2/\text{sec}$) yields a segregation thickness of 60 microns.

There are many other examples of ceramic processes which occur during nonisothermal annealing. As porcelain or refractories are processed in production kilns, much of the densification and reaction between granular components takes place during the heating cycle. We consider finally two examples of nonisothermal kinetic processes which are described in detail in Section 9.4 and Section 10.3 for isothermal conditions.

First, let us consider the nonisothermal decomposition reaction (Eq. 9.63) in which CaCO_3 decomposes to CaO and CO_2 . The reaction rate is determined by decomposition at the surface and obeys linear kinetics. The reaction rate R is equal to the change in weight per unit area of the CaCO_3 with time, $d(\omega/a)/dt$. Thus Eq. 9.4 can be rewritten

$$\frac{d(\omega/a)}{dt} = R = \frac{kT}{h} \exp \left(\frac{\Delta S^\ddagger}{R} \right) \exp \left(-\frac{\Delta H^\ddagger}{RT} \right) = A \exp \left(-\frac{\Delta H^\ddagger}{RT} \right) \quad (9.91)$$

at 1200°C in
I. Paulus. (b)

If the temperature of the CaCO_3 is changed at a constant rate, $T = \alpha t$, the weight change as a function of temperature is obtained from

$$\frac{d(\omega/a)}{dT} = \frac{A}{\alpha} \exp\left(-\frac{\Delta H^\ddagger}{RT}\right) \quad (9.92)$$

The integration of Eq. 9.92, assuming that A is not a strong function of temperature, yields the approximate solution

$$\frac{\Delta\omega}{\omega_0} \approx \frac{ART^2}{\alpha \Delta H^\ddagger} \exp\left(-\frac{\Delta H^\ddagger}{RT}\right) \quad (9.93)$$

The form of the equation is similar to Eq. 9.89. A plot of the non-isothermal decomposition in vacuum of a single crystal of CaCO_3 is given in Fig. 9.47. For this reaction and for several other endothermic decomposition reactions the activation energy for decomposition is identical with the heat of reaction (Eq. 9.63).

As a final example of nonisothermal kinetic processes consider the sintering of glass spheres (discussed in Chapter 10). The shrinkage rate $\frac{d(\Delta L/L_0)}{dt}$, which is a function of the surface tension γ , the viscosity $\eta = B e^{Q/RT}$, and the particle radius a , can be determined from nonisother-

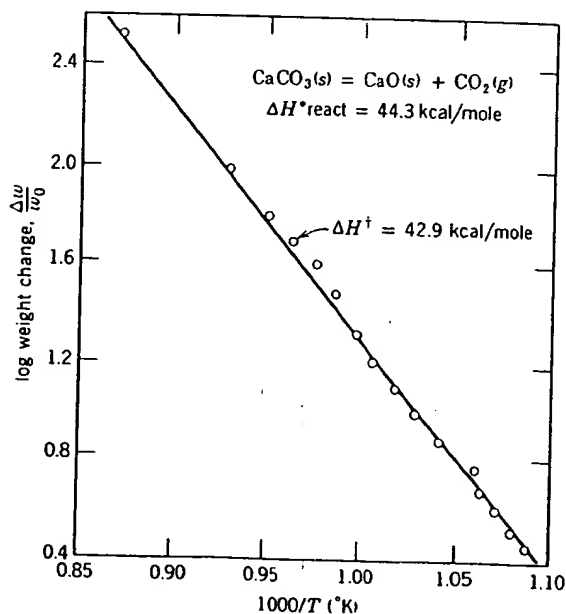


Fig. 9.47. Nonisothermal decomposition of CaCO_3 in vacuum.

Fig.
silica

mal

Kin
25-r
wat

1.
2.
3.
4.

*I

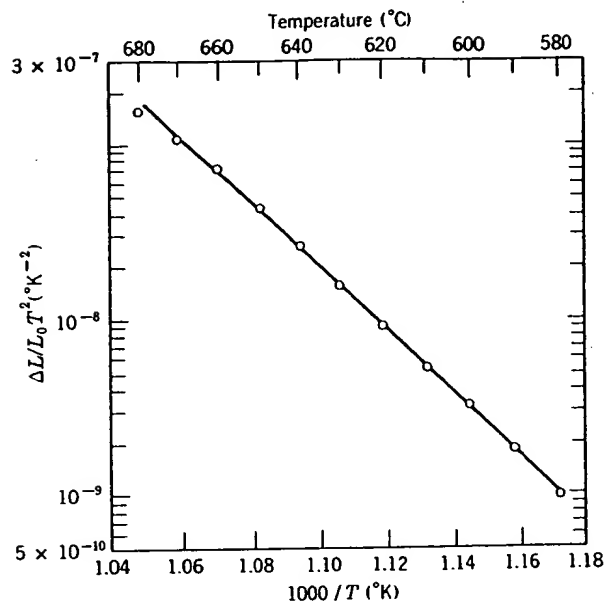


Fig. 9.48. Kinetic data for nonisothermal sintering of 0.25- μ m glass particles (soda-lime-silica). From I. B. Cutler, *J. Am. Ceram. Soc.*, 52, 14 (1969).

mal sintering from*

$$\frac{\Delta L}{L_0} \approx \left(\frac{\gamma R T^2}{2 \alpha \alpha B Q} \right) \exp(-Q/RT) \quad (9.94)$$

Kinetic data illustrating Eq. 9.94 are given in Fig. 9.48 for the sintering of 25-micron soda-lime-silica particles in an atmosphere of oxygen and water vapor.

Suggested Reading

1. H. Schmalzried, *Solid State Reactions*, Academic Press, New York, 1974.
2. G. C. Kuczynski, N. A. Hooton, and C. F. Gibbon, Eds., *Sintering and Related Phenomena*, Gordon and Breach, New York, 1967.
3. G. C. Kuczynski, Ed., "Sintering and Related Phenomena," *Materials Science Research*, Vol. 6, Plenum Press, New York, 1973.
4. T. J. Gray and V. D. Frechette, Eds., "Kinetics of Reaction in Ionic Systems," *Materials Science Research*, Vol. 4, Plenum Press, New York, 1969.

*I. B. Cutler, *J. Am. Ceram. Soc.*, 52, 14 (1969).

5. P. Kofstad, *Nonstoichiometry, Diffusion, and Electrical Conductivity in Binary Metal Oxides*, John Wiley & Sons, New York, 1972.
6. For a discussion of dissolution kinetics see A. R. Cooper, Jr., B. N. Samaddar, Y. Oishi, and W. D. Kingery, *J. Am. Ceram. Soc.*, **47**, 37 (1964); **47**, 249 (1964); and **48**, 88 (1965).
7. G. M. Schwab, Ed., *Reactivity of Solids*, Elsevier Publishing Company, New York, 1965.
8. W. D. Kingery, Ed., *Kinetics of High Temperature Processes*, John Wiley & Sons, New York, 1959.
9. M. E. Fine, *Introduction to Phase Transformations in Condensed Systems*, McGraw-Hill, New York, 1964; *Bull. Am. Ceram. Soc.*, **51**, 510 (1972).

Problems

- 9.1. Rates of solution can be controlled by (a) diffusion in the liquid, (b) diffusion through a reaction layer, or (c) phase-boundary reaction. How would you distinguish these?
- 9.2. While measuring the rate of decomposition of alumina monohydrate, a student finds the weight loss to increase linearly with time up to about 50% reacted during an isothermal experiment. Beyond 50%, the rate of the weight loss is less than linear. The linear isothermal rate increases exponentially with temperature. An increase of temperature from 451 to 493°C increases the rate tenfold. Compute the activation energy. Is this a diffusion-controlled reaction, a first-order reaction, or an interface-controlled reaction?
- 9.3. Consider formation of NiCr_2O_4 from spherical particles of NiO and Cr_2O_3 , when the rate is controlled by diffusion through the product layer.
 - (a) Carefully sketch an assumed geometry, and then derive a relation for the rate of formation early in the process.
 - (b) What governs the particles on which the product layer forms?
 - (c) At 1300°C, $D_{\text{Cr}} > D_{\text{Ni}} > D_{\text{O}}$ in NiCr_2O_4 . Which controls the rate of formation of NiCr_2O_4 ? Why?
- 9.4. Polymorphic transformations in solids result in polycrystalline materials of small size (fine-grained) or large size (coarse-grained), depending on the rates of nucleation and nuclei growth. How do these rates vary to produce fine-grained and coarse-grained products? Draw a time versus size for an individual grain illustrating the growth of a fine grain compared to a coarse grain. Start the time on the time axis at the moment of transformation.
- 9.5. According to Alper *et al.* [*J. Am. Ceram. Soc.*, **45**(6) 263-66 (1962)], Al_2O_3 is soluble in MgO to the extent of 3% by weight at 1700°C, 7% at 1800°C, 12% at 1900°C, and 0% at 1500°C. They observed crystallization of spinel crystals from the solid solution region on slow cooling. Fast quenching retained the solid solution as a single phase at room temperature. The exsolved spinel appeared uniformly without regard to grain boundaries within the periclase grains but on specific planes. (a) Is the nucleation of spinel homogeneous or heterogeneous within the periclase grains? (b) Account for the appearance of spinel crystals along specific planes of periclase crystals. Predict the shape of the rate of crystallization versus temperature for nucleated periclase solid solution containing 5% Al_2O_3 , over the temperature range 0°C to 1850°C.

- 9.6. In the previous problem, we described a solid solution of Al_2O_3 in MgO . Assuming a manufacturer of basic refractories uses MgO contaminated with 5 to 7% Al_2O_3 , what microstructure differences will exist in slow-cooled refractory compared to fast-cooled material? Would you predict sintering by self-diffusion (bulk), grain growth, and cation diffusion in this material would be different than in pure MgO ? Why?
- 9.7. Suppose that the formation of mullite from alumina and silica powder is a diffusion-controlled process. How would you prove it? If the activation energy is 50 kcal/mole and the reaction proceeds to 10% of completion at 1400°C in 1 hr, how far will it go in 1 hr at 1500°C ? in 4 hr at 1500°C ?
- 9.8. An amorphous SiO_2 film on SiC builds up, limiting further oxidation. The fraction of complete oxidation was determined by weight gain measurements and found to obey a parabolic oxidation law. For a particular-particle-sized SiC and pure O_2 the following data were obtained. Determine the apparent activation energy in kcal/mole. How can it be shown that this is a diffusion-controlled reaction?

Temp ($^\circ\text{C}$)	Fraction Reacted	Time (hr)
903	2.55×10^{-2}	100
1135	1.47×10^{-2}	10
	4.26×10^{-2}	100
1275	1.965×10^{-2}	10
	6.22×10^{-2}	100
1327	1.50×10^{-2}	5
	4.74×10^{-2}	50

- 9.9. The slow step in the precipitation of BaSO_4 from aqueous solution is the interface addition of the individual Ba^{++} and SO_4^{--} . Diffusion to the surface is assumed sufficiently fast that we may neglect any concentration differences in the solution. Assume that the rate of addition is first-order in both Ba^{++} and SO_4^{--} .
- Derive an expression for the approach to equilibrium in terms of the rate constants for the forward and back reaction and the surface area.
 - What is the effect of an excess of Ba^{++} ?
 - Why can you assume the surface area to be constant?
 - How would you modify your approach to include a correction for diffusion?
- 9.10. One-micron spheres of Al_2O_3 are surrounded by excess MgO powder in order to observe the formation of spinel. Twenty percent of the Al_2O_3 was reacted to form spinel during the first hour of a constant-temperature experiment. How long before all the Al_2O_3 will be reacted? Compute the time for completion on the basis of (a) no spherical geometry correction and (b) the Jander equation for correction of spherical geometry.
- 9.11. In fired chrome ore refractories, an R_2O_3 phase precipitates as platelets in the spinel phase matrix. Write the chemical equation for this reaction, and explain why it occurs. The precipitate is oriented so that the basal plane in the R_2O_3 phase is parallel to the (111) plane in the spinel. Explain why this should occur in terms of crystal structure.

Grain Growth, Sintering, and Vitrification

We have previously discussed phase changes, polymorphic transformations, and other processes independent of, or subsequent to, the fabrication of ceramic bodies. Phenomena that are of great importance are the processes taking place during heat treatment before use; these are the subject of this chapter.

During the usual processing of ceramics, crystalline or noncrystalline powders are compacted and then fired at a temperature sufficient to develop useful properties. During the firing process changes may occur initially because of decomposition or phase transformations in some of the phases present. On further heating of the fine-grained, porous compact, three major changes commonly occur. There is an increase in grain size; there is a change in pore shape; there is change in pore size and number, usually to give a decreased porosity. In many ceramics there may be solid-state reactions forming new phases, polymorphic transformations, decompositions of crystalline compounds to form new phases or gases, and a variety of other changes which are frequently of great importance in particular cases but are not essential to the main stream of events.

We shall be mainly concerned with developing an understanding of the major processes taking place. There are so many things which can happen, and so many variables that are occasionally important, that no mere cataloging of phenomena can provide a sound basis for further study. In general, we shall be concerned first with recrystallization and grain-growth phenomena, second with the densification of single-phase systems, and finally with more complex multiphase processes. There are many important practical applications for each of these cases.

10.1 Recrystallization

The terms *recrystallization* and *secondary recrystallization* have been used to describe the growth of new grains and other phenomena. The terms are mainly concerned with the process of *recrystallization* is the generation of new grains by the growth of plastically deformed grains. The grain size of the new grains is usually larger than that of the original grains. *Secondary recrystallization* is the growth of a few grains at the expense of the rest of the polycrystal. Although all these processes are secondary recrystallization.

Primary Recrystallization is the growth of new grains at the expense of the old grains. It is characterized by an increase in the number of grains and a decrease in the energy stored in the material. Although this process is a change to equilibrium, it is a change to equilibrium.

If the material is deformed at a constant rate, the grain size is d ,

where U is the time period. This process is characteristic of the chloride crystals at 470°C. The nucleation process is determined by the grain size.

The nucleation process is the growth of a new nucleus to the point at which the local surface free energy is required for the nucleus. If the grain size increases to

10.1 Recrystallization and Grain Growth

The terms recrystallization and grain growth have had a very broad and indefinite usage in much of the ceramic literature; they have sometimes been used to include phase changes, sintering, precipitation, exsolution, and other phenomena which produce changes in the microstructure. We are mainly concerned with three quite distinct processes. *Primary recrystallization* is the process by which nucleation and growth of a new generation of strainfree grains occurs in a matrix which has been plastically deformed. *Grain growth* is the process by which the average grain size of strainfree or nearly strainfree material increases continuously during heat treatment without change in the grain-size distribution. *Secondary recrystallization*, sometimes called abnormal or discontinuous grain growth, is the process by which a few large grains are nucleated and grow at the expense of a fine-grained, but essentially strain-free, matrix. Although all these processes occur in ceramic materials, grain growth and secondary recrystallization are the ones of major interest.

Primary Recrystallization. This process has as its driving force the increased energy of a matrix which has been plastically deformed. The energy stored in the deformed matrix is of the order of 0.5 to 1 cal/g. Although this is small compared with the heat of fusion, for example (which is a 1000 or more times this value), it provides a sufficient energy change to effect grain-boundary movement and changes in grain size.

If the isothermal change in grain size of strainfree crystals in a deformed matrix is measured after an initial induction period, there is a constant rate of grain growth for the new strainfree grains. If the grain size is d ,

$$d = U(t - t_0) \quad (10.1)$$

where U is the growth rate (cm/sec), t is the time, and t_0 is the induction period. This is illustrated in Fig. 10.1 for recrystallization of a sodium chloride crystal which had been deformed at 400°C and then annealed at 470°C. The induction period corresponds to the time required for a nucleation process, so that the overall rate of recrystallization is determined by the product of a nucleation rate and a growth rate.

The nucleation process is similar to those discussed in Chapter 8. For a nucleus to be stable, its size must be larger than some critical diameter at which the lowered free energy of the new grain is equal to the increased surface free energy. The induction period corresponds to the time required for unstable embryos present to grow to the size of a stable nucleus. If an unlimited number of sites is available, the rate of nucleation increases to some constant rate after an initial induction period. In

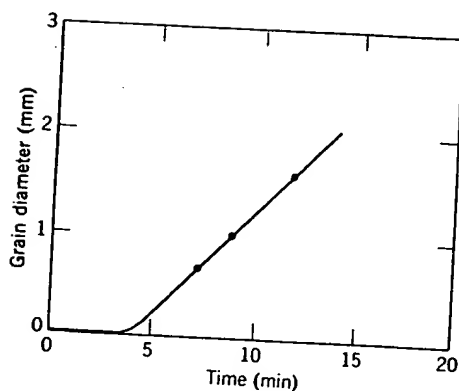


Fig. 10.1. Recrystallization of NaCl deformed at 400°C (stress = 4000 g/mm²) and recrystallized at 470°C. From H. G. Müller, *Z. Phys.*, 96, 279 (1935).

practice the number of favorable sites available is limited, and the rate of nucleation passes through a maximum as they are used up. H. G. Müller* observed that nuclei in sodium chloride tended to form first at grain corners, for example. As the temperature is increased, the rate of nucleation increases exponentially:

$$\frac{N}{dt} = N_0 \exp\left(-\frac{\Delta G_N}{RT}\right) \quad (10.2)$$

where N is the number of nuclei and ΔG_N is the experimental free energy for nucleation. Consequently, the induction period, $t_0 \sim 1/(dN/dt)$, decreases rapidly as the temperature level is raised.

As indicated in Eq. 10.1, the growth rate remains constant until the grains begin to impinge on one another. The constant in growth rate results from the constant driving force (equal to the difference in energy between the strained matrix and strainfree crystals). The final grain size is determined by the number of nuclei formed, that is, the number of grains present when they finally impinge on one another. The atomistic process necessary for grain growth is the jumping of an atom from one side of a boundary to the other and is similar to a diffusional jump in the boundary. Consequently the temperature dependence is similar to that of diffusion:

$$U = U_0 \exp\left(-\frac{E_U}{RT}\right) \quad (10.3)$$

where the activation energy E_U is normally intermediate between that for boundary and lattice diffusion. The growth-rate-temperature curve for

**Z. Phys.*, 96, 279 (1935).

recrystalliza
for diffusio

Since bot
temperature
rapidly with
different ter
recrystalliza
of cold worl
temperature
grains on on
and growth.
since the gr
However, a
rapidly, so
ments (Fig.
growth follo
creasing an
whereas the

In genera
required for
higher temp
increased ar

recrystallization of sodium chloride has a knee similar to that observed for diffusion and conductivity data, as discussed in Chapter 6.

Since both the nucleation rate and the growth rate are strongly temperature-dependent, the overall rate of recrystallization changes rapidly with temperature. For a fixed holding time, experiments at different temperatures tend to show either little or nearly complete recrystallization. Consequently, it is common to plot data as the amount of cold work or the final grain size as a function of the *recrystallization temperature*. Since the final grain size is limited by impingement of the grains on one another, it is determined by the relative rates of nucleation and growth. As the temperature is raised, the final grain size is larger, since the growth rate increases more rapidly than the rate of nucleation. However, at higher temperatures recrystallization is completed more rapidly, so that the larger grain size observed in constant-time experiments (Fig. 10.2) may be partly due to the greater time available for grain growth following recrystallization. The growth rate increases with increasing amounts of plastic deformation (increased driving force), whereas the final grain size decreases with increasing deformation.

In general, it is observed that (1) some minimum deformation is required for recrystallization, (2) with a small degree of deformation a higher temperature is required for recrystallization to occur, (3) an increased annealing time lowers the temperature of recrystallization, and

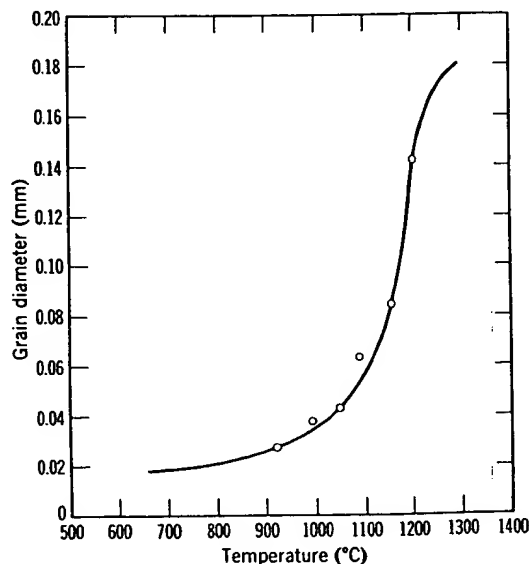


Fig. 10.2. Effect of annealing temperature on grain size of CaF_2 following compression at 80,000 psi and 10 hr at temperature. From M. J. Buerger, *Am. Mineral.*, 32, 296 (1947).

(4) the final grain size depends on the degree of deformation, the initial grain size, and the temperature of recrystallization. In addition, continued heat after recrystallization is completed leads to the continuation of grain growth.

Primary recrystallization is particularly common in metals which are extensively deformed in normal processing techniques. Ceramic materials are seldom plastically deformed during processing, so that primary recrystallization is not commonly observed. For relatively soft materials, such as sodium chloride or calcium fluoride, deformation and primary recrystallization do occur. It has also been observed directly in magnesium oxide; also, the polygonization process described in Chapter 4 (see Fig. 4.24) for aluminum oxide has many points of similarity.

Grain Growth. Whether or not primary recrystallization occurs, an aggregate of fine-grained crystals increases in average grain size when heated at elevated temperatures. As the average grain size increases, it is obvious that some grains must shrink and disappear. An equivalent way of looking at grain growth is as the rate of disappearance of grains. Then the driving force for the process is the difference in energy between the fine-grained material and the larger-grain-size product resulting from the decrease in grain-boundary area and the total boundary energy. This energy change corresponds to about 0.1 to 0.5 cal/g for the change from a 1-micron to a 1-cm grain size.

As discussed in Chapter 5, an interface energy is associated with the boundary between individual grains. In addition, there is a free-energy difference across a curved grain boundary which is given by

$$\Delta G = \gamma \bar{V} \left(\frac{1}{r_1} + \frac{1}{r_2} \right) \quad (10.4)$$

where ΔG is the change in free energy on going across the curved interface, γ is the boundary energy, \bar{V} is the molar volume, and r_1 and r_2 are the principal radii of curvature. (This relationship has been derived and discussed in Chapter 5. That part of Chapter 5 should be reviewed if its meaning is not clear.) This difference in the free energy of material on the two sides of a grain boundary is the driving force that makes the boundary move toward its center of curvature. The rate at which a boundary moves is proportional to its curvature and to the rate at which atoms can jump across the boundary.

Grain growth provides an opportunity to apply the absolute-reaction-rate theory already discussed in Chapter 6. If we consider the structure of a boundary (Fig. 10.3), the rate of the overall process is fixed by the rate at which atoms jump across the interface. The change in energy with an atom's position is shown in Fig. 10.3b, and the frequency of atomic jumps

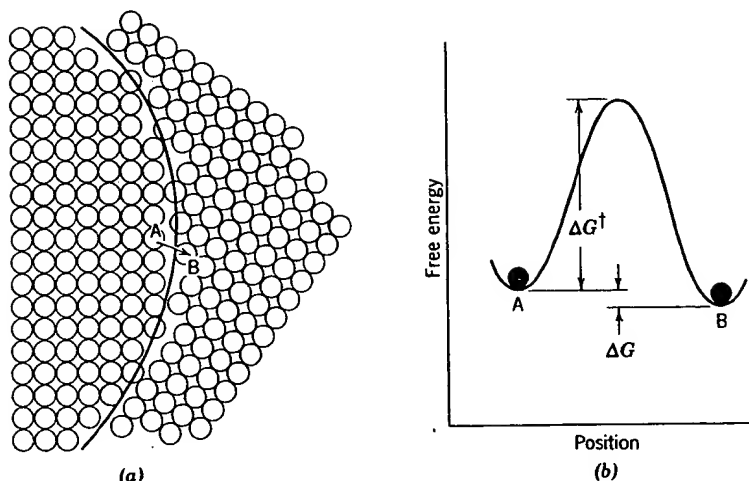


Fig. 10.3. (a) Structure of boundary and (b) energy change for atom jump.

in the forward direction is given by

$$f_{AB} = \frac{RT}{Nh} \exp\left(-\frac{\Delta G^\ddagger}{RT}\right) \quad (10.5)$$

and the frequency of reverse jumps is given by

$$f_{BA} = \frac{RT}{Nh} \exp\left(-\frac{\Delta G^\ddagger + \Delta G}{RT}\right) \quad (10.6)$$

so that the net growth process, $U = \lambda f$, where λ is the distance of each jump is given by

$$U = \lambda f = \lambda (f_{AB} - f_{BA}) = \frac{RT}{Nh} (\lambda) \exp\left(-\frac{\Delta G^\ddagger}{RT}\right) \left(1 - \exp\frac{\Delta G}{RT}\right) \quad (10.7)$$

and since $1 - \exp\frac{\Delta G}{RT} \approx \frac{\Delta G}{RT}$, where $\Delta G = \gamma \bar{V} \left(\frac{1}{r_1} + \frac{1}{r_2}\right)$ and $\Delta G^\ddagger = \Delta H^\ddagger - T \Delta S^\ddagger$,

$$U = \left(\frac{RT}{Nh}\right) (\lambda) \left[\frac{\gamma \bar{V}}{RT} \left(\frac{1}{r_1} + \frac{1}{r_2}\right)\right] \exp\frac{\Delta S^\ddagger}{R} \exp\left(-\frac{\Delta H^\ddagger}{RT}\right) \quad (10.8)$$

which is equivalent in form to Eq. 10.3 given previously. That is, the rate of growth increases exponentially with temperature. The unit step involved is the jump of an atom across the boundary, so that the activation energy should correspond approximately to the activation energy for boundary diffusion.

If all the grain boundaries are equal in energy, they meet to form angles of 120° . If we consider a two-dimensional example for illustrative purposes, angles of 120° between grains with straight sides can occur only for six-sided grains. Grains with fewer sides have boundaries that are concave when observed from the center of the grain. Shapes of grains having different numbers of sides are illustrated in Fig. 10.4; a sample with uniform grain size is shown in Fig. 10.5. Since grain boundaries migrate toward their center of curvature, grains with less than six sides tend to grow smaller, and grains with more than six sides tend to grow larger. For any one grain, the radius of curvature of a side is directly proportional to the grain diameter, so that the driving force, and therefore the rate of grain growth, is inversely proportional to grain size:

$$\dot{d} = \frac{d(d)}{dt} = \frac{k}{d} \quad (10.9)$$

and integrating,

$$d - d_0 = (2k)^{1/2} t^{1/2} \quad (10.10)$$

where d_0 is the grain diameter at time zero. Experimentally it is found that when $\log d$ is plotted versus $\log t$, a straight line is obtained (Fig. 10.6). Frequently the slope of curves plotted in this way is smaller than one-half,

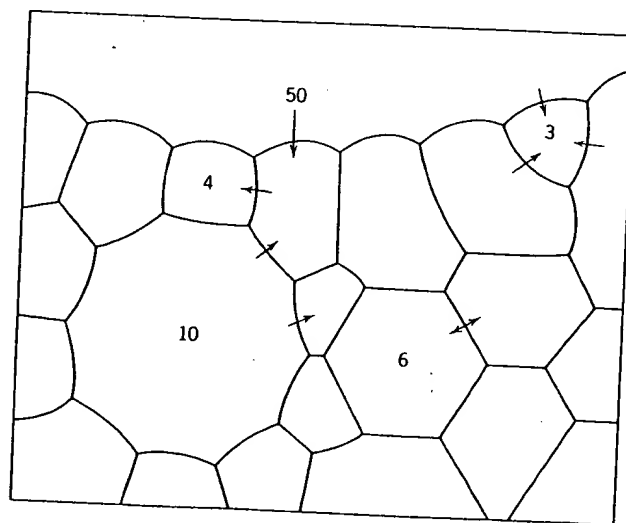


Fig. 10.4. Schematic drawing of polycrystalline specimen. The sign of curvature of the boundaries changes as the number of sides increases from less than six to more than six, and the radius of curvature is less, the more the number of sides differs from six. Arrows indicate the directions in which boundaries migrate. From J. E. Burke.



usually fall
one being
reason is th
growth.

A somev
 B_i such th
force F_i re

Fig. 10.6. L
Burke.

angles
trative
r only
at are
grains
ample
daries
sides
grow
rectly
efore

(10.9)

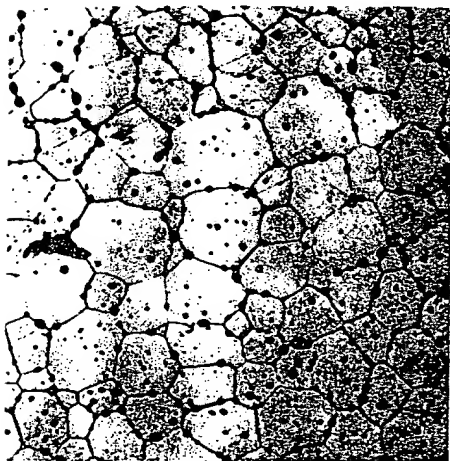


Fig. 10.5. Polycrystalline CaF_2 illustrating normal grain growth. Average angle at grain junctures is 120° .

10.10)

d that
10.6).
half,

usually falling between 0.1 and 0.5. This may occur for several reasons, one being that d_0 is not a large amount smaller than d ; another common reason is that inclusions or solute segregation or sample size inhibits grain growth.

A somewhat different approach is to define a grain-boundary mobility B_i such that the boundary velocity v is proportional to the applied driving force F_i resulting from boundary curvature:

$$v = B_i F_i \quad (10.11a)$$

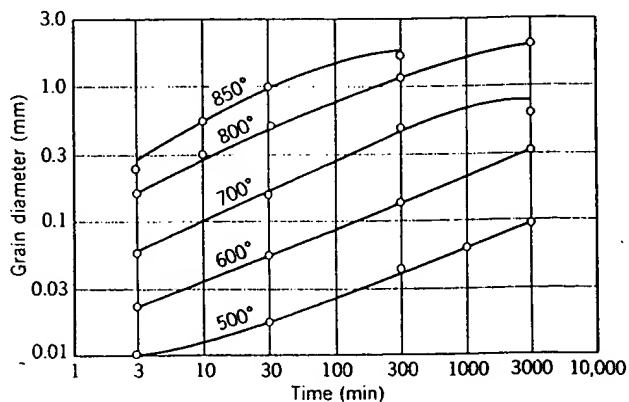


Fig. 10.6. Log grain diameter versus log time for grain growth in pure α -brass. From J. E. Burke.

of the
ix, and
idicate

For the atomic-jump mechanism illustrated in Fig. 10.3, the boundary mobility is given by the atomic mobility divided by the number of atoms involved, n_a :

$$B_i = \frac{B_a}{n_a} = \left(\frac{D_b}{kT} \right) \left(\frac{\Omega}{Sw} \right) \quad (10.11b)$$

where D_b is the grain-boundary diffusion coefficient, Ω is the atomic volume, S is the boundary area, and w is the boundary width. Since the average boundary velocity is equal to v and the driving force is inversely proportional to grain size, a grain-growth law of the form of Eqs. 10.9 and 10.10 results. However, as discussed in Chapter 5, the actual structure of a ceramic grain boundary is not quite so simple as pictured in deriving Eqs. 10.8 and 10.11b. Even for a completely pure material there is a space-charge atmosphere of lattice defects associated with the boundary and usually solute segregation as well, as shown in Figs. 5.11, 5.12, 5.17, and 5.18. The effect of this lattice defect and impurity atmosphere is to sharply reduce the grain-boundary velocity at low driving forces, as shown in Fig. 10.7 and analysed by J. Cahn* and K. Lücke and H. D. Stuwe.† The influence of this atmosphere becomes stronger as the grain

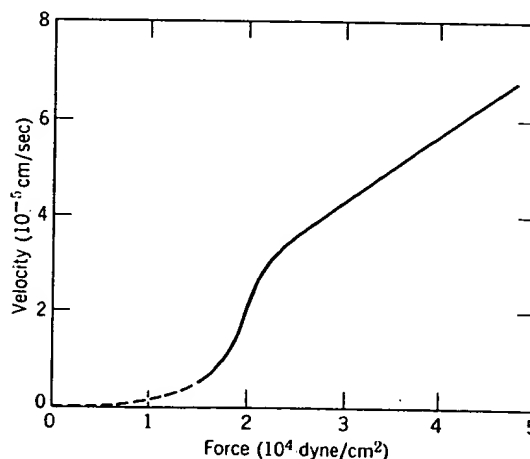


Fig. 10.7. Variation of boundary velocity v with driving force F at 750°C for a 20° tilt boundary in NaCl. From R. C. Sun and C. L. Bauer, *Acta Met.*, 18, 639 (1970).

size increases, the solute segregate concentration increases, and the average boundary curvature decreases. Additions of MgO to Al_2O_3 , $CaCl_2$

**Acta Met.*, 10, 789 (1962).

†*Acta Met.*, 19, 1087 (1971).

to KCl
proved

When
specim
when tl
to form
bounda
occurs.
movem
bounda
decrea
area of
pull it
includ
insuffi
It has l

where
and f_d
only a
creases
For
attache
Another

boundary
of atoms

(10.11b)

ie atomic
Since the
inversely
s. 10.9 and
ructure of
1 deriving
there is a
boundary
5.12, 5.17,
here is to
forces, as
and H. D.
the grain

to KCl and of ThO₂ to Y₂O₃ in amounts below the solubility limit have proved effective as grain-growth inhibitors.

When grains grow to such a size that they are nearly equal to the specimen size, grain growth is stopped. In a rod sample, for example, when the grain size is equal to the rod diameter, the grain boundaries tend to form flat surfaces normal to the axis so that the driving force for boundary migration is eliminated and little subsequent grain growth occurs. Similarly, inclusions increase the energy necessary for the movement of a grain boundary and inhibit grain growth. If we consider a boundary such as the one illustrated in Fig. 10.8, the boundary energy is decreased when it reaches an inclusion proportional to the cross-sectional area of the inclusion. The boundary energy must be increased again to pull it away from the inclusion. Consequently, when a number of inclusions are present on a grain boundary, its normal curvature becomes insufficient for continued grain growth after some limiting size is reached. It has been found that this size is given by

$$d_l \approx \frac{d_i}{f_{a_i}} \quad (10.12)$$

where d_l is the limiting grain size, d_i is the particle size of the inclusion, and f_{a_i} is the volume fraction of inclusions. Although this relationship is only approximate, it indicates that the effectiveness of inclusions increases as their particle size is lowered and the volume fraction increases.

For the process illustrated in Fig. 10.8, the boundary approaches, is attached to, and subsequently breaks away from a second-phase particle. Another possibility is that the grain boundary drags along the particle

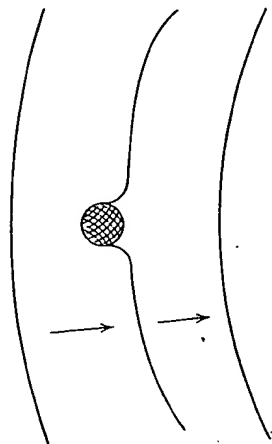


Fig. 10.8. Changing configuration of a boundary while passing an inclusion.

for a 20° tilt
(70).

s, and the
l₂O₃, CaCl₂

which remains attached to the boundary as it moves. This requires material transport across the particle, which may occur by interface or surface or volume diffusion, by viscous flow, or by solution (precipitation in a liquid or glass inclusion), or by evaporation (condensation in a gas inclusion). We can define an inclusion particle mobility B_p , relating the driving force and particle velocity $v_p = B_p F_p$ in the same way as has been done for the boundary (Eq. 10.11b) and for atomic diffusion in Chapter 6. When the inclusion is dragged by the boundary, their velocities are identical; in the case in which $B_p \ll B_b$ we can neglect the intrinsic boundary mobility, and the resulting grain-boundary velocity is controlled by the driving force on the boundary together with the mobility and number of inclusions per grain boundary, p :

$$v_b = \frac{B_p F_b}{p} \quad (10.13)$$

The inclusion particle moves along with the boundary, gradually becoming concentrated at boundary intersections and agglomerating into larger particles as grain growth proceeds. This is illustrated for the special case of pore agglomeration in Figs. 10.9 and 10.10.

Thus, second-phase inclusions can either (1) move along with boundaries, offering little impedance; (2) move along with boundaries, with the inclusion mobility controlling the boundary velocity; or (3) be so immobile that the boundary pulls away from the inclusion, depending on the relative values of the boundary driving force (inversely proportional to grain size), the boundary mobility (Fig. 10.7), and the inclusion particle mobility, which, depending on the assumed mechanism and particle shape, may be proportional to r_p^{-2} , r_p^{-3} , or r_p^{-4} .^{*} As grain growth proceeds, the driving force diminishes, and any inclusions dragged along by the boundary increase in size so that their mobility decreases. As a result, the exact way in which second-phase inclusions inhibit grain growth not only depends on the properties of the particular system but also can easily change during the grain-growth process. Sorting out these effects requires a careful evaluation of the microstructure evolution in combination with the kinetics of grain growth and a detailed knowledge of system properties. Inhibition of grain growth by solid second-phase inclusions has been observed for MgO additions to Al_2O_3 , for CaO additions to ThO_2 , and in other systems.

A second phase that is always present during ceramic sintering and in almost all ceramic products prepared by sintering is residual porosity

^{*}P. G. Shewmon, *Trans. A.I.M.E.*, 230, 1134 (1964); M. F. Ashby and R. M. A. Centamore, *Acta Met.*, 16, 1081 (1968).

Fig.
agglc

rem
com
(inte
sam
(inte
part
by 1
glon
early
forc
clus
resu
large
usua
gro

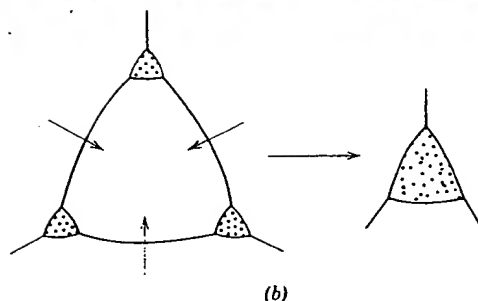
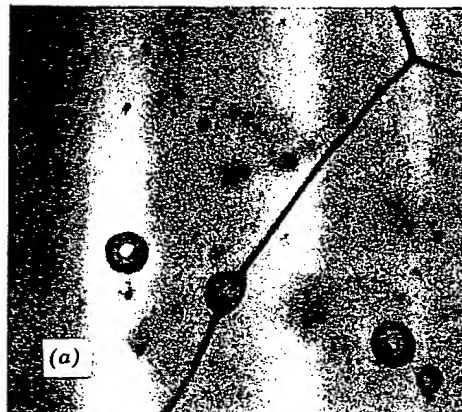


Fig. 10.9. (a) Pore shape distorted from spherical by moving boundary and (b) pore agglomeration during grain growth.

remaining from the interparticle space present in the initial powder compact. This porosity is apparent both on the grain boundaries (intergranular) and within the grains (intragranular) in the sintered CaF_2 sample shown in Fig. 10.5. It is present almost entirely at the grain corners (intergranular) in the sintered UO_2 samples shown in Fig. 10.10. As with particulate inclusions, pores on the grain boundaries may be left behind by the moving boundary or migrate with the boundary, gradually agglomerating at grain corners, as illustrated in Figs. 10.9 and 10.10. In the early stages of sintering, when the boundary curvature and the driving force for boundary migration are high, pores are often left behind, and a cluster of small pores in the center of a grain is a commonly observed result (see Fig. 10.5). In the later stages of sintering, when the grain size is larger and the driving force for boundary migration is lower, it is more usual for pores to be dragged along by the boundary, slowing grain growth.

s requires
terface or
ecipitation
n in a gas
elating the
s has been
Chapter 6.
cities are
e intrinsic
controlled
bility and

(10.13)

ly becom-
nto larger
ecial case

with boun-
s, with the
be so im-
ing on the
rtional to
n particle
d particle
proceeds,
ng by the
result, the
not only
can easily
s requires
tion with
n proper-
has been
 O_2 , and in

ng and in
porosity

Centamore,

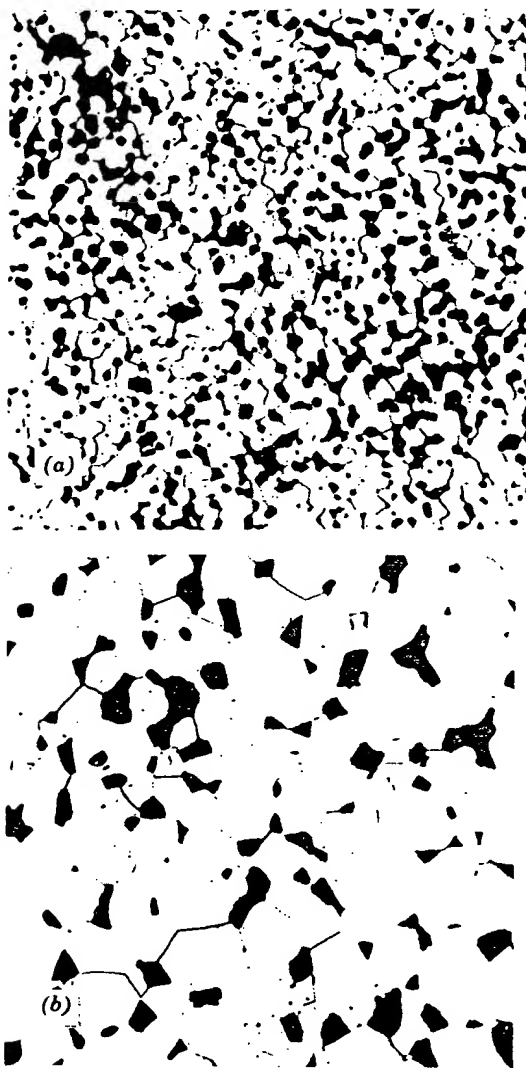


Fig. 10.10. Grain growth and pore growth in sample of UO_2 after (a) 2 min, 91.5% dense, and (b) 5 hr, 91.9% dense, at 1600°C ($400\times$). From Francois and Kingery.

Another factor that may restrain grain growth is the presence of a liquid phase. If a small amount of a boundary liquid is formed, it tends to slow grain growth, since the driving force is reduced and the diffusion path is increased. There are now two solid-liquid interfaces, and the driving force is the difference between them, that is, $(1/r_1 + 1/r_2)_A - (1/r_1 + 1/r_2)_B$, which

is smaller than the driving force for grain growth. Also, the precipitation of a second phase, even, this case, the presence of a liquid phase, as discussed in the next section, enhance secondary recrystallization. The amounts of secondary recrystallization described in the next section are a function of the amount of liquid phase present.

Secondary recrystallization, sometimes called abnormal grain growth, occurs when some grains grow at the expense of others. A grain that has many small pores and a high surface energy will grow at the expense of a grain that has a lower surface energy and fewer pores. This is shown in Fig. 10.11, where a uniform grain structure has evolved into a structure with a few large grains and many small grains.

Secondary recrystallization is a grain growth process. Under these conditions, the driving force for grain growth is the reduction of surface energy. The driving force is with high surface energy grains. The material resistance to grain growth is the grain boundary energy. The grain growth has much larger driving force than grain growth. It is determined by the grain boundary energy and the grain boundary formation energy. The grain size of secondary recrystallization is much larger than the grain size of primary recrystallization, even though the driving force is smaller.

Secondary recrystallization in ceramics is a process of secondary recrystallization. The resultant structure is a structure with a few large grains and many small grains.

is smaller than either alone; in addition, if the liquid wets the boundary, the interface energy must be lower than the pure-grain-boundary energy. Also, the process of solution, diffusion through a liquid film, and precipitation is usually slower than the jump across a boundary. However, this case is more complex in that grain growth may be enhanced by the presence of a reactive liquid phase during the densification process, as discussed in Section 10.4. In addition, a very small amount of liquid may enhance secondary recrystallization, as discussed later, whereas larger amounts of liquid phase may give rise to the grain-growth process described in Chapter 9. In practice, it is found that addition of a moderate amount of silicate liquid phase to aluminum oxide prevents the extensive grain growth which frequently occurs with purer materials.

Secondary Recrystallization. The process of secondary recrystallization, sometimes called discontinuous or exaggerated grain growth, occurs when some small fraction of the grains grow to a large size, consuming the uniform-grain-size matrix. Once a single grain grows to such a size that it has many more sides than the neighboring grains (such as the grain with fifty sides illustrated in Fig. 10.4), the curvature of each side increases, and it grows more rapidly than the smaller grains with fewer sides. The increased curvature on the edge of a large grain is particularly evident in Fig. 10.11, which shows a large alumina crystal growing at the expense of a uniform-particle-size matrix.

Secondary crystallization is particularly likely to occur when continuous grain growth is inhibited by the presence of impurities or pores. Under these conditions the only boundaries able to move are those with a curvature much larger than the average; that is, the exaggerated grains with highly curved boundaries are able to grow, whereas the matrix material remains uniform in grain size. The rate of growth of the large grains is initially dependent on the number of sides. However, after growth has reached the point at which the exaggerated grain diameter is much larger than the matrix diameter, $d_g \gg d_m$, the curvature is determined by the matrix grain size and is proportional to $1/d_m$. That is, there is an induction period corresponding to the increased growth rate and the formation of a grain large enough to grow at the expense of the constant-grain-size matrix. Therefore, the growth rate is constant as long as the grain size of the matrix remains unchanged. Consequently, the kinetics of secondary recrystallization is similar to that of primary recrystallization, even though the nature of the nucleation and driving force is different.

Secondary recrystallization is common for oxide, titanate, and ferrite ceramics in which grain growth is frequently inhibited by minor amounts of second phases or by porosity during the sintering process. A typical resultant structure is illustrated for barium titanate in Fig. 10.12, and the

11.5% dense,

of a liquid
ds to slow
on path is
ving force
2)B, which

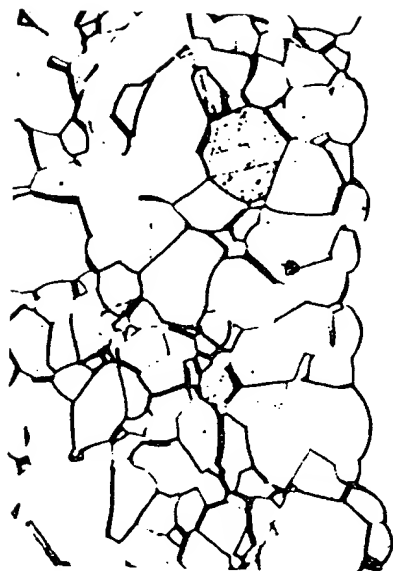


Fig. 10.11. Growth of a large Al_2O_3 crystal into a matrix of uniformly sized grains (495 \times). Compare with Fig. 10.4. Courtesy R. L. Coble.

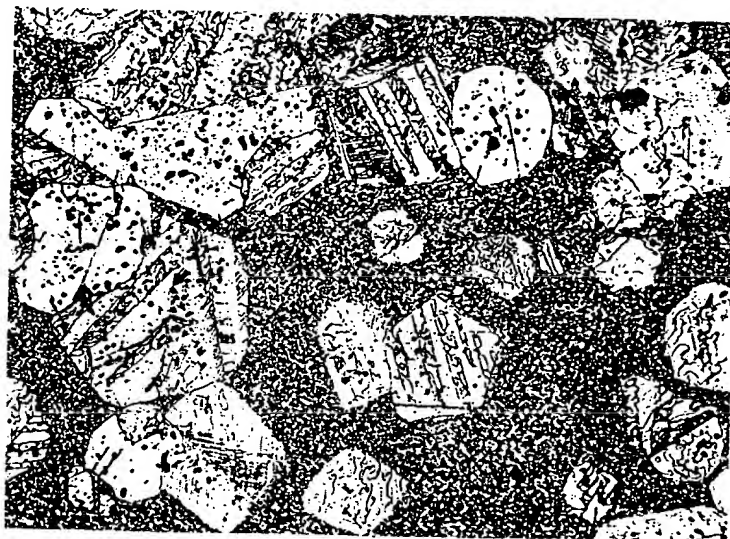
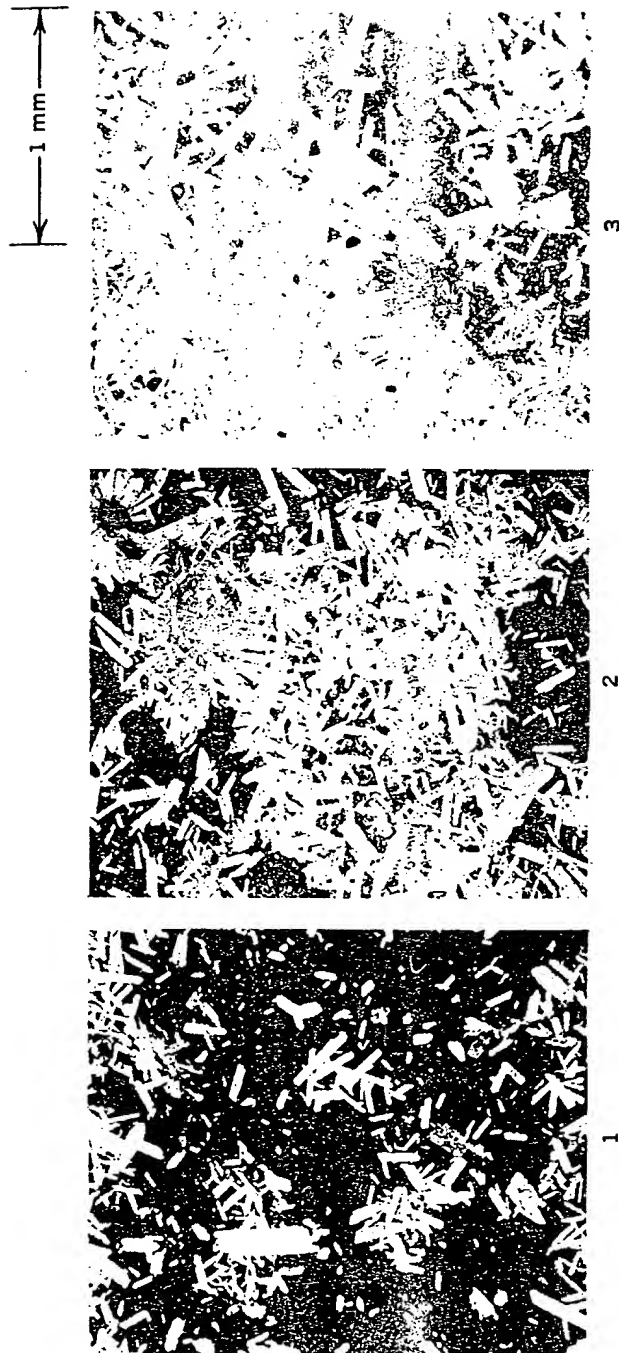


Fig. 10.12. Large grains of barium titanate growing by secondary recrystallization from a fine-grained matrix (250 \times). Courtesy R. C. DeVries.

from a

(495X).



Time at 1560°C (hr)

Fig. 10.13. Large grains of Al_2O_3 growing by secondary recrystallization from a fine-grained matrix. Courtesy I. B. Outler, in reference 5.

progressive growth of aluminum oxide crystals during secondary recrystallization is illustrated in Fig. 10.13.

When polycrystalline bodies are made from fine powder, the extent of secondary recrystallization depends on the particle size of the starting material. Coarse starting material gives a much smaller relative grain growth, as illustrated in Fig. 10.14 for beryllia. This is caused by both the rate of nucleation and the rate of growth. There are almost always present in the fine-grained matrix a few particles of substantially larger particle size than the average; these can act as embryos for secondary recrystallization, since already $d_s > d_m$, and growth proceeds to a rate proportional to $1/d_m$. In contrast, as the starting particle size increases, the chances of grains being present which are much larger in particle size than the average are much decreased, and consequently the nucleation of secondary recrystallization is much more difficult; the growth rate, proportional to $1/d_m$, is also smaller. In the data shown in Fig. 10.14, material having a starting particle size of 2 microns grows to a final particle size of about 50 microns, whereas material with an initial particle size of 10 microns shows a final grain size of only about 25 microns. This result of a much larger final grain size for a smaller initial particle size would be very puzzling if the process of secondary recrystallization was not known to occur.

Secondary recrystallization has been observed to occur with the boundaries of the large grains apparently perfectly straight (Fig. 10.15). Here the previous discussion of the surface tension and curvature of the phase boundary does not apply directly. That is, the boundary energy is

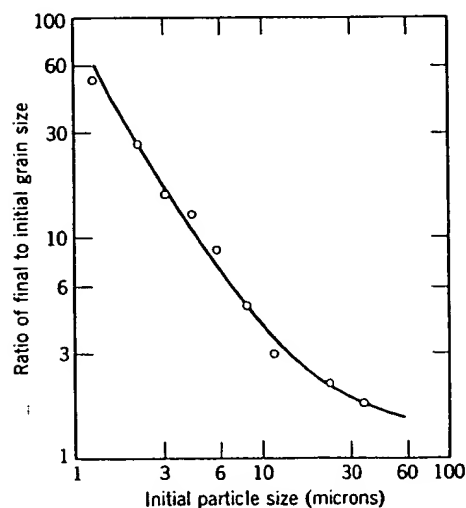


Fig. 10.14. Relative grain growth during secondary recrystallization of BeO heated $2\frac{1}{2}$ hr at 2000°C . From P. Duwez, F. Odell, and J. L. Taylor, *J. Am. Ceram. Soc.*, 32, 1 (1949).

not independent of surface energy. A small concentration of boundary plane with lower surface energy face material immediately boundaries of the system, amount of 1 and this kind of previous

Secondary recrystallization produces resultant polycrystalline mechanical properties improved polycrystalline literature as this is not true oxide with texture so that has left almost

Fig. 10.15. (a) straight, when
Courtesy R. I.

not independent of crystal directions, and the growth planes are those of low surface energy. These structures all seem to occur in systems having a small concentration of impurity which gives rise to a small amount of a boundary phase. The driving force for secondary recrystallization is the lower surface energy of the large grain compared with the high-surface-energy faces or small radius of curvature of adjacent grains. Transfer of material under these conditions can only occur when there is an intermediate boundary phase separating the surfaces of the small and large grains. The amount of second phase present tends to increase at the boundaries of the large crystals compared with that at other boundaries in the system, and a large grain continues to grow once it is initiated. If the amount of boundary phase is increased, however, normal grain growth and this kind of secondary recrystallization are both inhibited, as discussed previously.

Secondary recrystallization affects both the sintering of ceramics and resultant properties. Excessive grain growth is frequently harmful to mechanical properties (see Sections 5.5 and 15.5). For some electrical and magnetic properties either a large or a small grain size may contribute to improved properties. Occasionally grain growth has been discussed in the literature as if it were an integral part of the densification process. That this is not true can best be seen from Fig. 10.16. A sample of aluminum oxide with an initial fine pore distribution was heated to a high temperature so that secondary recrystallization occurred. The recrystallization has left almost the same amount of porosity as was present in the initial

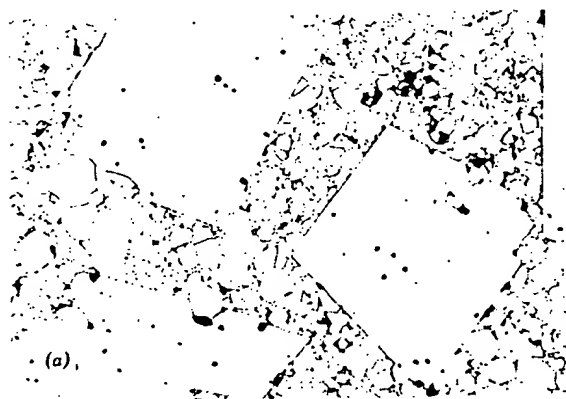


Fig. 10.15. (a) Idiomorphic grains in a polycrystalline spinel. The large grain edges appear straight, whereas the shape of the small grains is controlled by surface tension (350 \times). Courtesy R. L. Coble.

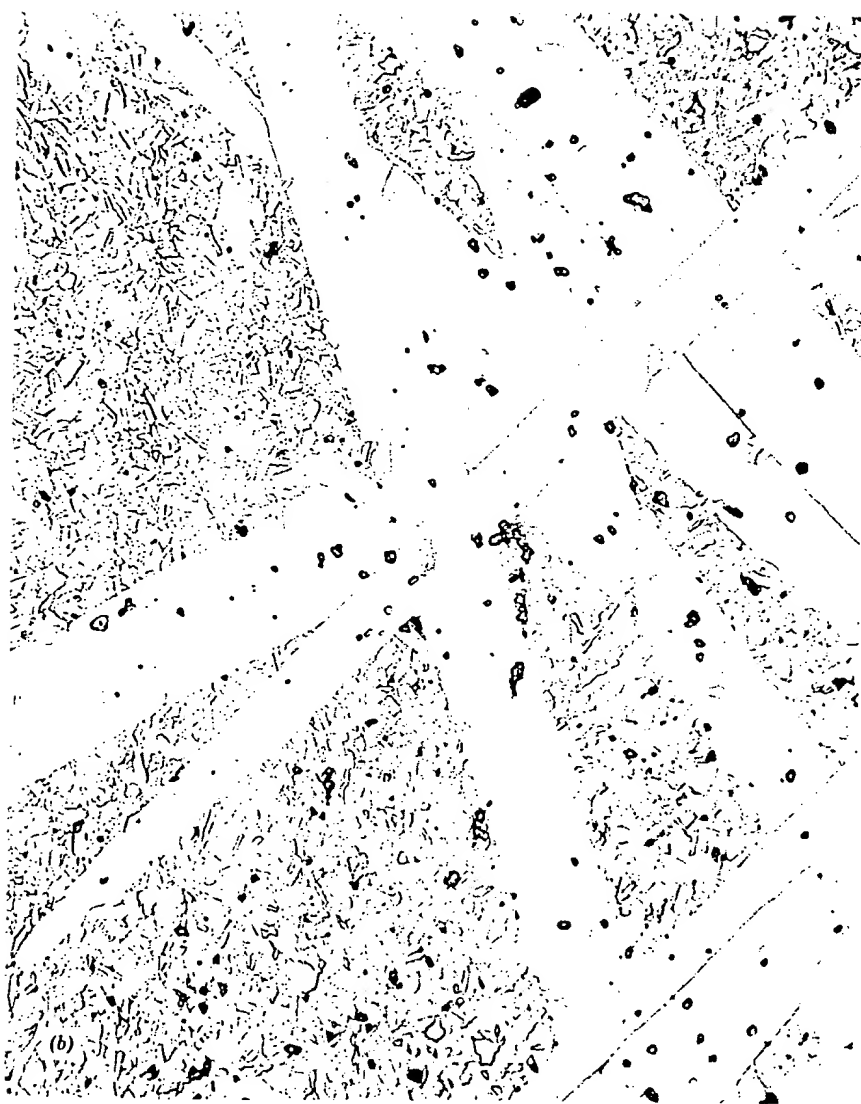


Fig. 10.15 (Continued). (b) Idiomorphic grains of α -6H SiC in a β -SiC matrix (1000 \times).

compact. Elimination of porosity is a related but separate subject and is considered in following sections. An application in which secondary recrystallization has been useful is in the development of preferred orientation on firing of the magnetically hard ferrite, $\text{BaFe}_{12}\text{O}_{19}$.^{*} For this

^{*}A. L. Stuijts, *Trans. Brit. Ceram. Soc.*, 55, 57 (1956).

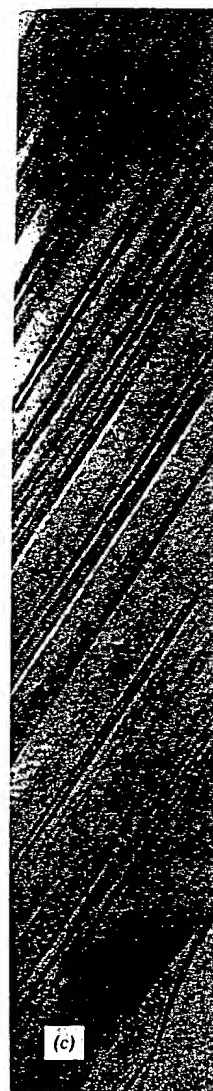


Fig. 10.15 (Continued)

magnetic material degree of preferred orientation of powdered material to a high magnetic alignment after l



Fig. 10.15 (Continued). (c) Detail of boundary (75,000 \times). Courtesy S. Prochazka.

magnetic material it is desirable to obtain a high density as well as a high degree of preferred orientation in the sintered product. Particles of the powdered material can be oriented to a considerable extent by subjecting them to a high magnetic field while forming. On sintering there was a 57% alignment after heating at 1250°C. On further heating at 1340°C the

rix (1000 \times).

ject and is
secondary
preferred
* For this

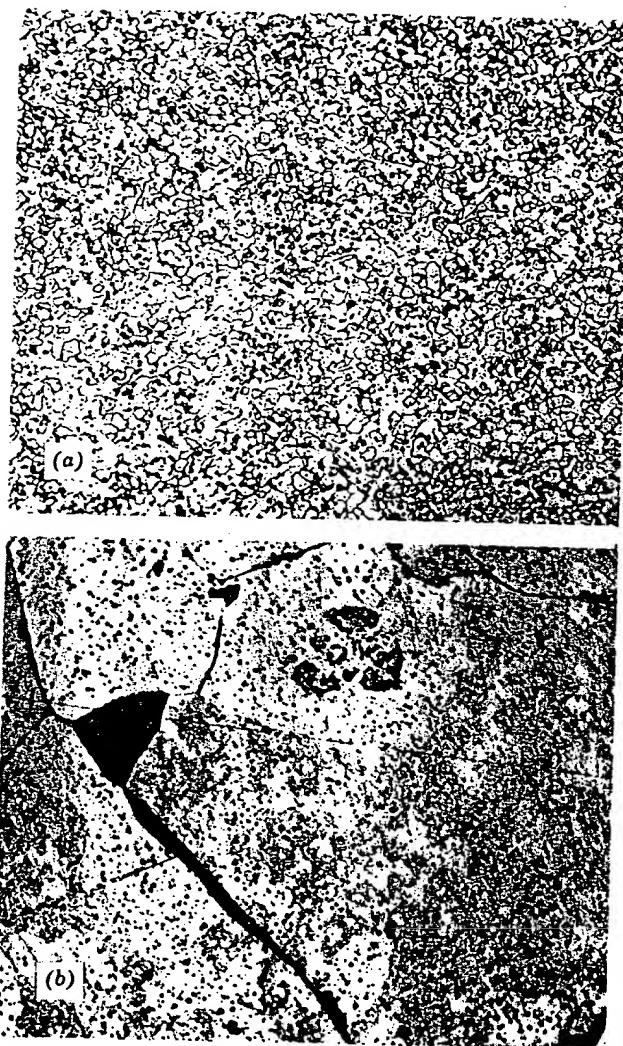


Fig. 10.16. A specimen of alumina (a) sintered 1 hr at 1800°C and (b) heated 1 hr at 1900°C to give secondary recrystallization. Note that the pore spacing has not changed. Courtesy J. E. Burke.

preferred orientation increased to 93% alignment, corresponding to the structural change brought about by secondary recrystallization. It seems apparent that the few large grains in the starting material are more uniformly aligned than the fine surrounding material. These grains serve as nuclei for the secondary recrystallization process and give rise to a highly oriented final product.

10.2 Solid-State

Changes that occur in grain size and shape. In Section 10.1, the following section, the change in grain size, that is, the change in grain size of a porous compact, before and after sintering, is separated by the change in grain size of a particular material. Properties such as strength, which are desirable to eliminate in applications, it may be that the gas permeability transfer of material of changes that are present can change. These changes necessarily change the shape of the pores, becoming more spherical.

Driving Force for densification is the free energy by which the process takes place with

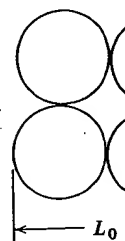


Fig. 10.17.

10.2 Solid-State Sintering

Changes that occur during the firing process are related to (1) changes in grain size and shape, (2) changes in pore shape, and (3) changes in pore size. In Section 10.1 we concentrated on changes in grain size; in this and the following section we are mainly concerned with changes in porosity, that is, the changes taking place during the transformation of an originally porous compact to a strong, dense ceramic. As formed, a powder compact, before it has been fired, is composed of individual grains separated by between 25 and 60 vol% porosity, depending on the particular material used and the processing method. For maximizing properties such as strength, translucency, and thermal conductivity, it is desirable to eliminate as much of this porosity as possible. For some other applications it may be desirable to increase this strength without decreasing the gas permeability. These results are obtained during firing by the transfer of material from one part of the structure to the other. The kind of changes that may occur are illustrated in Fig. 10.17. The pores initially present can change shape, becoming channels or isolated spheres, without necessarily changing in size. More commonly, however, both the size and shape of the pores present change during the firing process, the pores becoming more spherical in shape and smaller in size as firing continues.

Driving Force for Densification. The free-energy change that gives rise to densification is the decrease in surface area and lowering of the surface free energy by the elimination of solid-vapor interfaces. This usually takes place with the coincidental formation of new but lower-energy

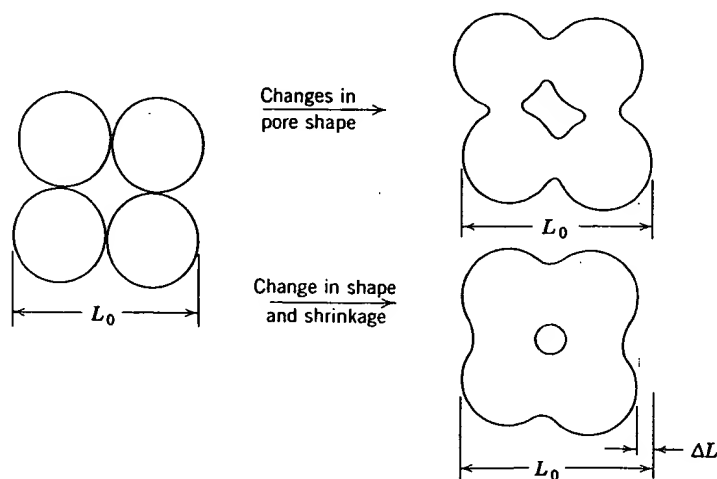


Fig. 10.17. Changes in pore shape do not necessarily require shrinkage.

solid-solid interfaces. The net decrease in free energy occurring on sintering a 1-micron particle size material corresponds to an energy decrease of about 1 cal/g. On a microscopic scale, material transfer is affected by the pressure difference and changes in free energy across a curved surface. These changes are due to the surface energy and have been discussed in Chapter 5 and referred to in Section 10.1. If the particle size, and consequently the radius of curvature, is small, these effects may be of a substantial magnitude. As indicated in Chapter 5, they become large when the radius of curvature is less than a few microns. This is one of the major reasons why much ceramic technology is based on and depends on the use of fine-particle materials.

Most of the insight into the effect of different variables on the sintering process has come from considering simple systems and comparing experimental data with simple models. Since our major aim is to be sure we understand the importance of different variables in traditional or new systems, we use this method here. Since the driving force is the same (surface energy) in all systems, considerable differences in behavior in various types of systems must be related to different mechanisms of material transfer. Several can be imagined—evaporation and condensation, viscous flow, surface diffusion, grain-boundary or lattice diffusion, and plastic deformation are among those that occur to us. Of these, diffusion and viscous flow are important in the largest number of systems; evaporation-condensation is perhaps the easiest to visualize.

Evaporation-Condensation. During the sintering process there is a tendency for material transfer because of the differences in surface curvature and consequently the differences in vapor pressure at various parts of the system. Material transfer brought about in this way is only important in a few systems; however, it is the simplest sintering process to treat quantitatively. We derive the sintering rate in some detail, since it provides a sound basis for understanding more complex processes.

Let us consider the initial stages of the process when the powder compact is just beginning to sinter and concentrate on the interaction between two adjacent particles (Fig. 10.18). At the surface of the particle there is a positive radius of curvature so that the vapor pressure is somewhat larger than would be observed for a flat surface. However, just at the junction between particles there is a neck with a small negative radius of curvature and a vapor pressure an order of magnitude lower than that for the particle itself. The vapor-pressure difference between the neck area and the particle surface tends to transfer material into the neck area.

We can calculate the rate at which the bonding area between particles increases by equating the rate of material transfer to the surface of the

Fig. 10.18. I

lens between
pressure of
of the sur
(Kelvin) eq

where p_1 is
molecular v
radius is m
pressure di
tion, $\ln p_1/r$

where Δp
negative ra
the nearly 1
to the diffe
given by th

where α is
rate of con

From the g
at the conti

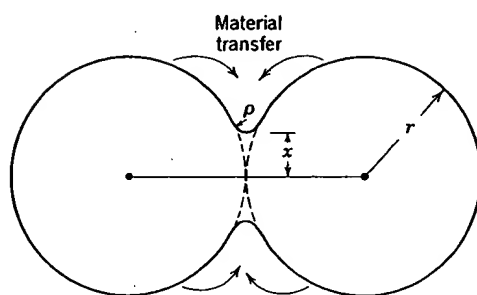


Fig. 10.18. Initial stages of sintering by evaporation-condensation.

lens between the spheres with the increase in its volume. The vapor pressure over the small negative radius of curvature is decreased because of the surface energy in accordance with the Thomson-Freundlich (Kelvin) equation discussed in Chapter 5:

$$\ln \frac{p_1}{p_0} = \frac{\gamma M}{dRT} \left(\frac{1}{\rho} + \frac{1}{x} \right) \quad (10.14)$$

where p_1 is the vapor pressure over the small radius of curvature, M is the molecular weight of the vapor, and d is the density. In this case the neck radius is much larger than the radius of curvature at the surface, ρ , and the pressure difference $p_0 - p_1$ is small. Consequently, to a good approximation, $\ln p_1/p_0$ equals $\Delta p/p_0$, and we can write

$$\Delta p = \frac{\gamma M p_0}{d \rho RT} \quad (10.15)$$

where Δp is the difference between the vapor pressure of the small negative radius of curvature and the saturated vapor in equilibrium with the nearly flat particle surfaces. The rate of condensation is proportional to the difference in equilibrium and atmospheric vapor pressure and is given by the Langmuir equation to a good approximation as

$$m = \alpha \Delta p \left(\frac{M}{2\pi RT} \right)^{1/2} \quad \text{g/cm}^2/\text{sec} \quad (10.16)$$

where α is an accommodation coefficient which is nearly unity. Then the rate of condensation should be equal to the volume increase. That is,

$$\frac{mA}{d} = \frac{dv}{dt} \quad \text{cm}^3/\text{sec} \quad (10.17)$$

From the geometry of the two spheres in contact, the radius of curvature at the contact points is approximately equal to $x^2/2r$ for x/r less than 0.3;

the area of the surface of the lens between spheres is approximately equal to $\pi^2 x^3/r$; the volume contained in the lenticular area is approximately $\pi x^4/2r$. That is,

$$\rho = \frac{x^2}{2r}; \quad A = \frac{\pi^2 x^3}{r}; \quad v = \frac{\pi x^4}{2r} \quad (10.18)$$

Substituting values for m in Eq. 10.16, A and v in Eq. 10.18 into Eq. 10.17 and integrating, we obtain a relationship for the rate of growth of the bond area between particles:

$$\frac{x}{r} = \left(\frac{3\sqrt{\pi}\gamma M^{3/2} p_0}{\sqrt{2} R^{3/2} T^{3/2} d^2} \right)^{1/3} r^{-2/3} t^{1/3} \quad (10.19)$$

This equation gives the relationship between the diameter of the contact area between particles and the variables influencing its rate of growth.

The important factor from the point of view of strength and other material properties is the bond area in relation to the individual particle size, which gives the fraction of the projected particle area which is bonded together—the main factor in fixing strength, conductivity, and related properties. As seen from Eq. 10.19, the rate at which the area between particles forms varies as the two-thirds power of time. Plotted on a linear scale, this decreasing rate curve has led to characterizations of *end point* conditions corresponding to a certain sintering time. This concept of an end point is useful, since periods of time for sintering are not widely changed; however, the same rate law is observed for the entire process (Fig. 10.19b).

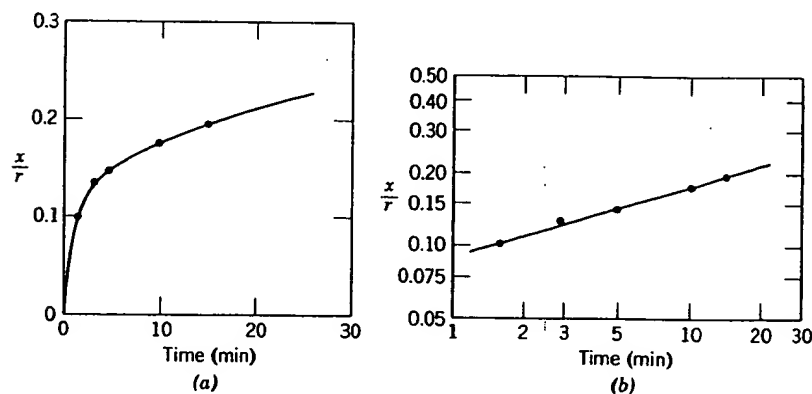


Fig. 10.19. (a) Linear and (b) log-log plots of neck growth between spherical particles of sodium chloride at 725°C.

If we c
such as
particles
particle
shrinkag
by vapo
changed.
propertie

The p
pore-sha
proportio
Since the
process
From a
control c
and the t
generally
condition

The n
fer is p
changes
particles

(a)

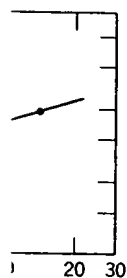
imately equal
approximately

(10.18)

into Eq. 10.17
th of the bond

(10.19)

of the contact
e of growth.
th and other
idual particle
rea which is
luctivity, and
hich the area
e. Plotted on
erizations of
g time. This
sintering are
for the entire



cal particles of

If we consider the changes in structure that take place during a process such as this, it is clear that the distance between centers of spherical particles (Fig. 10.18) is not affected by the transfer of material from the particle surface to the interparticle neck. This means that the total shrinkage of a row of particles, or of a compact of particles, is unaffected by vapor-phase-material transfer and that only the shape of pores is changed. This changing shape of pores can have an appreciable effect on properties but does not affect density.

The principal variables in addition to time that affect the rate of pore-shape change through this process are the initial particle radius (rate proportional to $1/r^{2/3}$) and the vapor pressure (rate proportional to $p_0^{1/3}$). Since the vapor pressure increases exponentially with temperature, the process of vapor-phase sintering is strongly temperature-dependent. From a processing point of view, the two main variables over which control can be exercised for any given material are the initial particle size and the temperature (which fixes the vapor pressure). Other variables are generally not easy to control, nor are they strongly dependent on conditions of use.

The negligible shrinkage corresponding to vapor-phase-material transfer is perhaps best illustrated in Fig. 10.20, which shows the shape changes that occur on heating a row of initially spherical sodium chloride particles. After long heating the interface contact area has increased; the

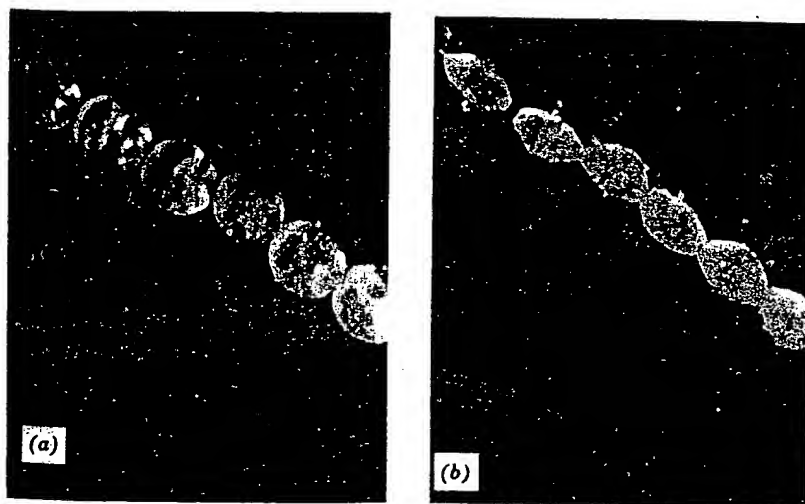


Fig. 10.20. Photomicrographs of sintering sodium chloride at 750°C: (a) 1 min; (b) 90 min.

particle diameter has been substantially decreased, but the distance between particle centers, that is, the shrinkage, has not been affected.

Vapor-phase-material transfer requires that materials be heated to a temperature sufficiently high for the vapor pressure to be appreciable. For micron-range particle sizes this requires vapor pressures in the order of 10^{-4} to 10^{-5} atm, a pressure higher than those usually encountered during sintering of oxide and similar phases. Vapor-phase transfer plays an important part in the changes occurring during treatment of halides such as sodium chloride and is important for the changes in configuration observed in snow and ice technology.

Solid-State Processes. The difference in free energy or chemical potential between the neck area and the surface of the particle provides a driving force which causes the transfer of material by the fastest means available. If the vapor pressure is low, material transfer may occur more readily by solid-state processes, several of which can be imagined. As shown in Fig. 10.21 and Table 10.1, in addition to vapor transport (process 3), matter can move from the particle surface, from the particle bulk, or from the grain boundary between particles by surface, lattice, or grain-boundary diffusion. Which one or more of these processes actually contributes significantly to the sintering process in a particular system depends on their relative rates, since each is a parallel method of lowering the free energy of the system (parallel reaction paths have been discussed in Chapter 9). There is a most significant difference between these paths for matter transport: the transfer of material from the surface to the neck by surface or lattice diffusion, like vapor transport, does not lead to any decrease in the distance between particle centers. That is, these processes do not result in shrinkage of the compact and a decrease in porosity. Only

Fig. 10.21.
Courtesy M.

Table 10.1. Alternate Paths for Matter Transport During the Initial Stages of Sintering^a

Mechanism Number	Transport Path	Source of Matter	Sink of Matter
1	Surface diffusion	Surface	Neck
2	Lattice diffusion	Surface	Neck
3	Vapor transport	Surface	Neck
4	Boundary diffusion	Grain boundary	Neck
5	Lattice diffusion	Grain boundary	Neck
6	Lattice diffusion	Dislocations	Neck

^aSee Fig. 10.21.

transfer of
between p
Let us c
to the nec
is exactly
vapor-pa
surface ar
The geom

The proce

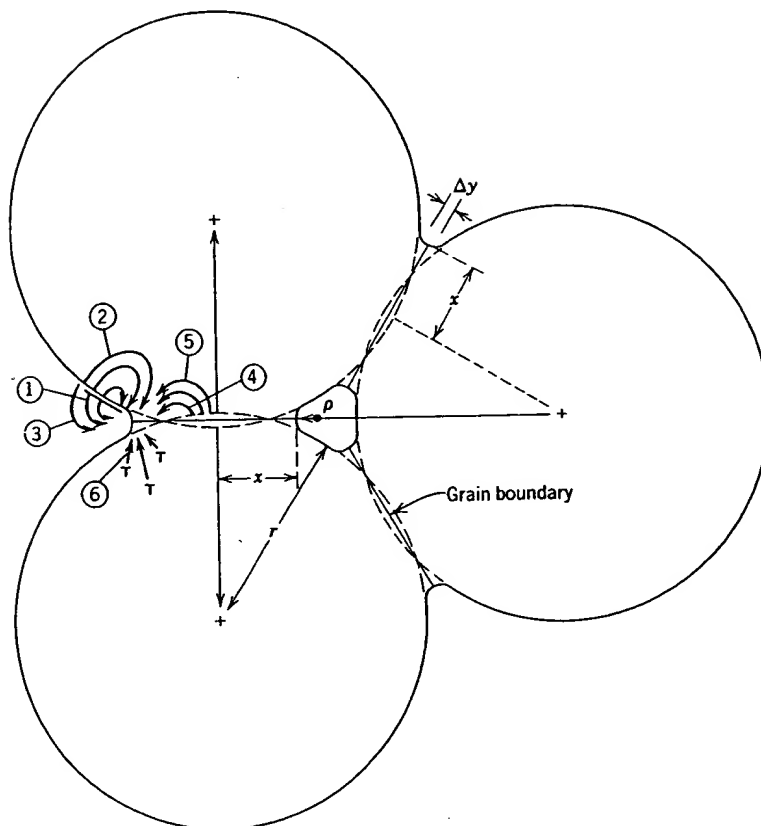


Fig. 10.21. Alternate paths for matter transport during the initial stages of sintering. Courtesy M. A. Ashby. (See Table 10.1.)

transfer of matter from the particle volume or from the grain boundary between particles causes shrinkage and pore elimination.

Let us consider mechanism 5, matter transport from the grain boundary to the neck by lattice diffusion. Calculation of the kinetics of this process is exactly analogous to determination of the rate of sintering by a vapor-phase process. The rate at which material is discharged at the surface area is equated to the increase in volume of material transferred. The geometry is slightly different:

$$\rho = \frac{x^2}{4r}; \quad A = \frac{\pi^2 x^3}{2r}; \quad V = \frac{\pi x^4}{4r} \quad (10.20)$$

The process can be visualized most easily by considering the rate of

migration of vacancies. In the same way that there are differences in vapor pressure between the surface of high negative curvature and the nearly flat surfaces, there is a difference in vacancy concentration. If c is the concentration of vacancies and Δc is the excess concentration over the concentration on a plane surface c_0 , then, equivalent to Eq. 10.15,

$$\Delta c = \frac{\gamma a^3 c_0}{kT\rho} \quad (10.21)$$

where a^3 is the atomic volume of the diffusing vacancy and k is the Boltzmann constant. The flux of vacancies diffusing away from the neck area per second per centimeter of circumferential length under this concentration gradient can be determined graphically and is given by

$$J = 4D_v \Delta c \quad (10.22)$$

Where D_v is the diffusion coefficient for vacancies, D_v equals $D^*/a^3 c_0$ if D^* is the self-diffusion coefficient. Combining Eqs. 10.22 and 10.21 with the continuity equation similar to Eq. 10.17, we obtain the result

$$\frac{x}{r} = \left(\frac{40\gamma a^3 D^*}{kT} \right)^{1/5} r^{-3/5} t^{1/5} \quad (10.23)$$

With diffusion, in addition to the increase in contact area between particles, there is an approach of particles centers. The rate of this approach is given by $d(x^2/2r)/dt$. Substituting from Eq. 10.23, we obtain

$$\frac{\Delta V}{V_0} = \frac{3 \Delta L}{L_0} = 3 \left(\frac{20\gamma a^3 D^*}{\sqrt{2}kT} \right)^{2/5} r^{-6/5} t^{2/5} \quad (10.24)$$

These results indicate that the growth of bond formation between particles increases as a one-fifth power of time (a result which has been experimentally observed for a number of metal and ceramic systems) and that the shrinkage of a compact densified by this process should be proportional to the two-fifths power of time. The decrease in densification rate with time gives rise to an apparent end-point density if experiments are carried out for similar time periods. However, when plotted on a log-log basis, the change in properties is seen to occur as expected from Eq. 10.24. Experimental data for sodium fluoride and aluminum oxide are shown in Fig. 10.22.

The relationships derived in Eqs. 10.23 and 10.24 and similar relationships for the alternate matter transport processes, which we shall not derive, are important mainly for the insight that they provide on the variables which must be controlled in order to obtain reproducible processing and densification. It is seen that the sintering rate steadily decreases with time, so that merely sintering for longer periods to obtain

GF

 $\frac{\Delta L}{L_0}$ $\frac{\Delta L}{L_0}$

0

0

Fig. 10.22. (Aluminum oxide compact)

improved
critical var
Control
roughly pr
diameter a
illustrated
even these
size is dec

differences in
ature and the
tration. If c is
centration over
to Eq. 10.15,

(10.21)

and k is the
from the neck
h under this
is given by

(10.22)

als D^*/a^3c_0 if
nd 10.21 with
result

(10.23)

area between
rate of this
, we obtain

(10.24)

tion between
ich has been
systems) and
ss should be
densification
experiments
plotted on a
pected from
um oxide are

ilar relation-
we shall not
vide on the
reproducible
rate steadily
ods to obtain

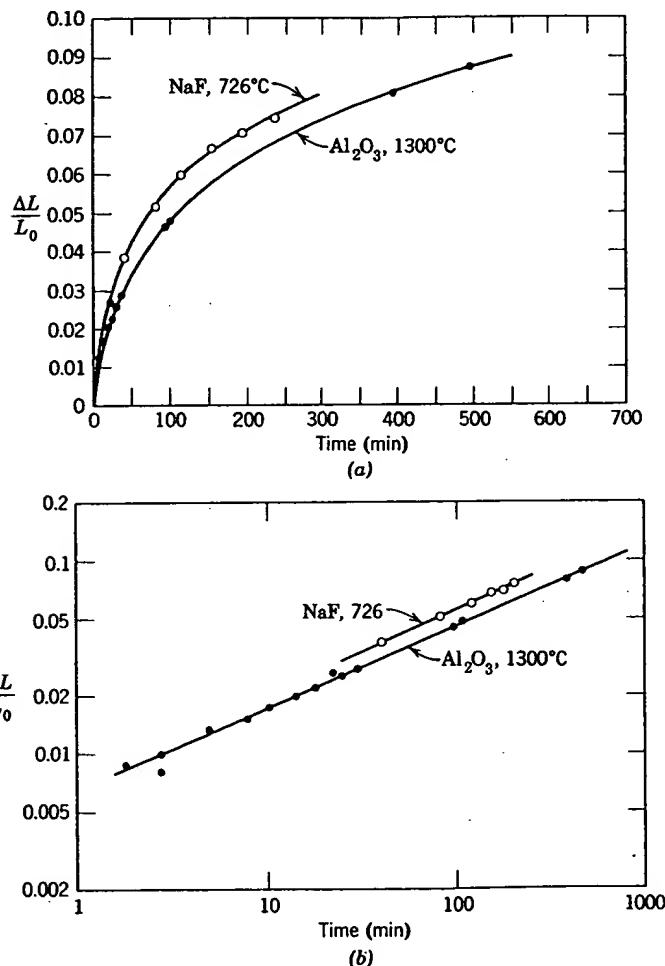


Fig. 10.22. (a) Linear and (b) log-log plots of shrinkage of sodium fluoride and aluminum oxide compacts. From J. E. Burke and R. L. Coble.

improved properties is impracticable. Therefore, time is not a major or critical variable for process control.

Control of particle size is very important, since the sintering rate is roughly proportional to the inverse of the particle size. The interface diameter achieved after sintering for a period of 100 hr at 1600°C is illustrated in Fig. 10.23 as a function of particle size. For large particles even these long periods do not cause extensive sintering; as the particle size is decreased, the rate of sintering is raised.

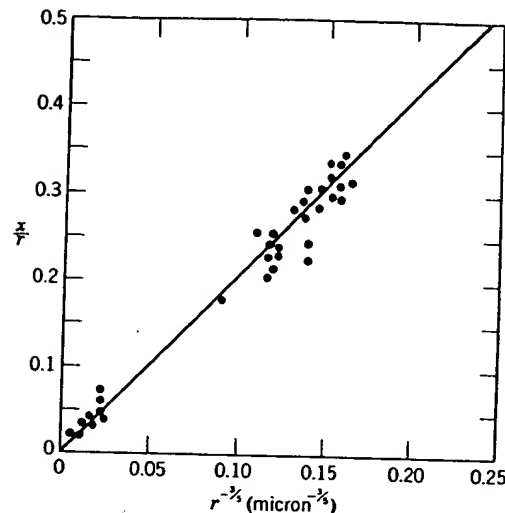


Fig. 10.23. Effect of particle size on the contact area growth in Al_2O_3 , heated 100 hr at 1600°C . From R. L. Coble.

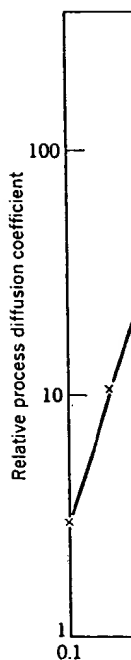
The other variable appearing in Eqs. 10.22 and 10.24 that is subject to analysis and some control is the diffusion coefficient; it is affected by composition and by temperature; the relative effectiveness of surfaces, boundaries, and volume as diffusion paths is affected by the microstructure. A number of relationships similar to Eqs. 10.23 and 10.24 have been derived, and it has been shown that surface diffusion is most important during early stages of sintering (these affect the neck diameter between particles but not the shrinkage or porosity); grain-boundary diffusion and volume diffusion subsequently become more important. In ionic ceramics, as discussed in Chapter 9, both the anion and the cation diffusion coefficients must be considered. In Al_2O_3 , the best studied material, oxygen diffuses rapidly along the grain boundaries, and the more slowly moving aluminum ion at the boundary or in the bulk controls the overall sintering rate. As discussed in Chapter 5, the grain-boundary structure, composition, and electrostatic charge are influenced strongly by temperature and by impurity solutes; as discussed in Chapter 6, the exact mechanism of grain-boundary diffusion remains controversial. Estimates of the grain-boundary-diffusion width from sintering data range from 50 to 600 Å. These complications require us to be careful not to overanalyze data in terms of specific numerical results, since the time or temperature dependence of sintering may be in accordance with several plausible models. In general the presence of solutes which enhance either

boundary or sintering. As coefficients sintering rate

In order to solid-state particle size temperature

As an example effect of titanium in a region processes as ally as Ti^{+3}

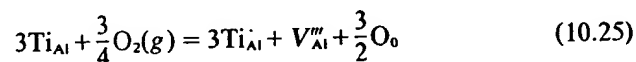
from which



boundary or volume diffusion coefficients enhance the rate of solid-state sintering. As discussed in Chapter 6, both boundary and volume diffusion coefficients are strongly temperature-dependent, which means that the sintering rate is strongly dependent on the temperature level.

In order to effectively control sintering processes which take place by solid-state processes, it is essential to maintain close control of the initial particle size and particle-size distribution of the material, the sintering temperature, the composition and frequently the sintering atmosphere.

As an example of the influence of solutes, Fig. 10.24 illustrates the effect of titania additions on the sintering rate of a relatively pure alumina in a region of volume diffusion. (Both volume and boundary diffusion processes are enhanced.) It is believed that Ti enters Al_2O_3 substitutionally as Ti^{+3} and Ti^{+4} (Ti_{Al} and Ti_{Al}''). At equilibrium



from which

$$K_1 = \frac{[\text{Ti}_{\text{Al}}]^3 [V_{\text{Al}}''']}{[\text{Ti}_{\text{Al}}]^3 [P_{\text{O}_2}]^{3/4}} \quad (10.26)$$

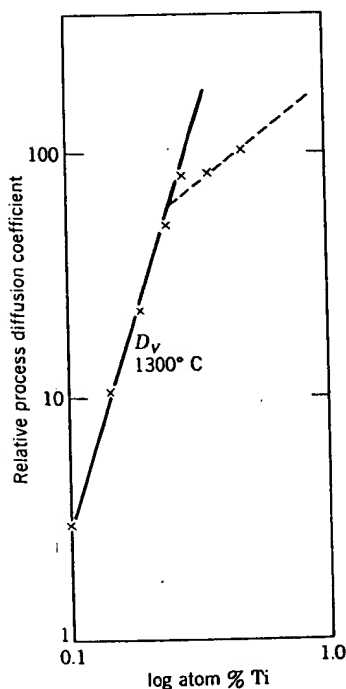


Fig. 10.24. Data for the relative sintering process diffusion coefficient with Ti additions to Al_2O_3 . $D\alpha[\text{Ti}]^3$. From R. D. Bagley, I. B. Cutler, and D. L. Johnson, *J. Am. Ceram. Soc.*, 53, 136 (1970); R. J. Brook, *J. Am. Ceram. Soc.*, 55, 114 (1972).

In the powders used, divalent impurities such as magnesium exceed in concentrations the intrinsic defect levels, so that overall charge neutrality at moderate titania levels is achieved by

$$[\text{Ti}_{\text{Al}}'] = [\text{Mg}_{\text{Al}}'] \quad (10.27)$$

and at constant impurity and oxygen pressure levels, combining Eqs. 10.26 and 10.27 gives

$$[V_{\text{Al}}'''] = K_2 [\text{Ti}_{\text{Al}}']^3 \quad (10.28)$$

Since the total Ti addition ($\text{Ti}_{\text{Al}} + \text{Ti}_{\text{Al}}'$) is much greater than the impurity levels, $[\text{Ti}]_{\text{Total}} \approx [\text{Ti}_{\text{Al}}']$ and $[V_{\text{Al}}'''] \approx K_2 [\text{Ti}]_{\text{Total}}^3$. The dependence of lattice defect concentrations on titania concentration is shown in Fig. 10.25 for the proposed model. As discussed in Chapter 6, the diffusion coefficient is proportional to the vacancy concentration; as a result the effect of this model is to anticipate an increase in the sintering rate proportional to the third power of titania concentration as experimentally observed (Fig. 10.24). At higher concentrations the dependence on titania concentration should become less steep, which is suggested by the sintering data.

Thus far our discussion of the variables influencing the sintering process has been based on the initial stages of the process, in which models are based on solid particles in contact. As the process continues, an intermediate microstructure forms in which the pores and solid are both continuous, followed by a later stage in which isolated pores are separated from one another. A number of analytical expressions have

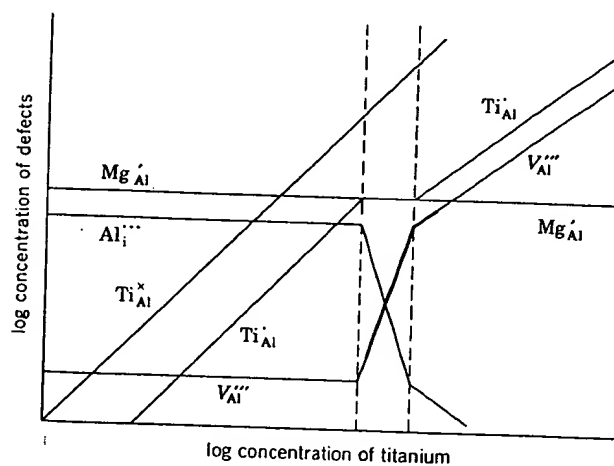


Fig. 10.25. Model for the dependence of defect concentrations on the Ti concentration in Al_2O_3 . From R. J. Brook, *J. Am. Ceram. Soc.*, 55, 114 (1972).

been deriv
processes li
mechanism
boundary a
spherical p

where D_v
concentrati
material-so
sort of anal

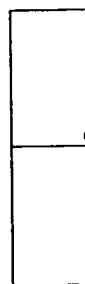


Fig. 10.26. more of the

with a large
diffusion
elimination
porosity. T
volume or
solute con
the geome
variety of

With fir
increase i
treatment
results fr
sinter rap
rapid grai
the bound

been derived from specific microstructural models for the transport processes listed in Table 10.1. In the later stages of the process only two mechanisms are important: boundary diffusion from sources on the boundary and lattice diffusion from sources on the boundary. For a nearly spherical pore the flux of material to a pore can be approximated as

$$J = 4\pi D_v \Delta c \left(\frac{rR}{R-r} \right) \quad (10.29)$$

where D_v is the volume diffusion coefficient, Δc is the excess vacancy concentration (Eq. 10.21), r is the pore radius, and R is the effective-material-source radius. The importance of microstructure in applying this sort of analysis to specific systems is illustrated in Fig. 10.26. For a sample

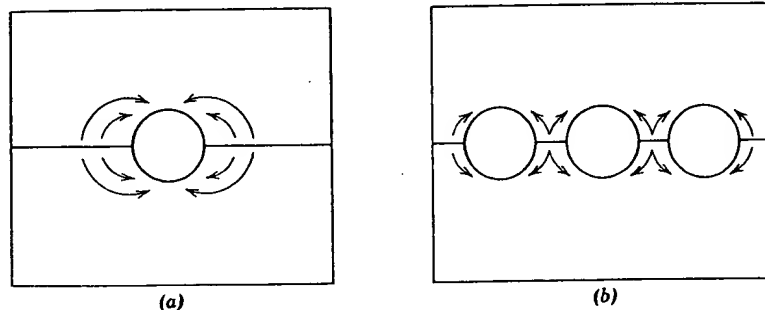


Fig. 10.26. The mean diffusion distance for material transport is smaller when there are more of the same size of pores in a boundary.

with a larger number of pores, all the same size, on a boundary the mean diffusion distance is smaller when there are more pores, and pore elimination is accomplished more quickly for the sample with the higher porosity. Thus, although the terms which influence the rate of sintering—volume or boundary diffusion coefficient (and therefore temperature and solute concentration) surface energy and pore size—are well established, the geometrical relationship of grain boundaries to the pores may have a variety of forms and is critical in determining what actually occurs.

With fine-grained materials such as oxides, it is usual to observe an increase in both grain size and pore size during the early stages of heat treatment, as illustrated for Lucalox alumina in Fig. 10.27. This partially results from the presence of agglomerates of the fine particles which sinter rapidly, leaving interagglomerate pores, and is partly due to the rapid grain growth during which pores are agglomerated by moving with the boundaries, as illustrated in Fig. 10.9. In cases in which agglomeration

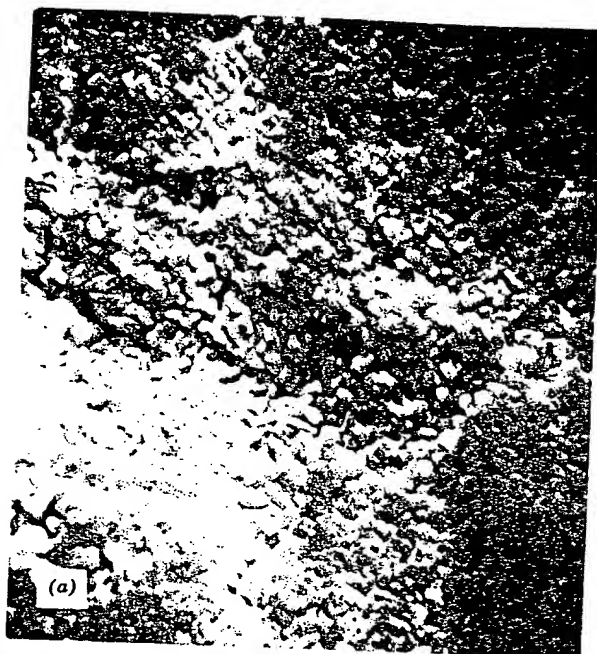


Fig. 10.27. Progressive development of microstructure in Lucalox alumina. Scanning electron micrographs of (a) initial particles in the compact (5000 \times), (b) after 1 min at 1700°C (5000 \times).

Fig. 10.27 (c and d) after variations in

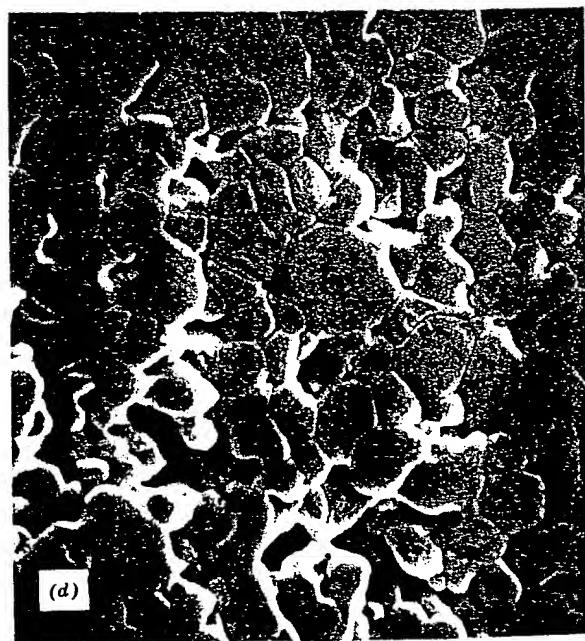
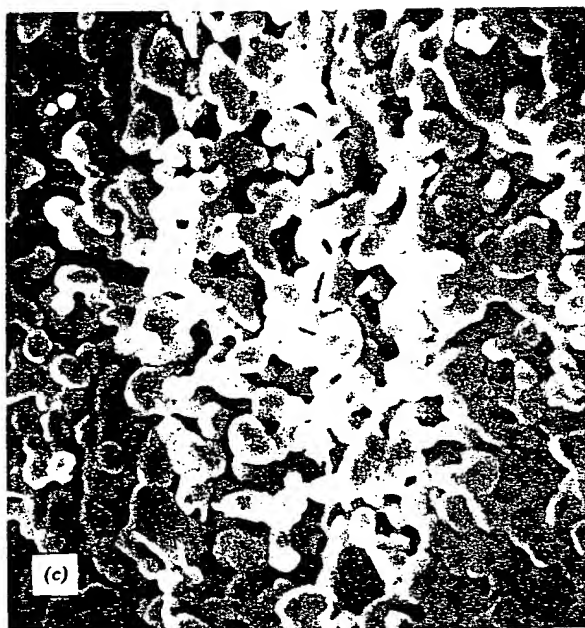


Fig. 10.27 (Continued) (c) Scanning electron micrographs after $2\frac{1}{2}$ min at 1700°C (5000 \times), and (d) after 6 min at 1700°C (5000 \times). Note that pores and grains increase in size, that there are variations in packing and in pore size, and that pores remain located between dense grains.

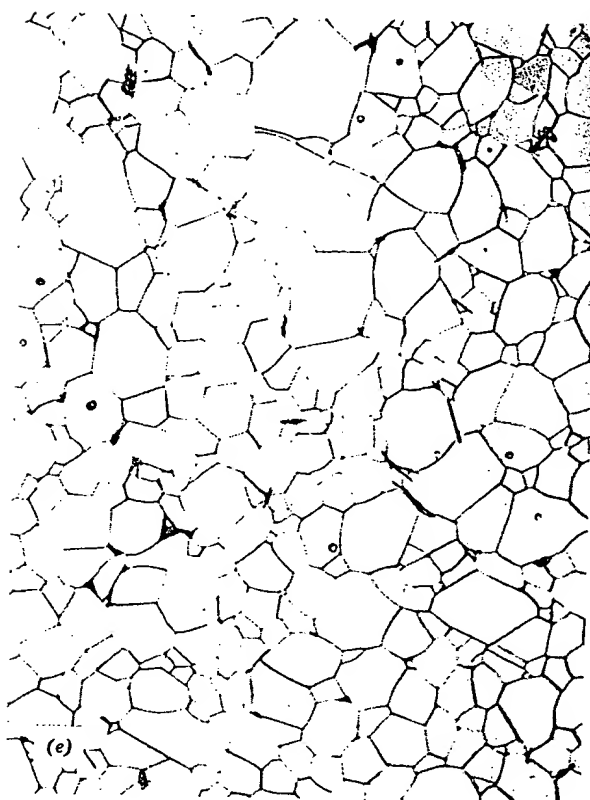


Fig. 10.27 (Continued) (e) The final microstructure is nearly porefree, with only a few pores located within grains (500 \times). Courtesy C. Greskovich and K. W. Lay.

of fine precipitated particles into clumps is severe, ball milling to break up the agglomerates leads to a remarkable increase in the sintering rate. Even minor variations in the original particle packing are exaggerated during the pore growth process; in addition, spaces between agglomerates and occasional larger voids resulting from the bridging of particles or agglomerates are present. As a result, during intermediate stages of the sintering process there is a range of pore sizes present, and the slower elimination of the larger pores leads to variations in pore concentration in the later stages of the sintering process, as illustrated in Fig. 10.28c.

In addition to local agglomerates and packing differences, pore-concentration variations in the later stages of sintering can result from particle-size variations in the starting material, from green density varia-

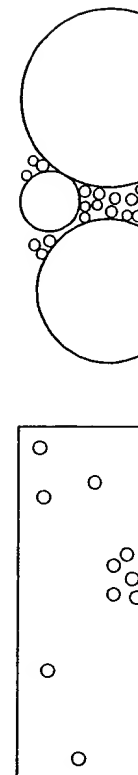


Fig. 10.28. Pore elimination near the die friction, (c) elimination near

tions caused by pore elimination during heating in pore concentration. That is, the adjacent grain orders of magnitude sintered oxide.

Not only residual pore thermodynamic

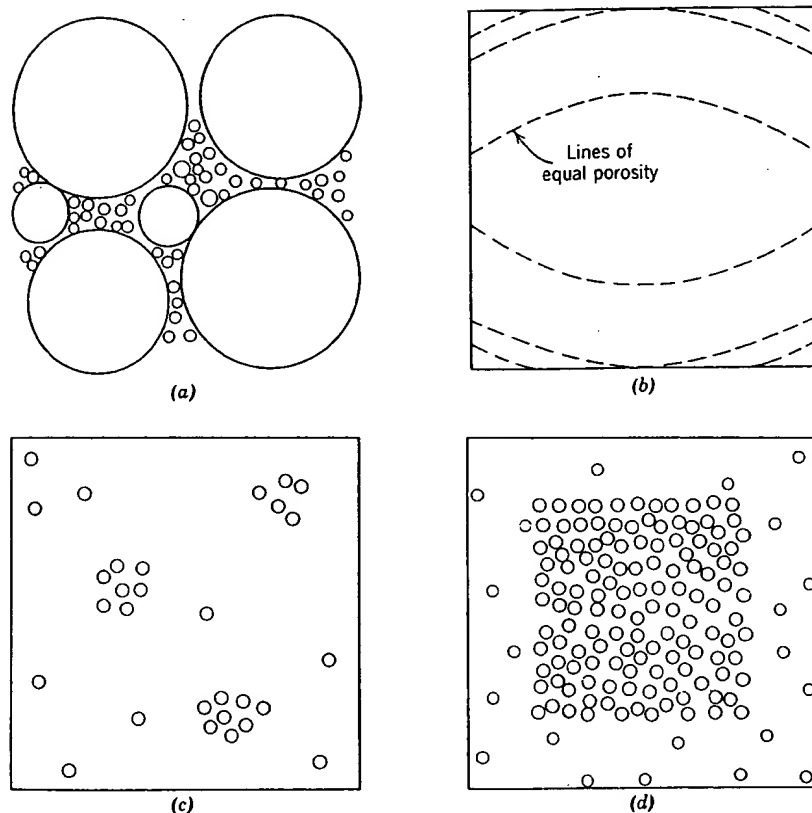


Fig. 10.28. Pore-concentration variations resulting from (a) a variation in grain sizes, (b) die friction, (c) local packing and agglomeration differences, and (d) more rapid pore elimination near surfaces.

tions caused by die-wall friction during pressing, and from the more rapid elimination of porosity near surfaces caused by temperature gradients during heating, as shown in Fig. 10.28. The importance of local variations in pore concentration results from the fact that the part of the sample containing pores tends to shrink but is restrained by other porefree parts. That is, the effective diffusion distance is no longer from the pore to an adjacent grain boundary but a pore-pore or pore-surface distance many orders of magnitude larger. An example of residual pore clusters in a sintered oxide is shown in Fig. 10.29.

Not only the kinetics of pore elimination can lead to "stable" and residual porosity, but it is also possible in some cases to have a thermodynamically metastable equilibrium pore configuration. In Fig.

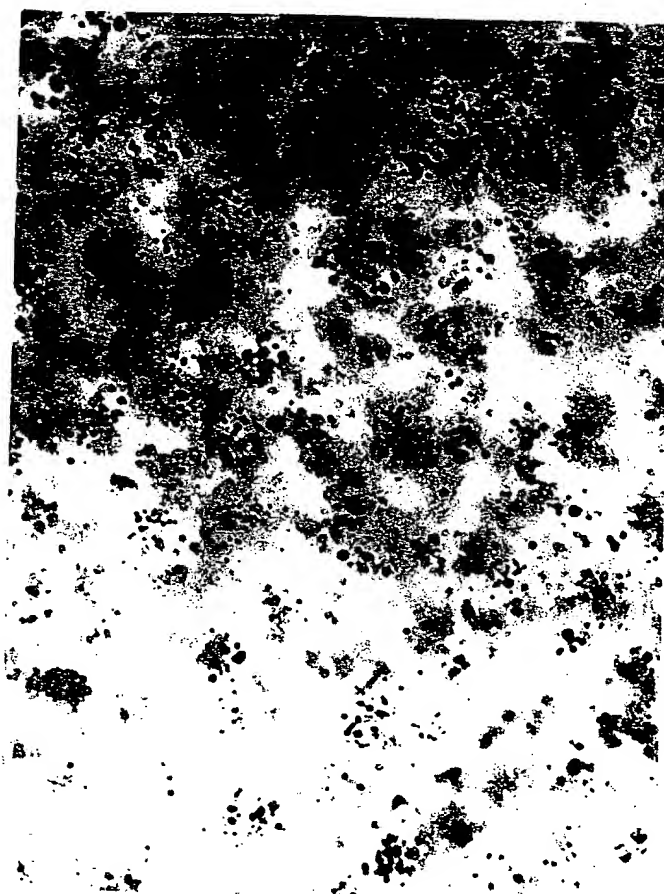


Fig. 10.29. Residual pore clusters resulting from improper powder processing in a sample of 90 mole % Y_2O_3 -10 mole % ThO_2 . Transmitted light, 137 \times . Courtesy C. Greskovich and K. N. Woods.

10.26 we have drawn spherical pores located on a grain boundary, the usual model description, but we know from our discussion of interface energies in Chapter 5 that there is a dihedral angle ϕ at the pore-boundary intersection determined by the relative interface energies;

$$\cos \frac{\phi}{2} = \frac{\gamma_{gb}}{2\gamma_s} \quad (10.30)$$

In most cases the dihedral angle for pure oxides is about 150° , and the spherical pore approximation is quite good; but for $\text{Al}_2\text{O}_3 + 0.1\% \text{MgO}$ the

value
carbide
nonsp

As c
and 10
on the
grains
polyhe
of the
angle
When

Ratio of circumscribed sphere radius to pore curvature (r/p)

Fig. 10
numbe

value is 130° , for $\text{UO}_2 + 30 \text{ ppm C}$ the value is 88° , and for impure boron carbide the value is about 60° . For these materials the consequences of nonspherical pores have to be considered.

As discussed for discontinuous grain growth and illustrated in Figs. 10.4 and 10.11, the boundary curvature between grains or phases depends both on the value of the dihedral angle and on the number of surrounding grains. If we take r as the radius of a circumscribed sphere around a polyhedral pore surrounded by grains, the ratio of the radius of curvature of the pore surfaces ρ to the spherical radius depends both on the dihedral angle and on the number of surrounding grains, as shown in Fig. 10.30a. When r/ρ decreases to zero, the interfaces are flat and have no tendency

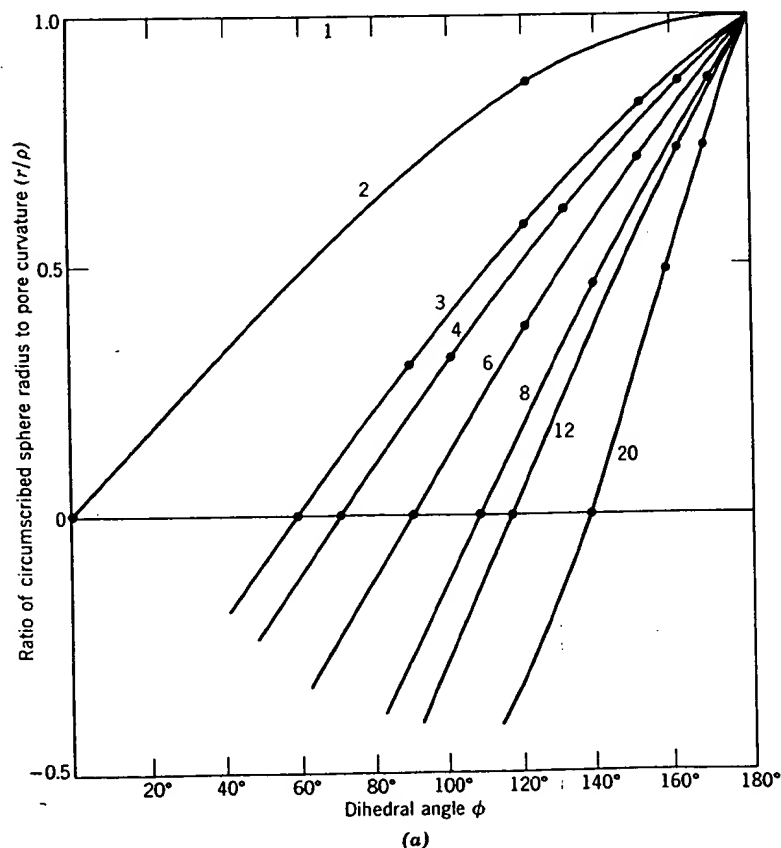


Fig. 10.30. (a) Change in the ratio (r/ρ) with dihedral angle for pores surrounded by different numbers of grains as indicated on individual curves.

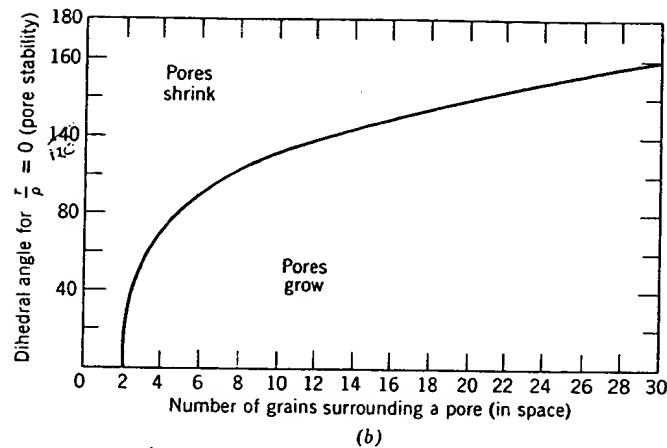


Fig. 10.30 (Continued). (b) Conditions for pore stability.

for shrinkage; when r/p is negative, the pore tends to grow. This is illustrated in Fig. 10.30b. For a uniform grain size the space-filling form is a tetrakaidecahedron with 14 surrounding grains. From an approximate relationship between the number of surrounding grains and the pore-diameter to grain-diameter ratio we can derive a relationship for pore stability as a function of dihedral angle and the ratio of pore size to grain size, as shown in Fig. 10.31. From this figure we can see why large pores present in poorly compacted powder such as shown in Fig. 10.32 not only remain stable but grow. It is also seen that an enormous disparity between

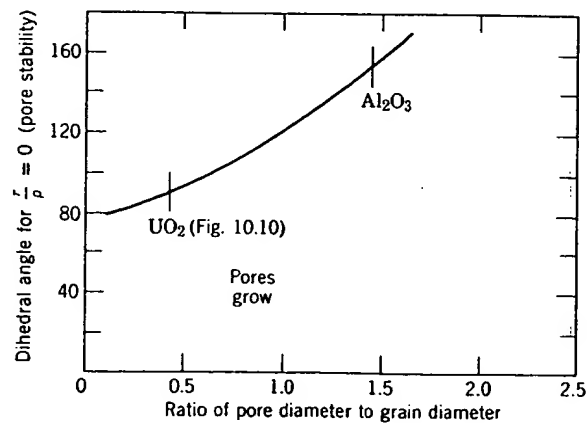


Fig. 10.31. Conditions for pore stability.

Fig. 10.32. L with scanning

grain size and size of affects the process.

The inter two-way sintering, grain growth can occur once the pore growth can temperature from grain grain bound illustrated has occurred reduction in oxide show discontinuous grain bound



Fig. 10.32. Large voids formed by bridging of agglomerates in fine Al_2O_3 powder viewed with scanning electron microscope at 2000 \times . Courtesy C. Greskovich.

grain size and pore size is not necessary for pore stability. That is, the site and size of the porosity relative to the grain-boundary network not only affects the necessary distance for diffusion but also the driving force for the process.

The interaction of grain boundaries and porosity is, of course, a two-way street. When many pores are present during the initial stages of sintering, grain growth is inhibited. However, as discussed in Section 10.1, once the porosity has decreased to a value such that secondary grain growth can occur, extensive grain growth may result at high sintering temperatures. When grain growth occurs, many pores become isolated from grain boundaries, and the diffusion distance between pores and a grain boundary becomes large, and the rate of sintering decreases. This is illustrated in Fig. 10.16b, in which extensive secondary recrystallization has occurred, with the isolation of pores in the interior of grains and a reduction in the densification rate. Similarly, the sample of aluminum oxide shown in Fig. 10.33 has been sintered at a high temperature at which discontinuous grain growth occurred. Porosity is only removed near the grain boundaries, which act as the vacancy sink. The importance of

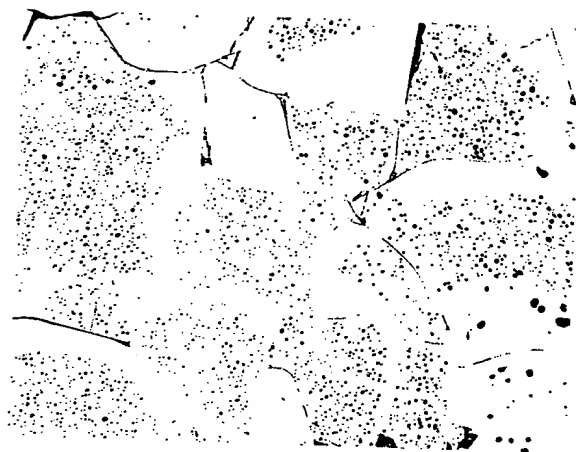


Fig. 10.33. Sintered Al_2O_3 illustrating elimination of porosity adjacent to grain boundaries with residual porosity remaining at grain centers. Courtesy J. E. Burke.

controlling grain growth as an integral part of controlling sintering phenomena cannot be overestimated. Consequently, the grain-growth processes discussed in Section 10.1 must be actively prevented in order to obtain complete densification. Usually densification continues by a diffusion process until about 10% porosity is reached; at this point rapid grain growth occurs by secondary recrystallization, and the rate of densification is sharply reduced. In order to obtain densification much beyond this level, prevention of secondary recrystallization is essential. The most satisfactory way of doing this is with additives which prevent or slow down boundary migration to a point at which it is possible to obtain pore elimination. Additions of MgO to Al_2O_3 , ThO_2 to Y_2O_3 , and CaO to ThO_2 , among others, have been found to slow boundary migration and allow complete pore elimination by solid-state sintering in these systems. The porefree microstructure of a polycrystalline ceramic having optical transparency suitable for use as a laser material is shown in Fig. 10.34.

10.3 Vitrification

To vitrify is to make glasslike and the vitrification process—densification with the aid of a viscous liquid phase—is the major firing process for the great majority of silicate systems. (In some current glossaries vitrification is defined as being identical to densification on firing, but the more specific usage is preferred.) A viscous liquid silicate is formed at the firing temperature and serves as a bond for the body. For

Fig. 10.34. Pol
Courtesy C. Gr

satisfactory
such that de
slumping or
rates of the
large extent
firing.

Process Ki
10.21), there

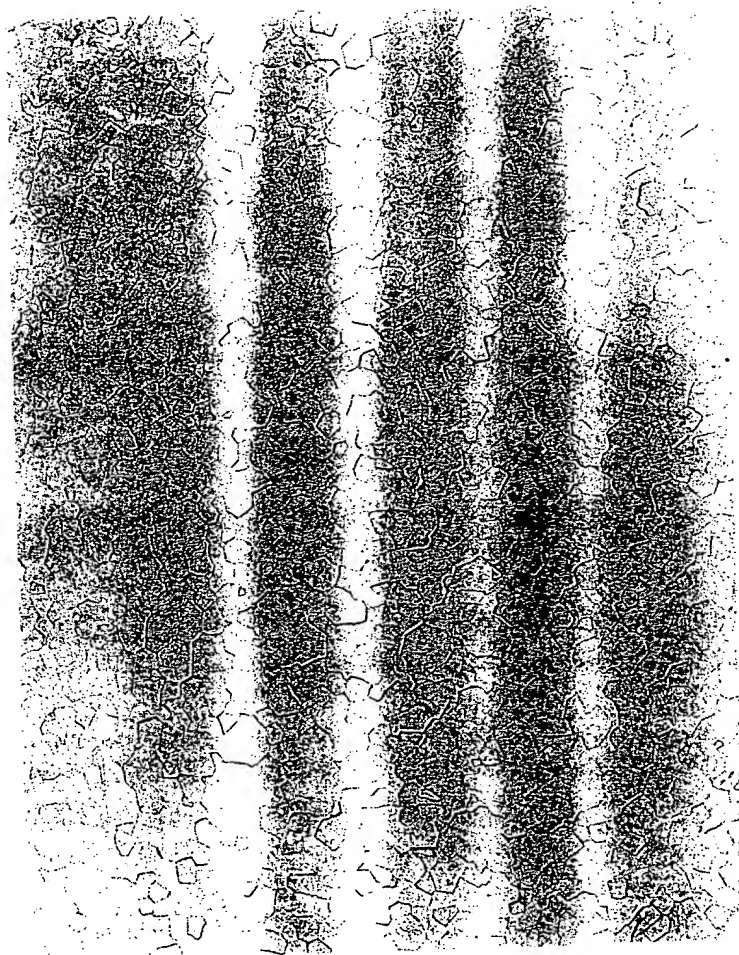


Fig. 10.34. Polished section of $Y_2O_3 + 10$ mole % ThO_2 sintered to porefree state. 100 \times . Courtesy C. Greskovich and K. N. Woods.

satisfactory firing the amount and viscosity of the liquid phase must be such that densification occurs in a reasonable time without the ware slumping or warping under the force of gravity. The relative and absolute rates of these two processes (shrinkage and deformation) determine to a large extent the temperature and compositions suitable for satisfactory firing.

Process Kinetics. If we consider two particles initially in contact (Fig. 10.21), there is a negative pressure at the small negative radius of

curvature ρ compared with the surface of the particles. This causes a viscous flow of material into the pore region. By an analysis similar to that derived for the diffusion process, the rate of initial neck growth is given as*

$$\frac{x}{r} = \left(\frac{3\gamma}{2\eta\rho} \right)^{1/2} t^{1/2} \quad (10.31)$$

The increase in contact diameter is proportional to $t^{1/2}$; the increase in area between particles is directly proportional to time. Factors of most importance in determining the rate of this process are the surface tension, viscosity, and particle size. The shrinkage which takes place is determined by the approach between particle centers and is

$$\frac{\Delta V}{V_0} = \frac{3 \Delta L}{L_0} = \frac{9\gamma}{4\eta r} t \quad (10.32)$$

That is, the initial rate of shrinkage is directly proportional to the surface tension, inversely proportional to the viscosity, and inversely proportional to the particle size.

The situation after long periods of time can best be represented as small spherical pores in a large body (Fig. 10.35). At the interior of each pore

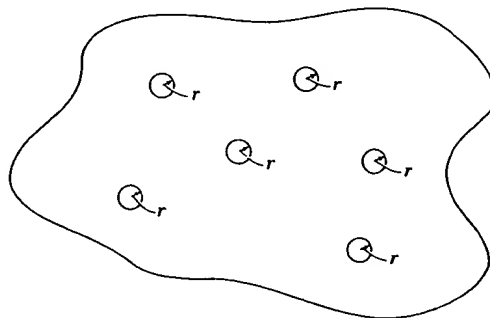


Fig. 10.35. Compact with isolated spherical pores near the end of the sintering process.

there is a negative pressure equal to $2\gamma/r$; this is equivalent to an equal positive pressure on the exterior of the compact tending to consolidate it. J. K. Mackenzie and R. Shuttleworth† have derived a relation for the rate of shrinkage resulting from the presence of isolated equal-size pores in a viscous body. The effect of surface tension is equivalent to a pressure of $-2\gamma/r$ inside all pores or, for an incompressible material, to the applica-

*J. Frenkel, *J. Phys (USSR)*, 9, 385 (1945).

†*Proc. Phys. Soc. (London)*, B62, 833 (1949).

tion of a hyc
is to deduce
viscosity of
an equation

where ρ' is
density or t
the number
pores depe

By combin

where r_0 is

The gene
plot of rel
10.36 follo
reach a rel
of the sir

Fig. 10.36.
material. Fr
(1949).

This causes a
similar to that
growth is given

(10.31)

the increase in
factors of most
surface tension,
pressure is deter-

(10.32)

on the surface
sely propor-

is noted as small
of each pore

sintering process.

to an equal
consolidate it.
for the rate
of pores in a
pressure of
the applica-

tion of a hydrostatic pressure of $+2\gamma/r$ to the compact. The real problem is to deduce the properties of the porous material from the porosity and viscosity of the dense material. The method of approximation used gives an equation of the form

$$\frac{d\rho'}{dt} = \frac{2}{3} \left(\frac{4\pi}{3} \right)^{1/3} n^{1/3} \frac{\gamma}{\eta} (1 - \rho')^{2/3} \rho'^{1/3} \quad (10.33)$$

where ρ' is the relative density (the bulk density divided by the true density or the fraction of true density which has been reached) and n is the number of pores per unit volume of real material. The number of pores depends on the pore size and relative density and is given by

$$n \frac{4\pi}{3} r^3 = \frac{\text{Pore volume}}{\text{Solid volume}} = \frac{1 - \rho'}{\rho'} \quad (10.34)$$

$$n^{1/3} = \left(\frac{1 - \rho'}{\rho'} \right)^{1/3} \left(\frac{3}{4\pi} \right)^{1/3} \frac{1}{r} \quad (10.35)$$

By combining with Eq. 10.33,

$$\frac{d\rho'}{dt} = \frac{3\gamma}{2r_0\eta} (1 - \rho') \quad (10.36)$$

where r_0 is the initial radius of the particles.

The general course of the densification process is best represented by a plot of relative density versus nondimensional time, illustrated in Fig. 10.36 following Eq. 10.33. Spherical pores are formed very quickly to reach a relative density of about 0.6. From this point until the completion of the sintering process about one unit of nondimensional time is

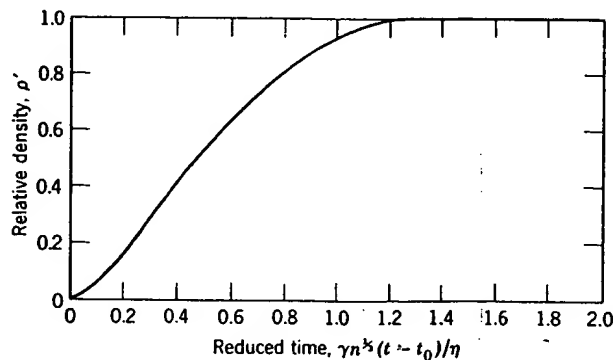


Fig. 10.36. Increase in relative density of compact with reduced time for a viscous material. From J. K. Mackenzie and R. Shuttleworth, *Proc. Phys. Soc. (London)*, B62, 833 (1949).

$$t_{\text{sec}} \sim \frac{1.5 r_0 \eta}{\gamma} \quad (10.37)$$

purposes
typical so
over an i
factor ov
be closely
discussed
by changi
The relati
viscosity
under the
makes it
stresses d
due to gr
supported
obtaining
fine-grain
ment is c
systems a
naturally
vitrificati

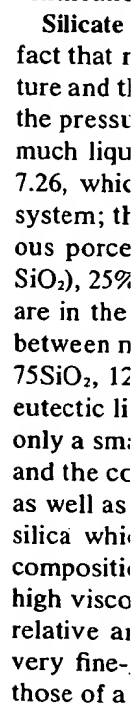


Fig. 10.37. Densification of a soda-lime-silica glass.

Important Variables. The particular importance of Eqs. 10.31 to 10.37 is the dependence of the rate of densification on three major variables—the particle size, viscosity, and surface tension. For silicate materials the surface tension is not changed much by composition, although there are some systems for which surface energy is particularly low, as illustrated in Chapter 5. However, surface tension is not a variable that normally causes difficulty during the design of compositions or the control of processing. The particle size has a strong effect on the sintering rate and must be closely controlled if the densification process is going to be controlled. In changing from a 10-micron to 1-micron particle, the rate of sintering is increased by a factor of 10. Even more important for control

purposes is the viscosity and its rapid change with temperature. For a typical soda-lime-silica glass the viscosity changes by a factor of 1000 over an interval of 100°C; the rate of densification changes by an equal factor over the temperature range. This means that the temperature must be closely controlled. Viscosity is also much changed by composition, as discussed in Chapter 3. The rate of densification, then, can be increased by changing the composition to lower the viscosity of the glassy material. The relative values of viscosity and particle size are also important; the viscosity must not be so low that appreciable deformation takes place under the forces of gravity during the time required for densification. This makes it necessary for the particle size to be in such a range that the stresses due to surface tension are substantially larger than the stresses due to gravitational forces. Materials sintered in a fluid state must be supported so that deformation does not occur. The best means of obtaining densification without excessive deformation is to use very fine-grained materials and uniform distribution of materials. This requirement is one of the reasons why successful compositions in silicate systems are composed of substantial parts of talc and clays that are naturally fine-grained and provide a sufficient driving force for the vitrification process.

Silicate Systems. The importance of the vitrification process lies in the fact that most silicate systems form a viscous glass at the firing temperature and that a major part of densification results from viscous flow under the pressure caused by fine pores. Questions that naturally arise are how much liquid is present and what are its properties. Let us consider Fig. 7.26, which shows an isothermal cut at 1200°C in the $K_2O-Al_2O_3-SiO_2$ system; this is the lower range of firing temperatures used for semivitreous porcelain bodies composed of about 50% kaolin (45% Al_2O_3 , 55% SiO_2), 25% potash-feldspar, and 25% silica. This and similar compositions are in the primary field of mullite, and at 1200°C there is an equilibrium between mullite crystals and a liquid having a composition approximately 75 SiO_2 , 12.5 K_2O , 12.5 Al_2O_3 , not much different in composition from the eutectic liquid in the feldspar-silica system (Fig. 7.14). In actual practice only a small part of the silica present as flint enters into the liquid phase, and the composition of the liquid depends on the fineness of the grinding as well as on the overall chemical composition. However, the amount of silica which dissolves does not have a large effect on the amount and composition of the liquid phase present. The liquid is siliceous and has a high viscosity; the major effect of compositional changes is to alter the relative amounts of mullite and liquid phases present. Since mullite is very fine-grained, the fluid flow properties of the body correspond to those of a liquid having a viscosity greater than the pure liquid phase. For

some systems the overall flow process corresponds to plastic flow with a yield point rather than to true viscous flow. This changes the kinetics of the vitrification process by introducing an additional term in Eqs. 10.33 and 10.36 but does not change the relative effects of different variables.

Although phase diagrams are useful, they do not show all the effects of small changes in composition. For example, a kaolinite composition should show equilibrium between mullite and tridymite at 1400°C with no glassy material. However, it is observed experimentally that even after 24 hr about 60 vol% of the original starting material is amorphous and deforms as a liquid. The addition of a small amount of lithium oxide as Li_2CO_3 has been observed to give a larger content of glass than additions of the same composition as the fluoride. Similar small amounts of other mineralizers can also have a profound effect in the firing properties of particular compositions. That fine grinding and intimate mixing reduce the vitrification temperature follows from the analysis in Eqs. 10.31 to 10.37. S. C. Sane and R. L. Cook* found that ball milling for 100 hr reduced the final porosity of a clay-feldspar-flint composition from 17.1 to 0.3% with the same firing conditions. This change is caused in part by increased tendencies toward fusion equilibrium and uniform mixing of constituents and in part by the smaller initial particle and pore size. In contrast to triaxial (flint-feldspar-clay) porcelains, which frequently do not reach fusion equilibrium, many steatite bodies and similar compositions which are prepared with fine-particle, intimately mixed material and form a less siliceous liquid reach phase equilibrium early in the firing process.

The time-temperature relationship and the great dependence of vitrification processes on temperature can perhaps be seen best in the experimental measurements illustrated in Fig. 10.38. As shown there, the time required for a porcelain body to reach an equivalent maturity changes by almost an order of magnitude with a 50° temperature change. There are changes in both the amount and viscosity of the glassy phase during firing, so that it is difficult to elucidate a specific activation energy for the process with which to compare the activation energy for viscous flow. However, the temperature dependence of the vitrification rate of a composition such as this (a mixture of clay, feldspar, and flint) is greater than the temperature dependence of viscosity alone. This is to be expected from the increased liquid content at the higher firing temperatures.

In summary, the factors determining the vitrification rate are the pore size, viscosity of the overall composition (which depends on amount of liquid phase present and its viscosity), and the surface tension. Equivalent

*J. Am. Ceram. Soc., 34, 145 (1951).

Fig. 10.38. E
from F. H. N.

densificatio
In controll
of the incre
tures. Chai
vitrification

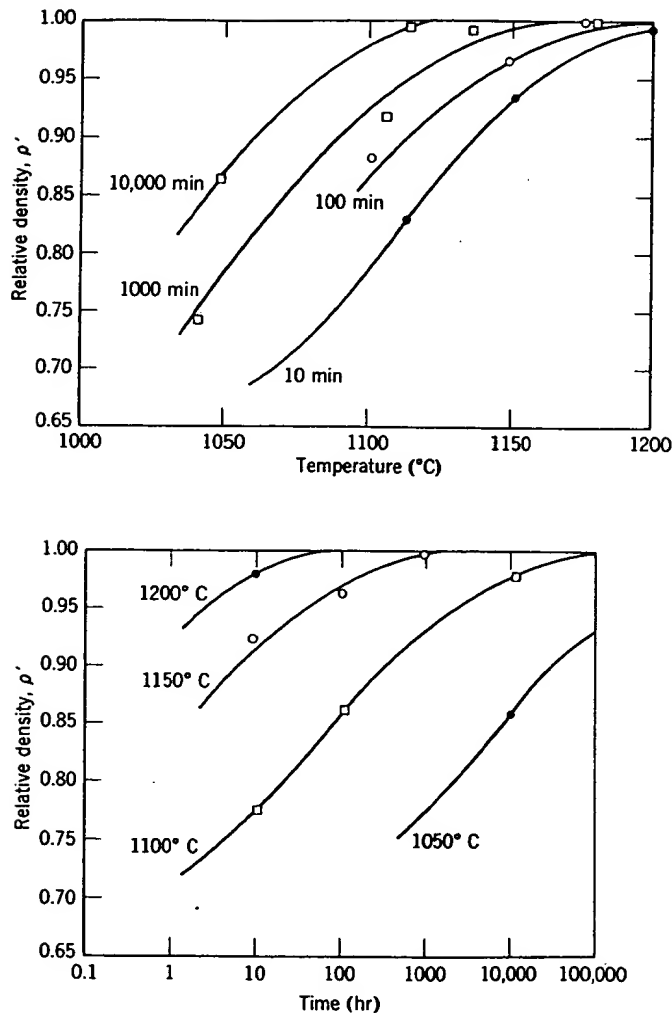


Fig. 10.38. Effect of time and temperature on the vitrification of a porcelain body. Data from F. H. Norton and F. B. Hodgdon, *J. Am. Ceram. Soc.*, 14, 177 (1931).

densification results from longer periods of time at the same temperature. In controlling the process, the temperature dependence is great because of the increase in liquid content and lowered viscosity at higher temperatures. Changes in processing and changes in composition affect the vitrification process as they affect these parameters.

10.4 Sintering with a Reactive Liquid

Another quite different process which leads to densification is sintering in the presence of a reactive liquid. Here we are referring to systems in which the solid phase shows a certain limited solubility in the liquid at the sintering temperature; the essential part of the sintering process is the solution and reprecipitation of solids to give increased grain size and density. This kind of process occurs in cermet systems such as bonded carbides and also in oxide systems when the liquid phase is fluid and reactive, such as magnesium oxide with a small amount of liquid phase present (Fig. 10.39), UO_2 with the addition of a small amount of TiO_2 (Fig. 7.11), and high-alumina bodies which have an alkaline earth silicate as a bonding material.

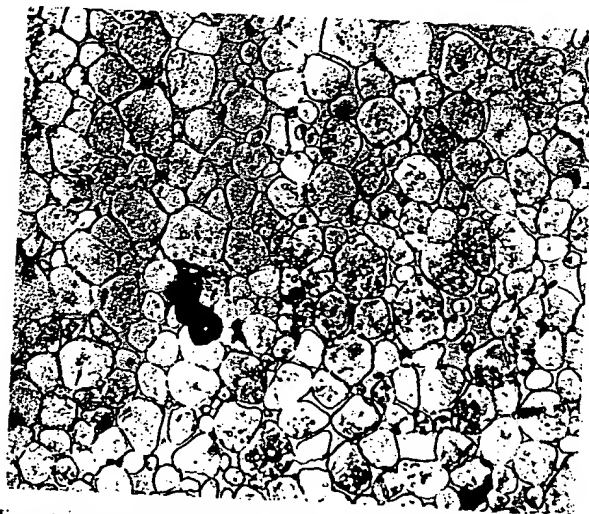


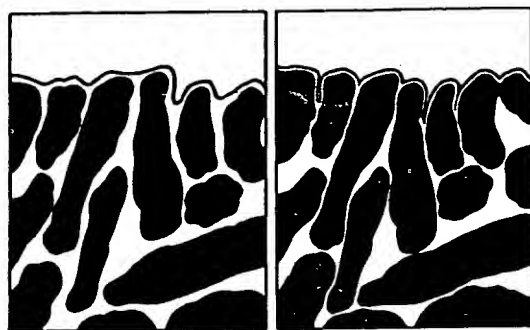
Fig. 10.39. Microstructure of magnesium—2% kaolin body resulting from reactive-liquid sintering (245 \times).

Studies of a large number of systems indicate that for densification to take place rapidly it is essential to have (1) an appreciable amount of liquid phase, (2) an appreciable solubility of the solid in the liquid, and (3) wetting of the solid by the liquid. The driving force for densification is derived from the capillary pressure of the liquid phase located between the fine solid particles, as illustrated in Fig. 10.40. When the liquid phase wets the solid particles, each interparticle space becomes a capillary in which a substantial capillary pressure is developed. For submicron particle sizes, capillaries with diameters in the range of 0.1 to 1 micron

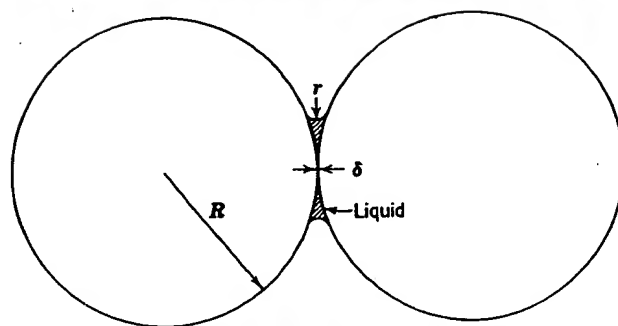


Fig. 10.40. (a) S
Drop of liquid bet
of forsterite cera

intering
stems in
id at the
s is the
ize and
bonded
uid and
d phase
O₂ (Fig.
ate as a



(a)



(b)



(c)

Fig. 10.40. (a) Surface of solid-liquid composite with varying amounts of liquid phase. (b) Drop of liquid between two solid spheres exerts pressure to pull them together. (c) Surface of forsterite ceramic showing liquid capillary depression between crystals.

ve-liquid

ition to
unt of
and (3)
ition is
etween
l phase
lary in
micron
micron

develop pressures in the range of 175 to 1750 psi for silicate liquids and in the range of 975 to 9750 psi for a metal such as liquid cobalt (see discussion in Chapter 5 and Table 5.2).

The capillary pressure results in densification by different processes which occur coincidentally. First, on formation of a liquid phase there is a rearrangement of particles to give a more effective packing. This process can lead to complete densification if the volume of liquid present is sufficient to fill in the interstices completely. Second, at contact points where there are bridges between particles high local stresses lead to plastic deformation and creep, which allow a further rearrangement. Third, there is during the sintering process a solution of smaller particles and growth of larger particles by material transfer through the liquid phase. The kinetics of this solution-precipitation process have already been discussed in Chapter 9. Because there is a constantly imposed capillary pressure, additional particle rearrangement can occur during grain-growth and grain-shape changes and give further densification. (As discussed for vapor transport and surface diffusion in solid-state sintering, mere solution-precipitation material transfer without the imposed capillary pressure would not give rise to densification). Fourth, in cases in which liquid penetrates between particles the increased pressure at the contact points leads to an increased solubility such that there is material transfer away from the contact areas so that the particle centers approach one another and shrinkage results; the increase in solubility resulting from the contact pressure has been discussed in Chapter 5. Finally, unless there is complete wetting, recrystallization and grain growth sufficient to form a solid skeleton occur, and the densification process is slowed and stopped.

Perhaps even more than for the solid-state process, sintering in the presence of a liquid phase is a complex process in which a number of phenomena occur simultaneously. Each has been shown to occur, but experimental systems in which a single process had been isolated and analysed during sintering have not been convincingly demonstrated. Clearly, the process requires a fine-particle solid phase to develop the necessary capillary pressures which are proportional to the inverse capillary diameter. Clearly, the liquid concentration relative to the solid particle packing must be in a range appropriate for developing the necessary capillary pressure. Clearly, if and when a solid skeleton develops by particle coalescence, the process stops.

A critical and still controversial question is the degree of wetting required for the process to proceed. In some important systems such as tungsten carbide-cobalt and titanium carbide-nickel-molybdenum the dihedral angle is zero. In other systems such as iron-copper and magnesia-silicate liquids this is not the case at equilibrium; but the dihedral angle is

low, and the necessary capillary pressure for the silicate liquid process, as essential for effective as

Fig. 10.41. G
compositions
Trans. Brit. C

10.5 Press

The sintering pressures required for densification at elevated temperatures are also removable at advantage by the use of a vacuum furnace.

*R. L. Cob

low, and the solid is wetted by the liquid phase, as required to develop the necessary capillary pressure. For grain growth of periclase particles in a silicate liquid, the dihedral angle has a large effect on the grain-growth process, as illustrated in Fig. 10.41. Although zero dihedral angle is not essential for liquid-phase sintering to occur, the process becomes more effective as this ideal is approached.

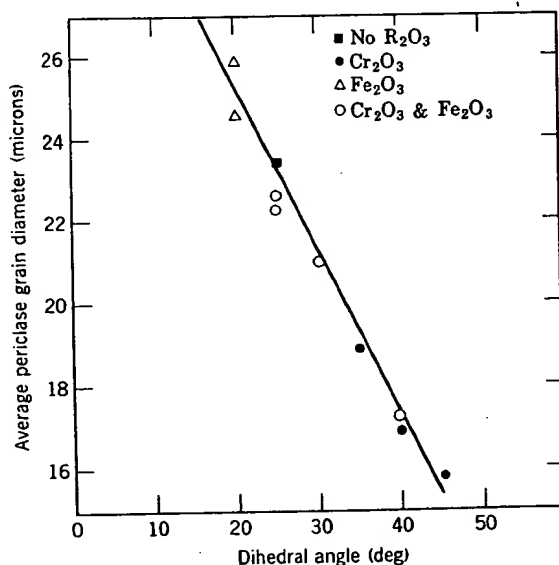


Fig. 10.41. Grain growth of periclase particles in liquid-phase-sintered periclase-silicate compositions as a function of dihedral angle. From B. Jackson, W. F. Ford, and J. White, *Trans. Brit. Ceram. Soc.*, 62, 577 (1963).

10.5 Pressure Sintering and Hot Pressing

The sintering processes thus far discussed depend on the capillary pressures resulting from surface energy to provide the driving force for densification. Another method is to apply an external pressure, usually at elevated temperature, rather than relying entirely on capillarity.* This is desirable in that it eliminates the need for very fine-particle materials and also removes large pores caused by nonuniform mixing. An additional advantage is that in some cases densification can be obtained at a temperature at which extensive grain growth or secondary recrystalliza-

*R. L. Coble, *J. Appl. Phys.* 41, 4798 (1970).

tion does not occur. Since the mechanical properties of many ceramic systems are maximized with high density and small grain size, optimum properties can be obtained by hot-pressing techniques. The effect of added pressure on the densification of a beryllium oxide body is illustrated in Fig. 10.42. The main disadvantages of hot pressing for oxide

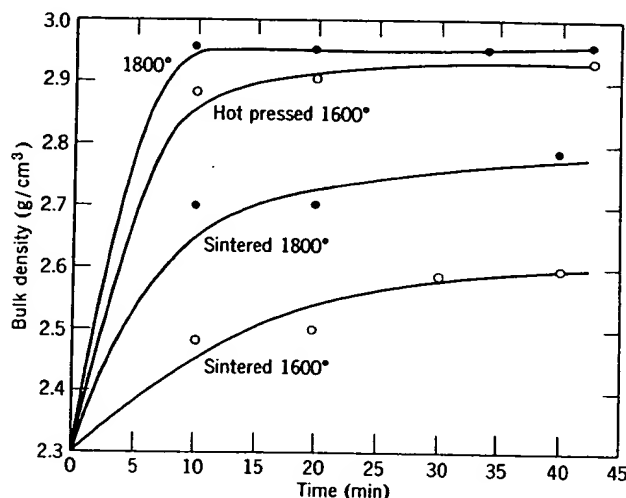


Fig. 10.42. Densification of beryllia by sintering and by hot pressing at 2000 psi.

bodies are the unavailability of inexpensive and long-life dies for high temperatures and the difficulty in making the process into an automatic one to achieve high-speed production. Both factors make the hot-pressing process an expensive one. For oxide materials which have to be pressed at temperature above 1200 or 1300°C (often at 1800 to 2000°C) graphite is the most satisfactory die material available; the maximum stress is limited to a few thousand pounds per square inch, and the life of dies is usually limited to seven or eight pieces. The entire die must be heated and cooled with the formation of each piece. Techniques for using high temperatures in a process in which the die is maintained cool with the material heated have shown some promise in laboratory tests but have not been developed for production.

For lower-temperature materials, such as glasses or glass-bonded compositions which can be pressed in metal dies at temperatures below 800 to 900°C, the hot-pressing process can be developed as an automatic and inexpensive forming method. This is similar to the normal pressing of

glass at
shape 1

Dens
which
liquid-
when h
materi
densifi
pressur
erature
optimu
nearly
carbide
It is of
MgO,
induce

10.6

The
connec
growth
these
occur
chemic
closed
pressu
genera
major
them
possib

Oxi
which
as bin
oxidiz
organi
tempe
tempe
this p
carbon
before
tempe

glass as a glass-forming method in which it is used to obtain the desired shape rather than as a means of eliminating porosity.

Densification during pressure sintering can occur by all the mechanisms which have been discussed for solid-state sintering, vitrification, and liquid-phase sintering. In addition, particularly during the early stages, when high stresses are present at the particle contact points, and for soft materials, such as the alkali halides, plastic deformation is an important densification mode. Since the grain-growth process is insensitive to pressure, pressure-sintering oxides at high pressures and moderate temperatures allows the fabrication of high-density-small-grain samples with optimum mechanical properties and with sufficiently low porosity to be nearly transparent. Covalent materials such as boron carbide, silicon carbide, and silicon nitride can be hot-pressed to nearly complete density. It is often advantageous to add a small fraction of liquid phase (i.e., LiF to MgO, B to silicon carbide, MgO to silicon nitride) to allow pressure-induced liquid phase, or liquid-film, sintering to occur.

10.6 Secondary Phenomena

The primary processes which occur on heating and are important in connection with the firing behavior of all ceramic compositions are grain growth and densification, as discussed in previous sections. In addition to these changes, there are a large number of other possible effects which occur during the firing of some particular compositions. These include chemical reactions, oxidation, phase transitions, effects of gas trapped in closed pores, effects of nonuniform mixing, and the application of pressure during heating. Although they are not processes of the most general importance, they frequently cause the main problems and the major phenomena observed during firing. Although we cannot discuss them in great detail, we should at least be familiar with some of the possibilities.

Oxidation. Many natural clays contain a few percent organic matter which must be oxidized during firing. In addition, varnishes or resins used as binders, as well as starches and other organic plasticizers, must be oxidized during firing, or difficulties result. Under normal conditions organic materials char at temperatures above 150°C and burn out at temperatures ranging from 300 to 400°C. Particularly with low-firing-temperature compositions, it is necessary to heat at a slow enough rate for this process to be completed before shrinkage becomes substantial. If the carbonaceous material is sealed off from the air by vitrification occurring before oxidation is completed, it acts as a reducing agent at higher temperatures. Sometimes this may merely affect the color, giving rise to

black coring of brick and heavy clay products whose interiors are in a reduced state, black in color. A typical example of a stoneware heated too rapidly for oxidation to be completed is illustrated in Fig. 10.43, which shows the central black core. Very often impurities present, particularly sulfides, may cause difficulties unless oxidized before vitrification. Sulfides in general react with oxygen in the temperature range of 350 to 800°C, forming SO_2 gas which escapes through open pores.

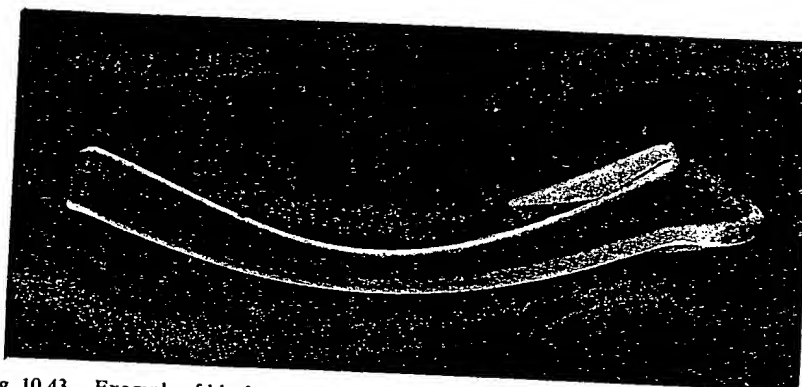


Fig. 10.43. Example of black core produced when time allowed for oxidation reactions was insufficient for completion of the reaction.

In ferrite and titania compositions control of oxidation reactions during firing is particularly important. As illustrated for the Ti-TiO_2 and Fe-O_2 systems (Chapter 7), the phases present depend on the oxygen pressure. In addition, as discussed in Chapter 4, the composition of these phases covers a substantial range of stoichiometry and depends on the oxygen pressure. It is common practice in the manufacture of ferrites to control the oxygen pressure during firing so that the composition of each phase present, and the overall phase composition of the body, is maintained to give the best magnetic properties.

Decomposition Reactions. Many of the constituents used in ceramic bodies are in the form of carbonates or hydrated compounds; these decompose during firing to form the oxide plus a gaseous product (CO_2 , H_2O). Many impurities are also incorporated as carbonates, hydrates, and sulfates and decompose during firing (see Section 9.4).

Hydrates decompose over a wide temperature range between 100 and 1000°C, depending on the particular composition. Carbonates decompose over a temperature range from 400 to 1000°C, also depending on the particular composition. For each temperature there is, of course, an

equilibrium further decomposition encountered at higher temperatures. Large pores, to form cell off before a phase that is particularly a temperature gradient and are the two firing.

Sulfates decompose they remain bodies. In a high sulfated burned brick salts to the barium calcium sulf

Decomposition. A particular of kyanite, to 1450°C. mullite and than kyanite composition other constituents Al_2O_3 to form magnesia a high-temperature heating car

Phase Transformations. Transformation or und anticipated transformation can since the temperature is such a large

equilibrium pressure of the gaseous product; if this pressure is exceeded, further decomposition does not take place, leading to the major problem encountered, the sealing of pores before complete dissociation. As the temperature is raised, the decomposition pressure increases and forms large pores, blistering, and bloating. (This is, of course, the method used to form cellular glass products in which the surface is intentionally sealed off before chemical reaction or decomposition takes place to form a gas phase that expands and produces a foamed product.) This kind of defect is particularly common when high heating rates are used, for then there is a temperature gradient between the surface and interior of the ware, and the surface layer vitrifies, sealing off the interior. This temperature gradient and the time required for oxidation of constituents or impurities are the two most important reasons for limiting the rate of heating during firing.

Sulfates create a particular problem in firing because they do not decompose until a temperature of 1200 to 1300°C is reached. Therefore they remain stable during the firing process used for burning many clay bodies. In particular, CaSO_4 is stable but slightly soluble in water, so that a high sulfate content leads to a high concentration of soluble salts in the burned brick. This causes efflorescence—the transport of slightly soluble salts to the surface, forming an undesirable white deposit. Addition of barium carbonate prevents the deposit from forming by reacting with calcium sulfate to precipitate insoluble barium sulfate.

Decomposition also occurs in some materials to form new solid phases. A particular example used in refractory technology is the decomposition of kyanite, $\text{Al}_2\text{O}_3 \cdot \text{SiO}_2$, to form mullite and silica at a temperature of 1300 to 1450°C. This reaction proceeds with an increase in volume, since both mullite and the silica glass or cristobalite formed have lower densities than kyanite. The reaction is useful, since the addition of kyanite to a composition can counteract a substantial part of the firing shrinkage if the other constituents are carefully selected. Similarly, reaction of MgO with Al_2O_3 to form spinel occurs with a decrease in volume. By incorporating magnesia and alumina in a refractory mix, or more commonly in a high-temperature ramming mix or cement, the shrinkage taking place on heating can be decreased.

Phase Transformations. Polymorphic transformations may be desirable or undesirable, depending on the particular composition and the anticipated use. If a large volume change accompanies the polymorphic transformation, difficulties result; owing to the induced stresses. Refractories cannot be made containing pure zirconium oxide, for example, since the tetragonal monoclinic transformation at about 1000° involves such a large volume change that the ware is disrupted. The source of these

stresses has been discussed in Chapter 5 in connection with boundary stresses caused by differential thermal expansion or contraction of different grains. The expansion or contraction of a crystal in a matrix leads to the same sort of stresses that may give rise to actual cracking, illustrated for quartz grains in a porcelain body in Fig. 10.44. The stresses in individual grains can be reduced if the grain size is reduced; properties of porcelains are improved if fine-grained flint is used rather than coarse material.

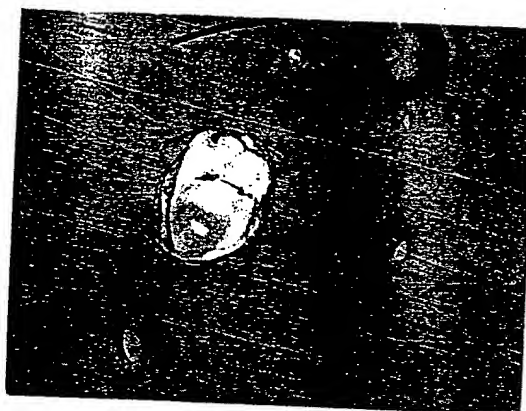


Fig. 10.44. Cracked quartz grain and surrounding matrix in a porcelain body. Differential expansion due mainly to the α - β quartz transition leads to cracking of larger grains but leaves small grains intact (500 \times).

Sometimes desirable phase transformations only occur sluggishly. This is what happens, for example, with the firing of refractory silica brick. The transition from quartz, the starting material, to tridymite and cristobalite, the desired end constituents, occurs only slowly. In order to increase the rate of transformation, calcium oxide is added as a mineralizer. The calcium oxide forms a liquid in which silica is soluble. Consequently the quartz dissolves and precipitates as tridymite, which is the more stable phase (Chapter 7). Some of the quartz transforms directly to cristobalite during the process as well. In general, mineralizers help in achieving equilibrium conditions by providing a mechanism of material transfer—solution or vaporization—that circumvents energy barriers to direct transformations. In silicate systems the addition of fluorides or hydroxyl ions is particularly helpful in this regard, since they greatly increase the fluidity of the liquid phase present.

Trapped Gases. In addition to the bloating occasioned by decomposition reactions, trapping of gases within closed pores imposes a limitation

on the ultimate water vapor pressure from close carbon monoxide solubility spherical of 0.8 atm. when the limited. A negative negative to $1/r$; this factor required, translucent

Nonuniform sintering, short of imperfections present. common. (that is, introduction of these porosity forming

Overfiring variety of a reduced titanates higher temperature there is optimum common cause of gases

10.7 Firing

As for amount forming removed

on the ultimate density that can be reached during firing. Gases such as water vapor, hydrogen, and oxygen (to a lesser extent) are able to escape from closed pores by solution and diffusion. In contrast, gases such as carbon monoxide, carbon dioxide, and particularly nitrogen have a lower solubility and do not normally escape from closed pores. If, for example, spherical pores are closed at a total porosity of 10% and a partial pressure of 0.8 atm nitrogen, the pressure has increased to 8 atm (about 110 psi) when they have shrunk to a total porosity of 1%, and further shrinkage is limited. At the same time that the gas pressure is increasing, however, the negative radius of curvature of the pore becomes small so that the negative pressure produced by surface tension is increased proportional to $1/r$; the gas pressure builds up proportional to $1/r^3$. For sintering in air this factor usually limits densification; where very high densities are required, as for optical materials or dental porcelains requiring high translucency, vacuum or hydrogen atmosphere is preferred.

Nonuniform Mixing. Although not mentioned in most discussions of sintering, the most important reason why densification and shrinkage stop short of complete elimination of pores is that gross defects caused by imperfect mixing and compact consolidation prior to firing are usually present. Examination of typical production ceramics shows that they commonly contain upward of 10% porosity in the millimeter size range (that is, pores much larger than the particle size of the raw materials introduced in the composition). These pores are caused by local variations induced during forming, and there is no tendency for elimination of these pores during firing. Corrective treatment must be taken in the forming method.

Overfiring. Ware is commonly referred to as overfired if for any of a variety of reasons a higher firing temperature leads to poorer properties or a reduced shrinkage. For solid-state sintering, such as ferrites and titanates, a common cause is secondary recrystallization occurring at the higher temperature before the elimination of porosity. Consequently, there is some maximum temperature at which the greatest density or optimum properties are obtained. For vitreous ceramics the most common cause of overfiring is the trapping of gases in pores or the evolution of gases which cause bloating or blistering.

10.7 Firing Shrinkage

As formed, green ware contains between 25 and 50 vol% porosity. The amount depends on the particle size, particle-size distribution, and forming method (Chapter 1). During the firing process this porosity is removed; the volume firing shrinkage is equal to the pore volume

eliminated. This firing shrinkage can be substantially decreased by addition of nonshrinking material to the mix; fire-clay brick is commonly manufactured with grog (prefired clay) additions which serve to decrease firing shrinkage. Similarly, this is one of the functions of the flint in the porcelain body; it provides a nonshrinking structure which reduces the shrinkage during firing. Terra-cotta compositions, composed of mixtures of fired grog and clay, can be made in large shapes because a large part of the raw material has been prefired and the firing shrinkage is low.

If firing is carried to complete densification, the fractional porosity originally present is equal to the shrinkage taking place during firing. This commonly amounts to as much as 35% volume shrinkage or 12 to 15% linear shrinkage and causes difficulty in maintaining close tolerances. However, the main difficulties are warping or distortion caused by different amounts of firing shrinkage at different parts of the ware. Nonuniform shrinking can sometimes even cause cracks to open.

Warping. A major cause of warping during firing is density variations in the green ware. There are many reasons for differences in porosity in the green ware. The density after firing is nearly uniform, and there is higher shrinkage for the parts that had a low density than for the parts that had a high density in the green ware. In pressed ware, pressure variations in the die (Chapter 1) cause different amounts of compaction at different parts of a pressed piece; usually the shrinkage at the center is larger than the shrinkage at the ends, and an hourglass shape results from an initially cylindrical sample (Fig. 10.45a).

Another source of warping during firing is the presence of temperature gradients. If ware is laid on a flat plate and heated from above, there is a temperature difference between the top and bottom of the ware that may cause greater shrinkage at the top than at the bottom and a corresponding warping. In some cases the gravitational stresses may be sufficient to make the ware lie flat, even though shrinkage is nonuniform. The relationship between temperature distribution, warpage, and deformation under the stresses developed is complicated and difficult to analyze quantitatively. Another source of warpage in firing is preferred orientation of the platy clay particles during the forming process. This causes the drying and firing shrinkage to have directional properties.

Vitreous ware is also warped by flow under forces of gravity. This is especially true for large heavy pieces in which substantial stresses are developed. In the forming of vitreous sanitary ware, the upper surface of a closet bowl (Fig. 10.45c) or a lavatory (Fig. 10.45d) must be designed with a greater curvature than is desired in the end product so that the settling which occurs on firing produces a final shape that is satisfactory. A final contributor to warpage during firing is the frictional force or *drag*

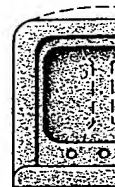


Fig. 10.45. Firing shrinkage with different frictional force

of the ware shrink less so that the

Difficulties and warping method to way that firing that forming m forming. The other source of length to mixes that variations cause a de settling ma tions. Duri an unsym Sometim can be ove in Fig. 10.4

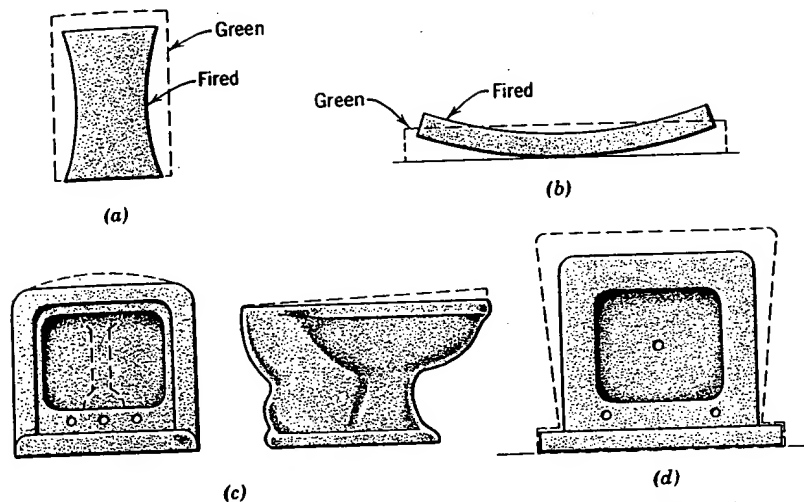


Fig. 10.45. Firing shrinkage of (a) pressed crucible with differential shrinkage due to green density variations, (b) tile with differential shrinkage due to temperature gradients, (c) ware with differential shrinkage due to gravity settling, and (d) differential shrinkage due to frictional force of setting.

of the ware against the setter. This means that the bottom surface tends to shrink less than the upper surface (Fig. 10.45d). Ware must be designed so that the final shape, including shrinkage, comes out to be rectangular.

Difficulties caused by differential firing shrinkage, resulting distortion, and warping can be eliminated in three ways: first, altering the forming method to minimize the causes of warping; second, designing shapes in a way that compensates for warping; and third, using setting methods in firing that minimize the effects of warping. One obvious improvement in forming methods is to obtain uniformity of the structure during initial forming. This requires elimination of pressure gradients, segregation, and other sources of porosity variation. Pressing samples that have long ratios of length to die diameter cause density variations. Extruded and pressed mixes that have low plasticity are particularly prone to large pressure variations and green density differences. Slip casting and extrusion both cause a degree of segregation and density differences during firing. Some settling may occur during the casting process, causing structural variations. During extrusion pressure differences at various parts of the die or an unsymmetrical setting for the die can cause variations.

Sometimes variations in firing shrinkage and difficulties from warping can be overcome by compensating the shapes. This is true, for example, in Fig. 10.45, in which the closet bowl and lavatory are designed in such a

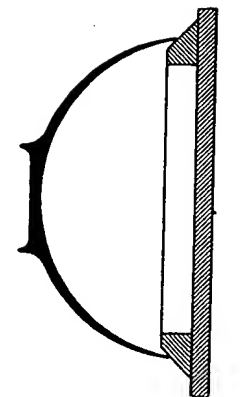
ally decreased by
brick is commonly
serve to decrease
of the flint in the
which reduces the
posed of mixtures
use a large part of
kage is low.

rational porosity
during firing. This
age or 12 to 15%
close tolerances.
ortion caused by
rts of the ware.
ks to open.

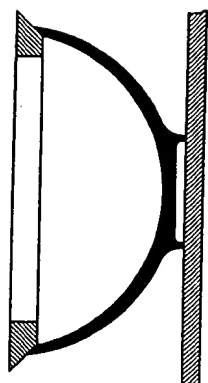
density variations
ces in porosity in
orm, and there is
for the parts that
ressure variations
action at different
ter is larger than
s from an initially

of temperature
above, there is a
he ware that may
a corresponding
be sufficient to
nonuniform. The
and deformation
difficult to analyze
referred orienta-
ness. This causes
erties.

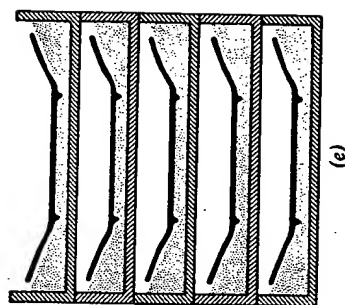
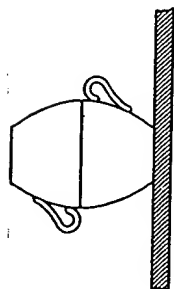
gravity. This is
tial stresses are
upper surface of
must be designed
duct so that the
t is satisfactory.
ial force or drag



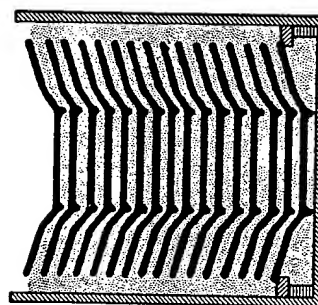
(b)



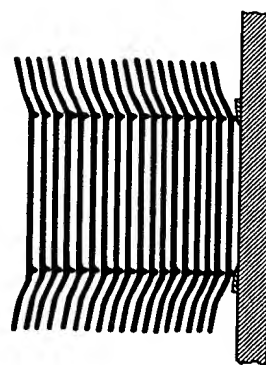
(a)



(e)



(d)



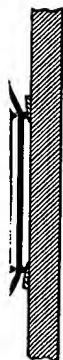
(c)



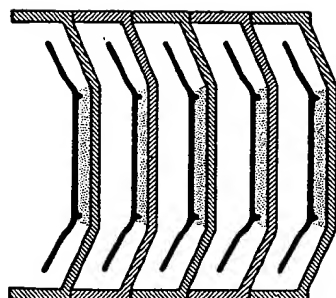
(e)



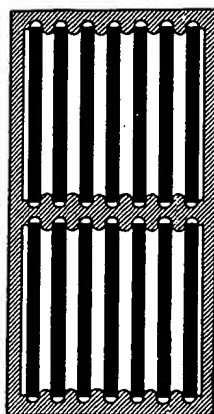
(d)



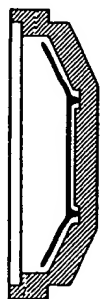
(c)



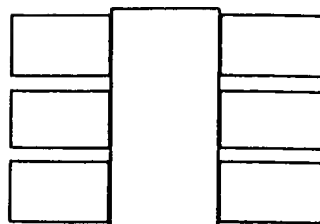
(b)



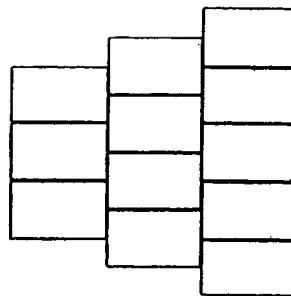
(h)



(g)



(i)



(j)

Fig. 10.46. Setting methods for (a) cups and bowls, (b) large bowls, (c) earthenware, (d) hotel china plates, (e) bone china plates, (f) frit porcelain plates, (g) hard porcelain plates, (h) tile, (i) brick checkerwork, (j) brick bench setting. From F. H. Norton.

way that the final shape is satisfactory. In the same way, when plates are fired in the horizontal position there is a tendency for the rims to settle; this can be compensated for by adjusting the shape of the initial piece.

Correct setting methods are important in eliminating difficulties caused by firing-shrinkage variations. These have been most extensively developed for porcelain compositions in which complete vitrification is desired and high shrinkages result. Some of the standard setting methods are illustrated in Fig. 10.46. Cups and bowls are commonly boxed as indicated in Fig. 10.46a. This keeps the rim circular, since warpage of one restricts warpage of the other; in addition, it prevents the thin rims from being too rapidly heated. For larger pieces, unfired setters are necessary as a means of controlling shrinkage and maintaining circular rims. A variety of methods is used for setting different kinds of plate compositions, depending on the amount of shrinkage expected. For ware fired to complete vitrification individual setting and support are essential. For ware fired to partial densification, plates can be stacked with no ill effects. In general, large tiles and brick do not cause much difficulty.

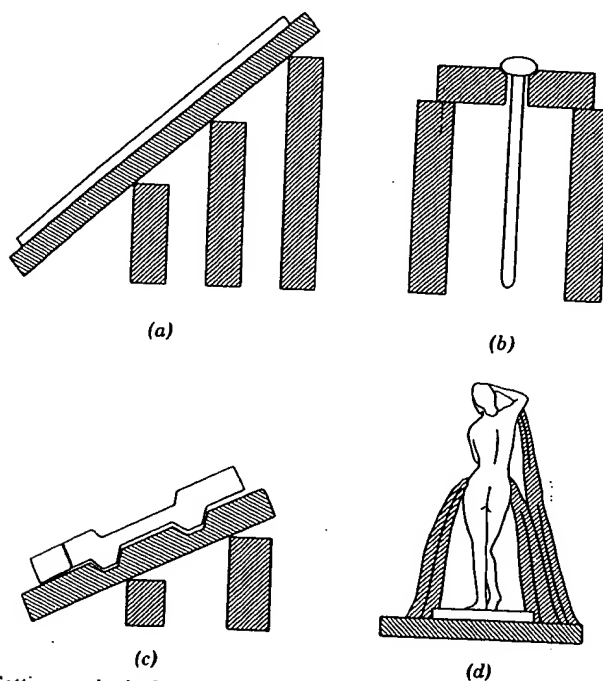


Fig. 10.47. Setting methods for special shapes. (a) Large tiles set at an angle of repose; (b) slender rod supported by collar; (c) special shape; (d) sculptured piece. From F. H. Norton.

G

Special sl
verse effect
angle of rep
shrink with
an inclined
10.47b). Gr
several feet
designed fo
handle uniq
are particul
from unfire

1. G. C. Ku
Phenome
2. G. C. Ku
Research,
3. R. L. Co
Burke, E
4. W. D. Ki
Cambridg
5. W. D. Ki
ogy Pres
6. J. E. Burl
Prog. Me
7. E. Schra
Bodies,"
8. For addi
(1970); D.

- 10.1. Disting
tallizat
import
- 10.2. Explai
approx
gradien
- 10.3. Can g
grain g

Special shapes may require special setting methods to eliminate adverse effects of firing shrinkage. Large refractory tile can be set at an angle of repose on a flat surface (Fig. 10.47a). This allows the tile to shrink without much stress. In the same way rods or tubes may be set in an inclined V groove or supported by a collar from the upper end (Fig. 10.47b). Gravitational forces keep the tubes straight up to lengths of several feet. Unique shapes can always be supported on special setters designed for the particular sample. Some experience is necessary to handle unique shapes efficiently. Small pieces of sculptured vitrified ware are particularly difficult. The safest setting provides complete support from unfired struts (Fig. 10.47d).

Suggested Reading

1. G. C. Kuczyuski, N. A. Hooton, and C. F. Gibson, Eds., *Sintering and Related Phenomena*, Gordon and Breach, New York, 1967.
2. G. C. Kuczyuski, Ed., "Sintering and Related Phenomena", *Materials Science Research*, Vol. 6, Plenum Press, New York, 1973.
3. R. L. Coble and J. E. Burke, *Progress in Ceramic Science*, Vol. III, J. E. Burke, Ed., Pergamon Press, 1963.
4. W. D. Kingery, Ed., *Ceramic Fabrication Process*, Part IV, Technology Press, Cambridge, Mass., and John Wiley & Sons, New York, 1958.
5. W. D. Kingery, Ed., *Kinetics of High-Temperature Process*, Part IV, Technology Press, Cambridge, Mass., and John Wiley & Sons, New York, 1959.
6. J. E. Burke and D. Turnbull, "Recrystallization and Grain Growth in Metals," *Prog. Met. Phys.*, 3, 220 (1952).
7. E. Schramm and F. P. Hall, "The Fluxing Effect of Feldspar in Whiteware Bodies," *J. Am. Ceram. Soc.*, 15, 159 (1936).
8. For additional papers on sintering see: R. L. Coble, *J. Appl. Phys.*, 41, 4798 (1970); D. L. Johnson and I. B. Cutler, *J. Am. Ceram. Soc.* 46, 541 (1963).

Problems

- 10.1. Distinguish between primary recrystallization, grain growth, and secondary recrystallization as to (a) source of driving force, (b) magnitude of driving force, and (c) importance in ceramic systems.
- 10.2. Explain why the activation energy for grain-boundary migration corresponds approximately with that for boundary diffusion, even though no concentration gradient exists in the former case.
- 10.3. Can grain growth during sintering cause compaction of ceramics? Explain. Can grain growth affect the sintering rate? Explain.

tes are
settle;
ce.
caused
ly de-
tion is
ethods
ved as
of one
s from
essary
ms. A
mposi-
ired to
d. For
ffects.

repose;
n F. H.

BRIEF ATTACHMENT C

IN THE UNITED STATES PATENT AND TRADEMARK OFFICE

In re Patent Application of

Applicants: Bednorz et al.

Serial No.: 08/479,810

Filed: June 7, 1995

Date: March 1, 2005

Docket: YO987-074BZ

Group Art Unit: 1751

Examiner: M. Kopec

For: NEW SUPERCONDUCTIVE COMPOUNDS HAVING HIGH TRANSITION
TEMPERATURE, METHODS FOR THEIR USE AND PREPARATION

Commissioner for Patents
P.O. Box 1450
Alexandria, VA 22313-1450

FIRST SUPPLEMENTAL AMENDMENT

Sir:

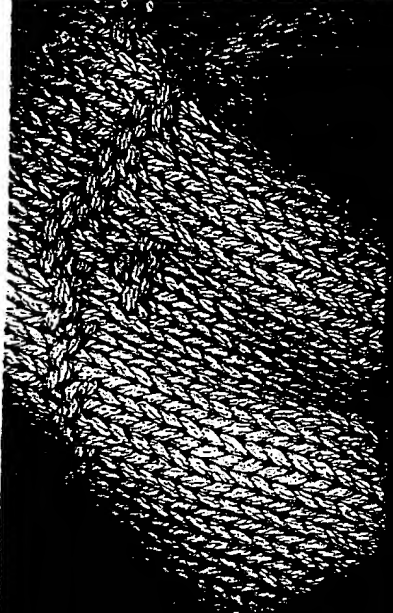
In response to the Office Action dated July 28, 2004, please consider the
following:

ATTACHMENT C

POLAR DIELECTRICS AND THEIR APPLICATIONS

JACK C. BURFOOT and GEORGE W. TAYLOR

University of California Press
Berkeley and Los Angeles



University of California Press
Berkeley and Los Angeles, California

ISBN: 0-520-03749-9

Library of Congress Catalog Card Number: 78-62835

Copyright © 1979 by Jack C. Burfoot and George W. Taylor

Printed in Great Britain

2

Preparation of Polar Materials

This chapter summarises the techniques used for fabricating polar materials in single crystal, ceramic, thin film and glass forms. It then goes on to discuss the various post-fabrication procedures such as annealing, poling, cutting, thinning, polishing and electroding which are usually needed before the polar materials can be used for either experiments or applications.

For basic studies, where the polar material should be as near perfect as possible, it is desirable to use single crystals. For applications, where dimensions, reproducibility and cost are crucial factors then the polar material is usually fabricated in ceramic, thin film or glass form. This division is not precise. For example, some materials have not yet been grown as single crystals and hence basic studies must be made in the ceramic form. In other cases, the larger dielectric, piezoelectric, pyroelectric, electro-optic, etc., coefficients obtainable with particular single crystal materials can make this fabrication form mandatory for certain applications. And yet again thin films offer an important advantage for studying surface layer physics.

The two major problems in fabricating large samples of high quality polar materials are the maintenance of the correct stoichiometry and the avoidance of strains. Chemical, thermal and optical methods, as well as sophisticated

techniques such as X-ray, electron, neutron and proton diffraction scattering are used to determine the quality of the fabricated material. By comparison, the fabrication techniques themselves are still much of an art, as evidenced by the variety of 'recipes' reported for particular materials. This however may be changing. For example, it is now customary to make a careful determination of the phase diagram of the material so as to choose the optimum fabrication conditions. These diagrams can be quite complex, as can be seen from figures 2.1 and 2.2, the phase diagrams for BaTiO_3 and $\text{Pb}(\text{ZrSnTiNb})\text{O}_3$. Note that in figure 2.2 because of the ternary nature of the material, (a) the material is best considered a Nb doped PbZrO_3 - PbSnO_3 - PbTiO_3 solid solution, (b) a different phase diagram is needed for each temperature. Another example of the scientific approach is the use of fluid dynamic principles to try to understand circulation currents in the melt during growth³.

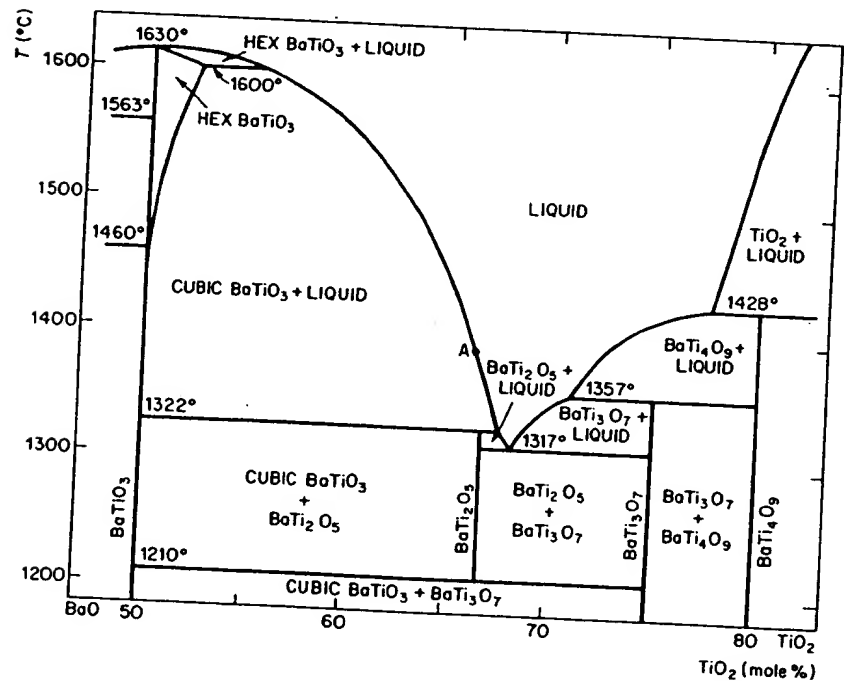


Figure 2.1 Barium titanate. Phase diagram (Rase and Roy¹)

Many measurements can be made to determine the degree to which a ceramic, thin film or glass material approaches the properties of its single crystal counterpart. The hysteresis loop is a simple yet powerful criterion for making this determination. The squarer the loop and the larger its polarisation, then the better the orientation of the crystallites and the smaller the

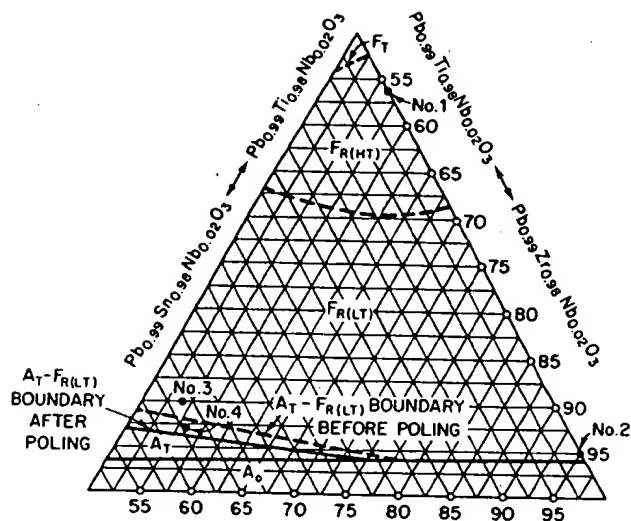


Figure 2.2 Part of the phase diagram of $\text{Pb}_{0.99}(\text{ZrSnTi})_{0.98}\text{Nb}_{0.02}\text{O}_3$ at 25°C (poled at 25°) F = Ferroelectric, A = antiferroelectric, T = tetragonal, R = rhombohedral, LT = low temperature phase, HT = high temperature phase (Raider and Cook²)

percentage of non-polar material and voids present. In general, doctor-bladed ceramics and epitaxial thin films are the fabrication techniques producing materials closest to the single crystal form, whilst the glasses and conventionally sintered ceramics are the furthest away.

2.1 Growth of Single Crystals

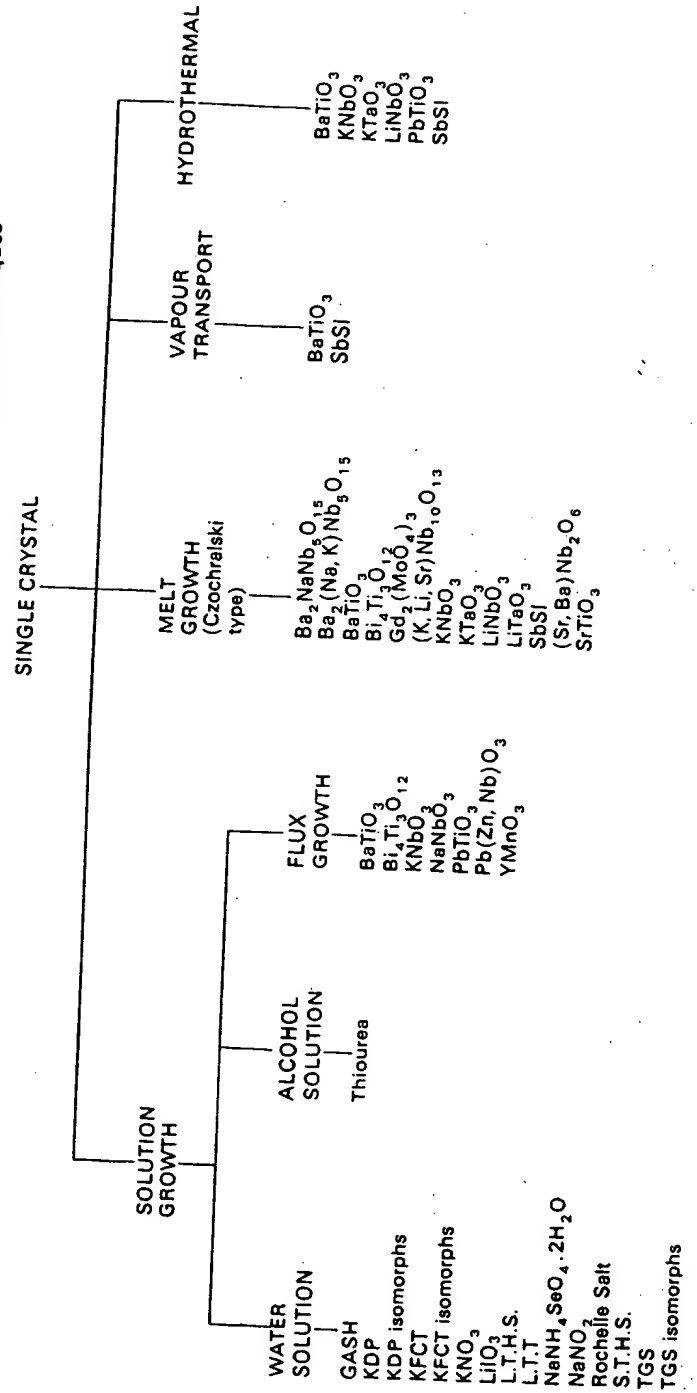
The two major methods that have been used to date for fabricating single crystals have been the solution (or flux) growth technique and the melt growth technique.

2.1a Solution Grown Crystals

This method has been successfully used for both water soluble materials and those that are soluble in other liquids or fluxes.

The first stage in growing a water soluble crystal is to prepare an aqueous saturated solution of the polar material. Crystals can be grown by either keeping the solution at a constant temperature and allowing a gradual evaporation of the solvent or by slowly lowering the temperature while keeping the solution saturated. Slow growth, taking a thousand hours or more, usually produces the best and largest crystals. Other factors which affect the crystal

Table 2.1 Single crystal polar materials that have been grown by various techniques



growth are the purity of the materials, the solubility-temperature characteristics of the solution, the fineness of the temperature control, the use of stirring to prevent temperature and concentration gradients from developing in the solution, and the use of seed crystals suspended in the solution to enhance growth.

Table 2.1 contains a fairly comprehensive listing of the polar materials which have been successfully grown from aqueous solution. Figure 2.3 shows a large solution-grown crystal of triglycine sulphate, TGS. The original seed crystal is visible in the centre of the photograph. The organic polar material thiourea can be grown from an aqueous solution; however, better results are obtained from an alcoholic solution.

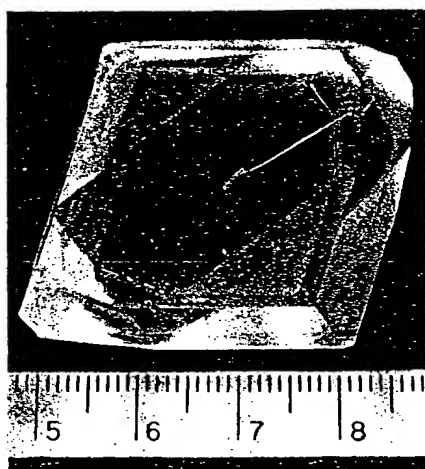


Figure 2.3 Photograph of a TGS crystal (Linz⁴)

Polar materials that are not soluble in water or alcohol can often be dissolved at high temperature in other materials, usually referred to as fluxes. For example, 26 different fluxes have been reported⁵ for barium titanate, BaTiO_3 . In some cases, an excess of one of the constituents can act as a flux. For example, additional Bi_2O_3 will serve as a flux in growing crystals of bismuth titanate, $\text{Bi}_4\text{Ti}_3\text{O}_{12}$.⁶

Besides the particular flux used there are many other variables in flux growth. They include the purity and particle size of the component materials, the time-temperature cycle used for forming the molten flux solution, the crucible material and its shape and size, the method of heating (both resistive and r.f. induction heating are used), the time-temperature cycle used for cooling, the thermal gradients established in the furnace (both vertical and

horizontal gradients have been used), and the atmosphere maintained in the furnace.

Some of the crystals that have been grown by flux techniques are shown in table 2.1. Space does not permit detailing the growth conditions used for each material. To give some idea, however, it is worth summarising the successful technique developed by Remeika⁷ for the flux growth of BaTiO_3 crystals. A platinum crucible containing 30% BaTiO_3 powder, 70% KF (the flux) and a small trace of Fe_2O_3 is heated for 8 h at 1175°C . The Fe_2O_3 compensates for the loss of oxygen at high temperature. The crucible is then cooled slowly to 875°C , at which stage the excess liquid flux is poured off. The crystals thus formed are then cooled slowly to room temperature. Any residual flux is removed by acid etching. The crystals have a plate-like morphology and some typical examples are shown in figure 2.4a.

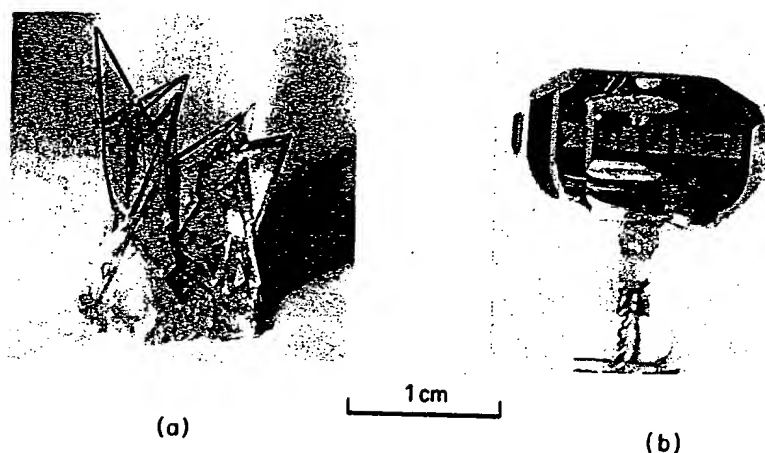


Figure 2.4 Photograph of barium titanate crystals.
(a) Crystals grown by flux method (Epstein⁸).
(b) Crystals grown by Czochralski method (Belruss *et al.*¹¹)

2.1b Melt Growth

If a polar material melts congruently, that is, if stoichiometry is maintained, then the crystal can be grown directly from the melt. As the crystal grows, either by spontaneous nucleation on to a chemically inert platinum or iridium wire or onto a seed crystal, it is gradually withdrawn from the molten liquid. In the Stockbarger method, this is done by withdrawal of the crucible containing the melt. In the Czochralski method (figure 2.5), the crystal is gradually 'pulled' out of the melt, and it is usual to rotate the crystal while pulling, to minimise thermal and stress gradients. Also suitable optics are provided for

viewin
growe
desigr
metho
and le
are pc
and a
used.
at 70
atmos
Bel
times
gradu
grown
crysta
132°C
figure

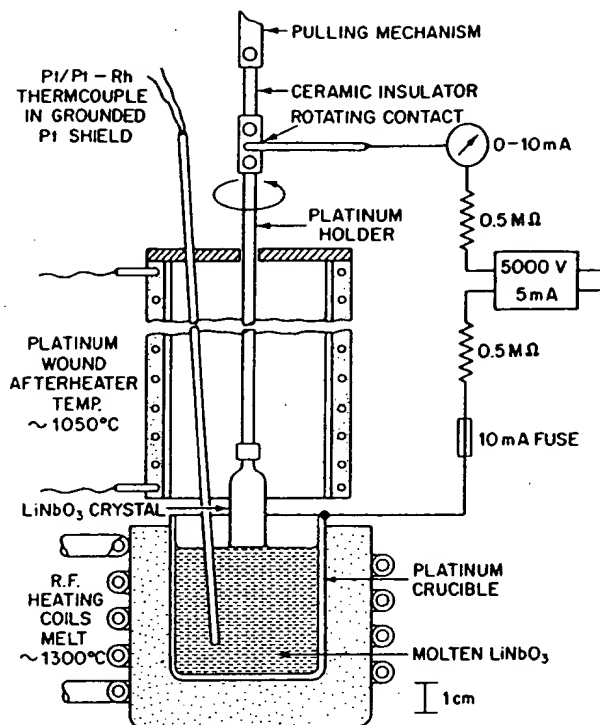


Figure 2.5 Czochralski crystal grower for lithium niobate (Nassau⁹)

viewing the crystal during growth. Figure 2.5 shows a Czochralski crystal grower used for growing lithium niobate, LiNbO_3 . The apparatus is also designed to pole the crystal during the growth process. The Czochralski method is usually the best for polar materials, in that it produces less strains and less twinning in the crystal. A large number of variations in the technique are possible including variation of the pulling and rotation rates, the method and amount of after-heating used as the crystal emerges, and the atmosphere used. Figure 2.6 is a photograph of a $\text{Gd}_2(\text{MoO}_4)_3$ crystal pulled by Kumada at 70 mm/h using a rotational speed of 100 rev/min in an oxygen rich atmosphere¹⁰. Most Czochralski grown crystals have the form of figure 2.6.

Belruss *et al.*¹¹ have developed a modified Czochralski technique, sometimes referred to as 'top seeding', in which the temperature of the melt is gradually dropped (0.2°C/h) as pulling proceeds. The crystal of figure 2.4b was grown by this technique, using a pulling rate of 0.7 mm/h. Pulled BaTiO_3 crystals have a polyhedral morphology and a transition temperature, T_c of 132°C . By comparison, the Remeika⁷ flux grown BaTiO_3 crystals, shown in figure 2.4a have a plate-like structure and a T_c of 120°C . The lower T_c is due to

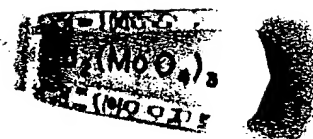


Figure 2.6 Single crystal of gadolinium molybdate (Kumada¹⁰)

the substitution of K atoms at some Ba sites and Fe at some Ti sites in the BaTiO_3 crystal lattice; the K and Fe impurities originate from the flux used.

The polar material single crystals that have been successfully grown from the melt by Czochralski type techniques are listed in table 2.1.

2.1c Other Techniques

Single crystals of both BaTiO_3 and antimony sulpho-iodide, SbSI , have been grown by vapour transport¹². Hydrothermal methods, which involve a combination of high pressure and temperature have been used to grow single crystals of several types of polar materials¹³⁻¹⁵—see also table 2.1.

2.2 Ceramic Fabrication

The classical technique for forming ceramics is sintering at atmospheric pressure. Recent variations on this process are doctor-blading and hot pressing.

2.2a Sintering

The constituents (or their oxides) of the polar material are mixed in the correct proportions with an organic binder and then pressed at room temperature into a structure having the desired shape and dimensions. In most cases this is a cylinder, although for some applications, for example sonar, more complex shapes are used. The pressed structure is sintered or fired at an appropriate temperature in an appropriate atmosphere. This causes the organic binder to be burnt out and the pressed materials to react chemically and form the desired polar material. Table 2.2 contains a list of some of the polar materials which have been fabricated as sintered ceramics.

Table 2.2 Ceramic polar materials that have been fabricated by various techniques

CERAMICS			
SINTERED	DOCTOR BLADED	HOT PRESSED	
AgNbO ₃	Pb(Fe, Nb)O ₆	BaTiO ₃	(Na, K)NbO ₃
AgTaO ₃	PbHfO ₃	PbNb(Zr, Sn, Ti)O ₃	Pb(Zr, Ti)O ₃
AgVO ₃	Pb ₃ (Mg, Nb ₂)O ₉	Pb(Zr, Ti)O ₃	PbBi(Zr, Ti)O ₃
Ba ₂ NaNb ₅ O ₁₅	PbNb ₂ O ₆		PbLa(Zr, Ti)O ₃
BaTiO ₃	PbTiO ₃		PbNb(Zr, Ti)O ₃
Bi ₄ Ti ₃ O ₁₂	PbZrO ₃		Pb(Sn, Zr, Ti)O ₃
Cd ₂ Nb ₂ O ₇	PbBi(Zr, Sn, Ti)O ₃		
CdTiO ₃	PbNb(Zr, Sn, Ti)O ₃		
(K, Li, Sr)Nb ₁₀ O ₁₃	PbBi(Zr, Ti)O ₃		
KNbO ₃	PbLa(Zr, Ti)O ₃		
KTaO ₃	PbNb(Zr, Ti)O ₃		
K(Nb, Ta)O ₃	RbTaO ₃		
LiNbO ₃	SrBaNb ₂ O ₆		
LiTaO ₃	SrTiO ₃		
(Na, K)NbO ₃	WO ₃		
NaNbO ₃			
NaTaO ₃			
Na(NbTa)O ₃			

2.2b Doctor-Blading

Doctor-Blading¹⁶ is particularly suited for forming large area, thin sheets of ceramic. The constituents of the polar materials are mixed in a liquid together with a suitable plasticiser and the resultant slurry is poured onto flat glass. A stainless steel blade, accurately positioned a small distance, *S*, above the substrate is then drawn through the slurry. The resulting sheet is allowed to dry after which it can be peeled off the glass. At this stage the material is termed 'green' because it can be easily cut or punched into any two dimensional shape. The sintering is done in a two step process, viz. a lower temperature firing to burn out the plasticiser and then a higher temperature firing in a controlled atmosphere to form the polar material.

Whenever a ceramic is sintered there is a large amount of shrinkage. For a doctor-bladed material, the shrinkage is particularly evident as a decrease in thickness. Figure 2.7 shows the relationship between the thickness of 'green' and fired materials for a PbNb(Zr, Sn, Ti)O₃ ceramic. A fired and electroded doctor-bladed ceramic strip is shown in figure 2.14.

2.2c Hot Pressing

In the hot-pressing process the ceramic is sintered under pressure, typically developed in a hydraulic press. Hot pressing can result in ceramic densities

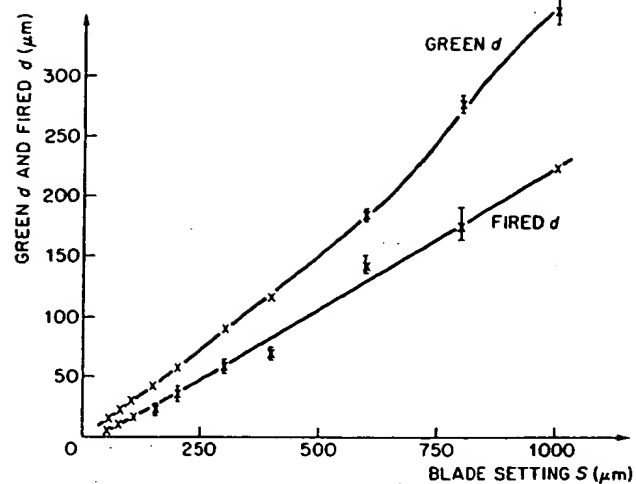


Figure 2.7 Thickness of 'green' and fired materials as a function of blade setting, S , for a doctor-bladed $\text{Pb}(\text{ZrSnTiNb})\text{O}_3$ ceramic (Wentworth and Taylor¹⁶)

even higher than 99.9% of the theoretical maximum. As a result, such materials have properties approaching those of a single crystal. For example, the hot-pressed ceramic can have a high value of remanent polarisation, a low value of coercive field and, as shown in figure 2.8, can be transparent.

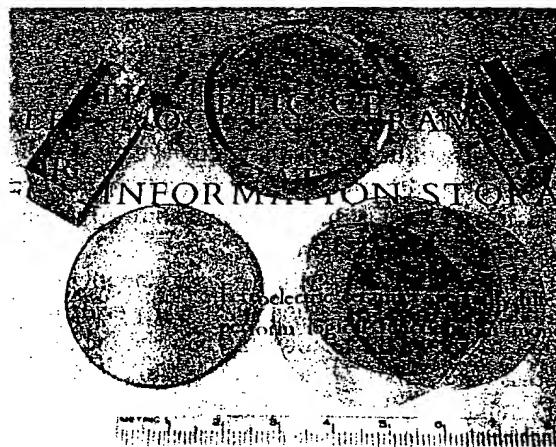


Figure 2.8 Photograph of polished transparent $\text{Pb}(\text{ZrTiLa})\text{O}_3$ hot-pressed ceramic samples. (Haertling and Land¹⁸)

Haertling^{17, 18} has extensively studied how the parameters of time, pressure, temperature, chemical purity and firing atmosphere affect the properties of hot-pressed Nb, Sn, Bi and La doped and Sn, Ba, and La modified^{*} $\text{Pb}(\text{Zr}, \text{Ti})\text{O}_3$ ceramics. Figure 2.9 is typical of such results. In this case the effects of time, pressure, and temperature, on grain size of a $\text{PbNb}(\text{Zr}, \text{Sn}, \text{Ti})\text{O}_3$ ceramic are shown. As discussed in section 15.2a the grain size is important in determining the electro-optic properties of certain ceramic compositions. It also affects many other properties of the ceramic including the permittivity. Other ceramics that have been hot pressed are listed in table 2.2.

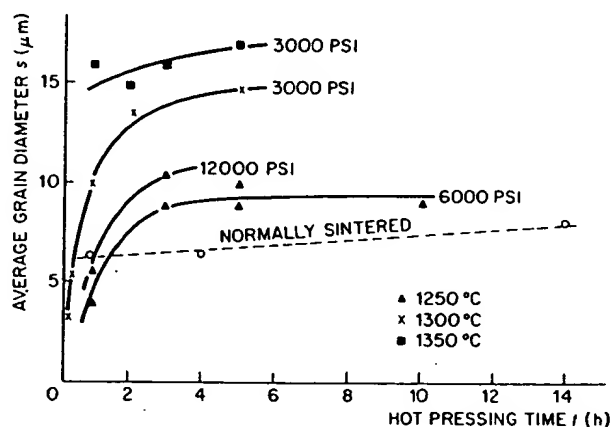


Figure 2.9 Effect of hot pressing time, temperature and pressure on average grain diameter of a hot pressed $\text{PbNb}(\text{ZrSnTi})\text{O}_3$ ceramic (Haertling¹⁷)

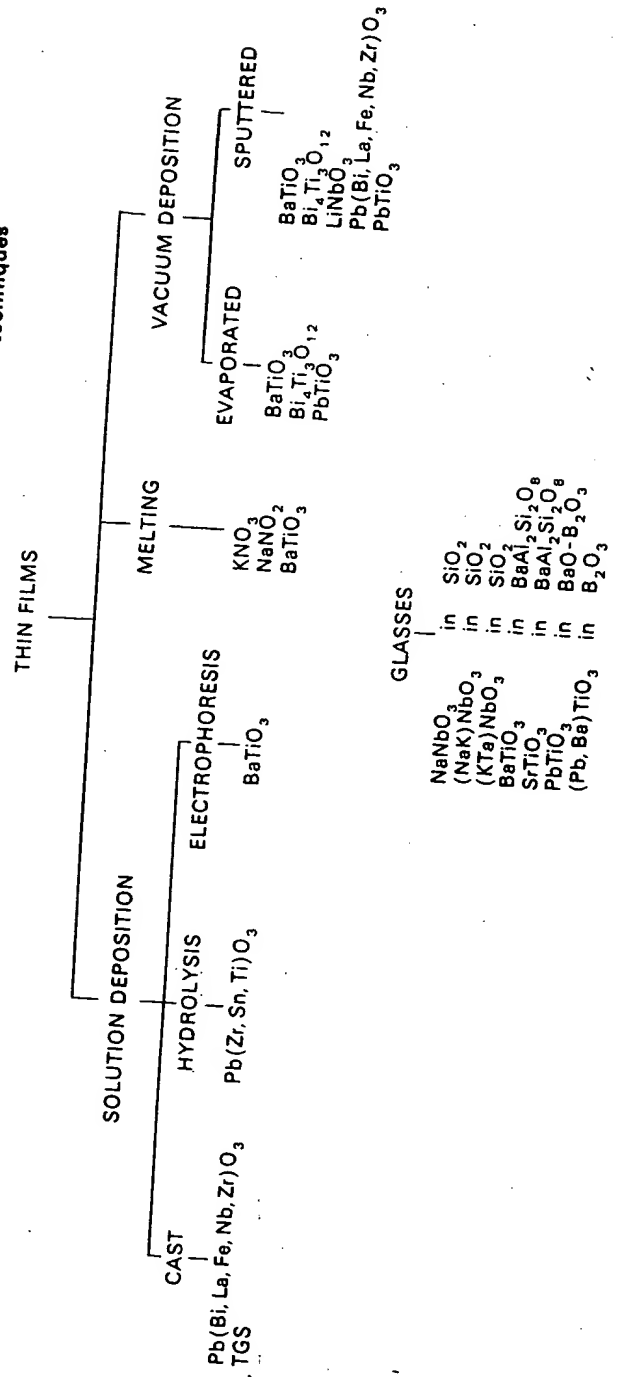
2.3 Thin Film Fabrication

There has recently been much general interest in thin films of polar materials (i.e. less than about $10 \mu\text{m}$ thick). In particular, for device applications, thin films have important advantages which include (a) formation of large capacitances, (b) low switching voltages, (c) the possibility of forming the film directly on the integrated semiconductor 'driving' circuits.

The various techniques used for making thin films are described below. The materials that have been made by these techniques are summarised in table 2.3. With the exception of r.f. sputtering, the fabrication techniques generally

* As described in sections 15.2 and 17.4, the properties of the $\text{Pb}(\text{Zr}, \text{Ti})\text{O}_3$ ceramics vary greatly depending on whether the amount of additive is less or greater than about 5 atom per cent. As a result it is convenient to use the term *doped* $\text{Pb}(\text{ZrTi})\text{O}_3$ when the additive is less than 5 atom per cent and the term *modified* $\text{Pb}(\text{ZrTi})\text{O}_3$ when the additive is greater than 5 atom per cent.

Table 2.3 Thin film polar materials that have been formed by various techniques



produce polycrystalline films, which have properties more similar to ceramics than to single crystals.

2.3a Solution Deposition

Three types of solution deposition have been used for forming thin films. They are casting, hydrolysis and electrophoresis.

Casting

Beerman¹⁹ has made thin films of TGS (a water soluble polar material) by spraying an aqueous solution of TGS onto a suitable substrate. Chapman²⁰ has formed thin films of the complex ferroelectric $\text{Pb}(\text{BiLaFeNbZr})\text{O}_3$ by first making a colloidal suspension, or slurry, of the basic oxides of the composition. The suspension was then centrifuged onto a metallic substrate and sintered at 900°C to form the ferroelectric thin film.

Hydrolysis

Lure *et al.*²¹ have deposited a mixture of Pb, Zr, Sn and Ti oxides on a metallic substrate by hydrolysing a solution of Pb, Zr, Sn and Ti tetrachlorides. The oxides were then sintered to form a ferroelectric film of $\text{Pb}(\text{ZrSnTi})\text{O}_3$.

Electrophoresis

Lamb *et al.*²² placed two noble metal electrodes into a suspension of BaTiO_3 particles in ether. The application of about 200 V cm^{-1} between the electrodes caused a film to be formed on the anode. Subsequent sintering in an atmosphere of 98% helium and 2% oxygen at 1350°C created a stable BaTiO_3 film.

2.3b Melting

Nolta *et al.*²³ have shown that a thin layer of potassium nitrate, KNO_3 , can be easily formed by melting KNO_3 powder onto a metal substrate. However, KNO_3 has the disadvantage that it is only ferroelectric at room temperature and atmospheric pressure for a short time, before reverting to a non-ferroelectric phase²⁴. Sodium nitrite, NaNO_2 , and barium titanate, BaTiO_3 films have also been prepared by melting.

2.3c Vacuum Deposition

Evaporation and sputtering techniques have been used for the vacuum deposition of thin films.

Evaporation

In his early work Feldman²⁵ evaporated BaTiO_3 from a coated tungsten

filament onto a metallic substrate in a vacuum of less than 5×10^{-5} mm Hg. Due to the difference in volatility of the constituent oxides, the resultant film consisted of separated layers of BaO and TiO₂. To combine the oxides the film had to be subsequently heated in air at 1100°C.

Flash evaporation onto a heated substrate is a technique developed by Müller *et al.*²⁶ and Burfoot *et al.*²⁷ which overcomes the dissociation problem. The polar material is evaporated in small-thickness increments, typically corresponding to a few crystal lattice spacings, by dropping the source material, a grain at a time, onto a filament heated to a temperature of about 2000°C. One variation which has proved successful in improving the quality of the evaporated films has been to leak a small amount of oxygen into the vacuum chamber. This improved stoichiometry by overcoming oxygen deficiencies. Another successful technique has been the use of multiple evaporation sources. For example, in forming BaTiO₃, a source of BaO and a source of TiO₂ are used. The multiple sources can reduce the amount of filament material in the film.

In addition to BaTiO₃, thin films of lead titanate, PbTiO₃, and bismuth titanate, Bi₄Ti₃O₁₂, have been evaporated. Films evaporated onto metal substrates such as platinum are polycrystalline in nature. An epitaxial film of BaTiO₃ with its *c*-axis uniformly aligned perpendicular to the substrate can be evaporated if the substrate is a freshly cleaved alkali halide crystal such as LiF or NaF. Burfoot²⁷ has developed a technique for removing the film from the insulating substrate, so that an electrode can be placed on the thin film for electrical measurements.

Sputtering

Francombe²⁸ has suggested that sputtering offers several advantages over evaporation, namely (a) better control of stoichiometry, especially for the more complex oxide materials, (b) better thickness control and (c) freedom from material contamination. Most sputtering has been r.f. sputtering from ceramic targets. However, diode, triode and tetrode sputtering has also been used. The polar materials which have been sputtered are listed in table 2.3. Two of these materials, BaTiO₃ and Bi₄Ti₃O₁₂, have also been sputtered epitaxially.

It is instructive to summarise the sputtering technique developed for monoclinic Bi₄Ti₃O₁₂, since the problems which occur are rather typical, and the results obtained have been the most impressive. Takei *et al.*²⁹ used a 10 cm² ceramic target of bismuth titanate mounted on a water-cooled metallic base and positioned 4 cm from a heated substrate. Using a 4 mm atmosphere of O₂ and Ar they were able to sputter Bi₄Ti₃O₁₂ films at a rate of about 1 Å s⁻¹ using a power level of 1 W cm⁻² and a self bias of 700 V.

The problem in vacuum deposition, as with single crystal and ceramic fabrication, is to develop the correct stoichiometry so that only the required phase is formed. In the case of sputtering Bi₄Ti₃O₁₂, this is done by using a

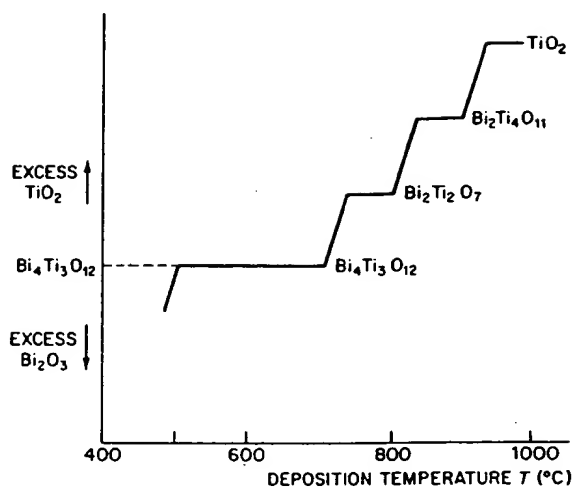


Figure 2.10 Dependence of composition on substrate temperature for films r.f. sputtered from a target of composition 80% $\text{Bi}_4\text{Ti}_3\text{O}_{12}$, 20% $\text{Bi}_{12}\text{TiO}_{20}$. (Francombe²⁸)

ceramic target of 0.8 $\text{Bi}_4\text{Ti}_3\text{O}_{12}$, 0.2 $\text{Bi}_{12}\text{TiO}_{20}$ and a substrate temperature of 650°C. The bismuth enriched target compensates for the high volatility of that oxide, while as can be seen from figure 2.10, the chosen substrate temperature favours $\text{Bi}_4\text{Ti}_3\text{O}_{12}$ over the other phases.

The $\text{Bi}_4\text{Ti}_3\text{O}_{12}$ film can be sputtered epitaxially and aligned along any preferred direction by choosing a substrate having a suitable crystal lattice. Substrates which have been used are Pt, single crystal $\text{Bi}_4\text{Ti}_3\text{O}_{12}$ and MgO and MgAl_2O_4 . Except for a higher coercive field, the electrical and optical properties of the epitaxial films closely match those of the bulk (single crystal) material; see, for example, figure 2.11. The most dramatic evidence of the quality of the sputtered films of $\text{Bi}_4\text{Ti}_3\text{O}_{12}$ is their ability, as shown in figure 2.12, to duplicate the complex electro-optic light valve switching properties of the single crystal material described in section 15.2a.

2.4 Fabrication of Polar Glasses

Borrelli, Herczog and colleagues^{31, 32} at Corning have succeeded in crystallising NaNbO_3 and $(\text{NaK})\text{NbO}_3$ in glass matrices of SiO_2 , and BaTiO_3 and SrTiO_3 in a matrix of $\text{BaAl}_2\text{Si}_2\text{O}_8$. Also, Isard and his colleagues^{33, 34} at Sheffield have made glasses of PbTiO_3 and $(\text{PbBa})\text{TiO}_3$ in B_2O_3 matrices and $(\text{K Ta})\text{NbO}_3$ in a SiO_2 matrix. These polar glasses are made by the rapid quench cooling of the appropriate molten oxides, followed by suitable annealing treatment to crystallise the polar material in the low permittivity,

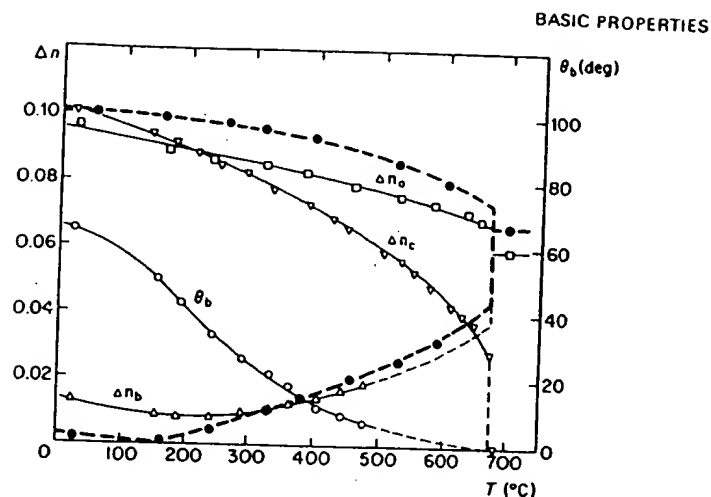


Figure 2.11 Birefringence values and extinction angle of bismuth titanate as a function of temperature measured at wavelength 5890 Å. The solid lines are from single crystal, and the dashed lines from film. The subscripts a, b, and c indicate the monoclinic axis along which light was directed for each measurement. (Wu *et al.*³⁰)

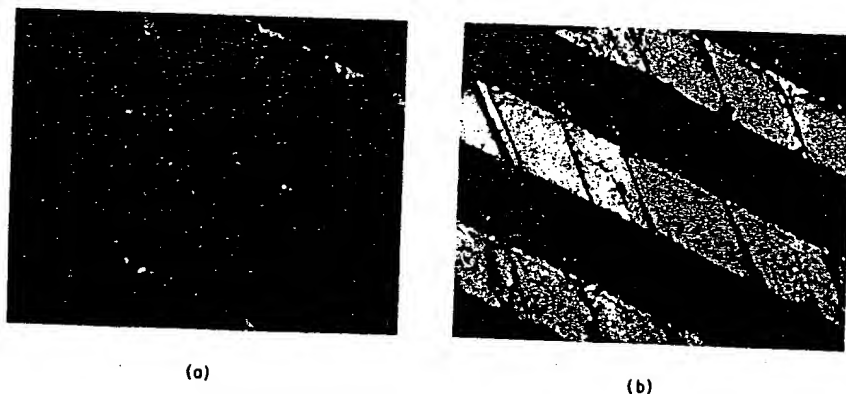


Figure 2.12 A sputtered bismuth titanate film viewed between crossed polarisers in (a) 'off' condition (b) 'on' condition (Wu *et al.*³⁰). Microphotographs of an interdigital electrode array.

high resistivity glass matrix. The volume per cent of glass matrix present should be kept as small as possible: 20% is an achievable amount. The electrical properties of the glasses are enhanced by a large crystallite grain size for the polar material portion, while the optical properties are favoured by a small grain size. For electro-optic applications, 0.5 μm is a typical compromise grain size.

The polar glass materials have the characteristic advantages associated with glass, namely an absence of pores and hence a high dielectric breakdown and mechanical strength. Also, they can be conveniently fabricated in thin uniform sheets. On the other hand, the presence of the glass matrix with its relatively low dielectric permittivity as compared to the polar materials means that the electrical and optical coefficients are smaller than those of the corresponding ceramic or single crystal material. The properties are, however, still sufficiently significant for some electro-optic applications and for some cryogenic temperature, capacitor applications.³²

2.5 Post-Fabrication Procedures

2.5a Annealing

Crystals grown from the melt often develop strains which lead to undesirable domain structures (twinning) and mechanical cracking. The strains are mainly caused by the mechanical constraints imposed during the growth process. The easiest way to remove these strains is by thermal annealing. This can be done by cooling the crystal through its transition temperature at a prescribed rate in a suitable temperature gradient. For example, Hopkins and Miller³⁵ have found that the strains due to domain structures in $\text{Bi}_4\text{Ti}_3\text{O}_{12}$ can be successfully annealed out by placing the crystals on an alumina surface in a tube furnace with a temperature gradient of 5°C cm^{-1} and cooling at the rate of 2°C min^{-1} . Annealing is also used to remove strains which can develop in thin film materials and ceramics while they are being fabricated.

2.5b Poling

In a newly fabricated ceramic, the crystallites, and hence the polar axis, can lie in a large number of directions. This will cause the material to have only a quasi-isotropic response in its electrical, optical, piezoelectric and other characteristics. A lack of orientation can also exist in certain freshly prepared single crystal and thin film materials due to there being more than one possible orientation for the polar axis. For example in BaTiO_3 there are three possible orientations for the polar axis and each orientation has two possible directions.

Before such unaligned materials can be used for measurements and applications, it is necessary to orient the polar axis in a common direction usually normal to the major surfaces. (However, in the case of the electro-optic PLZT ceramics it is necessary, for some modes of operation (see section 15.2), to pole parallel to the surface.)

Polar axis orientation is done by a poling technique which consists of applying a D.C. voltage for a sufficient time to suitable electrodes on the material. The amplitude and duration of the voltage required for poling vary substantially between materials. Some materials will pole easily and if used in



Figure 2.13 Single crystal bismuth titanate poled in central region, as viewed between crossed polarisers (Hopkins and Miller³⁵): scale has 1 mm divisions.

large-signal switching applications may not even require a preliminary poling cycle. Others can only be poled near their Curie point where the coercive field of the material is small. Sometimes the poling is done during the crystal growth—see figure 2.5. The maximum poling voltage that can be applied is limited by breakdown and arcing in the material. Hence poling is often done in an oil bath. Figure 2.13 shows a $\text{Bi}_4\text{Ti}_3\text{O}_{12}$ crystal which has been poled in its central section. The crystal is viewed between crossed polars and hence only the poled region is uniformly extinguished.

2.5c Cutting, Thinning and Polishing

Depending on the intended usage, it is often necessary to cut and thin the 'as grown' single crystal or the 'as sintered' ceramic slug or disc to smaller dimensions. If the material is water soluble then the cutting can be done with a water soaked string. Other materials may require cutting with a high speed diamond coated wire. The thinning can be done by slicing, mechanical grinding or etching. In the latter process, depending on the material, the etch solution can vary from water to aqua regia. Some materials will, with a suitably applied high impulse pressure, naturally cleave into thin platelets. Desputtering, where-in the polar material is made the sputtering source, is a technique that permits very carefully controlled thinning of a material.³⁸

For optical use it is almost mandatory to have a finely polished surface to minimise light scattering. Several methods are used for polishing. One of the most common is a series of polishes with alumina powder of progressively smaller particle size.

2.5d Electroding

Many measurements and most devices require the application of electric fields to the material. This is done by applying a voltage between electrodes placed on the surfaces of the polar material. Because of the high ϵ of polar materials, the electrodes must be in intimate contact with the surfaces. Virtually any airgap will cause an intolerable reduction in the voltage developed in the polar material.

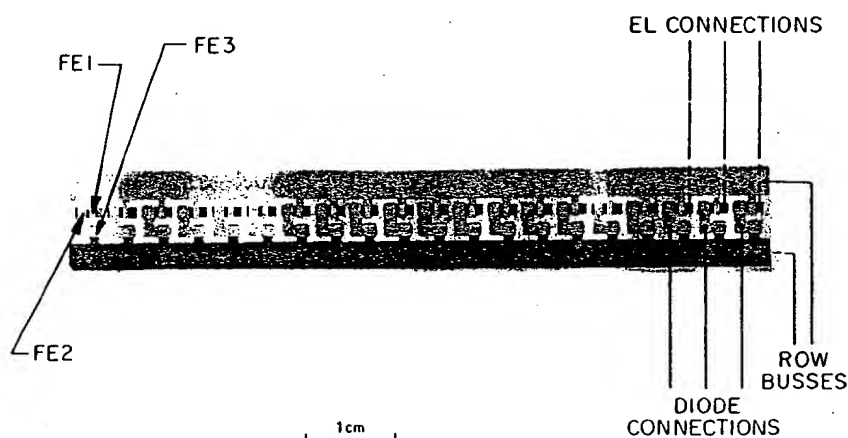


Figure 2.14 An evaporated gold electrode pattern on a doctor bladed ceramic strip (Taylor³⁶).

For quick measurements, air drying silver paste is often used as an electrode. For applications which require accurately defined electrodes, it is usual to evaporate metal through photomechanically formed masks. Figure 2.14 shows such an electrode pattern formed with evaporated gold on a doctor-bladed PZT-type ceramic. Silk screening and sputtering are two other techniques which have been used for forming electrodes. For electro-optic applications, it is often necessary to have transparent electrodes. Very thin (less than 500 Å thick) evaporated metal electrodes can sometimes be used. However, r.f. sputtered indium and/or tin oxide has proved to be a more satisfactory transparent electrode. Such electrodes can have a resistance of less than 10 Ω per square and an optical transmission of greater than 90% in the visible spectrum.

At first sight, electroding would seem to be no more than a technical process. However, as discussed in detail in section 3.2c, electrodes can have a significant effect on the ageing phenomena in polar materials. For example, if metal electrodes are used, single crystal BaTiO₃ ages after repeated polarisation reversals. With conducting liquid electrodes (e.g. an aqueous lithium chloride

solution) no ageing occurs³⁷. These and other results indicate that the surface physics involved is complicated and not well understood. The large electric field gradients which exist near the surfaces of polar materials undoubtedly contribute to the effects that the electrodes can have on the switching properties of polar materials.

References

1. D. E. Rase and R. Roy, *J. Am. ceram. Soc.*, **38**, 110 (1965)
2. M. E. Raider and W. R. Cook, *J. appl. Phys.*, **38**, 1977 (1967)
3. J. R. Carruthers and K. Nassau, *J. appl. Phys.*, **39**, 5205 (1968)
4. A. Linz, private communication
5. M. L. Sholokhovitch and I. N. Belyaev, *Zhur. Obschehei. Khim.*, **24**, 218 (1954); *ibid.*, 1118 (1954)
6. A. D. Morrison, F. A. Lewis and A. Miller, *Ferroelectrics*, **1**, 75 (1970)
7. J. P. Remeika, *J. Am. chem. Soc.*, **76**, 940 (1954)
8. D. J. Epstein, U. S. Air Force Contract Report AFAL-TR-70-172
9. K. Nassau, *Ferroelectricity* (ed. E. F. Weller), Elsevier, Amsterdam, p. 266 (1967)
10. A. Kumada, *Ferroelectrics*, **3**, 115 (1972)
11. V. Belruss, J. Kalnajs, A. Linz and R. Folweiler, *Materials Research Bulletin*, **6**, 899 (1971)
12. T. Mori, H. Tamura and E. Sawaguchi, *J. phys. Soc. Japan*, **20**, 1294 (1965)
13. V. I. Popolitov and B. N. Litvin, *Sov. Phys. Crystall.*, **13**, 483 (1968)
14. V. G. Hill and K. G. Zimmerman, *J. electrochem. Soc.*, **115**, 978 (1968)
15. A. A. Shternberg and V. A. Kuznetsov, *Sov. Phys. Crystall.*, **13**, 647 (1968)
16. C. Wentworth and G. W. Taylor, *Am. ceram. Soc. Bull.*, **46**, 1186 (1967)
17. G. H. Haertling, *J. Am. ceramic Soc.*, **42**, 679 (1963); *ibid.*, **49**, 113 (1966)
18. G. H. Haertling and C. E. Land, *J. Am. ceram. Soc.*, **54**, 1 (1971)
19. G. H. Haertling and C. E. Land, *Ferroelectrics*, **3**, 269 (1972)
20. H. P. Beerman, *Ferroelectrics*, **2**, 123 (1971)
21. D. W. Chapman, *J. appl. Phys.*, **40**, 2381 (1969)
22. M. S. Luré, E. I. Vasil'eva and I. V. Ignat'eva, *Bull. Acad. Sci. USSR*, **24**, 1372 (1960)
23. V. A. Lamb and H. I. Salmon, *Bull. Am. ceramic Soc.*, **41**, 781 (1962)
24. J. P. Nolte and N. W. Schubring, *Phys. Rev. Letters*, **9**, 285 (1962)
25. R. A. Dork, N. W. Schubring and J. P. Nolte, *J. appl. Phys.*, **35**, 1984 (1964)
26. N. W. Schubring, R. A. Dork and J. P. Nolte, *J. appl. Phys.*, **38**, 1671 (1967)
27. G. W. Taylor and B. J. Lechner, *J. appl. Phys.*, **39**, 2372 (1968)
28. C. Feldman, *Phys. Rev.*, **96**, 819 (1954)
29. C. Feldman, *Rev. scient. Instrum.*, **26**, 463 (1955)
30. E. K. Müller, B. J. Nicholson and M. H. Francombe, *Electrochem. Technology*, **1**, 158 (1963)

27. J. C. Burfoot and J. R. Slack, *Proc. European Meeting*, Saarbrücken (1969)
J. C. Burfoot and J. R. Slack, *J. phys. Soc. Japan*, **28**, Supplement, 417 (1970)
28. M. H. Francombe, *Ferroelectrics*, **3**, 199 (1972)
29. W. J. Takei, N. P. Formigoni and M. H. Francombe, *Appl. Phys. Letters*, **15**, 256 (1969)
W. J. Takei, N. P. Formigoni and M. H. Francombe, *J. Vacuum Sci. Tech.*, **7**, 442 (1970)
30. S. Y. Wu, W. J. Takei and M. H. Francombe, *Ferroelectrics*, **10**, 209 (1976)
31. N. F. Borrelli, A. Herczog and R. D. Mauer, *Appl. Phys. Letters*, **7**, 117 (1965)
N. F. Borrelli, *J. appl. Phys.*, **38**, 4243 (1967)
N. F. Borrelli and M. M. Layton, *IEEE Trans. Electron Devices*, **ED-16**, 511 (1969)
32. W. N. Lawless, *Ferroelectrics*, **3**, 287 (1972); *ibid.*, **7**, 379 (1974)
33. D. G. Grossman and J. O. Isard, *J. Phys. D. appl. Phys.*, **3**, 1058 (1970)
34. D. V. Keight and J. O. Isard, paper given at British Ceramic Society Meeting (Dec. 1972)
35. M. M. Hopkins and A. Miller, *Ferroelectrics*, **1**, 37 (1970)
36. G. W. Taylor, *IEEE Trans. Electron Devices*, **ED16**, 565 (1969)
37. G. W. Taylor, Ph.D. Thesis, University of London (1961)
38. J. Vossen, private communication

BRIEF ATTACHMENT D

IN THE UNITED STATES PATENT AND TRADEMARK OFFICE

In re Patent Application of

Applicants: Bednorz et al.

Serial No.: 08/479,810

Filed: June 7, 1995

For: NEW SUPERCONDUCTIVE COMPOUNDS HAVING HIGH TRANSITION
TEMPERATURE, METHODS FOR THEIR USE AND PREPARATION

Date: March 1, 2005

Docket: YO987-074BZ

Group Art Unit: 1751

Examiner: M. Kopec

Commissioner for Patents
P.O. Box 1450
Alexandria, VA 22313-1450

FIRST SUPPLEMENTAL AMENDMENT

Sir:

In response to the Office Action dated July 28, 2004, please consider the
following:

ATTACHMENT D

CERAMIC PROCESSING BEFORE FIRING

Edited by

George Y. Onoda, Jr.

and

Larry L. Hench

Department of Materials Science and Engineering
University of Florida, Gainesville

A Wiley-Interscience Publication

JOHN WILEY & SONS, New York • Chichester • Brisbane • Toronto

*To Karl Schwartzwalder and Frederick H. Norton
for their pioneering contributions to the science
and technology of modern ceramic processing*

Copyright © 1978 by John Wiley & Sons, Inc.

Library of Congress Cataloging in Publication Data:

Main entry under title:

Ceramic processing before firing.

"A Wiley-Interscience publication."

"Edited from the proceedings of the conference . . .
held at the University of Florida from January 27 to
30, 1975."

Includes index.

I. Ceramics. I. Onoda, George Y., 1938-

II. Hench, L. L., 1938- III. Florida.
University, Gainesville.

TP807.C45 666 77-10553

ISBN 0-471-65410-8

Printed in the United States of America

10 9 8 7 6 5 4 3 2 1

Contributors

- R. A. Alleigro, Norton Company, Worcester, Massachusetts
 R. B. Bennett, Battelle's Columbus Laboratories, Columbus, Ohio
 M. Berg, General Motors, Flint, Michigan
 J. E. Burke, General Electric Company, Schenectady, New York
 A. R. Cooper, Case Western Reserve University, Cleveland, Ohio
 W. B. Crandall, Alfred University, Alfred, New York
 I. B. Cutler, University of Utah, Salt Lake City, Utah
 R. E. Farris, Kaiser Refractories, Pleasonton, California
 W. M. Flock, Plessey Central Development Laboratories, Los Angeles, California
 D. W. Fuerstenau, University of California, Berkeley, California
 P. K. Gallagher, Bell Laboratories, Murray Hill, New Jersey
 D. W. Gates, NASA-Marshall Space Flight Center, Alabama
 R. S. Gordon, University of Utah, Salt Lake City, Utah
 Y. Harada, IIT Research Institute, Chicago, Illinois
 T. M. Hare, North Carolina State University, Raleigh, North Carolina
 D. P. H. Hasselman, Lehigh University, Bethlehem, Pennsylvania
 L. L. Hensch, University of Florida, Gainesville, Florida
 H. Heystek, U.S. Bureau of Mines, Tuscaloosa, Alabama
 E. J. Jenkins, University of Florida, Gainesville, Florida
 D. W. Johnson, Jr., Bell Laboratories, Murray Hill, New Jersey
 W. D. Kingery, Massachusetts Institute of Technology, Cambridge, Massachusetts
 W. G. Lawrence, Alfred University, Alfred, New York
 M. G. McLaren, Rutgers University, New Brunswick, New Jersey
 J. S. Masaryk, Kaiser Refractories, Pleasonton, California
 E. A. Metzbowler, Naval Research Laboratories, Washington, D.C.
 R. E. Mistler, Western Electric, Princeton, New Jersey
 D. E. Niesz, Battelle's Columbus Laboratories, Columbus, Ohio
 F. H. Norton, Gloucester, Massachusetts
 G. Y. Onoda, Jr., University of Florida, Gainesville, Florida
 C. Orr, Jr., Georgia Institute of Technology, Atlanta, Georgia

J. P. Page, Western Electric Company, Allentown, Pennsylvania
 H. Palmour, III, North Carolina State University, Raleigh, North Carolina
 J. A. Pask, University of California, Berkeley, California
 G. W. Phelps, Rutgers University, New Brunswick, New Jersey
 A. G. Pincus, Rutgers University, New Brunswick, New Jersey
 F. N. Rhines, University of Florida, Gainesville, Florida
 A. Roberts, Sel-Rex Company, Santa Ana, California
 G. C. Robinson, Clemson University, Clemson, South Carolina
 H. Rumpf, Universitat of Karlsruhe, Karlsruhe, Germany
 R. B. Runk, Western Electric Company, Princeton, New Jersey
 R. Russell, Jr., Ohio State University, Columbus, Ohio
 K. Schwartzwalder, Holly, Michigan
 D. J. Shanefield, Western Electric Company, Princeton, New Jersey
 H. Schubert, Universitat of Karlsruhe, Karlsruhe, Germany
 P. Somasundaran, Columbia University, New York, New York
 K. Sommer, Universitat of Karlsruhe, Karlsruhe, Germany
 R. T. Trempier, General Electric Company, Cleveland, Ohio
 K. K. Verma, Sel-Rex Company, Santa Ana, California
 O. J. Whittemore, Jr., University of Washington, Seattle, Washington
 W. O. Williamson, Pennsylvania State University, University Park, Pennsylvania

Preface

This book has been edited from the proceedings of the conference on "The Science of Ceramic Processing Before Firing" held at the University of Florida from January 27 to 30, 1975. The conference, the tenth in a series of university conferences on ceramic science, was attended by approximately 200 persons from industry, government, and universities.

It was the first conference in several decades that concentrated on subjects relevant to raw materials, batch processing, and forming of ceramics. Scientists and engineers were invited from throughout the United States to cover topics that were judged to be of particular importance to the theme of the conference. In addition, we were particularly fortunate in having Dr. H. Rumpf and Dr. K. Sommer of Karlsruhe, Germany, with us. A number of the contributors were not ceramists but were experts in areas that are directly related to problems in ceramic processing. Outside areas included fine-particle technology, surface chemistry, mineral dressing, and metallurgy.

At first we planned to have the proceedings published rapidly as a compiled book with a minimum of editing. However, contributors and conference participants encouraged us to prepare a book as close as possible to a textbook, since none exists that covers the topics of the conference. Therefore, many of the chapters were revised, shortened, and sometimes rearranged in an attempt to provide a style more closely approaching a single-author contribution. There were distinct limits in the editing, because in many cases we did not wish to lose the logic and intent of a paper that depended on the style of presentation.

The book is not a descriptive discourse on how ceramics are processed. Other books are available for this purpose. We concentrate on the principles of processing in rather detailed fashion, with the intention of bringing about a better understanding of the science of processing. Students in ceramics should find this book useful as a textbook in ceramic processing, particularly if their course stresses principles. From the response at the conference, where more than three-fourths of the registrants were from

industry, we believe that this book will also be useful for ceramic engineers throughout industry.

We are grateful to the U.S. Bureau of Mines (Tuscaloosa, Alabama and Washington, D.C.), the U.S. Army Research Office (Durham, N.C.), and the Department of Materials Science and Engineering, University of Florida, for their partial sponsorship of the conference that made this book possible. Finally, the editors would like to thank Arleen Weintraub for her diligent, competent, and cheerful preparation of the entire written manuscript and Becky McElowney for her valuable assistance in the administration of the conference.

G. Y. ONODA, JR.
L. L. HENCH
Editors

Gainesville, Florida
October 1977

Honoring KARL SCHWARTZWALDER



Dr. Karl Schwartzwaldner
(May 5, 1907-May 2, 1975)

Karl Schwartzwaldner was born on May 5, 1907 in Pomeroy, Ohio. As a youth he learned to work and play vigorously and with purpose. He was employed in the backroom of the Pomeroy Daily News, delivered newspapers covering a long route on foot, and did odd jobs to provide supplementary family income. His family included his fine parents, Frances and Frank, and three sisters, with whose families he has remained very close through the years. While not large physically, he was always naturally competitive and courageous, whether in swimming the Ohio River, participating in contact sports, or even as we attempted to pick winners at the racetrack in later years. He has never been one to back away from a cause in which he believes or to waiver in an encounter in support of right. Yet he has always been considerate of others and concerned with their personal welfare. He genuinely enjoys people and helping others is his greatest pleasure.

While Karl's fine intellect and creative genius enabled him to realize great professional success and recognition, he has remained completely unchanged in demeanor or true character from our first professional association some 40 years ago.

Following graduation from Pomeroy High School in 1925, he worked for a year before enrolling at Ohio State University in the fall of 1926. In the depths of the Great Depression he received the Bachelor of Ceramic Engineering degree in 1930 and the Master of Science degree in 1931. He was active in Tau Beta Pi, Techniko, Sigma Xi, Sigma Gamma Epsilon, Keramos, and the Student Branch of the American Ceramic Society while on campus.

Those years at Ohio State were the beginning of a long and close friendship with the late Dr. Arthur S. Watts, who for over 60 years contributed so much to the advancement of our American ceramic industry. It was Dr. Watts who encouraged Karl in 1931 to become associated with AC Spark Plug, now a division of the General Motors Corporation, an association that lasted until his retirement in 1972. Karl rose through various positions of responsibility in the Research and Development Laboratory to become Chief Ceramic Engineer in 1945 and then Director of Research and Development for all of AC in 1954. His ingenuity is evidenced by an imposing list of over 50 patents in the field of ceramics and metals. He has been a pioneer and vital force in the continuing development of technical ceramics in the United States, especially the refractory oxide types such as alumina ceramics, where his contributions to compositional and processing technology are well documented. Less well known is his role in the ultrasecret Manhattan Project of World War II, where his council and ceramic expertise were widely employed.

While Karl's technical contributions are generally well recognized,

perhaps less known is his influence in advancing the careers of the many people who worked under him through the years. His guidance and selfless concern for them have resulted in an imposing alumni body, whose influence will remain far-reaching.

Karl has always enjoyed travel, having visited many foreign countries, inspected countless research and manufacturing operations, and become acquainted with scientific and technical personnel worldwide. He has a peculiar ability to combine business and pleasure in the best sense. His insatiable curiosity has pervaded whatever he encountered in these extensive travels, benefiting both his company and those he contacted along the way.

Karl has been an active member of many technical and professional organizations, including, of course, the American Ceramic Society, for which he served as President from 1956 to 1957 and which has designated him both a Fellow and an Honorary Member. He has also been an active contributor in many other organizations, such as the National Institute of Ceramic Engineers, the American Society for Metals, the Society for Automotive Engineers, and the National Academy of Engineering. His technical affiliations and many committee services through the years are

patently too extensive to allow further review here but are indeed imposing. Karl somehow has also found time to be active in civic affairs in such organizations as the Flint, Michigan Chamber of Commerce, the Flint Science Fair, the Five Talents Program for talented high school students, which he founded and sponsored, the Industrial Executives Club, and Saint Rita's Catholic Church, which he long served as a member of the Board of Trustees, and in which Ruth and Karl Schwartzwalder were both uniquely active.

Perhaps among the least widely known facets of Karl's life and also that of his late, wonderful wife, Ruth, are their abiding faith in young people and their concerned interest in nature and wildlife. One must have been exposed to their country home, "their" animals, and the constant influx of young friends to realize the basic goodness of Ruth and Karl. They truly represent the best of human instincts.

It is only natural that many honors, awards, and accompanying responsibilities have come to Karl, including recognition as a Distinguished Alumnus and the Award of an Honorary Doctorate by his Alma Mater, Ohio State University, which he has tangibly supported in many ways throughout his career; the Arthur F. Greaves-Walker Award of the National Institute of Ceramic Engineers; the Bleining Memorial Award and John Jeppson Medal of the American Ceramic Society; the Man of the Year Award from *Ceramic Age*; the Liberty Bell Award of the Michigan State Bar; the Outstanding Michigan Inventor Award of the Michigan Patent Law Association; the Earl R. Wilson, Sr. Memorial Award of the Society of Automotive Engineers; and special citations from the National Association of Manufacturers and various governmental agencies that have sought and received his counsel.

Karl Schwartzwalder is truly a giant among men. I will ever be most grateful for a warm and enduring friendship with Karl accompanied by genuine feelings of brotherly love and mutual respect. Paraphrasing our Alma Mater, "Time and change will surely show, how firm our friendship." Thank you, Karl.

Ralston Russell, Jr.

On May 2, 1975, Karl Schwartzwalder died after an extended illness. This tribute by Ralston Russell Jr., was delivered at the conference three months before the untimely passing of Dr. Schwartzwalder.

Ed.

Honoring FREDERICK HAREWOOD NORTON



Frederick Harewood Norton
(October 23, 1896-)

Professor F. H. Norton was born on October 23, 1896, in Manchester, Massachusetts, and obtained a Bachelor of Science degree in Industrial Physics from the Massachusetts Institute of Technology in 1918.

His connections with M.I.T. have been close throughout his life. His father was head of the M.I.T. Physics Department, and his brother, John T. Norton, was a professor of metallurgy at M.I.T. for many years.

Soon after his graduation from M.I.T., he started work at Langley Field for NACA, the group that was largely responsible for early airframe development in this country. Dr. Norton worked in several areas, including the creep rates of heated steel. Before he left in 1923 to join Babcock and Wilcox as a ceramist, he was chief physicist for NACA. (NACA went on to develop supersonic aircraft and eventually turned into NASA.) Dr. Norton later became an expert on refractories.

After about 3 years at Babcock and Wilcox, he went to M.I.T. as a Babcock and Wilcox Research Fellow, and later joined the M.I.T. faculty to start a Division of Ceramics.

As a teacher he was one of the first to recognize the interdisciplinary nature of ceramic science. He required that his students study colloid

chemistry in the chemistry department, take X-ray crystallography from Warren, and geology and petrography from Martin Buerger. Considering the research interest both of these professors have had in the ceramics area, I suspect their interaction with Professor Norton was much more than just as teachers of his students.

Norton's success as a teacher is well known. At least two of his students are now deans in major universities and I shall not attempt to enumerate the leading ceramists in the country who have been directly or indirectly strongly influenced by him.

As a ceramist he has had the widest interests. His book on refractories was perhaps the first scientifically based book on ceramics to be published. It first appeared in the 1930s and has gone through four editions. It reflects his continuing close association with Babcock and Wilcox, but also his

intense interest in the mechanical techniques of ceramic processing, as well as the origin of the properties in the precursor and product materials. His is not theoretical knowledge only. He is responsible for the series of insulating firebrick that permitted the inner wall of furnaces to be insulated instead of requiring an inner course of solid firebrick.

He was one of the early workers to investigate the colloidal chemistry nature of the plasticity of clays and the methods of controlling it by dialysis and evaluating it by measuring base-exchange capacity.

Less well known, perhaps, is his seminal work on fiber optics with the American Optical Company. He may be considered the father of this technology, and certainly did a great deal of the early development work.

Finally, I must mention his invaluable work for the Manhattan District in the making of ceramics at the M.I.T. Branch of the project during the war. I was on the receiving end of the project at Los Alamos and recall the exquisite magnesia and beryllia crucibles we received for melting uranium and later plutonium.

Earlier, there had been a similar development on crucibles made of what was called "Brass," which was actually cerium sulfide. Leo Brewer, I believe, had guessed that the melting point of plutonium would be somewhere above 1600°C, where the vapor pressure of MgO would have been too high, so, Professor Norton and his group developed methods for fabricating this esoteric material. Luckily, the melting point of plutonium turned out to be lower than 700°C, so this material was not needed and MgO crucibles were used.

One could go on endlessly. Professor Norton is a Fellow and Honorary Life Member of the American Ceramic Society and the British Ceramic Society. He has honorary doctorates from Alfred and the University of Toledo. He is a most skillful sculptor and artist potter and has written several books in this area.

The most striking aspect that I repeatedly observed in conversations with many of his former students and coworkers is the very high regard in which Professor Norton was and is held. In addition, there were many expressions of gratitude to him for having provided the discipline, the insight, and, indeed, the demand that they understand what they were doing. Many feel that his precepts have guided them throughout their professional careers.

Joseph E. Burke

Contents

PART ONE INTRODUCTORY

<i>Chapter 1</i>	
Cycles in Ceramic History	3
<i>Frederick H. Norton</i>	
<i>Chapter 2</i>	
Processing Controls in Technical Ceramics	11
<i>Karl Schwartzwalder</i>	

PART TWO POWDERS

<i>Chapter 3</i>	
Active Powders	21
<i>I. B. Cutler</i>	
<i>Chapter 4</i>	
Characterization and Process Interactions	31
<i>W. M. Flock</i>	
<i>Chapter 5</i>	
Physical Characterization Terminology	35
<i>G. Y. Onoda, Jr. and L. L. Hench</i>	
<i>Chapter 6</i>	
Physical Characterization Techniques for Particles	39
<i>C. Orr, Jr.</i>	
<i>Chapter 7</i>	
Structure and Properties of Agglomerates	61
<i>D. E. Niesz and R. B. Bennett</i>	
<i>Chapter 8</i>	
Characterization of Agglomerates with Transmission Electron Microscopy	75
<i>L. L. Hench and E. J. Jenkins</i>	

xx	Contents	Contents	xxi
<i>Chapter 9</i> Bayer-Processed Aluminas <i>W. M. Flock</i>	85	<i>Chapter 20</i> Mixedness of Suspensions <i>K. Sommer and H. Rumpf</i>	253
<i>Chapter 10</i> Grinding of Aluminas <i>M. Berg</i>	101	<i>Chapter 21</i> Quantitative Theory of Cracking and Warping During the Drying of Clay Bodies <i>A. R. Cooper</i>	261
<i>Chapter 11</i> Theories of Grinding <i>P. Somasundaran</i>	105	<i>Chapter 22</i> Mineralogy of Curing and Drying of a Refractory Concrete <i>R. E. Farris and J. S. Masaryk</i>	277
<i>Chapter 12</i> Reactive Powders from Solution <i>D. W. Johnson, Jr. and P. K. Gallagher</i>	125		
<i>Chapter 13</i> Lattice Strain in Alumina Powders <i>J. P. Page, E. A. Metzbowler, D. J. Shanefield, and D. P. H. Hasselman</i>	141		
<i>Chapter 14</i> Agglomeration Effects on the Sintering of Alumina Powders Prepared by Autoclaving Aluminum Metal <i>R. T. Tremper and R. S. Gordon</i>	153	PART FOUR GREEN-BODY FORMATION AND MICROSTRUCTURE	291
<i>Chapter 15</i> Layer-Silicate Minerals <i>H. Heystek</i>	177	<i>Chapter 23</i> Firing—The Proof Test for Ceramic Processing <i>W. D. Kingery</i>	
		<i>Chapter 24</i> Effect of Process Optimization Properties of Alumina Sintered Under Rate Control <i>T. M. Hare and H. Palmour III</i>	307
PART THREE PARTICULATE-WATER SYSTEMS		<i>Chapter 25</i> Dynamic Particle Stacking <i>F. N. Rhines</i>	321
<i>Chapter 16</i> The Structure of Water and Its Role in Clay-Water Systems <i>W. G. Lawrence</i>	193	<i>Chapter 26</i> Particle Compaction <i>O. J. Whittemore, Jr.</i>	343
<i>Chapter 17</i> Particle-Size Distribution and Slip Properties <i>G. W. Phelps and M. G. McLaren</i>	211	<i>Chapter 27</i> Adhesion Forces in Agglomeration Processes <i>H. Rumpf and H. Schubert</i>	357
<i>Chapter 18</i> Viscosity of Concentrated Newtonian Suspensions <i>K. Sommer</i>	227	<i>Chapter 28</i> Strength and Microstructures of Dried Clay Mixtures <i>W. O. Williamson</i>	377
<i>Chapter 19</i> The Rheology of Organic Binder Solutions <i>G. Y. Onoda, Jr.</i>	235	<i>Chapter 29</i> Extrusion Defects <i>G. C. Robinson</i>	391

PART FIVE PROCESSES AND APPLICATIONS

<i>Chapter 30</i>		
Tape Casting of Ceramics	411	
<i>R. E. Mistler, D. J. Shanefield, and R. B. Runk</i>		
<i>Chapter 31</i>		
Zinc Orthotitanate Powders for Thermal-Control Coatings	449	
<i>Y. Harada and D. W. Gates</i>		
<i>Chapter 32</i>		
Characterization of Powders for Thick Films and Capacitors	463	
<i>K. K. Verma and A. Roberts</i>		
<i>Chapter 33</i>		
Future Directions in Processing Research	471	
<i>J. A. Pask, A. G. Pincus, R. Russell, Jr., J. E. Burke, R. A. Alleigro, W. B. Crandall, D. W. Fuerstenau</i>		
Index	479	

PART ONE

INTRODUCTORY

It is appropriate that the two introductory chapters are written by the scientist and the engineer who probably contributed most to modern concepts in ceramic processing. The history described in these chapters serves to highlight the changes in approach and philosophy of thinkers and doers in this industry. Before this century ceramics processing was purely an art, but the rapid technological developments in our society required that new materials be developed rapidly. Leisure was no longer an available luxury, and inventiveness and understanding of why processes did or did not work were crucial to meet the new demands of technology.

I

Cycles in Ceramic History

Frederick H. Norton

Anyone studying the world history of ceramics must be aware of the alternating periods of activity and quiescence. I have found the causes of these cycles of great interest and am therefore setting down some thoughts on this subject.

BEFORE THE CHRISTIAN ERA

Ceramic ware during this period was made largely from native clays, which produced a rather soft earthenware. Hand molding and wheel throwing was usual, but some ware, such as the Tanagra figurines, was formed in fired clay molds. Terra cotta was made in rather large pieces. Glazes containing lead and tin were commonly used with a variety of colors. An original surface finish for earthenware, called Terra Sgrillata, was used in Greece and Italy. The finish consisted of a fine fraction of clay separated by suspension in water. When applied as a glaze it could be dried and fired to a smooth dense layer on the ware.

In this period ceramics were used largely in the household, but art ware, such as painted Greek vases, was also produced. The ancient potter did not seem to have the social standing of sculptors and painters.

THE FIRST 17 CENTURIES OF THE CHRISTIAN ERA

In this period a great variety of pottery was made nearly everywhere, but most of it was earthenware. However, one of the most stupendous ceramic developments of all time occurred in China. The earthenware produced at the beginning of the period was gradually refined to a stoneware and finally to the pure white translucent porcelain. This ware reached such heights of perfection that fine specimens were treasured by the wealthy Chinese and by the Ruling Family as well. When specimens of this porcelain trickled into Europe in Marco Polo's days, they were viewed with wonder and awe.

At once the nobility of the Continent recruited potters to search for the secret of making this fine ware. Some progress was made with a frit porcelain, but for many years the secret of making hard porcelain was not discovered in the West.

Today old Chinese porcelains are exhibited in museums all over the world and there are many private collectors who pay enormous sums for fine specimens. I once held in my hand a little vase that had just been purchased for \$60,000, and extraordinary pieces have brought much higher prices than this at auctions.

These fine specimens can still be made today, as attested by the very fine forgeries that frequently come on the market. Museums such as the Boston Museum of Fine Arts have laboratories with the most modern equipment to evaluate Chinese pottery and detect forgeries.

What are the factors that permitted this remarkable ceramic development in China? One, undoubtedly, was the availability of a natural porcelain body, a partially decomposed feldspar. This raw body was found in the area of Ching-Te Chen, the center of fine porcelain making. Then there was the development of high-fire kilns capable of reaching a temperature of 1400°C, which is 200 or 300°C higher than could be reached in previous kilns. The Chinese potters used continuous chamber kilns in the form of a chain of chambers running up the hillside both to gain high temperatures and to conserve the scarce wood fuel.

Another factor encouraging fine porcelain manufacture was the intense desire of the Chinese people for beautiful objects. They cherished a cabinet of fine vases more than the architecture of their houses. The Emperor was intensely interested in porcelain, which caused him to subsidize many of the finest potters.

Sometime ago I had a student who was raised in Ching-Te Chen and whose ancestors had lived there for generations. He told a story about a potter who was sentenced to death for some political offence; however, my student's grandfather in some way was able to save his life. In return this

potter made a pair of exquisite vases as a present, which took him 5 years. They were small vases and the surfaces were covered with tiny dragons modeled in the finest detail. The eyes of the dragons twinkled when the vases were moved as the black and white eyeballs were free in their sockets.

It was not unusual for a master potter, subsidized by the Emperor, to spend a lifetime in producing just one superb vase for the palace collection. It would seem that the quality of the potter's ware was influenced by the unhurried life-style at this time and the uninterrupted apprenticeship of the young potter to the masters.

Why did the quality of the porcelain ware decline after the Ming Dynasty? Some believe it was due to the exhaustion of the natural body material before the Chinese had learned to make a controlled body of kaolin, feldspar, and quartz. Probably the main cause of deterioration was the artistic fussiness that sets in towards the end of all great art cycles.

EIGHTEENTH CENTURY EUROPE

In the Western World, at the start of the eighteenth century, there was continued production of generally undistinguished earthenware. On the other hand, strenuous efforts were being made on the Continent to duplicate Chinese porcelain. The early attempts produced a type of frit porcelain in which glass was added to the earthenware body. An excellent translucency was achieved, but the ware could not compare with hard porcelain. Then in 1709 a German chemist, Graph von Tschirnhaus, finally discovered the formula for fine porcelain. Attempts were made to keep this valuable knowledge a secret, but soon potters were enticed away from von Tschirnhaus, and many small factories started up all over the Continent, usually supported by wealthy nobles. Most of these enterprises lasted only a few years, but some are still known as producers of hard porcelain, such as Sèvres, Copenhagen, and Meissen.

Thus vitreous pottery produced on the Continent continues to be largely a hard porcelain body made of a kaolin-feldspar-quartz mixture, bisque fired at low temperature and glost fired at a high temperature. Thus a pattern was set for both tableware and artware in the continental area that is still going on.

THE NINETEENTH CENTURY

The earthenware potteries saw few changes during this period except for greater use of coal. However, Hoffman in Germany invented the

continuous-chamber kiln, quite unaware that this principle had been used in China many years earlier. Again, England was the original home of the steam engine, so this source of power became available at the end of the century and must have been a factor in modernizing the potteries. However, in 1935 when I visited a large English pottery, almost all work, even wedging, was done by hand.

Toward the end of the nineteenth century electric power pointed to exciting new possibilities of working at very much higher temperatures than had been possible before. Thus electrochemistry began in France and led rapidly to giant steps at the start of the next century.

THE TWENTIETH CENTURY TO 1930

The manufacture of ceramics in this period showed very few significant changes except for the powerful electric furnaces for making silicon carbide, fused alumina, and fused magnesia. Other changes were the increased use of gas and oil for kiln fuel, the start of tunnel kilns, and the use of electric motors for more powerful forming machines.

However, there was an increasing understanding of the various ceramic materials and their forming and firing, and improvements were made in treating clays and other minerals. All these things were building a foundation for the enormous leap in the next period.

A very significant step occurred near the end of the nineteenth century: the initiation of ceramic societies where ceramists could get together and discuss their problems. This did much to break up the years when each pottery was cloaked in a tight veil of secrecy. These societies also began to publish journals to disperse specialized knowledge. In England the British Ceramic Society was started and was carried on by Mellor and later by Green. In Germany an association was started by Seger and carried on actively, and in the United States the American Ceramic Society was conceived by Orton and carried on by Purdy. These organizations and many more that started later were instrumental in uniting the field of ceramics.

THE PERIOD FROM 1925 TO 1974

In 1926 I was asked to start a Ceramic Department at the Massachusetts Institute of Technology by Dr. Stratten, formerly chief of the United States Bureau of Standards. In preparation for this project, I visited a number of existing schools for ceramic engineering. My reaction after these visits was

that the schools were doing a fine job in preparing students for manufacturing plants, but the courses seemed rather narrow and inbred. The comments from these schools was general agreement that my lack of a degree in ceramic engineering doomed my project to failure.

The situation seemed to call for integration of other disciplines into the ceramic course to broaden it. This was already being done in Germany to a considerable extent by applying physical chemistry and thermodynamics to ceramic problems. At this time Dr. Bleininger, then at the Homer Laughlin Pottery, was a great influence in steering me toward ceramic science.

The petrographic microscope was extensively used by the mineralogist but only to a limited extent by the ceramist, as it was not adapted to examining the finer particles in clay. Crystal structure determination by X-ray diffraction, started by Bragg in England and carried on in this country by Warren at M.I.T., seemed to be pertinent to many ceramic problems. Also, differential thermal analysis methods seemed useful, so at this time equipment was built in our laboratory for research on clays. The electron microscope was found to be important in many problems, especially morphology of clay particles, so Warren designed and built one in the ceramic laboratory that was very useful in our research.

The precise measurement of temperature is of the greatest importance in the testing or firing of ceramic products. In early times the eye of the skilled fireman was the only judge of temperature. Excavations of old kiln sites indicate much overfired ware, so this method was far from precise. Wedgewood's shrinkage cylinders were a great step ahead and the pyrometric cones went even further. After World War I the optical pyrometer and the thermocouple began to be extensively used and provided better temperature control. Now there are excellent recording and controlling instruments available to hold temperatures to the 1°C tolerances needed for some of the electronic wares.

The colloidal chemist was becoming interested in clay suspensions, from which many aspects of casting slips were made clear. Hauser at M.I.T. was instrumental in sparking increased interest in clay colloids.

During this period great progress was made in the production of equilibrium diagrams applying to ceramics. The United States Bureau of Standards, United States Bureau of Mines, and various universities were instrumental in carrying out this fundamental work so essential to ceramic research and production. The American Society for Testing materials was making progress in setting standards and organizing definitions.

At this time great progress was made in the ceramic field through the study of crystal physics, for the atomic structure of many crystals became of interest to the ceramist.

During the World War II work was active on electrical ceramic bodies,

especially in Germany. For high-frequency use steatite porcelains were made in large quantities. At the same time research was going on in the field of titanates. In this country developments also occurred rapidly with ferroelectrics and later with ferromagnetics, largely under the leadership of Von Hippel at M.I.T. These materials were put into use at once and soon became one of the larger branches of ceramics. The miniature printed circuit, first developed by the United States Bureau of Standards for the proximity fuse, has found ever expanding use for printed-on sintered-alumina substrates. The spark plugs with triaxial or mica cores were not suitable for high-powered internal combustion engines, so the sintered-alumina core came into use and now is universally employed for this type of engine.

Around 1930 a new type of conference was started at M.I.T., the first of its kind there and, as far as I know, anywhere else. The idea was to set out a rather specific branch of the ceramic field and other disciplines that could reflect on it. The lecturers were given a reasonable honorarium and those attending paid an entrance fee, hopefully to cover expenses. When first suggested, the plan met with much skepticism from the administration, but finally I got permission to go ahead because it employed unused summer facilities of the school. We included not only lectures and discussions, but also a carefully prepared laboratory course so that those registered could become acquainted with apparatus not generally available at that time, such as the long-arm centrifuge and differential thermal analysis apparatus. Also, attention was given to laboratory note keeping, precision of measurements, patent records, temperature measurements, and many other details pertaining to the ceramic research laboratory.

This type of conference proved so successful that others like it were given annually until my retirement. Other departments began to develop these summer conferences until now there are hundreds every year. Looking back, it seems certain that these conferences have done much to bring up to date the plant worker who often feels rather alone in his domain. Also, the associations made in these groups lead to an excellent interchange of ideas. A further dividend is the opportunity for our graduate students to become acquainted with people in industry; a number of times this has led to excellent positions for the students.

Great progress was made in the refractories field after World War II. Higher-fired and high-alumina silica-alumina brick were commonly used for severe service. Basic brick, for the steel industry of $\text{MgO-Cr}_2\text{O}_3$, was greatly improved. Fused refractory blocks for the glass industry of alumina and zirconia became common. Perhaps one of the most interesting developments was the insulating refractory which allowed the insulating layer to be on the

inside of the furnaces instead of outside of a layer of heavy firebrick. This not only saved fuel, but allowed much quicker heating.

In the field of manufacturing processes, we may mention isostatic pressing used for many products in the last few years, such as spark plug porcelains and tank blocks. The vacuum auger has taken over the field of extrusion, and automated hydraulic presses have found considerable use. Slip casting under pressure is on the way. The roller former has now largely displaced the jigger for making flat and hollow ware. The kilns have been improved to give more even temperature distribution.

In the field of dinner ware, silk screen decoration has been mechanized and decals have been improved. The color maker, applying crystal physics methods, has devised new strains, such as those containing vanadia and zirconia.

Abrasives of the usual silicon carbide and fused alumina are now being made much as they have been for many years. However, the shape and brittleness of the alumina grains is better controlled. Among new materials are the man-made diamonds produced on the basis of the high-pressure carbon-phase diagram. Other hard materials, such as boron nitride, are finding new uses.

It is interesting to speculate on the reason for the tremendous advances of ceramics since World War II. The most important factor was the infiltration of science into the previously rather narrow and empirical ceramic sphere. This caused older processes to be better understood and mysteries to be unraveled and opened the door for original approaches to solve problems. Another factor was the precise determination of material properties, which opened up new uses for them. Lastly, we may look to the much greater interchange of ideas from our ceramic schools, ceramic societies, and technical publications digested by the increasing number of well-trained ceramists.

Has this present expansion in the ceramics field reached a peak or will it continue? I think anyone who reads this book must conclude that the field of ceramics is ready for a further climb.

2

Processing Controls in Technical Ceramics

Karl Schwartzwalder

It was the best of times: it was the worst of times
It was the age of wisdom: it was the age of foolishness
It was an epoch of disbelief: it was an epoch of incredulity
It was the season of hope: it was the winter of despair.

Charles Dickens

These times of challenge in ceramic processing are much like those that Dickens wrote about in the *Tale of Two Cities*, for in many plants therein lies the cause of nonuniformity, unreliability, nonreproducibility, and size limitation of products. In these times of rising material costs and nonavailability, soaring energy costs and shortages, and drops in productivity and profits, a challenge to use creative processing faces us.

In this paper I review (1) processing controls in technical ceramics and (2) major improvements resulting from such controls. Also, I point out the most fertile areas for future development.

CHANGING ATTITUDES IN THE 1930s

Years ago *Punch* had a cartoon captioned "The greatest of all research problems is the people who do research." I have not found this to be true as we were blessed with very capable people. As the problems unfold, I give the names of your peers who solved or contributed to the solution of these problems. The innovations developed in testing resulted in (1) a change from defensive to offensive tactics in processing controls and (2) a simplification in processing.

Let me take you back some 40 years. In those days under the guise of quality control, controls were more for defensive purposes should losses arise than for the improvement of processing or quality. The engineer was called upon to defend himself against management. Following the tactics of the metallurgist, the as-received materials were made into bars and processed (including firing). Test results on these pieces provided process control. There was no apparent reason for change from normal.

My first experience with the company for which I worked over 40 years was as a summer student. My impression as a student was that our plant was the most obsolete that I had ever seen. Professor Watts later convinced me that it was a golden opportunity. I am sure that many summer students feel the same way today.

The composition or body of our insulator was made by blunging, leaf-filter pressing, mixing, and shaping to a roll on French-kneading machines (ever hear of them?). It was then extruded from a cylinder into a block with an internal hole and counterbore and finally turned on a lathe into an insulator shape. Moisture content was measured by weighing and by feel, with feel determining the final decision. Modulus of rupture bars, tensile bars, thermal expansion, thermal diffusivity, T_c value discs, and breakdown voltage pieces were made daily. As many people were employed in this area as in development. The insulators were fired in a continuous kiln that Ross Purdy once called a toaster. Lindbergh flew the Atlantic with spark plugs containing insulators made by such methods!

From this method of processing in production, changes were made. Better materials were used in the composition; that is, a switch was made from mullite to alumina. In processing, a change was made to continuous filtration with vacuum drums and continuous extrusion by vacuum pug mills. The lathe continued to be the method for contouring. The salvage material from the operations was reprocessed. While the new materials were tested, they were usually passed as received. A closer control on moisture was maintained since this influenced shrinkage and hence size, which has to be maintained. The only pride in the process was cost, and the process was used at least in part up to the 1950s.

ROLE OF RESEARCH AND DEVELOPMENT

Several unique processing procedures were developed for use in production. Siemens-Halske in Germany developed a method to make a sintered alumina composition. The patent rights were purchased. The processing was to grind 20% fused alumina and 80% of a low-soda calcined alumina in steel mills to the desired fineness. This mix was then acid treated to remove the iron. The fineness and the pH were controlled by methods developed by Dr. Ralston Russell. The insulators were made by slip casting in plastic molds using chrome-plated copper core pins. The mold life was short. The insulators' shapes were finished on a lathe using a ceramic cutting tool. The processing was costly (as I recall, the company dropped about 500,000 in good depression dollars). But the experience did lead to other processes for making an insulator with alumina as the base material.

The first new processing methods developed in the thirties were the manufacture of insulators using thermosetting and thermoplastic resins as binders, and the application of new techniques developed by the plastics industry to form the insulators. No longer was processing dependent on the plasticity of clays. No longer was wet processing required. From this point on all compositions were prepared by dry grinding, the plastics being added as part of the mill charge. In the case of thermosetting resins, the ground dry powder was used as screened as the mill discharged. The powder was formed into preforms, the several preforms being used to simulate the shape of the formed insulators. Later the preformed system was abandoned and the granulated powder was volumetrically fed into hot 40-cavity dies and cured under pressure to form the insulators.

In the thermoplastic system the resins were part of the dry-milled batch, and the plasticizer was admixed to this material in a hot sigma mixer. The insulators were injection molded in insulator shapes in 40-cavity dies. The plasticizer was removed in a dryer, and the insulators were then fired in continuous tunnel kilns.

During this period of development and manufacture, new methods of control and testing were devised, the former based on resin systems and the latter on sections taken from insulators. Dr. Robert W. Smith, who had worked on the development of the spectrograph for our company at the University of Michigan, devised methods of analysis for the ingredients in raw materials and the insulator, except of course the alkalies. He also devised methods for determining physical characteristics such as thermal expansion, thermal diffusivity, and electrical resistance from sections cut from the insulator. Dr. Helen Bartlett cut thin bands from the insulators to determine modulus of rupture. Dr. Morris Berg, while at RCA, worked to improve the method and, as I recall, had it adopted by the American

Society for Testing Materials. Dr. Barlett also sought to determine the tensile strength by measuring internal pressure by closing the hole through the insulator and bursting it with fluid pressure. It was partially successful.

The plastic method of manufacture, utilized because it was a simplified process, required that the insulator be free from ribs on its exposed portion. Functionally this was permissible, since in operation the exposed portion of the spark plug was covered by a protective boot to avoid any flashover due to dirt accumulation. Madison Avenue and national competitors tested the spark plugs for the general public without the boots to show the increased voltage necessary for flashover on ribbed plugs. To this day, American spark plugs have ribs, while Bosch in Germany does not.

The secondary operation required to put on the ribs necessitated a further change in processing. The isostatic method of molding was adopted around 1950. By the way, Dr. Ralston Russell did development work on this process in the early thirties. Mr. Joseph Coors was very helpful in not only making the decision to go in this direction, but in giving us his ideas on processing. The plant facilities were completely changed, and new continuous kilns were built.

The body continued to be dry ground. The binders were added in liquid form in the wet mixing equipment. The blanks were pressed from spray-dried powder and were contoured on a resin-bonded abrasive wheel.

Mr. John Quirk, who at this time was working for Battelle, called our attention to work Battelle was doing for one of the carbon companies that had initiated a new process for making reactive alumina. This was an exciting subject, since at the same time we were also working with Monsanto on a similar matter and had failed. We discussed the potential with the alumina companies and, after several years of hard work, all were able to produce a satisfactory reactive product that has found good usage in a variety of markets. The future was reactive aluminas.

The objective then was to be able to dry grind the entire body and, after screening, feed the material directly to the presses. We also wanted to accelerate grinding. Dr. Walter Gitzen of Alcoa called our attention to the work that had been done on mineral aids, mentioning that naphthenic acid had been found to be an excellent aid in ball-milling Bayer aluminas, except that it was hydrophobic and hence was not suitable for alumina to be used in aqueous suspension. Subsequently, both companies undertook development programs. Dr. Gitzen, A. Pearson, and George MacZura worked on Bayer alumina, and at our plant Michael Fenerty in manufacturing, Dr. Morris Berg, and Arthur V. Somers in Research and Development worked on body compositions. Several patents on this manner of processing were issued to both companies.

The attempt to reduce the process to manufacturing practice was not successful. The material tended to bridge in the feeder, and when this happened, the molds were destroyed and replacement was costly, especially in time.

The mill grinding was successful, the output per mill increasing markedly. A system had been devised by Mr. Fenerty so that molding pressure that would yield a given firing shrinkage could be predicted. Losses now were more in handling in the firing operation than in the processing to that point.

MICROSTRUCTURE AND PROPERTIES

During the period of 1959 to 1965, Dr. William Shulhof and Dr. Dave Hinckley undertook to relate physical properties to the interdependent elements of microstructure. Examples were composition relating to phases, size, shape, and orientation and packing of grains. Modulus of rupture was predicted by a few simple measurements on ceramics on which there was good background, such as a production body.

They were also the first, at least in our company, to use designed experiments and statistical analysis to control composition and process variables and to design a ceramic to meet our specific property requirements. Robert Vernetti was the engineer under Mr. Fenerty, and with a few studies he was able to control the kilns to give maximum properties as required for our product.

Dr. Shulhof and Dr. Hinckley developed preparation techniques for sections that permitted better definition of various phases in the body. They may have been the first to use electron microscopy to look at the morphological changes in various phases caused by trace elements.

They also developed X-ray diffraction techniques that measured minor-phase constituents of ceramic bodies. The minor phases were often indications of process conditions; therefore, these techniques led to better process control. X-Ray measurements were found to be a method that predicted "reactivity" of alumina.

Dr. Hinckley developed techniques so that the amount and quality of clays could be measured accurately on production-type materials. For example, X-ray diffraction techniques gave complete analysis of the clay phases in a sample. Percent of bentonite was measured by an ethylene glycol expansion in conjunction with X-ray diffraction. He used base exchange techniques to characterize the "activity" of the clay, for instance, in comparing Florida kaolin with Georgia kaolin. Incidentally, Dr. Russell worked on similar base exchange techniques during the thirties.

Dr. William Flock simplified the control aspect of this analysis by correlating the X-ray data with simple optical examination of alumina aggregates. I recall one incident when we were visiting one of the alumina companies and were asked if we had any questions. Bill said, "Yes, why did you increase your rate of precipitation of alumina hydrate?" They were stunned that Bill knew this, and so he discussed his methods of analysis with them.

At the time of my retirement, Dr. Flock's insulator composition was the best that had been developed for our product.

Dr. Charles Ondrick simplified the processing procedures, which has reduced costs and improved quality.

You may wonder why so many worked on processing for relatively short periods of time. The top engineers or scientists move on to other areas for the simple reason that very capable men are always in demand whether we be in periods of depression, recession, or prosperity. Their capabilities saved the company millions of dollars and, at the same time, produced a superior product.

Process control is no longer a defensive measure. Management looks at process control as (1) cost control, (2) a means of lower processing costs and improving productivity through simplification of processing and decreasing salvage operations, and (3) a means of improving the quality and reproducibility of the product.

Our objective was to achieve this through the development of new techniques for the determination of the microstructure of the materials utilized and its relation to properties and microstructure of the final fired product. Like any method, it can and should be improved, and will be in the future. New techniques and instrumentation to cover organic and inorganic distribution are required.

FUTURE ADVANCES IN PROCESSING

To me, the most important advancement that will be made in the next few years is in new processing techniques. Some innovative changes are taking place in ceramics that could lead to new processing techniques in technical ceramics.

One innovation is a process developed by Howard Sunman of 3M that does not require melting and high-temperature firing for making continuous ceramic fibers. These have a visible appearance much like that of fiber glass. Viscous concentrates of salts solutions, sols, or mixture of these are spun into continuous filaments by extruding and drawing through multiple-holed spinnerettes at low temperatures. The drawn fibers can be collected as

a strand and fired continuously to decompose the compounds, the fugitives can be removed, and the material can be consolidated into strong continuous fibers. Numerous materials can be formed into fibers by this process. In addition to fiber products, this method should open a vast field for ceramic composites requiring process controls completely different than those now utilized.

About 20 years ago 3M developed a monolithic ceramic honeycomb that could operate at high temperature and radiate or transmit very large heat fluxes. These honeycombs are now being used in automotive catalytic converters made by several companies and, I assume, by different processes. I do not know who actually developed the extrusion process for making honeycombs. Many, I am sure, thought of this process. Corning was apparently the first to reduce the process to commercial practice. I am sure this process required a completely different set of controls and will open new fields in thin-walled ceramics.

One more example is a process developed by Kelsey-Hayes for hydrostatic molding of powders at high temperatures by using a glass or ceramic envelope in the shape of the product desired. The part produced from these powders is fired in an atmosphere best suited for the powder. Here again, a whole new set of process controls will be required. While presently this process is used for powdered metals, it can be used for ceramics.

PART TWO

POWDERS

The first requirement of a successful ceramic process is the availability of a good powder. Not only should the powder have the required purity, it should also have certain desirable characteristics, such as high packing density and good sinterability. Many existing processes have been improved through the use of better raw materials, and the past 20 years have been particularly fruitful in this regard. Methods for fine grinding have been significantly improved and active powders from solution are now providing a greater variety of starting materials. Available also are better powder-characterization techniques, and the practice of characterization is becoming more common. What to characterize is better appreciated, particularly in terms of how it relates to actual processing steps.

3

Active Powders

I. B. Cutler

The goal in processing ceramic powders is to obtain a product with the most desirable properties commensurate with an acceptable cost. Properties of a sintered product reflect the nature of the particle compact. A review of sintering theory and practice can help the processor of ceramic powders and powder compacts get the most active powders for the least effort.

Unfortunately, the term "active" powder may mean different things to different people. In terms of ceramic powders it generally means a sinterable powder. What makes a powder particularly active or responsive to temperature and promotes sintering is at least partially known at present. Among the voluminous literature are some excellent reviews.¹⁻⁴ An oversimplified approach clearly reflecting the bias of the author is given here.

DENSIFICATION THEORY

In the majority of sintering operations, densification accompanies sintering. Densification almost always requires shrinkage. The shrinkage takes place as a result of materials being transported by one or more of several diffusion processes. This may involve a liquid or reactive liquid or diffusion at grain boundaries or through the volume of particles. Clearly, any vapor transport or surface diffusion will not contribute to shrinkage and densifica-

tion. On the contrary, any vapor transport or surface diffusion will interfere with densification processes by dissipating the driving force for the densification and shrinkage processes. Although plastic deformation through dislocation motion has not been entirely eliminated as a mechanism of material transport, the number of instances where dislocation motion makes a contribution is thought to be small.

Considerable effort has been expended in attempting to delineate mechanisms of sintering. There appears to be little, if any, practical justification for much of the effort that has been expended in determining the particular equation(s) or the particular diffusion path(s) that best describes the sintering of a particular material. The theory has been of great practical importance in describing what can be done to change the sintering of many materials either to promote or inhibit densification.

PARTICLE SIZE

The theory makes it clear that particle size is a very important variable in the densification process. The rate of densification, regardless of which theory or equations and mechanisms are employed, is inversely proportional to particle size for a simple viscous system at any temperature and inversely proportional to particle size to the 1.5 power for volume diffusion. This means that the smaller the particle size of the material, the more active the powder will be toward sintering.

To put this in perspective, sufficient data on various Bayer-process alumina powders are available to give us some information on the sintering temperature for various particle sizes. A tenfold reduction in particle size reduces the sintering temperature by approximately 200°C. This, of course, assumes that all the other variables are held constant and that we are only altering the particle size and sintering temperature.

Most everyone agrees that particle size is an extremely important parameter. Confusion arises, however, because many small particles are held in rather tight agglomerates. The problem of agglomeration and the confusion over which is really the particle to consider in sintering are best illustrated in the case of Bayer alumina. The early work of Ryshkewitch⁸ emphasized the importance of grinding Bayer alumina to make it into an active powder. Actually, the crystal size was not altered during the grinding operation, but the particle size was altered as it was reduced from an agglomerate to a particle near the size of the crystals contained in the agglomerate. With the aid of scanning electron microscopy, we can visualize this much better today than when the principle was first discovered. Figure 3.1 shows an agglomerate of alpha alumina derived from

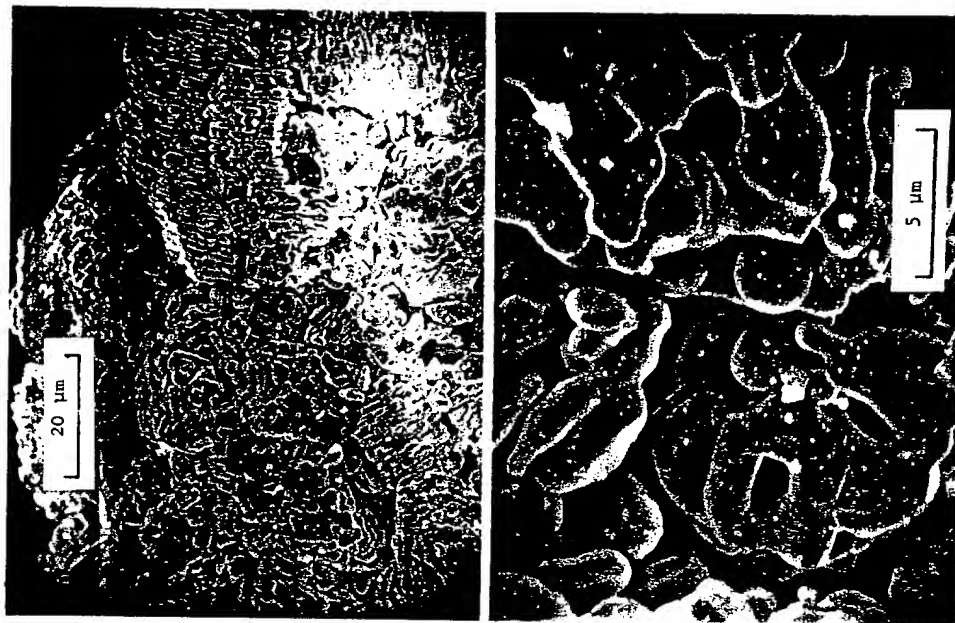


Figure 3.1. Bayer-process alumina (Alcoa A-14) as calcined to form alpha alumina from aluminum hydroxide. The particles retain the morphology of the original hydrate.

aluminum hydroxide by calcination. The particle still shows the morphology of the original aluminum hydroxide. Like so many powders derived by decomposition, there is some preferred orientation of the alpha alumina in the agglomerate. Each agglomerate acts as a spongy particle of very large size and, consequently, it is nearly impossible to sinter below the melt-



Figure 3.2 Ground alpha alumina (Alcoa A-14). Note that the fragments of the original agglomerate are only partially reduced to their ultimate crystalline size.

ing point. Upon grinding to release the individual crystals, an active powder is obtained. As shown in Figure 3.2, grinding does not always yield individual crystals, but rather smaller agglomerates, depending on the grinding efficiencies.

Even alpha alumina derived from alum and other sulfates produces agglomerates. Possibly the agglomerates from alum have lower preferred orientation of the individual crystallites than in the case of the Bayer alumina. As active as the aluminas derived from alum are, they can still be increased in activity by grinding.⁶ More important is the increase of green density resulting from the grinding of these spongy agglomerates.

The activation of alumina by grinding has, at times, been related to energy stored in alumina particles through the incorporation of defects. It is certainly possible to increase the defect content of materials through deformation, but it is doubtful that this contributes significantly to the sintering process. Such nonequilibrium vacancies and interstitials will rapidly anneal out at the sintering temperature during the initial stages of sintering and make only a very minor contribution to the sintering process.

PARTICLE SHAPE AND SIZE DISTRIBUTION

Because theory describes particle size in terms of spherical particles, realistic systems must incorporate a measure of the particles in terms of

their radii of curvature. As can be seen in Figure 3.2, the grinding of alumina produces angular particles. Judging from experience with angular glass particles in comparison with spherical glass particles this angularity may increase the activity of a powder by as much as four or five times the activity of the comparable spherical powder.⁷ This is significant, but, unfortunately, submicron-size particles in agglomerates are very difficult to effectively grind to their ultimate crystals. Thus it is not always possible to utilize the angularity with the more desirable sizes.

Size distribution is important in practical systems where shrinkage is to be minimized. Mostly large particles and sufficient small particles to fill in the interstices will give a particle compact of highest green density. For viscous systems that cannot maintain stress during sintering, the effective particle size in a distribution is simply the average of all particle sizes in the particle compact. It is more complicated for nonviscous systems, as discussed by Coble,⁸ and the effective particle size for up to something like 10% coarse particles appears to be essentially that of the fine-size fraction. It rapidly changes to the particle size of the coarse fraction for a distribution with over half coarse particles. From the point of view of minimizing shrinkage and maximizing density of the green compact, it would be nice to have particle compacts of mostly coarse particles. If this choice is made, it must be remembered that the particle compact with the distribution of mostly coarse particles will sinter as though it were made up entirely of coarse particles, and the sintering temperature must be increased accordingly.

PACKING OF PARTICLES

One of the chief arguments against using fine particle sizes ($<0.1 \mu$) is the decrease in green density of particle compacts of very fine powders and the resultant increase in sintering shrinkage. At least part of this problem is agglomeration. Close-packed spheres have the same density regardless of sphere size. The idea that physical forces between small particles begin to exert an influence on particle packing as particle sizes below 1μ are utilized is one explanation for poor packing of very fine particles. Ramsey and Avery⁹ have some interesting information regarding this factor in their work with ultrafine oxide powders prepared by electron-beam evaporation. They have compared individual particles produced by electron-beam evaporation with agglomerates of a similar surface area obtained by decomposition. The individual particles of MgO were compacted to 50% theoretical density at 66.7 kpsi and 64% of theoretical density at 133 kpsi. The MgO obtained by decomposition of nesquehonite (magnesium carbonate, $\text{MgCO}_3 \cdot 3\text{H}_2\text{O}$) gave significantly lower pressed densities. Sintering behavior of MgO parti-

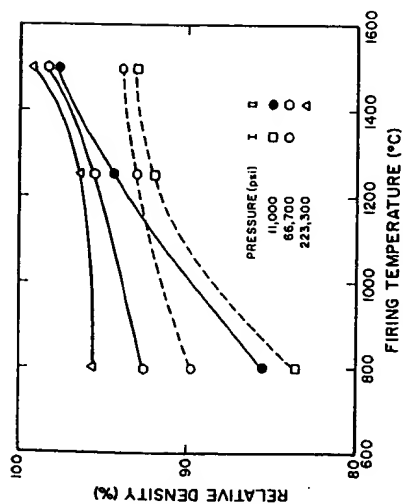


Figure 3.3. Data by Ramsey and Avery for (I) MgO from decomposition of $\text{MgCO}_3 \cdot 3\text{H}_2\text{O}$ in *vacuo* and (II) MgO from electron-beam evaporation, both of about the same surface area (319 and 360 m^2/g , respectively).

cles produced individually is compared with the agglomerated MgO obtained by decomposition in Figure 3.3. The conclusion reached from these and the data of Binns et al.⁶ is that the most important deterrent to the use of submicron particles is the difficulty of the packing of agglomerates rather than individual particles. Thus we need to be more clever in devising methods of obtaining unagglomerated crystals of submicron size by techniques other than grinding.

There appears to be some minimum density of packing of particles or minimum number of contacts per particle necessary to produce uniform shrinkage in a particle compact. Bruch¹⁰ showed that a lower limit of density of a particle compact had to be exceeded to produce full densification of alumina during sintering. Exner et al.¹¹ have noted that particle rearrangement can take place during the initial stages of sintering and result in pore growth, that is, when a limited number of particle-particle contacts are involved in the compact. Ordinarily, this threshold of green density is exceeded in many practical cases; however, we should be aware of the importance of low density in situations where minimum densification is desired.

ADDITIVES AND IMPURITIES

The sintering of stoichiometric oxides, such as aluminum oxide and magnesium oxide, may be dramatically affected by an additive that will enter solid

solution and disturb the stoichiometry of the oxide. This is shown in Figure 3.4 for a rather impure commercial aluminum oxide sintered at various temperatures compared with the same aluminum oxide for which the sintering temperature is held steady but the addition of TiO_2 is varied. It is easily seen that temperature and additions of TiO_2 have comparable effects. Both change the diffusion process by about equal amounts. A small addition of TiO_2 may alter the sintering temperature by as much as 200°C, which is about the same effect as reducing the particle size to one-tenth of the original size.

Not all additives that enter solid solution increase the rate of sintering, as has been discussed in the literature.^{14,15} Various solutes have different abilities for producing nonstoichiometry, some of which may increase while others decrease the rate of sintering. Finding additives that are grain-growth inhibitors and that promote elimination of porosity is similarly difficult and time consuming. In no field of endeavor is it more difficult to predict the effect that an additive will produce than in the area of sintering.

By exceeding the solubility limit of TiO_2 in aluminum oxide, the kinetics of densification are decreased. This appears to be typical of the sintering

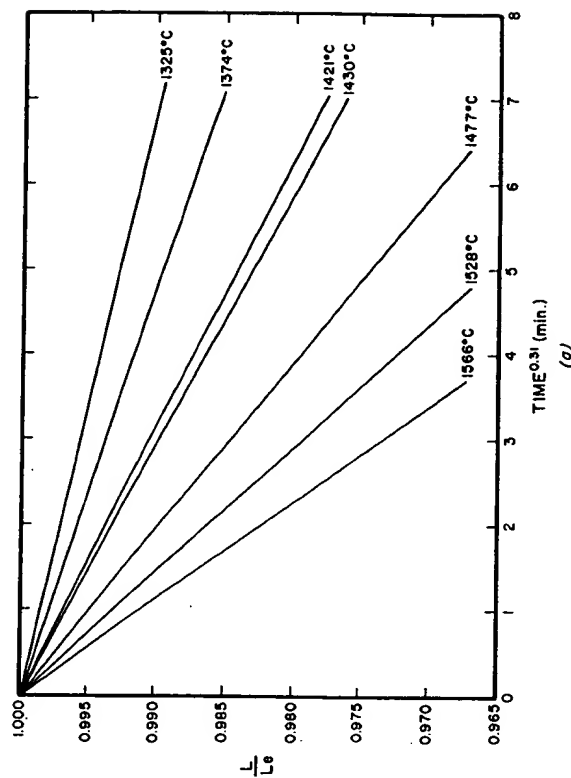


Figure 3.4. Isothermal shrinkage data for A-14 alumina (a) as a function of temperature¹⁴ and (b) as a function of TiO_2 content at $T = 1520^\circ\text{C}$.¹⁵ Additions of TiO_2 are expressed in terms of atomic percent of Ti.

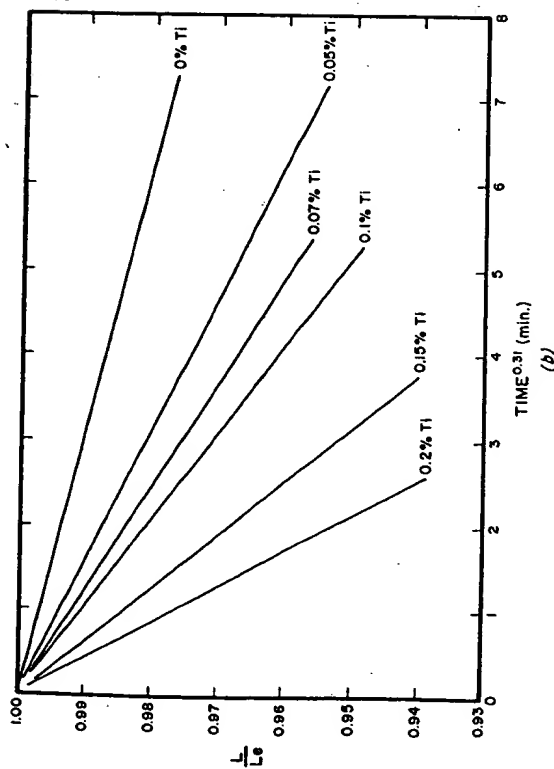


Figure 3.4 (Continued)

process. Additives that form a second phase without forming a liquid apparently inhibit the densification process. On the other hand, the liquids appear to increase densification. No example of this is more familiar to the ceramist than the case of porcelain where the feldspar contributes a liquid phase that promotes densification.

Reactive sintering in the presence of a liquid phase constitutes still another special case of active sintering. For example, forsterite (Mg_2SiO_4) may be sintered utilizing a eutectic liquid of magnesia and about 65% silica, along with periclase (MgO) at temperatures on the order of 1560 to 1600°C. By the time the liquid has reacted with the magnesium oxide the material will be well sintered and will yield a forsterite composition.

ATMOSPHERE

Although the sintering atmosphere has little to do with ceramic powder processing, it does have a great deal to do with the sintering process. For completeness, it is mentioned here that we should be cognizant of the atmosphere surrounding the particle compact as it is being sintered. Defect concentration can be altered by the atmosphere, and the atmosphere contributes to pore removal in the final stages of sintering.

References

CONCLUSION

Great progress has been made in understanding the sintering process of particle compacts. Particle size, agglomeration, particle shape, size distribution of particles, and packing in the compact all have a great influence on sintering and densification. Additives and atmosphere contribute to the sintering process as well. During processing most of these parameters may be changed to meet the needs of the ceramist and his sintered product.

REFERENCES

1. F. Thummler and W. Thomma, "The Sintering Process," *Metall. Rev.*, 12 (115), 69 (1967).
2. A. L. Stuijts, "Synthesis of Materials from Powders by Sintering," *Ann. Rev. Mater. Sci.*, 3, 363-395 (1973).
3. A. L. Stuijts, "Sintering Theories and Industrial Practice," *Sintering and Related Phenomena* (Materials Science Research, Vol. 6), G. C. Kuczynski, ed., Plenum Press, New York, 1973, pp. 331-350.
4. I. B. Cutler, "Sintered Alumina and Magnesia," *Refractory Materials*, Vols. 5-111, A. M. Alper, ed., Academic, New York, 1970, pp. 129-179.
5. E. Ryshkewitch, *Oxydkeramik*, Springer-Verlag, Berlin 1948.
6. D. B. Binns, P. Engel, and P. Popper, "Methods for Increasing the Compactibility of Powder," *Proc. Int. Conf. Compaction Consolidation Particulate Matter, 1st Brighton, England*, 1972.
7. I. B. Cutler and R. E. Heinrichsen, "Effect of Particle Shape on the Kinetics of the Sintering of Glass," *J. Amer. Ceram. Soc.*, 51 (10), 604-605 (1968).
8. R. L. Coble, "Effects of Particle-Size Distribution in Initial-Stage Sintering," *J. Amer. Ceram. Soc.*, 56, 461-466 (1973).
9. J. D. F. Ramsey and R. G. Avery, "Ultrafine Oxide Powders Prepared by Electron Beam Evaporation," *J. Mater. Sci.*, 9, 1681-1695 (1974).
10. C. A. Bruch, "Sintering Kinetics for the High-Density Alumina Process," *Bull. Amer. Ceram. Soc.*, 41 (12), 799-806 (1962).
11. H. E. Exner, G. Petzow, and P. Wellner, "Problems in the Extension of Sintering Theories to Real Systems," *Sintering and Related Phenomena*, Material Science Research, Vol. 6, G. C. Kuczynski, ed., Plenum Press, New York, 1973, pp. 351-362.
12. D. L. Johnson and I. B. Cutler, "Diffusion Sintering II: Initial Sintering Kinetics of Alumina," *J. Amer. Ceram. Soc.*, 46 (11), 545-550 (1963).
13. R. D. Bagley, I. B. Cutler and D. L. Johnson, "Effect of TiO_2 on the Initial Sintering of Al_2O_3 ," *J. Amer. Ceram. Soc.*, 53, 136-141 (1970).
14. P. Reijner, "Non-Stoichiometry and Sintering of Ionic Solids," *Proc. Int. Symp., Reactivity Solids, 6th, New York*, 1969, Wiley-Interscience, New York pp. 99-114.
15. D. W. Ready, "Mass Transport and Sintering of Impure Ionic Solids," *J. Amer. Ceram. Soc.*, 47, 366-369 (1969).

4

Characterization and Process Interactions

W. M. Flock

The process engineer must decide when, where, how, and what powder characterization parameters to measure. Furthermore, he is faced with the fact that they must be measured within a reasonable time, at a reasonable cost, and by average operators. Hence material characterization is often the most frustrating tasks facing the ceramic scientist.

Probably the first question that should be posed is, why characterize? Answers to this question are as variable as those to the question of what to characterize. A common answer is to ensure quality or obtain information for future references. Another more negative response is to reject defective material; if these are the only reasons for characterization, then an inactive process-control model results and data are collected and stored until a problem occurs.

If characterization is carried out to predict and adjust, an active process-control model is being employed. By predicting the material-process response and ceramic-product character, adjustments in processing can be made if these predictions are not in line with the desired performance or properties. It is the material characterization required for this active model that is discussed in this chapter. For an active process model, material characterization can be defined as the means by which the ceramic engineer interacts or communicates with the process on a real-time basis.

THE PROCESS-CONTROL-MODEL CONCEPT

To interact with a process on a real-time basis, a process model is required. The model shown in Figure 4.1 is used in principle for nearly all high-volume ceramic-manufacturing processes. Its use may be intentional or unintentional, and it may not be as rigorously developed as shown in Figure 4.1, but economics dictate that variation from this model must be slight.

If we assume that the process objectives are to develop consistent predictable products, then this model requires that processing conditions and raw materials be consistent and predictable. If variations occur in one, then adjustments must be made in the other, that is, raw material plus process equals predictable ceramic character. However, economic conditions require that if process adjustments are made, they must be inexpensive and rapid. In large-volume operations, process parameters such as tooling, body composition, organic composition, and firing profile must be held constant, while parameters such as mill time, forming pressure, and surfactants (grinding aids, viscosity aids, and lubricants) may be changed.

In summary, for this model to be operative, two conditions are required: (1) that constant raw materials or materials that have been sufficiently characterized to predict their material-process response be used and (2) that the process is sufficiently understood to make the required adjustments.

Since high-volume ceramic processing has been successfully carried out for over 50 years, and since the material scientists are in agreement that material characterization is, by in large, inadequate, then the scientific community is out of touch with reality and no problem exists, ceramic articles are not being made with consistent properties, or the above proposed model is incorrect and material variations have no effect on ceramic character, and some other unknown process is active. In actual practice, it is found that all the above are partially true, for in lieu of the capability to

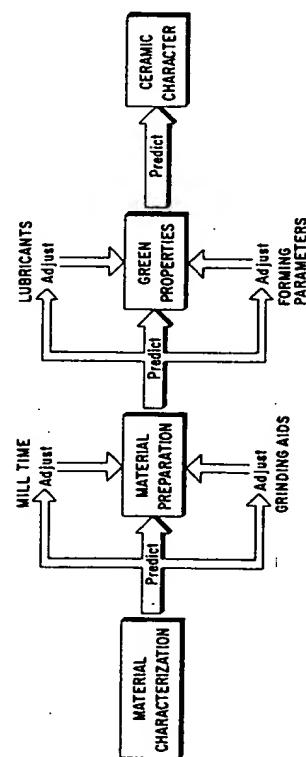


Figure 4.1. Active material process control model.

provide complete material characterization, the process engineer has survived by holding constant as many of the material variables as possible.

MATERIAL CHARACTERIZATION CONCEPT

What material variables must be held constant? Or stated differently, what parameters are required to define the material character? It has been found by a number of investigators that material character can be expressed by the following function:

$$C = f(s, sh, o, p \text{ and } c)$$

where C = character

s = size

sh = shape

o = orientation

p = packing

c = composition

The process model dictates that these variables either be held constant or be measured, but since the capability to measure or characterize such variables as shape, packing, and orientation is sorely lacking, the problem was solved, and continues to be solved for many processes, by the practice of single-source purchasing. The ceramic industry, and for that matter, most industries, has used, and continues to use, single-source raw materials made by a particular manufacturing process and specific manufacturing equipment. These sole source suppliers have learned from loud and quick customer response that process changes are forbidden. It is common to hear statements that only kiln A or pit B can be used for a customer and kiln B or pit C for another customer. The failure of the material scientist to provide meaningful characterization tools has fostered sole-source purchasing. This concept, based on human experience and not scientific concepts, has created misconceptions and doubts that will strew the road to progress with obstacles for years to come, that is, it has created an environment in which change is forbidden.

Another less detrimental but nevertheless costly technique is to negate the need for material characterization by eliminating the previous raw material history, that is, beginning the process over within the users control. This approach transfers the problem of material characterization to process control, which fortunately is much better developed. A typical example of this approach is the destruction of the Bayer-process characteristics by high-temperature sintering (tabular alumina) followed by steel-ball milling for

size reduction and an acid wash for iron removal; however, energy costs are making this concept prohibitive.

In summary, increasing costs dictate that material characterization must be advanced to the stage where total characterization can be made regardless of the previous process used and that it can be done sufficiently to predict the material-process response. This is an ambitious step, but the concept presented in Chapter 9 for Bayer-processed alumina is believed to be one approach that practical experience has shown to be in the right direction.

5

Physical Characterization Terminology

G. Y. Onoda, Jr.

L. L. Hensch

Particulate materials consist of small units of solid matter that have specific physical characteristics. A variety of small units have been described by various names, for example, primary particle, ultimate particle, particle, grain, colloid, agglomerate, conglomerate, aggregate, clump, cluster, crystallite, granule, and floc. Inconsistencies exist in the literature on the definitions and uses of these terms, partly because different disciplines (e.g., ceramics, powder metallurgy, fine particle technology) have tended to have their own preferences. In this chapter definitions are proposed that hopefully will aid in the establishment of consistent terminology in the ceramics field. These definitions are used in this book.

PRIMARY PARTICLES

A primary particle is a discrete, low-porosity unit. It may be a single crystal, a monophase polycrystal, a multiphase polycrystal, or a glass. The pores, if any, are isolated from each other and therefore the primary

particle is impervious to fluids. If the primary particle is one of several that make up larger agglomerates, it is common to refer to the size of such a particle as the "ultimate" particle size.

AGGLOMERATES

"Agglomerate" is a general term describing a small mass having a network of interconnective pores. It is comprised of primary particles bonded together by surface forces and/or solid bridges (see Chapter 27). The surface forces may be electrostatic or van der Waal attractions between particles or liquid capillary forces due to the presence of liquid within the agglomerate. Solid bridges are a result of sintering, fusion, chemical reaction, or setting of a binder.

Agglomerates with solid bridges can retain their identity under a wide variety of conditions. In contrast, agglomerates held together with surface forces are much more readily disrupted by small external forces. It is often convenient to have a simple terminology that distinguishes between the two general agglomerate types. Therefore, *solid agglomerates* are defined as agglomerates with solid bridges; *weak agglomerates* are agglomerates with surface forces as bonds.

PARTICLES

A "particle" may be a single primary particle or a solid agglomerate. As such, it is a small mass that is free to move as an entity¹ when the powder is dispersed by the breaking of the surface force bonds. Most particle-size measuring techniques operate on such particles.

GRANULES

The term "granules" is frequently used in ceramics to identify agglomerates that are intentionally formed by the addition of a granulating agent to promote the formation of large agglomerates. This definition is an operational one based on a deliberate forming process. An example of a granule is the product from a spray drier.

FLOCS

Flocs are a cluster of particles that form in a liquid suspension. The floc can be dispersed by appropriate modification of the interfacial forces through

alteration of the solution chemistry. The particles of a floc are held together by short-range interfacial forces or by organic flocculating agents.

COLLOIDS

Colloids are particles that, when dispersed in a fluid, are fine enough so that Brownian motion maintains them in suspension without settling. In general, colloids are particles of submicron size.

AGGREGATE

The term "aggregate" in ceramics refers to the coarse constituent in a batch material, usually in combination with a fine constituent called the bond. Some fine-particle technologists use the term "aggregate" to represent what we define as solid agglomerates. This practice is avoided to prevent confusion within the field of ceramics.

REFERENCE

1. E. R. Stover, "A Critical Survey of Characterization of Particulate Ceramic Raw Materials," Technical Report AFML-TR-67-56, Air Force Materials Laboratory, Wright-Patterson Air Force Base, Ohio, May 1967.

6

Physical Characterization Techniques for Particles

C. Orr, Jr.

This chapter assesses and reviews the fundamental measurement techniques for particle size, surface area, shape, and pore structure of particles. The basic concepts, assumptions involved, special attributes or deficiencies, and the meaning and value of results are discussed. Some of the simplified comparison techniques that may be adapted for routine process-control purposes are outlined.

PARTICLE SIZE

Particles considered in this chapter are restricted to those having dimensions greater than colloids ($\sim 0.1 \mu\text{m}$) and less than those that can be discerned without magnification or other aid ($\sim 1000 \mu\text{m}$). For want of a better term, "diameter" is employed as the measure of size, although it applies strictly to circles and spheres, and very few particles are spherical. Diameter is thus subject to interpretation.

Microscopy

When measured microscopically, particle diameter is usually taken as the distance between points on opposite sides of the particle using some convention with respect to particle orientation; only rarely is an accounting of even one right-angle dimension attempted. The result of a series of such particle measurements is a statistical number-based size distribution that most likely underestimates the contribution of the smallest particles. The tendency of particles to assume their most stable position when deposited on a substrate reveals their greatest dimensions to examination, which further biases the results.

Manual measurement of size is extremely tedious. There are several sophisticated electronic commercial systems in which the taking and analysis of size data is highly automated. Whether the system is manual or automatic, great care should be exercised in preparing representative samples. Appropriate numbers of particles should be examined so that neither too many nor too few are exposed on prepared slides or photographs. Since a magnification factor is always included in microscopic measurements, this factor is subject to error which can shift a distribution either towards greater or smaller sizes.¹

Microscopic techniques and data treatments have been described in detail in many publications.²⁻⁷ They are not pursued further here except to note that microscopy must be regarded as very useful as a check on other methods and as a guide to method selection. Since microscopic size analysis results directly in number-based data pertaining to particle profile, a mean diameter computed on this basis can differ quite significantly from a mass mean diameter (e.g., derived from a sieve analysis).

Sieving

This is the oldest of all particle characterization methods. Sieving has often been described in the technical literature⁸⁻⁹ and needs little further elaboration here. With care, a sieve analysis can be obtained down to about 1 μm in diameter⁸⁻⁹; analysis is relatively rapid, and as with microscopy, the obviousness of the method makes the results highly desirable. There are pitfalls here too, however. If analysis is carried out with a dry powder, electrostatic effects and particle agglomeration may cause problems. Particle agglomeration can still be a problem even in wet sieving, especially with the very small-opening sieves. Also commercial wire-sieve openings are likely to vary several percent from the nominal size. The finer meshes, particularly, are very easily damaged by careless handling. Particles of approximately the opening size tend to be caught in the sieves, which, if it occurs over

much of the powder, causes a distortion of the data. Results are highly dependent on operator technique. In general, sieving should be continued for a considerably longer time than is frequently allowed. Sieve analysis cannot yet be said to have succumbed to automation, but progress is being made.^{10,11} Success here should alleviate some of the problems noted.

The diameter obtained by sieving irregular particles is that of the smallest cross section that will pass an approximately square opening. Such a diameter can differ considerably from a microscopically measured diameter, and results also differ in that they are mass based. Thus sets of data for the same powder obtained from microscopy and from sieving often appear to be very different.

Stokes' Diameter

Measurement of the sedimentation rate of particles in a quiescent liquid affords a very important means of particle sizing. The size thus determined is known as the Stokes' or equivalent spherical diameter. It is the diameter of the sphere of the same density that would exhibit the identical free-fall velocity of the particle. As such it is a measure that readily correlates with many handling and processing parameters.

Data on sedimentation rates may be obtained using initially uniform liquid suspensions by measuring the concentration of particles remaining in suspension as a function of time. Sedimentation rates can also be obtained by measuring the quantity of sediment produced as a function of time. This method is less widely used and is not described here.

Hydrometers,¹² divers,¹³ light transmission,¹⁴ and X-ray absorption¹⁵⁻¹⁸ can be utilized. Hydrometers disturb the orderly sedimentation process, and use of both hydrometers and divers requires long times of analysis. Light transmission, or so-called turbidimetric analysis, is sensitive to particle refractive index unless only the light in a very small forward beam is detected,¹⁹ and even then corrections must be applied for submicrometer diameters. The diameter finally detected is representative of particle cross section and must be multiplied by particle diameter to put the results on a mass basis. These difficulties have so far prevented the development of a wide-ranging, generally satisfactory light extinction size analyzer.

X-Ray Absorption

A narrow beam of low-power X-rays constitutes a very satisfactory means for measuring concentration since adsorption is directly dependent on interposed mass. A commercial version of an instrument, shown in Figure 6.1, utilizes low-energy X-ray detection for concentration coupled with sedi-

mentation cell scanning to speed the analysis. It gives very satisfactory results for powders with atomic numbers greater than about 12. The concentration of particles remaining in suspension is detected as a function of time and depth within the sedimentation cell. By effectively solving Stokes' law throughout the course of an analysis, a plot of equivalent spherical diameter versus mass percent less than each diameter is developed.

A particle-size analysis with this equipment requires a dilute suspension, usually but not necessarily aqueous, of about 1.0% solids by volume. Particle- and liquid-density and liquid-viscosity data are required. Depending somewhat on density and viscosity values, particle diameters between about 150 and 0.1 μm can be measured.

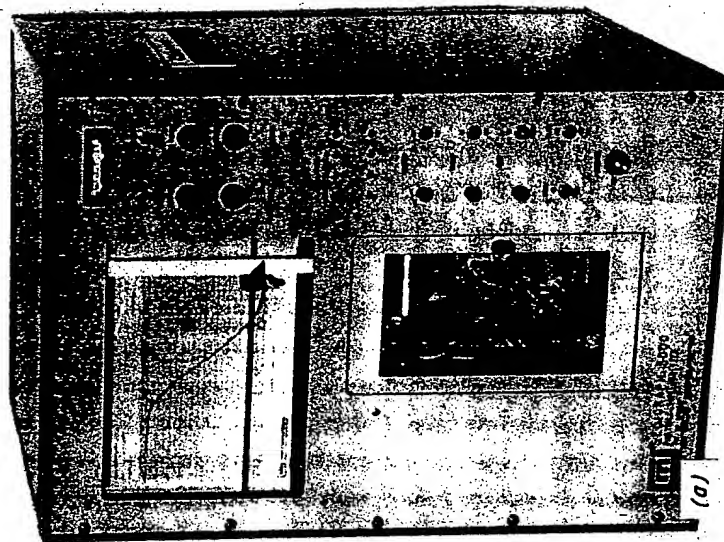


Figure 6.1. X-Ray sedimentation particle-size analyzer: (a) photograph of equipment, (b) schematic diagram.

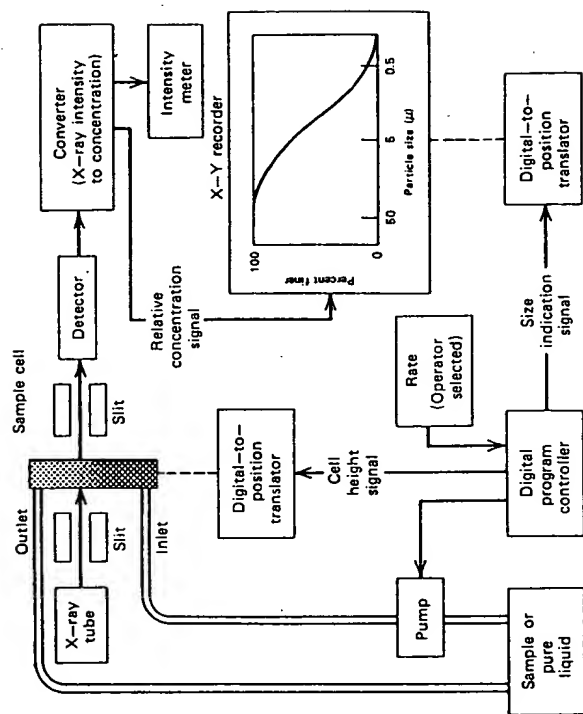


Figure 6.1 (Continued)

Electrical Resistance

The number and size of particles suspended in a weak electrolyte may be determined when the particles are made to flow through a small aperture with immersed electrodes on either side.²⁰⁻²⁴ The electrodes carry a current that also passes through the aperture. The most familiar instrument of this type is the Coulter Counter, shown in Figure 6.2, which was originally developed for blood-cell counting but was long ago adapted for industrial use. As a particle passes through the aperture, the accompanying resistance change results in a voltage pulse of short duration proportional in magnitude to particle volume. These pulses are amplified and discriminated to give results in terms of particle number versus particle volume.

Particle volume is essentially linearly related to resistance change irrespective of particle shape, provided the particle diameter is roughly 20% of the aperture diameter. If the particles are larger, deviations from a generally spherical shape introduce an error of a few percent.²⁵ Particles very much smaller than the orifice are counted with decreasing sensitivity.



Figure 6.2. Coulter Counter (Coulter Electronics, Inc., Hialeah, Fla.).

Particle resistivity is seldom a problem, because, whether conducting or not, particles normally behave in an electrolyte as if they had infinite resistance.

The shape of the electronic pulse occasioned by particle passage has been the subject of much investigation. It is apparently round-topped because of particle approach and emergence influences, and not rectangular as it would be if ideality could be achieved.²² This impedes the attainment of full amplifier response to the presence of a particle before it leaves the aperture, resulting in a slight undersizing of the coarser particles. Coincidental passage of more than one particle produces an erroneous indication of both size and number. This effect is substantially eliminated by diluting the measured suspension or correcting for coincidence by a relatively simple procedure.²³ Careful filtration and dust protection for the electrolyte are essential to a low background count. With an aqueous saline solution, a commonly employed electrolyte, it is advisable to add about 0.1% formaldehyde to prevent microorganism growth if the electrolyte is expected to be stored for a period of time.

A Coulter Counter is simple to use. A pinch of powder is added to the electrolyte and is well dispersed²⁴; the aperture most likely to avoid plugging—one about $2\frac{1}{2}$ times the largest particle is chosen, and appropriate control settings are entered. The analysis is essentially automatic thereafter. The results, as noted above, represent a number-based distribution of

particle volumes recorded in terms of particle diameter. The diameter spread measured with one aperture should not exceed one order of magnitude, for example, from 100 to 10 μm . By using several apertures, particle diameters from several hundred to about 0.5 μm may be encompassed.

Permeametry

Among simplified techniques for sizing particles, one of the most convenient is permeametry.²⁷ This technique is sometimes portrayed as indicating mean size and sometimes specific surface area. As ordinarily practiced, it probably measures neither. However, it does afford a relatively rapid and inexpensive means for establishing relative fineness and, as such, is useful in some routine control applications. One commercial permeameter requires the formation of a small compressed bed of dry powder through which dry air is forced at a fixed rate. An average particle size is then deduced from the pressure loss experienced by the air and the degree of particle packing. A still simpler version is known as the Blaine Fineness Tester^{28,29}; a glass-blower can fabricate one of these devices in a very short while.

SURFACE AREA

The definition of surface area for a truly plane surface is clear. Mica, for example, can be obtained molecularly flat by careful cleaving.³⁰ Most materials, unlike mica, do not have the centers of all atoms in the surface layer lying in one plane. Rather they have irregularities ranging from atomic scale to gross defects, including crystal imperfections, cracks, crevices, and pores. Their actual surface area can be many times the apparent geometric area.

Simple geometric considerations show that very small particles present a proportionally large fraction of the total surface area of a powder mass. The small particles are often overlooked in a size analysis but are included in a total surface area evaluation. Also, in many instances where powder-size distribution is essentially identical, surface-area measurement reveals distinct differences, because one powder has impervious particles and the other has particles containing cracks, crevices, or pores.

BET Gas Adsorption

Standard means for surface-area evaluation utilizes low-temperature absorption, or uptake on the powder surface, of a gas.³¹ Most commonly nitrogen is used at the temperature of liquid nitrogen, although a number of

other gases and temperatures may be employed. Adsorption reveals itself as the removal of a portion of a gas when a solid is exposed to it. At relatively low pressures the gas forms an incomplete layer of molecules attached to the solid surface. As the pressure increases a layer several molecules deep is formed. The critical factor is determining the conditions under which a layer of adsorbed gas precisely one molecule thick is formed.

The volume of gas adsorbed per unit mass of solid depends on the gas pressure, the absolute temperature, and the nature of the gas and solid. When the gas is adsorbed below its critical temperature it is convenient to express the pressure dependence in terms of the so-called relative pressure p/p_0 , where p_0 is the saturation vapor pressure of the adsorbing gas that is available in various handbooks. Adsorption isotherms are obtained by measuring at constant temperature the volume of gas adsorbed per unit sample weight versus relative pressure.

Tens of thousands of adsorption isotherms have been determined using a variety of gases and solids. A typical adsorption isotherm is shown in Figure 6.3; the asymptote point B is approximately where a single gas layer occurs. From the volume of gas required to attain this condition as read from the ordinate, the number of gas molecules per unit weight of solid can be calculated. Then the specific surface area of the solid can be computed by including the area occupied by each gas molecule, which is believed to be 16.2 \AA^2 for nitrogen. Areas occupied by a number of other adsorbed gas molecules have also been determined.³²

Since locating an asymptotic point such as B is subject to error, much theoretical and experimental effort has been expended over the past years in devising more satisfactory mathematical treatments for adsorption data. These are not discussed here, but they have resulted in relatively simple expressions from which the single-layer condition, hence sample surface area, can be calculated directly.

Apparatus for making gas adsorption determinations of powder surface area range from the homemade glass systems of earlier days to quite sophisticated devices (e.g., the computer-controlled system shown in Figure 6.4). The preferable technique involves measuring equilibrium gas pressures as outlined above, but by a gravimetric technique in which the weight of the adsorbed gas is determined and modified gas chromatographic systems have also been employed. The gravimetric procedure has certain advantages, but the very small weight changes involved make the procedure quite tedious and lengthy. Gas chromatographic systems must employ a carrier gas along with the gas to be adsorbed which leads to proportioning and other problems.

Gas-adsorption measurement of surface area is not above questioning. Particle surfaces are not energetically uniform. Along grain boundaries and

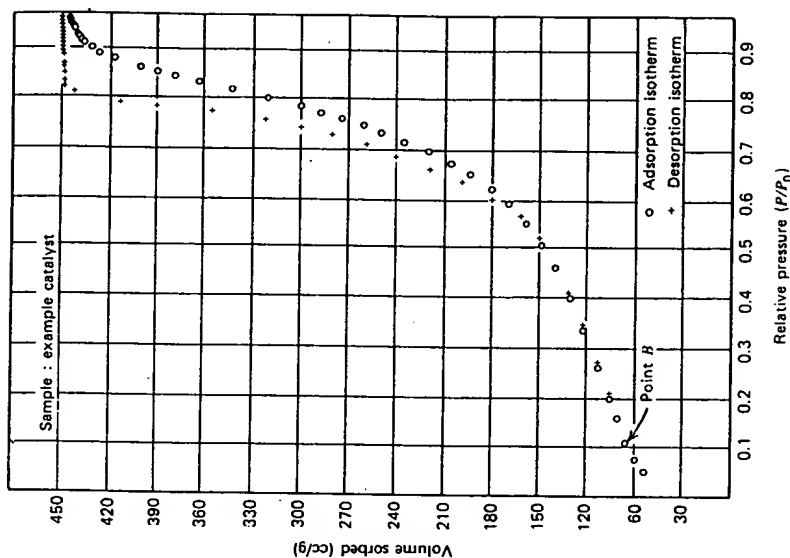


Figure 6.3. Nitrogen adsorption and desorption isotherms.

at the bottom of cracks there appear to exist enhanced adsorption sites, while less than normal energy sites are represented by protrusions. At these first regions it is entirely possible for second, and even higher, layer adsorption to begin before single-layer coverage is completed elsewhere, and it is equally possible that some of the protrusions remain bare until most of the other surface is covered. This condition, of course, contributes to error, but one effect tends to counter the other. Overall, it appears that abnormal adsorption is small in the context of total surface area. Surface-area values have been reproduced within a few percent by different investigators separated widely in both space and time. BET results have been confirmed many times by a number of other tests utilizing a variety of procedures.^{3,31} Low-temperature gas adsorption thus must be considered the standard to

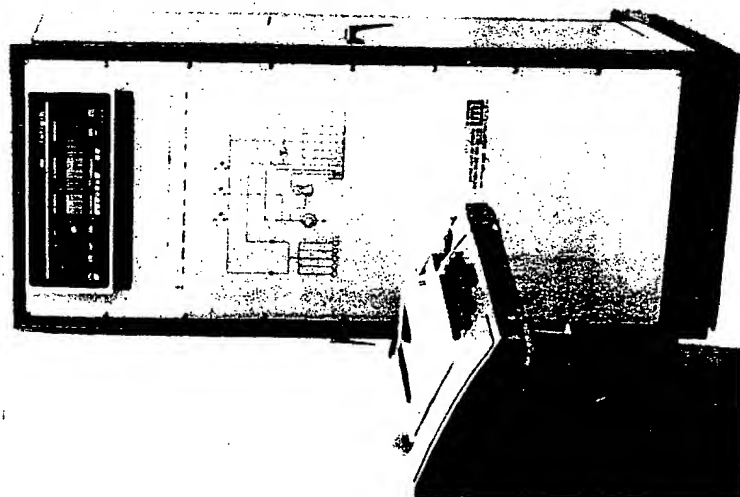


Figure 6.4. Automated surface and pore-volume analyzer (Micromeritics Instrument Corp., Norcross, Ga.).

which all other surface measurements are compared and, indeed, must be considered one of the few standards available for particle characterization.

Liquid-Phase Adsorption

The adsorption (or sorption as the phenomenon is often termed when involving liquids) of dyes, iodine, and a few other dissolved substances onto an immersed powder is often indicated as being a simple surface-measuring means. This is usually far from true. First, there is competition between the dissolved molecules and the dissolving liquid molecules for the available powder surface. Second, the area occupied by molecules in a liquid on a surface varies widely with concentration. There are also other factors to be

considered, such as molecule orientation when attached to a surface. However, if there are overriding reasons that make liquid-phase sorption attractive, if relative results are sufficient, as they might be in a process control application, and if results are initially correlated with low-temperature gas adsorption, then the suggested system would be nitrophenol dissolved in water or one of several other solvents. The nitrophenol molecule attaches to either polar or nonpolar solids; its concentration in solution is readily detected colorimetrically; and it has been shown to give fairly reliable results with several solids.^{34,35} Its constant-temperature sorption with increasing concentration often yields an isotherm somewhat resembling that in Figure 6.3 with one-layer coverage given by the point of inflection (point *B*). Single-molecule coverage, however, depends strongly on the nature of the solid, with values having been found to range from 15 to 50 Å², hence the necessity for correlation with gas adsorption. Results depend greatly on the care and uniformity with which the tests are conducted.

Low-Angle, X-Ray Scattering

X-Rays are partially deflected when they encounter an electron-density change such as they do upon passage into and out of powder particles. The extent of this density change can be related theoretically³⁶ to particle surface area. By measuring the intensity of the undeflected portion of an X-ray beam and energy scattered out to approximately 3°, it is possible to calculate a surface-area value.^{37,38} The calculations are somewhat tedious, however, and demand a detailed knowledge of the material not readily available. Another approach to determine directly the unknown surface area is to relate the deviated beam intensity for a material of unknown surface area to that for another sample of the same material having had its surface area established by low-temperature gas adsorption.³⁹ This technique has the potential for yielding surface areas in a minute or two, including sample preparation, and could become very useful in process control.⁴⁰

SHAPE

Particle shape is recognized as influencing powder flowability, bulk density, angle of repose, and packing characteristics, and may be as important as particle size in many cases. Shape is rarely measured, not because of a shortage of so-called shape-factor definitions, but because no one has yet found a completely satisfactory means for measuring shape, especially for particles with reentrant contours.

There are two-dimensional shape parameters based on microscopic determinations of the maximum particle diameter (i.e., length) and two maximum perpendicular radii, one on either side of the maximum diameter.⁴¹ "Elongation" and "flatness" ratios are defined in terms of the length, breadth, and thickness of a particle.⁴² Other considerations of shape involve particle perimeter and surface area. "Roundness" is the ratio of the perimeter of a circle of the same area as the particle to the actual perimeter of the particle, while "sphericity" is the ratio of the surface area of a sphere of the same volume as the particle to the actual surface area of the particle.⁴³ Such definitions are deficient for many purposes in that they do not adequately characterize the gross shape of a particle.

Other classifications categorize coarse grains as either generally spherical, intermediate in shape, or tabular, depending on the time required to slide, roll, or bounce down an inclined plane.⁴⁴ The suggestion has been offered⁴⁵ that measurement of the rate of sieve passage might be developed into a shape description, it having been found that elongated cylindrical particles pass a sieve at a slower rate than do short cylindrical ones. Finally, producing sieves with rectangular, triangular, and round instead of square openings has been suggested.

Perhaps the most fruitful approach to shape characterization is a dynamic method based on the representation of an irregular particle as an ellipsoid having equivalent radii of gyration about its principal axes.⁴⁶ Both two- and three-dimensional representations might be employed. Obtaining the two-dimensional data is straightforward; how to arrive at dimensions in three planes obviously presents problems. Treating the data, however generated, would be quite tedious were it not now possible to utilize electronic digitizing equipment and computers. The summary of the method given here considers only manual analysis in two dimensions to present the rudiments of the technique. The starting point is a photograph of the particle.

The outline of the particle is traced on graph paper (Figure 6.5). Then X and Y coordinates of small areas within the particle are tabulated. From these measures are calculated radii of gyration of the plan figure about its principal axis and the axis at right angles to the principal axis, assuming the figure actually to be a thin sheet of material of uniform thickness and density. Next is calculated an equivalent ellipse having these same radii. The ratio of the longer axis of the ellipse to the shorter is taken as the "anisometry," or unequal nature, of the particle. The area of the ellipse will be greater than that of the figure representing the particle; the ratio of the ellipse area to the figure area is taken as a measure of the "bulkiness" of the particle.

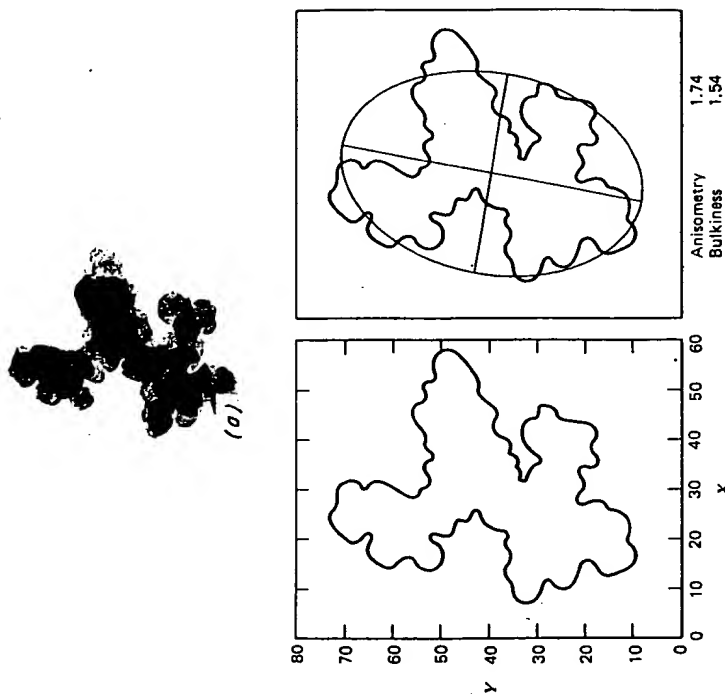


Figure 6.5. Shape factors for irregular particle.⁴⁶

Extension of the evaluation to a figure in three dimensions requires computation of radii of gyration about three principal axes coinciding with geometric axes. The "bulkiness" of the particle is then defined as the ratio of the volume of the equivalent ellipsoid to that of the particle, and "anisometry" is defined in terms of ratios of the lengths of the three axes by reducing these to two dimensionless factors: an "elongation ratio" and a "flatness ratio." An equivalent shape other than an ellipsoid, perhaps a prism, could be used as the basic geometrical form.

While the delineation of dynamic shape factors as given above represents a considerable advance, techniques and instrumentation suitable for routine

use are not currently available. Much work remains to be done to reduce particle shape to the useful parameter it should be.

PORE STRUCTURE

Quite a number of apparently solid particles have cracks, crevices, holes, and fissures within their structure, and, of course, objects formed from powders by consolidation and firing usually have internal spaces. While pores might run straight through a material, they are more likely to twist, turn, branch, and interconnect. They may start on one side and emerge on the same side, or they may never emerge. They may decrease in dimensions with depth or they may enlarge, giving so-called "ink-well" pores.

Pores are openings in rigid objects, while the term "voids" refers to the spaces abounding among the grains of an unconsolidated powder, for example. Void volume is thus easily altered; changing pore volume requires at least partial destruction of the porous object. A consolidated mass produced by compressing and sintering a powder is considered to contain only pores, even though some of the openings may be among individual grains and some in fissures within the grains themselves. Pores constitute the primary concern here. Unfortunately, measurements with loose powders may detect both pore and void volumes, so judicious examination of measurement data is necessary to distinguish the two.

Pore systems have to be described in terms of a geometric model, the right-cylinder model being most utilized. This convention is followed here. Thus pores hereafter are considered as though all were straight cylindrical openings having one of several diameters and various total lengths. There are basically two practical ways of measuring pore structure: (1) by forcing a nonwetting liquid into the pores under pressure and then analyzing the pressure-volume penetration curve and (2) by condensing a liquid within the pores, subsequently analyzing these data. Of course, particle and particle-formed structures can be evaluated by sectioning and microscopic examination. Although obvious, this is such a tedious procedure it is rarely employed.

Mercury is a nonwetting liquid for most solids, and it is used exclusively in the penetration technique. Mercury under pressure but outside a cylindrical pore experiences a force tending to push it into the cylinder expressed by the product of pressure and cylinder cross section. The opposing force tending to prevent the mercury from entering is the product of mercury surface tension, the perimeter of contact, and a term known as the contact angle. Equating these forces results in a simple expression between applied pressure and pore diameter involving as other terms the mercury surface

tension and its contact angle with the solid. At normal temperature the surface tension of mercury is about 474 dynes/cm, and mercury usually exhibits a contact angle of about 130° . The pressure-pore diameter relationship becomes then a simple proportionality, some values for which are given in Figure 6.6.

Appropriate apparatus for conducting pore evaluations by mercury penetration are simple in concept but complex in practice because they are required to operate at both low and high pressures. Every sample has to be evacuated initially to free it of atmospheric gases and vapors. Sensitive volume-measuring equipment is required to indicate accurately from very small to rather sizable volume changes of mercury. Present commercial equipment requires operator attendance and involves some sample manipulation; automated instrumentation is under development, however.

Typical penetration results are shown by Figure 6.7. The data of curve 1, for example, apply to an unconsolidated powder having a mean particle diameter of about $50\text{ }\mu\text{m}$, and the first step in the curve is seen to correspond approximately to this diameter. This portion of the curve must then apply to void, or interparticle, spaces. The second step in the curve, applying to considerably smaller pores, must represent pores within the particles.

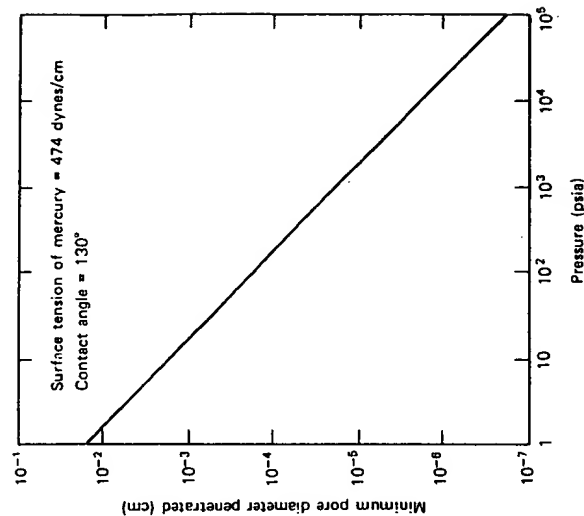


Figure 6.6. Mercury pressure-pore diameter relationship.

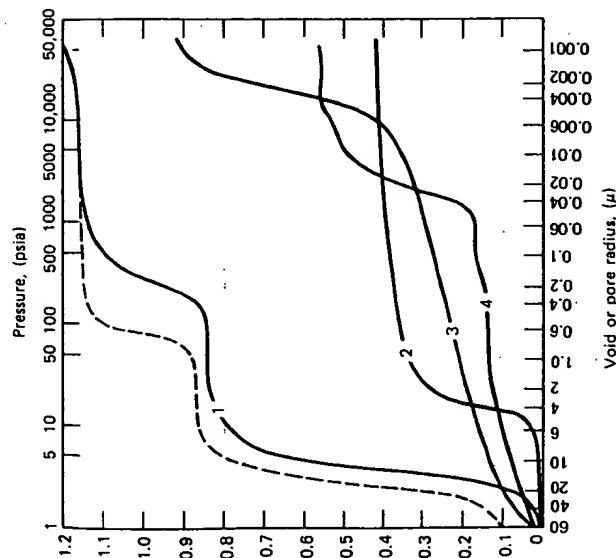


Figure 6.7. Mercury penetration results.

Many users go no further than this with a pore analysis, being content with information easily read from such a graph. In this example pore diameters are primarily between 1.2 and 0.2 μm and they represent a volume of approximately 0.30 cc/g of sample. Various ways have been suggested to fit penetration data to pore distribution functions from which the surface area associated with various pore sizes, for example, can be calculated. It is also possible to follow the expulsion of mercury from pores as the pressure is reduced to gain insight into pore shape.⁴⁷ Space precludes following these developments here.

Mercury penetration is fairly rapid, requires little sample preparation, covers a wide range of pore sizes, and gives results of considerable reliability. There are difficulties and uncertainties to be sure. With nonrigid materials, distortions may arise because of sample compression under high pressure; the mercury contact angle is difficult to evaluate accurately and may actually change with pressure; mercury surface tension may vary with radius of curvature in an unknown manner; and mercury amalgamates with some metals. This last item is often not an insurmountable problem; a thin

layer of fatty acid deposited on the metal surface will usually protect it for the duration of a test.

The other method of pore evaluation, an extension of the low-temperature adsorption technique for surface-area analysis, is applicable only to pores between about 20 and 600 \AA in diameter. This makes it particularly attractive for catalysts and catalyst-support analysis but eliminates it where large pores are encountered.

If the analysis that led to the results described in conjunction with Figure 6.3 is continued to high relative pressures and is then reversed, leading again toward lower pressures, a complete curve of data such as that given in Figure 6.3 will most likely be obtained. Preceding material described the first break in such a curve as signifying approximately the completion of a single layer of adsorbed gas molecules and subsequent portions to correspond to the formation of still thicker layers. Upon continuing to add gas almost to saturation, the layers within pores are thought to merge and eventually to fill the pores with condensed liquid. The curve for the reverse process, that is, the desorption curve, must then represent the evaporation of condensed liquid and the emptying of the pores. Both the filling and emptying curves contain data pertinent to the size and volume of the pores. Because the analysis of the desorption curve is perhaps easier to explain, it will be utilized here. The model retains cylindrical pores of various diameter and lengths as in the mercury penetration analysis.

It is well known that the tendency for any liquid, including liquid nitrogen, to evaporate is greater when the exposed liquid surface is flat (as it would be in a large open container) than when the liquid is confined in a small capillary tube. This means that nitrogen condensed in large pores evaporates more readily than that in small pores. The desorption curve then represents a progressive depletion of condensed liquid beginning with large pores and proceeding to smaller ones. When any pore empties of its condensed liquid, it still has on its surface an adsorbed layer of gas that may be several molecules thick. Accounting for these remnants of remaining gas complicates the calculations so that giving details will not be attempted here even though the procedure is quite straightforward. Basically it means that the calculations have to be performed in a stepwise manner.⁴⁸ Results from gas-desorption tests can be cast as a plot of volume represented by pores of decreasing diameter like the mercury penetration data or in several other ways. The surface area represented only by pore walls can also be computed.

The experimental procedure is straightforward but involved, and attempting to maintain stable conditions and carry out the several manipulations by hand inevitably leads to errors. For this reason an automated instrument under computer control, as mentioned earlier, is almost essential. One or

two attempts to carry out an analysis manually usually is convincing of the necessity for instrumental control.

A simple test based on powder-flow properties⁴⁹ indicates total pore volume with acceptable accuracy for some routine control purposes, particularly with highly porous powders. The applicability of the test under use conditions would, of course, need to be established by comparison with, say, mercury intrusion before adoption. The test is based on the fact that free-flowing powders appear dry and remain free-flowing with the addition of water up to a point, after which further additions bring about a marked change. Such behavior is attributed to the first additions of water filling pore spaces within the particles and later additions filling the void spaces among the particles. To carry out a test, about 25 g of dried powder is weighed and transferred to a screw-top bottle. A small quantity of water, or perhaps another liquid, is then added from a burette and the bottle is capped and shaken vigorously. The bottle is uncapped and lumps, if any, are broken with a spatula or by more vigorous shaking. The process is repeated with water being added in small increments until the powder does not flow freely when the bottle is upended, this condition indicating the filling of the pores and the beginning of spillover into the voids. The specific pore volume is calculated by dividing the volume of water to the end point by the weight of the sample.

Sorption from solution, for reasons given previously, must be approached with caution in attempts to apply it to pore evaluation. Nevertheless, there are apparently a few instances of reliable application.⁵⁰ Here the technique is based on the premise that the size of the dissolved molecule, usually a dye, determines the dimensions of the pore it might penetrate. There is considerable uncertainty in the size of the various dye molecules, so careful standardization against other pore measurements is essential in any attempted application of this technique.

REFERENCES

1. J. A. Davidson and H. S. Haller, "Latex Particle Size Analysis. V. Analysis of Errors in Electron Microscopy," *J. Colloid Interface Sci.*, **47**, 459-472 (1974).
2. J. M. DallaValle, *Micromeritics: The Technology of Fine Particles*, 2nd Ed., Pitman, New York, 1948.
3. C. Orr, Jr. and J. M. DallaValle, *Fine Particle Measurement*, Macmillan, New York, 1959.
4. G. Herdan, *Small Particle Statistics*, 2nd Ed., Academic, New York, 1960.
5. R. R. Irani and C. F. Callis, *Particle Size: Measurement, Interpretation, and Application*, Wiley, New York, 1963.

References

6. R. D. Cadle, *Particle Size: Theory and Industrial Applications*, Reinhold, New York, 1965.
7. T. T. Mercer, *Aerosol Technology in Hazard Evaluation*, Academic, New York, 1973.
8. J. D. Zwicker, "Sieve Analysis to Below Two Microns Using Micromesh Sieves," *Ceram. Bull.*, **45**, 716-719 (1966).
9. H. B. Carroll and I. B. Aksi, "Sieving and Particle Size Distribution in 10 through 1 Region," *Rev. Sci. Instrum.*, **37**, 620-623 (1966).
10. K. Schöner, W. Schwenk, and K. Steier, "A Fully Automatic Device for Screen Analyses," *Anforderungen—Technik*, **7**, 368-372 (1974).
11. C. Orr, Jr., Unreported development pending patent protection.
12. E. E. Bauer, "Hydrometer Computations in Soil Studies Simplified," *Eng. New-Rec.*, **118**, 662-664 (1937).
13. S. Berg, "Determination of Particle Size Distribution by Examining Gravitational and Centrifugal Sedimentation according to Pipet Method and With Divers," Symposium on Particle Size Measurement, ASTM Spec. Tech. Publ. No. 234, 1959, pp. 143-171.
14. C. C. McMahon, "Particle Size Analysis By the Method of Musgrave and Harner," *Ceram. Bull.*, **49**, 794-796 (1970).
15. J. Kalshoven, "Fast and Automatic Sedimentation Analysis," *Proc. Conf. Particle Size Anal.*, London, 1967, The Society for Analytical Chemistry, pp. 197-204.
16. J. P. Olivier, G. K. Hickin, and C. Orr, Jr., "Rapid Automatic Particle Size Analysis in the Subsieve Range," *Powder Tech.*, **4**, 257-263 (1971).
17. W. P. Hendrix and C. Orr, Jr., "Automatic Sedimentation Size Analysis Instrument," *Proc. Conf. Particle Size Analysis 1970*, The Society for Analytical Chemistry, London, 1972, pp. 133-144.
18. P. Sennett, J. P. Olivier, and G. K. Hickin, "Application of Rapid Automatic Particle Size Analysis to the Paper Industry," *Tappi*, **57**, 92-95 (1974).
19. J. R. Hodgkinson, "Dust Measurement by Light Scattering and Adsorption," Ph.D. Thesis, University of London, 1962.
20. W. H. Coulter, "High Speed Automatic Blood Cell Counter and Cell Size Analyzer," *Proc. Natl. Electron. Conf.*, **12**, 1034-1042 (1956).
21. R. H. Berg, "Electronic Size Analysis of Subsieve Particles by Flowing Through a Small Liquid Resistor," ASTM Symposium on Particle Size Measurement, Spec. Tech. Publ. No. 234, 1959, pp. 245-255.
22. H. E. Kubitschek, "Electronic Measurement of Particle Size," *J. Res. Natl. Bur. Stand.*, **A13**, 128-135 (1960).
23. T. Allen, "A Critical Evaluation of the Coulter Counter," *Proc. Conf. Particle Size Anal.*, London, 1967, The Society for Analytical Chemistry, pp. 110-127.
24. S. Kinsman, "Instrumentation for Filtration Tests," *Chem. Eng. Prog.*, **70**, 48-51 (1974).
25. H. Bader, H. R. Gordon, and O. B. Brown, "Theory of Coincidence Counts and Simple Practical Methods of Coincidence Count Correction for Optical and Resistive Pulse Particle Counters," *Rev. Sci. Instrum.*, **43**, 1407-1412 (1972).
26. R. W. Lines, "Some Observations on Sampling for Particle Size Analysis with the Coulter Counter," *Powder Tech.*, **7**, 129-136 (1973).
27. F. M. Lea and R. W. Nurse, "The Specific Surface of Fine Powders," *J. Soc. Chem. Ind. (London)*, **58**, 277-283 (1939).

28. R. L. Blaine, "A Simplified Air Permeability Fineness Apparatus," *ASTM Bull.*, 123, 51-55 (1943).
29. N. F. Schulz, "Measurement of Surface Areas by Permeametry," *Int. J. Miner. Proc.*, 1, 65-79 (1974).
30. F. P. Bowden, "The Nature and Topography of Solid Surfaces and the Study of Van der Waal's Forces in their Immediate Vicinity. The Surface Decomposition of Solids," *Fundamentals of Gas-Surface Interactions*, H. Saltsbur, J. N. Smith, Jr. and M. Rogers, eds., Academic, New York, 1967.
31. S. Brunauer, P. H. Emmett, and E. Teller, "The Adsorption of Gases in Multimolecular Layers," *J. Amer. Chem. Soc.*, 60, 309-319 (1939).
32. A. L. McCellan and H. F. Harnsberger, "Cross-Sectional Areas of Molecules Adsorbed on Solid Surfaces," *J. Colloid Interface Sci.*, 23, 577-599 (1967).
33. S. J. Gregg and K. S. W. Sing, *Adsorption, Surface Area, and Porosity*, Academic, New York, 1967.
34. C. H. Giles, T. H. MacEwan, S. N. Nakhwa, and D. Smith, "Studies in Adsorption, Part XI. A System of Classification of Solution Adsorption Isotherms and its Use in Diagnosis of Adsorption Mechanisms and in Measurements of Specific Surface Areas of Solids," *J. Chem. Soc., Part III*, 1960, 3973-3993.
35. C. H. Giles and S. N. Nakhwa, "Studies in Adsorption XVI. The Measurement of Specific Surface Areas of Finely Divided Solids by Solution Adsorption," *J. Appl. Chem.*, 12, 266-273 (1962).
36. E. D. Eanes and A. S. Posner, "Small-Angle X-Ray Scattering Measurements of Surface Areas," *The Solid-Gas Interface*, Vol. 2, E. A. Flood, ed., Dekker, New York, 1967, Chap. 33.
37. D. N. Winslow and S. Diamond, "The Specific Surface of Hydrated Portland Cement Paste as Measured by Low-Angle X-Ray Scattering," *J. Colloid Interface Sci.*, 45, 425-426 (1973).
38. D. N. Winslow and S. Diamond, "Specific Surface of Hardened Portland Cement Paste as Determined by Small-Angle X-Ray Scattering," *J. Amer. Chem. Soc.*, 57, 193-197 (1974).
39. R. A. Van Nordstrand and K. M. Hack, "Small Angle X-Ray Scattering of Silica and Alumina Gels," presented before the Division of Petroleum Chemistry, American Chemical Society, Chicago, Sept. 9-11, 1953.
40. R. W. Camp, private communication.
41. C. F. Royse, Jr., *Semimetric Analysis*, Arizona State University, Tempe, 1970.
42. H. Heywood, "The Scope of Particle Size Analysis and Standardization," Symposium on Particle Size Analysis, *Trans. Inst. Chem. Eng.*, 255, 14-24 (1947).
43. H. Wadell, "The Coefficient of Resistance as a Function of Reynolds Number for Solids of Various Shapes," *J. Franklin Inst.*, 217, 459-490 (1934).
44. W. H. Glezen and J. C. Ludwick, "An Automated Grain-Shape Classifier," *J. Sediment. Petrol.*, 33, 23-40 (1963).
45. N. S. Land, "A Feasibility Study of a Technique for Sorting Particles by Shape," *Mat. Res. Stand.*, 9, 26-29, 77 (1969).
46. A. I. Medalia, "Dynamic Shape Factors of Particles," *Powder Tech.*, 4, 117-118 (1970/1971).

References

47. M. Svata, "Determination of Pore Size and Shape Distribution from Porosimetric Hysteresis Curves," *Powder Tech.*, 5, 345-349 (1971/1972).
48. E. P. Barrett, L. G. Joynder, and P. P. Halenda, "The Determination of Pore Volume and Area Distributions in Porous Substances. I. Computation from Nitrogen Isotherms," *J. Amer. Chem. Soc.*, 73, 373-380 (1951).
49. W. B. Innes, "Total Porosity and Particle Density of Fluid Catalysts by Liquid Titration," *Anal. Chem.*, 28, 332-334 (1956).
50. C. H. Giles, A. P. D'Silva, and A. Cameron, "Determination of Pore-Size Distributions of Powders from Solute Adsorption," *Chem. Ind. (London)*, 1969, 239-240.

7

Structure and Properties of Agglomerates

D. E. Niesz

R. B. Bennett

The structure and properties of solid agglomerates in a powder often dominate powder-processing parameters, microstructure, and bulk properties. The origin, characterization, elimination, and effects of various types of solid agglomerates are discussed in this chapter. All agglomerates referred to in this chapter are solid agglomerates, unless otherwise stated.

ORIGIN OF SOLID AGGLOMERATES

The most common type of agglomerate in a ceramic powder is one bonded by a diffusion bond formed during calcination. Such agglomerates are strong enough to retain their identity during green forming. However, many reactive powders contain more than one type of agglomerate; therefore, reporting properties that reflect only the average properties of the various agglomerates types is inadequate. Figure 7.1 shows two types of agglomerates that make up one alumina powder. This situation often occurs in unmilled reactive alumina because of the numerous transition phases that



Figure 7.1. Electron micrograph of alumina I agglomerates.

can be present, as discussed in Chapter 9. Here the agglomerate containing the 100 to 200 Å particles is gamma alumina and represents 10 to 20 wt % of the powder. Because of its low bulk density, it leads to a very nonuniform green density even though it is weak enough to be broken down by a kitchen blender. Quantitative determination of the relative amounts of each type of agglomerate in this powder is essential for evaluating lot-to-lot variability.

PHYSICAL CHARACTERIZATION OF POWDERS AND AGGLOMERATES

The following physical characteristics of agglomerates are important:

1. Microstructure of agglomerates.
2. Percentage of each type of agglomerate in a powder.

3. Size distribution of the ultimate particles.
4. Size distribution of the agglomerates.
5. Bulk density of the agglomerates.
6. Strength of the agglomerates.
7. Character of the agglomerate bond.

In evaluating the features listed above, care must be taken not to alter the powder character by the characterization technique. The first characterization step is microscopic evaluation of the agglomerate. The depth of field of a scanning electron microscope (SEM) is valuable, but a transmission electron microscope is required to resolve the structure of very fine powders (Chapter 8). Some effort has been made toward automating the scanning electron microscopy technique,¹ and continued effort in this direction is needed if analysis of fine powders is to become more routine. The visual observation is invaluable in determining appropriate characterization techniques and in interpreting the results of various characterizations.

The agglomerates in calcined powders normally are broken down to their ultimate particles by ball milling in a water medium followed by granulation with a spray drier. Control of the characteristics of the spray-dried powder is a key element in many ceramic powder processes. The granules in a spray-dried powder are held together by organic binders, plastic materials such as clay or talc, and by decomposed gels or hydrates precipitated from solution during drying.

The bulk density of agglomerates has a marked effect on the bulk density of the powder and the compaction ratio. Surface area and the bulk and true density of a powder are also important, but they are related more to the bulk powder than the agglomerates in the powder. If the bulk density of agglomerates in a powder vary, the agglomerates with a bulk density well below that of the major agglomerate lead to a low local density and thus to a nonuniform die fill and green compact. Techniques for measuring the bulk density of agglomerates are lacking, although mercury porosimetry² has been used for this purpose (Chapter 6). For an agglomerated powder, a bimodal pore-size distribution is obtained when pore diameter is plotted against pore volume. In the porosimetry technique, if the pores of the agglomerate are infiltrated by mercury without crushing the agglomerate, the bulk density of the agglomerate can be calculated.

Agglomerates in calcined powders can also be broken down by dry milling, as discussed in Chapter 10. The resulting powder is composed of weak agglomerates or granules bonded by the small amount of dry milling aid used to facilitate dry grinding.

A type of agglomerate that is not widely recognized is one bonded by decomposed gels or hydrates. These agglomerates form by precipitation of cations from solution when water slurries are dried. Some bonding may also

occur between the hydrated surface layers of the powder particles. The strength of the resulting agglomerate depends on the percentage of bond phase. For high-surface-area powders, this bonding can produce strong agglomerates.

The lack of a good technique to characterize agglomerate bulk density is not a serious limitation on powder characterization, since strong, porous agglomerates cannot be tolerated in a powder to be used in powder processing. It often is enough to know that a powder does or does not contain strong, porous agglomerates. Agglomerates usually can be observed with a microscope and their strength can be measured. Powders must be pretreated by some technique, such as ball milling, to eliminate such agglomerates if an optimum powder process is desired.

The strength of agglomerates is also an important factor in determining a powder's compaction behavior and in determining the amount of milling required to eliminate strong agglomerates. It is important to characterize the agglomerate bond in powders to be used in powder processing. This is discussed in Chapter 27 as well.

AGGLOMERATE STRENGTH

The strength of agglomerates in a powder can be determined from powder-compaction data.⁹ By this technique the relative strength of the agglomerates in a powder is related to a break in the compaction curve when the logarithm of pressure is plotted against percentage of theoretical density. This relation can be derived from the formula first suggested by Duckworth⁹ in discussing Ryshkewitch's⁸ paper on the strength of porous sintered alumina and zirconia:

$$\sigma = \sigma_0 e^{-bp} \quad (1)$$

where σ = strength of a porous body

σ_0 = strength of a nonporous body of the same material

b = an empirical constant

p = porosity expressed as a fraction

If the strength is replaced by the pressing pressure, then

$$P = P_0 e^{-bp} \quad (2)$$

Taking the logarithm of both sides gives

$$\ln P = \ln P_0 - bp \quad (3)$$

This equation is a straight line when the logarithm of pressure is plotted against the volume fraction of porosity. The logarithm of pressure is also

linearly related to porosity expressed as a percentage and to density expressed as a fraction or as a percentage of theoretical density.

Figure 7.2 shows the compaction data for several materials plotted as the logarithm of pressure versus percentage of theoretical density. The breaks in the curves for aluminum and copper indicate the pressure at which plastic deformation of the powder particles at their contact points begins to control the compaction behavior.

Alumina I is an unmilled, calcined alumina containing two distinct types of agglomerates. An electron micrograph of this powder is shown in Figure 7.1. The break in the curve at 300 psi for this powder indicates the pressure at which crushing of the contact points of the porous agglomerates begins to control the compaction behavior of the powder.⁹ Thus the strength of the agglomerates composed of 100 to 200 Å ultimate particles is indicated by this break point. The minimum amount of this agglomerate that can be detected in this powder is about 5 wt %.

There is a slight break in the curve for alumina II⁹ at 12 psi. This powder is a dry-milled reactive alumina, and the break indicates the relative strength of the agglomerates bonded by the milling aid. The curve is straight between the 12 psi break and 100,000 psi. This type of curve indicates the absence of strong, porous agglomerates, such as those formed during calcination. During calcination the bond area at particle contact points is increased by diffusion processes. The sensitivity to change in agglomerate strength with calcination temperature was evaluated by calcining alumina II at progressively higher temperatures. The break points occurred at 60, 150, 875, and 2000 psi for calcination temperatures of 1800, 2000, 2200, and 2400°F, respectively.⁹

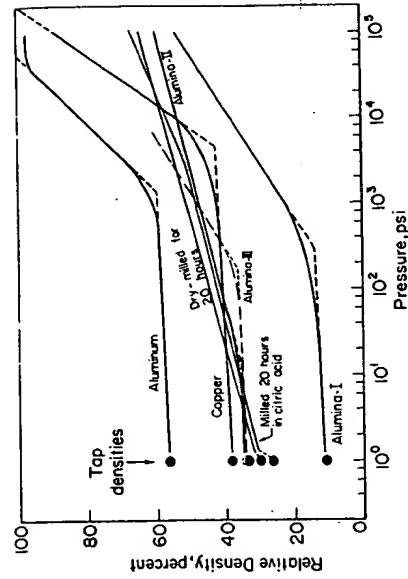


Figure 7.2. Compaction data for several powders.

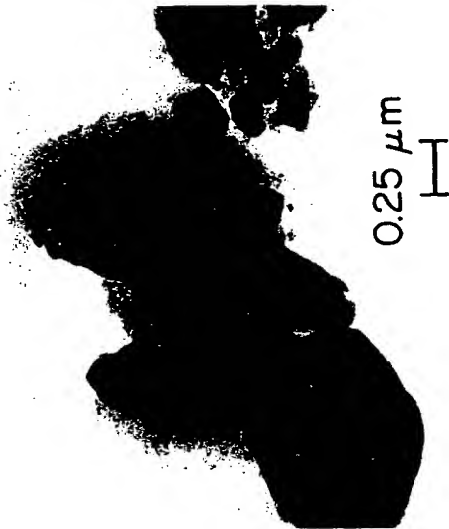


Figure 7.3. Electron micrograph of alumina I powder after water milling for 20 hours.

The curve for alumina I after milling in water for 20 hours shows a break point at approximately 3000 psi.⁶ This indicates the presence of strong agglomerates. Figure 7.3 shows an electron micrograph of this powder. A translucent, weblike material that can be seen around the edges of the agglomerates has been identified as aluminum monohydrate by thermogravimetric analysis. This hydrate acts as a cement that bonds the agglomerate particles together. The mechanism by which this bond forms is discussed later.

Alumina III is a wet-milled and spray-dried 96% commercial alumina body. The break point at 200 psi represents the strength of the spray-dried granules. This technique is quite sensitive to variations in the strength of spray-dried granules, and considerable variation can be detected in nominally identical lots of powder.

The curve for alumina I after dry milling for 20 hours does not exhibit any breaks between 10 and 100,000 psi.⁶ The only granules in this powder are those held together by the small amount of dry-milling aid. These are so weak that their presence is undetectable by this technique.

There is an upper limit of agglomerate strength that can be evaluated by this technique, and the presence of such agglomerates must be determined microscopically. The coarse-particle agglomerate in alumina I is an example of a agglomerate whose strength cannot be determined by this technique at pressures below 100,000 psi.

EFFECT OF AGGLOMERATES ON MICROSTRUCTURAL DEVELOPMENT

As an example of the significance of agglomerate structure and properties on microstructural development, the microstructural development during sintering is illustrated for three powders.⁹ All three powders were derived from alumina I. Electron micrographs of the three powders are shown in Figures 7.4 through 7.6. The as-received powder contains two types of agglomerates, as discussed earlier. In the dry-milled powder, the agglomerates are essentially all broken down into their primary particles. The 100 to 200 Å particles are dispersed on the surfaces of the larger particles. The wet-milled powder is composed of agglomerates bonded by aluminum monohydrate, as discussed earlier.

The differences in the microstructures developed from these three powders after isostatic pressing and sintering can best be illustrated by examining the fracture surfaces of compacts with densities between 90 and 95% of the theoretical value. The compact prepared from the as-received powder is shown in Figure 7.7. The very nonuniform microstructure consists of dense, coarse-grained regions and porous, fine-grained regions. On a polished surface the porous regions are isolated. The porous areas are remnants of the porous agglomerates in the powder that had 100 to 200 Å

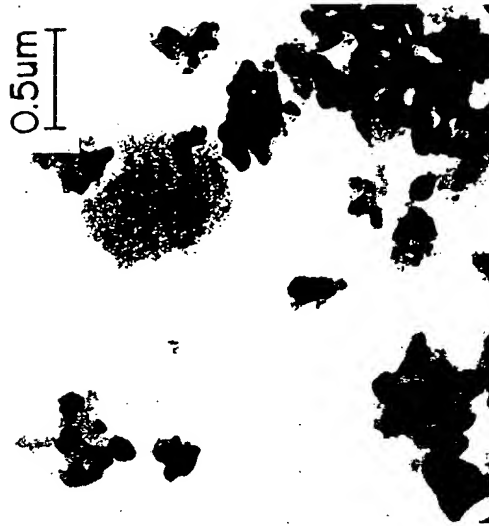


Figure 7.4. Electron micrograph of alumina I powder in the as-received condition.

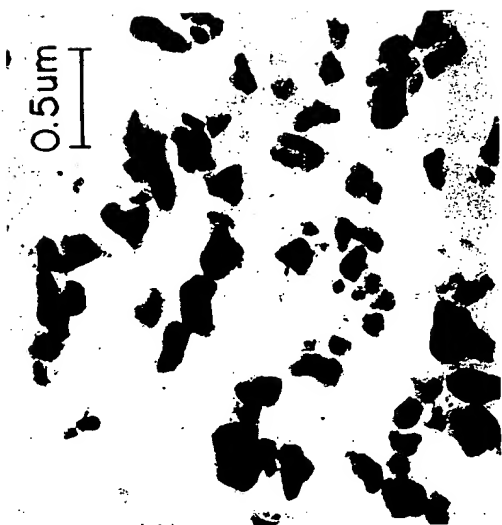


Figure 7.5. Electron micrograph of alumina I powder after dry-ball milling for 20 hours with naphtheneic acid as a dry-grinding aid.

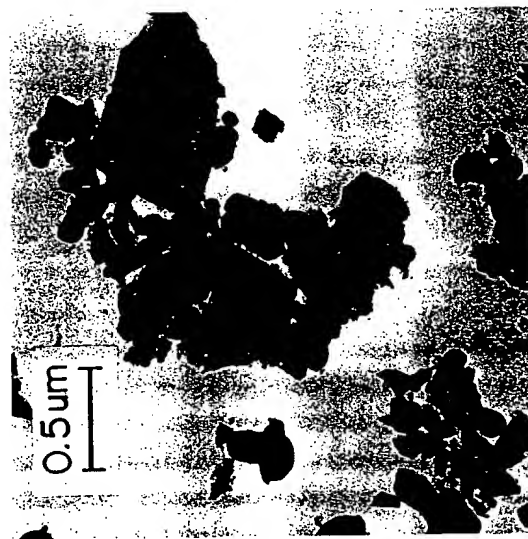


Figure 7.6. Electron micrograph of alumina I powder after water milling for 20 hours with citric acid.

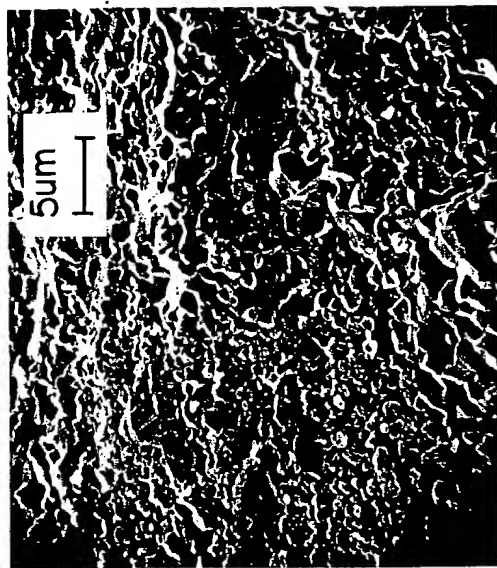


Figure 7.7. Fracture surface of 95% dense compact prepared from as-received alumina I powder.

primary particles. As sintering proceeds, the denser areas reach a limiting density and pockets of porosity remain. These pockets of porosity limit the attainable density, act as light-scattering centers, and act as critical flaws for fracture initiation.

By contrast, the fracture surface of the compact prepared from the dry-milled powder is uniform (Figure 7.8). This type of microstructure is required if a compact is to be sintered to theoretical density to achieve translucency and optimum mechanical strength. The microstructure of a theoretically dense compact prepared from this dry-milled powder is shown in Figure 7.9. Final microstructures of this quality cannot be obtained from powders that result in nonuniform microstructures, such as that shown in Figure 7.7.

The fracture surface of the compact prepared from the wet-milled powder appears to be quite uniform. However, closer examination reveals numerous separations in the microstructure (Figure 7.10). These separations appear to be the result of disruption of the particle contacts due to shrinkage and phase inversions in the hydrated phase that served as the bond phase in the powder agglomerates. Except for small samples, the disruption leads to bulk rupture of the compact during sintering.

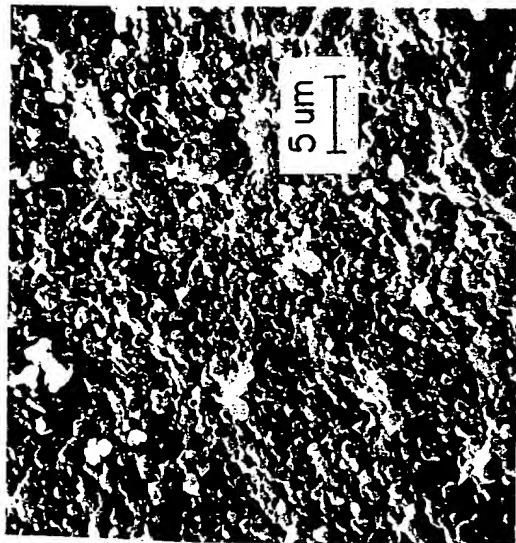


Figure 7.8. Fracture surface of 96% dense compact prepared from dry-milled alumina I powder.

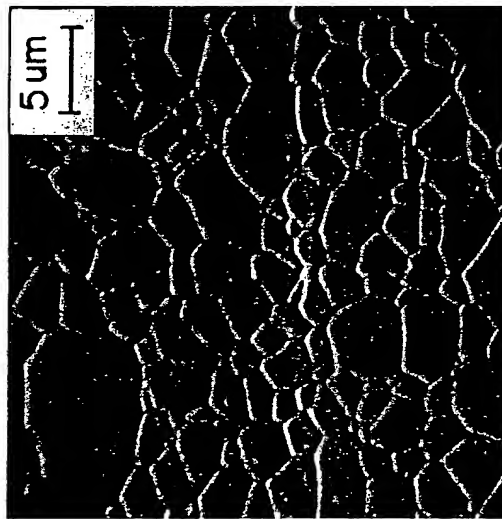


Figure 7.9. Microstructure of theoretically dense compact prepared from dry-milled alumina I powder.

70



Figure 7.10. Fracture surface of 92% dense compact prepared from water-milled alumina I powder.

MECHANISM OF AGGLOMERATE FORMATION DURING WET MILLING

The mechanism by which the agglomerates form during wet milling is shown in Figure 7.11.⁶ The left view depicts a water-solvated alumina particle, with hydrogen ions preferentially absorbed on the surface in a double-layer effect. The probable surface reaction is modeled in the right view, which depicts a fresh fracture surface exposed by milling attrition.

Exchange of hydrogen ions for aluminum ions permits the reaction to penetrate below the outer surface of the particle. The ion exchange normally produces an aluminum monohydrate layer on the particle⁷ and releases aluminum ions into the water medium. Normally this reaction is quite limited, since the monohydrate acts as a reaction barrier, but transition aluminas can be hydrated by aging in water.⁷ Thus the gamma alumina content of alumina I would be expected to have a strong influence on this reaction. For alumina I the extent of this reaction in 20 hours is normally slow. However, attrition during milling continuously removes the monohydrate reaction barrier, and the extent of the reaction during 20 hours of milling is quite significant for this powder. During drying, the aluminum-ion concentration in the liquid phase increases, and an aluminum

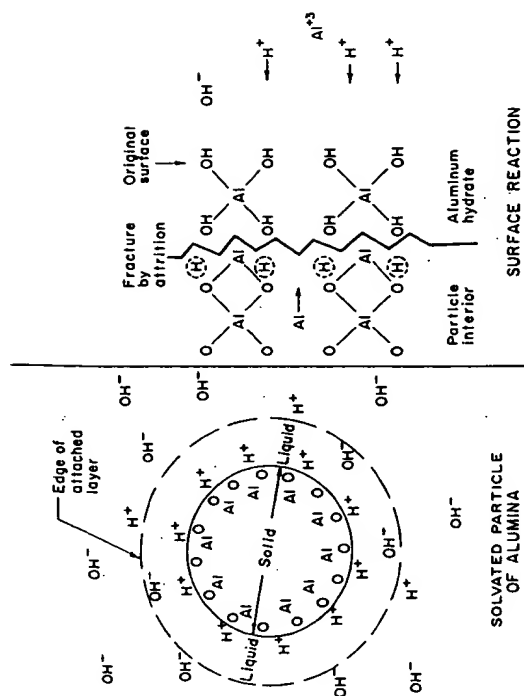


Figure 7.11. Schematic of alumina-water interaction during water milling.

hydroxide gel precipitates. With continued drying, the gel partially dehydrates, the extent depending on the drying conditions for the powder. Normally the gel ends up as a monohydrate with a surface of approximately 500 m²/g and a capillary pore structure. It serves as a bond for the agglomerates in the dried powder.

During heating to the sintering temperature, the remainder of the structural water is evolved, after which the bond goes through several intermediate phases. More importantly, however, it begins to shrink because of elimination of the capillary porosity by sintering at temperatures well below that at which the body begins to shrink. The sintering shrinkage and the volume changes associated with the phase changes lead to disruption of the particle contacts and a weakening or rupture of the compact. The mechanism described is believed to be the cause for poor sinterability of high-surface-area powders milled in water.

For alumina powders composed of 100% alpha alumina, the alumina-water reaction is of little significance, since they normally have surface areas below 20 m²/g.⁶ If the alumina is to be milled in water, particular emphasis should be placed on eliminating all transition phases, such as gamma, since they normally have surface areas above 100 m²/g. The high surface area of the hydrated reaction products also suggests that surface-

area data are inadequate to unambiguously characterize the effects of wet milling a reactive alumina powder, since a small amount of aluminum monohydrate can override the surface area of the bulk of the powder.

REFERENCES

1. J. Lebedzik, K. G. Burke, S. Troutman, G. G. Johnson, Jr., and E. W. White, "New Methods for Quantitative Characterization of Multiphase Particulate Materials Including Thickness Measurement," *Scanning Electron Microscopy*, Illinois Institute of Technology, Chicago, Illinois, 1973, pp. 121-128.
2. M. J. Orr, et al., "Applications of Mercury Penetration to Materials Analysis," *Micromeritics Instrument Corporation*, Norcross, Georgia, undated.
3. D. E. Niesz, R. B. Bennett, and M. J. Snyder, "Strength Characterization of Powder Aggregates," *Bull. Amer. Ceram. Soc.*, 51 (9), 677-680 (1972).
4. W. Duckworth, "Discussion of Ryshkewitch paper," *J. Amer. Ceram. Soc.*, 36 (2), 68 (1953).
5. E. Ryshkewitch, "Compression Strength of Porous Sintered Alumina and Zirconia—9th Communication to Ceramography," *J. Amer. Ceram. Soc.*, 36 (2), 65-68 (1953).
6. R. B. Bennett and D. E. Niesz, "Effect of Surface-Chemical Reactions During Wet Milling of Alumina," paper presented at the 74th Annual Meeting of the American Ceramic Society, Washington, D.C., May 9, 1972.
7. J. W. Newsome, H. W. Heiser, A. J. Russell, and H. C. Stumpf, "Alumina Properties," *Alcoa Research Laboratories Technical Paper No. 10*, 2nd revision (1960).
8. R. B. Bennett and D. E. Niesz, "Relation of Calcination to Character of Reactive Alumina," paper presented at the 76th Annual Meeting of the American Ceramic Society, Chicago, Illinois, April 29, 1974.

8

Characterization of Agglomerates with Transmission Electron Microscopy

L. L. Hench
E. J. Jenkins

In the previous chapter the importance of ceramic processing of agglomerates in powders was described. It was indicated that transmission electron microscopy is required to resolve the structure of fine powders.

This chapter describes methods for obtaining detailed information on localized, microstructural features by transmission electron microscopy. Means for characterizing solid agglomerates, weak agglomerates, and primary particles are discussed and limitations are noted.

TRANSMISSION ELECTRON MICROSCOPY (TEM) METHOD

In using transmission electron microscopy to characterize powders, severe approximations and assumptions are inherent in the analysis as it is usually

applied. Dry dusting of powders onto TEM grids preserves some of the structural relations. However, the observations may not be representative of the relations in bulk powder because the time and expense involved in the method necessitates a small sampling number. Single-plane TEM imaging of agglomerates is usually insufficient to obtain representative data because agglomerates are three-dimensional structural entities.

As an example of the limitation of single-plane imaging, consider Figure 8.1. Both pictures are the same agglomerate of Linde A (α - Al_2O_3), but at two different angles of tilt (0 and 45°) in a Phillips Model 301 Scanning Transmission Electron Microscope (STEM) at 80 kV electron accelerating

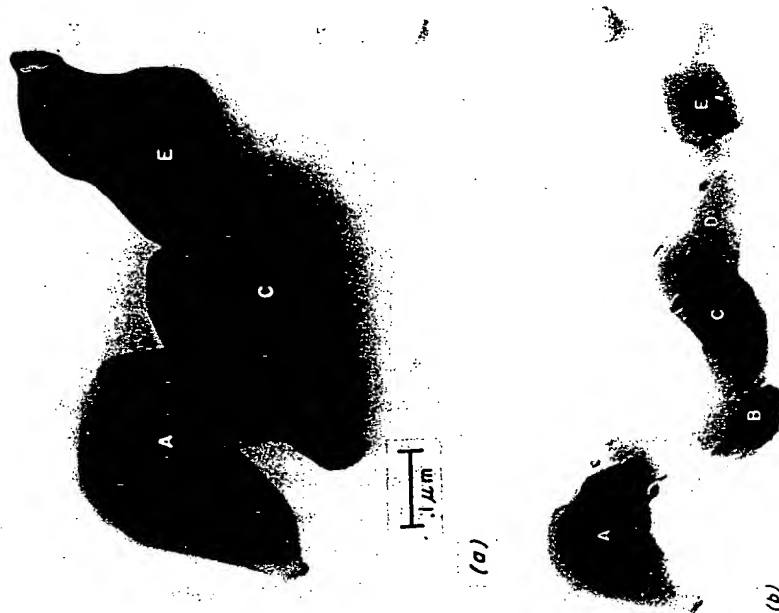


Figure 8.1. Transmission electron micrograph (TEM) of a Linde A Al_2O_3 solid agglomerate at (a) 0° tilt and (b) 45° tilt to the EM beam.

voltage. The agglomerate was one of several obtained by dry dusting Linde A onto a Cu EM grid.

The 0° tilt angle in Figure 8.1 suggests that the agglomerate consists of three particles (A, C, and E). The size of the agglomerate from this view can be characterized by maximum and minimum axes lengths of 0.9 and 0.5 μm . Changing the tilt angle to 45° reveals that the agglomerate is very much different than expected from the 0° tilt view alone. At least five particles are visible. Particles B and D were obscured by the other particles in the 0° view. Maximum and minimum axes of 1.3 and 0.3 μm , respectively, are observed from the 45° view.

Additional information, such as whether the particles are attached by weak or solid bonds, cannot be easily judged from one view direction alone. A weak agglomerate bond has a point contact character that can be seen only if viewed at the proper angle. Tilting provides different views to aid in the interpretation. For the agglomerate shown in Figure 8.1 the particles are clearly seen to be sintered together. As a larger number of particles per agglomerate are considered, it becomes even more difficult to distinguish the intraagglomerate features required for total characterization.

Tilting larger agglomerates in the TEM often provides less information because of particle overlap in the path of the EM beam, as shown by Figure 8.2. A major change in the agglomerate structure is apparent after tilting, but clear identification of even the number of particles present in the agglomerate is not possible. By comparing views at different angles, particles A, B, and C, D are found to exist as separate particles. Very careful rotation and tilting of the EM stage simultaneously might eventually reveal all the particle-particle interfaces in this agglomerate.

Since the particles in Figure 8.2 are sintered together, the only correct particle-size distribution for this powder clump would require a laborious analysis as outlined above. Particle-size analysis by any sedimentation-type technique will yield only a distribution of solid agglomerate sizes, not a distribution of particle sizes. Also, considering the wide range of axial ratios of agglomerates observed in a powder, the meaning of agglomerate-size distribution achieved by a sedimentation-type technique is unclear.

TEM ANALYSIS OF Al_2O_3 POWDER

Figures 8.1 and 8.2 show two small agglomerates representative of Linde A α - Al_2O_3 taken as a random sample from a commercial bag of powder. The agglomerates were shown to be solid agglomerates by use of the tilting stage. A larger agglomerate of Linde A is shown in Figure 8.3. This is also a solid agglomerate and is representative of the Linde A agglomerate struc-

tures. Although tilting does "open-up" some apparent particle-particle contacts, there is always at least one sinter bond holding a particle to the large agglomerate. The agglomerates have a large external and internal surface area because of the low-density packing of the particles in the agglomerate. The agglomerate shown in Figure 8.3 is especially dramatic with respect to this stringy-like feature and high surface area characteristic of the Linde A agglomerates.

The agglomerates also show attachment, probably by weak bonds, of ultrasmall ($0.1 \mu\text{m}$) debris particles. Quantitative characterization of features of this type of multiagglomerate system is a formidable challenge.

Altering Al_2O_3 production to change the size of primary particles has a strong influence on agglomerate features as well. Larger-particle-size aluminas such as A-17 have fewer particles per agglomerate, as shown in Figure 8.4. The particles also tend to be weak bonded as shown through TEM tilting (Figure 8.5). Primary particles contain substructural features, probably as remnants of their processing history.

Tabular alumina T-61 exhibits very little agglomeration tendency and remains mainly as large isolated particles (Figure 8.6).

EFFECT OF A BINDER ON POWDER STRUCTURE

Addition of 0.2 wt % of acrylic ester resin binder (acryloid B-7, Rohm and Haas) to A-17 alumina results in binder-bonded granules, as seen by comparing Figure 8.7 (A-17 with binder) with Figure 8.4 (A-17 without binder). However, complete dispersion of the binder in the powder is not achieved. In a TEM tilting stage analysis of a granule from the A-17 binder sample

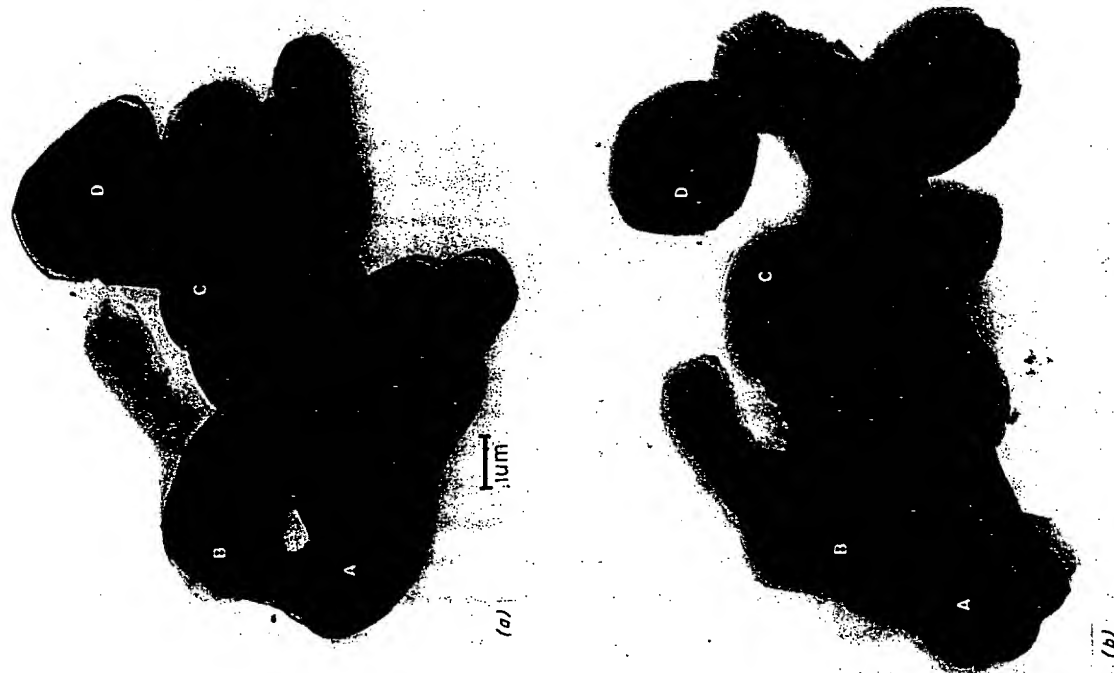


Figure 8.2. TEM of a large Linde A Al_2O_3 agglomerate at (a) 0° tilt and (b) 45° tilt.



Figure 8.3. TEM of a large Linde A Al_2O_3 agglomerate.

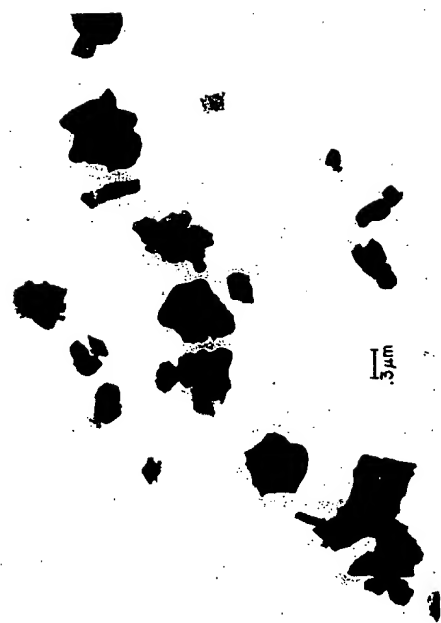


Figure 8.4. TEM of A-17 Al₂O₃ agglomerates.



Figure 8.5. TEM of an A-17 Al₂O₃ agglomerate at (a) 0° tilt and (b) 16° tilt.

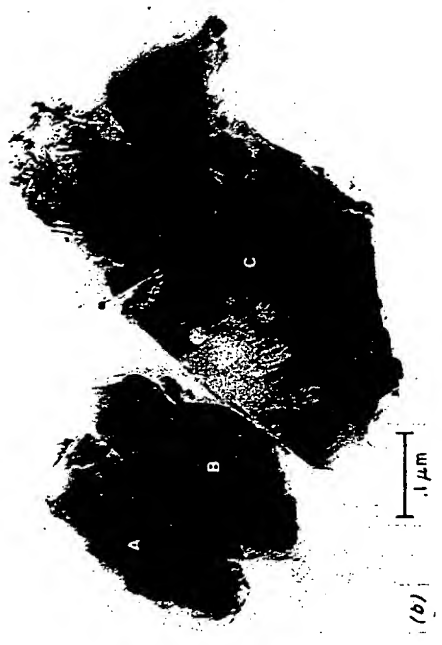


Figure 8.5 (Continued)



Figure 8.6. TEM of T-61 Al₂O₃ single particles.



Figure 8.7. TEM of a granule of A-17 Al_2O_3 with binder. A through D are individual agglomerates.



Figure 8.8. TEM of an agglomerate from an A-17 binder granule at (a) 0° tilt and (b) 45° tilt.

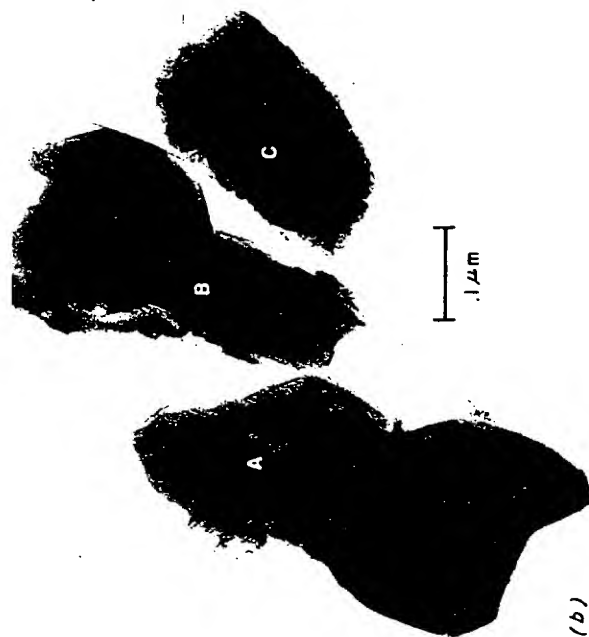


Figure 8.8 (Continued)

(Figure 8.8), particles A, B, and C all separate with tilting with no evidence of the binder being present.

SUMMARY

Transmission electron microscopy of ceramic powders can establish whether strong or weak agglomerates are present by tilting small powder agglomerates in the EM beam. Binder distribution in granules can also be analyzed. Particle- and void-size distributions in the agglomerates can be measured with fair accuracy by exposing the agglomerates to various beam orientations. The size distribution and axial ratios of agglomerates can also be determined with fair accuracy with the same technique. However, determination of the characterization features of large agglomerates and a cluster of agglomerates is only marginal because of particle overlap in the EM beam. Because submicron ceramic powders contain all the above com-

plexities, physical characterization of the powder structures leaves much room for improvement at this time.

ACKNOWLEDGMENT

The authors gratefully acknowledge the partial financial support of NIH grant NIGMS 1 PO1 GM 21056-01.

9

Bayer-Processed Aluminas

W. M. Flock

A wide variety of alumina powders are available for ceramic processing applications. The endless generation of new-product code numbers can be overwhelming to process and material engineers. It is hoped, at least for Bayer aluminas, that the characterization data presented in this chapter will impart some insight into the various differences among aluminas.

To define the material parameters to be measured for as-received aluminas, a brief review of the Bayer process is necessary and thus is presented first.

THE BAYER PROCESS

The Bayer process begins with bauxite ore, a naturally occurring weathered residue consisting of hydrated aluminum oxide, kaolin clays, hydrated iron oxides, and titanium dioxide. The bauxite is digested with caustic soda to dissolve aluminum into solution. Other undissolved matter is filtered off, and the filtrant solution is precipitated to yield aluminum trihydrate. The trihydrate is calcined to produce alumina.

PURITY OF ALUMINA TRIHYDRATES

The potential chemical contaminants in the final alpha alumina are restricted to silica from the kaolin clay, iron, titanium, and sodium that is

added as caustic soda during the digestion process. The amount of chemical contamination is largely determined in the precipitation step by the rate and manner of the trihydrate precipitation, that is, the amount of adsorbed or included contamination. Since these impurities are largely adsorbed, chemical purity dependence on this process step can be reduced by subsequent trihydrate washing. Another technique, which can be used to increase the chemical purity, is to precipitate the trihydrate from specially refined solutions, that is, those very low in silica, iron, and titanium.

The precipitation rate can also indirectly affect later calcining conditions and the resultant phase purity. Since trihydrate agglomerates are converted to alpha alumina by rotary calcining, the uniformity of phase conversion is directly affected by the agglomerate shape. Rapid precipitation produced by the addition of many nucleating sites (i.e., excessive seed crystals) can result in trihydrate agglomerate growth by accretion. This coalescence of rapidly growing agglomerates produces grape-like irregular clusters that are difficult to mix during rotary calcining. Slow precipitation, from a few nucleating sites, produces nearly spherical agglomerates, which mix more rapidly.

Trihydrate Calcination

During calcining, the alumina trihydrate, which consists of approximately 40% water, is converted to the final ceramic-grade alumina by the addition of heat and mineralizers. The latter additions are patented constituents (boric acid, chlorine and/or fluorine, and silica). These additions are required to reduce the sodium content (the major chemical impurity in Bayer-process aluminas) and to control the grain size. It should be noted that the various mineralizers produce differences in particle shape. Under controlled conditions, these slight variations in shape are not sufficient to exclude a mutual substitution of one supplier's alumina for another. It is, however, a factor that adds complexity to material characterization.

From a ceramic users point of view, two critical crystal structure changes occur during calcining that have a profound effect on later characterization and final ceramic character. These structural changes are the mode of trihydrate decomposition and the decomposition path. The decomposition path is through one or more of five well-defined intermediate crystalline phases (gamma, chi, delta, theta and kappa¹). Trihydrate decomposition occurs by way of a topotactic transformation.

Topotactic phase transformations have been described by Taylor² and Nicol.³ A topotactic transformation is one in which an earlier structure, in this case the close-packed oxygen ions of the OH radical, is maintained during dehydration. The hydrogen ions are lost and the aluminum ions rearrange without destroying the close-packed oxygen array. The crystalline

graphic orientation of the trihydrate structure is therefore maintained through these intermediate phases to the final alpha-phase agglomerates. These agglomerates are therefore defined as pseudomorphic structures.

It is this pseudomorphic trihydrate structure that forms the basis for the classification of Bayer aluminas presented in this chapter. The pseudomorphic structure preserves the Bayer-process history and therefore provides insights into the precipitation rate and calcining conditions. By studying the pseudomorphic agglomerates, estimates can be made concerning chemical and phase purity, particle shape, and size. Such information is useful in the design of more quantitative material characterization tests. The relations between individual alpha crystallites and the Bayer agglomerates are described in this chapter in the section on Surface Area and Its Significance.

The trihydrate decomposition path is of significant importance to ceramic processing since it encompasses a series of lower-molecular-density, high-surface-area phases. These phases are a potential source of contamination in as-received aluminas. The presence of such phases can result in misleading characterization data, and in some cases, adversely affect ceramic processing.

Commercial Aluminas

Considerable progress has been made in the characterization of Bayer aluminas. The three major alumina suppliers have made major strides in the development of tests for the routine characterization of aluminas. Table 9.1 is a tabulation of data supplied by Alcan, Alcoa, and Reynolds Aluminum Companies. The data cannot be directly compared in all cases, since several test methods are not standardized. This problem will soon be rectified, since a joint effort is being made by the alumina suppliers and the Alumina Ceramic Manufacturers Association (ACMA) to standardize these tests. The significant point of this table is that a great wealth of characterization information is available and that these data are routinely generated by the alumina suppliers. However, these data are not sufficient to make decisions regarding possible material substitutions. Further classification required for this purpose is presented in the remainder of this chapter.

CHARACTERIZATION OF BAYER-PROCESSED ALUMINA

The commercially available Bayer aluminas (Table 9.1) are characterized with respect to the expanded process model depicted in Figure 9.1. The major characterization tool is the petrographic microscope, and additional

Table 9.1. Ceramic grade Bayer aluminas

Type ^a	% Na ₂ O	Average Particle Size (μm)	Compaction	Fired Density	Surface Area (m ² /g)
RC-20	0.40	2.7	2.31 ^b	3.37 ^c	0.87
RC-24	0.23	2.9	2.35 ^b	3.50 ^c	0.53
RC-25	0.31	2.6	2.33 ^b	3.52 ^c	0.95
RC-122	0.03	2.6	2.35 ^b	3.46 ^c	0.35
C-70	0.50	2.5	2.28	3.18 ^c	0.66
C-71	0.75	2.2	2.24	3.33 ^c	0.71
C-72	0.03	1.61	2.27	3.58 ^c	1.28
C-73	0.02	3.1	2.28	2.99 ^c	0.34
C-75	0.01	2.8	2.25	2.97 ^c	0.49
A-2	0.46	3.25	2.21 ^c	3.22 ^c	—
A-5	0.35	4.7	2.30	3.07 ^c	—
A-12	0.24	—	—	—	0.5
A-14	0.06	—	—	—	0.6
A-10	0.06	—	—	—	0.2
A-3	0.36	0.63	1.79	3.64	9.0
A-15	0.07	—	—	—	—
A-16	0.06	0.6	—	—	—
XA-139	0.008	0.42	2.00	3.90 ^d	6.5
RC-23	0.30	0.6	1.91 ^b	3.86 ^c	7.5
RC-152	0.05	1.5	2.30 ^b	3.46 ^c	2.6
RC-172	0.04	0.6	2.21 ^c	3.94 ^d	4.0
ERC-HP	0.008	0.55	2.15 ^c	3.95 ^d	7.4

^a C = Alcan, A = Alcoa, RC = Reynolds.^b 20 g pellet pressed at 4000 psi, 4 hour grind.^c Fired densities obtained at 1620°C for 1 hr soak.^d Fired densities obtained at 1510°C for 2 hr soak.^e 10 g pellet pressed at 5000 psi, 4 hour grind.

characterization data are obtained by particle-size analysis, surface-area measurements, and compactional and functional tests such as shrinkage and fired density. A summary of these data is given in Table 9.1. A recent Alcan publication⁴ presents an excellent summary of the test methods used by both the suppliers and many ceramic users. Similar information can be obtained from Alcoa and Reynolds' brochures.

The characterization objectives are to provide information from which ceramic processing can be predicted and/or adjusted to meet the desired ceramic character. The concept used is that the material character is a

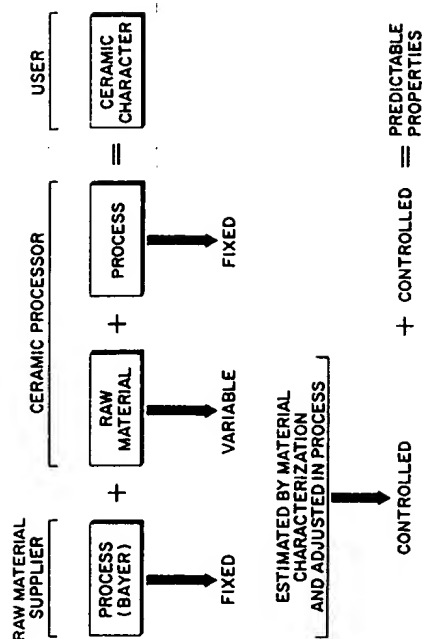


Figure 9.1. Expanded process control model.

function of the shape, size, orientation, packing, and composition of its constituents. The principal characterization criteria employed to estimate these parameters are refractive index and agglomerate structure (see Figure 9.2).

Definition of Terms

Before discussing the characterization criteria, several specific terms are defined:

Agglomerate. A genetic term used to describe mesh-size particles formed during the precipitation of alumina trihydrate.

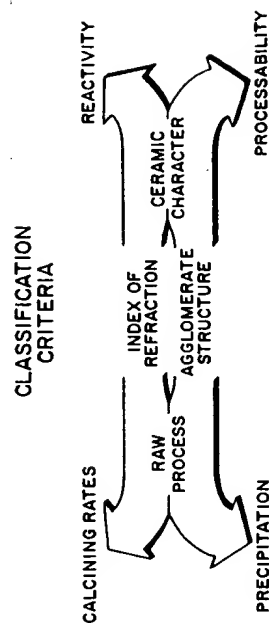


Figure 9.2. Genetic classification of Bayer agglomerates.

Pseudomorphic agglomerate. An agglomerate that has been subjected to partial or complete dehydration, but which retains the original trihydrate morphology.

Nonalpha phase. Any transition metastable aluminum oxide phase, such as gamma, kappa, chi, theta, or delta.

Alpha phase. The high-temperature, stable phase of aluminum oxide (Corundum mineralogical designation).

Reactive agglomerate. Alpha-phase agglomerates with high surface area and sufficient free energy to sinter to essentially theoretical density without the addition of glass-flux modifiers.

Beta alumina. The 12:1 sodium aluminate phase.

RELATION BETWEEN ALPHA CRYSTALLITES AND AGGLOMERATE STRUCTURE

The pseudomorphic trihydrate structure, which is described earlier, permits the characterization of alpha crystallites to be carried out as if they were orders of magnitude larger than their actual size of 0.2 to 10 μm . The occurrence of crystallites in 200 mm diameter agglomerates produces an effective magnification of 20,000 \times . This inherent magnification places the material into the ideal working range of the petrographic microscope. The additional magnifications of 50 to 200 \times obtained with the microscope produce a total useful magnification of one million to four million times.

The ability to use the petrographic microscope is a major asset, since it provides a link among the atomistic (angstrom), microstructural (micrometer), and phenomenological levels. It enables the simultaneous integration of texture parameters (size, shape, orientation, and packing) and chemical and mineralogical phase analysis. Such analyses for fine-grained material are normally possible only through the combined use of the electron probe and scanning microscopes. The petrographic microscope has, however, for the last 100 years provided the same information for coarse-grained material (i.e., 50 μ grains or larger) that these instruments provide today for fine-grained materials.

Throughout the remainder of this chapter, when agglomerate properties such as surface area, chemical purity and phase are discussed, it is implied that these are the properties of the individual primary particles.

Surface Area and Its Significance

The reactivity of an alumina is not simply related to its BET surface area. At one time it was generally believed that high surface area should be corre-

lated with high sintering reactivity. With alumina agglomerates, however, nonalpha phases (transition aluminas) may be present that have very high surface area but contribute little to reactivity. The transition aluminas have surface areas above 100 m^2/g . Reactive aluminas (alpha phase) have surface areas of 4 to 7 m^2/g , while nonreactive alpha aluminas have much smaller surface areas. The surface area contribution of the alpha aluminas is defined as "useful," while nonalpha-phase contributions are defined as "nonuseful."

The surface areas given in Table 9.1 are for as-received powders. Milled powders (deagglomerated) in general have approximately 2½ times the surface area of the powder before milling, provided no contamination has occurred. Since this increase is consistent and predictable, the surface areas stated in this chapter are for as-received aluminas.

Since the transition aluminas have surface areas equal to several hundred times those of the nonreactive alpha phase, the presence of 1 or 2% of these phases has a significant effect on the measured surface area. The A-2 and RC-20 alumina types typically have 1 or 2% nonalpha phase and yield surface areas of 0.7 to 0.9 m^2/g . A-12 and RC-24 types are typically free of nonalpha phase and have surface areas of 0.4 to 0.7 m^2/g . However, the RC-24 type is thermally more reactive than the A-2 or RC-20 types. Because of the nonalpha phases the surface area of the A-2 or RC-20 aluminas does not provide a meaningful index for describing thermal reactivity. Thus, in nonreactive aluminas, surface-area contributions from transition-phase agglomerates are a characterization nuisance and have little effect on final ceramic character. They are a serious nuisance, since the true physical surface area is used to predicate such processing parameters as binder concentration, drying time, and mill packing. The tape-casting process is very sensitive to surface area, since it affects such properties as drying time, belt release, and tape fixability.

Surface-area contributions from nonalpha-phase agglomerates in reactive aluminas such as A-16 or RC-172 are much more serious because they have a direct influence on ceramic processability. Since these materials have surface areas 10 to 15 times as high as nonreactives, a greater percentage of nonalpha-phase material is required to change the surface area. However, since reactive aluminas are calcined at a lower temperature, the possible occurrence of nonalpha phases is much higher. In addition to destroying the correlation between surface area and thermal reactivity, nonalpha material seriously effects processability. The reactive surfaces readily "cake" or reagglomerate during milling and cause incomplete size reduction. Furthermore, they adsorb large quantities of binder and affect, for example, viscosity and drying rates. These reactions are very detrimental in the tape casting of super-smooth alumina substrates. Finally, transition phases are

believed, by the writer, to produce spotty porosity in 99+% dense bodies. Since transition agglomerates are difficult to mill, and since they are of lower phase density, their sintering to the higher-density alpha phase results in a large volume reduction and produces localized high shrinkage.

For the above reasons, it is important to identify the surface-area source particularly for reactive aluminas. The presence of transition agglomerates in Bayer aluminas is a serious problem. Therefore, identification of these agglomerates with the petrographic microscope is an essential characterization process.

Characterization Criteria

Refractive Index. Refractive index differences are the basis of the optical-microscopy technique used to differentiate the transition phases and beta alumina from the stable alpha phase. The specimens are prepared as loose-grain mounts with the powder immersed in 1.720 refractive index oil. Analyses are carried out at low magnification (50 to 200 \times).

The selection of 1.720 index oil is of importance, since alpha (corundum) alumina has indices of refraction of 1.760 and 1.768 and the common phase impurities, beta alumina and the anhydrous transition phases, have refractive indices of 1.720 or less. Phase identification is based on this difference in refractive index (1.760 to 1.720). The optical principle employed is that transparent solids become practically invisible when placed in liquids with similar refraction index. Their boundaries form a continuous medium and light passes with little or no reflection or refraction. Secondly, as the differences in refractivity (refractive index) between the liquid and the solid become greater, the amount of the boundary light (refraction and reflection) increases. This increase in refractivity is observed as "relief"; the solid becomes plainly visible from the liquid as the difference in refractive index increases. By using the Becke method or central illumination method of refractive index measurement, a solid can be determined to have indices greater or less than the liquid. By careful measurement of these refractive indices, precise statements can be made concerning the chemical composition and internal structure of the solid phase.

In the present analysis the liquid refractive index was fixed at 1.720 and the difference in refractivity (relief) was used to identify the phases. Alpha-phase material presents distinct boundaries and blue colors, while nonalpha-phase agglomerates have indistinct boundaries and light brown colors. The color is a function of the amount of light dispersion.

Alpha-phase agglomerates are identified by their refractive index. These agglomerates have a refractive index slightly lower than the stable alpha phase and therefore exhibit a distinctive pale blue color.

It can be argued that another source for the distinctive pale blue color of the reactive agglomerates is the finer crystallite size. It is possible that a portion of the color dispersion is due to the greater number of crystal boundaries in reactive agglomerates. Whichever mechanism is active, a distinct color difference between reactive and nonreactive agglomerates exists and the author has found this to be the only definite method for clearly differentiating reactive materials.

Of the two mechanisms the lower-refractive-index mechanism is favored, since it also accounts for the high surface area of these agglomerates. A relation between refractive index and surface area can be formed on the basis that refractive index is a direct measure of electron density, and if cation or anion defects exist, the electron density would decrease, which in turn would slightly reduce the refractive index.

Birefringence. In addition to refractive indices, birefringence and optic axes orientation are other optical techniques used to characterize these aluminas. Because of the small differences in refractive index between the crystallographic axes (1.760 versus 1.768) of alpha alumina, its birefringence is increased to a workable range by inserting a gypsum plate into the optical path of the polarizing microscope with crossed Nicols. The first-order red of the gypsum plate provides a background color in the micrographs. For additional information on optical properties and use of the petrographic microscope, the reader is referred to any text on optical mineralogy⁶ or to a paper by Allen.⁸

It is the interaction of light with variations in the crystal electron density that produces birefringent colors that aid phase identification. Alpha-phase material exhibits low first-order grays and whites, while the other more anisotropic transition phases exhibit high first-order colors.

Agglomerate Structure and Shape. These are parameters that estimate chemical purity and, indirectly, phase purity. Agglomerate structure is a direct estimate of precipitation rate. In the Bayer process, as previously described, precipitation rate is a function of pH, temperature, and the number of nucleation sites, that is, seed crystals. If the rate is low because of any of the above conditions, agglomerate growth is slow and radiant growth occurs from the central nuclei. If precipitation is rapid, the radiant growth is replaced by coalescing agglomerates, which result in irregular, grape-like agglomerates with internal structures lacking areas of optical continuity.

The major significance of these two structures designated as random (grape-like with no initial crystal orientation) and oriented (spherical with distinct internal crystal orientation) is that they directly affect the chemical

purity of the final material. Since precipitation occurs from a sodium aluminate solution containing finely suspended iron, silica, and titania particles, inclusion due to physical adsorption in the nonoriented agglomerates is the contamination source.

An indirect effect of agglomerate shape is phase uniformity. Since the trihydrate conversion is accomplished in a rotary kiln, uniform agglomerate mixing is critical. Nonspherical, irregularly shaped particles are more difficult to mix and can result in incomplete or excessive phase conversion, that is, grain growth. The author has never observed a uniformly calcined product that did not have controlled trihydrate as its source material.

CLASSIFICATION OF BAYER ALUMINAS

The aluminas given in Table 9.1 are genetically classified in this section. The classification purpose is to relate raw-material process history to ceramic processability and final character. Secondly, the aluminas are classified to reduce the spread in properties so that quantitative characterization can be carried out. The final purpose is to aid in the selection of alumina types, that is, material substitution.

The classification criteria are shown in Figure 9.2. The interaction among these criteria, the previous raw material processing, and their ceramic behavior are discussed in a previous section. In this section eight alumina types are classified according to reactivity, agglomerate structure, and

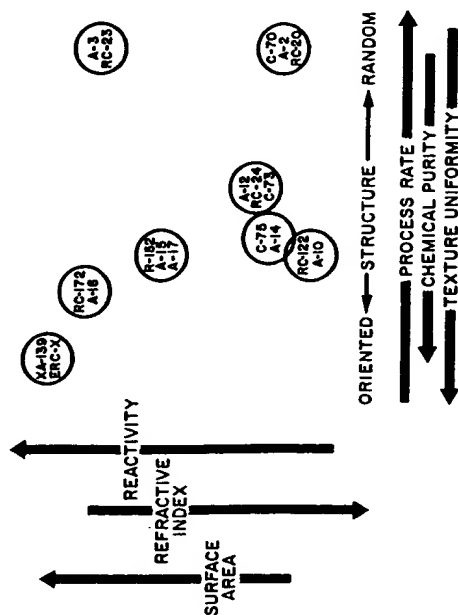


Figure 9.3. Classification of Bayer aluminas.

phase content, as shown in Figure 9.3. Surface areas, soda contents, and the range of average particle sizes are also stated. The variation in reactivity among types is indicated by an arrow. The direction of the arrow indicates increasing reactivity and the arrow length reflects the spread in reactivity. Several typical alumina types are placed on the reactivity arrow at their appropriate positions. A tight cluster of types indicates little or no difference in reactivity.

For discussion purposes, the eight alumina types are grouped into the following four larger classes:

1. Nonreactive; high purity.
2. Nonreactive; low purity.
3. Reactive; high purity.
4. Reactive; low purity.

The nonreactive alumina are discussed first.

Nonreactive Aluminas

Oriented—High-Purity Types. One of the first commercial Bayer aluminas marketed in the early forties was Alcoa A-10. Prior to A-10, tabular alumina was the only source of high-purity aluminum oxide. Tabular is a Bayer product that is further processed by sintering and is then reduced to a fine grain size by steel-ball milling. With respect to thermal reactivity, tabular alumina is completely inert, having an unmeasurable low BET surface area. A-10 does not require extensive ball milling, but like tabular, A-10 is a very nonreactive material, having surface areas of 0.15 to 0.25 m²/g and an average particle size greater than 5 μ m. There is no direct commercial substitute for A-10 alumina. Alcan C-6 was an early attempt and Kaiser KC-8 is a product with some similar properties.

Based on historical usage, A-10 has been produced in a greater volume for high-alumina bodies (refractory applications not included) than any other material. It has an excellent record of uniformity but is being replaced with lower-cost, more thermally reactive materials, such as A-12, C-73, and RC-24.

A-10 is characterized petrographically by a uniform deep blue alpha conglomerate. The majority of these agglomerates have oriented structures indicating slow precipitation. The chemical and phase purity confirm that A-10 is a highly controlled product. Nonalpha-phase agglomerates are never observed. The grain size is coarse, but the uniform size distribution results in excellent green densities and low-fired shrinkages but, conversely, produces a low surface area and low thermal reactivity, that is, a high firing

temperature. Although A-10 stands in a class alone, it has been combined with the alumina family of C-75, A-14, RC-122, and B-4. Like A-10 these aluminas are characterized by very uniform, nonreactive alpha agglomerates and high chemical purity. The agglomerates of B-4, RC-122, and A-14 are primarily the oriented type, while C-75 is closer to the random agglomerate. Because of similar calcining conditions, particle size, and distribution, A-14 and C-75 are very similar and result in materials capable of mutual substitution in most ceramic processes. RC-122 has an improved size distribution and yields higher compactions and lower-fired shrinkages than either A-14 or C-75. RC-122 and B-4 are both closer to A-10 but are more reactive. The surface areas of the four materials are a true reflection of the physical surface, since these aluminas are free of surface-active nonalpha-phase agglomerates. The surface area varies from 0.35 to 0.55 m²/g and the average particle size is 2.6 to 2.8 μ m.

Like A-10 these materials have been the standard for high-quality electrical grade ceramics and, like A-10, they are being replaced with either a lower-cost nonreactive alumina or a higher-cost transition reactive alumina.

The second family in the nonreactive, high-purity group is transitional between the high-purity and low-purity aluminas. These aluminas have intermediate soda levels but a highly uniform phase and particle size. The three members of this class are A-12, RC-24, and C-73.

This class is unique in many respects. All three aluminas can be substituted for one another. Their higher soda contents make them lower in cost than the previous materials, but their closely controlled agglomerate and phase composition make them well suited for close-tolerance technical ceramics. The increase in soda does lower the TE value several hundred degrees but has no effect on the dielectric strength of electrical ceramics made from these aluminas.

Their excellent particle size distribution yields compactions much higher than A-14 and C-75 but lower than A-10, hence shrinkage is moderate to low.

The surface area is real (physical only) and varies from 0.4 to 0.7 m²/g. Compared to the A-14 types, the thermal reactivity of this group is higher. The agglomerates are both random and oriented, reflecting lower chemical purity. RC-24 is predominantly an agglomerated material.

Commercially these materials are increasing in usage owing to their lower cost, higher compactions, thermal activity, and uniformity. They are used in practically all types of high-alumina ceramics.

Random—Low-Purity Types. The final nonreactive family is the A-2, RC-20, and C-70 type. Other members of this group are RC-25, A-5, and C-71. All these aluminas have random agglomerates (rapid precipitation)

and high soda contents and contain nonalpha-phase agglomerates. The surface areas are therefore high, 0.6 to 1.2 m²/g, with 0.9 to 1.0 m²/g being typical. Based on particle size, the true physical surface area should be 0.5 m²/g or less. The powder compaction of these aluminas is fair to moderate.

Their low phase and chemical purity exclude their use for close tolerance electrical grade ceramics. These aluminas, however, are widely used in lower-cost ceramics where the size control and electrical properties are not critical. Typical uses are for abrasion-resistant material, grinding media, and low-temperature refractories. A significant recent use has been as high-modulus fillers in whiteware products. The substitution of one material for another in these less-critical ceramic applications is usually possible.

Reactive Aluminas

There is no question that future ceramic bodies will be formulated with thermally reactive aluminas. Reactive aluminas are the newest Bayer products, having been introduced in 1966. Several product types are still in experimental pilot production (XA-139 and Reynolds ERC-HP). The production experience in the manufacture of these aluminas is much less than that in the case of nonreactive types, and the controls required for their production are much more extensive. Based on these two conditions, variations in as-received materials can be expected. Reactive alumina agglomerates are readily identified by their refractive index and light blue color in singularly polarized light (plain light).

Four families of reactive aluminas are recognized and distinguished based on phase purity, chemical purity, and the number of reactive agglomerates.

The highest purity, most-reactive aluminas require the tightest process control. Precipitation rates are greatly reduced and calcining is carried out using proprietary mineralizers to control grain growth. Because of these conditions and lower volume usage, reactive aluminas cost 3 to 10 times as much as the nonreactive aluminas. The benefits to the ceramic users are increased thermal reactivity and greatly improved ceramic character. Because of lower product maturity, process complexities, and the failure of the user to adequately characterize reactive materials, the expected ceramic benefits are not always achieved.

In fairness to the alumina suppliers, it should be noted that the alumina material improvements have not been matched by ceramic-process improvements and hence the problem of large-volume ceramic fabrication with reactive materials still faces the industry.

Transition Reactive. Because of the ceramic users inability to handle the high-surface-area reactive aluminas, the original product had to be scaled down to the users capability level. The high surface area and fine particle

size resulted in poor milling, and inadequate knowledge of binder-powder interactions resulted in poor green densities, laminations in parts, and low green strengths. These process defects produced high shrinkage (greater than 22%) and cracked and warped parts. RC-152 and A-15 were adjusted to provide a compromise between high-surface-area reactive aluminas and the low-surface-area nonreactives.

Light-microscopy analyses clearly show that these materials are mixtures of reactive and nonreactive agglomerates that have been precipitated under similar conditions but that have been subjected to different calcining temperatures. Such materials can be produced by the physical mixing of reactive and nonreactive agglomerates or by calcining at the critical conversion point and producing both reactive and nonreactive materials. From light-microscopy analyses, it is not possible to determine which procedure was used, nor is it critical to know. The important fact is that these materials are mixtures of two distinct agglomerate populations—reactive and nonreactive.

Both agglomerates have oriented structures and very good chemical purity. They are free of nonalpha-phase materials and the surface areas of 1.5 to 2.5 m²/g represent the true physical surface. The average particle size is 1.5 μm which is significantly finer than the previous nonreactives but much coarser than full reactive aluminas.

Commercially these aluminas are very important in that they are used for practically all 99.5% alumina bodies. The dual-agglomerate population produces a wide particle-size distribution, which in turn produces excellent compactions and low-fired shrinkage. However, since they are mixtures of reactive and nonreactive materials, wide variations in reactivity are possible, making surface area an important characterization tool.

Reactive—High Purity. With improved ceramic process experience and capability, the fully reactive aluminas were again placed on the market. These materials are A-16 and RC-172. They contain essentially all reactive agglomerates and, like the transition types, contain oriented agglomerates. Since they are calcined at a reduced temperature, some lots contain a percentage of nonalpha-phase material. Typical material surface areas are 4.0 to 6.5 m²/g. Higher values due to the nonalpha phase have also been measured. The average particle size is extremely fine, being less than 0.6 μm, and the soda level is very low (around 0.05%).

The major commercial use for these materials has been for super-smooth substrates (as-fired surface finishes of less than 5.0 μ in.). The need for super-smooth substrates produced to very close specifications has greatly improved the state of the art of reactive materials. Another important application has been for high-density, 99.5% grinding media. The 99+

material improves grinding efficiencies, greatly reduces ball wear, and improves final ceramic purity.

Reactive Mixed Phase—Low Purity. Two very interesting reactive aluminas are A-3 and RC-23. These materials are truly reactive, having surface areas greater than 7.5 m²/g, but are not produced with precise controls required for the other reactive materials. They are therefore produced at much lower costs and have excellent potential use in less-critical ceramic applications.

The problems in working with these materials are numerous. The abundance of nonalpha phase, particularly the beta phase, caused by the high soda content, makes milling extremely difficult. Mill problems, plus fine particle size, result in very poor compactions, low green strengths, and shrinkages greater than 25%. Standard material preparation procedures and forming by tablet pressing are impossible. However, additions of these materials to improve reactivity of other aluminas are possible.

As an interesting aside, the high reactivity of these materials points out that chemical purity itself is not a prerequisite for reactivity. Reactivity is a function of the degree of phase conversion, that is, defect structure.

Reactive Ultrahigh Purity. The finest example of controlled Bayer aluminas is found in the last family, which consists of two experimental production materials, XA-139 and ERC-HP. These aluminas have the highest purity (<0.01% Na₂O) and finest grain size (0.5 μm) and are the most reactive Bayer materials produced. XA-139 is particularly interesting in that the precipitation rate is so slow that single or twinned trihydrate crystals are developed instead of the typical trihydrate agglomerate.

This controlled precipitation is reflected in the materials high chemical and phase purity. The high surface area (6.5 to 7.5 m²/g) is a true reflection of the reactive alpha phase, since nonalpha-phase material has not been observed.

These aluminas are excellent base material for sintering studies. Their commercial usage is not known but they could be used to provide additional surface-finish improvement (super-smooth type) or for very-high-strength materials. Their typical properties are given in Table 9.1.

Classification Summary

The Bayer aluminas given in Table 9.1 have been classified into eight families based on agglomerate structure and refractive index. These criteria, their relations to other material characteristics, and ceramic reactivity are

shown in Figure 9.3. The relations of the eight classes to one another and with respect to their properties are also illustrated.

REFERENCES

1. H. P. Rooksby, "Oxides and Hydroxides of Aluminum and Iron," *The X-Ray Identification and Crystal Structures of Clay Minerals*, G. Brown, Ed., Mineralogical Society, London, 1961, pp. 354-392.
2. H. F. W. Taylor, "Crystallographic Aspects of High Temperature Transformations of Clay Minerals," *Proc. Natl. Conf., Clay and Clay Minerals*, 12th, 1964, Pergamon, London, pp. 9-10.
3. A. W. Nicol, "Topotactic Transformation of Muscovite under Mild Hydrothermal Conditions," *Proc. Natl. Conf. Clay and Clay Minerals*, 12th, 1964, Pergamon, London, pp. 11-19.
4. "Characterizing Aluminas," Alcan Company, 1973.
5. E. H. Kraus, W. F. Hunt, and L. S. Ramsdell, *Mineralogy*, McGraw-Hill, New York, 1951.
6. A. W. Allen, "Optical Microscopy in Ceramic Engineering," *Ceramic Microstructures*, R. M. Fulrath and J. A. Pask, eds., Wiley, 1966, pp. 71-158.

10

Grinding of Aluminas

M. Berg

Bayer-processed alumina, as is discussed in Chapter 9, consists of solid agglomerates rather than individual primary particles. Breaking down the agglomerates by grinding results in many advantages, including denser compacts, lower firing shrinkage, lower firing temperatures, lower tendency for lamination and warpage, and, most important of all, better-fired microstructures. Grinding does not break down the individual primary particles but instead fractures the agglomerates to form a combination of individual or several individual primary particles.

HISTORY OF ALUMINA-GRINDING TECHNOLOGY

Alumina grinding started in the early 1930s with two inventions. One invention was used at RCA for making a ceramic coating for vacuum tube filaments. The other related to work by Schwartzwalder on alumina at AC Spark Plug. Schwartzwalder's work was basically a continuation of the work by Seamen in Germany. These studies involved ball milling a combination of fused and calcined aluminas in steel mills, acid bleaching the iron that was trapped on the alumina during grinding, and then decanting and washing repeatedly. This work led to the first alumina spark-plug insulators in the United States. At RCA, because the process was too costly, mullite was eventually used for filaments.

A spark-plug insulator fits in a steel shell and serves as both a structural member and an insulator at high temperatures. In the early 1930s, spark-plug insulators were high alumina mullite compositions. Alumina insulators became important in the early 1940s. With the addition of organic resins to the aluminas, the finest aircraft spark plug became available for bombers in World War II. The insulators were typically 94 to 96% alumina.

Two schools developed in the approach for grinding aluminas, wet grinding and dry grinding. Wet grinding was done in a ball mill, which was followed by filter pressing and drying, or spray drying. In our case we used a continuous drum filter, pugged the material, and made it into an insulator.

The dry-grinding approach was carried out by Schwartzwalder in the early 1940s. This approach was adapted at AC Spark Plug and continues to be the method utilized. Suitable liners and balls for mills had to be developed that would not contaminate the alumina. They were usually matched very closely to the composition of the final batch. Special grinding aids were developed to prevent the rebounding of alumina in the mill.

Injection molding was the forming process for spark plugs at AC during the 1940s. This process was eventually phased out in favor of isostatic pressing because it was more costly to make the ribs of the insulator than to form the whole insulator.

In the 1950s isostatic pressing of insulators began. After the grinding operation, organic materials (binders) were added to a water-alumina slip and the slip was spray dried. The spray-dried granules were fed to the pressing operation.

During the 1960s Sommer received four patents in the area of dry grinding. In one contribution he changed the ball-mill loading ratio of alumina to balls. The normal ratio at that time was 3:1 or 4:1. Sommer showed how the ratio could be increased to between 10:1 and 20:1. With suitable grinding aids, he enhanced the milling and obtained more compactable powder.

PRESENT STATUS

Most grinding of aluminas today takes place dry in ball mills. Where wet grinding is being used, the vibratory mill is common. The fluid energy mill is being examined to grind various materials, such as gamma alumina for use in catalysts.

In milling an alumina, probably some of the most important items to consider are the alumina characteristics obtained from the incoming material. The bulk density will provide information concerning powder handling in the plant and on loading a mill. The flowability will indicate

how the material will flow in your mill and will give insight on the particle distribution. The grindability of the material is determined at AC by a test that is a spinoff of Sommer's so-called super grinding. This involves a very high loading (10 to 1) in a small gallon mill, and milling for 4 hr. The milled powder is tested for compaction behavior, surface area, and size distribution. With this knowledge large mills can be tailored by predicting to some degree how the powder will compact and how much grinding time is required. The surface area of the material yields information not only on the particle, but also on whether other materials are present (such as gamma alumina in an alpha). Chemical composition is important to determine the sintering behavior of the final product. Recognizing the important characteristics of the incoming alumina, it is possible to work with the various alumina companies so as to control this product and to use material from three or four alumina suppliers.

Grinding aids are used to promote flowability in the ball mill and to prevent caking. In theory the grinding aid tends to be a polar molecule that attaches itself to the active bond site that has been broken and prevents that grain from rebounding. Grinding aids include esters, organic salts such as sodium liquisulfonates, stearic acid, oleic acid, and monostearates. Even ethylene glycol, added as a binder, functions as a grinding aid as well. Also in grinding, lubricants are added so that we actually have a combination of binders, lubricants, and grinding aids.

11

Theories of Grinding

P. Somasundaran

The previous chapters have dealt with agglomerates and the breakdown of hard agglomerates by grinding. The grinding of coarse-grain material to produce fine powders is also of concern in many areas of ceramics. The science of fine grinding in ceramics appears to have lagged considerably behind the technological advances. Considering the large energy consumption and capital equipment costs in grinding, and the importance of the size and size distribution of the ground powder, it would be helpful to understand more about the mechanisms of grinding and the kinetics involved. These factors have received much attention in the field of mineral processing. This chapter reviews concepts in grinding and discusses the theoretical progress in fine grinding and effects of grinding aids.

STRENGTH OF INDIVIDUAL PARTICLES

The fracture of a particle involves the propagation of cracks that are present or initiated in the particle. The stress σ required for fracture is given by the Griffith relationship¹

$$\sigma = \sqrt{\frac{2E\gamma}{L}}$$

where E = Young's modulus
 γ = fracture energy
 L = crack length

For brittle materials, γ is between 10^3 and 10^4 erg/cm². With plastic deformation, γ is much greater than 10^4 erg/cm².

When a particle is repeatedly fractured, each new particle (fragment) tends to be stronger. The larger cracks existing in the original particle propagate first, leaving the finer cracks in the new particles. The probability of finding a flaw of a given minimum fracture stress decreases. As fragmentation continues, eventually the fracture stress required may increase to the extent that some plastic deformation is possible. With plastic deformation occurring, the particle cannot be ground further; consequently, a limit of fineness in grinding exists. This limit is reported to be 1 μ m for quartz and 3 to 5 μ m for limestone.

The possibility that new flaws are created during the fragmentation process has not been considered by past investigators. However, it can be expected that movement and merger of dislocations and other defects can produce additional flaws and can retard the tendency of increasing fracture strength with decreasing particle size. Another overlooked factor is that the amount of elastic energy that must be stored to propagate a crack is limited to the volume of the particle, and very small particles may not have sufficient stored energy.

The effect of rate of stress application is reported to be a gradual increase in the fracture stress initially when the rate is increased from that of slow compression tests to that of fast compression tests. Fracture stress further increases with low-velocity impact but then decreases when the velocity of the impact is further increased.² The initial increase is attributed to larger plastic deformation before failure when a higher rate of compression is used.

Increase in temperature of the fracture environment can be expected to cause an increase in plastic deformation. In this regard it is interesting to note that even under low-temperature conditions, the temperature near a propagating crack-tip can be very high owing to release of large quantities of energy in the form of heat. The magnitude of this energy is 10 to 10^6 times that of the surface energy requirement for fracture.³ The temperature at the crack tip under such conditions can even be above the melting point.³ After the propagation of the fracture, such a region, probably of the order of 100 Å to 1 μ , cools down rapidly, freezing amorphous or other high-energy structures at the fracture surface.

Newly forming, high-energy surfaces can react with the surrounding environment if the possible rate of penetration of the environment is equal to or larger than the speed of crack propagation. Figure 11.1 shows the effect of water vapor on the specific crack-extension energy of glass to be significant, but only when the crack velocity is less than about 0.1 to 10^{-4} cm/second. Below such crack velocity, cracking is assisted by water penetration

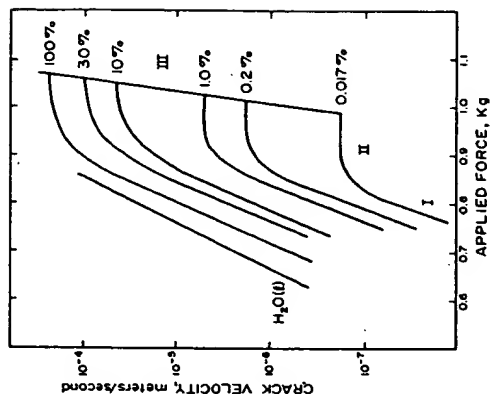


Figure 11.1. Crack velocity v in soda-lime glass as a function of the applied force, with relative humidity shown for each line. [S. M. Wiederhorn, *J. Amer. Ceram. Soc.* 50, 407 (1967).]

followed by "hydrolytic stress corrosion," whereas above this velocity water penetration is apparently not fast enough for it to be in contact with the advancing crack tip.

GRINDING MECHANISMS

During grinding several particles are simultaneously and repeatedly subjected to stress application in the grinding zone. With each stress application, several fractures may occur in each particle. Theories of crack initiation and propagation discussed above are therefore compounded by the interaction of flaws in a particle, secondary breakage, interaction of particles with each other and with the surface of the container, secondary interactions between particles and the grinding media, and physical and chemical interactions between particles and the grinding environment. In addition, the type of transport of the material through the grinding zone and size classification of it, if any, in the mill will also affect the nature of the product obtained. The present understanding of the above interactions is limited and in several cases is intuitive or speculative.

The distribution of cracks and the interaction among them during propagation will essentially determine the size distribution of the particles obtained during fracture of a single particle. Interaction of a propagating crack with a dormant crack can accelerate, decelerate, or terminate the

propagation and can possibly activate the dormant one during the process, depending possibly on the relative orientation between them. Shock waves generated in the specimen as a result of stress application or crack propagation can also activate dormant cracks. Shock waves that diverge from a peripheric point of contact in a sphere or disc can be focused at a point a distance of one-third the diameter from that point on the symmetrical axis to cause tensile fracture.¹

Fracture fragments possessing sufficient kinetic energy can undergo further fragmentation by impacting on the walls of the container. Slow compression tests on single spheres have shown that the particles, when allowed to undergo secondary breakage, produced 3.6 times as much surface area for a given specific energy input than those subjected to single fracture when they were embedded in gelatin.⁶ Primary fragments rich with flaws have been found to degrade much more readily than a new sphere comparatively free of surface flaws.^{7,8} During grinding a significant amount of secondary breaking can occur as a result of the impact of primary fragments with the grinding media and container wall, as well as with other particles.

Interaction among particles can be significant, depending on the grinding mechanism, relative hardness and size of particles, and the extent of size classification during grinding. A number of interaction phenomena can take place. Particles can nip each other and thereby remove chips, releasing a certain amount of elastic stress. They can also reduce their rugosity and even change their shape by abrasion, which in turn will alter the effects of subsequent comminution events. Most importantly, the presence of fines in the mill can reduce the grinding efficiency considerably because of the cushioning effect produced by a bed of fine particles.⁹ Energy is wasted in deformation and flow of the bed of fines. The above effect is more prominent under dry-grinding conditions than under wet-grinding conditions and all the more so for ball milling. In a rod mill coarse particles are considered to be preferentially ground, and the fines are protected by the wedging of the rods by the coarse particles.⁶

In addition to these physical interactions, chemical reactions have also been shown to occur, as in the case of prolonged grinding of a mixture of masticott and sulfur.⁹

While impact-type comminution will produce fragments with a more normal size distribution, nipping by the grinding media or the other particles will produce a distribution with more coarse particles. Also, abrasion will produce a distribution with more ultrafine particles. Intense point loading produces fine fragments of the intensely stressed region and much larger fragments of the remaining material.² The combination of the above types of fragmentation yields a product characteristic of the ground material and

the grinding media,¹⁰ as each type is active to a different extent with different machines and materials.

SIZE DISTRIBUTION

The size distribution of powders is most conveniently represented by comparing y versus x , where x is the size of the particle and y is the cumulative weight percent of all particles finer than size x .

A plot of $\log y$ versus $\log x$ often yields a straight line for the range $10 < y < 40$. However, for y values below 10 and above around 40, the linearity in the plot no longer applies. To describe the distribution over a broader range mathematically, several equations have been proposed.¹¹⁻²¹ Some are largely empirical fits to data, while others are based on models involving distribution of Griffith flaws,¹²⁻¹⁶ probability of survival under constant stress,¹¹ and statistical consideration of random division of particles.¹⁸⁻²⁰ Most equations are of the form

$$y = 1 - f(x/a)$$

where $f(x/a)$ is a function that involves exponents or power relationships and constants that determine the average size and breadth of the distribution. The various equations fit specific situations and no universal equation has yet been widely accepted.

RATE OF GRINDING

The size reduction as a function of time has been considered mainly in terms of the energy consumption. If the rate of energy consumption is constant with time, then the time and total energy consumption are directly proportional to each other. Major relationships between particle size and time or energy have been recently discussed by Agar and Somasundaran.²² Attempts have been made to relate energy consumption to surface area,^{23,24} volume, or weight of the particles,²⁵ size and size distribution parameters,^{3,26} and fracture stresses.²⁷ The more recent treatments satisfy specific experimental observations that were considered by the investigator, but none appear widely acceptable for all conditions.

Other approaches have involved the monitoring of the rate of disappearance of material coarser than a certain size^{28,29} or the rate of production of fine material from a narrowly sized feed.^{30,31} In some cases the forms of the equations can be shown to be equivalent to certain size versus time relationships mentioned previously.

Changes in the entire size distribution of ground material with time have been studied³²⁻³⁴ extensively. One of the simpler equations presented is one obtained by curve fitting a three-parameter equation³⁵:

$$y(x, t) = 1 - \left[1 - \left(\frac{x}{x_0} \right)^s \right] \frac{(t/p)}{t_0}$$

where t is time and s , p , and t_0 are constants. This equation fits several sets of data in the literature, particularly those for ball milling.

ULTRAFINE GRINDING

As grinding proceeds into an ultrafine region, it becomes more and more difficult to obtain further reduction in size because a grind limit is approached. A practical grind limit exists for most systems. This is most importantly determined by the tendency of the product particles to re-aggregate and establish a physical equilibrium between aggregation and fragmentation. In addition, the probability of a particle becoming involved in a comminution event, as well as that of its fracture when it is involved in the grinding as well as a decrease in volumetric capacity to store elastic stress energy, increases the required stress for initiating fracture. Difficulty in obtaining particles below a limiting size has also been attributed to "excessive clearance between impacting surfaces," diminished utilization of energy due to transmission of forces "through a long chain of particles few of which suffer sufficient strain to shatter," semifluid nature of the final product, and protection of smaller particles by the larger ones.³⁶

Additional flaws can probably be generated in the fine particles by applying thermal shocks. It is of interest to note that laser techniques, even though still uneconomical, have been studied for reducing the drilling strength of rocks.³¹

Aggregation can be retarded using a number of techniques. It can be minimized by removing the finest particles continuously using closed-circuit grinding. It is also considered advisable to successively reduce the size of the grinding medium (balls, pebbles, etc.) as the grinding proceeds into fine and ultrafine regions, since the ratio of the size of the grinding medium to the size of the particles should be kept within certain limits for maximum grinding efficiency. Cooling the machines by improving the ventilation or by external or internal watersprays minimizes agglomeration due to rising temperature.³² Addition of dispersive chemical agents is found to be bene-

ficial for ultrafine grinding.³³ Both grinding aids and grinding liquids have significant influence on ultrafine grinding.³⁴ Inorganic salts with multivalent ions or complex anions were found to be the most effective grinding aids. Adsorption of multivalent ions on the particles to increase the electrical repulsion between them is possibly the major reason for their influence. Formation of brittle or corrosive surface films has also been considered as a reason for their effect.

An "attritor ball mill" in which balls are rotated with a stirring arm was found to be significantly more efficient than use of a standard ball mill for fine grinding.³⁴ Milling time was 5 to 10 times less with the attritor ball mill for the same output. This grinding method is stated to be good also for alloy powders and refractory compounds. Vibration grinding,³⁵⁻³⁷ centrifugal grinding,³⁸ and fluid energy milling³⁹ have been considered recently for efficient fine grinding. Grinding time with a two-chamber (1.5 in. wide diameter) experimental vibratory ball mill was found to be less than 3 hours for producing graphite fines with a specific surface area of 400 m²/g.³⁸ This is to be compared with 26 hours of grinding with a 15 in. ball mill for the same surface-area development. Theories of rate of vibrational milling have been presented along with experimental analysis of the theories.⁴⁰

Relations described earlier become usually inapplicable in the fine-size region. The following equation, which takes into account the possible existence of a grind limit, was proposed⁴¹:

$$S = S_m [1 - \exp(-KE)] \quad (20)$$

where F is again the energy input, S is the specific surface area reaching a limiting value S_m , and K is a constant. Harris⁴² has a more general equation in which E is raised to a constant. The data fit however, is, better with another relation of Harris', developed on the basis of a logistic growth function model for fine grinding:

$$\frac{\Phi_m}{\Phi} = 1 + \left(\frac{h}{t} \right) h'$$

t is grinding time and h and h' are two constants. Φ is a measure of fineness reaching a maximum value of Φ_m . It is assumed to be proportional to specific surface area or to the inverse of size modulus. None of these relations, however, represent cases where the Φ_m exists at $0 < t < \infty$.

It is important to note that surface area and related surface activity are the parameters of importance in a system using very fine particles. It is therefore most meaningful to represent the fine-grinding system by surface area versus time or even cumulative surface area versus size models instead of weight versus time or cumulative weight versus size models.

MECHANOCHEMICAL EFFECTS

Both physical and chemical characteristics have been found to undergo significant changes during powder preparation by prolonged grinding.⁹ There is sufficient evidence in the literature^{43,48} that, in addition to desired and expected changes in physical properties such as specific surface area, changes occur also in shape, sintering activity, chemical reactivity, and so forth. The exact nature of alterations is dependent on, among other things, the conditions of grinding and the method of grinding used. Using gravimetric, thermogravimetric X-ray diffraction and electron microprobe analyses, the change in various properties of samples of quartz, calcite, and massicot ground in a pebble mill for several hundred hours was studied.⁹ It was found that the density of the particles decreased in the case of quartz as a function of grinding time (or particle size) apparently owing to the creation of deep amorphous layers on the particles. This effect however, was, absent when the grinding was done in water, possibly because of continuous dissolution of amorphous material in water. More than half of the quartz particles with diameters of $200\ \mu$ was converted to amorphous quartz during prolonged ball milling. Such effects have been also reported in several other cases.⁴⁴⁻⁴⁶ During grinding of hematite, a distinct change in color was observed owing to the production of ferrous oxide at the surface.⁴⁸ Work with clay minerals has provided additional evidence for the effects of prolonged grinding. Bloch,⁴⁷ for example, found that prolonged grinding of montmorillonite caused disruption of its crystalline structure and release of some alumina and magnesia. Reactivity of materials is in general found to be enhanced by comminution, as in the case of kaolinite and molybdenum sulfide, the latter becoming particularly reactive towards oxygen when ball milled in air. Researchers on catalytic activity of metallic oxides, ionic crystals, metal sheets, and wires have observed a favorable increase in such activity due to grinding. Ceramic powders activated by prolonged grinding are reported to sinter more readily. Snow and Luckie⁴⁹ and Naeser and Fielder⁴⁸ have recently reviewed these effects. Increase in catalytic and sintering activities has been proposed to occur as a result of an increase in the dislocation density of the materials. Even though no simultaneous work on both reactivity and dislocation density has been carried out by any of the above workers, it is not unreasonable to expect a change in sample reactivity owing to an increase in dislocation density that naturally occurs during most mechanical treatments.

Polymorphic transitions have been reported to occur during grinding^{49,50-53} possibly owing to temperature and pressure changes that take place locally as a result of the grinding process. Thus, during grinding of massicot and

calcite, such transitions altered the structure of these materials to those of litharge and aragonite, respectively.⁹

In addition to the above physical and structural changes, even solid-state reactions have been reported to occur during grinding. Figure 11.2 shows the changes in the massicot-sulfur system when it is ground for several hours.⁹ Massicot converts itself slowly to litharge up to about 20 hours; a chemical reaction then follows in which the oxide in both forms and sulfur are converted to galena. Such solid-state reactions have been reported to be most prominent during the grinding of carbonates. For example, zinc carbonate⁴⁵ and cadmium carbonate⁴⁴ with relatively low decomposition temperatures give carbon dioxide by mere grinding at room temperature. In the case of carbonates such as magnesium with higher decomposition temperatures, prolonged dry grinding lowered their decomposition temperatures significantly. Another important example of chemical decomposition during grinding is that of $\text{Na}_2\text{P}_2\text{O}_7 \cdot 6\text{H}_2\text{O}$ to form ortho- and pyrophosphates.⁷⁶ Several hydrated salts, such as $\text{FeSO}_4 \cdot 7\text{H}_2\text{O}$ and $\text{BaCl}_2 \cdot 2\text{H}_2\text{O}$, have been found to decompose during grinding.⁷⁶ These reactions are most prominent when the mill atmosphere is dry. An interesting complete chemical reaction that has been discovered to occur as a result of grinding is that between black lead sulfide and white cadmium sulfate to form white lead sulfate and yellow cadmium sulfide, the progress of the reaction being indicated by the gradual change in color.

A point to note is that contamination of the samples with the grinding medium can also occur during prolonged grinding. Mullite contamination

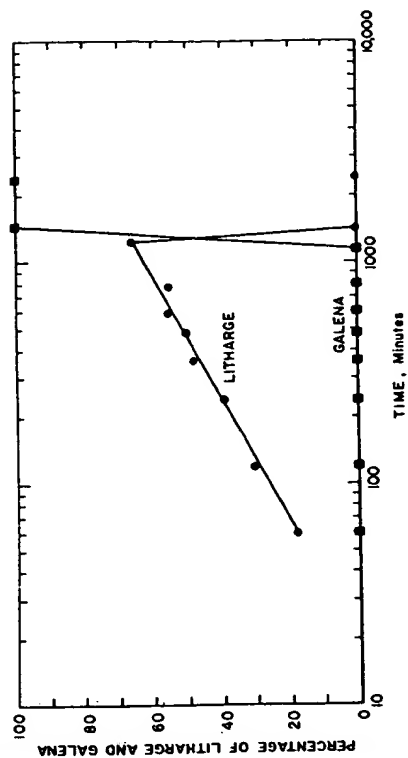


Figure 11.2. Amount of litharge and galena formed during grinding in a massicot-sulfur system.⁹

was found in a sample ground with a mortar and pestle.⁷⁷ The implications of these effects on powder preparation for various purposes, including sample preparation by grinding for chemical analysis, must be recognized.

GRINDING AIDS

Use of grinding aids and the mechanisms by which they act are discussed in a recent review by Somasundaran and Lin.⁸⁸ Grinding aids in vapor form, such as ethylene glycol, propylene glycol, butylene glycol, are used commercially in Germany and Yugoslavia for improving the efficiency of cement grinding.⁷⁹⁻⁸⁰ Amine acetates and diethylene glycol are used in Japan as grinding aids in plant-size mills.^{81,82} Any such attempt to improve the grinding efficiency is highly desirable, since the current grinding operations are notorious for their inefficiencies, which are of the order of 1%. Parts of our review⁸³ relevant to grinding aids are given below.

WATER (MOISTURE)

Grinding in water is usually more efficient than dry grinding.⁸⁴⁻⁸⁶ This effect of water has been ascribed by Lin and Mitzmager⁸⁶ to a reversible reaction between unsatisfied surface bonds and water molecules. Water in the form of vapor also should be expected to produce such hydrolytic corrosive effects. Even though there is no grinding work in the literature reported as a function of humidity, some evidence exists that this factor does affect the process. For example, the grinding rate of soda lime glass is higher in humid air than in a vacuum.⁸⁷ It must be noted that the increased efficiency of wet grinding can also be due to physical reasons. Cushioning effects due to the presence of a bed of fines will be less during wet grinding than during dry grinding, since the fine particles tend to remain suspended in the water in the former case. This would of course cause an increase in the efficiency of the grinding. In addition, effects of viscosity and specific gravity of the medium can also be significant.^{88,89}

Organic Liquids

Grinding in organic liquids is reported to be more efficient than in water. A 12-fold higher production of surface area for grinding in organic liquids, such as isoamyl alcohol, than for that in water was shown.⁹⁰ Higher grinding rates were obtained in carbon tetrachloride and methylcyclohexane than in nitrogen.⁹⁰ An interesting observation was that the grinding efficiency

was lower in the two organic liquids than in water but became the same when small amounts of water were present in the organic liquids in dissolved form.

Surface Active Agents

Surfactants have been widely reported as effective grinding aids. The effect of adding a flotation agent called Flotigam P on wet-ball milling of quartzite and limestone⁹¹ is shown in Figure 11.3 as an example. It can be seen that as much as 100% increase in specific surface area was obtained by additions of up to 0.3%. Additions in amounts higher than 0.03% caused a decrease in specific surface area. Sodium oleate in large concentrations has also been reported to produce a net decrease in specific surface area. The effect of Armac T on the grinding of quartz in a ball mill⁹² is shown in Figure 11.4. The effect is detrimental under all concentrations studied. It is not yet known whether these detrimental effects are due to experimental artifacts introduced by the aggregation of fines or are the result of change in interfacial properties due to adsorption of surfactant adsorption on particles. Flocs in the mill during grinding could consume some of the impact energy for deflocculation. In addition, hydrophobization of particles by the adsorbed surfactants can result in the attachment of air bubbles to them and consequent levitation. The grinding efficiency can be expected to be lower if the particles remain levitated. The beneficial effect of these grinding aids has been considered to be due to the reduction in surface energy upon

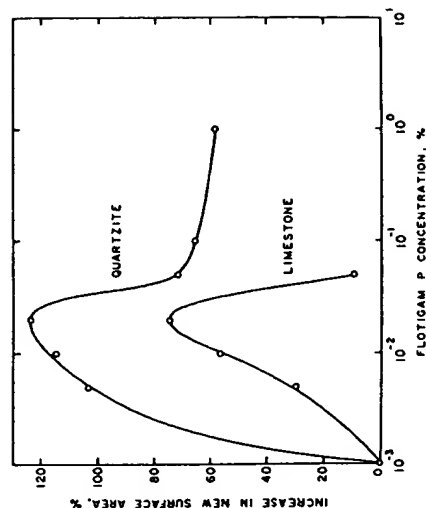


Figure 11.3. Effect of Flotigam P on grinding of quartzite and limestone in a rod mill.⁹¹

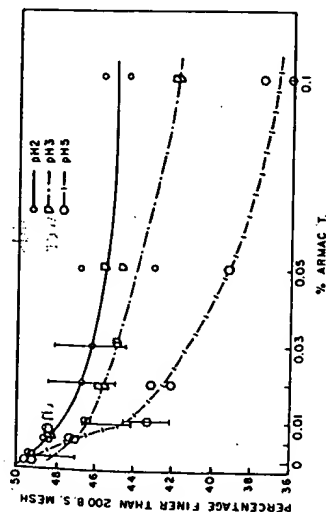


Figure 11.4. Effect of Armac T on the comminution of quartz in a ball mill at different pH values.⁹⁸

their adsorption, making it easier to produce new surfaces under such conditions. This reasoning is in line with the explanation offered by Reh binder and coworkers for the observed increase in drilling rate on the addition of these agents. On the other hand, it is also possible that it is an indirect result of several other phenomena that could occur in the system, such as the interaction of the surfactant molecules adsorbed on the surface and the resultant effects on various interfacial properties. In some cases it could also be the result of the ability of the reagents to enhance the dispersion of the particles and thus indirectly to facilitate fragmentation.

Examples of grinding aids used in the past include polysiloxane in the grinding of ultraporcelain and talc; silicones in the drop-weight crushing of limestone and quartz; glycols, amines, organosilicones, organic acetates, carbon blacks, and wool grease in the grinding of cement; silicones in the ball milling of quartz; acetones in nitromethane benzene, carbon tetrachloride and hexane in vibratory milling of ground glass, marble and quartz; and wool grease in the milling of gypsum, limestone, and quartz. Some of these reagents are reported to act by preventing ball coating but not aggregation of particles.⁹⁸ This effect of additives is very beneficial, since it is known that ball coating impairs the grinding efficiency.

Inorganic Electrolytes

Use of inorganic electrolytes during drilling was noted in the forties by Reh binder et al.⁹⁴ to increase the efficiency significantly. A number of workers have attempted to establish corresponding effects during grinding.⁹⁵⁻¹⁰⁰ Even though all the reported results are not in agreement, grinding is in general found to be more efficient in the presence of inorganic elec-

trolytes. In the ceramic industry, grinding of metallic and refractory-type materials is found to be more efficient when multivalent electrolytes are used as additives.¹⁰¹⁻¹⁰⁹ Effect of AlCl_3 and CuSO_4 on wet grinding is shown in Figure 11.5. Both reagents aid the grinding, the extent of the effect being determined both by the valency of the active ion of the salt and the manner of grinding. In some cases use of salts above certain levels is reported to cause poor grinding.^{98,99} In addition to any effect that these electrolytes might have on the hardness of the materials, the influence on the flocculation or dispersion of particles is also possibly a major reason for their overall observed effect.⁹⁸ This reasoning is supported by work that showed that the addition of dispersing agents always improved the comminution of solids.⁹⁸

Physical Nature of the Environment

Properties such as viscosity and density of the grinding environment can be expected to have an effect on the hydrodynamic behavior of particles, as well as of the grinding medium, and therefore on the grinding performance. Grinding is normally dependent on the viscosity of the medium up to about 20,000 mill revolutions and is then independent.¹¹⁰ Similar results were found for the viscosity of the environment.⁹⁹ The effect of density of the suspending fluid by grinding quartz and pyrite in air, water, and tetrabromoethane has been studied.⁹⁸ Grinding in water was more efficient than in air. The results obtained in tetrabromoethane however, were, inferior,

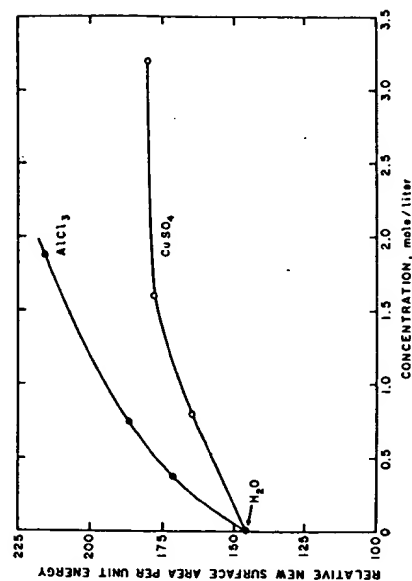


Figure 11.5. New surface area produced per unit energy applied during mill grinding in aqueous solutions as a function of CuSO_4 and AlCl_3 concentrations.⁹⁸

possibly because quartz particles, which are lighter than tetrabromoethane, remained partially afloat and thus out of the path of the impacting grinding media.

Mechanisms

The main two mechanisms proposed to explain the effects of comminution aids are Reh binder's¹¹ mechanism based on adsorption-induced surface energy changes and Westwood's^{12,13} mechanisms based on adsorption-induced mobility of near-surface dislocations. Reh binder's mechanism is based on the concept that a fruitful comminution event involves the production of new surfaces and that to accomplish this an amount of energy proportional to the free energy of the surface should be spent. Addition of chemical agents to reduce the effective surface energy of the solid particles should, on the basis of the above concept, enhance the grinding process. According to Westwood, the Reh binder effect is more likely due to changes in the electronic states near the surface and point and line defects caused by the adsorption of the additives on the solid. Such changes are known to influence the specific interactions between dislocations and point defects that control the dislocation mobility and hence the hardness. Hardness of materials has been recently proposed by Westwood et al. to be controlled by the zeta potential of the material in solutions.¹⁴ Since addition of surface active agents does affect the zeta potential significantly, it can be then expected to affect the grinding performance.

On the basis of the results obtained during abrasion and grinding tests on cement clinker in the presence of organic liquid vapor, it was found that the effectiveness of the vapor grinding aids in industrial ball milling is due to reduction of adhesive forces leading to prevention of aggregation of powder and of coating of balls and liners.¹⁵ Influence of adsorption of vapors on plastic deformation itself is considered to be significant only for cases where stresses are applied for long intervals and for grinding where stresses are applied rapidly.

REFERENCES

1. A. A. Griffith, "The Phenomena of Rupture and Flow in Solids," *Philos. Trans. Roy. Soc. London, Ser. A* 221, 163-198 (1920-1921).
2. C. C. Harris, "On the Role of Energy in Comminution," *Trans. Inst. Mining Metall. (London)*, 75, C37-C56 (1966).
3. H. Rumpf, "Physical Aspects of Comminution and New Formulation of a Law of Comminution," *Powder Tech.*, 7, 145-149 (1973).

References

4. H. Schonert, H. Umhauer, and W. Klemm, *Proc. Int. Conf. Fracture 2nd Brighton*, 1969, p. 474.
5. H. H. Gildemeister, and K. Schonert, "Berechnung Zur Wellenausbreitung in Kugeln Und Bruchphänomene in Kreisscheiben Bei Prallbeanspruchung," 3rd European Symposium on Comminution, paper 1-8, Canner, October 1971; *Dechema Monogr.*, 69 (1972).
6. B. H. Bergstrom, C. L. Sollenberger, and W. Jr. Mitchell, "Energy Aspects of Single Particle Crushing," *Trans. AIME*, 220, 367-372 (1961).
7. G. L. Fairs, "A Method of Predicting the Performance of Commercial Mills in the Fine Grinding of Brittle Materials," *Trans. Inst. Mining Metall. (London)* 63, 211 (1953).
8. P. Somasundaran and D. W. Fuerstenau, "Preferential Energy Consumption in Tumbling Mills," *Trans. AIME*, 229, 132-134 (1963).
9. I. J. Lin and P. Somasundaran, "Alterations in Properties of Samples During Their Preparation by Grinding," *Powder Tech.*, 6, 171-179 (1972).
10. D. D. Crabtree, R. S. Kinasevich, A. L. Mular, T. P. Meloy, and D. W. Fuerstenau, "Mechanisms of Size Reduction in Comminution Systems 1. Impact, Abrasion, and Chipping Grinding," *Trans. AIME*, 229, 201-206 (1964).
11. H. Heywood, "Principles of Crushing and Grinding," *Chemical Engineering Practice*, H. W. Cremer, and T. Davies, eds., Butterworths, London, Vol. 3, (1956), pp. 1-23.
12. J. J. Gilvarry and B. H. Bergstrom, "Fracture of Brittle Solids: Pt. 2—Distribution Functions for Fragment Size in Single Fracture, (Experimental)," *J. Appl. Phys.*, 32, 391-399 (1961).
13. J. J. Gilvarry and B. H. Bergstrom, "Fracture of Brittle Solids: Pt. 3—Experimental Results of the Distribution of Fragment Size in Single Fracture," *J. Appl. Phys.*, 33, 3211-3213 (1962).
14. J. J. Gilvarry, "Fracture of Brittle Solids Two Dimensional Distribution Function for Fragment Size in Single Fracture: Pt. 4 (Theoretical), Pt. 5 (Experimental)" *J. Appl. Phys.*, 33, 3214-3217 and 3218-3224 (1962).
15. J. J. Gilvarry and B. H. Bergstrom, "Fracture and Comminution of Brittle Solids (Theory and Experiment)," *Trans. AIME*, 220, 380-390 (1961).
16. J. J. Gilvarry, and B. H. Bergstrom, "Fracture and Comminution of Brittle Solids: Further Experimental Results," *J. Appl. Phys.*, 223, 419 (1962).
17. E. Evans, "A Contribution to the Theory of the Size Distribution of Broken Coal," *Proc. Conf. Sci. Use Coal*, London, Institute of Fuel, 1958, paper 14.
18. A. M. Gaudin and T. P. Meloy, "Model and a Comminution Distribution Equation for Repeated Fracture," *Trans. AIME*, 223, 43-50 (1962).
19. T. P. Meloy, "A Three Dimensional Derivation of the Gaudin Size Distribution Equation," *Trans. AIME*, 226, 447-448 (1963).
20. R. R. Klimpel and L. G. Austin, "The Statistical Theory of Primary Breakage Distributions for Brittle Materials," *Trans. AIME*, 232, 88-94 (1965).
21. C. C. Harris, "The Application of Size Distribution Equations to Multi-Event Comminution Process," *Trans. AIME*, 241, 343-358 (1968).
22. G. E. Agar and P. Somasundaran, "Rationalization of Energy—Particle Size Relationships in Comminution," *Xth Int. Miner. Proc. Cong. 10th, London*, 1973, Institute of Min. and Metallurgy, paper 16.
23. P. R. Von Rittinger, *Lehrbuch der Aufbereitungskunde*, Ernst und Korn, Berlin, 1867.

24. F. C. Bond, "The Third Theory of Comminution," *Trans. AIME*, 193, 484-494 (1952).
25. F. Kick, *Das Gesetz Der Proportionalen Widerstand und Seine Anwendung*, Arthur Felix, Leipzig, 1885.
26. R. J. Charles, "Energy—Size Reduction Relationships in Comminution," *Trans. AIME*, 208, 80-88 (1957).
27. J. A. Holmes, "A Contribution to the Study of Comminution—A Modified Form of Kick's Law," *Trans. Inst. Chem. Eng.*, 35, 125-141 (1957).
28. N. Arbib and C. C. Harris, "Particle Size Distribution/Time Relationships in Comminution," *Br. Chem. Eng.*, 10(4), 240-247 (1965).
29. F. W. Bowditch, "Theoretical and Experimental Studies of the Kinetics of Grinding in a Ball Mill," *Trans. AIME*, 217, 194-202 (1960).
30. N. Arbib and U. N. Bhargava, "Correlation of Product Size, Capacity and Power in Tumbling Mills," *Trans. AIME*, 217, 245-252 (1960).
31. D. W. Fuerstenau and P. Somasundaran, "Comminution Kinetics," *Proc. Int. Miner. Process. Congr. Cannes*, 1963, Pergamon, pp. 25-33.
32. G. F. Huttig, "Zur Kinetik Der Zermahlungsvorgange," *Z. Elektrochem.*, 57, 534-539 (1953).
33. O. Theimer, "Über Die Kinetik Von Zermahlungsvorg-Änge," *Kolloid Z.*, 132, 134-141 (1953).
34. L. Bass, "Zur Theorie Der Mahlvorgänge," *Z. Angew. Math. Phys.*, 5, 283-292 (1956).
35. B. Epstein, "Logarithmic—Normal Distribution in Breakage of Solids," *Ind. Eng. Chem.*, 40, 2289-2291 (1948).
36. R. P. Gardner and L. G. Austin, "The Use of a Radioactive Tracer Technique and a Computer in the Study of the Batch Grinding of Coal," *J. Inst. Fuel*, 35, 173-177 (1962).
37. R. P. Gardner and L. G. Austin, "A Chemical Engineering Treatment of Batch Grinding," *Symposium Zerkleinern*, H. Rumpf and D. Behrens, eds., Verlag Chemie, Düsseldorf, W. Germany, 1962, pp. 217-248.
38. C. C. Harris, "Batch Grinding Kinetics," *Trans. AIME*, 241, 359-364 (1968).
39. C. C. Harris, "Size Reduction—Time Relationships of Batch Grinding," *Trans. AIME*, 241, 449-454 (1968).
40. P. C. Kapur, "A Similarity Solution to an Integro-Differential Equation Describing Batch Grinding," *Chem. Eng. Sci.*, 25, 899-901 (1970).
41. D. F. Kelsall and K. J. Reid, "The Derivation of a Mathematical Model for Breakage in a Small, Continuous, Wet, Ball Mill," *Application of Mathematical Models in Chemical Engineering Research, Design, and Production*, Institute of Chemical Engineers, London, 1965, pp. 14-20.
42. T. S. Mika, L. M. Berlioz, and D. W. Fuerstenau, "An Approach to the Kinetics of Dry Batch Ball Milling," *Zerkleinern*, 2nd Symposium on Comminution, H. Rumpf and W. Pietsch, eds., Verlag Chemie, Weinheim, 1967, pp. 205-240.
43. J. A. Herbst, G. A. Grandy, and T. S. Mika, "On the Development and Use of Lumped Parameter Models for Continuous Open and Closed Circuit and Grinding Systems," *Trans. Inst. Mining Metall.*, 80, C193-C198 (1971).
44. J. A. Herbst, G. A. Grandy, and D. W. Fuerstenau, "Population Balance Models for the Design of Continuous Grinding Mills," 10th International Mineral Processing Conference, London, Institution of Mining and Metallurgy, 1973, paper 19.
45. P. C. Kapur and P. K. Agrawal, "Approximate Solutions to the Discretized Batch Grinding Equation," *Chem. Eng. Sci.*, 25, 1111-1113 (1970).
46. J. A. Herbst and D. W. Fuerstenau, "The Zero Order Production of Fine Sizes in Comminution and its Implications in Simulation," *Trans. AIME*, 241, 538-549 (1968).
47. J. A. Herbst and D. W. Fuerstenau, "Influence of Mill Speed and Ball Loading on the Parameters of the Batch Grinding Equation," *Trans. AIME*, 252, 169-176 (1972).
48. G. D. Gumtz and D. W. Fuerstenau, "Simulation of Locked-Cycle Grinding," *Trans. AIME*, 247, 330-335 (1970).
49. C. C. Harris, "Relationships for the $x y t$ Comminution Surface," *Trans. Inst. Mining Metall.*, 79, C157-C168 (1970).
50. A. L. Mular, "Comminution in Tumbling Mills—A Review," *Can. Metall. Q.*, 4 (1), 31-73 (1965).
51. W. N. Lucke, "Novel Methods of Rock Fracture," *Mining Congr. J.*, 64-69 (Aug. 1973).
52. B. Becke, *Principles of Comminution*, Akademiai Kiado, Budapest, 1964.
53. P. Somasundaran and I. J. Lin, "Effect of the Nature of Environment of Comminution Processes," *Industrial and Engineering Chemistry and Proc. Des. and Dev.*, 11, 321-331 (1972).
54. M. Quatinnetz, R. J. Schafer, and C. R. Smeal, "The Production of Submicron Metal Powders by Ball Milling with Grinding Aids," *Ultrafine Particles*, Ed. W. E. Kuhn, Wiley, New York, 1963, pp. 271-296.
55. E. A. Smith, "Some Special Functions of the Vibrational Ball Mill," *Chem. Ind. (London)*, 1967 (34), 1436-1442.
56. H. L. Podmore and E. S. G. Beasley, "Vibration Grinding in Close Packed Media Systems," *Chem. Ind. (London)*, 1967 (34), 1443-1450.
57. A. Kirk, "Practical Review of Vibration Milling," *Chem. Ind. (London)*, 1967 (3), 1378-1382.
58. R. Planiol, "Vacuum-Operated Centrifugal Grinder is Proposed for Powder Savings," *Eng. Min. J.*, 140-142 (Sept. 1968).
59. B. Dobson and E. Rothwell, "Particle Size Reduction in a Fluid Energy Mill," *Powder Tech.*, 3, 213-217 (1969/1970).
60. H. E. Rose, "Some Observations on the Application of Vibration Mills," *Chem. Ind. (London)*, 1967 (33), 1383-1389.
61. Cited by A. L. Mular, "Comminution in Tumbling Mills—A review," *Can. Metall. Q.*, 4, (1), 31-73 (1965).
62. C. C. Harris, "On the Limit of Comminution," *Trans. AIME*, 238, 17-30 (1967).
63. R. H. Snow and P. T. Luckie, "Annual Review of Size Reduction—1973," *Powder Tech.*, 10, 129-142 (1974); Snow, R. H., "Annual Review of Size Reduction—1972," *Powder Tech.*, 7, 69-83 (1973); R. H. Snow, "Annual Review of Size Reduction," *Powder Tech.*, 5, 351-364 (1971/1972); see *Ind. Eng. Chem.* for previous annual reviews.
64. R. C. Ray, "The Effect of Long Grinding on Quartz," *Proc. Roy. Soc. London, Ser. A*, A102, 640-642 (1923).
65. Y. J. Burton, "Change in the State of Solids Due to Milling Processes," *Trans. Inst. Chem. Eng.*, 44, 37-41 (1966).

66. C. Legrand and J. Nicolas, "Contribution of X-ray Diffraction and the Electron Microscope to the Study of Ground Kaolins," *Bull. Soc. Fr. Ceram.*, **44**, 61-69 (1959).
67. J. M. Bloch, "Effect of Grinding on the Crystal Structures and Properties of Montmorillonite," *Bull. Soc. Chimique Fr.*, 774-781 (1950).
68. G. Naessner and A. Fielder, "Mechanical Activation of Solids and Its Technical Significance," *Verfahrenstechnik*, **6** (9), 299-305 (1972).
69. J. H. Burns and M. A. Bredig, "Transformation of Calcite to Aragonite by Grinding," *J. Chem. Phys.*, **25**, 1281 (1956), D. O. Northwood and D. Lewis, *Can. Miner.*, **10**, 216-224 (1970).
70. R. B. Gammage and D. R. Glasson, *J. Appl. Chem.*, **13**, 1466 (1963).
71. A. Schiele and H. Gantzkow, *Z. Physik*, **15**, 184 (1923).
72. G. L. Clark and R. Rowan, "Polymorphic Transitions by Grinding. Distortion and Catalytic Activity in PbO," *J. Amer. Chem. Soc.*, **63**, 1302-1305 (1941).
73. F. Dachille and R. Roy, *Proc. Int. Congr. on Reactivity of Solids*, 4th, Elsevier, Amsterdam, 1960; M. Senna and H. Kuno, *J. Amer. Ceram. Soc.*, **54**, 259-262 (1971).
74. G. Naessner and W. Scholz, *Ber. Deut. Keram. Ges.*, **39**, 106 (1962).
75. D. Oceppek, "Mechanical and Mechano-Chemical Reactions in Crushing Processes," *Rudarsko-Met. Zbornik*, (1), 5-16 (1969); E. A. Prodan, et al., "Decomposition of Sodium Triphosphate Hydrate During Dry Grinding," *Dokl. Akad. Nauk Belorusk.*, **14**, (6) 526-529 (1970) [*Chem. Abstr.*, **73**, 72664z (1971)].
76. I. J. Lin and A. Metzger, "Changes in the State of Solids Due to Communion," Technion Faculty Civil Engineering Internal, Publication No. 140, 1970.
77. J. C. Jamieson and J. R. Goldsmith, "Some Reaction Produced in Carbonates by Grinding," *Amer. Mineral.*, **45**, 818-827 (1960).
78. F. W. Locher and H. M. V. Seebach, "Influence of Adsorption on Industrial Grinding," *Industrial and Engineering Chemistry Process Des. Dev.*, **11**, 190-197 (1972).
79. V. Korac, "Use of Grinding Auxiliary Agents in Cement Production," *Tehnika (Belgrade)*, **27**, 649-653 (1972), *Chem. Abstr.*, **77**, 922609.
80. K. Popovic, "Effects of Grinding Aids on Portland Cement Clinker," *Cement (Zagreb)*, **15**, 14-17 (1971); *Chem. Abstr.*, **76**, 144429p.
81. T. Furukawa, A. Anan, and K. Yamasaki, "Use of Grinding Agents in Closed Circuit Grinding System for Cement Clinker," *Semento Gijyusu Nempo*, **25**, 69-75 (1971); *Chem. Abstr.*, **77**, 14340g.
82. T. Furukawa, A. Anan, and K. Yamasaki, "Use of Grinding Agents in Closed Circuit Grinding System for Cement Clinker," *Semento Gijyusu Nempo*, **25**, 69-75 (1971); *Chem. Abstr.*, **77**, 14341g.
83. F. C. Bond, *Mining Congr. J.*, 38-40 (January 1975).
84. W. H. Goghil, and F. D. Devaney, "Ball Mill Grinding," U.S. Bureau of Mines, Tech. Paper No. 581 (1937).
85. H. E. Rose, R. M. E. Sullivan, *Ball, Tube and Rod Mills*, Chemical Publishing Co., New York, 1958, p. 30.
86. I. J. Lin, and A. Mitzmager, "The Influence of the Environment on the Communion on Quartz," *Trans. AIME*, **241**, 412-418 (1968).
87. F. W. Locher, W. Eichartz, and H. M. von Seebach, S. Sprung, "Environmental Effects in Grinding," Extended Abstracts, 163rd National Meeting of the American Chemical Society, Boston, April 10-14, 1972, p. 81.
88. P. C. Kapur, A. L. Mular, and D. W. Fuerstenau, "The Role of Fluids in Communion," *Can. J. Chem. Eng.*, **43**, 119-124 (1965).
89. W. A. Hockings, M. E. Volin, and A. L. Mular, Effect of Suspending Fluid Viscosity on Batch Mill Grinding," *Trans. AIME*, **232**, 59-62 (1965).
90. S. Z., Kieskalt, *Ver. Deut. Ing.*, **91**, 313-315 (1949).
91. E. Von Szanthe, "Der Einfluß Von Oberflächenaktiven Stoffen Bei der Feinzerkleinerung," *Erzbergbau Metallhüttenwes.*, **2**, 353-360 (1949).
92. L. A. Gilbert, and T. H. Hughes, "Some Experiments in Additive Grinding," *Symposium Zerkleinerung I*, Verlag Chem., Dusseldorf, Germany 1962, pp. 170-193.
93. L. Opoczky, *Epitoanag.*, **19**, 121-125 (1967).
94. P. A. Rehinder, L. A. Schreiner, and K. F. Zhigach, "Hardness Reducers in Drilling," Moscow Academy of Science, 1944; *Trans. Counc. Sci. Ind. Res.*, Melbourne, Australia, 1948, p. 163.
95. G. Beyer, *Rudy (Prague)*, **12** (7-8), 296-298 (1964).
96. J. H. Brown, "The Effects of Chemical Agents in Communion," M.I.T. Progress Report N.Y.O. 7172, 1955.
97. V. I. Byalkovskii and I. A. Kudinov, *Keram. Sb.*, 8-13 (1940); *Khim. Ref. Z.*, **4** (5), 114 (1941); *Ceram. Abstr.*, **22**, 121 (1943).
98. A. Z. Frangiskos, and H. G. Smith, "The Effect of Some Surface Active Reagents on the Communion of Limestone and Quartz," *Progress in Mineral Dressing, Trans. Int. Miner. Dressing Condr. Stockholm, Sweden*, 1957, 67-84.
99. R. Mallikarjunan, and K. M. Pai, and P. Halasyamani, "The Effect of Some Surface Active Agents on the Communion of Quartz and Calcite," *Trans. Indian Inst. Metals*, **18**, 79-82 (1965).
100. M. H. Stanzky, I. L. Feld, U.S. Bureau of Mines Report 7168, 1968, p. 28.
101. E. R. Dawley, *Pit Quarry*, **36**, 57 (1943).
102. V. H. Dodson, and F. G. Serafin, U.S. Patent 3,443,976 (May 13, 1969).
103. R. A. Knight, and C. A. Calow, AWRE Report 039-068, United Kingdom, April 1968.
104. M. Quatincez, R. J. Schafer, and C. Smeal, *Trans. AIME*, **221**, 1105-1110 (1961).
105. R. J. Schafer, and M. Quatincez, U.S. Patent 3,090,567 (May 21, 1963).
106. M. J. Sinnott, "The Influence of Surfaces on the Properties of Materials," in *Properties of Crystallizing Solids*, ASTM Technical Publication, No. 283, Philadelphia, 1961, pp. 28-39.
107. F. G. Serafin, U.S. Patent 3,443,975 (May 13, 1969).
108. F. G. Serafin, U.S. Patent 3,459,570 (August 5, 1969).
109. T. Tanaka, *Zement Kalk-Gipsstein*, **15**, 28 (1962).
110. H. E. Schweyer, *Ind. Eng. Chem.*, **34**, 1060-1064 (1942).
111. P. A. Rehinder, "On the Effect of Surface Changes on Cohesion, Hardness, and Other Properties of Crystals," *Proc. Phys. Congr. State Press, 6th Moscow*, 1928, 29.
112. A. R. C. Westwood, "Environment Sensitive Mechanical Behavior, Status and Problems," in *Environment-Sensitive Mechanical Behaviors*, A. R. C. Westwood and N. S. Stoloff, eds., Gordon and Breach, New York, 1966, pp. 1-65.
113. N. H. MacMillan and A. R. C. Westwood, "Surface Charge-Dependent Mechanical Behavior of Non-Metals," Office of Naval Research Project NR-032-524, RIAS, Martin Marietta Corp., Baltimore, September 1973.

12

Reactive Powders from Solution

D. W. Johnson, Jr.
P. K. Gallagher

A variety of techniques for preparing ceramic powders involve a liquid solution as an initial step. The aqueous or organic-based solutions contain dissolved salts with appropriate cations or anions. The solvent is removed, leaving a residue that is the final powder or that is thermally converted to the desired form.

The most critical step in solution techniques is the removal of the solvent. The solutions, if well prepared, are homogeneous on an atomic scale. The degree of homogeneity of the residue, however, depends on the mechanism of the solvent-removal technique.

Although generally straightforward, solution preparation requires careful consideration of the solubility of the critical cations and anions. Problems can arise, for example, in preparing barium ferrite; ferrous sulfate and barium nitrate salts cannot be used because the highly insoluble barium sulfate phase would precipitate out.

This chapter describes a number of solution techniques for preparing powders. The techniques involve solvent vaporization, solution combustion, or precipitation-filtration.

SOLVENT VAPORIZATION

The solute is separated from solution by removing the solvent as a vapor phase, either by evaporation or sublimation.

Direct Evaporation

Solvent can be removed using as simple a technique as heating in a beaker on a hot plate. Direct evaporation may be suitable for single-component solutions. With multicomponent solutions, large-scale segregation of the components often results. An exception to this problem is when a solid solution of multicomponent salts is formed. Ferrites have been prepared by using ammonium sulfate (schoenite type) salts that form solid solutions when precipitated.¹ Another exception involves a technique in which a filter paper is soaked, dried, and ashed to give presumably equilibrated phases in the subsolidus region of the $\text{NaAlO}_2\text{-Al}_2\text{O}_3$ system.² The filter paper aids in preventing large-scale segregation of the components.

Spray Drying

This common technique prevents segregation during evaporation by breaking the liquid into very small droplets. This promotes rapid evaporation to minimize segregation and assures that any segregation is confined to the small droplets, since no mass transport from droplet to droplet takes place. Spray driers usually consist of an atomizer, a drying chamber, and a powder collector. The atomizer is either a pneumatic nozzle or a centrifugal disc. Droplet diameters are on the order of 10 to 20 μm . The droplets are intercepted in the drying chamber by a heated air stream that quickly evaporates the solvent. The dried powder is collected in a cyclone separator.

Ferrite compositions and magnesium aluminate have been successfully produced from sulfate solutions using spray drying.³ Decomposing the sulfates at 800 to 1000°C gave agglomerates with crystallites about 0.2 μm in diameter. These could be pressed and sintered to practically the theoretical density. Nickel-zinc ferrites have also been prepared by spray drying sulfates.⁴ Sintered nickel-zinc ferrites had lower coercive force, higher initial permeability, and more-controlled stoichiometry and grain size when made from spray-dried powder rather than from conventionally ball-milled powders.

By increasing the temperature of the gases in the spray drier the salts can be dried and decomposed directly in the spray drier in a single step. This technique is termed "spray roasting" and has been used for the preparation of ferrite powders using nitrates or chlorides.^{5,6}

Fluid Bed Drying

This technique is similar to spray roasting except that the solution is trapped in a fluid bed for drying and decomposition. A pneumatic nozzle injects solution droplets into a heated fluid bed of the solid product. By varying the temperature, fluidizing gas flow rate and solution injection rate, the process could be made continuous, with a portion of the calcined product being removed from the bed periodically. It has been used to prepare and calcine uranyl nitrate and aluminum nitrate.⁷

Advantages of fluid bed drying include: (1) the absence of moving parts, (2) large capacity per unit volume of equipment, and (3) the formation of granulated powders of relatively high bulk density and large particle size. It appears well suited to powders for which the conditions for stable fluidization are known, but it may not be convenient to change compositions on a small laboratory scale. It is possible to obtain a controlled discharge of solid particles that have reached a specific size.⁸

Codecomposition

In this technique a solution (typically nitrates) is atomized and blown against a hot platinum (or other) surface to evaporate the solvent and decompose the salt in a single step.⁹ It appears to be most suitable for the preparation of laboratory batches.

Emulsion Drying

A solution can be separated into small droplets prior to drying as an emulsion of an aqueous solution and an immiscible liquid such as kerosene. This is stirred while being dried in a vacuum dryer to give a rather stable suspension of solid salt particles in kerosene. The particles are deflocculated, precipitated, filtered, washed, and decomposed. The behavior of the powders is comparable with that of spray-dried powders.¹⁰ The technique allows efficient transfer of heat to the emulsified droplets, but the homogeneity is probably dependent on the degree of emulsification that can be stabilized.

Gelation-Evaporation

A variety of techniques have been reported in which gravitational settling of precipitated phases or diffusion of components in an amorphous phase is hindered during solvent evaporation by the formation of a gelatinous or glassy matrix. Many processes termed "sol-gel techniques" are included

under this heading. Sol-gel usually refers to the preparation of spheres of nuclear reactor fuels. The process generally infers the preparation of a sol (an aqueous colloidal suspension of the desired oxides in hydrated form) from the nitrates or other salts by controlled precipitation or digestion of precipitates.^{11,12} The sol is converted to a gel by partial dehydration or by adding ammonia in various forms. In some cases the dehydration is achieved by evaporation and in other cases by dispersion of the sol as droplets in a column containing a long-chain alcohol and a surfactant. The gel is completely dried and can be fired to a very dense ceramic with no further processing.

The sol-gel technique is particularly useful for preparing dense microspheres at low sintering temperatures.¹³ In general the technique provides highly reactive agglomerates of very fine particles, but it is difficult to reform the agglomerates into other sinterable shapes.

Other gel processes do not involve the preparation of a sol. Silicates have been prepared where ethyl orthosilicate is dissolved in absolute ethyl alcohol and is added to a solution of the nitrate of other metals.¹⁴ The solution is hydrolyzed with water, and silica precipitates to a gel. This is then evaporated slowly to a dry powder and is calcined to give reactive oxides.

MgAl₂O₄ has been prepared by dissolving aluminum hydroxychloride in water and blending in a slurry of magnesium hydroxide.¹⁵ This mixture becomes a gel, which is dried, ball milled, and calcined.

A number of evaporative methods involve the immobilization of ions in a glassy or amorphous matrix other than those commonly considered to be gels. In the simplest case some salts can be dissolved in their waters of hydration by heating and then quenching to a glass without phase separation and can be carefully decomposed to the oxides. This technique has been used to prepare MgAl₂O₄ to Y₃Al₅O₁₂.¹⁶

Another technique involves the processing of a glassy matrix using organic polyfunctional acids possessing at least one hydroxy and one carboxylic function, such as citric, malic, tartaric, glycolic, and lactic acid.¹⁷ A solution is formed with the metallic salts and the organic acid. The solution is rapidly dehydrated in a rotating evaporator at a pressure of a few torrs. The solution is discharged from the evaporator before the viscosity is too high for removal and is further dehydrated in a vacuum oven. This forms a transparent glass that has mixing on an atomic scale and can be pyrolyzed to the oxides. Ferrites have been prepared by a similar technique using glasses made from a solution of maleic anhydride.¹⁸ Y₃Fe₅O₁₂ has been prepared using citric acid as the glass former.¹⁹

Freeze-Drying

Freeze-drying or cryochemical preparation of ceramic oxides was introduced by Schnettler et al.²⁰ A solution is separated into small droplets

by spraying it through a hydraulic nozzle at a pressure of a few psi. At this point the technique differs from the other volatilization methods in that segregation is prevented by a rapid freezing step. Solution droplets are sprayed into a bath of immiscible liquid, such as hexane chilled by Dry Ice-acetone, or by spraying directly into liquid nitrogen.²¹ The rapid freezing step is very important because the degree of ice-salt segregation is minimized. The hexane is not as cold as the liquid nitrogen but has better thermal contact with the droplets, since a gaseous layer of nitrogen around the droplets in liquid nitrogen impedes heat transfer. A continuous method of freezing involves introducing droplets of solution into the bottom of a chilled bath of refrigerant with a density higher than that of the frozen solution.²² The frozen product is skimmed from the top of the refrigerant. These freezing methods generally produce spherical frozen beads of solution with diameters in the 0.01 to 5 mm range.

The drying step²⁰ involves the sublimation of water from the frozen solution without melting. The frozen sample is introduced into a vacuum chamber that is evacuated to a pressure of about 1 torr or less, at which the water sublimates rather than melts. Heat can be applied to aid sublimation. To keep the partial pressure of water in the system as low as possible, a refrigerated condensing coil is usually introduced to collect the sublimed water. The drying can be done in a commercial freeze-drier or in a small glass apparatus for laboratory use consisting of a chamber with a sample and a liquid nitrogen trap all evacuated by a mechanical pump.

The freeze-drying technique gives spheres of aggregated crystallites that are replicas of the frozen beads of solution and that have a very low bulk density.²³ The crystallite size can be varied by changing the calcination step or the concentration of the solutions.^{20,23}

Reactive powders of Al₂O₃, prepared by freeze-drying, were easily sintered to 99.9% density.²⁴ A modified nickel ferrite composition was sintered to a high density using freeze-dried powders.²⁵ Drying, spray drying, and precipitation for the preparation of LiFe₂O₄ were compared and it was found that freeze drying allowed the most flexibility in terms of sintering temperature and grain size.²⁶ The sintering temperatures needed were much lower than those needed for conventionally prepared powders, and a large degree of control over grain size was available.

Lithiated NiO for catalytic studies has been prepared using freeze drying.²⁷ The very uniform mixing allowed the Li₂O to diffuse into the NiO lattice at about 400°C as compared to 950 to 1000°C for conventionally prepared mixtures. With such low-temperature preparation, surface areas up to 60 m²/g were preserved compared with less than 1 m²/g for conventionally prepared NiO.

Some low-freezing-point solutions have a tendency to form glasses when cooled rather than to freeze into ice and salt. When these are heated in a

freeze-drier they tend to flow and in some cases the homogeneity of the solution is lost. The addition of ammonium hydroxide to concentrated solutions of ferric sulfate has been shown to result in a raising of the freezing point and the promotion of salt-ice phase separation.²⁹ A variation of freeze-drying has been introduced for preparing actinide metal oxides from nitrate solutions, avoiding the problem of glass formation during freezing.³⁰ The nitrate solution is atomized, chilled to near Dry Ice temperatures, and contacted with NH_4OH to convert the nitrates to insoluble hydroxide at low temperatures. This is freeze-dried and decomposed to the oxides.

SOLUTION COMBUSTION

Solution combustion encompasses those preparation techniques in which solutions are actually burned to form solid particulates. It also includes to some degree those techniques that volatilize liquids for hydrolysis, decomposition, or oxidation from the gaseous state.

Alcohol Solutions

Ferrites have been produced by dissolving nitrates in alcohol and burning the solution in an atomizing burner.³⁰ The stoichiometric ratios of nitrates are dissolved in alcohol, the solution is atomized in oxygen, the dispersion is burned, and the powder is collected using a cyclone chamber. This technique is reproducible and more convenient and controllable than conventional mixing or coprecipitation.³⁰ The same technique has been used for ferrites except for the substitution of a water-spray tower for powder collection.³¹ The phases present in the ferrite were dependent on the oxygen pressure in the burner; the higher oxygen pressures produced single-phase ferrites.

Barium and titanium alcoholates mixed in an organic solvent have been burned in air or oxygen to give BaTiO_3 .³²

Organometallics

While some organometallics, such as metal alkyls, can burn in air or oxygen to give oxide particulates, it is an expensive process and is not widely used. Some organometallics are not readily combustible but are mixed with alcohols for burning,³³ as is discussed in the previous sections. However, some organometallics can be decomposed in a hot gas stream to give the oxides, as in the case of some transition metal alkoxides.³⁴ For zirconium tetratertiary butoxide, the material is vaporized, mixed with an inert

carrier gas, and fed into a decomposition chamber where it is contacted with another stream of hot (325 to 500°C) inert gas. The oxide, recovered by an electrostatic precipitator, has an average particle size of less than 100 Å and a purity greater than 99.95%.

Chlorides

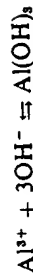
The vapor-phase decomposition or hydrolysis of metal chlorides in a flame is a fairly common technique. It is used commercially to make high-surface-area SiO_2 powders.³⁵ Silicon tetrachloride is reacted at high temperatures with hydrogen and oxygen (a highly exothermic reaction) to give silica and hydrochloric acid. The silica can be collected by a cyclone separator and calcined to remove traces of residual hydrochloric acid. This produces a very fine powder with a surface area in the range 175 to 200 m^2/g . Properties of silica and alumina made from chlorides have been reported.³⁶

A burner designed to prevent clogging of the orifice by the oxide has been described.³⁷ The burner has four concentric tubes admitting from the center out chloride vapor in oxygen, nitrogen, hydrogen, and oxygen. The nitrogen layer delays the hydrolysis until the gas is a few centimeters from the tip. Mixed oxides or doped oxides have been prepared in the flame reactor by using mixtures of chlorides.

PRECIPITATION-FILTRATION

Precipitation with subsequent removal of the solids by filtration is one of the most widely used techniques for the preparation of ceramic powders from solutions. Usually the equipment needed is very simple and can be found in most chemical laboratories. However, the precipitation step involves a large number of variables that can affect the process. Some of the more important ones are discussed briefly here.

The pH of an aqueous solution is important for several reasons. The influence of pH on the precipitation of hydroxides is obvious in that the OH^- -concentration appears in the solubility product. For example, in the precipitation of $\text{Al}(\text{OH})_3$ the equilibria is:



If the pH is too low, there are insufficient hydroxide ions in solution. At high pH the soluble complex $\text{Al}(\text{OH})_4^-$ is formed and again precipitation is not accomplished. The precipitation of $\text{Al}(\text{OH})_3$ is best done at a solution pH in the range of 4 to 9.

Precipitates can be conveniently broken into three categories: (1) single-compound precipitates, which decompose directly into the desired stoichiometry; (2) solid-solution precipitates, for which the desired stoichiometry can be incorporated into a single-phase solid solution precipitate; and (3) mixtures or polyphase precipitates.

Single Compounds

When possible this is the ideal form of a precipitate. The cation ratio of the desired product is incorporated directly into the precipitate as a compound. There is no need for accurate assays, since the stoichiometry is assured and the homogeneity of the precipitate is on the atomic scale. Some examples are BaTiO_3 from $\text{BaTiO}(\text{C}_2\text{O}_4)_2 \cdot 4\text{H}_2\text{O}$,⁴⁰ BaSnO_3 from $\text{BaSn}(\text{C}_2\text{O}_4)_2 \cdot 0.5\text{H}_2\text{O}$,⁴¹ and LaFeO_3 from $\text{LaFe}(\text{CN})_6 \cdot 5\text{H}_2\text{O}$.⁴²

One advantage of the homogeneity is the low-temperature reactivity. When BaSnO_3 is prepared by the reaction of milled BaCO_3 and SnO_2 , the reaction temperature is near 1000°C and Ba_2SnO_4 as a reaction intermediate is detected.⁴³ Using $\text{BaSn}(\text{C}_2\text{O}_4)_2 \cdot 0.5\text{H}_2\text{O}$ as a precursor, BaSnO_3 can be formed at about 700°C without any detectable intermediates.^{41,44} Also, the low reaction temperature widens the range of particle sizes that can be made.

With barium titanate, the precipitation process has been extended to include the direct doping with lanthanum during the precipitation process.⁴⁵ The availability of the rare earth, transition metal cyanides has proven useful in the preparation of highly reactive catalysts, such as LaCoO_3 , PrCoO_3 , and LaMnO_3 .^{46,47}

The principal disadvantage of the technique is the rarity of its applicability. Most practical compositions have no precursor of the same composition and other types of precipitation must be used.

Solid Solutions

A single-phase solid-solution precipitate assures homogeneity on an atomic scale but does not assure the proper cation ratio. The ratio must be set by very careful control of the precipitation process.

During the precipitation of a solid solution, the cation ratio in the solution is not necessarily found in the precipitate. For instance a barium titanate with partial substitution of strontium and lead for barium can be prepared using the standard oxalate process, which assures a 1:1 ratio of divalent metal to titanium.⁴⁸ Generally it is necessary to establish by careful chemical analyses the divalent metal ion ratio necessary in the solution to give the desired product. Again, the pH of the solution is important and

pH also plays a more subtle role in the precipitation of salts other than hydroxide. For instance, ammonium oxalate and oxalic acid are commonly used precipitating agents and the relative concentrations of $\text{H}_2\text{C}_2\text{O}_4$, HC_2O_4^- , and $\text{C}_2\text{O}_4^{2-}$ are strongly affected by pH. It can also affect the oxidation state of the ions of interest. At high pH, iron(II) will react rapidly with atmospheric oxygen because the iron(III) that is formed is removed from solution as the hydroxide.

Solution concentrations, temperature, and atmosphere also affect the equilibrium of a precipitation. However, equilibrium is seldom achieved during precipitation, and a number of nonequilibrium factors can also affect the precipitation process.

The order of mixing of the solution and the precipitating agent is important. Generally the solution of cations is added slowly with stirring to a solution containing the precipitating agent. This allows an excess of precipitating agent, and the solubility products of all the cations are likely to be exceeded simultaneously. Adding the precipitating agent to the cation solution will often cause the cations to be precipitated stepwise with the resulting inhomogeneities.

The rate of mixing is a variable that can affect the particle size of the precipitate by way of the degree of supersaturation and thus the number of nuclei formed. Finely divided precipitates are formed by rapidly mixing cold concentrated solutions.

Stirring rate can also affect the degree of supersaturation and the particle size. Stirring also prevents the formation of large agglomerates, which can hinder later steps of powder processing. The application of ultrasonic fields during precipitation can also reduce the agglomerate sizes.⁴⁹

The effect of other ions on the surface chemistry of precipitates can be important and is treated more completely elsewhere.⁴⁹ An important example involves the electrical double layer that surrounds many fine precipitates in suspension. The heavy concentration of electrolyte surrounding the particles after the precipitation often destroys this layer and allows the particles to flocculate and settle. When the precipitate is then washed free of this excess electrolyte the particles may deflocculate and form a stable colloid that is difficult to filter. This can be avoided by the addition of a small amount of an ammonium salt which can subsequently be removed by calcination.

Impurities in a precipitate can be incorporated though a precipitation from the solution either as a separate phase or in solid solution. Impurities can be adsorbed on the surface of a precipitate and subsequently incorporated by further growth or whole pockets of solvent can become occluded. In general, conditions that favor large particle size, slow growth, and equilibrium will produce the purest precipitates.

must be controlled, since the cation ratios in the precipitate change with pH.^{48,49} Generally the higher the pH, the more closely the cation ratios of the precipitate follow those of the solution.

Common examples of solid-solution precipitates are the divalent metal oxalates, which can be used for the preparation of ferrites.^{1,49-51} Sulfates also frequently form solid solutions that can yield oxide ferrites or sulfides.¹

Mixtures

In contrast to the first two types this precipitation technique does not give a single phase. The homogeneity of the original solution is partly lost, since segregation occurs during precipitation. However, the degree of mixing normally achieved is still far superior to that found by conventional mixing techniques. This type of precipitation is the most common, since systems in which the single compound or solid-solution precipitation will work are comparatively few. The cation ratio is usually easily controlled, because precipitation takes place under conditions where the solubility product of all components is exceeded and the desired cations are precipitated nearly quantitatively. Precipitates are often hydroxides or hydrated oxides but can also be oxalates, carbonates, and so forth.

The preparation of ferrites by coprecipitation of hydroxides or hydrated oxides is usually quite straightforward. However, the anion of the original soluble salt can apparently affect the sinterability of the final product. Nickel ferrite has been prepared by precipitating hydroxides from sulfate, chloride, and nitrate solutions.⁵² The powder precipitated from the sulfate solutions was superior for the purposes of high density and fine microstructure. The specific hydroxide used for the precipitation also affected the sintering properties. Using potassium hydroxide as the precipitating agent gave powders that showed inhibited grain growth during sintering; those precipitated using lithium hydroxide showed discontinuous grain growth.

Other examples of mixed hydroxide or hydrated oxide precipitates include the preparation of magnesium aluminates.⁵³ A spinel phase was formed at 400°C (compared with 1200 to 1600°C required using conventionally mixed powders). A mixed-oxide precipitate as a precursor to LaMnO_3 gives a powder that forms the compound at 400°C below the synthesis temperature needed for mixed oxides.⁵⁴

In cases where a single precipitating agent will not precipitate all desired cation species, a second precipitating agent can be used. Since lithium hydroxide is soluble, a stearate-hydroxide combination will precipitate a precursor for lithium ferrite.⁵⁵ In cases where a single solution is not readily available for all cations, separate solutions can be added at the proper rate to a single precipitating agent. For the preparation of lead titanate, titanium is most easily used as the chloride, but lead chloride is insoluble. Thus

separate solutions can be added to an oxalate to obtain a mixed precipitate.⁴⁸

Special Precipitation Techniques

The hydrolysis of organometallics is a versatile technique for the preparation of highly reactive powders. In this process the organometallic, often an alkoxide, is prepared and mixed with highly purified water for hydrolysis. Examples of oxides made from alkoxides are yttria-zirconia,⁵⁶ barium titanate,⁵⁷ and alumina.⁵⁸

Hydrothermal conditions at higher temperatures yield precipitates with relatively large and well-formed crystals. This has been demonstrated for various ferrite compositions^{59,60} and for ZrO_2 .⁶¹ In some cases the hydrothermal treatment⁶⁰ gives an oxide product rather than a hydroxide or a hydrated oxide.

For some hydroxide precipitations, prolonged digestion at high pH and at temperatures near boiling will form an oxide phase directly that can be filtered and used without needing a separate decomposition step. This technique is particularly useful for ferrites,^{62,63} but other materials, such as BaTiO_3 ⁶⁴ and even complex chalcogenides,⁶⁵ have been prepared by similar techniques.

While most precipitations are affected by the addition of a precipitating ion, the addition of an aqueous solution to a large excess of a second solvent in which the original solute is insoluble will also cause precipitation to occur. This principle forms the basis for a powder preparation technique termed "liquid drying."⁶⁶ For the preparation of some spinels the appropriate sulfates were dissolved in water and this solution was atomized and sprayed into a large excess of acetone. The small droplet size caused rapid precipitation and minimized the amount of segregation that took place. Other investigators have also reported the preparation of ferrite¹ and transition metal sulfides⁶⁷ using similar methods.

In cases where a single salt is being precipitated, a well-crystallized precipitate can be made by homogeneous precipitation.⁶⁸ This technique slowly raises the concentration of the precipitating ion, such as hydroxide or oxalate, which is formed by the slow hydrolysis of urea or ethyl oxalate. This provides a precipitation scheme where there is minimal supersaturation and relatively few nuclei form.

ADVANTAGES

The greater degree of homogeneity possible with solution-prepared powders compared with conventional ground, mixed, and calcined powders provides

a higher reactivity. The diffusion paths necessary to achieve the desired solid phases are short. This allows processing in a single step or at lower temperatures, which also gives greater control of powder particle size. Consequently, improvements in sinterability are the result. The solution preparation also offers: (1) the advantages of precise control of stoichiometry through gravimetric or volumetric combination of analyzed single cation solutions; (2) an ability to disperse trace additives uniformly; and (3) freedom from the contamination inherent in most powder grinding and mixing operations.

REFERENCES

1. Y. D. Tretyakov, I. Y. Kosinskaya, N. N. Oleinikov, and Y. G. Sakonov, "Synthesis of Ferrites from Solid Solutions of Salts," *Izv. Akad. Nauk. SSSR Neorg. Mater.*, **5** (7), 1255-1258 (1969); translation in *Inorg. Mater.*, **5** (7), 1067-1070 (1969).
2. A. G. Elliot and R. A. Huggins, "Phase Relations in the System $\text{NaAlO}_2\text{-Al}_2\text{O}_3$," *J. Amer. Ceram. Soc.*, **58** (11-12), 497-500 (1975).
3. J. G. M. DeLau, "Preparation of Ceramic Powders from Sulfate Solutions by Spray Drying and Roasting," *Amer. Ceram. Soc. Bull.*, **49** (6), 572-574 (1970).
4. A. Lagrange, J. Nicolas, and M. Hildebrandt, "Preparation and Properties of Hot-Pressed Ni-Zn Ferrites for Magnetic Head Application," *IEEE Trans. Mag.*, **8** (3), 494-497 (1972).
5. T. Akashi, T. Tsuji, and Y. Onoda, *Sintering and Related Phenomena*, G. C. Kuczynski, N. A. Hooton, and C. F. Gibbon, eds., 747-756, Gordon and Breach, New York, 1967.
6. M. J. Ruthner, H. G. Richter and I. L. Steiner, *Proc. Int. Conf. Ferrites Jap.*, 1970, Y. Hoshino, S. Iida, and M. Sugimoto, eds., University Park Press, Baltimore, 1971, pp. 75-78.
7. A. A. Jonke, E. J. Petkus, J. W. Loeding, and S. Lawroski, "The Use of Fluidized Beds for the Continuous Drying and Calcination of Dissolved Nitrate Salts," *Nucl. Sci. Eng.*, **2**, 303-319 (1957).
8. O. M. Todes, V. A. Seballo, Y. Y. Kaganovich, A. P. Goltsiken, S. P. Nalimov, and O. M. Rozanov, "Design Calculation of Processes for the Dehydration of Solutions in a Fluidized Bed with Selective Discharge," *Khim. Prom.*, **46** (8), 612-615 (1970). *Chem. Abstr.*, **74**, 5030x (1971).
9. R. Roy, "New Ceramic Materials Produced by Novel Processing Techniques," *International Journal of Powder Metallurgy*, **6** (1), 25-28 (1974).
10. A. L. Stuijts, *Proc. Int. Conf. Ferrites, Japan*, 1970, Y. Hoshino, S. Iida, and M. Sugimoto, eds., University Park Press, Baltimore, 1971, pp. 108-113.
11. D. W. Ferguson, O. C. Dean, and D. A. Douglas, "Sol-Gel Process for the Remote Preparation and Fabrication of Recycle Fuels," *Proc. Intern. Conf. Peaceful Uses At. Energy*, **3rd, Geneva**, 1964, **10**, 307-315 (1965).
12. "Sol-Gel Processes for Ceramic Nuclear Fuels," Proceedings of a Panel Held in Vienna, May 1968, International Atomic Energy Agency, Austria, 1968.

13. J. M. Fletcher and C. J. Hardy, "Applications of Sol-Gel Processes to Industrial Oxides," *Chem. Ind. (London)*, 1968 (2), 48-51.
14. D. M. Roy and R. Roy, "Experimental Study of Formation and Properties of Synthetic Serpentine and Related Layer Silicate Minerals," *Amer. Mineral.*, **39** (11,12), 957-975 (1954).
15. P. W. D. Mitchell, "Chemical Method For Preparing MgAl_2O_3 Spinel," *J. Am. Ceram. Soc.*, **55** (9), 484 (1972).
16. D. R. Messier and G. E. Gazza, "Synthesis of MgAl_2O_4 and $\text{Y}_2\text{Al}_2\text{O}_7$ by Thermal Decomposition of Hydrated Nitrate Mixtures," *Amer. Ceram. Soc. Bull.*, **51** (9), 692-697f (1972).
17. C. Marcilly, P. Courty, and B. Delmon, "Preparation of Highly Dispersed Mixed Oxides and Oxide Solid Solutions by Pyrolysis of Amorphous Organic Precursors," *J. Amer. Ceram. Soc.*, **53** (1), 56-57 (1970).
18. L. J. Koppens, "Improved Ferrite Memory Cores Obtained by a New Preparation Technique," *IEEE Trans. Mag.*, **8** (9), 303-305 (1972).
19. Th. J. A. Popma and A. M. Van Diepen, "Magnetization and Mossbauer Spectra of Non-Crystalline $\text{Y}_2\text{Fe}_2\text{O}_7$," *Mater. Res. Bull.*, **9** (9), 1119-1128 (1974).
20. F. J. Schnetler, F. R. Monforte, and W. W. Rhodes, *Science of Ceramics*, Vol. 4, G. H. Stewart, ed., The British Ceramic Soc., 1968, pp. 79-90, Stoke-on-Trent.
21. V. V. Merkovich and T. A. Wheat, "Use of Liquid Nitrogen in Spray Freezing," *Amer. Ceram. Soc. Bull.*, **49** (8), 724-725 (1970).
22. H. A. Sauer and J. A. Lewis, "Freezing Droplets of Aqueous Solutions for the Cryochemical Process," *Amer. Inst. Chem. Eng. J.*, **18** (2), 435-437 (1972).
23. D. W. Johnson and F. J. Schnetler, "Characterization of Freeze-Dried Al_2O_3 and Fe_2O_3 ," *J. Amer. Ceram. Soc.*, **53** (8), 440-444 (1970).
24. Y. S. Kim and F. R. Monforte, "Theoretically Dense (99.9%) Polycrystalline Alumina Prepared from Cryochemically Processed Powders," *Amer. Ceram. Soc. Bull.*, **50** (6), 532-535 (1971).
25. F. J. Schnetler and D. W. Johnson, *Proc. Int. Conf. Ferrites Jap.*, 1970, Y. Hoshino, S. Iida, and M. Sugimoto, eds., University Park Press, Baltimore, 1971, pp. 121-124.
26. D. W. Johnson, Jr., P. K. Gallagher, D. J. Nitti, and F. Schrey, "Effect of Preparation Technique and Calcination Temperature on the Densification of Lithium Ferrites," *Amer. Ceram. Soc. Bull.*, **53** (2), 163-167 (1974).
27. A. C. C. Tseung and H. L. Bevan, "Preparation and Characterization of High Surface Area Semiconducting Oxides," *J. Mater. Sci.*, **5**, 604-610 (1970).
28. R. E. Jaeger, T. J. Miller and J. C. Williams, "Effects of Ammonium Hydroxide on Phase Separation in the Cryochemical Processing of Salt Solutions," *Amer. Ceram. Soc. Bull.*, **53** (12), 850-852 (1974).
29. M. C. Tinkle, "Cryochemical Method for Forming Spherical Metal Oxide Particles from Metal Salt Solutions," U.S. Patent 3,776,988 (Dec. 4, 1973).
30. J. T. Wenckus and W. Z. Leavitt, "Preparation of Ferrites by the Atomizing Burner Technique," *Conf. Mag. Mater. Boston*, 1956, T-91, American Institute of Electrical Engineers, New York, 1957.
31. W. W. Malinofsky and R. W. Babbitt, "Fine-Grained Ferrites I. Nickel Ferrite," *J. Appl. Phys.*, **32** (3) (supplement), 237a-238s (1961).
32. S. DiVita and R. J. Fischer, "Barium Titanates," U.S. Patent 2,985,506 (May 23, 1961).

33. M. L. Nielson, P. M. Hamilton, and R. J. Walsh, Ultrafine Particles, W. E. Kuhn, ed., Wiley, New York, 1963, pp. 181-195.
34. K. S. Mazdiyasi, C. T. Lynch, and J. S. Smith, "Preparation of Ultra-High-Purity Submicron Refractory Oxides," *J. Amer. Ceram. Soc.*, **48** (7), 372-375 (1965).
35. G. J. Duffy, "Vapor-Phase Production of Colloidal Silica," *Ind. Eng. Chem.*, **51** (3), 232-238 (1959).
36. K. A. Loftman, Ultrafine Particles, W. E. Kuhn, ed., Wiley, New York, 1963, pp. 196-205.
37. M. Formenti, F. Juillet, P. Meriaudeau, S. J. Teichner and P. Vergnon, "Preparation in a Hydrogen Oxygen Flame of Ultrafine Metal Oxide Particles," *J. Colloid Interface Sci.*, **39** (1), 79-89 (1972).
38. F. I. Kukoz and E. M. Feigina, "Effect of Ultrasound and other Precipitation Conditions on the Particle Size Composition of Nickelous Hydroxide Precipitates," *Zh. Prikl. Khim. (Leningrad)*, **42** (9), 1978-1983 (1969); *Chem. Abstr.* **72**, 4736d (1970).
39. A. W. Adamson, *Physical Chemistry of Surfaces*, Wiley, New York, 1967.
40. W. S. Clabaugh, E. M. Swiggard, and R. Gilchrist, "Preparation of Barium Titanyl Oxalate Tetrahydrate for Conversion to Barium Titanate of High Purity," *J. Res. Natl. Bur. Stand.*, **56**, 289-291 (1956).
41. P. K. Gallagher and F. Schrey, *Proc. ICTA, 3rd*, **2**, H. G. Wiedemann, ed., 623-634, Burkhauer Verlag, Basel, 1972.
42. P. K. Gallagher, "A Simple Technique for the Preparation of R. E. FeO₃ and R. E. CoO₃," *Mater. Res. Bull.*, **3**, 225-232 (1968).
43. G. Wagner and H. Binder, "The Binary Systems BaO-SnO₂ and BaO-PbO₂, I. Phase Analysis," *Z. Anorg. U. Allgem. Chem.*, **297**, 328-346 (1958).
44. P. K. Gallagher and D. W. Johnson, Jr., "Kinetics of the Formation of BaSnO₃ from Barium Carbonate and Tin (IV) Oxide or Oxalate Precursors," *Thermochim. Acta*, **4**, 283-289 (1972).
45. P. K. Gallagher, F. Schrey, and F. V. DiMarcello, "Preparation of Semiconducting Titanates by Chemical Methods," *J. Amer. Ceram. Soc.*, **46** (8), 359-365 (1963).
46. D. W. Johnson, Jr. and P. K. Gallagher, "Studies of Some Perovskite Oxidation Catalysts Using DTA Techniques," *Thermochim. Acta*, **7**, 303-309 (1973).
47. P. K. Gallagher, D. W. Johnson, Jr., and F. Schrey, "Studies of Some Supported Perovskite Oxidation Catalysts," *Mater. Res. Bull.*, **9**, 1345-1352 (1974).
48. F. Schrey, "Effect of pH on the Chemical Preparation of Barium-Strontium Titanate," *J. Amer. Cer. Soc.*, **48** (8), 401-405 (1965).
49. P. K. Gallagher and F. Schrey, "Preparation and Thermal Analysis of Mixed Magnesium-Manganese-Iron Oxalates and Hydrated Oxides," *J. Amer. Ceram. Soc.*, **47** (9), 434-437 (1964).
50. W. J. Schuele, "Preparation of Fine Particles from Bimetal Oxalates," *J. Phys. Chem.*, **63** (1), 83-86 (1959).
51. P. K. Gallagher, H. M. O'Bryan, Jr., F. Schrey, and F. R. Monforte, "Preparation of Nickel Ferrite from Coprecipitated Ni₂Fe₂C₂O₇·2H₂O," *Amer. Ceram. Soc. Bull.*, **48** (11), 1053-1059 (1969).
52. H. M. O'Bryan, Jr., P. K. Gallagher, F. R. Monforte, and F. Schrey, "Microstructure Control in Nickel Ferrite," *Amer. Ceram. Soc. Bull.*, **48** (2), 203-208 (1969).
53. R. J. Bratton, "Cocrecipitates Yielding MgAl₂O₄ Spinel Powders," *Amer. Ceram. Soc. Bull.*, **48** (8), 759-762 (1969).

54. S. A. Prokudina, Y. S. Rubinchik, and M. M. Pavlyuchenko, "Kinetics of Low Temperature Synthesis of LaMnO₃," *Izv. Akad. Nauk SSSR, Neorg. Mater.* **10** (3), 488-492 (1974); translation in *Inorg. Mat.*, **10** (3), 416-419 (1974).
55. A. L. Micheli, "Preparation of Lithium Ferrites by Co-precipitation," *IEEE Trans. Magn.*, **6** (3), 606-608 (1970).
56. K. S. Mazdiyasi, C. T. Lynch, and J. S. Smith, II, "Cubic Phase Stabilization of Translucent Yttria-Zirconia at Very Low Temperatures," *J. Amer. Ceram. Soc.*, **50** (10), 532-537 (1967).
57. K. S. Mazdiyasi, R. T. Dolloff, and J. S. Smith, II, "Preparation of High-Purity Submicron Barium Titanate Powders," *J. Amer. Ceram. Soc.*, **52** (10), 523-526 (1969).
58. D. F. Saunders and A. Packter, "Effects of Rate and Temperature of Mixing on the Surface Area of Precipitated Alumina Hydrates," *Chem. Ind. (London)*, **18**, 594 (1970).
59. A. A. Van Der Giessen, "Hydrothermal Preparation of Ceramic Powders," *Klei Keram.*, **20** (2), 30-38 (1970); *Chem. Abstr.* **72**, 114604s (1970).
60. F. Schrey, "Hydrothermal Preparation of a Manganese-Zinc Ferrite," paper 17-El-67F, 1967 Annual Meeting of the American Ceramic Soc.; *Bull. Amer. Ceram. Soc.*, **46** (4), 788 (1967).
61. N. T. Okopnaya, V. I. Zelentsov, V. M. Chertov, and B. N. Lyashkevich, "Regulation of the Particle Size of Zirconium Dioxide by a Hydrothermal Method," *Adsorbtsiya Adsorbentry*, **2**, 108-109 (1974); *Chem. Abstr.*, **111783z** (1974).
62. P. E. D. Morgan, "Direct Aqueous Precipitation of Lithium Ferrite and Titanate," *J. Amer. Ceram. Soc.*, **57** (11), 499-500 (1974).
63. M. Kiyama, "Conditions for the Formation of Fe₂O₃ by the Air Oxidation of Fe(OH)₃ Suspensions," *Bull. Chem. Soc. Jap.*, **47** (7), 1646-1650 (1974).
64. S. S. Flaschen, "Aqueous Synthesis of Barium Titanate," *J. Amer. Chem. Soc.*, **77** (12), 6194 (1955).
65. P. W. D. Mitchell and P. E. D. Morgan, "Direct Precipitation Methods for Complex Crystalline Chalcogenides," *J. Amer. Ceram. Soc.*, **57** (6), 278 (1974).
66. R. E. Jaeger and T. J. Miller, "Preparation of Ceramic Oxide Powders by Liquid Drying," *Amer. Ceram. Soc. Bull.*, **53** (12), 855-859 (1974).
67. R. J. Bouchard, "The Preparation of Pyrite Solid Solutions of the Type Fe₂Co_{1-x}S₂, Co₂Ni_{1-x}S₂, and Cu₂Ni_{1-x}S₂," *Mater. Res. Bull.*, **3**, 563-570 (1968).
68. L. Gordon, M. L. Salutsky, and H. H. Willard, *Precipitation from Homogeneous Solution*, Wiley, New York, 1959.

13

Lattice Strain in Alumina Powders

J. P. Page

E. A. Metzbower

D. J. Shanefield

D. P. H. Hasselman

The fundamental factors underlying the densification kinetics of powder materials during sintering appear to be well understood. The effect of surface energy, particle size, and temperature, as well as the various mechanisms of material transport, such as viscous and plastic flow, evaporation and condensation, volume, and surface diffusion, all have been the object of a number of experimental and theoretical studies.¹⁻⁴ The shrinkage behavior of a powder compact, as theoretically derived, can be expressed as:

$$\frac{\Delta L}{L_0} = N \left[\frac{\gamma D a_0^3}{R^p K T} \right]^n t^m \quad (1)$$

where L is the linear shrinkage of the powder compact after time t , L_0 is the original length of the compact, N is a constant, γ is the surface energy, D is the diffusion coefficient, a_0 is the vacancy volume, R is the particle radius, K is the Boltzmann constant, T is the temperature, and p , n , m are exponents

whose values depend on the particular mechanism for material transport. Equation 1 is a simplified form of an equation given by Kingery.⁸

In practice we have observed that different batches of alumina made by the same chemical process and similar in surface area, particle size distribution, morphology, and purity can exhibit marked differences in their sinterability. The differences in sinterability cannot be explained in terms of surface energy, particle size, and purity.

One possible explanation for this behavior, suggested in Chapter 9, is the presence of transition aluminas (nonalpha phase) in the powder. Another possibility, presented in this chapter, is that the kinetics of material transport during sintering are different in each powder because of different levels of defects in the powders.

Defects can change the rate-controlling mechanism of material transport (e.g., substitution of surface diffusion for bulk diffusion). Also, defects can suppress or enhance the rate of material transport for a given sintering mechanism.

Enhancement of the rate of material transport can be due to increased concentrations of lattice defects, such as vacancies.⁶ In ionic compounds excess vacancy concentrations can be created by the addition of impurities.⁷ To conserve charge neutrality, impurities of a higher positive valence than the host material create cation vacancies. For example, TiO_2 impurities have been observed to increase densification rates of MgO .⁸ Similar effects have been observed for TiO_2 impurities in ZnO .⁹ However, additions of Ga^{3+} and Al^{3+} decreased sintering rates for ZnO as the result of decreases in cation-vacancy concentration.⁹

High concentrations of dislocations or subgrain boundaries can also significantly affect sintering rates, particularly in those materials for which sintering is controlled by bulk diffusion. This latter hypothesis is substantiated by the observations of Pines and Sirenko,¹⁰ who noted that the sinterability of cold-worked copper powders showed a positive correlation with the dislocation density. Also, Fedorchenko¹¹ ascribed the superior sintering of carbonyl nickel compared to electrolytic nickel to its having higher densities of dislocations and higher internal lattice strain. Additionally, it is well recognized that mechanically worked powders, such as ball-milled powders, generally show a greater sintering activity than annealed powders with the same particle size.^{12,13}

MEASURING LATTICE STRAIN

In the search for a suitable technique to establish the validity of this hypothesis, it should be noted that lattice strain can cause a distinct broadening of the lines obtained in X-ray analysis. As a result, if excess lat-

tice defects and internal strain have an effect on the sintering behavior of alumina powders, a correlation between sinterability and X-ray line broadening should be found.

The magnitude of average internal strain and coherently diffracting domain size can be measured by X-ray analysis using the Warren-Averbach method.¹⁴ Using nickel-filtered copper radiation, the (012) and the (113) peaks and their second-order reflections were step-scanned at intervals of $2\theta = 0.05^\circ$ using a time period of 20 sec. Each peak required a total of 81 measurements. The as-recorded X-ray data were corrected for polarization and geometric factors, atomic scattering factors, and the K_α doublet with the aid of a previously developed computer program.¹⁵ The corrected profiles were then further corrected for instrument broadening by the Stokes method,¹⁷ followed by the separation of the effects on internal strain and domain size by the Warren-Averbach method. The average ($\bar{\epsilon}$) of the mean strain perpendicular to the (012) and (113) planes at a depth of 50 Å was calculated.

Lattice-strain measurements were carried out on five alumina powders. These powders, prepared by the Bayer process and dry ball milled for a period of approximately 24 hr, were obtained from commercial sources and were designated A, B, C, D, and E. These powders were selected on the basis of previously established differences in sintering behavior. The powder characteristics and sintering behavior (described later) were measured in the as-received condition.

Powder purity was measured by optical emission and spark ion-mass spectroscopy and the results are recorded in Table 13.1. Powder surface area and particle size were determined by the B.E.T. and sedimentation methods, respectively. Particle shape and the presence of dislocations and internal strain were determined qualitatively by scanning electron microscopy and transmission electron microscopy.

SINTERABILITY OF POWDERS

The five powders were cold-pressed into compacts approximately $\frac{3}{8}$ in. in diameter by 0.1 in. thick in a circular steel die at 3000 psi and were fired at 1475°C for 7 hr. Prior to firing, green density was determined from the specimens' weight and dimension. After sintering, density was measured by ASTM C20-70 using toluene as the suspending fluid. The sinterability of the powders was expressed by the Hirschhorn densification parameter (D.P.)¹⁸ defined by:

$$\text{D.P.} = \frac{\text{final density} - \text{green density}}{\text{theoretical density} - \text{green density}}$$

Table 13.1. Impurities in alumina samples (ppm)

Impurity	Sample A	Sample B	Sample C	Sample D	Sample E
Iron	90	70	61	82	144
Magnesium	525	350	365	450	<250
Silicon	399	516	500	407	402
Titanium	<50	<50	<50	<50	<50
Calcium	250	<100	<100	250	360
Sodium	520	400	450	550	530
Gallium	25	23	18	20	72
Potassium	<50	<50	<50	<50	<50
Lithium	68	40	38	45	39
Barium	70	<50	<50	90	<50
Boron	7	12	NA	12	4
Fluorine	67	102	NA	69	109
Sulfur	93	106	NA	64	41

The parameter D.P. can vary from 0 to 1 and defines the ratio of the actual densification achieved under the sintering conditions selected to the total densification that could have been achieved theoretically.

To establish the time dependence of the densification, additional specimens measuring approximately $\frac{1}{2}$ in. diameter by 0.500 ± 0.002 in. long were isostatically pressed at 7500 psi, followed by sintering at 1475°C in a dilatometer.

Table 13.2 gives the experimental data for the median particle size, particle-size range,* surface area, strain domain size, and green density together with the data for fired density, densification parameter, and sintering constant.

MULTIPLE REGRESSION ANALYSIS

A multiregression analysis showed that the fired density can be expressed by:

$$\rho_f = 1.692 + 0.949\rho_g + 8.0 \times 10^{-2}\tau - 9.65 \times 10^{-3}A_s \quad (2)$$

where ρ_f = fired density in g/cc

ρ_g = green density in g/cc

τ = mean strain

A_s = surface area in m^2/g .

* Particle-size range between particle sizes corresponding to the 10 and 90% deciles, as determined by sedimentation.

Table 13.2. Alumina powder characteristics, X-Ray data and sintering behavior

Sample	Median Particle size	Band width (μ)	Surface Area (m^2/g)	Mean strain $\times 10^3$	Domain size (\AA)	Green Density (g/cc)	Fired Density (g/cc)	Densification Parameter	Sintering Constant (m in Eq. 1)
A	0.45	1.08	14.20	3.143	393	2.265	3.931	0.96	—
B	0.39	0.92	10.24	2.369	376	2.126	3.793	0.89	—
C	0.54	1.15	10.75	3.175	428	2.127	3.843	0.92	—
D	0.38	1.06	11.28	1.917	393	2.090	3.691	0.84	0.34
E	0.61	1.35	9.59	2.630	352	2.148	3.851	0.90	0.43

The analysis showed that the variation in fired density could be accounted for by 80.1, 13.2, and 6.7% of the variations in green density, strain, and surface area, respectively, with a multiple correlation coefficient of .994. The fired density was not affected by differences in median particle size, particle size range, or domain size.

Similarly, the densification parameter (D.P.) could be expressed by:

$$\text{D.P.} = -3.962 \times 10^{-3} + 0.397 \rho_g + 4.656 z - 3.33 \times 10^{-3} A_s \quad (3)$$

The variations in densification parameter could be accounted for by 81.7, 11.8, and 2.6% of the variations in green density, strain, and surface area, respectively, with a multiple correlation coefficient of .993. As for the fired density, the present results for the densification parameter were not affected by the variation in median particle size, particle-size range, and domain size.

As expected, of all the characteristics determined in the present study, green density has the major effect on final density values to be obtained. However, in agreement with the original hypothesis and as indicated by the percentage contributions, the internal strain also plays a vital role in the densification process. The positive coefficients of the internal strain terms in equations 2 and 3 indicate that high internal strain is desirable in achieving high fired densities.

The negative coefficients in Equations 2 and 3 suggest that the high final density requires low surface area, which in turn implies the requirement of large particle size. This appears contradictory, since high densification rates require small particle size, as indicated by Equation 1. In addition, the statistical analysis of the present data showed that particle size had no effect. A regression analysis of green density in terms of surface area, particle size, and particle-size range showed that green density can be expressed by:

$$\rho_g = 1.650 + 0.0387 A_s + 0.816 a - 0.287 \Delta a$$

in which the relative contribution by A_s , a , and Δa to ρ_g are 63, 22, and 4%, respectively. These results suggest that, in spite of the negative coefficients for the effect of surface area on fired density, high surface area is desirable in view of its greater effect on fired density by way of the green density compared to its direct effect on fired density.

LATTICE STRAIN AND SINTERABILITY

Since the firing conditions for all samples were identical, the significant effect of internal strain on final density must have been to accelerate the

rate of densification. In the absence of externally applied loads, any permanent internal strains in the individual particles can only result from the presence of lattice imperfections. In monocrystalline powder particles, lattice imperfections can exist in the form of dislocations, stacking faults, subgrain boundaries, and perhaps nonuniform vacancy concentrations. These lattice imperfections can affect material transport during sintering in two ways. First, the strain field associated with these imperfections can provide an additional driving force for mass transport as they are being annealed out at higher temperatures. This mechanism is expected to be effective primarily only during the initial stage of the densification process and is not thought to be sufficient to explain the observed results. More likely, as suggested earlier, lattice imperfections in the form of immobile dislocations serve as diffusion pipes, thereby accelerating material transport by lattice diffusion. This mechanism is expected to be effective over the total period of sintering and, in the opinion of the authors, presents the most likely explanation for the observed results. Further confirmation of this conclusion can be found by comparing the sintering curves shown in Figure 13.1, in which the slope of the relative density versus time curve corresponds to the value m in Equation 1. The numerical values for m are

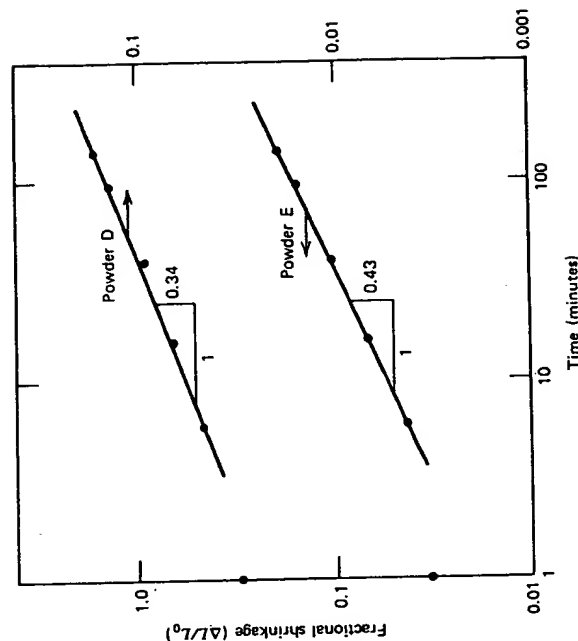


Figure 13.1. Sintering kinetics of two alumina powders.

given in Table 13.2. Sample D with the lower value of strain energy has a value for the sintering constant near $1/6$, which suggests that for this powder, grain-boundary diffusion was the primary mechanism for material transport. For powder E, however, the value of m approaches 0.5, which is representative of material transport by volume diffusion.¹⁹

The detection of the presence of dislocation within the particles by transmission electron microscopy presented difficulties. The majority of particles were too large for transmission of the electron beam so that only less representative platelike particles could be examined. Although the presence of dislocations could not be determined unambiguously, numerous particles showed evidence of the presence of internal strains in the form of extinction patterns, as shown in Figure 13.2 for powder sample E.

The dislocation densities within the particles can be estimated from the X-ray data. From the known value of domain size (D), the dislocation density (ρ_D) can be calculated from²⁰:

$$\rho_D = \frac{3n}{D^2} \quad (4)$$

where n is the number of dislocations per domain face. The dislocation density (ρ_S) can be determined from the strain (ϵ) by²⁰:

$$\rho_S = \frac{K(\epsilon)^2}{Fb^2} \quad (5)$$

where F = dislocation interaction factor

b = Burger's vector

$K = 20.6$, calculated by the procedure of Williamson and Smallman.²⁰

Values for ρ_D and ρ_S calculated by means of Equation 4 and 5 are given in Table 13.3. The values listed may be in error by as much as a factor of 5 in

Table 13.3. Dislocation densities in alumina powders

Powder Sample	Dislocation Calculated from Strain	Densities Calculated from Domain Size
A	1.36×10^{11}	1.94×10^{11}
B	0.77×10^{11}	2.21×10^{11}
C	1.39×10^{11}	1.64×10^{11}
D	0.51×10^{11}	1.94×10^{11}
E	0.95×10^{11}	2.42×10^{11}



Figure 13.2. Extinction pattern showing microstrain and possible dislocations in powder sample E.

view of the simplifying assumptions that underlie Equations 4 and 5. Nevertheless, it is of interest to note that the values for the dislocation densities approach those found for cold-worked metals.²⁰

It is most probable that these large dislocation densities were introduced during the ball-milling stage of the powder production process. Under these conditions, it is quite likely that during particle impact the stress exceeds the critical stress required for dislocation generation or multiplication. Indeed, the abrasion of aluminum oxide²¹ is known to introduce high densities of dislocations in the surface.

Of interest to the present study is the difference in dislocation densities for the various powders. It appears unlikely that dislocation densities on the order of those given in Table 13.3 could have been introduced during the chemical stage of the powder production process. An alternative explanation is based on the general observation that in the growth of single crystals, high rates of growth generally result in lattice imperfections. Undoubtedly, such lattice imperfections do exist in the present powders, even in relatively low concentrations. For the various powder samples differences in these concentrations of lattice imperfections may be the result of even slight variations in temperature during the growth process. It is well known that lattice imperfections in the form of properly oriented and pinned disloca-

tions can act as Frank-Read sources for the multiplication of additional dislocations during mechanical impact. During the ball-milling process, the multiplication of dislocations could result in the dislocation densities given in Table 13.3, with any differences between the powder samples related to initial differences in lattice imperfections prior to the ball-milling stage. It is suggested here that relating the particular growth conditions of the crystallites to the final densities of internal stress generated during ball milling may constitute a fruitful area for future research.

As is pointed out above, the accelerated sintering could also be due to excess vacancy concentrations as the result of certain types of impurities. In this present study, however, no correlation among impurity content, final density, and densification parameter could be found. As a result, it is felt that the present observation cannot be attributed to excess vacancy concentrations.

Regardless of the validity of the above explanations, the present results show that a high degree of internal strain is beneficial in achieving high final densities in a sintering operation. The results also suggest that a general internal strain be considered an important parameter for the characterization of powder samples.

REFERENCES

1. J. Frenkel, *J. Phys. (USSR)*, **9**, 385 (1945).
2. G. C. Kuczynski, *J. Appl. Physics*, **21**, 632 (1945).
3. D. L. Johnson, *Phys. Sintering*, **1** (Y3), (July 1969) B1.
4. B. Ya. Pines, *Uspekhi Fiz. Nauk*, **52**, 501 (1954); translation AES-TR 5563, 2/15, 1963.
5. W. D. Kingery, *Introduction to Ceramics*, Wiley, New York, 1963, p. 376.
6. P. Reyner, *Reactivity of Solids*, Wiley-Interscience, New York, 1969.
7. F. A. Kroger, *The Chemistry of Imperfect Crystals*, Wiley, New York, 1964.
8. D. N. Polyboyarinov, *Refractories (Moscow)*, **27**, 137 (1962).
9. W. A. Weyl, *Ceram. Age*, **60**, 28 (1952).
10. B. Ya. Pines and A. F. Sirenko, *Fiz Tverd. Tela*, **7**, 687 (1965).
11. I. M. Fedorchenko and V. V. Skorokhod, *Sov. Powder Metall.*, **10** (58) 805 (1967).
12. A. L. McLaren and P. W. M. Atkinson, *J. Nucl. Mater.*, **17**, 332 (1965).
13. V. A. Bron and N. V. Semkina, *Sov. Powder Metall.*, **5**, 332 (1962).
14. W. H. Gitzel, "Alumina as a Ceramic Material," *Amer. Ceram. Soc.*, Columbus, Ohio, 1970, p. 7.
15. B. E. Warren and B. L. Averbach, *J. Appl. Phys.*, **21**, 595 (1950).
16. E. A. Metzbowler, NRL Report 7253, 1971.
17. A. R. Stokes, *Proc. Phys. Soc., London*, **B61**, 382, (1948).

18. J. L. Hirschorn, *Introduction to Powder Metallurgy*, Colonial Press, New York, 1969, p. 206.
19. F. Thummler and W. Thomma, *Metal Rev.*, **12**, 69 (1967).
20. G. K. Williamson and R. E. Smallman, *Philos. Mag.*, **1**, 34 (1956).
21. B. J. Hockey, "Science of Ceramic Machining," S. J. Schneider and R. W. Rice, eds., National Bureau of Standards, Washington, 1972, p. 333.

14

Agglomeration Effects on the Sintering of Alumina Powders Prepared by Autoclaving Aluminum Metal

R. T. Tremper
R. S. Gordon

Aluminum oxide can be sintered to translucency with a density near theoretical by the addition of a small amount of magnesia and by firing in an appropriate atmosphere. This technique, first described by Coble,¹ has been studied intensively and the properties of high-density, sintered alumina allow it to be used as an arc chamber in high-pressure, sodium vapor lamps. For this application the sintered body must be as dense as possible. To achieve a total light transmission comparable to that which is possible with a single crystal, the porosity level in sintered Al_2O_3 must lie below 10^{-4} to 10^{-6} volume fraction for pore sizes in the range of 0.5 to $5\mu\text{m}$. It is well established² that voids and second-phase particles are primarily responsible

for the diffuse light transmission characteristics of polycrystalline Al_2O_3 and not grain boundaries. The optical anisotropy in Al_2O_3 is too small for grain boundaries to influence, to any significant degree, the total transmission through a dense polycrystalline body.

Most of the previous studies on the sintering kinetics of polycrystalline alumina focused on alum or Bayer-process powders that are frequently used in the production of commercial products. These powders are normally obtained by means of the high-temperature (1100 to 1200°C) thermal decomposition of an aluminum hydroxide (e.g., gibbsite and boehmite) or an alum salt. A new low-temperature process has recently been developed in this laboratory for the production of high-purity aluminum oxide. It consists of converting in an autoclave high-purity (99.99%) aluminum metal directly to the oxide at low temperatures (300 to 500°C) and moderate steam pressures (500 to 5000 psi).

By autoclaving, alumina powders can be prepared with a wide range of characteristics (e.g., surface areas, agglomerate sizes and distributions, and phase compositions). The purpose of the present study was to determine quantitatively the effects of these characteristics on "powder sinterability," with the ultimate goal of specifying the properties of an alumina powder that are necessary and sufficient for it to be sintered to densities up to and higher than 99.99% of theoretical, a level that is attractive for application in a sodium vapor lamp.

EXPERIMENTAL PROCEDURE

Synthesis of Autoclave Alumina

Using the previous results of Krischner and Torkar³ as a starting point, an extensive study was undertaken of the conversion of aluminum metal to an aluminum oxide powder by reaction with high-pressure steam. Since this work will be reported extensively elsewhere,⁴ only a brief description of the process is given here. In essence, by placing aluminum metal in any form (splatter, ingot, chopped rods) in a high-pressure steam chamber (autoclave) and subjecting it to the proper combination of temperature (350 to 450°C), steam pressure (1000 to 4500 psi), and time (up to 100 hours), alumina powders can be synthesized that contain up to 100% of the alpha phase and possess surface areas between 1 and 20 m²/g.

Two basic types of autoclave processes were used in synthesizing the alumina powders for this study. The first technique used was direct steam transfer. In this procedure the aluminum metal, which had been preheated in the reaction autoclave, was subjected directly to the final operating

Experimental Procedure

pressure by the transfer of steam from the reservoir autoclave. Pressures employed in this type of experiment were usually between 1500 and 4500 psi. By use of a double-chamber autoclave in this manner, the temperature in the reaction autoclave could be maintained at a point equal to or above the saturation temperature. The specific experiment that produced 100% alpha alumina involved the direct transfer of steam at the saturation temperature and pressure. This variation is referred to as the "transfer-saturation" method.

The second general type of process used in the production of alumina powders was the two-stage process. In this method the aluminum is subjected initially to steam at a relatively low pressure (1000 to 1500 psi) and temperatures above saturation (approximately 400°C); this is followed by a second steam transfer to pressures between 2200 and 3200 psi and temperatures of no more than 30°C over saturation. During the first stage, the reaction product is essentially all gamma alumina, which is converted to 100% alpha alumina during the second steam transfer. This technique allows for the production of an alumina powder with an agglomerate-size distribution different from that encountered in the single-stage, steam-transfer procedure.

Both the steam-transfer and two-stage processes are indicated schematically in Figure 14.1. Another possible reaction path is to heat the metal and steam together along the saturation curve and then into the

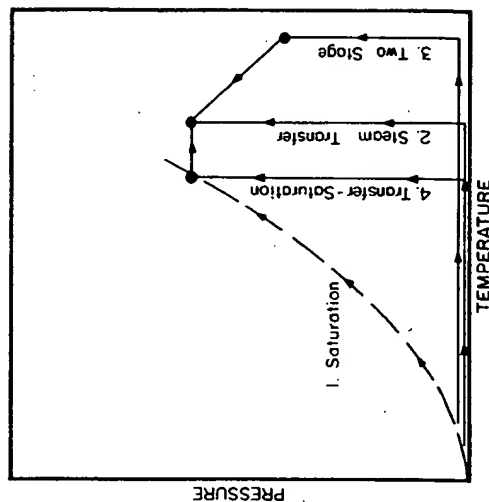


Figure 14.1. Schematic diagram of autoclave reaction path.

superheated region. This method is undesirable because of the formation of boehmite⁴ as a precursor.

Powder Characterization

The reader is referred elsewhere⁴ for a complete description of the technique used to characterize the autoclave alumina powders, namely, ignition loss, thermal gravimetric analysis, surface area measurement by BET, absolute density determination, X-ray diffraction, and transmission electron microscopy. In addition to these methods, the powders were further characterized by scanning electron microscopy* and for agglomerate-size distribution by determined by use of a Coulter Counter.

In addition to routine agglomerate-size studies at 1000 to 4000+, high-resolution micrographs of the agglomerate structure at 60,000+ were obtained.

Median agglomerate sizes and distributions were determined by Coulter Counter particle-size analysis.[†] Prior to analysis, each sample was dispersed in an electrolyte of 4% $\text{Na}_2\text{P}_2\text{O}_7$ by subjecting the suspension to a 5 minute ultrasonic treatment. In all measurements a 50 μm aperture with a 0.8 μm minimum detectable point was used. Agglomerates below 1 μm of course, were undetected in this analysis.

Sample Protection

Upon removal from the autoclave, the powders were screened through a 90 mesh nylon screen, and the fines of this process were called the as-prepared powder. Portions of the powders were doped with the appropriate amount of $\text{Mg}(\text{NO}_3)_2 \cdot 6\text{H}_2\text{O}$ to give 0.1 wt % MgO in the sintered ceramic. An aqueous slurry technique was used, followed by drying at 600°C and screening through a 100 mesh nylon screen. The sample to be milled (10 g lots) were placed in 500 ml polypropylene centrifuge bottles along with 125 g of alumina grinding media and a few drops of isopropanol as a milling aid. These were placed on an adapted laboratory vibratory mill and milled for 2 hours. The powders were then rescreened through 100 mesh. One gram portions of the processed powders were pressed into pellets (0.667 in diameter) in a tungsten carbide die in a hydraulic laboratory press with no binders or lubricants. A pressure of 15,000 psi was used yielding pellets of 40 to 55% theoretical density.

* JEOL 50 A Electron Probe Microanalyzer.

† Coulter Counter, Model B and Model T.

Sintering

The furnace used for this study was a tungsten mesh element vacuum furnace.* In all runs the temperature was programmed† to conform to the following schedule: (1) heat to 1200°C at 500°C/hour, (2) heat to the soak temperature at 125 to 150°C/hour, (3) soak for 6.7 hours, and (4) cool to room temperature at 350°C/hour. The vacuum was maintained at 1 to 5 $\times 10^{-4}$ torr throughout each sintering cycle. Typically, three to four pellets were sintered simultaneously, each separated by squares of tungsten foil.

Density and Ceramographic Preparation

The bulk density of the sintered pellets was determined by a normal weight and measurement technique. Samples whose density was > 90% had virtually all closed porosity, and their densities were redetermined by the fluid immersion technique in a temperature-controlled bath of monobromobenzene. The density of a single crystal of aluminum oxide was determined with each set of samples, and the relative densities (sample to single crystal value of that set) are reported as percent of theoretical. Cross sections of many of the sintered samples were prepared by normal ceramographic techniques, followed by thermal etching for 1 hour at 1600°C in hydrogen.

RESULTS

Effect of Autoclaving Conditions on Powder Sinterability

The principal objective of the sintering studies in the early stages of the program was to discover the powder properties that have the biggest influence on powder sinterability. In the synthesis of autoclave alumina, several powder characteristics were determined as a function of time in the autoclave at several steam pressures, using steam-transfer conditions at temperatures above saturation. Two of these were the relative amounts of $\alpha\text{-Al}_2\text{O}_3$, $\text{K1-Al}_2\text{O}_3$, and $\gamma\text{-Al}_2\text{O}_3$ in the powder and the powder surface area (BET). The K1 phase is unique to autoclaving conditions. Several autoclaving conditions were chosen for study. These are summarized in Table 14.1

* Astro Industries Model 1100 V.

† Data-Trak 5300 Programmer.

along with the equilibrium compositions (long autoclaving times) and the range of surface areas. For short autoclaving times the surface areas of the powders were high ($> 25 \text{ m}^2/\text{g}$) and $\gamma\text{-Al}_2\text{O}_3$ was the predominant phase. The approach to an equilibrium phase composition was rapid at the highest pressure (~ 5 hours) and fairly slow at the lower pressures (> 50 hours). From these four conditions, powders were available for sintering with a range of $\alpha\text{-Al}_2\text{O}_3$ contents and surface areas. In general, as the $\alpha\text{-Al}_2\text{O}_3$ content increased with autoclaving time, the surface area of the powder decreased, presumably because of the conversion of the fine $\gamma\text{-Al}_2\text{O}_3$.

From these four conditions several powders were selected at different autoclaving times for each pressure. These powders (as prepared) were pressed into pellets and sintered at 1625°C , a temperature suitably high for testing the powder's sintering characteristics and yet not too high to encounter problems with excessive and discontinuous grain growth. The results of these sintering studies are presented in Figure 14.2, in which bulk densities are plotted versus autoclaving time at each of the four pressures. The variations in $\alpha\text{-Al}_2\text{O}_3$ content and surface area of these powders with autoclaving time are also shown in Figure 14.2. (Of course, complete conversion to $\alpha\text{-Al}_2\text{O}_3$ occurs during sintering.)

This series of experiments indicates conclusively that the sinterability of autoclave alumina powders increases with increasing $\alpha\text{-Al}_2\text{O}_3$ content. In all cases in which the powder contained significant amounts of $\gamma\text{-Al}_2\text{O}_3$, poor sintering characteristics were observed. The surface area becomes an important variable after conversion to $\alpha\text{-Al}_2\text{O}_3$ (or an $\alpha\text{-KI}$ mixture) is complete. In some cases at 3100 and 4500 psi, converted powders with low surface areas ($\sim 2 \text{ m}^2/\text{g}$ at long autoclaving times) either sintered to low densities or did not sinter at all. The presence of the KI phase ($\sim 40\%$ in the 2400 and 3100 psi powders) appeared not to be deleterious to sintering in these initial experiments. Subsequent experiments, however, with powders containing essentially 100% $\text{KI-Al}_2\text{O}_3$, revealed rather poor sintering characteristics.

Table 14.1. Typical autoclaving conditions

Pressure (psi)	Temperature ($^\circ\text{C}$)	Equilibrium Phase Composition	Range of Surface Area (m^2/g)
1500	400	70% α , 30% γ	27-14
2400	420	60% α , 40% KI	26-2
3100	440	60% α , 40% KI	31-2
4500	420	90% α , 10% KI	25-2

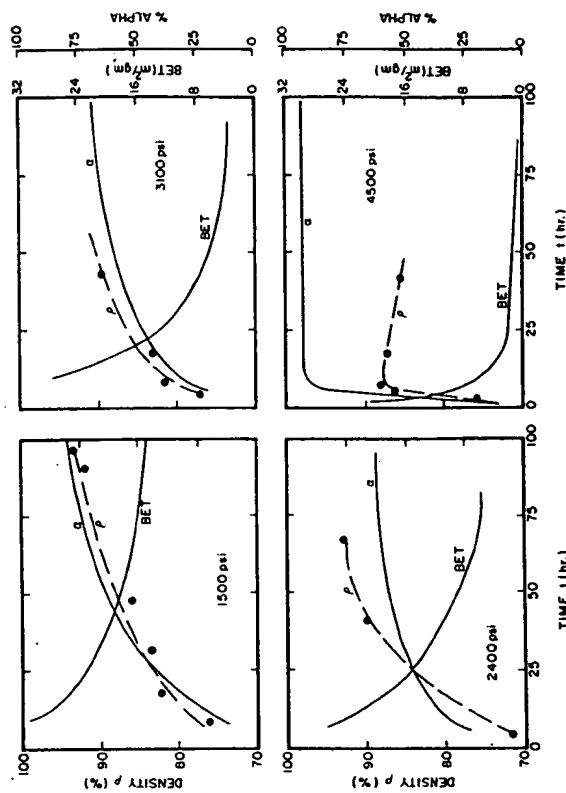


Figure 14.2. Powder properties and sintered densities versus autoclave time.

Final-Stage Sintering of Autoclave Powders

Based on the initial screening experiments (Figure 14.2), six autoclave powders were chosen for a systematic sintering study. Each powder, because of its phase composition (50 to 80% $\alpha\text{-Al}_2\text{O}_3$) and reasonably high surface area ($> 6 \text{ m}^2/\text{g}$) was believed to have a reasonable chance to be sintered in four conditions; as-prepared, milled only, doped (MgO) only, and milled and doped with MgO. Milling was introduced because of the highly agglomerated nature of the powders in the as-prepared (or autoclaved) condition. Pressed pellets of these powders in the four conditions were sintered in the temperature range between 1700 and 1900°C . For comparison, two commercial, high-purity (99.98 to 99.992%) powders were prepared in the doped condition.* One of these powders (CA) was highly agglomerated, while the other (CAF) was reported to be in an agglomerate-free state. After autoclaving, powder F was screened through a 400 mesh nylon screen with the fines retained for sintering in the four conditions. A summary of autoclaving conditions and powder characteristics for powders in this series is given in Table 14.2.

* Adolph Meller Co., Providence, Rhode Island.

Table 14.2. Autoclave conditions and properties of final stage powders

Powder	Source of Al Raw Material	Pressure (psi)	Temperature (°C)	Time (hours)	Surface Area (m ² /g)	Approximate Phase Composition
A	Ingot	1500	400	94	35	50% α , 50% γ
B	Chopped rod	1500	400	113	14	60% α , 40% γ
C	Chopped rod	3100	445	32	11	60% α , 40% KI
D	Ingot	3100	440	69	11	60% α , 40% KI
E	Chopped rod	4500	420	5.5	6	80% α , 20% KI
F ^a	Ingot	4500	425	19.5	8	70% α , 30% KI

^a Screened through 400 mesh.

In Figure 14.3A the sintered densities (percent of theoretical) at different sintering temperatures are given for the powders in Table 14.2 in the as-prepared condition. All powders exhibited rather poor sintering characteristics, as might be expected for undoped and agglomerated powders. Powder F, which had been screened to break up large agglomerates, sintered to the highest density (~97.5%). The relative ranking of the powders in terms of their densities was essentially independent of temperature. A typical microstructure of a specimen sintered in the "as-prepared" condition is shown in Figure 14.4A. In all these specimens the grains were quite small (10 to 24 μ m) and large pores were present, both on the grain boundaries and within the grains.

Sintering data for the milled-only series of powders are presented in Figure 14.3B. Two important features are to be noted. First, the relative differences in sinterability of the powders was significantly reduced by the milling procedure. However, even these small differences in reactivity appear to be significant, since the "ranking" of the powders remains roughly the same across the entire temperature range. The second important feature is that there is no increase in density with temperature, indicating that these specimens had reached their ultimate density at temperatures below 1700°C, and that sintering at higher temperatures resulted in essentially no further pore annihilation or removal. In support of this conclusion, a typical microstructure of a specimen sintered in the milled-only condition is shown in Figure 14.4B. In the entire series of samples, extremely large grains (100 to 300 μ m), each entrapping a large number of small pores, were encountered. Milling leads to the breakdown of large agglomerates and hence to the removal of large pores from the green powder compact. Small, well-dispersed pores are less effective in inhibiting discontinuous grain growth than the larger pores present in the

agglomerated structures. Furthermore, milling, by broadening the distribution of particle sizes, can lead to a larger driving force for discontinuous grain growth.⁸

The sintering data for the doped-only powders and the doped commercial powders (CA and CAF) used as a reference are shown in Figure 14.3C. Again, as in the as-prepared series, the trend of a gradual increase in sintered density with temperature was observed. Two autoclave powders (D and F) could be sintered to densities over 99% at 1900°C, while the remaining powders exhibited rather poor sintering characteristics. The commercial powders, especially the agglomerate-free powder, exhibited excellent sintering properties with the production of translucent pieces above 1800°C. It is perhaps significant that milling (Figure 14.3B) produced a greater improvement in sintered densities than did doping (Figure 14.3C), although doping alone did permit powders D and F to be sintered to a high density. These particular powders possessed the smallest agglomerates. These results indicate the effect of agglomerates and associated large pores in inhibiting the densification process.

A typical microstructure of a specimen sintered in the doped-only condition is shown in Figure 14.4C. As expected from the data in Figure 14.3C, a large number of pores remain both on the grain boundaries and within the grains. These large pores probably originate from large voids between the agglomerates in the powder compacts. Again the grains were fairly small, ranging from 15 to 35 μ m depending on the temperature. The inability of most of the doped-only powders to sinter to high densities is related to the agglomeration characteristics of the powders and possibly to a nonuniform dispersal of the dopant.

The sintering data from the doped and milled autoclave powders are presented in Figure 14.3D along with the results for the commercial powders (note that the density scale is greatly expanded). By doping and milling, virtually all the powders sintered to > 99% of theoretical density. In fact, at 1740 and 1800°C, the sinterability of powder B approached that of the commercial agglomerate-free powder, while powder D did the same at 1900°C. Virtually all the autoclave powders sintered to higher densities than the agglomerated commercial powder. Trends among the powders, although not immediately obvious from the graph, can be detected with careful scrutiny and are discussed later. The best of this series was very good indeed, with translucency comparable to that of the doped agglomerate-free commercial powder.

A typical microstructure of a 99.8% dense specimen from this series is given in Figure 14.4D. It is a classic equiaxed, nearly pore-free microstructure, with the few remaining pores trapped within grains (sometimes in

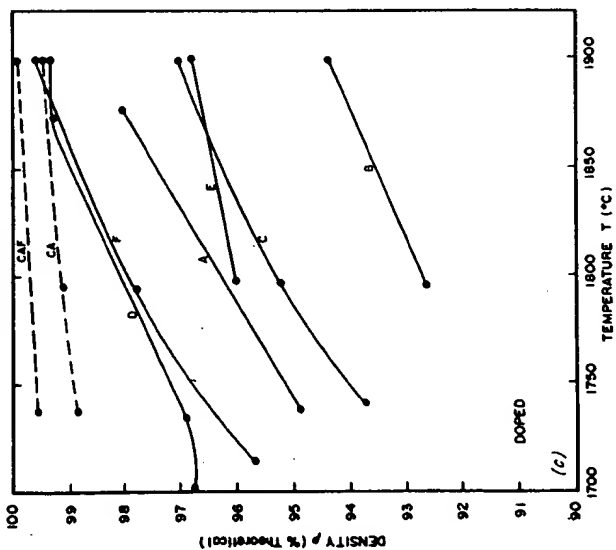
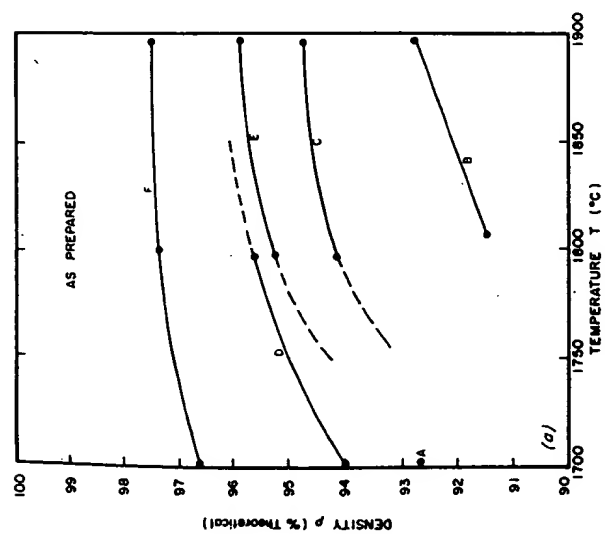


Figure 14.3. Sintered densities versus temperature: (a) as prepared, (b) milled only, (c) doped only, (d) doped and milled.

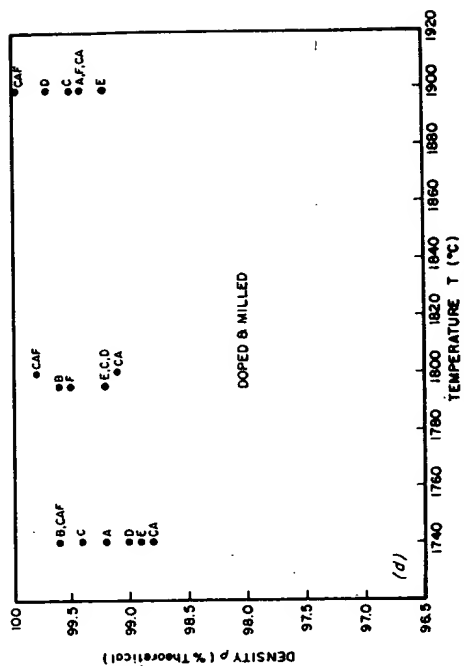
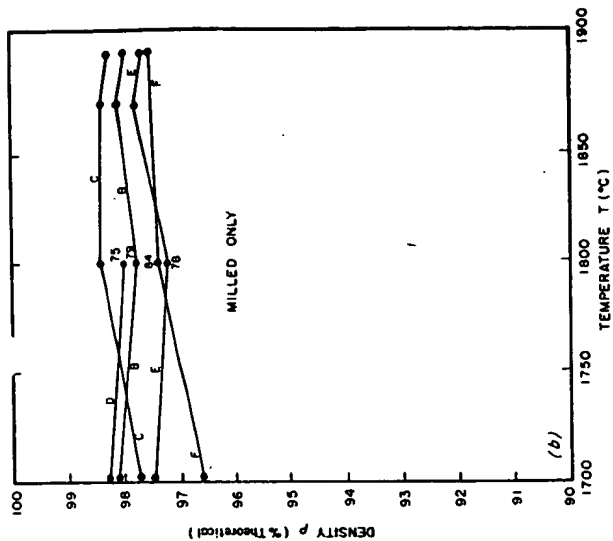


Figure 14.3. (Continued)

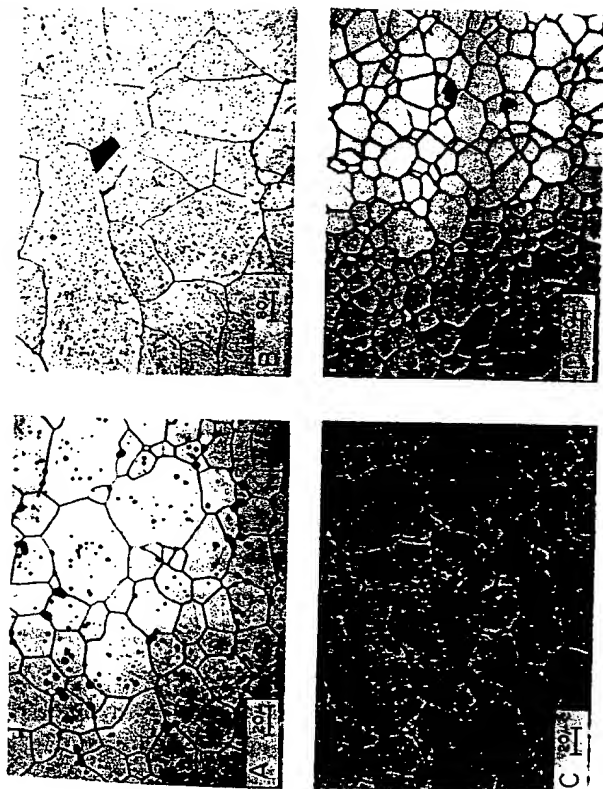


Figure 14.4. Typical microstructures; (A) as prepared, (B) milled only, (C) doped only, (D) doped and milled.

clusters). The milling step has probably done two things to promote final density: breakdown of agglomerates and dispersion of the dopant. The grain sizes of the samples in this series were between 20 and 40 μm .

Agglomeration Characteristics of Autoclave Powders

Early in the sintering program it became apparent that alumina powders prepared by autoclaving Al metal could only be sintered to theoretical density providing the powders were milled after synthesis. Preliminary examination of the autoclave powders by low-magnification scanning electron microscopy revealed that the powders were highly agglomerated, with individual agglomerates up to 20 μm in size.

Consequently, it was decided to make a thorough investigation into the nature of agglomerate formation by taking into account the variables of different Al metal reactants, autoclave temperature, steam pressure, and reaction conditions in the autoclave. In addition, a preliminary study was

conducted to determine what happens to the agglomerates during vibratory milling.

In Figure 14.5 Coulter Counter cumulative plots of agglomerate sizes are given for powders synthesized from an ingot reactant at four different pressures (1500, 2400, 3100, and 4500 psi) in steam-transfer experiments. Distribution curves for the other reactant metals were similar in shape to those at the same autoclave pressures and temperatures. At 1500 psi powders were prepared at $400 \pm 10^\circ\text{C}$ for reaction times exceeding 90 hours to insure 70 to 80% conversion to $\alpha\text{-Al}_2\text{O}_3$. For the 2400 and 3100 psi conditions the reaction times at 425 to 440°C were over 30 hours to insure 60 to 70% conversion to $\alpha\text{-Al}_2\text{O}_3$, with 30 to 40% $\text{KI-Al}_2\text{O}_3$ making up the balance. At 4500 psi the reactions times at 425°C were 7.5 hours to achieve at least a 90% conversion to $\alpha\text{-Al}_2\text{O}_3$. Included also in Figure 14.5 for comparison is the distribution curve for the deagglomerated commercial powder (CAF). The powder synthesized at 1500 psi was the "best" as-prepared autoclave powder in that its cumulative Coulter plot was closest to that of the commercial deagglomerated powder and nearly log-normal.

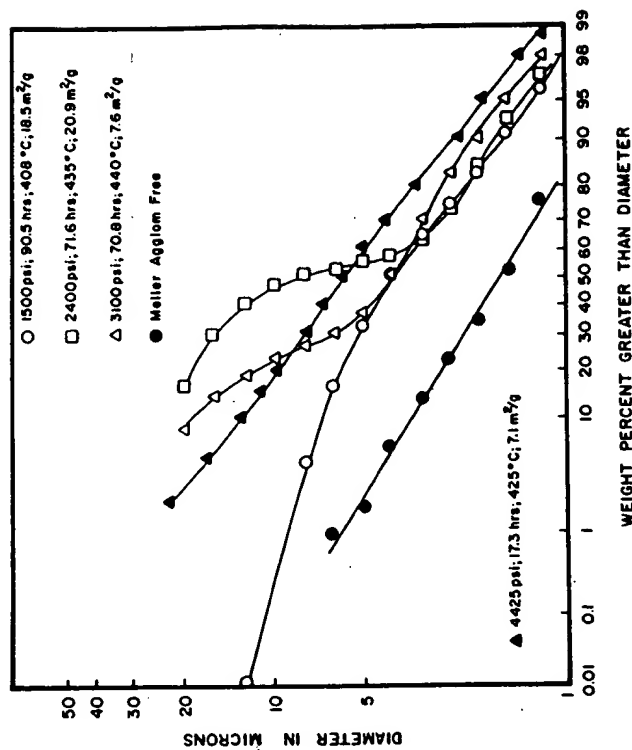


Figure 14.5. Effect of autoclave pressure on agglomerate-size distribution.

All the plots in Figure 14.5 are similar at small agglomerate sizes ($< 5 \mu\text{m}$). However, powders synthesized in the intermediate pressure regime (2400 to 3100 psi) under supersaturated conditions where $\text{KI-Al}_2\text{O}_3$ is a significant secondary phase (30 to 40%) to $\alpha\text{-Al}_2\text{O}_3$ possess sigmoidal distribution curves, and significant fractions (20 to 60%) of the agglomerates exceed $10 \mu\text{m}$ in size. This tendency for coarse-agglomerate formation is most pronounced in the powders synthesized at 2400 psi. Powders prepared at these intermediate pressures under steam-transfer conditions at saturation temperatures show only a slight tendency towards a duplex or sigmoidal agglomerate distribution. These powders are essentially pure $\alpha\text{-Al}_2\text{O}_3$, while the powders prepared under supersaturated conditions contain appreciable amounts of the KI phase. Powders prepared at 4500 psi possess a nearly log-normal agglomerate distribution curve (similar to powders prepared at 1500 psi), except that the agglomerates are much larger than those formed at the lower pressure.

To investigate the effect of Al raw material, three powders, each prepared from a different reactant (splatter, chopped rod, and ingot), were investigated. These powders were prepared by autoclaving at 1500 psi and $400 \pm 10^\circ\text{C}$ for reaction times in excess of 90 hours to insure 70 to 80% conversion to $\alpha\text{-Al}_2\text{O}_3$. Examination of these powders by low-magnification ($4000\times$) scanning electron micrographs revealed the presence of agglomerates of various sizes up to 10 to $20 \mu\text{m}$. Ultimate particle sizes, which can be estimated from the surface areas of the powders (12 to $35 \text{ m}^2/\text{g}$), are on the order of 0.05 to $0.1 \mu\text{m}$. Thus the agglomerates are considerably larger than the individual crystallite sizes. The largest agglomerates are present in the powders prepared from the splatter and chopped-rod reactants, while the smallest agglomerates form from the bulk ingot reactants.

In Figure 14.6 cumulative agglomerate-size plots from the Coulter measurements are given for these three powders. All the curves are of the same general shape. Consistent with the scanning microscope observations, powders prepared from the chopped rod possess agglomerates considerably larger (about two times as large) than those prepared from the ingot.

In Figure 14.7 high-resolution photomicrographs ($40,000$ to $60,000\times$) are presented to illustrate the fine structure of the agglomerates. Two distinct types of crystallites are present within the agglomerates: (1) relatively large (0.5 to $1.5 \mu\text{m}$) rhombohedral (hexagonal) crystals (Figure 14.7d) and (2) smaller (0.02 to $0.1 \mu\text{m}$), equiaxed crystals, where hexagonal facets or forms are readily apparent (Figure 14.7c). It appears that the micron-size crystals form from agglomerates of the smaller crystallites at an intermediate stage of the process.

Investigation of these powders by transmission electron microscopy and diffraction also revealed two forms of $\alpha\text{-Al}_2\text{O}_3$: (1) large rhombohedral

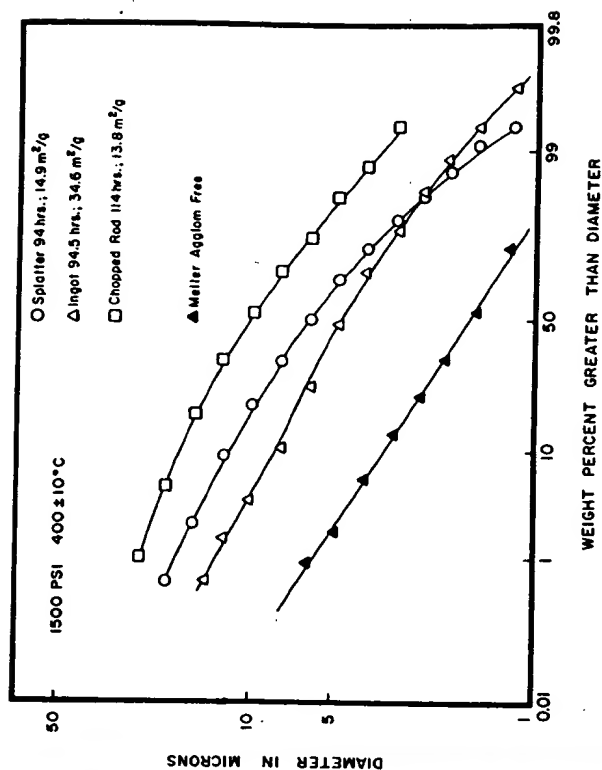


Figure 14.6. Effect of aluminum raw material on agglomerate-size distribution.

crystals $\sim 1 \mu\text{m}$ and (2) smaller crystallites $\sim 0.1 \mu\text{m}$. These observations are consistent with those obtained by high-resolution, scanning electron microscopy. Evidently the small crystallites ($\sim 0.1 \mu\text{m}$) are the "active" form of $\alpha\text{-Al}_2\text{O}_3$ reported by Krischner and Torkar.⁸ This phase is predominant at 1500 psi. For long reaction times agglomerates ($\sim 1 \mu\text{m}$) of these small crystals transform into larger single crystals of well-defined crystal habit.

For powders synthesized at higher pressures (≥ 2400 psi), very little effect was obtained by changing the initial reactant, and the data in Figure 14.5 are representative for all reactant types for these steam-transfer conditions.

The best agglomeration characteristics (i.e., log-normality and small median agglomerate sizes) were discovered in powders that had been synthesized in the two-stage, steam-transfer process. This process involved the prior formation of $\gamma\text{-Al}_2\text{O}_3$ at either 2400 or 3100 psi. The Coulter curves for these powders were nearly always log-normal and agglomerates were usually smaller than those shown for the 1500 psi powders in Figure 14.5.

As mentioned earlier, milling was found to be a necessary operation

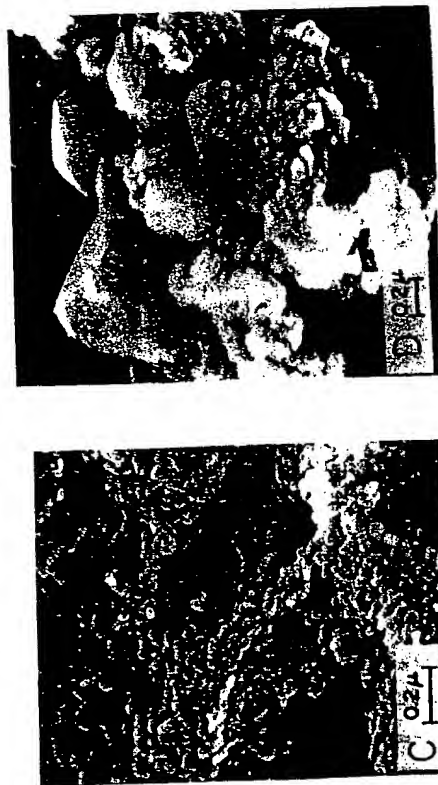
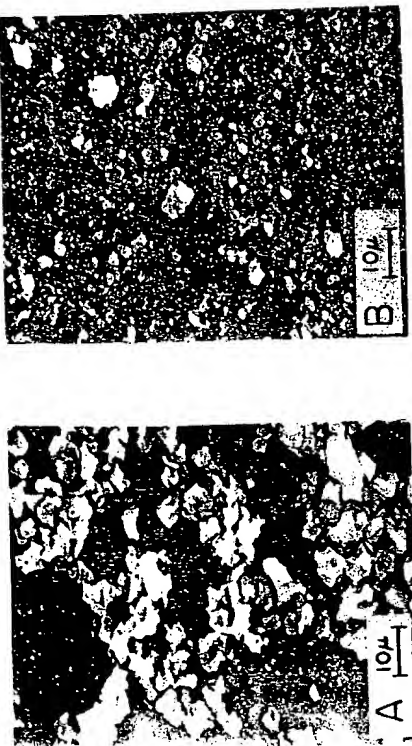


Figure 14.7. Agglomerate morphology by scanning electron microscopy: (A) as-prepared powder, (B) milled powder, (C) "active" alpha alumina, (D) transformation from "active" to "nonactive" alpha alumina.

before the autoclave powders could be sintered to theoretical density. As a result an exploratory study on the effects of milling on agglomerate size and distribution was initiated. In Figures 14.7a and 14.7b, scanning electron photomicrographs (1000 \times) show the effect of vibratory milling on a typical autoclave powder. While the effect of milling is clearly apparent, some large agglomerates (5 to 15 μ m) still persist in the powders even after comminu-

tion. The results of the milling study are summarized in Figure 14.8, in which the range of agglomerate sizes for the milled autoclave powders is indicated schematically. Powders on the low end of the indicated range exhibited the best sintering characteristics. The distribution curve for the commercial deagglomerated powder is included in Figure 14.8 for comparison.

Several facts become clear from the figure. (1) Vibratory milling reduces the median agglomerate size by about two to four times, depending on the extent of initial agglomeration. (2) All the milled powders have similar agglomerate sizes and cumulative distribution curves. The agglomerate distributions are slightly sigmoidal and indicate a pronounced coarse fraction over 5 μ m. (3) The lowest median agglomerate sizes (\sim 2.3 μ m) obtained by the laboratory milling procedure are still almost a factor of 2 higher than those in milled or deagglomerated commercial powder.

Correlation of Sintering Data with Powder Agglomeration Characteristics

The single most decisive change in sinterability of the autoclave powders was noticed at the time that milling was introduced as a process variable. Consequently, a method was sought to relate quantitatively the stage of agglomeration in an autoclave powder to its sintering characteristics. To this end, the agglomeration characteristics of the autoclave powders have been described by the use of an "agglomeration factor" described by

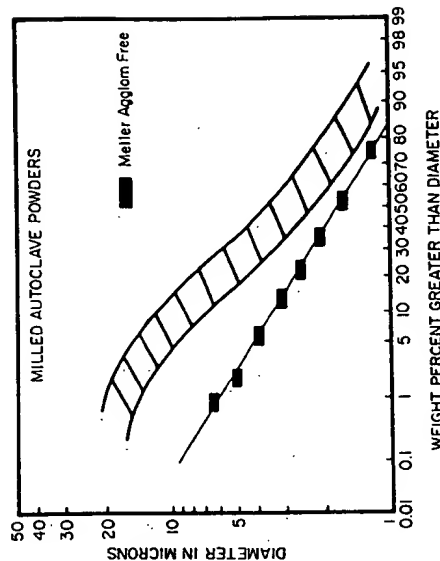


Figure 14.8. Range of agglomerate-size distributions for milled powders.

Johnson *et al.*⁶ and originally proposed by Balek.⁷ It is defined as the ratio of the median agglomerate diameter, as measured by the Coulter technique, to the equivalent spherical diameter of the individual crystallites, as measured by gas adsorption (BET). This agglomeration factor, AF(50), is defined as

$$AF(50) = \frac{\text{median agglomerate diameter (Coulter Counter)}}{\text{equivalent spherical diameter of crystallites (BET)}} \quad (1)$$

An agglomeration factor on the order of 1 corresponds to complete deagglomeration, while higher values indicate increased agglomeration. Since a number of the powders used in this study possessed a bimodal distribution of agglomerate sizes (particularly those synthesized at 2400 and 3100 psi) and since the authors agree with Cutler (Chapter 3) that it is the coarse fraction of the powder that limits its ability to be sintered to theoretical density, another agglomeration factor [AF (10)] has been defined as the ratio of the agglomerate diameter that 10% of the powder is larger than, to the equivalent spherical diameter of the individual crystallites, that is:

$$AF(10) = \frac{\text{diameter that 10\% of agglomerates are larger than (Coulter Counter)}}{\text{equivalent spherical diameter of crystallites (BET)}} \quad (2)$$

In Table 14.3 the two agglomeration factors [AF (50) and AF (10)] are given for the six powders studied in the final-stage sintering studies. The powders are ranked according to their overall sinterability in both the doped and undoped conditions for the unmilled and milled categories. The rankings were made subjectively using sintered densities and visually observed translucency as selection criteria. (Relative rankings for doped and undoped samples of the same powders were nearly always the same.)

An examination of the data in Table 14.3 reveals that, in general, the correlation between increased sinterability and decreased agglomeration factor (smaller agglomerates) is very good. In the unmilled category, the best powder was easily F, which had been screened through a 400 mesh screen; this sample had the second lowest AF(10). Powder D, which sintered not as well as powder F, had a lower AF(50) (25 to 29) but higher AF(10) (132 to 64), indicating that perhaps the assumption that the coarse fraction of agglomerates controls the sinterability is correct. The rest of the powders sintered in order of their agglomeration factors except powder B, which was made from the chopped rod raw material. It was our experience that all measurable quantities being equal, powders made from the chopped rod did not sinter as well as those synthesized from the more massive raw materials (ingot). It was noted also that powders synthesized from chopped rods of Al possess higher agglomeration factors than powders prepared from Al

Table 14.3. Correlation of sinterability with agglomeration factor

Rank	Sample No.	Agglomeration Factor (50)	Agglomeration Factor (10)	% Alpha	Surface Area (m ² /g)
Unmilled					
1	F	29	64	60	8
2	D	25	132	60	11
3	E	22	62	80	6
4	C	46	124	60	11
5	A	120	202	50	35
6	B	91	164	60	14
Milled					
1	D	17	56	60	11
2	C	16	55	60	11
3	B	23	64	60	14
4	A	62	200	50	35
Commercial					
	CAF (agglomerate free)	~12	~25	100	12-30
	CA (agglomerated)	~50	~110	100	~25

ingots. The top three powders in the unmilled category were ingot-derived powders.

In the milled category, the same general trends can be seen, with the most sinterable powders having the lowest agglomeration factors.

In Table 14.3 the agglomeration factors are given for the two commercial high-purity aluminas used in this study as standards. All through this study the best autoclave powders sintered better than the commercial agglomerate-free powder. Examination of the relative agglomeration factors shows this result to be reasonable.

Since a method of synthesis was developed in which both the surface area and the agglomerate-size distribution of an alumina powder could be obtained by specifying a particular autoclaving condition, a series of four powders, each with different agglomeration factors, AF(10), were synthesized and prepared for sintering studies. Pressures of 2400 and 3100 psi were chosen. At each pressure powders were synthesized by two techniques: (1) steam transfer at saturation and (2) two-stage steam transfer. The autoclaving times were chosen so that the surface areas of the powders would be similar. Under these autoclaving conditions the synthesized powders were pure α -Al₂O₃. The powders were doped and milled for sinter-

Table 14.4. Effect of agglomeration factor on final density

Sample	Surface Area (m ² /g)	AF(10)	Percent Theoretical Density
3100 (one-stage)	13	53	99.60
3100 (two-stage)	11	30	99.85
2400 (one-stage)	12	27	99.90
2400 (two-stage)	10	17	99.95
CAF	14	22	99.98

ing studies in the normal manner. The agglomerate-size distributions for the powders after milling are shown in Figure 14.9. Pellets of each powder were sintered at 1900°C in vacuum and the results are summarized in Table 14.4.

The results of this set of experiments clearly indicate the importance of the degree of agglomeration, as quantified by the agglomeration factor, in determining the final density of a sintered alumina ceramic. The autoclave powder with the lowest (AF(10)) agglomeration factor (2400 two-stage) sintered to the highest density (99.95%). The agglomerate characteristics of this powder were nearly identical to those of the commercial agglomerate-free powder, which also sintered to a very high density (99.98%).

Finally, for use in determining what agglomeration factors are necessary to sinter an autoclave powder of a given surface of high density, the data from a large number of sintering experiments are summarized in Figure 14.10. The density of 99.98% of theoretical was chosen arbitrarily to separate the powders into two groups. It is clear from these data that the agglomeration factor [AF(10)] alone cannot predict whether or not a given powder can be sintered to a high density. Powders with higher surface areas can evidently tolerate larger agglomeration factors than powders with smaller surface areas and still be sintered to high densities (>99.8%).

Optical Properties of Sintered Autoclave Alumina Bodies

As stated in the introduction, the objective of this study was to determine the powder characteristics that are necessary and sufficient for the achievement of high sintered densities in polycrystalline Al₂O₃. From the experiments to date, the following necessary powder properties have been identified:

1. Nearly complete conversion to α -Al₂O₃.
2. Doping with a requisite amount of MgO.

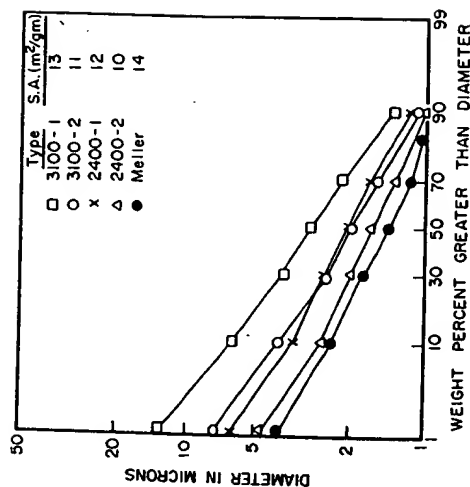


Figure 14.9. Agglomerate-size distributions for final-stage sintering experiments.

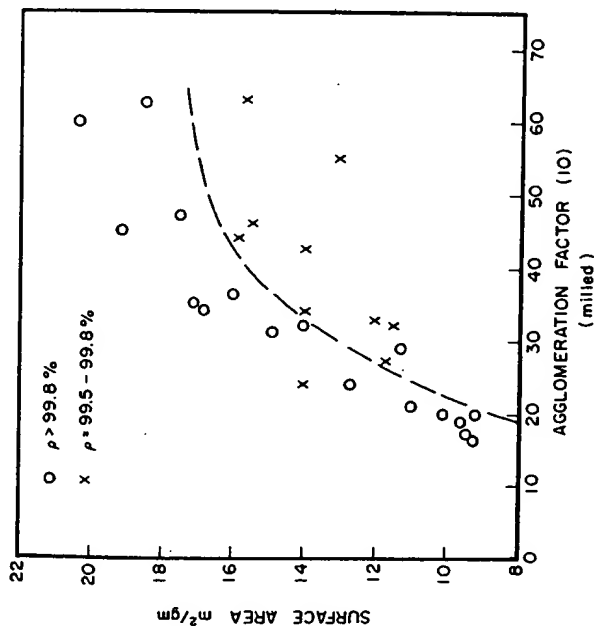


Figure 14.10. Agglomeration factor versus surface area for all doped and milled sintered specimens.

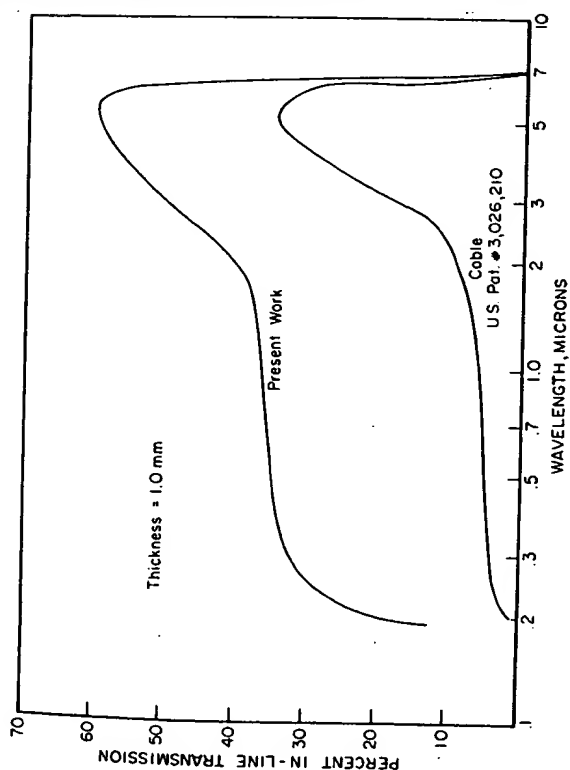


Figure 14.11. Comparison of optical transmission properties.

3. Milling to reduce the median agglomerate size below 1 to 2 μm and the AF(10) agglomeration factor below 10 to 20.
4. A powder surface area that is reasonably high ($> 8 \text{ m}^2/\text{g}$).

To achieve all these conditions, autoclave powders were prepared by the two-stage process at 2400 and 3100 psi (refer to Table 14.4). Typical in-line, optical transmission data for translucent polycrystalline Al_2O_3 (99.85 to 99.95% theoretical density) prepared from these two-stage powders are given in Figure 14.11. These data, particularly in the visible spectrum for the highest density (99.95%) specimen, are a significant improvement (two to five times) over the optical transmission data of conventionally prepared translucent alumina,⁶ shown also in Figure 14.11 for comparison.

To achieve further improvements, porosity levels will have to be reduced by approximately one order of magnitude (i.e., sintered densities over 99.99%). This result will probably require more efficient powder preparation procedures so that median agglomerate sizes are under 1 μm and no agglomerates over 2 to 3 μm exist in the powder.

CONCLUSION

The use of alumina powders synthesized hydrothermally in an autoclave has proven extremely valuable in determining which powder characteristics are important in sintering aluminum oxide to theoretical density. By choosing the appropriate autoclaving conditions, powders with varying $\alpha\text{-Al}_2\text{O}_3$ contents, surface areas, and agglomerate-size distributions were formed. A study of the sintering properties of these alumina powders has led to the conclusion that 100% $\alpha\text{-Al}_2\text{O}_3$ in the powder is necessary for doping with magnesium oxide and milling it to break up agglomerates has been reaffirmed. The sinterability of an alumina powder was also related to the relative number of ultimate particles in the agglomerates by an agglomeration factor. It was shown that the agglomeration factor required for sintering a powder to translucency varied with the surface area of the powder. The highest sintered densities (99.95%) and best optical-transmission characteristics were obtained by sintering autoclave powders synthesized by the two-stage process. These powders were completely converted to $\alpha\text{-Al}_2\text{O}_3$ and were reasonably fine (10 to 15 m^2/g). They possessed median agglomerate sizes after milling of under 2 μm and essentially a log-normal distribution of agglomerate sizes.

ACKNOWLEDGMENTS

The authors express their gratitude to I. Cisan, T. King, and W. L. Taylor of this laboratory for valuable help in sample preparation. E. S. Palik of the Quartz and Chemical Products Department and W. H. Thresh of this laboratory performed the many BET and Coulter analyses required for this work. E. Lifshin of Corporate Research and Development is responsible for the excellent SEM micrographs. The help of J. Cooper, D. McClellan, and D. C. Fries in performing the quantitative X-ray analyses is acknowledged.

REFERENCES

1. R. L. Coble, "Sintering Crystalline Solids. I. Intermediate and Final State Diffusion Models," *J. Appl. Phys.*, **32**, (5), 787-792 (1961); R. L. Coble, "II. Experimental Test of Diffusion Models in Powder Compacts," *J. Appl. Phys.*, **32**, (5), 793-799.
2. J. G. J. Peelen and R. Metselaar, "Light Scattering by Pores in Polycrystalline Materials: Transmission Properties of Alumina," *J. Appl. Phys.*, **45**, (1), 216-220 (1974).

3. (a) K. Torkar and H. Krischner, "Untersuchungen uber Aluminium-hydroxyde und-oxide," *Monatsh. Chem.*, **91**, 658-668. (1960); (b) H. Krischner and K. Torkar, "Microcrystalline Active Corundum," Vol. 1, G. H. Stewart, ed., *Science of Ceramics*, 1962, pp. 63-76, Academic Press, London.
4. R. S. Gordon and R. T. Tremper, unpublished work.
5. G. R. Chol, "Influence of Milled Powder Particle Size Distribution on the Microstructure and Electrical Properties of Sintered Mn-Zn Ferrites," *J. Amer. Ceram. Soc.*, **54**, 34-39 (1971).
6. (a) L. Berrin, D. W. Johnson, and D. J. Nitti, "High Purity Reactive Alumina Powders: I, Chemical and Powder Density," *Bull. Amer. Ceram. Soc.*, **51**, (11), 840 (1972); (b) L. Berrin, D. W. Johnson, and D. J. Nitti, "II, Particle Size and Agglomeration Study," *Bull. Amer. Ceram. Soc.*, **51**, (12), 896 (1972).
7. V. Balek, "Temperature Dependence of Characteristic Properties of α -Fe₂O₃ Powders," *J. Mater. Sci.*, **5**, (8), 714 (1970).
8. R. L. Coble, U. S. Patent 3,026,210. (1962).

15

Layer-Silicate Minerals

H. Heystek

Through the centuries the potter has always known that different clays and shales have different plastic, dry, and fired properties, but he did not know why. The dramatic advances in the development of research tools and techniques, especially in the last 25 years, allowed the ceramist to develop a basic understanding of the structure and composition of ceramic raw materials. Rapid and important changes have occurred in the manufacturing processes as a result of increased automation, production, and firing rates, and demands for improved products and quality control. This in turn requires the more accurate control and, in some cases, specific tailoring of raw material that can only be done when these materials are well characterized.

Clay mineralogists have evolved the modern concept of layer silicates (phyllosilicates) as small crystalline hydrous aluminum silicate particles, with magnesium and iron substituting wholly or in part for aluminum in some minerals, and with lithium, calcium, sodium or potassium in others. Ample evidence exists that the unique characteristics that predetermine the ceramic use and application of the layer silicates are as follows:

1. Composition and structure of the layer silicates.
2. Particle shape and size distribution.
3. Nature and amount of nonlayer-silicate constituents.

Characterization of a raw materials system requires a qualitative and quantitative mineralogical analysis and chemical analysis of all constituents, including gangue minerals, organics, and soluble salts. Therefore, knowing the mineralogy and classification scheme of layer silicates in general is particularly valuable. The behavior and properties of the raw material should also be characterized. This includes particle-size distribution, particle shape, exchangeable ions, rheological properties, workability, drying behavior, shrinkage, and strength.

In this chapter the classification scheme for layer silicates and methods for characterizing these materials are described. In 1969 the Clay Minerals Society Nomenclature Committee submitted to the Association International Pour L'Etude Des Argilles (AIEA) the latest version of a classification scheme¹ for the layer silicates. This classification (Table 15.1) represents a general agreement among clay scientists of 32 countries and is the result of many discussions at International and national clay mineral meetings and with the Commission on New Minerals and Mineral Names of the IMA (International Mineralogical Association).

LAYER-SILICATE CLASSIFICATION

The basic structural and compositional units in layer silicates are Si—O tetrahedral sheets and Mg—OH or Al—OH octahedral sheets combined to form the so-called 1:1, 2:1, and 2:1:1 layer types.

The 1:1 Types

As shown in Table 15.1, the combination of one silica tetrahedral and one octahedral sheet results in the kaolinite-serpentine group. The difference between kaolinite and serpentine is that in the former only two-thirds of the octahedral cation positions are filled by aluminum ions (dioctahedral), whereas in the latter, all the positions are filled by magnesium ions (trioctahedral).

The kaolinite group, with the general composition $Al_2Si_2O_5(OH)_4$, includes the minerals kaolinite, dickite, nacrite, and metahalloysite. This classification proposes that the term "halloysite" be used for the fully hydrated ($4H_2O$) variety and that is a layer-stacking notation be used for the structural varieties kaolinite, dickite, and nacrite analogous to the mica polymorphs. As yet no decision has been made on the appropriate symmetry symbols to be used.²

In the dioctahedral 1:1 layer silicates, there is no charge per formula unit, and very little if any substitution occurs within the structural unit.

Table 15.1. Classification scheme for layer silicates

Type	Group (x = charge per formula unit)	Subgroup	Species
1:1	Kaolinite-serpentine $x \sim 0$	Kaolinites Serpentines	Kaolinite, halloysite Chrysotile, lizardite, antigorite
	Pyrophyllite talc $x \sim 0$	Pyrophyllites Talc	Pyrophyllite Talc
	Smectite	Dioctahedral smectites	Montmorillonite, beidellite, nontronite
	$x \sim 0.25-0.6$	Trioctahedral smectites	Saponite, hectorite, sauconite
	Vermiculite	Dioctahedral vermi- culites	Dioctahedral vermi- culite
2:1	$x \sim 0.6-0.9$	Trioctahedral vermi- culites	Trioctahedral vermi- culite
	Mica $x \sim 1$	Dioctahedral micas Trioctahedral micas	Muscovite, paragonite Biotite, phlogopite
	Brittle mica	Dioctahedral brittle micas	Margarite
	$x \sim 2$	Trioctahedral brittle micas	Clintonite
2:1:1	Chlorite	Dioctahedral chlorites	Donbassite
	x variable	Di, trioctahedral chlorites	Cookeite, sudoite
		Trioctahedral chlorites	Pennine, clinochlore, prochlorite

However, some reports^{3,4} have suggested that iron and titanium can occur within the kaolinite structure. This is not the case with the trioctahedral 1:1 serpentine minerals listed below, where nickel, ferrous and ferric iron, and aluminum are substituted for magnesium in the octahedral positions, and aluminum is substituted for silicon in the tetrahedral sheet.

Chrysotile	$Mg_3Si_4O_{10}(OH)_2$ —tubular, monoclinic
Lizardite	$Mg_3Si_4O_{10}(OH)_2$ —platy, orthorhombic
Antigorite	$Mg_3Si_4O_{10}(OH)_2$ —platy, monoclinic

Amesite	$(\text{Al}_2\text{Mg}_2)(\text{Si}_2\text{Al}_2)\text{O}_{10}(\text{OH})_2$
Berthierine	$(\text{Al}, \text{Fe}^{3+}, \text{Fe}^{2+}, \text{Mg})(\text{Si}_2\text{Al})\text{O}_{10}(\text{OH})_2$
Garnierite	$(\text{Ni}, \text{Mg})_2\text{Si}_2\text{O}_{10}(\text{OH})_2$

The 2:1 Types

The 2:1 type of layer silicate refers to the fact that there is one octahedral sheet sandwiched between two tetrahedral sheets in the unit structure and includes the pyrophyllite talc, smectite, and mica groups. The different groups are a result of varying relative surface-charge densities ranging from an essentially zero electron change per formula unit for pyrophyllite and talc to a charge of about 2 for the brittle micas.

Pyrophyllite is a dioctahedral hydrous aluminum silicate, and talc is a trioctahedral hydrous magnesium silicate with limited substitution by aluminum possible.⁵ Commercial "talc" may or may not be predominantly talc, as associated minerals such as calcite, dolomite, quartz, magnesite, and chlorite are common. However, it is the commercial label of "talc" for material containing appreciable quantities of the chain silicates tremolite and anthophyllite that concerns the Health Division of the Mining Enforcement and Safety Administration (MESA) in the establishment of safety standards.⁶ Ceramists are aware of the presence of talc or tremolite $\text{Ca}_2\text{Mg}_5(\text{Si}_4\text{O}_{11})_2(\text{OH})_2$ because of the different body-pressing characteristics and fired mineralogy⁷ imparted by the particle shape or chemistry of these minerals.

For the 2:1 minerals with a layer charge of 0.25 to 0.6, there is still general national and international disagreement between smectite and montmorillonite-saponite as a group name. The present approach is to leave the question open and await the evolution of the most acceptable term through usage.

In the so-called expanded 2:1 minerals, substitution for silicon may occur in the tetrahedral sheet, while the ions commonly substituting for one another in the octahedral sheet are aluminum, magnesium, lithium, and ferrous and ferric iron. Frequently these substitutions are by ions of similar ionic radius rather than by those of the same charge. The subsequent deficit or excess charge on the layer structure is compensated by loosely held interlayer potassium, sodium, calcium, and magnesium ions and organic molecules.⁸ This explains the relatively high cation-exchange capacity of the smectites and their expansion in the *c*-direction when water enters between the unit layers. The interlamellar distances are variable, depending on water content and the exchangeable ion present. The nature of the initially absorbed water layers is considered to have a partially ordered structure⁹ that is affected specifically by the surface forces and structure of the smectites and the different exchangeable ions that may be present.

The dioctahedral smectites are montmorillonite, $\text{Al}_{1-x}\text{Mg}_x\text{Si}_4\text{O}_{10}(\text{OH})_2$, with all the substitution in the octahedral sheet; beidellite, $\text{Al}_2\text{Si}_4-x\text{Al}_x\text{O}_{10}(\text{OH})_2$, with all the substitution in the tetrahedral sheet; and nontronite, $(\text{Fe}, \text{Al})_2\text{Si}_4-x\text{Al}_x\text{O}_{10}(\text{OH})_2$, with substitution dominant in the tetrahedral sheet. The trioctahedral smectites are represented by the clay minerals hectorite, $\text{Mg}_{3-x}\text{Li}_x\text{Si}_4\text{O}_{10}(\text{OH})_2$; saponite, $\text{Mg}_{3-x}\text{Al}_x\text{Si}_4-x\text{Al}_x\text{O}_{10}(\text{OH})_2$; and saucornite, $\text{Zn}_{3-x}\text{Al}_x\text{Si}_4-x\text{Al}_x\text{O}_{10}(\text{OH})_2$.

The vermiculites have a higher charge per formula unit (0.6 to 0.9) than the smectites, and this charge deficiency is balanced by interlayer exchangeable magnesium ions. The magnesium ions are hydrated, resulting in an interlayer double sheet of water molecules and a *c*-axis dimension of 14 Å that collapses to 10 Å on heating. Most vermiculites are trioctahedral, $\text{Mg}_{3-x}\text{Fe}_x\text{Si}_4-x\text{Al}_x\text{O}_{10}(\text{OH})_2$, although the dioctahedral analogue has been reported to be common in soils.¹⁰ The industrially known macrocrystalline vermiculite, which has exfoliation properties when heated, is actually a hydrobiotite, which is an interstratified biotite and vermiculite.

The mica minerals have a 2:1 layer structure similar to the smectites except that the charge deficiency (the substitutions) is typically concentrated in the tetrahedral sheet. As counterions, potassium is tenaciously held in the interlayer space, resulting in a characteristic 10 Å basal spacing. Much isomorphous substitution occurs in addition to many possible variations in the manner of stacking of the structural units above each other. Some typical dioctahedral micas are muscovite, $\text{KAl}_2\text{Si}_4\text{AlO}_{10}(\text{OH})_2$, and paragonite, $\text{NaAl}_2\text{Si}_4\text{AlO}_{10}(\text{OH})_2$. Trioctahedral micas are phlogopite, $\text{K}(\text{Mg}, \text{Fe})_{2-x}(\text{Fe}, \text{Al})_{2-x}\text{Si}_{2+x}(\text{Al}, \text{Fe})_{2-x}\text{O}_{10}(\text{OH})_2$.

The micaceous minerals common in soils, clays, shales, and slates have been called illite as originally defined by Grim *et al.*¹¹ It has become clear, however, that the terms illite or hydromica have been used to cover a fairly wide range of minerals. These terms are considered useful field terms and presently are not included in the classification table.

The brittle micas represented by the dioctahedral variety margarite, $\text{CaAl}_2\text{Si}_2\text{Al}_2\text{O}_{10}(\text{OH})_2$, and the trioctahedral mineral clintonite, $\text{CaMg}_2\text{Al}_2\text{Si}_2\text{O}_{10}(\text{OH})_2$, have not been reported as occurring in clays. Although not of interest to ceramists, they are layer silicates and are included in the classification scheme.

The 2:1:1 Types

In chlorites the fundamental unit layer is a 2:1 structure plus an interlayer hydroxide sheet resulting in a 2:1:1 layer. The common chlorite minerals occurring in clays are trioctahedral, such as pennine, clinocllore, and donbassite, has been described by Lazarenko¹² (dioctahedral in both the 2:1 layer and the interlayer hydroxide sheet). Cookeite and sudoite¹³ are

examples of di, trioctahedral chlorites that are dioctahedral in the 2:1 layer but trioctahedral in the interlayer hydroxide sheet. It is known that the various chlorites (Mg, Fe, Al)₂(Si, Al)₄O₁₀(OH)₂ differ from each other in the kind or amount of substitution within the hydroxide sheet or the tetrahedral or octahedral sheets in the 2:1 layer. In addition, variations not only occur in the orientation of the sheets within a 2:1 layer, but also in the stacking sequence of chlorite units.

Interstratified-Layer Silicates

Considering the similarities in crystalline structure and chemical composition of the various layer silicates, it is not surprising that random and regular intimately interstratified units of two distinct species are quite common. In addition, the layer silicates usually originate as the weathered products of primary minerals, and alternation sequences such as biotite, vermiculite, chlorite, kaolinite; and mica, illite, vermiculite, montmorillonite in soils have been reported frequently¹⁴ and are supported by synthezation in laboratory experiments.¹⁵ It is to be expected, therefore, that interlaying of these minerals in various combinations would occur as a result of preferential weathering of some layers with respect to others.

No general agreement has yet been reached on the preferred terminology for interstratified minerals, but it has been suggested that with the random or irregularly interstratified-layer silicates the material should be described in terms of the component layers with the dominant component listed first, for example, "irregular chlorite-mica interstratification." Furthermore, if the minerals are regularly interstratified, distinctive names, such as corrensitite (1 chlorite/1 vermiculite), should not be used but rather the prefix "regular", for example, "regular chlorite-vermiculite interstratification." Reported in the literature are occurrences of interstratifications such as illite-montmorillonite, vermiculite-biotite, vermiculite-chlorite, mica-chlorite, montmorillonite-chlorite, saponite-chlorite, berthierite-chlorite, montmorillonite-kaolinite, and muscovite-kaolin.

LAYER-SILICATE CHARACTERIZATION

When considering the use of layer silicates in ceramic processing, we find that particle shape, fine particle size (frequently 2 μm or less), large surface area, and ion-exchange capacity of the materials are usually the principal factors that control viscosity, plasticity or workability, pressing behavior, green and dry strength, and drying shrinkage. Characterizing layer silicates as to their structural and chemical composition, particle morphology and

size distribution, and cation-exchange capacity is therefore absolutely necessary to the ceramist in designing bodies and controlling processing (Table 15.2).

The most valuable instrumental characterization techniques are X-ray diffraction, thermal methods, electron optical methods, and infrared spectroscopy. No one technique, however, is adequate on its own but should be used in combination with another and with total chemical analysis, cation-exchange capacity determinations, and surface-area measurements.

X-Ray Diffraction

Since the proposed layer-silicate classification is based on the structure and composition of these minerals, it is not surprising that X-ray diffraction has become indispensable in the identification of clay minerals. Much has been written¹⁶⁻¹⁸ on sample preparation and treatment techniques (orientation, glycolation, heating), so only brief mention is made here of the basic diagnostic parameters used to identify the different layer silicates.

The interplanar spacings normal to the (001) cleavage as shown in Table 15.3 are the most significant criteria used in X-ray differentiation between the layer silicates. The 7 Å minerals, kaolinites and serpentines, are further distinguished on the basis of their 060 reflections, which are 1.48 to 1.49 and 1.52 to 1.59 Å, respectively. This also applies to the 9.3 Å minerals, pyrophyllite talc. X-Ray diffraction patterns of the smectites (expanded 2:1 minerals) yield typical 12 to 15 Å basal spacings that change to 17 Å spacings after treatment with ethylene glycol. To separate the 14 Å chlorites and vermiculites, heat treatment followed by X-ray diffraction is used. The 14 Å spacing of chlorites persists up to 550°C, whereas at 350°C, dioctahedral and trioctahedral vermiculites show a shift of the spacing to 12 Å and 9 Å, respectively.

Frequently, samples for X-ray investigation are given extensive preparation to aid in the identification of natural mixtures of layer silicates. The material is ground, fractionated to obtain the minus 2 μm fraction, and sometimes chemically treated to remove iron or organic phases. This should be kept in mind when the bulk characterization of the material is considered, because the amount and type of the nonlayer silicate admixtures, such as free quartz, feldspar, carbonates, sulfates, oxides and hydroxides of iron, anatase, and amorphous material, could play a dominant role in its ceramic properties.

The problems of analyzing clay mineral mixtures quantitatively by X-ray diffraction are principally due to preferential orientation effects, variations in crystallinity,¹⁹ chemical composition, and particle size as well as to intimate layer interstratification. Most methods attempt to relate the diffrac-

Table 15.2. Simplified characterization of layer silicates

Mineral	Composition (%)			Cation exchange capacity (meq/100 g)	Particle		Ceramic Properties	Industrial Uses
	SiO ₂	Al ₂ O ₃	Other		Size (μm)	Shape		
Kaolinites	45	39		3-15	1-10	Hexagonal plates	White firing	Whitewares
Halloysite				10-40	0.2 x 1	Tubes	Refractory, c/32 + Low to medium: Plasticity Drying shrinkage Green strength	
Pyrophyllite	67	28		0		Plates		
Talc	63		32 MgO	0		Plates	White firing	
Smectites	55	20	Fe ₂ O ₃ MgO Li ₂ O	75-150	1	Plates	Usually red burning	Structural clay products
Vermiculite	35	15	25 MgO	100-150	2	Plates	c/04 to c/7	
Mica	55	25	5 K ₂ O	10-40	1	Plates	High: Plasticity	
Chlorites	29	20	30 MgO	10-40	2	Plates	Drying shrinkage Green strength	
Interstratified layer silicates	combinations of above			25-77	2	Plates		

Table 15.3. Interplanar spacings of layer silicates

Type	Group	Basal Spacing (Å)
1:1	Kaolinites-serpentine	7
2:1	Pyrophyllite-talc	9.3
	Smectite	12-15
	Vermiculite	14
	Mica	10-11
2:1:1	Chlorite	14

tion intensity from a given compound to its percentage in artificial mixtures²⁰ or use internal standards such as Zn(OH)₂,²¹ pyrophyllite,²² and aluminum powder.

If other techniques, such as selective dissolution analyses,²³ thermal gravimetric analyses, and cation-exchange capacities, are used in conjunction with X-ray diffraction, reasonably good quantitative mineralogical estimates can be made. Hussey²⁴ recently optimized chemical allocation to minerals within prescribed limits using a simultaneous linear equations program.

Thermal Methods

In conjunction with X-ray diffraction, thermal techniques such as differential thermal analysis,²⁵ thermogravimetry, and differential thermogravimetry are extremely useful in identifying such things as amorphous or poorly crystalline phases, organic material, pyrite, carbonates, and gibbsite. Improvements in commercially available equipment, such as increased sensitivity, atmosphere control, and registration of evolved gases, have made thermal techniques more effective in quantitative determinations. A committee on standardization established by the First International Conference on Thermal Analysis in 1965 recommended²⁶ a uniform reporting system for authors so that thermal data could be critically assessed.

Absorption Spectroscopy

Infrared absorption spectroscopy is now widely used to distinguish structural hydroxyl groups from structural and sorbed water²⁷ and is effective in investigating poorly crystallized and amorphous materials. It is a technique complementary to X-ray diffraction and thermal investigations in obtaining structural data.

Mossbauer spectroscopy²⁸ has become increasingly useful in the study of the coordination (octahedral or tetrahedral) or valence (Fe^{2+} or Fe^{3+}) of iron in layer silicates. In addition, siderite and goethite, common gangue minerals in clays and shales, can also be detected.

Ultraviolet visible spectroscopy²⁹ also shows promise as a quick method of determining the presence, location, and valance state of iron in a layer-silicate structure.

Electron-Optical Methods

Electron microscopy is of value in supplying morphological data and in the case of kaolinite (plates) and halloysite (tubes) results in conclusive identification. The use of high-resolution electron microscopy on samples that were ultramicrotomed³⁰ made possible direct photographs of the (001) atomic planes and representation of 7, 10, and 14 Å structures. This technique allows for the identification of interstratified clay minerals³¹ and the textural or fabric study of undisturbed samples of clays, shales, and slates. The scanning electron microscope with its great depth of focus is also uniquely suited to textural and fabric investigations of the fine-grained layer silicates.

A combination of selective-area electron diffraction with electron microscopy allows no one to obtain diffraction diagrams of single crystals with diameters of about 1000 Å. In addition, electron-microscope microprobe analysis⁴ can be carried out to determine the elemental composition of individual clay-mineral particles. Finally, direct electron-microscope measurements of dispersed clay particles provide a valuable check on results of standard³² particle-size-distribution methods.

Surface Area

In a clay-water system the surface area of the clay particles and the ion population in the aqueous media are the major factors affecting the properties of a slip; the extrusion or pressing of a body; and the strength, porosity, and drying characteristics of the processed ware. The most widely used method to determine surface area of fine dry particles involves the adsorption of gases as described by Brunauer *et al.*³³ (see Chapter 6). However, this technique does not record the so-called internal surfaces of the expandable 2:1 layer silicates. Simple and rapid procedures have been devised to overcome this problem, that is, measurement of the quantity of glycerol, dodecylamine hydrochloride,³⁴ or methylene blue³⁵ that is adsorbed by clays. In the last case, the cation-exchange capacity of the clay is also determined.

Cation-Exchange Capacity

Many procedures for determining the cation-exchange capacity (C.E.C.) of clays have been described in the literature, including the conventional Kjeldahl method and, most recently, the use of an ammonia electrode.³⁶ The C.E.C. of kaolinite, which is given in Table 15.2, is low³⁷ compared with that of other clay minerals but varies among different kaolinites. A detailed study of some Georgia kaolinites³⁸ has shown that their exchange capacity, surface area, and iron and titanium content increased as their crystalline stacking order decreased.

In addition to total C.E.C., it is important to determine the amount and type of naturally occurring exchangeable ions. These ions play an important role in the rheological properties and drying characteristics³⁹ of a raw material, especially in structural clay products, in which very little or no beneficiation is utilized.

NEED FOR COMPLETE CHARACTERIZATION

In all layer-silicate deposits, horizontal and vertical variability occurs to a greater or lesser degree, creating a problem for the ceramic manufacturer intent on producing products of uniform quality. In the past the practice was to use a large amount of different raw materials in a body in an attempt to offset changes in the properties of any one component. Today the trend is to use materials guaranteed by suppliers to conform to specified compositions and particular ranges of physical properties.

Much has been said and written about the characterization of "pure" layer silicates. But pure systems do not exist even with beneficiated materials such as kaolins, ball clays, and talcs used in the whiteware industry. Therefore, a suppliers data sheet should, in addition to such information as chemical analysis, percent of plus 325 mesh material, viscosity curve, and percent drying shrinkage, include a total quantitative mineralogical analysis, screen analysis, particle-size distribution to less than 1 μm , particle-shape and surface-area data, C.E.C., and exchangeable ions and soluble salts present. As an example, it is necessary to know (1) if a "talc" contains fibrous tremolite in addition to the platy talc; (2) the quantity of free quartz, calcite, or dolomite that may be present, or (3) in the case of a ball clay, how much quartz, smectite, mica, or organic material occurs with the predominant mineral kaolinite.

To the brick, clay pipe, or lightweight aggregate manufacturer, a careful mineralogical evaluation of his particular clay or shale deposit is imperative. If, for example, kaolinite, illite, chlorite, quartz, calcium carbonate,

iron hydroxide, and organic material are present, it is important to determine their quantitative distribution pattern. With additional information, such as soluble salts present, particle morphology, chemical analysis, and total size distribution available as presented in Table 15.4, a planned mining, stockpiling, blending, and quality-control program becomes feasible. In years past it was stated that this approach was too expensive for the industrial clay products industry—today it is too expensive not to do it. Once a deposit is completely characterized, it is possible to determine what compositional variables are the most critical and to concentrate on them for control purposes.

A complete detailed qualitative and quantitative characterization is also necessary of material used in rheological and viscosity studies. This must be the initial step toward developing precise methods for evaluating workability or plasticity and obtaining data that can be used in predicting or controlling the process behavior of ceramic bodies.

An aid toward a better understanding and correlation of characterization techniques and data from different laboratories should result from the Source Clay Minerals Project recently activated by the Clay Minerals Society.⁴⁰ A clay-minerals repository has been established at the Geology Department of the University of Missouri. Unbeneficiated, well-blended samples of natural clays are available for study. It is hoped that all data obtained by investigators will be accumulated in the repository for future evaluation.

Finally, it is necessary to stress again that to obtain quantitative characterization data, more than one investigative technique must be used. Also, it is imperative that the sample used for characterization be representative of the shipment, stockpile, or deposit considered for use by a consumer.

REFERENCES

1. S. W. Bailey, "Summary of National and International Recommendations on Clay Mineral Nomenclature," 1969-1970 CMS Nomenclature Committee, *Clays and Clay Minerals*, 19, 129-132 (1971).
2. S. W. Bailey, "Polymorphism of the Kaolin Minerals," *Amer. Miner.*, 48, 1196-1209 (1963).
3. D. L. Dolcater, J. K. Syers, and M. L. Jackson, "Titanium as Free Oxide and Substituted Forms in Kaolinites and Other Soil Minerals," *Clay Clay Miner.*, 18, 71-79 (1970).
4. W. B. Jepson and J. B. Rowe, "The Composition of Kaolinite—An Electron Microscope Microprobe Study," presented at 23rd Annual Clay Minerals Conference, Cleveland, Ohio, 1974.

References

5. I. S. Stemple and G. W. Brindley, "A Structural Study of Talc and Talc-Tremolite Relations," *J. Amer. Ceram. Soc.*, 43, 34-42 (1960).
6. A. Goodwin, ed., *Proc. Symp. Talc*, 1974, Bureau of Mines IC 8639.
7. H. Heystek and E. Planz, "Mineralogy and Ceramic Properties of Some California Talcs," *Bull. Amer. Ceram. Soc.*, 43, (8), 555-561 (1964).
8. J. Moum, C. N. Rao, and T. S. R. Ayyar, "A Natural 17 A Montmorillonite-Organic Complex from Alleppey, Kerala State—India," *Clays Clay Miner.*, 21, 89-95 (1973).
9. P. F. Low, "Physical Chemistry of Clay—Water Interaction," *Adv. Agronomy*, 13, 269-327 (1961).
10. G. Brown, "The Dioctahedral Analogue of Vermiculite," *Clay Miner. Bull.*, 2, 64-70 (1953).
11. R. E. Grim, R. H. Bray, and W. F. Bradley, "The Mica in Argillaceous Sediments," *Amer. Miner.*, 22, 813-829 (1937).
12. E. K. Lazarenko, "Donbassites, A New Group of Minerals from the Donetz Basin," *C. R. Acad. Sci., USSR*, 28, 519-521 (1940).
13. G. Muller, "The Identification of Dioctahedral Four Layer Phyllosilicates (Sudoit, in the series Sudoit-Chlorite)," *Int. Clay Conf., 1st. London*, 1963, Pergamon, pp. 121-130.
14. M. J. Wilson, "The Weathering of Biotite in Some Aberdeenshire Soils," *Mineral. Mag.*, 35, 1080-1093 (1966).
15. R. Roy and L. B. Sand, "A Note on Some Properties of Synthetic Montmorillonites," *Amer. Miner.*, 41, 505-509 (1956).
16. G. Brown, ed., *The X-Ray Identification and Crystal Structure of Clay Minerals*, Mineralogical Society, London, 1961.
17. D. Carroll, *Clay Minerals: A Guide to Their X-ray Identification*, The Geological Society of America, Special Paper 126, 1970.
18. K. G. Sansom and D. White, "Aggregation and Dispersion in Clays with Particular Reference to Montmorillonites," *Trans. Br. Ceram. Soc.*, 70, 163-165 (1971).
19. D. N. Hinkley, "Variability in Crystallinity Values Among the Kaolin Deposits of the Coastal Plain of Georgia and South Carolina," *Clays Clay Miner., 11th. Proc. Natl. Conf.*, 1963 pp. 229-235.
20. A. D. Buck, "Quantitative Mineralogical Analysis by X-ray Diffraction," U.S. Army Engineer Waterways Experiment Station Miscellaneous Paper C-72-2, February 1972.
21. M. H. Mossman, D. H. Freas, and S. W. Bailey, "Orienting Internal Standard Method for Clay Mineral X-Ray Analysis," *Proc. Natl. Conf., Clays Clay Miner., 15th*, 1967 pp. 441-453.
22. J. M. Roberts, "X-Ray Diffraction and Chemical Techniques for Quantitative Soil Clay Mineral Analysis," Ph.D. Thesis, Dept. Civil Eng., Pennsylvania State University, June 1974.
23. C. A. Alexiades and M. L. Jackson, "Quantitative Clay Mineralogical Analysis of Soils and Sediments," *Proc. Natl. Conf., Clays Clay Miner., 14th*, 1966, pp. 35-52.
24. G. A. Hussey, "Use of a Simultaneous Linear Equations Program for Quantitative Clay Analysis and the Study of Mineral Alteration During Weathering," Ph.D. Thesis, Department of Agronomy, Pennsylvania State University, August 1972.
25. R. C. Mackenzie, ed., *The Differential Thermal Investigation of Clays*, Mineralogical Society, London, 1957.

26. H. G. McAuliffe, "Recommendations for Reporting Thermal Analysis Data," *Anal. Chem.*, **39**, 4 (1967).
27. V. C. Farmer, ed., *The Infrared Spectra of Minerals*, The Mineralogical Society, London, 1974.
28. C. E. Weaver, J. M. Wampler, and T. E. Peculi, "Mossbauer Analysis of Iron in Clay Minerals," *Science*, **156**, 504-508 (1967).
29. S. W. Karickhoff and G. W. Bailey, "Optical Absorption Spectra of Clay Minerals," *Clay Clay Miner.* **21**, 59-70 (1973).
30. J. L. Brown and M. L. Jackson, "Chlorite Examination by Ultramicrotomy and High Resolution Electron Microscopy," *Clays Clay Miner.* **21**, 1-7 (1973).
31. T. Yoshida, "Elementary Layers in the Interstratified Clay Minerals as Revealed by Electron Microscopy," *Clays Clay Miner.*, **21**, 413-420 (1973).
32. O. Lauer, Grain Size Measurements on Commercial Powders," issued by Alpine Ag, Augsburg, 1966.
33. S. Brunauer, P. H. Emmett, and E. Teller, "Adsorption of Gases in Multimolecular Layers," *Amer. Chem. Soc.*, **60**, 309-319 (1938).
34. G. W. Kalb and R. B. Curry, "Determination of Surface Area by Surfactant Adsorption in Aqueous Suspension, I. Dodecylamine Hydrochloride," *Clays Clay Miner.*, **17**, 47-57 (1969).
35. P. T. Hang and G. W. Brindley, "Methylene Blue Adsorption by Clay Minerals. Determination of Surface Areas and Cation Exchange Capacities (Clay-Organic Studies XVIII)," *Clays Clay Miner.* **18**, 203-212 (1970).
36. E. Busenberg and C. V. Clemency, "Determination of the Cation Exchange Capacity of Clays and Soils Using an Ammonia Electrode," *Clays Clay Miner.* **21**, 213-217 (1973).
37. R. E. Grim, *Clay Mineralogy*, McGraw-Hill Book Co., Inc., New York, 1953.
38. H. H. Murray and S. C. Lyons, "Further Correlations of Kaolinite Crystallinity with Chemical and Physical Properties," *Proc. Natl. Conf., Clays Clay Miner.*, **8th**, 1960 pp. 11-16.
39. R. T. Bailey, "Measurement of Strength of Unfired Clays and Ceramic Bodies," *Trans. Br. Ceram. Soc.*, **71**, 272-277 (1972).
40. W. F. Moll, "Source Clay Minerals Project," *Clays Clay Miner.*, **21**, 71-73 (1973).

PART THREE

PARTICULATE-WATER SYSTEMS

Most ceramic processes at some stage involve a particulate-liquid state. Water is the most commonly used liquid for such purposes. The interactions of the aqueous phase with ceramic particles, the properties of slips, the rheology of solutions, and the phenomena associated with mixing and drying are important areas covered in the chapters that follow.

16

The Structure of Water and its Role in Clay-Water Systems

W. G. Lawrence

Many papers have been published on the effects of adding different ions on the properties of clay-water systems. However, little has been written from the viewpoint of the structure of water and how it relates to the effects in clay-water systems. In this chapter a review is presented of water structure and how ions affect this structure. This information is used to discuss possible structural effects in the interaction of aqueous solutions with clay surfaces.

WATER STRUCTURE

The water molecule has the configuration shown in Figure 16.1.¹ The H—O—H bond angle is $104^{\circ} 40'$, and therefore the molecule is a dipole with a dipole moment of 1.71 to 1.97×10^{-18} esu. Because of its dipole nature, a water molecule attracts ions and other molecules, forming combinations that are not related to electron transfer or sharing even though

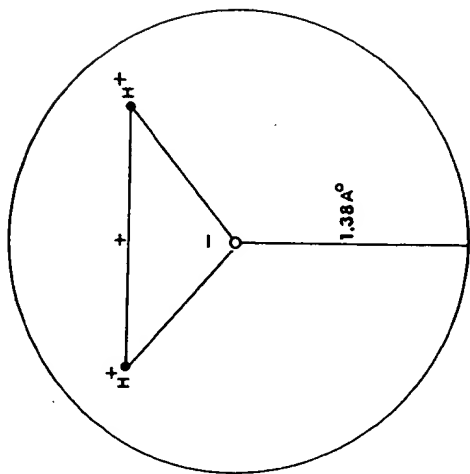


Figure 16.1. Structure of the water molecule.

these combinations may be stoichiometric. Among the types of interactions possible,² two that are important for our consideration are: (1) dipole-dipole attractions between water molecules, resulting in some type of structure found in associated liquids and (2) ion-dipole attractions, which are responsible for the fact that ions in water solutions are not separate entities but are associated with and travel with a certain number of water molecules.

With water and other liquids having angular intensity distributions of the molecular field, the arrangement of molecules deviates from a close-packed system. The molecules arrange in a structure that best satisfies the bond angles determined by the angular charge distribution.³

The details of the structure of water have been extensively investigated and many theories have evolved. However, this subject is still controversial and no single theory is widely accepted. Two general approaches have been to view water as association complexes and as defective crystalline systems. Association complexes are disconnected clusters of water molecules. By means of X-ray diffraction studies, Morgan and Warren⁴ showed that the average number of nearest neighbors around a water molecule is 4.6. This is close to the tetrahedral coordination of ice. However, they cautioned that their results cannot be interpreted in terms of certain number of neighbors at certain distances. At any given time, any given molecule may have more or less than four neighbors, and these neighbors may be at a continuous

variety of distances. The authors therefore suggest the possibility of having disconnected association complexes.

Lennard-Jones and Pople⁵ maintain that the presence of broken intermolecular bonds necessary for "disconnected association complexes" must be rejected because of thermodynamic considerations. They maintain that the weak, diffuse second maxima in the radial distribution curve is due to distortion rather than breaking of intermolecular bonds.

Eyring⁶ and Frenkel⁷ have introduced the concept of lattice defects to the water structure. Eyring considers the water molecules to be associated with regular lattice positions, but some of those lattice sites may be left vacant ("hole" theory of liquids). These holes or vacancies can then diffuse or move by the process of a molecule jumping into the vacant position and leaving behind another hole.

Figure 16.2 represents the idealized water lattice. Each water molecule has tetrahedral coordination, having four nearest neighbors at a distance of 2.85 Å at 1.5°C and 3 Å at 83°C.⁴ Megaw⁸ indicates the hexagonal axial ratio $c/a = 1.6289$ at 0°C. This is somewhat lower than the ideal ratio for the tetrahedral structure, which is $c/a = \sqrt{8/3} = 1.6330$. The unit cell of ice at 0°C is $a_0 = 4.5135$ Å and $c_0 = 7.3521$ Å, with each unit cell containing four molecules.

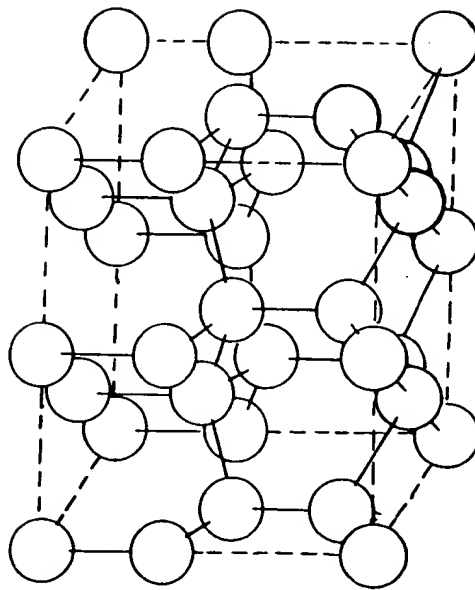


Figure 16.2. The ideal water lattice.

ROLE OF THE HYDROGEN BOND

Forslind⁸ has discussed in detail the process of molecular association and the hydrogen bond. For a hydrogen bond to form between two electronegative atoms, it is first necessary that there be a close approach of these atoms. The dipole-dipole interaction between water molecules themselves is apparently a slow, sluggish type based on the difficulty of nucleation of the condensed vapor phase. It appears that the initial approach between water molecules is due to the van der Waals and molecule dipole attraction until interpenetration of electron clouds is achieved. At this point the attraction between the hydrogen nuclei and the two unpaired electrons of the oxygen provides a significant orienting influence.

It is known that the hydrogen atom may be simultaneously attracted to two or more electronegative atoms, such as fluorine, oxygen, chlorine, and nitrogen. The hydrogen atom may thus act as a bond between oxygens. When a hydrogen is bonded to one electronegative element, such as oxygen in the case of H_2O , the strong pull exerted by the atom on the bonding electrons leaves an effective positive charge on the hydrogen sufficient to cause attraction for a second electronegative atom.

Frank and Wen⁹ present a resonance scheme for the hydrogen bond in water. This considers resonance between three types of structures. It recognizes that hydrogen bond formation is an acid-base interaction. When a bond is formed, one molecule becomes more acidic and the adjacent molecule more basic than the unbonded water molecule. Thus a cooperative-type bonding is pictured such that when one bond is formed the tendency is for several to form and when one bond is broken a cluster breaks down. This gives a picture of flickering clusters of various sizes and shapes first bonded or associated and then breaking down. The half-life of such clusters is 10^{-10} to 10^{-11} seconds, which corresponds to the dielectric and bulk relaxation time of water but is long enough (10^2 to 10^3 times a molecular vibration period) to be meaningful.

Tanford¹⁰ presents facts of interest in consideration of the water structure. The heat of sublimation of ice is 12,200 cal/mole at $0^\circ C$. Of this, 1400 cal/mole represents the heat required to give the water molecules the random motion they possess in the gaseous state (translational enthalpy). The remainder, 10,800 cal/mole, must be the energy required to break the hydrogen bonds holding the structure together. The heat of fusion of ice is 1400 cal/mole, only about 15% of the energy required to break the hydrogen bonds in the crystal. It is therefore obvious that liquid water must retain a considerable amount of structure, which is maintained by the hydrogen bonding mechanism.

These observations and the previously cited data that show the O—O

distance to be approximately 2.85 Å and the O—O bond angle to be tetrahedral indicate that the water molecules are hydrogen bonded, with the hydrogen located 1.00 Å from one oxygen and 1.76 Å from the other. It can jump from one equilibrium position to the other, which can temporarily create H_3O^+ and OH^- ions. A small number of these ions are always present in ice crystals.

EFFECTS OF NONPOLAR MOLECULES

Frank and Evans¹¹ present data on the temperature coefficient of solubility of simple nonpolar gas molecules in water. From such data the entropy loss in the solution process is calculated. For nonpolar gases in nonpolar solvents the entropy loss is in the 10 to 15 cal/degree mole range. In water, however, it is in the 25 to 40 cal/degree mole range. Since the entropy of a system is an indication of the degree of disorder present, the extra entropy loss in aqueous solutions of nonpolar gases means the water structure has become more ordered under the influence of the dissolved nonpolar molecules. As Frank and Evans describe it "the water builds a microscopic iceberg round the nonpolar molecule." This writer prefers to say that the water structure is immobilized adjacent to such molecules.

If one considers the flickering-cluster type of water structure in which the half-life of the cluster (10^{-10} to 10^{-11} seconds) depends on the resonance scheme of the hydrogen bonding, it seems reasonable that such a cluster having one side or a portion of its surface adjacent to a nonpolar molecule with which hydrogen bonding is not possible would have a longer half-life. It is being protected. This concept is borne out by the observation that the entropy loss is greatest for the larger solute molecules, such as radon and chloroform.

EFFECT OF IONS ON WATER STRUCTURE

If nonpolar molecules show such effects as previously described, one can imagine the greatly exaggerated effects that might be produced by ionic solutions. In addition to the possible effect of surface alone, there is the intense electric field due to the ionic charge. When small distances are involved, the field intensity is around 1 million V/cm, assuming the bulk dielectric constant of water (80) gives a field of 0.5×10^6 V/cm at a distance of 6 Å from the center of a monovalent ion. This value is certainly minimal, since the dielectric constant of water has been shown to be approximately 2 to 4 around a point charge such as an ion.

Frank and Wen⁹ present the simple model shown in Figure 16.3 for the structure modifications in water produced by a small ion. From previous discussions regarding the dipole nature of the water molecule, dipole-dipole interactions, ion-dipole interactions, and the cooperative type of bonding in water resulting in association of the liquid in clusters having a certain half-life, a picture of the effect of such ions emerges.

The high field strength of the ion will lead to immobilization of the nearest-neighbor water molecules as a result of the ion-dipole attraction (*A*). This type of attraction is shown in Figure 16.4. The second region (*B*) is one in which the arrangement is more random than normal, and the outer region (*C*) contains normal water having the normal water structure as a result of dipole-dipole attraction and hydrogen bonding. The inner region (*A*) will contain water molecules highly oriented with the negative side of the water molecule towards the positive side pointing away from the positive ion. The outer region (*C*) will maintain the tetrahedral arrangement as previously described. The intermediate region between *A* and *C* may be of finite width and will contain no more orientation disorder than either *A* or *C*.

Frank and Evans¹¹ believe that region *A* is composed of nearest-neighbor water molecules, with the extent of region *A* being increased by a small or multiply charged ion. Such ions induce additional structure (entropy loss)

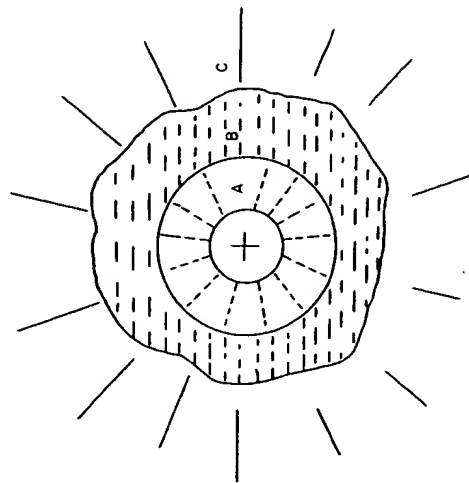


Figure 16.3. A simple model for the structure modifications produced by a small ion: (*A*) region of immobilization of water molecules due to ion-dipole attraction, (*B*) region of structure breaking, (*C*) structurally "normal" water.

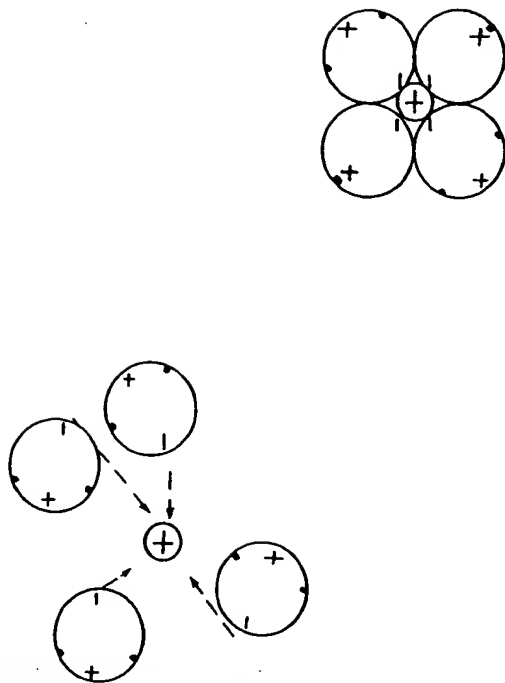


Figure 16.4. Ion-dipole attraction.

beyond the first water layer. Thus region *A* may be enlarged at the expense of region *B*. The large single charged ions, such as Cs^+ and I^- , seem to have enough structure-breaking effects to enlarge region *B* at the expense of *A* and may in some cases eliminate it entirely. This effect would involve entropy gain.

Thus it is possible to predict the structure-altering properties of a considerable number of ions from entropy data. Cations smaller or more highly charged than K^+ are structure formers, becoming more so the smaller and more highly charged they are. K^+ itself is slightly structure-breaking, with this tendency increasing through Rb^+ and Cs^+ . F^- is a structure former, but the other halide anions, which are larger, are structure breakers. OH^- is a structure former, and NO_3^- , ClO_4^- , and SO_4^{2-} are structure breakers.

In any concept pertaining to the effect of ions on water structure, the structure formed about any ion is not a rigid, firmly held layer resembling ice; instead it is a water structure, which on the average has a higher degree of order than does normal water. Although hydration numbers have been assigned to various ions to indicate how many water molecules are associated with an ion, the values are quite variable and meaningless. Thus one may find hydration numbers for the Na^+ ion varying from 71 to 1.

Samoilov¹² has provided an excellent dynamic picture of the hydration

process. His concept is based on the logical approach that the water molecules are in constant motion; thus continual exchange may take place between the water molecules closest to the ion and those farther away. The magnitudes defining the frequency of exchange of water molecules near the ions are the quantitative characteristics of ion hydration in solutions.

If a water molecule is in the immediate vicinity of other water molecules, then it spends an average time γ in the immediate vicinity of a certain selected water molecule. Time γ is the average time the two molecules remain as neighbors. The activation energy of exchange or the energy required to separate them as neighbors is E . The time a water molecule is in the immediate vicinity of an ion will not be γ , because an ion is not energetically equivalent to a water molecule. The time a molecule is associated with the ion will be γ_i where $\gamma_i \neq \gamma$ mainly because of the difference in the activation energy of exchange. This energy is no longer E but $E + \Delta E$.

γ_i/γ and ΔE are quantitative characteristics of ion hydration in solutions. If an ion firmly holds the water molecules it means the time a molecule spends in the vicinity of the ion is much greater than the time it spends associated with another water molecule and γ_i/γ is large. For permanent bonding to an ion $\gamma_i/\gamma = \infty$. Any decrease in γ_i/γ indicates weakening of the ion bond with the water molecules of the solution. γ_i/γ is related to ΔE by the relation $\gamma_i/\gamma = \exp(\Delta E/RT)$; thus finding ΔE for the ion results in a quantitative description of its hydration.

Samoilov¹² worked out the method for calculating ΔE for individual ions from experimental data on self-diffusion in water and the temperature coefficients of ion mobility in solutions and arrived at the following relationship

$$\frac{1}{U_i} \frac{dU_i}{dT} + \frac{1}{T} - \frac{1}{D} \frac{dD}{dT} = \frac{\Delta E}{RT^2} \frac{1}{1 + \alpha \exp(\Delta E/RT)}$$

where U_i = ion mobility

D = self-diffusion coefficient of water

α = numerical coefficient with a value of 0.0655

The values of ΔE and γ_i/γ calculated from the above equation are given in Table 16.1.

Table 16.1. ΔE and γ_i/γ for some monatomic ions (21.5°C)

Ion	Li ⁺	Na ⁺	K ⁺	Cs ⁺	Cl ⁻	Br ⁻	I ⁻	Mg ²⁺	Ca ²⁺
$\Delta E(\text{kcal/mole})$	0.73	0.25	-0.25	-0.33	-0.27	-0.29	-0.32	2.61	0.45
γ_i/γ	3.48	1.46	0.65	0.57	0.63	0.61	0.58	86.3	2.16

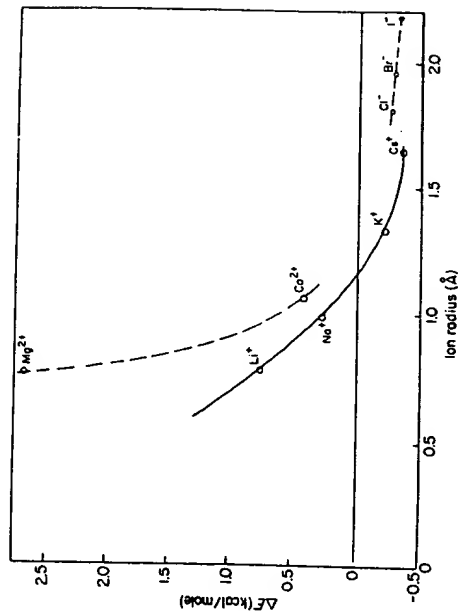


Figure 16.5. ΔE versus ion radius for some cations and anions.

The values for ΔE given in Table 16.1 are plotted against ionic radius in Figure 16.5. It is seen that ΔE decreases with increasing radius and that at approximately 1.20 Å, radius changes from positive to negative. In this case $\gamma_i/\gamma \sim 1$ and a water molecule in the vicinity of an ion is more mobile than in pure water. This provides a concept termed "negative hydrogen." Wang,¹³ in studying self-diffusion of water in solutions of KCl and KI, showed them to be higher than in pure water, which is supporting evidence of the negative hydration concept.

RELATIONS BETWEEN ION CHARACTERISTICS AND IMMOBILIZATION OF WATER MOLECULES

An increase in the ordered structure of water involves entropy loss, while a decrease in structure involves entropy gain. It is thus possible to use the entropy of solution ΔS which is the entropy change (calories per degree per mole) in passing the hypothetical mole fraction of unity in solution, as a basis for correlating structure effects of ions. It is thus possible to calculate ΔS° , which is the contribution to the entropy change ΔS due to the effect of ions on the structure of water. Robinson and Stokes¹⁴ present data for a number of ions (Table 16.2).

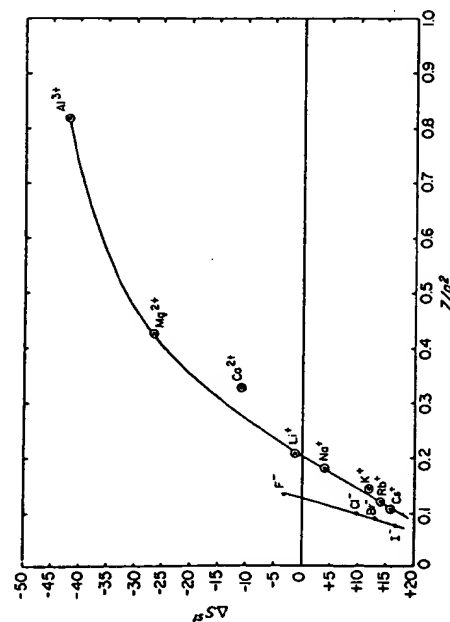
For all alkali and halide ions except the smallest (Li⁺ and F⁻) ΔS° indi-

Table 16.2. Entropy of solution of monatomic ions in water¹⁶.

Ion	ΔS	ΔS°
F ⁻	-40.9	-3.5
Cl ⁻	-26.6	+10.2
Br ⁻	-22.7	+13.9
I ⁻	-18.5	+17.9
H ⁺	-38.6	
Li ⁺	-39.6	-1.1
Na ⁺	-33.9	+4.0
K ⁺	-25.3	+12.0
Rb ⁺	-23.1	+14.1
Cs ⁺	-21.3	+15.7
Mg ²⁺	-84.2	-27.6
Ca ²⁺	-65.5	-10.7
Al ³⁺	-133.	-42.0

cates an increase of disorder in the structure of water, being the greatest for the largest ions (Cs⁺ and I⁻). The negative ΔS° for Mg²⁺, Ca²⁺, and Al³⁺, on the other hand, indicates these ions would promote a long-range order in the water structure.

There is obviously a size effect involved as well as a charge effect. A plot of the ionic field strength z/a^2 for the ions versus ΔS° from Tables 16.2 and

Figure 16.6. ΔS° versus z/a^2 for several cations and anions.

16.3 is shown in Figure 16.6. This shows good correlation for cations and anions if they are considered separately. One would expect some difference between the two because of the difference in bonding mechanism between a cation-H₂O and an anion-H₂O molecule. In the case of the anion-H₂O molecule interaction, the role of the hydrogen bonding must be considered. The hydrogen bonding mechanism is most effective between anions having high electronegativity. Thus F⁻, being the most electronegative of the anions in this series, has an abnormally high effect as far as increasing the ordered structure of water. This effect is reduced as the electronegativity of the anion is in the series of F⁻, Cl⁻, Br⁻, and I⁻ decreased.

Bingham¹⁸ presents data (Table 15.3) on the ionic elevations of fluidity for several cations. The plot of this data versus z/a^2 (Figure 16.7) for the ions results in a curve very similar to that of Figure 16.6. The correlation of this data is not as good as shown by the plot of the entropy ΔS° data.

Table 16.3. Ionic elevations, Δ , and z/a^2 for selected cations¹⁸.

Cation	R_c	R_{H_2O}	$R_c + R_{H_2O}$	a^2	z/a^2	Δ
Cs ⁺	1.69	1.38	3.07	9.42	0.106	2.59
Pb ²⁺	1.21		2.59	6.72	0.299	2.6
Rb ⁺	1.48		2.86	8.20	0.122	1.86
NH ₄ ⁺	1.43		2.81	7.9	0.126	0.44
K ⁺	1.33		2.71	7.35	0.136	0.28
H ⁺	1.38		2.76			-6.41
Ag ⁺	1.26		2.64	6.96	0.144	-8.91
Na ⁺	0.95		2.33	5.44	0.184	-9.60
Hg ²⁺	1.10		2.48	6.25	0.32	-12.2
Li ⁺	0.60		1.98	3.92	0.255	-14.0
Ba ²⁺	1.35		2.73	7.19	0.279	-25.3
Sr ²⁺	1.13		2.51	6.30	0.318	-28.4
Ca ²⁺	0.99		2.37	5.61	0.356	-31.3
Co ²⁺	0.72		2.10	4.42	0.450	-34.4
Cu ²⁺						-34.7
Mn ²⁺	0.80		2.18	4.75	0.421	-34.8
Cr ²⁺	0.65		2.03	4.12	0.730	-35.4
Zn ²⁺	0.74		2.12	4.50	0.444	-35.6
Mg ²⁺	0.65		2.03	4.12	0.484	-36.5
Cd ²⁺	0.97		2.35	5.52	0.361	-37.2
Ni ²⁺	0.69		2.07	4.30	0.465	-39.1
Be ²⁺	0.31		1.69	2.86	0.70	-45.0
Cr ³⁺	0.65		2.03	4.12	0.730	-49.6
Fe ³⁺	0.60		1.98	3.92	0.77	-52.2
Al ³⁺	0.50		1.88	3.53	0.855	-70.5

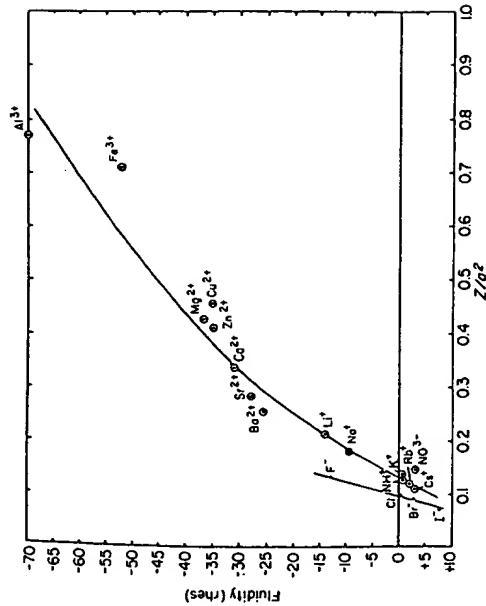


Figure 16.7. Ionic elevation of fluidity versus z/d^2 for several cations and anions.

Bingham's data indicate the Na^+ ion to be a structure promoter, while the entropy data show it to be a structure modifier. The structure-promoting tendency of ions is related to the field strength of the ion; the higher the field strength the greater the surface promotion due to the ion. This involves the size and charge of the ion, as the smaller the size and larger the charge, the greater the field strength.

THE "WATER HULL"

The concept of immobilization of water induced by ions of high charge and small size provides a basis for the mechanism of formation of a "water hull" or "solvated layer" surrounding a clay particle. Since the surface of a clay crystal is composed of positive and negative sites resulting from the exposure of such ions as Al^{3+} , Si^{4+} , O^{2-} , and OH^- , one would expect such active sites to exert an influence on the surrounding water. This influence might be even more pronounced, since these ions at the surface are part of a rigid crystal lattice. They have the capability of attracting the dipole water molecule or other positive or negative ions to satisfy their charge deficiency. The extent or thickness of the water layer built up will depend on the types of ions associated with the liquid. Those ions that are structure promoters, such as Ca^{2+} , Mg^{2+} , and Al^{3+} as shown in Figure 16.8, will result in a

larger, thicker solvated layer being built up around the particle. This would be comparable to enlargement of area *A* in Figure 16.3. This concept has been verified in part by East¹⁶ who has calculated the water-film thickness from shrinkage measurements and volume water loss. For a kaolinite in the size range 0.4 to 0.8 μ , the water-film thickness was 80 Å for H-kaolin, 86 Å for Na-kaolin, and 106 Å for Ca-kaolin. The experimental techniques involved in the precise measurement of these thicknesses are extremely difficult and these values are only qualitative indications of size that serve to confirm the theory.

The influence of the size of ions on their ability to enhance the development of the water structure has been pointed out by many investigators.

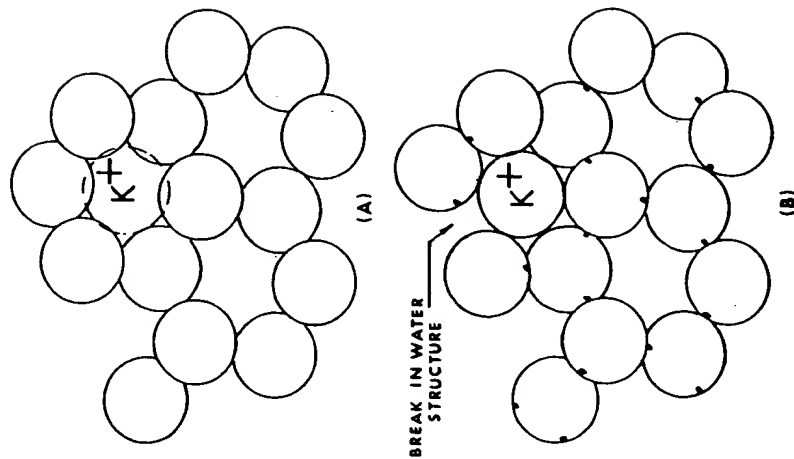


Figure 16.8. Water structure showing size of K^+ ion with respect to hole in hexagonal ring.

Forslind³ suggests that small ions that fit into the water structure without disrupting it would enhance its development. Larger ions would be expected to retard its development. From the data presented, the critical size radius for a monovalent cation is approximately 1.36 Å. This is in close agreement with the size of the "hole" in the hexagonal water structure. Ions such as K^+ or Cs^+ , being larger than this critical size, would disrupt this structure (Figure 16.8) unlike those ions that are smaller or more highly charged such as Ca^{2+} , Mg^{2+} , and Al^{3+} (Figure 16.9), which would retain the structure.

The extent or thickness of the water layer built up around a clay particle depends on the type of ions associated with the water, with such properties

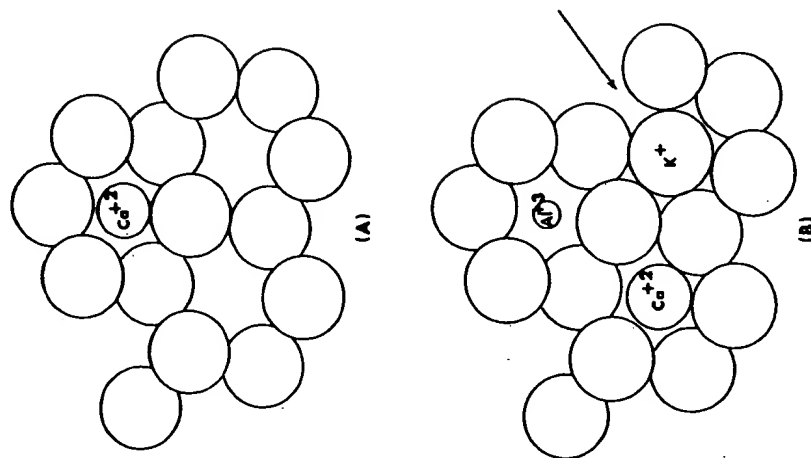


Figure 16.9. Accommodation of Ca^{2+} and Al^{3+} in water structure.

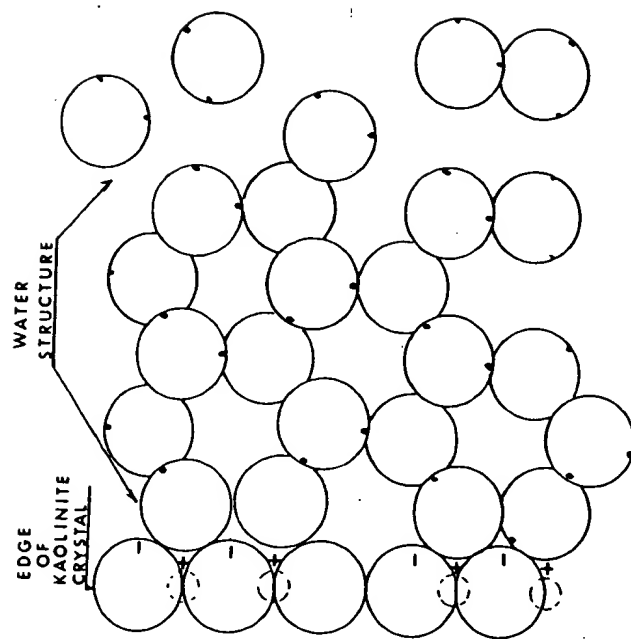


Figure 16.10. Kaolinite surface (left) and buildup of hexagonal water structure on this surface.

as plasticity and viscosity being greatly affected. In systems having small particle size, large surface area, and high solids content, the separation distance between particles may approach the water-film thickness. The properties of this interparticle water determine the behavior of the system.

The excellent geometric fit between the kaolinite crystal and the ice structure has been pointed out by Mason.¹⁷ Because of the small ($\sim 1.1\%$) misfit with ice, kaolinite is a natural effective nuclei for ice formation. Thus one would expect very little disorder at the kaolinite-water interface and good bonding between the two. Figure 16.10 shows the buildup of the water structure on the edge of a kaolinite crystal and the good fit and the hexagonal ring arrangement of the water molecules. Figure 16.11 shows the effect of the large K^+ ion on the structure. It is obvious that the addition of such ions disrupts the structure and prevents its buildup to any great distance, and it can be seen that it would take little force to shear such a system.

Figure 16.12 shows the case for the Ca^{2+} ion as the impurity. This strengthens the structure and enhances its development to larger distances,

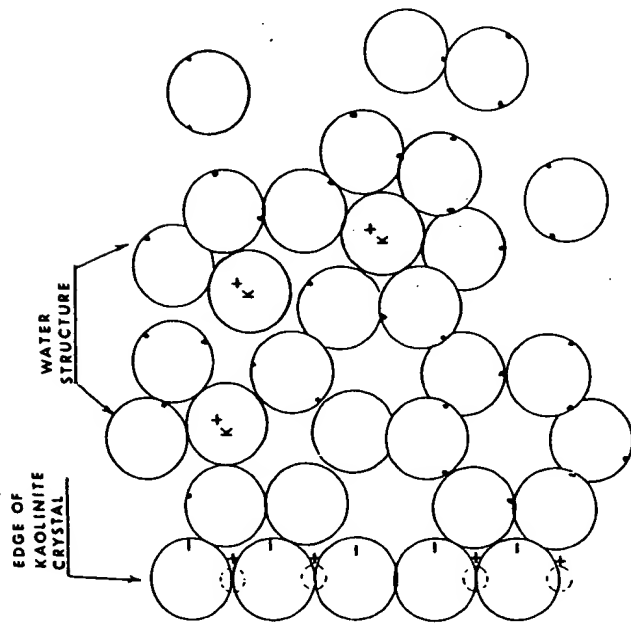


Figure 16.11. Weakening of water structure adjacent to kaolinite crystal surface by K^+ ion.

and if such a structure reaches dimensions approaching the interparticle distance, high forces would be required to shear the system.

CONCLUSIONS

It is obvious from this discussion that there is no one theory of water structure that completely explains its behavior. The theory proposed to explain the effect of ions on the structure as related to the behavior of clay-water systems is certainly not applicable in all instances. If size is a controlling influence, with the suggested 1.36 Å being critical, it does not explain the fact that the viscosity of clay suspensions is reduced equally by Li^+ , Na^+ , K^+ , and Cs^+ as shown by Johnson and Norton.¹⁸

As a ceramist studies the water structure it becomes evident that there are similarities between the water and glass structures. Both have tetrahedral coordination with oxygens bonded by a cation in a random network having only short-range order. The addition of the large monovalent ions disrupts or weakens the structure in both cases. The addition of the smaller

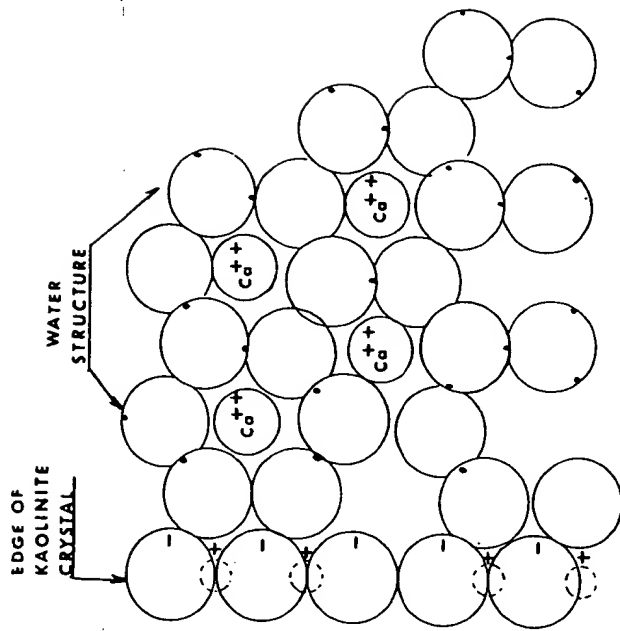


Figure 16.12. Water structure adjacent to kaolinite crystal surface containing Ca^{++} ions.

multiply charged ions strengthens the structure of each. Theories have been presented pertaining to the structures of water and glass that have nearly identical concepts, Tilton¹⁹ on glass structure and Pauling²⁰ on the water structure. Water containing high concentrations of ions, when cooled, becomes increasingly viscous and freezes without crystallization into a glasslike material.

Further clarification must await the development of techniques for more detailed study of the nature of the water structure in the immediate vicinity of ions and clay-particle surfaces.

REFERENCES

1. J. D. Bernal and R. H. Fowler, *J. Chem. Phys.*, **1**, 515 (1933).
2. T. Moeller, *Inorganic Chemistry*, Wiley, New York, 1952, p. 187.
3. E. Forslind, "A Theory of Water," Swedish Cement and Concrete Research Institute at the Royal Institute of Technology, Stockholm, 1952.
4. J. Morgan and B. E. Warren, *J. Chem. Phys.*, **6**, 666 (1938).

5. J. Lennard-Jones and J. A. Pople, *Proc. Roy. Soc. London, Ser. A.*, **205**, 155 (1951).
6. H. Eyring, *J. Chem. Phys.*, **4**, 283 (1936).
7. J. Frenkel, *Kinetic Theory of Liquids*, Clarendon Press, Oxford, 1946.
8. H. D. Megaw, *Nature*, **134**, 900 (1934).
9. H. S. Frank and Wen-Yong Wen, "Interactions in Ionic Solutions," *Discuss. Faraday Soc.*, **24**, 133-140 (1957).
10. C. Tanford, "The Structure of Water and Aqueous Solutions," *Temp. Measurement Control Sci. Ind.*, **3**, 123-129 (1963).
11. H. S. Frank and M. W. Evans, *J. Chem. Phys.*, **13**, 507 (1945).
12. O. Ya Samoilov, "A New Approach to the Study of Hydration of Ions in Aqueous Solutions," *Discuss. Faraday Soc.*, **24**, 141-146 (1957).
13. J. H. Wang, *J. Phys. Chem.*, **58**, 686 (1954).
14. R. A. Robinson and R. H. Stokes, *Electrolytic Solutions: Measurement and Interpretation of Conductance, Chemical Potential and Diffusion in Solutions of Simple Electrolytes*, Academic, New York, 1955, p. 50.
15. E. C. Bingham, *J. Phys. Chem.*, **45**, 885 (1941).
16. W. H. East, "Fundamental Study of Clay: X, Water Films in Monodispersed Kaolinite Fractions," *J. Amer. Ceram. Soc.*, **33**, 7, 211-218 (1950).
17. B. J. Mason, "The Growth of Snow Crystals," *Sci. Amer.*, **1**, 204 (1961).
18. A. L. Johnson and F. H. Norton, "Fundamental Study of Clay: II Mechanism of Deflocculation in the Clay-Water System," *J. Amer. Ceram. Soc.*, **24**, (6) 189-203 (1941).
19. L. W. Tilton, "Noncrystal Ionic Model for Silica Glass," *Jr. Res. Natl. Bur. Stand.*, **59**, (2) 139 (1957).
20. L. Pauling, *The Nature of the Chemical Bond*, Cornell University Press, Ithaca, New York, 1960, p. 464.

17

Particle-Size Distribution and Slip Properties

G. W. Phelps
M. G. McLaren

Casting slips are fluid suspensions of one or more particulate ceramic materials dispersed in a liquid (usually water) at high solids volume by deflocculating agents. A casting operation involves consolidation of suspended solids into a semirigid mass through removal of a portion of the liquid by an absorbent mold. Casting-slip suspension particles are normally predominantly noncolloidal ($>0.5 \mu\text{m}$), although some colloidal material must be present to insure slip stability and good rheological qualities.

Deflocculation of clay and clay-based aqueous suspensions by alkali hydroxides and hydrolyzable alkali salts has received detailed attention,^{1,2} as has the role of organic³ and inorganic⁴ polyions in promoting deflocculation of clay slips. The potential-determining functions of hydrogen and hydroxyl ions in deflocculation of oxide slips are well established.⁵⁻⁸ Selective adsorption of organic polyions in deflocculation of metal oxides has also been thoroughly investigated.⁹⁻¹²

Although interrelationships between rheological and deflocculation properties and slip casting have been the subject of a great many studies,¹³⁻¹⁷ the part played by particle size in general and by particle-size distribution in

particular seems to have received little attention in the literature.^{18,19} This discussion deals with literature of polydisperse systems and the role of particle-size distribution in governing deflocculation and rheology of ceramic suspensions.

SLIP RHEOLOGY AND PARTICLE-SIZE DISTRIBUTION

Some slips move easily at slower rates of shear but resist stirring at higher speeds, assuming a dry, grainy appearance. When allowed to stand quietly the dry-appearing slip returns to its original shiny, fluid state. This phenomenon is termed dilatancy,²⁰ although shear hardening has been found to occur in advance of actual volume increase in a number of systems,²¹ so some authorities²² prefer the term "shear thickening." Other kinds of slip become progressively more fluid as shearing rate rises, and upon cessation of stirring these systems thicken more or less rapidly. This phenomenon is usually termed "pseudoplastic," although some observers recommend the more general expression "shear thinning."²²

Alumina Slips

Calcined alumina powders with different particle-size distributions were compared for their flow behavior as slips. The flow characteristics were measured with a capillary tube viscometer (Cooke-Harrison).^{22,23} Size distributions were determined by a sedimentation technique (Numinco Sedigraph 5000, Micromeritics Instrument Co.) after the powder was dispersed with sodium hexametaphosphate in water in a Waring Blendor. For rheology measurements, a powder was deflocculated in water with Darvan 7. A "practical loading limit" was determined by the ability of a 0.1 hp mixer (Lightnin', Mixing Equipment Co., Inc.) to continue stirring the slip. All slips studied were loaded to this limit. Each powder, therefore, was characterized by a different limit.

Three alumina powders were studied individually and in two combinations: a "coarse" alumina, a "fine" alumina, and a commercial casting grade alumina. The combinations were a 4% fine alumina-96% coarse alumina mixture and a calculated body comprised of a mixture of casting-grade alumina, coarse alumina, and fine alumina. The particle-size distribution for the five resulting powders is given in Figure 17.1a.

The flow curves for the five slips are shown in Figure 17.1b. The coarse alumina was strongly shear thickening and, in fact, would not increase in flow rate at shear stresses above about 400 dynes/cm². The casting-grade alumina was slightly shear thickening. The fine alumina, in contrast, was shear thinning.

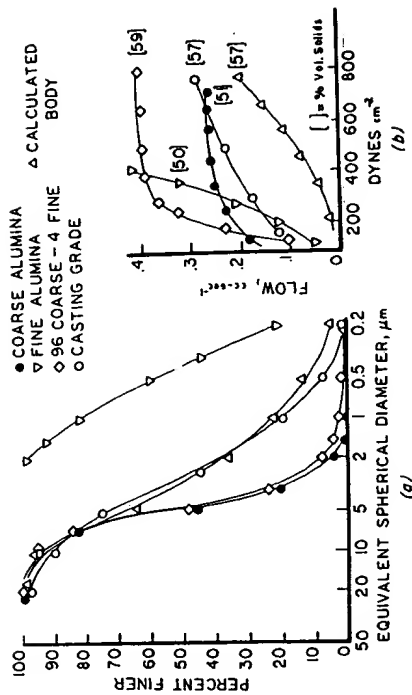


Figure 17.1. Particle-size distribution and rheology of alumina slips: (a) particle-size distribution and (b) flow behavior for different aluminas deflocculated in water.

Adding 4% fine alumina to the coarse alumina did not change the shear-thickening character possessed by the coarse alumina alone. However, the mixture flowed more rapidly at each shear stress (a decrease in the apparent viscosity). The calculated body was less fluid than the commercial casting alumina slip and showed moderate shear thinning.

The loading limits for the five alumina slips are noted in brackets in Figure 17.1b. The fine and coarse powders, having narrow size distributions, had a lower loading limit than the other three powders.

Quartz Slips

Figure 17.2a gives distributions for two air-elutriated quartz powders (A and B), each having minimal colloid and narrow size distribution. Slips deflocculated with sodium silicate in water attained volume loadings for quartz A and B of 48 and 50% percent, respectively. The flow rate-stress curves in Figure 17.2b show strong shear thickening. An equal parts blend of A and B had an extended distribution and gave a slip with much higher flow rate than did either component powder.

Whiteware Slips

Most whiteware casting bodies are heterogeneous mixtures of clays, ground feldspathic minerals, and powdered silica. Typical of such formulas are the sanitaryware bodies. Figure 17.3 gives particle-size distribution and the rheology data for the ball-clay component, the kaolin component, and the

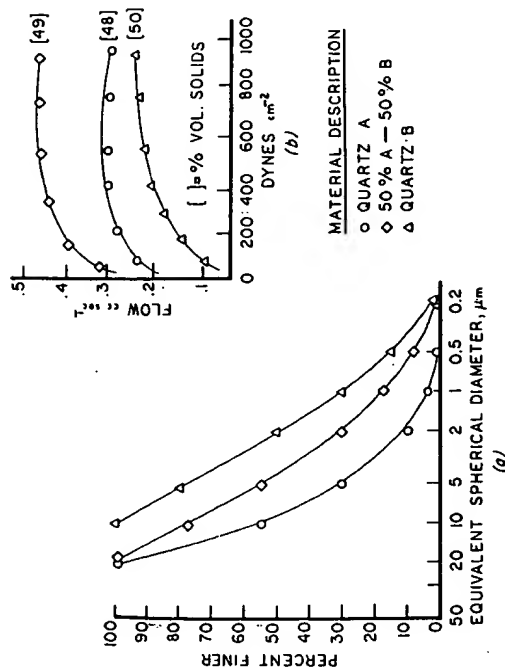


Figure 17.2. The effect on slip fluidity of combining dilatant slips prepared from two different narrow-size-range distributions of quartz (quartz A and quartz B); (a) size distribution and (b) flow behavior.

nonplastic component of a sanitaryware body. The clay components and nonplastic components each had narrow distributions.

The high-surface ball clay could be loaded only to 43% solids by volume and the slip was typically shear thinning. The low-area kaolin gave shear thickening at 49% solids by volume, while the very-low-area nonclay powder slip was strongly shear thickening at 52% solids.

A body was prepared by mixing the components. This mixing gave the very broad size distributions shown in Figure 17.3. The body exhibited moderate shear-thinning rheology and could be loaded to 54%. This slip could be cast, while none of the individual component slips would qualify as a sanitary-ware slip in terms of rheology and loading.

Occasionally the replacement of a particular low-specific-surface material by another of the same mineral character and surface area but having a different particle distribution results in markedly different defloculation response and slip rheology.²⁶ Figure 17.4 describes such an occurrence; in this instance the nonclays component of a sanitary-ware casting body (inverted triangles) was changed from a jointly ground feldspar-quartz (open circles) to a blend of separately ground (diamonds) feldspar and quartz. The distribution of the replacement body (upright triangles) in the intermediate range of sizes showed an apparently modest change. However,

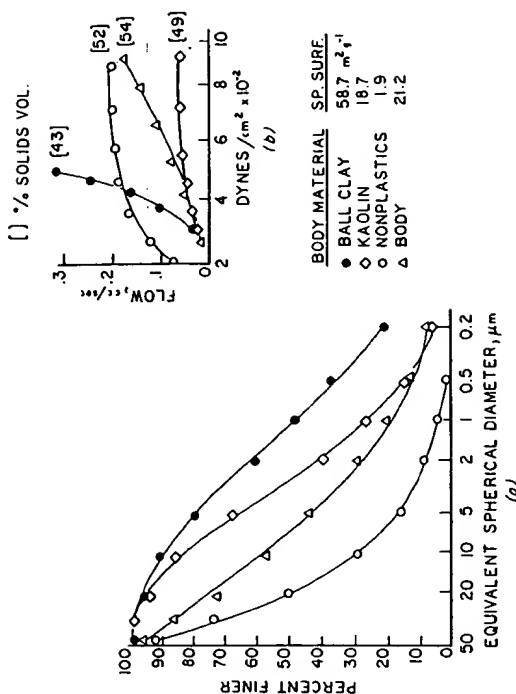


Figure 17.3. Size distributions (a) and flow behavior (b) of ball clay, kaolin, and nonplastic components of a sanitary casting body. The solid volumes represent pourable loading limits of defloculated aqueous slips. Specific surface areas are: (1) ball clay, $58.7 \text{ m}^2/\text{g}$; (2) kaolin, $18.7 \text{ m}^2/\text{g}$; (3) nonplastics, $1.9 \text{ m}^2/\text{g}$; and (4) body, $21.2 \text{ m}^2/\text{g}$. Numbers in brackets are the percent solids by volume.

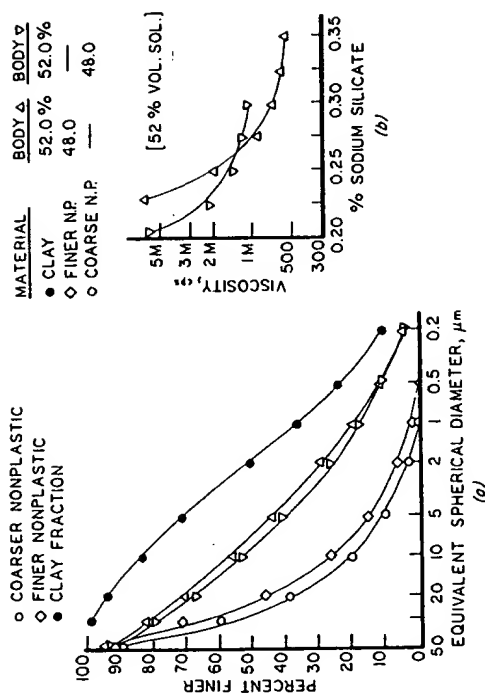


Figure 17.4. Sanitaryware casting body coinciding with moderate variation of intermediate-range particle-size distribution caused by a change in nonplastics component size distribution: (a) size distributions and (b) flow behavior with sodium silicate added.

the deflocculation curves for the respective bodies (Figure 17.4b) indicates a decided increase in initial-flow deflocculant requirement and much greater fully deflocculated fluidity for the body with separately ground nonplastics. Analogous rheological changes also occur where coarse china clays are interchanged in high-solids whiteware casting bodies.

FLOC STRUCTURE IN COMMERCIAL CASTING SLIPS

Commercial casting slips are usually maintained in a state of deflocculation that allows moderate thickening with time. Control laboratories in commercial plants use various flow-tube and rotational viscometric devices for consistency and gel-rate measurements. In Figure 17.5 are given deflocculation-curve and thickening-rate data for a commercial sanitaryware formula, obtained with the commonly used Gallenkamp²⁸ and Brookfield²⁷ rotational viscometers. Gel-rate data were determined with the Gallenkamp by rotating its flywheel through 360°, releasing it, recording degrees of overswing past the zero point for fresh slip, and then allowing the spindle to stand for 6 minutes in the cocked position before releasing again. The dif-

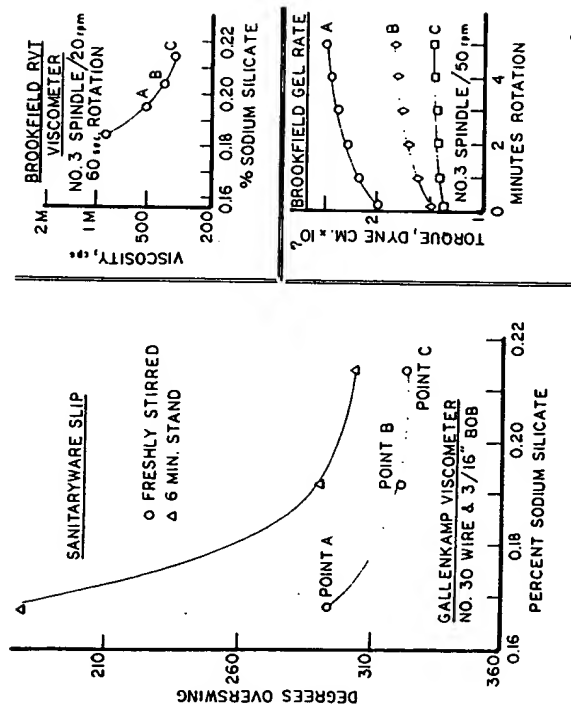


Figure 17.5. Rheological data for a commercial lot of sanitaryware slip using the Gallenkamp and Brookfield RVT rotational viscometer.

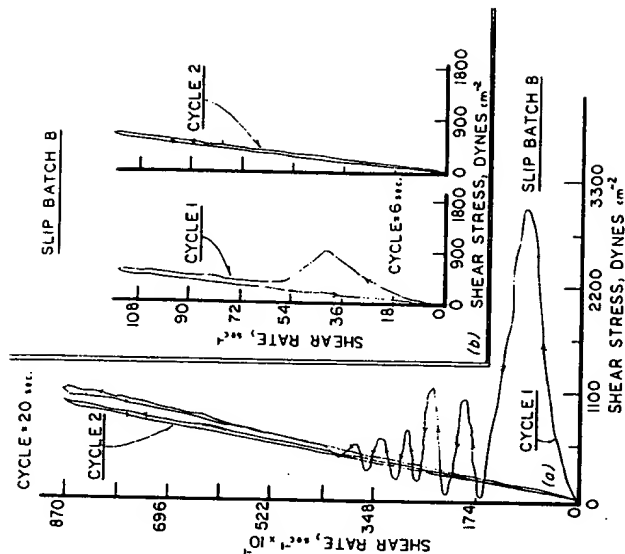


Figure 17.6. Shear rate-shear stress curves for a commercial sanitaryware slip using a Ferranti-Shirley cone-plate viscometer under two different conditions: (a) high shear and slow cycle of 20 seconds, (b) low shear and rapid cycle of 6 seconds.

ference between fresh and aged slip overings was reported as "thixotropy." Brookfield time-thickening data were obtained by allowing the spindle to rotate at constant speed over a period of time and observing the increase in torque.

A research viscometer, the Ferranti-Shirley coneplate instrument,²⁸ was used in obtaining the rate of shear-shear stress curves on slip B shown in Figure 17.6. Two sets of runs were made, one at high shear rate (0/500/0 rpm in a 20 second cycle) and another at low shear rate (0/30/0 rpm in 6 seconds). In each case the up-and-down cycle was repeated immediately following the initial cycle. The marked differences in curve configuration between first and second cycle traces of Figure 17.6 prompted an experiment in which a previously cycled (0/500/0 rpm) sample was left on the plate while cone and plate were separated and then repositioned. The sample was protected with a damp cloth to prevent moisture loss and allowed to stand 15 minutes, and the two-cycle sequence was repeated. The

curves obtained were similar to the original first and second high-shear-rate cycle traces. Beazley²⁹ has proposed that data of this nature show the slip to be in a state of aggregated, liquid-holding flocs (consisting of particles held together by a combination of coulombic and van der Waal's forces), forming a network. The initial impact of shearing shows strong stressing that breaks the network into individual flocs, each of which contains considerable liquid. Breaking of the flocs frees some liquid and extends the distribution of particles so that a sudden reduction in stress occurs. Subsequent oscillations, as rate of shear increases, are joint consequences of increasing stress and alternating shear thickening from Brownian-motion-induced particle contacts and continuing shear breakdown. The more gradual application of shear diagrammed in the insert graph of Figure 17.6 indicates, according to Moore,³⁰ an approach to equilibrium between breakdown and restructuring. Once the structure has been completely disrupted, there must be a period of time before it reforms, thus accounting for the disappearance of the bulge on second cycle traces. The reappearance of the bulge on "aged," previously cycled samples is evidence of time thickening.

CASTING RATE VERSUS PARTICLE SIZE AND SURFACE AREA

Casting rate, consistent with good drain, release, and a state of plastic firmness of the cast, is of primary concern to the manufacturing plant.¹⁸ Particle size has long been recognized as of prime importance in controlling rate of cast formation. One observer¹⁸ noted that the percentage of particles finer

BODY P.S. v. CAST RATE

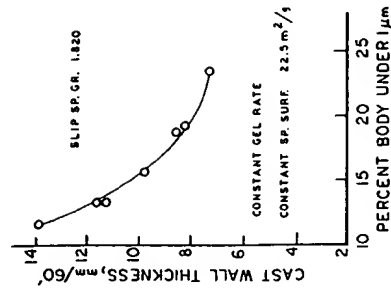


Figure 17.7. Effect of intermediate-range particle-size variation on rate of cast of organic-free sanitary-ware casting body at constant slip weight, gel rate, and specific surface.

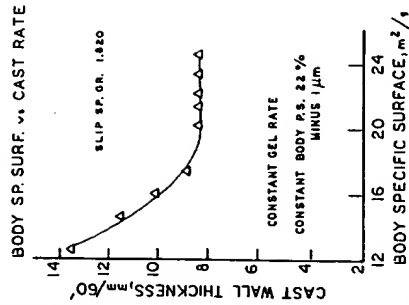


Figure 17.8. Effect of changes in casting rate of sanitary-ware (Figure 17.7) from variation in clay colloid content at constant slip weight, gel rate, and intermediate particle-size distribution.

than 1μ in a whiteware slip constituted an index of rate of cast. The data of Figure 17.7 show the changes in rate of cast with changes of minus 1μ variation of the clays component of a sanitary-ware-type organic-free, salt-free body at constant gel rate (Gallenkamp), constant slip weight, and constant specific surface. Although the trend is not linear, casting rate is definitely sensitive to apparently modest -1μ percentage changes. Figure 17.8 shows that for a constant 1μ the specific surface can be varied over a wide range with reasonably constant rate of cast. However, once the specific surface (i.e. colloid fineness) is reduced below some critical point, rate of cast will rise sharply.

SUMMARY AND DISCUSSION

The rheological curves of Figure 17.1 show the profound effect of quite small weight percentages of fine (i.e., colloidal and near colloidal) particles on the fluidity of deflocculated, crowded suspensions. The more extended a distribution (see Figures 17.1 and 17.3), the more fluid is the slip at high-volume solids. These data for casting slips parallel findings of Freundlich and Jones³¹ and of Pryce-Jones³² obtained with suspensions of narrow distributions of quartz particles in the range of 1 to 25μ . Clarke³³ observed sharp reductions in apparent viscosity of 50 vol % solids 30 to 175μ suspensions of quartz and glass particles upon addition of colloid-size polyamions. Eveson et al.³⁴ reported puzzlement at the anomalously low relative viscosities obtained for mixtures of suspensions of monosize spheres in water. These observations appear to be related to theoretical considerations of

Furnas¹⁸ and of Karlsson and Spring,³⁵ which point out that voids volume in packed polydisperse powders is a function of (a) the percentages of constituent monosize particles and (b) the ratio of the smallest to largest size particle. The smaller the S/L (ratio smallest size S to largest size L) and the more continuous the distribution, the lower the voids volume of the system. Furnas' argument is demonstrated by the graph of Figure 17.9. The voids volume for a monosize powder is assumed to be 40%. The addition of a second, smaller monosize powder to the larger-size powder has the effect of filling the voids of the predominant larger-size mass, thus reducing the voids volume of the combination. As the particles of the finer size are made still finer (i.e., more particles per unit volume), the combined powder voids volume drops to about 17% at $S/L = 0.01$ and remains constant regardless of the value of S . By using progressively smaller multiple monosize powders in combinations approaching a continuous distribution, the reduction in voids as S/L diminishes is less abrupt but approaches 5% at very low S/L (10^{-4} to 10^{-6}). Thus for a fixed liquid volume, that suspension whose particle-size distribution is most nearly continuous and whose S/L is low, would theoretically make maximum use of the liquid in flow. Of course, this neglects any interfacial effects between liquid and solid that might immobilize a portion of the liquid. Such an argument might account for the large

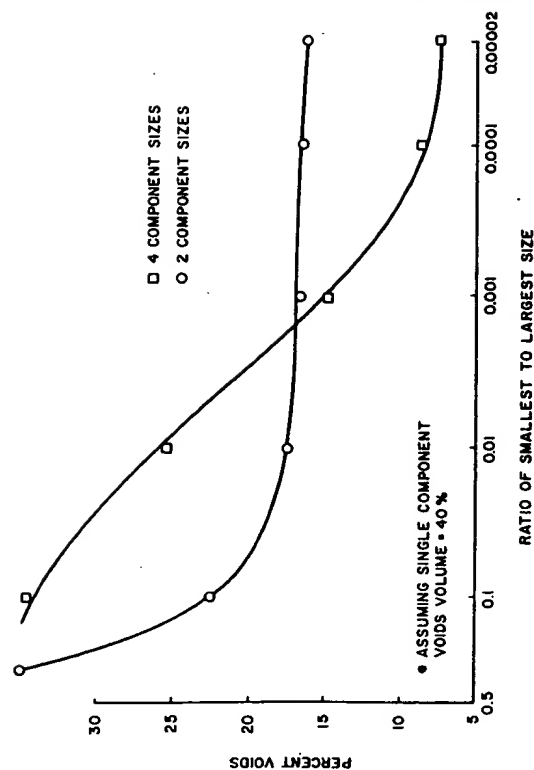


Figure 17.9. Data of Furnas¹⁸ drawn to show the effect of porosity of mixing a small amount of finer monosize spheres with a larger amount of large single-size spheres.

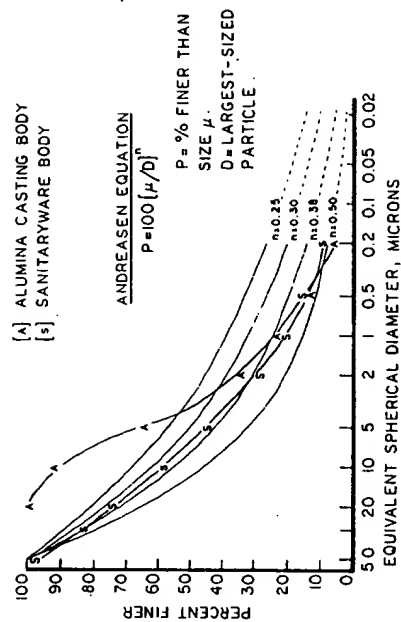


Figure 17.10. Plots of sanitary-ware-body and calcined-alumina-body distributions superimposed on a plot of Andreassen limit curves¹⁹ calculated for a maximum particle-size $D = 50 \mu$ over a range of 0.25 to 0.50. Note that the sanitary-ware distribution falls within the 0.33 to 0.50 limits established by Andreassen for optimum distributions.

increases in fluidity obtained by combining narrow distributions to make a more extended distribution or by adding small volumes of fines to a coarser distribution.

Andreassen¹⁹ studied continuous distributions of quartz grains and concluded that optimum packing for a distribution whose largest size D appeared in the relation

$$P = 100 \left(\frac{\mu}{D} \right)^{\eta}$$

where P is the percentage of particles finer than size μ , and η a fractional constant. Optimum packing was reported as lying between $\eta = 0.33$ and 0.50. Andreassen limits calculated for $D = 50 \mu$ over a range of η values are shown by Figure 17.10. Plots for a sanitary-ware body (from Figure 17.3) and an alumina casting body (from Figure 17.1) superimposed on the graph show that the sanitary-ware distribution more nearly approaches the Andreassen theoretical limits for optimum voids. An extrapolation of the A and S curves into the range of colloidal dimensions shows the sanitary-ware body to have a markedly smaller S/L value, hence lower theoretical voids. A similar calculation and plot for a refractory grain casting body is shown by Figure 17.11 and indicates that the distribution conforms to the Andreassen limits only in the lower size range.

The very sharp changes in fluidity and deflocculation response with small changes in intermediate particle size shown by Figure 17.4 and the marked

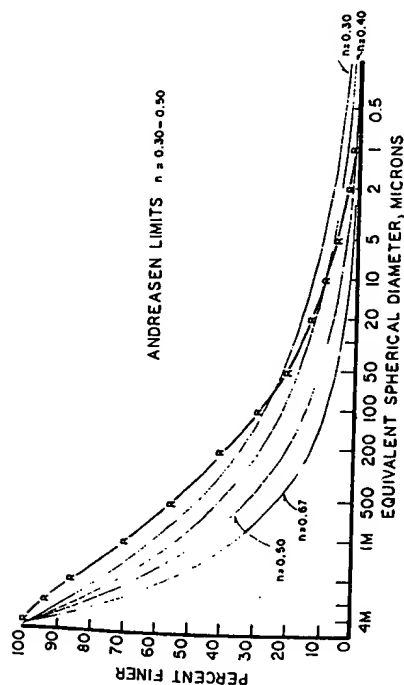


Figure 17.11. Andreason limits calculated for $D = 4750 \mu$. A plot of a refractory casting body [R] lies outside the 0.33 to 0.50 limits over most of its range.

changes in rate of cast with variation of the 1μ particle content at constant colloid shown by Figure 17.7 may possibly be due to changes in void volume (porosity) induced by small shifts in the intermediate range of an extended particle distribution. Figure 17.12 shows plots of data taken from a study by Bo et al.³⁶ of the role of particle-size distributions on the porosity and air permeability of continuous distributions of combinations of very-narrow-range distributions of glass spheres. Curves B and E represent optimum distributions of two different ranges. Curve B had a more extended range ($S/L = 0.05$) than curve E ($S/L = 0.27$). Where there is a deficit of intermediate-size particles (as in curves A and D), the curve becomes more concave, and porosity and permeability both increase. When there is an excess of intermediate-size particles (curves C and F), the curve configurations lie above the optimum traces B and E, and permeability diminishes, with porosity again increasing. The porosity and permeability changes coinciding with intermediate-particle-size shifts are proportionately very much larger for $S/L = 0.05$ than for $S/L = 0.27$. If this observation could be applied to the sanitary-ware body distribution where $S/L = 10^{-3}$, one might expect very small intermediate-size deficits to produce relatively quite large increases in porosity (higher liquid entrapment = higher viscosity) and permeability (higher casting rate). Moves in the direction of excess intermediate-size material would be expected to sharply reduce rate of cast (decreased permeability) and raise viscosity (increased porosity).

In recent years a number of rheological models have been proposed to describe the flow properties of colloidal suspensions. One model based on

References

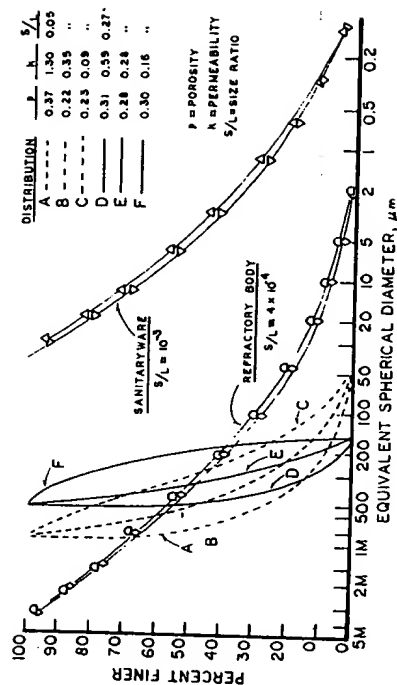


Figure 17.12. Graphical presentation of data of Bo et al.³⁶ showing the effect of particle distribution on porosity and permeability of packed distributions of glass spheres.

elementary reaction rate theory^{37,38} treats shear-thinning behavior in terms of a few empirically determined constants but does not take into account dependence of these constants on colloidal and surface properties of the dispersed particles. Although these models do appear to successfully picture suspension rheology over a fairly wide range of shear rate,³⁹ their basic assumptions were questioned⁴⁰ and a modified model was proposed in which the hydrodynamic-structural theory was extended to account for a distribution of relaxation times. The effect would be to widen the range over which shear thinning can occur. Another model based on particle collision and aggregation processes⁴¹ accounts for increased viscosity at both low and high rates of shear. A recent comparison of these two theories⁴² for shear thinning found the latter to more nearly agree with observed shear rate-shear stress data.

In light of these observations it seems possible to consider investigating deflocculated, high-solids ceramic suspensions within the context of packed powders. The particles of colloidal dimensions constitute a complicating factor because of their tendency to agglomerate and bind the system into a unit that breaks up into a distribution whose extension depends on the rate of shearing.

REFERENCES

1. A. L. Johnson and F. H. Norton, "Fundamental Study of Clay. II. Mechanism of Deflocculation in the Clay-Water System," *J. Amer. Ceram. Soc.*, **24**, 189-203 (1941).

2. R. K. Schofield and H. R. Samson, "Flocculation of Kaolinite Due to the Attraction of Oppositely Charged Crystal Faces," *Discuss. Faraday Soc.*, **18**, 134-145 (1954).
3. G. W. Phelps, "The Organic Colloid Fraction in Clay Slip Casting," *Proc. Fall Meetings ME/WW Div. Amer. Ceram. Soc.*, **1970**, 9-15.
4. F. J. Stevenson and J. H. A. Butler, "Chemistry of Humic Acids and Related Pigments," *Organic Geochemistry*, G. Eglington and M. T. J. Murphy, eds., Springer-Verlag, Berlin-Heidelberg, 1969, Chap. 22.
5. H. J. Modi and D. W. Fuerstenau, "Streaming Potential Studies on Corundum in Aqueous Solutions of Inorganic Electrolytes," *J. Phys. Colloid Chem.*, **61**, 640-643 (1957).
6. G. A. Parks and P. L. De Bruyn, "The Zero Point Charge of Oxides," *J. Colloid Sci.*, **63**, 967-973 (1962).
7. G. Y. Onoda and P. L. De Bruyn, "Proton Adsorption at the Liquid-Solid Interface. Pt. I. A Kinetic Study of Adsorption," *Surf. Sci.*, **4**, 48-63 (1966).
8. (a) S. M. Ahmed, "Studies of the Dissociation of Oxide Surfaces at the Liquid-Solid Interface," *Can. J. Chem.*, **44**, 1663-1670 (1966); (b) S. M. Ahmed and D. Marsimov, "Studies of the Oxide Surfaces at the Liquid-Solid Interface. Pt. II. Fe Oxides," *Can. J. Chem.*, **46**, 3841-3846 (1968).
9. D. W. Fuerstenau, "Streaming Potential Studies on Quartz in Solutions of Ammonium Acetates in Relation to the Formation of Hemimicelles at the Quartz-Solution Interface," *J. Phys. Chem.*, **60**, 981-985 (1956).
10. P. Somasundaran, T. W. Healy, and D. W. Fuerstenau, "Surfactant Adsorption at the Solid-Liquid Interface-Dependence of Mechanism on Chain Length," *J. Phys. Chem.*, **68**, 3562-3566 (1964).
11. P. Somasundaran and D. W. Fuerstenau, "Mechanisms of Alkyl Sulfonate Adsorption at the Alumina-Water Interface," *J. Phys. Chem.*, **70**, 90-96 (1966).
12. P. Somasundaran, T. W. Healy, and D. W. Fuerstenau, "The Aggregation of Colloidal Alumina Dispersions by Adsorbed Surfactant Ions," *J. Colloid Interface Sci.*, **22**, 599-605 (1966).
13. S. R. Hind, "Study of Factors Involved in Slip Casting," *Trans. Ceram. Soc.*, **22**, 90-104 (1923).
14. F. P. Hall, "The Casting of Clay Ware—A Resume," *J. Amer. Ceram. Soc.*, **13**, 751-766 (1930).
15. G. A. Loomis, "Properties of Clay Casting Slips," *J. Amer. Ceram. Soc.*, **23**, 159-162 (1940).
16. A. Dietzel and H. Mostetzky, "Mechanism of Dewatering of a Ceramic Slip by The Plaster Mold: I. Experimental Investigation of the Diffusion Theory of the Slip-Casting Process," *Ber. Deut. Keram. Ges.*, **33**, 7-18 (1956).
17. W. E. Worrall and W. Ryan, "The Mechanism of Slip Casting," *J. Br. Ceram. Soc.*, **1**, 270-271 (1964).
18. (a) C. C. Furnas, "The Relations Between Specific Volume, Voids, and Size Composition in Systems of Broken Solids of Mixed Sizes," U.S. Bur. Mines Report Invest. No. 2894 Oct. 1928. (b) C. C. Furnas, "Grading Aggregates, I. Mathematical Relations for Beds of Broken Solids of Maximum Density," *Ind. Eng. Chem.*, **23**, 1052-1058 (1931).
19. G. Herden, *Small Particle Statistics*, 2nd Ed., Butterworths, London, 1960, pp. 188-189.
20. M. Reiner, *Deformation, Strain and Flow*, Interscience, New York, 1960, Chap. XXI.
21. A. B. Metzner and M. Whitlock, "Flow Behavior of Concentrated (Dilant) Suspensions," *Trans. Soc. Rheol.*, **11**, 238-254 (1958).
22. F. R. Eirich, Ed., *Rheology: Theory and Applications*, Vol. 4, Academic, New York, 1967, Chap. 8.
23. R. D. Cooke, "The Plastic Properties of Enamel Slip," *J. Amer. Chem. Soc.*, **7**, 651-655 (1924).
24. W. N. Harrison, "Vitrenous Enamel Slips and Their Control," *J. Amer. Ceram. Soc.*, **10**, 970-994 (1927).
25. G. W. Phelps and A. Silwanowicz, "The Role of Nonclay Particle Size in Whiteware Slip Casting," *J. Can. Ceram. Soc.*, **39**, 17-19 (1970).
26. A. Clark and H. J. Hodsman, "Viscometer," *J. Soc. Chem. Ind.*, **56**, 671 (1937).
27. J. R. van Wazer, J. W. Lyons, K. Y. Kim, and R. E. Colwell, *Viscosity and Flow Measurement*, Interscience, New York, 1963, pp. 139-150.
28. R. McKennell, "Cone-Plate Viscometer Comparison with Coaxial Cylinder Viscometer," *Anal. Chem.*, **28**, 1710-1714 (1956).
29. K. M. Beazley, "Breakdown and Buildup in China Clay Suspensions," *Trans. Br. Ceram. Soc.*, **63**, 451-471 (1964).
30. F. Moore, "The Rheology of Ceramic Slips and Bodies," *Trans. Br. Ceram. Soc.*, **58**, 470-494 (1959).
31. H. Freundlich and A. D. Jones, "Sedimentation Volume, Dilatancy and Plastic Properties of Concentrated Suspensions," *J. Phys. Chem.*, **40**, 1217-1236 (1936).
32. J. Pryce-Jones, "Flow of Suspensions, Thixotropy and Dilatancy," *Durham Philos. Soc.*, **10**, 427-467 (1948).
33. B. Clarke, "Rheology of Coarse Settling Suspensions," *Trans. Inst. Chem. Eng. (London)*, **45**, T251-T256 (1967).
34. G. F. Eveson, S. G. Ward, and R. L. Whitmore, "Theory of Size Distribution in Paints, Coals, Greases, etc. Anomalous Viscosity in Model Suspensions," *Discuss. Faraday Soc.*, **(11)**, 11-14 (1951).
35. K. Karlsson and L. Spring, "Packing of Irregular Particles," *J. Mater. Sci.*, **5**, 340-344 (1970).
36. M. K. Bo, D. C. Freshwater, and B. Scarlett, "The Effect of Particle Size Distribution on the Permeability of Filter Cakes," *Trans. Inst. Chem. Eng.*, **43**, T228-T232 (1965).
37. D. A. Denny and R. S. Brodkey, "Kinetic Interpretation of Non-Newtonian Flow," *J. Appl. Phys.*, **33**, 2269-2274 (1962).
38. M. M. Cross, "Rheology of Non-Newtonian Flow: A New Flow Equation for Pseudoplastic Systems," *J. Colloid Sci.*, **20**, 417-439 (1965).
39. M. M. Cross, "Kinetic Interpretation of Non-Newtonian Flow," *J. Colloid Interface Sci.*, **33**, 30-35 (1970).
40. T. Gillespie, "Application of the Hydrodynamic-Structural Theory of Non-Newtonian Flow to Suspensions which Exhibit Moderate Shear Thickening with Particular Reference to 'Dilant Plastisols,'" *J. Colloid Interface Sci.*, **22**, 554-562 (1966).
41. A. S. Michaels and J. C. Bolger, "The Plastic Behavior of Flocculated Kaolin Suspensions," *Ind. Eng. Chem. Fund.*, **1**, 153-164 (1962).
42. R. J. Hunter and S. K. Nicol, "The Dependence of Plastic Flow Behavior of Clay Suspensions on Surface Properties," *J. Colloid Interface Sci.*, **28**, 250-259 (1968).

18

Viscosity of Concentrated Newtonian Suspensions

K. Sommer

The viscosity η of a dilute suspension of rigid spheres in a liquid was deduced by Einstein in 1905 to be given by

$$\eta = \eta_l (1 + 2.5c_v)$$

where η_l is the viscosity of the liquid and c_v is the ratio of the volume of the suspended matter to the total volume.

Subsequently, many new formulas have been developed for highly concentrated suspensions and nonspherical particles; however, these formulas are semiempirical and apply only to the particular suspension of the investigation. The differences in the various suspensions can be explained in terms of the differences in the materials and the interactions between their particles. New theoretical and experimental approaches are needed to separate the different effects in concentrated suspensions.

THEORY

The viscosity of a concentrated suspension is dependent on the rheology of the liquid phase and on the direct interactions between particles. These two effects can be separated theoretically as shown below.

For a unit volume of suspension, the rate of energy dissipation \dot{E}_o due to a shear flow is given by

$$\dot{E}_o = \tau \dot{\gamma} = \eta \dot{\gamma}^2 \quad (1)$$

where τ = external shear stress rate

$\dot{\gamma}$ = shear strain rate

η = apparent viscosity of the suspension

For a Newtonian liquid, η is independent of the shear strain rate. For other cases η depends on $\dot{\gamma}$.

The total dissipated energy is the sum of the energy \dot{E}_l dissipated by the liquid phase and the energy \dot{E}_s dissipated by the direct particle-particle interactions (or solid friction energy), that is,

$$\dot{E} = \dot{E}_l + \dot{E}_s \quad (2)$$

Dividing Equation 2 by the volume V of the suspension and dividing the first term on the right side of the equation by the volume V_l of the liquid yields

$$\dot{E}_o = \frac{V_l}{V} \frac{\dot{E}_l}{V_l} + \frac{\dot{E}_s}{V} \quad (3)$$

Letting C_o equal the volume concentration of the solid,

$$\dot{E}_o = (1 - C_o) \dot{E}_{o,l} + \frac{\dot{E}_s}{V} \quad (4)$$

where $\dot{E}_{o,l}$ is the dissipated energy per unit volume of liquid.

A parameter $\dot{\gamma}^*$ can be defined by

$$\dot{E}_{o,l} = \eta_l \dot{\gamma}^{*2} \quad (5)$$

where $\dot{\gamma}^*$ is a mean shear rate for the liquid phase and η_l is the apparent viscosity of the liquid.

Combining Equations 1, 4, and 5 gives

$$\tau \cdot \dot{\gamma} = (1 - C_o) \eta_l \dot{\gamma}^{*2} + \frac{\dot{E}_s}{V} \quad (6)$$

All the quantities in Equation 6 are measurable except $\dot{\gamma}^*$ and \dot{E}_s .

The solid friction energy \dot{E}_s can be determined if two suspensions are selected that allow certain simplifications to occur:

1. τ is measured for both suspensions at the same value of $\dot{\gamma}$ (thereby giving τ_1 and τ_2 for the first and second suspension).

2. Both suspensions have the same solid at the same C_o .
3. $\dot{\gamma}^*$ is assumed to be the same for both because $\dot{\gamma}$ and C_o are the same for both suspensions.
4. The two liquids have similar physical and chemical properties so that \dot{E}_s is the same as $\dot{E}_{s,s}$.
5. The only differences in the two liquids are their viscosities (η_{l1} and η_{l2}).

Writing Equation 6 for both suspensions, and making the above assumptions, we can combine the two equations to yield

$$\dot{\gamma}^* = \left[\frac{\dot{\gamma}(\tau_1 - \tau_2)}{(1 - C_o)(\eta_{l1}\eta_{l2})} \right]^{1/2} \quad (7)$$

and

$$\frac{\dot{E}_s}{\dot{E}} = 1 - \frac{(\tau_1/\tau_2) - 1}{(\eta_{l1}/\eta_{l2}) - 1} \quad (8)$$

EXPERIMENT

Figure 18.1 shows two flow curves of closely sized, glass spheres (mean size of 23 μm) suspended in two oils with similar chemistry but different vis-

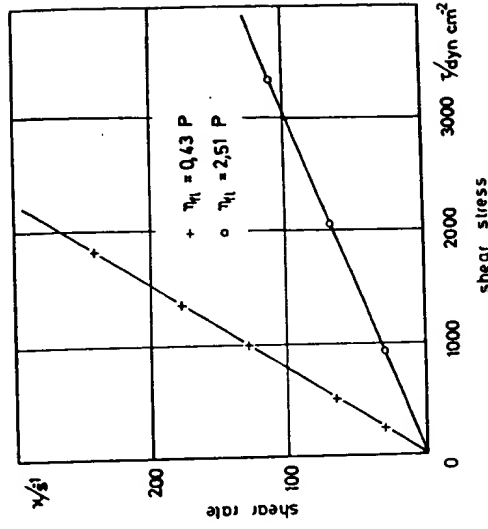


Figure 18.1. Flow curves of closely sized glass spheres with a mean particle size of 23 μm in two different oils with viscosities $\eta_{l1} = 0.43$ and 2.51 P.

cosities (0.43 and 2.51 P). For both suspensions $C_v = 0.4$. Newtonian behavior is found in both cases.

From the two sets of data, the value of γ^* is calculated with Equation 7 and plotted versus $\dot{\gamma}$ in Figure 18.2. A linear relation is found between γ^* and $\dot{\gamma}$.

Also shown in Figure 18.2 are similar results for cases where C_v is 0.20 and 0.35. These are also linear. The mean shear rate for a given external shear rate decreases as C_v decreases.

Experiments using different solid particles but the same liquid have been carried out. Two suspensions with the same liquid (and same liquid viscosity) are formed using glass spheres in one case and Plexiglas spheres of the same size in the second case. For both suspensions C_v was 0.4. The flow curves for the two cases are given in Figure 18.3. Both are Newtonian, but the suspension with glass spheres had a significantly larger apparent viscosity. However, the mean shear rates in the liquids were the same

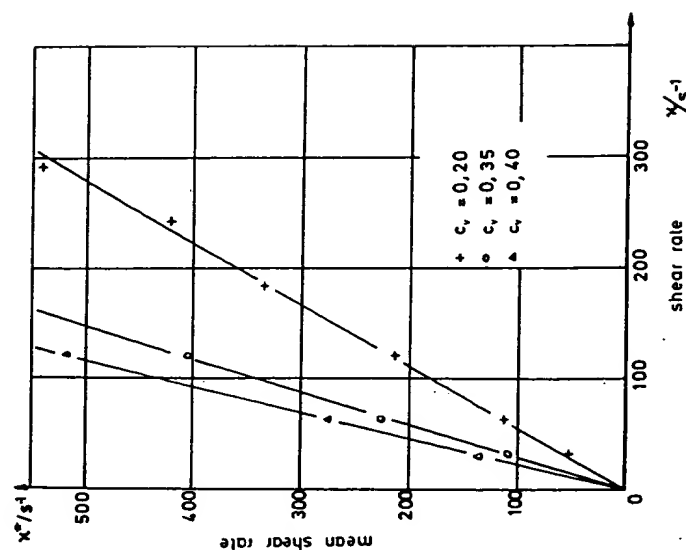


Figure 18.2. The mean shear rate γ^* as a function of the external shear rate γ by a glass sphere-oil suspension and different concentrations C_v .

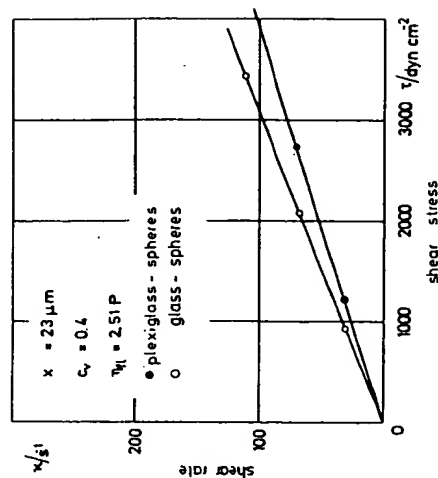


Figure 18.3. Flow curves of plexiglass spheres and glass spheres suspended in the same oil ($\eta_l = 2.51$ P).

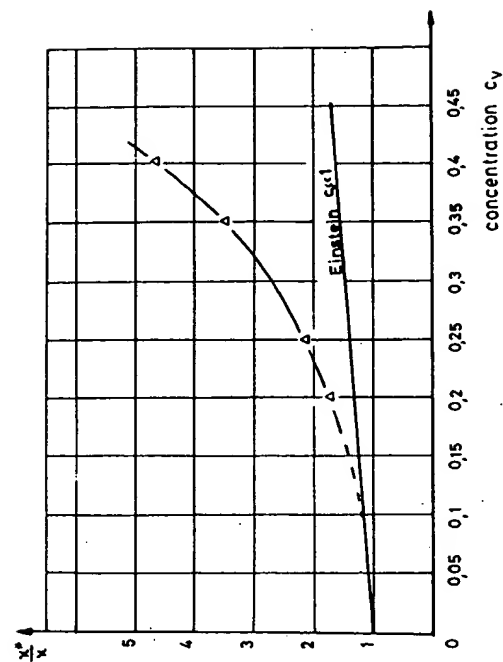


Figure 18.4. The ratio γ^*/γ as a function of concentration C_v of the glass spheres-oil suspensions ($x = 23 \mu\text{m}$).

throughout the whole range of the external shear rate examined. In both cases $\dot{\gamma}^*/\dot{\gamma}$ is equal to 4.45. Thus the flow properties of the liquid phase did not change. The differences in viscosity were due to the different particle-particle interactions.

The ratio $\dot{\gamma}^*/\dot{\gamma}$ was measured as a function of C_v for the glass-spheres suspension. The results, presented in Figure 18.4, show that a straight line is approached at dilute concentrations (at C_v values below 0.1). This straight line shows that Einstein's relationship is being approached at low concentrations. At higher concentrations the shear rate within the liquid phase increases more rapidly than expected by Einstein's theory because of the hydrodynamic interactions between particles.

The fraction E_r/E calculated from Equation 8 is very small at dilute concentrations. Above $C_v = 0.2$, E_r becomes a significant fraction of E because of the influence of the direct particle-particle interactions.

The above results demonstrate that the relative contributions of particle-particle interactions to the viscosity of suspensions can be determined experimentally. It was therefore of interest to examine chocolate, which exhibits shear thinning behavior that has been attributed often to the changing of the structure of the suspension. The viscosity of the liquid in the chocolate is altered by changing temperature. The overall flow behaviors at 40°C and 50°C are compared in Figure 18.5. Calculation of $\dot{\gamma}^*/\dot{\gamma}$ reveals that the quantity is independent of $\dot{\gamma}$, as shown in Figure 18.6. This indicates that the thinning behavior of chocolate cannot be due to changes in the flow properties but rather to a decrease of the direct particle-particle interaction; that is, the solid friction has changed.

SUMMARY

By defining a characteristic mean shear rate $\dot{\gamma}^*$, it is possible to determine the changing "structure" and flow properties of concentrated suspensions. A method of measurement has been given that permits the separation of the influence of a viscous liquid phase from that of the direct interactions between particles on the viscosity of the solution.

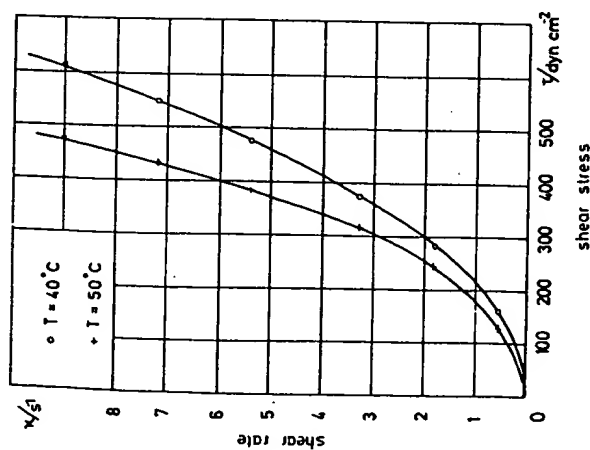


Figure 18.5. Flow curves of chocolate at two temperatures ($T_1 = 40^\circ\text{C}$ and $T_2 = 50^\circ\text{C}$).

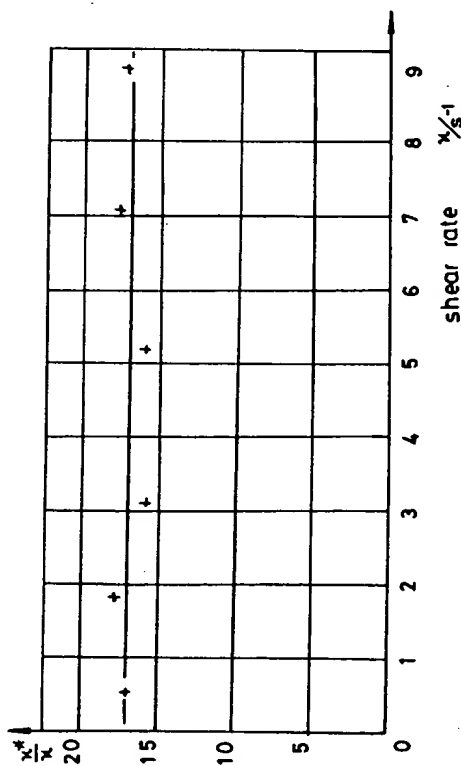


Figure 18.6. The ratio $\dot{\gamma}^*/\dot{\gamma}$ as a function of the external shear $\dot{\gamma}$ for chocolate.

19

The Rheology of Organic Binder Solutions

G. Y. Onoda, Jr.

Organic binders are essential additives for the processing of many commercial ceramics. The binders provide green strength and plasticity to clay-free ceramics so that bodies can be molded and retained in the desired shapes before firing. Ceramic processes that utilize organic binders include dry pressing, extrusion, tape casting, roll forming, thick-film printing, slip casting, injection molding, and compression molding.

A large number of organic substances have been utilized or advocated as binders for ceramics during the past 50 years. Several useful compilations and descriptions of various organic binders have appeared in the literature.¹⁻⁹ Certain classification schemes have been proposed for binders, based on origin,⁹ chemical composition, physical characteristics, molecular weight, polarity, affinity for water, and dominant adhesion mechanisms.¹⁰ However, actual comparisons of organic binders according to the proposed classification schemes were not carried out in most cases.

Of the ceramic processes listed above, all except injection molding and compression molding involve the use of binders that are dissolved or dispersed in a liquid. The binders are dissolved molecularly in water or an organic solvent or are dispersed in liquid as an "emulsion." The liquid phase is important for uniformly dispersing the binder throughout the

particulates. Also, the liquid is necessary for providing fluidity for slips or plasticity for extrusion or semidry pressing. Dry green strength in the body is developed by the evaporation of the liquid. The binder is retained in the body and provides organic bridges between the ceramic particles.

Organic binders strongly affect the rheology of the liquid phase. They increase the viscosity and change the flow characteristics from Newtonian (for pure water) to pseudoplastic in most cases. Also, with some binders gels can develop under various conditions. The rheology of the solution directly affects the behavior of suspensions and pastes formed by adding particulates to the solution.

The applicability of a given organic binder for a specific ceramic process is very much dependent on the rheological characteristics of the binder solution. In this chapter relationships between rheological variables and ceramic processing phenomena are discussed. A wide variety of organic binders are compared on the basis of rheology and in relation to processing.

CHEMICAL STRUCTURE

Most soluble organic binders are long-chain polymer molecules. The backbone of the molecule consists of covalently bonded atoms such as carbon, oxygen, and nitrogen. Attached to the backbone are side groups located at frequent intervals along the length of the molecule. The chemical nature of the side groups determines in part what liquids will dissolve the binder. If the side groups are highly polar, solubility in water is promoted. Binders soluble in polar organic solvents have side groups of intermediate polarity. Solubility in nonpolar liquids is promoted by nonpolar side groups.

The chemical polarity and resulting affinity for a liquid is a necessary but not a sufficient condition for effecting solubility in the liquid. The side groups of a molecule bond strongly to the side groups of adjacent molecules, thereby giving the binder a high cohesive strength. If the solvent molecule cannot disrupt this intermolecular bonding, solvation does not take place. This condition occurs, for example, with pure cellulose and pure poly(vinyl alcohol) binders. Both of these polymers must be modified chemically at their side groups to effect solubility. This is accomplished by making the side groups bulkier, thereby reducing the amount of interaction that can take place between molecules. In the case of poly(vinyl alcohol), approximately 12 to 20% of the OH side groups must be replaced by acetate groups to convert the polymer to the cold-water-soluble form. Cellulose is modified to water-soluble form by substituting hydroxyethyl, methyl, carboxymethyl, or hydroxypropyl side groups. These groups are not only

hydrophilic but also provide enough bulk so that solute molecules can penetrate between polymer molecules.

The long-chain molecules of binders consist of smaller units, called monomers, that are linked together. The number of monomers in a polymer is called the "degree of polymerization." The monomer is the smallest unit that characterizes the chemical structure of the molecule.

The carbohydrate-derived binders are characterized by a ring-type monomer, the ring being a modified α -glucose structure. The ring has five carbon atoms, as shown in Figure 19.1. Each carbon atom can be identified by a number, such as C-1 or C-2, according to its position indicated by the numbers in parenthesis in Figure 19.1. The linkages between rings occur by an ether bond ($-\text{O}-$) between C-1 of one monomer and C-4 of another.

The various modifications occur by side groups (R) attached to C-5, C-2, or C-3. The degree of substitution (DS) is the number of sites on which modifications are made in a monomer. When DS is one, the C-5 site possesses the side group. As the DS values increase above one (maximum of 3), the C-2 is the next favored position for substitutions (after C-5), and C-3 is the least favored. When not possessed by a special side group the R position on C-2 and C-3 is filled by an OH group.

The monomer formulas for a variety of water-soluble, carbohydrate-derived binders are given in Figure 19.2. The typical DS values are also given.

The monomer formulas for some important binders that are not of vegetable origin are given in Figure 19.3. These include the vinyls, acrylics, and polyethylene oxides. The vinyls are characterized by a linear backbone consisting of carbon-carbon linkages, with a side group attached to every other carbon atom. The acrylics are similar to vinyls in that they have the same backbone structure. However, some acrylics have two side groups attached to the carbon atom.

Both vinyls and acrylics have flexible backbones because of the rotatable carbon-carbon bonds and these can lead to a molecule with a coiled and curving configuration. Thus the spatial length of a molecule may be much

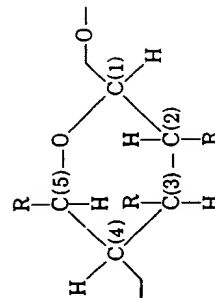


Figure 19.1. Modified α -glucose monomer.

Binder	R Groups	DS
Methylcellulose	$-\text{CH}_2-\text{O}-\text{CH}_3$	2
Hydroxypropylmethylcellulose	$-\text{CH}_2-\text{O}-\text{CH}_2-\text{CH}(\text{OH})-\text{CH}_3$	2
Hydroxyethylcellulose	$-\text{CH}_2-\text{O}-\text{C}_2\text{H}_4-\text{O}-\text{C}_2\text{H}_4-\text{OH}$ $-\text{CH}_2-\text{O}-\text{C}_2\text{H}_4-\text{OH}$	0.9-1.0
Sodium carboxymethylcellulose	$-\text{CH}_2-\text{O}-\text{CH}_2-\text{C}(=\text{O})\text{ONa}$	
Starches and dextrans	$-\text{CH}_2-\text{OH}$	
Sodium alginate	$-\text{C}(=\text{O})\text{ONa}$	
Ammonium alginate	$-\text{C}(=\text{O})\text{ONH}_4$	

Figure 19.2. Formula for some water-soluble, carbohydrate-derived binders.

smaller than the actual length of the molecule backbone. This has an important effect on the rheology of binder solutions, as is discussed later. The backbone of the carbohydrate-type binders is rather inflexible compared with those of the vinyls and acrylics. These molecules tend to remain extended, thereby having a larger spatial effect than those molecules that can coil and ball up into a compact configuration.

The monomer formulas for some binders that are soluble in organic solvents are given in Figure 19.4.

RHEOLOGY AND MOLECULAR STRUCTURE

The increase in viscosity of a liquid as large molecules (and colloids) are added is strongly influenced by their shape. The effectiveness of a molecule or colloid for increasing viscosity is dependent on its "sphere of influence" in the liquid. Molecules and colloids are constantly in motion (Brownian) because of thermal vibrations and impact by the liquid molecules. The solute molecules or colloids are tumbling and rotating, and the time-average

volume swept out by molecules or colloids is defined as their "sphere of influence." For a given molecular weight, a molecule has the largest sphere of influence when it has the largest length in one direction. Thus a linear molecule has a greater sphere of influence than a branched molecule of equivalent molecular weight. A fully extended linear molecule has a greater sphere of influence than the same molecule when it is coiled. The often dramatic increases in solution viscosity that are found with binders is a result of their long, linear chemical structure.

To a first approximation, the viscosity η of a solution is related to the concentration c of binder by an equation of the form

$$\log \eta = kc \quad (1)$$

where η is in centipoise and c is in weight percent. Although some significant departures from this equation exist, usually the viscosity changes are more easily represented on plots of $\log \eta$ versus c , and this has become common practice. Another limitation of representing rheology data by these plots is associated with the phenomenon of "pseudoplasticity," as is discussed below.

Pseudoplasticity is another important rheological characteristic that develops as binders are added to a liquid. The time-average volume of the binder molecule can be distorted by shear forces in the liquid. The molecules tend to line up in a manner that reduces the resistance to flow.

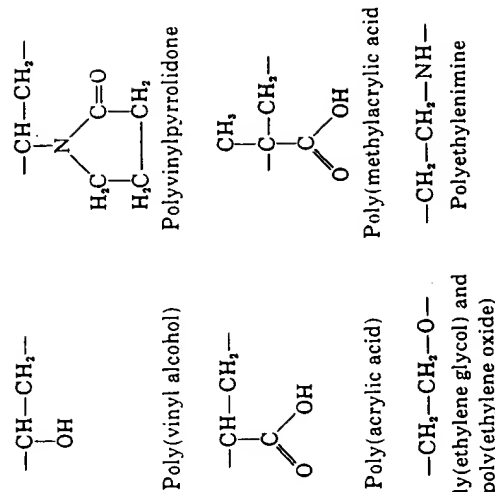
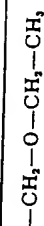


Figure 19.3. Formulas for some water-soluble binders not of vegetable origin.

Celluloses (see Figure 19.1)

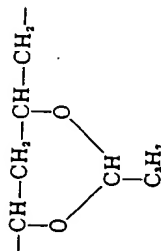
R Group



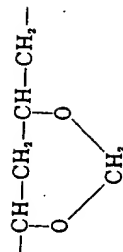
Ethyl cellulose

Vinyls

Poly(vinyl butyral)



Poly(vinyl formol)



Acrylics

Poly(methyl methacrylate)

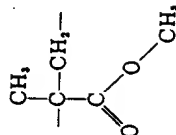


Figure 19.4. Formulas for some binders soluble in organic solvents.

This alignment has the effect of reducing the instantaneous viscosity with increasing shear strain rate. When the shear stress is removed, the alignment of molecules may disappear immediately. In this case the shear stress-strain rate dependency is reversible. If the alignment dissipates gradually, the lower-viscosity state is retained for some time after the higher shear stresses are removed. This time-dependent rheological behavior is known as thixotropy.

Because of the common pseudoplastic behavior of binder solution, the viscosity of binder solutions must be defined in terms of the specific measuring conditions (e.g., method of measurement and flow rate). Data available on viscosity for different binders are often obtained under different conditions, so comparing the viscosity of different binders must be made with appropriate precautions.

"Gelation" is a third rheological condition of importance in binder solu-

tions. Gels can be obtained by (1) cooling a warm solution, (2) heating a solution (thermal gelation), and (3) action of a chemical gelling agent (chemical gelation). Gels have elasticity up to a certain yield stress, beyond which tearing and fracture may occur. Therefore, gelled liquids do not flow and their behavior cannot be represented in terms of flow response to various shear strain rates.

Bonding between polymer molecules is responsible for gel formation. Gels formed by heating or cooling are usually reversible in that a liquid state can be reobtained by reversing the thermal conditions or by diluting the gel with the solvent. Formation of gels by a chemical gelling agent tends to be irreversible.

COMPARISON OF BINDER VISCOSITIES

Organic binders are often arbitrarily designated according to how effectively they increase the viscosity of a solution. Designations such as low, medium, and high viscosity grades of binders are commonly employed for specific binders that are available in different molecular weights. Such definitions have not been established for comparing different binders, however. For purposes of comparison, it is convenient to establish definitions for viscosity grades.

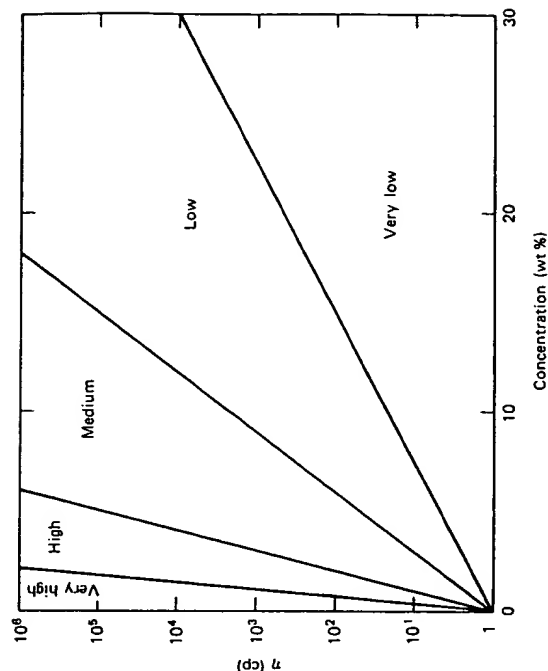


Figure 19.5. Criterion for viscosity grades based on viscosity-concentration relationship.

The graph in Figure 19.5 defines the criterion for categorizing viscosity grades that are used in this chapter. While the borderlines between grades are arbitrarily selected, they are convenient for the present purposes. The viscosity grade of a binder is determined by superimposing the viscosity-versus-concentration curve on the graph of Figure 19.4. The field within which the curve falls defines the viscosity grade (very low, low, medium, high, or very high).

From data given by binder suppliers and available in the literature, the viscosity grades of a wide variety of water-soluble binders have been

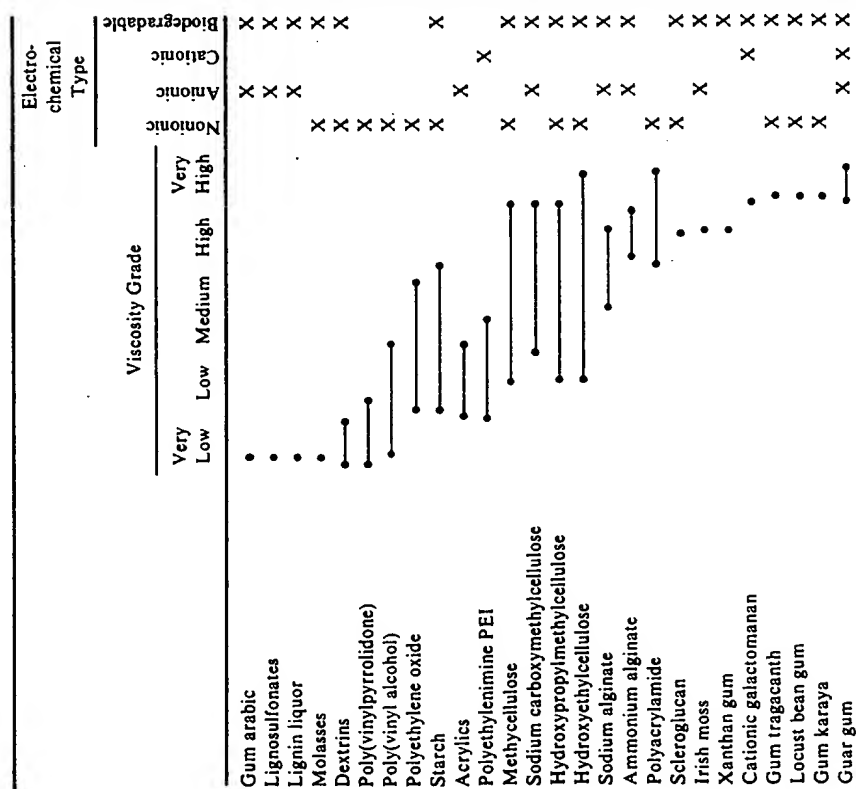


Figure 19.6. Viscosity grades for some water-soluble binders.

determined and are summarized in Figure 19.6. For many binders a range of viscosity grades are available by variation in molecular weight.

Examination of Figure 19.6 shows the trends in the viscosities for vinyl-, acrylic-, and carbohydrate-derived binders. The vinyls and acrylics have very low or low viscosity. The cellulose derivatives are predominantly in the medium- and high-viscosity ranges. Also, the alginates and most of the natural gums (which are carbohydrates) have high or very high viscosities.

EMULSIONS

A class of binders, called "emulsions," can also be considered as very-low viscosity binders. Emulsions are organic substances that are finely divided and dispersed in a liquid (e.g., water) with the aid of emulsifying agents (certain surfactants).

Wax emulsions were among the first important binders of the emulsion type. The properties of waxes have long been recognized as useful for binder applications. They provide a reasonable level of green strength for many applications. At the same time they are soft enough so that granules are readily crushed at relatively low pressing pressures. However, the use of waxes in processing was hindered for a time by the fact that they were available only in the solid (bulk) state. It was necessary to melt or dissolve them in organic solvents when adding them to a ceramic batch. When wax emulsions were developed, waxes could readily be incorporated into ceramic bodies with water.

During the past several decades, a variety of wax or waxlike binders in emulsion form have been developed, including paraffin wax, modified paraffin wax, microcrystalline wax, mineral wax, and synthetic waxes such as stearic acid derivatives.

SIGNIFICANCE OF VISCOSITY IN CERAMIC PROCESSING

The viscosity imparted by binders is one of the primary considerations in the selection of a binder for a specific process. While binder is added to provide the necessary green strength, it must also impart the appropriate viscosity to the liquid in the batch material. For slip casting, doctor blading, and spray drying, the slip must have a low enough viscosity to carry out the process. This requires that the solution in the batch have low enough viscosity. In contrast, the liquid present for extrusion processes must have high viscosity¹¹ (10^4 to 10^6 cP). If the liquid is too fluid, it would be too easily squeezed out and separated from the ceramic mass.

An equation useful for estimating what viscosity grade of binder is necessary for a ceramic application is derived below. In Equation 1 the parameter k is a measure of the viscosity grade of a binder. Using the definitions of Figure 19.4, the range of k for each viscosity grade is as follows:

viscosity grade	k value range
very low	0-0.133
low	0.133-0.333
medium	0.333-1.00
high	1.0-3.0
very high	3.0- ∞

The value of k required for a given ceramic process depends on the amount of liquid, the amount of binder, and the viscosity needed for the process.

The amount of liquid can be estimated from space-filling considerations. A dry powder packs to a certain packing density. If V is the total volume of the pack, this volume is the sum of the actual volume V_s occupied by the solid and the volume V_v of the void spaces. The packing density p expressed as percent of theoretical density, is given by

$$p = \frac{100V_s}{V_s + V_v} \quad (2)$$

When the volume V_L of liquid added to the powder exceeds V_v , the mixture is fluid. A plastic state arises when $V_L \approx V_v$ (assuming the liquid has a high viscosity). A semidry pressing condition exists when $V_L \approx 0.3 V_v$. It is useful to define a parameter y given by

$$y = \frac{V_L}{V_v} \quad (3)$$

which represents the fraction of void space actually occupied by the liquid. The concentration of binder c , expressed as percent of liquid weight, is given by

$$c = \frac{100\rho_B V_B}{\rho_L V_L} \quad (4)$$

where ρ_B and ρ_L are the densities of the dry binder and liquid, respectively.

Combining Equations 1 through 4 by eliminating c , V_v , and V_L , we arrive at

$$k = \left(\frac{100 - p}{p} \right) \left(\frac{\rho_L}{\rho_B} \right) \frac{y \log \eta}{100 (V_B/V_s)} \quad (5)$$

Thus k can be calculated by estimating the percent of theoretical packing density of the powder (p), the viscosity η , and the amount of binder (V_B/V_s) needed for the process.

To illustrate the use of the relation given by Equation 5, some typical cases for extrusion, slips, and semidry pressing are considered.

Typically, ceramic powders have a packing density of around 55% of the theoretical value. Binders have a density of around 1.25 g/cc in many cases. If the liquid is water, its density is 1.0 g/cc. Thus

$$\begin{aligned} p &= 55 \\ \rho_B &= 1.25 \\ \rho_L &= 1.0 \end{aligned}$$

For extrusion y is approximately 1 and η is around 10^5 cP; substituting these numbers and the typical values for p , ρ_B , and ρ_L , we can calculate k as a function of V_B/V_s from Equation 5. From the k values we can determine the viscosity grades corresponding to the specific conditions. In Figure 19.7, the grade binders required for different binder contents are shown based on the typical data of this example.

Similar results are shown in Figure 19.7 for slips and semidry pressed bodies. For slips y may range from 1.5 to 2.0 and so these two extreme cases are illustrated. The viscosity for slip solutions is assumed to be 10 cP. For the semidry batch material, y is around 0.3 and viscosity is around 10^3 cP.

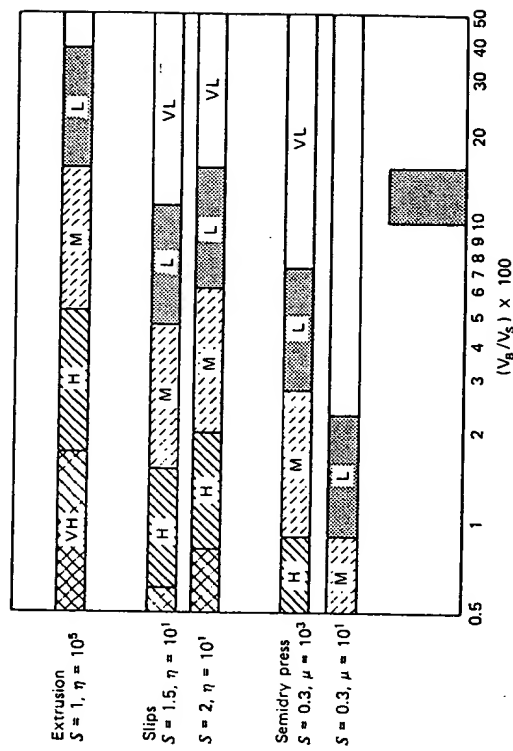


Figure 19.7. Binder grades calculated for different ceramic processes.

It is common in practice to find that the amount of binder used corresponds to V_B/V_s values between 0.08 to 0.15. This quantity is approximately the maximum amount that could be added without closing up the pore spaces in the body (which could be detrimental to burnout). The binder content range is designated by the width of the marker in Figure 19.7. We see that specific binder viscosity grades are identified for the three types of processes that fall into this V_B/V_s range. For extrusion processes medium-viscosity grade binders are needed. Low- or very-low-viscosity binders are needed for slips. Simidry pressing clearly requires very-low-viscosity binders.

The above conclusions explain why certain types of binders are used for certain processes. Starch, methylcellulose, and hydroxyethylcellulose are common binders for extrusion, for example, because they are of medium viscosity grade. Dry pressing preceded by spray drying utilizes gum arabic, poly(vinyl alcohol), and low-viscosity-grade starches. Semidry pressing utilizes very-low-viscosity binders of lower cost, including lignin liquor, lignosulfonates, dextrine, molasses, and poly(vinyl alcohol).

It should be remembered that Figure 19.7 was constructed on the basis of the "typical" conditions described in the text. For any specific application, the variables may be different and the necessary viscosity grades should be calculated from these variables.

Another reason for worrying about binder solution viscosities is that it is the high viscosities that limit how much binder can be dissolved in the liquid. Generally, once the viscosity reaches around 10^6 cP, the binder cannot dissolve any further because of kinetic reasons. If too much binder is added, undissolved binder would exist in the body. This can result in large pores after firing and in springback problems because of the low modulus of elasticity of the binder.

PSEUDOPLASTICITY AND ITS SIGNIFICANCE

The pseudoplasticity of solutions is important in many technologies, including ceramics. This property is very important in paints for the identical reasons that it is important in ceramics.

A suspension of solid particles tends to settle out in simple liquids such as water if the particles are larger than colloidal ($> 10^{-6}$ cm). The slips utilized in ceramics would not remain homogenous if settling occurred. One approach to slow down the settling is to increase the viscosity of the liquid. However, slips must be fluid enough to be sprayed or painted. To solve this problem, a pseudoplastic solution is utilized. The settling of a particle involves very small shear forces and shear strain rates. Under these condi-

tions a pseudoplastic solution may have a very high viscosity. At high shear forces, as in pouring, spraying, or painting, the viscosity of the solution may be several orders of magnitude lower.

Figure 19.8 shows a solution viscosity-shear rate relationship for a 2% solution of hydroxyethylcellulose, a typical, strongly pseudoplastic binder. The ranges of shear rate corresponding to particle suspensions, leveling of paints, pouring of solutions, mixing and stirring, spraying, brushing, and rolling are indicated. For this particular binder, the viscosity resisting the settling of particles is more than three orders of magnitude greater than the viscosity under spraying or painting conditions.

In thick-film printing, pseudoplasticity is important for having low viscosity during screening but high viscosity once deposited so that the slip

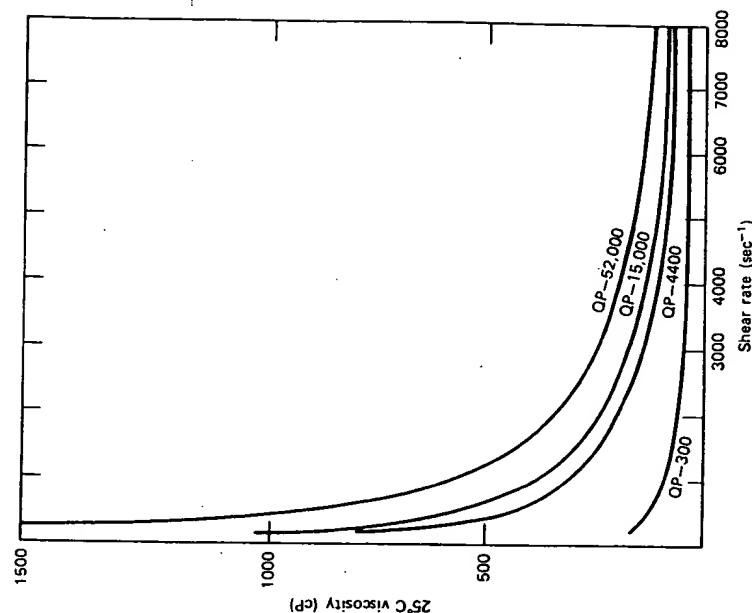


Figure 19.8. Typical viscosity-shear rate functions for 2% solutions of hydroxyethylcellulose. Different curves represent different HEC grades of varying molecular weight.

does not run and level out throughout the surface area. The time available before the slip is dry is only sufficient for a localized leveling between adjacent screen hole patches.

Thixotropy often is not a desirable feature when the pseudoplastic behavior is important. If the slip remains of low viscosity after being acted upon by the process step, the advantage of high viscosity at low shear rates become lost. A fast recovery of high viscosity when shear is reduced is essential.

Pseudoplasticity may also be an important factor in extrusion processes, although this has not yet been proven. Without external forces, the solution would have only small shear forces acting on it and may make the body more rigid by being at high viscosity. Under extrusion forces, the solution viscosity may be lower, thereby aiding the deformation process.

Most organic binders are pseudoplastic to some degree. While the effect is small in some, appreciable pseudoplasticity is exhibited by binders such as hydroxyethylcellulose, scleroglucan (Polytran FS), sodium carboxylethylcellulose, poly(ethylene oxide), poly(vinyl alcohol), and alginates. The pseudoplasticity increases with increasing binder concentrations.

MISCELLANEOUS PROPERTIES

Gelation

Under certain conditions, binder solutions can form gels. For example, poly(vinyl alcohol) (fully hydrolyzed grades) can be gelled by the addition of certain dyes (e.g., Congo red) and borax. Sodium alginates can be gelled with alkaline earth and heavy metal ions. Locust bean gum is gelled by borax. Gum karaya, Irish moss, and agar gel by the gradual swelling of the binder. Heating increases the fluidity, and cooling brings about gel formation. Under certain conditions starches and starch derivatives can also be gelled.

Thermal gelation is an unusual type of gel formation exhibited by methylcellulose and hydroxypropylmethylcellulose. They gel when the solution is heated to temperatures between 50 and 90°C, depending on the specific binder type.

Gel formation has not been stressed as useful in the ceramic literature. Bodies having gelled liquids dry much more slowly because the liquid does not flow to the surface during drying. Water must leave the body by diffusion within the gel structure. However, one advantage of a gelled structure is that the binder does not migrate to the drying surface,¹² as it would if it

were carried there by the flowing liquid as it moves to the surface. This advantage can be utilized with thermogelling solutions, since the gel is stable at higher temperatures. With higher temperatures the diffusion rate of water out of the gel is high and drying can be very rapid. Normal gels, which become liquid with heating, can only be dried at lower temperatures (if the gel is to be retained) where drying would be very slow.

Compatibility with Electrolytes

The rheological behavior of binder solutions can be affected by the presence of electrolytes in solution. The electrolytes may increase or decrease the viscosity, or cause gelation or precipitation of the binder.

In general, nonionic binders have higher tolerances for most electrolytes than ionic binders. For example, the nonionic binders of methylcellulose, hydroxyethylcellulose, and poly(vinyl alcohol) have stable viscosities over a wide pH range and can tolerate monovalent cations and multivalent metallic ions to fairly high concentrations with only a few exceptions. Ionic binders, such as carboxymethylcellulose, gum arabic, guar gum, and alginates, are particularly susceptible to alkaline earth ions, heavy metal ions, and trivalent cations. Stability with respect to pH changes exists over a smaller pH range.

When electrolytes are a problem in binder stability, one approach to remedy the problem, other than changing binders, by adding chelating agents that will tie up the detrimental cations.

Biodegradation

All carbohydrate-derivative binders are susceptible to degradation by enzymatic attack as a result of bacteria or fungi in the solution. Natural gums are particularly susceptible. Hydroxyethylcellulose is somewhat more resistant, while methylcellulose has rather high resistance to attack. In contrast, binders such as poly(vinyl alcohol), acrylics, polyethylene oxides, which are not derived from carbohydrates, are not susceptible to biodegradation.

Biodegradation reduces the molecular weight of the binders and consequently reduces the viscosity of the solutions. When this problem is encountered, a preservative or microbicide should be used to inhibit the degradation. The suppliers of the specific binder usually can recommend appropriate preservatives or microbicides. Care must be exercised that these agents do not introduce metallics that would be undesirable to the finished product.

Mixed-Binder Systems

Many binders are compatible with other binders. That is, a combination of two binders does not cause precipitation, unexpected gelation, or other detrimental effects. In some cases the use of two binders has certain merit. For example, poly(vinyl alcohol) has good bonding power and may be desired for green strength. However, this binder may not have enough thickening power for the desired application. It is possible to add hydroxyethylcellulose, for example, to obtain high viscosities. In another case the dispersion action of gum arabic may be very useful, but the strength and plasticizing capability of poly(vinyl alcohol) may be needed for dry pressing. Mixtures of poly(vinyl alcohol) and gum arabic are possible because of their compatibility. The compatibility of different binder combinations can often be ascertained by consulting the suppliers of the binders.

Plasticizers

When dry, binders often became hard and stiff. Granules for pressing often must be sufficiently soft and deformable to break down in the die under pressure. Plasticizers are additives that soften the binder in the dry or near-dry state. They are lower-molecular-weight organic species that dissolve in the same liquid as the binder. After drying, the binder and plasticizer are intimately mixed as a single material. The plasticizer disrupts the close aligning and bonding of the binder molecules, thereby increasing the flexibility of the material. While softening the binder, the plasticizer tends to reduce the strength.

Water-soluble plasticizers include substances such as glycerine, poly(ethylene glycol), poly(propylene glycol), and propylene glycol. These are effective for poly(vinyl alcohol), methylcellulose, hydroxyethylcellulose, poly(ethylene oxide), polyacrylamides, and several other binders.

Binder Burnout

The amount of foreign contaminants due to the binder left in the fired body depends largely on the chemistry of the binder. Some binders are anionic polyelectrolytes. These include lignosulfonates, carboxymethylcellulose, and alginates. They are often effective as dispersants for clay-based systems. However, these polymers are salts and contain cations such as sodium, potassium, calcium, and ammonium. The metals can be deleterious to many ceramics requiring high purity. The use of these polyelectrolytes as binders is usually with clay-based systems and certain refractories in which the introduced cations can be tolerated. Those with ammonium cations are employed when higher purity is required.

The nonionic binders do not contain metals except as impurities. However, some contain nitrogen, as with PVP, polyacrylamide, poly-ethylenimine, and PEI. The use of these nitrogen-containing binders appears to be very limited in ceramic processing, possibly because the nitrogen can be deleterious in firing or because the cost of these binders tends to be high. The use of protein binders during the 1940s suggests that nitrogen may not be harmful in many cases, however.

For those binders having only carbon, hydrogen, and oxygen as primary constituents, burnout problems can still be encountered. The ash content is a measure of the level of metallic contaminants. Most of the purer binders have ash contents in the 0.5 to 2% range. This can introduce metallic contaminants on the order of 100 to 500 ppm to a ceramic. Also, significant levels of carbon can remain if the binder does not undergo complete thermal degradation. Particularly in reducing atmospheres, the binders with pure carbon-carbon linkage in their backbone and with smaller side groups tend to carburize. Oxygen is required to convert the carbon to CO or CO₂.

REFERENCES

1. J. W. Whittenmore, "Industrial Use of Plasticizers, Binders, and Other Auxiliary Agents," *Bull. Amer. Ceram. Soc.*, **23** (11), 427-432 (1944).
2. E. P. McNamara and J. E. Comefora, "Classification of Natural Organic Binders," *J. Amer. Ceram. Soc.*, **28** (1), 25-31 (1945).
3. C. C. Treischel and E. W. Enrich, "Study of Several Groups on Organic Binders Under Low Pressure Extrusion," *J. Amer. Ceram. Soc.*, **29** (5), 129-132 (1946).
4. A. Wild, "Review of Organic Binders for Use in Structural Clay Products," *Amer. Ceram. Soc. Bull.*, **33** (12), 368-370 (1954).
5. T. Knapp, "Glaze Binders," *Bull. Amer. Ceram. Soc.*, **33** (1), 11 (1954).
6. H. Thurnauer, "Controls Required and Problems Encountered in Production Dry Pressing," *Ceramic Fabrication Processes*, W. D. Kingery, ed., Massachusetts Institute of Technology and Wiley, 1958.
7. S. Levine, "Organic (Temporary) Binders for Ceramic Systems," *Ceram. Age*, **75** (1), 39-42 (1960); **75** (2), 25-36 (1960).
8. T. A. Smith, "Organic Binders and Other Additives for Glazes and Engobes," *Trans. Br. Soc.*, **61** (9), 523-549 (1962).
9. A. R. Teter, "Binders for Machinable Ceramics," *Ceram. Age*, **82** (8), 30-32 (1966).
10. A. Pincus and L. Shipley, "The Role of Organic Binders in Ceramic Processing," *Ceramic Ind.*, **92** (4), 106 (1969).
11. J. F. White and A. L. Clavel, "Extrusion Properties of Non-Clay Oxides," *Bull. Amer. Ceram. Soc.*, **42** (11), 698-702 (1963).
12. J. E. Comefora, "Migration Characteristics of Organic Binders," *Ceram. Age*, **132** (April 1945).

20

Mixedness of Suspensions

K. Sommer

H. Rumpf

Obtaining homogeneous suspensions is one of the goals of processing slips and pastes for a variety of operations. To assess how well a slip or paste is mixed requires defining some parameter that serves as a measure of the degree of mixedness. The use of the variance, a statistical parameter, for various types of suspensions is described in this chapter.

CONCEPT OF VARIANCE

For a simple two-component system, the volume concentration X_1 for component 1 is given by

$$X_1 = \frac{V_1}{V_1 + V_2}$$

where V_1 and V_2 are the volumes of components 1 and 2. The system as a whole has an average value of X_1 . If small samples are taken that all have the same values of X_1 as the overall sample, the mixture is called ideally homogeneous.

Ideal homogeneity cannot be obtained in practice; that is, the concentration of a sample in a real mixture is generally larger or smaller than that for

the ideally homogeneous value. Obviously, the more the concentration varies from the ideal, the poorer the degree of mixing.

The well-known statistical parameter variance is a useful measure of mixedness. The variance σ^2 is the mean square deviation of concentration from the average:

$$\sigma^2(X_i) = \lim_{K \rightarrow \infty} \frac{1}{K} \sum_i (X_{i1} - P_1)^2$$

where P_1 = average, or ideal, value for the volume concentration of component 1

K = number of samples taken.

For a finite number of samples

$$\sigma^2(X_i) = \frac{1}{K} \sum_i (X_{i1} - P_1)^2$$

In the remaining text, the variance is also referred to as the mixedness.

If the two constituents of the mixing are entirely separated (e.g., at the beginning of mixing), every sample will contain either only constituent 1 or constituent 2. The variance for this system is

$$\sigma_{\text{ideal}}^2(X_i) = P_1(1 - P_1)$$

and is independent of the size of the sample and of the size of individual particles.

For an ideally homogeneous mixture,

$$\sigma_{\text{ideal}}^2(X_i) = 0$$

STOCHASTIC HOMOGENEITY

In contrast to the ideal homogeneity there is another final state of mixing that is characterized by the fact that it is not the composition of the samples that is the same in any part of the mixed material, but only the probability that their composition is the same. We call this a uniform random mix and its state is called stochastic homogeneity. What is often called a random mix is really a uniform random mix. A random mix can exist when the distribution of probabilities is different. A uniform random mix is the most homogeneous state of mixing that can be obtained by motion if there are no selective forces present.

When samples with a constant number of particles n are withdrawn from a composition, a generally valid variance of the numerical concentration for

stochastic homogeneity can be derived and is given as:

$$\sigma^2(x) = \frac{p(1-p)}{n}$$

Pawlowski¹ gave the following solution for the stochastic homogeneity of low-concentration suspensions, always assuming a constant total sample volume V :

$$\sigma^2(X_i) = P_1 \cdot \frac{v_1}{V}; \quad V = \text{const.} \quad P_1 \ll 1$$

where v_1 is the volume of a single particle.

Stange² dealt with a two-component system whose particle sizes differ only slightly. He assumed that for samples with a constant volume of all particles V_p , the mean number of particles per sample can be regarded as approximately constant, but in practice this is not so. Even when the ratio of the diameters of the two particle fractions to be mixed is $d_1/d_2 = 1.2$ there is, for $n = 150$, a range of variation between $n = 100$ and $n = 200$. This diameter ratio is still regarded as a monosize fraction for most practical chemical engineering purposes. Stange's equation

$$\sigma^2(X_i) = \frac{P_1(1-P_1)}{V_p} (P_1 \cdot v_2 + (1-P_1) \cdot v_1)$$

therefore only holds when $v_2 \approx v_1$.

Since the conditions of Stange and Pawlowski are sometimes not fulfilled, the present authors derived a general solution for samples having particle sizes that vary.³ For sampling at a constant particle volume V_p , the variance is given by:

$$\sigma^2(X_i) = P_1(1-P_1) \cdot \frac{j \cdot v_1}{V_p}$$

where j is a number defined by the simple fraction:

$$\frac{v_1}{v_2} = \frac{j}{j} \quad i, j = 1, 2, 3, \dots$$

For the special case when the particle volumes v_1 of one component are an integral multiple of the particle volume v_2 of the other, the variance of stochastic homogeneity reduces to:

$$\sigma^2(X_i) = P_1(1-P_1) \cdot \frac{v_1}{V_p} \quad (1)$$

SUSPENSION

When a monosize-particle fraction is mixed into a suspension, the liquid molecules v_2 are so small that it is perfectly fair to claim that the particle volume v_1 is an integral multiple of v_2 . Equation 1 therefore applies to this case, too. For a suspension the "sample particle volume" V_p consisting of the solid component and the liquid is identical to the total sample volume V . A comparison with Pawlowski's equations shows that in the limiting case $P_1 \rightarrow 0$ Equation 1 converts to that of Pawlowski. It differs from Stange's equation by the factor $(1 - P_1)$.

The same analysis as above can also be applied to random packing. In this case we do not regard liquid molecules but rather vanishingly small space units as the monosize-particle volume of the second component.

MIXING OF SEVERAL MONOSIZED-PARTICLE FRACTIONS OF UNEQUAL PARTICLE SIZES

For the mixing of several monosized-particle fractions it is assumed that the single-particle volumes v_i are always an integral multiple of the next smaller particle volumes v_{i+1} :

$$v_1 = \mu_2 \cdot v_2 = \mu_3 \cdot \mu_2 \cdot v_3 = \dots \quad \mu_i = 0, 1, 2, \dots \quad (2)$$

v_1 is the greatest single-particle volume and v_n is the smallest. From this we determine that the smallest ratio of different single-particle volumes v_i/v_{i+1} is 2, that is, the ratio of the equivalent particle sizes d_i/d_{i+1} is 1.26, where the value 1.2 is often regarded as a monosized fraction. Therefore Equation 2 is a practical simplification. With these assumptions an equation for the variance of the stochastic homogeneity can be formulated:

$$\sigma^2(X_k) = P_k(1 - P_k) \cdot \frac{v_k}{V_p} + P_k'^2 \cdot \sigma^2 \left(\sum_{i=1}^{k-1} X_i \right) \quad (3)$$

$$P_k' = \frac{P_k}{\left(1 - \sum_{i=1}^{k-1} X_i\right)}$$

and

$$\sigma^2 \left(\sum_{i=1}^k X_i \right) = P_k(1 - P_k) \cdot \frac{v_k}{V_p} + (1 - P_k')^2 \cdot \sigma^2 \left(\sum_{i=1}^{k-1} X_i \right)$$

X_i is the volume concentration in a sample and P_i is the theoretical volume concentration of the component i . The above formulas are relatively com-

plicated, because the concentration of a component i in a sample is correlated to the concentrations of each of the other components.

MIXEDNESS AND TEST ACCURACY

It can be shown that the following equation of the variance of the stochastic homogeneity of a two-component suspension holds quite generally

$$\sigma^2(X_i) = P_i(1 - P_i) \cdot \frac{v_i}{V}$$

where v_i is the particle volume of component 1 and V is the total volume of the sample. It has also become clear that this calculable final state depends only on the composition of the mix, the particle size or particle volume, and the size of the sample. Figure 20.1 shows the two latter correlations.

The calculations are made for a highly concentrated suspension with $P_1 = 0.5$. The total volume of the sample is plotted along the x-axis and the standard deviation σ_2 along the y-axis. The particle size d has been taken as the parameter of the straight line. The larger the sample volume and the smaller the particle size, the smaller is σ_2 . Just as the final state of stochastic homogeneity is not a characteristic of the mixer, neither is the initial

Standard deviation of random mixtures ($P_1 = 0.5$)

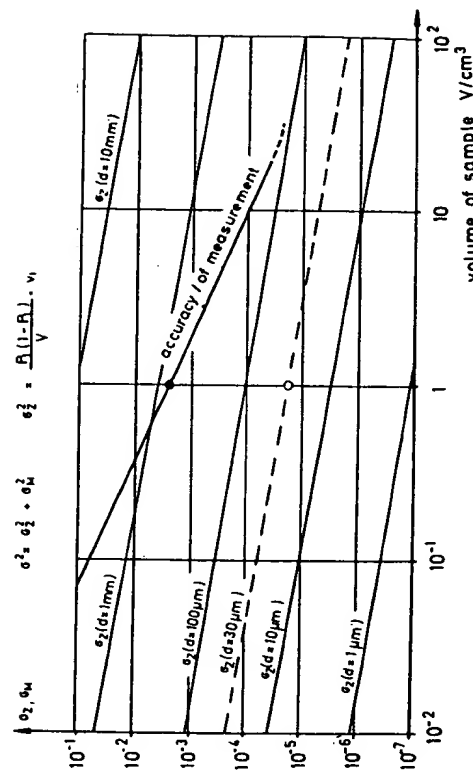


Figure 20.1. Standard deviation of random mixtures as a function of the sample volume V .

state of the completely separated components, for both are only characteristic of the composition of the mix.

For the assessment of mixing, the most important point is the way the variance changes from the initial to the final state. It is therefore necessary to examine which amount of the total variance is a material attribute and which is an attribute of the mixing.

Assuming mixing in which the components at time $t = t_0$ are completely separated the concentration distribution in space will approach a balance in the course of time ($t > t_0$). When repeating this mixing test under identical starting conditions, a perfectly characteristic concentration profile $P(r, t)$ will on the average develop at time t . When we compare the concentrations $X(r_j, t)$ of the various tests in position r_j at time t , they will vary randomly about the expected value $P(r_j, t)$ (Figure 20.2).

The deviation from the theoretical value is therefore affected by two variation factors: first by the systematic deviation of the mean concentration $P(r_j, t)$ and secondly by random variations of the concentration $X(r_j, t)$. It can now be shown that the total variance in the mixing is given by:

$$\sigma_{\text{total}}^2(t) = \sigma_M^2 + \sigma_Z^2 + \left(1 - \frac{v_1}{V}\right) \sigma_{\text{sys}}^2(t)$$

σ_M^2 and σ_Z^2 are variances that are independent of time. The change with time of the total variance $\sigma_{\text{total}}^2(t)$ is only determined by the change with time of the systematic deviation, and σ_{sys}^2 is the real criterion for assessing a mixer. Mixing is completed when this systematic variance becomes zero. The total variance in the final state is therefore a constant composed of σ_M^2 and σ_Z^2 .

In addition to the computable standard deviation σ_s , the inaccuracy of measurement σ_M determined in tests with chocolate or cocoa butter-sugar mixes is also presented in Figure 20.1. It can be seen that it is generally much greater in the given range than the random variations of stochastic homogeneity. That is why, for a discussion of $\sigma_{\text{total}}(t)$, the inaccuracy of measurement must at the latest be noted at or shortly before the end of mixing, and this is unfortunately often neglected in the literature.

Figure 20.3 shows how the standard deviation s of the sample composition of a mix changes during mixing. The mixing time is plotted along the x-axis and the empirically determined standard deviation s along the y-axis. A cocoa butter-sugar suspension containing 50% sugar by volume was mixed in a Werner-Pfleiderer kneader, which was completely filled.

The test points were obtained during a mixing test. They cannot lie below the accuracy of measurement. After a certain mixing time they are therefore bound to enter the band between σ_{M0} and σ_{Mu} . During the tests the mixing time was $t_M \approx 12$ minutes.

When σ_M is greater than σ_s it is impossible to ascertain whether

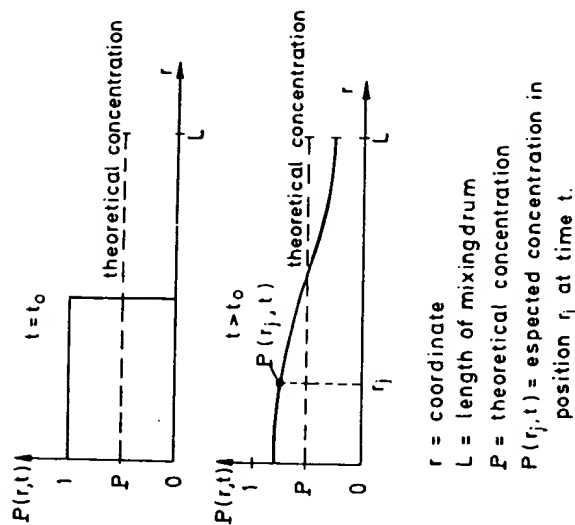


Figure 20.2. The concentration in a mixer as a function of the position r_j and the time t .

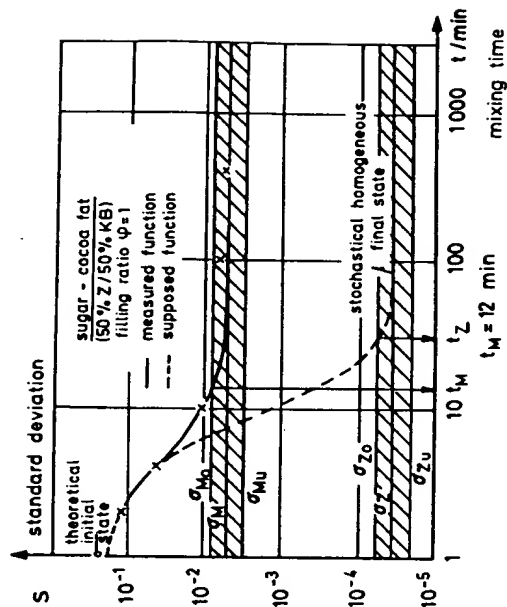


Figure 20.3. Time-dependent mixedness for a sugar-cocoa fat mixture.

stochastic homogeneity has been reached. During actual mixing it is only possible to determine the effective state of mixing when the inaccuracy of the method of measurement is less than σ_z . This would give a curve that enters the confidence limits for σ_z after a mixing time t_z . Stochastic homogeneity is reached at t_z . It is certain that t_z is not less than t_M , but is cannot safely be asserted that t_z is greater than t_M , nor by how much it is greater than t_M .

The question of how homogeneous a mixture has to be will ultimately be decided by technical requirements if, in the application, variations up to σ_M are admissible, the mixing test can be applied, and t_M is a sufficient mixing time. A longer mixing time produces neither a measurable nor a technically required advantage. In many cases the analytical determination of mixedness by measurement of the concentration is worse than the sensory judgment (e.g., homocopathy, taste, texture). If technical requirements demand a more homogeneous mix, the more accurate measuring method must be used, if indeed this is possible. If not, the demand for greater mixing homogeneity is absurd, because it cannot be checked.

REFERENCES

1. J. Pawlowski, "Zur Statistik der Homogenisierungsprozesse," *Chem.-Ing.-Techn.*, **36**, (11), 1089/98 (1964).
2. K. Stange, "Die Mischgüte einer Zufallsmischung als Grundlage zur Beurteilung von Mischversuchen," *Chem.-Ing.-Techn.*, **26**, 331/337 (1954).
3. K. Sommer and H. Rumpf, "Varianz der stochastischen Homogenität bei Körnermischungen und Suspensionen," *Chem.-Ing.-Techn.*, **46**, 257 (1974).
4. K. Sommer, "Einfluß des Probevolumens auf den mittleren Fehler der Korngrößenanalyse," *Chem.-Ing.-Techn.*, **47**, 1 (1975).

21

Quantitative Theory of Cracking and Warping During the Drying of Clay Bodies

A. R. Cooper

Cracking and warping of ceramic bodies during drying are a result of the nonuniform shrinkage that takes place throughout the body. From a physical viewpoint, drying behavior has been well described.¹⁻³ However, no quantitative treatment exists for describing the stresses and strains that arise during drying. To make this understanding quantitative, we have utilized the well-established theory describing the stresses, strains, and deformations that are caused by nonuniform temperature distributions in a material.⁴ The same theory can be applied to the problem of drying stresses and deformations caused by nonuniform water contents. Similar considerations have already been utilized for describing the stresses and deformations that develop from nonuniform concentration distributions.^{10,11}

The transport of water in soils and particularly in clays is a subject of intense interest in the field of soil science. While several methods^{12,13} have evolved for treatment of the process of water transport in soil-water

systems, most workers seem to follow the approach of Philip¹⁴ and treat water transport as a diffusion process. Since this approach is directly applicable to "thermal stress theory," and since careful measurements¹⁵ confirm the validity of the diffusion equations over an order of magnitude of time, we choose to follow this scheme. Further, progress¹⁶⁻¹⁸ in techniques of solution of the nonlinear concentration-dependent diffusion equation for cases of interest in soil science and the establishment of a thermodynamic basis¹⁹⁻²¹ for the drying process in soils may prove to be of direct utility in ceramics.

In this paper we do not utilize the sophisticated methods of the soil scientists for solution of the nonlinear diffusion equations. Rather, it is shown below that by being concerned about the magnitude of the effects due to variable water diffusivity and by accounting explicitly for approximations that will lead to significant errors, we can utilize a relatively simple theory to gain a quantitative understanding of drying stresses.

PHENOMENOLOGY OF SWELLING

A typical water-expansion curve for clay is shown schematically in Figure 22.1, where V is the total volume of the body, V_0 is the dry volume, and C is the volume fraction of water. If V_w and V_s are the actual volumes of water and solid in the body, C is equal to $V_w/(V_w + V_s)$. An abrupt change in expansion occurs at $C = \theta$. When a body is drying, it shrinks until the clay particles touch. Further drying occurs without shrinkage by replacing the water in the pores by air. The volume fraction θ is that point where the particles touch during drying.

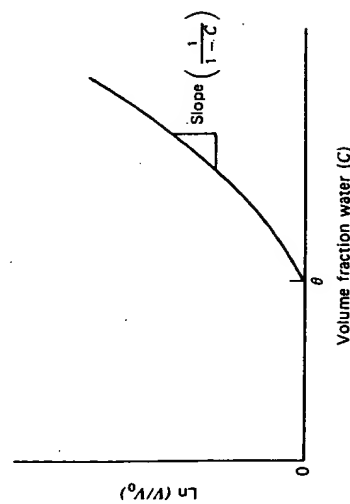


Figure 21.1. Schematic curve of water expansion of clay-water system.

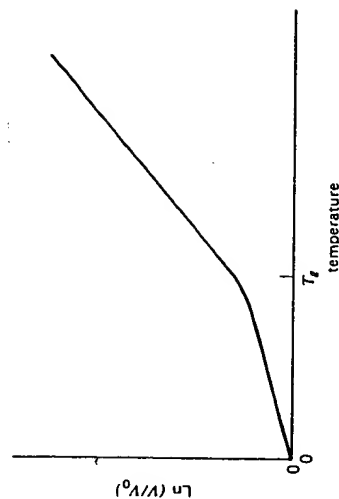


Figure 21.2. Schematic curve of thermal expansion of glass-forming system.

The water expansion can be described by a coefficient α_C as follows:

$$\alpha_C \equiv \frac{1}{V} \frac{\partial V}{\partial C} \equiv \frac{1}{V} \frac{\partial V}{\partial [V_w/(V_w + V_s)]} \quad (1)$$

Note that for $C > \theta$, $dV = dV_w$ and for $C < \theta$, $dV = 0$, we see that

$$\begin{aligned} \alpha_C &= 0 & C < \theta \\ \alpha_C &= \frac{1}{(1-C)} & C \geq \theta \end{aligned} \quad (2)$$

Since calculation of stresses involves linear strains, we are more concerned with linear expansion than with volume expansion. If L_x is a characteristic length in the x direction, the linear expansion coefficient α_{xc} is defined by $\alpha_{xc} = 1/L_x (\partial L_x / \partial C)$. The linear expansion coefficients in three orthogonal directions must always sum to the volume expansion coefficient, for example, $\alpha_x + \alpha_y + \alpha_z = \alpha$. When the material is isotropic, we can further simplify, since $\alpha_x = \alpha_y = \alpha_z = \frac{1}{3} \alpha$. Although we henceforth assume isotropy for simplicity, we realize that anisotropic water expansion exists^{1,6-8} and can be of decisive importance¹ in fracture and warping.

DEFORMATION BEHAVIOR

The water-expansion curve for clay has some similarity to the thermal-expansion curve of a glass-forming system, shown in Figure 21.2. For the glass, V_0 represents the volume at zero temperature. The temperature T is analogous to C for the water-expansion case. The expansion curve for glass also has an abrupt change in slope at the glass transition temperature (T_g). However, the glass still has a finite thermal expansion at $T < T_g$.

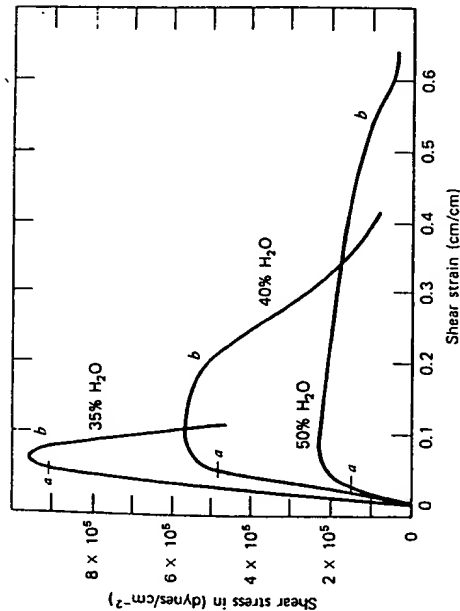


Figure 21.3. Stress-strain diagrams for a plastic clay at several water contents (taken from Norton¹⁷): *a* = yield point, *b* = fracture. Note: percent water is weight percent water *M*; $C = M/100[(M(1 - X) + X)]$ where X^{-1} = specific gravity of clay.

A characteristic difference between a clay-water system and a glass-forming system is that above their glass transition, glasses are viscous and can only support a hydrostatic stress. As seen in Figure 21.3, however, at water contents where $C \gg \theta$, the clay still has a finite modulus of elasticity. When clays are in the plastic range, they can maintain their shape against finite deformation forces, for example, those due to gravity.

Several additional points about Figure 21.3 deserve comment. (1) For a decrease of water concentration ΔC of about 0.30 (which is equivalent to 15 wt %), the modulus of elasticity increases by a factor of about 5. (2) The strain at the yield point remains remarkably constant over the entire range of water contents. (3) The occurrence of cracking as indicated by the points *b* on the curves occurs at higher strains but lower stress as *C* increases.

It is well known that so long as $C > \theta$, a clay-water paste will dry at a rate determined entirely by conditions external to the piece¹⁸; that is to say, water flow through the clay paste is always adequate to maintain the flux density of water *j* consistent with the evaporation kinetics. Typically, the volume of water evaporating per unit surface area per second, that is, the flux *j*, is given by

$$j = k(p_w - p_0)$$

where *k* = evaporation constant governed by the flow conditions

p_w = vapor pressure of water at the temperature of drying

p_0 = partial pressure of water in the surrounding atmosphere.

Since *k*, p_w , and p_0 are often held fixed, this portion of the drying cycle is often called the "constant-rate" period. As the system becomes dryer, water flow within the piece begins to influence the kinetics and causes a "falling rate."

KINETICS OF DRYING

As shown by Philip and Knight,^{16,17} the phenomenology of water flow through clay-water systems is best comprehended and related to permeability models when the flow relative to the clay particles is considered. This results in his using the moisture ratio γ , which is equal to V_w/V_s , to describe the water content and substituting a distance of solid variable *m*, where *m* is equal to *z/C*, in place of the usual distance variable *z*. However, he also shows that there is a direct conversion between the diffusion coefficient appropriate when the (γ , *m*) variables are utilized and the diffusion coefficient using the (*C*, *z*) variables, that is,

$$D(C, z) = (1 + \gamma)^2 D(\gamma, m)$$

This leaves us free to write the diffusion equation in the usual way as

$$\frac{\partial C}{\partial t} = \nabla(D \nabla C) \quad (3)$$

Our approach here is to consider solution of this equation for the case of a large slab of thickness $2w$ with an initial uniform water concentration C_0 and an equal drying rate *j* from both surfaces. Assuming at first that *D* is constant for all $C > \theta$, we get the solution¹²

$$C(z, t) = C(0, 0) - \frac{jw}{D} \left(\frac{z^2}{2w^2} + \frac{Dt}{w^2} - \frac{1}{6} \right) - \frac{2}{\pi^2} \sum_{n=1}^{\infty} \frac{(-1)^n}{(n)^2} \cos \left(\frac{n\pi z}{w} \right) \exp \left(-\frac{n^2 \pi^2 t}{w^2} \right) \quad (4)$$

This solution, displayed as Figure 21.4, reveals that after a short period of time, the form of the concentration profile becomes fixed; dC/dt is equal to $-j/w$, a constant everywhere, and the concentration distribution is parabolic.

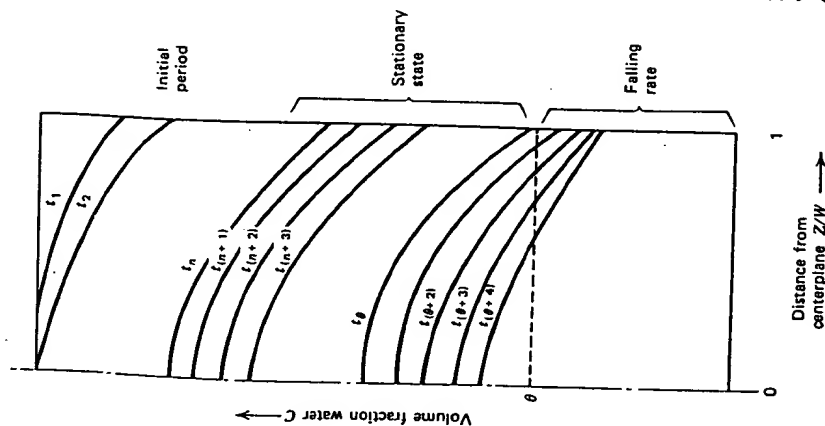


Figure 21.4. C versus z solutions of the water-diffusion equation for constant rate drying and constant D .

This "stationary-state" condition is asymptotically attained. An estimate of the time required before the distribution becomes parabolic is given by the fact that when $t > 0.3w^2/D$, the terms in the summation in Equation 4 always contribute less than 3% of the value of $C(z, t)$ for all z . Even when D is not constant, we may expect that the distribution will tend to the stationary state, that is, dC/dt is equal to $(-j/w)$.

For constant D in the stationary-state regime, it is easy to show that

$$C(w, t) - \bar{C}(t) = -1/3(jw/D) \quad (5)$$

This is also the maximum differential in water content between the average concentration \bar{C} and the concentration at any other point at any

time during the drying process with constant drying rate and constant water-diffusion coefficient.

Once the water concentration at the surface reaches θ , the drying rate begins to diminish. Since no volume change occurs in the region of $C < \theta$, there is little interest to us from the point of view of deformation and fracture once the entire specimen satisfies this condition.

While Equations 2 and 3 and Figure 21.4 are for a constant diffusion coefficient, the recent data on $D(\theta)$ for bentonite,²⁸ as well as the results quoted by Ward (see Figure 21.5), show that D is actually an increasing function of water concentration. This has two important consequences. First, the curves $C(z, t)$ during the stationary-state period are no longer simple parabola. Rather, as indicated in Figure 21.6, an increase in the diffusion coefficient in the higher-water-containing interior causes a decrease in the composition differentials over that obtained if the diffusion constant is fixed at its value at the outer surface. Thus if the diffusion coefficient at the surface D_w is substituted for D , Equation 3 still provides an upper

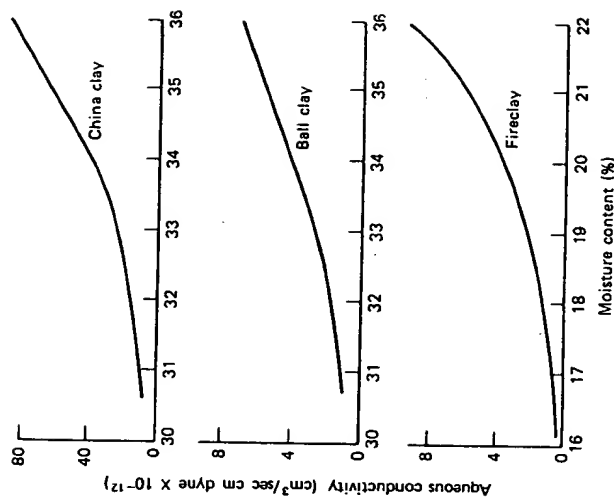


Figure 21.5. Variation in moisture conductivity (proportional to D) of three clays. Note moisture content is weight percent water M ; $C = M/[100M(1 - X) + X]$ where X^{-1} is specific gravity of clay. (From Ford,¹ Figure 28, p. 51.)

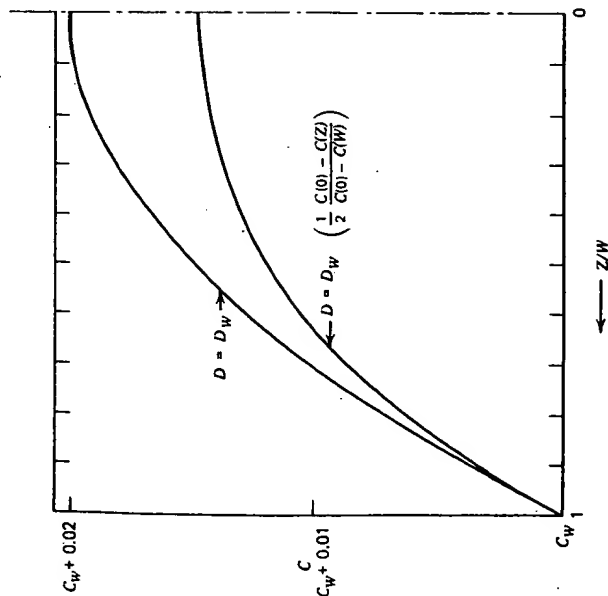


Figure 21.6. Comparison of water distribution for case of constant D (i.e., $D = D_w$) and variable D .

bound for the water concentration differentials. Second, the differentials $[C(w, t) - \bar{C}(t)]$, will increase as time advances during the stationary-state period. Actually, as seen in Figure 21.6, the estimate is quite good for a twofold variation in D across the piece. Because of the decrease of D_w with time, the maximum concentration differential occurs at the time when $C(w) = \theta$.

It is interesting that constant D solutions to Equation 3 for cylindrical or spherical symmetry and constant drying rate also yield stationary-state concentration distributions that are parabolic, just as those in Equation 4 and Figure 21.4, with the only replacement being fractional radius r/R for fractional thickness z/w . Likewise, the differentials are only slightly modified (because of the difference in averaging procedures) to:

$$C(R, t) - \bar{C}(t) = -\frac{1}{4} \frac{jR}{D} \quad \text{cylinder}$$

$$C(R, t) - \bar{C}(t) = -\frac{1}{5} \frac{jR}{D} \quad \text{sphere} \quad (6)$$

Drying also causes temperature differentials, as a result of the heat of vaporization, but these are ignored here for simplicity.

THERMAL STRESS THEORY

To understand the consequences of water differentials, such as those given in Equations 4 through 6, we look for an analogy to thermal stress theory. This methodology permits calculation of stresses, strains, deformation, and warping due to the presence of nonuniform temperatures. Explicit solutions exist for simple shapes such as slabs, cylinders, and spheres.⁶⁻⁸ For example, with constant thermal expansivity α , elastic modulus E , and Poisson's ratio ν , the normal stress σ in the plane of a slab of thickness $2w$ with the origin of the z axis placed at the slab midplane is:

$$\sigma(z) = \frac{aE}{1-\nu} \left(-T + \frac{1}{2w} \int_{-w}^{+w} T dz + \frac{3z}{2w^3} \int_{-w}^{+w} Tz dz \right) \quad (7)$$

If the temperature distribution T is linear, there is no stress anywhere, that is, $\sigma = 0$. If T is symmetric, that is, $T(z) = T(-z)$, then the last term drops out in Equation 7 and $\sigma(z) = Ea(\bar{T} - T(z)/(1-\nu))$. (This condition is also true for tangential stress at the surface of spheres and cylinders of radius R , that is, $\sigma(R) \sim [\bar{T} - T(R)]$. In this convention positive values of σ are tension. Hence, during cooling the maximum tension occurs at the surface $z = w$ or $r = R$.)

The normal strain in the plane ϵ_{xx} is given by

$$\epsilon_{xx}(z) = \epsilon_{yy}(z) = \frac{a}{w} \int_{-w}^{+w} T dz + \frac{3z}{2w^3} \int_{-w}^{+w} Tz dz \quad (8)$$

and the curvature ρ by

$$\rho^{-1} \approx -\frac{3}{2} \frac{a}{w^3} \int_{-w}^{+w} Tz dz \quad (9)$$

Notice that when temperature distribution is symmetric, $1/\rho = 0$, that is, a plane slab remains flat.

Materials that are capable of developing residual stresses can exist with a nonuniform temperature distribution T_0 without a stress. If they are quenched to a new temperature regime where stresses can be supported, the stress, strain, and curvature present at the new temperature distribution T are given by substituting $(T - T_0)$ for T in Equations 7 through 9.

A constant function of z is both linear and symmetric. Hence, for T a constant function of z , the stress and curvature are calculable by substitut-

ing $-T_0$ for T in Equations 7 and 9. The stresses obtained in tempering glass by quenching are approximately described in this way by letting the zero stress temperature distribution T_0 be that which is present when the center of the slab goes through the glass transition temperature T_g .

APPLICATION OF THERMAL STRESS THEORY TO DRYING

In the region where a clay-water paste exhibits elastic behavior (where $\sigma < \sigma_{yp}$), the equations of thermal stress apply with the substitution $C \rightarrow T$, $C_0 \rightarrow T_0$, and $a_c \rightarrow \alpha$. However, it is not appropriate to use Equations 7 and 8 directly because they apply exactly only for constant properties and, as we see in Figure 21.3, the elastic constant varies markedly with water concentration. Thus we must use an expression²⁴ that avoids the approximation of constant properties. For an isotropic slab dried at an equal rate from both surfaces, the result is:

$$\frac{\sigma(z, t)}{A(z, t)} = - \int_{C(z, 0)}^{C(z, t)} a_c(X) dx + \frac{\int_0^w A(\psi, t) \int_{C(z, 0)}^{C(\psi, t)} a_c(X) dX d\psi}{\int_0^w A(\psi, t) d\psi} \quad (10)$$

where $A = [E/(1 - \nu)]$ and water expansion a_c are functions of concentration, X is the dummy concentration variable, ψ is the dummy distance variable, and $C(z, 0)$ is a water distribution at which there is no stress. Provided this stress-free distribution is one of uniform concentration, we may replace $C(z, 0)$ with any constant water concentration, for example, $C(w, t)$. Then the maximum tension stress always occurs at the surface and

$$\sigma_{\text{Max}}(t) = \sigma(w, t) = \frac{A(w, t) \int_0^w A(\psi, t) \int_{C(w, t)}^{C(\psi, t)} a_c(X) dX d\psi}{\int_0^w A(\psi, t) d\psi} \quad (11)$$

It is not difficult to evaluate Equation 11 directly for a given case. By making some reasonable approximations, however, we can gain further insight. Since $a_c = \frac{1}{3} [(1 - C)]$ for an isotropic material

$$\int_{C(w, t)}^{C(\psi, t)} a_c(X) dX = \frac{1}{3} \ln \left\{ \frac{[1 - C(w, t)]}{[1 - C(\psi, t)]} \right\} \quad (12)$$

Further, since

$$\ln \frac{[1 - C(w, t)]}{[1 - C(\psi, t)]} \approx \left(\frac{C(\psi, t) - C(w, t)}{1 - C(w, t)} \right)$$

$$\frac{\sigma(w, t)}{A(w, t)} \approx \frac{1/3 [1 - C(w, t)] \int_0^w A(\psi, t) [C(\psi, t) - C(w, t)] d\psi}{\int_0^w A(\psi, t) d\psi} \quad (13)$$

The quotient of the two integrals in Equation 13 is just the average of the quantity $[C(\psi, t) - C(w, t)]$ weighted according to the elastic modulus. Since $A(\psi)$ is a decreasing function of ψ the water concentrations in the interior will not be weighted as heavily as the surface water concentration. Thus

$$\frac{\sigma(w, t)}{A(w, t)} < \frac{1}{3 [1 - C(w, t)]} [\bar{C}(t) - C(w, t)] \quad (14)$$

and substitution of numerical values suggests:

$$\frac{\sigma(w, t)}{A(w, t)_{\text{lab}}} \approx \frac{1}{3} [\bar{C}(t) - C(w, t)] = \frac{1}{9} \frac{jw}{D_w} \quad (15)$$

Thus we see now that the stress is directly proportional to the flux of water from the surface and the width of the sample and inversely proportional to the diffusion coefficient.

For spheres and cylinders of radius R , we can write analogous approximations for the tangential stress:

$$\frac{\sigma_{\theta\theta}(R, t)}{A(R, t)} \approx \frac{1}{12} \frac{j_R}{D_R} \quad \text{cylinder}$$

$$\frac{\sigma_{\theta\theta}(R, t)}{A(R, t)} \approx \frac{1}{15} \frac{j_R}{D_R} \quad \text{sphere} \quad (16)$$

The question remains as to what value of σ to select to avoid the development of cracks during drying. From Figure 21.3 it appears that (for the clay measured by Norton) if σ/E remains less than about 0.05, no chance of fracture exists. Also, if this condition is maintained there is likewise no opportunity for irreversible deformation. Then, assuming that no volume change occurs during elastic deformation and hence $\nu = \frac{1}{2}$, we may con-

clude that for safe drying

$$\begin{aligned}
 j_{\text{slab}} &\leq \frac{9D}{w} \left(\frac{0.05}{0.5} \right) \approx \frac{D_w}{w} \\
 j_{\text{cyl}} &\leq \frac{12D}{w} \left(\frac{0.05}{0.5} \right) \approx 1.2 \frac{D_R}{R} \\
 j_{\text{sphere}} &\leq \frac{15D}{w} \left(\frac{0.05}{0.5} \right) \approx 1.5 \frac{D_R}{R}
 \end{aligned} \quad (17)$$

Maintaining drying rates within these restrictions should avoid fracture, provided j , the drying rate, is kept equal at all points on the surface.

Warping is prevented during the drying of an isotropic system during the entire drying cycle if the water concentration distribution is symmetric, as is easily seen by substituting $(C - C_0)$ for T in Equation 9. It also follows from Equation 9 that even if the drying rate is nonuniform, there will be no shape change in a fully dried slab, cylinder, or sphere with an originally symmetric water distribution, provided no stress relaxation occurs during drying. For a material with the properties shown in Figure 21.3, this requires that $\sigma < \sigma_{yp}$. Retention of shape also is achieved if the conditions of Equation 17 are fulfilled.

Since D_w decreases as time of drying increases, Equation 17 suggests that minimum drying time is achieved if j decreases with time during the stationary-state period.

POSSIBILITY OF "TEMPERING" A CLAY DURING DRYING

The analogy of clay drying to glass cooling poses the question, Can residual compressive stresses be created in a dried piece by a method similar to that used to create stresses during rapid cooling of glass?" First this requires the creation of a water distribution that causes some stress relaxation. Such a result can be achieved if $\sigma > \sigma_{yp}$. It is clear from Figure 21.3 that this is most easily obtained at the higher water contents, which suggests drying initially at a rate such that j is greater than that permitted by Equation 17. While this is no doubt a useful idea, it is not clear without analysis beyond the scope of this paper whether the strong dependence of D on C prevents the possibility of obtaining stress relaxation during initial stages of drying without obtaining fracture near the end of the drying cycle.

RELATION TO OBSERVATIONS

The predictions from theory are consistent with the observation that the most critical period for fracture during drying is at the end of the constant-rate period. They are also consistent with the comments of Ward, "In general terms, cracking or warping of an article during drying is due to differential shrinkage of the body, which may have several causes: (1) Differential rate of loss of water from different positions, e.g., surface and interior. (2) Uneven distribution of moisture within the article prior to drying, resulting in non-uniform total shrinkage. (3) Anisotropic shrinkage because of the orientation of particles during shaping. (4) Mechanical restraint of shrinkage at a position where the article is in contact with the surface on which it is resting, particularly with heavy shapes and particles formed and dried on plaster moulds."

It is difficult, however, to obtain a quantitative agreement with the observations of Macey and Wilde,⁷ who measured the maximum rates of drying permissible for a brick clay. For example, for a slab of 1.27 cm half width, they found that $j_{\text{Max}} = 1.5 \times 10^{-6}$ cm²/cm² second. According to Equation 17, $j_{\text{Max}} \approx D_w/w = 0.8 D_w$. Hence, from drying data $D_w \approx 2 \times 10^{-6}$ cm²/second. For comparison, one can make estimates on diffusivity of water in clay from data presented by Ward. Comparing the water flux j with the concentration gradient at the surface, $(dC/dz)_w$ for ball clay (Figure 21.7), one gets $D_w \approx 1.6 \times 10^{-3}$ cm²/second. Likewise, using the aqueous conductivity data, Figure 21.4, and the relation between hydrostatic pressure P and equilibrium water concentration¹ $dP/dC = 1.1 \times 10^8$ dynes/cm², one obtains $D_w \approx 1 \times 10^{-3}$ cm²/second. A discrepancy of about two orders of magnitude is present.

Several explanations are possible: (1) Factors completely different from the stresses caused by water differentials govern the maximum permissible drying rate. (2) Nonuniformities of body and/or drying cause local stresses far in excess of those considered by our assumption of a uniform isotropic clay body and a uniform drying rate. (3) The drying rate, diffusion coefficient, and deformation characteristics were all measured on different clays and perhaps at different temperatures, and hence good agreement cannot be expected. Some support for the last point is found from the water-diffusion data on Smiles and Harvey²³ on the bentonite-water system. Extrapolating to the range of water concentrations of interest in clay drying, one obtains $D \approx 10^{-6}$ cm²/second, which is lower than the result obtained from Macey's observed safe drying rates.

Another discrepancy between Macey's results and Equation 17 is that Macey found in the drying of cubes that $j_{\text{Max}} \sim w^{-2.6}$. Although none of the

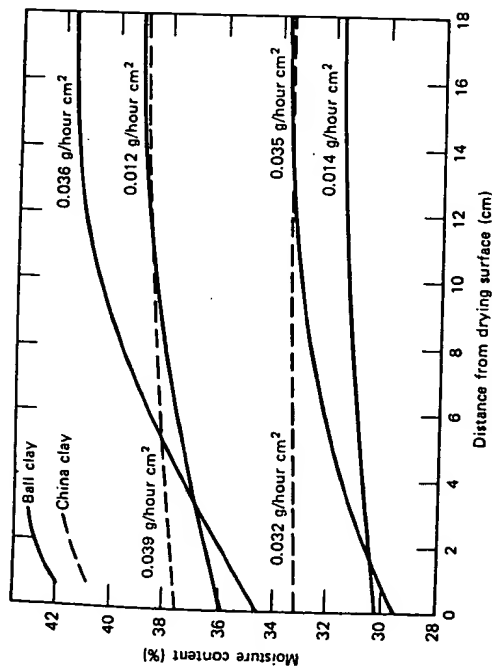


Figure 21.7. Moisture distribution during "constant rate" period for drying of very thick slabs.

simple shapes, spheres, cylinders, and slabs, considered in this paper are cubes, $j_{\text{Max}} \sim w^{-1}$ or R^{-1} .

CONCLUSIONS

It has been shown that by treating water flow as being analogous to heat flow, it is possible to calculate stresses and warping of simply shaped bodies during drying. The approximate results are simple enough to be readily useful. They suggest ways of optimizing the drying process, for example, steadily decrease the drying rate during the period when the body is shrinking; however, at present they lack experimental confirmation. Thus it is hoped that the theory will be useful in (a) provoking a more detailed analysis of the process using, for example, the methods of Philip¹⁶ and Parlange,¹⁸ and a more detailed description of the deformation characteristics and (b) providing a useful model for design of a series of experiments in drying kinetics of a single body involving determination of water-diffusion coefficients, a detailed determination of the deformation characteristics, and a study of drying fracture and warping.

References

ACKNOWLEDGMENT

A. H. Heuer critically reviewed the manuscript and made useful and welcome suggestions to improve its unity and clarity.

REFERENCES

1. R. W. Ford, "Institute of Ceramics Textbook Series 3. Drying," McLaren, London, England, 1964.
2. F. H. Norton, *Elements of Ceramics*, Addison-Wesley, Cambridge, Mass., 1952.
3. H. Salmang, *Ceramics Physical and Chemical Fundamentals*, translated by Marcus Francis, Butterworths, London, 1961.
4. F. H. Clews, *Heavy Clay Technology*, Academic, London, 1969.
5. A. J. Dale, *Modern Ceramic Practice*, McClaren, London, 1963.
6. H. H. Macey, "The Relative Safe Rates of Drying of Some Different Sizes and Shapes," *Trans. Br. Ceram. Soc.*, 38, 464 (1939). H. H. Macey and F. G. Wilde, "Experiments on the Drying of Clay," *Trans. Br. Ceram. Soc.*, 43, 93 (1944).
7. R. Q. Packard, "Moisture Stress in Unfired Ceramic Bodies," *J. Amer. Ceram. Soc.*, 50, 223 (1967).
8. H. H. Macey, "The Drying of Clay Ware, A Discussion," *Trans. Br. Ceram. Soc.*, 46, 207 (1947).
9. B. A. Boley and J. H. Weiner, "Theory of Thermal Stresses," Wiley, New York, 1960.
10. A. R. Cooper and D. A. Krohn, "Strengthening of Glass Fibers: II. Ion Exchange," *J. Amer. Ceram. Soc.*, 52, 665 (1969).
11. O. Richmond, W. C. Leslie, and H. A. Wreidt, "Theory of Residual Stresses due to Chemical Concentration Gradients," *Trans. American Society for Metals*, 57 (1), 294-300 (1964).
12. A. E. Scheidegger and K. H. Liao, "Thermodynamic Analogy of Mass Transport Processes in Porous Media," *Fundamentals of Transport Phenomena in Porous Media*, Elsevier, New York, 1972.
13. G. Dagan, "Some Aspects of Heat and Mass Transfer in Porous Media," *Fundamentals of Transport Phenomena in Porous Media*, Elsevier, New York, 1972.
14. J. R. Philip, "Hydrostatics and Hydrodynamics in Swelling Media," *Fundamentals of Transport Phenomena in Porous Media*, Elsevier, New York, 1972.
15. D. E. Smiles, "Infiltration into a Swelling Material," *Soil Sci.*, 117 (3), 140-147 (1974).
16. J. R. Philip, "Recent Progress in the Solution of Nonlinear Diffusion Equations," *Soil Sci.*, 117 (5), 257-262 (1974). (See numerous references to earlier work by this author.)
17. J. R. Philip and J. H. Knight, "On Solving the Unsaturated Flow Equation: 3. New Quasi-Analytical Technique," *Soil Sci.*, 117 (1), 1-13 (1974).
18. J. Y. Parlange, "Theory of Water Movement in Soils: 10. Cavities with Constant Flux," *Soil Sci.*, 116 (1), 1-7 (1973). (This paper gives reference to the nine earlier contributions by this author.)

19. G. Sposito, "Volume Changes in Swelling Clays," *Soil Sci.*, 115 (4), 315-320 (1973).
20. S. Iwata, "Thermodynamics of Soil Water: IV. Chemical Potential of Soil Water," *Soil Sci.*, 117 (3), 135-139 (1974).
21. S. Al-Khafaf, R. J. Hanks, "Evaluation of the Filter Paper Method for Estimating Soil Water Potential," *Soil Sci.*, 117, 194-199 (1974).
22. H. S. Carslaw and J. C. Jaeger, "Conduction of Heat in Solids," 2nd ed., Clarendon Press, Oxford, 1954, p. 112.
23. D. E. Smiles and A. G. Harvey, "Measurement of Moisture Diffusivity of Wet Swelling Systems," *Soil Sci.*, 116 (6), 391-399 (1973).
24. I. S. Alvarez and A. R. Cooper, Jr., "Thermal Stress Distribution for a Thin Plate with Temperature Variation through the Thickness," to be published by *J. Appl. Mech.*

22

Mineralogy of Curing and Drying of A Refractory Concrete

R. E. Farris

J. S. Masaryk

Tabular alumina aggregate bonded with calcium aluminate cement is a technically important refractory concrete. The mineralogical changes that occur during the curing and drying of this concrete greatly affect many of its properties. One important use of this concrete is in hardening UHF antennae for Minuteman Missile systems. The concrete protects against the heat and shock of a nuclear blast. In this application the dielectric and loss tangent characteristics (at UHF frequencies) must be consistent because the impedance of the antenna is matched. Mismatch causes gain loss, and transmitting power is not sufficient to contact the antenna.

Development studies during the past several years on hardened UHF antennae has led to a better understanding of the mineralogy of curing and drying of the refractory concrete. The phase that develop and their effects on processing and properties have been analyzed. The results of this work are discussed in this chapter.

MATERIALS, PROCESS DESCRIPTION, AND PROBLEMS

The concrete for the hardened antenna consists of a cylindrical mass weighing about 3000 lb. It consists of sized tabular alumina (6 mesh maximum size) bonded with calcium aluminate cement. The cement contains about 80% Al_2O_3 and 18% CaO . The overall concrete contains 94% Al_2O_3 . The process can be divided into four major steps:

1. *Mixing and casting.* The correct ratios of dry concrete and water are mixed and then properly placed in the mold.
2. *Curing.* The cement-water reactions occur and heat is liberated to form the initial bond in the system.
3. *Queueing.* The period where the castings are allowed to reach thermal and reaction equilibrium before the drying cycle commences.
4. *Drying.* Removal of the water to the required level.

Free water in the concrete causes dielectric losses in the antenna and must be removed. With a fairly rigid drying schedule, it was found over a period of time that residual moisture varied between 2.5 and 4.0%. The variable that correlated best to this variation was the cement lot used to manufacture the concrete, and possibly the CaO content of the cement. Other manufacturing variables that can have some effect are "casting water" or "concrete consistency," curing condition, and queueing conditions.

Another concern resulted from postmortem analysis of antennae that split during drying. This analysis revealed dehydration products that are not considered typical for normal low-temperature (275°C maximum) drying of concrete bonded with calcium aluminate cement. These dehydration products have been previously described in the literature, but not under the same conditions of pressure, temperature, and composition encountered in this particular system.

As a result of these concerns, studies were carried out to better define the effect of processing variables on bond-phase mineralogy during drying.

PREVIOUS LITERATURE

To follow the thermal response of the system of water, calcium aluminate cement, and aggregate, one must first establish the hydration reactions and temperatures and then follow the dehydration reactions that occur later. In the discussion of the hydration-dehydration reaction of calcium aluminate cement, the following notations are used: (1) C is for CaO , (2) A is for

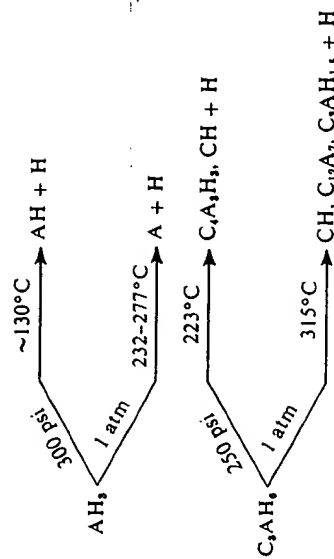


Figure 22.1. Decomposition of AH_6 and C_4AH_6 .

Al_2O_3 , and (3) H is for H_2O . For example, CA is for $\text{CaO} \cdot \text{Al}_2\text{O}_3$, which is the monocalcium aluminate.

The literature¹ discusses the reaction of CA with water at 1 atm pressure. The reactions are summarized in Table 22.1. The hydration of CA results in CAH_{10} and C_2AH_6 . These dehydrate at higher temperatures to C_3AH_6 and finally to C_{12}A_7 , along with the formation of A. At very high temperatures (600 to 1000°C), the excess A reacts to form various ceramic bonding phases, such as CA_2 and CA_3 , along with C_{12}A_7 .

Majumdar and Roy² studied reactions under hydrothermal conditions (high pressure and temperature). They investigated materials initially having C/A ratios of 3:1 and 4:3. In the hydration reaction, C_3A formed C_3AH_6 and the C_4A formed C_4AH_6 . During decomposition the C_3AH_6 formed C_3A , CH , and H at 223°C and 250 psi. Any AH_6 that formed converted to AH and H at 130°C and 3000 psi. The hydrothermal products are compared in Figure 22.1 with those formed at 1 atm. In general the decomposition of the major phases is lowered about 100°C in systems under pressure.

Table 22.1. Hydration-dehydration of CA cement at atmospheric pressure

Compounds and Reactions	Stable Temperature Range (°C)	Major Decomposition Temperature (°C)
$\text{CA} + \text{H} \rightarrow \text{CAH}_{10} + \text{C}_2\text{AH}_6$	—	—
$\text{CAH}_{10} \rightarrow \text{C}_3\text{AH}_6 + \text{AH}_3$	0-20	20
$\text{C}_2\text{AH}_6 \rightarrow \text{C}_3\text{AH}_6 + \text{AH}_3$	25-58	58
$\text{AH}_6 \rightarrow \text{A} + \text{H}$	27-350	232 and 277
$\text{C}_4\text{AH}_6 \rightarrow \text{C}_{12}\text{A}_7 + \text{H}$	58-350	310-320

POSTMORTEM PHASE ANALYSIS OF CONCRETE

Studies on production failures revealed that the predominant phases were AH (boehmite) and $C_3A_2H_5$. The curing was carried out in an ambient of 1 atm. Therefore, the presence of AH and $C_3A_2H_5$ was contrary to what was stated in the literature; these products are produced only under hydrothermal conditions. It was therefore hypothesized that the interiors of the large castings were subjected to hydrothermal conditions as a result of the pressure developed internally by trapped water vapor. To investigate this possibility, autoclave studies were initiated.

AUTOCLOAVE STUDIES

In this work it was assumed that during drying an antenna would behave similarly to a "leaky" autoclave. On this basis the maximum pressure in the large concrete mass at any temperature would be that of saturated steam at the temperature in question. The "leaky" portion of the assumption relates to the casting permeability. Casting permeability yields to several processing variables, the work relating to process variables is discussed in the next section.

The autoclave studies were straightforward. Dry concrete, the same as that used in antenna manufacture, was blended with 9% "casing water" and 3 in. diameter \times 6 in. high cylinders were cast at about 20 to 24°C. The cylinders were cured for 16 to 24 hours at 20 to 24°C and 90 to 95% relative humidity (RH). Cured cylinders were then placed in a standard autoclave for pressure-temperature treatments as shown in Table 22.2. The standard autoclave was limited to 166°C and 80 psi. For higher conditions the samples were placed in a model bomb over water and heated to the listed temperatures that yield the indicated pressures. Holding times at maximum pressures for 24 hours were found to be adequate to yield reaction products. In all cases the steam was released at temperature and then the bomb or autoclave was cooled. Analysis of mineral phases was made using X-ray diffraction techniques. The relative X-ray intensity of reaction product versus temperature and pressure is shown in Table 22.2 and the results are discussed in the following paragraphs.

Gibbsite (AH_3) decomposes between 115 and 130°C at 10 to 25 psig to form boehmite. Previous work suggested this reaction would occur in this temperature range but at very high pressures (3000 psi). This work and the work of others have shown that at atmospheric pressure, regardless of temperature, the AH_3 to AH reaction does not occur in high-purity

Table 22.2. Relative X-ray intensities of mineral phases in autoclaved concrete-calcium aluminate cement bond

Temperature (°C)	Gauge Pressure (psi)	CA	AH ₃	AH	C ₃ AH ₆	C ₃ A ₂ H ₅
115	10	3	16	3	21	—
130	25	—	—	10	21	—
148	50	—	—	13	23	—
166	80	—	—	15	14	—
177	120	—	—	12	15	—
204	233	—	—	25	17	—
232	410	—	—	26	14	—
246	525	—	—	29	3	13
260	665	—	—	41	2	17

concretes. Once formed, however, the boehmite is very stable and becomes a significant bonding phase to temperatures of 510 to 520°C.

Between 148 and 166°C (50 to 80 psig) a decreased intensity for $C_3A_2H_5$ was observed. Additional phases were not observed and there should be no tendency for the $C_3A_2H_5$ to decrease in crystallinity. The reason for the decrease is not readily apparent. However, an increase in the AH intensity was observed between 117 and 204°C (120 to 233 psig). This may indicate some tendency for the $C_3A_2H_5$ to decompose directly to AH and CH under these hydrothermal conditions.

The major decomposition reaction for the $C_3A_2H_5$ was seen to occur between 232 and 246°C (410 to 525 psig). The new compound $C_3A_2H_5$ was identified; however, CH was not. The CH was probably amorphous or masked by other reaction products. Longer exposure to the hydrothermal conditions may produce identifiable CH. Boehmite intensity increased again, either indicating greater crystallinity or a direct decomposition of $C_3A_2H_5$ to AH.

Work needs to be done to define the minimum temperature-pressure conditions under which the AH_3 and $C_3A_2H_5$ decompose. The work reported here was confined relative to those pressures of saturated steam at various temperatures because it was felt that these were the maximum pressures attainable during the drying of the concrete. Discrepancies that exist between this work and that cited earlier are shown in Figure 22.2.

As a result of this work, it was apparent that temperature ranges in the drying schedule that need be accommodated are 120 to 130°C for the AH,

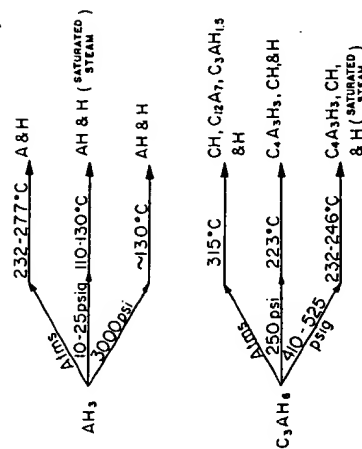


Figure 22.2. Comparison of reported decomposition of AH_3 and C_3AH_6 .

and 235 to 245°C for the C_3AH_6 decompositions. These accommodations are not necessarily for the water-release problem but rather for stresses caused by thermal gradients and strains caused by bond-phase changes to smaller volume (shrinkage). In large massive cylinders, center temperatures are depressed relative to surfaces because of the heat-sink effect resulting from the energy required for the decomposition reaction.

CASTING SIZE

During the early part of the program, several of the antennae suffered massive failure during drying. The typical fracture divides the shape in half, generally across the diameter. Samples of concrete obtained from these cross sections were submitted for analysis. Position samples were at about the halfway point vertically and were sampled along the radius surface to

Table 22.3. Relative X-Ray intensity and thermal analysis of mineral phases in dried concrete (typical)

Position	Relative X-Ray Intensity (Percent of total weight loss)			
	C_3AH_6	AH	C_3AH_6	$CaCO_3$
Surface	10-15 (40-60)	10-20 (20-30)	—	— (15-35)
Surface, 5 in.	4-7 (30-40)	20-40 (30-40)	tr-5 (5-15)	5-10 (10-30)
Surface, 10 in.	6-7 (25-35)	20-30 (30-40)	tr-5 (10-15)	5-10 (10-30)
Center	5-6 (30-50)	20-30 (30-40)	tr-5 (5-15)	5-10 (10-15)

center. Data from X-ray and thermal analyses of these samples are shown in Table 22.3. These data confirm the hydrothermal decomposition of the concrete. The thermal analysis data show an additional phase not identifiable by the X-ray method used—calcium carbonate.

The calcium carbonate is of concern because of specifications relative to residual weight after drying. Experiments are currently underway to determine preferred conditions for carbonate formation.

The antennae average about 32 in. in diameter and about 30 in. high above the outer conductor. To establish concrete thicknesses that respond to hydrothermal decomposition versus those that respond to thermal decomposition, three different sizes of castings were made, dried, and analyzed for decomposition products. The sizes were, for diameter and height, 6 × 12 in., 12 × 12 in., and 30 × 30 in. Results of this work are shown in Table 22.4. These data appear to indicate that the outer 1 to 2 in.

Table 22.4. Mineral phases versus casting diameter—relative X-Ray intensity

Size (in.)		Distance from Surface (in.)						Relative X-Ray Intensity			
Diameter	Height	0	1 1/2	3	0	1 1/2	3	C_3AH_6	AH	C_3AH_6	CH
6	12 ^a	0	1 1/2	3	0	1 1/2	3	6	3	—	—
								24	15	—	—
								27	16	—	—
6	12 ^b	0	1 1/2	3	0	1 1/2	3	PT	16	3	—
								PT	16	3	—
								PT	10	5	3
12	12 ^c	0-1	1-2	4	0-1	1-2	4	9	10	PT	—
								7	16	10	—
								6	21	11	—
								5	18	12	—
30	30 ^d	0-1	5	6	0-1	5	6	—	9	—	4
								—	24	16	8
								—	56	24	9
								—	75	24	5
30	30 ^e	0-1	7.5	15	0-1	7.5	15	13	19	5	—
								5	44	18	—
								3	49	20	—

^a Drying temperature = 400°F.

^b Drying temperature = 600°F.

^c Drying temperature = 540°F.

^d Drying temperature = 600°F (25°F/hour heating rate).

^e Drying temperature = 500°F (~5°F/hour heating rate).

of the casting surface respond solely to thermal decomposition, while the inner portions of the casting respond very well to hydrothermal decomposition. We have also found that certain processing variables contribute to the type of decomposition that takes place, and the limited information available is discussed later. Also of importance in this work was the fact that the residual mineralogy of the 12×12 in. casting was nearly identical to that found in production antennae (compare Tables 22.3 and 22.4). This allowed us to decrease our sample weight from ~ 2000 to ~ 150 lb.

PROCESS VARIABLES

The physical characteristic of the large concrete mass that must control the pressure in the casting during drying is the permeability. The counterpart to permeability relative to controllable variables would be heating rate during drying. Relatively small specimens with reasonable permeability, if heated rapidly enough, could create enough free water relative to its release rate at the surface to approach autoclave (saturated steam) conditions.

Heating rate has been specified for the concerns of this study; therefore, the variable that needs to be controlled to establish consistent drying behavior is permeability.

Conditions at the time of casting probably exert the greatest influence on permeability. Further, in any lot of concrete with constant aggregate sizing and cement behavior, the controllable variables that allow one to exert some influence on the castware permeability are "casting water" (amount of water required to achieve desired "casting consistency") and raw-material temperature, including casting-water temperature. Fixing material temperature allows one to measure independently the effect of casting water on resultant bond-phase mineralogy and, hence, indirectly on permeability.

As a result of these implications, 12 in. diameter \times 12 in. high castings were made using either 8 or 10% casting water. The normal casting water for this lot of concrete was 9%, dry weight basis. On the basis of thermal diffusivity, a drying schedule was estimated that would simulate the thermal gradient experienced by production-dried antennae. After the units were dried, strength was determined by diametral compression, and samples for mineral-phase analysis were chipped from the diametral cross section. The results of these analyses are shown in Table 22.5. A similar experiment was conducted using 8.5 and 9.5% casting water. Results for 8.5% casting water were similar to those obtained using 8% casting water, and those obtained using 9.5% casting water were similar to those found with 10% casting water. An exact quantitative comparison has not yet been obtained.

Table 22.5. The effect of casting water on bond phase mineralogy during drying to 540°F

Casting Water (%)	Distance from Surface (in.)	Relative X-Ray Intensity				
		C ₃ AH ₆	AH	C ₄ A ₃ H ₅	C ₃ AH _{4.5}	CA
8	0	13	12	3	PT	3
	2	7	27	14	PT	—
	4	7	27	14	PT	—
	(Center) 6	8	32	13	PT	—
10	0	12	10	—	PT	PT
	2	19	14	—	PT	—
	4	14	13	—	PT	—
	(Center) 6	18	15	PT	PT	—

These results indicate that for a particular lot of concrete, variation of casting water by $\frac{1}{2}$ to 1% can alter the bond-phase decomposition path from a strictly thermal to a hydrothermal response. These results also imply that temperature considerations for major thermal decomposition reactions should be adjusted relative to casting behavior or possibly cast density.

Curing and queuing conditions, once established, are held constant and yield relatively consistent mineralogy to commence the drying operation. These early conditions influence to some extent, however, the amount of residual CA in the concrete.

THERMAL DECOMPOSITION TEMPERATURES

Decomposition temperatures for the C₃AH₆ to C₄A₃H₅ have been confirmed on production units. Confirmation appears as a temperature lag or depression (endotherm) measured on the surface of the antenna, while heat input to the oven remains constant or is increased. This is noticed while casting surface temperatures are in the 230 to 250°C range.

The conditions have not been established where the casting permeability becomes sufficiently high to allow water transport and release without pressure buildup. This work has been largely confined to temperatures below 316°C (600°F). However, identification of mineral phases has been confirmed by thermal analysis. On the basis of these results, the major decomposition temperatures for several of the hydrate compounds have been measured. This technique has also allowed the detection of certain

Table 22.6. Thermal decomposition temperatures for CA cement bond phases in dried concrete

Compound	Temperature Range (°C)	Peak Reaction Temperature (°C)
AH ₃	210-240	~230
C ₃ AH ₆	240-370	~315
C ₃ AH _{1.5} ^a	465-482	~470
AH	480-565	~525
C ₄ A ₃ H ₅	565-620	~600
CaCO ₃	650-790	~745

^a Questionable—when this peak occurs, X-ray results generally indicate the presence of C₁₂A₇.

compounds that are difficult to identify by X-ray in this system, specifically calcium carbonate. Table 22.6 gives these phases and their measured decomposition temperature ranges at atmospheric pressure in flowing dry air.

Many times X-ray data indicate the presence of C₁₂A₇ when the system temperature has not been sufficiently high to form this compound. When thermal analyses of these samples are made, a second endotherm-decomposition peak occurs at about 470°C. X-Ray diffraction peaks for these compounds are similar; therefore, it is suggested that this TGA peak is that for C₃AH_{1.5}^a. Often some intensification of the AH peak is consistent with this reaction.

CONCLUSIONS

Small variations (0.5 to 1%) in casting water can cause significant variation in hydrated CA cement bond-phase mineralogy during the drying process. These variations result from changes in permeability, causing differences in the internal pressure of the concrete.

Increases in internal pressure cause initial decomposition reactions to occur at lower temperatures, on the order of 100°C. The products of these decomposition reactions, AH and C₄A₃H₅, still comprise a hydrate bonding phase that is more tenacious at higher temperatures than that observed with typical low-pressure decomposition.

Additional work is required to better define the pressure-temperature-hydrate phase decomposition interactions. Guidelines or limits for these

studies appear to be defined; however, certain inconsistencies are still prevalent.

In addition to casting water and heating rate, cement-to-aggregate ratio and sizing can influence the bond-phase decomposition reactions.

ACKNOWLEDGMENTS

Dr. Kaiser wishes to thank Boeing Aerospace Company, who is the major contractor funding this study. In addition, the authors wish to thank W. H. Boyer for the X-ray analysis results; R. W. Nimmer and W. R. Alder for thermal analysis results; and M. A. Stett, M. E. Green, and J. W. Meeds for carrying out the autoclave and 12 in. diameter cylinder studies.

REFERENCES

1. G. V. Givan, L. D. Hart, R. P. Helich, and G. Maczura, "Curing and Firing High Purity Calcium Aluminate Bonded Tabular Alumina Castable," presented at the Refractories Division meeting of the American Ceramic Society at Bedford Springs, Pa., Oct. 4, 1974.
2. A. J. Majumdar and R. Roy, "The System CaO-Al₂O₃-H₂O," *J. Amer. Ceram. Soc.*, 39, (12) 434-442 (1956).

PART FOUR

GREEN-BODY FORMATION AND MICROSTRUCTURE

The green body is the precursor to the fired body, and consequently the quality of the product depends heavily on the detailed characteristics of the unfired body. In these chapters attention is focused on physical behavior of powders during the formation of green bodies (mixing, packing, and compaction), on the forces of adhesion that provide green strength, and on defects within green bodies that affect the microstructure of the product.

23

Firing—The Proof Test for Ceramic Processing

W. D. Kingery

Processing before firing involves processes used to manipulate fine-particle-size solids and form shapes suitable for firing. After firing the formed shapes must have useful properties meeting more or less stringent requirements. In some cases the properties achieved are less critical than the shape or cost; in other cases the required shapes are simple but requirements imposed on resulting properties are very difficult to achieve. In all cases some minimum level of properties is a processing objective.

Almost all variations in the material as it is prepared for the kiln are amplified during the firing process. As a result, examination of fired ware not only serves as a test for successful processing, but also leads to inferences about the way in which processing must be modified or improved to obtain satisfactory ware.

A few of the ways in which the firing process can be interpreted as indicating the success of, and requirements for, prior processing are examined in this chapter.

A SPECTRUM OF RESULTS

During firing, a formed ceramic body tends toward chemical equilibrium, which is approached by reaction between components, chemical and diffu-

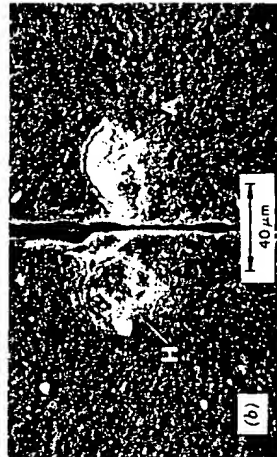
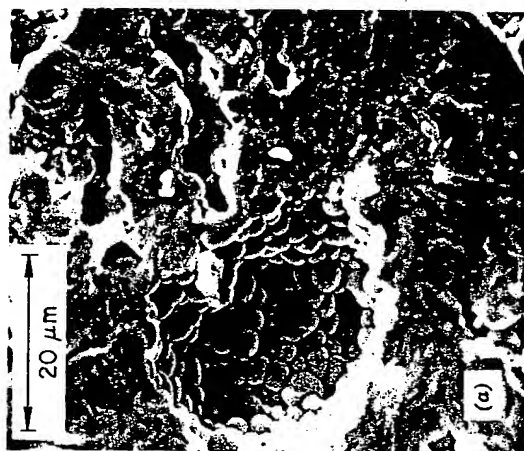
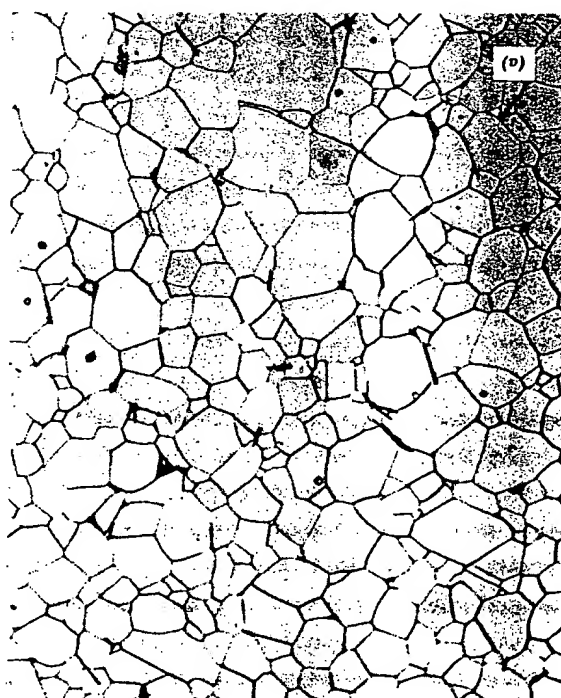
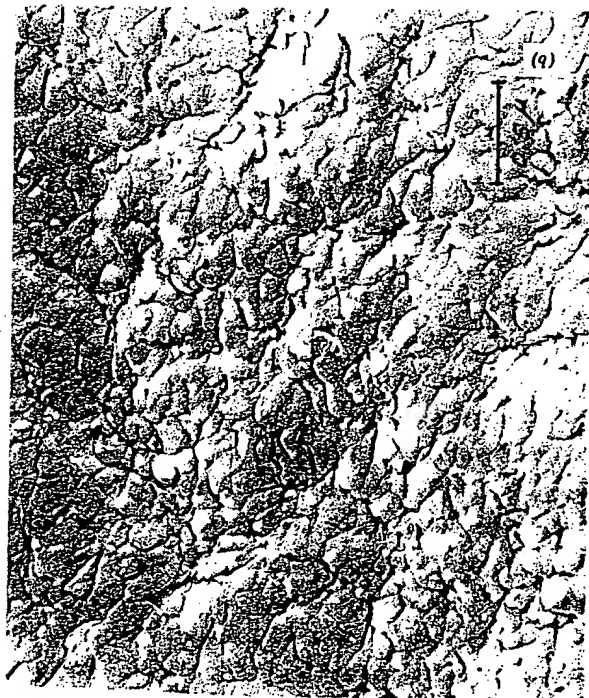


Figure 23.2. (a) Large internal pore in a sample of commercial PZT. (b) Foreign agglomerate in a sample of experimental Al_2O_3 . (Fractographs, courtesy Roy W. Rice.)

sion, and phase transformations; it also tends toward physical equilibrium, a minimization of the surface energy and strain energy, approached by grain growth, pore elimination, and phase separation on cooling. When a material is processed such that the final composition ready for firing is a uniform homogeneous fine-particle-size mixture, these processes occur at a relatively low temperature uniformly throughout the sample. The result for two single-phase compositions is shown in Figure 23.1 for a completely dense pore-free uniform-grain-size optically transparent sintered yttrium

Figure 23.1. (a) Polished section of $\text{Y}_2\text{O}_3 + 10\% \text{ThO}_2$ sintered to a uniform grain size nearly pore-free transparent ceramic. $100\times$ (courtesy C. Gresovich and K. N. Woods). (b) Fine-grain yttria-stabilized zirconium oxide ceramic hot-pressed at 1300°C . $30,000\times$ (courtesy T. Vasilos).



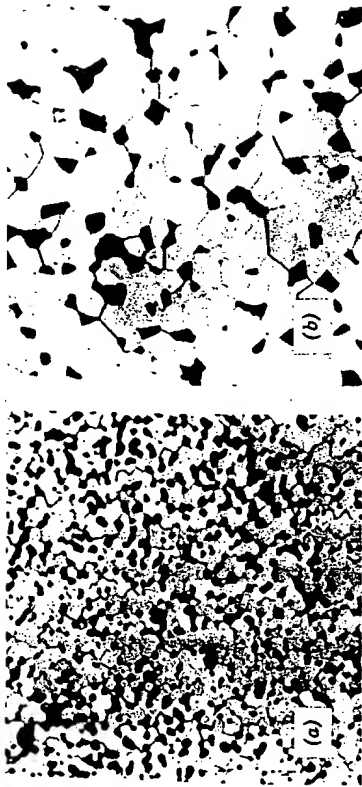


Figure 23.3. Grain growth and pore growth in sample of UO_2 containing small amount of carbon after (a) 2 minutes and (b) 5 hours at 1600°C . $312\times$ (Francois et al.).



Figure 23.4. Idiomorphic grains in polycrystalline spinel containing a small amount of liquid phase. $350\times$ (courtesy R. L. Coble). From W. D. Kingery, *Introduction to Ceramics*, Wiley, New York, 1960.

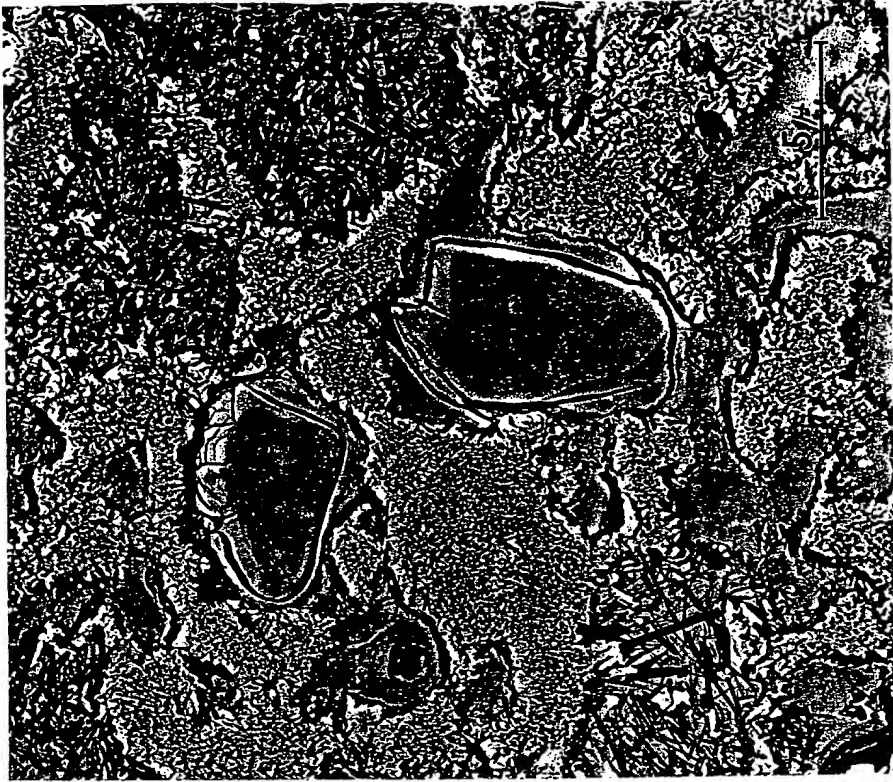


Figure 23.5. Electron micrograph of electrical insulator porcelain illustrating solution rims and cracks associated with large quartz grains. $1245\times$ (courtesy S. T. Lundin). From W. D. Kingery, *Introduction to Ceramics*, Wiley, New York, 1960.

oxide and for a hot-pressed zirconium oxide. When samples are prepared from uniform-particle-size material without agglomeration, nearly complete densification can be achieved at remarkably low temperatures as compared with ordinary firing requirements.

On the other hand, many samples are characterized by gross defects. Large internal voids and unconsolidated foreign agglomerates, such as

shown in Figure 23.2, are very common indeed; so common, that fracture of commercial ware almost always is found to originate at this kind of macroscopic defect.

COMPOSITIONAL CONTROL

One of the most spectacular examples of firing as a proof test for processing comes for ware that has been insufficiently dried. Many of us have had the experience, or seen the results of an overeager potter, firing poorly dried ware with excess water present. The steam generated literally explodes the product.

A related but somewhat less spectacular result was observed by Laurent and Bernard¹ in the preparation of alkali halide samples for diffusion measurements. They sintered imperfectly dry samples by rapidly heating to a temperature near the melting point; the residual porosity was substantially greater than in perfectly dry samples, and the measured diffusion charac-

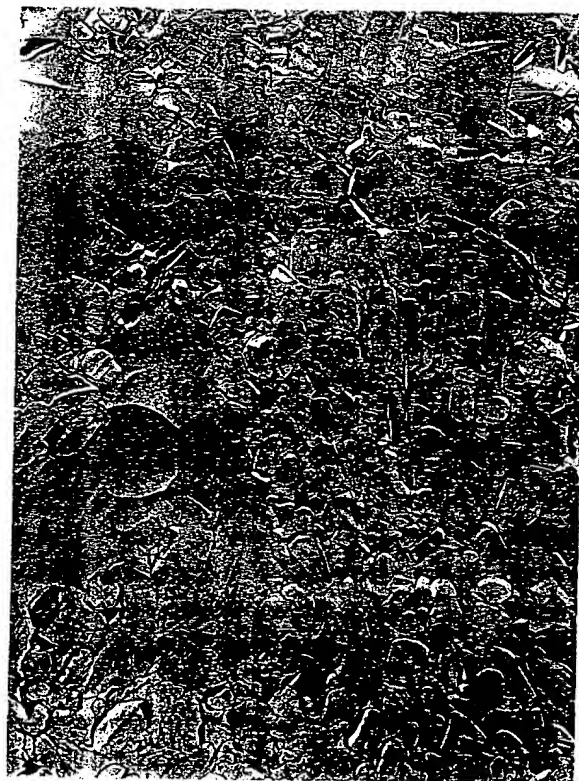


Figure 23.6. Irregular distribution of protoenstatite crystals in a steatite body. Major glass phase etched on a fractograph surface. 2700 \times (courtesy K. H. Schuller).

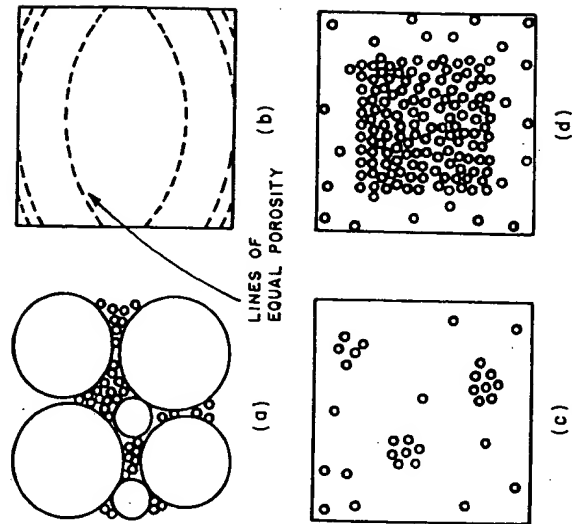


Figure 23.7. Pore concentration variations resulting from (a) a variation in grain sizes, (b) die friction, (c) local packing and agglomeration differences, and (d) more rapid pore elimination near surfaces.

teristics were markedly affected by the residual water content and its influence on grain boundary behavior. In a more definitive study, Francois et al.² investigated rapidly heated samples of uranium dioxide containing a small fraction of carbon. The surface was sealed during firing, with the result that gas generation in the pores led to a limitation of density that persisted during long heating; the pore configuration was such that pore growth occurred along with grain growth, essentially all the porosity remaining as intergranular pores (Figure 23.3).

Similarly, the control of composition, including minor constituents, has a major influence on the development of microstructure. If a small amount of wetting liquid is present, idiomorphic grain growth can take place, making it impossible to achieve a fine uniform grain size; the liquid phase formed at the boundaries of a largely crystalline material causes selected growth of large individual grains (Figure 23.4).

The results of compositional variations and the requirements for processing controls are classically illustrated by the influence of large grains of

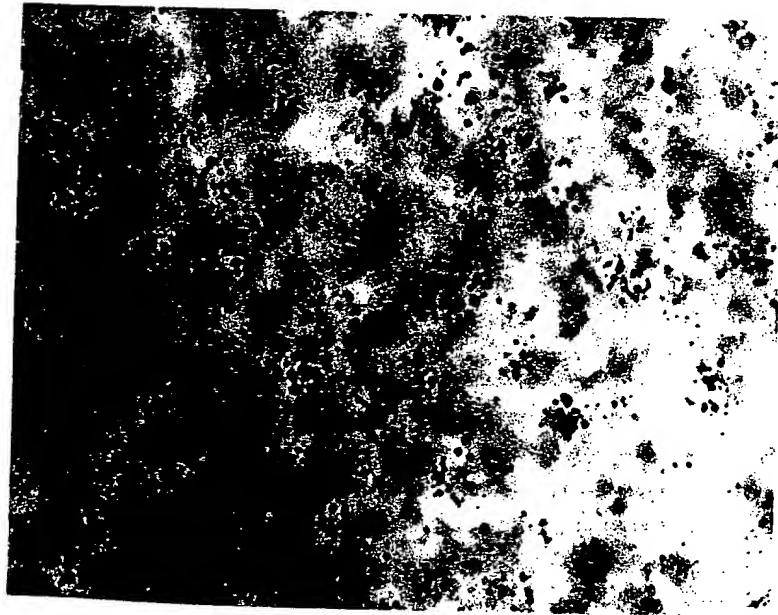


Figure 23.8. Residual pore clusters resulting from improper powder processing in a sample of 90 mole % Y_2O_3 -10 mole % ThO_4 . Transmitted light, 137 \times (courtesy C. Greskovich and K. N. Woods).

quartz in porcelain bodies. The rate of dissolution of the quartz grains is the slowest process taking place during chemical equilibration. As a result, for usual particle sizes the quartz will completely dissolve to form a glass only after long high-temperature firing. At lower temperatures a solution rim that has very different thermal-expansion characteristics forms around quartz grains and gives rise to stresses on cooling, often cracks as shown in Figure 23.5. Dramatic increases in the strength are obtained by using fine-particle-size silica as a body constituent or by replacing the quartz with another material such as alumina.

UNIFORMITY

In analytical treatments of the firing process it is implicitly or explicitly assumed that the starting material has been processed in such a way that it is physically uniform with regard to the distribution of components and the distribution of porosity. In products where particle sizing has been used to

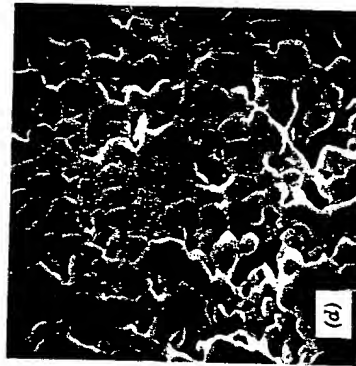
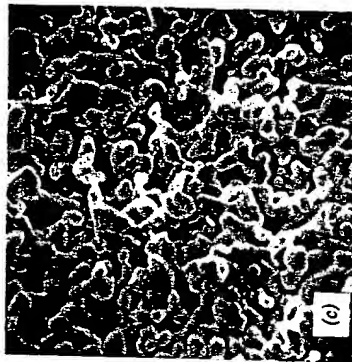
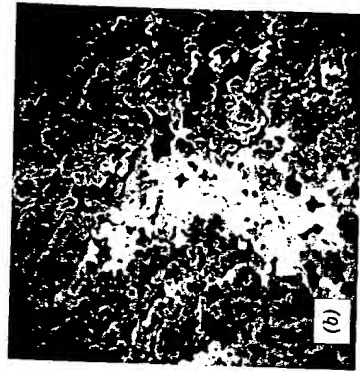
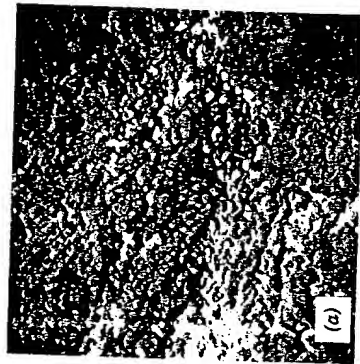


Figure 23.9. Progressive development of microstructure in Lucalox alumina. Scanning electron micrographs of (a) initial particles in the compact (3125 \times) (b) after 1 minute at 1700°C (3125 \times), (c) after 2 1/2 minutes at 1700°C (3125 \times), and (d) after 6 minutes at 1700°C (3125 \times). Note that pores and grains increase in size, that there are variations in packing and pore size, and that pores remain located between dense grains. (Courtesy C. Greskovich and K. W. Lay.)

maximize the green density, this is clearly, and intentionally, not true. Accidental and intentional variations of particle size and material distribution have strong consequences in the resulting structure.

For chemical equilibration processes the rate-limiting process is usually diffusion, and the time required is related to the nondimensional constant Dt/a^2 , where D is the diffusion coefficient ($\text{cm}^2 \text{ second}^{-1}$), t is the time (seconds), and a^2 is a characteristic dimension (cm^2). When this parameter is nearly unity, diffusively limited processes are approximately complete. For firing processes the maximum reasonable time is limited by economic considerations and by the boundaries of normal human patience. The diffusion coefficient depends on the particular system and the temperature used for the firing process. The characteristic dimension over which diffusion occurs depends on processing parameters, particularly the uniformity and the grain size of the constituents. Large grain-size materials do not reach chemical equilibrium, as illustrated for the quartz particles shown in Figure 23.5. A result of nonuniformity is shown in Figure 23.6.

In addition to chemical equilibration, the physical processes of pore elimination and grain growth are controlled by diffusion, either in the bulk

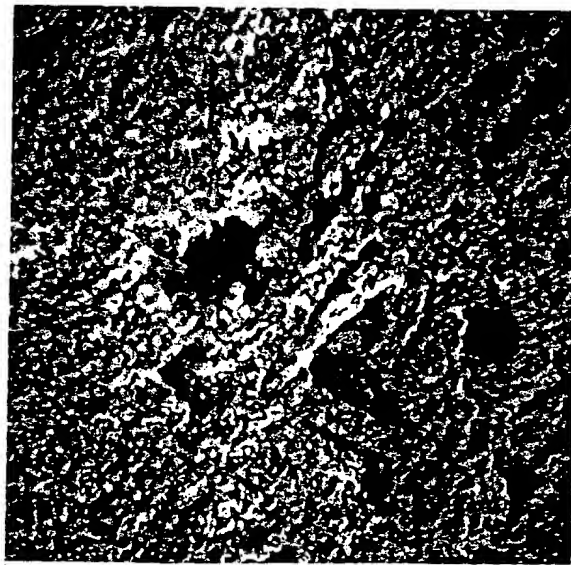


Figure 23.10. Large voids formed by bridging of agglomerates in fine Al_2O_3 powder viewed with scanning electron microscope at 2000 \times (courtesy C. Greskovich).

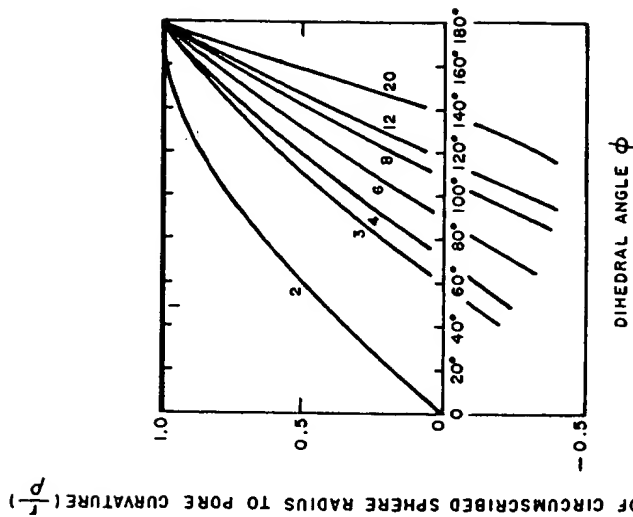


Figure 23.11. Change in the ratio (r/ρ) with dihedral angle for pores surrounded by different numbers of grains as indicated on individual curves.

or in the grain boundaries; a similar nondimensional parameter, Dt/a^2 , describes the time required for equilibration to occur. For an isothermal completely uniform mixture of uniform pore sizes, a corresponds approximately to the pore-separation distance. For processing variables that give rise to changes in pore distribution, as shown in Figure 23.7, the characteristic distance required for pore elimination corresponds to a much larger value related to the spacing between pore clusters or the distance for high-porosity regions to the surface. As a result, pore elimination is not feasible, and microstructures with residual pore clusters result, as shown in Figure 23.8.

The exaggeration of any initial nonuniformity during the firing process is seen in Figure 23.9, which shows the progressive development of pores and grains for a sample of Lucalox alumina prepared from Linde A material.

Initially the structure appears quite uniform in the compact. However, after 1 minute at 1700°C there is an increase in grain size and also an increase in pore size. In areas where agglomerates come together, the pores remain located between dense grains in which both grain size and pore size are increasing. This condition is substantially greater in some samples than others, depending on the effectiveness of processing. A sample containing large voids formed by bridging of agglomerates is shown in Figure 23.10.

When a pore is surrounded by grains, the surface curvature between the pore and the grains depends both on the value of the dihedral angle at the grain boundary intersection with the pore and on the number of surrounding grains. If we take r as the radius of a circumscribed sphere around a polyhedral pore, the ratio of this value to the radius of curvature of the pore surface is shown in Figure 23.11. When the ratio of pore size to radius of curvature (r/p) decreases to zero, the interface will be flat and there will be no tendency for pore shrinkage or growth. Pores will be stable, as shown in Figure 23.3 for cubic pores in UO_2 surrounded by six grains with a dihedral

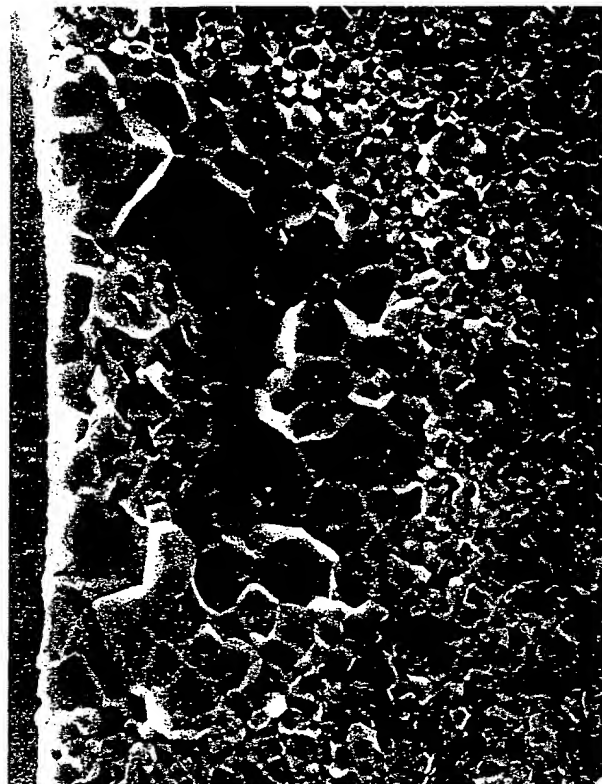


Figure 23.14. Origin of fracture at large grains surrounding an oblong impurity zone in hot-pressed alumina. 460× (courtesy W. H. Rhodes).

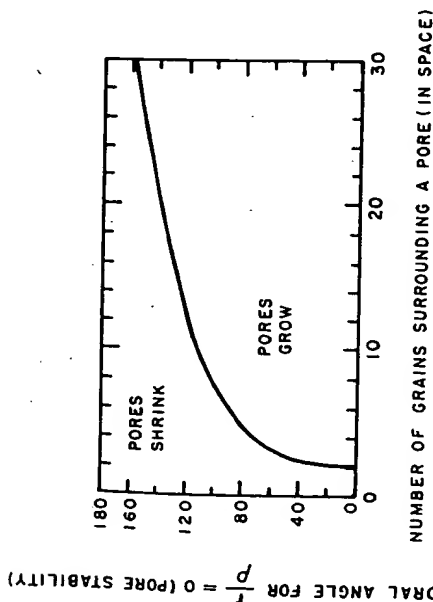


Figure 12.12. Conditions for pore stability.

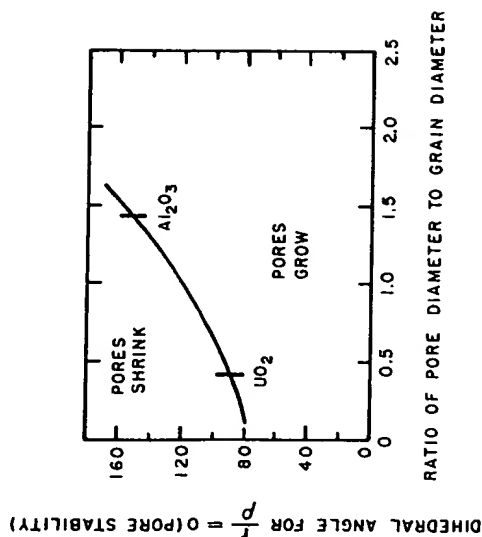


Figure 12.13. Conditions for pore stability.

angle of about 90° . When (r/p) becomes negative, there is a thermodynamic tendency for pore growth rather than shrinkage; that is, the direction of the change in pore shape depends on the ratio of pore size to grain size. This is shown for a range of dihedral angles and number of grains surrounding a pore in space in Figure 23.12, where a line of thermodynamic equilibrium separates regions of pore shrinkage (the usual case) from regions of pore growth. This is shown in a different way in Figure 23.13.

This relation between pore behavior and the pore size/grain size ratio accounts for most of the increase in pore size during the early stages of sintering fine powders and explains the extreme sensitivity of residual porosity to agglomerate formation and seemingly minor variations in processing. Large changes in structure occur in the early stages of firing (Figure 23.9) and strongly affect subsequent events. The same underlying phenomena accounts for the internal structure of the large pore shown in Figure 23.2a.

CONSEQUENCES

Because of the amplification of existing defects during firing, the arrangement and uniformity of body constituents resulting from processing before ware enters the kiln is the primary factor that determines many properties of ceramic products. As shown in Figures 23.2 and 23.14, fracture events are almost always initiated at regions of physical or chemical inhomogeneity. This is also true of other properties dependent on failure events, such as thermal shock resistance, dielectric strength, and high-temperature deformation. Defects can also be introduced by inadequate firing processes—warping, bloating, overfiring, black core, dunting, and so forth. However, even when these faults are avoided and the firing process itself is carried out to perfection, resulting properties are limited almost wholly by the ware that enters the kiln. Cases in which firing serves to correct inadequacies of processing are rare.

ACKNOWLEDGMENT

Work was supported by the U.S. Atomic Energy Commission under contract AT(11-1)2390. A fuller account of many of the principles involved is given in W. D. Kingery, H. K. Bowen, and D. R. Uhlmann, *Introduction to Ceramics*, 2nd Ed., Wiley, New York, 1975.

References

REFERENCES

1. J. F. Laurent and J. Bernard, *J. Phys. Chem. Solids*, **7**, 218 (1958); J. Cabance, *J. Chim. Phys. Physico Chim. Biol.*, **59**, 1123, 1135 (1962).
2. B. Francois, R. Dalmas, G. Cizeron, and W. D. Kingery, *Mem. Sci. Rev. Metall.*, **64**, 1079 (1967).

24

Effect of Process Optimization Properties of Alumina Sintered Under Rate Control

T. M. Hare
H. Palmour, III

INTRODUCTION

Systematic studies of the cumulative effects of prefiring variables on firing processes and subsequent properties have not been generally available in the open literature even for a single material. Prefiring variables include milling practice, binder and/or lubricant additions, forming procedures, burnout methods, and resulting fractional green densities.

Our work over a number of years¹⁻¹⁰ with several different high-purity aluminas of chemical- or conventional-Bayer-process origin has shown that improvements in firing methods are related to improvements in the prefiring processing of those materials.⁸ The importance of various process variables upon the bend strength of finished alumina bars¹⁰ is shown in Figure 24.1.

The correlations between processing and strength were found to be related to the flaws in the samples⁸; the effectiveness of a given preparative step is inversely related to the characteristic size of flaws that it generates in the final microstructure. An example of such process-related flaws is shown in Figure 24.2.

The current study is an extension of these earlier investigations of processing variables and their relationships to rate-controlled densification processes.¹⁻¹⁰ It is more quantitative and represents an attempt (within our experimental limits) to achieve for alumina a systematic optimization of the whole sequence of process steps that precede firing.

The apparatus used in rate-controlled sintering studies is a specially instrumented high-temperature dilatometer, described elsewhere,^{1,3,4,7} which permits monitoring and control of the shrinkage-time firing profile. Since linear shrinkage in any given direction is proportional to volume shrinkage, and hence to fractional density D , it is possible to preprogram the entire densification profile in terms of preselected densification rates $dD/D dt$, which are maintained over specific segments of the total density range to be traversed. Once such a program (usually comprised of three progressively

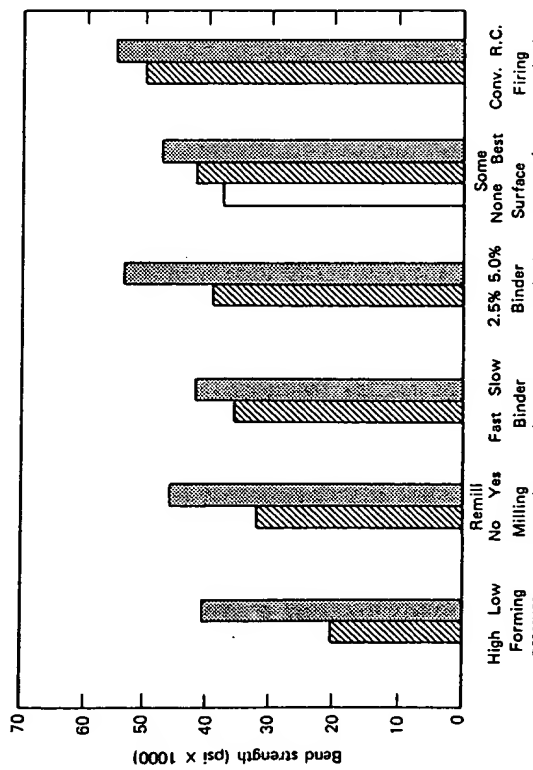


Figure 24.1. Examples of strength increases attributable to various process improvements (After Palmour et al.^{1,3}).

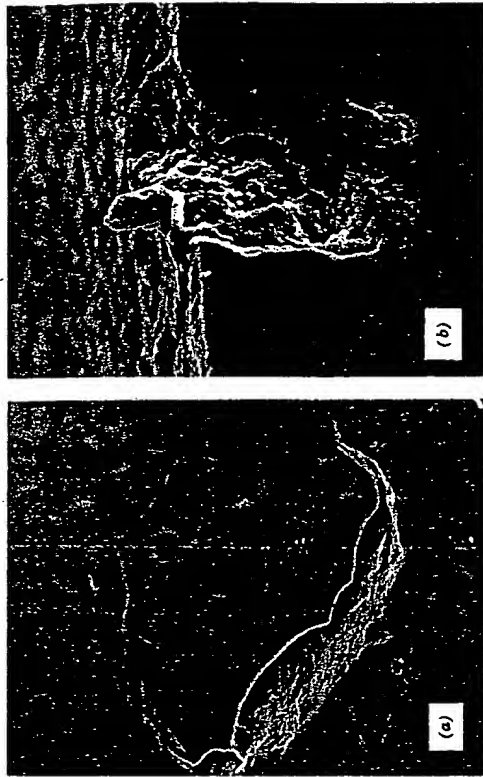


Figure 24.2. Gross processing flaws in conventionally sintered Kemalox alumina: (a) SEM 83x and (b) SEM 250x. After Palmour et al.^{1,3}

slower rate regimes) is designed, the dilatometer provides an instrumental means for assuring that the small test specimen follows the desired program from the onset of shrinkage D_0 at some elevated temperature T_0 (normally attained at some constant heating rate dT/dt) to completion of the firing at D_f , T_f . During the rate-controlled portion of the firing, the ceramic specimen itself provides its own feedback by means of the high-temperature dilatometer, calling for more or less power as required to maintain the preprogrammed shrinkage-time (and hence density-time) curve. During this phase, temperature becomes a monitored but wholly dependent variable; the resulting temperature-time trace is a consequence of the energy requirements of the specimen during sintering as it conforms to the programmed density-time profile.

When a temperature-time profile is determined in the dilatometer it may thereafter be used to program reproductions of the original rate-controlled firing.⁸ This makes it possible to achieve the desired density-time profile either in the dilatometer under temperature control or in conventionally instrumented kilns or furnaces. This ability to scale up, which has been successfully demonstrated for alumina processed in laboratory gas-fired periodic kilns,⁸ obviously is important in developing practical industrial applications for rate-controlled sintering technology.

EXPERIMENTAL PROCEDURES

The equipment and methods used in characterizing and processing the alumina samples have been described in detail elsewhere.⁹

An organic binder is necessary for use with these alumina materials to assure sample integrity after dry pressing and to attain adequate levels of fractional green density. The binder utilized in our study was Carbowax 4000 (Union Carbide). Although the waxy binder provides some degree of lubricity to aid in forming an additional lubricant additive, isostearic acid has proved effective. On the basis of prior studies, the level of each of these additives was fixed at either 0 or 5 wt % unless otherwise noted.

All milling and remilling reported in this study was carried out at ~60% of critical speed in a 3 gallon polyurethane-lined mill containing ~1.9 cm diameter 99% Al_2O_3 balls with a 20:1 ball-to-charge ratio. Before-and-after spectrographic analyses of alumina materials did not show any significant impurity increases attributable to dry milling (18 hours), remilling if any (18 hours), or organic binder or lubricant additives.

In those experiments calling for a fluid vehicle for binder suspension and distribution, the binder was premixed in an appropriate quantity of a selected solvent (e.g., 600 ml/200 g Al_2O_3), which was then slurried (under agitation) with previously dry-milled alumina powder. The mixed slurry was dried at room temperature in large Pyrex trays prior to (a) crushing, screening, and forming or (b) remilling, screening, and forming.

For dry processing, the as-received flaky binder material was added directly to previously dry-milled alumina powder in a clean dry mill along with lubricant, if any. After the first several hours of remilling, the mill was emptied and scraped down with a plastic spatula to remove and redistribute any adherent, binder-rich material. After reloading, remilling was continued to complete the 18 hour schedule. This redistribution step was found to be extremely important, particularly if the batch formulation called for a (liquid) lubricant.

Rectangular bar specimens measuring $\sim 0.25 \times 0.30 \times 1.4$ in. were formed by dry pressing a preweighed charge of prepared powder (~ 3.75 g) in a hardened steel die in an air-operated hydraulic press. Unless otherwise noted, dry pressing was carried out at 2000 psi for materials containing binders and at 1000 psi for binder-free materials. When repressing was needed, the formed bars were placed in small rubber balloons, evacuated, tied off, and repressed isostatically at 40,000 psi, unless otherwise noted. The repressed bars displayed very little shape distortion.

On the basis of prior thermogravimetric (TGA) and dynamic differential calorimetry (DDC) studies of binder oxidation and removal, a binder burnout schedule was designed. Formed bars were heated from 100 to

200°C over a 4 hour period and from 200 to 500°C over an additional 4 hour span and were cooled to room temperature in the oven.

Starting materials included several different lots of chemically prepared Kemalox aluminas (W. R. Grace & Co.), both undoped (KA-100) and MgO-doped ($\sim 0.09\%$, KA-210), together with two types of Alcoa superground, low-soda Bayer-process aluminas, including a moderate purity grade (A-16 SG) and a higher purity MgO-free grade (XA-139 SG). Detailed characterizations of these several materials along with descriptions of sintering behavior, microstructural features, and mechanical strengths have been described elsewhere.^{8-10,12}

Exploratory phases of the experiments reported here were carried out with the same lot of A-16 SG described above. Once the basic optimization of a refined preprocessing sequence was established with A-16 SG, the integrated process was applied to Linde A alumina (Union Carbide Corp.). This material was used both in the as-received undoped form (MgO-free) and with doping (0.1%) added as MgO during initial dry milling.

PREFIRING PROCESS OPTIMIZATIONS

Dry Milling

The importance of intensive dry milling in the sintering of alumina has been demonstrated previously.^{8,13-17} As in the earlier study, an 18 hour dry-milling operation was utilized with Linde A to break up and disperse agglomerates and to introduce annealable excess energy (internal strain). The superground Alcoa aluminas had already been subjected to intensive milling; they were advanced to the next process step in the as-received condition.

Binder Additions with Fluids

In a previous study⁸ binder additions were made in the form of methyl alcohol slurries, using procedures already described. In this investigation other solvents (water, cyclohexane) were included with methyl alcohol in a more detailed study of binder distribution using Alcoa A-16 SG material. A dry binder milled directly in the batch was included as a control.

Water added in various ways was effective in increasing green density but was less effective than methyl alcohol in improving fired density. As vehicles, methyl alcohol and water were found to have a small concentration dependence of their effect on green and fired densities, with a 3:1 vehicle-to-solid ratio being somewhat better than 1:1. The anhydrous vehicle,

cyclohexane, yielded poorer green densities but better fired densities than either water or methyl alcohol. However, the most promising fired densities were obtained with the directly added dry-remilled binder, even though green densities were somewhat low.

Results of this study emphasize the desirability of anhydrous processing of alumina. These findings are in good agreement with a recent study of deleterious $H_2O-Al_2O_3$ reactions.¹⁸

Dry Binder and Lubricant Additions

Experiments using dry additions of binder were carried out with Alcoa A-16 SG material. The influence of lubricant additions and isostatic repressing to increase green densities is summarized in Table 24.1.

The lubricant level had a much greater effect on green density than did binder level, both at constant weight volatiles (batches 1, 2, 5) and at constant binder content (batches 3, 4, 5). The highest green and fired densities were obtained with isostatic repressing and 2.5% lubricant; the 5% binder level yielded slightly higher values than 2.5%. At the highest lubricant level the conventionally pressed bars had nearly the same green density

Table 24.1. The effect of several processing variables on densities of A-16 SG alumina

Batch	Binder Content (%)	Lubricant Content (%)	Press Method	Green Density ^a	Fired Density	
					Conventional 1530°C + 2½ hr to 1550°C	Rate Controlled
1	2.5	2.5	Conv ^c	0.6010	0.9895	0.9904
			Iso ^d	0.6077	0.9910	0.9912
2	3.75	1.25	Conv.	0.5888	0.9885	
			Iso	0.5993	0.9887	0.9897
3	5.0	2.5	Conv	0.6061	0.9902	0.9904
			Iso	0.6111	0.9902	0.9916
4	5.0	1.25	Conv	0.5825	0.9902	0.9904
			Iso	0.5927	0.9904	0.9912
5	5.0	0	Conv.	0.5700	0.9898	
			Iso	0.5931		

^a Volatile-free basis.

^b Density-time profile optimized for earlier form of processing.

^c Conventional dry pressing at 20,000 psi.

^d Isostatic repressing at 40,000 psi.

Table 24.2. Green density as a function of pressing variables for milled, undoped, Linde A alumina, remilled with binder (B) and lubricant (L).

Initial Pressure (psi)	Iso Repressing (psi)	Fractional Green Density		
		B 2.5%; L 2.5%	B 5.0%; L 2.5%	B 5.0%; L 5.0%
1000	25,000	0.5938		0.5955
	50,000	0.6022		0.6039
2000	25,000	0.5992		0.6030
	50,000	0.6086		0.6130
4000	25,000	0.5985		0.6079
	50,000	0.6110		0.6190

as those repressed isostatically. When well-processed A-16 SG was sintered under rate control with a reasonably well optimized density-time profile, a fractional density of 0.992 was achieved. For conventional firings the density was limited to ~0.990.

With finer, higher-surface-area Linde A, similar results were obtained (Table 24.2), but a 5% binder, 5% lubricant addition was found to be slightly better than only 2½% lubricant. Green density increased with both initial forming pressure and isostatic repressing pressure. An initial forming pressure of 2000 psi and a final isostatic pressure of 40,000 psi was chosen as a standard condition.

For milled, undoped Linde A, use of optimized processing conditions (remilled with 5% binder, 5.0% lubricant, dry pressed at 2000 psi, followed by 40,000 psi isostatic repress and controlled slow binder burnout) produced bars that attained fractional green densities of 0.6055 (volatile-free basis). When fired conventionally (1530°C, 2½ hours), a density of 0.9880 was attained.

PREPROCESSING EFFECTS ON SINTERING OF LINDE A ALUMINA

Five batches of Linde A alumina were prepared by several methods to compare the effects of process variables on sintering characteristics. Table 24.3 shows some characteristics of the prepared materials.

Batches were characterized primarily by the fractional green density obtained during formation under an initial pressure of 2000 psi, followed by isostatic repressing at 40,000 psi. In the case of the binderless batch, an

Batches were dry milled for 18 hours under previously described "optimum" conditions except for batch 3, which had less initial dry milling. The fractional green density obtained was a function of the organic additives employed, as previously discussed.

The "best" processing method (batch 1) utilized 5% binder and 5% lubricant. "Poorly processed" material (batch 2) employed no additives, although it was well milled (18 hours + 18 hours remilled). The fractional green density obtained after slow burnout of organics was 0.05 higher than that obtained using the binder alone and ~0.10 higher than that obtained without the use of organics, when all were milled for a comparable time.

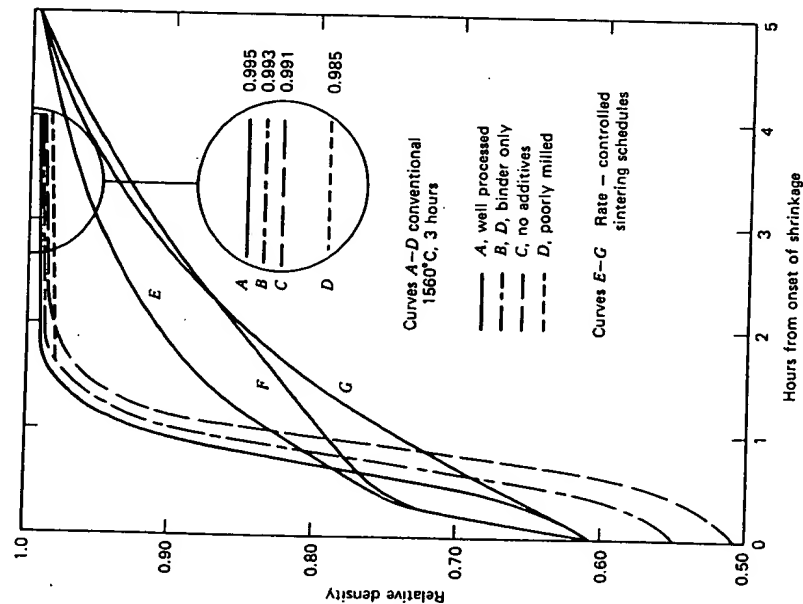


Figure 24.3.

Table 24.3. Processing parameters investigated in sinterability study for Linde A alumina

Batch	Condition	Milling Time (hours)	Remilling Time (hours)	% Binder	% Lubricant	Fractional Green Density
1	Doped (0.1% MgO)	18	18	5	5	0.6075
2	Doped	18	18	—	—	0.5055
3	Doped	~2	18	5	—	0.5502
4	Doped	18	19	5	—	0.5600
5	Undoped	18	19	5	5	0.6055

Differences in sinterability between batches 3 and 4 were not apparent from green density alone.

Figure 24.3 shows the relative importance of the prefiring process variables and the basic difference between the conventional sintering schedules and the rate-controlled sintering profiles employed in this study. The four conventional curves A through D represent typical densification paths for specimens conventionally fired at 8.7°C/minute to 1560°C and held for 3 hours. After 3 hours at 1560°C, the relative-density differences existing between various batches are small but significant (see inset). Curves A through C represent batches that received equal milling treatment; their final densities rank in the same order as their fractional green densities. Curve D shows the density-time path of the poorly milled batch with binder only (batch 3), which did not go beyond the 0.985 relative density level. The chief differences between conventional and rate-controlled densification profiles are the slower densification rates maintained for the latter between 0.75 and about 0.90 and the somewhat faster sintering rates near the end of the firing (curves E through G).

PROCESSING AND SINTERING EFFECTS ON MICROSTRUCTURE OF LINDE A ALUMINA

These studies have attempted to achieve high density and fine grain size, in keeping with an overall objective of increasing mechanical strength. This does not necessarily mean firing to extremely high density and achieving a high degree of translucency. Grain growth encountered in raising density from about 0.992 to 0.995, for example, certainly would reduce the bend strength by virtue of the increased grain size, probably offsetting any

advantage gained by reducing the porosity by that small amount. The exact level of a strength-maximizing density has been difficult to determine in view of confounding effects attributable to the many process-related flaws that become relevant as stress concentrators at very fine ($<2\ \mu$) grain sizes.

For alumina in the intermediate sintering range (<0.95) it has been well established that, given a starting fractional green density, grain size is a function of the final density attained. One of the objectives of this and related research has been to show that this simple grain size-density relationship is not strictly true for final-stage (>0.95) densification of MgO-doped alumina. Until recently the facts have been largely masked by variability attributable to processing.

This study has shown the importance of controlling preprocessing variables and firing schedules in the control of grain size. Figure 24.4 shows that well-processed material sintered for 1 hour at 1560°C had about the same density (within 0.1%) as poorly processed material sintered for 3 hours at the same temperature; however, the well-processed material had a considerably finer grain size.

Figure 24.5 shows an important comparison between a well-processed sample sintered according to rate-controlled profile *G* (Figure 24.3), and a

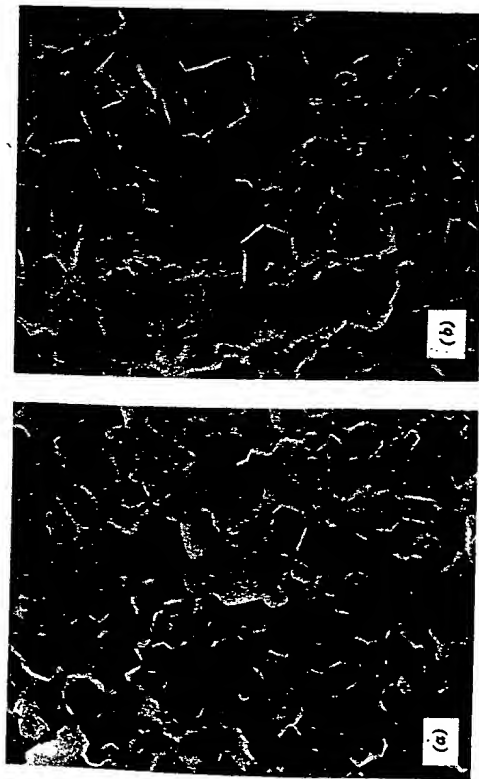


Figure 24.4. Microstructural comparison of MgO-doped Linde A sintered-conventionally at 1560°C to about equal densities, SEM 1840x. (a) best processing: 1 hour soak, $D = 0.992$; (b) poor processing: 3 hours soak, $D = 0.991$.

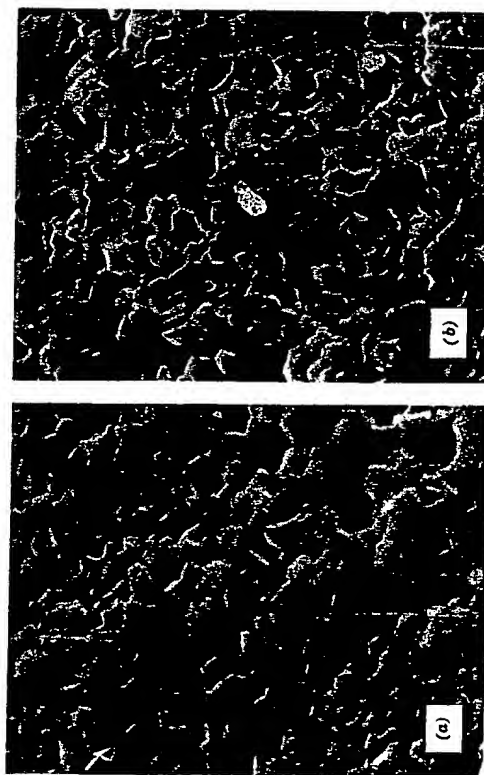


Figure 24.5. Microstructural comparison of well-processed, MgO-doped Linde A using different sintering methods, SEM 1800x. Note: about equal grain size. (a) conventional 1450°C , 3 hours, $D = 0.986$ and (b) rate controlled to 1560°C , $D = 0.993$.



Figure 24.6. Low-density region in MgO-doped, well-processed Linde A fired conventionally to 1450°C , 3 hours, SEM 3040x.

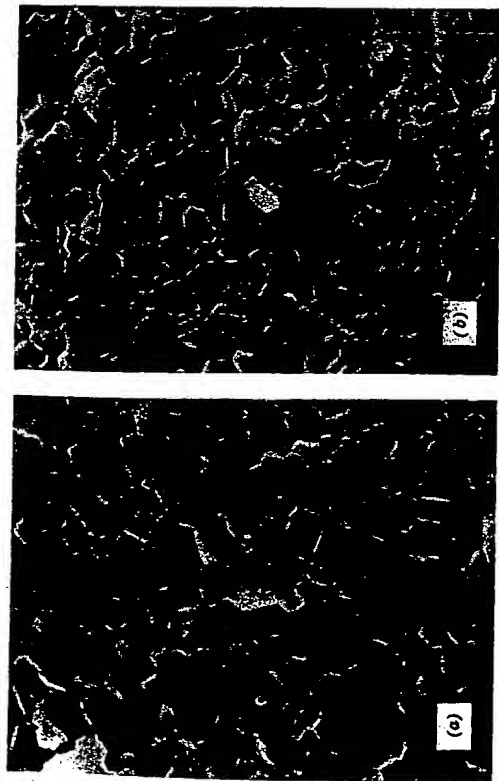


Figure 24.7. Microstructural comparison of well-processed, MgO-doped Linde A using different sintering methods, SEM 1840x. Note: comparable densities. (a) conventional 1560°C, 1 hour, $D = 0.992$ and (b) rate controlled to 1560°C, $D = 0.993$.

sample fired conventionally at 1450°C for 3 hours. Although the rate-controlled specimen did spend some time 1500°C, its grain size is not appreciably different from that of the conventionally sintered material. However, the rate-controlled specimen showed a considerably higher fractional density. Figure 24.6 shows a region of low density typical of the 1450°C conventional firing, illustrating that even the best processing obtained in this study is not yet fully optimized. Apparently a major advantage of rate-controlled sintering is that it permits such low-density regions to densify uniformly before pore-channel closure isolates them prior to final-stage sintering. Further evidence of this is seen in Figure 24.7. Specimens rate-control sintered according to profile G (Figure 24.3) had a finer grain size when compared at nearly equal density with conventionally sintered material.

ACKNOWLEDGMENTS

This work sponsored by the U.S. Navy, Naval Air Systems Command, under Contracts N00010-73-C-0134 and N00019-74-C-0265. We gratefully

References

acknowledge technical assistance by M. L. Huckabee, R. K. Boozer, E. M. Gregory, J. P. Kirkland, R. M. Roberts, Wanda K. Johnson, Betty L. Smith, E. H. Kendall, Jr., and R. Glenn Simpson, and secretarial assistance by Ann S. Ethridge and Anne Y. Gregory.

REFERENCES

1. H. Palmour III and D. R. Johnson, "Sintering and Related Phenomena," G. C. Kuczynski, N. A. Hooton, and C. F. Gibbon, eds., Gordon and Breach, New York, 1967, pp. 770-791.
2. H. Palmour III, R. A. Bradley, and D. R. Johnson, *Kinetics of Reactions in Ionic Systems*, T. J. Gray and V. D. Frechette, eds., Plenum Press, New York, 1969, pp. 392-407.
3. R. A. Lawhon, "Rate Controlled Sintering of Polyphase Ceramic Bodies by Direct Instrumentation," Master of Science Thesis, North Carolina State University, Raleigh, North Carolina, 1970.
4. D. R. Johnson, "Densification Kinetics of Spinel Sintered under Rate Control," Ph.D. Dissertation, North Carolina State University, Raleigh, North Carolina, 1970.
5. M. L. Huckabee and H. Palmour III, "Rate Controlled Sintering of Fine-Grained Al₂O₃," *Amer. Ceram. Soc. Bull.*, 51 (7), 574-576 (1972).
6. H. Palmour III and M. L. Huckabee, "Studies in Densification Dynamics," *Sintering and Related Phenomena*, G. C. Kuczynski, ed., Materials Science Research Ser., Vol. 6, Plenum, New York, 1973, pp. 275-282.
7. H. Palmour III and M. L. Huckabee, "Process for Sintering Finely Divided Particulates and Resulting Ceramic Products," U.S. Patent Application filed April 26, 1973, Serial No. 354,515.
8. H. Palmour, T. M. Hare, and M. L. Huckabee, "Optimal Densification of Ceramics by Rate Controlled Sintering," Final Technical Report, Contract No. N00019-73-00139, Naval Air Systems Command, March 1974.
9. H. Palmour III, T. M. Hare, and M. L. Huckabee, "Conventional vs. Rate Controlled Sintering of Alumina: I. Microstructural Comparisons," presented at the 77th Annual Meeting of the American Ceramic Society, Washington, D.C., May 3-8, 1975.
10. T. M. Hare, H. Palmour III, and M. L. Huckabee, "Conventional vs. Rate Controlled Sintering of Alumina: II. Strength Comparisons," presented at the 77th Annual Meeting of the American Ceramic Society, Washington, D.C., May 3-8, 1975.
11. D. E. Witter, R. A. Bradley, D. R. Johnson, and H. Palmour III, "Use of Computers in Ceramic Research," *Ceram. Age*, 84 (11), 28-31 (1968); *Errata*, *ibid.*, 85 (1), (1969).
12. T. M. Hare, M. L. Huckabee, and J. P. Kirkland, "Intermediate Stage Densification Kinetics for Alumina Sintered under Rate Control," presented at Fall Meeting, Basic Science Division of the American Ceramic Society, Pittsburgh, Pennsylvania, Sept. 24, 1973.
13. D. Lewis and M. W. Lindley, "Enhanced Activity and the Characterization of Ball Milled Alumina," *J. Amer. Ceram. Soc.*, 49 (1), 49 (1966).
14. A. Pearson, J. E. Marhanka, G. Maczura, and L. D. Hart, "Dense, Abrasion Resistant 99.8% Alumina," *Amer. Ceram. Soc. Bull.*, 47 (7), 654-658 (1968).

15. D. E. Niesz, R. B. Bennett, and M. J. Snyder, "Strength Characterization of Powder Aggregates," Technical Report Number 1, Contract Number N00014-68-0347, Office of Naval Research, Oct. 1970.
16. R. B. Bennett and D. E. Niesz, "Comminution of a Reactive Alumina Powder," Technical Report Number 2, Contract Number N00014-68-C-0342, Office of Naval Research, Oct. 1971.
17. R. B. Bennett and D. E. Niesz, "Strength Characterization of Powder Aggregates," Technical Report Number 3, Contract Number N00014-68-C-0342, Office of Naval Research, Oct. 1972.

25

Dynamic Particle Stacking

F. N. Rhines

It is widely recognized that the mode of stacking of particles in a powder compact greatly influences the properties of the green body, the course of subsequent sintering, and the properties of the sintered product. Efforts to explain this dependence, through an understanding of the nature of powder stacking, have often taken the form of constructing assemblies of spheres, either of identical or mixed sizes. This approach assumes that it is possible to represent a stack of powder in terms of a typical arrangement of particles, which is repeated many times to produce the stack.

The origin of the idea of modeling particle assemblies with spheres has been credited to Rene J. Haüy (1789),¹ who was concerned with the atomic arrangement in crystals. A century later W. Barlow² used the face-centered-cubic and close-packed-hexagonal models to describe particle stacking. In the 90 years since then, more than a score of investigators have contrived stacking models by the use of real or imagined spheres, of like or variable size, systematically or randomly stacked. One of the most comprehensive of such analyses was that of L. C. Graton and H. J. Fraser.³

Considering the great amount of effort that must have gone into these studies, as well as the length of time over which the results have been known to the public, it seems surprising that there are still no recognized laws of particle stacking, or even generally accepted industrial procedures based on these models. Thus this writer concludes that the unit-cell approach is inca-

pable of leading to a useful result in this type of natural process. This is not to imply that the work has been barren. A number of important trends and a few relationships that promise to apply to the general case of natural powder stacking have emerged, but these cannot be woven into a general understanding of stacking until a valid base for the subject has been established.

Except for the rare case in which the particles are so perfectly identical that they can assume a "crystalline arrangement,"¹⁴ the assumption of repeated, typical arrangements of particles is not valid for hard particles. For most powders the particles differ individually in the detail or their shapes and sizes.⁶ Since the particles can come to rest only through mutual contact, these differences result in an infinity of local arrangements, which cannot be represented by any iterative model. The stack, nevertheless, has a distinctive character that reflects the nature of the powder or power mix that has gone into its composition and the manner in which the stack has been formed, for example, poured, shaken down, or slip cast. Thus, to describe a stacking realistically it is necessary to characterize the powder and also the mode of stacking in terms of parameters that can be evaluated independently of the specific particle shape and size, as well as the difference from site to site in the structure of the stack. In other words, it is necessary to characterize the stack as a whole, rather than particle by particle.

STACKING PARAMETERS

Two appropriate parameters that are capable of evaluation without reference to particle size or shape are: (1) the number of particles P in the stack and (2) the number of interparticle contacts C in the stack. Both these numbers are subject, in principle, to direct and exact evaluation. The numerical difference between them is a measure of the topological connectivity G of the stacking⁴:

$$G = C - P + 1 \quad (1)$$

In this view the powder stack may be thought of as a three-dimensional network in which the individual particles represent nodes that are joined by interparticle contacts that serve as branches of the net. The connectivity of such a net is defined as the number of branches (interparticle contacts) that would have to be severed to reduce the net to a single chain of particles. As a chain there is one more particle than there are contacts; hence the connectivity is one more than the difference between the number of contacts and the number of particles. It is obvious that porous particles are already multiply connected and that their connectivity becomes part of the

connectivity of the system as a whole. Where porous particles are involved, a more elaborate method for evaluating the topological parameters of the system is required. In some cases it might be possible to determine an average connectivity of the powder particles by serial sectioning and to add this to the main-network connectivity. It is doubtful that the result would justify the great effort required.

DeHoff and coworkers⁷ have demonstrated the important principle that the course of geometric change in second-stage sintering is determined by the connectivity of the system, which is often the same as the connectivity of the original powder stack. The ratio of the surface area to the volume of the porosity in second-stage sintering remains constant and is proportional to the connectivity. This makes it possible to design and construct a sinter body of specified structure and properties. The same authors have shown also that the permeability of the porous body is a simple function of connectivity. Other properties that display a qualitative relationship to the connectivity, but which have not yet been studied in detail, include powder flow rate, sintering rate and, perhaps, electrical and thermal conductivity. In a somewhat less direct fashion it appears that the connectivity may prove to be involved in some of the mechanical properties of both green and sintered bodies.

The number of particles P in a powder mass may be determined directly by the use of a Coulter Counter, or equivalent device. Such a count must be made without distinguishing the sizes and shapes of the particles. It is necessary, however, to count the particles separately, not as disintegratable clumps. The particles should be counted in the form in which they will appear as individuals in the ultimate stack. If they will break up into pieces in the stack, then they should be disintegrated before counting. It is also required, in principle, that *all* the particles in the stack be counted, because any kind of segregation in the stack would tend to distort the count. In practice, it is impractical to make total counts, for which reason rather sophisticated sampling techniques may be required.

The number of interparticle contacts C in a powder mass has been counted directly by a number of investigators, of whom the first seem to have been Smith et al.⁸ They used lead shot wetted with acetic acid, which left a white deposit of lead acetate at each point of contact. The white marks were then counted as the stack was disassembled. Such methods are cumbersome at best and become impractical as the particle size becomes very small. Fortunately, it is possible to estimate C through a knowledge of apparent density.

Apparent density is another property that applies to the powder mass as a whole. It has been found that the apparent density is simply related to the number of interparticle contacts, at least over the range from half to fully dense (Figure 25.1).⁹ This important relationship, which makes possible the

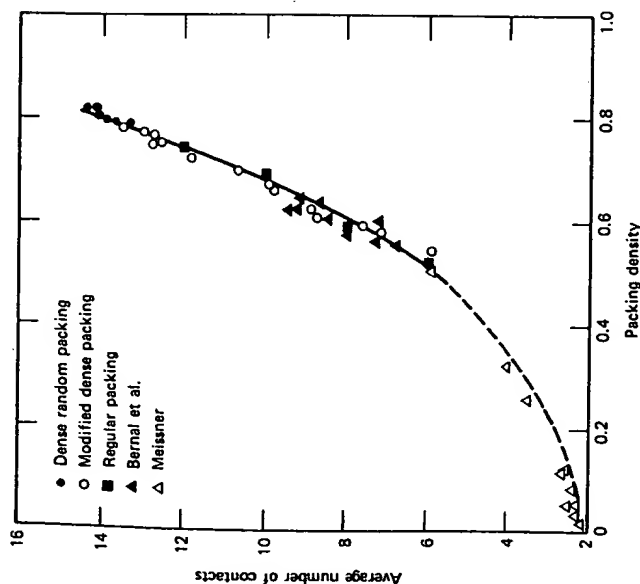


Figure 25.1. Average number of contacts per particle versus packing density. From Norman and Maust¹⁰.

estimation of the number of contacts from one simple measurement, was first reported by Smith et al.⁸ and has since been confirmed by others.^{10,11} The relationship displayed in Figure 25.1 is valid irrespective of particle size, but the slope of the curve varies with particle shape. That the relationship must differ with particle shape may be illustrated with a thought comparison of spherical versus dendritic particles, wherein it is evident that the apparent density of a stack of dendritic particles must be lower than that of a stack of spheres having the same total number of interparticle contacts. Thus powders of different shapes require special calibration for determination of the number of contacts through the apparent density.

EXPERIMENTAL INVESTIGATIONS

Having means by which the stack and the powder can be characterized in an exact and meaningful manner, it becomes of interest to inquire into the

question of how the characteristics of the stack can be controlled. It serves, for the present, to control the number of particles and the number of interparticle contacts. The number of particles per gram, or per unit volume, can be manipulated through the particle size and particle-size distribution. Since the quantities involved are directly additive it does not appear that the control of the number of particles requires special consideration at this time.

Control of the number of interparticle contacts can be had in two rather obvious ways, namely, through the orientation of the particles so as to contact a maximum number of neighbors and through the mixing of particle size and shape. Particle reorientation and relocation can be accomplished by mechanical agitation of the stack. The controlled mixing of powders involves suitable classification and blending of powders from selected sources. In so doing the apparent density of the stack provides an index of the number of contacts.

About 20 years ago, a study of the packing of powders became the subject of a series of theses at the Carnegie Institute of Technology sponsored by a luncheon club of Pittsburgh powder metallurgists. The results, which have not been published up to now, are summarized in this chapter and form the basis upon which a new analysis of powder stacking is proposed. The authors of these theses are John A. Brown (1950), R. J. MacDonald (1951), and Richard H. Vogt (1958). Although some aspects of their work have been duplicated by others, there remains much that is new.

A *mild steel powder* was made for the research by Arthur H. Grobe at the Vanadium Alloy Steel Company in Latrobe, Pennsylvania. The particles were typical of atomized powders, being ovate in form and spanning a large range of particle size. A water quench, which was part of the atomizing process, gave the particles a shiny, rust-resistant surface, which remained clean after 10 years of storage. The powder was first sized by taking cuts with consecutive sieves of a new Tyler Screen set (Table 25.1). Each cut was then tested for its apparent density. Duplicate measurements were made at four laboratories, namely, Kennametals, Westinghouse, Gibson Electric, and Carnegie Tech. In all cases the determination was made by the use of a Scott Volumeter. The results, which were mostly in good agreement, are summarized in Figure 25.2. It is to be noted that the apparent density diminished approximately in proportion to the particle size over most of the range. This is an effect that has been noted by nearly everyone who has carried out a similar experiment. The less-dense packing of the finer particles has been ascribed to bridging, or clumping, resulting from interparticle adherence that is more persistent the lighter the particle. The loss in density at the coarse end of this series is not commonly found. It is believed to be associated with a departure from the common particle

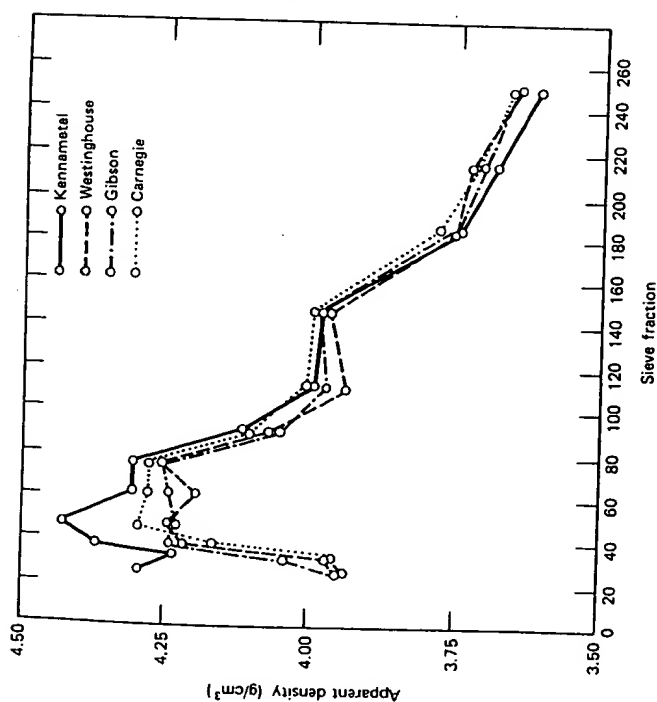


Figure 25.2. Apparent density of separate sieve fractions of steel powder. From Brown.

shape among the largest particles, for which reason the coarsest cuts were excluded from subsequent experiments.

Brown measured the apparent densities of binary mixtures of steel powders of different sizes. Weighed fractions of two cuts were blended by quartering and rolling on glossy paper, as in assaying practice, and then were passed through a Scott Volumeter to determine the weight of 1 in.³ of the mixture. Two typical results are displayed in Figure 25.3. Here the 408 μ powder is mixed, respectively, with 163 and 68 μ powder, giving size ratios of approximately 3:1 and 6:1. Both curves arch to a maximum density with slightly less than one-third of the finer cut present in the mixture. In all the nine series studied by Brown, the density attained a similar flat maximum near 30% of the finer cut in the mixture.

The same result as that described above has been obtained by essentially everyone who has conducted comparable experiments. Westman and Huggill proposed an explanation of this phenomenon in terms of the packing volume (Figure 25.4). In this diagram volume is plotted vertically and com-

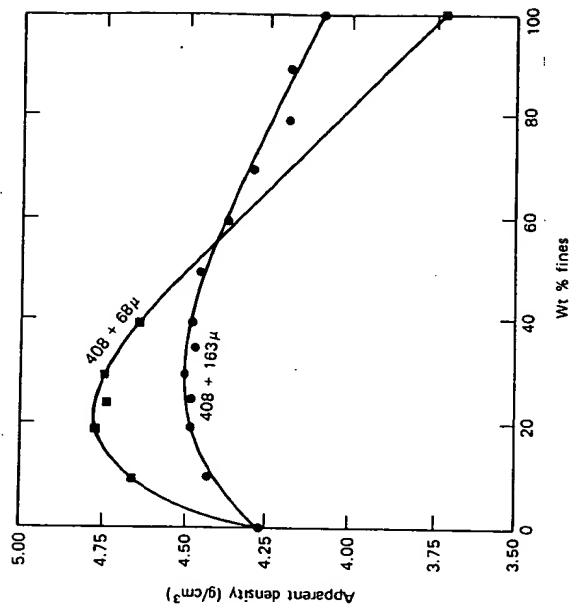


Figure 25.3. Some typical plots of apparent density versus weight percent of the fine fraction in binary mixtures: 408 μ powder mixed with 163 μ powder; 408 μ powder mixed with 68 μ powder. From Brown.

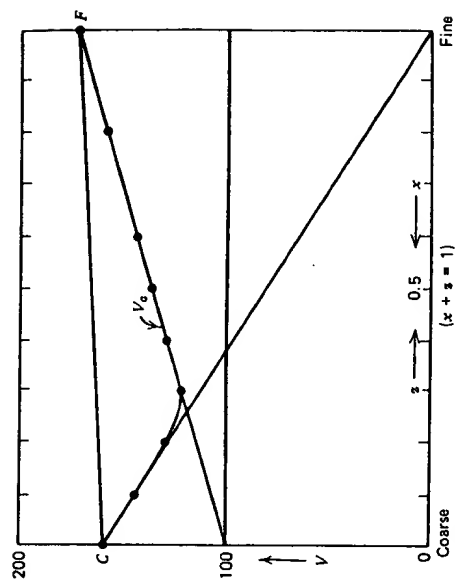


Figure 25.4. Diagrammatic representation of the Westman and Huggill hypothesis to account for the apparent density of binary mixtures of powders.

Table 25.1. Mean particle size, apparent density and flow rate of unmixed sieve fractions of atomized steel powder (Brown)

Lot No.	Sieve Fraction	Mean Particle Size (μ)	Apparent Density (g/cm^3)	Flow Rate (seconds)
0	-20 + 30	715	3.94	None
1	-30 + 35	505	3.96	None
2A	-35 + 40	460	4.16	34.6
2B	-40 + 50	408	4.29	29.8
2C	-50 + 70	253	4.27	24.6
2D	-70 + 80	199	4.27	22.8
3	-80 + 100	163	4.10	23.2
4	-100 + 120	137	3.98	23.1
5	-120 + 170	106	3.97	22.5 ^a
6	-170 + 200	81	3.78	24.0 ^a
7	-200 + 230	68	3.73	24.3 ^a
8	-230 + 270	58	3.65	24.7 ^a

^a A smooth flow was not observed. Stacking occurred.

position of the mix is plotted horizontally. The horizontal line at $V = 100$ represents the ideal volume of the fully dense material. The line CF represents the packing volume of mixtures, obtained by adding the packing volume of the unmixed components. The diagonal lines terminating at C and F are the contributions of the two cuts to the total volume, based on the concept that the coarse fraction is of primary importance in determining the skeleton of the stack and that the fine fraction first fills the void spaces among the coarse particles and, when the void spaces are filled, begins to add to the total volume of the stack. Accordingly, to the left of the intersection of the diagonal lines the portion connecting the point C represents the packing volume as determined by the coarse fraction alone, while the portion at the right, connecting to point F , consists of the fully dense contribution of the coarse fraction added to the normal volume of the fine fraction. As is seen later in this chapter, and as was in fact recognized by Westman and Hugill, this analysis constitutes an oversimplification. It has the charm, however, of providing a rather good simulation of the variation of apparent density with composition.

The maximum in the apparent density of the composition series becomes higher as the difference in particle size increases, up to at least a ratio of coarse to fine of 6:1 (Figure 25.5). A similar finding has been reported by

McGeary,¹² except that he carried the study to larger ratios and found very little change in the maximum density above a 6:1 ratio.

Flow rate is a property that may be expected to vary with the number of interparticle contacts in the system, because the displacement of a particle requires the rupture of contacts. With the number of interparticle contacts in a powder stack proportional to the apparent density, it is expected that the flow rate will be slower the greater the apparent density. Brown measured the flow rates of all the powder mixtures in the same nine series, using a Hall Flow Meter, ASTM Standard B 213-46T, and found the expected relationship (Figure 25.6). In each case the composition of slowest flow corresponded nearly with that of maximum density. Where deviations occurred, the minimum flow rate was at slightly larger content of fines in the mixture.

Ternary mixtures of the steel powders were examined by MacDonald. He found a flat maximum in the apparent density, higher than that of any of the associated binary maxima, located at about two-thirds of the coarsest fraction. This result has since been duplicated by other investigators.¹³

Segregation according to particle size became apparent as the foregoing studies progressed. In an attempt to deal with this factor, Vogt examined the effect of vibratory pucking upon the apparent density of binary mixtures. To observe directly any tendency for the particles to segregate according to size, he employed a white silica beach sand and dyed the finer cuts each a different color. The particle size range was somewhat shorter than that used by Brown (Table 25.2), but the particle shapes were similarly

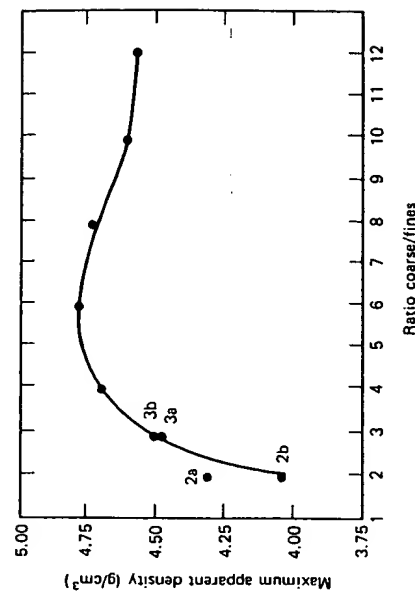


Figure 25.5. Maximum apparent density (composition not specified) versus the ratio of the sizes of the coarse and fine particles. From Brown.

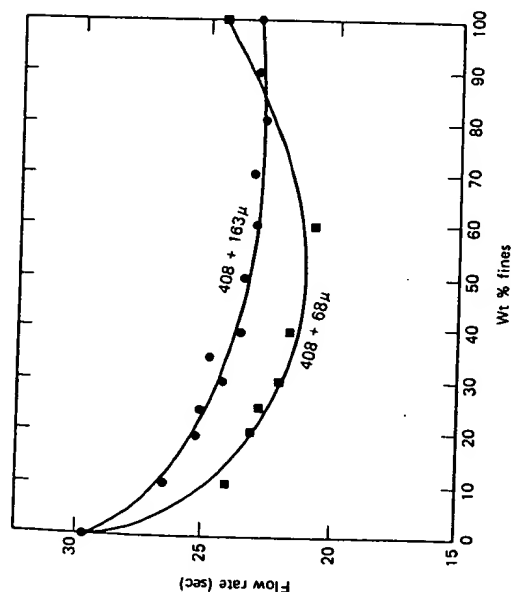


Figure 25.6. Some typical plots of powder flow rate versus weight percent of the fine powder in the mixture (same series depicted in Figure 25.3). From Brown.

ovate and smooth. Instead of using a Scott Volumeter, Vogt poured weighed portions of the powder into a 100 ml glass graduate cylinder and used the filling volume to calculate the apparent density. At the same time the glass container made it possible to observe segregation visually. The glass cylinder was strapped to a wooden base with rubber bands, and the base was vibrated by means of a small motor with an eccentric fly wheel

Table 25.2. Mean particle size, apparent density of as-poured and vibrated sieve fractions of white sand (Vogt)

Lot No.	Sieve Fraction	Mean Particle Size (μ)	Apparent Density As-Poured (g/cc)	Apparent Density Vibrated (g/cc)
A	-20 + 30	715	1.348	1.462
B	-30 + 40	506	1.306	1.466
C	-40 + 50	358		
D	-50 + 70	254		
E	-70 + 100	180	1.158	1.392
F	-100 + 140	127	1.073	1.322
G	-140 + 200	89	0.994	1.268

rotating at a speed of 1800 rpm. The cylinder was filled and the as-poured volume was measured before the vibrating motor was started. Thereafter, the vibrator was operated and readings of apparent density were made periodically, until a steady state was indicated by constant readings.

The powder was blended in two ways. One method, similar to that used by Brown, consisted of quartering and rolling the weighed portions of the mixture upon glossy paper and then pouring the blend directly into the glass cylinder. Particle-size segregation was apparent during blending, in the as-poured stack, and became more prominent as the powder was left undisturbed in the cylinder. In an effort to overcome this separation, the two powders of the binary combination were introduced into the cylinder through two funnels so arranged that the two streams of powder combined in fall. The mixing appeared, at first, to be more homogeneous, but after 24 hours of quiescent standing, gross separation of the fines to the bottom of the cylinder was evident. No homogeneous stack was ever achieved in these experiments.

It was first noticed that the apparent density increases with the height of the powder stack in the cylinder (Figure 25.7). The effect persists, moreover, through long vibration. For this reason a constant weight of powder was used in all subsequent experiments. The same effect has been

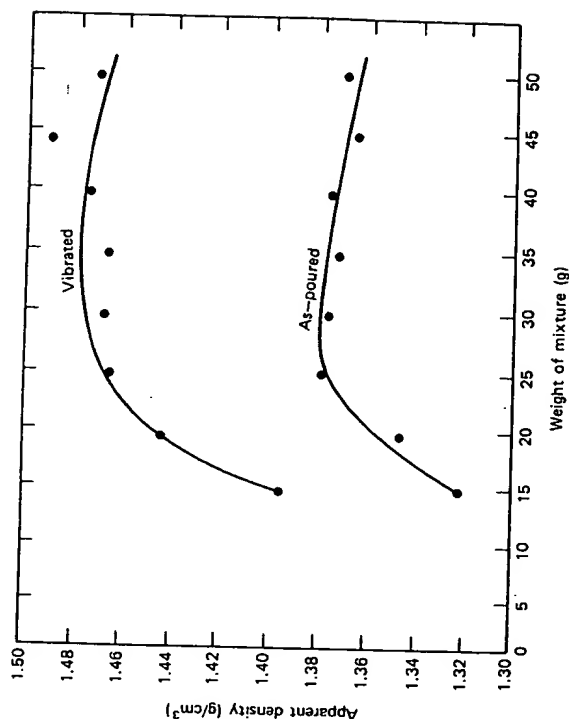


Figure 25.7. Apparent density versus height of the stack (i.e., weight of powder). From Vogt.

found by other experiments; for example, Bell et al.¹⁴ used an additional loading on the powder to secure increased densification. It may be surmised that the larger load tends to assist the breaking of bonds between particles, reducing bridging and clumping.

Vogt also found the now-familiar effect of particle size on the apparent density of single-size cuts (Figure 25.8). Again it can be seen that this effect persists in spite of vibratory packing, although the finer cuts densify most during vibration.

Vibratory settling of binary mixtures was found to increase the apparent density of all mixtures progressively, until no further change would take place (Figures 25.9 through 25.12). The composition of maximum density is preserved, although it tends to occur at slightly higher fines content after vibration. No reversal in densification, such as that reported by Gugel and Norton,¹⁵ was found. This may appear surprising in view of the additional fact that the size separation became distinct during vibration. Intuitively, it had been supposed that the most dense state, toward which the stack would

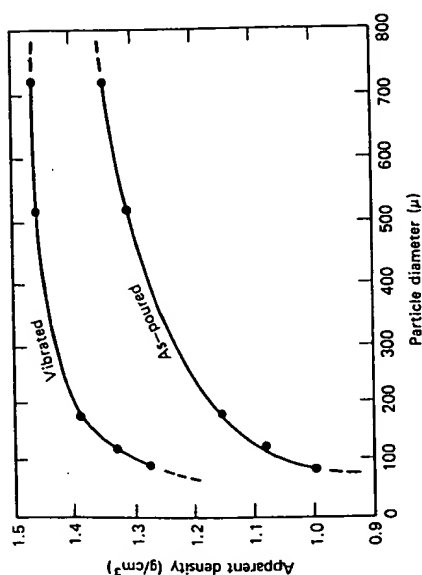


Figure 25.8. Apparent density versus particle size of individual sieve fractions. From Vogt.

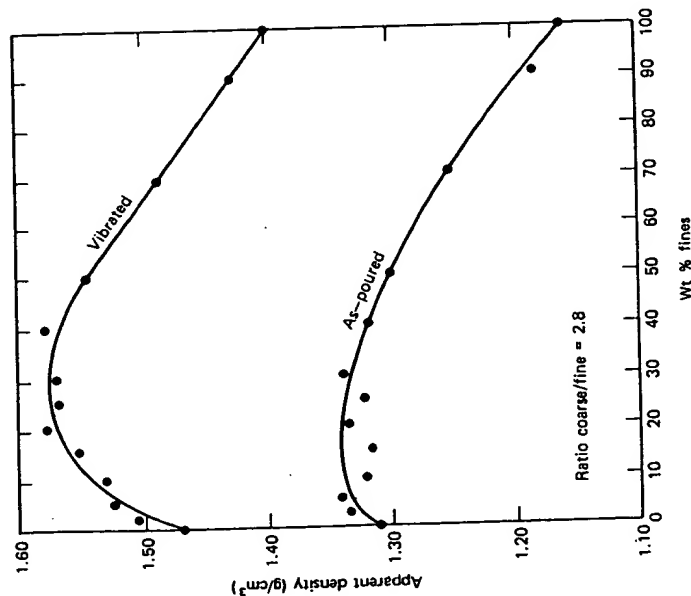


Figure 25.9. Apparent density versus weight percent of fines in mixtures of two powders (506 and 180 μ) with size ratio of 2.8:1. From Vogt.

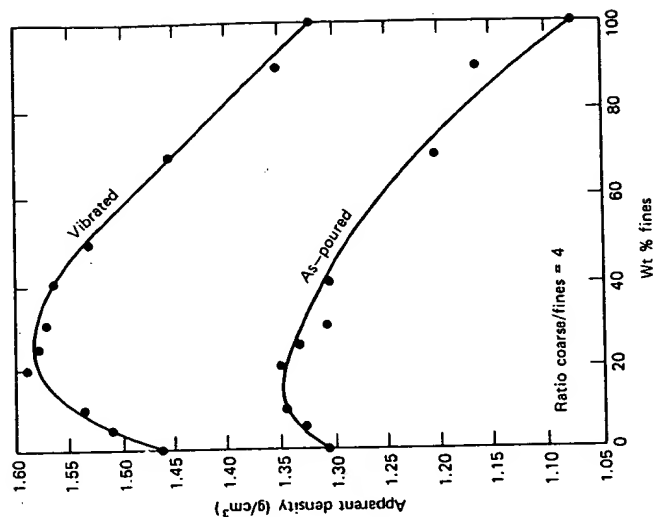


Figure 25.10. Apparent density versus weight percent of fines in mixtures of two powders (506 and 127 μ) with size ratio of 4:1. From Vogt.

tend, would be one in which the smaller particles would be held in interstices between larger particles. It had been supposed, accordingly, that any segregation of the two sizes would result in an expansion corresponding to the return of each cut to its individual stacking density. Clearly, these suppositions were not fulfilled.

The color distribution in the stack suggested a gradation in the mixture, somewhat as indicated schematically in Figure 25.13. Such a gradation does not exclude interstitial packing, but it makes the degree of interstitial placement a function of vertical position in the stack. It seems, therefore, that the steady-state stacking must be a dynamic equilibrium wherein the particles are kept in a state of partial mixing by the mechanical energy of vibration, acting against a natural tendency to segregate, under the influence of gravity.

The effect of particle-size difference on segregation was examined by

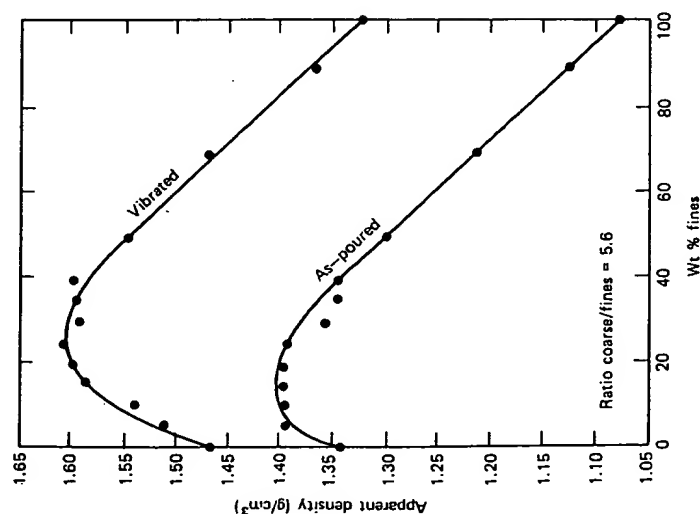


Figure 25.11. Apparent density versus weight percent of fines in mixtures of two powders (715 and 127 μ) with size ratio of 5.1:1. From Vogt.

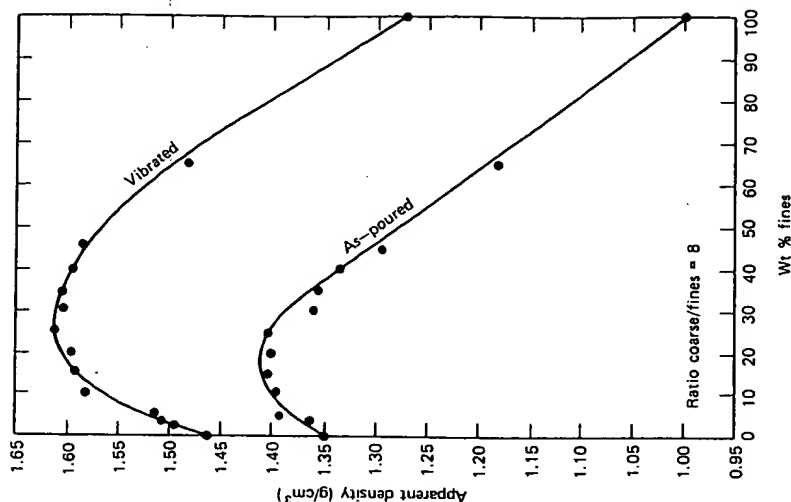


Figure 25.12. Apparent density versus weight percent of fines in mixtures of two powders (715 and 89 μ) with size ratio of 8:1. From Vogt.

sampling the extreme top layer of each of the mixes after stabilization by vibration. The particles of the sample were spread on a glass slide and were counted under a microscope. The ratio of the number of coarse to fine particles in the original mixture is plotted as a function of the ultimate ratio in the top layer of the stack after stabilization by vibration (Figure 25.14). Each line of this graph corresponds to a different size ratio of the powder mixture. The 45° line, labeled "stable mixture," represents the ideal case of no segregation. There was no case in which any of the mixtures approached this ideal line. The slopes of the experimental lines, which represent the degree of segregation in each case, are plotted as a function of the particle-

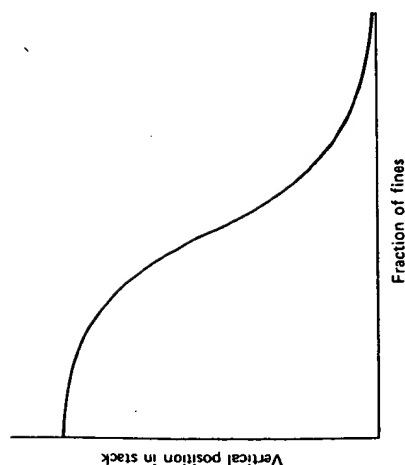


Figure 25.13. Schematic representation of the fraction of fines as a function of vertical position in the stack.

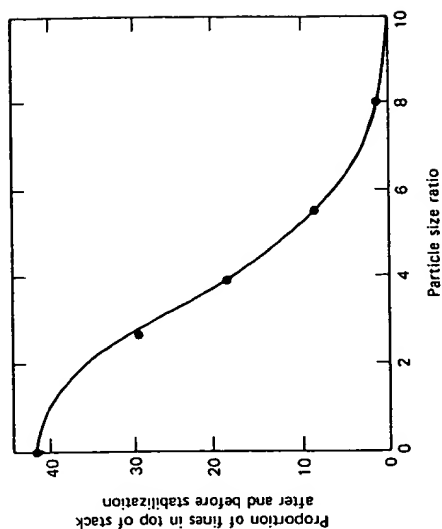


Figure 25.15. Ratio of fine to coarse particles remaining in the top of the stack after vibrating plotted as a function of the particle-size ratio of each mixture.

size ratio in Figure 25.15. Here it is seen that increasing size difference acts progressively to increase segregation, until the separation becomes almost complete, in the top of the stack, with a size ratio in excess of 8:1. It appears that there is no tendency for any particular size of particle to be most stable in the stack. The most stable finer cut was that nearest the size of the coarse fraction. This was indeed an unexpected result!

DISCUSSION

The picture of stacking that thus emerges is a dynamic one in which the system is seeking maximum density of packing for a given particle-size mixture and a given mechanical energy input. To be sure, the dynamic behavior may be thwarted by anchoring the particles in one way or another, but the tendency for the stacking to adjust itself dynamically must always be present, waiting for an opportunity to act.

Particle size varying, as it does, from top to bottom of the stack denies the usual simple ideas of interstitial filling as a direct reason for the higher density of mixed aggregates. Also, the progressive manner in which the density increases with size difference in binary mixtures does not argue for the conventional concept of hole filling by the finer particles. The effect of size mixing on the apparent density is something that involves the whole

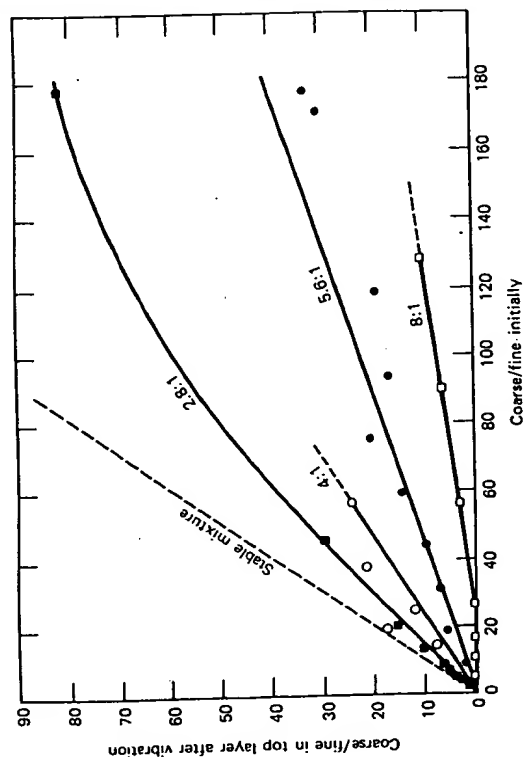


Figure 25.14. Ratio of the number of fine to the number of coarse particles in the top of the stack after vibrating versus the original ratio in the mixture. If there were no segregation all plots would superimpose on the line labeled stable mixture. Departure from homogeneity increases with the ratio of the particle sizes. From Vogt.

stack of powder, not merely local sites. Moreover, it affects the as-poured stack and the vibrated stack in like fashion and amount. This seems to limit rather severely even the general idea of best fit as an explanation for the existence of a composition of maximum density. The only solid ground that seems to remain is the correspondence between number of contacts and apparent density. The experiments indicate simply that the number of contacts tends to maximize when about two-thirds of the particles are of the coarser variety, irrespective of homogeneity of mixing, or perfection of fit.

Segregation according to particle size appears to be a gravity effect. The finer particles filter through the coarser particles until they are arrested by coming to a stratum of finer particles through which passage is difficult. The powder stack might be compared, in this respect, to a set of graded sieves, composed of the particles themselves. Some mechanical agitation seems necessary to give the particles mobility and to release particles from interstices in which they may be trapped. The same mechanical energy is expected, however, to promote mixing. The steady state to which the mixture tends during vibration amounts to an equilibrium between size separation and mixing, the mixing being the more pronounced the more energetic the mechanical input.

Densification by vibration has been shown by Bell et al.¹⁴ to proceed very rapidly at the beginning, most of the ultimate change in density being realized in a matter of 5 seconds or less. This argues for densification by the rotation of the particles, virtually *in situ*, to achieve more contacts, rather than by the time-consuming random diffusion of particles to sites of best fit. Indeed, it appears that the most significant result of particle migration must be size segregation. This too must result in an increase in the total number of contacts in the system and an increase in the stability of the structure.

Stability may be thought of as the resistance of the powder mass to change of stacking. This property is illustrated, for example, by resistance to flow, or by resistance to further densification under the influence of vibration, such as is displayed by the finer-size powders. In all cases the stability seems to increase with number of interparticle contacts, perhaps more fundamentally with the connectivity of the system.

The strength of the bond at the contact is also a stabilizing factor. The bond always has some strength, even when it consists of mere van der Waals forces, so that some mechanical force is needed to break it and to set readjustment of the stack in motion. Where a binder, such as a thin film of water, is present, the surface tension can provide a strong enough bond so that considerable force is required to produce particle motion. When the number of contacts and the strength of their bonds has become sufficient to immobilize the powder stack, no further densification occurs.

Bonding strength can also be diminished by chemical means. If a powder stack is filled with a wetting medium, so that the only internal surface becomes that between the solid particles and the liquid, the bonds may become relatively weak and spontaneous particle migration may be initiated. A typical example is that of water added to dry sand. An almost instant shrinkage of the sand mass occurs, because the weakening of the interparticle bonds allows particle rotation. Indeed, dynamic particle stacking appears to attain its ultimate perfection in a slowly moving aqueous medium. This is illustrated by the case of the formation of opal, which consists of a close-packed stacking of identical silica spheres, the color of the opal depending on the sphere size.* Stratification and stacking of the silica spheres develops in thin crevices in rocks where sand and slowly moving water interact. The large number of contacts of the close packing stabilizes the structure, but, as many a wearer has found to her dismay, water and agitation can destroy the stacking and with it the opal.

Particle shape has had much too little study as a variable in particle stacking. There can be no doubt of its importance, but systematic means for dealing with so complex a variable are not yet available. Fortunately, many of the particles of industrial interest are individually dense, approximately equiaxed, and nearly convex in form. For such particles it is possible to visualize some principles of stacking. When a particle falls on a stack, it tends to come to rest in contact with three other particles and, as the stack grows, three more particles are likely to rest on the first one, giving a total of six contacting neighbors, or an average of three contacts per particle. It is readily apparent that, by rotation, the subject particle might find a position in which it would contact more than six neighbors. Perfect spheres of identical size can assume a close-packed arrangement, like that of opal, in which they have up to 12 neighbors. Owe Berg et al.¹⁶ among others, have succeeded in causing a stack of steel spheres to assume close packing under the influence of three-dimensional vibration. It is geometrically possible for identical particles of any shape to be arranged in close packing, but orientational alignment, as well as spatial positioning, must be attained and this is not an event of high probability. It has been assumed that close packing sets a limit to the number of contacts that can occur in a stack. That this is an erroneous assumption is shown by the fact that the grains in a polycrystalline material average 14 neighbors (i.e., 7 contacts per particle). Still more contacts per particle seem possible where the particle shape is branched, and especially where the particles are not rigid. For example,

* According to recent studies at the University of Melbourne CSIRO, under the direction of Alan Moore.

there scarcely could be any limit to the number of contacts in a bucket of octopi. At the other end of the scale, a pile of straws may be expected to average considerably less than six contacting neighbors.

In real powder stacks, and especially under the influence of vibration, the increase in apparent density, above that corresponding to the three contacts per particle stack, may be thought of as a measure of the frequency of occurrence of higher-contact configurations. Similarity of particles should increase the likelihood of close-packed configurations, wherefore a size-segregated stack may consist of strata containing not only particles of like size, but a larger fraction of close-packed configurations than would be possible for unlike neighbors. These matters invite further investigation.

Characterization

It must now be apparent that the deductions drawn initially with respect to the kind of description that would be needed for a stack of powder were well justified. No kind of iterative geometry could describe the structure of the stack as it has revealed itself through experiment. The only parameters that can be applied are those that are totals for the entire stack. Number of particles, number of interparticle contacts, apparent density, and connectivity all apply to the stack as a whole. It is true that these parameters do not describe the stack completely, but there are additional parameters available. Total surface area and total curvature of surface are but two of a number of other parameters that can be evaluated for the stack as a whole and add to the detail of the description. Progress with the correlation of these geometric parameters with physical properties of the powder stack has been gratifying. Where correlations exist they have usually been found to be simple relationships, easy to apply in practice.

REFERENCES

1. R. J. Hally, "Exposition abrégé de la théorie de la structure des cristaux," *Anal. chem.* 1-28 (1789).
2. W. Barlow, *Nature* 29, 186-188, 205-207 (1883).
3. L. C. Gratton and H. J. Fraser, "Systematic Packing of Spheres with Particular Relation to Porosity and Permeability," *J. Geol.*, 43, 785-909 (1935).
4. R. M. Koerner, "Limiting Density Behavior of Quartz Powders," *Powder Tech.*, 3, 308-312 (1969/70).
5. J. E. Davis, V. G. Carithers, and D. R. Watson, "Practical Method for Using Particle Size Distribution of Calcined Aluminas to Predict their Compacting and Sintering Properties," *Amer. Ceram. Soc. Bull.*, 11, 906-912 (1971).

6. F. N. Rhines, "A New Viewpoint on Sintering," *Trans. Metal Powder Association*, 1958, 91-101, *Platsee Proc.*, 3, 38-53 (1958).
7. R. T. DeHoff and F. N. Rhines, Final Report to AEC, University of Florida, 1973.
8. W. O. Smith, P. D. Foote, and P. F. Busang, "Packing of Homogeneous Spheres," *Phys. Rev.*, 34, (11), 1271-1274 (1929).
9. Yu. E. Pivinskii, "Increasing the Density of Particle Packing in Forming Ceramics," *Sklelo Keram.*, 21 (9), 25-29 (1969), Translation, Consultants Bureau of Plenum Publishing Corp, New York, 1970.
10. A. E. R. Westman, "The Packing of Particles and Particle Shape," *J. Amer. Ceram. Soc.*, 20, 155-166 (1937).
11. J. J. Hauth, "Vibrationally Compacted Ceramic Fuels," U.S. Atomic Energy Commission HW 67777, 44, 1961.
12. R. K. McGeary, "Mechanical Packing of Spherical Particles," *J. Amer. Ceram. Soc.*, 44, (10), 513-522 (1961).
13. F. F. Pownes, "The Effect of Sand Grain Size on Packing Density," *Br. Foundryman*, 54 (11), 346-468 (1961).
14. W. C. Bell, R. D. Dillender, H. R. Lominac, and E. G. Manning, "Vibratory Compacting of Metal and Ceramic Powders," *J. Amer. Ceram. Soc.*, 38 (11), 396-404 (1955).
15. E. Gugel and F. H. Norton, "High Density Fire Brick," *Ceram. Bull.*, 41 (1), 8-11 (1962).
16. T. G. Owe Berg, R. L. McDonald, and R. J. Trainor, Jr., "The Packing of Spheres," *Powder Tech.*, 3, 183-188 (1969/1970).

26

Particle Compaction

O. J. Whittemore, Jr.

The largest number of polycrystalline ceramic products are formed by pressing. Products include insulators for electronic equipment and electrical appliances, refractory brick and other shapes, some building brick, grinding wheels, nuclear fuel, and many other special ceramics. Product sizes may vary from 1 mm to grinding wheels 2 m in diameter. The particle or grain sizes within the products may vary from 0.05 μm to 1 cm. The pharmaceutical and powder metallurgy industries also employ pressing as their principal forming process. Pressing processes include: (1) dry pressing, where less than 2% water is present; (2) semidry pressing, with 5 to 20% water; and (3) isostatic pressing, with less than 2% water. Advantages of pressing are the rapid molding rates (as high as 5000 pieces/minute in rotary presses) and the precision (molded tolerances on the order of 0.1 mm). The final product precision, however, depends on many factors, including powder mixing and sintering control.

EQUIPMENT

A variety of presses are available for compacting ceramics. Their designs display consideration of compact size and shape, material compaction characteristics, molding rate, product density, and powder abrasiveness.

The compacting force is applied by mechanical, hydraulic, or pneumatic means and sometimes by a combination of these. The force can also be applied repeatedly in some designs, in this way overcoming the rheological resistance to flow.

Mechanical

Many presses for molding small precise shapes compact by action of cams against push rods or plungers.^{1,2} Cams can be provided both above and below, and also in parallel so that secondary motion will achieve uniform compacting with different shape thicknesses. Developed originally for pharmaceuticals, these "pill" presses can be provided with hydraulic or pneumatic assists to equalize pressure. Rotary presses have a rotary table on which a number of dies are arranged in a circle, each being filled, compacted, and emptied in sequence. These presses are available with maximum pressures to 100 tons, although most are in the range of 1 to 20 tons.

Most refractory brick is formed in large mechanical toggle presses capable of pressures up to 800 tons. The toggle mechanism operates much like the elbow in a human arm.³ Toggles can also be driven hydraulically to provide pressures up to 1300 tons and to form deeper shapes (see Figure 26.1).

Friction presses have long been used to press tiles, and so forth.³ The plunger is attached to a large vertical screw, which is driven down by a large friction wheel. By the time the plunger compacts the fill, it has high velocity. The impact can be repeated rapidly and from three to five impacts are normally applied. Large friction presses are now being employed in molding large thick refractory shapes.⁴ Although the press is rated at 500 tons the density achieved is close to that obtained on 1000 ton mechanical toggle presses (see Figure 26.2).

Cam and toggle presses close to a given volume. Therefore, although the size is assured, the density achieved is determined by the mold fill. Friction presses close to that point where the inertial energy is absorbed.

Hydraulic

Presses compacting by fluid pressure against a piston are generally used in the abrasives industry⁵ and occasionally in other industries. Hydraulic press sizes vary from a few hundred kilograms to 5000 tons. Here, in contrast to mechanical presses, the density is determined by the pressure while the size is determined by the mold fill. An objection to hydraulic presses is the generally slower rate.

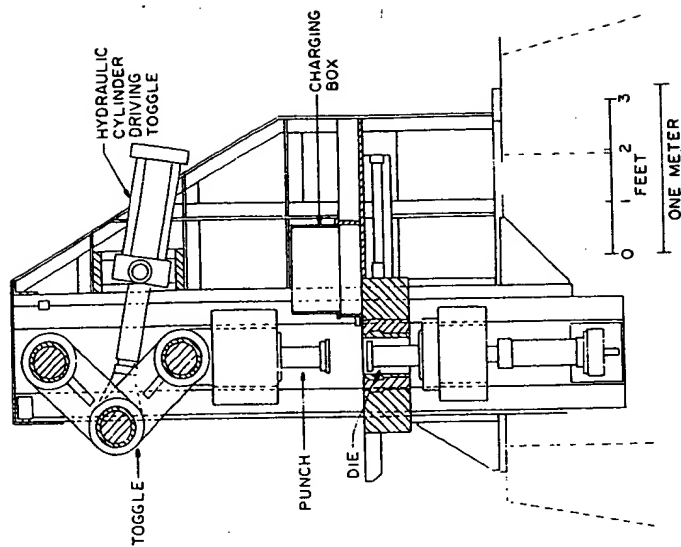


Figure 26.1. Hydraulic toggle press, 1300 ton capacity.

Pneumatic

Special refractory shapes are frequently compacted by hand using air hammers. Uniform high densities can be achieved with skill. Impact presses are constructed with one or more air hammers driving the mold plunger onto the fill. The assemblage is held together by low hydraulic pressure. Impact presses also can produce denser and more uniform products than toggle presses, but their operation is slower.

Isostatic

When a powder mixture is placed in a flexible rubber mold and hydrostatic pressure is applied to the mold exterior, this forming process is called isostatic or hydrostatic pressing.^{6,7} The two variations used are "wetbag," where the powder is loaded into a portable mold outside the pressure vessel,

and "dry-bag," where that part of the flexible mold that contacts the pressurizing liquid is an integral part or lining of the pressure vessel. In the latter, the mold is usually sufficiently rigid to hold its shape when filled. Products range from spark plug insulators (see Figure 26.3) to sewer pipe 2 m long and massive refractory blocks for glass furnace linings.

Roll-Compacting

If feed material is passed between two horizontal smooth rolls, a continuous sheet of product may be compacted.^{8,9} If indentations are cut in the surface of the rolls, briquets are formed that may be granulated for subsequent compacting or may be sintered for refractory grog.

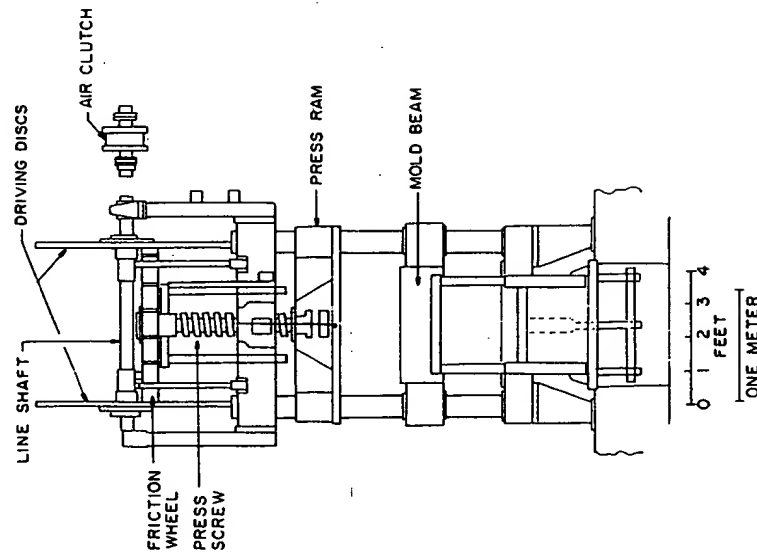


Figure 26.2. Friction press, 300 ton capacity.*

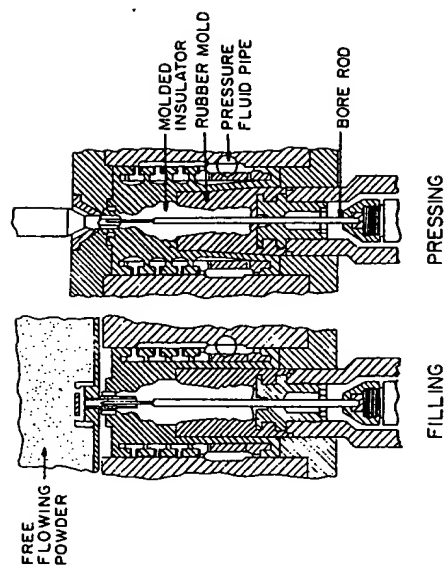


Figure 26.3. Isostatic press for spark plug insulators.*

Vibratory Compacting

When particles are poured into a mold that is then vibrated, considerable compaction can occur if the particle sizing is well graded and high accelerations of vibration are applied. Nuclear fuel rods have been produced at 90% of theoretical density.¹⁰ Experimentally, densities as high as 95% of theoretical have been produced.¹¹ These products are not subsequently fired, as they are not bonded sufficiently to be removed from their containers.

BINDERS AND LUBRICANTS

To assist the compaction process, a number of materials are employed as binders or lubricants.¹² If the ceramic composition includes clay in sufficient amount, other additions are not necessary. For example, foundry molds can be compacted readily of sand with only 2 to 3% of bentonite clay. However, many compositions preclude the inclusion of clay so a number of organic additives are used. These perform several functions.

Binders

When compact strength is required for subsequent handling or other uses, a number of organic materials are used, usually as water solutions. Examples

are the lignosulfonates (residues from the sulfite paper process), dextrans, starches, celluloses, and poly(vinyl alcohol). Amounts added may be as low as 0.5% and as much as 5% for coarse-grained mixtures.

Internal Lubricants

Some plastic flow may occur during compaction if a wax such as paraffin or poly(ethylene glycol) is added. These additives also contribute some strength but less than the binders. A large amount can be added and is contained in the void volume of the particle mass.¹³ This was illustrated by preparing three series of mixtures of aluminas with poly(ethylene glycol) wax (Carbowax 4000, Union Carbide Corp.).¹⁴ The aluminas used were 38900, 7 μm average size (Norton Co.); XA16, 0.5 μm average size (Aluminum Company of America); and Linde A, 0.3 μm average size (Union Carbide Corp.). The first two were well divided and the last contained aggregates. After pressing at 15,000 psi, densities were determined, samples were fired at 800°C where no shrinkage occurred, weight losses were determined, and pore-size distributions were determined by mercury porosimetry.

Volume percent of alumina in the compacts is plotted in Figure 26.4 versus weight percent wax and shows little densification of the alumina. The mid pore sizes determined by mercury porosimetry are also indicated in Figure 26.4 and show little change for the 7 and 0.5 μm aluminas with wax contents up to 10 wt % (27 vol %). The wax thus filled the interstices between particles up to this amount. At higher wax contents the particles were being held apart, as evidenced by larger pore diameters. No difference was noted for the 0.3 μm alumina up to 16 wt % wax (39 vol %).

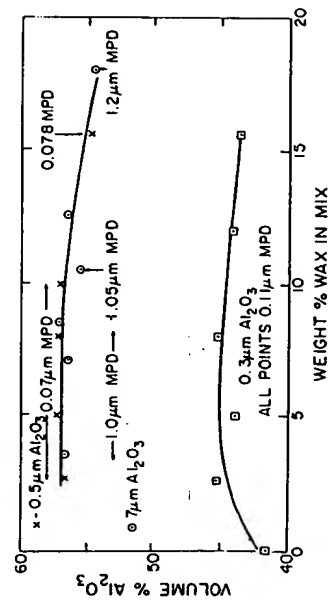


Figure 26.4. Effect of wax addition on compacted alumina density (midpore diameters, MPD, by mercury intrusion).

Of interest is the ratio of 7 between particle size and mid pore size for the 7 and 0.5 μm aluminas. The lower ratio for the 0.3 μm alumina is probably caused by the aggregates present; a bimodal pore distribution was noted, with the peak of smaller pores occurring at 0.04 μm , which also is a ratio of 7.

Mold Lubricants

To reduce the frictional effects at the mold walls, lubricants such as stearic acid and colloidal graphite are employed. These may be wiped or sprayed on the mold wall or pumped through porting.¹⁵

GRANULATION

Fine powders usually have low bulk densities and high compaction ratios (ratio of bulk density to compact density). Fine powders also do not flow well when the die is filled. To alleviate these problems, some form of granulation is often employed, usually a form of compaction. One method of granulating is spray-drying,¹⁶ where drops of liquid containing powder are sprayed into a chamber and fall through rising hot gases that evaporate the liquid. Surface tension of the liquid holds the drops in spherical form, which, when dry, are free flowing, feed uniformly into the die, and have little dust.

Granulation is also accomplished by pressing the powder into compacts that are chopped or crushed and then screened to obtain the desired granule size for die filling. A large reduction in the compaction ratio can be realized by precompacting and more uniform final products result. However, although high granule density will reduce the compaction ratio, coarse weak bodies may result, with greater density variations within the compact.¹⁷

COMPACTION EQUATIONS

For a basic understanding of powder compaction, an analytical equation of state would be desirable. However, information required includes the flow properties of powders under stress, stress or pressure distribution within compacts, the distribution of particle-to-particle stresses, and the strength distribution of ceramic particles. Some information has been determined on the last two factors on glass spheres.¹⁸

Because of the unsolved analytical problems, several empirical equations have been proposed that have value in understanding compaction. Walker¹⁹

determined pressure-volume relationships in compacting several powders and observed the plot of logarithm of pressure versus volume to be linear. Balshin²⁰ obtained a similar relationship assuming that incremental pressure is proportional to incremental energy expended.

$$\log p = V/L_0 + C$$

where p is pressure, V_0 is relative volume, C is a constant, and L is a constant called the pressing modulus, considered analogous to Young's modulus used in Hooke's law. The pressing modulus is a function of the initial material properties but was observed to vary during pressing. Balshin showed near linearity in plots of $\log p$ versus relative volume for pressing graphite and sodium carbonate, and Huffine and Bonilla²¹ later showed linearity for mixed sizes of salt.

An equation describing the compaction behavior of metals was proposed by Heckel,²²

$$\ln \left(\frac{1}{1-D} \right) = Kp + A$$

where D = relative density at pressure p

K = material constant

$A = \ln [1/(1 - D_0)] + B$ where D_0 is the initial relative density

He described three compaction stages as (1) densification by die filling, $\ln [1/(1 - D_0)]$, (2) densification by particle rearrangement, B ; and (3) densification by particle deformation. However, the equation did not describe the compaction behavior of alumina. Leiser²³ later found compaction of fused pure magnesia conformed to Heckel's equation but that of alumina, mullite, and glass did not. As fused pure magnesia has some ductility, this expression appears valid only for ductile materials.

A probabilistic approach was proposed by Cooper and Eaton²⁴ with an expression relating fractional volume compaction V^* with applied pressure P ,

$$V^* = \frac{V_0 - V}{V_0 - V_\infty} = a_1 \exp \frac{-k_1}{p} + a_2 \exp \frac{-k_2}{p}$$

where V_0 = initial volume of compact

V = volume of compact at pressure P

V_∞ = compact volume at infinite pressure or theoretical density

a_1, a_2, k_1, k_2 = constants calculated to give agreement with experiment

The two terms assume a two-stage process, described as (1) rearrangement of particles within the compact with accompanying slight fracture or elastic

deformation so as to fill voids about the size of the original particles and (2) major fragmentation and filling of small voids. The initial stage of compaction, or die filling, is eliminated by definition of V^* . Sized alumina, silica, magnesia, and calcite particles that vary in hardness on Mohs' scale from 3 to 9 were studied. As hardness increased, the relative compaction at pressure decreased.

The coefficients a_1 and a_2 indicate the fraction of compaction occurring in the two terms. When their sum is not unity, other processes become operative before the theoretical limit of compaction is reached. As hardness increased, the sum of a_1 and a_2 decreased from unity for calcite to 0.85 for alumina. The coefficient a_1 is chosen by data at the lower pressures and its value was found²⁵ to be dependent on the lower pressure chosen. Oudemans²⁶ studied compaction of fine alumina and iron oxide particles and was unable to apply either Cooper and Eaton's expression or that of Balshin.

Kawakita and Ludde²⁸ compared equations of 14 other investigators with his equation:

$$C = \frac{V_0 - V}{V_0} = \frac{abP}{1 + bP}$$

where C = degree of volume reduction

V_0 = initial volume

V = volume at pressure P

a and b = constants characteristic of the powder

This equation can be rearranged as:

$$\frac{P}{C} = \frac{1}{ab} + \frac{P}{a}$$

and if there is a linear relation between P/C and P , the constants can be evaluated. The linear relation held for soft, fluffy, and pharmaceutical powders and also for stainless steel and copper oxide powders except for deviation at the lower pressures. Linearity of the P/C versus P plot was not found to be exact using Leiser's data²³ for magnesia and alumina -35 + 42 mesh powders. Kawakita's equation has also been applied²⁸ to tapping compaction and vibratory compaction, replacing pressure with tapping number and vibrating time, respectively.

Although compaction equations have been criticized as only curve fitting and none have been found to be generally applicable, they all focus attention on important considerations, such as the stages of compaction, the mechanisms, and the variables.

MECHANISMS OF COMPACTION

Where the stages of ceramic powder compaction are die filling, particle rearrangement, and particle fracture, the mechanisms are considered to be particle sliding, elastic deformation, and fragmentation. Describing compaction can be difficult because two stages may be occurring simultaneously and mechanisms predominating during a stage cannot be clearly defined.

Particle fracture was shown by Gormly⁶ to occur in pressing a 24 grit grinding wheel. Although there was only a reduction from 50 to 40% retained on a 25 mesh sieve, this amount could result in collapse of many particle bridges. Kingery¹⁸ also showed reduction in size of fine fused alumina when pressed and repressed. Calkins¹⁹ studied the compaction of 250 μ m diameter glass spheres that had been vibrated to minimum volume. After compaction, he determined the pore size distribution by mercury porosimetry of the compact without removal from the mold. The void frequency is shown in Figure 26.5 for the as-packed state, after 20,000 psi compaction (23% fracture) and after 40,000 psi compaction (45% fracture). The filling of voids or void-size reduction thus is accompanied by an increase in small voids.

Fracture is accentuated, however, when single-size particles are compacted as in this latter study. When mixtures of two particle sizes are compacted, Chattopadhyay²⁷ found much less fracture of the coarser size. When -16 + 20 mesh fused-alumina particles were pressed at 24,000 psi, only 23% survived. When 70% of -16 + 20 mesh particles with 30% of one of

three finer sizes was compacted, much greater amounts of the coarse size survived. The greatest amount of coarse-particle survival occurred with the finest of the finer sizes. With the finest particles, the number of contacts increase, the stress per contact point decreases, and less fracture of coarse particles occurs.²⁸

Most compaction is not conducted at pressures where a large amount of particle fracture takes place. Instead, we rely on flow of the mixture of fine fractions together with the plasticizers present and some entrainment of the coarser particles to produce rearrangement of particles to obtain higher densities. Since we usually start with compaction ratios of 2 or larger, much of the compaction occurs at low pressures.

Particle sliding is more difficult to observe. Hartmann²⁹ microscopically observed scratches on coarse particles after compaction. The orientation of the layered silicates (clays and talc) under pressure was demonstrated by Berry et al.¹⁷ The distinction between particle sliding and rearrangement is not easy to make for these minerals.

STRESS DISTRIBUTION

A common method of determining stress distribution within a compact is to measure density distribution and correlate stress with density. In pressing grinding wheels, a characteristic X pattern of slightly higher density is found in the cross section of the wheel.⁶ Lower densities are found on the center exterior of faces and ends. Grinding wheels are pressed from both ends. When a compact is pressed from one end, the density decreases from the top to the bottom.

Actual measurements of stress within a compact during pressing were made by Train²⁸ by means of wire resistance gauges. The isobars of highest pressure in pressing from one direction were found to originate where the face of the moving plunger met the die wall and to pass diagonally through the compact meeting near the center. This work was done on magnesium carbonate, a relatively soft material.

Indirect "end point" measurements have been done by McRitchie³⁰ in large compacts by incorporating small pressure cells constructed as Brinell hardness testers. Cooper and Goodnow³¹ evaluated the deformation of lead grids placed within compacts of alumina and talc by radiography.

Analytically, Schwartz and Weinstein³² computed the stress distribution from a knowledge of the cohesion and the angle of internal friction of the powder mass as related in the Coulombs' yield criterion. The predicted results were compared with measured results on urania powders.

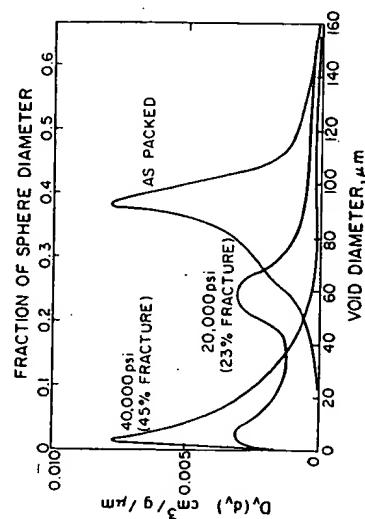


Figure 26.5. Void frequency of compacted 250 μ m glass spheres.

REFERENCES

1. H. Thurnauer, "Controls Required and Problems Encountered in Production Dry Pressing," *Ceramic Fabrication Processes*, W. D. Kingery, ed., M.I.T. Press, Cambridge, 1958, pp. 62-70.
2. F. H. Norton, *Fine Ceramics*, McGraw-Hill, New York, 1970, pp. 376, 401-403, 427, 437, 439, 442.
3. F. H. Norton, *Refractories*, 3rd Ed. McGraw-Hill, New York, 1949, pp. 130-139.
4. G. L. Barna, "Automatic Friction Press," presented at Pacific Coast Regional Meeting, American Ceramic Society, Oct. 24, 1974.
5. M. W. Gormly, "Technical Aspects of Vitrified Grinding Wheel Manufacture: III Mixing and Molding," *Amer. Ceram. Soc. Bull.*, 37 (4), 189-192 (1958).
6. B. A. Jeffery, "Method of and Apparatus for Shaping Articles," U.S. Patent 1,863,854 (1932) (to Champion Spark Plug Co.).
7. B. A. Jeffery, "Method of and Apparatus for Molding Materials," U.S. Patent 2,152,738 (1939) (to Champion Spark Plug Co.).
8. C. Orr, Jr., *Particulate Technology*, MacMillan, New York, 1966, pp. 400-427.
9. R. C. Ragan, "Method for Continuous Manufacture of Ceramic Sheets," U.S. Patent 3,007,222 (1961) (to Gladding-McBean & Co.).
10. R. B. Holden, *Ceramic Fuel Elements*, Gordon and Breach, Science Publishers, New York, 1966, pp. 27-49.
11. R. K. McGeary, "Mechanical Packing of Spherical Particles," *J. Amer. Ceram. Soc.*, 44 (10), 513-522 (1961).
12. S. Levine, "Organic (Temporary) Binders for Ceramic Use," *Ceram. Age*, 39-42 (January 1960) and 25-36 (February 1960).
13. C. A. Bruch, "Problems in Die Pressing Submicron Size Alumina Powder," *Ceram. Age*, 44-47 (October 1967).
14. O. J. Whittemore, Unpublished research, University of Washington, Seattle.
15. A. W. Mohr, "Pressing Problems Not Unique," *Ceram. Age*, 24 (December 1970).
16. B. A. Jeffery, "Preparing and Molding Material," U.S. Patent 2,251,454 (1941) (to Champion Spark Plug Co.).
17. T. F. Berry, W. C. Allen, and W. A. Hassett, "Role of Powder Density in Dry Pressed Ceramic Parts," *Amer. Ceram. Soc. Bull.*, 38 (8) 393-400 (1959).
18. D. J. Calkins, "Ceramic Powder Compaction by a Brittle Fracture Mechanism Using a Glass Sphere Model," Ph.D. Thesis, University of Washington, Seattle, 1970.
19. E. E. Walker, "The Compressibility of Powder," *Trans. Faraday Soc.*, 19, 73 (1923).
20. M. Y. Balshin, "The Theory of the Process of Pressing," *Vestnik Metalloform*, 18 (2) 124-137 (1938).
21. C. L. Huffine and C. F. Bonilla, "Particle-Size Effects in the Compression of Powders," *Amer. Inst. Chem. Eng. J.*, 8, (4), 490-493 (1962).
22. R. W. Heckel, "Analysis of Powder Compaction Phenomena," *AIIME Trans.*, 221 (5) 1001-1008 (1961).
23. D. B. Leiser and O. J. Jr., Whittemore, "Compaction Behavior of Ceramic Particles," *Amer. Ceram. Soc. Bull.*, 49 (8), 714-717 (1970).
24. A. R. Jr. Cooper and L. E. Eaton, "Compaction Behavior of Several Ceramic Powders," *J. Amer. Ceram. Soc.*, 45, 99, 97-101 (1962).
25. K. Kawakita and K. H. Ludde, "Some Considerations on Powder Compression Equations," *Powder Technol.*, 4, 61-68 (1970/1971).
26. W. D. Kingery, "Pressure Forming of Ceramics," *Ceramic Fabrication Processes* W. D. Kingery, ed., M.I.T. Press, Cambridge, 1958, pp. 55-61.
27. A. K. Chattopadhyay and O. J. Jr. Whittemore, "Powder Compaction in Systems of Bimodal Distribution," *Amer. Ceram. Soc. Bull.*, 52 (7), 575-577 (1973).
28. H. S. Hartmann, "Packing and Compaction in Dies of Spherical Particles," Sc.D. Thesis, Massachusetts Institute of Technology, Cambridge, 1964.
29. D. Train, "Transmission of Forces Through a Powder Mass During the Process of Pelleting," *Trans. Inst. Chem. Eng.*, 35 (4), 258-266 (1957).
30. F. H. McRitchie, "A Device for Determining Pressure Distribution in Dry Pressing Refractories," *Amer. Ceram. Soc. Bull.*, 43, (7), 501-504 (1964).
31. A. R. Jr. Cooper and W. H. Goodnow, "Density Distributions in Dry-Pressed Compacts of Ceramic Powders Examined by Radiography of Lead Grids," *Amer. Ceram. Soc. Bull.*, 41 (11), 760-761 (1962).
32. E. G. Schwartz and A. S. Weinstein, "Model for the Compaction of Ceramic Powders," *J. Amer. Ceram. Soc.*, 48 (7), 346-350 (1965).

27

Adhesion Forces in Agglomeration Processes

H. Rumpf

H. Schubert

Agglomeration occurs naturally in powders because of adhesion forces that always act between fine particles. In some important cases agglomerates (granules) are formed intentionally by the addition of a liquid or binder. Because the behavior of powders is so strongly affected by agglomeration processes, this chapter focuses on the nature of agglomeration forces and the factors that affect these forces.

GENERAL CONSIDERATIONS

For particles larger than 1 cm, gravity forces acting on particles are much larger than the natural adhesion forces between particles. If the particle size is reduced, the gravity force decreases very rapidly (by the third power of particle diameter), while natural adhesion decreases approximately by the first or second power of diameter. With 1 μm particles, for example, van

der Waals adhesion forces are about six orders of magnitude larger than gravity. Figure 27.1 shows this feature. Gold spheres of $10\text{ }\mu\text{m}$ diameter are adhering to a glass surface by van der Waals forces only. They stick as they come together, with negligible influence of gravity force. This is the world of fine particles; their behavior depends much more on surface phenomena than on volume forces.

To overcome adhesion forces by volume forces, we have to apply high centrifugal forces of about 10^6 to 10^8 times gravity. The result of such an experiment is shown in Figure 27.2. Gold particles of about $10\text{ }\mu\text{m}$ diameter, adhering to an originally plane anthracene surface, were submitted to high centrifugal forces until some of them flew off. Before flying away they plastically deformed the anthracene surface by van der Waals adhesion forces only.

Other adhesion mechanisms are realized by liquid or solid bridges. In the example shown in Figure 27.3 the solid bridges were formed during drying by crystallizing salts.

The principal bonding mechanisms of agglomerates are as follows:

1. Electrostatic.
2. Van der Waals.

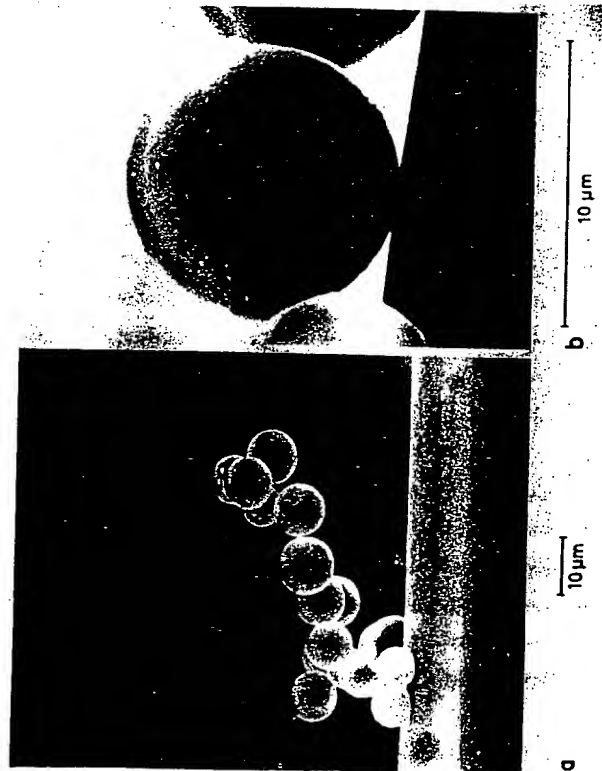


Figure 27.1. Gold spheres on glass fiber (Stereoscan).

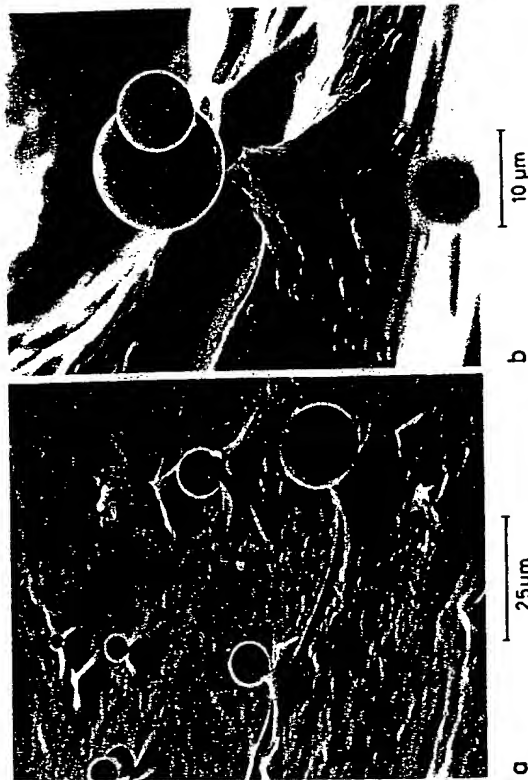


Figure 27.2. Gold spheres on an anthracene surface (Stereoscan).

3. Liquid bridges.
4. Capillary liquid.
5. Viscous binders.
6. Solid bridges.

As an approximate rule, the adhesion forces increase in order from 1 to 6. Chemical bonds are not specifically listed because they normally do not



Figure 27.3. Bridges between spheres: (a) liquid bridges and (b) salt-crystal bridges.

occur unless a solid bridge is formed. An exception is paper, where the fibers adhere by hydrogen bonds. Chemical bonds of course can be effective between solid surfaces and liquid and can cause adhesion by viscous binders. With liquids of low viscosity, surface tension and capillary phenomena are responsible for adhesion. The bonding mechanisms listed above are discussed in detail in the sections that follow.

BONDING MECHANISMS

Electrostatic Forces

When two different materials come into contact, electrons tend to flow from one to the other because of differences in the electronic work functions at both surfaces. This gives rise at equilibrium to a contact potential difference U that ranges between 0 and 0.5 V, depending on the two materials. The work functions of surfaces depend on local impurities and are often unknown.

The adhesion force F acting between two conducting spheres of radius R is given by¹

$$F = \frac{1}{2} \epsilon \epsilon_0 \pi \frac{U^2 R}{a_0}$$

where ϵ = dielectric constant of the gas

ϵ_0 = absolute dielectric constant of vacuum

a_0 = distance between the two surfaces in contact

a_0 is assumed to be on the order of interatomic dimensions (e.g., 4×10^{-8} cm). Similarly, expressions exist for sphere-plane surfaces and plane-plane surface interactions.¹

The adhesion forces between nonconductors are smaller than between conductors. In nonconductors the accumulated charges may extend up to a depth of about 1 μm , while conductors may have charges concentrated in a layer of a few angstroms at the surface.

After a quick separation of particles, half of the charge remains on the separated surfaces, giving a surplus charge that may be neutralized in time according to the conductive conditions. The largest surface charge densities are realized if particles are contacted and separated many times, for instance, by impact in pneumatic conveying or by impact grinding. The electrical charge distribution has been measured² for quartz and limestone particles that were subjected to a deagglomerating impact treatment. The

Bonding Mechanisms

maximum surplus charge density found was around 100 elementary charges per square micrometer, which corresponds to a potential gradient of 20,000 V/cm at the surface. Fracture also produces surplus charges on the new surfaces.

Spherical particles of opposite surplus charge densities σ_1 and σ_2 attract each other according to Coulomb's law:

$$F = \frac{\pi}{4 \epsilon_0} \frac{\sigma_1 \sigma_2 x^2}{[1 + (a/x)]^2}$$

where x = diameter of the spheres

a = distance of separation between the spheres

With ideal insulators, this formula also gives the adhesion forces in the case of contact.

Van der Waals Forces

When a chemist speaks of van der Waals forces, he thinks of small bonding forces between molecules that depend on the distance according to the -7 power law. We speak of the same forces, the London-van der Waals dispersion forces, which are due to fluctuating dipoles and which are found with every substance. These forces can be superimposed to a first approximation. Consequently, if two solid bodies are separated by a distance a between their surfaces, the van der Waals molecular forces can be integrated over the whole bodies. This yields the van der Waals adhesion force, according to the Hamaker theory. If the bodies are spheres with radii R , the van der Waals adhesion force F is inversely proportional to the square of the distance a between their surfaces according to the formula:

$$F = \frac{K\bar{w}}{16\pi} \frac{R}{a^2}$$

where $K\bar{w}$ is the Lifshitz-van der Waals constant, which ranges between 1 and 10 eV depending on the materials in contact. Thus van der Waals adhesion forces are not short-range chemical bonds between the surface molecules only. They depend on the whole solid continuum near the surfaces and also on the properties of a fluid phase between the solid bodies. They are still measurable up to distances a of about 500–1000 Å (far above the effective range of single chemical bonds). Lifshitz has derived a so-called macroscopic theory of van der Waals adhesion forces, applying Maxwell's equations to the electrodynamic fields in the solid continua. A study of the van der Waals interaction is given by Krupp.¹

Liquid-Bridge Forces

The best information is available for the liquid-bridge bonding mechanism. The shape of a liquid bridge is such that the capillary pressure in the bridge is the same in the whole volume (if gravity is negligible). This means that the mean radius of curvature is the same at all points of the surface. We have evaluated the exact solution of the corresponding differential equation for all radially symmetrical geometries of the contacting bodies with variable distances, bridge volumes, and contact angles. The results are available in the form of a set of diagrams.^{3,4}

Figure 27.4 gives the results of calculation for the case of two spheres where the contact angle δ is zero. Here, F is the adhesion force, γ is the surface tension, and x is the diameter of the spheres. The quantity $F/(\gamma \cdot x)$ is a dimensionless adhesion force F_H that can be conveniently plotted as a function of a/x , where a is the distance between the two spheres. Curves for different V_1/V_2 ratios are plotted, where V_1 and V_2 are the volumes of liquid and the two spheres, respectively. The maximum F_H is equal to π , when a/x is zero and V_1/V_2 is zero. With increasing V_1/V_2 , the force-distance curves become less inclined. For V_1/V_2 greater than 0.1, the force is nearly independent of distance.

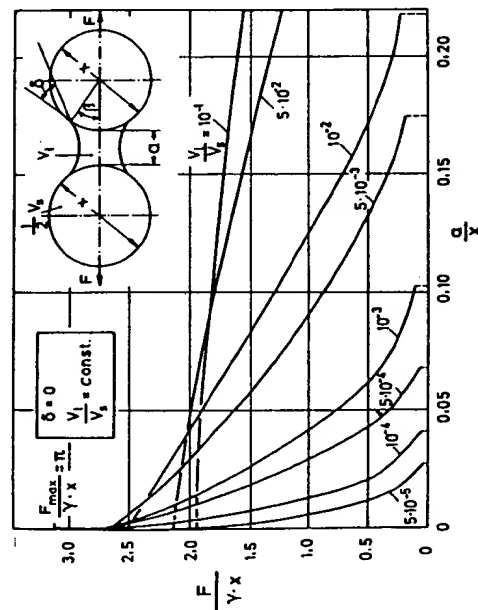


Figure 27.4. Dimensionless adhesion force $F/\gamma \cdot x$ of a liquid bridge between two spheres as a function of the distance ratio a/x .

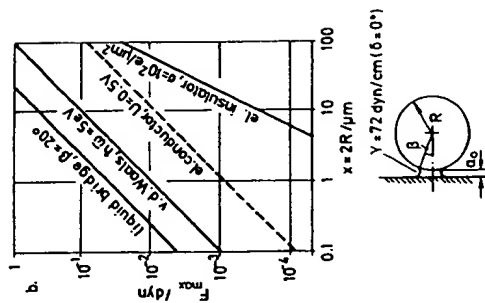


Figure 27.5. Adhesion force F_{\max} of liquid bridge, van der Waals, and electrostatic interaction between a smooth sphere and a half space as a function of the sphere diameter x . The surfaces of the two interacting bodies are in contact, $a_0 = 4 \times 10^{-8}$ cm.

Comparison of Adhesion Forces

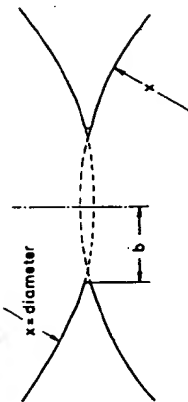
In Figure 27.5 the calculated adhesion force is plotted against sphere diameter for a sphere adjacent to a plane surface. The Lifshitz-van der Waals constant $\hbar\omega = 5$ eV is relatively high; the contact potential difference $U = 0.5$ V and the surface charge density $\sigma = 100$ C/ μm^2 are both maximum values; the liquid-bridge angle $\beta = 20^\circ$ gives a medium value of the liquid-bridge force. The liquid-bridge forces are about four times as large as the van der Waals forces, which are by an order of magnitude greater than electrostatic adhesion forces between conductors, due to contact potential, and these are again about 100 to 10 times as great as adhesion forces due to maximum surplus charges of opposite sign.

Solid Bridges

Solid bridges are formed by crystallizing salts or by sintering. The strength of agglomerates due to crystallizing salt depends sensitively on the drying conditions. Pietsch's experiments⁵ have illustrated rather comprehensively the different tendencies. We are presently investigating these effects under still more defined drying conditions.

Sintering is a field of research of its own. The different sintering mechanisms have been studied intensively by many researchers. We are

First stage of sintering

driving forces: 1) surface tension γ 2) force $F_i = F_{co} + F$ resistance: viscous flow [viscosity, η (T)]analytic solution for temp. $T = \text{const}$:
($t = \text{time}$)

$$\left(\frac{b}{x}\right)^2 = \left(\frac{4}{5} \frac{\gamma}{x} + \frac{2}{5\pi} \frac{F_i}{x^2}\right) \frac{1}{\eta} \quad \left(\begin{smallmatrix} \text{Rumpf} \\ \text{Sommer} \end{smallmatrix}\right)$$

Figure 27.6. Sinter neck between two spheres at the first stage of sintering.

interested in the first stage of sintering, where adhesion forces are reinforced by sintering effects. If, for instance, a powder with a relatively low melting point is stored for a long time, the particles stick together and the flowing properties of the powder change in an often very unwelcome way.

In this first stage of sintering, the driving forces are surface tension γ and a force F_i . The force F_i can be the sum of a compression force F_{co} and the adhesion force F_a due to van der Waals (or liquid-bridge) adhesion around the sinter neck. F_a changes with the growth of the sinter neck, but this may be neglected in the very first stage of sintering.

The resistance is usually related to viscous flow or creep, which is expressed by the viscosity η . We are interested in the growth with time of the sinter neck radius b (Figure 27.6) between two spheres of diameter x . The temperature is constant, and the variables are b , x , γ , η , F_i , and t . From a dimensional analysis it is found that

$$\frac{b}{x} = f\left(\frac{\gamma \cdot t}{\eta \cdot x}, \frac{F_i \cdot t}{\eta \cdot x^2}\right)$$

The analytical solution is based on a differential energy balance. In the time element dt , the dissipational energy due to viscous flow must be equal to the decrease of surface energy plus the work done by F_i . The exact calculation gives

$$\left(\frac{b}{x}\right)^2 = \left(\frac{4\gamma}{5x} + \frac{2}{5\pi} \frac{F_i}{x^2}\right) \frac{t}{\eta}$$

The factor $\frac{1}{5}$ differs from Frenkel's⁸ factor, which is $\frac{1}{4}$. The difference is practically unimportant. However, Frenkel's derivation of the velocity field in the sphere and sinter neck is not exact in the sense of a rigorous theory.

If the force F_i is only van der Waals adhesion, we get

$$\frac{F_i}{x^2} = \frac{F_{adv}}{x^2} = \frac{K\bar{\omega} p}{32\pi a_0^2 x}$$

$$\left(\frac{b}{x}\right)^2 = \left(\frac{4}{5}\gamma + \frac{K\bar{\omega}}{80\pi^2 a_0^2}\right) \frac{t}{x\eta}$$

The two terms in parentheses have a fixed relation, independent of x . For $\gamma = 500$ dynes/cm, $K\bar{\omega} = 5\text{eV}$, and $a_0 = 4 \times 10^{-8}$ cm, the relation of the surface force term ($\frac{1}{5}\gamma$) to the adhesion force term ($K\bar{\omega}/80\pi^2 a_0^2$) is 63:1. The van der Waals adhesion can therefore be neglected.

A compression force ($F_{co} \approx F_i$) has the same influence as the surface energy, if

$$\frac{F_{co}}{x^2} = 2\pi \frac{\gamma}{x}$$

For $\gamma = 500$ dynes/cm we get

$$\frac{\epsilon}{1 - \epsilon} \cdot P_{\text{isost}} \approx \frac{F_{co}}{x^2} = \frac{3.14 \times 10^2}{x/\mu\text{m}} \frac{\text{N}}{\text{cm}^2}$$

This equation allows an assessment of whether surface energy or compression forces have a greater influence on the early stage of sintering. If, for instance, the particles are of $100 \mu\text{m}$ size and $\epsilon = 0.5$, the influence of F_c is greater than that of γ , if an isostatic pressure is applied such that $F_{co}/x^2 > 3.14 \text{ N/cm}^2$. For a calculation of the sinter neck radius, the viscosity η should be known, but this value is generally not obtainable.

BONDING MECHANISMS AND STRENGTH OF AGGLOMERATES

For moist agglomerates having less than 30% of the void spaces filled with liquid, a theoretical tensile strength can be calculated from the mean value of the number of contact points times the adhesion force component in the tensile strength direction. The average adhesion force depends on the average a/x value in the system. Experimental values of strength indicate a value of 0.05 for the average a/x value. This is shown in Figure 27.7 in the region of $0 \leq S \leq 0.3$.

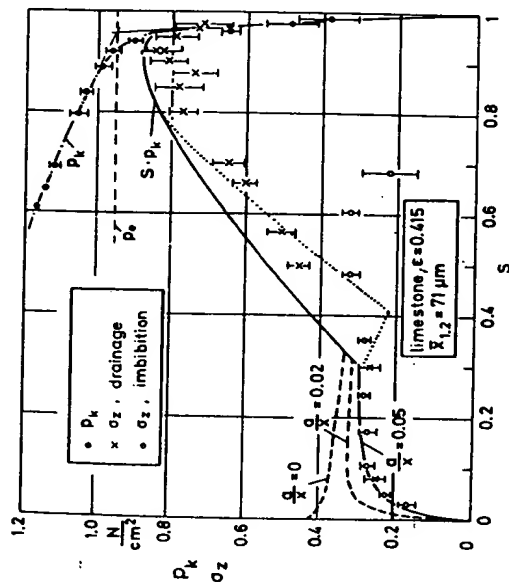


Figure 27.7. Capillary pressure P_k and tensile strength σ_z as a function of the liquid saturation S .

In reality, of course, the distance has a distribution. At some points there is real contact combined with elastic and probably plastic deformation. At other points the distance is still larger but small enough to transmit adhesion forces. Each contact is characterized by a force-elongation curve. If the whole agglomerate is strained, the total force, transmitted in a certain cross-sectional area, is the sum of the contact forces. At a certain total elongation a maximum total force T_{\max} is reached. The breakage occurs in the cross-sectional area with the smallest T_{\max} . This gives the tensile strength. In the simplified theory it is supposed that all contact forces in the normal direction are equal in the case of breakage. It has been shown experimentally that this simplified theory is applicable to large monosized spheres and the liquid-bridge bonding mechanism.⁷

If more than about 80% of the void space between the particles is filled with liquid (capillary state, liquid saturation $S > 0.8$), a capillary suction (pressure P_k) is formed in the liquid space and the agglomerate is held together by the outer pressure. The tensile strength σ_z equals the product P_k times S .

We have simultaneously measured capillary pressure in the agglomerate, saturation, and tensile strength with wet limestone powders. In Figure 27.7 capillary pressure (P_k) and tensile strength of agglomerates (σ_z) made from

71 μm limestone particles are plotted against saturation S . The measured values of tensile strength just reach up to the theoretical curve ($S \cdot P_k$), calculated from the measured capillary pressure. Figure 27.8 also shows that the capillary liquid mechanism, $S > 0.8$, gives a maximum tensile strength, which is about three times as great as the strength in the range $0 < S < 0.3$ (the liquid-bridge state).

The measured tensile strength is different, depending on whether the saturation is realized by drainage or by imbibition. The capillary pressure after drainage is much higher than after imbibition at comparable S (Figure 27.7), because the porous system is a sequence of caverns and necks. With drainage the capillary pressure depends on the radii of curvature in the necks; with imbibition it depends on the radii of curvature in the caverns.

The tensile stress/strain behavior of wet agglomerates is shown in Figure 27.8 for limestone pellets made from 65 μm particles. The maximum stress and maximum strain both increase with increasing saturation. If we compare the curves for drainage with $S = 0.65$ and those for imbibition with $S = 0.68$, we see that the somewhat smaller maximum stress in the case of imbibition is reached at a much greater strain. When, after imbibition, the agglomerate is strained, the liquid situation is changed into drainage. So approximately the same stress is reached, combined with much greater strain. This can quantitatively be derived from capillary-pressure hysteresis curves.

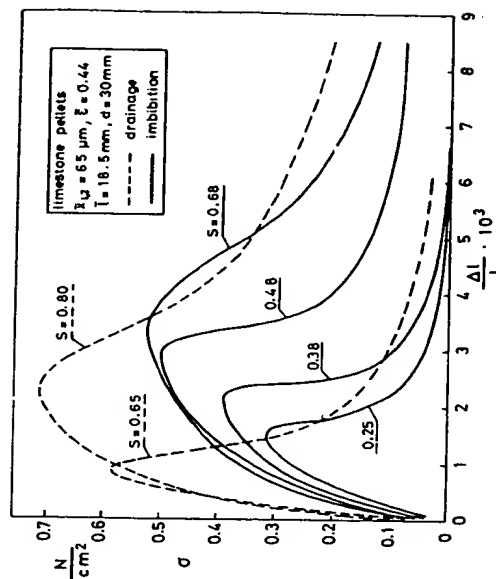


Figure 27.8. Tensile stress-strain curves of moist limestone agglomerates.

In general, tensile stress, shear stress, and strain experiments are necessary to understand and predict the mechanics of agglomerates.⁸⁻⁹

OTHER INFLUENCES ON ADHESION FORCES

Influence of Surface Roughness on the Adhesion Forces

In reality adhesion forces can be considerably changed by surface roughness. The influence of surface roughness is maximum with van der Waals forces, since they depend sensitively on the microgeometry in the contact region, while electrostatic adhesion of ideal insulators with opposite surplus charges is independent of the contact geometry and distance as long as $a/x \ll 1$.

The quantitative relations are demonstrated in Figure 27.9 for a sphere with radius R supporting a half-spherical roughness peak of radius r , which is in contact with the half space. The calculated adhesion force is plotted against the radius r of the roughness peak. The van der Waals forces are calculated for $R = 0.5, 5$, and $50 \mu\text{m}$. Each of the three curves has a sharp minimum that lies some orders of magnitude below the maximum value for the smooth sphere with $r = 0$ or $r = R$. At the minimum both the small and the large sphere contribute to the adhesion force. On the left side of the minimum, with smaller r , the attraction due to the large sphere increases,

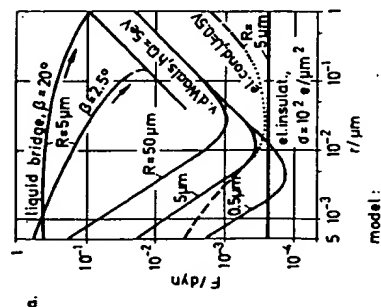


Figure 27.9. Adhesion force F of liquid bridge, van der Waals, and electrostatic interaction between a sphere and a half space as a function of the radius r of a roughness peak.

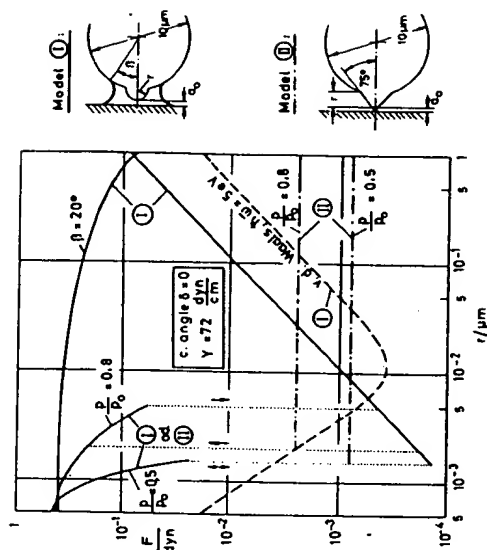


Figure 27.10. Adhesion force F of liquid bridges between sphere and half space as a function of the radius r of a roughness peak. Parameter is the relative vapor pressure p/p_0 .

since the distance r is decreasing. On the right side of the minimum, the large sphere has no more influence and the van der Waals adhesion force increases in proportion to r . We see that the van der Waals adhesion can drop to very low values, below electrostatic forces. The same lowering of van der Waals adhesion is produced if, instead of roughness peaks, fine particles of 10^{-2} to $10^{-1} \mu\text{m}$ are placed between the spheres. In practice this effect is utilized to prevent agglomeration of fine dry powders by adding a very fine silica powder of 10^{-2} to $10^{-1} \mu\text{m}$ particle size.

Liquid bridges are much less sensitive to roughness peaks if the bridge angle β is not too small. If β is very small, the liquid-bridge forces are also very sensitive to roughness peaks as shown in Figure 27.10 in the case of very small liquid bridges due to capillary condensation.

Again the adhesion force is plotted against roughness peak radius r . The radius of the large sphere is $R = 5 \mu\text{m}$. The liquid-bridge force for $\beta = 20^\circ$ and the van der Waals force have been taken from Figure 27.9. The volume of the liquid bridge formed by capillary condensation depends on the relative vapor pressure p/p_0 and is calculated according to Kelvin's law. At a very small radius r , the liquid bridge is formed between the large sphere and the plate. At a certain size r of the roughness peak, the bridge between the large sphere and the plate bursts and only a small bridge between the small sphere and the plate remains. The adhesion force drops abruptly and rises

again with increasing r . Here we see again a great influence of roughness peaks. We recognize also that in dry systems with relative humidities above 50% the liquid-bridge adhesion due to capillary condensation may be larger than van der Waals adhesion with small roughness peaks. Complete wetting has been assumed, that is, a contact angle $\delta = 0$ and the surface tension of water $\gamma = 72$ dynes/cm. In reality the two adhesion forces superimpose, whereby the van der Waals forces can be somewhat smaller because of the water volume.

As a consequence of these calculations, we conclude that adhesion is mainly due to liquid-bridge forces and van der Waals forces if there are no solid bridges or viscous binders. Only under special roughness geometries, where van der Waals forces have a minimum, electrical adhesion forces may reach the same order of magnitude.

If the particles are not in contact and the distance a increases, liquid bridges collapse at distances $a/x < 1$, depending on bridge volume. Van der Waals attraction forces drop practically to zero for $a > 1 \mu\text{m}$. Thus at distances larger than $1 \mu\text{m}$, that is, $a/x > 1$, only electrostatic attraction or repulsory forces are still effective. They play an important role in agglomeration kinetics of particles suspended in a gas by forcing particles together, and in diffusion, turbulence, and convection of particles.²

Influence of Elastic Deformation

The existence of adhesion forces causes bodies to undergo elastic deformation at their contact points. The elastic deformation occurs to the extent where the elastic repulsion force balances the attractive force. This elastic deformation causes the effective adhesion force to increase because the force required to separate the contacting surfaces must overcome the sum of the attractive and repulsive forces. Dahneke¹⁰ has analyzed the influence of elastic deformation on adhesion for a few specific cases and derived approximate relationships for the separation-force enhancement. New calculations, however, show that the results given by Dahneke should be reduced by a factor of 8. Hence it follows that the influence of elastic deformation on particle adhesion can be neglected in most cases.

Influence of Plastic Deformation

If plastic deformation occurs at the point of contact between two bodies, a permanent surface of contact is established. The van der Waals force of adhesion is greater for two plane surfaces in contact than for point contacts. The additional van der Waals attractive force due to plastic deformation is equal to $f_{pl} \cdot P''_{vaw}$, where P''_{vaw} is the force of attraction per unit area of

contact between two flat surfaces, and f_{pl} is the surface area of contact. The quantity P''_{vaw} is given by¹

$$P''_{vaw} = \frac{K\omega}{8\pi^2 a_0^3}$$

Since the additional adhesion force from plastic deformation depends on the area of permanently established contact (due to plastic deformation), this area must be determined. An elastic deformation of a particle produces a contact circle at the contact point. According to the theory of Hertz, the normal stress σ_1 within the contact circle varies from zero at the circumference to a maximum value p_0 in the center according to the formula

$$\left(\frac{\sigma_1}{p_0}\right)^2 = 1 - \frac{c}{C_0}$$

where C_0 = radius of the contact circle

c = distance from the center

σ_1 = stress at position c

If p_0 exceeds a certain limit, which we denote as p_{pl}^H , plastic deformation occurs in the center.

The stress at which plastic deformation begins with small particles and roughness peaks is much higher than the macroscopic yield strength. Faulhaber,¹¹ using a micro-compression test apparatus, found a value for p_{pl}^H of around 10^8 N/cm^2 for $10 \mu\text{m}$ quartz glass spheres.

As the compression force increases, p_0 becomes greater than p_{pl}^H and the area f_{pl} of the plastically deformed zone increases. The area f_{pl} is given by

$$f_{pl} = \frac{F_t}{p_{pl}^H} \cdot \frac{1 - (p_{pl}^H/p_0)^2}{1 - \frac{1}{8} (p_{pl}^H/p_0)^2}$$

where F_t is the total compressive force. A pseudo-yield strength p_{pl} can be defined as F_t/f_{pl} . It follows from the above equation that

$$p_{pl} = p_{pl}^H \frac{1 - \frac{1}{8} (p_{pl}^H/p_0)^2}{1 - (p_{pl}^H/p_0)^2} \quad (1)$$

If the plastic part of deformation is much greater than the elastic one, $p_0/p_{pl}^H \gg 1$ and hence $p_{pl} \approx p_{pl}^H$. For small glass spheres and predominant plastic deformation, $p_{pl} \approx p_{pl}^H \approx 10^8 \text{ N/cm}^2$. Similar values can be expected for crystalline materials, since in very small volumes the yield strength is much greater than the macroscopic yield strength owing to dislocation movement. In small volumes below $1 \mu\text{m}$ extension, there is very little chance for dislocation existence and dislocation movement. The yield

strength in this case approximates the molecular shear strength, while the macroscopic yield strength of metals is on the order of some 10^4 N/cm^2 .

If in addition to any adhesion force F_0 an outer compression force F_{co} is applied, the total plastic deformation is

$$f_{pl} = \frac{F_t}{p_{pl}} = \frac{F_0 + F_{co}}{p_{pl}}$$

In contrast to the case with elastic deformation (due to F_{co}), this plastically deformed area remains if the compression force is removed. It causes an additional van der Waals attraction force $f_{pl} \cdot P'_{vaw}$.

In the case of separation, the separation force must overcome the total adhesion force

$$\begin{aligned} F &= F_0 + f_{pl} P'_{vaw} \\ &= F_0 \left(1 + \frac{P'_{vaw}}{p_{pl}} \right) + F_{co} \frac{P'_{vaw}}{p_{pl}} \end{aligned}$$

With $\hbar\omega = 1$ to 2 eV as an estimated value for limestone and $a_0 = 4 \times 10^{-8} \text{ cm}$ we get

$$P'_{vaw} = (0.3-0.6) 10^4 \text{ N/cm}^2$$

$$\frac{P'_{vaw}}{p_{pl}} \leq 10^{-2} \quad \text{for hard materials}$$

$$F \approx F_0 + F_{co} \frac{P'_{vaw}}{p_{pl}} \quad (2)$$

Figure 27.11 shows some of the first results of measurements executed by Schutz of our Institute with $60 \mu\text{m}$ limestone particles. A set of particles were laid on a plane-polished steel substrate that could be fixed in a centrifuge in two opposite situations. In one situation the particles were pressed against the substrate by the centrifugal force, which then equaled the compression force F_{co} . After that, the substrate was fixed in the opposite situation and the particles were separated from the substrate by the centrifugal force, which then equaled the adhesion force F .

Each curve represents one measured distribution function of adhesion forces. The speed of the centrifuge, and therefore the separating centrifugal force, is increased stepwise. This force is plotted as the abscissa. At each step the percentage of particles that have left the substrate is measured (ordinate). They are all particles with a smaller adhesion force than the force indicated at the abscissa; the compression force F_{co} . The curve with

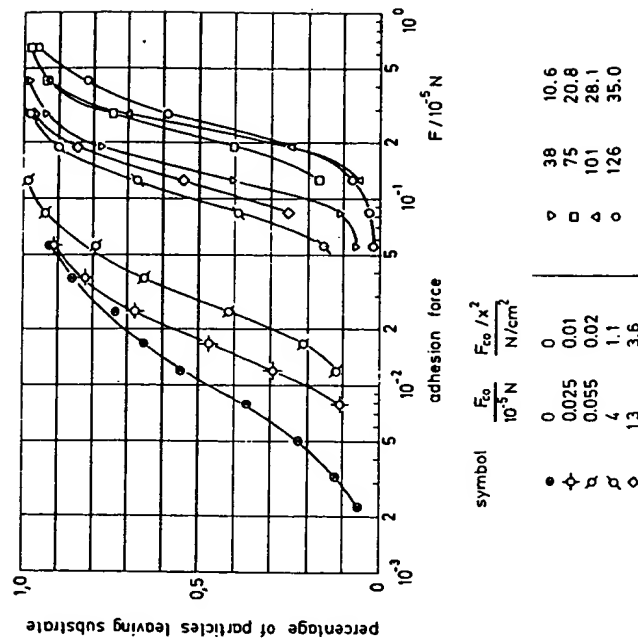


Figure 27.11. Distribution of adhesion forces of limestone particles that were pressed against a substrate by a centrifugal force.

$F_{co} = 0$ is flat. The particles have been spread very loosely on the substrate. In this case a one-point contact is very likely. Since the limestone particles are irregularly shaped, a great variety of contact geometries is possible. Therefore, the standard deviation of the measured adhesion force distribution curve is great. If the particles are pressed against the substrate by an increasing compression force, the distribution curves get steeper and shift to higher adhesion forces. The change in the inclination of the curves indicates that the particles are changing their position, probably from one-point to more-point contacts. The contact geometry becomes more homogeneous. Above $F_{co} = 4 \times 10^{-8} \text{ N}$ the curves remain parallel. It can be assumed that with higher compression forces the particles do not change their position any more. $F_{co} = 3.8$ dynes is about 400 times the median value of F for $F_{co} = 0$.

Such compression forces occur in practice when particles are compressed in a packing. If the packing is stochastically homogeneous with porosity ϵ

and the compression is isotatic, the relation between isostatic pressure P_{isot} and the compression force F_{co} at the contact points is

$$P_{\text{isot}} = \frac{1 - \epsilon}{\epsilon} \cdot \frac{F_{\text{co}}}{x^2}$$

In a bulk powder with $\epsilon \approx 0.5$, we get $P_{\text{isot}} \approx F_{\text{co}}/x^2$.

The values F_{co}/x^2 are given in Figure 27.11. Pressures between 1 and 10 N/cm² are very common in bulk powders.

In Figure 27.12 the median values F_{so} of the distribution curves in Figure 27.11 are plotted against the compression force F_{co} . At $F_{\text{co}} = 0$ the adhesion force is $F_{\text{so}}(0) = 10^{-7}$ N. It increases very steeply with relatively small compression forces until the threefold adhesion force $F_{\text{so}} = 1.2 \times 10^{-6}$ N is reached. This indicates that in this first region the contact position changes from one-point to more-point contact. Above $F_{\text{so}} \approx 10 F_{\text{so}}(0)$ the adhesion force increases linearly with F_{co} , with

$$\frac{dF_{\text{so}}}{dF_{\text{co}}} = 0.8 \times 10^{-8}$$

If the increase of adhesion is due to plastic deformation, we derive from

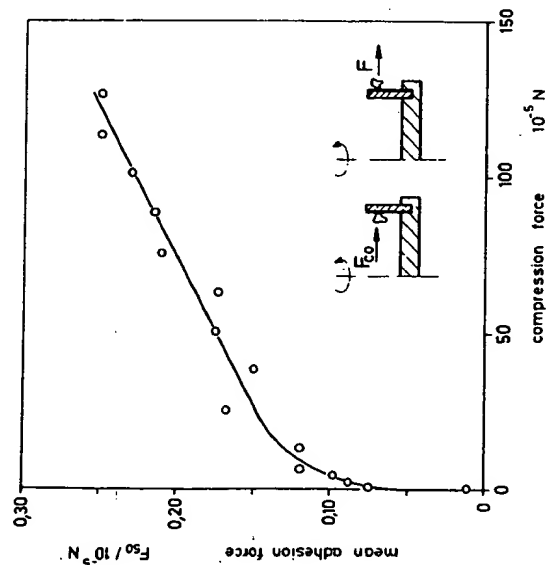


Figure 27.12. Mean adhesion force F_{so} as a function of the compression force F_{co} for limestone particles.

Equation 1

$$\frac{dF_{\text{so}}}{dF_{\text{co}}} = \frac{P'_{\text{vdw}}}{P_{\text{pl}}} = 0.8 \times 10^{-8}$$

with $P'_{\text{vdw}} = (0.3-0.6) \times 10^4 \text{ N/cm}^2$ we get

$$P_{\text{pl}} = (3.8-7.5) \times 10^8 \text{ N/cm}^2$$

This value is in satisfactory agreement with Equation 1 for $p_{\text{pl}}^{\text{H}} = 10^9 \text{ N/cm}^2$, measured with quartz-glass spheres.¹¹ $p_{\text{pl}} > p_{\text{pl}}^{\text{H}}$ indicates an elastic deformation superimposed on the plastic deformation at the contact edges of the particles. This remaining elastic stress diminishes the effect of the van der Waals adhesion pressure in the contact area. From Equation 1 $p_{\text{pl}}^{\text{H}}/p_0 = 0.9$ to 0.95 can be estimated.

In tableting and briquetting F_{co}/x^2 reaches values on the order of some 10^8 N/cm^2 instead of 126 N/cm^2 as in the experiments referred to above. It is not likely that the linear function $F_{\text{so}}(F_{\text{co}})$ can be extrapolated to much higher values of F_{co} for, in addition to the elastic stress, grinding will take place at the contact edges or in the whole particle. It will be necessary to determine experimentally how adhesion forces change with high compression forces.

In general, the calculation of adhesion forces and the relevant influences indicates the tendencies. But they are restricted to geometrical models that deviate considerably from reality if the particles have an irregular shape. All measurements of adhesion forces of irregularly shaped particles show a broad distribution of adhesion forces. They often are log-normal distributed and range over one to two orders of magnitude.

SUMMARY

Agglomeration is due to different adhesion mechanisms. We have a most comprehensive knowledge of the liquid capillary mechanism in moist agglomerates with above 80% saturation. The liquid-bridge adhesion mechanism has also been very well studied theoretically. Van der Waals adhesion can be calculated for spherical particles but depends very sensitively on contact geometry and surface roughness. Electrostatic adhesion forces are normally smaller. An additional compression force increases particle adhesion by changing the particle position from one-point to more-point contact and, after that, by plastic deformation if the compression force is higher than about 400 times the original adhesion force. A new formula for the first stage of sintering is presented that can be used to assess the influence of a compression force in comparison with surface tension.

ACKNOWLEDGMENT

The authors are indebted to Dr. Sommer for his substantial contribution to the sintering calculations, W. Schutz for his measurements of adhesion forces, W. Muhr for his calculations of electrostatic forces, and K. H. Sartor and K. Schaber for their calculations of liquid bridges. This work was kindly supported by the Deutsche Forschungsgemeinschaft, Bonn-Bad Godesberg.

REFERENCES

1. H. Krupp, "Particle Adhesion, Theory and Experiment," *Adv. Colloid Interface Sci.*, **1** (2), 111-239 (1967).
2. K. Borho, "Agglomeration und Wandansatz bei Gas-Feststoff-Stromungen aufgrund elektrostatischer Aufladungen," *Chem.-Ing.-Tech.*, **45**, 387-391 (1973).
3. H. Schubert, "Untersuchungen zur Ermittlung von Kapillardruck und Zugfestigkeit von feuchten Haufwerken aus körnigen Stoffen," Thesis University Karlsruhe, 1972.
4. H. Schubert, "Haftung zwischen Feststoffteilchen aufgrund von Flüssigkeitsbrücken," *Chem.-Ing.-Tech.*, **46**, 333-334 (1974).
5. W. Pietsch, "The Strength of Agglomerates Bound by Salt Bridges," *Can. J. Chem. Eng.*, **47**, 403-409 (1969).
6. J. Frenkel, "Viscous Flow of Crystalline Bodies under the Action of Surface Tension," *J. Phys.*, **9**, 385-391 (1945).
7. H. Schubert, "Tensile Strength of Agglomerates," *Powder Tech.*, **11**, 107-119 (1975).
8. H. Rumpf, "Die Wissenschaft des Agglomerierens," *Chem.-Ing.-Tech.*, **46**, 1-11 (1974).
9. H. Schubert, W. Herrmann, and H. Rumpf, "Deformation Behavior of Agglomerates Under Tensile Stress," *Powder Tech.*, **11**, 121-131 (1975).
10. B. Dähneke, "The Influence of Flattening on the Adhesion of Particles," *J. Colloid Interface Sci.*, **40**, 1-13 (1972).
11. F. R. Faulhaber, Thesis University Karlsruhe 1966.

28

Strength and Microstructures of Dried Clay Mixtures

W. O. Williamson

This account, based on published and unpublished information, reviews the relations between the transverse strength (modulus of rupture) of a dried fine-grained clay, with or without nonplastic additions, and the corresponding microstructures. The nonplastic additions were coarse or fine quartz, tremolitic talc, chrysotile asbestos, glass fragments, glass spheres, and Madagascar and Mexican graphite. All except the glass spheres had been comminuted industrially.

SOME FACTORS AFFECTING DRY STRENGTH

The bonds broken during dry strength tests are not commonly intracrystalline but are between clay-mineral platelets or their aggregates, or between these and nonplastic grains. Such grains, except those of graphite for instance, are not usually fractured during tests. The nature of the bonds

is discussed elsewhere.^{1,2} Evidence is presented that the bonds, although of several types, are often ionic. The ions involved may remain incompletely dehydrated, even in test pieces dried at 105 to 110°C.

Transverse strength tends to increase with the number of bonds per unit bulk volume and with the extent of the surface over which an individual bond produces effective adhesion. Strong bonds need not imply strong test pieces, as they help to maintain open porous structures, which are weak because they contain abundant flaws.^{1,2}

Transverse strength is influenced not only by bonds, but by the effectiveness of flaws in concentrating the applied stresses and thus breaking the bonds. A connection between this effectiveness and the porosity of the test piece may be anticipated. However, ions originally present in the interstitial water not only affect the porosity and pore characteristics of the dried test piece, but also contribute to the bonds. Thus bonds and the microstructures within which they exist are not independent variables.^{1,2}

Dried clay-containing test pieces, with or without nonplastic additions, often have apparent porosities of 20 to 40%, and their strength commonly increases with decreasing porosity. Frequently, however, no obvious quantitative relation is discernible between strength and porosity.^{1,2} Indeed, within limits, strength and porosity can increase together.^{1,2,4} The absence of a simple or universal relationship is not surprising, as percentage of apparent porosity represents merely the total void space, in a constant volume of material, accessible to the fluid used in determining it. It neglects pore size, shape, and size distribution. For instance, a pore may have an overall shape that makes it unlikely that it will operate as a dangerous flaw, while the really dangerous flaws might be slotlike spaces between clay-mineral platelets, or packets of platelets, in its walls.^{1,2} Moreover, the stepped edges of packets in contact with the basal planes of platelets in adjacent packets could constitute further regions of dangerous flaws, although the void spaces in these regions might contribute little to the total porosity.^{1,2}

Most clay-mineral crystals are flat and thin. The same is true, in greater or lesser degree, for Madagascar graphite flakes, cleavage fragments of tremolite, and grains of ground quartz, glass, and Mexican graphite. Tremolitic talc and especially asbestos contain fibrous particles.

During extrusion these shape factors promote particle orientation and, as a result, pore orientation and interconnection. Dry strength is thus anisotropic.^{1,2} Extruded test pieces are broken across, not along, planes or directions of particle and pore orientation, and thus higher, not lower, strength values are ascertained. These strength values may become higher still if the interstitial liquid in the plastic mixture contained dispersants, because these promote more intense particle parallelism and closer particle

packing. The dispersants may have been deliberately added or may have resulted from reactions between the interstitial liquid and solid particles of feldspar, nepheline syenite, glass,⁶ and so forth, which release alkali metal ions.

The interstitial solutions in clay-water systems are commonly somewhat acidic in the absence of extraneous sources of alkalis. However, interaction between the clay and the water occurs progressively and involves not only ion exchange, but also gradual chemical decomposition of the solid phases. The resulting changes in the nature and concentration of the ions produce corresponding changes in the degree of flocculation of the clay minerals and, ultimately, in the microstructure and the associated strength of the dried clay. Such changes are among the factors that cause dry strength to vary with the time and temperature of contact between the clay and water before and during the desiccation of the test pieces.^{2,6} Thus the dry strength of even a monomineralic, homoionic, monodispersed clay may be expected to change with the time and temperature of aging in the plastic state,² although no reference to relevant experiments has been found.

Extrusion produces not only particle parallelism resulting from laminar plastic flow, but also slip bands, caused by compression within which the clay-mineral platelets lie at large angles to the surface, which is under tension during cross-breaking (Figure 28.1). In some circumstances these slip bands weaken the test piece. Planes or directions of particle orientation that are favorable for higher strength are not in these slip bands but instead are in the matrix. Those in the bands are not as favorably oriented and can cause fracture.

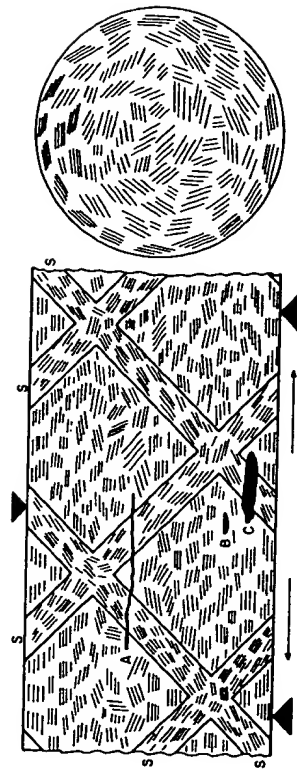


Figure 28.1. A schematic section containing the axes of an extruded clay cylinder (with corresponding transverse section). The cylinder is being broken by three-point loading, which produces tensile stresses in the directions of the arrows. Traces of the clay platelets are represented by lines.

METHODS AND MATERIALS

The preparative, extrusion, testing, microscopical, and fractographic techniques were essentially those already described,^{8,9} but in addition some specimens were examined by scanning electron microscopy. The plastic bodies had water contents slightly below those at their sticky points. Data on the materials used, summarized here, are given more fully elsewhere. Similarly, the results of strength determinations appear in simplified form, although their validity was checked statistically in many instances.

The clay was largely kaolinite^{8,9} with some micaceous minerals. Its particle-size distribution included 50 wt % < 1.0 μm esd (effective sieve diameter). An original water content of 39.6 wt % corresponded to a dry modulus of rupture of 775 psi.

The coarse and fine quartz particles were somewhat flat angular chips. A weight distribution^{8,9} of the coarse quartz, on U.S. Standard Screens, was +140/Tr., -140 + 200/2.3%, -200 + 230/4.1%, -230 \times 270/33.7%, -270/59.9%.

The two different samples⁷ of finer quartz were quartz A (specific surface 2 m^2g^{-1}) and quartz B (specific surface 0.5 m^2g^{-1}). They had an average particle size of 1.1 and 4.2 μm , respectively.

The tremolitic talc used also contained considerable talc and antigorite, as indicated by X-ray diffraction.⁸ Polarizing microscopy revealed many cleavage fragments of tremolite, with some fibrous mineral constituents. The particle-size distribution of the total material included 81, 43 and 12 wt % < 49, 15 and 1.3, μm esd, respectively.

The chrysotile asbestos had a wide range of fiber lengths, but 95% of its fibers were less than 13.5 mm long. The fibers were bundles of fibrils, each about 200 \AA across, and were not very open structured.⁴

The crushed glass was composed of rather flat, sharp chips that, on U.S. Standard Screens, gave approximately +100/0, -100 + 200/75, -200/25%. The glass spheres had a similar size distribution.⁸

Weight distributions, on U.S. Standard Screens, of the Madagascar (flaky) and Mexican (nonflaky) graphites appear in Table 28.1.

MICROSTRUCTURES OF EXTRUDED CYLINDERS

The cylinders contained packets of mutually parallel clay-mineral platelets. The plane of mutual parallelism within each packet, which is the basal plane of the clay-mineral crystals, was angularly related to the corresponding planes in neighboring packets, although the angular differences were

Table 28.1 Screen analysis of Madagascar (flaky)⁸ and Mexican (non-flaky)¹⁰ graphites

Source	Percentage Weights Retained on U.S. Standard Screens						
	20	30	40	50	60	70	80
Madagascar	0.2	1.1	16.5	68.2	81.0	92.6	ND
Mexico	ND	ND	8.3	46.5	79.5	88.8	97.9
							2.3

often small. As an approximation the packets can be regarded as lying in a series of cylindrical shells, coaxial with extruded cylinder, with the widest shell having the diameter of the cylinder. The cylinder underwent a large reduction in diameter when forced through the circular orifice of the die. Thus there was no obvious tendency for the packets to lie on paraboloidal surfaces, convexly curved in the direction of flow, although this tendency was very apparent in certain cylinders extruded under other conditions.¹¹ More specifically, the clay-mineral packets tended to be parallel to the axis of the cylinder and, towards the exterior, parallel to the curved surface (Figure 28.1).

The added nonplastic grains were mostly much coarser than the clay-mineral crystals. Except for the glass spheres, the nonplastic grains tended to be flat, and the preferred orientation of their greatest cross-sectional areas resembled that of the major surfaces (basal planes) in the clay-mineral packets. Elongated or fibrous grains, abundant in tremolitic talc or asbestos, tended to parallelism with the axis of the cylinder, especially in its outer layer (Figure 28.1).

Slip bands were very variable in thickness and often less than 12 μm wide. They crossed the planar and linear parallel structures just described. Ideally, they coincided with the curved surfaces of two sets of cones coaxial with the extruded cylinder. Within each set the cones followed each other successively and each cone protruded into the one ahead. One set pointed in the direction of extrusion and the other in the opposite direction.¹¹ Thus, in a section containing the axis of the cylinder, the traces of the slip bands intersected at about 90° and met those of the curved surface at approximately 45°. The clay-mineral packets in the slip bands lay at small angles to their wall (Figure 28.1).

Electron microscopy did not show conclusively whether the slip bands terminated at the actual curved surface of the cylinder or beneath the very thin, highly oriented layer of clay-mineral platelets sometimes found at this surface. At the magnification of the optical microscope, the slip bands appeared to reach the surface itself.

THE INFLUENCE OF SLIP BANDS ON BREAKING BEHAVIOR

Whether or not the slip bands ended at or beneath the curved surfaces, fractography demonstrated that test pieces frequently failed along them.⁸ Such bands contained slotlike pores between clay-mineral platelets or between their packets, which lay across the directions of the applied stresses and were thus likely to be sites for the initiation and propagation of the cracks that lead to failure. The measured transverse strength is probably affected, not only by the mere presence of slip bands, but by their periodicity and width and by variations of the microstructure within them. Among factors that might influence these characteristics are the mineralogy, particle-size distribution and water-content of the clay, the ratio between the diameters of the extruder reservoir and orifice, and the rate of extrusion. Relevant published information is minimal, although there is evidence that more rapid extrusion reduces the distance between the successive slip bands, while, at similar extrusion rates, the distance increases in coarser-grained bodies.¹²

Coarse quartz,⁸ tremolitic talc,⁸ asbestos,⁴ and crushed glass,⁸ when up to 25, 20, 25, and 25 wt % respectively, was added, produced corresponding increases in modulus of rupture of 4, 47, 27, and 9%, respectively. Reduction in the water content of the clay-quartz mixture from 39.6 to 29.3 wt % changed the strength increase from 4 to 16%. This was the only mixture for which the effects of varying the water content, as well as the proportion of nonplastic grains, were studied in detail.^{8,9}

Strengthening resulted from the simultaneous operation of two mechanisms, while, for glass, a third was involved concurrently. Added nonplastic grains tended to reduce the number of slip bands per unit length of extruded cylinder, so that fewer dangerous flaws occurred on the surfaces under tension and the test piece appeared stronger. It was noticed that the addition of most nonplastics increased the pressure required to initiate extrusion.^{8,9,10} This, presumably, implied that the plastic mass had become more resistant to the compressional stresses necessary for the formation of slip bands. Added glass, however, lowered the pressure required for extrusion⁸ because it produced an interstitial alkaline solution that dispersed the clay and allowed it to flow more readily. As might be expected, slip bands remained relatively abundant unless the mixtures were very rich in glass (50 wt %).

Many nonplastic particles were large enough to project into or across those slip bands that had been able to develop in their presence. These produced strengthening by impeding the propagation of cracks. For continued growth, cracks had to circumvent obstructing particles that, because

of the orientation caused by laminar plastic flow during extrusion, tended to lie with their greatest cross-sectional areas or, if prismatic or fibrous, their lengths across the slip bands and the paths of the cracks therein (Fig. 28.1). Cracks arising from flaws in the matrix of the slip bands would encounter similarly oriented nonplastic grains athwart their paths. However, it is not yet known whether nonplastic grains impede the nucleation and the continued growth of cracks.

Increasing additions of coarse quartz grains changed the fractography of test pieces from angular and faceted because of failure along intersecting systems of slip bands, to relatively smooth because the slip bands had been reduced in number and continuity.⁸ These changes were obvious to the unaided eye. Similar changes were observable in test pieces of some of the mixtures containing nonplastics other than quartz. However, mixtures containing asbestos⁴ were notable for irregularly fractured surfaces, often without marked faceting, from which fibers not only protruded, but sometimes linked the two halves of the broken test piece. Here part of the total fracture mechanism involved rupture at clay-fiber boundaries and the partial or complete withdrawal of fibers from their clay sheaths.

STRENGTH INCREASES PRODUCED BY CRUSHED GLASS

There was evidence that crushed glass caused strength increases, not only by reducing the number of slip bands and by inhibiting the ready propagation of cracks along them, but also by producing an interstitial alkaline solution that dispersed the clay.⁸ Thus the intermittent shaking of 50 wt % of glass in water, during 6 hours at room temperature, produced a supernatant solution of pH 10. When the clay was tempered with this solution, instead of with distilled water, its transverse strength increased by 9%. Although the interstitial solution in the clay-glass mixtures might not have attained so high a pH, it may be reasonably expected to disperse the clay and thus strengthen it. Dispersion was in fact suggested by the progressive decrease in the percentage of apparent porosities of the dried test pieces that accompanied the addition of increasing weights of glass to the clay.

At some time during the preparation, ageing, and drying of the mixture, the glass fragments developed mantles of clay-mineral crystals having their basal planes approximately parallel to the surface of the substrate. This was found by examining thin sections. Such occurrences resemble the isotropic deposition of clay-mineral platelets that occurs, for instance, around sodium chloride crystals that are in contact with aqueous suspensions of montmorillonite.¹³

The clay mantles around glass fragments implied the presence of boundary regions that, in the dry state, might be conducive to the overall strength of the clay-glass mixture. That such boundary regions were relatively strong was suggested by the reported adhesion between clay and glass, which became more marked when the original clay slurries were alkaline.¹⁴

If clay mantles developed around the other nonplastic grains studied, they were not obvious in thin sections, although they are known to form around quartz grains in soils¹⁵ and can be produced in the laboratory by percolating clay suspensions through columns of quartz grains.¹⁶

ADDITIONS CAUSING ONLY STRENGTH REDUCTIONS

Fine quartz A and B⁷ and Madagascar⁹ and Mexican¹⁰ graphites resulted in 15, 3, 15 and 24% reductions in the modulus of rupture, respectively, when as little as 10 wt % of quartz or 5 wt % of graphite was added. If any increases in strength occurred, which seems improbable, they must have accompanied smaller additions than those investigated.

Numerous slip bands still developed in the presence of the percentages of added quartz or graphite cited. The quartz grains, especially those in quartz A, were commonly too small to lie across the slip bands and thus too small to increase the strength in the manner possible for coarse quartz. Thus it could be argued that the modulus of rupture need not fall below that of the clay without admixture because, in this clay, the number of slip bands that exert some control on the measured strength is not less than that in the clay containing the fine quartz. The observed strength reduction could result, however, from the very numerous clay-quartz boundaries (potential sites for dangerous flaws) exposed on the surfaces under tension during testing. These boundaries are numerous because of the small size and extensive specific surface of the quartz grains. In accord with these concepts, quartz A, which had about four times the specific surface of quartz B, produced five times the percentage decrease in modulus of rupture caused by the latter. A further possibility is that, although developing slip bands tend to remove small nonplastic particles from their paths,¹² some quartz grains become trapped within them and modify their microstructure in such a way that cracks can be more readily initiated and propagated.

Both strengthening and weakening of clays and bodies by added quartz has been reported but without discussion of the mechanisms involved.^{17,18} Examination of the published data suggests that strengthening occurred when the quartz was markedly coarser than the associated clay-mineral crystals, as was found in the present study.

Many particles of Madagascar⁹ and Mexican¹⁰ graphite were large enough to lie across slip bands and thus to promote strengthening, yet they

caused weakening even when only 5 wt % was present. Grains of the two types of graphite differed in both internal structure¹⁹ and shape. Those of Madagascar graphite were flaky, while those of Mexican graphite were irregular but had a tendency to be simultaneously somewhat flat and elongated, but not flakelike.

The stresses accompanying extrusion often fractured Madagascar graphite into small blocks, many of which remained in mutual contact. Others, near the original surfaces of the flakes, were partially or completely separated by intrusive clay or protruded into their clay matrix.² The resulting clay-graphite boundary resembled the hooking adhiants that promote adhesion between certain pairs of materials. However, because of the numerous flaws at or near the boundary and within the graphite grain itself, weakening, not strengthening, resulted.

Optical microscopy suggested that Mexican, unlike Madagascar, graphite was relatively free from gross flaws, including those produced during extrusion. However, its presence weakened the test pieces, presumably because dangerous flaws developed at its boundary with the clay.

The curved surfaces of test pieces, especially of those containing Madagascar graphite, showed graphite grains, partially fractured during contact with the die surfaces to produce trails of finer fragments. Often there existed a larger fragment ahead of the trails that was a remnant of the parent grain. This was a further indication that graphite-produces dangerous flaws.

The nature of clay-graphite boundaries is worthy of further study. Clay minerals are hydrophilic, while graphite particles are sometimes regarded as essentially hydrophobic, which suggests that dried clay would not adhere strongly to graphite. However, the edge faces of graphite crystals, or surfaces produced by transverse fracture, as well as defect regions on the basal plane, can adsorb water,¹⁹ which indicates that at least part of the crystal surface is hydrophilic and thus might form an effective bond with clay. Moreover, natural graphite crystals contain fine-grained inorganic materials that could impart some hydrophilic character to their entire surface. A sample of Mexican graphite, for instance, left 13.3% of ash, and much of this was derived from kaolinite.¹⁹ Nevertheless, the outer clay layers of dried extruded cylinders sometimes flaked away spontaneously from underlying graphite grains, suggesting poor adhesion between the clay and at least part of the grain surface.

STRENGTH LOSS CAUSED BY SMALL GLASS ADDITIONS

The addition of 10 wt % of crushed glass to the clay decreased the modulus of rupture by 5%, although additions of 25 and 50 wt % increased it by 9

and 8%, respectively.⁹ During passage through the die, the glass fragments tore the clay surface and produced imperfections visible to the unaided eye. These could weaken the test piece and their effects can be overcome only when sufficient glass is present to strengthen the clay by the mechanisms previously discussed.

When 50 wt % of glass spheres, similar in size to the crushed glass fragments, was added to the clay, the surface imperfections just described were not obvious. However, the modulus of rupture was reduced by 25%. This weakening may be caused by the ability of a crack, propagating in a slip band or elsewhere, to circumvent a sphere more readily than an irregular glass chip, often lying with its greatest cross-sectional area across the path of the crack. The slower reaction of the spheres with interstitial water, because their specific surface was less than that of crushed glass, and the consequent less-effective dispersion of the clay, may be involved also. However, the different effects on clay strength, caused by the addition of irregular and of spherical glass particles, are worthy of detailed study.

STRENGTH REDUCTION CAUSED BY AN EXCESS OF NONPLASTICS

Mixtures containing sufficient coarse quartz, crushed glass, tremolitic talc, and asbestos declined in strength, although smaller percentages had produced strengths above that of the clay without admixture. In the mixtures studied, the clay content was always more than adequate to cover the surfaces of the nonplastic grains. Slip bands were rare or absent in such mixtures so that dangerous flaws must be associated with other types of microstructure, including those at or near the boundaries between the clay and the nonplastic grains. For instance, the adhesion at these boundaries may be less than the cohesion within the clay itself. Moreover, the nonplastics grains were commonly larger than the clay-mineral crystals in their matrix and, unlike this matrix, they did not shrink during drying. Hence they could influence the spatial distribution or orientation of the vector linear drying shrinkage in their vicinity. The linear shrinkage is unlikely to be scalar because of the flatness of most clay particles and their tendency to common orientation. Pores might thus develop in the dried clay, near the nonplastic grains, having shapes and sizes conducive to their operation as dangerous flaws.²⁰

Clay, in the interstices between nonplastic grains, may develop drying cracks. These reduce transverse strength and seem to form especially if increasing percentages of relatively coarse nonplastic grains are added to clay and the total water content of the various mixtures is kept constant.⁹ Because the clay is often more hydrophilic than the nonplastic grains and

Acknowledgment

has a more extended specific surface, the water tends to concentrate increasingly on the diminishing fractions of clay when the nonplastic content of the mixture is raised. The clay becomes more and more hydrous and its drying shrinkage, and the corresponding tendency to crack, increases.

Increasing amounts of nonplastic grains may become progressively more difficult to mix effectively with clay and thus the grains segregate and form local porous regions that diminish the strength of test pieces in which they occur. Fine quartz, especially quartz A, behaved in this way and whitish clumps of grains were obvious on fracture surfaces.⁷ The fracture surfaces of clay-asbestos mixtures showed a similar phenomenon because the more flexible of the fibrous components tended to roll up into tiny balls.⁴

CONCLUSIONS

The transverse strength of dried, extruded, clay-containing cylinders depends on interparticle or interaggregate bonds and on flaws in the microstructure. Slip bands, produced during extrusion, are one source of flaws, and fracture tends to occur along them. The propagation of cracks becomes more difficult and strength is increased if the nonplastic grains (coarse quartz, tremolite cleavage fragments, crushed glass) are broad enough, or long enough (fibers in tremolitic talc or asbestos), to lie across the slip bands. In addition to lying across slip bands, crushed glass reacts with interstitial water in the plastic mixture to produce an alkaline solution that disperses, and thus strengthens, its clay matrix. Nonplastic grains promote weakening if they are too small to lie across the slip bands (fine quartz). Grains of Madagascar and Mexican graphite, although large enough to lie across the slip bands, cause only strength reductions owing to weakness of the clay-graphite boundaries and the development, during extrusion, of flaws in the graphite grains.

Progressive additions of nonplastics reduce the number of slip bands, but any strengthening effect is finally annulled, and weakening supervenes, because of the increasing numbers of clay-nonplastic boundaries and thus of the dangerous flaws situated at or near these boundaries. In some circumstances segregation effects during mixing, or the development of drying cracks in the clay, accompany the addition of large quantities of nonplastics and contribute to the loss of strength.

ACKNOWLEDGMENT

The author is grateful to the students whose theses are cited in the references. Their experimental data, obtained under his supervision, con-

tributed substantially to the present account. Dr. E. W. White gave the author invaluable help in scanning electron microscopy.

REFERENCES

1. W. O. Williamson, "Strength of Dried Clay-A Review," *Amer. Ceram. Soc. Bull.*, **50** (7), 620-625 (1971).
2. W. O. Williamson, "The Strength of Clays at Small Moisture Contents," *Miner. Sci. Eng.*, **6** (1), 3-8 (1974).
3. F. L. Kennard III and W. O. Williamson, "Transverse Strength of Ball Clay," *Amer. Ceram. Soc. Bull.*, **50** (9), 745-748 (1971).
4. F. A. Beightol, "Effects of Asbestos on the Dry Strength of Clay," B.S. Thesis, Ceramic Science Section, Department of Material Sciences, Pennsylvania State University, 1974.
5. J. Brun, "Dry Strength of Clay-Glass Mixtures," B.S. Thesis, Ceramic Science Section, Department of Material Sciences, Pennsylvania State University, 1973.
6. F. L. Kennard III, "Factors Affecting the Dry Strength of Clay," M.S. Thesis, Ceramic Science Section, Department of Material Sciences, Pennsylvania State University, 1970.
7. F. K. Koons, "The Effect of Fine Silica on the Strength of Dried Clay," B.S. Thesis, Ceramic Science Section, Department of Material Sciences, Pennsylvania State University, 1974.
8. D. W. Wirth, "The Effect of Talc on the Dry Strength of Clay," B.S. Thesis, Ceramic Science Section, Department of Material Sciences, Pennsylvania State University, 1972.
9. D. L. Amig, "Effects of Graphite on the Dry Strength of Clay," B.S. Thesis, Ceramic Science Section, Department of Material Sciences, Pennsylvania State University, 1973.
10. J. M. Ceriani, "Effects of Non-Flake Graphite on the Dry Strength of Clay," B.S. Thesis, Ceramic Science Section, Department of Material Sciences, Pennsylvania State University, 1973.
11. J. H. Weymouth and W. O. Williamson, "Effects of Extrusion and Some Other Processes on the Microstructure of Clays," *Amer. J. Sci.*, **251** (2), 89-108 (1953).
12. F. Moore, "The Physics of Extrusion," *Claycraft*, **36** (2), 50-54 (1962).
13. W. T. Higdon, "Studies of Ionotropy—A Special Case of Gelation," *J. Phys. Chem.*, **62** (7), 1277-1281 (1958).
14. S. Anderson, D. Tandon, L. B. Kohlenberger, and F. G. Blair, "Strength of Adhesion of Dried Clay Slurries to Window Glass as a Function of Slurry pH," *J. Amer. Ceram. Soc.*, **52** (9), 521 (1969).
15. D. I. Sideri, "On the Formation of Structures in Soil: II. Synthesis of Aggregates; on the Bonds uniting Clay with Sand and Clay with Humus," *Soil Sci.*, **42**, 461-481 (1936).
16. R. J. Hunter and A. E. Alexander, "Surface Properties and Flow Behavior of Kaolinite. Part III: Flow of Kaolinite Sols through a Silica Column," *J. Colloid Sci.*, **18** (9), 846-862 (1963).
17. E. Kieffer, "On Testing the Binding Power of Ceramic Raw Materials," *Ber. Deut. Keram. Ges.*, **12** (9), 477-479 (1931).
18. V. Hofmann and A. Rothe, "Plasticity and Dry Bending Strength of Kaolins and Clays with and without the Addition of Quartz," *Ber. Deut. Keram. Ges.*, **47** (5), 296-299 (1970).

References

19. S. M. Kemberling and P. L. Walker, Jr., "Compaction of Natural Graphite," *Tanso*, **2** (52), 1-7 (1968).
20. W. O. Williamson, "Microstructures of Plastic or Dried Clay-Bodies," *Proc. Int. Seminar Clay Miner. Ceram. Processes Prod.*, Milan, 1974, F. Veniale and C. Palmonari, eds., Cooperativa Libreria Universitaria Editrice, Bologna, pp. 47-57.

29

Extrusion Defects

G. C. Robinson

Extrusion is the process of shaping an object by pushing a material through an opening the size and shape of the cross section of the object. Extrusion equipment may be of two types, the piston extruder and the auger extruder. There are many variations within each type. The products of extrusion may be very small, such as tubes of under 0.06 in. diameter, or very large, such as 36 in. diameter pipes. The process is used to form crude natural clays or refined nonplastics, including oxides, graphite, and metal powders.

A variety of green-body defects can arise during the forming process. These include lamination, surface and edge tearing, bridge and core cracking, column splitting, segregation, and preferred orientation of particles. The causes and potential cures for these problems are discussed in this chapter.

MATERIAL FLOW DURING EXTRUSION

Flow Characteristics

The flow pattern of material through the conveying zone of the equipment and then through the forming zone is significant to extrusion quality. Flow is the result of a force applied to the extruded mass that causes its forward

movement. Forcing a Newtonian liquid through an orifice in a cylinder results in a straight-line relationship between the applied force and the rate of flow. In contrast, a Bingham plastic substance requires an initial force to start flow. This behavior is characteristic of many bodies. The slope of the rate of flow versus pressure curve is a measure of the mobility of the substance. Departures from the linear flow-pressure relationships, characteristic of dilatant and thixotropic materials, are also encountered in extrusion of ceramic materials. To achieve extrusion control and minimize defects, such nonlinear behavior must be kept to a minimum.

Piston Extrusion

Flow patterns occurring during piston extrusion have been studied by Astbury et al.¹ Lines imprinted transversely to the direction of column flow showed that the center moves in advance of the exterior of the column. The amount of displacement increases with the taper of the die, as shown in Figure 29.1. The drag of the die tends to produce shear planes or cracks

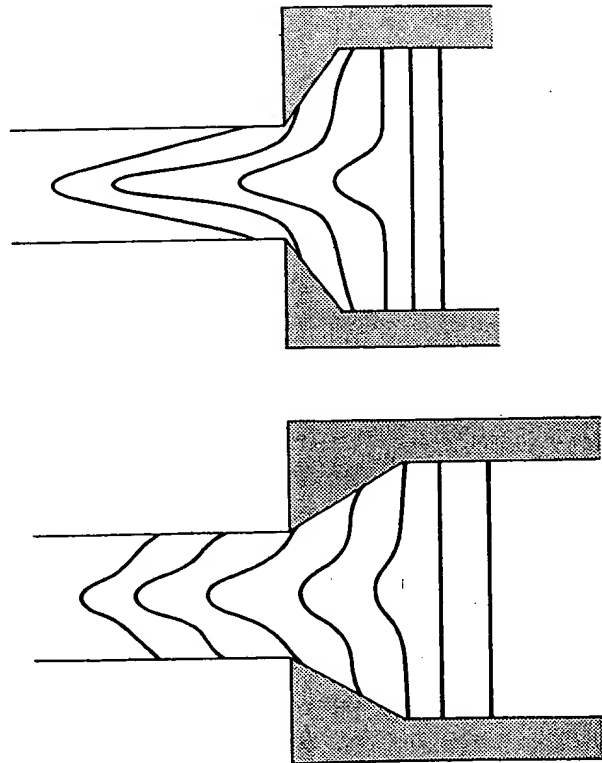


Figure 29.1. The influence of die taper on retardation of flow of exterior surfaces.

that extend from the surface of the column and cut across the flow lines into the interior of the column. One or both of these patterns may appear as cracks in the finished product.

Auger Extrusion

Auger extrusion will produce a pattern of flow similar to that produced by piston extrusion in the die section of the extruder. However, additional flow characteristics are developed by the auger.

Flow is not as efficient in the auger extruder. Forward movement depends on friction between the clay and the barrel lining to restrain the clay from turning with the auger. The clay must either slide on the surfaces of the auger or shear at intermediate surfaces between the auger surface and the interior barrel surface to move forward. The clay is discharged as a single rope (or multiple ropes for multiple wing augers) at the tip of the auger. The twisting of the auger causes the rope to be discharged as a coil, while the spacer and die tapers cause compression of the coil into a single column of extrudate. The hub of the auger produces the hole in the center of the coil. The coils may fracture in low-plasticity materials to produce a series of concentric and tapered cones, which are then forced together during travel through the die taper. Thus auger extrusion has the potential of producing a number of weakness planes that may develop into flaws in the finished product.

STRUCTURES PRODUCED BY EXTRUSION

Lamination

Lamination has been the curse of extrusion since inception. There is always laminar flow in extrusion, but correct design of the die and raw-material mixture can prevent laminar flow from developing into cracks or weaknesses. The development of laminar flow during auger extrusion is shown in Figure 29.2. Lumps of different-colored clays were alternately fed into an extruder and then the column was sectioned to show the flow patterns. The section cut perpendicular to the direction of extrusion shows the characteristic circular pattern, while longitudinal sections show twin peaks of forward displacement. There is a lag in the center of the column produced by the dead zone of the hub of the auger and the resulting hole in the coiled rope. There is also a lag at the exterior of the column produced by the drag of the die on the exterior surface of the extrudate. Failure of the column to be completely knitted together results in weak zones that may separate into



Figure 29.2. Laminar flow development from auger tip (top) to extruded column (bottom).

cracks as a result of forces developed during drying, firing, or even freezing if this uncommon treatment is applied.

Figure 29.3 shows lamination cracks appearing in the interior of an extruded object. These cracks, which are parallel to the flow patterns in both longitudinal and transverse sections, normally develop in materials that are difficult to dry. Elimination of lamination cracks (but not laminar flow) can be accomplished by improving the drying behavior of the material, changing the die design to minimize displacement, or achieving better knitting of the extrudate.



Figure 29.3. Laminations cracks in longitudinal section (left) and transverse section (right).

Surface and Edge Tearing

An extruded column may exhibit surface cracks. One type is predominant at the corners of a rectangular column. Small cracks enter at the edges and cut at an angle across the column. This cracking has been called "edge tearing," "dog teeth," or "feather edging" (Figure 29.4). The cracks arise from the greater friction at the corners of the die than on the faces. The presence of large particle sizes of nonplastics will increase the tendency for formation of this flaw.

Other cracks may appear over the entire surface. These cracks have a square to rectangular pattern and result from interfacial friction between

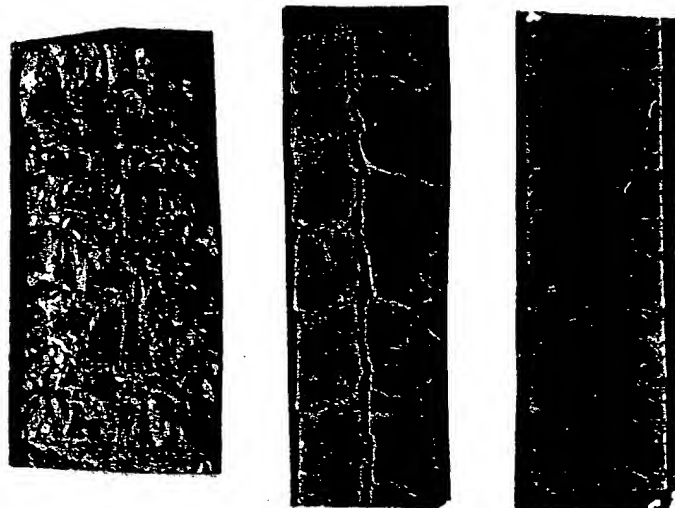


Figure 29.4. Edge tearing; pronounced in lower, severe in middle, and aggravated by large size grog in upper picture.

the die and the column. The clay has a low plastic strength and is incapable of surmounting the friction drag without cracking. This type of surface cracking and penetration of the cracks into the interior of the column is shown in Figure 29.5.

Particle Orientation

The process of extrusion causes particles of flaky habit to orient parallel to the faces of the die. This orientation causes a greater shrinkage in the direction perpendicular to extrusion than in the lengthwise direction. Thus the flaky particles are a source of a laminated structure in a direction transverse to the direction of extrusion.

The orientation may cause a differential expansion during the removal of the last 2% of water from an extruded material. For example, comparison of the transverse and linear expansion for a 40% clay, 60% sericite mixture with the expansion of a 40% clay, 60% sand mixture has shown that the micaceous flakes of sericite cause a larger expansion and a greater differential than the rounded grains of sand.

Particle and Water Segregation

Analyses performed by Astbury, et al¹ and Robinson, et al² have shown that there is a difference in composition between the surface and the interior of an extruded column. The skin of a die-slickened extrudate will show a higher percentage of fine particles and a higher water content than the interior of the column. The nonuniform particle size, water, and shrinkage in the column cross section can lead to cracks in the finished unit. Measurements were made at different points in the cross section of a conduit tile by Eighmie and Robinson.³ The water content was found to vary from 14.6 to 13.4% and the volume drying shrinkage varied from 9.3 to 7.5% on different locations in one plane of the cross section.

Bridge and Core Cracking

The introduction of cores and their supporting bridgework can produce weak zones and cracks in the finished product. The selection of bridge and core configuration has been the subject of many articles but remains an art. The separation in the column caused by insertion of the bridge has been minimized by streamlining, serrating edges, and changing the separation distance from the die.

A study of bridgework design has been presented by Merry.⁴ There is a choice of supporting the bridge with a single cross bar or the use of an H-



Figure 29.5. Surface cracks of low-plasticity materials.

shaped support. The best support configuration depends on variations in the sand content in the plant raw material. With high sand contents, the H-bridge configurations were desirable and prevented the development of cracks. In contrast, clays with low sand content required the use of a single cross-bar configuration. Bridgework not only causes separation of the extruded column, but also retards the flow in some parts of the cross section and may even direct and flow to other locations.

Column Splitting

The friction at the die interface working against the cohesion of the material can attempt to pull the column apart into a variety of patterns. A high-friction sandy material may pull apart in a continuous split as shown in Figure 29.6. A material of high cohesion and high strain together with high friction may split into four segments with a central twisting core as shown in Figure 29.7.

Enhancement of Extrusion Structure

A number of methods have been employed to make extrusion structure more apparent. When the plastic extrudate is frozen, expansion of the freezing water causes an opening of the laminar structure. Such a technique may be informative, but it should be remembered that a material that cracks under freezing conditions may not show such faults under normal drying and firing procedures.

Liquid penetrants and fluorescent-die penetrants have been used to examine extrusion structures. Cutting apart a fired product will frequently

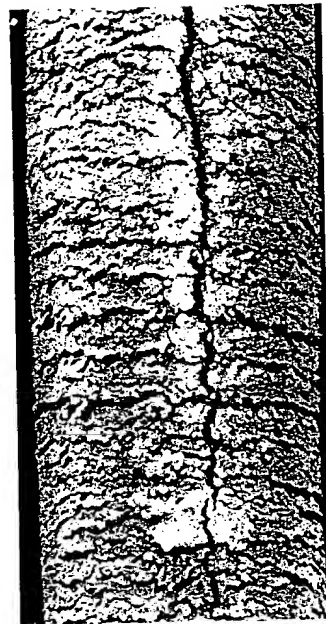


Figure 29.6. Column splitting in sandy material.



Figure 29.7. Splitting of column into four exterior segments and a central twisting core.

display internal lamination cracks. Examination of the fracture pattern occurring after strength determinations on plastic dry or fired products may reveal extrusion structures. The extrusion of different-colored materials or the application of patterns prior to extrusion may assist in examining the flow mechanisms occurring during extrusion.

RAW MATERIAL PROPERTIES DETERMINING EXTRUDABILITY

Adhesion

Adhesion of the extrudate to the metal parts of the extruder is significant in determining flow. This adhesion is responsible for the resistance against turning of clay with the auger, for the sliding of the clay on the auger, and for the drag between spacer lining and clay, and die lining and clay, which causes surface tearing and lamination.

The adhesion between substances can be evaluated by an experimental piston extruder operated without an orifice. The raw material for extrusion is packed into the cylinder by completely closing one end of the cylinder

and pushing the material against the closure until a preselected pressure level is applied to the piston. The closure is removed and the cylinder is reversed with the piston introduced into the closure side of the cylinder. The slug of clay is pushed downward away from the closure side and the force required to cause movement of the clay slug through the cylinder is determined and used to indicate adhesion. The surface area of this clay slug can be measured and the adhesion is expressed as the force per unit area. The cylinder metal and its surface finish should duplicate the barrel lining, auger surface, or die surface being evaluated.

Adhesion can be changed by changing the structure and composition of the metal or the extrudate. This provides a variety of potential control measures to decrease adhesion: (1) polishing the metal, (2) chrome plating the metal, (3) heating the metal, (4) increasing the water in the extrudate, (5) changing from angular to rounded particles in the extrudate, (6) adding lubricants to the extrudate, and (7) lubricating the interface between metal and extrudate. Extrusion quality and cost are optimum when the adhesion against turning is high and all other adhesions are low.

Internal Friction

The raw material must slide on itself whenever the die opening is smaller than the barrel diameter or when the compression of the rope coils is greater than the void space within the coil. The resistance against internal flow can be evaluated by the same device as used for adhesion measurement. Internal friction is evaluated by placing a die restriction on the open side of the reversed cylinder and measuring the increase in force required to extrude through the opening. A series of progressively smaller openings can be used and a curve is obtained of the force required versus increasing opposition to flow. Another approach is to measure the rate of flow through an opening versus the pressure causing flow.

The internal friction indicates the energy required for extrusion and the extent of "forging" desirable in extruder design. Materials of high internal friction should be extruded through equipment in which there is little size reduction occurring between the die diameter and the auger diameter. The size reduction can be large and coring extensive with materials of low internal friction.

Cohesion

Cohesion is the plastic strength of the extrudate. The stress at the elastic and plastic yield points can be determined on the extruded column by conventional means. The value is significant to extrusion quality.

A material of low cohesion will surface tear when the adhesion to the die is greater than the cohesion. The lower the cohesion, the more likely is the appearance of surface defects. Very high cohesion will favor carryover of auger twisting into the extruded column but will lessen the forward displacement caused by spacer and die drag.

Cohesion can be increased by increasing the quantity of colloidal material in the mix, reducing the water, or adding organic plasticizers or deflocculants. Cohesion can be reduced by adding grog or other nonplastics. The smaller the particle size of a nonplastic addition, the more effective it is in reducing cohesion.

Plastic Strain

Plastic strain indicates how much you can bend or stretch the extruded column before it cracks. Plastic strain is symptomatic of lamination behavior. The higher the value of strain, the greater the forward displacement and the greater the carryover of auger twist. Any material with a strain greater than 0.10 is likely to show lamination faults. Also, such materials are difficult to dry.

High or low values of strain are undesirable. Low values of strain foretell surface tearing. The raw material cannot be formed against the dragging interfacial friction and instead tears apart or cracks. Intermediate values of strain give the best extrusion. Strain can be increased by adding plasticizers and reduced by adding small-size nonplastic particles.

The low limit of strain is influenced by the cohesion of the extrudate and, as a result, surface tearing is better predicted by the product of stress and strain than by strain alone. A product of less than 1.0 predicts surface tearing, while a product between 1 and 4 indicates good extrusion.

Particle Shape

Platelike particles contribute their own characteristic laminar structure. These particles will orient and produce laminae across the cross section of the column without necessarily displaying any displacement structure in the direction of column flow.

Mica, sericite, vermiculite, and graphite are illustrations of flaky substances that can cause troublesome lamination. The lamination can be minimized by reducing the particle size, reducing the orientation force by minimizing die taper, or extruding at a soft consistency. Agglomerating the flaky particles into nodules of sufficient strength to resist collapse during extrusion will also produce lamination.

Drying Behavior

It is difficult to answer the question of whether or not lamination cracks are the fault of extrusion or of drying. The flow patterns and weak zones are developed during extrusion, but usually there is no visible crack in the plastic extrudate. The cracks develop during the drying process as the result of forces applied by shrinkage gradients. Reducing the shrinkage gradients will reduce or eliminate the lamination crack. Slower drying schedules can reduce lamination cracking, and changing the body composition to improve drying behavior will eliminate lamination cracks. The addition of nonplastic particles in two size classifications will improve drying behavior. Some nonplastic particles should be added in the size range between 28 and 65 mesh to reduce drying shrinkage, while particles of nonplastics in the -200 mesh size should be added to increase the permeability of the body. This combination will make a crack-free unit.

Abrasiveness

The abrasiveness of the material determines the rate of wear of the metal parts of the extruder. This property helps determine maintenance cost of

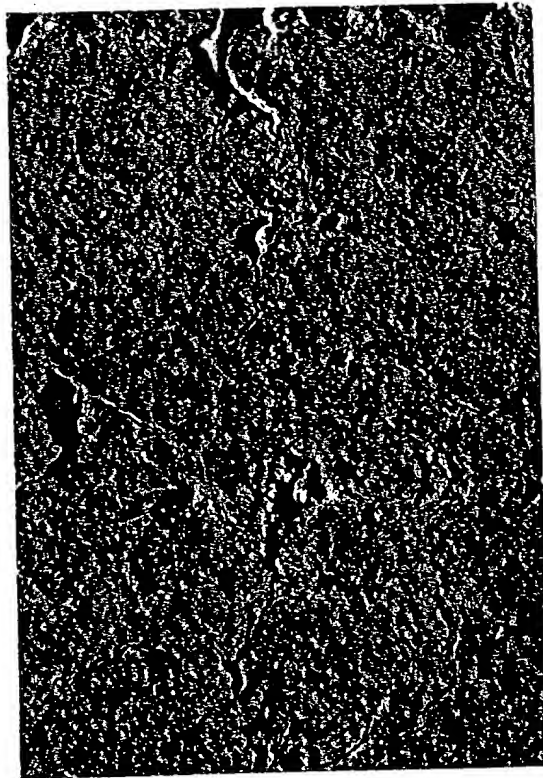


Figure 29.8. Drying cracks caused by Large-particle-size grog.



Figure 29.9. The transverse lamination cracking with -14 + 28 mesh grog.

extrusion and selection of materials for the extruder. Thus ceramic cores will give greater life because of greater abrasion resistance than metals.

Particle-Size Distribution

Particle-size distribution is an important raw material variable. Nonplastic particles larger than 28 mesh encourage edge tearing, drying cracks (Figure 29.8), and transverse lamination cracking (Figure 29.9). Particle sizes of nonplastics between 28 and 100 mesh will break up large lamination cracks into many small cracks. A combination of these particles with -200 mesh nonplastics will eliminate the small lamination cracks. The -200 mesh nonplastics are more effective than an equal quantity of larger-size particles in reducing plasticity and cohesion and working toward elimination of surface cracking.

The ideal particle-size distribution would be a somewhat uniform gradation of sizes with 30% nonplastics. Natural clays with good extrusion characteristics will approximate the foregoing suggestions for particle size and quantity of a nonplastic.

MACHINE VARIABLES THAT DETERMINE EXTRUSION

The Auger

The auger has been the subject of extensive study. It influences the rate of production, the cost of production, and the quality of the extrudate. The characteristics of the auger are explained in detail elsewhere.⁸⁻¹¹ The significant design features of the auger are its pitch, diameter, hub diameter, taper, and number of wings.

Speed of Auger Rotation

The speed of auger rotation can influence quality and productivity. The work of Goodson and Dodd¹¹ showed that the extrusion rate is a function of both the rate of rotation of the auger and the quantity of contained water. At any given water content there appears to be an optimum rpm that gives maximum output. Furthermore, the optimum shifts with changing water content.

The speed of rotation influences the friction developed between the barrel lining and the clay. The best speed to use depends on the type of clay. Insufficient speed will permit slipping and turning with the auger, while correct speed will hold the clay against twist of the auger. Insufficient speed will also produce heating of the material within the brick machine.

Turndown Ratio

The significance of the ratio of die diameter to auger diameter has been mentioned in previous sections. This should be selected to suit the characteristics of the material being extruded. Furthermore, this ratio will affect the rate of column output.

The Die

Die configuration has been studied from the standpoint of its role in energy consumption, but there have been very few studies of the relation between die design and the product quality. The design of extrusion dies remains an art with very few sources of supply in this country. The following studies are being made in our laboratories to help establish the relation between die design and quality of extrusion.

The die may be defined as the entire section of the machine forward of the auger or it may be separated into two zones—the spacer zone between the auger tip and the entrance point to the shaper cap, which approximates the cross-sectional dimensions of the extruded column. In the latter case, as used herein, the shaper cap is considered as the die.

Tests were made with three different brick raw materials using dies of different taper, different entrance angle, different diameter, and different length. The force required for extrusion, volume shrinkage, water of plasticity, dry bulk density, and column consistency was determined for each extrusion. A mass of data was compiled for this investigation and the results were disappointing. Variables of taper, entrance angle, and die length had only a small influence on the properties measured. Perhaps the key result of this work was to point out that a 1% change in forming water, say from 17 to 18%, had a much greater influence on all the properties evaluated than did the die parameters.

However, changes in die taper, die length, and entrance angle have been shown to have a significant influence on edge tearing, lamination, and plastic strength. Increasing die taper reduces edge tearing and increases internal laminations. Increase in extrusion speed at a single die taper reduces the tendency for edge tearing.

Vacuum

Evacuation or reducing the pressure within the extruder can dramatically improve the extrusion behavior of some materials. As a consequence, de-airing or vacuum extrusion is the common practice. However, the effects of de-airing are not linear with respect to pressure. Little improvement is

obtained with a pump operating to, say, 24 in. of mercury vacuum, whereas large improvements are observed by increasing the vacuum from 25 to 29 in.

Although de-airing is universally accepted, it is sometimes inappropriate to the particular material being extruded. Very plastic materials may give better performance with extrusion without evacuation instead of with de-airing.

Die Balance

The quality of the extrusion is influenced by the position of the die. The extent of separation between the tip of the auger and the die determines the tendency for one part of the column to deform forward with respect to the remainder of the column. A die position close to the auger tends to make the exterior of the column run faster than the interior. A lengthy separation between the auger tip and the die will cause the center to run fast. At a condition of balance, the column will move without a tendency for longitudinal displacements. The correct placement is a function of the material and also of the water in the material. A change in the quantity of water will change the correct die position. Incorrect placement of the die can produce column splitting or other defects in the extruded column.

Centering the die is also important to performance. An off-center die will encourage the column to twist in one direction or another and may introduce strains that will later appear as cracks. The die needs to be aligned with the center line of the auger and also with cores and bridge-work. However, in some instances, cores are displaced to encourage flow of materials into sections of the die that are normally slow moving.

REFERENCES

1. N. F. Astbury, H. R., Hodkinson, and F. Moore, "The Problem of the Clay Column," "The Mechanics of Extrusion," and "The Physics of Extrusion," papers presented at the 29th Annual Meeting of the Institute of Clay Technology, Sept. 29, 1962, Harrogate, England; Chambers Engineering News Letter No. 13.
2. G. C. Robinson, R. H. Kizer, Jr., and J. F. Duncan, "Raw Material Parameters Determining Extrudability," *Amer. Ceram. Soc. Bull.*, 47 (9), 822-832 (1968).
3. T. L. Eighmie, "The Influence of Die Parameters on the Extrusion of Structural Clay Products," Master of Science Thesis, Clemson University, 1970.
4. E. A. Hawk, "Handling the Difficult Extrusion Problem," *Amer. Ceram. Soc. Bull.*, 33 (11), 326-327 (1956).
5. J. George Seanor and W. P. Schweltzer, "Basic Theoretical Factors in Extrusion Augers," *Amer. Ceram. Soc. Bull.*, 41 (9), 560-563 (1962).

References

6. G. Caprix and A. Laratta, "Screw Extrusion of Bodies," *Trans. Br. Ceram. Soc.*, 64 19-26 (1965).
7. A. J. Reed, "Auger Design," *Amer. Ceram. Soc. Bull.*, 41 (9), 549 (1962).
8. W. J. Johnson, "Evaluation of NCPRC Research Auger," *Amer. Ceram. Soc. Bull.*, 41 (9), 550-555 (1962).
9. H. H. Lund, S. A. Bortz, and A. J. Reed, "Auger Design for Clay Extrusion," *Amer. Ceram. Soc. Bull.*, 41 (9), 554-559.
10. J. R. Parks and M. J. Hill, "Design of Extrusion Augers and the Characteristic Equation of Ceramic Extrusion Machines," *J. Amer. Ceram. Soc.*, 42 (1), 1-6 (1959).
11. F. J. Goodson and A. E. Dodd, *Conf. Mixing Agitation Liquid Media* July 1951, Institute Chemical Engineers pp. 333-341, London.

PART FIVE

PROCESSES AND APPLICATIONS

Tape casting is one of the latest ceramic processes practiced on a large commercial scale. The process is a major departure from the more traditional methods of ceramic processing. Because many details of the process have not been widely published, a rather extensive treatment appeared justified and is the subject of Chapter 30.

Two applications, thermal control coatings and thick films, illustrate the importance of powder characterization in these processes. In the final chapter, brief comments are provided by various members of a panel discussion on future directions in processing research.

30

Tape Casting of Ceramics

R. E. Mistler

D. J. Shanefield

R. B. Runk

Tape casting is an important process for forming large-area, thin, flat ceramic parts. A "tape" is formed by the use of a scraping blade, or "doctor blade," which evenly coats a moving surface with a slip. The coating dries to form a green tape that can be cut into different shapes. The cut tape is fired to form a flat ceramic body that is essentially two-dimensional.

The chief advantage of the tape-casting process over other forming techniques is that it is the best method of forming flat articles with thicknesses in the 1 to 50 mils range. These articles are virtually impossible to dry press and most difficult, if not impossible, to extrude. If the plate is to be pierced with numerous holes, dry pressing would be even more difficult because of problems in uniform die fill.

BACKGROUND

Tape casting or doctor-blading is really a very ancient art that is more commonly known as knife coating in many other fields, including the paper,

plastics, and paint industries. In the paint industry the technique is used to test the covering power of paint formulations.

The marriage of a more ancient art, slip casting, which is familiar to all ceramists, and doctor-blading took place within the past 25 years. Tape casting is more closely related to slip casting than to any other "traditional" ceramic-processing technique. Many of the tricks and problems in working with ceramic suspensions are common to both. The means for removing the liquid carrier or suspending agent during drying are different: tape casting involves evaporation, while slip casting utilizes absorption in a porous mold. Also the sizes and shapes of products, manufactured by the two processes differ considerably.

Use of tape casting to form ceramics apparently occurred first during World War II in the development of dielectric materials useful as substitutes for mica in high-quality capacitors. Glenn Howatt obtained a patent¹ describing such a process and founded a company that is now part of Gulton Industries. Howatt's patent is for "forming ceramic materials into flat plates, especially useful in the electrical and radio fields." This is still the principal field of application today, although the present end uses are in many cases far beyond anything imagined in 1945.

The Howatt patent teaches a process that is a combination of slip casting and doctor-blading, since the slurry is spread on absorbent bats where the liquid vehicle is removed.

The limitations of the tape-casting process are in thickness and lack of "three-dimensional" capability. Dry pressing and extrusion seem to have the production edge when thicknesses of $\frac{1}{8}$ in. or more are desired in plates. Tapes can be made this thick, but pressing seems to be less of a problem. As noted earlier, tapes are essentially two dimensional, and the technique is not practical for pieces that have lips, ledges, tapered holes, and blind holes.

At present the main ceramic applications of the tape-casting process are in the electronics industry. Capacitor dielectrics, piezoelectrics, and thick-tape glazes and metallizing preparations are the major products. Other products include thin-film substrates.

There are numerous other references and patents relating to tape casting in the ceramics field. The most important of these are included in reference 2.

This chapter covers binder-solvent selection, raw material characterization, dispersion of the ceramic powder, precasting treatments, casting process and apparatus, including precision casting, drying of the tape, punching to shape, and multilayer casting. We draw mostly on our experience in casting high-alumina ceramic substrates for the discussion and illustrative-examples. We have not been limited to this one material, however, and have experience in casting the following materials: lead

zirconate-lead titanate (PZT), lead zirconate-lead titanate doped with lanthanum (PLZT), barium titanate, steatite, forsterite, porcelain, glass, manganese-nickel-cobalt thermistor materials, ferrites, bonded silicon carbide varistor materials, and calcium-aluminum silicate compositions.

BINDER-SOLVENT SELECTION

There are two principal types of solvents, water and organic liquids. In either case the binder should meet the following criteria: (1) form a tough flexible film when dried and present in low concentrations, well under 10 wt %; (2) volatilize to a gas leaving no residual carbon or ash during firing; (3) not be adversely affected by ambient conditions during storing; (4) be relatively inexpensive; and (5) be soluble in an inexpensive, volatile, non-flammable solvent in the case of organic solvent systems.

The binder, or plastic, is thus of the "film-forming" type. These film formers usually are long-chain polymers that possess characteristics of internal flexibility in contrast to polymers that have substantial three-dimensional linkages, which tend to be rather rigid. Just about every plastic imaginable has been used to make tapes, but some of the more popular are poly(vinyl acetate), poly(vinyl chloride), poly(vinyl chloride-poly(vinyl acetate) copolymers, polystyrene, poly(vinylidene chloride), poly(vinyl alcohol) (water system), polymethacrylates of many types, and cellulose nitrates.

Some of the factors that must be considered in the selection of binder are: (1) thickness of tape to be made; (2) casting surface-glass, plastic, metal; and (3) solvent type desired. The extremely volatile solvents, such as acetone, are most suitable for the thinnest films, and the lower volatility solvents, such as toluene, seem best for the thicker films. When trying a new material in the laboratory we generally used a poly(vinyl chloride-poly(vinyl acetate) copolymer with MEK as the solvent for casting up to a thickness of 10 mils and poly(vinyl butyral) with toluene or trichloroethylene as the solvent for thicker casts. Table 30.1 gives the typical binder-solvent-plasticizer systems for thick and thin casting trials.

Plasticizers are normally added to obtain sufficient flexibility of the film for easy handling. The plasticizer is often present in amounts greater than the binder itself. The list of plasticizers is much too long to include here, but binder manufacturers are in a position to recommend those suitable for use with their products. Milling of the slip (discussed in a later section) is best done before additions of the binder and plasticizer because of the very high viscosity that results after their addition. After binders and so forth are added, the mill is run until all are thoroughly dissolved and mixed. In some

Table 30.1. Typical binder-solvent-plasticizer systems for tape casting

	Thick (0.010 in.)	Thin (0.010 in.)
Binder	3.0 poly(vinyl butyral) ^a	15 vinyl chloride-acetate ^b
Solvent	35.0 toluene	85.0 MEK
Plasticizer	5.6 poly(ethylene glycol)	1.0 butyl benzyl phthalate

Note: Numbers given are parts by weight per 100 parts ceramic powder.

^a Butvar Type B-76, Monsanto Company, St. Louis, Mo.

^b VVNS, 90:10 vinyl chloride-vinyl acetate; copolymer supplied by Union Carbide Corp.

cases the binders are predissolved in a portion of the solvent system for faster mixing.

STARTING MATERIALS

For any ceramic process it is essential that the starting powders be well characterized. This is especially true for tape casting. The important parameters that should be monitored on all powder lots are average particle size and distribution, surface area, and trace-impurity level.²

At this point we draw upon the vast amount of information that was generated in developing a process for the manufacture of fine-grained alumina substrates by tape casting. The characterization and processing would be very similar for any ceramic material. Briefly, the process consists of nonaqueous wet ball milling, followed by tape casting on pastic film, punching, and firing. A flow diagram in shown in Figure 30.1.

Table 30.2 gives the starting materials. The major component is a dry-ball-milled Bayer-process alumina, either Alcoa-A-16 or Reynolds RC-172 DBM. This powder is essentially alpha alumina, with a medium particle size of 0.4 μ , and a B.E.T. surface area of about 11 m²/g. As received, the alumina is agglomerated, and nearly spherical clusters of particles are visible at 300 \times magnification (Figure 30.2). Tap densities of 1.3 and 1.5 g/cc have been reported for this type of material. Figure 30.3 is a TEM of the alumina particles sprayed onto glass after ultrasonic dispersion in water. Shadowing was done with Pt-carbon evaporated at a 23 $^{\circ}$ angle without rotation of the sample. The length of the shadow indicates that the particles are not the flat platelets often observed³ in other types of alumina powder but are roughly as high as they are wide.

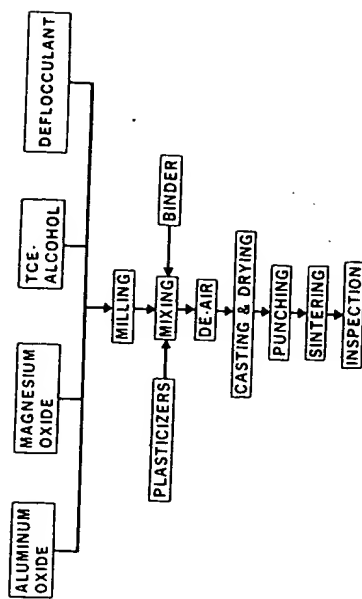


Figure 30.1. A flow diagram for an alumina-substrate tape-casting process.

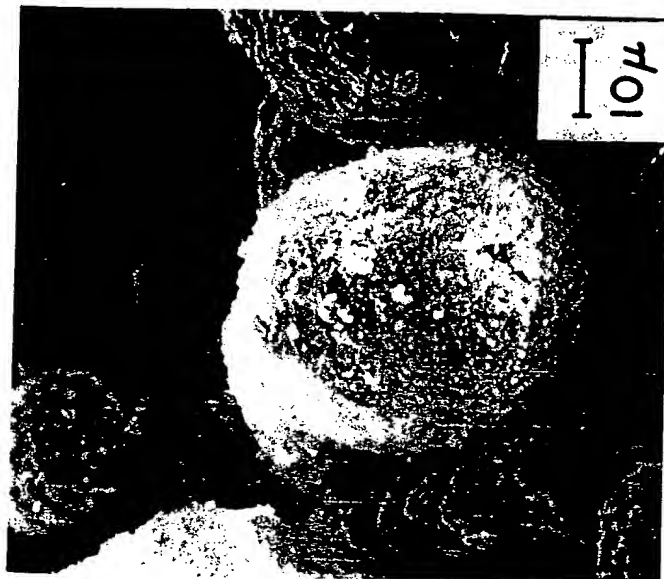


Figure 30.2. SEM of as-received agglomerated alumina powder.

Table 30.2. Materials and milling procedure

Process Step	Material	Function	Parts by Weight
Mill for (24 hours) (first stage)	Alumina powder	Substrate material	100.0
	Magnesium oxide	Grain growth inhibitor	0.25
	Menhaden fish oil ^a	Deflocculant	1.7
	Trichloroethylene	Solvent	39.0
	Ethyl alcohol	Solvent	15.0
Add to above and mill for 24 hours (second stage)	Poly(vinyl butyral) ^b	Binder	4.0
	Poly(ethylene glycol)	Plasticizer	4.3
	Octyl phthalate	Plasticizer	3.6

^a Haynie Type Z-3 (air treated), Jesse S. Young Company, New York, New York.^b Type B-98 (molecular weight approximately 32,000), Monsanto Company, St. Louis, Missouri.

DISPERSION OF THE CERAMIC POWDER

Milling Procedure

As shown in Table 30.2, the milling is done in two stages, with and without binder and plasticizers. An 85% alumina porcelain is satisfactory for use in the mill lining and grinding media. If there is concern with mill impurity pickup, many other mill and grinding-media materials are available. The advantages gained must be weighed against the added cost, particularly if the process is to be used in large-scale production. The mill is half filled with the media, which are $\frac{1}{16}$ in. cylinders. The milling is done at 65% of critical speed. The charge is added in proportion to 3000 g of dry alumina powder added to a mill having an empty capacity of 2.3 gal. This charge can be scaled up or down depending on the size of the mill used.

Figure 30.4 shows the effects of variations in the milling procedure. Black circles denote 24 hour, second-stage milling. Low densities resulted from either insufficient milling time or excessive milling time in the presence of the binder. The effects of excess milling are presently unexplained. The effects of insufficient milling are apparent from the discussion below.

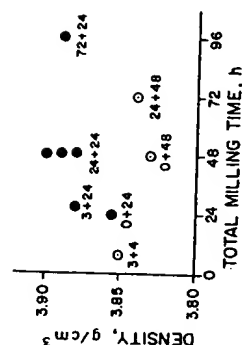


Figure 30.4. Densities of fired substrates versus milling time. First number denotes hours of ball milling in first stage (before adding binder and plasticizers); second number denotes hours of milling in second stage.

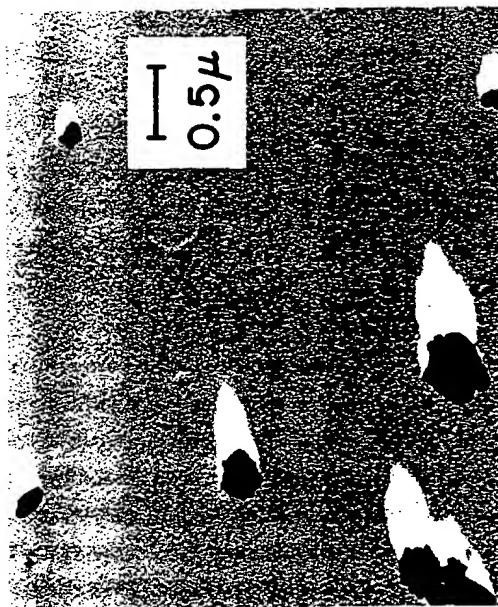


Figure 30.3. Transmission electron micrograph of alumina powder, spray dispersed and shadowed at 23° angle to the plane of the illustration. Length of shadow indicates that particles are not flat platelets.

Impurity Pickup

During milling, Ca and Si from the mill lining and grinding media are added to the slip, as shown by emission spectrographic analysis of the milled and dried slip, expressed as element ppm by weight as follows:

	As-received	Milled 2 days	
		100	300
Ca (ppm)	300	1500	
Si (ppm)			

If the milling is done with high-purity lining and media (99+ % Al_2O_3), the resulting tape does not sinter adequately under the firing conditions used, and the substrate has open porosity and a density of 3.80 g/cc or less. However, if talc is added to the higher-purity composition sufficient to provide the 1500 ppm of Si, the resulting tape sinters to 3.88 g/cc and contains essentially zero open porosity. Polymethylphenylsiloxane silicon resin (SR-82, General Electric Company, Waterford, New York) can be substituted for the talc, resulting in a fired density of 3.89 g/cc. The degree of dispersion of the impurities appears to be important, since equivalent additions of SiO_2 powder (Quso, Type 30, Philadelphia Quartz Company, Philadelphia, Pennsylvania) yield low-density substrates. Also, low density results when Mg is not included in the starting materials as a grain-growth inhibitor.

Deagglomeration

The term "weak agglomerate" is used to mean a group of particles that are weakly bonded together, which is consistent with the definition in Chapter 5. The term "solid agglomerate" is defined operationally in this paper as a group of particles that cannot be separated by 40 kHz ultrasonic treatment at 100 watts for 20 minutes in an aqueous dispersion.^{4,7} The word "floc" is used as defined in Chapter 5.

As mentioned earlier, the as-received alumina powder is highly agglomerated. We have found that ultrasonic treatment at 40 kHz and above reduces the measured particle size of this material to a limiting value, at which the agglomerates originally present were broken down. Wet and dry sieve analyses⁸ and other studies have differentiated between some levels of bond strength in these agglomerates.

It is generally true that a large surface area tends to favor agglomeration. (For an example of this correlation, see the data on nine different alumina powders in Figure 30.5 of reference 9.) The large area appears to offer more

possibilities for interparticle contact and adhesion, thus leading to porous, poorly packed agglomeration and low green density. However, good sinterability requires both the high surface area and the good packing. It is a remarkable feature of the present process that a powder with a surface area of about 11 m^2/g , which is high for alpha alumina, can be effectively deagglomerated and deflocculated, resulting ultimately in good packing.

Direct evidence of the deagglomeration produced by milling was obtained by sedimentation particle-size analysis. Slip of the composition given in Table 30.2 was milled for 2 days, and the relative particle size was determined as follows: 7.56 g of slip was added to 40 cc of a 50 vol % solution of benzene in ethanol, but ultrasonic dispersion was *not* used before the sedimentation measurement. The measured median size was 0.4 μ , but the absolute accuracy of this value was not trustworthy, because the density and viscosity of the solution were assumed to be the averages of the benzene and alcohol values. For relative comparison, however, the particle-size distribution of unmilled slip was determined after it was diluted in benzene-alcohol in the same manner and ultrasonically dispersed for 20 minutes. The particle sizes were within 15% of those of the milled slip, showing that 2 days of milling is equivalent to the ultrasonic dispersion in breaking down agglomerates.

Milled slip was also diluted in benzene-alcohol and, in addition, it was ultrasonically treated for 20 minutes. These particle sizes were also within 15% of those of the unmilled but ultrasonically dispersed slip, showing that the hard particles are not significantly reduced in size by the wet milling.

Particle-size determinations of A-16 alumina dispersed by other means are consistent with the above. The diameters of the particles that were separable by smearing and spraying using a TEM and the centrifugal action of the MSA particle-size analyzer⁸ were generally in the same size range.

Surface-Area Effects

Unmilled slip of the composition shown in Table 30.2 consisted of A-16 alumina with a surface area of 10.2 m^2/g . This powder was dried and heated in air at 500°C for 2 hours to remove the organic constituents. The resulting material was white powder that adhered together only about as strongly as powder pressed between two fingers, and sintering was therefore not great. After a 300°C outgassing, the BET surface area was 10.8 m^2/g . Slip samples milled for 1, 2, and 7 days were treated in the same manner and yielded surface area that were 11.2, 12.6, and 11.8 m^2/g , respectively indicating a slight increase in surface area with milling, but this small increase might be due to impurities from the grinding media.

Deflocculation

The Mechanism. If less than half the amount of menhaden oil indicated in Table 30.2 is used during milling, the slip viscosity becomes too high to allow grinding media motion when the mill is rotated. However, the presence of the full amount of deflocculant provides a paintlike fluidity with good milling action, in spite of the high solid-to-liquid ratio shown in Table 30.2, and in spite of the high surface area of the solid material present.

Two models that are commonly proposed¹⁰ to explain the action of deflocculants are charge repulsion and steric hindrance. Each assumes that the deflocculant is adsorbed onto the solid particles.

Generally the steric hindrance model is useful in explaining the stabilization on nonaqueous dispersions.^{11,12} However, traces of water were shown¹³ to influence the zeta potential and agglomerate size of TiO_2 dispersed in nitrobenzene, and charge effects might therefore be important in some essentially nonaqueous systems. For example, charge repulsion has been proposed as the mechanism for the deflocculation of alumina in xylene.¹⁴

In comparisons of the effectiveness of oleic acid versus stearic acid as deflocculants for alumina in nonaqueous liquids, the presence of a carbon-carbon double bond in the deflocculant has been reported^{14,15} to enhance the deflocculation effect. Also, infrared spectra of the adsorbed species have shown¹⁶ that the double bonds in oleic acid strongly influence the effective area covered by each molecule adsorbed on TiO_2 dispersed in benzene.

The influence of the carbon-carbon chain length on deflocculation has also been reported¹⁷ for alumina in various nonaqueous liquids. The chain-length influence on adsorption has been reported for alumina in water¹⁸ and for Fe_2O_3 in heptane.¹⁹ Generally an optimum length has been found for each of these effects.

The adsorption of various esters onto alumina has been shown²⁰ to be increased when the ester is less soluble in the solvent (toluene, chloroform, etc.).

To estimate the degree of adsorption, a solution of menhaden oil in the trichloroethylene-alcohol mixture was filtered through the alumina powder and evaporated to determine the unadsorbed residue. Additional blanks were run without the alumina and without the oil. The amounts of oil residues in the first two cases were indistinguishable to within the $\pm 5\%$ precision of the experiment. Therefore, there was little or no deflocculant adsorbed. In the third case the residue was less than one-tenth of the usual amount of oil in the composition, showing that there was not sufficient oil-like adsorbate (grinding aid, etc.) on the as-received alumina to dissolve and mask a significant adsorption of the menhaden oil. (These mixtures were

not milled because of difficulty in separating the milled alumina from the small amount of solvent.)

If trichloroethylene is substituted for the alcohol in the slip composition, the viscosity becomes excessive. The menhaden oil is very soluble in this liquid but less soluble in the alcoholic mixture and insoluble in pure ethanol.

A hypothesis consistent with the above is that a certain minimum amount of menhaden oil is required in solution to drive the adsorption process by mass action. Increasing the solubility decreases this effect. However, less than 5% of the oil is actually adsorbed.

The zeta potential of the alumina in trichloroethylene-alcohol in the presence of the menhaden oil was estimated to be $+74 \text{ mV}$, calculated from a measured²¹ electrophoretic mobility of $0.5 \text{ } \mu\text{m cm/V second}$. However, when the menhaden oil was omitted, the mobility was the same. This indicates that the deflocculant probably does not operate through charge repulsion, and the steric-hindrance model is likely to describe the system. It should be noted that the mobilities were measured on dilute, unmilled suspensions. It is known²² that the zero point of charge of alpha alumina can be altered by abrasion, but experimental difficulties prevented the use of concentrated, milled suspensions. Also, traces of water were probably present. However, if a strong charge-repulsion effect existed in this system, it would probably be detected here, even without milling.

The pH of water in contact with the standard milled slip is 8.0 ± 0.5 .

Chemical Characterization. Using A-16 with a surface area of approximately $11 \text{ m}^2/\text{g}$, a series of compounds was substituted for fish oil in otherwise standard mill batches. The 2.3 gal mill jar was used in all cases and at least one standard mill using menhaden oil was made from each bag of A-16 alumina. The results are reported in Table 30.3. A measure of the viscosity during the first day of milling was estimated qualitatively by the loudness of the ball sound.

All the slips marked "thixo." in the table were pseudoplastic and thixotropic and appeared highly viscous when not being agitated. However, the viscosity of the slip when nearly at rest is evidently not an important consideration, as shown by the fact that these thixotropic slips were sufficiently fluid when agitated and were easily cast.

Mill batch 236 adhered to the cellulose acetate carrier film after casting and drying, and the surfaces of the forcibly peeled-off tape were rough. Therefore, the amine has a deleterious effect on the overall system, although it deflocculates. Batch 251 was prepared using 120 g of the B-98 Butvar binder in place of the fish oil deflocculant in the first stage of milling. Fluidity was achieved during the first hour of milling and was maintained

Table 30.3. Substitute deflocculants

Mill Batch Number	Material Replacing Menhaden Oil, 55 g	Chemical Functional Groups Present	Results			
			Molecular Weight	Slip Viscosity	Tape	Fired Substrate
211	No Deflocculant	None	—	Solid		
185A	Nujol	(Possible C=C and high MW)		Solid		
252	Propylamine	Base	59	Viscous		
236	Octadecylamine	Base	270	Thixo.	One half cracked	Rough surface
—	Trichloroacetic acid	Acid	163	Solid		
191	Oleic acid	Acid, C=C	282	Solid		
209	Octadiene	C=C	110	Solid		
249	Glycerine	OH	92	Solid		
189	Phthalates and polyethylene glycol (plasticizers)	OH, COO	278, ect.	Solid		
182, 185	Octyl and other phthalates (plasticizer)	COO	278, etc.	Solid		
251	Poly(vinyl butyral) (binder)	COO, OH, (C=C)	32,000	Fluid	Sticks to cellulose acetate	
207	Glyceryl tristearate	OOO	891	Solid		
210	Ethyl oleate	COO, C=C	310	Solid		
237	Glyceryl monooleate	COO, C=C	357	Thixo.	One half cracked	
239	Ditto, but 1413 cc alcohol, no TCE	COO, C=C	357	Solid		
204, 208	Glyceryl trioleate	COO, C=C	885	Thixo.	Good	Good
250	Glyceryl trioate plus octadecylamine	COO, C=C, Base	885, 270	Thixo.		
177, 253	Corn Oil	COO, C=C; see Table 30.4	885; etc.	Fluid	Good	Good
296	Untreated menhaden oil (Haynie LCP)	COO, C=C (NH ₂); see Table 30.4	885, etc.	Fluid, slightly viscous		
215	Extra menhaden oil (110 g total)	COO, C=C (NH ₂); see Table 30.4	885, etc.	Fluid, slightly viscous		

during the remaining 23 hours. According to the supplier,²³ this material contains about 19% hydroxylated species and about 2% acetate ester. It might also contain residual, unpolymerized vinyl groups and, therefore, double bonds.

The odor of the menhaden oil indicates that an amine base might be present. Therefore, the composition of mill batch 250 was designed to duplicate the functional groups present in the menhaden oil (amines and double bonds, etc.), but with the use of only synthetic, characterizable materials. However, the viscosity was equally low in batches 204 and 208 using glyceryl trioleate alone as a defloculant. The glyceryl trioleate results demonstrate that the goal of a synthetic defloculant is achievable, at least experimentally.

Inspection of Table 30.3 indicates that a combination of a carbon-carbon double bond, an ester group, and a molecular weight of at least 357 was necessary in the series of defloculants that were studied here. For example, the ethyl oleate molecule contains a double bond and an ester group, but its molecular weight is too low, and the deflocculation was unsatisfactory. Glyceryl monooleate, with the same functional groups and also a higher molecular weight gave sufficiently fluid slip for casting.

Glyceryl tristearate has ester groups and a high molecular weight but no double bonds, and it was unsatisfactory. For comparison again, glyceryl monooleate has double bonds in addition and was satisfactory.

Nujol is a refined mineral oil commonly used for dispersing powder samples for infrared analysis. It is used for this purpose because its infrared spectrum does not usually show COO group absorptions or components other than carbon-carbon single and double bonds. Its viscosity indicates the probable presence of components with molecular weights on the order of a few hundred. This material, usually lacking COO groups, did not give effective deflocculation.

Corn oil is similar to menhaden oil in that it contains glyceryl esters of unsaturated fatty acids, as shown in Table 30.4, and therefore all three attributes mentioned above are present. This oil gave excellent results as a substitute for menhaden oil. The slip viscosity appeared slightly low, indicating excellent deflocculation.

Other complex materials, such as poly(vinyl butyral), evidently do deflocculate and might be worth further study. Also, glyceryl monooleate might be improvable, with the use of extra plasticizer to decrease the cracking during drying. It is soluble in alcohol but requires the presence of trichloroethylene (TCE) for effective deflocculation (see batch 239 results).

A wider range of materials appears to deflocculate the slip when the alumina surface areas are $\leq 10.5 \text{ m}^2/\text{g}$, but we have not thoroughly evaluated these compositions.

Table 30.4. Analysis of various oils

Material	Iodine Number ^a	Saponification Number ^a	Weight Percent of Fatty Acid Groups ^a			
			Saturated		Unsaturated	
			Stearic	Other	Oleic	Other
Untreated menhaden ^a	170	191	1	23	0	76
Air-treated menhaden ^a	100	185	—	—	—	(30% linolenic)
Untreated corn ^a	123	192	3	12	50	35
Glyceryl trioleate (calculated)	86	190	0	0	100	0
Glyceryl tristearate (calculated)	0	190	100	0	0	0

^a Defined in reference 5, p. 793. The iodine number is a measure of unsaturation, and the saponification number is a measure of ester content.

^a Percentage of total fatty acid groups only, not of total oil. Natural oils are reported in reference 5, p. 776 to be mostly glyceryl esters of fatty acids.

PRECASTING TREATMENTS AND CONTROLS

After the slip is milled it is transferred from the mill to storage vessels or chambers for de-airing. A vacuum is pulled on the slip using a roughing pump to a level below the boiling point, usually until agitation due to escaping air ceases. Some times the slip is actually permitted to boil for a few minutes at this point. One must be careful of excessive solvent loss if boiling is carried on for a long time.

For the alumina process, the slip is pumped into the casting machine through a series of two filters, one with $37 \mu\text{m}$ openings and one with $10 \mu\text{m}$ openings. A peristaltic-type finger pump is used with Tygon tubing. The filters, which are nylon, remove any large pieces of unground alumina or undissolved binder that may be present. Both of these can cause defects in the cast tape or fired product.

As in any slip-casting operation, the control of viscosity and specific gravity are important. Early in our development work it was standard practice to check these parameters on every batch of slip that was produced. Later we developed confidence in the process reproducibility and the "feel" of the operator and eliminated all but occasional checks on these

parameters. The normal operating viscosity of the slip in Table 30.2 was in the range of 2500 to 3500 cp* and the specific gravity was 1.9 to 2.0 g/cc.

CASTING PROCESS

The Casting Machine

There are a great many variations of this simple device. Basically, however, one has some type of container, one side of which can be moved vertically to form an opening or gate through which the slip escapes. The gate height is controlled by micrometer screw adjustments, often with large dial indicators for convenient viewing. The assembly is customarily fixed in position with a carrier or substrate material drawn under the gate. The substrate is most often a metal belt or a plastic film made of Mylar, polyethylene, or the like, or in some cases individual glass plates. Many factors influence the thickness of the wet cast film at a given gate opening, for example, the hydrodynamic head of the slip reservoir behind the blade, the viscosity of the slip, and the speed with which the film is cast. All these are susceptible to variation, and suitable controls must be instituted for uniform production.

The casting machine used in the alumina substrate work is shown in Figures 30.5 and 30.6. It is an enclosed chamber 4.75 in. \times 12 in. \times 25 ft. The floor of the machine is a smooth aluminum metal plate on which a strip of cellulose acetate film moves. The film is supplied continuously from a spool and enters the slip chamber through a slot in the end of the chamber. Electrostatic brushes can be mounted at this point to remove any dust particles from the carrier film.

The doctor blade at the exit side of the chamber is adjusted by means of micrometer screws. To produce the desired final substrate thickness of 0.026 in., about a 0.063 in. gap between the blade and the carrier film is used. The layer of slip passes through the gap with its thickness controlled by the micrometer settings. The thickness of the freshly cast layer of slip (just beyond the doctor blade) is continuously monitored by a gamma-ray back-scatter or X-ray transmission instrument, and the gap between the doctor blade and carrier film is adjusted accordingly. This can be done automatically or manually.

The normal casting speed utilized in this work was 6 in./minute. This rate is dependent on the length of the machine, the drying conditions, and whether the machine is to be operated in a continuous or batch mode.

* Brookfield Viscometer: #4 spindle, 20 rpm.

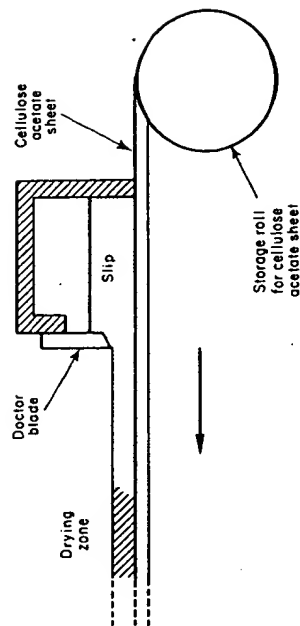


Figure 30.5. Schematic diagram of the doctor-blade casting machine.

Continuously variable speed controls were located at the payoff end of the machine so that a single operator could process the tape.

The Carrier Material

As mentioned above, many materials have been used as substrates or carrier films in the tape-casting process. One usually tries to use the material that

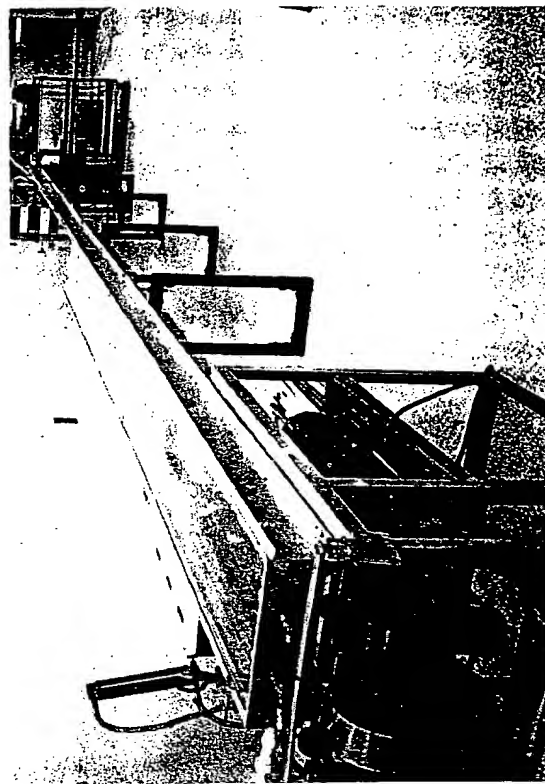


Figure 30.6. Laboratory model of the doctor-blade casting machine.

does the job for the lowest cost. In most cases the binder solvent system plays an important role in the selection of a carrier. A continuous stainless steel or chrome-plated steel belt may be the best carrier if the tape is to be stripped continuously at the end of the machine. The fine-grained alumina substrate process used a unique carrier material, cellulose triacetate (Kodacel TA401, Eastman Chemical Products, Inc., Kingsport, Tennessee). According to the supplier, this material, which is 0.015 in. thick, contains ≈ 15 wt % of diethyl phthalate plasticizer (bp 290°C), an organic liquid that is similar to one of the plasticizers given in Table 30.2. TGA and DTA studies of the film showed 16% weight loss in N_2 between 100 and 320°C and an endothermic peak at 280°C. After casting and drying, the cellulose acetate is 4.7% thicker and is an average of 3.3% narrower than as-received, probably because of absorption of solvent and/or exchange reactions among the plasticizers.

In our experiments thus far, substitute carrier-film materials that did not become narrowed did not yield satisfactory results, and the dry tape cracked and/or stuck to the film excessively or insufficiently. The cast material must stick to the carrier film sufficiently to prevent extreme curling during drying, but it must not stick so much as to prevent the film from being peeled away from the dry tape prior to firing.

The movie-grade cellulose triacetate also provided an extremely smooth and uniform casting surface, which we believe contributed to the smooth-surfaced, low-defect alumina substrates produced. Thicknesses down to 0.005 in. were used in the standard process with equivalent results.

DRYING

In the substrate process, the layer of slip dries slowly while it is carried through the machine on the moving plastic film. Filtered air is blown through the machine in a direction opposite to that of the moving slip. The air flow rate is 5 ft/minute. This arrangement provides dry air at the exit end in contact with the almost dry tape. At the other end in contact with the freshly cast wet slip is air that has passed through the entire casting machine and is saturated with solvent vapor. The difference in solvent content between the slip and the air is slight at any point in the machine. This controls the rate of solvent evaporation, allowing the remaining solvent in the slip layer to redistribute itself with only a small vertical gradient of concentration. This small gradient of concentration tends to minimize curling and cracking of the slip as it dries. Heat increases the drying rate, but its use is limited, because the boiling point of the solvent, 71°C, must not be exceeded if controlled, bubble-free drying of the slip is to be achieved.

Drying

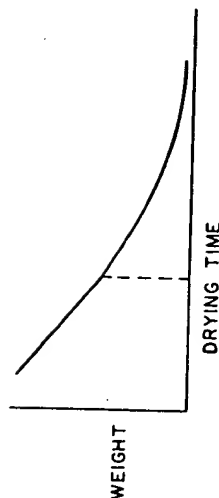


Figure 30.7. Schematic of weight versus time in a two-stage drying process.

The drying of slurries in general has been studied by other workers. A two-stage process is commonly observed with such materials,²⁴ the first stage of drying proceeding at constant rate, and the second stage at a gradually decreasing rate. These are shown in Figure 30.7. In either stage of drying, the solvent must move through three consecutive steps of transport: (1) solvent flows vertically through the slip to the surface, (2) solvent then evaporates at the surface, and (3) solvent vapor is swept away at the surface. The overall rate is determined by whichever is the slowest step.

In the first stage the slip is still fluid and solvent is easily transported through it (step 1) by liquid diffusion or capillary action. Step 2 is the slow step, being limited by the inflow of heat required to supply the latent heat of vaporization. In those cases involving very little air flow, step 3 can also be slow, causing a pileup of nearly saturated vapor at the surface and a consequent decrease in the evaporation rate. Therefore, the rate of total drying in this stage can be influenced by either temperature (step 2) or air flow (step 3). Neither of these is likely to be time dependent, and so a constant rate is usually observed for still-fluid slip.²⁴

In the second stage the slip has become solid, and the solvent no longer flows by capillary action or fast diffusion. The solid is gel-like, and step 1 is limited by the slow diffusion of solvent through the gel. This would be the slowest step, and like many diffusion processes, it might be expected to follow the same sort of equations as radioactive decay, having a rate that decreases with time.

A solution²⁵ to the well-known Fick's law diffusion equations, set up for the case of an initially uniform solvent distribution and evaporation from one surface of a slab, is given by

$$W = W_0 \left\{ e^{-Dl(\pi/2d)^2} + \frac{1}{9 \exp[-9Dl(\pi/2d)^2]} + \frac{1}{25 \exp[-25Dl(\pi/2d)^2]} + \dots \right\} \quad (1)$$

where W = weight
 W_0 = initial weight
 D = diffusivity
 t = time
 d = thickness of slip.

At relatively long times, only the first term of the series is significant. A plot of $\log W$ versus t should then give a straight line. It is apparent from the equation that an increase in the diffusivity would have a strong effect on the drying rate.

Diffusivities in solids tend to vary with temperature according to the Arrhenius activation energy equation:

$$D = D_0 \exp \frac{-E}{RT} \quad (2)$$

A special apparatus was used to determine the drying rates of the slip at various temperatures and air flows. This is shown in Figure 30.8. Nearly laminar flow was achieved by filling the rectifier chamber with 10,000 parallel drinking straws, thus improving the reproducibility by minimizing random eddy currents. Slip was cast onto a glass sheet on the pan of the scale using a movable doctor blade. The weight of the slip was noted periodically. A thermocouple was imbedded into the slip sample.

Figure 30.9 shows a plot of experimental data obtained with the laminar flow apparatus. Two stages of drying are indicated (run 1), as illustrated by the constant rate (linear) portion of the curve, and the changing rate

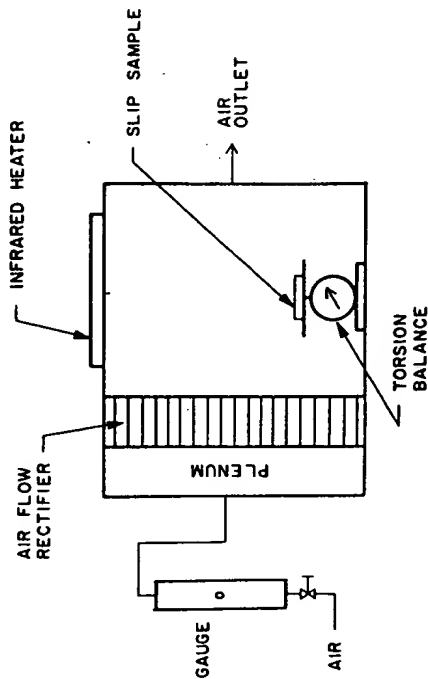


Figure 30.8. Experimental laminar flow-drying chamber.

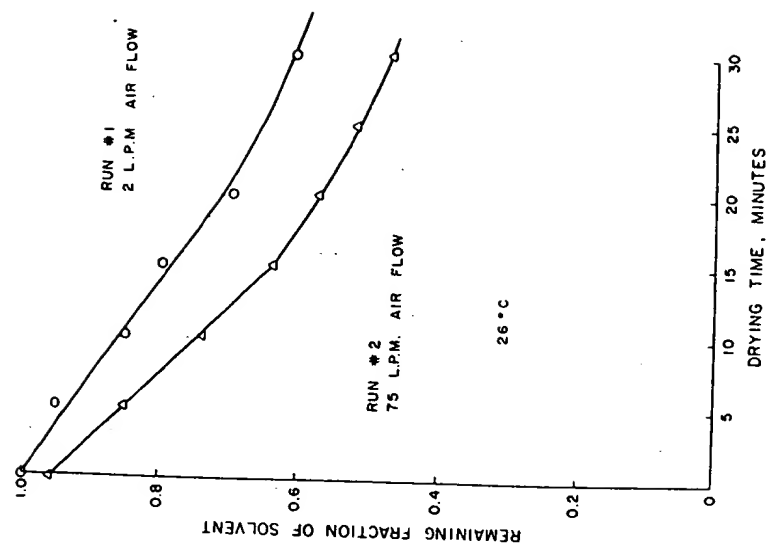


Figure 30.9. Drying data. Remaining fraction of solvent versus drying time at constant temperature.

(curved) portion. The experiment was repeated, but this time there was an air flow of 75 l/min. These data indicate that the air flow has an effect on the first stage, as predicted by the model.

Figure 30.10 shows the same data replotted on semilog paper. The straight lines during the second stages of drying confirm the predicted exponential relationship, assuming that only the first term of the series is significant. Note that air flow does not affect the second stage slope, showing that diffusion through the gel is probably the slowest step, not evaporation or vapor removal. Also shown in Figure 30.10 are data taken at a slip temperature of 60°C. The indication is a speedup of drying during both stages. This is consistent with the idea of a latent heat effect during the first

stage and an activation energy effect during the second stage. The diffusion through the solid was speeded to the limiting point where it was no longer the slowest step.

Five drying experiments were run at different temperatures, with the weighings being made only after the solidification of the slip (second-stage drying). A $\log W/W_0$ versus time plot for each experiment gave values of $\pi^2 D/4t^2$ as the slopes. To obtain the Arrhenius activation energy, these five slopes were plotted against the reciprocal absolute temperature in Figure 30.11. The slope of this plot is $-E/R$ in the Arrhenius equation, and the activation energy E was thus obtained. The experimental value is 22 Kcal/mole, which is a reasonable value for such polymer-solvent systems.²⁰

Several means of increasing the drying speed during actual casting runs were demonstrated by this experiment. Increased air flow during the first stage of drying is one method, and heat applied during either stage is another.

In the casting machine shown in Figure 30.6, it was found experimentally that air flow above 110 ft³/hour (5 ft³/minute) resulted in skin formation

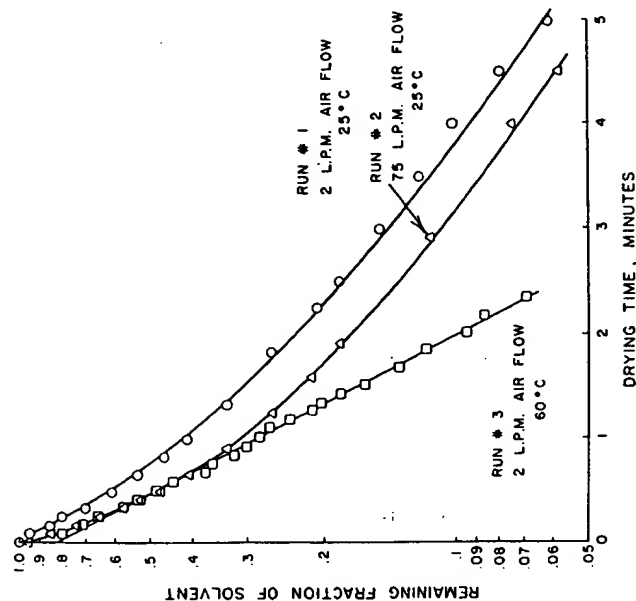


Figure 30.10. Semilog plot of drying data.

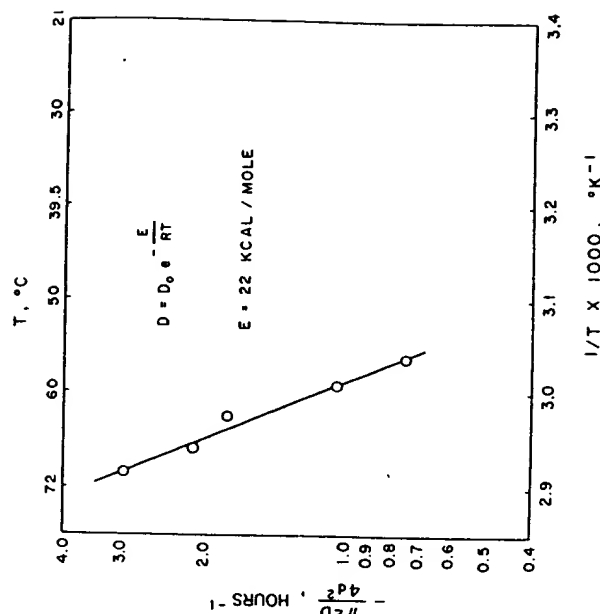


Figure 30.11. Arrhenius plot for diffusion-controlled stage of drying.

during the first stage of drying. Evidently the solvent is removed from the surface layer too fast for diffusion through the liquid to replenish the layer, even though this diffusion is fairly rapid. Once skin forms the first-stage drying is slowed, since all diffusion must then proceed through the solid skin. The formation of skin also has other detrimental effects on the quality of the final product. Therefore, the forced drying by increasing the air flow is limited to this level.

On our machine heat was applied to the drying slip by mounting nichrome heating elements on the glass top of the machine. The elements were positioned to bring the slip temperature up rapidly during the first stage of drying. A temperature of 50 to 80°C was maintained in the drying slip, with the highest temperature being at the driest end of the tape. Temperatures were measured by embedding a thermocouple in the traveling slip. The profiles of two typical forced-drying runs are shown in Figure 30.12.

This type of forced drying provided satisfactory results in that tapes were sufficiently dry to strip from the carrier at the end of a 25 ft casting machine.

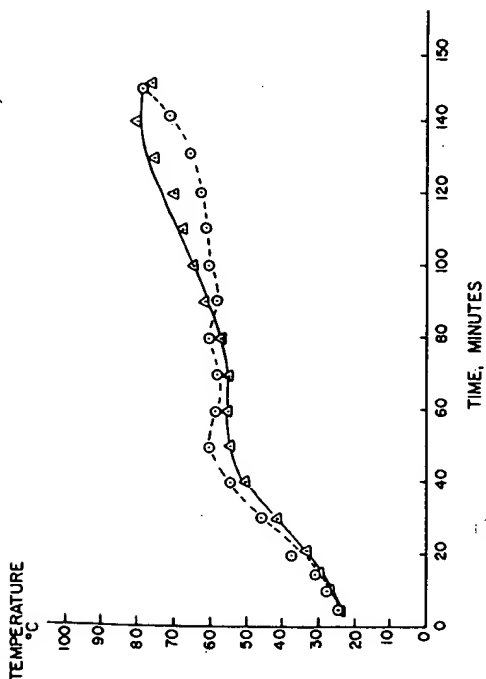


Figure 30.12. Slip temperature versus time in casting machine.

PRECISION CASTING

For some applications precise dimensional control of the final part and, therefore, of the as-cast tape is essential. This was the case in the development of a process for producing lead zirconate titanate tapes 1 to 12 mils thick with thickness tolerances of better than ± 0.3 mils over large areas.²⁷ Briefly, the primary requirement was to improve existing tape-casting technology by providing a precise gap between the blade and the casting surface. Further requirements were to provide a casting surface of a moving carrier tape of controlled thickness that would glide under the blade and over a supporting, laterally level bed with minimum friction. To provide these features we constructed a precision casting machine that had the following features:

1. A well-constructed, stable table base.
2. A curved bed, 1 ft wide and 14 ft long with its maximum height under the doctor blade.
3. A thin carrier tape with close thickness tolerances.
4. A doctor blade with an edge milled to a fraction of a mil in straightness.
5. A doctor-blade configuration to minimize the effects of hydrodynamic and surface tensile forces at the blade.

The major features of this machine are the curved bed of smooth tempered glass bent into the arc of a circle with a radius of 430 ft, and a two-bladed doctor blade. The curvature was provided to assure close contact between the thin carrier tape and the bed. The maximum height of the circle was located under the doctor blade so that the surface at this point would be horizontal in the longitudinal and the lateral direction, to prevent any tendency of the slip to flow under gravitational forces. The doctor-blade construction is shown in Figure 30.13. This construction with two blades was chosen to control the hydrodynamic and surface tensile forces as the slip passes under the blades. In Figure 30.13 the left blade is the casting blade. Because of hydrodynamic forces it is necessary to maintain a constant height of the casting pool at the right of the casting blade to maintain a constant height of the cast to the left of the blade. It is also beneficial to minimize the differential heights between the casting pool and the cast on the respective sides of the casting blade. The simple two-blade design satisfied these two conditions. By adjusting the relative heights of the two blades and the speed of the carrier tape, a constant low-level casting-pool height may be maintained for all but the initial and final few seconds of casting.

The other parameters that must be controlled to optimize casting thickness control include slip viscosity (function of percent solvent and temperature), casting speed, doctor blade setting, and drying shrinkage of the tape.

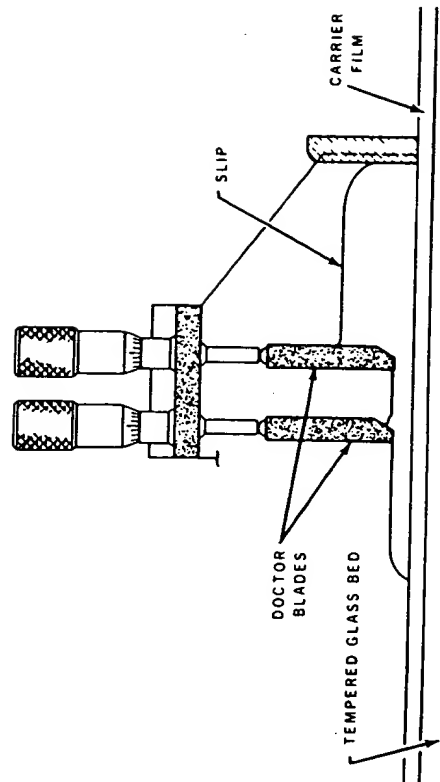


Figure 30.13. Side view of precision tape-casting doctor-blade showing two-blade construction and optimized flow conditions.

With the machine described above and by close control of the casting parameters mentioned, tapes of lead zirconate titanate have been reproducibly cast 8 in. wide and 10 ft long, with thicknesses from 1 to 12 mils and with thickness tolerances better than $\pm 4\%$ (e.g., 5.0 ± 0.2 mils).

TAPE CHARACTERIZATION

The density of unfired tape (often called the "green" density) is an important parameter for characterizing a tape-casting process. In experimental modifications of the tape, the green-density measurement can be useful in detecting poor packing of the powder or in detecting excessive polymeric binder content.

In the determination of bulk green density²⁸ the volume measurement can be made with a flat-faced micrometer caliper, provided about 15 thickness measurements are taken and averaged (for a substrate area of about 20 in.²). The same volume can be obtained by extrapolating mercury porosimeter data to zero pressure. Typical bulk densities for the alumina tapes produced in our laboratory were 2.5 to 2.6 g/cc. Taking the organic materials into account, these bulk densities correspond to an alumina volume percent of 56, which is a densely packed green body, considering that no pressing is involved and the alumina particles are small.

The volume for calculating the apparent density²⁹ of the tape can be measured by a mercury porosimeter at 20,000 psi or an air pycnometer at atmospheric pressure. In either case the measured apparent green density of the alumina substrate tape ranged from 2.9 to 3.0 g/cc.

Another technique used for measuring the density of the tape was the Archimedes' method³⁰ using water. A difficulty was encountered in that water immediately began to be absorbed into the tape as the immersed weightings were begun, causing changing weight values and preventing bulk-density determinations by this means. Another approach³¹ to bulk density determination is to thoroughly soak the tape sample with water and then weigh it while it is soaked but not immersed. This was not possible because the water immediately began evaporating, again causing continuously changing values. Also the tape expanded when immersed in all the liquids that we tried.

A method for extrapolating the water absorption back to zero immersion time was developed. The method rests on the assumption that the more water absorbed into the tape pores, the slower the further absorption. The amount absorbed should asymptotically approach a maximum value. One would then expect the following relationships to be observed.

$$\frac{dW}{dt} = k \left(\frac{\text{amount of unfilled open}}{\text{porosity remaining}} \right) = k(W_m - W) \quad (3)$$

where W = weight of tape plus absorbed water at time t ,
 W_m = maximum value of weight reached by the tape at long times
 k = empirical constant.

To simplify the calculations substitution can be made: Replace dW/dt with an equal quantity, $-d(W_m - W)/dt$. Then

$$\frac{d(W_m - W)}{W_m - W} = -kdt \quad (4)$$

Integration gives

$$\log(W_m - W) = -kt \quad (5)$$

This allows a linear plot to be obtained when $W_m - W$ is plotted versus t on semilog paper. Extrapolating back to zero time, one can obtain the initial weight of tape immersed in a buoyant fluid such as water before any swelling has taken place. From this and the unimmersed (dry) weight, one can calculate the bulk tape density using the Archimedes' method. The experimental plot did yield a straight line, and the calculated density of the alumina tape was 2.63 g/cc.

An estimate of the apparent density can also be obtained by a variation of this method. W_m minus the initial (extrapolated) weight is the amount of water absorbed. The volume of this is roughly the volume of the open porosity, subject to a possible error due to swelling. This volume can be combined with the other data to calculate³² the apparent density. It was found to be 2.91 g/cc, which is in agreement with the other techniques tried.

A comparison of the bulk and apparent densities given above indicates that the tape samples contain some kind of open porosity. It should be noted that the tape must be broken into small pieces for use in the pycnometers or the porosimeter, and many cross-sections are thus exposed. Therefore, it is possible that the major surfaces of the tape are sealed by polymer and the pores are only accessible through the cross-sections.

Visible-light examination with a variety of lighting techniques at magnifications from 1 to 800 \times does not show evidence of porosity on any of the surfaces. However, SEM pictures of the surface at 10,000 \times show submicron-size pits. It could not be determined whether the bottoms of these pits were sealed with polymer. Also, microtomed cross sections appeared to show porosity, under the SEM, although these could have been an artifact of the microtoming operation.

Assuming that the tape is not significantly compressible, the mercury porosimeter pressure versus volume curves can be used to calculate pore size. A curve of this type on the alumina tape indicates that 50% of the pores are $< 0.09 \mu$ in diameter. However, the tape is compressible, and this

method cannot distinguish between porosity and compressibility while the pressure is applied.

The porosimeter operators reported some degree of permanent penetration of the tape by the mercury, proving that there is some open porosity. However, the weight gain due to Hg absorption cannot be used as a quantitative separation of porosity from compressibility because some mercury flows back out of elastic porous materials when the applied pressure is removed. The weight gain is only a qualitative test, but nevertheless it is a definite indication of unoccupied space in the original tape.

It should be noted that it is difficult to distinguish between open porosity versus a molecular level of penetration of the water and air into the polymer structure itself. The polymer might be especially permeable to these fluids if it were in a stretched state, having shrunk between the alumina particles during drying. The mercury might be a better test for macroporosity, but at 20,000 psi the mercury could conceivably force its way into the stretched polymer, thus creating discrete pores. Therefore, the original "pore" size might be as large as 0.09μ or as small as a molecule.

As an increasing amount of polymeric binder is added to the tape composition, more of the interstitial space between the alumina particles is probably filled with binder. It has been found that an excess of binder above a certain level (4 g of binder for each 100 g of the alumina) causes maldistribution effects in the tape and curling or cracking during firing. The apparent density measured with an air pycnometer should be sensitive to the amount of organic chemical material (binder, etc.) present in the interstitial space, and this is probably why it was found to be useful in diagnostically assessing new formulations. A plot of bulk and apparent density versus percentage organics is shown in Figure 30.14. It should be noted that, while the apparent densities are sensitive to the amounts of organic materials, the bulk densities are less sensitive.

Attempts to correlate curling and cracking with the apparent-density measurements have only been made with data obtained by the use of the air pycnometer and not with other types of measurements. It is therefore unknown whether all the apparent-density methods are equally sensitive to excess binder or whether there are significant differences in fluid permeability. At any rate, the other apparent-density methods are less convenient than the air pycnometers.

It is well known¹⁰ that the sinterability of a powder compact is dependent on the degree to which the powder particles are packed together. In the tape process, poor deflocculation might be expected to cause poor packing of the alumina particles and thus low fired density. The degree of alumina packing can indirectly be measured by determining the bulk density, provided the amount of other material (binder, etc.) is known.

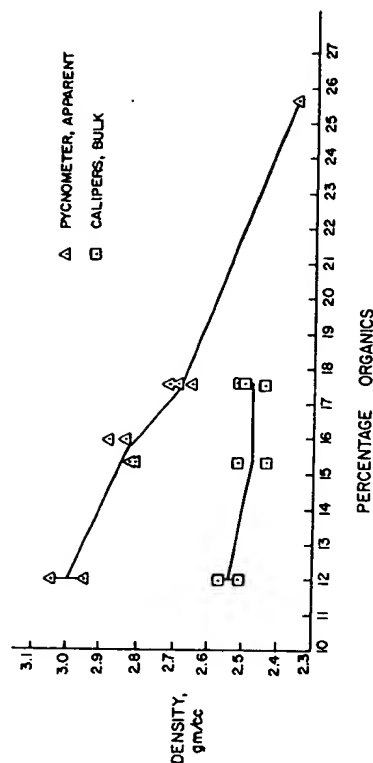


Figure 30.14. Green density versus organic content.

Bulk densities and the resulting fired densities are reported in Table 30.5 for various experimental tape compositions in which poor deflocculation and poor alumina packing probably occur. For comparison, data are also shown for standard tapes in which poor packing was not observed to occur. (It should be noted that good results have been reported when the other aluminas in Table 30.5 were used in other processes with increased firing temperatures.)

The packing factor in the tape can be calculated as follows: In 1 cc of standard tape the total weight is about 2.53 g (bulk density). Of this, 12.0% is organic material. Weight-loss measurements during 750°C binder

Table 30.5. Substitute aluminas

Alumina Powder Used	BET Surface Area (m ² /g)	Bulk Green Density (Caliper), (g/cc)	Bulk Fired Density (Archimedes), (g/cc)
Standard ^a	11.3-12.4	2.51-2.57	3.88-3.90
Linde A ^b	8.3	2.09	3.8, Porous
Calcined Al ₂ (SO ₄) ₃ ^c	9.1	2.01	3.8, Porous
Kappa-theta ^d	16.6	1.97	3.8, Porous

^a A-16, Aluminum Company of America, Pittsburgh, Pennsylvania.

^b Linde A, Union Carbide Company, East Chicago, Indiana.

^c Experimental, Western Electric Company, Princeton, New Jersey.

^d Experimental, E. I. duPont de Nemours and Company, Wilmington, Delaware.

removal have shown that the tapes exposed to ambient air for several months contain less than 1% residual solvent. Spectrographic analysis has shown that inorganic impurities comprise about 1% or less of the fired substrate composition. Neglecting residual solvent and inorganic impurities, the alumina is the other 88% of the 2.53 g, or 2.23 g. The bulk density of the alumina itself in this configuration is therefore 2.23 g/cc. This is 56% of the density of sapphire (3.986 g/cc as measured by Wachtman¹ on a variety of synthetic sapphire samples).

As calculated from the micrometer bulk density, it is interesting to compare the 56% packing factor of the tape A-16 alumina with the corresponding value for dry-pressed A-16.

After pressing at 5000 psi, with a small amount of stearic acid as a lubricant, micrometer green densities measured in this laboratory are typically 2.18 g/cc (single action press), and Alcoa reported² 2.24 g/cc (double action press). These correspond to packing factors of 55 to 56%. Therefore, the packing in the tape-cast material is excellent, considering the fact that no external pressure is applied during its formation.

In 1 cc of standard tape, the weights of alumina and organic materials were as reported above. Knowing the densities of the sapphire (3.986 g/cc, reference 31) and the mixed organic materials (1.06 g/cc), the volumes of these materials are easily calculated. Alumina (2.226 g) has a volume of 0.558 cc, while the binder (0.304 g) has a volume of 0.287 cc. Thus the total weight is 2.530 g and the total volume is 0.845 cc. The apparent density of the total solids from these calculations is 2.99 g/cc. This is indistinguishable from the range of apparent-density values reported previously. Therefore,

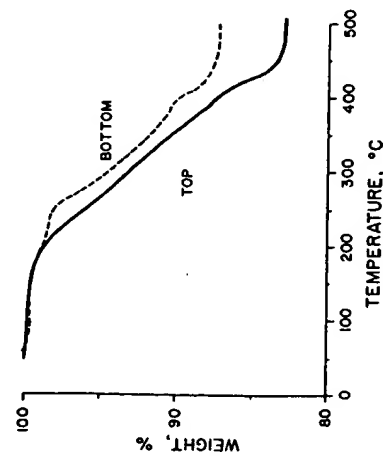


Figure 30.15. Nitrogen atmosphere TGA curves of thin slices cut from top and bottom sections of tape.

there is essentially no closed porosity, at least as measurable by these methods. These calculations are for 1 cc of tape, of which 0.845 cc is occupied by the total solids. Therefore, the open porosity is $\approx 15\%$ by these methods.

Figure 30.15 shows binder burnout TGA curves for thin sections cut from the top and bottom of the tape. The difference between the curves is related to slight warping during firing, but it is satisfactorily small. This also is an excellent characterization test to determine tape uniformity. If segregation of the solids and organics took place as a result of settling, there would be a large difference in binder content from side to side. The uniformity observed is a good measure of the degree of deflocculation, even during the drying stage. This, we believe, combined with a distribution of particle sizes leads to the excellent packing and relatively high bulk density achieved.

PUNCHING

The as-cast sheets of ceramic tape are usually cut to the desired sizes and shapes with a simple punch and die set actuated by a rotary punch press. This operation is called blanking. The pieces are punched oversize to allow for firing shrinkage.

In the case of the smooth-surfaced alumina substrate tapes, special care was taken to avoid scratching the relatively soft tape during handling and punching. Dust, punching scraps, and other foreign particles must not be pressed into the tape by the punch face or the ejector. A specially designed punch with a recessed central area that only contacted the tape at the very edges of the parts was used. In addition, careful vacuum-cleaning procedures between punching operations were instituted.

If holes are required in the finished ceramic, they can often be punched simultaneously with the blanking operation, especially if the holes are larger than 0.020 in. in diameter. For larger holes the operation is almost trivial and no serious problems are involved. But for many applications in the electronics industry, arrays of very small holes are desirable. Typical examples are alumina substrates for thin-film or thick-film microcircuits, in which electrically conductive metallization is applied to both sides, and holes must be provided for current to pass from one side to the other. The smaller the hole diameters, the more densely the components can be packed, and therefore the higher the scale of hybrid integration for designing a complex integrated circuit.

Punching is an inexpensive method for producing holes in tape-cast ceramics, because hundreds of holes can be produced in a single stroke of the punch into the die.

Alternative methods are available, such as laser drilling⁵⁶ and diamond drilling the fired ceramic. If holes are to be located within 1 mil of nominal, these are the preferred techniques. Piazza and Steele⁵⁴ have pointed out that multiple punching of unfired tapes can be utilized with reasonable yields if the tolerances on hole location are 8 mils or greater.

In determining whether punching will be less expensive for a given hole size, an important consideration is the expected life of the punch and die set. For holes of diameters greater than 0.020 in., punches made of hard materials, such as tungsten carbide, can be expected to last through several hundred thousand punch operations. A new punch and die set ordinarily costs several thousand dollars, and this method is therefore suitably inexpensive for mass production. However, when hole diameters approach 0.010 in., the punches are fragile, and laser drilling becomes cost competitive in spite of its necessarily time-consuming step-and-repeat mode of operation.

If the improved techniques of punching smaller-diameter holes reported below are used, the punching of the tape before firing can be restored as a good candidate for the less-expensive method.

Figure 30.16 shows a schematic cross section of a punch and die, in the middle of the operational sequence. As shown in the diagram, the punch has pushed a cylindrical slug of tape into the die cavity. The next step is for the punch to retract upwards, while the metal "stripper plate" keeps the tape from moving. The plate then rises also, the tape is removed (to be inspected and fired), and the next piece of tape to be punched is placed over the die.

Experiments in our laboratory, later confirmed at other facilities, have shown that 0.010 to 0.012 in. diameter punches tend to break or wear excessively during the first 20,000 operations unless the following design criteria are followed:

1. The larger-diameter shank of the punch should be 8 to 10 times the diameter of the punch itself, to provide rigidity against excessive flexing.
2. The punch tip should move down to a point below the bottom of the upper die hole (Figure 30.16) to prevent the tape slugs from remaining in the die after retraction and jamming the later operations by becoming compressively packed.
3. A partial vacuum should be applied to the larger-diameter die hole to aid in slug removal. This vacuum can conveniently be provided by a Bernoulli effect air jet in each die hole, emanating from a simple gallery of holes drilled at an angle down through the die block.
4. The punch-to-die clearance on each side is optimally about 0.0015 in. for alumina substrate tape. In other words, a punch diameter of 0.012 in. requires a die diameter of 0.015 in. Too small a clearance (0.0005 in. on

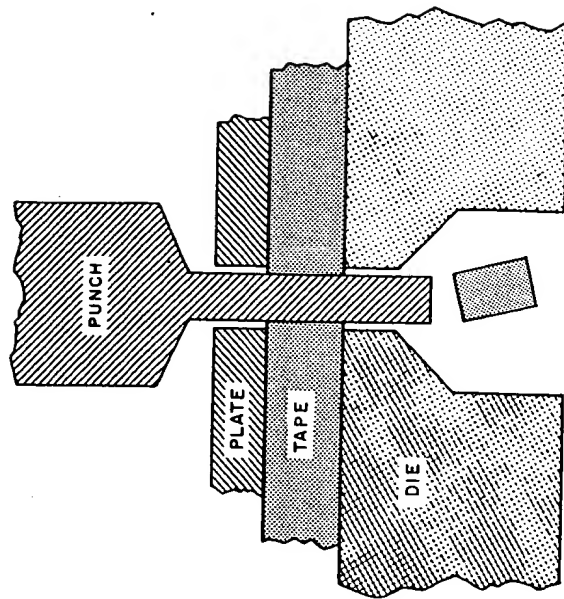


Figure 30.16. Schematic diagram of an optimized punch and die design for punching small holes in green ceramic tape.

each side) results in punch breakage, and too large a clearance (0.003 in.) results in irregular holes in the tape.

Because of irregularities in the tape, narrow punches occasionally flex sideways far enough to strike the die. Therefore, brittle punch materials, such as carbides, should be mated with relatively softer die materials, such as tool steel hardened to about Rockwell 60. After many thousands of operations with this combination of materials, dies were observed to have several "bites" taken out of them, but the tungsten carbide punches (available from Schneider and Marquard Company, Newton, New Jersey) did not break or visibly wear.

Another punch material having good wear properties for use with abrasive ceramic tape is boride-coated steel. (Borofuse, available from Materials Development Corporation, Medford, Mass.) This has the advantage of not requiring electrosark-discharge machining for punch fabrication, since boring can be done by the punch maker after some of the other fabrication procedures are completed.

It should be mentioned that ordinary tool-steel punches are not suffi-

ciently hard for large-scale production usage, and their tips become rounded after about 10,000 operations with alumina substrate tape. The holes in the tape produced by round tips are irregular and unpredictably small, especially after firing.

With the use of carefully designed punches and dies, hundreds of small holes having excellent cylindrical shapes can be punched simultaneously. No visible wear is typically observed on 0.012 in. tungsten carbide punches after 20,000 operations.

MULTILAYER STRUCTURES

A specialized technology commonly used in electronic ceramics, especially for multilayer capacitors, piezoelectric devices, transistor packages, hybrid circuit modules, and small printed circuit boards, is multilayer processing. Since the processing before sintering is an important part of this technology we cover it briefly in this section. Lamination and screened multilayer formation are two major techniques used to produce the multiple-layer structures.

Lamination

Schwartz and Wilcox³⁸ describe the lamination process as comprising the following steps: (1) tape casting thermoplastic sheets, (2) punching holes, (3) screen printing the metal electrode patterns, (4) laminating the sheets together, (5) punching the final shapes, and (6) sintering the monolithic structure.

Since we have described the processing steps before sintering with the exception of screen printing and laminating, we will concentrate on these latter aspects here. Metallization of the green ceramic sheets is accomplished by screen printing. Special vacuum chucks can be used to hold the tape in place and to provide suction for simultaneous metallization of through-holes. Close control of the metal-paste properties (viscosity and density) will aid reproducibility. The metal paste, which is screen-printed, must sinter compatibly with the ceramic material. Palladium, platinum, molybdenum, and tungsten have been used with various ceramic materials. There are numerous patents and papers³⁹⁻⁴¹ describing the different types of metallization used in multilayers.

The actual lamination process consists of applying pressure to several stacked green sheets at a suitable temperature to produce a monolithic structure. The temperatures used have ranged from room temperature to several hundred degrees Fahrenheit. Temperature and pressure depend to a

large degree on the type and amount of binder. A typical range of pressures is from 200 to 20,000 psi. Care should be taken to insure equal application of pressure over the entire surface of the part. Sufficient time must be allowed to permit the entire part to reach thermal equilibrium. Another technique described in the literature⁴² is continuous roll-to-roll lamination performed by passing two or more sheets of material between a set of nip rollers at pressures ranging from 100 to 1000 psi. This is done at room temperature at a speed of 20 ft/minute.

Screened Multilayer Structures

Recently a process has been reported⁴³ that eliminates the need for costly punching tools and allows low-cost, automatic processing of multilayered structures. It is known as the Screened Multilayer Ceramic (SMC). In the SMC process conductive layers and dielectric layers are alternately screen printed onto flexible unfired ceramic tape. For the conductive patterns, moly-manganese or tungsten are used, and a special screenable alumina paste is used for the dielectric layers when the base tape is alumina. The screened multilayer structure is cosintered at about 1600°C in a reducing atmosphere. The process avoids costs of alignment and punching, as well as the costs and time associated with tooling that are involved in lamination processes.

MULTILAYER CASTING

A multiple-layer casting technique has also been described in the recent literature.^{44,45} The technique is not used to produce ceramic packages with buried conductors. In the process described, it was used to cast three layers of material simultaneously on top of one another. The purpose was to produce a gradient of grain sizes from the surface layers to the internal layers, with the ultimate goal of producing a high-strength material. A schematic of the triple doctor blade is shown in Figure 30.17. Details of the

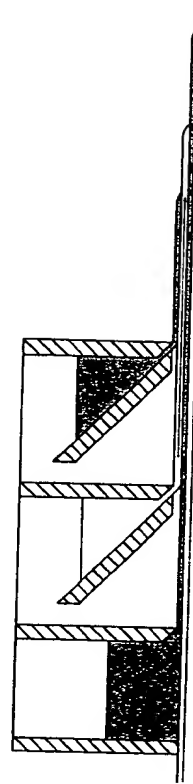


Figure 30.17. Schematic drawing of a doctor-blade arrangement for multiple-layer casting.

casting process are included in reference 44. This technique produced alumina substrates with flexural strengths of >100,000 psi.

SUMMARY

In this paper we have attempted to convey some of the many "tricks of the trade" a ceramist would use to develop a tape-casting process. Many of the examples we have used were taken from our own work in developing a process for producing high-quality fine-grained alumina substrates. Some areas have been emphasized more than others, mainly because of a lack of detailed literature in those areas. All steps before sintering were covered, however, in an attempt to create a coherent picture of the tape-casting process.

ACKNOWLEDGMENTS

Thanks are due to many Western Electric employees at the Engineering Research Center, both past and present, for aid in developing the technology described in this paper.

REFERENCES

1. G. N. Howatt, "Method of Producing High Dielectric, High Insulation Ceramic Plates," U.S. Patent 2,582,993, (Jan. 22, 1952).
2. (a) H. W. Stetson and W. J. Gyurk, "Alumina Substrates," U.S. Patent 3,698,923 (Oct. 17, 1972); (b) D. J. Shanefield and R. E. Mistler, "Manufacture of Fine-Grained Alumina Substrates for Thin Films," *West. Electr. Eng.*, 15 (2), 26-31 (1971); (c) G. N. Howatt, R. G. Breckenridge, and J. M. Brownlow, "Fabrication of Thin Ceramic Sheets for Capacitors," *J. Amer. Ceram. Soc.*, 30 (8), 237-242 (1947); (d) J. L. Park, Jr., "Manufacture of Ceramics," U.S. Patent 2,966,719 (Jan. 3, 1961); (e) J. J. Thompson, "Forming Thin Ceramics," *Amer. Ceram. Soc. Bull.*, 42 (9), 480-481 (1963); (f) D. J. Shanefield and R. E. Mistler, "Fine Grained Alumina Substrates: I, the Manufacturing Process," *Amer. Ceram. Soc. Bull.*, 53 (5), 416-420 (1974); (g) H. W. Stetson and W. J. Gyurk, "Use of Menhaden Oil of Deflocculate Dry Ground Alumina in Manufacture of Substrates," U.S. Patent 3,780,150 (Dec. 18, 1973); (h) J. F. Argyle, G. O. Medowski, D. W. Ports, and R. D. Sutch "Fine-Grain Alumina Bodies," U.S. Patent 3,819,785 (June 25, 1974).
3. J. E. Davis, V. G. Carithers, and D. R. Watson, "Practical Use of Particle Size Distribution to Predict Compacting and Sintering Properties of Calcined Aluminas," *Amer. Ceram. Soc. Bull.*, 50 (11), 906-912 (1971).
4. H. Burrell, "Solubility Parameters," *Interchem. Rev.*, 14 (1), 3-16 (1955).

References

5. F. A. Norris, *Encyclopedia of Chemical Technology*, Vol. 8, R. E. Kirk and D. F. Othmer, eds., Interscience, New York, 1965, pp. 776-793.
6. G. D. Parfitt, *Dispersion of Powders in Liquids*, American Elsevier, New York, 1969, pp. 82, 116, 160-169, 296.
7. Terminology used as defined in ASTM D 1356 and E20, Part 33, American Society for Testing and Materials, Philadelphia, 1970, p. 10.
8. D. W., Jr. Johnson, D. J. Nitti, and L. Berrin, "High Purity Reactive Alumina Powders: II, Particle Size and Agglomeration Study," *Amer. Ceram. Soc. Bull.* 51 (12), 896-900 (1972).
9. J. J. Burke, ed., *Ultrafine-Grain Ceramics*, Syracuse University Press, Syracuse, 1970, p. 146.
10. G. D. Parfitt, *Dispersion of Powders in Liquids*, American Elsevier, New York, 1969, p. 315.
11. V. T. Crowl and M. A. Malati, "Adsorption of Polymers and the Stability of Pigment Dispersions," *Discuss. Faraday Soc.*, 42, pp. 301-312 (1966).
12. D. H. Napper and A. Netschey, "Steric Stabilization of Colloidal Particles," *J. Colloid Interface Sci.*, 37 (3), 528-535 (1971).
13. F. J. Micala, Y. K. Lui, and A. C. Zettlemoyer, "Mechanism of Deaggregation and Stability of Rutile Dispersion in Organic Liquids," *Discuss. Faraday Soc.*, 42, pp. 238-247 (1966).
14. H. Koelmans and J. T. G. Overbeck, "Stability and Electrophoretic Deposition of Suspension in Nonaqueous Media," *Discuss. Faraday Soc.*, 18, pp. 52-63 (1954).
15. A. E. Lewis, "Polar-Screen Theory for the Deflocculation of Suspensions," *J. Amer. Ceram. Soc.*, 44 (5), 233-239 (1961).
16. A. F. Sherwood and S. M. Rybicka, "Surface Properties of Titanium Dioxide Pigments," *J. Oil Colour Chem. Assoc.*, 49 (8), 648-649 (1966).
17. L. A. Romo, "Effect of C₆, C₈, and C₁₀ Alcohols and Water on the Stability of Dispersions with Alumina and Aluminum Hydroxide," *Discuss. Faraday Soc.*, 42, pp. 238-247 (1966).
18. S. G. Dick, D. W. Fuerstenau, and T. W. Healy, "Adsorption of Alkylbenzene Sulfonate Surfactants at the Alumina-Water Interface," *J. Colloid Interface Sci.*, 37 (3), 595-602 (1971).
19. T. Allen and R. M. Patel, "Adsorption of Long-Chain Fatty Acids on Finely Divided Solids Using a Flow Microcalorimeter," *J. Colloid Interface Sci.*, 35 (4), 647-655 (1971).
20. R. R. Stromberg, A. R. Quasius, S. D. Toner, and M. S. Parker, "Adsorption of Polyesters on Glass, Silica, and Alumina," *J. Res. Natl. Bur. Stand.*, 62 (2), 71-77 (1959).
21. Zeta-Meter, Inc., New York, unpublished work.
22. D. J. O'Connor, P. G. Johansen, and A. S. Buchanan, Electrokinetic Properties and Surface Reactions of Corundum," *Trans. Faraday Soc.*, 52 (5), 229-236 (1956).
23. "Butvar," Technical Bulletin 6070, Monsanto Company, St. Louis, Missouri, p. 6.
24. A. F. Greaves-Walker, *Drying Ceramic Products*, Industrial Publications, Chicago, 1968, p. 19.
25. T. K. Sherwood, "The Drying of Solids—I," *Ind. Eng. Chem.*, 21 (1), 12-16 (1929).
26. L. Slifkin, *Encyclopedia of Physics*, R. M. Besancon, ed., Reinhold, New York, 1966, p. 171.

27. R. B. Runk and M. J. Andrejco, "A Precision Tape Casting Machine for Fabricating Thin, Organically Suspended Ceramic Tapes," *Amer. Ceram. Soc. Bull.*, **54** (2) 199-200 (1975).
28. Terminology used as defined in ASTM E 12-70. American Society for Testing and Materials, Philadelphia, 1970.
29. "Bulk Density, Apparent Porosity, and Apparent Specific Gravity of Fired Porous Whiteware Products," ASTM C373-56, Vol. 13, 1970, p. 326.
30. W. D. Kingery, *Introduction to Ceramics*, Wiley New York, 1960, p. 40.
31. J. B. Jr. Wachtman, National Bureau of Standards, private communication.
32. Alcoa Reactive Aluminas," Aluminum Company of America, Pittsburgh, Pennsylvania, 1967, p. 3.
33. J. Longfellow, "High Speed Drilling in Alumina Substrates with a CO₂ Laser," *Amer. Ceram. Soc. Bull.*, **50** (3), 251-253 (1971).
34. J. R. Piazza and T. G. Steele, "Positional Deviations of Preformed Holes in Substrates," *Amer. Ceram. Soc. Bull.*, **51** (6), 516-518 (1972).
35. B. Schwartz and D. L. Wilcox, "Laminated Ceramics," *Ceram. Age*, **83** (6), 40-44 (1967).
36. H. W. Stetson, "Method of Making Multilayer Circuits," U.S. Patent 3,189,978 (June 22, 1965).
37. B. M. Hargis, "Ceramic Metallic Composite Substrate," U.S. Patent 3,549,784 (Dec. 22, 1970).
38. M. Bennett, W. E. Boyd, and J. E. Nobile, "Fabrication of Multilevel Ceramic, Microelectronic Structures," U.S. Patent 3,518-756 (July 7, 1970).
39. G. N. Howatt, "Method of Eliminating Voids in Ceramic Bodies," U.S. Patent 3,635,759 (Jan. 18, 1972).
40. R. A. Gardner and R. W. Nufer, "Properties of Multilayer Ceramic Green Sheets," *Solid State Technol.*, **17** (5), 38-43 (1974).
41. D. L. Wilcox, "Ceramics for Packaging," *Solid State Technol.*, **14** (2), 55-60 (1971).
42. J. Ettore, and G. R. Castels, "Pressure-Fusible Tapes for Multilayer Structures," *Amer. Ceram. Soc. Bull.*, **51** (5), 482-485 (1972).
43. T. Ihochi, K. Otsuke, and H. Maejima, "Screened Multilayer Ceramics and the Automatic Fabrication Technology," *Proc. Semiconductor/IC Processing Prod. Conf. New York*, 1972, p. 71.
44. R. E. Mistler, "High Strength Alumina Substrates Produced by a Multiple-Layer Casting Technique," *Amer. Ceram. Soc. Bull.*, **52** (11), 850-854 (1973).
45. R. E. Mistler, "Strengthening Alumina Substrates by Incorporating Grain Growth Inhibitor in Surface and Promoter in Interior," U.S. Patent 3,652,378 (March 28, 1972).
46. "Marine Oils" (booklet), Haynie Products, Inc., Baltimore, Maryland.

31

Zinc Orthotitanate Powders for Thermal-Control Coatings

Y. Harada
D. W. Gates

The objective of the present study was to develop a process for producing a pigment (finely divided powder) for use in spacecraft thermal-control coatings. The desired pigment was Zn₂TiO₄, a binary oxide that normally requires temperatures of 900°C or greater for its formation from ZnO and TiO₂. Thus the studies were directed toward maintenance of the powder in a discrete particle state under the relatively rigorous temperature regimes that would ordinarily encourage sintering of particles (conglomeration). Although a sintered material can be comminuted to a pigment particle size by grinding, the potential introduction of contaminants in such a process makes its elimination desirable.

A process was developed in which Zn₂TiO₄ powder of pigment size, that is, submicron to 5 μ particles, could be obtained at temperatures up to 1200°C. This was accomplished by increasing the ZnO and TiO₂ reaction rate at lower temperatures through the use of intimately mixed, finely

divided oxalate precursors obtained by a mixed precipitation. Final heat treatment for complete reaction was conducted a very rapidly so as to minimize particle sintering.

TECHNICAL BACKGROUND

The temperature control of satellites and spacecraft is one of the most challenging technical problems confronting spacecraft designers and materials engineers. The ultimate objective of thermal design is to ensure that the spacecraft operates within a prescribed temperature range defined by the temperature limitations of the vehicle's materials and components.

One of the primary passive methods used to achieve thermal control has been the use of coatings with high reflectance or low solar absorptance (α_s) that are resistant to discoloration in a vacuum-ultraviolet environment. The inorganic pigment that has been found to exhibit high reflectance and stability is ZnO .¹ Two coatings that have been used extensively on various spacecrafts are Z-93 and S-13G. Both incorporate ZnO as a pigment, the former using potassium silicate as a binder and the latter using a methyl silicone.¹

However, ZnO is a strong absorber in the ultraviolet region, limiting its ability to reflect solar energy. Therefore, more recent work² has been involved with the development of another pigment, zinc orthotitanate (Zn_2TiO_4), which exhibits higher reflectance than ZnO in the near ultraviolet as shown in Figure 31.1.

Synthesis of Zn_2TiO_4 at elevated temperatures by a solid-solid reaction has been reported by several investigators. Bartram and Slepety's³ described its preparation from anatase titania and zinc oxide by reaction at 800 to 1000°C for 3 hours. Reaction times of 48 hours at 800°C to obtain Zn_2TiO_4 from a zinc oxide-titanic acid reaction has been reported.⁴ A phase diagram (Figure 31.2) for the ZnO-TiO_2 system proposed by Dulin and Rase⁵ shows the existence of a 1Zn to 1Ti compound, ZnTiO_3 , as well as the orthotitanate. Both investigations showed the presence of secondary phases, such as ZnTiO_3 , ZnO , and/or TiO_2 , in their Zn_2TiO_4 products, indicating the need for accurate stoichiometry control to obtain a pure product. The presence of secondary phases has been found to be deleterious to the optical stability of Zn_2TiO_4 .

The use of decomposable salt precursors to enhance reaction or sinterability of oxides has been reported by several investigators.⁶⁻⁷ An example of this enhancement is that of a high-purity BaTiO_3 produced from coprecipitated $\text{BaTiO}(\text{C}_2\text{O}_4)_x \cdot 4\text{H}_2\text{O}$.⁸

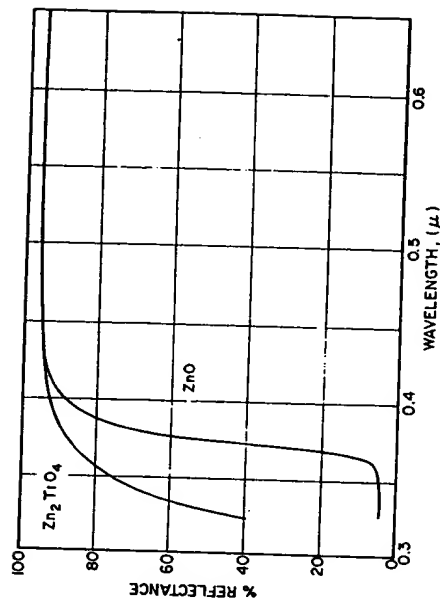


Figure 31.1. Spectra of ZnO and Zn_2TiO_4 .

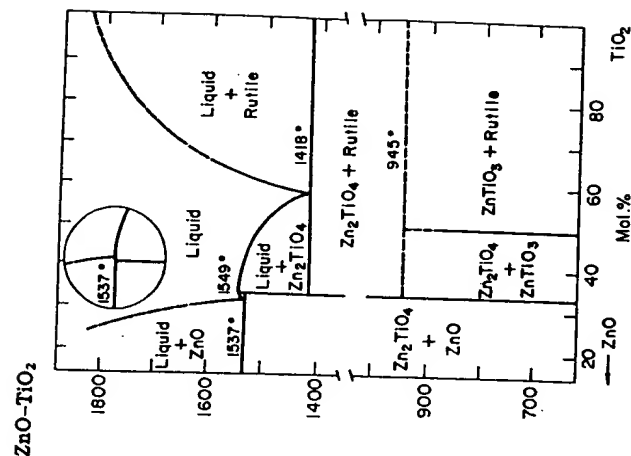


Figure 31.2. ZnO-TiO_2 system From Dulin and Rase.⁵

The present study was thus directed toward processing of the zinc- and titanium-source precursors so that rapid conversion to Zn_2TiO_4 under modest time/temperature requirements could be achieved. At the same time it was necessary to modify ultimate firing conditions to minimize sintering effects that are encouraged by such powder processing prior to firing. This paper describes the studies that were conducted in the areas of precipitation, decomposition, and firing, leading to the desired pigment material.

EXPERIMENTAL PROCEDURE

The zinc and titanium sources were reagent grade ZnCl_2 and purified TiCl_4 , and the oxalic acid was reagent grade. Zinc chloride and oxalic acid solutions were prepared by conventional dissolution of the crystals in distilled water at 40°C . The TiCl_4 solution was prepared by dropwise addition of the TiCl_4 into distilled water, which was cooled in an ice bath to prevent formation of hydrolyzed titanium.

Precipitation of mixed oxalates was conducted by addition of a mixed-chloride solution (having a 2.05:1.00 Zn/Ti ratio) to oxalic acid at 40°C . This was followed by heating of the system with stirring to 90°C , where it was held from 1 to 4 hours, depending on the batch size.

Filtration was performed in a buchner-funnel system under slight vacuum. The precipitate was washed thoroughly with hot water until there was no evidence of acid in the filtrate.

Calcination and firing were performed in standard atmospheric Global furnaces. Powders were contained in fused silica boats for firings up to 1300°C and in platinum crucibles at 1400°C .

RESULTS AND DISCUSSION

The solid-state process used to synthesize Zn_2TiO_4 in earlier work² is shown in Figure 31.3. The disadvantages of this oxide-oxide reaction are: (1) extensive grinding of the individual oxides and of the mixture prior to firing is necessary, (2) an extended period of 18 hours is required for complete reaction to form Zn_2TiO_4 , and (3) additional grinding is needed to obtain a particle size of about 1 to $5\ \mu$. The various comminution steps in this process present the danger of contamination from the milling media; the resulting impurities are a source of reflectance degradation and also can lower the stability to an ultraviolet-vacuum environment.

The precipitation process (Figure 31.4) was developed to minimize or eliminate such grinding and to decrease the processing times, both of which

Results and Discussion

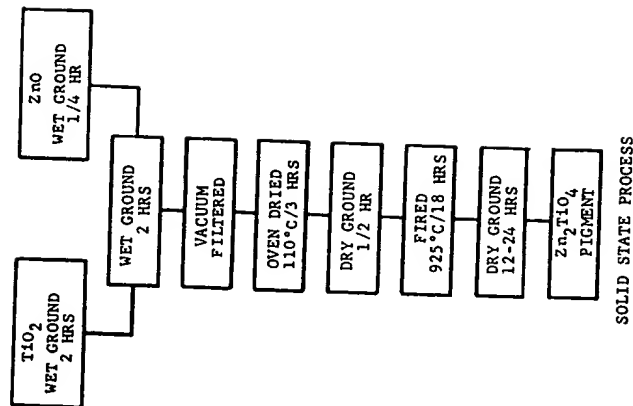


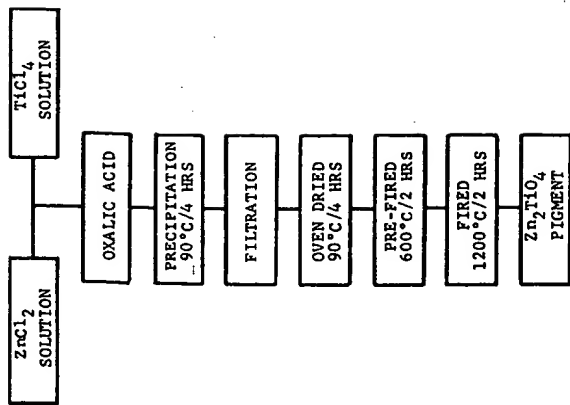
Figure 31.3. Solid-state process for forming Zn_2TiO_4 .

would be desirable for larger-scale pigment production. The studies leading to the process shown in Figure 31.4 are discussed in the following sections.

Precipitation Studies

Complete precipitation of the mixed zinc and titanium oxalates in the aqueous medium was found to require a 2 hour hold at 90°C under continued stirring. X-Ray powder pattern examination showed the precipitate to be a mixture of $\text{ZnC}_2\text{O}_4 \cdot 2\text{H}_2\text{O}$ and a second phase whose lines suggest orthorhombic crystallinity. The pattern for this titanium phase could not be found in the literature. This material, which is termed titanium oxalate in this paper, is presently being characterized.

Scanning electron microscope (SEM) photographs of the individual oxalates and the mixed precipitate are shown in Figures 31.5 through 31.7. The difference in particle size between $\text{ZnC}_2\text{O}_4 \cdot 2\text{H}_2\text{O}$ (2 to $10\ \mu$) and the titanium phase precipitate (submicron to $5\ \mu$) lead to a heterogeneous mixture in the mixed precipitate (Figure 31.7). Examination of different batches has shown uniform distribution of the two phases in each precipitation.



PRECIPITATION PROCESS

Figure 31.4. Precipitation process for forming Zn_2TiO_4 .



ZINC OXALATE

Figure 31.5. SEM microstructural view of zinc oxalate.



TITANIUM OXALATE

Figure 31.6. SEM microstructural view of titanium oxalate.



COPRECIPITATED ZINC-TITANIUM OXALATE (LH-52)

Figure 31.7. SEM microstructural view of mixed oxalates.

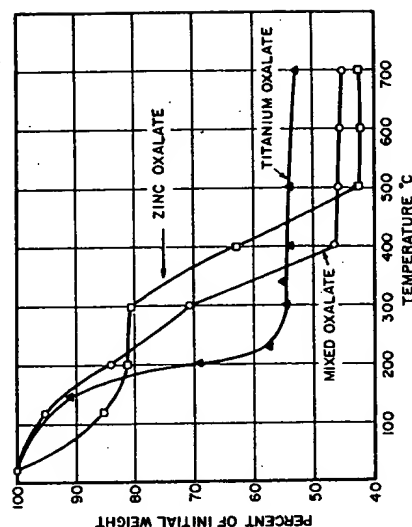
Decomposition Studies

Materials examined include the individual oxalates and the mixed precipitates. Samples were heated at temperatures from 120 to 700°C for 2 hours each, using direct insertion and removal from the furnace at temperature to minimize the effects of heat up and cool down.

The results of a gravimetric analysis (Figure 31.8) show that the titanium oxalate phase decomposes at a lower temperature than does the zinc oxalate. The weight-loss curve for the mixture lies between the curves for the individual components, reflecting the different rates of decomposition.

The appearance of the powders after heat treatment and the results of X-ray analysis using powder patterns are presented in Table 31.1. After the 400 and 500°C calcinations, the zinc oxalate material was gray and lumpy. The weight loss data show that this is the range where rapid decomposition occurs. D'Eyre and Sellman⁹ in their work with thorium oxalate attribute this coloring to the presence of carbon from the dissociation of carbon monoxide.

The titanium oxalate materials showed a lesser departure from white and were all free flowing. The mixed oxalate samples calcined at the various temperatures were also quite fine in particle size and did not display the aggregation shown by zinc oxalate samples. Samples calcined at 600 and



WEIGHT LOSS VS TEMPERATURE FOR ZINC OXALATE, TITANIUM OXALATE AND MIXED OXALATES

Figure 31.8. Weight loss versus temperature for zinc oxalate, titanium oxalate, and mixed oxalates.

Table 31.1. Appearance and phases present for zinc oxalate, titanium oxalate, and mixed oxalates as a function of temperature

Phases Present ^a	Appearance ^a			Phases Present ^a
	Zinc Oxalate	Titanium Oxalate	Coprecipitate Oxalates	
Temperature (°C)				
120	White	Light yellow	White	TiOX
200	White	Light yellow	Light yellow	TiOX + TiOx + X
300	White	Light yellow	Light yellow	TiOx
400	Gray, lumpy	Light yellow	Yellow	TiOx
500	Light gray, lumpy	Light yellow	Yellow	TiOx
600	Tan	White	White	ZnO + TiOx
700	Yellow	White	White	ZnO + TiOx + ZnO

Note: All samples calcined for 2 hours.

^a All powders free flowing unless otherwise indicated.

^a ZnOx, zinc oxalate; TiOx, titanium oxalate; X, apparently an intermediate phase in the decomposition of zinc oxalate.

700°C were white, although the lower-temperature samples showed some coloring.

X-Ray analysis of the various products revealed complete pyrolysis for Zn_2TiO_4 at 500°C, for titanium oxalate at 300°C, and for the mixed oxalates at 500°C. Formation of Zn_2TiO_4 was apparently initiated at 600°C. The existence of free ZnO but no TiO_2 in the X-ray pattern may be due to an extremely fine state of subdivision for the latter.

A SEM photograph of the 600°C material produced from mixed oxalates appears in Figure 31.9. A large range in particle size is evident for this partially reacted material, and the sharp edges of particle surfaces reflect the morphology of the as-precipitated material.

Heat-Treatment Studies

Complete conversion to Zn_2TiO_4 was conducted at temperatures from 900 to 1400°C. Firing times of 2 hours were used up to 1300°C; the 1400°C soak time was 5 minutes. To retain the material in unsintered form, samples were fired as loose powders using what may be termed "flash calcination." This involved direct insertion of the powder in a fused silica container into a furnace at the prescribed firing temperature. Approximately 15 minutes was needed for large batches (1000 g) to attain temperature. Samples were removed in a similar abrupt manner after the prescribed firing time.

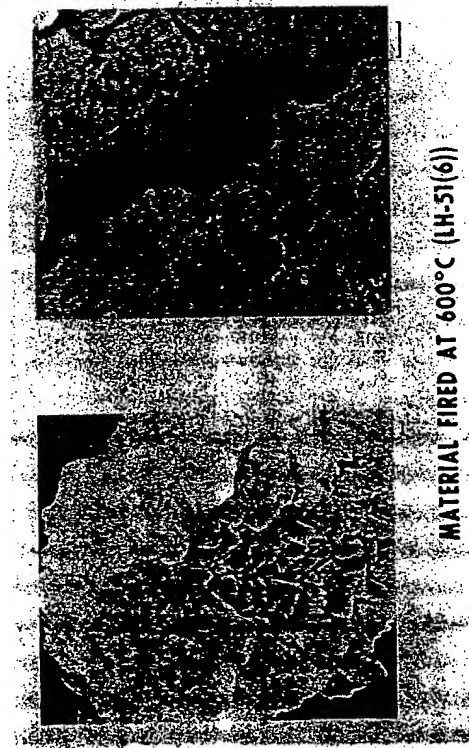


Figure 31.9. SEM microstructural view of mixed oxalates calcined at 600°C/2 hours.

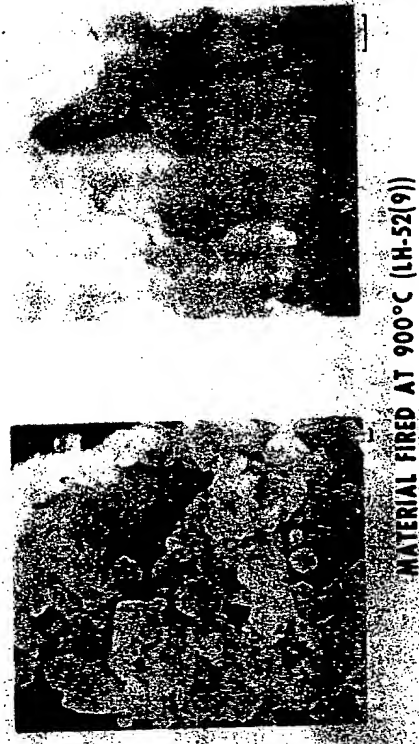


Figure 31.10. SEM microstructural view of mixed oxalates calcined at 900°C/2 hours.

All materials were precalcined at 600°C for 2 hours prior to the high-temperature (>900°C) treatments to eliminate the volatiles formed during decomposition. Flash calcination of the mixed precipitates without this pretreatment resulted in excessive blowing and loss of powder.

X-Ray evaluations revealed an essentially pure Zn_2TiO_4 after 2 hour firings at various temperatures from 900 to 1400°C. As designed for this study by the use of a 2.05 Zn to 1.00 Ti ratio, a slight excess of ZnO was also detected. Acetic acid leaching to form zinc acetate resulted in removal of the free ZnO. Gravimetric analysis showed the amounts to be from 2 to 4 wt % for various batches.

SEM studies showed that the 900°C material had a particle size range from submicron to about 2 μ (Figure 31.10). The particles exhibited rounded surfaces unlike the as-precipitated or 600°C materials. Material heated at 1200°C (Figure 31.11) showed an increase in size, exhibiting a range from about 2 to 5 μ , with no evidence of submicron particles. Sintering of particles was apparent from the necking behavior shown for the 1200°C material. Material heat treated at 1300°C/2 hours and 1400°C/5 minutes exhibited a similar morphology.

The final product at all heat-treatment conditions was a material that, although caked, could be reduced to a powder by manual crushing. Most importantly, the physical state of the Zn_2TiO_4 powder was amenable to direct incorporation into a silicone vehicle for use as a paint.

Thus the use of mixed-oxalate precursors to enhance the ZnO-TiO_2 reac-



MATERIAL FIRED AT 1200°C (LH-53(6-12))

Figure 31.11. SEM microstructural view of mixed oxalates calcined at 1200°C/2 hours.

tion at lower temperatures, coupled with a rapid-heat-treatment technique, flash calcination, provides a more rapid method for obtaining a Zn_2TiO_4 powder suitable for use as a pigment. Elimination of grinding of the powder, necessary in the solid-solid state process, yields a purer product less susceptible to color degradation in a space environment.

ACKNOWLEDGMENT

This work has been sponsored by the George C. Marshall Space Flight Center, National Aeronautics and Space Administration, under Contract No. NAS8-26791. The authors wish to express their appreciation to W. R. Logan for conducting the experimental studies and to J. E. Gilligan for his valuable contributions.

REFERENCES

1. G. A. Zerlaut, Y. Harada, and E. H. Tompkins, "Ultraviolet Irradiation in Vacuum of White Spacecraft Coatings," *Symposium on Thermal Radiation of Solids*, S. Katzoff, ed., NASA SP-35, Washington, D.C., 1965.
2. G. A. Zerlaut, J. E. Gilligan, and N. A. Ashford, "Space Radiation Environmental Effects in Reactively Encapsulated Zinc Orthotitanates and Their Paints," AIAA 6th Thermophysics Conference, April 1971, Paper No. 71-449.

References

3. S. R. Bartram and R. A. Slepety, "Compound Formation and Crystal Structure in the System $ZnO-TiO_2$," *J. Amer. Ceram. Soc.*, **44** (10), 493-499 (1961).
4. S. R. Dulin and D. E. Rase, "Phase Equilibria in the System $ZnO-TiO_2$," *J. Amer. Ceram. Soc.*, **43** (3), 125-131 (1960).
5. D. T. Livey, B. M. Wanklyn, M. Hewitt, and P. Murray, Properties of MgO Powders Prepared by Decomposition of $Mg(OH)_2$, " *Trans. Br. Ceram. Soc.*, **56**, (5), 217-236 (1957).
6. Y. Harada, Y. Baskin, and J. H. Handwerk, "Calcination and Sintering Study of Thoria," *J. Amer. Ceram. Soc.*, **45**, (6), 253-257 (1962).
7. R. E. Jaeger and T. J. Miller, "Preparation of Ceramic Powders by Liquid Drying," *Amer. Ceram. Soc. Bull.*, **53** (12) 855-859 (1974).
8. W. S. Clabaugh, E. M. Swiggard, and R. Gilchrist, "Preparation of Barium Titanate Oxalate Tetrahydrate for Conversion to Barium Titanate of High Purity," *J. Res. Natl. Bur. Stand.*, **56** (5), 289-291 (1956).
9. R. W. M. D'Eye, and P. G. Sellman, "The Thermal Decomposition of Thorium Oxalate," *J. Inorg. Nucl. Chem.*, **1** (1/2), 143-148 (1955).

32

Characterization of Powders for Thick Films and Capacitors

K. K. Verma
A. Roberts

In thick-film applications, powders are utilized to prepare resistor and conductor pastes. These pastes or inks are screen printed on substrates. Resistors include printed patterns of resistive paste systems using metals, metal oxides, and glass-frit mixtures. Conductors are printed patterns of conductive-paste systems consisting of metals, metal mixtures and alloys, and glass-powder mixtures. Some special applications, such as dielectric crossover and encapsulating layers, quite often are used on thick-film printed patterns but are covered in this chapter.

The capacitor industry uses powders for preparing a dielectric body and conducting electrodes. The latter includes internal electrodes between dielectric layers in multilayer capacitors, external or exposed electrodes for "single-plate" capacitors, and end termination of multilayer capacitors.

Pastes for use in thick-film and capacitor applications are prepared by grinding, blending, and dispersing powders in a liquid-vehicle system. Powder characterization is an important part of achieving the desired paste

rheology, firing behavior, and final properties. This chapter discusses the rheology of pastes, the effects of particle characteristics on rheology, and how these factors affect performance.

PERFORMANCE CHARACTERISTICS

For a given choice of materials and process parameters (such as drying and firing), the final performance of a capacitor or thick-film component depends on a proper choice of physical characteristics of the powders and on the powder-preparation method used in the manufacture of dielectric bodies and electrode and resistor inks. The parameters on which performance testing is based are given below.

For capacitors the parameters include: (1) micro- and macrostructure of the dielectric body, (2) leaching and dewetting of electrode metallization during soldering, (3) bond strength and solderability, (4) screenability and area coverage of the paste system, (5) capacitance and dielectric constant, (6) dissipation factor, (7) insulation resistance, (8) temperature coefficient of capacitance, and (9) shorts and voltage failure.

For thick films the parameters include: (1) macrostructure of the film, (2) leaching and dewetting, (3) adhesion with the substrate and bondability, (4) screenability and area coverage, (5) resistivity, (6) noise, (7) electrostatic discharge, and (8) temperature coefficient of resistance.

PASTE SYSTEMS

The screenability of thick-film pastes depends on the rheology of the system, which in turn depends on the nature of the powders, vehicle system, surface active agents, and other modifiers present in the paste. The particle-size distribution of the powders plays a considerable role in controlling rheology and, therefore, viscosity of the paste.

Figure 32.1 shows the commonly found flow behavior of paste systems. A theoretically ideal paste would show a Newtonian behavior, in which case the flow response (shear rate) of the paste is linear with applied stress. This type of behavior may only be expected from low-viscosity liquid systems, and common thick-film pastes very seldom act this way. They do not usually respond to the applied stress linearly. This nonlinear or non-Newtonian behavior is represented by curves 3 through 5 in Figure 32.1. Good screenable pastes fall into this category and may be classified as plastic or pseudoplastic systems. They usually have high viscosity, considerable interaction among organic vehicle systems and/or dispersed

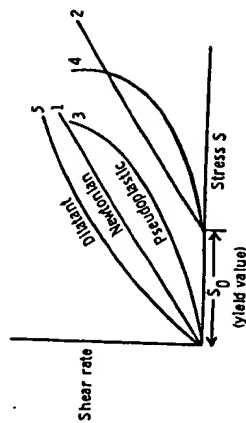


Figure 32.1. Typical flow curves. From Miller.¹

powders in the paste, and some gel structure. Another common form of screenable pastes showing non-Newtonian behavior exhibits a phenomenon known as thixotropy. This behavior, represented in Figure 32.2, shows characteristic hysteresis believed to be due to the breaking up of the secondary bonds that form a gel structure, with increasing stress. The gel structure, however, can reform if the material is allowed to stand. This characteristic of the paste system can be utilized to an advantage in screenable pastes, since such behavior can, to an extent, eliminate secondary flow of screened pastes.

EFFECTS OF PARTICLE SIZE, SHAPE, AND DISPERSION ON A PASTE SYSTEM

Increasing the percent solids in a paste system normally increases its viscosity. This relationship, however, is affected by a tendency of the fine particles to form flocs rather than an increased amount of dispersed solids in the paste. Particle shape and size asymmetry will promote non-Newtonian behavior in the pastes. For example, at reasonably high concentrations, nonspherical particles are far more effective than spherical particles in producing non-Newtonian behavior. Such paste systems would generally show high yield values.

Powder particles that tend to flocculate at even low concentration destroy Newtonian behavior of suspensions. The strong surface forces of fine parti-

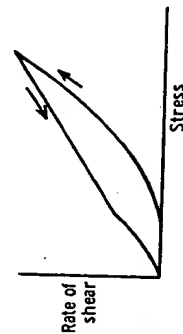


Figure 32.2. Thixotropic hysteresis. From Miller.¹

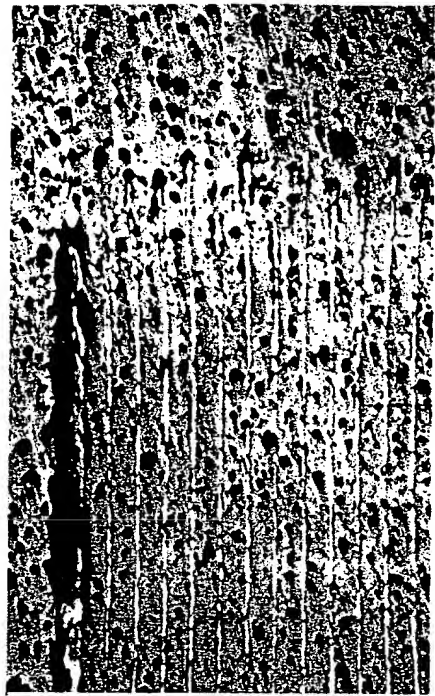
cles bring the particles together, causing the paste system to gel. The smaller the particles, the larger the surface area and, therefore, the stronger the surface forces. In a paste system proper wetting of the particles by the vehicle is necessary for good flow characteristics. Highly surface active powder particles also require more vehicle to cover the surface, thus reducing the effective amount of vehicle available for flow; consequently, such systems exhibit plastic behavior and high viscosity.

A real screening paste system rarely consists of only one type of powder and vehicle. A practical system may consist of the following: (1) a mixture of powders, (2) more than one type of solvent and/or vehicle, (3) modifiers such as gelation materials, (4) surface-active agents, and (5) ingredients to control sensitivity of a paste to environment, temperature, drying, and firing.

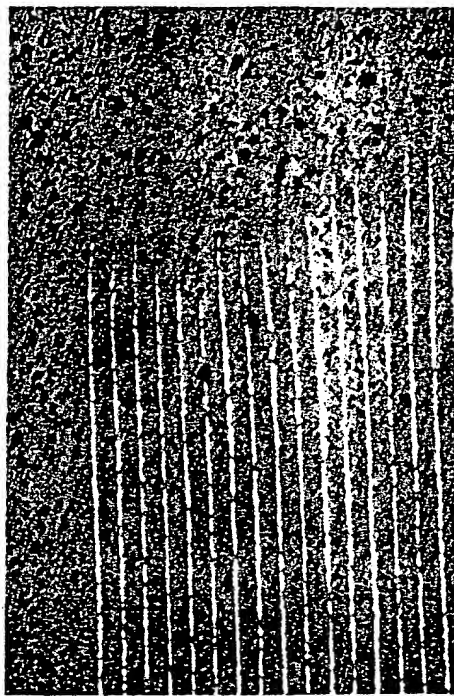
EFFECTS OF POWDER PREPARATION AND POWDER CHARACTERISTICS ON PERFORMANCE

Experience has shown that in many instances more than one performance characteristic of a capacitor or thick-film component can be affected simultaneously by a choice of powder characteristic, such as a certain particle-size distribution or shape, and a processing parameter, such as longer time for mixing and dispersing of powder particles. An example is the poor and good macrostructures of two multilayer capacitor chips shown in Figure 32.3. A poor structure is represented by the discontinuity of the electrodes, and the voids and cracks in the dielectric body. These voids and discontinuities have been caused mainly by poor dispersion of organic binder in the dielectric body, which burns off during firing and leaves the poor structure. The essentially void-free structure obtained in the lower part of the figure by homogenizing dispersion of the binder system in a colloid mill simultaneously improved the capacitance, dissipation factor, insulation resistance, and temperature and voltage response of the capacitor chip.

Final quality and performance of a capacitor depends on both macro- and microstructure. Microstructure refers to the size and structure of grains in the dielectric body. A grain size of $\sim 1 \mu$ is considered optimum for the most favorable combination of capacitance, loss, and dissipation factor. A homogeneous mixture and controlled particle-size distribution are necessary to achieve the above requirements. With an excessive amount of fines, a homogeneous and better sintered body may be obtained, but extra fines may cause increased sintering and excessive grain growth. However, this can be restricted by small additions of grain-growth inhibitors. Again, increased amounts of blending and mixing are required for its homogeneous disper-



"Poor Physical Structure"



"Good Physical Structure"

Figure 32.3. Multilayer capacitor quality. From Capozzi.*

sion. It may be necessary to adjust firing time to permit and compensate for optimization of powder characteristics.

Capacitors

Microstructure of the dielectric body and macrostructure of the capacitor have already been covered above. In the rest of this section the electrode inks for capacitors are discussed separately as internal and external or end-termination electrodes.

Internal electrodes consist of metallization between the dielectric layers in multilayer capacitors. These normally do not use any glass frit and may normally be fired at high temperatures simultaneously with the dielectric body. In this case the area covered by printed electrode paste on a dielectric tape is of major importance.

Fine particle size and adequate mixing and dispersion of powders increase the possibility of uniformly sintered, continuous metallization, especially when mixtures of metal powders are used. Particle shape also influences processing and performance. A uniform, homogenous, and continuous layer of internal electrode provides a capacitor with high capacitance, low dissipation factor, fewer shorts, and fewer voltage failures.

In the case of external electrodes or end terminations, glass frit is normally used with a mixture of metals or alloys; these systems are fired at lower temperature. A densely sintered electrode is desired to resist leaching and dewetting in the solder melt.

Blisters, cracks, and voids on the surface can be minimized by increased mixing, proper choice of vehicle, and higher degree of powder dispersion in the paste system. If excessive fusion and flow of glass frit at the firing temperature can be avoided, finer glass-frit size gives a denser electrode layer with improved adhesion, as well as improved temperature and voltage response of capacitance.

Thick Films

A significant part of this area has been covered under the heading of paste systems, in reference to the screenability and rheology of pastes.

In thick films where the resistor systems have glass frit as an important ingredient, the conductor systems may use very little or may even be fritless. For example, two developments in recent years are fritless gold and fritless platinum/silver conductor systems.

For quality testing of thick-film components, the performance characteristics listed above, such as macrostructure, leaching and dewetting, adhesion with the substrate, bondability, screenability, and area

coverage, are common to both resistor and conductor systems. Therefore, their response to powder preparation and characterization will be similar.

Increased grinding and mixing to obtain better dispersion of solids in the paste system seem to improve macrostructure defects, such as pinholes and cavities on the surface of the film. Leaching and dewetting improve because of better sintering of the film and adhesion with the substrate. Electrical performance is also generally dependent on milling time.

For a given size range denser particles show better leaching and dewetting resistance, though they do not necessarily improve adhesion and bondability at the same time. It would appear, however, that adhesion and bondability should be improved by a suitable choice of glass frit or low-melting metal or alloy mixture, and that leaching and dewetting may be improved by a proper choice of metal, alloy, or oxide mixtures. For example, it may be expected that in a Pd/Ag system, leaching of Ag into a solder bath is reduced when the allow of Pd and Ag is formed.

REFERENCES

1. L. F. Miller, "Screenability and Rheology," *Solid State Technol.* 17, 54-60 (Oct. 1974).
2. V. F. Capozzi, "Multilayer Ceramic Capacitor Materials and Manufacture," EMD, Sel-Rex Co., Santa Ana, Ca., 92705.

33

Future Directions in Processing Research

OPENING REMARKS BY PANEL LEADER—J. A. PASK

This timely conference reflects progress during the last 10 to 15 years on the science of ceramic processing. While we are far from providing all the answers, this conference has taken a long step in that direction.

Microstructure is a key toward understanding processing. Around 20 years ago we started talking about how it was necessary to characterize materials, characterize processes, and correlate character features with features of microstructure. To do that, the microstructure must be observed. The availability of exotic tools and microscopes makes the job possible. We have seen important applications of the scanning electron microscope and the transmission electron microscope, and see that the petrographic microscope is now being used again because features can be seen with this microscope that cannot be seen with the others. The major point is that we can now observe microstructure in great detail. Features can be seen on a microscale rather than only a macroscale. But we still have to quantify much more than we have been able to do so far.

This chapter summarizes the presentations given by panel members at the conference. The subject of the panel was processing research needs. The speakers represented different branches of industry, including traditional ceramics, technical ceramics, refractories, and materials for energy, and an

academic perspective. Also, comments given earlier in the conference by A. G. Pincus on particle characterization have been added in this chapter.

POWDER CHARACTERIZATION—A. G. PINCUS

Why characterize particulates? One reason is that characterization is needed at the transfer point between powder supplier and the plant because the vendor and buyer have to be able to talk to each other. They have to agree on a set of specifications if they are to do business with each other. Also, the characterization of particulates has even more significance because, unless you can properly characterize a particulate, you will not have the subsequent forming and firing steps under control. The character of the particulate is going to affect the processing and certainly affect the product all the way through until it is shipped out of the factory, and maybe even in service. We think maybe some of this character of the particulates is wiped out in firing, but it has a way of hanging on until it shows itself.

Several years ago we talked of it being completely wiped out if you make your crystalline ceramics by way of melting or vapor-deposition routes. This wipes out any surface-history effects and you are no longer dependent upon fabrication of particulates. I even predicted one time that forming as a glass and then crystallizing to make a ceramic is so far superior to powder processing that it is going to displace powder processing entirely. We've seen now that after more than 15 years of glass-ceramics being around, it hasn't happened. The attendance at this conference is an example of the fact that powder processing is very much alive. We will be staying with powder processing and we have to learn how to do the characterization job well all the way through, from the preparation of the powders themselves on through to the shipping of the material out of the factory.

The problem that man and plant face is a bewildering array of tools, techniques, and instruments to do a characterization job. Particle-size measurement again is a good example of this. We talk about characterization as if it just got invented in this era of the new ceramics, this whole post World War II development, which has seen technical ceramics move into so many new fields. I think if you go back into the history of ceramics there has always had to be an intuitive or even quantitative understanding of characterization. The new feature we face now is the explosion of instrumentation. There are more and more instruments to do the job and more and more data piling out needing to be interpreted and applied. When you hook the computer up to the rapid electronic measuring device, you really have a problem. It is not only how to characterize, but how much data to accumulate. An incident quoted by a colleague relates to this question. He

visited a ceramic whiteware plant and saw many file cabinets, and he asked the ceramist in charge, "What is all of this, what have you got in there?" "Particle-size measurements," was the response. "Do you measure particle size?" and he said every shipment that comes in he measures. So my colleague asked what he did with the information once he gets it, and the ceramist said, "I put it in my files!" This has always been a prime problem; how do you effectively use your characterization data.

Now if you shorten the time for making measurements from a day or more to a half an hour or minutes, and then have the computer able to absorb all this data and feed it back to you, a mammoth job of data selection must be faced. This leads us back to the kind of papers that have been presented at this meeting, where there is a real striving for understanding. Understanding the process and tying processing into the characterization well enough so that maybe just a few measurements will give you the controls that you need in large-scale manufacturing must be our prime objective.

TRADITIONAL CERAMICS—R. RUSSELL, JR.

A little boy rushed excitedly into the house and said, "Wow! Our new neighbors have a new lawnmower that doesn't require gasoline or oil or anything, all you do is push it!" I believe that story has some implications to ceramic processing in that it does say that there may be some good ideas in old technology and progress can come through better understanding of old technology and its application. During this panel I am to deal with traditional ceramics which have old technologies. First, I identify traditional ceramics as products such as triaxial porcelain and other whitewares for nonelectronic use; for example, dinnerware, sanitary ware, floor tiles, and various types of pottery. I also include structural clay products, enamels, abrasives, ceramic cements, etc.

It is a difficult challenge to say in a few minutes something relevant to such a wide product line. That is why I have chosen to talk, more or less, philosophically. My experience in production, research, education, and consulting has emphasized over and over the critical importance of ceramic processing. I'm not sure when I first fully recognized that a ceramic product represents a combination of many complex processes. But, the awakening came very early in my career and has been reconfirmed continually for some 40 years. I keep emphasizing this fact to my students, but I suspect they will accept only the thesis that "processing is vital" when ceramic production, development, quality, or characterization problems confront them in real-life situations.

When we set about some 12 years ago to define the criteria in ceramic engineering education, the significance of ceramic processing in justifying our various ceramic engineering curricula was a central theme, distinguishing us from the metallurgical or polymer engineering people, for example. The resulting objective criteria in the ceramic engineering education report of the American Society for Engineering Education included considerable emphasis on ceramic processing. However, I've wondered if any modern curriculum is doing justice to this area; and I doubt that any of our graduates, confronted with material-engineering problems, would claim overexposure to processing technology despite the sincere efforts of some of my peers. One has only to examine the ceramic literature in recent years, or for that matter, our Masters and Doctorate dissertations to gain some insight into the lack of emphasis on ceramic processing compared with basic and applied research on materials and their behavior. While processing is by no means ignored in our current literature, its coverage is hardly prolific or, in my opinion, adequate.

Now, rather than continuing to emphasize the negative, let us take the positive view. If we agree that ceramic processing is vital, why do we not understand it more fully, do it better, and publish more widely? I summarize a number of factors which I think are involved:

1. Institutional research and development is largely sponsored, with recent sponsorship being highly science and materials-properties oriented.
2. The processing research that is sponsored tends to relate overwhelmingly to modern or advanced materials needs, rather than traditional ceramics.
3. The processing of conventional ceramics tends to be traditionalized, and a natural resistance to change plus a resignation to the status quo is in effect all too often.
4. Lack of a general realization that a more thorough study of traditional ceramics and their processing has the potential rewards to justify an extensive effort.
5. Individual manufacturers, and in some cases groups of manufacturers, that study or develop processing technology often consider the information proprietary or just don't care to make it available publicly. (I've had some experience in that direction that I've thought was unfortunate.)
6. The demise of engineering experiment stations with ceramic-processing orientation and the greater science emphasis in such organizations as the National Bureau of Standards, the Bureau of Mines, and governmental and private research organizations tends to deemphasize traditional ceramic processing research.
7. Ceramic technical curricula are controlled by fewer and fewer engineering-oriented educators and reflect the character of the available

research funding as well as national trends in education, neither of which has favored an engineering or processing emphasis.

Now, while other factors are involved, the pertinent question is how to shift some of the research, development, and publication emphasis to processing, technology, and fundamentals, especially as regards to more traditional ceramics, which I assure you are an important part of our field, both volumewise and dollarwise. There are no easy answers, but some obvious changes based on part on my above-listed items are needed. First and foremost is the recognition of the great potential in ceramic-processing studies. Conferences, such as this, must increase. These must be developed to promote the processing studies needed for progress. Ceramic processing must be elevated in status, and those willing and able to contribute must be encouraged. There is great opportunity here for the talented and energetic ceramist who can lead the way and do much to encourage this direction. It is my hope that this conference has been one firm step towards better and more economical processing.

TECHNICAL CERAMICS—J. E. BURKE

One of the major goals of industrial ceramics is to obtain reproducible powders and to characterize them decently. For theoretical purposes we tend to think of powders as monodispersed, individual particles, and that their behavior can be characterized by measuring the surface area. In fact, surface area so frequently tells us very little about the activity (sinterability) of the powder.

We also must learn more about powder activity. Use of sintered density as a measure of powder activity is indirect and too often misleading. The activity of a powder, from the viewpoint of how it affects sinterability, is strongly dependent upon agglomeration. The small particles of the agglomerates sinter very rapidly, but big holes remain forever. A coarse powder may sinter more slowly but may go to a higher density because of the absence of large voids due to agglomerates.

Let us summarize what I think are some of the important points that have been made in this conference. Hard agglomerates do not break down during processing. The role of the strength of agglomerates is not yet clear. Some sintering-rate measurements are very helpful in indicating what role hard agglomerates are playing. Finally, a very good way to obtain information about the characteristics of powders is to look at the microstructure, because that indicates all of the factors of concern.

REFRACTORIES—R. A. ALLEIGRO

This conference did not cover the problems of the refractory industry in much detail. The papers mainly were associated with fine particles. Refractories are concerned with the other end of the spectrum. We start with rocks and try to find materials to put with them to get some degree of bonding. I would like to talk about the bonding of these large aggregates with fine particulates and clays. These aggregates are not micron- or submicron-size particles, but range up to 3000 μ in size (in some cases even larger). Yet when refractories are formed, the same consideration of particle size, shape, orientation, packing, and composition are important.

It has been mentioned (Chapter 23) that the examination of the fired product gives an indication of process character and control. In refractories we are continuously guided by those final results, with feedback to raw materials and processes involved in consolidation and firing. Examination of the fired product gives an indication of process character and control. This is essential before second-guessing the cause of rejects. Microstructural examination provides information on the amount and distribution of glassy phases bonding the coarse particles, the possible fractures in the bonding phases or in the large grain due to thermal shock, and the quality of adhesion.

The large particles, or aggregates, can have a wide range of physical and chemical variation. Some are dense, while others are quite open; others are rough or smooth. Some may be blocky or angular platelets. These characteristics greatly affect the bonding mechanism between the matrix and the aggregate. Chemical variations, either intentional by mixing of two types or through impurities often affect the final product.

What we strive for is to determine the desired product characteristics and feed this back to specifications which reflect a reasonable degree of constancy and an acceptable rejection level. Characterization of raw materials must be tied to those critical attributes upon which performance is based.

ENERGY-RELATED MATERIALS—W. B. CRANDALL

I would like to focus on the processing and characterization of oxynitride powders, which have been neglected so far in this conference, but offer outstanding potential for achieving superior high-temperature performance. An important factor in the processing of sialons, a solid solution of alumina and silicon nitride, is a large volume expansion that occurs as the solid solution is formed. Consequently, continuous application of pressure in hot pressing is largely compensated by the volume change. However, char-

acterization of the alumina and silicon nitride powder end-members led to significant processing improvements. The petrographic microscope was found to be the most useful powder-characterization tool. Calcination of aluminum trihydroxide could be controlled to an optimum activity for the solid-solution-densification reaction by measuring the index of refraction.

Secondly, we found that the powder activity could be maintained during hot pressing by keeping the oxygen pressure below 10^{-18} atm and nitrogen about 10^{-3} atm. By use of a two-stage pressure and temperature application in the controlled atmosphere, powder activity is preserved and high-density compacts can be achieved.

ACADEMIC RESEARCH—D. W. FUERSTENAU

The title of this conference was the Science of Ceramic Processing before Firing, and I notice that at least two-thirds, if not three-fourths, of the topics talked about were "after firing." However, what you saw was that a lot of the problems that end up in your end products result from various factors in the preparation in the raw materials, in the preparation of the green bodies, and eventually the firing characteristics of the compacts. I thought there would be considerably more discussion on how do you actually characterize a particle and what kind of physical/chemical characteristics must be used for doing this. I once had a tour of Coors alumina plant and I noticed that a lot of their alumina products are made by filling molds with granules, yet only once did I hear some discussion about the effects of these granules. An area that certainly deserves study is what is the structure and size distribution of these granules, what do they do to the active behavior and flow characteristics in the die. I think one has to start right at the very beginning of particle preparation and work your way all the way along to sintering. I can see that some of the items briefly mentioned must tie very directly to the factors that control particle activity. One problem restricting progress in this field, as I see it, is that not one single professor of ceramics in this country devotes his entire professional interest to processing—someone who studies the preparation of particles. I've done a lot of work on grinding, but my interest in grinding is on the scale of boulders compared to what you people are dealing with. The kinds of products that are involved in the mineral processing industry in something like 100 to 300 microns in size and the phenomenon that exists in grinding at this relatively coarse size is far different from that encountered when you are down in the micron size. I think there is a whole world of study in particle preparation followed by particle characterization or mixing

or formation of agglomerates, packing, and stresses that exist within packed powders. I imagine this is what contributes considerably to the nonuniformity and is worthy of basic studies without worrying about the final product. I think this is a good opportunity for some person to set as his life's goal. This is really what I've done in the world of mineral processing. I'm not personally concerned with whether I am going to be able to make a slurry of such and such a grade of ore and produce a concentrate or metal from that grade of ore; but I've really devoted many years to understanding basics and intend to continue this effort.

Index

- | | |
|---|---|
| Abrasion, 108 | Air pycnometer, 436 |
| Abrasive, 9 | Alcan, 87 |
| Abrasiveness, 402 | Alcan C-6, 95 |
| Absorbed, 71 | AlCl ₃ , 117 |
| Absorbance, 450 | Alcoa, 87 |
| Absorption, X-ray, 41 | Alkaline solution, 383 |
| Academic research, 477 | Alleigro, R. A., 476 |
| Acid, boric, 86 | Alumina, 8, 12, 61, 101, 112, 129, 131,
135, 141, 153, 277, 293, 307, 348, 412 |
| naphenic, 14 | A-2, 91 |
| Acrylics, 237 | A-3, 97 |
| Active Al ₂ O ₃ , 167 | A-10, 95 |
| Activity, clay, 15 | A-12, 91 |
| Additives, 26, 136 | A-16, 91, 98 |
| Adhesion, 386, 399 | A-17, 79 |
| Adhesion forces, 357 | activation of, 24 |
| Adsorption, 55, 111 | alpha, 85, 155 |
| liquid-phase, 48 | Bayer, 85, 14 |
| Agar, 109 | Bayer-process, 22, 311, 414 |
| Ageing, 383 | Bayer-processed, 101 |
| Agglomerate, 22, 36, 61, 86, 89, 164, 293,
295, 414, 418 | beta, 90 |
| characterization of, 75 | calcined, 65 |
| formation, 71 | classification of Bayer, 94 |
| pseudomorph, 87, 90 | fused, 9, 13 |
| reactive, 90 | gamma, 62, 71 |
| shape, 86, 93 | low-soda calcined, 13 |
| strength, 63, 64, 365 | non-reactive, 95 |
| weak, 36 | reactive, 14, 61, 65, 97 |
| Agglomeration, 40, 153, 164, 357, 401, 475 | sintered, 13 |
| Agglomeration factor, 170 | Alumina Ceramic Manufacturers Association
(ACMA), 87 |
| Agglomeration kinetics, 370 | Alumina porcelain, 417 |
| Aggregate, 37, 337 | Alumina slips, 212 |
| Aggregated, 129 | Aluminate, sodium, 90 |
| Aggregation, 110 | Alumina trihydrates, 85 |
| Aids, grinding, 32 | Aluminum, 153 |
| mineral, 14 | Aluminum hydroxide, 71-72, 131 |
| viscosity, 32 | |

- Alum salt, 154
- American Ceramic Society, 6
- Amesite, 180
- Ammonia electrode, 187
- Ammonium alginate, 238
- Amorphous quartz, 112
- Analysis, differential thermal, 8
 - particle-size, 88
 - turbidimetric, 41
- Andraesen limit curves, 221
- Angle of repose, 49
- Anthracene, 458
- Antigorite, 179, 380
- Apparent density, 323, 438
- Aragonite, 113
- Archimedes' method, 436
- Area, BET surface, 90
 - surface, 39, 63, 79, 88, 95, 108, 111, 144, 156, 186, 218, 323, 414, 475
- Armstrong, 115
- Arrhenius activation energy, 432
- Asbestos, 377, 383
- Atmosphere, sintering, 28
- Attritor ball mill, 111
- Auger, 391, 404
 - vacuum, 9
- Auger rotation, speed of, 404
- Autoclave studies, 280
- Average particle size, 88
- Avery, 25
- Balek, 170
- Ball clay, 213
- Ball milled, 143
- Ball milling, 14, 63, 95, 102, 149
- Balshin, 350
- Bar, tensile, 12
- Barium titanate, 135
- Bartlett, 14
- Bartlett, Helen, 13
- BaSnO₃, 133
- BaTiO₃, 133, 450
- Bayer process, 33, 85, 143, 154, 307
 - aluminas, 22, 311, 414
- Beazley, 218
- Bennett, R. B., 61
- Bentonite, 15, 267
- Benzyl phthalate, 414
- Berg, M., 13, 101
- Berthierine, 180
- BET gas adsorption, 45, 156
- Binders, 13, 79, 91, 98, 347, 413, 422
 - additions, 311
 - burnout, 250
 - organic, 63, 310, 466
 - potassium silicate, 450
- Bingham, 203
- plastic substance, 392
- Binns, 26
- Biodegradation, 249
- Birefringence, 93
- Blaine Fineness Tester, 45
- Bleining, 7
- Block, 112
- Blunging, 12
- Bo, *et al.*, 222
- Boehmite, 154, 280
- Bond, 77
 - diffusion, 61
- Bonding mechanisms, 365
- Bonding strength, 339
- Boundaries, crystal, 93
 - grain, 46
- Bragg, 7
- Bridge, 396
- Bridgework design, 396
- Briquetting, 375
- British Ceramic Society, 6
- Brown, John A., 325
- Bruch, 26
- Brunauer, 186
- Bulk density, 49, 62, 102, 438
- Bulk green density, 436
- Burger's vector, 148
- Burke, J. E., 475
- Butylene glycol, 114
- Cadmium carbonate, 113
- Cadmium sulfide, 113
- Calcination, 61, 452, 458
- Calcined, 91
- Calcining, 86
- Calcite, 112, 113
- Calcium aluminate cement, 277
- Calcium carbonate, 282
- Calkins, 352
- Capacitor, 463, 468
 - multilayer, 463
- Capacitor dielectrics, 412
- Capillary, 359

- Capillary action, 429
- Capillary pressure, 366
- Carbide, silicon, 9
- Carbohydrate-derived binders, 237
- Carbonates, 113
 - magnesium, 25
- Carbon tetrachloride, 114
- Carbowax 400, 310
- Carrier film, 427
- Carrier-film materials, 428
- Casting, slip, 9
- Cast layer, thickness of, 426
- Casting machine, 425
- Casting rate, 218
- Casting size, 282
- Casting slips, 211
- Cation-exchange capacity, 180, 187
- Cellulose acetate, 421
- Cement, 278
 - centrifugal force, 372
 - centrifugal grinding, 111
 - centrifuge, 8
- Ceramics, electrical grade, 96
 - technical, 11
- Ceramographic, 157
- Chalcogenides, 135
- Characterization, 31, 35, 39, 86, 156, 340, 414, 477
 - chemical, 421
 - of layer silicates, 184
 - physical, 62
 - of powders, 463, 472
 - of tape, 436
- Chattopadhyay, 352
- Chi, 86
- China, 4
- Chlorine, 86
- Chlorite, 179
- Chrysotile, 179, 377
- Classification of layer-silicate, 178
- Clay, 13, 63, 213, 377, 391
 - fine-grained, 377
 - kaolin, 85
 - native, 3
- Clay bodies, drying of, 261
- Clay minerals, 112
- Clay "tempering," 272
- Clay-water paste, 264
- Clay-water systems, 193, 379
- Clintonite, 179
- Coatings, thermal-control, 449
- Coble, 25, 153
- Codecomposition, 127
- Cohesion, 386, 400
- Cohesive strength, 236
- Colloids, 37, 39, 238
- Color difference, 93
- Column splitting, 391
- Comminution, 108, 452
- Compact, 25
- Compaction, 88, 98, 103, 343
- Compaction equations, 349
- Compression force, 372
- Compression molding, 235
- Concrete, casting, 278
 - curing, 278
 - drying schedule, 281
 - mixing, 278
 - refractory, 277
- Conductor pastes, 463
- Contact potential, 360
- Contamination, 136
- Converters, catalytic, 17
- Cooke-Harrison, 212
- Cooper, A. R., 261, 350
- Coors, Joseph, 14
- Copenhagen, 5
- Core cracking, 396
- Coulter Counter, 43, 156, 323
- Crack, 98, 383, 393, 468
 - surface, 395
- Cracking, 261, 264, 391, 438
- Crack velocity, 106
- Crandall, W. B., 476
- Crystallite, 90
- Crystallite sizes, 166
- Crystallizing salts, 363
- Curing, refractory concrete, 277
- Curling, 438
- CuSO₄, 117
- Cutler, I. B., 21
- Dahneke, 370
- Deagglomeration, 360
- Deagglomeration, 418
- De-airing, 406, 425
- Decomposition, 154, 456
 - trihydrate, 86
- Defects, 142, 295
- Deflocculants, 401, 417, 422

- Deflocculation, 115, 211, 420
 Deformations, 261
 DeHoff, 323
 Dehydration products, 278
 Delta, 86
 Densification, 21, 141, 146, 308
 by vibration, 338
 Densities, 112, 309
 bulk, 49, 62, 102, 438
 fired, 88
 green, 25, 26, 62, 98, 144, 313, 436
 true, 63
 Dextrins, 238
 Diameter, 39
 pore, 54
 Stokes', 41
 Diamond, 9
 Diamond drilling, 442
 Dickite, 178
 Die, 393, 405, 441
 Die balance, 406
 Dielectric body, 466
 Dielectric strength, 96
 Differential thermal analysis, 185
 Differential thermogravimetry, 185
 Diffraction, X-ray, 7, 15
 Diffusion, 21, 147
 Diffusion coefficient, 300
 Diffusion-controlled state of drying, 433
 Diffusivities, 430
 thermal, 12
 Dihedral angle, 303
 Dilatancy, 212, 392
 Dilatometer, 308
 Disco, T_g value, 12
 Dislocations, 142
 Dislocation density, 148
 Dispersants, 378
 Dispersion, 383, 417, 465, 469
 Distributions, particle-size, 77, 211, 382, 404, 419
 pore-size, 63, 352
 size, 24, 63, 107, 108, 177
 void-size, 83
 Divers, 41
 "Doctor blade," 411
 Dodd, 404
 "Dog teeth," 395
 Double-layer, 71
 Dried clay mixture, 377

- Extrusion, 9, 16, 235, 245, 378, 412
 Extrusion defects, 391
 Eying, 195
 Farris, R. E., 277
 Faulhaber, 371
 "Feather edging," 395
 Fedorchenko, 142
 Feldspar, 4, 379
 Feranti-Shirley cone-plate viscometer, 217
 Ferrites, 126
 Ferromagnetics, 8
 Fibers, ceramic, 16
 Fibrous grains, 381
 Flick's law, 429
 Fielder, 112
 Films, thick, 463
 Filtration, 12
 Fine particles, 357
 Firing, 291, 307, 394, 458, 466
 Flaws, 308, 378
 Flickering-cluster, 197
 Flocc, 36, 418
 Flocculation, 379
 Flock, W. M., 16, 85
 Flocc structure, 216
 Flotigam P, 115
 Flowability, 49
 Flow characteristics, 391
 Flow-pressure relationships, 392
 Flow rate, 329
 Fluid bed drying, 127
 Fluid energy milling, 111
 Fluorescent-die penetrants, 398
 Fluorine, 86
 Forces, interfacial, 36
 Forming, 391
 Forslind, 196
 Forsterite, 28
 Fractography, 382
 Fracture, 105
 Fragment, glass, 377
 Fragmentation, 110
 Frank, 196, 198
 Freeze-drying, 128
 Freezing, 398
 Frenkel, 365, 195
 Friction presses, 344
 Fuerstenau, D. W., 477
 Furnas, 220

- Galene, 113
 Gallagher, P. K., 125
 Gallenkamp and Brookfield RVT rotational viscometer, 216
 Gamma, 86
 Gamma alumina, 155
 Gamma-ray back-scatter, 426
 Garnierite, 180
 Gas-desorption, 55
 Gates, D. W., 449
 Gel, 63, 429
 Gelation, 240, 248
 Gelation-evaporation, 127
 Gibbsite, 154, 280
 Gitzen, Walter, 14
 Glass, 377
 Glass-ceramics, 472
 Glass frit, 468
 Glass spheres, 229, 349, 377
 Glaze, 3
 Glycerine, 422
 Glyceryl monooleate, trioleate, and tristearate, 423
 Gold, 358
 Goodson, 404
 Gordon, R. S., 153
 Gormly, 352
 Grain boundary behavior, 397
 Grain boundary diffusion, 148
 Grain growth, 294, 397
 Grain-growth inhibitors, 466
 Grain size, 292, 297, 315
 Granulation, 63, 349
 Granules, 36, 63, 79, 243, 357, 477
 spray dried, 102
 Graphite, 391, 401
 Gravimetric analysis, 456
 Green, 6
 Green body, 321, 391
 formation, 289
 Green density, 25, 26, 62, 98, 144, 313, 436
 Griffith, 109
 Griffith relationship, 105
 Grinding, 22, 101, 375
 dry, 102, 108
 mechanisms of, 105
 theory, 105
 wet, 102, 108
 Grinding aids, 103, 105, 114

- Grinding media, 97
 Gyration, radii of, 50
 Hall Flow Meter, 329
 Halloysite, 178
 Harada, Y., 449
 Hardness, 118
 Hare, T. M., 307
 Harris, 111
 Hasselman, D. P. H., 141
 Heckel, 350
 Hematite, 112
 Hensch, L. L., 35, 75
 Hertz, 371
 Heystek, H., 177
 Hinchley, Dave, 15
 Hirschorn densification parameter, 143
 History, 3
 Hoffman, 5
 Homogeneity, 125, 254
 Honeycomb, 17
 Hugill, 326
 Hydrate, 63
 Hydrated surface layers, 64
 Hydration, 199
 Hydraulic press, 344
 Hydrogen bond, 196
 Hydrometers, 41
 Hydrophilic, 237, 385
 Hydrophobic, 385
 Hydrostatic pressing, 345
 Hydrothermal, 135
 Hydroxyethylcellulose, 238
 Hydroxypropylmethylcellulose, 238
 Ice, 196
 Illite, 181
 Impact grinding, 110
 Impact presses, 345
 Impurities, 26, 86
 Insulators, 12
 Insulation during milling, 418
 Index, refractive, 41, 92
 Infrared adsorption spectroscopy, 185
 Injection molding, 13, 102, 235
 Inorganic electrolytes, 116
 Insulators, 12
 spark-plug, 101
 Intergranular pores, 297
 Internal friction, 400
 Interstitials, 24
 Ion hydration, 200
 Iron, 85
 Isopropanol, as milling aid, 156
 Isostatic, 14
 Isostatic compression, 374
 Isostatic pressing, 9, 67, 102, 343
 Isostatic repressing, 312
 Isotherms, adsorption, 46
 Jenkins, E. J., 75
 Johnson, *et al.*, 170
 Johnson, D. W., Jr., 125, 208
 Kaolin, 5, 213
 Florida and Georgia, 15
 Kaolinite, 178, 207, 380
 Kappa, 86
 Kawakita, 351
 KC-8, 95
 Kemalox alumina, 309
 KI-A1, O₂, 157
 Kilns, chamber and high-fire, 4
 Kinetics, 141, 154
 of drying, 265
 Kingery, W. D., 142, 291, 352
 Kjeldahl method, 187
 Knife coating, 411
 Knight, 265
 Krichner, 154, 167
 Krupp, 361
 LaFeO₃, 133
 Laminar flow, 393
 Laminations, 98, 101, 391, 393, 444
 Laser drilling, 442
 Lattice defects, 195
 Lattice strain, 141
 Lawrence, W. G., 193
 Layer silicates, 177
 Lead sulfate, 113
 LiFe₂O₄, 129
 Lifshitz-van der Waals constant, 361
 Light transmission, 153
 Limestone, 106, 115, 360
 Limestone powders, 366
 Lin, 114
 Linde A (α -Al₂O₃), 76, 301, 311
 Liquid bridges, 359
 Liquid drying, 135
 Litharge, 113

- Lizardite, 179
 Loading, 103
 Lubricants, 32, 347
 Lucalox alumina, 299
 Luckie, 112
 Ludde, 351
 MacDonald, R. J., 325
 Macey, 273
 McGeary, 329
 Machines, French kneading, 12
 McLaren, 211
 Madagascar graphite, 377
 Magnesite, 112
 Magnesium aluminate, 134
 Majumdar, 279
 Masaryk, J. S., 277
 Massachusetts Institute of Technology, 6
 Massicot, 112
 Mechanical strength, 315
 Mechanisms of compaction, 352
 Mechanochemical effects, 112
 Meissen, 5
 Mellor, 6
 Menhaden fish oil, 417, 420
 Mercury porosimetry, 63, 348, 436
 Merry, 396
 Metalloxytite, 178
 Metallic contaminants, 251
 Metallization, 444, 468
 Methyl alcohol, 311
 Methylcellulose, 238
 Methylcyclohexane, 114
 Methyl silicone, 450
 Metzbow, E. A., 141
 Mexican graphite, 377
 MgAl₂O₄, 128
 MgO, 25, 159
 sintering behavior of, 25
 surface area, 26
 MgO-Cr₂O₃, 8
 MgO-doped Linde A, 316
 Mica, 178, 401
 Microbicide, 249
 Microscope, electron, 7
 petrographic, 7, 87, 477
 transmission electron, 63
 Microscopy, 40
 scanning electron, 22, 156, 380, 453
 transmission electron, 75, 148, 156
 Microspheres, 128
 Microstructural, 75, 459
 Microstructure, 62, 67, 101, 160, 289, 315, 377, 466, 471
 of extruded cylinders, 380
 Mill atmosphere, 113
 Milling, 33, 91, 99, 111, 310, 417
 on agglomerate size, 168
 ball, 14, 63, 95, 102, 199
 dry, 63, 311
 wet, 71
 Mineral, 183
 Mineralogical analysis, 178
 Mineralogy, 277, 382
 Mineral wax, 243
 Ming Dynasty, 5
 Mistler, R. E., 411
 Mitzmager, 114
 Mixed binder systems, 250
 Mixedness of suspensions, 253
 Mixed-oxide precipitate, 134
 Mixing, 12, 132, 331, 466, 477
 Mixtures, 98
 Modulus of rupture, 377, 380
 Moisture distribution, 274
 Molding, hand, 3
 hydrostatic, 17
 injection, 13, 102, 235
 Mold lubricants, 349
 Molybdenum sulfide, 112
 Monohydrate, aluminum, 66
 Monooleate, 423
 Montmorillonite, 112, 179, 383
 Moore, 218
 Morphology, 7
 Mossbauer spectroscopy, 186
 Mullite, 12
 Multilayer casting, 445
 Multilayer structures, 444
 screened, 445
 Nacrite, 178
 Naeser, 112
 Na, O, 88
 Nepheline syenite, 379
 Newtonian behavior, 464
 Newtonian flow, 236
 Newtonian liquid, 392
 Nickel-zinc ferrites, 126
 Nicot, 86

INDEX

- Pyrophosphates, 113
Pyrophyllites, 179
Quartz, 5, 106, 112, 360, 377
Quartz glass spheres, 371
Quartz grains, 384
Quartzite, 115
Quartz slips, 213
Queueing (concrete), 278
Quirk, John, 14
Ramsey, 25
Random mix, 254
Rase, 450
Rate, precipitation, 93
Rate control, 307
RC-20, 91
RC-23, 99
RC-24, 91
RC-172, 91, 98
Reactive powders, 61, 125
Reactivity, 90, 94, 136
Reflectance, 450
Refractories, 476
 insulating, 8
 low-temperature, 97
Refracton, 89
Refractory concrete, 277
Rehbinder, 115
Relative humidities, 370
Research, future directions, 471
Residual stresses, 269
Resins, thermosetting and thermoplastic, 13
Resistor, 463
Reynolds aluminum, 87
Rheological, 211
Rheological properties, 187
Rheology, 464
 of organic binder solutions, 235
Rhines, F. N., 321
Roberts, A., 463
Robinson, G. C., 201, 391
Rod mill, 115
Roll-compacting, 346
Roll forming, 235
Rotary presses, 344
Rotary punch press, 441
Roy, 279
Rumpf, H., 253, 357

INDEX

- Polymethylphenylsiloxane silicon resin, 418
Polymorphic transitions, 112
Polysiloxane, 116
Polyvinylpyrrolidone, 239
Porcelains, 4, 295
 frit, 5
 steatite, 8
Pore, 35
Pore growth, 294
Pore size distribution, 63, 352
Pore stability, 302
Porosimeter, 438
Porosimetry, mercury, 63, 348, 436
Porosity, 27, 69, 92, 153, 223, 378
 open, 438
Pottery, 4
Powder, 19, 141, 153
 active, 21
 reactive, 61, 125
Powder activity, 475, 477
Powder characterization, 463, 472
Powder compact, 321
Powder compaction, 64
Powder mixing, 343
Powder purity, 143
Precipitates, 72, 133
Precipitation, 63, 86
Precipitation-filtration, 131
Precipitation process, 452
Precision casting, 434
Preservative, 249
Pressing, 343, 440
 filter, 102
 isostatic, 9, 67, 102, 343
 leaf filter, 12
Process, Bayer, 33, 85, 143, 154, 307
Products, whiteware, 97
Proof test, ceramic processing, 291
Propagation of cracks, 382
Properties, powder flow, 56
Propylene glycol, 114
Propylamine, 422
Pseudoplastic, 212
Pseudoplasticity, 239, 246
Punching, 441
Purdy, 6, 12
Purity, 85
 high, 98
 ultrahigh, 99

- Particle-size mixture, 293
Particle stacking, 321
Particulate, 472
Particulate-water systems, 191
Pask, J. A., 471
Paste systems, 464
Pawlowaki, 255
Penetration, mercury, 52
Permeability, 223, 284, 323
Permeability models, 265
Permeametry, 45
Petrographic microscope, 7, 87, 477
PH, 13, 93, 131
Phase, alpha, 90
 liquid, 28
 nonalpha, 90
 transition, 91
Phase content, 95
Phelps, G. W., 211
Philip, 262, 265
Phthalates, 422
Phyllosilicates, 177
Piazza, 442
Pietsch, 363
Piezoelectrics, 412
Pigment, 449
Pincus, A. G., 472
Pines, 142
Piston extruder, 391
Plastic deformation, 106, 370
Plastic flow, 379
Plasticizers, 13, 250, 414, 422
Plastic state of clay, 379
Plastic strain, 401
Plugs, spark, 12
Polarizing microscopy, 380
Poly (acrylic acid), 239
Poly (ethylene glycol), 239, 348, 414
Poly (methacrylic acid), 239
Poly (methyl methacrylate), 240
Poly (vinyl acetate), 413
Poly (vinyl alcohol), 239
Poly (vinyl butyral), 240, 413, 422
Poly (vinyl chloride), 413
Poly (vinyl formol), 240
Polyethylene glycol, 422
Polyethylene oxides, 237
Polyethylenimine, 239
Polymer, 413
Polymer molecules, 236

- Runk, R. B., 411
 Rupture, modulus of, 12
 Russell, R., Jr., 13, 473
 Ryshkewitch, 22, 64

 Samoilov, 199
 Sanitaryware, 213
 Saturation, 366
 Scanning electron microscopy, 22, 156, 380, 453
 Schubert, H., 357
 Schwartz, 444
 Schwartzwalder, Karl, 11
 Scott Volumeter, 325
 Screen printed, 463
 Sedimentation rate, 41
 Sedimentation-type, 77
 Segregation, 329, 331, 338, 391, 396
 difference on, 334
 Segur, 6
 Self-diffusion coefficient of water, 200
 SEM, 63, 437, 459
 Semidry pressing, 343
 Sericite, 401
 Serpentine, 178
 Shanefield, D. J., 141, 411
 Shape, 39, 108
 agglomerate, 86, 93
 particle, 24, 33, 49, 86, 177, 329, 339, 401, 465
 Shear strain rate, 228
 Shear stress rate, 228
 Shear thickening, 212
 Shear thinning, 212
 Shock waves, 108
 Shrinkage, 21, 88, 95, 98, 101, 141
 fired, 98
 Shulhof, William, 15
 Sieve analyses, 418
 Sieving, 40
 Silica, 85, 86
 Silica powder, 369
 Silicate, 128
 Silicate minerals, 177
 Silicoes, 116
 Sinterability, 72, 134, 146, 157, 315, 419, 438, 475
 Sintered, 77, 129, 307
 Sintering, 21, 36, 67, 153, 141, 313, 321, 343, 363, 419

 rate controlled, 308
 SiO₂, 131
 Sirenko, 142
 Sivres, 5
 Size, grain, 86
 particle, 22, 33, 46, 39, 218, 257, 334, 337, 465
 range of average particle, 95
 Size distribution, 24, 63, 107, 108, 177
 Size reduction, 109
 Slip, 411
 Slip bands, 381
 in clay, 379
 Slip casting, 235, 412
 Slip properties, 211
 Slip rheology, 212
 Smallman, 148
 Smectite, 179
 Smith, *et al.*, 324
 Smith, Robert, W., 13
 Snow, 112
 Soda contents, 95
 Sodium, 85
 Sodium alginate, 238
 Sodium carboxymethylcellulose, 238
 Sodium chloride, 383
 Sodium oleate, 115
 Sodium silicate, 213
 Solder, 469
 Sol-gel techniques, 127
 Solid bridges, 359
 Solid-solid reaction, 450
 Solid solutions, 133
 Solubility in water, 236
 Solution, solid, 27
 Solution techniques, 125
 Solvated layer, 204
 Solvent, 413
 Solvent vaporization, 126
 Somasundaran, P., 105, 109, 114
 Sommer, K., 227, 253
 Specific gravity, 425
 Speed of auger rotation, 404
 Sphericity, 50
 Spinel, 135, 294
 Spray drying, 126
 Spray roasting, 126
 Stability, 338
 Stacking parameters, 322
 Standards, Bureau of, 8

 Stange, 255
 Starches, 238
 Stearic acid, 420
 Steele, 442
 Steric hindrance model, 420
 Stoichiometry, 27, 136
 Stokes, 201
 Stokes method, 143
 Stoneware, 4
 Strain, 261
 Strain domain size, 144
 Strength, 98, 105, 377
 Strength of agglomerates, 63, 64, 365
 Strength distribution of ceramic particles, 349
 Stress, 261
 Stress distribution, 353
 Structural clay products, 473
 Structure, 89
 agglomerate, 93, 94
 pore, 39, 52
 Structure of water, 193
 Subgrain boundaries, 142
 Sublimation, 129
 Substrates, 91
 Sunman, Howard, 16
 Surface fracture, 69
 Surface active agents, 115
 Surface area, 39, 63, 79, 88, 95, 108, 111, 144, 156, 186, 218, 323, 414, 475
 Surface-area effects, 419
 Surface cracks, 395
 Surface roughness, 368
 Surfactants, 32, 115
 Suspension, 256
 liquid, 36
 Swelling, 262
 Synthesis of autoclave alumina, 154

 Tableting, 375
 Tabular alumina, 278
 Tabular alumina T-61, 79
 Talcs, 63, 116, 179, 418
 Tanford, 196
 Tape-castings, 91, 235, 411
 Taylor, 86
 TE, 96
 Tearing, 391
 Technical ceramics, 475
 Techniques, 39

 TEM, 414
 Temperature, 106
 Tensile strength, 366
 Terra Corta, 3
 Terra Sigrillata, 3
 Tetrabromoethane, 117
 TGA, 441
 Thermal decomposition, 285
 Thermal gravimetric analysis, 156
 Thermal shocks, 110
 Thermal stress theory, 269
 Thermogravimetric, 66, 112, 310
 Thermogravimetry, 185
 Theta, 86
 Thick film, 463
 Thick-film printing, 235
 Thick-film substrates, 412
 Thixotropic slips, 421
 Thixotropy, 248, 392
 Throwing wheel, 3
 TiO₂, 420, 449
 addition to aluminum oxides, 27
 Titanates, 8
 Titanium, 85
 Titanium oxalate, 455
 Toggle presses, 344
 Topological connectivity, 322
 Torkar, 154, 167
 Train, 353
 Transfer-saturation, 155
 Transformation, topotactic, 86
 Translucency, 315
 Transmission, light, 41
 Transmission electron microscopy, 75, 148, 156
 Transverse strength, 378
 Tremolite, 180
 Tremolitic talc, 377
 Tremper, R. T., 153
 Triaxial porcelain, 473
 Trichloroacetic acid, 422
 Trichloroethylene-alcohol mixture, 420
 Trioctate, 423
 Tristearate, 423
 Tschonhaus, Graph von, 5
 Turndown ratio, 405

 Ultimate particle sizes, 166
 Ultrafine grinding, 110
 Ultraporcelain, 116

- Ultrasonic dispersion, 419
- Uniformity, 299
- UO₂, 294, 303
- Urania powders, 353
- Vacancies (alumina), 24
- Vacuum, 405
- Van der Waals forces, 358
- Vapor pressure, 369
- Variance, 253
- Verma, K. K., 463
- Vermiculites, 179, 181, 401
- Vibration grinding, 111
- Vibratory compacting, 347
- Vibratory settling, of binary mixtures, 333
- Vinyls, 237
- Viscosity, 117, 464, 425
 - in ceramic processing, 243
 - of concentrated Newtonian suspensions, 227
- Viscous binders, 359
- Vogt, Richard H., 325
- Void, 468
- Void frequency, 352
- Void space, 378
- Voltage, breakdown, 12
- Volume, void, 525
- Von Hippel, 8
- Waal, van der, 36
- Walker, 349
- Ward, 273
- Warpage, 101, 261
- Warped, 98
- Warren, 7
- Warren-Averbach method, 143
- Washing, 86
- Water, interstitial, 378
- Water diffusivity, 262
- Water-expansion, 262
- Water flow, 265
- Water (moisture), 114
- Water vapor, 106
- Watts, 12
- Wax emulsions, 243
- Weight-loss measurements, 439
- Wen, 196
- Werner-Pfleiderer kneader, 258
- Westman, 326
- Westwood, 118
- Wet-grinding, 102, 108
- White ware, 473
- White ware slips, 213
- Whittemore, O. J., Jr., 343
- Wilcox, 444
- Wilde, 273
- Williamson, W. O., 148, 377
- XA-139, 97
- X-ray analysis, 456
- X-ray diffraction, 112, 156, 183, 194, 280, 380
- X-ray line broadening, 143
- X-ray scattering, low angle, 49
- X-ray transmission instrument, 426
- Y₂Al₂O₃, 128
- Yield strength, 372
- Y₂O₃ + 10 7/8 ThO₂, 292
- Y₂O₃-10 mole% ThO₂, 298
- Yttria-zirconia, 135
- Zero point of charge, 421
- Zeta potential, 118, 420
- Zinc carbonate, 113
- Zinc orthotitanate powders, 449
- Zinc oxalate, 454
- ZnO, 449
- ZrO₂, 135

BRIEF ATTACHMENT E

IN THE UNITED STATES PATENT AND TRADEMARK OFFICE

In re Patent Application of

Applicants: Bednorz et al.

Serial No.: 08/479,810

Filed: June 7, 1995

For: NEW SUPERCONDUCTIVE COMPOUNDS HAVING HIGH TRANSITION
TEMPERATURE, METHODS FOR THEIR USE AND PREPARATION

Date: March 1, 2005

Docket: YO987-074BZ

Group Art Unit: 1751

Examiner: M. Kopec

Commissioner for Patents
P.O. Box 1450
Alexandria, VA 22313-1450

FIRST SUPPLEMENTAL AMENDMENT

Sir:

In response to the Office Action dated July 28, 2004, please consider the
following:

ATTACHMENT E

STRUCTURE,
PROPERTIES AND
PREPARATION OF
PEROVSKITE-TYPE
COMPOUNDS

BY
FRANCIS S. GALASSO,
United Aircraft Research Laboratories



PERGAMON PRESS

OXFORD · LONDON · EDINBURGH · NEW YORK
TORONTO · SYDNEY · PARIS · BRAUNSCHWEIG

Pergamon Press Ltd., Headington Hill Hall, Oxford
 4 & 5 Fitzroy Square, London W.1
 Pergamon Press (Scotland) Ltd., 2 & 3 Teviot Place, Edinburgh 1
 Pergamon Press Inc., Maxwell House, Fairview Park, Elmsford
 New York 10523
 Pergamon of Canada Ltd., 207 Queen's Quay West, Toronto 1
 Pergamon Press (Aust.) Pty. Ltd., 19a Boundary Street,
 Rushcutters Bay, N.S.W. 2011, Australia
 Pergamon Press S.A.R.L., 24 rue des Écoles, Paris 5^e
 Vieweg & Sohn GmbH, Burgplatz 1, Braunschweig

Copyright © 1969
 Pergamon Press Inc.

First edition 1969

CONTENTS

PREFACE	ix
1. INTRODUCTION	1
2. STRUCTURE OF PEROVSKITE-TYPE COMPOUNDS	3
2.1. Ternary Oxides	4
2.2. Complex Oxides	11
2.3. Madelung Energy	39
2.4. Ionic Radii	41
3. X-RAY DIFFRACTION AND ELECTRON PARAMAGNETIC STUDIES	50
3.1. X-ray Diffraction	50
3.2. Electron Paramagnetic Resonance Studies	57
4. CONDUCTIVITY	60
4.1. Conductors	60
4.2. Superconductors	63
4.3. Semiconductors	64
4.4. Thermoelectricity	73
4.5. Hall Effect	76
5. FERROELECTRICITY	79
5.1. Ternary Perovskites	80
5.2. Solid Solutions	90

Library of Congress Catalog Card No. 68-21881

PRINTED IN HUNGARY
 08 012744 4

5.3. Complex Perovskites	99
5.4. Effect of Nuclear Irradiation	103
5.5. Applications of Ferroelectric Materials	105
5.6. Theories of Ferroelectricity	109
6. PHASE TRANSITIONS	115
6.1. Ternary Perovskites	115
6.2. Complex Perovskite-type Compounds	118
7. FERROMAGNETISM	122
8. OPTICAL PROPERTIES	129
8.1. Transmittance	129
8.2. Coloration by Light	133
8.3. Electro-optic Effect	133
8.4. Lasers	134
9. OTHER PROPERTIES	140
9.1. Catalysts	140
9.2. Thermal Conductivity	141
9.3. Melting Points	141
9.4. Heats of Formation	142
9.5. Thermal Expansion	143
9.6. Density	143
9.7. Mechanical Properties	144
10. PREPARATION OF PEROVSKITE-TYPE OXIDES	159
10.1. Powders	159

10.2. Thin Films	162
10.3. Single Crystals	165
11. OTHER PEROVSKITE-TYPE COMPOUNDS	182
11.1. Preparation of Perovskite-type Phases	182
11.2. Structure	184
11.3. Properties	187
INDEX	191
OTHER TITLES IN THE SERIES	209

PREFACE

SINCE 1945, when the ferroelectric properties of barium titanate were reported by von Hippel in the United States and independently by workers in other countries, ABO_3 compounds with the perovskite structure have been studied extensively. These studies have resulted in the discovery of many new ferroelectric and piezoelectric materials. Most of the literature written on perovskite-type compounds has been concentrated on these properties.

In addition, a number of solid-state chemists devoted many years to producing new ternary perovskite compounds of all kinds and studying their structures. By 1955 it appeared that most of the possible combinations of large A cations and smaller B ions needed to form perovskite-type compounds had been tried. At that time, as part of a thesis problem at the University of Connecticut, I found that new perovskite-type compounds could be prepared by introducing more than one element in the B position of the perovskite structure.

At the United Aircraft Research Laboratories in 1960, J. (Pyle) Pinto, W. Darby and I continued this research by initiating an extensive program to study the preparation, structure and properties of these perovskite-type compounds. Because these compounds contained two different B ions with different valence states, many combinations of elements and, therefore, the formation of many compounds were possible. These studies as well as research conducted by other workers throughout the world resulted in large amounts of new structural and property data on perovskite-type compounds. During the same time renewed interest in ternary perovskite compounds was generated as a result of studies which showed that they might prove useful as laser host materials, for laser modulation, as thermistors, as superconductors and as infrared windows.

The purpose of this book is to attempt to bring together the information obtained from these studies, including the

various methods of preparing powders, thin films and single crystals of perovskite-type compounds, the structure of these compounds and their properties. The properties covered are electrical conductivity, ferroelectricity, ferromagnetism, optical transmittance the electro-optical effect, catalytic properties, melting points, heats of formation, thermal expansion, densities and mechanical properties. Because of the growing number of applications for perovskite-type compounds, I felt that this information might prove valuable to applied researchers. In addition, structural data are included for scientists who are interested in correlating the structure and properties of materials.

I am grateful to Professor Roland Ward and Professor Lewis Katz for introducing me to this field of research and to my previous fellow workers at the University of Connecticut for their studies on many unusual perovskite-type compounds. I must also acknowledge Professor Aaron Wold and Professor Rustum Roy for their discussions on perovskite compound preparations, Dr. Michael Kestigian and Professor A. Smakula for helpful advice on crystal growing, Dr. Alexander Wells and Professor Martin Buerger for pointing out the need for a compilation and discussion of structural data of the type presented herein, Dr. Fredrick Seitz for helpful discussions on ordering and to Dr. John Goodenough for information on the ferromagnetic properties and conductivity in perovskites. I would also like to thank Dr. V. Nicolai of O.N.R. Washington, D.C., for information on lasers, Dr. Charleton of Fort Monmouth, New Jersey, for discussions on dielectrics and Dr. Fredricks of Wright-Patterson A.F.B. for reports on microwave properties of perovskites. I am indebted to United Aircraft Research Laboratories, my colleagues J. Pinto and W. Darby; R. Fanti, Chief of Materials Sciences, and Professor P. Duwez, a member of the Advisory Committee for United Aircraft Corporation. I wish to thank Professor R. Smoluchowski, Dr. R. Graf, Professor A. Wold and Dr. M. Kestigian for helpful suggestions and for checking through the manuscript. Finally, I am grateful to my wife, Lois, Miss Kathy Donahue, Miss Joyce Hurlburt, Mrs. Jean Kelly and Mrs. Nancy Letendre for their patience and effort in preparing this manuscript.

CHAPTER 1

INTRODUCTION

THIS book contains details on the structure, properties, and preparation of perovskite-type compounds. Because of the growing number of applications for these compounds, information on their preparation is becoming more in demand. The long fluorescence lifetimes observed for Cr^{3+} in LaAlO_3 , and the large room-temperature electro-optical effect in $\text{K}(\text{Ta}_{0.45}\text{Nb}_{0.55})\text{O}_3$, for example, have caused considerable interest in obtaining these materials as optical quality single crystals. In addition, the better known ferroelectric and piezoelectric properties of perovskites have induced researchers to continue the effort to prepare them as larger and more perfect single crystals, polycrystalline compacts and thin films. Materials scientists also are continuously trying to prepare new perovskite compounds with new and improved properties. One of the best ways of accomplishing this is to use the insight gained from structure-property relationships. An objective of this book is to point out some of these structure-property relationships as well as to provide the reader with enough data so that he can deduce some of his own.

In this book, the oxide phases have been divided into two types, the ternary ABO_3 type and their solid solutions, where A is a large metal cation and B is a smaller metal cation and the newer complex $\text{A}(\text{B}'\text{B}'')\text{O}_3$ type compounds where B' and B'' are two different elements in different oxidation states and $x+y=1$. First, the structural data are presented in a systematic manner for quick and easy reference. A chapter is included on the identification of distortions in the structure of ternary perovskite-type compounds and of ordering in the structure of complex perovskite-type compounds using X-ray diffraction techniques. The properties of the perovskite

compounds described herein are electrical conductivity, ferroelectricity, ferromagnetism, optical, catalytic, melting points, heats of formation, thermal expansion and mechanical properties. Then, the preparation of these compounds as powders, thin films and single crystals are described. In addition, a chapter is included on other compounds besides oxides with the perovskite structure.

CHAPTER 2

STRUCTURE OF PEROVSKITE-TYPE COMPOUNDS

Most of the compounds with the general formula ABO_3 have the perovskite structure. The atomic arrangement in this structure was first found for the mineral perovskite, $CaTiO_3$. It was thought that the unit cell of $CaTiO_3$ could be represented by calcium ions at the corners of a cube with titanium ions at the body center and oxygen ions at the center of the faces (Fig. 2.1). This simple cubic structure has retained the name perovskite, even though $CaTiO_3$ was later determined to be orthorhombic by Megaw.⁽¹⁾ Through the years it has been found that very few perovskite-type oxides

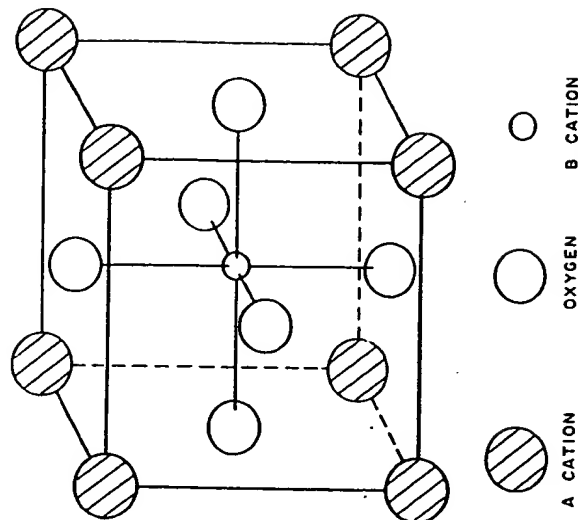


Fig. 2.1. Perovskite structure, ABO_3 .

have the simple cubic structure at room temperature, but many assume this ideal structure at higher temperatures.

In the perovskite structure, the A cation is coordinated with twelve oxygen ions and the B cation with six. Thus, the A cation is normally found to be somewhat larger than the B cation. In order to have contact between the A, B, and O ions, $R_A + R_O$ should equal $\sqrt{2}(R_B + R_O)$, where R_A , R_B and R_O are the ionic radii. Goldschmidt⁽²⁾ has shown that the cubic perovskite structure is stable only if a tolerance factor, t defined by $R_A + R_O = t\sqrt{2}(R_B + R_O)$, has an approximate range of $0.8 < t < 0.9$, and a somewhat larger range for distorted perovskite structures. It should be noted that conflicting reports in the literature make it difficult to assign the correct unit cell dimensions for these distorted perovskite structures.

The ternary perovskite-type oxides described in this chapter will be divided into $A^1+B^3+O_3$, $A^2+B^4+O_3$, $A^3+B^3+O_3$ types and oxygen- and cation-deficient phases. The oxygen- and cation-deficient phases will be regarded as those which contain considerable vacancies and not those phases which are only slightly non-stoichiometric. Many of these contain B ions of one element in two valence states and should not be confused with the complex perovskite compounds which contain different elements in different valence states.

The complex perovskite type compounds, $A(B'_x B''_y)O_3$, will be divided into compounds which contain twice as much lower valence state element as higher valence state element, $A(B'_{0.67} B''_{0.33})O_3$, those which contain twice as much of the higher valence state element as the lower valence state element, $A(B'_{0.33} B''_{0.67})O_3$, those which contain the two B elements in equal amounts, $A(B'_0.5 B''_0.5)O_3$, and oxygen-deficient phases $A(B'_x B''_y)O_{3-z}$.

2.1. TERNARY OXIDES

Oxides of the $A^1+B^3+O_3$ Type

The $A^1+B^3+O_3$ type oxides are of particular interest because of their ferroelectric properties. Potassium niobate, $KNbO_3$, has a structure which can be described by an ortho-

rhombic unit cell of $a=3.9714$ Å, $b=5.6946$ Å and $c=5.7203$ Å where b and c equal approximately $\sqrt{2}a$ or the length of face diagonals of the simple perovskite cell, and exhibits ferroelectric properties. The sodium niobate, $NaNbO_3$, structure also can be described by an orthorhombic unit cell but is antiferroelectric. The unit cell is pseudotetragonal at 420°C, tetragonal at 560°C and cubic at 640°C. Unlike the structure of niobates the $KTaO_3$ structure is described by a cubic unit cell. The structure of $NaTaO_3$ is orthorhombic with the space group $Pc2_1n$ and all the atoms are placed in the unit cell in positions:⁽³⁾

$$(4a) \quad xyz; \bar{x}, y + \frac{1}{2}, \bar{z}; x + \frac{1}{2}, y + \frac{1}{2}, \frac{1}{2} - z; \frac{1}{2} - x, y, z + \frac{1}{2}$$

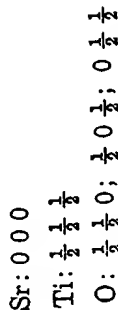
	x	y	z
Na	-0.01	0.78	0.02
Ta	0.50	0.00	0.00
O(1)	-0.02	0.76	0.52
O(2)	0.29	-0.03	0.29
O(3)	0.29	0.50	0.29

Smith and Welch⁽⁴⁾ found that potassium iodate, KIO_3 , and thallous iodate, $TlIO_3$, also adopt the perovskite structure. Single-crystal studies showed that KIO_3 had a rhombohedral structure with unit cell parameters $a=4.410$ Å, $\alpha=89.41^\circ$. Powder diffraction studies on $TlIO_3$ powders indicated that it also had a rhombohedral structure with cell dimensions, $a=4.510$ Å, $\alpha=89.34^\circ$, while the structures of $CsIO_3$ and $RbIO_3$, on the other hand, have been reported to be cubic.

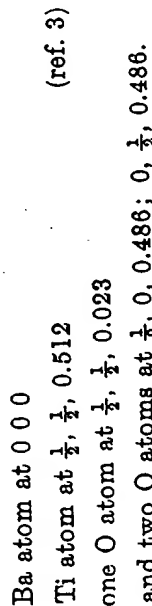
Oxides of the $A^2+B^4+O_3$ Type

Probably the largest number of perovskite-type compounds are described by the general formula $A^2+B^4+O_3$, where the A cations are alkaline earth ions, cadmium or lead and the B^4+ ions include Ce, Fe, Pr, Pu, Sn, Th, Hf, Ti, Zr, Mo and U. The best known compounds of this type are the titanates because of the ferroelectric properties that the barium and lead compounds exhibit. Calcium titanate, as previously mentioned, was the original example of a compound with an "ideal" cubic perovskite structure, but it was later

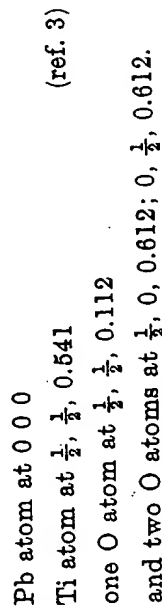
determined to have an orthorhombic structure. The structure of strontium titanate, however, is truly cubic; the space group is $Pm\bar{3}m$, and its atoms are in the following positions in the unit cell:



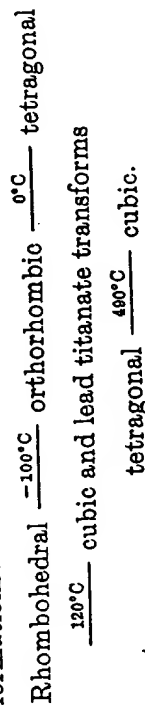
Barium titanate and lead titanate are of more interest because the atomic displacements in their structures produce ferroelectric properties. Neutron diffraction studies show that the displacements are greater in lead titanate than they are in barium titanate. For barium titanate the atoms in the unit cell are in the following positions:



The room temperature tetragonal form of lead titanate has its atoms in these positions in its unit cell:



While the structure of calcium titanate exhibits orthorhombic symmetry at room temperature, it becomes cubic above 900°C. Barium titanate undergoes the following transformations:



Roth^(s) regards BaZrO_3 as another compound with an "ideal" cubic perovskite structure. While his conclusion has

been questioned, it is logical that this compound with a tolerance factor of 0.88 should adopt the same structure as SrTiO_3 which has a tolerance factor of 0.86. Strontium zirconate and calcium zirconate probably have an orthorhombic structure, although Smith and Welch⁽⁴⁾ felt that the SrZrO_3 powder pattern should be indexed on a "doubled" cubic perovskite

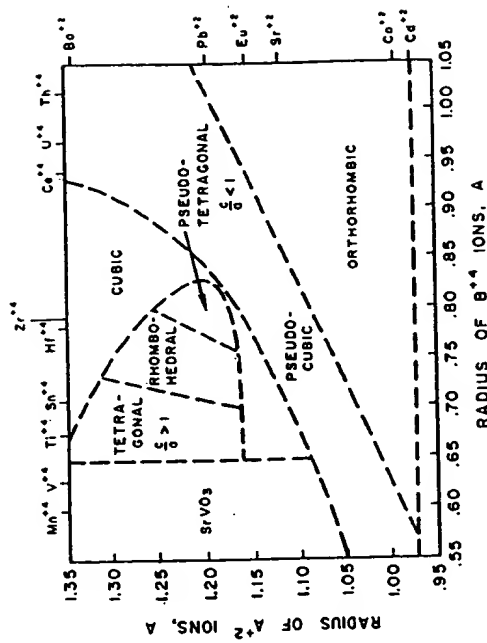


Fig. 2.2. Classification of perovskite-type compounds, $\text{A}^{2+}\text{B}^{4+}\text{O}_3$ (after Roth^(s)).

cell. The lead zirconate structure originally was thought to be tetragonal, but was found to be orthorhombic by X-ray and neutron diffraction studies.

The compound BaSnO_3 also has been reported by Smith and Welch⁽⁴⁾ to have the "ideal" cubic perovskite structure. This selection of the unit cell was confirmed by Roth^(s) and Megaw⁽¹⁾ independently.

Another interesting compound is CaUO_3 , because although it has a tolerance factor of only 0.71 it still has the perovskite structure. Roth^(s) points out that a minimum tolerance factor of 0.77 was previously set for $\text{A}^{2+}\text{B}^{4+}\text{O}_3$ type compounds, but because of this new information can be assumed to be incorrect. The compound CaUO_3 was not found to have a cubic structure but was found to adopt the CaTiO_3 structure.

A diagrammatic presentation of radius data for $A^{2+}B^{4+}O_3$ type compounds is shown in Fig. 2.2. The regions are determined from experimental data for room-temperature studies. While this diagram holds well for compounds, there are some discrepancies in the boundaries of the ferroelectric field for solid solutions. The diagram, however, is still a useful summary of structural data.

Oxides of the $A^{3+}B^{3+}O_3$ Type

The largest number of $A^{3+}B^{3+}O_3$ type compounds were found by Geller and Wood⁽⁶⁾ to have an orthorhombic structure similar to that for $GdFeO_3$, Fig. 2.3. The space group for these compounds is $Pbnm$ and the atoms are in the following positions:

Four Gd atoms at $\pm(x, y, \frac{1}{4}; \frac{1}{2} - x, y + \frac{1}{2}, \frac{1}{4})$ $x = -0.018$
 $y = 0.060$.

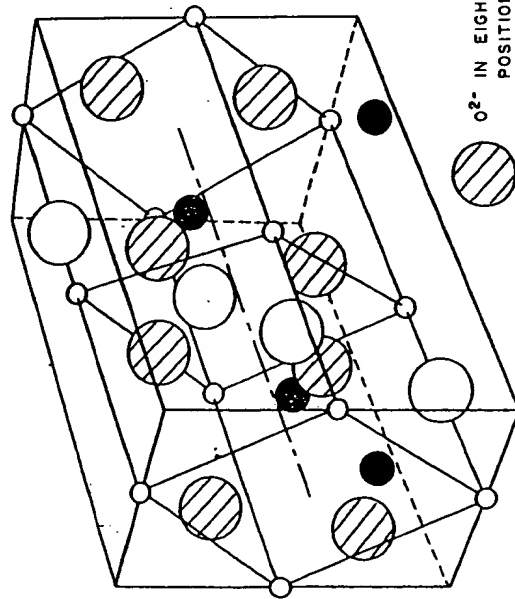


Fig. 2.3. Structure of $GdFeO_3$ (after Geller⁽⁶⁾).

Four Fe atoms at $\frac{1}{2} 0 0; \frac{1}{2} 0 \frac{1}{2}; 0 \frac{1}{2} 0; 0 \frac{1}{2} \frac{1}{2}$.

Four O atoms at the same positions listed for Gd atoms, but with $x = 0.05$, $y = 0.47$ (ref. 3)

and

eight O atoms at $\pm(xyz; \frac{1}{2} - x, y + \frac{1}{2}, \frac{1}{2} - z; \bar{x}, \bar{y}, z + \frac{1}{2}; x + \frac{1}{2}, \frac{1}{2} - y, \bar{z})$

where $x = -0.29$, $y = 0.275$, $z = 0.05$.

The relationship of the orthorhombic unit cell to that of the perovskite structure can be seen in Fig. 2.3. The unit cell for the $GdFeO_3$ structure, $a_0 = 5.346$ Å, $b_0 = 5.616$ Å, $c = 7.668$ Å contains four distorted perovskite units.

Looby and Katz⁽⁷⁾ thought they had found a new type of structure adopted by $YCrO_3$, and indexed the powder pattern on the basis of a monoclinic cell, but pointed out that the correct unit cell might be orthorhombic. Geller and Wood⁽⁶⁾ were able to show from single crystal studies that the structure of $YCrO_3$ was similar to that of $GdFeO_3$. Thus, it is quite possible that many additional $A^{3+}B^{3+}O_3$ compounds which have been reported to have monoclinic structures could really have orthorhombic structures. Some of the compounds which were confirmed as having the $GdFeO_3$ structure are $EuAlO_3$, $EuFeO_3$, $GdAlO_3$, $GdCrO_3$, $GdVO_3$, $LaAlO_3$, $LaCrO_3$, $LaGaO_3$, $LaScO_3$, $NdAlO_3$, $NdCrO_3$, $NdFeO_3$, $NdVO_3$, $NdGaO_3$, $PrCrO_3$, $PrFeO_3$, $PrGaO_3$, $PrScO_3$, $PrVO_3$, $SmAlO_3$, $SmCrO_3$, $SmFeO_3$, $YScO_3$, $YAlO_3$, $YCrO_3$, $YFeO_3$, $NdScO_3$ and $GdScO_3$. Two of these compounds, $LaGaO_3$ and $SmAlO_3$ transform to a rhombohedral form at 900° and 850° C respectively. The compounds $LaAlO_3$, $NdAlO_3$ and $PrAlO_3$ also have this rhombohedral structure which is probably quite similar to that of $GdFeO_3$.

Figure 2.4 presents a classification of $A^{3+}B^{3+}O_3$ type compounds according to the constituent ionic radii. All of the compounds in the upper left of the diagram form perovskite-type structures. Where both the A and B ions are small, the compounds have the corundum- or ilmenite-type structures. When both the A and B ions are large, the phases form La_2O_3 type structures.

While none of the $A^{3+}B^{3+}O_3$ type compounds have the "ideal" cubic perovskite structure, the rhombohedral perovskites such as $LaAlO_3$ are only slightly distorted. The search for laser host materials with cubic crystallographic sites for Cr^{3+} substitution has produced considerable interest in these compounds. Lanthanum aluminum oxide, $LaAlO_3$, with $\alpha = 90.4'$, has been widely studied as a laser host material. However, the phase transition at 435° has presented considerable problems in trying to grow it in single crystal form.

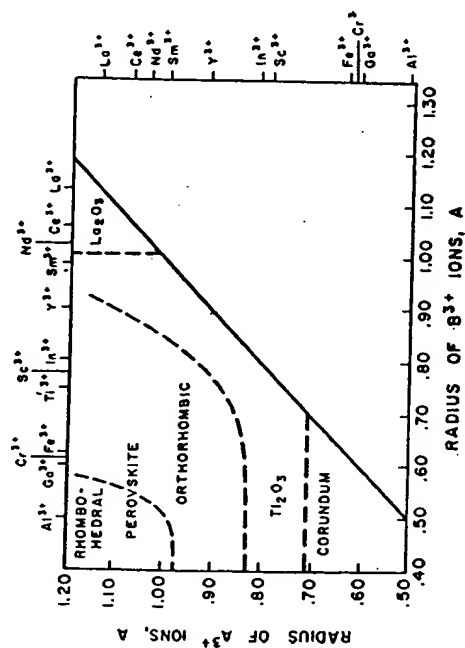


Fig. 2.4. Classification of perovskite-type compounds, $A^{3+}B^{3+}O_3$ (after Roth⁽⁶⁾).

Non-stoichiometric Ternary Oxides

Probably the best known non-stoichiometric ternary oxides are the tungsten bronzes. The phases Na_xWO_3 have been found to have the cubic perovskite structure in the range $0.3 < x < 0.95$ ⁽⁸⁾ and the phases Li_xWO_3 in the range $0.35 < x < 0.57$.⁽⁹⁾ The lattice constants of these materials vary linearly with increasing amounts of alkali metal ion. A smaller range of non-stoichiometry exists in the strontium niobium bronzes⁽⁹⁾ where the alkaline earth metal ion mole fraction can vary from 0.7 to 0.9 and in La_xVO_3 where $0.66 < x < 1$.

Rooksby *et al.*⁽¹⁰⁾ reported the preparation of a group of perovskite-type rare earth niobates and tantalates. The struc-

ture of these $A_{0.33}B_{0.33}O_3$ type compounds was tetragonal, orthorhombic or monoclinic.

The existence of these cation deficient compounds is not surprising in view of the fact that ReO_3 is stable without A ions. The deficiencies can be tolerated over ranges of composition without changes in structure. However, different amounts of A ion are necessary to stabilize the structure depending on which B ion is in the octahedrally coordinated sites.

Oxygen deficiencies have also been observed in the perovskite structure. The phases $SrB_{0.3-x}O_3$ where B is Ti or V have been found to have the perovskite structure over the range $0 < x < 0.5$ for the titanium phases and $0 < x < 0.25$ for the vanadium phases. Both $SrVO_{2.75}$ and $SrTiO_{2.5}$ were found to have cubic structures. Similar phases have been reported in the $SrFeO_{3-x}$,⁽¹¹⁻¹³⁾ $CaMnO_{3-x}$,^(13, 14) and $SrCoO_{3-x}$,⁽¹⁵⁾ systems although the oxygen deficiency is not as great.

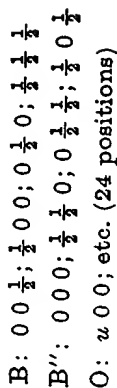
Coates and McMillan showed that cubic perovskite structures could be obtained in calcium perovskites, which are normally distorted, by producing oxygen vacancies. The phases $CaMnO_3$ and $CaTiO_3$ become cubic with the introduction of deficiencies. As these authors point out, studies in this area are not abundant enough to obtain a good understanding of the effect of nonstoichiometry on the perovskite structure.

2.2. COMPLEX OXIDES

Oxides of the $A^{2+}(B_0^{2+}B_0^{2+}B_0^{2+})O_3$ Type

The structure of compounds which contain twice as many B^{3+} ions as B^{2+} ions is not well established. Fresia *et al.*,⁽¹⁶⁾ who prepared one of the first compounds of this type, $Ba(Sc_{0.67}W_{0.33})O_3$, felt that it probably had an ordered perovskite structure described by Steward and Rooksby.⁽¹⁶⁾ In this structure the two different B ions alternate at the corners of the simple cubic unit cell of the perovskite structure so that the cell edge has to be doubled (see Fig. 2.5). The space group is $Fm\bar{3}m$ and the atomic positions are:

$$A: \frac{1}{4} \frac{1}{4} \frac{1}{4}; \frac{1}{4} \frac{1}{4} \frac{1}{4}; \frac{3}{4} \frac{1}{4} \frac{1}{4}; \frac{3}{4} \frac{3}{4} \frac{1}{4}; \frac{3}{4} \frac{1}{4} \frac{3}{4}; \frac{1}{4} \frac{3}{4} \frac{3}{4}; \frac{1}{4} \frac{1}{4} \frac{3}{4}; \frac{3}{4} \frac{3}{4} \frac{3}{4}$$



Since the B' and B'' have to be present in equal amounts in this structure, $\text{Ba}(\text{Sc}_{0.57}\text{W}_{0.33})\text{O}_3$ should probably be written

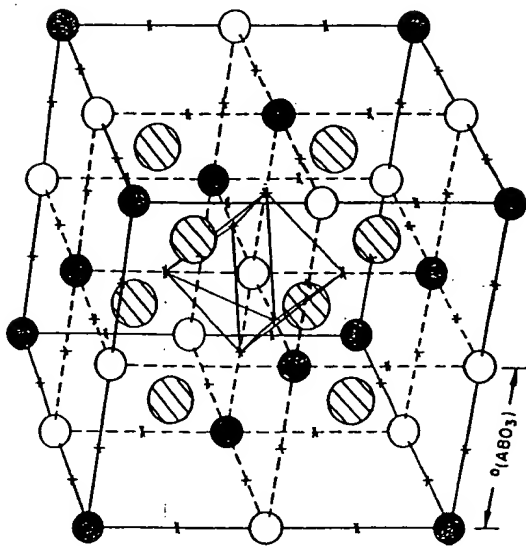


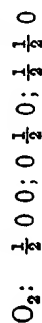
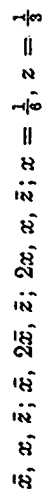
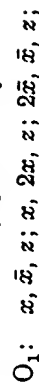
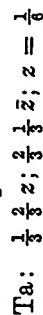
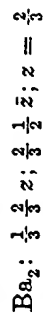
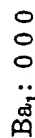
FIG. 2.5. The $(\text{NH}_4)_2\text{FeF}_6$ structure: cubic ordered perovskite-type $\text{A}(\text{B}'_{0.57}\text{B}''_{0.33})\text{O}_3$ (after L. Pauling, *J. Am. Chem. Soc.* 46, 2738 (1924)).

$\text{Ba}[\text{Sc}_{0.5}(\text{Sc}_{0.12}\text{W}_{0.33})\text{O}_3]$ where three-quarters of the Sc ions are on the B' sites and one-quarter of the Sc ions are randomly distributed with the W atoms on the B'' sites. Sleight and Ward⁽¹⁷⁾ also found that it was necessary to use the doubled unit cell to index all observed lines in the X-ray patterns of $\text{A}(\text{B}'_{0.57}\text{U}_{0.33})\text{O}_3$ and $\text{A}(\text{B}'_{0.57}\text{Re}_{0.33})\text{O}_3$ ⁽¹⁸⁾ compounds. When

the compound $\text{Sr}(\text{Cr}_{0.5}\text{Re}_{0.5})\text{O}_3$ was changed in composition to obtain $\text{Sr}(\text{Cr}_{0.57}\text{Re}_{0.33})\text{O}_3$ no new phase appeared but the lattice expanded and the intensities of the superlattice lines in the X-ray patterns showed a marked decrease. However, no detailed structure studies have been conducted to determine the arrangement of atoms in these phases.

Oxides of the $\text{A}^{2+}(\text{B}_{0.33}^{2+}\text{B}_{0.67}^{5+})\text{O}_3$ Type

A large number of compounds containing niobium and tantalum as one of the B ions in perovskite structure and a divalent ion as the other B ion were prepared by Roy⁽¹⁹⁾ and independently by Galasso *et al.*⁽²⁰⁾ Both workers originally could not account for the extra lines which most of the X-ray patterns of these compounds contained. Once Galasso *et al.*⁽²¹⁾ found that one of the compounds, $\text{Ba}(\text{Sr}_{0.33}\text{Ta}_{0.67})\text{O}_3$, had a new ordered perovskite structure; subsequent studies showed that many of the $\text{A}^{2+}(\text{B}_{0.33}^{2+}\text{B}_{0.67}^{5+})\text{O}_3$ adopted this structure. The structure of $\text{Ba}(\text{Sr}_{0.33}\text{Ta}_{0.67})\text{O}_3$ is based on space group $P\bar{3}m1$ with atoms in the unit cell at the following locations:



The structure is shown in Figs. 2.6 and 2.7. Note that if the perovskite structure is described as close-packed layers of A and oxygen ions perpendicular to the [111] direction with small B ions in the octahedral holes between the layers, then these B ions Sr and Ta each form planes of atoms. These planes are parallel to the close-packed layers and, since there are twice as many tantalum ions as strontium ions, the repeat scheme is two layers of tantalum ions and one of strontium ions. It is interesting that the ordered structure of $\text{A}(\text{B}'_{0.5}\text{B}''_{0.5})\text{O}_3$ type compounds when observed in the same way in the [111]

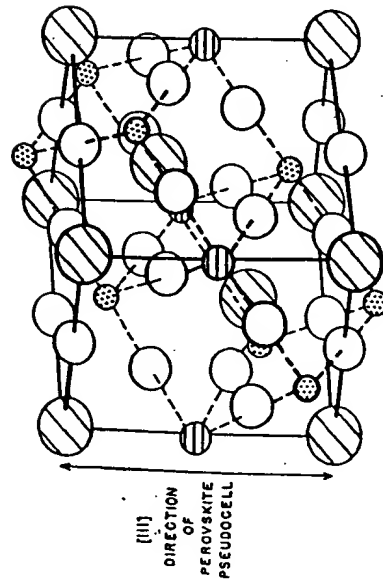


FIG. 2.6. The $\text{Ba}(\text{Sr}_{0.33}\text{Ta}_{0.67})\text{O}_3$ structure (after Galasso *et al.* (11)).

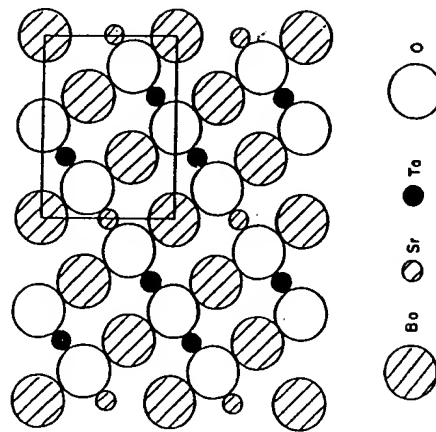


FIG. 2.7. Three-layer repeat sequence in $\text{Ba}(\text{Sr}_{0.33}\text{Ta}_{0.67})\text{O}_3$. The (110) plane (after Galasso *et al.* (11)).

direction, consists of alternating layers, one of which contain B' ions and the other B'' ions.

A study of $\text{Ba}(\text{B}_{0.33}^{2+}\text{Ta}_{0.67}^{5+})\text{O}_3$ compounds showed a decrease in the ordering as the difference in the size of the B^{2+} and Ta^{5+} ions became smaller. (22) The results were confirmed in a later investigation of $\text{Ba}(\text{B}_{0.33}^{2+}\text{Nb}_{0.67}^{5+})\text{O}_3$ compounds. (23) In some cases the ordering lines in the X-ray patterns were very broad and became sharp when the samples were annealed at high temperatures. This observation was attributed to the existence of small ordering domains which grew at higher temperatures. Thus the X-ray patterns of some of the compounds which might be expected to be ordered because of the large size difference of the B' and B'' ions did not show the ordering lines if they could not be annealed at high temperatures because of low melting points.

Oxides of the $\text{A}^{2+}(\text{B}_{0.5}^{3+}\text{B}_{0.5}^{5+})\text{O}_3$, $\text{A}^{2+}(\text{B}_{0.5}^{3+}\text{B}_{0.5}^{5+})\text{O}_3$, $\text{A}^{3+}(\text{B}_{0.5}^{3+}\text{B}_{0.5}^{5+})\text{O}_3$ Types

The largest group of complex perovskite type compounds has the general formula $\text{A}(\text{B}'_x\text{B}''_{1-x})\text{O}_3$. When the structure of these compounds is ordered, and most of them are, they adopt the structure shown in Fig. 2.5. It was postulated by Galasso *et al.* (20) that an ordered distribution of the B ions is most probable when a large difference existed in either their charges or ionic radii. This hypothesis can be validated qualitatively by looking at the data below in Table 2.1.

TABLE 2.1. Structural Data for $\text{A}(\text{B}'_x\text{B}''_{1-x})\text{O}_3$ Type Compounds

Compound	Difference in charge of B ions	Difference in ionic radii of B ions	Arrangement of B ions
$\text{Ba}(\text{Fe}_{0.5}^{2+}\text{Ta}_{0.5}^{5+})\text{O}_3$	2	0.04	Random ²⁰
$\text{Ba}(\text{Mg}_{0.5}^{2+}\text{W}_{0.5}^{6+})\text{O}_3$	4	0.05	Ordered ¹⁶
$\text{Ba}(\text{La}_{0.5}^{3+}\text{Ta}_{0.5}^{5+})\text{O}_3$	2	0.46	Ordered ²¹
$\text{Ba}(\text{Sr}_{0.5}^{2+}\text{Ta}_{0.5}^{5+})\text{O}_3$	3	0.44	Ordered ²¹
$\text{Ba}(\text{Zr}_{0.5}^{4+}\text{Nb}_{0.5}^{5+})\text{O}_3$	3	0.05	Random ²⁰

A study of $\text{Ba}(\text{Mg}_{0.5}^2\text{Nb}_{0.5}^5)\text{O}_3$ ⁽²⁴⁾ type compounds indicated that the critical percentage difference in ionic radii between B ions which causes ordering lies between 7% and 17%.

The first compounds with this ordered structure were reported by Steward and Rooksby,⁽¹⁶⁾ who found that a number of alkaline earth tungstates and molybdates of the $\text{A}(\text{A}_{0.5}\text{B}_{0.5}')\text{O}_3$ type where A is an alkaline earth ion and B' is Mo or W have this structure. The structures of $\text{Ba}(\text{Ca}_{0.5}\text{W}_{0.5})\text{O}_3$ and $\text{Ba}(\text{Ca}_{0.5}\text{Mo}_{0.5})\text{O}_3$ were reported to be cubic at room temperature while the $\text{Ba}(\text{Sr}_{0.5}\text{W}_{0.5})\text{O}_3$ structure was distorted and became cubic only after heating to 500°C. Fresia *et al.*⁽¹⁵⁾ found that other ions such as Zn^{2+} , Fe^{2+} , Co^{2+} and Ni^{2+} could be used as the B' ion in the ordered perovskite structure without distortion. However, when compounds were prepared with strontium in the A position the structures were distorted. It should be noted at this point that some authors index the tetragonal and orthorhombic distortion of the cubic ordered unit cell by using the ~ 8 Å edges, while others use an ~ 5.7 Å face diagonal for two axes and ~ 8 Å edge for the third.

Sleight and Ward⁽¹⁷⁾ in a study of $\text{A}(\text{B}_{0.5}^2\text{U}_{0.5})\text{O}_3$ type perovskites also found that all of the compounds containing strontium in the A position had distorted structures. The unit cells were pseudomonoclinic, but the powder patterns were indexed on a smaller orthorhombic unit cell. Using a tolerance factor

$$t = R_A + R_O / \sqrt{2} [(R_B^{2+} + R_B^{5+})/2 + R_O]$$

they calculated that a number of compounds containing barium in the A position should form the cubic ordered perovskite structure, and observed that they did form this structure.

Some of the most interesting compounds were those containing Mo^{5+} , W^{5+} or Re^{5+} as one of the B ions and another paramagnetic ion as the other because of the ferromagnetic properties they exhibited. These compounds will be discussed in detail in another section.

By adjustment of the oxidation state by valence compensation the compounds $\text{Ba}(\text{Li}_{0.5}\text{Os}_{0.5})\text{O}_3$ and $\text{Ba}(\text{Na}_{0.5}\text{Os}_{0.5})\text{O}_3$

were prepared.⁽¹⁸⁾ It appears that the osmium has a valence state of 7 in these compounds, a value not reported previously for this element. Similar compounds also were prepared with Re^{7+} as the B' ion.

Lanthanum also has been introduced in the A position of the perovskite structure with two ions in the B position. The symmetry of the structure of these compounds has not been resolved, but it appears that they adopt some modification of the ordered perovskite structure. Preliminary single crystal studies indicate that they could have ordered cubic unit cells.⁽²⁵⁾ This would be interesting in light of the fact that there are no $\text{A}^{3+}\text{B}^{3+}\text{O}_3$ type ternary oxides with the simple cubic perovskite structure.

Oxides of the $\text{A}^{2+}(\text{B}_{0.25}^1\text{B}_{0.75}^{3+})\text{O}_3$ Type

It was expected, because of the large charge difference in the B ions, that $\text{Ba}(\text{Nb}_{0.25}\text{Ta}_{0.75})\text{O}_3$ and $\text{Sr}(\text{Nb}_{0.25}\text{Ta}_{0.75})\text{O}_3$ would be ordered. However, no superstructure lines were observed in the X-ray patterns of these two compounds.⁽²⁷⁾ It should be noted that attempts to prepare compounds with smaller amounts of the B ion than 0.25 were not successful.

Oxygen-deficient Oxides of the $\text{A}^{2+}(\text{B}_{0.5}^3\text{B}_{0.5}^{4+})\text{O}_{2.75}$ and $\text{A}^{2+}(\text{B}_{0.5}^2\text{B}_{0.5}^{5+})\text{O}_{2.75}$ Types

All compounds with the general formula $\text{A}^{2+}(\text{B}_{0.5}'\text{B}_{0.5}'')\text{O}_{2.75}$ were found to have the ordered structure. Compounds containing tantalum as the B' ions were first reported by Brixner.⁽²⁴⁾ Later uranium and molybdenum were also found to form these oxygen-deficient compounds.^(17, 28)

A summary of the oxides with the perovskite structure and structural data are presented in Table 2.2.

TABLE 2.2. Unit Cell Data for Perovskite-type Compounds

A ²⁺ B ⁴⁺ O ₃				
Compound	a (Å)	b (Å)	c (Å)	Remarks
AgNbO ₃	7.888	15.660	7.888	$\beta = 90.57^\circ$
AgTaO ₃	3.931	3.914	3.931	$\beta = 90.36^\circ$
CaIO ₃	9.324 } or			cubic
	4.66 } or			cubic
KIO ₃	8.92 } or			$\alpha = 80^\circ 24'$ rhom-
	4.410 } or			bohedral
KNbO ₃	3.9714	5.6948	5.7203	orthorhombic
KTaO ₃	3.9885			cubic
NaNbO ₃	5.512	5.577	3.885	orthorhombic
NaTaO ₃	3.8851	5.4778	5.5239	orthorhombic
RbIO ₃	4.62 } or			cubic
	9.04 } or			$\alpha = 89.34^\circ$ rhom-
TlIO ₃	4.510			bohedral

A²⁺B⁴⁺O₃

A ²⁺ B ⁴⁺ O ₃				
Compound	a (Å)	b (Å)	c (Å)	Remarks
BaCeO ₃	4.397			4, 5, 35, 42
BaFeO ₃	3.98		4.01	tetragonal
BaMoO ₃	4.0404			43, 44
BaPbO ₃	4.273			45
BaPrO ₃	8.708 } or			46
	4.354 } or			31, 47
BaPuO ₃	4.39			48
BaSnO ₃	4.117			1, 4, 5
BaThO ₃	4.480			4, 35, 42, 47
	8.985			monoclinic
BaTiO ₃	3.989		4.029	tetragonal
BaUO ₃	4.387			pseudocubic
BaZrO ₃	4.192			cubic
CaCeO ₃	7.70			cubic
CaHfO ₃				31, 50
CaMnO ₃	10.683	7.449	10.476	orthorhombic
				orthorhombic
CaMoO ₃	7.80	7.77	7.80	$\beta = 91^\circ 23'$ mono-
				clinic

TABLE 2.2 (cont.)

A²⁺B⁴⁺O₃ (cont.)

Compound	a (Å)	b (Å)	c (Å)	Remarks	Refer- ences
CaSnO ₃	5.518	7.884	5.684	orthorhombic	4, 54
CaThO ₃	8.74			monoclinic,	
				pseudocubic	31
CaTiO ₃	5.381	7.845	5.443	orthorhombic	54
CaUO ₃	5.78	8.29	5.97	orthorhombic	49
CaVO ₃	5.326	7.547	5.352	orthorhombic	52
CaZrO ₃	5.597	8.008	5.758	orthorhombic	55
CdCeO ₃	7.65			orthorhombic	
				or cubic	31, 50
CdSnO ₃	5.547	5.577	7.867	orthorhombic	5
CdThO ₃	8.74			pseudocubic	31
CdTiO ₃	5.301	7.806	5.419	orthorhombic	5
CdZrO ₃				orthorhombic	31
EuTiO ₃	3.897				56
MgCeO ₃	8.54				31
PbCeO ₃	7.62			orthorhombic	31, 50
PbHfO ₃				pseudotetragonal	57
PbSnO ₃	7.86	8.13		tetragonal	31
PbTiO ₃	3.896	4.136		tetragonal	58
PbZrO ₃	9.28			pseudocubic,	
				orthorhombic	1
SrCeO ₃	5.986	8.531	6.125	orthorhombic	4, 5, 31
SrCoO ₃	7.725				13
SrFeO ₃	3.869				13
SrHfO ₃	4.069 } or			orthorhombic	31
	8.138 } or				
SrMoO ₃	3.9751				45
SrPbO ₃	5.864	5.949	8.336	orthorhombic	46
SrRuO ₃				cubic	59
SrSnO ₃	4.0334 } or			cubic	1, 4, 60
	8.070 } or				
SrThO ₃	8.84			pseudocubic	31
SrTiO ₃	3.904			cubic	5
SrUO ₃	6.01	8.60	6.17	orthorhombic	49
SrZrO ₃	5.792 } or	8.189	5.818	orthorhombic	4, 5, 31
	8.218 } or			cubic	

A²⁺B³⁺O₃

A ²⁺ B ³⁺ O ₃				
Compound	a (Å)	b (Å)	c (Å)	Remarks
BaAlO ₃	7.61		7.94	tetragonal
				31

TABLE 2.2 (cont.)

 $A^{3+}B^{3+}O_3$ (cont.)

Compound	a (Å)	b (Å)	c (Å)	Remarks	References
BiCrO ₃	3.90	3.87	3.90	$\alpha = \gamma = 90^\circ 35'$ triglinio	61
BiMnO ₃	3.93	3.98	3.93	$\beta = 89^\circ 10'$ $\alpha = \gamma = 91^\circ 25'$ triglinio	61
CeAlO ₃	3.767			$\beta = 90^\circ 55'$ tetragonal	62, 63
CeCrO ₃	3.866		3.794		63, 64, 65
CeFeO ₃	3.900			pseudocubic, orthorhombic	64, 63
CeGaO ₃	3.879			cubic, orthorhombic orthorhombic	64
CeSeO ₃	3.80				64
CeVO ₃	7.77				65, 66
CrBiO ₃	5.21	8.08		tetragonal	31
DyAlO ₃	5.30	5.31	7.40	orthorhombic	67
DyFeO ₃	3.70	5.60	7.62	orthorhombic	67
DyMnO ₃	5.271	5.292	7.458	cubic	68
EuAlO ₃	3.803			GdFeO ₃ structure	63, 69
EuCrO ₃	5.371	5.611	7.686	GdFeO ₃ structure	63
EuFeO ₃					6, 63, 69
FeBiO ₃	7.64 } or 3.965 }			$\alpha = 89^\circ 28'$ rhom- bohedral	70, 71, 72
GdAlO ₃	5.247	5.304	7.447	GdFeO ₃ structure	63, 67, 69
GdCoO ₃	3.732	3.807	3.676	orthorhombic	73
GdCrO ₃	5.312	5.514	7.611	GdFeO ₃ structure	74
GdFeO ₃	5.346	5.616	7.668	orthorhombic	6, 75
GdMnO ₃	3.82	5.756	7.925	GdFeO ₃ structure	14
GdScO ₃	5.487	5.623	7.638	GdFeO ₃ structure	74
GdVO ₃	5.345			$\alpha = 90^\circ 4'$ rhom- bohedral	74
LaAlO ₃	3.788				5

TABLE 2.2 (cont.)

 $A^{3+}B^{3+}O_3$ (cont.)

Compound	a (Å)	b (Å)	c (Å)	Remarks	References
LaCoO ₃	3.824 } or 7.651 }			$\alpha = 90^\circ 42'$ rhom- bohedral	13, 63, 65, 76, 77, 78
LaCrO ₃	5.477	5.514	7.755	GdFeO ₃ structure	74
LaFeO ₃	5.556	5.565	7.862	GdFeO ₃ structure	5, 6
LaGaO ₃	5.496	5.524	7.787	GdFeO ₃ structure	74
LaInO ₃	5.723	8.207	5.914	orthorhombic $\alpha = 90^\circ 41'$	5, 64
LaNiO ₃	7.676			pseudocubic	78, 79
LaRhO ₃	3.94			GdFeO ₃ structure	76, 80
LaScO ₃	5.678	5.787	8.098	GdFeO ₃ structure	64, 74
LaTiO ₃	3.92			cubic	81, 82
LaVO ₃	3.99 } or 7.842 }			orthorhombic rhombohedral	65, 66, 83
LaYO ₃	3.752				84
NdAlO ₃	3.777			GdFeO ₃ structure	63, 67, 69
NdCoO ₃	5.412	5.494	7.695	GdFeO ₃ structure	85, 73
NdCrO ₃	5.441	5.573	7.753	GdFeO ₃ structure	74
NdFeO ₃	5.428	5.502	7.706	GdFeO ₃ structure	6, 64
NdGaO ₃	5.627	8.121	5.891	orthorhombic	74
NdInO ₃	3.80	5.771	7.998	GdFeO ₃ structure	5, 64
NdMnO ₃	5.574	5.589	7.733	GdFeO ₃ structure	68
NdScO ₃	5.440			$\alpha = 60^\circ 20'$ rhombohedral	64, 74
NdVO ₃	3.757 } or 5.31 }			$\alpha = 90^\circ 13'$ rhombohedral	74
PrAlO ₃	3.787			GdFeO ₃ structure	48, 63, 69
PrCoO ₃	5.444	5.484	7.710	GdFeO ₃ structure	65, 73
PrCrO ₃					74

TABLE 2.2 (cont.)

 $A^{3+}B^{3+}O_3$ (cont.)

Compound	a (Å)	b (Å)	c (Å)	Remarks	References
PrFeO ₃	5.495	5.578	7.810	GdFeO ₃ structure	74
PrGaO ₃	5.465	5.495	7.729	GdFeO ₃ structure	74
PrMnO ₃	3.82				68
PrScO ₃	5.615	5.776	8.027	GdFeO ₃ structure	74
PrVO ₃	5.477	5.545	7.759	GdFeO ₃ structure	74
PuAlO ₃	5.33			$\alpha = 56^\circ 4'$ structure	74
PuCrO ₃	5.46	5.51	7.76	GdFeO ₃ structure	48
PuMnO ₃	3.86			pseudocubic structure	48
PuVO ₃	5.48	5.51	7.78	GdFeO ₃ structure	48
SmAlO ₃	5.285	5.290	7.473	GdFeO ₃ structure	48
SmCoO ₃	3.747	3.803	3.728	orthorhombic structure	64, 63, 89, 74
SmCrO ₃	5.372	5.502	7.650	GdFeO ₃ structure	85, 73
SmFeO ₃	5.394	5.592	7.711	GdFeO ₃ structure	74
SmInO ₃	5.589	8.082	5.886	orthorhombic structure	6, 64
SmVO ₃	3.89				5, 65
YAlO ₃	5.179	5.329	7.370	GdFeO ₃ structure	6
YCrO ₃	5.247	5.518	7.540	GdFeO ₃ structure	6, 7, 64, 74
YFeO ₃	5.302	5.559	7.622	GdFeO ₃ structure	65
YSrO ₃	5.431	5.712	7.894	GdFeO ₃ structure	74

 A_2BO_3 and ABO_{3-x}

Ce _{0.33} NbO ₃	3.89	3.91	7.86	orthorhombic	10
Ce _{0.33} TaO ₃	3.90	3.91	7.86	orthorhombic	10

TABLE 2.2 (cont.)

 A_2BO_3 and ABO_{3-x} (cont.)

Compound	a (Å)	b (Å)	c (Å)	Remarks	References
Dy _{0.33} TaO ₃	3.83	3.83	7.75	$\gamma = 90.8^\circ$ monoclinic	10
Gd _{0.33} TaO ₃	3.87	3.89	7.73	orthorhombic	10
La _{0.33} NbO ₃	3.91		7.90	tetragonal	10
La _{0.33} TaO ₃	3.92		7.88	tetragonal	10
Nd _{0.33} NbO ₃	3.90	3.91	7.76	orthorhombic	10
Nd _{0.33} TaO ₃	3.91		7.77	tetragonal	10
Pr _{0.33} NbO ₃	3.91	3.92	7.77	orthorhombic	10
Pr _{0.33} TaO ₃	3.91	3.92	7.78	orthorhombic	10
Sm _{0.33} TaO ₃	3.89		7.75	tetragonal	10
Y _{0.33} TaO ₃	3.82	3.83	7.74	$\gamma = 90.9^\circ$ monoclinic	10
Yb _{0.33} TaO ₃	3.79	3.80	7.70	$\gamma = 91.6^\circ$ monoclinic	10
Ca _{0.33} TaO ₃	11.088 ($x=1$)	7.505	5.378	orthorhombic	85
Li ₂ WO ₃	3.72			cubic $x = 0.35-0.57$	86
Na ₂ WO ₃	($x=1$)			cubic $x = 0.7-1.0$	8, 50, 87, 88, 89, 80, 91, 92
Sr _{0.33} Nb _{0.22} Nb _{0.22} O ₃	($x=0.2$)			cubic	9
CaMnO _{3-x}	3.981				9
SrCoO _{3-x}	($x=0.45$)			$x = 0.7-0.9$	13, 14
SrFeO _{3-x}	4.016				13
SrTiO _{3-x}					11, 12, 13
SrVO _{3-x}					83

 $A(B'_{0.47}B''_{0.33})O_3$

Ba(Al _{0.47} W _{0.33})O ₃					93
Ba(Dy _{0.47} W _{0.33})O ₃	8.386			(NH ₄) ₂ FeF ₆ structure	93

TABLE 2.2 (cont.)

 $A(B_{0.67}B'_{0.33})O_3$ (cont.)

Compound	a (Å)	b (Å)	c (Å)	Remarks	References
Ba(Er _{0.67} W _{0.33})O ₃	8.386			(NH ₄) ₂ FeF ₆ structure	93
Ba(Eu _{0.67} W _{0.33})O ₃	8.605			(NH ₄) ₂ FeF ₆ structure	93
Ba(Fe _{0.67} U _{0.33})O ₃	8.232			(NH ₄) ₂ FeF ₆ structure	17
Ba(Gd _{0.67} W _{0.33})O ₃	8.411			(NH ₄) ₂ FeF ₆ structure	93, 94
Ba(In _{0.67} U _{0.33})O ₃	8.512			(NH ₄) ₂ FeF ₆ structure	17
Ba(In _{0.67} W _{0.33})O ₃	8.321			ordered structure	93
Ba(La _{0.67} W _{0.33})O ₃	8.58			(NH ₄) ₂ FeF ₆ structure	94
Ba(Lu _{0.67} W _{0.33})O ₃	8.513			(NH ₄) ₂ FeF ₆ structure	93
Ba(Nd _{0.67} W _{0.33})O ₃	8.49			(NH ₄) ₂ FeF ₆ structure	17
Ba(Sc _{0.67} U _{0.33})O ₃	8.24			(NH ₄) ₂ FeF ₆ structure	15, 93
Ba(Y _{0.67} U _{0.33})O ₃	8.70			(NH ₄) ₂ FeF ₆ structure	17
Ba(Y _{0.67} W _{0.33})O ₃	8.374			(NH ₄) ₂ FeF ₆ structure	93
Ba(Yb _{0.67} W _{0.33})O ₃	8.01			(NH ₄) ₂ FeF ₆ structure	93
Pb(Fe _{0.67} W _{0.33})O ₃	8.00			(NH ₄) ₂ FeF ₆ structure	95, 96
Sr(Cr _{0.67} Re _{0.33})O ₃	7.89			(NH ₄) ₂ FeF ₆ structure	18
Sr(Fe _{0.67} U _{0.33})O ₃	3.945			(NH ₄) ₂ FeF ₆ structure	17
Sr(In _{0.67} Re _{0.33})O ₃	8.297			(NH ₄) ₂ FeF ₆ structure	18
Sr(La _{0.67} Nb _{0.33})O ₃	5.58	5.58	7.89	tetragonal structure	47, 94
Sr(La _{0.67} Sb _{0.33})O ₃	5.57	5.57	7.89	orthorhombic structure	18

TABLE 2.2 (cont.)

 $A^{2+}(B_{0.33}^{2+}B'_{0.67})O_3$ (cont.)

Compound	a (Å)	b (Å)	c (Å)	Remarks	References
Ba(Ca _{0.33} Nb _{0.67})O ₃	5.92		7.25	hex. ordered Ba(Sr _{0.33} Ta _{0.67})O ₃ structure	23
Ba(Ca _{0.33} Ta _{0.67})O ₃	5.895		7.284	hex. ordered Ba(Sr _{0.33} Ta _{0.67})O ₃ structure	21, 97, 98
Ba(Cd _{0.33} Nb _{0.67})O ₃	4.168				23
Ba(Cd _{0.33} Ta _{0.67})O ₃	4.167				22
Ba(Co _{0.33} Nb _{0.67})O ₃	4.09				20
Ba(Co _{0.33} Ta _{0.67})O ₃	5.778		7.082	hex. ordered Ba(Sr _{0.33} Ta _{0.67})O ₃ structure	19, 22
Ba(Cu _{0.33} Nb _{0.67})O ₃	8.04		8.40	tetragonal structure	94
Ba(Fe _{0.33} Nb _{0.67})O ₃	4.085				23
Ba(Fe _{0.33} Ta _{0.67})O ₃	4.10				20
Ba(Mg _{0.33} Nb _{0.67})O ₃	5.77		7.08	hex. ordered Ba(Sr _{0.33} Ta _{0.67})O ₃ structure	20, 23, 94
Ba(Mg _{0.33} Ta _{0.67})O ₃	5.782		7.067	hex. ordered Ba(Sr _{0.33} Ta _{0.67})O ₃ structure	22, 98
Ba(Mn _{0.33} Nb _{0.67})O ₃	5.819		7.127	hex. ordered Ba(Sr _{0.33} Ta _{0.67})O ₃ structure	93
Ba(Mn _{0.33} Ta _{0.67})O ₃	4.074				22
Ba(Ni _{0.33} Nb _{0.67})O ₃	5.758		7.052	hex. ordered Ba(Sr _{0.33} Ta _{0.67})O ₃ structure	19, 23, 98
Ba(Ni _{0.33} Ta _{0.67})O ₃	4.26				19, 22, 98
Ba(Pb _{0.33} Nb _{0.67})O ₃	4.25				23
Ba(Pb _{0.33} Ta _{0.67})O ₃	5.95		7.47	hex. ordered Ba(Sr _{0.33} Ta _{0.67})O ₃ structure	22
Ba(Zn _{0.33} Nb _{0.67})O ₃	4.094				20, 21
Ba(Zn _{0.33} Ta _{0.67})O ₃	5.782		7.097	hex. ordered Ba(Sr _{0.33} Ta _{0.67})O ₃ structure	20, 23, 96
Ca(Ni _{0.33} Nb _{0.67})O ₃	3.88				20, 22, 98
Ca(Ni _{0.33} Ta _{0.67})O ₃	3.93				96
Pb(Co _{0.33} Nb _{0.67})O ₃	4.04				19
Pb(Co _{0.33} Ta _{0.67})O ₃	4.01				96, 99

TABLE 2.2 (cont.)

 $A^{3+}(B_{0.33}^{1+}B_{0.67}^{4+})O_3$ (cont.)

Compound	a (Å)	b (Å)	c (Å)	Remarks	References
Pb(Mg _{0.33} Nb _{0.67})O ₃	4.041				96, 100
Pb(Mg _{0.33} Ta _{0.67})O ₃	4.02				96, 99
Pb(Mn _{0.33} Nb _{0.67})O ₃					96
Pb(Ni _{0.33} Nb _{0.67})O ₃	4.025				96, 100
Pb(Ni _{0.33} Ta _{0.67})O ₃	4.01				96, 99
Pb(Zn _{0.33} Nb _{0.67})O ₃	4.04				99
Sr(Ca _{0.33} Nb _{0.67})O ₃	5.76		7.16	hex. ordered Ba(Sr _{0.33} Ta _{0.67})O ₃ structure (NH ₄) ₂ FeF ₆ structure	23
Sr(Ca _{0.33} Sb _{0.67})O ₃	8.17				94
Sr(Ca _{0.33} Ta _{0.67})O ₃	5.764		7.086	hex. ordered Ba(Sr _{0.33} Ta _{0.67})O ₃ structure	22
Sr(Cd _{0.33} Nb _{0.67})O ₃	4.089			(NH ₄) ₂ FeF ₆ structure	23
Sr(Co _{0.33} Nb _{0.67})O ₃	8.01			(NH ₄) ₂ FeF ₆ structure	94
Sr(Co _{0.33} Sb _{0.67})O ₃	7.99			structure	94
Sr(Co _{0.33} Ta _{0.67})O ₃	5.630		6.937	hex. ordered Ba(Sr _{0.33} Ta _{0.67})O ₃ structure	20, 22
Sr(Cu _{0.33} Sb _{0.67})O ₃	7.84		8.19	tetragonal	94
Sr(Fe _{0.33} Nb _{0.67})O ₃	3.997		4.018	tetragonal	23
Sr(Mg _{0.33} Nb _{0.67})O ₃	5.66		6.98	hex. ordered Ba(Sr _{0.33} Ta _{0.67})O ₃ structure	23
Sr(Mg _{0.33} Sb _{0.67})O ₃	7.96			(NH ₄) ₂ FeF ₆ structure	94
Sr(Mg _{0.33} Ta _{0.67})O ₃	5.652		6.951	hex. ordered Ba(Sr _{0.33} Ta _{0.67})O ₃ structure	19, 22
Sr(Mn _{0.33} Nb _{0.67})O ₃					93
Sr(Mn _{0.33} Ta _{0.67})O ₃	5.64		6.90	hex. ordered Ba(Sr _{0.33} Ta _{0.67})O ₃ structure	23, 96
Sr(Ni _{0.33} Nb _{0.67})O ₃					93
Sr(Ni _{0.33} Ta _{0.67})O ₃	5.607		6.923	hex. ordered Ba(Sr _{0.33} Ta _{0.67})O ₃ structure	20, 22
Sr(Pb _{0.33} Nb _{0.67})O ₃					93
Sr(Pb _{0.33} Ta _{0.67})O ₃					93

TABLE 2.2 (cont.)

 $A^{3+}(B_{0.33}^{1+}B_{0.67}^{4+})O_3$ (cont.)

Compound	a (Å)	b (Å)	c (Å)	Remarks	References
Sr(Zn _{0.33} Nb _{0.67})O ₃	5.66		6.95	hex. ordered Ba(Sr _{0.33} Ta _{0.67})O ₃ structure	20, 23
Sr(Zn _{0.33} Ta _{0.67})O ₃	5.664		6.951	hex. ordered Ba(Sr _{0.33} Ta _{0.67})O ₃ structure	20, 22
$A^{3+}(B_{0.33}^{1+}B_{0.67}^{4+})O_3$					
Ba(Bi _{0.33} Nb _{0.67})O ₃	8.630			(NH ₄) ₂ FeF ₆ structure	101
Ba(Bi _{0.33} Ta _{0.67})O ₃	8.568			(NH ₄) ₂ FeF ₆ structure	101
Ba(Ce _{0.33} Nb _{0.67})O ₃	4.293				102
Ba(Ce _{0.33} Pa _{0.67})O ₃	8.800			(NH ₄) ₂ FeF ₆ structure	103
Ba(Co _{0.33} Nb _{0.67})O ₃	4.06			(NH ₄) ₂ FeF ₆ structure	94
Ba(Co _{0.33} Re _{0.67})O ₃	8.086			(NH ₄) ₂ FeF ₆ structure	18
Ba(Cr _{0.33} W _{0.67})O ₃	7.88		8.61	tetragonal (NH ₄) ₂ FeF ₆ structure	104
Ba(Cu _{0.33} W _{0.67})O ₃	8.437			(NH ₄) ₂ FeF ₆ structure	94
Ba(Dy _{0.33} Nb _{0.67})O ₃	8.740			(NH ₄) ₂ FeF ₆ structure	25, 102
Ba(Dy _{0.33} Pa _{0.67})O ₃	8.740			(NH ₄) ₂ FeF ₆ structure	103
Ba(Dy _{0.33} Ta _{0.67})O ₃	8.545			(NH ₄) ₂ FeF ₆ structure	105
Ba(Er _{0.33} Nb _{0.67})O ₃	8.427			(NH ₄) ₂ FeF ₆ structure	25, 102
Ba(Er _{0.33} Pa _{0.67})O ₃	8.716			(NH ₄) ₂ FeF ₆ structure	103
Ba(Er _{0.33} Re _{0.67})O ₃	8.354			(NH ₄) ₂ FeF ₆ structure	18
Ba(Er _{0.33} Ta _{0.67})O ₃	8.423			(NH ₄) ₂ FeF ₆ structure	105
Ba(Er _{0.33} U _{0.67})O ₃	8.67			(NH ₄) ₂ FeF ₆ structure	104
Ba(Eu _{0.33} Nb _{0.67})O ₃	8.507			(NH ₄) ₂ FeF ₆ structure	25, 102
Ba(Eu _{0.33} Pa _{0.67})O ₃	8.783			(NH ₄) ₂ FeF ₆ structure	103

TABLE 2.2 (cont.)

TABLE 2.2 (cont.)		$A^{2+}(B_0^{2+}B_0^{2+})O_3$ (cont.)			Refer- ences
Compound	a (Å)	b (Å)	c (Å)	Remarks	
Ba(Eu _{0.5} Ta _{0.5})O ₃	8.506			(NH ₄) ₃ FeF ₆ structure	105
Ba(Fe _{0.5} Mo _{0.5})O ₃	8.08				28
Ba(Fe _{0.5} Nb _{0.5})O ₃	4.06				20, 25, 106
Ba(Fe _{0.5} Re _{0.5})O ₃	8.05			(NH ₄) ₃ FeF ₆ structure	18
Ba(Fe _{0.5} Ta _{0.5})O ₃	4.056			(NH ₄) ₃ FeF ₆ structure	20, 103
Ba(Gd _{0.5} Nb _{0.5})O ₃	8.496			(NH ₄) ₃ FeF ₆ structure	25, 102
Ba(Gd _{0.5} Pa _{0.5})O ₃	8.774			(NH ₄) ₃ FeF ₆ structure	103
Ba(Gd _{0.5} Re _{0.5})O ₃	8.431			(NH ₄) ₃ FeF ₆ structure	18
Ba(Gd _{0.5} Sb _{0.5})O ₃	8.44			(NH ₄) ₃ FeF ₆ structure	94
Ba(Gd _{0.5} Ta _{0.5})O ₃	8.487			(NH ₄) ₃ FeF ₆ tetragonal	105
Ba(Ho _{0.5} Nb _{0.5})O ₃	8.434	8.513		(NH ₄) ₃ FeF ₆ structure	25, 102
Ba(Ho _{0.5} Pa _{0.5})O ₃	8.730			(NH ₄) ₃ FeF ₆ structure	103
Ba(Ho _{0.5} Ta _{0.5})O ₃	8.442			(NH ₄) ₃ FeF ₆ structure	105
Ba(In _{0.5} Nb _{0.5})O ₃	8.279			(NH ₄) ₃ FeF ₆ structure	25, 107
Ba(In _{0.5} Os _{0.5})O ₃	8.224			(NH ₄) ₃ FeF ₆ structure	18
Ba(In _{0.5} Pa _{0.5})O ₃	8.596			(NH ₄) ₃ FeF ₆ structure	103
Ba(In _{0.5} Re _{0.5})O ₃	8.258			(NH ₄) ₃ FeF ₆ structure	18
Ba(In _{0.5} Sb _{0.5})O ₃	8.269			(NH ₄) ₃ FeF ₆ structure	94, 108
Ba(In _{0.5} Ta _{0.5})O ₃	8.280			(NH ₄) ₃ FeF ₆ structure	93
Ba(In _{0.5} U _{0.5})O ₃	8.52			(NH ₄) ₃ FeF ₆ structure	104
Ba(La _{0.5} Nb _{0.5})O ₃	8.007	8.690		(NH ₄) ₃ FeF ₆ tetragonal	25, 102, 106
Ba(La _{0.5} Pa _{0.5})O ₃	8.885			(NH ₄) ₃ FeF ₆ structure	103

TABLE 2.2 (cont.)

TABLE 2.2 (cont.)		$A^{2+}(B_0^{2+}B_0^{2+})O_3$ (cont.)			Refer- ences
Compound	a (Å)	b (Å)	c (Å)	Remarks	
Ba(La _{0.5} Re _{0.5})O ₃	8.58			(NH ₄) ₃ FeF ₆ structure	18
Ba(La _{0.5} Ta _{0.5})O ₃	8.611	8.639	8.764	(NH ₄) ₃ FeF ₆ structure	24, 93, 106
Ba(Lu _{0.5} Nb _{0.5})O ₃	8.364			(NH ₄) ₃ FeF ₆ structure	25, 102
Ba(Lu _{0.5} Pa _{0.5})O ₃	8.606			(NH ₄) ₃ FeF ₆ structure	103
Ba(Lu _{0.5} Ta _{0.5})O ₃	8.372			(NH ₄) ₃ FeF ₆ structure	105
Ba(Mn _{0.5} Nb _{0.5})O ₃	4.083			(NH ₄) ₃ FeF ₆ structure	106
Ba(Mn _{0.5} Re _{0.5})O ₃	8.18			(NH ₄) ₃ FeF ₆ structure	18
Ba(Mn _{0.5} Ta _{0.5})O ₃	4.076			(NH ₄) ₃ FeF ₆ structure	106
Ba(Nd _{0.5} Nb _{0.5})O ₃	8.540			(NH ₄) ₃ FeF ₆ structure	25, 102, 106
Ba(Nd _{0.5} Pa _{0.5})O ₃	8.840			(NH ₄) ₃ FeF ₆ structure	103
Ba(Nd _{0.5} Re _{0.5})O ₃	8.51			(NH ₄) ₃ FeF ₆ structure	18
Ba(Nd _{0.5} Ta _{0.5})O ₃	8.556			(NH ₄) ₃ FeF ₆ structure	105, 106
Ba(Ni _{0.5} Nb _{0.5})O ₃	4.1			(NH ₄) ₃ FeF ₆ structure	94
Ba(Pr _{0.5} Nb _{0.5})O ₃	4.27			(NH ₄) ₃ FeF ₆ hexagonal	102, 106
Ba(Pr _{0.5} Pa _{0.5})O ₃	8.862			(NH ₄) ₃ FeF ₆ structure	103
Ba(Pr _{0.5} Ta _{0.5})O ₃	4.27			(NH ₄) ₃ FeF ₆ structure	108
Ba(Rh _{0.5} Nb _{0.5})O ₃	8.17			(NH ₄) ₃ FeF ₆ hexagonal	94
Ba(Rh _{0.5} U _{0.5})O ₃				BaTiO ₃	104
Ba(Sco _{0.5} Nb _{0.5})O ₃	4.121			(NH ₄) ₃ FeF ₆ structure	96, 102
Ba(Sco _{0.5} Os _{0.5})O ₃	8.152			(NH ₄) ₃ FeF ₆ structure	18
Ba(Sco _{0.5} Pa _{0.5})O ₃	8.549			(NH ₄) ₃ FeF ₆ structure	103
Ba(Sco _{0.5} Re _{0.5})O ₃	8.163			(NH ₄) ₃ FeF ₆ structure	18
Ba(Sco _{0.5} Sb _{0.5})O ₃	8.197			(NH ₄) ₃ FeF ₆ structure	108
Ba(Sco _{0.5} Ta _{0.5})O ₃	8.222			(NH ₄) ₃ FeF ₆ structure	93, 96

TABLE 2.2 (cont.)

 $A^{2+}(B_0^{2+}B_0^{3+})O_3$ (cont.)

Compound	a (Å)	b (Å)	c (Å)	Remarks	References
Ba($Sc_{0.5}U_{0.5}$)O ₃	8.49			(NH ₄) ₂ FeF ₆ structure	104
Ba($Sm_{0.5}Nb_{0.5}$)O ₃	8.518			(NH ₄) ₂ FeF ₆ structure	25, 102, 106
Ba($Sm_{0.5}Pa_{0.5}$)O ₃	8.792			(NH ₄) ₂ FeF ₆ structure	103
Ba($Sm_{0.5}Ta_{0.5}$)O ₃	8.519			(NH ₄) ₂ FeF ₆ structure	105, 106
Ba($Tb_{0.5}Nb_{0.5}$)O ₃	4.229				102
Ba($Tb_{0.5}Pa_{0.5}$)O ₃	8.753			(NH ₄) ₂ FeF ₆ structure	103
Ba($Tl_{0.5}Ta_{0.5}$)O ₃	8.42			(NH ₄) ₂ FeF ₆ structure	108
Ba($Tm_{0.5}Nb_{0.5}$)O ₃	8.408			(NH ₄) ₂ FeF ₆ structure	25, 102
Ba($Tm_{0.5}Pa_{0.5}$)O ₃	8.692			(NH ₄) ₂ FeF ₆ structure	103
Ba($Tm_{0.5}Ta_{0.5}$)O ₃	8.406			(NH ₄) ₂ FeF ₆ structure	105
Ba($Y_{0.5}Nb_{0.5}$)O ₃	4.200			(NH ₄) ₂ FeF ₆ structure	102, 106
Ba($Y_{0.5}Pa_{0.5}$)O ₃	8.718			(NH ₄) ₂ FeF ₆ structure	103
Ba($Y_{0.5}Re_{0.5}$)O ₃	8.372			(NH ₄) ₂ FeF ₆ structure	18
Ba($Y_{0.5}Ta_{0.5}$)O ₃	8.433			(NH ₄) ₂ FeF ₆ structure	105, 106
Ba($Y_{0.5}U_{0.5}$)O ₃	8.69			(NH ₄) ₂ FeF ₆ structure	104
Ba($Yb_{0.5}Nb_{0.5}$)O ₃	8.374			(NH ₄) ₂ FeF ₆ structure	25, 96, 102
Ba($Yb_{0.5}Pa_{0.5}$)O ₃	8.678			(NH ₄) ₂ FeF ₆ structure	103
Ba($Yb_{0.5}Ta_{0.5}$)O ₃	8.390			(NH ₄) ₂ FeF ₆ structure	96, 105
Ca($Al_{0.5}Nb_{0.5}$)O ₃	3.81	3.80	3.81	$\beta = 90^\circ 15'$ monoclinic	109
Ca($Al_{0.5}Ta_{0.5}$)O ₃	3.81	3.80	3.81	$\beta = 90^\circ 17'$ monoclinic	109
Ca($Co_{0.5}W_{0.5}$)O ₃	5.60	5.43	7.73	orthorhombic	94
Ca($Cr_{0.5}Mo_{0.5}$)O ₃	5.49	7.70	5.36	orthorhombic	28

TABLE 2.2 (cont.)

 $A^{2+}(B_0^{2+}B_0^{3+})O_3$ (cont.)

Compound	a (Å)	b (Å)	c (Å)	Remarks	References
Ca($Cr_{0.5}Nb_{0.5}$)O ₃	3.85	3.85	3.85	$\beta = 90^\circ 47'$ monoclinic	109
Ca($Cr_{0.5}Os_{0.5}$)O ₃	5.38	7.66	5.47	orthorhombic	18
Ca($Cr_{0.5}Re_{0.5}$)O ₃	5.38	7.67	5.47	orthorhombic	18
Ca($Cr_{0.5}Ta_{0.5}$)O ₃	3.85	3.85	3.85	$\beta = 90^\circ 45'$ monoclinic	109
Ca($Cr_{0.5}W_{0.5}$)O ₃	5.47	7.70	5.35	orthorhombic	28
Ca($Dy_{0.5}Nb_{0.5}$)O ₃	4.03	4.03	4.03	$\beta = 92^\circ 25'$ monoclinic	109
Ca($Dy_{0.5}Ta_{0.5}$)O ₃	4.03	4.03	4.03	$\beta = 92^\circ 24'$ monoclinic	109
Ca($Er_{0.5}Nb_{0.5}$)O ₃	4.02	4.01	4.02	$\beta = 92^\circ 11'$ monoclinic	109
Ca($Er_{0.5}Ta_{0.5}$)O ₃	4.02	4.01	4.02	$\beta = 92^\circ 10'$ monoclinic	109
Ca($Fe_{0.5}Mo_{0.5}$)O ₃	5.53	7.73	5.42	orthorhombic	109
Ca($Fe_{0.5}Nb_{0.5}$)O ₃	3.89	3.88	3.89	$\beta = 91^\circ 2'$ monoclinic	28
Ca($Fe_{0.5}Sb_{0.5}$)O ₃	5.54	5.47	7.74	orthorhombic	109
Ca($Fe_{0.5}Ta_{0.5}$)O ₃	3.89	3.88	3.89	$\beta = 91^\circ 7'$ monoclinic	94
Ca($Gd_{0.5}Nb_{0.5}$)O ₃	4.03	4.04	4.03	$\beta = 92^\circ 42'$ monoclinic	109
Ca($Gd_{0.5}Ta_{0.5}$)O ₃	4.03	4.04	4.05	$\beta = 92^\circ 41'$ monoclinic	109
Ca($Ho_{0.5}Nb_{0.5}$)O ₃	4.02	4.02	4.02	$\beta = 92^\circ 19'$ monoclinic	109
Ca($Ho_{0.5}Ta_{0.5}$)O ₃	4.03	4.02	4.03	$\beta = 92^\circ 16'$ monoclinic	109
Ca($In_{0.5}Nb_{0.5}$)O ₃	3.97	3.95	3.97	$\beta = 91^\circ 53'$ monoclinic	109
Ca($In_{0.5}Ta_{0.5}$)O ₃	3.97	3.96	3.97	$\beta = 91^\circ 51'$ monoclinic	109
Ca($La_{0.5}Nb_{0.5}$)O ₃	4.07	4.07	4.07	$\beta = 92^\circ 8'$ monoclinic	109
Ca($La_{0.5}Ta_{0.5}$)O ₃	4.07	4.07	4.07	$\beta = 92^\circ 9'$ monoclinic	109
Ca($Mn_{0.5}Ta_{0.5}$)O ₃	3.90	3.87	3.90	$\beta = 91^\circ 9'$ monoclinic	109
Ca($Nd_{0.5}Nb_{0.5}$)O ₃	4.05	4.05	4.05	$\beta = 92^\circ 28'$ monoclinic	109

TABLE 2.2 (cont.)

A²⁺(B₁³⁺B₂³⁺)O₃ (cont.)

Compound	a (Å)	b (Å)	c (Å)	Remarks	References
Ca(Nd _{0.5} Ta _{0.5})O ₃	4.05	4.05	4.05	$\beta = 92^\circ 25'$ monoclinic	109
Ca(Ni _{0.5} W _{0.5})O ₃	5.55	5.40	7.70	orthorhombic	94
Ca(Pr _{0.5} Nb _{0.5})O ₃	4.06	4.05	4.08	$\beta = 92^\circ 25'$ monoclinic	109
Ca(Pr _{0.5} Ta _{0.5})O ₃	4.06	4.05	4.06	$\beta = 92^\circ 22'$ monoclinic	109
Ca(Sc _{0.5} Re _{0.5})O ₃	5.49	7.86	5.63	monoclinic	109
Ca(Sm _{0.5} Nb _{0.5})O ₃	4.04	4.04	4.04	orthorhombic $\beta = 92^\circ 42'$	18
Ca(Sm _{0.5} Ta _{0.5})O ₃	4.05	4.04	4.05	monoclinic $\beta = 92^\circ 28'$	109
Ca(Tb _{0.5} Nb _{0.5})O ₃	4.03	4.03	4.03	monoclinic $\beta = 92^\circ 35'$	109
Ca(Tb _{0.5} Ta _{0.5})O ₃	4.03	4.03	4.03	monoclinic $\beta = 92^\circ 36'$	109
Ca(Y _{0.5} Nb _{0.5})O ₃	4.03	4.02	4.03	monoclinic $\beta = 92^\circ 23'$	109
Ca(Y _{0.5} Ta _{0.5})O ₃	4.03	4.02	4.03	monoclinic $\beta = 92^\circ 23'$	109
Ca(Yb _{0.5} Nb _{0.5})O ₃	4.01	4.00	4.01	monoclinic $\beta = 92^\circ 0'$	109
Ca(Yb _{0.5} Ta _{0.5})O ₃	4.01	4.00	4.01	monoclinic $\beta = 92^\circ 3'$	109
Pb(Fe _{0.5} Nb _{0.5})O ₃	4.017			monoclinic	109
Pb(Fe _{0.5} Ta _{0.5})O ₃	4.011				26, 110
Pb(In _{0.5} Nb _{0.5})O ₃	4.11				28
Pb(Ho _{0.5} Nb _{0.5})O ₃	4.160			monoclinic	111
Pb(Lu _{0.5} Nb _{0.5})O ₃	4.162			monoclinic	111
Pb(Lu _{0.5} Ta _{0.5})O ₃	4.163			monoclinic	111
Pb(Sc _{0.5} Nb _{0.5})O ₃	4.078			tetragonal	26, 112
Pb(Sc _{0.5} Ta _{0.5})O ₃	4.072				26, 112
Pb(Yb _{0.5} Nb _{0.5})O ₃	4.15				96, 111,
					96, 111
Pb(Yb _{0.5} Ta _{0.5})O ₃	4.13			(NH ₄) ₃ FeF ₆ structure	94
Sr(Co _{0.5} Nb _{0.5})O ₃	3.93			(NH ₄) ₃ FeF ₆ structure	28
Sr(Co _{0.5} Sb _{0.5})O ₃	7.88				94, 107
Sr(Cr _{0.5} Mo _{0.5})O ₃	7.82				
Sr(Cr _{0.5} Nb _{0.5})O ₃	3.9421				

TABLE 2.2 (cont.)

A²⁺(B₁³⁺B₂³⁺)O₃ (cont.)

Compound	a (Å)	b (Å)	c (Å)	Remarks	References
Sr(Cr _{0.5} Os _{0.5})O ₃	7.84			(NH ₄) ₃ FeF ₆ structure	18
Sr(Cr _{0.5} Re _{0.5})O ₃	7.82			(NH ₄) ₃ FeF ₆ structure	18
Sr(Cr _{0.5} Sb _{0.5})O ₃	7.862			(NH ₄) ₃ FeF ₆ structure	94, 108
Sr(Cr _{0.5} Ta _{0.5})O ₃	3.94			(NH ₄) ₃ FeF ₆ structure	19
Sr(Cr _{0.5} W _{0.5})O ₃	7.82				28
Sr(Dy _{0.5} Ta _{0.5})O ₃					93
Sr(Er _{0.5} Ta _{0.5})O ₃					93
Sr(Eu _{0.5} Ta _{0.5})O ₃					93
Sr(Fe _{0.5} Mo _{0.5})O ₃	7.89			(NH ₄) ₃ FeF ₆ structure	28
Sr(Fe _{0.5} Nb _{0.5})O ₃	3.97			(NH ₄) ₃ FeF ₆ structure	20
Sr(Fe _{0.5} Sb _{0.5})O ₃	7.916				94, 108
Sr(Fe _{0.5} Ta _{0.5})O ₃	3.96			(NH ₄) ₃ FeF ₆ tetragonal	113
Sr(Ga _{0.5} Nb _{0.5})O ₃	3.946				18
Sr(Ga _{0.5} Os _{0.5})O ₃	7.82			(NH ₄) ₃ FeF ₆ structure	18
Sr(Ga _{0.5} Re _{0.5})O ₃	7.843			(NH ₄) ₃ FeF ₆ structure	18
Sr(Ga _{0.5} Sb _{0.5})O ₃					108
Sr(Gd _{0.5} Ta _{0.5})O ₃	7.84			tetragonal	93
Sr(Ho _{0.5} Ta _{0.5})O ₃					93
Sr(In _{0.5} Nb _{0.5})O ₃	4.0569				107
Sr(In _{0.5} Os _{0.5})O ₃	8.06			(NH ₄) ₃ FeF ₆ structure	18
Sr(In _{0.5} Re _{0.5})O ₃	8.071			(NH ₄) ₃ FeF ₆ structure	18
Sr(In _{0.5} U _{0.5})O ₃	8.33			(NH ₄) ₃ FeF ₆ structure	104
Sr(La _{0.5} Ta _{0.5})O ₃	8.27			(NH ₄) ₃ FeF ₆ structure	24
Sr(Lu _{0.5} Ta _{0.5})O ₃					93
Sr(Mn _{0.5} Mo _{0.5})O ₃	7.98			(NH ₄) ₃ FeF ₆ structure	28
Sr(Mn _{0.5} Sb _{0.5})O ₃					114
Sr(Nd _{0.5} Ta _{0.5})O ₃					93
Sr(Ni _{0.5} Sb _{0.5})O ₃				tetragonal	94

TABLE 2.2 (cont.)

 $A^{2+}(B_{0.5}^{2+}B_{0.5}^{2+})O_3$ (cont.)

Compound	a (Å)	b (Å)	c (Å)	Remarks	References
Sr(Rh _{0.5} Sb _{0.5})O ₃	5.77		7.99	orthorhombic (NH ₄) ₂ FeF ₆	94
Sr(Sc _{0.5} Os _{0.5})O ₃	8.02	5.55		(NH ₄) ₂ FeF ₆ structure	18
Sr(Sc _{0.5} Re _{0.5})O ₃	8.02				18
Sr(Sm _{0.5} Ta _{0.5})O ₃					93
Sr(Tm _{0.5} Ta _{0.5})O ₃					93
Sr(Yb _{0.5} Ta _{0.5})O ₃					93

 $A^{2+}(B_{0.3}^{2+}B_{0.7}^{2+})O_3$

Ba(Ba _{0.3} Os _{0.7})O ₃	8.66		8.34	tetragonal	18
Ba(Ba _{0.3} Re _{0.7})O ₃	8.65		8.33	tetragonal (NH ₄) ₂ FeF ₆	18
Ba(Ba _{0.3} U _{0.7})O ₃	8.89			structure (NH ₄) ₂ FeF ₆	17
Ba(Ba _{0.3} W _{0.7})O ₃	8.6			structure (NH ₄) ₂ FeF ₆	16
Ba(Ca _{0.3} Mo _{0.7})O ₃	8.355			structure (NH ₄) ₂ FeF ₆	16
Ba(Ca _{0.3} Os _{0.7})O ₃	8.362			structure (NH ₄) ₂ FeF ₆	18
Ba(Ca _{0.3} Re _{0.7})O ₃	8.356			structure (NH ₄) ₂ FeF ₆	18, 115
Ba(Ca _{0.3} Ta _{0.7})O ₃	8.393			structure (NH ₄) ₂ FeF ₆	108
Ba(Ca _{0.3} U _{0.7})O ₃	8.67			structure (NH ₄) ₂ FeF ₆	17
Ba(Ca _{0.3} W _{0.7})O ₃	8.39			structure (NH ₄) ₂ FeF ₆	15, 16
Ba(Cd _{0.3} Os _{0.7})O ₃	8.325			structure (NH ₄) ₂ FeF ₆	18
Ba(Cd _{0.3} Re _{0.7})O ₃	8.322			structure (NH ₄) ₂ FeF ₆	18, 115
Ba(Cd _{0.3} U _{0.7})O ₃	6.13	8.64	6.07	orthorhombic	17
Ba(Co _{0.3} Mo _{0.7})O ₃	4.0429				107
Ba(Co _{0.3} Re _{0.7})O ₃	8.086			(NH ₄) ₂ FeF ₆ structure	18, 115
Ba(Co _{0.3} U _{0.7})O ₃	8.374			(NH ₄) ₂ FeF ₆ structure	17

TABLE 2.2 (cont.)

 $A^{2+}(B_{0.5}^{2+}B_{0.5}^{2+})O_3$ (cont.)

Compound	a (Å)	b (Å)	c (Å)	Remarks	References
Ba(Co _{0.5} W _{0.5})O ₃	8.098			(NH ₄) ₂ FeF ₆ structure	15, 107
Ba(Cr _{0.5} U _{0.5})O ₃	8.297			(NH ₄) ₂ FeF ₆ structure	17
Ba(Cu _{0.5} U _{0.5})O ₃	8.18		8.84	tetragonal (NH ₄) ₂ FeF ₆	17
Ba(Fe _{0.5} Re _{0.5})O ₃	8.05			structure (NH ₄) ₂ FeF ₆	18, 115
Ba(Fe _{0.5} U _{0.5})O ₃	8.312			structure (NH ₄) ₂ FeF ₆	17
Ba(Fe _{0.5} W _{0.5})O ₃	8.133			structure (NH ₄) ₂ FeF ₆	15
Ba(Mg _{0.5} Os _{0.5})O ₃	8.08			structure (NH ₄) ₂ FeF ₆	18
Ba(Mg _{0.5} Re _{0.5})O ₃	8.082			structure (NH ₄) ₂ FeF ₆	18, 115
Ba(Mg _{0.5} Ta _{0.5})O ₃	8.13			structure (NH ₄) ₂ FeF ₆	108, 116
Ba(Mg _{0.5} U _{0.5})O ₃	8.381			structure (NH ₄) ₂ FeF ₆	17
Ba(Mg _{0.5} W _{0.5})O ₃	8.099			structure (NH ₄) ₂ FeF ₆	15, 16
Ba(Mn _{0.5} Re _{0.5})O ₃	8.18			structure (NH ₄) ₂ FeF ₆	18, 115
Ba(Mn _{0.5} U _{0.5})O ₃	8.52			structure (NH ₄) ₂ FeF ₆	17
Ba(Ni _{0.5} Mo _{0.5})O ₃	4.0225			structure (NH ₄) ₂ FeF ₆	107
Ba(Ni _{0.5} Re _{0.5})O ₃	8.04			structure (NH ₄) ₂ FeF ₆	18, 115
Ba(Ni _{0.5} U _{0.5})O ₃	8.336			structure (NH ₄) ₂ FeF ₆	17
Ba(Ni _{0.5} W _{0.5})O ₃	8.068			structure (NH ₄) ₂ FeF ₆	15, 107
Ba(Pb _{0.5} Mo _{0.5})O ₃	8.43		8.72	tetragonal	117
Ba(Sr _{0.5} Os _{0.5})O ₃	8.60		8.29	tetragonal (NH ₄) ₂ FeF ₆	18
Ba(Sr _{0.5} Re _{0.5})O ₃	8.84			structure (NH ₄) ₂ FeF ₆	18, 115
Ba(Sr _{0.5} U _{0.5})O ₃	8.5			structure (NH ₄) ₂ FeF ₆	17
Ba(Sr _{0.5} W _{0.5})O ₃	8.095			structure (NH ₄) ₂ FeF ₆	16
Ba(Zn _{0.5} Os _{0.5})O ₃				structure (NH ₄) ₂ FeF ₆	18

TABLE 2.2 (cont.)

 $A^{++}(B_{0.5}^{2+}B_{0.5}^{2+})O_3$ (cont.)

Compound	a (Å)	b (Å)	c (Å)	Remarks	References
Ba(Zn _{0.5} Re _{0.5})O ₃	8.106			(NH ₄) ₂ FeF ₆ structure	18, 115
Ba(Zn _{0.5} U _{0.5})O ₃	8.397			(NH ₄) ₂ FeF ₆ structure	17
Ba(Zn _{0.5} W _{0.5})O ₃	8.116			(NH ₄) ₂ FeF ₆ structure	15
Ca(Ca _{0.5} Os _{0.5})O ₃	5.73	7.87	5.80	orthorhombic	18
Ca(Ca _{0.5} Re _{0.5})O ₃	5.67	8.05	5.78	orthorhombic	18
Ca(Ca _{0.5} W _{0.5})O ₃	8.0			(NH ₄) ₂ FeF ₆ structure	18
Ca(Cd _{0.5} Re _{0.5})O ₃	5.64	7.99	5.77	orthorhombic	16
Ca(Co _{0.5} Os _{0.5})O ₃	5.47	7.70	5.59	orthorhombic	18
Ca(Co _{0.5} Re _{0.5})O ₃	5.46	7.71	5.58	orthorhombic	18
Ca(Fe _{0.5} Re _{0.5})O ₃	5.41	7.69	5.53	orthorhombic	18, 115
Ca(Mg _{0.5} Re _{0.5})O ₃	5.48	7.77	5.56	orthorhombic	18
Ca(Mg _{0.5} W _{0.5})O ₃	7.7			(NH ₄) ₂ FeF ₆ structure	16
Ca(Mn _{0.5} Re _{0.5})O ₃	5.52	7.82	5.55	orthorhombic	18
Ca(Ni _{0.5} Re _{0.5})O ₃	5.45	7.67	5.55	orthorhombic	18
Ca(Sr _{0.5} W _{0.5})O ₃	8.1			(NH ₄) ₂ FeF ₆ structure	16
Pb(Ca _{0.5} W _{0.5})O ₃				$\beta = 90^\circ 57'$	98
Pb(Cd _{0.5} W _{0.5})O ₃	4.150	4.101	4.150		118
Pb(Co _{0.5} W _{0.5})O ₃	7.99			(NH ₄) ₂ FeF ₆ structure	119
Pb(Mg _{0.5} Te _{0.5})O ₃					116
Pb(Mg _{0.5} W _{0.5})O ₃	4.0				95, 96
Sr(Ca _{0.5} Mo _{0.5})O ₃	8.21				117
Sr(Ca _{0.5} Os _{0.5})O ₃				(NH ₄) ₂ FeF ₆ structure	18
Sr(Ca _{0.5} Re _{0.5})O ₃	5.76	8.21	5.85	orthorhombic	18
Sr(Ca _{0.5} U _{0.5})O ₃	6.06	8.46	5.93	orthorhombic	17
Sr(Ca _{0.5} W _{0.5})O ₃	8.2			(NH ₄) ₂ FeF ₆ structure	16
Sr(Cd _{0.5} Re _{0.5})O ₃	5.73	8.16	5.91	orthorhombic	18
Sr(Cd _{0.5} U _{0.5})O ₃	6.03	8.42	5.91	orthorhombic	17
Sr(Co _{0.5} Mo _{0.5})O ₃	3.9367		3.9764		107, 113
Sr(Co _{0.5} Os _{0.5})O ₃	7.88		7.92	tetragonal	18
Sr(Co _{0.5} Re _{0.5})O ₃	7.86		7.98	tetragonal	18
Sr(Co _{0.5} U _{0.5})O ₃	8.19			(NH ₄) ₂ FeF ₆ structure	17

TABLE 2.2 (cont.) $A^{++}(B_{0.5}^{2+}B_{0.5}^{2+})O_3$ (cont.)

Compound	a (Å)	b (Å)	c (Å)	Remarks	References
Sr(Co _{0.5} W _{0.5})O ₃	7.89		7.98	tetragonal (NH ₄) ₂ FeF ₆ structure	15, 113
Sr(Cr _{0.5} U _{0.5})O ₃	8.09			tetragonal (NH ₄) ₂ FeF ₆ structure	17
Sr(Cu _{0.5} W _{0.5})O ₃	7.66		8.40	tetragonal (NH ₄) ₂ FeF ₆ structure	94
Sr(Fe _{0.5} Os _{0.5})O ₃	7.85			structure	18
Sr(Fe _{0.5} Re _{0.5})O ₃	7.86		7.89	tetragonal (NH ₄) ₂ FeF ₆ structure	18, 115
Sr(Fe _{0.5} U _{0.5})O ₃	8.11			structure	17
Sr(Fe _{0.5} W _{0.5})O ₃	7.96			(NH ₄) ₂ FeF ₆ structure	94
Sr(Mg _{0.5} Mo _{0.5})O ₃				structure	117
Sr(Mg _{0.5} Os _{0.5})O ₃	7.86		7.92	tetragonal (NH ₄) ₂ FeF ₆ structure	18
Sr(Mg _{0.5} Re _{0.5})O ₃	7.88		7.94	tetragonal (NH ₄) ₂ FeF ₆ structure	18
Sr(Mg _{0.5} Te _{0.5})O ₃	7.94			structure	116
Sr(Mg _{0.5} U _{0.5})O ₃	8.19			(NH ₄) ₂ FeF ₆ structure	17
Sr(Mg _{0.5} W _{0.5})O ₃	7.9			(NH ₄) ₂ FeF ₆ structure	16
Sr(Mn _{0.5} Re _{0.5})O ₃	8.01			(NH ₄) ₂ FeF ₆ structure	18
Sr(Mn _{0.5} U _{0.5})O ₃	8.28			(NH ₄) ₂ FeF ₆ structure	17
Sr(Mn _{0.5} W _{0.5})O ₃	8.01			(NH ₄) ₂ FeF ₆ structure	94
Sr(Ni _{0.5} Mo _{0.5})O ₃	3.9237		3.9474	tetragonal	107, 113
Sr(Ni _{0.5} Re _{0.5})O ₃	7.85		7.92	tetragonal (NH ₄) ₂ FeF ₆ structure	18
Sr(Ni _{0.5} U _{0.5})O ₃	8.15			structure	17
Sr(Ni _{0.5} W _{0.5})O ₃	7.86		7.91	tetragonal	15, 107, 113
Sr(Pb _{0.5} Mo _{0.5})O ₃					117
Sr(Sr _{0.5} Os _{0.5})O ₃	8.32		8.12	tetragonal	18
Sr(Sr _{0.5} Re _{0.5})O ₃	8.41		8.13	tetragonal	18
Sr(Sr _{0.5} U _{0.5})O ₃	6.22	8.65	6.01	orthorhombic	17
Sr(Sr _{0.5} W _{0.5})O ₃	8.2			(NH ₄) ₂ FeF ₆ structure	16
Sr(Zn _{0.5} Re _{0.5})O ₃	7.89		8.01	tetragonal	18
Sr(Zn _{0.5} W _{0.5})O ₃	7.92		8.01	tetragonal	15, 113

TABLE 2.2 (cont.)

Compound	<i>a</i> (Å)	<i>b</i> (Å)	<i>c</i> (Å)	Remarks	References
Ba(Ag _{0.5} I _{0.5})O ₃	8.46			(NH ₄) ₃ FeF ₆ structure	108
Ba(Li _{0.5} Os _{0.5})O ₃	8.100			(NH ₄) ₃ FeF ₆ structure	18
Ba(Li _{0.5} Re _{0.5})O ₃	8.118			(NH ₄) ₃ FeF ₆ structure	18
Ba(Na _{0.5} I _{0.5})O ₃	8.33			(NH ₄) ₃ FeF ₆ structure	18, 108
Ba(Na _{0.5} Os _{0.5})O ₃	8.291			(NH ₄) ₃ FeF ₆ structure	18
Ba(Na _{0.5} Re _{0.5})O ₃	8.296			(NH ₄) ₃ FeF ₆ structure	18
Ca(Li _{0.5} Os _{0.5})O ₃	7.83			(NH ₄) ₃ FeF ₆ structure	18
Ca(Li _{0.5} Re _{0.5})O ₃	7.83			(NH ₄) ₃ FeF ₆ structure	18
Sr(Li _{0.5} Os _{0.5})O ₃	7.86			(NH ₄) ₃ FeF ₆ structure	18
Sr(Li _{0.5} Re _{0.5})O ₃	7.87			(NH ₄) ₃ FeF ₆ structure	18
Sr(Na _{0.5} Os _{0.5})O ₃	8.13			(NH ₄) ₃ FeF ₆ structure	18
Sr(Na _{0.5} Re _{0.5})O ₃	8.13			(NH ₄) ₃ FeF ₆ structure	18

$$A^3+(B_{0.5}^2+B_{0.6}^4)O_2$$

$\text{La}(\text{Co}_{0.5}\text{Ir}_{0.5})\text{O}_3$	94	orthorhombic monoclinic	$(\text{NH}_4)_2\text{FeF}_6$ structure
$\text{La}(\text{Cu}_{0.5}\text{Ir}_{0.5})\text{O}_3$	94		
$\text{La}(\text{Mg}_{0.5}\text{Ge}_{0.5})\text{O}_3$	19		
$\text{La}(\text{Mg}_{0.5}\text{Ir}_{0.5})\text{O}_3$	93		
$\text{La}(\text{Mg}_{0.5}\text{Nb}_{0.5})\text{O}_3$	26, 94		
$\text{La}(\text{Mg}_{0.5}\text{Ru}_{0.5})\text{O}_3$	26		
$\text{La}(\text{Mg}_{0.5}\text{Ti}_{0.5})\text{O}_3$	19, 96		
$\text{La}(\text{Mn}_{0.5}\text{Ir}_{0.5})\text{O}_3$			
$\text{La}(\text{Mn}_{0.5}\text{Ru}_{0.5})\text{O}_3$	26		
$\text{La}(\text{Ni}_{0.5}\text{Ir}_{0.5})\text{O}_3$	26		
$\text{La}(\text{Ni}_{0.5}\text{Ru}_{0.5})\text{O}_3$	26, 94		
$\text{La}(\text{Ni}_{0.5}\text{Ti}_{0.5})\text{O}_3$	26		
$\text{La}(\text{Zn}_{0.5}\text{Ru}_{0.5})\text{O}_3$	19		
$\text{Nd}(\text{Mg}_{0.5}\text{Ti}_{0.5})\text{O}_3$	26		
	19		

TABLE 2.2 (cont.)

Compound	a (Å)	b (Å)	c (Å)	Remarks	References
$\text{Ba}(\text{Na}_{0.25}\text{Ta}_{0.75})\text{O}_3$ $\text{Sr}(\text{Na}_{0.25}\text{Ta}_{0.75})\text{O}_3$	4.137 4.055				27 27

$\text{A}(\text{B}_{0.5}^{2+}\text{B}_{0.5}^{4+})\text{O}_{2.75}$					
Compound	a (Å)	b (Å)	c (Å)	Remarks	References
$\text{Ba}(\text{In}_{0.5}\text{U}_{0.5})\text{O}_{2.75}$	8.551			$(\text{NH}_4)_2\text{FeF}_6$ structure	104

$\text{A}(\text{B}_{0.5}^{2+}\text{B}_{0.5}^{5+})\text{O}_{3.75}$					
Compound	a (Å)	b (Å)	c (Å)	Remarks	References
$\text{Ba}(\text{Ba}_{0.5}\text{Ta}_{0.5})\text{O}_{3.75}$	8.89			$(\text{NH}_4)_2\text{FeF}_6$ structure	24
$\text{Ba}(\text{Fe}_{0.5}\text{Mo}_{0.5})\text{O}_{3.75}$	8.08			$(\text{NH}_4)_2\text{FeF}_6$ structure	28
$\text{Sr}(\text{Sr}_{0.5}\text{Ta}_{0.5})\text{O}_{3.75}$	8.34			$(\text{NH}_4)_2\text{FeF}_6$ structure	24

2.3. MADELUNG ENERGY

The calculation of the binding energy of a crystal is one of the fundamental problems in the theory of solids. In this calculation, the basic assumption in the theory of cohesive energy of ionic crystals is that the solid can be considered as a system of positive and negative ions. In the NaCl structure, the shortest interionic distance is given by L . Each sodium ion is surrounded by 6 Cl^- ions at a distance L , 12 Na^+ ions at a distance $L/\sqrt{2}$, 8 Cl^- ions at a distance $L/\sqrt{3}$, etc. The Coulomb energy of the sodium ion in the field of all other ions is therefore,

$$U_M = -\frac{e^2}{L} \left(\frac{6}{\sqrt{1}} - \frac{12}{\sqrt{2}} + \frac{8}{\sqrt{3}} - \frac{6}{\sqrt{4}} + \frac{24}{\sqrt{5}} \right)$$

where e is the charge per ion. The coefficient of e^2/L is a pure number, determined only by the crystal structure and called the Madelung constant, M_L .

The Madelung constant for the cubic perovskite structure is 24.755. Using the equation

$$U_M = -M_L e^2/L$$

the Madelung energy for an assumed ideal structure for CaTiO_3 calculates out to be 4280.5 (117)

Rosenstein and Schor⁽¹²¹⁾ determined the superlattice Madelung energy of idealized ordered cubic perovskites. These calculations were based on formulas $A_2^{2+}B^{4-}B'^{4+}O_6$ which is twice the $A(B'_2B''_2)O_3$ type formulas used throughout this report. In their formula $4 \pm n$ denoted a net charge of $4 \pm$ plus $n \pm$ charges. The ordered structure for these compounds is shown in Fig. 2.5.

The method used for computing the change in Madelung energy due to charge ordering of the B ions is in accordance with the technique of superposition employed by Templeton,⁽¹²²⁾ since the ordering charges n^+ and n^- for an ordered perovskite were at alternate sites in a rocksalt structure. Using $M_L = 1.74756$ and $L = \frac{1}{4}$ supercell edge they derived the Madelung energy due to charge ordering,

$$U_M = -1.74756 \times 331.984 \times 0.5 n^2/L.$$

The Madelung energies are given in Table 2.3 below.

TABLE 2.3. Table of Madelung Energies for Idealized Ordered Perovskite Compounds (after Rosenstein and Schor⁽¹²¹⁾)

n	Compound	Supercell edge (Å)	Madelung energy ordering	Kcal mole ⁻¹ total
0	$\text{Ca}_2\text{Ti}_2\text{O}_6$	7.68	—	8561
1	$\text{Ba}_2\text{Sc}^{3+}\text{Re}^{5+}\text{O}_6$	8.16	142	8199
2	$\text{Ba}_2\text{Ni}^{2+}\text{Re}^{5+}\text{O}_6$	8.04	577	8755
3	$\text{Ba}_2\text{Li}^{1+}\text{Re}^{5+}\text{O}_6$	8.12	1286	9383

The results showed that the energy due to charge ordering was in some cases a significant fraction of the total Madelung

energy especially where the charge difference in the B ions was large.

In a later study, Saltzman and Schor⁽¹²³⁾ calculated the Madelung energy of tetragonal perovskite structure. Madelung constants were determined for the 4-4, 3-5, and 1-7 tetragonal perovskite structures for axial ratios $\alpha = c/a$ varying from 0.90 to 1.10. Least-squares fits expressing the Madelung constant as a function of $(1-\alpha)$ also were reported. The results are given in Table 2.4.

TABLE 2.4. Table of Madelung Energies (after Saltzman and Schor⁽¹²³⁾)

Compound	$\alpha = c/a$	Madelung constant	Madelung energy ordering	Total Madelung energy
$\text{Ba}_2\text{BaOsO}_6$	0.993	53.70	543	8235
$\text{Ba}_2\text{BaReO}_6$	0.993	53.70	544	8244
$\text{Ba}_2\text{SrOsO}_6$	0.994	53.68	547	8289
$\text{Ba}_2\text{SrReO}_6$	1.034	52.43	545	8260
$\text{Sr}_2\text{CoReO}_6$	1.013	52.78	587	8896
$\text{Sr}_2\text{FeReO}_6$	1.004	52.94	590	8945
$\text{Sr}_2\text{MgOsO}_6$	1.008	52.87	589	8934
$\text{Sr}_2\text{MgReO}_6$	1.008	57.87	588	8911
$\text{Sr}_2\text{NiReO}_6$	1.009	52.85	590	8941
$\text{Sr}_2\text{SrOsO}_6$	0.976	53.45	563	8631
$\text{Sr}_2\text{SrReO}_6$	0.967	53.62	559	8468
$\text{Sr}_2\text{ZnReO}_6$	1.016	52.74	585	8878

2.4. IONIC RADII

The ionic radii of the ions as given by Ahrens and as calculated in perovskite-type compounds are listed in Table 2.5. The ionic radii of the B ion was obtained in ABO_3 -type compounds, while those of B' and B'' were obtained in complex perovskite compounds. There are a number of ions which appear to differ considerably in radius in the structure of perovskite-type compounds as compared with those of Ahrens. In addition, the ionic radii of W^{6+} and Os^{7+} were calculated for the first time.

TABLE 2.5. *Ionic Radii*

	Ahrens	B [†]	B [†]	B [‡]
Ag ^{†+}	1.26			
Au	1.37			
Cs	1.67			
Cu	0.96			
Fr	1.80			
I	0.82			
K	1.33			
Li	0.68			
Na	0.94			
Rb	1.47			
Tl	1.47			
Ag ²⁺	0.89			
Ba	1.34			
Be	0.35			
Ca	0.99		0.99	
Cd	0.97		0.97	
Co	0.73		0.73	
Cu	0.72			
Fe	0.74			
Ge	0.73			
Hg	1.10			
Mg	0.67			
Mn	0.80		0.74	
Ni	0.69		0.80	
Pb	1.20		0.69	
Pd	0.80		1.20	
Pt	0.80			
Ra	1.43			
Sn	0.93			
Sr	1.12		1.12	
Ti	0.76			
V	0.95			
Zn	0.74		0.74	
Ac ³⁺	1.18			
Al	0.55	0.558		
Am	1.07			
As	0.58			

TABLE 2.5 (cont.)

	Ahrens	B [†]	B [†]	B [‡]
Au	0.85			
B	0.23			
Bi	0.93			
Ce	1.07		1.06	
Co	0.63	0.56		
Cr	0.63	0.808		
Dy	0.92			
Er	0.89		0.94	
Eu	0.98		0.91	
Fe	0.64		0.99	
Ga	0.62	0.628	0.63	
Gd	0.97	0.613		
Ho	0.91		0.97	
In	0.81		0.93	
La	1.14	0.714	0.78	
Lu	0.85		1.14	
Mn	0.66		0.86	
Np	1.10	0.625	0.67	
Nd	1.04			
P	0.44		1.04	
Pa	1.13			
Pm	1.06			
Pr	1.06		1.02	
Pu	1.08			
Rh	0.68			
Sb	0.76			
Sc	0.81	0.686	0.74	
Sm	1.00		1.00	
Tb	0.93			
Ti	0.76	0.61		
Tl	0.95			
Tm	0.87		0.90	
V	0.74	0.625		
Y	0.92	0.773	0.92	
Yb	0.86		0.88	
Am ⁴⁺	0.92			
C	0.16			

TABLE 2.5 (cont.)

	Ahrens	B [†]	B [†]	B [†]
Ce	0.94			
Ge	0.53			
Hf	0.78			
Ir	0.68			
Mn	0.60			
Mo	0.69			
Nb	0.74			
Np	0.95			
Os	0.69			
Pa	0.98			
Pb	0.84			
Pd	0.65			
Pr	0.92			
Pt	0.65			
Pu	0.93			
Rh	0.65			
Ru	0.67			
S	0.37			
Se	0.50			
Si	0.42			
Sn	0.71			
Tb	0.81			
Te	0.70			
Th	1.02			
Ti	0.68			
U	0.97			
V	0.63			
W	0.70			
Zr	0.78			
As ^{††}	0.46			
Bi	0.74			
Nb	0.69			
Os			0.69	
P			0.67	
Pa	0.35			
Re	0.89			
Sb	0.62			0.68

TABLE 2.5 (cont.)

	Ahrens	B [†]	B [†]	B [†]
Ta	0.68			
V	0.59			0.68
W				0.59
				0.66
Cr ^{††}	0.52			
Mo	0.62			
Po	0.67			
Re	0.52			
S	0.30			
Se	0.42			
Te	0.56			
U	0.80			
W	0.62			0.62
At ^{††}	0.62			
Br	0.39			
Cl	0.27			
F	0.08			
I	0.50			
Mn	0.46			
Np	0.71			
Re	0.56			
Te	0.57			
Os				0.55

[†] Calculated for ABO₃-type compounds by S. Geller, *Acta Cryst.* 10, 248 (1957).

^{††} Ionic radii of B^{††}: Calculated from complex perovskite compounds A(B_{0.5}Ta_{0.5})O₃ by F. Galasso *et al.*, UACRL D910289-5, Final Report, July 1965. Ionic radii of B^{††}: Calculated from complex perovskite compounds A(B_{0.5}Ta_{0.5})O₃.

[‡] Calculated from A(B_{0.5}B_{0.5})O₃ perovskite-type compounds.

REFERENCES

1. H. D. MEGAW, *Proc. Phys. Soc.* 58, 133, 326 (1946).
2. V. M. GOLDSCHMIDT, *Skrifter Norske Videnskaps-Akad. Oslo, I. Mat.-Naturv. Kl.*, No. 8 (1926).
3. R. W. G. WYCKOFF, *Crystal Structures* 2, 359 (1964).
4. A. J. SMITH and A. J. E. WELCH, *Acta Cryst.* 18, 653 (1960).
5. R. S. ROTH, *J. Research NBS*, RP 2736, 58, (1957).
6. S. GELLER and A. E. WOOD, *Acta Cryst.* 9, 563 (1956).
7. J. T. LOOBY and L. KATZ, *J. Am. Chem. Soc.* 76, 6029 (1954).
8. W. F. DEJONG, *Z. Krist.* 81, 314 (1932).
9. D. RIDGE and R. WARD, *J. Am. Chem. Soc.* 77, 6132 (1955).
10. H. P. ROOKSBY, E. A. D. WHITE and S. A. LANGSTON, *J. Am. Ceram. Soc.* 48, 447 (1965).
11. C. BRISI, *Ricerca Sci.* 24, 1858 (1954).
12. G. H. JONKER, *Physica* 20, 1118 (1954).
13. H. L. YAKEL, *Acta Cryst.* 8, 394 (1955).
14. G. H. JONKER and J. H. VAN SANTEN, *Physica*, 16, 337 (1950).
15. F. J. FRESIA, L. KATZ and R. WARD, *J. Am. Chem. Soc.* 81, 4783 (1959).
16. E. G. STEWARD and H. P. ROOKSBY, *Acta Cryst.* 4, 503 (1951).
17. A. W. SLEIGHT and R. WARD, *Inorg. Chem.* 1, 790 (1962).
18. A. W. SLEIGHT, J. LONGO and R. WARD, *Inorg. Chem.* 1, 245 (1962).
19. R. ROY, *J. Am. Ceram. Soc.* 27, 581 (1954).
20. F. GALASSO, L. KATZ and R. WARD, *J. Am. Chem. Soc.* 81, 820 (1959).
21. F. GALASSO, J. R. BARRANTE and L. KATZ, *J. Am. Chem. Soc.* 88, 2830 (1961).
22. F. GALASSO and J. PYLE, *Inorg. Chem.* 2, 482 (1963).
23. F. GALASSO and J. PYLE, *J. Phys. Chem.* 67, 1561 (1963).
24. L. BRIKNER, *J. Am. Chem. Soc.* 80, 3214 (1958).
25. F. GALASSO and W. DARBY, *J. Phys. Chem.* 66, 131 (1962).
26. F. GALASSO and W. DARBY, *Inorg. Chem.* 4, 71 (1965).
27. F. GALASSO and J. PINTO, *Inorg. Chem.* 4, 255 (1965).
28. F. K. PATTERSON, C. W. MOELLER and R. WARD, *Inorg. Chem.* 2, 196 (1963).
29. M. H. FRANCOMBE and B. LEWIS, *Acta Cryst.* 11, 175 (1958).
30. W. H. ZACHARIASEN, *Skrifter Norske Videnskaps-Akad. Oslo, I. Mat.-Naturv. Kl.* No. 4 (1928).
31. I. NÁRAY-SZABÓ, *Műegyetemi Közlemények* 1, 30 (1947).
32. R. P. OZEROV, N. V. RANNEV, V. I. PAKHOMOV, I. S. REZ and G. S. ZHDANOV, *Kristallografiya* 7, 620 (1962).
33. I. NÁRAY-SZABÓ and A. KALMÁN, *Acta Cryst.* 14, 791 (1961).
34. J. H. SMITH, *Nature* 115, 334 (1925).
35. E. A. WOOD, *Acta Cryst.* 4, 353 (1951).
36. L. L. QUITL, *Z. Anorg. Allgem. Chem.* 208, 257 (1932).

37. P. VOUSDEN, *Acta Cryst.* 4, 373 (1951).
38. M. WELLS and D. MEGAW, *Proc. Phys. Soc.* 78, 1258 (1961).
39. H. F. KAY and J. L. MILES, *Acta Cryst.* 10, 213 (1957).
40. D. SANTANA, *Anales Real. Soc. Españ. Fis. Quím. (Madrid)*, Ser. A, 44, 557 (1948).
41. L. RIVOIR and M. ABBAD, *Anales Fis. Quím. (Madrid)*, 48, 1051 (1947).
42. A. F. WELLS, *Structural Inorganic Chemistry*, Oxford University Press, Aiken House, London (1950).
43. W. W. MALINOVSKY and H. KEDDES, *J. Am. Chem. Soc.* 76, 3090 (1954).
44. S. W. DERBYSHIRE, A. C. FRAKER and H. H. STADELMAIER, *Acta Cryst.* 14, 1293 (1961).
45. L. H. BRIKNER, *J. Inorg. Nucl. Chem.* 14, 226, (1960).
46. R. WEISS, *Compt. Rend.* 246, 3073, (1958).
47. A. HOFFMAN, *Z. Physik. Chem.* 28, 65 (1953).
48. L. E. RUSSELL, J. D. L. HARRISON and N. H. BRETT, *J. Nucl. Mater.* 2, 310 (1960).
49. S. M. LANG, F. P. KNUDSEN, C. L. FILLMORE, R. S. ROTH, NBS Circ. 568 (1956).
50. I. NÁRAY-SZABÓ, *Naturwiss.* 31, 466 (1943).
51. C. E. CURTIS, L. M. DONEY and J. R. JOHNSON, Oak Ridge Natl. Lab. ORNL-1681 (1964).
52. R. WARD, B. GUSHEE, W. MCCARROLL and D. H. RIDGE, Univ. Conn. 2d Tech. Rep., NR-052-268, Contract ONR-367(00) (1953).
53. W. H. MCCARROLL, R. WARD and L. KATZ, *J. Am. Chem. Soc.* 78, 2809 (1956).
54. L. W. COUGHANOUR, R. S. ROTH, S. MARZULLO and F. E. SENNETT, *J. Research NBS*, RP 2576, 54, 149 (1955).
55. L. W. COUGHANOUR, R. S. ROTH, S. MARZULLO and F. E. SENNETT, *J. Research NBS*, RP 2580, 54, 191 (1955).
56. J. BROUS, I. FANKUCHEN and E. BANKS, *Acta Cryst.* 6, 67 (1953).
57. G. SHIRANE and R. PEFINSKY, *Phys. Rev.* 91, 812 (1953).
58. B. JAFFE, R. S. ROTH and S. MARZULLO, *J. Research NBS*, RP 2628, 55, 239 (1955).
59. J. J. RANDALL and R. WARD, *J. Am. Chem. Soc.* 81, 2629 (1959).
60. W. W. COFFEEN, *J. Am. Ceram. Soc.* 36, 207 (1953).
61. F. SUGAWARA and S. IDA, *J. Phys. Soc. Japan* 20, 1529 (1955).
62. W. H. ZACHARIASEN, *Acta Cryst.* 2, 388 (1949).
63. A. RUGGIERO and R. FERRO, *Gazz. Chim. Ital.* 85, 892 (1955).
64. M. L. KEITH and R. ROY, *Am. Mineralogist* 39, 1 (1954).
65. A. WOLD and R. WARD, *J. Am. Chem. Soc.* 76, 1029 (1954).
66. W. RÜDORFF and H. BECKER, *Z. Naturforsch.* 9b, 613 (1954).
67. J. A. W. DALZIEL and A. J. E. WELCH, *Acta Cryst.* 18, 856 (1960).
68. R. C. VIOKERY and A. KLANN, *J. Chem. Phys.* 27, 1161 (1957).
69. S. GELLER and V. B. BALA, *Acta Cryst.* 9, 1019 (1956).
70. V. S. FILIP'EV, N. P. SMOLYANTNOV, E. G. FRESKO and I. N. BELYAEV, *Kristallografiya* 5, 958 (1960).

71. A. I. ZASLAVSKII and A. G. TUTOV, *Dokl. Akad. Nauk SSSR* 185, 815 (1960).
72. S. A. FEDULOV, Y. N. VENEVTSEV, G. S. ZHDANOV and E. G. SMACHEVSKAYA, *Kristallografiya* 6, 795 (1961).
73. A. RUGGIERO and R. FERRO, *Atti. Accad. Nazl. Lincei, Rend., Classe Sci. Fis. Mat. Nat.* 17, 254 (1964).
74. S. GELLER, *Acta Cryst.* 10, 243 (1957).
75. S. GELLER, *J. Chem. Phys.* 24, 6 (1956).
76. A. WOLD, B. POST and E. BANKS, *J. Am. Chem. Soc.* 79, 6365 (1957).
77. F. ASKHAM, I. FANKUCHEN, and R. WARD, *J. Am. Chem. Soc.* 72, 3799 (1950).
78. W. C. KOEHLER and E. O. WOLLAN, *Phys. Chem. Solids* 2, 100 (1957).
79. M. FOËX, A. MANCHERON and M. LINÉ, *Compt. Rend.* 250, 3027 (1960).
80. D. D. KHANOLKAR, *Current Sci. (India)* 30, 52 (1961).
81. M. KESTIGIAN and R. WARD, *J. Am. Chem. Soc.* 76, 6027 (1954).
82. W. D. JOHNSON and D. SESTRICH, *J. Inorg. Nucl. Chem.* 20, 32 (1961).
83. M. KESTIGIAN, J. G. DICKINSON and R. WARD, *J. Am. Chem. Soc.* 79, 5598 (1957).
84. N. N. PADUROV and C. SCHUSTERUS, *Ber. Deut. Keram. Ges.* 32, 292 (1955).
85. L. JÄRNBERG, S. ANDERSSON and A. MAGNÉLI, *Acta Chem. Scand.* 13, 1248 (1959).
86. A. MAGNÉLI and R. NILSSON, *Acta Chem. Scand.* 4, 398 (1950).
87. G. HÄGG, *Z. Physik. Chem.* 29 B, 192 (1935).
88. D. VAN DUYN, *Rec. Trav. Chim.* 61, 669 (1942).
89. A. MAGNÉLI, *Arkiv. Kemi.* 1, 269 (1949).
90. E. O. BRIMM, J. C. BRANTLEY, J. H. LORENZ and M. H. JELLINEK, *J. Am. Chem. Soc.* 73, 5427 (1951).
91. B. W. BROWN and E. BANKS, *J. Am. Chem. Soc.* 76, 983 (1954).
92. M. ATOJI and R. E. RUNDLE, *J. Chem. Phys.* 32, 627 (1960).
93. F. GALASSO, W. DARBY and J. PYLE, prepared at the United Aircraft Corporation Research Laboratories — not reported.
94. G. BLASSE, *J. Inorg. Nucl. Chem.* 27, 993 (1965).
95. G. A. SMOLENSKII, A. I. AGRANOVSKAYA and V. A. ISUPOV, *Sov. Phys. Solid State* 1, 907 (1959).
96. A. I. AGRANOVSKAYA, *Bulletin of Acad. Sciences of U.S.S.R. Physics Series* 24, 1271 (1960).
97. F. GALASSO and J. PYLE, *J. Phys. Chem.* 67, 533 (1963).
98. F. GALASSO and J. PRATO, *Nature* 207, 70 (1965).
99. V. A. BOKOV and I. E. MYL'NIKOVA, *Sov. Phys., Solid State* 2, 2428 (1961).
100. I. G. ISMAILZADE, *Sov. Phys., Cryst.* 5, 292 (1960).
101. A. S. VISKOV, YU. N. VENEVTSEV and G. S. ZHDANOV, *Sov. Phys. Dokl.* 10, 391 (1965).
102. L. BRINKER, *J. Inorg. Nucl. Chem.* 15, 352 (1960).
103. C. KELLER, *J. Inorg. Nucl. Chem.* 27, 321 (1965).
104. A. W. SLEIGHT and R. WARD, *Inorg. Chem.* 1, 799 (1962).
105. F. GALASSO, G. LAYDEN and D. FINORBAUGH, *J. Chem. Phys.* 44, 2703 (1966).
106. V. S. FILIP'EV and E. G. FESENKO, *Sov. Phys., Cryst.* 6, 616 (1962).
107. L. BRINKER, *J. Phys. Chem.* 64, 165 (1960).
108. A. W. SLEIGHT and R. WARD, *Inorg. Chem.* 3, 292 (1964).
109. V. S. FILIP'EV and E. G. FESENKO, *Sov. Phys., Cryst.* 10, 243 (1965).
110. G. A. SMOLENSKII, A. I. AGRANOVSKAYA, S. N. POPOV and V. A. ISUPOV, *Sov. Phys., Tech. Phys.* 3, 1981 (1958).
111. M. F. KUPRIYANOV and E. G. FESENKO, *Sov. Phys. Cryst.* 10, 189 (1965).
112. I. G. ISMAILZADE, *Sov. Phys. Cryst.* 4, 389 (1960).
113. M. F. KUPRIYANOV and E. G. FESENKO, *Sov. Phys. Cryst.* 7, 358 (1962).
114. G. BLASSE, *Philips Research Reports* 20, 327 (1965).
115. J. LONGO and R. WARD, *J. Am. Chem. Soc.* 83, 2816 (1961).
116. G. BAYER, *J. Am. Ceram. Soc.* 46, 804 (1963).
117. I. N. BELYAEV, L. I. MEDVEDEVA, E. G. FESENKO and M. F. KUPRIYANOV, *Izv. Akad. Nauk SSSR Neorgan. Materialy*, 1 6, (1965).
118. YU. E. ROZINSKAYA and YU. N. VENEVTSEV, *Sov. Phys., Cryst.* 10, 275 (1965).
119. YU. YA. TOMASHPOL'SKII and YU. N. VENEVTSEV, *Sov. Phys. Solid State* 6, 2388 (1965).
120. Q. C. JOHNSON and D. H. TEMPLETON, *J. Chem. Phys.* 34, 2004 (1961).
121. R. D. ROSENSTEIN and R. SCHOR, *J. Chem. Phys.* 1, 789 (1963).
122. D. H. TEMPLETON, *J. Chem. Phys.* 23, 1826 (1955).
123. M. N. SALTZMAN and R. SCHOR, *J. Chem. Phys.* 42, 3698 (1965).

11. A. FERRETTI, D. B. ROGERS and J. B. GÓDENOUGH, *J. Phys. Chem. Solids*, **26**, (1966).
12. A. R. SWEDLER, C. J. RAUB and B. T. MATTHEIAS, *Phys. Letters* **16**, 108 (1966).
13. J. F. SCOOLEY, W. R. HOSLER and M. L. COHEN, *Phys. Rev. Letters* **12**, 474 (1964).
14. A. R. SWEDLER, private communication.
15. F. GALASSO and W. DABBY, *Inorg. Chem.*, **1**, 71 (1965).
16. D. D. GLOWER and R. C. HECKMAN, *J. Chem. Phys.*, **41**, 877 (1964).
17. E. K. WEISE and I. A. LESKE, *J. Chem. Phys.*, **21**, 801 (1953).
18. E. J. W. VERWEY, P. W. HAAIJMAN, F. C. ROMERYN and G. W. VAN OOSTERHOUT, *Philips Res. Rep.*, **5**, 173 (1950).
19. G. H. JONKER and J. H. VAN SANTEN, *Physica*, **16**, 337 (1950).
20. G. H. JONKER, *Physica*, **20**, 1118 (1954).
21. P. W. HAAIJMAN, R. W. DAM and H. A. KLASSENS, *Method of Producing Semiconducting Materials*, German Pat. 929,350, June 23 (1956).
22. H. A. SAUER and S. S. FLASCHEN, *Proc. Electronic Components Symp.*, 7th Washington D.C., May, 41 (1956).
23. G. G. HARMAN, *Phys. Rev.*, **106**, 1358 (1957).
24. O. SABURI, *J. Phys. Soc. Japan*, **14**, 1159 (1959).
25. C. SABURI, *J. Am. Ceram. Soc.*, **44**, 54 (1961).
26. J. TENNERY and R. COOK, *J. Am. Ceram. Soc.*, **44**, 187 (1961).
27. W. T. PERIA, W. R. BRATSON and R. P. FENITTY, *J. Am. Ceram. Soc.*, **44**, 249 (1961).
28. W. HEYWANG, *Solid State Elec.*, **8**, 51 (1961).
29. F. M. RYAN and E. C. SUBBARAO, *App. Phys. Letters*, **1**, 69 (1962).
30. G. GOODMAN, *J. Am. Ceram. Soc.*, **46**, 49 (1963).
31. H. A. SAUER and J. R. FISHER, *J. Am. Ceram. Soc.*, **43**, 297 (1960).
32. P. K. GALLAGHER, F. SCHEY and F. DIMARCELLO, *J. Am. Ceram. Soc.*, **46**, 359 (1963).
33. P. K. GALLAGHER and F. SCHEY, *J. Am. Ceram. Soc.*, **46**, 567 (1963).
34. J. W. DAVISON and J. PASTERNAK, U.S. Naval Res. Labs. Memorandum Rpt. No. 1037 (March 1960).
35. General Ceramics, *Oxide Thermoelectric Materials Final Rpt.* (2 Feb. 60-2 Feb. 61), Contract NOBS-78414.

CHAPTER 5

FERROELECTRICITY

DURING World War II extensive investigations were conducted on titanates by von Hippel *et al.* at MIT under wartime restrictions.⁽¹⁾ After the war, the work was released along with studies conducted in England,⁽²⁻⁴⁾ Russia⁽⁵⁻⁷⁾ and Japan.⁽⁸⁾ As a result of these investigations, barium titanate was found to be a ferroelectric.⁽⁷⁾ The term ferroelectric was used because these materials are analogous in some ways to ferromagnetic materials. For example, when an alternating potential is applied to a capacitor containing a ferroelectric material, the instantaneous relation between charge and potential, or polarization and field, produces a hysteresis loop on a cathode-ray oscilloscope (see Fig. 5.1). Ferromagnetic

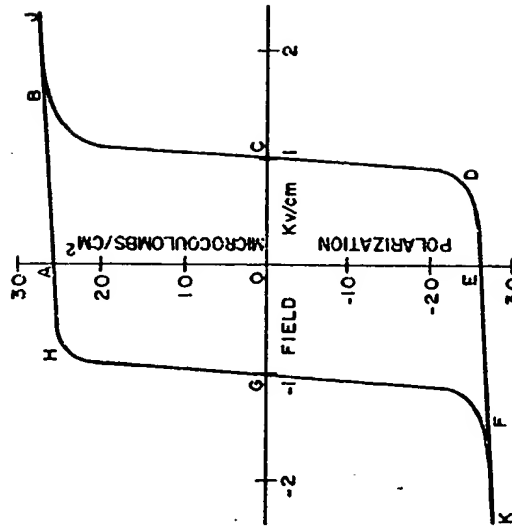


Fig. 5.1. Ferroelectric hysteresis loop.

materials also exhibit a hysteresis loop which represents the relation between magnetic induction B and magnetic field H .

A ferroelectric has been defined as a dielectric having a spontaneous polarization which can be reversed in sign. It therefore must have a polar structure with no center of symmetry. In changing the direction of the polar axis the structure must pass through an intermediate non-polar stage and the polar structure is a distortion of this more symmetrical form. The structure of ferroelectric materials becomes less distorted as the temperature increases and undistorted at and above a temperature called the Curie point.

5.1. TERNARY PEROVSKITES

Titanates

Barium titanate has the ideal cubic perovskite structure above the Curie point, but on cooling below this temperature the oxygen and titanium ions shift to form a tetragonal structure with the c -axis about 1% longer than the other two. At about 0°C the symmetry of the crystal becomes orthorhombic, and at -90°C trigonal (see Fig. 5.2). When a crystal of barium titanate is cooled below 120°C it breaks up into many domains with c -axes oriented perpendicularly.

Merz⁽⁹⁾ found that the switching time required to change the domain configuration depended on the applied field and the size of the sample. This dependence of switching time on thickness was postulated to be caused by a surface layer different from the bulk of the order of 10^{-4} cm on the crystal. The switching time depends linearly on the thickness of the sample if the field is kept constant (see Fig. 5.3).

The presence of the surface layer on BaTiO_3 also was reported by Känzig from electron diffraction experiments which indicated that there was a tetragonal strain in the surface layer which was slightly larger than the tetragonal strain in the bulk below the Curie temperature.⁽¹⁰⁾ The tetragonal strain in the surface did not vanish even when the crystal was heated above the Curie temperature of the bulk. As further support for the postulation, Chynoweth reported that pyroelectric currents could be produced in single crystals of

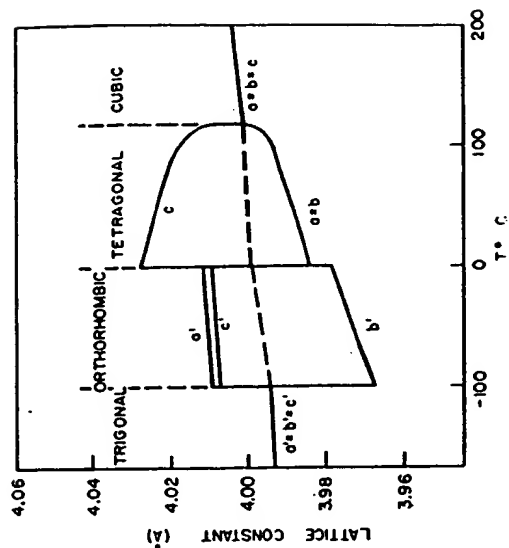


FIG. 5.2. Lattice constants of BaTiO_3 as functions of temperature (after H. F. Kay and P. Vousden, *Phil. Mag.* 40, 229 (1948)).

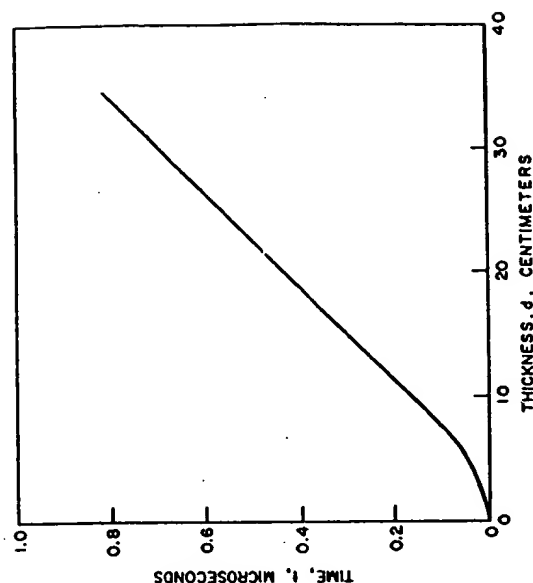


FIG. 5.3. Switching time for infinite field vs. thickness of the sample (after Merz⁽⁹⁾).

barium titanate above the Curie temperature even though no electric field was applied,⁽¹¹⁾ but in spite of these studies, there still appears to be considerable doubt as to the existence of the space-charge layer on the surface.

The tetragonal distortion in the structure of BaTiO_3 resulted in the formation of dipoles. Merz⁽¹²⁾ measured the dipole moment of BaTiO_3 single crystals and found it to be 18×10^{-6} coulombs/cm² at 120°C and 26×10^{-6} at ambient temperature. In addition, he⁽¹³⁾ also measured the dielectric constant and found that it was much greater perpendicular to the c-axis than along it (see Fig. 5.4).

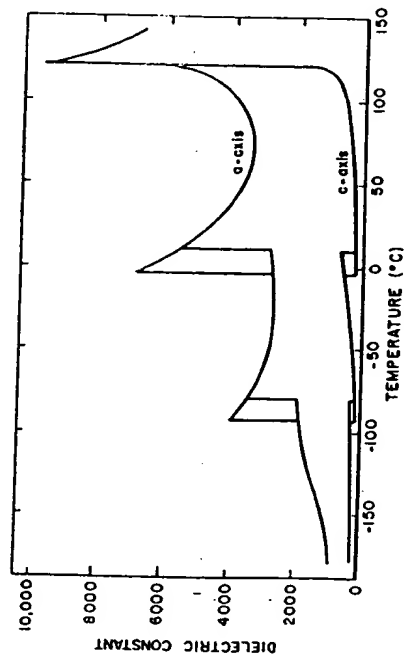


FIG. 5.4. Dielectric constant of BaTiO_3 as a function of temperature (after Merz⁽¹²⁾).

The dielectric constant of ceramic barium titanate was found to be about 1500, which falls between the values obtained along the c-axis and a-axis of the single crystal. The value decreases slowly with frequency to 10^6 c/s, and then decreases further to a value of 126 at 24×10^3 Mc. When the measurement is made under pressure, the dielectric constant increases⁽¹⁴⁾ and the Curie point shifts to lower temperatures.⁽¹⁵⁾

Because of this high dielectric constant, experimental studies have been conducted to improve the properties of barium titanate for energy converter and capacitor applications.⁽¹⁶⁾ A figure of merit for capacitor applications is de-

noted as (time constant) RC which is the time for a capacitor to discharge to $1/e$ of the charging voltage. Time constants were measured for various grades of BaTiO_3 and for BaTiO_3 with different additives. The results are presented in Table 5.1.

TABLE 5.1. Measurements on BaTiO_3 Compositions Fired 1 hr at 1450°C (after Hoh and Pirig⁽¹⁶⁾)

BaTiO_3 starting material grade	Additive	RC in sec.
1. C.P.	none	10
2. Commercial capacitor	none	52
3. Commercial piezoelectric	none	220
4. High purity	none	700
5. Commercial capacitor	0.1 wt% Cr_2O_3	3,000
6. High purity	0.1 wt% Cr_2O_3	12,500
7. High purity	0.15 wt% Cr_2O_3	10,500
8. Commercial capacitor	3.0 wt% CaSnO_3	9,800
9. Commercial capacitor	0.1 wt% Cr_2O_3	12,000
10. High purity	+ 1 wt% CaSnO_3	
	0.1 wt% Cr_2O_3 as	
	CrF_3	3,500
11. Commercial capacitor	0.5 mole % UO_2 as	10,500
12. Commercial capacitor	U_2O_5	
	0.5 mole % UO_2 as	8,000
13. Commercial capacitor	UF_4	
	0.5 mole % UO_2 as	
	UF_4 + 3 mole % CaSnO_3	13,000

The results showed that the additives improved the time constant by several orders of magnitude. The compounds Cr_2O_3 and CaSnO_3 improved RC only at room temperature, but the solid fluoride additives showed the most promise.

MacChesney *et al.*⁽¹⁷⁾ improved the stability of the properties with respect to temperature by adding La_2O_3 . The temperature coefficient of capacitance and dissipation factor was reduced to low values by adding 1 mole % La_2O_3 .

In other studies, increased stability of BaTiO_3 has been

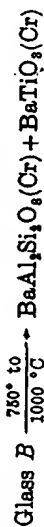
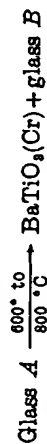
reported for materials with the following additives: 1% NiZrO_3 , $(\text{Ti}, \text{Zr}, \text{Sn})\text{O}_2 + \text{Bi}_2\text{O}_3$, 6% $(\text{Bi}_2\text{O}_3, 2\text{ZrO}_2)$, $(\text{Zr}, \text{Sn})\text{O}_2 + \text{Li}_2\text{O}$, $(\text{Zr}, \text{Sn})\text{O}_2 + \text{Al}_2\text{O}_3$, 2.37% $(\text{CaTiO}_3) + 1.43\% (\text{Bi}_2\text{SnO}_6) + 2.85\text{SnO}_2$, 1–25% (CaZrO_3) , and 41% $\text{Fe}_2\text{O}_3 + 10\text{TiO}_2 + 9\text{FeO} + 5\text{NiO} + 5\text{CoO}$.

High dielectric constants have been produced in barium titanate after reduction and re-oxidation and with metal additives. However, it is probable that the high dielectric constants reported for these materials are high because of semi-conductivity of the samples or the presence of a thin non-conducting skin on a conducting medium.

Khodakov⁽¹⁸⁾ attempted to modify the properties of BaTiO_3 by using a fine particle size of BaTiO_3 (1–20 μ) and found that the peaks in the dielectric constant versus temperature curves were flatter with decreasing particle size. This is an important method of obtaining materials whose dielectric constants are high and relatively independent of temperature.

Blinton and Havel⁽¹⁹⁾ studied the properties of flame-sprayed barium titanate ceramic coatings. The coatings were predominantly the cubic phase. The metastable cubic phase transforms to the tetragonal phase by annealing the ceramic at 1400°C for 2 hr in air or helium. A study of the dielectric constant as a function of temperature revealed that the curves were much flatter than that for normal barium titanate.

Interesting dielectric materials also were prepared by crystallizing BaTiO_3 with feldspar $\text{BaAl}_2\text{Si}_2\text{O}_8$ by heat-treating glasses having compositions corresponding to $x\text{BaTiO}_3 + (100-x)\text{(BaAl}_2\text{Si}_2\text{O}_8)$. Herczog⁽²⁰⁾ proposed the mechanism of crystallization as being



If the heating rate and the final temperature of heat treatment were controlled the particle size could be varied from 0.01 to 1 μ . The size of the particles were quite uniform for any treatment. For particles below 0.2 μ the dielectric constant was nearly independent of temperature, and materials with a particle size of 1 μ were found to have the highest

dielectric constant. Resistivity and dielectric strength were high compared with ceramic materials.

Barium titanate also exhibits piezoelectric properties which means that electric polarization takes place when it is subjected to mechanical strain, and inversely the material mechanically deforms upon application of an electric field. This effect reverses in sign upon reversal of the electric field. This is in contrast to electrostriction exhibited by all dielectrics under an applied field.

Determination of the piezoelectric properties of single-crystal BaTiO_3 gave 950×10^{-8} statcoul/dyne for d_{33} and -310×10^{-8} statcoul/dyne for d_{31} where d_{33} is the proportionality between the charge developed on the two faces perpendicular to its c -axis and d_{31} is the proportionality between the charge on the same two faces and the force applied when the force is perpendicular to the c -axis.^(21–24)

In order to obtain this effect in ceramic barium titanate, it must be first poled by d.c. voltages of 20–30 kV/cm which line up approximately 10% of the c -axis of the crystallites. The piezoelectric moduli measured for ceramics depend on the effectiveness of the poling operation.

Lead titanate is also a ferroelectric with a tetragonal distortion of the perovskite structure. Shirane and Pepinsky⁽²⁵⁾ studied the structure with X-ray and neutron diffraction. The results indicated a shift of 0.30 Å for the Ti ion along the c -axis and 0.47 Å for the Pb ions which were much larger displacements than those found in barium titanate (see Fig. 5.5). At 490°C, PbTiO_3 changes from a tetragonal form to a cubic form (see Fig. 5.6). The energy absorption at this transformation temperature is 1150 cal/mol.⁽²⁶⁾

The dielectric constant of PbTiO_3 is about 100 at room temperature and reaches a peak of about 1000 at 490°C.⁽²⁷⁾ Studies on single crystals indicate that the Curie point is at 495°C. The domain structures of these single crystals were reported to be essentially the same as that observed in BaTiO_3 .

The piezoelectric coefficient d_{33} for PbTiO_3 with additives was found to be less than 30×10^{-12} coulombs/newton except for specimens containing 1 mole % CaF_2 which gave values as high as 130×10^{-12} coulombs/newton.⁽²⁸⁾

Strontium titanate has the cubic perovskite structure, and is not ferroelectric at room temperature even though it has a dielectric constant of 200. There are conflicting reports on

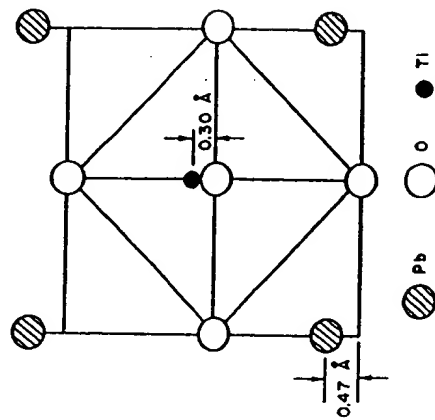


FIG. 5.5. Structure of PbTiO_3 (after G. Shirane, R. Pepinsky and G. B. Frazer, *Acta Cryst.* 9, 131 (1956)).

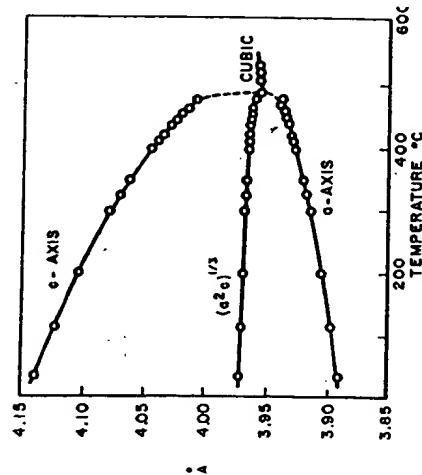


FIG. 5.6. Temperature dependence of volume and lattice constants for PbTiO_3 (after Shirane *et al.*⁽⁷⁰⁾).

the possibility of it being ferroelectric at very low temperatures, even though Gränicher⁽²⁰⁾ did report the observation of a hysteresis loop with a field of 300 V/cm at 4°K. The spon-

taneous polarization was reported to be 3×10^{-6} coulomb/cm² and the remnant polarization 1×10^{-6} coulomb/cm².

Calcium titanate has an orthorhombic structure at room temperature, the structure becomes tetragonal at 600°C and cubic at 1000°C.⁽³⁰⁾ It has a room-temperature dielectric constant of 100, but it is not ferroelectric.

Niobates and Tantalates

Potassium niobate, KNbO_3 , is the best-known compound of this group. The transition temperature on heating is -12°C for the rhombohedral to orthorhombic transforma-

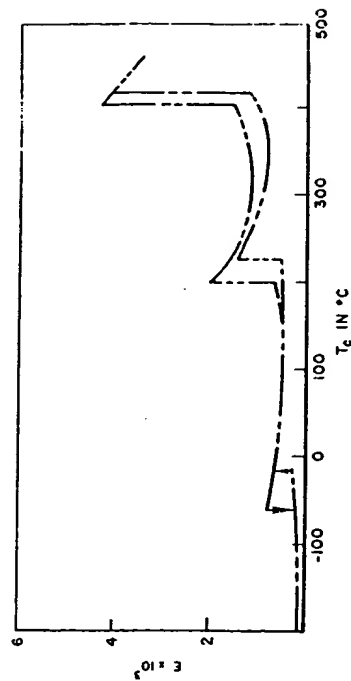


FIG. 5.7. Dielectric constant of KNbO_3 as a function of temperature (after Shirane *et al.*⁽³¹⁾).

tion, 224°C for the orthorhombic to tetragonal transformation, 412°C for the tetragonal to cubic transformation and -59°, 200° and 407°C on cooling (see Fig. 5.7). The loss tangent at these transitions is approximately 0.3.^(31, 32) This is about ten times as high as the value for BaTiO_3 . The values of saturation polarization have been obtained from hysteresis loops and found to be 0.9×10^{-6} coulombs/cm² at room temperature.

Sodium niobate is not ferroelectric and may be antiferroelectric, but ferroelectricity can be induced by the application of a strong field of the order of 10 kV/cm. Once ferroelectricity is induced, the crystals remain ferroelectric from -55°C to 200°C. Vousden⁽³³⁾ and Francombe⁽³⁴⁾ indicated

that there are several transformations in NaNbO_3 at 20° , 390° , 420° , 560° and 640°C . The last is the tetragonal to cubic transformation. The temperature dependence of the dielectric constant is given in Fig. 5.8.

A rectangular hysteresis loop with the same saturation polarization value of BaTiO_3 was investigated by Matthias⁽³⁵⁾ who reported the Curie temperature for NaTaO_3 to be 475°C .

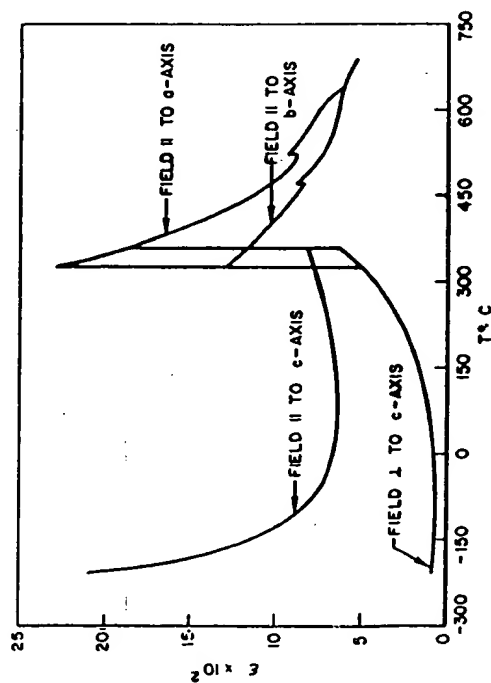


Fig. 5.8. Temperature dependence of dielectric constant of NaNbO_3 (after L. E. Cross and B. J. Nicholson⁽¹¹⁾).

Potassium tantalate was reported as having a phase transformation between 10°K and 20°K and a hysteresis loop below 13°K ⁽³⁶⁾. Smolenskii reported a Curie temperature of 247°C for RbTaO_3 .⁽³⁷⁾

Zirconates and Hafnates

Lead zirconate, PbZrO_3 , is antiferroelectric, that is although there is a dipole moment in each unit cell, the arrangement of the moments in adjacent cells is such as to cause a net dipole moment of zero. At 230°C , the symmetry of the structure changes from orthorhombic to cubic (see Fig. 5.9). The temperature variation of the dielectric constant of lead zirconate is given in Fig. 5.10.

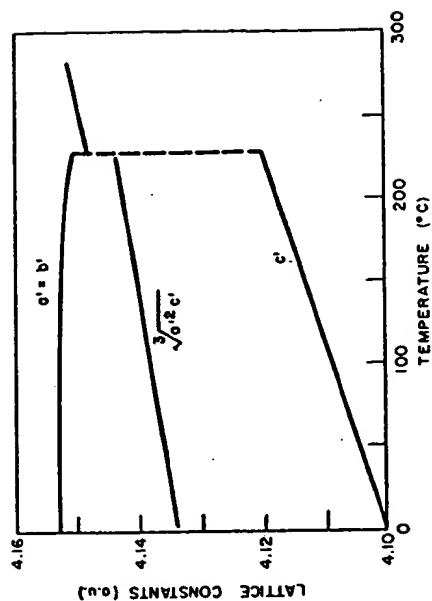


Fig. 5.9. Temperature variation of the lattice constants of lead zirconate (after E. Sawaguchi, *J. Phys. Soc. Japan* 8, 615 (1953)).

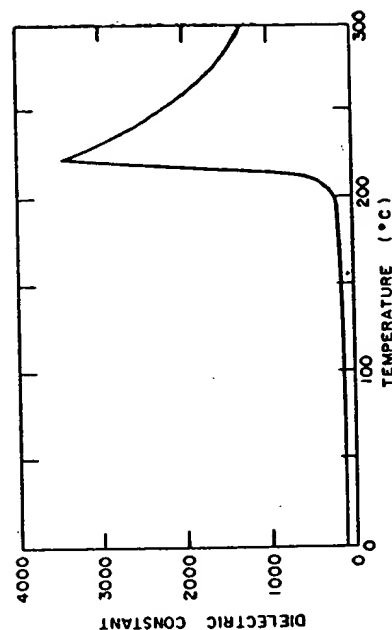


Fig. 5.10. Dielectric constant of lead zirconate as a function of temperature (after Roberts⁽³⁸⁾).

Lead hafnate transforms to a new structure at 160°C and transforms at 210°C to a cubic form. The two lower forms are antiferroelectric and the high-temperature form is paraelectric.⁽³⁸⁾

5.2. SOLID SOLUTIONS

BaTiO_3 - SrTiO_3

One of the most widely studied solid solution systems is that between BaTiO_3 and SrTiO_3 . There is complete solid

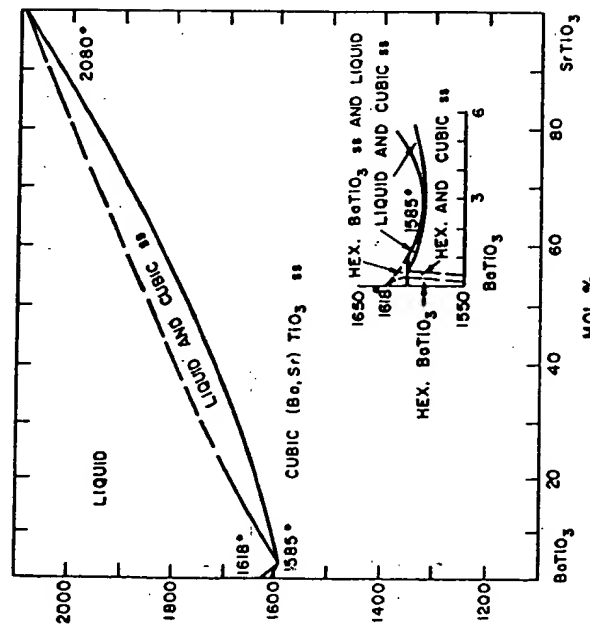


FIG. 5.11. Phase diagram for the BaTiO_3 - SrTiO_3 system (after J. D. Basmajian and R. C. DeVries, *J. Am. Ceram. Soc.* 40, 374 (1957)).

solution in this system, with the size of the unit cells decreasing linearly with the substitution of Sr in BaTiO_3 ^(39, 40) (see Fig. 5.11). The Curie point also decreases with increasing

amounts of strontium substitution (see Fig. 5.12). With the first additions of strontium the ambient temperature dielectric constant increases, reaches a maximum of 8000 at about 30 mole % addition, and then decreases. It is interesting that the low-temperature Curie point materials do not show the decrease in dielectric constant that is found for barium titanate at 10° cycles.⁽⁴¹⁻⁴³⁾ A minimum in the activation energy obtained from d.c. measurements was found at 40% SrTiO_3 .⁽⁴³⁾

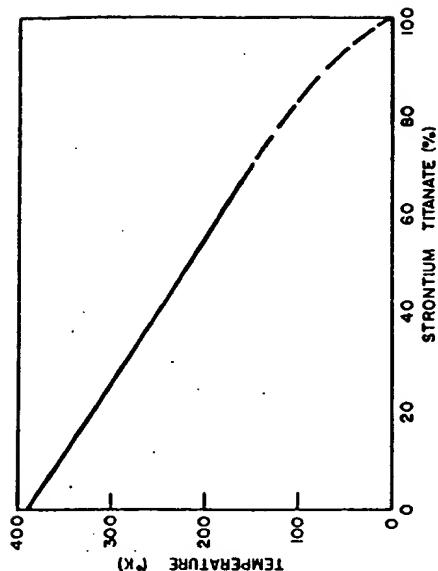


FIG. 5.12. Variation of Curie temperature as a function of composition, $(\text{Ba}, \text{Sr})\text{TiO}_3$ (after Rushman *et al.*⁽⁴³⁾).

BaTiO_3 - PbTiO_3

Lead titanate also forms complete solid solution with barium titanate. The addition of lead titanate lowers the room temperature dielectric constant, increases the Curie temperature (see Fig. 5.13),⁽³⁴⁾ decreases the d.c. resistivity and the activation energy⁽⁴³⁾, and improves the piezoelectric properties of barium titanate.^(44, 45)

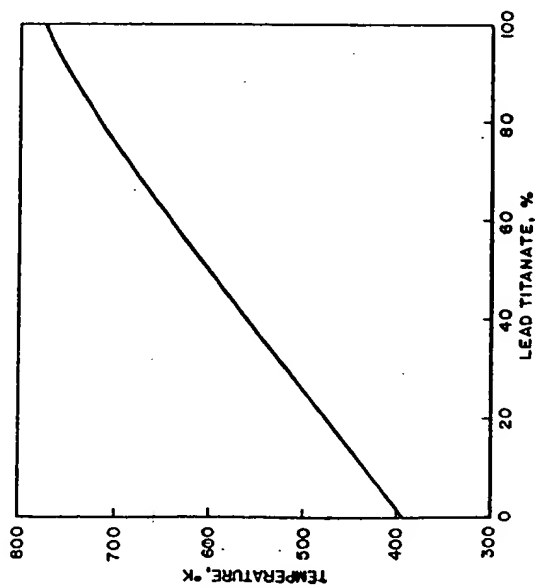


FIG. 5.13. Variation of Curie temperature with composition, (Ba, Pb)TiO₃ (after G. Shirane, S. Hoshino and K. Suzuki, *J. Phys. Soc. Japan* 5, 466 (1950)).

BaTiO₃-CaTiO₃

Calcium titanate is soluble in BaTiO₃ up to 25 mole % and BaTiO₃ dissolves in CaTiO₃ to about the same extent (see Fig. 5.14). The addition of calcium to barium titanate lowers the room-temperature dielectric constant, and small amounts improve the piezoelectric properties.

BaTiO₃-(Ba, Sr, Ca)ZrO₃

The BaTiO₃-BaZrO₃ phase diagram is shown in Fig. 5.15. The addition of barium, strontium and calcium zirconate to barium titanate lowers the Curie point and broadens the maximum dielectric constant.⁽⁴⁾

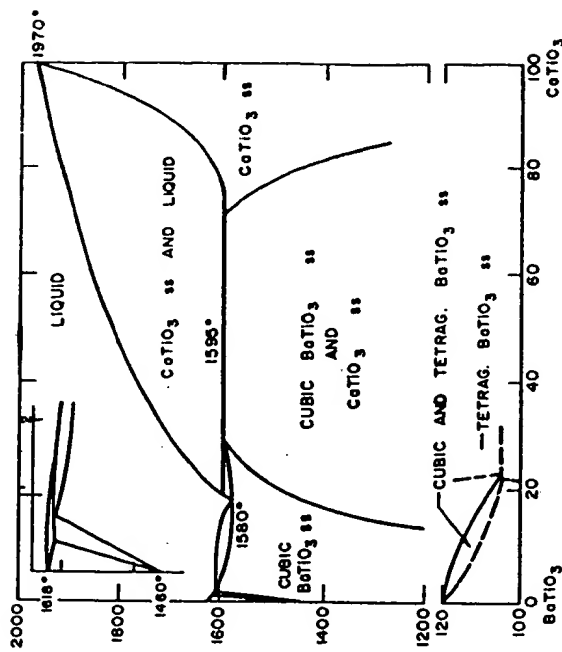


FIG. 5.14. Phase diagram for the BaTiO₃-CaTiO₃ system (after R. C. DeVries and R. Roy, *J. Am. Ceram. Soc.* 88, 145 (1965)).

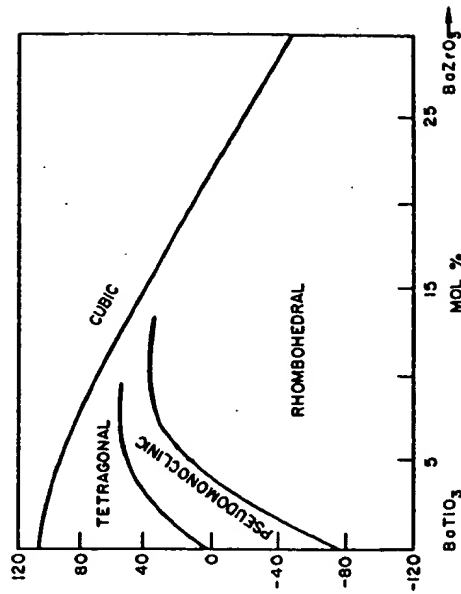


FIG. 5.15. Phase diagram for the system BaTiO₃-BaZrO₃ (after T. N. Verbitskaya, G. S. Zhdanov, Yu. N. Voznetsev and S. P. Solov'ev, *Kristallografiya*, 8, 189 (1958)).

BaTiO₃-BaSnO₃

Dungan *et al.*⁽⁴⁷⁾ found that additions of BaSnO₃ to BaTiO₃ lowers the Curie temperature, and increases the unit cell size. Figure 5.16 shows the variation in Curie temperature with additions of BaSnO₃.

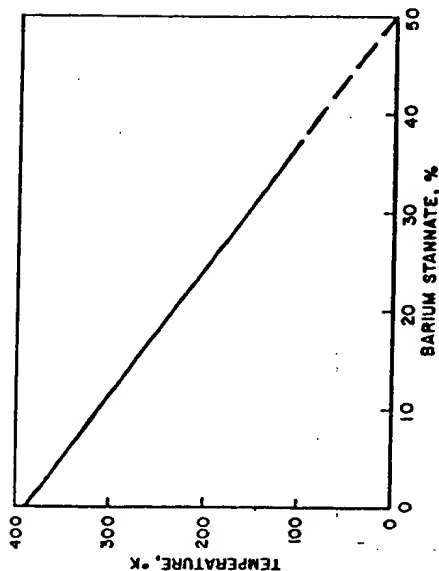


Fig. 5.16. Variation of Curie point of barium titanate with the addition of barium stannate (after Dungan *et al.*⁽⁴⁷⁾).

BaTiO₃-BaHfO₃

A study of the BaTiO₃-BaHfO₃ system by Fresenko and Prokopolov⁽⁴⁸⁾ showed that it was quite similar to those of BaTiO₃-BaZrO₃ and BaTiO₃-BaSnO₃. Payne and Tenny⁽⁴⁹⁾ made dielectric measurements and X-ray diffraction studies in this system and found that the dielectric constant for each sample increased as the BaHfO₃ concentration was increased to 16 mole % BaHfO₃ and then decreased with further BaHfO₃ additions. They suggest that the ferroelectric-paraelectric transition for the composition containing 16 mole % BaHfO₃ was of second order and occurred between a ferroelectric rhombohedral phase and a paraelectric cubic phase.

Other BaTiO₃ Solid Solutions

More complex systems with barium titanate as one of the constituents have also been studied. The phase diagram for the system BaSnO₃-BaTiO₃-PbSnO₃-PbTiO₃ is shown in Fig. 5.17.

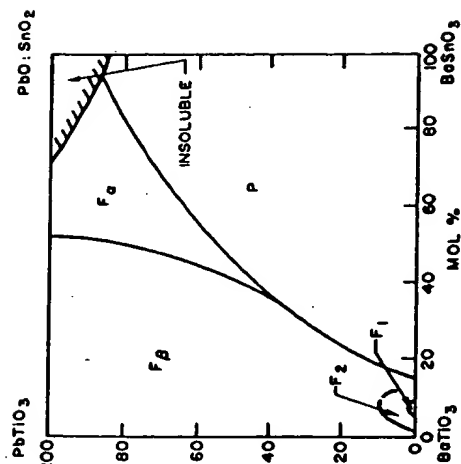


Fig. 5.17. Phase diagram for the PbTiO₃-BaTiO₃-PbO:SnO₂-BaSnO₃ system, P = paraelectric, cubic phase, F_1 = ferroelectric, rhombohedral phase, F_2 = ferroelectric, tetragonal phase, F_3 = ferroelectric, rhombohedral phase, F_4 = ferroelectric, orthorhombic phase (after T. Ikeda, *J. Phys. Soc. Japan* 14, 1292 (1959)).

PbTiO₃-KNbO₃

The phase diagram of the PbTiO₃-KNbO₃ system and dielectric properties of the solid solutions were determined by Tien *et al.*⁽⁵⁰⁾ Where solid solution was formed between compounds with one common cation, the Curie temperature varied more or less linearly with composition. Figure 5.18 presents this data for the KNbO₃-NaNbO₃, PbTiO₃-PbZrO₃, PbTiO₃-BaTiO₃, PbTiO₃-NaNbO₃ and the KNbO₃-KTaO₃ systems. In the PbTiO₃-KNbO₃ system where no ions are

common the preparation of homogeneous specimens proved to be difficult. Tien *et al.* feel that the minimum that exists is common for all systems which involve ferroelectric or antiferroelectric compounds not containing a common ion, point-

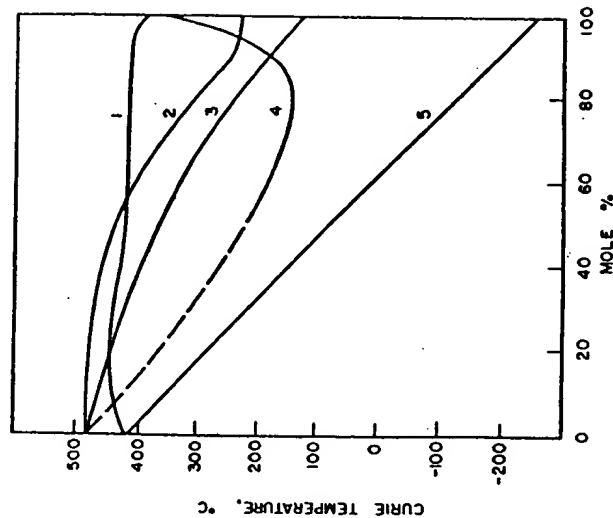


FIG. 5.18. Curie temperatures in perovskite systems: (1) $\text{KNbO}_3\text{-NaNbO}_3$, (2) $\text{PbTiO}_3\text{-PbZrO}_3$, (3) $\text{PbTiO}_3\text{-BaTiO}_3$, (4) $\text{PbTiO}_3\text{-NaNbO}_3$, (5) $\text{KNbO}_3\text{-KTaO}_3$ (after Tien *et al.* (50)).

ing out that this is true of the $\text{BaTiO}_3\text{-PbZrO}_3$, $\text{NaNbO}_3\text{-PbZrO}_3$, $\text{NaNbO}_3\text{-PbTiO}_3$ as well as the $\text{PbTiO}_3\text{-KNbO}_3$ system.

$\text{PbZrO}_3\text{-PbTiO}_3$

Addition of barium, strontium and titanium ions destroys the antiferroelectric properties of PbZrO_3 . Figure 5.19 shows a phase diagram of the $\text{PbZrO}_3\text{-PbTiO}_3$ system. The addition of lead titanate to lead zirconate appears to lower the dielec-

tric constant and increases the temperature of its maximum.⁽⁵¹⁾

Jaffe *et al.* (52) found that in systems where compositional boundaries exist between ferroelectric phases of slightly differing structure the induced piezoelectric effects are enhanced as the composition approaches the phase boundary. In the system lead titanate-lead zirconate, lead titanate-lead oxide:tin oxide, lead zirconate-lead oxide:tin oxide and the lead titanate-lead hafnate, one of the compositions 45%

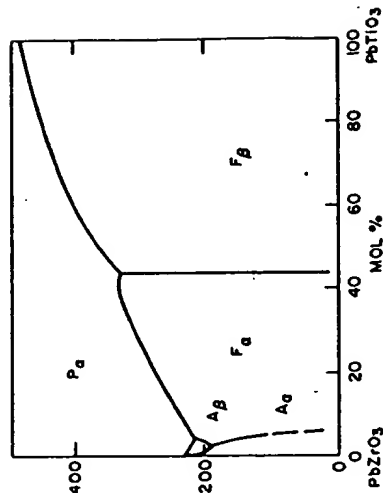


FIG. 5.19. Phase diagram for the $\text{PbTiO}_3\text{-PbZrO}_3$ system, P = paraelectric, cubic phase, A_a = antiferroelectric, orthorhombic phase, A_b = antiferroelectric, F_f = ferroelectric, rhombohedral phase, F_a = ferroelectric, tetragonal phase (after E. Sawaguchi, *J. Phys. Soc. Japan* 8, 616 (1953)).

$\text{PbTiO}_3\text{-55% PbZrO}_3$ has a Curie temperature of 340°C and a radial coupling coefficient of 0.3 at 275°C which is twice that of barium titanate. Another containing 47.25% PbTiO_3 , 22.75% PbZrO_3 and 30% $\text{PbO}:\text{SnO}_2$ had the highest piezoelectric coefficient (d_{31}) of all compositions studied— 74×10^{-12} coulomb/newton.

Ikedo⁽⁵³⁾ reported that the addition of LaFeO_3 to $\text{Pb}(\text{Ti}, \text{Zr})\text{O}_3$ ceramics near the phase boundary improved the piezoelectric performance. In more detailed studies Ikeda⁽⁵⁴⁾ showed that improved piezoelectric ceramics were obtained when $\text{Pb}(\text{Ti}, \text{Zr})\text{O}_3$ was modified by the addition of $A^{1+}B^{5+}O_3$ ($A = \text{K}, \text{Na}, \text{B} = \text{Sb}, \text{Bi}$) or $A^{3+}B^{3+}O_3$ ($A = \text{Bi}, \text{La}$; $B = \text{Fe}, \text{Al}$,

Cr). Dielectric constants above 1500 and radial coupling coefficients above 0.6 were obtained with Na^+ and Sb^{5+} substitution.

PbZrO_3 - BaZrO_3

When barium replaces lead in PbZrO_3 , the dielectric maximum of lead zirconate is shifted to lower temperatures.⁽⁵³⁾ In addition, the maximum dielectric constant becomes great-

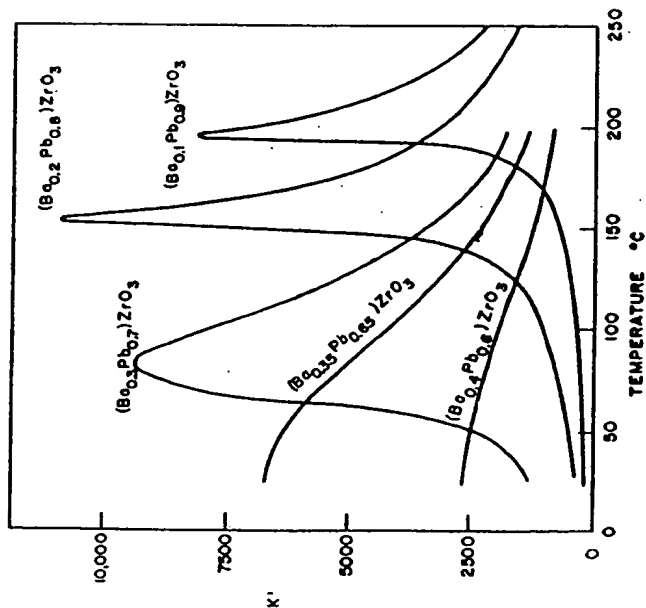


Fig. 5.20. Dielectric constant of $(\text{Ba}, \text{Pb})\text{ZrO}_3$ compositions at varying temperatures (after Roberts⁽⁵³⁾).

er and the high values are maintained over a broader range of temperature (see Fig. 5.20). The largest value is obtained for a composition of $(\text{Ba}_{0.20}\text{Pb}_{0.80})\text{ZrO}_3$ and when still larger percentages of barium are substituted, the dielectric maximum is lowered, but the temperature range of high dielectric constant values become broader. The dielectric constant of $\text{Ba}_{0.35}\text{Pb}_{0.65}\text{ZrO}_3$ stays above 6000 from room temperature up to 60°C making it useful for capacitor application.

5.3. COMPLEX PEROVSKITES

Viskov *et al.*⁽⁵⁴⁾ reported that the compounds $\text{Ba}(\text{Bi}_{0.5}\text{Nb}_{0.5}\text{O}_3)$, $\text{Ba}(\text{Bi}_{0.5}\text{Ta}_{0.5}\text{O}_3)$, $\text{Ba}(\text{Bi}_{0.5}\text{U}_{0.5}\text{O}_3)$, $\text{Ba}(\text{Bi}_{0.5}\text{W}_{0.5}\text{O}_3)$ and $\text{Ba}(\text{Bi}_{0.5}\text{Mo}_{0.5}\text{O}_3)$ had distorted unit cells and high dielectric constants which peaked with temperature. They reported anomalies in dielectric constants at temperatures of 420°, 410°, 320°, 400° and 260°C for the compounds con-

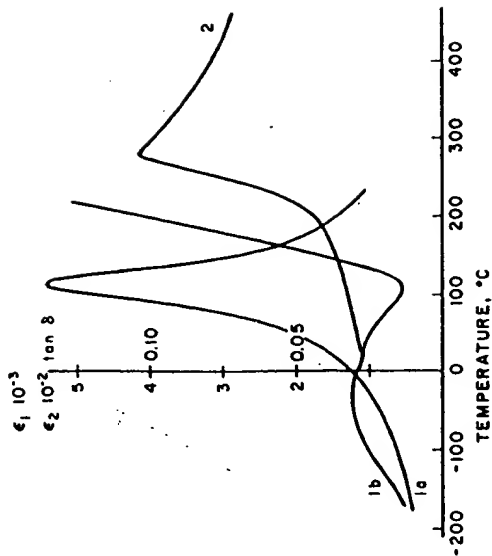


Fig. 5.21. Temperature dependence of ϵ' for $\text{Pb}(\text{Fe}_{0.5}\text{Nb}_{0.5})\text{O}_3$ and $\text{Pb}(\text{Y}_{0.5}\text{Nb}_{0.5})\text{O}_3$: (1a and 1b) ϵ' and $\tan \delta$ for $\text{Pb}(\text{Fe}_{0.5}\text{Nb}_{0.5})\text{O}_3$; (2) ϵ' for $\text{Pb}(\text{Y}_{0.5}\text{Nb}_{0.5})\text{O}_3$ (after Smolenskii *et al.*⁽⁵⁷⁾).

taining Nb, Ta, V, W and Mo, respectively, and felt that the first three were ferroelectric and the last two antiferroelectric. However, evidence for this assumption was lacking.

Smolenskii *et al.*⁽⁵⁷⁾ found from studies on powder compacts that $\text{Pb}(\text{Fe}_{0.5}\text{Nb}_{0.5})\text{O}_3$ and $\text{Pb}(\text{Y}_{0.5}\text{Nb}_{0.5})\text{O}_3$ might be ferroelectrics with Curie temperatures of 112°C and 280°C, respectively. The temperature dependence of permittivity and loss tangent for these compounds are shown in Fig. 5.21. The compound $\text{Pb}(\text{Fe}_{0.5}\text{Nb}_{0.5})\text{O}_3$ exhibited a hysteresis loop, but $\text{Pb}(\text{Y}_{0.5}\text{Nb}_{0.5})\text{O}_3$ only showed a maximum in its permittivity and therefore may be antiferroelectric.

Smolenskii *et al.*⁽⁵⁸⁾ also found that $\text{Pb}(\text{Sc}_{0.5}\text{Nb}_{0.5})\text{O}_3$ and $\text{Pb}(\text{Sc}_{0.5}\text{Ta}_{0.5})\text{O}_3$ were ferroelectric materials. The dielectric constant of the niobium- and tantalum-containing compounds exhibited a maximum at 90° and 20°C, respectively (see Fig. 5.22). The characteristic drop in the loss tangent corresponds to a maximum of the dielectric constant. Hysteresis loops were obtained for both compounds at 18°C. The spontaneous polarization for $\text{Pb}(\text{Sc}_{0.5}\text{Nb}_{0.5})\text{O}_3$ at 18° equaled 3.6 microcoulombs and the coercive force 6 kV/cm.

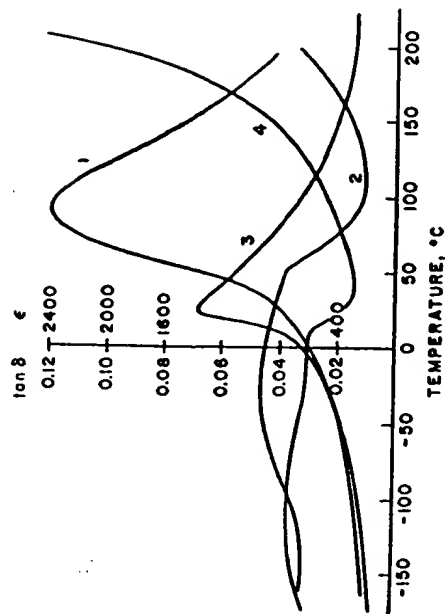


Fig. 5.22. Temperature dependence of ϵ and $\tan \delta$ of $\text{Pb}(\text{Sc}_{0.5}\text{Nb}_{0.5})\text{O}_3$ and $\text{Pb}(\text{Sc}_{0.5}\text{Ta}_{0.5})\text{O}_3$: (1, 2) ϵ and $\tan \delta$ of $\text{Pb}(\text{Sc}_{0.5}\text{Nb}_{0.5})\text{O}_3$; (3, 4) ϵ and $\tan \delta$ of $\text{Pb}(\text{Sc}_{0.5}\text{Ta}_{0.5})\text{O}_3$ (after Smolenskii *et al.*⁽⁵⁸⁾).

Maxima in dielectric constant with temperatures were observed for $\text{Pb}(\text{Lu}_{0.5}\text{Nb}_{0.5})\text{O}_3$, $\text{Pb}(\text{Yb}_{0.5}\text{Ta}_{0.5})\text{O}_3$ and $\text{Pb}(\text{In}_{0.5}\text{Nb}_{0.5})\text{O}_3$ at 280° for the first two compounds and 90° for the last, but they were probably antiferroelectric.⁽⁵⁹⁾ Studies on single crystals of $\text{Pb}(\text{Co}_{0.5}\text{W}_{0.5})\text{O}_3$ ⁽⁶⁰⁾ showed that it had a maximum in its dielectric constant at 32°C and exhibited a double hysteresis-loop characteristic of an antiferroelectric material.

Measurements on $\text{Pb}(\text{Fe}_{0.47}\text{W}_{0.53})\text{O}_3$ and $\text{Pb}(\text{Fe}_{0.5}\text{Ta}_{0.5})\text{O}_3$ indicate that these compounds are true ferroelectrics, while $\text{Pb}(\text{Mg}_{0.5}\text{W}_{0.5})\text{O}_3$ appears to be antiferroelectric.⁽⁶¹⁾ A sharp

permittivity peak was observed at 38°C in the dielectric constant-temperature curve for $\text{Pb}(\text{Mg}_{0.5}\text{W}_{0.5})\text{O}_3$. The compounds $\text{Pb}(\text{Fe}_{0.47}\text{W}_{0.53})\text{O}_3$ and $\text{Pb}(\text{Fe}_{0.5}\text{Ta}_{0.5})\text{O}_3$ exhibited hysteresis loops at liquid-oxygen temperature and the latter compound exhibited a maximum in its dielectric constant at -30°C.

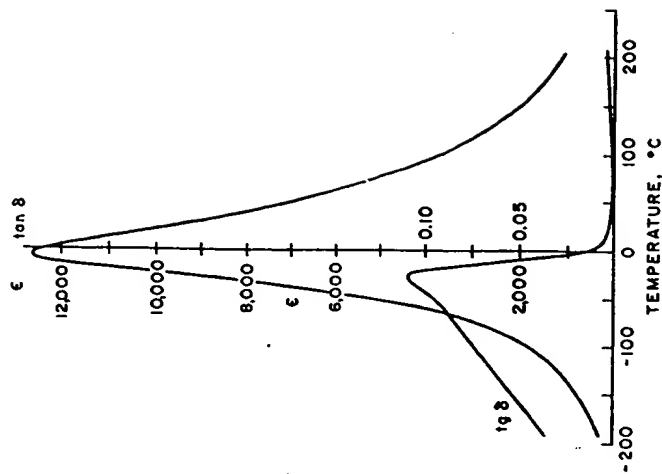


Fig. 5.23. Temperature dependence of ϵ and $\tan \delta$ values for $\text{Pb}(\text{Mg}_{0.33}\text{Nb}_{0.67})\text{O}_3$ (1 kc) (after Smolenskii *et al.*⁽⁶²⁾).

Single crystals of $\text{Pb}(\text{Ni}_{0.33}\text{Nb}_{0.67})\text{O}_3$ were prepared by Myl'nikova and Bokov and reported to be ferroelectric. A maximum was observed in a plot of its dielectric constant versus temperature, and a hysteresis loop was observed at a temperature of -196 °C.⁽⁶²⁾

Smolenskii and Agranovskaya⁽⁶³⁾ studied a large number of perovskite-type compounds and found two new ferroelectric materials, $\text{Pb}(\text{Mg}_{0.33}\text{Nb}_{0.67})\text{O}_3$ and $\text{Pb}(\text{Ni}_{0.33}\text{Nb}_{0.67})\text{O}_3$. Figure 5.23 shows the temperature dependence of the dielec-

tric constant and loss tangent for $\text{Pb}(\text{Mg}_{0.33}\text{Nb}_{0.67})\text{O}_3$. The dielectric constant reached a maximum value of 12,600 at -15°C when a frequency of 1 kc/s was used in the measurements. A hysteresis loop was observed at -130°C and a spontaneous polarization value of 14×10^{-6} coulombs was calculated. The compound $\text{Pb}(\text{Ni}_{0.33}\text{Nb}_{0.67})\text{O}_3$ also appears to be a ferroelectric material.

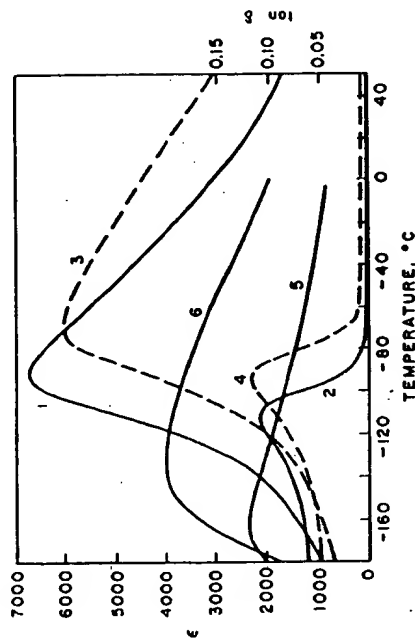


FIG. 5.24. The temperature dependences of ϵ and $\tan \delta$: (1, 2) ϵ and $\tan \delta$ for single crystals $\text{Pb}(\text{Mg}_{0.33}\text{Ta}_{0.67})\text{O}_3$ (1 kc); (3, 4) ϵ and $\tan \delta$ for single crystals $\text{Pb}(\text{Co}_{0.33}\text{Nb}_{0.67})\text{O}_3$ (1 kc); (5) ϵ for single-crystal $\text{Pb}(\text{Ni}_{0.33}\text{Ta}_{0.67})\text{O}_3$ (450 kc), (6) ϵ for single-crystal $\text{Pb}(\text{Co}_{0.33}\text{Ta}_{0.67})\text{O}_3$ (1 kc), (after Bokov *et al.*⁽⁴⁴⁾).

Bokov and Myl'nikova⁽⁴⁴⁾ prepared single crystals of compounds $\text{Pb}(\text{Ni}_{0.33}\text{Ta}_{0.67})\text{O}_3$, $\text{Pb}(\text{Mg}_{0.33}\text{Ta}_{0.67})\text{O}_3$, $\text{Pb}(\text{Co}_{0.33}\text{Nb}_{0.67})\text{O}_3$, $\text{Pb}(\text{Co}_{0.33}\text{Ta}_{0.67})\text{O}_3$ and $\text{Pb}(\text{Zn}_{0.33}\text{Nb}_{0.67})\text{O}_3$ and showed that the compounds were ferroelectrics. The temperature dependence of the dielectric constant and loss tangent for these compounds are shown in Figs. 5.24 and 5.25. The loss tangent maximum occurred at a slightly lower temperature than the permittivity maximum which is characteristic of ferroelectrics. The authors attributed the differences of the phase transitions to the absence of ordering of the B ions in the octahedral positions. The data obtained from the hysteresis loops are the following for $\text{Pb}(\text{Co}_{0.33}\text{Nb}_{0.67})\text{O}_3$, $E_{\text{max}} = 28$ kV/cm, at $t = -150^\circ\text{C}$, for $\text{Pb}(\text{Zn}_{0.33}\text{Nb}_{0.67})\text{O}_3$,

$E_{\text{max}} = 38$ kV/cm, at $t = 20^\circ\text{C}$, for $\text{Pb}(\text{Mg}_{0.33}\text{Ta}_{0.67})\text{O}_3$, $E_{\text{max}} = 45$ kV/cm, at $t = 182^\circ\text{C}$, for $\text{Pb}(\text{Co}_{0.33}\text{Ta}_{0.67})\text{O}_3$, $E_{\text{max}} = 70$ kV/cm, at $t = -196^\circ\text{C}$, and for $\text{Pb}(\text{Ni}_{0.33}\text{Ta}_{0.67})\text{O}_3$, $E_{\text{max}} = 150$ kV/cm, at $t = -196^\circ\text{C}$. The Curie temperatures of compounds $\text{Pb}(\text{Mg}_{0.33}\text{Nb}_{0.67})\text{O}_3$, $\text{Pb}(\text{Mg}_{0.33}\text{Ta}_{0.67})\text{O}_3$, $\text{Pb}(\text{Co}_{0.33}\text{Nb}_{0.67})\text{O}_3$, $\text{Pb}(\text{Co}_{0.33}\text{Ta}_{0.67})\text{O}_3$, $\text{Pb}(\text{Ni}_{0.33}\text{Nb}_{0.67})\text{O}_3$, $\text{Pb}(\text{Ni}_{0.33}\text{Ta}_{0.67})\text{O}_3$ and $\text{Pb}(\text{Zn}_{0.33}\text{Nb}_{0.67})\text{O}_3$ are -12°C , -98°C , -70°C , -140°C , -120°C , -180°C and 140°C , respectively.

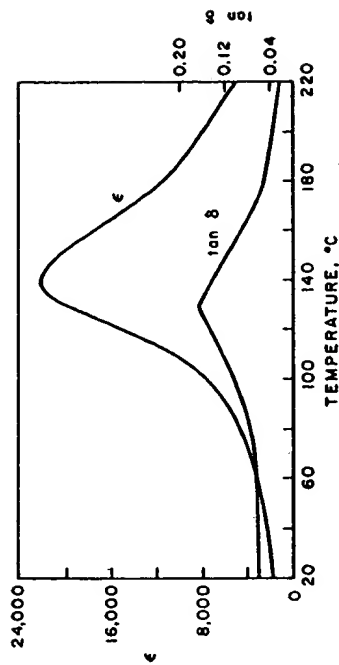


FIG. 5.25. The temperature dependence of ϵ and $\tan \delta$ of single crystal $\text{Pb}(\text{Zn}_{0.33}\text{Nb}_{0.67})\text{O}_3$ (1 kc) (after Bokov *et al.*⁽⁴⁴⁾).

Johnson *et al.*⁽⁴⁵⁾ conducted an extensive study of complex ferroelectric solid solutions $\text{Pb}(\text{Sc}_{0.5}\text{Nb}_{0.5})_x\phi_{1-x}\text{O}_3$ where ϕ is either Ti, Zr, or Hf, finding that the maximum value of the spontaneous polarization of a system decreased as Ti was replaced by Zr and Zr by Hf and the Curie temperature increased as ϕ increased. In addition, the Curie points decreased in value as Ti was replaced by Zr and Zr by Hf. A complete list of ferroelectric compounds, Curie points and polarization values are given in Table 5.2.

5.4. EFFECT OF NUCLEAR IRRADIATION

In recent years there has been considerable interest in the effect of nuclear radiation on the properties of ferroelectric materials. In one study, Glower and Hester⁽⁴⁶⁾ found that

TABLE 5.2. *Ferroelectrics Data*

	$T^{\circ}\text{C}$	P_s (at $T^{\circ}\text{C}$)	Refs.
BaTiO ₃	120	10 ⁻⁶	69
PbTiO ₃	490	26.0 (23)	70
KNbO ₃	435	750.0 (23)	35
		0.9 (23)	
		30 (250)	
KTaO ₃	-260		35
NaNbO ₃	-200		71
CdTiO ₃	-218		72
Pb(Cd _{0.5} W _{0.5})O ₃			73
Pb(Sc _{0.5} Nb _{0.5})O ₃	90		58
Pb(Sc _{0.5} Ta _{0.5})O ₃	26	3.6 (18)	74
Pb(Fe _{0.47} W _{0.53})O ₃	-75		75
Pb(Fe _{0.5} Nb _{0.5})O ₃	112		76
Pb(Fe _{0.5} Ta _{0.5})O ₃	-30		64
Pb(Mg _{0.33} Nb _{0.67})O ₃	-12	14 (-130)	64
Pb(Ni _{0.33} Nb _{0.67})O ₃	-120		64
Pb(Ni _{0.33} Ta _{0.67})O ₃	-180		64
Pb(Mg _{0.33} Ta _{0.67})O ₃	-98		64
Pb(Co _{0.33} Nb _{0.67})O ₃	-70		64
Pb(Co _{0.33} Ta _{0.67})O ₃	-140		64
Pb(Zn _{0.33} Nb _{0.67})O ₃	140		64

nuclear reactor irradiation of single crystal of BaTiO₃ produced increases in the coercive field (E_c) and a decrease in the remnant polarization (P_r). Crystals in the polarized state during irradiation were more resistant to radiation damage than were virgin crystals and the radiation damage rate was only slightly dependent upon crystal thickness. In their conclusions, they interpreted the changes in E_c and P_r in terms of a radiation model involving a build-up of a space charge due to the trapping of ionized carriers in the domain walls of the crystals.

Hilczert⁽⁶⁷⁾ reported that irradiation of barium titanate with 10¹⁹ neutrons/cm² reduced the dielectric constant by up to 40%. Doses of 10¹⁴-10¹⁹ neutrons/cm² of (a) pile neutrons containing 10% fast neutrons; and (b) fast neutrons only that had passed through a 0.4-mm Cd foil gave the same effect, implying that fast neutrons produced the damage.

Schenk⁽⁶⁸⁾ found that tetragonal BaTiO₃ when irradiated with neutron doses of 4.2×10^{18} neutrons/cm² at 35°C transformed to cubic with radiation damage. The lattice expanded 2.26% for a and 1.17% for c .

5.5. APPLICATIONS OF FERROELECTRIC MATERIALS

Use of Ferroelectric Properties

The high dielectric constants and ferroelectric behavior of perovskite-type compounds are probably the most important properties they exhibit.

Materials such as barium titanate cannot be used as capacitors in tuned circuits or filters where high-frequency stability is needed. However, they can be used as by-pass, blocking and smoothing capacitors which present a low-impedance path to an alternating current above a certain frequency.

The room-temperature dielectric constant of barium titanate can be raised by the addition of strontium titanate which lowers the Curie temperature. However, a flattening of the permittivity peak by using mixtures of alkali titanates and zirconates is more important. To date most of these ceramic capacitors have been used at low voltages as by-pass capacitors.

In addition, the hysteresis loop of ferroelectric single crystals makes them of potential use for information storage in electronic computers. Ferroelectrics also have been used as dielectric amplifiers. These are analogous to magnetic amplifiers, which require magnetic materials with narrow rectangular hysteresis loops.

The International Telephone and Telegraph Corporation recently reported a new use for ferroelectrics. This method for producing high-voltage a.c. or d.c. power was based on the fact that the dielectric constant of a ferroelectric is sensitive to temperature at the Curie point. The capacitor is held at the Curie point and then heated, lowering the dielectric constant. Since the charge cannot decrease because of a diode in the circuit, there must be a rise in capacitor voltage. This increased voltage also means an increase of electrical energy, thus there is a conversion of heat energy into elec-

trical energy. This scheme has been proposed for use in a space vehicle which spins so it alternately faces toward and away from the sun.

Use of Piezoelectric Properties

One of the best known uses of piezoelectric materials is for the measurement of force or pressure. However, since there is a current leakage with time, they have best been used for measuring dynamic pressures, in blast gauges and accelerometers. Recently, the Spark Pump, the heart of which is two lead zirconate-lead titanate piezoelectric elements, was introduced by Clevite as an ignition source for gasoline engines. These elements were capable of achieving voltages of 20,000 volts when mechanical pressure was applied.

Another use of piezoelectrics is the phonograph pick-up which transforms the mechanical energy from the phonograph needle to an electrical signal. One of the methods of accomplishing this involves the use of two piezoelectric plates combined into a sandwich which is subjected to bending forces.

Piezoelectric transducers have also been used for sound transmission and reception, and ultrasonic cleaning devices.

Quartz has been used for electric frequency control. The piezoelectric coupling causes a reaction with an electric driving circuit which forces the circuit to oscillate at an exact frequency.

In a wave filter application, the impedance property of a crystal near a resonance point is used to allow passage of an electric signal which falls within a prescribed band of frequencies, while other frequencies are not passed.

The selection of materials for these applications depends on their piezoelectric constant. Some constants are listed in Fig. 5.26 and the units in Table 5.3 for perovskite-type ceramics. Note that the k , electromechanical coupling coefficient, values show the relationship between the mechanical energy stored and the electrical energy applied or the electrical energy stored and the mechanical energy applied. A high coupling coefficient, that is the ability to convert from one form of energy to another, is desirable in most of the applications.

PIEZOELECTRIC CERAMICS—BASIC ACTIONS

AXES	ELECTROMECHANICAL EFFECTS	PIEZOELECTRIC ELASTIC AND DIELECTRIC CONSTANTS
PLATES, BARS 	THICKNESS EXPANDER POLED FIELD STRAIN LENGTH EXPANDER POLED FIELD STRAIN	d_{33}, d_{31}, d_{32} $\epsilon_{33}, \epsilon_{31}, \epsilon_{32}$ K_3 γ_{11}, γ_{22} K_3
DISCS 	RADIAL EXPANDER POLED FIELD STRAIN THICKNESS EXPANDER POLED FIELD STRAIN	d_{31}, d_{32}, d_{33} $\epsilon_{31}, \epsilon_{32}, \epsilon_{33}$ K_3 γ_{11}, γ_{22} K_3
SHEAR PLATE 	SHEAR FIELD STRAIN	d_{15}, d_{25}, d_{33} $\epsilon_{15}, \epsilon_{25}, \epsilon_{33}$ K_1
TUBES 	THICKNESS EXPANDER LENGTH EXPANDER (Circumference Expander)	d_{33}, d_{31}, d_{32} $\epsilon_{33}, \epsilon_{31}, \epsilon_{32}$ K_3 γ_{11}, γ_{22} K_3

Fig. 5.26. Piezoelectric ceramics—basic actions (after Bulletin 9247 (1962), Clevite Corp.).

The constant d is the ratio of the strain developed to the applied field or the short circuit charge density to the applied stress. The constant g is the ratio of the open circuit field to the applied stress or the strain developed to the applied charge density. A high d constant is desired for high amplitude production and a high g constant for high voltage production. Other constants are K , relative dielectric constant in the material to space, and N , the frequency constant which is the controlling dimension times the resonant frequency.

TABLE 5.3. *Ceramic Properties Definitions (after Bulletin 9247 (1962), Clevite Corp.)*

Property	Definition	MKS units
Electro-mechanical coupling coefficient k	$\sqrt{\frac{\text{mechanical energy stored}}{\text{electrical energy applied}}}$	
	$\sqrt{\frac{\text{electrical energy stored}}{\text{mechanical energy applied}}}$	
Piezoelectric constants d	$\frac{\text{strain developed}}{\text{applied field}}$	$\frac{\text{meter/meter}}{\text{volts/meter}}$
	$\frac{\text{short circuit charge density}}{\text{applied stress}}$	$\frac{\text{coulombs/meter}^2}{\text{newtons/meter}^2}$
g	$\frac{\text{open circuit field}}{\text{applied stress}}$	$\frac{\text{volts/meter}}{\text{newtons/meter}^2}$
	$\frac{\text{strain developed}}{\text{applied charge density}}$	$\frac{\text{meter/meter}}{\text{coulombs/meter}^2}$
Relative dielectric constant K	$\frac{\epsilon(\text{permittivity of material})}{(\text{permittivity of space})}$	
Modulus of elasticity Y	$\frac{\text{stress}}{\text{strain}}$	$\frac{\text{newtons/meter}^2}{\text{meter/meter}}$
Density ρ		$\frac{\text{kg}}{\text{meters}^3}$
Frequency constant N	Controlling dimension \times resonant frequency	cps-meters

The subscripts 1, 2 and 3 indicate the x -, y - and z -axes, respectively, and the subscripts 4, 5 and 6 represent a double subscript which stands for a plane. For example, 4 represents the yz -plane, 5 represents the xz -plane and 6 represents the xy -plane. The first subscript describes the direction of the field, the second the direction of the strain. For K the subscript p means planar coupling.

In the constant Y , the first subscript refers to the direction of stress and the second to the direction of the strain. The subscript for the dielectric constant refers only to the field. Table 5.4 presents the elastic, piezoelectric and dielectric properties of several ceramic compositions. The PZT materials are special commercial ceramic compositions. The PZT materials are special commercial ceramic compositions of lead zirconate-lead titanate solid solutions. Using this data, the best materials for a particular application can be selected.

5.6. THEORIES OF FERROELECTRICITY

Because of the importance of perovskite-type compounds as ferroelectrics, a brief review of theories which have been proposed to explain the phenomena associated with this property is presented. For more details, the original papers or the excellent treatment of this subject by Jona and Shirane in a book entitled *Ferroelectric Crystals*, published by Macmillan Company of New York, can be consulted.

Devonshire proposed a phenomenological theory for BaTiO_3 .^{7a, m} He assumes that BaTiO_3 in all forms can be considered to be a strained cubic crystal with a free energy which can be expressed as a function of temperature, stress and polarization. If the stress is initially taken as zero, an equation can be written as a series involving powers of the polarization P . The coefficients are functions of the stress-free condition and have subscripts X . Devonshire gives the equation with separate terms and coefficients for the components of polarization in the axial directions x , y , z . The equation is:

$$G_1 - G_{10} = \frac{1}{2} A^x (P_x^2 + P_y^2 + P_z^2) + \frac{1}{4} B^x (P_x^4 + P_y^4 + P_z^4) + \frac{1}{6} C^x (P_x^6 + P_y^6 + P_z^6) + \frac{1}{2} D (P_x^2 P_y^2 + P_x^2 P_z^2 + P_y^2 P_z^2),$$

TABLE 5.4. *Elastic, Piezoelectric and Dielectric Properties of Several Ceramic Compositions (after D. Berlincourt, B. Jaffe, H. Jaffe, and H. H. A. Krueger, IRE Nat'l Convention (1959))*

	95w % BaTiO ₃	PZT-4	PZT-5
	5w % CaTiO ₃		
Coupling coefficients			
k_{33}	0.49	0.64	0.675
k_p	0.325	0.52	0.54
k_{31}	0.19	0.31	0.32
k_{15}	0.495	0.65	0.655
Piezoelectric constants			
d_{33}	150	256	320
d_{31}	-58	-111	-140
d_{15}	257	450	495
Free dielectric constants			
K_1	1280	1360	1285
K_3	1200	1200	1500
Frequency constants			
N_1	2290	1650	1500
N_3	2840	2000	1890
Elastic constants			
$1/s_{11}^E = Y_{11}^E$	11.6	8.15	6.75
$1/s_{33}^E = Y_{33}^E$	11.1	6.7	5.85
$1/s_{12}^E = Y_{12}^E$	4.4	2.6	2.0
$1/s_{13}^E = Y_{13}^E$	5.5	7.5	7.5
Density	500	600	75
Mechanical Q	115 °C	340 °C	360 °C
Curie point			

where G_{10} is the value of G_1 for the unpolarized, unstressed crystal and the last term indicates that there is an interaction between the components of polarization along the x -, y - and z -axis.

From the equation given above, four sets of solutions which may correspond to minima in free energy can be obtained:

$$\begin{aligned} P_x &= P_y = P_z = 0; \\ P_x &= P_y = 0, \quad P_z \neq 0 \\ P_z &= 0, \quad P_x = P_y \neq 0 \\ P_x &= P_y = P_z \neq 0 \end{aligned}$$

These represent the cubic phase, in which the polarization is zero, and the tetragonal, orthorhombic (referred to monoclinic axes) and the rhombohedral forms respectively. The relative depths of the minima of the free energy function change with the coefficient A^X . If this decreases steadily and constant values are chosen for the coefficients, the temperatures at which the transitions occur are those actually observed.

On determining the constants, Devonshire drew theoretical curves for the spontaneous polarization, the free energy and the dielectric constants, over a range of temperatures. Qualitative agreement between calculated and experimental data was quite good.

Devonshire also gave equations for calculating spontaneous strain for a clamped crystal and discussed the effect of clamping on the nature of the transition. Probably one of the most important conclusions that can be made from the use of these equations is that the transition of the clamped crystal would be of the second order, even though that of the free crystal is of the first order.

Using Devonshire's approach of determining the coefficients for his equations from certain properties and employing them to predict others, a number of quantities were calculated. For example, the entropy change at the transition was determined for BaTiO₃ and KNbO₃, in reasonable agreement with experimental data.

Using a model approach, Mason and Matthias⁽⁷⁸⁾ suggest that the stable position for the Ti⁴⁺ ion in barium titanate is not at the center of the oxygen octahedra. Instead it is at any of the six positions which correspond to slight displacements from the center toward the oxygen ions. When the Ti⁴⁺ ion was in any of these positions the unit cell would have a dipole moment. However, if any dipole theory were correct, a number of polar liquids would be ferroelectrics which is not the case. In addition, with this theory it is not

possible to obtain good agreement with experimental calculations.

Jaynes proposed a model in which oxygen ions are displaced rather than titanium ions⁽⁷⁶⁾ and also a theory which does not require the attribution of dipole moments to atomic displacement.⁽⁸⁰⁾ Only the electronic states of the TiO_6 octahedra are considered. The theory was adequate for determining the entropy change, but it predicts an infrared absorption line at $\sim 10\mu$, which was not detected.

Devonshire's model theory considers the dipole of an atom vibrating in the field of the neighbors. The dipole moment is not fixed in magnitude, but depends on the displacement from the equilibrium position.

Slater's theory⁽⁸¹⁾ is similar to Devonshire's model theory. However, in addition, he assumes that each atom has an electronic polarization and titanium also has an ionic polarization. It predicts that the direction of spontaneous polarization is along the z -axis, but this is a disadvantage when it is applied to some structures.

In a structural approach, ferroelectricity and antiferroelectricity are associated with the off-center position of a high-valency cation in an octahedron. Megaw^(82, 83) added the emphasis on the covalent bond character in the occurrence of ferroelectricity. The problem with Megaw's theory is that the origin of ferroelectricity is sought in abrupt changes in the character of the bonds at each transition. Like all of the theories described above, the structural approach has its limitation.

REFERENCES

1. A. VON HIPPEL *et al.*, RPTPB 4860 (1944).
2. W. JACKSON and W. REDDISH, *Nature* 156, 717 (1945).
3. H. MEGAW, *Nature* 155, 484 (1945).
4. H. P. ROOKSBY, *Nature* 155, 484 (1945).
5. B. M. VUL, *Nature* 156, 480 (1945).
6. B. M. VUL and I. M. GOLDMAN, *C.R. Acad. Sci. URSS* 46, 139 (1945).
7. V. GINZBURG, *J. Phys. USSR* 10, 107 (1946).
8. S. MIYAKE and R. UEDA, *J. Phys. Soc. Japan* 1, 32 (1945).
9. W. J. MERZ, *J. Appl. Phys.* 17, 938 (1946).
10. W. KANZIG, *Phys. Rev.* 98, 549 (1955).
11. A. G. CHRYNOWETZ, *Phys. Rev.* 102, 705 (1956).

12. W. J. MERZ, *Phys. Rev.* 91, 513 (1953).
13. W. J. MERZ, *Phys. Rev.* 75, 687 (1949).
14. B. M. VUL and L. WERESHCHAGIN, *C.R. Acad. Sci. URSS* 48, 634 (1945).
15. W. J. MERZ, *Phys. Rev.* 78, 52 (1950).
16. S. H. HOH and F. E. PRIGY, *J. Am. Ceram. Soc.* 46, 516 (1963).
17. J. B. MACCHESNEY, P. K. GALLAGHER and F. V. DIMARCELLO, *J. Am. Ceram. Soc.* 46, 197 (1963).
18. A. L. KHODAKOV, *Sov. Phys., Solid State* 2, 1904 (1960).
19. J. L. BLINTON and R. HAVELL, *Cer. Bull.*, Part II, 41, 762 (1962).
20. A. HERCZOG, *J. Am. Ceram. Soc.* 47, 107 (1964).
21. W. L. CHERRY and R. ADLER, *Phys. Rev.* 72, 981 (1948).
22. W. P. MASON, *Phys. Rev.* 74, 1134 (1948).
23. F. SAWAGUCHI and T. AKIOKA, *J. Phys. Soc. Japan* 4, 117 (1949).
24. S. NOMURA and S. SAWADA, *J. Phys. Soc. Japan* 5, 227 (1950).
25. G. SHIRANE and R. PEPINSKY, *Phys. Rev.* 97, 1179 (1955).
26. G. SHIRANE and E. SAWAGUCHI, *Phys. Rev.* 81, 458 (1951).
27. G. SHIRANE and S. HOSHINO, *J. Phys. Soc. Japan* 6, 265 (1951).
28. T. Y. TEN and W. G. CARLSON, *J. Am. Ceram. Soc.* 45, 567 (1962).
29. H. GRANTICHER, *Helv. Phys. Acta* 29, 210 (1956).
30. H. F. KAY, *Rpt. Brit. Elec. Res. Assoc.*, Ref. L/T, 257 (1951).
31. G. SHIRANE, H. DANNER, A. PAVLOVIC and R. PEPINSKY, *Phys. Rev.* 98, 612 (1954).
32. S. TRIEBWASSER, *Phys. Rev.* 101, 998 (1956).
33. P. VOUSDEN, *Acta Cryst.* 4, 545 (1951).
34. M. H. FRANCOMBE, *Acta Cryst.* 9, 258 (1954).
35. B. T. MATTHIAS, *Phys. Rev.* 75, 1771 (1949).
36. J. K. HULM, B. T. MATTHIAS and A. LONG, *Phys. Rev.* 79, 885 (1950).
37. G. A. SMOLENSKII *et al.*, *Dokl. Akad. Nauk SSSR*, 76, 519 (1951).
38. G. SHIRANE and R. PEPINSKY, *Phys. Rev.* 91, 812 (1953).
39. D. F. RUSHMAN and M. A. STRIVENS, *Trans. Faraday Soc.* 42A, 231 (1946).
40. G. DURST, M. GROTEHURTS and A. G. BARKOW, *J. Am. Ceram. Soc.* 33, 133 (1950).
41. J. G. POWLES, *Nature* 162, 655 (1958).
42. H. IWAYANAGI, *J. Phys. Soc. Japan* 8, 525 (1953).
43. S. NOMURO and S. SAWADA, *J. Phys. Soc. Japan* 5, 227 (1950).
44. E. J. BRAUER, H. JAFFEE and F. KULCSAR, *J. Acoust. Soc. Am.* 24, 117 (1952).
45. D. A. BERLINCOURT and F. KULCSAR, *J. Acoust. Soc. Am.* 24, 709 (1952).
46. R. G. GRAF, *Ceram. Age* 58, 16 (1951).
47. R. H. DUNGAN, D. F. KANE and L. R. BICKFORD, *J. Am. Ceram. Soc.* 35, 318 (1952).
48. E. G. FESSENKO and O. I. PROKOPOLO, *Sov. Phys., Cryst.* 6, 373 (1961).
49. W. H. PAYNE and V. J. TENNERY, *J. Am. Ceram. Soc.* 48, 413 (1965).

50. T. Y. TIEN, E. C. SUBBARAO and H. HRIZO, *J. Am. Ceram. Soc.* 46, 572 (1962).
51. G. SHIRANE, *Phys. Rev.* 86, 219 (1952).
52. B. JAFFE, R. S. ROTH and S. MORZULLO, *J. Appl. Phys.* 25, 809 (1954).
53. T. IKEDA, *J. Appl. Phys. Japan* 3, 493 (1964).
54. T. IKEDA and T. OKANO, *J. Appl. Phys. Japan* 3, 63 (1964).
55. S. ROBERTS, *J. Am. Ceram. Soc.* 38, 86 (1950).
56. A. S. VIKOV, YU. N. VENEVTSEV and G. S. ZHDANOV, *Sov. Phys. Doklady* 10, 391 (1965).
57. G. A. SMOLENSKII, A. I. AGRANOVSKAYA, S. N. POPOV and V. A. ISUPOV, *Sov. Phys. Tech. Phys.* 3, 1981 (1958).
58. G. A. SMOLENSKII, V. A. ISUPOV and A. I. AGRANOVSKAYA, *Sov. Phys., Solid State* 1, 150 (1959).
59. M. F. KUPRIYANOV and E. G. FESENKO, *Sov. Phys., Cryst.* 10, 189 (1966).
60. V. A. BOKOV, S. A. KIZHAEV, I. E. MYL'NIKOVA and A. G. TUTOV, *Sov. Phys., Solid State* 6, 2419 (1965).
61. G. A. SMOLENSKII, A. I. AGRANOVSKAYA and V. A. ISUPOV, *Sov. Phys., Solid State* 1, 907 (1959).
62. I. E. MYL'NIKOVA and V. A. BOKOV, *Sov. Phys., Cryst.* 4, 408 (1960).
63. G. A. SMOLENSKII and A. I. AGRANOVSKAYA, *Sov. Phys., Solid State* 1, 1429 (1960).
64. V. A. BOKOV and I. E. MYL'NIKOVA, *Sov. Phys., Solid State* 2, 2428 (1961).
65. V. J. JOHNSON, M. W. VALENTA, J. E. DOUGHERTY, R. M. DOUGLASS and J. W. MEADOWS, *J. Phys. Chem. Soc.* 24, 85 (1963).
66. D. D. GLOWER and D. L. HESTER, *J. Appl. Phys.* 36, 2175 (1965).
67. B. HILTZER, *Phys. Status Solidi* 5, 113 (1964).
68. M. SCHENK, *Phys. Status Solidi* 4, 25 (1964).
69. A. VON HIPPEL, R. G. BRECKENRIDGE, F. C. CHESLEY and L. TISZA, *Ind. Eng. Chem.* 88, 1097 (1946).
70. G. SHIRANE, S. HOSHINO and K. SUZUKI, *Phys. Rev.* 80, 1105 (1950).
71. H. L. E. CROSS and B. J. NICHOLSON, *Phil. Mag.*, Ser. 7, 46, 453 (1955).
72. G. A. SMOLENSKII, *Dokl. Akad. Nauk SSSR* 70, 405 (1950).
73. V. A. ISUPOV and L. T. ELEM'YANOVA, *Kristallografiya* 11, 776 (1966).
74. A. I. AGRANOVSKAYA, *Bull. Acad. Sciences, U.S.S.R., Phys. Sciences* 24, 1271 (1960).
75. G. A. SMOLENSKII, A. I. AGRANOVSKAYA, S. N. POPOV and V. A. ISUPOV, *Sov. Phys. Tech. Phys.* 8, 1981 (1960).
76. A. F. DEVONSHIRE, *Phil. Mag.* 40, 1040 (1949).
77. A. F. DEVONSHIRE, *Phil. Mag. Suppl.* 3, 85 (1954).
78. W. P. MASON and B. T. MATTHIAS, *Phys. Rev.* 74, 1622 (1948).
79. E. T. JAYNES, *Phys. Rev.* 79, 1008 (1950).
80. E. T. JAYNES, *Ferroelectricity*, Princeton University Press, (1953).
81. J. C. SLATER, *Phys. Rev.* 78, 748 (1950).
82. H. D. MEGAW, *Acta Cryst.* 5, 739 (1952).
83. H. D. MEGAW, *Acta Cryst.* 7, 187 (1954).

CHAPTER 6

PHASE TRANSITIONS

THE phase transitions in perovskite-type compounds are often associated with a change in ferroelectric properties. Some of these were described in the previous chapter. In this chapter, an attempt will be made to describe phase transitions reported for perovskite-type compounds, whether or not they involve a ferroelectric transition. These phase transitions can be divided into those of the first kind which are associated with the absorption or liberation of heat along with discontinuous changes in entropy and in lattice parameters, and those of the second kind which involve a peak in heat capacity, in the coefficient of thermal expansion and in compressibility. A list of perovskite-type compounds with transition temperatures and references is given in Table 6.1.

6.1. TERNARY PEROVSKITES

The phase transitions in barium titanate are probably the best characterized. The cubic phase is stable down to 120°C, and below this temperature the tetragonal ferroelectric phase appears, and remains stable to about 5°C. Below 5°C a new phase is formed, which has a unit cell with orthorhombic symmetry and still is ferroelectric with the direction of spontaneous polarization being parallel to one of the original cubic $\langle 110 \rangle$ directions. At -90°C another transition occurs and the symmetry of the structure becomes rhombohedral. The polar axis lies along one of the original cubic $\langle 111 \rangle$ directions. The thermal expansion of the cell parameters in each of these phases is shown in Fig. 5.2. The volume changes at the phase transitions with rising temperature are 0.0006,

TABLE 6.1. Phase Transitions

Compound	Transition temp., °C (to cubic at highest temp. listed)	Refer- ences
AgNbO ₃	325, 550	1
AgTaO ₃	485	1
BaTiO ₃	-90, 5, 120	2
KNbO ₃	-10, 225, 435	3
KTaO ₃	-260	4
NaNbO ₃	-200, 354, 562, 840	5, 6
NaTaO ₃	470	4, 7
PbHfO ₃	163, 215	8
PbTiO ₃	490	9
PbZrO ₃	230	10, 11, 7
SrTiO ₃	-220	7, 12, 13
Pb(Co _{0.5} W _{0.5})O ₃	32	14, 15
Pb(Cd _{0.5} W _{0.5})O ₃	410	16
Pb(Lu _{0.5} Nb _{0.5})O ₃	280	16, 17
Pb(Lu _{0.5} Ta _{0.5})O ₃	280	16, 17
Pb(Yb _{0.5} Nb _{0.5})O ₃	280	17, 14, 18
Sr(Co _{0.5} Mo _{0.5})O ₃	320	19
Sr(Co _{0.5} W _{0.5})O ₃	400	19
Sr(Fe _{0.5} Nb _{0.5})O ₃	250	20
Sr(Fe _{0.5} Ta _{0.5})O ₃	250	20
Sr(Ni _{0.5} Mo _{0.5})O ₃	230	19
Sr(Ni _{0.5} W _{0.5})O ₃	300	19
Sr(Y _{0.5} Nb _{0.5})O ₃	630	21
Sr(Y _{0.5} Ta _{0.5})O ₃	640	21
Sr(Zn _{0.5} Mo _{0.5})O ₃	420	19
Sr(Zn _{0.5} W _{0.5})O ₃	430	19

0.014 and 0.062 Å³ and the transition heats are 8, 22 and 50 cal/mole.

The cubic to tetragonal transition in barium titanate also is characterized by the appearance of domain patterns. Observation of ferroelectric domains between crossed nicols is an excellent method of studying phase transitions in ferro-

electric materials. Examining crystals after etching and after electrostatically charged particles have been deposited on the surface are other methods which have been used to investigate the domain pattern.

Studies on tetragonal barium titanate using a polarizing microscope have shown that it is possible for domains to be polarized at 90° to each other. When the polar axis is perpendicular to the plane of a (001) plate, the domain is called a "c" domain, and when it lies within the plane of the plate, the domain is called an "a" domain. These domains are easily observed under polarized light, and their appearance or disappearance indicates the cubic to tetragonal or tetragonal to cubic transition.

If domains are polarized antiparallel to each other, they are called 180° domains and a field must be applied perpendicular to the polar axis to make them visible.

Considering phase transitions involving other A²⁺B⁴⁺O₃-type compounds, the structure of strontium titanate becomes cubic at -220°C and that of calcium titanate changes to cubic at 1280°C. Lead titanate has a transition from a tetragonal ferroelectric phase to a cubic phase at 490°C, Fig. 5.6, the pseudotetragonal antiferroelectric PbZrO₃ phase undergoes a first-order phase transition to cubic at 230°C (Fig. 5.9) with a heat of transition of 440 cal/mole and PbHfO₃ shows transitions at 163°C and 215°C. The transition for PbHfO₃ at 215°C is probably an antiferroelectric transformation to cubic symmetry.

The phase transitions at 435°C, 225°C and -10°C in KNbO₃ are quite similar to those found for BaTiO₃ except that the spontaneous strain in KNbO₃ is larger in all three phases. The transition energies are 190, 85 and 32 cal/mole, see Fig. 5.7, and the *c/a* for the unit cell of tetragonal KNbO₃ is 1.017 compared with the value of 1.010 for that of BaTiO₃. All of the phase changes are first order and exhibit temperature hysteresis. The structure of KTaO₃ changes to cubic symmetry at -260°C.

The structure of NaNbO₃ is monoclinic below -200°C and is ferroelectric. Above this temperature the structure of NaNbO₃ has orthorhombic symmetry. This antiferroelectric phase changes to a nonpolar pseudotetragonal phase at

354°C. At 502°C the structure of NaNbO_3 becomes tetragonal, and cubic at 640°C. At room temperature, a polar structure can be induced by the application of a field and a double hysteresis loop can be observed.

A transition at 480° to cubic symmetry was found for NaTaO_3 ; however, no anomaly in the dielectric constant has been detected.

X-ray studies on AgNbO_3 indicate that the structure transforms from orthorhombic symmetry to tetragonal symmetry at 325°C and from tetragonal to cubic symmetry at 550°C. AgTaO_3 shows similar phase transitions at 370°C and 485°C.

6.2. COMPLEX PEROVSKITE-TYPE COMPOUNDS

The onset of ferroelectricity in the complex perovskite-type compounds listed in Table 5.2 must be associated with phase transitions. However, very few such transitions have

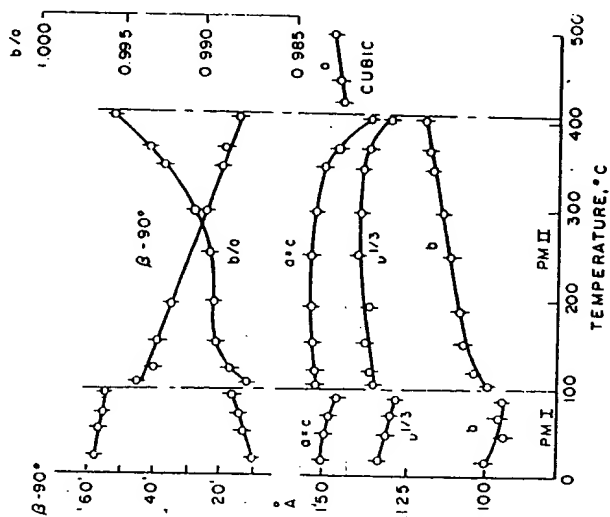


Fig. 6.1. Parameters of the perovskite pseudocell of $\text{Pb}(\text{Cd}_{0.5}\text{W}_{0.5})\text{O}_3$ as functions of temperature (after Roginskaya *et al.* (18)).

been reported with the ferroelectric data. In some cases, the back reflections in the X-ray patterns have been too poor to prove that small distortions existed in the ferroelectric phases.

Phase transitions for a few complex perovskite compounds have been studied. A pseudomonoclinic form of $\text{Pb}(\text{Cd}_{0.5}\text{W}_{0.5})\text{O}_3$ has been found to exist up to 100°C, at which temperature it transforms to a second monoclinic form and at 410°C it becomes cubic (see Fig. 6.1). The cubic form has the ordered

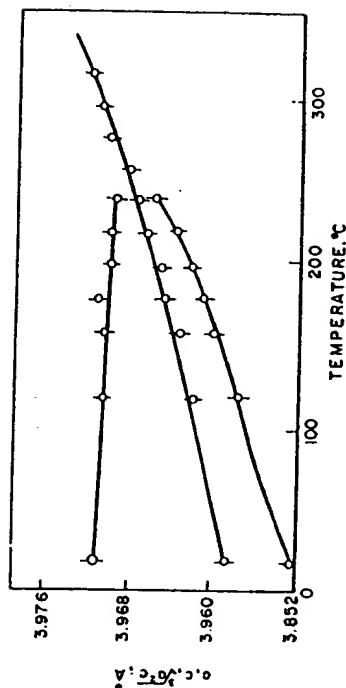


Fig. 6.2. Parameters of $\text{Sr}(\text{Fe}_{0.5}\text{Nb}_{0.5})\text{O}_3$ as a function of temperature (after Kupriyanov *et al.* (17)).

perovskite structure with a unit cell of "a" approximately equal to 8 Å. The authors feel that the monoclinic form of $\text{Pb}(\text{Cd}_{0.5}\text{W}_{0.5})\text{O}_3$ below 100°C is antiferroelectric.

The phase transformation of $\text{Sr}(\text{Fe}_{0.5}\text{Nb}_{0.5})\text{O}_3$ involves a change from a tetragonal to cubic form at 220°C (see Fig. 6.2). From the unit cell size given there does not appear to be any ordering of the B ions in this compound. A similar phase transition was reported for $\text{Sr}(\text{Fe}_{0.5}\text{Ta}_{0.5})\text{O}_3$.

The compound $\text{Sr}(\text{Y}_{0.5}\text{Ta}_{0.5})\text{O}_3$ was found to transform from a rhombohedral form to a cubic form at 640°C, similar to that in $\text{Sr}(\text{Y}_{0.5}\text{Nb}_{0.5})\text{O}_3$ (see Fig. 6.3).

Tetragonal to cubic phase transformations have been reported for $\text{Sr}(\text{Ni}_{0.5}\text{W}_{0.5})\text{O}_3$, $\text{Sr}(\text{Co}_{0.5}\text{W}_{0.5})\text{O}_3$, $\text{Sr}(\text{Zn}_{0.5}\text{W}_{0.5})\text{O}_3$, $\text{Sr}(\text{Ni}_{0.5}\text{Mo}_{0.5})\text{O}_3$, $\text{Sr}(\text{Co}_{0.5}\text{Mo}_{0.5})\text{O}_3$ and $\text{Sr}(\text{Zn}_{0.5}\text{Mo}_{0.5})\text{O}_3$ at temperatures of 300°, 400°, 430°, 230°, 320° and 420°C, re-

spectively. The X-ray diffraction data indicates ordering of the B ions, but in Fig. 6.4 the cell size used for convenience was that of the simple perovskite structure. This figure shows the variation in cell size with temperature.

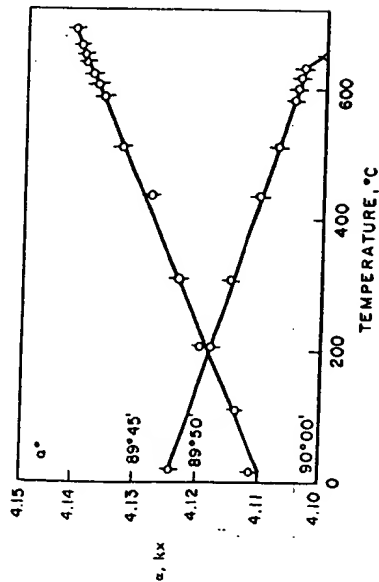


FIG. 6.3. Parameters of $\text{Sr}(\text{Y}_{0.5}\text{Ta}_{0.5})\text{O}_3$ as a function of temperature (after Smolenskii *et al.* (18)).

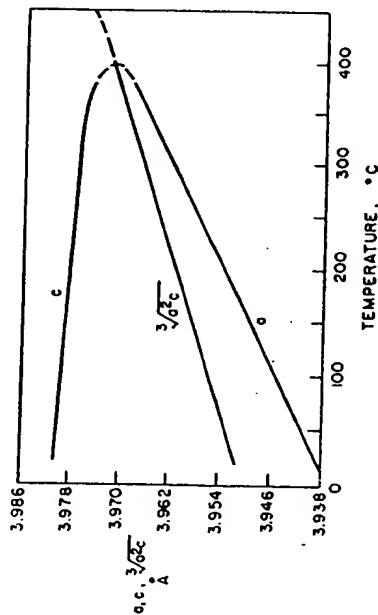


FIG. 6.4. Parameters of $\text{Sr}(\text{Co}_{0.5}\text{W}_{0.5})\text{O}_3$ as a function of temperature (after Kupriyanov *et al.* (19)).

Filip'ev and Fesenko studied the phase transition in $\text{Pb}(\text{Co}_{0.5}\text{W}_{0.5})\text{O}_3$ and found that it involved a change in symmetry from orthorhombic to cubic at 25°C. Superstructure was observed in both phases. A peak in the dielectric con-

stant was seen at the phase transition, indicating that the compound was ferro- or antiferroelectric.

Antiferroelectric phase transitions from monoclinic to cubic symmetry were reported for the compounds $\text{Pb}(\text{Lu}_{0.5}\text{Nb}_{0.5})\text{O}_3$, $\text{Pb}(\text{Lu}_{0.5}\text{Ta}_{0.5})\text{O}_3$ and $\text{Pb}(\text{Yb}_{0.5}\text{Nb}_{0.5})\text{O}_3$ at 280°C. However, the transition temperature does not coincide with the temperatures at which the peak in the dielectric constants occurred for these compounds.

REFERENCES

1. M. H. FRANCOMBE and B. LEWIS, *Acta Cryst.* 11, 175 (1958).
2. H. F. KAY and P. VOUSDEN, *Phil. Mag.* 40, 1019 (1949).
3. G. SHIRANE, H. DANNER, A. PAYLOV, and R. PEPINSKY, *Phys. Rev.* 98, 672 (1954).
4. B. T. MATTHIAS, *Phys. Rev.* 75, 1771 (1949).
5. G. SHIRANE, R. NEWNHAM and R. PEPINSKY, *Phys. Rev.* 96, 581 (1954).
6. M. H. FRANCOMBE, *Acta Cryst.* 9, 256 (1956).
7. G. A. SMOLENSKII, *Zhur. Tekh. Fiz.* 20, 137 (1950).
8. G. SHIRANE and R. PEPINSKY, *Phys. Rev.* 91, 812 (1953).
9. G. SHIRANE and S. HOSKINO, *J. Phys. Soc. Japan* 6, 265 (1951).
10. E. SAWAGUCHI, G. SHIRANE and Y. TAKAGI, *J. Phys. Soc. Japan* 6, 333 (1951).
11. G. SHIRANE, E. SAWAGUCHI and Y. TAKAGI, *Phys. Rev.* 84, 476 (1951).
12. G. A. SMOLENSKII, *Dokl. Akad. Nauk SSSR* 70, 405 (1950).
13. G. A. SMOLENSKII, *Izvest. Akad. Nauk SSSR Ser. Fiz.* 20, 166 (1956).
14. Y. TOMASHPOL'SKII and Y. N. VENEVTSEV, *Sov. Phys., Solid State* 6, 2388 (1965).
15. V. A. BOKOV, S. A. KIZHAEV, I. E. MYL'NIKOVA and A. G. TUTOV, *Sov. Phys., Solid State* 6, 2419 (1965).
16. Y. E. ROGINSKAYA and Y. N. VENEVTSEV, *Sov. Phys. Cryst.* 10, 275 (1965).
17. M. F. KUPRIYANOV and E. G. FESENKO, *Sov. Phys. Cryst.* 10, 189 (1965).
18. G. A. SMOLENSKII, A. I. AGRAPOVSKAYA, S. W. POPOV and V. A. ISUPOV, *Sov. Phys. Techn. Phys.* 3, 1981 (1968).
19. M. F. KUPRIYANOV and E. G. FESENKO, *Sov. Phys., Cryst.* 7, 358 (1962).
20. M. F. KUPRIYANOV and E. G. FESENKO, *Sov. Phys., Cryst.* 6, 639 (1961-2).
21. M. F. KUPRIYANOV and E. G. FESENKO, *Sov. Phys., Cryst.* 7, 282 (1962).

found between Mn^{3+} - Mn^{3+} and Mn^{3+} - Cr^{3+} pairs at low temperatures. The saturation magnetization increased up to a composition of 30% LaCrO_3 and then the increasing number of Cr^{3+} - Cr^{3+} strong negative interactions lowered the saturation magnetization. The maximum was found in the region of the transition point from a monoclinic to a pseudocubic structure.⁽³⁾

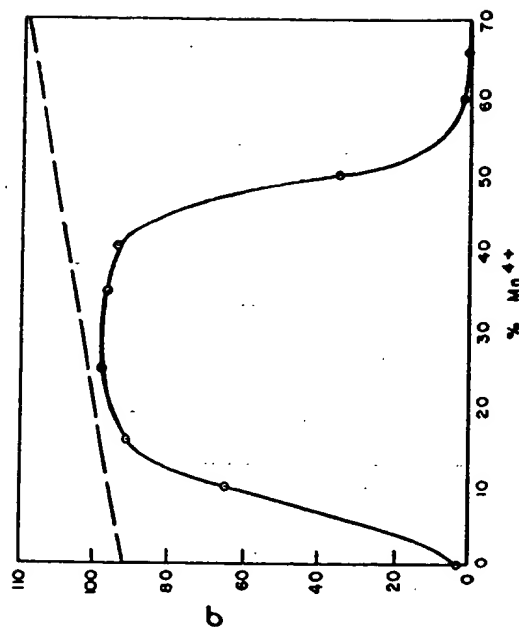


FIG. 7.1.1. Saturation magnetization at 20.4°K of LaMnO_3 - CaMnO_3 (after G. H. Jonker, *Physica* 22, 707 (1956)).

In a similar study of the $(\text{La}, \text{Ba})_x(\text{Mn}^{3+}, \text{Ti}^{4+})_{1-x}\text{O}_3$ system, Jonker found that a maximum in the saturation magnetization existed at the composition which produced a change from a monoclinic to a cubic structure. Since the titanium ion is diamagnetic the positive interaction between Mn^{3+} ions is the only one possible in these phases.

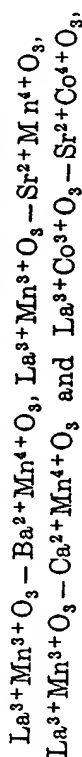
Goodenough *et al.*^(4, 5) investigated the $\text{La}(\text{Mn}_{1-x}\text{Co}_x)\text{O}_3$ series of phases and reported that the ferromagnetic saturation varied nearly linearly between $x = 0.20$ and $x = 0.70$. This was attributed to a positive interaction between Mn ions, with Co ions being in the diamagnetic low spin state. However, the similarity between the ferromagnetic saturation

CHAPTER 7

FERROMAGNETISM

THE common exchange energy in magnetic oxides is of the indirect (super-exchange) type. The energy between spins of neighboring metal ions in perovskite-type structures is often found to be negative so that antiparallel alignment has the lowest energy. It has been proposed that this alignment is caused by mutual interaction of the metal ions with the oxygen ion which is situated between them.

The magnetic oxides with the perovskite structure,



studied by Jonker and van Santen appear to be exceptions.⁽¹⁾ These studies indicated that a weak magnetic interaction between Mn^{3+} ions, a negative interaction between Mn^{4+} ions and strong positive interaction between Mn^{3+} and Mn^{4+} ions existed in the manganites. It was found that in the solid solution range $\text{LaMn}^{2+}\text{O}_3 - 25-35\% \text{AMn}^{4+}\text{O}_3$ ($A = \text{Ca}, \text{Sr}, \text{Ba}$) the magnetic saturation values agreed with the sum of the moments of Mn^{3+} and Mn^{4+} ions and the highest values of the Curie temperatures occurred in this region. The saturation magnetization at 90°K is given in Fig. 7.1 for mixed crystals of $(\text{La}, \text{Ca})\text{MnO}_3$. A corresponding situation was found for compounds containing Co^{3+} and Co^{4+} ions, but not for compounds containing Cr^{3+} and Cr^{4+} , or with Fe^{3+} and Fe^{4+} , as the B ions were found to be antiferromagnetic⁽²⁾. All of these phases with the B metal ions in two valence states were highly conducting.

In order to avoid the high conductivity, Jonker studied $\text{La}(\text{Mn}_{1-x}\text{Cr}_x)\text{O}_3$ solid solutions which contained B ions of different elements with the same electronic configuration as the Mn^{3+} and Mn^{4+} ions. Positive magnetic interactions were

tion versus composition curve for the $\text{La}(\text{Mn}_{1-x}\text{Cr}_x^{3+})\text{O}_3$ and $\text{La}(\text{Mn}_{1-x}\text{Co}_x)\text{O}_3$ series led Jonker to believe that there might be another explanation for the magnetic behavior of the former series.⁽⁶⁾ His studies indicated that there was a rather strong positive interaction between the Co and Mn ions as well as the positive interaction between Mn^{3+} ions suggested by Goodenough. In addition, the results suggested that neighboring pairs of Co and Mn ions were present in the divalent

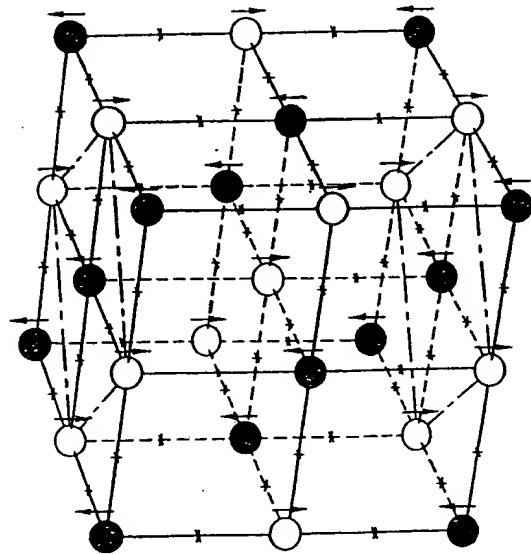


Fig. 7.2. Magnetic ordering in $\text{Ba}(\text{B}'_{0.5}\text{B}''_{0.5})\text{O}_3$ type compounds (after Longo and Ward⁽⁶⁾).

and tetravalent valence states respectively in the solid solutions.

Wold *et al.*⁽⁷⁾ reported ferromagnetism in the $\text{La}(\text{Mn}_{1-x}\text{Ni}_x)\text{O}_3$ system. This may be caused by Ni^{3+} - Mn^{3+} and Ni^{3+} - Ni^{3+} interactions. However, it is possible that the Mn^{4+} and Ni^{2+} may be present in some sites and also could interact.

Sugawara and Iida⁽⁸⁾ prepared BiMnO_3 at 40 kbar and 700°C. The compound was found to be ferromagnetic at 130°K.

In the magnetic-ordered perovskite-type compounds with the general formula $\text{A}(\text{B}'_{0.5}\text{B}''_{0.5})\text{O}_3$ where B' is W^{5+} , Mo^{5+} , or Re^{5+} and B'' also is a parametric ion, Longo and Ward propose that a negative interaction between the B' and B'' exists.⁽⁹⁾ The ordered arrangement of the two B cations is shown in Fig. 7.2. The compounds $\text{Ba}(\text{Fe}_{0.5}\text{Re}_{0.5})\text{O}_3$, $\text{Sr}(\text{Fe}_{0.5}\text{Re}_{0.5})\text{O}_3$ and $\text{Ca}(\text{Fe}_{0.5}\text{Re}_{0.5})\text{O}_3$ were found to have Curie temperatures of 43°C, 128°C and 265°C, respectively. By analogy with the

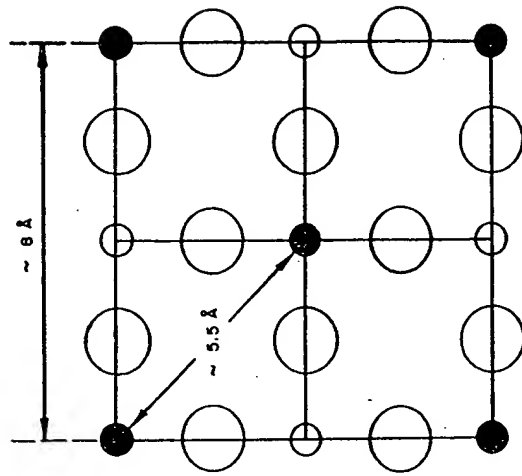


Fig. 7.3. Face of cubic ordered perovskite structure (100).
● = B', ○ = B'', ○ = 0, A ions omitted (after Blasse⁽¹³⁾).

magnetic properties of these compounds, an increase in Curie temperature with decreasing A cation size might have been anticipated for compounds containing W^{5+} and Mo^{5+} as the B'' ion. However, the $\text{A}(\text{Cr}_{0.5}\text{Mo}_{0.5})\text{O}_3$, $\text{A}(\text{Cr}_{0.5}\text{Mo}_{0.5})\text{O}_3$ and $\text{A}(\text{Fe}_{0.5}\text{Mo}_{0.5})\text{O}_3$ compounds showed a lower Curie temperature for Ca^{2+} compounds.⁽¹⁰⁾ In fact, for the phases in the system (Ba, Sr, Ca)($\text{Fe}_{0.5}\text{Mo}_{0.5}$) O_3 a maximum in the Curie point was found for $\text{Sr}(\text{Fe}_{0.5}\text{Mo}_{0.5})\text{O}_3$ at an Fe-O-Mo bond distance of approximately 3.95 Å.⁽¹¹⁾

Blasse, in a study of perovskites $\text{La}(\text{B}'_{0.5}\text{Mn}_{0.5})\text{O}_3$ ($\text{B}' = \text{Mg, Co, Ni and Cu}$), found that the magnetic exchange interactions between B' and Mn^{4+} ions in ferromagnetic compounds appear to be positive.⁽¹²⁾ The saturation moment of $\text{La}(\text{Co}_{0.5}\text{Mn}_{0.5})\text{O}_3$ and $\text{La}(\text{Ni}_{0.5}\text{Mn}_{0.5})\text{O}_3$ was increased by annealing the compounds, which increased the ordering of the B ions and decreased the number of antiferromagnetic $\text{B}'\text{-O-B}$ and $\text{Mn}^{4+}\text{-O-Mn}^{4+}$ interactions, so that a decreasing Curie temperature was expected and found experimentally. Table 7.1 presents the ferromagnetic perovskite compounds and their Curie points.

TABLE 7.1. Ferromagnetic Compounds

	Curie temp. (°C)	References
$\text{Ba}_2\text{FeMoO}_6$	64	10, 11
$\text{Sr}_2\text{FeMoO}_6$	146	10, 11
$\text{Ca}_2\text{FeMoO}_6$	104	10
$\text{Sr}_2\text{CrMoO}_6$	200	10
$\text{Ca}_2\text{CrMoO}_6$	-125	10
Sr_2CrWO_6	180	10
Ca_2CrWO_6	-130	10
$\text{Ba}_2\text{FeReO}_6$	43	9
$\text{Ba}_2\text{FeReO}_6$	43	9
$\text{Sr}_2\text{FeReO}_6$	128	9
$\text{Ca}_2\text{FeReO}_6$	265	9
$\text{Sr}_2\text{CrReO}_6$	Magnetic R.T.	17
$\text{Ca}_2\text{CrReO}_6$	Magnetic R.T.	17
BiMnO_3	-170	8

In a study of antiferromagnetic ordered perovskites $\text{A}(\text{B}'_0\text{B}'_{0.5})\text{O}_3$ where B' is the only paramagnetic ion, Blasse showed that the mechanism for magnetic interaction between the paramagnetic B' ions is of the type $\text{B}'\text{-O-B}''\text{-O-B}'$ (see Fig. 7.3). This is a new type of superexchange in the perovskite structure.

In a study of $\text{Sr}(\text{B}'_{0.5}\text{W}_{0.5})\text{O}_3$ type compounds where $\text{B}' = \text{Mn, Fe, Co and Ni}$, Blasse⁽¹⁴⁾ found that the Néel temperature (see Fig. 7.4) increased as it did in the $\text{B}'\text{O}$ compounds

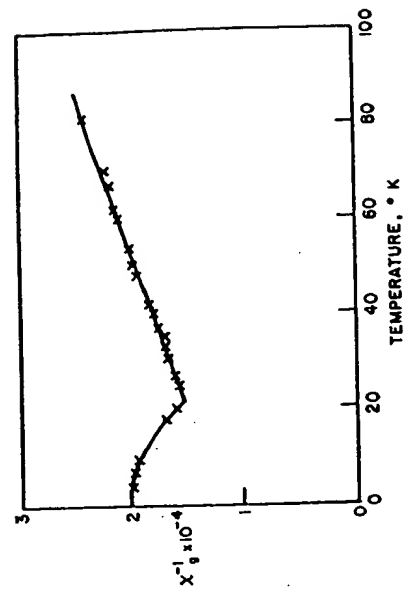


FIG. 7.4. Reciprocal susceptibility per gram vs. temperature of $\text{Sr}(\text{Co}_{0.5}\text{W}_{0.5})\text{O}_3$ (after Blasse⁽¹⁴⁾).

(rocksalt structure) and $\text{KB}'\text{F}_3$ compounds (perovskite structure). See Table 7.2.

TABLE 7.2. Magnetic Properties of Compounds $\text{Sr}(\text{B}'_{0.5}\text{W}_{0.5})\text{O}_3$, $\text{B}'\text{O}$ and $\text{KB}'\text{F}_3$ (after Blasse⁽¹⁴⁾)

B'	$\text{Sr}(\text{B}'_{0.5}\text{W}_{0.5})\text{O}_3$ T_N (°K)	$\text{B}'\text{O}$ T_N (°K)	$\text{KB}'\text{F}_3$ T_N (°K)
Mn^{3+}	10	116	88
Fe^{3+}	16	186	113
Co^{3+}	22	292	114
Ni^{3+}	54	523	275
Cu^{3+}	—	—	243

In the complex perovskite structures the B' ions are separated by an OWO array, and in MeO by a single oxygen ion. Since the Néel temperature is linearly related to the exchange constant of the $180^\circ \text{B}'\text{-O-W-O-B}'$ and $\text{B}'\text{-O-B}'$ interactions, the data in Table 7.2 shows that the $\text{B}'\text{-O-B}'$ interaction is about 10 times as strong as the $\text{B}'\text{-O-W-O-B}'$ interaction.

In addition, from measurements on $\text{Ca}(\text{Fe}_{0.5}\text{Sb}_{0.5})\text{O}_3$ and

$\text{Sr}(\text{Fe}_{0.5}\text{Sb}_{0.5})\text{O}_3$, Blasse found that the magnetic interactions became stronger for shorter distances, $T_N(^{\circ}\text{K}) = 31$ and 21, respectively. If incomplete ordering exists, such as is found in $\text{Sr}(\text{Mn}_{0.5}\text{Sb}_{0.5})\text{O}_3$, a strongly positive $\text{Mn}^{3+}-\text{O}-\text{Mn}^{3+}$ interaction can be present.

Parasitic ferromagnetism has also been observed in perovskites. It was reported in GdFeO_3 , for temperatures between 78° and 295°K ,⁽¹⁵⁾ the magnetization varied for high fields ($H > 6000$ oe) according to the expression $\sigma = \sigma^0 + \chi H$, where the parasitic ferromagnetization σ^0 amounted to about 1% of the $\sigma(\text{Fe})$ available. It was attributed to imperfectly compensated antiferromagnetism of the Fe^{3+} ion sublattice. Wold⁽¹⁶⁾ has prepared samples of LaFeO_3 with reduced parasitic ferromagnetism by careful control of sample stoichiometry, concluding that the use of careful preparation conditions should be a requirement before measurements are made on ferromagnetic materials.

REFERENCES

1. G. H. JONKER and J. H. VAN SANTEN, *Physica* 16, 337 (1950).
2. G. H. JONKER and J. H. VAN SANTEN, *Physica* 19, 120 (1953).
3. G. H. JONKER, *Physica* 22, 707 (1956).
4. J. B. GOODENOUGH, in LANDOLT-BORNSTEIN, *Eigenschaften der Materie in ihren Aggregatzuständen* 9, 2. Springer-Verlag, Berlin (1962).
5. J. B. GOODENOUGH, A. WOLD, R. J. ARNOTT and M. MENYUK, *Phys. Rev.* 124, 373 (1961).
6. G. H. JONKER, *J. Appl. Phys.* 37, 1424 (1966).
7. A. WOLD, R. J. ARNOTT and J. B. GOODENOUGH, *J. Appl. Phys.* 29, 337 (1958).
8. F. SUGAWARA and S. IIDA, *J. Phys. Soc. Japan*, 20, 1529 (1965).
9. J. LONGO and R. WARD, *J. Am. Chem. Soc.* 83, 2816 (1961).
10. F. K. PATTERSON, C. W. MOELLER and R. WARD, *Inorg. Chem.* 2, 196 (1963).
11. F. GALASSO, F. DOUGLAS and R. KASPER, *J. Chem. Phys.* 44, 1672 (1966).
12. G. BLASSE, *J. Phys. Chem. Sol.* 26, 1969 (1965).
13. G. BLASSE, *Proc. Int. Conf. Magnetism*, Nottingham, 350 (1964).
14. G. BLASSE, *Phil. Res. Rpt.* 20, 327 (1965).
15. M. A. GILLES, *J. Chem. Phys.* 24, 1239 (1956).
16. A. WOLD, private communication.
17. A. W. SLEIGHT, J. LONGO, and R. WARD, *Inorg. Chem.* 1, 245 (1962).

CHAPTER 8

OPTICAL PROPERTIES

8.1. TRANSMITTANCE

Merz⁽¹⁾ studied the optical properties of single-domain crystals of BaTiO_3 at various temperatures. The refractive index of the crystal was nearly a constant value of ~ 2.4 from 20° to 90°C and reached a maximum value of 2.46 at 120°C (see Fig. 8.1). At the transition temperature a sudden change in n is observed (see Fig. 8.2).

Lawless and DeVries⁽²⁾ also measured the index of refraction of BaTiO_3 at 5893 \AA in the range of 20 – 160° . A constant index of 2.368 was obtained from 20° to 105°C and above the Curie point the index increased 1.3% to 2.398 and remained constant to 160°C .

The single crystal of BaTiO_3 , 0.25 mm thick, was found to transmit from 0.5μ to 6μ . Complete absorption was found

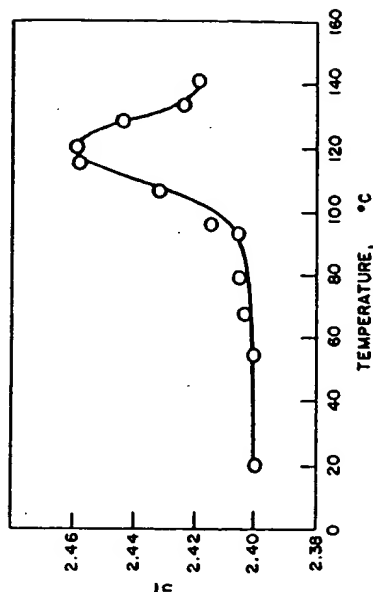


FIG. 8.1. Refractive index \bar{n} as a function of temperature (after Merz⁽¹⁾).

for wavelengths greater than $11\ \mu$ and a feeble absorption band existed near $8\ \mu$ (see Fig. 8.3).

The optical properties of strontium titanate single crystals produced by a flame fusion process were reported by Noland.⁽³⁾ The optical coefficient was obtained from $0.20\ \mu$ to $17\ \mu$ in wavelength (see Fig. 8.4). Transmission of better than 70% was measured from $0.55\ \mu$ to $5\ \mu$. The index of

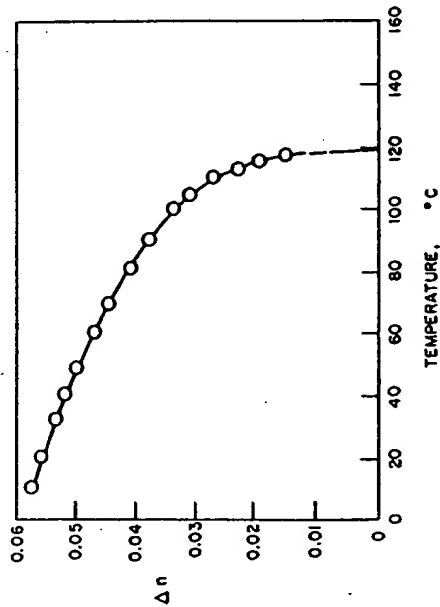


Fig. 8.2. Birefringence Δn as a function of temperature (after Merz⁽¹⁾).

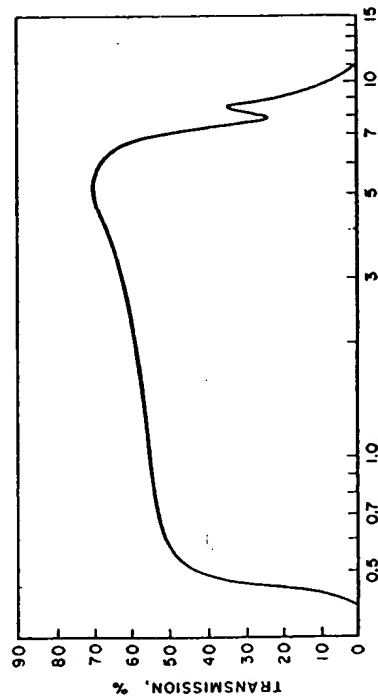


Fig. 8.3. Transmission spectrum of barium titanate single crystal, $d = 0.25\ \text{mm}$ (after A. F. Tatsenko, *Sov. Phys. Techn. Phys.* 8, 2267 (1957)).

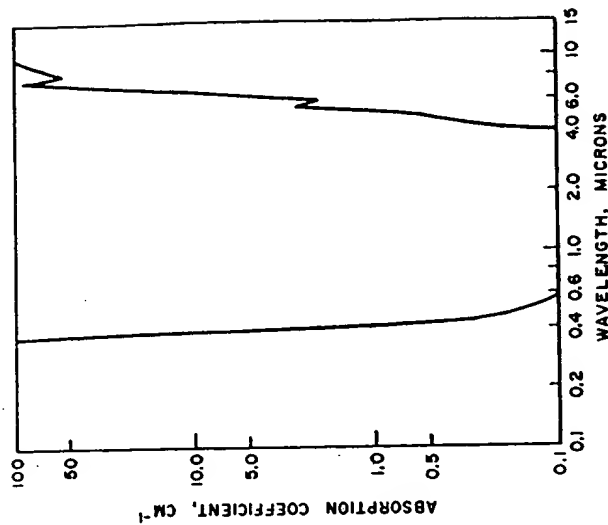


Fig. 8.4. Absorption coefficient of single crystal SrTiO_3 as a function of wavelength (after Noland⁽³⁾).

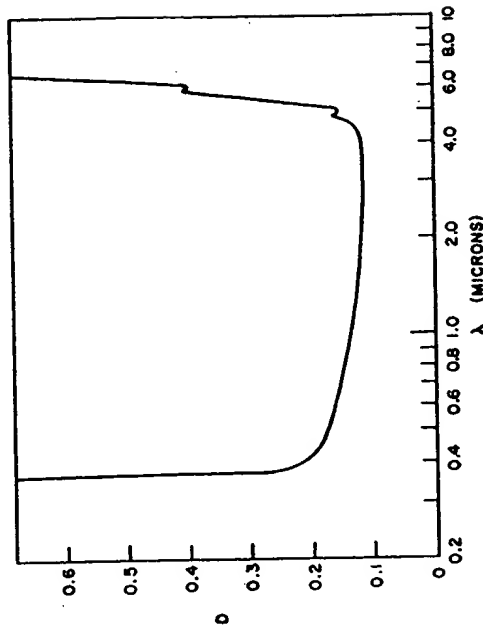


Fig. 8.5. Optical density vs. wavelength of $1.9\ \text{mm}\ \text{CaTiO}_3$ crystal (after Linz *et al.*⁽⁴⁾).

refraction of these crystals is 2.407 at 5893 Å, the dielectric constant is 310 and the loss tangent 0.00025.

The optical density of CaTiO_3 was reported by Linz and Herrington.⁽⁴⁾ The crystals were prepared by the flame fusion technique (see Fig. 8.5). The absorption characteristics are quite similar to those of SrTiO_3 crystals with the exception that the absorptions are shifted to shorter wavelengths. Index of refraction data for CaTiO_3 and SrTiO_3 as a function of wave-

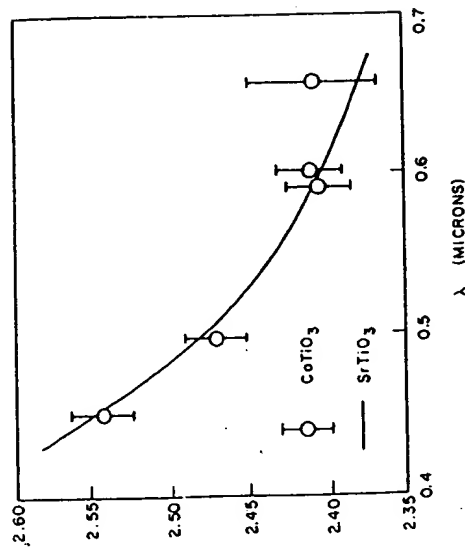


Fig. 8.6. Dispersion of CaTiO_3 and SrTiO_3 (after Linz *et al.*⁽⁴⁾).

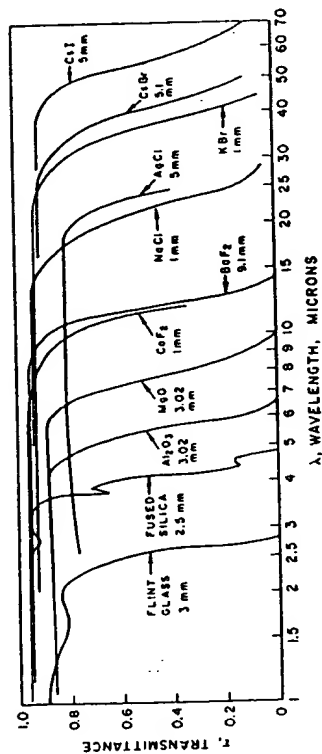


Fig. 8.7. Infrared transmittance of crystalline window and prism materials after L. J. Neuringer (*Electrical Manufacturing*) (March 1960), copyright (Conover-Mast publications, Inc.).

length are plotted in Fig. 8.6. The data are quite similar and the deviation at 657 Å can be attributed to the difficulty in the measuring technique at that wavelength.

BaTiO_3 and SrTiO_3 have been considered for high-temperature infrared windows. Typical materials which are presently being used are shown in Fig. 8.7. Note that the titanates are useful in the same wavelength range as silica and Al_2O_3 . In addition, strontium titanate is considered as an excellent material for use with optically immersed infrared detectors. For many applications the detector-lens combinations are cooled to solid CO_2 and liquid N_2 temperatures to increase the sensitivity. Salzberg⁽⁵⁾ made successive transmittance measurements on strontium titanate from room temperature to -187°C showing that there was no decrease in the transmittance of strontium titanate down to -187°C .

8.2. COLORATION BY LIGHT

MacNevin and Ogle⁽⁶⁾ noticed that the alkaline earth titanates took on a purplish color when exposed to light and heating reversed the effect. The effect presumably was caused by impurities.

8.3. ELECTRO-OPTIC EFFECT

The electro-optic properties of KTaO_3 , $\text{K}(\text{Ta}_{0.95}\text{Nb}_{0.05})\text{O}_3$ (KTN), BaTiO_3 and SrTiO_3 in the paraelectric phase were measured by Geusic *et al.*⁽⁷⁾ The electro-optic coefficients of these perovskites are nearly constant with temperature and from material to material when the distortions of the optical indicatrix are expressed in terms of the induced polarization. Thus, the coefficients might be fundamental properties of the perovskite lattice. These studies also showed that KTN has a large room-temperature electro-optic effect, low electrical losses and a large saturation polarization. An induced birefringence of 0.0057 has been reported with an applied field of 13,000 V/cm, which corresponds to a retardation of 180 half-waves per cm of light path length at 6828 Å. Thus, for polarization of amplitude modulators, the power and voltage requirements can be satisfied by transistor circuitry. The large value of Δn also should make possible a light-scan-

ning system using a prism or a partially electroded cube which can scan over 500 resolvable beam diameters.

Cohen and Gordon⁽⁸⁾ described experiments which involve propagating an electromagnetic wave through an electro-optic medium. Using 2.5 μ sec microwave pulses with a peak power of a few hundred watts at 9.5 GC, 5% of the light in the zero-order beam was transferred to the higher orders at frequencies 750 GC. Therefore, when the beam is polarized at 45° to the direction of the microwave electric field, it should be possible to extinguish the zero-order beam and pass 75% of the deflected beam.

I. P. Kaminov⁽⁹⁾ described experiments in which ferroelectric barium titanate was used at 70 MC as an optical phase modulator. Focused fundamental gaussian mode passed through the edge of a crystal plate with both the higher order "donut" mode of a 0.633- μ He-Ne maser and the fundamental mode maintaining their identity.

Borrelli *et al.*⁽¹⁰⁾ observed the electro-optic effect of ferroelectric microcrystals in a glass matrix. Crystals of NaNbO_3 containing small amounts of cadmium were formed by controlled crystallization of a glass with a high silica glass remaining as a matrix. The cadmium was used to make antiferroelectric NaNbO_3 ferroelectric. The crystal size was varied from 50 to 500 Å (less than the wavelength of light) and the dielectric constant from 50 for the glass to 550 for the transparent crystallized material. Materials which had larger crystallite sizes had the higher dielectric constants. In these experiments the difference in refractive index was measured as a function of electric field. No electro-optical activity was observed for the glass, but the retardation was proportional to the square of the electric field for the crystallized glass. In addition, the materials with the higher dielectric constants produce the largest index differences, see Fig. 8.8.

8.4. LASERS

In recent years there has been considerable interest in materials to be used for laser application. The operating laser systems are listed in Table 8.1.

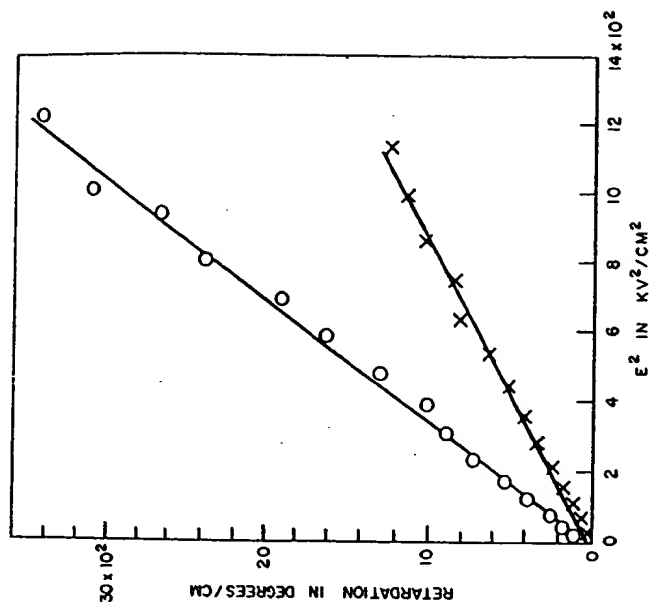


FIG. 8.8. Retardation in degrees of arc per cm vs. the square of the applied electric field (O, sample with ϵ of 540; X, sample with ϵ of 356). Measurements made at 6328 Å (after Borrelli⁽¹⁰⁾).

In selecting perovskite laser host materials a great deal can be learned from an examination of these systems.

The ion Nd^{3+} appears to be the most popular for introduction into relatively large crystallographic sites. However, except when LaF_3 is used as a host, compensating ions are required in these substitutions. Divalent Tm^{2+} and Dy^{2+} can be substituted in CaF_2 without compensating ions but these divalent rare earth ions are relatively unstable. For Al_2O_3 whose structure contains octahedrally coordinated crystallographic sites for the Al^{3+} , Cr^{3+} proved to be ideal for substitution. Other small ions which have been used to produce laser action are Fe^{3+} and Mn^{4+} , but these ions have not been employed to the extent Cr^{3+} has.

The perovskite structure should be a promising one since

TABLE 8.1. Data for Operating Laser Systems

Laser	Output (μ)	Operating temp. ($^{\circ}$ K)
1. $\text{Al}_2\text{O}_3(\text{Cr}^{3+})$	0.6944	300 (Cont.) 77
2. $\text{CaF}_2(\text{U}^{3+})$	2.556	77 (Cont.)
3. $\text{SrF}_2(\text{U}^{3+})$	2.407	77
4. $\text{BaF}_2(\text{U}^{3+})$	2.556	77
5. Glass (Nd^{3+})	1.06	300
6. $\text{CaWO}_4(\text{Nd}^{3+})$	1.0646	300 (Cont.)
7. $\text{SrMoO}_4(\text{Nd}^{3+})$	1.0843	300
	1.084	77 (Cont.)
8. $\text{CaMoO}_4(\text{Nd}^{3+})$	1.087	300
9. $\text{PbMoO}_4(\text{Nd}^{3+})$	1.0586	300
10. NaLaMoO_4 (Nd^{3+})	1.0586	300
11. $\text{CaF}_2(\text{Nd}^{3+})$	1.046	300
12. $\text{SrF}_2(\text{Nd}^{3+})$	1.06	300
13. $\text{BaF}_2(\text{Nd}^{3+})$	1.06	300
14. $\text{LaF}_3(\text{Nd}^{3+})$	1.06	300
15. $\text{CaWO}_4(\text{Ho}^{3+})$	2.046	77
16. $\text{CaF}_2(\text{Ho}^{3+})$	2.05	77
17. $\text{CaWO}_4(\text{Tm}^{3+})$	1.116	77
18. $\text{SrF}_2(\text{Tm}^{3+})$	1.91	300
19. $\text{CaWO}_4(\text{Fe}^{3+})$	1.612	77
20. $\text{CaWO}_4(\text{Pr}^{3+})$	1.05	77
21. Glass (Yb^{3+})	1.01	77
22. Glass (Sm^{3+})	0.71	77
23. Glass (Gd^{3+})	0.31	77
24. $\text{Y}_3\text{Al}_5\text{O}_{12}(\text{Nd}^{3+})$		300 (Cont.)
25. $\text{Y}_3\text{Al}_5\text{O}_{12}$ (Nd^{3+} , Cr^{3+})		300 (Cont.)
26. $\text{CaF}_2(\text{Sm}^{3+})$	0.7082	77
27. $\text{CaF}_2(\text{Tm}^{3+})$	1.116	4
28. $\text{CaF}_2(\text{Dy}^{3+})$	2.36	77 (Cont.)

it contains a large A site suitable for Nd^{3+} and smaller B site for Cr^{3+} . In the ideal structure these sites are cubic and centrosymmetric, a condition theoreticians feel should be necessary for obtaining long fluorescence lifetimes for activator ions. However, as was pointed out previously no simple cubic perovskite-type compounds exist which will accept trivalent activator ions without producing defects or require charge

compensating ions. The compound LaAlO_3 , however, has a structure which is only slightly distorted from cubic symmetry. The fluorescence lifetime for Cr^{3+} in LaAlO_3 has been reported to be as high as 46 msec as compared with 3 msec for the lifetime of Cr^{3+} in Al_2O_3 .⁽¹¹⁾ This enhancement in lifetime has been attributed to the nearly cubic symmetry of the site containing the Cr^{3+} ion. The transition of LaAlO_3 at 435°C presents a problem in obtaining single crystals of thin material. However, flux-grown and hydrothermally grown crystals big enough for fluorescence measurements have been prepared.⁽¹²⁾ The measurements showed the fluorescence line at 7356 Å which is characteristic of Cr^{3+} .

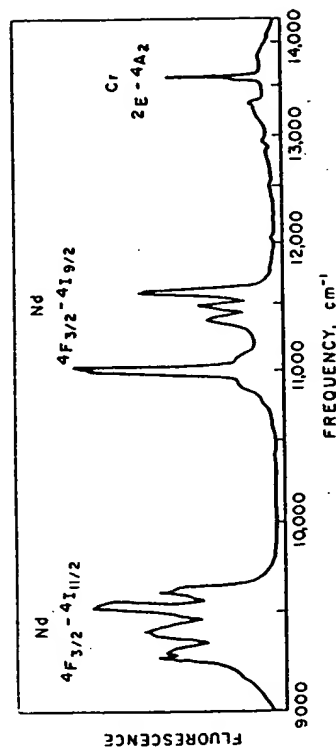


FIG. 8.9. Fluorescence spectrum of $\text{LaAlO}_3\text{-Cr}$, Nd excited with high-pressure mercury lamp (after Murphy *et al.*⁽¹¹⁾).

Murphy *et al.*⁽¹¹⁾ reported on energy transfer between Cr^{3+} and Nd^{3+} in LaAlO_3 . These studies were conducted on powder samples. The fluorescence spectrum of $\text{LaAlO}_3\text{:Cr}$, Nd is presented in Fig. 8.9. The line at 7356 Å is due to Cr^{3+} and the remaining two groups are associated with the fluorescence of Nd^{3+} . Lifetimes of Nd^{3+} and Cr^{3+} were found to be 0.46 and 4.6 msec, respectively, at room temperature. Their studies indicated that energy transfer existed between the $^4\text{T}_2$ level of Cr^{3+} and the D levels of Nd^{3+} .

Ohlmann and Mazelsky⁽¹³⁾ also found transfer of excitation radiation from Cr^{3+} to Nd^{3+} ions in GdAlO_3 . The purpose of the studies was to increase the efficiency of lasers from the usual 2% or less. The low efficiency was attributed to the poor

spectral mismatch between the broad bands of the pump lamps and the relatively narrow absorption bands of the paramagnetic ions. Thus, Cr^{3+} was added to GdAlO_3 to produce broad absorption bands which could transfer the energy it absorbed to the Nd^{3+} ion. The fluorescence spectrum showed two groups occurring around 0.9μ and 1.07μ from Nd^{3+} and fluorescence at 0.727μ due to chromium. When the Cr^{3+} levels were excited, the fluorescence of neodymium showed an intensity increase of several times in the doubly doped samples over the singly doped samples. The lifetimes of Nd^{3+} and Cr^{3+} in GdAlO_3 were 0.130 msec and 15 msec, respectively.

Other simple perovskite compounds considered for laser host materials were SrTiO_3 , SrSnO_3 , BaSnO_3 and BaZrO_3 . However, divalent or tetravalent laser activating ions would be required for substitution so that the symmetry would not be destroyed by compensating ions. The activating ions in these valence states are not particularly stable.

Because of the enhancement of lifetimes observed for Cr^{3+} in LaAlO_3 and GdAlO_3 as compared with its lifetime in Al_2O_3 , a search was made by Galasso *et al.*⁽¹⁴⁾ for cubic perovskite compounds which would accept trivalent rare earth ions. They found that compounds of the $\text{Ba}(\text{B}_0^{3+}\text{Ta}_{0.5})\text{O}_3$ had an ordered structure in which the B ions alternate so that the symmetry about the B site is retained. Barium was selected since compounds of this type containing barium are usually least distorted, and Ta^{5+} is one of the B ions because of its resistance to reduction and the other B ion should not produce energy levels which would interfere with those of the doping ions. The fluorescence lifetimes of powders of these compounds containing activator ions are presented in Table 8.2. The values obtained, i.e. 850 msec for Nd^{3+} in $\text{Ba}(\text{Lu}_{0.5}\text{Ta}_{0.5})\text{O}_3$ and 800 msec in Nd^{3+} in $\text{Ba}(\text{Gd}_{0.5}\text{Ta}_{0.5})\text{O}_3$, indicate that there may be some enhancement in lifetimes due to cubic symmetry about the substituted ion. However, the increase is small and it appears that the neodymium lifetime is not influenced as much by environment as that of Cr^{3+} .

The fluorescence spectra of Er^{3+} ion studied in a $\text{Ba}(\text{Gd}_{0.5}\text{Nb}_{0.5})\text{O}_3$ host confirmed the fact that a center of symmetry existed at the B site in the structure of these cubic complex oxides.⁽¹⁵⁾

TABLE 8.2. *Fluorescent Lifetime Data (after Galasso et al.⁽¹⁴⁾)*

Doped $\text{Ba}(\text{B}_0^{3+}\text{Ta}_{0.5})\text{O}_3$ phases Nd^{3+} doped	Emission line (μ)	Lifetime at 300°K (μ sec)	Lifetime at 77°K (μ sec)
$\text{Ba}(\text{La}_{0.48}\text{Nd}_{0.02}\text{Ta}_{0.50})\text{O}_3$	1.06	500	650
$\text{Ba}(\text{Gd}_{0.48}\text{Nd}_{0.02}\text{Ta}_{0.50})\text{O}_3$		700	800
$\text{Ba}(\text{Y}_{0.48}\text{Nd}_{0.02}\text{Ta}_{0.50})\text{O}_3$		200	250
$\text{Ba}(\text{Lu}_{0.48}\text{Nd}_{0.02}\text{Ta}_{0.50})\text{O}_3$		400	850
$\text{Ba}(\text{In}_{0.48}\text{Nd}_{0.02}\text{Ta}_{0.50})\text{O}_3$		150	250
$\text{Ba}(\text{Sn}_{0.48}\text{Nd}_{0.02}\text{Ta}_{0.50})\text{O}_3$		200	220
Sm^{3+} doped			
$\text{Ba}(\text{Y}_{0.48}\text{Sm}_{0.02}\text{Ta}_{0.50})\text{O}_3$	0.70	1450	
Yb^{3+} doped			
$\text{Ba}(\text{Y}_{0.48}\text{Yb}_{0.02}\text{Ta}_{0.50})\text{O}_3$	1.01	1800	

REFERENCES

1. W. J. MERR, *Phys. Rev.* 76, 1221 (1949).
2. W. N. LAWLESS and R. C. DEVRIES, *J. Appl. Phys.* 35, 2638 (1964).
3. J. A. NOLAND, *Phys. Rev.* 94, 724 (1954).
4. A. LINZ, JR. and K. HERRINGTON, *J. Chem. Phys.* 28, 824 (1958).
5. C. D. SALZBERG, *J. Opt. Soc.* 51, 1149 (1961).
6. W. M. MACNEVIN and P. R. OGLE, *J. Am. Chem. Soc.* 76, 3849 (1954).
7. J. E. GEUSIO, S. K. KURTZ, L. G. VAN UITERT and S. H. WEMPLE, *Appl. Phys. Letters* 4, 14 (1964).
8. M. G. COHEN and E. I. GORDON, *Appl. Phys. Letters* 5, 181 (1964).
9. I. P. KAMINOW, *Appl. Phys. Letters* 7, 123 (1965).
10. N. F. BORRELLI, A. HERCZOG and R. D. MAUREL, *Appl. Phys. Letters* 7, 117 (1965).
11. J. MURPHY, R. C. OHLMANN and R. MAZELSKY, *Phys. Rev. Letters* 18, 135 (1964).
12. *Airtron Semiannual Tech. Sum. Rpt.*, NONR 4816(00) (1 July-31 Dec. 65).
13. R. C. OHLMANN and R. MAZELSKY, to be published.
14. F. GALASSO, G. LAYDEN and D. FLINCHBAUGH, *J. Chem. Phys.* 44, 2703 (1966).
15. G. BLASSE, A. BRIL and W. C. NIEUWFOORT, *J. Phys. Chem. Soc.* 27, 1587 (1966).

trodes in fuel cells. Dickens and Whittingham⁽²⁾ studied the recombination of oxygen atoms on the surfaces of phases with the formula M_xWO_3 where M is Li, Na or K and $0 < x < 0.80$. The pattern of catalytic activity for oxygen atom recombination is approximately the same for Li_xWO_3 , Na_xWO_3 and K_xWO_3 phases. In the semiconducting range, from $x = 0$ to $x = 0.25$, the catalytic activity decreased, but in the range above $x = 0.25$ the catalytic activity increased sharply to a maximum at $x = 0.55$. Above $x = 0.25$ the conductivity of the bronzes is metallic. Thus, the catalytic activities of the tungsten bronzes appear to be closely related to the electronic properties of the bronzes.

Heterogeneous Catalysis

Parravano⁽³⁾ studied the effect of the electronic rearrangement of ferroelectric materials at their transition temperatures on the electron exchange occurring during a catalytic process. From data obtained for carbon monoxide oxidation on $KNbO_3$, he concluded that the change in the rate of catalytic oxidation of CO is affected by the electronic transition. This supported the evidence for an electronic mechanism as being rate determining for the catalytic oxidation of CO.

9.2. THERMAL CONDUCTIVITY

The thermal conductivity values for the titanates are listed in Table 9.1. They are quite low, with the conductivity of barium titanate being lower than that of strontium titanate and calcium titanate at 50°C.

9.3. MELTING POINTS

The melting points of many of the ternary oxides have been determined, but none of complex perovskite type compounds (see Table 9.1). It should be realized that in many cases these are only approximate values; however, they do serve as guides for crystal growth experiments, for example, note that zirconates are extremely high melting-point materials along with hafnates and thorates, the titanates have

CHAPTER 9

OTHER PROPERTIES

9.1. CATALYSTS

Fuel Cell

A detailed study was conducted by Epperly *et al.*⁽¹⁾ to evaluate complex perovskites of the general formula $A(B'_3B''_3)O_3$ with $A = Li, Os, Ca, Sr, Ba, La, Ti, Pb$ and Bi , $B' = V, Cr, Mn, Fe, Co, Ni, Ru, Rh, Ir$ and Pt and $B'' = Ti, Zr, Sn, Hf, V, Nb, Ta, Mo$ and W for fuel cell application. The B' ions were selected from those which are known to have catalytic properties and B'' ions were selected for the corrosion resistance they impart to a compound. The problem was to tailor the compounds so that they would have high conductivity and high resistance to attack by dilute solutions of sulfuric acid. While it is dangerous to generalize, the information generated can be quite useful if it is realized that it is qualitative in nature.

They found that most of the perovskite compounds studied were quite acid resistant, but were poor conductors. It is important to note that the B ions were used in their highest oxidation states. The incorporation of oxygen vacancies improved the conductivity but the acid resistance was not as good. Compounds containing Ni had good acid resistance, especially when Ni^{2+} ions were added to the acid, but were poor conductors. The compounds containing cobalt were made conductive by producing oxygen vacancies, but then became soluble in the acid. Compounds containing Nb or Ta were more acid resistant than those containing Mo or W. Compounds containing Ti, Zr or Hf had relatively poor acid resistance. The most satisfactory perovskites were those containing manganese in more than one valence state.

The tungsten bronzes also have been considered for elec-

TABLE 9.1. Other Properties

Phase	Thermal conductivity (W/cm ² C)	Coeff. of thermal expansion ($\times 10^{-6}/^{\circ}\text{C}$)	ΔH (kcal/mole)	Melting point ($^{\circ}\text{C}$)
BaThO ₃	0.022-0.032 (50-230)	19 (10-90)	394.8	2299
BaTiO ₃		14 (140-1200)		1610
BaZrO ₃	0.043-0.046 (50-135)	7.79 (25-500)	397.4	2688
CaHfO ₃		8.52 (25-1000)		2471
CaTiO ₃		3.6 (100-800)		1975
CaZrO ₃	0.037-0.058 (50-140)	12.1 (800-1300)	398.9	2343
GdAlO ₃		7.08 (1000-1300)		2080
KNbO ₃		13.04 (25-500)		1888
KTaO ₃		14.05 (25-1000)		1412
LaAlO ₃		-16 (below 490)		1780
LaFeO ₃		25 (above 490 $^{\circ}$)		2080
NaNbO ₃		8.63		2799
NaTaO ₃	0.037-0.058 (50-140)	9.43 (25-500)	398.9	1950
PbTiO ₃		8.84 (25-1000)		
SrTiO ₃		9.64 (25-1000)		
SrZrO ₃	0.037-0.058 (50-140)	13.19	398.9	
YAlO ₃		10.99		
Ba(Fe _{0.5} Ta _{0.5})O ₃	0.037-0.058 (50-140)	13.19	398.9	1950
Sr(Fe _{0.5} Ta _{0.5})O ₃				

intermediate melting points, and the niobates and tantalates are relatively low melting.

9.4. HEATS OF FORMATION

Only the heats of formation of the titanates have been measured. These values shown in Table 9.1 are quite similar for barium, strontium and calcium titanate.

9.5. THERMAL EXPANSION

There does not appear to be a trend in the thermal expansion of the perovskites in relation to the ion in the A position (see Table 9.1). Note that for the titanates, the coefficient of thermal expansion of barium titanate above the Curie point is similar to that of calcium titanate and larger than that of strontium titanate. For the zirconates the coefficient of thermal expansion of SrZrO₃ is greater than that for BaZrO₃, while the coefficient of thermal expansion of Ba(Fe_{0.5}Ta_{0.5})O₃ is greater than that of Sr(Fe_{0.5}Ta_{0.5})O₃. Lead titanate is unusual, having a negative coefficient up to 490 $^{\circ}\text{C}$ and above this temperature it behaves like the other titanates.

9.6. DENSITY

The densities of perovskite-type compounds were calculated from X-ray data using the equation in a computer program

$$D = \frac{\text{Molecular weight} \times \text{no. of molecules per unit cell}}{\text{Volume of unit cell} \times 6.023 \times 10^{23} \text{ molecules/mole}}$$

In the program, the equation for the volume of a triclinic cell was used

$$V = a \times b \times c \sqrt{(1 - \cos^2 \alpha - \cos^2 \beta - \cos^2 \gamma + 2 \cos \alpha \cos \beta \cos \gamma)}$$

and the appropriate parameters from Table 2.2 were introduced for each compound. The molecular weight was obtained by introducing the periodic table with atomic weights into the computer and then inserting the data deck with the appropriate atomic symbols and multipliers. The cube root of

$$\frac{\text{volume of the unit cell}}{\text{no. of molecules per unit cell}}$$

was also calculated to obtain a' , the unit cell edge of a cubic cell which represents the same volume allowed in the true unit cell for a molecule of a perovskite-type compound. This permits a comparison to be made between the ionic radii of the ions in these compounds even when they are indexed on cells with different symmetry. Table 9.2 presents the molecular weight, a' , and the density of the perovskite compounds.

9.7. MECHANICAL PROPERTIES

Only very little information is available on the mechanical properties of perovskites (see Table 9.1). The modulus of barium titanate has been measured to be 16×10^6 psi.

The modulus of SrZrO_3 has been found to be 12×10^6 psi, the bend strength 13×10^3 psi and the compressive strength 5×10^3 psi. Strontium zirconate has an interesting stress-strain curve as shown in Fig. 9.1.⁽⁴⁾ The small yield observed was attributed to domain motion or crystal twinning similar to that which takes place in ferroelectric BaTiO_3 under an electric stress.

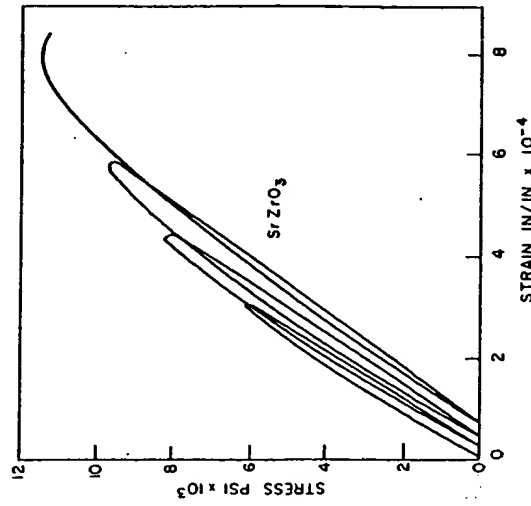


Fig. 9.1. Stress-strain behavior of hot-pressed SrZrO_3 (after Tinklepaugh⁽⁴⁾).

TABLE 9.2. Data for Perovskite-type Compounds

Compound	Formula weight	Volume	Z	a' , Å	Density
$A^{1+}B^{2+}O_3$					
AgNbO_3	248.774	974.325	16	3.934	6.782
AgTaO_3	336.816	60.481	1	3.925	9.244
CaIO_3	307.808	101.195	1	4.680	6.049
KIO_3	214.005	85.752	1	4.410	4.143
KNbO_3	180.008	129.368	2	4.014	4.620
KTaO_3	268.048	63.450	1	3.988	7.013
NaNbO_3	163.894	119.427	2	3.909	4.556
NaTaO_3	251.936	117.498	2	3.887	7.119
RbIO_3	260.373	92.345	1	4.520	4.680
TiIO_3	379.273	91.716	1	4.510	6.865
$A^{2+}B^{4+}O_3$					
BaCeO_3	325.458	85.010	1	4.397	6.355
BaFeO_3	241.185	63.520	1	3.990	6.303
BaMoO_3	281.278	65.959	1	4.040	7.079
BaPbO_3	392.528	78.019	1	4.273	8.352
BaPrO_3	326.245	82.540	1	4.354	6.561
BaPuO_3	427.338	84.605	1	4.390	8.385
BaSnO_3	304.028	69.782	1	4.117	7.232
BaThO_3	417.376	90.217	1	4.485	7.680
BaTiO_3	233.238	64.110	1	4.002	6.039
BaUO_3	423.368	84.431	1	4.387	8.324
BaZrO_3	276.558	73.665	1	4.192	6.232
CaCeO_3	228.198	460.683	8	3.862	6.578
CaHfO_3	266.568	—	—	—	—
CaMnO_3	143.016	833.656	8	4.706	2.278
CaMoO_3	184.018	472.590	8	3.895	5.171
CaSnO_3	206.768	246.406	4	3.949	5.672
CaThO_3	320.116	667.628	8	4.370	6.368
CaTiO_3	135.978	223.913	4	3.825	4.032
CaUO_3	326.108	280.060	4	4.151	7.570
CaVO_3	139.020	215.125	4	3.775	4.291
CaZrO_3	179.298	257.617	4	4.008	4.621
CdCeO_3	300.518	447.697	8	3.825	8.914
CdSnO_3	279.088	243.371	4	3.933	7.615
CdThO_3	392.436	667.628	8	4.370	7.806
CdTiO_3	208.298	218.491	4	3.794	6.330
CdZrO_3	251.618	—	—	—	—
EuTiO_3	247.858	59.182	1	3.897	6.952
MgCeO_3	212.430	622.836	8	4.270	4.529

TABLE 9.2 (cont.)

Compound	Formula weight	Volume	Z	α' , Å	Density
$A^{2+}B^{4+}O_3$ (cont.)					
Gd SO_3	250.204	250.297	4	3.970	6.638
GdVO $_3$	256.190	229.580	4	3.857	7.410
LaAlO $_3$	213.890	54.354	1	3.788	6.532
LaCoO $_3$	245.841	55.906	1	3.824	7.300
LaCrO $_3$	238.904	234.202	4	3.883	6.773
LaFeO $_3$	242.755	243.086	4	3.932	6.631
LaGaO $_3$	256.628	236.413	4	3.895	7.208
LaInO $_3$	186.908	277.773	4	4.110	4.468
LaNiO $_3$	245.618	452.246	8	3.838	7.212
LaRhO $_3$	289.813	61.163	1	3.940	7.866
LaSeO $_3$	231.864	266.089	4	4.052	6.786
LaTiO $_3$	234.808	60.236	1	3.920	6.471
LaVO $_3$	237.850	63.521	1	3.990	6.216
LaYO $_3$	276.813	—	—	—	—
NdAlO $_3$	219.220	52.819	1	3.752	6.890
NdCoO $_3$	261.171	53.882	1	3.777	7.738
NdCrO $_3$	244.234	228.799	4	3.853	7.088
NdFeO $_3$	248.085	235.092	4	3.888	7.007
NdGaO $_3$	261.958	230.054	4	3.860	7.561
NdInO $_3$	192.238	269.200	4	4.068	4.742
NdMnO $_3$	247.176	54.872	1	3.800	7.478
NdSO $_3$	237.194	257.276	4	4.007	6.122
NdVO $_3$	243.180	236.115	4	3.888	6.868
PrAlO $_3$	215.887	37.778	1	3.355	9.486
PrCoO $_3$	247.838	54.310	1	3.787	7.575
PrCrO $_3$	240.901	230.181	4	3.861	6.948
PrFeO $_3$	244.752	239.385	4	3.912	6.789
PrGaO $_3$	268.626	232.103	4	3.871	7.399
PrMnO $_3$	243.843	55.743	1	3.820	7.262
PrSeO $_3$	233.861	260.334	4	4.022	5.965
PrVO $_3$	239.847	235.641	4	3.891	6.759
PuAlO $_3$	316.980	97.324	1	4.600	5.407
PuCrO $_3$	341.994	233.456	4	3.879	9.727
PuMnO $_3$	344.936	57.512	1	3.860	9.956
PuVO $_3$	340.940	239.179	4	3.910	9.465
SmAlO $_3$	225.330	208.928	4	3.738	7.161
SmCoO $_3$	257.281	53.123	1	3.759	8.040
SmCrO $_3$	250.344	226.109	4	3.838	7.352
SmFeO $_3$	254.195	232.589	4	3.874	7.257
SmInO $_3$	198.348	265.872	4	4.051	4.954
SmVO $_3$	249.290	58.864	1	3.890	7.030
YAlO $_3$	163.885	203.404	4	3.705	5.350

TABLE 9.2 (cont.)

Compound	Formula weight	Volume	Z	α' , Å	Density
$A^{2+}B^{4+}O_3$ (cont.)					
PbCeO $_3$	395.308	442.451	8	3.810	11.865
PbHfO $_3$	433.678	—	—	—	—
PbSnO $_3$	373.878	502.268	8	3.974	9.885
PbTiO $_3$	303.088	62.780	1	3.974	8.014
PbZrO $_3$	346.408	799.179	8	4.640	5.756
SrCeO $_3$	275.738	312.783	4	4.276	5.854
SrCoO $_3$	194.551	460.994	8	3.862	5.605
SrFeO $_3$	191.465	57.916	1	3.869	5.488
SrHfO $_3$	314.108	67.369	1	4.069	7.740
SrMoO $_3$	231.568	62.812	1	3.975	6.120
SrPbO $_3$	342.808	290.801	4	4.174	7.828
SrRuO $_3$	236.688	—	—	—	—
SrSnO $_3$	254.308	65.617	1	4.033	6.434
SrThO $_3$	367.656	690.807	8	4.420	7.068
SrTiO $_3$	183.518	59.502	1	3.904	5.120
SrUO $_3$	373.648	318.903	4	4.304	7.780
SrZrO $_3$	226.838	275.952	4	4.101	5.458
$A^{3+}B^{3+}O_3$					
BAlO $_3$	283.960	459.822	8	3.859	8.201
BiCrO $_3$	308.974	58.851	1	3.890	8.715
BiMnO $_3$	311.916	61.424	1	3.946	8.430
CeAlO $_3$	215.100	53.838	1	3.776	6.632
CeCrO $_3$	240.114	57.781	1	3.866	6.898
CeFeO $_3$	243.965	59.319	1	3.900	6.827
CeGaO $_3$	257.838	58.366	1	3.879	7.333
CeSeO $_3$	233.074	—	—	—	—
CeVO $_3$	239.060	59.319	1	3.900	6.690
CrBiO $_3$	308.974	487.813	8	3.936	8.411
DyAlO $_3$	237.480	204.722	4	3.713	7.702
DyFeO $_3$	266.345	226.162	4	3.838	7.820
DyMnO $_3$	265.436	50.653	1	3.700	8.699
EuAlO $_3$	226.940	208.034	4	3.733	7.243
EuCrO $_3$	251.954	55.002	1	3.803	7.604
EuFeO $_3$	255.805	231.631	4	3.869	7.333
FeBiO $_3$	312.825	62.335	1	3.965	8.331
GdAlO $_3$	232.230	207.251	4	3.728	7.440
GdCoO $_3$	264.181	52.228	1	3.738	8.397
GdCrO $_3$	257.244	222.929	4	3.820	7.662
GdFeO $_3$	261.095	230.217	4	3.861	7.531
GdMnO $_3$	260.186	55.743	1	3.820	7.748

TABLE 9.2 (cont.)

Compound	Formula weight	Volume	Z	α' , Å	Density
$A^{2+}B^{3+}O_3$ (cont.)					
YCrO ₃	188.899	218.305	4	3.793	6.746
YFeO ₃	192.750	225.862	4	3.836	5.667
YScO ₃	181.859	244.887	4	3.941	4.931
A_2BO_3					
Ce _{0.33} NbO ₃	187.144	119.550	2	3.910	6.197
Ce _{0.33} TaO ₃	275.186	119.857	2	3.913	7.623
Dy _{0.33} TaO ₃	282.571	113.684	2	3.845	8.252
Gd _{0.33} TaO ₃	280.839	116.370	2	3.875	8.012
La _{0.33} NbO ₃	186.744	120.776	2	3.923	5.133
La _{0.33} TaO ₃	274.786	121.087	2	3.927	7.534
Nd _{0.33} NbO ₃	188.503	118.332	2	3.897	5.289
Nd _{0.33} TaO ₃	276.545	118.789	2	3.902	7.729
Pr _{0.33} NbO ₃	187.404	119.092	2	3.905	5.224
Pr _{0.33} TaO ₃	275.446	119.246	2	3.907	7.669
Sm _{0.33} TaO ₃	278.562	117.274	2	3.885	7.886
Y _{0.33} TaO ₃	258.285	113.227	2	3.840	7.573
Yb _{0.33} TaO ₃	286.049	110.852	2	3.813	8.567
Ca _{0.8} TaO ₃	248.986	446.725	4	4.816	3.701
Li ₂ WO ₃ , $x=1$	238.787	51.479	1	3.720	7.700
Ni ₂ WO ₃	254.838	57.602	1	3.862	7.344
Sr _{0.7} NbO ₃	202.238	63.092	1	3.981	5.321
Sr _{0.5} NbO ₃	224.143	64.771	1	4.016	5.745
CaMnO _{3-x} , $x=6$	143.000	—	—	—	—
SrCoO _{3-x} , $x=0$	194.535	—	—	—	—
SrFeO _{3-x} , $x=0$	191.449	—	—	—	—
SrTiO _{3-x} , $x=0$	183.502	—	—	—	—
SrVO _{3-x} , $x=0$	186.544	—	—	—	—
$A(B'_{0.67}B''_{0.33})O_3$					
Ba(Al _{0.67} W _{0.33})O ₃	264.086	—	—	—	—
Ba(Dy _{0.67} W _{0.33})O ₃	354.884	589.745	8	4.193	7.991
Ba(Er _{0.67} W _{0.33})O ₃	358.073	589.745	8	4.193	8.063
Ba(Eu _{0.67} W _{0.33})O ₃	347.822	637.166	8	4.302	7.249
Ba(Fe _{0.67} W _{0.33})O ₃	301.306	557.848	8	4.116	7.173
Ba(Gd _{0.67} W _{0.33})O ₃	351.366	595.036	8	4.205	7.842
Ba(In _{0.67} W _{0.33})O ₃	246.009	578.138	8	4.160	5.671
Ba(La _{0.67} W _{0.33})O ₃	339.078	631.629	8	4.290	7.129
Ba(Lu _{0.67} W _{0.33})O ₃	263.888	616.730	8	4.256	5.682
Ba(Nd _{0.67} W _{0.33})O ₃	363.239	—	—	—	—
Ba(Sc _{0.67} W _{0.33})O ₃	342.649	616.947	8	4.256	7.376
Ba(Sm _{0.67} W _{0.33})O ₃	294.009	611.960	8	4.245	6.380

TABLE 9.2 (cont.)

Compound	Formula weight	Volume	Z	α' , Å	Density
$A(B'_{0.67}B''_{0.33})O_3$ (cont.)					
Ba(Sc _{0.67} W _{0.33})O ₃	276.129	559.476	8	4.120	6.554
Ba(Y _{0.67} U _{0.33})O ₃	323.454	658.503	8	4.350	6.523
Ba(Y _{0.67} W _{0.33})O ₃	305.575	587.217	8	4.187	6.911
Ba(Yb _{0.67} W _{0.33})O ₃	361.945	—	—	—	—
Pb(Fe _{0.67} W _{0.33})O ₃	353.276	—	—	—	—
Sr(Cr _{0.67} Re _{0.33})O ₃	231.902	513.922	8	4.005	5.992
Sr(Cr _{0.67} U _{0.33})O ₃	249.005	512.000	8	4.000	6.459
Sr(Fe _{0.67} Re _{0.33})O ₃	234.482	491.169	8	3.945	6.340
Sr(Fe _{0.67} W _{0.33})O ₃	233.706	61.490	1	3.947	6.309
Sr(In _{0.67} Re _{0.33})O ₃	197.064	571.167	8	4.148	4.582
La(Co _{0.67} Nb _{0.33})O ₃	257.052	245.066	4	3.945	6.948
La(Co _{0.67} Sb _{0.33})O ₃	266.571	244.166	4	3.937	7.249
$A(B'_{0.33}B''_{0.67})O_3$					
Ba(Ce _{0.33} Nb _{0.67})O ₃	260.812	220.045	3	4.186	5.903
Ba(Ce _{0.33} Ta _{0.67})O ₃	319.800	219.214	3	4.181	7.265
Ba(Cd _{0.33} Nb _{0.67})O ₃	284.677	72.407	1	4.168	6.526
Ba(Cd _{0.33} Ta _{0.67})O ₃	343.665	72.355	1	4.167	7.884
Ba(Co _{0.33} Nb _{0.67})O ₃	267.033	68.418	1	4.090	6.479
Ba(Co _{0.33} Ta _{0.67})O ₃	326.021	204.617	3	4.086	7.935
Ba(Cu _{0.33} Nb _{0.67})O ₃	268.553	542.989	8	4.079	6.568
Ba(Fe _{0.33} Nb _{0.67})O ₃	266.015	68.167	1	4.085	6.478
Ba(Fe _{0.33} Ta _{0.67})O ₃	325.003	68.921	1	4.100	7.828
Ba(Mg _{0.33} Nb _{0.67})O ₃	255.608	204.134	3	4.083	6.236
Ba(Mg _{0.33} Ta _{0.67})O ₃	314.596	204.608	3	4.086	7.657
Ba(Mn _{0.33} Nb _{0.67})O ₃	265.715	—	—	—	—
Ba(Mn _{0.33} Ta _{0.67})O ₃	324.703	208.994	3	4.115	7.737
Ba(Ni _{0.33} Nb _{0.67})O ₃	266.980	67.618	1	4.074	6.554
Ba(Ni _{0.33} Ta _{0.67})O ₃	325.948	202.482	3	4.072	8.017
Ba(Pb _{0.33} Nb _{0.67})O ₃	315.958	77.309	1	4.260	6.784
Ba(Pb _{0.33} Ta _{0.67})O ₃	374.946	76.766	1	4.250	8.108
Ba(Sr _{0.33} Ta _{0.67})O ₃	335.488	229.026	3	4.242	7.295
Ba(Zn _{0.33} Nb _{0.67})O ₃	269.157	68.619	1	4.084	6.511
Ba(Zn _{0.33} Ta _{0.67})O ₃	328.145	205.476	3	4.091	7.953
Ca(Ni _{0.33} Nb _{0.67})O ₃	169.700	58.411	1	3.880	4.823
Ca(Ni _{0.33} Ta _{0.67})O ₃	228.688	60.698	1	3.930	6.254
Pb(Co _{0.33} Nb _{0.67})O ₃	336.883	65.939	1	4.040	8.481
Pb(Co _{0.33} Ta _{0.67})O ₃	395.871	64.481	1	4.010	10.191
Pb(Mg _{0.33} Nb _{0.67})O ₃	325.458	65.988	1	4.041	8.187
Pb(Mg _{0.33} Ta _{0.67})O ₃	384.446	64.965	1	4.020	8.823
Pb(Mn _{0.33} Nb _{0.67})O ₃	335.565	—	—	—	—
Pb(Ni _{0.33} Nb _{0.67})O ₃	336.810	65.208	1	4.025	8.574

TABLE 9.2 (cont.)

Compound	Formula weight	Volume	Z	α' , Å	Density
$A(B_{0.3}^{2+}B_{0.7}^{4+})O_3$ (cont.)					
Ba(Eu _{0.3} Nb _{0.7})O ₃	307.771	615.643	8	4.253	6.639
Ba(Eu _{0.3} Pa _{0.7})O ₃	376.818	677.530	8	4.391	7.386
Ba(Eu _{0.3} Ta _{0.7})O ₃	351.792	615.426	8	4.253	7.591
Ba(Fe _{0.3} Mo _{0.7})O ₃	261.232	527.514	8	4.040	6.576
Ba(Fe _{0.3} Nb _{0.7})O ₃	269.715	569.923	1	4.060	6.442
Ba(Fe _{0.3} Re _{0.7})O ₃	306.362	521.680	8	4.026	7.799
Ba(Fe _{0.3} Ta _{0.7})O ₃	303.736	66.726	1	4.056	7.556
Ba(Gd _{0.3} Nb _{0.7})O ₃	310.416	613.258	8	4.248	6.722
Ba(Gd _{0.3} Pa _{0.7})O ₃	379.463	675.449	8	4.387	7.401
Ba(Gd _{0.3} Re _{0.7})O ₃	357.063	599.290	8	4.215	7.912
Ba(Gd _{0.3} Sb _{0.7})O ₃	324.838	601.212	8	4.220	7.175
Ba(Gd _{0.3} Ta _{0.7})O ₃	354.437	613.184	8	4.248	7.676
Ba(Ho _{0.3} Nb _{0.7})O ₃	314.256	599.930	8	4.217	6.956
Ba(Ho _{0.3} Pa _{0.7})O ₃	383.303	605.339	8	4.305	7.051
Ba(Ho _{0.3} Re _{0.7})O ₃	358.277	601.639	8	4.221	7.908
Ba(In _{0.3} Nb _{0.7})O ₃	231.791	587.468	8	4.139	5.425
Ba(In _{0.3} Pa _{0.7})O ₃	280.438	556.223	8	4.112	6.896
Ba(In _{0.3} Re _{0.7})O ₃	300.838	635.189	8	4.298	6.290
Ba(In _{0.3} Sb _{0.7})O ₃	278.438	563.151	8	4.129	6.566
Ba(In _{0.3} Ta _{0.7})O ₃	246.213	565.404	8	4.134	5.783
Ba(La _{0.3} U _{0.7})O ₃	275.812	567.684	8	4.140	6.452
Ba(La _{0.3} U _{0.7})O ₃	304.353	618.470	8	4.260	6.535
Ba(La _{0.3} Nb _{0.7})O ₃	301.246	643.769	8	4.317	6.214
Ba(La _{0.3} Pa _{0.7})O ₃	370.293	701.411	8	4.442	7.011
Ba(La _{0.3} Re _{0.7})O ₃	347.893	631.629	8	4.290	7.314
Ba(La _{0.3} Ta _{0.7})O ₃	345.267	651.958	8	4.336	7.033
Ba(Lu _{0.3} Nb _{0.7})O ₃	319.276	585.116	8	4.182	7.246
Ba(Lu _{0.3} Pa _{0.7})O ₃	388.323	650.813	8	4.333	7.924
Ba(Lu _{0.3} Re _{0.7})O ₃	363.297	586.797	8	4.186	8.222
Ba(Mn _{0.3} Nb _{0.7})O ₃	259.260	68.067	1	4.083	6.323
Ba(Mn _{0.3} Re _{0.7})O ₃	305.907	547.343	8	4.090	7.422
Ba(Mn _{0.3} Ta _{0.7})O ₃	255.283	67.718	1	4.076	6.258
Ba(Nd _{0.3} Nb _{0.7})O ₃	303.911	622.836	8	4.270	6.480
Ba(Nd _{0.3} Pa _{0.7})O ₃	372.958	690.807	8	4.420	7.170
Ba(Nd _{0.3} Re _{0.7})O ₃	350.558	616.295	8	4.255	7.554
Ba(Nd _{0.3} Ta _{0.7})O ₃	347.932	626.343	8	4.278	7.377
Ba(Ni _{0.3} Nb _{0.7})O ₃	261.146	68.921	1	4.100	6.290
Ba(Ni _{0.3} Re _{0.7})O ₃	302.245	77.854	1	4.270	6.444
Ba(Pr _{0.3} Nb _{0.7})O ₃	371.292	695.978	8	4.431	7.085
Ba(Pr _{0.3} Pa _{0.7})O ₃	346.266	77.854	1	4.270	7.383
Ba(Pr _{0.3} Re _{0.7})O ₃	283.244	545.338	8	4.085	6.898
Ba(Rh _{0.3} Nb _{0.7})O ₃	355.806	—	—	—	—

TABLE 9.2 (cont.)

Compound	Formula weight	Volume	Z	α' , Å	Density
$A(B_{0.3}^{2+}B_{0.7}^{4+})O_3$ (cont.)					
Pb(Ni _{0.3} Ta _{0.7})O ₃	395.798	64.481	1	4.010	10.189
Pb(Zr _{0.3} Nb _{0.7})O ₃	339.007	65.939	1	4.040	8.534
Sr(Ca _{0.3} Nb _{0.7})O ₃	211.092	205.726	3	4.093	5.110
Sr(Ca _{0.3} Sb _{0.7})O ₃	230.417	545.338	8	4.085	5.611
Sr(Ca _{0.3} Ta _{0.7})O ₃	270.080	204.170	3	4.083	6.588
Sr(Cd _{0.3} Nb _{0.7})O ₃	234.957	68.368	1	4.089	5.705
Sr(Co _{0.3} Nb _{0.7})O ₃	217.313	513.922	8	4.005	5.615
Sr(Co _{0.3} Pa _{0.7})O ₃	236.639	610.082	8	3.995	6.161
Sr(Co _{0.3} Re _{0.7})O ₃	276.301	190.423	3	3.989	7.226
Sr(Cu _{0.3} Sb _{0.7})O ₃	238.159	503.403	8	3.977	6.283
Sr(Fe _{0.3} Nb _{0.7})O ₃	216.295	64.192	1	4.004	5.593
Sr(Mg _{0.3} Nb _{0.7})O ₃	205.888	193.651	3	4.011	5.295
Sr(Mg _{0.3} Pa _{0.7})O ₃	225.214	504.358	8	3.980	5.930
Sr(Mg _{0.3} Re _{0.7})O ₃	264.876	192.301	3	4.002	6.859
Sr(Mn _{0.3} Nb _{0.7})O ₃	215.995	—	—	—	—
Sr(Mn _{0.3} Pa _{0.7})O ₃	274.983	—	—	—	—
Sr(Mn _{0.3} Re _{0.7})O ₃	217.240	190.081	3	3.987	5.692
Sr(Ni _{0.3} Ta _{0.7})O ₃	276.228	188.489	3	3.975	7.298
Sr(Ph _{0.3} Nb _{0.7})O ₃	266.238	—	—	—	—
Sr(Pb _{0.3} Ta _{0.7})O ₃	325.226	—	—	—	—
Sr(Zr _{0.3} Nb _{0.7})O ₃	219.437	192.818	3	4.006	5.667
Sr(Zr _{0.3} Pa _{0.7})O ₃	278.425	193.119	3	4.008	7.180
$A(B_{0.3}^{2+}B_{0.7}^{4+})O_3$					
Ba(Bi _{0.3} Nb _{0.7})O ₃	336.281	642.736	8	4.315	6.948
Ba(Bi _{0.3} Ta _{0.7})O ₃	380.302	628.982	8	4.284	8.030
Ba(Ce _{0.3} Nb _{0.7})O ₃	301.851	79.119	1	4.293	6.333
Ba(Ce _{0.3} Pa _{0.7})O ₃	370.898	681.472	8	4.400	7.228
Ba(Co _{0.3} Nb _{0.7})O ₃	261.258	68.923	1	4.060	6.480
Ba(Co _{0.3} Re _{0.7})O ₃	307.905	528.690	8	4.043	7.734
Ba(Cr _{0.3} Os _{0.7})O ₃	306.436	—	—	—	—
Ba(Cr _{0.3} Re _{0.7})O ₃	304.436	—	—	—	—
Ba(Cr _{0.3} U _{0.7})O ₃	330.351	—	—	—	—
Ba(Cu _{0.3} W _{0.7})O ₃	309.033	534.633	8	4.058	7.676
Ba(Dy _{0.3} Nb _{0.7})O ₃	313.041	600.571	8	4.218	6.922
Ba(Dy _{0.3} Pa _{0.7})O ₃	382.088	667.628	8	4.370	7.600
Ba(Dy _{0.3} Ta _{0.7})O ₃	357.062	623.930	8	4.272	7.000
Ba(Er _{0.3} Nb _{0.7})O ₃	315.421	598.438	8	4.213	7.711
Ba(Er _{0.3} Pa _{0.7})O ₃	384.468	662.143	8	4.358	7.711
Ba(Er _{0.3} Re _{0.7})O ₃	362.068	583.020	8	4.177	8.247
Ba(Er _{0.3} Ta _{0.7})O ₃	359.442	597.586	8	4.211	7.988
Ba(Er _{0.3} U _{0.7})O ₃	387.983	651.714	8	4.335	7.906

TABLE 9.2 (cont.)

Compound	Formula weight	Volume	Z	$a', \text{\AA}$	Density
$A(B_{0.5}B_{0.5}')O_3$ (cont.)					
Ba($Sc_{0.5}Nb_{0.5}$) O_3	254.269	69.985	1	4.121	6.031
Ba($Sc_{0.5}Os_{0.5}$) O_3	302.916	541.742	8	4.076	7.426
Ba($Sc_{0.5}Pr_{0.5}$) O_3	323.316	624.807	8	4.274	6.872
Ba($Sc_{0.5}Re_{0.5}$) O_3	300.916	543.938	8	4.081	7.347
Ba($Sc_{0.5}Sb_{0.5}$) O_3	268.691	550.763	8	4.098	6.479
Ba($Sc_{0.5}Ta_{0.5}$) O_3	298.290	555.818	8	4.111	7.127
Ba($Sc_{0.5}U_{0.5}$) O_3	326.831	611.960	8	4.245	7.092
Ba($Sm_{0.5}Nb_{0.5}$) O_3	306.966	618.035	8	4.259	6.596
Ba($Sm_{0.5}Pa_{0.5}$) O_3	376.013	679.616	8	4.396	7.347
Ba($Sm_{0.5}Ta_{0.5}$) O_3	350.987	618.262	8	4.259	7.539
Ba($Tb_{0.5}Nb_{0.5}$) O_3	311.253	75.633	1	4.229	6.831
Ba($Tb_{0.5}Pa_{0.5}$) O_3	380.300	670.611	8	4.376	7.631
Ba($Tb_{0.5}Ta_{0.5}$) O_3	377.997	596.948	8	4.210	8.409
Ba($Tm_{0.5}Nb_{0.5}$) O_3	316.258	594.399	8	4.204	7.096
Ba($Tm_{0.5}Pa_{0.5}$) O_3	385.305	656.688	8	4.346	7.792
Ba($Tm_{0.5}Ta_{0.5}$) O_3	360.279	593.975	8	4.203	8.055
Ba($Y_{0.5}Nb_{0.5}$) O_3	276.244	74.088	1	4.200	6.189
Ba($Y_{0.5}Pa_{0.5}$) O_3	345.291	662.599	8	4.359	6.920
Ba($Y_{0.5}Re_{0.5}$) O_3	322.891	586.797	8	4.186	7.307
Ba($Y_{0.5}Ta_{0.5}$) O_3	320.265	599.717	8	4.216	7.092
Ba($Y_{0.5}U_{0.5}$) O_3	348.806	656.235	8	4.345	7.059
Ba($Yb_{0.5}Nb_{0.5}$) O_3	318.311	587.217	8	4.187	7.199
Ba($Yb_{0.5}Pa_{0.5}$) O_3	387.358	653.520	8	4.339	7.871
Ba($Yb_{0.5}Ta_{0.5}$) O_3	362.332	590.590	8	4.195	8.147
Ca($Al_{0.5}Nb_{0.5}$) O_3	148.022	55.161	1	3.807	4.455
Ca($Al_{0.5}Th_{0.5}$) O_3	192.043	55.161	1	3.807	5.779
Ca($Co_{0.5}W_{0.5}$) O_3	209.470	235.054	4	3.888	5.917
Ca($Cr_{0.5}Mo_{0.5}$) O_3	162.046	226.583	4	3.841	4.749
Ca($Cr_{0.5}Nb_{0.5}$) O_3	160.529	57.061	1	3.850	4.670
Ca($Cr_{0.5}Os_{0.5}$) O_3	209.176	225.423	4	3.834	6.161
Ca($Cr_{0.5}Re_{0.5}$) O_3	207.176	226.717	4	3.836	6.095
Ca($Cr_{0.5}Ta_{0.5}$) O_3	204.550	57.062	1	3.850	5.951
Ca($Cr_{0.5}W_{0.5}$) O_3	206.001	225.337	4	3.833	6.070
Ca($Dy_{0.5}Nb_{0.5}$) O_3	215.781	65.392	1	4.029	5.478
Ca($Dy_{0.5}Ta_{0.5}$) O_3	259.802	65.393	1	4.029	6.595
Ca($Er_{0.5}Nb_{0.5}$) O_3	218.161	64.756	1	4.016	5.592
Ca($Er_{0.5}Ta_{0.5}$) O_3	262.182	64.757	1	4.016	6.721
Ca($Fe_{0.5}Mo_{0.5}$) O_3	163.972	231.688	4	3.869	4.699
Ca($Fe_{0.5}Nb_{0.5}$) O_3	162.455	58.703	1	3.886	4.594
Ca($Fe_{0.5}Ta_{0.5}$) O_3	176.877	234.551	4	3.885	5.007
Ca($Fe_{0.5}Sb_{0.5}$) O_3	206.476	58.701	1	3.886	5.839
Ca($Gd_{0.5}Nb_{0.5}$) O_3	213.156	65.540	1	4.032	5.399

TABLE 9.2 (cont.)

Compound	Formula weight	Volume	Z	$a', \text{\AA}$	Density
$A(B_{0.5}B_{0.5}')O_3$ (cont.)					
Ca($Gd_{0.5}Ta_{0.5}$) O_3	257.177	65.541	1	4.032	6.514
Ca($Ho_{0.5}Nb_{0.5}$) O_3	216.996	64.912	1	4.019	5.549
Ca($Ho_{0.5}Ta_{0.5}$) O_3	261.017	65.237	1	4.026	6.842
Ca($In_{0.5}Nb_{0.5}$) O_3	134.531	62.222	1	3.963	3.589
Ca($In_{0.5}Ta_{0.5}$) O_3	178.562	62.381	1	3.986	4.761
Ca($La_{0.5}Nb_{0.5}$) O_3	203.986	67.373	1	4.069	5.028
Ca($La_{0.5}Ta_{0.5}$) O_3	248.007	67.372	1	4.069	6.111
Ca($Mn_{0.5}Ta_{0.5}$) O_3	206.021	58.851	1	3.890	5.811
Ca($Na_{0.5}Nb_{0.5}$) O_3	206.651	66.368	1	4.049	5.169
Ca($Na_{0.5}Ta_{0.5}$) O_3	250.672	66.371	1	4.049	6.270
Ca($Ni_{0.5}W_{0.5}$) O_3	209.358	230.769	4	3.884	8.024
Ca($Pr_{0.5}Nb_{0.5}$) O_3	204.985	66.699	1	4.056	5.102
Ca($Pr_{0.5}Ta_{0.5}$) O_3	249.008	66.701	1	4.056	6.197
Ca($Sc_{0.5}Ta_{0.5}$) O_3	203.656	242.942	4	3.931	5.566
Ca($Sm_{0.5}Nb_{0.5}$) O_3	209.708	65.866	1	4.039	5.285
Ca($Sm_{0.5}Ta_{0.5}$) O_3	253.727	66.205	1	4.045	6.362
Ca($Tb_{0.5}Nb_{0.5}$) O_3	213.993	65.384	1	4.029	5.433
Ca($Tb_{0.5}Ta_{0.5}$) O_3	258.014	65.383	1	4.029	6.551
Ca($Y_{0.5}Nb_{0.5}$) O_3	178.984	65.232	1	4.026	4.555
Ca($Y_{0.5}Ta_{0.5}$) O_3	223.005	65.232	1	4.006	5.675
Ca($Yb_{0.5}Nb_{0.5}$) O_3	221.051	64.281	1	4.006	5.708
Ca($Yb_{0.5}Ta_{0.5}$) O_3	265.072	64.279	1	4.006	6.845
Pb($Fe_{0.5}Nb_{0.5}$) O_3	329.585	64.819	1	4.017	8.440
Pb($Fe_{0.5}Ta_{0.5}$) O_3	373.586	64.529	1	4.011	9.610
Pb($In_{0.5}Nb_{0.5}$) O_3	301.641	69.427	1	4.110	7.212
Pb($Ho_{0.5}Nb_{0.5}$) O_3	384.106	71.057	1	4.142	8.973
Pb($Lu_{0.5}Nb_{0.5}$) O_3	389.126	70.646	1	4.134	9.143
Pb($Lu_{0.5}Ta_{0.5}$) O_3	433.147	70.835	1	4.138	10.161
Pb($Sc_{0.5}Nb_{0.5}$) O_3	324.119	67.901	1	4.080	7.924
Pb($Sc_{0.5}Ta_{0.5}$) O_3	368.140	67.519	1	4.072	9.051
Pb($Yb_{0.5}Nb_{0.5}$) O_3	388.161	71.473	1	4.150	9.015
Pb($Yb_{0.5}Ta_{0.5}$) O_3	432.182	70.445	1	4.130	10.184
Sr($Co_{0.5}Nb_{0.5}$) O_3	211.538	60.698	1	3.930	5.785
Sr($Co_{0.5}Sb_{0.5}$) O_3	225.960	489.304	8	3.940	6.133
Sr($Cr_{0.5}Mo_{0.5}$) O_3	209.586	478.212	8	3.910	5.820
Sr($Cr_{0.5}Nb_{0.5}$) O_3	208.069	61.261	1	3.942	5.638
Sr($Cr_{0.5}Os_{0.5}$) O_3	256.716	481.890	8	3.920	7.075
Sr($Cr_{0.5}Re_{0.5}$) O_3	254.716	478.212	8	3.910	7.074
Sr($Cr_{0.5}Sb_{0.5}$) O_3	222.491	485.958	8	3.931	6.080
Sr($Cr_{0.5}Ta_{0.5}$) O_3	252.090	61.163	1	3.940	6.842
Sr($Cr_{0.5}W_{0.5}$) O_3	253.541	478.212	8	3.910	7.041
Sr($Dy_{0.5}Ta_{0.5}$) O_3	307.342	—	—	—	—

TABLE 9.2 (cont.)

Compound	Formula weight	Volume	Z	α' , Å	Density
$A(B_0^{2+}B_0^{3+})O_3$ (cont.)					
Sr($Er_{0.5}Ta_{0.5}$) O_3	309.722	—	—	—	—
Sr($Eu_{0.5}Ta_{0.5}$) O_3	302.072	—	—	—	—
Sr($Fe_{0.5}Mo_{0.5}$) O_3	211.512	491.169	8	3.945	5.719
Sr($Fe_{0.5}Nb_{0.5}$) O_3	209.995	62.571	1	3.970	5.571
Sr($Fe_{0.5}Sb_{0.5}$) O_3	224.417	496.041	8	3.958	6.008
Sr($Fe_{0.5}Ta_{0.5}$) O_3	254.016	62.428	1	3.967	6.754
Sr($Ga_{0.5}Nb_{0.5}$) O_3	216.931	61.443	1	3.946	5.861
Sr($Ga_{0.5}Os_{0.5}$) O_3	265.578	478.212	8	3.910	7.375
Sr($Ga_{0.5}Ru_{0.5}$) O_3	263.578	482.444	8	3.921	7.255
Sr($Ga_{0.5}Sb_{0.5}$) O_3	231.353	486.193	8	3.932	6.319
Sr($Gd_{0.5}Ta_{0.5}$) O_3	304.717	—	—	—	—
Sr($Hf_{0.5}Nb_{0.5}$) O_3	308.557	—	—	—	—
Sr($In_{0.5}Nb_{0.5}$) O_3	182.071	66.770	1	4.057	4.527
Sr($In_{0.5}Os_{0.5}$) O_3	230.718	523.607	8	4.030	5.852
Sr($In_{0.5}Re_{0.5}$) O_3	228.718	526.753	8	4.036	5.777
Sr($In_{0.5}U_{0.5}$) O_3	254.033	578.009	8	4.165	5.850
Sr($La_{0.5}Ta_{0.5}$) O_3	295.547	565.609	8	4.135	6.939
Sr($Lu_{0.5}Ta_{0.5}$) O_3	313.577	—	—	—	—
Sr($Mn_{0.5}Mo_{0.5}$) O_3	211.057	508.170	8	3.990	5.516
Sr($Mn_{0.5}Sb_{0.5}$) O_3	223.982	—	—	—	—
Sr($Nd_{0.5}Ta_{0.5}$) O_3	298.212	—	—	—	—
Sr($Ni_{0.5}Sb_{0.5}$) O_3	225.848	—	—	—	—
Sr($Rh_{0.5}Sb_{0.5}$) O_3	247.946	255.868	4	3.999	6.434
Sr($Sc_{0.5}Os_{0.5}$) O_3	253.196	515.850	8	4.010	6.518
Sr($Sc_{0.5}Re_{0.5}$) O_3	251.190	515.850	8	4.010	6.467
Sr($Sm_{0.5}Ta_{0.5}$) O_3	301.287	—	—	—	—
Sr($Tm_{0.5}Ta_{0.5}$) O_3	310.559	—	—	—	—
Sr($Yb_{0.5}Ta_{0.5}$) O_3	312.612	—	—	—	—
$A(B_0^{2+}B_0^{3+})O_3$					
Ba($Ba_{0.5}Os_{0.5}$) O_3	349.108	625.463	8	4.276	7.412
Ba($Ba_{0.5}Re_{0.5}$) O_3	347.108	623.271	8	4.271	7.396
Ba($Ba_{0.5}U_{0.5}$) O_3	373.023	702.595	8	4.445	7.051
Ba($Ba_{0.5}W_{0.5}$) O_3	345.933	636.056	8	4.300	7.223
Ba($Ca_{0.5}Mo_{0.5}$) O_3	253.348	583.229	8	4.177	5.769
Ba($Ca_{0.5}Os_{0.5}$) O_3	300.478	584.696	8	4.181	6.825
Ba($Ca_{0.5}Re_{0.5}$) O_3	298.478	583.439	8	4.178	6.794
Ba($Ca_{0.5}Ta_{0.5}$) O_3	269.178	591.223	8	4.196	6.046
Ba($Ca_{0.5}U_{0.5}$) O_3	324.393	651.714	8	4.335	6.610
Ba($Ca_{0.5}W_{0.5}$) O_3	297.303	590.590	8	4.195	6.685
Ba($Cd_{0.5}Os_{0.5}$) O_3	336.638	576.969	8	4.182	7.748
Ba($Cd_{0.5}Re_{0.5}$) O_3	334.638	576.346	8	4.161	7.711

TABLE 9.2 (cont.)

Compound	Formula weight	Volume	Z	α' , Å	Density
$A(B_0^{2+}B_0^{3+})O_3$ (cont.)					
Ba($Cd_{0.5}U_{0.5}$) O_3	360.553	321.487	4	4.316	7.447
Ba($Co_{0.5}Mo_{0.5}$) O_3	262.775	66.081	1	4.043	6.801
Ba($Co_{0.5}Re_{0.5}$) O_3	307.905	528.890	8	4.043	7.734
Ba($Co_{0.5}U_{0.5}$) O_3	333.820	587.217	8	4.187	7.549
Ba($Co_{0.5}W_{0.5}$) O_3	308.730	531.047	8	4.049	7.670
Ba($Cr_{0.5}U_{0.5}$) O_3	330.351	571.167	8	4.148	7.681
Ba($Cr_{0.5}U_{0.5}$) O_3	336.123	591.506	8	4.197	7.546
Ba($Fe_{0.5}Re_{0.5}$) O_3	308.362	521.660	8	4.025	7.799
Ba($Fe_{0.5}U_{0.5}$) O_3	332.277	574.271	8	4.156	7.684
Ba($Fe_{0.5}W_{0.5}$) O_3	305.187	537.963	8	4.066	7.534
Ba($Mg_{0.5}Os_{0.5}$) O_3	292.594	527.514	8	4.040	7.366
Ba($Mg_{0.5}Re_{0.5}$) O_3	290.504	527.006	8	4.041	7.310
Ba($Mg_{0.5}Ta_{0.5}$) O_3	261.294	537.368	8	4.065	6.457
Ba($Mg_{0.5}U_{0.5}$) O_3	316.509	588.091	8	4.190	7.140
Ba($Mg_{0.5}W_{0.5}$) O_3	289.419	531.244	8	4.049	7.235
Ba($Mn_{0.5}Re_{0.5}$) O_3	305.907	547.343	8	4.090	7.422
Ba($Mn_{0.5}U_{0.5}$) O_3	331.822	618.470	8	4.260	7.125
Ba($Ni_{0.5}Mo_{0.5}$) O_3	262.663	65.086	1	4.022	6.699
Ba($Ni_{0.5}Re_{0.5}$) O_3	307.793	519.718	8	4.020	7.865
Ba($Ni_{0.5}U_{0.5}$) O_3	333.708	579.259	8	4.168	7.651
Ba($Ni_{0.5}W_{0.5}$) O_3	306.618	524.777	8	4.033	7.759
Ba($Pb_{0.5}Mo_{0.5}$) O_3	336.903	—	—	—	—
Ba($Sr_{0.5}Os_{0.5}$) O_3	324.248	613.128	8	4.263	6.949
Ba($Sr_{0.5}Re_{0.5}$) O_3	322.248	613.128	8	4.248	6.980
Ba($Sr_{0.5}U_{0.5}$) O_3	348.163	690.807	8	4.420	6.693
Ba($Sr_{0.5}W_{0.5}$) O_3	321.073	614.125	8	4.250	6.943
Ba($Zn_{0.5}Os_{0.5}$) O_3	313.123	530.457	8	4.047	7.839
Ba($Zn_{0.5}Re_{0.5}$) O_3	311.123	532.623	8	4.053	7.757
Ba($Zn_{0.5}U_{0.5}$) O_3	337.038	592.069	8	4.198	7.560
Ba($Zn_{0.5}W_{0.5}$) O_3	309.948	534.596	8	4.058	7.699
Ca($Ca_{0.5}Os_{0.5}$) O_3	293.218	261.552	4	4.029	5.159
Ca($Ca_{0.5}Re_{0.5}$) O_3	201.218	263.819	4	4.040	5.064
Ca($Ca_{0.5}U_{0.5}$) O_3	200.943	512.000	8	4.000	5.189
Ca($Cd_{0.5}Re_{0.5}$) O_3	237.378	260.017	4	4.021	6.062
Ca($Co_{0.5}Os_{0.5}$) O_3	212.945	235.445	4	3.890	5.997
Ca($Co_{0.5}Re_{0.5}$) O_3	210.645	234.899	4	3.887	5.954
Ca($Fe_{0.5}Re_{0.5}$) O_3	209.102	230.064	4	3.860	6.035
Ca($Mg_{0.5}Re_{0.5}$) O_3	193.334	236.743	4	3.897	5.423
Ca($Mg_{0.5}W_{0.5}$) O_3	192.159	466.533	8	3.850	5.590
Ca($Mn_{0.5}Re_{0.5}$) O_3	208.647	239.574	4	3.913	5.783
Ca($Ni_{0.5}Re_{0.5}$) O_3	210.533	231.998	4	3.871	6.026
Ca($Sr_{0.5}W_{0.5}$) O_3	223.813	531.441	8	4.050	5.593

TABLE 9.2 (cont.)

Compound	Formula weight	Volume	Z	a' , Å	Density
$A(B_{0.5}^{2+}B_{0.5}^{4+})O_3$ (cont.)					
Pb(Ca _{0.5} W _{0.5})O ₃	367.153	—	1	4.133	—
Pb(Cd _{0.5} W _{0.5})O ₃	403.313	70.620	1	—	9.480
Pb(Co _{0.5} W _{0.5})O ₃	376.580	—	8	3.995	8.621
Pb(Mg _{0.5} Te _{0.5})O ₃	331.144	510.082	1	4.000	9.319
Pb(Mg _{0.5} W _{0.5})O ₃	369.269	64.000	—	—	—
Sr(Ca _{0.5} Mo _{0.5})O ₃	203.628	—	8	4.105	6.018
Sr(Ca _{0.5} Os _{0.5})O ₃	260.758	553.388	4	4.105	5.971
Sr(Ca _{0.5} Re _{0.5})O ₃	248.758	276.644	4	4.236	5.999
Sr(Ca _{0.5} U _{0.5})O ₃	274.673	304.017	8	4.100	5.963
Sr(Cd _{0.5} W _{0.5})O ₃	247.583	551.368	4	4.080	6.964
Sr(Cd _{0.5} U _{0.5})O ₃	284.9182	271.657	4	4.217	6.878
Sr(Co _{0.5} Mo _{0.5})O ₃	310.833	300.066	1	3.950	5.739
Sr(Co _{0.5} Os _{0.5})O ₃	213.055	81.025	8	3.940	7.039
Sr(Co _{0.5} Re _{0.5})O ₃	260.185	489.294	8	3.950	6.987
Sr(Co _{0.5} U _{0.5})O ₃	268.185	495.513	8	3.925	7.100
Sr(Cr _{0.5} U _{0.5})O ₃	284.100	549.353	8	4.055	6.992
Sr(Cu _{0.5} W _{0.5})O ₃	257.010	496.772	8	3.980	7.035
Sr(Cr _{0.5} U _{0.5})O ₃	280.631	529.475	8	3.940	6.727
Sr(Cu _{0.5} W _{0.5})O ₃	259.313	492.875	8	3.950	—
Sr(Fe _{0.5} Os _{0.5})O ₃	258.842	483.737	8	3.925	6.592
Sr(Fe _{0.5} Re _{0.5})O ₃	258.642	487.441	8	3.935	6.488
Sr(Fe _{0.5} U _{0.5})O ₃	282.557	533.412	8	4.055	5.613
Sr(Fe _{0.5} W _{0.5})O ₃	255.467	504.358	8	3.980	6.449
Sr(Mg _{0.5} Mo _{0.5})O ₃	195.744	—	—	—	6.450
Sr(Mg _{0.5} Os _{0.5})O ₃	242.874	489.294	8	3.940	6.620
Sr(Mg _{0.5} Re _{0.5})O ₃	240.874	493.030	8	3.950	6.800
Sr(Mg _{0.5} Te _{0.5})O ₃	211.574	500.566	8	3.970	6.590
Sr(Mg _{0.5} U _{0.5})O ₃	266.789	549.353	8	4.095	6.817
Sr(Mn _{0.5} Re _{0.5})O ₃	239.999	493.039	8	3.950	7.022
Sr(Mn _{0.5} U _{0.5})O ₃	266.187	513.922	8	4.005	6.967
Sr(Mn _{0.5} W _{0.5})O ₃	282.102	567.664	8	4.140	6.981
Sr(Ni _{0.5} Os _{0.5})O ₃	255.012	513.922	8	4.005	—
Sr(Ni _{0.5} Mo _{0.5})O ₃	212.943	60.772	1	3.932	6.486
Sr(Ni _{0.5} Re _{0.5})O ₃	268.073	488.050	8	3.937	6.294
Sr(Ni _{0.5} U _{0.5})O ₃	283.988	541.343	8	4.075	6.128
Sr(Ni _{0.5} W _{0.5})O ₃	266.898	488.677	8	3.938	6.536
Sr(Pb _{0.5} Mo _{0.5})O ₃	287.183	—	—	—	6.962
Sr(Sr _{0.5} Os _{0.5})O ₃	274.528	562.086	8	4.126	—
Sr(Sr _{0.5} Re _{0.5})O ₃	272.528	575.019	8	4.158	6.486
Sr(Sr _{0.5} U _{0.5})O ₃	298.443	323.356	4	4.324	6.294
Sr(Sr _{0.5} W _{0.5})O ₃	271.353	551.368	8	4.100	6.128
Sr(Zn _{0.5} Re _{0.5})O ₃	261.403	498.639	8	3.965	6.536

TABLE 9.2 (cont.)

Compound	Formula weight	Volume	Z	a' , Å	Density
$A(B_{0.5}^{2+}B_{0.5}^{4+})O_3$ (cont.)					
Sr(Zn _{0.5} W _{0.5})O ₃	260.228	502.438	8	3.975	6.878
$A(B_{0.5}^{2+}B_{0.5}^{4+})O_3$					
Ba(Ag _{0.5} Ir _{0.5})O ₃	302.725	605.496	8	4.230	6.840
Ba(Li _{0.5} Os _{0.5})O ₃	283.908	531.441	8	4.050	7.094
Ba(Li _{0.5} Re _{0.5})O ₃	281.908	534.992	8	4.059	6.998
Ba(Na _{0.5} Ir _{0.5})O ₃	260.285	578.010	8	4.165	5.980
Ba(Na _{0.5} Os _{0.5})O ₃	291.933	567.869	8	4.140	6.827
Ba(Na _{0.5} Re _{0.5})O ₃	289.933	570.961	8	4.148	6.744
Ca(Li _{0.5} Os _{0.5})O ₃	186.648	480.049	8	3.915	5.163
Ca(Li _{0.5} Re _{0.5})O ₃	184.648	480.049	8	3.915	5.108
Sr(Li _{0.5} Os _{0.5})O ₃	234.188	485.588	8	3.930	6.405
Sr(Li _{0.5} Re _{0.5})O ₃	232.188	487.443	8	3.935	6.326
Sr(Na _{0.5} Os _{0.5})O ₃	242.213	537.368	8	4.065	5.986
Sr(Na _{0.5} Re _{0.5})O ₃	240.213	537.368	8	4.065	5.936
$A^{2+}(B_{0.5}^{2+}B_{0.5}^{4+})O_3$					
La(Co _{0.5} Ir _{0.5})O ₃	216.375	—	—	—	—
La(Cu _{0.5} Ir _{0.5})O ₃	218.678	—	—	—	—
La(Mg _{0.5} Ir _{0.5})O ₃	235.359	59.319	1	3.900	6.586
La(Mg _{0.5} Te _{0.5})O ₃	199.064	496.793	8	3.960	5.321
La(Mg _{0.5} Ti _{0.5})O ₃	245.517	—	—	—	—
La(Mg _{0.5} U _{0.5})O ₃	249.599	494.914	8	3.955	6.697
La(Mn _{0.5} Ti _{0.5})O ₃	223.014	60.791	1	3.932	6.090
La(Mn _{0.5} U _{0.5})O ₃	214.377	485.588	8	3.930	5.863
La(Ni _{0.5} Ir _{0.5})O ₃	264.912	481.890	8	3.920	7.300
La(Ni _{0.5} Re _{0.5})O ₃	216.263	493.039	8	3.950	5.825
La(Ni _{0.5} Ti _{0.5})O ₃	266.798	493.039	8	3.950	7.186
La(Zn _{0.5} U _{0.5})O ₃	240.213	60.698	1	3.930	6.569
La(Zn _{0.5} U _{0.5})O ₃	270.128	506.262	8	3.885	7.086
Nd(Mg _{0.5} Ti _{0.5})O ₃	228.344	59.319	1	3.900	6.390
$A(B_{0.5}^{2+}B_{0.5}^{4+})O_3$					
Ba(Na _{0.5} Te _{0.5})O ₃	326.797	70.804	1	4.137	7.662
Sr(Na _{0.5} Te _{0.5})O ₃	277.077	66.676	1	4.055	6.898
$A(B_{0.5}^{2+}B_{0.5}^{4+})O_{3.75}$					
Ba(In _{0.5} U _{0.5})O _{3.75}	300.353	625.246	8	4.275	6.379
$A(B_{0.5}^{2+}B_{0.5}^{4+})O_{2.75}$					
Ba(Ba _{0.5} Te _{0.5})O _{2.75}	340.482	656.235	8	4.345	6.890
Ba(Fe _{0.5} Mo _{0.5})O _{2.75}	267.232	527.514	8	4.040	6.476
Sr(Sr _{0.5} Te _{0.5})O _{2.75}	265.902	580.094	8	4.170	6.087

There also is a small amount of mechanical property data available on perovskite solid solutions of the PZT type, $\text{Pb}(\text{Zr}_{1-x}\text{Ti}_x)\text{O}_3$.⁽³⁾ The interest in these materials as piezoelectrics was discussed in Chapter 5. Tensile strength measurements on hot-pressed specimens of $\text{Pb}(\text{Zr}_{0.43}\text{Ti}_{0.57})\text{O}_3$, $\text{Pb}(\text{Zr}_{0.73}\text{Ti}_{0.27})\text{O}_3$ and $\text{Pb}(\text{Zr}_{0.33}\text{Ti}_{0.67})\text{O}_3$ containing 1 wt% Nb_2O_5 balanced with PbO gave values of 9700, 11,150, 12,550 and 14,600 psi respectively. The nominal grain size of these particles was 3 microns and the densities of the specimens were at least 95% theoretical. The moduli of the hot-pressed specimens of $\text{Pb}(\text{Zr}_{0.55}\text{Ti}_{0.45})\text{O}_3$, $\text{Pb}(\text{Zr}_{0.75}\text{Ti}_{0.25})\text{O}_3$ and $\text{Pb}(\text{Zr}_{0.55}\text{Ti}_{0.45})\text{O}_3$ were found to be 14×10^6 psi for the former two phases and 16×10^6 for the latter phase.

REFERENCES

1. W. R. EPPERLY *et al.*, *Semiannual Report* No. 7 (1 Jan. 1965-30 June 1965).
2. P. G. DICKENS and M. S. WHITTINGHAM, *Trans. Faraday Soc.* 61, 1226 (1967).
3. G. PARRAVANO, *J. Chem. Phys.* 20, 342 (1952).
4. J. R. TINKLEPAUGH, presented at the 12th Sygamore Army Mat. Res. Conf. (24-27 Aug. 1965).
5. R. H. DUNGAN, Development Report SC-DR-66-593, Sandia Corp. (Nov. 1966).

CHAPTER 10

PREPARATION OF PEROVSKITE-TYPE OXIDES

10.1. POWDERS

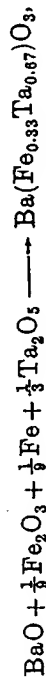
Many of the perovskite-type oxides can be prepared by a high-temperature solid-state reaction between binary oxide powders which are stable in air. However, it is often advantageous to use carbonates, nitrates, etc., instead of the oxides, if they can be obtained in smaller particle sizes to insure quicker reactions or if they are much purer. In a typical preparation of barium titanate powder, barium carbonate and titanium oxide are weighed out in equal molar quantities, mixed thoroughly and fired at 1000°C for 24 hr in zirconium silicate boats or in platinum crucibles. However, the material often will react with the platinum or impurities in the boats as evidenced by coloration of the sample. Therefore, if extremely pure material is desired it is advantageous to fire the mixture on top of a barium titanate compact. In addition, since the oxides often can not be entirely reacted by a single firing, repeated regrinding and reheating is required.

Some of the perovskite-type compounds can only be prepared using special techniques. These are discussed below. Compounds containing lead in the A position of the perovskite structure are often difficult to prepare because of the volatility of lead oxide. Sometimes this problem can be alleviated by heating the reactants in a lead oxide atmosphere, or by using an excess of lead oxide in the reaction mixture, or by heating the reactants at a relatively low temperature to allow them to combine before the final firing. When lead is the A ion and pentavalent ions are used as the B ions,

compounds with the pyrochlore structure very often are formed early in the reaction sequence and are difficult to react further even with repeated mixing and reheating of the product.

Fresia *et al.*⁽¹⁾ found that in the preparation of compounds with the general formula $A(B_{0.5}^{2+}W_{0.5}^{6+})O_3$, where $A = \text{Sr, Ba, } B^{2+} = \text{Fe, Co, Ni and Zn, alkaline earth tungstates always could be detected in the final products. Similar results have been observed for molybdenum compounds. Regrinding and refiring of the samples often helps to reduce the amount of tungstate or molybdate present, but each compound has to be treated as a separate case for which the best firing temperature and firing time must be determined.$

In preparing perovskite-type compounds containing divalent iron and cobalt, the valence state is retained by heating the sample in an evacuated sealed silica capsule or in a non-oxidizing atmosphere. Divalent Fe or Cr ions can be obtained in a compound by mixing equal amounts of metallic Fe and Fe_2O_3 or Cr and Cr_2O_3 , respectively, with the other oxide constituents. For example, Galasso *et al.*⁽²⁾ prepared $\text{Ba}(\text{Fe}_{0.33}^{2+}\text{Ta}_{0.67})\text{O}_3$ by mixing the reactants according to the equation:



compacting the sample and firing it at 1000°C for 24 hr in an evacuated sealed silica capsule.

Sleight and Ward⁽³⁾ in forming compounds of the $\text{A}(\text{B}_{0.5}^{2+}\text{U}_{0.5}^{6+})\text{O}_3$ type found it advantageous to use $\text{UO}_2(\text{NO}_3)_2 \cdot 6\text{H}_2\text{O}$ as a source of hexavalent uranium. Compounds containing pentavalent uranium were prepared by heating UO_2 and UO_3 in equal proportions with the other oxide reactants. The UO_3 was obtained by heating $\text{UO}_2(\text{NO}_3)_2 \cdot 6\text{H}_2\text{O}$ at 400°C in air and the UO_2 was prepared by heating UO_3 at 1000°C in hydrogen.

Sleight *et al.*⁽⁴⁾ also produced other complex perovskite compounds such as $\text{Sr}(\text{Na}_{0.5}\text{Re}_{0.5})\text{O}_3$ and $\text{Sr}(\text{Na}_{0.5}\text{Os}_{0.5})\text{O}_3$ which contained heptavalent rhenium and osmium by heating the metal with sodium carbonate and strontium oxide in air. A similar procedure was used to prepare compounds with hexavalent osmium as one of the B ions. The reaction

is given as:

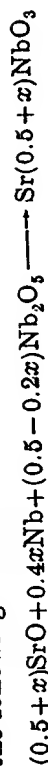


where $A = \text{Sr or Ca}$, and $B = \text{a divalent metal ion}$.

A mixture of $(\text{ReO}_3 + \text{Re})$ was used in the preparation of compounds containing pentavalent rhenium with other trivalent ions in the B position.

Patterson *et al.*⁽⁵⁾ found that they could prepare $\text{A}(\text{B}_{0.5}^{2+}\text{W}_{0.5}^{6+})\text{O}_3$ and $\text{A}(\text{B}_{0.5}\text{Mo}_{0.5})\text{O}_3$ type compounds by using a mixture of the metal trioxides and the metals to obtain pentavalent tungsten and pentavalent molybdenum respectively.

Ridgley and Ward⁽⁶⁾ prepared the strontium-niobium bronzes which contained some niobium ions in the tetraavalent state. These phases adopted the perovskite structure when x varied between 0.7 and 0.95 in Sr_xNbO_3 . Two procedures were used to prepare these bronzes. The first involved the following reaction:



where Nb metal was used to reduce part of the pentavalent niobium and the second required that NbO_2 be formed first and reacted with SrO and Nb_2O_5 . The NbO_2 was prepared by reducing Nb_2O_5 with hydrogen at 1200°C for 36 hr.

Other methods for producing compounds containing elements in unusual oxidation states have been reported by McCarroll *et al.*⁽⁷⁾ Randall and Ward⁽⁸⁾ and Kestigian *et al.*⁽⁹⁾ McCarroll *et al.* prepared CaMoO_3 using a mixture of molybdenum metal and MoO_3 as a source of tetravalent molybdenum, Randall and Ward prepared SrRuO_3 by heating strontium oxide and ruthenium metal in air, and Kestigian *et al.* prepared LaVO_3 by mixing and heating La_2O_3 and V_2O_5 together in vacuum. The V_2O_5 was obtained by heating vanadium pentoxide in hydrogen at 800° for 14 hr.

Many of the ions in binary oxides which are unstable become stabilized in the perovskite structure. For example, $\text{BaFe}^{4+}\text{O}_3$ can be prepared although heating Fe_2O_3 in oxygen will not produce Fe^{4+} . As another example, the addition of a rare earth oxide or Y_2O_3 to barium titanate produces some Ti^{3+} when the mixture is heated to 1000°C in air. This material is extremely stable, even though heating Ti_2O_3 in air

would result in the formation of TiO_2 . This factor is used to advantage in the preparation of many of the perovskite type compounds.

The preparation of the magnetic perovskites BiMnO_3 and BiCrO_3 created an interesting new area of research on perovskite type compounds.⁽¹⁰⁾ These compounds were formed by heating the oxides at 700°C under a pressure of 40 kbar, and then quenching them. In both cases, they formed compounds which had distorted perovskite structures with triclinic unit cells.

10.2. THIN FILMS

The need for special elements in microcircuitry has caused considerable interest in the formation of thin films of dielectric materials. The perovskite-type compounds which have high dielectric constants are most attractive for this purpose. However, the problems of forming binary oxides in thin film form have not been entirely solved, thus, researchers have been reluctant to attempt the preparation of thin films of more complicated materials. Of the studies which have been conducted on perovskites, most of them have been on BaTiO_3 films. Films $7.5\ \mu$ thick have been formed by a special slip method⁽¹¹⁾ but thinner films could not be prepared. In addition, thin single crystal films have been prepared by first growing crystals from solution⁽¹²⁾ and then etching in hot phosphoric acid.⁽¹³⁻¹⁴⁾ Films also have been obtained by spreading small amounts of molten BaTiO_3 on a platinum sheet.⁽¹⁵⁾

In 1955 Feldman prepared ferroelectric films of BaTiO_3 approximately 1 to $2\ \mu$ thick by vapor deposition.⁽¹⁶⁾ In this process, the BaTiO_3 powder was mixed with alcohol, placed on a tungsten-wire filament and vacuum evaporated onto a platinum substrate. The BaO evaporated first and the TiO_2 later, but after firing the film at 1000 – 1100°C the barium titanate was again formed. X-ray diffraction studies indicated that the films consisted of mainly BaTiO_3 with traces of BaO_2 and TiO_2 and with minor amounts of BaTi_2O_6 , BaTi_3O_9 , and Ba_2TiO_4 . The samples were prepared for property measurements by placing a gold dot on the surface to act as an elec-

trode. The films were found to be ferroelectric and had dielectric constants as high as 270. This, of course, is one of the simpler techniques of forming barium titanate films, but is not satisfactory for obtaining pure materials.

Using a more elaborate method, Green⁽¹⁷⁾ deposited alternating layers of BaO and TiO_2 by successive evaporation from several tungsten coils and then heating the films in air at 1150°C . Frankl *et al.*⁽¹⁸⁾ used two electron beams to evaporate TiO_2 and BaO and Moll⁽¹⁹⁾ evaporated barium titanate in an electric field to obtain single-crystal titanate films; however, Roder's studies⁽²⁰⁾ left some doubt as to the reliability of Moll's process.

The best technique for producing thin films of barium titanate was used by Muller *et al.*⁽²¹⁾ who prepared thin films with thicknesses of the order of $1\ \mu$ by vacuum evaporating grain by grain of powder. In addition, solid solutions of BaTiO_3 with SrTiO_3 and BaSnO_3 were prepared in thin film form by the same technique. The samples were formed into pellets crushed and sieved to form grains of 100/200-mesh size. The grains then were delivered by a V-shaped niobium trough and were moved by taps from a gear wheel transmitted through a rod (see Fig. 10.1). The grains were dropped onto an iridium boat where a liquid pool of the material was maintained and from which the material was evaporated onto a substrate held at approximately 500°C . The boat temperature was held 2300°C for the BaTiO_3 evaporation, slightly lower for those containing some BaSnO_3 . When the substrate was held at room temperature, amorphous films were formed, but using a substrate temperature of 500°C resulted in the formation of crystalline films. The crystalline films of BaTiO_3 were found to have a dielectric constant of 400 to 700. Substitution of strontium or tin into the barium titanate before evaporation resulted in films with lower dielectric constants, 250–300 for $\text{Ba}(\text{Ti}_{0.9}\text{Sn}_{0.1})\text{O}_3$ and 200–400 for $\text{Sr}_{0.73}\text{Ba}_{0.27}\text{TiO}_3$. The dissipation factor at 1 kc/s for $0.2\ \mu$ films was larger for crystalline films of barium titanate than for the amorphous films and the breakdown strength of the amorphous films exceeded $1.5 \times 10^6\ \text{V/cm}$ while that of the crystalline films was 2 to 3 times lower. However, the dielectric constant of the amorphous films was only from 13–20.

It should be noted that the films also were prepared using a flash evaporation technique where the grain is evaporated from the boat before the next one arrives, but the technique of using a molten pool was preferred by Müller because it reduced contamination from the boat and permitted the use of lower heating temperatures.

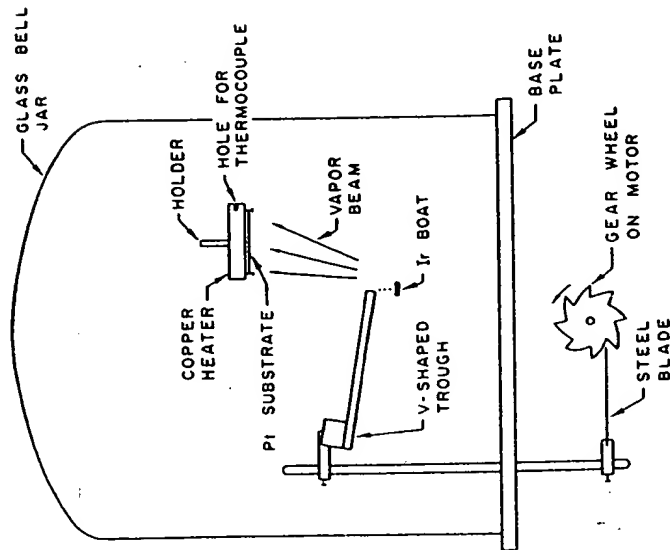


FIG. 10.1. Diagrammatic view of evaporation system (after Müller *et al.* (31)).

Müller *et al.* also deposited thin films of SrTiO_3 , CaTiO_3 , BaSnO_3 , SrSnO_3 , BaCeO_3 and NaNbO_3 using the grain by grain evaporation technique. (22) A cleaved LiF substrate was rigidly fastened to a copper block and heated to 700°C . The results of these experiments indicate that the technique may be feasible for producing single crystals of these materials.

Attempts also have been made to produce thin films of PbTiO_3 with tolerances of $\pm 0.1 \mu$ by generating a plasma of

the bulk material in a vacuum chamber and forming the thin films on a low temperature substrate. (23) Thin films have been formed with capacitances of the order $50 \mu\text{F}/\text{in}^2$ indicating a dielectric constant of over 100. The breakdown voltage of the thinnest films has been found to be 10 volts.

10.3. SINGLE CRYSTALS

Of the large number of compounds with the perovskite structure, those with ferroelectric and magnetic properties and those with potential application as laser host materials have received the most attention from single-crystal researchers.

KNbO_3

Single crystals of potassium niobate, KNbO_3 and BaTiO_3 have been studied most extensively. Matthias and Remeika (24)

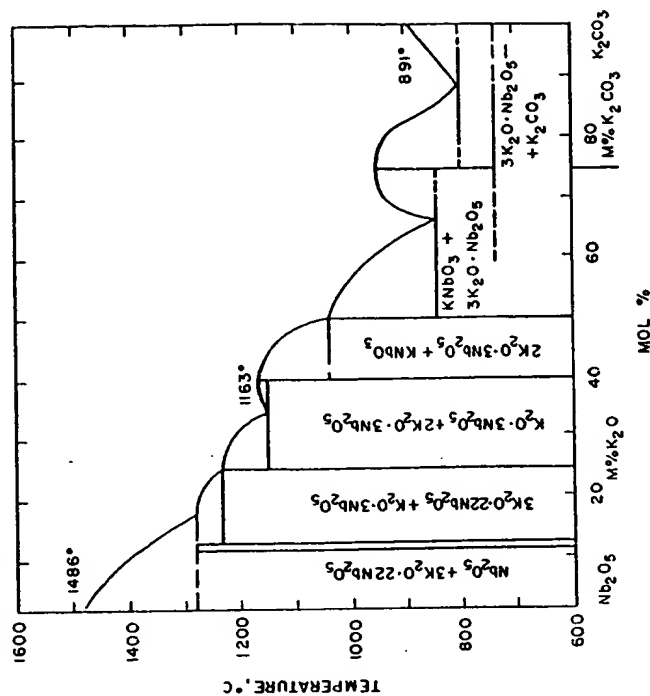


FIG. 10.2. Phase diagram of the $\text{K}_2\text{CO}_3\text{-Nb}_2\text{O}_5$ system (after A. Reisman and F. Holtzberg, *J. Am. Chem. Soc.* 77, 2117 (1955)).

have reported the growth of KNbO_3 single crystals using KCl or KF as a flux. In later studies, Shirane *et al.*⁽²⁵⁾ and Triebwasser⁽²⁶⁾ also grew KNbO_3 from a flux. The phase diagram is shown in Fig. 10.2. Pulvari⁽²⁷⁾ evaluated the methods of these previous workers and tried additional fluxes and flux combinations to obtain pure crystals. The fluxes used were K_2CO_3 , KCl , NaCl , KF , CaCl_2 , KBO_2 , K_2SiO_3 with K_2CO_3 being selected as the most satisfactory one for growing ferroelectric crystals. The purest crystals were grown with 5–10% excess of K_2CO_3 and a soak time in the 1080–1100°C temperature range before slowly cooling the melt. Repeated recrystallization resulted in clearer and less colored crystals. The problem with the flux technique in general is that the crucible is often attacked and the crucible material and solvent enters in the growth process.

NaNbO_3

Sodium niobate, NaNbO_3 , crystals have been grown from a mixture of sodium carbonate and niobium pentoxide in a sodium fluoride flux.⁽²⁸⁾ In this process, the mixture is preheated to 1000°C, soaked for 2 hr at 1350°C and then cooled at 5°/hr. The crystals prepared in this manner grew in the form of small cubes.

NaTaO_3

Kay⁽²⁹⁾ gives the following method for growing single crystals of sodium tantalate, NaTaO_3 . A mixture of Na_2CO_3 , $\text{Na}_2\text{B}_4\text{O}_7$, and Ta_2O_5 in the proportions 7:1:4 is heated at 1200°C for 12 hr and then cooled over a period of 6 hr resulting in crystals whose dimensions are $1 \times 2 \times 2$ mm.

KTaO_3

Potassium tantalate, KTaO_3 , crystals have been prepared using a KF flux.⁽³⁰⁾ In a typical run, a mixture with a flux to sample ratio of 5:1 mole % is melted in a platinum crucible, soaked at $> 1300^\circ\text{C}$ for 4 hr, cooled at $30^\circ/\text{hr}$ to 900°C , and then cooled more quickly to room temperature. The dark blue-black crystals produced are leached from the flux with water and are then used as seeds to pull clear KTaO_3 crystals from a melt. These blue crystals are not adequate for ferroelectric applications since they are highly conducting.

In the process used by Wemple⁽³⁰⁾ to pull crystals of KTaO_3 , a typical charge of 70 g of Ta_2O_5 , 42.10 g of K_2CO_3 , 24 mg of MnO_2 and 12 mg SnO_2 are mixed, placed in a 100-ml platinum crucible, and set into a vertical furnace. An oxygen atmosphere is maintained in the furnace (see phase diagram, Fig. 10.3). The mixture is slowly heated to a temperature

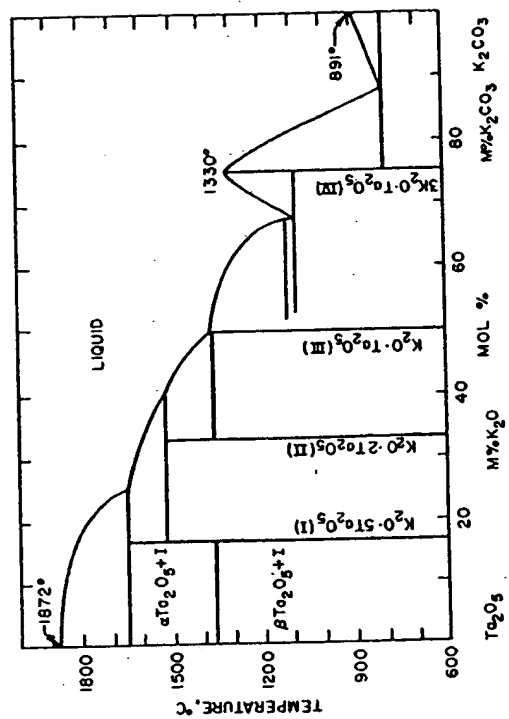


FIG. 10.3. Phase diagram of the K_2CO_3 - Ta_2O_5 system (after A. Reisman, F. Holtzberg, M. Berkenblit and M. Berry, *J. Am. Chem. Soc.* 78, 4514 (1956)).

10 – 20°C above the liquidus over a 12–15-hr period and soaked for 4–6-hr. The KTaO_3 seed then is lowered to within 0.5 cm from the melt surface, the temperature of the melt is raised 5°C above the liquidus temperature, T_L , and slowly cooled at the rate of $3.5^\circ\text{C}/\text{hr}$. When the melt passed through a temperature 2 – 3°C above T_L , the seed is lowered to touch the melt and lifted 1 – 2 mm, pulling a small meniscus. The seed drive motor then is set to rotate at 60 rev/min with reversal every 30 sec. During the growth period the cooling rate is maintained at $3.5^\circ/\text{hr}$ and at various times the seed is lifted 1 – 2 mm. When the crystal is at the desired size, it is lifted above the melt surface but still kept in the furnace, and the cooling rate is changed to 25 – $30^\circ\text{C}/\text{hr}$ until room tem-

perature is attained. The color of the crystals grown in this manner changed from a bright green to colorless at room temperature and the crystals weighed from 4-10 g.

KTN

A similar procedure was used by Wemple⁽³⁰⁾ and Bonner *et al.*⁽³¹⁾ to grow crystals of KTN, $K(Ta_{0.35}Nb_{0.37})O_3$, which exhibit a large room-temperature electro-optic effect, low electrical losses and a large saturation polarization. A mixture of K_2CO_3 , Ta_2O_5 , Nb_2O_5 and SnO_2 in appropriate proportions to obtain a composition $K_{1+x}(Ta_{0.29}Nb_{0.71})O_3Sn_{0.001}$, where x depends on volatilization losses, were placed in a platinum crucible and set in a vertical tube furnace. The composition was selected from the phase diagram so that crystals of $K(Ta_{0.35}Nb_{0.37})O_3$ would be pulled from the melt (see Fig. 10.4). The crucible was placed on a pedestal which was rotated

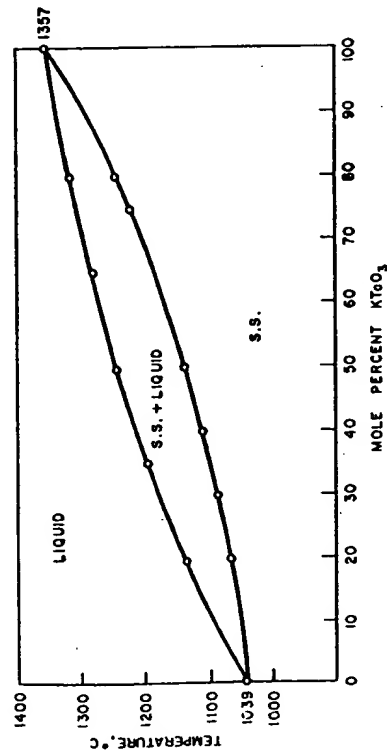


FIG. 10.4. Phase diagram of the $KNbO_3$ - $KTaO_3$ system (after A. Reisman, S. Triebwasser and F. Holtzberg, *J. Am. Chem. Soc.* 77, 4228 (1955)).

ed at 60 rev/min with reversals every 30 sec. The top of the muffle which contained the crucible was closed by a split ring with a hole to accommodate the rod that held the seed. The furnace was held at approximately 1225°C, oxygen flow was maintained up through the muffle, and the bottom of the crucible was kept 50°C warmer than the top of the melt. The melt was then cooled 0.1°C/hr while the seed was rotated

ed at the surface. The seed was allowed to grow laterally from 2 to 3 days, and then the growing crystal was lifted at $\frac{1}{4}$ in. per day until it was cool enough to remove from the furnace. It is difficult in this process to produce a crystal with a uniform composition throughout.

$BaTiO_3$

Because of its ferroelectric properties, $BaTiO_3$ single crystals have been studied extensively. Crystals of $BaTiO_3$ have been grown from fluxes, by the Czochralski technique, the Verneuil technique and also using zone melting methods.

Some of the fluxes used to grow $BaTiO_3$ include $BaCl_2$,⁽³²⁾ KF ,⁽³³⁾ and BaF_2 .⁽³⁴⁾ Linars obtained small blue butterfly twins (shaped like butterfly wings) and cubes using BaF_2 as a flux.

Potassium fluoride is a more popular flux than the above-mentioned fluxes for growing $BaTiO_3$ single crystals. In this technique, a mixture of 10 mole % $BaTiO_3$ and 90 mole % KF is soaked at temperatures of 980 to 1200°C for 4 hr followed by cooling rates of 10°C/hr, resulting in butterfly crystals being formed. DeVries⁽³⁵⁾ conducted detailed studies on these butterfly twin crystals and concluded that they were probably formed when (111) twinning of the (100) habit takes place.

Single crystals of $BaTiO_3$ also have been grown by pulling from a BaO - TiO_2 melt by von Hippel *et al.* The phase diagram is shown in Fig. 10.5. A detailed schematic of the crystal growth furnace is shown in Fig. 10.6. The mixture used was made up of 67 mole % TiO_2 and 33 mole % BaO . The mixture was soaked at 1420°C, the temperature was lowered to 1396° and the seed then was immersed about 1 mm below the surface with air flowing through the seed rod. After 30 min the melt was cooled 5°C/hr for 1 hr. The crystal then was pulled at 0.25 mm/hr and the melt was cooled at 2 to 3°C/hr. The seed was rotated at 60 rev/min and reversed at 30-sec intervals. Then, the crystal was removed from the melt at 1335°C and annealed to room temperature. Single crystals of $BaTiO_3$ up to 2 cm diameter by 1 cm long have been grown by this method.

Attempts also were made by von Hippel *et al.*⁽³⁰⁾ to grow single crystals of BaTiO_3 by the flame-fusion technique. For this technique powders with small particle size but with good flow characteristics are necessary. In order to produce the powder, a solution of titanium tetrachloride, prepared by dripping 1.50 moles of TiCl_4 into 500 ml of water below 20°C , was added to a solution of oxalic acid, 5 moles $(\text{COOH})_2$ in 1320 ml of water and held at 20°C . A solution of barium chloride at 70°C , 1.60 moles $\text{BaCl}_2 \cdot 2\text{H}_2\text{O}$ dissolved in 900 ml

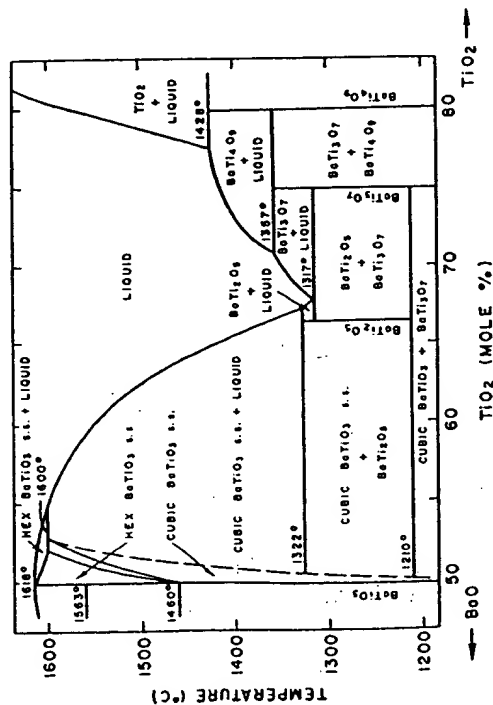


Fig. 10.5. Phase diagram of the BaO-TiO₂ system (after D. E. Rase and R. Roy, *J. Am. Ceram. Soc.* 38, 110 (1955)).

H₂O, was added to the mixture with rapid stirring. After 5 hr of stirring, barium titanyl oxalate was filtered, washed and ignited for 2 hr at 1000°C. Powder was passed through a sieve, and was used in the flame-fusion apparatus (see Fig. 10.7). Small crystals of BaTiO₃ were obtained, but they were not of optical quality.

Brown and Toat⁽⁸⁾ found that they could grow single crystals 2.5 cm long by 0.32 cm diameter of BaTiO_3 which contain 1.5%, SrTiO_3 by a floating zone process. The heating source was a ring burner closely surrounding the molten zone.

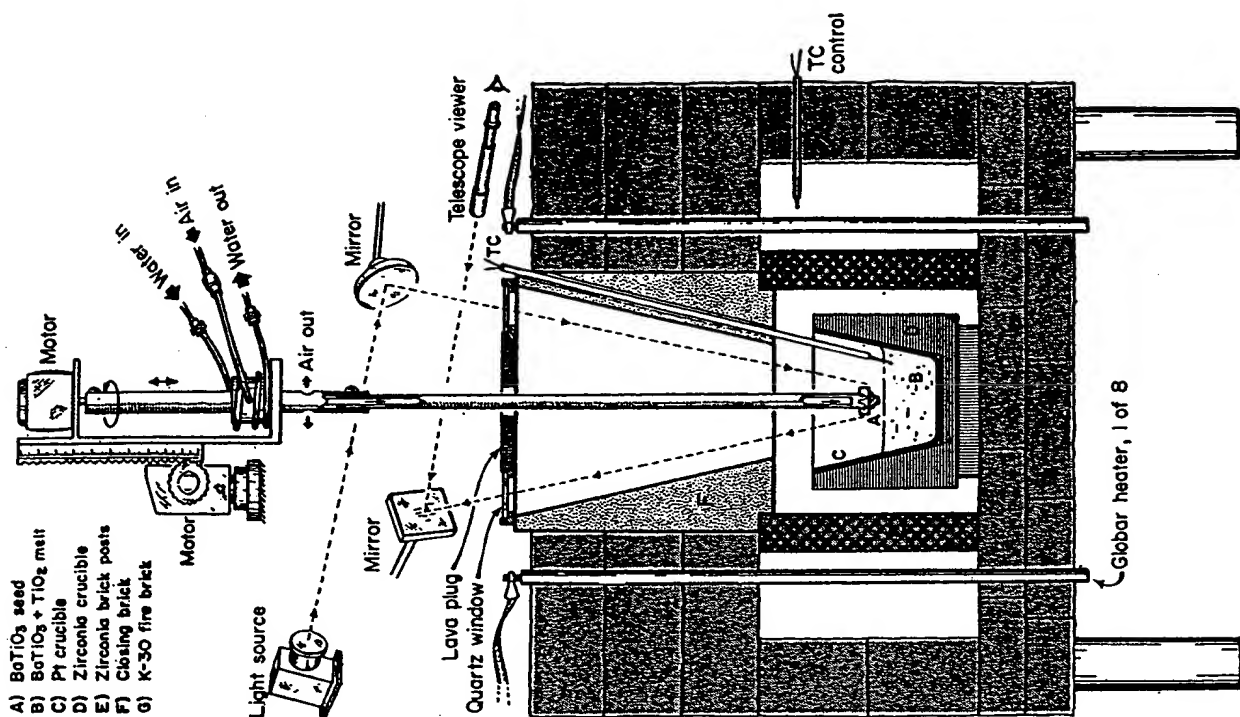


FIG. 10.6. Crystal-pulling furnace (after von Hippel *et al.* (38)).

Pressed bars of the material were fused to a seed crystal and were withdrawn at a rate of 3.5 cm/hr into an auxiliary heater maintained at temperature of 1300–1500°C (see Fig. 10.8).

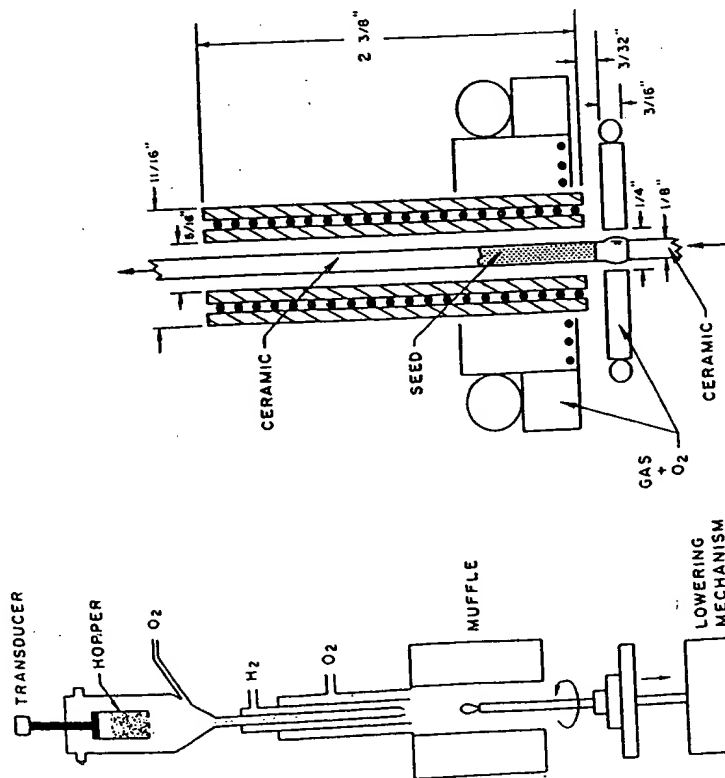


FIG. 10.8. Zone melter (after Brown and Toat⁽³⁷⁾).

FIG. 10.7. Flame-fusion apparatus (after von Hippel *et al.*⁽³⁸⁾).

In an interesting study, DeVries⁽³⁸⁾ obtained large grains of barium titanate in a polycrystalline rod by lowering it through a steep gradient. The center of the furnace coil was only at 1300°C and the rod was lowered at the rate of 0.6 mm/hr. In addition, he grew large grains of BaTiO₃ by seeding a polycrystalline aggregate.

Of these methods for growing barium titanate, the KF flux method is probably the most successful, since other tech-

niques such as pulling from the melt and the Verneuil method involve relatively rapid and uneven cooling of the crystal through a phase transition which causes the crystal to crack, but there are problems with all of the crystal-growing techniques. The flux technique and the Czochralski method both require the use of a crucible which may dissolve and be introduced into the crystal. In the Verneuil technique special powders must be prepared and the resulting crystals are highly strained. The floating-zone process produces crystals with less strain than the Verneuil technique, but with more defects than crystals grown by flux and Czochralski techniques.

CaTiO₃

Single crystals of CaTiO₃ have been obtained using CaCl₂, BaCl₂, CaCl₂-BaCl₂ and Na₂CO₃-K₂CO₃ fluxes. The chloride solutions were soaked at 1150°C and the carbonates at 1000°C for 30–40 hr. Cooling rates used varied from 50°C to 100°C/hr. The crystals produced were of the order of 1 mm.⁽³⁹⁾

Larger crystals of CaTiO₃, 25 mm long and 12 mm in diameter, have been grown by Merker using the flame-fusion technique.⁽⁴⁰⁾ The feed material was prepared by mixing solutions of titanium tetrachloride, calcium chloride and oxalic acid in molar proportions of 1.0/1.4/4.0. Then the calcium titanyl oxalate formed was transformed to CaTiO₃ by heating to 1000°C. After passing the CaTiO₃ through a 100-mesh sieve, the powder was placed in the flame-fusion apparatus and the crystal was grown. Initially, the boules fractured after growth, but this was overcome by annealing and slowly cooling the crystal.

SrTiO₃

Strontium titanate crystals also have been prepared by Merker.⁽⁴¹⁾ The feed material was formed by nearly the same process reported for preparing BaTiO₃ boule powder. A solution of oxalic acid was added to dilute titanium tetrachloride, followed by the addition of a solution of strontium chloride. The solution temperature was held at 70°C under agitation. After aging, the crystal salt was filtered, heated at 1000°C, sieved and used. The crystal as prepared had an opaque black appearance; however, a colorless transparent crystal was obtained by annealing the crystal in air.

PbTiO₃

Single-crystal growth of PbTiO₃ is of interest because PbTiO₃ is a high-temperature ferroelectric. Rogers⁽⁴²⁾ grew clear crystals 5 × 3 × 0.2 mm of PbTiO₃ using a Bridgman-Stockbarger method with excess PbO. Nomura and Sawada also obtained similar results using a PbCl₂ flux.⁽⁴³⁾

CdTiO₃

Single crystals of CdTiO₃, 0.12 × 0.06 × 0.06 mm, have been grown from a NaCl flux.⁽⁴⁴⁾

PbZrO₃

Pulvari⁽⁴⁵⁾ grew crystals of PbZrO₃ using the techniques reported by Jona *et al.*,⁽⁴⁶⁾ which involved placing a mixture of 2.4 g of PbF₂ and 6.9 g of PbZrO₃ in a covered platinum crucible, heated it at 1250°C for 1 hr and cooling at a rate of 50°/hr. The crystals grown were in the shape of cubes, 3 mm on edge.

(R.E.) BO₃

A large number of small perovskite crystals with Y, La, Pr, Nd, Eu, Sm and Gd in the A position and Al, Sc, Cr, Fe, Co and Ga in the B position were grown by Remeika.⁽⁴⁷⁾ A constituent oxide to lead monoxide ratio of 1:6 by weight was mixed and a platinum crucible was used to hold the mixture. The mixture was maintained at a temperature of 1300°C for a short period, except for compounds containing Al³⁺ or Sc³⁺ where the soaking time used was 4 hr. The temperature was then reduced to 850°C at a rate of 30°/hr and the crystals were leached from the mixture and crucible with hot dilute nitric acid.

LaAlO₃

Because of the longer fluorescence lifetime of Cr³⁺ in LaAlO₃ compared to Cr³⁺ in any other laser host material, the crystal is considered a good candidate for a high power-pulsed laser. However, the phase transition LaAlO₃ exhibits at 435°C presents a problem for growing it as a single crystal by many of the popular techniques.

Single crystals of pale yellow LaAlO₃ measuring $\frac{1}{2} \times \frac{1}{2} \times \frac{1}{4}$ in. have been grown by Airtron⁽⁴⁸⁾ in 250-ml crucibles from Bi₂O₃-B₂O₃ flux. A Bi₂O₃ flux containing 18.93 mole % B₂O₃ and 81.7 mole % Bi₂O₃ was mixed in proportions with the other oxides so that there were 10.97 and 10.77 moles of La₂O₃ and Al₂O₃ respectively. The platinum crucible was placed in a furnace, heated for 16 hr at 1340°C while rotating it and cooling it slowly to 960°C. The flux was poured off and the crystals washed with dilute HNO₃. All of the crystals were in the form of rectangular parallelepipeds. Airtron also has produced growth on a seed using a hydrothermal synthesis process where LaAlO₃ powder was used for a nutrient. The K₂CO₃ concentration used was 7 molal, the pressure was 20,000 psi, and the growth temperature was approximately 500°C.

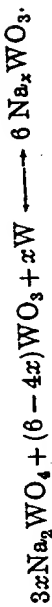
Single crystals of LaAlO₃ also have been prepared by pulling from the melt.⁽⁴⁹⁾ The crucible was charged with La₂O₃ and Al₂O₃ powder in equal quantities. The melting point of LaAlO₃ was found to be 2075–2080°C. From this melt, crystals up to 43 g in weight were grown and a total of five different boule axis orientations were obtained.

GdAlO₃

In a study of laser host materials, Mazelsky *et al.*⁽⁵⁰⁾ prepared gadolinium aluminum oxide, GdAlO₃, single crystals from a melt. The seed was inserted in the melt and pulled at a temperature of 2030°C while rotating the rod holding the seed at 65 rev/min. Using a pull rate of 6–7 mm/hr crystals $\frac{1}{2}$ in. in diameter and 1 in. long were obtained. The crystals, however, were not of good optical quality.

Na_xWO₃

The sodium tungsten bronzes, Na_xWO₃, were prepared by Straumanis.⁽⁵¹⁾ The method is based on the reaction



To prepare orange to yellow bronzes, perovskite type, in which x is 0.6 to 0.9, it was necessary to use mole ratios of reactants 4:2:1 to 9:2:1. The mixture was heated to 850°C

in an inert atmosphere and then slowly cooled. The crystals were recovered by leaching the solid in boiling water, sodium hydroxide solution and then HF.

$\text{Pb}(\text{B}_{0.33}^{\text{Ta}_{0.67}})\text{O}_3$

Bokov and Myl'nikova⁽⁵²⁾ prepared single crystals of the ferroelectric compounds $\text{Pb}(\text{Ni}_{0.33}\text{Ta}_{0.67})\text{O}_3$, $\text{Pb}(\text{Mg}_{0.33}\text{Ta}_{0.67})\text{O}_3$, $\text{Pb}(\text{Co}_{0.33}\text{Nb}_{0.67})\text{O}_3$, $\text{Pb}(\text{Co}_{0.33}\text{Ta}_{0.67})\text{O}_3$, $\text{Pb}(\text{Zn}_{0.33}\text{Nb}_{0.67})\text{O}_3$ using a lead oxide flux. A mixture of 60–80 mole % PbO and reagent grade oxides in proper proportions was placed in a platinum crucible and heated to 1200–1300°C. The melt was cooled at a rate of between 30–100°C/hr to a temperature of 800°C and then cooled more rapidly to room temperature. Crystals were separated by boiling in 20% HNO_3 except for $\text{Pb}(\text{Zn}_{0.33}\text{Nb}_{0.67})\text{O}_3$ crystals which were washed in acetic acid. The crystals were in the form of imperfect cubes, 1–2 mm on edge.

Later, Bokov *et al.*⁽⁵³⁾ grew $\text{Pb}(\text{Co}_{0.5}\text{W}_{0.5})\text{O}_3$ single crystals using a similar technique. Cobalt carbonate, H_2WO_4 and PbO were mixed in amounts corresponding to 10 mole % CoO, 20–30 mole % WO_3 , and 70–80% PbO. The soaking temperature was 1200°C and the cooling rate to 800°C was 5°C/hr. The crystals formed were small cubes.

$\text{Ba}(\text{B}_{0.33}^{\text{Ta}_{0.67}})\text{O}_3$

Single crystals of $\text{Ba}(\text{B}_{0.33}^{\text{Ta}_{0.67}})\text{O}_3$ type compounds⁽⁵⁴⁾ where B^{2+} is Ca, Mg, Zn or Ni were grown by Galasso and Pinto using a BaF_2 flux. The details of the process for each compound and results are presented in Table 10.1.

$\text{Pb}(\text{B}_{0.33}^{\text{Ta}_{0.67}})\text{O}_3$

Ferroelectric crystals of $\text{Pb}(\text{B}_{0.33}^{\text{Ta}_{0.67}})\text{O}_3$ type compounds, where B^{3+} is Sc or Fe and B^{5+} is Nb or Ta, were prepared by Galasso and Darby⁽⁵⁵⁾ using PbO and PbO-PbF_2 fluxes. The conditions of growth and the results are as in Table 10.2.

TABLE 10.1. Crystal Growth Data for $\text{Ba}(\text{B}_{0.33}^{\text{Ta}_{0.67}})\text{O}_3$ -type Compounds (after Galasso and Pinto⁽⁵⁴⁾)

Compound	Max. temp. (°C)	Soaking time	Sample wt(g)	Flux wt(g)	Cooling rate (°C/hr)	Crystal size (mm)	Color
$\text{Ba}(\text{Ca}_{0.33}\text{Ta}_{0.67})\text{O}_3$	1385	1.0 hr	6.4	24.0	13	1.0	yellow
$\text{Ba}(\text{Mg}_{0.33}\text{Ta}_{0.67})\text{O}_3$	1400	8.5 hr	6.4	43.0	10	2.0	yellow
$\text{Ba}(\text{Ni}_{0.33}\text{Ta}_{0.67})\text{O}_3$	1380	0.5 hr	6.3	18.0	40	0.5	green
$\text{Ba}(\text{Zn}_{0.33}\text{Ta}_{0.67})\text{O}_3$	1380	2.0 hr	11.2	65.0	10	1.5	red

TABLE 10.2. Crystal Growth Data for $\text{Pb}(\text{B}_{0.33}^{\text{Ta}_{0.67}})\text{O}_3$ -type Compounds (after Galasso and Darby⁽⁵⁵⁾)

Compound	Flux	Flux (wt%)	Temp range (°C)	Cooling rate (°C/hr)	Crystal size (mm) on edge
$\text{Pb}(\text{Fe}_{0.33}\text{Nb}_{0.67})\text{O}_3$	PbO	64	1230–800	6	1
$\text{Pb}(\text{Fe}_{0.33}\text{Ta}_{0.67})\text{O}_3$	PbO	64	1230–800	6	1
$\text{Pb}(\text{Sc}_{0.33}\text{Nb}_{0.67})\text{O}_3$	PbO	86	1150–900	30	1
$\text{Pb}(\text{Sc}_{0.33}\text{Ta}_{0.67})\text{O}_3$	PbO-PbF ₂	42.5	1325–1025	25	1

$\text{Ba}(\text{B}_{0.33}^{\text{Ta}_{0.67}})\text{O}_3$

Galasso *et al.* studied $\text{Ba}(\text{B}_{0.33}^{\text{Ta}_{0.67}})\text{O}_3$ -type materials for laser application.⁽⁵⁶⁾ Single crystals of these compounds with $\text{B}^{3+} = \text{La, Gd, Lu, Sc}$ and Y were grown using BaF_2 flux, but more satisfactory results were obtained with B_2O_3 as the flux. Crystals of $\text{Ba}(\text{Y}_{0.33}\text{Ta}_{0.67})\text{O}_3$ up to 0.5 cm on edge were formed by mixing 566.3 g BaCO_3 , 164.1 g of Ta_2O_5 , 83.9 g Y_2O_3 and 112 g B_2O_3 , placing the mixture in a 250-ml platinum crucible, soaking it for 12 hr at 1470°C and cooling it at 1.3°C/hr to 1110°C. A polished crystal is shown in Fig. 10.9.

Growth of $\text{Ba}(\text{Y}_{0.33}\text{Ta}_{0.67})\text{O}_3$ crystals from a flux in a temperature gradient using a seed crystal suspended below the

melt surface also was attempted. In this method, an excess of nutrient material (i.e. material of the composition to be grown) is available in the bottom of the crucible, which is maintained at a higher temperature than the surface of the melt. When the seed crystal is placed in the cooler region of the crucible, some of the nutrient dissolves, is transported by diffusion through the flux, and deposits on the rotating seed as it is slowly withdrawn from the melt.

In these experiments a 400-g charge of composition $\text{BaO}:\text{YTbO}_3:\text{B}_2\text{O}_3 = 52:35:13$ was equilibrated for 20 hr. The melt surface was held 8°C cooler than the bottom of the crucible. The seed was lowered into the melt, rotated at about 100 rev/min and withdrawn at a rate of 0.0025 in./hr. In a 4-day growth period, the linear growth rate was of the order of 0.025 mm/hr. The material which was grown showed large single crystal regions; however, with better control of the volatilization of B_2O_3 large single crystals could probably be grown.

Another technique^(6a) considered was one developed with J. Davis, also of the United Aircraft Research Laboratories, to grow Al_2O_3 single crystals. The apparatus (see Fig. 10.10) is similar to an electron beam zone melter except that it requires no anode wire around the insulator and it can be used in partial pressures of oxygen or other gases. The material to be used is made into a polycrystalline rod and passed through a ring (cold cathode) which impinges electrons on a small zone and melts it. As the molten zone passes along the material it purifies the rod as it transforms it into a single crystal. The technique seems to be well suited for high melting point oxides.

$\text{La}(\text{B}_{0.5}^{2+}\text{B}_{0.5}^{4+})\text{O}_3$

Single crystals of $\text{La}(\text{B}_{0.5}^{2+}\text{B}_{0.5}^{4+})\text{O}_3$ -type compounds where B^{2+} is Ni, Mg, Zn and B^{4+} is Ir or Ru were grown from fluxes in platinum crucibles⁽⁵⁵⁾. The amount and composition of the fluxes, firing conditions and cooling rates are listed in Table 10.3.

The crystals produced in this manner were found to be electrically conducting.

TABLE 10.3. Crystal Growth Data for $\text{La}(\text{B}_{0.5}^{2+}\text{B}_{0.5}^{4+})\text{O}_3$ -type Compounds (after Galasso and Darby⁽⁵⁵⁾)

Compound	Flux	Flux (wt%)	Temp. range ($^\circ\text{C}$)	Cooling rate ($^\circ\text{C/hr}$)	Crystal size (mm) on edge
$\text{La}(\text{Mg}_{0.5}\text{Ru}_{0.5})\text{O}_3$	PbO-PbF ₂	85	1320-1000	30	1.0
$\text{La}(\text{Ni}_{0.5}\text{Ir}_{0.5})\text{O}_3$	PbO-PbF ₂	85	1300-1000	30	0.5
$\text{La}(\text{Ni}_{0.5}\text{Ru}_{0.5})\text{O}_3$	PbO-PbF ₂	85	1300-1000	30	2.0
$\text{La}(\text{Zn}_{0.5}\text{Ru}_{0.5})\text{O}_3$	PbO	85	1300-850	30	0.5
	PbO	85	1300-25	30	0.1

REFERENCES

1. E. J. FRESIA, L. KATZ and R. WARD, *J. Am. Chem. Soc.* **81**, 4783 (1959).
2. F. GALASSO, L. KATZ and R. WARD, *J. Am. Chem. Soc.* **81**, 820 (1959).
3. A. SLEIGHT and R. WARD, *Inorg. Chem.* **1**, 790 (1962).
4. A. SLEIGHT, J. LONGO and R. WARD, *Inorg. Chem.* **1**, 245 (1962).
5. F. PATTERSON, C. W. MOELLER and R. WARD, *Inorg. Chem.* **2**, 196 (1963).
6. D. RIDGLEY and R. WARD, *J. Am. Chem. Soc.* **77**, 8135 (1955).
7. W. MCCABROLLE, R. WARD and L. KATZ, *J. Am. Chem. Soc.* **78**, 2909 (1956).
8. J. RANDALL and R. WARD, *J. Am. Chem. Soc.* **81**, 2629 (1959).
9. M. KESTIGIAN, J. G. DIKENSON and R. WARD, *J. Am. Chem. Soc.* **79**, 5598 (1957).
10. F. SUGAWARA and S. IIDA, *J. Phys. Soc. Japan* **20**, 1529 (1965).
11. C. FELDMAN, *Rev. Sci. Instr.* **26**, 463 (1955).
12. R. C. DEVRIES, *J. Am. Ceram. Soc.* **45**, 225 (1962).
13. J. T. LAST, *Rev. Sci. Instr.* **28**, 720 (1959).
14. H. PFISTERER, E. FUCHS and W. LIESKE, *Naturwiss.* **49**, 178 (1962).
15. F. V. BURSIA and N. P. SMIRNOVA, *Fiz. Tverd. Tela.* **4**, 1675 (1962).
16. C. FELDMAN, *Rev. Sci. Instr.* **26**, 463 (1955).
17. J. P. GREEN, *A Method for Fabricating Thin Ferroelectric Films of BaTiO₃*, Tech. Mem. ESL-TM-105, MIT (April 1961).

18. D. FRANKL, A. HAGENLOCHER, E. O. HAFNER, P. H. KLECK, A. SANDOR, E. BOTH and H. J. DEGENHART, *Proc. Electron Components, Conf.* 44, (1962).
19. A. MOLL, *Z. Angew. Phys.* 10, 410 (1958).
20. O. RÖDER, *Z. Angew. Phys.* 12, 323 (1960).
21. E. K. MÜLLER, B. J. NICHOLSON and M. H. FRANCOMBE, *Electrochem. Techn.* 1, 158 (1963).
22. E. K. MÜLLER, B. J. NICHOLSON and G. TURNER, *J. Electrochem. Soc.* 110, 989 (1963).
23. *Electronics*, P. 54 (1 Sept. 1961).
24. B. T. MATTHEIAS and J. P. REMEIK, *Phys. Rev.* 78, 1886 (1949).
25. G. SHIRANE, H. DANNER, A. PAVLOVIO and R. PEPIŃSKY, *Phys. Rev.* 98, 612 (1954).
26. S. TRUBWASSER, *Phys. Rev.* 101, 993 (1956).
27. C. PULVARI, WADD Technical Report 60-146, Cath. Univ. of Am. (April 1960).
28. L. E. CROSS and B. J. NICHOLSON, *Phil. Mag.* 48, 453 (1955).
29. H. F. KAY, *Report Prog. Phys.* 18, 230 (1955).
30. S. H. WEMPLE, Ph.D. Thesis, MIT (1963).
31. W. A. BONNER, E. F. DEARBORN and L. G. VAN UTERT, *Cer. Bulletin* 44, 19 (1965).
32. H. BLATTNER, B. MATTHEIAS, and W. MERZ, *Helv. Chim. Acta* 20, 225 (1947).
33. J. P. REMEIK, *J. Am. Chem. Soc.* 76, 940 (1954).
34. R. C. LINARES, *J. Am. Chem. Soc.* 64, 941 (1942).
35. R. C. DEVRIES, *J. Am. Ceram. Soc.* 42, 547 (1959).
36. A. von HIPPEL *et al.*, Technical Report 178, Lab. Ins. Res., MIT (March 1963).
37. F. BROWN and W. H. TOAT, *J. Appl. Phys.* 85, 1594 (1964).
38. R. DEVRIES, *J. Am. Ceram. Soc.* 47, 134 (1964).
39. H. F. KAY, Report L/S 257, Brit. Elec. Res. Assoc. (1951).
40. L. MERKER, *J. Am. Ceram. Soc.* 45, 388 (1962).
41. L. MERKER, *Mining Eng.* 202, 647 (1955).
42. H. H. ROGERS, Tech. Report No. 56, Lab. for Inst. Res. MIT (1952).
43. S. NOMURA and S. SAWADA, *Report Inst. Sci. Tech., Univ. Tokyo* 6, 11 (1952).
44. H. F. KAY and J. L. MILES, Report L/T 303, Brit. Elec. Res. Assoc., 5 (1954).
45. C. PULVARI, WADC Technical Note 56-467, Cath. Univ. of Am. (Feb. 1957).
46. F. JONA, G. SHIRANE and R. PEPIŃSKY, *Phys. Rev.* 97, 1586 (1955).
47. J. P. REMEIK, *J. Am. Chem. Soc.* 78, 4258 (1956).
48. Airtron Semiannual Tech. Summ. Rpt. NONR-4618(00) (1 July 1965-31 Dec. 1965).
49. C. D. BRANDLE, H. FAY and O. H. NESTOR, Final Rpt. (Jan. 1965-May 1965) NONR-4793(00).
50. R. C. OHLMANN, R. MAZELSKY and J. MURPHY, Final Tech. Rpt. (16 Apr. 1964-16 Oct. 1965), NONR-4658(00).

51. M. E. STRAUMANN, *J. Am. Chem. Soc.* 71, 679 (1949).
52. V. A. BOKOV and I. E. MYL'NIKOVA, *Sov. Phys., Solid State* 2, 2428 (1961).
53. V. A. BOKOV, S. A. KIZHAEV, I. E. MYL'NIKOVA and A. G. TUTOV, *Sov. Phys., Solid State* 6, 2419 (1965).
54. F. GALASSO and J. PINTO, *Nature* 207, 70 (1965).
55. F. GALASSO and W. DABBY, *Inorg. Chem.* 4, 71 (1965).
56. F. GALASSO, G. LAYDEN and D. FINCHBAUGH, *J. Chem. Phys.* 44, 2703 (1966).

Many fluorides with the perovskite structure also have been prepared by a solid-state reaction between an alkali metal halide and a divalent metal oxide at 500–800°C.⁽⁶⁾ The same type of reactions have been conducted between the binary fluorides.

Single crystals of a number of fluorides have been prepared by Knox using fluorides precipitated from aqueous solutions as the reactants.⁽⁶⁾ The fluorides were heated in anhydrous HF, mixed with KHF₂, melted and slowly cooled in an inert atmosphere. Crystals of KMnF_3 , KFeF_3 , KCoF_3 , KNiF_3 , KCuF_3 and KZnF_3 have been grown in this manner.

Single crystals of KMnF_3 have been grown by the Czochralski technique by Nassau.⁽⁷⁾ In these studies, special equip-

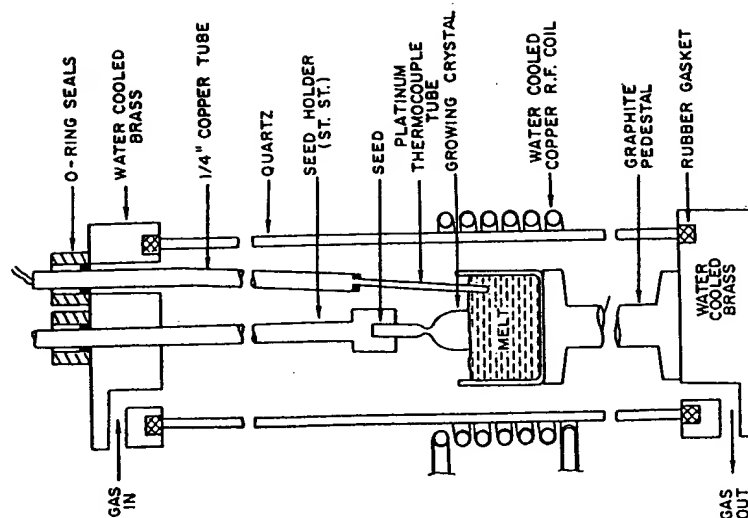


Fig. 11.1. Apparatus for Czochralski-pulling (after Nassau⁽⁷⁾).

CHAPTER 11

OTHER PEROVSKITE-TYPE COMPOUNDS

The oxides are by far the most numerous and most interesting materials with the perovskite structure. However, there are some carbides, halides, hydrides and nitrides with this structure which have been investigated because of their magnetic properties and possible use as hosts for transition metal activating ions. Some of the data on their preparation, structure and properties is presented in this chapter.

11.1. PREPARATION OF PEROVSKITE-TYPE PHASES (OTHER THAN OXIDES)

The ternary carbides with the perovskite structure have been prepared predominantly by two techniques. The first involves melting the appropriate proportions of the two metals and carbon under argon and cooling them. Whenever pronounced coring exists, the samples are annealed for long periods.⁽¹⁾ The second technique is a solid-state reaction between the reactants after they are placed in an evacuated sealed silica capsule.⁽²⁾ In a variation of this method, one metal is heated with carbon and the alloy is ground, mixed with the other metal and heated again.

Perovskite-type fluorides have been prepared by precipitation from aqueous solutions. However, crystals prepared in this manner are not stoichiometric.⁽³⁾ Therefore, other techniques are used when possible. The halides $\text{K}(\text{Na}_{0.5}\text{Cr}_{0.5})\text{F}_3$, $\text{K}(\text{Na}_{0.5}\text{Fe}_{0.5})\text{F}_3$ and $\text{K}(\text{Na}_{0.5}\text{Ga}_{0.5})\text{F}_3$ were formed by reacting the trifluorides with KHF_2 and NaHF_2 in a platinum crucible over an open flame.⁽⁴⁾ The melt was cooled, leached with water and ethyl alcohol, and the product dried.

ment had to be fabricated to prevent any oxygen from reacting with the melt (see Fig. 11.1).

Kestigian *et al.*⁽⁶⁾ grew crystals of RbFeF_3 and CsFeF_3 using a horizontal Bridgman technique. Anhydrous fluorides were used in dense graphite containers under an HF -argon atmosphere. Single crystals 2×0.5 in. in dimensions were grown by this method.

The ternary hydrides, LiBaH_3 and LiSrH_3 , were prepared by placing mixtures of the metals in a stainless-steel boat in a stainless-steel bomb and heating the mixture under a hydrogen atmosphere.⁽⁶⁾ The metals were ground and treated in a dry box under an argon atmosphere.

The nitrides Fe_3NiN , Fe_3PtN , Fe_3N and Fe_3PdN were prepared by Stadelmaier and Fraker⁽¹⁰⁾ using an induction unit to melt the alloy, which they then nitrided. The alloy was ground into powders and a mixture of NH_3 and hydrogen was used as the nitriding gas. Weiner and Berger⁽¹¹⁾ found that they could obtain nitrides by first processing the ingots into strips before nitriding. If the strips were very thin, homogeneous nitrides were obtained.

11.2. STRUCTURE

In the structure of the ternary carbides described in this chapter the Al, Sn or Ga metal atoms are in the A position, the C atom in the B position, and the transition metal atoms in the oxygen atom positions of the perovskite structure. This makes the X-ray pattern of these phases look like that produced by a face centered cubic arrangement of atoms with a superstructure. In the unit cell of Mn_3AlC structure the manganese atoms are located at the face centers, the aluminum atom is at the cube corners and the carbon atom is at the body centered position.

The nitrides Fe_3NiN and Fe_3PtN also adopt the perovskite structure. Studies by Wiener and Berger indicate that there is complete ordering in the structure of these nitrides. Because of the low scattering factor of nitrogen the powder patterns of these compounds also look as though they had a structure with a face-centered cubic lattice.

TABLE 11.1. Unit Cell Parameters for Perovskite-type Phases (other than oxides)

Phases	a (Å)	c (Å)	References
Carbides			
AlFe_3C	3.719		12
AlMn_3C	3.869		1
Fe_3SnC	3.85		5
GaMn_3C	8.376		12
Mn_3ZnC	3.92		2
Halides			
CaCaF_3	4.522		5
CsCdBr_3	10.70		13
CsCdCl_3	5.20		13
CaFeF_3	6.168	14.855	8
CaGeCl_3	5.47		13, 14
CaHgBr_3	5.77		13
CaHgCl_3	5.44	8.72	13
CaMgF_3	9.39	8.39	5
CaPbBr_3	5.874		
CaPbCl_3	5.590	5.630	
CsZnF_3	9.90	9.05	
KCaF_3	8.742		5
KCdF_3	4.293		5
KCoF_3	4.071		16
KO_2F_3	4.274	4.019	6
KCuF_3	4.140	3.926	6
KMgF_3	4.120		6
KMnF_3	3.973		5
KNiF_3	4.182		6
KNiF_3	4.012		6
KZnF_3	4.055		6
LiBaF_3	3.996		5
NaZnF_3	7.76	8.75	5
RbCaF_3	4.452		5
RbCoF_3	4.062		15
RbFeF_3	4.174		8
RbMgF_3	8.19		5
		$\beta = 98^\circ 30'$ monocl.	

TABLE 11.1 (cont.)

Phases	d (Å)	c (Å)	References
RbMnF ₃	4.250	8.01	17
RbZnF ₃	8.71		5
K(Cr _{0.5} Na _{0.5})F ₃	8.286		4
K(Fe _{0.5} Na _{0.5})F ₃	8.323		4
K(Ge _{0.5} Na _{0.5})F ₃	8.246		4
<i>Hydrides</i>			
LiBaH ₃	4.023		9
LiEuH ₃	3.796		18
LiSrH ₃	3.833		9
<i>Nitrides</i>			
Fe ₃ N	3.795		11
Mn ₃ N	3.857		11
Fe ₃ NiN	3.790		11
Fe ₃ PtN	3.857		11

As can be seen in Table 11.1, many of the fluorides have the "ideal" cubic perovskite structure. Of the series with the formula $\text{KBF}_3(\text{B}^{3+} = \text{Mn, Fe, Co, Ni, Cu, Cr and Zn})$, only KCuF_3 and KCrF_3 have distorted structures. Many of the others have structures related to the various modification of the perovskite type.

The complex fluorides $\text{K}(\text{Na}_{0.5}\text{Cr}_{0.5})\text{F}_3$ and $\text{K}(\text{Na}_{0.5}\text{Fe}_{0.5})\text{F}_3$ were found to adopt the ordered perovskite structure of the $(\text{NH}_4)_3\text{FeF}_6$ type. The fluoride ions in this structure move closer to the transition metal ion and away from the sodium ion.

The ternary hydrides LiBaH_3 and LiSrH_3 have the inverse perovskite structure with the lithium ions in the B position and alkaline earth metal ions in the A position. The crystallographic data for these phases as well as for the carbides, halides and nitrides are listed in Table 11.1.

11.3. PROPERTIES

Many of the carbides and nitrides with the perovskite structure are ferromagnetic materials. The carbide Mn_3AlC has been studied extensively. Butters and Myers^(a) found that it was strongly magnetic at low temperature and has a Curie temperature of 15°C. They also found that Mn_3ZnC was ferromagnetic with a Curie temperature of 80°C. The Curie temperatures of both of these materials varied with the Mn/Al or Zn ratio. Figure 11.2 shows the variation of Curie

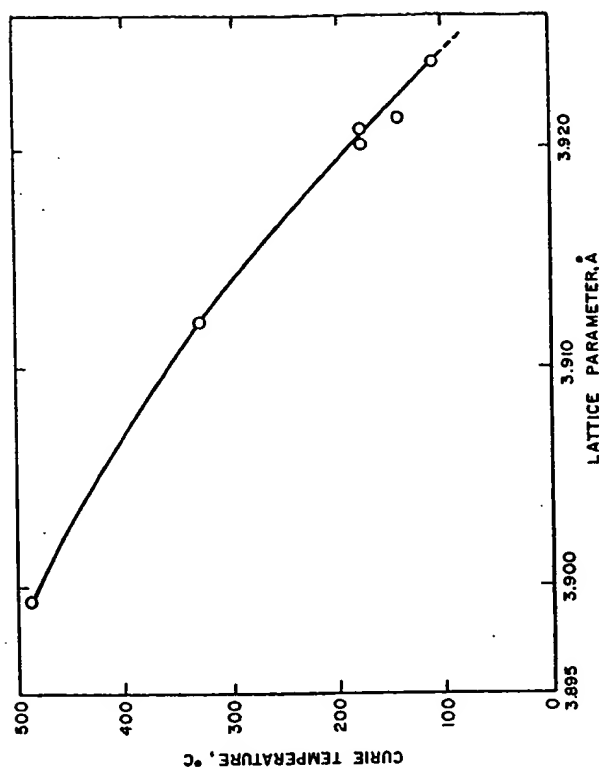


Fig. 11.2. Variation of Curie temperature with lattice parameters (after Butters and Myers^(a))

temperature with lattice constant for the Mn_3ZnC phases. Note that the Curie temperature increases as the lattice constant decreases.

The electrical resistivity of Mn_3ZnC is $770 \times \text{cat}^\circ \text{ ohm-cm}$ at 20° and decreases with increasing temperature. It is not stable in moist air and must be kept in a desiccator.

The nitrides Fe_3N , Mn_3N , Fe_3NiN and Fe_3PtN were also found to be ferromagnetic with Curie points of 488° , 465° , 487° and 369°C , respectively.

Studies by Machin *et al.*⁽¹⁹⁾ showed that many of the ternary perovskite-type fluorides also had interesting magnetic properties. The fluorides KFeF_3 , KCoF_3 and KNiF_3 are antiferromagnetic with Néel points of 112° , 135° and 280°K . The evidence for antiferromagnetism below 80°K for KMnF_3 and 215°K for KCuF_3 appears to be less certain. However, a study of the absorption spectra of KMnF_3 as a function of temperature does show anomalies in the maxima at 184°K and at 88°K . The first the authors attribute to a phase transformation and the latter to electron spin coupling.

Other fluorides which were found to be antiferromagnetic are RbFeF_3 ⁽²⁰⁾ and RbMnF_3 ⁽²¹⁾ with Néel temperatures of 75° and 83°K respectively. Small changes in the fluorescent properties in the vicinity of the Néel temperature have been reported for the latter compound and KMnF_3 .^(22, 23) At about half the Néel temperatures larger and more strongly temperature-dependent changes were observed in the fluorescence of these materials. This effect may involve the coupling of the lattice and magnetic interaction of the excited Mn^{2+} ion.

REFERENCES

1. R. G. BUTTERS and H. P. MYERS, *Phil. Mag.* 46, 895 (1955).
2. R. G. BUTTERS and H. P. MYERS, *Phil. Mag.* 40, 132 (1955).
3. W. G. PALMER, *Experimental Inorganic Chemistry*, Cambridge University Press (1954).
4. K. KNOX and D. W. MITCHELL, *J. Nucl. Chem.* 21, 253 (1961).
5. W. L. W. LUTHEKENS and A. J. E. WELCH, *Acta Cryst.* 5, 841 (1952).
6. K. KNOX, *Acta Cryst.* 14, 583 (1961).
7. K. NASSAU, *J. Appl. Phys.* 32, 1820 (1961).
8. M. KESTIGIAN, F. D. LEIFZIGER, W. J. CROFT and R. GUIDOBONI, *Inorg. Chem.* 5, 1462 (1966).
9. C. E. MESSER, J. C. EASTMAN, R. G. MEERS and A. J. MAELAND, *Inorg. Chem.* 3, 776 (1964).
10. H. H. STADELMAYER and A. C. FRAKER, *Trans. AIME* 218, 571 (1960).
11. G. W. WIENER and J. A. BERGER, *J. Metals* 7, 360 (1955).
12. H. P. MYERS, University of British Columbia (1956).

13. I. NARAY-SZABÓ, *Művelget Zsemlen* 1, 30 (1947).
14. A. N. CHRISTENSEN, *Acta Chem. Scand.* 19, 42 (1965).
15. W. RUDORFF, J. KANDLER, G. LINCKE and D. BABEL, *Angew. Chem.* 71, 672 (1959).
16. C. BRISI, *Ann. Chem.* 42, 356 (1952).
17. A. OKAZAKI and Y. SUEMUNE, *J. Phys. Soc. Japan* 17, 204 (1962).
18. C. E. MESSER and K. HARDCASTLE, *Inorg. Chem.* 3, 1327 (1964).
19. D. J. MACHIN, R. L. MARTIN and R. S. NYHOLM, *J. Chem. Soc.* 281, 1490 (1963).
20. F. F. Y. WANG and M. KESTIGIAN, *J. Appl. Phys.* 37, 975 (1966).
21. V. L. MORUZZI and D. T. TEANEY, *Bull. Am. Phys. Soc.* 9 (1964).
22. W. W. HOLLOWAY, JR., M. KESTIGIAN, R. NEWMAN and E. W. PROHOFKY, *Phys. Rev. Letters* 11, 82 (1963).
23. W. W. HOLLOWAY, JR., E. W. PROHOFKY and M. KESTIGIAN, *Phys. Rev.* 139, A954 (1965).

INDEX

OXIDES

- A¹⁺B³⁺O₃
- AgNbO₃
crystallography 18
density 145
phase transition 116, 118
- AgTaO₃
crystallography 18
density 145
phase transition 116, 118
- CaIO₃
crystallography 5, 18
density 145
- KIO₃
crystallography 5, 18
density 145
- (K₁Na₁)NbO₃
ferroelectricity 95
- KNbO₃
crystallography 4, 18
density 145
dielectric constant 87
ferroelectricity 96
melting point 142
phase transition 87, 116, 117
preparation, single crystal 165
- K(Nb,Ta)O₃
ferroelectricity 96
optical properties 1
preparation, single crystal 168
- KTaO₃
crystallography 5, 18
density 145
ferroelectricity 88
melting point 142
optical properties 133
phase transition 116, 117
preparation, single crystal 166
- NaNbO₃
crystallography 5, 18
density 145
dielectric constant 88
ferroelectricity 87
melting point 142
optical properties 134
- phase transition 5, 88, 116, 117
preparation
single crystal 166
thin film 164
- NaTaO₃
crystallography 18
density 145
ferroelectricity 88
melting point 142
phase transition 116, 118
preparation, single crystal 166
- RbIO₃
crystallography 18
density 145
- RbTaO₃
ferroelectricity 88
- TiIO₃
crystallography 5, 18
density 145
- A²⁺B⁴⁺O₃
- (Ba,Ca,Sr)TiO₃
electrical conductivity 70
- (Ba,Ca,Sr)(Ti,Zr)O₃
dielectric constant 92
ferroelectricity 92
- (Ba,Ca)TiO₃
dielectric constant 92
piezoelectricity 92
- (Ba,Ce,Mg)TiO₃
electrical conductivity 70
- BaCeO₃
crystallography 18
density 145
preparation, thin film 164
- BaFeO₃
crystallography 18
density 145
- Ba(Hf,Ti)O₃
dielectric constant 94
ferroelectricity 94
phase transition 94

- (Ba,La)(Mn,Ti)O₃
ferromagnetism 123
phase transition 123
- (Ba,La)TiO₃
electrical conductivity 70
thermoelectricity 76
- BaMoO₄
crystallography 18
density 145
- BaPbO₃
crystallography 18
density 145
- (Ba,Pb)(Sn,Ti)O₃
ferroelectricity 95
- (Ba,Pb)TiO₃
dielectric constant 91
electrical conductivity 70
ferroelectricity 91
piezoelectricity 98
- (Ba,Pb)ZrO₃
dielectric constant 98
ferroelectricity 98
- BaPrO₃
crystallography 18
density 145
- BaPuO₃
crystallography 18
density 145
- Ba(Si,Ti)O₃
electrical conductivity 70
- BaSnO₃
crystallography 7, 18
density 145
preparation, thin film 164
- Ba(Sn,Ti)O₃
ferroelectricity 94
- (Ba,Sr)(Sn,Ti)O₃
electrical conductivity 70
- (Ba,Sr)TiO₃
crystallography 90
dielectric constant 90
electrical conductivity 90
ferroelectricity 96
superconductivity 64
- BaThO₃
crystallography 18
density 145
melting point 142
- BaTiO₃
crystallography 6, 18
density 145
dielectric constant 82
electrical conductivity 68
electron paramagnetic resonance 57
- ferroelectricity 80
heat of formation 142
melting point 142
nuclear irradiation 104
optical properties 129
phase transition 6, 80, 115
piezoelectricity 110
preparation
single crystal 169
thin film 162
thermal conductivity 142
X-ray diffraction 50
- Ba(Ti,Zr)O₃
electrical conductivity 70
- BaUO₃
crystallography 18
density 145
- BaZrO₃
crystallography 6, 18
density 145
melting point 142
thermal conductivity 142
- CaCeO₃
crystallography 18
density 145
- CaHfO₃
crystallography 18
density 145
- (Ca,La)MnO₃
ferromagnetism 122
thermoelectricity 76
- CaMnO₃
crystallography 18
density 145
electrical conductivity 68
- CaMoO₃
crystallography 18
density 145
electrical conductivity 64
preparation, powder 161
- CaSnO₃
crystallography 19
density 145
superconductivity 64
- (Ca,Sr)TiO₃
CaThO₃
crystallography 19
density 145
- CaTiO₃
crystallography 3, 5, 19
density 145
dielectric constant 87
electrical conductivity 68

- CaTiO₃ (cont.)
heat of formation 142
Melting constant 40
melting point 142
optical properties 132
phase transition 87, 117
preparation
single crystal 173
thin film 164
thermal conductivity 142
thermal expansion 142
- CaUO₃
crystallography 7, 19
density 145
- CaVO₃
crystallography 19
density 145
- CaZrO₃
crystallography 7, 19
density 145
melting point 142
- CdCeO₃
crystallography 19
density 145
- CdSnO₃
crystallography 19
density 145
- CdThO₃
crystallography 19
density 145
- CdTiO₃
crystallography 19
density 145
- CdZrO₃
crystallography 104
ferroelectricity 174
preparation, single crystal 174
- EuTiO₃
crystallography 19
density 145
- MgTiO₃
crystallography 19
density 145
- PbCeO₃
crystallography 19
density 145
- PbHfO₃
crystallography 19
density 145
ferroelectricity 89
phase transition 89, 116, 117
- PbSnO₃
crystallography 19
density 146
- PbTiO₃
crystallography 6, 19
density 146
dielectric constant 85
ferroelectricity 85
phase transition 6, 85, 116, 117
piezoelectricity 85
preparation
single crystal 174
thin film 165
thermal expansion 142
X-ray diffraction 50
- PbTiO₃-KNbO₃
dielectric constant 95
- PbTiO₃-NaNbO₃
ferroelectricity 96
- Pb(Ti,Zr)O₃
dielectric constant 97
ferroelectricity 97
mechanical properties 168
piezoelectricity 97, 110
- PbZrO₃
crystallography 7, 19
density 146
dielectric constant 88
ferroelectricity 88
phase transition 88, 116, 117
preparation, single crystal 174
- SrCeO₃
crystallography 19
density 146
- SrCoO₃
crystallography 19
density 146
- SrFeO₃
crystallography 19
density 146
- SrHfO₃
crystallography 19
density 146
- SrMoO₃
crystallography 19
density 146
electrical conductivity 64
- SrPbO₃
crystallography 19
density 146
- SrRuO₃
crystallography 19
density 146
- SrSnO₃
preparation, powder 161
crystallography 19
density 146

- SrSnO₃ (*cont.*)
 preparation, thin film 164
 SrThO₃
 crystallography 19
 density 146
 SrTiO₃
 crystallography 6, 19
 density 146
 dielectric constant 86
 electrical conductivity 68
 electron paramagnetic resonance 58
 ferroelectricity 86
 heat of formation 142
 melting point 142
 optical properties 130
 phase transition 116, 117
 preparation, single crystal 173
 thermal conductivity 142
 thermal expansion 142
 SrUO₃
 crystallography 19
 density 146
 SrZrO₃
 crystallography 7, 19
 density 146
 mechanical properties 144
 melting point 142
 thermal expansion 142
- A²⁺B²⁺O₃
 BiAlO₃
 crystallography 19
 density 146
 BiCrO₃
 crystallography 20
 density 146
 preparation, powder 162
 BiMnO₃
 crystallography 20
 density 146
 ferromagnetism 126
 preparation, powder 162
 CeAlO₃
 crystallography 20
 density 146
 ferromagnetism 128
 X-ray diffraction 51
 GdMnO₃
 crystallography 20
 density 146
 GdScO₃
 crystallography 9, 20
 density 147
- CeGaO₃
 crystallography 20
 density 146
 CeScO₃
 crystallography 20
 density 146
 CeVO₃
 crystallography 20
 density 146
 CrBiO₃
 crystallography 20
 density 146
 DyAlO₃
 crystallography 20
 density 146
 DyFeO₃
 crystallography 20
 density 146
 DyMnO₃
 crystallography 20
 density 146
 EuAlO₃
 crystallography 9, 20
 density 146
 EuCrO₃
 crystallography 20
 density 146
 EuFeO₃
 crystallography 9, 20
 density 146
 FeBiO₃
 crystallography 20
 density 146
 GdAlO₃
 crystallography 9, 20
 density 146
 melting point 142
 preparation, single crystal 175
 GdCoO₃
 crystallography 20
 density 146
 GdCrO₃
 crystallography 9, 20
 density 146
 GdFeO₃
 crystallography 8, 20
 density 146
 ferromagnetism 128
 X-ray diffraction 51

- GdVO₃
 crystallography, 9, 20
 density 147
 LaAlO₃
 crystallography 9, 10, 20
 density 147
 laser properties 1
 melting point 142
 phase transition 10
 preparation, single crystal 174
 LaCoO₃
 crystallography 21
 density 147
 electrical conductivity 69
 preparation, single crystal 174
 La(Co,Mn)O₃
 ferromagnetism 123
 LaCrO₃
 crystallography 9, 21
 density, 147
 electrical conductivity 69
 La(Cr,Mn)O₃
 ferromagnetism 122
 LaFeO₃
 crystallography 21
 density 147
 electrical conductivity 68
 melting point 142
 LaGdO₃
 crystallography 9, 21
 density 147
 phase transition 9
 LaInO₃
 crystallography 21
 density 147
 LaMnO₃
 electrical conductivity 68
 La(Mn,Ni)O₃
 ferromagnetism 124
 LaNiO₃
 crystallography 21
 density 147
 LaRhO₃
 crystallography 21
 density 147
 LaScO₃
 crystallography 9, 21
 density 147
 (La,Sr)CoO₃
 electrical conductivity 69
 (La,Sr)CrO₃
 electrical conductivity 69
- (La,Sr)FeO₃
 electrical conductivity 89
 thermoelectricity 76
 (La,Sr)MnO₃
 electrical conductivity 69
 LaTiO₃
 crystallography 21
 density 147
 electrical conductivity 60
 LaVO₃
 crystallography 21
 density 147
 electrical conductivity 60
 preparation, powder 161
 LaYO₃
 crystallography 21
 density 147
 NdAlO₃
 crystallography 9, 21
 density 147
 NdCoO₃
 crystallography 21
 density 147
 NdCrO₃
 crystallography 9, 21
 density 147
 NdFeO₃
 crystallography 9, 21
 density 147
 NdGaO₃
 crystallography 9, 21
 density 147
 NdInO₃
 crystallography 21
 density 147
 NdMnO₃
 crystallography 21
 density 147
 NdScO₃
 crystallography 9, 21
 density 147
 NdVO₃
 crystallography 9, 21
 density 147
 PrAlO₃
 crystallography 9, 21
 density 147
 PrCoO₃
 crystallography 21
 density 147
 PrCrO₃
 crystallography 9, 21
 density 147

INDEX

[illegible]

INDEX

- KCoF₃ crystallography 186
 KCrF₃ crystallography 185
 KCoF₃ crystallography 185
 RbCoF₃ crystallography 185
 RbFeF₃ crystallography 185
 ferromagnetism 188
 preparation, single crystal 184
 RbMgF₃ crystallography 185
 RbMnF₃ crystallography 186
 ferromagnetism 188
 RbZnF₃ crystallography 186
 K(Cr_{0.5}Na_{0.5})O₃ crystallography 186
 preparation 182
 K(Fe_{0.5}Na_{0.5})O₃ crystallography 186
 preparation 182
 K(Ge_{0.5}Na_{0.5})O₃ crystallography 186
 preparation 182

HYDRIDES

- LiBaH₃ crystallography 186
 preparation 184
 LiEuH₃ crystallography 186
 preparation 184

NITRIDES

- Fe₃N crystallography 186
 ferromagnetism 188
 preparation 184
 Fe₃PtN crystallography 186
 ferromagnetism 188
 preparation 184

INDEX

- La(Mg_{0.5}Ru_{0.5})O₃ crystallography 38
 density 167
 electrical conductivity 66
 preparation, single crystal 178
 La(Ni_{0.5}Ti_{0.5})O₃ crystallography 38
 density 167
 X-ray diffraction 56
 La(Mg_{0.5}Ti_{0.5})O₃ crystallography 38
 density 167
 electrical conductivity 66
 La(Mn_{0.5}Ir_{0.5})O₃ crystallography 38
 density 167
 La(Mn_{0.5}Ru_{0.5})O₃ crystallography 38
 density 167
 La(Ni_{0.5}Ir_{0.5})O₃ crystallography 38
 density 167
 electrical conductivity 66
 preparation, single crystal 178
 Nd(Mg_{0.5}Ti_{0.5})O₃ crystallography 38
 density 167
 A²⁺(B¹⁺B³⁺)O₃ crystallography 39
 density 167
 Ba(Ba_{0.5}Ta_{0.5})O₃ crystallography 39
 density 167
 Ba(Fe_{0.5}Mo_{0.5})O₃ crystallography 39
 density 167
 Sr(Sr_{0.5}Ta_{0.5})O₃ crystallography 39
 density 167
 A²⁺(B¹⁺B³⁺)O₃ crystallography 39
 density 167
 Ba(Ne_{0.5}Ta_{0.5})O₃ crystallography 39
 density 167

CARBIDES

- AlFe₃C crystallography 185
 AlMn₃C crystallography 185
 ferromagnetism 187
 Fe₃SnC crystallography 185

HALIDES

- CsCaF₃ crystallography 185
 CsCdBr₃ crystallography 185
 CsCdCl₃ crystallography 185
 CsFeF₃ crystallography 185
 preparation, single crystal 184
 CsGeCl₃ crystallography 185
 CsHgBr₃ crystallography 185
 CsHgCl₃ crystallography 185
 CsHgI₃ crystallography 185
 CsMgF₃ crystallography 185
 CsPbBr₃ crystallography 185
 CsPbCl₃ crystallography 185
 CsZnF₃ crystallography 185
 KCaF₃ crystallography 185
 KCdF₃ crystallography 185

OTHER TITLES IN THE
SERIES IN SOLID STATE PHYSICS

VOL. 1 F. P. JONA & G. SHIRANE—Ferroelectric Crystals

VOL. 2 J. H. SCHULMAN & W. D. COMPTON—Colour Centers
in Solids

VOL. 3 J. FRIEDEL—Dislocations

VOL. 4 S. V. VONSOVSKII—Ferromagnetic Resonance

BRIEF ATTACHMENT F

IN THE UNITED STATES PATENT AND TRADEMARK OFFICE

In re Patent Application of

Applicants: Bednorz et al.

Serial No.: 08/479,810

Filed: June 7, 1995

For: NEW SUPERCONDUCTIVE COMPOUNDS HAVING HIGH TRANSITION
TEMPERATURE, METHODS FOR THEIR USE AND PREPARATION

Date: March 1, 2005

Docket: YO987-074BZ

Group Art Unit: 1751

Examiner: M. Kopec

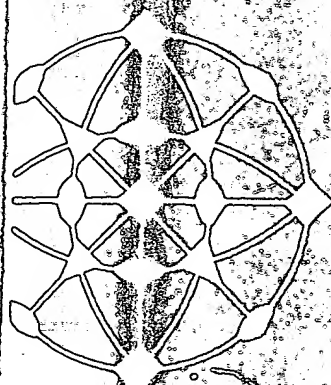
Commissioner for Patents
P.O. Box 1450
Alexandria, VA 22313-1450

FIRST SUPPLEMENTAL AMENDMENT

Sir:

In response to the Office Action dated July 28, 2004, please consider the
following:

ATTACHMENT F



Journal of Solid State Chemistry

ACADEMIC PRESS

New York and London

A Subsidiary of Harcourt Brace Jovanovich, Publishers



Oxygen Defect K_2NiF_4 -Type Oxides: The Compounds $La_{2-x}Sr_xCuO_{4-x/2+\delta}$

NINH NGUYEN, JACQUES CHOISNET,¹ MARYVONNE HERVIEU,
AND BERNARD RAVEAU

*Laboratoire de Cristallographie et Chimie du Solide, L.A. 251, ISMRA,
Université de Caen, 14032 Caen Cedex, France*

Received December 29, 1980; in final form February 18, 1981

Oxygen defect K_2NiF_4 -type oxides $La_{2-x}Sr_xCuO_{4-x/2+\delta}$ have been synthesized for a wide composition range: $0 \leq x \leq 1.34$. From the X-ray and electron diffraction study three domains have been characterized: orthorhombic compounds with La_2CuO_4 structure for $0 \leq x < 0.10$, tetragonal oxides similar to $LaSrCuO_4$ for $0.10 \leq x < 1$ and several superstructures derived from the tetragonal cell ($a = n \cdot a_{LaSrCuO_4}$, with $n = 3, 4, 4.5, 5, 6$) for $1 \leq x \leq 1.34$. The compounds corresponding to $0 < x < 1$ differ from the other oxides in that they are characterized by the presence of copper with two oxidation states: +2 and +3. A model structure for $La_{0.8}Sr_{1.2}CuO_{3.4}$, in which copper has only the +2 oxidation state, and for which the actual cell is tetragonal— $a = 18.80$ Å and $c = 12.94$ Å—has been established. The particular structural evolution of these compounds is discussed in terms of a competition between the capability of Cu(II) to be oxidized to Cu(III) and the ordering of oxygen vacancies.

Introduction

A lot of oxides, with the A_2MO_4 formula, characterized by the intergrowth of perovskite- and sodium chloride-type layers are known at the present time. Contrary to the perovskite oxides, no oxygen defect has been observed for this structural series to our knowledge. Copper, due to its ability to take different coordinations smaller than six, is a potential candidate which could form such anion defect compounds. However the only isostructural copper compounds which have been synthesized, La_2CuO_4 (1, 2) and $SrLaCuO_4$ (3) are stoichiometric. Nevertheless, the recent results concerning the oxides $La_{2-x}A_{1+x}O_{6-x/2}$ ($A = Ca, Sr$) (4), whose

structure is strongly related to that of $Sr_3Ti_2O_7$ (5) suggest the possibility of oxygen defect for A_2CuO_4 compounds. Thus, the present work deals with the oxides $La_{2-x}Sr_xCuO_{4-x/2+\delta}$, for which the replacement of lanthanum by strontium leads to the formation of oxygen vacancies, involving order phenomena.

Experimental

For the synthesis of the compounds of the system La_2CuO_4 – Sr_2CuO_3 , $SrCO_3$, CuO and La_2O_3 were mixed according to the following ratios: $(2-x)/2 La_2O_3/x SrCO_3/1 CuO$. All these reactions were made in a platinum crucible in air. The synthesis of the compounds with high purity strongly depends on the temperature for a fixed pressure. The mixtures were thus first heated for 5 hr at 900°C, and then at tem-

peratures ranging 12 hr.

The oxidation of the compounds by reactions were followed using a Setaram

The crystallography was established by two complementary X-ray diffraction with a Philips goniometer using an X-ray tube.

Results

Study of the System $La_{2-x}Sr_xCuO_{4-x/2+\delta}$

According to the results described, K_2NiF_4 -type oxides corresponding to the $La_{2-x}Sr_xCuO_{4-x/2+\delta}$ large composition range were studied by microthermogravimetry under hydro-

Range	x	
I	0	0
	0.08	0.0
II	0.25	0.0
	0.33 _a	0.1
	0.50	0.1
	0.66 _a	0.0
	0.88 _a	0.0
III	1.00 ^a	0.0
	1.28 ^a	0.0
	1.34 ^a	0.0
	1.20	0.0

^a The "a" parameters are given in

¹ Author to whom reprint requests should be addressed.

peratures ranging from 1000 to 1200°C for 12 hr.

The oxidation state of copper, i.e., the oxygen defect, was determined by reducing the compounds by hydrogen: the reduction reactions were followed by thermogravimetry using a Setaram microbalance.

The crystallographic data were established by two complementary methods: X-ray diffractometry using $CuK\alpha$ radiation with a Philips goniometer and electron diffraction using an EM 200 Philips microscope.

Results

Study of the System La_2CuO_4 - Sr_xCuO_3 : The Compounds $La_{2-x}Sr_xCuO_{4-x/2+\delta}$

According to the methods previously described, K_2NiF_4 -type compounds corresponding to the nominal composition $La_{2-x}Sr_xCuO_{4-x/2}$ were synthesized in a large composition range: $0 \leq x \leq 1.34$. The microthermogravimetric study of these oxides under hydrogen showed, however, that a part of Cu(II) had been oxidized to

Cu(III), leading to the formula $La_{2-x}Sr_xCuO_{4-x/2+\delta}$ with $0 \leq \delta < 0.12$. For $x > 1.34$ a mixture of the K_2NiF_4 -type phase and Sr_2CuO_3 (6) was observed.

The crystallographic data of different compositions are summarized in Table I. The study of the X-ray patterns showed a continuous evolution of the structure and allowed to characterize three composition ranges which were studied by electron diffraction.

(I) $0 \leq x < 0.10$. The X-ray patterns very similar to that of La_2CuO_4 (1) were indexed in an orthorhombic cell with:

$$a_1 = 2a_p \sin \beta/2 = a_{La_2CuO_4},$$

$$b_1 = 2a_p \cos \beta/2 = b_{La_2CuO_4},$$

$$c_1 = c_{La_2CuO_4},$$

where a_p is the parameter of the perovskite cubic cell, and β defines the monoclinic distortion of the cell.

From the conditions limiting possible reflections— $hkl: h+k, l+h, k+l = 2n$ —three space groups are possible: $Fmmm$, $Fmm2$, and $F222$.

TABLE I
CRYSTALLOGRAPHIC DATA OF $La_{2-x}Sr_xCuO_{4-x/2+\delta}$ COMPOUNDS

Range	x	δ	Composition	a (Å)	b (Å)	c (Å)	Heating temperature (°C)
I	0	0	La_2CuO_4	5.366(2)	5.402(2)	13.149(4)	1100
	0.08	0.030(1)	$La_{1.92}Sr_{0.08}CuO_{3.99}$	5.351(1)	5.368(2)	13.200(5)	1000
II	0.25	0.060(4)	$La_{1.75}Sr_{0.25}CuO_{3.935}$	3.775(2)		13.247(5)	1000
	0.33 ₃	0.119(4)	$La_{1.66}Sr_{0.33}CuO_{3.95}$	3.776(1)		13.250(2)	1100
	0.50	0.100(4)	$La_{1.50}Sr_{0.50}CuO_{3.85}$	3.773(1)		13.204(3)	1160
	0.66 ₆	0.092(4)	$La_{1.33}Sr_{0.66}CuO_{3.75}$	3.775(1)		13.150(4)	1170
	0.88 ₈	0.088(4)	$La_{1.12}Sr_{0.88}CuO_{3.64}$	3.773(1)		13.073(5)	1170
III	1.00 ^a	0.0	$LaSrCuO_{3.50}$	3.767(1)		13.002(3)	1200
	1.28 ^a	0.0	$La_{0.72}Sr_{1.28}CuO_{3.36}$	3.761(2)		12.922(9)	1200
	1.34 ^a	0.0	$La_{0.66}Sr_{1.34}CuO_{3.33}$	3.759(3)		12.907(9)	1200
	1.20	0.0	$La_{0.80}Sr_{1.20}CuO_{3.40}$	18.803(7)		12.941(7)	1200

^a The "a" parameters of these compounds (range III) are those of the tetragonal subcell; n values for every composition are given in Table II.

(II) $0.10 \leq x < 1$. The symmetry is tetragonal like that of LaSrCuO_4 (3); the cell parameters are related to the latter and to I in the following manner:

$$a_{II} \approx a_I/2^{1/2} \approx a_p \approx a_{\text{LaSrCuO}_4},$$

$$c_{II} \sim c_I \sim c_{\text{LaSrCuO}_4}.$$

The reflection conditions are those of LaSrCuO_4 — $hkl: h+k+l=2n$ —involving the space groups: $I4/mmm$, $I4/m$, $I422$ and $I42m$.

(III) $1 \leq x \leq 1.34$. The X-ray diffractograms are characterized by the existence of a system of strong peaks, which was already observed for the compounds (II), involving at least the existence of a tetragonal subcell of the same type. However, for all these patterns, weak peaks were always observed which could not be indexed in this cell. An electron diffraction study was thus undertaken: about 50 crystals were examined for each value of x given in Table II. Several types of crystals were isolated:

—Small number of crystals, about 10%, were characterized by a tetragonal cell similar to that of LaSrCuO_4 :

$$a_{III} \sim a_{II} \sim a_p \sim a_{\text{LaSrCuO}_4},$$

$$c_{III} \approx c_{II} \approx c_I \sim c_{\text{LaSrCuO}_4}.$$

—Most of the crystals, i.e., about 90%, presented, in addition to the fundamental reflections previously described, superstructure reflections with a variable inten-

sity. The electron diffraction patterns allowed us to find the following relations for the actual tetragonal cell for a composition x :

$$a_{III}^* = na_{II} \sim na_{II},$$

$$c_{III}^* = c_{II} \neq c_{II} \approx c_I.$$

For a same composition x , several sorts of superstructures were generally observed, characterized either by integral n values ($n = 4, 5$, or 6) or nonintegral values of n (n ranging from 4.5 to 5.6), as shown for several compositions in Table II. Figure 1 shows, as an example, the electron diffraction patterns of the (001) planes for $\text{La}_{2/3}\text{Sr}_{4/3}\text{CuO}_{3.33}$. From Table II it can be seen that a pure term, characterized by a superstructure with an integral value of n ($n = 5$), is only obtained for $x = 1.20$. It has thus been attempted to elaborate a structural model for this phase.

A Structural Model for $\text{La}_{0.8}\text{Sr}_{1.2}\text{CuO}_{3.4}$

The actual cell of this compound is tetragonal: $a = 18.80_4 \text{ \AA}$ and $c = 12.94 \text{ \AA}$ ($Z = 50$). The conditions limiting possible reflections are the same as those of the subcell ($a = 3.760$, $c = 12.94 \text{ \AA}$; $Z = 2$), leading to the space groups $I4/mmm$, $I4/m$, $I422$, and $I42m$. The intensity calculations were first made in the K_2NiF_4 type cell, with the most symmetric space group $I4/mmm$. For these calculations, reflections corresponding only to the subcell were used. Copper atoms were placed on $2(a)$, lanthanum and strontium atoms were statistically distributed on $4e$, and oxygen atoms and anionic vacancies were statistically distributed over two sorts of sites $4e$ (O_I) and $4c$ (O_{II}). After refinement of the atomic parameters the discrepancy factor could not be lowered below $R = 0.104$. The possibility of an order of the oxygen atoms and vacancies over the O_I and O_{II} sites was thus considered. The occupancy factors of both sites



FIG. 1. Electron diffraction patterns of the (001) planes for $\text{La}_{2/3}\text{Sr}_{4/3}\text{CuO}_{3.33}$.

were refined successively and the best fit (Table IV) was obtained.

TABLE II

n VALUES OBSERVED BY ELECTRON DIFFRACTION FOR COMPOUNDS OF RANGE III

Composition	x	n
$\text{LaSrCuO}_{3.5}$	1.00	1; 4.5
$\text{La}_{0.88}\text{Sr}_{1.12}\text{CuO}_{3.44}$	1.12	1; 4.5; 5
$\text{La}_{0.80}\text{Sr}_{1.20}\text{CuO}_{3.40}$	1.20	5
$\text{La}_{0.72}\text{Sr}_{1.28}\text{CuO}_{3.36}$	1.28	1; 4.6; 5; 5.3; 5.4
$\text{La}_{0.66}\text{Sr}_{1.34}\text{CuO}_{3.33}$	1.34	1; 4; 5; 5.6; 6

TABLE III

$\text{La}_{0.80}\text{Sr}_{1.20}\text{O}_{3.40}$: ATOM POSITIONS

Sites	x	y
La		
Sr		
Cu		
O_I		
O_{II}		

$$^a a = 3.760 \text{ \AA}; c = 12.94$$

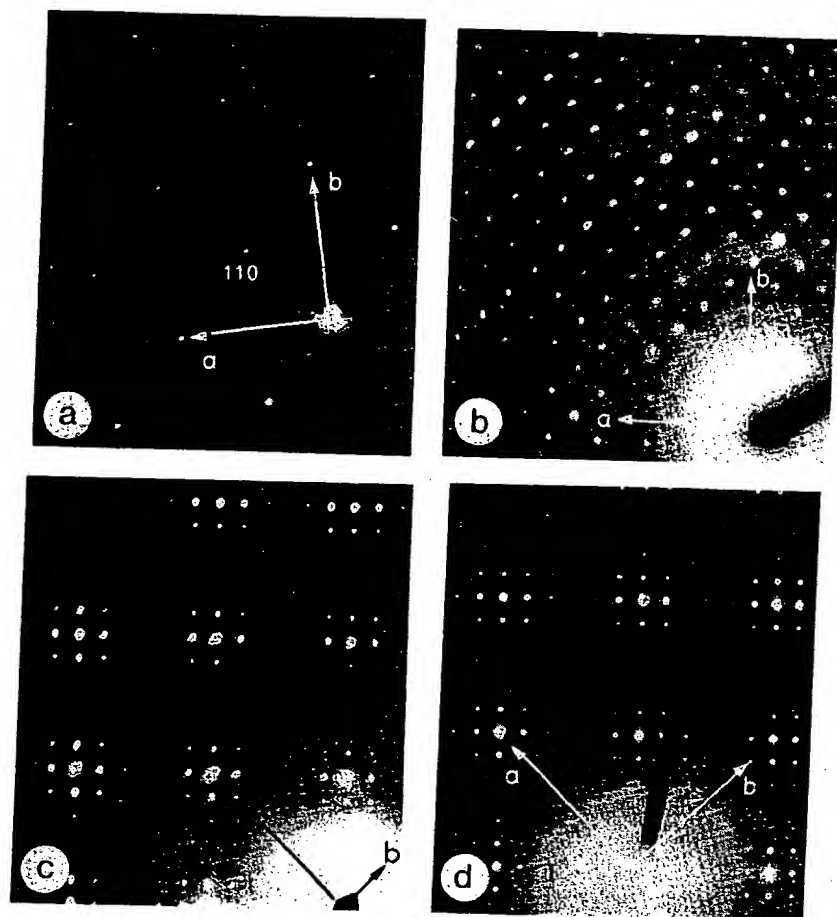


FIG. 1. Electron diffraction patterns of the (001) planes for $La_{2/3}Sr_{4/3}CuO_{3.33}$: (a) $n = 1$; (b) 4; (c) 5.6; (d) 6.

were refined successively and then simultaneously and the best value of $R = 0.081$ (Table IV) was obtained for a total occupa-

TABLE III

$La_{0.80}Sr_{1.20}O_{3.40}$: ATOM POSITIONS IN THE SUBCELL^a

	Sites	x	y	z	B (Å ²)
La	4(e)	0	0	0.357 ± 0.001	0.88
Sr	4(e)	0	0	0	0.85
Cu	2(a)	0	0	0	1.68
O _I	4(c)	0	0.5	0	4.25

^a $a = 3.760$ Å; $c = 12.94$ Å.

tion of the O_I sites, while vacancies and oxygen atoms were distributed over the O_{II} sites. The location of the vacancies preferentially on the O_{II} sites, at the same level as the copper atoms, can be considered as significant, on account of the relatively weak scattering factor of oxygen. This is confirmed by the high R value ($R = 0.153$) obtained for a total occupation of the O_{II} sites, vacancies and oxygen atoms being distributed on the O_I sites. The first results which are summarized in Table III show the atoms are located in positions very close to those usually observed in K_2NiF_4 type structures. The main difference with

TABLE IV
 $\text{La}_{0.8}\text{Sr}_{1.2}\text{CuO}_{3.4}$: OBSERVED AND
 CALCULATED INTENSITIES FOR ATOMIC
 POSITIONS OF TABLE III^a

<i>h k l</i>	<i>I</i> _{obs}	<i>I</i> _{calc}
0 0 2	4.0	4.0
1 0 1	13.0	15.1
0 0 4	17.0	16.9
1 0 3	164.0	156.1
1 1 0	114.0	115.1
1 1 2	0.1	1.7
0 0 6	29.0	23.6
1 0 5	27.0	23.5
1 1 4	35.0	34.6
2 0 0	44.0	49.8
2 0 2	0.1	0.4
1 1 6	26.0	25.2
2 1 1	3.9	3.8
1 0 7	12.0	11.1
2 0 4	10.3	8.2
0 0 8	6.6	5.3
2 1 3	48.0	48.1
2 0 6	15.8	18.1
2 1 5	8.1	9.4
1 1 8	9.0	7.5
1 0 9	0.1	1.7
2 2 0	9.0	12.4
2 2 2	0.1	0.1
0 0 10	0.1	0.8
3 0 1	0.1	0.7
2 1 7	6.0	7.0
2 2 4	3.3	3.0
2 0 8	7.6	6.9
3 0 3	7.0	8.8

^a Subcell, space group $I4/mmm$; $R = 0.081$.

the ideal structure concerns the existence of vacancies located in the same plane as the copper atoms (Fig. 2). Moreover, the high B value for oxygen of O_1 sites (4.2 \AA^2) suggests that in this plane oxygen and vacancies were ordered.

Calculations in the actual cell in space group $I4/m$, were undertaken with 136 possible reflections, including superstructure reflections. Using the position and distributions determined from the subcell, the R factor increased to 0.104, showing, of course, a weak contribution of the superstructure reflections to the R value. The

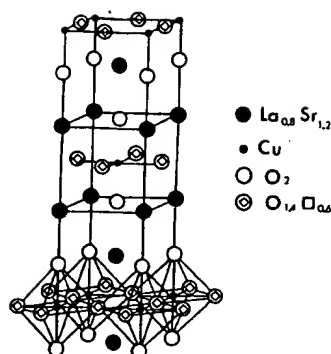


FIG. 2. Ideal drawing of the tetragonal K_2NiF_4 -type structure showing the localization of oxygen vacancies for $\text{La}_{0.8}\text{Sr}_{1.2}\text{CuO}_{3.4}$.

atomic parameters were then refined and the R value was lowered to 0.07 for the final atomic parameters given in Table V. From this table it can be seen that copper atoms are not significantly displaced from their ideal positions, while the bigger cations La, Sr, and the oxygen atoms are only slightly displaced from their ideal positions, but enough to produce the superstructure reflections. These small displacements are certainly induced by an order of the oxygen vacancies, whose contribution to intensities is too small to be detected here. Thus, on account of the numerous possibilities of order between vacancies, and oxygen atoms, and of the weak scattering power of these atoms, we did not try any hypothesis of distribution. Nevertheless, the very likely ordering of vacancies in the "copper plane," should also involve an ordering of lanthanum and strontium over the different sites. Refining the occupancy factors of La and Sr, led to an R value of 0.064 which is not very significant due to the weak contribution of La and Sr to the superstructure reflexions; a preferential occupation of the different sites is, however, likely: A_1 , A_4 , and A_5 would only be occupied by strontium, while lanthanum would occupy 90% of A_6 sites, the remaining strontium and lanthanum atoms being located statistically over the A_2 and A_3 sites.

$\text{La}_{0.8}\text{Sr}_{1.2}\text{CuO}_{3.4}$: AT
ACI

Sites	<i>x</i>
$A_1(4e)$	0
$A_2(16n)$	0.194
$A_3(16n)$	0.403
$A_4(16m)$	0.200
$A_5(16m)$	0.410
$A_6(32O)$	0.389
$A_7(2a)$	0
$A_8(8i)$	0.200
$A_9(8i)$	0.400
$A_{10}(8h)$	0.200
$A_{11}(8h)$	0.405
$A_{12}(16l)$	0.403
$A_{13}(4e)$	0
$A_{14}(16n)$	0.216
$A_{15}(16n)$	0.382
$A_{16}(16m)$	0.182
$A_{17}(16m)$	0.400
$A_{18}(32O)$	0.400
$A_{19}(8i)$	0.100
$A_{20}(8i)$	0.300
$A_{21}(4c)$	0
$A_{22}(16l)$	0.214
$A_{23}(16l)$	0.430
$A_{24}(16l)$	0.300
$A_{25}(16l)$	0.390
$A_{26}(8j)$	0.200
$A_{27}(8j)$	0.400

^a $a = 18.804 \text{ \AA}$; $c = I_4/mmm$.

Discussion

The stabilization, Cu(III) by only heati worthy of note. But characteristic of this existence of a Cu(III) $< x < 1$) which lies regions ($x = 0$ and x strongly related one t be explained by two o are competitive: the stoichiometric K_2NiF_4 La_2CuO_4 and LaSrCu form a related defect :

TABLE V
 $La_{0.8}Sr_{1.2}CuO_{3.4}$: ATOMIC PARAMETERS OF THE
 ACTUAL CELL^a

Sites	x	y	z	B (Å ²)
A ₁ (4e)	0	0	0.347	0.35
A ₂ (16n)	0.194	0	0.359	1.00
A ₃ (16n)	0.403	0	0.356	0.39
A ₄ (16m)	0.200	0.200	0.357	0.32
A ₅ (16m)	0.410	0.410	0.358	1.00
A ₆ (32O)	0.389	0.192	0.357	0.86
A ₇ (2a)	0	0	0	0.80
A ₈ (8i)	0.200	0	0	0.51
A ₉ (8j)	0.400	0	0	0.43
A ₁₀ (8h)	0.200	0.200	0	0.31
A ₁₁ (8h)	0.405	0.405	0	1.00
A ₁₂ (16f)	0.403	0.205	0	0.37
A ₁₃ (4e)	0	0	0.168	1.00
A ₁₄ (16n)	0.216	0	0.168	1.00
A ₁₅ (16n)	0.382	0	0.168	1.00
A ₁₆ (16m)	0.182	0.182	0.172	1.00
A ₁₇ (16m)	0.400	0.400	0.168	1.00
A ₁₈ (32O)	0.400	0.202	0.163	1.00
A ₁₉ (8i)	0.100	0	0	1.00
A ₂₀ (8j)	0.300	0	0	1.00
A ₂₁ (4c)	0	0.500	0	1.00
A ₂₂ (16f)	0.214	0.100	0	1.00
A ₂₃ (16f)	0.430	0.100	0	1.00
A ₂₄ (16f)	0.300	0.200	0	1.00
A ₂₅ (16f)	0.390	0.310	0	1.00
A ₂₆ (8j)	0.200	0.500	0	1.00
A ₂₇ (8j)	0.400	0.500	0	1.00

^a $a = 18.804$ Å; $c = 12.941$ Å (space group I_4/mmm).

Discussion

The stabilization, in this system, of Cu(III) by only heating the oxides in air is worthy of note. But the most important characteristic of this system concerns the existence of a Cu(III) composition range ($0 < x < 1$) which lies between two Cu(II) regions ($x = 0$ and $x \geq 1$), for structures strongly related one to the other. This can be explained by two opposite effects which are competitive: the trend to preserve a stoichiometric K_2NiF_4 structure as for La_2CuO_4 and $LaSrCuO_4$ and the trend to form a related defect structure but with an

ordering of the oxygen vacancies. Thus, rather close to the stoichiometric compound La_2CuO_4 ($x < 1$), the trend to stoichiometry is favored and the vacancies formed from the nominal compositions involving only Cu(II) are partly balanced by the oxidation of Cu(II) to Cu(III). For $x \geq 1$, i.e., rather far from stoichiometry, the La_2CuO_4 or "LaSrCuO₄" stoichiometric compounds cannot be stabilized any more and orderings of the oxygen vacancies appear leading to different microphases as observed from the electron diffraction study, favoring Cu(II) with smaller coordinations (2, 5).

Structure is not, of course, the only factor governing the relative stability of Cu(II) and Cu(III) in these oxides. Kinetics play an important part for determining the ratio Cu(III)/Cu(II) in the richer Cu(III) oxides. For $0 < x < 1$, we have indeed noticed that the pure compounds could only be synthesized by heating at least 12 hr at the formation temperature (Table I) in order to ensure a good crystallization. Annealing the same samples at the same temperature, during longer periods (24 hr) allows us to prepare pure phases with the same structure, but with greater amount of Cu(III). The oxygen pressure will also influence the Cu(III)/Cu(II) ratios. Heating, for example, some Cu(III) samples at low temperature under vacuum, involves a decrease of Cu(III) amount without destroying the structure. In the same way, a reaction under oxygen allows us to increase the Cu(III) amount.

The influence of the Cu(III) amount can also be detected by considering the structural evolution, especially the c parameter, of these compounds as a function of composition (Fig. 3). This evolution is rather complex and quite different from that usually observed for single solid solutions. The substitution of strontium for lanthanum, should not affect this evolution, due to the similar sizes of these cations. It seems interesting to take the Cu(II) compounds as

The influence of the oxygen pressure on the formation of these structures will be investigated. The relations between the electrical properties and the structure of these oxides will be studied.

References

1. J. M. LONGO AND P. M. RACCAH, *J. Solid State Chem.* **6**, 526 (1973).
2. B. GRANDE, H. K. MÜLLER-BUSCHBAUM, AND M. SCHWEIZER, *Z. Anorg. Allg. Chem.* **428**, 120 (1977).
3. J. B. GOODENOUGH, G. DEMAZEAU, M. POUCHARD, AND P. HAGENMULLER, *J. Solid State Chem.* **8**, 325 (1973).
4. N. NGUYEN, L. ER-RAKHO, C. MICHEL, J. CHOISNET, AND B. RAVEAU, *Mater. Res. Bull.* **15**, 891 (1980).
5. S. N. RUDDLESSEN AND P. POPPER, *Acta Crystallogr.* **11**, 54 (1958).
6. C. H. R. L. TESKE AND H. K. MÜLLER-BUSCHBAUM, *Z. Anorg. Allg. Chem.* **371**, 325 (1969).

II) ratio
s previ-
(3). At-
ters for
heating
t 500°C
ncrease
/Cu(II)

nber of
e struc-
plained
are and
During
ena are
u³⁺ for
cancies
phases.

BRIEF ATTACHMENT G

IN THE UNITED STATES PATENT AND TRADEMARK OFFICE

In re Patent Application of

Applicants: Bednorz et al.

Serial No.: 08/479,810

Filed: June 7, 1995

For: **NEW SUPERCONDUCTIVE COMPOUNDS HAVING HIGH TRANSITION
TEMPERATURE, METHODS FOR THEIR USE AND PREPARATION**

Date: March 1, 2005

Docket: YO987-074BZ

Group Art Unit: 1751

Examiner: M. Kopec

Commissioner for Patents
P.O. Box 1450
Alexandria, VA 22313-1450

FIRST SUPPLEMENTAL AMENDMENT

Sir:

In response to the Office Action dated July 28, 2004, please consider the
following:

ATTACHMENT G

THE OXYGEN DEFECT PEROVSKITE $\text{BaLa}_4\text{Cu}_5\text{O}_{13.4}$, A METALLIC CONDUCTOR

C. Michel, L. Er-Rakho and B. Raveau
Laboratoire de Cristallographie, Chimie et Physique des Solides, U.A. 251
ISMRA-Université de Caen, 14032 Caen Cedex, France

(Received March 14, 1985; Refereed)

ABSTRACT

A new oxygen defect perovskite $\text{BaLa}_4\text{Cu}_5\text{O}_{13.4}$, characterized by a mixed valence of copper has been isolated; the parameters of the tetragonal cell are closely related to that of the cubic perovskite: $a = 8.644(4) \text{ \AA}$ $= a_p \sqrt{5}$ and $c = 3.867(3) \text{ \AA} = a_p$. The X-ray diffraction study shows that the atoms are displaced from their ideal positions in the cubic cell, owing to the presence of ordered oxygen vacancies. The study of conductivity, magnetic susceptibility and thermoelectric power versus temperature shows that this oxide is a very good metallic conductor.

INTRODUCTION

Oxygen defect perovskites, have been more extensively studied these last years owing to their potential applications in catalysis, electrocatalysis or as gauges (1-3). In this respect mixed valence copper oxides offer a wide field for investigation: several perovskites (4) or perovskite-related structures have been isolated (5-6). These materials in which copper takes several coordinations simultaneously and a valence state intermediate between II and III can intercalate large amounts of oxygen according to the oxygen pressure and the temperature. Their electron transport properties ranging from semi-conductive to metallic (7) are closely correlated to the amount of intercalated oxygen.

The present paper deals with a new oxygen defect perovskite $\text{BaLa}_4\text{Cu}_5\text{O}_{13.4}$, which is like $\text{La}_3\text{Ba}_2\text{Cu}_6\text{O}_{14.8}$ (4) a mixed valence copper oxide but whose behavior is quite different.

EXPERIMENTAL

Synthesis

Samples were prepared in platinum crucible and in air from appropriate mixtures of dried oxides La_2O_3 , CuO and carbonate BaCO_3 . The mixtures were first heated a few hours at 900°C , ground and heated at 1000°C during several hours. They were then ground again, and mixed with an organic binder, compressed into bars and then slowly heated up to 1000°C . After 24 hours or more at 1000°C , the bars were finally quenched to room temperature. The use of a binder was necessary to avoid that the compressed bars break before

heating. In these conditions the compactness of bars was of about 80 %.

Chemical analysis

In order to determine the oxidation state of the transition metal ions, chemical analysis were carried out by iodometric titration using KI and by reduction in a flow of 25 % hydrogen in argon up to about 1000°C using a SETARAM microbalance for weight loss measurements.

Structural analysis

The cell parameters were determined from X-ray powder diffractograms registered with a Philips goniometer using Cu K α radiation. The space group was determined by electron diffraction using a JEOL 120CX electron microscope.

Magnetic and electrical measurements

The magnetic susceptibility was measured on powders by the Faraday method in the range 80-300K using a Cahn RG microbalance.

The conductivity was measured by the four points method on sintered bars. It was calculated by measuring the intensity/voltage ratio between the points in each current circulation direction in order to minimise the dissymmetry effect between the contacts. The Seebeck coefficient was measured on the same sintered bars held between two Pt heads.

Measurements were carried out up to 600K under an helium pressure of 200 mbars for T < 290K and in air for T > 290K in order to avoid possible departure of oxygen.

RESULTS AND DISCUSSION

The scanning of the system La₂O₃-BaO-CuO for the compositions corresponding to the molar ratio (La + Ba)/Cu = 1 allowed us to isolate a perovskite for La/Ba = 4. The X-ray diffraction pattern of this compounds presents besides the intense lines which can be indexed in a cubic perovskite cell, extra lines which are rather weak. This feature is confirmed by the electron diffraction study, which shows superstructure reflections, leading to a tetragonal cell whose parameters are related to the cubic perovskite subcell (a_p) as follows :

$$a = a_p \sqrt{5} \quad c = a_p$$

all the lines of the X-ray diffraction patterns can be then indexed with accuracy in the tetragonal system with $a = 8.644(4)$ Å and $c = 3.867(3)$ Å. No reflection conditions are observed. The analysis of the oxygen content leads to the formulation BaLa₄Cu₅O_{13.4} involving the presence simultaneously of Cu(II) and Cu(III) in spite of the presence of numerous oxygen vacancies (10.7 %). The measure of the density by pycnometry in benzene at 25°C ($d_{exp} = 7.05$) confirms this composition for one mole per cell ($d_{calc} = 7.03$). Thus it appears that the oxide BaLa₄Cu_{II}_{2.2}Cu_{III}_{2.8}O_{13.4} 1.6 exhibits a great similarity with the oxygen defect perovskite Ba₃La₃Cu_{II}_{5.26}Cu_{III}_{1+26.14%} previously described. However, this compound is very different from Ba₃La₃Cu₅O_{14.6} from the point of view of the oxygen intercalation : no intercalation or deintercalation of oxygen has been observed by annealing this phase at low temperature (400°C to 500°C) and under different oxygen pressures up to 1 bar contrary to Ba₃La₃Cu₅O_{14.6}. In the same way, no oxygen loss has been observed by TGA measurements for temperatures up to 650, 750 and 850°C and under oxygen pressures of 0.02, 0.2 and 1 bar respectively.

Taking into account the fact that the fundamental lines are indexed in a cubic perovskite cell and are strong with respect to the superstructure lines it was interesting to determine whether the metallic atoms were displaced from their ideal positions in the perovskite, or if the superstructure lines

Vol.

were
small
but
stud
posi
spac
king
were
from
Phk1
angle
te c
ideal
of th
R = f
B(0)
from
ties
(Tabl
from
oxygen
0.083
1 Å²
veral

Atomi
the s

in thi
rather
ctions

1.6 1C
ty p v
ty fro
(γ = 4

of tem

80 %.

metal ions,
I and by re-
ag a SETARAMctograms
pace group
microscope.

araday me-

intered bars.
the points
symetry ef-
a the samessure of
ossible de-s correspon-
erovskite
esents be-
cell, extra
ctron dif-
o a tetra-
bcell (a)
pthen
and c =
of the oxy-
resence
umerous oxy-
in benzene
ll (d_{calc} =
1.6 exhibits
Cu^{III} 1+2δ^{0.14δ}
on
: no inter-
ing this pha-
pressures up
oss has been
50°C andindexed in a
cture lines
displaced
ture lines

were only due to the ordering of oxygen vacancies. However, owing to the small amount of oxygen vacancies it was not likely to determine the distribution of the oxygen atoms by X-ray powder diffraction. Thus the structural study was undertaken for the composition La₄BaCu₅O₁₅ just to determine the positions of the atoms with respect to the cubic perovskite subcell. Eight space groups were possible, they were reduced to three P4, P4 and P4/m taking into account the analogy with the perovskite structure. Calculations were carried out in the most symmetrical space group P4/m. For a ranging from 0 to 48°, 37 peaks i.e. 84 hkl were registered. The disparity between Fhkl and F hkl led us to introduce 139 hkl in the calculations. In the same angle range 13 diffraction peaks (14 hkl) were indexed in the cubic perovskite cell with a = 3.867 Å, and used in a calculation with the atoms in the ideal positions of the cubic perovskite cell, involving only a refinement of the thermal factors B; this first refinement led to a discrepancy factor, $R = \frac{\sum |I_{obs} - I_{calc}|}{\sum I_{obs}}$ of 0.066 with B(La, Ba) = 1.2 Å², B(Cu) = 2.6 Å², B(O) = 3.9 Å². The high B values let us think that the atoms were displaced from their ideal positions. A calculation carried out with all the intensities in the P4/m space group and the same ideal positions and overall B = 1 Å² (Table 1a), led to R = 0.35 in agreement with this point of view. Starting from these ideal positions, and assuming a statistical distribution of the oxygen vacancies in the oxides BaLa₄Cu₅O_{13.4}, the R factor was lowered to 0.083, by refinement of the atomic parameters, the B factor being fixed at 1 Å². From the final atomic parameters (Table 1.b) it can be seen that several atoms are displaced from their ideal positions in the cubic perovskite.

TABLE 1

Atomic Parameters of BaLa₄Cu₅O_{13.4} (a) ideal positions (b) after refinement in the space group P4/m

Atom	Site	(a)			(b)		
		X	Y	Z	X	Y	Z
Ba, La	1(d)	0.5	0.5	0.5	0.5	0.5	0.5
Ba, La	4(k)	0.1	0.3	0.5	0.124(1)	0.277(1)	0.5
Cu	1(a)	0.0	0.0	0.0	0.0	0.0	0.0
Cu	4(j)	0.4	0.2	0.0	0.415(3)	0.168(2)	0.0
O	1(b)	0.0	0.0	0.5	0.0	0.0	0.5
O	2(e)	0.0	0.5	0.0	0.0	0.5	0.0
O	4(j)	0.3	0.4	0.0	0.261(7)	0.384(8)	0.0
O	4(j)	0.2	0.1	0.0	0.229(8)	0.063(6)	0.0
O	4(k)	0.4	0.2	0.5	0.428(10)	0.155(6)	0.5

Further refinements, concerning the ordered distribution of oxygen in this structure, which is most probable, were not carried out due to the rather low content of oxygen vacancies, and the too small number of reflections.

This oxide is a very good conductor: its conductivity is about $1.6 \cdot 10^3 (\Omega \text{ cm})^{-1}$ at room temperature. Figure 1 which represents the resistivity ρ versus temperature, shows that this oxide exhibits a metallic conductivity from 200 to 600K. The γ value deduced from the equation $\rho = \rho_0(1 + \gamma T)$ ($\gamma = 4.1 \cdot 10^{-3} \text{ }^\circ\text{C}^{-1}$) is very close to that of free electrons ($\gamma = 3.7 \cdot 10^{-3} \text{ }^\circ\text{C}^{-1}$).

The molar magnetic susceptibility is very weak and nearly independent of temperature. This suggests a Pauli paramagnetism which is characteris-

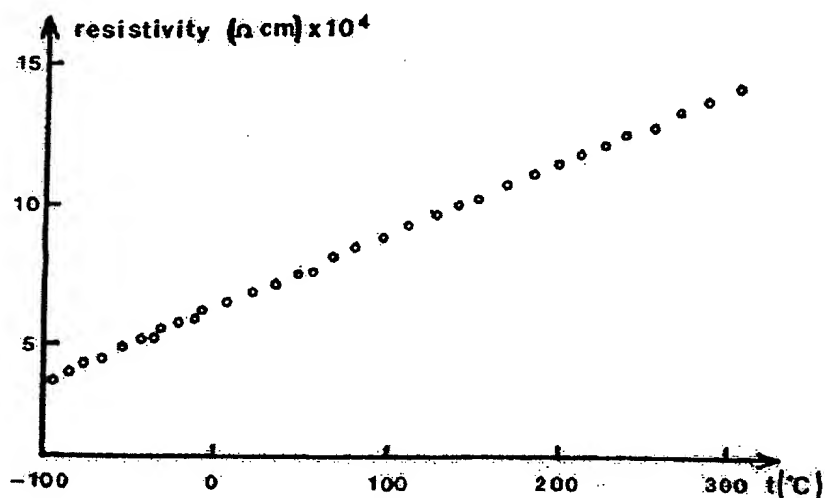


FIG. 1

Resistivity plotted as a function of temperature

tic of delocalized carriers. The Pauli susceptibility (8) calculated with $m^*/m = 1$ and for one carrier per Cu(III) ($\chi_M = 5.3 \cdot 10^{-5}$ e.m.u) is however one order of magnitude lower than the experimental value : $\chi_M = 6 \cdot 10^{-4}$ e.m.u. The increasing of the Pauli susceptibility up to the experimental value needs $m^*/m = 10$. This suggests a strongly correlated carriers gas (degenerated spin polaron gaz) which was introduced by Mott (9) to explain the magnetic susceptibility of LaCuO_3 and LaNiO_3 which are metals (10). At room temperature, the Seebeck coefficient is also very weak and positive ($\alpha = 9 \mu\text{V K}^{-1}$) and increases slightly with temperature ($\alpha_{500\text{K}} = 18 \mu\text{V K}^{-1}$) (Fig. 2). This

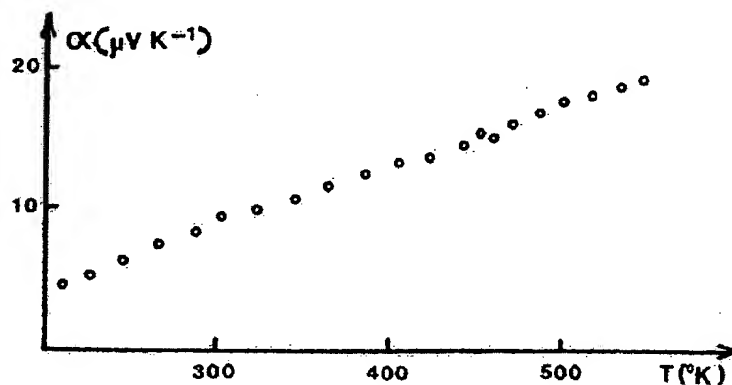


FIG. 2

Evolution of the thermoelectric power as un function of absolute temperature.

This

Mat. Res. Bull., 8, 647 (1973).

perature.

BRIEF ATTACHMENT H

IN THE UNITED STATES PATENT AND TRADEMARK OFFICE

In re Patent Application of

Applicants: Bednorz et al.

Serial No.: 08/479,810

Filed: June 7, 1995

For: NEW SUPERCONDUCTIVE COMPOUNDS HAVING HIGH TRANSITION
TEMPERATURE, METHODS FOR THEIR USE AND PREPARATION

Date: March 1, 2005

Docket: YO987-074BZ

Group Art Unit: 1751

Examiner: M. Kopec

Commissioner for Patents
P.O. Box 1450
Alexandria, VA 22313-1450

FIRST SUPPLEMENTAL AMENDMENT

Sir:

In response to the Office Action dated July 28, 2004, please consider the
following:

ATTACHMENT H

Avec la collaboration de :

AMIEL J. (Paris)	HOLTZBERG P. (G. B. M., New York)
AREND H. (Zürich)	HOPPS R. (Glencoe)
BOBERT J. (Nancy)	HUGBL R. (Reims)
BARTLETT N. (Bristol)	HUGGINS R. A. (Stanford)
BERNARD J. (Paris)	HURF J. (Commissariat à l'Énergie Atomique)
BERNARD J. (Besençon)	LANDRILL A. (Geneva)
BERNARD J. (Besençon)	JELLINEK P. (Geneva)
BERNARD J. (Besençon)	JERGENSEN C. K. (Geneva)
BEVAN D. J. M. (Bedford, Australia)	KLEIM W. (Münster in Westfalen)
BOYNTON E. (Geneva)	KOLDITZ J. (Berlin)
BRONCHER W. (Aachen)	LANG J. (Geneva)
BRUCE-WAGNER J. G. (Tampa)	LEBERER J. (Paris)
CHANG T. L. (Beijing, Pékin)	MAGNELI A. (Stockholm)
CHE M. (Paris)	MAURIN G. (Monsieul)
CHENHADAD R. (Lyon)	OSKAM A. (Amsterdam)
COTTON R. A. (Geneva & M. University)	PALCZYSKA W. (Warszawa)
COUSINS J. C. (Chernobyl-Ferraro)	POUCHARD M. (Bordeaux)
DECEANVRES A. (Lyon)	RABENAU A. (Stuttgart)
DUNCAN J. F. (Wellington, New Zealand)	RAO C. N. R. (Bangalore)
FREUNDLICH W. (Paris)	REID A. R. (Geneva)
FUEKI X. (Tokyo)	ROBERT A. P. (Paris)
GALLAIS F. (Toulouse)	RODUEL J. (Nantes)
GAMBLE F. R. (Baton, Liège)	SAITO N. (Toho University)
GIGUERE P. A. (Québec)	SERATOSA J. M. (Madrid)
GILBERT R. J. (Hamilton, Ontario)	SHULTZ M. (Geneva)
GONZALEZ-GARCIA P. (Sevilla)	SMITH A. (Stuttgart)
GOODENOUGH A. B. (Oxford)	SLEIGHT A. W. (Dr. Pont de Nemours Wilmington)
GRONVOLD B. (Oslo)	SPISTYNE V. (Medina)
GUTMANN V. (Wien)	TAL A. P. (Nantes)
HAERTEL J. (Nantes)	TAKI S. (Geneva)
HAGNMULLER J. (Bordeaux)	TAKIS P. (Lille)
HANNAY N. B. (Ed. Lab., Murray Hill)	VLECK A. (Paris)
HARALDSEN H. (Oslo-Bergen)	WIEBER W. (Berlin)
HEROLD A. (Nancy)	WYART J. (Paris)
HEUBEL J. (Lille)	

Sous la direction de A. CHRISTEN

Secrétaire Général : P. SILBER
 Université Pierre-et-Marie-Curie — Chimie Minérale — Tour 44,
 4, Place Jussieu, 75230 PARIS — CEDEX 05

Relations with Foreign Countries: P. HAGNMULLER
 Directeur du Laboratoire de Chimie du solide du C. N. R. S.,
 351, cours de la Libération, 33405 TALENCE Cedex

ABONNEMENTS — SUBSCRIPTIONS

C. D. R. — Centrale des Revues
 11, rue Gossin, 92543 Montrouge Cedex, France. Tél. 636-52-66

6 numéros par an — 6 issues à year — 6 Heft pro Jahr
 Parution : 10 mars, 10 mai, 10 juillet, 10 septembre, 10 novembre, 10 janvier

Tarif d'abonnement annuel	France	700 F
Annual Subscription (including postage)	Autres pays	1 000 FF
Jahresbezugspreis (einschließlich Porto)	Other countries	

Envoi d'un spécimen sur simple demande. Specimen copy graciously sent on request

The appearance of the code at the bottom of the first page of an article in this journal indicates the copyright owner's consent that copies of the article may be made for personal or internal use of specific clients. This consent is given on the condition that the copier pay the stated fee directly to the Copyright Clearance Center, Inc., 21 Congress St., Salem, Mass. 01970. For those organizations that have been granted a photocopy licence by CCC, a separate system of payment has been arranged. The fee code for users of the Transactional Reporting Service is 0020-7179/84 \$01.00. This consent does not extend to other kinds of copying, such as that for general distribution, for advertising or promotional purposes, for creating new collective works, or for resale.

Table des matières

CHIMIE DOUCE — SOFT CHEMISTRY

La réaction d'échange isotopique $\text{LiNO}_3 \rightarrow \text{HNO}_3$, en milieu acide.	383
J.-L. FOURQUET, M.-P. RENOU & R. DE PAPA	
Ion exchange and intercalation properties of some oxides with a layer and an intersecting tunnel structure.	391
B. RAYBAUD	
Oxygen intercalation in mixed valence copper oxides related to the perovskite.	407
C. MICHEL & B. RAYBAUD	
Soft chemistry in the MPS, series: EXAFS characterization of $\text{Mn}-\text{Zn}_2\text{P}_2\text{S}_6$ heterometallic layers.	426
R. CHÉRY & A. MICHALOWICZ	
Lithium insertion/extraction reactions with manganese oxides.	435
J.-B. GOODENOUGH, M. M. THACKERAY, W. L. P. DAVID & P. G. BRUCE	
Lithium insertion reactions in oxide bronzes.	456
I. D. RAISTRICK	
Soft chemistry: the derivatives of two-dimensional silicols.	468
M. FOURLON & M. ANAND	
Hydrolysis-polyolysis process applied to $\text{K}_2\text{Ti}_2\text{O}_7$.	476
R. MARCEAU, L. BROUAY, R. M'BEDE & M. TOURNON	
Sol-gel derived electrochromic layers.	487
A. CHANGSUDING, M. HENRY & J. LIVAUGH	
A novel nickel (+ II) hydride obtained by soft chemistry.	496
J. J. BRACONNIER, C. DELMAS, C. FODASSIER, M. FOLANZ, B. BEAUDOIN & P. HAGENMULLER	
Labilité des cations dans les chalcogénures ternaires de molybdène : rôle d'acides et de nouvelles synthèses.	509
M. POTT, P. GOUSSON, R. CHAVAZ & M. SERONT	
Chemical and electrochemical alkali metal intercalation in the 3D-framework of $\text{K}_2(\text{MoO}_4)_2$.	537
A. NADRI, C. DELMAS, R. SALMON & P. HAGENMULLER	
Orthorhombic tungsten dihydride: formation and properties.	545
R. SCHÜLLER, U. BERNHARD & W. PAULUS	
Metastable configurations during lithium intercalation into 2H-TaS_2 .	556
T. BORTZ, A. LEUR & J. O. BERNHARD	

(Received November 30, 1983).

Oxygen intercalation in mixed valence copper oxides related to the perovskites

by

Claude MICHEL and Bernard RAYEAU

Equipe Oxydes du Laboratoire de Cristallographie,

Chimie et Physique des Solides, L. A. 231, ISMRA,

Université, 14032 Caen Cedex, France.

Abstract.— Intercalation of oxygen in ternary copper oxides has been studied for three series of compounds: $\text{Ba}_x\text{La}_{1-x}\text{Cu}_2\text{O}_{4+x}$, $\text{La}_{1-x}\text{A}_x\text{Cu}_2\text{O}_{4+x}$ and $\text{La}_{1-x}\text{A}_x\text{CuO}_{2-x/2}$ ($\text{A} = \text{Ca}, \text{Sr}, \text{Ba}$). These mixed valence copper oxides, characterized by the presence of Cu(II) and Cu(III) simultaneously are oxygen defect compounds whose structure is closely related to that of the perovskite, and to those of the two members of the intergrowth SrO-perovskite : Sr_2TiO_6 and K_2NiF_4 , respectively. The localization of the oxygen vacancies in (001) planes of these structures makes that two of these families: $\text{Ba}_x\text{La}_{1-x}\text{Cu}_2\text{O}_{4+x}$ and $\text{La}_{1-x}\text{A}_x\text{Cu}_2\text{O}_{4+x}$ can be considered in their most reduced state as oxides with low dimensionality. The influence of oxygen intercalation on its structure is described. The electrical properties of these phases are described and discussed: they are strongly influenced by the intercalation process. A progressive transition from a p type semiconductive to a p type semi-metallic or metallic state is indeed observed which depends on the oxygen pressure and on the nature of the oxides.

Résumé.— L'intercalation d'oxygène dans les oxydes ternaires de cuivre a été étudiée pour trois séries de composés : $\text{Ba}_x\text{La}_{1-x}\text{Cu}_2\text{O}_{4+x}$, $\text{La}_{1-x}\text{A}_x\text{Cu}_2\text{O}_{4+x}$ et $\text{La}_{1-x}\text{A}_x\text{CuO}_{2-x/2}$ ($\text{A} = \text{Ca}, \text{Sr}, \text{Ba}$). Ces oxydes de cuivre à valence mixte, caractérisés par la présence simultanée de Cu(II) et Cu(III) , sont des composés déficients en oxygène dont la structure est étroitement liée respectivement à celle de la pérovskite et à celles des deux membres de la série d'intercroissances pérovskite- SrO : Sr_2TiO_6 et K_2NiF_4 . La localisation des lacunes anioniques dans les plans (001) de ces structures fait que deux de ces familles : $\text{Ba}_x\text{La}_{1-x}\text{Cu}_2\text{O}_{4+x}$ et $\text{La}_{1-x}\text{A}_x\text{Cu}_2\text{O}_{4+x}$ peuvent être considérées, dans leur état le plus réduit, comme des oxydes de basse dimensionnalité. L'influence de l'intercalation d'oxygène dans la structure est décrite. Les propriétés électriques de ces phases sont décrites et discutées : elles sont fortement influencées par le processus d'intercalation. Une transition progressive d'un état semi-conducteur de type p à un état semi-métallique ou métallique de même type, qui dépend de la pression d'oxygène et de la nature des oxydes, est en effet observée.

REVUE DE CHIMIE MINÉRALE, 0035-1032/84/04/407/19\$ 3.90/© Gauthier-Villars

INTRODUCTION

Intercalation of oxygen in an oxide, by a simple reversible exchange with O_2 in air or in a gaseous atmosphere can be used for different applications such as electrocatalysis, or gauges for materials with electrical properties sensitive to the oxygen content. Thus it appears that such oxides must exhibit rather large oxygen defects in their "reduced" form, and must be able to absorb oxygen from atmosphere tending towards a stoichiometric phase in their "oxidized" state. This phenomenon supposes a reversible change of the oxidation state and of the coordination number of the metallic atoms which participate to the framework of the oxide. In this respect, copper oxides are very good candidates, owing to the ability of copper to take several coordinations—octahedral, square pyramidal, square planar—and several oxidation states: $+1$, $+2$, $+3$. $Cu(II)$ and $Cu(III)$ must be especially considered owing to their possibility to take the same octahedral coordination in similar structures as shown from previous works on $La_2Cu^{II}O_4$ [1-2] and $LaSrCu^{III}O_4$ [3], which are isostructural with K_2NiF_4 . Ternary oxides $AxCuO_3$ containing $Cu(III)$ are more difficult to prepare than those with $Cu(II)$, since oxygen pressures ranging from 1 bar [4-7] to several kbars [3-8] are most of the time necessary to synthesize these compounds. However, the presence of A elements like barium favours the formation of $Cu(III)$ in normal pressure conditions [9-10]. The present paper deals with the soft intercalation of oxygen, i.e. at low pressure ($p \leq 1$ atm) and at low temperature ($T \sim 400-500^\circ C$) in three series of ternary copper oxides related to the perovskite [11-13] and belonging to the systems La_2O_3 -AO-CuO with A = Ca, Sr, Ba. The influence of oxygen intercalation on the electron transport properties of these phases are discussed.

STRUCTURAL CONSIDERATIONS

Three families with an oxygen defect structure have been isolated in the systems La_2O_3 -AO-CuO:

- The oxygen defect perovskites $La_2Ba_xCu_4O_{1+x}$
- The oxygen defect intergrowths $Sr_2Ti_2O_7$ type,
- The oxygen defect intergrowth K_2NiF_4 type, $La_{2-x}A_xCuO_{4-x/2+x}$.

The most reduced form which has been isolated for the defect perovskites $La_2Ba_xCu_4O_{1+x}$ corresponds to the formulation $La_2Ba_xCu_3O_{1+x}$. Its

structure (fig. 1) can be described as an ordered oxygen defect perovskite. All the metallo sites corresponding to the stoichiometric perovskite are occupied by copper ions and lanthanum and barium ions respectively, whereas only 7/9 of the anionic sites are occupied in an ordered manner.

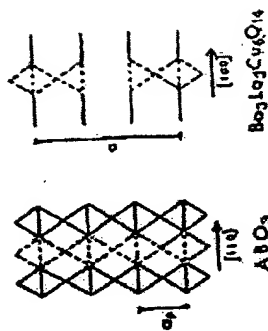


Fig. 1. — Schematic structure of a stoichiometric ABO_3 perovskite and the defect oxygen perovskite $Ba_2LaCu_4O_{11}$.

Considering the tetragonal cell of this compound ($a \approx a_p\sqrt{2} = 5.525$ Å, $c \approx 3a_p = 11.721$ Å), it can indeed be seen that the basal planes of the octahedra, parallel to (001) are preserved, that one apex out of two is missing at the levels $z = 1/6$ and $5/6$, whereas all the apices of these octahedra are missing at $z = 1/2$. It results that this reduced form can be considered as a true layer structure: double defect perovskite layers $[Ba_2La_{2-x}Cu_3O_7]_x$ built up from corner-sharing octahedra CuO_6 square pyramids CuO_5 and square groups CuO_4 are observed whose cohesion is ensured by lanthanum ions located at $z = 1/2$. It is remarkable that such an oxide is characterized by a high $Cu(III)$ content in spite of the high oxygen defect content. Site potential calculations confirm that the Cu^{3+} ions are located preferentially on the octahedral sites. It must also be noted that this limit compound has not really been synthesized. By heating in air at $1000^\circ C$ for 24 h the mixture of La_2O_3 , CuO and $BaCO_3$ and quenching the samples at room-temperature a slight excess of oxygen is indeed observed corresponding to the formulation $La_2Ba_xCu_4O_{1+x}$. The most reduced phase $La_2Ba_xCu_3O_{1+x}$ is then synthesized by annealing the sample $La_2Ba_xCu_4O_{1+x}$ at $400^\circ C$ under low oxygen pressure ($\sim 5 \cdot 10^{-3}$ bar) during several hours.

The deviation from stoichiometry in the oxides $La_2-xA_{1+x}Cu_4O_{6-x/2+x}$ is more complex owing to the possibility of substitution of calcium or strontium for lanthanum, in a small homogeneity range ($0 \leq x \leq 0.14$ for

strontium and $x = 0.10$ for calcium). The most reduced oxide which has been isolated in this family corresponds to the formulation $\text{La}_2\text{SrCu}_2\text{O}_6$. Its tetragonal cell ($a = 3.865 \text{ \AA}$, $c = 19.387 \text{ \AA}$), corresponds to a structure closely related to that of $\text{Sr}_2\text{Ti}_2\text{O}_7$ (fig. 2a). Cu^{2+} ions are indeed located on the Ti^{4+} sites, La^{3+} and Sr^{2+} ions are located on the Sr^{2+} sites, whereas six anionic sites out of seven are occupied by oxygen in an ordered manner; thus, this oxide can be considered as an intergrowth of double oxygen perovskite layers and SrO type layers. The perovskite layer exhibits some similarity with those observed for $\text{La}_2\text{Ba}_3\text{Cu}_6\text{O}_{14}$: the basal planes of the octahedra parallel to (001) are also preserved whereas at $z = 0$ and $z = 1/2$ all the apices of the oxygen octahedra are missing. However, the resulting configuration of the framework is different from $\text{La}_2\text{Ba}_3\text{Cu}_6\text{O}_{14}$. $\text{Cu}(\text{II})$ exhibits here only one coordination which is square pyramidal. Nevertheless this oxide, like $\text{La}_2\text{Ba}_3\text{Cu}_6\text{O}_{14}$, must be considered as a structure with low dimensionality. It can indeed be described as built up from slabs $|\text{LaSrCu}_2\text{O}_6|_\infty$ parallel to (001) whose cohesion is ensured by Sr^{2+} and La^{3+} ions located at $z = 0$ and $z = 1/2$. The $|\text{LaSrCu}_2\text{O}_6|_\infty$ slabs are themselves an intergrowth of SrO -type layers and corner-sharing square pyramidal layers. Such slabs are in fact derived from the K_2NiF_6 structure: the latter corresponds indeed to the superposition of two $|\text{K}_2\text{Ni}_2\text{F}_6|_\infty$ slabs which would share the face of their square pyramids, forming NiF_6 octahedra (fig. 2b). Like $\text{La}_2\text{Ba}_3\text{Cu}_6\text{O}_{14}$, $\text{La}_2\text{SrCu}_2\text{O}_6$ is

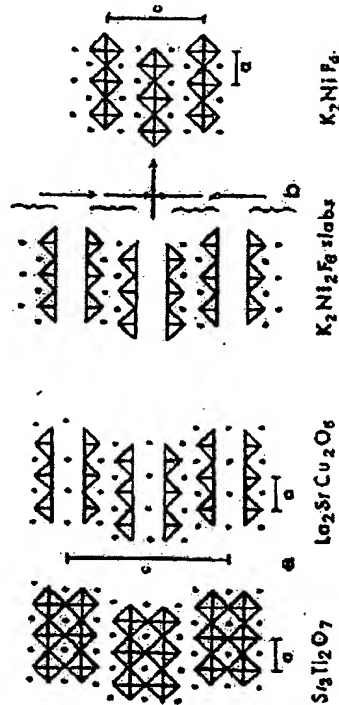


Fig. 2.

- a) Schematic structure of $\text{Sr}_2\text{Ti}_2\text{O}_7$ and $\text{La}_2\text{SrCu}_2\text{O}_6$ (projection on to (100) plane), showing the oxygen vacancies.
b) Schematic representation of $\text{K}_2\text{Ni}_2\text{F}_6$ slabs sharing the square faces of the NiF_6 pyramids to give the K_2NiF_6 structure.

characterized by a great stability in spite of its oxygen defect structure: it is indeed synthesized by heating the stoichiometric mixture of CuO , La_2O_3 and SrCO_3 at $1050-1100^\circ\text{C}$ for 24 h in air and by quenching them at room temperature in order to avoid their oxidation at lower temperature. Contrary to $\text{La}_2\text{Ba}_3\text{Cu}_6\text{O}_{14}$, copper is in its lower oxidation state, $\text{Cu}(\text{II})$ in this oxide.

The oxides $\text{La}_{2-x}\text{A}_x\text{CuO}_{4-x/2+x}$ exhibit an oxygen defect K_2NiF_6 type structure involving different coordinations of copper: octahedral, square pyramidal and eventually square planar (fig. 3). Their oxygen content

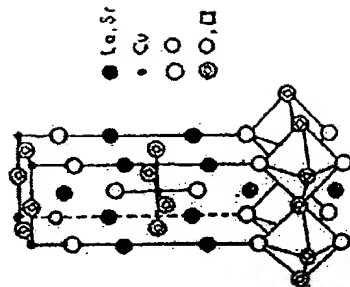


Fig. 3. — Perspective view of the structure of the oxides $\text{La}_{2-x}\text{Sr}_x\text{CuO}_{4-x/2+x}$ with oxygen vacancies located in the basal plane of the octahedra.

depends on the nature of the A ions ($A = \text{Ca}, \text{Sr}, \text{Ba}$) and on the substitution rate x which can lead to wide homogeneity ranges: $0 \leq x \leq 0.20$ for $A = \text{Ca}$ and Ba and $0 \leq x \leq 4/3$ for $A = \text{Sr}$. The most reduced phase which exhibits the highest deviation from stoichiometry has been synthesized in the case of strontium for $x = 4/3$: $\text{La}_{2/3}\text{Sr}_{4/3}\text{CuO}_{3.33}$. Contrary to the two other series, the oxygen vacancies are located in the basal plane of the octahedra which are parallel to the (001) plane of the tetragonal cell ($a = 3.759 \text{ \AA}$, $c = 12.907 \text{ \AA}$). It must also be emphasized that this type of localization of the oxygen vacancies is always observed whatever the nature of the A ions, and whatever the rate of substitution x may be. However, symmetry changes and order-disorder phenomena in this plane may appear according to the nature of A and x value (table I). So, the calcium and barium oxides are characterized by a monoclinic distortion of the tetragonal K_2NiF_6 structure, whatever the x value may be $0 \leq x \leq 0.20$; the same

is true for the strontium compounds with $0 \leq x \leq 0.10$. Thus, the oxides corresponding to these homogeneity ranges exhibit an orthorhombic cell related to that of K_2NiF_4 in the following way: $a \approx b \approx aK_2NiF_4 \sqrt{2}$ and $c \approx cK_2NiF_4$.

TABLE I

The oxides $La_{1-x}A_xCuO_{4-y/2+z}$: crystallographic data and analytical results (quenched materials).

A	x	δ	Cell parameters (Å)			Heating temperature °C
			a	b	c	
Ba	0		5.364	3.402	13.149	1,100
	0.05	0.01	5.363	3.380	13.201	1,100
	0.1	0.02	5.359	3.364	13.245	1,100
Ca	0.2	0.03	5.356		13.320	1,100
	0.05	0.04	5.351	3.387	13.150	1,100
	0.02	0.02	5.356	3.385	13.174	1,100
Sr	0.2	0.03	5.357	3.380	13.210	1,100
	0.08	0.03	5.351	3.368	13.200	1,000
	0.16	0.04	5.374		13.231	1,000
	0.25	0.07	5.375		13.247	1,000
	0.33	0.11	5.374		13.254	1,100
	0.50	0.10	5.376		13.210	1,160
	0.66	0.075	5.375		13.160	1,170
	0.88	0.06	5.369		13.070	1,170
	1.0	0.005	5.367 (*)		13.002	1,200
	1.20	0.0	5 x 5.376		12.940	1,200
	1.33	0.0	5.359 (*)		12.907	1,200

(*) These a parameters are those of the tetragonal subcell.

On the other hand, the strontium compounds exhibit a tetragonal symmetry similar to that of K_2NiF_4 or $LaSrCuO_4$ [3] for $0.10 < x < 1$ ($a \approx aK_2NiF_4$; $c \approx cK_2NiF_4$), whereas for $1 \leq x \leq 4/3$, superstructures appear on the electron diffraction patterns which involve tetragonal cells with $a = b \approx aK_2NiF_4$, n ranging from 1 to 6 according to the composition, c remaining unchanged ($c \approx cK_2NiF_4$). These oxides are very stable in spite of the high deviation from stoichiometry; for instance $La_{2/3}Sr_{1/3}CuO_{3.2}$ is prepared by heating a mixture of the compounds La_2O_3 , CuO and $SrCO_3$ at 1 200°C and quenching the phase at room temperature. It appears here that the most reduced phase exhibits also only $Cu(II)$ like $La_2SrCu_3O_6$ belonging to the second series. The oxides $La_{1-x}A_xCuO_{4-y/2+z}$ appear very closely related to the second series formulated $La_{2-2x}A_xCu_2O_{6-y/2+z}$ in that they can be considered as being respectively the members $n = 1$ and 2 of a series of oxygen defect intergrowths between perovskite and

SrO structures, corresponding to the general formulation $A_{n-1}B_nO_{3n+1}$. However the behaviour of $La_{2-2x}A_xCuO_{4-y/2+z}$ is very different from the two other series in that it cannot be considered in its most reduced form as an oxide with low dimensionality.

OXYGEN INTERCALATION AND DESINTERCALATION: INFLUENCE ON THE STRUCTURE

Oxygen can be intercalated in these three series of oxides by simple annealing of the materials at low temperature, i. e. 400°C-500°C, under different oxygen pressures.

The oxygen defect perovskite $La_3Ba_3Cu_6O_{14.10}$ synthesized in air can absorb rather important oxygen amounts by annealing the samples at 400°C under oxygen pressures ranging from 10^{-2} to 1 bar as shown from table II. In the same way, oxygen can be deintercalated from the structure of $La_3Ba_3Cu_6O_{14.10}$ or from more oxidized compounds by simply annealing the samples always at 400°C under lower oxygen pressure, 5.10^{-3} bar (table II). Thus it appears that the intercalated oxides $La_3Ba_3Cu_6O_{14.10}$

TABLE II

Evolution of δ as a function of the oxygen pressure after annealing the oxide $La_3Ba_3Cu_6O_{14.10}$ at 400°C.

PO_2 (bar)	5.10^{-3}	10^{-2}	2.10^{-1}	5.10^{-1}	0.1	0.2	1
δ	0.05	0.19	0.25	0.31	0.33	0.37	0.43

exhibit a rather wide homogeneity range $0.05 \leq \delta \leq 0.43$. The intercalation of oxygen in this structure does not influence the cell parameters, since the most oxidized compound, $La_3Ba_3Cu_6O_{14.43}$, is characterized by parameters very similar to those of $La_3Ba_3Cu_6O_{14.10}$, $a = 5.529$ Å and $c = 11.729$ Å, whereas no parameter change with respect to the air synthesized oxide is observed when δ tends towards zero. It is of course not possible to localize the additional oxygen in the structure by X ray diffraction; however site potential calculations [14], assuming that Cu^{2+} is octahedrally coordinated, show that this additional oxygen should be located between two square pyramids CuO_4 , i. e. at $z = 1/2$, between the layers described above, forming corner-sharing ribbons of CuO_4 octahedra running along c . The electron transport properties of these compounds, which will be discussed further, are in agreement with this hypothesis. The fact that

the c parameter does not vary, in spite of the intercalation of rather great amounts of oxygen is easily explained by the high oxygen defect content in the structure: the slabs $[\text{Ba}_1,3\text{La}_{0,3}\text{Cu}_2\text{O}_7]_{\infty}$ exhibit, themselves, oxygen defects, which may favour slight displacements of the copper and oxygen atoms along c during oxygen intercalation, between the slabs, without changing the c parameter.

The oxygen intercalation in the second series, $\text{La}_{2-x}\text{A}_{1+x}\text{Cu}_2\text{O}_{6-x/2+x}$, depends on the nature of the A ions, calcium or strontium, on the rate of substitution x , and on the oxygen pressure as shown from table III. It can

TABLE III
Crystallographic data and analytical results for the oxides
 $\text{La}_{2-x}\text{A}_{1+x}\text{Cu}_2\text{O}_{6-x/2+x}$

Quenched oxides (in air)			Annealed oxides (in O_2)		
Composition	δ	Cell parameters	Composition	δ	Cell parameters
$\text{La}_2\text{SrCu}_2\text{O}_6$	0	$a = 3.865 \text{ \AA}$ $c = 19.667 \text{ \AA}$	$\text{La}_2\text{SrCu}_2\text{O}_{6.20}$	0.20	$a = 3.865 \text{ \AA}$ $c = 20.055 \text{ \AA}$
$\text{La}_{1.98}\text{Sr}_{0.02}\text{Cu}_2\text{O}_{6.02}$	0.02	$a = 3.863 \text{ \AA}$ $c = 19.963 \text{ \AA}$			
$\text{La}_{1.99}\text{Sr}_{0.01}\text{Cu}_2\text{O}_{6.04}$	0.04	$a = 3.859 \text{ \AA}$ $c = 19.956 \text{ \AA}$	$\text{La}_{1.99}\text{Sr}_{0.01}\text{Cu}_2\text{O}_{6.29}$	0.29	$a = 3.863 \text{ \AA}$ $c = 20.051 \text{ \AA}$
$\text{La}_{1.98}\text{Ca}_{0.02}\text{Cu}_2\text{O}_{6.02}$	0.02	$a = 3.825 \text{ \AA}$ $c = 19.404 \text{ \AA}$	$\text{La}_{1.98}\text{Ca}_{0.02}\text{Cu}_2\text{O}_{6.08}$	0.08	$a = 3.825 \text{ \AA}$ $c = 19.404 \text{ \AA}$

Indeed be seen for the strontium oxides synthesized in air, like $\text{La}_2\text{SrCu}_2\text{O}_6$, that δ increases with the strontium content leading towards the formulation $\text{La}_{2-x}\text{A}_{1+x}\text{Cu}_2\text{O}_6$. It results that the Cu^{2+} content increases with the divalent A ion content, in order to compensate the oxygen vacancies due to the substitution of Sr^{2+} or Ca^{2+} for La^{3+} . The annealing of the latter oxides at 400°C under an oxygen pressure of one bar shows the ability of these phases to intercalate oxygen, δ ranging from 0 to 0.29 for $\text{La}_{2-x}\text{Sr}_{1+x}\text{Cu}_2\text{O}_{6-x/2+x}$ whereas $0.02 \leq \delta \leq 0.08$ for $\text{La}_{2-x}\text{Ca}_{1+x}\text{Cu}_2\text{O}_{6-x/2+x}$. One can see that the rate of intercalation is higher for the strontium oxides than for the calcium compound. Moreover, it seems that in the strontium oxides the maximum rate of intercalation increases with the strontium content. Contrary to the oxides $\text{La}_2\text{Ba}_2\text{Cu}_2\text{O}_{6+x}$, the compounds $\text{La}_{2-x}\text{Sr}_{1+x}\text{Cu}_2\text{O}_{6-x/2+x}$ exhibit a variation of the interlayer distances: the c parameter of the tetragonal cell increases with the oxygen content δ , for a same x value. This influence of

intercalation on the c parameter, can be explained by the fact that the $[\text{La}_{1-x}\text{Sr}_x\text{Cu}_2\text{O}_6]_{\infty}$ slabs, which are stoichiometric and formed of SrO -type layers are more rigid than the $[\text{Ba}_{1-x}\text{La}_x\text{Cu}_2\text{O}_7]_{\infty}$ slabs, and are only displaced by the introduction of oxygen between them. However the behaviour of the oxides $\text{La}_{1-x}\text{Ca}_x\text{Cu}_2\text{O}_{6-x/2+x}$, where c parameter is independent of δ is not explained; nevertheless in this latter case δ remains rather weak ($\delta \leq 0.08$). The oxygen desintercalation of these oxides is similar to that observed for the first family: for instance heating the most oxidized compound $\text{La}_2\text{SrCu}_2\text{O}_{6.30}$ at 400°C under low oxygen pressures ($\sim 10^{-3}$ bar) leads progressively to the reduced phase $\text{La}_2\text{SrCu}_2\text{O}_6$.

The behaviour of the oxides $\text{La}_{2-x}\text{A}_x\text{Cu}_2\text{O}_{6-x/2+x}$ is much more complex owing to the wide homogeneity ranges observed for these oxides especially in the case of strontium. For instance, the δ values observed for the strontium oxides synthesized in air (table I) do not increase progressively with x contrary to $\text{La}_{2-x}\text{Sr}_x\text{Cu}_2\text{O}_{6-x/2+x}$, but increase up to $x \approx 1/3$ and then decrease again up to $x \approx 1$. These δ values are difficult to compare owing to the fact that the different compositions were not synthesized at the same temperature in order to obtain pure oxides. It is sure that equilibrium is rarely reached for this series. So, for $0 \leq x \leq 1$ the δ values given in table I correspond to heating times of 12 h and annealing these samples in the same conditions, but for longer times (24 h to 48 h) allowed us to prepare pure phases with the same structure but characterized by greater δ values. Thus it appears that kinetics plays an important part for oxygen intercalation in this phase at a given temperature and a given oxygen pressure. Like for the two other series, oxygen can be intercalated or desintercalated by annealing the samples synthesized in air, at 400°C under an oxygen pressure of one bar or under vacuum (10^{-3} bar) respectively. The curves $\delta = f(x)$ are given in figure 4 for the strontium compounds where they are compared with the line $\delta = x/2$ which represents the maximum rate of intercalation available in this structure. It can be seen that oxygen can easily be desintercalated, leading towards the most oxygen defect structure; it appears that intercalation tends to be maximum for low x values ($0 \leq x \leq 0.25$), whereas it is only partial for higher x values ($0.33 \leq x \leq 1.20$), 11 % to 33 % of the available anionic sites being only occupied in this latter composition range. From these results it seems that intercalation is governed by two opposite effects which are competitive: the trend to preserve a stoichiometric K_2NiF_4 structure as for $\text{La}_2\text{Cu}^{10}\text{O}_4$ and $\text{LaSrCu}^{10}\text{O}_4$, and the trend to form a related defect structure but with an ordering of the oxygen vacancies. Thus, rather close to the stoichiometric compound La_2CuO_4 , the trend to stoichiometry is favoured by partial oxi-

dation of Cu(II) to Cu(I)), whereas rather far from La_2CuO_4 , for example for $x = 1$, the stoichiometric oxide LaSrCuO_4 [3] cannot be stabilized any more under normal oxygen pressure, and oxygen vacancies are favoured; the resulting great amount of anionic vacancies are ordered, leading to different microphases as observed by electron diffraction. The « a » parameter which characterizes the corresponding K_2NiF_4 type tetragonal cell is generally not influenced by the intercalation-deintercalation process except for high x values which exhibit superstructures. For such oxygen defect oxides, an order-disorder phenomenon of the oxygen vacancies appears in the (0 0 1) plane which contributes to the variation of the « a » parameter of the K_2NiF_4 subcell. It is for instance the case of the strontium oxide corresponding to $x = 1.20$. The sample quenched in air ($\delta = 0$) exhibits a superstructure in the (0 0 1) plane with a « a » subcell parameter of 3.76 Å (table I). The annealing at 400°C in oxygen of this phase involves an important decrease of the rate of the oxygen vacancies ($\delta = 0.33$). It results that the order disappears, leading to a true tetragonal cell with « a » greater than that of the quenched specimen ($a = 3.791$ Å), c being smaller ($c = 12.900$ Å). The evolution of the a parameter versus composition for quenched and annealed compounds is complex (fig. 5). It results from the influence of several factors: copper (III) and oxygen vacancies contents, size of Sr^{2+} which is slightly larger than La^{3+} . For every x value, c increases with the rate of intercalation, i. e. with the $\text{Cu}^{3+}/\text{Cu}^{2+}$ ratio, except for high x values which exhibit order-disorder phenomena. This behavior is in agreement with the observation previously made by Goodenough *et al.* [3].

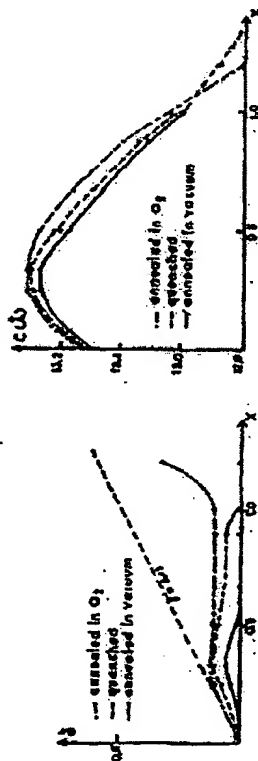


Fig. 4.

Fig. 4. — The oxides $\text{La}_{1-x}\text{Sr}_x\text{CuO}_{4-\delta}$: evolution of δ as a function of x for oxides resulting from different thermal treatments.

Fig. 5. — The oxides $\text{La}_{1-x}\text{Sr}_x\text{CuO}_{4-\delta}$: evolution of the a parameter as a function of x for oxides resulting from different thermal treatments.

The evolution of « c » can be interpreted by two opposite effects: increasing due to substitution of Sr^{2+} for La^{3+} and decreasing due to oxygen vacancies. For small x values ($x < 0.25$) the number of oxygen vacancies remains low and tends towards zero so that c increases owing to the replacement of La^{3+} by Sr^{2+} . For $x > 0.25$ the number of oxygen vacancies becomes very large and its effects prevails on that of substitution $\text{Sr}^{2+}/\text{La}^{3+}$, involving a decrease of « c ».

INFLUENCE OF THE INTERCALATION PROCESS ON THE ELECTRICAL PROPERTIES OF THE MIXED VALENCE COPPER OXIDES

Most of the oxides described above are characterized by the presence simultaneously of Cu(II) and Cu(III), and are thus mixed-valence oxides. The electron transport properties of these phases, which are p type semiconductors or p type semi-metals or metals are strongly influenced by the rate of intercalation.

The evolution of conductivity versus reciprocal temperature for different

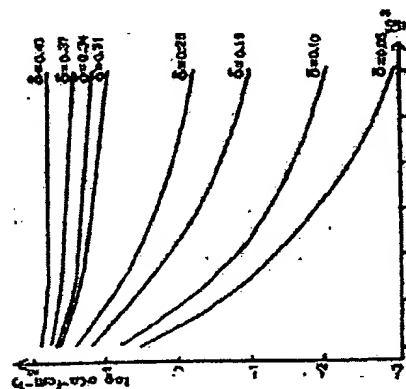


Fig. 6.

Fig. 6. — The oxides $\text{Ba}_{1-x}\text{La}_x\text{CuO}_{4-\delta}$: variation of the conductivity (logarithmic scale) as a function of reciprocal temperature for different δ values.

Fig. 7. — The oxides $\text{Ba}_{1-x}\text{La}_x\text{CuO}_{4-\delta}$: variation of the thermoelectric power as a function of T for different δ values.

Fig. 7.

δ values of the oxides $\text{La}_2\text{Ba}_3\text{Cu}_6\text{O}_{14+x}$ (fig. 6) shows that the conductivity increases drastically with the intercalation of oxygen, contrary to the structure which remains unchanged. In the same way the thermoelectric power of these phases (fig. 7) is very sensitive to the intercalation rate. These properties are interpreted by a conduction band model whose configuration is mainly determined by the splitting of the $3d$ Cu orbitals by the crystal field [15] (fig. 8 a). Every composition can indeed be considered as a mixing of the two limits: the reduced form $\text{Ba}_3\text{La}_3\text{Cu}_6\text{O}_{14}$, characterized by ribbons of one octahedron and two tetragonal pyramids running along c , and the oxidized form $\text{Ba}_3\text{La}_3\text{Cu}_6\text{O}_{15}$ which exhibits infinite octahedral ribbons along c . The $\sigma_{x^2-y^2}$ bands result from Cu—O—Cu interactions and strong electron-electron interactions split the $d_{x^2-y^2}$ and d_{z^2} levels by a few eV like the $\sigma_{x^2-y^2}$ and σ_{z^2} bands. It results that the band structure of $\text{La}_2\text{Ba}_3\text{Cu}_6\text{O}_{14}$ (fig. 8 b) is that of an insulator but this limit has not been synthesized; on the other hand, the only level configuration which can lead to a semi-metallic or metallic conduction for the limit $\text{Ba}_3\text{La}_3\text{Cu}_6\text{O}_{15}$ corresponds to a d_{z^2} empty level located just above or across the filled

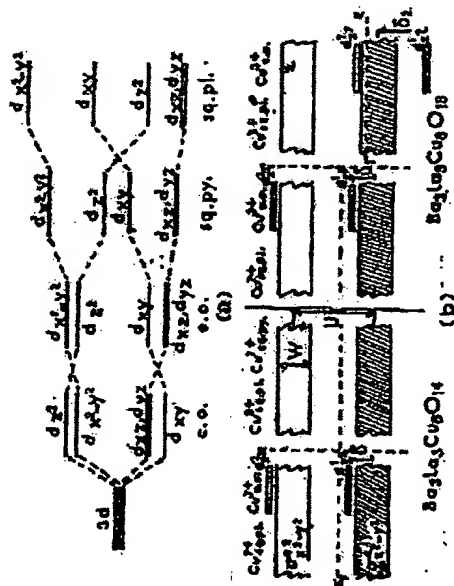


Fig. 8.

a) Crystal field splitting for d elements in different environments: o. o.: compressed octahedron, e. o.: elongated octahedron, sq. py.: square pyramid, sq. pl. square plane.
b) Schematic band diagram for $\text{Ba}_3\text{La}_3\text{Cu}_6\text{O}_{14}$ and $\text{Ba}_3\text{La}_3\text{Cu}_6\text{O}_{15}$. Δ denotes the intra-atomic Coulomb energy, δ , δ_1 and δ_2 the splitting due to the axial distortion of the octahedra and W the estimated band width.

$\sigma_{x^2-y^2}$ band (fig. 8 b). Thus, it appears that intercalation of oxygen which corresponds to a local change of copper coordination, will involve an increase of the density of the $d_{x^2-y^2}$ levels above the filled $\sigma_{x^2-y^2}$ band, i. e. an increase of the number of holes in the conduction band. The approximately linear evolution of $\log \sigma$ vs δ at 293 K is in agreement with this model. This progressive transition from a semi-conductive to a semi-metallic state can be explained by the Mott model [16] of quasi localized holes trapped at the top of the filled $3d_{x^2-y^2}$ band.

The oxides $\text{La}_{2-x}\text{A}_{1+x}\text{Cu}_2\text{O}_{6-2/3+x}$ exhibit a similar behaviour [17]. From the evolution of the curves $\log \sigma = f(1/T)$, between 80 K and 300 K (fig. 9) it can be seen that a continuous transition from a semi-conductive to a semi-metallic state is observed as the oxygen intercalation rate increases from $\delta = 0$ ($\text{La}_2\text{SrCu}_2\text{O}_6$) to $\delta = 0.29$ ($\text{La}_{1.86}\text{Sr}_{0.14}\text{Cu}_2\text{O}_{6.22}$). The conductivity depends also on the nature of the A ion which influences drastically the c parameter: the calcium oxide $\text{La}_{1.80}\text{Ca}_{0.20}\text{Cu}_2\text{O}_{6.27}$ is indeed much more conductor than the corresponding strontium oxide $\text{La}_{1.80}\text{Sr}_{0.20}\text{Cu}_2\text{O}_{6.27}$. The Seebeck coefficient curves $\alpha = f(T)$ (fig. 10) confirm this influence of intercalation: α increases continuously with T for

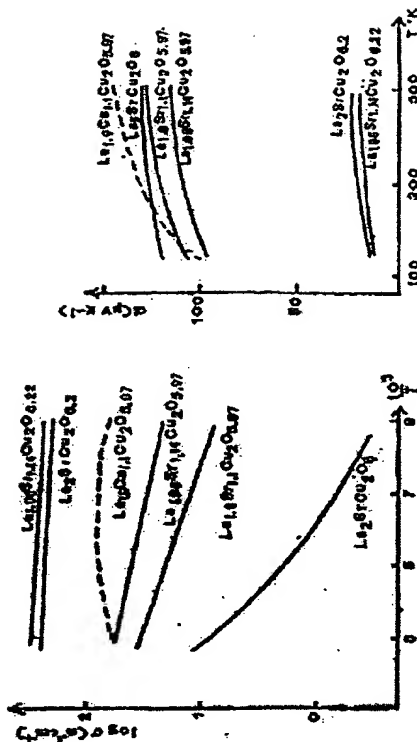


Fig. 9.

Fig. 10.

Fig. 9. — The oxides $\text{La}_{2-x}\text{A}_{1+x}\text{Cu}_2\text{O}_{6-2/3+x}$: evolution of the conductivity (logarithmic scale) vs $1/T$ for different compositions.

Fig. 10. — The oxides $\text{La}_{2-x}\text{A}_{1+x}\text{Cu}_2\text{O}_{6-2/3+x}$: evolution of the thermoelectric power vs T for different compositions.

the small intercalation rates ($\delta = 0$ to 0.04) i. e. for small Cu^{3+} contents, whereas it becomes weak and nearly independent of the temperature, for high intercalation rates ($\sigma = 0.20$ to 0.29), i. e. for high hole concentration. These properties very similar to those obtained for $\text{La}_2\text{Ba}_2\text{Cu}_2\text{O}_{4+x}$ can be explained by the same Mott model of holes trapped at the top of the $\sigma_{x^2-y^2}^*$ band. However the rather high conductivity of $\text{La}_2\text{SrCu}_2\text{O}_4$ in spite of the very weak Cu^{3+} content— $\delta \approx 0$ —let us think that the intra-atomic energy U is in this case of the same order of magnitude as the band width W_e (fig. 11). In the same manner the relatively high and metallic conductivity of the calcium oxide $\text{La}_{1.90}\text{Ca}_{0.10}\text{Cu}_2\text{O}_{4.99}$ compared to the corresponding strontium oxide shows that the band width W_e must be larger than U in the calcium compound so that the overlapping of the two $\sigma_{x^2-y^2}^*$ bands gives rise to a higher mobility.

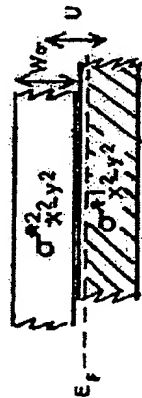


Fig. 11.—The oxides $\text{La}_{1-x}\text{Sr}_x\text{Cu}_2\text{O}_{4+x}$; schematic band diagram as deduced from electron transport properties.

The highest conductivities are observed for the oxides $\text{La}_{1-x}\text{Sr}_x\text{Cu}_2\text{O}_{4+x}$ [15]. For a given substitution rate x , the conductivity increases with the rate of intercalation δ as shown from figure 12 for temperature ranging from 80 K to 300 K. However the evolution of $\log \sigma$ vs $1/T$ as well as $\alpha = \sigma(T)$ is more complex than the two other series: δ is not the only factor governing the electron transport properties of the phases. Three domains must in fact be distinguished: $0 \leq x \leq 0.16$, $0.16 < x \leq 0.50$ and $0.50 < x \leq 1.20$ for the oxides quenched in air and annealed in oxygen. The compounds of the first domain ($0 \leq x \leq 0.16$) are characterized by a semi-metallic behaviour and their properties can be interpreted by the model developed by Goodenough for La_2CuO_4 [19] involving the presence of holes in the filled band $\sigma_{x^2-y^2}^*$. The weak variation of conductivity which does not correspond to the metallic model $\rho = \rho_0(1 + \gamma)$ (fig. 12 a), as well as the thermoelectric power values (fig. 13) greater than those of a metal are in agreement with this model. The fact that the holes may be trapped on localized levels at the top of the $\sigma_{x^2-y^2}^*$ band—according to the Mott Model—is also confirmed by the fact that α increases with temperature (fig. 13). The

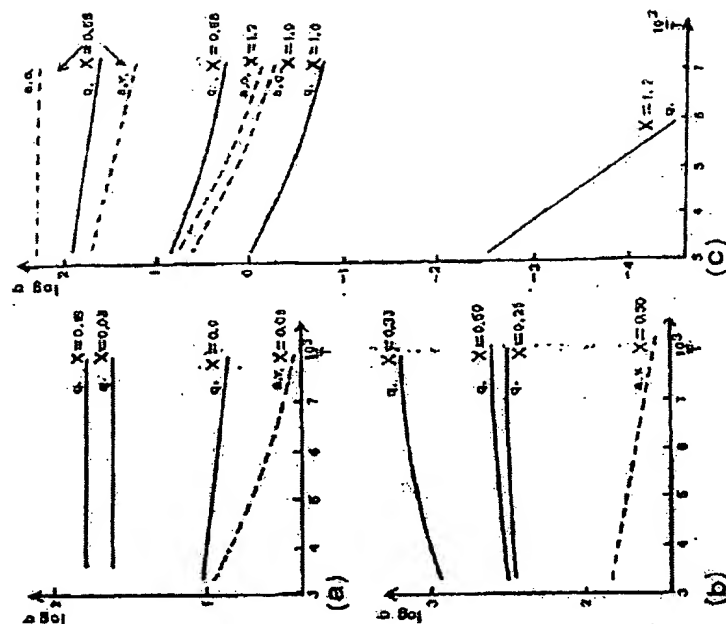


Fig. 12.—The oxides $\text{La}_{1-x}\text{Sr}_x\text{Cu}_2\text{O}_{4+x}$; variation of the conductivity vs T^{-1} (g: quenched in air, a. o.: annealed in O_2 , a. v.: annealed in vacuum).

a) $0 \leq x \leq 0.16$; b) $0.16 < x \leq 0.50$; c) $0.50 < x \leq 1.20$.

oxides belonging to the second domain ($0.16 < x \leq 0.50$), exhibit a metallic conductivity (fig. 12 b) which increases with the intercalation rate: ρ increases linearly with temperature and the thermoelectric power values are weak and nearly temperature independent (fig. 13). The highest x compositions ($0.50 < x \leq 1.20$), exhibit for the less oxidized compounds synthesized in air ($\delta < 0.07$) a semi-conductive behaviour: σ decreases drastically with δ (fig. 12 c), and correlatively α increases as δ decreases (fig. 13). These latter oxides and especially the compositions corresponding to $x = 0.88$, 1 and 1.2 exhibit a variation of the conductivity according to the Mott relation $\sigma = A \exp [-(Q/k_B T)^{1/4}]$ which characterizes a variable range hopping

ing of holes located in the $d_{x^2-y^2}$ band close to the Fermi level. It must be noted that the electrical properties of the oxides $\text{La}_{1-x}\text{Sr}_x\text{CuO}_{4-x/2+x}$ do not depend on the δ value only. So, for instance, the oxides corresponding to $0.33 \leq x \leq 1.0$ which have been annealed under an oxygen pressure of 1 bar exhibit the same δ value ($\delta \approx 0.11$), but are characterized by a decrease

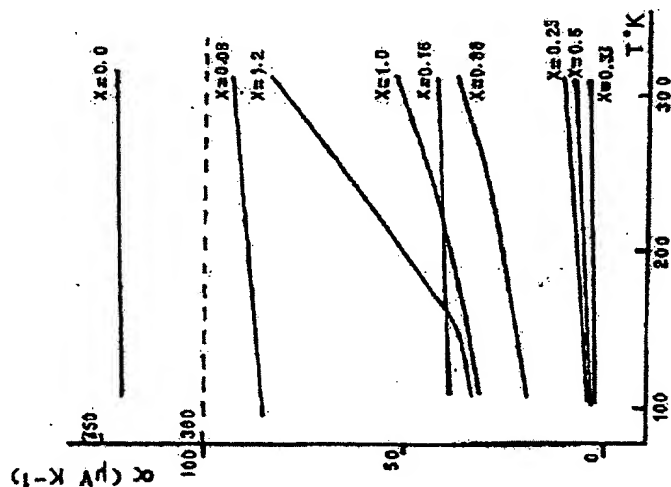


Fig. 13. — The oxides $\text{La}_{1-x}\text{Sr}_x\text{CuO}_{4-x/2+x}$: thermoelectric power vs T for quenched oxides with different x values.

of σ as x increases as shown figure 14. This shows the influence of the rate of anionic vacancies ($x/2-\delta$) on the carrier mobility. Moreover the distribution of the oxygen defects *i. e.*; the order-disorder phenomena, may influence the electron transport properties of these compounds.

The great sensitivity of these compounds to oxygen makes that their electrical conductivity can vary drastically, under a given oxygen pressure, owing to the intercalation or desintercalation of oxygen. For this reason

TOME 21 — 1984 — N° 4

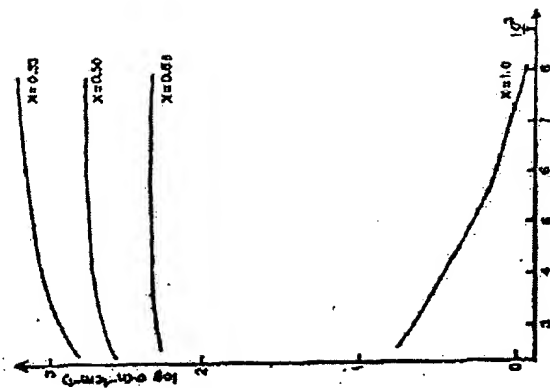


Fig. 14. — The oxides $\text{La}_{1-x}\text{Sr}_x\text{CuO}_{4-x/2+x}$: evolution of the conductivity as a function of reciprocal temperature for oxides annealed under an oxygen pressure of 1 bar ($\delta \approx 0.11$, $0.33 \leq x \leq 1.0$).

we have only discussed above the electrical properties of these phases at relatively low temperatures ($T < 300$ K), where all the compounds of the three families are not sensitive to intercalation or desintercalation. Such anomalies of the conductivity have indeed been observed for the oxides $\text{La}_{1-x}\text{Sr}_x\text{CuO}_{4-x/2+x}$ corresponding to $0 \leq x \leq 0.16$ and synthesized in air ($0 \leq \delta \leq 0.04$). One indeed observes (fig. 15), beyond 300 K under an oxygen pressure of 0.2 bar that σ decreases first drastically in the temperature range 300 K-420 K and then increases again in the temperature range 420 K-650 K. The thermogravimetric curves of these phases, characterized successively by a weight loss and weight gain, show clearly that this behaviour results from desintercalation and intercalation of oxygen successively. Similar properties are observed for the oxides $\text{La}_{1-x}\text{Sr}_{1-x}\text{Cu}_2\text{O}_{6-x/2+x}$ synthesized in air for $x = 0.1$ and 0.14 (fig. 15) and for which the thermogravimetric measurements confirm the oxygen desintercalation-intercalation process. The reversibility of the intercalation process in these phases is illustrated by the evolution of the conductivity of $\text{La}_{1-x}\text{Ca}_x\text{Cu}_2\text{O}_{6-x/2+x}$ versus reciprocal

REVUE DE CHIMIE NOUVELLE

FEB 12 '03 15:59

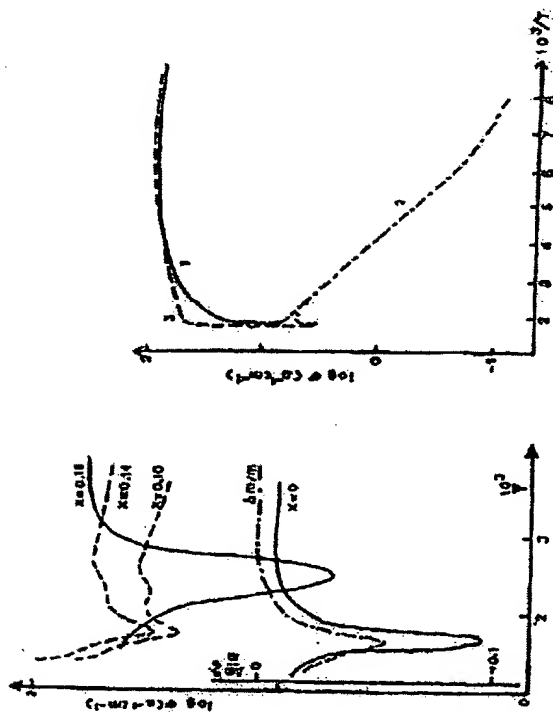


Fig. 15.

Fig. 15. — Variation of conductivity vs T^{-1} for some oxides in the $\text{La}_{0.8-x}\text{Sr}_x\text{CuO}_{4-x}$ series (solid line) and in the $\text{La}_{0.8-x}\text{Sr}_x\text{CuO}_{4-x}$ series (dotted line). A TG curve for $x = 0$ (first series), with the same temperature scale is given as example to illustrate the close relation between variation of conductivity and oxygen amount.

Fig. 16. — Variation of conductivity vs T^{-1} for the oxides $\text{La}_{0.8}\text{Ca}_{0.2}\text{CuO}_{4.2}$ under different atmospheres:

- 1) — first heating under inert atmosphere,
- 2) - - - first cooling and second heating under inert atmosphere,
- 3) - - - air introduction and second cooling (in air).

temperature under argon and air (fig. 16). The behaviour of this phase is indeed very different in argon and in air. The conductivity decreases under argon as soon as the temperature is greater than 300 K owing to the departure of oxygen and at about 570 K σ decreases drastically. At this stage of the experiment, heating is stopped and the sample is cooled progressively down to 77 K. In this latter temperature range a semi-conductive behaviour is observed owing to the lower oxygen rate of intercalation. Heating again up to 500 K under argon leads to the same curve. However

TOUS 21 — 1984 — N° 4

REVUE DE CHIMIE MINÉRALE

beyond 500 K, σ decreases again; this phenomenon is due to the fact that the thermodynamical equilibrium is not yet reached when we stop heating at 570 K. At 570 K argon is replaced by air, and heating is stopped. It can be seen that the conductivity increases immediately owing to the oxygen intercalation. The behaviour observed from 570 K to 77 K is then similar to that observed for the starting material.

REFERENCES

- [1] J. M. LORON, P. M. RACCAH, *J. Solid State Chem.*, 1973, 6, p. 526.
- [2] S. CHANDR, H. MULLER-BUCHHAUD, M. SCHWEITZER, *Z. Anorg. Allg. Chem.*, 1977, 428, p. 120.
- [3] J. B. GOODENOUGH, O. DEMAZEAU, M. TOUCHARD, P. HAGENMULLER, *J. Solid State Chem.*, 1973, 8, p. 323.
- [4] W. KLUM, O. WEHLMAYER, H. BADL, *Elektrochem. Ber. Deutsche Phys. Chem.*, 1959, 63, p. 36.
- [5] K. HESTERMAN, R. HOPPE, *Z. Anorg. Allg. Chem.*, 1969, 367, p. 249.
- [6] K. HESTERMAN, R. HOPPE, *Z. Anorg. Allg. Chem.*, 1969, 367, p. 261.
- [7] K. HESTERMAN, R. HOPPE, *Z. Anorg. Allg. Chem.*, 1969, 367, p. 270.
- [8] O. DEMAZEAU, C. PARANT, M. TOUCHARD, P. HAGENMULLER, *Mot. Res. Bull.*, 1972, 7, p. 913.
- [9] M. ARMAND, D. MACHIN, *J. Chem. Soc. Dalton Trans.*, 1975, p. 1051.
- [10] H. N. MCDON, F. JEANROT, M. ZANNA, J. AUBRY, *Rev. Chim. Miner.*, 1976, 13, p. 440.
- [11] N. NOUYEN, L. BRACHO, C. MICHEL, J. CHOINET, B. RAVEAU, *Mat. Res. Bull.*, 1980, 15, p. 891.
- [12] L. BRACHO, C. MICHEL, J. PROVOST, B. RAVEAU, *J. Solid State Chem.*, 1981, 37, p. 151.
- [13] N. NOUYEN, J. CHOINET, M. HERVIER, B. RAVEAU, *J. Solid State Chem.*, 1981, 39, p. 120.
- [14] J. PROVOST, F. STUBER, C. MICHEL, B. RAVEAU, *Synthetic Metals*, 1981, 4, p. 147.
- [15] J. PROVOST, F. STUBER, C. MICHEL, B. RAVEAU, *Synthetic Metals*, 1981, 4, p. 157.
- [16] N. F. MOTT, *Metal-Insulator Transitions*, Taylor and Francis, London, 1974.
- [17] N. NOUYEN, C. MICHEL, P. STUBER, B. RAVEAU, *Mot. Chem.*, 1982, 7, p. 413.
- [18] N. NOUYEN, F. STUBER, B. RAVEAU, *J. Phys. Chem. Solids*, 1983, 44, p. 389.
- [19] J. B. GOODENOUGH, *Mot. Res. Bull.*, 1973, 8, p. 423.

(Received December 12, 1983)

BRIEF ATTACHMENT I

IN THE UNITED STATES PATENT AND TRADEMARK OFFICE

In re Patent Application of

Applicants: Bednorz et al.

Serial No.: 08/479,810

Filed: June 7, 1995

For: NEW SUPERCONDUCTIVE COMPOUNDS HAVING HIGH TRANSITION
TEMPERATURE, METHODS FOR THEIR USE AND PREPARATION

Date: March 1, 2005

Docket: YO987-074BZ

Group Art Unit: 1751

Examiner: M. Kopec

Commissioner for Patents
P.O. Box 1450
Alexandria, VA 22313-1450

FIRST SUPPLEMENTAL AMENDMENT

Sir:

In response to the Office Action dated July 28, 2004, please consider the
following:

ATTACHMENT I



Thermal Analysis

Vol. 2 Inorganic Chemistry/Metallurgy
Earth Sciences
Organic Chemistry/Polymers
Biological Sciences/Medicine/Pharmacy

Editor
W. Hemminger
Institut für Werkstoffkunde
Universität Braunschweig
Federal Republic of Germany

UNIVERSITY OF CALIFORNIA
LIBRARY

SEP 25 1981

CATALOGING - PREP.

1980



Birkhäuser Verlag
Basel · Boston · Stuttgart

Proceedings of the Sixth International
Conference on Thermal Analysis

Bayreuth, Federal Republic of Germany
July 6-12, 1980



T

Vol. 1 Theory
Instrumentation
Applied Sciences
Industrial Applications

Vol. 2 Inorganic Chemistry/Metallurgy
Earth Sciences
Organic Chemistry/Polymers
Biological Sciences/Medicine/Pharmacy

Vol. 2 Inor
Eart
Org
Biol

Edit
W. I
Insti
Uni
Fed

B

Fore

Although the use of thermal analysis began in the 19th century, the effects of heat on materials in the 20th century. In the 19th century, it was broadly applicable for a demonstration of quality control of materials. From a scientific field of endeavour, it has grown to become a common ground for the application of these tools for the scientific field of endeavour. Others employ them and chemical processes. Growth in the value of the number of nations on a common ground and application of these tools for a similar but broadening an opportunity for common interests: of experts continue to work, to find solutions. The end is

Onta
Miss

CIP-Kurztitelaufnahme der Deutschen
Bibliothek

Thermal analysis. - Basel, Boston, Stuttgart:
Birkhäuser.

Bd. 1971 mit d. Erscheinungsorten: Basel,
Stuttgart. - Bd. 1977 im Verl. Heyden, Lon-
don, Bellmawr (NJ), Rhine.

ISBN 3-7643-1202-5

1980.

Vol. 2. Inorganic chemistry, metallurgy,
earth sciences, organic chemistry, polymers,
biological sciences, medicine, pharmacy:
proceedings of the 6. Internat. Conference
on Thermal Analysis, Bayreuth, Fed.
Republic of Germany, July 6-12, 1980/ed.
W. Hemminger. - 1980.

ISBN 3-7643-1086-3

NE: Hemminger, Wolfgang (Hrsg.): ICTA
(06, 1980, Bayreuth)

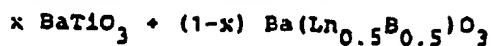
All rights reserved. No part of this publica-
tion may be reproduced, stored in a
retrieval system, or transmitted in any form
or by any means, electronic, mechanical,
photocopying, recording or otherwise, with-
out the prior permission of the copyright
owner.

© Birkhäuser Verlag Basel, 1980

ISBN 3-7643-1086-3

Printed in Switzerland

THERMAL BEHAVIOUR OF COMPOSITIONS IN THE SYSTEMS



V.S. Chincholkar* and A.R. Vyawahare

Department of Chemistry, Institute of Science, Nagpur

ABSTRACT

The effect of temperature on the dielectric constant (ϵ), $\tan \delta$ (loss tangent) and the ferroelectric properties of compositions in the systems $x \text{BaTiO}_3 + (1-x) \text{Ba}(\text{Ln}_{0.5}\text{B}_{0.5})\text{O}_3$ ($0 \leq x \leq 1$, Ln^{3+} = a rare earth cation and Y^{3+} , B^{5+} = Ta, Nb, V) reveal that in the Ta^{5+} system at $x = 0.8$, the ϵ_{max} (ϵ at T_c) and T_c (the Curie-point) exhibit an increasing trend with decreasing ionic radii of the Ln^{3+} ions, whereas in the analogous Nb^{5+} system, an almost linear behaviour has been observed. In the V^{5+} system, the pure phases ($x = 0$) exhibit increasing trend of ϵ_{max} and T_c values with decreasing rare earth cation size. Phases with $x = 0.8$, exhibit a break at Nd^{3+} in ϵ_{max} values, in contrast to an increasing trend in T_c values with decreasing rare earth cation size. Similar behaviour is observed for the polarization data. The increasing trend in the T_c values in the direction Ta^{5+} - Nb^{5+} - V^{5+} at $x = 0.8$ is perhaps reminiscent of the nephelauxetic effect.

The T_c values for these first order transitions have been confirmed by recording DTA curves against inert $\alpha\text{-Al}_2\text{O}_3$, the enthalpy change, however, being appreciably low in the present series.

INTRODUCTION

Recently emphasis has been placed on laser research and a concentrated effort has brought new and improved materials which can be used as hosts for transition. An important part of this effort has been directed towards finding potential laser materials having fluorescent energy states with long life times. In order to determine if symmetry conditions in

THERMAL ANALYSIS . ICTA 80 . BIRKHAUSER VERLAG, BASEL, BOSTON, STUTTGART

crystals also affect the life time of rare earth ion fluorescence, a series of ordered perovskite compounds having the general formula $A(B'_{0.5}B''_{0.5})O_3$ were studied [1]-[7]. However, temperature effects and doping characteristics were not studied. The present work concerns with the formation and the thermal characteristics of compositions in the systems $x BaTiO_3 + (1-x) Ba(Ln_{0.5}B_{0.5})O_3$ where $0 \leq x \leq 1$, Ln^{3+} = a rare earth cation and $B^{5+} = Nb^{5+}, Ta^{5+}$ and V^{5+} .

EXPERIMENTAL PROCEDURE

The compositions were prepared by the solid state reaction of the parent compounds (carbonates, oxides) at high temperature as described elsewhere [8], [9]. Room temperature X-ray structure was determined using Debye-Scherrer camera (14 cm diameter) and nickel-filtered $Cu-K\alpha$ radiation. Temperature effects on the dielectric constant (capacitance) and loss tangent ($\tan \delta$) were measured using a 716-C GR capacitance bridge together with type 1340-B type audiobeat frequency generator and 1231-B type u null detector and amplifier with 1231 P_5 type variable filter in a sample holder designed in this laboratory [10].

Modified [11] Sawyer-Tower type circuit was used to record hysteresis loops as a function of temperature in the above sample holder and a MOM Derivatograph was used to record DTA curves against $\alpha-Al_2O_3$ as reference.

RESULTS AND DISCUSSION

Tables 1-3 show the room temperature ϵ values as also the ϵ_{max} and the Curie-point (T_c) values evaluated from the capacitance measurements for compositions in the various systems. The temperature study was restricted to $x = 0.8$ compositions in the Ta^{5+} , Nb^{5+} systems and over the entire composition range in the V^{5+} system which exhibited the transition in the whole range of compositions. Table 4 shows these parameters at $x = 0$ for compositions in the V^{5+} system. In all the sy-

stems, an increase in ϵ_{max} with decreasing rare earth content of the lanthanide

ϵ_{max} , P_5 and T_c values

Composition

$Ba(La_{0.1}Ta_{0.1}Ti_{0.8})$
 $Ba(Nd_{0.1}Ta_{0.1}Ti_{0.8})$
 $Ba(Sm_{0.1}Ta_{0.1}Ti_{0.8})$
 $Ba(Gd_{0.1}Ta_{0.1}Ti_{0.8})$
 $Ba(Dy_{0.1}Ta_{0.1}Ti_{0.8})$
 $Ba(Y_{0.1}Ta_{0.1}Ti_{0.8})$

ϵ_{max} , P_5 and T_c values

$Ba(La_{0.1}Nb_{0.1}Ti_{0.8})$
 $Ba(Nd_{0.1}Nb_{0.1}Ti_{0.8})$
 $Ba(Sm_{0.1}Nb_{0.1}Ti_{0.8})$
 $Ba(Gd_{0.1}Nb_{0.1}Ti_{0.8})$
 $Ba(Dy_{0.1}Nb_{0.1}Ti_{0.8})$
 $Ba(Y_{0.1}Nb_{0.1}Ti_{0.8})$

ϵ_{max} , P_5 and T_c values

$Ba(La_{0.1}V_{0.1}Ti_{0.8})$
 $Ba(Nd_{0.1}V_{0.1}Ti_{0.8})$
 $Ba(Sm_{0.1}V_{0.1}Ti_{0.8})$
 $Ba(Gd_{0.1}V_{0.1}Ti_{0.8})$
 $Ba(Dy_{0.1}V_{0.1}Ti_{0.8})$
 $Ba(Y_{0.1}V_{0.1}Ti_{0.8})$

252

253

res-
ie
er,
itu-
ie

stems, an increasing trend in ϵ_{\max} as also T_c is observed with decreasing rare earth cation size, and is perhaps reminiscent of the lanthanide contraction.

Table 1

ϵ_{\max} , P_s and T_c values for compositions in the Ta^{5+} system

rare"

Composition	$\epsilon_{25^\circ C}$	P_s [$\mu C/cm^2$]	ϵ_{\max}	T_c [$^\circ C$]
Ba(La _{0.1} Ta _{0.1} Ti _{0.8})O ₃	200	4.5	780	85
Ba(Nd _{0.1} Ta _{0.1} Ti _{0.8})O ₃	250	6.0	850	90
Ba(Sm _{0.1} Ta _{0.1} Ti _{0.8})O ₃	342	8.1	1050	92
Ba(Gd _{0.1} Ta _{0.1} Ti _{0.8})O ₃	480	8.5	1120	96
Ba(Dy _{0.1} Ta _{0.1} Ti _{0.8})O ₃	530	8.9	1400	100
Ba(Y _{0.1} Ta _{0.1} Ti _{0.8})O ₃	580	9.6	1830	110

Table 2

ϵ_{\max} , P_s and T_c values for compositions in the systems Nb^{5+}

in
era-
ay
cm
e
e
with
in
d
e
DTA

Ba(La _{0.1} Nb _{0.1} Ti _{0.8})O ₃	232	5.3	580	90
Ba(Nd _{0.1} Nb _{0.1} Ti _{0.8})O ₃	260	6.2	900	100
Ba(Sm _{0.1} Nb _{0.1} Ti _{0.8})O ₃	290	8.4	1100	107
Ba(Gd _{0.1} Nb _{0.1} Ti _{0.8})O ₃	380	9.2	1220	110
Ba(Dy _{0.1} Nb _{0.1} Ti _{0.8})O ₃	415	9.8	1350	115
Ba(Y _{0.1} Nb _{0.1} Ti _{0.8})O ₃	530	10.2	1600	118

Table 3

ϵ_{\max} , P_s and T_c values for compositions in the V^{5+} system

apa-
ems.
tions
the
rs
y-

Ba(La _{0.1} V _{0.1} Ti _{0.8})O ₃	170	4.5	1100	93
Ba(Nd _{0.1} V _{0.1} Ti _{0.8})O ₃	225	3.5	840	124
Ba(Sm _{0.1} V _{0.1} Ti _{0.8})O ₃	280	7.5	1130	130
Ba(Gd _{0.1} V _{0.1} Ti _{0.8})O ₃	350	8.2	1290	135
Ba(Dy _{0.1} V _{0.1} Ti _{0.8})O ₃	480	8.2	1600	135
Ba(Y _{0.1} V _{0.1} Ti _{0.8})O ₃	530	12.2	2200	125

Table 4
 ϵ_{\max} , P_s and T_c values for compositions in the V^{5+} system at $x = 0$

Composition	ϵ_{\max}	P_s	T_c
$Ba(La_{0.5}V_{0.5})O_3$	60	--	--
$Ba(Nd_{0.5}V_{0.5})O_3$	20	7.8	260
$Ba(Sm_{0.5}V_{0.5})O_3$	30	10.7	500
$Ba(Gd_{0.5}V_{0.5})O_3$	35	11.3	850
$Ba(Dy_{0.5}V_{0.5})O_3$	25	12.5	1020
$Ba(Y_{0.5}V_{0.5})O_3$	40	17.9	1250

Covalency of the B-O bond is reported [12] to increase with decreasing rare earth cation size and may be responsible for the above occurrence. The behaviour, however, is linear in case of Nb^{5+} and non-linear in the case of Ta^{5+} , V^{5+} .

Table 5 shows the T_f and ΔH values as evaluated from the DTA curves, for some representative samples.

Table 5

Composition	T_f (°C)	ΔH (cal mole ⁻¹)
$Ba(La_{0.1}Ta_{0.1}Ti_{0.8})O_3$	80	25
$Ba(La_{0.1}Nb_{0.1}Ti_{0.8})O_3$	90	45
$Ba(La_{0.1}V_{0.1}Ti_{0.8})O_3$	95	65

A glance at the ΔH values reveal dilution of the ΔH value of the 120°C transition of $BaTiO_3$ (46 cal/mole) [13] by the addition of Ta^{5+} phases, no change with addition of Nb^{5+} phases and a substantial increase with incorporation of V^{5+} phases.

Another significant result of the present study is the observation of increasing T_c (T_f) values with decreasing B^{5+} radii, keeping the Ln^{3+} ion fixed, in the sequence $Ta^{5+}-Nb^{5+}-V^{5+}$.

Considering the energy level diagram of an octahedrally surrounded metal ion with configuration $(np)^6$, we expect Ta^{5+} to

be more ionic this the elec will be less justified by these ions T Jørgensen has that the elec $Nb^{5+}-V^{5+}$ and transition me cal bond beco Our results a

Fifth ionizati

Ion

V^{5+}

Nb^{5+}

Ta^{5+}

[1] F. Galasso Report OAS

[2] F. Galasso 81 (1959)

[3] F. Galasso 83 (1961)

[4] F. Galasso

[5] F. Galasso

[6] F. Galasso

[7] F. Galasso

[8] V.S. Chinc

254

255

be more ionically bonded than Nb^{5+} and V^{5+} . As a result of this the electron density in the t_{2g} -orbital of the Ta^{5+} ion will be less than that in the case of Nb^{5+} , V^{5+} . This is also justified by considering the fifth ionization potential of these ions T (Table 6) which also increases in this sequence. Jørgensen has concluded from the electron transfer spectra that the electron affinity increases in the sequence Ta^{5+} - Nb^{5+} - V^{5+} and from the reduced Racah parameters of several transition metal ions (nephelauxetic effect) that the chemical bond becomes more covalent in the sequence 5d-4d-3d group. Our results are consistent with the observations of Jørgensen.

Table 6

Fifth ionization potential and electron configuration of B^{5+} metal ions

Ion	Electron configuration	I_5 (eV)
V^{5+}	$3s^2 3p^6$	65
Nb^{5+}	$4s^2 4p^6$	52
Ta^{5+}	$5s^2 5p^6$	45

REFERENCES

- [1] F. Galasso, United Aircraft Corporation Laboratory, Report UAR-B10, Jan 1963
- [2] F. Galasso, L. Katz, and R. Ward, J.Amer.Chem.Soc. 81 (1959) 820
- [3] F. Galasso, J.R. Barrante, and L. Katz, J.Amer.Chem.Soc. 83 (1961) 2830
- [4] F. Galasso, and W.J. Darby, J.Phys.Chem. 66 (1962) 131
- [5] F. Galasso, and J. Pyle, J.Phys.Chem. 67 (1963) 533
- [6] F. Galasso, and J. Pyle, J.Phys.Chem. 67 (1963) 1561
- [7] F. Galasso, and J. Pyle, Inorg.Chem. 2 (1963) 482
- [8] V.S. Chincholkar, J.Inorg.Nucl.Chem. 34 (1972) 2973

- [9] K. Gade, and V.S. Chincholkar, J.Chem.Soc. (Dalton) 12 (1979) 1959
- [10] V.S. Chincholkar, Z.Angew.Chem. 26 (1970) 288
- [11] V.S. Chincholkar, Ph.D.Thesis. Pune University, 1967
- [12] R.S.Roth, J.Research NBS 58 (1957) 75
- [13] J. Volger, Philips Res.Rep. 7 (1952) 21
- [14] C.K.Jørgensen, "Absorption spectra and chemical bonding in complexes" Pergamon Press, 1962, pp. 147, 306 and 310-12

* Present address: Forensic Science Laboratory, Bombay-8

STUDIES

A.

Bhabha

The formation of
by Solid State re
 $\text{La}_2(\text{C}_2\text{O}_4)_3$, $\text{La}(\text{C}_2\text{O}_4)_3$
The reaction occu
depending upon th
kinetics of forms
and MoO_3 is evalu
controlled mechar
activation energy
 mole^{-1} .

A reversible phase
observed at 823 K
x-ray diffraction

The solid state :
 $\text{La}_2(\text{C}_2\text{O}_4)_3$, $\text{La}(\text{C}_2\text{O}_4)_3$
to gain better un
general and the
formation of tri
particular.
Several $\text{Ln}_2(\text{MoO}_4)_3$
been extensively
electrical, magn
kinetics and mecl
reported scantil
reactivity of th
re-examine this
detail.

THERMAL ANALYSIS . ICI

BRIEF ATTACHMENT J

IN THE UNITED STATES PATENT AND TRADEMARK OFFICE

In re Patent Application of

Applicants: Bednorz et al.

Serial No.: 08/479,810

Filed: June 7, 1995

For: NEW SUPERCONDUCTIVE COMPOUNDS HAVING HIGH TRANSITION
TEMPERATURE, METHODS FOR THEIR USE AND PREPARATION

Date: March 1, 2005

Docket: YO987-074BZ

Group Art Unit: 1751

Examiner: M. Kopec

Commissioner for Patents
P.O. Box 1450
Alexandria, VA 22313-1450

FIRST SUPPLEMENTAL AMENDMENT

Sir:

In response to the Office Action dated July 28, 2004, please consider the
following:

ATTACHMENT J

Model family of high-temperature superconductors: $\text{Ti}_m\text{Ca}_{n-1}\text{Ba}_2\text{Cu}_n\text{O}_{2(n+1)+m}$ ($m=1, 2$; $n=1, 2, 3$)

S. S. P. Parkin, V. Y. Lee, A. I. Nazzari, R. Savoy, T. C. Huang, G. Gorman, and R. Beyers
IBM Research Division, Almaden Research Center, 650 Harry Road,

San Jose, California 95120-6099

(Received 31 May 1988)

We describe the structures and superconducting properties of six compounds in the Ti-Ca-Ba-Cu-O system of the general form, $\text{Ti}_m\text{Ca}_{n-1}\text{Ba}_2\text{Cu}_n\text{O}_{2(n+1)+m}$, where $m=1$ or 2 and $n=1, 2$, or 3. One of the compounds displays the highest known superconducting transition temperature, $T_c=125$ K. The structures of these compounds consist of copper perovskitelike blocks containing 1, 2, or 3 CuO_2 planes separated by one or two Ti-O layers and thus form a model family of structures in which both the size and separation of the copper oxide blocks can be independently varied. The superconducting transition temperature increases with the number of CuO_2 planes in the perovskitelike block for both the Ti-O monolayer and bilayer compounds. For each pair of compounds ($m=1, 2$) with the same number of CuO_2 planes (same n), the transition temperatures are similar but are consistently 15–20 K lower in the materials with single Ti-O layers. Variations in the transition temperatures in the double and triple CuO_2 -layer compounds are observed to correlate with increased densities of intergrowths of related structures.

Recently¹⁻⁷ several new high-temperature superconductors have been synthesized in the Ti-Ca-Ba-Cu-O system, including $\text{Ti}_2\text{Ca}_2\text{Ba}_2\text{Cu}_3\text{O}_{10\pm x}$, which displays the highest superconducting transition temperature yet found, $T_c=125$ K.³ In this article we present data on the structures and superconducting properties of six compounds of the form $\text{Ti}_m\text{Ca}_{n-1}\text{Ba}_2\text{Cu}_n\text{O}_{2(n+1)+m}$, where $m=1$ or 2 and $n=1, 2$, or 3. The structures consist of copper perovskitelike blocks containing 1, 2, or 3 CuO_2 planes separated by one or two Ti-O layers. These compounds thus form a model family of structures in which both the size and separation of the copper blocks can be independently varied. We present data that establish that the superconducting transition temperature increases with the number of CuO_2 planes in the perovskitelike block for both the Ti-O monolayer and bilayer compounds. For each pair of compounds ($m=1, 2$) with the same number of CuO_2 planes (same n), the transition temperature is 15–20 K lower in the material with single Ti-O layers. Variations in the transition temperatures in the double and triple CuO_2 layer compounds are observed to correlate with increased densities of intergrowths of related structures.

The samples were prepared by thoroughly mixing suitable amounts of Ti_2O_3 , CaO , BaO_2 , and CuO , and forming a pellet of this mixture under pressure. The pellet was then wrapped in gold foil, sealed in a quartz tube containing slightly less than 1 atm of oxygen, and baked for approximately 3 h at $\approx 880^\circ\text{C}$. A wide range of starting compositions was studied. In most cases the resulting pellet was comprised of several phases. However, for certain ranges of starting compositions, the pellets contained only one superconducting phase of the form $\text{Ti}_m\text{Ca}_{n-1}\text{Ba}_2\text{Cu}_n\text{O}_{2(n+1)+m}$ together with minor amounts ($< \approx 20\%$) of insulating oxides such as those of Cu, Ca-Cu, Ba-Cu, and Ti-Ba. The relative amounts of each phase depended on the annealing time and temperature and the rate of

cooling from this temperature. In particular, for slow cooling rates ($\approx 100^\circ\text{C/h}$) the composition of the major $\text{Ti}_m\text{Ca}_{n-1}\text{Ba}_2\text{Cu}_n\text{O}_{2(n+1)+m}$ phase more closely matched that of the starting composition. The composition and microstructure of the pellets were determined from complementary powder x-ray diffraction, electron microprobe, electron diffraction, and high-resolution transmission electron microscopy (TEM) studies. The superconducting properties of each pellet were examined by resistivity and dc Meissner susceptibility studies. The latter was measured with a SHE SQUID magnetometer. Cooling in a field of 100 Oe, the magnitude of the Meissner susceptibility at 5.5 K ranged from 10% to 35% of the susceptibility of a perfect diamagnet of the same volume, neglecting small demagnetizing corrections. The magnitude of the diamagnetic shielding signal is very dependent on the distribution of the normal and superconducting phases within the multiphase pellets and in most cases did not give useful information. The susceptibility data revealed that for some pellets the presence of a minority superconducting phase resulted in the resistance of the pellet dropping to zero at substantially higher temperatures than the T_c of the majority superconducting phase. This type of behavior emphasizes the importance of determining the transition temperature from a flux exclusion measurement in this complex quinary system. These results are summarized in Table I.

We have previously described the preparation and properties of the three members of the $\text{Ti}_m\text{Ca}_{n-1}\text{Ba}_2\text{Cu}_n\text{O}_{2(n+1)+m}$ family, namely $\text{Ti}_2\text{Ca}_2\text{Ba}_2\text{Cu}_3\text{O}_{10}$ (2:2:2:3),³ $\text{Ti}_2\text{Ca}_1\text{Ba}_2\text{Cu}_2\text{O}_8$ (2:1:2:2),³ and $\text{Ti}_1\text{Ca}_2\text{Ba}_2\text{Cu}_3\text{O}_9$ (1:2:2:3),⁴ which display superconducting transition temperatures of 125, 108, and 110 K, respectively. By systematically varying the starting composition of the pellets, the related compounds, $\text{Ti}_2\text{Ca}_0\text{Ba}_2\text{Cu}_1\text{O}_x$ (2:0:2:1), $\text{Ti}_1\text{Ca}_0\text{Ba}_2\text{Cu}_1\text{O}_x$ (1:0:2:1), and $\text{Ti}_1\text{Ca}_1\text{Ba}_2\text{Cu}_2\text{O}_x$ (1:1:2:2) were synthesized. The unit cells for each phase

Model family of high-temperature superconductors: $\text{Tl}_m\text{Ca}_{n-1}\text{Ba}_2\text{Cu}_n\text{O}_{2(n+1)+m}$ ($m=1,2; n=1,2,3$)

S. S. P. Parkin, V. Y. Lee, A. I. Nazzari, R. Savoy, T. C. Huang, G. Gorman, and R. Beyers
IBM Research Division, Almaden Research Center, 650 Harry Road,

San Jose, California 95120-6099

(Received 31 May 1988)

We describe the structures and superconducting properties of six compounds in the Tl-Ca-Ba-Cu-O system of the general form, $\text{Tl}_m\text{Ca}_{n-1}\text{Ba}_2\text{Cu}_n\text{O}_{2(n+1)+m}$, where $m=1$ or 2 and $n=1, 2$, or 3 . One of the compounds displays the highest known superconducting transition temperature, $T_c \approx 125$ K. The structures of these compounds consist of copper perovskitelike blocks containing 1, 2, or 3 CuO_2 planes separated by one or two Tl-O layers and thus form a model family of structures in which both the size and separation of the copper oxide blocks can be independently varied. The superconducting transition temperature increases with the number of CuO_2 planes in the perovskitelike block for both the Tl-O monolayer and bilayer compounds. For each pair of compounds ($m=1,2$) with the same number of CuO_2 planes (same n), the transition temperatures are similar but are consistently 15–20 K lower in the materials with single Tl-O layers. Variations in the transition temperatures in the double and triple CuO_2 -layer compounds are observed to correlate with increased densities of intergrowths of related structures.

Recently¹⁻⁷ several new high-temperature superconductors have been synthesized in the Tl-Ca-Ba-Cu-O system, including $\text{Tl}_2\text{Ca}_2\text{Ba}_2\text{Cu}_3\text{O}_{10 \pm x}$, which displays the highest superconducting transition temperature yet found, $T_c = 125$ K.³ In this article we present data on the structures and superconducting properties of six compounds of the form $\text{Tl}_m\text{Ca}_{n-1}\text{Ba}_2\text{Cu}_n\text{O}_{2(n+1)+m}$, where $m=1$ or 2 and $n=1, 2$, or 3 . The structures consist of copper perovskitelike blocks containing 1, 2, or 3 CuO_2 planes separated by one or two Tl-O layers. These compounds thus form a model family of structures in which both the size and separation of the copper blocks can be independently varied. We present data that establish that the superconducting transition temperature increases with the number of CuO_2 planes in the perovskitelike block for both the Tl-O monolayer and bilayer compounds. For each pair of compounds ($m=1, 2$) with the same number of CuO_2 planes (same n), the transition temperature is 15–20 K lower in the material with single Tl-O layers. Variations in the transition temperatures in the double and triple CuO_2 layer compounds are observed to correlate with increased densities of intergrowths of related structures.

The samples were prepared by thoroughly mixing suitable amounts of Tl_2O_3 , CaO , BaO_2 , and CuO , and forming a pellet of this mixture under pressure. The pellet was then wrapped in gold foil, sealed in a quartz tube containing slightly less than 1 atm of oxygen, and baked for approximately 3 h at $\approx 880^\circ\text{C}$. A wide range of starting compositions was studied. In most cases the resulting pellet was comprised of several phases. However, for certain ranges of starting compositions, the pellets contained only one superconducting phase of the form $\text{Tl}_m\text{Ca}_{n-1}\text{Ba}_2\text{Cu}_n\text{O}_{2(n+1)+m}$ together with minor amounts ($< \approx 20\%$) of insulating oxides such as those of Cu, Ca-Cu, Ba-Cu, and Tl-Ba. The relative amounts of each phase depended on the annealing time and temperature and the rate of

cooling from this temperature. In particular, for slow cooling rates ($\approx 100^\circ\text{C/h}$) the composition of the major $\text{Tl}_m\text{Ca}_{n-1}\text{Ba}_2\text{Cu}_n\text{O}_{2(n+1)+m}$ phase more closely matched that of the starting composition. The composition and microstructure of the pellets were determined from complementary powder x-ray diffraction, electron microprobe, electron diffraction, and high-resolution transmission electron microscopy (TEM) studies. The superconducting properties of each pellet were examined by resistivity and dc Meissner susceptibility studies. The latter was measured with a SHE SQUID magnetometer. Cooling in a field of 100 Oe, the magnitude of the Meissner susceptibility at 5.5 K ranged from 10% to 35% of the susceptibility of a perfect diamagnet of the same volume, neglecting small demagnetizing corrections. The magnitude of the diamagnetic shielding signal is very dependent on the distribution of the normal and superconducting phases within the multiphase pellets and in most cases did not give useful information. The susceptibility data revealed that for some pellets the presence of a minority superconducting phase resulted in the resistance of the pellet dropping to zero at substantially higher temperatures than the T_c of the majority superconducting phase. This type of behavior emphasizes the importance of determining the transition temperature from a flux exclusion measurement in this complex quinary system. These results are summarized in Table I.

We have previously described the preparation and properties of the three members of the $\text{Tl}_m\text{Ca}_{n-1}\text{Ba}_2\text{Cu}_n\text{O}_{2(n+1)+m}$ family, namely $\text{Tl}_2\text{Ca}_2\text{Ba}_2\text{Cu}_3\text{O}_{10}$ (2:2:2:3),³ $\text{Tl}_2\text{Ca}_1\text{Ba}_2\text{Cu}_2\text{O}_8$ (2:1:2:2),³ and $\text{Tl}_1\text{Ca}_2\text{Ba}_2\text{Cu}_3\text{O}_9$ (1:2:2:3),⁴ which display superconducting transition temperatures of 125, 108, and 110 K, respectively. By systematically varying the starting composition of the pellets, the related compounds, $\text{Tl}_2\text{Ca}_0\text{Ba}_2\text{Cu}_1\text{O}_x$ (2:0:2:1), $\text{Tl}_1\text{Ca}_0\text{Ba}_2\text{Cu}_1\text{O}_x$ (1:0:2:1), and $\text{Tl}_1\text{Ca}_1\text{Ba}_2\text{Cu}_2\text{O}_x$ (1:1:2:2) were synthesized. The unit cells for each phase

TABLE I. Summary of properties of $Tl_mCa_{n-1}Ba_2Cu_nO_x$

Conc. ratio	Tl	Relative composition				Symmetry	Lattice parameters		Superlattice wave vector (k)	T_c (K)
		Ca	Ba	Cu	O		a (Å)	c (Å)		
$Tl_1Ca_{n-1}Ba_2Cu_nO_x$										
1:0:2:1	1.2	0.0	2	0.7	4.8	$P4/mmm$	3.869(2)	9.694(9)	a	b
1:1:2:2	1.1	0.9	2	2.1	7.1	$P4/mmm$	3.8505(7)	12.728(2)	$\langle 0.29, 0, 0.5 \rangle$	65–85
1:2:2:3	1.1	0.8	2	3.0	9.7	$P4/mmm$	3.8429(6)	15.871(3)	$\langle 0.29, 0, 0.5 \rangle$	100–110
$Tl_2Ca_{n-1}Ba_2Cu_nO_x$										
2:0:2:1	1.9	0.0	2	1.1	6.4	F/mmm^c	$a = 5.445(2)$ $b = 5.492(1)$	23.172(6)	$\langle 0.08, 0.24, 1 \rangle^c$	b
2:0:2:1 ^d	1.8	0	2	1.1	6.4	F/mmm^c	$a = 5.4634(3)$ $b \sim a$	23.161(1)	$\langle 0.08, 0.24, 1 \rangle^c$	20
2:0:2:1	1.8	0.02	2	1.1	6.3	$I4/mmm$	3.8587(4)	23.152(2)	$\langle 0.16, 0.08, 1 \rangle^e$	15–20
2:1:2:2	1.7	0.9	2	2.3	8.1	$I4/mmm$	3.857(1)	29.39(1)	$\langle 0.17, 0, 1 \rangle$	95–108
2:2:2:3	1.6	1.8	2	3.1	10.1	$I4/mmm$	3.822(4)	36.26(3)	$\langle 0.17, 0, 1 \rangle$	118–125

^aNo superlattice spots observed.^bNonmetallic or weakly metallic samples with no superconducting transition observed in resistivity and magnetic susceptibility studies for temperatures down to 4.2 K.^cThe symmetry of the structure is *orthorhombic* if the observed superlattice is ignored. Taking the superlattice into account lowers the symmetry to *monoclinic*.^dSample prepared from a Cu-rich starting composition, $Tl_2Ba_2Cu_2$.^eThe superstructure is identical to that for the orthorhombic 2:0:2:1 polymorph.

were determined from powder x-ray diffraction patterns extending from $2\theta = 3^\circ$ to 70° and verified by electron diffraction studies. These studies showed that all of the $Tl_mCa_{n-1}Ba_2Cu_nO_{2(n+1)+m}$ compounds have tetragonal cells at room temperature. The $Tl_1Ca_{n-1}Ba_2Cu_nO_{2n+3}$ compounds contain Tl-O monolayers, resulting in primitive tetragonal cells, whereas the $Tl_2Ca_{n-1}Ba_2Cu_nO_{2n+4}$ compounds contain Tl-O bilayers, resulting in body-centered tetragonal cells. The lattice parameters and symmetries of the various structures are included in Table I. As discussed later, the 2:0:2:1 compound also has an orthorhombic polymorph. As shown in Fig. 1, each oxide has a single peak in the low-angle portion ($3^\circ \leq 2\theta \leq 10^\circ$) of its x-ray diffraction pattern which results from the large c/a ratio in each structure. These peaks, (001) for $m=1$ and (002) for $m=2$, serve as fingerprints with which each of the compounds within the

$Tl_mCa_{n-1}Ba_2Cu_nO_{2(n+1)+m}$ family can be uniquely identified. The peak systematically shifts to lower angles as n increases within both the $Tl_1Ca_{n-1}Ba_2Cu_nO_{2n+3}$ and $Tl_2Ca_{n-1}Ba_2Cu_nO_{2n+4}$ families, consistent with an expansion of the unit cell along the c axis by the addition of extra CuO_2 and Ca planes. The peaks are in all cases at lower angles in the $Tl_2Ca_{n-1}Ba_2Cu_nO_{2n+4}$ compounds compared to the corresponding $Tl_1Ca_{n-1}Ba_2Cu_nO_{2n+3}$ compound, consistent with the increased number of Tl-O layers in the $Tl_2Ca_{n-1}Ba_2Cu_nO_{2n+4}$ compounds. The peaks are asymmetrically broadened to low angles because of geometrical aberrations in the focusing condition resulting from the flat specimens used.⁸ The arrangement of the cations in the various compounds is shown in Fig. 2. The positions of the oxygen atoms are inferred by comparison with related structures in the $La_{2-x}Sr_xCuO_4$, $YBa_2Cu_3O_x$, and $Bi_2Sr_2CaCu_2O_x$ families.^{9–11} The six structures are comprised of Cu perovskitelike blocks containing one, two, or three CuO_2 planes sandwiched between Tl-O monolayers (1:0:2:1, 1:1:2:2, and 1:2:2:3 compounds) or bilayers (2:0:2:1, 2:1:2:2, 2:2:2:3 compounds). The Ba cations are located in planes adjacent to the Tl-O unit and the Ca cations form planes within the interior of the Cu perovskitelike unit.

Since the preparation, structure, and properties of the double and triple CuO_2 layer oxides appear to be much less complex than those of the single CuO_2 layer oxides for both the monolayer and bilayer Tl-O compounds, we will discuss these groups of compounds separately. As described earlier, for each of the $n=2$ and $n=3$ compounds a single tetragonal structure was found. An important structural feature of these compounds observed by TEM, scanning electron microscopy (SEM), and electron microprobe studies are intergrowths of structures related to the primary phase by the addition or removal of CuO_2 or Tl-O layers. For some samples SEM images showed contrast striations $\approx 5\text{--}10\text{ }\mu\text{m}$ in width within individual

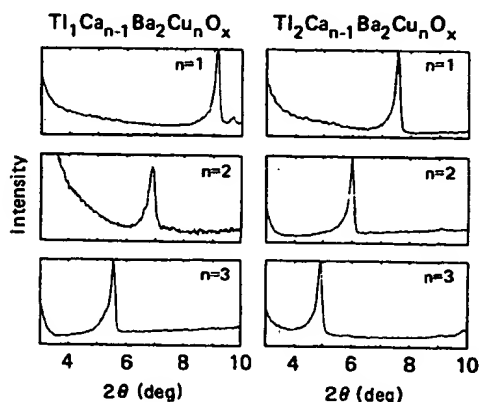


FIG. 1. Low-angle section of the powder x-ray diffraction patterns for the six phases $Tl_mCa_{n-1}Ba_2Cu_nO_{2(n+1)+m}$ ($m=1, 2$; $n=1, 2, 3$).

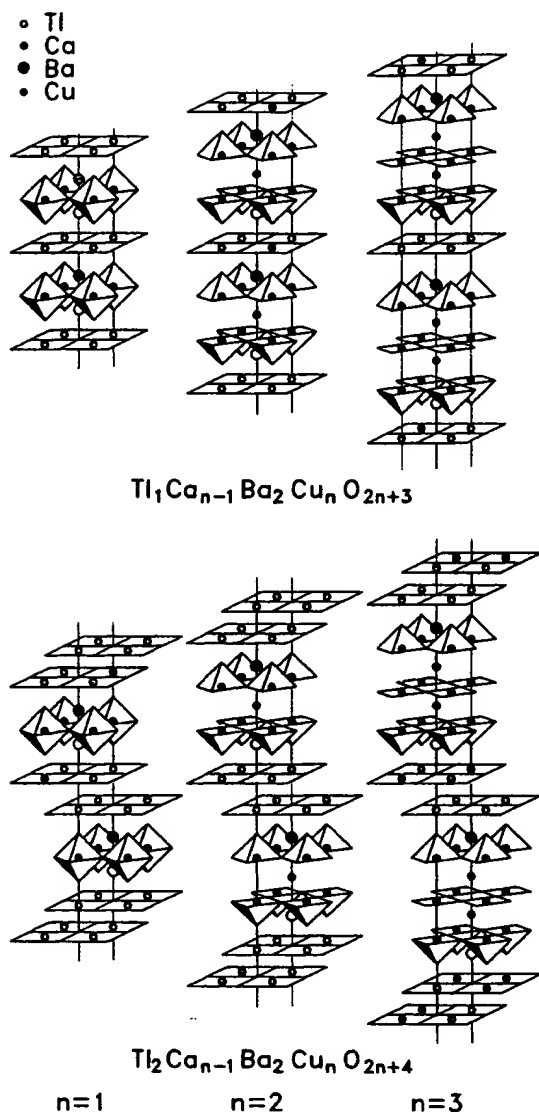


FIG. 2. Nominal structures of the six $\text{Tl}_m\text{Ca}_{n-1}\text{Ba}_2\text{Cu}_n\text{O}_{2(n+1)+m}$ phases for $n=1, 2$ and $m=1, 2, 3$.

grains which result from intergrowths of regions with different proportions of heavy atoms. TEM studies revealed the existence of intergrowths on much finer length scales, as demonstrated in Fig. 3 for a sample prepared from a starting composition of $\text{Tl}_{0.85}\text{Ca}_1\text{Ba}_2\text{Cu}_2$. Figure 3(a) shows a selected area diffraction pattern along b^* which indicates that this grain contains both 1:1:2:2 and 1:2:2:3 phases. Indeed Meissner data on this sample [included in Fig 4(d)] indicate two superconducting transitions with $T_c \approx 65$ and ≈ 105 K, consistent with the presence of extended regions of two distinct phases. Coincidentally, the c lattice parameters of the 1:1:2:2 and 1:2:2:3 phases are almost exactly in the ratio of 4/5 so that every fifth 1:2:2:3 $h0l$ spot coincides with every fourth 1:1:2:2 $h0l$ spot in Figure 3(a). High-resolution TEM micrographs in Figs. 3(b) and 3(c) show intergrowths of the

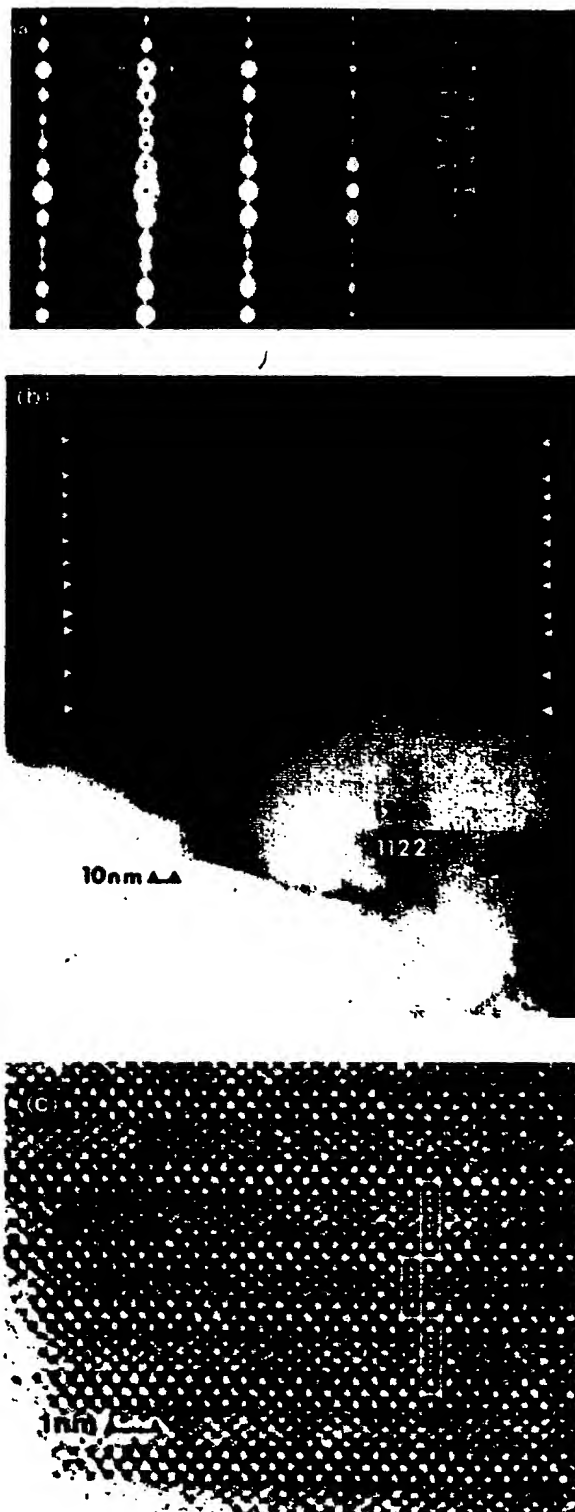


FIG. 3. (a) [010] selected area diffraction (SAD) pattern and (b) corresponding image of crystallites containing regions of 1:2:2:3 and 1:1:2:2. The arrows in (b) denote unit-cell thick intergrowths of 1:1:2:2 in 1:2:2:3. (c) High-resolution transmission electron micrograph of one unit-cell thick 1:1:2:2 intergrowth in 1:2:2:3.

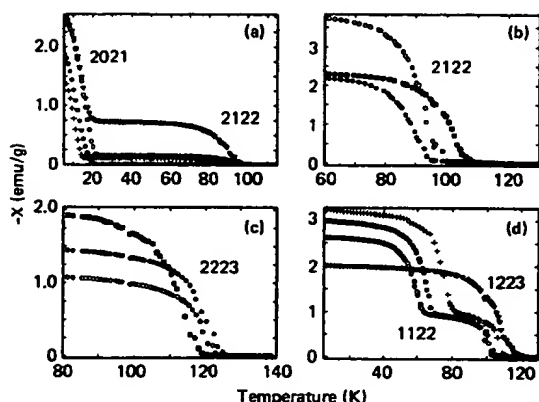


FIG. 4. Meissner susceptibility vs temperature for an applied field of 100 Oe for materials with starting cation composition, (a) $\text{Ti}_2\text{Ba}_2\text{Cu}_2$ (●), $\text{Ti}_2\text{Ca}_{0.05}\text{Ba}_2\text{Cu}_{1.05}$ (○, +), and $\text{Ti}_2\text{Ca}_{0.15}\text{Ba}_2\text{Cu}_{1.15}$ (▼); (b) $\text{Ti}_1\text{Ca}_2\text{Ba}_2\text{Cu}_3$ (●), $\text{Ti}_2\text{Ca}_1\text{Ba}_2\text{Cu}_2$ (○), and $\text{Ti}_{2.25}\text{Ca}_1\text{Ba}_2\text{Cu}_2$ (■); (c) $\text{Ti}_1\text{Ca}_2\text{Ba}_2\text{Cu}_3$ (■), $\text{Ti}_1\text{Ca}_{2.5}\text{Ba}_1\text{Cu}_3$ (○), and $\text{Ti}_1\text{Ca}_3\text{Ba}_1\text{Cu}_3$ (●); (d) $\text{Ti}_{0.45}\text{Ca}_1\text{Ba}_2\text{Cu}_2$ (○), $\text{Ti}_1\text{Ca}_1\text{Ba}_2\text{Cu}_2$ (●, +), and $\text{Ti}_{0.45}\text{Ca}_2\text{Ba}_2\text{Cu}_3$ (▼). The phases present in the pellet giving rise to the diamagnetic susceptibility are (a) 2:0:2:1 and 2:1:2:2, (b) 2:1:2:2, (c) 2:2:2:3, and (d) 1:1:2:2 and 1:2:2:3.

1:1:2:2 and 1:2:2:3 phases on length scales extending from $\approx 1\mu\text{m}$ down to one unit cell. The intergrowths are randomly distributed along the stacking axis. Isolated intergrowths comprising four CuO_2 planes were found in some samples (see Fig. 5) but no evidence was found for extended intergrowths comprising greater than three CuO_2 layers in these or other samples especially prepared from Cu- and Ca-rich starting compositions. A second type of intergrowth was observed in samples of the 1:2:2:3 phase in which an extra Ti-O plane was occasionally inserted between the Cu perovskitelike units, creating local regions of the 2:2:2:3 phase. Microprobe data show that the Ti content is systematically high in the compounds containing single Ti-O layers and systematically low in those com-

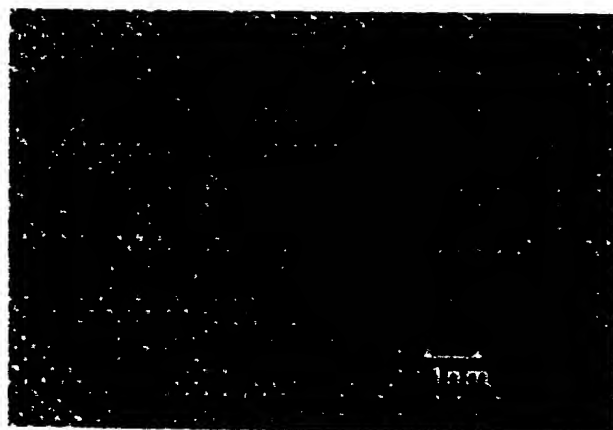


FIG. 5. High-resolution TEM image of an isolated four- CuO_2 -layer intergrowth. The markers denote the positions of the Cu columns.

pounds with Ti-O bilayers (see Table I) thus suggesting that intergrowths of Ti-O monolayers in the Ti-O bilayers materials and Ti-O bilayers in the Ti-O monolayer compounds are a general feature of these materials.

Meissner data (see Fig. 4) established that T_c can take a range of values for all of the double and triple CuO_2 layer compounds— $T_c \approx 95\text{--}108\text{ K}$ for 2:1:2:2, $T_c \approx 118\text{--}125\text{ K}$ for 2:2:2:3, $T_c \approx 65\text{--}85\text{ K}$ for 1:1:2:2, and $T_c \approx 100\text{--}110\text{ K}$ for 1:2:2:3. For a given compound, x-ray diffraction and microprobe studies did not detect any obvious difference between the samples with different transition temperatures. TEM studies, however, showed a clear correlation between the density of intergrowths and T_c . For the 2:1:2:2, 2:2:2:3, and 1:2:2:3 phases the material with no intergrowths displayed the highest transition temperature, whereas for the 1:1:2:2 compound the sample with the lowest density of intergrowths had the lowest T_c . As the density of intergrowths increased we observed that T_c systematically decreases or increases, respectively. It is possible that the structural or electronic modifications caused by the intergrowths are directly responsible for the decreased transition temperatures. Alternatively the presence of the intergrowths may simply reflect a means whereby the system accommodates, to some extent, off-stoichiometry in the cation sites which in turn may influence T_c . It is difficult to determine whether it is the local change in structure or composition which is responsible for the decrease in T_c since these are concurrent changes.

A second important structural feature found in all of the double and triple CuO_2 layer compounds is the presence of weak superlattice reflections in the selected area electron diffraction patterns. These reflections are considerably weaker than those previously found in the $\text{Bi}_2\text{Sr}_2\text{Ca}_1\text{Cu}_2\text{O}_x$ compound¹²⁻¹⁶ and indicate different structural modulations than those in the $\text{Bi}_2\text{Sr}_2\text{Ca}_1\text{Cu}_2\text{O}_x$ compound. The patterns can be described by a set of symmetry-related wave vectors, \mathbf{k} . Each wave vector describes a pair of reflections symmetrically disposed a reciprocal distance $|\mathbf{k}|$ along \mathbf{k} on either side of each Bragg peak, which would be consistent with a sinusoidal modulation of the charge density along this direction.¹⁷ The possibility that each \mathbf{k} corresponds to a different crystal variant with lowered symmetry is unresolved. The Ti-O monolayer and bilayer families each display a distinctive pattern of superlattice reflections, shown schematically in Figs. 6(a) and 6(b). One example of electron diffraction patterns showing the superlattice reflections is given in Fig. 7 for the 1:1:2:2 phase.

The structure and properties of the single CuO_2 layer compounds are more sensitive to the preparation conditions than those of the double and triple CuO_2 layer compounds. When prepared from a $\text{Ti}_2\text{Ba}_2\text{Cu}_1$ starting composition, the 2:0:2:1 compound has a face-centered orthorhombic cell and is not superconducting. The material is heavily twinned with twin planes of $\{110\}$ type in the orthorhombic cell. This cell is related to the tetragonal cell by a rotation of $\approx 45^\circ$ about the c axis with a and b increased in size by a factor of $\approx \sqrt{2}$. However when the 2:0:2:1 compound is prepared from a Cu-rich starting composition, $\text{Ti}_2\text{Ba}_2\text{Cu}_2$, the compound is superconduct-

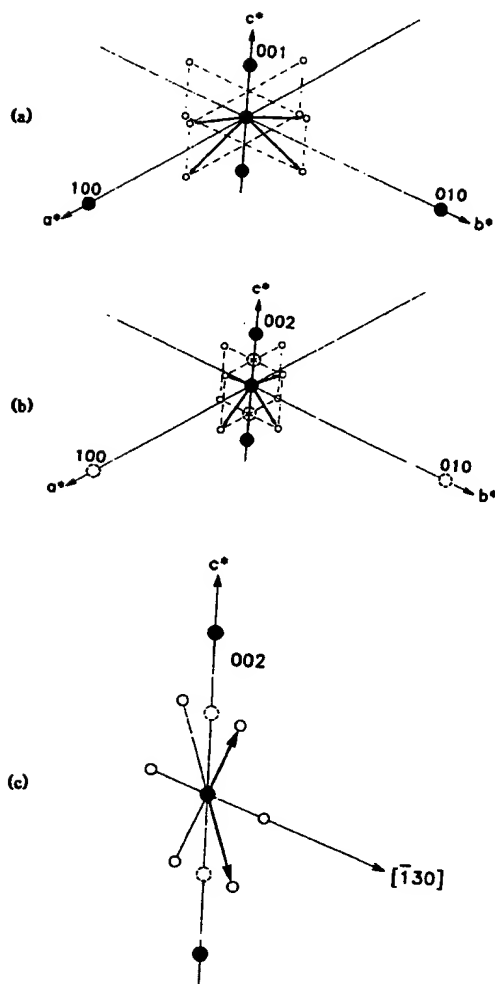


FIG. 6. Schematic diagram of the arrangement of superlattice reflections about the fundamental reflections for (a) the 1:1:2:2 and 1:2:2:3 phases, (b) the 2:1:2:2 and 2:2:2:3 phases, (c) the 2:0:2:1 phase. The fundamental reflections are shown as solid circles, and those which are systematically absent are shown as dashed circles. The superstructure is shown by open circles and the corresponding wave vectors by bold arrows.

ing at ≈ 20 K. While x-ray data indicate the structure is pseudotetragonal, transmission electron micrographs reveal a tweed pattern which is consistent with local orthorhombic distortion. A tetragonal polymorph with no evidence from TEM studies of either an average or local orthorhombic distortion can be formed by preparing the compound from a pellet containing a small amount of Ca ($\text{Ti:Ca:Ba:Cu} = 2:y:2:1+y$, with $y \approx 0.05-0.15$). This polymorph is also superconducting with a T_c which is independent of the amount of Ca in the starting composition but weakly dependent on the annealing time— $T_c \approx 15$ and 20 K for anneal times at 880°C of 3 and 9 h, respectively. As suggested by the Meissner data in Fig. 4(a) these pellets contain, in addition to the tetragonal 2:0:2:1 phase, a substantial amount of the 2:1:2:2 phase which increases as the proportion of Ca in the starting composition is increased. There is a sufficient amount of this phase that the resistance of these pellets actually drops to zero at

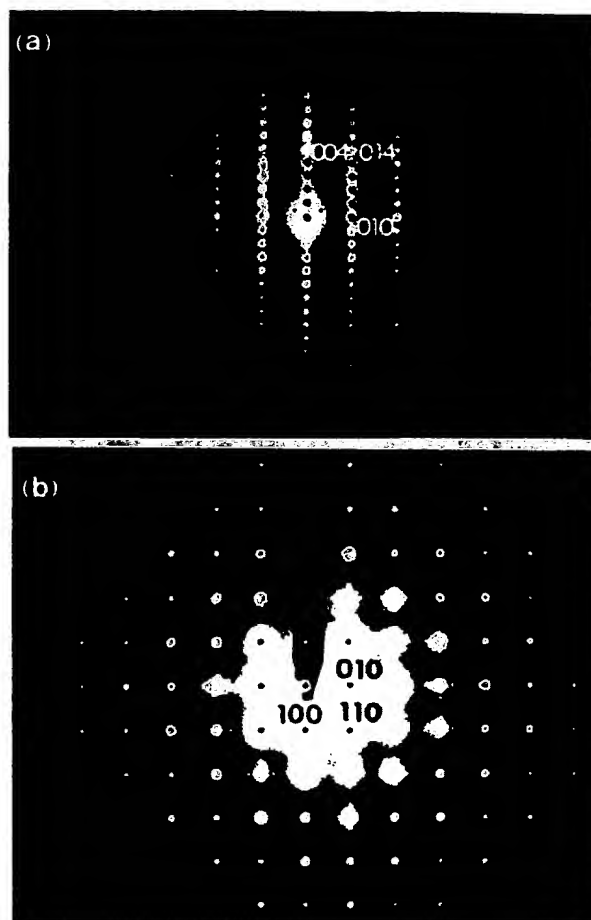


FIG. 7. (a) [100] and (b) [001] selected area diffraction patterns from crystallites of 1:1:2:2 showing superlattice reflections.

$T_c \approx 100$ K. The Meissner data in Fig. 4(a) show that for $y \approx 0.05$ the ratio of 2:1:2:2 to 2:0:2:1 is about 8% and for $y \approx 0.15$ the ratio is increased to $\approx 30\%$. Electron microprobe analysis shows that only a small amount of Ca (≈ 0.2 at.%) is incorporated into the 2:0:2:1 grains and consequently the role of the Ca doping in changing the structure and properties of the 2:0:2:1 material is unclear. Moreover there are reports that the 2:0:2:1 phase can be prepared without Ca with a transition temperature as high as ≈ 85 K.⁵ Both polymorphs of the 2:0:2:1 structures display a similar superlattice with an approximate wave vector, $\mathbf{k} = [0.08, 0.24, 1]$ in the orthorhombic setting. Taking the superlattice into account lowers the symmetry of both the orthorhombic and tetragonal structures to monoclinic with the c axis being unique. As shown in Fig. 8 this superstructure is different from those found in the double and triple CuO_2 layer compounds.

The other member of the $\text{Ti}_m\text{Ca}_{n-1}\text{Ba}_2\text{Cu}_n\text{O}_{2(n+1)+m}$ family which contains single CuO_2 layers, the 1:0:2:1 phase, has a primitive tetragonal cell and is not superconducting for the wide range of preparative conditions considered in this study, including growth from Cu-rich or Ca-doped starting compositions. No superstructures have been observed in these crystals so far.

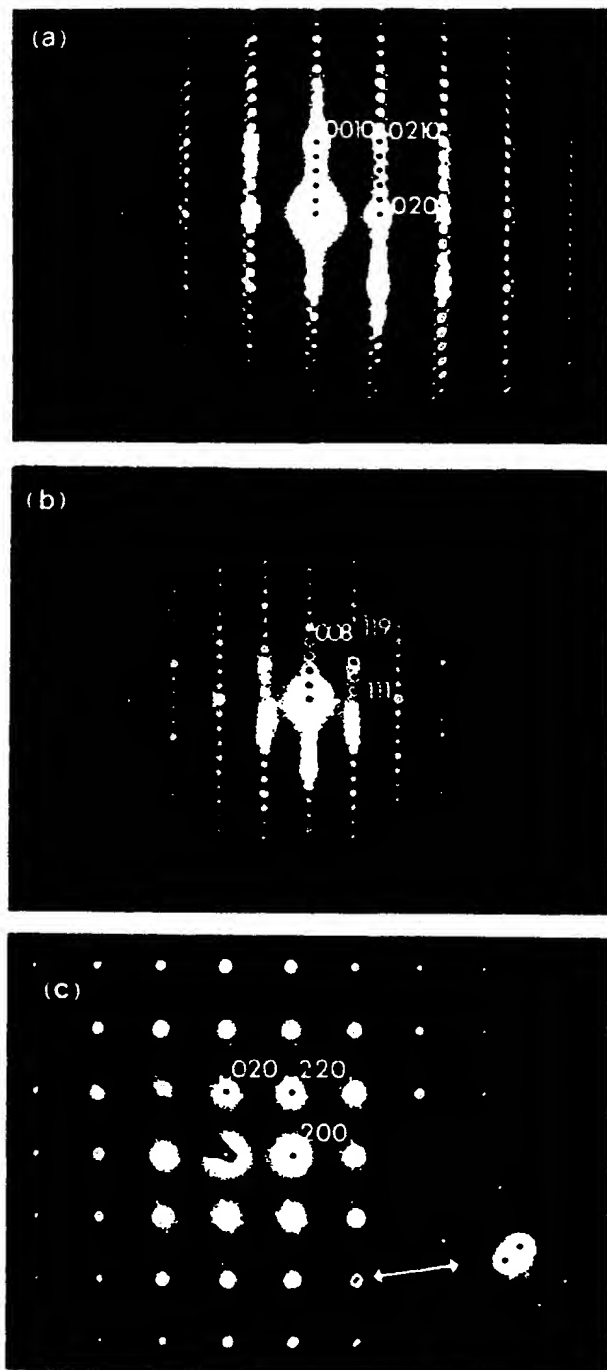


FIG. 8. (a) [100], (b) [110], and (c) [001] selected area diffraction patterns from a crystallite of 2:0:2:1.

As shown in Table I there is no obvious correlation of superlattice structure with the superconducting properties of the $\text{Tl}_m\text{Ca}_{n-1}\text{Ba}_2\text{Cu}_n\text{O}_{2(n+1)+m}$ compounds. Note that in the closely related compound, $\text{Bi}_2\text{Sr}_1\text{Ca}_2\text{Cu}_2\text{O}_x$, it has recently been proposed that the observed incommensurate superlattice corresponds to a distortion of both the Bi-O and CuO_2 planes resulting from ordered vacancies

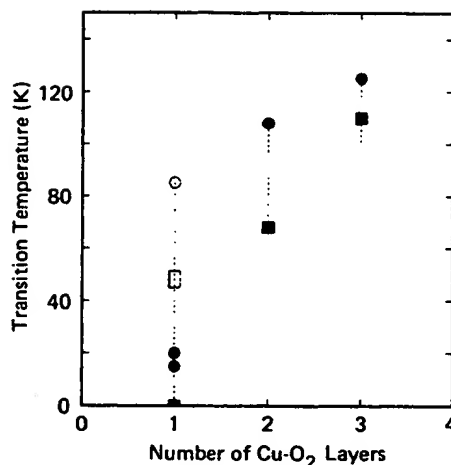


FIG. 9. Dependence of T_c on the number of CuO_2 planes within the Cu perovskitelike unit for the $\text{Tl}_1\text{Ca}_{n-1}\text{Ba}_2\text{Cu}_n\text{O}_{2n+3}$ (■) and $\text{Tl}_2\text{Ca}_{n-1}\text{Ba}_2\text{Cu}_n\text{O}_{2n+4}$ (●, this work; ○, Ref. 5) series of compounds. The dashed vertical lines correspond to the variations in T_c found for each phase. □ corresponds to data for $(\text{Tl}, \text{Bi})_1(\text{Ca}, \text{Sr})_2\text{Cu}_1\text{O}_x$ (Ref. 21).

on the Sr sites.¹⁶ The vacancies are postulated to determine the carrier density on the CuO_2 planes and so influence the T_c in a manner similar to that first noted by Schafer, Penney, and Olsen for the $\text{La}_{2-x}\text{Sr}_x\text{CuO}_{4-y}$ compounds.¹⁸ The number of different superlattice structures found in the Tl-Ca-Ba-Cu-O system provides a more extensive basis with which to test such hypotheses. Indeed it may be significant that, as shown in Table I, there are important variations in stoichiometry away from the ideal stoichiometries expected for the various $\text{Tl}_m\text{Ca}_{n-1}\text{Ba}_2\text{Cu}_n\text{O}_{2(n+1)+m}$ phases. In particular, the $[\text{Tl}]/[\text{Ba}]$ ratio is higher for the $n=1$ compounds compared to those for $n=2$ and $n=3$. Band-structure calculations of both the $\text{Tl}_m\text{Ca}_{n-1}\text{Ba}_2\text{Cu}_n\text{O}_{2(n+1)+m}$ compounds and $\text{Bi}_2\text{Sr}_1\text{Ca}_2\text{Cu}_2\text{O}_x$ indicate that the stoichiometry of the Tl-O and Bi-O layers would have a profound impact on the carrier density in these materials.^{19,20} The extent of off-stoichiometry on the cation or the oxygen sites in the Tl-Ca-Ba-Cu-O phases requires further study. Note also that one group has recently prepared a complex material of the form $(\text{Tl}, \text{Bi})_1(\text{Ca}, \text{Sr})_2\text{Cu}_1\text{O}_x$ with the 1:0:2:1 structure which appears to superconduct at temperatures of up to 50 K (Ref. 21). The variation of properties of the single CuO_2 layers compounds provides a fertile area for further study and highlights the difficulties in preparing these multicomponent oxides in a controlled manner.

In conclusion, these studies have shown that the superconducting transition temperature increases with the number of CuO_2 planes in the perovskitelike unit for both the $\text{Tl}_1\text{Ca}_{n-1}\text{Ba}_2\text{Cu}_n\text{O}_{2n+3}$ and $\text{Tl}_2\text{Ca}_{n-1}\text{Ba}_2\text{Cu}_n\text{O}_{2n+4}$ structures (Fig. 9). A similar dependency is found in both series of compounds with an increased spread of T_c as the number of CuO_2 planes is reduced. The range of T_c in the double and triple CuO_2 layer compounds correlates with the density of intergrowth defects. No such defects have been observed so far in the single CuO_2 layer compounds,

even when doped with Ca. One might speculate that in this case the variation in transition temperature may result from variations in cation or oxygen site occupancy. The increase in T_c as n increases may be accounted for by various theories, including several based on the BCS theory¹⁹ and others invoking more exotic mechanisms such as the resonating-valence-bond model.²² The variety of structures and properties in the Tl-Ca-Ba-Cu-O system provides a model family of compounds with which various

theories of high-temperature superconductivity can be evaluated.

We are indebted to S. J. La Placa, F. Herman, and J. B. Torrance for many useful discussions. We thank C. C. Torardi, R. B. Flippen, and R. M. Hazen for discussions regarding the 2:0:2:1 compound. We are grateful to Professor Sinclair at Stanford for the use of his electron microscope.

- ¹Z. Z. Sheng and A. M. Hermann, *Nature (London)* **332**, 138 (1988); **332**, 55 (1988).
- ²R. M. Hazen, L. W. Finger, R. J. Angel, C. T. Prewitt, N. L. Ross, C. G. Hadidiacos, P. J. Heaney, D. R. Veblen, Z. Z. Sheng, A. El Ali, and A. M. Hermann, *Phys. Rev. Lett.* **60**, 1657 (1988).
- ³S. S. P. Parkin, V. Y. Lee, E. M. Engler, A. I. Nazzari, T. C. Huang, G. Gorman, R. Savoy, and R. Beyers, *Phys. Rev. Lett.* **60**, 2539 (1988).
- ⁴S. S. P. Parkin, V. Y. Lee, A. I. Nazzari, R. Savoy, R. Beyers, and S. J. La Placa, *Phys. Rev. Lett.* **61**, 750 (1988).
- ⁵C. C. Torardi, M. A. Subramanian, J. C. Calabrese, J. Gopalakrishnan, K. J. Morrissey, T. R. Askew, R. B. Flippen, U. Chowdry, and A. W. Sleight, *Science* **240**, 631 (1988).
- ⁶M. A. Subramanian, J. C. Calabrese, C. C. Torardi, J. Gopalakrishnan, T. R. Askew, R. B. Flippen, K. J. Morrissey, U. Chowdry, and A. W. Sleight, *Nature (London)* **332**, 420 (1988).
- ⁷S. Kondoh, Y. Ando, M. Onoda, and M. Sato, *Solid State Commun.* **65**, 1329 (1988).
- ⁸W. Parrish, *X-ray and Electron Methods of Analysis* (Plenum, New York, 1968).
- ⁹J. M. Tarascon, Y. Le Page, P. Barboux, B. G. Bagley, L. H. Greene, W. R. McKinnon, G. W. Hull, M. Giroud, and D. M. Hwang, *Phys. Rev. B* **37**, 9382 (1988).
- ¹⁰S. A. Sunshine, T. Siegrist, L. F. Schneemeyer, D. W. Murphy, R. J. Cava, B. Batlogg, R. B. van Dover, R. M. Fleming, S. H. Glarum, S. Nakahara, R. Farrow, J. J. Krajewski, S. M. Zahurak, J. V. Waszczak, J. H. Marshall, P. Marsh, L. W. Rupp, and W. F. Peck, *Phys. Rev. B* **38**, 893 (1988).
- ¹¹J. B. Torrance, Y. Tokura, S. J. LaPlaca, T. C. Huang, R. J. Savoy, and A. I. Nazzari, *Solid State Commun.* **66**, 703 (1988).
- ¹²T. M. Shaw, S. A. Shivashankar, S. J. LaPlaca, J. J. Cuomo, T. R. McGuire, R. A. Roy, K. H. Kelleher, and D. S. Yee, *Phys. Rev. B* **37**, 9856 (1988).
- ¹³D. R. Veblen, P. J. Heaney, R. J. Angel, L. W. Finger, R. M. Hazen, C. T. Prewitt, N. L. Ross, C. W. Chu, P. H. Hor, and R. L. Meng, *Nature (London)* **332**, 334 (1988).
- ¹⁴E. A. Hewat, M. Dupuy, P. Bordet, J. J. Capponi, C. Chailout, J. L. Hodeau, and M. Marezio, *Nature (London)* **333**, 53 (1988).
- ¹⁵H. W. Zandbergen, Y. K. Huang, M. J. V. Menken, J. N. Li, K. Kadowaki, A. A. Menovsky, G. van Tendeloo, and S. Amelinckx, *Nature (London)* **332**, 620 (1988).
- ¹⁶P. L. Gai and P. Day (unpublished).
- ¹⁷P. M. De Wolff, *Acta Crystallogr. Sec. A* **30**, 777 (1974).
- ¹⁸M. W. Shafer, T. Penney, and B. L. Olsen, *Phys. Rev. B* **36**, 4047 (1987).
- ¹⁹M. S. Hybertson and L. F. Mattheiss, *Phys. Rev. Lett.* **60**, 1661 (1988).
- ²⁰F. Herman, R. V. Kasowski, and W. Y. Hsu, *Phys. Rev. B* **38**, 204 (1988); F. Herman, R. V. Kasowski, S. J. La Placa, and S. S. P. Parkin (unpublished).
- ²¹P. Haldar, A. Roig-Janicki, S. Sridhar, and B. C. Giessen (unpublished).
- ²²J. M. Wheatley, T. C. Hsu, and P. W. Anderson, *Nature (London)* **333**, 121 (1988).

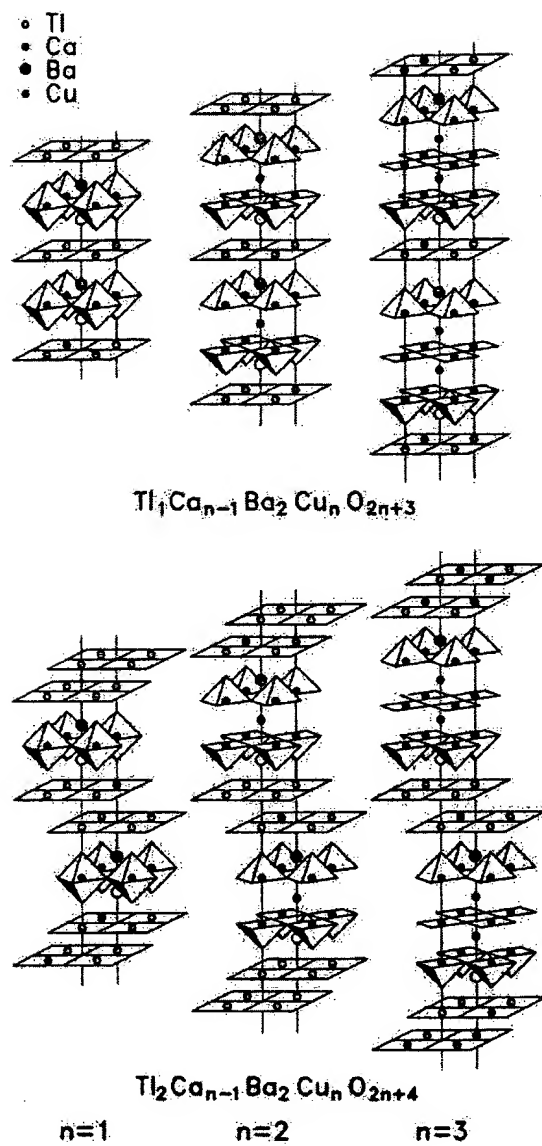


FIG. 2. Nominal structures of the six $\text{Ti}_m\text{Ca}_{n-1}\text{Ba}_2\text{Cu}_n\text{O}_{2(n+1)+m}$ phases for $n=1, 2$ and $m=1, 2, 3$.

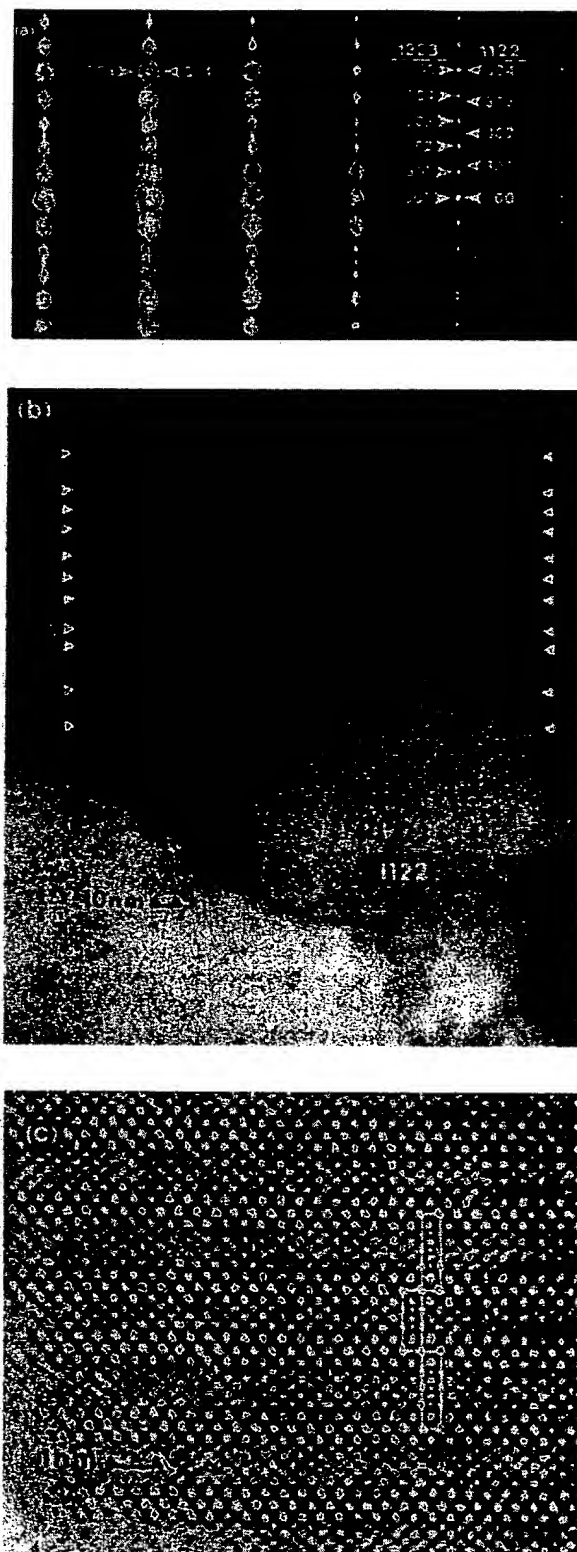


FIG. 3. (a) [010] selected area diffraction (SAD) pattern, and (b) corresponding image of crystallites containing regions of 1:2:2:3 and 1:1:2:2. The arrows in (b) denote unit-cell thick intergrowths of 1:1:2:2 in 1:2:2:3. (c) High-resolution transmission electron micrograph of one unit-cell thick 1:1:2:2 intergrowth in 1:2:2:3.

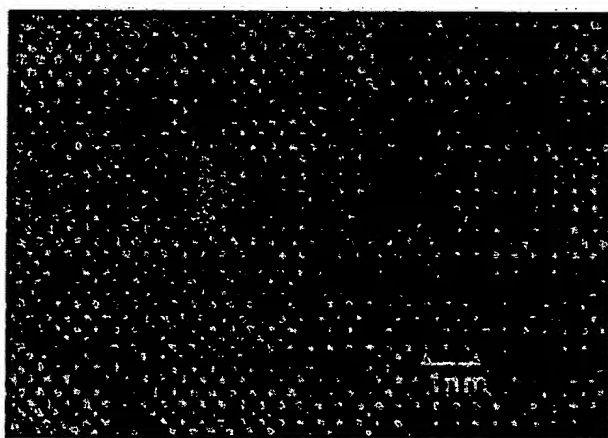


FIG. 5. High-resolution TEM image of an isolated four-CuO₂-layer intergrowth. The markers denote the positions of the Cu columns.

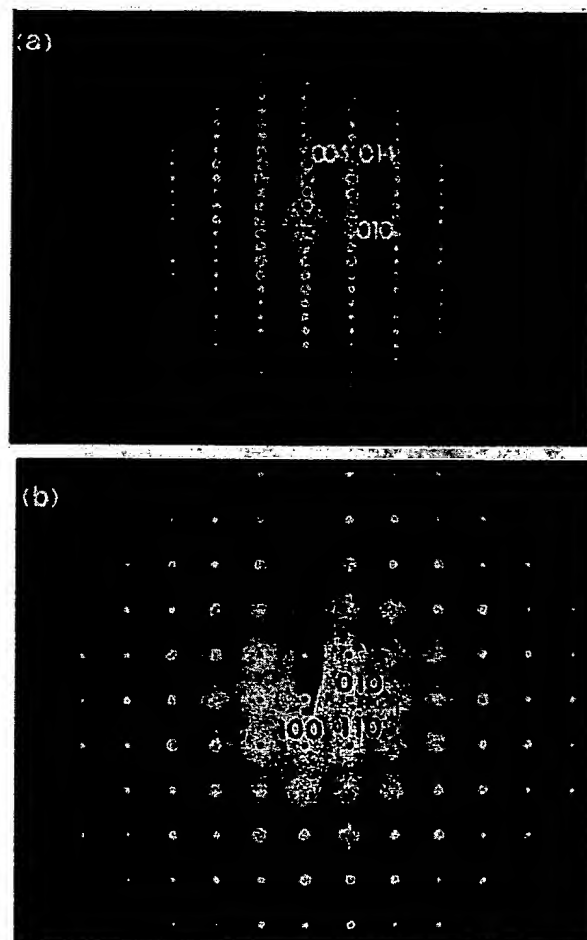


FIG. 7. (a) [100] and (b) [001] selected area diffraction patterns from crystallites of 1:1:2:2 showing superlattice reflections.

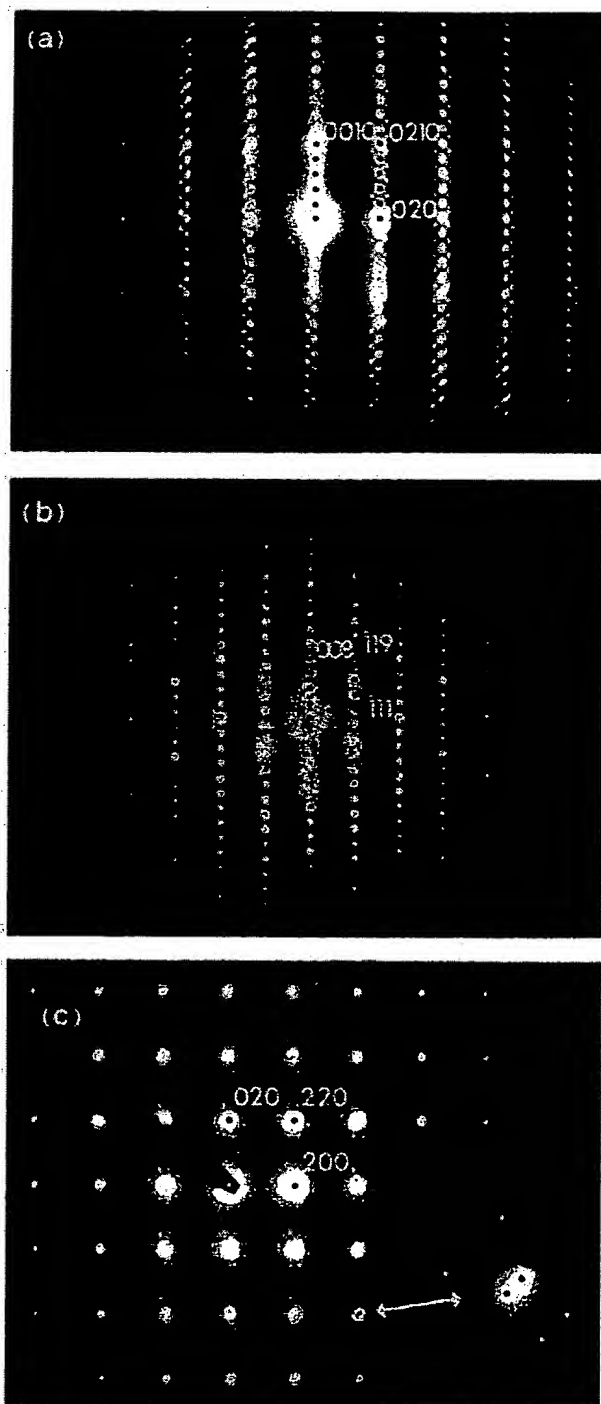


FIG. 8. (a) [100], (b) [110], and (c) [001] selected area diffraction patterns from a crystallite of 2:0:2:1.

BRIEF ATTACHMENT K

IN THE UNITED STATES PATENT AND TRADEMARK OFFICE

In re Patent Application of

Applicants: Bednorz et al.

Serial No.: 08/479,810

Filed: June 7, 1995

For: NEW SUPERCONDUCTIVE COMPOUNDS HAVING HIGH TRANSITION
TEMPERATURE, METHODS FOR THEIR USE AND PREPARATION

Date: March 1, 2005

Docket: YO987-074BZ

Group Art Unit: 1751

Examiner: M. Kopec

Commissioner for Patents
P.O. Box 1450
Alexandria, VA 22313-1450

FIRST SUPPLEMENTAL AMENDMENT

Sir:

In response to the Office Action dated July 28, 2004, please consider the
following:

ATTACHMENT K

A New High- T_c Oxide Superconductor without a Rare Earth Element

Hiroshi MAEDA, Yoshiaki TANAKA, Masao FUKUTOMI and Toshihisa ASANO

National Research Institute for Metals, Tsukuba Laboratories, Ibaraki 305

(Received January 22, 1988; accepted for publication January 23, 1988)

We have discovered a new high- T_c oxide superconductor of the Bi-Sr-Ca-Cu-O system without any rare earth element. The oxide $\text{BiSrCaCu}_2\text{O}_x$ has T_c of about 105 K, higher than that of $\text{YBa}_2\text{Cu}_3\text{O}_7$ by more than 10 K. In this oxide, the coexistence of Sr and Ca is necessary to obtain high T_c .

KEYWORDS: oxide superconductor, Bi-Sr-Ca-Cu-O system, rare earth, high T_c , new stable superconductor

Soon after the discovery of high- T_c superconductors of the layered perovskites $(\text{LaBa})_2\text{CuO}_4$ ¹⁾ and $(\text{LaSr})_2\text{CuO}_4$ ²⁾ with T_c of about 40 K, $\text{YBa}_2\text{Cu}_3\text{O}_7$ ³⁾ with T_c of 94 K was synthesized. The discovery of these materials stimulated many researchers to investigate new oxide superconductors of still higher T_c and extensive studies have been carried out to search for these oxides. Up to now, however, no new stable superconductors with T_c higher than that of $\text{YBa}_2\text{Cu}_3\text{O}_7$ have been reported. The values of T_c have not improved by the substitution of other rare earth elements for yttrium.

In order to find high- T_c superconductors, we believe that it is important to investigate other classes of oxides which do not include rare earth elements. This led us to study the superconducting oxide system including the Vb-element group such as Bi and Sb of trivalent elements, and we discovered a new high- T_c superconducting material $\text{BiSrCaCu}_2\text{O}_x$. This oxide has T_c of about 105 K, being higher than that of $\text{YBa}_2\text{Cu}_3\text{O}_7$ by more than 10 K.

The value of T_c in the Bi-Sr-Cu-O oxide system which does not include Ca is very low being about 8 K.^{4,5)} In order to obtain high T_c , the coexistence of Sr and Ca in the Bi oxide system is found to be absolutely necessary.

The Bi-Sr-Ca-Cu-O oxide samples were prepared from powder reagents of Bi_2O_3 , SrCO_3 , CaCO_3 and CuO . The appropriate amounts of powders were mixed, calcined at 800–870°C for 5 h, thoroughly reground and then cold-pressed into disk-shape pellets (20 mm in diameter and 2 mm in thickness) at a pressure of 2 ton/cm². Most of the pellets were sintered at about 870°C in air or in an oxygen atmosphere and then furnace-cooled to room temperature.

The electrical resistivity was measured by the standard four-probe method for a bar-shaped specimen of about 1×2×20 mm³ cut out from the pellets. Magnetization measurements were carried out with a vibrating sample magnetometer. The temperature was measured by Au7%Fe-Chromel thermocouples. Figure 1 shows the resistivity vs temperature curves of $\text{BiSrCaCu}_2\text{O}_x$ oxides thus prepared. Specimen (a) was sintered at a relatively low temperature of 800°C for 8 h while specimen (b) was sintered at a higher temperature of 882°C for 20 min followed by annealing at 872°C for 9 h. In the case of the lower sintering temperature, the onset temperature (T_c^{on}) of the superconducting transition is about 83 K and the zero resistance state (T_c^{off}) is reached at 75 K (low- T_c

phase). On the other hand, in the case of a higher sintering temperature, a high- T_c phase appears, the onset temperature of which is about 120 K and T_c extrapolated to zero resistance is as high as 105 K. The value of T_c^{off} is higher than that of $\text{YBa}_2\text{Cu}_3\text{O}_7$ by more than 10 K. Since a little amount of the low- T_c phase still remained in the sample, a complete zero resistance state is achieved at 75 K which corresponds to that of the low- T_c phase. We have not succeeded in synthesizing the oxides with a single phase of the high- T_c material at this moment. From our preliminary experiments, we know that sintering at high temperatures for a short duration of time is effective enough to increase the relative amount of the high- T_c phase. This may indicate that the high- T_c phase is stable at elevated temperatures.

Figure 2 shows the magnetization vs temperature curve for the specimen (b) in Fig. 1 which was sintered at the higher temperatures. A Meissner effect showing a perfect diamagnetic state is observed exactly in the same temperature range as in curve (a) shown in Fig. 1. We conclude, therefore, that the present high- T_c phase is indeed superconducting.

The high- T_c phase appears near the composition ratios of Bi:Sr:Ca=1:1:1. As the composition deviates from

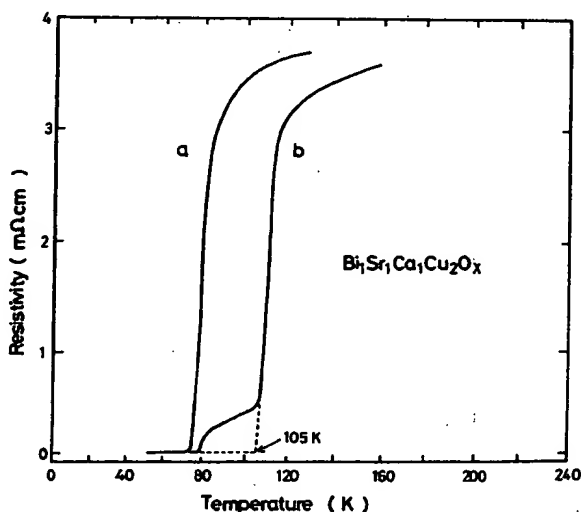


Fig. 1. Temperature dependence of resistivities in $\text{BiSrCaCu}_2\text{O}_x$ oxides (a) sintered in air at 800°C for 8 h, then cooled in a furnace and (b) sintered at 882°C for 20 min followed by annealing at 872°C for 9 h.

A New High- T_c Oxide Superconductor without a Rare Earth Element

Hiroshi MAEDA, Yoshiaki TANAKA, Masao FUKUTOMI and Toshihisa ASANO

National Research Institute for Metals, Tsukuba Laboratories, Ibaraki 305

(Received January 22, 1988; accepted for publication January 23, 1988)

We have discovered a new high- T_c oxide superconductor of the Bi-Sr-Ca-Cu-O system without any rare earth element. The oxide $\text{BiSrCaCu}_2\text{O}_x$ has T_c of about 105 K, higher than that of $\text{YBa}_2\text{Cu}_3\text{O}_7$ by more than 10 K. In this oxide, the coexistence of Sr and Ca is necessary to obtain high T_c .

KEYWORDS: oxide superconductor, Bi-Sr-Ca-Cu-O system, rare earth, high T_c , new stable superconductor

Soon after the discovery of high- T_c superconductors of the layered perovskites $(\text{LaBa})_2\text{CuO}_4$ ¹⁾ and $(\text{LaSr})_2\text{CuO}_4$ ²⁾ with T_c of about 40 K, $\text{YBa}_2\text{Cu}_3\text{O}_7$ ³⁾ with T_c of 94 K was synthesized. The discovery of these materials stimulated many researchers to investigate new oxide superconductors of still higher T_c and extensive studies have been carried out to search for these oxides. Up to now, however, no new stable superconductors with T_c higher than that of $\text{YBa}_2\text{Cu}_3\text{O}_7$ have been reported. The values of T_c have not improved by the substitution of other rare earth elements for yttrium.

In order to find high- T_c superconductors, we believe that it is important to investigate other classes of oxides which do not include rare earth elements. This led us to study the superconducting oxide system including the Vb-element group such as Bi and Sb of trivalent elements, and we discovered a new high- T_c superconducting material $\text{BiSrCaCu}_2\text{O}_x$. This oxide has T_c of about 105 K, being higher than that of $\text{YBa}_2\text{Cu}_3\text{O}_7$ by more than 10 K.

The value of T_c in the Bi-Sr-Cu-O oxide system which does not include Ca is very low being about 8 K.^{4,5)} In order to obtain high T_c , the coexistence of Sr and Ca in the Bi oxide system is found to be absolutely necessary.

The Bi-Sr-Ca-Cu-O oxide samples were prepared from powder reagents of Bi_2O_3 , SrCO_3 , CaCO_3 and CuO. The appropriate amounts of powders were mixed, calcined at 800–870°C for 5 h, thoroughly reground and then cold-pressed into disk-shape pellets (20 mm in diameter and 2 mm in thickness) at a pressure of 2 ton/cm². Most of the pellets were sintered at about 870°C in air or in an oxygen atmosphere and then furnace-cooled to room temperature.

The electrical resistivity was measured by the standard four-probe method for a bar-shaped specimen of about $1 \times 2 \times 20 \text{ mm}^3$ cut out from the pellets. Magnetization measurements were carried out with a vibrating sample magnetometer. The temperature was measured by Au7%Fe-Chromel thermocouples. Figure 1 shows the resistivity vs temperature curves of $\text{BiSrCaCu}_2\text{O}_x$ oxides thus prepared. Specimen (a) was sintered at a relatively low temperature of 800°C for 8 h while specimen (b) was sintered at a higher temperature of 882°C for 20 min followed by annealing at 872°C for 9 h. In the case of the lower sintering temperature, the onset temperature (T_c^{on}) of the superconducting transition is about 83 K and the zero resistance state (T_c^{off}) is reached at 75 K (low- T_c

phase). On the other hand, in the case of a higher sintering temperature, a high- T_c phase appears, the onset temperature of which is about 120 K and T_c extrapolated to zero resistance is as high as 105 K. The value of T_c^{off} is higher than that of $\text{YBa}_2\text{Cu}_3\text{O}_7$ by more than 10 K. Since a little amount of the low- T_c phase still remained in the sample, a complete zero resistance state is achieved at 75 K which corresponds to that of the low- T_c phase. We have not succeeded in synthesizing the oxides with a single phase of the high- T_c material at this moment. From our preliminary experiments, we know that sintering at high temperatures for a short duration of time is effective enough to increase the relative amount of the high- T_c phase. This may indicate that the high- T_c phase is stable at elevated temperatures.

Figure 2 shows the magnetization vs temperature curve for the specimen (b) in Fig. 1 which was sintered at the higher temperatures. A Meissner effect showing a perfect diamagnetic state is observed exactly in the same temperature range as in curve (a) shown in Fig. 1. We conclude, therefore, that the present high- T_c phase is indeed superconducting.

The high- T_c phase appears near the composition ratios of Bi:Sr:Ca = 1:1:1. As the composition deviates from

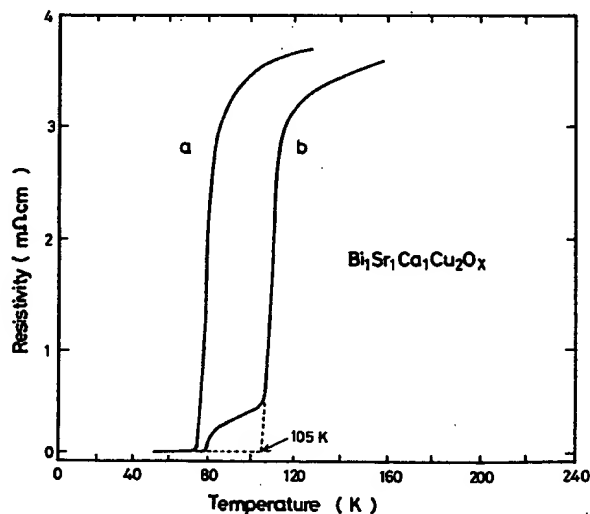


Fig. 1. Temperature dependence of resistivities in $\text{Bi}_1\text{Sr}_1\text{Ca}_1\text{Cu}_2\text{O}_x$ oxides (a) sintered in air at 800°C for 8 h, then cooled in a furnace and (b) sintered at 882°C for 20 min followed by annealing at 872°C for 9 h.

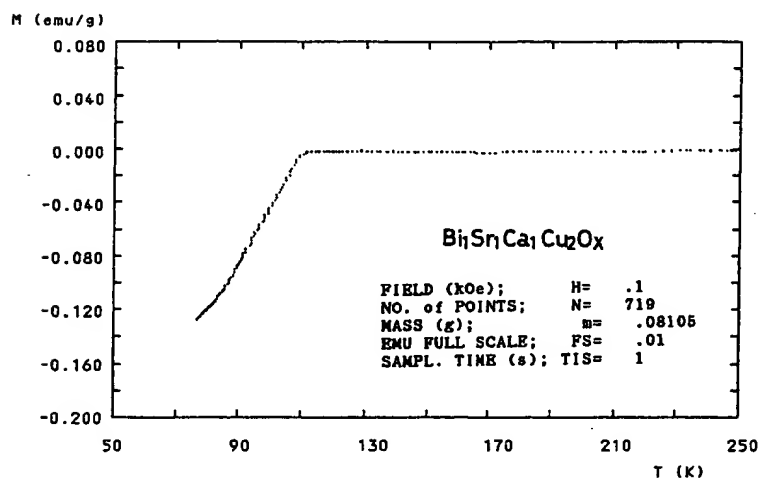


Fig. 2. Magnetization of $\text{Bi}_1\text{Sr}_1\text{Ca}_1\text{Cu}_2\text{O}_x$ for the sample (b) in Fig. 1 in a field of 100 Oe.

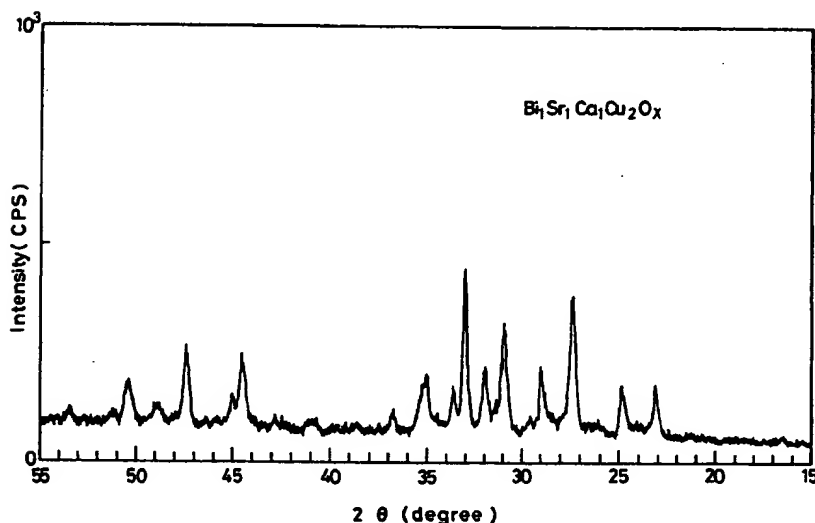


Fig. 3. X-ray ($\text{Cu K}\alpha$) diffraction pattern of the $\text{Bi}_1\text{Sr}_1\text{Ca}_1\text{Cu}_2\text{O}_x$ oxide superconductor for the sample (b) in Fig. 1.

this ratio, a low- T_c phase tends to appear irrespective of the sintering conditions. In $\text{BiSrCaCu}_x\text{O}_x$ oxides, the oxide of $y=1$ is not superconducting. According to the results of the X-ray diffraction analyses, the starting material corresponding to the composition of $\text{Bi}_1\text{Sr}_1\text{Ca}_1\text{Cu}_2\text{O}_x$ seems to form a single phase. While in the nominal composition of oxides with $y>2$, unreacted CuO remained in the sample. A typical X-ray diffraction pattern for the oxide of $y=2$ (sample (b) in Fig. 1) is shown in Fig. 3. Although the structure of this oxide is not identified yet, it appears to be different from those of $(\text{LaSr})_2\text{CuO}_4$ and $\text{YBa}_2\text{Cu}_3\text{O}_7$.

This material having high T_c above 105 K may have potential application in various industrial fields in the near future. It should be noted that these oxides are extremely stable in water and moisture and that no change in the superconducting properties has been observed even after the thermal cyclings between 4 K and room temperature or above.

Furthermore, the oxide has two phases with different

T_c and their structures seem to be different from those of high- T_c oxide superconductors discovered up to now. We believe that this new oxide will contribute greatly to elucidating the high- T_c superconducting mechanism.

Acknowledgements

We would like to thank Dr. M. Uehara for the measurements of magnetization and Dr. K. Ogawa for his useful discussions.

References

- 1) J. G. Bednorz and K. A. Müller: *Z. Phys.* **B64** (1986) 189.
- 2) S. Uchida, H. Takagi, K. Kitazawa and S. Tanaka: *Jpn. J. Appl. Phys.* **26** (1987) L1.
- 3) M. K. Wu, J. R. Ashburn, C. J. Torng, P. H. Hor, R. L. Meng, L. Gao, Z. J. Haang, Y. Q. Wang and C. W. Chu: *Phys. Rev. Lett.* **58** (1987) 908.
- 4) J. Akimitsu, A. Yamazaki, H. Sawa and H. Fujiki: *Jpn. J. Appl. Phys.* **26** (1987) L2080.
- 5) C. Michel, M. Hervieu, M. M. Borel, A. Grandin, F. Deslandes, J. Provost and B. Raveau: *Z. Phys.* **B68** (1987) 421.

BRIEF ATTACHMENT L

IN THE UNITED STATES PATENT AND TRADEMARK OFFICE

In re Patent Application of

Applicants: Bednorz et al.

Serial No.: 08/479,810

Filed: June 7, 1995

For: NEW SUPERCONDUCTIVE COMPOUNDS HAVING HIGH TRANSITION
TEMPERATURE, METHODS FOR THEIR USE AND PREPARATION

Date: March 1, 2005

Docket: YO987-074BZ

Group Art Unit: 1751

Examiner: M. Kopec

Commissioner for Patents
P.O. Box 1450
Alexandria, VA 22313-1450

FIRST SUPPLEMENTAL AMENDMENT

Sir:

In response to the Office Action dated July 28, 2004, please consider the
following:

ATTACHMENT L



The resulting map (Fig. 1e) shows that the absorption feature has a mean W of 0.2 nm and stretches from roughly north to south across the entire emission line region, corresponding to a length of >30 kpc (the map presents only the area with good signal-to-noise ratio). Its spatial width is rather uncertain, because it is unresolved in the east-west direction ($<1.5''$). It cannot be narrower than $0.5''$ because otherwise even a 100% obscuration would be washed out by our beam into a relative depression of $<25\%$ (0.25 nm). So we assume a projected size of 10×10 kpc² for the absorber, with a deconvoluted equivalent width of about 0.5 nm.

Such an absorber can either consist of one or more clouds located well in front of 4C41.17 (if the blueshift of the absorption is cosmological, the absorber sits at a comoving distance of 5 Mpc). On the other hand, the velocity in the EELR itself is large enough to cover this blueshift; otherwise we would be unable to detect the feature. Thus, a dense, partially ionized cloud at the edge of 4C41.17 could equally explain the absorption. In this latter case more detailed observations are necessary for a physical interpretation. We therefore would like to pursue the former possibility of a physically separated absorber. Such clouds—commonly known as Lyman-forest clouds—and their properties have been extensively studied in the absorption line spectra of high redshift quasars.

For comparison we make use of a spectrum¹⁴ of the quasar Q0000-263 ($z=4.11$), the Lyman-forest of which covers the λ range of our observation. We smoothed the original spectrum (resolution, 0.1 nm) to our instrumental resolution of 1.0 nm. The comparison between smoothed and original spectrum reveals that any absorption feature as deep as that observed in 4C41.17 typically consists of two or more narrow absorption lines. We have to realize therefore, that our 'absorption cloud' is likely to be a superposition of several individual Lyman-forest clouds. Nevertheless, we believe that the outline of the absorber in the W map (Fig. 1e) is most likely to be determined by one single cloud which made the feature strong enough to become detectable, and we assign half of the measured equivalent width (0.25 nm) to this cloud. Assuming a Doppler parameter $b=35$ km s⁻¹ and $N_{\text{H}}/N_{\text{H}^+}=10^{-4}$ as typical for Lyman clouds of that depth (refs 1, 3), we find a column density $N_{\text{H}} \sim 10^{15}$ cm⁻². A cigar-shaped cloud of 40 kpc length and 10 kpc diameter would contain a total hydrogen mass of $\sim 3 \times 10^7 M_{\odot}$.

What is the probability of detecting such an absorption feature in front of 4C41.17? Both the smoothed spectrum of Q0000-263 (ref. 14) and the standard $dN(W, z)/dz$ relation¹⁵ yield ~ 25 features with $W > 0.4$ nm on each line of sight and within one z unit at the observed wavelength. Considering the 'useful' wavelength range of ~ 1.2 nm (the blue half of the width of the emission line) in our search for line features, and the area of the EELR inspected of ~ 20 arcsec², the probability of detecting a cloud of a typical size of a few arcsec² is close to 1.

In conclusion, we believe that we have succeeded in obtaining the first direct observation of a Lyman absorption cloud. Either this cloud belongs directly to the mass concentration around 4C41.17 or it is a physically separated foreground object. In the latter case it would represent the population of Lyman-forest clouds known from the absorption spectra of quasars. In either case, our observations indicate that the relevant absorbers have projected sizes of some 100 kpc² and an elongated shape, like a cigar or a sheet seen almost edge-on in the case of 4C41.17. □

Received 23 September 1992; accepted 19 January 1993.

- Chaffee, F. H., Foltz, C. R., Bechtold, J. & Weymann, R. J. *Astrophys. J.* **301**, 116–123 (1986).
- Carswell, R. F., Webb, J. K., Baklanov, A. A. & Atwood, B. *Astrophys. J.* **319**, 709–722 (1987).
- Rauch, M. *et al.* *Astrophys. J.* **390**, 387–404 (1992).
- Foltz, C. B., Weymann, R. J., Röser, H. J. & Chaffee, F. H. *Astrophys. J.* **281**, L1–L4 (1984).
- Smeth, A. *et al.* *Astrophys. J.* **389**, 39–62 (1992).
- Tyler, D. *Astrophys. J.* **321**, 69–79 (1987).
- Pettini, M., Hunstead, R. W., Smith, L. J. & Mar, D. P. *Mon. Not. R. astr. Soc.* **246**, 545–564 (1990).
- Kneib, S. in *Dark Matter in the Universe* (eds Sato, H. & Kotama, H.) 50–62 (Springer, Berlin, 1990).

- Spirad, H. in *Epoch of Galaxy Formation* (eds Frenk, C. S. *et al.*) 33–56 (Kluwer, Dordrecht, 1988).
- Lilly, S. *Astrophys. J.* **333**, 161–167 (1988).
- Chambers, K. C., Miley, G. K. & van Breugel, W. *Astrophys. J.* **363**, 21–39 (1990).
- Meisenheimer, K. & Hippelein, H. *Astr. Astrophys.* **264**, 455–471 (1992).
- Röser, S. & Bastian, U. *FW Star Catalogue* (Spektrum Akad., Heidelberg, 1991).
- Webb, J. K. *et al.* *ESO Messenger* **51**, 15–18 (1988).
- Murdoch, H. S., Hunstead, R. W., Pettini, M. & Blades, J. C. *Astrophys. J.* **309**, 19–32 (1986).

ACKNOWLEDGEMENTS. We thank R. Carswell for the spectrum of Q0000-236 and H. Röser for discussions.

Superconductivity at 94 K in $\text{HgBa}_2\text{CuO}_{4+\delta}$

S. N. Putilin[†], E. V. Antipov^{*}, O. Chmaissem[†] & M. Marezio^{††}

^{*} Chemical Department, Moscow State University, 119899 Moscow, Russia

[†] Laboratoire de Cristallographie CNRS-UF, BP 166, 38042 Grenoble Cedex 09, France

^{††} AT&T Bell Laboratories, Murray Hill, New Jersey 07974, USA

FOLLOWING the discovery¹ of high-transition-temperature (high- T_c) superconductivity in doped La_2CuO_4 , several families of related compounds have been discovered which have layers of CuO_2 as the essential requirement for superconductivity: the highest transition temperatures so far have been found for thallium-bearing compounds². Recently the mercury-bearing compound $\text{HgBa}_2\text{R}_2\text{Cu}_2\text{O}_{8+\delta}$ (Hg-1212) was synthesized³ (where R is a rare-earth element), with a structure similar to the thallium-bearing superconductor $\text{TlBa}_2\text{CaCu}_2\text{O}_7$ (Tl-1212), which has one TlO layer and two CuO_2 layers per unit cell, and a T_c of 85 K (ref. 2). But in spite of its resemblance to Tl-1212, Hg-1212 was found not to be superconducting. Here we report the synthesis of the related compound $\text{HgBa}_2\text{CuO}_{4+\delta}$ (Hg-1201), with only one CuO_2 layer per unit cell, and show that it is superconducting below 94 K. Its structure is similar to that of Tl-1201 (which has a T_c of <10 K)⁴, but its transition temperature is considerably higher. The availability of a material with high T_c but only a single metal oxide (HgO) layer may be important for technological applications, as it seems that a smaller spacing between CuO_2 planes leads to better superconducting properties in a magnetic field⁵.

The samples were prepared by solid state reaction between stoichiometric mixtures of $\text{Ba}_2\text{CuO}_{3+\delta}$ and yellow HgO (98% purity, Aldrich). The precursor $\text{Ba}_2\text{CuO}_{3+\delta}$ was obtained by the same type of reaction between BaO_2 (95% purity, Aldrich) and CuO (NormaPur, Prolabo) at 930 °C in oxygen, according to the procedure described by De Leeuw *et al.*⁶. The powders were ground in an agate mortar and placed in silica tubes. All these operations were carried out in a dry box. After evacuation, the tubes were sealed, placed in steel containers, as described in ref. 3, and heated for 5 h to reach ~ 800 °C. The samples were then cooled in the furnace, reaching room temperature after ~ 10 h.

The formation of the new phase $\text{HgBa}_2\text{CuO}_{4+\delta}$ was revealed by X-ray powder analysis, performed with a Guinier-Hägg focusing camera and Fe K α radiation (1.93730 Å). Finely powdered silicon ($a=5.43088$ Å at 25 °C) was used as an internal standard. The intensities of the reflections were evaluated by means of an automatic film scanner and indexed on a tetragonal cell with lattice parameters $a=3.8797$ (5) Å, $c=9.509$ (2) Å and assignment $Z=1$. No systematic absences were observed, leading to the number of molecules per unit cell of the space group $P4/mmm$. The c parameter corresponded to the value calculated from the formula $c \approx 9.5 + 3.2(n-1)$, similar to that deduced for the $\text{TlBa}_2\text{R}_{n-1}\text{Cu}_n\text{O}_{2n+3}$ homologous series. We took this as a strong indication that the powder pattern corresponded to that of the first member of the $\text{HgBa}_2\text{R}_{n-1}\text{Cu}_n\text{O}_{2n+4+\delta}$ series.

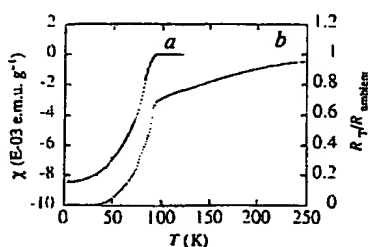


FIG. 1 AC magnetic susceptibility χ (a) and normalized resistivity (b) as a function of temperature for $\text{HgBa}_2\text{CuO}_{4+\delta}$.

Scanning electron microscopy using a JEOL SM 840A equipped with an energy-dispersive spectroscopy (EDS) attachment revealed that the sample was well crystallized with particle sizes of several micrometres. EDS analysis of several well crystallized, flat and oriented grains was performed. Beside Hg, Ba, Cu and O, no other element was detected in the spectra. The average metal ratio found for eight grains was $\text{Hg}:\text{Ba}:\text{Cu} = 28(1):47(2):25(1)$, where the numbers between parentheses are the standard deviations. Determination of the oxygen content by EDS analysis was not possible, so it was estimated by structural analysis and iodometric titration. The cation stoichiometry is in qualitatively good agreement with the proposed formula of the new compound.

Alternating-current magnetic susceptibility measurements between 4.2 and 120 K, done without any additional oxygen treatment, showed that $\text{HgBa}_2\text{CuO}_{4+\delta}$ samples undergo a transition from paramagnetic to diamagnetic with an onset as high as 94 K (Fig. 1a, where the susceptibility is in electromagnetic units g^{-1}). The estimated magnetic susceptibility at 4.2 K. corresponds to $>50\%$ of the ideal diamagnetic values.

The resistivity was measured between 4.2 and 250 K by the four-probe technique. The sample was a pressed pellet which was annealed in oxygen for 2 h. The temperature dependence of the normalized resistivity, shown in Fig. 1, exhibits a sharp drop at T_c , but the transition is broad and it reaches the value of zero resistance only at 35 K. This behaviour indicates that the sample is not homogeneous.

To determine the structure of $\text{HgBa}_2\text{CuO}_{4+\delta}$, X-ray powder data were collected by a $\theta/2\theta$ STADI P diffractometer in transmission mode. The experimental conditions were as follows: 2θ range $= 6-115^\circ$ (0.02° steps) with fixed counting time 60 s and a rotating sample. An absorption correction was applied and the sample thickness was calculated from the primary beam absorption ($\mu R = 1.7$, where μ is absorption coefficient and R is thickness). The structural refinements were done by the Rietveld method. The initial positional parameters were deduced from a structural model containing the sequence $(\text{Hg})(\text{BaO})(\text{CuO}_2)(\text{BaO})(\text{Hg})$. After convergence (intensity discrepancy factor, $R_i = 0.039$), a Fourier difference map revealed that the position at $(\frac{1}{2}, \frac{1}{2}, 0)$ of the Hg layer was partially occupied. During the final cycle of refinement, the occupancy factor of a third oxygen atom placed in this position was varied together with the positional and thermal parameters for all atoms (except for the thermal parameter of O(3) which was kept fixed at 1.0 \AA^2). The final intensity (R_i) and profile (R_p) discrepancy factors based on 84 reflections were $R_i = 0.0367$ and $R_p = 0.116$, with a GOF (goodness of fit) $= 0.33$.

The final positional and thermal parameters together with the relevant interatomic distances are given in Table 1. Observed, calculated and difference diffraction patterns are shown in Fig. 2. A schematic representation of the structure is shown in Fig. 3. Preliminary structural refinements based on powder neutron diffraction data support the presence of oxygen in the O(3) position with an occupancy factor slightly larger than that found by X-ray powder diffraction data. The neutron data also

TABLE 1 Crystallographic data for $\text{HgBa}_2\text{CuO}_{4+\delta}$

Positional, thermal and occupancy parameters						
Atom	Position	x	y	z	B_{iso} (\AA^2)	Occupancy
Hg	1a	0	0	0	2.55 (5)	1.00
Ba	2h	0.5	0.5	0.2979 (1)	1.43 (4)	1.00
Cu	1b	0	0	0.5	0.88 (9)	1.00
O(1)	2e	0.5	0	0.5	0.4 (3)	1.00
O(2)	2g	0	0	0.206 (2)	2.2 (3)	1.00
O(3)	1c	0.5	0.5	0	1.0	0.10 (3)
Selected interatomic distances (\AA)						
Hg-O(2) ($\times 2$)	1.95 (2)	Cu-O(1) ($\times 4$)	1.940 (1)	Ba-O(1) ($\times 4$)	2.730 (1)	
Hg-O(3)*	2.742 (1)	Cu-O(2) ($\times 2$)	2.79 (2)	Ba-O(2) ($\times 4$)	2.880 (5)	
				Ba-O(3)*	2.831 (1)	

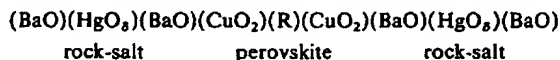
Data obtained using monochromatized $\text{CuK}\alpha_1$ radiation ($\lambda = 1.54056 \text{ \AA}$), giving $a = 3.87766(4) \text{ \AA}$, $c = 9.5073(1) \text{ \AA}$.

* Partially occupied sites.

confirm the large value for the mercury thermal factors. As in the case of the X-ray data, the anisotropic model shows a very slight difference between $B_{11} = B_{22}$ and B_{33} , the thermal factors along x, y and z respectively.

$\text{HgBa}_2\text{CuO}_{4+\delta}$ has a structure related to that of Hg-1212 (ref. 3). Its lattice parameters correspond to four-layered packing along the c-axis of a unit cell: $a = a_{\text{per}}$, $c = 2a_{\text{per}}$ (where a_{per} is the parameter of the perovskite subcell) and its structure contains the sequence $(\text{CuO}_2)(\text{BaO})(\text{HgO}_\delta)(\text{BaO})(\text{CuO}_2)$. The Cu cations are octahedrally coordinated, while the coordination of the other cations depends upon the value of δ . This, as obtained from powder X-ray data, is 0.10(3). An important consequence is that most of the Hg cations have two oxygen atoms near them in a 'dumb-bell' configuration, an appropriate coordination for Hg^{2+} cations. Because δ is small and different from zero (within about three standard deviations) X-ray powder data alone are insufficient to determine which sites of the rock-salt positions in the HgO layer are occupied and how they affect the Hg coordination. The extra oxygen atoms are needed in order to increase the average oxidation number of the Cu and to create the concentration of holes necessary for superconductivity. Iodometric titration performed with a large excess of KI leads to 16% of Cu^{3+} , corresponding to $\delta = 0.08$.

Similarly, the structure of $\text{HgBa}_2\text{RCu}_2\text{O}_{6+\delta}$ (the second member of the $\text{HgBa}_2\text{R}_{n-1}\text{Cu}_n\text{O}_{2n+2+\delta}$ series) can be described as six-layered blocks made of rock-salt and perovskite-type structures. In the structure of Hg-1212 the layer sequence is:



The CuO_2 monolayer in Hg-1201 has been replaced by the $(\text{CuO}_2)(\text{R})(\text{CuO}_2)$ block. As a consequence the Cu cations are

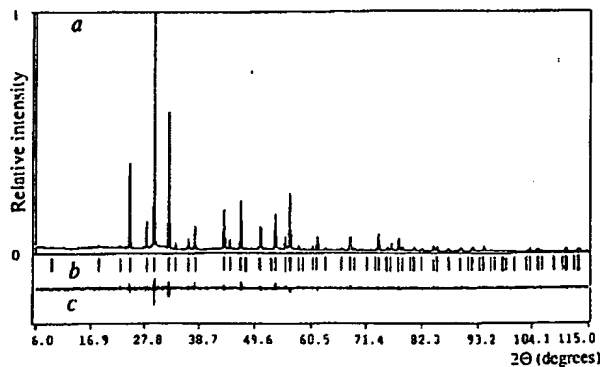


FIG. 2 Observed (a), calculated (b) and difference (c) powder patterns after Rietveld refinement for $\text{HgBa}_2\text{CuO}_{4+\delta}$.

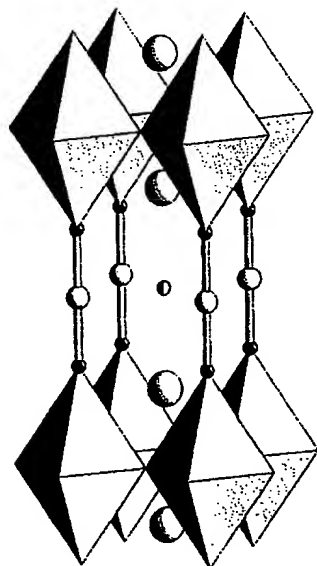


FIG. 3 Structure of $\text{HgBa}_2\text{CuO}_{4+\delta}$. The large, medium and small circles represent the Ba, Hg and O atoms, respectively. The Cu atoms are inside the octahedra. Note that the partially occupied oxygen O(3) site on the Hg layer is represented by a partially filled circle.

pyramidally coordinated. The coordination of the Ba and Hg cations in Hg-1212 is similar to that of the same cations in Hg-1201. The R cations are surrounded by 8 oxygen atoms arranged as a prism. The valence of the Cu cations depends upon the value of δ and the valence of the R cations: if the same Cu valence or hole concentration as in Hg-1201 is needed to induce the superconducting state in Hg-1212, then the R cations should be $2+$ and δ_{1212} should be appreciably greater than δ_{1201} . For the previously reported Hg-1212, R was a mixture of Eu and Ca, and δ was not precisely determined³. It is possible that δ was not large enough to compensate for the higher valence of the R cations and to transfer the needed extra charges to CuO_2 layers.

As stated above, the structural arrangement of $\text{HgBa}_2\text{CuO}_{4+\delta}$ is similar to that of $\text{TlBa}_2\text{CuO}_{3-\delta}$, except for the oxygen stoichiometry of the HgO_δ and $\text{TlO}_{1-\delta}$ layers respectively. For the former, δ is very small and this depletion is possible because the dumb-bell coordination is appropriate for the Hg^{2+} cations. For the latter, the $\text{TlO}_{1-\delta}$ layer is only slightly oxygen depleted, creating the appropriate coordination for the thallium cations, resulting in either a distorted octahedron or a five-coordinated polyhedron. These different requirements for attaining the optimal concentration of holes are due to the different preferred coordination geometries of the Tl^{3+} and Hg^{2+} cations.

The first member of the latter series (Tl-1201) has been reported and found to become superconducting at <10 K (ref. 4). By doping the Ba sites with La this value can be increased to 52 K (ref. 7). The second member of the mono-Tl series becomes superconducting at 85 K (ref. 2). This increase is a general rule for the first few members of this series of compounds. If this behaviour holds for the Hg-series, the second member could reach values for T_c as high as those of the thallium.

The possible advantages for technical applications of $\text{HgBa}_2\text{CuO}_{4+\delta}$, in analogy with one-Tl-layer materials, would be due to the relatively short distance between CuO_2 layers. This might lead to lower anisotropy of the superconducting properties and to higher flux-melting temperatures than those of two-TlO-layer superconductors⁵. □

Received 18 December 1992; accepted 12 February 1993.

1. Bednorz, J. G. & Müller, K. A. *Z. Phys.* **B64**, 189–193 (1986).
2. Parkin, S. S. P. *et al.* *Phys. Rev.* **B38**, 6531–6537 (1988).
3. Putlin, S. N., Bryntse, I. & Antipov, E. V. *Mater. Res. Bull.* **26**, 1299–1307 (1991).
4. Gopalswamy, I. K., Yashin, I. V. & Iyer, R. M. *Physica C* **175**, 183–186 (1991).
5. Kim, D. H. *et al.* *Physica C* **177**, 431–437 (1991).
6. De Loeuw, D. M., Mutsaers, C. A. H. A., Langerets, C., Smoorenburg, H. C. A. & Rommels, P. J. *Physica C* **152**, 39–49 (1988).
7. Subramanian, M. A., Kwei, G. H., Parise, J. B., Goldstone, J. A. & Von Dreele, R. B. *Physica C* **166**, 19–24 (1990).

ACKNOWLEDGEMENTS. The authors thank R. V. Shpanchenko and J. L. Tholence for their collaboration. S.N.P. thanks D. Massenet for a grant to attend the Laboratoire de Cristallographie of the CNRS, Grenoble. S.N.P. and E.V.A. are supported by grants from the Project "Polak" of the Russian Scientific Council on Superconductivity.

Dependence of aggregate morphology on structure of dimeric surfactants

R. Zana* & Y. Talmon

Department of Chemical Engineering, Technion-Israel Institute of Technology, Haifa 32000, Israel

SURFACTANT molecules in water form organized assemblies of various shapes, such as micelles and bilayer lamellae, which are of interest as analogues of biological structures, as model systems for studying complex phase behaviour and because of their technological importance, for example to the food and paint industries. The polar head groups are usually arranged randomly at the surface of these assemblies. We have studied the effect on the microstructure of these assemblies of imposing constraints on the head-group spacing. We investigate the structures formed by 'double-headed' surfactants in which two quaternary ammonium species ($\text{C}_m\text{H}_{2m+1}\text{N}^+(\text{CH}_3)_2$) are linked at the level of the head groups by a hydrocarbon spacer (C_sH_{2s}). Here we report the microstructures formed by these dimeric surfactants with $m = 12$ and $s = 2, 3$ or 4 in aqueous solution, by rapidly cooling the micellar solutions and investigating the vitrified structures with transmission electron microscopy. The surfactants with a short spacer ($s = 2, 3$) form long, thread-like and entangled micelles even at low concentrations, whereas the corresponding monomeric ammonium surfactants can form only spherical micelles. The dimeric surfactants with $s = 4$ form spheroidal micelles. Thus short spacers (which impose reduced head-group separation) appear to promote lower spontaneous curvature in the assemblies. This approach may afford a new way to control amphiphile self-aggregation.

Conventional surfactant molecules generally comprise two distinct parts that are incompatible with each other: one polar head and either one or two alkyl chains. These molecules tend to self-associate in water, where they produce micellar solutions in the dilute range, and lyotropic mesophases at higher concentrations. Whatever the structure, the surfactant polar heads are located at the interface between the hydrocarbon and water regions. Their relative positions and distances are determined mainly by their electrostatic interactions, and also by the packing requirements of the disordered alkyl chains^{1–3}. In caesium or rubidium soaps at low temperature in the presence of water, for example the head groups form well developed hexagonal or rectangular crystalline arrays⁴. Generally, however, they are arranged randomly, and little is known of their packing geometry or the width of their spacing distribution.

To investigate the effect of a perturbation of the local arrangement of polar heads on the micellar and mesomorphic properties

* To whom correspondence should be addressed in Haifa. On leave of absence from Institut Charles Sadron (CNRS), 6 rue Boursingault, 67083 Strasbourg Cedex, France.

BRIEF ATTACHMENT M

IN THE UNITED STATES PATENT AND TRADEMARK OFFICE

In re Patent Application of

Applicants: Bednorz et al.

Serial No.: 08/479,810

Filed: June 7, 1995

For: **NEW SUPERCONDUCTIVE COMPOUNDS HAVING HIGH TRANSITION
TEMPERATURE, METHODS FOR THEIR USE AND PREPARATION**

Date: March 1, 2005

Docket: YO987-074BZ

Group Art Unit: 1751

Examiner: M. Kopec

Commissioner for Patents
P.O. Box 1450
Alexandria, VA 22313-1450

FIRST SUPPLEMENTAL AMENDMENT

Sir:

In response to the Office Action dated July 28, 2004, please consider the
following:

ATTACHMENT M

Superconductivity near 70 K in a new family of layered copper oxides

R. J. Cava, B. Batlogg, J. J. Krajewski, L. W. Rupp, L. F. Schneemeyer, T. Siegrist, R. B. vanDover, P. Marsh, W. F. Peck, Jr, P. K. Gallagher, S. H. Glarum, J. H. Marshall, R. C. Farrow, J. V. Waszczak, R. Hull & P. Trevor

AT&T Bell Laboratories, Murray Hill, New Jersey 07974, USA

A new family of high-temperature superconductors is described, with the general formula $Pb_2Sr_2ACu_3O_{8+\delta}$. Although they have the planes of CuO_2 square pyramids characteristic of the other copper-oxide superconductors, the new compounds belong to a distinct structural series, with wide scope for elemental substitution. Their unusual electronic configuration also gives new insight into the role of charge distribution among the structural building blocks in controlling superconductivity.

SINCE the first observation¹ of high-transition-temperature (high- T_c) superconductivity in La-Ba-Cu-O, progress in the understanding of this remarkable phenomenon has been coupled to the discovery of new materials. Until now, three families of copper-oxide-based high- T_c superconductors have been identified, based on $(La,M)_2CuO_4$, $LnBa_2Cu_3O_7$, and $(Ti,Bi)_{2n}(Ba,Sr)_{2n+1}Cu_nO_{4n+2n+2}$ (ref. 2). (Here M represents a metal cation that may substitute on some La sites, and Ln represents a lanthanide.) Here we report the discovery of a new family of planar copper-oxide superconductors with general formula $Pb_2Sr_2ACu_3O_{8+\delta}$ (where A is a lanthanide or a mixture of Ln+Sr or Ca), and describe the synthesis, crystal structure and properties of prototype compounds. We find, for example, that one preliminary optimal composition $Pb_2Sr_2Y_{0.5}Ca_{0.5}Cu_3O_8$ has a superconducting T_c of 68 K. The new family displays the same kind of rich substitutional chemistry as is observed for $LnBa_2Cu_3O_7$, with the phase forming for Y and at least La, Pr, Nd, Sm, Eu, Gd, Dy, Ho, Tm, Yb and Lu, spanning the entire rare-earth series. Wide ranges of large-metal-atom solid solution and oxygen stoichiometry are observed, suggesting many possible avenues to be explored for the optimization of superconducting properties.

Superconductivity is induced in the host compounds $Pb_2Sr_2LnCu_3O_{8+\delta}$ ($\delta=0$) either by partial substitution of a divalent ion (such as Sr or Ca) on the lanthanide site, or possibly by the accommodation of excess oxygen ($\delta>0$), or a combination of both. The compounds can be synthesized only under mildly reducing conditions, which are necessary to maintain Pb in a 2+ oxidation state. Oxidation of $\delta=0$ compounds is possible, but only at low temperatures, where decomposition to a Pb(IV)-containing perovskite is sluggish. Remarkably, the formal average oxidation state of copper in the superconductors is less than 2+, but a clear structural distinction between different types of copper layers leads us to hypothesize that holes are nonetheless present on electronically active CuO pyramidal planes.

Synthesis

The preparative conditions for the new materials are considerably more stringent than for the previously known copper-based superconductors. Direct synthesis of members of this family by reaction of the component metal oxides or carbonates in air or oxygen at temperatures below 900 °C is not possible because of the stability of the oxidized $SrPbO_3$ -based perovskite. Successful synthesis is accomplished by the reaction of PbO with pre-reacted (Sr, Ca, Ln) oxide precursors. The precursors are prepared from oxides and carbonates in the appropriate metal ratios, calcined for 16 hours (in dense Al_2O_3 crucibles) at 920–980 °C in air with one intermediate firing. Some of the

$Pb_2Sr_2LnCu_3O_{8+\delta}$ compounds can be prepared in air from $PbO+LnSr_2Cu_3O_x$ precursor mixtures, which are not reacted at temperatures below ~850 °C. For example, single-phase $Pb_2Sr_2YCu_3O_{8+\delta}$ ($\delta=0$) can be prepared by reacting PbO with $YSr_2Cu_3O_x$ at 920 °C for 1 h, followed by quenching. Slower cooling results in partial decomposition through oxidation. Short reaction times are generally sufficient to obtain single-phase products. The same air-heating/quenching process does not appear to work, however, for $Pb_2Sr_2LaCu_3O_{8+\delta}$ or $Pb_2Sr_2LuCu_3O_{8+\delta}$.

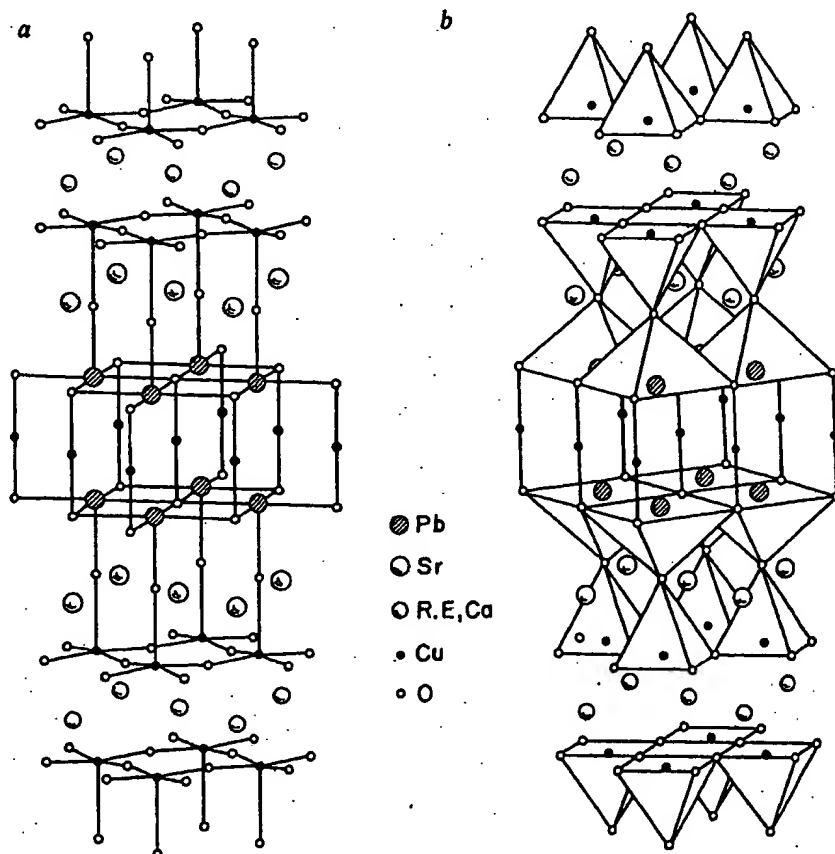
The best synthetic conditions found so far involve the reaction of PbO with the cuprate precursors in thoroughly mixed pressed pellets. Reaction temperatures are between 860 and 925 °C, for times between 1–16 h, in a flowing gas stream of 1% O_2 in N_2 , a mildly reducing atmosphere. For $Pb_2Sr_2Y_{1-x}Ca_xCu_3O_{8+\delta}$, for example, single-phase materials are obtained for $0 \leq x < 0.5$ in 1% O_2 after heating overnight at 865 °C and cooling in the gas stream to room temperature in 15 minutes. Using higher temperatures, higher p_{O_2} in the gas stream or higher Ca contents of the starting mixture results in the intergrowth of 123-type $YSr_2(Pb,Cu)_3O_x$ with the new compound, or the formation of an $SrPbO_3$ -based second phase. Similar procedures are successful for other Sr/rare-earth/Ca combinations. The oxygen contents of $Pb_2Sr_2Y_{1-x}Ca_xCu_3O_{8+\delta}$ for $0 \leq x \leq 0.50$, prepared under these conditions, are measured by reduction in H_2 and are uniformly $\delta=0 \pm 0.1$. Ca is employed as a dopant on the Ln site because it has an ionic size similar to the intermediate rare-earths. We have not yet found synthetic conditions under which $Pb_2Sr_{2+x}Ln_{1-x}Cu_3O_{8+\delta}$ solid solutions can be prepared as single-phase polycrystalline samples that are good bulk superconductors, although superconducting single crystals of that stoichiometry have been prepared.

Single crystals of the superconducting compounds were grown from PbO- and CuO-rich melts using a similar precursor technique. Melt compositions were generally $Pb_{3.5}Sr_3YCu_4O_x$. Following a 30-min soak at 1,025 °C, samples were cooled at 2 °C min^{-1} in the 1% O_2 atmosphere to temperatures between 800 and 400 °C, and were then rapidly cooled to room temperature in the same gas stream. Crystals are plate-like in habit, but are generally more equiaxed than those of $LnBa_2Cu_3O_7$.

Stoichiometry and crystal structure

Compounds of stoichiometry $Pb_2Sr_2LnCu_3O_8$ ($\delta=0$) are not bulk superconductors, although we often observe small amounts of superconductivity (1% or less) in materials of that stoichiometry prepared either by the quench or by the 1%- O_2 synthetic techniques. The non-bulk superconductivity may be due to inhomogeneities in either oxygen content or Sr/Ln distribution.

Fig. 1 Two representations of the crystal structure for the new superconducting compounds, for the case of $\text{Pb}_2\text{Sr}_{2.24}\text{Nd}_{0.76}\text{Cu}_3\text{O}_{8+\delta}$. Representation *a* emphasizes the Cu-O and Pb-O bonding scheme, and representation *b* emphasizes the manner in which Cu-O and Pb-O coordination polyhedra are arranged.



The range of oxygen contents possible for these compounds is remarkable. $\text{Pb}_2\text{Sr}_2\text{YCu}_3\text{O}_{8+\delta}$, $\delta=0$, for example, can be oxidized by heating in O_2 to temperatures below 500 °C for short times (2–4 h) to δ values of ~ 1.6 , retaining the same basic crystal structure. We have observed values as large as $\delta=1.8$ for $\text{Pb}_2\text{Sr}_2\text{Y}_{0.75}\text{Ca}_{0.25}\text{Cu}_3\text{O}_{8+\delta}$. Oxidation at temperatures higher than 500 °C, or for longer reaction periods, generally results in decomposition to the SrPbO_3 -based perovskite. Powder samples of $\text{Pb}_2\text{Sr}_2\text{YCu}_3\text{O}_{8+\delta}$ with large values of δ are not superconducting. Single crystals of the $\text{Pb}_2\text{Sr}_{2+x}\text{Ln}_x\text{Cu}_3\text{O}_{8+\delta}$ type are superconductors with transition temperatures between 10 and 70 K. These crystals may have non-zero values of δ but have not yet been fully characterized. The range of T_c s observed suggests a complex and interesting relationship between T_c , δ and the Sr:Ln ratio.

Powder X-ray diffraction indicates that the new phases have an orthorhombic unit cell which is based on a many-layer perovskite structure. The characteristic X-ray pattern for the prototype compound $\text{Pb}_2\text{Sr}_2\text{YCu}_3\text{O}_8$ is presented in Table 1. The compound deviates only slightly from tetragonal symmetry. The simplest cell consistent with the X-ray pattern is *c*-centred, with lattice parameters $a=5.40$, $b=5.43$, and $c=15.74$ Å. Systematic absences are consistent with a *c*-centred cell down to the detectability limit of 1% maximum intensity. The orthorhombic cell gives an excellent fit to the powder diffraction pattern but a hint of a shoulder on the high 2θ side of the 314 reflection indicates that the true symmetry may be weakly monoclinic. Although the lattice parameters for this family of compounds are very similar to those reported for $\text{TiBa}_2\text{Ca}_2\text{Cu}_3\text{O}_8$ (ref. 3), the crystal structures are quite different. Electron microscope investigations indicate that for some crystals, weak (but sharp) reflections are present which violate the *c*-centring. Furthermore, these studies show the presence of long-period, long-range-ordered superlattices in the *a*-*b* plane, suggesting that a variety of structural distortions and stoichiometry-driven atom-ordering schemes can occur.

The crystal structure of compounds in this family, determined for a superconducting Nd-based single crystal of approximate stoichiometry $\text{Pb}_2\text{Sr}_{2.24}\text{Nd}_{0.76}\text{Cu}_3\text{O}_{8+\delta}$ (determined by structure refinement) is shown in Fig. 1. The crystal employed in the structural determination was twinned, as expected from the pseudo-tetragonal symmetry. The atomic coordinates are reported in the *c*-centred orthorhombic cell to be consistent with the powder data, but a primitive cell with *a* and *b* rotated by 45° and reduced by $\sqrt{2}$ gives an equally good description of the single-crystal data. The very small scattering cross-section of oxygen precludes determination of δ by refinement. The data are well fitted by the structural model (refinement parameter $R=3.7\%$), but a microscopic explanation of the orthorhombic symmetry is not apparent; if the origin is primarily in the oxygen sublattice we would not be able to detect it in the X-ray structure determination.

The basis of the structure comprises infinite planes of corner-shared CuO_4 pyramids separated by eight-coordinate rare-earth atoms, as are common to all the presently known copper-based superconductors with $T_c > 50$ K. The four in-plane copper-oxygen distances are ~ 1.9 Å, and the distance to the apical oxygen is ~ 2.3 Å, both of which are very similar to those observed in $\text{YBa}_2\text{Cu}_3\text{O}_7$. The structural components unique to the new class of materials are the $\text{PbO}-\text{CuO}_4-\text{PbO}$ planes shown in the centre of the Fig. 1. For $\delta=0$, Pb has a distorted flattened square pyramid coordination (sharing edges with adjacent pyramids), with the lone pair pointing toward the vacant sixth site of the coordination octahedron. The PbO_4 pyramids are separated by a single copper layer, which, for $\delta=0$, is oxygen-free, and displays an O-Cu-O coordination characteristic of Cu^{1+} (Cu-O distance ~ 1.8 Å), as is observed in non-superconducting $\text{YBa}_2\text{Cu}_3\text{O}_6$. During the low-temperature oxidation process, oxygen is apparently accommodated in this copper layer, resulting in a large expansion of the *c* axis. The PbO_4 and CuO_4 pyramidal planes are joined by the common oxygens at their apices. The Sr atoms are coordinated to nine oxygens, as in (La,

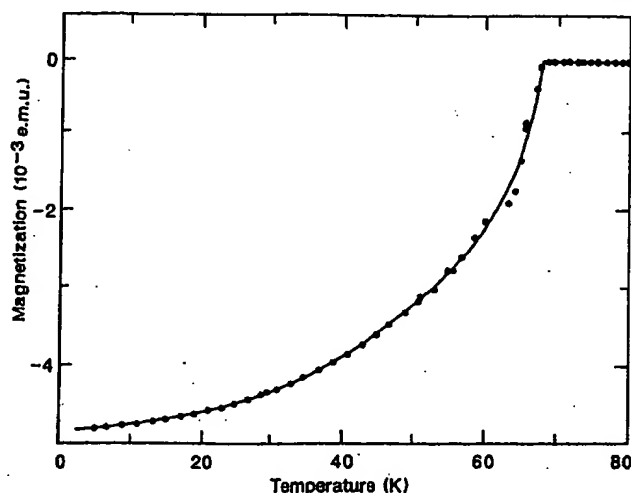


Fig. 2 Magnetization data (d.c. field-cooled at 25 Oe) for $\text{Pb}_2\text{Sr}_2\text{Y}_{0.5}\text{Ca}_{0.5}\text{Cu}_3\text{O}_8$.

$\text{Sr})\text{CuO}_4$, and the Ln site is eight-coordinate, as in the $\text{LnBa}_2\text{Cu}_3\text{O}_7$ family, sandwiched between the CuO_2 pyramidal planes. In the superconducting compound $\text{Pb}_2\text{Sr}_2\text{Y}_{1-x}\text{Ca}_x\text{Cu}_3\text{O}_{8+\delta}$, Ca partially substitutes for Y in the eight-coordinate site.

The crystal structures of all the known copper-oxide-based superconductors are generally described as many-layered perovskites. The similarities and differences among them are most easily illustrated in terms of the stacking sequences of rocksalt-like (AO) and perovskite-like (BO_2) layers². Taking, for example, representatives from the superconductor families that have double CuO_2 pyramidal layers, the stacking sequences are:

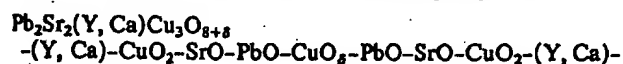


Table 1 Characteristic X-ray powder diffraction pattern for $\text{Pb}_2\text{Sr}_2\text{YCu}_3\text{O}_8$

<i>hkl</i>	<i>d</i>	<i>I/I</i> ₀	<i>hkl</i>	<i>d</i>	<i>I/I</i> ₀
001	15.74	7	116	2.164	11
002	7.87	3	025	2.057	12
003	5.25	2	205	2.050	10
004	3.94	10	008	1.967	7
110	3.831	11	220	1.915	25
111	3.722	24	118, 009	1.750	2
112	3.444	1	027, 207	1.730	1
005	3.148	11	224	1.722	2
113	3.094	11	130	1.717	2
114	2.745	100	310, 131	1.708	3
020	2.717	43	311	1.699	2
200	2.701	43	225	1.636	3
021	2.677	7	133	1.632	3
201	2.662	7	313	1.625	1
006	2.623	6	028	1.593	11
023	2.412	1	208, 119	1.591	11
203	2.401	1	134	1.574	18
024	2.236	2	314	1.568	14
204	2.227	1			

Cu K α radiation, 0–60° 2 θ c-centred orthorhombic cell, preliminary indexing, true symmetry may be weakly monoclinic. Lattice parameters $a = 5.4019(15)$, $b = 5.4333(15)$, $c = 15.7388(1)$.

The new superconductors, then, can be seen to be intimately related in structure to those previously described. They can be considered as related to $\text{Ti}_2\text{Ba}_2\text{CaCu}_3\text{O}_8$ by insertion of a single CuO_2 layer between adjacent polarizable AO layers, or related to $\text{YBa}_2\text{Cu}_3\text{O}_{6+\delta}$ by sandwiching of the CuO_2 'chain' layer by two PbO layers. We believe that it is the electronic screening of the CuO_2 planes from the CuO_2 layers by the PbO layers that makes the new superconductors of considerable interest. Furthermore, we expect these materials to be even more anisotropic in their physical properties than those previously known, as the double pyramidal CuO_2 -A- CuO_2 layers are widely separated.

Superconducting properties

We have studied the composition dependence of the superconducting properties of compounds in the series $\text{Pb}_2\text{Sr}_2\text{Y}_{1-x}\text{Ca}_x\text{Cu}_3\text{O}_8$ for $0 \leq x \leq 0.75$, by estimating the flux expulsion measured on cooling in a field of 25 Oe in a d.c. SQUID magnetometer (S.H.E. model 905). The greatest flux expulsion occurs for $x = 0.5$, and is ~20% of the ideal value (see Fig. 2). Because flux becomes trapped in the pores of these low-density ceramics, this is an underestimate of the true volume fraction of superconductivity. For $x \geq 0.5$, the materials were not entirely single-phase, with one or more impurity peaks having a maximum intensity of 5% of the strongest peak in the powder X-ray pattern. This, coupled with the estimate of the volume fraction of superconductivity, suggests that the optimal superconducting composition may have x somewhat greater than 0.5. This could be achieved if different synthetic methods can be found that allow a larger range of solid solution to be attained. We have measured the normal-state susceptibility (in a 20-kOe field) for temperatures below 400 K of apparently single-phase samples (no unindexed X-ray lines to 0.5% maximum intensity) of the non-superconducting endmember $\text{Pb}_2\text{Sr}_2\text{YCu}_3\text{O}_8$ and superconducting $\text{Pb}_2\text{Sr}_2\text{Y}_{0.625}\text{Ca}_{0.375}\text{Cu}_3\text{O}_8$. The susceptibility of the superconductor (χ) is essentially temperature independent ($\chi \approx 1 \times 10^{-4}$ e.m.u. per mole formula unit), with only a slight decrease at low temperatures. This temperature dependence is similar to that of high-quality $\text{YBa}_2\text{Cu}_3\text{O}_7$, and is characterized by the absence of a Curie-Weiss contribution. Furthermore, this supports our conclusion that the copper atoms between the PbO layers are Cu^{2+} . Post-oxidation at 500 °C results in oxidation of this copper to magnetic Cu^{2+} . $\text{Pb}_2\text{Sr}_2\text{YCu}_3\text{O}_8$ appears to be magnetic (–0.5 μB per Cu atom), but further studies are necessary to clarify whether this is intrinsic or is due to the presence of highly magnetic impurity phases that are undetectable by X-ray diffraction.

Figure 3 shows the temperature dependence of the resistivity for a single crystal of $\text{Pb}_2\text{Sr}_2\text{Dy}_{1-x}\text{Ca}_x\text{Cu}_3\text{O}_{8+\delta}$. The midpoint of the superconducting transition is at 51.5 K (indicated by an arrow in Fig. 3), although there is a small foot which gives a zero-resistance T_c of 46 K. Above T_c the temperature

Table 2 Crystallographic data for $\text{Pb}_2\text{Sr}_2\text{Nd}_{0.76}\text{Cu}_3\text{O}_{8+\delta}$

Atom	Position	<i>x</i>	<i>y</i>	<i>z</i>	<i>B</i> _{iso} [Å ²]
Pb	4l	1/2	0	0.38858 (4)	1.09 (2)
Sr	4k	0	0	0.22184 (9)	0.74 (4)
Nd, Sr*	2a	0	0	0	0.69 (3)
Cu1	2d	0	0	1/2	0.86 (9)
Cu2	4l	1/2	0	0.11074 (13)	0.46 (5)
O1	4l	1/2	0	0.2546 (8)	1.5 (5)
O2	4k	0	0	0.384 (3)	13 (5)
O3	8m	1/4	1/4	0.0995 (5)	0.9 (3)

Orthorhombic cell (pseudotetragonal substructure); $a = 5.435(1)\text{Å}$, $b = 5.463(1)\text{Å}$, $c = 15.817(3)\text{Å}$; space group *Cmmm*, $z = 2$; observed reflections 707, $R_w = 0.037$.

* Mixed occupancy site: (1) Sr, 0.76(1) Nd.

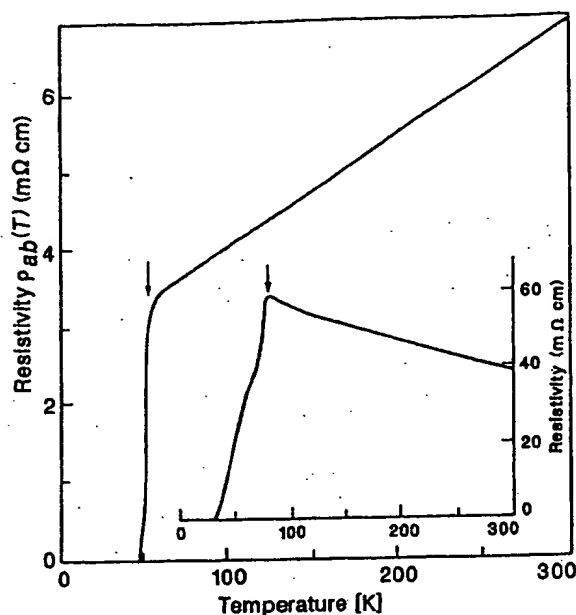


Fig. 3 Resistivity in the a - b plane as a function of temperature for a single crystal of $\text{Pb}_2\text{Sr}_2(\text{Dy,Ca})\text{Cu}_3\text{O}_{8+\delta}$. Inset, typical temperature-dependent resistivity for a polycrystalline sample of $\text{Pb}_2\text{Sr}_2(\text{Y,Ca})\text{Cu}_3\text{O}_8$.

dependence is fairly linear, but near T_c there is a region of positive curvature which, along with the resistivity foot, we attribute to small inhomogeneities in the metal and/or oxygen distribution. The scale of the resistivity is a factor of ten greater than for previous oxide superconductors. It is not yet clear whether this is an intrinsic property.

A typical resistivity curve for a ceramics sample is shown in the inset to Fig. 3, illustrating the typically broad transitions observed. The transition in this sample begins at 79 K (arrow) but zero resistance is achieved (within instrumental accuracy) as 32 K. Note that the resistivity scale is again quite high. We attribute the breadth of the transition and the negative normal-state temperature coefficient to inhomogeneity in the metal and/or oxygen distribution, rather than to exogenous phases at the grain boundaries. The behaviour of this system seems to be very similar to that of $(\text{La,Sr})_2\text{CuO}_4$ (ref. 4).

Electronic aspects

Given that the average formal copper valence of previously known superconductors has always been greater than +2, the new superconductors are unique and, at first sight, anomalous. For the series $\text{Pb}_2\text{Sr}_2\text{Y}_{1-x}\text{Ca}_x\text{Cu}_3\text{O}_8$, the average formal copper valence increases from 1.67 in the non-superconducting $x=0$ member to ~ 1.92 at the maximum Ca concentration studied. At our current estimate of the optimal superconducting composition ($x=0.5$), the average formal valence is 1.83. The linear coordination of the copper atom sandwiched between the PbO sheets, characteristic of Cu^{1+} , and the probable electronic isolation of this layer from the conducting CuO pyramidal planes, imply that the formal charge formulation becomes $\text{Pb}_2\text{Sr}_2\text{YCu}^{1+}\text{Cu}_2^{2+}\text{O}_8$ in the non-superconducting compound. When Ca is substituted for Y, we propose that holes are accommodated only in the CuO_2 planes, and at the $x=0.5$ stoichiometry the formal charge formulation becomes $\text{Pb}_2\text{Sr}_2\text{Y}_{0.5}\text{Ca}_{0.5}\text{Cu}^{1+}\text{Cu}_2^{2.25+}\text{O}_8$, which is consistent with the cur-

rent assumption for previously known high- T_c materials that holes are present in the CuO_2 pyramidal planes.

For $\text{Pb}_2\text{Sr}_2\text{ACu}_3\text{O}_{8+\delta}$ compounds with $\delta > 0$, excess oxygen must be accommodated near the Cu^{1+} planes, and a more complex hole-doping scheme may be operating. We expect that in that case the compound does not respond in a simple fashion to the change in charge through doping of a rigid band; the oxygen inserted in the bonding neighbourhood of the reduced Cu and Pb ions may create the electronic states in which the charge is partly or fully accommodated.

This new family of compounds has a unique crystal structure, yet it also reflects a concept common to all copper-oxide-based superconductors. By now it is well established that superconductivity is associated with layers of Cu-O octahedra, pyramids and squares. The remaining structural building blocks are seen as the electron acceptors which induce the holes necessary for superconductivity in the Cu-O layers. For $\text{YBa}_2\text{Cu}_3\text{O}_{6+\delta}$, for example, we have shown in detail how the CuO_2 chains act as charge reservoirs, and how superconductivity depends on charge transfer between chains and planes⁵.

To illustrate the concept of local charge distribution, one may rewrite the formulae of the high- T_c copper-oxide superconductors as follows: $\text{YBa}_2\text{Cu}_3\text{O}_6[\text{CuO}_2]$; $\text{Sr}_2\text{CaCu}_2\text{O}_6[\text{Bi}_2\text{O}_2]$; $\text{Ba}_2\text{CaCu}_2\text{O}_6[\text{Ti}_2\text{O}_2]$; $\text{Sr}_2(\text{Y,Ca})\text{Cu}_2\text{O}_6[\text{Pb}_2\text{CuO}_{2+\delta}]$; where the structural components in square brackets act as reservoirs which control the charge on the superconducting Cu-O planes. The $\text{PbO-CuO}_2\text{-PbO}$ reservoir layer is likely to be exceptionally flexible in accommodation of charge, and we therefore expect that a relationship between T_c and oxygen stoichiometry as unusual as that for $\text{YBa}_2\text{Cu}_3\text{O}_{6+\delta}$ will eventually be observed. The wide ranges of metal-atom and oxygen-atom stoichiometries in this new family of superconductors are of considerable interest, and warrant further study with the aim of understanding and optimizing the superconducting properties.

We thank D. W. Murphy and K. Rabe for helpful discussions.

Received 21 October; accepted 28 October 1988.

1. Bednorz, J. G. & Müller, K. A. *Z. Phys.* **B64**, 189-193 (1986).
2. Santoro, A., Beech, F., Marelli, M. & Cava, R. J. *Physica C* (in the press).
3. Parkin, S. S. P. et al. *Phys. Rev. Lett.* **61**, 750-753 (1988).

4. Van Dover, R. B., Cava, R. J., Batlogg, B. & Rietman, E. A. *Phys. Rev. B* **35**, 5337-5339 (1987).
5. Cava, R. J. et al. *Physica C* (in the press).

BRIEF ATTACHMENT N

IN THE UNITED STATES PATENT AND TRADEMARK OFFICE

In re Patent Application of

Applicants: Bednorz et al.

Serial No.: 08/479,810

Filed: June 7, 1995

For: NEW SUPERCONDUCTIVE COMPOUNDS HAVING HIGH TRANSITION
TEMPERATURE, METHODS FOR THEIR USE AND PREPARATION

Date: March 1, 2005

Docket: YO987-074BZ

Group Art Unit: 1751

Examiner: M. Kopec

Commissioner for Patents
P.O. Box 1450
Alexandria, VA 22313-1450

FIRST SUPPLEMENTAL AMENDMENT

Sir:

In response to the Office Action dated July 28, 2004, please consider the
following:

ATTACHMENT N

LANDOLT-BÖRNSTEIN

Numerical Data and Functional Relationships
in Science and Technology

New Series

Editor in Chief: K.-H. Hellwege

Group III: Crystal and Solid State Physics

Volume 4

Magnetic and Other Properties
of Oxides and Related Compounds

Part a

J. B. Goodenough · W. Gräper · F. Holtzberg · D. L. Huber
R. A. Lefever · J. M. Longo · T. R. McGuire · S. Methfessel

Editors: K.-H. Hellwege and A. M. Hellwege



Springer-Verlag Berlin · Heidelberg · New York 1970

N LANDOLT-BÖRNSTEIN

is

Zahlenwerte und Funktionen
aus Naturwissenschaften und Technik

Neue Serie

Gesamtherausgabe: K.-H. Hellwege

Gruppe III: Kristall- und Festkörperphysik

Band 4

Magnetische und andere Eigenschaften
von Oxiden und verwandten Verbindungen

Teil a

J. B. Goodenough · W. Gräper · F. Holtzberg · D. L. Huber
R. A. Lefever · J. M. Longo · T. R. McGuire · S. Methfessel

Herausgeber: K.-H. Hellwege und A. M. Hellwege



1970

Springer-Verlag Berlin · Heidelberg · New York 1970

3 Crystallographic and magnetic properties of perovskite and perovskite-related compounds *)

3.0 Introduction — Einleitung

3.0.1 General remarks — Allgemeines

The perovskites form a family of compounds having a crystal structure similar to that of the mineral perovskite, CaTiO_3 . There are two classes of materials crystallizing with this general structure type: primarily ionic materials having the ideal chemical formula ABX_3 (A = larger cation, B = smaller cation, X = anion), and alloys having the ideal formula M^cXM_i^f (X = interstitial atom, M^c and M^f are metal atoms). Of these two classes, the former is much larger and the more important.

The stability of the ABX_3 perovskite structure is primarily derived from the electrostatic (Madelung) energy achieved if cations occupy corner-shared octahedra. Thus the first prerequisite for a stable ABX_3 perovskite is the existence of stable, polar octahedral-site building blocks. This, in turn, requires that the B cation have a preference for octahedral coordination and that there be an effective charge on the B cation. Since any A cation must occupy the relatively large anionic interstice created by corner-shared octahedra, a second prerequisite is an appropriate size for the A cation. Where it is too large, the B-X bond length cannot be optimized, and hexagonal stacking with face-shared octahedra becomes competitive. Where the A cation is too small, A-X bonding stabilizes structures having a smaller anionic coordination about the A cation. Thus ABX_3 perovskites are commonly found in fluorides and oxides having B cations with a preference energy for octahedral coordination. By contrast, the chlorides and sulfides, having larger anions, not only require the largest A cations, but also form layer structures, where the A cations are missing, because they have anionic d orbitals energetically available for orbital hybridization.

There are many perovskite-related structures, and these have been included in these tables. For example, the structure can tolerate mixed systems such as $\text{A}_{1-x}\text{A}_2'\text{BX}_3$ and $\text{AB}_{1-x}\text{B}_2'\text{X}_3$, A-cationic vacancies \square as in $\square_{1-x}\text{A}_2\text{BX}_3$, and cationic ordering as in $\text{A}_2\text{BB}'\text{X}_6$. Although anion-deficient perovskites have been reported many times, the anion vacancies \oplus are probably not distributed randomly. In compounds containing Fe^{3+} ions, for example, they appear to condense in pairs at individual B-site octahedra to convert the local anion interstice from an octahedron to a tetrahedron. In

Die Perovskite sind eine Gruppe von Verbindungen mit der gleichen Kristallstruktur wie das Mineral Perowskit, CaTiO_3 . Man unterscheidet zwei Klassen von Substanzen, die in diesem allgemeinen Strukturtyp kristallisieren: in erster Linie Ionenverbindungen mit der idealen chemischen Formel ABX_3 (A = größeres Kation, B = kleineres Kation, X = Anion) und Legierungen mit der idealen Formel M^cXM_i^f (X = Zwischengitteratom, M^c und M^f = Metallatome). Von diesen beiden Klassen ist die erstere wesentlich umfangreicher und wichtiger.

Die Stabilität der ABX_3 -Perowskitstruktur beruht in erster Linie auf der elektrostatischen (Madelung-) Energie, die dann zustande kommt, wenn Kationen Oktaeder mit gemeinsamen Ecken besetzen. So ist die Existenz von stabilen, polaren Oktaeder-Bausteinen die erste Vorbedingung für ein stabiles ABX_3 -Perowskit. Dies wiederum erfordert, daß das B-Kation die Oktaeder-Koordination bevorzugt und daß beim B-Kation eine effektive Ladung existiert. Da ein jedes A-Kation die relativ große Anionen-Lücke besetzen muß, die zwischen Oktaedern mit gemeinsamen Ecken entsteht, ist die passende Größe des A-Kations die zweite Vorbedingung. Wenn das A-Kation zu groß ist, läßt sich der optimale B-X-Bindungsabstand nicht erreichen, und eine hexagonale Packung von Oktaedern mit gemeinsamen Flächen kann ebenso auftreten. Wenn das A-Kation zu klein ist, ergibt die A-X-Bindung Strukturen mit einer kleineren Anionen-Koordination um das A-Kation. Daher sind ABX_3 -Perowskite gewöhnlich unter den Fluoriden und Oxiden zu finden, in denen die B-Kationen Oktaeder-Koordination energetisch bevorzugen. Dagegen erfordern Chloride und Sulfide, die größere Anionen haben, nicht nur die größten A-Kationen, sondern sie bilden, weil sie anionische d -Elektronenbahnen mit der richtigen Energie für eine Bahn-Hybridisierung haben, auch Schichtstrukturen, bei denen die A-Kationen ganz fehlen.

Es gibt viele dem Perowskit verwandte Strukturen, die in diese Tabellen aufgenommen wurden. Zum Beispiel können gemischte Systeme wie $\text{A}_{1-x}\text{A}_2'\text{BX}_3$ und $\text{AB}_{1-x}\text{B}_2'\text{X}_3$ mit dieser Struktur auftreten, weiter A-Kationenlücken \square wie in $\square_{1-x}\text{A}_2\text{BX}_3$ und geordnete Kationen wie in $\text{A}_2\text{BB}'\text{X}_6$. Über Perowskite mit Anionenlücken ist schon häufig berichtet worden, vermutlich sind die Anionenleerstellen \oplus nicht willkürlich verteilt. In Verbindungen, die Fe^{3+} -Ionen enthalten, scheinen sie z. B. paarweise im Oktaeder eines einzelnen B-Platzes zusammenzutreffen und die

*) This work was sponsored by the U. S. Air Force.

compou
it is mor
anions
deficien
cations,
contain
across v
edges (
ciencies
alloys.
B-occup
perovsl
cation
an inte
(Fig. 2:
stackin
nal sta
cies (F
(AX)_m
rocksa
stacke
also oc
an A c
struct
with i
classif
and I
rather
for ex
18). S
of the

Tl
ing pl
BaTi
ferro
cond
ducti
lator
tor a
patit
trans
ture
ABX
mult
[Sm
ferro
ed f
Ba,
perc
and
mag
of f
mag
app
tura
tha

*) 7
c
1

compounds containing Ti^{4+} ions, on the other hand, it is more probable that local rearrangements of the anions form trigonal bipyramidal sites. Anion-deficient, ionic materials in which there are no A-cations, such as $\square WO_{3-x}$, have been shown to contain $\square BX_3$ blocks connected by "shear" planes across which the occupied octahedra share common edges (Fig. 22). On the other hand, anion deficiencies may occur randomly in the $M^cX_{1-x}M_f^f$ alloys. B-cation defects cannot occur, because the B-occupied octahedra form the basis of the ABX_3 -perovskite structure. Where there are apparent B-cation vacancies, as in $A_mB_{m-1}X_{3m}$, there is either an interleaving of perovskite layers with A_2X_2 layers (Fig. 23) or an interleaving of cubic (perovskite) stacking of AO_3 layers with regularly spaced hexagonal stackings at which are located the B-ion vacancies (Fig. 24). Similarly, the series of compounds $(AX)_m(ABX_3)_n$ crystallize with an interleaving of rocksalt layers (Fig. 25). Interleaving of cubic-stacked AO_3 layers and hexagonal-stacked layers also occurs in ABX_3 compounds having too large an A cation to be accommodated by the perovskite structure (Fig. 3). Finally, there are a few alloys with interesting magnetic properties that can be classified as $A_2BB'X_6$ compounds if the symbols B and B' are allowed to represent atomic clusters rather than single cations. These are illustrated, for example, by the alloy $Al_2(AlCo_{12})(Co)_8B_6$ (Fig. 18). Sections 3.1 and 3.2 are devoted to descriptions of the perovskite and perovskite-related structures.

The ABX_3 perovskites exhibit several interesting physical properties such as ferroelectricity (as in $BaTiO_3$), ferromagnetism (as in $SrRuO_3$), weak ferromagnetism (as in $LaFeO_3$ or $HoFeO_3$), superconductivity (as in $SrTiO_{3-x}$), a large thermal conductivity due to exciton transport ($LaCoO_3$), insulator-to-metallic transitions of interest for thermistor applications (as in $LaCoO_3$), fluorescence compatible with laser action (as in $LaAlO_3:Nd$), and transport properties of interest for high-temperature thermoelectric power (as in La_2CuO_4). A few ABX_3 perovskites have been found that are simultaneously antiferromagnetic and ferroelectric [Sm16, Mi7, Sm9]. The simultaneous occurrence of ferroelectricity and ferromagnetism has been reported for systems like $Sr_{0.25}La_{0.75}MnO_3-ATiO_3$ ($A = Ba, Pb, Bi_{0.5}K_{0.5}$) [To3, To6]. Many of the $M^cXM_f^f$ perovskite alloys are ferromagnetic or ferrimagnetic, and a few exhibit first-order ferrimagnetic-to-ferromagnetic transitions. Nevertheless, the significance of the entire perovskite family for the field of magnetism*) lies not yet in their technological applications, but in their provision of an isostructural series of compounds having outer d electrons that are localized and spontaneously magnetic in

*) The technologically important dielectric properties are outside the scope of this summary. See Vol. III/3 of the New Series of Landolt-Börnstein.

dortige Anionenlücke von einem Oktaeder in einen Tetraeder umzuwandeln. Bei Verbindungen, die Ti^{4+} -Ionen enthalten, ist es dagegen wahrscheinlicher, daß die lokale Anordnung der Anionen trigonale Doppelpyramiden-Plätze bildet. Für Ionenverbindungen mit Anionenlücken, die keine A-Kationen haben, wie $\square WO_{3-x}$, ist gezeigt worden, daß sie $\square BX_3$ -Blöcke enthalten, die durch „Gleit“-ebenen verbunden sind, in denen die besetzten Oktaeder gemeinsame Kanten innehaben (Fig. 22). In $M^cX_{1-x}M_f^f$ -Legierungen können jedoch Anionenlücken auch beliebig auftreten. B-Kationenlücken können nicht vorkommen, weil die von B besetzten Oktaeder die Basis der ABX_3 -Perowskitstruktur bilden. Wo scheinbare B-Kationenleerstellen auftreten, wie in $A_mB_{m-1}X_{3m}$, sind entweder A_2X_2 -Schichten zwischen Perowskitschichten eingeschoben (Fig. 23), oder kubische (Perowskit-) Anordnungen von AO_3 -Schichten wechseln mit regelmäßig verteilten hexagonalen Anordnungen, in denen die B-Ionenlücken auftreten, ab (Fig. 24). Ähnlich kristallisieren die Verbindungen der Reihe $(AX)_m(ABX_3)_n$ mit einer Einschiebung von Steinsalzschichten (Fig. 25). Einschiebungen von kubisch gepackten AO_3 -Schichten und hexagonal gepackten Schichten treten auch in solchen ABX_3 -Verbindungen auf, deren A-Kation für die Perowskit-Struktur zu groß ist (Fig. 3). Schließlich gibt es einige wenige Legierungen mit interessanten magnetischen Eigenschaften, die als $A_2BB'X_6$ -Verbindungen eingeordnet werden können, wenn man unter den Symbolen B und B' Atomgruppen statt einzelner Kationen versteht. Dies gilt z. B. für die Legierung $Al_2(AlCo_{12})(Co)_8B_6$ (Fig. 18). Die Abschnitte 3.1 und 3.2 sind der Beschreibung der Perowskit- und verwandter Strukturen gewidmet.

Die ABX_3 -Perowskite weisen einige interessante physikalische Eigenschaften auf, wie Ferroelektrizität (in $BaTiO_3$), Ferromagnetismus (in $SrRuO_3$), schwachen Ferromagnetismus (in $LaFeO_3$ oder $HoFeO_3$), Supraleitfähigkeit (in $SrTiO_{3-x}$), große Wärmeleitfähigkeit durch Exzitonentransport (in $LaCoO_3$), für Thermistoren interessante Übergänge zwischen Nichtleiter und metallischem Leiter (in $LaCoO_3$), für Laser-Anwendungen geeignete Fluoreszenz (in $LaAlO_3:Nd$), und Transporteigenschaften, die für Thermospannungen bei hohen Temperaturen von Interesse sind (in La_2CuO_4). Einige wenige ABX_3 -Perowskite wurden gefunden, die sowohl ferromagnetisch als auch ferroelektrisch sind [Sm16, Mi7, Sm9]. Das gleichzeitige Auftreten von Ferroelektrizität und Ferromagnetismus wurde bei Systemen wie $Sr_{0.25}La_{0.75}MnO_3-ATiO_3$ ($A = Ba, Pb, Bi_{0.5}K_{0.5}$) [To3, To6] beschrieben. Viele $M^cXM_f^f$ -Perowskitlegierungen sind ferromagnetisch oder ferrimagnetisch, und einige zeigen Übergänge erster Ordnung von Ferri- zu Ferromagnetismus. Trotzdem liegt die Bedeutung der gesamten Perowskit-Familie für den Magnetismus*) noch nicht in der technologischen Anwendung, sondern im Vorhandensein einer isostrukturellen Reihe von Verbin-

*) Die technologisch wichtigen dielektrischen Eigenschaften liegen nicht im Rahmen dieser Zusammenstellung. Siehe Band III/3 der Neuen Serie des Landolt-Börnstein.

one member, collective and spontaneously magnetic in another, and collective and Pauli paramagnetic in yet another. This permits a systematic experimental investigation of the properties of the d electrons on passing through the transition from a localized character, where crystal-field plus superexchange and/or double-exchange theories apply, to an uncorrelated (except below a superconducting transition temperature) collective-electron character, where the conventional band theory applies. In addition, the simplicity of the perovskite ABX_3 structure minimizes competitive magnetic interactions between neighboring magnetic cations. Therefore from a study of magnetic order, as revealed by neutron diffraction, together with detailed structural information, as revealed by x-ray diffraction, it has been possible to test the semi-empirical rules for 180° cation-anion-cation isotropic superexchange interactions between localized electrons, the double-exchange hypothesis, antisymmetric exchange, and predictions of magnetic order and spontaneous atomic moments due to collective electrons.

Section 3.3 presents the general phenomenological exchange Hamiltonian for localized electrons and summarizes the microscopic models for isotropic superexchange, double exchange, and antisymmetric exchange. From these models, general rules for the interactions responsible for magnetic order are developed for comparison with the tabulated magnetic data.

Section 3.4 presents the fundamental physical concepts needed to construct a qualitative phase diagram for the outer d electrons as a function of the number n_i of electrons per relevant orbital, the magnitude of a nearest-neighbor transfer energy b , and the temperature T . It also summarizes the various characters of several physical properties imparted by outer electrons to show how they can be used to distinguish the electronic phases in different perovskites. Information from the tabulated data is used to show the influence of covalence and intra-atomic exchange, which help determine the parameter b , on the character of the electrons. Spontaneous collective-electron magnetism is seen to occur only in a narrow transitional interval of b between localized-electron magnetism and collective-electron Pauli paramagnetism.

Section 3.5 provides schematic energy diagrams for the alloys $M^cXM_f^d$. These are shown to be useful guides to predictions of the magnitudes of the atomic moments and the magnetic order.

dungen mit äußeren d -Elektronen, die lokalisiert und spontan magnetisch in der einen Verbindung, kollektiv und spontan magnetisch in einer anderen, und kollektiv und Pauli-paramagnetisch in noch einer weiteren sind. Dies erlaubt systematische experimentelle Untersuchungen der Eigenschaften der d -Elektronen, indem man von einem lokalisierten Zustand, in dem Kristallfeld plus Superaustausch- und/oder Doppelaustausch-Theorien gelten, zu einem Zustand unkorrelierter Kollektivelektronen (außer bei Temperaturen unterhalb des Übergangs zur Supraleitung) übergeht, in dem die konventionelle Bändertheorie anzuwenden ist. Weiterhin führt die Einfachheit der Perowskit- ABX_3 -Struktur zu minimalen konkurrierenden Wechselwirkungen zwischen benachbarten magnetischen Kationen. Aufgrund der Untersuchung der magnetischen Ordnung, die man durch die Neutronenbeugung kennt, und einer genauen Kenntnis der Struktur, wie man sie durch Röntgenbeugung gewonnen hat, war es deshalb möglich, die halbempirischen Gesetze über die isotrope 180° -Kation-Anion-Kation-Superaustausch-Wechselwirkung zwischen lokalisierten Elektronen, die Doppelaustausch-Hypothese, den antisymmetrischen Austausch und Voraussagen für magnetische Ordnung und spontane Atom-Momente, die von Kollektivelektronen herrühren, zu prüfen.

Der Abschnitt 3.3 enthält den allgemeinen phänomenologischen Hamilton-Austausch-Operator für lokalisierte Elektronen und faßt die mikroskopischen Modelle für den isotropen Superaustausch, den Doppelaustausch und den antisymmetrischen Austausch zusammen. Aus diesen Modellen werden allgemeine Regeln für die Wechselwirkungen, die für die magnetische Ordnung verantwortlich sind, zum Vergleich mit den tabellierten Daten entwickelt.

Der Abschnitt 3.4 enthält die grundlegenden physikalischen Ideen, die für die Herstellung eines qualitativen Phasendiagramms für die äußeren d -Elektronen als Funktion der Elektronenzahl n_i pro betreffenden Bahnzustand, der Größe einer Übertragungsenergie b zwischen nächsten Nachbarn und der Temperatur T notwendig sind. Außerdem werden hier verschiedene Charakteristika einiger durch die äußeren Elektronen gegebenen physikalischen Eigenschaften zusammengestellt, um zu zeigen, wie man mit ihrer Hilfe die elektronischen Phasen verschiedener Perowskite unterscheiden kann. Auf Grund der tabellierten Werte wird der Einfluß von Kovalenz und intra-atomarem Austausch, die den Parameter b mitbestimmen, auf den Charakter der Elektronen gezeigt. Spontane Magnetisierung der Kollektivelektronen tritt, wie man sieht, nur in einem schmalen Übergangsintervall von b zwischen dem Magnetismus lokalisierter Elektronen und dem Pauli-Paramagnetismus der Kollektivelektronen auf.

Der Abschnitt 3.5 enthält schematische Energiediagramme für die Legierungen $M^cXM_f^d$. Es wird gezeigt, daß sie zu brauchbaren Voraussagen über die Größe der Atom-Momente und die magnetische Ordnung führen können.

In the introductions to the sections 3.2...3.5 we have referenced the principle theoretical contribution discussed, but no attempt was made to do this systematically for the experimental contributions, which are thoroughly referenced in the tables. — In the crystallographic tables, the crystal parameters quoted either represent the most complete analysis, in our judgment, or belong to the most complete set of parameters for a series of similar compounds. They do not necessarily represent the historical reference that established the unit-cell dimensions.

Literature was considered up to 1969.

Finally, we would like to thank DAVID MAHONEY for his willing assistance, the library and publications personnel of Lincoln Laboratory for their efficient support, and Mrs. G. E. BOYD for her help with all the foreign references.

In den Einleitungen zu den Abschnitten 3.2...3.5 haben wir die grundlegenden theoretischen Beiträge, die diskutiert werden, mit Literaturhinweisen versehen; für die experimentellen Beiträge haben wir dies nicht systematisch durchzuführen versucht, da die entsprechenden Tabellen vollständig mit Literaturhinweisen versehen sind. — In den kristallographischen Tabellen stellen die angeführten Kristallparameter entweder die nach unserer Beurteilung vollständigste Analyse dar, oder sie gehören zum vollständigsten Satz von Parametern für eine Reihe ähnlicher Verbindungen. Sie geben nicht notwendigerweise den historischen Literaturhinweis, der die Dimensionen der Einheitszelle festlegte.

Die Literatur wurde bis 1969 berücksichtigt.

Schließlich möchten wir DAVID MAHONEY für seine bereitwillige Hilfe, den Angestellten der Bibliothek und der Veröffentlichungsabteilung des Lincoln-Laboratoriums für ihre wirksame Unterstützung und Mrs. G. E. BOYD für ihre Hilfe bei der ausländischen Literatur danken.

3.0.2 Symbols and units used in tables and figures

Crystallographic structure

symmetry

a, b, c [Å]
 α, β, γ [deg]
 $\Theta_{\text{trans}}, \Theta_{\text{ord}}$ [°K]
 Θ_D [°K]
 T_{melt} [°K]
 c_{ij}
 ϵ_i
 $r_{A,B,B'}$ [Å]

symmetry classification for perovskite structures: C = cubic, H = hexagonal, R = rhombohedral, O = orthorhombic ($a < c/\sqrt{2}$), O' = orthorhombic ($c/\sqrt{2} < a$), T = tetragonal, M = monoclinic, Tr = triclinic
 lattice parameters
 angle between crystallographic axes
 crystallographic transition and ordering temperatures
 Debye temperature
 melting temperature
 elastic constants
 crystalline strains
 radius of A, B, B' cation

Magnetic properties (static measurements)

magnetic order

n_A, n_B^A
 \bar{n}_m
 n_{eff}
 Θ_C [°K]
 Θ_N [°K]
 Θ_r [°K]
 Θ_p [°K]
 Θ' [°K]
 C_m [emu °K mole⁻¹]
 χ_g [emu/g], [cm³/g]
 χ_m [emu/mole]
 p_A, p^A [μ_B]
 $p_m, p^{(xy)}$
 p^*
 J_{nn}/k [°K]
 d
 σ_w [erg/cm²]
 W_{nn}

see magnetic structure type from Fig. 26
 atomic moment and component of atomic moment parallel to net ferromagnetic moment in numbers of Bohr magnetons: $p_A = n_A \mu_B$
 net magnetization per molecule in numbers of Bohr magneton: $p_m = \bar{n}_m \mu_B$
 $n_{\text{eff}} = \sqrt{8C_m}$ is the effective paramagnetic moment: $p_{\text{eff}} = n_{\text{eff}} \mu_B$
 Curie temperature
 Néel temperature; extrapolated Néel temperature
 temperature for spin reorientation
 paramagnetic Curie temperature ($\Theta_p < 0$ if antiferromagnetic coupling)
 temperature below which parasitic n_i^A deviates appreciably from 0.05
 molar Curie constant determined from Curie-Weiss law $\chi_m = C_m/(T - \Theta_p)$
 specific paramagnetic susceptibility
 molar paramagnetic susceptibility
 atomic moment, atomic moment of element A
 molecular moment (of molecule xy)
 effective paramagnetic moment: $p^* = \sqrt{\chi_m T}$
 isotropic exchange constant of Eq. (16) for near-neighbor interactions
 Ln-Fe interaction parameter defined by
 $M(t) = \sigma_0(0) B(t) [1 + (d/t)]$, where $t = T/\Theta_C$ and $B(t)$ is the Brillouin function
 domain wall energy density
 net near-neighbor Weiss molecular field constant: $H_{w1} = \sum_{j=1}^z W_{ij} M_j$

σ { [Gauss cm ³ /g] [emu/g]	magnetic moment per gram = specific magnetization
σ_0 [emu/g]	specific parasitic (weak) magnetization as obtained from $\sigma = \sigma_0 + \chi_g H_a$
σ_{sp}	spontaneous specific magnetization
H_a [Oe]	externally applied field
H_{crit} [Oe]	critical applied field for antiferromagnetic-ferromagnetic transition or for spin-flop transition
H_c	coercivity
α	cant angle
b_1, b_2 [dyn/cm ²]	magnetoelectric coefficients
λ_{100}	magnetostriction constant for [100] direction: $\lambda_{100} = -4b_1/3(c_{11} - c_{12})$
C_{ijk}	components of the tensor describing the quadratic dependence of magnetization on applied field: Eq. (36)
μ_B	the Bohr magneton = 5585 cmu/g
T [erg/g]	torque: $T = \sigma \times H_a$
Magnetic properties (resonance measurements)	
H_A	effective crystalline-anisotropy field
H_{ex}	exchange field
H_D	spin-canting field (Dzialoshinskii field)
H_{int}	internal magnetic field at the nucleus
H_n	axial hyperfine field arising from nuclear polarization
H_{hfp}	hyperfine field $I \cdot A \cdot S$, where I = nuclear spin, S = net atomic spin, and the components of the interaction tensor are $A_s, A_{ns}, A_\sigma, A_\pi, A_{2p}$.
f_s^A, f_n^A, f_π^A	fraction of unpaired s, p_σ or p_π electron spins involved in covalent bonding: $f_s^A = 2SA_s/A_{ns} = \frac{1}{3} N_0^2 \lambda_s^2, f_n^A = 2SA_\sigma/A_{2p} = \frac{1}{3} N_0^2 \lambda_\sigma^2, f_\pi^A = 2SA_\pi/A_{2p} = \frac{1}{3} N_0^2 \lambda_\pi^2$.
$\epsilon, \Delta E$	See Eq. (4) for $N_e, N_i, \lambda_s, \lambda_\sigma, \lambda_\pi$.
F_{ij}, G_{ij}	nuclear quadrupole coupling constant and quadrupole splitting dipolar and quadrupolar magnetoelastic coefficients: $\delta g_i = \sum_{j=1}^6 F_{ij} \epsilon_j$ and $d_i = \sum_{j=1}^6 G_{ij} \epsilon_j$, where $\mathcal{H}_{spin-lattice} = \mu_B H_a \cdot \delta g \cdot S + S \cdot d \cdot S$
ν_R [Hz]	resonance frequency for NMR
$\Delta \nu$ [Hz]	half-line width
T_1 [sec]	nuclear spin-lattice relaxation time
T_2 [sec]	nuclear spin-spin relaxation time
T_{le} [sec]	nuclear spin-lattice relaxation time during a locking pulse
Optical measurements	
n	index of refraction
ϵ_0	low-frequency dielectric constant
ρ [°/cm]	Faraday rotation
ν_{TO}, ν_{LO} [Hz]	frequency of transverse and longitudinal optical modes
Transport measurements	
θ_{cs}	superconducting critical temperature
E_F	Fermi energy
E_a	activation energy for a small-polaron hop
ρ [Ω cm]	electrical resistivity
S [μ V/°K]	Seebeck coefficient
e [esu]	magnitude of the electronic charge
c, n_1, n_\pm [cm ⁻³]	charge-carrier density
μ [cm ² /Vsec]	charge-carrier mobility
τ [sec]	charge-carrier collision time
m^* [g]	charge-carrier effective mass
D_0 [cm ² /sec]	charge-carrier diffusion coefficient at $E_a = 0$
N_\pm	density of unoccupied states: $2(2\pi m_\pm^* k T / h^2)^{3/2}$
General properties	
T [°K]	temperature
p	pressure
c_p	specific heat at constant pressure

Abbreviations for text and indices

AFMR	antiferromagnetic resonance
APR	acoustic paramagnetic resonance
BPW	Bethe-Peierls-Weiss method
C, cub	cubic
DS	Danielson-Stevens method
DTA	differential thermal analysis
ESR	electron spin resonance = paramagnetic resonance
f.c.	face-centered permutation
FMR	ferromagnetic resonance
F _R	ferromagnetic with reduced n_A
H, hex, hex (nL)	hexagonal, hexagonal n-layer structure
I.R.	infrared
Ln	Lanthanone = any of the rare-earth elements
MF	molecular field approximation
M, mon	monoclinic
NAR	nuclear acoustic resonance
NMR	nuclear magnetic resonance
ncub	noncubic
O, O', orth	orthorhombic (O: $a < c/\sqrt{2}$; O': $c/\sqrt{2} < a$)
P & S	reference to preparation and structural information
Prep.	reference to material preparation
Prop.	reference to material properties
pscub	pseudocubic
psmon	pseudomonoclinic
R, rh	rhombohedral
RW	Rushbrooke-Wood method
S. G.	space group
S.S.	solid solution
T, tetr	tetragonal
Tr, tr	triclinic

3.1 Descriptions of stoichiometric ABX₃ and M^eXM₃^f structures

3.1.1 The ideal perovskite structure

The ideal perovskite structure has the cubic unit cell of Fig. 1 with space group Pm3m. Fig. 1(a) shows the corner-sharing octahedral units (BX₃ array in ABX₃ and XM₃^f array in M^eXM₃^f), which form the stable skeleton of the structure. The A cation (or M^e atom) occupies the body-center position. Fig. 1(b) shows the unit cell with the A cation (or M^e atom) at the origin, or corner position. This shows the face-centered-cubic character (with Cu₃Au-type order) of the AX₃ or M^eM₃^f subarrays. Fig. 1(c) shows the cubic perovskite on a hexagonal basis, with the *c* axis along the cubic [111] direction. The alternate AX₃ and B ionic layers each have cubic stacking. Also indicated is the ordering of B and B' layers in the ordered A(B_{2/3}B'_{1/3})X₃ structures.

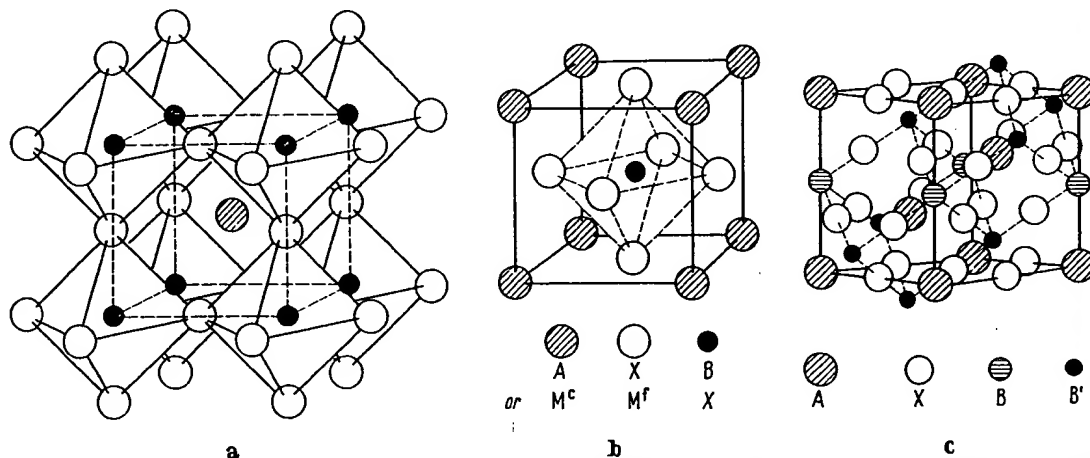


Fig. 1. ABX₃, M^eXM₃^f. Ideal perovskite structure: a) B cation (or X atom) at origin. b) M^e atom (or A cation) at origin. c) A cation at origin in hexagonal basis [Ga10].

The alloys M^cXM^f are stabilized by covalent M-X bonding and by metallic M-M bonding, so that they are generally cubic. Only in phases exhibiting complex magnetic order are there distortions to lower symmetry. On the other hand, the ABX₃ perovskites, which are primarily stabilized by the Madelung energy, are rarely cubic at normal temperatures. Madelung energy calculations are available [Ro15a, Sa2b, Mi1].

Although cubic at high temperatures, most ABX₃ compounds exhibit distortions to lower symmetry below some temperature Θ_{trans} as a result of atomic displacements. Such displacive transitions can be described by a finite set of normal vibrational modes that become soft, their vibrational frequency increasing with $T > \Theta_{\text{trans}}$. From LANDAU's [La2] theory of phase transitions, it may be argued [Ha1, Co2] that at a second-order displacive transition, the frequency of one normal mode becomes zero. Thus the occurrence of ferroelectricity in perovskite-type crystals such as BaTiO₃ has been correlated both theoretically and experimentally [An2, Co1, Ba17, Co28, Ne8, Sh26] with the existence of a transverse optic mode of lattice vibration having wave number $k \approx 0$ and a temperature-dependent frequency $\omega \sim (T - \Theta_{\text{trans}})^{1/2}$.

Similarly, in the case of LaAlO₃, softening of a single normal mode can produce the R $\bar{3}c$ -to-cubic transition, and this transition is probably second-order. Investigation [Ha1] of the atomic displacements involved in other distortions from cubic symmetry, on the other hand, has shown that several normal modes are involved, and these displacive transitions are first-order.

SrTiO₃ exhibits a tetragonal (D_{4h}^{18} with $c/a = 1.00056$) to cubic transition at $\Theta_{\text{trans}} = 110^\circ \text{K}$ [Ly2, Ri5] that appears to illustrate the softening of a triply degenerate phonon at the R point of the Brillouin zone in the cubic phase. For $T < \Theta_{\text{trans}}$, it splits into two zone-center phonons having a frequency dependence $\omega \sim (\Theta_{\text{trans}} - T)^{0.31}$ [Fl2]. In the presence of an external electric field E_a the symmetry is further reduced to C_{4v} if $E_a \parallel c$ -axis, or C_{2v} if $E_a \perp c$ -axis, and the critical modes have the same symmetry as the ferroelectric TO modes. "Anticrossing" of the modes occurs for $E_a = 1.5 \text{ kV/cm}$ and 15 kV/cm [Ne7, Wo19]. Thus the observed [He5] maximum in the electric susceptibility of SrTiO₃ at very low temperatures does not appear to be associated with a ferroelectric transition.

Theoretical interest in the analytic description of these phase transitions continues [Go1a, Mu4a, Ta14a, Th3].

The physical origins of the various crystallographic distortions may be separated into three parts: relative ionic sizes, electron ordering among localized electrons, and electron ordering among collective electrons.

3.1.2 The influence of relative ionic sizes

3.1.2.1 Tolerance factor

The first prerequisite for a stable perovskite structure is the existence of a stable BX₃ skeletal subarray. If the B-cation radius is $r_B < 0.51 \text{ \AA}$ in oxides, for example, the B cation does not achieve its optimum B-O separation in an octahedral site and therefore stabilizes a structure with a smaller anion coordination. The Al³⁺ ion is borderline, being stable in four, five or six coordination. However, Ga³⁺, Ge⁴⁺ and V⁵⁺ ions are definitely more stable in tetrahedral sites at ambient pressures.

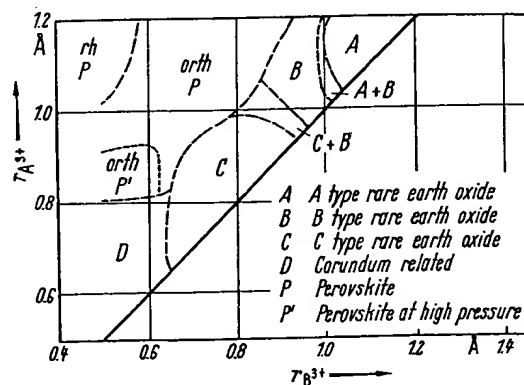
Given the BX₃ skeletal subarray, additional stabilization is achieved by accommodating a large A cation within this skeleton. Because there is an optimum A-X bond length, the presence of an A atom generally distorts the BX₃ array so as to optimize the A-X bonding. However, if this distortion is too large, then other space groups become competitive. GOLDSCHMIDT [Go2] defined the tolerable limits on the size of the A cation via a tolerance factor

$$t = (r_A + r_X) / \sqrt{2} (r_B + r_X) \quad (1)$$

where r_A , r_B , r_X are empirical radii of the respective ions. By geometry, the ideal cubic structure should have $t = 1$. The perovskite structure occurs only within the range $0.75 < t < 1.00$. However, this is not a sufficient condition, since the A and B cations must, in themselves, be stable in twelvefold (12 or 8 + 4 or 6 + 6) and sixfold coordinations. This sets lower bounds for the cationic radii. In oxides these bounds are $r_A > 0.90 \text{ \AA}$ and $r_B > 0.51 \text{ \AA}$. In addition, MEGAW [Me5] noted that, if $0.75 < t < 0.9$, a cooperative buckling of the corner-shared octahedra to optimize the A-X bond lengths enlarges the unit cell; on the other hand, if $0.9 < t < 1$, such buckling may not be found, although small distortions to rhombohedral symmetry occur. These structures are to be distinguished from perovskites that exhibit additional distortions as a result of electron ordering. The cubic phase is found at high temperatures or where the A-X bond is more ionic (especially if $t \approx 1$).

Where the A cation is too small ($r_A < 0.9 \text{ \AA}$) to accommodate twelve nearest neighbors, a structure in which the A and B cations are both six-coordinated becomes competitive. From the phase diagram of Fig. 2 for the oxides $A^{2+}B^{3+}O_3$, which has been adapted from SCHNEIDER, ROTH, and WARING [Sc13], the initial competition is the C-M₂O₃ structure, which contains two unusual types of corner-shared, six-coordinated sites. The C-M₂O₃ structure consists of a face-centered-cubic array of cations with anions occupying $\frac{1}{2}$ of the tetrahedral interstices in an ordered manner. Thus each cation has six out of eight near-neighbor anions at the corners of a circumscribing cube: $\frac{1}{2}$ of the cations have two anions missing at the ends of a body diagonal and $\frac{1}{2}$ of the cations have two anions missing at the end of a face diagonal of the circumscribing cube. This arrangement minimizes the electrostatic repulsive forces between the cations.

Fig. 2. General $r_A - r_B$ phase diagram for $A^{2+}B^{3+}O_3$ compounds based on ionic-size considerations. Exceptions may occur where considerations other than ionic radii r_A, r_B become important, as in the case $A = Bi$. A similar plot for $A^{2+}B^{4+}O_3$ perovskites is not useful because secondary considerations are amplified by ferroelectric distortions and the possibility of different layer sequences where larger A cations are present. [Adapted from *Sc13*].



Given smaller A cations, however, electrostatic screening between face-shared octahedra can be achieved by displacements of the cations away from the shared face, and the structure competitive with perovskite is generally built from an hexagonal-close-packed anion array, which has octahedral holes sharing common faces along the c -axis. With one octahedral hole per anion and a cation/anion ratio 2/3, the cations are ordered among these holes so as to minimize the electrostatic energy. If the A and B cations carry the same charge, as in $A^{2+}B^{3+}O_3$, only pairs of cations share common octahedral-site faces and there is no ordering of A and B within the cationic array. This allows the electrostatic force between two cations sharing a common octahedral face to be reduced by displacements of the cations away from each other, thus distorting the octahedra. The result is the corundum structure of Al_2O_3 . If the cations A and B carry different charges, as in $A^{2+}B^{4+}O_3$, then the A and the B cations order into alternate puckered cationic (111) planes of the rhombohedral corundum structure to form the ilmenite structure. However, where there is a large difference in the cationic charges, as in $Li^+Sb^{5+}O_3$ and $Li^+Nb^{5+}O_3$, two other alternatives become competitive: (1) The A^+ ions order in strings of face-shared octahedra so as to permit the B^{5+} -ion octahedra to share only edges with near-neighbor occupied octahedra. This structure is illustrated by $LiSbO_3$ [Ed1]. (2) After ordering B^{5+} and Li^+ ions within each cationic (111) plane of the corundum structure in such a way that B^{5+} and Li^+ ions share common octahedral-site faces, each A^+ cation is then displaced into the far face of its octahedron, where it is equally spaced from B^{5+} cations above and below so long as the B^{5+} cations remain in the centers of their octahedra. This is the structure of paraelectric $LiNbO_3$ and $LiTaO_3$ [Ab3].

Where the A cation is too large ($t > 1.0$), the close-packed AX_3 layers of Fig. 1(c) tend to change their stacking sequence from cubic to hexagonal. However, the change from the all-cubic stacking of the rhombohedral perovskite structure to the all-hexagonal stacking of the hexagonal (hex. 2L) $CsNiCl_2$ structure goes via the three intermediate steps shown in Fig. 3 [Lo1]. The first step is the hexagonal $BaTiO_3$ structure of Fig. 3(c). It is a six-layer structure with stacking sequence $a-b-c-a-c-b-a$, corresponding to one hexagonal stacking out of three. In this structure (hex. 6L), two-out-of-three B cations form pairs sharing a common octahedral-site face, and one-out-of-three B cation shares only common octahedral-site corners as in the perovskite structure. Many ordered compounds $A_2B_2B'O_6$ are known to have this structure. The second step, illustrated by the hexagonal $BaMnO_3$ structure of Fig. 3(d), alternates hexagonal and cubic stackings with the sequence $a-b-c-b-a$. This four-layer structure (hex. 4L), contains only B-cation pairs sharing common octahedral-site faces. The electrostatic forces between paired B-cations in Figs. 3(c), (d) displace the paired cations from one another along the c axis, exactly as in the corundum

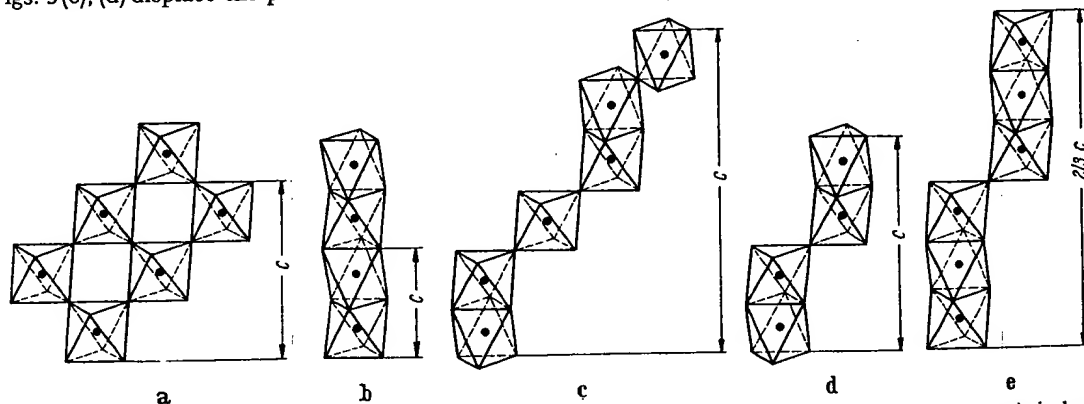


Fig. 3. Stable structures intermediate to a) cubic perovskite and b) the two-layer hexagonal $CsNiCl_2$ structure, c) six-layer hexagonal $BaTiO_3$ structure, d) four-layer hexagonal $BaMnO_3$ structure, e) nine-layer hexagonal $BaRuO_3$ structure. [Adapted from *Ca2*].

structure. The third step is the nine-layer (hex. 9L) structure of BaRuO_3 , which has two hexagonal stackings out of three in the sequence $a-b-c-b-c-a-c-a-b-a$. Here the B cations form strings of three sharing common octahedral-site faces along the c -axis. Electrostatic forces displace the two end-member B cations away from the center B cation of each string, as shown in Fig. 3(e). Because cubic stacking is stabilized by hydrostatic pressure, it is possible to convert under pressure and high temperature the hexagonal structures to the perovskite structure through the successive sequence of steps. This is well illustrated by the $\text{Ba}_{1-x}\text{Sr}_x\text{RuO}_3$ system as shown in Fig. 4(a). These particular intermediate structures appear to be stabilized by the cation displacements, but at the cost of alternating the stacking sequence. The (hex. 4L) structure, which has the maximum alternation of stacking, is not always found, and the intermediate structures tend to be stabilized by smaller B cations, as illustrated in Fig. 4(b).

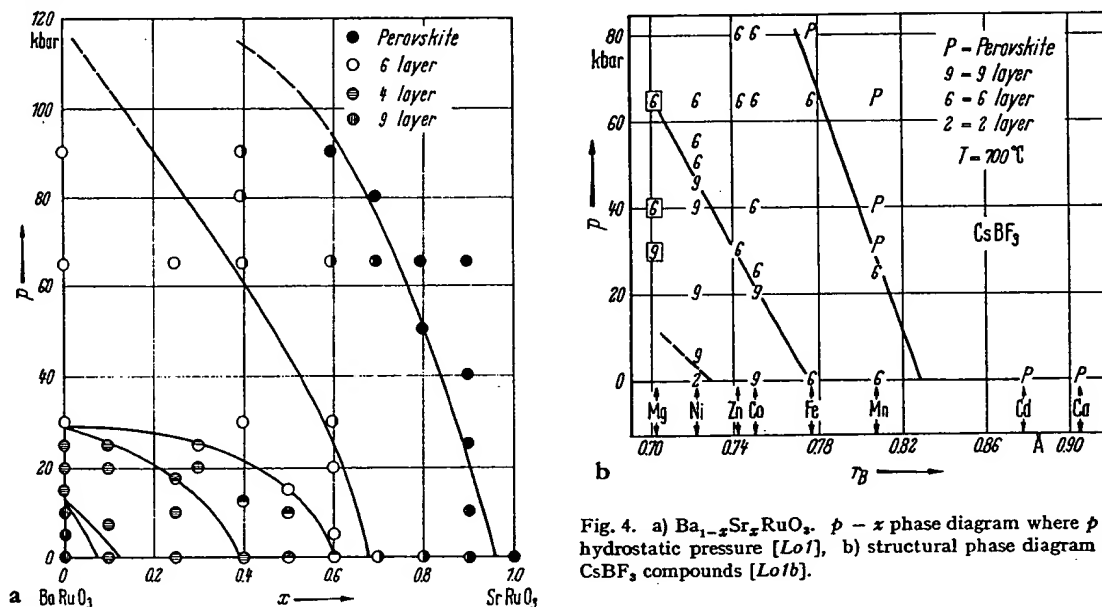


Fig. 4. a) $\text{Ba}_{1-x}\text{Sr}_x\text{RuO}_3$, p - x phase diagram where p is hydrostatic pressure [Lo1], b) structural phase diagram of CsBF_3 compounds [Lo1b].

3.1.2.2 O-orthorhombic structure

Cooperative buckling of corner-shared octahedra, although indexed on a monoclinic pseudocell in earlier work, may produce the orthorhombic primitive cell of Fig. 5 containing four formula units. It was first identified in single crystals of GdFeO_3 [Ge1] and later confirmed [Co2f]. Powder photographs taken with CrK_α radiation could be indexed on the monoclinic pseudocell containing a single GdFeO_3 molecule, which is the origin of the earlier classification. The pseudocell dimensions of GdFeO_3 are $a = c = 3.87 \text{ \AA}$, $b = 3.83 \text{ \AA}$, $\beta = 92.8^\circ$, where $2b_{\text{pseudocell}} = c_{\text{true cell}}$. The true orthorhombic cell is referred to in the tables as O-orthorhombic and is distinguished from the O'-orthorhombic structure by a lattice-parameter ratio

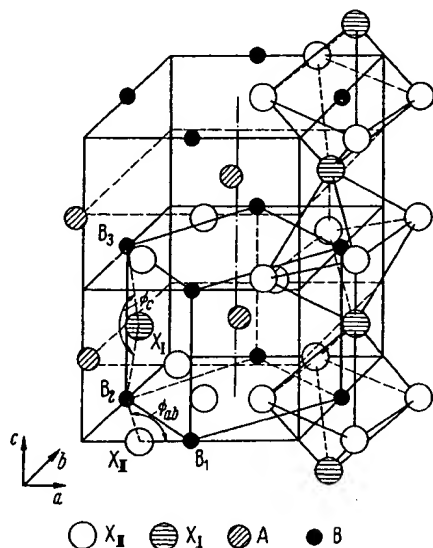


Fig. 5. GdFeO_3 , O-orthorhombic structure.

$\phi_{ab} = \angle \text{B}_1\text{X}_1\text{B}_2$, $\phi_c = \angle \text{B}_1\text{X}_1\text{B}_2$.

Fig. from [Ve12], structure [Ge1], coordinates [Co2f].

ion	position	coordinates		
		x	y	z
Gd^{3+}	4(c)	-0.018	0.060	$\frac{1}{2}$
Fe^{3+}	4(b)	$\frac{1}{2}$	0	0
O_I^{2-}	4(c)	0.05	0.470	$\frac{1}{2}$
O_{II}^{2-}	8(d)	-0.29	0.275	0.05

$c/a > \sqrt{2}$, where $a < b$. The O'-orthorhombic structure, which has $c/a < \sqrt{2}$, is the result of a superposed Jahn-Teller (with or without spin-orbit coupling) distortion. It is also to be distinguished from ferroelectric O_B⁺-orthorhombic and O_B⁻-orthorhombic distortions in which each B cation is removed from the center of symmetry of its interstice. Other orthorhombic distortions have been reported for NdGaO₃ [Br26] and NaCoF₃ [Ok5].

The O-orthorhombic unit cell has the probable space group Pbnm with A cations in positions 4(c): $\pm(x, y, \frac{1}{2}; \frac{1}{2} - x, \frac{1}{2} + y, \frac{1}{2})$, the B cations in 4(b): $(\frac{1}{2}, 0, 0; \frac{1}{2}, 0, \frac{1}{2}; 0, \frac{1}{2}, 0; 0, \frac{1}{2}, \frac{1}{2})$, eight anions X_{II} in 8(d): $\pm(x, y, z; \frac{1}{2} - x, \frac{1}{2} + y, \frac{1}{2} - z; \bar{x}, \bar{y}, \frac{1}{2} + z; \frac{1}{2} + x, \frac{1}{2} - y, \bar{z})$, and the remaining four anions X_I in 4(c). Coordinates for the ions in GdFeO₃ are also given in Fig. 5.

The buckling of the corner-shared octahedra decreases the cation-anion-cation angle Φ from 180°. If the B cations and the anions are distinguished as B₁($\frac{1}{2}, 0, 0$), B₂($0, \frac{1}{2}, 0$), B₃($\frac{1}{2}, 0, \frac{1}{2}$), X_{II}($\frac{1}{2} + x, \frac{1}{2} - y, \bar{z}$), and X_I($\frac{1}{2} - x, \frac{1}{2} + y, \frac{1}{2}$), then the two representative angles are $\Phi_{ab} = (B_1 - X_{II} - B_2)$ and $\Phi_c = (B_2 - X_I - B_3)$. GILLES [Gi4] has estimated that in La(Co_{0.2}Mn_{0.8})O₃ these angles are $\Phi_{ab} = 150^\circ \pm 3^\circ$ and $\Phi_c = 177^\circ \pm 3^\circ$ with B₁ - O_{II} = 1.95 Å, B₂ - O_{II} = 2.10 Å, B₁ - O_I = B₃ - O_I = 1.96 Å. The angles in GdFeO₃ are similar.

3.1.2.3 Rhombohedral structures

Where there is no buckling of the octahedra, the perovskites ABX₃ may have a small deformation from cubic to rhombohedral symmetry. Where this deformation does not enlarge the unit cell, it is possible to index it either on a unit cell containing two formula units, as shown in Fig. 6, or on a unit cell containing one formula unit. The corresponding rhombohedral angles are $\alpha \approx 60^\circ$ or $\alpha \approx 90^\circ$. In the early literature, detailed anion positions were not known, and it was common to use the smaller cell with $\alpha \approx 90^\circ$. However, the anions are generally displaced so as to require the larger unit cell of Fig. 6, which has $\alpha \approx 60^\circ$.

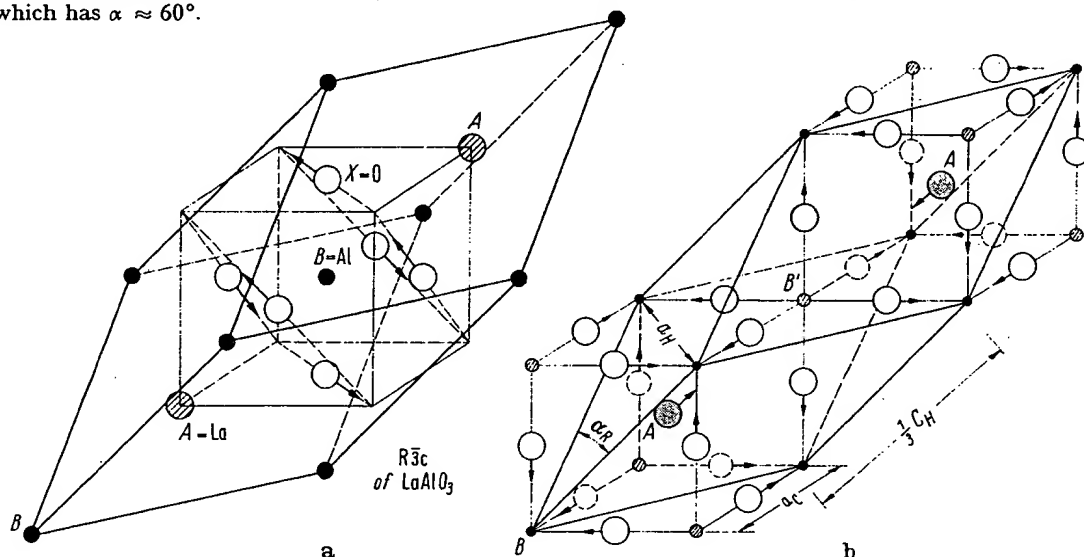


Fig. 6. Rhombohedral ABX₃ structures: a) anion shifts for symmetry $R\bar{3}c$; b) the simplest ionic displacements, corresponding to symmetry $R\bar{3}m$ for ordered A₂BB'₂X₆ structures having $r_{B'} > r_B$ [Ra3].

Anion displacements from their ideal positions may be of three different types: (1) AX₃(111) planes remain equidistant from neighboring B-cation (111) planes, leaving all the B-cations equivalent. Within these planes, three A-X distances are reduced and three are enlarged via cooperative rotations of the B-cation octahedra, as shown in Fig. 6(a). (2) The anions may move within pseudocubic {110} planes including the B-B axes so as to create two distinguishable B positions: B positions having a shorter B-X separation and B' positions having a larger B'-X separation. This gives the symmetry $R\bar{3}m$, which allows the A cations to be displaced along the [111] axis so as to make the separations B-A \neq B'-A. (3) In the most general case, the anion displacements may be decomposed into $R\bar{3}c$ and $R\bar{3}m$ components. The resulting symmetry $R\bar{3}$ also gives distinguishable B and B' positions via its $R\bar{3}m$ component.

Although the distinction between these possibilities has been determined in only a few cases, it appears that $R\bar{3}c$ can be anticipated unless there is a physical reason for creating two distinguishable positions B and B'. This conclusion is based on the fact that LaAlO₃ has been shown to have the symmetry $R\bar{3}c$ by neutron diffraction, [De14] nuclear quadrupole resonance [Mu5], electron-spin resonance, [Ki3] and x-ray techniques [Ge4b, De17]. It is strongly supported by the observation [Ra3] that LaCoO₃ has the symmetry $R\bar{3}c$ at low temperatures, where all of the trivalent cobalt are in their low-spin state, but has the symmetry $R\bar{3}$ at higher temperatures where thermal activation creates a nearly equal population of high-spin and low-spin cobalt ions. These are crystallographically distinguishable, via different ionic radii, as B and B'.

3.1.3 The influence of localized-electron ordering

3.1.3.1 Crystal-field theory

Crystal-field theory rests on the assumption that the outer electrons to be described are localized at discrete atomic positions. This assumption is valid for outer *f* electrons; it is valid for *d* electrons in fluorides and in many oxides. Given this assumption, the Schrodinger equation $\mathcal{H}\psi = E\psi$ that describes the localized orbitals and their energies contains the Hamiltonian

$$\mathcal{H} = \mathcal{H}_0 + V_{el} + V_{cub} + (V_{LS} + V_{ncub} + V_{\lambda} + \sum_j V_{ij}) \quad (2)$$

where \mathcal{H}_0 is the Hamiltonian for a hydrogen-like, spherical potential, V_{el} is the atomic correction for spherical symmetry that enters if there is more than one outer *d* electron, and V_{cub} is the energy correction due to the cubic component of the crystalline fields. For outer *d* electrons, V_{el} and V_{cub} are generally ≈ 1 eV, and the ion is in a high-spin or a low-spin state depending upon the relative magnitudes of these two terms. In the case of 3*d* electrons, the perturbations listed within the parentheses are all < 0.1 eV, and they must be considered simultaneously. $V_{LS} = \lambda \mathbf{L} \cdot \mathbf{S}$ is the spin-orbit coupling energy, and covalent mixing reduces slightly the parameter λ from its free-atom value. V_{ncub} is the noncubic component of the crystalline field, V_{λ} is the elastic coupling energy associated with cooperative local distortions, and V_{ij} is the magnetic exchange energy coupling localized atomic moments on neighboring cations.

Solution of the zero-order equation $\mathcal{H}_0\psi = E\psi$ gives hydrogenic wave functions $f_{lm} = R_l(r) Y_l^m(\theta, \phi)$. From the spherical harmonics $Y_l^m(\theta, \phi)$, the *d* electrons ($l = 2$) have the following angular dependence and azimuthal-angular-momentum quantum number *m* derived from $L_x f = -i\hbar \partial f / \partial \phi = m\hbar f$:

$$\begin{aligned} f_A &\sim (3z^2 - r^2)/r^2 &= (3\cos^2\theta - 1); & m = 0 \\ (f_D \pm if_E) &\sim 2(xz \pm iyz)/r^2 &= \sin 2\theta \exp(\pm i\phi); & m = \pm 1 \\ (f_B \pm if_C) &\sim (x^2 - y^2 \pm i2xy)/r^2 &= \sin^2\theta \exp(\pm i2\phi); & m = \pm 2 \end{aligned} \quad (3)$$

where θ, ϕ are conventional spherical coordinates. The perturbation V_{el} reflects the fact that outer electrons of parallel spin are excluded from one another and therefore screen each other less from the positive atomic nucleus than do those of antiparallel spin. This correction is responsible for Hund's highest-multiplicity rule for the free atoms. It influences the radial part of the wave function, and hence the relative energies of states of different spin, but not the angular part.

Given the cartesian axes at a B cation formed by the principal axes of its octahedral interstice, the five *d* orbitals of Eq. (3) are separated into two symmetry groups; f_A and f_B , which are directed along the cartesian axes toward near-neighbor anions, have E_g symmetry and are referred to as e_g orbitals; f_C, f_D , and f_E , which are more stable because they are directed away from the near-neighbor anions, have T_{2g} symmetry and are referred to as t_{2g} orbitals. The principal contribution to the cubic-field splitting 10 Dq of T_{2g} and E_g energies is due to covalent mixing, not to electrostatic energies as calculated on a point-charge model. If covalent mixing with the near-neighbor anionic and A-cationic orbitals is introduced, then the crystalline localized orbitals of t_{2g} and e_g symmetry become

$$\begin{aligned} \psi_t &= N_t(f_t - \lambda_n \phi_n + \lambda_A \phi_A) \\ \psi_e &= N_e(f_e - \lambda_s \phi_s - \lambda_\sigma \phi_\sigma) \end{aligned} \quad (4)$$

where f_t and f_e are linear combinations of the atomic f_C, f_D, f_E and f_A, f_B orbitals. The symmetrized anionic p_n *s* and p_σ orbitals are ϕ_n, ϕ_s and ϕ_σ ; the symmetrized A-cationic *s, p* orbitals are ϕ_A . The covalent-mixing parameters $\lambda_\sigma, \lambda_n, \lambda_A, \lambda_s$ are roughly proportional to the overlap integral for atomic orbitals on neighboring ions and inversely proportional to their energy separation. Initially, the energy separations of cationic *d* and ϕ_σ or ϕ_n are given by $E_M - E_I$, the difference between the Madelung energy and ionization potentials for the "effective" ionic charges, so that by symmetry

$$10Dq = \Delta_M + (\lambda_\sigma^2 - \lambda_n^2)(E_M - E_I), \lambda_n < \lambda_\sigma \quad (5)$$

where Δ_M is any electrostatic contribution to 10 Dq. The one-electron crystal-field splitting of the *d*-state manifold is shown in Fig. 7(a). The relationship $\lambda_n < \lambda_\sigma$ has been confirmed by nuclear magnetic resonance studies of KMnF_3 , KNiF_3 , and K_2NiCrF_6 [Sh30, Hu4]. In these experiments the fractional occupancies by unpaired spins of the 2*s*, 2*p_σ*, and 2*p_n* orbitals are:

$$f_{x_s} \equiv 2SA_s/A_{2s} \sim N_s^2 \lambda_s^2, \quad f_{x_\sigma} = 2SA_\sigma/A_{2p} \sim N_\sigma^2 \lambda_\sigma^2, \quad f_{x_n} = 2SA_n/A_{2p} \sim N_n^2 \lambda_n^2$$

where A_s is the isotropic component and A_σ, A_n the anisotropic components of the hyperfine interaction tensor A_{ij} entering the nuclear spin-electron spin coupling energy $\sum_j \mathbf{I}_j \cdot \mathbf{A}_{ij} \cdot \mathbf{S}_j$. Interpretation of the phenomenological parameters $\lambda_n, \lambda_\sigma$ and 10 Dq has been discussed extensively [Hu4].

With more than one outer *d* electron or *d* hole, it is necessary to introduce V_{el} , which is responsible for Hund's highest multiplicity rule (highest net *S* and *L*) for the free atoms. For four outer electrons, the atomic ground term is therefore 5D . In a crystal, this rule may break down as a result of the crystalline

field
may
with
(Δ_{ex})

Fig.
a) \angle

Hu
sio:
Sir
is:
pa:
pe:
the
va:
ste

on
 t_2
ti

fields. Schematically, the Hund splitting Δ_{ex} for states of different spin and the one-electron splitting $10 Dq$ may be represented on the same energy diagram, as shown in Fig. 7 (b). It follows from this figure that with four to eight outer d electrons, the magnitude of the net ground-state spin depends upon whether $(\Delta_{\text{ex}} - 10 Dq)$ is positive or negative. If $\Delta_{\text{ex}} > 10 Dq$, the ion is in a high-spin state; if $\Delta_{\text{ex}} < 10 Dq$,

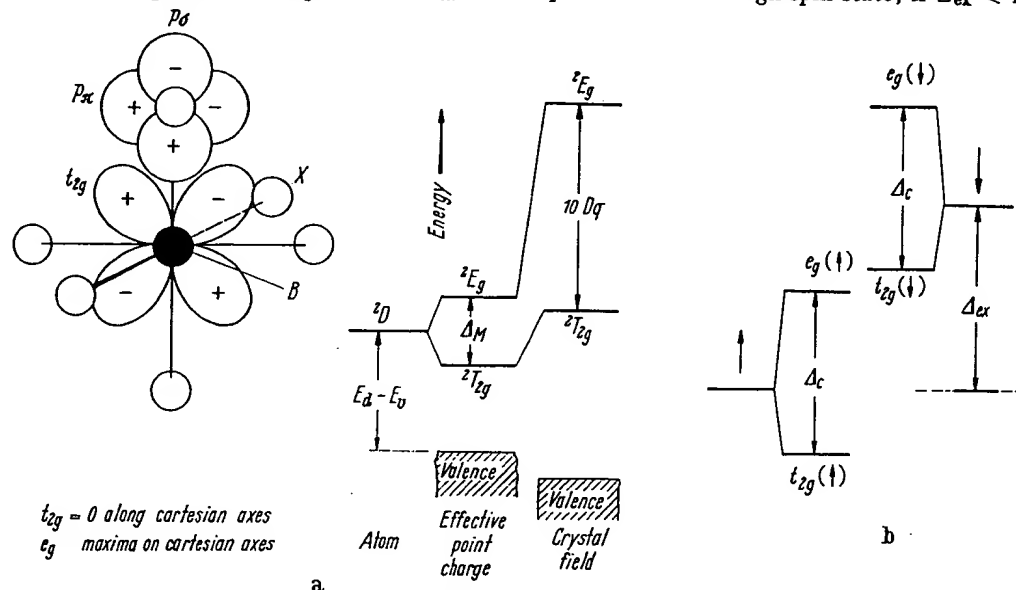


Fig. 7. One-electron crystal-field splitting of the d -state manifold of a transition-metal B cation in a cubic perovskite: a) $\Delta_{\text{ex}} = 0$ and b) schematically for $\Delta_{\text{ex}} \neq 0$, corresponding to more than one outer d electron.

Hund's rule breaks down and the ion is in a low-spin state. Since Δ_{ex} decreases with larger radial extension of the crystalline wave functions, it decreases with increasing covalent-mixing parameters λ_{σ} , λ_{π} . Simultaneously, from Eq. (5) it follows that $10 Dq$ increases with increasing covalency. Therefore there is a critical amount of covalent bonding beyond which Hund's rule breaks down. Covalency with a particular anionic sublattice increases with cationic charge and on going to the right through any long period of the periodic table. In oxides with the perovskite structure, only divalent and trivalent ions of the first long period are high-spin. Of these, trivalent nickel is low-spin and trivalent cobalt exhibits a variable high-spin to low-spin population as a function of temperature.

In general, it is necessary to use a multi-electron notation for the outer d electrons. Whereas atomic D states are split by the crystalline fields as shown in Fig. 7, atomic F states are split as shown in Fig. 8.

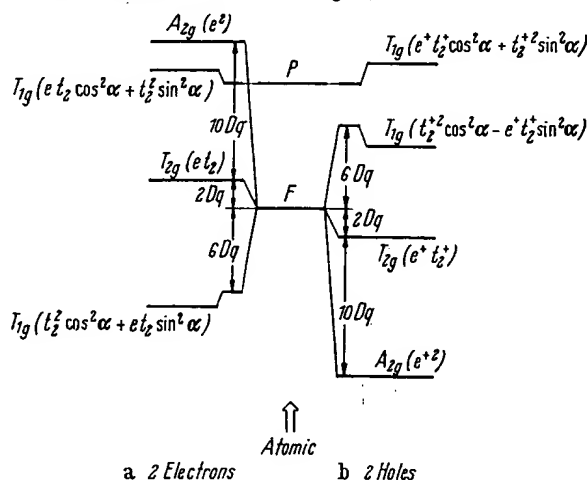


Fig. 8. Octahedral-site splitting of atomic F states: a) two-electron $3F$ states and b) two-hole $3F$ states.

Because the operator $L_z = -i\hbar\partial/\partial\phi$ is imaginary, the crystal-field splitting of f_B and f_C quenches the orbital angular momentum associated with these orbitals, so that the e_g orbitals have $m = 0, 0$ and the t_{2g} orbitals have $m = 0, \pm 1$. An isomorphism between f_C , f_D , f_E and atomic P orbitals simplifies calculation of V_{LS} . It is possible to treat the t_{2g} orbitals as atomic P orbitals if the sign of the spin-orbit-coupling

parameter λ is reversed [Gr9]. Therefore ground states having an orbital degeneracy and $m \neq 0$ are split by V_{LS} into $(2J + 1)$ multiplet states corresponding to states of different $J = L + S$. However, the order of the levels is inverted (largest J lowest for less than five d electrons, smallest J lowest for more than five d electrons) because of the change in sign of λ . According to the Landé interval rule, the separation between states J and $J + 1$ is $|\lambda| (J + 1)$. The first-order multiplet splittings, which do not include mixing of higher states of similar symmetry, are shown in Fig. 9 for Fe²⁺ and Co²⁺ ions. Note that the term is now identified by its symmetry character T_{2g} or T_{1g} rather than by its atomic orbital-momentum character D or F . Tab. 1 summarizes the various symmetry notations for different spin states.

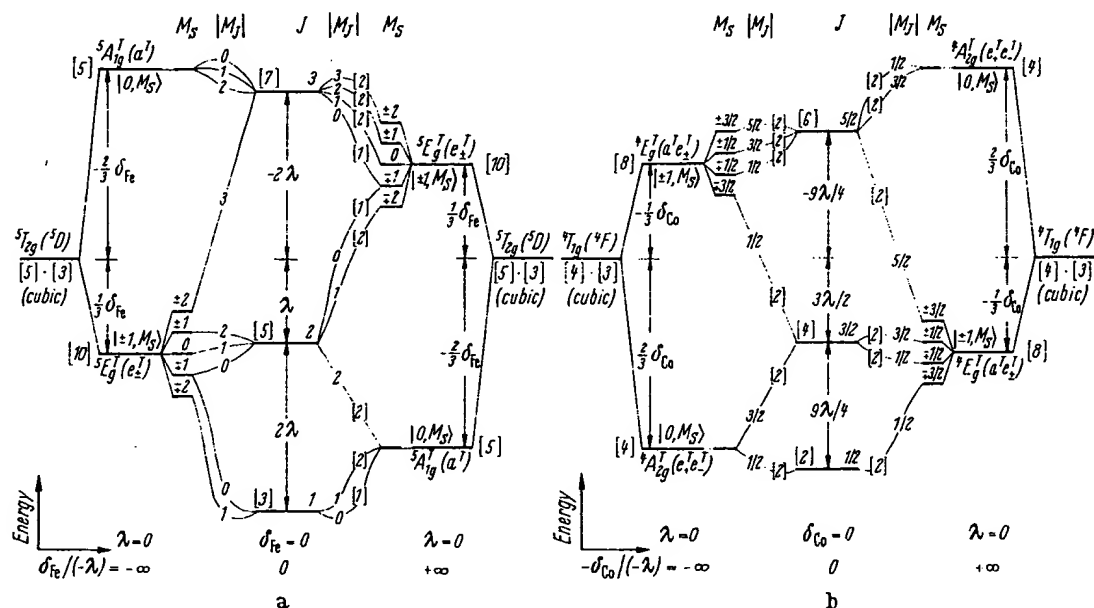


Fig. 9. Schematic spin-orbit plus trigonal-field, or tetragonal-field, splittings of cubic-field levels as a function of the ratio $\delta/(-\lambda)$ for a) ${}^5T_{2g}$ level of Fe²⁺ and b) ${}^4T_{1g}$ level of Co²⁺.

Spin-orbit coupling introduces an axial symmetry to the charge distribution, where the spin (or atomic-moment) defines the axis. Therefore, if there is a noncubic component to the crystalline field ($V_{ncub} \neq 0$), then there is a spin-lattice interaction via the orbital-lattice interaction that introduces a magnetic anisotropy. For localized electrons, this is a local, one-ion anisotropy. Conversely, if the spins are ordered below some transition temperature, then the local interstices have time to relax about the noncubic charge distribution, thereby distorting the octahedral site. Therefore there is an intimate connection between the noncubic symmetry and the magnitude of the multiplet splitting. The noncubic component is usually parametrized as

$$V_{ncub} = \delta(L_z^2 - \frac{3}{2}), \quad (6)$$

and Fig. 9 includes the total perturbation $V_{LS} + V_{ncub}$ of the one-electron and two-electron ground states.

With one or two holes in a half-shell, the one-electron and two-electron energy diagrams are inverted. In these cases $M_L = \sum m_l = 0$, so that $V_{LS} = 0$, and there is no multiplet splitting.

Tab. 1 also displays the general ground-state wave functions for a magnetically ordered phase having collinear spins. The coefficients a_1, a_2, a_3 of the Kramers' doublets and b_1, b_2 of the singlets all depend upon the relative magnitudes of the five perturbation terms $V_{LS} + V_{ncub} + V_\lambda + \mathcal{H}_Z$ where \mathcal{H}_Z is the Zeeman energy due to the internal molecular field resulting from magnetic order. The molecular-field approximation is used for the first-order, isotropic magnetic-coupling energy \mathcal{H}_{ex} , which is the dominant term in $\sum V_{ij}$ [see discussion of Eq. (13)]. This gives

$$\mathcal{H}_Z \approx 2J_p \langle S \rangle S_z \quad (7)$$

where J_p , the sum of all near-neighbor exchange parameters, can be determined from the temperature dependence of the magnetic susceptibility and z is along the axis of the average spin $\langle S \rangle$ on the neighboring cations. This term contributes to the spectroscopic-splitting factor g , and hence to the net atomic moment, if $V_{LS} \neq 0$. In Tab. 1, the components of the wave functions are designated by the notation $|M_L, M_S\rangle$, where M_L, M_S are the azimuthal quantum numbers for the net orbital and spin momenta.

Tab. 1. Lowest terms and ground state wave function for octahedral-site cations having *n* localized outer *d* electrons

<i>n</i>	Ion	<i>t_{2g}ⁿ</i>	<i>V_{el}</i>	<i>V_{cub}</i>	<i>V_{LS}</i>	$V_{LS} + V_{\text{nucb}}(\delta < 0) + \mathcal{H}_Z$	$V_{LS} + V_{\text{nucb}}(\delta > 0) + \mathcal{H}_Z$
1	Ti ³⁺ , V ⁴⁺ , W ⁵⁺ , Re ⁶⁺	<i>t_{2g}¹</i>	² D	² T _{2g}	$J = \frac{3}{2}$	$ +1, +\frac{1}{2}\rangle$	$a_1 0, +\frac{1}{2}\rangle + a_3 +1, -\frac{1}{2}\rangle$
2	V ³⁺ , Cr ⁴⁺ , Mo ⁵⁺	<i>t_{2g}²</i>	³ F	³ T _{1g}	$J = 2$	$ +1, +1\rangle$	$b_1 +1, -1\rangle + b_2 0, 0\rangle + b_3 -1, +1\rangle$
3	V ²⁺ , Cr ³⁺ , Mn ⁴⁺ , Mo ³⁺	<i>t_{2g}³</i>	⁴ F	⁴ A _{2g}	$J = \frac{3}{2}$	$ 0, +\frac{3}{2}\rangle$	$ 0, +\frac{3}{2}\rangle$
4	Cr ²⁺ , Mn ³⁺	<i>t_{2g}⁴</i>	⁵ D	⁵ E _g	$J = 2$	${}^5B_{1g} 0, +2\rangle$	${}^5A_{1g} 0, +2\rangle$
5	Fe ⁴⁺ , Ru ^{IV} , Os ^{IV}	<i>t_{2g}⁵</i>		³ T _{1g}	$J = 0$	$b_1 +1, -1\rangle + b_2 0, 0\rangle + b_3 -1, +1\rangle$	$b_1' +1, -1\rangle + b_2' 0, 0\rangle + b_3' -1, +1\rangle$
	Mn ²⁺ , Fe ³⁺	<i>t_{2g}⁵</i>	⁶ S	⁶ A _{1g}	$J = \frac{5}{2}$	$ 0, +\frac{5}{2}\rangle$	$ 0, +\frac{5}{2}\rangle$
	Ir ^{IV}	<i>t_{2g}⁵</i>		² T _{2g}	$J = \frac{1}{2}$	$a_1 0, +\frac{1}{2}\rangle + a_3 +1, -\frac{1}{2}\rangle$	$a_1' 0, +\frac{1}{2}\rangle + a_3' +1, -\frac{1}{2}\rangle$
6	Fe ³⁺ , Co ³⁺	<i>t_{2g}⁶</i>	⁵ D	⁵ T _{2g}	$J = 1$	$a_1 -1, +2\rangle + a_2 0, +1\rangle + a_3 +1, 0\rangle$	$b_1 +1, -1\rangle + b_2 0, 0\rangle + b_3 -1, +1\rangle$
	Co ^{III} , Rh ^{III} , Pt ^{IV}	<i>t_{2g}⁶</i>		¹ A _{1g}	$J = 0$	$ 0, 0\rangle$	$ 0, 0\rangle$
7	Co ²⁺	<i>t_{2g}⁷</i>	⁴ F	⁴ T _{1g}	$J = \frac{1}{2}$	$a_1 -1, +\frac{3}{2}\rangle + a_2 0, +\frac{1}{2}\rangle + a_3 +1, -\frac{1}{2}\rangle$	$a_1' -1, +\frac{3}{2}\rangle + a_2' 0, +\frac{1}{2}\rangle + a_3' +1, -\frac{1}{2}\rangle$
	Ni ^{III}	<i>t_{2g}⁷</i>		² E _g	$J = \frac{1}{2}$	${}^2B_{1g} 0, +\frac{1}{2}\rangle$	${}^2A_{1g} 0, +\frac{1}{2}\rangle$
8	Ni ²⁺ , Pd ²⁺	<i>t_{2g}⁸</i>	³ F	³ A _{2g}	$J = 1$	$ 0, +1\rangle$	$ 0, +1\rangle$
9	Cu ²⁺	<i>t_{2g}⁹</i>	² D	² E _g	$J = \frac{1}{2}$	${}^2B_{1g} 0, +\frac{1}{2}\rangle$	${}^2A_{1g} 0, +\frac{1}{2}\rangle$

3.1.3.2 Jahn-Teller distortions

If the cubic-field ground state of the B cation is an orbitally two-fold-degenerate E_g state, then the t_{2g} orbitals are either full or half-filled, so that $M_L = 0$, and there is no spin-orbit coupling ($V_{LS} = 0$). JAHN and TELLER [Ja6] have shown that, if there is no perturbation available to remove a ground-state orbital degeneracy, then there will be a spontaneous distortion to lower local symmetry below some transition temperature $\Theta_{\text{trans}} < T_{\text{melt}}$ where T_{melt} is the melting point. Since the energy gained by a local distortion is reduced by the work done against the elastic restoring forces of the crystal, transition temperatures Θ_{trans} are small for isolated ions. However, if all of the B cations are similar, then cooperative distortions are possible, and the net energy gained per ion is much greater because of the elastic-coupling energy V_λ of Eq. (2). Such a cooperative phenomenon is characterized by thermal hysteresis and a definite (usually first-order) transition temperature. Since they are due to electronic ordering, such transitions are martensitic.

VAN VLECK [Va15] pointed out that the normal vibrational modes that split an E_g electronic state are themselves twofold-degenerate with symmetry E_g . One mode gives the interstice a tetragonal distortion, the other an orthorhombic distortion. It follows that, from first-order theory, there is no static distortion of the interstice, only a dynamic coupling between the electronic charge density and the vibrational modes. Moreover, this dynamic coupling greatly enhances the two E_g vibrational modes and gives a dynamic splitting of the electronic E_g state. This mechanism has important consequences for the acoustic properties and, as discussed in 3.3, for the sign of the magnetic superexchange coupling.

Inclusion in the theory of higher-order coupling terms and anharmonic elastic terms shows that a static, tetragonal ($c/a > 1$) distortion of the interstice is stable below some Θ_{trans} [Ka10]. This sign for the static distortion was first established experimentally through the interpretation [Go15] and further study of cooperative tetragonal-to-cubic transitions in spinel systems. However, application to the perovskites requires a solution of the lowest-energy cooperative distortion via inclusion of the elastic-coupling energy V_λ . GOODENOUGH [Go6] proposed that individual tetragonal ($c/a > 1$) octahedra order their long axes alternately along [100] and [010] axes of the pseudocubic cell. KANAMORI [Ka10] generalized this solution to include an orthorhombic component to the local-octahedron distortions. This gives B-B separations within (001) planes having a long (l) and a short (s) B-X separation and along the [001] axis two intermediate (m) B-X separations where $s < m < (l + s)/2$. This prediction was later verified by HEPWORTH and JACK [He9] for $\square \text{MnF}_3$ and by OKAZAKI [Ok1] for KCuF_3 (see Fig. 10). Superposition of this distortion on an O-orthorhombic cell stabilizes the unique axis along the orthorhombic c -axis, and

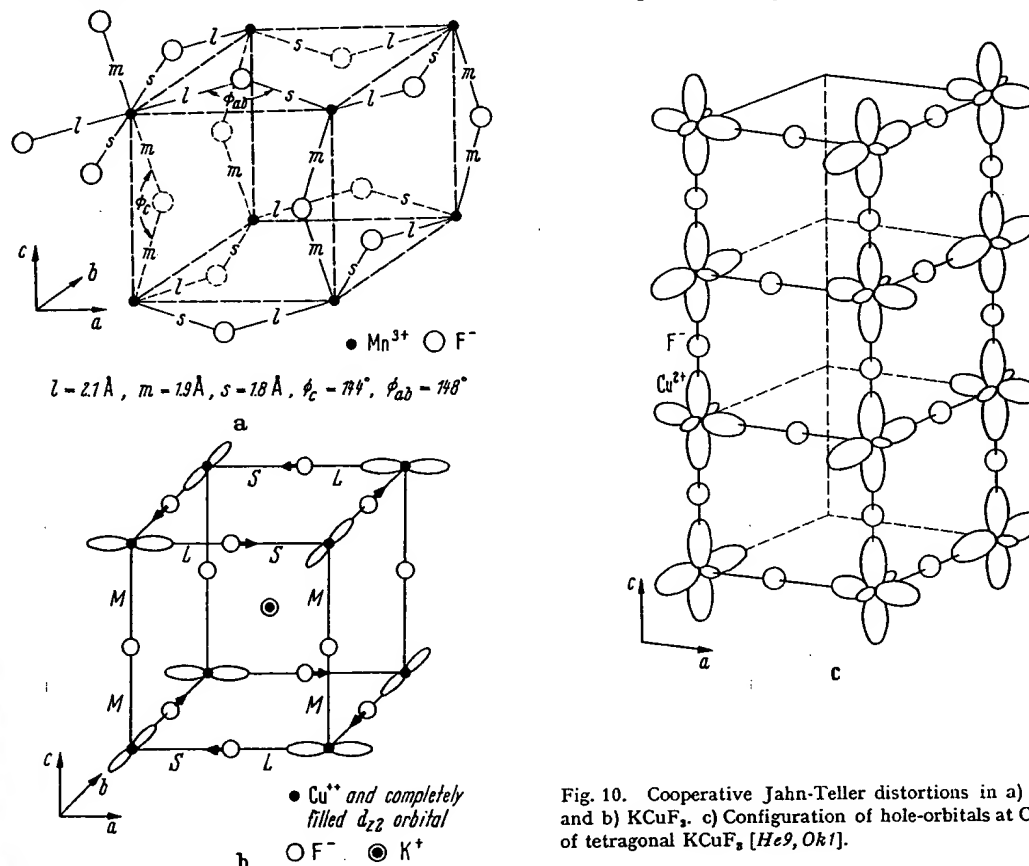


Fig. 10. Cooperative Jahn-Teller distortions in a) $\square \text{MnF}_3$ and b) KCuF_3 , c) Configuration of hole-orbitals at Cu^{2+} ions of tetragonal KCuF_3 [He9, Ok1].

the axial ratios of the O-orthorhombic cell are transformed from $a < c/\sqrt{2}$ to $c/\sqrt{2} < a$. To signal the fact that a Jahn-Teller distortion (with or without spin-orbit coupling) has been superposed on a distortion due to relative ionic sizes, the notation O'-orthorhombic is used in Tab. 2 wherever $c/\sqrt{2} < a$.

The important B cations that exhibit dynamic and static JAHN-TELLER stabilizations in the absence of spin-orbit coupling are: Cu^{2+} ${}^3E_g(t_{2g}^6 e_g^2)$, Cr^{2+} and Mn^{3+} ${}^5E_g(t_{2g}^3 e_g^2)$, Ni^{III} ${}^2E_g(t_{2g}^6 e_g^1)$, where Roman numerals are used for the valence state of a low-spin cation. Tab. 2 shows that O'-orthorhombic symmetry above a magnetic-ordering temperature is associated with these ions, provided the d electrons are localized, and only with these ions, with the exception of LaVO_3 and CeVO_3 , where sharply enhanced distortions appear abruptly below Θ_N [Ro3; Go10]. The cubic ${}^3T_{1g}$ state of V^{3+} is orbitally threefold-degenerate, so that it may induce small distortions above Θ_N , larger distortions below Θ_N (see discussion Go14). LaNiO_3 remains R3c because the e_g electrons are collective. In $\text{La}_2\text{Li}_{0.5}\text{Ni}_{0.5}\text{O}_4$ crystals, on the other hand, the ordered Ni^{III} ions have localized e_g electrons, and there is a tetragonal ($c/a > 1$) distortion. The sign of this distortion is manifest by the large c/a ratio. Strictly speaking, this is not a Jahn-Teller distortion, since the K_2NiF_4 structure is tetragonal, but ordering of the localized electron of unpaired spin in the tetragonal field distorts the Ni^{III} octahedra to tetragonal symmetry with axes parallel to the unique axis. Pure Jahn-Teller distortions can be distinguished from distortions associated with spin-orbit coupling because they are independent of magnetic order and generally occur at a Θ_{trans} above the magnetic-ordering temperature.

3.1.3.3 Spin-orbit coupling

B cations having cubic-field ground-state terms T_{2g} or T_{1g} are orbitally threefold-degenerate with $M_L = 0, \pm 1$, so that $V_{LS} \neq 0$. The combined perturbations $V_{LS} + V_{\text{ncub}}$ separate into secular equations for different M_J , as shown in Fig. 9. With a single outer electron, the ${}^2T_{2g}$ cubic-field term is split in two, the energies for different M_J shifting by

$$\begin{aligned} E_{3/2} &= \frac{1}{3}\delta - \frac{1}{2}\lambda \\ E_{1/2}^\pm &= -\frac{1}{3}\delta + \frac{1}{4}\lambda \pm \frac{1}{2}\{\delta^2 + \lambda\delta + (\frac{3}{2}\lambda)^2\}^{1/2} \end{aligned} \quad (8)$$

where $\lambda > 0$. In a cubic field

$$E_{3/2} = E_{1/2}^- = E_{1/2}^+ - \frac{3}{2}\lambda, \quad (9)$$

and spin-orbit coupling leaves an orbitally twofold-degenerate ground state. Therefore it is necessary to consider an additional Jahn-Teller stabilization via $V_{\text{ncub}} + V_1 + \mathcal{H}_Z$. GOODENOUGH [Go14] has shown that it is necessary to consider two temperature regions: $T > \Theta_N$ and $T < \Theta_N$, where Θ_N is the temperature below which the spins order collinearly. In the paramagnetic domain $T > \Theta_N$, the molecular fields vanish ($\langle S \rangle = 0$) and, from Eq. (7), $\mathcal{H}_Z = 0$. In this case, the ground-state energy varies as (δ^2/λ) . Since the work done against elastic restoring forces is $q_2\delta^2$, there is a spontaneous Jahn-Teller distortion, corresponding to $\delta > 0$, at a $\Theta_{\text{trans}} > \Theta_N$ only if the product λq_2 is relatively small. In the magnetically ordered state ($T < \Theta_N$), on the other hand, there is an internal molecular field H_{int} at each atom, which produces a Zeeman splitting of the orbitals of different spin. The magnitude of this splitting depends upon the spectroscopic splitting factor, which has the components

$$g_{\parallel} = 2 - 2g_1(\delta/\lambda) \text{ and } g_{\perp} = 2 + g_1(\delta/\lambda) \quad (10)$$

where $g_1 > 0$. Therefore the Zeeman splitting in the molecular fields is maximized by making $\delta < 0$ and having the spins parallel to the unique axis defined by δ . Further, this energy is linear in δ , so that a spontaneous distortion should occur at some $\Theta_{\text{trans}} < \Theta_N$. A similar argument holds for the orbitally twofold-degenerate $J = 1$ and $J = \frac{1}{2}$ states of octahedral-site Fe^{2+} ${}^5T_{2g}$ and Co^{2+} ${}^4T_{1g}$.

In summary, if multiplet splitting leaves a ground state with a twofold, accidental orbital degeneracy, then there is a spontaneous Jahn-Teller distortion at some Θ_{trans} that removes this degeneracy. If $\Theta_{\text{trans}} > \Theta_N$, then $\delta > 0$. However, this alternative requires special crystallographic conditions that do not appear to be met in perovskites. On the other hand, a $\Theta_{\text{trans}} \leq \Theta_N$ and $\delta < 0$ can be generally anticipated wherever the spins order collinearly and the d electrons are localized. Further, from Eqs. (3) and (6), it follows that T_{2g} states (one outer t_{2g} electron) have $\delta < 0$ if the site symmetry is tetragonal ($c/a > 1$), whereas T_{1g} states (two outer t_{2g} electrons) have $\delta < 0$ if it is tetragonal ($c/a < 1$). Alternatively, distortions of the site symmetry may be to trigonal symmetry. A $\delta < 0$ corresponds to $\alpha < 60^\circ$ for T_{2g} states, to $\alpha > 60^\circ$ for T_{1g} states. These relationships are also summarized in Tab. 1. Experimentally, Fe^{2+} ${}^5T_{2g}$ octahedra become trigonal ($\alpha < 60^\circ$) below Θ_N , as exhibited by KFeF_3 , whereas Co^{2+} ${}^4T_{1g}$ octahedra become tetragonal ($c/a < 1$) below Θ_N , as exhibited by KCoF_3 . Where $\Theta_{\text{trans}} = \Theta_N$, the magnetic-ordering temperature may be first-order. In addition, the spontaneous distortions introduce large magnetostriiction and magnetic anisotropy.

The cubic-field ground state of V^{3+} ${}^3T_{1g}$ is orbitally threefold-degenerate. As a result, any spontaneous distortion must correspond to $\delta < 0$, i.e., tetragonal ($c/a < 1$) or trigonal ($\alpha > 60^\circ$). However, as in the other cases, a $\Theta_{\text{trans}} \lesssim \Theta_N$ is to be expected in the perovskite structure. The V^{3+} ion generally occurs in an O-orthorhombic perovskite, and superposition of a tetragonal ($c/a < 1$) distortion with coincident unique axes again results in O'-orthorhombic symmetry. The perovskite LaVO_3 exhibits an abrupt contraction of the c -axis on cooling through Θ_N .

3.1.4 The influence of collective-electron ordering

3.1.4.1 Band theory

Conventional band theory rests on three principal assumptions: (1) A description of the outer electrons may be built up from solutions of a single electron moving in a periodic potential. (2) Multiplet structure on individual atoms may be disregarded. (3) Electron-phonon interactions may be treated as a small perturbation. For an infinite crystal, the unperturbed solution of running waves in a periodic potential gives the Bloch functions and energies

$$\psi_{\mathbf{k}\mathbf{m}} = \exp(i\mathbf{k} \cdot \mathbf{r}) u_{\mathbf{k}\mathbf{m}}(\mathbf{r}); E_{\mathbf{k}} = E_0 + \hbar^2 k^2 / 2m^* \quad (11)$$

where $\hbar \mathbf{k}$ is the momentum of an electron of effective mass m^* and $u_{\mathbf{k}}(\mathbf{r})$ is a periodic function. In the tight-binding approximation appropriate for narrow bands, the Bloch functions are

$$\psi_{\mathbf{k}}(\mathbf{r}) = 1/\sqrt{N} \sum_{\mathbf{R}_n} \exp(i\mathbf{k} \cdot \mathbf{R}_n) w(\mathbf{r} - \mathbf{R}_n)$$

where $w(\mathbf{r} - \mathbf{R}_n)$ is a localized wave function for the atom at \mathbf{R}_n defined by

$$w(\mathbf{r} - \mathbf{R}_n) = 1/\sqrt{N} \sum_{\mathbf{n}} \exp[i\mathbf{k} \cdot (\mathbf{r} - \mathbf{R}_n)] u_{\mathbf{k}}(\mathbf{r})$$

and $u_{\mathbf{k}}(\mathbf{r})$ is a localized crystalline orbital. At the Brillouin-zone boundaries defined by

$$2\mathbf{k} \cdot \mathbf{K} + |\mathbf{K}|^2 = 0, \quad (12)$$

where \mathbf{K} is a reciprocal lattice vector, there are energy discontinuities in energy-momentum space. In polar insulators, this introduces an energy gap E_g between occupied, primarily anionic states and empty, primarily cationic states. Cooperative displacements δ of the cationic sublattice relative to the anionic sublattice may increase this gap, thereby stabilizing the total energy of the occupied states by $\epsilon_2 \delta^2$. Since the resulting elastic-strain energy is $q_2 \delta^2$, there can be a spontaneous displacement only for the exceptional case $q_2 < \epsilon_2$ and a ground state corresponding to a small distortion parameter δ . In this case vibrational entropy may stabilize the higher symmetry at the higher temperatures. This differs from the usual criterion for spontaneous distortions, where a term linear in δ is identified. There appear to be two situations occurring in perovskites where the requirement $q_2 < \epsilon_2$ is met: (1) Where B-cations have empty d orbitals, there is a critical range of covalent-mixing parameters through which the site preference changes from octahedral to tetrahedral. In this range q_2 is very small for B-cation displacements within an octahedron that reduce the coordination number from six towards four. The origin of the small q_2 is a balance of the electrostatic energy lost and covalent-bond energy gained on going to smaller anion coordination. (2) The high polarizability of the outer core electrons of Pb^{2+} and Bi^{3+} ions makes q_2 relatively small, so that displacements that permit a relatively large ϵ_2 can occur spontaneously.

What distinguishes these spontaneous distortions from those due to an ordering of localized electrons is the displacement of the cations from the centers of symmetry of their interstices. (The Jahn-Teller distortions, with or without spin-orbit coupling, leave the cations in the centers of symmetry of their interstices.) Unlike the structures, such as corundum, where pairs of octahedra share a common face, these cationic displacements from the centers of symmetry of their interstices do not follow from point-charge electrostatic arguments. In polar insulators, these displacements lead to ferroelectricity or antiferroelectricity, and they often induce displacements of neighboring cations. Further, where the requirement $q_2 \approx \epsilon_2$ occurs just above Θ_{trans} , there must be a strong interaction of the bonding (mostly anionic) electrons with those vibrational modes that anticipate the cooperative ionic displacements below Θ_{trans} . These "soft" vibrational modes impart several anomalous physical properties, including a high electric susceptibility.

3.1.4.2 Distortions due to B-X bonding

Transition-metal cations having no outer d electrons have the following site preferences:

Sc^{3+}	<u>Ti^{4+}</u>	<u>V^{5+}</u>	Cr^{6+}	Mn^{7+}
Y^{3+}	<u>Zr^{4+}</u>	<u>Nb^{5+}</u>	<u>Mo^{6+}</u>	Tc^{7+}
	Hf^{4+}	<u>Ta^{5+}</u>	<u>W^{6+}</u>	<u>Re^{7+}</u>

where cations at the left of each row have definite octahedral-site (or larger anion coordination) preference and those to the right have definite tetrahedral-site preference. Those underlined by a solid line may be stabilized in the octahedral sites of a perovskite-type structure, but they tend to induce spontaneous ferroelectric or antiferroelectric distortions, the ions moving cooperatively out of the centers of symmetry of their interstices. The ions underlined by dashed lines only occur in ordered perovskites $\text{A}_2\text{BB}'\text{O}_6$ and $\text{A}_3\text{BB}'_2\text{O}_9$. In general, they are found in tetrahedral sites or in strongly distorted octahedral sites. However, in the ordered perovskites they are able to strongly polarize the anion near neighbors so as to stabilize the octahedral symmetry.

trar
site
nun
Y³⁺
stal
any
at t
the
non

neo
sym
this
cha
axis
orb
alor
pos

tha
bor
nur
stro
que
illu
pol
elec
cat
by
the
a fe
tur
the
dis
orl

OC

Fig
oct

OC

It is significant that spontaneous ferroelectric distortions are only induced by B cations if these are transition-metal cations having empty d orbitals. It is also significant that the change from octahedral-site to tetrahedral-site preference is associated with a relative stabilization of the d orbitals (larger atomic number in any long period) as well as with a decrease in ionic size. (The ionic radii decrease in the order Y^{3+} , Sc^{3+} , Hf^{4+} , Zr^{4+} , Ta^{5+} , Nb^{5+} , Ti^{4+} , W^{6+} , Mo^{6+} , Re^{7+} , V^{5+} , Tc^{7+} , Cr^{6+} , Mn^{7+}). The greater the relative stability of the d orbitals, the larger are the parameters λ_σ and λ_π of Eq. (4), and these are enhanced by any displacement that decreases a B-X separation. Such an enhancement stabilizes the occupied states at the expense of the d states, and a net stabilization can occur if the d states are empty. Also the smaller the cationic size, the smaller the elastic resistance to displacements within an octahedral interstice. (Phenomenological ionic models for the ferroelectric distortions have also been given [Me7, Ha33].)

There are three B-cation displacements relative to their octahedral interstices that would simultaneously stabilize the occupied anionic p_π orbitals relative to the unoccupied t_{2g} orbitals: (1) *Tetragonal symmetry*. Displacements along an [001] axis that create alternate long and short B-X distances along this axis would stabilize s , p_σ and the two p_π orbitals per anion on this axis and strongly polarize the charge density toward the short B-X separation. (2) *Orthorhombic symmetry*. Displacement along a [110] axis that created two shortest and two longest B-X distances would stabilize the s , p_σ and the two p_π orbitals per anion on two out of the three cartesian axes. (3) *Rhombohedral symmetry*. Displacement along a [111] axis would stabilize the s , p_σ and the two p_π orbitals per anion on all the anions. These three possibilities are illustrated in Fig. 11.

Such distortions also induce changes in the A-X separations, and the particular cooperative distortion that is stabilized depends upon the character of the A-X bonding. The covalency contribution to the A-X bond increases with formal A cationic charge; for a fixed charge it decreases with increasing atomic number of the A cation down any column of the periodic table. If A-X covalent bonding is relatively strong and the perovskite is distorted to O-orthorhombic symmetry, all ferroelectric distortions may be quenched because the p_π orbitals are stabilized by σ -bonding with the A cations. This appears to be illustrated by $CaTiO_3$, and almost so by $SrTiO_3$. On the other hand, if the A atom is stabilized by a polarization of its outer core electrons (Pb^{2+} and Bi^{3+} as discussed in 3.1.4.3), then a tetragonal, ferroelectric distortion is stabilized so as to allow a cooperative displacement of the A and B cations, the A cation moving along the [001] axis to stabilize two p_π orbitals per anion not on [001] axes. This is illustrated by the $PbTiO_3$ structure of Fig. 12. If the covalency contribution to the A-X bonding is relatively weak, then the B-X covalency contribution should dominate. For large A cations ($t > 0.9$), this would stabilize a ferroelectric, rhombohedral distortion at lowest temperatures, as illustrated by $BaTiO_3$. As the temperature increases, successive distorted structures ($R_F^B \rightarrow O_F^B \rightarrow T_F^B \rightarrow C$) introduce incremental additions to the entropy. However, a small A cation and weak A-X covalency contribution may lead to a ferroelectric distortion superposed on the O-orthorhombic structure to give the O_F^B -orthorhombic structure of $CdTiO_3$ or $NaTaO_3$ shown in Fig. 13. Even more complex distortions are found in $NaNbO_3$ [Vo6]. The room-tem-

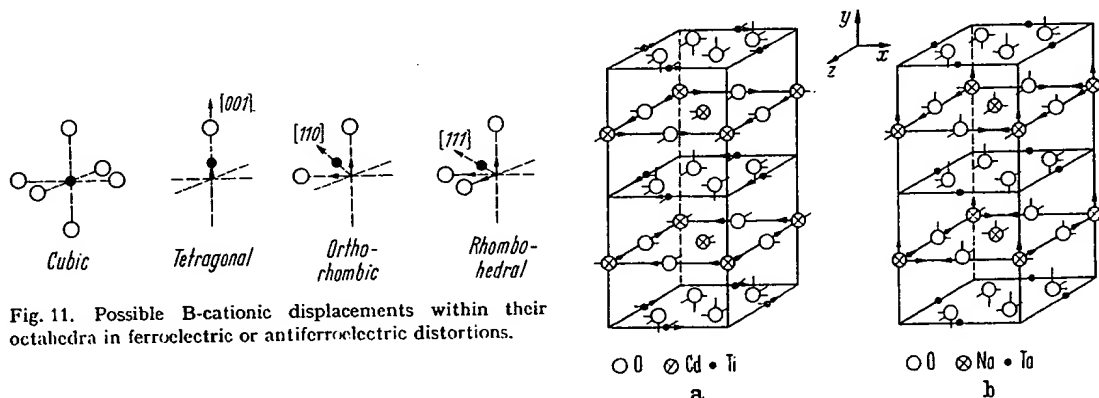


Fig. 11. Possible B-cationic displacements within their octahedra in ferroelectric or antiferroelectric distortions.

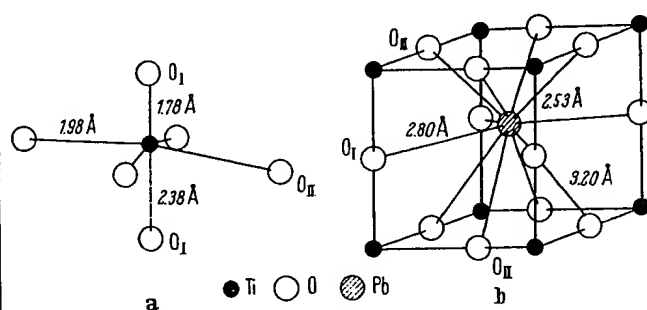


Fig. 12. Tetragonal $PbTiO_3$: a) environment of Ti and b) environment of Pb [Sh21].

perature form has parallel pairs of (001) NbO₂ planes coupled antiparallel to give an antiferroelectric phase, as shown in Fig. 14. The Na atoms are also displaced antiparallel to one another.

3.1.4.3 Distortions due to core polarization: Pb²⁺ and Bi³⁺

Lead and bismuth are heavy ions, and the 6s orbitals are sufficiently more stable than the 6p orbitals that Pb²⁺ and Bi³⁺ ions are commonly stable. However, the outer 6s² core electrons have a relatively large radial extension, making the ionic radius large, and this reduces the overlap of the 6p orbitals with the orbitals on near-neighbor anions. This reduction in overlap reduces the strength of the A-X bond. However, hybridization of 6s and 6p orbitals, which costs the energy separation of 6s and 6p orbitals, produces a polarization of the outer-core electrons, so that the effective ionic radius is much smaller on one side of the cation than on the other. This permits the formation of a much more stable bond on one side of the cation, and the energy gained in this bonding may be greater than the hybridization energy required to polarize the core. It is for this reason that Pb²⁺ and Bi³⁺ ions are stabilized in many crystals with an asymmetric anion coordination.

There are three possible displacements of the A cations that would stabilize the anion p_{π} orbitals (which σ -bond with the A cations): (1) *Tetragonal symmetry*. Displacement of the A cations along [001] axes to stabilize the two p_{π} orbitals per anion not on [001] axes, as found for PbTiO₃ (see Fig. 12). (2) *Orthorhombic symmetry*. Displacement of the A cations along [110] axes to stabilize strongly one p_{π} orbital per anion on [001] axes and less strongly one p_{π} orbital per anion not on [001] axes. The smallest induced distortion of the B-cation octahedra occurs for an antiferroelectric displacement of the type illustrated by PbZrO₃, Fig. 15. (3) *Rhombohedral symmetry*. Displacement of the A cations along [111] axes to stabilize strongly one p_{π} orbital per anion. To be cooperative, such a distortion must be ferroelectric, as in BiFeO₃, Fig. 16. Further, since the A cation is moved toward a B cation, there is an electrostatic repulsion between them that displaces the B cation from the center of symmetry of its interstice.

Given spontaneous distortions due to A-cation displacements, there remains the possibility that electron ordering among localized d electrons on B cations can superpose an additional distortion. Whether this is the origin of the triclinic symmetry reported for ferromagnetic BiMnO₃, where Mn³⁺ is a Jahn-Teller ion, is not known.

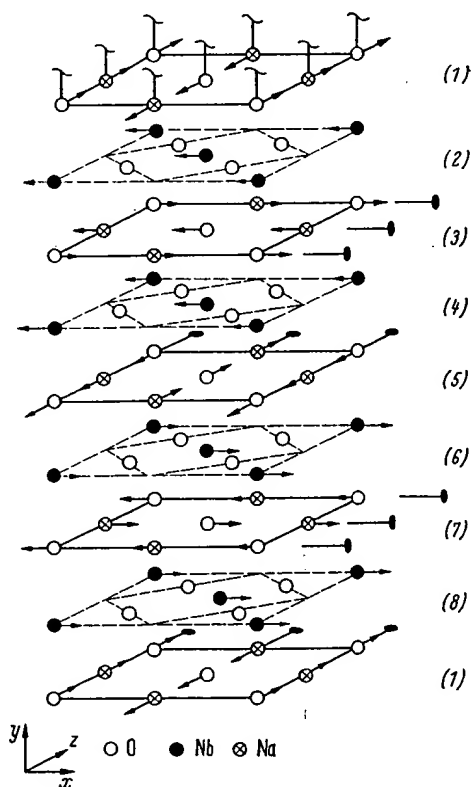


Fig. 14. Ionic displacements in orthorhombic NaNbO₃. The shifts of the anions in NbO₂ planes and the small x shifts of the Nb ions have been omitted for clarity [Vog].

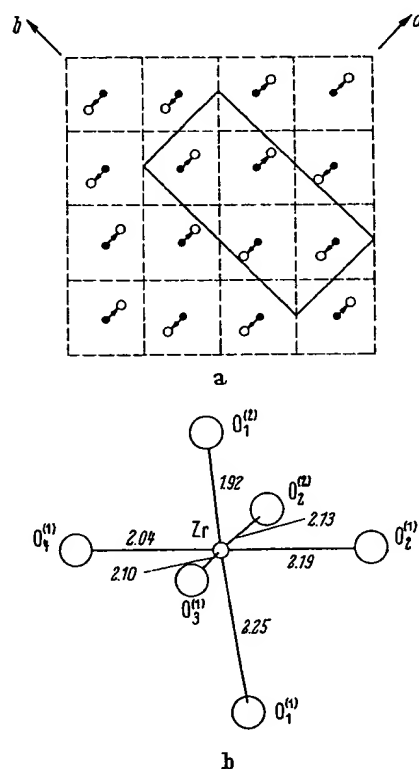


Fig. 15. a) Pb-ion shifts (≈ 0.26 Å) in a (001) plane of antiferroelectric PbZrO₃. b) Distorted Zr octahedra as a result of simultaneous anion displacements. Zr-O distances are given in Å [Sas, Jos].

3.1.4.4 Competitive phases

A few compounds have atomic radii compatible with the formation of a perovskite phase and yet are stabilized in other structures at ordinary temperature and pressure. Two important competitive structures of this type are represented by YAlO_3 and PbRuO_3 . Both of these compounds convert to the perovskite structure under hydrostatic pressure.

The hexagonal YAlO_3 structure of Fig. 17(a) consists of close-packed layers having the sequence $b-a-b'-a-b-c-b'-c-b$, where b is an A-cation layer, b' is a B-X layer with anions stacked beneath A cations (b stacking) and B cations in the trigonal bipyramids formed by face-shared tetrahedra in the hexagonal $a-b-a$ or $c-b-c$ anion-stacking sequence. The structure apparently forms because both the A cations and the B cations simultaneously approach the lower limit for cationic size: $r_B = 0.51 \text{ \AA}$, $r_A = 0.90 \text{ \AA}$. The small Al^{3+} ion is relatively stable in the five-fold coordination of the trigonal-bipyramid sites, and the small Y^{3+} ion is more stable in an eightfold (or $6 + 2$) coordination instead of a twelvefold (or $9 + 3$) coordination. These site preferences reflect an increased stabilization of the bonding, anionic orbitals as a result of closer cation-anion distances.

The antiferromagnetic, ferroelectric compound YMnO_3 has a similar structure, but with an a -axis $\sqrt{3}$ larger than that of YAlO_3 to give six molecules per unit cell. The Mn^{3+} ion can be stabilized in a trigonal-bipyramid site because it has four outer d electrons with configuration $e_g^2 e_g^2 a_1^0$, where the empty a_1 orbital is directed along the c -axis to bond covalently with the two collinear oxygen ions. The larger unit cell and the ferroelectricity are reflected in the complex magnetic order shown in Fig. 17(b). Below Θ_N , exchange striction favors antiferromagnetic Mn-O-O-Mn interactions. The ferroelectric transition that occurs above 600°C is apparently due to the relatively large size of the Mn^{3+} ion, which creates a large enough interstice for the Y^{3+} ion that it is stabilized by a displacement from the center of symmetry of its interstice so as to lower its near-neighbor anion coordination from eight toward seven.

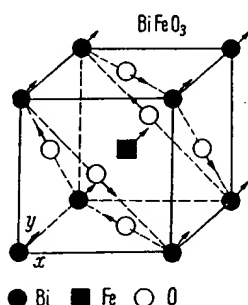


Fig. 16. Structure of BiFeO_3 showing displacements in perovskite subcell [M10].

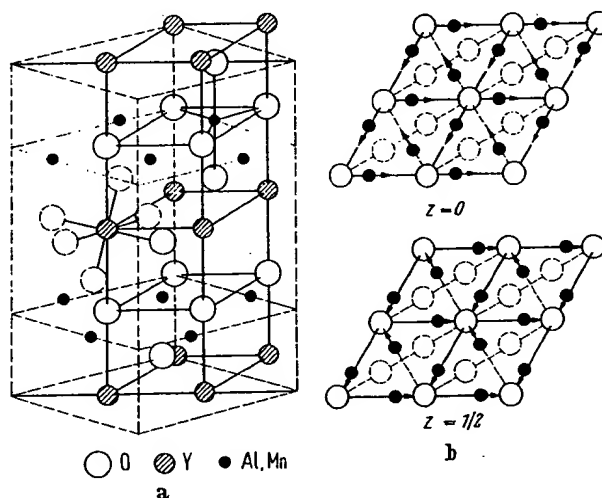


Fig. 17. a) Comparison of the unit cells of YAlO_3 (solid lines) and YMnO_3 (dashed lines). b) Magnetic structure of YMnO_3 [Be36, Be39].
 $a = 3.678 \text{ \AA}$, $c = 10.52 \text{ \AA}$ for YAlO_3 .

Cubic PbRuO_3 gives an x-ray pattern of the pyrochlore structure, corresponding to chemical formula $\text{A}_2\text{B}_2\text{O}_7$, and therefore may be written as $\text{Pb}_2\text{Ru}_2\text{O}_7\oplus$. This structure is competitive with the perovskite structure in several $\text{PbB}^{4+}\text{O}_3$ compounds. It has been shown [Lo4] that the anion vacancies \oplus are located at the centers of Pb^{2+} -ion tetrahedra sharing common corners and that the electrostatic repulsion between the Pb ions may be counteracted by a transfer of the two outer-core electrons per Pb ion to the \oplus sites, which act as traps for four electrons per vacancy. Thus the outer core electrons at the Pb^{2+} ions induce a completely new structure rather than a ferroelectric-type displacement of the A-cations within the perovskite structure. This new structure contains B cations in corner-shared octahedra, as in perovskite, but the B-X-B angle is reduced to about 135° . This structure is also stabilized in AgSbO_3 [Sc22] presumably because there is a small effective charge on the Ag^+ ions. The pyrochlore $\text{A}_2\text{B}_2\text{O}_7$ structure itself is competitive if attempts are made to force a low valence state on one of the cations.

3.1.5 Structures encountered with ordered B, B' cations

3.1.5.1 Same B atom

There are three ways of creating two different cations from the same atom:

(1) Two A cations of different valence can create two different valence states of the same B atom, and these may order at lower temperature as a result of different cationic charge. The ordering temperature may be quite low, since only electron transfers are required for cationic ordering. This is illustrated by (La_{0.5}Ca_{0.5})(Mn³⁺_{0.5}Mn⁴⁺_{0.5})O₃, which has the Mn³⁺, Mn⁴⁺ ordering in a rocksalt-type array. Because Mn³⁺(*t*_{2g}⁴*e*_g²) is a Jahn-Teller ion having localized outer *d* electrons, there is also a cooperative distortion to tetragonal (*c/a* > 1) symmetry of the Mn³⁺-occupied octahedra, and the ordering of these distortions gives a macroscopic distortion to tetragonal (*c/a* < 1) symmetry (see Fig. 26).

(2) Where the energy difference between the high-spin and low-spin states of the B cation are nearly equal, the populations of the two energy states approach each other at higher temperatures. In LaCoO₃, high-spin Co³⁺ and low-spin Co^{III} are separated by only $E_{3+} - E_{III} \approx 0.08$ eV, and the populations of the two spin states are nearly equal at 400 °K. This temperature is sufficiently low that ordering of the two different spin states occurs above this temperature, and the symmetry changes from R $\bar{3}c$ to R $\bar{3}$ [R $\bar{a}3$]. In this case, it is the difference in ionic size and covalent bonding, which results in a difference in the effective ionic charge—not the formal ionic charge—that is the driving force for the ionic ordering.

(3) Disproportionation of B^{m+} cations into B^{(m-1)+} and B^{(m+1)+} cations may create ions of different size and charge that become ordered. This is illustrated by □PdF₃, which has been shown by magnetic susceptibility measurements to be Pd²⁺Pd^{IV}F₆ [Ba19]. (The A cation is missing.) Such a disproportionation permits the formation of (PdF₆)²⁻ clusters in which the anionic orbitals are stabilized by strong covalent mixing with the σ -bonding 4*d* orbitals of *e*_g symmetry. This is accomplished by a shifting of the F⁻ ions toward the Pd⁴⁺ ions and away from the Pd²⁺ ions. Simultaneously, the anionic shift reduces covalent mixing in the occupied, antibonding 4*d* orbitals of *e*_g symmetry at the Pd²⁺ ions. These orbitals are therefore localized and further stabilized by intra-atomic exchange (Hund splitting), so that each Pd²⁺ ion carries an atomic moment of 2 μ_B . Were there no disproportionation, the single electron per low-spin Pd^{III} ion would occupy antibonding *e*_g orbitals that were more unstable than the occupied, localized *e*_g orbitals at the Pd²⁺ ions. However, the transformation 2 Pd^{III} → Pd²⁺ + Pd^{IV} costs ionization energy, and this is usually too large (as in LaNiO₃) for disproportionation to occur.

3.1.5.2 Different B atoms

There are many examples of ordered B, B' structures in compounds having different B atoms: A₂B²⁺B'³⁺F₆; A₂B²⁺B'³⁺B'⁵⁺O₆; A₂B²⁺B'³⁺B'⁶⁺O₆; A₂B²⁺B'³⁺B'⁷⁺O₆; A₂B²⁺B'³⁺B'⁴⁺O₆; A₂B²⁺B'³⁺B'⁵⁺O₆; and A₂B²⁺B'³⁺B'⁶⁺O₆. In the A₂BB'₂X₆ group, ordering is on alternate (111) planes of B cations, in the A₂B₂B'₂X₆ group the B' cations occupy every third B-cation (111) layer, Fig. 1(c). The probability for an ordered arrangement of the B, B' cations is determined by the differences between their ionic charges and their ionic radii [Fe22, Fe23, Ga1, Ga10]. To first approximation, the order-disorder transition temperature Θ_{ord} induced by the charge difference $\Delta q = (q' - q)$ at cations B' and B is $\Theta_{ord} \sim (\Delta q)^2$. Thus superstructure has been observed in all the known compounds having $(\Delta q)^2 = 36$ and 16, whereas those having $(\Delta q)^2 = 4$ are disordered unless there is a relatively large difference in ionic sizes. The minimum difference in ionic size that results in ordered A₂B²⁺B'³⁺B'⁵⁺O₆ compounds is $|r_B - r_{B'}|/r_B \approx 0.09$, and this has been achieved where B' = Nb or Ta, having empty *d* orbitals for the formation of stable (B'O₆)²⁻ clusters, while the B cation has no relatively stable, empty *d* orbitals.

Given the formation of (B'X₆) octahedra, a confusion arises as to where the structure corresponds to an ordered A₂BB'O₆ perovskite built up of corner-shared octahedra plus A cations and where it corresponds to the isostructural (NH₄)₃FeF₆ structure, which consists of discrete (B'X₆) octahedra separated by A and B cations. (The cubic K₂NaAlF₆ structure with space group T_h^h(Pa3) is similar to (NH₄)₃FeF₆, but has a lower symmetry because there are very small rotations of the (B'X₆) octahedra.) Some authors [Fe22] select as a criterion for the perovskite structure the cationic radius ratio $r_B/r_A < 0.8$ where $r_B > r_{B'}$. This decision is based on the observation that a plot of the cubic lattice parameter *a*₀ vs. B-cation radius *r*_B is a straight line for $r_B/r_A < 0.8$, but bends over for $r_B/r_A > 0.8$. However, this probably reflects the ratio at which electrostatic forces inhibit (or reverse) any A-cation displacements rather than the ratio at which discrete (B'X₆) octahedra are formed. For most physical properties this criterion is probably arbitrary.

Without electron-ordering distortions superposed on the size effects, ordered A₂BB'₂X₆ perovskites can be described by either the O-orthorhombic cell of Fig. 5 or by the rhombohedral R $\bar{3}$ (or R $\bar{3}m$) cell of Fig. 6. Where $\alpha = 60^\circ$, a tetramolecular cubic cell may be chosen provided the A cations are not displaced from their ideal positions. Like cubic (NH₄)₃FeF₆, the cubic cell has the space group O_h^h(Fm3m) with B cations in 4(b) ($\frac{1}{2}, \frac{1}{2}, \frac{1}{2}$); f.c., A cations in 8(c) ($\frac{1}{2}, \frac{1}{2}, \frac{1}{2}$); f.c., B' cations in 4(a) (0, 0, 0); f.c., and X-anions in 24(e) ($\pm(u, 0, 0; 0, u, 0; 0, 0, u)$); f.c. with $0.2 < u < 0.25$. However, even where $\alpha = 60^\circ$, motions of the A cations along the [111] axes may occur, thereby destroying the cubic symmetry.

If an electron-ordering transition superposes a distortion at every other octahedron of Fig. 5, either the B or the B' octahedra remaining cubic, cooperative elastic interactions between the distorted octahedra give a further reduction in symmetry. The resulting monoclinic cell [Fi9, B18], which is pseudotriclinic, is not to be confused with the pseudomonoclinic symmetry reported in early work for the O-orthorhombic structures. The origin of the superposed electron-ordering transition could be either a Jahn-Teller ordering of localized electrons or a ferroelectric-type displacement of the anions about a (B'X₆) octahedron.

Several Ca₂B³⁺Ta⁵⁺O₆ and Sr₂B³⁺Nb⁵⁺O₆ perovskites having B = rare-earth atom exhibit the monoclinic symmetry of a distorted O-orthorhombic cell [Fi8]. Since the 4f electrons at the rare-earth ions are localized, it is tempting to attribute this to a Jahn-Teller distortion with spin-orbit coupling. Although Fig. 9 shows that the octahedral site splitting of one-electron 4f orbitals gives orbitally threefold-degenerate levels having an accidental degeneracy that is not removed by spin-orbit coupling, nevertheless there are two reasons why this explanation cannot be correct: (1) There is no magnetic ordering of the 4f electrons at room temperature and (2) Sr₂GdNbO₆ shows the distortion even though Gd³⁺ has a half-filled 4f⁷ shell, which has no orbital degeneracy associated with the ground state. It is therefore concluded that the additional distortions are due to the potentially ferroelectric cations Nb⁵⁺ and Ta⁵⁺.

3.1.5.3 Complex alloys A₂BB'X₆, where B = M₁₃, B' = M₈

Several complex interstitial alloys have a formal structural relationship to the ordered perovskite A₂BB'X₆ as well as interesting magnetic properties. In this group, having space group Fm3m, the B position is occupied by a thirteen-atom cluster consisting of a metal atom at position 4(a) at the center of a cubo-octahedral, twelve-atom cluster of M atoms at positions 48(h); the B' position is occupied by a simple cube of eight M' atoms at 32(f). The three principal axes of each cluster are along the cubic axes of the perovskite cell, as shown schematically in Fig. 18, so that each X atom at positions 24(e) has eight near neighbors. The eight A atoms of the tetra-molecular cell are at the 8(c) positions. The 4(b) position at the center of the M₈ clusters is empty. Alloys with this structure include the ferromagnetic borides Al₂[(AlM₁₂)(M'₈)]B₆, where M = Fe, Co, Ni, as well as Cr₂₃C₆.

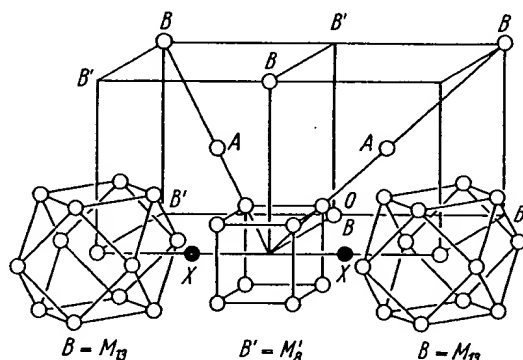


Fig. 18. One quadrant of the A₂BB'X₆ structure showing the atomic positions of the B = M₁₃ and B' = M₈ clusters [We19].

3.1.6 First-order magnetic transition in M^cXM₁₂^f perovskites

Many perovskites M^cXM₁₂^f exhibit first-order phase changes at magnetic-ordering transitions. Most of these are reported to be cubic-to-cubic transitions, but in ZnCMn₁₂ it is a tetragonal (ferrimagnetic)-to-cubic (ferromagnetic) transition. These crystallographic changes are induced by a complex interplay of collective electrons in overlapping bands. Because of the intimate connection with the magnetic properties and because of the necessarily speculative character of any model at this time, discussion of these compounds is deferred to 3.5.

3.1.7 Data: Crystallographic properties of ABX₃, A₂BB'X₆, A₃B₂BX₉ and A(B_xB'_yB''_z)X₃ compounds with perovskite or perovskite-related structure (Tab.2)

Tab. 2.

Within any section, the compounds are in general first ordered according to the atomic number of the B cation and then by the basicity of the A cation. For the ordered perovskites of Tab. 2b, c, d, the compounds are further ordered by the atomic number of the other B cation. The order of the sections is as follows:

Tab. 2a — ABX₃

A²⁺LiH₃
 A(H₂O) (Li_{1/3})₃; A = I⁻¹, Br⁻¹
 A²⁺B²⁺X₃; X = F⁻¹, Cl⁻¹, Br⁻¹
 A²⁺B³⁺O₃; B = V, Nb, Sb, Ta, I, Pa, U
 A²⁺B⁴⁺O₃; B = Ti, V, Cr, Mn, Fe, Co, Ni, Ge, Zr, Mo, Tc, Ru, Sn, Ce, Pr, Hf, Re, Ir, Pb, Th, U, Np, Pu
 A²⁺B⁴⁺X₃ or A²⁺B³⁺X₃; X = S or Se, B = Ti, Zr, Ta, In, Ga
 A²⁺B³⁺O₃; B = Al, Sc, Ti, V, Cr, Mn, Fe, Co, Ni, Ga, Y, Nb, Rh, In, Ho, Er, Tm, Yb, Lu

Tab. 2b — A₂BB'X₆

A₂BB³⁺X₆; X = F⁻¹, Cl⁻¹, B³⁺ = Al, Sc, Ti, V, Cr, Mn, Fe, Co, Ni, Cu, Ga, Ag, In, Ce, Pr, Au, Tl
 A²⁺A³⁺B³⁺B⁴⁺O₆; B⁴⁺ = Ti, Ir
 A₂BBⁿ⁺O₆; B⁴⁺ = Ti, Mn, Ge, Zr, Ru, Ir
 B⁵⁺ = V, Nb, Sb, Ta, Bi, Pa, Pu
 B⁶⁺ = Mo, Te, W, Re^{6+,5+}, Os^{6+,5+}, U^{6+,5+}, Np⁶⁺, Pu⁶⁺
 B⁷⁺ = Tc, Re, Os, I

Tab. 2c — A₃BB₂O₉

A₃BB₂⁵⁺O₉; B⁵⁺ = Nb, Ru, Sb, Ta
 La₃Co₂B⁵⁺O₉; B⁵⁺ = Nb, Sb
 A₃B₂B⁶⁺O₉; B⁶⁺ = Mo, W, Re, U

Tab. 2d — A²⁺(B_xB'_yB''_z)O₃

Abbreviations in Tab. 2:

Symmetry: C = cubic, H = hexagonal, M = monoclinic, O = orthorhombic ($a < c/\sqrt{2}$), O' = orthorhombic ($c/\sqrt{2} < a$), R = rhombohedral, T = tetragonal, Tr = triclinic.
Remarks: for abbreviations, see p. 131.

Tab. 2a. ABX₃ compounds

Compound	Sym	a Å	b Å	c Å	angle	Ref.	Remarks	Magnetic Data
A ²⁺ Li ⁺ H ₃ ⁻¹								
BaLiH ₃	C	4.023				Me25	P & S [Me26]; Neutron diffraction shows S.G. Pm3m [Ma11a]	
BaLiD ₃	C	4.02				Ma11a	Neutron diffraction shows S.G. Pm3m [Ma11a]	
SrLiH ₃	C	3.833				Me25	P & S [Me26]	
EuLiH ₃	C	3.796				Me24		
BaLiF ₃	C	3.996				Lu1	P & S [Ro20, Be22a, Bu3a]	
A(H ₂ O) (Li _{1/3}) ₃ ; A = I ⁻¹ , Br ⁻¹								
I(H ₂ O) (Li _{1/3}) ₃	C	4.296				We6		
Br(H ₂ O) (Li _{1/3}) ₃	C	3.99				Ke14		
A ²⁺ B ²⁺ X ₃ ; X = F ⁻¹ , Cl ⁻¹ , Br ⁻¹								
CsMgF ₃	H	6.04		14.45		Lo1b	Hex (6L), high pressure phase	
	H	6.16		22.13		Lo1b	Hex (9L), high pressure phase	
	T	9.39		8.72		Lu1	Prep. [Be22a, Bu3a]	
RbMgF ₃	M	8.19	8.19	8.19	$\beta = 98^\circ 30'$	Lu1	S.S. with Co, Hex (6L), $\Theta_0 = 15^\circ \text{K}$ (50% Co) [Sh1a]	
KMgF ₃	C	3.973				Re6	P & S [De22, Lu1, Be53], I.R. spectra [Pe5, Yo2] NMR, F ¹⁹ [Al1a], elastic properties [Re7a]	
NaMgF ₃	O	5.363		7.676		Ch5	P & S [Lu1, Be53, Ru8, Ba1], NMR, F ¹⁹ [Al1a]	
	T	3.942	5.503	3.933		Ch5	T = 760 °C, tetr. 760 < T < 900 °C	
	C	3.955				Ch5	T = 900 °C, cubic T ≥ 900 °C	
NH ₄ MgF ₃	C	4.06				Ch8a	Pseudocubic	
CsMgCl ₃	H	7.278		6.19		Yd1	Hex (2L)	
KMgCl ₃	O	6.954	6.971	9.922		Br28	Absorption spectra: Ni [Br28], ESR: Mn [Zd1]	
CsCaF ₃	C	4.523				Lu1		
RbCaF ₃	C	4.457				Lu1		
KCaF ₃	C	8.76				Br9		
CsCaCl ₃	C	5.396				Yd1	P & S [Lu1]	
CsTiCl ₃	H	7.297		6.048		Yd1	Hex (2L)	

in 3.3.4,
Tab.

Compound	Sym	a Å	b Å	c Å	angle	Ref.	Remarks	Magnetic Data
A ⁺ B ³⁺ X ₃ ; X = F ⁻ , Cl ⁻ , Br ⁻ (continued)								
CsVCl ₃	H	7.23		6.03		Se1b	Hex (2L), P & S [Yd1]	in 3.3.4, Tab.
RbVCl ₃	H	7.04		6.0		Gr8a	Hex (2L), optical and magnetic properties	
KVCl ₃	H	6.90		5.98		Se1b	Hex (2L), P & S [Yd1]	
RbCrF ₃	T	6.149		8.088		Vo1	P & S [Co27]	6
KCrF ₃	T	6.04		8.01		Co27		
	C	4.158				Co27	T = 500 °C, P & S [Ed2, Vo1, Kn3, Yo1, Pe2a]	
NaCrF ₃	M	8.544		7.968		Se1	Neutron diffraction	
(NH ₄)CrF ₃	T	5.695	5.885	7.639		Vo1	a and b axis said to double	
TiCrF ₃	T	6.232		7.954		Vo1		
CsCrCl ₃	T	6.194		8.064		Vo1		
RbCrCl ₃	H	7.249		6.228		Yd1	Hex (2L), P & S [Se2]	
	H	7.03		6.08		Se2	Hex (2L) pseudohexagonal	
CsMnF ₃	H	6.213		15.074		Za1	Hex (6L), $\Theta_N = 54^\circ\text{K}$, P & S [Si14, Be19], neutron diffraction [Pi1], optical properties [Si28, Si30], NMR [Mi4, Wei1], AFMR [Wi14], magnetic properties [Le3, Le4, Se1], S.S. with K and Na [Be19a]	6
							High pressure phase, P & S [Sy1]	
RbMnF ₃	C	4.328				Lo1b	P & S [Si14, Be19, Co25, Ho17], cubic to T = 20 °K	
	C	4.2396				Wa8	[Te4], dielectric properties [Ig1, Ch4a], compressibility [Si29], I.R. spectra [Ax2, Pe5], bibliography [Fr10a]	6
KMnF ₃	C	4.186				Be3	P & S [Be14, Si14, Cr4, Be2, Be4, Kn3, Ok2, Ok3, Ok4, Be53, Ok6, Ho17, Gu1a], S.S. with Co + Ni [Ha28], I.R. spectra [Ax2, Pe5, Yo2], bibliography [Fr10a]	
							T = 95 °K, $c/a > \sqrt{2}$, 184 > T > 84 °K [Be3, De3, Ok6]	
NaMnF ₃	O	5.885	5.885	8.376		Be3	T = 65 °K, $c/a < \sqrt{2}$, T < 84 °K [Be3, De3, Ok6]	6
	O	5.900	5.900	8.330		Be3	Prep. [Ho17, Be19b], a and b axis doubled [Si14], P & S [Ma9]	
	O	5.568	5.760	8.000		Si14	P & S [Cr4, Ho17, Co25], neutron diffraction [Pi1]	
(NH ₄)MnF ₃	C	4.238				Si14		6
TiMnF ₃	C	4.250				Ki9		
CsMnCl ₃	H	7.288		27.44		Ke7	Hex (9L), $\Theta_N = 69^\circ\text{K}$, AFMR [Ke1, Sh5]	
RbMnCl ₃	H	7.164		17.798		Ke7	Hex (6L), $\Theta_N = 86^\circ\text{K}$, AFMR & ESR [Ke1, Sh3, Sh5]	6
							Cubic T > 458 °C, AFMR & ESR [Ke1, Sh5]	
KMnCl ₃	T	10.024		9.972		Cr6		

Compound	Sym	a Å	b Å	c Å	angle	Ref.	Remarks	Magnetic Data
A+B ²⁺ X ₃ ; X = F ⁻¹ , Cl ⁻¹ , Br ⁻¹ (continued)								
CsFeF ₃	H	6.158		14.855		Ke19	Hex (6L), structure [Ba5], $\Theta_c = 60^\circ$ K [Po9a, Po9b]	in 3.3.4, Tab.
	C	4.283				Lo1b	High pressure phase	
RbFeF ₃	C	4.173				Wa12	P & S [Ke19], neutron diffraction [Wa14], cubic $T > 97^\circ$ K, tetra. $97 > T > 86^\circ$ K, orth. $86 > T > 45^\circ$ K, mon. $T < 45^\circ$ K [Te17]	
KFeF ₃	C	4.122				Ok6	P & S [Kn3, Ma29, Ok2, Ok3, Ok4], neutron diffrac- tion [Se1]	6
NaFeF ₃	R	4.108			$\alpha = 89^\circ 51'$	Ok6	$T = 78^\circ$ K, rhombohedral $T < 121^\circ$ K	6
NH ₄ FeF ₃	O	5.495	5.672	7.890		Tr2	P & S [Vo1, Ma9, Po9a]	6
TlFeF ₃	C	4.177				Po9a		6
CsFeCl ₃	C	4.188				Yo1	P & S [Po9a]	6
RbFeCl ₃	H	7.237		6.045		Yd1	Hex (2L), P & S [Se2a]	6
CsCoF ₃	H	7.060		6.020		Se2a	Hex (9L), magnetic properties [Ru6], P & S [Ba4]	
	H	6.194		22.61		Ba5	Hex (6L), high pressure phase	
	H	6.09		14.67		Lo1b	Hex (6L), high pressure phase	
RbCoF ₃	C	4.116				Ru6	P & S [Ru8, Cr4], S.S. with Mg [Sh1a]	6
KCoF ₃	C	4.069				Ok6	P & S [Kn3, Ma29, Ok2, Ok3, Ok4, Ru8, Cr4] I.R. spectra [Ax1, Ax2, Pe5, Yo2, Pe2a]	6
	C	4.057		4.049		Ok6	$T = 78^\circ$ K	
NaCoF ₃	T	5.420		7.792		Ru6	P & S [Ru8, Og2, Tu5, Ma10]	6
NH ₄ CoF ₃	O	4.127	5.603			Ru6	P & S [Cr4, Ru8]	6
TlCoF ₃	C	4.138				Ru6	P & S [Ru8]	6
CsCoCl ₃	H	7.202		6.032		Yd1	Hex (2L), complete structure and magnetic prop- erties [So1]	
RbCoCl ₃	H	6.996		5.996		En1	Hex (2L)	
CsNiF ₃	H	6.236		5.225		Ba2	Hex (2L)	
	H	6.15		22.32		Lo1b	Hex (9L), high pressure phase	
	H	6.05		14.54		Lo1b	Hex (6L) high pressure form: $\Theta_c = 111^\circ$ K	
RbNiF ₃	H	5.843		14.31		Ru5	Hex (6L), P & S [St14], $\Theta_c = 139^\circ$ K, magnetic properties [St19b, Mc1a, Sm32, Sm31, Sh1, Go3, Ku2, Go3a], S.S. with Co [Bo13, Su11, Pi16], optical properties [Sm32, Sm31, Sm22, Sh1, Ty1, Pi8, Pi14, Pi15, Za1a, Be19c, Pi16], Raman scattering [Ch14a], NMR [Sm32a]	
	C	4.074				Ka4	High pressure phase, P & S [Sy1]	6
KNiF ₃	C	4.015				Ok6	P & S [Ok3, Ok4, Kn3, Ma10, Ru5, Ok2], I.R. spec- tra [Pe5, Ba17a]	6
	C	4.002				Ok6	$T = 78^\circ$ K	

Compound	Sym	a Å	b Å	c Å	angle	Ref.	Remarks	Magnetic Data
A ⁺ B ²⁺ X ₃ ; X = F ⁻ , Cl ⁻ , Br ⁻ (continued)								
NaNiF ₃	O	5.360	5.524	7.688		Ru8	P & S [Og2, Ru5, Ok5]	in 3.3.4,
NH ₄ NiF ₃	C	8.145				Ru5	P & S [Ru8]	Tab.
TiNiF ₃	H	5.87		14.37		Ko4	Hex (6L)	6
	C	4.10				Ko4	High pressure phase, P & S [Sy1]	6
CsNiCl ₃	H	7.169		5.940		Yd1	Hex (2L), P & S [As4], structure determination [Ti4]	
(CH ₃) ₄ NNiCl ₃	H	9.019		6.109		Si44	Hex (2L)	
CsNiBr ₃	H	7.488		12.480		As4	Related to Hex (2L)	
CsCuF ₃	H	12.55		11.56		Ba2	Related to Hex (2L), optical properties [Sc10a]	
RbCuF ₃	T	6.001		7.894		Ru6	Optical properties [Sc10a]	6
KCuF ₃	T	5.855		7.846		Ru6	P & S [Ed2, Kn3, Ok1, Ok2, Ok6], neutron diffraction [Sc1], optical properties [Pe2a, Oe1, Sc10a]	6
	T	4.121		3.913		Ok6	T = 78 °K	
NaCuF ₃	M	11.01	11.37	7.521	β = 86° 54'	Ru6	P & S [Ru3]	6
NH ₄ CuF ₃	T	6.09		7.78		Cy4		
TiCuF ₃	T	6.083		7.866		Ru6	P & S [Ru3]	6
CsCuCl ₃	H	7.20		18.00		Yd1	Related to Hex (2L), P & S [Sc7, We9] magnetic properties Θ _p = -3.5 °K, μ _{eff} (300 °K) = 1.95 μ _B [Ri8c, Fi2]	6
	M	4.029	13.785	8.736	β = 97° 20'	Ki10	Not perovskite, magnetic properties Θ _N = 17.5 °K [Ma1, Sh5]	
KCuCl ₃	M	4.066		9.003	β = 97° 30'	Ki10	Not perovskite	
NH ₄ CuCl ₃	M	4.05	14.189	9.30	β = 96° 5'	Ki10	Not perovskite, magnetic properties [In3]	
KCuBr ₃	M		14.43					
CsZnF ₃	T	9.90		9.05		Lu1	Hex (6L), high pressure phase	
RbZnF ₃	H	6.09		14.67		Lo1b	P & S [Cy4, Lu1]	
	C	4.110				Ba1	Hex (6L) high temperature form	
KZnF ₃	H	5.896		14.44		Ba1	P & S [Lu1, Ma29], thermal conductivity [Su8], optical properties: Ni, Mn [Fe11, Fe15], I.R. spectra [Yo2, Pe2a]	
	C	4.055				Kn3	P & S [Lu1, Ru8, Ba1, Ma9, Ma10, Sc10]	
NaZnF ₃	O	5.404		7.743		Tu5		
NH ₄ ZnF ₃	C	4.115	5.569			Cy4	Hex (6L)	
AgZnF ₃	C	3.98				De22		
TlZnF ₃	H	5.934		14.52		Vo1		
CsGeCl ₃	R	5.444			α = 89° 38'	Ch15	Nuclear quadrupole resonance [Vo0]	
	C	5.475				Ch15	Cubic T > 155 °C, ferroelectric transition at 155 °C	

Compound	Sym	a Å	b Å	c Å	angle	Ref.	Remarks	Magnetic Data
A ⁺ B ³⁺ X ₃ ; X = F ⁻ , Cl ⁻ , Br ⁻ (continued)								
CsSrF ₃	C	5.589				Yd1	[Be22a, Bu3a] no cell dimensions	in 3.3.4, Tab.
CsSrCl ₃								
CsPdF ₃							Prep. + Prop. [Ba20, Fi3]	
CsCdF ₃	C	4.47				Kl1	P & S [Co27a]	
RbCdF ₃	C	4.395				Vo1	Mn emission [Kl1], P & S [Co27a]	
KCdF ₃	T	6.101		8.652		Ba5b	P & S [Ma29, Br9, Kl1, Co27a, Co26, Vo1], Mn emission [Kl1]	
(NH ₄)CdF ₃	T	4.368		4.447		Co27a		
TiCdF ₃	C	4.400				Co27a	T _{melt} = 765 °C	
CsCdCl ₃	C	5.20				Fe20	Slight distortion [Na15], P & S [Si3]	
	H	7.418		18.39		Si3	Hex (6L)	
CsCdBr ₃	C	10.70				Na15	P & S [Na19]	
CsSnCl ₃	C	5.58				Do5		
CsSnBr ₃	C	5.94				Do5		
CsEuF ₃	C	4.77				Bo31		
CsHgCl ₃	C	10.88				Na15	P & S [Na19, Na18]	
CsHgBr ₃	C	5.77				Na15	P & S [Na19]	
CsPbF ₃	C	4.81				Sc9		
CsPbCl ₃	T	5.590		5.630		Mo2	Phase transition at 40 °C [Sa2a]	
CsPbBr ₃	C	5.599				Mo2	Cubic T > 47 °C [Mo3]	
A ⁺ B ³⁺ O ₃		5.874						
AVO ₃	O	5.720	5.739	3.984		Fe7	Not perovskite, A = Na, K, Rb, Cs and Ag	6
RbNbO ₃						Wo15	Not perovskite	
KNbO ₃	T	4.00		4.07		Wo15	Structure [Ka19, Vo4, Vo5], crystal growth [Bu2, Sh25], optical properties [Ka8, Ch13]; S.S. with: BaTiO ₃ [Br2], NaNbO ₃ [Du3, Te8c], Li [Ni2a] T = 260 °C, Tetr. 435 > T > 225 °C, S.S. with KTaO ₃ (see KTaO ₃) T = 500 °C, cubic T > 435 °C	
	C	4.024				Wo15	T = -140 °C, neutron diffraction	
	R	4.016				Sh23		
	C	4.2			α = 89° 50'	Ad1	2Na + Nb ₂ O ₆	
NaNbO _{2.5}								

Compound	Sym	a Å	b Å	c Å	angle	Ref.	Remarks	Magnetic Data
A+B ³⁺ O ₃ (continued)								
NaNbO ₃	O	5.505	5.568	15.518		Vo6	Structure determined, P & S [Vo4, Vo5, We10, Ba18, Fe7, Wo15]; S.S. with: KNbO ₃ [Du3, Te8c], NaTaO ₃ [W4, Is7, Is14], SrNb ₂ O ₆ [Is16, Te7], CdTiO ₃ [Le2], AgNbO ₃ [Br24], Cd and Sr [Te8b]	in 3.3.4, Tab.
NaNbO ₃	O	5.51	5.57	7.77		Wo17	50 kV/cm applied to crystal; other phase transformations [Te6, So1b, Le5, Fr1, Sh20a, Cr6a, So1a, Is7a]; heat of transformations [Te8a]	
Na _{0.973} K _{0.027} NbO ₃	O	5.528	5.582	7.782		We10	Structure determined	
LiNbO ₃	H	5.1483		13.8631		Ab4	Not perovskite, see text	
AgNbO ₃	M	7.888	7.888	15.660	β = 90° 34'	Fr2	S.S. with KNbO ₃ [We5]	
AgSbO ₃	C	3.595				Fr2	T = 550 °C, cubic T > 550 °C	
AgSbO ₃	C	10.32				Sc22	Defect pyrochlore	
RbTaO ₃	T	3.92		4.51		Sm11	[Fe7] says not perovskite	
KTaO ₃	C	3.9885				Vo4	P & S [Vo5], crystal growth [Sh25, Wi4, We13], optical properties [Fr20, Fr2, Di7, Di8, Be27, Aπ1, Pe4, Jo15, Sh20, Ka7, Sc5, St20, La7a], Faraday rotation [Ba7], electrooptic properties [Fr20, Fa7, Fa8, Fr21, Fr22, Ge13, Zo3], S.S. with: KNbO ₃ [Fu3, Ha2, Ch13, Ge9, We12, We14, Di6, Hi2a, La7a], Ca [Se4]; Raman spectrum [Fl1a, Pe6, Fl1b]; ESR: Eu, Gd [Un1], Fe, Ni [Ha9a, We18b]; ultrasonic attenuation [Ba17b]; Nuclear spin resonance [Gr7a]	
NaTaO ₃	O	5.494	5.513	7.751		Ka22	Crystal structure, P & S [Vo4, Vo5], S.S. with: NaNbO ₃ [Is14, Is7]	
NaTaO ₃	C	3.929				Is5	630 °C, cubic T ≥ 630 °C, tetr. 630 > T > 550 °C	
LiTaO ₃	H	5.154		13.783		Ab2	Not perovskite, neutron diffraction [Ab3] (see text)	
CuTaO ₃	M	7.862	7.862	3.914	β = 90° 21'	Sh12	Actually Cu _{0.5} TaO ₃ , see "Bronze" section	
AgTaO ₃	C	3.949				Fr2	P & S [Br27]	
CsIO ₃	C	4.674				Fr2	485 °C; cubic T > 485 °C	
RbIO ₃	C	4.541				Bo30	P & S [Na15]	
KIO ₃	R	8.94	8.94	8.94	α = 89° 44'	Bo30	P & S [Na15]	
TiIO ₃	M	4.410			β = 89° 12'	Na16	Perovskite (?), P & S [Na15]	
NH ₄ IO ₃	R	4.510			α = 89° 25'	Sm3	P & S [Ri9]	
CsPaO ₃	C	9.18			α = 89° 20'	Sm3		
CsPaO ₃	C	4.368				Na15		
CsPaO ₃	C					Ke5		

Compound	Sym	a Å	b Å	c Å	angle	Ref.	Remarks	Magnetic Data
A ⁺ B ³⁺ O ₃ (continued)								
KPaO ₃	C	4.341				<i>Ke5</i>		
NaPaO ₃	O	5.82	5.97	8.36		<i>Ke5</i>	P & S [<i>Ru3a</i> , <i>Ip1</i>], Prop. [<i>Ke13</i>]	in 3.3.4, Tab.
RbUO ₃	C	4.323				<i>Ke12</i>	P & S [<i>Ru3a</i> , <i>Ch1b</i>], Prop. [<i>Ke13</i>]	6
KUO ₃	C	4.290				<i>Ke12</i>	P & S [<i>Ru3a</i>], Prop. [<i>Ke13</i>]	6
NaUO ₃	O	5.775	5.905	8.25		<i>Ke12</i>		6
A ³⁺ B ⁴⁺ O ₃								
BaTiO ₃	C	4.012				<i>Me1</i>	T = 200 °C, cubic 120 < T < 1372 °C [<i>Ed5</i>], cubic T > 133 °C [<i>We11a</i>], high temperature phase [<i>Me4</i> , <i>Me6</i> , <i>Me2</i> , <i>Ka23</i>]	
	T	3.994		4.034		<i>Me1</i>	T = 20 °C, tetragonal 5 < T < 120 °C; struc- ture determination: by x-rays [<i>Ev2</i> , <i>Ev3</i> , <i>Ev4</i> , <i>Ch2</i>], by neutrons [<i>Sh18</i> , <i>Fr4</i>], by electron mi- croscopy [<i>Pl2</i>]; P & S [<i>De1</i> , <i>Sa5</i>], further re- marks: *)	
	O	5.682	5.669	3.990		<i>Vo5</i>	T = -10 °C, orthorhombic -90 < T < 5 °C [<i>Ka24</i>]	
	R	3.998			α = 89° 52'	<i>Ka24</i>	T = -100 °C, rhombohedral T < -90 °C	
	H	5.735		14.05		<i>Bu4</i>	Hex (6L); structure determination [<i>Bu4</i> , <i>Ev1</i>]. Further remarks: **)	
SrTiO ₃	C	3.905				<i>Me4</i>	T = 293 °K; cubic T > 110 °K, thermal expan- sion α = 9.4 · 10 ⁻⁶ Å/deg, may be tetr. with c/a = 1.00008 [<i>Ly2</i>]	
	T	3.8972		3.8991		<i>Ly2</i>	T = 100 °K, Tetr. 65 < T < 110 °K, c/a = 1.00056, on single crystal [<i>Ly2</i>]. Further remarks: ***) See page 156	
	O					<i>Ly2</i>	a:b:c 0.9998:1:1.0002, orthorhombic 35 < T < 65 °K [<i>Ly2</i>]	
	R					<i>Ly2</i>	Possibly rhombohedral at 10°K	

*) Complete bibliography to 1961 [*Ha7*]; Raman scattering [*Di8*, *Du2*, *Pa6*, *Pt3*, *Ri3*, *Di8a*, *Ro19a*]; study of structural changes [*Ca4*, *Co15a*, *Co6*, *Me6*, *Se8*, *Ka24*, *We11a*]; pressure dependence of dielectric properties [*Go27*, *Ka1*, *Le9*, *Me23*, *Mo7*, *Mo8*, *Pa3*, *Pa4*, *Pa5*, *Pa6*, *Sa3*]; radiation damage [*Sc6*, *We3*]; refractive index [*Sh37*, *Ho3*, *Ho3a*]; thermal conductivity [*Di9*, *Ma23*, *Sw7*, *In2b*]; surface layers [*Or1*, *Le12*, *Ho10*, *Du1*, *Cr2*, *Ca1*, *Br3*]. Optical properties [*Mu1*, *Mu12*, *Mu13*, *Ve8*, *Ve6*, *Ha15*, *Jo1*, *Co30*, *Sh24*, *Re4*, *Pa7*, *Na8*, *Kh3*, *Ba9*, *We11a*]; ultrasonic propagation [*Gr10*]; ESR: Ti [*Da4*, *Ta4*, *Ta6*], Mn [*Ik1*, *Ik2*, *Ik3*, *Ve10*], Pt [*Si3*], Eu [*Ta7*, *Ta8*], Gd [*Bu7*, *Ta3*, *Ta5*, *Ta8*, *Ri5*]; dielectric properties [*De9*, *Hu11*, *Si17*, *Fr17*, *We11a*]. Transport properties [*Ue1*, *Ue2*, *Ta9*, *Se15*, *Ry1*, *Mu10*, *Ma32*, *Ma3*, *Ko9*, *Ka21*, *Ik5*, *Be28*, *An4*], electromicroscopic observation [*Mo12*]. Lattice vibration [*Ax1*, *Ha14*, *Ka3*, *Dr3*], shock-wave compression [*Do4*], elastic properties [*Ru5*], grain size influence on θ_0 [*Ri2*], relaxation time [*Wi5*, *Bo4*]. Properties with additives: Mg [*Is13*], Mn [*Bh1*, *As2*], Fe [*Sc25*], Co, Ni [*Ku1*, *Co23a*], Zn [*Si16*], Nb + Ta [*Gw1*, *Ku1*], Ln [*Co4*, *As2*, *Bo4*, *Jo11*], Sr [*He14*, *Al1*, *He6*], Bi [*Bo3*, *Jo11*], Sb [*He13*, *Jo11*], Pb [*Bo3*, *Jo11*], Halogens [*Jo10*], PbNb₂O₆ [*Sr1*], Ca, Zr, Si, Fe, Mg [*Br22a*]; defect study [*Co24*, *Mu9*, *No8*], neutron scattering [*Ya2a*].

**) P & S [*Wo16*, *Me4*, *Ma36*, *St19c*, *Ra5*, *Bl14a*, *Di4*]; effect of additives on occurrence [*Ra5*, *Ro20a*, *Di4*], hex. form due to oxygen vacancies or metal substitution for Ti [*Di4*], magnetic properties with Ti, Cr, V, Mn, Re, Fe, Co, Ru, Ir, Pt substitution [*Di4*].

Compound	Sym	a Å	b Å	c Å	angle	Ref.	Remarks	Magnetic Data
A ²⁺ B ⁴⁺ O ₃ (continued)								
CaTiO ₃	O	5.381	5.443	7.645		Pe3	P & S [Ba18, Ze1, Ze2, Le10, Na13, Na15, Me4, Ku3], optical properties [St21, Pe8, Mu13], de-tailed structure [Ka21a]	in 3.3.4, Tab.
CdTiO ₃	C O	5.348	5.417	7.615		Gr3a Ka22	Structure determined Pbn2 ₁ [Ka22], structure questioned [Ge3a], P & S [Me4], S.S. with NaNbO ₃ [Le2], electrical properties [Sh24a], perovskite-ilmenite transformation [Li0]	
PbTiO ₃	T	3.904		4.152		Sh21	Complete structure [Sh21], P & S [Me4, Sh19, Co13, Sh15, Sh24b], optical properties [Pe8, Fu5], piezoelectric properties [Ue3, Fe2, Fe1, Is14a], slow neutron scattering [So2], S.S. with (Ba, Sr, Ca, Pb) (Ti, Zr, Sn)O ₃ [Sh19, Ta14, Ha20, Ba12, No7, Ou1, Ou2, Th2, Ok7, Ta6, Kl7, Ou1a, Pe9, Is1, Uc2, St34, Fe1, Bu10, Fe3, Fe9, Fu5, He14, Iw3, St35, Di1a], radiation damage [Ha30], S.S. with PbGeO ₃ [Di5b]	
(CuA)TiO ₃	C C	3.960 ≈ 7.4				Sh21 De18	T = 535 °C, cubic T > 490 °C A = Ca (25%) a = 7.393 Å; Cd (25%) a = 7.399 Å; Sr (20%) a = 7.420 Å	
EuTiO ₃	C	7.810				Ho12	P & S [Br20, Mc1b], Prop. [Mc2, Mc3, Mc4, Si4]	6
La _{0.5} K _{0.5} TiO ₃	C	3.914				Ro20	Dielectric properties [Sm8, Ag1]	
La _{0.5} Na _{0.5} TiO ₃	C	3.86				Ag1	Dielectric properties [Sm8]	
Ce _{0.5} K _{0.5} TiO ₃	C	3.90				Ro20	S.S. with La	
Nd _{0.5} K _{0.5} TiO ₃	C	3.874				Ro20		
Y _{0.5} Na _{0.5} TiO ₃	C	5.326	5.443	7.614		Re2	Dielectric properties [Ag1, Bu3, Sm8, Sm26]	
Bi _{0.5} K _{0.5} TiO ₃	T	3.913		3.993		Io2	Dielectric properties [Ag1, Bu3, Sm8, Sm26]	
Bi _{0.5} Na _{0.5} TiO ₃	R	3.891			α = 89° 36'	Io2	S.S. with SrTiO ₃ [Ti1, Ve9, Wei6]	
La _{0.5} TiO ₃	C	3.887				Ke18		
SrVO _{3.5}	C	3.848				Ke18		
SrVO _{3.0}	C	3.838				Wo14	P & S [Re8]	6

*** Superconductivity [Am2, Ap2, Ea2, Fr10, Ko7, Sc19, Sc20, Sc21]; Raman scattering [Sc4, Sc3, Ri6, Os1, N41a, F11b]; Mössbauer: Co²⁺ [Bh3]. Optical properties [Ba6, Ba15, Ba16, Ca6, Co9, Du1, Ea1, Gr1, Ka9, Mu11, Mu12, Mu13, Si12, Va6, Zo2, Am3, Fa4a, Fe10a]; Hall mobility [Fr6, Fr9, Pa5, Tu1]; ESR: Co²⁺ [Ri7], Fe³⁺ [K12, Ba8, Ri7, Un2], Ni²⁺ [Ho1], Gd³⁺ [Ri7, Ri5, Sa2, Si11]; magnetoresistance [Fr7, Tu3, Ya3b]; piezoelectric properties [Tu2]; Shubnikov-deHaas effect [Fr8]; thermal conductivity (33 < T < 110 °K) [Su7]; diffusion and formation of oxygen defects [Pa3, Pa4, Wa9, Wa10]; radiation damage [Sc6, Ro4]; band structure [Ka6]; dielectric properties: doped with Fe and Cr [Ma3] with Nb [Ti2]; elastic constants from sound wave attenuation [Be6, Jo5a]; electromechanical behavior [Ru2]; pressure dependence of dielectric properties [He6a, Sa3]; photoconduction [Ya4, Ya5, Ya6a, Ya3b]; magnetic properties [Fr5]; vibrational modes [Ja8, Jo14]; thermal expansion [De19b], inelastic neutron scattering [Sh16a], electrooptic effect [So3].

Compound	Sym	a Å	b Å	c Å	angle	Ref.	Remarks	Magnetic Data
----------	-----	--------	--------	--------	-------	------	---------	------------------

Y₂B₆); magnetic properties [F75]; vibrational modes [Jad, Jo14]; thermal expansion [De190], inelastic neutron scattering [Sh16a], electrooptic effect [So3].

Compound	Sym	a Å	b Å	c Å	angle	Ref.	Remarks	Magnetic Data
A ²⁺ B ⁴⁺ O ₃ (continued)								
CaVO _{3.0}	C	3.767	5.352	7.547		Wo14	P & S [Ru7, De2, Re8, Re9]	in 3.3.4, Tab. 6
CaVO _{3.85}	O	5.326				Ro16		
BaCrO ₃	C	3.780		22.95		Wo14	Hex (9L), high pressure phase, semiconducting, ΔE = 0.09 eV	
	H	5.62				Ch1a	Hex (4L), high pressure phase, semiconducting, ΔE = 0.11 eV	
	H	5.659		9.359		Ch1a	Hex (6L), high pressure phase	
	H	5.627		13.690		Ch1a	Hex (12L), high pressure phase	
	H	5.662		27.752		Ch1a	Hex (14L), high pressure phase	6
	H	5.652		32.515		Ch1a	Hex (27L), high pressure phase	
	H	5.649		62.706		Ch1a		
	C	3.818				Ch1		
SrCrO ₃	O	5.287	5.316	7.486		Go17		
CaCrO ₃	C	4.00				Ro19	P & S [De21]	
PbCrO ₃	C	5.672		4.71		Ha7	Hex (2L), P & S [Ha16, Sy1]	6
BaMnO ₃	H	5.667		20.948		Sy1	Hex (9L), high pressure phase	
	H	5.669		9.375		Ha7	Hex (4L), high pressure phase, P & S [Ha16]	
	H	5.645		9.264		Sy1	Hex (4L), high temperature phase	
SrMnO ₃	H	5.449		9.085		Sy1	Hex (4L), S.S. with (Bi, Ba, La)MnO ₃ [Jo17]	
	H	5.431		13.396		Sy1	Hex (6L), high pressure phase	
CaMnO ₃	O	5.270	5.275	7.464		Ma6	96% Mn ⁴⁺ , P & S [Vo12, To13, Yui1, Yui8], S. S. with Bi [Bo6, Bo12, Sri9]	6
	O	5.302	5.304	7.488		Ma6		
Ca _{0.75} Sr _{0.25} MnO ₃	O	4.099			α = 88° 47'	Mo10	α = 0.36 P & S [De15, Er1, Mo11, Ma22, Va8]	
BaFeO _{3-x}	C	3.997				Mo10	α = 0.25; K _β X-ray spectra [Ko6a]	
	T	7.956		8.006		Mo10	α = 0.19	
	H	5.672		13.90		Mo10	Hex (6L); α = 0.08	
BaFeO _{2.5}	O	5.83	16.98	5.54		Gal8	Brownmillerite structure, see Fig. 21	6
	C	4.15				Mo11	T = 1000 °C, T = 20 °C (triclinic)	
SrFeO _{3.0}	C	3.850				Ma4	P & S [Wa17, Ya1, Ga17, Sh17], S.S. with La [Ga16, Wa17, Wa20], Bi [Ma8], Ti [Cl2, Br18]	
	C					Ma4		
SrFeO _{2.84}	T	3.851		3.867		Ma4	P & S [Ba23], S.S. with Al [Ba24, Ba25], Brownmillerite structure, see Fig. 21	
SrFeO _{2.80}	O	5.671	15.59	5.528		Ma4	P & S [Be39, Sm4], neutron diffraction [Ta10, Fr16, Co22], Mössbauer [Go4, Gr6, Ge7, Ge8, Wi15, Wi16, Ta10, Gr4]	
CaFeO _{2.80}	O	5.64	14.68	5.39		Be40	Prop. [Gr5, Po1, Wh4, Be40, Sm4]	6
CaFe _{0.5} Al _{0.5} O _{2.5}	O	5.58	14.50	5.34		Ha10	P & S [Mo15]	
PbFeO _{2.5}	T	7.79		15.85		Be26		6

Compound	Sym	a Å	b Å	c Å	angle	Ref.	Remarks	Magnetic Data
A ³⁺ B ⁴⁺ O ₃ (continued)								
BaCoO _{3.72}	H	5.59		4.83		Gu7	Hex (2L), P & S [Si47]	in 3.3.4, Tab.
SrCoO _{3-x}	C	7.725				Ya1	1.4% Co ⁴⁺ , S.S. with La [Wa17]	
BaNiO _{3.8}	H	5.58		4.832		La4	Hex (2L) [La3, Gu7]	
CaGeO ₃	C	3.723				Ri8a	High pressure phase; doubled cell [Si3a]	
CdGeO ₃	C	3.70				Ri8a	High pressure phase, pseudocubic	
BaZrO ₃	C	4.20				Ha20	P & S [Ho2, Me4, Be24]; S.S. with BaTiO ₃ [Ve7], PbTiO ₃ [Ha20]; optical properties [Pe7, Du5]	
	C	4.26				Fo4	T = 2000 °C	
SrZrO ₃	O	5.792	5.818	8.189		Pe3	P & S [Ho2, Me4, Sm3, Sc18a], D.T.A., T < 1000 °C [Ca5], optical properties [Pe7, Du5], S.S. with Hf [Be24a]	
	C	4.18				Fo4	T = 2000 °C, cubic T > 1300 °C	
CaZrO ₃	O	5.587	5.758	8.008		Ti3	P & S [Si15, Me4, Ru9, Ru14], S.S. with Cr [Ni2]	
	C	4.10				Fo4	T = 2000 °C, cubic T > 1600 °C	
PbZrO ₃	O	5.872	11.744	8.202		Sa8	P & S [Is1, Me4, Sa7], phase transitions [Go28, Go29, Go30, Sa8, Te5, Te8, Ue1, Sh15a, Te8d], radiation damage [Ha30], optical properties [Pe7], neutron diffraction [Jo5], dielectric properties [Kh4, Kh6, Kh8, Go29], piezo-electric effect [Ro1, Th2, Is14a], S.S. with Ca [Kh4, Si15], (BiNa) and (BiK) [Bu3], Pb(Ni _{1/3} Nb _{2/3})O ₃ [Bu10], BiFeO ₃ [Ge10], Hf [Go31]	
	C	4.149				Sa8	T = 230 °C, cubic T > 230 °C	
EuZrO ₃	C	4.099				Ho12	P & S [Mc4]	6
Bi _{0.5} K _{0.5} ZrO ₃							Prep. + Prop. [Sm33, Bu3]	
Bi _{0.5} Na _{0.5} ZrO ₃							Prep. + Prop. [Sm33, Bu3]	
BaMoO ₃	C	4.04				Sc17	P & S [Bo19, Sc16, Ro2a], S.S. with Sr [Br15]	6
SrMoO ₃	C	3.98				Sc17	P & S [Bo19, Sc16, Ro2a], S.S. with Ti [Ro2a, Br17], S.S. with Zr [Br17]	6
CaMoO ₃	O	5.45	5.58	7.77		Mc1	P & S [Sc16, Go17, Ro2a]	6
BaTcO ₃	H	5.758		14.046		Mu7	Hex (6L)	
	C	8.140				Ke9		
SrTcO ₃	C	3.95				Mu7	Slight distortion, P & S [Ke9]	
CaTcO ₃	O	3.87	3.96	3.76		Ke9		
PbTcO ₃	C	10.360				Mu7	Defect pyrochlore structure	
BaRuO ₃	H	5.75		21.60		Ra6	Hex (9L), structure determination [Do2], Prop. [Ca2], S.S. with Sr [Do3, Lo1], S.S. with Zr, Mn, Ir, Ni [Do3a]	
	H	5.73		9.50		Lo1	Hex (4L), high pressure phase	

Compound	Sym	a Å	b Å	c Å	angle	Ref.	Remarks	Magnetic
----------	-----	--------	--------	--------	-------	------	---------	----------

LT, HT (1000°C)	Lo1	9.50	5.73	H
Hex (4L), high pressure phase				

Compound	Sym	a Å	b Å	c Å	angle °	Ref.	Remarks	Magnetic Data
A ²⁺ B ⁴⁺ O ₃ (continued)								
BaRuO ₃	H	5.71		14.00		Lo1	Hex (6L), high pressure phase	in 3.3.4, Tab. 6
SrRuO ₃	O	5.53	5.57	7.85		Ra6	P & S [K _h 1], Prop. [Ca2, Lo3]	
CaRuO ₃	O	5.36	5.53	7.67		Ra6	Prop. [Ca2, Lo3]	6
SrRu _{0.8} Ir _{0.2} O ₃	O	5.55	5.58	7.84		Ra6		
PbRuO ₃	C	10.25				Lo4	P & S [Ra6], Defect pyrochlore structure	
	O	5.56	5.61	7.86		Lo1a	High pressure phase	
BaSnO ₃	C	4.117				Me4	P & S [Wa2, Co8, Sm3], S.S. with Sr [Sm3], (Ba, Sr, Pb)TiO ₃ [Na9, Du4, My2], optical properties [Du5, Ya3], Mössbauer in S.S. with Ti [Be7, Bo9, Kr6]; S.S. with Ti, tetragonal at 91% Ti [Do1]	
SrSnO ₃	C	8.070		7.885		Sm3	P & S [Ho2, Me4, Co8], optical properties [Du5]	
CaSnO ₃	O	5.519	5.668			Sm2	P & S [Ro12, Co8, Me4]; optical properties [Du5]; S.S. with BaTiO ₃ cubic at 13% CaSnO ₃ [Do1]	
CdSnO ₃	O	5.457	5.577	7.867		Sm2	P & S [Na13, Co8]	
PbSnO ₃	M	4.076	4.076	4.043		Su9	High pressure preparation	
	C	4.07			$\beta = 89^\circ 45'$	Su9	T = 125 °C, cubic T > 125 °C	
BaCeO ₃	C	4.397				Sm3	P & S [Ho2], optical properties [Du5], S.S. with Sr [Sm3], dielectric properties [Sm7a]	
SrCeO ₃	O	6.011	6.156	8.588		Sm3	P & S [Ho2], optical properties [Du5], dielectric properties [Sm7a]	
CaCeO ₃	C	7.70				Na14	Pseudocubic	
CdCeO ₃	C	7.65				Na14	Pseudocubic	
PbCeO ₃	C	7.62				Na14	Pseudocubic	
BaPrO ₃	C	8.708				Na15	P & S [Ho2]	
BaHfO ₃	C	4.172				Sh16	S.S. with CaZrO ₃ [Be24], P & S [Sc18a]	
SrHfO ₃	C	4.069				Ho2	P & S [Na15], S.S. with SrZrO ₃ [Be24a]	
CaHfO ₃	O	5.568	5.732	7.984		De7	Prep. [Ru14]	
CdHfO ₃	M	3.942	3.982	3.942	$\beta = 91^\circ 36'$	Av1		
PbHfO ₃	C	4.136		4.099		Sh16	Cubic T > 215 °C, S.S. with PbZrO ₃ [Go31]	
	C	4.134				Sh16	T = 250 °C, cubic T > 215 °C	
PbReO ₃	C	10.425				Lo4	Defect pyrochlore type	
BaIrO ₃	H	5.76		44.4		Do3	S.S. with Sr [Do3], distorted Hex. (9L); structure [Ro2b]	
SrIrO ₃	M	5.60	9.62	14.17	$\beta = 93^\circ 16'$	Lo1a	Prep. [Ro2a], distorted Hex (6L)	
	O	5.58	5.60	7.89		Lo1a	High pressure phase (Perovskite)	
PbIrO ₃	C	10.271				Lo4	P & S [Ra6], defect pyrochlore type	
CaIrO ₃	O	3.145	9.855	7.293		Ro2b	Not perovskite	
BaPbO ₃	C	4.265				Wa2	P & S [We7, Ni3], electrical properties [Ik4]	
SrPbO ₃	O	5.864	5.949	8.336		We7		

Compound	Sym	a Å	b Å	c Å	angle	Ref.	Remarks	Magnetic Data
A ³⁺ B ⁴⁺ O ₃ (continued)								
BaThO ₃	C	8.985				Sm30	P & S [Ho2, Na15, Me4, Be24]	in 3.3.4, Tab.
SrThO ₃	C	8.84				Na15	Pseudocubic, S.S. with Ba [Be24]	
CaThO ₃	C	8.74				Na15	Pseudocubic	
CdThO ₃	C	8.74				Na15	Pseudocubic	
PbThO ₃	C	8.960				Na15	Pseudocubic	
BaUO ₃	C	4.387				La5	P & S [Sc16, Ru4, Tr9], S.S. with BaTiO ₃ [Va9]	
BaNpO ₃	C	4.384				Ke4		
BaPuO ₃	C	4.357				Ke3	Pseudocubic	
SrPuO ₃	C	4.28				Ke3	Pseudocubic	
A ³⁺ B ⁴⁺ X ₃ or A ³⁺ B ³⁺ X ₃ ; X = S, Se								
BaTiS ₃	H	6.77		5.74		Cl1	Hex (2L), P & S [No9, As3b], orthorhombic and tetragonal modifications [Ha6]	
BaTiSe ₃	H	7.054		6.033		As3a	Hex (2L), P & S [No9]	
SrTiS ₃	H	6.730		5.829		Ha6	Hex (2L), P & S [No9], orthorhombic and tetragonal modifications [Ha6]	
PbTiS ₃	T	4.16		11.752		St27	"Layer structure" P & S [No9]	
BaZrS ₃	O	7.037	9.983	7.050		Cl3	Distorted perovskite, P & S [Ha6, No9, As3b]	
BaZrSe ₃	H	7.188		6.025		As3a	Hex (2L), P & S [No9]	
SrZrS ₃	O	13.49	9.79	14.23		Cl1	Distorted perovskite, P & S [No9]	
CaZrS ₃	O	13.07	9.58	14.05		Cl1	Distorted perovskite, P & S [No9]	
BaTaS ₃	H	6.847		5.742		As3b	Hex (2L) P & S [No9]	
BaTaSe ₃	H	7.134		5.987		As3a	Hex (2L) P & S [No9]	
ATaSe ₃	O	11.0	6.8	11.9		No9	A = Sr and Pb—not perovskite	
LnInS ₃	O	≈ 3.95	≈ 11.78	20.98		Ka13	Ln = La, Ce, Pr, Nd and Sm; T _{melt} ≈ 1100 °C	
LnGaSe ₃	H	≈ 10.3		≈ 6.2		Ka12a	Ln = La, Ce, Pr, Nd, Sm; T _{melt} = 1100 °C	
A ³⁺ B ³⁺ O ₃								
LaAlO ₃	R	5.357			α = 60° 6'	Ge5	P & S [Be34, Da1, Re5, De14], ESR: Gd, Cr [Kt3, St16a], Luminescence: Eu [Ya3, Bl13, Bl14], Pr [Ma30, De8], Cr [Bl15, Bo14]; twinning + detwinning [Fa9, Fa10]; nuclear quadrupole resonance [De17]; S.S. with BaTiO ₃ [Sm15, Is2b]; space group, R3c [Ra3, Ge4b], Review [Ge4b] T = 650 °C; cubic T > 522 °C [Wo15a, Ge4b, Ax3], inelastic neutron scattering [Ax3]	6
CeAlO ₃	C	3.818			α = 60° 15'	Ge5	P & S [Be34, Ro16, Sc13, Ke2]	
PrAlO ₃	R	5.327 5.307			α = 60° 22'	Kt1 Ge5	P & S [Be34, Ma27, Yu4, Zol, Re5, Li2, Ru10, Sc13]	

PrAlO ₃	R	5.307		$\alpha = 60^\circ 22'$	Ge5	P & S [Be34, Ma27, Yu4, Zo1, Re5, Li2, Ru10, Sc13]	6
--------------------	---	-------	--	-------------------------	-----	--	---

Compound	Sym	a Å	b Å	c Å	angle	Ref.	Remarks	Magnetic Data
A ³⁺ B ³⁺ O ₃ (continued)								
PrAlO ₃	T	3.74		3.76		Ma27	Discussion of disagreement between [Ge5] and [Ma27] given in [Ge4a] and [To12a]	in 3.3.4, Tab. 6
NdAlO ₃	R	5.286			$\alpha = 60^\circ 25'$	Ge5	P & S [Be34, Da2, Zo1, Ke2, Ge5, Re5, Li2, Ru10, Sc13, Da1]	6
SmAlO ₃	O	5.285 7.46	5.290 7.46	7.473 7.43		Ge5 Ma27	P & S [Be34, Ke2, Re5, Li2, Sc13, Zo1]	6
EuAlO ₃	O	5.316	5.292	7.458	$\alpha = 60^\circ 19'$	Ge2	Discussion of disagreement between [Ge5] and [Ma27] given in [Ge4a] and [To12a]	
GdAlO ₃	H	5.271		10.52		Ge5	T = 850 °C, rhombohedral T > 800 °C	6
	O	3.760 5.247	5.304	7.447		Be36 Ge5	P & S [Bo14, Re5, Li2] Prep. T < 900 °C, see Fig. 17a	
TbAlO ₃	H	3.73	5.308	10.51		Be36	P & S [Be34, Da1, Ga28, Sc13, Li2, Ma39]; optical properties [Bi13, Bl14, Bl16, Ga8, Oh1]; NMR, Al ³⁺ [Bo2a]	6
	O	5.229		7.415		Bi2	Prep. < 900 °C, see Fig. 17a	
DyAlO ₃	H	3.730	5.31	10.51		Be36	Neutron diffraction [Bi2], P & S [Ga28, Sc13], optical properties [Hu6, Hu6a]	6
	O	5.23		7.40		Gi3	Prop. < 900 °C, see Fig. 17a	
HoAlO ₃	H	3.700		10.50		Be36	P & S [Be34, Ga28, Da1, Da2, Sc13], neutron diffraction [Bi1, He12], optical properties [Hu5, Sc24, Fa5]	6
	O	5.18	5.33	7.36		Sc13	Prep. < 900 °C, see Fig. 17a	
ErAlO ₃	H	3.670		10.51		Be36	P & S [Ga28]	6
	O	5.16	5.32	7.33		Sc13	Prep. < 900 °C, see Fig. 17a	
TmAlO ₃	H	3.660		10.50		Be36	P & S [Ga28]	6
YbAlO ₃	O	5.15	5.33	7.29		Sc13	Prep. < 900 °C, see Fig. 17a	
LuAlO ₃	O	5.128	5.332	7.317		Sc13	P & S [Ga28]	
YAlO ₃	O	5.179	5.329	7.370		Ga28		
BiAlO ₃	H	3.68		10.52		Ge6	No perovskite [Ga28, Sc13]	
PuAlO ₃	T	7.61		7.94		Be36	P & S [Mi8, Be34], ESR: Fe ³⁺ and Gd ³⁺ [Wh3]; decomposition of YAG [Ma26]	
AmAlO ₃	R	3.78			$\alpha = 90^\circ 24'$	Na15	Prep. < 900 °C, see Fig. 17a	
LaScO ₃	R	3.75			$\alpha = 90^\circ 28'$	Ru13	Not able to be reproduced [Bu3]	
CeScO ₃	O	5.678	5.787	8.098		Ke8		
PrScO ₃	O					Ge2	P & S [Sc13, Ke2]	
NdScO ₃	O	5.615	5.776	8.027		Ke2	No dimensions	
SmScO ₃	O	5.574	5.771	7.998		Ge2	P & S [Sc13]	
	O	5.53	5.76	7.95		Sc13	P & S [Sc13, Ke2]	

Goodenough/Longo

Compound	Sym	a Å	b Å	c Å	angle	Ref.	Remarks	Magnetic Data
A ³⁺ B ³⁺ O ₃ (continued)								
EuScO ₃	O	5.51	5.76	7.94	$\alpha = \gamma = 90^\circ 41'$ $\beta = 91^\circ 52'$	Sc13	P & S [Sc13], Prop. [Bo36]	in 3.3.4, Tab.
GdScO ₃	O	5.487	5.756	7.925		Ge2		
DyScO ₃	O	5.43	5.71	7.89		Sc13		
HoScO ₃	O	5.42	5.71	7.87		Sc13		
YScO ₃	O	5.431	5.712	7.894		Ge2		
BiScO ₃	Tr	4.042	4.127	4.042		To11b		
LaTiO _{3-x}	C	3.934				We16		
La _{0.87} TiO ₃	C	3.887				Ke18		
CeTiO ₃	T	5.513		7.760		We16		
PrTiO ₃	T	5.508		7.742		We16		
NdTiO ₃	O	5.482	5.521	7.728		We16	P & S [Be33, Ho12, Si4]	6
SmTiO ₃	O	5.398	5.568	7.651		We16	P & S [Be33, Ho12, Si4]	6
GdTlO ₃	O	5.353	5.655	7.616		We16	P & S [Be33, Si4, Mc1c]	6
EuTiO ₃	C	7.810				Ho12	P & S [Bo36, Ho12, Si4, Mc1c]	6
TbTiO ₃	O	5.388	5.648	7.676		Mc1c	P & S [Br20, Mc1b], Prop. [Mc3, Mc4, Si4], neutron diffraction [Mc2]	6
DyTiO ₃	O	5.361	5.659	7.647		Mc1c		
HoTiO ₃	O	5.339	5.665	7.626		Mc1c		
ErTiO ₃	O	5.318	5.657	7.613		Mc1c		
TmTiO ₃	O	5.306	5.647	7.607		Mc1c		
YbTiO ₃	O	5.293	5.633	7.598		Mc1c		
LuTiO ₃	O	5.274	5.633	7.580		Mc1c		
YTiO ₃	O	5.340	5.665	7.624		Mc1c		
LaVO ₃	O'	5.540	5.540	7.83		Wo14	P & S [Si5, Be33, Ke16, Re8, Wo4, Ke18, Ke15, Yal, Ro3], S.S. with: SrVO _{3.8} [Ke18, Wo14], S.S. with CaVO _{2.8} [Wo14]	6
CeVO ₃	O'	5.486	5.486	7.74		Wo14	P & S [Be33, Re8, Wo4]	6
PrVO ₃	O'	5.487	5.562	7.751		Wo14	P & S [Be33, Re8, Wo4, Vi2, Ge2]	6
NdVO ₃	O	5.451	5.579	7.734		Wo14	P & S [Be33, Re8, Wo4, Vi2, Ge2]	6
SmVO ₃	O	5.393	5.588	7.672		Wo14	P & S [Be33, Re8, Wo4]	6
GdVO ₃	O	5.343	5.614	7.637		Wo14	P & S [Be33, Bo36, Re8, Ge2]	6
DyVO ₃	O	5.302	5.602	7.601		Wo14	P & S [Re8]	6
ErVO ₃	O	5.262	5.604	7.578		Wo14	P & S [Re8]	6
YVO ₃	O	5.284	5.605	7.587		Wo14	P & S [Re8]	6
PuVO ₃	O	5.45	5.58	7.76		Ru13	P & S [Ro3, Re8]	6
AmVO ₃	O	5.48	5.61	7.78		Ke8		6

Compound	Sym	a Å	b Å	c Å	angle	Ref.	Remarks	Magnetic Data
A ³⁺ B ³⁺ O ₃ (continued)								
LaCrO ₃	O	5.479	5.515	7.753		Qu1	Semiconducting 0.6 eV [Ru11], neutron diffraction [Ko1], optical properties [Ru11], dielectric properties [Ra8], P & S [Ge2, Ru11, Wo4, Ke2, Na14], S.S. with Ni, Mn [Be33, Be21]; T _{melt} = 2500 °C [Fo2], EPR [We4] T = 280 °C, rhombohedral 280 < T < 1030 °C T = 1230 °C	in 3.3.4, Tab. 6
La _{0.9} Bi _{0.1} CrO ₃ La _{0.9} Si _{0.1} CrO _{3-x}	R	5.47			α = 60° 32'	Ru11		6
	C	3.92	5.50	7.75		Ru11		6
	O	5.47				Iw1		6
	C	7.754				Ya1		6
CeCrO ₃	O	5.475	5.475	7.740		Qu1	P & S [Ru10, Be33, Wo4, Ke2] P & S [Ge2, Ru10, Be33, Wo4], T _{melt} = 2420 °C [Fo2], dielectric properties [Ra8]	6
PrCrO ₃	O	5.448	5.479	7.718		Qu1	P & S [Ru10, Ge2, Be33, Wo4, Ke2], T _{melt} = 2405 °C [Fo2]	6
NdCrO ₃	O	5.425	5.478	7.694		Qu1	P & S [Ru10, Ge2, Be33, Wo4, Ke2], T _{melt} = 2385 °C [Fo2]	6
SmCrO ₃	O	5.367	5.508	7.643		Qu1	P & S [Ru10]	6
EuCrO ₃	O	5.340	5.515	7.622		Qu1	P & S [Ru10, Ge2, Be33], T _{melt} = 2370 °C [Fo2]	6
GdCrO ₃	O	5.312	5.525	7.606		Qu1	Neutron diffraction [Be42, Ma24], specific heat [De1a]	6
TbCrO ₃	O	5.291	5.518	7.576		Qu1	Neutron diffraction [Be38], T _{melt} = 2345 °C [Fo2]; dielectric hysteresis disappears at ≈ 540 °C indicating no center of symmetry [Ra8]	6
DyCrO ₃	O	5.265	5.520	7.552		Qu1	Neutron diffraction [Be32, Be47, Be50], dielectric properties [Co6], T _{melt} = 2330 °C [Fo2], dielectric hysteresis disappears at ≈ 460 °C indicating no center of symmetry [Ra8], S.S. with HoMnO ₃ [4p1b]	6
HoCrO ₃	O	5.243	5.519	7.538		Qu1	Dielectric properties [Co6], T _{melt} = 2325 °C [Fo2]	6
ErCrO ₃	O	5.223	5.516	7.519		Qu1	T _{melt} = 2320 °C [Fo2], dielectric hysteresis disappears at ≈ 520 °C indicating no center of symmetry [Ra8]	6
TmCrO ₃	O	5.209	5.508	7.500		Qu1	Dielectric hysteresis disappears at ≈ 480 °C indicating no center of symmetry [Ra8]	6
YbCrO ₃	O	5.195	5.510	7.490		Qu1	P & S [Ge6, Ge2, Lo5, Ka18, Pa14, Yu5], dielectric properties [Ra8], T _{melt} = 2340 °C [Fo2] High pressure preparation	6
LuCrO ₃	O	5.176	5.497	7.475		Qu1		6
YCrO ₃	O	5.241	5.521	7.532		Qu1		6
InCrO ₃	O	5.170	5.355	7.543		Sh9		6

Compound	Sym	a Å	b Å	c Å	angle	Ref.	Remarks	Magnetic Data
A ³⁺ B ³⁺ O ₃ (continued)								
TlCrO ₃	O	5.302	5.405	7.647	$\alpha = \gamma = 90^\circ 35'$ $\beta = 89^\circ 10'$	Sh9	High pressure preparation	in 3.3.4, Tab.
BiCrO ₃	Tr	3.90	3.87	3.90		Su10	High pressure preparation; S.S. with BiMnO ₃ [To11a]	
PuCrO ₃	O	5.46	5.51	7.76	$\alpha = 90^\circ 36'$	Ru13	P & S [Na14], neutron diffraction [Ko1, Wo12], S.S. with Ba, Sr, Ca [Wo12, Ja4, Ja5, Jo8, Jo12, Ha22, Jo7, Jo9, Ya1, Ro11], S.S. with Cr, Fe, Co, Ni [Be33, Be21, Gi4, Jo7, Jo8, Jo9, Wo2, Wo6, Fu2, Bl7], S.S. with (Ba, Sr, Ca, Pb)TiO ₃ [Ha31, Ha32, To3, To6, To12], S.S. with GdCoO ₃ [De23], 24% Mn ⁴⁺	6
LaMnO ₃	O'	5.533	5.722	7.694		Wo2		
CeMnO ₃	R	3.892				Ve12	P & S [Be33, Vi1], complete structure [Qu2]	
PrMnO ₃	O'	5.537	5.557	7.818		Ve12	P & S [Be33, Vi1, Sz1], complete structure [Qu2]	
NdMnO ₃	O'	5.445	5.787	7.575		Ve12	P & S [Be33]	
SmMnO ₃	O'	5.380	5.854	7.557		Ve12	P & S [Sz1]	
EuMnO ₃	O'	5.359	5.843	7.482		Ve12	P & S [Be33, Sz1], S.S. with LaCoO ₃ [De23]	
GdMnO ₃	O'	5.338	5.842	7.453		Ve12	Complete structure determination [Qu2]	
TbMnO ₃	O'	5.313	5.853	7.432		Ve12	P & S [Sz1]	
DyMnO ₃	O'	5.297	5.831	7.403		Ve12	Preparation temperature 1600 °C, see Fig. 17a	
HoMnO ₃	H	5.275	5.828	7.375	Sz1	Magnetic properties [Ve12, Be32], dielectric properties [Be35, Co7], P & S [Sz1], see Fig. 17a	6	
	H	6.177		11.43	Ya2	High pressure phase, P & S [Wa5, Vi1, Sz1]	6	
	O'	6.136		11.42		Wa4	Magnetic properties [Ve12, Be32], dielectric properties [Be35, Co7], see Fig. 17a	6
ErMnO ₃	H	5.26	5.84	7.35		Ya2	High pressure phase	6
	O'	6.115		11.41		Wa4	Magnetic properties [Ve12, Be32], dielectric properties [Be35, Co7], see Fig. 17a	6
TmMnO ₃	H	5.24	5.82	7.335		Ya2	High pressure phase	6
	O'	6.062		11.40		Wa4	Magnetic properties [Ve12, Be32, Ro8, Bo11], dielectric properties [Be35, Ro8, Bo11, Co7, Is11], P & S [Sz1], see Fig. 17a	6
YbMnO ₃	H	5.23	5.81	7.32		Ya2	High pressure phase	6
	O'	6.062		11.40		Wa4	Magnetic properties [Ve12, Be32], dielectric properties [Be35, Co7], see Fig. 17a	6
LuMnO ₃	H	5.22	5.80	7.30		Ya2	High pressure phase	6
	O'	6.042		11.37		Wa4	Magnetic properties [Ve12, Be32], dielectric properties [Be35, Co7], see Fig. 17a	6
YMnO ₃	H	5.205	5.79	7.31		Ya2	High pressure phase	6
	O'	6.125		11.41			Dielectric or magnetic properties [Ta13, Ro8, Be35, Co5, Co7, Co3, Bo11, Is11, Pe17, Pe16, Be32, Be39, Be43, Be44, Be49, Ko3, Ki8], see Fig. 17a	6

Berichtigungen zu Band III/4a

- S. 177, letzte Zeile: statt $\text{Ba}_2\text{TdPaO}_6$ lies $\text{Ba}_2\text{TbPaO}_6$
S. 219, Zeile 16 von unten: statt $\text{KMg}_{1-x}\text{Ni}_x\text{Fe}_3$ lies $\text{KMg}_{1-x}\text{Ni}_x\text{F}_3$
S. 252, Zeile 26 von oben (Überschrift): statt $\text{Sr}_3\text{Fe}_3\text{UO}_9$ lies $\text{Sr}_3\text{Fe}_2\text{UO}_9$

Errata in Vol. III/4a

- p. 177, bottom line: instead of $\text{Ba}_2\text{TdPaO}_6$ read $\text{Ba}_2\text{TbPaO}_6$
p. 219, line 16 from the bottom: instead of $\text{KMg}_{1-x}\text{Ni}_x\text{Fe}_3$ read $\text{KMg}_{1-x}\text{Ni}_x\text{F}_3$
p. 252, line 26 from above (headline): instead of $\text{Sr}_3\text{Fe}_3\text{UO}_9$ read $\text{Sr}_3\text{Fe}_2\text{UO}_9$

Compound	Sym	a Å	b Å	c Å	angle	Ref.	Remarks	Magnetic Data
A ³⁺ B ³⁺ O ₃ (continued)								
YMnO ₃	O'	5.26	5.84	7.35		Wa3	High pressure phase; S.S. with: Fe, perovskite at 15% Fe [Ch6]	6
BiMnO ₃	M	10.93	11.31	7.98	$\beta = 92^\circ 24'$	Bo12	P & S [Su10]; S.S. with Ca [Bo6, Bo12, Si19], PbTiO ₃ [Bo6, Bo7], Sr [Iv1], La [Iv1], BiCrO ₃ [To11a]; crystallographic transformation T = 210 °C [To11a]	
PuMnO ₃ LaFeO ₃	C O	3.86 5.556	5.565	7.862		Ru13 Ge6	Pseudocubic P & S [Be33, Fo5, Re5, Wo3, Ke2, Da2, Na14, Ya1], S.S. with Ni, Mn [Be33], S.S. with Al, Co, Cr, Sc [Ka17, Wo3], rhombohedral T > 980 °C [Da1], S.S. with: PbNb ₂ O ₆ [Fr11], Pb [Re5a], Bi [Re5b]	6
CeFeO ₃ PrFeO ₃	O O	5.541 5.495	5.577 5.578	7.809 7.810		Ro1a Ge6	P & S [Ke2, Be33] P & S [Be33, Fo5, Re5], S.S. with Al, Co, Cr, Sc [Ka17]	
NdFeO ₃	O	5.441	5.573	7.753		Ge6	P & S [Be33, Fo5, Re5, Wo3], S.S. with Pb [Re5a], Bi [Re5b]	6
SmFeO ₃	O	5.394	5.592	7.711		Ge6	P & S [Be33, Fo5, Re5, Wo3], S.S. with Pb [Re5a], Bi [Re5b]	
EuFeO ₃ GdFeO ₃	O O	5.371 5.346	5.611 5.616	7.686 7.668		Ge6 Ge6	P & S [Re5], S.S. with Pb [Re5a], Bi [Re5b] P & S [Be33, Re5], crystal structure [Co21], S.S. with Pb [Re5a], Bi [Re5b]	6
TbFeO ₃ DyFeO ₃ HoFeO ₃	O O O	5.326 5.302 5.278	5.602 5.598 5.591	7.635 7.623 7.602		Ei1 Ei1 Ei1	P & S [Ko6], S.S. with: Pb [Re5a], Bi [Re5b] P & S [Da2], S.S. with: Pb [Re5a], Bi [Re5b] P & S [Ko6], S.S. with: Pb [Re5a], Bi [Re5b], HoMnO ₃ [Ap1a]	
ErFeO ₃	O	5.263	5.582	7.591		Ei1	P & S [Fo5], crystal structure [Wi7], S.S. with: Pb [Re5a], Bi [Re5b]	6
TmFeO ₃	O	5.251	5.576	7.584		Ei1	Crystal structure [Wi8], S.S. with: Pb [Re5a], Bi [Re5b]	
YbFeO ₃	O	5.233	5.557	7.570		Ei1	P & S [Ko6, Be1, Ha21], S.S. with: Pb [Re5a], Bi [Re5b]	6
LuFeO ₃ YFeO ₃	O O	5.213 5.283	5.547 5.592	7.565 7.603		Ei1 Ei1	P & S [Sa6], S.S. with: Pb [Re5a], Bi [Re5b] P & S [Fo5, Ru11, Ko6, Wo3, Ge4, Ma26, Va7, Sh12a], crystal structure [Co21], S.S. with: Pb [Re5a], Bi [Re5b]	
TiFeO ₃	O	5.319	5.448	7.796		Sh9		6

Compound	Sym	a Å	b Å	c Å	angle	Ref.	Remarks	Magnetic Data
A ³⁺ B ³⁺ O ₃ (continued)								
BiFeO ₃	R	5.62			α = 59° 41'	Mi0	P & S [Fi12, Is10, Ko5, Kr4, To7, To9, To12, Yu3, Yu1, Za2, Sm34, To10, Ge10a, Ro22], neutron diffraction [Ph1, Ki4, Ki5, Ki6, Bh2], S.S. with: LaAlO ₃ [Fe5], LnFeO ₃ [Kr5, Kh5, Ro7, Ro9, Is10b, Ro10, Ki6], Pb(Ti, Zr)O ₃ [La6, Fe8, Ge10, Fe2, Sm7], BaTiO ₃ [Ve5, Ka15], SrTiO ₃ [Fe6], LaCrO ₃ [Ro5], SrSnO ₃ [Hi1], Bi ₄ Ti ₃ O ₁₂ [Is12], SrFeO ₃ [Ma8], Pb ₂ FeNbO ₆ [Ro10, Yu1, Yu2, Sm12, Sm13, Is10a, Zh1, Is8, Kr3, Kr5], Sr(Sn _{1/3} Mn _{2/3})O ₃ [Mi6, Vi4], Sr _{0.7} La _{0.3} MnO ₃ [Ro10], PbNb ₂ O ₆ [Fr11]; BiMnO ₃ [Ma31], Pb(Fe _{1/3} W _{1/3})O ₃ [Sm26], PrFeO ₃ [Vi4a], complete structure S.G. R3c [Mi10] R3c, T < 375 °C; R3, T > 375 °C [Ra3]; P & S [As3, Wo4, He7, Sc23], Prop. [Me17, Ko1, Ra3, Ge12, Ra3, Jo9, Go16, Na1, Bl6, He7, Mu4, Me18], S.S. with Sr [Me18, Ra4, Jo13], S.S. with Sr and Th [Sc23] T = 937 °C: atomic positions demand R3 symmetry	in 3.3.4, Tab. 6
LaCoO ₃	R	5.436			α = 60° 48'	Wo9		6
PrCoO ₃	R	5.52			α = 60° 0'	Ra3		
NdCoO ₃	O	5.331	5.373	7.587		Be33	P & S [Wo4]	6
SmCoO ₃	O	5.336	5.336	7.547		Be33	P & S [Wo4], thermal conductivity [Ge12]	
GdCoO ₃	O	5.289	5.354	7.541		Be33	P & S [Wo4]	6
TbCoO ₃	O	5.228	5.404	7.436		Be33	P & S [As5]	6
BiCoO ₃	C	4.228				To11b	Studied in review of TbBO ₃ compounds [Ma24]. No cell dimension	6
LaNiO ₃	R	5.461				Wo8	High pressure preparation [To11a]	6
BiNiO ₃	C	4.173			α = 60° 49'	To11b	P & S [Wo6], neutron diffraction [Ko1]	6
LaGaO ₃	O	5.496	5.524	7.787		Ge2	High pressure preparation [To11a]	6
CeGaO ₃	R	5.544			α = 60° 25'	Ge2	P & S [Ke2, Da2, Be34, Br25, Da1, Ma25a] T = 900 °C, rhombohedral T > 875 °C (by DTA)	
PrGaO ₃	C	3.87				Ke2	Distorted	
NdGaO ₃	O	5.465	5.495	7.729		Ge2	P & S [Be34, Br25, Ma25a]	
	O	5.426	5.502	7.706		Ge2	P & S [Da1, Be34, Br25, Ke2, Ma25a], complete structure [Br26], S.S. with LaGaO ₃ [Br25]	6
SmGaO ₃	O	5.369	5.520	7.650		Ma25a	High pressure preparation	
EuGaO ₃	O	5.351	5.528	7.628		Ma25a	High pressure preparation	
GdGaO ₃	O	5.322	5.537	7.606		Ma25a	High pressure preparation [Ma25]	
TbGaO ₃	O	5.307	5.531	7.578		Ma25a	High pressure preparation	

Compound	Sym	a Å	b Å	c Å	angle	Ref.	Remarks	Magnetic Data
----------	-----	--------	--------	--------	-------	------	---------	------------------

Compound	Sym	a Å	b Å	c Å	angle	Ref.	Remarks	Magnetic Data
A ³⁺ B ³⁺ O ₃ (continued)								
DyGaO ₃	O	5.282	5.534	7.556		Ma25a	High pressure preparation	in 3.3.4, Tab.
HoGaO ₃	O	5.251	5.531	7.536		Ma25a	High pressure preparation	
ErGaO ₃	O	5.239	5.527	7.522		Ma25a	High pressure preparation	
TmGaO ₃	O	5.224	5.515	7.505		Ma25a	High pressure preparation [Ma25]	
YbGaO ₃	O	5.208	5.510	7.490		Ma25a	High pressure preparation	
LuGaO ₃	O	5.188	5.505	7.484		Ma25a	High pressure preparation [Ma26]	
YGaO ₃	O	5.257	5.536	7.533		Ma25	High pressure preparation [Ma26]	
LaYO ₃	O	5.868	6.071	8.438		Ge3	P & S [Pa2, Mo6], optical properties (Eu ³⁺) [B113]	
BiYO ₃	C	4.2				To11b	High pressure preparation [To11a]	
LaNbO ₃	C	4.02				Si5	Pseudocubic	
LaRhO ₃	O	5.524	5.679	7.900		Wo5	P & S [Ch11, Wo9, Kh1]	
PrRhO ₃	O	5.4143	5.7473	7.8026		Sh8a	P & S [Ch11]	
NdRhO ₃	O	5.3778	5.7551	7.7745		Sh8a	P & S [Wo5]	
SmRhO ₃	O	5.3211	5.7613	7.7083		Sh8a	P & S [Ch11]	
EuRhO ₃	O	5.2985	5.7607	7.6802		Sh8a		
GdRhO ₃	O	5.2774	5.7605	7.6584		Sh8a	P & S [Ch11]	
TbRhO ₃	O	5.2541	5.7492	7.6226		Sh8a		
DyRhO ₃	O	5.2449	5.7314	7.6002		Sh8a		
HoRhO ₃	O	5.2299	5.7257	7.5823		Sh8a	P & S [Ch11]	
ErRhO ₃	O	5.2160	5.7117	7.5610		Sh8a	P & S [Ch11]	
TmRhO ₃	O	5.2028	5.6974	7.5428		Sh8a		
LuRhO ₃	O	5.1861	5.6700	7.5125		Sh8a		
InRhO ₃	O	5.301	5.435	7.586		Sh9	P & S [Ge3, Pa2]	
LaInO ₃	O	5.723	5.914	8.207		Ro16		
NdInO ₃	O	5.627	5.891	8.121		Ro16		
SmInO ₃	O	5.589	5.886	8.082		Ro16		
EuInO ₃	O	5.567	5.835	8.078		Sh9	High pressure preparation	
GdInO ₃	O	5.548	5.842	8.071		Sh9	High pressure preparation	
DyInO ₃	O	5.519	5.751	8.041		Sh9	High pressure preparation	
YInO ₃	O	5.500	5.787	8.053		Sh9		
LaHoO ₃	O	5.888	6.092	8.480		Mo6		6
LaErO ₃	O	5.85	6.07	8.43		Sc12	P & S [Sc13, Mo6]	6
LaTmO ₃	O	5.85	6.06	8.42		Sc12	P & S [Sc13, Mo6]	6
LaYbO ₃	O	5.85	6.02	8.41		Sc12	P & S [Sc13, Mo6], complete structure determined, S.G. Pbn2 ₁ , [Mu8], T _{melt} = 2120 °C [T70]	6
LaLuO ₃	C	4.325				T70	T = 2080 °C	
PrLuO ₃	O	5.82	6.02	8.37		Sc12	P & S [Sc13, Mo6]	
	O	5.751	5.977	8.320		Mo6		

Tab. 2b. A₃B'BX₃ compounds

Compound	Sym	a Å	b Å	c Å	angle	Ref.	Remarks	Magnetic Data
A ₃ B ⁺ B ³⁺ X ₆ ; X = F ⁻¹ , Cl ⁻¹								in 3.3.4, Tab.
Cs ₃ NaAlF ₆	H	6.168		29.76		Ba5a	Hex (12 L)	
Rb ₃ NaAlF ₆	C	8.29				Ba5a	Hex (12L)	
Rb ₃ LiAlF ₆	H	5.802		28.02		Ba5a	R perovskite	
K ₃ LiAlF ₆	H	5.574		13.648		Wi11b	Hex (6L), Prep. T > 470 °C	
	H	5.614		13.754		Me21		
K ₃ NaAlF ₆	C	8.105				St33		
K ₃ KAlF ₆	C	8.65				Na17		
Na ₃ NaAlF ₆	M	5.46				Pa9	P & S [St33, Me19, Cr5a], S.S. with Fe [Cr5a]	
(NH ₄) ₃ (NH ₄)AlF ₆	C	8.90	5.61	7.80	β = 90° 11'	Ho16a	P & S [Pa10, Me20] Prep. [Ba0]	
Cs ₃ CsScF ₆	C	9.32				Bo2	Prep. [Ba0]	
Cs ₃ KScF ₆	C					Th1	Prep. [Ba0]	
Rb ₃ RbScF ₆	C	17.46				Bo2	T < 680 °C	
K ₃ KScF ₆	C	5.60		8.12		Bo2		
Na ₃ NaScF ₆	M	6.49	5.81	9.45	β = 90° 45'	Br7	High temperature form P & S [Ba5], magnetic properties, n _{eff} = 1.70, Θ _p = 0 °K [Eh1]	
(NH ₄) ₃ (NH ₄)ScF ₆	T	9.26		8.75		Br7	Structure determined [Bu4a]	
K ₃ KTiF ₆	T	8.56				Br7	P & S [Ba5]	
K ₃ NaTiF ₆	C	8.367				Br7		
Na ₃ NaTiF ₆	M	5.53				Br7		
Cs ₃ KVF ₆	C	9.04	5.83	7.99	β ≅ 90°	Ba5a		
Cs ₃ NaVF ₆	C	6.267				Ba5a		
Rb ₃ KVF ₆	H	8.88		30.40		Ba5a	Hex (12L)	
Rb ₃ NaVF ₆	C	8.47				Ba5a		
Rb ₃ LiVF ₆	C	5.891		28.77		Ba5a		
K ₃ KVF ₆	H					Ba5a	Hex (12L)	
K ₃ NaVF ₆	C	8.315				Ba5	Magnetic properties, 80 < T < 300 °K, n _{eff} = 2.79, Θ _p = -14 °K [Fi4]	
(NH ₄) ₃ (NH ₄)VF ₆	C	9.04				Pa6a		
Cs ₃ RbCrF ₆	C	9.15				Ba5a		
Cs ₃ KCrF ₆	C	8.99				Ba5a		
Cs ₃ NaCrF ₆	C	6.231				Ba5a		
Rb ₃ KCrF ₆	H	8.81		30.24		Ba5a	Hex (12L)	
Rb ₃ NaCrF ₆	C	8.42				Ba5a		
Rb ₃ LiCrF ₆	C	5.865				Ba5a		
K ₃ KCrF ₆	H	8.56		28.61		K16	Hex (12L)	
K ₃ KCrF ₆	T	8.54		8.62		Bo2	P & S [Pe2] High temperature form	

Compound	Sym	a Å	b Å	c Å	angle	Ref.	Remarks	Magnetic Data
A ²⁺ B ³⁺ +X ₆ ; X = F ⁻¹ , Cl ⁻¹ (continued)								
K ₂ NaCrF ₆	C	8.266		7.878	β ≈ 90°	<i>Kn5</i>	Prop. [Sh28]	in 3.3.4, Tab.
Na ₂ NaCrF ₆	M	5.468	5.679			<i>Vo1</i>		
(NH ₄) ₂ (NH ₄)CrF ₆	C	9.01				<i>Pa6a</i>		
K ₂ KMnF ₆	T	17.50		16.60		<i>Pe2</i>	Magnetic properties, $p^* = 4.95 \mu_B$ [Pe2]	
K ₂ NaMnF ₆	T	8.171		8.577		<i>Kn4</i>		
Cs ₂ CsFeF ₆	C	10.46				<i>Mi2</i>		
Cs ₂ KFeF ₆	C	9.05				<i>Ba5a</i>	P & S [Ho16a]	
Cs ₂ NaFeF ₆	H	6.260		30.40		<i>Ba5a</i>	Hex (12L)	
Rb ₂ RbFeF ₆	C	8.88				<i>Bo2</i>		
Rb ₂ KFeF ₆	C	8.87				<i>Ba5a</i>		
Rb ₂ NaFeF ₆	C	8.47				<i>Ba5a</i>	Hex (12L)	
Rb ₂ LiFeF ₆	H	5.891		28.77		<i>Ba5a</i>		
K ₂ KFeF ₆	C	8.58				<i>Bo2</i>		
K ₂ NaFeF ₆	C	8.323				<i>Kn5</i>		
Na ₂ NaFeF ₆	M	5.506	5.719	7.925	β = 90° 28'	<i>Cr5a</i>	P & S [Mi5], magnetic properties, 92 < T < 296 °K, $n_{\text{eff}} = 5.85$, $\Theta_p = -2^\circ \text{K}$ [Fi1]	
Li ₂ LiFeF ₆	C	8.88				<i>Mi2</i>	Magnetic properties, 93 < T < 293 °K, $n_{\text{eff}} = 6.00$, $\Theta_p = 0^\circ \text{K}$ [Fi1]	
(NH ₄) ₂ (NH ₄)FeF ₆	T	6.39		9.30		<i>Si33</i>	Low temperature form	
	C	9.10				<i>Pa9</i>	P & S [Si33, Ki6]; magnetic properties, 92 < T < 294 °K, $n_{\text{eff}} = 5.86$, $\Theta_p = -2^\circ \text{K}$ [Fi1]	
Cs ₂ CsCoF ₆	C	9.23				<i>Ki6</i>	Magnetic properties, 90 < T < 290 °K, $n_{\text{eff}} = 5.28$, $\Theta_p = +2^\circ \text{K}$ [Ki6]	
Rb ₂ RbCoF ₆	C	8.90				<i>Ki6</i>	P & S [Ho13], magnetic properties, 90 < T < 290 °K, $n_{\text{eff}} = 5.48$, $\Theta_p = -2^\circ \text{K}$ [Ki6]	
K ₂ KCoF ₆	C	8.57				<i>Ki6</i>	P & S [Me27, Ho13], magnetic properties, 73 < T < 300 °K, $n_{\text{eff}} = 5.53$, $\Theta_p = -10^\circ \text{K}$ [Co23, Ki6]	
K ₂ NaCoF ₆	C	8.22				<i>Me27</i>	Pseudocubic, P & S [Ho13], magnetic properties, 90 < T < 290 °K, $n_{\text{eff}} = 5.39$, $\Theta_p = -5^\circ \text{K}$ [Ki6]	
Na ₂ NaCoF ₆	C	7.91				<i>Ki6</i>		
K ₂ KNiF ₆	C	8.44				<i>Bo2</i>	P & S [Ki6], magnetic properties, 90 < T < 295 °K, does not obey Curie-Weiss law [Ki2, Ki3, We20]	
K ₂ KCuF ₆	C	8.50				<i>Ki6</i>	Magnetic properties, $n_{\text{eff}} = 2.8$ [Ki2]	
Cs ₂ KGaF ₆	C	8.975				<i>Ho16a</i>		
K ₂ NaGaF ₆	C	8.246				<i>Kn5</i>		
(NH ₄) ₂ (NH ₄)GaF ₆	C	9.041				<i>Sc26</i>		
Cs ₂ KAgF ₆	C	9.175				<i>Ho16</i>		

Compound	Sym	a Å	b Å	c Å	angle	Ref.	Remarks	Magnetic Data
A ²⁺ B ³⁺ B ³⁺ X ₆ ; X = F ⁻¹ , Cl ⁻¹ (continued)								
Cs ₂ CsInF ₆	C	9.50				Bo2		
Cs ₂ KInF ₆	C	9.219				Ho16a		
Rb ₂ RbInF ₆	C	9.20				Bo2		
K ₂ KInF ₆	C	17.71				Bo2		
(NH ₄) ₂ (NH ₄)MoO ₃ F ₃	C	9.10				Pa9		
Cs ₂ NaCeF ₆	C	9.26				Be52a		
Cs ₂ KCeF ₆	C	9.61				Be52a		
Cs ₂ RbCeF ₆	C	9.75				Be52a		
Cs ₂ CsCeF ₆	C	9.84				Be52a		
Cs ₂ KKCeF ₆	C	9.36				Be52a		
CsRbRbCeF ₆	C	9.60				Be52a		
Rb ₂ KCeF ₆	C	9.40				Be52a		
Rb ₂ RbCeF ₆	C	9.49				Be52a		
RbKKCeF ₆	C	9.20				Be52a		
K ₂ KCeF ₆	C	9.07				Be52a		
Rb ₂ RbPrF ₆	C	9.48				Bo2		
Cs ₂ NaSmF ₆	C	9.163				Al4		
Rb ₂ NaSmF ₆	C	8.988				Al4		
Cs ₂ NaTbF ₆	C	9.107				Al4		
Rb ₂ NaTbF ₆	C	9.9208				Al4		
Rb ₂ NaHoF ₆	C	8.881				Al4		
Cs ₂ NaErF ₆	C	9.061				Al4		
Rb ₂ NaErF ₆	C	8.867				Al4		
Cs ₂ NaYbF ₆	C	9.022				Al4		
Rb ₂ NaYbF ₆	C	8.824				Al4		
Cs ₂ NaYF ₆	C	9.056				Al4		
Rb ₂ NaYF ₆	C	8.8693				Al4		
Cs ₂ AgAuCl ₆	T	7.38				El3		
Cs ₂ AgAuCl ₆	C	5.28				El3		
Cs ₂ AuAuCl ₆	T	7.49				El3		
Cs ₂ KTlF ₆	C	9.36				Ho16a		
K ₂ KTlF ₆	C	11.86				Bo2		
(A ³⁺ A ³⁺) (B ³⁺ B ³⁺)O ₆								
BaLaMnTiO ₆	C	3.960				Ha32		
SrLaMnTiO ₆	R	3.912			α = 90° 12'	Ha32	S.S. with Sr, rhombohedral > 30% Sr Cubic > 700 °C	
CaLaMnTiO ₆	R	3.872			α = 90° 6'	Ha32		
CaYMnTiO ₆	O	5.32	5.53	7.54		Ha32	S.S. with La	
PbLaMnTiO ₆	R	3.933			α = 90° 12'	Ha32	S.S. with x = Pb ₂ NbMnO ₆ ; cubic ≥ 50%	

Compound	Sym	a Å	b Å	c Å	angle	Ref.	Remarks	Magnetic Data
PbLaMnTiO ₆	R	3.933			$\alpha = 90^\circ 12'$	Ha32	S.S. with $x = \text{Pb}_x\text{NbMnO}_6$; cubic $\geq 50\%$	
(A ³⁺ A ³⁺) (B ³⁺ B ⁴⁺)O ₆ (continued)								in 3.3.4, Tab.
SrLaFeTiO ₆	C	3.92				Bi8		
SrLaMnIrO ₆	C	3.93				Bi8		
SrLaFeIrO ₆	C	3.94				Bi8		
A ₃ ⁺ BB'O ₆								
La ₂ MgTiO ₆	C	3.96						
Nd ₂ MgTiO ₆	C	3.90				Ag1	P & S [Ro20], Eu ³⁺ fluorescence [Bi14], S.S. with: Ni and optical properties [Re4a]	
LaCeMgTiO ₆	C	3.929				Ro20	Slight distortion	
Bi ₂ MgTiO ₆	C	3.98				Ro20	Slight distortion	
Y ₂ Ni _{0.4} Mg _{0.6} TiO ₆	C	3.83				Su5	Some question on atom positions	
La ₂ MgMnO ₆	C					Re4a	Optical properties	
La ₂ CoMnO ₆						Bi7		
La ₂ NiMnO ₆						Bi7	See LaMnO ₃ systems for magnetic properties	
						Bi7	See LaMnO ₃ systems for magnetic properties, P & S [Fu2]	
						Bi7	See LaMnO ₃ systems for magnetic properties	
La ₂ CuMnO ₆						Ro20		
La ₂ MgGeO ₆	C	3.90				Re4a		
Y ₂ MgGeO ₆	C	3.88				Ra1	S.S. with Ni and optical properties [Re4a]	
La ₂ MgZrO ₆	C	4.06				Ra1		
La ₂ CaZrO ₆	C	4.174				Ra1		
La ₂ LiNbO ₆	O	5.59				Bi1a		
La ₂ MgRuO ₆	C	7.91	5.76	7.92		Ga5	Eu ³⁺ fluorescence [Bi14]	
La ₂ MnRuO ₆	C	7.84				Ga5	Semiconducting, $\Delta E = 0.046$ eV	
La ₂ NiRuO ₆	C	7.90				Ga5	Semiconducting, $\Delta E = 0.12$ eV	
La ₂ ZnRuO ₆	C	7.97				Ga5	Optical properties	
La ₂ Ni _{0.4} Mg _{0.6} SnO ₆	C	4.02				Re4a		
La ₂ MgReO ₆	C	7.926				Ba25a		
La ₂ NiReO ₆	C	7.908				Ba25a		
La ₂ CoReO ₆	T	5.611		7.968		Ba25a	Disproportionates [Ba25a]	
La ₂ FeReO ₆	C	7.92				Ga5	"Complex magnetic properties" [Bi7], P & S [Bi8]	
La ₂ MgIrO ₆	C	7.86				Ga5		
La ₂ MnIrO ₆	O	5.60	5.60	7.92		Bi8	"Complex magnetic properties" [Bi7]	
La ₂ CoIrO ₆	C	7.90				Ga5	"Complex magnetic properties" [Bi7], P & S [Bi8]	
La ₂ NiIrO ₆	C	5.80	5.60	7.72	$\gamma = 86^\circ 56'$	Bi8	"Complex magnetic properties" [Bi7]	
La ₂ CuIrO ₆	M							
A ₃ ⁺ BV ⁵⁺ O ₆	O	6.123	6.180	8.622		Ve2	P & S [Vi3, Ve3], dielectric properties [Vi2b]	
Ba ₂ BiVO ₆	C	4.372				Ve2	Cubic $> 320^\circ\text{C}$	

Compound	Sym	a Å	b Å	c Å	angle	Ref.	Remarks	Magnetic Data
A ₂ ²⁺ BNb ⁵⁺ O ₆								in 3.3.4, Tab.
Ba ₂ ScNbO ₆	C	8.220				Fi10	P & S [Ag1, Br16]	6
Ba ₂ VNbO ₆	C	4.051				Ch10		
Ba ₂ MnNbO ₆	C	4.090				Ha32	P & S [Ag1]	
Ba ₂ FeNbO ₆	C	4.057				Ga1	P & S [Ga13, Fi10, Ag1]	
Ba ₂ CoNbO ₆	C	4.06				Bl8		
Ba ₂ NiNbO ₆	C	4.1				Bl8		
Ba ₂ SrNbO ₆ ^{1,5}	C	8.54				Ga1	P & S [Fi10]	
Ba ₂ YNbO ₆	C	4.180				Br16		
Ba ₂ RhNbO ₆	C	8.17				Bl8	P & S [Ga1]	
Ba ₂ InNbO ₆	C	8.279				Br16		
Ba ₂ BaNbO ₆ ^{1,5}	C	8.68				Ga1		
Ba ₂ LaNbO ₆	T	8.607		8.690		Ga1	P & S [Br16], cubic T > 300 °C [Fi10]	
Ba ₂ CeNbO ₆	C	4.293				Br16	Probably ordered	
Ba ₂ PrNbO ₆	C	4.285				Br16	Probably ordered, cubic T > 300 °C [Fi10]	
Ba ₂ NdNbO ₆	C	8.540				Ga1	P & S [Br16], cubic T > 300 °C [Fi10]	
Ba ₂ SmNbO ₆	C	8.518				Ga1	P & S [Br16], cubic T > 300 °C [Fi10]	
Ba ₂ EuNbO ₆	C	8.507				Ga1	P & S [Br16]	
Ba ₂ GdNbO ₆	C	8.496				Ga1	P & S [Br16], fluorescences [Bl11, Ni1, Bl14]	6
Ba ₂ TbNbO ₆	C	4.229				Br16	Probably ordered	
Ba ₂ DyNbO ₆	C	8.437				Ga1	P & S [Br16]	
Ba ₂ HoNbO ₆	C	8.434				Ga1	P & S [Br16]	
Ba ₂ ErNbO ₆	C	8.427				Ga1	P & S [Br16]	
Ba ₂ TmNbO ₆	C	8.408				Ga1	P & S [Br16]	
Ba ₂ YbNbO ₆	C	8.374				Ga1	P & S [Br16], dielectric properties [Ag1]	
Ba ₂ LuNbO ₆	C	8.364				Ga1	P & S [Br16]	
Ba ₂ TiNbO ₆	C	8.42				Sl6		
Ba ₂ BiNbO ₆	R	6.086			α = 60° 21'	Ve2	P & S [Vi3, Ve3], dielectric properties [Vi2b]	
Sr ₂ AlNbO ₆	C	7.784				Fi10	P & S [Sl7]	
Sr ₂ CaNbO ₆ ^{1,5}	C	8.20				Ga13		
Sr ₂ VNbO ₆	C	3.965				Ch10		
Sr ₂ CrNbO ₆	C	7.87				Bl8	P & S [Br14]	
Sr ₂ MnNbO ₆	R	3.97			α ≈ 90°	Ha32	P & S [Ku12], cubic T > 200 °C [Ku12]	6
Sr ₂ FeNbO ₆	T	3.960				Ku6	P & S [Ga13, Ku12]	
	C	3.968				Ku6	T = 250 °C, cubic T ≥ 250 °C	
	C	3.93				Bl8		
Sr ₂ CoNbO ₆	C	3.9477				Br14		
Sr ₂ GaNbO ₆	C	8.34				Ga13		
Sr ₂ SrNbO ₆ ^{1,5}	C	5.184			α = 59° 51'	Ku12	Cubic T > 630 °C	
Sr ₂ YNbO ₆	R	8.106				Fi10	P & S [Br14]	
Sr ₂ InNbO ₆	C							

Compound	Sym	a Å	b Å	c Å	angle	Ref.	Remarks	Magnetic Data
A ₃ BNb ₅ O ₈ (continued)								
Sr ₂ PrNbO ₆	T	5.822		8.431		Ku12		
Sr ₂ NdNbO ₆	T	5.780		8.367		Ku12		
Sr ₂ SmNbO ₆	M	5.85	5.94	8.30	$\beta = 90^\circ 12'$	Fi10	P & S [Ku12]	
Sr ₂ EuNbO ₆	M	5.84	5.91	8.30	$\beta = 90^\circ 12'$	Fi10		
Sr ₂ GdNbO ₆	M	5.83	5.90	8.28	$\beta = 90^\circ 15'$	Fi10		
Sr ₂ TbNbO ₆	M	5.82	5.88	8.27	$\beta = 90^\circ 8'$	Fi10		
Sr ₂ DyNbO ₆	M	5.81	5.87	8.26	$\beta = 90^\circ 9'$	Fi10		
Sr ₂ HoNbO ₆	M	5.81	5.86	8.23	$\beta = 90^\circ 6'$	Fi10		
Sr ₂ ErNbO ₆	M	5.80	5.84	8.23	$\beta = 90^\circ 4'$	Fi10		
Sr ₂ TmNbO ₆	C	8.20				Fi10	Slight distortion	
Sr ₂ YbNbO ₆	C	8.196				Ku12	Cubic $T > 540^\circ\text{C}$	
Sr ₂ LuNbO ₆	C	8.19				Ku12	Cubic $T > 540^\circ\text{C}$	
SrLaCoNbO ₆	C	7.99				Bi8		6
SrLaNiNbO ₆	C	7.95				Bi8		6
SrLaCuNbO ₆	T	7.80		8.28		Bi8		
La ₂ LiNbO ₆							Ordered perovskite (Eu ³⁺ fluorescence) [Bi14]	
Ca ₂ AlNbO ₆	O	5.382	5.408	7.614		Fi8		
Ca ₂ VNbO ₆	O	5.44	5.51	7.77		Ch9		
Ca ₂ CrNbO ₆	O	5.418	5.494	3.858		Fi8		
Ca ₂ MnNbO ₆	O	5.44	5.55	7.74		Ha32		
Ca ₂ FeNbO ₆	O	5.451	5.551	3.881		Fi8		
Ca ₂ YNbO ₆	O	5.580	5.819	8.046		Fi8		
Ca ₂ InNbO ₆	O	5.532	5.715	7.913		Fi8		
Ca ₂ LaNbO ₆	O	5.652	5.866	8.140		Fi8	Possibly lower symmetry	
Ca ₂ PrNbO ₆	O	5.623	5.866	8.116		Fi8	Possibly lower symmetry	
Ca ₂ NbNbO ₆	O	5.612	5.858	8.104		Fi8		
Ca ₂ SmNbO ₆	M	5.590	5.860	8.090	$\beta = 90^\circ 10'$	Fi8		
Ca ₂ GdNbO ₆	M	5.572	5.841	8.080	$\beta = 90^\circ 12'$	Fi8		
Ca ₂ TbNbO ₆	O	5.571	5.830	8.072		Fi8		
Ca ₂ DyNbO ₆	O	5.580	5.819	8.062		Fi8		
Ca ₂ HoNbO ₆	O	5.580	5.812	8.050		Fi8		
Ca ₂ ErNbO ₆	O	5.575	5.794	8.020		Fi8		
Ca ₂ YbNbO ₆	O	5.571	5.769	8.000		Fi8		
Pb ₂ AlNbO ₆	C	10.53				Fi11	Defect pyrochlore type P & S [Ag1, Ve4]	
Pb ₂ ScNbO ₆	T	4.074		4.083		Is2	Dielectric properties [Jo3, Sm18, Te82], S.S. with Pb(Ti, Zr, Hf)O ₃ [Jo3], crystal growth [Ga5]	
Pb ₂ Sc _{0.5} Cr _{0.5} NbO ₆	C	4.060				To1	Possible rhombohedral distortion	
Pb ₂ CrNbO ₆	C	10.54				Fi11	Defect pyrochlore type	
Pb ₂ MnNbO ₆	C	4.023				Fi11	P & S [Ha32], S.S. with Fe and PbTiO ₃ [Ha31]	6

Compound	Sym	a Å	b Å	c Å	angle	Ref.	Remarks	Magnetic Data
A ₂ ²⁺ BNb ⁵⁺ O ₆ (continued)								in 3.3.4, Tab. 6
Pb ₂ FeNbO ₆	R	4.014			α = 89° 55'	Ku10	P & S [Ro8], S.S. with BiFeO ₃ [Sm12, Is8, Yu2], complete structure [Pl3], crystal growth [Ga5], dielectric properties [Kh8, Sm25, Sm16, Bo8, Sh32, Sh1, Sh33], optical spectra [Pi5], B site ordering [Yu9], S.S. with Ta [Sh33]	6
Pb ₂ CoNbO ₆	C	8.084				Ro8	Dielectric properties [Ku10, Ag1, Ve4]	6
Pb ₂ NiNbO ₆	C	4.030				Ku10	Dielectric properties [Ku10] with 5% Ba [Sh32]	6
Pb ₂ GaNbO ₆	C					Fi11	High pressure preparation, no dimension [To11a]	
Pb ₂ YNbO ₆	C	10.65				Ku9	Pyrochlore type	
Pb ₂ InNbO ₆	C	4.110				Ku9	Dielectric properties [Ku10]	
Pb ₂ HoNbO ₆	O	5.86	5.91	8.21		Ku9	Dielectric properties [Ku10]	
Pb ₂ TmNbO ₆	O	5.858	5.936	8.178		Ku10		
Pb ₂ YbNbO ₆	O	5.848	5.918	8.186		Fi11		
Pb ₂ LuNbO ₆	O	5.850	5.902	8.176		Ku9	Cubic T > 280 °C, dielectric properties [Sm25, Ku9, Ku10, Ag1, Is17], S.S. with PbFe _{0.8} W _{1.2} O ₆ [To5, To11, Ro11]	
Pb ₂ BiNbO ₆	M	10.777	10.643	10.777	β = 90° 29'	Ku9	Cubic T > 280 °C, dielectric properties [Ku9, Ku10, Is17]	
Pb ₂ Mg _{0.5} Mn _{0.5} NbO ₆	C	4.018				Vi3	Defect pyrochlore type	
Pb ₂ Co _{0.5} Mn _{0.5} NbO ₆	C	4.020				Vi5	Dielectric properties [Ve4, Vi5]	6
Pb ₂ Ni _{0.5} Mn _{0.5} NbO ₆	C	4.018				Vi5	Dielectric properties [Ve4, Vi5]	6
Pb ₂ Zn _{0.5} Mn _{0.5} NbO ₆	C	4.028				Vi5	Dielectric properties [Ve4, Vi5]	6
Pb ₂ Cd _{0.5} Mn _{0.5} NbO ₆	C	4.060				Ro8	Dielectric properties [Ve4, Vi5, Ro8, Ve3]	
A ₂ ²⁺ BSb ⁵⁺ O ₆								
Ba ₂ ScSbO ₆	C	8.197				Sl6	Not perovskite [Bl8]	
Ba ₂ CrSbO ₆						Bl8	Not perovskite [Bl8]	6
Ba ₂ MnSbO ₆						Bl8	Hex (6L), P & S [Sl6, Bl3]	
Ba ₂ FeSbO ₆	H	5.79		14.22		Bl8	Hex (6L)	
Ba ₂ CoSbO ₆	H	5.72		14.00		Bl8	Not perovskite [Bl8]	
Ba ₂ NiSbO ₆						Bl8	Hex (6L)	
Ba ₂ RhSbO ₆	H	5.78		14.20		Sl6	P & S [Bl3, Bl8]	6
Ba ₂ InSbO ₆	C	8.269				Bl8	P & S [Sl6, Bl3]	6
Ba ₂ GdSbO ₆	C	8.44				Bl8	P & S [Sl6, Bl3]	6
Sr ₂ CrSbO ₆	C	7.87				Bl8	P & S [Sl6, Bl3]	6
Sr ₂ MnSbO ₆	T	7.86		8.08		Bl8	Not single phase (no dimensions)	6
Sr ₂ FeSbO ₆	C	7.90				Bl8		
Sr ₂ CoSbO ₆	C	7.88				Bl8		
Sr ₂ NiSbO ₆	T					Bl8		

Compound	Sym	a Å	b Å	c Å	angle	Ref.	Remarks	Magnetic Data in 3,3,4, Tab.
A ₂ ³⁺ BSb ⁵⁺ O ₆ (continued)								
Sr ₂ GaSbO ₆	T	7.84		7.91		Sl6		6
Sr ₂ RhSbO ₆	O	5.55		7.99		Bi8		
Ca ₂ FeSbO ₆	O	5.47	5.77	7.74		Bi8		
SrLaMgSbO ₆	C					Bi14		
SrLaCoSbO ₆	C	7.99				Bi8	Eu ³⁺ fluorescence, no dimensions	6
SrLaNiSbO ₆	C	7.93				Bi8		6
SrLaCuSbO ₆	T	7.80		8.35		Bi8		6
A ₂ ³⁺ BTa ⁵⁺ O ₆								
Ba ₂ AlTaO ₆								
Ba ₂ ScTaO ₆								
Ba ₂ VTaO ₆	C	8.220				Fi10	No compound [Ag1, Sm8]	
Ba ₂ CrTaO ₆	C	8.104				Sl1	Dielectric properties [Ag1, Br13, Br14], P & S [Ga15]	
Ba ₂ MnTaO ₆	H					Sl1	P & S [Ch10]	
Ba ₂ FeTaO ₆	C	4.076				Fi5	Hex (6L) no dimensions	
	C	4.048				Fi5	P & S [Sl1]	
	C					Sl1	P & S [Ga13], dielectric properties [Ag1], S.S. with BaTiO ₃ [Na2]	
Ba ₂ NiTaO ₆	C	8.152				Fi10	P & S [Ag1, Br13, Br14, Fi5, La9], doped with Nd, Sm, Yb [Ga15]	
Ba ₂ YTaO ₆	C	8.424				Fi10	P & S [Ag1, Ga15] doped with Nd, Sm, Yb [Ga15]	
Ba ₂ InTaO ₆	C	8.282				Fi10	P & S [Br13, Fi5] cubic T > 300 °C [Fi5]	
Ba ₂ BaTaO ₆ .3	C	8.70				Ga13	P & S [Br13, Fi5] cubic T > 300 °C [Fi5]	
Ba ₂ LaTaO ₆	R	6.07			α = 60° 25'	Ga15	P & S [Br13], doped with Nd [Ga15], cubic > 300 °C [Fi5]	
Ba ₂ PrTaO ₆	R	6.05			α = 60° 10'	Fi10	P & S [Br13, Fi5] cubic T > 300 °C [Fi5]	
Ba ₂ NdTaO ₆	R	6.04			α = 60° 4'	Fi10	P & S [Br13, Fi5] cubic T > 300 °C [Fi5]	
Ba ₂ SmTaO ₆	R	6.01			α = 60° 4'	Fi10	P & S [Br13, Fi5] cubic T > 300 °C [Fi5]	
Ba ₂ EuTaO ₆	C	8.486				Fi10	P & S [Ga15]	
Ba ₂ GdTaO ₆	C	8.470				Fi10	Doped with Nd [Ga15]	
Ba ₂ TbTaO ₆	C	8.440				Fi10		
Ba ₂ DyTaO ₆	C	8.420				Fi10		
Ba ₂ HoTaO ₆	C	8.416				Fi10	P & S [Ga15]	
Ba ₂ ErTaO ₆	C	8.398				Fi10	P & S [Ga15]	
Ba ₂ TmTaO ₆	C	8.388				Fi10	P & S [Ga15]	
Ba ₂ YbTaO ₆	C	8.378				Fi10	P & S [Ga15], dielectric properties [Ag1]	
Ba ₂ LuTaO ₆	C	8.354				Fi10	P & S [Ga15], doped with Nd [Ga15]	
Ba ₂ ITaO ₆	C	8.42				Sl1		
Ba ₂ BITaO ₆	R	6.047			α = 60° 15'	Ve2	Dielectric properties [Vi3, Ve3]	
Sr ₂ AlTaO ₆	C	7.786				Fi10	P & S [Sl1], B-B' ordering [Sl1]	

Compound	Sym	a Å	b Å	c Å	angle	Ref.	Remarks	Magnetic Data
A ₂ ⁺ BTa ⁵⁺ O ₆ (continued)								
Sr ₂ VTaO ₆	C	3.967				Ch10	P & S [Ro20], S.S. with Fe [Na7]	in 3.3.4, Tab. 6
Sr ₂ CrTaO ₆	C	3.94				Na7		
Sr ₂ MnTaO ₆	C	3.994				Ku12		
Sr ₂ FeTaO ₆	T	3.960		3.981		Ku7	P & S [Ku12, Si1, Na5, Na6, Na7], B-B' ordering [Si1, Be5], S.S. with SrTiO ₃ and Ba ₂ FeTaO ₆ [Na5, Be5], S.S. with BaTiO ₃ [Na6] Cubic at 250 °C [Ku7, Na5, Na6]	
Sr ₂ GaTaO ₆	C	3.973				Ku7		
Sr ₂ SrTaO ₆	C	7.892				Si1	P & S [Br13]	
Sr ₂ YTaO ₆	C	8.34			α = 59° 46'	Ga13		
Sr ₂ RhTaO ₆	R	5.837				Ku12		
Sr ₂ InTaO ₆	C	7.936				Si1		
Sr ₂ LaTaO ₆	C	8.110				Fi10	P & S [Si1]	
Sr ₂ PrTaO ₆	T	5.853		8.387		Ku12	P & S [Br13]	
Sr ₂ NdTaO ₆	M	5.87	5.98	8.35	β = 90° 9'	Fi10	P & S [Ku12]	
Sr ₂ SmTaO ₆	M	5.86	5.96	8.34	β = 90° 9'	Fi10	P & S [Ku12]	
Sr ₂ EuTaO ₆	M	5.85	5.93	8.31	β = 90° 11'	Fi10	P & S [Ku12]	
Sr ₂ GdTaO ₆	M	5.84	5.91	8.30	β = 90° 12'	Fi10	P & S [Ku12]	
Sr ₂ TbTaO ₆	M	5.83	5.90	8.29	β = 90° 13'	Fi10	P & S [Ku12]	
Sr ₂ DyTaO ₆	M	5.82	5.88	8.28	β = 90° 9'	Fi10		
Sr ₂ HoTaO ₆	M	5.82	5.87	8.26	β = 90° 8'	Fi10		
Sr ₂ ErTaO ₆	M	5.81	5.85	8.23	β = 90° 8'	Fi10		
Sr ₂ TmTaO ₆	M	5.80	5.84	8.23	β = 90° 4'	Fi10	Slight distortion	
Sr ₂ YbTaO ₆	C	8.20				Ku12		6 6
Sr ₂ LuTaO ₆	C	8.196				Fi10	Slight distortion	
SrLaCoTaO ₆	C	8.18				Bi8		
SrLaNiTaO ₆	C	7.99				Bi8		
SrLaCuTaO ₆	C	7.95				Bi8		
Ca ₂ AlTaO ₆	T	7.80		8.28		Bi8		
Ca ₂ VTaO ₆	O	5.381	5.407	7.612		Fi8		
Ca ₂ CrTaO ₆	O	5.45	5.49	7.76		Ch9		
Ca ₂ MnTaO ₆	O	5.418	5.491	3.857		Fi8		
Ca ₂ FeTaO ₆	O	5.462	5.571	3.873		Fi8	P & S [Si1]	
Ca ₂ YTaO ₆	O	5.451	5.560	3.880		Fi8		
Ca ₂ InTaO ₆	O	5.580	5.819	8.044		Fi8		
Ca ₂ LaTaO ₆	O	5.531	5.714	7.924		Fi8		
Ca ₂ PrTaO ₆	O	5.654	5.890	8.146		Fi8		
Ca ₂ NdTaO ₆	O	5.629	5.867	8.116		Fi8	Possibly lower symmetry	
Ca ₂ SmTaO ₆	O	5.616	5.857	8.106		Fi8	Possibly lower symmetry	
	O	5.606	5.853	8.096		Fi8		

Compound	Sym	a Å	b Å	c Å	angle	Ref.	Remarks	Magnetic Data
A ₂ ⁺ BTa ⁵⁺ O ₆ (continued)								
Ca ₂ GdTbTaO ₆	M	5.572	5.841	8.080	β = 90° 12'	Fi8		in 3.3.4, Tab.
Ca ₂ TbTaO ₆	M	5.574	5.833	8.076	β = 90° 12'	Fi8		
Ca ₂ DyTaO ₆	O	5.582	5.820	8.064		Fi8		
Ca ₂ HoTaO ₆	O	5.586	5.811	8.054		Fi8		
Ca ₂ ErTaO ₆	O	5.582	5.796	8.033		Fi8		
Ca ₂ YbTaO ₆	O	5.570	5.772	8.002		Fi8		
Pb ₂ AlTaO ₆	C	10.51				Fi11		
Pb ₂ ScTaO ₆	C	4.080				Ga5	Defect pyrochlore type, P & S [Ag1] P & S [Is2, Ag1], crystal growth [Ga5], dielectric properties [Sm18]	
Pb ₂ MnTaO ₆	C	10.73				Fi11	Defect pyrochlore type, 5% Sr for Pb gives perovskite [Sh32]	6
Pb ₂ FeTaO ₆	C	4.011				Ga5	P & S [Ag1], crystal growth [Ga5], Prop. [Sh32]	6
Pb ₂ CoTaO ₆	C	4.038				Ku11	Dielectric properties [Ku11, Sh32]	6
Pb ₂ YTaO ₆	C	10.70				Fi11	Defect pyrochlore type	
Pb ₂ PrTaO ₆	C	10.75				Fi11	Defect pyrochlore type	
Pb ₂ NdTaO ₆	C	10.68				Fi11	Defect pyrochlore type	
Pb ₂ SmTaO ₆	C	10.70				Fi11	Defect pyrochlore type	
Pb ₂ YbTaO ₆	O	5.85	5.90	8.22		Ku9	Dielectric properties [Ag1, Is17, Fi11]	
Pb ₂ LuTaO ₆	O	5.848	5.899	8.214		Ku9	Cubic T > 280 °C; dielectric properties [Is17]	
Pb ₂ BiTaO ₆	T	10.686		10.816		Vi3	Distorted defect pyrochlore type	
Pb ₂ Mg _{0.5} Mn _{0.5} TaO ₆	C	4.015				Vi5	Dielectric properties [Vi5, Ve4]	6
Pb ₂ Ni _{0.5} Mn _{0.5} TaO ₆	C	4.009				Vi5	Dielectric properties [Vi5, Ve4]	6
A ₂ ⁺ BB'O ₆ ; B' = Bi ³⁺ , Pb ²⁺ , Pu ³⁺								
Ba ₂ LaBiO ₆	C	8.759				Sc18b	No dimensions, Bi ³⁺ -Bi ³⁺	
Ba ₂ BiBiO ₆	C					Sc18b		
Ba ₂ ScPaO ₆	C	8.549				Ke5		
Ba ₂ SrPaO ₆	C	8.860				Ke5		
Ba ₂ YPaO ₆	C	8.718				Ke5		
Ba ₂ InPaO ₆	C	8.596				Ke5		
Ba ₂ BaPaO ₆	C	8.932				Ke5		
Ba ₂ LaPaO ₆	C	8.885				Ke5		
Ba ₂ CePaO ₆	C	8.800				Ke5		
Ba ₂ PrPaO ₆	C	8.862				Ke5		
Ba ₂ NdPaO ₆	C	8.840				Ke5		
Ba ₂ SmPaO ₆	C	8.792				Ke5		
Ba ₂ EuPaO ₆	C	8.783				Ke5		
Ba ₂ GdPaO ₆	C	8.770				Ke5		
Ba ₂ TdPaO ₆	C	8.753				Ke5		

Compound	Sym	a Å	b Å	c Å	angle	Ref.	Remarks	Magnetic Data
A ₃ ²⁺ BB'O ₆ ; B' = Bi ³⁺ , Pa ⁵⁺ , Pu ⁵⁺ (continued)								
Ba ₂ DyPaO ₆	C	8.740				Ke5		in 3.3.4, Tab.
Ba ₂ HoPaO ₆	C	8.730				Ke5		
Ba ₂ ErPaO ₆	C	8.716				Ke5		
Ba ₂ TmPaO ₆	C	8.692				Ke5		
Ba ₂ YbPaO ₆	C	8.678				Ke5		
Ba ₂ LuPaO ₆	C	8.666				Ke5		
Ba ₂ PuPaO ₆	C	8.748				Ke5		
Ba ₂ AmPaO ₆	C	8.793				Ke5		
Sr ₂ LuPaO ₆	C	8.462				Ke5		
BaSrSrPaO ₆ ^s	C	8.784				Ke5		
Ba ₂ MnPuO ₆	C	8.32				Aw2		
Ba ₂ InPuO ₆	C	8.50				Aw2		
Ba ₂ LaPuO ₆	C	8.63				Aw2	Pseudocubic	
Ba ₂ CePuO ₆	C	8.72				Aw2		
Ba ₂ NdPuO ₆	C	8.66				Aw2		
Ba ₂ TiPuO ₆	C	8.06				Aw2	Pu ⁴⁺	
Ba ₂ ZnPuO ₆	C	8.38				Aw2	Pseudocubic	
Ba ₂ PbPuO ₆	C	8.58				Aw2		
A ₃ ²⁺ BMo ⁶⁺ O ₆								
Ba ₂ CaMoO ₆	C	8.355				St32	No compound [Pa7]	6
Ba ₂ CrMoO ₆	C	8.08				Pa7	S.S. with Sr [Ga12]	
Ba ₂ FeMoO ₆	C	4.043				Br14	Probably ordered	
Ba ₂ CoMoO ₆	C	4.022				Br14	Probably ordered	
Ba ₂ NiMoO ₆	C	3.91				Br14		6
Sr ₂ CrMoO ₆	C	7.98				Br14		6
Sr ₂ MnMoO ₆	T	7.888		7.909		Ga12	P & S [Pa7], Prop. [Ga12, Na4], S.S. with Ba and Ca [Ga12], neutron diffraction [Na11]	6
Sr ₂ FeMoO ₆	T	5.581		7.940		Ku8	P & S [Br14]	6
	C	7.918				Ku8	Cubic at 320 °C; no dielectric anomaly	
Sr ₂ NiMoO ₆	T	5.560		7.886		Ku8	P & S [Br14], semiconducting, ΔE = 0.78 eV ≤ 181 °C ≤ 1.30 eV [No1], S.S. with Ba, cubic at 22% Ba [No1, No3]	6
	C	7.878				Ku8	Cubic at 230 °C [Ku8, No3], no dielectric anomaly [Ku8]	
Sr ₂ ZnMoO ₆	T	5.561		7.966		Ku8	Cubic at 420 °C; no dielectric anomaly	
	C	7.954				Ku8		

Compound	Sym	a Å	b Å	c Å	angle	Ref.	Remarks	Magnetic Data
A ₂ ²⁺ BMo ⁶⁺ O ₆ (continued)								in 3.3.4, Tab. 6
Ca ₂ CrMoO ₆	O	5.36	5.49	7.70		Pa7		6
Ca ₂ FeMoO ₆	O	5.42	5.53	7.73		Pa7		6
A ₂ ²⁺ BTa ⁵⁺ O ₆								
Ba ₂ MgTeO ₆	C	8.13				Sl6	P & S [Ba26, Re4a]	
Ba ₂ CaTeO ₆	C	8.393				Sl6	P & S [Ba26], S.S. with Ni [Re4a]	
BaPbMgTeO ₆	C	8.08				Ba26		
Sr ₂ MgTeO ₆	C	7.94				Ba26		
SrPbMgTeO ₆	C	7.955				Ba26		
Sr ₂ NiTeO ₆	C	3.95				Re4a	Optical properties and S. S. with Ba	
Sr ₂ CuTeO ₆	T	7.680		8.465		Re4b	Optical properties	
Ca ₂ CaTeO ₆	O	5.55	5.77	7.98		Bl1a		
Pb ₂ MgTeO ₆	C	7.99				Ba26		
A ₂ ²⁺ BW ⁶⁺ O ₆								
Ba ₂ MgWO ₆	C	8.099				Sl32	P & S [Be18], dielectric properties [Ag7]	
Ba ₂ CaWO ₆	C	8.390				Be18	P & S [Sl32], S.S. with Ni [Re4a]	
Ba ₂ CrWO ₆	C					Pa7	No perovskite	
Ba ₂ FeWO ₆	C	8.133				Fr14		6
Ba ₂ CoWO ₆	C	8.098				Fr14	P & S [Br14], Prop., semiconducting, ΔE = 0.81 eV [Bo1], neutron diffraction [Co31]	6
Ba ₂ NiWO ₆	C	8.066				Fr14	P & S [Br14, Ag7], S.S. with Sr [No2], neutron diffraction [Co31], optical properties [Re4a]	6
Ba ₂ CuWO ₆	T	7.88		8.61		Bl8	P & S [Ka12, Ve2, Ve3], complete structure [Pl3]	6
Ba ₂ ZnWO ₆	C	8.116				Fr14	P & S [Be18]	
Ba ₂ SrWO ₆	C	8.53				Be18	P & S [Fr10, Sl32], S.S. with Sr ₃ WO ₆ [Be18]	
Ba ₂ CdWO ₆	C	8.383				Be18	Slightly distorted; cubic T > 805 °C [Ch4]	
Ba ₂ BaWO ₆	C	8.62				Sl32	P & S [Sl32]	
BaSrMgWO ₆	C	8.02				Be18	P & S [Be18]	
Ba _{1.5} Ca _{0.5} CaWO ₆	C	8.387				Sl32	Distorted	
BaSrCaWO ₆	C	8.29				Sl32	Composition questionable	
BaCaCaWO ₆	C	8.363				Be18	Distorted	
BaSrZnWO ₆	C	8.07				Be18	Composition questionable	
BaCaZnWO ₆	C	8.38				Be18	Composition questionable	
Sr ₂ MgWO ₆	C	7.8				Be18	P & S [Sl32], distorted	
Sr ₂ CaWO ₆	C	8.2				Be18	Distorted	6
Sr ₂ CrWO ₆	C	7.82				Pa7	Prop. [Bl4]	6
Sr ₂ MnWO ₆	C	8.01				Bl8	Prop. [Bl4]	6
Sr ₂ FeWO ₆	C	7.96				Bl8		6

Compound	Sym	a Å	b Å	c Å	angle	Ref.	Remarks	Magnetic Data
A ₃ +BW ⁶ +O ₆ (continued)								in 3.3.4, Tab. 6
Sr ₂ CoWO ₆	T	7.89		7.98		Fr14	P & S [Br14], Prop. [No1, Ku8, Bi2, Bi4] T ≈ 400 °C, cubic T > 400 °C; no dielectric anomaly	6
Sr ₂ NiWO ₆	C	7.904		7.91		Ku8	P & S [Br14], Prop. [No1, Bi2, Bi4, No2, Ve1, No2, Re4a], S.S. with LaFeO ₃ [Sm23], S.S. with Ba [No2], ESR [No4], S.S. with Ca [Re4a]	6
Sr ₂ CuWO ₆	T	7.86				Fr14	T ≈ 300 °C, cubic T > 300 °C [Ku8, No4] P & S [Ka12], dielectric properties [Ve2]	6
Sr ₂ ZnWO ₆	C	7.908		8.40		Ku8	P & S [Ku8, Be18], S.S. with Ba, cubic > 40% Ba [Fr14]	
	T	7.66		8.01		Bi8	T ≈ 430 °C, cubic T > 430 °C [Ku8, Fr14], no dielectric anomaly [Ku8]	
	C	7.92				Fr14	Distorted, P & S [Si32]; cubic T > 1100 °C, S.S. with Ca [Ch3]	
Sr ₂ SrWO ₆	C	7.956				Ku8	Distorted, P & S [Si32]	
SrCaMgWO ₆	C	8.3				Be18	Distorted, P & S [Be18]	
SrCaCaWO ₆	C	7.87				Bi8	Distorted, P & S [Be18]	
Ca ₂ MgWO ₆	C	8.1				Si32	Distorted, P & S [Be18]	
Ca ₂ CaWO ₆	C	7.75				Si32	Distorted, P & S [Be18]; not cubic T < 1500 °K, S.S. with Sr [Ch3, Ch4]	
Ca ₂ CrWO ₆	O	8.02				Pa7	Prop. [Bi2, Ki7]	6
Ca ₂ CoWO ₆	O	5.35	5.47	7.70		Bi8	Optical properties [Re4a]	6
Ca ₂ NiWO ₆	O	5.43	5.60	7.73		Bi8	Not perovskite [Bi8]	
Ca ₂ CuWO ₆	O	5.40	5.55	7.70		Be8	Dielectric properties [Sm8, Ag1, Sm13, Kh5, Mi1a, Kh6, Si42], piezoelectric properties, S.S. with Ti, Zr [Si34], S.S. with Cd [Is15], S.S. with PbFe _{2/3} W _{1/3} O ₆ [Sm10], S.S. with PbTiO ₃ , Ca ₂ MgWO ₆ , Pb ₂ MgNb ₂ O ₉ [Sm20, Si35]	
Pb ₂ MgWO ₆	C	8.0				Be8	Distorted, dielectric properties [Ag1] Prop. [Ve2, Ve4, Ro8]	6
Pb ₂ CaWO ₆	C	4.2	5.756	8.066		Be8	Prop., no cell dimensions [Ve4]	6
Pb ₂ MnWO ₆	O	5.736				Ve3	P & S [Fi11, Be18], Prop. [Te13, Bo10, Ki7, Fi6], B site ordering [Yu9], S.S. with BaTiO ₃ [To2]	6
Pb ₂ FeWO ₆	O	5.661	5.676	9.976		Bo10	T ≈ 20 °C, cubic T > 20 °C	6
Pb ₂ CoWO ₆	O	8.017				Fi6	Dielectric properties, P & S [To11a, To11b]	6
Pb ₂ NiWO ₆	C	7.997				No6	T = 173 °K - tetragonal below 290 °K	
Pb ₂ NiWO ₆	T	8.006		7.920		No6	Distorted, dielectric properties [Ro6], S.S. with Mg [Is15]	6
Pb ₂ CdWO ₆	C	4.1				Be18	Cubic at 400 °C, transformations [Po8], S.S. with Pb (Li _{1/3} Nb _{1/3} W _{1/3})O ₃ [Di5]	
Pb ₂ CdWO ₆	C	4.15				Fi7		

Compound	Sym	a Å	b Å	c Å	angle	Ref.	Remarks	Magnetic Data
A ₂ ⁺ BW ⁶⁺ O ₆ (continued)								
Pb ₂ Na _{0.5} Sc _{0.5} WO ₆						Ve4	Dielectric properties, no cell dimensions	in 3.3.4, Tab.
Pb ₂ Na _{0.5} Fe _{0.5} WO ₆						Ve4	Dielectric properties, no cell dimensions	
Pb ₂ Na _{0.5} Yb _{0.5} WO ₆	T	8.202		8.104		Ve4	Dielectric properties [Vi5, Ve4]	
Pb ₂ Mg _{0.5} Mn _{0.5} WO ₆	T	8.082		8.018		Vi5	Dielectric properties [Vi5, Ve4]	
Pb ₂ Co _{0.5} Mn _{0.5} WO ₆						Vi5	Dielectric properties [Vi5, Ve4]	6
Pb ₂ Ni _{0.5} Mn _{0.5} WO ₆						Vi5	No cell dimensions, Prop. [Vi5]	6
Pb ₂ Li _{0.5} Fe _{0.5} WO ₆	C	8.008				Ve3	Dielectric properties [Vi5, Ve2, Ve3, Ve4]	
Pb ₂ Li _{0.5} Co _{0.5} WO ₆	C	4.013				Ve3	Dielectric properties [Ve3]	
Pb ₂ Li _{0.5} La _{0.5} WO ₆	C	8.04				Vi5	Dielectric properties [Vi5]	
Pb ₂ Li _{0.5} Yb _{0.5} WO ₆	C	4.100				Ve3	Dielectric properties [Ve2, Ve3, Ve4]	
Pb ₂ Li _{0.5} Mn _{0.5} WO ₆						Ve4	Dielectric properties, no cell dimensions	
Pb ₂ Li _{0.5} Zr _{0.5} WO ₆						Ve4	Dielectric properties, no cell dimensions	
Pb ₂ Li _{0.5} Hf _{0.5} WO ₆						Ve4	Dielectric properties, no cell dimensions	
Pb ₂ Yb _{0.5} W _{0.5} O ₆	C	4.124				Ve4	Dielectric properties [Ve2, Ve3, Ve4]	
Pb ₂ FeMn _{0.5} W _{0.5} O ₆	C	4.037				Ro8	Dielectric properties [Ve4]	6
A ₂ ⁺ BReO ₆ , Re ³⁺ and Re ⁶⁺								
Ba ₂ MgReO ₆	C	8.082				Si8	P & S [Lo2, Sc18], single crystal [Si7]	
Ba ₂ CaReO ₆	C	8.356				Si8	P & S [Lo2, Sc18]	
Ba ₂ ScReO ₆	C	8.163				Si8	P & S [Sc18]	
Ba ₂ MnReO ₆	C	8.18				Si8	P & S [Lo2, Wa15], single crystal + Prop. [Si7]	6
Ba ₂ FeReO ₆	C	8.05				Si8	P & S [Lo2, Wa15], single crystal + Prop. [Si7], [Ba25a] suggests Ba ₂ Fe _{1-x} Re _x O ₆	6
Ba ₂ CoReO ₆	C	8.086				Si8	P & S [Lo2, Wa15], single crystal + Prop. [Si7]	6
Ba ₂ NiReO ₆	C	8.04				Si8	P & S [Lo2, Wa15], single crystal + Prop. [Si7]	6
Ba ₂ ZnReO ₆	C	8.106				Si8	P & S [Lo2, Wa15], single crystal + Prop. [Si7]	6
Ba ₂ SrReO ₆	T	8.60		8.43		Si8	P & S [Lo2], single crystal + Prop. [Si7]	
Ba ₂ YReO ₆	C	8.372				Si8	P & S [Sc18]	
Ba ₂ CdReO ₆	C	8.322				Si8	P & S [Lo2]	
Ba ₂ InReO ₆	C	8.258				Si8	P & S [Sc18]	
Ba ₂ BaReO ₆	T	8.65		8.33		Si8	P & S [Sc18]	
Ba ₂ LaReO ₆	C	8.547				Ba25a	Prep. 900 °C, a ₀ increases with prep. temperature suggesting Ba ₂ Re _{1-x} Re _x ³⁺ La _{1-x} Ba _x O ₆ ; P & S [Si8]	
Ba ₂ NdReO ₆	C	8.51				Si8	Prop. [Lo2], P & S [Sc18]	
Ba ₂ SmReO ₆	C	8.458				Ba25a		
Ba ₂ EuReO ₆	C	8.438				Ba25a		
Ba ₂ GdReO ₆	C	8.431				Si8		
Ba ₂ TbReO ₆	C	8.399				Ba25a		

Compound	Sym	a Å	b Å	c Å	angle	Ref.	Remarks	Magnetic Data
A ₃ ⁺ BReO ₆ , Re ⁶⁺ and Re ⁵⁺ (continued)								
Ba ₂ DyReO ₆	C	8.391				Ba25a		in 3.3.4, Tab.
Ba ₂ HoReO ₆	C	8.375				Ba25a		
Ba ₂ ErReO ₆	C	8.354				Sl8	Prop. [Lo2], P & S [Sc18]	
Ba ₂ TmReO ₆	C	8.342				Ba25a		
Ba ₂ YbReO ₆	C	8.329				Ba25a		
Ba _{2-x} Sr _x YbReO ₆	C	8.230				Ba25a	$x = 1.2$, small positive deviation from Vegard's law	
BaSrFeReO ₆							Prop. [Sl8, Lo2] Single crystal [Sl7], Prep. [Sc18] P & S [Sc18]	
Ba ₂ YReO ₆	T	7.88		7.94		Sl8	distorted	6
Sr ₂ MgReO ₆	O	5.76	5.85	8.21		Sl8		
Sr ₂ CaReO ₆	C	8.02				Sl8		
Sr ₂ CrReO ₆	C	7.82				Sl8		
Sr ₂ MnReO ₆	C	8.01				Sl8	distorted	6
Sr ₂ FeReO ₆	T	7.86		7.89		Sl8		
Sr ₂ CoReO ₆	T	7.88		7.98		Sl8		
Sr ₂ NiReO ₆	T	7.85		7.92		Sl8		
Sr ₂ ZnReO ₆	T	7.89		8.01		Sl8	P & S [Lo2, Wa15]	
Sr ₂ GaReO ₆	C	7.843				Sl8		
Sr ₂ SrReO ₆	T	8.41		8.13		Sl8	P & S [Sc18]	
Sr ₂ YReO ₆	C	8.197	5.81			Ba25b		
Sr ₂ CdReO ₆	O	5.73		8.16		Sl8		
Sr ₂ InReO ₆	O	8.071				Sl8		
Sr ₂ GdReO ₆	C	8.239				Ba25b		6
Sr ₂ TbReO ₆	C	8.223				Ba25b		6
Sr ₂ DyReO ₆	C	8.210				Ba25b		6
Sr ₂ HoReO ₆	C	8.200				Ba25b		6
Sr ₂ ErReO ₆	C	8.181				Ba25b		
Sr ₂ TmReO ₆	C	8.167				Ba25b		
Sr ₂ YbReO ₆	C	8.155				Ba25b		
Ca ₂ MgReO ₆	O	5.48	5.56	7.77		Sl8	P & S [Sc18]	
Ca ₂ CaReO ₆	O	5.67	5.78	8.05		Sl8	P & S [Sc18]	
Ca ₂ ScReO ₆	O	5.49	5.63	7.86		Sl8		6
Ca ₂ CrReO ₆	O	5.38	5.47	7.67		Sl8		
Ca ₂ MnReO ₆	O	5.52	5.55	7.82		Sl8		6
Ca ₂ FeReO ₆	O	5.41	5.53	7.69		Sl8		
Ca ₂ CoReO ₆	O	5.46	5.58	7.71		Sl8	P & S [Lo2]	6

Compound	Sym	a Å	b Å	c Å	angle	Ref.	Remarks	Magnetic Data
A ₃ ⁺ BReO ₆ , Re ³⁺ and Re ⁴⁺ (continued)								
Ca ₃ NiReO ₆	O	5.45	5.55	7.67		Sl8		in 3.3.4, Tab. 6 6
Ca ₃ CdReO ₆	O	5.64	5.77	7.99		Sl8		
Pb ₃ MnReO ₆	O	5.69	5.74	8.024		Ro8	Claim Mn ³⁺ - Re ⁴⁺ , Prop. [Ro8, Ro11]	
Pb ₃ MnReO ₆	O	5.67	5.75	8.008		Ro8	Claim Mn ³⁺ - Re ⁴⁺ , Prop. [Ro8, Ve4]	
A ₃ ⁺ BOsO ₆								
Ba ₃ MgOsO ₆	C	8.08				Sl8		6
Ba ₃ CaOsO ₆	C	8.362				Sl8		
Ba ₃ ScOsO ₆	C	8.152				Sl8		
Ba ₃ MnOsO ₆	H	5.82		14.2		Sl8	Hex (6L)	
Ba ₃ FeOsO ₆	H	5.76		14.1		Sl8	Hex (6L)	
Ba ₃ ZnOsO ₆	C	8.095				Sl8		
Ba ₃ SrOsO ₆	T	8.43		8.72		Sl8		
Ba ₃ CdOsO ₆	C	8.325				Sl8		
Ba ₃ InOsO ₆	C	8.224				Sl8		
Ba ₃ BaOsO ₆	C	8.66		8.34		Sl8		
Sr ₃ MgOsO ₆	T	7.86		7.92		Sl8		
Sr ₃ CaOsO ₆	C	8.21				Sl8	Distorted	
Sr ₃ ScOsO ₆	C	8.02				Sl8	Distorted	
Sr ₃ CrOsO ₆	C	7.84				Sl8		
Sr ₃ FeOsO ₆	C	7.85				Sl8	Distorted	
Sr ₃ CoOsO ₆	C	7.86		7.92		Sl8		
Sr ₃ GaOsO ₆	T	7.82				Sl8		
Sr ₃ SrOsO ₆	C	8.32		8.12		Sl8		
Sr ₃ InOsO ₆	T	8.06				Sl8		
Ca ₃ CaOsO ₆	O	5.73	5.80	7.87		Sl8		
Ca ₃ CrOsO ₆	O	5.38	5.47	7.66		Sl8		
Ca ₃ CoOsO ₆	O	5.47	5.59	7.70		Sl8		
A ₃ ⁺ BUO ₆								
Ba ₃ BeUO ₆	C	8.82				Aw1	Doubtful	6
Ba ₃ MgUO ₆	C	8.381				Sl5		
Ba ₃ CaUO ₆	C	8.67				Sl5	Distorted, P & S [Ru4]	
Ba ₃ ScUO ₆	C	8.49				Sl5		
Ba ₃ TiUO ₆	C	8.05				Aw1	Ti ⁴⁺	
Ba ₃ CrUO ₆	C	8.297				Sl5	Also prepared as Hex (6L)	
Ba ₃ MnUO ₆	C	8.52				Sl5	P & S [Aw1]	
Ba ₃ FeUO ₆	C	8.312				Sl5	Prop. [Dis]	
Ba ₃ CoUO ₆	C	8.372				Sl5		

Compound	Sym	a Å	b Å	c Å	angle	Ref.	Remarks	Magnetic Data
A ₃ ⁺ BUO ₆ (continued)								
Ba ₂ NiUO ₆	C	8.336				Sl5	Optical properties [Re4a]	in 3.3.4, Tab.
Ba ₂ CuUO ₆	T	8.18		8.84		Sl5		
Ba ₂ ZnUO ₆	C	8.397				Sl5		
Ba ₂ GeUO ₆	C	8.56				Aw1	Doubtful	
Ba ₂ SrUO ₆	C	8.84				Sl5	Distorted, P & S [Ru4]	
Ba ₂ YUO ₆	C	8.69				Sl5	Distorted	
Ba ₂ ZrUO ₆	C	8.35				Aw1		
Ba ₂ RhUO ₆	H	5.84		14.9		Sl5	Hex (6L)	
Ba ₂ CdUO ₆	O	6.07	6.13	8.64		Sl5		
Ba ₂ InUO ₆	C	8.521				Sl5		
Ba ₂ InUO ₆ ¹⁵	C	8.551				Sl5		Complete structure determined, P & S [Sl5, Ru4]
Ba ₂ BaUO ₆	T	6.285		8.943		Ru4	Distorted	
Ba ₂ LaUO ₆	C	8.73				Aw1	Ce ⁴⁺	
Ba ₂ CeUO ₆	C	8.87				Aw1		
Ba ₂ NdUO ₆	C	8.76				Aw1		
Ba ₂ SmUO ₆	C	8.76				Aw1		
Ba ₂ EuUO ₆	C	8.68				Aw1		
Ba ₂ GdUO ₆	C	8.66				Aw1		
Ba ₂ DyUO ₆	C	8.65				Aw1		
Ba ₂ HoUO ₆	C	8.65				Aw1	Distorted	
Ba ₂ ErUO ₆	C	8.67				Aw1		Distorted
Ba ₂ YbUO ₆	C	8.60				Aw1		
Ba ₂ LuUO ₆	C	8.57				Aw1		
Ba ₂ HfUO ₆	C	8.31				Aw1		
Ba ₂ HgUO ₆	C	8.83				Aw1	Doubtful	
Ba ₂ PbUO ₆	C	8.85				Aw1	Doubtful	
Ba ₂ SrUO ₆	C	8.66				Ru4		
Sr ₂ MgUO ₆	C	8.19				Sl5	Distorted	
Sr ₂ CaUO ₆	O	5.93	6.06	8.46		Sl5		
Sr ₂ CrUO ₆	C	8.09				Sl5	Distorted	6
Sr ₂ MnUO ₆	C	8.28				Sl5	Distorted	
Sr ₂ FeUO ₆	C	8.11				Sl5	Distorted	
Sr ₂ CoUO ₆	C	8.19				Sl5	Distorted	
Sr ₂ NiUO ₆	C	8.15				Sl5	Distorted, optical properties [Re4a]	
Sr ₂ SrUO ₆	M	5.959	6.179	8.553	$\beta = 90^\circ 11'$	Ru4	Complete structure; P & S [Sl5, Ru4, Be25, Ip1]	
Sr ₂ CdUO ₆	O	5.91	6.03	8.42		Sl5		
Sr ₂ InUO ₆	C	8.33				Sl5	Distorted; Prop. [Ke13]	
SrCaCaUO ₆	O	5.83	6.01	8.36		Sl5		6

Compound	Sym	a Å	b Å	c Å	angle	Ref.	Remarks	Magnetic Data
----------	-----	--------	--------	--------	-------	------	---------	------------------

Compound	Sym	a Å	b Å	c Å	angle	Ref.	Remarks	Magnetic Data
in 3.3.4, Tab.								
Al ³⁺ BUO ₆ (continued)								
Ca ₂ CaUO ₆	M	5.728	5.958	8.301	$\beta = 90^\circ 33'$	Rt4	Complete structure determined, P & S [Sl5, Ru4, Be25, Ipt]	
Pb ₂ PbUO ₆	O	13.71	12.36	8.21		Sl26	Not perovskite	
Al ³⁺ BB'O ₆ ; B' = Np ⁴⁺ , Pu ⁴⁺								
Ba ₂ SrNpO ₆	C	8.799				Ke4		
Ba ₂ BaNpO ₆	C	8.860				Ke4		
Ba ₂ SrNpO ₆	C	8.735				Ke4		
Ba ₂ SrPuO ₆	C	8.780				Ke3		
Ba ₂ BaPuO ₆	C	8.840				Ke3		
Ba ₂ SrPuO ₆	C	8.717				Ke3		
Sr ₂ SrPuO ₆						Ke3	Not perovskite	
Al ³⁺ B+B'O ₆ ; B' = Tc ⁴⁺ , Re ⁴⁺ , Os ⁴⁺ , Ir ⁴⁺								
Ba ₂ LiTcO ₆	C	8.092				Wa16	P & S [Ke9]	
Ba ₂ NaTcO ₆	C	8.292				Wa16	P & S [Ke9]	
Sr ₂ LiTcO ₆	C	7.84				Wa16	Distorted, P & S [Ke9]	
Sr ₂ NaTcO ₆	T	8.09		8.14		Wa16	P & S [Ke9]	
Ca ₂ LiTcO ₆						Sl4	Not able to be made [Wa16]	
Ba ₂ LiReO ₆	C	8.118				Sl4	S.S. with Na [Sl4]	
Ba ₂ NaReO ₆	C	8.296				Sl4		
Sr ₂ LiReO ₆	C	7.87				Sl8		
Sr ₂ NaReO ₆	C	8.13				Sl8		
Ca ₂ LiReO ₆	C	7.83				Sl8	Distorted	
Ba ₂ LiOsO ₆	C	8.100				Sl8	S.S. with Re [Sl8]	
Ba ₂ NaOsO ₆	C	8.282				Sl8		
Sr ₂ LiOsO ₆	C	7.86				Sl8		
Sr ₂ NaOsO ₆	C	8.13				Sl8		
Ca ₂ LiOsO ₆	C	7.83				Sl8	Distorted	
Ba ₂ NaIO ₆	C	8.33				Sl6		
Ba ₂ AgIO ₆	C	8.46				Sl6		

6

Tab. 2c. A₃BB₂O₉ (for H symmetry see Fig. 1c)

Compound	Sym	a Å	b Å	c Å	angle	Ref.	Remarks	Magnetic Data
A ₃ BB ₂ ⁴⁺ O ₉								in 3.3.4, Tab.
Ba ₃ MgNb ₂ O ₉	H	5.77		7.08		Ga9	P & S [Ga13, Bl8], see Fig. 1 (c)	
Ba ₃ CaNb ₂ O ₉	H	5.92		7.25		Ga9	See Fig. 1 (c)	
Ba ₃ FeNb ₂ O ₉	C	4.085				Ga9		
Ba ₃ CoNb ₂ O ₉	C	4.09				Ga13		
Ba ₃ NiNb ₂ O ₉	C	4.074				Ga9		
Ba ₃ CuNb ₂ O ₉	T	8.04		8.40		Bl8	P & S [Ro20, Ag1], dielectric properties [Sm8], optical properties [Re4a]	
Ba ₃ ZnNb ₂ O ₉	C	8.166				Ve2	Dielectric properties [Ka12, Ve3]	
Ba ₃ CdNb ₂ O ₉	C	4.094				Ga9	Cubic > 653 °K	
Ba ₃ BaNb ₂ O ₉	C	4.168				Ga9	P & S [Ga13, Ag1]	
Ba ₃ PbNb ₂ O ₉	H	6.01		8.0		Ga9		
Ba ₃ MgNb ₂ O ₉	C	4.26				Ga9	P & S [Bl8], see Fig. 1 (c)	
Sr ₃ MgNb ₂ O ₉	H	5.66		6.98		Ga9	See Fig. 1 (c)	
Sr ₃ CaNb ₂ O ₉	H	5.76		7.16		Ga9	See Fig. 1 (c)	
Sr ₃ FeNb ₂ O ₉	T	3.997		4.018		Ga9		
Sr ₃ CoNb ₂ O ₉	C	8.01				Bl8		
Sr ₃ NiNb ₂ O ₉	H	5.64		6.90		Ga9	P & S [Ag1], optical properties of S.S. with Ba and Ca [Re4a], see Fig. 1 (c)	
Sr ₃ CuNb ₂ O ₉	T	7.888		8.148		Ka12	Prop. [Ve2]	
Sr ₃ ZnNb ₂ O ₉	H	5.66		6.95		Ga9	P & S [Ga13], see Fig. 1 (c)	
Sr ₃ CdNb ₂ O ₉	C	4.089				Ga9	Distorted perovskite	
Ca ₃ CaNb ₂ O ₉	C					Bl8		
Ca ₃ NiNb ₂ O ₉	C	3.88				Ag1		
Pb ₃ MgNb ₂ O ₉	C	4.04				Ag1	Dielectric properties [Sm27, Ag1, Ou1, Ou1a, Ou2, Bo5, Is4, Bo16, Be23, Kh5, Kh4, Kh8, Sm14, Sm20, Sm29, Sm8, Cr6b], crystal growth [Ba5, My3], electrooptic effect [Sm29]	
Pb ₃ MnNb ₂ O ₉							No cell dimensions	
Pb ₃ CoNb ₂ O ₉	C	4.05				Ag1	Dielectric properties [Bo5, Ag1]	
Pb ₃ NiNb ₂ O ₉	C	4.02				Bo5	Dielectric properties [Ag1, Sm8, Bo5, Is4], crystal growth [Bo5, My3], S.S. with Mg [Sm20, Sm27, Sm14, Is4, Cr6b], S.S. with Pb(Ti, Zr)O ₈ [Bu10], electrooptic effect [Sm29a]	
Pb ₃ ZnNb ₂ O ₉	C	4.05				Bo5	Dielectric properties [Bo5, Kh7, Be23a]	
Pb ₃ Sc _{1/3} W _{2/3} NbO ₉	C	4.074				To1	Dielectric properties [Ve4]	
Pb ₃ CdNb ₂ O ₉	C	8.246				To1	Dielectric properties [Ve2, Ve3, Ve4]	

Compound	Sym	a Å	b Å	c Å	angle	Ref.	Remarks	Magnetic Data
A ₃ BB ₂ X ₆ (continued)								in 3.3.4, Tab.
Ba ₃ MgRu ₂ O ₉	H					Ca2	Hex (6L), magnetic properties 84 < T < 948 °K, Θ _N = 390 °K [Ca2]	
Ba ₃ MgSb ₂ O ₉	H	5.83		14.26		Bl8	Hex (6L)	
Ba ₃ CaSb ₂ O ₉	H	5.99		14.84		Bl8	Hex (6L)	
Ba ₃ CoSb ₂ O ₉	H	5.84		14.35		Bl8	Hex (6L)	
Ba ₃ NiSb ₂ O ₉	H	5.82		14.25		Bl8	Hex (6L), optical properties of S.S. with Sr and Nb [Re4a]	
Ba ₃ CuSb ₂ O ₉	H	5.82		14.22		Bl8	Hex (6L)	
Ba ₃ SrSb ₂ O ₉	H	6.15		15.6		Bl8	Hex (6L)	
Ba ₃ BaSb ₂ O ₉	H	6.09		15.9		Bl8	Hex (6L)	
Sr ₃ MgSb ₂ O ₉	C	7.96				Bl8		
Sr ₃ CaSb ₂ O ₉	C	8.17				Bl8		
Sr ₃ CoSb ₂ O ₉	C	7.99				Bl8		
Sr ₃ NiSb ₂ O ₉	C	3.98				Bl8		
Sr ₃ CuSb ₂ O ₉	C	7.84				Bl8		
Sr ₃ SrSb ₂ O ₉	T	7.84				Re4a	Cell probably doubled, optical properties [Re4a]	
Sr ₃ La _{0.5} Li _{0.5} Sb ₂ O ₉	O	5.78	5.80	8.19		Bl8	Optical properties [Re4b]	
Ba ₃ MgTa ₂ O ₉	O	5.62	5.68	8.34		Bl8		
Ba ₃ CaTa ₂ O ₉	H	5.782		8.00		Bl8		
Ba ₃ MnTa ₂ O ₉	H	5.895		7.067		Ga10	Crystal growth [Ga7], see Fig. 1 (c)	
Ba ₃ FeTa ₂ O ₉	H	5.819		7.284		Ga10	P & S [Ga8], crystal growth [Ga7], see Fig. 1 (c)	
Ba ₃ CoTa ₂ O ₉	C	4.10		7.127		Ga10	See Fig. 1 (c)	
Ba ₃ NiTa ₂ O ₉	C	5.776				Ga13		
Ba ₃ CuTa ₂ O ₉	H	5.758		7.082		Ga10	P & S [Ro20], see Fig. 1 (c)	
Ba ₃ ZnTa ₂ O ₉	T	8.132		7.052		Ga10	P & S [Ro20], crystal growth [Ga7], optical properties [Re4a], see Fig. 1 (c)	
Ba ₃ SrTa ₂ O ₉	H	5.782		8.432		Ka12	P, S + Prop. [Ve2, Ve3]	
Ba ₃ CdTa ₂ O ₉	H	5.95		7.097		Ga10	P & S [Ga13], crystal growth [Ga7], see Fig. 1 (c)	
Ba ₃ BaTa ₂ O ₉	C	4.167		7.47		Ga11	P & S [Ga13], see Fig. 1 (c)	
Ba ₃ PbTa ₂ O ₉	C	6.10				Ga10	See Fig. 1 (c)	
Ba ₃ Zn _{0.5} Ni _{0.5} Ta ₂ O ₉	C	4.250		8.05		Bl8		
Sr ₃ MgTa ₂ O ₉	C	4.08				Ga10		
Sr ₃ CaTa ₂ O ₉	H	5.652		6.951		Ga10	P & S [Ro20], see Fig. 1 (c)	
Sr ₃ CoTa ₂ O ₉	H	5.764		7.096		Ga10	See Fig. 1 (c)	
Sr ₃ NiTa ₂ O ₉	H	5.630		6.937		Ga10	P & S [Ga13], see Fig. 1 (c)	
Sr ₃ CuTa ₂ O ₉	H	5.607		6.923		Ga10	P & S [Ga13], see Fig. 1 (c)	
Sr ₃ ZnTa ₂ O ₉	T	7.860		8.248		Ka12	P, S + Prop. [Ve2, Ve3]	
Pb ₃ MgTa ₂ O ₉	H	5.664		6.951		Ga10	P & S [Ga13], see Fig. 1 (c)	
Pb ₃ CoTa ₂ O ₉	C	4.03				Bo5	Prep. [Ag1], electrooptic effect [Sm29a]	
Pb ₃ NiTa ₂ O ₉	C	4.02				Bo5	Prep. [Ag1]	

Compound	Sym	a Å	b Å	c Å	angle	Ref.	Remarks	Magnetic Data
La ₃ Co ₂ B ³⁺ O ₉	O	5.58	5.58	7.89		Bl8		in 3.3.4, Tab.
La ₃ Co ₂ NbO ₉	O	5.57	5.57	7.87		Bl8		
La ₃ Co ₂ SbO ₉								
A ₃ B ₂ B ³⁺ O ₉								
Ba ₃ Cr ₂ MoO ₉	H	5.72		14.02		Pa7	Hex (6L)	
Ba ₃ Fe ₂ MoO ₉	H	5.74		14.08		Bl8	Hex (6L)	
Ba ₃ In ₂ MoO ₉	C	4.168				Ka12		
Ba ₃ Bi ₂ MoO ₉	O	6.148	6.184	8.642		Ve2	P & S [Vi3, Ve3], dielectric properties [Vi2b]	
	C	4.37				Vi2b	T > 500 °C	
Ba ₃ LiNbMoO ₉	R	4.091				Ka12		
Ba ₃ LiTaMoO ₉	C	4.090				Ka12		
Pb ₃ Bi ₂ MoO ₉	T	11.262		11.452	α = 89° 50'	Vi3	Defect pyrochlore type	
Ba ₃ Sc ₂ WO ₉	C	8.24				Fr14	P & S [Ga15], dielectric properties [Ka12]	
Ba ₃ Cr ₂ WO ₉	H	5.75		14.35		Pa7	Hex (6L)	
Ba ₃ Fe ₂ WO ₉	H	5.74		14.08		Bl8	Hex (6L)	
Ba ₃ Co ₂ WO ₉	H	5.74		14.10		Bl8	Hex (6L)	
Ba ₃ Y ₂ WO ₉	C	8.374				Ga15		
Ba ₃ Rh ₂ WO ₉	H	5.74		14.15		Bl8	Hex (6L)	
Ba ₃ In ₂ WO ₉	C	8.321				Ga15	Structure + Prop. [Ka12]	
Ba ₃ La ₂ WO ₉	C	8.58				Bl8		
Ba ₃ Nd ₂ WO ₉	C	8.513				Ga15		
Ba ₃ Eu ₂ WO ₉	C	8.605				Ga15	P & S [Bl8]	
Ba ₃ Gd ₂ WO ₉	C	8.411				Ga15	Structure + Prop. [Ka12]	
Ba ₃ Dy ₂ WO ₉	C	8.386				Ka12	Probably ordered	
Ba ₃ Ho ₂ WO ₉	C	4.252				Ga15		
Ba ₃ Er ₂ WO ₉	C	8.386				Ga15	No cell dimensions	
Ba ₃ Yb ₂ WO ₉						Ga15	No cell dimensions	
Ba ₃ Lu ₂ WO ₉						Ve2	Dielectric properties [Vi3, Ve3, Vi2b]	
Ba ₃ Bi ₂ WO ₉	R	6.131			α = 60° 23'			
Ba ₃ LiNbWO ₉	R	4.098			α = 89° 52'	Ka12		
Ba ₃ LiTaWO ₉	R	4.095			α = 89° 53'	Ka12		
Sr ₃ Fe ₂ WO ₉	T	3.945		3.951		Ga15	P & S [Bl8], S.S. with Sr ₃ Fe ₂ UO ₉ [Se6a]	
SrLa ₂ Mg ₂ WO ₉	C	7.91				Bl8		
SrLa ₂ Co ₂ WO ₉	C	7.90				Bl8		
Pb ₃ Sc ₂ WO ₉	C	8.134				Ve3	Dielectric properties [Ve4, Ve2, Ve3, To1]	
Pb ₃ Mn ₂ WO ₉	C					Ro8	No cell dimensions, Prop. [Ve4, Ro8], S.S. with PbTiO ₃ [Di5a]	6
Pb ₃ Fe ₂ WO ₉	C	4.02				Ro8	Prop. [Ag1, Ro8, Sm10, Sm16, Sm28, To3, To11, Te13, Pl1, K16], B site ordering [Yu9]	6
Pb ₃ Bi ₂ WO ₉	T	10.637		10.799		Vi3	Defect pyrochlore type	

Compound	Sym	a Å	b Å	c Å	angle	Ref.	Remarks	Magnetic Data
A ₃ B ₂ B ⁶⁺ O ₉ (continued)								
Pb ₃ ScMnWO ₉						Ve4	No cell dimensions	in 3.3.4, Tab.
Pb ₃ CrMnWO ₉						Ve4	No cell dimensions	6
Pb ₃ FeMnWO ₉						Ve4	No cell dimensions	6
Pb ₃ CdMnWO ₉	O	5.80	5.90	8.138		Ro8	Prop. [Ve4, Ro8]	6
Pb ₃ CoFeWO ₉						Ve4	No cell dimensions	6
Pb ₃ LiNbWO ₉	C	8.090				Vi5	Dielectric properties [Ve2, Ve4, Vi5]	
Pb ₃ Cd _{1/3} Nb _{2/3} WO ₉	O	5.813				To1	Dielectric properties [Ve2, Ve4]	
Ba ₃ Cr ₂ ReO ₉	H	5.70		8.178		Si8	Hex (6L)	
Ba ₃ Fe ₂ ReO ₉	H	5.81		13.8		Si8	Hex (6L)	
Sr ₃ Cr ₂ ReO ₉	C	8.015		14.10		Si8	Hex (6L)	
Sr ₃ Fe ₂ ReO ₉	C	7.890				Si8		
Sr ₃ In ₂ ReO ₉	C	8.297				Si8		
Ba ₃ Sc ₂ UO ₉	C	8.49				Si5	Hex (6L)	
Ba ₃ Cr ₂ UO ₉	H	5.82				Si5	P & S [Ro14]	
Ba ₃ Fe ₂ UO ₉	C	8.232		14.6		Si5	Slight distortion	
Ba ₃ Y ₂ UO ₉	C	8.70				Si5		
Ba ₃ In ₂ UO ₉	C	8.512				Si5		
Sr ₃ Cr ₂ UO ₉	C	8.00				Si5		
Sr ₃ Fe ₂ UO ₉	C	8.066				Ro14	Prop. [Be51], S.S. with Sr ₃ Fe ₂ WO ₉ [Se6a]	6
Tab. 2d. A ³⁺ (B ₂ B ⁶⁺)O ₉								
Compound	Sym	a Å	b Å	c Å	angle	Ref.	Remarks	Magnetic Data
Ba[Zn _{0.2} Fe _{0.8} Nb _{0.4}]O ₉	C	4.08				Ga13		
Ba[Zn _{0.2} Fe _{0.2} Ta _{0.8}]O ₉	C	4.08				Ga13		
Sr[Zn _{0.2} Fe _{0.2} Ta _{0.8}]O ₉	C	4.01				Ga13		
Ba[Li _{0.25} Nb _{0.75}]O ₉	C	4.095				Ka12		
Ba[Na _{0.25} Nb _{0.75}]O ₉	C	4.107				Ka12		
Ba[Na _{0.25} Ta _{0.75}]O ₉	C	4.137				Ga6		
Sr[Na _{0.25} Ta _{0.75}]O ₉	C	4.055				Ga6		
Ba[Fe _{0.75} Nb _{0.25}]O ₉	C	4.07				Ga13		
Ba[Fe _{0.75} Ta _{0.25}]O ₉	C	4.07				Ga13		
Sr[Fe _{0.7} Nb _{0.3}]O ₉	C	3.96				Ga13		
Ba[Fe _{1/7} Fe _{6/7} Ta _{4/7}]O ₉	C	4.08				Ga13		
Ba[Co _{1/7} Co _{6/7} Ta _{4/7}]O ₉	C	4.09				Ga13		
Sr[Co _{1/7} Co _{6/7} Ta _{4/7}]O ₉	C	4.00				Ga13		
Ba[Na _{0.4} W _{0.6}]O ₉	C	4.158				Ka12		

3.2 Descriptions of perovskite-related structures

3.2.1 A-cation vacancies

3.2.1.1 No A cations

Because a skeleton of shared-corner octahedra is stable, it is possible to remove all the A cations from the perovskite structure without collapsing the BX_3 subarray. In the case of $\square \text{ReO}_3$, for example, the structure remains cubic. However, a partial or a complete collapse of the skeleton is found in many $\square BX_3$ compounds. The completely collapsed structure has hexagonal-close-packed X layers with one-third of the octahedral sites occupied by B atoms, as indicated in Fig. 19. This results in a simple-cubic array of B cations with corner-shared octahedra having a B-X-B angle of 132° . For comparison, Fig. 19 also shows the corner-shared octahedra across a close-packed $\square X_3$ plane of the cubic $\square \text{ReO}_3$ structure, where the B-X-B angle is 180° . It is possible to go from one structure to the other by a simple increase of the B-X-B angle, the B cations forming a simple-cubic array in all structures. In the partially collapsed structure, represented by CrF_3 , and B-X-B angle is intermediate, $\approx 150^\circ$. Trifluorides of the first-row transition metals have the partially collapsed structure, those of the second- and third-row transition metals have the ReO_3 structure where the number of outer d electrons per cation is ≤ 3 , but the completely collapsed structure where it is ≥ 6 . The B cations of the latter group either have no atomic moment (Rh^{III} and Ir^{III} have $t_{2g}^6 e_g^0$) or disproportionate into magnetic and nonmagnetic ions (Pd^{2+} , $t_{2g}^6 e_g^2$ and Pd^{IV} , $t_{2g}^6 e_g^0$), so that there are no magnetic interactions between neighboring cations. The other trifluorides, on the other hand, are all antiferromagnetic, and coupling between like atoms of the second and third long periods is stronger than that between like atoms of the first long period. Since the B-X-B superexchange interaction is enhanced by a larger B-X-B angle, it is reasonable to assume that the interactions between neighboring B cations stabilizes the ReO_3 structure. These interactions may be either weaker interactions between localized electrons, as in the magnetic fluorides, or stronger interactions, as in metallic ReO_3 . In this connection, stabilization of the cubic structure in the tungsten bronzes $\text{A}_x^m \text{WO}_3$ for $m \times > 0.3$ is significant. The conduction electrons introduce cation-anion-cation interactions while simultaneously reducing the energy gained by a ferroelectric distortion.

Electron-ordering distortions may be superposed on the array of corner-shared octahedra. MnF_3 , for example, exhibits the Jahn-Teller distortions shown in Fig. 10(a) superposed on the partially collapsed structure. WO_3 , on the other hand, exhibits several low-temperature phases characteristic of an interplay of antiferroelectric distortions and different degrees of the collapse of the B-X-B angle.

3.2.1.2 The bronze structures

Although $\square BX_3$ compounds with the ReO_3 structure and cubic ABX_3 compounds have the same BX_3 array, complete solid solutions $\square_x \text{A}_{1-x} \text{BX}_3$, $0 \leq x \leq 1$, are not possible. Although there is no ordering of the vacancies for larger x , except for $\text{Na}_{0.75} \text{WO}_3$ [Atf], for smaller x there is ordering accompanied by a collapse of the BX_3 array within basal planes perpendicular to a unique axis. Such a collapse creates the tetragonal and hexagonal tunnel structures of Fig. 20. The tetragonal structure contains three types of tunnels, one containing cubic, twelve-coordinated A' sites, one containing pentagonal-prism, fifteen-coordinated A'' sites, and one small tunnel containing nine-coordinated A''' sites, which are only occupied by Li^+ ions. Without Li^+ ions, all these sites are filled at $\text{A}_0 \text{A}_0' \text{A}_0'' \text{BX}_3$. This phase, which may occur for a

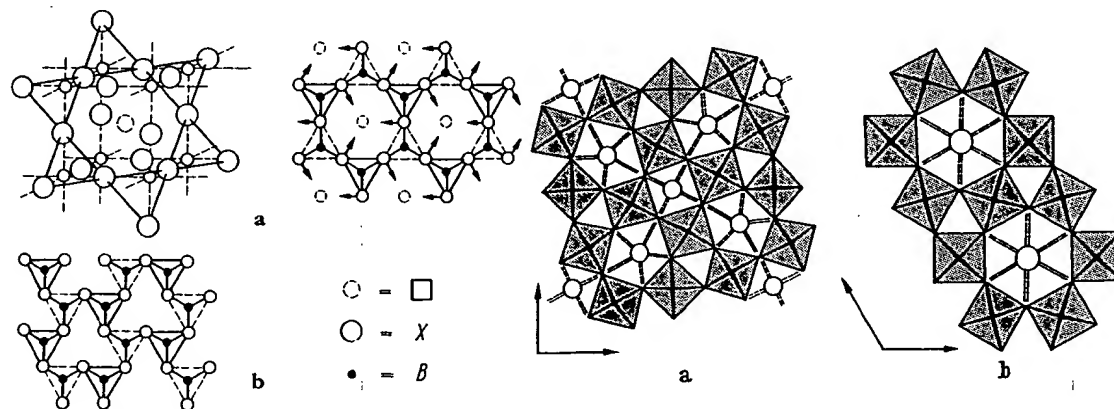


Fig. 19. Projections on B-cation planes of two $\square BX_3$ structures. Triangles in full and dotted lines represent faces of octahedra below or above the B-cation plane. a) Cubic $\square \text{ReO}_3$ structure DO_3 . Arrows indicate cooperative atomic motions that collapse the structure. b) Completely collapsed $\square \text{RhF}_3$ structure.

Fig. 20. Bronze structures found in $\text{A}_x \square_{1-x} \text{BX}_3$ systems. a) Tetragonal (II) structure occurring for $x \leq 0.6$. b) Hexagonal structure occurring for $x \leq 0.33$ [Wat].

range of $x \leq 0.6$, is labelled tetragonal (II) in Tab. 3 to distinguish it from the antiferroelectric tetragonal (I) phase of WO_3 . The hexagonal structure contains hexagonal-prism, eighteen-coordinated A sites and is restricted to the range of composition $x \leq 0.33$. An orthorhombic tunnel structure has also been identified for AB_2O_6 compounds [Ga15a].

Tab. 3. Color vs. x for Na_xWO_3 and compositional ranges for the bronze structures in the A^{1+}WO_3 perovskites. Adapted from [Di3]

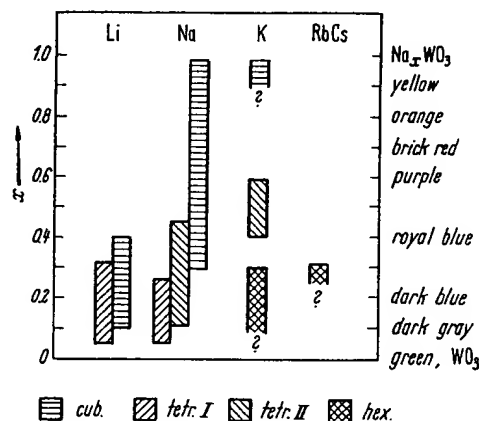


Fig. 21. Projections onto (110) planes of a) cubic perovskite and b) brownmillerite structures. Brownmillerite structure is formed by removing alternate [110] strings of oxygen from central row of a) and regrouping remaining oxygen into the tetrahedra shown in b) [Wa1].

3.2.2 Anion-deficient compounds

3.2.2.1 Compounds ABX_{3-x}

Several systems ABX_{3-x} , where $0 \leq x \leq 0.5$, have been reported as anion-deficient perovskites. $\text{SrTiO}_{2.5}$ and $\text{SrVO}_{2.5}$, for example, both give simple x-ray powder patterns in qualitative agreement with the assumption of a perovskite structure having one-sixth of the anions missing at random. Further, the homogeneity range of SrTiO_{3-x} is reported [Wa1] to extend over $0 \leq x \leq 0.5$ without any change of lattice parameter. However, if an anion is removed from a close packed structure, the metal atoms to which it was formerly bonded will have highly unsymmetrical coordination, and some local rearrangement of the anion can be expected. The nature of this local rearrangement depends upon the character of the B cation. In order to learn what rearrangements may occur locally, it is necessary to examine those special cases where long-range order occurs, since local changes of cation coordination are difficult to detect by x-ray diffraction and have not been investigated by other methods.

In the system $\text{SrFe}_{2-x}^{2+}\text{Fe}_{1-2x}^{3+}\text{O}_{3-x}$, $0 \leq x \leq 0.5$, it is known that the Fe^{3+} ions are stable in either tetrahedral or octahedral coordination. Therefore, it is reasonable to anticipate the creation of fourfold coordination about half of the Fe^{3+} ions in the system. This is possible because the d electrons of Fe^{3+} ions are localized, so that Fe^{3+} and Fe^{4+} ions are distinguishable, even though the d electrons of the end member $\text{SrFe}^{4+}\text{O}_3$ appear to be collective. Support for the creation of tetrahedral sites, as well as a suggestion of how the tetrahedra might be arranged, is given by $\text{Ca}_2\text{Fe}_2\text{O}_6$, which has the brownmillerite structure [Be41] of Fig. 21. Within every other (001) BX_2 plane of the cubic perovskite, alternate [110] rows of anions are removed. The remaining anions in these planes are displaced alternately along [110] and $[\bar{1}\bar{1}0]$ directions toward the anion vacancies, the B cations shifting slightly also to maintain equal B-X distances with all four near-neighbor anions. The result is fourfold coordination for all B cations in these (001) BX_2 planes, sixfold coordination for all B cations in the alternate (001) BX_2 planes.

The x-ray pattern of $\text{K}_2\text{Ti}_2\text{O}_6$ has a strong resemblance to that of perovskite. However, $\text{KTiO}_{2.5}$ is not an anion-deficient perovskite, but is completely ordered, each Ti^{4+} ion having five oxygen near neighbors forming a trigonal bipyramid [An3]. It has little similarity to perovskite.

The oxygen-deficient, tetragonal compounds $(\text{Ba}_{2x}\text{Bi}_{1-2x})\text{BiO}_{3-x}$, $0.22 < x < 0.5$, retain an octahedral grouping for Bi in the B sites, but the A positions have only six oxygen near neighbors, two each at 2.7, 3.1 and 3.6 Å [Au1].

These examples indicate that a variety of orderings must occur in anion-deficient perovskites. Further structural work needs to be done.

3.2.2.2 Alloys $M^cX_{1-x}M^f$

Since the alloys M^cXM^f are generally considered to represent interstitial X atoms in an ordered, face-centered-cubic M^cM^f alloy, it is not surprising that the phase is stable over a considerable range of anion deficiency. Since these alloys are metallic, it is probable that the X-atom vacancies are randomly distributed.

3.2.2.3 Shear structures $\square BO_{3-x}$

Ranges of composition have been reported for BO_{3-x} , where B = Mo or W. MAGNÉLI [Ma14] has shown that these compositional ranges consist of a series of discrete phases having an x-ray diffraction pattern dominated by a cubic $\square ReO_3$ -type (DO_6) subcell, but exhibiting superlattice lines. The superlattice of any discrete phase is not due to an ordering of anion vacancies within this basic structure, but to a regular interruption of the DO_6 structure by planes of discontinuity across which octahedra share edges rather than corners. In these structures the oxygen vacancies condense into regularly spaced planes and are then eliminated by a shear displacement of the type shown schematically in Fig. 22. These "shear" planes may be constituted in different ways: For the series of phases B_nO_{3n-2} , six octahedra in a group share edges, and for the phases B_nO_{3n-1} groups of four octahedra share edges. In both cases the discontinuities continue in two dimensions throughout the structure where they separate DO_6 blocks n octahedra thick. The $\beta-WO_{3-x}$ phases, $0.10 \leq x \leq 0.17$, belong to the series B_nO_{3n-2} with $12 < n \leq 20$. The observed compositional range $(W, Mo)O_{3-x}$, $0.07 \leq x \leq 0.12$, contains six discrete B_nO_{3n-1} phases corresponding to $n = 8, 9, 10, 11, 12$, and 14 [Ma17a]. The origin of the shear planes appears to be an interplay between electrostatic and elastic forces: Electrostatic repulsive energies between B cations sharing common octahedral-site edges is minimized by cationic displacements (of ferroelectric type) away from the center of symmetry of the interstice and the shared octahedral edge. These displacements can be cooperative, costing a minimum of elastic energy, if the shared edges are coplanar. The origin of the regular spacing between planes is not established. Presumably it is primarily due to elastic energy, although collective-electron effects [Go11] probably play a contributing role.

3.2.3 Structures deficient in B cations

3.2.3.1 Bismuth compounds

Bismuth compounds with chemical formula $(Bi_2A_{m-2})B_{m-1}O_{3m}$ have the structural formula $(Bi_2O_2)^{2+}(A_{n-1}B_nO_{3n+1})^{2-}$, $n = m - 1$. These compounds consist of a regular intergrowth of the perovskite structure with Bi_2O_2 sheets consisting of BiO_4 square pyramids sharing edges [Au2], as indicated in Fig. 23. Between the Bi_2O_2 sheets are n layers of corner-shared octahedra and $(n - 1)$ layers of perovskite-type A cations in the twelve-coordinated interstices. Where $n = 1$, the pyramidal sheets alternate with

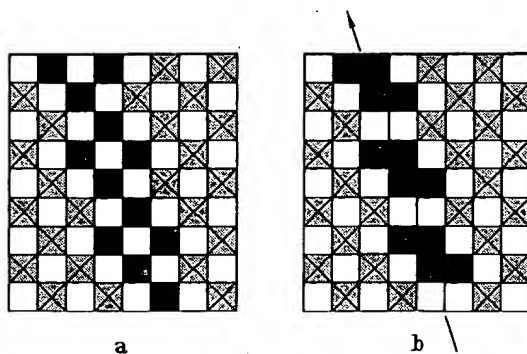
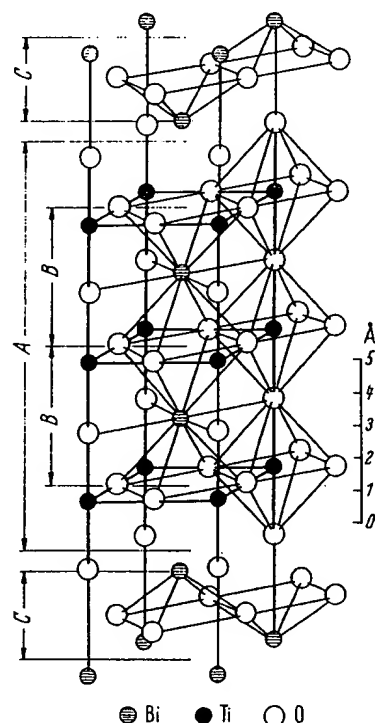


Fig. 22. Projection onto (001) planes of a) cubic $\square ReO_3$ structure and b) B_nO_{3n-1} shear plane. Anions are removed from black octahedra, which then move to adjacent positions to form configuration b) [Wa1].

Fig. 23. One half of the pseudo-tetragonal unit cell of $Bi_4Ti_2O_{14}$ (from $x \approx 0.25$ to $x \approx 0.75$). A denotes the perovskite layer $(Bi_2Ti_2O_{10})^{2-}$, C the $(Bi_2O_2)^{2+}$ layers, and B the unit cells of the hypothetical perovskite structure $BiTiO_3$ [Au3].



single octahedral layers, and no sites are available for A cations. This particular phase has been prepared in a large number of oxides and oxyfluorides, where $B = \text{Ti, Nb, Ta}$ and the O/F ratio depends upon the valencies of the A and B cations (see Tab. 4).

Many of these compounds are reported to exhibit ferroelectric distortions within the perovskite layers, and they will certainly be important for technical applications in the future.

3.2.3.2 Hexagonal $A_nB_{n-1}X_{3n}$ structures

As shown in Fig. 1(c), the cubic perovskite may be indexed on an hexagonal basis. It consists of cubic stacking of close-packed AX_3 layers with B cations in the all-anion octahedral interstices. Within a (110) plane, B-cation octahedra share common corners as shown schematically in Fig. 3(a). In the $Ba_5Ta_4O_{15}$ structure [Ga5a], the stacking sequence of the AX_3 layers is $a-b-c-b-c-a$, as shown in Fig. 24, and the B-cation vacancies are where the stacking is hexagonal. Thus the structure consists of perovskite blocks n AX_3 layers and $(n - 1)$ B layers thick, separated by a stacking fault at a layer of B-cation vacancies. These hexagonal structures appear to be stabilized where the tolerance factor is $t > 1$.

3.2.3.3 $AX \cdot (ABX_3)_n$ structures

Materials having compositions intermediate between ABX_3 and A_2BX_4 may have similar diffraction patterns. However, this compositional region contains several phases having the structural formula $AX \cdot (ABX_3)_n$. Each phase contains perovskite sheets n units thick separated by AX (NaCl-type) sheets. The limiting composition A_2BX_4 , corresponding to $n = 1$, is shown in Fig. 25. It is important for the theory of magnetism because, if A is nonmagnetic, then by symmetry there is no net molecular field within an antiferromagnetic layer from cations in adjacent antiferromagnetic layers. This permits the study of two-dimensional antiferromagnetism. The A_2BX_4 structure also permits the study of B^{3+} cations in oxides with a smaller B-X-B separation (hence stronger interaction) than is found in the BO compounds with rocksalt structure. The possible significance of this is illustrated by La_2NiO_4 . The Ni^{2+} electrons of e_g symmetry appear to be collective in La_2NiO_4 , localized in NiO .

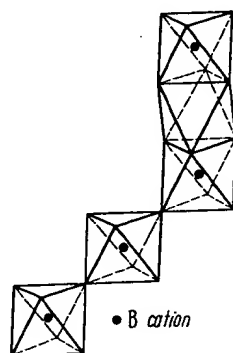


Fig. 24. Schematic (110) projection of the $Ba_5Ta_4O_{15}$ structure. Horizontal lines refer to BaO_3 close-packed layers with stacking a , b , or c .

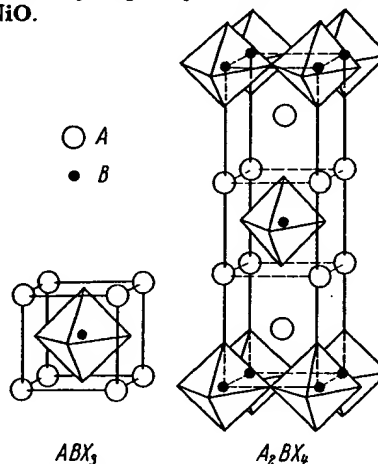


Fig. 25. Comparison of ABX_3 and A_2BX_4 structures [Tr1].

3.2.4 Data: Crystallographic properties of non- ABX_3 compounds of composition A_nBX_{3n} , $\square BX_3$, $(AX)_n(ABX_3)_m$ and $Bi_2O_2(A_{n-1}B_nO_{3n+1})$ with perovskite-related structure (Tab. 4)

Tab. 4.

See Fig. 20(a) for the tetragonal II bronze structure with $a \approx 12.5 \text{ \AA}$, $c \approx 4 \text{ \AA}$ and Fig. 20(b) for the hexagonal bronze structure with $a \approx 7.4 \text{ \AA}$, $c \approx 7.5 \text{ \AA}$.

Within any section, the compounds are ordered by B-cation atomic number, and the order of the sections is as follows:

Tab. 4a — A_nBX_{3n}

A_nBO_{3n} ; $B = \text{Nb, Mo, Ta, W, Re}$

A_nFeF_{3n}

Tab. 4b — $\square BX_3$

Tab. 4c — $\square BB'X_3$

Tab. 4d — $(AX)_n(ABX_3)_m$

$X = F^{-1}, Cl^{-1}$; $B^{2+} = \text{Mg, Cr, Mn, Fe, Co, Ni, Cu, Zn, Cd}$

$X = O^{-2}$; $B = \text{Al, Ti, Cr, Mn, Fe, Co, Ni, Cu, Ga, Ge, Zr, Nb, Mo, Tc, Ru, Rh, Sn, Hf, Ir, Pb, U}$

Tab. 4e — $Bi_2O_2(A_{n-1}B_nO_{3n+1})$

$n = 1$; $B = \text{Mo, W}$ $n = 2$; $B = \text{Nb, Ta}$ $n = 3$; $B = \text{Nb, Ti}$ $n = 4, 5 \text{ and } 8$; $B = \text{Ti}$

For abbreviations, see p. 131. Tab. 4a. A_2BX_3 compounds							Magnetic Data
Compound	Sym	a Å	b Å	c Å	angle	Ref.	
A_2NbO_3							
$Ba_{0.5}NbO_3$	O	12.17	20.5	7.87		<i>Fr1b</i>	Structure and review [<i>Ga15a</i>], S. S. with (Pb, Ca, Sr) $_{0.5}NbO_3$ [<i>Su4c</i> , <i>Fr1b</i> , <i>Is3a</i>], dielectric properties [<i>Gl0</i>]
$Ba_{0.5}NbO_{2.5}$	T	12.60		3.95		<i>Ga14</i>	Studied $x = 0.5 \dots 1.0$
$Sr_{0.95}NbO_3$	C	4.016				<i>Ri3</i>	
$Sr_{0.7}NbO_3$	C	3.981				<i>Ri3</i>	
$Sr_{0.5}NbO_3$	O	11.021	7.33	5.604		<i>He12a</i>	Dielectric properties [<i>Go20</i> , <i>Su4b</i>], S. S. with (Ba, Sr) Nb_2O_6 [<i>Ba25c</i> , <i>Fr1b</i> , <i>Is2a</i> , <i>Kr7</i> , <i>Sm16a</i> , <i>Su4c</i>], P & S [<i>Ro16a</i>], S. S. with Ti, Zr, Sn [<i>Su1a</i> , <i>Su4b</i> , <i>Su4c</i>], S. S. with Li, Na, K, Rb, Cs, Y, La, Sm [<i>Su4b</i> , <i>Su4c</i>]
$Ca_{0.5}NbO_3$	O	5.764	15.09	5.232		<i>He12a</i>	Prep. $T < 1250^\circ C$
$Pb_{0.5}NbO_3$	O	17.51	17.81	7.72		<i>Fr2a</i>	$T = 570^\circ C$
$La_{0.33}NbO_3$	R	8.664		3.907	$\alpha = 88^\circ 30'$	<i>Fr1a</i>	P & S [<i>Ke8</i> , <i>Ro13</i> , <i>Sa6a</i>]; dielectric properties, S. S. with $KSr_3Nb_2O_{15}$ [<i>Bu5</i>]
	T	12.46		7.908		<i>Fr2a</i>	P & S [<i>Ke8</i> , <i>Ro13</i>]
	O	3.911	3.917			<i>Iy1</i>	P & S [<i>Ke8</i> , <i>Ro13</i>]
$Ce_{0.33}NbO_3$	O	3.901	3.917	7.886		<i>Iy1</i>	(Ln = Sm \dots Lu) not able to be prepared
$Ce_{0.25}NbO_3$	O	3.881	3.897	7.843		<i>Ko10</i>	P & S [<i>Ko10</i>], detailed structure [<i>Tr7</i>]
$Pr_{0.33}NbO_3$	O	3.891	3.915	7.862		<i>Iy1</i>	
$Nd_{0.33}NbO_3$	O	3.878	3.907	7.840		<i>Iy1</i>	
$Ln_{0.33}NbO_3$						<i>Ro13</i>	
$Th_{0.25}NbO_3$	T	7.783		7.837		<i>Ke6</i>	
$Pa_{0.25}NbO_3$	T	7.75		7.81		<i>Ke6</i>	
$U_{0.25}NbO_3$	T	7.727		7.792		<i>Ke6</i>	
$NP_{0.25}NbO_3$	T	7.69		7.76		<i>Ke6</i>	
$Pu_{0.25}NbO_3$	T	7.67		7.74		<i>Ke6</i>	
$Am_{0.33}NbO_3$	T	3.819		7.835		<i>Ke8</i>	
$Ba_2KNb_2O_{15}$	T	12.55		4.019		<i>Bu5a</i>	$T_{\text{melt}} = 1395^\circ C$
$Ba_2NaNb_2O_{15}$	O	17.626	17.592	3.995		<i>Va13</i>	Dielectric and optical properties [<i>Va13</i> , <i>Ge14</i> , <i>Sm6a</i> , <i>Bu5a</i> , <i>Va11a</i>], Raman effect [<i>Bu4b</i>]; S. S. with K [<i>Bu5a</i>], Sr [<i>Va11a</i>]; elastic proper- ties [<i>Sp0</i>], piezoelectric properties [<i>Wa15a</i>] Dielectric + optical properties [<i>Gi1a</i> , <i>Bu5</i>]
$Sr_2KNb_2O_{15}$	T	13.47		3.942		<i>Gi1a</i>	

Compound	Sym	a Å	b Å	c Å	angle	Ref.	Remarks	Magnetic Data in 3.3.4, Tab.
$A_x\text{NbO}_3$ (continued)								
$\text{Sr}_2\text{NaNb}_2\text{O}_{15}$	O	17.4	17.4	3.90		<i>Va13</i>	Dielectric + optical properties [<i>Va11a</i> , <i>Va13</i>]	
$\text{Na}_3\text{LaNb}_2\text{O}_{15}$	C	3.918				<i>Is5b</i>		
$\text{Na}_2\text{BiNb}_2\text{O}_{15}$	C	3.925				<i>Is5b</i>		
$\text{K}_3\text{Li}_2\text{Nb}_2\text{O}_{15}$	T	12.47		4.01		<i>Fu2a</i>	Tetr. W bronze type — dielectric + optical properties [<i>Va12</i> , <i>Va13</i> , <i>Va11a</i>] P & S [<i>Is5b</i>]	
$\text{K}_2\text{LaNb}_2\text{O}_{15}$	T	12.580		3.930		<i>Sc27</i>		
$\text{K}_2\text{CeNb}_2\text{O}_{15}$	T	12.545		3.913		<i>Sc27</i>		
$\text{K}_2\text{PrNb}_2\text{O}_{15}$	T	12.530		3.918		<i>Sc27</i>		
$\text{K}_2\text{NdNb}_2\text{O}_{15}$	T	12.497		3.924		<i>Sc27</i>		
$\text{K}_2\text{SmNb}_2\text{O}_{15}$	T	12.474		3.917		<i>Sc27</i>		
$\text{K}_2\text{EuNb}_2\text{O}_{15}$	T	12.457		3.914		<i>Sc27</i>		
$\text{K}_2\text{GdNb}_2\text{O}_{15}$	T	12.450		3.912		<i>Sc27</i>		
$\text{K}_2\text{TbNb}_2\text{O}_{15}$	T	12.440		3.910		<i>Sc27</i>		
$\text{K}_2\text{DyNb}_2\text{O}_{15}$	T	12.431		3.903		<i>Sc27</i>		
$\text{K}_2\text{HoNb}_2\text{O}_{15}$	T	12.426		3.899		<i>Sc27</i>		
$\text{K}_2\text{YNb}_2\text{O}_{15}$	T	12.424		3.901		<i>Sc27</i>		
$\text{K}_2\text{BiNb}_2\text{O}_{15}$	O	17.75	17.90	7.84		<i>Is5b</i>	P & S [<i>Kr2</i> , <i>Kr8</i>]	
$\text{Rb}_2\text{LaNb}_2\text{O}_{15}$	T	12.633		3.945		<i>Sc27</i>		
$\text{Ba}_3(\text{Ti}_2\text{Nb}_2)\text{O}_{80}$	T	12.54		4.01		<i>Si23</i>	Tetr. W bronze type, structure determined [<i>Ja9</i>]	
$\text{Ba}_3(\text{Zr}_2\text{Nb}_2)\text{O}_{80}$	T	17.95	17.95	7.98		<i>Fa1</i>	Tetr. W bronze	
$\text{Ba}_3(\text{FeNb}_2)\text{O}_{80}$	O	17.50	17.50	7.72		<i>Is5b</i>	Prop. [<i>Fa2</i> , <i>Fa1</i>] S.S. with Nd, Sm, Eu, Gd [<i>Fa1</i> , <i>Fa2</i>]	
$\text{Sr}_2(\text{FeNb}_2)\text{O}_{80}$	O	≈ 12.5		≈ 3.9		<i>Is5b</i>	Tetr. W bronze type, A = Ba, Sr, Pb, Bi, La, Ce, Nd, Sm, Gd, K; B = Fe, Ni, Mg; dielectric properties [<i>Kr2</i>] gives review of the tetr. W bronze structure type	
$\text{A}_3(\text{B}_2\text{Nb}_{10-2})\text{O}_{30}$	T					<i>Kr2</i>		
$\text{Ba}_2\text{MgNb}_{14}\text{O}_{45}$	O	18.00	18.00	8.02		<i>Is5b</i>		
$\text{Sr}_2\text{MgNb}_{14}\text{O}_{45}$	O	17.55	17.55	7.82		<i>Is5b</i>		
$\text{Ba}_{0.37}\text{Sr}_{0.76}\text{Nb}_2\text{O}_{6.78}$	T	12.4032		3.9134		<i>Ja8a</i>	T = 25 °C, complete structure determination	
$\text{K}_{0.3}\text{NbO}_{3.5}\text{F}_{0.5}$	T	12.632		3.950		<i>Ma19a</i>	Tetragonal tungsten bronze	
A_2MoO_3								
$\text{Rb}_{0.37}\text{MoO}_3$	H	7.321		7.683		<i>Bi6</i>	High pressure preparation, metallic conductivity, P & S [<i>Ch1b</i>]	
$\text{K}_{0.98}\text{MoO}_3$	C	3.917				<i>Bi6</i>	High pressure preparation, metallic conductivity, P & S [<i>Ch1b</i>]	
$\text{K}_{0.99}\text{MoO}_3$	C	3.920				<i>Bi6</i>	High pressure preparation, metallic conductivity	
$\text{K}_{0.8}\text{MoO}_3$	T	12.32		3.859		<i>Bi6</i>	High pressure preparation, metallic conductivity, $\Theta_{\infty} = 4.2$ °K [<i>Si7a</i>]	

Compound	Sym	a Å	b Å	c Å	angle	Ref.	Remarks	Magnetic Data
$A_x\text{MoO}_3$ (continued)								in 3.3.4, Tab.
$\text{K}_{0.23}\text{MoO}_3$	M	18.249	7.560	9.855	$\beta = 117^\circ 32'$	Gr2	"Blue Mo bronze"; Prep. [Wol10], metallic conductivity [Bo20], structural discussion [St22], optical properties [Di2a]	
$\text{K}_{0.24}\text{MoO}_3$	M	14.278	7.723	6.387	$\beta = 92^\circ 34'$	St24	"Red Mo bronze"; Prep. [Wol10]. Semiconducting [Bo20], structural discussion [St22]	
$\text{Na}_{0.47}\text{MoO}_3$	C	3.853				Bi6	High pressure preparation, $\Theta_{\infty} < 1.3^\circ\text{K}$ [St7a]	
$\text{Na}_{0.50}\text{MoO}_3$	C	3.847				Bi6	High pressure preparation	
$\text{Na}_{0.15}\text{MoO}_{2.38}$	M	9.57	5.50	12.95		St25	Complete structure, random vacancies [St25]; optical properties [Di2a]	
A_xTaO_3								
$\text{Ba}_{0.5}\text{TaO}_{3-z}$	T	12.60		3.95		Ga14	($x = 0 \dots 0.5$), P & S [Is2a]	
$\text{Ba}_{0.5}\text{TaO}_3$	H	21.14		3.917		La8	Dielectric properties, P & S [Is2a, Ga14], review [Ga15a]	
$\text{Sr}_{0.5}\text{TaO}_{3-z}$	T	12.41		3.90		Ga14	($x = 0 \dots 0.5$), review [Ga15a]	
$\text{Ca}_{0.5}\text{TaO}_3$	C	3.886				Ja7	Review [Ga15a]	
$\text{Pb}_{0.5}\text{TaO}_3$	O	17.635	17.695	7.757		Is9	Review of literature, P & S [Is2a]	
$\text{Pb}_{0.5}\text{TaO}_3$	T	17.71		7.788		Is9	$T = 300^\circ\text{C}$, tetr. $T > 270^\circ\text{C}$	
$\text{Cu}_{0.5}\text{TaO}_3$	C	7.522				Ka16	P & S [Sh12], optical properties [Ka16]	
$\text{La}_{0.33}\text{TaO}_3$	T	3.918		7.913		Iy1	P & S [Ke8, Ro13, Tr8], Prep. [Sa6a]	
$\text{Ce}_{0.33}\text{TaO}_3$	T	3.915		7.878		Iy1	P & S [Ke8, Ro13], Prep. [Sa6a]	
$\text{Pr}_{0.33}\text{TaO}_3$	O	3.895	3.910	7.836		Iy1	P & S [Ke8, Ro13], Prep. [Sa6a]	
$\text{Nd}_{0.33}\text{TaO}_3$	O	3.876	3.916	7.829		Iy1	P & S [Ke8, Ro13], Prep. [Sa6a]	
$\text{Sm}_{0.33}\text{TaO}_3$	O	3.882	3.896	7.785		Iy1	P & S [Ke8, Ro13], Prep. [Sa6a]	
$\text{Eu}_{0.33}\text{TaO}_3$	O	3.871	3.885	7.792		Ke8	P & S [Ke8, Ro13]	
$\text{Gd}_{0.33}\text{TaO}_3$	T	3.874		7.795		Iy1	P & S [Ke8, Ro13]	
$\text{Tb}_{0.33}\text{TaO}_3$	T	3.851		7.780		Ke8	P & S [Ke8, Ro13]	
$\text{Dy}_{0.33}\text{TaO}_3$	T	3.847		7.769		Iy1	P & S [Ke8, Ro13]	
$\text{Ho}_{0.33}\text{TaO}_3$	T	3.841		7.756		Iy1	P & S [Ke8]	
$\text{Er}_{0.33}\text{TaO}_3$	T	3.825		7.754		Iy1	P & S [Ke8]	
$\text{Yb}_{0.33}\text{TaO}_3$	M	3.828	7.749	3.839	$\beta = 90^\circ 54'$	Ro13	P & S [Ke8, Tr8, Ro13, Ly1]	
$\text{Y}_{0.33}\text{TaO}_3$	T	3.824		7.758		Iy1	P & S [Ko10]	
$\text{Th}_{0.23}\text{TaO}_3$	C	7.810				Ke6	P & S [Ko10]	
$\text{Pa}_{0.23}\text{TaO}_3$	T	7.77		7.78		Ke6	P & S [Ko10]	
$\text{U}_{0.23}\text{TaO}_3$	T	7.739		7.773		Ke6	P & S [Ko10]	
$\text{NP}_{0.23}\text{TaO}_3$	T	7.70		7.75		Ke6	P & S [Ko10]	
$\text{Pu}_{0.23}\text{TaO}_3$	T	7.654		7.731		Ke6	P & S [Ko10]	
$\text{Am}_{0.33}\text{TaO}_3$	T	3.889		7.820		Ke8	P & S [Ko10]	
$\text{K}_{0.5}\text{TaO}_{2.5}\text{F}_{0.5}$	T	12.569		3.961		Ma19a	Tetragonal tungsten bronze	

Compound	Sym	a Å	b Å	c Å	angle	Ref.	Remarks	Magnetic Data in 3.3.4, Tab.
A_xWO_3								
$Ca_{0.32}WO_3$	H	7.42		7.63		Ma17	Superconducting, $\Theta_{cs} = 1.12^\circ K$ [Sw3]	
$Ca_{0.30}WO_3$	H	7.38		7.59		Ma17	Thermal expansion to $720^\circ C$ [We15]	
$Rb_{0.32}WO_3$	H	7.386		7.54		Si7	P & S [Ma17], metallic conduction and magnetic susceptibility [Si7, Si9], optical properties [Do6]	
$Rb_{0.27}WO_3$	H	7.394		7.516		We15	Superconductivity, $\Theta_{cs} = 1.98^\circ K$ [Sw3], thermal expansion to $970^\circ C$ [We15]	
$(NH_4)_{0.38}WO_3$	H	7.395		7.525		Gi1	Superconductivity $2.2^\circ K \geq \Theta_{cs}$ [Gi1]	
$(NH_4)_{0.08}WO_3$	T	7.60		6.36		Ne8a		
$K_{0.9}WO_3$	C	3.926				Bi6		
$K_{0.56}WO_3$	T	12.326		3.845		We15	High pressure preparation (metallic conductivity), P & S [Ch1b]	
$K_{0.3}WO_3$	H	7.385		7.513		We15	Magnetic susceptibility ($x = 0.53$) [Ku5], electric properties ($x = 0.57$ and 0.63) [Si43], thermal expansion to $750^\circ C$ ($x = 0.3 \dots 0.55$) [We15]	
$K_{0.13}WO_3$	H	7.370		7.515		Ba11	Electric + magnetic properties [Si8, Si9, Si7], S.S. with Li [Ba11], S.S. with Na [Br8], P & S [Ma12, Ma17, De19], review [Di3, Ma15, Ma18, Si9]	
Na_xWO_3	C	3.8				Br22	Superconductivity, Θ_{cs} (Hex) = $0.5^\circ K$, Θ_{cs} (Tetr.) = $1.5^\circ K$ [Sw3], magnetic properties [Ku5, Fu1, Gr8, Si43]	
							$a = [0.0819 x + 3.7846] \text{ Å}$ [Br22, We2]; cubic, $0.26 < x < 1.0$; early preparation [Bo17, W+1, Ph1, Wo1, Sp1, Sp2, Ka5], P & S [Si37, Si38, Si39, Va5, De6, Ha5, Br8, Ha4, Bi6, Ch1b]; neutron diffraction ($0.56 < x < 0.86$) [At1]; electrical properties [Hu8, Hu9, Hu10, Mu3, Mu4, Br21, Fu1, Ga2], reviews [Di3, Ma15, Ma18, Ri1, Si7], optical properties [Di3a]	
	T	12.094		3.748		Ma13	$x = 0.28$, tetragonal II [Ri1]. Superconductivity, $\Theta_{cs} < 1^\circ K$ [Sw3, Ra12], optical properties [Br22, Da3], NMR [Fr18, Fr19, Na12]	
	T	5.248		3.895		Ma16	$x = 0.10$, tetragonal I [Ri1]; thermal properties [Sh7, Fu1, Ge11, Ta2, Ve11], Na diffusion [Sm6], electrostatic energy calculated [Sm5]	
$Li_{0.30}WO_3$	H	7.405		7.554		Gi1	Metallic conductivity, superconducting $\Theta_{cs} < 1.3^\circ K$ [Gi1]	
$Li_{0.394}WO_3$	C	3.715				Si10	Magnetic properties, Pauli paramagnetic or diamagnetic [Si10, Co17], metallic conductivity [Co17, Si10, Si7, Sh8], P & S [Ma19, Ma16, Si40]	
$Li_{0.56}WO_3$	C	3.718				Co17	Review [Di3]	

Compound	Sym	a Å	b Å	c Å	angle	Ref.	Remarks	Magnetic Data
in 3.3.4, Tab.								
$A_x\text{WO}_3$ (continued)								
$\text{Li}_{0.05}\text{WO}_3$	C	3.723		3.88		Co17	I. R. spectra [Si7a]	
$\text{H}_{0.5}\text{WO}_3$	C	3.755				Gi1	Structure determination by x-ray and neutron dif-	
$\text{H}_{0.23}\text{WO}_3$	T	5.22				Di2	fraction, I. R. spectra [Si7a]	
$\text{H}_{0.1}\text{WO}_3$	O	7.247	7.502	3.84		Gi1	I. R. spectra [Si7a]	
$\text{Ba}_{0.12}\text{WO}_3$	T	12.16		3.843		Co19	$x = 0 \dots 0.13$; $\chi_m = 20 \cdot 10^{-6}$ emu/mole, Novel preparation [Co16]; superconductivity, $x = 0.13$, $\theta_{cs} = 1.9^\circ\text{K}$ [Sw4]	
$\text{Ba}_{0.10}\text{Na}_{0.33}\text{WO}_3$	T	12.12		3.834		Co19	Metallic conductivity	
Ca_xWO_3	O	7.340	7.420	3.840		Va2	$x = 0.02$, $0 < x < 0.01$ (monoclinic); $0.01 < x < 0.03$ (orthorhombic), studied as function of T [Va2, Va4]	
	T	5.240		3.854		Va2	$x = 0.035$, $0.03 \leq x < 0.40$ (tetragonal); $0.04 < x < 0.095$ (two phase)	
	T	5.292		3.832		Va2	$x = 0.10$, $0.095 \leq x < 0.105$ (tetragonal); $0.105 \leq x < 0.125$ (cubic $a = 3.790 \text{ Å}$); $x > 0.125$ (two phase)	
$\text{Sr}_{0.24}\text{WO}_3$	H	7.430		7.581		Gi1	Metallic conductivity, superconducting $\theta_{cs} < 1.3^\circ\text{K}$ [Gi1]	
$\text{Sr}_{0.19}\text{WO}_3$	T	12.241		3.774		Gi1	Superconducting $\theta_{cs} < 1.3^\circ\text{K}$ [Gi1]	
$\text{Pb}_{0.17}\text{WO}_3$	T	12.163		3.767		Be30	$x = 0.057 \dots 0.16$ monoclinic, $x = 0.16 \dots 0.35$ tetr.	
$\text{Pb}_{0.35}\text{WO}_3$	T	12.207		3.782		Be30	Novel preparation [Co16]	
$\text{La}_{0.08}\text{WO}_3$	C	3.829				Br23	Cubic, ($x = 0.08 \dots 0.19$), metallic conductivity [Sh6]	
$\text{La}_{0.02}\text{WO}_3$	T	7.52		3.89		Br23		
$\text{Ce}_{0.1}\text{WO}_3$	C	3.828				Os2	$n_{\text{eff}} = 2.5$, all rare-earth bronzes blue-violet	
$\text{Pr}_{0.1}\text{WO}_3$	C	3.827				Os2	$n_{\text{eff}} = 3.6$	
$\text{Nd}_{0.1}\text{WO}_3$	C	3.822				Os2	$n_{\text{eff}} = 3.8$	
$\text{Sm}_{0.1}\text{WO}_3$	C	3.817				Os2	$n_{\text{eff}} = 1.6$ (temperature dependent), crystal growth [Co14]	
$\text{Eu}_{0.15}\text{WO}_3$	C	3.828				Os2	$n_{\text{eff}} = 3.4$ (temperature dependent), P & S [Sh6]	
$\text{Eu}_{0.10}\text{WO}_3$	C	3.815				Os2		
$\text{Eu}_{0.08}\text{WO}_3$	C	3.808				Os2	$n_{\text{eff}} = 7.9$, crystal growth [Co14], P & S [Sh6], relation of a vs. x [We2]	
$\text{Gd}_{0.1}\text{WO}_3$	C	3.810				Os2	$n_{\text{eff}} = 9.6$	
$\text{Tb}_{0.1}\text{WO}_3$	C	3.808				Os2	$n_{\text{eff}} = 10.6$	
$\text{Dy}_{0.1}\text{WO}_3$	C	3.805				Os2	$n_{\text{eff}} = 10.6$, P & S [Sh6]	
$\text{Ho}_{0.1}\text{WO}_3$	C	3.801				Os2	$n_{\text{eff}} = 9.5$	
$\text{Er}_{0.1}\text{WO}_3$	C	3.797				Os2	$n_{\text{eff}} = 7.5$, crystal growth [Co14]	
$\text{Tm}_{0.1}\text{WO}_3$	C	3.794				Os2		

Compound	Sym	a Å	b Å	c Å	angle	Ref.	Remarks	Magnetic Data
----------	-----	--------	--------	--------	-------	------	---------	------------------

Compound	Sym	a Å	b Å	c Å	angle	Ref.	Remarks	Magnetic Data
A_xWO_3 (continued)								in 3.3.4, Tab.
$Yb_{0.1}WO_3$	C	3.791				Os2	$n_{\text{eff}} = 4.5$	
$Lu_{0.1}WO_3$	C	3.788				Os2	$n_{\text{eff}} = 0$	
$Y_{0.08}WO_3$	C	3.800				Br23	Tetr. $x < 0.09$, metallic conductivity [Sh6]	
$Al_{0.25}WO_3$	O	7.368	7.476	3.850		Po10	$x = 0.015, 0.010 < x < 0.030$ orthorhombic; 0.030 $< x < 0.105$, two phase; studied as func- tion of T [V44]	
$Cu_{0.77}WO_3$	O	5.387	5.440	3.784		Po10	$0.105 < x \leq 0.135$; $x > 0.135$, two phase	
$Cu_{0.28}WO_3$	Tr	5.73 5.85	3.88 6.65	7.74 4.88	$\alpha = 134^\circ 45'$ $\beta = 91^\circ 40'$ $\gamma = 93^\circ 37'$	Co18	Semiconducting ≈ 0.15 eV	
$Ag_{0.01}WO_3$	O	3.73	3.85	7.35		Co18	Magnetic susceptibility $\chi_m = 34 \cdot 10^{-6}$ emu/mole	
Cd_xWO_3	O	7.316	7.532	3.867		Si8	Metallic conductivity, P & S [Po2]	
$In_{0.02}WO_3$	T	5.244		3.867		Va3	$x = 0.005, 0.005 \leq x < 0.02$ orthorhombic	
$In_{0.30}WO_3$	T	5.233		3.863		Va3	$x = 0.020, 0.02 \leq x < 0.04$ tetragonal	
$In_{0.30}WO_3$	H	7.384		7.508		Bo21	$x = 0.01 \dots 0.05$, P & S ($x = 0.11$) [Bi3]	
$In_{0.33}WO_3$	H	7.50		7.56		Bo21	$x = 0.2 \dots 0.3$, metallic conductivity, weak dia- magnetism	
$Tl_{0.38}WO_3$	T	7.31		12.80		Sw1	$x = 0.26 \dots 0.33$; metallic conductivity	
$U_{0.085}WO_3$	C	3.812				Si6	Metallic conductivity, $x = 0.19 \dots 0.36$, novel prep- aration [Co16]	
$U_{0.125}WO_3$	C	3.821				Ko10	relationship of a vs. x [We2]	
$Cs_{0.3}(Ta_{0.3}W_{0.7})O_3$	C	7.450		7.821		Ko10	P & S [Sh9]	
$Rb_{0.3}(Ta_{0.3}W_{0.7})O_3$	H	7.342		7.715		Ga4	Thermal expansion and resistivity ($10^8 \Omega \text{cm}$)	
$K_{0.3}(Ta_{0.3}W_{0.7})O_3$	H	7.333		7.685		Ga4	Thermal expansion and resistivity ($10^8 \Omega \text{cm}$)	
$K_{0.3}(Ta_{0.3}W_{0.3})O_3$	T	12.36		3.90		Ga4	Thermal expansion and resistivity ($10^8 \Omega \text{cm}$)	
A_xReO_3							Entire range of S. S. with Ta and Nb [De19a]	
$K_{0.05}ReO_3$	C	3.895				Si2	Metallic conductivity	
$K_{0.3}ReO_3$	H	7.318		7.485		Ch1b	High pressure preparation, $\Theta_{\infty} = 3.6^\circ \text{K}$ [Si7a]	
$Na_{0.05}ReO_3$	T	3.825		3.841		Si7a	Metallic, $\Theta_{\infty} < 1.3^\circ \text{K}$, P & S [Si2]	
A_xFeF_3								
$Rb_{0.25}FeF_3$	H	7.36		7.53		Tr1	Hex ($x = 0.18 \dots 0.30$); P & S [De13a]	
$K_{0.95}FeF_3$	C	4.113				De11	($x = 0.95 \dots 1.0$) cubic	
$K_{0.50}FeF_3$	T	12.60		3.936		De11	($x = 0.40 \dots 0.60$) tetr	
$K_{0.25}FeF_3$	H	7.385		7.510		De11	($x = 0.18 \dots 0.25$) hex	
$Na_{0.11}FeF_3$	R	5.37			$\alpha = 59^\circ$	Tr1	$x = 0.0 \dots 0.16$; P & S [De13a]	
$Tl_{0.30}FeF_3$	H	7.35		7.52		Tr1	Hex ($x = 0.20 \dots 0.31$); P & S [De13a]	

Tab. 4b. □ BX₃ compounds

Compound	Sym	a Å	b Å	c Å	angle	Ref.	Remarks	Magnetic Data
AlF ₃	R	5.029			$\alpha = 58^\circ 31'$	Ke20		in 3.3.4, Tab.
ScF ₃	R	5.708			$\alpha = 59^\circ 32'$	No10		
TiF ₃	R	5.519			$\alpha = 58^\circ 53'$	Si2	P & S [En2]	
TiOF ₂	C	3.798				Vo3		6
VF ₃	R	5.373			$\alpha = 57^\circ 31'$	Ja2a	Neutron diffraction [Wo13]	6
CrF ₃	R	5.2643			$\alpha = 56^\circ 37'$	Kn2	Prop. [Bi7, Ha11, Ha12, Bo33, Ra9], structure [Ja3], neutron diffraction [Wo13] 300 °C	6
MnF ₃	R	5.332			$\alpha = 56^\circ 37'$	Kn2	Neutron diffraction [Wo13], Prop. [Bo33, Bo34, Ny1, Kl5, He10, Sm1]	6
	M	8.904	5.037	13.448	$\beta = 92^\circ 44'$	He9	Neutron diffraction [Wo13], Prop. [Bi7, Sh5, We17, Bu1], crystal transformation [Cr5]	6
FeF ₃	R	5.362			$\alpha = 58^\circ 0'$	He11	Neutron diffraction [Wo13], Prop. [He8, Ny1]	6
CoF ₃	R	5.279			$\alpha = 57^\circ 0'$	He11		6
GaF ₃	R	5.20			$\alpha = 57^\circ 30'$	Br6		6
ZrF ₃	C	3.96				Ek3		6
NbF ₃	C	3.903				Ek4	P & S [Sc2], "doubtful"	6
NbO ₂ F	C	3.902				Fr15		6
MoF ₃	C	3.8985				Gu8	Neutron diffraction [Wi6], P & S [La7]	6
RuF ₃	R	5.408			$\alpha = 54^\circ 90'$	He11	Neutron diffraction [Wi6]	6
RhF ₃	R	5.330			$\alpha = 54^\circ 25'$	He11		6
PdF ₃	R	5.5234			$\alpha = 53^\circ 55'$	He11	Neutron diffraction [Wi6], Prop. [Ba19, Ba20, Ny1, Fi3]	6
InF ₃	R	5.722			$\alpha = 56^\circ 15'$	Mu1		6
TeO ₃	R	5.180			$\alpha = 56^\circ 25'$	Du2	Prep. [Lo8]	
TaF ₃	C	3.9012				Gu8	Prop. [Ny1], "doubtful"	
TaO ₂ F	C	3.896				Fr15		6
WO ₃	M	7.297	7.539	7.688	$\beta = 90^\circ 55'$	Lo6	Structure [Br1, Ta15], neutron diffraction [Lo6], Prop. [Cr7, Cr8, Ta15, Co16, Be22, Iw2, De16, Ke10], optical properties [Di3a], phase transformations [Pe3a]	
Re _{0.33} W _{0.67} O ₃	C	3.7574				Si2		
ReO ₃	C	3.7477				Si2	P & S, [Me11, Bi4, Bi5], crystal growth [Fe21], Prop. [Si2, Fe21, Fe10, Gu6a], structure vs. oxygen content [Si2], DeHaas-Van Alphen effect [Ma27a], NMR [Na11a]	
IrF ₃	R	5.418			$\alpha = 54^\circ 8'$	He11	P & S [Ro2]	
UO ₃	C	4.156				Wa6	P & S [En2]	

Tab. 4c. □ BB'X₆ compounds

Compound	Sym	a Å	b Å	c Å	angle	Ref.	Remarks	Magnetic Data
BB'X ₆	R						Structural review [Gi2, Ke11, Co29]	in 3.3.4, Tab.
NaVF ₆	R	5.63			$\alpha = 56^\circ 30'$	Ke11		
LiVF ₆	R	5.30			$\alpha = 56^\circ 18'$	Ke11		
CaMnF ₆	R	5.59			$\alpha = 55^\circ 36'$	Ho14		
MgMnF ₆	R	5.26			$\alpha = 56^\circ 54'$	Ke11		
NaNbF ₆	C	8.26				Ke11	P & S [Co29]	
LiNbF ₆	R	5.47			$\alpha = 58^\circ 6'$	Ed3	Magnetic properties $80 < T < 300^\circ \text{K}$, $n_{\text{eff}} = 1.66$, $\theta_p = -218^\circ \text{K}$ [Ha18]	
NaMoF ₆	C	8.194						
LiMoF ₆	R	5.43			$\alpha = 57^\circ 6'$	Bo18		
NaTcF ₆	R	5.77			$\alpha = 55^\circ 48'$	Ed4		
NaRuF ₆	R	5.80			$\alpha = 54^\circ 30'$	Bo18	P & S [Hu7]	
LiRuF ₆	R	5.39			$\alpha = 56^\circ 0'$	Bo18		
GePdF ₆	R	5.53			$\alpha = 54^\circ 0'$	Ba21	Magnetic properties, $n_{\text{eff}} = 2.82$, $\theta_p = 31^\circ \text{K}$ [Ba21]	
PdPdF ₆	R	5.52			$\alpha = 53^\circ 54'$	Ba21	P & S [He11], see PdF ₆	
SnPdF ₆	R	5.70			$\alpha = 53^\circ 6'$	Ba21	Magnetic properties, $n_{\text{eff}} = 2.98$, $\theta_p = 28^\circ \text{K}$ [Ba21]	
PtPdF ₆	R	5.55			$\alpha = 54^\circ 0'$	Ba21	Magnetic properties, $n_{\text{eff}} = 2.72$, $\theta_p = 1.2^\circ \text{K}$ [Ba21]	
NaSbF ₆	C	8.184				Te12	P & S [Sc22]	
LiSbF ₆	C	5.44			$\alpha = 57^\circ 0'$	Bu6	Complete structure; P & S [Ke11]	
CaHF ₆	C	8.462				Ke7		
NaTaF ₆	C	8.28				Ke11		
LiTaF ₆	C	5.48			$\alpha = 58^\circ 0'$	Ke11		
NaWF ₆	C	8.18				Ke11	P & S [Co29]	
LiWF ₆	R	5.45			$\alpha = 57^\circ 24'$	Ke11	Magnetic properties $80 < T < 300^\circ \text{K}$, $n_{\text{eff}} = 0.5$, $\theta_p = -125^\circ \text{K}$ [Ha18]	
NaReF ₆	C	8.18				Ke11		
NaOsF ₆	R	5.80			$\alpha = 55^\circ 12'$	Bo18	P & S [Pe1]; magnetic properties $80 < T < 300^\circ \text{K}$, $n_{\text{eff}} = 1.57$, $\theta_p = -100^\circ \text{K}$ [Ha19]	
LiOsF ₆	R	5.43			$\alpha = 55^\circ 30'$	Bo18		
NaIrF ₆	R	5.80			$\alpha = 55^\circ 12'$	Bo18		
LiIrF ₆	R	5.41			$\alpha = 56^\circ 0'$	Bo18		
PdPtF ₆	R	5.55			$\alpha = 54^\circ 0'$	Ba21		
CaPbF ₆	C	8.476				Ho15		

Tab. 4d. $(AX)_n(ABX_3)_m$ compounds

Compound	Sym	a Å	b Å	c Å	angle	Ref.	Remarks	Magnetic Data
Halides								in 3.3.4, Tab.
Cs ₂ MgF ₄	T	4.055		13.79		Ba1	No cell dimensions [Be22a]	
Rb ₂ MgF ₄	T	3.955		13.706		Re6	P & S [Wi12], S.S. with K ₂ NiF ₄ [We20]	
K ₂ MgF ₄	T	4.07		13.88		Ch8a		
(NH ₄) ₂ MgF ₄	T	4.007		14.43		Vo1		
Tl ₂ MgF ₄	T							
Na ₂ CrF ₄	M	3.344	9.533	5.657	$\beta = 87^\circ 12'$	Vo1	Not K ₂ NiF ₄ type	
Cs ₂ CrCl ₄	T	5.215		16.46		Se2		
Rb ₂ CrCl ₄	T	5.143		15.73		Se2	Possibly distorted K ₂ NiF ₄ [Se2]	
K ₂ CrCl ₄								
Cs ₂ MnF ₄	T	4.31		14.63		Co25		
Cs ₂ MnCl ₄	T					Le7	K ₂ NiF ₄ type	6
Rb ₂ MnF ₄	T	4.228		13.89		Co25	P & S [Vo1], Prop. [De20, Br5]	6
K ₂ MnF ₄	T	4.20		13.14		Br5	P & S [Vo1, Co25], Prop. [De20, Co15]	6
Rb ₂ FeF ₄	T	4.20		13.38		Tr1		6
K ₂ FeF ₄	T	4.140		12.98		De12		
K ₃ Fe ₂ F ₇	T	4.130		21.15		De12		
Tl ₂ FeF ₄	T	4.194		13.91		Vo1		
Rb ₂ CoF ₄	T	4.135		13.67		Ru6	P & S [Ru3, Ru8]	6
K ₂ CoF ₄	T	4.07		13.08		Ru6	Prop. [Ru8, Sr3, Sr2, Va1, Le8], dielectric proper- ties [La1a]	6
Tl ₂ CoF ₄	T	4.11		14.05		Ru6	P & S [Ru3, Ru8]	
Rb ₂ NiF ₄	T	4.087		13.71		Ru8	Prop. [Ru5]	6
K ₂ NiF ₄	T	4.006		13.076		Ba10	Prop. [Sr2, Go26, De20, Ru5, Ti5, We20], dielectric properties [La1b], neutron diffraction [Pl4, Pl5, Pl6, Pl7, Le6, Le7]	6
(NH ₄) ₂ NiF ₄	T	4.08		13.78		Ru8		6
Tl ₂ NiF ₄	T	4.051		14.22		Ru8		6
Rb ₂ CuF ₄	T	4.238		13.28		Ru6	P & S [Ru3], optical properties [Sc10a]	6
K ₂ CuF ₄	T	4.145		12.72		Ru6	Prop. [Ru6, Va1], P & S [Kn1, Gu1a]	6
Na ₂ CuF ₄	M	3.261	9.354	5.601	$\beta = 87^\circ 30'$	Ba3	P & S [Ru3] — not K ₂ NiF ₄ type	6
Tl ₂ CuF ₄	T	4.199		13.66		Ru6	P & S [Ru3]	6
(NH ₄) ₂ CuCl ₄	T	7.20	7.20	15.46		Wi9		
(CH ₃ NH ₂) ₂ CuCl ₄	O	7.30	7.54	18.55		Gr7	Prop. [De20, Bo15, Ko8], Prep. [Re7]	6
(C ₂ H ₅ NH ₂) ₂ CuCl ₄	O	7.35	7.47	21.18		Wi9	Prop. [De20, Bo15, Ko8], Prep. [Re7]	6
Rb ₂ ZnF ₄	T	4.125		13.67		Ba1	P & S [Sc10]	
K ₂ ZnF ₄	T	4.02		13.05		Sc10		
K ₂ Zn ₂ F ₇	T	4.063		21.22		Br12		

Compound	Sym	a Å	b Å	c Å	angle	Ref	Remarks	Magnetic Data
$K_2Zn_2F_7$	T	4.063		21.22		Br12		
Halides (continued)								
$(NH_4)_2ZnF_4$	T	4.14		13.97		Cr3		in 3,3,4, Tab.
Tl_2ZnF_4	T	4.105		14.10		Vol		
Rb_2CdF_4	T	4.414		13.98		Co27a		
$Rb_2Cd_2F_7$	T	4.403		22.71		Co27a	Prep. [Co26, Co27a] Prep. [Co26, Co27a]	
K_2CdF_4	T							
$K_2Cd_2F_7$	T	5.26		16.88		Si3		
Oxides								
$SrLaAlO_4$	T	3.75		12.5		Ru1	Eu ³⁺ fluorescence [Ni1]	
Sr_2TiO_4	T	3.88		12.58		Ba10	P & S [Ru1, Br11, Lu2, Po9, Ha19a], Eu ³⁺ fluores- cence [Ni1]	
$Sr_3Ti_2O_7$	T	3.90		20.38		Ru2	P & S [Lu2]	
$Sr_4Ti_3O_{10}$	T	3.90		28.1		Ru2		
$Ca_3Ti_2O_7$	O	5.412	5.426	19.50		Pe3	P & S [Ro17]	
$Ca_4Ti_3O_{10}$	O	5.404	5.435	27.14		Pe3	P & S [Ro17]	
$NaLaTiO_4$	T	3.76		12.95		Bl12	(Na and Ln ordered). Fluorescence: Eu [Bl12a]	
$NaNdTiO_4$	T	3.76		12.79		Bl12		
$NaSmTiO_4$	T	3.77		12.59		Bl12	Fluorescence: Eu [Bl12a]	
$NaGdTiO_4$	T	3.77		12.46		Bl12		
$NaDyTiO_4$	T	3.77		12.22		Bl12		
$NaTmTiO_4$	T	3.78		12.05		Bl12		
$NaLuTiO_4$	T	3.78		11.92		Bl12		
$NaYTiO_4$	T	3.786		12.209		Re2	Fluorescence: Eu [Bl12a]	
$Na_3Y_3Ti_3O_{14}$	T	3.79		20.2		Re2		
$Na_3Y_3Ti_3O_{10}$	T	3.79		28.2		Re2		
Eu_3TiO_4	T	3.89		12.53		Ro21	P & S [Mc1b]	
$Eu_3Ti_2O_7$	T	3.899		20.295		Ro21	P & S [Mc1b]	
Sr_2CrO_4	T	3.82		12.4		Lo1a	Cr ⁴⁺ , high pressure preparation	
$Sr_2Cr_2O_7$	T	3.82		20.1		Lo1a	Cr ⁴⁺ , high pressure preparation	
$SrLaCrO_4$	T	3.84		12.52		Bl9		
Sr_2MnO_4	T	3.79		12.43		Ba10	Substitution of La [Sr2]	
Ca_2MnO_4	T	3.667		12.063		Ma6	P & S [Ru1, Br11]	6
$Ca_2Mn_2O_7$	T	3.709		19.44		Ma6	97% Mn ⁴⁺ ; P & S [Ru1, Br11]	6
$Ca_4Mn_3O_{10}$	T	3.724		26.90		Ma6	97% Mn ⁴⁺ ; P & S [Ru1, Br11]	6
$Sr_{1-x}La_xMnO_4$	T					Le7		6
$SrLaMnO_4$	T	3.88		12.5		Bl9		
Sr_2FeO_{4-x}	T	3.864		12.390		Gal9	$x = 0.3$	6
$Sr_3Fe_2O_{7-x}$	T	3.853		20.149		Gal9	$x = 0.1$, P & S [Br10], Prop. [Ma7]	6

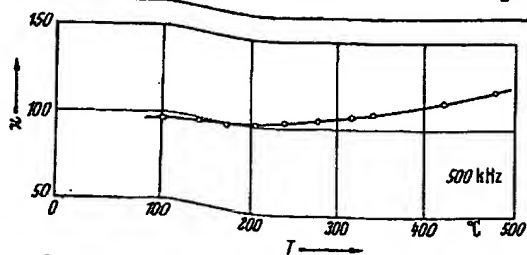
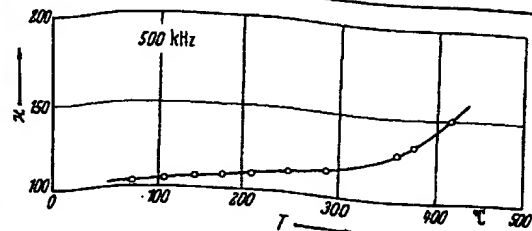
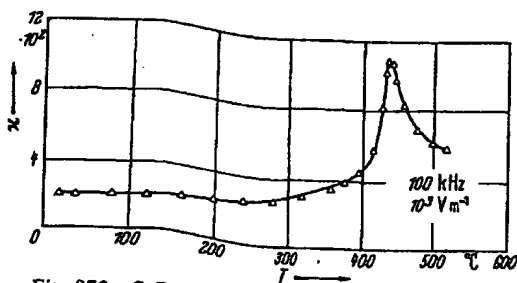
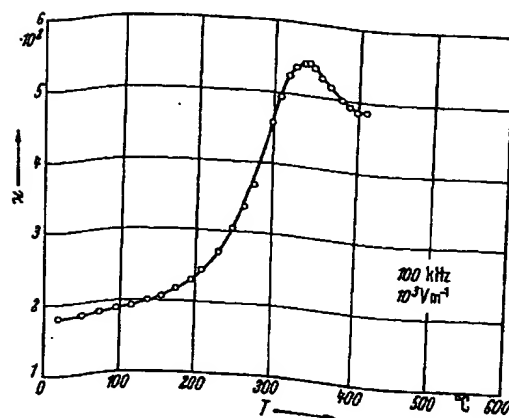
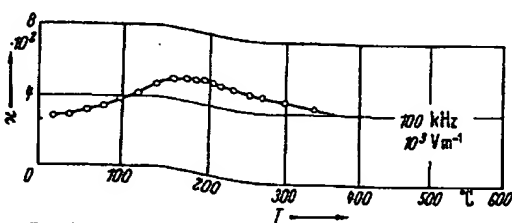
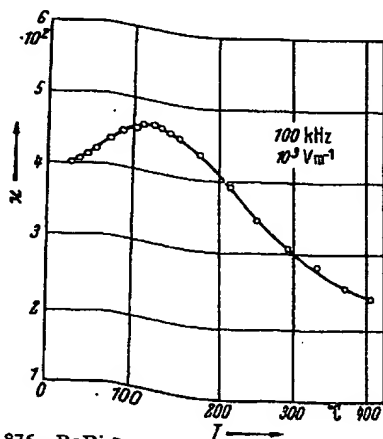
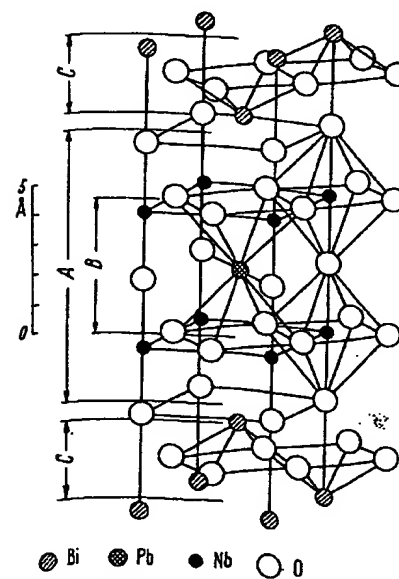
Compound	Sym	a Å	b Å	c Å	angle	Ref.	Remarks	Magnetic Data
Oxides (continued)								
$\text{Sr}_2\text{Fe}_2\text{O}_{7-x}$ cont.	T	3.892		20.054		Ga19	$x = 1$, Prop. [Ma7]	in 3.3.4, Tab.
$\text{Sr}_2\text{FeO}_5\text{F}$	T	3.84		12.98		Ga3		
SrLaFeO_4	T	3.86		12.69		Bl9	Prop. [As6]	6
SrLaCoO_4	T	3.80		12.50		Bl9		
La_2CoO_4	O	5.482	5.539	12.66		Ra2	Prop. [Fo1, Fo3] substitution of Sr [Sr2, Go6]	
$\text{La}_2\text{Co}_{0.5}\text{Li}_{0.5}\text{O}_4$	T	3.77		12.58		Bl9	Prop. [Sr2, Go26]	6
$\text{La}_{1.5}\text{Sr}_{0.5}\text{CoO}_4$	T	3.82		12.58		Bl9		6
$\text{La}_{1.5}\text{Sr}_{0.5}\text{Co}_{0.5}\text{Mg}_{0.5}\text{O}_4$	T	3.85		12.62		Bl9		6
$\text{Sr}_{1.5}\text{La}_{0.5}\text{Co}_{0.5}\text{Ti}_{0.5}\text{O}_4$	T	3.855		12.652		Ra2	P & S [Fo1, Fo3], Prop. [Sm34, Sm24]	6
La_2NiO_4	T						Prop. [Sm34]	6
Pr_2NiO_4	T	3.81		12.31		Fo1	Prop. [Sm34, Sm24]	6
Nd_2NiO_4	T	3.80		12.51		Bl9		6
SrLaNiO_4	T	3.75		12.89		Bl9		6
$\text{La}_2\text{Ni}_{0.5}\text{Li}_{0.5}\text{O}_4$	O	5.36	5.41	13.17		Lo1c	Prop. [Fr25, Fo1, Fo3] at 420 °C, tetr. $T > 250$ °C	6
La_2CuO_4	T	3.81		13.24		Lo1c		
Pr_2CuO_4	T	3.96		12.23		Fr25		
Nd_2CuO_4	T	3.94		12.15		Fo1	P & S [Fr25]	
Sm_2CuO_4	T	3.91		11.93		Fo1	P & S [Fr25]	
Eu_2CuO_4	T	3.91		11.92		Fr25		
Gd_2CuO_4	T	3.89		11.85		Fo1	P & S [Fr25]	
SrLaGaO_4	T	3.84		12.71		Bl9		
Ca_2GeO_4	T	3.70		11.88		Re2	100 kbars, 900 °C required, P & S [Ri8b]	
Ba_2ZrO_4	T	4.187		13.48		Sc18a		
Sr_2ZrO_4	T	5.801		12.445		Pe3	P & S [Sc18a]	
$\text{Sr}_2\text{Zr}_2\text{O}_7$	T	5.798		20.94		Pe3		
$\text{Sr}_4\text{Zr}_3\text{O}_{10}$	O	5.795	5.808	29.34		Pe3		
$\text{K}_2\text{NbO}_5\text{F}$	O	3.96	5.814	12.67		Ga2		
Sr_2MoO_4	T	3.92		12.84		Ba10	P & S [Sc16], Prop. [Ro2a]	6
Ba_2TeO_4	T	4.011		13.40		Ke9		
Sr_2TeO_4	T	3.902		12.72		Ke9		
Sr_2RuO_4	T	3.870		12.74		Ra6	Prop. [Ca2]	6
Sr_2RhO_4	T	3.85		12.90		Ra6		
SrLaRhO_4	T	3.92		12.78		Bl9		
Ba_2SnO_4	T	4.130		13.27		We8	P & S [Wa2]	
Sr_2SnO_4	T	4.037		12.53		We8	P & S [Wa2]	
Ca_2SnO_4	T						Not K_2NiF_4 type, [We8]	
Ba_2HfO_4	T	4.161		13.45		Sc18a		
Sr_2HfO_4	T	4.089		12.52		Sc18a		

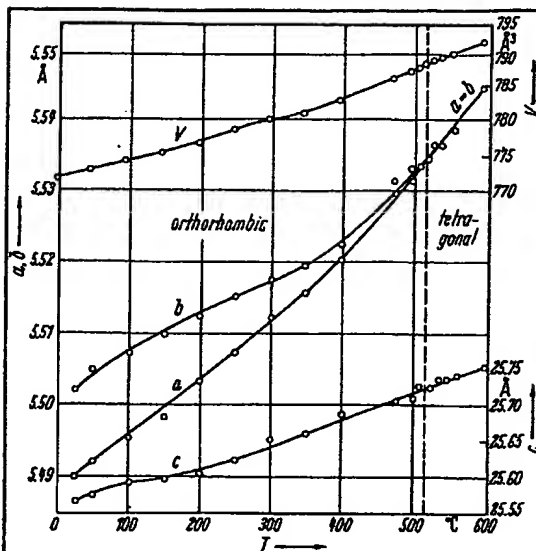
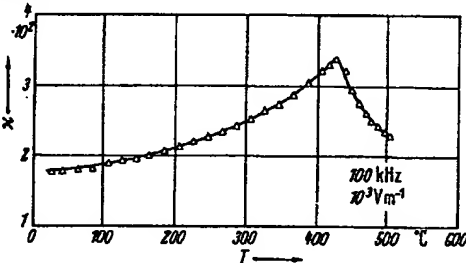
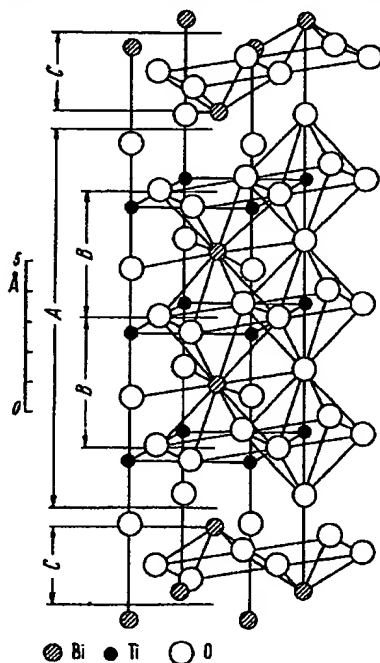
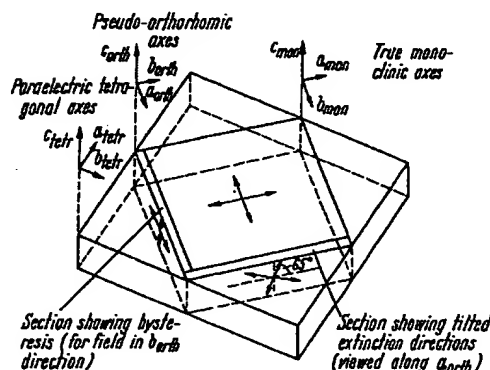
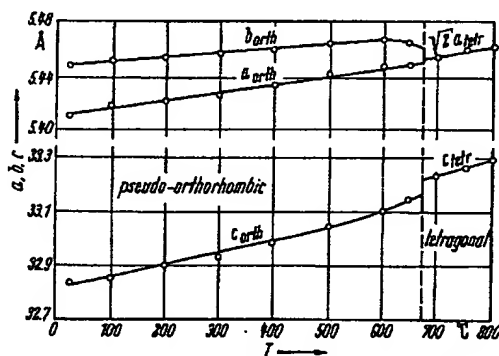
Compound	Sym	a Å	b Å	c Å	angle	Ref.	Remarks	Magnetic Data
Oxides (continued)								
Sr ₂ IrO ₄	T	3.89		12.92		Ra7	Prop. [Ro2a]	in 3.3.4, Tab. 6
Ca ₂ IrO ₄	H	9.423		3.195		Ba2a	Not K ₂ NiF ₄ type	
Ba ₂ PbO ₄	T	4.296		13.30		We8	P & S [Wa2]	
A ₂ PbO ₄						We8	A = Sr + Ca, not K ₂ NiF ₄ type	
Cs ₂ UO ₄	T	4.38		14.79		Ko11		
Rb ₂ UO ₄	T	4.345		13.83		Ko11		
K ₂ UO ₄	T	4.335		13.10		Ko11		
β-Na ₂ UO ₄	O	5.795	5.97	11.68		Ko11		

Tab. 4e: see next page

Tab. 4e. $\text{Bi}_2\text{O}_3(\text{A}_{n-1}\text{B}_n\text{O}_{3n+1})$ compounds

Compound	Sym	a Å	b Å	c Å	angle	Ref.	Remarks	Magnetic Data
Bi_2MoO_6	O	5.49	5.50	16.24		Bl10	P & S [Zej]	in 3.3.4, Tab.
Bi_2WO_6	O	5.49	5.50	16.24		Bl10		
$\text{BaBi}_2\text{Nb}_2\text{O}_9$	O	5.533	5.533	25.55		Au2	P & S [Su3], S.S. with Sr and Ca [Sm19]	
$\text{SrBi}_2\text{Nb}_2\text{O}_9$	O	5.504	5.504	25.05		Au2	P & S [Sm19; Su3]	
$\text{CaBi}_2\text{Nb}_2\text{O}_9$	O	5.435	5.485	24.87		Au2	P & S [Sm19; Su3], dielectric properties [Is3]	
$\text{PbBi}_2\text{Nb}_2\text{O}_9$	O	5.492	5.503	25.53		Au2	P & S [Su2; Su3], S.S. with Ba and Sr [Sm19], dielectric properties [Sm19, Is3] $T = 520^\circ\text{C}$	
$\text{K}_{0.5}\text{Bi}_{2.5}\text{Nb}_2\text{O}_9$	T	5.535		25.72		Is3		
$\text{Na}_{0.5}\text{Bi}_{2.5}\text{Nb}_2\text{O}_9$	O	5.506	5.506	25.26		Au2		
$\text{BaBi}_2\text{Ta}_2\text{O}_9$	O	5.47	5.47	26.94		Au2		
$\text{SrBi}_2\text{Ta}_2\text{O}_9$	O	5.556	5.556	25.60		Su4	P & S [Sm19; Su3]	
$\text{CaBi}_2\text{Ta}_2\text{O}_9$	O	5.509	5.509	25.06		Au2	P & S [Sm19; Su3]	
$\text{PbBi}_2\text{Ta}_2\text{O}_9$	O	5.435	5.468	24.97		Is3	Dielectric properties $T = 600^\circ\text{C}$	
$\text{PbBi}_2\text{Ta}_2\text{O}_9$	T	5.479		25.085		Is3		
$\text{Bi}_3\text{NbTiO}_9$	O	5.496	5.496	25.40		Su4	P & S [Sm19, Su2, Su3]	
$\text{Bi}_3\text{TaTiO}_9$	O	5.405	5.442	25.11		Au2	P & S [Su3, Sm19], dielectric properties [Is11b, Is3]	
$\text{BaBi}_3\text{Ti}_2\text{NbO}_{12}$	O	5.402	5.436	25.15		Au2	P & S [Su3], dielectric properties [Is11b]	
$\text{PbBi}_3\text{Ti}_2\text{NbO}_{12}$	T	3.874		33.70		Su2		
$\text{Bi}_4\text{Ti}_3\text{O}_{12}$	T	3.867		33.55		Su2		
$\text{Bi}_4\text{Ti}_3\text{O}_{12}$	O	5.410	5.448	32.84		Au3	Dielectric properties [Kr1, Su4, Sm19, Va11], S.S. with BaTiO_3 [Is6], S.S. with $\text{Pb}_2\text{Nb}_2\text{O}_7$ [Su7], tetragonal at 675°C [Su7], Electrooptic properties [Cu2], switching behavior [Cu7], monoclinic symmetry [Cu2]	
$\text{BaBi}_4\text{Ti}_4\text{O}_{15}$	T	5.461		41.85		Su4	P & S [Su3, Sm19, Au4, Is6, Su2]	
$\text{SrBi}_4\text{Ti}_4\text{O}_{15}$	T	5.428		40.95		Su4	P & S [Su3, Sm19]	
$\text{CaBi}_4\text{Ti}_4\text{O}_{15}$	T	5.418		40.75		Su4	P & S [Su3, Sm19]	
$\text{PbBi}_4\text{Ti}_4\text{O}_{15}$	T	5.437		41.35		Su4	P & S [Su2, Sm19, Su3]	
$\text{Bi}_4\text{Ti}_3\text{GaO}_{15}$	T	5.408		41.05		Su4	P & S [Su3]	
$\text{Bi}_4\text{Ti}_3\text{FeO}_{15}$	O	5.445	5.455	41.31		Is12	Tetr. $T > 740^\circ\text{C}$, Prop. [Is11a]	
$\text{K}_{0.5}\text{Bi}_{4.5}\text{Ti}_4\text{O}_{15}$	T	5.440		41.15		Su4	P & S [Su3]	
$\text{Na}_{0.5}\text{Bi}_{4.5}\text{Ti}_4\text{O}_{15}$	T	5.427		40.65		Su4	P & S [Su3, Ha2], structure determination [Ne2]	
$\text{Ba}_2\text{Bi}_4\text{Ti}_3\text{O}_{18}$	O	5.514	5.526	50.37		Is6	P & S [Su3], tetr. at 310°C [Is6]	
$\text{Ba}_2\text{Bi}_4\text{Ti}_3\text{Fe}_2\text{O}_{18}$	O	5.490	5.500	50.185		Is12		
$\text{Sr}_2\text{Bi}_4\text{Ti}_3\text{O}_{18}$	T	5.461		48.80		Su4	Probably orthorhombic	
$\text{Pb}_2\text{Bi}_4\text{Ti}_3\text{O}_{18}$	T	5.461		49.70		Su4	P & S [Su3]	
$\text{Ba}_5\text{Bi}_4\text{Ti}_3\text{Fe}_3\text{O}_{17}$	O	5.491	5.502	76.20		Is12		


 Fig. 871. $\text{CaBi}_2\text{Nb}_2\text{O}_9$ (ceramics). κ vs. T [61S11].

 Fig. 872. $\text{CaBi}_2\text{Ta}_2\text{O}_9$ (ceramics). κ vs. T [61S11].

 Fig. 873. $\text{SrBi}_2\text{Nb}_2\text{O}_9$ (ceramics). κ vs. T [62S17].

 Fig. 874. $\text{SrBi}_2\text{Ta}_2\text{O}_9$ (ceramics). κ vs. T [62S17].

 Fig. 875. $\text{BaBi}_2\text{Nb}_2\text{O}_9$ (ceramics). κ vs. T [62S17].

 Fig. 876. $\text{BaBi}_2\text{Ta}_2\text{O}_9$ (ceramics). κ vs. T [62S17].

 Fig. 877. $\text{PbBi}_2\text{Nb}_2\text{O}_9$. Schematic drawing of crystal structure. One half of the pseudotetragonal unit cell from $x \approx 0.25$ to $x \approx 0.75$ is given. A denotes the perovskite layer $\text{PbNb}_2\text{O}_7^{2-}$, B denotes a unit of hypothetical perovskite structure PbNbO_3 and C denotes $(\text{Bi}_2\text{O}_7)^{4+}$ layers [62S15].


 Fig. 878. PbBi₂Nb₂O₉ (ceramics). Lattice parameters vs. T (601°).

 Fig. 880. PbBi₂Ta₂O₉ (ceramics). κ vs. T (625°).

 Fig. 882. Bi₄Ti₃O₁₂. Schematic drawing of crystal structure. One half of the pseudotetragonal unit cell from $z \approx 0.25$ to $z \approx 0.75$ is given. A denotes the perovskite layer Bi₂Ti₂O₇, B denotes a unit of hypothetical perovskite structure BiTiO₃, and C denotes (Bi₄O₁₂)²⁺ layers [62S15].

 Fig. 881. Bi₄Ti₃O₁₂. Relationship between the three sets of crystallographic axes [67C6].

 Fig. 883. Bi₄Ti₃O₁₂. Lattice parameters vs. T [61S16].

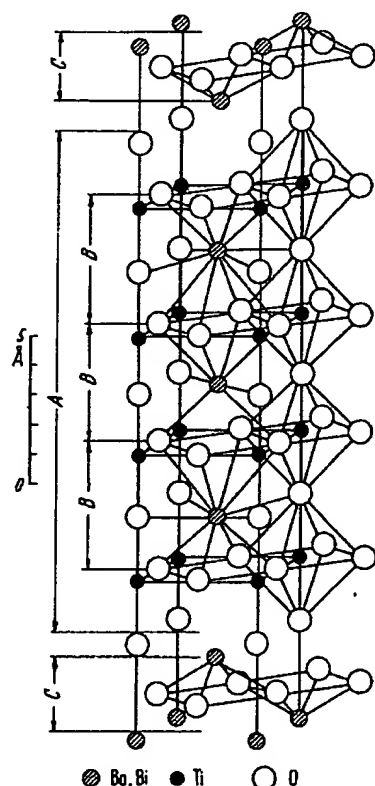


Fig. 890. $\text{BaBi}_4\text{Ti}_4\text{O}_{18}$. Schematic drawing of crystal structure. One half of the pseudotetragonal unit cell from $x \approx 0.25$ to $x \approx 0.75$ is given. A denotes the perovskite layer $\text{BaBi}_2\text{Ti}_2\text{O}_{12}$, B denotes a unit of hypothetical perovskite structure $(\text{Ba}, \text{Bi})\text{TiO}_3$, C denotes $(\text{Bi}_4\text{O}_6)^{4+}$ layers [62S15].

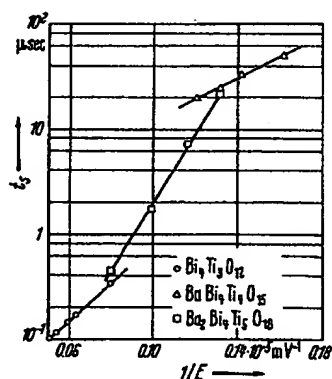


Fig. 892. $\text{BaBi}_4\text{Ti}_4\text{O}_{18}$, $\text{Ba}_2\text{Bi}_4\text{Ti}_4\text{O}_{18}$, $\text{Bi}_4\text{Ti}_3\text{O}_{12}$. t_s vs. $1/E$. [62F1]. t_s : switching time.

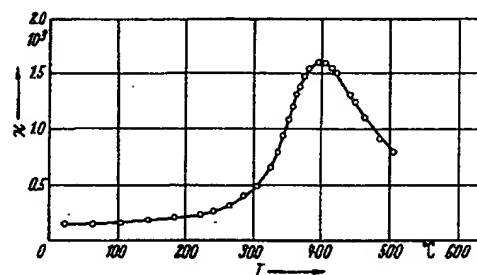


Fig. 891. $\text{BaBi}_4\text{Ti}_4\text{O}_{18}$ (ceramics). χ vs. T [61S15].

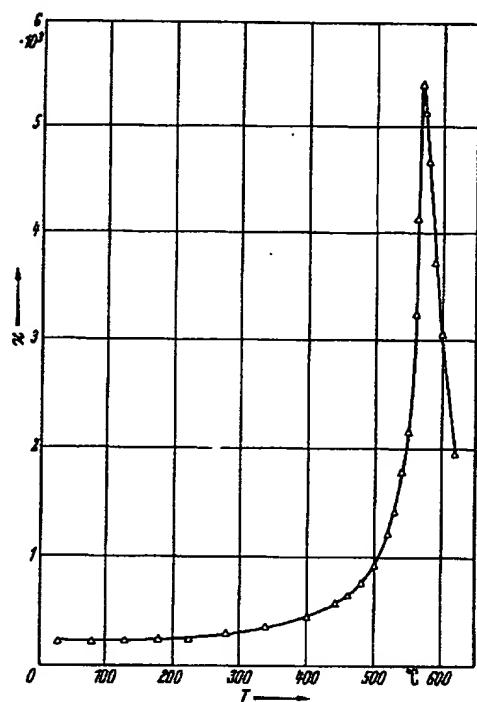


Fig. 893. $\text{PbBi}_4\text{Ti}_4\text{O}_{18}$ (ceramics). χ vs. T [61S15].

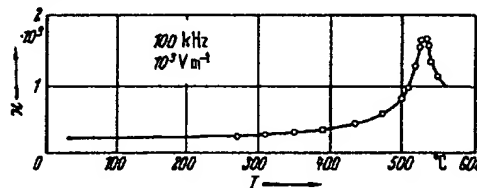


Fig. 894. $\text{SrBi}_4\text{Ti}_4\text{O}_{18}$ (ceramics). χ vs. T [62S17].

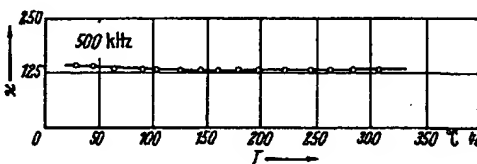


Fig. 895. $\text{CaBi}_4\text{Ti}_4\text{O}_{18}$ (ceramics). χ vs. T [61S17].

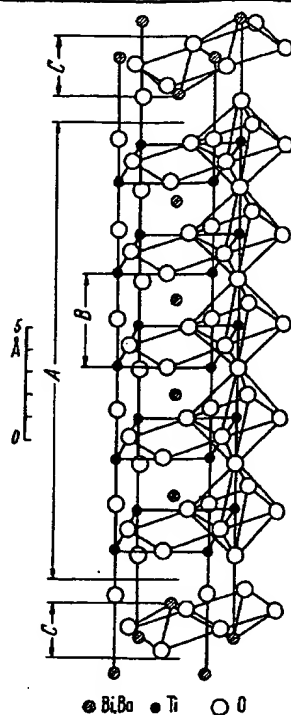


Fig. 896. $\text{Ba}_2\text{Bi}_4\text{Ti}_4\text{O}_{18}$. Schematic drawing of the crystal structure. One half of the tetragonal unit cell from $x = 0.25$ to $x = 0.75$ is given. A denotes the perovskite layer of $\text{Ba}_2\text{Bi}_4\text{Ti}_4\text{O}_{18}$, B denotes a unit cell of the hypothetical perovskite structure $(\text{Ba}, \text{Bi})\text{TiO}_3$, and C denotes the layers of $(\text{Bi}_2\text{O}_2)^{2+}$ [62A5].

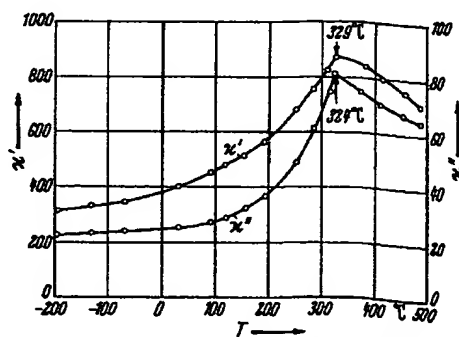


Fig. 898. $\text{Ba}_2\text{Bi}_4\text{Ti}_4\text{O}_{18}$. x' and x'' vs. T [62A5].

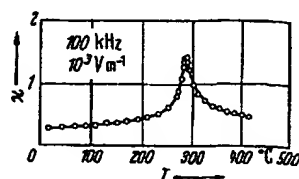


Fig. 900. $\text{Sr}_2\text{Bi}_4\text{Ti}_4\text{O}_{18}$ (ceramics). x' vs. T [62S17].

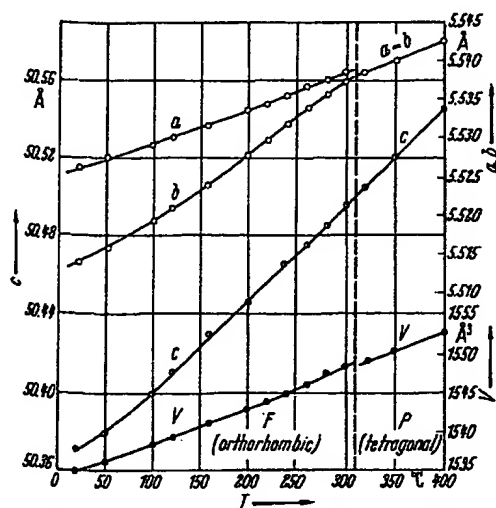


Fig. 897. $\text{Ba}_2\text{Bi}_4\text{Ti}_4\text{O}_{18}$. Lattice parameters vs. T [6315].

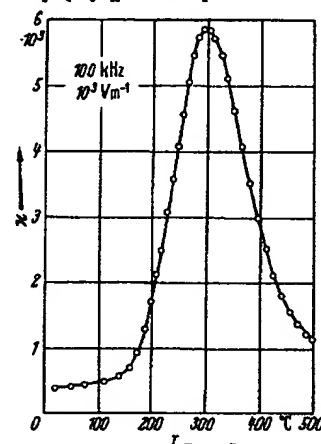


Fig. 899. $\text{Pb}_2\text{Bi}_4\text{Ti}_4\text{O}_{18}$ (ceramics). x' vs. T [62S17].

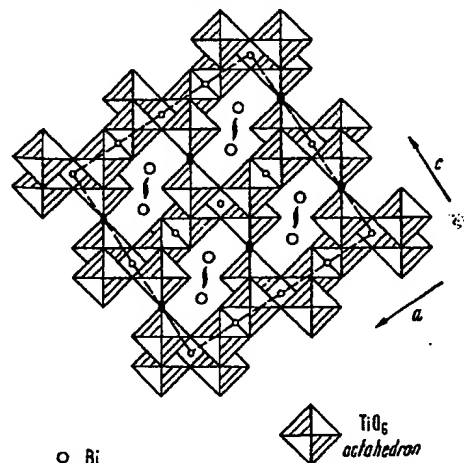


Fig. 901. $\text{Bi}_2\text{Ti}_4\text{O}_{11}$. Schematic projection of structure on $(010)_z$ [65J4].

BRIEF ATTACHMENT O

IN THE UNITED STATES PATENT AND TRADEMARK OFFICE

In re Patent Application of

Applicants: Bednorz et al.

Serial No.: 08/479,810

Filed: June 7, 1995

For: NEW SUPERCONDUCTIVE COMPOUNDS HAVING HIGH TRANSITION
TEMPERATURE, METHODS FOR THEIR USE AND PREPARATION

Date: March 1, 2005

Docket: YO987-074BZ

Group Art Unit: 1751

Examiner: M. Kopec

Commissioner for Patents
P.O. Box 1450
Alexandria, VA 22313-1450

FIRST SUPPLEMENTAL AMENDMENT

Sir:

In response to the Office Action dated July 28, 2004, please consider the
following:

ATTACHMENT O

LANGENSCHIEDT'S

GERMAN-English
English-German
DICTIONARY

OVER 20,000 ENTRIES

TWO VOLUMES IN ONE • 592 PAGES

LANGENSCHIEDT'S

Deutsch-Englisches
Englisch-Deutsches
WORTERBUCH

**LANGENSCHIEDT'S GERMAN-ENGLISH
ENGLISH-GERMAN DICTIONARY**

A Washington Square Press edition

1st printing.....January, 1953

37th printing.....August, 1969

New Revised and Enlarged Edition

1st printing.....January, 1970

This WASHINGTON SQUARE PRESS edition is published by arrangement with Langenscheidt KG, Publishers, Berlin and Munich, Germany, and is printed from brand-new plates made from newly set, clear, easy-to-read type.



Published by Washington Square Press,
a division of Simon & Schuster, Inc., 630 Fifth Avenue, New York, N.Y.

WASHINGTON SQUARE PRESS editions are distributed in the U.S. by Simon & Schuster, Inc., 630 Fifth Avenue, New York, N.Y. 10020 and in Canada by Simon & Schuster of Canada, Ltd., Richmond Hill, Ontario, Canada.

Standard Book Number: 671-47825-7.

Copyright, ©, 1952, 1969, 1970, by Langenscheidt KG, Berlin and Munich, Germany. All rights reserved. Published on the same day in Canada by Simon & Schuster of Canada, Ltd. Printed in the U.S.A. This WASHINGTON SQUARE PRESS edition may not be sold in Germany, Switzerland, and Austria. A hard-bound edition of this book is available in the U.S. from McGraw-Hill Book Company.

For over 100
have been an
several decades
aries have been

However, lan
To bring you a
compiled this e
which have ente
last few years i
Mondfähre, M
lunar probe, hea

Langenscheidt
another new and
ing user: it prov
sion and conjuga
entries (see pp. 7

The phonetic
headwords follow
national Phonetic

In addition to
special quick-refe
date with names
breviations and w

Designed for
Dictionary, with
of great value to
in home and offic

ne Fläche; (gleiche) Höhe, Niveau
n, Stand *m*; *fig.* Maßstab *m*; Was-
serwaage *f*; sea ~ Meeresspiegel *m*;
on the ~ F offen, aufrichtig; 3. *v/t.*
gleichmachen, ebenen; *fig.* anpassen;
richten, zielen mit; ~ up erhöhen;
v/i. ~ at, against zielen auf (*acc.*);
~headed vernünftig, nüchtern.
lever ['li:və] Hebel *m*; Hebestange *f*;
~age [ˌæridʒ] Hebelkraft *f*.
levity ['leviti] Leichtfertigkeit *f*.
levy ['levi] 1. Erhebung *f* von Steu-
ern; 2. Aushebung *f*; Aufgebot *n*;
3. Steuern erheben; 4. ausheben.
lewd [lud] licherlich, unzuchtig.
liability [laɪˈbɪləti] Verantwortlich-
keit *f*; 2. Haftpflicht *f*; Verpflich-
tung *f*; *fig.* Hang *m*; liabilities *pl.*
Verbindlichkeiten *f/pl.*, † Passiva
pl.
liable [ˈlaɪəbəl] verantwortlich;
haftpflichtig; verpflichtet; ausge-
setzt (to *dat.*); be ~ to neigen zu.
liar ['laɪə] Lügner(in).
libel ['laɪbəl] 1. Schmähschrift *f*;
Verleumdung *f*; 2. schmähen; ver-
unglimpfen.
liberal ['libərəl] 1. □ liberal (*a.*
pol.); freigebig; reichlich; freisin-
nig; 2. Libérale(r) *m*; ~ity [lib-
ˈræliti] Freigebigkeit *f*; Freisinnig-
keit *f*.
liberate ['libəreɪt] befreien; frei-
lassen; ~ion [libəˈreɪʃən] Befreiung
f; ~or ['libəreɪtə] Befreier *m*.
libertine ['libə(:)teɪn] Wüstling *m*.
liberty ['libəti] Freiheit *f*; take
liberties sich Freiheiten erlauben;
be at ~ frei sein.
librarian [laɪˈbreəriən] Bibliothe-
kar(in); ~y ['laɪbrəri] Bibliothek *f*.
lice [laɪs] *pl.* von louse.
license [ˈlɪsəns] 1. Li-
zenz *f*; Erlaubnis *f*; Konzession *f*;
Freiheit *f*; Zügellosigkeit *f*; driving
~ Führerschein *m*; 2. lizenzieren,
berechtigen; *et.* genehmigen; ~see
[ˈlaɪsənˈsi:] Lizenznehmer *m*.
licentious [ˈlaɪsənʃəs] unzuchtig;
ausschweifend.
lichen ɔ, ʒ ['laɪkən] Flechte *f*.
lick [lɪk] 1. Lecken *n*; Salzlecke *f*;
F Schlag *m*; 2. (be)lecken; F ver-
dreschen; übertreffen; ~ the dust
im Staub kriechen; fallen; geschla-
gen werden; ~ into shape zurecht-
stutzen.
licorice ['likərɪs] Lakritze *f*.
lid [lɪd] Deckel *m*; (Augen)Lid *n*.
lie¹ [laɪ] 1. Lüge *f*; give s.o. the ~
j-n Lügen strafen; 2. lügen.
lie² [ˌli:] 1. Lage *f*; 2. [irr.] liegen; ~ by
still-, brachliegen; ~ down sich nie-
derlegen; ~ in wait for j-m auf-
lauern; let sleeping dogs ~ *fig.* daran
rühren wir lieber nicht; ~down
[ˈlaɪˈdaʊn] Nickerchen *n*; ~in: have
a ~ sich gründlich ausschlafen.
lien ɔ, ʒ ['liən] Pfandrecht *n*.

lieu [lju:] in ~ of (an)statt.
lieutenant [leɪˈtenənt; ɔ leˈtenənt]
Am. luˈtenənt] Leutnant *m*; Statt-
halter *m*; ~commander & Korvet-
tenkapitän *m*.
life [laɪf], *pl.* lives [laɪvz] Leben *n*;
Menschenleben *n*; Lebensbeschrei-
bung *f*; for ~ auf Lebenszeit; for
one's ~, for dear ~ ums (Liebe) Le-
ben; to the ~ naturgetreu; ~ sen-
tence lebenslängliche Zuchthaus-
strafe; ~ assurance Lebensver-
sicherung *f*; ~belt ['laɪfbelt] Ret-
tungsgürtel *m*; ~boat Rettungs-
boot *n*; ~guard Leibwache *f*;
Badewärter *m* am Strand; ~insur-
ance Lebensversicherung *f*; ~
jacket & Schwimweste *f*; ~less
□ ['laɪflɪs] leblos; matt (*a. fig.*);
~like lebenswahr; ~long lebens-
länglich; ~preserver Am. ['laɪf-
ˈpreɪzə:və] Schwimmgürtel *m*; Tot-
schläger *m* (Stock mit Bleikopf);
~time Lebenszeit *f*.
lift [lɪft] 1. Heben *n*; *phys.* & Auf-
trieb *m*; *fig.* Erhebung *f*; Fahrstuhl
m; give s.o. a ~ j-m helfen; j-n (im
Auto) mitnehmen; 2. *v/t.* (auf)he-
ben; erheben; beseitigen; sl. klauen,
stehlen; *v/i.* sich heben.
ligature ['lɪɡətʃuə] Binde *f*; 2.
Verband *m*.
light¹ [laɪt] 1. Licht *n* (*a. fig.*); Fen-
ster *n*; Aspekt *m*, Gesichtspunkt
m; Feuer *n*; Glanz *m*; *fig.* Leuchte
f; ~s *pl.* Fähigkeiten *f/pl.*; will you
give me a ~ darf ich Sie um Feuer
bitten; put a ~ to anzünden; 2. licht,
hell; blond; 3. [irr.] *v/t.* oft ~ up
be-, erleuchten; anzünden; *v/i.*
mit ~ up aufleuchten; ~ out Am. sl.
schnell losziehen, abhauen.
light² [ˌlaɪt] 1. *adj.* □ *u. adv.* leicht
(*a. fig.*); ~ current & Schwachstrom
m; make ~ of *et.* leicht nehmen;
2. ~ (up)on stoßen od. fallen auf
(*acc.*), geraten an (*acc.*); sich nieder-
lassen auf (*dat.*).
lighten ['laɪtn] blitzen; (sich) erhel-
len; leichter machen; (sich) er-
leichtern.
lighter ['laɪtə] Anzünder *m*; (Ta-
schen)Feuerzeug *n*; & L(e)ichter *m*.
light-headed ['laɪtˈhedɪd] wirr im
Kopf, irr; ~hearted □ [ˌhɑ:tɪd]
leichterzig; fröhlich; ~house
['laɪthaus] Leuchtturm *m*.
lighting ['laɪtɪŋ] Beleuchtung *f*;
Anzünden *n*.
light-minded ['laɪtˈmaɪndɪd] leicht-
sinnig; ~ness ['laɪtnɪs] Leichtigkeit
f; Leichtsinns *m*.
lightning ['laɪtnɪŋ] Blitz *m*; ~ bug
Am. zo. Leuchtkafer *m*; ~conduc-
tor, ~rod & Blitzableiter *m*.
light-weight ['laɪtweɪt] Sport:
Leichtgewicht *n*.
like [laɪk] 1. gleich; ähnlich; wie;
such ~ dergleichen; feel ~ F sich

legt fühlen
he ~ wie
2. Gleich-
ungen *f/pl.*
the ~ de-
gen, gern ha-
don? wie g
should ~ to
sen.
lihood ['laɪ-
hʊd] 1. Mög-
lichkeit *f*; 2. ly
geeignet;
srscheinlich
[ˈlaɪkən] 1.
[ˈlaɪknɪs]
n; Gestalt
sch-, ebenfa-
[ˈlaɪkɪŋ] 1.
Gefallen
[ˈlaɪlɪk] 1.
[ˈlɪlɪ] Lü-
glöckchen
[ˈlɪm] Kö-
ber [ˈlɪmb
meidig; 2.
[ˈlaɪm] K-
Limonen *f*;
[ˈlaɪlɪt] Kall
ter(licht *n*;
des öffentli-
[ˈlɪmɪt] 1.
tritt gestat-
is the ~/
ist (doch)
F bis zu
begrenzen
); ~ation
ng *f*, Besch-
Verfahr-
mpany Ge-
ränkter H-
ter; ~less
[ˈlɪmp] 1.
schlaff; w
[ˈlɪpɪd] □ 1.
chtig.
[ˈlaɪn] 1.
e *f*; Ven-
rche *f*; (C
e *f*; V
senbahnli-
itung *f*;
e *f*, S
ichtung *f*;
ont *f*; ~
undlage
e *f*; h
ch *n*; in
ung mit;
n; draw
ntmachen
pparat bl
stellen;
sen; Kl
verfen; *v/i.*
[ˈlɪn] 1.
amie *f*;
[ˈlɪl] gera

BRIEF ATTACHMENT P

IN THE UNITED STATES PATENT AND TRADEMARK OFFICE

In re Patent Application of

Applicants: Bednorz et al.

Serial No.: 08/479,810

Filed: June 7, 1995

For: NEW SUPERCONDUCTIVE COMPOUNDS HAVING HIGH TRANSITION
TEMPERATURE, METHODS FOR THEIR USE AND PREPARATION

Date: March 1, 2005

Docket: YO987-074BZ

Group Art Unit: 1751

Examiner: M. Kopec

Commissioner for Patents
P.O. Box 1450
Alexandria, VA 22313-1450

FIRST SUPPLEMENTAL AMENDMENT

Sir:

In response to the Office Action dated July 28, 2004, please consider the
following:

ATTACHMENT P

LANDOLT-BÖRNSTEIN

LA

Numerical Data and Functional Relationships
in Science and Technology

New Series

Editor in Chief: K.-H. Hellwege

Group III: Crystal and Solid State Physics

Volume 3

Ferro- and Antiferroelectric Substances

by Toshio Mitsui and

R. Abe · Y. Furuhashi · K. Gesi · T. Ikeda · K. Kawabe

Y. Makita · M. Marutake · E. Nakamura · S. Nomura

E. Sawaguchi · Y. Shiozaki · I. Tatsuzaki · K. Toyoda

Editors: K.-H. Hellwege and A. M. Hellwege



Springer-Verlag Berlin · Heidelberg · New York 1969

Sprir

II Data

Oxides

1 Perovskite-type oxides

1A Simple perovskite-type oxides

Nr. 1A-1 NaNbO_3 , Sodium niobate

a	It was reported by MARTIAS et al. in 1951 that NaNbO_3 was ferroelectric. Cross et al., however, proved in 1955 that at room temperature it is not ferroelectric but antiferroelectric.					51M2 55C2
b	phase	V	IV	III*	II	I
	state	F	A			P
	crystal system	monoclinic	orthorhombic	pseudo-tetragonal	tetragonal	cubic
	space group		Pbma^a - D_{2h}^{11}			$\text{Pm}3\text{m-O}_h^1$
	Θ^{**}	-200	354	562	640	a)61W2 58R3
	$P_r \parallel [001]$ in phase V. Phase IV: $a = 5.568 \text{ \AA}$ ($\cong \sqrt{2}a_0$), $b = 5.505 \text{ \AA}$ ($\cong \sqrt{2}a_0$), $c = 15.518 \text{ \AA}$ ($\cong 4a_0$), where a_0 is the lattice constant of the cubic cell of phase I. In phase IV (orthorhombic system) the longest edge of a unit cell is taken as the c axis (see Fig. 1). This system of the axes is adopted here. In Well and Megaw's analysis b and c axes were interchanged. The orthorhombic structure is also represented by a pseudomonoclinic unit cell (see Fig. 1), where $b' = c$, $a' = c'$ ($\cong a_0$), $\beta' \cong \pi/2$.					51V3 61W2
2a	Cooling method from a molten mixture of Na_2CO_3 , Nb_2O_5 , and NaF .					51W1
3	Crystal structure: In phase IV, $Z = 8$. Tab. 1; Fig. 1, 2.					
4	Lattice distortions (thermal expansion): For phase I, II, III, IV: Tab. 2,3; Fig. 3. For phase V, at -160°C : $a = 5.564 \text{ \AA}$ ($\cong \sqrt{2}a_0$), $b = 5.548 \text{ \AA}$ ($\cong \sqrt{2}a_0$), $c = 7.812 \text{ \AA}$ ($\cong 2a_0$), $\beta = 91^\circ 09'$. Fig. 4.					57J1
5a	Dielectric constants: Fig. 5. Curie-Weiss law: $\kappa = C/(T - \Theta_p)$, $T > \Theta_{\text{III-IV}}$, where $C = 2 \cdots 4 \cdot 10^5 \text{ } ^\circ\text{K}$ and $\Theta_p = 60 \cdots 80^\circ\text{C}$.					54S3 55C2
c	Spontaneous polarization: $P_s \cong 12 \cdot 10^{-3} \text{ C m}^{-2}$ ($\parallel c$, in phase V). Coercive and critical field for normal and double hysteresis curve: Fig. 6.					
9a	Birefringence: Fig. 7, 8.					
14a	Domain structure: See					55C2, 64p1, 62M9, 62W3
b	Dynamic properties: Fig. 9, 10.					

Tab. 1. NaNbO_3 . Fractional coordinates x, y, z of atoms in unit cell at RT. [61W2]

	x	y	z
Na(1)	$\frac{1}{2}$	0.250	0
Na(2)	0.769	0.251	$\frac{1}{2}$
Nb	0.261	0.257	0.125
O(1)	$\frac{1}{2}$	0.208	0
O(2)	0.271	0.290	$\frac{1}{2}$
O(3)	0.010	0.532	0.121
O(4)	0.446	0.972	0.126

* According to Ismailzade phase III consists of 4 phases (see Fig. 3). [63I4]

Transitions exhibit large temperature hysteresis, and the transition temperatures measured with decreasing temperature are given here.

Tab. 2. NaNbO_3 . Lattice parameters at various temperatures. [56F1] and [54S3]

$T [^\circ\text{C}]$	Crystal symmetry	Lattice parameters	
		[56F1]	[54S3]
20	Monoclinic	$a' = c' = 3.914 \text{ \AA}$ $b' = 4 \cdot 3.881 \text{ \AA}$ $\beta' = 90^\circ 39'$	$a' = c' = 3.915 \text{ \AA}$ $b' = 4 \cdot 3.881 \text{ \AA}$ $\beta' = 90^\circ 40'$
390	Pseudotetragonal	$a = 2 \cdot 3.920 \text{ \AA}$ $c = 4 \cdot 3.926 \text{ \AA}$ $c/a = 2.0032$	$a = 2 \cdot 3.919 \text{ \AA}$ $c = 4 \cdot 3.927 \text{ \AA}$ $c/a = 2.0040$
420	Pseudotetragonal	$a = 2 \cdot 3.924 \text{ \AA}$ $c = 4 \cdot 3.924 \text{ \AA}$ $c/a \approx 2.0000$	$a = 2 \cdot 3.921 \text{ \AA}$ $c = 4 \cdot 3.927 \text{ \AA}$ $c/a = 2.0028$
560	Tetragonal (changing to simple perovskite-type cell)	$a = 2 \cdot 3.933 \text{ \AA}$ $c = 4 \cdot 3.940 \text{ \AA}$ $c/a = 2.0038$	— — —
640	Cubic	$a = 3.942 \text{ \AA}$	—

Tab. 3. NaNbO_3 . Lattice parameters of the subcell at various temperatures. [63I4]. See Fig. 3

$T [^\circ\text{C}]$	Subcell parameters				
	pseudomonoclinic I ($a' = c' > b'$, $\beta' > 90^\circ$)				
	$a' [\text{\AA}]$	$b' [\text{\AA}]$	$\beta' - 90^\circ$	a'/b'	$V [\text{\AA}^3]$
18 ... 20	3.914 ₇	3.885	40'	1.0075 ₅	59.5 ₃
100	3.917 ₆	3.893 ₆	37	1.0060	59.7 ₄
150	3.919 ₆	3.898 ₇	33	1.0055	59.9
200	3.922 ₄	3.902 ₄	29	1.0050	60.0 ₅
250	3.924 ₃	3.907 ₅	26	1.0040	60.1 ₇
300	3.925 ₅	3.914	22	1.0030	60.3 ₃
340	3.926 ₅	3.917 ₆	18	1.0025	60.4
350	3.926 ₅	3.919	17	1.0020 ₂	60.4 ₂
pseudomonoclinic II					
360	3.927 ₂	3.920	6	1.0020	60.45
380	3.927 ₈	3.921 ₃	5	1.0015 ₅	60.50
400	3.928 ₃	3.922 ₃	4	1.0015	60.5 ₂
pseudomonoclinic III					
420	3.929 ₄	3.923	3	1.0015	60.5 ₅
440	3.930	3.924	3	1.0015	60.60
460	3.932	3.926 ₃	3	1.0015	60.70
pseudomonoclinic IV					
480	3.933 ₅	3.927 ₅	3	1.0015 ₂	60.7 ₇
500	3.934 ₆	3.928 ₈	2	1.0015	60.8 ₂
510	3.935	3.929 ₅	2	1.0015	60.85
tetragonal I					
$T [^\circ\text{C}]$	$c [\text{\AA}]$	$a = b [\text{\AA}]$	c/a	$V [\text{\AA}^3]$	
520	3.936 ₇	3.929 ₅	1.0015 ₅	60.80	
540	3.938	3.930 ₂	1.0020	60.85	
560	3.939 ₈	3.931 ₆	1.0020 ₈	60.90	
tetragonal II					
580	3.941 ₄	3.934 ₂	1.0020	61.00	
600	3.943 ₄	3.937 ₈	1.0015	61.15	
620	3.945 ₆	3.942	1.0010	61.30	
630	3.945	≈ 3.945	≈ 1.0000	61.40	
cubic					
$T [^\circ\text{C}]$	$a_0 [\text{\AA}]$	$V [\text{\AA}^3]$	$T [^\circ\text{C}]$	$a_0 [\text{\AA}]$	$V [\text{\AA}^3]$
640	3.947 ₂	61.50	700	3.949 ₇	61.6 ₂
650	3.947 ₆	61.5 ₂	720	3.950 ₆	61.6 ₇
680	3.949	61.5 ₇			

Furuhata/Marutake

Nr. 1A-2 KNbO_3 , Potassium niobate

1a	Ferroelectricity in KNbO_3 was first discovered by MATTHIAS in 1949.				49M4
b	phase	IV	III	II	I
	state	F	F	F	P
	crystal system	rhombohedral	orthorhombic	tetragonal	cubic
	space group		$\text{Bmm}2^{\text{a}}\text{-C}_{2v}^{\text{14}}$		$\text{Pm}3\text{m-O}_h^{\text{1}}$
	θ	-10	225	435	$^{\circ}\text{C}$
	$P_s \parallel [001]$ in phase II (along $[001]$ of phase I), $P_s \parallel [001]$ in phase III (along $[110]$ of phase I), $P_s \parallel [111]$ in phase IV (along $[111]$ of phase I). $T_{\text{melt}} = 1050^{\circ}\text{C}$ $\rho = 4.590 \cdot 10^3 \text{ kg m}^{-3}$ $a = 5.697 \text{ \AA}$, $b = 3.971 \text{ \AA}$, $c = 5.720 \text{ \AA}$ at RT. Transparent. Light yellow.				55R3, 58M3 52L1 67K4
2	Flux method (K_2CO_3 flux). Phase diagram of $\text{K}_2\text{CO}_3\text{-Nb}_2\text{O}_5$ system; see Pulling method from the $\text{K}_2\text{CO}_3\text{-Nb}_2\text{O}_5$ mixture Crystal form: square plate				51W1 55R3 58M3
3	Crystal structure: $Z = 1$ in phase I, II, IV. $Z = 2$ in phase III. Tab. 4, 5; Fig. 11.				
4	Temperature dependence of lattice parameters: Tab. 6; Fig. 12.				
5	Dielectric constant: Fig. 13, 14. $\kappa = C/(T - \theta_p)$, $T > \theta_{\text{II-I}}$, where $C = 2.42 \cdot 10^5 \text{ }^{\circ}\text{K}$, $\theta_p = 360^{\circ}\text{C}$. Nonlinear dielectric properties: $\xi = -1.62 \cdot 10^9 \text{ J C}^{-4} \text{ m}^5$, $\zeta = 1.79 \cdot 10^{10} \text{ J C}^{-6} \text{ m}^9$. Spontaneous polarization and coercive field: Fig. 15. $P_s = 26 \cdot 10^{-2} \text{ C m}^{-2}$ at $T = \theta_p$.				56T3 56T3 56T3 56T3
6	Transition heat, transition entropy: Tab. 7.				56T3
7	Piezoelectricity: Fig. 16.				
12	NQR: Tab. 8; Fig. 17 ... 20.				

Tab. 4. KNbO_3 . Atomic positions in fractional coordinates at RT in phase III. [67K4]

Nb	0, 0, 0
K	$0, \frac{1}{2}, \frac{1}{2} + z_K$
O(1)	$0, \frac{1}{2}, z_1$
O(2)	$\frac{1}{2} + x_2, 0, \frac{1}{2} + z_2$
z_K	+0.017
z_1	+0.021
z_2	+0.035
x_2	+0.004

Tab. 5. KNbO_3 . Interatomic distances and bond angles at RT. [67K4]

	*	distance \AA	**	*	angle $^{\circ}$
Nb-O(1)	(2)	1.991 ± 0.001	O(2)(s)-Nb-O(2)(s)	(1)	97.4 ± 1.2
Nb-O(2)	(2)	1.863 ± 0.007	O(2)(l)-Nb-O(2)(l)	(1)	83.4 ± 1.0
Nb-O(2)	(2)	2.180 ± 0.009	O(2)(s)-Nb-O(2)(l)	(2)	89.7 ± 0.5
K-O(1)	(1)	2.837 ± 0.014	O(1)-Nb-O(2)(s)	(4)	92.3 ± 0.6
K-O(1)	(2)	2.848 ± 0.001	O(1)-Nb-O(2)(l)	(4)	87.5 ± 0.6
K-O(1)	(1)	2.883 ± 0.014	Nb-O(1)-Nb	(1)	172.8 ± 0.7
K-O(2)	(4)	2.792 ± 0.008	Nb-O(2)-Nb	(2)	168.6 ± 0.6
K-O(2)	(4)	2.873 ± 0.010			
O(1)-O(2)	(4)	2.780 ± 0.012			
O(1)-O(2)	(4)	2.884 ± 0.012			
O(2)-O(2)	(1)	2.802 ± 0.024			
O(2)-O(2)	(1)	2.894 ± 0.024			
O(2)-O(2)	(2)	2.860 ± 0.001			

* Numbers in this column indicate numbers of equal bonds or angles per formula unit.

* For the O-Nb-O angles, the letter s or l indicates whether the Nb-O(2) bond involved is short or long.

Tab. 6. KNbO_3 . Lattice constants and volume of unit cell at various temperatures. [54S3]. a' , c' : lattice parameters of pseudotetragonal cell

T °C	$a' = c'$ Å	b Å	b/a	β	V Å ³
25	4.0375	3.9711	1.0167	90° 15'	64.73
125	4.0374	3.9797	1.0145	90° 15'	64.87
185	4.0363	3.9830	1.0134	90° 13'	64.89
205	4.0369	3.9839	1.0133	90° 14'	64.93
	$a = b$	c	c/a		
220	3.9972	4.0636	1.0166		64.92
230	3.9978	4.0640	1.0166		64.95
270	3.9992	4.0647	1.0164		65.01
320	4.0023	4.0639	1.0154		65.10
375	4.0048	4.0620	1.0143		65.15
410	4.0080	4.0567	1.0122		65.18
425	4.0214				65.03
450	4.0225				65.09
510	4.0252				65.22

Tab. 7. KNbO_3 . Transition heat and transition entropy per mole. [54S1]

Transition	ΔQ_m cal mol ⁻¹	ΔS_m cal °K ⁻¹ mol ⁻¹
IV → III	32	0.12
III → II	85	0.17
II → I	190	0.28
	134	—

Tab. 8. KNbO_3 . NQR spectrum. [54C1]. The measured frequency ratios intersect the calculated ratios in a straight line at constant $\eta = 0.806 \pm 0.002$. η = asymmetry parameter

Crystal structure	f MHz	Measured ratio	Calculated ratio ($\eta = 0.806$)	Identification	e^2qQ/h MHz
orthorhombic (20 °C)	3.648			(9/2, 7/2)	23.120 ± 0.05
	3.030	1.204	1.204	(3/2, 1/2)	
	2.527	1.198	1.196	(7/2, 5/2)	
	2.085	1.214	1.213	(5/2, 3/2)	
rhombohedral (-196 °C)	2.674		($\eta = 0.0$)	(9/2, 7/2)	16.0 ± 0.1
	2.004	1.335	1.333	(7/2, 5/2)	
	1.335	1.503	1.500	(5/2, 3/2)	

Nr. 1A-3 NaTaO_3 , Sodium tantalate

1a	It was reported by MATTHIAS in 1949 that NaTaO_3 is ferroelectric below 480 °C. No anomalies of the dielectric constants, however, were observed by SMOLENSKII et al.					49M1 57S3
b	phase	IV	III	II	I	57K1 57K1 62I4 51V2
	state	(F)				
	crystal system	orthorhombic	orthorhombic	tetragonal	cubic	
	space group	$\text{Pc}2_1\text{n-C}_{2v}^2$				
	θ	480	550	630	°C	
	$a = 5.4941 \text{ Å}$, $b = 7.7508 \text{ Å}$, $c = 5.5130 \text{ Å}$ at RT. The cubic cell in phase I becomes pseudomonoclinic in phase IV. Relation between the orthorhombic unit cell and the pseudomonoclinic cell: Fig. 21.					
3	Crystal structure: $Z = 4$. Atomic positions: Tab. 9; Fig. 22.					
4	Temperature dependence of lattice parameters: Tab. 10; Fig. 23.					

Tab. 9. NaTaO₃. Fractional coordinates of atoms in the unit cell. [57K1]

Na	x :	$0 - 0.01$	$0 + 0.01$	$\frac{1}{2} - 0.01$	$\frac{1}{2} + 0.01$
	y :	$\frac{1}{4} + 0.03$	$\frac{1}{4} + 0.03$	$\frac{1}{4} + 0.03$	$\frac{1}{4} + 0.03$
	z :	$0 + 0.02$	$0 - 0.02$	$\frac{1}{2} - 0.02$	$\frac{1}{2} + 0.02$
Ta*	x :	$\frac{1}{2}$	$\frac{1}{2}$	0	0
	y :	0	$\frac{1}{2}$	$\frac{1}{2}$	0
	z :	0	0	$\frac{1}{2}$	$\frac{1}{2}$
O(1)	x :	$0 - 0.02$	$0 + 0.02$	$\frac{1}{2} + 0.02$	$\frac{1}{2} - 0.02$
	y :	$\frac{3}{4} + 0.01$	$\frac{1}{4} + 0.01$	$\frac{3}{4} + 0.01$	$\frac{1}{4} + 0.01$
	z :	$\frac{1}{2} + 0.02$	$\frac{1}{2} - 0.02$	$0 + 0.02$	$0 - 0.02$
O(2)	x :	$\frac{1}{4} + 0.04$	$\frac{1}{4} - 0.04$	$\frac{3}{4} - 0.04$	$\frac{3}{4} + 0.04$
	y :	$0 - 0.03$	$0 - 0.03$	$\frac{1}{2} - 0.03$	$\frac{1}{2} - 0.03$
	z :	$\frac{1}{4} + 0.04$	$\frac{3}{4} + 0.04$	$\frac{3}{4} - 0.04$	$\frac{1}{4} - 0.04$
O(3)	x :	$\frac{1}{4} + 0.04$	$\frac{1}{4} - 0.04$	$\frac{3}{4} - 0.04$	$\frac{3}{4} + 0.04$
	y :	$\frac{1}{2} + 0.06$	$\frac{1}{2} + 0.06$	$0 + 0.06$	$0 + 0.06$
	z :	$\frac{1}{4} + 0.04$	$\frac{3}{4} + 0.04$	$\frac{3}{4} - 0.04$	$\frac{1}{4} - 0.04$

Tab. 10. NaTaO₃. Temperature dependence of the pseudo-cell parameters. [62I4].
For the notations, see Fig. 21

T [°C]	23	100	200	300	400	450	480	500	550	580	600
$a' = c'$ [Å]	3.889 _s	3.893 _s	3.899 _s	3.907	3.912 _s	3.916	3.918	3.920	3.923	3.925 _s	3.927
b' [Å]	3.885 _s	3.890 _s	3.896 _s	3.903 _s	3.910 _s	3.913 _s	3.915 _s	3.918	3.923	≈3.925 _s	≈3.927
$\beta - 90^\circ$	22'00"	16'00"	9'00"	6'00"	4'00"	3'30"	2'00"	≈2'00"	1'30"	0'00"	0'00"
a'/b'	1.0010	1.0009	1.0009	1.0008	1.0006	1.0006	1.0005	1.0005	1.000	1.000	1.000
V [Å ³]	58.8 ₀	59.0 ₀	59.2 _s	59.5 _s	59.8 _s	60.0 ₀	60.1 ₀	60.2 ₀	60.3 _s	60.4 _s	60.5 _s

T [°C]	630	660	680
$b = a = c$ [Å]	3.929	3.931	3.932 _s
V [Å ³]	60.6 _s	60.7 _s	60.8 ₀

Nr. 1A-4 KTaO₃, Potassium tantalate

1a	Ferroelectric activity was first reported by MATTHIAS in 1949; ^{a)} however, recent studies by WEMPLE have proved that the ferroelectric transition does not occur, at least above 1.6 °K. ^{b)}	^{a)} 49M1, 49M4 ^{b)} 64W2, 65W2
b	KTaO ₃ is cubic and its space group is Pm3m-O _h . $T_{\text{melt}} = (1357 \pm 3)^\circ\text{C}$. $\rho = 6.97 \cdot 10^3 \text{ kg m}^{-3}$. $a = 3.9885 \text{ Å}$ at RT. Transparent, colorless or pale blue (blue in oxygen-deficient crystals). Cleavage: along (100) planes. Hardness: nearly the same as quartz.	64W2, 65W2, 51V2 55R2, 56R2 58R1 51V2 64W2
2a	Flux method: KF flux, ^{a)} dark small crystals; K ₂ CO ₃ flux, ^{b)} large (≈10 mm) transparent crystals. Czochralski-Kyropoulos method: large (≈10 mm) good quality crystals. Floating technique: planar single crystals. Phase diagram of system K ₂ CO ₃ -Ta ₂ O ₅ : Fig. 24. Hydrothermal phase diagram K ₂ O-Ta ₂ O ₅ -H ₂ O at 400 °C:	^{a)} 62T5, 64W2 ^{b)} 66U1 64W2, 65W2, 67B7 66W8 67M2
3	$Z = 1$ Crystal structure: cubic perovskite type, (Pm3m-O _h). K at 1a position; Ta at 1b position; 3O at 3c position.	51V1, 51V2

* All positions ± 0.002 .

Figuren S. 221 ff.

II 1 Oxide des Perowskit-Typs

4	Nr. 1A-4 KTaO_3 , continued $a = 3.9885 \text{ \AA}$ at RT; $a = 4.0026 \text{ \AA}$ at 450°C .	51V2, 59B1
5a	Dielectric constant at low frequencies: earlier studies showed a peak in the κ vs. T curve; ^{a)} recent measurements have shown that no peak exists down to 1.6°K . ^{b)} Fig. 25. $\kappa = 243$ at RT. $\kappa = \kappa_0 + C/(T - \Theta_p)$, $T > 30^\circ\text{K}$, where $\kappa_0 = 48$, $C = 5.7 \cdot 10^4^\circ\text{K}$, $\Theta_p = 4^\circ\text{K}$. Loss tangent: $\tan \delta \approx 0.001$ at 200 kHz at RT. Dielectric constant in the GHz range: Fig. 26. Q values in the GHz range: $Q = 10^3 \dots 10^4$. Dielectric loss in the far infrared frequency range: See 1A-4-9 below (Figs. 34, 35). Hydrostatic pressure dependence of the reciprocal dielectric constant: Fig. 27.	^{a)} 50H3 ^{b)} 65W2, 64W2 65W2 64W2 64R3 64W2
b	Effects of dc bias on κ at 4.2°K and at RT: Figs. 28, 29. Coefficients in free energy expansion: $\xi = 9 \cdot 10^9 \text{ V m}^5 \text{ C}^{-3}$ at 4.2°K , $\xi = (4 \pm 1) \cdot 10^9 \text{ V m}^5 \text{ C}^{-3}$ at 295°K .	65K1 65W2 64W2
c	D vs. E curves show no hysteresis character down to 1.6°K . P vs. E at 4.2°K : see	
9a	Refractive index in visible region: Fig. 30. Reflectivity in far infrared region and the dispersion: Figs. 31, 32. Reflectivity data were used to obtain transverse optical modes of the lattice vibration by means of Kramers-Kronig relation (cf. Tab. 42). Transverse optical modes as a function of temperature: Tab. 11; Fig. 33. The square of the wave number $\tilde{\nu}_{11}$ for the "ferroelectric mode" is approximately linear to T : $\tilde{\nu}_{11}^2 \propto (T - \Theta_p)$. (Additional data are given on the ferroelectric soft mode, see 1A-4-13b). Effect of lattice vibration on the fluorescent spectrum of Eu^{3+} in KTaO_3 : see Imaginary part of the dielectric constant and the conductivity in the far infrared region: Figs. 34, 35. Absorption coefficient α depends on the degree of oxygen reduction in KTaO_3 . Absorption coefficient near the interband absorption edge (about 3.6 eV) for insulating and semiconducting KTaO_3 : Fig. 36 (for additional data, see Fig. 2 of reference). Absorption vs. wavelength of light: Fig. 37. Absorption vs. carrier concentration in semiconducting KTaO_3 : Fig. 38. Optical absorption in impurity doped single crystals: for impurities Fe, Mn, Co and Cr, see	63M4, 67P4 67P4, 67F2 65S9 65W2 67B1 64W2 64G3, 63G3 67F4
b	Quadratic electrooptic constants (6328 \AA , $2 \dots 77^\circ\text{K}$): $M_{11} - M_{12} = (0.16 \pm 0.01) \text{ m}^4 \text{ C}^{-2}$; $M_{44} = (0.12 \pm 0.01) \text{ m}^4 \text{ C}^{-2}$. Electroreflectance and electroabsorption were studied using semiconducting KTaO_3 . Effect of interface dc field on the reflectance of the (100) surface: Fig. 39. Electroreflectance spectra of (100) and (111) surfaces: Figs. 40, 41. Effect of polarization of light on the electroreflectance: Fig. 42. Electroreflectance as a function of the surface polarization: Fig. 43. Electroreflectance singularities and the corresponding energies: Tab. 12. Electroabsorption near the absorption edge: Fig. 44. Fundamental absorption edge ($\approx 3.6 \text{ eV}$) shifts to higher energies with dc bias: Fig. 45.	67B1, 66B2 67F2
d	Faraday rotation near the band edge: Fig. 46; Tab. 44.	65S9
f	Electric-field-induced Raman effect: Fig. 47. (For the ferroelectric soft mode obtained from the Raman scattering, see Fig. 33). Fluorescence spectrum of Eu^{3+} in KTaO_3 : see	
10	Resistivity of insulating single crystal: $\rho > 10^9 \Omega \text{ m}$ at RT. Most data on the transport properties have been obtained using oxygen-deficient semiconducting KTaO_3 . Resistivity of oxygen-deficient single crystals as a function of temperature: Fig. 48. Hall mobility: $\mu_H = 3 \cdot 10^{-3} \text{ m}^2 \text{ V}^{-1} \text{ sec}^{-1}$ at RT (see also Tab. 13). $\mu_H \approx 8 \cdot 10^4 \text{ T}^{-3} \text{ m}^2 \text{ V}^{-1} \text{ sec}^{-1}$, $T > 100^\circ\text{K}$; Fig. 49. Hall coefficient and Hall mobility at 4.2°K and RT for several semiconducting KTaO_3 : Tab. 13. Hall mobility vs. carrier concentration: Fig. 50. Scattering cross section vs. carrier concentration: see Ca concentration in doped KTaO_3 vs. net ionized donor concentration: see Electrical conductivity vs. hydrostatic pressure: Fig. 51. Conductivity in the far infrared region: see Fig. 35. Seebeck coefficient: $Q = 550 \mu\text{V}^\circ\text{K}^{-1}$ at RT. (Oxygen-deficient KTaO_3 with $N = 3.5 \cdot 10^{23} \text{ m}^{-3}$). Effective mass estimated from the Seebeck coefficient: $m^* = (0.8 \pm 0.28) m_0$. Photoconductivity vs. $h\nu$ shows a peak at $h\nu = 3.58 \text{ eV}$.	65W2 65W2 65W2 66S17 66W5 65W2 65W2 65W2

Sawaguchi

12a	Nr. 1A-4 KTaO_3 , continued
b	Dielectric constant at low frequencies: earlier studies showed a peak in the κ vs. T curve; ^{a)} recent measurements have shown that no peak exists down to 1.6°K . ^{b)} Fig. 25.
13b	Effects of dc bias on κ at 4.2°K and at RT: Figs. 28, 29.
17	Refractive index in visible region: Fig. 30.
Tab. mode The soft 1	
T [°K]	
12a	
12b	
12c	
12d	
12e	
12f	
12g	
12h	
12i	
12j	
12k	
12l	
12m	
12n	
12o	
12p	
12q	
12r	
12s	
12t	
12u	
12v	
12w	
12x	
12y	
12z	

12a	NMR of ^{181}Ta in KTaO_3 : spin-lattice relaxation time, $T_1 \approx 10^{-3}$ sec at RT; spin-spin relaxation time, $T_2 = \approx 10^{-5}$ sec at RT; nuclear magnetic moment of ^{181}Ta ($I = 7/2$): $p_n = (2.340 \pm 0.001) \mu_n$ (uncorrected); ($p_n = (2.35 \pm 0.01) \mu_n$, after estimated corrections). Nuclear magnetic acoustic resonance: the absorption data were given for $\Delta m = \pm 2$ transition of ^{181}Ta as a function of the angle between magnetic field and sound axis [100].	60B2 67M4 66U1 64W2 67H3 67H3 63W5, 64W2 67H3, 65H2 64W2															
b	ESR of Eu^{3+} and Gd^{3+} in KTaO_3 : Tab. 14. ESR of Fe^{3+} : $g = 1.99 \pm 0.01$; $ a = (345 \pm 10) \cdot 10^{-2} \text{ m}^{-1}$ at 4.2 °K; $a = (288 \pm 5) \cdot 10^{-2} \text{ m}^{-1}$ at RT (Fe^{3+} is on the Ta^{5+} site). $a = (30 \pm 1) \cdot 10^{-2} \text{ m}^{-1}$ at RT (Fe^{3+} is on the K^{1+} site). ESR Stark effect for Fe^{3+} : E_{bias} along [100] induces axial splitting term D ($D = 12 \cdot 10^{-2} \text{ m}^{-1}$ at $E_{\text{bias}} = 1.0 \text{ MV m}^{-1}$ at 4.2 °K; $D \propto E_{\text{bias}}^2$). ESR of Ni^{3+} located on Ta^{5+} site (low spin state) and on K^{1+} site: see ESR in Mn-doped, Co-doped and Cr-doped KTaO_3 : see																
13b	Phonon dispersion relation for the transverse optical branch: Fig. 52; Tab. 15. Temperature dependence of the ferroelectric soft mode: Fig. 53. The square of the phonon energy of the ferroelectric soft mode can be approximated by $(\hbar\nu)^2 = 10^4 A/\kappa$, $40^\circ\text{K} < T < 295^\circ\text{K}$; where $A = 2.825 (\text{meV})^2$, $\kappa(T)$ is the dielectric constant. For the ferroelectric soft mode, see also 1A-4-9a. Phonon energies of the acoustic modes: Fig. 54.	67S11 67S11															
17	Etchant: single crystal is slowly etched by dilute HF. Band structure and the related properties: see references; also 1A-4-9a, 9b, 9d, 10, and Tab. 12. Band gap energies determined by various methods:	64W2 67F4, 67B1															
<table border="1"> <thead> <tr> <th>Method</th><th>296 °K</th><th>77 °K</th></tr> </thead> <tbody> <tr> <td>Faraday rotation</td><td>3.77 eV 3.62 eV</td><td>3.79 eV 3.65 eV</td></tr> <tr> <td>Electroreflectance singularities</td><td>3.57 eV 3.80 eV</td><td></td></tr> <tr> <td>Absorption data</td><td>3.75 eV</td><td></td></tr> <tr> <td>Energy at which $\alpha \approx 10^6 \text{ m}^{-1}$</td><td>3.79 eV</td><td></td></tr> </tbody> </table>			Method	296 °K	77 °K	Faraday rotation	3.77 eV 3.62 eV	3.79 eV 3.65 eV	Electroreflectance singularities	3.57 eV 3.80 eV		Absorption data	3.75 eV		Energy at which $\alpha \approx 10^6 \text{ m}^{-1}$	3.79 eV	
Method	296 °K	77 °K															
Faraday rotation	3.77 eV 3.62 eV	3.79 eV 3.65 eV															
Electroreflectance singularities	3.57 eV 3.80 eV																
Absorption data	3.75 eV																
Energy at which $\alpha \approx 10^6 \text{ m}^{-1}$	3.79 eV																
Cyclotron resonance of semiconducting KTaO_3 at 70 GHz and 1.4 °K: microwave skin depth, about 30 μm ; see reference paper for the microwave absorption vs. magnetic field curves.																	
		67B1 65S13															

Tab. 11. KTaO_3 . Transverse optical modes at various temperatures [67P4]. The wave number $\tilde{\nu}_{t1}$ (ferroelectric soft mode) is temperature dependent.

$T [^\circ\text{K}]$	$\tilde{\nu}_{t1}$	$\tilde{\nu}_{t2}$	$\tilde{\nu}_{t3}$
	$\cdot 10^3 \text{ m}^{-1}$		
12	25	196	—
126	58	198	551
232	79	198	551
295	88	199	550
463	106	199	—

Tab. 12. KTaO_3 (Ca-doped). Singularities observed in electroreflectance spectra (in eV) [67F4]. See Figs. 40, 41

	E_1	E_2	A_1	A'_1	A_2
	[eV]				
KTaO_3 (100)	3.57	3.80	4.40	4.88	5.50
KTaO_3 (111)	—	3.77	4.45	4.90	5.47
KTaO_3 (110)	3.55	3.80	4.47	4.85	5.50

Tab. 13. KTaO_3 (reduced). Hall coefficient R_H and Hall mobility μ_H at 295 °K and 4.2 °K for single crystals [65W2]. Carrier concentrations N are calculated from the 4.2 °K Hall coefficient using $R_H = -1/Ne$

Sample Nr.	N_{calc} m^{-3}	R_H $\text{m}^2 \text{ C}^{-1}$		μ_H $\text{m}^2 \text{ V}^{-1} \text{ sec}^{-1}$	
		(295°K)	(4.2°K)	(295°K)	(4.2°K)
1	$3.5 \cdot 10^{23}$	$20.3 \cdot 10^{-6}$	$18 \cdot 10^{-6}$	$2.7 \cdot 10^{-3}$	2.3
2	$6.0 \cdot 10^{23}$	$12.9 \cdot 10^{-6}$	$10.4 \cdot 10^{-6}$	$2.9 \cdot 10^{-3}$	1.9
3	$6.6 \cdot 10^{23}$	$11.5 \cdot 10^{-6}$	$9.4 \cdot 10^{-6}$	$3.1 \cdot 10^{-3}$	1.9
4	$2.4 \cdot 10^{24}$	$3.0 \cdot 10^{-6}$	$2.6 \cdot 10^{-6}$	$3.0 \cdot 10^{-3}$	1.1
5	$7.8 \cdot 10^{24}$	$1.0 \cdot 10^{-6}$	$0.80 \cdot 10^{-6}$	$3.0 \cdot 10^{-3}$	0.53
6	$1.3 \cdot 10^{25}$	$0.62 \cdot 10^{-6}$	$0.48 \cdot 10^{-6}$	$3.1 \cdot 10^{-3}$	0.34

Tab. 14. KTaO_3 . Parameters of ESR spectrum of Eu^{2+} and Gd^{3+} ions, doped in single crystals of KTaO_3 [66U1]

Tab. 14. KLaO_3 . Parameters for KLaO_3 [6607]

Para-magnetic center	Site	S	\mathcal{H}	ν GHz	T °K	g-factor	FS	HFS	
							b_{40}, b_{60} 10^{-2} m^{-1}	I	A 10^{-2} m^{-1}
Eu^{2+}	K^+	7/2	(8)	9.1	77	1.990 ± 0.002	$b_{40} = (\pm)16 \pm 2$ $b_{60} = (\pm)1.2 \pm 0.6$	5/2 5/2	$ ^{151}\text{A} = 36 \pm 1$ $ ^{153}\text{A} = 16 \pm 1$
Gd^{3+}		7/2			4.2	1.990 ± 0.002	$b_{40} = -8.14 \pm 0.27$ $b_{60} = +0.47 \pm 0.3$		
					77	1.990 ± 0.002	$b_{40} = -7.0 \pm 0.3$ $b_{60} = +0.5 \pm 0.5$		

Tab. 15. KTaO_3 . Phonon energies of the soft ferroelectric mode (transverse optical mode) at various temperatures [67S11]. The wave vector q at the zone boundary is 0.788 \AA^{-1} ($= \pi/a$). See Fig. 52

T °K	Phonon energy [meV] for $q [\text{\AA}^{-1}] =$		
	0	0.1	0.2
295	10.7	11.5	13.5
230	9.7		
170	8.6	10.0	12.5
120	7.3		
77	5.7	7.5	10.7
40	4.2	6.0	
28	3.6	5.9	10.5
15	3.0	5.3	
10	3.2	5.2	
4	3.1	5.3	9.8

Nr. 1A-5 CaTiO_3 , Calcium titanate (Perovskite)Tab. 16. CaTiO_3 . Ion positions. [57K2]

4 Ti in 4(a):	$\frac{1}{2}, 0, 0; 0, 0, \frac{1}{2}; \frac{1}{2}, \frac{1}{2}, 0; 0, \frac{1}{2}, \frac{1}{2}$.
4 Ca in 4(c):	$x, \frac{1}{2}, z; \bar{x}, \frac{1}{2}, \bar{z}; \frac{1}{2} + x, \frac{1}{2}, \frac{1}{2} - z; \frac{1}{2} - x, \frac{1}{2}, \frac{1}{2} + z;$ with $x = 0, z = 0.030$.
4 O in 4(c):	with $x = \frac{1}{2} - 0.037, z = -0.018$.
8 O in 8(d):	$x, y, z; \frac{1}{2} - x, \frac{1}{2} - y, \frac{1}{2} + z;$ $\bar{x}, \frac{1}{2} + y, \bar{z}; \frac{1}{2} + x, \bar{y}, \frac{1}{2} - z;$ $\bar{x}, \bar{y}, \bar{z}; \frac{1}{2} + x, \frac{1}{2} + y, \frac{1}{2} - z;$ $x, \frac{1}{2} - y, z; \frac{1}{2} - x, y, \frac{1}{2} + z;$ with $x = \frac{1}{4} - 0.018, y = -0.026, z = \frac{1}{4} - 0.018$.

1a Specific heat anomaly associated with a phase transition was observed in CaTiO_3 at about 1260°C by NAYLOR et al. in 1946. GRÄNICHER et al. reported that CaTiO_3 becomes cubic above 1260°C .

b	phase	II	I
	state		P
	crystal system	orthorhombic	cubic
	space group	Pcmn-D_{2h}^{16}	

$\Theta \approx 1260^\circ\text{C}$

$\rho = 4.10 \cdot 10^3 \text{ kg m}^{-3}$ at RT.

$T_{\text{melt}} = 1960^\circ\text{C}$

$a = 5.3670 \text{ \AA}, b = 7.6438 \text{ \AA}, c = 5.4439 \text{ \AA}$ at RT.

The ideal perovskite cubic unit cell becomes pseudo-monoclinic in phase II in the same manner as shown in Fig. 21. $\beta' = 90^\circ 48'$ at RT.

Transparent, colorless.

2 Flux method; flux: $\text{CaCl}_2, \text{BaCl}_2, \text{CaCl}_2 + \text{BaCl}_2, \text{Na}_2\text{CO}_3 + \text{K}_2\text{CO}_3$.
Flame fusion method:

3 Crystal structure: $Z = 4$ in phase II.
Fig. 55; Tab. 16.

4 Lattice distortion: Fig. 56.

5a Dielectric constant: $\kappa = 186, \tan \delta = 3 \cdot 10^{-4}$ at RT.
Fig. 57.

6a Specific heat: Fig. 58.
Transition heat: $\Delta Q = 550 \text{ cal mol}^{-1}$ at $\Theta_{\text{II-I}}$.

46N1, 54G1

54G1

57K2

46N1

62M3

62M3

57K2

57K2
58L1, 62M3

57K2

62M3

46N1

9a	Nr. 1A-5 CaTiO ₃ , continued Refractive indices: Fig. 59. Reflection and absorption: Fig. 60, 61.			
17	Hardness: Mohs 6.5 ... 7, Knoop 986			62M3
Nr. 1A-6 SrTiO ₃ , Strontium titanate				
1a	Ferroelectric-like behavior of SrTiO ₃ was first observed by GRÄNICHER in 1956.			56G2
b	phase	II*	I	62R1
	state	(F)	P	
	crystal system	tetragonal	cubic**	
	space group		Pm3m-O _h ¹	
	Θ	110 °K		
	T _{melt} ≈ 2000 °C. ρ = 5.11 · 10 ³ kg m ⁻³ . a = 3.905 Å at RT. Transparent, colorless			63f2, 64l1 63f2 64L4
2a	Crystal growth: Flux method (flux: KF or 50% Na ₂ CO ₃ + 50% K ₂ CO ₃). Flame-fusion (Verneuil) method. Phase diagram of the system SrO-TiO ₂ is given in Figs. 297 and 289 of [64l1].			57N1 61G1 64l1
3	Crystal structure: Z = 1. Fig. 62.			
4	Thermal expansion: Fig. 63.			
5a	Dielectric constant: Figs. 64 ... 76. Expression of κ vs. T curve: Curie-Weiss law: κ = C/(T - Θ _p), T > 70 °K, where C = 7.83 · 10 ⁴ °K, Θ _p = 28 °K κ = M/[(T ₁ /2) coth(T ₁ /2T) - T ₀], T < 50 °K, where T ₀ = 38 °K, T ₁ = 84 °K, M = 9 · 10 ⁴ °K.			61M3 59W2, 62S2
b	Coefficients of free energy expansion at low temperatures:			66C6
c	Saturation polarization: Fig. 77. Remanent polarization: Fig. 78.			
d	Electrocaloric effect: Fig. 79. For additional data, see			64K5, 65H4, 61H1
6a	Specific heat: Fig. 80. Specific heat below 1 °K, see			61g1, 66A4
b	Thermal conductivity: Figs. 81, 82. For ceramics: see also			58Y1, 60Y1, 61g1, 66H9
7a	Piezoelectricity (dc bias induced piezoelectricity): Figs. 83, 84, 85.			
b	Electrostriction: Fig. 86.			
8a	Elastic compliances and stiffnesses: Tab. 17; Figs. 87, 88, 89.			
9a	Refractive indices: Tabs. 18, 19; Fig. 90. Reflectivity, absorption coefficient and dielectric constant: (i) Infrared region: Figs. 91 ... 95. See also Tab. 42. (ii) Visible and ultraviolet region: Figs. 96 ... 102. See also Tab. 43.			
b	Quadratic electrooptic effect: M ₁₁ - M ₁₂ = (0.14 ± 0.01) m ⁴ C ⁻² at 6328 Å (4.2 ... 300 °K).			64G3
c	Piezooptic effect: Tabs. 20, 21.			

* In phase II a hysteresis loop is observed,^{a)} b) but the remanent polarization depends upon the amplitude of the applied field. According to LYTLE, phase II consists of three phases. ^{a)} [59W2], ^{b)} [61M3], [64L4]

** Generally the phase I is believed to be cubic but evidence of pseudo-cubic structure was reported by a few authors. [64L4], [66C6]

* In phase II a hysteresis loop is observed, a), b) but the remanent polarization depends upon the amplitude of the applied field. According to LYTLE, phase II consists of three phases. a) [59W2], b) [61M3], [64L4]

** Generally the phase I is believed to be cubic but evidence of pseudo-cubic structure was reported by a few authors. [64L4], [66C6]

9d	Nr. 1A-6 SrTiO ₃ continued	67B1
e	Faraday rotation: Fig. 103. See also Tab. 44. Raman effect: Fig. 104. Brillouin scattering: Fig. 105. See	66K1
10	Electrical resistivity: $\rho > 10^7 \Omega\text{m}$ (good quality single crystal) at RT. Fig. 106. For additional data, see Tab. 22. Resistivity, Hall coefficient and Hall mobility of semiconductive samples: Tab. 23; Figs. 107 ... 110. For additional data, see Hall mobility for photo-excited electron: see Fig. 115. Piezoresistivity: Figs. 111, 112, 113. Photoconductivity: Figs. 114, 115. Photoemission: Fig. 116. Superconductivity: discovered in semiconductive SrTiO ₃ by SCHOOLEY et al. in 1964. Figs. 117 ... 120. Tab. 24. Penetration depth of static magnetic field in superconductive SrTiO ₃ is of the order of 10^{-5} m.	61g1 61g1 64F5, 67T6 66T10 64S5 66S16
11	Magnetic susceptibility: Tab. 25.	
12a	NMR: Fig. 121.	
b	ESR: Tab. 26; Figs. 122 ... 130.	
c	Mössbauer effect: Figs. 131, 132.	
13c	Inelastic neutron scattering: Tab. 27; Figs. 133, 134, 135.	
14a	Domain structure: A fine twin structure was observed in phase II. The appearance of the twin structure is similar to that of the 90° domains in tetragonal BaTiO ₃ . The dc field, however, does not change the twin structure.	61M3, 64L4
16	Radiation damage: Fig. 136.	66R6
17	Etching and chemical polishing: Band structure and related properties: The band structure was determined theoretically by KAHN et al: Fig. 137. For discussions, see Magnetoresistance, Shubnikov-deHaas effect. The conduction band consists of spheroids along [100] having 3 minima at X_3 . The transverse and longitudinal effective electron mass: $m_t = 1.5 m_0 (\pm 15\%)$, $m_l = 6.0 m_0 (\pm 30\%)$.	64K1 65S18 66F3, 67F3 67F3

Tab. 17. SrTiO₃. Elastic constants at RT

s_{11}	s_{12}	s_{13}	c_{11}	c_{12}	c_{13}	Method	Note	Reference
$10^{-12} \text{ m}^2 \text{ N}^{-1}$			10^{11} N m^{-2}					
3.3	-0.74	8.4	3.48	1.01	1.19	composite-bar	c calculated from s	58p5
3.729	-0.909	8.091	3.181	1.025	1.236	pulse	s calculated from c	63B2
3.772 ± 0.023	-0.926 ± 0.010	8.233 ± 0.040	3.156 ± 0.027	1.027 ± 0.027	1.215 ± 0.006		s calculated from c	63W1

Tab. 18. SrTiO₃. n vs. λ at 21 °C. [57G1]

λ Å	n	λ Å	n	λ Å	n
4200	2.6050	5400	2.4386	6600	2.3771
4300	2.5810	5500	2.4312	6700	2.3737
4400	2.5585	5600	2.4245	6800	2.3703
4500	2.5394	5700	2.4182	6900	2.3674
4600	2.5236	5800	2.4122	7000	2.3645
4700	2.5101	5900	2.4069	7100	2.3617
4800	2.4970	6000	2.4019	7200	2.3590
4900	2.4846	6100	2.3971	7300	2.3564
5000	2.4734	6200	2.3928	7400	2.3538
5100	2.4636	6300	2.3886	7500	2.3514
5200	2.4548	6400	2.3846	7600	2.3490
5300	2.4464	6500	2.3807	7700	2.3468

Tab. 19. SrTiO₃. n vs. λ [65B9]

λ μm	n	λ μm	n
0.45	2.537	1.8	2.270
0.5	2.472	2.0	2.264
0.6	2.402	2.2	2.258
0.7	2.363	2.4	2.2524
0.8	2.340	2.6	2.2490
0.9	2.326	2.8	2.2395
1.0	2.315	3.0	2.2315
1.1	2.306	3.2	2.2236
1.2	2.299	3.4	2.2143
1.4	2.287	3.6	2.2058
1.6	2.279	3.8	2.1951

Tab. 20. SrTiO_3 . Π_{66} vs. λ at $(27 \pm 1)^\circ\text{C}$. [57G1]

λ Å	Π_{66} $10^{-13} \text{ m}^2 \text{ N}^{-1}$	λ Å	Π_{66} $10^{-13} \text{ m}^2 \text{ N}^{-1}$
4200	-3.69	6000	-4.92
4300	-3.74	6100	-4.99
4400	-3.78	6200	-5.05
4500	-3.99	6300	-5.12
4600	-3.965	6400	-5.13
4700	-4.13	6500	-5.18
4800	-4.09	6600	-5.22
4900	-4.22	6700	-5.29
5000	-4.33	6800	-5.52
5100	-4.32	6900	-5.48
5200	-4.41	7000	-5.555
5300	-4.51	7100	-5.62
5400	-4.59	7200	-5.77
5500	-4.575	7300	-5.73
5600	-4.62	7400	-5.78
5700	-4.69	7500	-5.79
5800	-4.79	7600	-5.825
5900	-4.85	7700	-5.98

Tab. 21. SrTiO_3 . $\Pi_{21} - \Pi_{11}$ vs. λ at $(27 \pm 1)^\circ\text{C}$. [57G1]

λ Å	$\Pi_{21} - \Pi_{11}$ $10^{-13} \text{ m}^2 \text{ N}^{-1}$	λ Å	$\Pi_{21} - \Pi_{11}$ $10^{-13} \text{ m}^2 \text{ N}^{-1}$
4200	9.03	6000	9.95
4300	9.23	6100	9.94
4400	9.03	6200	9.91
4500	9.26	6300	9.84
4600	9.12	6400	9.82
4700	9.12	6500	9.88
4800	9.14	6600	9.96
4900	9.16	6700	9.92
5000	9.35	6800	9.98
5100	9.44	6900	9.99
5200	9.61	7000	9.91
5300	9.54	7100	9.92
5400	9.68	7200	9.94
5500	9.56	7300	9.99
5600	9.85	7400	10.05
5700	9.85	7500	9.90
5800	9.86	7600	9.92
5900	9.88	7700	10.02

Tab. 22. SrTiO_3 (single crystal). Effects of electrode material on the apparent conductivity [65C6]. Measurements were made by the two terminal method at $T = 130^\circ\text{C}$, $t = 24$ hours after the application of the field $E = 100 \text{ kV m}^{-1}$

Electrode material	σ [$\Omega^{-1} \text{ m}^{-1}$] after 24 h at 130°C	Form of σ vs. t curve
Au	$4.8 \cdot 10^{-7}$	Fall then rise
Ag	$8.8 \cdot 10^{-8}$	As for gold
Sn	$8.8 \cdot 10^{-9}$	Fall followed by slow rise but without saturation
Cr	$6.0 \cdot 10^{-11}$	Continuous fall tending toward steady value
Cd	$9.5 \cdot 10^{-11}$	Similar to chromium
Al	$2.9 \cdot 10^{-10}$	Similar to chromium (for a field of 400 kV m^{-1} behavior is like that of gold)

Tab. 23. SrTiO_3 (single crystal). The 300°K and 2°K Hall coefficient R_H and Hall mobility μ_H values and the 300°K electron concentrations for semiconductive single crystals. [67T6]. In the first column, (Nb) means Nb-doped samples, the other samples are reduced ones

Sample	300°K		2°K		$n = \frac{1}{eR_H(300^\circ\text{K})}$ m^{-3}
	R_H $10^{-6} \text{ m}^3 \text{ C}^{-1}$	μ_H $10^{-4} \text{ m}^2 \text{ V}^{-1} \text{ sec}^{-1}$	R_H $10^{-6} \text{ m}^3 \text{ C}^{-1}$	μ_H $10^{-1} \text{ m}^2 \text{ V}^{-1} \text{ sec}^{-1}$	
5	0.26	6.5	0.25	1.0	$2.4 \cdot 10^{25}$
2	0.62	5.2	0.77	1.8	$1.0 \cdot 10^{25}$
3	1.8	7.2	3.9	2.7	$3.5 \cdot 10^{24}$
6	5.3	8.0	11.0	3.1	$1.2 \cdot 10^{24}$
12	14.0	8.0			$4.5 \cdot 10^{23}$
9	23.0	5.8			$2.7 \cdot 10^{23}$
13(Nb)	0.22	5.5	0.22	3.3	$2.8 \cdot 10^{25}$
8(Nb)	0.58	4.8	0.63	8.2	$1.1 \cdot 10^{25}$
10(Nb)	3.4	6.2	3.3	12.0	$1.8 \cdot 10^{24}$
14(Nb)	14.0	6.7	11.0	13.0	$4.5 \cdot 10^{23}$
15(Nb)	22.0	5.4	18.0	19.0	$2.8 \cdot 10^{23}$
11(Nb)	44.0	6.0	33.0	22.0	$1.4 \cdot 10^{23}$

Tab. 24 see page 50

Tab. 25. SrTiO₃. Susceptibility in pure and reduced single crystals [66F7].

$\Delta\chi_{\text{magn}}$ represents the contribution from the charge carriers; $\Delta\chi_{\text{magn}}$ is obtained by measuring the N = carrier concentration; T_{deg} = degeneracy temperature; m^* = density-of-state effective mass

Sample	N at 4.2 °K m^{-3}	T_{deg} °K	χ_{magn} or $\Delta\chi_{\text{magn}} \cdot 10^{-7} \text{ cm}^3 \text{ g}^{-1}$		m^* at 4.2 °K [m_0]
			300 °K	78 °K	
pure 28 h, 950 °C hydrogen 5 h, 1200 °C hydrogen (carbon boat) reoxidized 18 h, 700 °C, air	$6 \cdot 10^{24}$ $7.5 \cdot 10^{25}$	28 148	-1.02	-1.00	-
			+0.037	+0.073	-
			+0.270	+0.523	5.1
			-	-	-
27 h, 1370 °C hydrogen (carbon boat)	$5.3 \cdot 10^{25}$	550	-1.016	-1.012	-
			+1.704	+1.763	4.9

Tab. 27. SrTiO₃. The frequency of the lowest transverse optic mode at $q = 0$ for five different temperatures. [62C4]

T °K	10^{13} sec^{-1}	
	Neutron	Far infrared
90	1.23 ± 0.03	1.2 ^{a)}
142	1.72 ± 0.04	
203	2.24 ± 0.05	
296	2.73 ± 0.05	
430	3.32 ± 0.07	3.0 ^{a)} 2.63 ^{b)}

a) [62B2] b) [62S12]

Tab. 26. SrTiO₃. Summary of the properties of ESR spectrum in SrTiO₃ for various doped paramagnetic ions

Para-magnetic center	Site	S	\mathcal{H}	ν GHz	T °K	g -factor		FS D, E, a [10^{-3} m^{-1}]	I	HFS		Ref.	Literature
						g_{\parallel}	g_{\perp}			aA [10^{-3} m^{-1}]	bA [10^{-3} m^{-1}]		
Cr ³⁺	Ti ⁴⁺	3/2	(5)	9	80	1.9788 ± 0.007	(isotropic)	$D = 2 \pm 0.3, E = 0$	3/2	$aA = 0$		f)	58M7
					300	1.9780 ± 0.007	(isotropic)	$D = 0, E = 0$		$aA = 16.2 \pm 0.3$			62M6
Mn ²⁺	Ti ⁴⁺	3/2	(5)	10	77	1.994 ± 0.001	(isotropic)	$D = +1.0, E = 0$	5/2	$aA = -69.4 \pm 1$			59M4
					RT	1.994 ± 0.001	(isotropic)	$D = -0.7, E = 0$		$aA = -69.4 \pm 1$		a) b) c) d) e)	59D2
Fe ³⁺	Ti ⁴⁺	5/2	(7)	9	1.9	2.004 ± 0.001	(isotropic)	$D = +17.9 \pm 1.0, E = 0$ $a = -230 \pm 10, E = 0$					58M8
					4.2	2.004 ± 0.001	(isotropic)	$D = +16.1 \pm 0.7, E = 0$ $a = -225.6 \pm 1.9$					
Ni ²⁺	Ti ⁴⁺	1	(4)	10	77	2.004 ± 0.001	(isotropic)	$D = +7.3 \pm 0.3, E = 0$ $a = -220.8 \pm 1.1$				e)	62R3
					300	2.004 ± 0.001	(isotropic)	$D = 1.0, E = 0$ $a = -197.7 \pm 0.7$					62R3
Ni ¹⁺ or Ni ³⁺	Ti ⁴⁺	1/2	(2)	10	80	2.204 ± 0.001	(isotropic)						
					20	2.204 ± 0.001	(isotropic)					e)	62R3
					80	2.029 ± 0.001							62R3
					203	2.029 ± 0.001		2.352 ± 0.001				e)	62R3

Ni ²⁺	Ti ⁴⁺	1	(4)	10	20	2.029 ± 0.001	2.352 ± 0.001	e)
Ni ²⁺ or Ni ³⁺	Ti ⁴⁺	1/2	(2)	10	20			
				80				
				203				

Para-magnetic center	Site	S	J	ν GHz	T °K	g-factor		FS D, E, a [10 ⁻³ m ⁻¹]	HFS I ^a A , ^a A _⊥ [10 ⁻² m ⁻¹]	Ref.	Literature
						g	g _⊥				
Ni ³⁺	Ti ⁴⁺	1/2	(2)	10	4.2	2.110 ± 0.002	2.213 ± 0.002			e)	62R3
					20	2.136 ± 0.001	2.202 ± 0.001				
					80	2.172 ± 0.001	2.184 ± 0.001				
					203	(isotropic)	2.180 ± 0.002				
Ce ³⁺	—	1/2	(2)	10	4.2	3.005 ± 0.005	1.118 ± 0.003			e)	62R3
					4.2	2.609 ± 0.003	2.472 ± 0.003				
Nd ³⁺	—	1/2	(2)	16	2	2.61 ± 0.01	2.470 ± 0.005			e)	62R2
					35	2.62 ± 0.01	2.470 ± 0.005				
					16	2.11 ± 0.01	2.780 ± 0.005				
Yb ³⁺	—	1/2	(3)	35	2	2.10 ± 0.005					62R2
					50	2.18 ± 0.01	2.720 ± 0.005		1/2 ^a A = 530 ± 20 ^a A _⊥ = 720 ± 5		
					65	(2.25)	2.70 ± 0.01		5/2 ^a A = 211 ± 5		
Eu ²⁺	—	7/2	(8)	16	2	1.99 ± 0.001	-10 ± 4	106.6 ± 2	5/2 ^a A = 36.2 5/2 ^a A _⊥ = 17.6	f)	62R2
					300	1.99 ± 0.001	0	105.9 ± 2			
					2	1.992 ± 0.002	-362.5 ± 0.5	-3.2 ± 0.5			
Gd ³⁺	Sr ²⁺	7/2	(8)	16	2	1.992 ± 0.002	-362.5 ± 0.5	-3.24 ± 0.5		f) b)	62R2 62R1
					12, 18	1.992 ± 0.002	-362.5 ± 0.5	-4.8 ± 0.5			
					77	1.992 ± 0.002	-233.6 ± 0.5	-0.25 ± 0.5			
					300	1.992 ± 0.002		-5.7 ± 0.2	0.5 ± 0.3		

a) $\xi = [100]$, $\eta = [010]$, $\zeta = [001]$.

b) Deviations from spin Hamiltonian (7) is ascribed to a covalent bonding by MÜLLER. However, AISENBERG et al. find a negligible contribution of the covalent bonding. [59A].

c) Spectrum is due to a double quantum absorption between $S_g = -1$ and $S_g = +1$ levels.

d) At least fifteen inequivalent sites are observed.

e) Three inequivalent spectra are observed with axes parallel to the cubic [100], [010] and [001].

f) Effects of temperature and pressure on Cr³⁺, Fe³⁺, Eu³⁺, and Gd³⁺ spectra. [64R2].g) Fe³⁺ spectra due to nearest charge compensation. [64K7].h) Electric field dependence of Gd³⁺ spectra. [66S7].

Tab. 24. SrTiO_3 (ceramics containing Ba or Ca in mol%). Superconductive properties of $(\text{Ba}_x\text{Sr}_{1-x})\text{TiO}_3$ and $(\text{Ca}_x\text{Sr}_{1-x})\text{TiO}_3$ [67S8]. H_{c1} is the point at which the magnetization curve first deviates from linearity; $H_{c1}(0)$ is the extrapolated value for $T \rightarrow 0^\circ\text{K}$.
 N = Carrier concentration Θ_c = superconducting transition temperature

% Ba or Ca	N 10^{25} m^{-3}	Θ_c $^\circ\text{K}$	$H_{c1}(0)$ Oe	% Ba or Ca	N 10^{25} m^{-3}	Θ_c $^\circ\text{K}$	$H_{c1}(0)$ Oe
—	2.7	0.18		10.0	4.2	0.25	
—	5.8	0.30	2.8	12.5	4.5	<0.10	
—	6.4	0.25	2.8				
—	1.7	0.10		2.5 (Ca)	5.0	0.32	
—	12.0	0.17		5.0	9.2	0.30	
—	23.0	0.10		7.5	74.0	<0.06	
2.5 (Ba)	6.0	0.52		7.5	8.7	0.43	
2.5	0.3	0.23		7.5	0.2	<0.06	(3.5) ^{a)}
5.0	6.7	0.50	3.9	7.5	0.6	0.37	
7.5	7.0	0.29		7.5	33.0	<0.07	
7.5	0.05	0.22		7.5	2.0	0.48	
7.5	34.0	0.09		7.5	0.06 ^{b)}	<0.06	
7.5	0.5	0.25		10.0	9.3	0.39	
7.5	2.3	0.27		20.0	13.0	0.29	
7.5	15.0	0.45		30.0	6.7	0.50	1.9
				30.0	0.6	<0.05	

Nr. 1A-7 CdTiO_3 , Cadmium titanate

1a	CdTiO ₃ was reported by SMOLENSKII in 1950 to be ferroelectric below 50 ... 60 °K. In 1950 HULM et al. denied its ferroelectricity but HEGENBARTH supported SMOLENSKII's findings.			50S7, 50H2, 59H4
b	phase	II	I	
	state	(F) ^{a)}		
	crystal system		orthorhombic ^{b)}	a) 50S7
	space group		Pc2 ₁ n ^{b)} -C _{2v} ^{b)}	b) 57K1
	Θ	-223... -213 °C		
	Lattice constants: a = 5.348 Å, b = 7.615 Å, c = 5.417 Å at RT. The relation between the orthorhombic unit cell and the pseudo-cubic monoclinic cell is the same as in the case of NaTaO ₃ ; see Fig. 21.			50S7 57K1
2	Flux method (flux: 40 wt% NaCl + 40 wt% NaBO ₂ + 20 wt% Na ₂ CO ₃).			
3	Z = 4. Crystal structure in phase I: Tab. 28; Fig. 138.			57K1
5a	Dielectric constant: κ = 250 at RT. κ = C/(T - Θ _p), C = 4.5 · 10 ⁴ °K.			
b	Effect of E _{bias} on κ: Fig. 139.			50S7, 50H2

		Positions				Estimated error
Tab. 28. CdTiO_3 . Fractional coordinates of atoms in the unit cell. [57K1]						
Cd	x :	$0 + 0.006$	$0 - 0.006$	$\frac{1}{2} + 0.006$	$\frac{1}{2} - 0.006$	± 0.002
	y :	$\frac{1}{2}$	$\frac{1}{2}$	$\frac{1}{2}$	$\frac{1}{2}$	
	z :	$0 + 0.016$	$0 - 0.016$	$\frac{1}{2} - 0.016$	$\frac{1}{2} + 0.016$	± 0.002
Ti	x :	$\frac{1}{2} + 0.005$	$\frac{1}{2} - 0.005$	$0 + 0.005$	$0 - 0.005$	± 0.005
	y :	0	$\frac{1}{2}$	$\frac{1}{2}$	0	
	z :	$0 - 0.065$	$0 + 0.065$	$\frac{1}{2} + 0.065$	$\frac{1}{2} - 0.065$	± 0.010
O(1)	x :	$0 - 0.03$	$0 + 0.03$	$\frac{1}{2} + 0.03$	$\frac{1}{2} - 0.03$	± 0.015
	y :	$\frac{1}{2}$	$\frac{1}{2}$	$\frac{1}{2}$	$\frac{1}{2}$	± 0.025
	z :	$\frac{1}{2} + 0.05$	$\frac{1}{2} - 0.05$	$0 + 0.05$	$0 - 0.05$	± 0.015
O(2)	x :	$\frac{1}{2} + 0.05$	$\frac{1}{2} - 0.05$	$\frac{1}{2} - 0.05$	$\frac{1}{2} + 0.05$	± 0.005
	y :	$0 - 0.03$	$0 - 0.03$	$\frac{1}{2} - 0.03$	$\frac{1}{2} - 0.03$	± 0.015
	z :	$\frac{1}{2} + 0.06$	$\frac{1}{2} + 0.06$	$\frac{1}{2} - 0.06$	$\frac{1}{2} - 0.06$	± 0.015
O(3)	x :	$\frac{1}{2} + 0.05$	$\frac{1}{2} - 0.05$	$\frac{1}{2} - 0.05$	$\frac{1}{2} + 0.05$	± 0.005
	y :	$\frac{1}{2} + 0.07$	$\frac{1}{2} + 0.07$	$0 + 0.07$	$0 + 0.07$	± 0.015
	z :	$\frac{1}{2} + 0.06$	$\frac{1}{2} + 0.06$	$\frac{1}{2} - 0.06$	$\frac{1}{2} - 0.06$	± 0.015

^{a)} This specimen is not spherical, so that the value of $H_{c1}(0)$ quoted is only approximate.
^{b)} Hall coefficient appeared to be affected by magnetic history of specimen at liquid helium temperature.

Nr. 1A-8 BaTiO₃, Barium titanate

(Responsible authors for this section are as follows: IKEDA, NAKAMURA, NOMURA, SAWAGUCHI, SHIOZAKI and TOYODA, abbreviated as INaNoSaShiTo).

1a	The anomalous dielectric properties of BaTiO ₃ were discovered on ceramic specimens independently by WAINER and SOLOMON in 1942, by OGAWA in 1944 and by WUL in 1945. The ferroelectric activity of BaTiO ₃ was reported independently by VON HIPPEL and co-workers in 1944 and by WUL in 1946. The structural change associated with the cubic-tetragonal phase transition was observed, by means of x-rays, by MEGAW in 1945, independently of the above dielectric studies.					42W1, 44O1, 45W1, 44V2, 46W2, 45M1	
b	phase	IV ^{a)}	III ^{a)}	II ^{b)}	I ^{b)}	*)49K2, 49R1 b)45M1 c)46V1, 46W1 d)55R1	
	state	F ^{a)}	F ^{a)}	F ^{c)}	P ^{b)}		
	crystal system	rhombohedral ^{a)}	orthorhombic ^{a)}	tetragonal ^{b)}	cubic ^{b)}		hexagonal ^{d)} *
	space group	R3m-C _{3v} ^{a)}	Amm2-C _{2v} ^{a)}	P4mm-C _{4v} ^{b)}	Pm3m-O _h ^{b)}		C63/mmc-D _{6h} ^{d)}
	θ	-90 ^{a)} 5 ^{a)} 120 ^{b)} ** 1460 ^{d)} °C					
<p>$P_a \parallel [001]$ in phase II (along $[100]$ of phase I). $P_a \parallel [001]$ in phase III (along $[110]$ of phase I). $P_a \parallel [111]$ in phase IV (along $[111]$ of phase I). The directions of P_a are illustrated along with lattice distortions in Fig. 140. $T_{\text{melt}} = 1618^\circ\text{C}$. Tetragonal form (phase II): $\rho = 6.02 \cdot 10^3 \text{ kg m}^{-3}$ (calculated from lattice constants) $a = 3.9920 \text{ \AA}$, $c = 4.0361 \text{ \AA}$ at 20°C. Transparent, light brown. Hexagonal form: $a_{\text{hex}} = 5.735 \text{ \AA}$, $c_{\text{hex}} = 14.05 \text{ \AA}$ at RT. $\rho = (6.1 \pm 0.1) \cdot 10^3 \text{ kg m}^{-3}$.</p>							51W2 51R1 48B3
2a	Crystal growth: Flux method (flux KF ^{a)} or TiO ₂ -rich melt ^{b)}). Pulling method (top-seeded solution growth technique using excess TiO ₂ as the solvent). Melting method (with limited success). Tab. 29; Fig. 141.					*)54R1, b)65S8 63L3 50V2	
b	Crystal forms: For butterfly-type: Fig. 142. For chunky type: Fig. 143. For hexagonal form: Fig. 144.						
3	Crystal structure of phase I: $Z = 1$. Tab. 30. Crystal structure of phase II: $Z = 1$. Tab. 31. Crystal structure of phase III: $Z = 2$. Tab. 32; Fig. 145, 146; Tab. 33. Crystal structure of phase IV: $Z = 1$. Crystal structure of hexagonal form: $Z = 6$. Tab. 34, 35; Fig. 147.						
4	Lattice constants of phase I, II, III, and IV: Phase I: $a = 3.996 \text{ \AA}$ at 120°C . Phase II: $a = 3.9920 \text{ \AA}$, $c = 4.0361 \text{ \AA}$ at 20°C . Phase III: $a = 3.990 \text{ \AA}$, $b = 5.669 \text{ \AA}$, $c = 5.682 \text{ \AA}$ at -10°C . Phase IV: $a = 4.001 \text{ \AA}$, $\alpha = 89^\circ 51'$ at -168°C . Thermal expansion: Fig. 148, 149; Tab. 36, 37; Fig. 150. Lattice distortion due to p : Fig. 151.					47M3 51R1 57S2 57J2	
5a	Dielectric constant: Fig. 152, 153, 154, 192. Dielectric dispersion: Fig. 155 ... 159. Further data from optical measurements: Fig. 201; Tab. 42. Effect of p on κ : Fig. 160, 161, 162. Phase diagram in regard to p : Fig. 163, 164. Effect of E_{bias} on θ_f : $d\theta_f/dE_{\text{bias}} = 1.43 \cdot 10^{-5} \text{ }^\circ\text{K V}^{-1} \text{ m}$; on κ : Fig. 165.					53M2	
b	Non-linear dielectric properties: Fig. 166. $\xi = -5.5 \cdot 10^8 \text{ J C}^{-4} \text{ m}^5$, $\zeta = 1.7 \cdot 10^{10} \text{ J C}^{-6} \text{ m}^9$.					53M2	

* The transition from the hexagonal form to the cubic one is very sluggish and the hexagonal form can be produced by rapid cooling from above 1460°C .

** In most papers this Curie point has been reported to be about 120°C , but it seems to be about 130°C for pure BaTiO₃ [65J2].

5c	Nr. 1A-8 BaTiO ₃ continued Spontaneous polarization: Fig. 167, 168, 169. Coercive field: Fig. 170, 171, 172. Effect of p on P_s : Fig. 173.	
d	Electrocaloric effect: Fig. 174. Pyroelectricity: Fig. 175.	
6a	Specific heat: Fig. 176, 177. Transition heat, transition entropy: Tab. 38.	
b	Thermal conductivity: Fig. 178, 179.	
7a	Piezoelectricity: Tab. 39, 40; Fig. 180 ... 183.	
b	Electrostriction: Fig. 184, 185.	
8a	Elastic compliances and stiffnesses: Tab. 41. See also Tab. 40. Fig. 186 ... 193.	
b	Non-linear elastic properties: Fig. 194.	
9a	Refractive indices: Fig. 195, 196, 197. Birefringence: Fig. 198, 199. Reflection and absorption: (i) Far-infrared region. Fig. 200, 201; Tab. 42. (ii) Infrared region. Fig. 202, 203, 204. (iii) Visible region. Fig. 205, 206, 207. (iv) Ultraviolet region. Fig. 208; Tab. 43; Fig. 209, 210, 211. For the effect of E_{bias} on the absorption edge, see	67G1
b	Linear electrooptic effect: Fig. 212 ... 215. Quadratic electrooptic effect: $(M_{11} - M_{12}) = (+ 0.13 \pm 0.02) \text{ m}^4 \text{ C}^{-2}$ at 408 ... 433 °K, measured at 6328 Å.	64G3
d	Faraday rotation: Fig. 216; Tab. 44.	64M2
e	Non-linear optical properties: Susceptibility for SHG (second harmonic generation) (relative values, see Sec. I C): $d_{15} = 35 \pm 3$, $d_{31} = 37 \pm 3$, $d_{33} = 14 \pm 1$, determined with the Nd-doped CaWO ₄ laser beam. Fig. 217.	
f	Raman scattering: Fig. 218.	
g	Luminescence: Fig. 219, 220.	
10	Conductivity of as-grown crystals and ceramics: The data vary from sample to sample depending on the purity and the method of preparation: only representative data are given here. Fig. 221 ... 225. Conductivity associated with doping or reduction (including PTC (Positive Temperature Coefficient) or resistivity: $d\rho/dT > 0$): Fig. 226 ... 230. Reference papers on PTC anomaly: Tab. 45. Piezoresistivity: Fig. 231, 232. For additional data, see Breakdown strength: Fig. 233, 234. For additional data, see Photoconductivity and photoemission: Fig. 235, 236. Other transport properties: In n -type single-domain crystals, the electron mobility is anisotropic at RT; $\mu_{\perp c} \approx 1.2 \cdot 10^{-4} \text{ m}^2 \text{ V}^{-1} \text{ sec}^{-1}$, and $\mu_c \approx 0.13 \cdot 10^{-4} \text{ m}^2 \text{ V}^{-1} \text{ sec}^{-1}$ In n -type single-domain crystals, the energy separation ($\Delta u = 10^{-2} \dots 10^{-1} \text{ eV}$) between the c -axis conduction band minima and the a -axis conduction band minima has been estimated vs. T . In n -type single-domain crystals, the density-of-state mass $m^* = (6.5 \pm 2) m_0$. Data are available on the Hall coefficient and conductivity of single domain crystals having donor concentrations of $N = 8.5 \cdot 10^{24} \text{ m}^{-3}$ and of $N = 2.5 \cdot 10^{23} \text{ m}^{-3}$. Fig. 237. Seebeck-effect: Fig. 238.	59S1, 63M1, 67G4 58I3, 59F1, 64K3, 64U1 67B2 67B2 67B2 67B2
12b	ESR: Tab. 46; Fig. 239 ... 243.	
c	Mössbauer effect: Fig. 244 ... 247.	
13b	Diffuse X-ray scattering: Fig. 248, 249, 250. Inelastic neutron scattering: Fig. 251.	

14a	Domain structure: Domains have been observed by various methods: polarized light ^{a)} , X-rays ^{b)} , electron microscope ^{c)} , etching method ^{d)} , powder pattern method ^{e)} , and decoration method ^{f)} . Fig. 252 ... 255.	a) 48M1, 49F1, 52M3 b) 63B13, 64N1, 65C3, 64L1 c) 62T1, 63B9, 67R4, 64T2, 66R5, 67R2 d) 55H2 e) 59P1 f) 66S8
b	Domain wall motion: Domain wall motion has been observed optically ^{a)} and by repeated differential etching ^{b)} . The domain shapes in motion depend on the applied field and temperature. ^{c)} Fig. 256. The wall velocity is proportional to $\exp(-\delta/E)$ at relatively low field. δ = activation field for domain wall motion. Fig. 257 ... 267.	a) 59M2, 60S2 b) 63S13 c) 63S13 58M4, 59M3
15	Surface layer: The first suggestion about the existence of surface layers of BaTiO ₃ crystals was made by KÄNZIG ^{a)} on the basis of electron diffraction studies of very small particles of BaTiO ₃ ^{b)} . The dependence of the following quantities on the thickness of the crystals has been observed as evidence of the existence of surface layers: domain wall velocity ^{c)} , dielectric constant ^{d)} , optical absorption coefficient ^{e)} and electroluminescence spectra ^{f)} . Pyroelectric current was observed above the Curie point and discussed in connection with surface layers ^{g)} . A few models of surface layers have been proposed ^{h)} . According to TANAKA and HONJŌ ⁱ⁾ , the surface layer, if it exists, seems to be very thin.	a) 55K1 b) 54A1 c) 56M4, 61M2, 65C1 d) 61S4, 62C3 e) 60C3 f) 58H1, 65B7, 66B6 g) 56C1 h) 56M4, 61F2, 59D3, 65C1 i) 64T2
16	Radiation damage: Fig. 268, 269.	
17	Energy band structure: Fig. 270.	

Tab. 29. BaTiO₃. Solubility in KF solution. [54K1]

T	1000	1050	1100	1150	1200	1250	1300	°C
BaTiO ₃	4	6	9	12.5	17	22.5	28.5	mole %

Tab. 30. BaTiO₃. Fractional coordinates of atoms in the unit cell of phase I. [52M2]

	x	y	z
Ba	0	0	0
Ti	$\frac{1}{2}$	$\frac{1}{2}$	$\frac{1}{2}$
O	$\frac{1}{2}$	$\frac{1}{2}$	0
	$\frac{1}{2}$	0	$\frac{1}{2}$
	0	$\frac{1}{2}$	$\frac{1}{2}$

Tab. 31. BaTiO₃. Shift of atoms in fractional coordinates of phase II from the positions of phase I. [51K1], [55F1], [61E3]

δz_{Ti}	$\delta z_{O(1)}$	$\delta z_{O(2)}$	Ba		Ti		O(1)		O(2)			References
			B_{11}	B_{33}	B_{11}	B_{33}	B_{11}	B_{22}	B_{11}	B_{22}	B_{33}	
0.014	-0.032	0	0.48		0.13		0.13		0.48			51K1
0.014	-0.023	-0.014	0.273		0.152		0.334		0.267			55F1
0.015	-0.024	-0.020	0.27	0.28	0.53	0.21	0.90	0.08	0.60	0.49	0.07	61E3
0.012	-0.026	0	0.27	0.28	0.46	0.30	0.90	0.50	0.60	0.90	0.90	61E3

The positions of atoms in the unit cell are Ba at (0, 0, 0), Ti at ($\frac{1}{2}$, $\frac{1}{2}$, $\frac{1}{2} + \delta z_{Ti}$), O(1) at ($\frac{1}{2}$, $\frac{1}{2}$, $\delta z_{O(1)}$) and O(2) at ($\frac{1}{2}$, 0, $\frac{1}{2} + \delta z_{O(2)}$).

Tab. 32. BaTiO₃. Fractional coordinates of atoms in the unit cell of phase III. [57S2]

	x	y	z
Ba	0	0	0
Ti	0	$\frac{1}{2}$	$\frac{1}{2}$
	$\frac{1}{2}$	0	$\frac{1}{2} + \delta z_{Ti}$
	$\frac{1}{2}$	$\frac{1}{2}$	δz_{Ti}
O(1)	0	0	$\frac{1}{2} + \delta z_{O(1)}$
	0	$\frac{1}{2}$	$\delta z_{O(1)}$
	$\frac{1}{2}$	$\frac{1}{2} + \delta y_{O(2)}$	$\frac{1}{2} + \delta z_{O(2)}$
O(2)	$\frac{1}{2}$	$\frac{1}{2} + \delta y_{O(2)}$	$\frac{1}{2} + \delta z_{O(2)}$
	$\frac{1}{2}$	$\frac{1}{2} - \delta y_{O(2)}$	$\frac{1}{2} + \delta z_{O(2)}$
	$\frac{1}{2}$	$\frac{1}{2} - \delta y_{O(2)}$	$\frac{1}{2} + \delta z_{O(2)}$

$$\delta z_{Ti} = +0.010; \delta z_{O(1)} = -0.010; \delta z_{O(2)} = -0.013; \delta y_{O(2)} = +0.003.$$

Tab. 33. BaTiO₃. Comparison of atomic shifts in phase III and phase II with respect to different origins. The coordinate of atoms of [55F1] and [57S2] are used for phase II and III, respectively. [57S2]

	Orthorhombic	Tetragonal
Ba at (000)		
δz { Ti	+0.06 Å	+0.06 Å
O(1)	-0.06 Å	-0.09 Å
O(2)	-0.07 Å	-0.06 Å
$\delta y_{O(2)}$	± 0.02 Å	—
Origin is chosen to give $\delta z_{O(2)} = 0$		
δz { Ti	+0.13 Å	+0.15 Å
Ba	+0.07 Å	+0.09 Å
O(1)	+0.02 Å	-0.03 Å

Tab. 34. BaTiO₃. Fractional coordinates of atoms in the unit cell of hexagonal structure. [48B3]

2Ba(1) at (b),	
4Ba(2) at (f),	$z = 0.097$,
2Ti(1) at (a),	
4Ti(2) at (f),	$z = 0.845$,
6O(1) at (h),	$z = 0.522$,
12O(2) at (k),	$z = 0.836, z = 0.076$

Tab. 35. BaTiO₃. Interatomic distances of hexagonal structure. [48B3]

in the Ti ₂ O ₇ group	
O(1) — O(1) = 2.49 Å	in the shared face.
= 3.25 Å	in the same layer but the atoms do not belong to the same shared face.
O(2) — O(2) = 2.91 Å	
O(1) — O(2) = 2.91 Å	
Ti(2) — O(1) = 1.96 Å	
Ti(2) — O(2) = 2.02 Å	
in the TiO ₆ octahedra	
O(2) — O(2) = 2.82 Å	in the same layer.
O(2) — O(2) = 2.69 Å	between adjacent layers.
Ti(1) — O(2) = 1.95 Å	

Tab. 36. BaTiO₃. Lattice constants and unit cell volume at various T . [51R1]

T °C	a Å	b Å	c Å	V Å ³
+ 20	3.9920	3.9920	4.0361	64.317
+ 4	3.9910	3.9911	4.0357	64.282
Θ_{III-II}				
+ 4	4.0185	3.9860	4.0162	64.319
- 99	4.0170	3.9750	4.0150	64.093
Θ_{IV-III}				
- 99	4.0015	4.0015	4.0020	64.079
- 160	3.9996	3.9996	3.9997	63.981

Accuracy of measurement below RT was ± 0.0007 Å.Tab. 37. BaTiO₃. Linear thermal expansion coefficients along a , b , and c axes. [51R1]

T °C	α_a $10^{-6} \text{ } ^\circ\text{C}^{-1}$	α_b $10^{-6} \text{ } ^\circ\text{C}^{-1}$	α_c $10^{-6} \text{ } ^\circ\text{C}^{-1}$
+20 ... + 4	15.7	15.7	6.2
+ 4 ... - 99	4.9	28.4	-0.9
-99 ... -160	7.8	7.8	8.2

Tab. 38. BaTiO₃. Transition heats and transition entropies

Transition	ΔQ_m cal mol ⁻¹	ΔS_m cal mol ⁻¹ °K ⁻¹	References
IV → III	8 ± 2	0.04	52S5
	14.3	0.07	52V1
	12	0.06	52T1
III → II	22 ± 4	0.076	52S5
	15.5	0.054	52V1
	16	0.058	52T1
II → I	50 ± 5	0.125	52S5
	47	0.12	52V1
	47	0.12	48B1

Tab. 39. BaTiO₃ (single crystal and ceramic). Piezoelectric constants and electromechanical coupling factor. [66b1]

	d_{15}	d_{31}	d_{33}	10^{-12} CN ⁻¹			k_p	10^8 N C ⁻¹			T °C	References
				g_{15}	g_{31}	g_{33}		e_{15}	e_{31}	e_{33}		
single crystal	392	—	57.7	132	15.3	—23.1	0.560				20	50C2
	—	34.5	85.6								25	58B2
	—	33.3									RT	59H7
ceramic	270	—	79	191	18.8	—4.7	0.378	11.6	—4.4	18.6	14.8	56B3
	260	—	78	190	20.2	—5.2	0.36	11.4	—4.35	17.5	15.6	64b1

Tab. 40. BaTiO₃ (ceramic, plain and modified, commercial). Dielectric, piezoelectric, electromechanical and elastic constants (at 25 °C, except for Ca_{0.13}Pb_{0.08}Ba_{0.80}TiO₃). [66b1]

Composition	χ_{15}^T	d_{15}^T	d_{31}^T	d_{33}^T	10^{-12} CN $^{-1}$			k_p	10^{-12} m 2 N $^{-1}$			s_{66}^D				
					g_{15}	g_{31}	g_{33}		s_{11}^D	s_{13}^D	s_{33}^D					
BaTiO $_3$ Ca $_{0.05}$ Ba $_{0.95}$ TiO $_3$ Ca $_{0.05}$ Ba $_{0.95}$ TiO $_3$ (ceramic B) $^a)$ Ca $_{0.05}$ Ba $_{0.95}$ TiO $_3$ Pb $_{0.04}$ Ba $_{0.96}$ TiO $_3$ Pb $_{0.04}$ Ba $_{0.96}$ TiO $_3$ Ca $_{0.05}$ Pb $_{0.05}$ Ba $_{0.90}$ TiO $_3$ Ca $_{0.05}$ Pb $_{0.05}$ Ba $_{0.90}$ TiO $_3$ Ca $_{0.05}$ Pb $_{0.13}$ Ba $_{0.87}$ TiO $_3$ Ca $_{0.13}$ Pb $_{0.08}$ Ba $_{0.80}$ TiO $_3$	1350 ... 1700 1380 1200	242	—56 —53 —58	130 ... 160 135 149		—5.5 14.1	0.48	0.33	8.47 8.20 8.6	—2.38 —2.45 —2.6	21.7 21.3 22.4					
	910 1000 1180 800 600 450 600		—41 —38 —53 —40 —29 —20 —35	118 105 129 115 80 60 90			0.34 0.113 0.12 0.30 0.22	0.48	0.19 0.22	8.00 8.77 9.09 8.06 7.63 7.8 13	—2.40 —2.58 —2.64 —2.34 —2.87 —2.3	20.79 22.7 23.64 20.8 20.0 20.2				
	χ_{11}^T	χ_{31}^T	χ_{33}^T	e_{15}	e_{31}	e_{33}	s_{11}^D	s_{13}^D	s_{33}^D	s_{44}^D	s_{44}^D	s_{44}^D				
	Ca $_{0.05}$ Ba $_{0.95}$ TiO $_3$ (ceramics B) $^a)$ Ca $_{0.05}$ Pb $_{0.13}$ Ba $_{0.80}$ TiO $_3$	1300	1000	910	10.9	—3.1	13.5	8.3	9.1	7.0	—2.9	—2.7	—1.9	22.2	17.1	
				395				7.7	8.1	7.15	—2.4					
		h_{15}	h_{31}	h_{33}	c_{11}^D	c_{15}^D	c_{33}^D	c_{13}^D	c_{15}^D	c_{33}^D	c_{44}^D	c_{44}^D	c_{44}^D	c_{66}^D		
		10^9 N m $^{-2}$														
	Ca $_{0.05}$ Ba $_{0.95}$ TiO $_3$ (ceramics B) $^a)$	12.3	—3.8	16.7	158	159	150	177	69	70	67.5	62	45	58.5	45	
		10^9 N C $^{-1}$														

$^a)$ Trade Mark: Clevite Corporation, Cleveland, Ohio, USA.

^{a)} Trade Mark: Clevite Corporation, Cleveland, Ohio, USA.

Tab. 41. BaTiO₃ (single crystal and ceramics). Elastic constants. [66b7]

	$10^{-12} \text{ m}^2 \text{ N}^{-1}$										T °C	References
	s_{11}^E	s_{11}^H	s_{12}^E	s_{12}^H	s_{13}^E	s_{13}^H	s_{14}^E	s_{14}^H	s_{44}^E	s_{44}^H		
single crystal	9.26 11.2	7.25	15.7	10.8	-2.35	-3.15	-5.24	-3.26	18.4	12.4	25 RT	50C2 51B1 58B2
ceramics	8.55 9.1	8.18 8.7	8.93 9.5	6.76 7.1	-2.61 -2.7	-2.98 -3.0	-2.85 -2.9	-1.95 -1.9	23.3 22.8	18.3 17.5	25	56B3 64b1
	c_{11}^E	c_{11}^H	c_{33}^E	c_{33}^H	c_{13}^E	c_{13}^H	c_{44}^E	c_{44}^H	c_{66}^E	c_{66}^H	25	
single crystal	275.1	282.6 206	164.9	178.1	179.0	186.5 140	151.6	141.6	54.34	80.64 126	25 RT	66b1, 58B2 51B1
ceramics	166 150 165.6	168 150	162 146	189 171 180.7	76.6 66	78.2 68	77.5 66	71.0 57	42.9 44	54.6 57	25	56B3 64b1 55H5
									42.48	53.02	25	

Tab. 42 ... 45 see page 58

Tab. 46. BaTiO₃. Summary of the ESR parameters for various paramagnetic centers in doped BaTiO₃.

Para-magnetic center	Site	S	g	ν GHz	T °K	g-factor	FS		HFS		Ref.	Literature
							$D, E, a, F [10^{-3} \text{ m}^{-1}]$		I	$A, B [10^{-3} \text{ m}^{-1}]$		
Mn ²⁺	Ti ⁴⁺	5/2	(7)	9.3	78	2.0016 ± 0.0005	$D = 56 \pm 5$		5/2	$^{55}\text{A}_{ } = ^{55}\text{A}_{\perp} = 79.8 \pm 0.5$	a)	60I1
					300	2.0023 ± 0.0005	$D = 65 \pm 5$			$^{55}\text{A}_{ } = 78.6 \pm 0.5$	b)	63O1
					440	2.0009 ± 0.001	$a = 14 \pm 5$			$^{55}\text{A}_{ } = 79 \pm 0.5$	c)	64I5
	Ba ²⁺	5/2	(7)	9.3	RT	2.002 ± 0.001	$D = +(215 \pm 2)$ $a = +(16.76 \pm 0.94)$			$^{55}\text{A}_{ } = -(77.4 \pm 0.6)$ $^{55}\text{A}_{\perp} = -(82.3 \pm 0.8)$		
					438	2.002 ± 0.001	$D = 0$ $a = +(12.11 \pm 0.94)$			$^{55}\text{A}_{ } = ^{55}\text{A}_{\perp} = -(79.3 \pm 0.4)$		66I31 ^{a)}

Para-magnetic center	Site	S	g	ν GHz	T °K	g-factor	FS		HFS		Ref.	Literature
							$D, E, a, F, b [10^{-3} \text{ m}^{-1}]$		I	$A, B [10^{-3} \text{ m}^{-1}]$		

$D\delta^{\circ}$	γ/ω					
438		2.002 ± 0.001	$D = 0$ $a = +(12.11 \pm 0.94)$	$E = 0$	${}^{55}A_{ } = {}^{56}A_{\perp}$ ${}^{55}A_{ } = -(79.3 \pm 0.4)$	$001\gamma' /$

Para- magnetic center	Site	S	J	ν GHz	T °K	g-factor	FS			HFS		Ref.	Liter- ature
							D, E, a, F, b [10 ⁻³ m ⁻¹]			I	A, B [10 ⁻³ m ⁻¹]		
Fe ³⁺	Ti ⁴⁺	5/2	(7)	5 ... 7.5, 10, 16.3 10	393, 433	2.003	D = 0 a = 102 ± 12				d)	59H5, 62R1	
					300	2.0036 ± 0.002	D = +929 a = +91 ± 20	E = 0		e)	63S2 ^a		
					276	2.0036 ± 0.002	D = -530 ± 10 a = +105 ± 20			f)			
					213	2.0036 ± 0.002	D = -640 ± 10 E = 0 ± 1.3						
					77	2.0036 ± 0.002	D = 0 a = +115 ± 10	E = 0					
Co ²⁺	Ti ⁴⁺	1/2	(3)	9	173	2.003 ± 0.002	D = -23 ± 5 a - F = +113 ± 10					64S3 ^a ²	
					4	4.347 (isotropic)		7/2	$^{59}A_{ } = ^{59}A_{\perp}$ $^{59}A_{ } = 109$		67Z2		
Gd ³⁺	Ba ²⁺	7/2	(8)	12, 18 10	300	1.995 ± 0.003	b ₂₀	b ₄₀	b ₆₀			62R1	
					425	1.995 ± 0.003	-	-	-				
					RT	1.992	-	24 ± 0.9	-3.7 ± 2.8		64T1		
					436	1.992		23.3 ± 0.4	-1.8 ± 0.4		66T3		
						$g_{ }$	g_{\perp}						
Pr ³⁺	Ti ⁴⁺	1/2	(3)	10	4	1.950 ± 0.005	2.459 ± 0.003		1/2	$^{136}A = 0 \pm 5$ $^{136}B = 135 \pm 5$	66S21		
					78	1.935 ± 0.005	2.51 ± 0.02			$^{136}A < 28$ $^{136}B = 135 \pm 10$	63S12		
Electron	oxygen vacancy	1/2	(2)	10	55	1.930	1.911				g)	63S11, 66T2, 67T3	

^a Temperature dependence of D^a in the tetragonal phase is linear. [65V4].

a) Temperature dependence of D^s in the tetragonal phase is linear. [65V4].
b) Forbidden transition lines ($\Delta M = \pm 1, \Delta m = \pm 1$) are observed. [63O1], [64I5]. Forbidden transition lines ($\Delta M = \pm 1, \Delta m = \pm 2$) are observed. [65I1], [66I3].

- a) Temperature dependence of ω_M . [67Z1].
- b) Forbidden transition lines ($\Delta M = \pm 1, \Delta m = \pm 1$) are observed. [65O1], [64L3]. Forbidden transition lines ($\Delta M = \pm 1, \Delta m = \pm 1$) are observed. [62A1], [60L2].
- c) Fe^{2+} spectra are studied with a d.c. bias electric field near transition temperature from cubic to tetragonal phase and from tetragonal to orthorhombic phase. [63S2], [64E1].

(d) Fe^{3+} spectra are studied with a d.c. bias electric field near transition temperature from cubic to rhombohedral phase. [64S3].

f) Forbidden transition lines ($\Delta M = 2, 3, 4, 5$) are observed in the rhombohedral phase. $[65G']$.

f) Fe^{3+} spectra due to the oxygen vacancy; $g_{\parallel} \cong 2$, $g_{\perp} = 6.0 \pm 0.1$ at 77°K.

- 2) Hypertine structure of an electron captured by an oxygen vacancy. [o^+D^+].
- 1) Mn^{3+} ion takes the place of Ti^{4+} lattice site in ceramics, while it takes the place of Ba^{2+} in a single crystal.

- 1) Mn^{2+} ion takes the place of Mn^{3+} ion.
- 2) Positive a is assumed.

3) Fe^{3+} spectra in a single-domain specimen.

$$x' = x_{\infty} + \sum_i 4\pi \varrho_i v^2 \frac{v_i^2 - v^2}{(v_i^2 - v^2)^2 + \gamma_i^2 v^2} \quad x'' = \sum_i 4\pi \varrho_i v_i^2 \frac{\gamma_i v}{(v_i^2 - v^2)^2 + \gamma_i^2 v^2}$$

	BaTiO ₃ Ordinary ray	SrTiO ₃	TiO ₂ Ordinary ray	KTaO ₃
$\lambda_1; \nu_1$	20.4; 491	18.4; 544	20.0; 500	18.2 ± 0.2; 549 ± 6
γ_1/ν_1	0.059 ± 0.002	0.049 ± 0.002	0.044 ± 0.004	0.043 ± 0.009
$4\pi\epsilon_1$	0.60 ± 0.03	1.56 ± 0.06	2.0 ± 0.2	2.4 ± 0.5
$\lambda_2; \nu_2$	54.8; 183	56.3 ± 0.5; 178 ± 2.0	25.8; 388	49.8; 200.8
γ_2/ν_2	0.030 ± 0.006	0.039 ± 0.004	0.058 ± 0.006	0.055 ± 0.011
$4\pi\epsilon_2$	2.2 ± 0.4	3.6 ± 0.4	1.08 ± 0.1	7.6 ± 1.5
$\lambda_3; \nu_3$	296 ± 8; 33.8 ± 0.9	114.3 ± 1.1; 87.7 ± 0.9	54.8 ± 0.5; 183 ± 1.8	107.5 ± 2.0; 93.0 ± 2.0
γ_3/ν_3	2.5 ± 0.1	0.5 ± 0.1	0.19 ± 0.01	0.5 ± 0.1
$4\pi\epsilon_3$	1830 ± 70	311 ± 62	81.5 ± 4.1	163 ± 33

Resonance wavelength λ_i in 10^{-8} m; resonance frequency ν_i in 10^{12} m $^{-1}$; width γ_i ; strength $4\pi q_i$.

Tab. 43. BaTiO₃, SrTiO₃, TiO₂. Energies of fundamental absorption edges (in eV) at RT. [65C2]

[illegible]

Tab. 44. BaTiO_3 , SrTiO_3 , KTaO_3 , $\text{KTa}_{0.35}\text{Nb}_{0.65}\text{O}_3$ (KTN), TiO_2 . Band gap energies $\hbar\omega_g$ (in eV). [67B1]. See Fig. 46, 103, 216, 430. F_1, F_2 : different dispersion functions $F_i(\omega/\omega_g)$, see [67B1]

	SrTiO ₃		BaTiO ₃	KTaO ₃		KTN	TiO ₂	
	296 °K	77 °K	403 °K	296 °K	77 °K	296 °K	296 °K	
Faraday rotation $\hbar\omega_g$ for F_1	3.40	3.43	3.25	3.77	3.79	3.54	3.62	eV
Faraday rotation $\hbar\omega_g$ for F_2	3.21	3.26	3.11	3.62	3.65	3.36	3.37	eV
Energy of reflectivity peak or shoulder	3.20	—	3.20	—	—	3.70	—	eV
Energy of electrorreflectance singularity	—	—	3.20	3.57	—	3.60	3.00	eV
$\hbar\omega_g$ from absorption data	3.40	—	—	3.80	—	—	3.30	eV
Energy at which absorption coefficient $\alpha \approx 10^4 \text{ cm}^{-1}$	3.37	—	3.26	3.75	—	—	—	eV
				3.79	—	3.45	3.18	eV

Tab. 45. BaTiO₃ (reduced or doped). List of reference papers on PTC anomaly

Materials (dopants)	References	Materials (dopants)	References
Single crystal BaTiO ₃ : reduced	57H1, 63K3, 64I4, 64G4, 65M1, 65U2	Ceramics BaTiO ₃	63H5, 65U2
BaTiO ₃ : Nb	64B11	BaTiO ₃ : La	59S1, 63T3, 64J1, 65M1
		BaTiO ₃ : Ce	63T3
		BaTiO ₃ : Sm	63G5
		BaTiO ₃ : Gd	65U2
		BaTiO ₃ : Sb	65A3
		(Ba-Sr)TiO ₃	61H5, 65A3
		(Ba-Sr)TiO ₃ : La	59S1, 61T1, 63T3
		BaTiO ₃ : Sr, Ce, Sn	61S1
		BaTiO ₃ : Sr, Ca, Sn	61S1
		BaTiO ₃ : Sr, Bi	63T3
		BaTiO ₃ : Mg, Ce	61S1
		BaTiO ₃ : Zr, Ce	61S1
		BaTiO ₃ : Si, Ce	61S1

Nr. 1A-		
1a	For	
b	St	
	pl	
	st	
	cr	
	sp	
	θ	
	a	
2a	Cr	
b	Cr	
3	C	
	P	
4	T	
	D	
5a	D	
	a	
6a	S	
	Δ	
	Δ	
c	T	
7a	F	
9a	E	
	I	
	F	
12b	E	
14a	D	
16	F	
	T	
	P	
	—	
	—	

* Phase

Nr. 1A-9 PbTiO₃, Lead titanate

1a	Ferroelectric activity was reported independently by SHIRANE et al. and by SMOLENSKII in 1950.			50S4 50S6
b	phase	III ^b *)	II ^a)	I ^a)
	state		F ^a)	P ^a)
	crystal system		tetragonal ^c)	cubic ^a)
	space group		P4mm-C _{4v} ¹	Pm3m-O _h ¹
	Θ	-100 ^b)	490 ^a)	°C
	$a = 3.904_4 \text{ \AA}$, $c = 4.152_4 \text{ \AA}$ at RT (in phase II).			46M2
2a	Crystal growth: KF flux method; PbCl ₂ flux method.			58K1, 52N2
b	Crystal form: Fig. 271.			
3	Crystal structure: Positional parameters: Tab. 47, 48. Projection of crystal structure: Fig. 272, 273.			
4	Thermal expansion: Fig. 274 ... 280. Dependence of lattice parameters on hydrostatic pressure: Fig. 281.			
5a	Dielectric constants: Fig. 282. Small dielectric anomaly was observed at about -100 and -150 °C. Curie-Weiss constant: $C = 1.1 \cdot 10^5 \text{ °K}$ (single crystal).			56K2 62B4
6a	Specific heat: Fig. 283.			
		II-I		
	ΔQ_m	1150	cal mol ⁻¹	51S7
	ΔS_m	1.6	cal °K ⁻¹ mol ⁻¹	51S7
c	Thermal conductivity: Fig. 284.			
7a	Piezoelectric properties: Tab. 49.			
9a	Birefringence: Fig. 285. Infrared absorption: Fig. 286, 287. Frequencies of infrared modes: Tab. 50.			
12b	ESR: Tab. 51.			
14a	Domain structures were observed by polarized light.			52N2, 58K1, 59K1
16	Radiation damage: Fig. 288.			

Tab. 47. PbTiO₃. Positional parameters of atoms at RT. [56S5]

	x	y	z
Pb	0	0	0
Ti	$\frac{1}{2}$	$\frac{1}{2}$	0.540
O(1)	$\frac{1}{2}$	$\frac{1}{2}$	0.112
O(2)	$\frac{1}{2}$	0	0.612
	0	$\frac{1}{2}$	0.612

Tab. 48. PbTiO₃. Bond lengths in Å at RT (phase II) and at 490 °C (phase I) [56S5]. O(1)₊ represents the O(1) ion closer to, O(1)₋ that further away from Ti. Similarly O(2)₊ is closer to Pb

phase	II (at RT)	I (at 490 °C)
Ti-O(1) ₊	1.78	1.89
Ti-O(1) ₋	2.38	
Ti-O(2)	1.98	
Pb-O(1)	2.80	2.80
Pb-O(2) ₊	2.53	
Pb-O(2) ₋	3.20	

* Phase transition II-III was reported to occur only if the cooling rate is extremely slow. [55K3]

Tab. 49. PbTiO_3 (modified ceramics). Electromechanical constants at RT. [68U1]

Additive	$\text{PbNb}_{4/5}\text{O}_3$ 5.0 mol%	$\text{BiZn}_{1/2}\text{Ti}_{1/2}\text{O}_3$ 5.0 mol%	$\text{Bi}_{2/3}\text{Zn}_{1/3}\text{Nb}_{2/3}\text{O}_3$ 5.0 mol%	
a	3.915	3.904	3.911	Å
c	4.104	4.148	4.133	Å
c/a	1.049	1.062	1.057	
ρ	7.19	7.68	7.12	10^3 kg m^{-3}
porosity	0.105	0.036	0.10	
Θ	466	524	494	$^\circ\text{C}$
κ_{11}^T	—	195	244	
κ_{33}^T	226	147	203	
d_{31}	10	3.9	7.4	$10^{-12} \text{ C N}^{-1}$
d_{33}	37	37	47	$10^{-12} \text{ C N}^{-1}$
g_{31}	5.2	3.0	4.1	$10^{-8} \text{ m}^2 \text{ C}^{-1}$
g_{33}	16	28	28	$10^{-8} \text{ m}^2 \text{ C}^{-1}$
s_{11}^E	1.2	1.2	1.1	$10^{-11} \text{ m}^2 \text{ N}^{-1}$
s_{33}^E	1.1	0.95	1.1	$10^{-11} \text{ m}^2 \text{ N}^{-1}$
Q_{mech} for s_{11}	—336	54	326	
for s_{33}	71	74	76	
k_{15}	—	0.40	0.36	
k_{31}	0.068	0.031	0.052	
k_{33}	0.23	0.32	0.35	

Tab. 50. PbTiO_3 . Wave numbers in 10^3 m^{-1} and symmetries of infrared modes of lattice vibration obtained from Kramers-Kronig analysis of the reflectance data at RT. [65P4]

$\tilde{\nu}_1$ (Ti-O stretch)	$\tilde{\nu}_2$ (Ti-O ₃ torsion)	$\tilde{\nu}_3$ (O-Ti-O bend)	$\tilde{\nu}_4$ (cation-TiO ₃ lattice mode)
530 (E_u, A_1)	400 (B_1, E_u)	220 (E_u, A_1) 172	83 (E_u, A_1)

Tab. 51. PbTiO_3 . g -factors at RT. [64G1]

Paramagnetic center	Site	S	\mathcal{H}	ν GHz	T $^\circ\text{K}$	g -factor	
						g_{\parallel}	g_{\perp}
Fe^{3+}	Ti^{4+}	1/2*	(2)	8.8	RT	2.009 ± 0.005	5.97 ± 0.02

The spectrum up to 300 $^\circ\text{C}$ and down to -120 $^\circ\text{C}$ did not show any fundamental change.

Nr. 1A-10 CaZrO_3 , Calcium zirconate

1	A few physical properties of CaZrO_3 were studied in comparison with those of some perovskite-type ferroelectrics. The crystal was reported to be orthorhombic with the cell dimensions $a = 5.587$ Å, $b = 8.008$ Å, $c = 5.758$ Å at RT.	
4	Linear thermal expansion: $\alpha = 8.55 \cdot 10^{-6} \text{ }^\circ\text{C}^{-1}$ between 23 $^\circ\text{C}$ and 223 $^\circ\text{C}$; $\alpha = 9.53 \cdot 10^{-6} \text{ }^\circ\text{C}^{-1}$ between 223 $^\circ\text{C}$ and 333 $^\circ\text{C}$ for ceramics of bulk density $\rho = 4.95 \cdot 10^3 \text{ kg m}^{-3}$	55C1 65B10
9	Infrared absorption: Fig. 289, 290; Tab. 52.	

Tab. 52. CaZrO_3 . Wave numbers in 10^3 m^{-1} and symmetry of infrared modes of lattice vibration obtained from Kramers-Kronig analysis of the reflectance data at RT. [65P4]

$\tilde{\nu}_1$ (Zr-O stretch)	$\tilde{\nu}_2$ (Zr-O ₃ torsion)	$\tilde{\nu}_3$ (O-Zr-O bend)	$\tilde{\nu}_4$ (cation-ZrO ₃ lattice mode)
515 (B_1, B_2, A_1)	340 (B_1, B_2, A_2) (377) (418)	228 (B_1, B_2, A_1) 186	153 (B_1, B_2, A_1) 96

* The fictitious spin is $\frac{1}{2}$ [64G1].

Nr. 1A-11 SrZrO₃, Strontium zirconate

1	A few physical properties of SrZrO ₃ were studied in comparison with those of some perovskite-type ferroelectrics. The crystal was reported to be pseudo-cubic with $a' = 4.099 \text{ \AA}$ at RT.	57R2
4	Linear thermal expansion: $\alpha = 8.75 \cdot 10^{-6} \text{ }^\circ\text{C}^{-1}$ between 23 °C and 320 °C; $\alpha = 9.34 \cdot 10^{-6} \text{ }^\circ\text{C}^{-1}$ between 320 °C and 700 °C for ceramics of bulk density $\rho = 5.00 \cdot 10^3 \text{ kg m}^{-3}$.	65B10
9	Infrared absorption: Fig. 291, 292; Tab. 53.	

Tab. 53. SrZrO₃. Wave numbers in 10^3 m^{-1} and symmetry of infrared modes of lattice vibration obtained from Kramers-Kronig analysis of the reflectance data at RT. [65P4]

$\tilde{\nu}_1$ (Zr-O stretch)	$\tilde{\nu}_2$ (Zr-O ₃ torsion)	$\tilde{\nu}_3$ (O-Zr-O bend)	$\tilde{\nu}_4$ (cation-ZrO ₃ lattice mode)
522 (B_1, B_2, A_1)	325 (B_1, B_2, A_2) (357) (379)	240 (B_1, B_2, A_1)	143 (B_1, B_2, A_1)

Nr. 1A-12 BaZrO₃, Barium zirconate

1	A few properties of BaZrO ₃ were reported in comparison with those of some perovskite-type ferroelectrics. The crystal was reported to be cubic with the cell dimensions $a = 4.192 \text{ \AA}$ at RT.	57R2
4	Linear thermal expansion: $\alpha = 5.64 \cdot 10^{-6} \text{ }^\circ\text{C}^{-1}$ between 23 °C and 214 °C; $\alpha = 6.54 \cdot 10^{-6} \text{ }^\circ\text{C}^{-1}$ between 214 °C and 324 °C for ceramics of bulk density $\rho = 6.73 \cdot 10^3 \text{ kg m}^{-3}$.	65B10
9	Infrared absorption: Fig. 293, 294; Tab. 54.	

Tab. 54. BaZrO₃. Wave numbers in 10^3 m^{-1} and symmetries of infrared modes of lattice vibration obtained from Kramers-Kronig analysis of the reflectance data at RT. [65P4]

$\tilde{\nu}_1$ (Zr-O stretch)	$\tilde{\nu}_2$ (Zr-O ₃ torsion)	$\tilde{\nu}_3$ (O-Zr-O bend)	$\tilde{\nu}_4$ (cation-ZrO ₃ lattice mode)
505 (F_{1u})	— (F_{2u})	210 (F_{1u})	115 (F_{1u})

Nr. 1A-13 PbZrO₃, Lead zirconate

1a	Dielectric anomaly of PbZrO ₃ associated with a phase transition was reported independently by ROBERT and by SMOLENSKII in 1950. Antiparallel ionic shifts on the (001) projection of crystal structure were found by SAWAGUCHI et al. in 1951. In the same year antiferroelectric double hysteresis loops were discovered by SHIRANE et al.. PbZrO ₃ is the first compound in which double hysteresis loops were observed.		50R1, 50S7 51S3 51S8
b.	phase	II ^a)	I ^a)
	state	A ^b)	P ^a)
	crystal system	orthorhombic ^c)	cubic ^c)
	space group	Pba2-C _{2v} ^c)	Pm3m-O _h ^c)
	θ	230 °C ^a)	
	$a = 5.87 \text{ \AA}$, $b = 11.74 \text{ \AA}$, $c = 8.20 \text{ \AA}$ at RT (in phase II). The cubic unit cell in phase I becomes pseudo-tetragonal in phase II. The pseudo-tetragonal cell constants a' and c' are related with the orthorhombic cell constants a , b and c : $a = \sqrt{2} a'$, $b = 2\sqrt{2} a'$ and $c = 2c'$, where $a' = 4.15 \text{ \AA}$, $c' = 4.10 \text{ \AA}$ at RT. Relation between the pseudo-tetragonal and orthorhombic cells: Fig. 295.		51S3
	Crystal growth: PbCl ₂ flux method.		55J2

3	Nr. 1A-13 PbZrO ₃ , continued Z = 8 (in phase II). The crystal is polar along the <i>c</i> axis and antipolar along the <i>a</i> axis in phase II. Fig. 295 shows schematically the shifts of Pb ions. Positional parameters and shifts from ideal perovskite positions: Tab. 55. Projection of ZrO ₆ : Fig. 296, 297, 298. Bond distances between Zr and O: Fig. 299.	51S3, 57J4, 51S3 57J4
4	Thermal expansion: Fig. 300 ... 303. $\alpha_a \cong -0.05 \cdot 10^{-5} \text{ }^\circ\text{K}^{-1}$ and $\alpha_c \cong 2.80 \cdot 10^{-5} \text{ }^\circ\text{K}^{-1}$ in phase II; $\alpha_a \cong 1.10 \cdot 10^{-5} \text{ }^\circ\text{K}^{-1}$ in phase I, where α_a and α_c are the linear thermal expansion coefficients along the pseudo-tetragonal <i>a'</i> and <i>c'</i> axes, respectively.	52S1
5a	Dielectric constants: Fig. 304. $C = 1.36 \cdot 10^5 \text{ }^\circ\text{K}$ (determined with ceramics). Effect of pressure: Fig. 305. $(d\epsilon_a/dp)_{p \rightarrow 0} = (4.1 \pm 0.2) 10^{-8} \text{ }^\circ\text{K N}^{-1} \text{ m}^2$.	50R1 66R2
c	Critical field: Fig. 306.	
6a	Specific heat: Fig. 307. For the transition II-I: $\Delta Q_m = 440 \text{ cal mol}^{-1}$; $\Delta S_m = 0.88 \text{ cal }^\circ\text{K}^{-1} \text{ mol}^{-1}$.	52S2
b	Thermal conductivity: Fig. 308.	
8	Elastic compliances: Fig. 309.	
9a	Birefringence: Fig. 310. Infrared absorption: Fig. 311, 312; Tab. 56.	
16	Radiation damage: Fig. 313.	

Tab. 55. PbZrO₃ (ceramics). Atomic coordinates and shifts from ideal perovskite positions at RT. [57J4]

Atom	<i>x</i>	<i>y</i>	<i>z</i>	Wyckoff notation	Total shift Å
Pb'	0.706	0.127	0	4 <i>c</i>	0.26
Pb''	0.706	0.127	0.500	4 <i>c</i>	0.26
Zr'	0.243	0.124	0.250	4 <i>c</i>	0.04
Zr''	0.243	0.124	0.250	4 <i>c</i>	0.04
O(1)'	0.270	0.150	0.980	4 <i>c</i>	0.35
O(1)''	0.270	0.100	0.480	4 <i>c</i>	0.35
O(2)'	0.040	0.270	0.300	4 <i>c</i>	0.53
O(2)''	0.040	0.270	0.750	4 <i>c</i>	0.34
O(3)'	0	0.500	0.250	2 <i>b</i>	0
O(3)''	0	0.500	0.800	2 <i>b</i>	0.41
O(4)'	0	0	0.250	2 <i>a</i>	0
O(4)''	0	0	0.800	2 <i>a</i>	0.41

Tab. 56. PbZrO₃. Wave numbers in 10² m⁻¹ and symmetries of infrared modes of lattice vibration obtained from Kramers-Kronig analysis of the reflectance data at RT. [65P4]

$\tilde{\nu}_1$ (Zr-O stretch)	$\tilde{\nu}_2$ (Zr-O ₃ torsion)	$\tilde{\nu}_3$ (O-Zr-O bend)	$\tilde{\nu}_4$ (cation-ZrO ₃ lattice mode)
508 (<i>E_u</i> , <i>A₁</i>)	290 (<i>B₁</i> , <i>E_u</i>)	221 (<i>E_u</i> , <i>A₁</i>)	80 (<i>E_u</i> , <i>A₁</i>) 34

Nr. 1A-14 PbHfO₃, Lead hafnate

1a	A dielectric anomaly associated with a phase transition was observed, and the possibility of the antiferroelectricity was discussed by SHIRANE et al. in 1953.				53S3
b	phase	III	II	I	53S3
	state	(A)		P	
	crystal system	pseudo-tetragonal	tetragonal	cubic	
	Θ	163	215	°C	
Lattice constants for the pseudo-tetragonal phase: <i>a'</i> = 4.136 Å, <i>c'/a'</i> = 0.991 at RT.					53S3

4

Thermal expansion: Fig. 314.
Cubic thermal expansion coefficients: below 158 °C: $20 \cdot 10^{-6} \text{ deg}^{-1}$;
above 215 °C: $27 \cdot 10^{-6} \text{ deg}^{-1}$.

53S3

5a

Dielectric constant: Fig. 315.
 $C = 9.5 \cdot 10^4 \text{ °K (ceramics)}$.

53S3

Nr. 1A-15 BiFeO₃, Bismuth ferrite

1a

In 1960*) it was pointed out on the basis of x-ray studies of the solid solution, PbTiO₃-BiFeO₃, that BiFeO₃ could have a ferroelectric Curie point at high temperatures. The Curie point was estimated to be about 850 °C from studies of the same solid solution^{b)}. Disagreement, however, exists among many experimental data reported so far, therefore reservation is necessary in deciding whether BiFeO₃ is ferroelectric or anti-ferroelectric. Antiferromagnetic anomaly in BiFeO₃ was observed by direct magnetic measurements at about 370 °C^{c)}.

b

phase

state

crystal system

space group

θ

IV

(A) or (F),
 A_{magn}^*

rhombohedral

R3m-C_{3v}^{**}

370

III

(A) or (F),
 P_{magn}

rhombohedral

\approx 575

II

(A) or (F),
 P_{magn}

rhombohedral

850

I

(P),
 P_{magn}

cubic
(possibly)

°C

$a = (3.962 \pm 0.001) \text{ Å}$, $\alpha = 89^\circ 31' \pm 3'$ at RT.
Further references are available on unit cell parameters.

3

Crystal structure: From the x-ray diffraction studies, BiFeO₃ was found to belong to one of the five space groups: R 3, R $\bar{3}$, R 32, R3m and R $\bar{3}m$. Neutron diffraction studies suggested that BiFeO₃ belongs to the non-centrosymmetric space group R3m. The crystal structure can be regarded as consisting of alternating FeO₆ and BiO₆ trigonal pyramids: Fig. 316; Tab. 57. According to the electron diffraction study, BiFeO₃ belongs to the non-centrosymmetric space group R3m at RT. Atomic coordinates: Tab. 58. The space group R3m was, however, rejected by SMOLENSKII et al., because it does not satisfy the conditions for the existence of weak ferromagnetism. The magnetic structure of BiFeO₃ was proved to be G-type by the neutron diffraction experiments. Fig. 317, 318.

60Z2
63K5

64T6

64S9
63K5

4

Unit cell parameters: Fig. 319, 320. See also

66R8, 64T5

5a

Dielectric constant: Fig. 321, 322, 323.
No reliable data on the dielectric constant in the high temperature region near 850 °C are available.

11

Magnetic susceptibility: Fig. 324.
At RT, no spontaneous magnetic moment was observed in the fields up to 22 kOe.

12c

Mössbauer effect: Fig. 325, 326.

17

Calculations of the internal electric fields and their gradients in BiFeO₃ crystals were made on the basis of an ionic model.

67T7

Tab. 57. BiFeO₃. Values of the interatomic distances [Å]. [63K5]. See Fig. 316. See also [64T6]

520 °C

20 °C

Bi-Fe (A)

3.841

3.857

Bi-Fe (B)

3.006

2.994

Bi-O (C)

2.903

2.907

Bi-O (D)

2.680

2.693

Fe-O (F)

2.233

2.214

Fe-O (G)

1.754

1.774

O-O (H)

2.841

2.859

O-O (K)

2.800

2.800

O-O (L)

2.680

2.724

Tab. 58. BiFeO₃. Atomic coordinates. [64T6]

Atom

x

y

z

Bi

0.0337

0.0337

0.0337

Fe

0.5000

0.5000

0.5000

O(1)

-0.0280

0.5000

0.5000

O(2)

0.5000

-0.0280

0.5000

O(3)

0.5000

0.5000

-0.0280

* This state is presumably weak ferromagnetic. [66Y2]

** See subsection 3.

Nr. 1A-16 KIO_3 , Potassium iodate

1a	Ferroelectric behavior in KIO_3 was reported by HERLACH in 1961.					61H3
b	phase	V ^{a)}	IV ^{a)}	III ^{a)}	II ^{a)}	^{a)} 61H3
	state		F ^{a)}	F ^{a)}	F ^{a)}	
	crystal system			trigonal ^{b)} *		^{b)} 60S5
	Θ	-190 ^{a)}	-18, -10 ^{a)} **	70 ^{a)}	212 ^{a)}	°C
	$T_{\text{melt}} = 560^\circ\text{C}$. $\rho = 3.979^{1)} \cdot 10^3 \text{ kg m}^{-3}$. ¹⁾ A different value, 3.802, is also given in the same reference. $a = (4.410 \pm 0.005) \text{ \AA}$, $\alpha = 89,41^\circ$ at RT, adopting trigonal system. $a = 8.921 \text{ \AA}$, $b = 8.916 \text{ \AA}$, $c = 8.885 \text{ \AA}$, $\alpha \cong \beta \cong \gamma \cong 90^\circ \pm 30'$ at RT, adopting triclinic system. Transparent					66H17 08g1 60S5 65F3
2a	Hydrothermal method: Fig. 327. Growth from the supersaturated solution with 10 ... 14% HIO_3 at a constant temperature: Fig. 328.					61H3 27m1
3	$Z = 1$ in phase III, adopting trigonal system. $Z = 8$ in phase III, adopting triclinic system.					61H3 65F3
4	Lattice deformation: $a = [4.44 + 0.00022 (T - 220)] \text{ \AA}$, $\alpha = 89^\circ 20' - 0.09 (T - 220)'$ in phase I (T in $^\circ\text{C}$).					61H3
5a	Dielectric constants: Fig. 329, 330.					66H17
c	Spontaneous polarization: Fig. 331.					61H3
9a	Absorption edge: Fig. 332.					67V2
12a	NMR: Fig. 333.					61H3

1B Complex perovskite-type oxides

Nr. 1B1-i $(\text{K}_{1/2}\text{Bi}_{1/2})\text{TiO}_3$, Potassium bismuth titanate

1a	Ferroelectricity in $(\text{K}_{1/2}\text{Bi}_{1/2})\text{TiO}_3$ was found by SMOLENSKII and AGRANOVSKAYA in 1959.				59S6
b	phase	III	II	I	
	state	(F)	(A)	P	
	crystal system	tetragonal	pseudo-cubic	cubic	62I5
	space group			$\text{Pm}3\text{m}-\text{O}_h$	^{a)} 60S6
	Θ	270	410, 380 ^{a)}	°C	
	$a = (3.913 \pm 0.003) \text{ \AA}$, $c = (3.993 \pm 0.003) \text{ \AA}$ at RT.				
3	Crystal structure: Disordered perovskite.				62I5
4	Lattice distortion: Fig. 334. Thermal expansion: Fig. 335.				
5a	Dielectric constant: Fig. 336.				

Nr. 1B1-ii $(\text{Na}_{1/2}\text{Bi}_{1/2})\text{TiO}_3$, Sodium bismuth titanate

1a	Ferroelectricity in $(\text{Na}_{1/2}\text{Bi}_{1/2})\text{TiO}_3$ was found by SMOLENSKII and AGRANOVSKAYA in 1959.	59S6
----	--	------

* Various crystal systems have been proposed: trigonal [60S5], triclinic [65F3].
 ** -10°C on heating, -18°C on cooling.

* Various crystal systems have been proposed: trigonal [60S5], triclinic [65F3].
 ** -10 $^\circ\text{C}$ on heating, -18 $^\circ\text{C}$ on cooling.

1b	phase	III	II	I	62I5
	state	F	(A)	P	
	crystal system	rhombohedral	pseudo-cubic	cubic	
	space group			Pm3m-O _h	
	Θ	≈200 ^a 320 °C			
a = (3.891 ± 0.002) Å, α = 89° 36' ± 3' at RT.					
3	Crystal structure: Disordered perovskite.				62I5
4	Thermal expansion: Fig. 337.				
5a	Dielectric constant: Fig. 338.				60S6
c	Spontaneous polarization and coercive field: P _s ≈ 8.0 · 10 ⁻² C m ⁻² ; E _c ≈ 14 · 10 ² kV m ⁻¹ at 116 °C.				
Nr. 1B2-i Pb(Mg _{1/2} W _{1/2})O ₃					
1a	Antiferroelectric properties of Pb(Mg _{1/2} W _{1/2})O ₃ were discovered by SMOLENSKII et al. in 1959.				59S7
b	phase	II	I		62Z1
	state	A	P		
	crystal system	orthorhombic	cubic		
	space group	C222 ₁ -D ₂ ²			
	Θ	38 °C			
a = 22.74 Å, b = 22.79 Å, c = 15.90 Å at RT. Orthorhombic unit cell: see Fig. 339.					
2a	Crystal growth: Crystal growth of Pb(Mg _{1/2} W _{1/2})O ₃ was reported by MYL'NIKOVA.				60M2
3	Crystal structure: Pb(Mg _{1/2} W _{1/2})O ₃ has the structure of perovskite type. Fig. 339. Z = 64 (molecular unit: Pb ₂ MgWO ₆).				62Z1
4	Lattice distortion associated with the phase transition. Thermal expansion: Fig. 340.				62Z1
5a	Dielectric constants: Fig. 341, 342, 343. dε _a /dp = -5.84 · 10 ³ °K N ⁻¹ m ² .				
6	Specific heat: Fig. 344. Transition heat (II → I): ΔQ _m = 276 cal mol ⁻¹ .				66S28
8a	Elastic compliance: Fig. 345. Ultrasound absorption: Fig. 346, 347.				
Nr. 1B2-ii Pb(Cd _{1/2} W _{1/2})O ₃					
1a	Synthesis of Pb(Cd _{1/2} W _{1/2})O ₃ was reported by BELYAEV et al. in 1963.				63B3
b	phase	II	I		65F4
	state	(A)	P		
	crystal system	monoclinic	cubic		
	Θ	400 °C			
	a = (4.156 ± 0.002) Å, b = (4.074 ± 0.002) Å, β = 91° 9' ± 5' at RT. ROGINSKAYA and VENEVTSEV reported that another transition exists at 120 °C, in addition to the transition at 400 °C.				
3	Crystal structure: Superstructure lines, indicating ordered location of the octahedral voids of the perovskite lattice, were observed.				65R4
4	Lattice distortion: Fig. 348, 349.				65F4
5a	Dielectric constant: Fig. 350.				

1.1 Oxide des Perowskit-Typs

Nr. 1B2-iii $\text{Pb}(\text{Mn}_{1/2}\text{W}_{1/2})\text{O}_3$

1a	A synthesis of $\text{Pb}(\text{Mn}_{1/2}\text{W}_{1/2})\text{O}_3$ was reported by VENEVTSEV et al.			64V3
b	phase	II	I	65R5
	state	(A), P_{magn}	P, P_{magn}	
	crystal system	monoclinic	cubic	
	Θ	423	°K	
$a = 4.063 \text{ \AA}$, $b = 4.033 \text{ \AA}$, $\beta = 90^\circ 12'$ at RT.				
5a	Dielectric constant: Fig. 351.			65R5
10	Electrical conductivity: $\sigma = 8 \cdot 10^{-8} \Omega^{-1} \text{ m}^{-1}$.			65R5
11	Magnetic susceptibility: see Fig. 351.			

Nr. 1B2-iv $\text{Pb}(\text{Co}_{1/2}\text{W}_{1/2})\text{O}_3$

1a	Antiferro- and ferroelectric properties in $\text{Pb}(\text{Co}_{1/2}\text{W}_{1/2})\text{O}_3$ were discovered by FILIP'EV et al.					63F1
b	phase	IV	III	II	I	65B8
	state	F, F_{magn} (weak)	F, P_{magn}	A, P_{magn}	P, P_{magn}	a) 66K6
	crystal system			orthorhombic	cubic	b) 64F4
	Θ	9a)	83 ... 103	293b)	305	°K
$a = 4.008 \text{ \AA}$ at 298 °K.						
2a	Crystal growth: Flux method with PbO .					65B8
3	Crystal structure: A superstructure was observed which was completely explained by alternation of the population of the oxygen octahedra by Co^{2+} and W^{6+} cations along the three directions. The real elementary lattice is a cubic face centered one with the parameter $A = 2a$ for phase I and with the parameters $A = 2 \cos(\beta/2)$, $B = 2b$, and $C = 2a \sin(\beta/2)$ for II, where a , b and β are the parameters of the perovskite sub-lattice.					64F4
4	phase	lattice parameters				64F4
	I	$A = 8.017 \text{ \AA}$ at 298 °K				
	II	$A = 5.669 \text{ \AA}$, $B = 7.956 \text{ \AA}$, $C = 5.689 \text{ \AA}$ at 258 °K				
Lattice distortion: Fig. 352.						
5a	Dielectric constant: Fig. 353, 354, 355.					
c	Polarization: Fig. 356.					
11	Magnetic susceptibility and magnetization: Fig. 357, 358.					

Nr. 1B2-v $\text{Pb}(\text{Mn}_{1/2}\text{Re}_{1/2})\text{O}_3$

1a	A synthesis of $\text{Pb}(\text{Mn}_{1/2}\text{Re}_{1/2})\text{O}_3$ was reported by VENEVTSEV et al.			64V3
b	phase	III	II	I
	state	(A), F_{magn}	(A), P_{magn}	P, P_{magn}
	crystal system		monoclinic	cubic
	Θ	103	393	°K
$a = 4.043 \text{ \AA}$, $b = 4.012 \text{ \AA}$, $\beta = 90^\circ 33'$ at RT.				
3	Crystal structure: Ordered perovskite.			65R5

66

4	
10	
11	
Nr. 1	
1a	
b	
3	
5a	
c	
Nr. 1	
1a	
Nr. 1	
1a	
b	
2a	
3	
5a	
9a	
11	
12b	
c	

4	Lattice distortion: Fig. 359.			65R5
10	Electrical conductivity: $\sigma = 1 \cdot 10^{-1} \Omega^{-1} \text{ m}^{-1}$.			65R5
11	Magnetic susceptibility and magnetic moment: Fig. 360. The linear temperature dependence of χ_{magn}^{-1} with a positive value of $\Theta_{\text{p magn}} = 85^\circ \text{ K}$, and the appearing of the spontaneous moment at 103° K , may indicate the presence of ferromagnetic properties in this compound, which is in agreement with the positive sign of the indirect exchange interaction proposed by GOODENOUGH for Mn^{2+} and Re^{5+} ions. However, the magnitudes of the calculated theoretical spontaneous moments agree with the experimental values only on the assumption of an anti-ferromagnetic interaction between ions distributed in an ordered fashion over the octahedral vacancies.			65R5
Nr. 1B3-i $\text{Pb}(\text{Sc}_{1/2}\text{Nb}_{1/2})\text{O}_3$				
1a	Ferroelectricity in $\text{Pb}(\text{Sc}_{1/2}\text{Nb}_{1/2})\text{O}_3$ was discovered by SMOLENSKII et al. in 1959.			59S9
b	phase	II	I	59S9
	state	F	P	
	crystal system	tetragonal ^a) (possibly)	cubic	
	Θ	90 $^\circ \text{ C}$		
	$a = (4.074 \pm 0.001) \text{ \AA}$, $c = (4.083 \pm 0.001) \text{ \AA}$ at RT. ^a)			
3	Crystal structure: In the powder patterns, additional to the principal lines of the perovskite structure, superstructural lines were observed indicating a doubling of the lattice period.			59I3
5a	Dielectric constant: Fig. 361.			59S9
c	Spontaneous polarization: $P_s \approx 3.6 \cdot 10^{-2} \text{ cm}^{-2}$ at 18° C .			
Nr. 1B3-ii $\text{Pb}(\text{Mn}_{1/2}\text{Nb}_{1/2})\text{O}_3$				
1a	A synthesis of $\text{Pb}(\text{Mn}_{1/2}\text{Nb}_{1/2})\text{O}_3$ with perovskite structure was reported by VENEV-TSEV et al.			64V3
Nr. 1B3-iii $\text{Pb}(\text{Fe}_{1/2}\text{Nb}_{1/2})\text{O}_3$				
1a	Ferroelectricity in $\text{Pb}(\text{Fe}_{1/2}\text{Nb}_{1/2})\text{O}_3$ was discovered by SMOLENSKII et al. in 1958.			58S4
b	phase	III	II	I
	state	F, A_{magn}	F, P_{magn}	P, P_{magn}
	crystal system	rhombohedral	rhombohedral	cubic
	space group			$\text{Pm}\bar{3}\text{m-O}_h^1$
	Θ	143	387	$^\circ \text{ K}$
	$a = 4.014 \text{ \AA}$, $\alpha = 89.92^\circ$ at RT.			62B10
2a	Crystal growth: Flux method with PbO .			62B7
3	Crystal structure: Disordered perovskite; X-ray studies have not shown any ionic ordering in the octahedral sites of perovskite structure. The magnetic peak was found in the neutron diffraction experiments at 78° K . The effective magnetic moment of the Fe^{3+} ion was found to be $(0.80 \pm 0.16) \mu_B$ at 78° K from the calculation of the intensity of the (111) reflection, which is about 90% of the magnetic moment at 0° K . Fig. 362.			64S8 65D6
5a	Dielectric constant: Fig. 363.			
9a	Optical absorption: Fig. 364.			
11	Magnetic susceptibility: Fig. 365. $\mu_{\text{eff}} = 5.4 \mu_B$.			62B7
12b	ESR: Fig. 366.			66S22
c	Mössbauer effect: Fig. 367, 368. The quadrupile splitting $\Delta E_{\text{qu}} = (0.37 \pm 0.02) \text{ mm sec}^{-1}$, the isomer shift $\delta = (0.52 \pm 0.02) \text{ mm sec}^{-1}$, corresponding to trivalent iron (at 20° C).			

Nr. 1B3-iv $\text{Pb}(\text{Co}_{1/2}\text{Nb}_{1/2})\text{O}_3$			
1a	A synthesis of $\text{Pb}(\text{Co}_{1/2}\text{Nb}_{1/2})\text{O}_3$ with perovskite structure was reported by VENEV-TSEV et al.		64V3
b	Informations on the dielectric and magnetic properties are available;		65R5
Nr. 1B3-v $\text{Pb}(\text{Ni}_{1/2}\text{Nb}_{1/2})\text{O}_3$			
1a	$\text{Pb}(\text{Ni}_{1/2}\text{Nb}_{1/2})\text{O}_3$ with perovskite structure was synthesized by the addition of 5 mol % BaO.		65S17
Nr. 1B3-vi $\text{Pb}(\text{In}_{1/2}\text{Nb}_{1/2})\text{O}_3$			
1a	Dielectric anomaly in $\text{Pb}(\text{In}_{1/2}\text{Nb}_{1/2})\text{O}_3$ was found by KUPRIYANOV and FESENKO in 1965.		65K9
b	phase	II	I
	state	(F)	P
	crystal system	monoclinic (possibly)	cubic
	θ	90	$^{\circ}\text{C}$
	$a = 4.11 \text{ \AA}$ at RT.		65K9
5a	Dielectric constant: Fig. 369.		
Nr. 1B3-vii $\text{Pb}(\text{Yb}_{1/2}\text{Nb}_{1/2})\text{O}_3$			
1a	Antiferroelectric properties in $\text{Pb}(\text{Yb}_{1/2}\text{Nb}_{1/2})\text{O}_3$ were reported by FILIP'EV et al. in 1963.		63F1
b	phase	II	I
	state	AF	P
	crystal system	monoclinic	cubic
	θ	300, 310*	$^{\circ}\text{C}$
	$a = 4.168 \text{ \AA}$, $b = 4.107 \text{ \AA}$, $\beta = 90^{\circ} 27'$ at RT*).		*64T4
3	Crystal structure: Superstructure lines, corresponding to ordering of Yb^{3+} and Nb^{5+} ions were found.		64T4
4	Lattice distortion: Fig. 370. Thermal expansion: Fig. 371.		
5a	Dielectric constant: Fig. 372.		
Nr. 1B3-viii $\text{Pb}(\text{Ho}_{1/2}\text{Nb}_{1/2})\text{O}_3$			
1a	Dielectric anomaly in $\text{Pb}(\text{Ho}_{1/2}\text{Nb}_{1/2})\text{O}_3$ was found by KUPRIYANOV and FESENKO.		65K9
b	phase	II	I
	state	(A)	P
	crystal system	monoclinic	cubic
	θ	240	$^{\circ}\text{C}$
	$a = 4.160 \text{ \AA}$, $b = 4.106 \text{ \AA}$, $\beta = 90^{\circ} 30'$ at RT.		65K9
5a	Dielectric constant: Fig. 373.		
Nr. 1B3-ix $\text{Pb}(\text{Lu}_{1/2}\text{Nb}_{1/2})\text{O}_3$			
1a	Dielectric anomaly in $\text{Pb}(\text{Lu}_{1/2}\text{Nb}_{1/2})\text{O}_3$ was found by SMOLENSKII and AGRANOV-SKAYA in 1958.		58S3

1b	phase	II	I	65K9
	state	(A)	P	
	crystal system	monoclinic	cubic	
	Θ	270 °C		
	$a = 4.152 \text{ \AA}, b = 4.093 \text{ \AA}, \beta = 90^\circ 30' \text{ at RT.}$			
4	Thermal expansion: Fig. 374.			
5a	Dielectric constant: Fig. 375.			
Nr. 1B3-x Pb(Sc _{1/2} Ta _{1/2})O ₃				
1a	Ferroelectricity in Pb(Sc _{1/2} Ta _{1/2})O ₃ was discussed by SMOLENSKII et al. in 1959.			59S9
b	phase	II	I	59S9 *)59I3
	state	F	P	
	crystal system	tetragonal ^a (possibly)	cubic	
	Θ	26 °C		
	$a = (4.072 \pm 0.001) \text{ \AA}, c = (4.072 \pm 0.001) \text{ \AA} \text{ at RT}^*$.			
3	Crystal structure: The large number of superstructure lines and their great intensity in Pb(Sc _{1/2} Ta _{1/2})O ₃ indicates that the degree of ordering of Sc ³⁺ and Ta ⁵⁺ ions is greater than in Pb(Sc _{1/2} Nb _{1/2})O ₃ . See 1B3-i-3.			59I3
5a	Dielectric constant: Fig. 376.			
Nr. 1B3-xi Pb(Mn _{1/2} Ta _{1/2})O ₃				
1a	Pb(Mn _{1/2} Ta _{1/2})O ₃ with perovskite structure was synthesized by the addition of 5 mol% SrO.			65S17
Nr. 1B3-xii Pb(Fe _{1/2} Ta _{1/2})O ₃				
1a	Ferroelectricity in Pb(Fe _{1/2} Ta _{1/2})O ₃ was discovered by SMOLENSKII et al. in 1959.			59S7
b	phase	III	II	68N1 *)65S17
	state	F, A _{magn}	F, P _{magn}	
	crystal system	rhombohedral	rhombohedral ^a)	
	space group		Pm3m-O _h	
	Θ	143, 133 ^a)	243, 233 ^a) °K	
	$P_s \parallel [111]$ (probably). $a = (4.007 \pm 0.001) \text{ \AA} \text{ at RT.}$ black (dark orange for thin samples).			
2a	Crystal growth: Flux method with PbO. When the soak temperature is higher than 1200 °C, crystals are obtained having both pyrochloride and perovskite structure.			68N1
3	Crystal structure: Disordered perovskite.			65S17
4	phase	lattice constants		68N1
	I	$a = (4.007 \pm 0.001) \text{ \AA} \text{ at RT.}$		
	II	$a = (4.006 \pm 0.001) \text{ \AA} \text{ at } 90^\circ \text{ K}$ $\alpha = 89.89^\circ \pm 0.02^\circ$		
5a	Dielectric constant: Fig. 377, 378.			
c	Spontaneous polarization: Fig. 379.			
11	Magnetic susceptibility: Fig. 380. $\mu_{\text{eff}} = 5.92 \mu_B; \Theta_{\text{p magn}} = -370^\circ \text{ K.}$			68N1

Series of Perovskite Types

Nr. 1B3-xiii $\text{Pb}(\text{Co}_{1/2}\text{Ta}_{1/2})\text{O}_3$

1a	A synthesis of $\text{Pb}(\text{Co}_{1/2}\text{Ta}_{1/2})\text{O}_3$ with perovskite structure was reported by SHVORNEVA and VENEVTSEV. The compound was stabilized by the addition of 1 mol% La_2O_3 .	65S17
----	---	-------

Nr. 1B3-xiv $\text{Pb}(\text{Yb}_{1/2}\text{Ta}_{1/2})\text{O}_3$

1a	Dielectric anomaly in $\text{Pb}(\text{Yb}_{1/2}\text{Ta}_{1/2})\text{O}_3$ was reported by ISUPOV and KRANIK in 1964.		64I6
b	phase	II	I
	state	(A)	F
	crystal system	monoclinic	cubic
	θ	280, 285*) °C	
	$a = 4.154 \text{ \AA}$, $b = 4.108 \text{ \AA}$, $\beta = 90^\circ 30'$ at RT.		
4	Thermal expansion: Fig. 381.		
5a	Dielectric constant: Fig. 382.		

a)65K9

Nr. 1B3-xv $\text{Pb}(\text{Lu}_{1/2}\text{Ta}_{1/2})\text{O}_3$

1a	Dielectric anomaly in $\text{Pb}(\text{Lu}_{1/2}\text{Ta}_{1/2})\text{O}_3$ was found by SMOLENSKII and AGRANOV-SKAYA in 1958.		58S3
b	phase	II	I
	state	(A)	P
	crystal system	monoclinic	cubic
	θ	280 °C	
	$a = 4.153 \text{ \AA}$, $b = 4.107 \text{ \AA}$, $\beta = 90^\circ 30'$ at RT.		
4	Lattice distortion: Fig. 383. Thermal expansion: Fig. 384.		
5	Dielectric constant: Fig. 385.		

65K9

Nr. 1B3-xvi $\text{Pb}(\text{Fe}_{1/2}\text{W}_{1/2})\text{O}_3$

1a	A synthesis of $\text{Pb}(\text{Fe}_{1/2}\text{W}_{1/2})\text{O}_3$ with perovskite structure was reported by VENEVTSEV et al.	64V3
b	The magnetic measurements confirmed the presence of the spinel phase in a sample of this composition.	65R5

Nr. 1B3-xvii $\text{Pb}(\text{Li}_{1/4}\text{Nb}_{1/4}\text{W}_{1/2})\text{O}_3$ and sister crystals

1a	Following composite perovskite compounds containing Pb were synthesized:			64V3
	$\text{Pb}(\text{Li}_{1/4}\text{Nb}_{1/4}\text{W}_{1/2})\text{O}_3$	$\text{Pb}(\text{Zn}_{1/4}\text{Mn}_{1/4}\text{Nb}_{1/2})\text{O}_3$	$\text{Pb}(\text{Co}_{1/4}\text{Mn}_{1/4}\text{W}_{1/2})\text{O}_3$	65V3
	$\text{Pb}(\text{Mg}_{1/4}\text{Mn}_{1/4}\text{Nb}_{1/2})\text{O}_3$	$\text{Pb}(\text{Cd}_{1/4}\text{Mn}_{1/4}\text{Nb}_{1/2})\text{O}_3$	$\text{Pb}(\text{Ni}_{1/4}\text{Mn}_{1/4}\text{W}_{1/2})\text{O}_3$	
	$\text{Pb}(\text{Co}_{1/4}\text{Mn}_{1/4}\text{Nb}_{1/2})\text{O}_3$	$\text{Pb}(\text{Mg}_{1/4}\text{Mn}_{1/4}\text{Ta}_{1/2})\text{O}_3$	$\text{Pb}(\text{Cd}_{1/4}\text{Mn}_{1/4}\text{W}_{1/2})\text{O}_3$	
	$\text{Pb}(\text{Ni}_{1/4}\text{Mn}_{1/4}\text{Nb}_{1/2})\text{O}_3$	$\text{Pb}(\text{Mg}_{1/4}\text{Mn}_{1/4}\text{W}_{1/2})\text{O}_3$	$\text{Pb}(\text{Sc}_{1/4}\text{Cr}_{1/4}\text{Nb}_{1/2})\text{O}_3$	

Nr. 1B4-i $\text{Pb}(\text{Mg}_{1/3}\text{Nb}_{2/3})\text{O}_3$

1a	Ferroelectricity in $\text{Pb}(\text{Mg}_{1/3}\text{Nb}_{2/3})\text{O}_3$ was discovered by SMOLENSKII and AGRANOV-SKAYA in 1958.		58S3, 59S6
b	phase	II	I
	state	F	P
	crystal system		cubic
	space group		$\text{Pm}3\text{m-O}_h^h$
	θ	265*) °K	
	$\rho = 8.12 \cdot 10^3 \text{ kg m}^{-3}$, $a = 4.04 \text{ \AA}$ at RT. Transparent, pale yellow.		

61B5, 60S7

a)67B9

67B18

70

2a	Crystal growth: Flux method (using PbO). Kyropoulos method.	59M5 67B18															
3	Crystal structure: Disordered perovskite.	61B5															
4	Thermal expansion: Fig. 386.																
5a	Dielectric constant: Fig. 387, 388, 389.																
b	Nonlinear dielectric properties: $E = [(T - \Theta_p)(\epsilon_0 C)^{-1}] P + \xi P^3 + \zeta P^5 + \dots$, where $\Theta_p = 265^\circ\text{K}$, $C = (3.7 \pm 1.0) \cdot 10^5^\circ\text{K}$, and $\xi \cong 5.6 \cdot 10^8 \text{ V m}^5 \text{ C}^{-3}$.	67B9															
c	Spontaneous polarization and coercive field: Fig. 390.																
7a	Piezoelectricity: Fig. 391.																
9a	Refractive index: $n = 2.56$ for 6328 \AA at 299°K . Birefringence: It was found that the crystals $\text{Pb}(\text{Mg}_{1/3}\text{Nb}_{2/3})\text{O}_3$ behave like optically isotropic crystals. An applied electric field causes double refraction. Fig. 392.	67B9															
e	Quadratic electrooptic effect: $M_{11} - M_{13} = +0.015 \text{ m}^4 \text{ C}^{-2}$, $M_{44} = +0.008 \text{ m}^4 \text{ C}^{-2}$ for 6328 \AA at 299°K .	67B9															
14a	Domain structure: Clear domains were observed only in very thin wafers (e. g., $20 \cdot 10^{-6} \text{ m}$).	61B5															
Nr. 1B4-ii $\text{Pb}(\text{Zn}_{1/3}\text{Nb}_{2/3})\text{O}_3$																	
1a	Ferroelectric $\text{Pb}(\text{Zn}_{1/3}\text{Nb}_{2/3})\text{O}_3$ crystal was synthesized by Bokov and MYL'NIKOVA in 1960.	60B7															
b	<table border="1"> <tr> <td>phase</td><td>II</td><td>I</td></tr> <tr> <td>state</td><td>F</td><td>P</td></tr> <tr> <td>crystal system</td><td></td><td>cubic</td></tr> <tr> <td>Θ</td><td>140</td><td>$^\circ\text{C}$</td></tr> </table> <p>$a = 4.04 \text{ \AA}$ at RT. light yellow.</p>	phase	II	I	state	F	P	crystal system		cubic	Θ	140	$^\circ\text{C}$	60B7			
phase	II	I															
state	F	P															
crystal system		cubic															
Θ	140	$^\circ\text{C}$															
2a	Crystal growth: Flux method with PbO. The crystals were separated from the matrix solution by washing in acetic acid at RT for a long time.	60B7															
5a	Dielectric constant: Fig. 393.																
Nr. 1B4-iii $\text{Pb}(\text{Cd}_{1/3}\text{Nb}_{2/3})\text{O}_3$																	
1b	Dielectric anomaly in $\text{Pb}(\text{Cd}_{1/3}\text{Nb}_{2/3})\text{O}_3$ was reported by VENEVTSEV et al. in 1966.	65T5, 66V5															
Nr. 1B4-iv $\text{Pb}(\text{Co}_{1/3}\text{Nb}_{2/3})\text{O}_3$																	
1a	Ferroelectricity in $\text{Pb}(\text{Co}_{1/3}\text{Nb}_{2/3})\text{O}_3$ was found by Bokov and MYL'NIKOVA in 1960.	60B7															
b	<table border="1"> <tr> <td>phase</td><td>II</td><td>I</td></tr> <tr> <td>state</td><td>F</td><td>P</td></tr> <tr> <td>crystal system</td><td></td><td>cubic</td></tr> <tr> <td>space group</td><td></td><td>$\text{Pm}3\text{m-O}_h^1$</td></tr> <tr> <td>Θ</td><td>-98</td><td>$^\circ\text{C}$</td></tr> </table> <p>$a = 4.04 \text{ \AA}$ at RT. brown.</p>	phase	II	I	state	F	P	crystal system		cubic	space group		$\text{Pm}3\text{m-O}_h^1$	Θ	-98	$^\circ\text{C}$	60B7
phase	II	I															
state	F	P															
crystal system		cubic															
space group		$\text{Pm}3\text{m-O}_h^1$															
Θ	-98	$^\circ\text{C}$															
2a	Crystal growth: Flux method with PbO.	60B7															
5a	Dielectric constant: Fig. 394.																

11-11 Cardes des Perovskit-Typs

Nr. 1B4-v $\text{Pb}(\text{Ni}_{1/3}\text{Nb}_{2/3})\text{O}_3$				
1a	Ferroelectricity in $\text{Pb}(\text{Ni}_{1/3}\text{Nb}_{2/3})\text{O}_3$ was discovered by SMOLENSKII and AGRANOV-SKAYA in 1958.			58S3, 59S6
b	phase	II	I	61B5, 60S7
	state	F	P	
	crystal system		cubic	
	space group		$\text{Pm}3\text{m}-\text{O}_h^1$	
	θ	153	$^{\circ}\text{K}$	
	$a = 4.03 \text{ \AA}$ at RT. $\rho = 8.55 \cdot 10^3 \text{ kg m}^{-3}$. yellowish green.			59M5
2a	Crystal growth: Flux method with PbO .			59M5
3	Crystal structure: Disordered perovskite.			59M5
4	Thermal expansion: Fig. 395.			61B5
5a	Dielectric constant: Fig. 396, 397, 398.			
9a	Birefringence: Fig. 399.			
Nr. 1B4-vi $\text{Pb}(\text{Mg}_{1/3}\text{Ta}_{2/3})\text{O}_3$				
1a	Ferroelectricity in $\text{Pb}(\text{Mg}_{1/3}\text{Ta}_{2/3})\text{O}_3$ was found by БОКОВ and МЫЛ'НИКОВА in 1960.			60B7
b	phase	II	I	60B7
	state	F	P	
	crystal system		cubic	
	space group		$\text{Pm}3\text{m}-\text{O}_h^1$	
	θ	-98	$^{\circ}\text{C}$	
	$a = 4.02 \text{ \AA}$ at RT. light yellow.			
2a	Crystal growth: Flux method with PbO .			60B7
3	Crystal structure: Disordered perovskite.			60B7
5a	Dielectric constant: Fig. 400.			
Nr. 1B4-vii $\text{Pb}(\text{Co}_{1/3}\text{Ta}_{2/3})\text{O}_3$				
1a	Ferroelectricity in $\text{Pb}(\text{Co}_{1/3}\text{Ta}_{2/3})\text{O}_3$ was found by БОКОВ and МЫЛ'НИКОВА in 1960.			60B7
b	phase	II	I	60B7
	state	F	P	
	crystal system		cubic	
	space group		$\text{Pm}3\text{m}-\text{O}_h^1$	
	θ	-140	$^{\circ}\text{C}$	
	$a = 4.01 \text{ \AA}$ at RT. brown.			
2a	Crystal growth: Flux method with PbO .			60B7
3	Crystal structure: Disordered perovskite.			60B7
5a	Dielectric constant: Fig. 401.			

72

Nr. 1B4-viii $\text{Pb}(\text{Ni}_{1/3}\text{Ta}_{2/3})\text{O}_3$					
1a	Ferroelectricity in $\text{Pb}(\text{Ni}_{1/3}\text{Ta}_{2/3})\text{O}_3$ was found by BOKOV and MYL'NIKOVA in 1960.			60B7	
b	phase	II	I	60B7	
	state	F	P		
	crystal system		cubic		
	space group		$\text{Pm}\bar{3}\text{m}-\text{O}_h^1$		
	Θ	-180 °C			
	$a = 4.01 \text{ \AA}$ at RT. green.				
2a	Crystal growth: Flux method.			60B7	
3	Crystal structure: Disordered perovskite.			60B7	
5a	Dielectric constant: Fig. 402.				
Nr. 1B5-i $\text{Pb}(\text{Mn}_{2/3}\text{W}_{1/3})\text{O}_3$					
1a	Dielectric and magnetic anomalies in $\text{Pb}(\text{Mn}_{2/3}\text{W}_{1/3})\text{O}_3$ were reported by ROGINSKAYA et al. in 1965.			65R5	
b	phase	III	II	I	65R5
	state	(A), (A_{magn})	(A), P_{magn}	P, P_{magn}	
	crystal system		monoclinic	cubic	
	Θ	203	473	°K	
	$a = c = 4.098 \text{ \AA}$, $b = 4.014 \text{ \AA}$, $\beta = 90^\circ 23'$ at RT.				
5a	Dielectric constant: Fig. 403.				
10	$\sigma = 2 \cdot 10^{11} \Omega^{-1} \text{ m}^{-1}$.			65R5	
11	Magnetic susceptibility: see Fig. 403. $\Theta_{\text{p magn}} = -75^\circ \text{K}$.				
Nr. 1B5-ii $\text{Pb}(\text{Fe}_{2/3}\text{W}_{1/3})\text{O}_3$					
1a	Ferroelectricity in $\text{Pb}(\text{Fe}_{2/3}\text{W}_{1/3})\text{O}_3$ was discovered by SMOLENSKII et al. in 1959.			59S7	
b	phase	III	II	I	62B7
	state	F, A_{magn}	P, A_{magn}	P, P_{magn}	
	crystal system		cubic	cubic	
	Θ	178	363	°K	
	$a = 4.02 \text{ \AA}$ at RT.				
2a	Flux method (PbO).			62B7	
5a	Dielectric constant: Fig. 404.				
11	Magnetic susceptibility: see Fig. 404. Magnetization is a linear function of the magnetic field intensity up to 8000 Oe. Effective magnetic moment: $4.2 \mu_B$.			62B7	
12b	ESR: Fig. 405.				
1C Solid solutions with perovskite-type oxides as end members					
Nr. 1C-a1 $\text{NaNbO}_3\text{-KNbO}_3$					
1b	Phase diagram: Fig. 406, 407, 408. Lattice parameters: Fig. 409.				
5a	Dielectric constant: Fig. 410; see Tab. 60. Polarization and coercive field: Fig. 411.				
6a	Transition energy: Tab. 59.				
7a	Electromechanical properties: Fig. 412 ... 417; Tab. 60.				

Tab. 59. $(\text{Na}_{1-x}\text{K}_x)\text{NbO}_3$. Transition energy ΔQ_m . [54S3]

x	Lower phase change	Upper phase change
1.00 (KNbO_3)	85 cal/mole	190 cal/mole
0.10	20 cal/mole	60 cal/mole
0 (NaNbO_3)	—	50 cal/mole

Tab. 60. $(\text{Na}_{0.5}\text{K}_{0.5})\text{NbO}_3$ (ceramics). Electric and electromechanical constants. [59E1]

Dielectric constant (100 kHz)	290
Dissipation factor (100 kHz)	$\approx 4.0\%$
Specific resistivity ρ	$10^{10} \Omega \text{m}$
Density ρ	$4.25 \cdot 10^3 \text{ kg m}^{-3}$
Poisson's ratio (assumed)	0.27
Coupling factor k_p	$0.34 \dots 0.39$
Frequency constant $f_R \tau$	1.67 kHz m
Mechanical Q_{mech} (radial)	130
Young's modulus E	$1.04 \cdot 10^{11} \text{ N m}^{-2}$
Piezoelectric constant $-d_{31}$	$32 \cdot 10^{-12} \text{ C N}^{-1}$
Piezoelectric constant $-g_{31}$	$12.6 \cdot 10^{-3} \text{ m}^2 \text{ C}^{-1}$
Piezoelectric constant d_{33}^*	$80 \cdot 10^{-12} \text{ C N}^{-1}$
Piezoelectric constant g_{33}^*	$31.5 \cdot 10^{-3} \text{ m}^2 \text{ C}^{-1}$
Coupling factor k_{33}^*	0.51

Nr. 1C-a2 NaNbO_3 - NaTaO_3

1b	Phase diagram: Fig. 418. Lattice parameters: Fig. 419.
4	Thermal expansion: Fig. 420.
5a	Dielectric constant: Fig. 421.
9a	Birefringence: Fig. 422.

Nr. 1C-a3 NaNbO_3 - NaSbO_3

1a	Curie temperature: Fig. 423.
----	------------------------------

Nr. 1C-a4 KNbO_3 - KTaO_3

1	Phase diagram: Fig. 424, 425.
5a	Dielectric properties: Fig. 426, 427. Θ_f : see Tab. 61.
6	Thermal properties: Fig. 428; Tab. 61.
9	See 1C-a5 for optical properties of $\text{K}(\text{Ta}_{0.35}\text{Nb}_{0.65})\text{O}_3$ (KTN).

Tab. 61. $\text{K}(\text{Nb}_{1-x}\text{Ta}_x)\text{O}_3$. L : latent heat, Θ_f : Curie point, A : constant in the formula for free energy = $A(T - \Theta_f)P^2 + \dots$, P_{calc} : P_s calculated for $T = \Theta_f$. [59H1]

x	L cal mol $^{-1}$	Θ_f °K	A 10^5 °K^{-1}	P_{calc} 10^{-3} C m^{-2}
0	110 \pm 10	679	2.6	27
0.06	46 \pm 4	656	2.7	17.7
0.12	10 \pm 2	623	2.85	7.9
0.18	4.0 \pm 2	591	3.05	5.1

Nr. 1C-a5 $\text{K}(\text{Ta}_{0.35}\text{Nb}_{0.65})\text{O}_3$ (KTN)For general properties of KNbO_3 - KTaO_3 , see 1C-a4.

9b	Electroreflectance: Fig. 429.
d	Faraday rotation: Fig. 430. See also Tab. 44.

Nr. 1C-a6 CaTiO_3 - SrTiO_3

1b	Phase diagram: Fig. 431, 432, 433. Lattice parameters: Fig. 434.
5a	Dielectric constant: Fig. 435, 436.
c	Spontaneous polarization: Fig. 437.

Nr. 1C-a7 CaTiO_3 - BaTiO_3

1b	Phase diagram: Fig. 438, 439, 440. Lattice parameters: Fig. 441.
5a	Dielectric constant: Fig. 442, 443.
6b	Thermal conductivity: Fig. 444.
7a	Electromechanical property: Tab. 62. See Fig. 183 and Tab. 40.

* Estimated values.

Tab. 62. $(\text{Ba}_{1-x}\text{Ca}_x)\text{TiO}_3$ (ceramics, pure BaTiO_3 base). d_{31} and d_{33} at RT. [57B4]

x	ρ 10^3 kg m^{-3}	ρ_x 10^3 kg m^{-3}	d_{31} $10^{-12} \text{ C N}^{-1}$	d_{33} $10^{-12} \text{ C N}^{-1}$	$-d_{33}/d_{31}$	Porosity ($1 - (\rho/\rho_x)$)
0	5.85	6.017	-97.5	229	2.35	0.028
0.05	5.70	5.85	-66.6	167	2.51	0.026
0.07	5.68	5.80	-58.0	150	2.58	0.021
0.09	5.65	5.74	-52.1	139	2.67	0.016
0.12	5.55	5.66	-43.4	124.5	2.88	0.019

Nr. 1C-a8 $\text{CaTiO}_3\text{-PbTiO}_3$ 1b | Curie temperature: Fig. 445.
Lattice parameter: Fig. 446.Nr. 1C-a9 $\text{SrTiO}_3\text{-BaTiO}_3$ 1b | Phase diagram: Fig. 447 ... 450.
Lattice parameter: Fig. 451; see Fig. 448.5a | Dielectric constant: Fig. 452.
Microwave dielectric loss: Tab. 63.

6a | Specific heat: Fig. 453.

10b | Conductivity associated with doping: Fig. 454, 455, 456.

Tab. 63. $(\text{Ba}_{1-x}\text{Sr}_x)\text{TiO}_3$. Dielectric loss: α, β, γ at 20 GHz. [62R4]. $(T - \Theta_p) \tan \delta = \alpha + \beta T + \gamma T^2$.

Sample		Heat treatment	Grain size μ	Θ_p $^\circ\text{K}$	α $^\circ\text{K}$	$\beta \cdot 10^4$	$\gamma \cdot 10^4$ ($^\circ\text{K}$) $^{-1}$
Polycrystalline	SrTiO_3	Hot pressed and fired in air at 900 $^\circ\text{C}$ for 10 h	1	37	0.33	7.7	4.3
		Refired at 1200 $^\circ\text{C}$ in air for 10 h	3	37	0.26	5.5	4.7
		Refired at 1400 $^\circ\text{C}$ in air for 10 h	15	37	0.17	4.4	4.2
		Refired at 1500 $^\circ\text{C}$ in O_2 for 6 h	30	37	0.08	4.5	3.7
	$\text{Ba}_{0.2}\text{Sr}_{0.8}\text{TiO}_3$	Hot pressed and fired in O_2 at 1500 $^\circ\text{C}$ for 10 h	30	105	0.6	9	2.5
	$\text{Ba}_{0.5}\text{Sr}_{0.5}\text{TiO}_3$	Hot pressed and fired in O_2 at 1500 $^\circ\text{C}$ for 10 h	30	218	2.0	(9) ^{a)}	(2.5)
	$\text{Ba}_{0.7}\text{Sr}_{0.3}\text{TiO}_3$	Ceramic fired to 1375 $^\circ\text{C}$ in air for 1 h	8	280	2.2	(9)	(2.5)
Single crystal	$\text{Ba}_{0.8}\text{Sr}_{0.2}\text{TiO}_3$	Ceramic fired to 1300 $^\circ\text{C}$ in air for 1 h	8	324	1.6	(9)	(2.5)
	SrTiO_3	None	∞	37	0	6.53	2.54
	$\text{SrTiO}_3 + 0.1\% \text{ Gd}^{3+}$	None	∞	37	0.033	(6.53)	(2.54)
	$\text{SrTiO}_3 + 0.03\% \text{ Fe}^{3+}$	None	∞	37	0.043	(6.53)	(2.54)

Nr. 1C-a10 $\text{SrTiO}_3\text{-PbTiO}_3$ 1b | Curie temperature: Fig. 457.
Lattice parameter: Fig. 458.5a | Dielectric constant: Fig. 459.
Curie constant: Fig. 460.

6a | Transition heat: Fig. 461.

Nr. 1C-a11 $\text{BaTiO}_3\text{-PbTiO}_3$ 1b | Phase diagram: Fig. 462.
Lattice parameter: Fig. 463.

5a | Dielectric constant: Fig. 464.

6a | Specific heat: Fig. 465.
Transition heat: Fig. 466.

7 | Electromechanical properties: see 1A-8.

16 | Radiation damage: Fig. 467.

^{a)} Values in parentheses indicate that these values were assumed in order to determine α .

Nr. 1C-a12 $\text{CaZrO}_3\text{-BaZrO}_3$

1b | Lattice parameter: Fig. 468.

Nr. 1C-a13 $\text{CaZrO}_3\text{-PbZrO}_3$

1b | Phase diagram: Fig. 469.

4 | Thermal expansion: Fig. 470.

5a | Dielectric constant: Fig. 471.

Nr. 1C-a14 $\text{SrZrO}_3\text{-PbZrO}_3$ 1b | Phase diagram: Fig. 472, 473.
Lattice parameter: Fig. 474.

4 | Thermal expansion: Fig. 475, 476, 477; Tab. 64.

5a | Dielectric constant: Fig. 478, 479.

c | Polarization: Fig. 480.

6a | Specific heat: Fig. 481.
Transition heat: Tab. 65.Tab. 64. PbZrO_3 , $(\text{Pb}_{0.95}\text{Sr}_{0.05})\text{ZrO}_3$, and $(\text{Pb}_{0.925}\text{Ba}_{0.075})\text{ZrO}_3$. $\Delta V/V$: anomalous volume change at the transition point. [54S2]

Composition	$\Delta V/V$ [10^{-4}]	
	Lowest phase	Intermediate phase
PbZrO_3	-41 at 230 °C	—
$(\text{Pb}_{0.925}\text{Ba}_{0.075})\text{ZrO}_3$	-43 at 150 °C	+24 at 190 °C
$(\text{Pb}_{0.95}\text{Sr}_{0.05})\text{ZrO}_3$	-30 at 210 °C	-20 at 230 °C

Tab. 65. PbZrO_3 , $(\text{Pb}_{0.95}\text{Sr}_{0.05})\text{ZrO}_3$, and $(\text{Pb}_{0.925}\text{Ba}_{0.075})\text{ZrO}_3$. ΔQ_m . [52S2]

Composition	ΔQ_m [cal mol $^{-1}$]	
	Lower transition	Upper transition
PbZrO_3	—	440
$(\text{Pb}_{0.925}\text{Ba}_{0.075})\text{ZrO}_3$	190	230
$(\text{Pb}_{0.95}\text{Sr}_{0.05})\text{ZrO}_3$	180	230

Nr. 1C-a15 $\text{BaZrO}_3\text{-PbZrO}_3$ 1b | Phase diagram: Fig. 482.
Lattice parameter: Fig. 483.

4 | Thermal expansion: Fig. 484.

5a | Dielectric constant: Fig. 485 ... 488.

c | Coercive field: Fig. 489.

8 | Elastic properties: Fig. 490.

Nr. 1C-a16 $\text{CaHfO}_3\text{-PbHfO}_3$

1b | Phase diagram: Fig. 491.

5a | Dielectric constant: Fig. 492.

Nr. 1C-a17 $\text{SrHfO}_3\text{-PbHfO}_3$

1b | Phase diagram: Fig. 493.

5a | Dielectric constant: Fig. 494.

Nr. 1C-a18 $\text{BaHfO}_3\text{-PbHfO}_3$

1b | Phase diagram: Fig. 495.

Nr. 1C-a19 $\text{CaSnO}_3\text{-SrSnO}_3$

1b | Lattice parameter: Fig. 496.

Nr. 1C-a20 $\text{BaSnO}_3\text{-SrSnO}_3$

1b | Lattice parameter: see Fig. 496.

Nr. 1C-a21 $\text{BaSnO}_3\text{-PbO:SnO}_2$

1b | Phase diagram: Fig. 497.

5a | Dielectric constant: Fig. 498.

Nr. 1C-a22 $\text{CaTiO}_3\text{-CaZrO}_3$

1b | Lattice parameter: Fig. 499.

Nr. 1C-a23 BaTiO ₃ -BaZrO ₃	1b	Phase diagram: Fig. 500. Lattice parameter: Fig. 501.	
	2a	Phase diagram: Fig. 502.	
	5a	Dielectric constant: Fig. 503.	
	8a	Elastic property: Fig. 504	
Nr. 1C-a24 BaTiO ₃ -BaHfO ₃	1b	Phase diagram: Fig. 505. Lattice parameter: Fig. 506.	
	5a	Dielectric constant: Fig. 507.	
Nr. 1C-a25 BaTiO ₃ -BaSnO ₃	1b	Phase diagram: Fig. 508. See also	5912
	2a	Phase diagram: Fig. 509.	
	4	Thermal expansion: Fig. 510.	
	5a	Dielectric constant: Fig. 511.	
Nr. 1C-a26 BaTiO ₃ -BaUO ₃	1b	Lattice parameter: Fig. 512.	
Nr. 1C-a27 PbTiO ₃ -PbZrO ₃ Pb(Zr _x Ti _{1-x})O ₃ with $x = 0.5 \dots 0.6$; for electromechanical properties of these very important piezo- electric materials, see 1C-a28.			
1a	Ferro- and antiferroelectric phase transitions in the PbTiO ₃ -PbZrO ₃ system were revealed in 1952 by SHIRANE, SUZUKI and TAKEDA.		52S6, 52S4, 52S3
b	Phase diagram at high temperature: Fig. 513. Phase diagram: Fig. 514, 515. Lattice parameter: Fig. 516, 517.		
2	Flux method:		62I1, 64F6, 67F7
4	Lattice distortion: Fig. 518a, b, 519. Thermal expansion: Fig. 520, 521, 522.		
5a	Dielectric constant: Fig. 523 ... 526.		
c	Spontaneous polarization: Fig. 527. Critical field: Fig. 528.		
6	Specific heat: Fig. 529, 530. Transition energy: Tab. 66.		
7 } 8 }	Electromechanical properties: see 1C-a28.		
9	Birefringence: Fig. 531a, b, c.		
16	Radiation damage: Fig. 532.		

Tab. 66. Pb(Zr-Ti)O₃. Transition energy and entropy. [53S1]. x : atomic percent of PbTiO₃; $d\theta/dx$: shift of the transition temperature with x ; $dS(d\theta/dx)$: it may be assumed that the free energy should decrease with the rate of $dS(d\theta/dx)$ with increasing x .

Kind of the phase change	θ °C	ΔQ_m cal mol ⁻¹	ΔS_m cal mol ⁻¹ °K ⁻¹	$d\theta/dx$	$dS(d\theta/dx)$
A _α → P _α	230 > T > 225	400	0.8	—	(-5.8)
A _α → A _β	225	110	0.22	-16	-3.5
A _β → P _α	230	290	0.58	-4	-2.3
A _α → F _α	240	—	—	-19	—
F _α → P _α	217	250	0.51	+ 1.0	+0.5
A _β → F _α	—	40	0.08	—	—

Nr. 1C-a28 $\text{Pb}(\text{Zr}_x\text{Ti}_{1-x})\text{O}_3$ ($x = 0.5 \dots 0.6$, lead zirconate-titanate)For general properties of PbTiO_3 - PbZrO_3 see 1C-a27.

1a	JAFÉ, ROTH, and MARZULLO discovered the excellent piezoelectric performances of Pb(Zr-Ti)O ₃ ceramics in 1954. PZT is the trade mark of this substance developed by Clevite Corporation, Cleveland, Ohio, USA.										54J1	
5a	Dielectric constants: Fig. 533 and Fig. 539, 540, 541, 543, 544.											
7) 8)	Electromechanical properties (ceramics): Tab. 67; Fig. 534 ... 538; Tab. 68 ... 72; Fig. 539 ... 542; Tab. 73; Fig. 543 ... 554.											
10	Electrical conductivity: see For breakdown, see										63G1, 61S14 59G2	
Tab. 67. Pb(Ti _{1-x} Zr _x)O ₃ [x = 0.48 ... 0.60] (ceramics). Electromechanical constants at RT. [60B3]												
Zr/Ti atom ratio	k ₃₁	k _p	k ₁₅	k ₃₃	κ ₁₁ ^T	κ ₁₁ ^S	κ ₃₃ ^T	κ ₃₃ ^S obs	κ ₃₃ ^S calc			
48/52	0.170	0.289	0.408	0.435	663	551	666	540	537			
50/50	0.230	0.397	0.504	0.546	855	631	846	585	585			
52/48	0.313	0.529	0.694	0.670	1180	612	730	399	389			
54/46	0.280	0.470	0.701	0.626	990	504	450	253	268			
56/44	0.267	0.450	0.657	0.619	840	477	423	246	258			
58/42	0.254	0.428	0.646	0.607	751	437	397	243	246			
60/40	0.238	0.400	0.625	0.585	672	410	376	240	245			
											Density ρ	
10 ⁻¹² m ² N ⁻¹											10 ³ kgm ⁻³	
48/52	10.8	10.5	10.9	8.83	28.3	23.6	28.3	-3.35	-3.66	-3.21	-2.40	7.59
50/50	12.4	11.7	13.3	9.35	32.8	24.5	32.9	-4.06	-4.72	-4.22	-2.60	7.55
52/48	13.8	12.4	17.1	9.35	48.2	25.0	38.4	-4.07	-5.38	-5.80	-2.56	7.55
54/46	11.6	10.7	14.8	9.0	45.0	22.9	29.9	-3.33	-4.24	-4.97	-2.68	7.62
56/44	11.0	10.2	14.0	8.65	39.8	22.6	28.4	-3.22	-4.01	-4.63	-2.57	7.59
58/42	10.5	9.85	12.8	8.10	37.7	21.9	27.1	-3.07	-3.75	-4.12	-2.33	7.64
60/40	10.4	9.75	12.05	7.92	36.9	22.5	26.7	-2.96	-3.55	-3.72	-2.17	7.60

Tab. 68. $(\text{Pb}_{1-x}\text{Sr}_x)(\text{Zr}_{1-y}\text{Ti}_y)\text{O}_3$ and $(\text{Pb}_{1-x}\text{Ca}_x)(\text{Zr}_{1-y}\text{Ti}_y)\text{O}_3$ (modified ceramics). Effects of Ca and Sr on electromechanical properties. [59K4]

Intended composition	ϵ_a 10^3 kgm^{-3}	κ at 1 kHz	24 hours after poling						Θ_f $^{\circ}\text{C}$
			κ at 1 kHz	$\tan \delta$ % at 1 kHz	k_p	d_{31} 10^{-12} CN^{-1}	g_{31} 10^{-3} m^2C^{-1}	$(s_{11}^E)^{-1}$ 10^{10} Nm^{-2}	
$\text{Pb}(\text{Zr}_{0.53}\text{Ti}_{0.47})\text{O}_3$	7.40	736	544	0.5	0.48	71	14.7	7.67	385
$\text{Pb}(\text{Zr}_{0.53}\text{Ti}_{0.47})\text{O}_3$	7.39	707	542	0.4	0.47	69	14.4	7.76	
$\text{Pb}_{0.99}\text{Ca}_{0.01}(\text{Zr}_{0.53}\text{Ti}_{0.47})\text{O}_3$	7.42	729	624	0.5	0.49	77	13.9	7.89	
$\text{Pb}_{0.99}\text{Sr}_{0.01}(\text{Zr}_{0.53}\text{Ti}_{0.47})\text{O}_3$	7.42	755	584	0.6	0.49	75	14.5	7.68	
$\text{Pb}_{0.95}\text{Ca}_{0.05}(\text{Zr}_{0.53}\text{Ti}_{0.47})\text{O}_3$	7.26	832	973	0.5	0.44	88	10.2	7.62	
$\text{Pb}_{0.95}\text{Sr}_{0.05}(\text{Zr}_{0.53}\text{Ti}_{0.47})\text{O}_3$	7.47	920	1002	0.4	0.50	101	11.4	7.65	360
$\text{Pb}_{0.92}\text{Ca}_{0.08}(\text{Zr}_{0.53}\text{Ti}_{0.47})\text{O}_3$	6.86	794	888	0.4	0.32	60	7.6	7.85	
$\text{Pb}_{0.925}\text{Sr}_{0.075}(\text{Zr}_{0.53}\text{Ti}_{0.47})\text{O}_3$	7.29	942	1094	0.3	0.50	103	10.6	7.94	
$\text{Pb}_{0.90}\text{Sr}_{0.10}(\text{Zr}_{0.53}\text{Ti}_{0.47})\text{O}_3$	7.22	997	1129	0.3	0.49	103	10.3	7.95	290
$\text{Pb}_{0.875}\text{Sr}_{0.125}(\text{Zr}_{0.47}\text{Ti}_{0.53})\text{O}_3$	7.09	609	663	0.3	0.28	40	6.8	9.91	
$\text{Pb}_{0.875}\text{Sr}_{0.125}(\text{Zr}_{0.50}\text{Ti}_{0.50})\text{O}_3$	7.11	813	880	0.3	0.33	57	7.3	9.05	
$\text{Pb}_{0.875}\text{Sr}_{0.125}(\text{Zr}_{0.52}\text{Ti}_{0.48})\text{O}_3$	7.10	973	1149	0.3	0.44	91	9.0	8.32	
$\text{Pb}_{0.875}\text{Sr}_{0.125}(\text{Zr}_{0.53}\text{Ti}_{0.47})\text{O}_3$	7.14	1076	1237	0.4	0.47	100	9.1	8.06	265
$\text{Pb}_{0.875}\text{Sr}_{0.125}(\text{Zr}_{0.54}\text{Ti}_{0.46})\text{O}_3$	7.16	1095	1325	0.6	0.51	119	10.1	7.51	
$\text{Pb}_{0.875}\text{Sr}_{0.125}(\text{Zr}_{0.56}\text{Ti}_{0.44})\text{O}_3$	7.14	1105	1210	0.4	0.51	116	10.8	7.31	
$\text{Pb}_{0.875}\text{Sr}_{0.125}(\text{Zr}_{0.59}\text{Ti}_{0.41})\text{O}_3$	7.17	919	585	0.4	0.45	66	12.7	8.39	
$\text{Pb}_{0.85}\text{Sr}_{0.15}(\text{Zr}_{0.53}\text{Ti}_{0.47})\text{O}_3$	6.90	1106	1260	0.5	0.43	97	8.7	7.68	242
$\text{Pb}_{0.80}\text{Sr}_{0.20}(\text{Zr}_{0.50}\text{Ti}_{0.50})\text{O}_3$	6.56	941	970	0.6	0.29	56	6.5	8.11	
$\text{Pb}_{0.80}\text{Sr}_{0.20}(\text{Zr}_{0.53}\text{Ti}_{0.47})\text{O}_3$	6.48	1212	1257	0.5	0.34	86	7.8	7.05	
$\text{Pb}_{0.80}\text{Sr}_{0.20}(\text{Zr}_{0.54}\text{Ti}_{0.46})\text{O}_3$	6.36	1182	1341	0.8	0.35	91	7.7	6.18	
$\text{Pb}_{0.80}\text{Sr}_{0.20}(\text{Zr}_{0.55}\text{Ti}_{0.45})\text{O}_3$	6.36	1200	1337	0.8	0.34	86	7.3	6.42	
$\text{Pb}_{0.80}\text{Sr}_{0.20}(\text{Zr}_{0.56}\text{Ti}_{0.44})\text{O}_3$	6.35	1107	1113	0.7	0.35	81	8.2	6.50	

Tab. 69. $\text{Pb}(\text{Zr-Ti})\text{O}_3$ (ceramics, modified). Electromechanical properties of $\text{Pb}(\text{Zr}_{0.54}\text{Ti}_{0.46})\text{O}_3$ with five-valent additives. [59K5]. $f_R \cdot r$: radial frequency constant

Addition wt. %	ϵ_a 10^3 kgm^{-3}	Before poling		24 hours after poling						Θ_f $^{\circ}\text{C}$
		κ at 1 kHz	$\tan \delta$ % at 1 kHz	κ at 1 kHz	$\tan \delta$ % at 1 kHz	k_p	$f_R \cdot r$ $\text{Hz} \cdot \text{m}$	d_{31} 10^{-12} CN^{-1}	Q_{mech}	
None	7.41	707	0.3	537	0.4	0.49	1641	71		390
None	7.29	706	0.4	513	0.5	0.50	1687	69		387
0.1 Nb_2O_5	7.26	598	0.3	508	0.4	0.38	1643	54		
0.5 Nb_2O_5	6.96	732	2.1	790	2.0	0.46	1443	94		
0.8 Nb_2O_5	7.36	965	1.6	1166	1.5	0.48	1606	105		
1.0 Nb_2O_5	7.36	1064	1.8	1308	1.6	0.53	1563	126	61	
1.0 Nb_2O_5	7.60	1055	2.2	1242	2.2	0.54	1538	125		361
1.2 Nb_2O_5	7.34	1011	2.0	1167	1.7	0.48	1614	104	70	
1.4 Nb_2O_5	7.37	1057	2.2	1218	1.9	0.50	1584	113	69	
1.7 Nb_2O_5	7.39	1058	2.0	1218	1.8	0.47	1594	105		
2.0 Nb_2O_5	7.37	1074	2.1	1202	2.0	0.50	1550	115		344
0.5 Nb_2O_5 } 0.5 La_2O_3 }	7.39	1169	2.1	1377	2.0	0.57	1491	146	48	369
1.0 Ta_2O_5	7.31	989	1.5	1187	1.5	0.49	1563	111	61	
1.0 Ta_2O_5	7.22	918	2.0	1121	2.1	0.50	1525	114		368
2.0 Ta_2O_5	7.49	1062	2.2	1230	2.1	0.50	1547	115		
2.0 Ta_2O_5	7.40	1077	1.8	1275	1.8	0.48	1581	111		364
2.5 Ta_2O_5	7.23	959	2.7	1112	2.4	0.36	1518	82	28	
5.0 Ta_2O_5	6.75	995	2.5	1052	2.6	0.33	1508	76		

Tab. 70. $\text{Pb}(\text{Zr-Ti})\text{O}_3$ (ceramics, modified). Electromechanical properties of $\text{Pb}(\text{Zr}_{0.54}\text{Ti}_{0.46})\text{O}_3$ with three-valent additives. [59K5]. $f_R \cdot r$: radial frequency constant

Addition wt. %	ϵ_a 10^3 kgm^{-3}	Before poling		24 hours after poling					Θ_f $^\circ\text{C}$
		κ at 1 kHz	$\tan \delta$ % at 1 kHz	κ at 1 kHz	$\tan \delta$ % at 1 kHz	k_p	$f_R \cdot r$ $\text{Hz} \cdot \text{m}$	d_{31} 10^{-12} CN^{-1}	
None	7.41	707	0.3	537	0.4	0.49	1641	71	390
None	7.29	706	0.4	513	0.5	0.50	1687	69	387
1.0 Y_2O_3	7.26	796	0.9	841	1.0	0.34	1547	66	374
1.0 La_2O_3	7.46	1187	1.9	1483	2.0	0.53	1510	138	
1.0 La_2O_3	7.47	1139	2.2	1387	2.1	0.52	1522	130	339
1.0 Nd_2O_3	7.43	1111	1.6	1395	1.8	0.49	1512	123	
1.0 Nd_2O_3	7.37	1101	1.9	1354	1.8	0.48	1511	119	348
1.0 didymia	7.41	1122	2.2	1341	2.2	0.50	1499	125	
2.0 La_2O_3	7.49	1296	2.6	1545	2.3	0.51	1545	132	
1.0 La_2O_3	7.20	1375	2.1	1792	1.7	0.51	1528	147	
1.0 Nd_2O_3	7.35	1362	2.2	1776	1.9	0.49	1558	136	
0.1 La_2O_3	6.75	790	0.4	870	0.6	0.42	1505	88	
0.2 La_2O_3	6.45	686	0.7	735	0.9	0.37	1419	78	
0.4 La_2O_3	6.44	942	1.4	1100	1.5	0.42	1407	109	
0.8 La_2O_3	7.19	1288	1.8	1682	1.8	0.49	1516	139	
1.0 La_2O_3	7.50	1255	2.4	1532	2.4	0.50	1550	128	

Tab. 71. Electromechanical properties of $\text{Pb}(\text{Zr}_{1-x}\text{Ti}_x)\text{O}_3$ (ceramics), modified with additives of 1 wt% Nb. [59K5]. $f_R \cdot r$: radial frequency constant

Base composition	ϵ_a 10^3 kgm^{-3}	Before poling		24 hours after poling					
		κ at 1 kHz	$\tan \delta$ % at 1 kHz	κ at 1 kHz	$\tan \delta$ % at 1 kHz	k_p	$f_R \cdot r$ $\text{Hz} \cdot \text{m}$	d_{31} 10^{-12} CN^{-1}	Q_{mech}
$\text{Pb}(\text{Zr}_{0.50}\text{Ti}_{0.50})\text{O}_3$	7.38	879	1.5	1041	1.2	0.42	1696	82	81
$\text{Pb}(\text{Zr}_{0.51}\text{Ti}_{0.49})\text{O}_3$	7.31	975	1.6	1188	1.3	0.45	1642	97	73
$\text{Pb}(\text{Zr}_{0.52}\text{Ti}_{0.48})\text{O}_3$	7.39	985	1.5	1200	1.4	0.45	1640	97	76
$\text{Pb}(\text{Zr}_{0.53}\text{Ti}_{0.47})\text{O}_3$	7.43	1092	1.8	1371	1.4	0.53	1547	130	61
$\text{Pb}(\text{Zr}_{0.54}\text{Ti}_{0.46})\text{O}_3$	7.44	1051	1.8	1296	1.7	0.54	1549	128	62
$\text{Pb}(\text{Zr}_{0.55}\text{Ti}_{0.45})\text{O}_3$	7.40	955	2.4	973	2.0	0.56	1524	117	55
$\text{Pb}(\text{Zr}_{0.56}\text{Ti}_{0.44})\text{O}_3$	7.38	818	2.8	745	2.5	0.53	1601	93	56
$\text{Pb}(\text{Zr}_{0.57}\text{Ti}_{0.43})\text{O}_3$	7.41	750	3.0	684	2.5	0.50	1636	82	60
$\text{Pb}(\text{Zr}_{0.58}\text{Ti}_{0.42})\text{O}_3$	7.41	713	3.0	630	2.8	0.49	1676	75	62

Tab. 72. Electromechanical properties of $(\text{Pb}_{0.95}\text{Sr}_{0.05})(\text{Zr}_{0.54}\text{Ti}_{0.46})\text{O}_3$ (ceramics) with Nb_2O_5 or Ta_2O_5 . [59K5]. $f_R \cdot r$: radial frequency constant

Addition wt. %	ϵ_a 10^3 kgm^{-3}	Before poling		24 hours after poling					Θ_f $^\circ\text{C}$
		κ at 1 kHz	$\tan \delta$ % at 1 kHz	κ at 1 kHz	$\tan \delta$ % at 1 kHz	k_p	$f_R \cdot r$ $\text{Hz} \cdot \text{m}$	d_{31} 10^{-12} CN^{-1}	
1.0 Nb_2O_5	7.34	1291	2.0	1609	2.0	0.56	1512	153	306
2.0 Nb_2O_5	7.22	1380	2.4	1662	2.1	0.47	1562	127	
3.0 Nb_2O_5	6.63	1125	2.1	1301	2.1	0.36	1550	91	
2.0 Ta_2O_5	7.33	1343	2.3	1695	2.0	0.54	1517	151	296

Tab. 73. PZT (commercial modified ceramics). Electromechanical constants at RT. [666]

Substance	κ_{11}^T	κ_{11}^S	κ_{33}^T	κ_{33}^S	$10^{-12} \text{ C N}^{-1}$			C m^{-2}			$10^{-3} \text{ m}^2 \text{ C}^{-1}$			h_{15}	10^9 NC^{-1}				
					d_{15}	d_{31}	d_{33}	e_{15}	e_{31}	e_{33}	g_{15}	g_{31}	g_{33}						
PZT-2	990	504	450	260	440	60.2	152	9.8	1.86	9.0	50.3	15.1	38.1	21.9					
PZT-4	1475	730	1300	635	496	123	289	12.7	5.2	15.1	39.4	11.1	26.1	19.7					
PZT-5A	1730	916	1700	830	584	171	374	12.3	5.4	15.8	38.2	11.4	24.8	15.2					
PZT-5H	3130	1700	3400	1470	741	274	593	17.0	6.55	23.3	26.8	7.9	19.7	11.3					
PZT-6A			1100			77	195						17.0						
PZT-6B	515	441	500	420	135	29	76	4.8	0.96	7.4	29.6	6.6	17.3	12.2					
PZT-7A	840	450	425	235	368	61	153	9.3	2.15	9.7	49.5	16.2	40.7	23.4					
PZT-8			1000			95	215					10.5	24.5						
	h_{31}	h_{33}	k_{15}	k_{33}	k_{31}	k_p	$10^{-12} \text{ m}^2 \text{ N}^{-1}$												
							s_{11}^E	s_{12}^E	s_{13}^E	s_{22}^E	s_{23}^E	s_{33}^E	s_{11}^D	s_{12}^D	s_{13}^D	s_{33}^D			
PZT-2	—	8.1	39.2	0.701	0.28	0.626	0.47	11.6	10.7	14.8	9.0	3.33	—4.24	—4.97	—2.68				
PZT-4	—	9.2	26.8	0.71	0.334	0.70	0.58	12.3	10.9	15.5	7.90	4.05	—5.42	—5.31	—2.10				
PZT-5A	—	7.3	21.5	0.685	0.344	0.705	0.60	16.4	14.4	18.8	9.46	5.74	—7.71	—7.22	—2.98				
PZT-5H	—	5.05	18.0	0.675	0.388	0.752	0.65	16.5	14.05	20.7	8.99	4.78	—7.27	—8.45	—3.05				
PZT-6A					0.229	0.54	0.39	11.5	10.9	9.35	8.05	3.45	—4.05	—3.1	—2.6				
PZT-6B	—	2.6	19.9	0.377	0.145	0.375	0.25	9.0	8.8	13.9	7.65	3.0	—3.2	—4.6	—2.3				
PZT-7A	—	10.4	46.6	0.68	0.306	0.67	0.52	10.7	9.7										
PZT-8					0.295	0.60	0.50	11.1	10.1	13.9	8.9								
	s_{44}^E	s_{44}^D	s_{66}	$10^{-12} \text{ m}^2 \text{ N}^{-1}$										c_{44}^E	c_{44}^D	c_{66}			
				$10^{-12} \text{ m}^2 \text{ N}^{-1}$															
PZT-2	45.0	22.9	29.9	135	136	113	148	67.9	69.3	68.1	61.2	22.2	43.7	33.4					
PZT-4	39.0	19.3	32.7	139	145	115	159	77.8	83.9	74.3	60.9	25.6	51.8	30.6					
PZT-5A	47.5	25.2	44.3	121	126	111	147	75.4	80.9	75.2	65.2	21.1	39.7	22.6					
PZT-5H	43.5	23.7	42.6	126	130	117	157	79.5	82.8	84.1	72.2	23.0	42.2	23.5					
PZT-6A			29.9																
PZT-6B	28.2	24.2	24.0	168	169	163	177	85.1	86.2	84.0	82.4	35.4	41.3	41.7					
PZT-7A	39.5	21.2	27.8	148	157	131	175	76.2	85.4	74.2	73.0	25.3	47.2	36.0					
PZT-8			29.6																

r Ta₂O₅

% Nb.

Q_{mech}

ith

θ_r
°C90
187
174

339

348

306

296

Nr. 1C-a29 $\text{PbTiO}_3\text{-PbHfO}_3$	1b	Phase diagram: Fig. 555, 556
Nr. 1C-a30 $\text{PbTiO}_3\text{-PbO:SnO}_2$	1b	Phase diagram: Fig. 557.
	5a	Dielectric constant: Fig. 558.
Nr. 1C-a31 $\text{PbZrO}_3\text{-PbHfO}_3$	1b	Phase diagram: Fig. 559.
Nr. 1C-a32 $\text{PbZrO}_3\text{-PbO:SnO}_2$	1b	Phase diagram: Fig. 560. Lattice parameter: Fig. 561.
	4	Thermal expansion: Fig. 562, 563.
	5a	Dielectric constant: Fig. 564a, b.
Nr. 1C-a33 $\text{LaFeO}_3\text{-BiFeO}_3$	1b	Phase diagram: Fig. 565. Lattice parameter: Fig. 566a, b.
	5a	Dielectric constant: Fig. 567.
	11	Magnetization: see Fig. 565.
Nr. 1C-b1 $\text{NaNbO}_3\text{-KTaO}_3$	1b	Phase diagram: Fig. 568. Lattice parameter: Fig. 569.
	4	Thermal expansion: Fig. 570.
	5a	Dielectric constant: Fig. 571.
Nr. 1C-b2 $\text{NaNbO}_3\text{-KSbO}_3$	1a	Curie temperature: see Fig. 423.
Nr. 1C-b3 $\text{BaTiO}_3\text{-PbZrO}_3$	4	Thermal expansion: Fig. 572.
	5a	Dielectric constant: Fig. 573.
Nr. 1C-b4 $\text{BaTiO}_3\text{-PbO:SnO}_2$	1b	Phase diagram: Fig. 574.
	5a	Dielectric constant: Fig. 575.
Nr. 1C-b5 $\text{PbTiO}_3\text{-CaZrO}_3$	1b	Phase diagram: Fig. 576. Lattice parameter: Fig. 577.
	5a	Dielectric constant: Fig. 578.
Nr. 1C-b6 $\text{PbTiO}_3\text{-CaSnO}_3$	1b	Phase diagram: see Fig. 576. Lattice parameter: Fig. 579.
	5a	Dielectric constant: Fig. 580.
Nr. 1C-b7 $\text{PbTiO}_3\text{-SrZrO}_3$	1b	Phase diagram: Fig. 581. Lattice parameter: Fig. 582a, b.
	5a	Dielectric constant: Fig. 583.
Nr. 1C-b8 $\text{PbTiO}_3\text{-SrSnO}_3$	1b	Phase diagram: Fig. 584. Lattice parameter: Fig. 585a, b.
	5a	Dielectric constant: Fig. 586.
Nr. 1C-b9 $\text{PbTiO}_3\text{-BaZrO}_3$	1b	Phase diagram: Fig. 587. Lattice parameter: Fig. 588a, b.
	5a	Dielectric constant: Fig. 589.
	7a	Electromechanical property: Tab. 74.

Tab. 74. $(1-x)\text{PbTiO}_3 - x\text{BaZrO}_3$ (ceramics). k_p and d_{33} at RT. [63B15]

x	Poling field $\cdot 10^5 \text{ V m}^{-1}$ [T in $^\circ\text{C}$]	k_p	d_{33} $\cdot 10^{-12} \text{ C N}^{-1}$
0.25	29 [185 ... 40]	0.16	40
0.30	27 [170 ... 40]	0.23	50
0.35	39 [145 ... 40]	0.30	110
0.40	30 [120 ... 40]	0.17	45

Nr. 1C-b10 $\text{PbTiO}_3\text{-BaSnO}_3$	1b Phase diagram: Fig. 590. Lattice parameter: Fig. 591a, b.
Nr. 1C-b11 $\text{LaAlO}_3\text{-BiFeO}_3$	1b Phase diagram: Fig. 592. Lattice parameter: Fig. 593. 5a Dielectric constant: Fig. 594.
Nr. 1C-b12 $\text{LaCrO}_3\text{-BiFeO}_3$	1b Phase diagram: Fig. 595. Lattice parameter: Fig. 596a, b. 4 Thermal expansion: Fig. 597. 11 Spontaneous magnetization: see Fig. 595.
Nr. 1C-c1 $\text{NaNbO}_3\text{-CaTiO}_3$	1b Phase diagram: Fig. 598. 5a Dielectric constant: Fig. 599.
Nr. 1C-c2 $\text{NaNbO}_3\text{-BaTiO}_3$	1b Phase diagram: Fig. 600.
Nr. 1C-c3 $\text{NaNbO}_3\text{-PbTiO}_3$	1b Transition temperature: Fig. 601. 5a Dielectric constant: Fig. 602.
Nr. 1C-c4 $\text{NaNbO}_3\text{-PbZrO}_3$	1b Phase diagram: Fig. 603. 5a Dielectric constant: Fig. 604a, b.
Nr. 1C-c5 $\text{KNbO}_3\text{-BaTiO}_3$	1b Phase diagram: Fig. 605. Lattice parameter: Fig. 606. 5a Dielectric constant: Fig. 607a, b, c.
Nr. 1C-c6 $\text{KNbO}_3\text{-PbTiO}_3$	1b Phase diagram: Fig. 608. Lattice parameter: Fig. 609. 5a Dielectric constant: Fig. 610a, b.
Nr. 1C-c7 $\text{SrTiO}_3\text{-BiFeO}_3$	1b Phase diagram: Fig. 611. Lattice parameter: Fig. 612. 5a Relaxation phenomena are observed in the range II [65F1].
Nr. 1C-c8 $\text{BaTiO}_3\text{-LaAlO}_3$	1b Lattice parameter and Curie temperature: Tab. 75.

Tab. 75. $\text{BaTiO}_3\text{-LaAlO}_3$. Lattice parameters and Θ_f . [5814]

Concentration mol%		a Å	c Å	c/a	V Å ³	Θ_f °C
BaTiO_3	LaAlO_3					
100.0	—	3.9956	4.0352	1.0100	64.42	+120
99.0	1.0	3.9951	4.0345	1.0098	64.39	+ 87
97.5	2.5	3.9949	4.0293	1.0086	64.30	+ 46
95.0	5.0	4.0050	—	1.0000	64.24	— 14
92.5	7.5	4.0011	—	1.0000	64.05	— 85
90.0	10.0	3.9984	—	1.0000	63.92	—133
87.5	12.5	3.9950	—	1.0000	63.76	—
85.0	15.0	3.9906	—	1.0000	63.55	—
75.0	25.0	3.9800	—	1.0000	63.04	—
—	100.0	3.7950	—	1.000	54.65	—

Nr. 1C-c9 $\text{BaTiO}_3\text{-BiFeO}_3$	11, 12	Néel temperature and magnetic resonance line width: Fig. 613.
Nr. 1C-c10 $\text{PbTiO}_3\text{-LaAlO}_3$	1b, 5a	Phase diagram: Fig. 614. Lattice parameter: Fig. 615. Dielectric constant: Fig. 616.
Nr. 1C-c11 $\text{PbTiO}_3\text{-LaMnO}_3$	1b	Transition temperatures: Fig. 617. Lattice parameters: Fig. 618.
Nr. 1C-c12 $\text{PbTiO}_3\text{-LaFeO}_3$	1b, 5a	Phase diagram: Fig. 619. Lattice parameter: Fig. 620. Dielectric constant: Fig. 621.
Nr. 1C-c13 $\text{PbTiO}_3\text{-BiFeO}_3$	1b, 4, 5a	Phase diagram: Fig. 622a, b. Lattice parameter: Fig. 623a, b. Thermal expansion: Fig. 624. Dielectric constant: Fig. 625.
Nr. 1C-c14 $\text{PbZrO}_3\text{-BiFeO}_3$	1b, 5a	Phase diagram: Fig. 626. Lattice parameter: Fig. 627. Dielectric constant: Fig. 628.
Nr. 1C-c15 $\text{SrSnO}_3\text{-BiFeO}_3$	1b, 12c	Phase diagram: Fig. 629. Mössbauer absorption: Fig. 630.
Nr. 1C-c16 $\text{SrFeO}_3\text{-BiFeO}_3$	1a, 11	Unit cell volume: Fig. 631. Magnetization: Fig. 632.
Nr. 1C-d1 $\text{SrTiO}_3\text{-Sr}(\text{Fe}_{1/2}\text{Ta}_{1/2})\text{O}_3$	1b	Phase diagram: Fig. 633.
Nr. 1C-d2 $\text{BaTiO}_3\text{-Ba}(\text{Fe}_{1/2}\text{Ta}_{1/2})\text{O}_3$	2b	Phase diagram: Fig. 634.
Nr. 1C-d3 $\text{BaTiO}_3\text{-(K}_{1/2}\text{Bi}_{1/2})\text{TiO}_3$	1b	Curie temperature: Fig. 635. Lattice parameters: Fig. 636.
Nr. 1C-d4 $\text{PbTiO}_3\text{-(Na}_{1/2}\text{Bi}_{1/2})\text{TiO}_3$	1b, 5a	Phase diagram and lattice parameters: Fig. 637. Dielectric constant: Fig. 638.
Nr. 1C-d5 $\text{PbTiO}_3\text{-(K}_{1/2}\text{Bi}_{1/2})\text{TiO}_3$	1b	Curie temperature and lattice parameters: Fig. 639.
Nr. 1C-d6 $\text{PbTiO}_3\text{-(Li}_{1/2}\text{La}_{1/2})\text{TiO}_3$	1b	Curie temperature and lattice parameters: Fig. 640.

Nr. 1C-d7 $\text{PbTiO}_3\text{-(Na}_{1/2}\text{La}_{1/2})\text{TiO}_3$	1b Curie temperature and lattice parameters: Fig. 641.																																		
Nr. 1C-d8 $\text{PbTiO}_3\text{-(Li}_{1/2}\text{Ce}_{1/2})\text{TiO}_3$	1b Lattice parameters: Fig. 642.																																		
Nr. 1C-d9 $\text{PbTiO}_3\text{-(Li}_{1/2}\text{Nd}_{1/2})\text{TiO}_3$	1b Lattice parameters: Fig. 643.																																		
Nr. 1C-d10 $\text{PbTiO}_3\text{-Pb(Mg}_{1/2}\text{W}_{1/2})\text{O}_3$	1b Phase diagram: Fig. 644. Lattice parameters: Fig. 645.																																		
Nr. 1C-d11 $\text{PbTiO}_3\text{-Pb(Fe}_{1/2}\text{Ta}_{1/2})\text{O}_3$	1b Curie temperature: Fig. 646.																																		
Nr. 1C-d12 $\text{PbTiO}_3\text{-Pb(Sc}_{1/2}\text{Nb}_{1/2})\text{O}_3$	1b Curie temperature: Fig. 647.																																		
Nr. 1C-d13 $\text{PbTiO}_3\text{-Pb(Mn}_{1/2}\text{Nb}_{1/2})\text{O}_3$	1b Transition temperature: Fig. 648. Lattice parameters: Fig. 649.																																		
Nr. 1C-d14 $\text{PbZrO}_3\text{-Pb(Sc}_{1/2}\text{Nb}_{1/2})\text{O}_3$	1b Curie temperature: see Fig. 647.																																		
Nr. 1C-d15 $\text{PbZrO}_3\text{-Pb(Fe}_{1/2}\text{Ta}_{1/2})\text{O}_3$	1b Curie temperature: Fig. 650.																																		
Nr. 1C-d16 $\text{PbZrO}_3\text{-(Na}_{1/2}\text{Bi}_{1/2})\text{ZrO}_3$	1b Phase diagram: Fig. 651.																																		
	4 Lattice distortion: Fig. 652.																																		
	5a Dielectric constant: Fig. 653.																																		
Nr. 1C-d17 $\text{PbZrO}_3\text{-(K}_{1/2}\text{Bi}_{1/2})\text{ZrO}_3$	1b Phase diagram: Fig. 654. Lattice parameters: Tab. 76.																																		
	4 Lattice distortion: Fig. 655.																																		
	5a Dielectric constants: Fig. 656.																																		
Tab. 76. $(1-x)\text{PbZrO}_3 - x(\text{K}_{1/2}\text{Bi}_{1/2})\text{ZrO}_3$. Lattice constants at RT [62B10]																																			
x	<table><tr><th>a Å</th><th>b Å</th><th>c Å</th><th></th></tr><tr><td>0</td><td>5.884</td><td>11.768</td><td>8.220</td><td>orthorhombic</td></tr><tr><td>0.10</td><td>5.882</td><td>11.764</td><td>8.227</td><td>orthorhombic</td></tr><tr><td>0.20</td><td>5.877</td><td>11.755</td><td>8.237</td><td>orthorhombic</td></tr><tr><td>0.30</td><td>5.876</td><td>11.751</td><td>8.248</td><td>orthorhombic</td></tr><tr><td>0.40</td><td>4.151</td><td>—</td><td>—</td><td>cubic</td></tr><tr><td>0.50</td><td>4.152</td><td>—</td><td>—</td><td>cubic</td></tr></table>	a Å	b Å	c Å		0	5.884	11.768	8.220	orthorhombic	0.10	5.882	11.764	8.227	orthorhombic	0.20	5.877	11.755	8.237	orthorhombic	0.30	5.876	11.751	8.248	orthorhombic	0.40	4.151	—	—	cubic	0.50	4.152	—	—	cubic
a Å	b Å	c Å																																	
0	5.884	11.768	8.220	orthorhombic																															
0.10	5.882	11.764	8.227	orthorhombic																															
0.20	5.877	11.755	8.237	orthorhombic																															
0.30	5.876	11.751	8.248	orthorhombic																															
0.40	4.151	—	—	cubic																															
0.50	4.152	—	—	cubic																															
Nr. 1C-d18 $\text{PbHfO}_3\text{-Pb(Sc}_{1/2}\text{Nb}_{1/2})\text{O}_3$	1b Curie temperature: see Fig. 647.																																		
Nr. 1C-d19 $\text{Pb(Mg}_{1/2}\text{W}_{1/2})\text{O}_3\text{-Pb(Mg}_{1/3}\text{Nb}_{2/3})\text{O}_3$	1b Phase diagram: Fig. 657.																																		
Nr. 1C-d20 $(\text{Na}_{1/2}\text{Bi}_{1/2})\text{TiO}_3\text{-(K}_{1/2}\text{Bi}_{1/2})\text{TiO}_3$	1b Curie temperature: see Fig. 635. Lattice parameters: see Fig. 636.																																		
Nr. 1C-d21 $\text{PbZrO}_3\text{-(Na}_{1/2}\text{Bi}_{1/2})\text{TiO}_3$	1b Phase diagram: Fig. 658. Lattice parameters: Fig. 659.																																		
Nr. 1C-d22 $\text{BiFeO}_3\text{-Sr(Sn}_{1/3}\text{Mn}_{2/3})\text{O}_3$	1b Phase diagram: Fig. 660. Lattice parameters: Fig. 661.																																		
	12c Mössbauer effect: see [65M8]																																		
Nr. 1C-d23 $\text{BiFeO}_3\text{-Pb(Fe}_{1/2}\text{Nb}_{1/2})\text{O}_3$	1b Lattice parameters: Fig. 662.																																		
	5a Dielectric constant: Fig. 663.																																		
	11 Magnetic susceptibility: Fig. 664. Néel temperature and spontaneous magnetization: Fig. 665.																																		

Nr. 1C-e1 NaNbO₃-LiNbO₃

1b | Phase diagram: Fig. 666.
5a | Dielectric constant: Fig. 667.

Nr. 1C-e2 NaNbO₃-NaVO₃

5a | Dielectric constant: Fig. 668.
14b | Switching: see Fig. 9.

Nr. 1C-e3 NaNbO₃-CaNb₂O₆

1b | Phase diagram: Fig. 669.
5a | Dielectric constant: Fig. 670.

Nr. 1C-e4 NaNbO₃-CdNb₂O₆

1b | Phase diagram: Fig. 671, 672.
Lattice parameter: Fig. 673.
5a | Dielectric constant: Fig. 674; Tab. 77.
7a | Piezoelectricity: Fig. 675; Tab. 78.

Tab. 77. $(1-x)\text{NaNbO}_3 - (x/2)\text{CdNb}_2\text{O}_6$ [56L2]. r : capacitance ratio; C : Curie constant; Θ_r , Θ compare Fig. 671, 672

Composition x	Firing conditions			x_{RT}	r	Θ °C	x_{max}	Θ_r °C	C $\cdot 10^4$ °C	Θ_p °C	g 10^3 kg m^{-3}
	T °C	t hr	atmos- phere								
0.02	1250	1	CdO	230	—	200	2700	375	12	345	3.9
0.05	1250	1	CdO	500	1200	60	4000	375	12	345	4.2
0.10	1250	1	CdO	1000	130	75	4100	320	18	275	4.3
0.15	1250	1	CdO	1400	40	50	8500	285	24	260	4.3
0.20	1250	1	CdO	2300	20	20	10000	250	14	250	4.4
0.25	1250	1	CdO	3500	10	5	15000	220	20	230	4.5
0.30	1220	2	CdO	2700	12	-25	11000	210	20	205	4.6

Tab. 78. $(1-x)\text{NaNbO}_3 - (x/2)\text{CdNb}_2\text{O}_6$ (ceramics) [62K4]

x	0.05	0.10	0.15	0.20	0.25	0.30	
g	4.2	4.3	4.3	4.3	4.4	4.2	10^3 kg m^{-3}
$f_R \cdot 2r$	3.0	3.0	3.0	3.15	3.36	3.25	10^3 Hz m
s_{11}^E	11.9	11.6	11.6	10.5	9.0	10.1	$10^{-12} \text{ m}^2 \text{ N}^{-1}$
$\tan \delta$	0.01	0.01	0.02	0.01	0.01	0.03	
x at Θ_r	4	4.1	8.5	16	13	11	10^3

Nr. 1C-e5 NaNbO₃-SrNb₂O₆

1b | Phase diagram: Fig. 676.
Lattice parameter: Fig. 677.
5a | Dielectric constant: Fig. 678.
7a | Electromechanical properties: Fig. 679, 680, 681.

Nr. 1C-e6 NaNbO₃-PbNb₂O₆

1b | Phase diagram: Fig. 682.
Lattice parameter: Fig. 683.
7a | Electromechanical properties: Fig. 684.

Nr. 1C-e7 CdTiO₃-LiNbO₃, CdTiO₃-LiTaO₃

5a | Dielectric constant: Fig. 685.

Nr. 1C-e8 SrTiO₃-Bi₂O₃ · 3TiO₂

1b | Lattice parameter: Fig. 686.
5a | Dielectric constant: Fig. 687, 688.

Nr. 1C-e9 BaTiO₃-BaNb₂O₆

1b | Phase diagram: Fig. 689.

Nr. 1C-e10 BaTiO ₃ -BaTa ₂ O ₆	1b	Lattice parameter: Fig. 690.
	5a	Dielectric constant: Fig. 691.
Nr. 1C-e11 BaTiO ₃ -A ₂ B ₂ O ₇	1b	Curie temperature: Fig. 692.
	5a	Dielectric constant: Fig. 693 ... 697.
Nr. 1C-e12 PbZrO ₃ -PbNb ₂ O ₆		
For the solid solution with PbNb ₂ O ₆ as an end material see 5B-8.		
	1b	Phase diagram: Fig. 698.
	4	Thermal expansion: Fig. 699.
	5	Dielectric constant: Fig. 700.
Nr. 1C-e13 PbZrO ₃ -PbTa ₂ O ₆	1b	Phase diagram: Fig. 701.
	4	Thermal expansion: see Fig. 699.
	5	Dielectric constant: Fig. 702.
Nr. 1C-f1 CaTiO ₃ -SrTiO ₃ -BaTiO ₃	1b	Phase diagram: Fig. 703.
Nr. 1C-f2 CaTiO ₃ -BaTiO ₃ -PbTiO ₃	1b	Phase diagram: Fig. 704, 705. Curie temperature: Fig. 706.
	7a	Electromechanical properties: see Nr. 1A-8, 7a.
Nr. 1C-f3 PbTiO ₃ -PbZrO ₃ -PbO:SnO ₂	1b	Phase diagram: Fig. 707.
	8b	Elastic properties: Fig. 708, 709.
Nr. 1C-f4 PbTiO ₃ -PbHfO ₃ -PbO:SnO ₂	1b	Phase diagram: Fig. 710.
Nr. 1C-f5 PbTiO ₃ -PbZrO ₃ -LaFeO ₃	1b	Phase diagram: Fig. 711. Lattice parameters: Fig. 712.
	1b	Phase diagram: Fig. 713. Lattice parameters: Fig. 714.
Nr. 1C-f6 PbTiO ₃ -PbZrO ₃ -BiFeO ₃	1b	Phase diagram: Fig. 713. Lattice parameters: Fig. 714.
	1b	Phase diagram: Fig. 715. Lattice parameters: Fig. 716.
Nr. 1C-f7 PbTiO ₃ -PbZrO ₃ -Pb(Mg _{1/3} Nb _{2/3})O ₃	1b	Phase diagram: Fig. 715. Lattice parameters: Fig. 716.
	7a	Electromechanical property: Fig. 717, 718.
Nr. 1C-f8 PbTiO ₃ -PbZrO ₃ -Pb(Fe _{1/2} Nb _{1/2})O ₃	1b	Lattice parameters: Fig. 719. Curie temperature: Fig. 720.
	7a	Electromechanical property: Fig. 721.
Nr. 1C-f9 PbTiO ₃ -PbZrO ₃ -ABO ₃	1b	Phase diagram: Fig. 722.
Nr. 1C-f10 PbTiO ₃ -SrTiO ₃ -LaMnO ₃	1b	Curie temperature: Fig. 723.
Nr. 1C-f11 PbTiO ₃ -LaMnO ₃ -LaMeO ₃ (Me = Fe, Co, Ni, Cr)		
	1b	Transition temperatures: Fig. 724.
	5a	Dielectric constant: Fig. 725.
	11	Magnetic susceptibility: see Fig. 725. Magnetization: Fig. 726.

Nr. 1C-f12 BaTiO ₃ -SrTiO ₃ -LaYO ₃ -LaInO ₃	1b Phase diagram: Fig. 727.
Nr. 1C-f13 CaSnO ₃ -SrSnO ₃ -BaSnO ₃	1b Phase diagram: Fig. 728.
Nr. 1C-f14 (Na-K)(Nb-Ta)O ₃	1b Phase diagram: Fig. 729.
Nr. 1C-f15 (Ca-Ba)(Ti-Zr)O ₃	1b Phase diagram: Fig. 730.
Nr. 1C-f16 (Sr-Pb)(Ti-Zr)O ₃	1b Phase diagram: Fig. 731. Lattice parameter: Fig. 732. Transition temperature: Fig. 733.
	5a Dielectric constant: Fig. 734, 735.
Nr. 1C-f17 (Ba-Pb)(Ti-Zr)O ₃	1b Phase diagram: Fig. 736. Lattice parameter: Fig. 737. Transition temperature: Fig. 738.
	7a Electromechanical properties: Fig. 739, 740.
Nr. 1C-f18 (Ba-Pb)(Ti-Sn)O ₃	1b Phase diagram: Fig. 741, 742. Lattice parameter: Fig. 743. Transition temperature: Fig. 744.
Nr. 1C-f19 BaTiO ₃ -PbTiO ₃ -BaNb ₂ O ₆ -PbNb ₂ O ₆	1b Phase diagram: Fig. 745. Lattice parameter: Fig. 746.

2 WO₃

2A Pure compound

Nr. 2A-1 WO₃, Tungsten trioxide

1a	The anomalous dielectric properties of ceramic specimens of WO ₃ were discovered by OGAWA ^{a)} in 1948. Possibility of ferroelectricity in WO ₃ was pointed out by MATTHIAS ^{b)} in 1949.								a)48N1,48N2 b)49M2 c)49M2 d)60T1 e)60T2 f)52K1 g)56S1
b	phase	VII	VI	V	IV	III	II	I	
	state	F ^{a)}							
	crystal system	mono-clinic ^{b)}	tri-clinic ^{b)}	mono-clinic ^{c)}	ortho-rhombic ^{b)}	tetra-gonal ^{d)}	tetra-gonal ^{b)}	tetra-gonal ^{b)}	
	space group			P2 ₁ /n ^{e)} -C _{2h} ⁵		P4/nmm ^{d)} -D _{2h} ⁷			
	θ	-40 ^{b)}	17 ^{b)}	330 ^{a)}	740 ^{e)}	910 ^{e)}	1230 ^{e)}	°C	
	T _{melt} = 1473 °C. ρ = 7.157 · 10 ³ kg m ⁻³ at RT. a = 7.30 Å, b = 7.53 Å, c = 7.68 Å, β = 90° 54' at 30 °C. Transparent, bluish green.								21J1 04S1 60T1
2a	Crystal growth: Sublimation method.								51U1, 56T2, 59S3
b	Crystal form: Plate-like.								
3	Crystal structure: Fig. 747, 748; Tab. 79; Fig. 749.								
	phase	VII	VI	V	IV	III	II	I	
	Z	4	8	8					60T1
4	Lattice distortion: Tab. 80. Thermal expansion: Fig. 750 ... 754.								
5a	Dielectric constant: κ = 100 ... 300 at liquid air temperature. No reliable dielectric measurements could be carried out at and above room temperature because of high electrical conductivity. dθ _{IV-III} /dp = -8.46 · 10 ⁻⁸ °K N ⁻¹ m ² .								49M2 66T4 49M2
c	Dielectric hysteresis loop was observed at liquid air temperature.								

* As to the crystal system in the phase VII, possibility of triclinic symmetry was discussed by TANISAKI [60T1].

V Index of substances — Substanzenverzeichnis

This index consists of two parts: part A is for pure compounds (including complex compounds such as $\text{Pb}(\text{Co}_{1/2}\text{Nb}_{1/2})\text{O}_3$ or $\text{Na}_{0.5}\text{Bi}_{4.5}\text{Ti}_4\text{O}_{15}$) and part B is for solid solutions.

V A: In the 1st column the substances are ordered according to the alphabetically arranged gross formula. When their names (e.g. Rochelle salt) and/or their abbreviated names (e.g. TGS) are widely used, they are also included in this column. In the gross formula the numbers of the elements are determined by simple addition.

Compounds containing water of crystallization are, however, listed twice: (1) H and O of the water molecules are included in the gross formula, (2) the water molecules are attached separately to the gross formula. For instance, Rochelle salt is listed in the 1st column as $\text{C}_4\text{H}_4\text{KNaO}_6 \cdot 4\text{H}_2\text{O}$, $\text{C}_4\text{H}_{12}\text{KNaO}_{10}$ and also as Rochelle salt, RS, Seignette salt.

Crystals in which H is replaced by D (e.g. KD_2PO_4) are not listed separately, since data on their properties are presented in the same section as the data on the non-deuterated crystals (e.g. KH_2PO_4).

V B: In the 1st column the gross formula of each end material of a solid solution (e.g. BaTiO_3 or PbTiO_3 for the solid solution $\text{BaTiO}_3\text{--PbTiO}_3$) is listed in the same manner as in the case of pure compounds. Thus the solid solution $\text{BaTiO}_3\text{--PbTiO}_3$ can be found in the 2nd column by looking first for either BaO_3Ti or O_3PbTi in the 1st column of Part B. If the solid solution is expressed by the formula such as $(\text{Sb}_x\text{Bi}_{1-x})\text{SI}$, the end material can be obtained by putting x equal to either 0 or 1. When solid solutions have abbreviated names (e.g. KTN), these are also included in the 1st column.

Since in general one section corresponds to one substance in this volume, the 3rd column gives the section number and the 4th column gives the first page of the section.

Dieses Verzeichnis besteht aus zwei Teilen: Teil A enthält die reinen Verbindungen (einschließlich komplexer Verbindungen wie $\text{Pb}(\text{Co}_{1/2}\text{Nb}_{1/2})\text{O}_3$ oder $\text{Na}_{0.5}\text{Bi}_{4.5}\text{Ti}_4\text{O}_{15}$) und Teil B enthält die Mischkristalle.

V A: In der 1. Spalte sind die Substanzen nach der alphabetisch angeordneten Bruttoformel aufgeführt. Wenn ihre Namen (z. B. Seignette-Salz) und/oder ihre abgekürzten Bezeichnungen (z. B. TGS) häufig gebraucht werden, sind auch sie in dieser Spalte zu finden. In der Bruttoformel ist die Anzahl jedes Elements durch einfache Addition bestimmt.

Verbindungen, die Kristallwasser enthalten, sind zweimal aufgeführt: 1. H und O der Wassermoleküle sind in der Bruttoformel enthalten. 2. die Wassermoleküle werden getrennt der Bruttoformel hinzugefügt (z. B. Seignette-Salz ist in der 1. Spalte aufgeführt als $\text{C}_4\text{H}_4\text{KNaO}_6 \cdot 4\text{H}_2\text{O}$, $\text{C}_4\text{H}_{12}\text{KNaO}_{10}$ und auch als Rochelle-Salz, RS, Seignette-Salz).

Kristalle, in denen H durch D ersetzt ist (z. B. KD_2PO_4), werden nicht gesondert aufgeführt. Daten von ihren Eigenschaften erscheinen in demselben Abschnitt an der gleichen Stelle wie die Daten von den nicht deuterierten Kristallen (z. B. KH_2PO_4).

V B: In der 1. Spalte ist die Bruttoformel jeder Endsubstanz einer Mischkristallreihe (z. B. BaTiO_3 oder PbTiO_3 für die Mischkristallreihe $\text{BaTiO}_3\text{--PbTiO}_3$) in derselben Weise aufgeführt wie im Fall von reinen Verbindungen. So kann die Mischkristallreihe $\text{BaTiO}_3\text{--PbTiO}_3$ in der zweiten Spalte gefunden werden, wenn man zunächst entweder BaO_3Ti oder O_3PbTi in der ersten Spalte von Teil B sucht. Wenn die Mischkristallreihe durch die Formel $(\text{Sb}_x\text{Bi}_{1-x})\text{SI}$ ausgedrückt wird, kann man die Endsubstanz finden, indem man x gleich 0 oder 1 setzt. Wenn Mischkristalle abgekürzte Namen haben (z. B. KTN), sind diese auch in der 1. Spalte enthalten.

Da in diesem Band jeweils ein Abschnitt einer Substanz entspricht, gibt die 3. Spalte die Abschnittsnummer und die 4. Spalte die erste Seite des Abschnitts an.

VA Pure compounds

Gross formula	Chemical formula	Nr.	Page
ADP	$\text{NH}_4\text{H}_2\text{PO}_4$	13A-7	143
$\text{AgC}_2\text{H}_3\text{N}_3\text{O}_5$	$\text{NH}_2\text{CH}_2\text{COOH} \cdot \text{AgNO}_3$	29A-1	191
$\text{Ag}_2\text{H}_3\text{IO}_6$	$\text{Ag}_2\text{H}_3\text{IO}_6$	35-22	209
AgNbO_3	AgNbO_3	35-16	207
AgO_3Ta	AgTaO_3	35-18	207
AgO_3V	AgVO_3	35-20	208
$\text{AlCH}_3\text{NO}_3\text{S}_2 \cdot 12\text{H}_2\text{O}$	$\text{CH}_3\text{NH}_2\text{Al}(\text{SO}_4)_2 \cdot 12\text{H}_2\text{O}$	18A-4	158
$\text{AlCH}_3\text{N}_3\text{O}_3\text{S}_2 \cdot 6\text{H}_2\text{O}$	$\text{C}(\text{NH}_2)_3\text{Al}(\text{SO}_4)_2 \cdot 6\text{H}_2\text{O}$	19A-1	161
$\text{AlCH}_3\text{N}_3\text{O}_3\text{S}_2$	$\text{C}(\text{NH}_2)_3\text{Al}(\text{SO}_4)_2 \cdot 6\text{H}_2\text{O}$	19A-1	161
$\text{AlCH}_3\text{NO}_3\text{Se}_2 \cdot 12\text{H}_2\text{O}$	$\text{CH}_3\text{NH}_2\text{Al}(\text{SeO}_4)_2 \cdot 12\text{H}_2\text{O}$	18A-4	158
$\text{AlCH}_3\text{N}_3\text{O}_3\text{Se}_2 \cdot 6\text{H}_2\text{O}$	$\text{C}(\text{NH}_2)_3\text{Al}(\text{SeO}_4)_2 \cdot 6\text{H}_2\text{O}$	18A-10	161
$\text{AlCH}_3\text{N}_3\text{O}_3\text{Se}_2$	$\text{C}(\text{NH}_2)_3\text{Al}(\text{SeO}_4)_2 \cdot 6\text{H}_2\text{O}$	19A-5	166
$\text{AlCH}_3\text{NO}_3\text{Se}_2$	$\text{C}(\text{NH}_2)_3\text{Al}(\text{SeO}_4)_2 \cdot 6\text{H}_2\text{O}$	19A-5	166
Ammonium metaphosphate	$\text{CH}_3\text{NH}_2\text{Al}(\text{SeO}_4)_2 \cdot 12\text{H}_2\text{O}$	18A-10	161
AsCsH_2O_4	CsH_2AsO_4	35-14	205
AsH_2KO_4	KH_2AsO_4	13A-6	143
		13A-4	141

V Substanzenverzeichnis

Gross formula	Chemical formula	Nr.	Page
AsH ₆ NO ₄	NH ₄ H ₂ AsO ₄	13A-8	147
AsH ₂ O ₄ Rb	RbH ₂ AsO ₄	13A-5	143
Azobenzene	C ₁₂ H ₁₀ N ₂	37-5	216
Azoxybenzene	C ₁₂ H ₁₀ N ₂ O	37-6	216
B ₇ BrCd ₃ O ₁₃	Cd ₃ B ₇ O ₁₃ Br	9A-18	120
B ₇ BrCo ₃ O ₁₃	Co ₃ B ₇ O ₁₃ Br	9A-14	119
B ₇ BrCr ₃ O ₁₃	Cr ₃ B ₇ O ₁₃ Br	9A-11	118
B ₇ BrCu ₃ O ₁₃	Cu ₃ B ₇ O ₁₃ Br	9A-16	119
B ₇ BrFe ₃ O ₁₃	Fe ₃ B ₇ O ₁₃ Br	9A-13	119
B ₇ BrMg ₃ O ₁₃	Mg ₃ B ₇ O ₁₃ Br	9A-10	118
B ₇ BrMn ₃ O ₁₃	Mn ₃ B ₇ O ₁₃ Br	9A-12	119
B ₇ BrNi ₃ O ₁₃	Ni ₃ B ₇ O ₁₃ Br	9A-15	119
B ₇ BrO ₁₃ Zn ₃	Zn ₃ B ₇ O ₁₃ Br	9A-17	120
B ₆ Ca ₂ H ₁₀ O ₁₆	Ca ₂ B ₆ O ₁₁ · 5H ₂ O	21A-1	173
B ₆ Ca ₂ O ₁₁ · 5H ₂ O	Ca ₂ B ₆ O ₁₁ · 5H ₂ O	21A-1	173
B ₇ Cd ₃ ClO ₁₃	Cd ₃ B ₇ O ₁₃ Cl	9A-9	118
B ₇ Cd ₃ IO ₁₃	Cd ₃ B ₇ O ₁₃ I	9A-25	122
B ₇ ClCo ₃ O ₁₃	Co ₃ B ₇ O ₁₃ Cl	9A-5	117
B ₇ ClCr ₃ O ₁₃	Cr ₃ B ₇ O ₁₃ Cl	9A-2	116
B ₇ ClCu ₃ O ₁₃	Cu ₃ B ₇ O ₁₃ Cl	9A-7	118
B ₇ ClFe ₃ O ₁₃	Fe ₃ B ₇ O ₁₃ Cl	9A-4	117
B ₇ ClMg ₃ O ₁₃	Mg ₃ B ₇ O ₁₃ Cl	9A-1	115
B ₇ ClMn ₃ O ₁₃	Mn ₃ B ₇ O ₁₃ Cl	9A-3	117
B ₇ ClNi ₃ O ₁₃	Ni ₃ B ₇ O ₁₃ Cl	9A-6	117
B ₇ ClO ₁₃ Zn ₃	Zn ₃ B ₇ O ₁₃ Cl	9A-8	118
B ₇ Co ₃ IO ₁₃	Co ₃ B ₇ O ₁₃ I	9A-22	121
B ₇ Cr ₃ IO ₁₃	Cr ₃ B ₇ O ₁₃ I	9A-19	120
B ₇ Fe ₃ IO ₁₃	Fe ₃ B ₇ O ₁₃ I	9A-21	120
B ₇ IMn ₃ O ₁₃	Mn ₃ B ₇ O ₁₃ I	9A-20	120
B ₇ INi ₃ O ₁₃	Ni ₃ B ₇ O ₁₃ I	9A-23	121
B ₇ IO ₁₃ Zn ₃	Zn ₃ B ₇ O ₁₃ I	9A-24	121
Ba ₄ Bi ₂ Fe ₂ Nb ₈ O ₃₀	Ba ₄ Bi ₂ Fe ₂ Nb ₈ O ₃₀	5C-g1	104
BaBi ₂ Nb ₈ O ₉	BaBi ₂ Nb ₈ O ₉	7A-7	109
BaBi ₃ NbO ₁₂ Ti ₂	BaBi ₃ Ti ₂ NbO ₁₂	7A-12	110
BaBi ₂ O ₉ Ta ₂	BaBi ₂ Ta ₂ O ₉	7A-8	109
BaBi ₄ O ₁₅ Ti ₄	BaBi ₄ Ti ₄ O ₁₅	7A-14	111
Ba ₂ Bi ₄ O ₁₈ Ti ₅	Ba ₂ Bi ₄ Ti ₅ O ₁₈	7A-19	112
BaC ₁₈ Ca ₂ H ₃₀ O ₁₂	Ca ₂ Ba(CH ₃ CH ₂ COO) ₆	26A-3	184
Ba ₄ Ce ₂ Nb ₈ Ni ₈ O ₃₀	Ba ₄ Ce ₂ Ni ₈ Nb ₈ O ₃₀	5C-d1	104
Ba ₄ Fe ₂ Gd ₂ Nb ₈ O ₃₀	Ba ₄ Gd ₂ Fe ₂ Nb ₈ O ₃₀	5C-g4	104
Ba ₂ Fe ₃ Nb ₇ Nd ₄ O ₃₀	Ba ₂ Nd ₄ Fe ₃ Nb ₇ O ₃₀	5C-h1	104
Ba ₄ Fe ₂ Nb ₈ Nd ₂ O ₃₀	Ba ₄ Nd ₂ Fe ₂ Nb ₈ O ₃₀	5C-g2	104
Ba ₆ FeNb ₉ O ₃₀	Ba ₆ FeNb ₉ O ₃₀	5C-f1	104
Ba ₂ Fe ₃ Nb ₇ O ₃₀ Sm ₄	Ba ₂ Sm ₄ Fe ₃ Nb ₇ O ₃₀	5C-h2	104
Ba ₄ Fe ₂ Nb ₈ O ₃₀ Sm ₂	Ba ₄ Sm ₂ Fe ₂ Nb ₈ O ₃₀	5C-g3	104
Ba ₂ KNb ₅ O ₁₅	KBa ₂ Nb ₅ O ₁₅	5C-b3	103
Ba ₉ MgNb ₁₄ O ₄₅	Ba ₉ MgNb ₁₄ O ₄₅	5C-e1	104
Ba ₂ NaNb ₅ O ₁₅	NaBa ₂ Nb ₅ O ₁₅	5C-b2	103
Ba ₂ Nb ₈ Nd ₄ Ni ₂ O ₃₀	Ba ₂ Nd ₄ Ni ₂ Nb ₈ O ₃₀	5C-c1	104
Ba ₂ Nb ₈ Ni ₂ O ₃₀ Sm ₄	Ba ₂ Sm ₄ Ni ₂ Nb ₈ O ₃₀	5C-c2	104
Ba ₂ Nb ₅ O ₁₅ Rb	RbBa ₂ Nb ₅ O ₁₅	5C-b5	103
Ba ₆ Nb ₈ O ₃₀ Ti ₂	Ba ₆ Ti ₂ Nb ₈ O ₃₀	5C-j1	104
BaNb _{1.5} O _{5.25} Zr _{0.25}	BaZr _{0.25} Nb _{1.5} O _{5.25}	5C-j3	105
BaO ₆ Ta ₂	BaTa ₂ O ₆	5A-3	98
BaO ₃ Ti	BaTiO ₃	1A-8	51
BaO ₃ Zr	BaZrO ₃	1A-12	61
BeC ₆ F ₄ H ₁₇ N ₈ O ₆	(NH ₂ CH ₂ COOH) ₃ H ₃ BeF ₄	28A-3	190
BeF ₄ H ₃ N ₂	(NH ₄) ₂ BeF ₄	14A-2	154
BiBrS	BiSBr	10A-7	126
BiBrSe	BiSeBr	10A-10	127
Bi ₂ CaNb ₂ O ₉	CaBi ₂ Nb ₂ O ₉	7A-3	107
Bi ₂ CaO ₉ Ta ₂	CaBi ₂ Ta ₂ O ₉	7A-4	108
Bi ₄ CaO ₁₅ Ti ₄	CaBi ₄ Ti ₄ O ₁₅	7A-17	112

V Index of substances

Gross formula	Chemical formula	Nr.	Page
BiClS	BiSCL	10A-6	125
BiClSe	BiSeCl	10A-9	126
Bi ₂ Fe ₄ Nb ₆ Nd ₄ O ₃₀	Bi ₂ Nd ₄ Fe ₄ Nb ₆ O ₃₀	5C-i2	104
BiFeO ₃	BiFeO ₃	1A-15	63
Bi ₅ GaO ₁₅ Ti ₃	BiBi ₄ Ti ₃ GaO ₁₅	7A-18	112
BiIS	BiSI	10A-8	126
BiISe	BiSeI	10A-11	127
BiK ₂ Nb ₅ O ₁₅	K ₂ BiNb ₅ O ₁₅	5C-a2	102
Bi _{1/2} K _{1/2} O ₃ Ti	(K _{1/2} Bi _{1/2})TiO ₃	1B1-i	64
Bi _{4.5} K _{0.5} O ₁₅ Ti ₄	K _{0.5} Bi _{4.5} Ti ₄ O ₁₅	7B-4	114
Bi _{1/2} Na _{1/2} O ₃ Ti	(Na _{1/2} Bi _{1/2})TiO ₃	1B1-ii	64
Bi _{4.5} Na _{0.5} O ₁₅ Ti ₄	Na _{0.5} Bi _{4.5} Ti ₄ O ₁₅	7B-3	114
Bi ₂ Nb ₂ O ₉ Pb	PbBi ₂ Nb ₂ O ₉	7A-9	109
Bi ₂ NbO ₁₂ PbTi ₂	PbBi ₃ Ti ₂ NbO ₁₂	7A-13	110
Bi ₂ Nb ₂ O ₉ Sr	SrBi ₂ Nb ₂ O ₉	7A-5	108
Bi ₃ NbO ₉ Ti	BiBi ₂ TiNbO ₉	7A-1	107
Bi ₂ O ₉ PbTa ₂	PbBi ₂ Ta ₂ O ₉	7A-10	110
Bi ₄ O ₁₅ PbTi ₄	PbBi ₄ Ti ₄ O ₁₅	7A-15	111
Bi ₄ O ₁₈ Pb ₂ Ti ₅	Pb ₂ Bi ₄ Ti ₅ O ₁₈	7A-20	112
Bi ₂ O ₉ SrTa ₂	SrBi ₂ Ta ₂ O ₉	7A-6	109
Bi ₄ O ₁₅ SrTi ₄	SrBi ₄ Ti ₄ O ₁₅	7A-16	111
Bi ₄ O ₁₈ Sr ₂ Ti ₅	Sr ₂ Bi ₄ Ti ₅ O ₁₈	7A-21	113
Bi ₃ O ₉ TaTi	BiBi ₂ TiTaO ₉	7A-2	107
Bi ₂ O ₁₁ Ti ₄	Bi ₂ Ti ₄ O ₁₁	7A-22	113
Bi ₄ O ₁₂ Ti ₃	BiBi ₃ Ti ₂ TiO ₁₂	7A-11	110
Br ₃ C ₄ H ₁₂ HgN	N(CH ₃) ₄ HgBr ₃	24A-2	179
Br ₃ C ₄ H ₁₂ HgP	P(CH ₃) ₄ HgBr ₃	24A-3	180
BrH	H · Br	35-12	203
BrSSb	SbSBr	10A-1	122
BrSbSe	SbSeBr	10A-3	124
C ₃ CaCl ₂ H ₂₁ N ₃ O ₆	(CH ₃ NHCH ₂ COOH) ₃ · CaCl ₂	32A-1	192
C ₁₈ Ca ₂ H ₃₀ O ₁₂ Pb	Ca ₂ Pb(CH ₃ CH ₂ COO) ₆	26A-2	183
C ₁₈ Ca ₂ H ₃₀ O ₁₂ Sr	Ca ₂ Sr(CH ₃ CH ₂ COO) ₆	26A-1	182
C ₃ Cl ₃ H ₁₂ HgN	N(CH ₃) ₄ · HgCl ₃	24A-1	178
C ₄ Cl ₂ H ₁₀ MnN ₂ O ₄ · 2H ₂ O	(NH ₂ CH ₂ COOH) ₂ · MnCl ₂ · 2H ₂ O	31A-1	192
C ₄ Cl ₂ H ₁₀ MnN ₂ O ₆	(NH ₂ CH ₂ COOH) ₂ · MnCl ₂ · 2H ₂ O	31A-1	192
C ₂ ClH ₂ NO ₂	CH ₂ ClCOONH ₄	27A-1	184
C ₄ Cl ₂ H ₂ NO ₄	(CH ₂ ClCOO) ₂ H · NH ₄	27A-2	184
CCrH ₆ NO ₈ S ₂ · 12H ₂ O	CH ₃ NH ₂ Cr(SO ₄) ₂ · 12H ₂ O	18A-6	160
CCrH ₆ N ₂ O ₈ S ₂ · 6H ₂ O	C(NH ₂) ₃ Cr(SO ₄) ₂ · 6H ₂ O	19A-2	164
CCrH ₃₀ NO ₂₀ S ₂	CH ₃ NH ₂ Cr(SO ₄) ₂ · 12H ₂ O	18A-6	160
CCrH ₁₈ N ₃ O ₁₄ S ₂	C(NH ₂) ₃ Cr(SO ₄) ₂ · 6H ₂ O	19A-2	164
CCrH ₆ N ₂ O ₈ Se ₂ · 6H ₂ O	C(NH ₂) ₃ Cr(SeO ₄) ₂ · 6H ₂ O	19A-6	167
CCrH ₁₈ N ₃ O ₁₄ Se ₂	C(NH ₂) ₃ Cr(SeO ₄) ₂ · 6H ₂ O	19A-6	167
C ₂ CuH ₂ O ₄ · 4H ₂ O	Cu(HCOO) ₂ · 4H ₂ O	25A-1	180
C ₂ CuH ₁₀ O ₃	Cu(HCOO) ₂ · 4H ₂ O	25A-1	180
C ₆ FeH ₆ K ₄ N ₆ O ₃	K ₄ Fe(CN) ₆ · 3H ₂ O	22A-2	174
CFeH ₆ NO ₈ S ₂ · 12H ₂ O	CH ₃ NH ₂ Fe(SO ₄) ₂ · 12H ₂ O	18A-7	160
CFeH ₃₀ NO ₂₀ S ₂	CH ₃ NH ₂ Fe(SO ₄) ₂ · 12H ₂ O	18A-7	160
C ₆ FeK ₄ N ₆ · 3H ₂ O	K ₄ Fe(CN) ₆ · 3H ₂ O	22A-2	174
CGaH ₆ NO ₈ S ₂ · 12H ₂ O	CH ₃ NH ₂ Ga(SO ₄) ₂ · 12H ₂ O	18A-5	160
CGaH ₆ N ₂ O ₈ S ₂ · 6H ₂ O	C(NH ₂) ₃ Ga(SO ₄) ₂ · 6H ₂ O	19A-3	165
CGaH ₁₈ N ₃ O ₁₄ S ₂	C(NH ₂) ₃ Ga(SO ₄) ₂ · 6H ₂ O	19A-3	165
CGaH ₃₀ NO ₂₀ S ₂	CH ₃ NH ₂ Ga(SO ₄) ₂ · 12H ₂ O	18A-5	160
CGaH ₆ N ₂ O ₈ Se ₂ · 6H ₂ O	C(NH ₂) ₃ Ga(SeO ₄) ₂ · 6H ₂ O	19A-7	167
CGaH ₁₈ N ₃ O ₁₄ Se ₂	C(NH ₂) ₃ Ga(SeO ₄) ₂ · 6H ₂ O	19A-7	167
C ₄ H ₁₂ HgI ₃ N	N(CH ₃) ₄ HgI ₃	24A-4	180
C ₆ H ₆ K ₄ MnN ₆ O ₃	K ₄ Mn(CN) ₆ · 3H ₂ O	22A-1	174
C ₆ H ₆ K ₄ N ₆ O ₃ Os	K ₄ Os(CN) ₆ · 3H ₂ O	22A-4	176
C ₆ H ₆ K ₄ N ₆ O ₃ Ru	K ₄ Ru(CN) ₆ · 3H ₂ O	22A-3	176
C ₄ H ₄ KNaO ₆ · 4H ₂ O	NaKC ₄ H ₄ O ₆ · 4H ₂ O	33A-1	193
C ₄ H ₁₂ KNaO ₁₀	NaKC ₄ H ₄ O ₆ · 4H ₂ O	33A-1	193
C ₄ H ₄ LiNO ₆ · H ₂ O	LiNH ₄ · C ₄ H ₄ O ₆ · H ₂ O	34A-1	199

V Substanzenverzeichnis

Gross formula	Chemical formula	Nr.	Page
$C_4H_{10}LiNO_7$	$LiNH_4 \cdot C_4H_4O_6 \cdot H_2O$	34A-1	199
$C_4H_4LiO_6Ti \cdot H_2O$	$LiTiC_4H_4O_6 \cdot H_2O$	34A-2	199
$C_4H_6LiO_7Ti$	$LiTiC_4H_4O_6 \cdot H_2O$	34A-2	199
$C_4H_8NNaO_6 \cdot 4H_2O$	$NaNH_4C_4H_4O_6 \cdot 4H_2O$	33A-2	197
$C_4H_{16}NNaO_{10}$	$NaNH_4C_4H_4O_6 \cdot 4H_2O$	33A-2	197
$C_4H_{11}N_9O_7$	$(NH_2CH_2COOH)_2 \cdot HNO_3$	30A-1	191
$C_6H_{17}N_3O_{10}S$	$(NH_2CH_2COOH)_3 \cdot H_2SO_4$	28A-1	185
$CH_3NO_8S_2V \cdot 12H_2O$	$CH_3NH_3V(SO_4)_2 \cdot 12H_2O$	18A-8	161
$CH_3N_3O_8S_2V \cdot 6H_2O$	$C(NH_2)_3V(SO_4)_2 \cdot 6H_2O$	19A-4	166
$CH_{16}N_3O_{14}S_2V$	$C(NH_2)_3V(SO_4)_2 \cdot 6H_2O$	19A-4	166
$CH_3NO_{20}S_2V$	$CH_3NH_3V(SO_4)_2 \cdot 12H_2O$	18A-8	161
$C_6H_{17}N_3O_{10}Se$	$(NH_2CH_2COOH)_3 \cdot H_2SeO_4$	28A-2	190
CH_4N_2S	$SC(NH_2)_2$	23A-1	177
$C_4H_4NaO_6Rb \cdot 4H_2O$	$NaRbC_4H_4O_6 \cdot 4H_2O$	33A-3	198
$C_4H_{12}NaO_{10}Rb$	$NaRbC_4H_4O_6 \cdot 4H_2O$	33A-3	198
$CH_3InNO_8S_2 \cdot 12H_2O$	$CH_3NH_3In(SO_4)_2 \cdot 12H_2O$	18A-9	161
$CH_{30}InNO_{20}S_2$	$CH_3NH_3In(SO_4)_2 \cdot 12H_2O$	18A-9	161
$C_6K_4MnN_6 \cdot 3H_2O$	$K_4Mn(CN)_6 \cdot 3H_2O$	22A-1	174
$C_6K_4N_6Os \cdot 3H_2O$	$K_4Os(CN)_6 \cdot 3H_2O$	22A-4	176
$C_6K_4N_6Ru \cdot 3H_2O$	$K_4Ru(CN)_6 \cdot 3H_2O$	22A-3	176
CaO_3Ti	$CaTiO_3$	1A-5	44
CaO_3Zr	$CaZrO_3$	1A-10	60
$Cd_2H_8N_2O_{12}S_3$	$(NH_4)_2Cd_2(SO_4)_3$	16A-1	156
$Cd_{1/4}Mn_{1/4}Nb_{1/2}O_3Pb$	$Pb(Cd_{1/4}Mn_{1/4}Nb_{1/2})O_3$	1B3-xvii	70
$Cd_{1/4}Mn_{1/4}O_3PbW_{1/2}$	$Pb(Cd_{1/4}Mn_{1/4}W_{1/2})O_3$	1B3-xvii	70
$Cd_2Nb_2O_7$	$Cd_2Nb_2O_7$	6A-1	105
$Cd_{1/3}Nb_{2/3}O_3Pb$	$Pb(Cd_{1/3}Nb_{2/3})O_3$	1B4-iii	71
$Cd_{1/2}O_3PbW_{1/2}$	$Pb(Cd_{1/2}W_{1/2})O_3$	1B2-ii	65
CdO_3Ti	$CdTiO_3$	1A-7	50
Cl_3CsGe	$CsGeCl_3$	35-21	208
ClH	HCl	35-11	202
ClK	KCl	35-28	211
$CoCrH_2N_2O_8S_2 \cdot 12H_2O$	$Co(NH_2)_2HCr(SO_4)_2 \cdot 12H_2O$	18A-11	161
$CoCrH_{29}N_2O_{20}S_2$	$Co(NH_2)_2HCr(SO_4)_2 \cdot 12H_2O$	18A-11	161
Colemanite	$Ca_2B_6O_{11} \cdot 5H_2O$ or $CaB_3O_4(OH)_3 \cdot H_2O$	21A-1	173
$Co_{1/4}Mn_{1/4}Nb_{1/2}O_3Pb$	$Pb(Co_{1/4}Mn_{1/4}Nb_{1/2})O_3$	1B3-xvii	70
$Co_{1/4}Mn_{1/4}O_3PbW_{1/2}$	$Pb(Co_{1/4}Mn_{1/4}W_{1/2})O_3$	1B3-xvii	70
$Co_{1/3}Nb_{2/3}O_3Pb$	$Pb(Co_{1/3}Nb_{2/3})O_3$	1B4-iv	71
$Co_{1/2}Nb_{1/2}O_3Pb$	$Pb(Co_{1/2}Nb_{1/2})O_3$	1B3-iv	68
$Co_{1/3}O_3PbTa_{2/3}$	$Pb(Co_{1/3}Ta_{2/3})O_3$	1B4-vii	72
$Co_{1/2}O_3PbTa_{1/2}$	$Pb(Co_{1/2}Ta_{1/2})O_3$	1B3-xiii	70
$Co_{1/2}O_3PbW_{1/3}$	$Pb(Co_{1/2}W_{1/2})O_3$	1B2-iv	66
$Cr_{1/4}Nb_{1/2}O_3PbSc_{1/4}$	$Pb(Sc_{1/4}Cr_{1/4}Nb_{1/2})O_3$	1B3-xvii	70
CsH_2O_4P	CsH_2PO_4	13A-3	141
$CsH_3O_6Se_2$	$CsH_3(SeO_3)_2$	20A-3	172
$CsNO_3$	$CsNO_3$	12A-3	134
Deoxyribonucleic acid	Deoxyribonucleic acid	35-33	212
DNA	Deoxyribonucleic acid	35-33	212
$ErMnO_3$	$ErMnO_3$	4A-2	95
$Eu_2Mo_3O_{12}$	$Eu_2(MoO_4)_3$	35-2	200
$F_7H_8N_2P$	$NH_4PF_6NH_4F$	35-24	210
$FeH_4NO_8S_2 \cdot 12H_2O$	$NH_4Fe(SO_4)_2 \cdot 12H_2O$	18A-1	157
$FeH_{28}NO_{20}S_2$	$NH_4Fe(SO_4)_2 \cdot 12H_2O$	18A-1	157
$Fe_2Nb_6Nd_4O_{30}$	$Nd_6Fe_4Nb_6O_{30}$	5C-i1	104
$Fe_2Nb_7Nd_4O_{30}Pb_2$	$Pb_2Nd_4Fe_2Nb_7O_{30}$	5C-h3	104
$Fe_{1/2}Nb_{1/2}O_3Pb$	$Pb(Fe_{1/2}Nb_{1/2})O_3$	1B3-iii	67
$FeNb_9O_{30}Sr_6$	$Sr_6FeNb_9O_{30}$	5C-f2	104
$Fe_2Nb_8O_{30}Sr_4Yb_2$	$Sr_4Yb_2Fe_2Nb_8O_{30}$	5C-g5	104
$Fe_{1/2}O_3PbTa_{1/2}$	$Pb(Fe_{1/2}Ta_{1/2})O_3$	1B3-xii	69
$Fe_{1/2}O_3PbW_{1/2}$	$Pb(Fe_{1/2}W_{1/2})O_3$	1B3-xvi	70
$Fe_{2/3}O_3PbW_{1/3}$	$Pb(Fe_{2/3}W_{1/3})O_3$	1B5-ii	73

V Index of substances

Page	Gross formula	Chemical formula	Nr.	Page
199	GASH	$C(NH_2)_3Al(SO_4)_2 \cdot 6H_2O$	19A-1	161
199	$Gd_2Mo_3O_{12}$	$Gd_2(MoO_4)_3$	35-3	200
199	GeTe	GeTe	36-1	212
197	HI	HI		
197	$H_{11}In_2O_6$	$(NH_4)_2H_3IO_6$	35-13	204
191	$H_4InNO_3S_2 \cdot 12H_2O$	$NH_4In(SO_4)_2 \cdot 12H_2O$	35-23	209
185	$H_{28}InNO_{20}S_2$	$NH_4In(SO_4)_2 \cdot 12H_2O$	18A-3	158
161	H_2KO_4P	KH_2PO_4	18A-3	158
166	$H_5LiN_2O_4S$	$Li(N_2H_5)SO_4$	13A-1	134
166	$H_3LiO_6Se_2$	$LiH_3(SeO_3)_2$	35-15	205
161	$H_4NNaO_4S \cdot 2H_2O$	$NaNH_4SO_4 \cdot 2H_2O$	20A-1	168
190	H_5NNaO_6S	$NaNH_4SO_4 \cdot 2H_2O$	17A-1	157
177	H_6NO_4P	$NH_4H_2PO_4$	17A-1	157
198	H_5NO_4S	$(NH_4)HSO_4$	13A-7	143
198	$H_5N_2O_4S$	$(NH_4)_2SO_4$	15A-1	154
161	$H_4NO_3S_2V \cdot 12H_2O$	$NH_4V(SO_4)_2 \cdot 12H_2O$	14A-1	148
161	$H_{28}NO_{20}S_2V$	$NH_4V(SO_4)_2 \cdot 12H_2O$	18A-2	158
174	$H_3NaO_6Se_2$	$NaH_3(SeO_3)_2$	18A-2	158
176	H_2O (Ice)	H_2O	20A-2	169
44	H_2O_4PRb	RbH_2PO_4	35-29	211
60	HO_4RbS	$RbHSO_4$	13A-2	141
156	HfO_3Pb	$PbHfO_3$	15A-2	155
70	HoMnO ₃	HoMnO ₃	1A-14	62
70	$Ho_{1/2}Nb_{1/2}O_3Pb$	$Pb(Ho_{1/2}Nb_{1/2})O_3$	4A-3	95
105			1B3-viii	68
71	Ice	H_2O		
65	IKO ₃	KIO ₃	35-29	211
50	ISSb	SbSI	1A-16	64
208	ISbSe	SbSeI	10A-2	122
202	ISbTe	SbTeI	10A-4	125
211	$In_{1/2}Nb_{1/2}O_3Pb$	$Pb(In_{1/2}Nb_{1/2})O_3$	10A-5	125
161			1B3-vi	68
161	KDP	KH_2PO_4		
173	$K_2LaNb_5O_{15}$	$K_2LaNb_5O_{15}$	13A-1	134
70	$K_{0.6}Li_{0.4}NbO_3$	$K_{0.6}Li_{0.4}NbO_3$	5C-a1	102
70	$K_{0.6}Li_{0.4}Nb_{0.3}O_3Ta_{0.7}$	$K_{0.6}Li_{0.4}(Ta_{0.7}Nb_{0.3})O_3$	5C-k1	105
71	$KLiO_4S$	$KLiSO_4$	5C-k2	105
68	KNO_2	KNO_2	35-27	211
72	KNO_3	KNO_3	11A-2	130
70	$KNbO_3$	$KNbO_3$	12A-1	131
66	$KNb_5O_{15}Sr_2$	$KSr_2Nb_5O_{15}$	1A-2	39
70	KO_3Ta	$KTaO_3$	5C-b1	102
141			1A-4	41
172	Lecontite	$NaNH_4SO_4 \cdot 2H_2O$		
134	$LiNbO_3$	$LiNbO_3$	17A-1	157
	$Li_{1/4}Nb_{1/4}O_3PbW_{1/2}$	$Pb(Li_{1/4}Nb_{1/4}W_{1/2})O_3$	3A-1	89
212	LiO_3Ta	$LiTaO_3$	1B3-xvii	70
212	$LuMnO_3$	$LuMnO_3$	3A-2	92
	$Lu_{1/2}Nb_{1/2}O_3Pb$	$Pb(Lu_{1/2}Nb_{1/2})O_3$	4A-6	97
95	$Lu_{1/2}O_3PbTa_{1/2}$	$Pb(Lu_{1/2}Ta_{1/2})O_3$	1B3-ix	68
200			1B3-xv	70
210	MASD	$CH_3NH_2Al(SO_4)_2 \cdot 12H_2O$		
157	$Mg_{1/4}Mn_{1/4}Nb_{1/2}O_3Pb$	$Pb(Mg_{1/4}Mn_{1/4}Nb_{1/2})O_3$	18A-4	158
157	$Mg_{1/4}Mn_{1/4}O_3PbTa_{1/2}$	$Pb(Mg_{1/4}Mn_{1/4}Ta_{1/2})O_3$	1B3-xvii	70
104	$Mg_{1/4}Mn_{1/4}O_3PbW_{1/2}$	$Pb(Mg_{1/4}Mn_{1/4}W_{1/2})O_3$	1B3-xvii	70
104	$Mg_{1/3}Nb_{2/3}O_3Pb$	$Pb(Mg_{1/3}Nb_{2/3})O_3$	1B3-xvii	70
67	$MgNb_{11}O_{45}Sr_9$	$Sr_9MgNb_{11}O_{45}$	1B4-i	70
104	$Mg_{1/3}O_3PbTa_{2/3}$	$Pb(Mg_{1/3}Ta_{2/3})O_3$	5C-e2	104
104	$Mg_{1/2}O_3PbW_{1/2}$	$Pb(Mg_{1/2}W_{1/2})O_3$	1B4-vi	72
69	$Mn_{1/4}Nb_{1/2}Ni_{1/4}O_3Pb$	$Pb(Ni_{1/4}Mn_{1/4}Nb_{1/2})O_3$	1B2-i	65
70	$Mn_{1/2}Nb_{1/2}O_3Pb$	$Pb(Mn_{1/2}Nb_{1/2})O_3$	1B3-xvii	70
73	$Mn_{1/4}Nb_{1/2}O_3PbZn_{1/4}$	$Pb(Zn_{1/4}Mn_{1/4}Nb_{1/2})O_3$	1B3-ii	67
	$Mn_{1/4}Ni_{1/4}O_3PbW_{1/2}$	$Pb(Ni_{1/4}Mn_{1/4}W_{1/2})O_3$	1B3-xvii	70
			1B3-xvii	70

V Substanzenverzeichnis

Gross formula	Chemical formula	Nr.	Page
MnO ₂	MnO ₂	35-31	212
Mn _{1/2} O ₃ PbRe _{1/2}	Pb(Mn _{1/2} Re _{1/2})O ₃	1B2-v	66
Mn _{1/2} O ₃ PbTa _{1/2}	Pb(Mn _{1/2} Ta _{1/2})O ₃	1B3-xi	69
Mn _{1/2} O ₃ PbW _{1/2}	Pb(Mn _{1/2} W _{1/2})O ₃	1B2-iii	66
Mn _{2/3} O ₃ PbW _{1/3}	Pb(Mn _{2/3} W _{1/3})O ₃	1B5-i	73
MnO ₃ Tm	TmMnO ₃	4A-4	96
MnO ₃ Y	YMnO ₃	4A-1	94
MnO ₃ Yb	YbMnO ₃	4A-5	96
Mo ₃ O ₁₅ Sm ₂	Sm ₂ (MoO ₄) ₃	35-1	200
Mo ₃ O ₁₅ Tb ₂	Tb ₂ (MoO ₄) ₃	35-4	201
NNO ₃	NaNO ₂	11A-1	128
NO ₃ Rb	RbNO ₃	12A-2	133
NaNbO ₃	NaNbO ₃	1A-1	37
NaO ₃ Ta	NaTaO ₃	1A-3	40
NaO ₃ V	NaVO ₃	35-19	208
Nb _{1/2} Ni _{1/2} O ₃ Pb	Pb(Ni _{1/2} Nb _{1/2})O ₃	1B3-v	68
Nb _{2/3} Ni _{1/3} O ₃ Pb	Pb(Ni _{1/3} Nb _{2/3})O ₃	1B4-v	72
Nb ₂ O ₆ Pb	PbNb ₂ O ₆	5A-1	97
Nb ₂ O ₇ Pb ₂	Pb ₂ Nb ₂ O ₇	6A-2	106
Nb _{1/2} O ₃ PbSc _{1/2}	Pb(Sc _{1/2} Nb _{1/2})O ₃	1B3-i	67
Nb _{1/2} O ₃ PbYb _{1/2}	Pb(Yb _{1/2} Nb _{1/2})O ₃	1B3-vii	68
Nb _{2/3} O ₃ PbZn _{1/3}	Pb(Zn _{1/3} Nb _{2/3})O ₃	1B4-ii	71
Nb ₂ O ₁₅ RbSr ₂	RbSr ₂ Nb ₅ O ₁₅	5C-b4	103
Ni _{1/3} O ₃ PbTa _{2/3}	Pb(Ni _{1/3} Ta _{2/3})O ₃	1B4-viii	73
O ₃ PbSc _{1/2} Ta _{1/2}	Pb(Sc _{1/2} Ta _{1/2})O ₃	1B3-x	69
O ₆ Pb ₄ Si	Pb ₄ SiO ₆	35-26	210
O ₆ PbTa ₂	PbTa ₂ O ₆	5A-4	98
O ₃ PbTa _{1/2} Yb _{1/2}	Pb(Yb _{1/2} Ta _{1/2})O ₃	1B3-xiv	70
O ₃ PbTi	PbTiO ₃	1A-9	59
O ₆ Pb ₃ V ₂	Pb ₃ V ₂ O ₆	35-25	210
O ₃ PbZr	PbZrO ₃	1A-13	61
O ₃ RbTa	RbTaO ₃	35-17	207
O ₃ Sn	SnO ₂	35-32	212
O ₄ SrTa ₂	SrTa ₂ O ₆	5A-2	98
O ₇ Sr ₂ Ta ₂	Sr ₂ Ta ₂ O ₇	6A-3	106
O ₃ SrTi	SrTiO ₃	1A-6	45
O ₃ SrZr	SrZrO ₃	1A-11	61
O ₂ Ti	TiO ₂	35-30	212
O ₃ W	WO ₃	2A-1	88
p-azoxyanisole	C ₁₄ H ₁₄ N ₂ O ₃	37-1	215
p-azoxyphenetole	C ₁₆ H ₁₈ N ₂ O ₃	37-2	215
p-butoxybenzoic acid	C ₁₁ H ₁₄ O ₃	37-3	215
Perovskite	CaTiO ₃	1A-5	44
p-methoxycinnamic acid	C ₁₀ H ₁₀ O ₃	37-4	216
Pyrolusite	MnO ₂	35-31	212
Rochelle salt	NaKC ₄ H ₄ O ₆ · 4H ₂ O	33A-1	193
RS	NaKC ₄ H ₄ O ₆ · 4H ₂ O	33A-1	193
Rutile	TiO ₂	35-30	212
Seignette salt	NaKC ₄ H ₄ O ₆ · 4H ₂ O	33A-1	193
SiV ₃	V ₃ Si	36-4	214
SnTe	SnTe	36-2	213
TGS	(NH ₂ CH ₂ COOH) ₃ H ₂ SO ₄	28A-1	185
Tri-glycine tellurate		28A-4	190

V Index of substances

VB Solid solutions

Gross formula	Chemical formula	Nr.	Page
ABO ₃	ABO ₃ -PbTiO ₃ -PbZrO ₃	1C-f9	87
Al ₂ BaO ₄	BaAl ₂ O ₄ -BaLi ₂ F ₄	8B-1	115
AlLaO ₃	LaAlO ₃ -BaTiO ₃	1C-c8	83
AlLaO ₃	LaAlO ₃ -BiFeO ₃	1C-b11	83
AlLaO ₃	LaAlO ₃ -PbTiO ₃	1C-c10	84
AsH ₂ NO ₄	NH ₄ H ₂ AsO ₄ -TiH ₂ AsO ₄	13B-3	148
AsH ₂ O ₄ Ti	TiH ₂ AsO ₄ -NH ₄ H ₂ AsO ₄	13B-3	148
AsIS	AsSI-SbSI	10B-1	127
BaBi ₂ Nb ₂ O ₉	(Ba-Pb)Bi ₂ Nb ₂ O ₉	7B-5	114
BaBi ₂ Nb ₂ O ₉	Bi ₂ BaNb ₂ O ₉ -Bi ₂ TiNbO ₉	7B-1	113
BaBi ₂ NbO ₁₂ Ti ₂	Bi ₂ BaTi ₂ NbO ₁₂ -Bi ₂ Ti ₂ O ₁₂	7B-2	113
BaF ₄ Li ₂	BaLi ₂ F ₄ -BaAl ₂ O ₄	8B-1	115
BaFe _{1/2} O ₃ Ta _{1/2}	Ba(Fe _{1/2} Ta _{1/2})O ₃ -BaTiO ₃	1C-d2	84
BaHfO ₃	BaHfO ₃ -BaTiO ₃	1C-a24	77
BaHfO ₃	BaHfO ₃ -PbHfO ₃	1C-a18	76
BaNb ₂ O ₆	BaNb ₂ O ₆ -BaTiO ₃	1C-e9	86
BaNb ₂ O ₆	BaNb ₂ O ₆ -BaZrO ₃	5C-j2	105
BaNb ₂ O ₆	BaNb ₂ O ₆ -CaNb ₂ O ₆	5B-1	99
BaNb ₂ O ₆	BaNb ₂ O ₆ -PbNb ₂ O ₆	5B-5	100
BaNb ₂ O ₆	BaNb ₂ O ₆ -SrNb ₂ O ₆	5B-3	99
BaNb ₂ O ₆	BaNb ₂ O ₆ -BaTiO ₃ -PbTiO ₃ -PbNb ₂ O ₆	1C-f19	88
BaNb ₂ O ₆	(Ba-Pb-Sr)(Nb-Ta) ₂ O ₆	5B-15	102
BaNb ₂ O ₆	(Ba-Pb-Ca)(Nb-Ta) ₂ O ₆	5B-15	102
BaO ₂ Sn	BaZr _{0.25} Nb _{1.5} O _{5.25}	5C-j3	105
BaO ₂ Sn	BaSnO ₃ -BaTiO ₃	1C-a25	77
BaO ₂ Sn	BaSnO ₃ -PbO:SnO ₂	1C-a21	76
BaO ₂ Sn	BaSnO ₃ -PbTiO ₃	1C-b10	83
BaO ₂ Sn	(Ba-Pb)(Sn-Ti)O ₃	1C-f18	88
BaO ₂ Sn	BaSnO ₃ -SrSnO ₃	1C-a20	76
BaO ₂ Ta ₂	BaTa ₂ O ₆ -BaTiO ₃	1C-f13	88
BaO ₂ Ta ₂	(Ba-Pb-Ca)(Ta-Nb) ₂ O ₆	1C-e10	87
BaO ₂ Ta ₂	(Ba-Pb-Sr)(Ta-Nb) ₂ O ₆	5B-15	102
BaO ₂ Ti	BaTiO ₃ -Ba(Fe _{1/2} Ta _{1/2})O ₃	5B-15	102
BaO ₂ Ti	BaTiO ₃ -BaHfO ₃	1C-d2	84
BaO ₂ Ti	BaTiO ₃ -BaNb ₂ O ₆	1C-a24	77
BaO ₂ Ti	BaTiO ₃ -BaSnO ₃	1C-e9	86
BaO ₂ Ti	BaTiO ₃ -BaTa ₂ O ₆	1C-a25	77
BaO ₂ Ti	BaTiO ₃ -BaUO ₃	1C-e10	87
BaO ₂ Ti	BaTiO ₃ -BaZrO ₃	1C-a26	77
BaO ₂ Ti	BaTiO ₃ -BiFeO ₃	1C-a23	77
BaO ₂ Ti	BaTiO ₃ -Bi ₂ Ti ₂ O ₁₂	1C-c9	84
BaO ₂ Ti	BaTiO ₃ -CaTiO ₃	7B-6	114
BaO ₂ Ti	BaTiO ₃ -Co ₂ Nb ₂ O ₇	1C-a7	74
BaO ₂ Ti	BaTiO ₃ -Co ₂ Ta ₂ O ₇	1C-e11	87
BaO ₂ Ti	BaTiO ₃ -(K _{1/2} Bi _{1/2})TiO ₃	1C-e11	87
BaO ₂ Ti	BaTiO ₃ -KNbO ₃	1C-d3	84
BaO ₂ Ti	BaTiO ₃ -LaAlO ₃	1C-c5	83
BaO ₂ Ti	BaTiO ₃ -Mn ₂ Nb ₂ O ₇	1C-c8	83
BaO ₂ Ti	BaTiO ₃ -Mn ₂ Ta ₂ O ₇	1C-e11	87
BaO ₂ Ti	BaTiO ₃ -NaNbO ₃	1C-e11	87
BaO ₂ Ti	BaTiO ₃ -Ni ₂ Nb ₂ O ₇	1C-c2	83
BaO ₂ Ti	BaTiO ₃ -Ni ₂ Ta ₂ O ₇	1C-e11	87
BaO ₂ Ti	BaTiO ₃ -PbO:SnO ₂	1C-e11	87
BaO ₂ Ti	BaTiO ₃ -PbTiO ₃	1C-b4	82
BaO ₂ Ti	BaTiO ₃ -PbZrO ₃	1C-a11	75
BaO ₂ Ti	BaTiO ₃ -SrTiO ₃	1C-b3	82
BaO ₂ Ti	BaTiO ₃ -CaTiO ₃ -PbTiO ₃	1C-a9	75
BaO ₂ Ti	BaTiO ₃ -CaTiO ₃ -SrTiO ₃	1C-f2	87
		1C-f1	87

V Substanzenverzeichnis

Gross formula	Chemical formula	Nr.	Page
BaO ₃ Ti	BaTiO ₃ -LaInO ₃ -LaYO ₃ -SrTiO ₃	1C-f12	88
BaO ₃ Ti	BaTiO ₃ -PbTiO ₃ -BaNb ₂ O ₆ -PbNb ₂ O ₆	1C-f19	88
BaO ₃ Ti	(Ba-Ca)(Ti-Zr)O ₃	1C-f15	88
BaO ₃ Ti	(Ba-Pb)(Ti-Sn)O ₃	1C-f18	88
BaO ₃ Ti	(Ba-Pb)(Ti-Zr)O ₃	1C-f17	88
BaO ₃ U	BaUO ₃ -BaTiO ₃	1C-a26	77
BaO ₃ Zr	BaZrO ₃ -BaNb ₂ O ₆	5C-j2	105
BaO ₃ Zr	BaZrO ₃ -BaTiO ₃	1C-a23	77
BaO ₃ Zr	BaZrO ₃ -CaZrO ₃	1C-a12	76
BaO ₃ Zr	BaZrO ₃ -PbTiO ₃	1C-b9	82
BaO ₃ Zr	BaZrO ₃ -PbZrO ₃	1C-a15	76
BaO ₃ Zr	(Ba-Ca)(Zr-Ti)O ₃	1C-f15	88
BaO ₃ Zr	(Ba-Pb)(Zr-Ti)O ₃	1C-f17	88
BaO ₃ Zr	BaZr _{0.25} Nb _{1.5} O _{5.25}	5C-j3	105
BeF ₄ H ₈ N ₂	(NH ₄) ₂ BeF ₄ -(NH ₄) ₂ SO ₄	14B-1	154
BiFeO ₃	BiFeO ₃ -BaTiO ₃	1C-c9	84
BiFeO ₃	BiFeO ₃ -LaAlO ₃	1C-b11	83
BiFeO ₃	BiFeO ₃ -LaCrO ₃	1C-b12	83
BiFeO ₃	BiFeO ₃ -LaFeO ₃	1C-a33	82
BiFeO ₃	BiFeO ₃ -Pb(Fe _{1/2} Nb _{1/2})O ₃	1C-d23	85
BiFeO ₃	BiFeO ₃ -PbTiO ₃	1C-c13	84
BiFeO ₃	BiFeO ₃ -PbZrO ₃	1C-c14	84
BiFeO ₃	BiFeO ₃ -SrFeO ₃	1C-c16	84
BiFeO ₃	BiFeO ₃ -Sr(Sn _{1/3} Mn _{2/3})O ₃	1C-d22	85
BiFeO ₃	BiFeO ₃ -SrSnO ₃	1C-c15	84
BiFeO ₃	BiFeO ₃ -SrTiO ₃	1C-c7	83
BiFeO ₃	BiFeO ₃ -PbTiO ₃ -PbZrO ₃	1C-f6	87
Bi ₅ GaO ₁₅ Ti ₃	Bi ₅ Ti ₃ GaO ₁₅ -Bi ₄ PbTi ₄ O ₁₅	7B-7	114
BiIS	BiSI-SbSI	10B-5	128
Bi _{1/2} K _{1/2} O ₃ Ti	(K _{1/2} Bi _{1/2})TiO ₃ -BaTiO ₃	1C-d3	84
Bi _{1/2} K _{1/2} O ₃ Ti	(K _{1/2} Bi _{1/2})TiO ₃ -(Na _{1/2} Bi _{1/2})TiO ₃	1C-d20	85
Bi _{1/2} K _{1/2} O ₃ Ti	(K _{1/2} Bi _{1/2})TiO ₃ -PbTiO ₃	1C-d5	84
Bi _{1/2} K _{1/2} O ₃ Zr	(K _{1/2} Bi _{1/2})ZrO ₃ -PbZrO ₃	1C-d17	85
Bi _{1/2} Na _{1/2} O ₃ Ti	(Na _{1/2} Bi _{1/2})TiO ₃ -(K _{1/2} Bi _{1/2})TiO ₃	1C-d20	85
Bi _{1/2} Na _{1/2} O ₃ Ti	(Na _{1/2} Bi _{1/2})TiO ₃ -PbTiO ₃	1C-d4	84
Bi _{1/2} Na _{1/2} O ₃ Ti	(Na _{1/2} Bi _{1/2})TiO ₃ -PbZrO ₃	1C-d21	85
Bi _{1/2} Na _{1/2} O ₃ Zr	(Na _{1/2} Bi _{1/2})ZrO ₃ -PbZrO ₃	1C-d16	85
BiNbO ₆	Bi(Nb-Ti)O ₆ -PbNb ₂ O ₆	5B-14	102
Bi ₂ Nb ₆ O ₁₈	Bi ₂ O ₃ · 3Nb ₂ O ₅ -PbNb ₂ O ₆	5B-13	102
Bi ₂ Nb ₂ O ₅ Pb	Bi ₂ PbNb ₂ O ₅ -Bi ₃ TiNbO ₉	7B-1	113
Bi ₂ Nb ₂ O ₅ Pb	Bi ₂ PbNb ₂ O ₅ -BaBi ₂ Nb ₂ O ₉	7B-5	114
Bi ₃ NbO ₁₂ PbTi ₂	Bi ₃ PbTi ₂ NbO ₁₂ -Bi ₄ Ti ₃ O ₁₂	7B-2	113
Bi ₃ Nb ₂ O ₅ Sr	Bi ₃ SrNb ₂ O ₅ -Bi ₃ TiNbO ₉	7B-1	113
Bi ₃ NbO ₁₂ SrTi ₂	Bi ₃ SrTi ₂ NbO ₁₂ -Bi ₄ Ti ₃ O ₁₂	7B-2	113
Bi ₃ NbO ₅ Ti	Bi ₃ TiNbO ₉ -Bi ₂ BaNb ₂ O ₉	7B-1	113
Bi ₃ NbO ₅ Ti	Bi ₃ TiNbO ₉ -Bi ₂ PbNb ₂ O ₉	7B-1	113
Bi ₃ NbO ₅ Ti	Bi ₃ TiNbO ₉ -Bi ₂ SrNb ₂ O ₉	7B-1	113
Bi ₄ O ₁₅ PbTi ₄	Bi ₄ PbTi ₄ O ₁₅ -Bi ₅ Ti ₃ GaO ₁₅	7B-7	114
BiO ₆ Ti	Bi(Ti-Nb)O ₆ -PbNb ₂ O ₆	5B-14	102
Bi ₂ O ₃ Ti ₃	Bi ₂ O ₃ · 3TiO ₂ -PbNb ₂ O ₆	5B-14	102
Bi ₂ O ₃ Ti ₃	Bi ₂ O ₃ · 3TiO ₂ -SrTiO ₃	1C-e8	86
Bi ₄ O ₁₂ Ti ₃	Bi ₄ Ti ₃ O ₁₂ -BaTiO ₃	7B-6	114
Bi ₄ O ₁₂ Ti ₃	Bi ₄ Ti ₃ O ₁₂ -Bi ₃ BaTi ₂ NbO ₁₂	7B-2	113
Bi ₄ O ₁₂ Ti ₃	Bi ₄ Ti ₃ O ₁₂ -Bi ₃ PbTi ₂ NbO ₁₂	7B-2	113
Bi ₄ O ₁₂ Ti ₃	Bi ₄ Ti ₃ O ₁₂ -Bi ₃ SrTi ₂ NbO ₁₂	7B-2	113
BrSSb	SbSBr-SbSI	10B-3	127
C ₆ FH ₁₇ N ₃ O ₉ P	(NH ₂ CH ₂ COOH) ₃ · H ₂ PO ₃ F-		
C ₆ FeH ₆ K ₄ N ₆ O ₃	(NH ₂ CH ₂ COOH) ₃ · H ₂ SO ₄	28B-2	191
C ₆ FeH ₆ K ₄ N ₆ O ₃	K ₄ Fe(CN) ₆ · 3H ₂ O-(NH ₄) ₄ Fe(CN) ₆ · 3H ₂ O	22B-1	176
C ₆ FeH ₆ K ₄ N ₆ O ₃	K ₄ Fe(CN) ₆ · 3H ₂ O-Rb ₄ Fe(CN) ₆ · 3H ₂ O	22B-2	176
C ₆ FeH ₁₆ N ₁₀ · 3H ₂ O	K ₄ Fe(CN) ₆ · 3H ₂ O-Tl ₄ Fe(CN) ₆ · 3H ₂ O	22B-3	177
C ₆ FeH ₂₂ N ₁₀ O ₃	(NH ₄) ₄ Fe(CN) ₆ · 3H ₂ O-K ₄ Fe(CN) ₆ · 3H ₂ O	22B-1	176
	(NH ₄) ₄ Fe(CN) ₆ · 3H ₂ O-K ₄ Fe(CN) ₆ · 3H ₂ O	22B-1	176

V Index of substances

Gross formula	Chemical formula	Nr.	Page
$C_6FeH_5N_6O_4Rb_4$	$Rb_4Fe(CN)_6 \cdot 3H_2O - K_4Fe(CN)_6 \cdot 3H_2O$	22B-2	176
$C_6FeH_5N_6O_4Ti_4$	$Ti_4Fe(CN)_6 \cdot 3H_2O - K_4Fe(CN)_6 \cdot 3H_2O$	22B-3	177
$C_6FeK_4N_6 \cdot 3H_2O$	$K_4Fe(CN)_6 \cdot 3H_2O - (NH_4)_4Fe(CN)_6 \cdot 3H_2O$	22B-1	176
$C_6FeK_4N_6 \cdot 3H_2O$	$K_4Fe(CN)_6 \cdot 3H_2O - Rb_4Fe(CN)_6 \cdot 3H_2O$	22B-2	176
$C_6FeK_4N_6 \cdot 3H_2O$	$K_4Fe(CN)_6 \cdot 3H_2O - Ti_4Fe(CN)_6 \cdot 3H_2O$	22B-3	177
$C_6FeN_4Rb_4 \cdot 3H_2O$	$Rb_4Fe(CN)_6 \cdot 3H_2O - K_4Fe(CN)_6 \cdot 3H_2O$	22B-2	176
$C_6FeN_4Ti_4 \cdot 3H_2O$	$Ti_4Fe(CN)_6 \cdot 3H_2O - K_4Fe(CN)_6 \cdot 3H_2O$	22B-3	177
$C_4H_4KNaO_6 \cdot 4H_2O$	$NaKC_4H_4O_6 \cdot 4H_2O - NaNH_4C_4H_4O_6 \cdot 4H_2O$	33B-1	198
$C_4H_4KNaO_6 \cdot 4H_2O$	$NaKC_4H_4O_6 \cdot 4H_2O - NaTiC_4H_4O_6 \cdot 4H_2O$	33B-2	198
$C_4H_{12}KNaO_{10}$	$NaKC_4H_4O_6 \cdot 4H_2O - NaNH_4C_4H_4O_6 \cdot 4H_2O$	33B-1	198
$C_4H_{12}KNaO_{10}$	$NaKC_4H_4O_6 \cdot 4H_2O - NaTiC_4H_4O_6 \cdot 4H_2O$	33B-2	198
$C_4H_8NNaO_6 \cdot 4H_2O$	$NaNH_4C_4H_4O_6 \cdot 4H_2O - NaKC_4H_4O_6 \cdot 4H_2O$	33B-1	198
$C_4H_{16}NNaO_{10}$	$NaNH_4C_4H_4O_6 \cdot 4H_2O - NaKC_4H_4O_6 \cdot 4H_2O$	33B-1	198
$C_6H_{17}N_5O_{10}S$	$(NH_2CH_2COOH)_3 \cdot H_2SO_4 - (NH_2CH_2COOH)_3 \cdot H_2PO_3F$	28B-2	191
$C_6H_{17}N_5O_{10}S$	$(NH_2CH_2COOH)_3 \cdot H_2SO_4 - (NH_2CH_2COOH)_3 \cdot H_2SeO_4$	28B-1	191
$C_6H_{17}N_5O_{10}Se$	$(NH_2CH_2COOH)_3 \cdot H_2SeO_4 - (NH_2CH_2COOH)_3 \cdot H_2SO_4$	28B-1	191
$C_4H_4NaO_6Ti \cdot 4H_2O$	$NaTiC_4H_4O_6 \cdot 4H_2O - NaKC_4H_4O_6 \cdot 4H_2O$	33B-2	198
$C_4H_{12}NaO_{10}Ti$	$NaTiC_4H_4O_6 \cdot 4H_2O - NaKC_4H_4O_6 \cdot 4H_2O$	33B-2	198
$CaHfO_3$	$CaHfO_3 - PbHfO_3$	1C-a16	76
$CaNb_2O_6$	$CaNb_2O_6 - BaNb_2O_6$	5B-1	99
$CaNb_2O_6$	$CaNb_2O_6 - NaNbO_3$	1C-e3	86
$CaNb_2O_6$	$CaNb_2O_6 - PbNb_2O_6$	5B-2	99
$CaNb_2O_6$	$(Ca-Ba-Pb)(Nb-Ta)_2O_6$	5B-15	102
$Ca_2Nb_2O_7$	$Ca_2Nb_2O_7 - Cd_2Nb_2O_7$	6B-1	106
CaO_3Sn	$CaSnO_3 - PbTiO_3$	1C-b6	82
CaO_3Sn	$CaSnO_3 - SrSnO_3$	1C-a19	76
CaO_3Sn	$CaSnO_3 - SrSnO_3 - BaSnO_3$	1C-f13	88
CaO_3Ta_2	$(Ca-Ba-Pb)(Ta-Nb)_2O_6$	5B-15	102
$Ca_2O_7Ta_2$	$Ca_2Ta_2O_7 - Sr_2Ta_2O_7$	6B-6	106
CaO_3Ti	$CaTiO_3 - BaTiO_3$	1C-a7	74
CaO_3Ti	$CaTiO_3 - CaZrO_3$	1C-a22	76
CaO_3Ti	$CaTiO_3 - NaNbO_3$	1C-c1	83
CaO_3Ti	$CaTiO_3 - PbTiO_3$	1C-a8	75
CaO_3Ti	$CaTiO_3 - SrTiO_3$	1C-a6	74
CaO_3Ti	$CaTiO_3 - BaTiO_3 - PbTiO_3$	1C-f2	87
CaO_3Ti	$CaTiO_3 - BaTiO_3 - SrTiO_3$	1C-f1	87
CaO_3Ti	$(Ca-Ba)(Ti-Zr)O_3$	1C-f15	88
CaO_3Zr	$CaZrO_3 - BaZrO_3$	1C-a12	76
CaO_3Zr	$CaZrO_3 - CaTiO_3$	1C-a22	76
CaO_3Zr	$CaZrO_3 - PbTiO_3$	1C-b5	82
CaO_3Zr	$CaZrO_3 - PbZrO_3$	1C-a13	76
CaO_3Zr	$(Ca-Ba)(Zr-Ti)O_3$	1C-f15	88
$CdNb_2O_6$	$CdNb_2O_6 - NaNbO_3$	1C-e4	86
$CdNb_2O_6$	$CdNb_2O_6 - PbNb_2O_6$	5B-10	101
$Cd_2Nb_2O_7$	$Cd_2Nb_2O_7 - Ca_2Nb_2O_7$	6B-1	106
$Cd_2Nb_2O_7$	$Cd_2Nb_2O_7 - Cd_2Ta_2O_7$	6B-3	106
$Cd_2Nb_2O_7$	$Cd_2Nb_2O_7 - Mg_2Nb_2O_7$	6B-4	106
$Cd_2Nb_2O_7$	$Cd_2Nb_2O_7 - Pb_2Nb_2O_7$	6B-2	106
$Cd_2O_7Ta_2$	$Cd_2Ta_2O_7 - Cd_2Nb_2O_7$	6B-3	106
CdO_3Ti	$CdTiO_3 - LiNbO_3$	1C-e7	86
CdO_3Ti	$CdTiO_3 - LiTaO_3$	1C-e7	86
$Ce_{1/2}Li_{1/2}O_3Ti$	$(Li_{1/2}Ce_{1/2})TiO_3 - PbTiO_3$	1C-d8	85
$CoLaO_3$	$LaCoO_3 - PbTiO_3 - LaMnO_3$	1C-f11	87
$Co_2Nb_2O_7$	$Co_2Nb_2O_7 - BaTiO_3$	1C-e11	87
$Co_2O_7Ta_2$	$Co_2Ta_2O_7 - BaTiO_3$	1C-e11	87
$CrLaO_3$	$LaCrO_3 - BiFeO_3$	1C-b12	83
$CrLaO_3$	$LaCrO_3 - PbTiO_3 - LaMnO_3$	1C-f11	87
$CsNO_3$	$CsNO_3 - RbNO_3$	12B-4	134
$Eu_2Mo_3O_{12}$	$(Eu-Gd)_2(MoO_4)_3$	35-5	201
$Eu_2Mo_3O_{12}$	$(Eu-Tb)_2(MoO_4)_3$	35-6	201

V Substanzenverzeichnis

Gross formula	Chemical formula	Nr.	Page
FeLaO ₃	LaFeO ₃ -BiFeO ₃	1C-a33	82
FeLaO ₃	LaFeO ₃ -PbTiO ₃	1C-c12	84
FeLaO ₃	LaFeO ₃ -PbTiO ₃ -LaMnO ₃	1C-f11	87
FeLaO ₃	LaFeO ₃ -PbTiO ₃ -PbZrO ₃	1C-f5	87
Fe _{1/2} Nb _{1/2} O ₃ Pb	Pb(Fe _{1/2} Nb _{1/2})O ₃ -BiFeO ₃	1C-d23	85
Fe _{1/2} Nb _{1/2} O ₃ Pb	Pb(Fe _{1/2} Nb _{1/2})O ₃ -PbTiO ₃ -PbZrO ₃	1C-f8	87
Fe _{1/2} O ₃ PbTa _{1/2}	Pb(Fe _{1/2} Ta _{1/2})O ₃ -PbTiO ₃	1C-d11	85
Fe _{1/2} O ₃ PbTa _{1/2}	Pb(Fe _{1/2} Ta _{1/2})O ₃ -PbZrO ₃	1C-d15	85
FeO ₃ Sr	SrFeO ₃ -BiFeO ₃	1C-c16	84
Fe _{1/2} O ₃ SrTa _{1/2}	Sr(Fe _{1/2} Ta _{1/2})O ₃ -SrTiO ₃	1C-d1	84
Gd ₂ Mo ₃ O ₁₂	(Gd-Eu) ₂ (MoO ₄) ₃	35-5	201
Gd ₂ Mo ₃ O ₁₂	(Gd-Nd) ₂ (MoO ₄) ₃	35-8	202
Gd ₂ Mo ₃ O ₁₂	(Gd-Tb) ₂ (MoO ₄) ₃	35-9	202
Gd ₂ Mo ₃ O ₁₂	(Gd-Y) ₂ (MoO ₄) ₃	35-7	202
Gd ₂ Mo ₃ O ₁₂	Gd ₂ ((Mo-W)O ₄) ₃	35-10	202
Gd ₂ O ₁₂ W ₃	Gd ₂ ((W-Mo)O ₄) ₃	35-10	202
GeTe	GeTe-SnTe	36-3	214
H ₂ KO ₄ P	KH ₂ PO ₄ -NH ₄ H ₂ PO ₄	13B-1	148
H ₄ N ₂ O ₃	NH ₄ NO ₃ -KNO ₃	12B-1	134
H ₆ NO ₄ P	NH ₄ H ₂ PO ₄ -KH ₂ PO ₄	13B-1	148
H ₆ NO ₄ P	NH ₄ H ₂ PO ₄ -TiH ₂ PO ₄	13B-2	148
H ₈ N ₂ O ₃ S	(NH ₄) ₂ SO ₄ -(NH ₄) ₂ BeF ₄	14B-1	154
H ₂ O ₄ PTl	TiH ₂ PO ₄ -NH ₄ H ₂ PO ₄	13B-2	148
HfO ₃ Pb	PbHfO ₃ -BaHfO ₃	1C-a18	76
HfO ₃ Pb	PbHfO ₃ -CaHfO ₃	1C-a16	76
HfO ₃ Pb	PbHfO ₃ -Pb(Sc _{1/2} Nb _{1/2})O ₃	1C-d18	85
HfO ₃ Pb	PbHfO ₃ -PbTiO ₃	1C-a29	82
HfO ₃ Pb	PbHfO ₃ -PbZrO ₃	1C-a31	82
HfO ₃ Pb	PbHfO ₃ -SrHfO ₃	1C-a17	76
HfO ₃ Pb	PbHfO ₃ -PbTiO ₃ -PbO:SnO ₂	1C-f4	87
HfO ₃ Sr	SrHfO ₃ -PbHfO ₃	1C-a17	76
IK	KI-KNO ₃	12B-3	134
IOSb	SbOI-SbSI	10B-2	127
ISSb	SbSI-AsSI	10B-1	127
ISSb	SbSI-BiSI	10B-5	128
ISSb	SbSI-SbOI	10B-2	127
ISSb	SbSI-SbSBr	10B-3	127
ISSb	SbSI-SbSeI	10B-4	128
ISbSe	SbSeI-SbSI	10B-4	128
InLaO ₃	LaInO ₃ -BaTiO ₃ -LaYO ₃ -SrTiO ₃	1C-f12	88
KNO ₃	KNO ₃ -KI	12B-3	134
KNO ₃	KNO ₃ -NH ₄ NO ₃	12B-1	134
KNO ₃	KNO ₃ -RbNO ₃	12B-2	134
KNbO ₃	KNbO ₃ -BaTiO ₃	1C-c5	83
KNbO ₃	KNbO ₃ -KTaO ₃	1C-a4	74
KNbO ₃	KNbO ₃ -NaNbO ₃	1C-a1	73
KNbO ₃	KNbO ₃ -PbNb ₂ O ₆	5B-11	101
KNbO ₃	KNbO ₃ -PbTiO ₃	1C-c6	83
KNbO ₃	KNbO ₃ -SrNb ₂ O ₆	5C-b6	103
KNbO ₃	(K-Na)(Nb-Ta)O ₃	1C-f14	88
KNbO ₃	K _{0.6} Li _{0.4} (Nb _{0.3} Ta _{0.7})O ₃	5C-k2	105
KNbO ₃	K(Nb _{0.65} Ta _{0.35})O ₃ (KTN)	1C-a5	74
KO ₃ Sb	KSbO ₃ -NaNbO ₃	1C-b2	82
KO ₃ Ta	KTaO ₃ -KNbO ₃	1C-a4	74
KO ₃ Ta	KTaO ₃ -NaNbO ₃	1C-b1	82
KO ₃ Ta	K(Ta _{0.35} Nb _{0.65})O ₃ (KTN)	1C-a5	74
KO ₃ Ta	(K-Na)(Ta _{0.7} Nb _{0.3})O ₃	1C-f14	88
KO ₃ Ta	K _{0.6} Li _{0.4} (Ta _{0.7} Nb _{0.3})O ₃	5C-k2	105
KTN	K(Ta _{0.35} Nb _{0.65})O ₃	1C-a5	74

V Index of substances

Page	Gross formula	Chemical formula	Nr.	Page
82	LaFeO ₃	LaFeO ₃ -PbTiO ₃	1C-c12	84
84	La _{1/2} Li _{1/2} O ₃ Ti	(Li _{1/2} La _{1/2})TiO ₃ -PbTiO ₃	1C-d6	84
87	LaMnO ₃	LaMnO ₃ -PbTiO ₃	1C-c11	84
87	LaMnO ₃	LaMnO ₃ -LaCoO ₃ -PbTiO ₃	1C-f11	87
85	LaMnO ₃	LaMnO ₃ -LaCrO ₃ -PbTiO ₃	1C-f11	87
87	LaMnO ₃	LaMnO ₃ -LaFeO ₃ -PbTiO ₃	1C-f11	87
85	LaMnO ₃	LaMnO ₃ -LaNiO ₃ -PbTiO ₃	1C-f11	87
85	LaMnO ₃	LaMnO ₃ -PbTiO ₃ -SrTiO ₃	1C-f10	87
84	La _{1/2} Na _{1/2} O ₃ Ti	(Na _{1/2} La _{1/2})TiO ₃ -PbTiO ₃	1C-d7	85
84	La ₂ Nb ₆ O ₁₈	La ₂ O ₃ · 3Nb ₂ O ₅ -PbNb ₂ O ₆	5B-12	101
	LaNiO ₃	LaNiO ₃ -LaMnO ₃ -PbTiO ₃	1C-f11	87
201	LaO ₃ Y	LaYO ₃ -BaTiO ₃ -LaInO ₃ -SrTiO ₃	1C-f12	88
202	LiNbO ₃	LiNbO ₃ -CdTiO ₃	1C-e7	86
202	LiNbO ₃	LiNbO ₃ -LiTaO ₃	3B-1	94
202	LiNbO ₃	LiNbO ₃ -NaNbO ₃	1C-e1	86
202	LiNbO ₃	LiNbO ₃ -PbNb ₂ O ₆	5B-11	101
214	Li _{1/2} Nd _{1/2} O ₃ Ti	Li _{0.4} K _{0.6} (Nb _{0.5} Ta _{0.7})O ₃	5C-k2	105
	LiO ₃ Ta	(Li _{1/2} Nd _{1/2})TiO ₃ -PbTiO ₃	1C-d9	85
148	LiO ₃ Ta	LiTaO ₃ -CdTiO ₃	1C-e7	86
134	LiO ₃ Ta	LiTaO ₃ -LiNbO ₃	3B-1	94
148	LiO ₃ Ta	Li _{0.4} K _{0.6} (Ta _{0.7} Nb _{0.3})O ₃	5C-k2	105
	Mg ₂ Nb ₂ O ₇	Mg ₂ Nb ₂ O ₇ -Cd ₂ Nb ₂ O ₇	6B-4	106
154	Mg _{1/3} Nb _{2/3} O ₃ Pb	Pb(Mg _{1/3} Nb _{2/3})O ₃ -Pb(Mg _{1/2} W _{1/2})O ₃	1C-d19	85
148	Mg _{1/3} Nb _{2/3} O ₃ Pb	Pb(Mg _{1/3} Nb _{2/3})O ₃ -PbTiO ₃ -PbZrO ₃	1C-f7	87
76	Mg _{1/2} O ₃ PbW _{1/2}	Pb(Mg _{1/2} W _{1/2})O ₃ -Pb(Mg _{1/3} Nb _{2/3})O ₃	1C-d19	85
76	Mg _{1/2} O ₃ PbW _{1/2}	Pb(Mg _{1/2} W _{1/2})O ₃ -PbTiO ₃	1C-d10	85
85	Mn _{1/2} Nb _{1/2} O ₃ Pb	Pb(Mn _{1/2} Nb _{1/2})O ₃ -PbTiO ₃	1C-d13	85
82	Mn _{2/3} O ₃ Sn _{1/3} Sr	Sr(Sn _{1/3} Mn _{2/3})O ₃ -BiFeO ₃	1C-d22	85
82	Mn ₂ Nb ₂ O ₇	Mn ₂ Nb ₂ O ₇ -BaTiO ₃	1C-e11	87
76	Mn ₂ O ₇ Ta ₂	Mn ₂ Ta ₂ O ₇ -BaTiO ₃	1C-e11	87
87	Mo ₃ Nd ₂ O ₁₂	(Nd-Gd) ₂ (MoO ₄) ₃	35-8	202
76	Mo ₃ O ₁₂ Tb ₂	(Tb-Eu) ₂ (MoO ₄) ₃	35-6	201
	Mo ₃ O ₁₂ Tb ₂	(Tb-Gd) ₂ (MoO ₄) ₃	35-9	202
	Mo ₃ O ₁₂ Y ₂	(Y-Gd) ₂ (MoO ₄) ₃	35-7	202
134	NO ₃ Rb	RbNO ₃ -CsNO ₃	12B-4	134
127	NO ₃ Rb	RbNO ₃ KNO ₃	12B-2	134
128	NaNbO ₃	NaNbO ₃ -BaTiO ₃	1C-c2	83
127	NaNbO ₃	NaNbO ₃ -CaNb ₂ O ₆	1C-e3	86
127	NaNbO ₃	NaNbO ₃ -CaTiO ₃	1C-c1	83
128	NaNbO ₃	NaNbO ₃ -CdNb ₂ O ₆	1C-e4	86
128	NaNbO ₃	NaNbO ₃ -KNbO ₃	1C-a1	73
88	NaNbO ₃	NaNbO ₃ -KSbO ₃	1C-b2	82
	NaNbO ₃	NaNbO ₃ -KTaO ₃	1C-b1	82
134	NaNbO ₃	NaNbO ₃ -LiNbO ₃	1C-e1	86
134	NaNbO ₃	NaNbO ₃ -NaVO ₃	1C-e2	86
134	NaNbO ₃	NaNbO ₃ -NaSbO ₃	1C-a3	74
83	NaNbO ₃	NaNbO ₃ -NaTaO ₃	1C-a2	74
74	NaNbO ₃	NaNbO ₃ -PbNb ₂ O ₆	1C-e6,	86
73	NaNbO ₃	NaNbO ₃ -PbTiO ₃	5B-11	101
101	NaNbO ₃	NaNbO ₃ -PbZrO ₃	1C-c3	83
83	NaNbO ₃	NaNbO ₃ -SrNb ₂ O ₆	1C-c4	83
103	NaNbO ₃	(Na-K)(Nb-Ta)O ₃	1C-e5	86
88	NaO ₃ Sb	NaSbO ₃ -NaNbO ₃	1C-f14	88
105	NaO ₃ Ta	NaTaO ₃ -NaNbO ₃	1C-a3	74
74	NaO ₃ Ta	(Na-K)(Ta-Nb)O ₃	1C-a2	74
82	NaO ₃ V	NaVO ₃ -NaNbO ₃	1C-f14	88
74	Nb ₂ Ni ₂ O ₇	Ni ₂ Nb ₂ O ₇ -BaTiO ₃	1C-e2	86
74	Nb ₂ O ₆ Pb	PbNb ₂ O ₆ -BaNb ₂ O ₆	1C-e11	87
88	Nb ₂ O ₆ Pb	PbNb ₂ O ₆ -Bi ₂ O ₃ · 3Nb ₂ O ₅	5B-5	100
105	Nb ₂ O ₆ Pb	PbNb ₂ O ₆ -Bi ₂ O ₃ · 3TiO ₂	5B-13	102
74	Nb ₂ O ₆ Pb	PbNb ₂ O ₆ -CaNb ₂ O ₆	5B-14	102
			5B-2	99

V Substanzenverzeichnis

Gross formula	Chemical formula	Nr.	Page
$\text{Nb}_2\text{O}_5\text{Pb}$	$\text{PbNb}_2\text{O}_6\text{-CdNb}_2\text{O}_6$	5B-10	101
$\text{Nb}_2\text{O}_5\text{Pb}$	$\text{PbNb}_2\text{O}_6\text{-KNbO}_3$	5B-11	101
$\text{Nb}_2\text{O}_5\text{Pb}$	$\text{PbNb}_2\text{O}_6\text{-La}_2\text{O}_3 \cdot 3\text{Nb}_2\text{O}_5$	5B-12	101
$\text{Nb}_2\text{O}_5\text{Pb}$	$\text{PbNb}_2\text{O}_6\text{-LiNbO}_3$	5B-11	101
$\text{Nb}_2\text{O}_5\text{Pb}$	$\text{PbNb}_2\text{O}_6\text{-NaNbO}_3$	1C-e6,	86
$\text{Nb}_2\text{O}_5\text{Pb}$		5B-11	101
	$\text{PbNb}_2\text{O}_6\text{-PbO:SnO}_2$	5B-9	101
$\text{Nb}_2\text{O}_5\text{Pb}$	$\text{PbNb}_2\text{O}_6\text{-PbTa}_2\text{O}_6$	5B-6	101
$\text{Nb}_2\text{O}_5\text{Pb}$	$\text{PbNb}_2\text{O}_6\text{-PbTiO}_3$	5B-7	101
$\text{Nb}_2\text{O}_5\text{Pb}$	$\text{PbNb}_2\text{O}_6\text{-PbZrO}_3$	5B-8,	101
		1C-e12	87
	$\text{PbNb}_2\text{O}_6\text{-RbNbO}_3$	5B-11	101
$\text{Nb}_2\text{O}_5\text{Pb}$	$\text{PbNb}_2\text{O}_6\text{-Sm}_2\text{O}_3 \cdot 3\text{Nb}_2\text{O}_5$	5B-12	101
$\text{Nb}_2\text{O}_5\text{Pb}$	$\text{PbNb}_2\text{O}_6\text{-SrNb}_2\text{O}_6$	5B-4	100
$\text{Nb}_2\text{O}_5\text{Pb}$	$\text{PbNb}_2\text{O}_6\text{-Y}_2\text{O}_3 \cdot 3\text{Nb}_2\text{O}_5$	5B-12	101
$\text{Nb}_2\text{O}_5\text{Pb}$	$\text{PbNb}_2\text{O}_6\text{-Bi(Nb-Ti)O}_3$	5B-14	102
$\text{Nb}_2\text{O}_5\text{Pb}$	$\text{PbNb}_2\text{O}_6\text{-BaNb}_2\text{O}_6\text{-BaTiO}_3\text{-PbTiO}_3$	1C-f19	88
$\text{Nb}_2\text{O}_5\text{Pb}$	$(\text{Pb-Ba-Ca})(\text{Nb-Ta})_2\text{O}_6$	5B-15	102
$\text{Nb}_2\text{O}_5\text{Pb}$	$(\text{Pb-Ba-Sr})(\text{Nb-Ta})_2\text{O}_6$	5B-15	102
$\text{Nb}_2\text{O}_5\text{Pb}$	$\text{Pb}_2\text{Nb}_2\text{O}_7\text{-CdNb}_2\text{O}_7$	6B-2	106
$\text{Nb}_2\text{O}_7\text{Pb}_2$	$\text{Pb}(\text{Sc}_{1/2}\text{Nb}_{1/2})\text{O}_3\text{-PbHfO}_3$	1C-d18	85
$\text{Nb}_{1/2}\text{O}_3\text{PbSc}_{1/2}$	$\text{Pb}(\text{Sc}_{1/2}\text{Nb}_{1/2})\text{O}_3\text{-PbTiO}_3$	1C-d12	85
$\text{Nb}_{1/2}\text{O}_3\text{PbSc}_{1/2}$	$\text{Pb}(\text{Sc}_{1/2}\text{Nb}_{1/2})\text{O}_3\text{-PbZrO}_3$	1C-d14	85
$\text{Nb}_{1/2}\text{O}_3\text{PbSc}_{1/2}$	$\text{RbNbO}_3\text{-PbNb}_2\text{O}_6$	5B-11	101
NbO_3Rb	$\text{Sm}_2\text{O}_3 \cdot 3\text{Nb}_2\text{O}_5\text{-PbNb}_2\text{O}_6$	5B-12	101
$\text{Nb}_6\text{O}_{18}\text{Sm}_2$	$\text{SrNb}_2\text{O}_6\text{-BaNb}_2\text{O}_6$	5B-3	99
$\text{Nb}_2\text{O}_5\text{Sr}$	$\text{SrNb}_2\text{O}_6\text{-KNbO}_3$	5C-b6	103
$\text{Nb}_2\text{O}_5\text{Sr}$	$\text{SrNb}_2\text{O}_6\text{-NaNbO}_3$	1C-e5	86
$\text{Nb}_2\text{O}_5\text{Sr}$	$\text{SrNb}_2\text{O}_6\text{-PbNb}_2\text{O}_6$	5B-4	100
$\text{Nb}_2\text{O}_5\text{Sr}$	$(\text{Sr-Ba-Pb})(\text{Nb-Ta})_2\text{O}_6$	5B-15	102
$\text{Nb}_2\text{O}_5\text{Sr}$	$\text{Sr}_2\text{Nb}_2\text{O}_7\text{-Sr}_2\text{Ta}_2\text{O}_7$	6B-5	106
$\text{Nb}_2\text{O}_7\text{Sr}_2$	$\text{Ni}_2\text{Ta}_2\text{O}_7\text{-BaTiO}_3$	1C-e11	87
$\text{Ni}_2\text{O}_7\text{Ta}_2$	$\text{Y}_2\text{O}_3 \cdot 3\text{Nb}_2\text{O}_5\text{-PbNb}_2\text{O}_6$	5B-12	101
$\text{Nb}_2\text{O}_{18}\text{Y}_2$		1C-a21	76
O_3PbSn	$\text{PbO:SnO}_2\text{-BaSnO}_3$	1C-b4	82
O_3PbSn	$\text{PbO:SnO}_2\text{-BaTiO}_3$	5B-9	101
O_3PbSn	$\text{PbO:SnO}_2\text{-PbNb}_2\text{O}_6$	1C-a30	82
O_3PbSn	$\text{PbO:SnO}_2\text{-PbTiO}_3$	1C-a32	82
O_3PbSn	$\text{PbO:SnO}_2\text{-PbZrO}_3$	1C-f4	87
O_3PbSn	$\text{PbO:SnO}_2\text{-PbHfO}_3\text{-PbTiO}_3$	1C-f3	87
O_3PbSn	$\text{PbO:SnO}_2\text{-PbTiO}_3\text{-PbZrO}_3$	1C-f18	88
O_3PbSn	$(\text{Pb-Ba})(\text{Sn-Ti})\text{O}_3$	5B-6	101
O_3PbTa_2	$\text{PbTa}_2\text{O}_6\text{-PbNb}_2\text{O}_6$	1C-e13	87
O_3PbTa_2	$\text{PbTa}_2\text{O}_6\text{-PbZrO}_3$	5B-16	102
O_3PbTa_2	$\text{PbTa}_2\text{O}_6\text{-SrTa}_2\text{O}_6$	5B-15	102
O_3PbTa_2	$(\text{Pb-Ba-Ca})(\text{Ta-Nb})_2\text{O}_6$	5B-15	102
O_3PbTa_2	$(\text{Pb-Ba-Sr})(\text{Ta-Nb})_2\text{O}_6$	1C-b10	83
O_3PbTi	$\text{PbTiO}_3\text{-BaSnO}_3$	1C-a11	75
O_3PbTi	$\text{PbTiO}_3\text{-BaTiO}_3$	1C-b9	82
O_3PbTi	$\text{PbTiO}_3\text{-BaZrO}_3$	1C-c13	84
O_3PbTi	$\text{PbTiO}_3\text{-BiFeO}_3$	1C-b6	82
O_3PbTi	$\text{PbTiO}_3\text{-CaSnO}_3$	1C-a8	75
O_3PbTi	$\text{PbTiO}_3\text{-CaTiO}_3$	1C-b5	82
O_3PbTi	$\text{PbTiO}_3\text{-CaZrO}_3$	1C-d5	84
O_3PbTi	$\text{PbTiO}_3\text{-(K}_{1/2}\text{Bi}_{1/2})\text{TiO}_3$	1C-c6	83
O_3PbTi	$\text{PbTiO}_3\text{-KNbO}_3$	1C-c10	84
O_3PbTi	$\text{PbTiO}_3\text{-LaAlO}_3$	1C-c12	84
O_3PbTi	$\text{PbTiO}_3\text{-LaFeO}_3$	1C-c11	84
O_3PbTi	$\text{PbTiO}_3\text{-LaMnO}_3$	1C-d8	85
O_3PbTi	$\text{PbTiO}_3\text{-(Li}_{1/2}\text{Ce}_{1/2})\text{TiO}_3$	1C-d6	84
O_3PbTi	$\text{PbTiO}_3\text{-(Li}_{1/2}\text{La}_{1/2})\text{TiO}_3$	1C-d9	85
O_3PbTi	$\text{PbTiO}_3\text{-(Li}_{1/2}\text{Nd}_{1/2})\text{TiO}_3$	1C-d4	84
O_3PbTi	$\text{PbTiO}_3\text{-(Na}_{1/2}\text{Bi}_{1/2})\text{TiO}_3$	1C-d7	85
O_3PbTi	$\text{PbTiO}_3\text{-(Na}_{1/2}\text{La}_{1/2})\text{TiO}_3$		

Furuhata/Makita

V Index of substances

Page	Gross formula	Chemical formula	Nr.	Page
101	O_3PbTi	$PbTiO_3-NaNbO_3$	1C-c3	83
101	O_3PbTi	$PbTiO_3-Pb(Fe_{1/2}Ta_{1/2})O_3$	1C-d11	85
101	O_3PbTi	$PbTiO_3-PbHfO_3$	1C-a29	82
101	O_3PbTi	$PbTiO_3-Pb(Mg_{1/2}W_{1/2})O_3$	1C-d10	85
86	O_3PbTi	$PbTiO_3-Pb(Mn_{1/2}Nb_{1/2})O_3$	1C-d13	85
101	O_3PbTi	$PbTiO_3-PbNb_2O_6$	5B-7	101
101	O_3PbTi	$PbTiO_3-PbO:SnO_2$	1C-a30	82
101	O_3PbTi	$PbTiO_3-Pb(Sc_{1/2}Nb_{1/2})O_3$	1C-d12	85
101	O_3PbTi	$PbTiO_3-PbZrO_3$	1C-a27	77
101	O_3PbTi	$PbTiO_3-SrSnO_3$	1C-b8	82
87	O_3PbTi	$PbTiO_3-SrTiO_3$	1C-a10	75
101	O_3PbTi	$PbTiO_3-SrZrO_3$	1C-b7	82
101	O_3PbTi	$PbTiO_3-ABO_3-PbZrO_3$	1C-f9	87
100	O_3PbTi	$PbTiO_3-BaTiO_3-CaTiO_3$	1C-f2	87
101	O_3PbTi	$PbTiO_3-BiFeO_3-PbZrO_3$	1C-f6	87
102	O_3PbTi	$PbTiO_3-LaCoO_3-LaMnO_3$	1C-f11	87
88	O_3PbTi	$PbTiO_3-LaCrO_3-LaMnO_3$	1C-f11	87
102	O_3PbTi	$PbTiO_3-LaFeO_3-LaMnO_3$	1C-f11	87
102	O_3PbTi	$PbTiO_3-LaFeO_3-PbZrO_3$	1C-f5	87
106	O_3PbTi	$PbTiO_3-LaMnO_3-LaNiO_3$	1C-f11	87
85	O_3PbTi	$PbTiO_3-LaMnO_3-SrTiO_3$	1C-f10	87
85	O_3PbTi	$PbTiO_3-Pb(Fe_{1/2}Nb_{1/2})O_3-PbZrO_3$	1C-f8	87
85	O_3PbTi	$PbTiO_3-PbHfO_3-PbO:SnO_2$	1C-f4	87
101	O_3PbTi	$PbTiO_3-Pb(Mg_{1/3}Nb_{2/3})O_3-PbZrO_3$	1C-f7	87
101	O_3PbTi	$PbTiO_3-PbO:SnO_2-PbZrO_3$	1C-f3	87
99	O_3PbTi	$PbTiO_3-BaTiO_3-BaNb_2O_6-PbNb_2O_6$	1C-f19	88
103	O_3PbTi	$(Pb-Ba)(Ti-Sn)O_3$	1C-f18	88
86	O_3PbTi	$(Pb-Ba)(Ti-Zr)O_3$	1C-f17	88
100	O_3PbTi	$Pb(Ti-Zr)O_3$	1C-a28	78
102	O_3PbTi	$(Pb-Sr)(Ti-Zr)O_3$	1C-f16	88
106	O_3PbZr	$PbZrO_3-BaTiO_3$	1C-b3	82
87	O_3PbZr	$PbZrO_3-BaZrO_3$	1C-a15	76
101	O_3PbZr	$PbZrO_3-BiFeO_3$	1C-c14	84
	O_3PbZr	$PbZrO_3-CaZrO_3$	1C-a13	76
76	O_3PbZr	$PbZrO_3-(K_{1/2}Bi_{1/2})ZrO_3$	1C-d17	85
82	O_3PbZr	$PbZrO_3-(Na_{1/2}Bi_{1/2})TiO_3$	1C-d21	85
101	O_3PbZr	$PbZrO_3-(Na_{1/2}Bi_{1/2})ZrO_3$	1C-d16	85
82	O_3PbZr	$PbZrO_3-NaNbO_3$	1C-c4	83
82	O_3PbZr	$PbZrO_3-Pb(Fe_{1/2}Ta_{1/2})O_3$	1C-d15	85
87	O_3PbZr	$PbZrO_3-PbHfO_3$	1C-a31	82
87	O_3PbZr	$PbZrO_3-PbNb_2O_6$	5B-8,	101
88			1C-e12	87
101	O_3PbZr	$PbZrO_3-PbO:SnO_2$	1C-a32	82
87	O_3PbZr	$PbZrO_3-Pb(Sc_{1/2}Nb_{1/2})O_3$	1C-d14	85
102	O_3PbZr	$PbZrO_3-PbTa_2O_6$	1C-e13	87
102	O_3PbZr	$PbZrO_3-PbTiO_3$	1C-a27	77
102	O_3PbZr	$PbZrO_3-SrZrO_3$	1C-a14	76
83	O_3PbZr	$Pb(Zr-Ti)O_3$ (PZT)	1C-a28	78
75	O_3PbZr	$PbZrO_3-ABO_3-PbTiO_3$	1C-f9	87
82	O_3PbZr	$PbZrO_3-BiFeO_3-PbTiO_3$	1C-f6	87
84	O_3PbZr	$PbZrO_3-LaFeO_3-PbTiO_3$	1C-f5	87
82	O_3PbZr	$PbZrO_3-Pb(Fe_{1/2}Nb_{1/2})O_3-PbTiO_3$	1C-f8	87
75	O_3PbZr	$PbZrO_3-Pb(Mg_{1/2}Nb_{1/2})O_3-PbTiO_3$	1C-f7	87
82	O_3PbZr	$PbZrO_3-PbO:SnO_2-PbTiO_3$	1C-f3	87
84	O_3PbZr	$(Pb-Ba)(Zr-Ti)O_3$	1C-f17	88
83	O_3PbZr	$(Pb-Sr)(Zr-Ti)O_3$	1C-f16	88
84	O_3SnSr	$SrSnO_3-BaSnO_3$	1C-a20	76
84	O_3SnSr	$SrSnO_3-BiFeO_3$	1C-c15	84
84	O_3SnSr	$SrSnO_3-CaSnO_3$	1C-a19	76
85	O_3SnSr	$SrSnO_3-PbTiO_3$	1C-b8	82
84	O_3SnSr	$SrSnO_3-BaSnO_3-CaSnO_3$	1C-f13	88
85	O_6SrTa_2	$SrTa_2O_6-PbTa_2O_6$	5B-16	102
84	O_6SrTa_2	$(Sr-Ba-Pb)(Ta-Nb)_2O_6$	5B-15	102
85	$O_7Sr_2Ta_2$	$Sr_2Ta_2O_7-Ca_2Ta_2O_7$	6B-6	106

V Substanzenverzeichnis

Gross formula	Chemical formula	Nr.	Page
$O_7Sr_2Ta_2$	$Sr_2Ta_2O_7-Sr_2Nb_2O_7$	6B-5	106
O_3SrTi	$SrTiO_3-BaTiO_3$	1C-a9	75
O_3SrTi	$SrTiO_3-BiFeO_3$	1C-c7	83
O_3SrTi	$SrTiO_3-Bi_2O_3 \cdot 3TiO_2$	1C-e8	86
O_3SrTi	$SrTiO_3-CaTiO_3$	1C-a6	74
O_3SrTi	$SrTiO_3-PbTiO_3$	1C-a10	75
O_3SrTi	$SrTiO_3-Sr(Fe_{1/2}Ta_{1/2})O_3$	1C-d1	84
O_3SrTi	$SrTiO_3-BaTiO_3-CaTiO_3$	1C-f1	87
O_3SrTi	$SrTiO_3-LaMnO_3-PbTiO_3$	1C-f10	87
O_3SrTi	$SrTiO_3-BaTiO_3-LaInO_3-LaYO_3$	1C-f12	88
O_3SrZr	$(Sr-Pb)(Ti-Zr)O_3$	1C-f16	88
O_3SrZr	$SrZrO_3-PbTiO_3$	1C-b7	82
O_3SrZr	$SrZrO_3-PbZrO_3$	1C-a14	76
O_3SrZr	$(Sr-Pb)(Zr-Ti)O_3$	1C-f16	88
PZT	$Pb(Zr-Ti)O_3$	1C-a28	78
SnTe	SnTe-GeTe	36-3	214

BRIEF ATTACHMENT Q

IN THE UNITED STATES PATENT AND TRADEMARK OFFICE

In re Patent Application of

Applicants: Bednorz et al.

Serial No.: 08/479,810

Filed: June 7, 1995

For: NEW SUPERCONDUCTIVE COMPOUNDS HAVING HIGH TRANSITION
TEMPERATURE, METHODS FOR THEIR USE AND PREPARATION

Date: March 1, 2005

Docket: YO987-074BZ

Group Art Unit: 1751

Examiner: M. Kopec

Commissioner for Patents
P.O. Box 1450
Alexandria, VA 22313-1450

FIRST SUPPLEMENTAL AMENDMENT

Sir:

In response to the Office Action dated July 28, 2004, please consider the
following:

ATTACHMENT Q

J. C. Beckwith

STRUCTURE AND
PROPERTIES OF
INORGANIC SOLIDS

BY

FRANCIS S. GALASSO
United Aircraft Research Laboratories

ILLUSTRATED BY

W. DARBY



PERGAMON PRESS
Oxford · New York · Toronto
Sydney · Braunschweig

Pergamon Press Ltd., Headington Hill Hall, Oxford
Pergamon Press Inc., Maxwell House, Fairview Park, Elmsford, New York 10523
Pergamon of Canada Ltd., 207 Queen's Quay West, Toronto 1
Pergamon Press (Aust.) Pty. Ltd., 19a Boundary Street, Rushcutters Bay,
N.S.W. 2011, Australia

Vieweg & Sohn GmbH, Burgplatz 1, Braunschweig

Copyright © 1970

Pergamon Press Inc.

All Rights Reserved. No part of this publication may be reproduced,
stored in a retrieval system, or transmitted, in any form or by any
means, electronic, mechanical, photocopying, recording or otherwise,
without the prior permission of Pergamon Press Inc.

First edition 1970

P 712 412: 7



Ser.

Kat.

3. DEZ. 1970

Library of Congress Catalog Card No. 70-104123

PRINTED IN GREAT BRITAIN BY PAGE BROS. (NORWICH) LTD.
08 006873 1

CONTENTS

PREFACE

ix

1. INTRODUCTION

1

1.1. Crystallography

1

1.2. Properties

12

2. COMMON STRUCTURES

26

2.1. Body-centered Cubic, A2

26

2.2. Face-centered Cubic, A1

28

2.3. Close-packed Hexagonal, A3

30

2.4. Structure of Other Elements

32

2.5. Alloys (Ordering)

35

2.6. Discussion

36

3. THE CsCl TYPE AND RELATED STRUCTURES

39

3.1. CsCl, B2

39

3.2. Cuprite, C3

43

3.3a. Rutile, C4

44

3.3b. Trirutile

46

3.4. CaB₆, D2₁

48

3.5. BiF₃, D0₃

50

3.6. Discussion

52

4. THE NaCl TYPE AND RELATED STRUCTURES

59

4.1. NaCl, B1

59

4.2. FeS₂, C2

68

4.3. CaC₂, C11

70

4.4. Cu₂AlMn, L2₁

73

4.5. Discussion

75

5. ZnS TYPE AND RELATED STRUCTURES

82

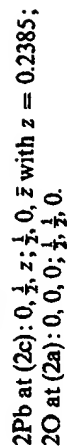
5.1. Diamond Cubic, A4

82

5.2. ZnS, Zinc Blende, B3

84

cell is elongated in the c direction; the lead atoms are displaced vertically downwards in the front and back faces and upwards in the side faces. This arrangement corresponds to placement of the atoms in the following special positions in space group $P4/nmm$:



In this structure both the lead and oxygen atoms are in fourfold coordination with atoms of the other type. The oxygen atoms are in a tetrahedron of lead atoms, while the lead atoms are at the vertex of a square pyramid with oxygen atoms at the base. In the horizontal oxygen sheets, the atoms are in square planar coordination or roughly cubic packing. This structure is illustrated in Fig. 7.1. Other compounds which adopt this structure are listed in Table 7.1.

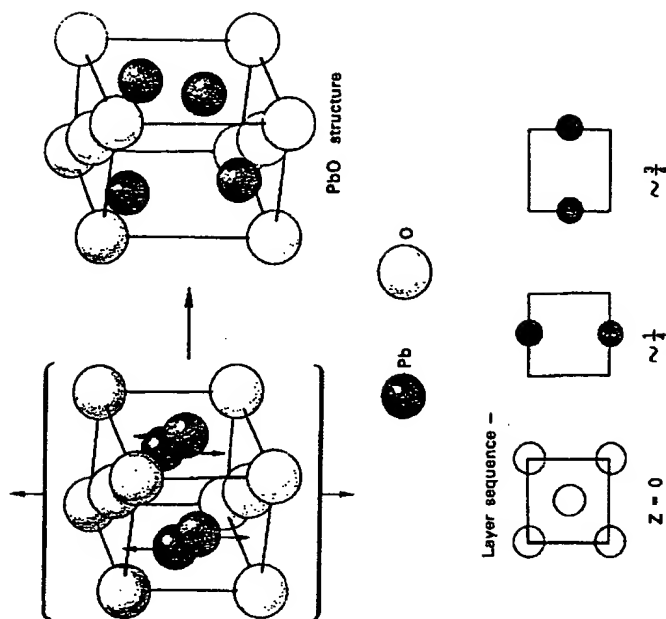


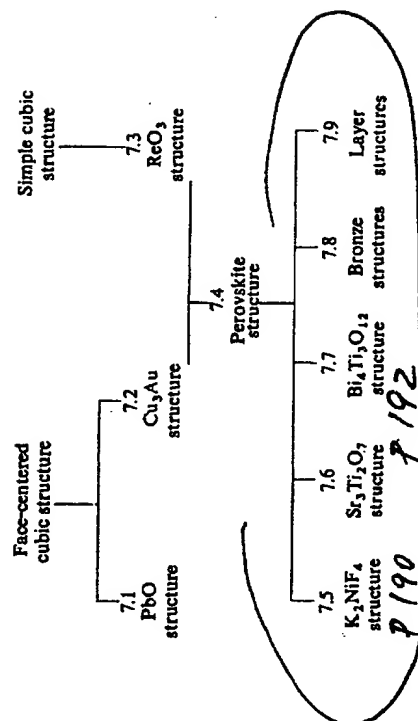
Fig. 7.1 Lead oxide structure

CHAPTER 7

PEROVSKITE TYPE AND RELATED STRUCTURES

THE perovskite-type structures are formed by ABX_3 -type compounds where the A atoms replace some of the X atoms in close-packed cubic layers and the B atoms fit in the octahedrally coordinated sites. In the ordered Cu_3Au structure there are no B atoms; in the ReO_3 structure the A atoms are missing so that there are holes in the close-packed X atom layers. These close-packed layers are perpendicular to the $\langle 111 \rangle$ directions (body diagonals) in the cubic unit cell. Related structures can be built up as close-packed layers of X atoms or by stacking cubic unit cells. The flow diagram showing the relationships between these structures is presented in Table 7.0.

TABLE 7.0.

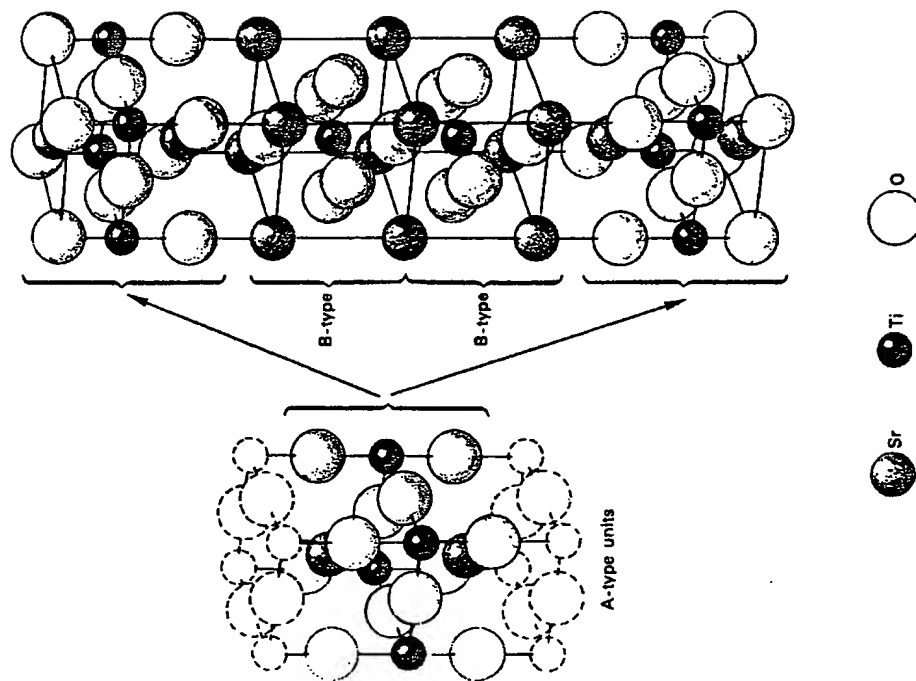


7.1. Red Lead Oxide, PbO , B10 , $P4/nmm$, Tetragonal

This lead oxide structure can be visualized by starting with an ordered cubic close-packed structure. Lead atoms are placed in the centered positions on the vertical faces of a unit cell and the oxygen atoms in the centered position on the top and bottom faces as well as at the cell corners. The cubic

TABLE 7.5. Phases with the K_2NiF_4 Structure

Phases	Cell size (Å)		Atomic parameters		Refs.
	a_0	c_0	x (A cation)	z (anion)	
Halides, Oxylhalides	5.215	16.46			1
	4.074	13.08			2
	4.155	12.74	0.356	0.153	3
	3.977	13.16	0.35	0.15	4
	4.01	13.08	0.352	0.151	5
	3.96	13.67			6
	4.017	13.05			7
	4.084	13.79			8
	4.087	13.71			8
	4.104	13.28			7
	3.84	12.98			9
	4.10	14.1			2
	4.051	14.22			8
Oxides	4.296	13.30	0.355	0.155	10
	4.130	13.27	0.355	0.155	10
	3.67	12.08			11
	4.38	14.79			12
	3.89	11.85			13
	4.34	13.10	0.36	0.145	14
	3.855	12.652	0.360	1.170	15
	3.94	12.15			13
	3.81	12.31			13
	4.345	13.83			12
	3.91	11.93			13
	3.89	12.92	0.347	0.151	16
	3.79	12.43			5
	3.92	12.84			5
Complex Oxides	3.85	12.90			17
	3.870	12.74			17
	4.037	12.53	0.353	0.153	10
	3.884	12.60	0.355	0.152	18
	3.77	12.58			19
	3.75	12.89			19
	3.75	12.5			11
	3.80	12.50			19
	3.85	12.62			19
	3.84	12.52			19
	3.82	12.58			19
	3.86	12.69			19
	3.84	12.71			19
	3.88	12.5			19
	3.80	12.51			19
	3.92	12.78			19

FIG. 7.6 The $Sr_3Ti_2O_7$ structure

BRIEF ATTACHMENT R

IN THE UNITED STATES PATENT AND TRADEMARK OFFICE

In re Patent Application of

Applicants: Bednorz et al.

Serial No.: 08/479,810

Filed: June 7, 1995

For: NEW SUPERCONDUCTIVE COMPOUNDS HAVING HIGH TRANSITION
TEMPERATURE, METHODS FOR THEIR USE AND PREPARATION

Date: March 1, 2005

Docket: YO987-074BZ

Group Art Unit: 1751

Examiner: M. Kopec

Commissioner for Patents
P.O. Box 1450
Alexandria, VA 22313-1450

FIRST SUPPLEMENTAL AMENDMENT

Sir:

In response to the Office Action dated July 28, 2004, please consider the
following:

ATTACHMENT R

9. DEC 1963

CRYSTAL STRUCTURES

Second Edition

Ralph W. G. Wyckoff, *University of Arizona, Tucson, Arizona*

VOLUME 4

Miscellaneous Inorganic Compounds, Silicates, and
Basic Structural Information

INTERSCIENCE PUBLISHERS

a division of John Wiley & Sons, New York • London • Sydney • Toronto

Preface

The presentation of data in this volume follows without significant change the pattern established in preceding volumes of this edition. As in Volume V, which was issued earlier, right-hand axes are used in all new drawings.

Since this edition was planned, it has been decided not to enlarge its scope by including intermetallic compounds. Instead, Chapter XIII is devoted to a very abbreviated statement of basic ideas about symmetry and valence. The writer has found that there are many people wishing to use structural data whose training has not prepared them to read with understanding the descriptions of structure now standard. Chapter XIII aims to give this information in as condensed a form as possible. Considering the rapidity with which valence theory is developing, its discussion of valence will undoubtedly seem inadequate to chemists concerned with the subject. In the writer's experience, however, there is little middle ground between a cursory statement such as that given here and a treatment, dealing mostly with organic structures, too long and detailed to be appropriate to the present series.

RALPH W. G. WYCKOFF

Copyright © 1951, 1953, 1959, 1960 by Interscience Publishers, Inc.
Copyright © 1968 by John Wiley & Sons, Inc.

ALL RIGHTS RESERVED

No part of this book may be reproduced by any means, nor transmitted, nor translated into a machine language without the written permission of the publisher.

Library of Congress Catalog Card Number 48-9169
SBN 470 96866
Printed in the United States of America

TABLE XI,45

Positions and Parameters of the Atoms in $\text{PbBi}_2\text{Nb}_2\text{O}_8$

Atom	Position	x	y	z
Pb	(4a)	0	0	0.500
Bi	(8c)	0	0.50	0.200
Nb	(8c)	0	0.50	0.422
O(1)	(4a)	0	0	0.00
O(2)	(8b)	$1/4$	$1/4$	0.25
O(3)	(8b)	$1/4$	$1/4$	0.079
O(4)	(8b)	$1/4$	$1/4$	-0.079
O(5)	(8c)	0	0.50	0.156

with the parameters of Table XI,45.

This structure, like those of $\text{Bi}_2\text{Ti}_2\text{O}_{12}$ (IX,f12) and $\text{BaBi}_2\text{Ti}_2\text{O}_{16}$ (XI,13) is built up of alternating Bi_2O_3 and perovskite-like layers.

The following compounds are isostructural:

Crystal	a_0 , Å	b_0 , Å	c_0 , Å
$\text{BaBi}_2\text{Nb}_2\text{O}_8$	5.533	5.533	25.55
$\text{Bi}_2\text{Ta}_2\text{TiO}_8$	5.402	5.436	25.15
$\text{Bi}_2\text{TiNbO}_8$	5.409	5.453	25.16
$\text{CaBi}_2\text{Nb}_2\text{O}_8$	5.435	5.485	24.87
$\text{CaBi}_2\text{Ta}_2\text{O}_8$	5.435	5.468	24.97
$\text{SrBi}_2\text{Nb}_2\text{O}_8$	5.504	5.504	25.06
$\text{SrBi}_2\text{Ta}_2\text{O}_8$	5.509	5.509	25.06
$\text{KBi}_2(\text{Nb}_2\text{O}_8)_2^*$	5.506	5.506	25.26
$\text{NaBi}_2(\text{Nb}_2\text{O}_8)_2^*$	5.47	5.47	26.94

*Two molecules per cell.

At elevated temperatures a_0 approaches b_0 and the symmetry of these compounds becomes tetragonal.

XI,78. The oxychloride mineral *perite*, PbBiO_2Cl , is orthorhombic with a tetramolecular unit of the edge lengths:

$$a_0 = 5.627(50) \text{ Å}; \quad b_0 = 5.575(20) \text{ Å}; \quad c_0 = 12.425(90) \text{ Å}.$$

Its space group is V_{17}^v ($Bmmb$) with atoms in the positions:

$$\begin{aligned} \text{Pb: } (4c) & \pm (0 \frac{1}{4} u, \frac{1}{4}, u + \frac{1}{2}) & \text{with } u = 0.385 \\ \text{Bi: } (4c) & \text{with } u = 0.090 \\ \text{Cl: } (4c) & \text{with } u = 0.75 \\ \text{O: } (8e) & \pm (u00; u \frac{1}{2} 0; u + \frac{1}{2} 0, \frac{1}{2}; u + \frac{1}{2} \frac{1}{2}, \frac{1}{2}; u + \frac{1}{2} \frac{1}{2}, \frac{1}{2}) \end{aligned}$$

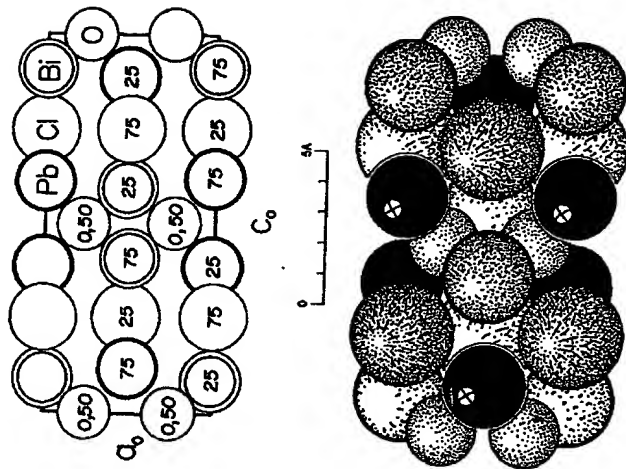


Fig. XI,60a (top). The orthorhombic structure of PbBiO_2Cl projected along its b_0 axis. Fig. XI,60b (bottom). A packing drawing of the orthorhombic PbBiO_2Cl structure seen along its b_0 axis. The lead atoms are black; the bismuth are heavily outlined and black shaded. The still larger dot-and-line shaded circles are chlorine; atoms of oxygen are smaller and dotted.

The resulting structure is shown in Figure XI,60. Each lead atom has four oxygen neighbors 2.45 Å. away and four more distant chlorine atoms (3.25 and 3.30 Å.). The environment of bismuth is similar, with Bi-O = 2.27 Å. and Bi-Cl = 3.42 and 3.45 Å.

The corresponding antimony compound, which occurs as the mineral *nadorite*, PbSbO_2Cl , is isostructural. For it:

$$a_0 = 5.59 \text{ Å}; \quad b_0 = 5.43 \text{ Å}; \quad c_0 = 12.20 \text{ Å}.$$

The atomic positions and parameters are:

$$\begin{aligned} \text{Pb: } (4c) & \text{ with } u = 0.380 \\ \text{Sb: } (4c) & \text{ with } u = 0.078 \\ \text{Cl: } (4c) & \text{ with } u = 0.756 \\ \text{O: } (8e) & \text{ with } u = 0.25 \end{aligned}$$

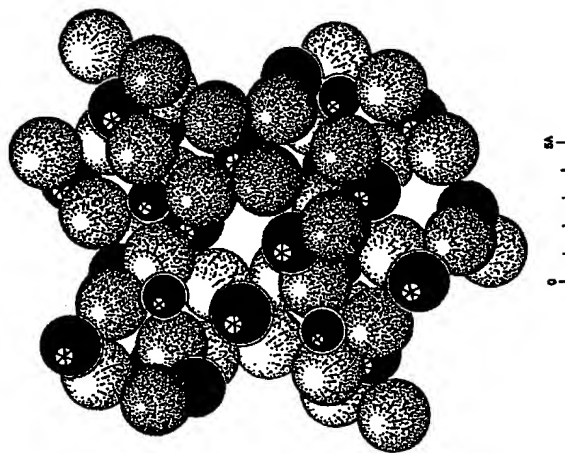
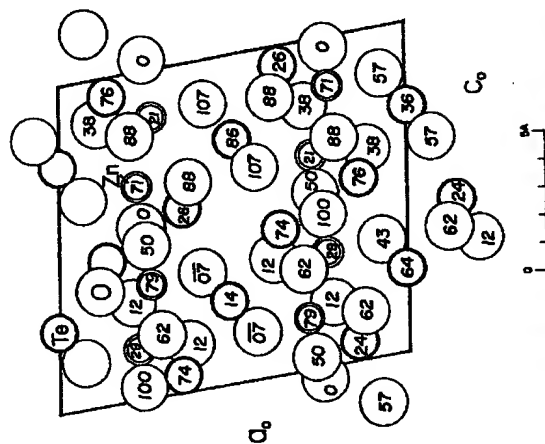


Fig. XI, 90a (top). The monoclinic structure of $\text{Zn}_7\text{Te}_2\text{O}_8$ projected along its b_0 axis.
Fig. XI, 90b (bottom). A packing drawing of the monoclinic structure of $\text{Zn}_7\text{Te}_2\text{O}_8$ seen along its b_0 axis. The zinc are the small, the tellurium the larger black circles. Atoms

BIBLIOGRAPHY TABLE, CHAPTER XI

Compound	Paragraph	Literature
$\text{Ag}(\text{CN})_2$	2	1966: K&B
$\text{AgCN} \cdot 2\text{AgNO}_3$	1	1965: B&D
$\text{Ag}_2\text{V}_2\text{O}_7$	3	1965: A
$\text{Ag}_2\text{O} \cdot 4\text{B}_2\text{O}_3$	4	1965: KM
$\text{AlBr}_3 \cdot \text{H}_2\text{S}$	6	1956: W,P&W
$\text{Al}_2\text{O}_3\text{C}$	7	1963: J&S
$\text{Al}_2\text{Ta}_2\text{O}_{11}(\text{F},\text{OH})$ (simpsenite)	9	1962: B&B
$\text{Al}_2\text{B}_4(\text{OH})_{10}\text{O}_{18}$ (geramejevite)	5	1934: G&K; 1938: S; 1955: G,B&B
$\text{Al}_2\text{C}_2\text{N}_4$	8	1963: J&W; 1966: J&W
$\text{Al}_2\text{C}_2\text{N}_4$	8	1963: J&W
$\text{Al}_2\text{C}_2\text{N}_4$	8	1963: J&W; 1966: J&W
$\text{B}_2\text{S}_2\text{Br}_2$	10	1958: Z
$\text{B}_2\text{H}_4\text{I}_2$	11	1965: H,B&P
BaB_2O_7	12	1965: B&P
$\text{BaBi}_2\text{Nb}_2\text{O}_{10}$	77	1949: A
$\text{BaBi}_2\text{Ti}_2\text{O}_{10}$	13	1950: A
$\text{Ba}_2\text{TiNb}_2\text{O}_{15}$	14	1965: S
$\text{Ba}_2\text{Bi}_2\text{O}_7$	15	1943: A
$\text{Bi}_2\text{Ta}_2\text{TiO}_7$	77	1949: A
$\text{Bi}_2\text{TiNbO}_7$	77	1949: A; 1960: I
$\text{Bi}_2\text{RO}_7\text{X}_2$	16	1938: S; 1939: S; 1940: S; 1941: S; S&GH; 1942: S; S&J; 1943: A; 1952: A
$\text{CaB}_2\text{O}_7(\text{OH})$	17	1962: C,C&A
$\text{CaBi}_2\text{Nb}_2\text{O}_{15}$	77	1949: A; 1960: I
$\text{CaBi}_2\text{Ta}_2\text{O}_{15}$	77	1960: I
$\text{Ca}_2\text{Be}_2\text{O}_8$	18	1966: H&Y
$\text{Ca}_2\text{Bi}_2\text{O}_7$	15	1943: A
CdBi_2O_7	19	1966: I&KM
$\text{CaBi}_2\text{Be}_2\text{Al}_2\text{O}_{11}$ (rhodizite)	20	1938: S; 1966: B&T
$\text{Ca}_2\text{Re}_2\text{Br}_{11}$	21	1965: E&P; 1966: E&P
$\text{Ca}_2\text{UO}_2\text{Br}_2$	22	1965: M,K&K
$\text{Ca}_2\text{UO}_2\text{Cl}_2$	23	1966: H,R&W
$\text{Ca}_2\text{RhCl}_6 \cdot \text{NH}_4\text{NO}_3$	55	1944: Z&S
$\text{Ca}_2(\text{UO}_2)\text{OCl}_2$	24	1964: A&W
$\text{CuCN} \cdot \text{N}_2\text{H}_4$	26	1966: C,L&R
$\text{CuPb}_2\text{Sb}_2\text{S}_4$ (meneghinite)	27	1938: H,P,R&W; 1960: E&H

BRIEF ATTACHMENT S

IN THE UNITED STATES PATENT AND TRADEMARK OFFICE

In re Patent Application of

Applicants: Bednorz et al.

Serial No.: 08/479,810

Filed: June 7, 1995

For: **NEW SUPERCONDUCTIVE COMPOUNDS HAVING HIGH TRANSITION
TEMPERATURE, METHODS FOR THEIR USE AND PREPARATION**

Date: March 1, 2005

Docket: YO987-074BZ

Group Art Unit: 1751

Examiner: M. Kopec

Commissioner for Patents
P.O. Box 1450
Alexandria, VA 22313-1450

FIRST SUPPLEMENTAL AMENDMENT

Sir:

In response to the Office Action dated July 28, 2004, please consider the
following:

ATTACHMENT S

MODERN OXIDE MATERIALS

Preparation, Properties and Device Applications

Edited by

B. COCKAYNE

Royal Radar Establishment, Malvern, England

and

D. W. JONES

*Centre for Materials Science,
University of Birmingham, England*

1972



ACADEMIC PRESS • London and New York

formed. Both the non-polar high temperature and polar phases can be either orthorhombic and/or tetragonal. It is the single crystal form of the tungsten bronze type ferroelectric compounds which has been primarily studied for both ferroelectric and electro-optic properties.

The first compound of this crystal class reported to be ferroelectric was lead metaniobate, $\text{Pb}_5\text{Nb}_{10}\text{O}_{30}$ (Goodman, 1953), with both orthorhombic a and b axes polar, an exception to the rule for these compounds. Lead metaniobate has a high Curie temperature, 843°K , and was developed as a piezoelectric ceramic for use over a wide temperature range. It is an unusual material with low permittivity, moderate piezoelectric activity and very low mechanical Q. This last point is a serious drawback for many applications but is of considerable use in ultrasonic flow detection where it helps to suppress the phenomenon known as ringing.

A number of solid solutions of lead metaniobate have been studied in the polycrystalline ceramic form but the only one of any practical significance is $(\text{Pb}_{5-x}\text{Ba}_x)\text{Nb}_{10}\text{O}_{30}$. The optimum piezoelectric properties are found near a phase boundary occurring at $x = 2$, which separates two ferroelectric orthorhombic phases. Subbarao (1960) found that for $x < 2$ the polarisation was in the $\langle 110 \rangle$ direction whilst for $x > 2$ the polarisation was parallel to the $\langle 001 \rangle$ direction indicating marked influence of the highly polarisable lead ion on the polar axis. Compositions around the phase boundary possess a relatively low temperature coefficient of the resonance frequency, high mechanical Q and moderately strong piezoelectric activity which renders them suitable for resonant piezoelectric devices requiring frequency stability with temperature.

More complex compounds exhibiting the tungsten bronze structure were reported by Roth and Fang (1960), Ainger et al. (1970) and Isupov (1964). One of the more interesting compounds, barium gadolinium iron niobate, $\text{Ba}_2\text{Gd}_2\text{Fe}_2\text{Nb}_8\text{O}_{30}$, was reported to be a ferroelectric and ferromagnetic ceramic, but investigations with similar ceramics showed that the weak magnetic properties were due to the presence of a second phase, barium hexaferrite.

C. LAYER STRUCTURE OXIDES AND COMPLEX COMPOUNDS

A large number of layer structure compounds of general formula $(\text{Bi}_2\text{O}_5)^{2+}(\text{A}_{x-1}\text{B}_x\text{O}_{3x+1})^{2-}$ have been reported (Smolenskii et al. 1961; Subbarao, 1962), where $\text{A} = \text{Ca}, \text{Sr}, \text{Ba}, \text{Pb}, \text{etc.}$, $\text{B} = \text{Ti}, \text{Nb}, \text{Ta}$ and $x = 2, 3, 4$ or 5 . The structure had been previously investigated by Aurivillius (1949) who described them in terms of alternate $(\text{Bi}_2\text{O}_5)^{2+}$ layers and perovskite layers of oxygen octahedra. Few have been found to be ferroelectric and include $\text{SrBi}_2\text{Ta}_2\text{O}_9$ ($T_c = 583^\circ\text{K}$), $\text{PbBi}_2\text{Ta}_2\text{O}_9$ ($T_c = 703^\circ\text{K}$), $\text{BiBi}_3\text{Ti}_2\text{Ti}_{10}\text{O}_{12}$ or $\text{Bi}_4\text{Ti}_3\text{O}_{12}$ ($T_c = 948^\circ\text{K}$), $\text{Ba}_2\text{Bi}_4\text{Ti}_5\text{O}_{18}$ ($T_c = 598^\circ\text{K}$) and $\text{Pb}_2\text{Bi}_4\text{Ti}_5\text{O}_{18}$ ($T_c = 583^\circ\text{K}$). Only bismuth titanate $\text{Bi}_4\text{Ti}_3\text{O}_{12}$ has been investigated in detail in the single crystal form and is finding applications in optical stores (Cummins, 1967) because of its unique ferroelectric-optical switching properties. The ceramics of other members have some interest because of their dielectric properties.

More complex compounds and solid solutions are realisable in these layer structure oxides but none have significant practical application.

formed. Both the non-polar high temperature and polar phases can be either orthorhombic and/or tetragonal. It is the single crystal form of the tungsten bronze type ferroelectric compounds which has been primarily studied for both ferroelectric and electro-optic properties.

The first compound of this crystal class reported to be ferroelectric was lead metaniobate, $\text{Pb}_5\text{Nb}_{10}\text{O}_{30}$ (Goodman, 1953), with both orthorhombic a and b axes polar, an exception to the rule for these compounds. Lead metaniobate has a high Curie temperature, 843°K , and was developed as a piezoelectric ceramic for use over a wide temperature range. It is an unusual material with low permittivity, moderate piezoelectric activity and very low mechanical Q. This last point is a serious drawback for many applications but is of considerable use in ultrasonic flow detection where it helps to suppress the phenomenon known as ringing.

A number of solid solutions of lead metaniobate have been studied in the polycrystalline ceramic form but the only one of any practical significance is $(\text{Pb}_{5-x}\text{Ba}_x)\text{Nb}_{10}\text{O}_{30}$. The optimum piezoelectric properties are found near a phase boundary occurring at $x = 2$, which separates two ferroelectric orthorhombic phases. Subbarao (1960) found that for $x < 2$ the polarisation was in the $\langle 110 \rangle$ direction whilst for $x > 2$ the polarisation was parallel to the $\langle 001 \rangle$ direction indicating marked influence of the highly polarisable lead ion on the polar axis. Compositions around the phase boundary possess a relatively low temperature coefficient of the resonance frequency, high mechanical Q and moderately strong piezoelectric activity which renders them suitable for resonant piezoelectric devices requiring frequency stability with temperature.

More complex compounds exhibiting the tungsten bronze structure were reported by Roth and Fang (1960), Ainger et al. (1970) and Isupov (1964). One of the more interesting compounds, barium gadolinium iron niobate, $\text{Ba}_2\text{Gd}_2\text{Fe}_2\text{Nb}_9\text{O}_{30}$, was reported to be a ferroelectric and ferromagnetic ceramic, but investigations with similar ceramics showed that the weak magnetic properties were due to the presence of a second phase, barium hexaferrite.

C. LAYER STRUCTURE OXIDES AND COMPLEX COMPOUNDS

A large number of layer structure compounds of general formula $(\text{Bi}_2\text{O}_5)^{2+}(\text{A}_{x-1}\text{B}_x\text{O}_{3x+1})^{2-}$ have been reported (Smolenskii et al. 1961; Subbarao, 1962), where $\text{A} = \text{Ca}, \text{Sr}, \text{Ba}, \text{Pb}, \text{etc.}$, $\text{B} = \text{Ti}, \text{Nb}, \text{Ta}$ and $x = 2, 3, 4$ or 5 . The structure had been previously investigated by Aurivillius (1949) who described them in terms of alternate $(\text{Bi}_2\text{O}_5)^{2+}$ layers and perovskite layers of oxygen octahedra. Few have been found to be ferroelectric and include $\text{SrBi}_2\text{Ta}_2\text{O}_9$ ($T_c = 583^\circ\text{K}$), $\text{PbBi}_2\text{Ta}_2\text{O}_9$ ($T_c = 703^\circ\text{K}$), $\text{BiBi}_3\text{Ti}_2\text{TiO}_{12}$ or $\text{Bi}_4\text{Ti}_3\text{O}_{12}$ ($T_c = 948^\circ\text{K}$), $\text{Ba}_2\text{Bi}_4\text{Ti}_5\text{O}_{18}$ ($T_c = 598^\circ\text{K}$) and $\text{Pb}_2\text{Bi}_4\text{Ti}_5\text{O}_{18}$ ($T_c = 583^\circ\text{K}$). Only bismuth titanate $\text{Bi}_4\text{Ti}_3\text{O}_{12}$ has been investigated in detail in the single crystal form and is finding applications in optical stores (Cummins, 1967) because of its unique ferroelectric-optical switching properties. The ceramics of other members have some interest because of their dielectric properties.

More complex compounds and solid solutions are realisable in these layer structure oxides but none have significant practical application.

BRIEF ATTACHMENT T

IN THE UNITED STATES PATENT AND TRADEMARK OFFICE

In re Patent Application of

Applicants: Bednorz et al.

Serial No.: 08/479,810

Filed: June 7, 1995

For: NEW SUPERCONDUCTIVE COMPOUNDS HAVING HIGH TRANSITION
TEMPERATURE, METHODS FOR THEIR USE AND PREPARATION

Date: March 1, 2005

Docket: YO987-074BZ

Group Art Unit: 1751

Examiner: M. Kopec

Commissioner for Patents
P.O. Box 1450
Alexandria, VA 22313-1450

FIRST SUPPLEMENTAL AMENDMENT

Sir:

In response to the Office Action dated July 28, 2004, please consider the
following:

ATTACHMENT T

LANDOLT-BÖRNSTEIN

Numerical Data and Functional Relationships
in Science and Technology

New Series

Editor in Chief: K.-H. Hellwege

Group III: Crystal and Solid State Physics

Volume 3

Ferro- and Antiferroelectric Substances

by Toshio Mitsui and

R. Abe · Y. Furuhashi · K. Gesi · T. Ikeda · K. Kawabe
Y. Makita · M. Marutake · E. Nakamura · S. Nomura
E. Sawaguchi · Y. Shiozaki · I. Tatsuzaki · K. Toyoda

Editors: K.-H. Hellwege and A. M. Hellwege



Springer-Verlag Berlin · Heidelberg · New York 1969

7 Layer-structure oxides

7A Pure compounds of simple type

Nr. 7A-1 $\text{Bi}_2\text{TiNbO}_6$

1a	Dielectric anomaly associated with a phase transition was reported by ISMAILZADE in 1960.		60I1
b	phase	II	I
	state		P ^{a)}
	crystal system	orthorhombic ^{b)}	tetragonal ^{b)}
	space group	Fmm2-C _{2v} ¹⁴	I4/mmm-D _{2h} ¹⁷
	Θ^*	900 ... 950 °C ^{b)}	
	$\rho = 6.4 \cdot 10^3 \text{ kg m}^{-3}$, $a = 5.40 \text{ \AA}$, $b = 5.44 \text{ \AA}$, $c = 25.1 \text{ \AA}$ at RT.		62S17
4	Temperature dependence of lattice parameters: Fig. 868. Linear thermal expansion: Fig. 869.		
5a	Dielectric constant: Fig. 870. $\kappa \approx 100$ at RT. The dielectric constant was not measured in the vicinity of the transition point because of high conductivity. Extrapolation of the Curie temperatures of the solid solution system obtained by the dielectric measurements indicates a transition temperature between 900° and 950 °C for $\text{Bi}_2\text{TiNbO}_6$.		61S11

Nr. 7A-2 $\text{Bi}_2\text{TiTaO}_6$

1a	Phase transition similar to that of $\text{Bi}_2\text{TiNbO}_6$ was reported by SUBBARAO in 1962.		62S17
b	phase	II	I
	state		P
	crystal system	orthorhombic	tetragonal
	space group	Fmm2-C _{2v} ¹⁴	I4/mmm-D _{2h} ¹⁷
	Θ	870 °C	
	$\rho = 8.5 \cdot 10^3 \text{ kg m}^{-3}$, $a = 5.39 \text{ \AA}$, $b/a = 1.007$, $c = 25.1 \text{ \AA}$ at RT.		62S17
4	Linear thermal expansion: see Fig. 869.		
5a	Dielectric constant: $\kappa \approx 140$ at RT.		62S17

Nr. 7A-3 $\text{CaBi}_2\text{Nb}_2\text{O}_9$

1a	Dielectric anomaly associated with a phase transition was discovered by ISMAILZADE in 1960.		60I1
b	phase	II	I
	state		P
	crystal system	orthorhombic	tetragonal
	space group	Fmm2-C _{2v} ¹⁴	I4/mmm-D _{2h} ¹⁷
	Θ	625 °C	
	$\rho = 5.0 \cdot 10^3 \text{ kg m}^{-3}$, $a = 5.39 \text{ \AA}$, $b/a = 1.006$, $c = 25.15 \text{ \AA}$ at RT.		62S17
4	Temperature dependence of lattice parameters: Tab. 104.		
5a	Dielectric constant: Fig. 871. $\kappa \approx 80$ at RT.		62S17

* According to [60I1] Θ is 600 ... 650 °C.

Tab. 104. Temperature dependence of the lattice parameters of $\text{CaBi}_2\text{Nb}_2\text{O}_9$ and $\text{CaBi}_2\text{Ta}_2\text{O}_9$ [60I1]

T	20	100	150	200	250	300	350	400	°C
$\text{CaBi}_2\text{Nb}_2\text{O}_9$									
a	5.442	—	5.453	—	5.458	—	5.465	—	Å
b	5.482 ₈	—	5.484	—	5.487	—	5.491	—	Å
c	24.920	—	24.955	—	24.990	—	25.035	—	Å
b/a	1.0075	—	1.0056	—	1.005 ₃	—	1.0047	—	Å
V	743.5	—	746.0	—	748.5	—	751.0	—	Å ³
$\text{CaBi}_2\text{Ta}_2\text{O}_9$									
a	5.435	5.438	—	5.444	—	5.452	—	5.464	Å
b	5.468 ₈	5.471	—	5.475 ₈	—	5.479	—	5.482 ₄	Å
c	24.970	24.980	—	25.015	—	25.040	—	25.060	Å
b/a	1.006	1.006	—	1.005 ₈	—	1.005	—	1.003 ₈	Å
V	742.0	743.2	—	745.6	—	748.0	—	750.6	Å ³
T	450	500	550	575	600	650	700	°C	
$\text{CaBi}_2\text{Nb}_2\text{O}_9$									
a	5.480	5.485	5.488 ₃	5.495 ₃	—	5.502 ₃	5.504	Å	
b	5.496 ₈	5.501 ₃	5.502 ₃	5.503 ₇	—	5.502 ₃	5.504	Å	
c	25.070	25.080	25.090	25.105	—	25.125	25.140	Å	
b/a	1.0036	1.0029	1.0025	1.0015	—	1.000	1.000	Å	
V	755.0	756.8	758.0	759.3	—	760.7	761.6	Å ³	
$\text{CaBi}_2\text{Ta}_2\text{O}_9$									
a	—	5.470	5.473	—	5.479	5.484	—	Å	
b	—	5.483 ₇	5.484	—	5.479	5.484	—	Å	
c	—	25.070	25.083	—	25.085	25.105	—	Å	
b/a	—	1.002 ₈	1.002 ₄	—	1.000	1.000	—	Å	
V	—	751.9	752.8	—	730.0	755.0	—	Å ³	

Nr. 7A-4 $\text{CaBi}_2\text{Ta}_2\text{O}_9$

1a	Dielectric anomaly associated with a phase transition was discovered by ISMAILZADE in 1960.		60I1
b	phase	II I	60I1
	state		
	crystal system	orthorhombic P	
	space group	Fmm2-C _{2v} ¹⁸ I4/mmm-D _{2h} ¹⁷	
	θ	575 °C	
	ε = 7.5 · 10 ³ kg m ⁻³ s.		
	a = 5.428 Å, b/a = 1.006, c = 24.90 Å at RT.		60I1
4	Temperature dependence of lattice parameter: see Tab. 104.		61S11
5a	Dielectric constant: Fig. 872.		

Nr. 7A-5 $\text{SrBi}_2\text{Nb}_2\text{O}_9$

1a	Dielectric anomaly associated with a phase transition was discovered by SMOLENSKII in 1961.		61S11
b	phase	II I	61S11 *) 62S17
	state		
	crystal system	orthorhombic P	
	space group		
	θ	420 440*) °C	
	ε = 6.9 · 10 ³ kg m ⁻³ s.		
	a = 5.506 Å, b/a = 1.000, c = 25.05 Å at RT.		
5a	Dielectric constant: Fig. 873. * ≈ 190 at RT.		62S15
	* = C/(T - θ _p), where C = 0.55 · 10 ⁵ °C, θ _p = 390 °C.		
7a	Piezoelectricity: d ₃₃ = 1.0 · 10 ⁻¹¹ C N ⁻¹ .		62S17

Nr. 7A-6 $\text{SrBi}_2\text{Ta}_2\text{O}_9$		
1a	Ferroelectricity in $\text{SrBi}_2\text{Ta}_2\text{O}_9$ was reported by SMOLENSKII in 1961.	61S11
b	phase	II I
	state	F P
	crystal system	orthorhombic tetragonal
	Θ	310 °C
	$\rho = 7.5 \cdot 10^3 \text{ kg m}^{-3}$.	61S11
	$a = 5.512 \text{ \AA}$, $b/a = 1.000$, $c = 25.00 \text{ \AA}$ at RT.	62S15
5a	Dielectric constant: Fig. 874. $\kappa \approx 180$ at RT. $\kappa = C/(T - \Theta_p)$, $C = 2.0 \cdot 10^5 \text{ °C}$, $\Theta_p = 190 \text{ °C}$.	62S17
c	Spontaneous polarization: $P_s = 5.8 \cdot 10^{-2} \text{ C m}^{-2}$ at 25 °C.	62S17
7a	Piezoelectric constant: $d_{33} = 2.3 \cdot 10^{-11} \text{ C N}^{-1}$.	62S17
Nr. 7A-7 $\text{BaBi}_2\text{Nb}_2\text{O}_9$		
1a	Dielectric anomaly associated with a phase transition was discovered by SMOLENSKII in 1961.	61S11
b	phase	II I
	state	P
	crystal system	orthorhombic tetragonal
	Θ	210 °C 200 ^{a)} °C
	$\rho = 6.3 \cdot 10^3 \text{ kg m}^{-3}$.	61S11 ^{a)} 62S17
	$a = 5.554 \text{ \AA}$, $b/a = 1.000$, $c = 25.60 \text{ \AA}$ at RT.	62S15
5a	Dielectric constant: Fig. 875. $\kappa = 280$ at RT.	62S17
Nr. 7A-8 $\text{BaBi}_2\text{Ta}_2\text{O}_9$		
1a	Dielectric anomaly associated with a phase transition was discovered by SMOLENSKII in 1961.	61S11
b	phase	II I
	state	P
	crystal system	orthorhombic tetragonal
	Θ	110 ^{a)} °C
	According to [61S11] Θ is 70 °C. $\rho = 8.4 \cdot 10^3 \text{ kg m}^{-3}$.	61S11 61S11
	$a = 5.556 \text{ \AA}$, $b/a = 1.000$, $c = 25.50 \text{ \AA}$ at RT.	62S15
5a	Dielectric constant: Fig. 876. $\kappa = 400$ at RT.	62S17
Nr. 7A-9 $\text{PbBi}_2\text{Nb}_2\text{O}_9$		
1a	Dielectric anomaly associated with a phase transition in $\text{PbBi}_2\text{Nb}_2\text{O}_9$ was reported by SMOLENSKII in 1959.	59S8
b	phase	II I
	state	P
	crystal system	orthorhombic tetragonal
	Θ	526 °C 550 ^{a)} °C
	$\rho = 7.6 \cdot 10^3 \text{ kg m}^{-3}$.	59S8 ^{a)} 61S15
	$a = 5.488 \text{ \AA}$, $b/a = 1.002$, $c = 25.55 \text{ \AA}$ at RT.	62S15
3	Crystal structure: Fig. 877.	
4	Temperature dependence of lattice parameters: Fig. 878.	
5a	Dielectric constant: Fig. 879. $\kappa = 170$ at RT. $\kappa = C/(T - \Theta_p)$, $C = 1.3 \cdot 10^5 \text{ °K}$, $\Theta_p = 510 \text{ °C}$.	62S17
7a	Piezoelectric constant: $d_{33} = 1.5 \cdot 10^{-11} \text{ C N}^{-1}$.	62S17

... die Kristallstruktur

Nr. 7A-10 PbBi₂Ta₂O₉

1a	Ferroelectricity was reported by SUBBARAO ^{a)} and SMOLENSKII ^{b)} independently in 1961.			^{a)} 61S15 ^{b)} 61S11
b	phase	II	I	
	state	F	P	
	crystal system	orthorhombic	tetragonal	
	Θ	430 °C		61S15 61S11
	$\rho = 9.0 \cdot 10^3 \text{ kg m}^{-3}$ $a = 5.496 \text{ \AA}$, $b/a = 1.000$, $c = 25.40 \text{ \AA}$ at RT.			62S15
5a	Dielectric constant: Fig. 880. $\kappa = 180$ at RT. $\kappa = C/(T - \Theta_p)$, $C = 3.7 \cdot 10^4 \text{ °C}$, $\Theta_p = 325 \text{ °C}$.			62S17
7a	Piezoelectric constant: $d_{33} = 5 \cdot 10^{-12} \text{ C N}^{-1}$.			62S17

Nr. 7A-11 Bi₄Ti₃O₁₃

1a	Ferroelectricity in Bi ₄ Ti ₃ O ₁₃ was reported by VAN UITERT et al. in 1961.			61V2
b	phase	II	I	
	state	F	P	
	crystal system	monoclinic ^{a)} (pseudo-orthorhombic)	tetragonal	61V2 ^{a)} 67C6
	Θ	675 °C		
	Unit cell is very nearly orthorhombic with the lattice parameters: $a_{\text{orth}} = 5.411 \text{ \AA}$, $b_{\text{orth}} = 5.448 \text{ \AA}$, $c_{\text{orth}} = 32.85 \text{ \AA}$ at RT. Relations between crystallographic axes: Fig. 881. P_s lies in a direction tilted at approximately 7° (or less) from the major crystal surface in a plane parallel to the pseudo-orthorhombic $b - c$ plane.			
2a	Crystal growth: Cooling method from melt consisting of 100 Bi ₂ O ₃ and 5 TiO ₂ (weight ratio).			67C6
3	Crystal structure: Fig. 882.			61V2
4	Temperature dependence of lattice parameter: Fig. 883. Thermal expansion: Fig. 884.			
5a	Dielectric constant: Fig. 885.			
c	P_s and E_c : Fig. 886, 887. TAMBOVSEV et al. measured P_s and E_c by applying a field parallel to the c_{orth} direction, $P_s = 1.99 \cdot 10^{-3} \text{ C m}^{-2}$, $E_c = 1.13 \cdot 10^4 \text{ V m}^{-1}$. According to [67C6], the spontaneous polarization lies in the pseudo-orthorhombic (100) plane and has a value larger than $30 \cdot 10^{-3} \text{ C m}^{-2}$.			63T1 67C6
	7	Piezoelectric constant: $d_{33} = 2.0 \cdot 10^{-11} \text{ C N}^{-1}$.		
10	Conductivity: see			61S17
14a	Domain structure: see Domains have been observed by polarized light.			64P3
b	Switching: Fig. 888, 889. See also Fig. 892, Tab. 105 and:			64P3 66C7
	Twining structure: see			66P6

Nr. 7A-12 BaBi₂Ti₂NbO₁₁

1a	Dielectric anomaly associated with a phase transition was reported by SUBBARAO in 1961.			61S15
b	phase	II	I	
	state		P	
	crystal system	pseudo-tetragonal	tetragonal	
	Θ	270 °C		61S15
	$a = 3.874 \text{ \AA}$, $c = 33.70 \text{ \AA}$ at RT.			

Nr. 7A-13 PbBi₂Ti₂NbO₁₁

1a	Dielectric anomaly associated with a phase transition was reported by SUBBARAO in 1961.			61S15
----	---	--	--	-------

* Point group is m.

110

* Point group is m.

1b	phase	II	I	
	state		P	
	crystal system	pseudo-tetragonal	tetragonal	
	Θ	290 °C		61S15
	$a = 3.687 \text{ \AA}, c = 33.55 \text{ \AA}$ at RT.			61S15

Nr. 7A-14 BaBi₄Ti₄O₁₅

1a	Dielectric anomaly associated with a phase transition was reported independently by SUBBARAO ^{a)} and by SMOLENSKI ^{b)} in 1961. Ferroelectric activity was reported independently by FANG et al. in 1961 ^{c)} .			^{a)} 61S15 ^{b)} 61S11 ^{c)} 61F7
b	phase	II	I	
	state	F	P	61F7
	crystal system	orthorhombic (or pseudo-orthorhombic)	tetragonal	
	Θ	375 °C 395 ^{a)} °C		^{a)} 61S15
	$\rho = 5.7 \cdot 10^3 \text{ kg m}^{-3}$ $a = 5.461 \text{ \AA}, b/a = 1.000, c = 41.85 \text{ \AA}$ at RT.			62S15
3	Crystal structure: Fig. 890.			
5a	Dielectric constant: Fig. 891. $\kappa = 150$ at RT. $\kappa = C/(T - \Theta_p)$, $C = 2.5 \cdot 10^5 \text{ °K}$, $\Theta_p = 335 \text{ °C}$.			61S15
7a	Piezoelectric constant: $d_{33} = 2.3 \cdot 10^{-11} \text{ C N}^{-1}$.			62S17
14b	Switching: Fig. 892; Tab. 105.			

Tab. 105. BaBi₄Ti₄O₁₅, Ba₂Bi₄Ti₄O₁₅, Bi₄Ti₄O₁₅, BaTiO₃ (for comparison). Switching parameters in comparison with those of BaTiO₃ [62F7]. $t_s = t_{\infty} \exp(+\alpha/E)$, t_s = switching time

	BaTiO ₃	Bi ₄ Ti ₄ O ₁₅	BaBi ₄ Ti ₄ O ₁₅	Ba ₂ Bi ₄ Ti ₄ O ₁₅	
α	6.1	41	23	76	10^5 V m^{-1}
t_{∞}	0.4	10^{-2}	1.5	10^{-2}	$\mu \text{ sec}$

Nr. 7A-15 PbBi₄Ti₄O₁₅

1a	Dielectric anomaly associated with a phase transition was reported by SUBBARAO in 1961.			61S15
b	phase	II	I	
	state		P	
	crystal system	orthorhombic (possibly)	tetragonal	61S15
	Θ	570 °C		
	$\rho = 6.6 \cdot 10^3 \text{ kg m}^{-3}$ $a = 5.437 \text{ \AA}, b/a = 1.000, c = 41.35 \text{ \AA}$ at RT.			62S15
5a	Dielectric constant: Fig. 893. $\kappa = 220$ at RT. $\kappa = C/(T - \Theta_p)$, $C = 1.4 \cdot 10^5 \text{ °C}$, $\Theta_p = 552 \text{ °C}$.			61S15 62S17
7a	Piezoelectric constant: $d_{33} = 2.3 \cdot 10^{-11} \text{ C N}^{-1}$.			62S17

Nr. 7A-16 SrBi₄Ti₄O₁₅

1a	Dielectric anomaly associated with a phase transition was reported by SUBBARAO in 1961.			61S15
b	phase	II	I	
	state		P	
	crystal system	orthorhombic (possibly)	tetragonal	61S15
	Θ	530 °C		
	$\rho = 5.2 \cdot 10^3 \text{ kg m}^{-3}$ $a = 5.428 \text{ \AA}, b/a = 1.000, c = 40.95 \text{ \AA}$ at RT.			62S17 62S15
5a	Dielectric constant: Fig. 894. $\kappa = 190$ at RT. $\kappa = C/(T - \Theta_p)$, $C = 0.68 \cdot 10^5 \text{ °C}$, $\Theta_p = 485 \text{ °C}$.			62S17
7a	Piezoelectric constant: $d_{33} = 1.5 \cdot 10^{-12} \text{ C N}^{-1}$.			62S17

Chemical Abstracts

Nr. 7A-17 $\text{CaBi}_4\text{Ti}_4\text{O}_{15}$

1a	$\text{CaBi}_4\text{Ti}_4\text{O}_{15}$ was investigated by SUBBARAO in 1962. No dielectric anomaly has been detected.	62S17
b	Orthorhombic: $a = 5.418 \text{ \AA}$, $b/a = 1.002$, $c = 40.75 \text{ \AA}$ at RT. $\rho = 4.7 \cdot 10^3 \text{ kg m}^{-3}$.	62S15
5a	Dielectric constant: Fig. 895. $\kappa = 120$ at RT.	61S11

Nr. 7A-18 $\text{Bi}_5\text{Ti}_5\text{GaO}_{15}$

1a	$\text{Bi}_5\text{Ti}_5\text{GaO}_{15}$ was investigated by SUBBARAO in 1962. No dielectric anomaly has been detected.	62S17
b	Orthorhombic: $a = 5.408 \text{ \AA}$, $b/a = 1.006$, $c = 41.05 \text{ \AA}$ at RT. $\rho = 7.3 \cdot 10^3 \text{ kg m}^{-3}$.	62S15
5a	Dielectric constant: $\kappa = 150$ at RT.	62S17

Nr. 7A-19 $\text{Ba}_2\text{Bi}_4\text{Ti}_5\text{O}_{18}$

1a	Ferroelectric activity of $\text{Ba}_2\text{Bi}_4\text{Ti}_5\text{O}_{18}$ was observed by AURIVILLIUS in 1962.	62A5												
b	<table> <tr> <th>phase</th><th>II</th><th>I</th></tr> <tr> <td>state</td><td>F</td><td>P</td></tr> <tr> <td>crystal system</td><td>orthorhombic</td><td>tetragonal</td></tr> <tr> <td>Θ</td><td colspan="2">325 °C</td></tr> </table> <p>$a = 5.527 \text{ \AA}$, $b = 5.514 \text{ \AA}$, $c = 50.37 \text{ \AA}$ at RT.</p>	phase	II	I	state	F	P	crystal system	orthorhombic	tetragonal	Θ	325 °C		62A5 63I5
phase	II	I												
state	F	P												
crystal system	orthorhombic	tetragonal												
Θ	325 °C													
3	Crystal structure: Fig. 896; Tab. 106.													
4	Temperature dependence of lattice parameter: Fig. 897.													
5a	Dielectric constant: Fig. 898. $\kappa' = 360$, $\kappa'' = 22$ at RT.	62A5 62A5												
c	Remanent polarization: $P_r = 2 \cdot 10^{-4} \text{ C m}^{-2}$ at RT. Coercive field: $E_c = 1.0 \cdot 10^6 \text{ V m}^{-1}$ at RT.													
14b	Switching: see Fig. 892; Tab. 105.													

Tab. 106. $\text{Ba}_2\text{Bi}_4\text{Ti}_5\text{O}_{18}$. Fractional coordinates of atoms [62A5]. Space group of $I4/mmm$ was assumed.

$I4/mmm$	$(0, 0, 0; 1/2, 1/2, 1/2) +$	
4 Bi in 4(e):	$\pm 0, 0, z$:	$z = 0.2255$
4 (Bi, Ba) in 4(e):		$z = 0.0420$
4 (Bi, Ba) in 4(e):		$z = 0.1300$
2 Ti in 2(b):	$\pm 0, 0, 1/2$	
4 Ti in 4(e):		$z = 0.3370$
4 Ti in 4(e):		$z = 0.4185$
4 O in 4(c):	$0, 1/2, 0; 1/2, 0, 0$	
4 O in 4(d):	$0, 1/2, 1/4; 1/2, 0, 1/4$	
4 O in 4(e):		$z = 0.2962$
4 O in 4(e):		$z = 0.3378$
4 O in 4(e):		$z = 0.4593$
8 O in 8(g):	$\pm (0, 1/2, z; 1/2, 0, z)$	$z = 0.0815$
8 O in 8(g):		$z = 0.1630$

Nr. 7A-20 $\text{Pb}_2\text{Bi}_4\text{Ti}_5\text{O}_{18}$

1a	Ferroelectric activity in $\text{Pb}_2\text{Bi}_4\text{Ti}_5\text{O}_{18}$ was observed by SUBBARAO in 1962.	62S17												
b	<table> <tr> <th>phase</th><th>II</th><th>I</th></tr> <tr> <td>state</td><td>F</td><td>P</td></tr> <tr> <td>crystal system</td><td>orthorhombic (possibly)</td><td>tetragonal</td></tr> <tr> <td>Θ</td><td colspan="2">310 °C</td></tr> </table> <p>$\rho = 6.6 \cdot 10^3 \text{ kg m}^{-3}$. $a = 5.461 \text{ \AA}$, $b/a = 1.000$, $c = 49.70 \text{ \AA}$ at RT.</p>	phase	II	I	state	F	P	crystal system	orthorhombic (possibly)	tetragonal	Θ	310 °C		62S17 62S15
phase	II	I												
state	F	P												
crystal system	orthorhombic (possibly)	tetragonal												
Θ	310 °C													

5a	Dielectric constant: Fig. 899. $\kappa = 400$ at RT. $\kappa = C/(T - \theta_p)$, $C = 4.1 \cdot 10^5$ °K, $\theta_p = 280$ °C.			62S17
c	Spontaneous polarization: $P_s = 6 \cdot 10^{-3}$ C m ⁻² at 235 °C.			62S17
7a	Piezoelectric constant: $d_{33} = 2.5 \cdot 10^{-12}$ C N ⁻¹ .			62S17
Nr. 7A-21 $\text{Sr}_2\text{Bi}_4\text{Ti}_5\text{O}_{18}$				
1a	Ferroelectric activity in $\text{Sr}_2\text{Bi}_4\text{Ti}_5\text{O}_{18}$ was observed by SUBBARAO in 1962.			62S17
b	phase	II	I	
	state	F	P	
	crystal system	orthorhombic (possibly)	tetragonal	
	θ	285 °C		
	$\rho = 5.3 \cdot 10^3$ kg m ⁻³ .			62S17
	$a = 5.461$ Å, $b/a = 1.000$, $c = 48.80$ Å at RT.			62S15
5a	Dielectric constant: Fig. 900. $\kappa = 280$ at RT. $\kappa = C/(T - \theta_p)$, $C = 0.47 \cdot 10^5$ °K, $\theta_p = 255$ °C.			62S17
c	Spontaneous polarization: $P_s = 3.5 \cdot 10^{-3}$ C m ⁻² at 255 °C.			62S17
7a	Piezoelectric constant: $d_{33} = 2.5 \cdot 10^{-12}$ C N ⁻¹ .			62S17
Nr. 7A-22 $\text{Bi}_2\text{Ti}_4\text{O}_{11}$				
1a	Dielectric anomaly associated with a phase transition was observed in $\text{Bi}_2\text{Ti}_4\text{O}_{11}$ by SUBBARAO in 1962.			62S16
b	phase	III	II	65J4
	crystal system	monoclinic	monoclinic	
		space group	$C2/c-C_{2h}^*$	
	θ	250*) 1200*) °C		*)62S16
	$\rho = (6.12 \pm 0.02) \cdot 10^3$ kg m ⁻³ .			65J4
	$a = (14.612 \pm 0.006)$ Å, $b = (3.799 \pm 0.004)$ Å, $c = (14.946 \pm 0.006)$ Å,			65J4
	$\beta = (93.13 \pm 0.01)^\circ$ at RT.			
3	Crystal structure: $Z = 2$ in phase II. $Z = 4$ in phase III. Fig. 901, 902; Tab. 107.			65J4
4	Thermal expansion: Fig. 903.			
5a	Dielectric constant: Fig. 904.			
c	No hysteresis loops could be obtained between 25 °C and 290 °C.			62S16
Tab. 107. $\text{Bi}_2\text{Ti}_4\text{O}_{11}$. Atomic parameters at RT [65J4]				
Atom		x	y	z
O(1)		0.0	0.262 \pm 0.012	0.250
O(2)		0.1828 \pm 0.0024	0.246 \pm 0.007	0.2207 \pm 0.0024
O(3)		0.1408 \pm 0.0024	0.256 \pm 0.007	0.0338 \pm 0.0024
O(4)		0.0814 \pm 0.0024	0.760 \pm 0.007	0.1259 \pm 0.0024
O(5)		0.2662 \pm 0.0024	0.747 \pm 0.007	0.0880 \pm 0.0024
O(6)		0.0546 \pm 0.0024	0.770 \pm 0.007	0.9221 \pm 0.0024
Ti(1)		0.0530 \pm 0.0006	0.250 \pm 0.002	0.1406 \pm 0.0006
Ti(2)		0.1461 \pm 0.0006	0.759 \pm 0.002	0.0162 \pm 0.0006
Bi		0.3211 \pm 0.00015	0.1747 \pm 0.0005	0.1798 \pm 0.00015
Thermal parameter $B = 0.33$ Å ² for all atoms. Coordinates and standard deviations in cell fractions.				
7B Complex compounds and solid solutions				
Nr. 7B-1 $\text{Bi}_{1-x}\text{Me}_2^{3+}\text{Ti}_{1-x}\text{Nb}_{1+x}\text{O}_9$ ($\text{Me}^{3+} = \text{Ba, Sr, Pb}$)		1b	Lattice parameter: Fig. 905. Transition temperature: Fig. 906.	
		5	Dielectric constant: Fig. 907.	
Nr. 7B-2 $\text{Bi}_{1-x}\text{Me}_2^{3+}\text{Ti}_2\text{Nb}_x\text{O}_{12}$ ($\text{Me}^{3+} = \text{Ba, Sr, Pb}$)		1b	Lattice parameter: Fig. 908. Transition temperature: Fig. 909.	
		5	Dielectric constant: Fig. 910.	
* The unit cell of phase II has about half the volume of the unit cell of phase III.				

Nr. 7B-3 $\text{Na}_{0.5}\text{Bi}_{4.5}\text{Ti}_4\text{O}_{15}$		
1a	Dielectric anomaly associated with a phase transition was reported by SUBBARAO in 1962.	62S17
b	phase	II I
	state	P
	crystal system	orthorhombic tetragonal
	Θ	650 °C
	$q = 6.3 \cdot 10^3 \text{ kg m}^{-3}$, $a = 5.427 \text{ \AA}$, $b/a = 1.006$, $c = 40.65 \text{ \AA}$ at RT.	62S17 62S15
5a	Dielectric constant: Fig. 911. $\kappa = 200$ at RT. $\kappa = C/(T - \Theta_p)$, $C = 0.79 \cdot 10^5 \text{ °K}$, $\Theta_p = 610 \text{ °C}$.	62S17
7a	Piezoelectric constant: $d_{33} = 1.0 \cdot 10^{-11} \text{ C N}^{-1}$.	62S17
Nr. 7B-4 $\text{K}_{0.5}\text{Bi}_{4.5}\text{Ti}_4\text{O}_{15}$		
1a	Dielectric anomaly associated with a phase transition was reported by SUBBARAO in 1962.	62S17
b	phase	II I
	state	P
	crystal system	orthorhombic tetragonal
	Θ	550 °C
	$q = 6.7 \cdot 10^3 \text{ kg m}^{-3}$, $a = 5.440 \text{ \AA}$, $b/a = 1.004$, $c = 41.15 \text{ \AA}$ at RT.	62S17 62S15
5a	Dielectric constant: Fig. 912. $\kappa = 140$ at RT. $\kappa = C/(T - \Theta_p)$, $C = 0.74 \cdot 10^5 \text{ °K}$, $\Theta_p = 515 \text{ °C}$.	62S17
7a	Piezoelectric constant: $d_{33} = 1.0 \cdot 10^{-11} \text{ C N}^{-1}$.	62S17
Nr. 7B-5 $(\text{Pb}_{1-x}\text{Ba}_x)\text{Bi}_2\text{Nb}_2\text{O}_9$ and $(\text{Pb}_{1-x}\text{Sr}_x)\text{Bi}_2\text{Nb}_2\text{O}_9$		
	1b Transition temperature: Fig. 913.	
	5 Dielectric constant: Fig. 914.	
Nr. 7B-6 $(1-x)\text{Bi}_4\text{Ti}_3\text{O}_{15} - x\text{BaTiO}_3$		
	5 Transition temperature: Fig. 915.	
Nr. 7B-7 $\text{Bi}_{4+x}\text{Pb}_{1-x}\text{Ti}_4\text{Ga}_x\text{O}_{15}$		
1a	Another formula for this solid solution is $(1-x)\text{PbBi}_4\text{Ti}_4\text{O}_{15} \cdot x\text{Bi}_2\text{Ti}_2\text{GaO}_{15}$. Properties of this solid solution were studied by SUBBARAO in 1962.	62S17
b	$x = 0.25$:	62S17
	phase	II I
	state	P
	crystal system	orthorhombic (pseudo-tetragonal) tetragonal
	Θ	600 °C
	Pseudo-tetragonal cell parameter: $a = 3.842 \text{ \AA}$, $c = 41.40 \text{ \AA}$ at RT. Dielectric constant: $\kappa = 180$ at RT; $\kappa = 3035$ at Θ .	
	$x = 0.5$:	
	phase	II I
	state	P
	crystal system	orthorhombic (pseudo-tetragonal) tetragonal
	Θ	620 °C
	Pseudo-tetragonal cell parameter: $a = 3.842 \text{ \AA}$, $c = 41.40 \text{ \AA}$ at RT. Dielectric constant: $\kappa = 179$ at RT; $\kappa = 1930$ at Θ .	62S17

BRIEF ATTACHMENT U

IN THE UNITED STATES PATENT AND TRADEMARK OFFICE

In re Patent Application of

Applicants: Bednorz et al.

Serial No.: 08/479,810

Filed: June 7, 1995

For: NEW SUPERCONDUCTIVE COMPOUNDS HAVING HIGH TRANSITION
TEMPERATURE, METHODS FOR THEIR USE AND PREPARATION

Date: March 1, 2005

Docket: YO987-074BZ

Group Art Unit: 1751

Examiner: M. Kopec

Commissioner for Patents
P.O. Box 1450
Alexandria, VA 22313-1450

FIRST SUPPLEMENTAL AMENDMENT

Sir:

In response to the Office Action dated July 28, 2004, please consider the
following:

ATTACHMENT U

STRUCTURE, PROPERTIES AND PREPARATION OF PEROVSKITE-TYPE COMPOUNDS

BY
FRANCIS S. GALASSO
United Aircraft Research Laboratories

INDEX

OXIDES

- $A^{2+}B^{4+}O_3$
phase transition: 6, 88, 116, 117
preparation:
 single crystal: 166
 thin film: 164
- $AgNbO_3$
crystallography: 18
density: 145
phase transition: 116, 118
- $AgTaO_3$
crystallography: 18
density: 145
phase transition: 116, 118
- $CaTiO_3$
crystallography: 5, 18
density: 145
- $KTiO_3$
crystallography: 5, 18
density: 145
- $(K,Na)NbO_3$
ferroelectricity: 95
- $KNbO_3$
crystallography: 4, 18
density: 145
dielectric constant: 87
ferroelectricity: 95
melting point: 143
phase transition: 87, 116, 117
preparation, single crystal: 166
- $K(Nb,Ta)O_3$
ferroelectricity: 96
optical properties: 1
preparation, single crystal: 166
- $KTiO_3$
crystallography: 5, 18
density: 145
ferroelectricity: 88
melting point: 143
optical properties: 123
phase transition: 116, 117
preparation, single crystal: 166
- $NaNbO_3$
crystallography: 5, 18
density: 145
dielectric constant: 88
ferroelectricity: 97
melting point: 142
optical properties: 134
- $NaTaO_3$
crystallography: 18
density: 145
ferroelectricity: 88
melting point: 143
phase transition: 116, 118
preparation, single crystal: 166
- $RbTiO_3$
crystallography: 18
density: 145
- $RbTaO_3$
ferroelectricity: 88
- TiO_2
crystallography: 5, 18
density: 145
- $A^{2+}B^{4+}O_3$
 $(Ba,Ca,Sr)TiO_3$
electrical conductivity: 70
- $(Ba,Ca,Sr)(Ti,Zr)O_3$
dielectric constant: 82
ferroelectricity: 92
- $(Ba,Ca)TiO_3$
dielectric constant: 93
piezoelectricity: 92
- $(Ba,Ca,Mg)TiO_3$
electrical conductivity: 70
- $BaCoO_3$
crystallography: 18
density: 145
preparation, thin film: 164
- $BaFeO_3$
crystallography: 18
density: 145
- $Ba(Hf,Ti)O_3$
dielectric constant: 84
ferroelectricity: 94
phase transition: 94

- (Ba,La)(Mn,Ti)O₃
ferromagnetism 123
phase transition 123
- (Ba,La)TiO₃
electrical conductivity 70
thermoelectricity 76
- BaMoO₄
crystallography 18
density 145
- BaPbO₃
crystallography 18
density 145
- (Ba,Pb)(Sn,Ti)O₃
ferroelectricity 95
- (Ba,Pb)TiO₃
dielectric constant 91
electrical conductivity 70
ferroelectricity 91
piezoelectricity 95
- (Ba,Pb)ZrO₃
dielectric constant 93
ferroelectricity 95
- BaPbO₃
crystallography 18
density 145
- BaPbO₃
crystallography 18
density 145
- Ba(Si,Ti)O₃
electrical conductivity 70
- BaSnO₃
crystallography 7, 18
density 145
preparation, thin film 184
- Ba(Sn,Ti)O₃
ferroelectricity 94
- (Ba,Sr)(Sn,Ti)O₃
electrical conductivity 70
- (Ba,Sr)TiO₃
crystallography 20
dielectric constant 80
electrical conductivity 90
ferroelectricity 98
superconductivity 64
- BaThO₃
crystallography 18
density 145
melting point 142
- BaTiO₃
crystallography 6, 18
density 145
dielectric constant 82
electrical conductivity 95
electron paramagnetic resonance 67
ferroelectricity 90
heat of formation 142
melting point 142
nuclear irradiation 104
optical properties 120
phase transition 85, 80, 116
piezoelectricity 110
preparation
single crystal 169
thin film 162
thermal conductivity 142
X-ray diffraction 60
- Ba(Ti,La)O₃
electrical conductivity 70
- BaVO₃
crystallography 18
density 145
- BaZrO₃
crystallography 6, 18
density 145
melting point 142
thermal conductivity 142
- CaCeO₃
crystallography 18
density 145
- CaErO₃
crystallography 18
density 145
melting point 142
thermal expansion 142
- (Ca,La)MnO₃
ferromagnetism 123
thermoelectricity 76
- CaMnO₃
crystallography 18
density 145
electrical conductivity 68
- CaMoO₃
crystallography 18
density 145
electrical conductivity 64
preparation, powder 181
- CaSnO₃
crystallography 10
density 145
- (Ca,Sr)TiO₃
superconductivity 64
- CaThO₃
crystallography 18
density 145
- CaTiO₃
crystallography 8, 6, 19
density 145
dielectric constant 87
electrical conductivity 68

- CaTiO_3 (cont.)
 heat of formation 142
 Madelung constant 40
 melting point 142
 optical properties 112
 phase transition 87, 117
 preparation
 single crystal 173
 thin film 164
 thermal conductivity 142
 thermal expansion 142
 CaVO_3
 crystallography 7, 19
 density 145
 CaVO_4
 crystallography 19
 density 145
 CaZrO_3
 crystallography 7, 19
 density 145
 melting point 142
 CeCrO_3
 crystallography 19
 density 145
 CeFeO_3
 crystallography 19
 density 145
 CeThO_3
 crystallography 19
 density 145
 CeTiO_3
 crystallography 19
 density 145
 ferroelectricity 104
 preparation, single crystal 174
 CdZrO_3
 crystallography 19
 density 145
 EuTiO_3
 crystallography 19
 density 145
 MgTiO_3
 crystallography 19
 density 145
 PbCoO_3
 crystallography 19
 density 145
 PbHfO_3
 crystallography 19
 density 145
 ferroelectricity 89
 phase transition 89, 115, 117
 PbSnO_3
 crystallography 19
 density 145
 PbTiO_3
 crystallography 6, 19
 density 145
 dielectric constant 85
 ferroelectricity 85
 phase transition 6, 85, 116, 117
 piezoelectricity 86
 preparation
 single crystal 174
 thin film 165
 thermal expansion 142
 X-ray diffraction 60
 $\text{PbTiO}_3\text{-KNO}_3$
 dielectric constant 85
 $\text{PbTiO}_3\text{-NaNbO}_3$
 ferroelectricity 86
 PbTiZrO_3
 dielectric constant 87
 ferroelectricity 87
 mechanical properties 153
 piezoelectricity 87, 110
 PtZrO_3
 crystallography 7, 19
 density 145
 dielectric constant 83
 ferroelectricity 83
 phase transition 83, 116, 117
 preparation, single crystal 174
 SrCoO_3
 crystallography 19
 density 145
 SrCoO_4
 crystallography 19
 density 145
 SrFeO_3
 crystallography 19
 density 145
 SrHfO_3
 crystallography 19
 density 145
 SrMoO_3
 crystallography 19
 density 145
 electrical conductivity 64
 ErPbO_3
 crystallography 19
 density 145
 ErRuO_3
 crystallography 19
 density 145
 preparation, powder 161
 ErTiO_3
 crystallography 19
 density 145

- SrFeO_3 (cont.)
 preparation, thin film 164
 SrTiO_3
 crystallography 19
 density 148
 SrTiO_3
 crystallography 6, 19
 density 148
 dielectric constant 85
 electrical conductivity 88
 electron paramagnetic resonance 53
 ferroelectricity 86
 heat of formation 142
 melting point 142
 optical properties 120
 phase transition 116, 117
 preparation, single crystal 175
 thermal conductivity 142
 thermal expansion 142
 SrUO_4
 crystallography 10
 density 148
 SrZrO_3
 crystallography 7, 19
 density 148
 mechanical properties 144
 melting point 142
 thermal expansion 142
- $\text{A}^{2+}\text{B}^{2+}\text{O}_4$
 HfAlO_4
 crystallography 19
 density 148
 BiO_2O_3
 crystallography 20
 density 148
 preparation, powder 162
 BiMnO_3
 crystallography 20
 density 148
 ferromagnetism 126
 preparation, powder 162
 CaAlO_3
 crystallography 20
 density 148
 CaCoO_3
 crystallography 20
 density 148
 CaFeO_3
 crystallography 20
 density 148
- CeGaO_3
 crystallography 20
 density 148
 CeSeO_3
 crystallography 20
 density 148
 CeVO_3
 crystallography 20
 density 148
 CrBiO_3
 crystallography 20
 density 148
 DyAlO_3
 crystallography 20
 density 148
 DyFeO_3
 crystallography 20
 density 148
 DyMnO_3
 crystallography 20
 density 148
 ErAlO_3
 crystallography 9, 20
 density 148
 EuCoO_3
 crystallography 20
 density 148
 EuFeO_3
 crystallography 9, 20
 density 148
 PbBiO_3
 crystallography 20
 density 148
 GdAlO_3
 crystallography 9, 20
 density 148
 melting point 142
 preparation, single crystal 176
 GdO_2O_3
 crystallography 20
 density 148
 GdO_2O_3
 crystallography 6, 20
 density 148
 GdFeO_3
 crystallography 8, 20
 density 148
 ferromagnetism 123
 X-ray diffraction 61
 GdMnO_3
 crystallography 20
 density 148
 GdSeO_3
 crystallography 9, 20
 density 147

- GdVO₃,
crystallography 9, 20
density 147
- LaAlO₃,
crystallography 9, 10, 20
density 147
basic properties 1
melting point 162
phase transition 10
preparation, single crystal 174
- LaCoO₃,
crystallography 21
density 147
electrical conductivity 69
preparation, single crystal 174
- La(Co,Mn)O₃,
ferromagnetism 153
- LaCrO₃,
crystallography 9, 21
density 147
electrical conductivity 69
- La(O₂,Mn)O₃,
ferromagnetism 153
- LaFeO₃,
crystallography 21
density 147
electrical conductivity 69
melting point 145
- LaGaO₃,
crystallography 9, 21
density 147
phase transition 9
- LaInO₃,
crystallography 21
density 147
- LaMnO₃,
electrical conductivity 69
- La(Mn,Ni)O₃,
ferromagnetism 124
- LaNiO₃,
crystallography 21
density 147
- LaRhO₃,
crystallography 21
density 147
- LaSiO₃,
crystallography 9, 21
density 147
- (La,Sr)CoO₃,
electrical conductivity 69
ferromagnetism 123
- (La,Sr)CrO₃,
electrical conductivity 69
- (La,Sr)FeO₃,
electrical conductivity 69
thermoelectricity 76
- (La,Sr)MnO₃,
electrical conductivity 69
- LaTiO₃,
crystallography 21
density 147
electrical conductivity 60
- LaVO₃,
crystallography 21
density 147
electrical conductivity 60
preparation, powder 161
- LaWO₃,
crystallography 21
density 147
- NdAlO₃,
crystallography 9, 21
density 147
- NdCoO₃,
crystallography 21
density 147
- NdCrO₃,
crystallography 9, 21
density 147
- NdFeO₃,
crystallography 9, 21
density 147
- NdGaO₃,
crystallography 9, 21
density 147
- NdInO₃,
crystallography 21
density 147
- NdMnO₃,
crystallography 21
density 147
- NdScO₃,
crystallography 9, 21
density 147
- NdVO₃,
crystallography 9, 21
density 147
- PrAlO₃,
crystallography 9, 21
density 147
- PrCoO₃,
crystallography 21
density 147
- PrCrO₃,
crystallography 9, 21
density 147

- PrFeO_3
 crystallography 9, 22
 density 147
 PrGaO_3
 crystallography 9, 22
 density 147
 PrMnO_3
 crystallography 22
 density 147
 PrScO_3
 crystallography 9, 22
 density 147
 PrVO_3
 crystallography 9, 22
 density 147
 PuAlO_3
 crystallography 22
 density 147
 PuCrO_3
 crystallography 22
 density 147
 PuMnO_3
 crystallography 22
 density 147
 PuVO_3
 crystallography 22
 density 147
 SmAlO_3
 crystallography 9, 22
 density 147
 phase transition 9
 SmCoO_3
 crystallography 22
 density 147
 SmCrO_3
 crystallography 9, 22
 density 147
 SmFeO_3
 crystallography 9, 22
 density 147
 SmInO_3
 crystallography 22
 density 147
 SmVO_3
 crystallography 22
 density 147
 YAlO_3
 crystallography 9, 22
 density 147
 melting point 142
 YCrO_3
 crystallography 9, 22
 density 148
 YFeO_3
 crystallography 9, 22
 density 148
 YScO_3
 crystallography 9, 22
 density 148
 ABO_3 and ABO_{4-x}
 $\text{Ce}_{0.8}\text{NbO}_3$
 crystallography 22
 density 148
 $\text{Ce}_{0.8}\text{TaO}_3$
 crystallography 23
 density 148
 $\text{Dy}_{0.8}\text{TaO}_3$
 crystallography 23
 density 148
 $\text{Gd}_{0.8}\text{TaO}_3$
 crystallography 23
 density 148
 $\text{La}_{0.8}\text{NbO}_3$
 crystallography 23
 density 148
 $\text{La}_{0.8}\text{TaO}_3$
 crystallography 23
 density 148
 $\text{Nd}_{0.8}\text{NbO}_3$
 crystallography 23
 density 148
 $\text{Nd}_{0.8}\text{TaO}_3$
 crystallography 23
 density 148
 $\text{Pr}_{0.8}\text{NbO}_3$
 crystallography 23
 density 148
 $\text{Pr}_{0.8}\text{TaO}_3$
 crystallography 23
 density 148
 $\text{Sm}_{0.8}\text{TaO}_3$
 crystallography 23
 density 148
 $\text{Y}_{0.8}\text{TaO}_3$
 crystallography 23
 density 148
 $\text{Yb}_{0.8}\text{TaO}_3$
 crystallography 23
 density 148
 $\text{Ce}_{0.1}\text{TaO}_3$
 crystallography 23
 density 148
 LaWO_3
 catalyst 141
 crystallography 10, 23

- Li_2WO_4 (cont.)
 density 148
 electrical conductivity 62
 Na_2WO_4
 crystals 141
 crystallography 10, 23
 density 148
 electrical conductivity 60
 preparation, single crystal 176
 Sr_2NbO_7
 crystallography 10, 23
 density 148
 preparation, powder 161
 BaTiO_3
 electrical conductivity 66
 CaMoO_4
 crystallography 11, 23
 density 148
 CaTiO_3
 electrical conductivity 66
 SrCoO_3
 crystallography 11, 23
 density 148
 SrFeO_3
 crystallography 11, 23
 density 148
 SrTiO_3
 crystallography 11, 23
 density 148
 electrical conductivity 66
 superconductivity 63
 SrVO_3
 crystallography 11, 23
 density 148
 electrical conductivity 60
 $\text{A}(\text{B}_{1-x}\text{B}_x)\text{O}_3$
 $\text{Ba}(\text{Al}_{1-x}\text{W}_x)\text{O}_3$
 crystallography 23
 density 148
 $\text{Ba}(\text{Bi}_{1-x}\text{W}_x)\text{O}_3$
 dielectric constant 60
 $\text{Ba}(\text{Dy}_{1-x}\text{W}_x)\text{O}_3$
 crystallography 23
 density 148
 $\text{Ba}(\text{S}_{1-x}\text{W}_x)\text{O}_3$
 crystallography 24
 density 148
 $\text{Ba}(\text{Sn}_{1-x}\text{W}_x)\text{O}_3$
 crystallography 24
 density 148
 $\text{Ba}(\text{Fe}_{1-x}\text{U}_x)\text{O}_3$
 crystallography 24
 density 148
 $\text{Ba}(\text{Ga}_{1-x}\text{W}_x)\text{O}_3$
 crystallography 24
 density 148
 $\text{Ba}(\text{In}_{1-x}\text{U}_x)\text{O}_3$
 crystallography 24
 density 148
 $\text{Ba}(\text{In}_{1-x}\text{W}_x)\text{O}_3$
 crystallography 24
 density 148
 $\text{Ba}(\text{La}_{1-x}\text{W}_x)\text{O}_3$
 crystallography 24
 density 148
 $\text{Ba}(\text{La}_{1-x}\text{W}_x)\text{O}_3$
 crystallography 24
 density 148
 $\text{Ba}(\text{Nd}_{1-x}\text{W}_x)\text{O}_3$
 crystallography 24
 density 148
 $\text{Ba}(\text{Sb}_{1-x}\text{U}_x)\text{O}_3$
 crystallography 24
 density 148
 $\text{Ba}(\text{Sb}_{1-x}\text{W}_x)\text{O}_3$
 crystallography 24
 density 148
 $\text{Ba}(\text{Y}_{1-x}\text{U}_x)\text{O}_3$
 crystallography 24
 density 148
 $\text{Ba}(\text{Y}_{1-x}\text{W}_x)\text{O}_3$
 crystallography 24
 density 148
 $\text{Ba}(\text{Yb}_{1-x}\text{W}_x)\text{O}_3$
 crystallography 24
 density 148
 $\text{La}(\text{Co}_{1-x}\text{Nb}_x)\text{O}_3$
 crystallography 24
 density 148
 $\text{La}(\text{Co}_{1-x}\text{Sb}_x)\text{O}_3$
 crystallography 24
 density 148
 $\text{Pb}(\text{Fe}_{1-x}\text{W}_x)\text{O}_3$
 crystallography 24
 density 148
 ferroelectricity 100
 $\text{Sr}(\text{Co}_{1-x}\text{Fe}_x)\text{O}_3$
 crystallography 15, 24
 density 148
 $\text{Sr}(\text{Co}_{1-x}\text{U}_x)\text{O}_3$
 crystallography 24
 density 148
 $\text{Sr}(\text{Fe}_{1-x}\text{Ba}_x)\text{O}_3$
 crystallography 24
 density 148
 $\text{Sr}(\text{Fe}_{1-x}\text{W}_x)\text{O}_3$
 crystallography 24
 density 148

- $\text{Sr}(\text{In}_{0.5}\text{Re}_{0.5})\text{O}_6$
 crystallography 24
 density 149
 $\text{A}^{2+}(\text{B}^{2+}\text{B}^{4+})\text{O}_6$
 $\text{Ba}(\text{Co}_{0.5}\text{Nb}_{0.5})\text{O}_6$
 crystallography 25
 density 149
 $\text{Ba}(\text{Co}_{0.5}\text{Ta}_{0.5})\text{O}_6$
 crystallography 25
 density 149
 preparation, single crystal 177
 $\text{Ba}(\text{Co}_{0.5}\text{Nb}_{0.5})\text{O}_6$
 crystallography 25
 density 149
 $\text{Ba}(\text{Co}_{0.5}\text{Ta}_{0.5})\text{O}_6$
 crystallography 25
 density 149
 $\text{Ba}(\text{Co}_{0.5}\text{Nb}_{0.5})\text{O}_6$
 crystallography 25
 density 149
 $\text{Ba}(\text{Co}_{0.5}\text{Ta}_{0.5})\text{O}_6$
 crystallography 25
 density 149
 $\text{Ba}(\text{Co}_{0.5}\text{Nb}_{0.5})\text{O}_6$
 crystallography 25
 density 149
 $\text{Ba}(\text{Fe}_{0.5}\text{Nb}_{0.5})\text{O}_6$
 crystallography 25
 density 149
 $\text{Ba}(\text{Fe}_{0.5}\text{Ta}_{0.5})\text{O}_6$
 crystallography 25
 density 149
 preparation, powder 180
 $\text{Ba}(\text{Mg}_{0.5}\text{Nb}_{0.5})\text{O}_6$
 crystallography 25
 density 149
 $\text{Ba}(\text{Mg}_{0.5}\text{Ta}_{0.5})\text{O}_6$
 crystallography 25
 density 149
 preparation, single crystal 177
 X-ray diffraction 55
 $\text{Ba}(\text{Mn}_{0.5}\text{Nb}_{0.5})\text{O}_6$
 crystallography 25
 density 149
 $\text{Ba}(\text{Mn}_{0.5}\text{Ta}_{0.5})\text{O}_6$
 crystallography 25
 density 149
 $\text{Ba}(\text{Ni}_{0.5}\text{Nb}_{0.5})\text{O}_6$
 crystallography 25
 density 149
- $\text{Ba}(\text{Ni}_{0.5}\text{Ta}_{0.5})\text{O}_6$
 crystallography 25
 density 160
 preparation, single crystal 177
 $\text{Ba}(\text{Pb}_{0.5}\text{Nb}_{0.5})\text{O}_6$
 crystallography 25
 density 160
 $\text{Ba}(\text{Pb}_{0.5}\text{Ta}_{0.5})\text{O}_6$
 crystallography 25
 density 160
 $\text{Ba}(\text{Sb}_{0.5}\text{Ta}_{0.5})\text{O}_6$
 crystallography 11, 15, 25
 density 160
 X-ray diffraction 55
 $\text{Ba}(\text{Zn}_{0.5}\text{Nb}_{0.5})\text{O}_6$
 crystallography 15, 25
 density 160
 $\text{Ba}(\text{Zn}_{0.5}\text{Ta}_{0.5})\text{O}_6$
 crystallography 15
 density 160
 preparation, single crystal 177
 $\text{Ca}(\text{Ni}_{0.5}\text{Nb}_{0.5})\text{O}_6$
 crystallography 25
 density 160
 $\text{Ca}(\text{Ni}_{0.5}\text{Ta}_{0.5})\text{O}_6$
 crystallography 25
 density 160
 $\text{Pb}(\text{Co}_{0.5}\text{Nb}_{0.5})\text{O}_6$
 crystallography 25
 density 160
 dielectric constant 102
 ferroelectricity 102
 preparation, single crystal 176
 $\text{Pb}(\text{Co}_{0.5}\text{Ta}_{0.5})\text{O}_6$
 crystallography 25
 density 160
 dielectric constant 102
 ferroelectricity 102
 preparation, single crystal 176
 $\text{Pb}(\text{Mg}_{0.5}\text{Nb}_{0.5})\text{O}_6$
 crystallography 25
 density 160
 dielectric constant 101
 ferroelectricity 101
 $\text{Pb}(\text{Mg}_{0.5}\text{Ta}_{0.5})\text{O}_6$
 crystallography 25
 density 160
 dielectric constant 102
 ferroelectricity 102
 preparation, single crystal 177
 $\text{Pb}(\text{Ni}_{0.5}\text{Nb}_{0.5})\text{O}_6$
 crystallography 25
 density 160

- $\text{Pb}(\text{Ni}_{0.5}\text{Nb}_{0.5})\text{O}_3$
 crystallography 26
 density 150
 dielectric constant 101
 ferroelectricity 101
 $\text{Pb}(\text{Ni}_{0.5}\text{Ta}_{0.5})\text{O}_3$
 crystallography 26
 density 150
 dielectric constant 102
 ferroelectricity 102
 preparation, single crystal 176
 $\text{Pb}(\text{Zn}_{0.5}\text{Nb}_{0.5})\text{O}_3$
 crystallography 26
 density 150
 dielectric constant 102
 ferroelectricity 102
 preparation, single crystal 176
 $\text{Sr}(\text{Co}_{0.5}\text{Nb}_{0.5})\text{O}_3$
 crystallography 26
 density 150
 $\text{Sr}(\text{Co}_{0.5}\text{Sb}_{0.5})\text{O}_3$
 crystallography 26
 density 150
 $\text{Sr}(\text{Co}_{0.5}\text{Ta}_{0.5})\text{O}_3$
 crystallography 26
 density 150
 $\text{Sr}(\text{Co}_{0.5}\text{Ti}_{0.5})\text{O}_3$
 crystallography 26
 density 150
 $\text{Sr}(\text{Co}_{0.5}\text{Zr}_{0.5})\text{O}_3$
 crystallography 26
 density 150
 $\text{Sr}(\text{Cu}_{0.5}\text{Nb}_{0.5})\text{O}_3$
 crystallography 26
 density 150
 $\text{Sr}(\text{Co}_{0.5}\text{Sb}_{0.5})\text{O}_3$
 crystallography 26
 density 150
 $\text{Sr}(\text{Co}_{0.5}\text{Ta}_{0.5})\text{O}_3$
 crystallography 26
 density 150
 $\text{Sr}(\text{Co}_{0.5}\text{Ti}_{0.5})\text{O}_3$
 crystallography 26
 density 150
 $\text{Sr}(\text{Co}_{0.5}\text{Zr}_{0.5})\text{O}_3$
 crystallography 26
 density 150
 $\text{Sr}(\text{Fe}_{0.5}\text{Nb}_{0.5})\text{O}_3$
 crystallography 26
 density 150
 $\text{Sr}(\text{Mg}_{0.5}\text{Nb}_{0.5})\text{O}_3$
 crystallography 26
 density 150
 $\text{Sr}(\text{Mg}_{0.5}\text{Ta}_{0.5})\text{O}_3$
 crystallography 26
 density 150
 $\text{Sr}(\text{Mg}_{0.5}\text{Ti}_{0.5})\text{O}_3$
 crystallography 26
 density 150
 $\text{Sr}(\text{Mg}_{0.5}\text{Zr}_{0.5})\text{O}_3$
 crystallography 26
 density 150
 $\text{Sr}(\text{Ni}_{0.5}\text{Nb}_{0.5})\text{O}_3$
 crystallography 26
 density 150
 $\text{Sr}(\text{Ni}_{0.5}\text{Ta}_{0.5})\text{O}_3$
 crystallography 26
 density 150
 $\text{Sr}(\text{Ni}_{0.5}\text{Zr}_{0.5})\text{O}_3$
 crystallography 26
 density 150
 $\text{Sr}(\text{Ta}_{0.5}\text{Nb}_{0.5})\text{O}_3$
 crystallography 26
 density 150
 $\text{Sr}(\text{Ta}_{0.5}\text{Ta}_{0.5})\text{O}_3$
 crystallography 26
 density 150
 $\text{Sr}(\text{Ta}_{0.5}\text{Zr}_{0.5})\text{O}_3$
 crystallography 26
 density 150
 $\text{Sr}(\text{Zn}_{0.5}\text{Nb}_{0.5})\text{O}_3$
 crystallography 27
 density 150
 $\text{Sr}(\text{Zn}_{0.5}\text{Ta}_{0.5})\text{O}_3$
 crystallography 27
 density 150

$\text{A}^{2+}(\text{B}^{3+}\text{B}^{5+})\text{O}_3$

- $\text{Ba}(\text{Bi}_{0.5}\text{Mo}_{0.5})\text{O}_3$
 dielectric constant 59
 $\text{Ba}(\text{Bi}_{0.5}\text{Nb}_{0.5})\text{O}_3$
 crystallography 27
 density 150
 dielectric constant 59
 ferroelectricity 59
 $\text{Ba}(\text{Bi}_{0.5}\text{Ta}_{0.5})\text{O}_3$
 crystallography 27
 density 150
 dielectric constant 59
 ferroelectricity 59
 $\text{Ba}(\text{Bi}_{0.5}\text{U}_{0.5})\text{O}_3$
 dielectric constant 59
 $\text{Ba}(\text{Co}_{0.5}\text{Nb}_{0.5})\text{O}_3$
 crystallography 27
 density 150
 $\text{Ba}(\text{Co}_{0.5}\text{Ta}_{0.5})\text{O}_3$
 crystallography 27
 density 150
 $\text{Ba}(\text{Co}_{0.5}\text{Zr}_{0.5})\text{O}_3$
 crystallography 27
 density 150

Page 150 of 159

201

Page 101 of 109

- $\text{Ca}(\text{Ho}_{0.4}\text{Ta}_{0.6})\text{O}_3$
 crystallography 21
 density 163
 $\text{Ca}(\text{In}_{0.4}\text{Nb}_{0.6})\text{O}_3$
 crystallography 21
 density 163
 $\text{Ca}(\text{In}_{0.4}\text{Ta}_{0.6})\text{O}_3$
 crystallography 21
 density 163
 $\text{Ca}(\text{La}_{0.4}\text{Nb}_{0.6})\text{O}_3$
 crystallography 21
 density 163
 $\text{Ca}(\text{La}_{0.4}\text{Ta}_{0.6})\text{O}_3$
 crystallography 21
 density 163
 $\text{Ca}(\text{Mn}_{0.4}\text{Ta}_{0.6})\text{O}_3$
 crystallography 21
 density 163
 $\text{Ca}(\text{Nd}_{0.4}\text{Nb}_{0.6})\text{O}_3$
 crystallography 21
 density 163
 $\text{Ca}(\text{Nd}_{0.4}\text{Ta}_{0.6})\text{O}_3$
 crystallography 21
 density 163
 $\text{Ca}(\text{Ni}_{0.4}\text{W}_{0.6})\text{O}_3$
 crystallography 22
 density 163
 $\text{Ca}(\text{Pr}_{0.4}\text{Nb}_{0.6})\text{O}_3$
 crystallography 22
 density 163
 $\text{Ca}(\text{Pr}_{0.4}\text{Ta}_{0.6})\text{O}_3$
 crystallography 22
 density 163
 $\text{Ca}(\text{Sc}_{0.4}\text{Ta}_{0.6})\text{O}_3$
 crystallography 22
 density 163
 $\text{Ca}(\text{Sm}_{0.4}\text{Nb}_{0.6})\text{O}_3$
 crystallography 21
 density 163
 $\text{Ca}(\text{Sm}_{0.4}\text{Ta}_{0.6})\text{O}_3$
 crystallography 22
 density 163
 $\text{Ca}(\text{Tb}_{0.4}\text{Nb}_{0.6})\text{O}_3$
 crystallography 22
 density 163
 $\text{Ca}(\text{Tb}_{0.4}\text{Ta}_{0.6})\text{O}_3$
 crystallography 22
 density 163
 $\text{Ca}(\text{Y}_{0.4}\text{Nb}_{0.6})\text{O}_3$
 crystallography 22
 density 163
 $\text{Ca}(\text{Y}_{0.4}\text{Ta}_{0.6})\text{O}_3$
 crystallography 22
 density 163
 $\text{Ca}(\text{Yb}_{0.4}\text{Nb}_{0.6})\text{O}_3$
 crystallography 22
 density 163
 $\text{Ca}(\text{Yb}_{0.4}\text{Ta}_{0.6})\text{O}_3$
 crystallography 22
 density 163
 $\text{Pb}(\text{Fe}_{0.4}\text{Nb}_{0.6})\text{O}_3$
 crystallography 22
 density 163
 ferroelectricity 99
 preparation, single crystal 176
 $\text{Pb}(\text{Fe}_{0.4}\text{Ta}_{0.6})\text{O}_3$
 crystallography 22
 density 163
 dielectric constant 101
 ferroelectricity 101
 preparation, single crystal 176
 $\text{Pb}(\text{Ho}_{0.4}\text{Nb}_{0.6})\text{O}_3$
 crystallography 22
 density 163
 $\text{Pb}(\text{In}_{0.4}\text{Nb}_{0.6})\text{O}_3$
 crystallography 22
 density 163
 dielectric constant 100
 ferroelectricity 100
 $\text{Pb}(\text{La}_{0.4}\text{Nb}_{0.6})\text{O}_3$
 crystallography 22
 density 163
 $\text{Pb}(\text{La}_{0.4}\text{Ta}_{0.6})\text{O}_3$
 crystallography 22
 density 163
 phase transition 121
 $\text{Pb}(\text{Sc}_{0.4}\text{Nb}_{0.6})\text{O}_3$
 crystallography 22
 density 163
 dielectric constant 100
 ferroelectricity 100
 phase transition 121
 $\text{Pb}(\text{Sc}_{0.4}\text{Ta}_{0.6})\text{O}_3$
 crystallography 22
 density 163
 phase transition 121
 $\text{Pb}(\text{Sm}_{0.4}\text{Nb}_{0.6})\text{O}_3$
 crystallography 22
 density 163
 dielectric constant 100
 ferroelectricity 100
 preparation, single crystal 176
 $\text{Pb}(\text{Sc}_{0.4}\text{Ta}_{0.6})\text{O}_3$
 crystallography 22
 density 163
 dielectric constant 100
 preparation, single crystal 176
 $\text{Pb}(\text{Yb}_{0.4}\text{Nb}_{0.6})\text{O}_3$
 crystallography 22
 density 163
 ferroelectricity 99
 phase transition 121
 $\text{Pb}(\text{Yb}_{0.4}\text{Ta}_{0.6})\text{O}_3$
 crystallography 22
 density 163
 dielectric constant 100
 ferroelectricity 100
 preparation, single crystal 176
 $\text{Sr}(\text{Co}_{0.4}\text{Nb}_{0.6})\text{O}_3$
 crystallography 22
 density 163
 $\text{Sr}(\text{Co}_{0.4}\text{Sb}_{0.6})\text{O}_3$
 crystallography 22
 density 163
 $\text{Sr}(\text{Co}_{0.4}\text{Ta}_{0.6})\text{O}_3$
 crystallography 22
 density 163
 ferroelectricity 100
 $\text{Sr}(\text{Co}_{0.4}\text{W}_{0.6})\text{O}_3$
 crystallography 22
 density 163
 $\text{Sr}(\text{Cr}_{0.4}\text{Nb}_{0.6})\text{O}_3$
 crystallography 22
 density 163
 $\text{Sr}(\text{Cr}_{0.4}\text{Ta}_{0.6})\text{O}_3$
 crystallography 22
 density 163
 $\text{Sr}(\text{Cr}_{0.4}\text{W}_{0.6})\text{O}_3$
 crystallography 22
 density 163
 $\text{Sr}(\text{Dy}_{0.4}\text{Ta}_{0.6})\text{O}_3$
 crystallography 22
 density 163
 $\text{Sr}(\text{Er}_{0.4}\text{Ta}_{0.6})\text{O}_3$
 crystallography 22
 density 163
 $\text{Sr}(\text{Eu}_{0.4}\text{Ta}_{0.6})\text{O}_3$
 crystallography 22
 density 163
 $\text{Sr}(\text{Fe}_{0.4}\text{Mo}_{0.6})\text{O}_3$
 crystallography 22
 density 164
 ferromagnetism 126
 $\text{Sr}(\text{Fe}_{0.4}\text{Nb}_{0.6})\text{O}_3$
 crystallography 22
 density 164
 ferromagnetism 126
 $\text{Sr}(\text{Fe}_{0.4}\text{Ta}_{0.6})\text{O}_3$
 crystallography 22
 density 164

203

Page 153 of 159

Page 154 of 159

- $\text{Sr}(\text{Co}_{0.4}\text{W}_{0.6})\text{O}_6$ (cont.)
 density 168
 ferromagnetism 127
 phase transition 119
 $\text{Sr}(\text{Co}_{0.4}\text{U}_{0.6})\text{O}_6$
 crystallography 37
 density 168
 $\text{Sr}(\text{Cu}_{0.4}\text{W}_{0.6})\text{O}_6$
 crystallography 37
 density 168
 $\text{Sr}(\text{Fe}_{0.4}\text{Co}_{0.6})\text{O}_6$
 crystallography 37
 density 168
 Madelung constant 41
 $\text{Sr}(\text{Fe}_{0.4}\text{Re}_{0.6})\text{O}_6$
 crystallography 37
 density 168
 Madelung constant 41
 $\text{Sr}(\text{Fe}_{0.4}\text{U}_{0.6})\text{O}_6$
 crystallography 37
 density 168
 $\text{Sr}(\text{Fe}_{0.4}\text{W}_{0.6})\text{O}_6$
 crystallography 37
 density 168
 ferromagnetism 126
 $\text{Sr}(\text{Mg}_{0.4}\text{Mo}_{0.6})\text{O}_6$
 crystallography 37
 density 168
 $\text{Sr}(\text{Mg}_{0.4}\text{Os}_{0.6})\text{O}_6$
 crystallography 37
 density 168
 $\text{Sr}(\text{Mg}_{0.4}\text{Re}_{0.6})\text{O}_6$
 crystallography 37
 density 168
 $\text{Sr}(\text{Mg}_{0.4}\text{Ta}_{0.6})\text{O}_6$
 crystallography 37
 density 168
 $\text{Sr}(\text{Mg}_{0.4}\text{U}_{0.6})\text{O}_6$
 crystallography 37
 density 168
 $\text{Sr}(\text{Mg}_{0.4}\text{W}_{0.6})\text{O}_6$
 crystallography 37
 density 168
 $\text{Sr}(\text{Mn}_{0.4}\text{Re}_{0.6})\text{O}_6$
 crystallography 37
 density 168
 $\text{Sr}(\text{Mn}_{0.4}\text{U}_{0.6})\text{O}_6$
 crystallography 37
 density 168
 $\text{Sr}(\text{Mn}_{0.4}\text{W}_{0.6})\text{O}_6$
 crystallography 37
 density 168
 ferromagnetism 126
- $\text{Sr}(\text{Ni}_{0.4}\text{Mo}_{0.6})\text{O}_6$
 crystallography 37
 density 168
 phase transition 119
 $\text{Sr}(\text{Ni}_{0.4}\text{Re}_{0.6})\text{O}_6$
 crystallography 37
 density 168
 $\text{Sr}(\text{Ni}_{0.4}\text{U}_{0.6})\text{O}_6$
 crystallography 37
 density 168
 Madelung constant 41
 $\text{Sr}(\text{Ni}_{0.4}\text{W}_{0.6})\text{O}_6$
 crystallography 37
 density 168
 ferromagnetism 126
 phase transition 119
 $\text{Sr}(\text{Pb}_{0.4}\text{Mo}_{0.6})\text{O}_6$
 crystallography 37
 density 168
 $\text{Sr}(\text{S}_{0.4}\text{O}_{0.6})\text{O}_6$
 crystallography 37
 density 168
 Madelung constant 41
 $\text{Sr}(\text{S}_{0.4}\text{Re}_{0.6})\text{O}_6$
 crystallography 37
 density 168
 $\text{Sr}(\text{S}_{0.4}\text{W}_{0.6})\text{O}_6$
 crystallography 37
 density 168
 $\text{Sr}(\text{Zn}_{0.4}\text{Mo}_{0.6})\text{O}_6$
 phase transition 119
 $\text{Sr}(\text{Zn}_{0.4}\text{Re}_{0.6})\text{O}_6$
 crystallography 37
 density 168
 Madelung constant 41
 $\text{Sr}(\text{Zn}_{0.4}\text{W}_{0.6})\text{O}_6$
 crystallography 37
 density 167
 phase transition 119
- $\text{A}^{2+}(\text{B}^{1+}\text{B}^{3+})\text{O}_6$
 $\text{Ba}(\text{Ag}_{0.4}\text{I}_{0.6})\text{O}_6$
 crystallography 38
 density 167
 $\text{Ba}(\text{Li}_{0.4}\text{Os}_{0.6})\text{O}_6$
 crystallography 16
 38
- density 167
 $\text{Ba}(\text{Li}_{0.4}\text{Re}_{0.6})\text{O}_6$
 crystallography 38
 density 167
 Madelung constant 40
 $\text{Ba}(\text{Na}_{0.4}\text{I}_{0.6})\text{O}_6$
 crystallography 38
 density 167
 $\text{Ba}(\text{Na}_{0.4}\text{Os}_{0.6})\text{O}_6$
 crystallography 16, 38
 density 167
 $\text{Ba}(\text{Na}_{0.4}\text{Re}_{0.6})\text{O}_6$
 crystallography 38
 density 167
 $\text{Ca}(\text{La}_{0.4}\text{Os}_{0.6})\text{O}_6$
 crystallography 38
 density 167
 $\text{Ca}(\text{La}_{0.4}\text{Re}_{0.6})\text{O}_6$
 crystallography 38
 density 167
 $\text{Sr}(\text{Li}_{0.4}\text{Os}_{0.6})\text{O}_6$
 crystallography 38
 density 167
 $\text{Sr}(\text{Li}_{0.4}\text{Re}_{0.6})\text{O}_6$
 crystallography 38
 density 167
 $\text{Sr}(\text{Na}_{0.4}\text{Os}_{0.6})\text{O}_6$
 crystallography 38
 density 167
 $\text{Sr}(\text{Na}_{0.4}\text{Re}_{0.6})\text{O}_6$
 crystallography 38
 density 167
 preparation, powder 160
- $\text{A}^{2+}(\text{B}^{1+}\text{B}^{3+})\text{O}_6$
 $\text{La}(\text{Os}_{0.4}\text{I}_{0.6})\text{O}_6$
 crystallography 38
 density 167
 $\text{La}(\text{Os}_{0.4}\text{Re}_{0.6})\text{O}_6$
 crystallography 38
 density 167
 $\text{La}(\text{Mg}_{0.4}\text{Os}_{0.6})\text{O}_6$
 crystallography 38
 density 167
 $\text{La}(\text{Mg}_{0.4}\text{I}_{0.6})\text{O}_6$
 crystallography 38
 density 167
 $\text{La}(\text{Mg}_{0.4}\text{Nb}_{0.6})\text{O}_6$
 crystallography 38
 density 167

KCoF_6 ,
 crystallography 185
 KCoF_6 ,
 crystallography 185
 KCoF_6 ,
 crystallography 185
 ferromagnetism 185
 preparation 183
 KFeF_6 ,
 crystallography 185
 ferromagnetism 185
 preparation 183
 KMgF_6 ,
 crystallography 185
 KMnF_6 ,
 crystallography 185
 ferromagnetism 185
 preparation 183
 KNiF_6 ,
 crystallography 185
 ferromagnetism 185
 preparation 183
 KZnF_6 ,
 crystallography 185
 LiBaF_6 ,
 crystallography 185

NaZnF_6 ,
 crystallography 185
 RbCoF_6 ,
 crystallography 185
 RbCoF_6 ,
 crystallography 185
 RbFeF_6 ,
 crystallography 185
 ferromagnetism 185
 preparation, single crystal 184
 RbMgF_6 ,
 crystallography 185
 RbMnF_6 ,
 crystallography 185
 ferromagnetism 185
 RbZnF_6 ,
 crystallography 185
 $\text{K}(\text{Ga}_{1-x}\text{Na}_x)\text{O}_6$,
 crystallography 185
 preparation 183
 $\text{K}(\text{Fe}_{1-x}\text{Na}_x)\text{O}_6$,
 crystallography 185
 preparation 183
 $\text{K}(\text{Ga}_{1-x}\text{Na}_x)\text{O}_6$,
 crystallography 185
 preparation 183

HYDRIDES

LiBaH_6 ,
 crystallography 185
 preparation 184
 LiSnH_6 ,

 crystallography 185
 LiSnH_6 ,
 crystallography 185
 preparation 184

NITRIDES

Fe_3N ,
 crystallography 185
 ferromagnetism 185
 preparation 184
 Mn_3N ,
 crystallography 185
 ferromagnetism 185
 preparation 184

Fe_3NIN ,
 crystallography 185
 ferromagnetism 185
 preparation 184
 Fe_3FeN ,
 crystallography 185
 ferromagnetism 185
 preparation 184

BRIEF ATTACHMENT V

IN THE UNITED STATES PATENT AND TRADEMARK OFFICE

In re Patent Application of

Applicants: Bednorz et al.

Serial No.: 08/479,810

Filed: June 7, 1995

For: NEW SUPERCONDUCTIVE COMPOUNDS HAVING HIGH TRANSITION
TEMPERATURE, METHODS FOR THEIR USE AND PREPARATION

Date: March 1, 2005

Docket: YO987-074BZ

Group Art Unit: 1751

Examiner: M. Kopec

Commissioner for Patents
P.O. Box 1450
Alexandria, VA 22313-1450

FIRST SUPPLEMENTAL AMENDMENT

Sir:

In response to the Office Action dated July 28, 2004, please consider the
following:

ATTACHMENT V

ARKIV FÖR KEMI Band 1 nr 54

Communicated 15 September 1949 by ARNE WESTGREN and ARNE TISELIUS

Mixed bismuth oxides with layer lattices

I. The structure type of $\text{CaNb}_2\text{Bi}_2\text{O}_9$

By BENGT AURIVILLIUS

With 5 figures in the text

In the course of a comprehensive investigation of mixed bismuth oxides, the system $\text{Bi}_2\text{O}_3-\text{TiO}_2$ was studied. At about 40 atomic % of TiO_2 a phase with a body-centered pseudo-tetragonal unit cell with $a = 3.84$ and $c = 32.8 \text{ \AA}$ was found. X-ray analysis (to be published later) seemed to show that the structure was built up of $\text{Bi}_2\text{O}_2^{2+}$ layers parallel to the basal plane, and sheets of composition $\text{Bi}_2\text{Ti}_3\text{O}_{10}^{2-}$. The atomic arrangement within the $\text{Bi}_2\text{Ti}_3\text{O}_{10}^{2-}$ sheets seemed to be the same as in structures of the perovskite type and the structure could then be described as consisting of $\text{Bi}_2\text{O}_2^{2+}$ layers between which double perovskite layers are inserted.

An attempt was then made to synthesize compounds where the $\text{Bi}_2\text{O}_2^{2+}$ layers alternate with single perovskite layers. The general formula for such compounds could be expected to be: $(\text{MeBi})_6\text{R}_4\text{O}_{18}$. In actual fact compounds with this structure could be prepared with Me: Na K Ca Ba Sr Pb R: Ti Nb Ta.

Procedure: Weighed amounts of the appropriate oxides or carbonates were mixed and heated in platinum or gold crucibles to about 1000°C . A number of compounds with the general formula $(\text{Bi, Me})_6\text{R}_4\text{O}_{18}$ were prepared. Out of these the following were found to have a body-centered tetragonal or pseudo-tetragonal unit cell. The real unit cells, however, appeared to be face-centered-orthorhombic.

Composition	Orthorhombic description			Pseudo-tetragonal description	
	a	b	c	a	c
$\text{Bi}_3\text{NbTiO}_9$	5.405	5.442	25.11	3.836	25.11
$\text{Bi}_3\text{TaTiO}_9$	5.402	5.436	25.15	3.832	25.15
$\text{CaBi}_2\text{Nb}_2\text{O}_9$	5.435	5.435	24.87	3.860	24.87
$\text{SrBi}_2\text{Nb}_2\text{O}_9$	5.504	5.504	25.05	3.892	25.05
$\text{SrBi}_2\text{Ta}_2\text{O}_9$	5.509	5.509	25.06	3.895	25.06
$\text{BaBi}_2\text{Nb}_2\text{O}_9$	5.533	5.533	25.55	3.912	25.55
$\text{PbBi}_2\text{Nb}_2\text{O}_9$	5.492	5.503	25.53	3.887	25.53
$\text{KBi}_6\text{Nb}_4\text{O}_{18}$	5.506	5.506	25.26	3.893	25.26
$\text{NaBi}_6\text{Nb}_4\text{O}_{18}$	5.47	5.47	26.94	3.87	26.94

B. AURIVILLIUS, *Mixed bismuth oxides with layer lattices*

Single crystals were prepared from the $\text{PbBi}_2\text{Nb}_2\text{O}_9$ and $\text{Bi}_2\text{NbTiO}_9$ phases. Weissenberg photographs of $0kl$ and $1kl$ (pseudo-tetragonal cell) were taken. In the powder photographs of $\text{Bi}_2\text{NbTiO}_9$ (Table 6a) the reflections 110 , 211 , 215 , 220 and 310 were clearly split up. No cleavage was found for the reflections $10l$, $20l$, and $30l$, (in all cases pseudo-tetragonal indices). From this it was concluded that the structure might be described by means of orthorhombic unit cells, having the same c axes as the pseudo-tetragonal cells, and a and b axes equal to the diagonals of the pseudo-tetragonal cells. Using orthorhombic units the Weissenberg photographs register hkl and $h, h+2, l$. In Table 6a the $\sin^2 \theta$ of $\text{Bi}_2\text{NbTiO}_9$ are calculated on the assumption of an orthorhombic unit cell.

A few discrepancies occur between the intensities of the spots as found in the Weissenberg photographs (first layer) and in the powder photographs. In the Weissenberg photographs ($h, h+2, l$), no difference was found between reflections hkl and hhl . From the powder photographs it is seen that 024 might be < 204 and that $311 < 131$ and $3111 < 1311$. The reason might be the orientation of the powder.

 $\text{PbBi}_2\text{Nb}_2\text{O}_9$ phase

The powder photographs of $\text{PbBi}_2\text{Nb}_2\text{O}_9$ (Table 6b) could be explained assuming a tetragonal cell with $a = 3.887 \text{ \AA}$ and $c = 25.53 \text{ \AA}$, but for two lines being split up, which indicated an orthorhombic unit cell with axes $a = 5.492$, $b = 5.503$ and $c = 25.53 \text{ \AA}$. As in $\text{Bi}_2\text{NbTiO}_9$, it was thus assumed that the real symmetry is $D_{2h} - mmm$, though nothing in the Weissenberg photographs indicated a lower Laue symmetry than $D_{2h} - 4/mmm$. The observed density was 7.91 , thus allowing 4 formula units/unit cell ($d_{\text{calc.}} = 8.22$).

With the exception of the criterion for face-centering that hkl occurring only with h, k, l all odd or all even, no systematic extinctions were found. This is characteristic of the space groups D_{2h}^{22} , D_2^7 and C_{2h}^{12} .

Positions of the metal atoms

As the scattering factors for the Pb and the Bi atoms are almost the same, it makes no difference in the intensity calculations whether the Pb and the Bi atoms occupy separate positions or are mixed at random. Therefore no difference will be made between Pb and Bi; they will both be denoted by Me.

The intensities of the reflections seemed to depend mainly on the value of l (see Table 1a). It therefore seemed probable that at least the Me and the Nb atoms are placed along the lines: $(000; \frac{1}{2}\frac{1}{2}0; \frac{1}{2}0\frac{1}{2}; 0\frac{1}{2}\frac{1}{2}) + 00z$. The sum of $\sum I_{00l} \cos 2\pi lz$ and $\sum I_{11l} \cos 2\pi lz$ will under such conditions represent the Patterson function along $00z$. In Fig. 1a these sums are plotted as functions of z . It is seen from the graph that high maxima occur for $z = 0.20$ and $z = 0.40$.

The unit cell of $\text{PbBi}_2\text{Nb}_2\text{O}_9$ contains 12 Me atoms and 8 Nb atoms.

If the space groups are assumed to be D_{2h}^{22} , D_2^7 or C_{2h}^{12} a or b , the only way of placing 12 Me atoms on the lines $00z$ is in one 4-fold and one 8-fold position. With these assumptions the only 4-fold positions possible are 000 or $00\frac{1}{2}$.

The crystals in the vicinity of maximum tetragonal indices $10l, 11l, 20l$ have been determined.

1
2
4
6
8
10
12
14
16
18
20
22
24
26
28
30
32
1
3
5
7
9
11
13
15
17
19
21
23
25
27
29
31

ARKIV FÖR KEMI. Bd 1 nr 54

Table 1a

Weissenberg Photographs of $\text{PbBi}_2\text{Nb}_2\text{O}_9$. Cu K_α radiation

The crystals form very thin plates, and therefore considerable absorption occurs. Spots in the vicinity of the lines described by WELLS (2) will therefore be weakened. The regions of maximum absorption are denoted by dotted lines. In the tables 1, 2 and 3 pseudotetragonal indices are used, and observed and calculated intensities for the reflections: 001, 101, 111, 201, and 211 are given. With orthorhombic description these reflections would have been denoted by: 001, 021 or 201, 221, 131 or 311.

l	I_1	I_2	I_{001}	$I_{\text{obs.}} I_{111}$	I_{201}
2	18	1.2		vw	vw
4	9.0	34	m^-	m	w
6	0.1	8.4	vw	m	—
8	25	14	m^-	w	w
10	350	340	vst	m^+	m
12	19	0.2	w	—	—
14	36	100	m^+	vw	w
16	9.6	4.8	vw	—	—
18	45	31	m	w	w
20	280	230	st	m^+	m^+
22	22	0.04	—	—	—
24	71	200	m^+	m	m^+
26	27	14	w	vw	vw
28	85	26	m^-	w	w
30	190	130	m	m	
32	25	8.4	w		

l	I_1	I_2	I_{101}	$I_{\text{obs.}} I_{211}$	
1	1.7	17	m	—	
3	20	6.3	m^-	vw	
5	380	370	vst	st	
7	18	0.0	—	—	
9	12	63	m	w	
11	3.2	5.3	—	—	
13	32	23	w	vw	
15	320	280	st	w	
17	20	0.2	—	—	
19	55	160	m^+	w^+	
21	18	7.8	vw	—	
23	61	32	m	w^+	
25	230	170	m^+	m	
27	24	1.7	—	—	
29	85	250	m^+		
31	48	23	w		

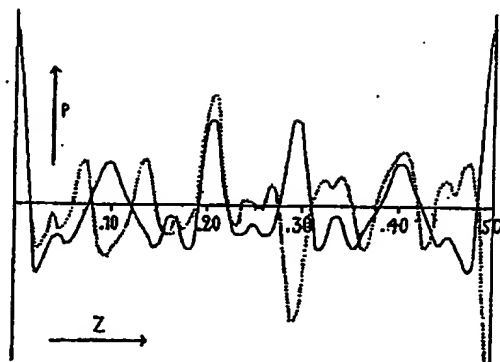
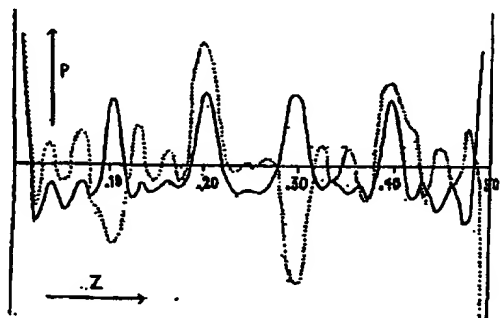
B. AURIVILLIUS, *Mixed bismuth oxides with layer lattices*

Table 1b
Weissenberg Photographs of $\text{PbBi}_2\text{Nb}_2\text{O}_9$

Zero layer				First layer			
00l	I'_1	$I_{\text{obs.}}$	I'_2	21l	I'_1	$I_{\text{obs.}}$	I'_2
4	11	m ⁻	32	1	1.7	—	14
6	1.4	vw	1.4	3	18	vw	4.8
8	28	m ⁻	14	5	330	st	340
10	360	vst	360	7	18	—	0.4
12	45	w	11	9	23	w	67
14	50	m ⁺	88	11	4.8	—	3.8
16	6.3	vw	5.8	13	26	vw	23
18	70	m	38	15	300	w	280
20	280	st	230	17	13	—	0.3
22	25	—	0.4	19	42	w ⁺	150
24	58	m ⁺	250	21	14	—	7.8
26	21	w	10	23	66	w ⁺	36
28	85	m ⁻	21	25	210	m	170
30	240	m	120	27	23	—	2.9
32	17	w	6.8				
10l				11l			
10l	I'_1	$I_{\text{obs.}}$	I'_2	11l	I'_1	$I_{\text{obs.}}$	I'_2
1	1.0	m	8.4	2	18	vw	1.2
3	14	m ⁻	4.0	4	9.0	m	34
5	320	vst	340	6	0.1	m	8.4
7	16	—	0.5	8	25	w	14
9	24	m	67	10	350	m ⁺	340
11	6.3	—	2.0	12	19	—	0.2
13	24	w	24	14	36	vw	100
15	310	st	280	16	9.6	—	4.8
17	13	—	0.5	18	45	w	31
19	42	m ⁺	150	20	280	m ⁺	230
21	14	vw	7.8	22	22	—	0.0
23	64	m	38	24	71	m	200
25	210	m	170	26	27	vw	14
27	23	—	2.9	28	85	w	26
29	81	m ⁺	220	30	190	m	130
31	32	w	24				
20l							
20l	I'_1	$I_{\text{obs.}}$	I'_2				
2	12	vw	1.4				
4	10	w	36				
6	0.5	—	4.8				
8	31	w ⁻	14				
10	350	m	350				
12	41	—	7.8				
14	50	w ⁻	88				
16	6.3	—	6.3				
18	69	w	40				
20	280	m ⁺	230				
22	25	—	0.4				
24	59	m ⁺	240				
26	20	vw	11				
28	85	w	21				

Of
It
Usi
sibiliti

The
0.20 s
In
the r
directi
course
actual
areas
alone.

Figure 1a. Patterson function of $\text{PbV}_2\text{Bi}_2\text{Nb}_2\text{O}_{10}$ along $00z$ Full curve: $\sum I_{00l} \cos 2\pi lz$ Dotted curve: $\sum I_{11l} \cos 2\pi lz$ (orthorhombic indices).Figure 1b. Patterson function of $\text{Bi}_3\text{NbTiO}_{10}$ along $00z$

Of 8-fold positions only $\pm 00z$ is possible.

It was assumed arbitrarily that 4 Me occupy the position 000.

Using the distances found with the aid of the Patterson function, two possibilities for placing the Nb atoms arose:

- | | | |
|---------------------------|-------------|------------------------|
| 1. 8 Nb in $\pm 00\ 0.20$ | 4 Me in 000 | 8 Me in $\pm 00\ 0.40$ |
| 2. 8 Nb in $\pm 00\ 0.40$ | 4 Me in 000 | 8 Me in $\pm 00\ 0.20$ |

The two curves on the graph were added and the areas under the peaks at 0.20 and 0.40 calculated. The ratio 1.5:1 was found for 0.20/0.40.

In case 1, the ratio was calculated to be 0.91:1 and in case 2, 1.1:1 if the ratio $f_{\text{Nb}}/f_{\text{Bi}}$ was assumed to be 0.46. These figures cannot be compared directly with the observed ratio 1.5:1 since the zero level in figure 1 is of course uncertain. Case 2 agrees slightly better insofar as the peak at 0.20 is actually higher. It seemed, however, that the uncertainty in determining the areas was so large that case 1 could not be excluded by these measurements alone.

B. AURIVILLIUS, *Mixed bismuth oxides with layer lattices*

Case 1

In calculating the structure amplitudes z_{Nb} was varied around 0.20 and z_{Me} around 0.40. The average ratio $f_{\text{Nb}}/f_{\text{Me}}$ was assumed to be 0.46. The intensities were compared with calculated values of A^2 :

$A = 10 (\cos 2\pi lz_{\text{Me}} + 0.46 \cos 2\pi lz_{\text{Nb}} + 0.5) = 10 F/4 f_{\text{Me}}$. In this way the best values for the parameters were found to be:

$z_{\text{Me}} = 0.397 \pm 0.002$ and $z_{\text{Nb}} = 0.192 \pm 0.004$. In Table 1a I_{calc} is compared with the observed intensities.

Case 2

z_{Nb} was varied about 0.40 and z_{Me} around 0.20. The best values were found to be $z_{\text{Nb}} = 0.412 \pm 0.004$ and $z_{\text{Me}} = 0.202 \pm 0.002$.

The observed and calculated values are compared in Table 1a.

It was found that arrangement 2 accounted slightly better for the experimental data than 1. It must, however, be borne in mind that the intensity ratios of weak spots might be changed through the influence of the oxygen atoms and that this influence was neglected in the calculations. The differences did not seem to be as large as to allow a decision between 1 and 2. It was therefore tried to find possible oxygen positions both for 1 and 2. The results were then compared.

Case 1. Positions of the oxygen atoms

The positions of the metal atoms were assumed to be: $(000; 0\frac{1}{2}\frac{1}{2}; \frac{1}{2}0\frac{1}{2}; \frac{1}{2}\frac{1}{2}0) + 000 (4 \text{ Me}_1) \pm 00 0.397 (8 \text{ Me}_2) \pm 00 0.192 (8 \text{ Nb})$. Since all point positions of D_{2d}^{20} can be described by positions of D_2^7 or $C_{2v}^{18} a$, only D_2^7 and $C_{2v}^{18} a$ have been considered.

At first only D_2^7 will be discussed. If the interatomic distances O—O, Me—O and Nb—O should not be smaller than 2.5, 2.2 and 1.8 Å, oxygen atoms could only be situated in the following positions:

$$\begin{array}{llll}
 4(b) \ 00\frac{1}{2} & 4(c) \ \frac{1}{2}\frac{1}{2}\frac{1}{2} & 4(d) \ \frac{1}{2}\frac{1}{2}\frac{1}{2} & 8(g) \ \pm 00z \\
 8(h) \ \frac{1}{2}\frac{1}{2}z; \frac{1}{2}\frac{1}{2}\frac{1}{2}-z & & & 0.086 \leq z \leq 0.122 \\
 & 0.039 \leq |z| \leq 0.061 & & 0.262 \leq z \leq 0.311 \\
 & 0.148 \leq |z| \leq 0.201 & & \\
 8(i) \ \frac{1}{2}y\frac{1}{2}; \frac{1}{2}\frac{1}{2}-y\frac{1}{2} & 8(j) \ x\frac{1}{2}\frac{1}{2}; \frac{1}{2}-x\frac{1}{2}\frac{1}{2} & & \\
 y=0 & x=0 & &
 \end{array}$$

An attempt was made to find positions for the oxygen atoms giving approximately regular octahedra around Nb, since from known structures containing Nb^{5+} and O^{2-} this seemed to be the normal configuration $\text{Nb}^{5+} - \text{O}^{2-}$. The maximum distance of contact Nb—O was assumed to be 2.5 Å.

With these assumptions 8(g) and 8(h) are the only positions where oxygen atoms in contact with Nb can be situated.

With oxygen atoms in three 8-fold positions 8(h) the distances O—O would be too short. It then only remains to consider the case of oxygen atoms in two 8-fold positions 8(g) and two 8 fold positions 8(h). For the oxygen

atoms in contact with Nb, reasonable interatomic distances were obtained assuming: 8 O₂ in 8(g) $z_2 = 0.100$ 8 O₃ in 8(g) $z_3 = 0.264$ 8 O₄ in 8(h) $z_4 = 0.168$ 8 O₅ in 8(h) $z_5 = -0.168$. Even if small adjustments of these parameters are admitted for the remaining 4 O there is room only in the position $00\frac{1}{2}$ (O₁).

With these assumptions the distances would be:

Me ₁ -4 O ₁ = 2.75	Me ₂ -4 O ₂ = 2.75	Nb - O ₂ = 2.34
Me ₁ -2 O ₂ = 2.55	Me ₂ -2 O ₄ = 2.55	Nb - 2 O ₄ = 2.04
	Me ₂ -2 O ₅ = 2.55	Nb - O ₅ = 2.04
O ₄ -4 O ₅ = 2.74		Nb - O ₃ = 1.84
O ₃ -2 O ₄ = 2.60		
O ₃ -2 O ₅ = 2.60		
O ₁ -2 O ₂ = 2.55		

It is seen that the positions given might equally well be described by D_{2h}^{22} or if the pseudo-tetragonal unit cell ($a = 3.89$ $c = 25.53$ Å) is chosen by D_{4h}^{17} .

As $a \sim b$ and the positions of the oxygen atoms must be chosen from space considerations, the discussion will be the same for C_{2v}^{18a} as for C_{2v}^{18b} . For C_{2v}^{18a} it is found that the oxygen atoms can be only in the planes $y = 0$ $y = 0.25 \pm 0.03$ $y = \frac{1}{2}$ and $y = 0.75 \pm 0.03$. For $y = 0$ or $\frac{1}{2}$, z must either be 0 or $\frac{1}{2}$ or lie between the limits $0.049 < |z| < 0.451$, otherwise the distance O-O will be < 2.5 Å. For $y = \frac{1}{4}$ or $\frac{3}{4}$, z must have the values 0, $\frac{1}{2}$, $\frac{1}{4}$ or $\frac{3}{4}$ or lie between the limits $0.049 < |z| < 0.201$ $0.299 < |z| < 0.451$.

In figure 2a sections of the unit cell are made for $y = 0$ and $y = \frac{1}{2}$. Possible regions with space group C_{2v}^{18a} are denoted in the figure by shaded areas. For these areas the distances O-O ≥ 2.5 Me-O ≥ 2.2 and Nb-O ≥ 1.8 Å.

With space group C_{2v}^{18a} it thus seems that no basically new atomic positions are obtained, although this symmetry allows the atoms to be slightly shifted from the positions of D_2^7 .

In Table 1 the intensities have been calculated from the parameters found and compared with the observed ones. (The calc. intensities are denoted by I_1^1). The mode of calculation is shown by the calculation of I_{001} . $I = A^2$.

$A = 10 (0.5 + \cos 2\pi lz_{Me} + (f_{Nb}/f_{Me}) \cos 2\pi lz_{Nb} + (f_O/f_{Me}) (0.5 + \cos 2\pi lz_2 + \cos 2\pi lz_3 + 2 \cos 2\pi lz_4))$. Since the ratios f_{Nb}/f_{Me} and f_O/f_{Me} vary with $\sin \theta/\lambda$ they were interpolated from values given in the *International Tables* (1).

Case 2. Positions of the oxygen atoms

The positions of the metal atoms were assumed to be: $(000; \frac{1}{2} \frac{1}{2} 0; 0 \frac{1}{2} \frac{1}{2}; \frac{1}{2} 0 \frac{1}{2}) + 000$ (4 Me₁) ± 00 0.202 (8 Me₂) ± 00 0.412 (8 Nb).

With D_2^7 the following positions are available for the oxygen atoms 4(b) $00\frac{1}{2}$

8(g) $\pm 00z$	8(h) $\frac{1}{4} \frac{1}{4} z, \frac{1}{4} \frac{1}{4} -z$
$0.086 \leq z \leq 0.116$	$0.039 \leq z \leq 0.161$
$0.288 \leq z \leq 0.342$	
4(c) $\frac{1}{4} \frac{1}{4} \frac{1}{4}$	4(d) $\frac{1}{4} \frac{1}{4} \frac{1}{4}$
	16(k) $xyz, \bar{x}\bar{y}z, x\bar{y}\bar{z}, \bar{x}y\bar{z}$
	$x = 0$ $x = 0.25 \pm 0.03$
	$y = 0.25 \pm 0.03$ or $y = 0$
	$z \sim 0.135$.

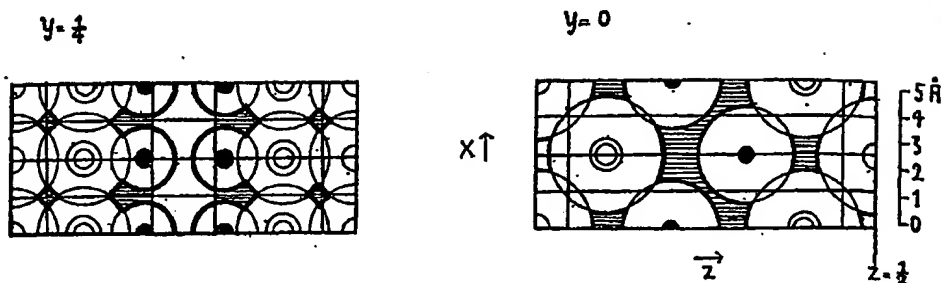
B. AURIVILLIUS, *Mixed bismuth oxides with layer lattices*

Figure 2 a (see Case 1 in the text.)

The projection of the positions of the Nb, Me₁ and Me₂ atoms on the planes $y=0$ and $y=\frac{1}{4}$ are denoted by: black circles, white circles and double circles respectively.

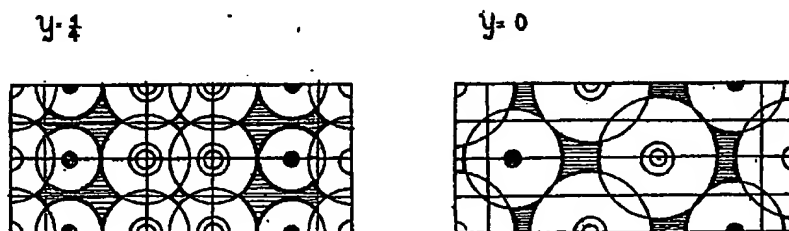


Figure 2 b (see Case 2 in the text.)

It was found that oxygen atoms in the positions 4(c), 4(d) or 16(k) could not be part of an octahedron around Nb. With O in the remaining positions 4(b), 8(g) and 8(h), octahedra around Nb might be achieved in the following ways: ($1.8 \leq \text{Nb}-\text{O} \leq 2.5$).

With oxygen atoms in three 8-fold positions 8(h), it seemed impossible to find positions for the remaining 12 oxygen atoms giving O—O distances ≤ 2.5 Å.

With two 8-fold positions 8(h) + 4(b) + one 8-fold position 8(g) the following positions were assumed for oxygen atoms in contact with Nb:

$$\begin{array}{lll} 4 \text{ O}_1 \text{ in } 4(b) & 8 \text{ O}_2 \text{ in } 8(g) & z = 0.324 \\ 8 \text{ O}_3 \text{ in } 8(h) & z = 0.088 & 8 \text{ O}_4 \text{ in } 8(h) \quad z = -0.088. \end{array}$$

For the remaining 8 oxygen atoms there was only room in the positions 4(c) and 4(d). (O₅, O₆).

With the above assumptions the distances would be:

$$\begin{array}{lll} \text{Me}_1 - 4 \text{ O}_1 = 2.75 & \text{Me}_2 - 2 \text{ O}_5 = 2.29 & \text{Nb} - \text{O}_1 = 2.24 \\ \text{Me}_1 - 4 \text{ O}_3 = 2.96 & \text{Me}_2 - 2 \text{ O}_6 = 2.29 & \text{Nb} - 2 \text{ O}_3 = 1.94 \\ \text{Me}_1 - 4 \text{ O}_4 = 2.96 & \text{Me}_2 - 4 \text{ O}_2 = 2.82 & \text{Nb} - 2 \text{ O}_4 = 1.94 \\ & & \text{Nb} - \text{O}_2 = 2.24 \\ \\ \text{O}_5 - 4 \text{ O}_6 = 2.75 & \text{O}_2 - 2 \text{ O}_5 = 2.70 & \text{O}_2 - 2 \text{ O}_3 = 2.96 \\ \text{O}_3 - 4 \text{ O}_4 = 2.75 & \text{O}_2 - 2 \text{ O}_6 = 2.70 & \text{O}_2 - 2 \text{ O}_4 = 2.96 \\ & \text{O}_1 - 4 \text{ O}_3 = 2.96 & \\ & \text{O}_1 - 4 \text{ O}_4 = 2.96 & \end{array}$$

The above positions might be equally well described by D_{2h}²³ or if a pseudotetragonal unit cell is assumed ($a = 3.89$ c = 25.53) by D_{4h}¹⁷.

In Figure 2
positions possible
are denoted by
positions given
O—O be attain

Thus no
In Table
The calculation
same as we
in which case
well for the
I₁ and I₂, v
Although the
described by
(see for inst
107:109). I
PbBi₂NbO₉

Just as f
to indicate
graphs (Tab
with axes c
The inter
the metal a
(Fig. 1b) s
are made as

A. 4 Nb
8 Bi³⁺
8 Bi³⁺
C₂

The area
and the ra
C₁ and C₂
the observe
were consid
f_{Ti}/f_{BIND}, f_{Nb},
calculated &
these calcul
agreement

ARKIV FÖR KEMI. Bd 1 nr 54

In Figure 2b sections are made of the unit cell for $y = 0$ and $y = \frac{1}{2}$ showing the positions possible for the oxygen atoms if the space group C_{2v}^{18} is assumed. Possible regions are denoted by shaded areas. It was found that only with oxygen atoms situated near the positions given above, could octahedra of O around all Nb atoms and reasonable distances Nb-O be attained.

Thus no new arrangements were found when space group C_{2v}^{18} was assumed. In Table 1 the intensities are calculated from the parameters given above. The calculated intensities are denoted by I_2 . The mode of calculation is the same as was used in case 1. It is seen from the Table that both 1 and 2, in which cases the influence of the oxygen atoms was neglected, account fairly well for the experimental data. From this follows that the calculated intensities I_1 and I_2 , where regard was taken to the O atoms, do not differ much either. Although the ratio 211:213 (see Table 1 (pseudo-tetragonal indices)) is best described by 1', 2' on the whole seemed to satisfy the observed intensities best (see for instance the intensity ratios 112:114 116:118 202:204 101:103 and 107:109). No definite conclusions could however be drawn from the study of $PbBi_2Nb_2O_9$ alone.

 Bi_2NbTiO_9

Just as for $PbBi_2Nb_2O_9$, there was nothing in the Weissenberg photographs to indicate a lower Laue symmetry than $D_{4h}-4/mmm$. From the powder photographs (Table 6a) it is however seen that the actual unit cell is orthorhombic with axes $a = 5.405$ $b = 5.442$ $c = 25.11$ Å.

The intensities of the spots in the Weissenberg photographs indicate that the metal atoms are probably placed on the lines $00z$. The Patterson function (Fig. 1b) showed high maxima at 0.20 and 0.40. If the same assumptions are made as for $PbBi_2Nb_2O_9$, the following arrangements seemed to be possible:

A. 4 Nb in 000	B. 4 Ti in 000	C_1 4 Bi in 000
8 BiTi in $\pm 00z_1$	8 BiNb in $\pm 00z_1$	8 NbTi in $\pm 00z_1$
8 BiTi in $\pm 00z_2$	8 BiNb in $\pm 00z_2$	8 Bi in $\pm 00z_2$
C_2 4 Bi in 000		
8 NbTi in $\pm 00z_2$	$z_1 \sim 0.20$	$z_2 \sim 0.40$
8 Bi in $\pm 00z_1$		

The areas under the peaks at 0.20 and 0.40 were calculated as for $PbBi_2Nb_2O_9$, and the ratio 0.20/0.40 was found to be 1.4. The calculated ratios for A, B, C_1 and C_2 were 1.0, 1.0, 0.84 and 1.2. The area ratio for C_2 agreed best with the observed one. The differences are however small, so that all alternatives were considered. The intensities were calculated as for $PbBi_2Nb_2O_9$. The ratios f_{Ti}/f_{BiNb} , f_{Nb}/f_{BiTi} and f_{NbTi}/f_{Bi} were assumed to be 0.26, 0.57 and 0.34. The calculated and observed intensities for A and B are compared in Table 2. In these calculations the influence of the oxygen atoms was neglected. The best agreement was found for

	z_1	z_2
A	0.198	0.400
B	0.196	0.400

B. AURIVILLIUS, *Mixed bismut oxides with layer lattices*

Table 2
Weissenberg photographs of $\text{Bi}_3\text{NbTiO}_9$.

h	I_A	I_B	I_{00l}	$I_{\text{obs.}} I_{11l}$	I_{20l}
2	4.0	12	—	vw	vw
4	7.3	22	m	st	m ⁺
6	2.3	5.3	w	st	m
8	7.3	22	m	w	m
10	510	440	st	st	st
12	1.4	2.6	w	—	vw
14	15	52	m ⁺	vw	w
16	0.2	0.0	w	vw	—
18	11	30	m ⁺	w	vw
20	500	400	st	st	m ⁺
22	0.1	0.4	—	—	—
24	27	94	m	m	m
26	0.5	2.0	w	m	m
28	14	31	m	m ⁺	m ⁺
30	490	350	m	m ⁺	—
h	I_A	I_B	I_{10l}	I_{21l}	
1	4.4	12	st	m ⁺	
3	5.8	17	m	vw	
5	520	450	vst	vst	
7	2.6	6.3	—	—	
9	11	35	m	m	
11	0.8	1.4	w	w	
13	9.0	27	vw	w	
15	510	420	st	w	
17	0.6	0.3	—	—	
19	20	70	w	w	
21	0.0	0.5	w	w	
23	12	31	m	m	
25	500	380	m ⁺	m ⁺	
27	0.0	3.2	—	—	
29	34	120	m	—	
31	1.4	4.4	m	—	

From Table 2 it is seen that A and B account quite well for the observed intensities.

With A and B, Bi and Ti or Bi and Nb would occupy the same point position. This seemed *a priori* unlikely and if it was assumed that $\text{Bi}_3\text{NbTiO}_9$ and $\text{PbBi}_2\text{Nb}_2\text{O}_9$ were built up in the same way, arrangements A and B would imply that Pb, Bi and Nb were distributed over one point position, in $\text{PbBi}_2\text{Nb}_2\text{O}_9$. Therefore, although arrangements A and B cannot be excluded from intensity discussions alone, they seem very improbable and will not be dealt with in the following.

One half
notes the

The f
8 NbTi i
following

4 ()
8 ()
8 ()

In Tal

4 Bi i
In case :
4 O₁ in

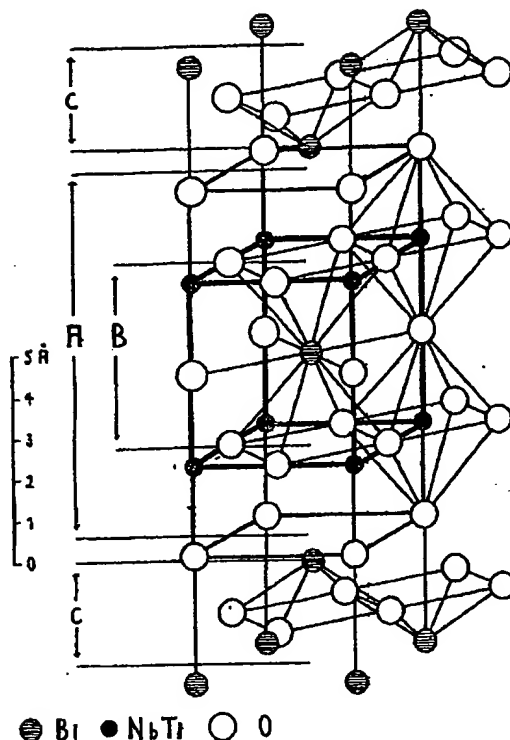


Figure 3.

One half of the pseudo-tetragonal unit cell of $\text{Bi}_2\text{NbTiO}_9$ (from $z \approx 0.25$ to $z \approx 0.75$). A denotes the perovskitic layer BiNbTiO_7 , C Bi_2O_3 layers and B the unit cell of a hypothetical perovskite structure $\text{BiNb}_{0.5}\text{Ti}_{0.5}\text{O}_3$.

Case C_1

The following positions were assumed: 4 Bi in 000, 8 Bi in $\pm 00\ 0.396$, 8 NbTi in $\pm 00\ 0.192$. By the same arguments as used for $\text{PbBi}_2\text{Nb}_2\text{O}_9$ the following positions were arrived at:

$$\begin{array}{lll} 4\ \text{O}_1\ \text{in}\ 00\frac{1}{2} & 8\ \text{O}_2\ \text{in}\ \pm 00\ 0.092 & 8\ \text{O}_3\ \text{in}\ \pm 00\ 0.268 \\ 8\ \text{O}_4\ \text{in}\ \frac{1}{4}\frac{1}{4}z; \frac{1}{4}\frac{1}{4}\frac{1}{2}-z & z = 0.164 & \\ 8\ \text{O}_5\ \text{in}\ \frac{1}{4}\frac{1}{4}z; \frac{1}{4}\frac{1}{4}\frac{1}{2}-z & z = -0.164. & \end{array}$$

In Table 3 the intensities are calculated from these parameters.

Case C_2

4 Bi in 000, 8 Bi in $\pm 00\ 0.200$ and 8 NbTi in $\pm 00\ 0.412$ were assumed. In case 2' (see $\text{PbBi}_2\text{Nb}_2\text{O}_9$) the parameters for the oxygen atoms would be 4 O_1 in $00\frac{1}{2}$, 8 O_2 in $\pm 00\ 0.324$, 4 O_3 in $\frac{1}{4}\frac{1}{4}\frac{1}{2}$.

$$\begin{array}{lll} 4\ \text{O}_6\ \text{in}\ \frac{1}{4}\frac{1}{4}\frac{1}{2} & 8\ \text{O}_4\ \text{in}\ \frac{1}{4}\frac{1}{4}z; \frac{1}{4}\frac{1}{4}\frac{1}{2}-z & z = 0.088 \\ & 8\ \text{O}_5\ \text{in}\ \frac{1}{4}\frac{1}{4}z; \frac{1}{4}\frac{1}{4}\frac{1}{2}-z & z = -0.088 \end{array}$$

B. AURIVILLIUS, *Mixed bismuth oxides with layer lattices*

Table 3
Weissenberg photographs of $\text{Bi}_2\text{NbTiO}_9$

Zero layer				First layer			
00l	$I_{C'_1}$	$I_{\text{obs.}}$	$I_{O'_2}$	21l	$I_{C'_1}$	$I_{\text{obs.}}$	$I_{C'_2}$
4	13	m	36	1	2.6	m ⁺	22
6	0.5	w	10	3	35	vw	6.3
8	48	m	16	5	290	vst	300
10	310	st	330	7	19	—	1.0
12	46	w	12	9	27	m	55
14	38	m ⁺	59	11	3.6	w	18
16	2.6	w	29	13	52	w	26
18	100	m ⁺	48	15	270	w	270
20	240	st	240	17	6.8	—	0.8
22	12	—	0.5	19	45	w	90
24	42	m	140	21	14	w	40
26	29	w	42	23	110	m	46
28	100	m	35	25	200	m ⁺	200
30	190	m	150				
10l	$I_{C'_1}$	$I_{\text{obs.}}$	$I_{O'_2}$	11l	$I_{C'_1}$	$I_{\text{obs.}}$	$I_{C'_2}$
1	2.0	st	17	2	34	vw	2.6
3	29	m	5.3	4	2.9	st	41
5	270	vst	300	6	6.8	st	69
7	17	—	1.2	8	62	w	22
9	29	m	56	10	360	st	310
11	5.8	w	15	12	14	—	1.0
13	49	vw	28	14	29	vw	76
15	270	st	270	16	10	vw	40
17	5.3	—	0.6	18	64	w	16
19	44	w	92	20	250	st	210
21	16	w	38	22	21	—	0.0
23	110	m	46	24	66	m	92
25	200	m ⁺	200	26	32	m	61
27	4.4	—	1.2	28	130	m ⁺	27
29	65	m	110	30	150	m ⁺	200
31	41	m	76				
20l	$I_{C'_1}$	$I_{\text{obs.}}$	$I_{O'_2}$				
2	18	vw	2.9				
4	12	m ⁺	37				
6	0.1	m	16				
8	48	m	17				
10	300	st	320				
12	33	vw	5.8				
14	37	w	58				
16	2.6	—	31				
18	100	vw	45				
20	240	m ⁺	240				
22	12	—	0.5				
24	42	m	140				
26	29	m	45				
28	100	m ⁺	35				

In T
from tl
202:204
fluence
0.396 a
discrepa
to be
certainly
to be t
Thus
consider
3' seem
With
 $D_{2h}^{23} - m$
(000;

With
 $D_{4h}^{17} - I$
(000;

Val

In Table 3 the intensities are calculated with these assumptions.. It is seen from the Table that with C_1 the order of the reflections 101:103, 211:213, 202:204 and 107:109 are reversed. The same result was obtained if the influence of the oxygen atoms was neglected. If z_{Bi} and z_{NbTi} were varied around 0.396 and 0.192 so as to give correct ratios for some of these reflections, large discrepancies occurred for other reflections. With C_2 the intensities turned out to be of the right order. There are however a few discrepancies. 00 20 is certainly stronger than 0018 and $00\ 30 > 0028$, but the calculated ratios seem to be too large. On the whole the agreement is however good.

Thus if the X ray data for only one of $PbBi_2Nb_2O_9$ or Bi_3NbTiO_9 were considered, different atomic arrangements appeared to be possible, whereas only one seems to explain the observed data both for $PbBi_2Nb_2O_9$ and Bi_3NbTiO_9 .

With orthorhombic description the positions will be:

$D_{2h}^{22} - mmm$

$(000; 0\frac{1}{2}\frac{1}{2}; \frac{1}{2}0\frac{1}{2}; \frac{1}{2}\frac{1}{2}0) +$

4 Bi_1 (Me_1) in 4 (a) 000
 8 Bi_2 (Me_2) in 8 (i) $\pm 00\ 0.200$ (0.202)
 8 NbTi (Nb) in 8 (i) $\pm 00\ 0.412$ (0.412)
 4 O_1 in 4 (b) $00\frac{1}{2}$
 8 O_2 in 8 (i) $00\ 0.324$ (0.324)
 8 O_3 in 8 (f) $\frac{1}{4}\frac{1}{4}\frac{1}{4}; \frac{1}{4}\frac{1}{4}\frac{3}{4}$
 16 O_4 in 16 (g) $\frac{1}{4}\frac{1}{4}z; \frac{1}{4}\frac{1}{4}\bar{z}; \frac{1}{4}\frac{3}{4}z; \frac{1}{4}\frac{3}{4}\bar{z}$
 $z = 0.088$.

With pseudo-tetragonal description the positions will be:

$D_{4h}^{17} - I\ 4/mmm$

$(000; \frac{1}{2}\frac{1}{2}\frac{1}{2}) +$

2 Bi_1 (Me_1) in 2 (a) 000
 4 Bi_2 (Me_2) in 4 (e) $\pm 00\ 0.200$ (0.202)
 4 NbTi (Nb) in 4 (e) $\pm 00\ 0.412$ (0.412)
 2 O_1 in 2 (b) $00\frac{1}{2}$
 4 O_2 in 4 (e) $\pm 00\ 0.324$ (0.324)
 4 O_3 in 4 (d) $0\frac{1}{2}\frac{1}{2}; \frac{1}{2}0\frac{1}{2}$
 8 O_4 in 8 (g) $\pm (0\frac{1}{2}z; \frac{1}{2}0z) z = 0.088$.

Table 4

Values of the tolerance factor, t , for different compounds having the $CaBi_2Nb_2O_9$ structure.

Compound	$t \cdot 100$
Bi_3NbTiO_9	91
Bi_3TaTiO_9	91
$CaBi_2Nb_2O_9$	91
$SrBi_2Nb_2O_9$	99
$SrBi_2Ta_2O_9$	99
$BaBi_2Nb_2O_9$	106
$PbBi_2Nb_2O_9$	101
$NaBi_2Nb_4O_{18}$	91
$KBi_2Nb_4O_{18}$	97

B. AURIVILLIUS, *Mixed bismuth oxides with layer lattices*

Table 5

Table 5 (co

Powder photographs of $\text{CaBi}_2\text{Nb}_2\text{O}_9$ and $\text{SrBi}_2\text{Nb}_2\text{O}_9$. Cr K radiation. Pseudo-tetragonal indices.

$\text{CaBi}_2\text{Nb}_2\text{O}_9$				
hkl	$I_{\text{obs.}}$	I_{α}	I_{β}	I_{γ}
006	—	8.4	0.8	0.01
008	m	61	9.6	0.6
114+00 10	(m)	230	230	230
00 12	—	0.5	19	47
00 14	vw	29	46	56
00 16	vw	2.6	0.6	4.0
00 18	w	100	34	13
101	—	1.2	0.5	2.9
103	st	36	1.4	1.4
105	vst	200	200	200
107	w	21	0.3	7.8
109	vvw	18	32	43
10 11	—	7.0	0.2	0.5
10 13	m ⁺	79	19	4.4
20 10+10 15	(st)	160	160	160
21 11+10 17	(w)	22	0.2	9.0
112	—	26	0.04	4.8
00 10+114	(m)	4.4	14	22
116	w	4.4	17	26
118	m	69	13	1.7
204+11 10	(st)	200	200	200
11 12	—	22	0.1	8.4
11 14	w	41	61	72
202	w	27	0.1	4.4
11 10+204	(st)	3.6	13	20
206	w	3.2	0.04	1.4
215+208	(st)	59	9.0	0.5
10 15+20 10	(st)	220	220	220
20 12	vw	1.4	15	41
211	w	0.1	2.3	6.3
213	w	38	2.0	1.0
208+216	(st)	210	210	210
217	—	21	0.3	7.8
219	vvw	18	33	43
10 17+21 11	(w)	4.4	0.01	1.4
$\text{SrBi}_2\text{Nb}_2\text{O}_9$				
006	—	3.2	0.1	0.2
008	vw	45	11	2.6
114+00 10	(m)	260	260	260
00 12	vw	0.2	16	35
00 14	m	42	68	64
00 16	—	0.3	1.4	4.4
00 18	w	83	35	18
00 20	st	160	160	160

One half
tioned in
determine
00 0.202.
Ca, Sr, Ba
 $\text{KBi}_2\text{Nb}_2\text{O}_9$
do not diff
valid for tl
Ca, Sr, Ba

α Only 1
 β Rando
 γ Only 1

ARKIV FÖR KEMI. Bd 1 nr 54

Table 5 (cont.)

Pseudo

<i>hkl</i>	<i>I</i> _{obs.}	<i>I</i> _α	<i>I</i> _β	<i>I</i> _γ
101	—	0.0	2.0	4.0
103	vw	24	2.0	0.1
105	st	230	240	230
107	—	12	0.01	3.6
109	w	28	42	49
10 11	—	2.3	0.01	0.8
10 13	m	61	20	8.4
20 10+10 15	(st)	190	200	200
β 00 20+220+10 17	(m)	13	0.01	4.0
10 19	m	88	110	120
112	—	16	0.3	1.7
00 10+114	(m)	10	20	26
116	vw	10	22	29
118	w	52	14	4.4
11 10	st	230	240	230
11 12	—	13	0.0	3.6
11 14	w	56	74	81
11 16	—	0.1	4.0	8.4
11 18	m	40	10	2.3
202	—	17	0.4	1.4
204	—	9.0	19	24
206	—	0.5	0.6	2.3
β 11 14+208	(w)	43	10	2.3
10 15+20 10	(st)	250	260	250
β 21 13+20 12	(vw)	0.01	12	29
20 14	w	42	58	64
20 16	—	0.2	1.7	4.8
211	w	0.6	4.8	7.8
213	w	26	2.6	0.01
215	st	240	240	240
217	—	12	0.01	3.6
219	vw	27	42	49
21 11	—	1.2	0.4	2.0
21 13	m	59	19	7.8
20 10+21 15	(st)	190	190	190

One half of the pseudo-tetragonal unit cell is pictured in figure 3. As mentioned in the discussion on $\text{PbBi}_2\text{Nb}_2\text{O}_9$, it was impossible in this phase to determine how Pb and Bi are distributed over the point positions 000 and 00 0.202. It therefore seemed of interest to try to determine the positions of Ca, Sr, Ba and K in the compounds $\text{CaBi}_2\text{Nb}_2\text{O}_9$, $\text{SrBi}_2\text{Nb}_2\text{O}_9$, $\text{BaBi}_2\text{Nb}_2\text{O}_9$ and $\text{KBi}_2\text{Nb}_2\text{O}_9$. As the cell dimensions of the Pb, Ca, Sr, Ba and K compounds do not differ much it was assumed that the parameters of $\text{PbBi}_2\text{Nb}_2\text{O}_9$ are also valid for the other compounds. There were three extreme ways of distributing Ca, Sr, Ba and K over the positions 000 and 00 0.202:

- α Only Bi in 00 202
- β Random distribution
- γ Only Bi in 000.

B. AURIVILLIUS, *Mixed bismuth oxides with layer lattices*

Table 6a

Powder photographs of $\text{Bi}_3\text{NbTiO}_9$. Cr K radiation.

Orthorhombic indices.

hkl	$10^4 \sin^2 \theta_{\text{calc.}}$	$10^4 \sin^2 \theta_{\text{obs.}}$	$I_{\text{obs.}}$	hkl	$10^4 \sin^2 \theta_{\text{calc.}}$	$10^4 \sin^2 \theta_{\text{obs.}}$	$I_{\text{obs.}}$	hkl	I
111	0914	0909	m	02 14	5856	5874	m	101	
113	1080	1072	w ⁺	20 14	5878			103	
008	1333	1319	w ⁺	—	—	5990	vw	008	
115	1414	1413	vst	139	6128	6129	w ⁺	105	
020	1774	1767	m ⁺	319	6172	6175	w ⁺	110	
200	1796	1790	m	—	—	6250	vw	00 10	
00 10	2083	2078	m	22 12	6569	6573	vw	114	
204	2129	2131	w	00 18	6747	6747	vw	β 109	
β 119	2136			13 11	6961	6961	w	116	
—	—	2324	vw	040	7097			109	
026	2524	2530	m	02 16	7105	7097	m	β 200	
206	2546	2546	m	20 16	7127			00 12	
119	2580	2586	m	042	7180	7182	m	118	
—	—	2739	vw	400	7185			10 11	
028	3107	3129	w	β 240	7357	7388	w	200	
208	3129			β 420	7420			11 10	
11 11	3413	3415	w	044	7430			00 14	
—	—	3523	w	22 14	7652	7648	w	10 13	
220	3570	3576	st	046	7847	7836	vw	211	
222	3653	3648	vw	406	7935			208	
β 11 13	3654			13 13	7960	8005	w	215	
02 10	3857	3860	st	31 13	8004			10 15	
20 10	3879			331	8054			20 10	
00 14	4082	4089	w	00 20	8330	8330	m		
β 135	4103			11 19	8411	8409	m		
—	—	4236	vw	048	8430				
226	4320	4324	w	20 18	8543	8558	st		
11 13	4412	4414	w	335	8554				
131	4462	4454	w	240	8887	8888	m		
311	4506	4504	vw	22 16	8901				
β 11 15	4521	4623	w	420	8959	8963	m		
133	4628			242	8970				
313	4672	4676	w	13 15	9127	9105	st		
β 22 10	4679			31 15	9171	9156	vst		
228	4903	4896	w	04 10	9180	9189	m		
135	4962	4956	st	40 10	9268	9264	m		
315	5006	5006	st	424	9292				
—	—			426	9709	9712	w		
11 15	5579	5581	st	339	9720				
22 10	5653	5652	st						

The intensities were calculated for these possibilities by calculations similar to those for $\text{PbBi}_2\text{Nb}_2\text{O}_9$, and compared with the observed ones. See Table 5. It was found that in no case did γ explain the observed intensities. For the Sr, Ba and K compounds the observed intensities did not permit any decision between α and β . For $\text{CaBi}_2\text{Nb}_2\text{O}_9$, however, only α seemed to give correct intensities. It was therefore concluded that the compounds discussed have the α arrangement.

The struc
 BiNbTiO_9 l
skite struct
view was
was observe
would allow
it is calculat
between the
(see Table
to be stable

† was calcul

In the calc
ionic radii we
 K^+ 1.33, Nb^{5+}
distributed ove

ARKIV FÖR KEMI. Bd 1 nr 54

Table 6b

Powder photographs of $\text{PbBi}_2\text{Nb}_2\text{O}_9$. Cr K radiation.

Pseudo-tetragonal indices.

$I_{\text{obs.}}$	hkl	$10^4 \sin^2 \theta_{\text{calc.}}$	$10^4 \sin^2 \theta_{\text{obs.}}$	$I_{\text{obs.}}$	hkl	$10^4 \sin^2 \theta_{\text{calc.}}$	$10^4 \sin^2 \theta_{\text{obs.}}$	$I_{\text{obs.}}$
m	101	0889	0892	vw	1114	5682	5699	m
vw	103	1050	1052	vw	219	5974	5990	m
w+	008	1288	1285	vw	0018	6520	6529	w
w+	105	1872	1871	vst	0020	6663	6664	vw
vw	110	1738	1763	m	1017	6685		
vw	0010	2012	2019	m	1116	6889	6924	m
vw	114	2060			β 305	6903		
vw	β 109	2069	2068	vw				
w	116	2462	2469	m	220	6950	6934	m
	109	2499	2499	m			6976	m
m	β 200	2877	2881	m	2014	7419	7435	m
	0012	2898			2113	7744	7749	m
m	118	3026	3028	w	301	7839	7846	vw
	1011	3304	3300	vw	0020	8049	8052	m
w	200	3475	3475	st	1019	8133	8131	m+
	1110	3750	3755	st	228	8238	8268	vw
w	0014	3944	3946	w+	1118	8258		
w	1013	4269	4270	w+	305	8332	8339	m+
vw	211	4364	4365	vw			8673	m+
	208	4763	4770	vw	310	8688	8690	m+
w	215	4847	4850	st			8874	st
	1015	5397	5416	st	2115	8872		
m	2010	5487	5493	st	2210	8962	8980	m
					314	9010		
					309	9449	9450	vw

The structure of $\text{Bi}_2\text{NbTiO}_9$ is thus built up of $\text{Bi}_2\text{O}_3^{2+}$ layers between which BiNbTiO_7^- layers are inserted. The structure may be looked upon as a perovskite structure where perovskite layers are separated by $\text{Bi}_2\text{O}_3^{2+}$ layers. This view was supported by the fact that in all cases where the above structure was observed the radii of the ions in the layers lying between the $\text{Bi}_2\text{O}_3^{2+}$ layers would allow for the formation of a perovskite structure. If the tolerance factor t is calculated from the ionic radii of the elements constituting the layers between the $\text{Bi}_2\text{O}_3^{2+}$ layers, it is found to lie between the limits 0.9 and 1.1 (see Table 4), the same limits within which perovskite structures are found to be stable.

t was calculated from the formula: $1.06 (R_A + R_O) = 0.95 t \sqrt{2} (R_B + R_O)$. (See (3).)

$$A = (K + \text{Bi})/2 \text{ Ca, Sr, Ba etc.}$$

$$B = (\text{Nb} + \text{Ti})/2 (\text{Ta} + \text{Ti})/2 \text{ Nb, Ta.}$$

In the calculations case a was assumed. For calculating t the following values for the ionic radii were used: Bi^{3+} 1.00, Ba^{2+} 1.39, Sr^{2+} 1.20, Ca^{2+} 1.02, Pb^{2+} 1.26, Na^+ 0.97, K^+ 1.33, Nb^{5+} 0.69, Ta^{5+} 0.69, Ti^{4+} 0.66 and O^{2-} 1.36. If, for instance, 1 K + 1 Bi are distributed over one 2-fold position the radius of (K, Bi) was taken as $(r_K + r_{\text{Bi}})/2$.

B. AURIVILLIUS, *Mixed bismuth oxides with layer lattices*

The structure proposed for $\text{CaBi}_2\text{Nb}_2\text{O}_9$ reminds one of the structure of beyerite $\text{CaBi}_2\text{O}_3(\text{CO}_3)_2$ described by LAGERCRANTZ and SILLÉN (4). The unit cell of beyerite is body-centered tetragonal with $a = 3.767$ and $c = 21.690$ Å. The positions of the Ca and the Bi atoms in beyerite are Ca 000 and Bi ± 00 0.19 (space group D_{2h}^{11}) as compared with $a = 3.860$ $c = 24.87$, Ca in 000 and Bi in ± 00 0.20 for $\text{CaBi}_2\text{Nb}_2\text{O}_9$.

The "rotating" CO_3^{2-} groups in beyerite correspond to octahedral sheets $\text{Nb}_4\text{O}_7^{2-}$ in $\text{CaBi}_2\text{Nb}_2\text{O}_9$. Following the notations given by LAGERCRANTZ and SILLÉN (4) the structure described above might also be denoted by X_{11} .

SUMMARY

A series of tetragonal or pseudo-tetragonal phases of general composition $(\text{Bi}, \text{Me})_6\text{R}_4\text{O}_{18}$ have been investigated.

Me: Na, K, Ca, Sr, Ba, Pb.

R: Nb, Ta, Ti.

The positions of the Me and R atoms were determined from the observed intensities and the positions of the O atoms were deduced from space considerations.

The following structure is proposed:

$D_{2h}^{21} - F mmm$

$(000; 0\frac{1}{2}\frac{1}{2}; \frac{1}{2}0\frac{1}{2}; \frac{1}{2}\frac{1}{2}0) +$
 4 Bi in 4 (a) 000
 8 Bi in 8 (c) ± 00 0.200
 8 NbTi in 8 (c) ± 00 0.412
 4 O in 4 (b) $00\frac{1}{2}$
 8 O in 8 (e) ± 00 0.324
 8 O in 8 (f) $\frac{1}{4}\frac{1}{4}\frac{1}{2}; \frac{1}{4}\frac{1}{4}\frac{1}{2}$
 16 O in 16 (g) $\frac{1}{4}\frac{1}{4}z; \frac{1}{4}\frac{1}{4}\bar{z}; \frac{1}{4}\frac{1}{2}z; \frac{1}{4}\frac{1}{2}\bar{z}$ $z = 0.088$.

From intensity calculations it was found that Ca in $\text{CaBi}_2\text{Nb}_2\text{O}_9$ and Sr, Ba and K in the corresponding compounds are probably situated in the position 000. The proposed structure is built up of $\text{Bi}_2\text{O}_7^{2+}$ layers alternating with single perovskite layers. The resemblance to the structure of beyerite is pointed out.

I wish to thank Professor L. G. SILLÉN for valuable discussions concerning this work.

Stockholms Högskola, Institute of Inorganic and Physical Chemistry, June 1949.

REFERENCES. 1. Internationale Tabellen zur Bestimmung von Kristallstrukturen, Berlin 1935. — 2. Wells, A. F. Z. Krist. 96, 451, 1937. — 3. Stillwell, Ch. Crystal Chemistry, New York and London, 1938, p. 272. — 4. Lagercrantz, A. and Sillén, L. G. Arkiv Kemi etc. 26, No 20, 1948.

Tryckt den 31 december 1949

Uppsala 1949. Almqvist & Wiksells Boktryckeri AB

It
in t
form

has
also
with
little
water
tinu
M
know
not
Ano
solu
is re
water
(Fig
inne
In
cape
M
met
benz
T
also
with
are
As
thar
qua
be
per

BRIEF ATTACHMENT W

IN THE UNITED STATES PATENT AND TRADEMARK OFFICE

In re Patent Application of

Applicants: Bednorz et al.

Serial No.: 08/479,810

Filed: June 7, 1995

For: NEW SUPERCONDUCTIVE COMPOUNDS HAVING HIGH TRANSITION
TEMPERATURE, METHODS FOR THEIR USE AND PREPARATION

Date: March 1, 2005

Docket: YO987-074BZ

Group Art Unit: 1751

Examiner: M. Kopec

Commissioner for Patents
P.O. Box 1450
Alexandria, VA 22313-1450

FIRST SUPPLEMENTAL AMENDMENT

Sir:

In response to the Office Action dated July 28, 2004, please consider the
following:

ATTACHMENT W

ARKIV FÖR KEMI Band 1 nr 58

Communicated 15 September 1949 by ARNE WESTGREN and ARNE TISELIUS

Mixed bismuth oxides with layer lattices

II. Structure of $\text{Bi}_4\text{Ti}_3\text{O}_{12}$

By BENGT AURIVILLIUS

With 5 figures in the text

By means of X ray analysis it has been found that the crystal structures of a number of bismuth oxyhalides consist of $\text{Bi}_2\text{O}_3^{2+}$ layers alternating with layers of halogen ions (1, 2). In all these cases the symmetry was found to be tetragonal and the lengths of the a axes almost constant ≈ 3.8 Å.

On making an X ray study of the system Bi_2O_3 — TiO_2 a phase (of composition about 40 atomic % TiO_2) was found, the powder photographs of which could be explained by assuming a pseudo-tetragonal cell with $a = 3.84$ and $c = 32.8$ Å. It seemed of interest to make a closer study of this phase since the cell dimensions and composition seemed to indicate a layer lattice with $\text{Bi}_2\text{O}_3^{2+}$ layers, but of a type hitherto uninvestigated.

Procedure: Weighed amounts of Bi_2O_3 (puriss) and TiO_2 (puriss) were mixed and heated to about 1100°C for some hours in a weighed platinum crucible. After cooling the crucible was weighed again and the composition calculated by assuming that the loss of weight could be ascribed to the volatility of Bi_2O_3 . Powder photographs of various preparations in the system Bi_2O_3 — TiO_2 indicated that there is a phase with a body-centered pseudo-tetragonal unit cell with $a = 3.841$ and $c = 32.83$ Å at compositions about 40 mole % TiO_2 . It was, however, impossible to get samples which were quite free from impurities so the powder photographs always contained a few extra lines.

The lines 21 $\bar{1}$, 22 $\bar{1}$ and 31 $\bar{1}$ were found to be split up. No cleavage was, however, found for the lines 10 $\bar{1}$, 20 $\bar{1}$ and 30 $\bar{1}$. This could be explained by assuming a face-centered orthorhombic unit cell with the same c axis as the pseudo-tetragonal cell and with its a and b axes equal to the diagonals ($a\sqrt{2}$) of the pseudo cell.

The orthorhombic axes will be: $a = 5.410$ $b = 5.448$ $c = 32.84$ Å. The observed density (40 mole % TiO_2) is 7.85. If the composition is assumed to be $\text{Bi}_4\text{Ti}_3\text{O}_{12}$ (43 mole % TiO_2) and 4 formula units are assumed per unit cell the calculated density will be 8.04 which agrees fairly well with the observed value.

Single crystals, thin plates, were picked out and Weissenberg photographs (zero layer and first layer) were taken around the 3.84 axes, thus registering $h0l$ and $h1\bar{l}$ (pseudo cell) or hhl and $h, h+2, l$ (orthorhombic cell).

B. AURIVILLIUS, *Mixed bismuth oxides with layer lattices. II*

Though there was nothing in the Weissenberg photographs to indicate lower Laue symmetry than $D_{4h} - 4/mmm$, it was — as has already been mentioned — found from the powder photographs that the real symmetry was not higher than orthorhombic (Laue symmetry $D_{2h} - mmm$).

Except for the extinctions following from the face-centering (hkl occurring only for h, k, l all odd or even) no systematic extinctions were found, which is characteristic of the space groups C_{2v}^{18} , D_2^7 and D_{2h}^{23} .

Positions of the bismuth atoms

Since the intensities of hkl with h, k, l all odd on one side and the intensities of hkl with h, k, l all even on the other side appeared to vary in the same way with l (see Table 1), it seemed probable that at least the bismuth atoms are situated on the lines: $(000; \frac{1}{2}\frac{1}{2}0; 0\frac{1}{2}\frac{1}{2}; \frac{1}{2}0\frac{1}{2}) + 00z$. The sum of $\sum I_{00l} \cos 2\pi lz$ and $\sum I_{11l} \cos 2\pi lz$ will under such conditions represent the Patterson function along $00z$. These two sums are pictured in figure 1. It is seen from the graph that high maxima occur at $z = 0.144, 0.280$ and 0.428 . If $C_{2v}^{18}c$ is not considered, only the following positions on the lines $00z$

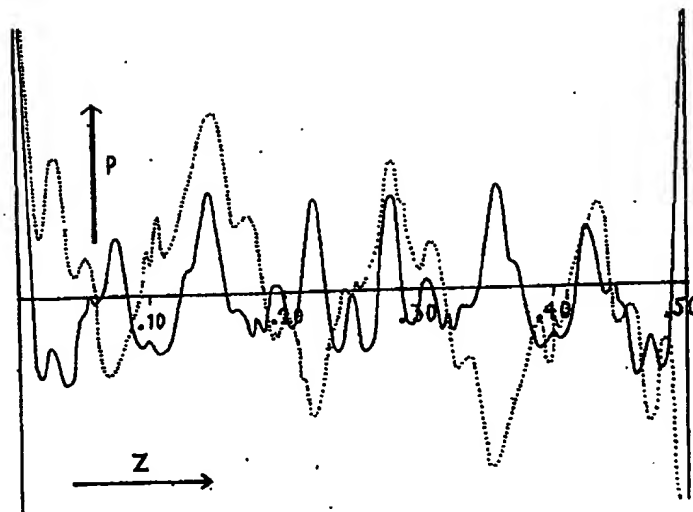
Table 1
Weissenberg Photographs of $Bi_4Ti_3O_{12}$. Cu K_α radiation

l	I _{calc.}	I _{obs.}				l	I _{calc.}	I _{obs.}		
		00	20 or 02	22	42 or 24			11	31 or 13	33
2	4.4		—	vvw	—	1	130	vst	m	m
4	20		w	w	—	3	14	w	—	—
6	85	m	m	m	w	5	18	m	vvw	—
8	180	m	m	m	w ⁺	7	390	vst	m ⁺	m ⁺
10	8.4	w	m	vvw	—	9	0.01	—	—	—
12	42	m	m	w	—	11	26	w	vw	vw
14	360	vst	m	m	m	13	42	w	vw	vw
16	3.6	m ⁺	—	vvw	—	15	230	w	vw	—
18	32	m	w	vvw	—	17	4.4	—	—	—
20	12	m	w	—	—	19	74	m	vvw	vw
22	260	st	st	m	m	21	300	st	m	w
24	2.0	w	w	vw	—	23	14	m	w	vw
26	110	m	st	st	m ⁺	25	37	m	m	w
28	240	m	st	st	st	27	0.09	—	—	—
30	27	w	m	m	m	29	280	st	st	st
32	40	m	st	m	st	31	0.6	w	w	—
34	7.8	vw	w	vw	—	33	150	st	st	st
36	280	m	vst	vst	—	35	170	st	st	—
38	0.1	vw	w	vw	—	37	41	m	m	—
40	190	m	vst	—	—	39	40	st	—	—
42	110	m	—	—	—	41	36	m	—	—

are possible
8-fold pos
found that
that the 1
three possi

If the in
will have

If the tw
culated, th
these figu
the zero le
order of m

Figure 1. Patterson function of $\text{Bi}_4\text{Ti}_3\text{O}_{12}$ along $00z$

$$\text{Full curve: } \sum_i I_{00i} \cos 2\pi iz$$

$$\text{Dotted curve: } \sum_i I_{11i} \cos 2\pi iz \quad (\text{orthorhombic indices})$$

are possible for the Bi atoms: The two 4-fold positions 000 and $00\frac{1}{2}$ and the 8-fold positions $\pm 00z$. Assuming that the unit cell contains 16 Bi it was found that the observed maxima in the graph could be explained by assuming that the 16 Bi atoms are situated in two 8-fold positions $\pm 00z$. In this way three possibilities arose:

- a. $z_1 = 0.215$ $z_2 = 0.356$
- b. $z_1 = 0.072$ $z_2 = 0.356$
- c. $z_1 = 0.072$ $z_2 = 0.215$.

If the influence of the Ti and the O atoms is neglected the Patterson maxima will have the following relative weights:

	a	b	c
0.144	2	1	3
0.280	1	3	2
0.428	3	2	1

If the two curves in figure 1 are added and the areas under the peaks calculated, the ratio of $(0.144):(0.280):(0.428)$ is found to be: $4.4:2.6:1.0$. Now, these figures cannot be directly compared with the figures given above, since the zero level in the graph is unknown. It is, however, seen that the observed order of magnitude of the peaks (0.144) (0.280) and (0.428) is the same as

B. AURIVILLIUS, *Mixed bismuth oxides with layer lattices. II*

that calculated for c. Case c was therefore assumed, and z_1 and z_2 were varied around 0.072 and 0.215. The observed intensities were found to agree quite well with those calculated for $z_1 = 0.067 \pm 0.004$ and $z_2 = 0.211 \pm 0.004$. In Table 1 the observed intensities are compared with intensities calculated as follows: $I = A^2$ $A = 10 \cdot (\cos 2\pi lz_1 + \cos 2\pi lz_2) = 10 F/4 f_{Bi}$. In Table 1 the lines of maximum absorption (see (4)) are indicated by dotted lines. If allowance is made for the polarisation factors and the absorption effect (4), it is seen that for h, k, l all odd the observed and calculated intensities agree quite well. For h, k, l all even the calculated ratios of 0016:0018 and 2216:2218 are inversed in comparison with the observed ratios. This might be due to the influence of the Ti and the O atoms.

The ir
culated i
be made
to find r

Space
assumed:

8 F

4 T

Positions of the Ti atoms

With the formula assumed the unit cell contains 12 Ti atoms. If the space group $C_{2v}^{18}c$ is not considered, the only 4-fold positions possible are:

- 4 (a) $x00$ or $0y0$ ($C_{2v}^{18} a$ or b), 4 (a) 000 4 (b) $00\frac{1}{2}$ (D_2^7, D_{2h}^{22}),
4 (c) $\frac{1}{2}\frac{1}{2}\frac{1}{2}$ 4 (d) $\frac{1}{2}\frac{1}{2}\frac{1}{2}$ (D_2^7)

The positions 000 , $\frac{1}{2}\frac{1}{2}\frac{1}{2}$ and $\frac{1}{2}\frac{1}{2}\frac{1}{2}$ seemed very improbable since the distance Bi—Ti would then be only 2.2—2.4 Å. For the remaining positions $00\frac{1}{2}$, $x00$ (or $0y0$) x (or y) must lie within the limits 0.38—0.62, if the minimum distance Bi—Ti is assumed to be 3.0 Å. If the distance Ti—Ti is assumed to be ≥ 3.0 Å, only 4 Ti can be situated in 4-fold positions and the remaining 8 Ti must occupy one 8-fold position. Of 8-fold positions the following seemed to be possible:

By ass
the follow

- 8 (d) $x0z$, $x0\bar{z}$ (or $0yz$, $0y\bar{z}$) $C_{2v}^{18} a$ or b , 8 (g) $\pm 00z$ (D_2^7, D_{2h}^{22}),
8 (h) $\frac{1}{2}\frac{1}{2}z$, $\frac{1}{2}\frac{1}{2}\bar{z} - z$ (D_2^7)

Thus there seemed to be two ways of arranging the Ti atoms:

1. 4 Ti_1 in $00\frac{1}{2}$, 8 Ti_2 in $\frac{1}{2}\frac{1}{2}z$, $\frac{1}{2}\frac{1}{2}\bar{z} - z$ $0.133 \leq z \leq 0.147$
2. 4 Ti_1 in $00\frac{1}{2}$, $x00$ (or $0y0$) $0.38 \leq x \leq 0.62$ (or $0.32 \leq y \leq 0.68$)
8 Ti_2 in $\pm 00z$ $0.324 \leq z \leq 0.398$, $x0z$, $x0\bar{z}$ (or $0yz$, $0y\bar{z}$)
 $0.38 \leq x \leq 0.62$ (or $0.38 < y < 0.62$) $0.102 \leq z \leq 0.176$

Two regio

Both for 1 and 2 the parameters are chosen as to make the distances Bi—Ti ≥ 3.0 Å. The region possible for the Ti_2 atoms — assuming arrangement 2 — is shown by the shaded area in figure 2.

By calculating the intensities of 001 for various z_{Ti} values, it was found that the calculated ratio 0016:0018 (see the discussion on the Bi positions) was best for $z \sim 0.13_0$ or 0.37_0 .

No cor
and octa
structures

The intensities of the spots in the Weissenberg photographs were then calculated for the arrangements 1 and 2 but no decision between 1 and 2 could be made by comparison with the observed intensities. It was therefore tried to find possible arrangements for the O atoms with both 1 and 2.

Case 1

Space group D_2^7 and the following positions for the metal atoms were assumed:

8 Bi₁ in 8 (g) $z_1 = 0.067 \pm 0.004$ 8 Bi₂ in 8 (g) $z_2 = 0.211 \pm 0.004$
 4 Ti₁ in 4 (b) $00\frac{1}{2}$ 8 Ti₂ in 8 (h) $0.133 \leq z \leq 0.147$

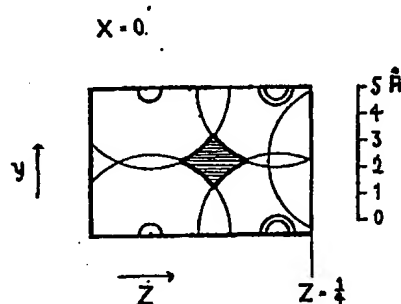


Figure 2.

By assuming that the distances $\text{Bi}-\text{O} \geq 2.2$, $\text{Ti}-\text{O} \geq 1.8$ and $\text{O}-\text{O} \geq 2.5$ Å, the following positions were found possible for the O atoms:

4 (a) 000 4 (c) $\frac{1}{4}\frac{1}{4}\frac{1}{4}$ 4 (d) $\frac{1}{4}\frac{1}{4}\frac{3}{4}$
 8 (g) $\pm 00z$ 8 (h) $\frac{1}{4}\frac{1}{4}z; \frac{1}{4}\frac{1}{4}\frac{1}{2}-z$
 $0.130 \leq z \leq 0.148$ $0 \leq |z| \leq 0.040$
 $0.274 \leq z \leq 0.445$ $-0.183 \leq z \leq -0.095$

16 (k) $xyz; \bar{x}\bar{y}z; x\bar{y}\bar{z}; \bar{x}y\bar{z}$

$x \approx 0$ $y \approx 0$
 $y = 0.27$ or $x = 0.27$

Two regions are possible:

$z = 0.113$ (for $z_{\text{Ti}} = 0.147$) and $z = 0.165$ (for $z_{\text{Ti}} = 0.132$)

No combinations of these positions could be found giving reasonable distances and octahedra around the Ti atoms, as is the case in previously investigated structures containing Ti^{4+} and O^{2-} . Arrangement 1 seemed therefore improbable.

B. AURIVILLIUS, *Mixed bismuth oxides with layer lattices. II*

Case 2

The positions of the metal atoms are assumed to be:

$$8 \text{ Bi}_1 \text{ in } \pm 00z_1 \quad z_1 = 0.067 \pm 0.004 \quad 8 \text{ Bi}_2 \text{ in } \pm 00z_2 \quad z_2 = 0.211 \pm 0.004$$

$$4 \text{ Ti}_1 \text{ in } 00\frac{1}{2}, x00 \text{ (or } 0y0) \quad 0.38 \leq x, y \leq 0.62 \quad 8 \text{ Ti}_2 \text{ in } \pm 00z, \\ 0.324 \leq z \leq 0.398$$

$$x0z; x0\bar{z} \text{ (or } 0yz; 0y\bar{z}) \quad 0.38 \leq x, y \leq 0.62 \\ 0.102 \leq z \leq 0.176$$

At first only space group D_2^7 was considered (Ti_1 in $00\frac{1}{2}$ and Ti_2 in $\pm 00z$). The following positions were found possible for the O atoms making the same assumptions as in case 1:

$$\begin{array}{lll} 4 \text{ (a) } 000 & 4 \text{ (c) } \frac{1}{4}\frac{1}{4}\frac{1}{4} & \\ 4 \text{ (d) } \frac{1}{4}\frac{1}{4}\frac{1}{4} & 8 \text{ (g) } \pm 00z & 8 \text{ (h) } \frac{1}{4}\frac{1}{4}z; \frac{1}{4}\frac{1}{4}\bar{z} - z \\ & 0.130 \leq z \leq 0.148 & 0 < |z| < 0.040 \\ & 0.379 \leq z \leq 0.445 & 0.095 < |z| < 0.183 \\ & 0.274 \leq z \leq 0.343 & \end{array}$$

$$16 \text{ (k) } xyz; \bar{x}\bar{y}z; x\bar{y}\bar{z}; \bar{x}y\bar{z} \\ x = 0.25 \pm 0.02 \quad \text{or} \quad y = 0.25 \pm 0.02 \\ y \sim 0 \quad \text{or} \quad x \sim 0 \\ 0.114 < z < 0.163$$

It was tried to find positions for the O atoms so that Ti_1 and Ti_2 would be surrounded by regular or almost regular octahedra of O atoms with distances $1.8 \leq \text{Ti} - \text{O} \leq 2.5 \text{ \AA}$. For O atoms in contact with Ti_1 , the following point positions are possible: 8 (h) $0 < |z| < 0.040$, 8 (g) $0.424 \leq z \leq 0.445$. With 8 O situated at $\frac{1}{4}\frac{1}{4}0$; $\frac{1}{4}\frac{1}{4}\frac{1}{4}$ and 8 O at ± 00.442 regular octahedra of O would surround Ti_1 . It, therefore, seemed probable that oxygen atoms are situated near these positions.

For oxygen atoms in contact with Ti_2 , the following positions are possible:

$$\begin{array}{ll} 8 \text{ (g}_1\text{)} \quad 0.379 \leq z_1 \leq 0.445 & 8 \text{ (h)} \quad 0.095 \leq |z| \leq 0.183 \\ 8 \text{ (g}_2\text{)} \quad 0.274 \leq z_2 \leq 0.343 & 16 \text{ (k)} \quad 0.114 \leq z \leq 0.163 \end{array}$$

With one set of oxygen atoms situated at 8 (h) or 16 (k), every Ti_2 atom will be in contact with two oxygen atoms, while if oxygen atoms are situated at 8 (g_1) or 8 (g_2), Ti_2 will be in contact with only one oxygen atom. It was

found the
8 (g_1) an
tions 8 (l
6 O are 1

With a
of oxygen
c. Wit
($z_1 \approx 0.10$
around Ti
position
rangement
With d
distances
was, there
The fo
 Ti_1 or Ti_2

Even i
room for
The pos
as follows

ARKIV FÖR KEMI. Bd 1 nr 58

found that only one set of oxygen atoms could occupy the positions 16 (k), 8 (g_1) and 8 (g_2), while at most 32 oxygen atoms could be situated in positions 8 (h). The following arrangements allowing Ti_2 to be in contact with 6 O are possible:

- a. 16 O (k) + 8 O (h) + 8 O (h)
- b. 16 O (k) + 8 O (g_1) + 8 O (g_2) + 8 (h)
- c. 8 O (h) + 8 O (h) + 8 O (h)
- d. 8 O (h) + 8 O (h) + 8 O (g_1) + 8 O (g_2)

With a and b no combination of positions could be found, giving octahedra of oxygen atoms around Ti_2 .

c. With 8 O in $\frac{1}{2}\frac{1}{2}0$; $\frac{1}{2}\frac{1}{2}\frac{1}{2}$, 8 O in 00 0.442 and 24 O in positions 8 (h) ($z_1 \approx 0.102$ $z_2 \approx -0.139$ $z_3 \approx 0.177$) so as to form octahedra of oxygen atoms around Ti_1 and Ti_2 , there was room for the remaining 8 O atoms only in the position $\pm 00z$ $z = 0.274$ or in the positions 4 (c) + 4 (d). With these arrangements, however, the distances O — O would be short (≈ 2.4 Å).

With d, positions for the oxygen atoms could be chosen, allowing reasonable distances and giving octahedra of oxygen atoms around Ti_2 . Arrangement d was, therefore, preferred to the arrangements a, b and c.

The following parameters were assumed for oxygen atoms in contact with Ti_1 or Ti_2 :

- $8 O_1$ in 8 (h) $z = 0$
 $8 O_4$ in 8 (g) $z = 0.436$
 $(z_{Ti_1} = 0.372)$ $8 O_5$ in 8 (g) $z = 0.308$
 $8 O_6$ in 8 (h) $z = 0.128$
 $8 O_7$ in 8 (h) $z = -0.128$

Even if these parameters are varied considerably around the values given, room for the remaining 8 O is left only in the positions 4 (c) and 4 (d) ($0_8, 0_9$).

The positions arrived at might also be described with space group $D_{2h}^{23} - F m m m$ as follows:

- $8 O_1$ in 8 (e) $\frac{1}{2}\frac{1}{2}0$; $\frac{1}{2}\frac{1}{2}\frac{1}{2}$
 $8 O_2$ in 8 (f) $\frac{1}{2}\frac{1}{2}\frac{1}{2}$; $\frac{1}{2}\frac{1}{2}\frac{1}{2}$
 $8 O_3$ in 8 (i) $\pm 00z$ $z = 0.436$
 $8 O_4$ in 8 (i) $\pm 00z$ $z = 0.308$
 $16 O_5$ in 16 (j) $\frac{1}{2}\frac{1}{2}z$; $\frac{1}{2}\frac{1}{2}\bar{z}$;
 $\frac{1}{2}\frac{1}{2}z$; $\frac{1}{2}\frac{1}{2}\bar{z}$
 $z = 0.128$

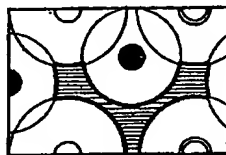
B. AURIVILLIUS, *Mixed bismuth oxides with layer lattices. II*

The distances and coordination will be:

$\text{Bi}_1 - 4 \text{ O}_1 = 2.92$	$\text{Ti}_2 - \text{O}_3 = 2.10$	$\text{Ti}_1 - 4 \text{ O}_1 = 1.92$
$\text{Bi}_1 - 4 \text{ O}_3 = 2.72$	$\text{Ti}_2 - \text{O}_4 = 2.10$	$\text{Ti}_1 - 2 \text{ O}_3 = 2.10$
$\text{Bi}_1 - 4 \text{ O}_5 = 2.76$	$\text{Ti}_2 - 4 \text{ O}_5 = 1.92$	
$\text{Bi}_2 - 4 \text{ O}_2 = 2.79$	$\text{O}_1 - 4 \text{ O}_1 = 2.71$	
$\text{Bi}_2 - 4 \text{ O}_4 = 2.79$	$\text{O}_3 - 4 \text{ O}_1 = 2.83$	
$\text{Bi}_2 - 4 \text{ O}_5 = 2.29$	$\text{O}_4 - 4 \text{ O}_2 = 2.70$	
	$\text{O}_4 - 4 \text{ O}_5 = 2.83$	
	$\text{O}_5 - 4 \text{ O}_5 = 2.71$	

No new combinations were found if the space group D_{2h}^{23} was assumed instead of D_2^7 .

$x = 0$



$x = \frac{1}{4}$

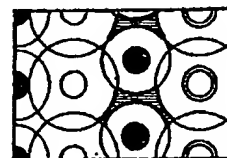
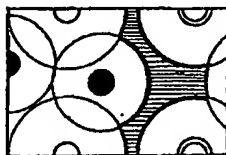


Figure 3 a.

$x = 0$



$x = \frac{1}{4}$

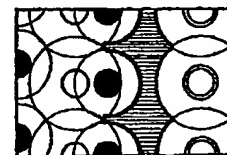


Figure 3 b.

Since $a \approx b$ and the positions of the O atoms must be chosen from space considerations, it does not matter whether space group $C_{2v}^{18} a$ or b is assumed. $C_{2v}^{18} b$ was assumed arbitrarily. It was found that oxygen atoms could only be situated in the planes $x=0$, $x=0.25 \pm 0.02$, $x=\frac{1}{2}$ and $x=0.75 \pm 0.02$. Thus the following positions are possible:

4 (a) $0y0$	8 (b) $\frac{1}{4}y\frac{1}{4}; \frac{1}{4}y\frac{3}{4}$	8 (c) $0yz; 0y\bar{z}$
8 (d) $xyz; \bar{x}y0$	16 (e) $xyz; \bar{x}y\bar{z}; \bar{x}yz; xyz$	
$x = 0.25 \pm 0.02$	$x = 0.25 \pm 0.02$	

ARKIV FÖR KEMI. Bd 1 nr 58

Table 2

Weissenberg Photographs of $\text{Bi}_4\text{Ti}_3\text{O}_{12}$. Cu K_α radiation

Zero Layer

001	I _{calc.}	I _{obs.}	201	I _{calc.}	I _{obs.}
6	56	m	2	1.0	vvw
8	61	m	4	12	w
10	12	w	6	59	m
12	58	m	8	81	m
14	450	vst	10	12	vvw
16	88	m ⁺	12	55	w
18	30	m	14	440	m
20	19	m ₋	16	64	vvw
22	200	st	18	31	vvw
24	27	w	20	19	—
26	120	m	22	200	m
28	230	m	24	26	vw
30	62	w	26	120	st
32	140	m ₋	28	230	st
34	4.0	vvw	30	62	m ₋
36	300	m	32	120	m
38	9.0	vw	34	4.0	vvw
40	110	m	36	290	vst
42	93	m	38	8.0	vw
101	I _{calc.}	I _{obs.}	301	I _{calc.}	I _{obs.}
1	52	vst	1	69	m
3	7.0	w	3	8.0	—
5	17	m ₋	5	18	—
7	470	vst	7	470	m ⁺
9	2.0	—	9	3.0	—
11	23	w	11	22	vw
13	46	w	13	45	vw
15	120	w	15	130	—
17	23	—	17	21	—
19	98	m	19	93	vw
21	320	st	21	320	w
23	36	m	23	36	vw
25	52	m	25	53	w
27	0.6	—	27	0.8	—
29	270	st	29	270	st
31	19	w	31	19	—
33	110	st			
35	140	st			
37	53	m			
39	75	st			
41	44	m			

instead

ations,
trarily.
± 0.02,

B. AURIVILLIUS, *Mixed bismuth oxides with layer lattices. II*

Table 2 (cont.)

First Layer

111	I _{calc.}	I _{obs.}	311	I _{calc.}	I _{obs.}
2	1.0	—	2	1.0	—
4	12	w	4	12	—
6	64	m	6	66	w
8	220	m	8	180	w ⁺
10	15	m ⁻	10	14	—
12	57	m ⁻	12	58	—
14	410	m	14	410	m
16	15	—	16	16	—
18	41	w	18	40	—
20	20	w	20	19	—
22	220	st	22	220	m
24	2.0	w	24	3.0	—
26	98	st	26	98	m ⁺
28	210	st	28	220	st
30	47	m	30	47	m
32	74	st	32	67	st
34	9.0	w			
36	310	vst			
38	4.0	w			
40	180	vst			
101	I _{calc.}	I _{obs.}	211	I _{calc.}	I _{obs.}
5	17	w	1	67	m
7	470	vst	3	8.0	—
9	2.0	vw	5	18	vw
11	23	m	7	470	m ⁺
13	46	m	9	2.0	—
15	120	m ⁺	11	23	vw
17	23	w	13	46	vw
19	98	m ⁺	15	130	vw
21	320	st	17	22	—
23	36	m	19	96	vw
25	52	m	21	320	m
27	0.6	—	23	36	w
29	270	st	25	50	m
31	19	w	27	0.8	—
33	110	st	29	270	st
35	140	st	31	19	w
37	53	m	33	110	st
39	75	st	35	140	st
41	44	st	37	53	m

Pow

λ
0
1
1
—
—
1
—
0
0
2
0
$\beta 0$
2
0
0
2
0
0
2
2
1
0
2
0
$\beta 1$
2
$\beta 3$
2
1
1
1
3
3
0
0
2
2
0
1
3
3

The pc

ARKIV FÖR KEMI. Bd 1 nr 58

Table 3

Powder Photographs of $\text{Bi}_4\text{Ti}_3\text{O}_{12}$. Cr K radiation, orthorhombic description

hkl	$10^4 \sin^2 \theta_{\text{calc.}}$	$10^4 \sin^2 \theta_{\text{obs.}}$	$I_{\text{obs.}}$	hkl	$10^4 \sin^2 \theta_{\text{calc.}}$	$10^4 \sin^2 \theta_{\text{obs.}}$	$I_{\text{obs.}}$
008	0779	0771	st	11 19	5282	5292	m
111	0903	0895	m	22 12	5314		
115	1195	1188	vw	02 18	5710	5734	vw
—	—	1288	m	20 18	5735		
—	—	1336	w	00 22	5887	5892	m
117	1487	1480	vst	13 11	5900		
—	—	1614	vw	22 14	5946	5949	m
00 12	1752	1752	m	31 11	5950		
020	1769			11 21	6255	6267	st
200	1794	1790	w	02 20	6635		
024	1964	1952	vw	20 20	6660	6664	vw
β 00 14	1974	1974	m	22 18	6676		
204	1989			040	7074	7070	vw
00 14	2384	2384	vst	13 15	7165	7172	m
028	2548			400	7174		
208	2573	2565	st	31 15	7215	7221	m
11 13	2947	2947	m	402	7223		
β 220	2953			11 23	7326	7335	w
02 10	2985			22 18	7503	7511	w
β 11 15	3003	3005	w	046	7512		
20 10	3010			02 22	7656	7674	m
00 16	3114	3115	m	20 22	7681		
02 12	3521	3538	vw	00 26	8223	8223	w
20 12	3546			11 25	8494	8495	w
220	3562	3567	m	337	8611	8611	m
11 15	3628	3638	m	20 24	8801		
00 18	3941	3942	w	13 19	8819	8806	vw
226	4000	4006	w	04 12	8826		
02 14	4153			240	8868	8859	w
β 137	4159	4171	st	31 19	8869		
20 14	4178			242	8917	8934	vw
β 317	4200			40 12	8926		
228	4341	4333	w	420	8943		
11 17	4406	4418	vw	22 22	9449	9458	st
131	4440	4428	vw	04 14	9458		
311	4482	4490	vw	00 28	9537	9551	m
00 20	4866	4880	w	40 14	9558		
02 16	4883			248	9647	9652	vw
20 16	4908	4923	w	428	9722	9714	vw
β 22 14	4922			13 21	9792	9785	w
137	5024	5029	m				
317	5074	5078	m				

The positions of the Ti atoms are assumed to be:

$$4 \text{ Ti}_1 \text{ in } 4 \text{ (a)} \quad 0.38 \leq y_1 \leq 0.62$$

$$8 \text{ Ti}_2 \text{ in } 8 \text{ (c)} \quad 0.38 \leq y_2 \leq 0.62 \quad 0.102 \leq z_2 \leq 0.176$$

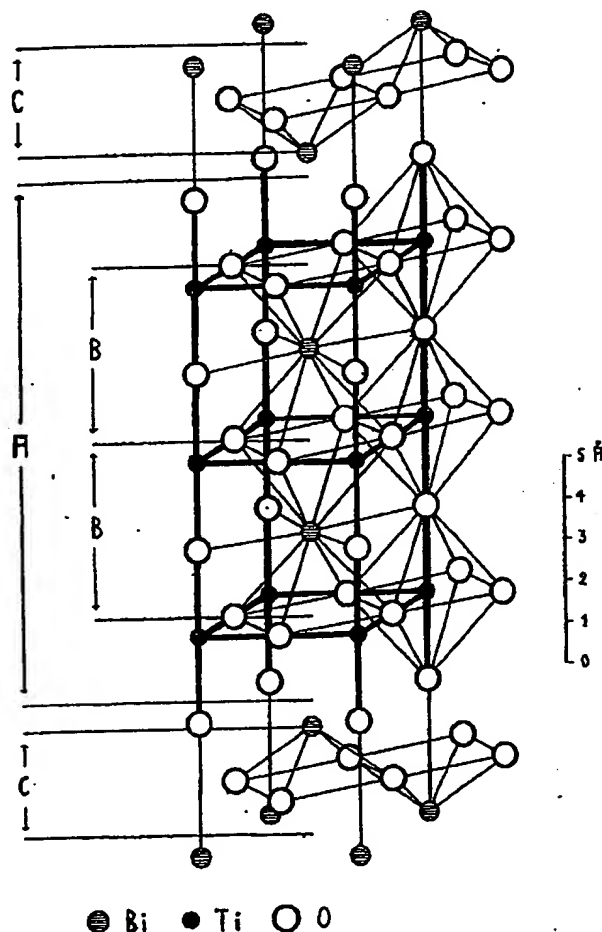
B. AURIVILLIUS, *Mixed bismuth oxides with layer lattices. II*

Figure 4.

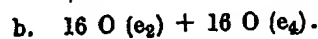
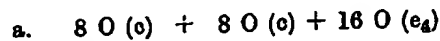
One half of the pseudo-tetragonal unit cell of $\text{Bi}_4\text{Ti}_3\text{O}_{12}$ (from $z \approx 0.25$ to $z \approx 0.75$). A denotes the perovskitic layer $\text{Bi}_2\text{Ti}_2\text{O}_{10}$, C $\text{Bi}_2\text{O}_5^{2+}$ layers and B unit cells of the hypothetical perovskite structure BiTiO_3 .

In figures 3 a and 3 b sections of one fourth of the unit cell are made for $z = 0$ and $z = 0.25$. (The projections of the positions of the Bi_1 , Bi_2 and Ti atoms are denoted by: white circles, double circles and black circles respectively. The same scale is used as for figure 2). Regions where oxygen atoms might be situated are shown by shaded areas. In figure 3 a the positions of the Ti atoms are assumed to be: $00\frac{1}{2}$ and $0y\bar{z}$; $0y\bar{z}$ $y = 0.62$ $z = 0.139$ and in figure 3 b, $0y0$ $y = 0.62$ and $\pm 00z$ $z = 0.324$.

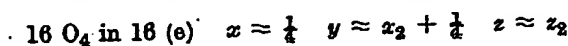
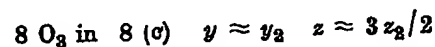
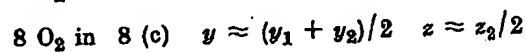
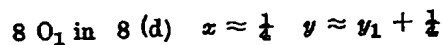
As in the discussion above it was tried to find positions for the O atoms giving an octahedral arrangement around Ti_1 and Ti_2 . Only with O atoms situated in the positions 8 (d) $x \approx \frac{1}{4}$ $y \approx y_1 + \frac{1}{4}$ and 8 (c) $y \approx y_1$ $z \approx 0.058$ would Ti_1 be surrounded by regular octahedra (see figure 3). It was therefore assumed that these positions are occupied by oxygen atoms. For oxygen atoms in contact with Ti_2 , the point positions 8 (c) and 16 (e) are possible. With 8 O situated at 8 (c), every Ti atom is in contact with one oxygen atom; with 16 O in 16 (e), Ti_2 may be in contact with 2 O (e_2) or 4 O ($y \approx y_2 + \frac{1}{4}$ $z \approx z_2$) (e_4). Bear-

ARKIV FÖR KEMI. Bd 1 nr 58

ing in mind that the unit cell contains 48 O and assuming 16 O to be situated at 8 (c) + 8 (d) (so as to form an octahedron around Ti_1), the following arrangements giving 6 O around Ti_2 seemed possible:



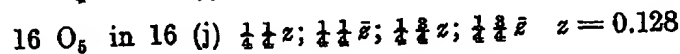
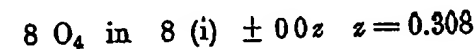
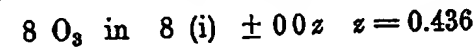
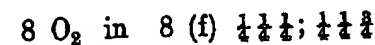
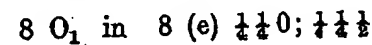
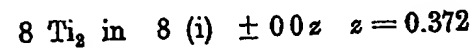
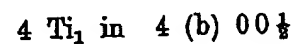
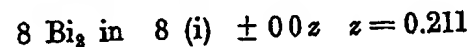
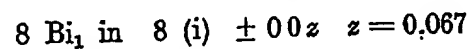
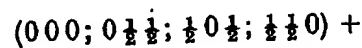
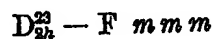
With b. no combination giving octahedra of O around Ti_2 could be found. With a., however, arrangements could be found allowing Ti_2 to be surrounded by an almost regular octahedron. The following parameters for oxygen atoms in contact with Ti_1 or Ti_2 were assumed:



For the remaining 8 O there seemed to be room only in the position 8 (b) $y \approx \frac{1}{4}$. It is seen that these positions are basically the same as were arrived at when space group D_2^7 was assumed, except for possible small shifts in the y direction.

Thus no new arrangement was found by assuming C_{2h}^{18} a or b. In Table 2 (pseudo-tetragonal indices) the intensities, calculated by means of the formula $I = (10 F/4 f_{Bi})^2$, are compared with the observed ones. Since the ratios f_{Ti}/f_{Bi} and f_O/f_{Bi} vary with $\sin \theta/\lambda$ they were interpolated for every reflection from values taken from the International Tables (3). Table 2 shows good agreement between the calculated and observed intensities.

The following structure is thus proposed:



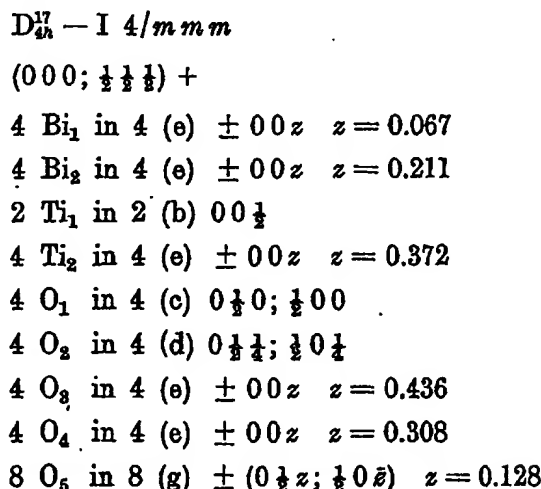
A de-
octahedral

= 0 and
oted by:
figure 2).
e 3 a the
39 and in

an octa-
positions
y regular
y oxygen
are pos-
om; with
d). Bear-

B. AURIVILLIUS, *Mixed bismuth oxides with layer lattices. II*

For the pseudo-tetragonal cell the positions will be:



In figure 4 one half of the pseudo-tetragonal unit cell is pictured. The structure consists of $\text{Bi}_2\text{O}_7^{2+}$ layers alternating with $\text{Bi}_2\text{Ti}_2\text{O}_{10}^{2-}$ layers. The arrangements of the atoms within the $\text{Bi}_2\text{Ti}_2\text{O}_{10}^{2-}$ layers seems to be the same as that found for perovskite structures, and it is easily found by calculation that the geometrical properties of the Bi^{3+} , Ti^{4+} and O^{2-} ions make a perovskite structure possible. Thus the structure might be looked upon as a layer structure where perovskitic layers $\text{Bi}_2\text{Ti}_2\text{O}_{10}^{2-}$ — corresponding to a hypothetical perovskite structure BiTiO_3 — alternate with $\text{Bi}_2\text{O}_7^{2+}$ layers. With the notations given by LAGERCRANTZ and SILLÉN (5), the above structure might be denoted by X_{III} .

I wish to thank Professor L. G. SILLÉN for valuable discussions concerning this work.

Stockholms Högskola, Institute of Inorganic and Physical Chemistry, 1949.

REFERENCES. 1. Bannister, F. A. and Hey, M. H., *Miner. Mag.* 24 (1935), 49. — 2. Sillén, L. G., *Dissert. Stockholm* 1940. — 3. Internationale Tabellen zur Bestimmung von Kristallstrukturen, Berlin 1935. — 4. Wells, A. F., *Z. Krist.* 96 (1937), 451. — 5. Lagercrantz, A. and Sillén, L. G., *Arkiv f. Kemi etc.* 25 (1947), 49.

Tryckt den 10 januari 1950

Uppsala 1950. Almqvist & Wiksells Boktryckeri AB

In a
concern
WO_{2.96}
contin

As w
are rat
triplets
taking
thin it
axis).
with Ch
using P
starting
tion. I
of a "c
amplitu
(1 + cos
The
showin
observe
network
b axis i
one for
consiste
lowing

¹ No
in the r
² The
were giv

BRIEF ATTACHMENT X

IN THE UNITED STATES PATENT AND TRADEMARK OFFICE

In re Patent Application of

Applicants: Bednorz et al.

Serial No.: 08/479,810

Filed: June 7, 1995

For: NEW SUPERCONDUCTIVE COMPOUNDS HAVING HIGH TRANSITION
TEMPERATURE, METHODS FOR THEIR USE AND PREPARATION

Date: March 1, 2005

Docket: YO987-074BZ

Group Art Unit: 1751

Examiner: M. Kopec

Commissioner for Patents
P.O. Box 1450
Alexandria, VA 22313-1450

FIRST SUPPLEMENTAL AMENDMENT

Sir:

In response to the Office Action dated July 28, 2004, please consider the
following:

ATTACHMENT X

ARKIV FÖR KEMI Band 2 nr 37

Communicated 24 May 1950 by ARNE WESTGREN and PERCY QUENSEL

Mixed oxides with layer lattices

III. Structure of $\text{BaBi}_4\text{Ti}_4\text{O}_{15}$

By BENGT AURIVILLIUS.

With 4 figures in the text

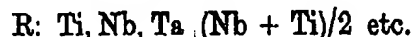
X ray studies on the compounds $\text{CaBi}_2\text{Nb}_2\text{O}_9$ (1) and $\text{Bi}_4\text{Ti}_3\text{O}_{12}$ (2) have shown that the comparatively complicated chemical formulae of these compounds can be explained by simple layer structures being built up from $\text{Bi}_2\text{O}_3^{2+}$ layers and perovskite layers. The unit cells are pictured schematically in Figs. 1 a and 1 c. It was found both for $\text{CaBi}_2\text{Nb}_2\text{O}_9$ and $\text{Bi}_4\text{Ti}_3\text{O}_{12}$ that the symmetry was body-centered pseudo-tetragonal and that the length of the a axes had the same value (3.8 Å) while the length of the c -axis was 25 Å for $\text{CaBi}_2\text{Nb}_2\text{O}_9$ and 33 Å for $\text{Bi}_4\text{Ti}_3\text{O}_{12}$. In both structures the heavy atoms form approximately a "substructure" with a smaller body-centered tetragonal cell with $a = 3.8$ Å and $c = 25/5$ Å for $\text{CaBi}_2\text{Nb}_2\text{O}_9$ or $c = 33/7$ Å for $\text{Bi}_4\text{Ti}_3\text{O}_{12}$.

The Bi_2O_2 layers and perovskite layers lie perpendicular to the c -axis. Similar layer structures have been found for a number of bismuth oxicomounds (3,4,5). The common structural element in all these compounds is quadratic Bi_2O_2 layers between which halides or certain radicals are inserted. This explains the fact that the a axes of all these compounds are of about the same length. For a survey see (5).

For the $\text{CaBi}_2\text{Nb}_2\text{O}_9$ type each perovskite layer has the composition $(\text{CaNb}_2\text{O}_7)_n$ and the height of the layer is equal to four distances Nb—O or approximately to the height of two $\text{E}2_1$ (perovskite) unit cells (see Fig. 1 a). A compound with a somewhat similar structure has previously been investigated by LAGERCRANTZ and SILLÉN (5). In this structure (see Fig. 1 b), beyerite $\text{CaBi}_2\text{O}_3(\text{CO}_3)_2$, the point positions corresponding to the positions of the Nb atoms in $\text{CaBi}_2\text{Nb}_2\text{O}_9$ are occupied by "rotating" CO_3^{2-} groups.

For the $\text{Bi}_4\text{Ti}_3\text{O}_{12}$ type the perovskite layers have the composition $(\text{Bi}_2\text{Ti}_3\text{O}_{10})_n$ and the height of the layer is equal to six distances Ti—O or approximately to the height of three $\text{E}2_1$ unit cells.

The general formula for a compound built up in a way similar to $\text{CaBi}_2\text{Nb}_2\text{O}_9$ but where the height of the perovskite layer enclosed between a pair of Me_2O_2 layers is equal to the height of m $\text{E}2_1$ cells, will be:



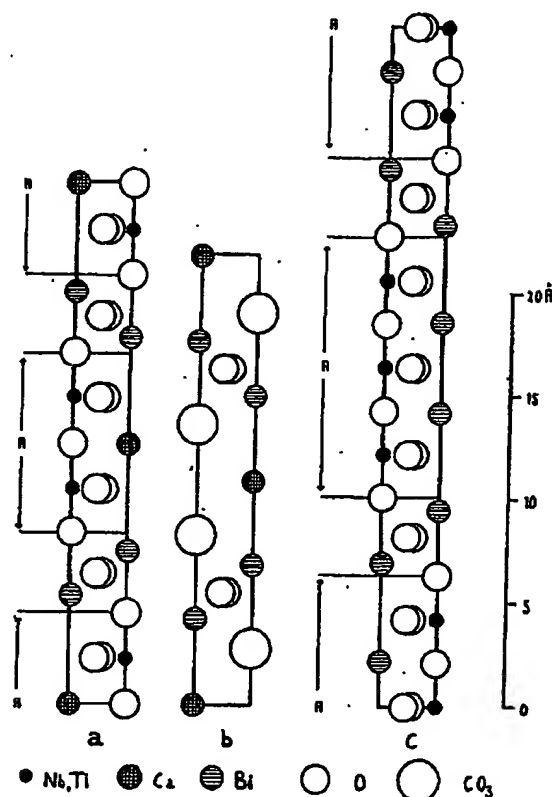
B. AURIVILLIUS, *Mixed oxides with layer lattices. III.*

Fig. 1. Schematic pictures of the structures of a. $\text{CaBi}_2\text{Nb}_2\text{O}_9$, b. $\text{CaBi}_2\text{O}_5(\text{CO}_3)_2$ and c. $\text{Bi}_4\text{Ti}_4\text{O}_{18}$. The vertical lines indicate the lines $00z$ and $\frac{1}{2}\frac{1}{2}z$ in the unit cells. A denotes perovskitic ($E2_1$) regions in the structures.

It seemed of interest to investigate whether compounds could be synthesized with $m = 4$. The present investigation shows that structures of the above type with $m = 4$ exist.

Mixtures of Bi_2O_3 , BaCO_3 and TiO_2 , corresponding to the composition $\text{BaBi}_4\text{Ti}_4\text{O}_{18}$, were prepared and heated to 1100°C . Single crystals, thin plates, were picked out and Weissenberg photographs were taken. These could be interpreted by means of a body-centered tetragonal cell with $a = 3.86 \text{ \AA}$ and $c = 41.7 \text{ \AA}$. The strong lines of the powder photographs (taken from preparations heated to 900°C (Au crucible) or 1100°C (Pt crucible)) were easily identified since they could all be described with the aid of the "sub-lattice" ($a = 3.86$ $c = 41.7/9$). If the c axis were 9 fold even the weak lines could be explained (Table 3). In this way the cell edges were found to be $a = 3.864 \text{ \AA}$ and $c = 41.76 \text{ \AA}$. The observed density was 7.2, which agrees fairly well with the assumption of 2 formula units/unit cell (calculated density 7.49).

The Weissenberg photographs registered $0kl$, $1kl$, hhl and $h, h+1, l$. In the Weissenberg and powder photographs there was nothing to indicate a lower Laue symmetry than $D_{4h}-4/mmm$. Except for the extinctions due to the body-centering, hkl occurring only for $h+k+l=2n$, no systematic extinctions were found, which is characteristic of the space groups C_{4v}^9 , $D_{2d}^{9,11}$ and D_{4h}^{17} . Fig. 2



Fig. 2. Patterson



Fig. 3. Three dim.
material was used
the amplitudes are
The ver

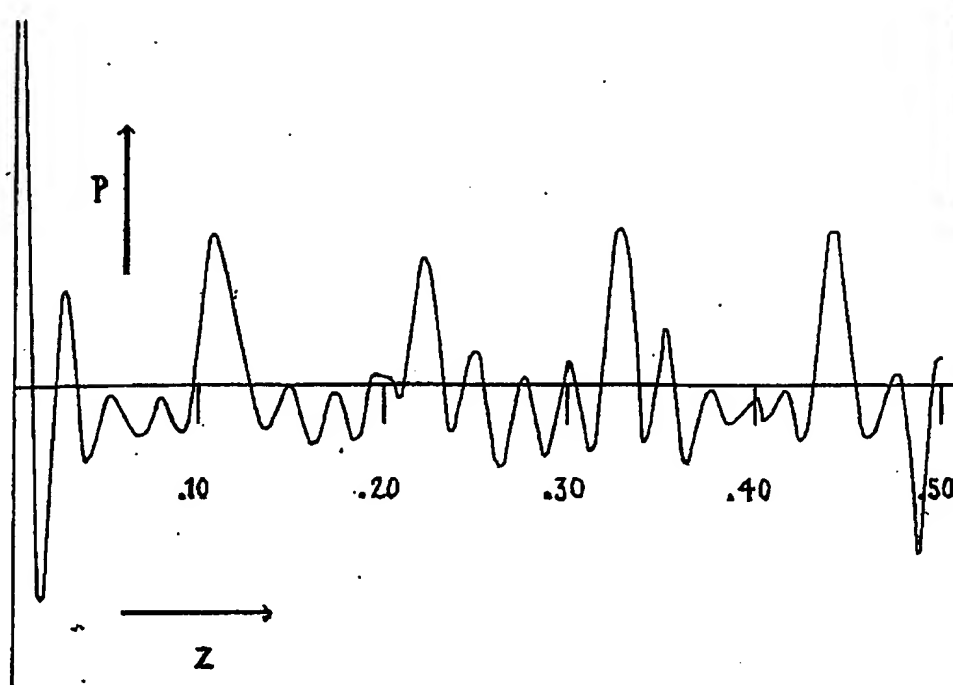


Fig. 2. Patterson Harker function of $\text{BaBi}_4\text{Ti}_4\text{O}_{15}$ along $00z$. All observed reflexions were used for this calculation.

$\text{O}_2)_2$ and
denotes

thesized
ve type

position
plates,
could be
Å and
prepara-
ly iden-
3" ($a =$
could be
3.864 Å
ell with

1, 1. In
a lower
ie body-
ns were
Fig. 2

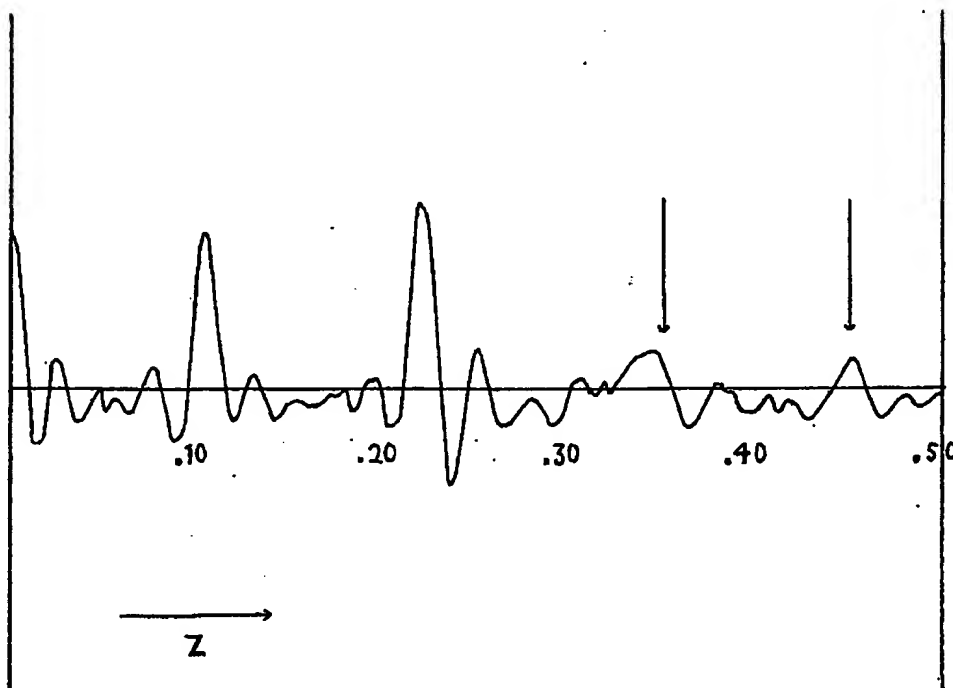


Fig. 3. Three dimensional Fourier cut along $00z$ for $\text{BaBi}_4\text{Ti}_4\text{O}_{15}$. The same intensity material was used as for the Patterson Harker analysis pictured in Fig. 2. The signs of the amplitudes are the same as those obtained in the structure factor calculation for Table 2. The vertical arrows correspond to the z_{T1} values actually assumed.

B. AURIVILLIUS, *Mixed oxides with layer lattices. III.*

shows the Patterson Harker function along 00z. For all observed reflexions the F^2 values were estimated from: $F^2 \approx I_{\text{obs.}} \frac{\sin^2 \theta}{1 + \cos^2 2\theta}$. As expected large peaks appear at $z \approx 1/9, 2/9, 3/9$ and $4/9$.

It is interesting to compare the cell dimensions found above with the ones which might be expected if the compound $\text{BaBi}_4\text{Ti}_4\text{O}_{15}$ is assumed to have a structure similar to that of $\text{CaBi}_2\text{Nb}_2\text{O}_9$ but with $m = 4$. In this case the a axis would have about the same value as found. The length of the c axis might be estimated in the following way: The c axis of $\text{Bi}_2\text{NbTiO}_9$ ($m = 2$ see (1)) is 25.11 Å; the value for $\text{Bi}_4\text{Ti}_3\text{O}_{12}$ ($m = 3$ see (2)) is 32.83, the difference is 7.72. If twice this value is added to the c axis of $\text{BaBi}_2\text{Nb}_2\text{O}_9$ ($m = 2$) the value 41.0 Å is obtained. The value actually found was, as mentioned above, 41.76 Å.

From the composition, cell dimensions, and crystal symmetry it seemed *a priori* probable that the structure of $\text{BaBi}_4\text{Ti}_4\text{O}_{15}$ was the one we anticipated. Therefore, the parameters were worked out with the aid of the parameters found for

Table 1

Weissenberg photographs of $\text{BaBi}_4\text{Ti}_4\text{O}_{15}$. Cu K_α radiation. For zero order photographs the regions of maximum absorption (see Wells (6)) are indicated by dotted lines. The intensities of 101, 103 and 105 have been taken from a zero order photograph, those of 1027–1049 from a first order photograph rotated around (100).

l	001	201	221	401	111	311	331
2		—	vw	—	—	—	vw
4		—	—	—	vw	—	vvw
6	vw	vvw	vw	—	w	—	vvw
8	m	m	w	—	m	vvw	vvw
10	m	m	w	—	st	vw	w
12	w	vvw	vw	—	vvw	—	w
14	w	—	vvw	—	w	—	—
16	st	w	m ⁺	vvw	m	vvw	m
18	vst	m	st	w	vst	w	st
20	st	w	w	vvw	w	—	—
22	m ⁺	vvw	vvw	vvw	vw	—	vw
24	w	vvw	vvw	vvw	vw	—	w
26	w	vvw	—	—	w	vvw	w
28	st	m ⁺	w ⁺	m ⁺	m	vw	—
30	w	w	w	m ⁺	—	vw	—
32	w	w ⁺	w	—	m	w	—
34	m	m	m ⁺	—	m	m	—
36	st	st	st	—	m ⁺	m	—
38	vvw	—	—	—	w	—	—
40	st	st	st	—	st	st	—
42	vvw	—	—	—	vw	—	—
44	—	—	—	—	—	—	—
46	m	m	—	—	st	—	—
48	w	m	—	—	st	—	—
50	w ⁺	—	—	—	m	—	—
52	w ⁺	—	—	—	—	—	—

$\text{Bi}_2\text{NbTiO}_9$
to be: 2
The pc

4 Ti in :
 $\frac{1}{2} 0(\frac{1}{2} - z_3)$
4 O in \pm
 $z_1 \approx 1/9$

These at
same values
ones only i
be an incorr

The par
of the Ba
(000 + 00
agreement
 $\pm 0.004, z_4$

Table 1 (cont.)

Weissenberg photographs of $\text{BaBi}_4\text{Ti}_4\text{O}_{15}$. Cu K_α radiation.

h	101	211	301	321	411
1	m	w	vw	vw	—
3	vvw	vvw	—	vvw	—
5	vvw	—	—	—	—
7	w	vw	vvw	w	—
9	vst	st	m	m	w
11	—	—	—	—	—
13	w	—	—	—	—
15	w ⁺	—	vvw	—	—
17	m	vvw	vvw	—	—
19	st	vw	vvw	vvw	vvw
21	w	—	vvw	vvw	vvw
23	w	—	vvw	vvw	m
25	m ⁺	vw	vw	vw	m ⁺
27	st	m	w	m	—
29	m	vw	vvw	vvw	—
31	m	w	vw	vw	—
33	vw	vvw	vvw	vw	—
35	—	—	—	—	—
37	m ⁺	m	m	—	—
39	vw	w	m	—	—
41	w	w	w ⁺	—	—
43	w ⁺	m	—	—	—
45	m	m ⁺	—	—	—
47	—	—	—	—	—
49	st	—	—	—	—
51	—	—	—	—	—

$\text{Bi}_3\text{NbTiO}_9$ and $\text{Bi}_4\text{Ti}_3\text{O}_{12}$. The positions of the heavy atoms might be expected to be: 2 Ba in 000, 4 Bi in $\pm 00z_1$, 4 Bi in $\pm 00z_2$.

The positions of the Ti and O atoms might be expected to be:

4 Ti in $\pm 00z_3$, 4 Ti in $\pm 00z_4$, 2 O in $00\frac{1}{2}$, 8 O in $\pm (0\frac{1}{2}(\frac{1}{2}-z_3), \frac{1}{2}0(\frac{1}{2}-z_3))$, 8 O in $\pm (0\frac{1}{2}(\frac{1}{2}-z_4), \frac{1}{2}0(\frac{1}{2}-z_4))$, 4 O in $\pm 00(z_3 + z_4)/2$, 4 O in $\pm 00(z_3 - (z_4 - z_3)/2)$, 4 O in $0\frac{1}{2}\frac{1}{2}, \frac{1}{2}0\frac{1}{2}$
 $z_1 \approx 1/9$ $z_2 \approx 2/9$ $z_3 \approx 0.350$ $z_4 \approx 0.450$

These atomic positions would give rise to high peaks in the Patterson-Harker plot at the same values as actually found. The calculated area ratios agree, however, with the observed ones only in as much as the biggest area is found for the peak at 1/9. The reasons might be an incorrect choice of the zero level and errors in the estimation of the intensities.

The parameters were varied around the above values for different positions of the Ba atoms: 2 Ba in 000, $00z_1$ or $00z_2$, 2 Ba equally distributed over $(000 + 00z_1)$, $(000 + 00z_2)$, $(00z_1 + 00z_2)$ or $(000 + 00z_1 + 00z_2)$. The best agreement seemed to be for $z_1 = 0.106 \pm 0.001$, $z_2 = 0.221 \pm 0.001$, $z_3 = 0.352 \pm 0.004$, $z_4 = 0.452 \pm 0.004$ with 2 Ba equally distributed over $(000 + 00z_1 +$

B. AURIVILLIUS, *Mixed oxides with layer lattices. III*

Table 2

Weissenberg photographs of $\text{BaBi}_4\text{Ti}_4\text{O}_{15}$. Cu K_α radiation

$$I_{\text{calc.}} = (2.5 F/t_{\text{BI}})^2$$

l	$I_{\text{obs.}}$ 101	$I_{\text{calc.}}$ 101	$I_{\text{obs.}}$ 211	$I_{\text{calc.}}$ 211	$I_{\text{obs.}}$ 301	$I_{\text{calc.}}$ 301
1	m	73	w	90	vw	94
3	vw	5.8	vw	7.3	—	8.4
5	vw	4.8	—	5.8	—	5.8
7	w	30	vw	31	vw	32
9	vst	620	st	610	m	630
11	—	13	—	12	—	14
13	w	25	—	24	—	24
15	w ⁺	62	—	60	vw	60
17	m	94	vw	92	vw	90
19	st	160	vw	170	vw	170
21	w	15	—	12	vw	12
23	w	19	—	18	vw	18
25	m ⁺	120	vw	120	vw	120
27	st	320	m	320	w	320
29	m	45	vw	45	vw	44
31	m	160	w	160	vw	160
33	vw	56	vw	56	vw	56
35	—	13	—	12	—	12
37	m ⁺	300	m	300	m	300
39	vw	12	w	13	m	13
41	w	15	w	14	w ⁺	15
43	w ⁺	200	m	200	—	—
45	m	180	m ⁺	180	—	—
47	—	18	—	—	—	—
49	st	250	—	—	—	—
51	—	3.6	—	—	—	—

l	$I_{\text{obs.}}$ 001	$I_{\text{calc.}}$ 001	$I_{\text{obs.}}$ 111	$I_{\text{calc.}}$ 111	$I_{\text{obs.}}$ 221	$I_{\text{calc.}}$ 221
2	—	—	—	0.5	vw	0.6
4	—	—	vw	4.8	—	5.3
6	vw	21	w	23	vw	24
8	m	110	m	100	w	110
10	m	62	st	280	w	98
12	w	12	vw	6.3	vw	9.6
14	w	14	w	16	vw	14
16	st	83	m	79	m ⁺	81
18	vst	440	vst	430	st	450
20	st	170	w	36	w	120
22	m ⁺	100	vw	79	vw	92
24	w	81	vw	86	vw	78
26	w	39	w	36	—	39
28	st	280	m	240	w	280
30	w	2.6	—	11	w	1.4
32	w	11	m	20	w	12
34	m	140	m	110	m ⁺	140
36	st	240	m ⁺	240	st	240
38	vw	19	w	35	—	21
40	st	380	st	230	st	340
42	vw	11	vw	22	—	—
44	—	3.2	—	4.8	—	—
46	m	240	st	230	—	—
48	w	69	st	46	—	—
50	w ⁺	53	m	110	—	—
52	w ⁺	280	—	—	—	—

hkl
0010
101
105
109
110
0016
116
118
0018
1110
1015
0020
1017
200
1019
1116
208
1118
1021
2010
211
213
217
1120
2014
219

00₂). Oth.
seen the thr
following M
over the po
From Tal
 $\approx I_{221} \approx I_4$
be expected
00₂, $\frac{1}{2}\frac{1}{2}\frac{1}{2}$,
for the rows
senberg pho
the observed
more clearly
 ≥ 3039 . Th
the z parame
structure fac
are 222:22.
reflexions the
be introduced
the agreemen

ARKIV FÖR KEMI. Bd 2 nr 37

Table 3

Powder photographs of $\text{BaBi}_4\text{Ti}_4\text{O}_{15}$ Cr K_α radiation.

hkl	$10^4 \sin^2 \theta_{\text{calc.}}$	$10^4 \sin^2 \theta_{\text{obs.}}$	$I_{\text{obs.}}$	hkl	$10^4 \sin^2 \theta_{\text{calc.}}$	$10^4 \sin^2 \theta_{\text{obs.}}$	$I_{\text{obs.}}$
0010	753	745	w	2018	5443	5440	vw
101	887	878	m	1025	5582	5581	w
105	1067	1058	vw	2113	5667	5669	vw
109	1489	1481	st	0028	5900	5892	vw
110	1758	1751	m	2018	5954	5960	m
0016	1927	1915	vw	2115	6088	6089	vw
116	2031	2018	vw	1124	6093	6089	vw
118	2240	2236	vw	1027	6365	6364	m
0018	2438	2423	m	2020	6526	6529	vw broad
1110	2511	2504	m	220	7032		
1015	2572	2567	vw	222	7064	7070	w broad
0020	3010	2992	w	2119	7112		
1017	3054	3051	w	305	8099		
200	3516	3514	m	1031	8111	8104	vw
1019	3596	3600	w	2214	8114		
1116	3685	3681	w	2123	8376	8365	vw
208	3998	3996	vw	2214	8507		
1118	4196	4186	m	309	8521	8520	m
1021	4198			1130	8531		
2010	4269	4265	w	310	8802		
211	4403	4402	vw	3011	8812	8802	m
213	4418			312	8820		
217	4764	4774	vw	1033	9074	9092	w broad
1120	4768			2125	9098		
2014	4991	5009	m	1132	9464	9484	w broad
219	5005			2218	9470		

00 z_2). Other distributions of Ba should, however, not be excluded; as will be seen the three dimensional Fourier cut along 00 z (see Fig. 3) seems to favour the following Me arrangement: 4 Bi \pm 00 z_2 and (2 Ba + 4 Bi) equally distributed over the positions 000 and \pm 00 z_1 .

From Table 1 it is seen that roughly for the same value of l : $I_{00l} \approx I_{20l} \approx I_{22l} \approx I_{40l}$, $I_{11l} \approx I_{31l} \approx I_{33l}$, $I_{10l} \approx I_{21l} \approx I_{30l} \approx I_{32l} \approx I_{41l}$ as might be expected from the above atomic positions with atoms only on the lines 00 z , $\frac{1}{2}\frac{1}{2}z$, $0\frac{1}{2}z$ and $\frac{1}{2}0z$. Table 2 gives calculated and observed intensities for the rows 00 l , 10 l , 11 l , 21 l , 22 l and 30 l . It was found from the Weissenberg photographs that 0028 > 0030 and 1037 > 1039 (see Table 2) but the observed ratios do not seem to be as large as those calculated. This is more clearly seen for the rows 40 l and 30 l where 4028 < 4030 and 3037 > 3039. These discrepancies could neither be removed by small variations in the z parameters nor by assuming other distributions of the Ba atoms for the structure factor calculations. Other discrepancies found from Tables 1 and 2 are 222:224, 332:334, 0050:0052 and 1148:1152. However, for most reflexions the agreement is quite good and considering the errors which might be introduced by absorption effects and errors in the ratios $f_{\text{Ti}}/f_{\text{Bi}}$ and f_0/f_{Bi} the agreement might on the whole be classified as fairly good.

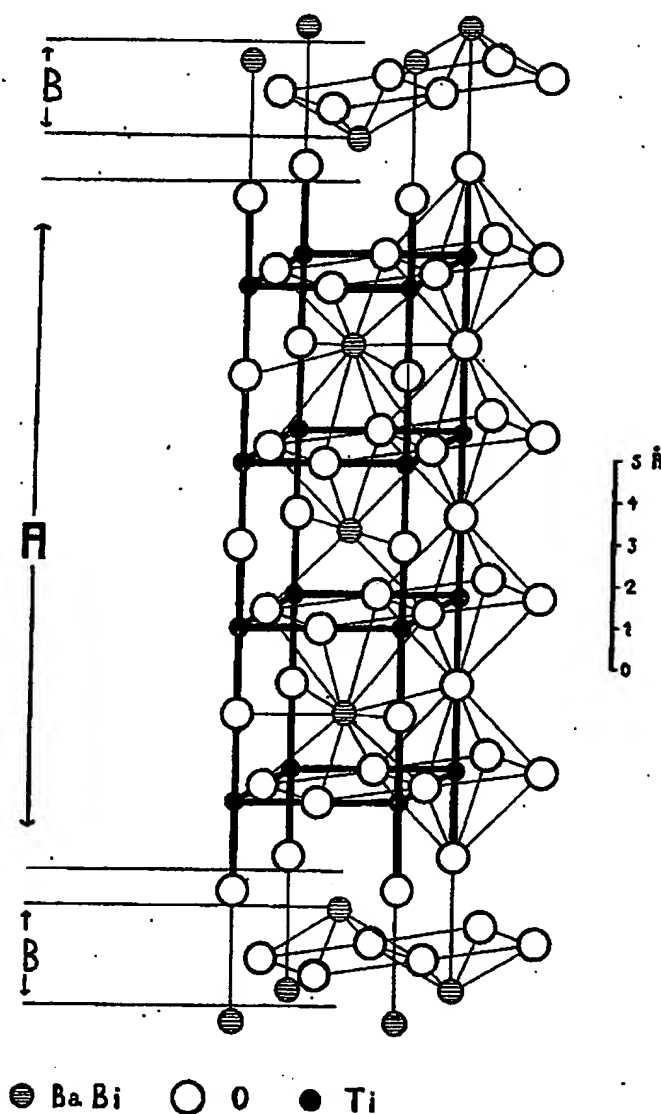
B. AURIVILLIUS, *Mixed oxides with layer lattices. III*

Fig. 4. One half of the unit cell of $\text{BaBi}_4\text{Ti}_4\text{O}_{15}$. A denotes the perovskitic region and B the Me_2O_2 layers.

The following structure is therefore proposed:
 $D_{2d}^{17} - I4/mmm$
 $(000, \frac{1}{2}\frac{1}{2}\frac{1}{2}) +$

2 Me_1 in 2 (a) 000
 2 O_1 in 2 (b) $00\frac{1}{2}$
 8 O_2 in 8 (g) $0\frac{1}{2}z; 0\frac{1}{2}\bar{z}; \frac{1}{2}0z; \frac{1}{2}0\bar{z}$ $z = 0.048$
 4 Ti_1 in 4 (e) $00z; 00\bar{z}$ $z = 0.452$
 4 O_3 in 4 (e) $z = 0.402$

Ba a1

If 1
the st
 $\frac{1}{2}\frac{1}{2}0$;
 $\frac{1}{2}\frac{1}{2}z$;
8 (i) z
8 Me_2

The

$\text{O}_1 - \frac{1}{2}$
 $\text{O}_3 - \frac{1}{2}$
 $\text{O}_3 - \frac{1}{2}$
 $\text{O}_5 - \frac{1}{2}$

One h

I wi

Stoc

REF.

499. —
 G., Dis
 No 20,

ARKIV FÖR KEMI. Bd 2 nr 37

4 Me ₂ in 4 (e)	$z = 0.106$
8 O ₄ in 8 (g)	$z = 0.148$
4 Ti ₂ in 4 (e)	$z = 0.352$
4 O ₅ in 4 (e)	$z = 0.302$
4 Me ₃ in 4 (e)	$z = 0.221$
4 O ₆ in 4 (d) $0\frac{1}{2}\frac{1}{2}; \frac{1}{2}0\frac{1}{2}$	

Ba and Bi equally distributed over all Me positions.

If the structure is described by means of an orthorhombic space group (D_{2h}^{23}), as used for the structures of Bi₃NbTiO₉ and Bi₄Ti₃O₁₂, the positions will be: $D_{2h}^{23} - F m m m$ (000; $\frac{1}{2}\frac{1}{2}0$; $0\frac{1}{2}\frac{1}{2}$; $\frac{1}{2}0\frac{1}{2}$) + 4 Me₁ in 4 (a) 000, 4 O₁ in 4 (b) $00\frac{1}{2}$, 16 O₂ in 16 (j) $\frac{1}{4}\frac{1}{4}z$; $\frac{1}{4}\frac{1}{4}\bar{z}$; $\frac{1}{4}\frac{1}{4}z$; $\frac{1}{4}\frac{1}{4}\bar{z}$; $z = 0.048$, 8 Ti₁ in 8 (i) 00 z ; 00 \bar{z} $z = 0.452$, 8 O₃ in 8 (i) $z = 0.402$, 8 Me₂ in 8 (i) $z = 0.106$, 16 O₄ in 16 (j) $z = 0.148$, 8 Ti₂ in 8 (i) $z = 0.352$, 8 O₅ in 8 (i) $z = 0.302$, 8 Me₃ in 8 (i) $z = 0.221$, 8 O₆ in 8 (f) $\frac{1}{4}\frac{1}{4}\frac{1}{4}$; $\frac{1}{4}\frac{1}{4}\frac{3}{4}$.

The distances (Å) and coordination will be:

O ₁ —8 O ₂ = 2.78	O ₂ —4 O ₃ = 2.73	Me ₂ —4 O ₂ = 3.10	Ti ₁ —O ₃ = 2.09
O ₃ —4 O ₃ = 2.84	O ₄ —4 O ₄ = 2.73	Me ₂ —4 O ₃ = 2.75	Ti ₁ —4 O ₂ = 1.93
O ₃ —4 O ₄ = 2.84	O ₅ —4 O ₆ = 2.73	Me ₂ —4 O ₄ = 2.61	Ti ₁ —O ₁ = 2.00
O ₅ —4 O ₆ = 2.91			
	Me ₁ —8 O ₂ = 2.78	Me ₃ —4 O ₆ = 2.28	Ti ₂ —O ₃ = 2.09
	Me ₁ —4 O ₁ = 2.73	Me ₃ —4 O ₅ = 2.89	Ti ₂ —4 O ₄ = 1.93
		(Me ₃ —4 O ₄ = 3.64)	Ti ₂ —O ₅ = 2.09

One half of the unit cell is shown in Fig. 4.

I wish to thank Professor L. G. SILLÉN for valuable discussions on this work.

Stockholms Högskola, Institute of Inorganic and Physical Chemistry. May 1950.

REFERENCES. 1. Aurivillius, B., Arkiv Kemi 1 (1950) 463. — 2. —, Ibid, 1 (1950) 499. — 3. Bannister, F. A. and Hey, M. H., Miner. Mag. 24. (1935) 49. — 4. Sillén, L. G., Dissert., Stockholm 1940. — 5. Lagercrantz, A. and Sillén, L. G., Arkiv Kemi 25 No 20, 1948. — 6. Wells, A. F., Z. Krist. 96 (1937) 451.

Tryckt den 14 oktober 1950

Uppsala 1950. Almqvist & Wiksells Boktryckeri AB

BRIEF ATTACHMENT Y

IN THE UNITED STATES PATENT AND TRADEMARK OFFICE

In re Patent Application of

Applicants: Bednorz et al.

Serial No.: 08/479,810

Filed: June 7, 1995

For: NEW SUPERCONDUCTIVE COMPOUNDS HAVING HIGH TRANSITION
TEMPERATURE, METHODS FOR THEIR USE AND PREPARATION

Date: March 1, 2005

Docket: YO987-074BZ

Group Art Unit: 1751

Examiner: M. Kopec

Commissioner for Patents
P.O. Box 1450
Alexandria, VA 22313-1450

FIRST SUPPLEMENTAL AMENDMENT

Sir:

In response to the Office Action dated July 28, 2004, please consider the
following:

ATTACHMENT Y

ARKIV FÖR KEMI Band 5 nr 4

Communicated 14 May 1952 by ARNE WESTGREN

The structure of $\text{Bi}_2\text{NbO}_5\text{F}$ and isomorphous compounds

By BENGT AURIVILLIUS

With 1 figure in the text

X-ray studies made previously on the compounds $\text{CaBi}_2\text{Nb}_2\text{O}_9$, $\text{Bi}_4\text{Ti}_3\text{O}_{13}$ and $\text{BaBi}_4\text{Ti}_4\text{O}_{15}$ (1) showed that they have very similar structures. The symmetry is tetragonal or pseudotetragonal, and the structures are each built up of quadratic Bi_2O_3 layers alternating with perovskite layers, the latter having different heights in the three different cases. The generalized formula for the compounds might be written $\text{Me}_2\text{O}_3 (\text{Me}'_{m-1} \text{R}_m \text{O}_{3m+1})$ where Me' is the 12 coordinated metal atom in the perovskite layers and R the 6 coordinated atom. The formulae for the above compounds, $\text{Bi}_2\text{O}_3(\text{CaNb}_2\text{O}_7)$, $\text{Bi}_2\text{O}_3(\text{Bi}_2\text{Ti}_3\text{O}_{10})$ and $\text{Bi}_2\text{O}_3[(\text{BaBi}_2)\text{Ti}_4\text{O}_{13}]$ thus have m values of 2, 3 and 4. The simplest case, $m=1$, would correspond to the formula $\text{Me}_2\text{O}_3(\text{RO}_6)$ and to a structure built up of Me_2O_3 layers and layers of RO_6 octahedra each octahedron sharing four corners. Compounds of this type have, however, not been successfully synthesized as yet.

The present paper deals with the compounds $\text{Bi}_2\text{NbO}_5\text{F}$, $\text{Bi}_2\text{TaO}_5\text{F}$ and $\text{Bi}_2\text{TiO}_4\text{F}_2$, which correspond to the simplest case, $m=1$ above, except that some of the O atoms are replaced by F atoms. The formulae of the compounds might thus be written: $\text{Bi}_2(\text{O}, \text{F})_2\text{Nb}(\text{O}, \text{F})_4$ etc.

Preparation, powder photographs and analyses

$\text{Bi}_2\text{NbO}_5\text{F}$: When a mixture of BiF_3 and Nb_2O_5 in the mol ratio 4:1 was heated in air at 800°C for a short time, a few single crystals (very thin plates) were obtained. Powder photographs of this sample indicated a tetragonal unit cell with the same cell dimensions as would be expected for the above general type when $m=1$. The best conditions for the formation of this phase were then studied by heating 2.5 g mixtures ($2\text{BiF}_3 + \frac{1}{2}\text{Nb}_2\text{O}_5$) in air at 640°C , this low temperature being chosen to reduce the volatility of the BiF_3 . The reaction times were varied from 5–40 hours, and powder photographs were taken of each product. For reaction times of 7–15 hours the lines of the above tetragonal phase predominated in the powder photographs, the few extra lines were very weak (see Table 1).

The fluorine content was found to vary from 4.0 % (7 hours) to 2.4 % (15 hours), whereas the calculated value for $\text{Bi}_2\text{NbO}_5\text{F}$ is 3.2 %. No variation in the size of the cell with the fluorine content was found, and it therefore seems probable that the composition of the phase is constant and that the observed variation in the F content is due to the presence of small impurities which are not visible in the powder photo-

B. AURIVILLIUS, *The structure of $\text{Bi}_2\text{NbO}_5\text{F}$ and isomorphous compounds*

Table 1

Powder photographs of $\text{Bi}_2\text{NbO}_5\text{F}$ (sample with 2.8 % F)
 Cr K radiation $\lambda_{\text{Cr K}\alpha} = 2.2909 \text{ \AA}$

hkl	$10^4 \cdot \sin^2 \theta_{\text{calc}}$	$10^4 \cdot \sin^2 \theta_{\text{obs}}$	I_{obs}
103	1319	1332	st
006	1708	1711	m
110	1784	1795	m
112	1974	1989	vw
105	2078	2083	vw
114	2543	2547	m
—	—	2785	vw
008	3036	3033	w
—	—	3093	vw
116	3492	3490	st
200	3568	3567	st
202	3758	3754	vw
—	—	3808	vw
{109}	4734	4737	st
{0010}	4743		
118	4820	4827	w
213	4888	4891	st
206	5276	5292	m
215	5647	5658	w
1110	6527	6529	vw
1011	6631	6630	w
0012	6830	6841	w
220	7137	7139	w
222	7327	7330	vw
301	8076	8080	vw
{219}	8303	8304	st
{2010}	8311		
303	8456	8456	m
1112	8614	8611	m
226	8845	8844	m
{1013}	8908	8919	m
{310}	8921		
312	9111	9119	vw
305	9215	9195	vw
0014	9297	9292	vw

Fig. 1. C

Bi_2TiO_5
 2:1 (total)
 photographs
 assuming
 the same
 phase are
 of the mi
 variation
 are 7.8 %
 fluorine a
 of $\text{Bi}_2\text{NbO}_5\text{F}$
 $\text{Bi}_2\text{TiO}_5\text{F}_2$

Method
 with NaOI
 (3). The di

Bismuti
 was deter
 precipitate
 as such.

The dim
 with focusi

graphs. To check that the Bi/Nb ratio had not changed essentially during the heating, a complete analysis was made on one sample (9 hours heating). The following values were obtained as the mean of three analyses: Bi: $68.0 \pm 0.6\%$, Nb: $14.2 \pm 0.6\%$, F: $3.7 \pm 0.2\%$.

The values calculated for $\text{Bi}_2\text{NbO}_5\text{F}$ are:

Bi: 68.5, Nb: 15.2%, F: 3.2%.

From these figures it seems probable that the formula of the compound is $\text{Bi}_2\text{NbO}_5\text{F}$.

$\text{Bi}_2\text{TaO}_5\text{F}$ was prepared in exactly the same way as $\text{Bi}_2\text{NbO}_5\text{F}$. No analysis was made since the powder photographs were similar to those of $\text{Bi}_2\text{NbO}_5\text{F}$ and niobium and tantalum compounds are usually isomorphous.

ARKIV FÖR KEMI. Bd 5 nr 4

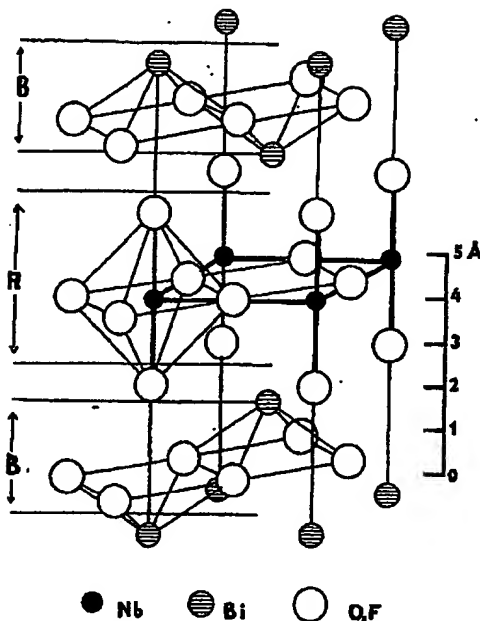


Fig. 1. One half of the unit cell of $\text{Bi}_2\text{NbO}_6\text{F}$. A denotes the region of $\text{Nb}(\text{O},\text{F})_6$ octahedra and B the $\text{Bi}_2(\text{O},\text{F})_2$ layers.

$\text{Bi}_2\text{TiO}_4\text{F}_2$: Mixtures of bismuth fluoride and titanium oxide in the mol ratio 2:1 (total 2.3 g) were heated in air at 640° for various lengths of time. The powder photographs obtained from samples heated for 3 or 5 hours could be interpreted by assuming a mixture of BiOF (2) and a phase whose cell dimensions were nearly the same as those of $\text{Bi}_2\text{NbO}_6\text{F}$. (See Table 2, where the reflexions from the BiOF phase are designated by b and those from the other phase by a). The fluorine contents of the mixed samples were found to be 6.4 % (5 hours) and 8.4 % (3 hours) but no variation of the cell size with the fluorine content was found. The calculated values are 7.8 % for BiOF and 6.7 % for $\text{Bi}_2\text{TiO}_4\text{F}_2$. From the original Bi/Ti ratio, from the fluorine analysis and from the similarity of the powder photographs with those of $\text{Bi}_2\text{NbO}_6\text{F}$ (Tables 1 and 2), it was concluded that the formula of the phase is $\text{Bi}_2\text{TiO}_4\text{F}_2$.

Methods of analysis: Fluorine. The samples were first decomposed by fusing with NaOH , and were then distilled with HClO_4 as described by WILLARD and WINTER (3). The distillate was titrated with $\text{Th}(\text{NO}_3)_4$ using Na-alizarinsulphonate as indicator.

Bismuth and Niobium. The samples were brought into solution, and niobium was determined as described in Scott's "Standard Methods" (4). Bismuth was first precipitated as Bi_2S_3 , which was then redissolved, converted to Bi_2O_3 and weighed as such.

Unit cells and space group

The dimensions of the unit cells were determined from powder photographs taken with focusing cameras of the Phragmén type (Tables 1 and 2). The radiation used

B. AURIVILLIUS, *The structure of $\text{Bi}_2\text{NbO}_5\text{F}$ and isomorphous compounds*

Table 2

Powder photographs of $\text{Bi}_2\text{TiO}_4\text{F}_2$ (mixed with BiOF) Cr K radiation ($\lambda_{\text{Cr K}_\alpha} = 2.2909 \text{ \AA}$). a denotes the $\text{Bi}_2\text{TiO}_4\text{F}_2$ phase and b the BiOF phase

hkl	phase	$10^4 \sin^2 \theta_{\text{calc}}$	$10^4 \sin^2 \theta_{\text{obs}}$	I_{obs}
101	a	957	941	vw
101	b	1270	1265	m
{103	a	1351		
{002	b	1352	1354	st
006	a	1771	1767	m
110	a	1816	1811	m
110	b	1864	1858	vw
112	a	2013	1999	w
105	a	2138	2132	w+
102	b	2284	2288	vw
114	a	2603	2601	m
—	—	—	3074	vw
112	b	3216	3231	w
107	a	3319	3320	vw
116	a	3587	3600	st
200	a	3631	3624	st
200	b	3728	3744	w
202	a	3828	3822	w
103	b	3974	3982	w
—	—	—	4352	vw
204	a	4418	4426	vw
211	a	4538	4590	w
—	—	—	4674	vw
{109	a	4893		
{113	b	4906	4904	st
{00 10	a	4919		
213	a	4982	4979	st
202	b	5080	5084	w
{206	a	5402		
{004	b	5408	5416	m+
215	a	5769	5788	m
212	b	6012	6025	m
104	b	6340	6353	w
{203	b	6770		
{208	a	6779	6786	m
10 11	a	6860	6869	m
217	a	6950	6950	vw
00 12	a	7084	7075	m
{220	a	7262		
{114	b	7272	7262	m
{220	b	7455		
{222	a	7459	7456	w
213	b	7702	7709	m
—	—	—	8049	vw
301	a	8210	8210	vw
—	—	—	8352	vw
{219	a	8524		
{20 10	a	8550	8524	st
303	a	8613	8603	m
301	b	8736	8725	w
222	b	8814	8807	w
11 12	a	8900	8900	m

was (be int

The The agrees calcul Zerc was n than l $h+k+$ Pow and fre

Bi_2N unit ce the ma for l od the Pat sity val here) sh of other position or 000. gave th No de For B meter. A occupy t was obt

ARKIV FÖR KEMI. Bd 5 nr 4

Table 2 (continued)

hkl	phase	$10^4 \sin^2 \theta_{\text{calc}}$	$10^4 \sin^2 \theta_{\text{obs}}$	I_{obs}
2 2 6	<i>a</i>	9033	9027	m
3 1 0	<i>a</i>	9078	9072	w
2 0 4	<i>b</i>	9136	9136	vw
3 1 2	<i>a</i>	9275	9272	m
3 1 0	<i>b</i>	9319	9319	w
{ 1 0 5	<i>b</i>	9382 }	9384	m
{ 3 0 5	<i>a</i>	9400 }		

was $Cr K$ ($\lambda_{Cr K_\alpha} = 2.2909 \text{ \AA}$). As mentioned above the powder photographs could be interpreted by assuming tetragonal unit cells; the cell dimensions are given below.

	a (Å)	c (Å)
$\text{Bi}_2\text{NbO}_5\text{F}$	3.835	16.63
$\text{Bi}_2\text{TaO}_5\text{F}$	3.829	16.64
$\text{Bi}_2\text{TiO}_4\text{F}_2$	3.802	16.33

The errors in these figures are estimated to be $\pm 0.1 \%$.

The observed density was 8.0 for $\text{Bi}_2\text{NbO}_5\text{F}$ (preparation with 2.8% F), which agrees fairly well with the assumption of 2 formula units per unit cell, giving a calculated density of 8.26.

Zero and first order Weissenberg photographs around the a axis were taken. There was nothing in the Weissenberg photographs to indicate a Laue symmetry lower than $D_{4h} - 4/mmm$. The only extinctions found were that h, k, l were absent for $h+k+l$ odd, which is characteristic of the space groups C_{4v}^9 , D_{2d}^9 , D_{2d}^{11} and D_{4h}^{11} .

Powder photographs only were taken of the compounds $\text{Bi}_2\text{TaO}_5\text{F}$ and $\text{Bi}_2\text{TiO}_4\text{F}_2$, and from these it was concluded that these substances are isomorphous with $\text{Bi}_2\text{NbO}_5\text{F}$.

Positions of the metal atoms

$\text{Bi}_2\text{NbO}_5\text{F}$: With 2 formula units per unit cell there are 4 Bi and 2 Nb atoms per unit cell. The intensities of the spots in the Weissenberg photographs seemed in the main to depend only on the l values. Thus for l even $I_{00l} \approx I_{11l} \approx I_{20l}$ etc. and for l odd: $I_{10l} \approx I_{21l} \approx I_{30l}$ etc. With these intensity values a good approximation of the Patterson-Harker function along $00z$ could be obtained by using only the intensity values of $h0l$ and $h1l$. The Patterson-Harker function thus calculated (not given here) showed only one, big, maximum, at $z=0.34$. This maximum, and the absence of others, could be explained only by assuming that 4 Bi atoms are situated at the positions $\pm 00z$ with $z=0.17$ or $z=0.33$, and the Nb atoms at the positions $00\frac{1}{2}$ or 000 . Arbitrarily choosing 000 as the position for Nb, trial and error calculations gave the value 0.325 for the Bi parameter.

No determination of z_{Bi} was made for $\text{Bi}_2\text{TaO}_5\text{F}$.

For $\text{Bi}_2\text{TiO}_4\text{F}_2$ the powder photograph data were used to determine the Bi parameter. Assuming the Ti atoms to be situated at 000 and the O and the F atoms to occupy the same positions as given below for $\text{Bi}_2\text{NbO}_5\text{F}$, the value $z_{Bi} = 0.327 \pm 0.006$ was obtained from trial and error calculations.

B. AURIVILLIUS, *The structure of $\text{Bi}_2\text{NbO}_5\text{F}$ and isomorphous compounds*Table 3
Weissenberg photographs of $\text{Bi}_2\text{NbO}_5\text{F}$

Zero layer

<i>l</i>	<i>h k</i>		0 0		2 0		4 0		<i>l</i>
			<i>I</i> _{calc}	<i>I</i> _{obs}	<i>I</i> _{calc}	<i>I</i> _{obs}	<i>I</i> _{calc}	<i>I</i> _{obs}	
0			—	—	170	vst	37	w	0
2			—	—	10	w	3	vw	2
4			0.3	—	0.04	—	0.05	—	4
6			220	vst	67	w	34	vw	6
8			12	w	5	vw	6	vvw	8
10			3	vw	2	—	2	—	10
12			44	st	26	w	86	st	12
14			15	m	11	w			14
16			10	w	10	w			16
18			16	m	28	m			18
20			22	m					20

<i>l</i>	<i>h k</i>		1 0		3 0		<i>l</i>
			<i>I</i> _{calc}	<i>I</i> _{obs}	<i>I</i> _{calc}	<i>I</i> _{obs}	
1			7	w	1	vw	1
3			270	vst	42	w	3
5			40	w	8	vw	5
7			1	—	0.2	—	7
9			75	m	30	vw	9
11			18	w	10	vw	11
13			3	vw	3	vw	13
15			20	m	19	m	15
17			12	w			17
19			14	w			19

Positions of the O and the F atoms

The positions of the O and the F atoms could not be distinguished either from the diffraction data, or from space considerations because of the similarity in the reflecting power and ionic radii of O^{2-} and F^- . The problem is therefore treated as though O and F were the same atomic species. In the following, the O and the F atoms are denoted by (O, F) and the discussion relates to $\text{Bi}_2\text{NbO}_5\text{F}$ for which z_{Bi} could be accurately determined from the Weissenberg photographs.

It seemed reasonable to assume that the Nb atoms are surrounded by a regular or nearly regular octahedron of (O, F) atoms with distances $\text{Nb}-(\text{O}, \text{F}) \approx 2.0 \text{ \AA}$. Neglecting the polar space group C_{4v}^9 , these conditions are fulfilled only if 4 (O, F) atoms, here called (O, F)₁, are situated at the positions $\pm 00z$ with $z \approx 0.12$, and 4 (O, F) atoms, (O, F)₂, at the positions $0\frac{1}{2}0, \frac{1}{2}00$. Assuming the distance (O, F)–(O, F) to be $\geq 2.5 \text{ \AA}$ and the distance $\text{Bi}-(\text{O}, \text{F})$ to be $\geq 2.2 \text{ \AA}$ there is only room for the remaining 4 (O, F) atoms, (O, F)₃, at the positions $0\frac{1}{2}\frac{1}{2}, \frac{1}{2}0\frac{1}{2}$.

The co

The pro
ties for th
derived asThe line
indicated b
the agree

ARKIV FÖR KEMI. Bd 5 nr 4

Tabl
photographs of BiNbO_5F $\text{Cu K}\alpha$ radiation

First layer

40		hk		11		31	
I_{calc}	I_{obs}	l		I_{calc}	I_{obs}	I_{calc}	I_{obs}
37	w	0		210	vst	36	w
3	vw	2		17	w	4	vvw
0.05	—	4		11	w	2	—
34	vw	6		110	m	33	w
6	vvw	8		27	vw	9	vw
.....							
2	—	10		2	vvw	1	—
		12		21	m	20	w
86	st	14		14	w	20	w
		16		5	w	17	w
		18		19	m		
		20		58	st		

hk		01		21		41	
l		I_{calc}	I_{obs}	I_{calc}	I_{obs}	I_{calc}	I_{obs}
1		7	—	2	vw	1	vvw
3		270	vst	74	m	33	w
5		40	m	13	w	7	—
7		1	—	0.3	—	0.2	—
.....							
9		75	vst	40	w	53	w
11		18	m	12	vvw	51	w
.....							
13		3	vw	3	vw		
15		20	m	19	m		
17		12	w	19	m		
19		14	w				

The coordination and distances in Å will be:

$$\begin{array}{ll}
 \text{Bi}-4 (\text{O}, \text{F})_3 = 2.29 & \text{Nb}-2 (\text{O}, \text{F})_1 = 2.0 \\
 \text{Bi}-4 (\text{O}, \text{F})_1 = 2.9 & \text{Nb}-4 (\text{O}, \text{F})_2 = 1.92 \\
 (\text{O}, \text{F})_3-4 (\text{O}, \text{F})_3 = 2.71 & (\text{O}, \text{F})_2-4 (\text{O}, \text{F})_2 = 2.71 \\
 (\text{O}, \text{F})_1-4 (\text{O}, \text{F})_3 = 2.9 & (\text{O}, \text{F})_1-4 (\text{O}, \text{F})_2 = 2.8
 \end{array}$$

The proposed structure is given in the summary. Calculated and observed intensities for the reflexions in the Weissenberg photographs are given in Table 3. I_{calc} is derived as follows:

$$I_{\text{calc}} = \frac{1 + \cos^2 2\theta}{1600 \cdot \sin 2\theta} \cdot F^2 \text{ where } F = \sum f \cos 2\pi(hx + ky + lz).$$

The lines of maximum absorption in the Weissenberg photographs (see 5) are indicated by dotted lines in Table 3. If the absorption effects are taken into account, the agreement between calculated and observed intensities is quite good.

either from the
arity in the re-
fore treated as
ae O and the F
F for which z_{Bi}
ed by a regular
(O, F) ≈ 2.0 Å
only if 4 (O, F)
th $z \approx 0.12$, and
distance (O, F)–
is only room for

B. AURIVILLIUS, *The structure of $\text{Bi}_2\text{NbO}_6\text{F}$ and isomorphous compounds*

Discussion of the structure

Even if the $(\text{O}, \text{F})_1$ atoms (see above) are assumed to occupy such a position that the distance $\text{Bi}-4(\text{O}, \text{F})_1$ is as small as possible [$z(\text{O}, \text{F})_1 = 0.15$, $(\text{O}, \text{F})_1 = (\text{O}, \text{F})_3 = 2.5$, $\text{Nb}-2(\text{O}, \text{F})_1 = 2.5$, $\text{Bi}-4(\text{O}, \text{F})_1 = 2.7$], the distance $\text{Bi}-4(\text{O}, \text{F})_1$ will still be much longer than the distance $\text{Bi}-4(\text{O}, \text{F})_3$. It therefore seems appropriate to describe the structure of $\text{Bi}_2\text{NbO}_6\text{F}$ as being built up of $\text{Bi}_2(\text{O}, \text{F})_2$ layers alternating with octahedral layers having the composition $\text{Nb}(\text{O}, \text{F})_4$, both layers being perpendicular to the c -axis. It might be pointed out that the structure of $\text{Bi}_2(\text{O}, \text{F})_2\text{Nb}(\text{O}, \text{F})_4$ is basically of the same type as the " X_1 structures", $\text{Me}_2\text{O}_2\text{X}$, previously investigated by SILLÉN (6). Thus the octahedral sheets $\text{Nb}(\text{O}, \text{F})_4$ correspond to single layers of halogen atoms, X , in $\text{Me}_2\text{O}_2\text{X}$.

Discussion of the distribution of the O and the F atoms

As seen above, the distance $\text{Bi}-4(\text{O}, \text{F})_3$ is 2.29 \AA for $\text{Bi}_2\text{NbO}_6\text{F}$. For $\text{Bi}_2\text{TiO}_6\text{F}$, the corresponding distance is calculated to be $2.26 \pm 0.06 \text{ \AA}$. These distances are very nearly the same as the corresponding distances, $\text{Bi}-4 \text{ O}$, within the Bi_2O_2 layers of other bismuth oxicompsounds (6). This need not, however, necessarily mean that the $\text{Bi}_2(\text{O}, \text{F})_2$ layers (see the figure) are free from F atoms, since compounds with $\text{Bi}_2(\text{O}, \text{F})_2$ layers which certainly contain F atoms have not been investigated hitherto, and thus the distances within such layers are unknown.

For the present it seems therefore best to make no special assumptions as to the distribution of the O and F atoms.

SUMMARY

The crystal structure of $\text{Bi}_2\text{NbO}_6\text{F}$ has been investigated by means of Weissenberg and powder photographs. From powder photographs the compounds $\text{Bi}_2\text{TaO}_6\text{F}$ and $\text{Bi}_2\text{TiO}_6\text{F}$ have been found to be isomorphous with $\text{Bi}_2\text{NbO}_6\text{F}$. The following structure is proposed for $\text{Bi}_2\text{NbO}_6\text{F}$:

$D_{4h}^{17} - I 4/mmm$		
$(000, \frac{1}{2}\frac{1}{2}\frac{1}{2}) +$		
2 Nb in 2 (a) :	000	
4 Bi in 4 (e) :	$\pm 00z$	$z = 0.325 \pm 0.001$
4 (O, F) ₁ in 4 (c) :	$0\frac{1}{2}0, \frac{1}{2}00$	
4 (O, F) ₃ in 4 (e) :	$\pm 00z$	$z = 0.12 \pm 0.01$
4 (O, F) ₂ in 4 (d) :	$0\frac{1}{2}\frac{1}{2}, \frac{1}{2}0\frac{1}{2}$	

The cell dimensions are $a = 3.835 \text{ \AA}$, $c = 16.63 \text{ \AA}$ for $\text{Bi}_2\text{NbO}_6\text{F}$. The positions of the metal atoms were determined from the diffraction data, those of the (O, F) atoms from space considerations. Although it does not seem improbable that O atoms alone occupy the positions $0\frac{1}{2}\frac{1}{2}, \frac{1}{2}0\frac{1}{2}$, Bi and O thus forming Bi_2O_2 layers as in other bismuth oxicompsounds, nothing can be definitely stated as to the distribution of the O and F atoms.

The structure is built up of quadratic $\text{Bi}_2(\text{O}, \text{F})_2$ layers alternating with octahedral sheets having the composition $\text{Nb}(\text{O}, \text{F})_4$ (see figure) and the formula might thus be written: $\text{Bi}_2(\text{O}, \text{F})_2\text{Nb}(\text{O}, \text{F})_4$. The structure is formally related to a series of

previo
represe

Univ

REF.
Mineral.
Ed. 5 (1
edited b
(1937) 4

ds

ARKIV FÖR KEMI. Bd 5 nr 4

previously investigated structures of general formula $Me_2O_2 (Me'_{m-1}R_mO_{3m+1})$ and represents the simplest case of this series, i.e. $m=1$.

University of Stockholm, Institute of Inorganic and Physical Chemistry, May 1952.

such a position
=0.15, (O, F)₁₋₄
3i-4 (O, F)₁ will
efore seems ap-
ip of Bi₂ (O, F)₁
Nb (O, F)₄, both
at the structure
ures", Me_2O_2X
(O, F)₄ correspond

REFERENCES. 1. Aurivillius, B., Arkiv Kemi 2 (1950) 519. — 2. —, Arkiv Kemi Mineral. Geol., 26 B (1948) no 2. — 3. Willard, H. H. and Winter, O. B., Ind. Eng. Chem. Anal. Ed. 5 (1933) 7. — 4. Standard Methods of Chemical Analysis by W. W. Scott, fifth edition, edited by N. H. Furman, New York 1925, p. 335 and p. 338. — 5. Wells, A. F., Z. Krist. 96 (1937) 451. — 6. Sillén, L. G., Dissert. Stockholm 1940.

toms.

For Bi₂TiO₄F₂
se distances are
within the Bi₂O₃
necessarily mean
ince compounds
een investigated

ptions as to the

of Weissenberg
s Bi₂TaO₅F and
following struc-

The positions of
e of the (O, F)
le that O atoms
Bi₂O₃ layers as
to the distribu-

with octahedral
ula might thus
l to a series of

Tryckt den 24 november 1952

Uppsala 1952. Almqvist & Wiksells Boktryckari AB

888

The content enclosed with or attached to this notice has been reproduced from that publication by permission of the copyright owner. It may not be further reproduced or publicly displayed without express permission of the copyright owner. Any unauthorized reproduction or use may subject you to financial and other penalties.

R dpmorris@us.ibm.com/--354936Daniel P. Morris

Copies: **1**

ORDER ARKIV FOER KEMI VOL 5

AUTHOR Aurivillius, B.,

AGE 39-EOA

AY

EAR 1952

SSN 03656128

DDEN BLK_02/17/05_0365-6128_307395

CHECKSUM 00090130048007110

CLLING 888

SERVICE REGULAR

INF. # BESG090130048-1

CONTACT Alma Gardner almag@us.ibm.com Phone 914-642-6811 Fax 914-642-6820

COMMENT

FAX*

dpmorris@us.ibm.com

Scan ID

**888**Alma Gardner
IBM InfoGate

LH, SU

Dept. 40L, L/2C908, MD/238
1133 Westchester Avenue
White Plains, NY 10604
USA

February 17, 2005



ØE

YV0939

888 T 3472

For questions about this order contact us at orderhelp@ieonline.com.

BRIEF ATTACHMENT Z

IN THE UNITED STATES PATENT AND TRADEMARK OFFICE

In re Patent Application of

Applicants: Bednorz et al.

Serial No.: 08/479,810

Filed: June 7, 1995

For: NEW SUPERCONDUCTIVE COMPOUNDS HAVING HIGH TRANSITION
TEMPERATURE, METHODS FOR THEIR USE AND PREPARATION

Date: March 1, 2005

Docket: YO987-074BZ

Group Art Unit: 1751

Examiner: M. Kopec

Commissioner for Patents
P.O. Box 1450
Alexandria, VA 22313-1450

FIRST SUPPLEMENTAL AMENDMENT

Sir:

In response to the Office Action dated July 28, 2004, please consider the
following:

ATTACHMENT Z

D. Hachwitz



Superconductivity

Charles P. Poole, Jr.

Horacio A. Farach

Richard J. Creswick

Department of Physics and Astronomy
University of South Carolina
Columbia, South Carolina



Academic Press

San Diego London Boston New York Sydney Tokyo Toronto

This book is printed on acid-free paper. (∞)

Copyright © 1995 by ACADEMIC PRESS

All Rights Reserved.

No part of this publication may be reproduced or transmitted in any form or by any means, electronic or mechanical, including photocopy, recording, or any information storage and retrieval system, without permission in writing from the publisher.

Academic Press

A Division of Harcourt Brace & Company

525 B Street, Suite 1900, San Diego, California 92101-4495

United Kingdom Edition published by

Academic Press Limited

24-28 Oval Road, London NW1 7DX

Library of Congress Cataloging-in-Publication Data

Poole, Charles P.

Superconductivity / by Charles P. Poole, Jr., Horacio A. Farach,

Richard J. Creswick.

p. cm.

Includes index.

ISBN 0-12-561455-1. -- ISBN 0-12-561456-X (pbk.)

I. superconductivity. I. Farach, Horacio A. II. Creswick,

Richard J. III. Title.

QC611.92.P66 1995

537.6'23--dc20

94-31853

CIP.

PRINTED IN THE UNITED STATES OF AMERICA

97 98 99 00 01 02 QW 9 8 7 6 5 4 3 2

Perovskite and Cuprate Crystallographic Structures

I. INTRODUCTION

Chapter 3 shows that the majority of single-element crystals have highly symmetrical structures, generally fcc or bcc, in which their physical properties are the same along the three crystallographic directions x , y , and z . The NaCl-type and A15 compounds are also cubic. Some compounds do have lower symmetries, showing that superconductivity is compatible with many different types of crystallographic structure, but higher symmetries are certainly more common. In this chapter we will describe the structures of the high-temperature superconductors, almost all of which are tetragonal or orthorhombic.

In Chapter 3, we also gave some examples of the role played by structure in determining the properties of superconductors. The highest transition tempera-

tures in alloys of transition metals are at the boundaries of instability between the bcc and hcp forms. The NaCl-type compounds have ordered vacancies on one or another lattice site. The magnetic and superconducting properties of the Chevrel phases depend on whether the large magnetic cations (i.e., positive ions) occupy eightfold sites surrounded by chalcogenide ions or whether the small magnetic ions occupy octahedral sites surrounded by Mo ions.

The structures described here are held together by electrons that form ionic or covalent bonds between the atoms. No account is taken of the conduction electrons, which are delocalized over the copper oxide planes and form Cooper pairs responsible for the superconducting properties below T_c . The following chapter will be devoted to explaining the role of these

conduction electrons within the frameworks of the Hubbard model and band theory. Whereas the present chapter describes atom positions in coordinate space, the following chapter relies on a reciprocal lattice elucidation of these same materials.

We begin with a description of perovskite and explain some reasons that perovskite undergoes various types of distortions. This prototype exhibits a number of characteristics that are common to the high-temperature superconducting cuprates (see Section V). We will emphasize the structural commonalities of these materials and make frequent comparisons between them. Our earlier work (Poole *et al.*, 1988) and the comprehensive review by Yvon and François (1989) may be consulted for more structural detail on the atom positions, interatomic spacings, site

and thallium high temperature superconductors (Medvedeva *et al.*, 1993).

We assume that all samples are well made and safely stored. Humidity can affect composition, and Garland (1988) found that storage of $\text{YBa}_2\text{Cu}_3\text{O}_{7-\delta}$ in 98% humidity exponentially decreased the diamagnetic susceptibility with a time constant of 22 days.

II. PEROVSKITES

Much has been written about the high-temperature superconductors being perovskite types, so we will begin by describing the structure of perovskites. The prototype compound barium titanate, BaTiO_3 , exists in three crystallographic forms with the following lattice constants and unit cell volumes (Wyckoff, 1964):

cubic:	$a = b = c = 4.0118 \text{ \AA}$	$V = 64.57 \text{ \AA}^3$	
tetragonal:	$a = b = 3.9947, c = 4.0336$	$V = 64.37 \text{ \AA}^3$	(7.1)
orthorhombic:	$a = 4.009\sqrt{2} \text{ \AA}, b = 4.018\sqrt{2} \text{ \AA}, c = 3.990 \text{ \AA}$	$V = 2(64.26) \text{ \AA}^3$	

symmetries, etc., of these compounds. There have been reports of superconductivity in certain other cuprate structures (e.g., Murphy *et al.*, 1987), but these will not be reported on in this chapter.

There is a related series of layered compounds $\text{Bi}_2\text{O}_2(M_{m-1}R_m\text{O}_{3m+1})$ called Aurivillius (1950, 1951, 1952) phases, with the 12-coordinated $M = \text{Ca}, \text{Sr}, \text{Ba}, \text{Bi}, \text{Pb}, \text{Cd}, \text{La}, \text{Sm}, \text{Sc}, \text{etc.}$, and the 6-coordinated transition metal $R = \text{Nb}, \text{Ti}, \text{Ta}, \text{W}, \text{Fe}, \text{etc.}$ The $m = 1$ compound Bi_2NbO_6 belongs to the same tetragonal space group $I4/mmm, D_{4h}^{17}$ as the lanthanum, bismuth,

For all three cases the crystallographic axes are mutually perpendicular. We will comment on each case in turn.

A. Cubic Form

Above 201°C barium titanate is cubic and the unit cell contains one formula unit BaTiO_3 with a titanium atom on each apex, a barium atom in the body center, and an oxygen atom on the center of each edge of the cube, as illustrated in Fig. 7.1. This corresponds to the barium atom, titanium atom, and three oxygen atoms being placed in positions with the following x, y , and z coordinates:

E site: Ti	$(0, 0, 0)$	Ti on apex	
F site: O	$(0, 0, \frac{1}{2}); (0, \frac{1}{2}, 0); (\frac{1}{2}, 0, 0)$	three oxygens	(7.2)
C site: Ba	$(\frac{1}{2}, \frac{1}{2}, \frac{1}{2})$	centered on edges	
		Ba in center.	

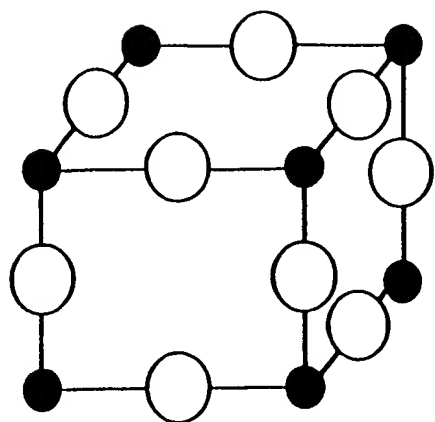


Figure 7.1 Barium titanate (BaTiO_3) perovskite cubic unit cell showing titanium (small black circles) at the vertices and oxygen (large white circles) at the edge-centered positions. Ba, not shown, is at the body center position (Poole *et al.*, 1988, p. 73).

The barium in the center has 12 nearest-neighbor oxygens, so we say that it is 12-fold coordinated, while the titanium on each apex has 6-fold (octahedral) coordination with the oxygens, as may be seen from the figure. (The notation *E* for edge, *F* for face, and *C* for center is adopted for reasons that will become clear in the discussion which follows.) Throughout this chapter we will assume that the *z*-axis is oriented vertically, so that the *x* and *y* axes lie in the horizontal plane.

Ordinarily, solid-state physics texts place the origin (0,0,0) of the perovskite unit cell at the barium site, with titanium in the center and the oxygens at the centers of the cube faces. Our choice of origin facilitates comparison with the structures of the oxide superconductors.

This structure is best understood in terms of the sizes of the atoms involved. The ionic radii of O^{2-} (1.32 Å) and Ba^{2+} (1.34 Å) are almost the same, as indicated in Table 7.1, and together they form a perfect fcc lattice with the smaller Ti^{4+} ions (0.68 Å) located in octahedral holes surrounded entirely by oxygens. The octahedral holes of a close-packed oxygen lattice have a radius of 0.545 Å; if these holes were empty the lattice constant would be $a = 3.73$ Å, as noted in Fig. 7.2a. Each

titanium pushes the surrounding oxygens outward, as shown in Fig. 7.2b, thereby increasing the lattice constant. When the titanium is replaced by a larger atom, the lattice constant expands further, as indicated by the data in the last column of Table 7.2. When Ba is replaced by the smaller Ca (0.99 Å) and Sr (1.12 Å) ions, by contrast, there is a corresponding decrease in the lattice constant, as indicated by the data in columns 3 and 4, respectively, of Table 7.2. All three alkaline earths, Ca, Sr, and Ba, appear prominently in the structures of 3 high-temperature superconductors.

B. Tetragonal Form

At room temperature barium titanate is tetragonal and the deviation from cubic, $(c - a)/\frac{1}{2}(c + a)$, is about 1%. All of the atoms have the same *x, y* coordinates as in the cubic case, but are shifted along the *z*-axis relative to each other by ≈ 0.1 Å, producing the puckered arrangement shown in Fig. 7.3. The distortions from the ideal structure are exaggerated in this sketch. The puckering bends the Ti-O-Ti group so that the Ti-O distance increases while the Ti-Ti distance remains almost

Table 7.1 Ionic Radii for Selected Elements^a

Small Small-Medium	Cu^{2+}	0.72 Å	Bi^{5+}	0.74 Å
	Cu^{+}	0.96 Å	Y^{3+}	0.94 Å
	Bi^{3+}	0.96 Å	Ti^{3+}	0.95 Å
	Ca^{2+}	0.99 Å	Bi^{3+}	0.96 Å
Medium-Large	Nd^{3+}	0.995 Å		
	Hg^{2+}	1.10 Å		
	Sr^{2+}	1.12 Å	La^{3+}	1.14 Å
	Pb^{2+}	1.20 Å	Ag^{+}	1.26 Å
Large	K^{+}	1.33 Å	O^{2-}	1.32 Å
	Ba^{2+}	1.34 Å	F^{-}	1.33 Å

^a See Table VI-2 of Poole *et al.* (1988) for a more extensive list.

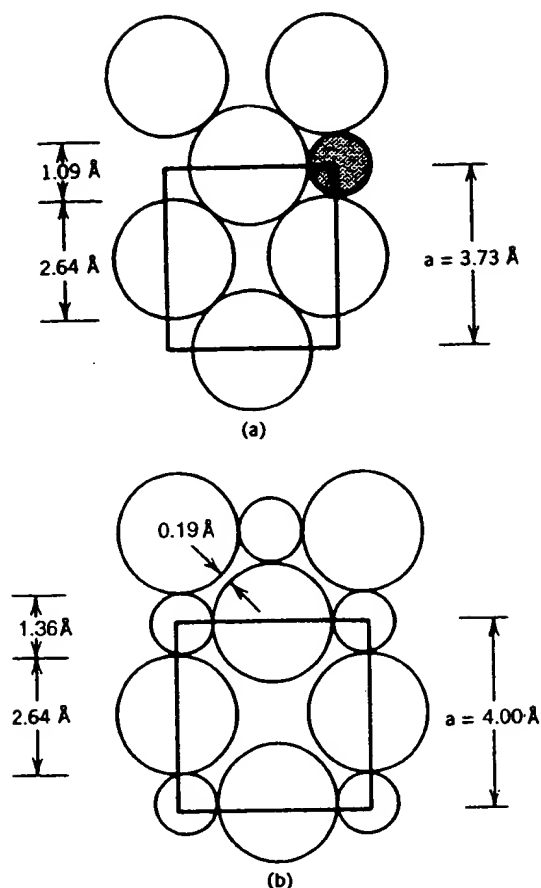


Figure 7.2 Cross section of the perovskite unit cell in the $z = 0$ plane showing (a) the size of the octahedral hole (shaded) between oxygens (large circles), and (b) oxygens pushed apart by the transition ions (small circles) in the hole sites. For each case the lattice constant is indicated on the right and the oxygen and hole sizes on the left (Poole *et al.*, 1988, p. 77).

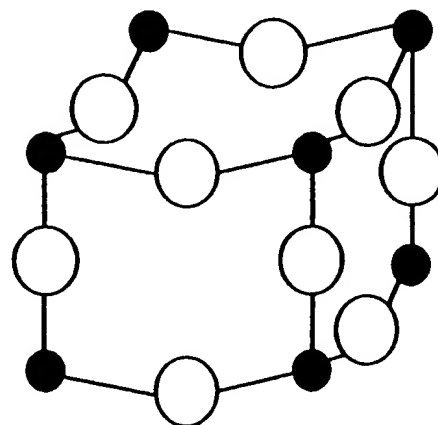


Figure 7.3 Perovskite tetragonal unit cell showing puckering of Ti-O layers that are perfectly flat in the cubic cell of Fig. 7.1. The notation of Fig. 7.1 is used (Poole *et al.*, 1988, p. 75).

the same. This has the effect of providing more room for the titanium atoms to fit in their lattice sites. We will see later that a similar puckering distortion occurs in the high-temperature superconductors as a way of providing space for the Cu atoms in the planes.

C. Orthorhombic Form

There are two principal ways in which a tetragonal structure distorts to form an orthorhombic phase. The first, shown at

Table 7.2 Dependence of Lattice Constants a of Selected Perovskites AMO_3 on Alkaline Earth A and Ionic Radius of Transition Metal Ion M^{+4} ; the Alkaline Earth Ionic Radii are 0.99 Å (Ca), 1.12 Å (Sr), and 1.34 Å (Ba)^a

Transitional metal	Transitional metal radius, Å	Lattice constant a , Å		
		Ca	Sr	Ba
Ti	0.68	3.84	3.91	4.01
Fe	—	—	3.87	4.01
Mo	0.70	—	3.98	4.04
Sn	0.71	3.92	4.03	4.12
Zr	0.79	4.02	4.10	4.19
Pb	0.84	—	—	4.27
Ce	0.94	3.85	4.27	4.40
Th	1.02	4.37	4.42	4.80

^a Data from Wyckoff (1964, pp. 391ff).

the top of Fig. 7.4, is for the b -axis to stretch relative to the a -axis, resulting in the formation of a rectangle. The second, shown at the bottom of the figure, is for one diagonal of the ab square to stretch and the other diagonal to compress, resulting in the formation of a rhombus. The two diagonals are perpendicular, rotated by 45° relative to the original axes, and become the a' , b' dimensions of the new orthorhombic unit cell, as shown in Fig. 7.5. These a' , b' lattice constants are $\approx \sqrt{2}$ times longer than the original constants, so that the volume of the unit cell roughly doubles; thus, it contains exactly twice as many atoms. (The same $\sqrt{2}$ factor appears in Eq. 7.1 in our discussion of the lattice constants for the orthorhombic form of barium titanate.)

When barium titanate is cooled below 5°C it undergoes a diagonal- or rhombal-type distortion. The atoms have the same z coordinates ($z=0$ or $\frac{1}{2}$) as in the cubic phase, so the distortion occurs entirely in the x, y -plane, with no puckering of the atoms. The deviation from tetragonality, as

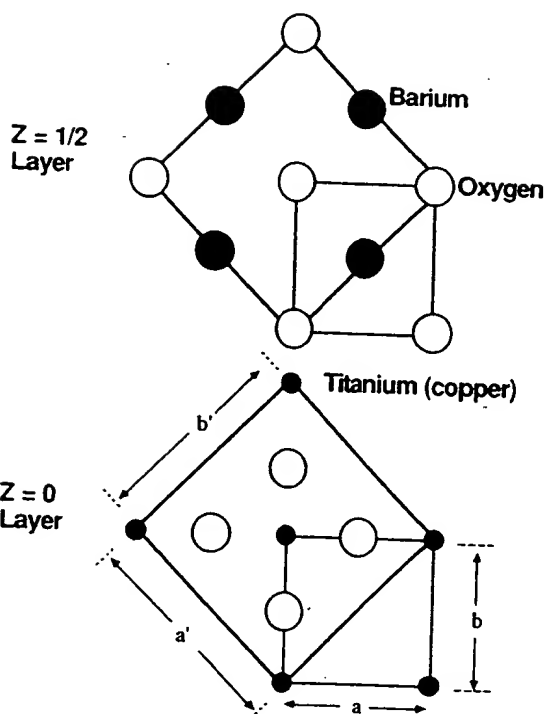


Figure 7.5 Rhombal expansion of monomolecular tetragonal unit cell (small squares, lower right) to bimolecular orthorhombic unit cell (large squares) with new axes 45° relative to the old axes. The atom positions are shown for the $z=0$ and $z=\frac{1}{2}$ layers (Poole *et al.*, 1988, p. 76).

given by the percentage of anisotropy,

$$\% \text{ ANIS} = \frac{100|b-a|}{\frac{1}{2}(b+a)} = 0.22\%, \quad (7.3)$$

is less than that of most orthorhombic copper oxide superconductors. We see from Fig. 7.5 that in the cubic phase the oxygen atoms in the $z=0$ plane are separated by 0.19 \AA . The rhombal distortion increases this O-O separation in one direction and decreases it in the other, in the manner indicated in Fig. 7.6a, to produce the Ti nearest-neighbor configuration shown in Fig. 7.6b. This arrangement helps to fit the titanium into its lattice site.

The transformation from tetragonal to orthorhombic is generally of the rhombal type for $(\text{La}_{1-x}\text{Sr}_x)_2\text{CuO}_4$ and of the rectangular type for $\text{YBa}_2\text{Cu}_3\text{O}_{7-\delta}$.

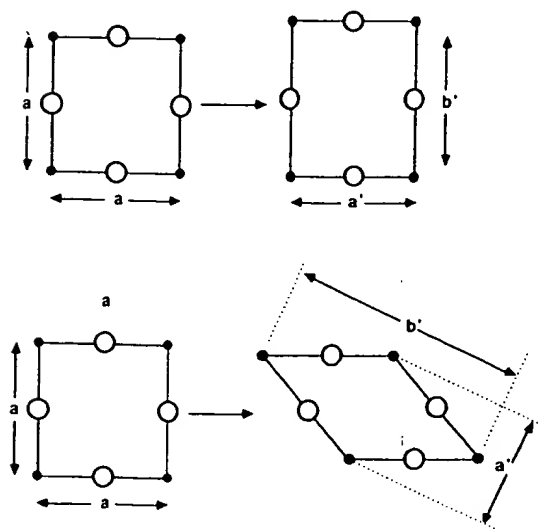


Figure 7.4 Rectangular- (top) and rhombal- (bottom) type distortions of a two-dimensional square unit cell of width a (Poole *et al.*, 1989).

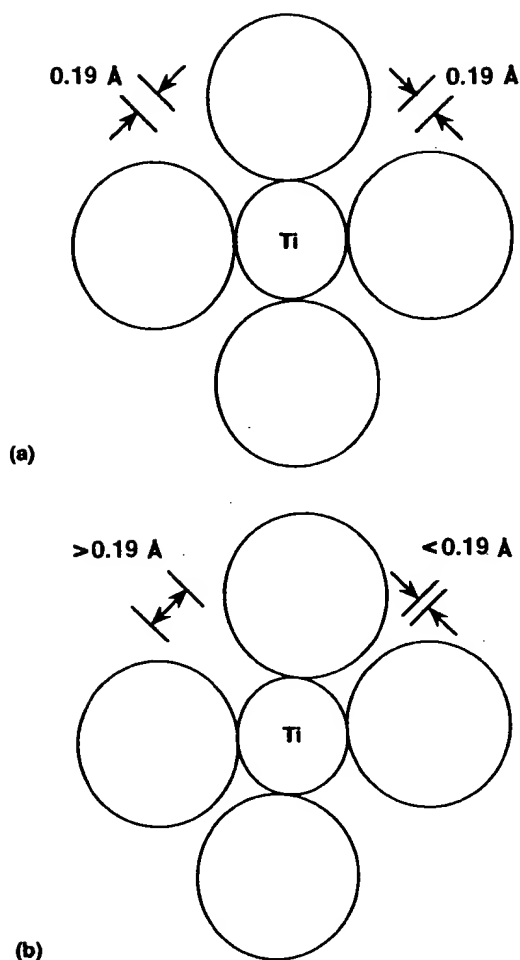


Figure 7.6 Shift of the oxygens in the a, b -plane around the titanium atom of perovskite from the room-temperature tetragonal (and cubic) configuration (a) to the rhombal configuration (b) of its low-temperature orthorhombic structure.

D. Planar Representation

Another way of picturing the structure of perovskite is to think of the atoms as forming horizontal planes. If we adopt the notation [E F C] to designate the occupation of the E, F, and C sites, the sketches of perovskite presented in Figs. 7.1 and 7.3 follow the scheme

$$\begin{array}{lll}
 z = 1 & [\text{TiO}_2^-] & \text{Ti at E, O at two F sites} \\
 z = \frac{1}{2} & [\text{O}-\text{Ba}] & \text{O at E, Ba at C} \\
 z = 0 & [\text{TiO}_2^-] & \text{Ti at E, O at two F sites.}
 \end{array} \quad (7.4)$$

The planes at the heights $z = 0, \frac{1}{2},$ and 1 can be labeled using this notation. The

usefulness of this labeling scheme will be clarified in Section V.

This completes our treatment of the structure of perovskite. We encountered many features that we will meet again in the analogous superconductor cases, and established notation that will be useful in describing the structure of the cuprates. However, before proceeding we present details about a cubic and a close-to-cubic perovskite superconductor in the following two sections.

III. CUBIC BARIUM POTASSIUM BISMUTH OXIDE

The compound



which forms for $x > 0.25$, crystallizes in the cubic perovskite structure with $a = 4.29 \text{ \AA}$ (Cava *et al.*, 1988; Jin *et al.*, 1992; Mattheiss *et al.*, 1988). K^+ ions replace some of the Ba^{2+} ions in the C site, and Bi ions occupy the E sites of Eq. (7.2) (Hinks *et al.*, 1988b; Kwei *et al.*, 1989; Pei *et al.*, 1990; Salem-Sugui *et al.*, 1991; Schneemeyer *et al.*, 1988). Some oxygen sites are vacant, as indicated by y . Hinks *et al.* (1989) and Pei *et al.* (1990) determined the structural phase diagram (cf. Kuentzler *et al.*, 1991; Zubkus *et al.*, 1991). We should note from Table 7.1 that the potassium (1.33 \AA) and barium (1.32 \AA) ions are almost the same size, and that Bi^{5+} (0.74 \AA) is close to Ti^{4+} (0.68 \AA). Bismuth represents a mixture of the valence states Bi^{3+} and Bi^{5+} which share the Ti^{4+} site in a proportion that depends on x and y . The larger size (0.96 \AA) of the Bi^{3+} ion causes the lattice constant a to expand 7% beyond its cubic BaTiO_3 value. Oxygen vacancies help to compensate for the larger size of Bi^{3+} .

It is noteworthy that $\text{Ba}_{1-x}\text{K}_x\text{BiO}_{3-y}$ becomes superconducting at a temperature ($\approx 40 \text{ K}$ for $x \approx 0.4$) that is higher than the T_c of all of the A15 compounds. This compound, which has no copper, has

been widely studied in the quest for clues that would elucidate the mechanism of high-temperature superconductivity. Features of $\text{Ba}_{1-x}\text{K}_x\text{BiO}_{3-y}$, such as the fact that it contains a variable valence state ion and utilizes oxygen vacancies to achieve charge compensation, reappear in the high-temperature superconducting compounds.

IV. BARIUM LEAD BISMUTH OXIDE

In 1983 Mattheiss and Hamann referred to the 1975 "discovery by Sleight *et al.* of high-temperature superconductivity" in the compound $\text{BaPb}_{1-x}\text{Bi}_x\text{O}_3$ in the composition range $0.05 \leq x \leq 0.3$ with T_c up to 13 K. Many consider this system, which disproportionates $2\text{Bi}^{4+} \rightarrow \text{Bi}^{3+} + \text{Bi}^{5+}$ in going from the metallic to the semiconducting state, as a predecessor to the LaSrCuO system.

The metallic compound BaPbO_3 is a cubic perovskite with the relatively large lattice constant (Wyckoff, 1964; cf. Nitta *et al.*, 1965; Shannon and Bierstedt, 1970) listed in Table 7.3. At room temperature semiconducting BaBiO_3 is monoclinic ($a \approx b \approx c/\sqrt{2}$, $\beta = 90.17^\circ$), but close to orthorhombic (Chaillout *et al.*, 1985; Cox and Sleight, 1976, 1979; cf. Federici *et al.*, 1990; Jeon *et al.*, 1990; Shen *et al.*, 1989). These two compounds form a solid solution series $\text{BaPb}_{1-x}\text{Bi}_x\text{O}_3$ involving cubic, tetragonal, orthorhombic, and monoclinic modifications. Superconductivity appears in the tetragonal phase, and the metal-to-insulator transition occurs at the tetragonal-to-orthorhombic phase boundary $x \approx 0.35$ (Gilbert *et al.*, 1978; Koyama and Ishimaru, 1992; Mattheiss, 1990; Mattheiss and Hamann, 1983; Sleight, 1987; cf. Bansil *et al.*, 1991; Ekino and Akimitsu, 1989a, b; Papaconstantopoulos *et al.*, 1989).

The compound resembles



with its variable Bi valence states, but it differs in not exhibiting superconductivity in the cubic phase.

V. PEROVSKITE-TYPE SUPERCONDUCTING STRUCTURES

In their first report on high-temperature superconductors Bednorz and Müller (1986) referred to their samples as "metallic, oxygen-deficient ... perovskite-like mixed-valence copper compounds." Subsequent work has confirmed that the new superconductors do indeed possess these characteristics.

In the oxide superconductors Cu^{2+} replaces the Ti^{4+} of perovskite, and in most cases the TiO_2 -perovskite layering is retained as a CuO_2 layering with two oxygens per copper. Because of this feature of CuO_2 layers, which is common to all of the high-temperature superconductors, such superconductors exhibit a uniform lattice size in the a, b -plane, as the data in Table 7.3 demonstrate. The compound BaCuO_3 does not occur because the Cu^{4+} ion does not form, but this valence constraint is overcome by replacement of Ba^{2+} by a trivalent ion, such as La^{3+} or Y^{3+} , by a reduction in the oxygen content, or by both. The result is a set of "layers" containing only one oxygen per cation located between each pair of CuO_2 layers, or none at all. Each high-temperature superconductor has a unique sequence of layers.

We saw from Eq. (7.2) that each atom in perovskite is located in one of three types of sites. In like manner, each atom at the height z in a high-temperature superconductor occupies either an Edge (E) site on the edge $(0, 0, z)$, a Face (F) site on the midline of a face $((0, \frac{1}{2}, z)$ or $(\frac{1}{2}, 0, z)$ or both), or a Centered (C) site centered within the unit cell on the z -axis $(\frac{1}{2}, \frac{1}{2}, z)$. The site occupancy notation [E F C] is used because many cuprates contain a succession of $[\text{Cu O}_2 -]$ and $[- \text{O}_2 \text{Cu}]$ layers in which the Cu atom switches between edge and centered sites, with the oxygens

Table 7.3 Crystallographic Characteristics of Oxide Superconducting and Related Compounds^a

Compound	Symbol	Symm	Type	Enlarg.	Form. units	a_0 (Å)	c_0 (Å)	c_0/Cu	%Anis	T_c (K)	Comments
BaTiO ₃	—	C	A	1	1	4.012	4.012	—	0	—	$T > 200^\circ\text{C}$
BaTiO ₃	—	T	A	1	1	3.995	4.03	—	0	—	20°C
BaTiO ₃	—	O	A	$\sqrt{2}$	2	$4.013\sqrt{2}$	3.990	—	0.23	—	$T < 5^\circ\text{C}$
BaPbO ₃	—	C	A	1	1	4.273	4.273	—	0	0.4	
BaPb _{0.7} Bi _{0.3} O ₃	—	T	S	$\sqrt{2}$	4	$4.286\sqrt{2}$	4.304	—	0	12	
BaBiO ₃	—	M	A	$\sqrt{2}$	2	$4.355\sqrt{2}$	4.335	—	0.13	—	$\beta = 90.17^\circ$
Ba _{0.6} K _{0.4} BiO ₃	—	C	A	1	1	4.293	4.293	—	0	30	
La ₂ CuO ₄	0201	T	S	1	2	3.81	13.18	6.59	0	35	Sr, doped
La ₂ CuO ₄	0201	O	S	$\sqrt{2}$	4	$3.960\sqrt{2}$	13.18	6.59	6.85	35	Sr, doped
YBa ₂ Cu ₃ O ₈	0213	T	A	1	1	3.902	11.94	3.98	0	—	
YBa ₂ Cu ₃ O ₇	0213	O	A	1	1	3.855	11.68	3.89	1.43	92	
Bi ₂ Sr ₂ CaCu ₂ O ₈	2212	T	S	$5\sqrt{2}$	20	$3.81\sqrt{2}$	30.6	7.65	0	84	
Bi ₂ Sr ₂ Ca ₂ Cu ₃ O ₁₀	2223	O	S	$5\sqrt{2}$	20	$3.83\sqrt{2}$	37	6.17	0.57	110	
Tl ₂ Ba ₂ CuO ₆	2201	T	S	1	2	3.83	23.24	11.6	0	90	
Tl ₂ Ba ₂ CaCu ₂ O ₈	2212	T	S	1	2	3.85	29.4	7.35	0	110	
Tl ₂ Ba ₂ Ca ₂ Cu ₃ O ₁₀	2223	T	S	1	2	3.85	35.88	5.98		125	
TlBa ₂ CuO ₅	1201		A	1	1		9.5	9.5		< 17	
TlBa ₂ CaCu ₂ O ₇	1212		A	1	1		12.7	6.35		91	
TlBa ₂ Ca ₂ Cu ₃ O ₉	1223		A	1	1		15.9	5.3		116	
TlBa ₂ Ca ₃ Cu ₄ O ₁₁	1234		A	1	1		19.1	4.78		122	
TlBa ₂ Ca ₄ Cu ₅ O ₁₃	1245		A	1	1		22.3	4.46		< 120	
HgBa ₂ CuO ₄	1201	T	A	1	1	3.86	9.5	9.5		95	
HgBa ₂ CaCu ₂ O ₆	1212	T	A	1	1	3.86	12.6	6.3		122	
HgBa ₂ Ca ₂ Cu ₃ O ₈	1223	T	A	1	1	3.86	17.7	5.2		133	

^a Symbol, symmetry (cubic C, tetragonal T, orthorhombic O, monoclinic M); type (aligned A, staggered S); enlargement in a , b -plane (diagonal distortion $\sqrt{2}$, superlattice 5); formula units per unit cell; lattice parameters (a_0 , c_0 , c_0 , and c_0 per Cu ion); % anisotropy; and transition temperature T_c . For the orthorhombic compounds tabulated values of a_0 are averages of a_0 and b_0 .

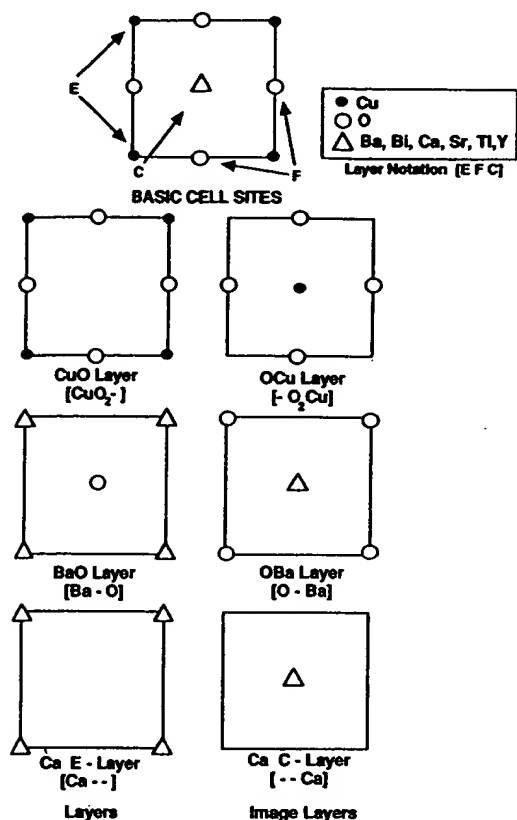


Figure 7.7 Types of atom positions in the layers of a high-temperature superconductor structure, using the edge, face, center notation $[E F C]$. Typical site occupancies are given in the upper right (Poole *et al.*, 1989).

remaining at their face positions. Similar alternations in position take place with Ba, O, and Ca layers, as illustrated in Fig. 7.7.

Hauck *et al.* (1991) proposed a classification of superconducting oxide structures in terms of the sequence (1) superconducting layers $[\text{Cu O}_2^-]$ and $[-\text{O}_2 \text{ Cu}]$, (2) insulating layers, such as $[\text{Y} - -]$ or $[- - \text{Ca}]$, and (3) hole-donating layers, such as $[\text{Cu O}^b -]$ or $[\text{Bi} - \text{O}]$.

The high-temperature superconductor compounds have a horizontal reflection plane (\perp to z) called σ_h at the center of the unit cell and another σ_h reflection plane at the top (and bottom). This means that every plane of atoms in the lower half of the cell at the height z is duplicated in the upper half at the height $1-z$. Such atoms, of course, appear twice in the unit cell, while atoms right on the symmetry planes only occur once since they cannot be reflected. Figure 7.8 shows a $[\text{Cu O}_2^-]$ plane at a height z reflected to the height $1-z$. Note how the puckering preserves the reflection symmetry operation. Superconductors that have this reflection plane, but lack end-centering and body-centering op-

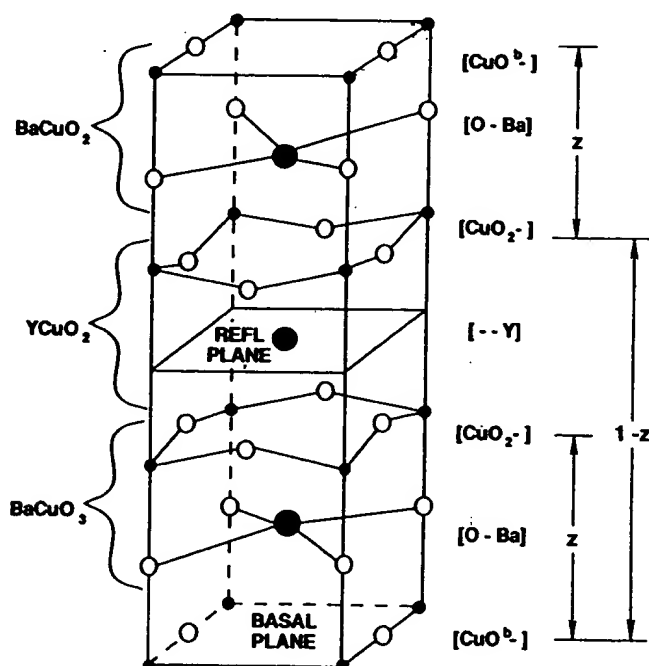


Figure 7.8 Unit cell of $\text{YBa}_2\text{Cu}_3\text{O}_7$ showing the molecular groupings, reflection plane, and layer types.

erations (see Section VII), are called *aligned* because all of their copper atoms are of one type; either all on the edge $(0,0,z)$ in E positions or all centered $(\frac{1}{2}, \frac{1}{2}, z)$ at C sites. In other words, they all lie one above the other on the same vertical lines, as do the Cu ions in Fig. 7.8.

VI. ALIGNED $\text{YBa}_2\text{Cu}_3\text{O}_7$

The compound $\text{YBa}_2\text{Cu}_3\text{O}_7$, sometimes called YBaCuO or the 123 compound, in its orthorhombic form is a superconductor below the transition temperature $T_c \approx 92$ K. Figure 7.8 sketches the locations of the atoms, Fig. 7.9 shows the arrangement of the copper oxide planes, Fig. 7.10 provides more details on the unit cell, and Table 7.4 lists the atom positions and unit cell dimensions (Benoit *et al.*, 1987; Capponi *et al.*, 1987; Hazen *et al.*, 1987; Jorgensen *et al.*, 1987; Le Page *et al.*, 1987; Siegrist *et al.*, 1987; Yan and Blanchin,

1991; see also Schuller *et al.*, 1987). Considered as a perovskite derivative, it can be looked upon as a stacking of three perovskite units BaCuO_3 , YCuO_2 , and BaCuO_2 , two of them with a missing oxygen, and this explains why $c \approx 3a$. It is, however, more useful to discuss the compound from the viewpoint of its planar structure.

A. Copper Oxide Planes

We see from Fig. 7.9 that three planes containing Cu and O are sandwiched between two planes containing Ba and O and one plane containing Y. The layering scheme is given on the right side of Fig. 7.8, where the superscript b on O indicates that the oxygen lies along the b -axis, as shown. The atoms are puckered in the two $[\text{Cu O}_2^-]$ planes that have the $[- - \text{Y}]$ plane between them. The third copper oxide plane $[\text{Cu O}^b -]$, often referred to as

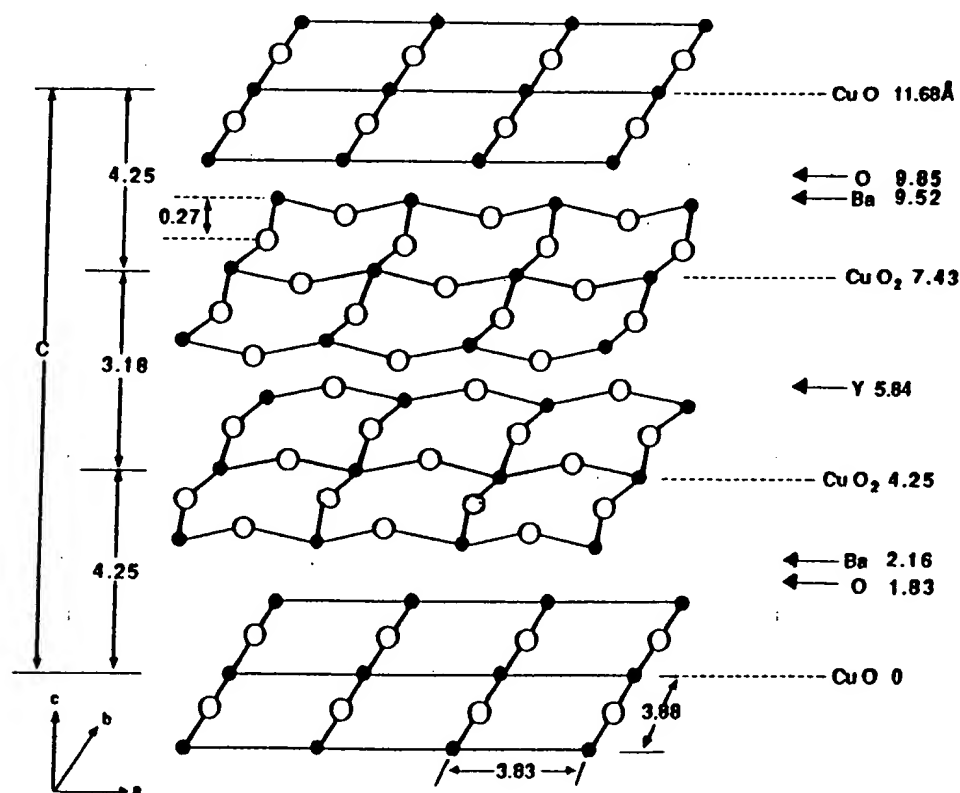


Figure 7.9 Layering scheme of orthorhombic $\text{YBa}_2\text{Cu}_3\text{O}_7$ with the puckering indicated. The layers are perpendicular to the c -axis (Poole *et al.*, 1988, p. 101).

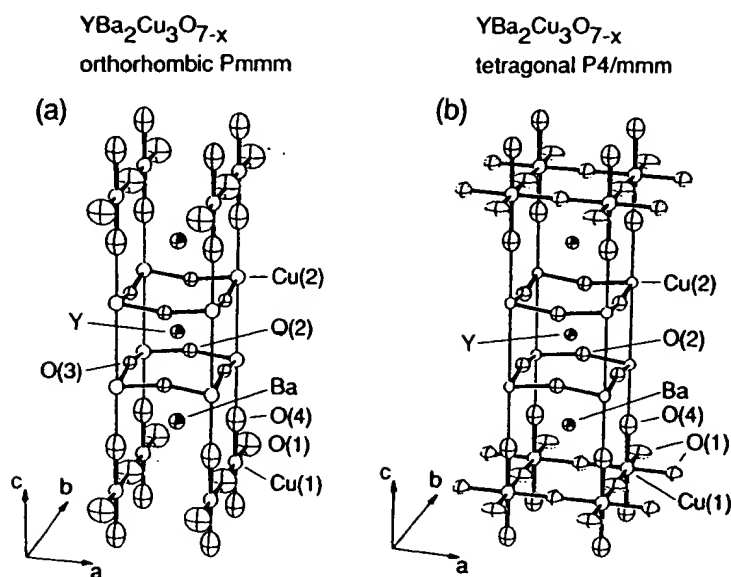


Figure 7.10 Sketches of the superconducting orthorhombic (left) and nonsuperconducting tetragonal (right) YBaCuO unit cells. Thermal vibration ellipsoids are shown for the atoms. In the tetragonal form the oxygen atoms are randomly dispersed over the basal plane sites (Jorgensen *et al.*, 1987a,b; also see Schuller *et al.*, 1987).

Table 7.4 Normalized Atom Positions in the $\text{YBa}_2\text{Cu}_3\text{O}_7$ Orthorhombic Unit Cell (dimensions $a=3.83 \text{ \AA}$, $b=3.88 \text{ \AA}$, and $c=11.68 \text{ \AA}$)

Layer	Atom	x	y	z
[Cu O -]	Cu(1)	0	0	1
	O(1)	0	$\frac{1}{2}$	1
[O - Ba]	O(4)	0	0	0.8432
	Ba	$\frac{1}{2}$	$\frac{1}{2}$	0.8146
[Cu O ₂ -]	Cu(2)	0	0	0.6445
	O(3)	0	$\frac{1}{2}$	0.6219
	O(2)	$\frac{1}{2}$	0	0.6210
[- - Y]	Y	$\frac{1}{2}$	$\frac{1}{2}$	$\frac{1}{2}$
[Cu O ₂ -]	O(2)	$\frac{1}{2}$	0	0.3790
	O(3)	0	$\frac{1}{2}$	0.3781
	Cu(2)	0	0	0.3555
[O - Ba]	Ba	$\frac{1}{2}$	$\frac{1}{2}$	0.1854
	O(4)	0	0	0.1568
	O(1)	0	$\frac{1}{2}$	0
[Cu O -]	Cu(1)	0	0	0

"the chains," consists of $-\text{Cu}-\text{O}-\text{Cu}-\text{O}-$ chains along the b axis in lines that are perfectly straight because they are in a horizontal reflection plane σ_h ; where no puckering can occur. Note that, according to the figures, the copper atoms are all stacked one above the other on edge (E) sites, as expected for an aligned-type superconductor. Both the copper oxide planes and the chains contribute to the superconducting properties.

B. Copper Coordination

Now that we have described the planar structure of YBaCuO it will be instructive to examine the local environment of each copper ion. The chain copper ion $\text{Cu}(1)$ is square planar-coordinated and the two coppers $\text{Cu}(2)$ and $\text{Cu}(3)$ in the plane exhibit fivefold pyramidal coordination, as indicated in Fig. 7.11. The ellipsoids at the atom positions of Fig. 7.10 provide a measure of the thermal vibrational motion which the atoms experience, since the amplitudes of the atomic vibrations are indicated by the relative size of each of the ellipsoids.

C. Stacking Rules

The atoms arrange themselves in the various planes in such a way as to enable them to stack one above the other in an efficient manner, with very little interference from neighboring atoms. Steric effects prevent large atoms such as Ba (1.34 Å) and O (1.32 Å) from overcrowding a layer or from aligning directly on top of each other in adjacent layers. In many cuprates stacking occurs in accordance with the following two empirical rules:

1. Metal ions occupy either edge or centered sites, and in adjacent layers alternate between E and C sites.
2. Oxygens are found in any type of site, but they occupy only one type in a particular layer, and in adjacent layers they are on different types of sites.

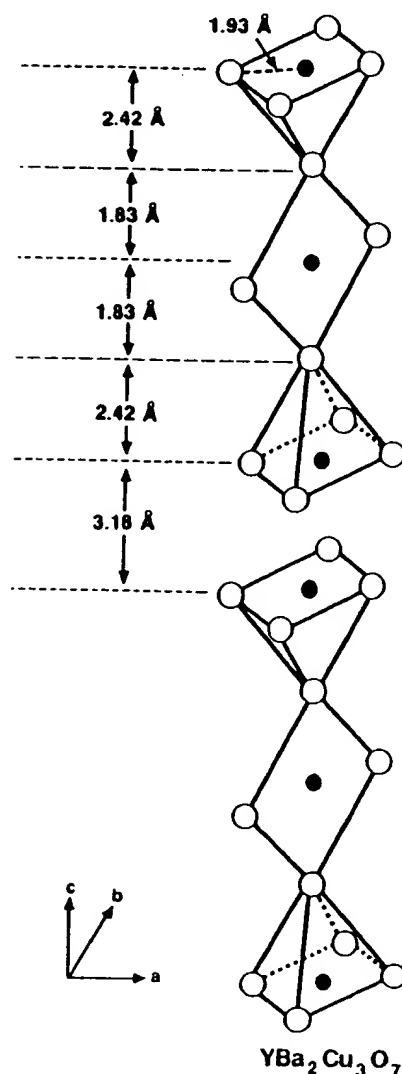


Figure 7.11 Stacking of pyramid, square-planar, and inverted pyramid groups along the c -axis of orthorhombic $\text{YBa}_2\text{Cu}_3\text{O}_7$ (adapted from Poole *et al.*, 1988, p. 100).

Minor adjustments to make more room can be brought about by puckering or by distorting from tetragonal to orthorhombic.

D. Crystallographic Phases

The $\text{YBa}_2\text{Cu}_3\text{O}_{7-\delta}$ compound comes in tetragonal and orthorhombic varieties, as shown in Fig. 7.10, and it is the latter phase which is ordinarily superconducting. In the tetragonal phase the oxygen sites in the chain layer are about half occupied

VI.
in
the
-C
oxy
cat
tha
of
Inc
cau
can
the
goe
750-
ous
pou
atur
thro
(Rot
is lo
phas
at at
thorh

1.0
0.8
0.6
0.4
0.2
0.0
0
Fractional Site Occupancy

Figure 7
(bottom)
the oxyg
right) fo
range 0-
age of th
Jorgenser
see also I

in a random or disordered manner, and in the orthorhombic phase are ordered into $-\text{Cu}-\text{O}-$ chains along the b direction. The oxygen vacancy along the a direction causes the unit cell to compress slightly so that $a < b$, and the resulting distortion is of the rectangular type shown in Fig. 7.4a. Increasing the oxygen content so that $\delta < 0$ causes oxygens to begin occupying the vacant sites along a . Superlattice ordering of the chains is responsible for the phase that goes superconducting at 60 K.

YBaCuO is prepared by heating in the 750–900°C range in the presence of various concentrations of oxygen. The compound is tetragonal at the highest temperatures, increases its oxygen content through oxygen uptake and diffusion (Rothman *et al.*, 1991) as the temperature is lowered, and undergoes a second-order phase transition of the order–disorder type at about 700°C to the low-temperature orthorhombic phase, as indicated in Fig. 7.12

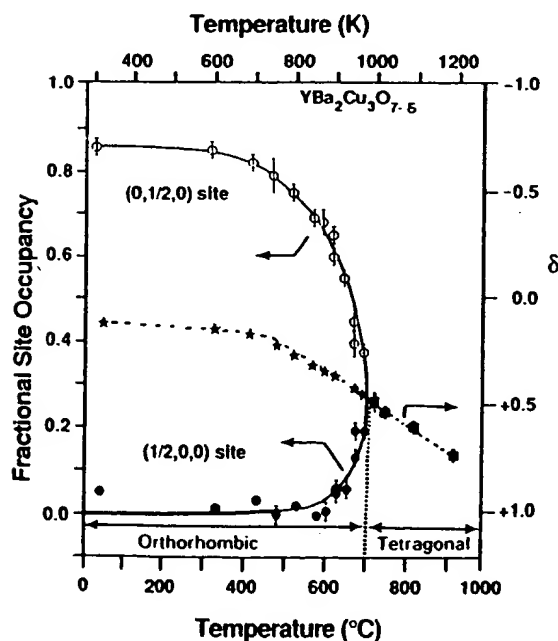


Figure 7.12 Fractional occupancies of the $(\frac{1}{2}, 0, 0)$ (bottom) and $(0, \frac{1}{2}, 0)$ (top) sites (scale on left), and the oxygen content parameter δ (center, scale on right) for quench temperatures of YBaCuO in the range 0–1000°C. The δ parameter curve is the average of the two site-occupancy curves (adapted from Jorgensen *et al.*, 1987a; also see Schuller *et al.*, 1987; see also Poole *et al.*, 1988).

(Jorgensen *et al.*, 1987, 1990; Schuller *et al.*, 1987; cf. Beyers and Ahn, 1991; Metzger *et al.*, 1993; Fig. 8). Quenching by rapid cooling from a high temperature can produce at room temperature the tetragonal phase sketched on the right side of Fig. 7.10, and slow annealing favors the orthorhombic phase on the left. Figure 7.12 shows the fractional site occupancy of the oxygens in the chain site $(0, \frac{1}{2}, 0)$ as a function of the temperature in an oxygen atmosphere. A sample stored under sealed conditions exhibited no degradation in structure or change in T_c four years later (Sequeira *et al.*, 1992). Ultra-thin films tend to be tetragonal (Streiffer *et al.*, 1991).

E. Charge Distribution

Information on the charge distributions around atoms in conductors can be obtained from knowledge of their energy bands (see description in Chapter 8). This is most easily accomplished by carrying out a Fourier-type mathematical transformation between the reciprocal k_x, k_y, k_z -space (cf. Chapter 8, Section II) in which the energy bands are plotted and the coordinate x, y, z -space, where the charge is distributed. We will present the results obtained for $\text{YBa}_2\text{Cu}_3\text{O}_7$ in the three vertical symmetry planes (x, z , y, z , and diagonal), all containing the z -axis through the origin, shown shaded in the unit cell of Fig. 7.13.

Contour plots of the charge density of the valence electrons in these planes are sketched in Fig. 7.14. The high density at the Y^{3+} and Ba^{2+} sites and the lack of contours around these sites together indicate that these atoms are almost completely ionized, with charges of +3 and +2, respectively. It also shows that these ions are decoupled from the planes above and below. This accounts for the magnetic isolation of the Y site whereby magnetic ions substituted for yttrium do not interfere with the superconducting properties. In contrast, the contours surrounding the Cu and O ions are not characteristic of an

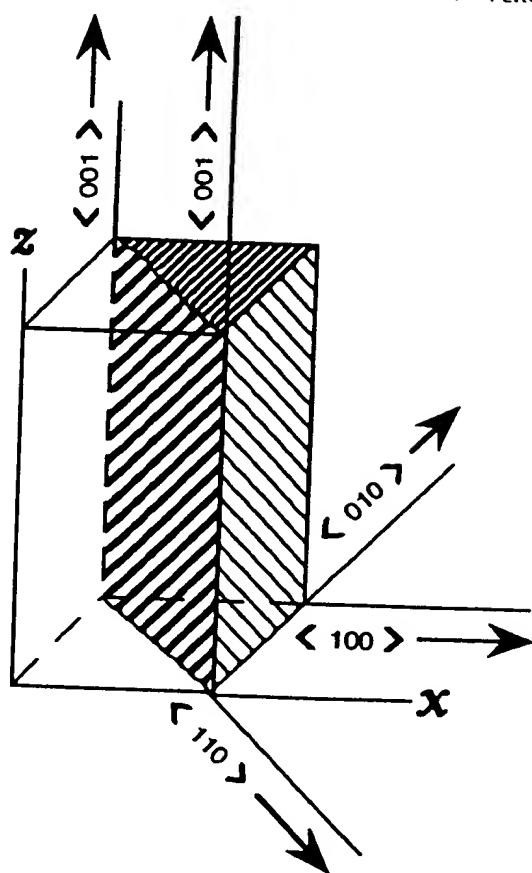


Figure 7.13 Three vertical crystallographic planes (x, z , y, z , and diagonal) of a tetragonal unit cell of $\text{YBa}_2\text{Cu}_3\text{O}_7$, and standard notation for the four crystallographic directions.

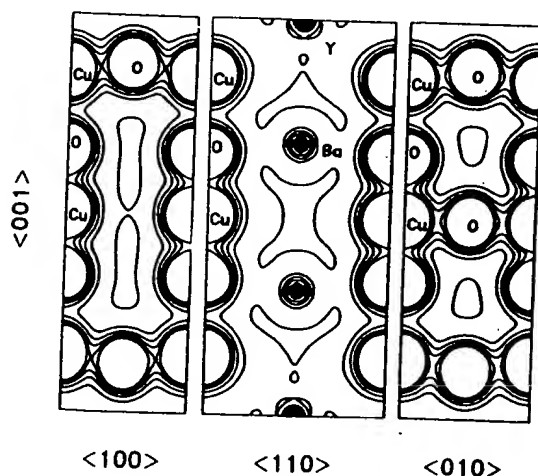
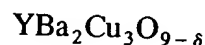


Figure 7.14 Charge density in the three symmetry planes of YBaCuO shown shaded in Fig. 7.13. The x, z , diagonal and the y, z planes are shown from left to right, labeled $\langle 100 \rangle$, $\langle 110 \rangle$, and $\langle 010 \rangle$, respectively. These results are obtained from band structure calculations, as will be explained in the following chapter (Krakauer and Pickett, 1988).

ordinary ionic compound. The short Cu-O bonds in the planes and chains (1.93–1.96 Å) increase the charge overlap. The least overlap appears in the Cu(2)–O(4) vertical bridging bond, which is also fairly long (2.29 Å). The Cu, O charge contours can be represented by a model that assigns charges of +1.62 and –1.69 to Cu and O, respectively, rather than the values of +2.33 and –2.00 expected for a standard ionic model, where the charge +2.33 is an average of +2, +2, and +3 for the three copper ions. Thus the Cu–O bonds are not completely ionic, but partly covalent.

F. YBaCuO Formula

In early work the formula



was used for YBaCuO because the prototype triple perovskite $(\text{YCuO}_3)(\text{BaCuO}_3)_2$ has nine oxygens. Then crystallographers showed that there are eight oxygen sites in the 14-atom YBaCuO unit cell, and the formula $\text{YBa}_2\text{Cu}_3\text{O}_{8-\delta}$ came into widespread use. Finally, structure refinements demonstrated that one of the oxygen sites is systematically vacant in the chain layers, so the more appropriate expression $\text{YBa}_2\text{Cu}_3\text{O}_{7-\delta}$ was introduced. It would be preferable to make one more change and use the formula $\text{Ba}_2\text{YCu}_3\text{O}_{7-\delta}$ to emphasize that Y is analogous to Ca in the bismuth and thallium compounds, but very few workers in the field do this, so we reluctantly adopt the usual “final” notation. In the Bi–Tl compound of Section IX, B, $\text{Ba}_2\text{YCu}_3\text{O}_{7-\delta}$ would be called a 0213 compound. We will follow the usual practice of referring to $\text{YBa}_2\text{Cu}_3\text{O}_{7-\delta}$ as the 123 compound.

G. $\text{YBa}_2\text{Cu}_4\text{O}_8$ and $\text{Y}_2\text{Ba}_4\text{Cu}_7\text{O}_{15}$

These two superconductors are sometimes referred to as the 124 compound and the 247 compound, respectively. They have the property that for each atom at position (x, y, z) there is another identical atom at

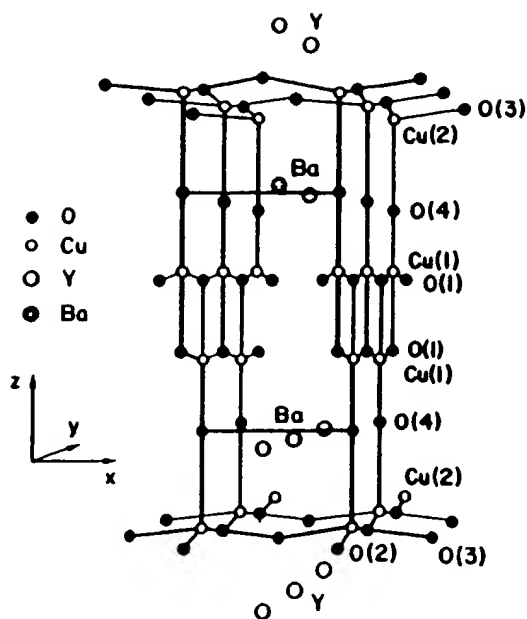
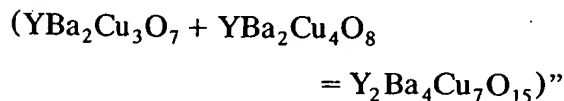


Figure 7.15 Crystal structure of $\text{YBa}_2\text{Cu}_4\text{O}_8$ showing how, as a result of the side-centering symmetry operation, the atoms in adjacent Cu-O chains are staggered along the y direction, with Cu above O and O above Cu (Heyen *et al.*, 1991; modified from Campuzano *et al.*, 1990).

position $(x, y + \frac{1}{2}, z + \frac{1}{2})$. In other words, the structure is side centered. This property prevents the stacking rules of Section C from applying.

The chain layer of $\text{YBa}_2\text{Cu}_3\text{O}_7$ becomes two adjacent chain layers in $\text{YBa}_2\text{Cu}_4\text{O}_8$, with the Cu atoms of one chain located directly above or below the O atoms of the other, as shown in Fig. 7.15 (Campuzano *et al.*, 1990; Heyen *et al.*, 1990a, 1991; Iqbal, 1992; Kaldis *et al.*, 1989; Marsh *et al.*, 1988; Morris *et al.*, 1989a). The transition temperature remains in the range from 40 K to 80 K when Y is replaced by various rare earths (Morris *et al.*, 1989). The double chains do not exhibit the variable oxygen stoichiometry of the single ones.

The other side-centered compound, $\text{Y}_2\text{Ba}_4\text{Cu}_7\text{O}_{15}$, may be considered according to Torardi, "as an ordered 1:1 intergrowth of the 123 and 124 compounds



(Bordel *et al.*, 1988, Gupta and Gupta, 1993). The 123 single chains can vary in their oxygen content, and superconductivity onsets up to 90 K have been observed. This compound has been synthesized with several rare earths substituted for Y (Morris *et al.*, 1989b).

VII. BODY CENTERING

In Section V we discussed aligned-type superconductor structures that possess a horizontal plane of symmetry. Most high-temperature superconductor structures have, besides this σ_h plane, an additional symmetry operation called body centering whereby for every atom with coordinates (x, y, z) there is an identical atom with coordinates as determined from the following operation:

$$x \rightarrow x \pm \frac{1}{2}, \quad y \rightarrow y \pm \frac{1}{2}, \quad z \rightarrow z \pm \frac{1}{2} \quad (7.5)$$

Starting with a plane at the height z this operation forms what is called an image plane at the height $z + \frac{1}{2}$ in which the edge atoms become centered, the centered atoms become edge types, and each face atom moves to another face site. In other words, the body-centering operation acting on a plane at the height z forms a body centered plane, also called an image plane, at the height $z \pm \frac{1}{2}$. The signs in these operations are selected so that the generated points and planes remain within the unit cell. Thus if the initial value of z is greater than $\frac{1}{2}$, the minus sign must be selected, viz., $z \rightarrow z - \frac{1}{2}$. Body centering causes half of the Cu-O planes to be $[\text{Cu O}_2 -]$, with the copper atoms at edge sites, and the other half to be $[- \text{O}_2 \text{ Cu}]$, with the copper atoms at centered sites.

Let us illustrate the symmetry features of a body-centered superconductor by considering the example of $\text{Tl}_2\text{Ba}_2\text{CaCu}_2\text{O}_8$. This compound has an initial plane $[\text{Cu O}_2 -]$ with the copper and oxygen atoms at the vertical positions $z = 0.0540$ and 0.0531 , respectively, as shown in Fig.

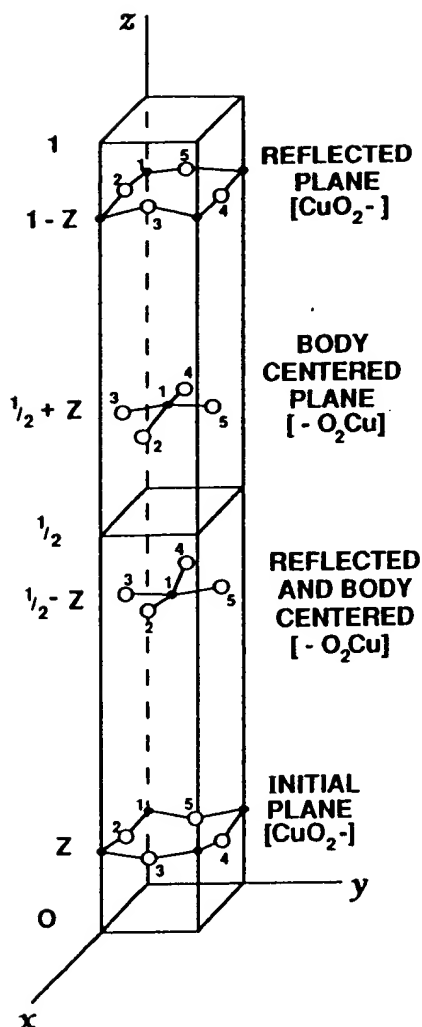


Figure 7.16 Body-centered tetragonal unit cell containing four puckered CuO_2 groups showing how the initial group (bottom) is replicated by reflection in the horizontal reflection plane ($z = \frac{1}{2}$), by the body centering operation, and by both.

7.16. For illustrative purposes the figure is drawn for values of z closer to 0.1. We see from the figure that there is a reflected plane $[\text{Cu O}_2 -]$ at the height $1 - z$, an image (i.e., body centered) plane $[-\text{O}_2 \text{Cu}]$ of the original plane at the height $\frac{1}{2} + z$, and an image plane $[-\text{O}_2 \text{Cu}]$ of the reflected plane (i.e., a reflected and body centered plane) at the height $\frac{1}{2} - z$. Figure 7.16 illustrates this situation and indicates how the atoms of the initial plane can be transformed into particular atoms in other planes (see Problem 5). Figure 7.17 shows how the configurations of the

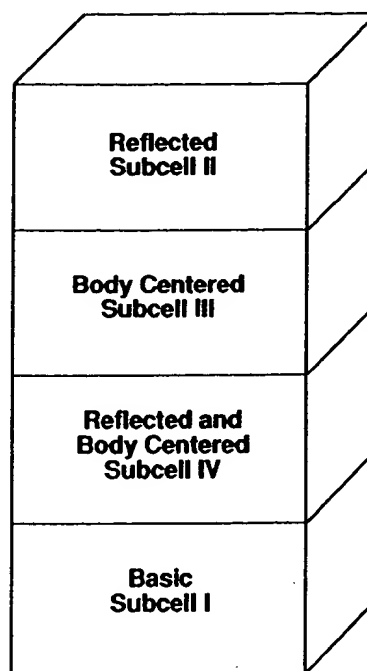


Figure 7.17 Body-centered unit cell divided into four regions by the reflection and body centering operations.

atoms in one-quarter of the unit cell, called the *basic subcell*, or subcell I, determine their configurations in the other three subcells II, III, and IV through the symmetry operations of reflection and body centering.

VIII. BODY-CENTERED La_2CuO_4 AND Nd_2CuO_4

The body-centered compound



has three structural variations in the same crystallographic space group, namely the $M = \text{La}$ and $M = \text{Nd}$ types, and a third mixed variety (Xiao *et al.*, 1989). Table 7.5 lists the atom positions of the first two types, and Fig. 7.18 presents sketches of the structures of all three. Each will be discussed in turn.

A. Unit Cell Generation of La_2CuO_4 (T Phase)

The structure of the more common La_2CuO_4 variety, often called the T phase,

Table 7.5 Atom Positions in the La_2CuO_4 and Nd_2CuO_4 Structures

La ₂ CuO ₄ structure					Nd ₂ CuO ₄ structure					
Layer	Atom	x	y	z	Layer	Atom	x	y	z	
[Cu O ₂ -]	O(1)	$\frac{1}{2}$	0	1	[Cu O ₂ -]	O(1)	$\frac{1}{2}$	0	1	
	Cu	0	0	1		Cu	0	0	1	
	O(1)	0	$\frac{1}{2}$	1		O(1)	0	$\frac{1}{2}$	1	
	La	$\frac{1}{2}$	$\frac{1}{2}$	0.862		[- - Nd]	Nd	$\frac{1}{2}$	$\frac{1}{2}$	0.862
[O - La]	O(2)	0	0	0.818	[- O ₂ -]	O(3)	0	$\frac{1}{2}$	$\frac{3}{4}$	
[La - O]	O(2)	$\frac{1}{2}$	$\frac{1}{2}$	0.682		O(3)	$\frac{1}{2}$	0	$\frac{3}{4}$	
	La	0	0	0.638		[Nd - -]	Nd	0	0	0.638
	O(1)	$\frac{1}{2}$	0	$\frac{1}{2}$		O(1)	$\frac{1}{2}$	0	$\frac{1}{2}$	
	[- O ₂ Cu]	Cu	$\frac{1}{2}$	$\frac{1}{2}$	$\frac{1}{2}$	[- O ₂ Cu]	Cu	$\frac{1}{2}$	$\frac{1}{2}$	$\frac{1}{2}$
O(1)		0	$\frac{1}{2}$	$\frac{1}{2}$	O(1)	0	$\frac{1}{2}$	$\frac{1}{2}$		
La		0	0	0.362	[Nd - -]	Nd	0	0	0.362	
[La - O]		O(2)	$\frac{1}{2}$	$\frac{1}{2}$	0.318	[- O ₂ -]	O(3)	$\frac{1}{2}$	0	$\frac{1}{4}$
[O - La]	O(2)	0	0	0.182	O(3)		0	$\frac{1}{2}$	$\frac{1}{4}$	
	La	$\frac{1}{2}$	$\frac{1}{2}$	0.138	[- - Nd]		Nd	$\frac{1}{2}$	$\frac{1}{2}$	0.138
	O(1)	0	$\frac{1}{2}$	0	O(1)		0	$\frac{1}{2}$	0	
	[Cu O ₂ -]	Cu	0	0	0	[Cu O ₂ -]	Cu	0	0	0
O(1)		$\frac{1}{2}$	0	0	O(1)	$\frac{1}{2}$	0	0		

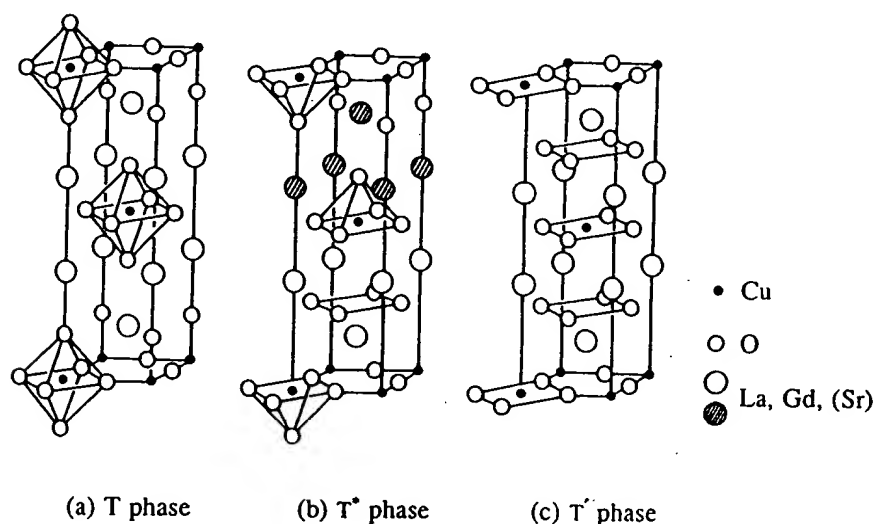


Figure 7.18 (a) Regular unit cell (T phase) associated with hole-type $(\text{La}_{1-x}\text{Sr}_x)_2\text{CuO}_4$ superconductors, (b) hybrid unit cell (T* phase) of the hole-type $\text{La}_{2-x-y}\text{R}_y\text{Sr}_x\text{CuO}_4$ superconductors, and (c) alternate unit cell (T' phase) associated with electron-type $(\text{Nd}_{1-x}\text{Ce}_x)_2\text{CuO}_4$ superconductors. The La atoms in the left structure become Nd atoms in the right structure. The upper part of the hybrid cell is T type, and the bottom is T'. The crystallographic space group is the same for all three unit cells (Xiao *et al.*, 1989; see also Oguchi, 1987; Ohbayashi *et al.*, 1987; Poole *et al.*, 1988, p. 83; Tan *et al.*, 1990).

can be pictured as a stacking of CuO_4La_2 groups alternately with image (i.e., body centered) $\text{La}_2\text{O}_4\text{Cu}$ groups along the c direction, as indicated on the left side of Fig. 7.19 (Cavaet *et al.*, 1987; Kinoshita *et al.*, 1992; Longo and Raccach, 1973; Ohbayashi *et al.*, 1987; Onoda *et al.*, 1987; Zolliker *et al.*, 1990). Another way of visualizing the structure is by generating it from the group $\text{Cu}_2\text{O}_2\text{La}$, comprising the layers $[\text{O}-\text{La}]$ and $\frac{1}{2}[\text{Cu O}_2 -]$ in subcell I shown on the right side of Fig. 7.19 and also on the left side of Fig. 7.20. (The factor $\frac{1}{2}$ appears because the $[\text{Cu O}_2 -]$ layer is shared by two subcells.) Subcell II is formed by reflection from subcell I, and subcells III and IV are formed from I and II via the body-centering operation in the manner of Figs. 7.16 and 7.17. Therefore, subcells I

and II together contain the group CuO_4La_2 , and subcells III and IV together contain its image (body centered) counterpart group $\text{La}_2\text{O}_4\text{Cu}$. The BiSrCaCuO and TlBaCaCuO structures to be discussed in Section IX can be generated in the same manner, but with much larger repeat units along the c direction.

B. Layering Scheme

The La_2CuO_4 layering scheme consists of equally-spaced, flat CuO_2 layers with their oxygens stacked one above the other, the copper ions alternating between the $(0,0,0)$ and $(\frac{1}{2}, \frac{1}{2}, \frac{1}{2})$ sites in adjacent layers, as shown in Fig. 7.21. These planes are body-centered images of each other, and are perfectly flat because they are

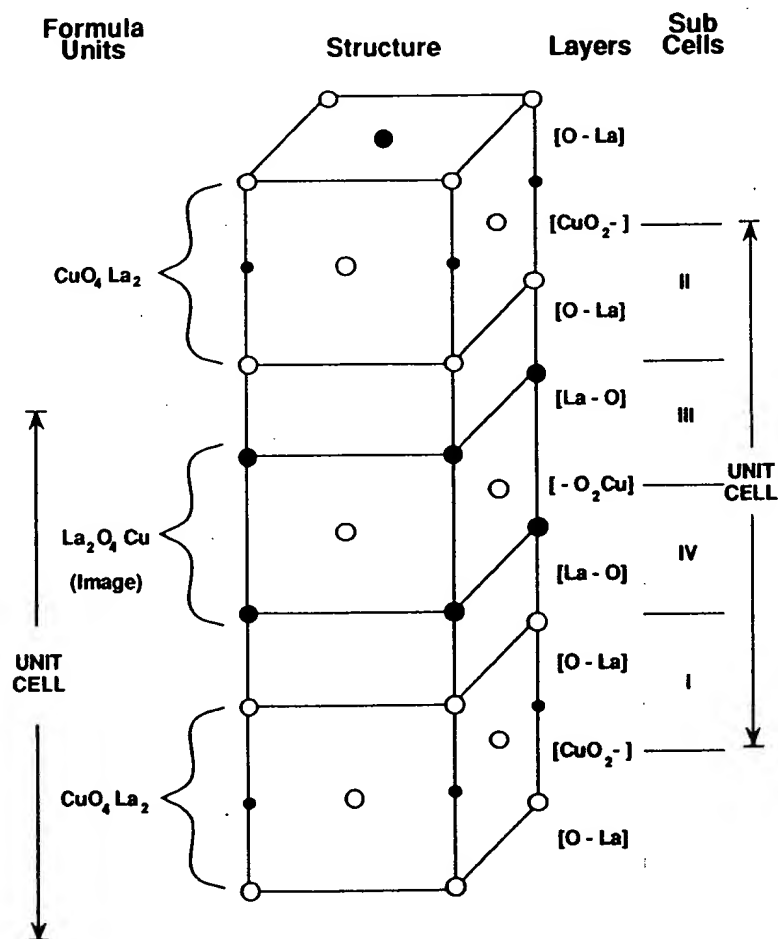


Figure 7.19 Structure of La_2CuO_4 (center), showing the formula units (left) and the level labels and subcell types (right). Two choices of unit cell are indicated, the left-side type unit cell based on formula units, and the more common right-side type unit cell based on copper-oxide layers.

Figure
left) a
tions c
in the

Fi
atc

La_2CuO_4	Sub Cell	Nd_2CuO_4
$[\text{CuO}_2^-]$	—	$[\text{CuO}_2^-]$
$[\text{O} - \text{La}]$	II	$[- - \text{Nd}]$
$[\text{La} - \text{O}]$	—	$[- \text{O}_2^-]$
	III	$[\text{Nd} - -]$
$[- \text{O}_2\text{Cu}]$	—	$[- \text{O}_2\text{Cu}]$
$[\text{La} - \text{O}]$	IV	$[\text{Nd} - -]$
$[\text{O} - \text{La}]$	—	$[- \text{O}_2^-]$
	I	$[- - \text{Nd}]$
$[\text{CuO}_2^-]$	—	$[\text{CuO}_2^-]$

Figure 7.20 Layering schemes of the La_2CuO_4 (T, left) and Nd_2CuO_4 (T', right) structures. The locations of the four subcells of the unit cell are indicated in the center column.

reflection planes. Half of the oxygens, O(1), are in the planes, and the other half, O(2), between the planes. The copper is octahedrally coordinated with oxygen, but the distance 1.9 Å from Cu to O(1) in the CuO_2 planes is much less than the vertical distance of 2.4 Å from Cu to the apical oxygen O(2), as indicated in Fig. 7.22. The La is ninefold coordinated to four O(1) oxygens, to four O(2) at $(\frac{1}{2}, \frac{1}{2}, z)$ sites, and to one O(2) at a $(0, 0, z)$ site.

C. Charge Distribution

Figure 7.23 shows contours of constant-valence charge density on a logarithmic scale drawn on the back x, z -plane and on the diagonal plane of the unit cell sketched in Fig. 7.13. These contour plots are obtained from the band structure calculations described in Chapter 8, Section XIV. The high-charge density at the lanthanum site and the low charge density around this site indicate an ionic state

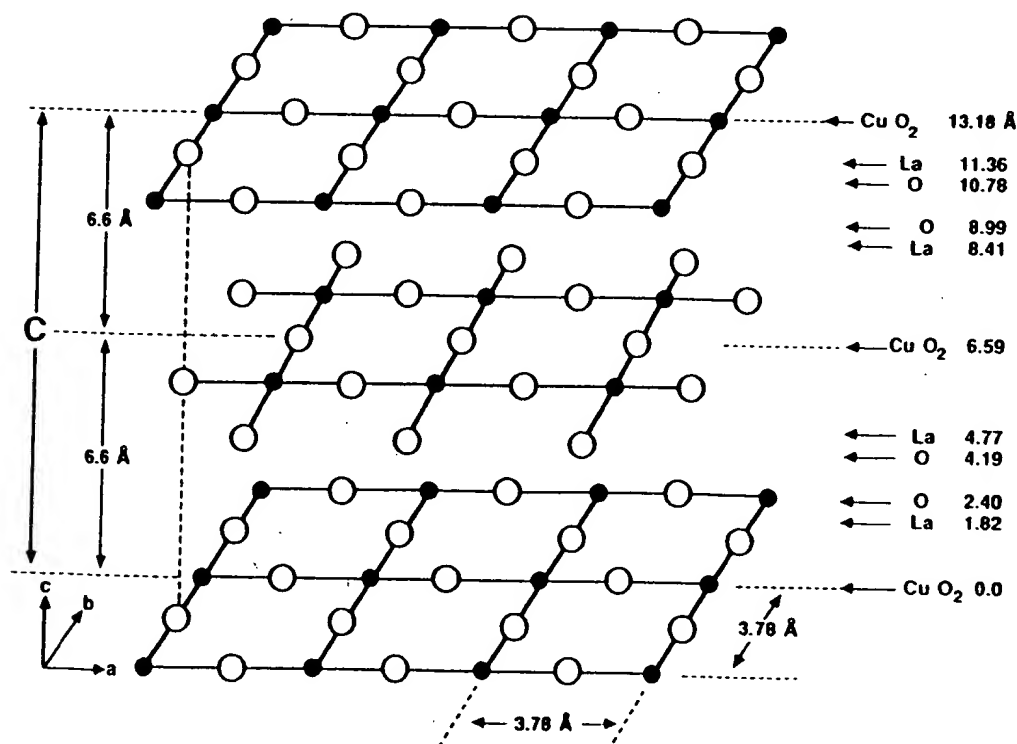


Figure 7.21 CuO_2 layers of the La_2CuO_4 structure showing horizontal displacement of Cu atoms in alternate layers. The layers are perpendicular to the c -axis (Poole *et al.*, 1988, p. 87).

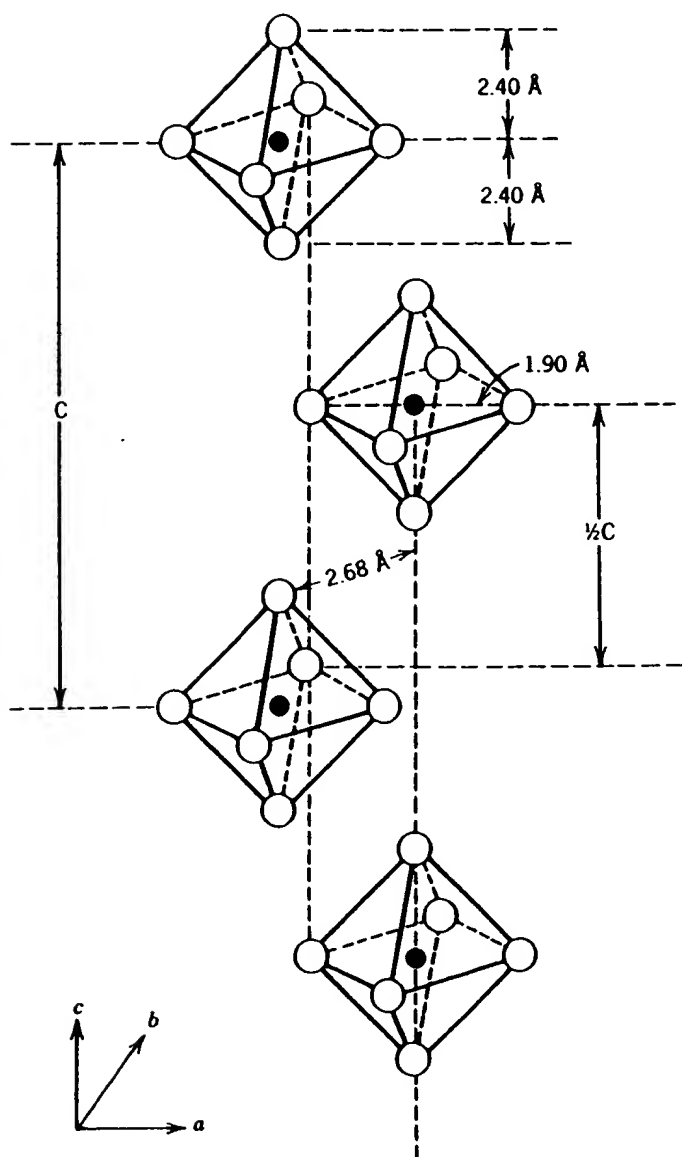


Figure 7.22 Ordering of axially distorted CuO_6 octahedra in La_2CuO_4 (Poole *et al.*, 1988, p. 88).

La^{3+} . The charge density changes in a fairly regular manner around the copper and oxygen atoms, both within the CuO_2 planes and perpendicular to these planes, suggestive of covalency in the Cu–O bonding, as is the case with the $\text{YBa}_2\text{Cu}_3\text{O}_7$ compound.

D. Superconducting Structures

The compound La_2CuO_4 is itself an antiferromagnetic insulator and must be doped, generally with an alkaline earth, to exhibit pronounced superconducting prop-

erties. The compounds $(\text{La}_{1-x}\text{M}_x)_2\text{CuO}_4$, with 3% to 15% of $M = \text{Sr}$ or Ba replacing La , are orthorhombic at low temperatures and low M contents and are tetragonal otherwise; superconductivity has been found on both sides of this transition. The orthorhombic distortion can be of the rectangular or of the rhombal type, both of which are sketched in Fig. 7.4. The phase diagram of Fig. 7.24 shows the tetragonal, orthorhombic, superconducting, and antiferromagnetically ordered regions for the lanthanum compound (Weber *et al.*, 1989; cf. Goodenough *et al.*, 1993). We see that

F.
L.
T.
or
th
sc

TEMPERATURE (K)

Fig.
La₂-
roma
Figur
data
line.
regio

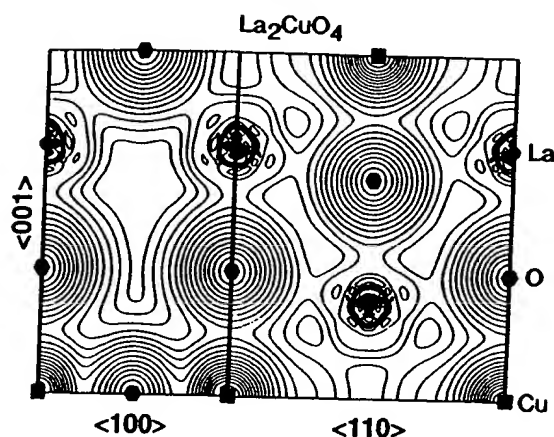


Figure 7.23 Contour plots of the charge density of La_2CuO_4 obtained from band structure calculations. The x, z -crystallographic plane labeled $\langle 100 \rangle$ is shown on the left and the diagonal plane labeled $\langle 110 \rangle$ on the right. The contour spacing is on a logarithmic scale (Pickett, 1989).

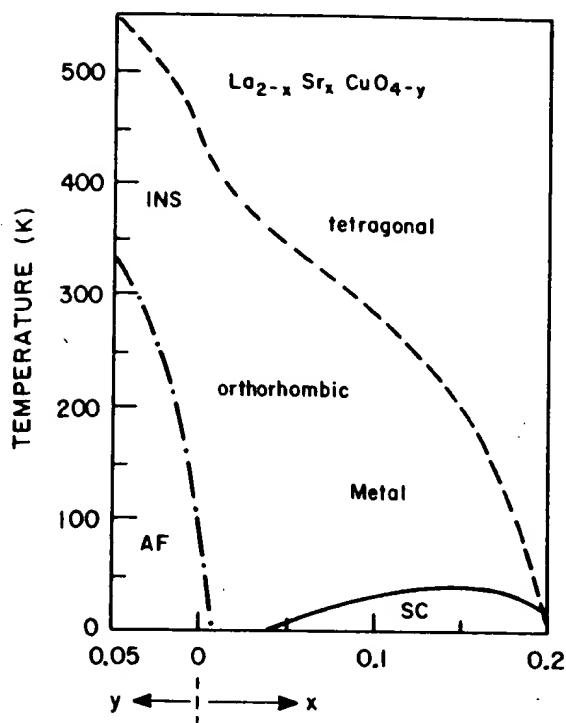


Figure 7.24 Phase diagram for hole-type $\text{La}_{2-x}\text{Sr}_x\text{CuO}_{4-y}$ indicating insulating (INS), antiferromagnetic (AF), and superconducting (SC) regions. Figure VI-6 of Poole *et al.* (1988) shows experimental data along the orthorhombic-to-tetragonal transition line. Spin-density waves (SDW) are found in the AF region (Weber *et al.*, 1989).

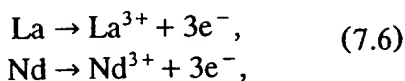
the orthorhombic phase is insulating at high temperatures, metallic at low temperatures, and superconducting at very low temperatures. Spin-density waves, to be discussed in Chapter 8, Section XIX, occur in the antiferromagnetic region.

E. Nd_2CuO_4 Compound (T' Phase)

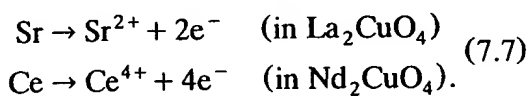
The rarer Nd_2CuO_4 structure (Skanakumar *et al.*, 1989; Sulewski *et al.*, 1990; Tan *et al.*, 1990) given on the right side of Fig. 7.18 and Table 7.5 has all of its atoms in the same positions as the standard La_2CuO_4 structure, except for the apical O(2) oxygens in the [O-La] and [La-O] layers, which move to form a $[-\text{O}_2-]$ layer between $[-\text{La}]$ and $[\text{La}-]$. These oxygens, now called O(3), have the same x, y coordinate positions as the O(1) oxygens, and are located exactly between the CuO_2 planes with $z = \frac{1}{4}$ or $\frac{3}{4}$. We see from Fig. 7.18 that the CuO_6 octahedra have now lost their apical oxygens, causing Cu to become square planar-coordinated CuO_4 groups. The Nd is eightfold coordinated to four O(1) and four O(3) atoms, but with slightly different Nd-O distances. The CuO_2 planes, however, are identical in the two structures. Superconductors with this Nd_2CuO_4 structure are of the electron type, in contrast to other high-temperature superconductors, in which the current carriers are holes. In particular, the electron superconductor $\text{Nd}_{1.85}\text{Ce}_{0.15}\text{CuO}_{4-\delta}$ with $T_c = 24$ K has been widely studied (Fontcuberta and Fàbrega, 1995, a review chapter; Allen 1990; Alp *et al.*, 1989b; Barlingay *et al.*, 1990; Ekino and Akimitsu, 1989a, b; Lederman *et al.*, 1991; Luke *et al.*, 1990; Lynn *et al.*, 1990; Sugiyama *et al.*, 1991; Tarason *et al.*, 1989a). Other rare earths, such as Pr (Lee *et al.*, 1990) and Sm (Almasan *et al.*, 1992) have replaced Nd.

The difference of structures associated with different signs attached to the current carriers may be understood in terms of the doping process that converts undoped material into a superconductor. Lanthanum and neodymium are both trivalent, and in the undoped compounds they each con-

tribute three electrons to the nearby oxygens,



to produce O^{2-} . To form the superconductors a small amount of La in La_2CuO_4 can be replaced with divalent Sr, and some Nd in Nd_2CuO_4 can be replaced with tetravalent Ce, corresponding to



Thus, Sr doping decreases the number of electrons to produce hole-type carriers, while Ce doping increases the electron concentration and the conductivity is electron type.

There are also copper-oxide electron superconductors with different structures, such as $\text{Sr}_{1-x}\text{Nd}_x\text{CuO}_2$ (Smith *et al.*, 1991) and $\text{TlCa}_{1-x}R_x\text{Sr}_2\text{Cu}_2\text{O}_{7-\delta}$, where R is a rare earth (Vijayaraghavan *et al.*, 1989). Electron- and hole-type superconductivity in the cuprates has been compared (Katti and Risbud, 1992; Medina and Regueiro, 1990).

F. $\text{La}_{2-x-y}\text{R}_x\text{Sr}_y\text{CuO}_4$ Compounds (T* Phase)

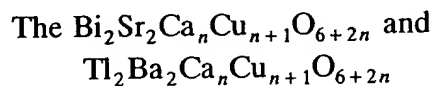
We have described the T structure of La_2CuO_4 and the T' structure of Nd_2CuO_4 . The former has O(2) oxygens and the latter O(3) oxygens, which changes the coordinations of the Cu atoms and that of the La and Nd atoms as well. There is a hybrid structure of hole-type superconducting lanthanum cuprates called the T* structure, illustrated in Fig. 7.18b, in which the upper half of the unit cell is the T type with O(2) oxygens and lower half the T' type with O(3) oxygens. These two varieties of halfcells are stacked alternately along the tetragonal c -axis (Akimitsu *et al.*, 1988; Cheong *et al.*, 1989b; Kwei *et al.*, 1990; Tan *et al.*, 1990). Copper, located in the base of an oxygen pyramid, is fivefold-coordinated CuO_5 . There are two inequivalent rare earth sites; the ninefold-coordinated site in the T-type halfcell is

preferentially occupied by the larger La and Sr ions, while the smaller rare earths R (i.e., Sm, Eu, Gd, or Tb) prefer the eightfold-coordinated site in the T' half-cell. Tan *et al.* (1991) give a phase diagram for the concentration ranges over which the T and T* phases are predominant.

IX. BODY-CENTERED BiSrCaCuO AND TlBaCaCuO

Early in 1988 two new superconducting systems with transition temperatures considerably above those attainable with YBaCuO , namely the bismuth- and thallium-based materials, were discovered. These compounds have about the same a and b lattice constants as the yttrium and lanthanum compounds, but with much larger unit cell dimensions along c . We will describe their body-centered structures in terms of their layering schemes. In the late 1940s some related compounds were synthesized by the Swedish chemist Bengt Aurivillius (1950, 1951, 1952).

A. Layering Scheme



compounds, where n is an integer, have essentially the same structure and the same layering arrangement (Barry *et al.*, 1989; Siegrist *et al.*, 1988; Torardi *et al.*, 1988a; Yvon and François, 1989), although there are some differences in the detailed atom positions. Here there are groupings of CuO_2 layers, each separated from the next by Ca layers with no oxygen. The CuO_2 groupings are bound together by intervening layers of BiO and SrO for the bismuth compound, and by intervening layers of TlO and BaO for the thallium compound. Figure 7.25 compares the layering scheme of the $\text{Tl}_2\text{Ba}_2\text{Ca}_n\text{Cu}_{n+1}\text{O}_{6+2n}$ compounds with $n = 0, 1, 2$ with those of the lanthanum and yttrium compounds. We also see from the figure that the groupings of $[\text{Cu O}_2 -]$ planes and $[- \text{O}_2 \text{ Cu}]$ image

(i.e., bc the c -a: that are ing prop A , shows th tioned ; scheme adjacent and cent never ha sites. Th at the ce is also c and that staggered Figure sents a the infor

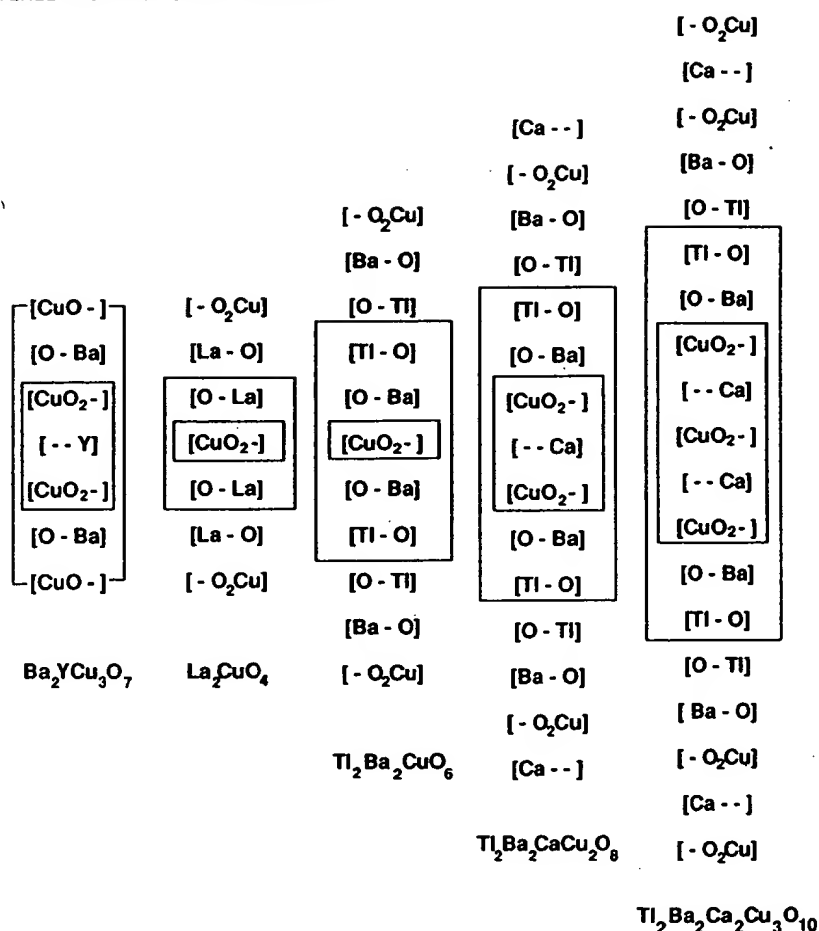


Figure 7.25 Layering schemes of various high-temperature superconductors. The CuO_2 plane layers are enclosed in small inner boxes, and the layers that make up a formula unit are enclosed in larger boxes. The Bi-Sr compounds $Bi_2Sr_2Ca_nCu_{n+1}O_{6+2n}$ have the same layering schemes as their Tl-Ba counterparts shown in this figure.

(i.e., body centered) planes repeat along the c -axis. It is these copper-oxide layers that are responsible for the superconducting properties.

A close examination of this figure shows that the general stacking rules mentioned in Section VI.C for the layering scheme are satisfied, namely metal ions in adjacent layers alternate between edge (E) and centered (C) sites, and adjacent layers never have oxygens on the same types of sites. The horizontal reflection symmetry at the central point of the cell is evident. It is also clear that $YBa_2Cu_3O_7$ is aligned and that the other four compounds are staggered.

Figure 7.26 (Torardi *et al.*, 1988a) presents a more graphical representation of the information in Fig. 7.25 by showing the

positions of the atoms in their layers. The symmetry and body centering rules are also evident on this figure. Rao (1991) provided sketches for the six compounds $Tl_mBa_2Ca_nCu_{n+1}O_x$ similar to those in Fig. 7.26 with the compound containing one ($m = 1$) or two thallium layers ($m = 2$), where $n = 0, 1, 2$, as in the Torardi *et al.* figure.

B. Nomenclature

There are always two thalliums and two bariums in the basic formula for $Tl_2Ba_2Ca_nCu_{n+1}O_{6+2n}$, together with n calciums and $n + 1$ coppers. The first three members of this series for $n = 0, 1$, and 2 are called the 2201, 2212, and 2223 compounds, respectively, and similarly for their

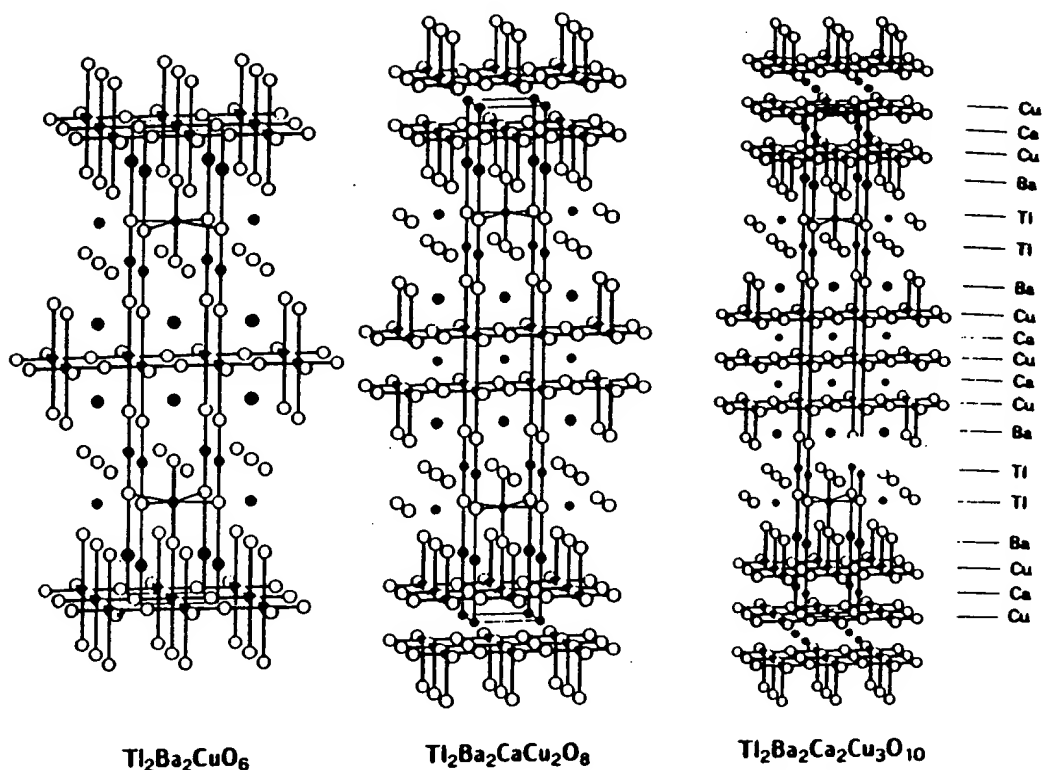


Figure 7.26 Crystal structures of $\text{Tl}_2\text{Ba}_2\text{Ca}_n\text{Cu}_{n+1}\text{O}_{6+2n}$ superconducting compounds with $n = 0, 1, 2$ arranged to display the layering schemes. The $\text{Bi}_2\text{Sr}_2\text{Ca}_n\text{Cu}_{n+1}\text{O}_{6+2n}$ compounds have the same respective structures (Torardi *et al.*, 1988a).

BiSr analogues $\text{Bi}_2\text{Sr}_2\text{Ca}_n\text{Cu}_{n+1}\text{O}_{6+2n}$. Since Y in $\text{YBa}_2\text{Cu}_3\text{O}_7$ is structurally analogous to Ca in the Tl and Bi compounds, it would be more consistent to write $\text{Ba}_2\text{YCu}_3\text{O}_7$ for its formula, as noted in Section VI.F. In this spirit $\text{Ba}_2\text{YCu}_3\text{O}_{7-\delta}$ might be called the 0213 compound, and $(\text{La}_{1-x}\text{M}_x)_2\text{CuO}_{4-\delta}$ could be called 2001.

C. Bi-Sr Compounds

Now that the overall structures and interrelationships of the BiSr and TlBa high-temperature superconductors have been made clear in Figs. 7.25 and 7.26 we will comment briefly about each compound. Table 7.3 summarizes the characteristics of these and related compounds.

The first member of the BiSr series, the 2201 compound with $n = 0$, has octahedrally coordinated Cu and $T_c \approx 9$ K (Torardi *et al.*, 1988b). The second mem-

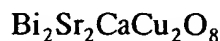
ber, $\text{Bi}_2(\text{Sr}, \text{Ca})_3\text{Cu}_2\text{O}_{8+\delta}$, is a superconductor with $T_c \approx 90$ K (Subramanian *et al.*, 1988a; Tarascon *et al.*, 1988b). There are two $[\text{Cu O}_2 -]$ layers separated from each other by the $[- - \text{Ca}]$ layer. The spacing from $[\text{Cu O}_2 -]$ to $[- - \text{Ca}]$ is 1.66 Å, which is less than the corresponding spacing of 1.99 Å between the levels $[\text{Cu O}_2 -]$ and $[- - \text{Y}]$ of YBaCuO . In both cases the copper ions have a pyramidal oxygen coordination of the type shown in Fig. 7.11. Superlattice structures have been reported along a and b , which means that minor modifications of the unit cells repeat approximately every five lattice spacings, as explained in Sect. IX.E. The third member of the series, $\text{Bi}_2\text{Sr}_2\text{Ca}_2\text{Cu}_3\text{O}_{10}$, has three CuO_2 layers separated from each other by $[- - \text{Ca}]$ planes and a higher transition temperature, 110 K, when doped with Pb. The two Cu ions have pyramidal coordination, while the third is square planar.

indical
Cu-O
and L
cate v
cent [I

D. Tl-
Th

have h
their t
1989; S
et al.,
series,
no [-
transiti
second
called t

Charge-density plots of



indicate the same type of covalency in the Cu-O bonding as with the $\text{YBa}_2\text{Cu}_3\text{O}_7$ and La_2CuO_4 compounds. They also indicate very little bonding between the adjacent [Bi - O] and [O - Bi] layers.

D. Tl-Ba Compounds

The TlBa compounds



have higher transition temperatures than their bismuth counterparts (Iqbal *et al.*, 1989; Subramanian *et al.*, 1988b; Torardi *et al.*, 1988a). The first member of the series, namely $\text{Tl}_2\text{Ba}_2\text{CuO}_6$ with $n = 0$, has no [- - Ca] layer and a relatively low transition temperature of ≈ 85 K. The second member ($n = 1$), $\text{Tl}_2\text{Ba}_2\text{CaCu}_2\text{O}_8$, called the 2212 compound, with $T_c = 110$ K

has the same layering scheme as its Bi counterpart, detailed in Figs. 7.25 and 7.26. The $[\text{Cu O}_2 -]$ layers are thicker and closer together than the corresponding layers of the bismuth compound (Toby *et al.*, 1990). The third member of the series, $\text{Tl}_2\text{Ba}_2\text{Ca}_2\text{Cu}_3\text{O}_{10}$, has three $[\text{Cu O}_2 -]$ layers separated from each other by [- - Ca] planes, and the highest transition temperature, 125 K, of this series of thallium compounds. It has the same copper coordination as its BiSr counterpart. The 2212 and 2223 compounds are tetragonal and belong to the same crystallographic space group as La_2CuO_4 .

We see from the charge-density plot of $\text{Tl}_2\text{Ba}_2\text{CuO}_6$ shown in Fig. 7.27 that Ba^{2+} is ionic, Cu exhibits strong covalency, especially in the Cu-O plane, and Tl also appears to have a pronounced covalency. The bonding between the [Tl - O] and [O - Tl] planes is stronger than that between the [Bi - O] and [O - Bi] planes of Bi-Sr.

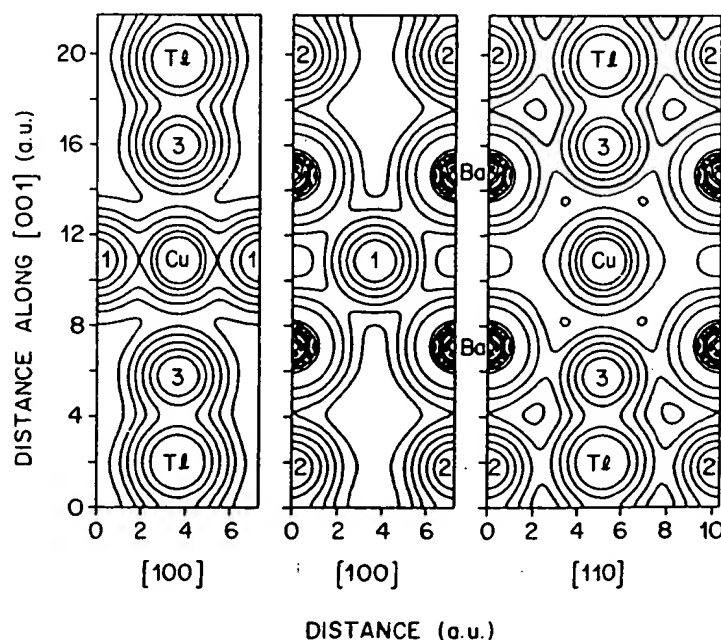
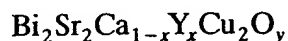


Figure 7.27 Contours of constant charge density on a logarithmic scale in two high-symmetry crystallographic planes of $\text{Tl}_2\text{Ba}_2\text{CuO}_6$. Oxygen atoms O(1), O(2), and O(3) are denoted 1, 2, and 3, respectively. The planar Cu-O1 binding is strongest (Hamann and Mattheiss, 1988; see Pickett, 1989).

E. Modulated Structures

The x-ray and neutron-diffraction patterns obtained during crystal structure determinations of the bismuth cuprates $\text{Bi}_2\text{Sr}_2\text{Ca}_n\text{Cu}_{n+1}\text{O}_{6+2n}$ exhibit weak satellite lines with spacings that do not arise from an integral multiple of the unit cell dimensions. These satellites have modulation periods of 21 Å, 19.6 Å, and 20.8 Å, respectively, for the $n = 0, 1$, and 2 compounds (Li *et al.*, 1989). Since the lattice constant $a = 5.41$ Å ($b = 5.43$ Å) for all three compounds, this corresponds to a superlattice with unit cell of dimensions $\approx 3.8a, b, c$, with the repeat unit along the a direction equal to $\approx 3.8a$ for all three compounds. A modulation of $4.7b$ has also been reported (Kulik *et al.*, 1990). This structural modulation is called incommensurate because the repeat unit is not an integral multiple of a .

Substitutions dramatically change this modulation. The compound



has a period that decreases from about $4.8b$ for $x = 0$ to the commensurate value $4.0b$ for $x = 1$ (Inoue *et al.*, 1989; Tamegai *et al.*, 1989). Replacing Cu by a transition metal (Fe, Mn, or Co) produces nonsuperconducting compounds with a structural modulation that is commensurate with the lattice spacing (Tarascon *et al.*, 1989b). A modulation-free bismuth-lead cuprate superconductor has been prepared (Manivannan *et al.*, 1991). Kistenmacher (1989) examined substitution-induced superstructures in $\text{YBa}_2(\text{Cu}_{1-x}\text{M}_x)_3\text{O}_7$. Superlattices with modulation wavelengths as short as 24 Å have been prepared by employing ultra-thin deposition techniques to interpose insulating planes of $\text{PrBa}_2\text{Cu}_3\text{O}_7$ between superconducting Cu-O layers of $\text{YBa}_2\text{Cu}_3\text{O}_7$ (Jakob *et al.*, 1991; Lowndes *et al.*, 1990; Pennycook *et al.*, 1991; Rajagopal and Mahanti, 1991; Triscone *et al.*, 1990). Tanaka and Tsukada (1991) used the Kronig-Penney model (Tanaka and

Tsukada, 1989a,b) to calculate the quasi-particle spectrum of superlattices.

F. Aligned Tl-Ba Compounds

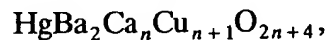
A series of aligned thallium-based superconducting compounds that have the general formula $\text{TlBa}_2\text{Ca}_n\text{Cu}_{n+1}\text{O}_{5+2n}$ with n varying from 0 to 5 has been reported (Ihara *et al.*, 1988; Rona, 1990). These constitute a series from 1201 to 1245. They have superconducting transition temperatures almost as high as the $\text{Tl}_2\text{Ba}_2\text{Ca}_n\text{Cu}_{n+1}\text{O}_{6+2n}$ compounds. Data on these compounds are listed in Table 7.3.

G. Lead Doping

In recent years a great deal of effort has been expended in synthesizing lead-doped superconducting cuprate structures (Itoh and Uchikawa, 1989). Examples involve substituting Pb for Bi (Dou *et al.*, 1989; Zhengping *et al.*, 1990), for Tl (Barry *et al.*, 1989; Mingzhu *et al.*, 1990), or for both Bi and Tl (Iqbal *et al.*, 1990). Different kinds of Pb, Y-containing superconductors have also been prepared (cf. Mattheiss and Hamann, 1989; Ohta and Maekawa, 1990; Tang *et al.*, 1991; Tokiwa *et al.*, 1990, 1991).

X. ALIGNED HgBaCaCuO

The series of compounds



where n is an integer, are prototypes for the Hg family of superconductors. The first three members of the family, with $n = 0, 1, 2$, are often referred to as Hg-1201, Hg-1212, and Hg-1223, respectively. They have the structures sketched in Fig. 7.28 (Tokiwa-Yamamoto *et al.*, 1993; see also Martin *et al.*, 1994; Putilin *et al.*, 1991). The lattice constants are $a = 3.86$ Å for all of them, and $c = 9.5, 12.6$, and 15.7 Å for $n = 0, 1, 2$, respectively. The atom positions of the $n = 1$ compound are listed in Table 7.6 (Hur *et al.*, 1994). The figure is drawn

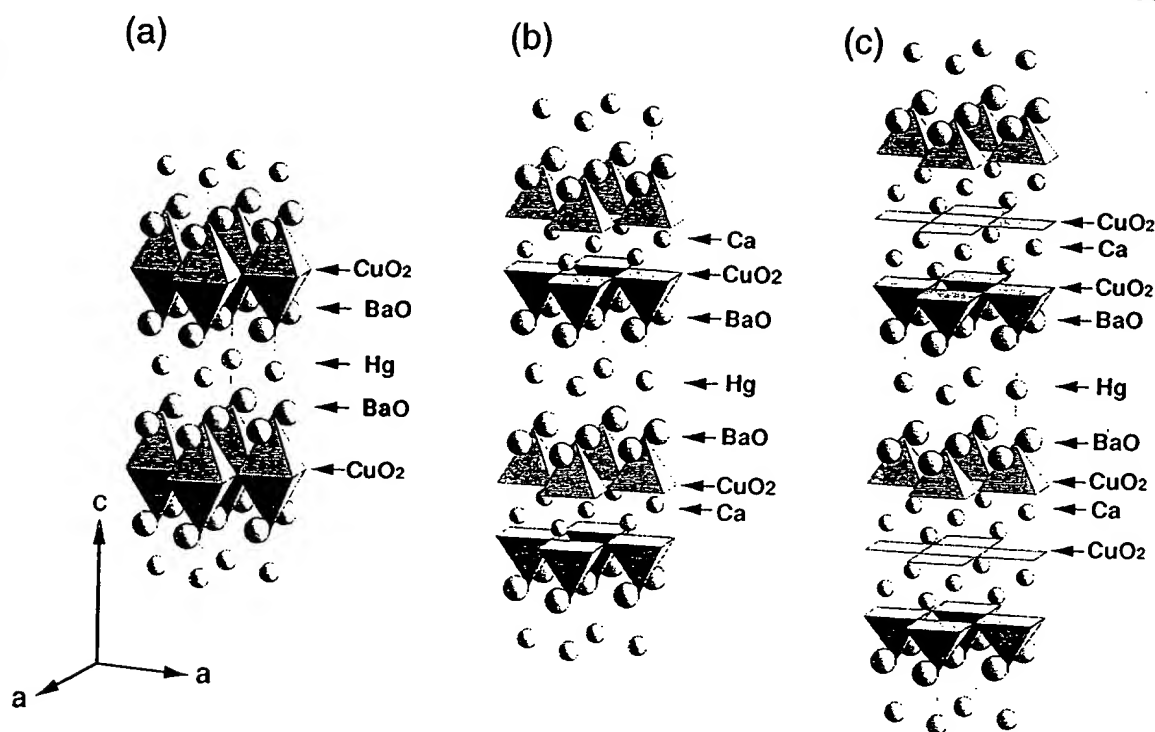


Figure 7.28 Structural models for the series $\text{HgBa}_2\text{Ca}_n\text{Cu}_{n+1}\text{O}_{2n+4}$. The first three members with $n = 0, 1, 2$ are shown (parts a, b, and c, respectively) (Tokiwa-Yamamoto *et al.*, 1993).

Table 7.6 Normalized Atom Positions in the Tetragonal Unit Cell of $\text{HgBa}_2\text{Ca}_{0.86}\text{Sr}_{0.14}\text{Cu}_2\text{O}_{6+\delta}$ ^a

Layer	Atom	<i>x</i>	<i>y</i>	<i>z</i>
[Hg - -]	Hg	0	0	1
	O(3)	$\frac{1}{2}$	$\frac{1}{2}$	1
	O(2)	0	0	0.843
[O - Ba]	Ba	$\frac{1}{2}$	$\frac{1}{2}$	0.778
	Cu	0	0	0.621
	O(1)	0	$\frac{1}{2}$	0.627
[Cu O ₂ -]	O(1)	$\frac{1}{2}$	0	0.627
	Ca, Sr	$\frac{1}{2}$	$\frac{1}{2}$	$\frac{1}{2}$
	O(1)	$\frac{1}{2}$	0	0.373
[Cu O ₂ -]	O(1)	0	$\frac{1}{2}$	0.373
	Cu	0	0	0.379
	Ba	$\frac{1}{2}$	$\frac{1}{2}$	0.222
[O - Ba]	O(2)	0	0	0.157
	O(3)	$\frac{1}{2}$	$\frac{1}{2}$	0
[Hg - -]	Hg	0	0	0

^a Unit cell dimensions $a = 3.8584 \text{ \AA}$ and $c = 12.6646 \text{ \AA}$, space group is $P4/mmm$, D_{4h}^1 . The Hg site is 91% occupied and the O(3) site is 11% occupied ($\delta = 0.11$). The data are from Hur *et al.* (1994).

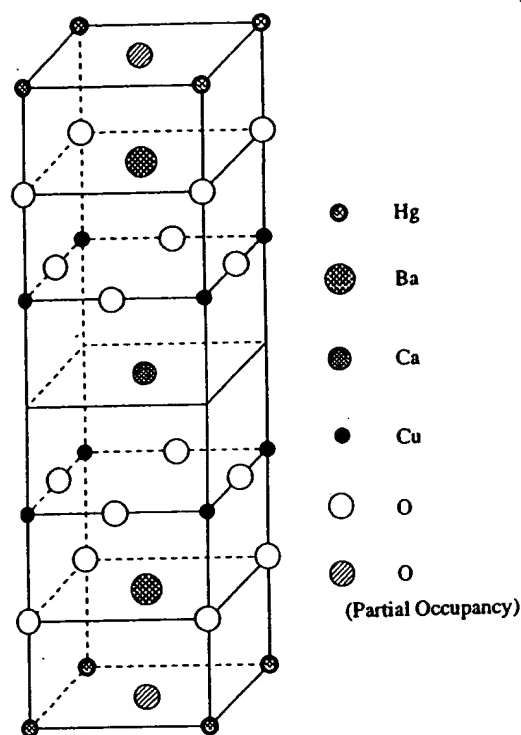


Figure 7.29 Schematic structure of the $\text{HgBa}_2\text{CaCu}_2\text{O}_{6+\delta}$ compound which is also called Hg-1212 (Meng *et al.*, 1993a).

with mercury located in the middle layer of the unit cell, while the table puts Hg at the origin (000) and Ca in the middle ($\frac{1}{2} \frac{1}{2} \frac{1}{2}$). Figure 7.29 presents the unit cell for the $n = 1$ compound $\text{HgBa}_2\text{CaCu}_2\text{O}_{6+\delta}$ drawn with Ca in the middle (Meng *et al.*, 1993a). The symbol δ represents a small excess of oxygen located in the center of the top and bottom layers, at positions $\frac{1}{2} \frac{1}{2} 0$ and $\frac{1}{2} \frac{1}{2} 1$ which are labeled "partial occupancy" in the figure. If this oxygen were included the level symbol would be [Hg - O] instead of [Hg - -]. These Hg compound structures are similar to those of the series $\text{TlBa}_2\text{Ca}_n\text{Cu}_{n+1}\text{O}_{2n+4}$ mentioned above in Section IX.F.

We see from Fig. 7.28 that the copper atom of Hg-1201 is in the center of a stretched octahedron with the planar oxygens O(1) at a distance of 1.94 Å, and the apical oxygens O(2) of the [O - Ba] layer much further away (2.78 Å). For $n = 1$ each copper atom is in the center of the

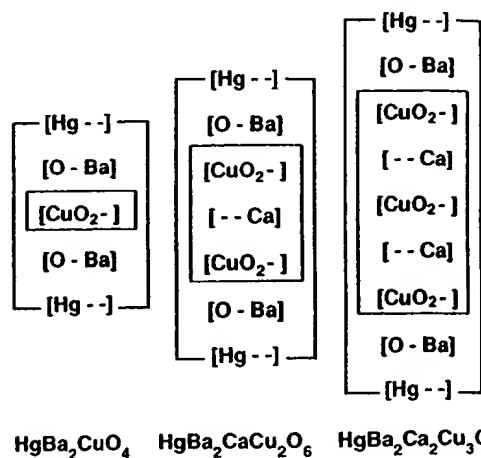
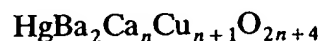


Figure 7.30 Layering schemes of three $\text{HgBa}_2\text{Ca}_n\text{Cu}_{n+1}\text{O}_{2n+4}$ compounds, using the notation of Fig. 7.25.

base of a tetragonal pyramid, and for $n = 2$ the additional CuO_2 layer has Cu atoms which are square planar coordinated. The layering scheme stacking rules of Section VI.C are obeyed by the Hg series of compounds, with metal ions in adjacent layers alternating between edge (E) and centered (C) sites, and oxygen in adjacent layers always at different sites. We see from Table 7.6 that the [O - Ba] layer is strongly puckered and the [Cu O₂ -] layer is only slightly puckered.

The relationships between the layering scheme of the $\text{HgBa}_2\text{Ca}_n\text{Cu}_{n+1}\text{O}_{2n+4}$ series of compounds and those of the other cuprates may be seen by comparing the sketch of Fig. 7.30 with that of Fig. 7.25. We see that the $n = 1$ compound $\text{HgBa}_2\text{CaCu}_2\text{O}_6$ is quite similar in structure to $\text{YBa}_2\text{Cu}_3\text{O}_7$ with Ca replacing Y in the center and Hg replacing the chains [Cu O -]. More surprising is the similarity between the arrangement of the atoms in the unit cell of each

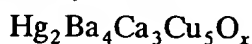


compound and the arrangement of the atoms in the semi-unit cell of the corresponding



compound. They are the same except for the replacement of the [Ti - O] layer by [Hg - -], and the fact that the thallium compounds are body centered and the Hg ones are aligned.

Supercells involving polytypes with ordered stacking sequences of different phases, such as Hg-1212 and Hg-1223, along the c direction have been reported. The stoichiometry is often



corresponding to equal numbers of the Hg-1212 and Hg-1223 phases (Phillips, 1993; Schilling *et al.*, 1993, 1994).

Detailed structural data have already been reported on various Hg family compounds such as $\text{HgBa}_2\text{CuO}_{4+\delta}$ (Putlin *et al.*, 1993) and the $n = 1$ compound with partial Eu substitution for Ca (Putlin *et al.*, 1991). The compound



has Hg in the position (0.065, 0, 0), slightly displaced from the origin of the unit cell (Martin *et al.*, 1994). Several researchers have reported synthesis and pretreatment procedures (Adachi *et al.*, 1993; Itoh *et al.*, 1993; Isawa 1994a; Meng, 1993b; Paranthaman, 1994; Paranthaman *et al.*, 1993). Lead doping for Hg has been used to improve the superconducting properties (Iqbal *et al.*, 1994; Isawa *et al.*, 1993; Martin *et al.*, 1994).

XI. BUCKMINSTERFULLERENES

The compound C_{60} , called buckminsterfullerene, or fullerene for short, con-

sists of 60 carbon atoms at the vertices of the dotriacontahedron (32-sided figure) that is sketched in Fig. 3.35 and discussed in Chapter 3, Section XVI. The term fullerene is used here for a wider class of compounds C_n with n carbon atoms, each of whose carbon atoms is bonded to three other carbons to form a closed surface, with the system conjugated such that for every resonant structure each carbon has two single bonds and one double bond. The smallest possible compound of this type is tetrahedral C_4 , which has the three resonant structures shown in Fig. 7.31. Cubic C_8 is a fullerene, and we show in Problem 17 that it has nine resonant structures. Icosahedral C_{12} is also a fullerene, but octahedral C_6 and dodecahedral C_{20} are not because their carbons are bonded to more than three neighbors. These hypothetical smaller C_n compounds have never been synthesized, but the larger ones, such as C_{60} , C_{70} , C_{76} , C_{78} , and C_{82} , have been made and characterized. Some of them have several forms, with different arrangements of polygons. Clusters of buckminsterfullerenes, such as icosahedral $(\text{C}_{60})_{13}$, have also been studied (T. P. Martin *et al.*, 1993).

There are several interesting geometrical characteristics of fullerenes (Chung and Sternberg, 1993). Since each carbon (vertex) joins three bonds (edges) and each edge has two vertices, the number of edges E in a structure C_n is 50% greater than the number of vertices V . There is a general theorem in topology, called Euler's Theorem, that the number of faces F of a

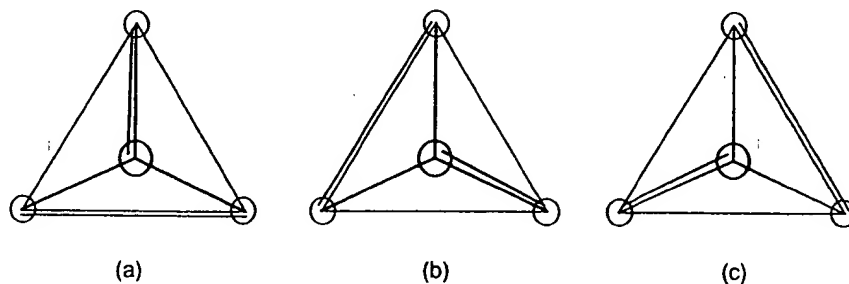


Figure 7.31 The three resonant structures of the (hypothetical) tetrahedral compound C_4 .

polyhedron is given by the formula

$$F = E - V + 2. \quad (7.8)$$

In a fullerene C_n where $n = V$ three edges meet at each vertex, so we have

$$E = 3V/2, \quad (7.9)$$

$$F = \frac{V}{2} + 2. \quad (7.10)$$

It is shown in Problem 16 that

$$E = \frac{1}{2} \sum_s s F_s, \quad (7.11a)$$

$$V = \frac{1}{3} \sum_s s F_s, \quad (7.11b)$$

where F_s is the number of faces with s sides, and of course,

$$F = \sum_s F_s. \quad (7.12)$$

Combining Eqs. (7.10)–(7.12) gives the fullerene face formula

$$\sum_s (6 - s) F_s = 12. \quad (7.13)$$

This expression does not place any restrictions on the number of hexagons (F_6), but it does severely limit the number of other polyhedra. The two smallest hypothetical fullerenes, the tetrahedron and the cube, have no hexagons, and the larger ones consist of 12 pentagons (F_5), from Eq. (7.13), and numerous hexagons. For example, the molecule C_{60} with $V = 60$ has 12 pentagons and 20 hexagons. Table 7.7 gives the geometric characteristics of the five Platonic solids, the solids generated by truncating all of their vertices, and several other regular polygons, most of which are fullerenes. The fullerenes of current interest are C_{60} and larger molecules consisting of 12 pentagons and numerous hexagons, such as C_{70} , C_{76} , C_{78} , and C_{82} . Some have several varieties, such as the isomers of C_{78} with the symmetries C_{2v} , D_3 , and D_{3h} (Diederich and Whetten, 1992).

The outer diameter of the C_{60} molecule is 7.10 Å and its van der Waals separation is 2.9 Å, so that the nearest-neighbor distance (effective diameter) in a

Table 7.7 Characteristics of Several Regular Solids^a

Figure	Vertices	Edges	Faces	Face (polygon) type
Tetrahedron	4	6	4	all equilateral triangles
Octahedron ^b	6	12	8	all equilateral triangles
Cube	8	12	6	all squares
Icosahedron ^b	12	30	20	all equilateral triangles
Dodecahedron (pentagonal)	20	30	12	all regular pentagons
Hexadecahedron	28	42	16	12 pentagons, 4 hexagons
Truncated tetrahedron	12	18	8	4 equilateral triangles, 4 hexagons
Truncated octahedron	24	36	14	6 squares, 8 hexagons
Truncated cube	24	36	14	8 equilateral triangles, 6 octagons
Dotriacontohedron (truncated icosahedron)	60	90	32	12 regular pentagons, 20 hexagons
Truncated dodecahedron	60	90	32	20 equilateral triangles, 12 decagons
Heptatriacontohedron	70	105	37	12 pentagons (2 regular), 25 hexagons
Tetracontahedron	76	114	40	12 pentagons, 28 hexagons
Hentetracontohedron	78	116	41	12 pentagons, 29 hexagons
Dotetracontohedron	84	126	44	12 pentagons, 32 hexagons
Large Fullerene	n	$\frac{3}{2}n$	$\frac{1}{2}n + 2$	12 pentagons, $\frac{1}{2}n - 10$ hexagons

^a The first five solids are the Platonic solids, and the seventh to eleventh are truncations of the Platonic solids. When carbons occupy the vertices all correspond to fullerenes except the octahedron and the icosahedron for which $3V \neq 2E$. The smallest compounds in this table have never been synthesized.

^b Not a fullerene because the vertices have more than three edges.

solid is 10.0 Å. The bonds shared by a five-membered and a six-membered ring are 1.45 Å long, while those between two adjacent six-membered rings are 1.40 Å long. Above 260 K these molecules form a face centered cubic lattice with lattice constant 14.2 Å; below 260 K it is simple cubic with $a = 7.10$ Å (Fischer *et al.*, 1991; Kasatani *et al.*, 1993; Troullier and Martins, 1992). When C_{60} is doped with alkali metals to form a superconductor it crystallizes into a face centered cubic lattice with larger octahedral and smaller tetrahedral holes for the alkalis. The C_{60} ions are orientationally disordered in the lattice (Gupta and Gupta, 1993).

XII. SYMMETRIES

Earlier in this chapter we mentioned the significance of the horizontal reflection plane σ_h characteristic of the high-temperature superconductors, and noted that most of these superconductors are body centered. In this section we will point out additional symmetries that are present. Table VI-14 of our earlier work (Poole *et al.*, 1988) lists the point symmetries at the sites of the atoms in a number of these compounds.

In the notation of group theory the tetragonal structure belongs to the point group $4/mmm$ (this is the newer international notation for what in the older Schönflies notation was written D_{4h}). The unit cell possesses the inversion operation at the center, so when there is an atom at position (x, y, z) , there will be another identical atom at position $(-x, -y, -z)$. The international symbol $4/mmm$ indicates the presence of a fourfold axis of symmetry C_4 and three mutually perpendicular mirror planes m . The Schönflies notation D_{4h} also specifies the fourfold axis, h signifying a horizontal mirror plane σ_h and D indicating a dihedral group with vertical mirror planes.

We see from Fig. 7.32 that the z -axis is a fourfold (90°) symmetry axis called C_4 , and that perpendicular to it are twofold (180°) symmetry axes along the x and y directions, called C_2 , and also along the diagonal directions (C'_2) in the midplane. There are two vertical mirror planes σ_v , two diagonal mirror planes σ_d which are also vertical, and a horizontal mirror plane σ_h . Additional symmetry operations that are not shown are a 180° rotation C_2^z around the z axis,

$$C_2^z = C_4^z C_4^z, \quad (7.14)$$

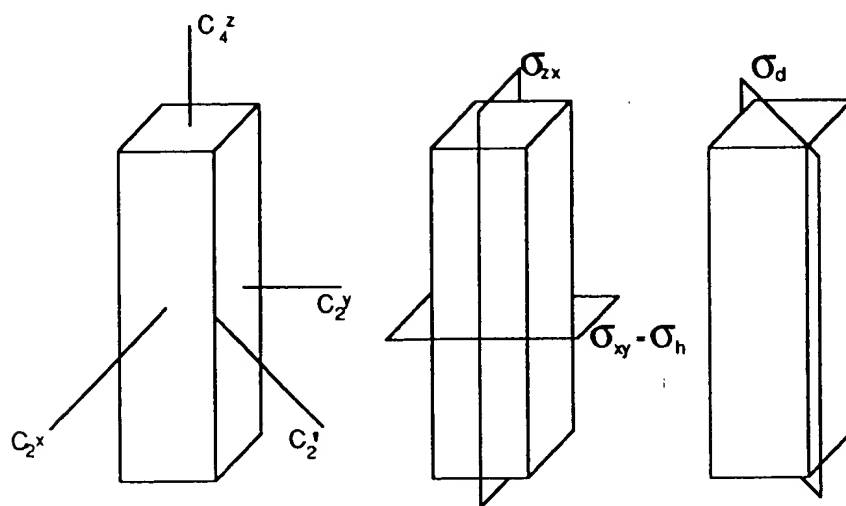


Figure 7.32 Symmetry operations of the tetragonal unit cell showing a fourfold rotation axis C_4 , three twofold axes C_2 , and reflection planes of the vertical $\sigma_{zx} = \sigma_v$, horizontal $\sigma_{xy} = \sigma_h$, and diagonal σ_d types.

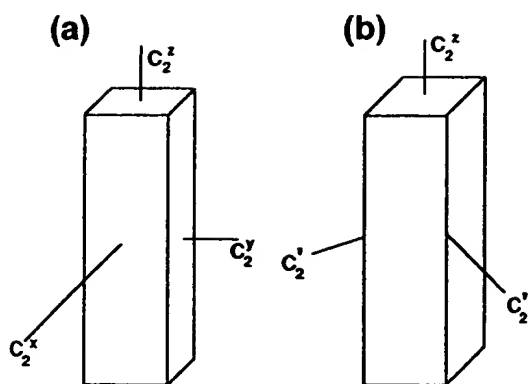


Figure 7.33 Rotational symmetry operations of an orthorhombic unit cell (a) with rectangular distortion, and (b) with rhombal distortion from an originally tetragonal cell.

and the improper fourfold rotation S_4^z around z that corresponds to C_4^z followed by, or preceded by, σ_h ,

$$S_4^z = C_4^z \sigma_h = \sigma_h C_4^z, \quad (7.15)$$

where C_4^z and σ_h commute.

The orthorhombic structure has mmm , D_{2h} symmetry. We see from Fig. 7.33 that both the rectangular and rhombal unit cells, which correspond to Figs. 7.4a and 7.4b, respectively, have three mutually perpendicular twofold axes, and that they also have three mutually perpendicular mirror planes σ , which are not shown. The two cases differ in having their horizontal axes and vertical planes oriented at 45° to each other.

Cubic structures, being much higher in symmetry, have additional symmetry operations, such as fourfold axes C_4^x , C_4^y , and C_4^z along each coordinate direction, threefold axes C_3 along each body diagonal, and numerous other mirror planes. These can be easily seen from an examination of Fig. 7.1. Buckyballs belong to the icosahedral group, which has twofold (C_2), fivefold (C_5), and sixfold (C_6) rotation axes, horizontal reflection planes, inversion symmetry, and sixfold (S_6) and tenfold (S_{10}) improper rotations, for a total of 120 individual symmetry operations in all (Cotton, 1963).

XIII. CRYSTAL CHEMISTRY

In Chapter 3 we briefly described the structures of some classical superconductors, and in this chapter we provided a more detailed discussion of the structures of the cuprate superconductors. The question arises of how structure is related to the presence of metallic and superconducting properties.

Villars and Phillips (1988; Phillips, 1989a) proposed to explain the combinations of elements in compounds that are favorable for superconductivity at relatively high temperatures by assigning three metallic coordinates to each atom, namely an electron number N_e , a size r , and an electronegativity X . The electron numbers are given in Table 3.1 for most of the elements, with $N_e = 3$ for all of the rare earths and actinides; several correlations of N_e with T_c have already been given in Chapter 3. The sizes and electronegativities were determined empirically from a study of some 3,000 binary intermetallic compounds of types AB , AB_2 , AB_3 , and A_2B_5 . The resulting values for each atom are listed in Fig. 7.34 together with their electron numbers. These values, although arrived at empirically on the basis of the constraint of self-consistency, do have a spectroscopic basis, and thus are called, respectively, *spectroscopic radii* and *spectroscopic electronegativities*.

The metallic coordinates of the atoms can be employed to calculate the three Villars–Phillips (VP) coordinates for each compound, namely (a) average number of valence electrons $N_v = \langle N_e \rangle_{av}$, (b) spectroscopic electronegativity difference ΔX , and (c) spectroscopic radius difference ΔR , where we are using the VP notation. For example, for the compound NbN, with $T_c = 17.3$ K, we have, using the data from Fig. 7.34,

$$\begin{aligned} N_v &= \frac{1}{2}(4 + 5) = 4.5, \\ \Delta R &= 2.76 - 0.54 = 2.22, \\ \Delta X &= 2.03 - 2.85 = -0.82. \end{aligned} \quad (7.16)$$

T
P
la

TI
V.
co
60
sit
10

po
are
nat
the
but
 T_c
clu:
sho
Al
met
Nbl

H 1 2.10* 1.25*																
Li 1 0.90 1.61	Be 2 1.45 1.08															
Na 1 0.89 2.65	Mg 2 1.31 2.03															
K 1 0.80 3.69	Ca 2 1.17 3.00	Sc 3 1.50 2.75	Ti 4 1.86 2.58	V 5 2.22 2.43	Cr 6 2.00 2.44	Mn 7 2.04 2.22	Fe 8 1.67 2.11	Co 9 1.72 2.02	Ni 10 1.76 2.18	Cu 11 1.08 2.04	Zn 12 1.44 1.88	Ga 3 1.70 1.695	Ge 4 1.99 1.56	As 5 2.27 1.415	Se 6 2.54 1.285	Br 7 2.83 1.20
Rb 1 0.80 4.10	Sr 2 1.13 3.21	Y 3 1.41 2.94	Zr 4 1.70 2.825	Nb 5 2.03 2.76	Mo 6 1.94 2.72	Tc 7 2.18 2.65	Ru 8 1.97 2.605	Rh 9 1.99 2.52	Pd 10 2.08 2.45	Ag 11 1.07 2.375	Cd 12 1.40 2.215	In 3 1.63 2.05	Sn 4 1.88 1.88	Sb 5 2.14 1.765	Te 6 2.38 1.67	I 7 2.76 1.585
Cs 1 0.77 4.31	Ba 2 1.08 3.402	La 3 1.35 3.08	Hf 4 1.73 2.91	Ta 5 1.94 2.79	W 6 1.79 2.735	Re 7 2.06 2.64	Os 8 1.85 2.65	Ir 9 1.87 2.624	Pt 10 1.91 2.70	Au 11 1.19 2.66	Hg 12 1.49 2.41	Tl 3 1.69 2.235	Pb 4 1.92 2.09	Bi 5 2.14 1.997	Po 6 2.40 1.90	At 7 2.64 1.83
Fr 1 0.70* 4.37*	Ra 2 0.90* 3.53*	Ac 3 1.10* 3.12*														
Ce 3 1.1* 4.50*	Pr 3 1.1* 4.48*	Nd 3 1.2* 3.99*	Pm 3 1.15* 3.99*	Sm 3 1.2* 4.14*	Eu 3 1.15* 3.94*	Gd 3 1.1* 3.91*	Tb 3 1.2* 3.89*	Dy 3 1.15* 3.67*	Ho 3 1.2* 3.65*	Er 3 1.2* 3.63*	Tm 3 1.2* 3.60*	Yb 3 1.1* 3.59*	Lu 3 1.2* 3.37*			
Th 3 1.3* 4.98*	Pa 3 1.5* 4.96*	U 3 1.7* 4.72*	Np 3 1.3* 4.93*	Pu 3 1.3* 4.91*	Am 3 1.3* 4.89*											

Figure 7.34 Periodic table listing metallic valences (upper right), sizes (center), and electronegativities (bottom) in the box of each element, according to the Villars-Phillips model (Phillips, 1989a, p. 321).

The VP coordinates for the A15 compound Ge_3Nb with $T_c = 23.2$ K are calculated as follows:

$$N_v = \frac{1}{4}(4 + 3 \times 5) = 4.75,$$

$$\Delta R = \frac{1}{2}(1.56 - 2.76) = -0.60, \quad (7.17)$$

$$\Delta X = \frac{1}{2}(1.99 - 2.03) = -0.02.$$

The text by Phillips (1989a) tabulates the VP coordinates for more than 60 superconductors with $T_c > 10$ K and for about 600 additional superconductors with transition temperatures in the range $1 < T_c < 10$ K.

When the points for the 600 compounds with lower transition temperatures are plotted on a three-dimensional coordinate system with axes N_v , ΔX , and ΔR , they scatter over a large range of values, but when the points for compounds with $T_c > 10$ K are plotted, they are found to cluster in three regions, called islands, as shown in Fig. 7.35. Island A contains the A15 compounds plus some complex intermetallics, island B consists mainly of the NbN family plus some borides and car-

bides, and island C has closely clustered Chevrel phases, with the high- T_c cuprates on the left. When ternary ferroelectric oxides with Curie temperatures that exceed 500°C are plotted in the same diagram as the superconductors they cluster between the Chevrel group and the cuprates. These ferroelectric oxides are not superconductors, though Phillips (1989a) suggested that doping them with Cu and alkaline earths could produce superconductors with high transition temperatures.

Thus we see that the high transition temperatures of classical superconductors are favored by particular structures and by particular combinations of metallic coordinates for each of these structures. The Villars-Phillips approach provides both structural and atomic criteria for the presence of high T_c .

We have discussed the Phillips approach to a crystal chemistry explanation of the superconductivity of the cuprates. Other researchers have offered alternate, in some cases somewhat related, approaches to understanding the commonali-

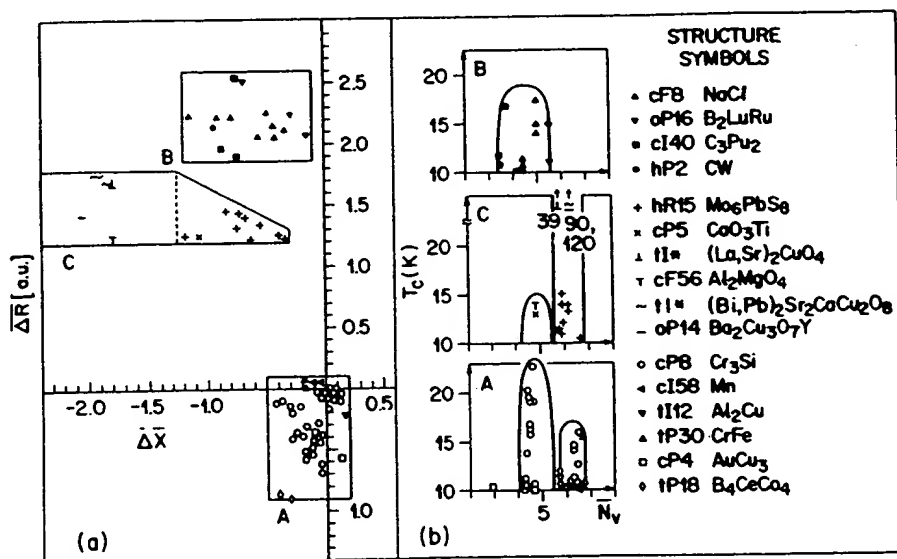


Figure 7.35 Regions in the Villars-Phillips configuration space where superconductivity occurs at relatively high temperatures (Phillips, 1989a, p. 324; Villars and Phillips, 1988).

ties of the various high-temperature and classical superconductors (Adrian, 1992; Schneider, 1992; Tajima and Kitazawa, 1990; Whangbo and Torardi, 1991; Torrace, 1992; Yakhmi and Iyer, 1992; Zhang and Sato, 1993).

XIV. COMPARISON WITH CLASSICAL SUPERCONDUCTOR STRUCTURES

Many elements such as copper and lead are face centered cubic, while many other elements, such as niobium, are body centered cubic, with $a = 3.30 \text{ \AA}$ for Nb. The A15 compounds, such as Nb_3Se , are (simple) cubic with lattice constant $a \approx 3.63\sqrt{2}$ and have parallel chains of Nb atoms 5.14 \AA apart. Other types of classical superconductors, such as the Laves and Chevrel phases, are cubic or close to cubic. The new oxide superconductors are tetragonal or orthorhombic close to tetragonal, and they all have $a \approx b \approx 3.85 \text{ \AA}$, which is somewhat greater than the value for the A15 compounds. The third lattice constant c varies with the compound, with the values 13.2 \AA for $LaSrCuO$, 11.7 \AA for $YBaCuO$, and ≈ 23 to 36 \AA for the

$BiSrCaCuO$ and $TlBaCaCuO$ compounds. These differences occur because the number of copper-oxygen and other planes per unit cell, as well as the spacings between them, vary from compound to compound due to the diverse arrangements of atoms between the layers. Thus relatively high-symmetry crystal structures are characteristic of many superconductors.

XV. CONCLUSIONS

Almost all the high-temperature oxide superconductors have point symmetry D_{4h} ($a = b$) or symmetry close to D_{4h} ($a \approx b$). These superconductors consist of horizontal layers, each of which contains one positive ion and either zero, one, or two oxygens. The copper ions may be coordinated square planar, pyramidal, or octahedral, with some additional distortion. Copper oxide layers are never adjacent to each other, and equivalent layers are never adjacent. The cations alternate sites vertically, as do the oxygens. The copper oxide layers are either flat or slightly puckered, in contrast to the other metal oxide layers, which are generally far from planar. The highest T_c compounds have metal layers

PROBLEMS

(e.g., Ca)
copper oxide

FURTHER

The Wy
1; 1964, Vol.
comprehensi
many import
A15 compou
Tables for λ
dale, 1965,
symmetries
groups. The
 Nb_3Ge , is e

Details
given by Bey
and Glazer
Chapter 6),
(1989). Phill
sion of the
earlier work
symmetries
Billinge *et al.*
temperature
viewed stru

The ir
conductors
viewed by C
and Koelle
stoichiomet
drashekhar
and by Rou
supercondu
(1991) and

The P
Chemical I
reviews of
are edited
Kroto and
haus *et al.*
thallium co
Yakhimi (C
Chu (1995).

PROBLE

1. Show
hole
aton
 $1/r_0$
the
2. Show
hole
ator

(e.g., Ca) with no oxygens between the copper oxide planes.

FURTHER READING

The Wyckoff series, *Crystal Structures* (1963, Vol. 1; 1964, Vol. 2; 1965, Vol. 3; 1968, Vol. 4) provides a comprehensive tabulation of crystal structures, but many important classical superconductors such as the *A15* compounds are not included. The *International Tables for X-Ray Crystallography* (Henry and Lonsdale, 1965, Vol. 1) provide the atom positions and symmetries for all of the crystallographic space groups. The Strukturbericht notation, e.g., *A15* for Nb_3Ge , is explained in Pearson's compilation (1958).

Details of cuprate crystallographic structures are given by Beyers and Shaw (1989; $\text{YBa}_2\text{Cu}_3\text{O}_7$), Burns and Glazer (1990), Hazen (1990), Poole *et al.* (1988, Chapter 6), Santoro (1990), and Yvon and François (1989). Phillips (1989a) provides an extensive discussion of the crystal chemistry of the cuprates. Our earlier work (Poole *et al.*, 1988, p. 107) lists the site symmetries in perovskite and cuprate structures. Billinge *et al.* (1994) reviewed lattice effects in high temperature superconductors, and Zhu (1994) reviewed structural defects in $\text{YBa}_2\text{Cu}_3\text{O}_{7-\delta}$.

The microstructure of high temperature superconductors studied by electron microscopy are reviewed by Chen (1990), Gai and Thomas (1992), Gross and Koelle (1994), and Shekhtman (1993). Oxygen stoichiometry in HTSC's is reviewed by Chandrasekhar *et al.*, (1994), Green and Bagley (1990) and by Routbert and Rothman (1995). Electron-doped superconductors are reviewed by Almasan and Maple (1991) and by Fontcuberta and Fàbrega (1995).

The March 1992 special issue of *Accounts of Chemical Research* (Vol. 25, No. 3) is devoted to reviews of buckminsterfullerenes. Two recent books are edited by Billups and Ciofolini (1993) and by Kroto and Walton (1993), and the review by Dresselhaus *et al.* (1994) are devoted to fullerenes. The thallium compounds were reviewed by Hermann and Yakhimi (1993) and the mercury superconductors by Chu (1995).

PROBLEMS

1. Show that the radius of the octahedral hole in an fcc close-packed lattice of atoms of radius r_0 is equal to $[\sqrt{2} - 1]r_0$. What is the radius of the hole if the lattice is formed from oxygen ions?
2. Show that the radius of the tetrahedral hole in an fcc close-packed lattice of atoms of radius r_0 is equal to $[(3/2)^{1/2} - 1]r_0$. What is the radius of the hole if the lattice is formed from oxygen ions?

3. The "image perovskite" unit cell is generated from the unit cell of Fig. 7.1 by shifting the origin from the point (0,0,0) to the point $(\frac{1}{2}, \frac{1}{2}, \frac{1}{2})$. Sketch this "image" cell. Show that the planes of atoms in this cell are the image planes related by the body centering operation to those of the original perovskite. This image cell is the one that usually appears to represent perovskite in solid-state physics texts.
4. Calculate the distance between the yttrium atom and its nearest-neighbor Ba, Cu, and O atoms in the superconductor $\text{YBa}_2\text{Cu}_3\text{O}_7$.
5. Write down the x, y, z coordinates for the five numbered atoms in the initial plane of Fig. 7.16. Give the explicit symmetry operations, with the proper choice of sign in Eq. (7.5) for each case, that transform these five atoms to their indicated new positions on the other three planes.
6. Explain how the international and Schönflies symbols, mmm and D_{2h} respectively, are appropriate for designating the point group for the orthorhombic superconductors.
7. What are the symmetry operations of the *A15* unit cell of Fig. 3.19?
8. The D_{2h} point group consists of eight symmetry operations that leave an orthorhombic cell unchanged, namely an identity operation E that produces no change, three twofold rotations C_2^i along $i = x, y, z$, three mirror reflection planes σ_{ij} , and an inversion i . Examples of these symmetry operations are

E	$x \rightarrow x$	$y \rightarrow y$	$z \rightarrow z$
C_2^x	$x \rightarrow x$	$y \rightarrow -y$	$z \rightarrow -z$
σ_{xy}	$x \rightarrow x$	$y \rightarrow y$	$z \rightarrow -z$
i	$x \rightarrow -x$	$y \rightarrow -y$	$z \rightarrow -z$

A group has the property that successive application of two symmetry oper-

ations produces a third. Thus, we have, for example,

$$C_2^x \sigma_{xy} = \sigma_{zx}$$

$$C_2^y C_2^x = C_2^z$$

$$i C_2^y = \sigma_{zx}$$

$$\sigma_{zx} \sigma_{yz} = C_2^z.$$

These results have been entered into the following multiplication table for the D_{2h} group. Fill in the remainder of the table. Hint: each element of a group appears in each row and each column of the multiplication table once and only once.

	E	C_2^x	C_2^y	C_2^z	i	σ_{xy}	σ_{yz}	σ_{zx}
E								
C_2^x								
C_2^y								
C_2^z								
i								
σ_{xy}								
σ_{yz}								
σ_{zx}								

- Construct the multiplication table for the D_{4h} point group which contains the 16 symmetry elements that leave a tetragonal unit cell unchanged. Which pairs of symmetry elements A and B do not commute, i.e., such that $AB \neq BA$? Hint: follow the procedures used in Problem 8.
- Draw diagrams analogous to those in Fig. 7.25 for the first two members of the aligned series $\text{TiBa}_2\text{Ca}_n\text{Cu}_{n+1}\text{O}_{5+2n}$, where $n = 0, 1$.
- Draw the analogue of Fig. 7.19 for the Nd_2CuO_4 compound, showing the location of all of the Cu and O atoms. How do Figs. 7.21 and 7.22 differ for Nd_2CuO_4 ?
- Calculate the Villars–Phillips coordinates for the three superconductors MoP_3 , V_3Sn , and NbTi .
- Select one of the compounds ($\text{Ti}_2\text{Ba}_2\text{CuO}_6$, $\text{Bi}_2\text{Sr}_2\text{CaCu}_2\text{O}_8$, $\text{Bi}_2\text{Sr}_2\text{Ca}_2\text{Cu}_3\text{O}_{10}$, $\text{Ti}_2\text{Ba}_2\text{Ca}_2\text{Cu}_3\text{O}_6$) and construct a table for it patterned after Tables 7.5 or 7.6.
- Locate a twofold (C_2), fivefold (C_5), and sixfold (C_6) rotation axis, and also a reflection plane σ_h in the buckyball sketch of Fig. 3.35. How many of each type of operation are there?
- We can see by examining Fig. 3.35 that a buckyball has inversion symmetry. Identify a sixfold (S_6) and tenfold (S_{10}) improper rotation axis, where an improper rotation is understood to involve a sequential inversion and a proper rotation. How many S_6 and how many S_{10} axes are there?
- Show that the total number of edges E in a fullerene is given by

$$E = \frac{1}{2} \sum_s s F_s,$$
 and the number of vortices is

$$V = \frac{1}{3} \sum_s s F_s,$$
 where F_s is the number of faces with s sides.
- Show that the cubic fullerene compound C_8 has nine resonant structures.

I.

the
ter
In
atc
rot
ne:
Ca
the
gen
Ti³
len
elec
bon
did
are
hen

References

- J. Aarts, J. Meiresonne, H. Sprey, W. Maj, and P. Zagwijn, *Phys. Rev. B* **41**, 4739 (1990).
- M. Abbate, M. Sacchi, J. J. Wnuk, L. W. M. Schreurs, Y. S. Wang, R. Lof, and J. C. Fuggle, *Phys. Rev. B* **42**, 7914 (1990).
- M. Abramowitz and I. A. Stegun, Eds., "Handbook of Mathematical Functions," NBS, U.S. Gov. Printing Off., Washington, DC, 1964.
- A. A. Abrikosov, *Zh. Eksp. Teor. Fiz.* **35**, 1442 (1957); *Sov. Phys. JETP* **5**, 1174 (1957).
- D. Achkir, D. Poirier, C. Bourbonnais, G. Quirion, C. Lenoir, P. Batail, and D. Jérôme, *Phys. Rev. B* **47**, 11595 (1993).
- J. V. Acrivos, L. Chen, C. M. Burch, P. Metcalf, J. M. Honig, R. S. Liu, and K. K. Singh, *Phys. Rev. B*, in press.
- S. Adachi, A. Tokiwa-Yamamoto, M. Itoh, K. Isawa, and H. Yamauchi, *Physica C* **214**, 313 (1993).
- F. J. Adrian, *Phys. Rev. Lett.* **61**, 2148 (1988); see also **63**, 688, 690 (1989).
- F. J. Adrian, *Chem. Eng. News* *Dec.* **21**, 24 (1992).
- G. Aepli, S. M. Hayden, H. A. Mook, Z. Fisk, S.-W. Cheong, D. Rytz, J. P. Remeika, G. P. Espinosa, and A. S. Cooper, *Phys. Rev. Lett.* **62**, 2052 (1989).
- N. Agraït, J. G. Rodrigo, and S. Vieira, *Phys. Rev. B* **46**, 5814 (1992).
- N. Agraït, J. G. Rodrigo, and S. Vieira, *Phys. Rev. B* **47**, 12345 (1993).
- I. J. R. Aitchison and N. E. Mavromatos, *Phys. Rev. B* **39**, 6544 (1989).
- M. Akera and T. Andu, in "Proc. 8th Int. Conf. on Elect. Prop. of 2-Dimensional Systems," Grenoble, France, 1989.
- H. Akera, A. H. MacDonald, S. M. Girvin, and M. R. Norman, *Phys. Rev. Lett.* **67**, 2375 (1991).
- J. Akimitsu, S. Suzuki, M. Wantanabe, and H. Sawa, *Jpn. J. Appl. Phys.* **27**, L1857 (1988).
- S. Aktas, "A Numerical Study of Magnetic Vortices in High Kappa Superconductors," Ph.D. thesis, University of South Carolina, 1993.
- S. Aktas, C. P. Poole, Jr., and H. A. Farach, *J. Phys. Condens. Matter* **6**, 7373 (1994).
- N. E. Alekseevskii, N. M. Dobrovolskii, D. Ekkert, and V. I. Tsebro, *JETP* **72**, 1145 (1977).
- M. Alexander, H. Romberg, N. Nücker, P. Adelman, J. Fink, J. T. Markert, M. B. Maple, S. Uchida, H. Takagi, Y. Tokura, A. C. W. P. James, and D. W. Murphy, *Phys. Rev. B* **43**, 333 (1991).
- A. A. Aligia, *Phys. Rev. B* **39**, 6700 (1989).
- K. Allan, A. Campion, J. Zhou, and J. B. Goode-nough, *Phys. Rev. B* **41**, 11572 (1990).

- P. B. Allen, Z. Fisk, and A. Migliori, in "Physical Properties of High Temperature Superconductors" (D. M. Ginsberg, Ed.), Vol. 1, Chap. 5, World Scientific, Singapore, 1989.
- P. B. Allen, in "High-Temperature Superconductivity" (J. W. Lynn, Ed.), Chap. 9, Springer-Verlag, Berlin, 1990.
- J. W. Allen, C. G. Olson, M. B. Maple, J.-S. Kang, L. Z. Liu, J.-H. Park, R. O. Anderson, W. P. Ellis, J. T. Market, Y. Dalichaouch, and R. Liu, *Phys. Rev. Lett.* **64**, 595 (1990).
- H. Alloul, T. Ohno, and P. Mendels, *Phys. Rev. Lett.* **63**, 1700 (1989).
- H. Alloul, A. Mahajan, H. Casalta, and O. Klein, *Phys. Rev. Lett.* **70**, 1171 (1993).
- C. C. Almasan, J. Estrada, C. P. Poole, Jr., T. Datta, H. A. Farach, D. U. Gubser, S. A. Wolf, and L. E. Toth, *Mater. Res. Soc. Symp. Proc.* **99**, 451 (1987).
- C. C. Almasan and M. B. Maple, in "Chemistry of High Temperature Superconductors" (C. N. R. Rao, Ed.), World Scientific, Singapore, 1991.
- C. C. Almasan, S. H. Han, E. A. Early, B. W. Lee, C. L. Seaman, and M. B. Maple, *Phys. Rev. B* **45**, 1056 (1992).
- E. E. Alp, J. C. Campuzano, G. Jennings, J. Guo, D. E. Ellis, L. Beaulaigue, S. Mini, M. Faiz, Y. Zhou, B. W. Veal, and J. Z. Liu, *Phys. Rev. B* **40**, 9385 (1989).
- A. Amato, C. Geibel, F. N. Gyax, R. H. Heffner, E. Knetsch, D. E. MacLaughlin, C. Schank, A. Schenck, F. Steglich, and M. Weber, *Z. Phys. B* **86**, 159 (1992).
- V. Ambegaokar and A. Baratoff, *Phys. Rev. Lett.* **10**, 468 (1963a); **11**, 104 (1963b).
- V. Ambegaokar and U. Eckern, *Phys. Rev. B* **44**, 10358 (1991).
- J. R. Anderson, D. A. Papaconstantopoulos, J. W. McCaffrey, and J. E. Schirber, *Phys. Rev. B* **7**, 5115 (1973).
- P. W. Anderson, *Phys. Rev.* **112**, 1900 (1958).
- P. W. Anderson, *Phys. Rev. B* **115**, 2 (1959).
- P. W. Anderson, *Phys. Rev. Lett.* **9**, 309 (1962).
- P. W. Anderson and J. M. Rowell, *Phys. Rev. Lett.* **10**, 230 (1963).
- P. W. Anderson and Y. B. Kim, *Rev. Mod. Phys.* **36**, 39 (1964).
- P. W. Anderson, *Science* **235**, 1196 (1987a); *Phys. Rev. Lett.* **59**, 2497 (1987b).
- P. W. Anderson, in "Frontiers and Borderlines of Many Particle Physics," Int. School of Physics "Enrico Fermi," North-Holland, Varenna, 1987.
- P. W. Anderson and Z. Zou, *Phys. Rev. Lett.* **60**, 132 (1988). (Reprinted in Halley, 1988).
- P. W. Anderson, *Phys. Rev. Lett.* **64**, 1839 (1990a); **65**, 2306 (1990b).
- P. W. Anderson, *Physica C* **185-189**, 11 (1991).
- P. W. Anderson and R. Schrieffer, *Physics Today*, June 1991, p. 54.
- P. W. Anderson, *Science* **256**, 1526 (1992).
- P. W. Anderson, "A Career in Theoretical Physics," World Scientific, Singapore, 1994a.
- P. W. Anderson, *Amer. Scientist* **82**, 379 (1994b).
- M. Andersson and Ö. Rapp, *Phys. Rev. B* **44**, 7722 (1991).
- Y. Ando, N. Motohira, K. Kitazawa, J. Takeya, and S. Akita, *Jpn. J. Appl. Phys.* **30**, L1635 (1991a); *Phys. Rev. Lett.* **67**, 2737 (1991b).
- B. Andraka, J. S. Kim, G. R. Stewart, K. D. Carlson, H. H. Wang, and J. M. Williams, *Phys. Rev. B* **40**, 11345 (1989).
- O. A. Anikeenok, M. V. Eremin, R. Sh. Zhdanov, V. V. Naletov, M. P. Rodionova, and M. A. Teplov, *JETP Lett.* **54**, 149 (1991).
- V. I. Anisimov, M. A. Korotin, J. Zaanen, and P. L. Andersen, *Phys. Rev. Lett.* **68**, 345 (1992).
- S. M. Anlage, M. Pambianchi, A. T. Findikoglu, C. Doughty, D.-H. Wu, J. Mao, S.-N. Mao, X. X. Xi, T. Venkatesan, J. L. Peng, and R. L. Greene, *Proc. SPIE Conf. on Oxide Superconductivity*, Vol. 2158 (D. Pavuna, Ed.), in press, 1994.
- J. F. Annett, N. Goldenfeld, and S. R. Renn, in "Physical Properties of High Temperature Superconductors" (D. M. Ginsberg, Ed.), Vol. 2, Chap. 9, World Scientific, Singapore, 1990.
- E. J. Ansaldo, C. Niedermayer, H. Glückler, C. E. Stronach, T. M. Riseman, R. S. Cary, D. R. Noakes, X. Obradors, A. Fuetes, J. M. Navarro, P. Gomez, N. Casañ, B. Martinez, F. Perez, J. Rodriguez-Carvajal, and K. Chow, *Physica C* **185-189**, 1213 (1991a).
- E. J. Ansaldo, C. Niedermayer, and C. E. Stronach, *Nature* **353**, 121 (1991b).
- V. P. Antropov, I. I. Mazin, O. K. Andersen, A. I. Liechtenstein, and O. Jepsen, *Phys. Rev. B* **47**, 12373 (1993).
- J. Aponte, H. C. Abache, A. Sa-Neto, and M. Octavio, *Phys. Rev. B* **39**, 2233 (1989).
- B. Arfi, *Phys. Rev. B* **45**, 2352 (1992).
- G. Arfken, "Mathematical Methods for Physicists," 3rd ed., Wiley, New York, 1985.
- T. A. Arias and J. D. Joannopoulos, *Phys. Rev. B* **39**, 4071 (1989).
- D. N. Aristov, S. V. Maleyev, and A. G. Yashenkin, *Phys. Rev. B* **48**, 3527 (1993).
- A. J. Arko, R. S. List, R. J. Bartlett, S.-W. Cheong, Z. Fisk, J. D. Thompson, C. G. Olson, A.-B. Yang, R. Liu, C. Gu, B. W. Veal, J. Z. Liu, A. P. Plaulikas, K. Vandervoort, H. Claus, J. C. Campuzano, J. E. Schirber, and N. D. Shinn, *Phys. Rev. B* **40**, 2268 (1989).
- G. B. Arnold, F. M. Mueller, and J. C. Swihart, *Phys. Rev. Lett.* **67**, 2569 (1991).
- A. G. Aronov, S. Hikami, and A. I. Larkin, *Phys. Rev. Lett.* **62**, 965, 2236(E), (1989).
- D. Arovas, J. R. Schrieffer, and F. Wilczek, *Phys. Rev. Lett.* **53**, 722 (1984).
- E. Arrigoni, G. Strinati, and C. Castellani, *Phys. Rev. B* **41**, 4838 (1990).

- E. Arrigoni and G. C. Strinati, *Phys. Rev. B* **44**, 7455 (1991).
- K. Asayama, G.-Q. Zheng, Y. Kitaoka, K. Ishida, and K. Fujiwara, *Physica C* **178**, 281 (1991).
- N. W. Ashcroft and N. D. Mermin, "Solid State Physics," Saunders, Philadelphia, 1976.
- M. Ashida, S. Aoyama, J. Hara, and K. Nagai, *Phys. Rev. B* **40**, 8673 (1989).
- M. Ashida, J. Hara, and K. Nagai, *Phys. Rev. B* **45**, 828 (1992).
- J. Ashkenazi, S. E. Barnes, F. Zuo, G. C. Vezzoli, and B. M. Klein, Eds., "High Temperature Superconductivity," Plenum, New York, 1991.
- T. R. Askew, R. B. Flippen, K. J. Leary, M. N. Kunchur, *J. Mater. Res.* **6**, 1135 (1991).
- L. G. Aslamazov and A. I. Larkin, *Fiz. Tverd. Tela* **10**, 1104 (1968) [*Sov. Phys. Solid State* **10**, 875 (1968)].
- W. Assmus, M. Herrmann, U. Rauchschwalbe, S. Riegel, W. Lieke, H. Spille, S. Horn, G. Weber, F. Steglich, and G. Cordier, *Phys. Rev. Lett.* **52**, 469 (1984).
- K. S. Athreya, O. B. Hyun, J. E. Ostenson, J. R. Clem, and D. K. Finnemore, *Phys. Rev. B* **38**, 11846 (1988).
- A. Auerbach, "Interacting Electrons and Quantum Magnetism," Springer-Verlag, Berlin, 1994.
- B. Aurivillius, *Ark. Kemi* **1**, 463, 499 (1950).
- B. Aurivillius, *Ark. Kemi* **2**, 519 (1951).
- B. Aurivillius, *Ark. Kemi* **5**, 39 (1952).
- C. Ayache, I. L. Chaplygin, A. I. Kirilyuk, N. M. Kreines, and V. I. Kudinov, *Solid State Commun.* **81**, 41 (1992).
- J. Azoulay, *Phys. Rev. B* **44**, 7018 (1991).
- E. Babic, M. Prester, D. Drobac, Ž. Marohnic, and N. Biškup, *Phys. Rev. B* **43**, 1162 (1991).
- E. Babic, M. Prester, D. Drobac, Ž. Marohnic, P. Nozar, P. Stastny, F. C. Maticcotta, and S. Bernik, *Phys. Rev. B* **45**, 913 (1992).
- P. K. Babu and J. Ramakrishna, *Supercond. Rev.* **1**, 75 (1992).
- D. C. Baird and B. K. Mukherjee, *Phys. Rev. Lett.* **21**, 996 (1968).
- D. C. Baird and B. K. Mukherjee, *Phys. Rev.* **3**, 1043 (1971).
- C. K. Bak and N. F. Pedersen, *Appl. Phys. Lett.* **22**, 149 (1973).
- O. N. Bakharev, A. V. Dooglav, A. V. Egorov, V. V. Naletov, M. P. Rodionova, M. S. Tagirov, and M. A. Teplov, *Appl. Magn. Reson.* **2**, 559 (1991).
- J. Bala and A. M. Oleś, *Phys. Rev. B* **47**, 515 (1993).
- C. J. Ballhausen, "Introduction to Ligand Field Theory," McGraw-Hill, New York, 1962.
- M. Ban, T. Ichiguchi, and T. Onogi, *Phys. Rev. B* **40**, 4419 (1989).
- A. Bansil, P. E. Mijnarends, and L. C. Smedskjaer, *Phys. Rev. B* **43**, 3667 (1991).
- A. Bansil and S. Kaprzyk, *Phys. Rev. B* **43**, 10335 (1991).
- A. Bansil (Ed.), "Proc. Conf. Spectroscopies in Novel Superconductors," *J. Phys. Chem. Solids*, in press.
- A. Baratoff and G. Binnig, *Physica B* **188**, 1335 (1981).
- B. Barbiellini, P. Genoud, J. Y. Henry, L. Hoffmann, T. Jarlborg, A. A. Manuel, S. Massidda, M. Peter, W. Sadowski, H. J. Scheel, A. Shukla, A. K. Singh, and E. Walker, *Phys. Rev. B* **43**, 7810 (1991).
- J. Bardeen, L. N. Cooper, and J. R. Schrieffer, *Phys. Rev.* **108**, 1175 (1957).
- J. Bardeen and M. P. Stephen, *Phys. Rev. A* **140**, 1197 (1965).
- R. Bar-Deroma, J. Felsteiner, R. Brenner, J. Ashkenazi, and D. van der Marel, *Phys. Rev. B* **45**, 2361 (1992).
- C. Barlingay, V. Garcia-Vázquez, C. M. Falco, S. Mazumdar, and S. H. Risbud, *Phys. Rev. B* **41**, 4797 (1990).
- A. Barone and G. Paterno, "Physics and Applications of the Josephson Effect," Wiley, New York, 1982.
- S. E. Barrett, D. J. Durand, C. H. Pennington, C. P. Slichter, T. A. Friedmann, J. P. Ricé, and D. M. Ginsberg, *Phys. Rev. B* **41**, 6283 (1990).
- S. E. Barrett, J. A. Martindale, D. J. Durand, C. H. Pennington, C. P. Slichter, T. A. Friedmann, J. P. Rice, and D. M. Ginsberg, *Phys. Rev. Lett.* **66**, 108 (1991).
- J. C. Barry, Z. Iqbal, B. L. Ramakrishna, H. Eckhardt, F. Reidinger, and R. Sharma, *Appl. Phys. Lett.* No. 71.70-b (1989).
- S. G. Barsov, A. L. Getalov, V. P. Koptev, L. A. Kuz'min, S. M. Mikirtych'yants, N. A. Tarasov, G. V. Shcherbakov, N. M. Kotov, A. S. Nigmatulin, Ya. M. Mukovskii, V. G. Grebinnik, V. N. Duginov, V. A. Zhukov, A. B. Lazarev, V. G. Ol'shevskii, S. N. Shilov, and E. P. Krasnoperov, *JETP Lett.* **46**, 499 (1987).
- K. Bartkowski, R. Horyn, A. J. Zaleski, Z. Bukowski, M. Horobiowski, C. Marucha, J. Rafalowicz, K. Rogacki, A. Stepień-Damm, C. Sulkowski, E. Trojanar, and J. Klamut, *Phys. Status Solidi* **103**, K37 (1987).
- F. E. Bates, *Phys. Rev. B* **39**, 322 (1989).
- B. Batlogg, A. P. Ramirez, R. J. Cava, R. B. van Dover, and E. A. Reitman, *Phys. Rev. B* **35**, 5340 (1987).
- B. Batlogg, R. J. Cava, L. W. Rupp, Jr., A. M. Muijsce, J. J. Krajewski, J. P. Remeika, W. F. Peck, Jr., A. S. Cooper, and G. P. Espinosa, *Phys. Rev. Lett.* **61**, 1670 (1988).
- P. E. Batson, T. M. Shaw, D. Dimos, and P. R. Duncombe, *Phys. Rev. B* **43**, 6236 (1991).
- B. W. Batterman and C. S. Barrett, *Phys. Rev. Lett.* **13**, 390 (1964).
- G. Baym and C. Pethick, "Landau Fermi-Liquid Theory," Wiley, New York, 1991.
- C. P. Bean, *Phys. Rev. Lett.* **8**, 250 (1962).
- C. P. Bean, *Rev. Mod. Phys.* **36**, 31 (1964).
- M. R. Beasley, R. Labusch, and W. W. Webb, *Phys. Rev.* **181**, 682 (1969).

- J. G. Bednorz and K. A. Müller, *Z. Phys. B* **64**, 189 (1986).
- J. G. Bednorz and K. A. Müller (Eds.), "Earlier and Recent Aspects of Superconductivity," Springer-Verlag, Berlin, 1990.
- C. W. J. Beenakker and H. van Houten, *Phys. Rev. Lett.* **66**, 3056 (1991).
- V. P. Belash, E. Z. Kurmaev, and S. A. Nemnonov, *Fiz. Met. Metalloved* **37**, 659 (1974).
- D. Belitz, in "High Temperature Superconductivity" (J. W. Lynn, Ed.), Chap. 2, Springer-Verlag, Berlin, 1990.
- R. Benedek and H.-B. Schüttler, *Phys. Rev. B* **41**, 1789 (1990).
- L. H. Bennett, Y. Flom, and G. C. Vezzoli, in "Proceedings High T_c Superconductors: Magnetic Interactions, Gaithersburg, MD," World Scientific, Singapore, 1989.
- M. A. Beno, L. Soderholm, D. W. Capone II, D. G. Hinks, J. D. Jorgensen, J. D. Grace, I. K. Schuller, C. U. Segre, and K. Zhang, *Appl. Phys. Lett.* **51**, 57 (1987).
- V. L. Berezinskii, *Sov. Phys. JETP* **34**, 610 (1972).
- D. D. Berkley, E. F. Skelton, N. E. Moulton, M. S. Osofsky, W. T. Lechter, V. M. Browning, and D. H. Liebenberg, *Phys. Rev. B* **47**, 5524 (1993).
- A. J. Berlinsky, C. Kallin, G. Rose, and A.-C. Shi, *Phys. Rev. B* **48**, 4074 (1993).
- R. Berman and D. K. C. MacDonald, *Proc. R. Soc. London Ser. A* **211**, 122 (1952).
- R. Beyers and T. M. Shaw, *Solid State Phys.* **42**, 135 (1989).
- R. Beyers and B. T. Ahn, *Annu. Rev. Mater. Sci.* **21**, 335 (1991).
- A. Bezing, K. Yvon, and J. Muller, *Solid State Commun.* **63**, 141 (1987).
- R. Bhagavatula, C. Ebner, and C. Jayaprakash, *Phys. Rev. B* **45**, 4774 (1992).
- K. V. Bhagwat and P. Chaddah, *Physica C* **166**, 1 (1990).
- K. V. Bhagwat and P. Chaddah, *Physica C* **190C**, 444 (1992).
- A. Bharathi, C. S. Sundar, W. Y. Ching, Y. C. Jean, P. H. Hor, Y. Y. Xue, and C. W. Chu, *Phys. Rev. B* **42**, 10199 (1990).
- A. K. Bhatnagar, R. Pan, D. G. Naugle, P. J. Squitrito, A. Clearfield, Z. Z. Sheng, Q. A. Shams, and A. M. Hermann, *Solid State Commun.* **73**, 53 (1990).
- R. N. Bhatt, *Phys. Rev. B* **16**, 1915 (1977).
- R. N. Bhatt, *Phys. Rev. B* **17**, 2947 (1978).
- A. Bhattacharya and C. S. Wang, *Phys. Rev. B* **45**, 10826 (1992).
- J. B. Bieri and K. Maki, *Phys. Rev. B* **42**, 4854 (1990).
- B. D. Biggs, M. N. Kunchur, J. J. Lin, S. J. Poon, T. R. Askew, R. B. Flippen, M. A. Subramanian, J. Gopalakrishnan, and A. W. Sleight, *Phys. Rev. B* **39**, 7309 (1989).
- S. J. L. Billinge, G. H. Kwei, and J. D. Thompson, in "Strongly Correlated Electronic Materials" (K. S. Bedell, Ed.) Addison-Wesley, New York, 1994.
- W. E. Billups and M. A. Ciufolini (Eds.), "Buckminster Fullerenes," VCH, New York, 1993.
- K. Binder and A. P. Young, *Rev. Mod. Phys.* **58**, 801 (1986).
- B. Binnig, A. C. Castellano, M. De Santis, P. Rudolf, P. Lagarde, A. M. Frank, and A. Marcelli, *Solid State Commun.* **63**, 1009 (1980).
- M. A. Biondi and M. P. Garfunkel, *Phys. Rev.* **116**, 853 (1959).
- R. J. Birgeneau, C. Y. Chen, D. R. Gabbe, H. P. Jenssen, M. A. Kastner, C. J. Peters, P. J. Picone, T. Thio, T. R. Thurston, H. L. Tuller, A. D. Axe, P. Böni, and G. Shirane, *Phys. Rev. Lett.* **59**, 1329 (1987).
- R. J. Birgeneau, D. R. Gabbe, H. P. Jenssen, M. A. Kastner, P. J. Picone, T. R. Thurston, G. Shirane, Y. Endoh, M. Sato, K. Yamada, Y. Hidaka, M. Oda, Y. Enomoto, M. Suzuki, and T. Murakami, *Phys. Rev. B* **38**, 6614 (1988).
- R. J. Birgeneau and G. Shirane, in "Physical Properties of High Temperature Superconductors" (D. M. Ginsberg, Ed.), Vol. 1, Chap. 4, World Scientific, Singapore, 1989.
- P. Birrer, F. N. Gyax, B. Hitti, E. Lippelt, A. Schenck, M. Weber, D. Cattani, J. Cors, M. Decroux, and Ø. Fischer, *Phys. Rev. B* **48**, 15689 (1993).
- D. Bishop, C. M. Varma, B. Batlogg, E. Bucher, Z. Fisk, and J. L. Smith, *Phys. Rev. Lett.* **53**, 1009 (1984).
- H. D. Bist, T. Datta, T. S. Little, J. C. Thigpen, Jr., J. R. Durig, P. R. Broussard, and D. D. Berkley, *J. Raman Spectrosc.* **22**, 639 (1991).
- F. Bitter, *Phys. Rev.* **38**, 1903 (1931).
- B. L. Blackford and R. H. March, *Canad. J. Phys.* **46**, 141 (1968).
- H. A. Blackstead, *J. Supercond.* **5**, 67 (1992).
- H. A. Blackstead, *Phys. Rev. B* **47**, 11411 (1993).
- E. J. Blagoeva, G. Busiello, L. De Cesare, Y. T. Millev, I. Rabuffo, and D. I. Uzunov, *Phys. Rev. B* **40**, 7357 (1989).
- E. J. Blagoeva, G. Busiello, L. De Cesare, Y. T. Millev, I. Rabuffo, and D. I. Uzunov, *Phys. Rev. B* **42**, 6124 (1990).
- G. Blatter, J. Rhyner, and V. M. Vinokur, *Phys. Rev. B* **43**, 7826 (1991a).
- G. Blatter, V. B. Geshkenbein, and V. M. Vinokur, *Phys. Rev. Lett.* **66**, 3297 (1991b).
- G. Blatter, B. I. Ivlev, and J. Rhyner, *Phys. Rev. Lett.* **66**, 2392 (1991c).
- G. Blatter, V. B. Geshkenbein, and A. I. Larkin, *Phys. Rev. Lett.* **68**, 875 (1992).
- G. Blatter and B. Ivlev, *Phys. Rev. Lett.* **70**, 2621 (1993).
- G. Blatter, M. V. Feigel'man, V. B. Geshkenbein, A. I. Larkin, and V. M. Vinokur, *Rev. Mod. Phys.* **66**, 1125 (1994).

- K. W. Blazey, K. A. Müller, J. G. Bednorz, W. Berlinger, G. Amoretti, E. Buluggiu, A. Vera, and F. C. Matarotta, *Phys. Rev. B* **36**, 7241 (1987).
- J. E. Blendell, C. K. Chiang, D. C. Cranmer, S. W. Freiman, E. R. Fuller, Jr., E. Drescher-Krasicka, W. L. Johnson, H. M. Ledbetter, L. H. Bennett, L. J. Swartzendruber, R. B. Marinenko, R. L. Mykleburst, D. S. Bright, and D. E. Newbury, *ACS Symp. Ser.* **351**, 240 (1987).
- B. Blok and H. Monien, *Phys. Rev. B* **47**, 3454 (1993).
- N. Bluzer, *Phys. Rev. B* **44**, 10222 (1991).
- G. S. Boebinger, T. T. M. Palstra, A. Passner, M. J. Rosseinsky, D. W. Murphy, and I. I. Mazin, *Phys. Rev. B* **46**, 5876 (1992).
- M. Boekholt, M. Hoffmann, and G. Güntherodt, *Physica C* **175C**, 127 (1991).
- C. A. Bolle, P. I. Gammel, D. G. Grier, C. A. Murray, D. J. Bishop, D. B. Mitzi, and A. Kapitulnik, *Phys. Rev. Lett.* **66**, 112 (1991).
- J. E. Bonevich, K. Harada, T. Matsuda, H. Kasai, T. Yoshida, G. Pozzi, and A. Tonomura, *Phys. Rev. Lett.* **70**, 2952 (1993).
- P. Böni, J. D. Axe, G. Shirane, R. J. Birgeneau, D. R. Gabbe, H. P. Jenssen, M. A. Kastner, C. J. Peters, P. J. Picone, and T. R. Thurston, *Phys. Rev. B* **38**, 185 (1988).
- E. Bonjour, R. Calemczuk, J. Y. Henry, and A. F. Khoder, *Phys. Rev. B* **43**, 106 (1991).
- D. A. Bonn, A. H. O'Reilly, J. E. Greedan, C. V. Stager, T. Timusk, K. Kamarás, and D. B. Tanner, *Phys. Rev. B* **37**, 1574 (1988).
- B. P. Bonner, R. Reichlin, S. Martin, H. B. Radousky, T. J. Folkerts, and R. N. Shelton, *Phys. Rev. B* **41**, 11576 (1990).
- N. Bontemps, D. Davidov, P. Monod, and R. Even, *Phys. Rev. B* **43**, 11512 (1991).
- P. Boolchand, C. Blue, K. Elgaid, I. Zitkovsky, D. McDaniel, W. Huff, B. Goodman, G. Lemon, D. E. Farrell, and B. S. Chandrasekhar, *Phys. Rev. B* **38**, 11313 (1988).
- P. Boolchand, S. Pradhan, Y. Wu, M. Abdelgadir, W. Huff, D. Farrell, R. Coussement, and D. McDaniel, *Phys. Rev. B* **45**, 921 (1992).
- P. Bordet, C. Chaillout, J. Chenavas, J. L. Hodeau, M. Marezio, J. Karpinski, and E. Kaldis, *Nature (London)* **334**, 596 (1988).
- H. J. Bornemann, D. E. Morris, C. Steinleitner, and G. Czjzek, *Phys. Rev. B* **44**, 12567 (1991).
- F. Borsa, A. Rigamonti, M. Corti, J. Ziolo, O. Hyun, and D. R. Torgeson, *Phys. Rev. Lett.* **68**, 698 (1992).
- I. Bose, *Phys. Rev. B* **43**, 13602 (1991).
- R. Böttner, N. Schroeder, E. Dietz, U. Gerhardt, W. Assmus, and J. Kowalewski, *Phys. Rev. B* **41**, 8679 (1990).
- L. Bottyán, B. Molnár, D. L. Nagy, I. S. Szücs, J. Tóth, J. Dengler, G. Ritter, and J. Schober, *Phys. Rev. B* **38**, 11373 (1988).
- R. Boyn, K. Löbe, H.-U. Habermeier, and N. Pruß, *Physica C* **181C**, 75 (1991).
- I. Božovic, K. Char, S. J. B. Yoo, A. Kapitulnik, M. R. Beasley, T. H. Geballe, Z. Z. Wang, S. Hagen, N. P. Ong, D. E. Aspnes, and M. K. Kelly, *Phys. Rev. B* **38**, 5077 (1988).
- I. Božovic, J. H. Kim, J. S. Harris, Jr., and W. Y. Lee, *Phys. Rev. B* **43**, 1169 (1991).
- I. Božovic, *J. Supercond.* **4**, 193 (1991).
- I. Božovic, J. H. Kim, J. S. Harris, Jr., E. S. Hellman, E. H. Hartford, and P. K. Chan, *Phys. Rev. B* **46**, 1182 (1992).
- A. I. Braginski, *Physica C* **180**, 642 (1991).
- B. H. Brandow, *J. Solid State Chem.* **88**, 28 (1990).
- E. H. Brandt, *Physica C* **162C-164C**, 1167 (1989).
- E. H. Brandt, *Physica B* **165-166**, 1129 (1990); *Int. Conf. Low Temperature Phys.*, Brighton, U.K., August 1990.
- E. H. Brandt and A. Sudbø, *Physica C* **180C**, 426 (1991).
- E. H. Brandt, *Phys. Rev. Lett.* **69**, 1105 (1992).
- A. Brass, H. J. Jensen, and A. J. Berlinsky, *Phys. Rev. B* **39**, 102 (1989).
- A. Brass and H. J. Jensen, *Phys. Rev. B* **39**, 9587 (1989).
- D. A. Brawner, A. Schilling, H. R. Ott, R. J. Haug, K. Ploog, and K. von Klitzing, *Phys. Rev. Lett.* **71**, 785 (1993).
- Y. J. M. Brechet, B. Douçot, H. J. Jensen, and A.-C. Shi, *Phys. Rev. B* **42**, 2116 (1990).
- E. Brézin, A. Fujita, and S. Hikami, *Phys. Rev. Lett.* **65**, 1949 (1990).
- G. Briceño, M. F. Crommie, and A. Zettl, *Phys. Rev. Lett.* **66**, 2164 (1991).
- D. Brinkmann and M. Mali, in "NMR Basic Principles and Progress," Vol. 31, Springer-Verlag, Berlin, 1994.
- M. B. Brodsky, R. C. Dynes, K. Kitazawa, and H. L. Tuller (Eds.), "High Temperature Superconductors," Vol. 99, Materials Research Society, Pittsburgh, 1988.
- C. Broholm, G. Aeppli, R. N. Kleiman, D. R. Harshman, D. J. Bishop, E. Bucher, D. Li. Williams, E. J. Ansaldo, and R. H. Heffner, *Phys. Rev. Lett.* **65**, 2062 (1990).
- N. B. Brookes, A. J. Viescas, P. D. Johnson, J. P. Remeika, A. S. Cooper, and N. V. Smith, *Phys. Rev. B* **39**, 2736 (1989).
- J. S. Brooks, C. C. Agosta, S. J. Klepper, M. Tokumoto, N. Kinoshita, H. Anzai, S. Uji, H. Aoki, A. S. Perel, G. J. Athas, and D. A. Howe, *Phys. Rev. Lett.* **69**, 156 (1992).
- S. D. Brorson, A. Kazeroonian, J. S. Moodera, D. W. Face, T. K. Cheng, E. P. Ippen, M. S. Dresselhaus, and G. Dresselhaus, *Phys. Rev. Lett.* **64**, 2172 (1990).
- P. R. Broussard, *Phys. Rev. B* **43**, 2783 (1991).
- P. Brüll, D. Kirchgässner, and P. Liederer, *Physica C* **182C**, 339 (1991).
- T. Brun, M. Grimsditch, K. E. Gray, R. Bhadra, V. Maroni, and C. K. Loong, *Phys. Rev. B* **35**, 8837 (1987).

- L. C. Brunel, S. G. Louie, G. Martinez, S. Labdi, and H. Raffy, *Phys. Rev. Lett.* **66**, 1346 (1991).
- O. Brunner, L. Antognazza, J.-M. Triscone, L. Miéville, and Ø. Fischer, *Phys. Rev. Lett.* **67**, 1354 (1991).
- R. Brusetti, A. J. Dianoux, P. Gougeon, M. Potel, E. Bonjour, and R. Calemczuk, *Phys. Rev. B* **41**, 6315 (1990).
- W. Buckel, "Superconductivity, Fundamentals and Applications," VCH, Weinheim, Germany, 1991.
- R. C. Budhani, L. Lesyna, D. DiMarzio, H. Wiesmann, and G. P. Williams, *Phys. Rev. B* **44**, 7087 (1991).
- J. I. Budnick, A. Golnik, Ch. Niedermayer, E. Recknagel, M. Rossmanith, A. Weidinger, B. Chamberland, M. Filipkowski, and D. P. Yang, *Phys. Lett. A* **124**, 103 (1987).
- J. I. Budnick, B. Chamberland, D. P. Yang, Ch. Niedermayer, A. Golnik, E. Recknagel, M. Rossmanith, and A. Weidinger, *Europhys. Lett.* **5**, 651 (1988).
- L. N. Bulaevskii, *Zh. Eksp. Teor. Fiz.* **64**, 2241 (1973); *Sov. Phys. JETP (Engl. Trans.)* **37**, 1133 (1988).
- L. N. Bulaevskii, O. V. Dolgov, and M. O. Pitsyn, *Phys. Rev. B* **38**, 11290 (1988).
- L. N. Bulaevskii and M. V. Zyskin, *Phys. Rev. B* **42**, 10230 (1990).
- L. N. Bulaevskii and I. D. Vagner, *Phys. Rev. B* **43**, 8694 (1991).
- L. N. Bulaevskii, *Phys. Rev. B* **44**, 910 (1991).
- L. N. Bulaevskii, M. Ledvij, and V. G. Kogan, *Phys. Rev. B* **46**, 366, 11807 (1992).
- N. Bulut and D. J. Scalapino, *Phys. Rev. B* **45**, 2371 (1992).
- G. Burns, "Solid State Physics," Academic Press, Orlando, FL 1985.
- G. Burns, B. V. Chandrashekhar, F. H. Dacol, M. W. Shafer, and P. Strobel, *Solid State Commun.* **67**, 603 (1988).
- G. Burns, P. Strobel, G. V. Chandrashekhar, F. H. Dacol, F. Holtzberg, and M. W. Shafer, *Phys. Rev. B* **39**, 2245 (1989).
- G. Burns and A. M. Glazer, "Space Groups for Solid State Scientists," Academic Press, San Diego, 1990.
- G. Burns, "High Temperature Superconductivity: An Introduction," Academic Press, Boston, 1992.
- M. J. Burns, *Phys. Rev. B* **40**, 5473 (1989).
- R. Busch, G. Ries, H. Werthner, G. Kreiselmeier, and G. Saemann-Ischenko, *Phys. Rev. Lett.* **69**, 522 (1992).
- G. Busiello and D. I. Uzunov, *Phys. Rev. B* **42**, 1018 (1990).
- G. Busiello, L. De Cesare, Y. T. Millev, I. Rabuffo, and D. I. Uzunov, *Phys. Rev. B* **43**, 1150 (1991).
- A. Bussmann-Holder and A. R. Bishop, *Phys. Rev. B* **44**, 2853 (1991).
- A. I. Buzdin, *Phys. Rev. B* **47**, 11416 (1993).
- B. Cabrera, C. E. Cunningham, and D. Saroff, *Phys. Rev. Lett.* **62**, 2040 (1989).
- Z.-X. Cai and D. O. Welch, *Phys. Rev. B* **45**, 2385 (1992).
- J. Callaway, "Energy Band Theory," Academic Press, New York, 1964.
- H. B. Callen, "Thermodynamics and an Introduction to Thermostatistics," Wiley, New York, 1985.
- P. Calvani, M. Capizzi, S. Lupi, P. Maselli, and E. Agostinelli, *Physica C* **180C**, 116 (1991).
- I. A. Campbell, L. Fruchter, and R. Cabanel, *Phys. Rev. Lett.* **64**, 1561 (1990).
- J. C. Campuzano, G. Jennings, M. Faiz, L. Beaulaigue, B. W. Veal, J. Z. Liu, A. P. Paulikas, K. Vandervoort, H. Claus, R. S. List, A. J. Arko, and R. L. Bartlett, *Phys. Rev. Lett.* **64**, 2308 (1990).
- J. C. Campuzano, L. C. Smedskjaer, R. S. Benedek, G. Jennings, and A. J. Bansil, *Phys. Rev. B* **43**, 2788 (1991).
- J. J. Capponi, C. Chaillout, A. W. Hewat, P. LeJay, M. Marezio, N. Nguyen, B. Raveau, J. L. Soubeyrou, J. L. Tholence, and R. Tournier, *Europhys. Lett.* **3**, 1301 (1987).
- J. P. Carbotte, *Rev. Mod. Phys.* **62**, 1027 (1990).
- J. R. Carbotte and C. Jiang, *Phys. Rev. B* **48**, 4231 (1993).
- M. Cardona, *Physica C* **185C-189C**, 65 (1991).
- G. Carneiro, *Phys. Rev. B* **45**, 2391 (1992).
- P. Carretta and M. Corti, *Phys. Rev. Lett.* **68**, 1236 (1992).
- P. Carretta and M. Corti, *Phys. Rev. Lett.* **68**, 1236 (1992).
- P. Carretta, M. Corti, A. Rigamonti, R. De Renzi, F. Licci, C. Paris, L. Bonoldi, M. Sparpaglione, and L. Zini, *Physica C* **191C**, 97 (1992).
- C. Castellani, M. Grilli, and G. Kotliar, *Phys. Rev. B* **43**, 8000 (1991).
- R. J. Cava, A. Santoro, D. W. Johnson, Jr., and W. W. Rhodes, *Phys. Rev. B* **35**, 6716 (1987).
- R. J. Cava, B. Batlogg, J. J. Krajewski, R. Farrow, L. W. Rupp, Jr., A. E. White, K. Short, W. F. Pick, and T. Kometani, *Nature* **332**, 814 (1988).
- M.-C. Cha, M. P. A. Fisher, S. M. Girvin, M. Wallin, and A. P. Young, *Phys. Rev. B* **44**, 6883 (1991).
- P. Chaddah, K. V. Bhagwat, and G. Raulkumaer, *Physica C* **159C**, 570 (1989).
- P. Chaddah and K. Bhagwat, in "High Temperature Superconductivity" (S. K. Malik and S. S. Shah, Eds.), Nova Science, New York, 1992.
- C. Chaillout, J. P. Remeika, A. Santoro, and M. Marezio, *Solid State. Commun.* **56**, 829 (1985).
- T. K. Chaki and M. Rubinstein, *Phys. Rev. B* **36**, 7259 (1987).
- B. Chakraborty, *Phys. Rev. B* **43**, 378 (1991).
- S. Chakravarty, B. I. Halperin, and D. R. Nelson, *Phys. Rev. Lett.* **60**, 1057 (1988).
- S. Chakravarty, B. I. Ivlev, and Y. N. Ovchinnikov, *Phys. Rev. B* **42**, 2143 (1990).
- S. Chakravarty, A. Sudbø, P. W. Anderson, and S. Strong, *Science* **261**, 337 (1993).

- L. P. Chan, D. R. Harshman, K. G. Lynn, S. Mas-sidda, and B. D. Mitzi, *Phys. Rev. Lett.* **67**, 1350 (1991).
- B. S. Chandrasekhar, *Appl. Phys. Lett.* **1**, 7 (1962).
- B. S. Chandrasekhar, in "Superconductivity" (R. D. Parks, Ed.), Vol. 1, Chap. 1, Dekker, New York, 1969.
- N. Chandrasekhar, O. T. Valls, and A. M. Goldman, *Mod. Phys. Letters* **8**, 1863 (1994).
- C. L. Chang, A. Kleinhammes, W. G. Moulton, and L. R. Testardi, *Phys. Rev. B* **41**, 11564 (1990).
- M. Charalambous, J. Chaussy, and P. Lejay, *Phys. Rev. B* **45**, 5091 (1992).
- T. Chattopadhyay, P. J. Brown, B. C. Sales, L. A. Boatner, H. A. Mook, and H. Maletta, *Phys. Rev. B* **40**, 2624 (1989).
- P. Chaudhari, R. T. Collins, P. Freitas, R. J. Gambino, J. R. Kirtley, R. H. Koch, R. B. Laibowitz, F. K. LeGoues, T. R. McGuire, T. Penney, Z. Schlesinger, A. P. Segmüller, S. Foner, and E. J. McNiff, Jr., *Phys. Rev. B* **36**, 8903 (1987).
- S. V. Chekalin, V. M. Farztdinov, V. V. Golovlyov, V. S. Letokhov, Yu. E. Lozovik, Yu. A. Matveets, and A. G. Stepanov, *Phys. Rev. Lett.* **67**, 3860 (1991).
- J. Chela-Flores, M. P. Das, and A. G. Saif, *Solid State Commun.* **65**, 77 (1988).
- D.-X. Chen, R. B. Goldfarb, J. Nogués, and K. V. Rao, *J. Appl. Phys.* **63**, 980 (1988).
- D.-X. Chen and R. B. Goldfarb, *J. Appl. Phys.* **66**, 2489 (1989).
- G. H. Chen, J. H. Wang, D. N. Zheng, Y. F. Yan, S. L. Jia, Q. S. Yang, Y. M. Ni, and Z. X. Zhao, *Mod. Phys. Lett. B* **3**, 295 (1989).
- H. Chen and J. Callaway, *Phys. Rev. B* **40**, 8800 (1989).
- C. H. Chen, in "Physical Properties of High Temperature Superconductors" (D. M. Ginsberg, Ed.), Vol. 2, Chap. 4, World Scientific, Singapore, 1990.
- J. H. Chen, *Solid State Commun.* **75**, 557, 563, 567, 573 (1990a); *Phys. Rev. B* **42**, 3952, 3957 (1990b).
- D.-X. Chen, A. Sanchez, J. Nogués, and J. S. Muñoz, *Phys. Rev. B* **41**, 9510 (1990a).
- D.-X. Chen, A. Sanchez, and J. Muñoz, *J. Appl. Phys.* **67**, 3430 (1990b).
- D.-X. Chen, A. Sanchez, T. Puig, L. M. Martinez, and J. S. Muñoz, *Physica C* **168C**, 652 (1990c).
- C. Y. Chen, R. J. Birgeneau, M. A. Kastner, N. W. Preyer, and T. Thio, *Phys. Rev. B* **43**, 392 (1991).
- D.-X. Chen, J. A. Brug, and R. B. Goldfarb, *IEEE Trans. Magn.* **27**, 3601 (1991).
- D.-X. Chen and A. Sanchez, *J. Appl. Phys.* **70**, 5463 (1991).
- C.-C. Chen, S. P. Kelty, and C. M. Lieber, *Science* **253**, 886 (1991).
- B. Chen and J. Dong, *Phys. Rev. B* **44**, 10206 (1991).
- C. T. Chen, L. H. Tjeng, J. Kwo, H. L. Kao, P. Rudolf, F. Sette, and R. M. Fleming, *Phys. Rev. Lett.* **68**, 2543 (1992).
- T.-P. Chen, Z. X. Zhao, H. D. Yang, E. L. Wolf, R. N. Shelton, and P. Klavins, *Phys. Rev.* **45**, 7945 (1992).
- Q. Y. Chen, in "Magnetic Susceptibility of Superconductors and other Spin Systems" (R. A. Hein, T. L. Francavilla, and D. H. Liebenberg, Eds.), Plenum, New York, 1992.
- L. Chengren and D. C. Larbalestier, *Cryogenics* **27**, 171 (1987).
- S.-W. Cheong, S. E. Brown, Z. Fisk, R. S. Kwok, J. D. Thompson, E. Zirngiebl, G. Gruner, D. E. Peterson, G. L. Wells, R. B. Schwarz, and J. R. Cooper, *Phys. Rev. B* **36**, 3913 (1987).
- S.-W. Cheong, M. F. Hundley, J. D. Thompson, and Z. Fisk, *Phys. Rev. B* **39**, 6567 (1989a).
- S.-W. Cheong, Z. Fisk, J. D. Thompson, and R. B. Schwarz, *Physica C* **159C**, 407 (1989b).
- H.-F. Cheung, Y. Gefen, E. K. Riedel, and W.-H. Shih, *Phys. Rev. B* **37**, 6050 (1988).
- X.-F. Chen, M. J. Marone, G. X. Tessema, M. J. Skove, M. V. Nevitt, D. J. Miller, and B. W. Veal, *Phys. Rev. B* **48**, 1254 (1993).
- C. C. Chi and C. Vanneste, *Phys. Rev. B* **42**, 9875 (1990).
- T. R. Chien, T. W. Jing, N. P. Ong, and Z. Z. Wang, *Phys. Rev. Lett.* **66**, 3075 (1991).
- J. H. Cho, F. Borsa, D. C. Johnston, and D. R. Torgeson, *Phys. Rev. B* **46**, 3179 (1992).
- C. H. Choi and P. Muzikar, *Phys. Rev. B* **39**, 11296 (1989); *Phys. Rev. B* **40**, 5144 (1989).
- J. Choi and J. V. José, *Phys. Rev. Lett.* **62**, 320 (1989).
- M. Y. Choi and S. Kim, *Phys. Rev. B* **44**, 10411 (1991).
- M. Y. Choi, C. Lee, and J. Lee, *Phys. Rev. B* **46**, 1489 (1992).
- H. Chou, K. Yamada, J. D. Axe, S. M. Shapiro, G. Shirane, I. Tanaka, K. Yamane, and H. Kojima, *Phys. Rev. B* **42**, 4272 (1990).
- D. B. Chrisey and G. K. Hubler (Eds.), "Pulsed Laser Deposition of Thin Films," Wiley, New York, 1994.
- C. W. Chu, P. H. Hor, R. L. Meng, L. Gao, and Z. J. Huang, *Science* **235**, 567 (1987).
- C. W. Chu, P. H. Hor, R. L. Meng, L. Gao, Z. J. Huang, and Y. Q. Wang, *Phys. Rev. Lett.* **58**, 405 (1987).
- C. W. Chu, P. H. Hor, R. L. Meng, L. Gao, Z. J. Huang, J. Bechtold, M. K. Wu, and C. Y. Huang, *Mater. Res. Soc. Symp. Proc.* **99**, 15 (1987).
- C. W. Chu, J. Bechtold, L. Gao, P. H. Hor, Z. J. Huang, R. L. Meng, Y. Y. Sun, Y. Q. Wang, and Y. Y. Xue, *Phys. Rev. Lett.* **60**, 941 (1988).
- C. W. Chu, L. Gao, F. Chen, Z. J. Huang, R. L. Meng, and Y. Y. Xue, *Nature* **365**, 323 (1993b).
- C. W. Chu, *J. Superconductivity* **7**, 1 (1994).
- C. W. Chu, "Unusual High Temperature Superconductors," *Proc. Symp. Quantum Theory of Real Materials*, Berkeley, California, Aug. 1994, in press.
- E. M. Chudnovsky, *Phys. Rev. B* **40**, 11355 (1989).
- E. M. Chudnovsky, *Phys. Rev. Lett.* **65**, 3060 (1990).

- E. M. Chudnovsky, *Phys. Rev. B* **43**, 7831 (1991).
- F. Chung and S. Sternberg, *Amer. Scientist* **81**, 56 (1993).
- L. Civale, A. D. Marwick, M. W. McElfresh, T. K. Worthington, A. P. Malozemoff, F. H. Holtzberg, J. R. Thompson, and M. A. Kirk, *Phys. Rev. Lett.* **65**, 1164 (1990).
- L. Civale, T. K. Worthington, and A. Gupta, *Phys. Rev. B* **43**, 5425 (1991).
- L. Civale, A. D. Marwick, T. K. Worthington, M. A. Kirk, J. R. Thompson, L. Krusin-Elbaum, Y. Sun, J. R. Clem, and F. Holtzberg, *Phys. Rev. Lett.* **67**, 648 (1991).
- J. H. Claassen, J. F. Evetts, R. E. Somekh, and Z. H. Barber, *Phys. Rev. B* **44**, 9605 (1991).
- J. Clarke, *Phys. Rev. Lett.* **28**, 1363 (1972).
- J. Clarke and J. L. Paterson, *J. Low Temp. Phys.* **15**, 491 (1974).
- J. Clayhold, N. P. Ong, P. H. Hor and C. W. Chu, *Phys. Rev. B* **38**, 7016 (1988).
- J. R. Clem, *Physica C* **162-164**, 1137 (1989).
- J. R. Clem and M. W. Coffey, *Phys. Rev. B* **42**, 6209 (1990).
- J. R. Clem, *Phys. Rev. B* **43**, 7837 (1991).
- J. Clem, "A. C. Losses in Type-II Superconductors, Chap. in *Magnetic Susceptibility of Superconductors and Other Spin Systems*," (R. A. Hein, T. L. Francavilla, and D. H. Liebenberg, Eds.), Plenum, New York, 1992.
- J. R. Clem and Z. Hao, *Phys. Rev. B* **48**, 13774 (1993).
- A. M. Clogston and J. Jaccarino, *Phys. Rev.* **121**, 1357 (1961).
- A. M. Clogston, *Phys. Rev. Lett.* **9**, 266 (1962).
- M. W. Coffey and J. R. Clem, *Phys. Rev. B* **44**, 6903 (1991).
- M. W. Coffey, *Phys. Rev. B* **46**, 567 (1992).
- M. W. Coffey, *Phys. Rev. B* **47**, 12284 (1993).
- M. W. Coffey, *Phys. Rev. B* **49**, 9774 (1994).
- R. W. Cohen, G. D. Cody, and L. J. Vieland, in *Electronic Density of States*, NBS Spec. Publ. (U.S.) **323**, 767 (1971).
- M. L. Cohen, in "Novel Superconductivity" (S. A. Wolf and V. Z. Kresin, Eds.), p. 1095. Plenum, New York, 1987.
- M. L. Cohen and D. R. Penn, *Phys. Rev. B* **42**, 8702 (1990).
- R. E. Cohen, *Computers in Phys.*, in press, 1994.
- J. L. Cohn, S. A. Wolf, V. Selvamanickam, and K. Salama, *Phys. Rev. Lett.* **66**, 1098 (1991).
- M. B. Cohn, M. S. Rzechowski, S. P. Benz, and C. J. Lobb, *Phys. Rev. B* **43**, 12823 (1991).
- J. L. Cohn, S. A. Wolf, and T. A. Vanderah, *Phys. Rev. B* **45**, 511 (1992).
- J. L. Cohn, E. F. Skelton, S. A. Wolf, J. Z. Liu, and R. N. Shelton, *Phys. Rev. B* **45**, 13144 (1992).
- J. L. Cohn, E. F. Skelton, S. A. Wolf, J. Z. Liu, and R. N. Shelton, *Phys. Rev. B* **45**, 13140, 13144 (1992).
- B. R. Coles, *Cont. Phys.* **28**, 143 (1987).
- G. Collin and R. Comes, *C. R. Acad. Sci. Paris* **304**, 1159 (1987).
- R. T. Collins, Z. Schlesinger, F. Holtzberg, and C. Feild, *Phys. Rev. Lett.* **63**, 422 (1989).
- R. T. Collins, Z. Schlesinger, G. V. Chandrasekhar, and M. W. Shafer, *Phys. Rev. B* **39**, 2251 (1989).
- R. T. Collins, Z. Schlesinger, F. Holtzberg, P. Chaudhari, and C. Feild, *Phys. Rev. B* **39**, 6571 (1989).
- R. T. Collins, Z. Schlesinger, F. Holtzberg, C. Feild, U. Welp, G. W. Crabtree, J. Z. Liu, and Y. Fang, *Phys. Rev. B*, **43**, 8701 (1991).
- S. J. Collocott, R. Driver, and E. R. Vance, *Phys. Rev. B* **41**, 6329 (1990a).
- S. J. Collocott, N. Savvides, and E. R. Vance, *Phys. Rev. B* **42**, 4794 (1990b).
- S. Collocott, R. Driver, and C. Andrikidis, *Phys. Rev. B* **45**, 945 (1992).
- R. Combescot, *Phys. Rev. Lett.* **67**, 148 (1991a); *Phys. Rev. B* **42**, 7810 (1991b).
- E. Compans and F. Baumann, *Jpn. J. Appl. Phys.* **26** Suppl. 3, 805 (1987).
- L. D. Cooley, G. Stejic, and D. C. Labalestier, *Phys. Rev. B* **46**, 2964 (1992).
- L. N. Cooper, *Phys. Rev.* **104**, 1189 (1956).
- S. L. Cooper, G. A. Thomas, J. Orenstein, D. H. Rapkine, M. Capizzi, T. Timusk, A. J. Millis, L. F. Schneemeyer, and J. V. Waszczak, *Phys. Rev. B* **40**, 11358 (1989).
- S. L. Cooper, A. L. Kotz, M. A. Karlow, M. V. Klein, W. C. Lee, J. Giapintzakis, and D. M. Ginsberg, *Phys. Rev. B* **45**, 2549 (1992).
- S. L. Cooper, D. Reznik, A. Kotz, M. A. Karlow, R. Liu, M. V. Klein, W. C. Lee, J. Giapintzakis, D. M. Ginsberg, B. W. Veal, and A. P. Paulikas, *Phys. Rev. B* **47**, 8233 (1993).
- S. L. Cooper and K. E. Gray in "Physical Properties of High Temperature Superconductors" (D. M. Ginsberg, Ed.), Vol. 4, Chap. 3, World Scientific, Singapore, 1994.
- C. Coretsopoulos, H. C. Lee, E. Ramli, L. Raven, T. B. Rauchfuss, and E. Oldfield, *Phys. Rev. B* **39**, 781 (1989).
- D. L. Cox and M. B. Maple, *Phys. Today*, Feb. 1995, p. 32.
- L. A. Curtiss and S. W. Tam, *J. Mater. Res.* **3**, 1269 (1988).
- J. Costa-Quintana, F. López-Aguilar, S. Balle, and R. Salvador, *Phys. Rev. B* **39**, 9675 (1989).
- L. Cota, L. Morales de la Garza, G. Hirata, L. Martínez, E. Orozco, E. Carrillo, A. Mendoza, J. L. Albarrán, J. Fuentes-Maya, J. L. Boldú, J. G. Pérez-Ramírez, R. Pérez, J. Reyes Gasga, M. Avalos, and M. José-Yacamán, *J. Mater. Res.* **3**, 417 (1988).
- R. Côte and A. Griffin, *Phys. Rev. B* **48**, 10404 (1993).
- F. A. Cotton, "Chemical Applications of Group Theory." Wiley, New York, 1963.
- D. E. Cox and A. W. Sleight, *Solid State Commun.* **19**, 969 (1976).

- D. E. Cox and A. W. Sleight, *Acta Cryst. B* 35, 1 (1979).
- D. L. Cox and M. B. Maple, *Phys. Today*, February 1995, p. 32.
- G. W. Crabtree, J. Z. Liu, A. Umezawa, W. K. Kwok, C. H. Sowers, S. K. Malik, B. W. Veal, D. J. Lam, M. B. Brodsky, and J. W. Downey, *Phys. Rev. B* 36, 4021 (1987).
- M. K. Crawford, G. Burns, and F. Holtzberg, *Solid State Commun.* 70, 557 (1989).
- M. K. Crawford, G. Burns, G. V. Chandrashekhar, F. H. Dacol, W. E. Farneth, E. M. McCarron III, and R. J. Smalley, *Phys. Rev. B* 41, 8933 (1990a).
- M. K. Crawford, G. Burns, G. V. Chandrashekhar, F. H. Dacol, W. E. Farneth, E. M. McCarron III, and R. J. Smalley, *Solid State Commun.* 73, 507 (1990b).
- R. J. Creswick, H. A. Farach, C. P. Poole, Jr., "Introduction to Renormalization Group Methods in Physics," Wiley, New York, 1992.
- M. Crisan, *Phys. Lett. A* 124, 195 (1987).
- M. F. Crommie, A. Zettl, T. W. Barbee, III, and M. L. Cohen, *Phys. Rev. B* 37, 9734 (1988).
- M. F. Crommie, G. Briceño, and A. Zettl, *Physica C* 162C-164C, 1397 (1989).
- M. F. Crommie and A. Zettl, *Phys. Rev. B* 43, 408 (1991).
- R. W. Cross and R. B. Goldfab, *Appl. Phys. Lett.* 58, 415 (1991).
- J. E. Crow and N.-P. Ong, in "High Temperature Superconductivity" (J. W. Lynn, Ed.), Chap. 7, Springer-Verlag, Berlin, 1990.
- M. A. Crusellas, J. Fontcuberta, S. Piñol, T. Grenet, and J. Beille, *Physica C* 180, 313 (1991).
- A. M. Cucolo, R. Di Leo, P. Romano, L. F. Schneemeyer, and J. V. Waszczak, *Phys. Rev. B* 44, 2857 (1991).
- S.-M. Cui and C.-H. Tsai, *Phys. Rev. B* 44, 12500 (1991).
- J. C. Culbertson, U. Strom, S. A. Wolf, P. Skeath, E. J. West, and W. K. Burns, *Phys. Rev. B* 39, 12359 (1989).
- J. C. Culbertson, U. Strom, S. A. Wolf, and W. W. Fuller, *Phys. Rev. B* 44, 9609 (1991).
- L. A. Curtiss and S. W. Tam, *J. Mater. Res.* 3, 1269 (1988).
- L. A. Curtiss and S. W. Tam, *Phys. Rev. B* 41, 1824 (1990).
- L. L. Daemen and J. E. Gubernatis, *Phys. Rev.* 43, 413, 2625 (1991).
- L. L. Daeman, L. J. Campbell, and V. G. Kogan, *Phys. Rev. B* 46, 3631 (1992).
- L. L. Daemen, L. J. Campbell, A. Yu Simonov, and V. G. Kogan, *Phys. Rev. Lett.* 70, 2948 (1993).
- L. L. Daemen and A. W. Overhauser, *Phys. Rev. B* 40, 10778 (1989).
- L. L. Daemen and J. E. Gubernatis, *Phys. Rev. B* 45, 314 (1992b).
- E. Dagotto, A. Moreo, R. Joynt, S. Bacci, and E. Gagliano, *Phys. Rev. B* 41, 2585, (1990).
- E. Dagotto, *Rev. Mod. Phys.* 66, 763 (1994).
- E. Dagotto, A. Moreo, F. Ortolani, D. Poilblanc, and J. Riera, *Phys. Rev. B* 45, 10741 (1992).
- P. Dai, Y. Zhang, and M. P. Sarachik, *Phys. Rev. Lett.* 67, 136 (1991).
- Y. Dalichaouch, M. B. Maple, J. Y. Chen, T. Kohara, C. Rossel, M. S. Torikachvili, and A. L. Giorgi, *Phys. Rev.* 41, 1829 (1990a).
- Y. Dalichaouch, B. W. Lee, C. L. Seaman, J. T. Markert, and M. B. Maple, *Phys. Rev. Lett.* 64, 599 (1990b).
- Y. Dalichaouch, B. W. Lee, S. E. Lambert, M. P. Maple, J. L. Smith, and Z. Fisk, *Phys. Rev. B* 43, 299 (1991).
- M. Das, in "Studies in High Temperature Superconductors" (A. V. Narlikar, Ed.), Vol. 3, Nova Sci., New York, 1989.
- C. Dasgupta and T. V. Ramakrishnan, *Physica C* (Amsterdam) 183C, 62 (1991).
- T. Datta, C. P. Poole, Jr., H. A. Farach, C. Almasan, J. Estrada, D. U. Gubser, and S. A. Wolf, *Phys. Rev. B* 37, 7843 (1988).
- M. Däumling and G. V. Chandrashekhar, *Phys. Rev. B* 46, 6422 (1992).
- D. Davidov, P. Monod, and N. Bontemps, *Phys. Rev. B* 45, 8036 (1992).
- M. C. de Andrade, C. C. Almasan, Y. Dalichaouch, and M. B. Maple, *Physica C* 184C, 378 (1991).
- L. De Cesare, *Phys. Rev. B* 43, 10555 (1991).
- P. G. de Gennes, *Rev. Mod. Phys.* 36, 225 (1964).
- P. G. de Gennes, "Superconductivity of Metals and Alloys," Benjamin, New York, 1966.
- L. Degiorgi, P. Wachter, G. Grüner, S.-M. Huang, J. Wiley, and R. B. Kaner, *Phys. Rev. Lett.* 69, 2987 (1992).
- L. J. de Jongh, *Europ. J. Solid State Inorg. Chem.*, in press.
- C. Dekker, W. Eidelloth, and R. H. Koch, *Phys. Rev. Lett.* 68, 3347 (1992).
- O. L. de Lange and V. V. Gridin, *Phys. Rev. B* 46, 5735 (1992).
- P. Delsing, K. K. Likharev, L. S. Kuzmin, and T. Claeson, *Phys. Rev. Lett.* 63, 1180, 1861 (1989).
- H. Dersch and G. Blatter, *Phys. Rev. B* 38, 11391 (1988).
- S. M. DeSoto, C. P. Slichter, H. H. Wang, U. Geiser, and J. M. Williams, *Phys. Rev. Lett.* 70, 2956 (1993).
- D. S. Dessau, B. O. Wells, Z.-X. Shen, W. E. Spicer, A. J. Arko, R. S. List, D. B. Mitzi, and A. Kapitulnik, *Phys. Rev. Lett.* 66, 2160 (1991).
- D. S. Dessau, Z.-X. Shen, B. O. Wells, D. M. King, W. E. Spicer, A. J. Arko, L. W. Lombardo, D. B. Mitzi, and A. Kapitulnik, *Phys. Rev. B* 45, 5095 (1992).
- G. Deutscher and P. Chaudhari, *Phys. Rev. B* 44, 4664 (1991).
- F. Devaux, A. Manthiram, and J. B. Goodenough, *Phys. Rev. B* 41, 8723 (1990).

- M. J. DeWeert, D. A. Papaconstantopoulos, and W. E. Pickett, *Phys. Rev. B* **39**, 4235 (1989).
- F. W. de Wette, A. D. Kulkarni, J. Prade, U. Schröder, and W. Kress, *Phys. Rev. B* **42**, 6707 (1990).
- A. DiChiara, F. Fontana, G. Peluso, and F. Tafuri, *Phys. Rev. B* **44**, 12026 (1991).
- A. DiChiara, F. Fontana, G. Peluso, and F. Tafuri, *Phys. Rev. B* **48**, 6695 (1993).
- F. Diederich and R. L. Whetten, *Acc. Chem. Res.* **25**, 119 (1992).
- D. DiMarzio, H. Wiesmann, D. H. Chen, and S. M. Heald, *Phys. Rev. B* **42**, 294 (1990).
- H.-Q. Ding, *Phys. Rev. Lett.* **68**, 1927 (1992).
- T. R. Dinger, T. K. Worthington, W. J. Gallagher, and R. L. Sandstrom, *Phys. Rev. Lett.* **58**, 2687 (1987).
- M. I. Dobroliubov and S. Yu. Khlebnikov, *Phys. Rev. Lett.* **67**, 2084 (1991).
- R. K. Dodd, J. C. Eilbeck, J. D. Gibbon, and H. C. Morris, "Solitons and Nonlinear Wave Equations." Academic Press, New York, 1982.
- I. Doi, K. Sano, and K. Takano, *Phys. Rev. B* **45**, 274 (1992).
- G. J. Dolan, G. V. Chandrashekhar, T. R. Dinger, C. Feild, and F. Holtzberg, *Phys. Rev. Lett.* **62**, 827 (1989a).
- G. J. Dolan, F. Holtzberg, C. Feild, and T. R. Dinger, *Phys. Rev. Lett.* **62**, 2184 (1989b).
- S. Doniach, in "Proceedings Los Alamos Symposium, High Temp. Supercond.," p. 406. Addison-Wesley, New York, 1989.
- S. Doniach and M. Inui, *Phys. Rev. B* **41**, 6668 (1990).
- G. Dopf, A. Muramatsu, and W. Hanke, *Phys. Rev. Lett.* **68**, 353 (1992).
- M. M. Doria, J. E. Gubernatis, and D. Rainer, *Phys. Rev. B* **41**, 6335 (1990).
- A. T. Dorsey, M. Huang, and M. P. A. Fisher, *Phys. Rev. B* **45**, 523 (1992).
- S. X. Dou, H. K. Liu, A. J. Bourdillon, M. Kviz, N. X. Tan, and C. C. Sorrell, *Phys. Rev. B* **40**, 5266 (1989).
- R. A. Doyle, O. L. deLange, and V. V. Gridin, *Phys. Rev. B* **45**, 12580 (1992).
- T. B. Doyle and R. A. Doyle, *Phys. Rev. B* **47**, 8111 (1993).
- P. G. Drizin and R. S. Johnson, "Solitons: An Introduction." Cambridge Univ. Press Cambridge, U.K., 1989.
- L. Dresner, *Cryogenics*, May, p. 285, 1978.
- M. S. Dresselhaus, G. Dresselhaus, and R. Saito, in "Physical Properties of High Temperature Superconductors" (D. M. Ginsberg, Ed.), Vol. 4, Chap. 7, World Scientific, Singapore, 1994.
- H. Drulis, Z. G. Xu, J. W. Brill, L. E. De Long, and J.-C. Hou, *Phys. Rev. Lett.* **44**, 4731 (1991).
- Q. Du, M. D. Gunzberger, and J. S. Peterson, *Phys. Rev. B* **46**, 9027 (1992).
- L. Dubeck, P. Lindenfeld, E. A. Lynten, and H. Rohrer, *Rev. Mod. Phys.* **36**, 110 (1964).
- A. Dulčić, R. H. Crepeau, and J. H. Freed, *Phys. Rev. B* **39**, 4249 (1989).
- B. D. Dunlap, M. Slaski, Z. Sungaila, D. G. Hinks, K. Zhang, C. Segre, S. K. Malik, and E. E. Alp, *Phys. Rev. B* **37**, 592 (1988).
- C. Duran, J. Yazzi, F. de la Cruz, D. J. Bishop, D. B. Mitzi, and A. Kapitulnik, *Phys. Rev. B* **44**, 7737 (1991).
- C. H. Eab and I. M. Tang, *Phys. Rev. B* **40**, 4427 (1989).
- D. E. Eastman, *Solid State Commun.* **7**, 1697 (1969).
- C. Ebner and D. Stroud, *Phys. Rev. B* **31**, 165 (1985).
- C. Ebner and D. Stroud, *Phys. Rev. B* **39**, 789 (1989).
- U. Eckern and E. B. Sonin, *Phys. Rev. B* **47**, 505 (1993).
- G. L. Eesley, J. Heremans, M. S. Meyer, G. L. Doll, and S. H. Liou, *Phys. Rev. Lett.* **65**, 3445 (1990).
- H. Eikmans and J. E. van Himbergen, *Phys. Rev.* **44**, 6937 (1991).
- R. Eisberg and R. Resnick, "Quantum Physics," Wiley, New York, 1974.
- J. W. Ekin, H. R. Hart, and A. R. Gaddipati, *J. Appl. Phys.* **68**, 2285 (1990).
- J. W. Ekin, K. Salama, and V. Selvamanickam, *Appl. Phys. Lett.* **59**, 360 (1991).
- T. Ekino and J. Akimitsu, *Phys. Rev. B* **40**, 6902, 7364 (1989a).
- T. Ekino and J. Akimitsu, *J. Phys. Soc. Jpn.* **58**, 2135 (1989b).
- T. Ekino and J. Akimitsu, *Phys. Rev. B* **42**, 8049 (1990).
- G. M. Eliashberg, *Zh. Eksp. Teor. Fiz.* **38**, 966 (1960a).
- G. M. Eliashberg, *Zh. Eksp. Teor. Fiz.* **39**, 1437 (1960b).
- B. Ellman, J. Yang, T. F. Rosenbaum, and E. Bucher, *Phys. Rev. Lett.* **64**, 1569 (1990).
- V. J. Emery, *Phys. Rev. Lett.* **58**, 2794 (1987) (reprinted in Halley, 1988, p. 227).
- V. J. Emery and G. Reiter, *Phys. Rev. B* **38**, 4547 (1988).
- J. W. Emsley, J. Feeney, and L. H. Sutcliffe, "High Resolution Nuclear Magnetic Resonance Spectroscopy, Pergamon, New York, 1965, Vol. 1.
- D. Emin, *Phys. Rev. B* **49**, 9157 (1994).
- P. Entel and J. Zielinski, *Phys. Rev. B* **42**, 307 (1990).
- O. Entin-Wohlman and Y. Imry, *Phys. Rev. B* **40**, 6731 (1989).
- L. E. Erickson, *Phys. Rev. B* **43**, 12723 (1991).
- R. Escudero, E. Guarner, and F. Morales, *Physica C* **162C-164C**, 1059 (1989).
- R. Escudero, F. Morales, and E. Guarner, *Physica C* **166C**, 15 (1990).
- D. Estève, J. M. Martinis, C. Urbina, M. H. Devoret, G. Collin, P. Monod, M. Ribault, and A. Revcolevschi, *Europhys. Lett.* **3**, 1237 (1987).
- J. P. Estrera and G. B. Arnold, *Phys. Rev. B* **39**, 2094 (1989).
- L. M. Falicov and C. R. Proetto, *Phys. Rev. B* **47**, 14407 (1993).

- M. M. Fang, J. E. Ostenson, D. K. Finnemore, D. E. Farrell, and N. P. Bansal, *Phys. Rev. B* **39**, 222 (1989).
- H. A. Farach, E. Quagliata, T. Mzoughi, M. A. Mesa, C. P. Poole, Jr., and R. Creswick, *Phys. Rev. B* **41**, 2046 (1990).
- D. E. Farrell, B. S. Chandrasekhar, M. R. DeGuire, M. M. Fang, V. G. Kogan, J. R. Clem, and D. K. Finnemore, *Phys. Rev. B* **36**, 4025 (1987).
- D. E. Farrell, C. M. Williams, S. A. Wolf, N. P. Bansal, and V. G. Kogan, *Phys. Rev. Lett.* **61**, 2805 (1988).
- D. E. Farrell, M. M. Fang, and N. P. Bansal, *Phys. Rev. B* **39**, 718 (1989a).
- D. E. Farrell, S. Bonham, J. Foster, Y. C. Chang, P. Z. Jiang, K. G. Vandervoort, D. J. Lam, and V. G. Kogan, *Phys. Rev. Lett.* **63**, 782 (1989b).
- D. E. Farrell, R. G. Beck, M. F. Booth, C. J. Allen, E. D. Bukowski, and D. M. Ginsberg, *Phys. Rev. B* **42**, 6758 (1990a).
- D. E. Farrell, C. J. Allen, R. C. Haddon, and S. V. Chichester, *Phys. Rev. B* **42**, 8694 (1990b).
- D. E. Farrell, J. P. Rice, D. M. Ginsberg, and J. Z. Liu, *Phys. Rev. Lett.* **64**, 1573 (1990c).
- D. E. Farrell, J. P. Rice, and D. M. Ginsberg, *Phys. Rev. Lett.* **67**, 1165 (1991).
- D. E. Farrell, in "Physical Properties of High Temperature Superconductors," (D. M. Ginsberg, Ed.), Vol. 4, Chap. 2, World Scientific, Singapore, 1994.
- E. Faulques and R. E. Russo, in "Applications of Analytical Techniques to the Characterization of Materials" (D. L. Perry, Ed.), p. 59. Plenum, New York, 1991.
- R. Fazio and G. Schön, *Phys. Rev. B* **43**, 5307 (1991).
- J. F. Federici, B. I. Greene, H. Hartford, and E. S. Hellman, *Phys. Rev. B* **42**, 923 (1990).
- R. Feenstra, D. K. Christen, C. Klabunde, and J. D. Budai, *Phys. Rev. B* **45**, 7555 (1992).
- R. Fehrenbacher, V. B. Geshkenbein, and G. Blatter, *Phys. Rev. B* **45**, 5450 (1992).
- D. Feinberg and C. Villard, *Phys. Rev. Lett.* **65**, 919 (1990).
- L. F. Feiner, M. Grilli, and C. DiCastro, *Phys. Rev. B* **45**, 10647 (1992).
- L. F. Feiner, *Phys. Rev. B* **48**, 16857 (1993).
- I. Felner, U. Yaron, Y. Yeshurun, G. V. Chandrasekhar, and F. Holtzberg, *Phys. Rev. B* **40**, 5329 (1989).
- J. C. Fernandez, R. Grauer, K. Pinnow, and G. Reinisch, *Phys. Rev. B* **42**, 9987 (1990).
- M. J. Ferrari, M. Johnson, F. C. Wellstood, J. Clarke, D. Mitzi, P. A. Rosenthal, C. B. Eom, T. H. Geballe, A. Kapitulnik, and M. R. Beasley, *Phys. Rev. Lett.* **64**, 72 (1989).
- M. J. Ferrari, F. C. Wellstood, J. J. Kingston, and J. Clarke, *Phys. Rev. Lett.* **67**, 1346 (1991).
- R. A. Ferrell, in "High Temperature Superconductivity" (J. W. Lynn, Ed.), Chap. 3, Springer-Verlag, Berlin, 1990.
- K. Fesser, U. Sum, and H. Büttner, *Phys. Rev. B* **44**, 421 (1991).
- A. L. Fetter and J. D. Walecka, "Quantum Theory of Many Particle Systems." McGraw-Hill, New York, 1971.
- R. P. Feynman, "Lectures on Physics," Vol. 3, Chap. 21. Addison-Wesley, New York, 1965.
- W. A. Fietz, M. R. Beasley, J. Silcox, and W. W. Webb, *Phys. Rev.* **136**, A335 (1964).
- A. T. Fiory, M. Gurvitch, R. J. Cava, and G. P. Espinosa, *Phys. Rev. B* **36**, 7262 (1987).
- A. T. Fiory, G. P. Espinosa, R. M. Fleming, G. S. Grader, M. Gurvitch, A. F. Hebard, R. E. Howard, J. R. Kwo, A. F. J. Levi, P. M. Mankiewich, S. Martin, C. E. Rice, L. F. Schneemeyer, and A. E. White, International Conference on Electronic Materials, Tokyo, 1988.
- A. T. Fiory, S. Martin, R. M. Fleming, L. F. Schneemeyer, J. V. Waszczak, A. F. Hebard, and S. A. Sunshine, *Physica C* **162C-164C**, 1195 (1989).
- A. T. Fiory, M. A. Paalanen, R. R. Ruel, L. F. Schneemeyer, and J. V. Waszczak, *Phys. Rev. B* **41**, 4805 (1990).
- O. Fischer, *Appl. Phys.* **16**, 1 (1978).
- O. Fischer, in "Earlier and Recent Aspects of Superconductivity" (J. G. Bednorz and K. A. Müller, Eds.), p. 96, Springer, Berlin, 1990.
- P. Fischer, K. Kakurai, M. Steiner, K. N. Clausen, B. Lebeck, F. Hulliger, H. R. Ott, P. Brüesch, and P. Unternährer, *Physica C* **152C**, 145 (1988).
- P. Fischer, H. W. Neumüller, B. Roas, H. F. Braun, and G. Saemann-Ischenko, *Solid State Commun.* **72**, 871 (1989).
- J. E. Fischer, P. A. Heiney, A. R. McGhie, W. J. Romanow, A. M. Denenstein, J. P. McCauley, Jr., and A. B. Smith, III, *Science* **252**, 1288 (1991).
- J. E. Fischer, P. A. Heiney, and A. B. Smith, III, *Acc. Chem. Res.* **25**, 97 (1992).
- K. H. Fischer, *Physica C* **178C**, 161 (1991).
- D. S. Fisher and D. A. Huse, *Phys. Rev. B* **38**, 373, 386 (1988).
- M. P. A. Fisher, *Phys. Rev. Lett.* **62**, 1415 (1989).
- R. A. Fisher, S. Kim, B. F. Woodfield, N. E. Phillips, L. Taillefer, K. Hasselbach, J. Flouquet, A. L. Giorgi, and J. L. Smith, *Phys. Rev. Lett.* **62**, 1411 (1989).
- M. P. A. Fisher, *Phys. Rev. Lett.* **65**, 923 (1990).
- D. S. Fisher, M. P. A. Fisher, and D. A. Huse, *Phys. Rev. B* **43**, 130 (1991).
- R. S. Fishman, *Phys. Rev. B* **38**, 11996 (1988).
- R. S. Fishman, *Phys. Rev. Lett.* **63**, 89 (1989).
- Z. Fisk, P. C. Canfield, W. P. Beyermann, J. D. Thompson, M. F. Hundley, H. R. Ott, E. Felder, M. B. Maple, M. A. Lopez de la Torre, P. Visani, and C. L. Seaman, *Phys. Rev. Lett.* **67**, 3310 (1991).
- M. D. Fiske, *Rev. Mod. Phys.* **36**, 221 (1964).

- M. J. DeWeert, D. A. Papaconstantopoulos, and W. E. Pickett, *Phys. Rev. B* **39**, 4235 (1989).
- F. W. de Wette, A. D. Kulkarni, J. Prade, U. Schröder, and W. Kress, *Phys. Rev. B* **42**, 6707 (1990).
- A. DiChiara, F. Fontana, G. Peluso, and F. Tafuri, *Phys. Rev. B* **44**, 12026 (1991).
- A. DiChiara, F. Fontana, G. Peluso, and F. Tafuri, *Phys. Rev. B* **48**, 6695 (1993).
- F. Diederich and R. L. Whetten, *Acc. Chem. Res.* **25**, 119 (1992).
- D. DiMarzio, H. Wiesmann, D. H. Chen, and S. M. Heald, *Phys. Rev. B* **42**, 294 (1990).
- H.-Q. Ding, *Phys. Rev. Lett.* **68**, 1927 (1992).
- T. R. Dinger, T. K. Worthington, W. J. Gallagher, and R. L. Sandstrom, *Phys. Rev. Lett.* **58**, 2687 (1987).
- M. I. Dobroliubov and S. Yu. Khlebnikov, *Phys. Rev. Lett.* **67**, 2084 (1991).
- R. K. Dodd, J. C. Eilbeck, J. D. Gibbon, and H. C. Morris, "Solitons and Nonlinear Wave Equations." Academic Press, New York, 1982.
- I. Doi, K. Sano, and K. Takano, *Phys. Rev. B* **45**, 274 (1992).
- G. J. Dolan, G. V. Chandrashekhar, T. R. Dinger, C. Feild, and F. Holtzberg, *Phys. Rev. Lett.* **62**, 827 (1989a).
- G. J. Dolan, F. Holtzberg, C. Feild, and T. R. Dinger, *Phys. Rev. Lett.* **62**, 2184 (1989b).
- S. Doniach, in "Proceedings Los Alamos Symposium, High Temp. Supercond.," p. 406. Addison-Wesley, New York, 1989.
- S. Doniach and M. Inui, *Phys. Rev. B* **41**, 6668 (1990).
- G. Dopf, A. Muramatsu, and W. Hanke, *Phys. Rev. Lett.* **68**, 353 (1992).
- M. M. Doria, J. E. Gubernatis, and D. Rainer, *Phys. Rev. B* **41**, 6335 (1990).
- A. T. Dorsey, M. Huang, and M. P. A. Fisher, *Phys. Rev. B* **45**, 523 (1992).
- S. X. Dou, H. K. Liu, A. J. Bourdillon, M. Kviz, N. X. Tan, and C. C. Sorrell, *Phys. Rev. B* **40**, 5266 (1989).
- R. A. Doyle, O. L. deLange, and V. V. Gridin, *Phys. Rev. B* **45**, 12580 (1992).
- T. B. Doyle and R. A. Doyle, *Phys. Rev. B* **47**, 8111 (1993).
- P. G. Drazin and R. S. Johnson, "Solitons: An Introduction." Cambridge Univ. Press Cambridge, U.K., 1989.
- L. Dresner, *Cryogenics*, May, p. 285, 1978.
- M. S. Dresselhaus, G. Dresselhaus, and R. Saito, in "Physical Properties of High Temperature Superconductors" (D. M. Ginsberg, Ed.), Vol. 4, Chap. 7, World Scientific, Singapore, 1994.
- H. Drulis, Z. G. Xu, J. W. Brill, L. E. De Long, and J.-C. Hou, *Phys. Rev. Lett.* **44**, 4731 (1991).
- Q. Du, M. D. Gunzberger, and J. S. Peterson, *Phys. Rev. B* **46**, 9027 (1992).
- L. Dubeck, P. Lindenfeld, E. A. Lynten, and H. Rohrer, *Rev. Mod. Phys.* **36**, 110 (1964).
- A. Dulčić, R. H. Crepeau, and J. H. Freed, *Phys. Rev. B* **39**, 4249 (1989).
- B. D. Dunlap, M. Slaski, Z. Sungaila, D. G. Hinks, K. Zhang, C. Segre, S. K. Malik, and E. E. Alp, *Phys. Rev. B* **37**, 592 (1988).
- C. Duran, J. Yazzi, F. de la Cruz, D. J. Bishop, D. B. Mitzi, and A. Kapitulnik, *Phys. Rev. B* **44**, 7737 (1991).
- C. H. Eab and I. M. Tang, *Phys. Rev. B* **40**, 4427 (1989).
- D. E. Eastman, *Solid State Commun.* **7**, 1697 (1969).
- C. Ebner and D. Stroud, *Phys. Rev. B* **31**, 165 (1985).
- C. Ebner and D. Stroud, *Phys. Rev. B* **39**, 789 (1989).
- U. Eckern and E. B. Sonin, *Phys. Rev. B* **47**, 505 (1993).
- G. L. Eesley, J. Heremans, M. S. Meyer, G. L. Doll, and S. H. Liou, *Phys. Rev. Lett.* **65**, 3445 (1990).
- H. Eikmans and J. E. van Himbergen, *Phys. Rev.* **44**, 6937 (1991).
- R. Eisberg and R. Resnick, "Quantum Physics," Wiley, New York, 1974.
- J. W. Ekin, H. R. Hart, and A. R. Gaddipati, *J. Appl. Phys.* **68**, 2285 (1990).
- J. W. Ekin, K. Salama, and V. Selvamanickam, *Appl. Phys. Lett.* **59**, 360 (1991).
- T. Ekino and J. Akimitsu, *Phys. Rev. B* **40**, 6902, 7364 (1989a).
- T. Ekino and J. Akimitsu, *J. Phys. Soc. Jpn.* **58**, 2135 (1989b).
- T. Ekino and J. Akimitsu, *Phys. Rev. B* **42**, 8049 (1990).
- G. M. Eliashberg, *Zh. Eksp. Teor. Fiz.* **38**, 966 (1960a).
- G. M. Eliashberg, *Zh. Eksp. Teor. Fiz.* **39**, 1437 (1960b).
- B. Ellman, J. Yang, T. F. Rosenbaum, and E. Bucher, *Phys. Rev. Lett.* **64**, 1569 (1990).
- V. J. Emery, *Phys. Rev. Lett.* **58**, 2794 (1987) (reprinted in Halley, 1988, p. 227).
- V. J. Emery and G. Reiter, *Phys. Rev. B* **38**, 4547 (1988).
- J. W. Emsley, J. Feeney, and L. H. Sutcliffe, "High Resolution Nuclear Magnetic Resonance Spectroscopy, Pergamon, New York, 1965, Vol. 1.
- D. Emin, *Phys. Rev. B* **49**, 9157 (1994).
- P. Entel and J. Zielinski, *Phys. Rev. B* **42**, 307 (1990).
- O. Entin-Wohlman and Y. Imry, *Phys. Rev. B* **40**, 6731 (1989).
- L. E. Erickson, *Phys. Rev. B* **43**, 12723 (1991).
- R. Escudero, E. Guarner, and F. Morales, *Physica C* **162C-164C**, 1059 (1989).
- R. Escudero, F. Morales, and E. Guarner, *Physica C* **166C**, 15 (1990).
- D. Estève, J. M. Martinis, C. Urbina, M. H. Devoret, G. Collin, P. Monod, M. Ribault, and A. Revcolevschi, *Europhys. Lett.* **3**, 1237 (1987).
- J. P. Estrera and G. B. Arnold, *Phys. Rev. B* **39**, 2094 (1989).
- L. M. Falicov and C. R. Proetto, *Phys. Rev. B* **47**, 14407 (1993).

- M. M. Fang, J. E. Ostenson, D. K. Finnemore, D. E. Farrell, and N. P. Bansal, *Phys. Rev. B* **39**, 222 (1989).
- H. A. Farach, E. Quagliata, T. Mzoughi, M. A. Mesa, C. P. Poole, Jr., and R. Creswick, *Phys. Rev. B* **41**, 2046 (1990).
- D. E. Farrell, B. S. Chandrasekhar, M. R. DeGuire, M. M. Fang, V. G. Kogan, J. R. Clem, and D. K. Finnemore, *Phys. Rev. B* **36**, 4025 (1987).
- D. E. Farrell, C. M. Williams, S. A. Wolf, N. P. Bansal, and V. G. Kogan, *Phys. Rev. Lett.* **61**, 2805 (1988).
- D. E. Farrell, M. M. Fang, and N. P. Bansal, *Phys. Rev. B* **39**, 718 (1989a).
- D. E. Farrell, S. Bonham, J. Foster, Y. C. Chang, P. Z. Jiang, K. G. Vandervoort, D. J. Lam, and V. G. Kogan, *Phys. Rev. Lett.* **63**, 782 (1989b).
- D. E. Farrell, R. G. Beck, M. F. Booth, C. J. Allen, E. D. Bukowski, and D. M. Ginsberg, *Phys. Rev. B* **42**, 6758 (1990a).
- D. E. Farrell, C. J. Allen, R. C. Haddon, and S. V. Chichester, *Phys. Rev. B* **42**, 8694 (1990b).
- D. E. Farrell, J. P. Rice, D. M. Ginsberg, and J. Z. Liu, *Phys. Rev. Lett.* **64**, 1573 (1990c).
- D. E. Farrell, J. P. Rice, and D. M. Ginsberg, *Phys. Rev. Lett.* **67**, 1165 (1991).
- D. E. Farrell, in "Physical Properties of High Temperature Superconductors," (D. M. Ginsberg, Ed.), Vol. 4, Chap. 2, World Scientific, Singapore, 1994.
- E. Faulques and R. E. Russo, in "Applications of Analytical Techniques to the Characterization of Materials" (D. L. Perry, Ed.), p. 59. Plenum, New York, 1991.
- R. Fazio and G. Schön, *Phys. Rev. B* **43**, 5307 (1991).
- J. F. Federici, B. I. Greene, H. Hartford, and E. S. Hellman, *Phys. Rev. B* **42**, 923 (1990).
- R. Feenstra, D. K. Christen, C. Klabunde, and J. D. Budai, *Phys. Rev. B* **45**, 7555 (1992).
- R. Fehrenbacher, V. B. Geshkenbein, and G. Blatter, *Phys. Rev. B* **45**, 5450 (1992).
- D. Feinberg and C. Villard, *Phys. Rev. Lett.* **65**, 919 (1990).
- L. F. Feiner, M. Grilli, and C. DiCastro, *Phys. Rev. B* **45**, 10647 (1992).
- L. F. Feiner, *Phys. Rev. B* **48**, 16857 (1993).
- I. Felner, U. Yaron, Y. Yeshurun, G. V. Chandrasekhar, and F. Holtzberg, *Phys. Rev. B* **40**, 5329 (1989).
- J. C. Fernandez, R. Grauer, K. Pinnow, and G. Reinisch, *Phys. Rev. B* **42**, 9987 (1990).
- M. J. Ferrari, M. Johnson, F. C. Wellstood, J. Clarke, D. Mitzi, P. A. Rosenthal, C. B. Eom, T. H. Geballe, A. Kapitulnik, and M. R. Beasley, *Phys. Rev. Lett.* **64**, 72 (1989).
- M. J. Ferrari, F. C. Wellstood, J. J. Kingston, and J. Clarke, *Phys. Rev. Lett.* **67**, 1346 (1991).
- R. A. Ferrell, in "High Temperature Superconductivity" (J. W. Lynn, Ed.), Chap. 3, Springer-Verlag, Berlin, 1990.
- K. Fesser, U. Sum, and H. Büttner, *Phys. Rev. B* **44**, 421 (1991).
- A. L. Fetter and J. D. Walecka, "Quantum Theory of Many Particle Systems." McGraw-Hill, New York, 1971.
- R. P. Feynman, "Lectures on Physics," Vol. 3, Chap. 21. Addison-Wesley, New York, 1965.
- W. A. Fietz, M. R. Beasley, J. Silcox, and W. W. Webb, *Phys. Rev.* **136**, A335 (1964).
- A. T. Fiory, M. Gurvitch, R. J. Cava, and G. P. Espinosa, *Phys. Rev. B* **36**, 7262 (1987).
- A. T. Fiory, G. P. Espinosa, R. M. Fleming, G. S. Grader, M. Gurvitch, A. F. Hebard, R. E. Howard, J. R. Kwo, A. F. J. Levi, P. M. Mankiewich, S. Martin, C. E. Rice, L. F. Schneemeyer, and A. E. White, International Conference on Electronic Materials, Tokyo, 1988.
- A. T. Fiory, S. Martin, R. M. Fleming, L. F. Schneemeyer, J. V. Waszczak, A. F. Hebard, and S. A. Sunshine, *Physica C* **162C-164C**, 1195 (1989).
- A. T. Fiory, M. A. Paalanen, R. R. Ruel, L. F. Schneemeyer, and J. V. Waszczak, *Phys. Rev. B* **41**, 4805 (1990).
- O. Fischer, *Appl. Phys.* **16**, 1 (1978).
- O. Fischer, in "Earlier and Recent Aspects of Superconductivity" (J. G. Bednorz and K. A. Müller, Eds.), p. 96, Springer, Berlin, 1990.
- P. Fischer, K. Kakurai, M. Steiner, K. N. Clausen, B. Lebeck, F. Hulliger, H. R. Ott, P. Brüesch, and P. Unternährer, *Physica C* **152C**, 145 (1988).
- P. Fischer, H. W. Neumüller, B. Roas, H. F. Braun, and G. Saemann-Ischenko, *Solid State Commun.* **72**, 871 (1989).
- J. E. Fischer, P. A. Heiney, A. R. McGhie, W. J. Romanow, A. M. Denenstein, J. P. McCauley, Jr., and A. B. Smith, III, *Science* **252**, 1288 (1991).
- J. E. Fischer, P. A. Heiney, and A. B. Smith, III, *Acc. Chem. Res.* **25**, 97 (1992).
- K. H. Fischer, *Physica C* **178C**, 161 (1991).
- D. S. Fisher and D. A. Huse, *Phys. Rev. B* **38**, 373, 386 (1988).
- M. P. A. Fisher, *Phys. Rev. Lett.* **62**, 1415 (1989).
- R. A. Fisher, S. Kim, B. F. Woodfield, N. E. Phillips, L. Taillefer, K. Hasselbach, J. Flouquet, A. L. Giorgi, and J. L. Smith, *Phys. Rev. Lett.* **62**, 1411 (1989).
- M. P. A. Fisher, *Phys. Rev. Lett.* **65**, 923 (1990).
- D. S. Fisher, M. P. A. Fisher, and D. A. Huse, *Phys. Rev. B* **43**, 130 (1991).
- R. S. Fishman, *Phys. Rev. B* **38**, 11996 (1988).
- R. S. Fishman, *Phys. Rev. Lett.* **63**, 89 (1989).
- Z. Fisk, P. C. Canfield, W. P. Beyermann, J. D. Thompson, M. F. Hundley, H. R. Ott, E. Felder, M. B. Maple, M. A. Lopez de la Torre, P. Visani, and C. L. Seaman, *Phys. Rev. Lett.* **67**, 3310 (1991).
- M. D. Fiske, *Rev. Mod. Phys.* **36**, 221 (1964).

- S. A. FitzGerald, S. G. Kaplan, A. Rosenberg, A. J. Sievers, and R. A. S. McMordie, *Phys. Rev. B* **45**, 10165 (1992).
- R. L. Fleisher, H. R. Hart, Jr., K. W. Lay, and F. E. Luborsky, *Phys. Rev. B* **40**, 2163 (1989).
- R. B. Flippen, *Phys. Rev. B* **44**, 7708 (1991).
- M. Florjanczyk and M. Jaworski, *Phys. Rev. B* **40**, 2128 (1989).
- R. Flükiger and W. Klose, "Landolt-Börnstein, Group III Solid State Physics," Vol. 21, Superconductors. Springer-Verlag, Berlin/New York, 1993.
- M. Foldeaki, M. E. McHenry, and R. C. O'Handley, *Phys. Rev. B* **39**, 2883 (1989).
- W. Folkerts and C. Haas, *Phys. Rev. B* **41**, 6341 (1990).
- S. Foner, E. J. McNiff, Jr., D. Heiman, S.-M. Huang, and R. B. Kaner, *Phys. Rev. B* **46**, 14936 (1992).
- J. Fonteberta and L. Fàbrega, in "Studies in High Temperature Superconductors" (A. V. Narlikar, Ed.), Vol. 16, Nova Sci., New York, in press.
- A. Forkl, T. Dragon, and H. Kronmüller, *J. Appl. Phys.* **67**, 3047 (1990).
- A. Forkl, H. U. Habermeyer, B. Liebold, T. Dragon, and H. Kronmüller, *Physica C* **180C**, 155 (1991).
- M. Forsthuber and G. Hilscher, *Phys. Rev. B* **45**, 7996 (1992).
- N. A. Fortune, K. Murata, K. Ikeda, and T. Takahashi, *Phys. Rev. Lett.* **68**, 2933 (1992).
- C. M. Foster, K. F. Voss, T. W. Hagler, D. Mihailovic, A. S. Heeger, M. M. Eddy, W. L. Olsen, and E. J. Smith, *Solid State Commun.* **76**, 651 (1990).
- H. Frahm, S. Ullah, and A. T. Dorsey, *Phys. Rev.* **66**, 3067 (1991).
- Z. Frait, D. Fraitová, and L. Pust, *J. Phys. Colloque C* **8**, 2235 (1988a); Z. Frait, D. Fraitová, E. Pollert, and L. Pust, *Phys. Status Solidi* **146**, K119 (1988b).
- J. P. Franck, in "Physical Properties of High Temperature Superconductors," (D. M. Ginsberg, Ed.), Vol. 4, Chap. 4, World Scientific, Singapore (1994).
- G. Frank, Ch. Ziegler and W. Göpel, *Phys. Rev. B* **43**, 2828 (1991).
- A. Freimuth, C. Hohn, and M. Galfy, *Phys. Rev. B* **44**, 10396 (1991).
- T. Freltoft, G. Shirane, S. Mitsuda, J. P. Remeika, and A. S. Cooper, *Phys. Rev. B* **37**, 137 (1988).
- T. Freltoft, H. J. Jensen, and P. Minnhagen, *Solid State Commun.* **78**, 635 (1991).
- T. A. Friedmann, J. P. Rice, J. Giapintzakis, and D. M. Ginsberg, *Phys. Rev. B* **39**, 4258 (1989).
- B. Friedl, C. Thomsen, and M. Cardona, *Phys. Rev. Lett.* **65**, 915 (1990).
- T. A. Friedmann, M. W. Rabin, J. Giapintzakis, J. P. Rice, and D. M. Ginsberg, *Phys. Rev. B* **42**, 6217 (1990).
- H. Fröhlich, *Phys. Rev.* **79**, 845 (1950).
- L. Fruchter and I. A. Campbell, *Phys. Rev. B* **40**, 5158 (1989).
- A. Fujimori, S. Takekawa, E. Takayama-Muromachi, Y. Uchida, A. Ono, T. Takahashi, Y. Okabe and H. Katayama-Yoshida, *Phys. Rev. B* **39**, 2255 (1989).
- H. Fujishita, M. Sera, and M. Sato, *Physica C* **175**, 165 (1991).
- K. Fujiwara, Y. Kitaoka, K. Ishida, K. Asayama, Y. Shimakawa, T. Manako, and Y. Kubo, *Physica C* **184**, 207 (1991).
- T. Fukami, T. Kamura, A. A. Youssef, Y. Hori, and S. Mase, *Physica C* **159**, 427 (1989).
- T. Fukami, K. Hayashi, T. Yamamoto, T. Nishizaki, Y. Horie, F. Ichikawa, T. Aomine, V. Soares, and L. Rinderer, *Physica C* **184**, 65 (1991a).
- T. Fukami, T. Yamamoto, K. Hayashi, T. Nishizaki, Y. Hori, F. Ichikawa, and T. Aomine, *Physica C* **185**, 2255 (1991b).
- T. A. Fulton, P. L. Gammei, D. J. Bishop, L. N. Dunkleberger, and G. J. Dolan, *Phys. Rev. Lett.* **63**, 1307 (1989).
- P. Fumagalli and J. Schoenes, *Phys. Rev. B* **44**, 2246 (1991).
- A. Furusaki, H. Takayanagi, and M. Tsukada, *Phys. Rev. Lett.* **67**, 132 (1991).
- A. Furusaki and M. Tsukada, *Phys. Rev. B* **43**, 10164 (1991).
- A. Furusaki and M. Ueda, *Phys. Rev. B* **45**, 10576 (1992).
- A. Furusaki, H. Takayanagi, and M. Tsukada, *Phys. Rev. B* **45**, 10563 (1992).
- M. Furuyama, N. Kobayashi, and Y. Muto, *Phys. Rev. B* **40**, 4344 (1989).
- E. Gagliano and S. Bacci, *Phys. Rev. B* **42**, 8772 (1990).
- P. L. Gai and J. M. Thomas, *Supercond. Rev.* **1**, 1 (1992).
- M. C. Gallagher, J. G. Adler, J. Jung, and J. P. Franck, *Phys. Rev. B* **37**, 7846 (1988).
- W. J. Gallagher, *J. Appl. Phys.* **63**, 4216 (1988).
- C. F. Gallo, L. R. Whitney, and P. J. Walsh, in "Novel Superconductivity" (S. A. Wolf and V. Z. Kresin, Eds.), p. 385, Plenum, New York, 1987.
- C. F. Gallo, L. R. Whitney, and P. J. Walsh, *Mater. Res. Soc. Symp. Proc.* **99**, 165 (1988).
- P. L. Gammel, D. J. Bishop, G. J. Dolan, J. R. Kwo, C. A. Murray, L. F. Schneemeyer, and J. V. Waszczak, *Phys. Rev. Lett.* **59**, 2592 (1987).
- P. L. Gammel, L. F. Schneemeyer, J. K. Waszczak, and A. J. Bishop, *Phys. Rev. Lett.* **61**, 1666 (1988).
- P. L. Gammel, A. Hebard, and D. J. Bishop, *Phys. Rev. B* **40**, 7354 (1989).
- J. T. Gammel, R. J. Donohoe, A. R. Bishop, and B. I. Swanson, *Phys. Rev. B* **42**, 10566 (1990).
- P. L. Gammel, L. F. Schneemeyer, and D. J. Bishop, *Phys. Rev. Lett.* **66**, 953 (1991).
- P. L. Gammel, D. J. Bishop, T. P. Rice, and D. M. Ginsberg, *Phys. Rev. Lett.* **68**, 3343 (1992).
- F. Gao, G. L. Carr, C. D. Porter, D. B. Tanner, S. Etemad, T. Venkatesan, A. Inam, B. Dutta, X. D. Wu, G. P. Williams, and C. J. Hirschmugl, *Phys. Rev. B* **43**, 10383 (1991).

- L. Gao, R. L. Meng, Y. Y. Xue, P. H. Hor and C. W. Chu, *Appl. Phys. Lett.* **58**, 92 (1991).
- L. Gao, Z. J. Huang, R. L. Meng, J. G. Lin, F. Chen, L. Beauvais, Y. Y. Sun, Y. Y. Xue, and C. W. Chu, *Physica C* **213**, 261 (1993).
- L. Gao, Y. Y. Xue, F. Chen, Q. Xiong, R. L. Meng, D. Ramirez, C. W. Chu, J. H. Eggert, and H. K. Mao, submitted for publication.
- M. M. Garland, *J. Mater. Res.* **3**, 830 (1988).
- P. Garoche, R. Bruset, D. Jérôme, and K. Bechgaard, *J. Physique Lett.* **43**, L147 (1982).
- L. J. Geerligs, M. Peters, L. E. M. de Groot, A. Verbruggen, and J. E. Mooij, *Phys. Rev. Lett.* **63**, 326 (1989).
- I. I. Geguzin, I. Ya. Nikiforov, and G. I. Alperovitch, *Fiz. Tverd. Tela.* **15**, 931 (1973).
- C. Geibel, S. Thies, D. Kaczorowski, A. Mehner, A. Grauel, B. Seidel, U. Ahlheim, R. Helfrich, K. Petersen, C. D. Bredl, and F. Steglich, *Z. Phys. B—Cond. Matt.* **83**, 305 (1991a).
- C. Geibel, C. Schank, S. Thies, H. Kitzawa, C. D. Bredl, A. Böhm, M. Rau, A. Grauel, R. Caspary, R. Helfrich, U. Ahlheim, G. Weber, and F. Steglich, *Z. Phys. B—Cond. Matt.* **84**, 1 (1991b).
- C. Geibel, U. Ahlheim, C. D. Bredl, J. Diehl, A. Grauel, R. Helfrich, H. Kitazawa, R. Köhler, R. Modler, M. Lang, C. Schank, S. Thies, F. Steglich, N. Sato, and T. Komatsubara, *Physica C* **185**, 2651 (1991c).
- A. K. Geim, I. V. Grigorieva, and S. V. Dubonos, *Phys. Rev. B* **46**, 324 (1992).
- B. Y. Gelfand and B. I. Halperin, *Phys. Rev. B* **45**, 5517 (1992).
- A. Gerber, Th. Grenet, M. Cyrot, and J. Beille, *Phys. Rev. B* **45**, 5099 (1992).
- W. Gerhäuser, G. Ries, H. W. Neumüller, W. Schmidt, O. Eibl, G. Saemann-Ischenko, and S. Klauwinzer, *Phys. Rev. Lett.* **68**, 879 (1992).
- V. B. Geshkenbein, V. M. Vinokur, and R. Fehrenbacher, *Phys. Rev. B* **43**, 3748 (1991).
- S. K. Ghatak, A. Mitra, and D. Sen, *Phys. Rev. B* **45**, 951 (1992).
- J. Ghijsen, L. H. Tjeng, H. Eskes, G. A. Sawatzky, and R. L. Johnson, *Phys. Rev. B* **42**, 2268 (1990).
- I. Giaever and H. R. Zeller, *Phys. Rev. Lett.* **20**, 1504 (1968).
- J. Giapintzakis, W. C. Lee, J. P. Rice, D. M. Ginsberg, I. M. Robertson, R. Wheeler, M. Kirk, and M.-Q. Ruault, *Phys. Rev. B* **45**, 10677 (1992).
- M. A. M. Gijs, D. Scholten, Th. van Rooy, and A. M. Gerrits, *Phys. Rev. B* **41**, 11627 (1990a).
- M. A. M. Gijs, A. M. Gerrits, and C. W. J. Beenakker, *Phys. Rev. B* **42**, 10789 (1990b).
- L. R. Gilbert, R. Messier, and R. Roy, *Thin Solid Films* **54**, 129 (1978).
- D. B. Gingold and C. J. Lobb, *Phys. Rev. B* **42**, 8220 (1990).
- M. J. P. Gingras, *Phys. Rev. B* **45**, 7547 (1992).
- D. M. Ginsberg (Ed.), "Physical Properties of High Temperature Superconductors," Vol. 1, World Scientific, Singapore, 1989.
- D. M. Ginsberg (Ed.), "Physical Properties of High Temperature Superconductors," Vol. 2, World Scientific, Singapore, 1990.
- D. M. Ginsberg (Ed.), "Physical Properties of High Temperature Superconductors," Vol. 3, World Scientific, Singapore, 1992.
- D. M. Ginsberg (Ed.), "Physical Properties of High Temperature Superconductors," Vol. 4, World Scientific, Singapore, 1994.
- V. L. Ginzburg and L. Landau, *Zh. Eksp. Teor. Fiz.* **20**, 1064 (1950).
- V. L. Ginzburg and D. A. Kirzhnits, "High Temperature Superconductivity," Nauka, Moscow, 1977 [Engl. Transl. Consultants Bureau, New York, 1982].
- S. L. Ginzburg, V. P. Khavronin, G. Yu. Logvinova, I. D. Luzyanin, J. Herrmann, B. Lippold, H. Börner and H. Schmiedel, *Physica C* **174**, 109 (1991).
- J. I. Gittleman and B. Rosenblum, *J. Appl. Phys.* **39**, 2617 (1968).
- S. H. Glarum, L. F. Schneemeyer, and J. V. Waszczak, *Phys. Rev. B* **41**, 1837 (1990).
- N. E. Glass and D. Rogovin, *Phys. Rev. B* **39**, 11327 (1989).
- D. Glatzer, A. Forkl, H. Theuss, H. U. Habermeier, and Kronmüller, *Phys. Status Solidi* **170**, 549 (1992).
- L. I. Glazman and A. E. Koshelev, *Phys. Rev. B* **43**, 2835 (1991a); *Physica C* **173**, 180 (1991b).
- H. R. Glyde, L. K. Moleko, and P. Findeisen, *Phys. Rev. B* **45**, 2409 (1992).
- A. Gold and A. Ghazali, *Phys. Rev. B* **43**, 12952 (1991).
- R. B. Goldfarb, A. F. Clark, A. I. Braginski, and A. J. Panson, *Cryogenics* **27**, 475 (1987a); R. B. Goldfarb, A. F. Clark, A. I. Braginski, and A. J. Panson, in "High Temperature Superconductors" (D. U. Grubser and M. Schluter, Eds.), p. 261, Mater. Res. Soc., Pittsburgh (1987b).
- D. Goldschmidt, *Phys. Rev. B* **39**, 2372 (1989).
- M. J. Goldstein and W. G. Moulton, *Phys. Rev. B* **40**, 8714 (1989).
- M. Golosovsky, D. Davidov, E. Farber, T. Tsach, and M. Schieber, *Phys. Rev. B* **43**, 10390 (1991).
- M. Golosovsky, Y. Naveh, and D. Davidov, *Phys. Rev. B* **45**, 7495 (1992).
- J. B. Goodenough and J.-S. Zhou, *Phys. Rev. B* **42**, 4276 (1990).
- J. B. Goodenough, J.-S. Zhou, and J. Chan, *Phys. Rev. B* **47**, 5275 (1993).
- L. F. Goodrich, A. N. Srivastava, and T. C. Stauffer, *J. Res. NIST* **96**, 703 (1991).
- L. F. Goodrich and A. N. Srivastava, *Supercond. Industry Spring*, 28 (1992).
- L. P. Gor'kov, *Zh. Eksp. Teor. Fiz.* **36**, 1918. [Sov. Phys. JETP **36**, 1364] (1959).
- L. P. Gor'kov, *Sov. Phys. JETP* **38**, 830 (1973).

- L. P. Gor'kov, *Sov. Phys. JETP Lett.* 20, 260 (1974).
- U. Gottwick, R. Held, G. Sparn, F. Steglich, H. Rietschel, D. Ewert, B. Renker, W. Bauhofer, S. von Molnar, M. Wilhelm, and H. E. Hoenig, *Europhys. Lett.* 4, 1183 (1987).
- C. E. Gough, M. S. Colclough, E. M. Forgan, R. G. Jordan, M. Keene, C. M. Muirhead, A. I. M. Rae, N. Thomas, J. S. Abell, and S. Sutton, *Nature* 326, 855 (1987).
- M. E. Gouvêa, G. M. Wysin, A. R. Bishop, and F. G. Mertens, *Phys. Rev. B* 39, 11840 (1989).
- G. S. Grader, P. K. Gallagher, and E. M. Gyorgy, *Appl. Phys. Lett.* 51, 1115 (1987).
- J. E. Gaebner, R. C. Haddon, S. V. Chichester, and S. M. Glarum, *Phys. Rev. B* 41, 4808 (1990).
- R. Graham, M. Schlautmann, and D. L. Shepelyansky, *Phys. Rev. Lett.* 67, 255 (1991).
- K. E. Gray, R. T. Kampwirth, and D. E. Farrell, *Phys. Rev. B* 41, 819 (1990).
- K. E. Gray, D. H. Kim, B. W. Veal, G. T. Seidler, T. F. Rosenbaum, and D. E. Farrell, *Phys. Rev. B* 45, 10071 (1992).
- K. E. Gray, *Appl. Supercond.*, (D. Shi, Ed.), in press.
- L. H. Green and B. G. Bagley, in "Physical Properties of High Temperature Superconductors" (D. M. Ginsberg, Ed.), Vol. 2, Chap. 8, World Scientific, Singapore, 1990.
- R. L. Greene, in "Organic Superconductivity" (V. Z. Kresin and W. A. Little, Eds.), p. 7, Plenum, New York, 1990.
- E. Gregory, T. S. Kreilick, J. Wong, A. K. Ghosh, and W. B. Sampson, *Cryogenics* 27, 178 (1987).
- V. V. Gridin, P. Pernambuco-Wise, C. G. Trendall, W. R. Datars, and J. D. Garrett, *Phys. Rev. B* 40, 8814 (1989).
- D. G. Grier, C. A. Murray, C. A. Bolle, P. L. Gammel, D. J. Bishop, D. B. Mitzi, and A. Kapitulnik, *Phys. Rev. Lett.* 66, 2770 (1991).
- R. Griessen, *Phys. Rev. Lett.* 64, 1674 (1990).
- M. Grilli, R. Raimondi, C. Castellani, C. DiCastro, and G. Kotliar, *Phys. Rev. Lett.* 67, 259 (1991).
- H. H. Gröbke, *Phys. Rev. B* 41, 11047 (1990).
- N. Grønbech-Jensen, *Phys. Rev. B* 45, 7315 (1992).
- N. Grønbech-Jensen, N. F. Pedersen, A. Davidson, and R. D. Parmentier, *Phys. Rev. B* 42, 6035 (1990).
- N. Grønbech-Jensen, S. A. Hattel, and M. R. Samuelsen, *Phys. Rev.* 45, 12457 (1991).
- R. Gross, P. Chaudhari, M. Kawasaki, and A. Gupta, *Phys. Rev. B* 42, 10735 (1990a).
- R. Gross, P. Chaudhari, M. Kawasaki, M. B. Ketchen, and A. Gupta, *Appl. Phys. Lett.* 57, 727 (1990b).
- R. Gross and D. Koelle, *Rept. Prog. Phys.*, 57, 651 (1994).
- D. Y. Gubser and M. Schluter, Eds., "High Temperature Superconductors," *Proc. Symp.*, Spring Meet., Anaheim, CA, Apr. 1987, Mater. Res. Soc., Pittsburgh, 1987.
- S. Guha, D. Peebles, and T. J. Wieting, *Phys. Rev. B* 43, 13092 (1991).
- F. Guinea and G. Zimanyi, *Phys. Rev. B* 47, 501 (1993).
- B. Gumhalter and V. Zlatic, *Phys. Rev. B* 42, 6446 (1990).
- J. Guo, D. E. Ellis, E. E. Alp, and G. L. Goodman, *Phys. Rev. B* 42, 251 (1990).
- A. Gupta, P. Esquinazi, and H. F. Braun, *Physica C* 184, 393 (1991).
- R. P. Gupta and M. Gupta, *Phys. Rev. B* 47, 11635 (1993a); *Phys. Rev. B* 48, 16068 (1993b).
- A. Gurevich and H. K  pfer, *Phys. Rev. B* 48, 6477 (1993).
- M. Gurvitch and A. T. Fiory, *Phys. Rev. Lett.* 59, 1337 (1987a); *Appl. Phys. Lett.* 51, 1027 (1987b); in "Novel Superconductivity" (S. A. Wolf and V. Z. Kresin, Eds.), p. 663, Plenum, New York, 1987c.
- M. Gurvitch, A. T. Fiory, L. F. Schneemeyer, R. J. Cava, G. P. Espinosa, and J. V. Waszczak, *Physica C* 153-155, 1369 (1988).
- H. Gutfreund and W. A. Little, in "Highly Conducting One Dimensional Solids" (J. T. Devreese, R. P. Evrard, and V. E. van Doren, Eds.), Chap. 7, Plenum, New York, 1979.
- F. Gygi and M. Schl  ter, *Phys. Rev. Lett.* 65, 1820 (1990a); *Phys. Rev. B* 41, 822 (1990b); 43, 7609 (1991).
- R. C. Haddon, *Acc. Chem. Res.* 25, 127 (1992).
- S. J. Hagen, T. W. Jing, Z. Z. Wang, J. Horvath, and N. P. Ong, *Phys. Rev. B* 37, 7928 (1988).
- S. J. Hagen, C. J. Lobb, R. L. Greene, M. G. Forrester and J. H. Kang, *Phys. Rev. B* 41, 11630 (1990a).
- S. J. Hagen, C. J. Lobb, R. L. Greene, M. G. Forrester and J. Talvacchio, *Phys. Rev. B* 42, 6777 (1990b).
- R. R. Hake, *Phys. Rev.* 166, 471 (1968).
- K. Hallberg, A. G. Rojo, and C. A. Balseiro, *Phys. Rev. B* 43, 8005 (1991).
- J. W. Halley, (Ed.), "Theories of High Temperature Superconductivity," Addison Wesley, Reading, MA, 1988.
- B. I. Halperin, *Phys. Rev. Lett.* 52, 1583, 2390 (1984).
- N. Hamada, S. Massidda, A. J. Freeman, and J. Redinger, *Phys. Rev. B* 40, 4442 (1989).
- D. R. Hamann and L. F. Mattheiss, *Phys. Rev. B* 38, 5138 (1988).
- P. D. Hambourger and F. J. Di Salvo, *Physica B* 99, 173 (1980).
- C. A. Hamilton, *Phys. Rev. B* 5, 912 (1972).
- P. C. Hammel, M. Takigawa, R. H. Heffner, Z. Fisk, and K. C. Ott, *Phys. Rev. Lett.* 63, 1992 (1989).
- P. C. Hammel, A. P. Reyes, Z. Fisk, M. Takigawa, J. D. Thompson, R. H. Heffner, W.-W. Cheong, and J. E. Schirber, *Phys. Rev. B* 42, 6781 (1990).
- D. P. Hampshire, X. Cai, J. Seuntjens, and D. C. Larbalestier, *Supercond. Sci. Technol.* 1, 12 (1988).
- S. Han, L. F. Cohen, and E. L. Wolf, *Phys. Rev. B* 42, 8682 (1990a).

REI
S. I
Z. J
Z. I
I
S. F
I
T. H
P
M. F
R
Z. H
(1
Z. Ha
M
28
Z. Ha
J. Har
11
A. B.
(19
R. K.
tros
D. C.
Gar
D. R. F
G. J
E. J
39, 8
D. R. H
Chic
T. P.
Lett.
D. R. H
1068
M. Hase
Kimu
Physic
T. Haseg
Prope
ductor
World
S. Hasega
Igaras
and R.
K. C. Hase
N. Hatake
Rev. B
J. Hauck,
Mika, 2
D. B. Havi
Rev. Le
R. M. Haze
N. L. R
Hor, A.
7238 (19

- S. G. Han, Z. V. Vardeny, K. S. Wong, and O. G. Symko, *Phys. Rev. Lett.* **65**, 2708 (1990b).
- Z. P. Han, R. Dupree, D. McK. Paul, A. P. Howes, and L. W. J. Caves, *Physica C* **181**, 355 (1991).
- Z. P. Han, R. Dupree, A. Gencten, R. S. Liu, and P. P. Edwards, *Phys. Rev. Lett.* **69**, 1256 (1992).
- S. H. Han, C. C. Almasan, M. C. de Andrade, Y. Dalichaouch, and M. B. Maple, *Phys. Rev. B* **46**, 14290 (1992).
- T. Hanaguri, T. Fukase, I. Tanaka, and H. Kojima, *Phys. Rev. B* **48**, 9772 (1993).
- M. Hangyo, N. Nagasaki, and S. Nakashima, *Phys. Rev. B* **47**, 14595 (1993).
- Z. Hao and J. R. Clem, *Phys. Rev. Lett.* **67**, 2371 (1991).
- Z. Hao, J. R. Clem, M. W. McElfresh, L. Civale, A. P. Malozemoff, and F. Holtzberg, *Phys. Rev. B* **43**, 2844 (1991).
- Z. Hao and J. R. Clem, *Phys. Rev. B* **46**, 5853 (1992).
- J. Hara, M. Ashida, and K. Nagai, *Phys. Rev. B* **47**, 11263 (1993).
- A. B. Harris and R. V. Lange, *Phys. Rev.* **157**, 295 (1967).
- R. K. Harris, "Nuclear Magnetic Resonance Spectroscopy," Halsted, 1986.
- D. C. Harris, S. T. Herbert, D. Stroud, and J. C. Garland, *Phys. Rev. Lett.* **67**, 3606 (1991).
- D. R. Harshman, L. F. Schneemeyer, J. V. Waszczak, G. Aeppli, R. J. Cava, B. Batlogg, L. W. Rupp, E. J. Ansaldo, and D. Li. Williams, *Phys. Rev. B* **39**, 851 (1989).
- D. R. Harshman, R. N. Kleiman, R. C. Haddon, S. V. Chichester-Hicks, M. L. Kaplan, L. W. Rupp, Jr., T. Pfiz, D. Li. Williams, D. B. Mitzi, *Phys. Rev. Lett.* **64**, 1293 (1990).
- D. R. Harshman and A. P. Mills, Jr., *Phys. Rev. B* **45**, 10684 (1992).
- M. Hase, I. Terasaki, A. Maeda, K. Uchinokura, T. Kimura, K. Kishio, I. Tanaka, and H. Kojima, *Physica C* **185-189**, 1855 (1991).
- T. Hasegawa, H. Ikuta, and K. Kitazawa, in "Physical Properties of High Temperature Superconductors" (D. M. Ginsberg, Ed.), Vol. 3, Chap. 7, World Scientific, Singapore, 1992.
- S. Hasegawa, T. Matsuda, J. Endo, N. Osakabe, M. Igarashi, T. Kobayashi, M. Naito, A. Tonomura, and R. Aoki, *Phys. Rev. B* **43**, 7631 (1991).
- K. C. Hass, *Solid State Phys.* **42**, 213 (1989).
- N. Hatakenaka, S. Kurihara, and H. Takayanagi, *Phys. Rev. B* **42**, 3987 (1990).
- J. Hauck, S. Denker, H. Hindriks, S. Ipta, and K. Mika, *Z. Phys. B* **84**, 31 (1991).
- D. B. Haviland, Y. Liu, and A. M. Goldman, *Phys. Rev. Lett.* **62**, 2180 (1989).
- R. M. Hazen, L. W. Finger, R. J. Angel, C. T. Prewitt, N. L. Ross, H. K. Mao, C. G. Hadjidakos, P. H. Hor, A. L. Meng, and C. W. Chu, *Phys. Rev. B* **35**, 7238 (1987).
- R. M. Hazen, L. W. Finger, R. J. Angel, C. T. Prewitt, N. L. Ross, C. G. Hadjidakos, P. J. Heaney, D. R. Veblen, Z. Z. Sheng, A. El Ali, and A. M. Hermann, *Phys. Rev. Lett.* **60**, 1657 (1988).
- R. M. Hazen, in "Physical Properties of High Temperature Superconductors" (D. M. Ginsberg, Ed.), Vol. 2, Chap. 3, World Scientific, Singapore, 1990.
- A. F. Hebard, P. L. Gammel, C. E. Rice, and A. F. J. Levi, *Phys. Rev. B* **40**, 5243 (1989).
- A. F. Hebard and M. A. Paalanen, *Phys. Rev. Lett.* **65**, 927 (1990).
- A. F. Hebard, M. J. Rosseinsky, R. C. Haddon, D. W. Murphy, S. H. Glarum, T. T. M. Palstra, A. P. Ramirez, and A. R. Kortan, *Nature*, **350**, 600 (1991).
- A. F. Hebard, in "Proc. R. L. Orbach Symp. Random Magnetism and High T_c Supercond.," World Scientific, Singapore, 1994.
- A. F. Hebard, in "Strongly Correlated Electronic Materials" (K. S. Bedell, Ed.), Addison-Wesley, New York, 1994.
- S. E. Hebboul and J. C. Garland, *Phys. Rev. B* **43**, 13703 (1991).
- P. Hedegård and M. B. Pedersen, *Phys. Rev. B* **42**, 10035 (1990).
- R. H. Heffner, J. L. Smith, J. O. Willis, P. Birrer, C. Baines, F. N. Gygax, B. Hitti, E. Lippelt, H. R. Ott, A. Schenck, E. A. Knetsch, J. A. Mydosh, and D. E. MacLaughlin, *Phys. Rev. Lett.* **65**, 2816 (1990).
- R. Heid, *Phys. Rev. B* **45**, 5052 (1992).
- R. A. Hein, T. L. Francavilla, and D. H. Liebenberg (Eds.), "Magnetic Susceptibility of Superconductors and Other Spin Systems," Plenum, New York, 1991.
- C. S. Hellberg and E. J. Mele, *Phys. Rev. B* **48**, 646 (1993).
- E. S. Hellman, B. Miller, J. M. Rosamilia, E. H. Hartford, and K. W. Baldwin, *Phys. Rev. B* **44**, 9719 (1991).
- F. Hellman and T. H. Geballe, *Phys. Rev. B* **36**, 107 (1987).
- N. F. M. Henry and K. Lonsdale, "International Tables for X-Ray Crystallography," Kynbo, Birmingham, England, 1965.
- J. Heremans, D. T. Morelli, G. W. Smith, and S. C. Strite III, *Phys. Rev. B* **37**, 1604 (1988).
- F. Herman, R. V. Kasowski, and W. Y. Hsu, *Phys. Rev. B* **36**, 6904 (1987).
- A. M. Hermann and J. V. Yakhmi, "Thallium Based High Temperature Superconductors," Dekker, Basel, 1993.
- S. L. Herr, K. Kamarás, D. B. Tanner, S.-W. Cheong, G. R. Stewart, and Z. Fisk, *Phys. Rev. B* **43**, 7847 (1991).
- D. W. Hess, T. A. Tokuyasu, and J. A. Sauls, *Phys. Condens. Matt.* **1**, 8135 (1989).
- H. F. Hess, R. B. Robinson, R. C. Dynes, J. M. Valles, Jr., and J. V. Waszczak, *Phys. Rev. Lett.* **62**, 214 (1989).

- H. F. Hess, R. B. Robinson, and J. V. Waszczak, *Phys. Rev. Lett.* **64**, 2711 (1990).
- H. F. Hess, R. B. Robinson, and J. V. Waszczak, *Physica B* **169**, 422 (1991).
- J. D. Hettinger and D. G. Steel, in "High Temperature Superconducting Science" (D. Shi, Ed.), Pergamon, New York, 1994.
- J. M. Hettinger, A. G. Swanson, W. J. Skocpol, J. S. Brooks, J. M. Graybeal, P. M. Mankiewicz, R. E. Howard, B. L. Straughn, and E. G. Burkhardt, *Phys. Rev. Lett.* **62**, 2044 (1989).
- R. E. Hetzel, A. Sudbø, and D. Huse, *Phys. Rev. Lett.* **69**, 518 (1992).
- E. T. Heyen, R. Liu, C. Thomsen, R. Kremer, M. Cardona, J. Karpinski, E. Kaldis, and S. Rusiecki, *Phys. Rev. B* **41**, 11058 (1990a).
- E. T. Heyen, S. N. Rashkeev, I. I. Mazin, O. K. Andersen, R. Liu, M. Cardona, and O. Jepsen, *Phys. Rev. Lett.* **65**, 3048 (1990b).
- E. T. Heyen, G. Kliche, W. Kress, W. König, M. Cardona, E. Rampf, J. Prade, U. Schröder, A. D. Kulkarni, F. W. de Wette, S. Piñol, D. McK. Paul, E. Morán, and M. A. Alario-Franco, *Solid State Commun.* **74**, 1299 (1990c).
- E. Heyen, M. Cardona, J. Karpinski, E. Kaldis, and S. Rusiecki, *Phys. Rev. B* **43**, 12958 (1991).
- Y. Hidaka, Y. Enomoto, M. Suzuki, M. Oda, and T. Murakami, *Jpn. J. Appl. Phys.* **26**, L377 (1987).
- S. Hikami and A. I. Larkin, *Mod. Phys. Lett. B* **2**, 693 (1988).
- S. Hikami and A. Fujita, *Prog. Theor. Phys.* **83**, 443 (1990a); *Phys. Rev. B* **41**, 6379 (1990b).
- S. Hikami, A. Fujita, and A. Larkin, *Phys. Rev. B* **44**, 10400 (1991).
- M. Hikita, Y. Tajima, A. Katsui, Y. Hidaka, T. Iwata, and S. Tsurumi, *Phys. Rev. B* **36**, 7199 (1987).
- M. Hikita and M. Suzuki, *Phys. Rev. B* **39**, 4756 (1989).
- G. Hilscher, H. Michor, N. M. Hong, T. Holubar, W. Perthold, M. Vybornov, and P. Rogl, in *Int. Conf. Strongly Correlated Electron Systems*, Amsterdam, Netherlands, Aug. 1994.
- D. G. Hinks, D. R. Richards, B. Dabrowski, D. T. Marx, and A. W. Mitchell, *Nature* **335**, 419 (1988).
- D. G. Hinks, B. Dabrowski, D. R. Richards, J. D. Jorgensen, S. Pei, and J. F. Zasadzinski, *Mat. Res. Soc. Symp. Proc.* **156**, 357 (1989).
- J. E. Hirsch, *Phys. Rev. B* **31**, 4403 (1985a); *Phys. Rev. Lett.* **54**, 1317 (1985b).
- J. E. Hirsch, *Phys. Rev. Lett.* **59**, 228 (1987).
- T. Hocquet, P. Mathieu, and Y. Simon, *Phys. Rev. B* **46**, 1061 (1992).
- J. A. Hodges, P. Imbert, and G. Jéhanho, *Solid State Commun.* **64**, 1209 (1987).
- U. Hofmann and J. Keller, *Z. Phys. B. Cond. Matter* **74**, 499 (1989).
- C. Hohn, M. Galfy, A. Dasculidou, A. Freimuth, H. Soltner, and U. Poppe, *Z. Phys. B* **85**, 161 (1991).
- K. Holczer, O. Klein, G. Grüner, J. D. Thompson, F. Deiderich, and R. L. Whetten, *Phys. Rev. Lett.* **67**, 271 (1991).
- T. Holst, J. B. Hansen, N. Grønbech-Jensen, and J. A. Blackburn, *Phys. Rev. B* **42**, 127 (1990).
- T. Holst and J. B. Hansen, *Phys. Rev. B* **44**, 2238 (1991).
- X. Q. Hong and J. E. Hirsch, *Phys. Rev. B* **46**, 14702 (1992).
- T. Honma, K. Yamaya, F. Minami, and S. Takekawa, *Physica C* **176**, 209 (1991).
- B. Hopfengärtner, B. Hensel, and G. Saemann-Ischenko, *Phys. Rev. B* **44**, 741 (1991).
- M. L. Horbach, F. L. J. Vos, and W. van Saarloos, *Phys. Rev. B* **48**, 4061 (1993).
- M. L. Horbach, F. L. J. Vos, and W. van Saarloos, *Phys. Rev. B* **49**, 3539 (1994).
- M. Horvatic, T. Auler, C. Berthier, Y. Berthier, P. Butaud, W. G. Clark, J. A. Gillet, P. Ségransan, and J. Y. Henry, *Phys. Rev. B* **47**, 3461 (1993).
- A. Houghton, R. A. Pelcovits, and A. Sudbø, *Phys. Rev. B* **40**, 6763 (1989); **41**, 4785(E) (1990).
- A. P. Howes, R. Dupree, D. McK. Paul, and S. Male, *Physica C* **185-189**, 1137 (1991).
- T. C. Hsu and P. W. Anderson, *Physica C* **162-164**, 1445 (1989).
- Q. Hu and M. Tinkham, *Phys. Rev. B* **39**, 11358 (1989).
- Q. Hu, C. A. Mears, P. L. Richards, and F. L. Lloyd, *Phys. Rev. Lett.* **64**, 2945 (1990).
- G. Y. Hu and R. F. O'Connell, *Phys. Rev. B* **47**, 8823 (1993).
- W. F. Huang, P. J. Ouseph, K. Fang, and Z. J. Xu, *Solid State Commun.* **66**, 283 (1988).
- Z. J. Huang, Y. Y. Xue, P. H. Hor, and C. W. Chu, *Physica C* **176**, 195 (1991a).
- Z. J. Huang, H. H. Fang, Y. Y. Xue, P. H. Hor, C. W. Chu, M. L. Norton, and H. Y. Tang, *Physica C* **180**, 331 (1991b).
- M.-Z. Huang, Y.-N. Xu, and W. Y. Ching, *Phys. Rev. B* **46**, 6572 (1992).
- Z. J. Huang, Y. Y. Xue, R. L. Meng, and C. W. Chu, *Phys. Rev. B* **49**, 4218 (1994).
- J. Hubbard, *Proc. Royal Soc. London A* **276**, 238 (1963).
- J. Hubbard, *Proc. Royal Soc. London A* **281**, 401 (1964).
- R. P. Huebener, R. T. Kampwirth, and A. Seher, *J. Low Temp. Phys.* **2**, 113 (1970).
- R. P. Huebener, "Magnetic Flux Structures in Superconductors," Springer Verlag, Berlin, 1979.
- R. P. Huebener, A. V. Ustinov, and V. K. Kaplunenko, *Phys. Rev. B* **42**, 4831 (1990).
- R. P. Huebener, *Physica C* **168**, 605 (1990).
- H. J. Hug, A. Moser, I. Parashikov, O. Fritz, B. Stiefel, H.-J. Güntherodt, and H. Thomas, *Physica*, to be published.
- N. H. Hur, H.-G. Lee, J.-H. Park, H.-S. Shin, and I.-S. Yang, *Physica C* **218**, 365 (1993).

- N. H. Hur, N. H. Kim, S. H. Kim, Y. K. Park, and J. C. Park, *Physica C*, **231**, 227 (1994).
- M. S. Hybertsen, E. B. Stechel, W. M. C. Foulkes, and M. Schlüter, *Phys. Rev. B* **45**, 10032 (1992).
- T. L. Hylton and M. R. Beasley, *Phys. Rev. B* **41**, 11669 (1990).
- O. B. Hyun, D. K. Finnemore, L. Schwartzkopf, and J. R. Clem, *Phys. Rev. Lett.* **58**, 599 (1987).
- O. B. Hyun, J. R. Clem, and D. K. Finnemore, *Phys. Rev. B* **40**, 175 (1989).
- M. Iansiti, M. Tinkham, A. T. Johnson, W. F. Smith, and C. J. Lobb, *Phys. Rev. B* **39**, 6465 (1989).
- H. Ihara, R. Sugise, K. Hayashi, N. Terada, M. Jo, M. Hirabayashi, A. Negishi, N. Atoda, H. Oyanagi, T. Shimomura, and S. Ohashi, *Phys. Rev. B* **38**, 11952 (1988).
- H. Ihara, M. Hirabayashi, H. Tanino, K. Tokiwa, H. Ozawa, Y. Akahama, and H. Kawamura, *Jpn. J. Appl. Phys.* **32**, L1732 (1993).
- J. Ihm and B. D. Yu, *Phys. Rev. B* **39**, 4760 (1989).
- S. Ikegawa, T. Wada, A. Ichinose, T. Yamashita, T. Sakurai, Y. Yaegashi, T. Kaneko, M. Kosuge, H. Yamauchi, and S. Tanaka, *Phys. Rev. B* **41**, 11673 (1990).
- S. Ikegawa, T. Wada, T. Yamashita, H. Yamauchi, and S. Tanaka, *Phys. Rev. B* **45**, 5659 (1992).
- J.-M. Imer, F. Patthey, B. Dardel, W. D. Schneider, Y. Baer, Y. Petroff, and A. Zettl, *Phys. Rev. Lett.* **62**, 336 (1989).
- T. Inabe, H. Ogata, Y. Maruyama, Y. Achiba, S. Suzuki, K. Kikuchi, and I. Ikemoto, *Phys. Rev. Lett.* **69**, 3797 (1992).
- S. E. Inderhees, M. B. Salamon, J. P. Rice, and D. M. Ginsberg, *Phys. Rev. Lett.* **66**, 232 (1991).
- Y. Inoue, Y. Shichi, F. Munakata, and M. Yamanaka, *Phys. Rev. B* **40**, 7307 (1989).
- M. Inui, P. B. Littlewood, and S. N. Coppersmith, *Phys. Rev. Lett.* **63**, 2421 (1989).
- L. Ioffe and G. Kotliar, *Phys. Rev. B* **42**, 10348 (1990).
- I. Ioffe and V. Kalmeyer, *Phys. Rev. B* **44**, 750 (1991).
- Z. Iqbal, J. C. Barry, and B. L. Ramakrishna, in "Studies in High Temperature Superconductors" (A. V. Narlikar, Ed.), Nova Sci., New York, 1989.
- Z. Iqbal, G. H. Kwei, B. L. Ramakrishna, and E. W. Ong, *Physica C* **167**, 369 (1990).
- Z. Iqbal, R. H. Baughman, B. L. Ramakrishna, S. Khare, N. S. Murthy, H. J. Bornemann, and D. E. Morris, *Science* **254**, 826 (1991).
- Z. Iqbal, *Supercond. Rev.* **1**, 49 (1992).
- Z. Iqbal, T. Datta, D. Kirven, A. Longu, J. C. Barry, F. J. Owens, A. G. Rinzier, D. Yang, and F. Reidinger, *Phys. Rev. B* **49**, 12322 (1994).
- F. Irie and K. Yamafuji, *J. Phys. Soc. Jpn.* **23**, 255 (1976).
- E. D. Isaacs, D. B. McWhan, R. N. Kleiman, D. J. Bishop, G. E. Ice, P. Zschack, B. D. Gaulin, T. E. Mason, J. D. Garrett, and W. J. L. Buyers, *Phys. Rev. Lett.* **65**, 3185 (1990).
- K. Isawa, A. Tokiwa-Yamamoto, M. Itoh, S. Adachi, and H. Yamauchi, *Physica C* **217**, 11 (1993).
- K. Isawa, A. Tokiwa-Yamamoto, M. Itoh, S. Adachi, and H. Yamauchi, *Physica C* **222**, 33 (1994a).
- K. Isawa, T. Higuchi, T. Machi, A. Tokiwa-Yamamoto, S. Adachi, M. Murakami, and H. Yamauchi, *Appl. Phys. Lett.* **64**, 1301 (1994b).
- T. Ishida and R. B. Goldfarb, *Phys. Rev. B* **41**, 8937 (1990).
- T. Ishida, R. B. Goldfarb, S. Okayasu, and Y. Kazumata, *Physica C* **185-189**, 2515 (1991).
- T. Ishiguro and K. Yamaji, "Organic Superconductors," Springer-Verlag, Berlin, 1990.
- A. Isihara, "Statistical Physics," Academic Press, New York, 1971.
- Y. Ishii and J. Ruvalds, *Phys. Rev. B* **48**, 3455 (1993).
- T. Itoh and H. Uchikawa, *Phys. Rev. B* **39**, 4690 (1989).
- M. Itoh, A. Tokiwa-Yamamoto, S. Adachi, and H. Yamauchi, *Physica C* **212**, 271 (1993).
- R. Itti, F. Munakata, K. Ikeda, H. Yamauchi, N. Koshizuka, and S. Tanaka, *Phys. Rev. B* **43**, 6249 (1991).
- Yu. M. Ivanchenko, *Phys. Rev. B* **48**, 15966 (1993).
- B. I. Ivlev and N. B. Kopnin, *Phys. Rev. Lett.* **64**, 1828 (1990).
- B. I. Ivlev, N. B. Kopnin, and M. M. Salomaa, *Phys. Rev. B* **43**, 2896 (1991a).
- B. I. Ivlev, Yu. N. Ovchinnikov, and R. S. Thompson, *Phys. Rev. B* **44**, 7023 (1991b).
- B. I. Ivlev and R. S. Thompson, *Phys. Rev. B* **45**, 875 (1992).
- Y. Iwasa, K. Tanaka, T. Yasuda, T. Koda, and S. Koda, *Phys. Rev. Lett.* **69**, 2284 (1992).
- Y. Iye, T. Tamegai, T. Sakakibara, T. Goto, and N. Miura, *Physica C* **153-155**, 26 (1988).
- Y. Iye, S. Nakamura, T. Tamegai, T. Terashima, K. Yamamoto, and Y. Bundo, "High-Temperature Superconductors: Fundamental Properties and Novel Materials Processing" (D. Christen, J. Narayan, and L. Schneemeyer, Eds.), MRS Symposia Proceedings, No. 169, p. 871. Material Research Soc., Pittsburgh, 1990.
- Y. Iye, in "Physical Properties of High Temperature Superconductors" (D. M. Ginsberg, Ed.), Vol. 3, Chap. 4, World Scientific, Singapore, 1992.
- J. D. Jackson, "Classical Electrodynamics," Wiley, New York, 1975.
- H. M. Jaeger, D. B. Haviland, B. G. Orr, and A. M. Goldman, *Phys. Rev.* **40**, 182 (1989).
- K. P. Jain and D. K. Ray, *Phys. Rev. B* **39**, 4339 (1989).
- R. C. Jaklevic, J. Lambe, J. E. Mercereau, and A. H. Silver, *Phys. Rev. A* **140**, 1628 (1965).
- G. Jakob, P. Przyszlupski, C. Stölzel, C. Tomé-Rose, A. Walkenhorst, M. Schmitt, and H. Adrian, *Appl. Phys. Lett.* **59**(13), 1626 (1991).
- G. M. Japiassú, M. A. Continentino, and A. Troper, *Phys. Rev. B* **45**, 2986 (1992).

- M. Jarrell, H. R. Krishnamurthy, and D. L. Cox, *Phys. Rev. B* **38**, 4584 (1988).
- B. Jeanneret, Ph. Flückiger, J. L. Gavilano, Ch. Lee-mann, and P. Martinoli, *Phys. Rev. B* **40**, 11374 (1989).
- C. S. Jee, B. Andraka, J. S. Kim, H. Li, M. W. Meisel, and G. R. Stewart, *Phys. Rev. B* **42**, 8630 (1990).
- J. H. Jefferson, H. Eskes, and L. F. Feiner, *Phys. Rev. B* **45**, 7959 (1992).
- C. D. Jeffries, Q. H. Lam, Y. Kim, C. M. Kim, A. Zettl and M. P. Klein, *Phys. Rev. B* **39**, 11526 (1989).
- H. J. Jensen, A. Brass, An-C. Shi, and A. J. Berlinsky, *Phys. Rev. B* **41**, 6394 (1990).
- H. J. Jensen and P. Minnhagen, *Phys. Rev. Lett.* **66**, 1630 (1991).
- Y. Jeon, G. Liang, J. Chen, M. Croft, M. W. Ruckman, D. Di Marizo, and M. S. Hegde, *Phys. Rev. B* **41**, 4066 (1990).
- L. Ji, R. H. Sohn, G. C. Spalding, C. J. Lobb, and M. Tinkham, *Phys. Rev. B* **40**, 10936 (1989).
- Y. X. Jia, J. Z. Liu, M. D. Lan, P. Klavins, R. N. Shelton, and H. B. Radousky, *Phys. Rev. B* **45**, 10609 (1992).
- H. Jiang, Y. Huang, H. How, S. Zhang, C. Vittoria, A. Widom, D. B. Chrisey, J. S. Horwitz, and R. Lee, *Phys. Rev. Lett.* **66**, 1785 (1991).
- C. Jiang and J. P. Carbotte, *Phys. Rev. B* **45**, 10670 (1992a).
- C. Jiang and J. P. Carbotte, *Phys. Rev. B* **45**, 7368 (1992b).
- W. Jin, C. K. Loong, D. G. Hinks, P. Vashishta, R. K. Kalia, M. H. Degani, D. L. Price, J. D. Jorgensen, and B. Dabrowski, *Mat. Res. Soc. Symp. Proc.* **209**, 895 (1991).
- S. Jin, G. W. Kammlott, S. Nakahara, T. H. Tiefel, and J. Graebner, *Science* **253**, 427 (1991).
- S. Jin, T. H. Tiefel, R. C. Sherwood, M. E. Davis, R. B. van Dover, G. W. Kammlott, R. A. Fastnacht, and H. D. Keith, *Appl. Phys. Lett.* **52**, 2074 (1988).
- W. Jin, M. H. Dagani, R. K. Kalia, and P. Vashishta, *Phys. Rev. B* **45**, 5535 (1992).
- T. W. Jing and N. P. Ong, *Phys. Rev. B* **42**, 10781 (1990).
- R. Job and M. Rosenberg, *Supercond. Sci. Technol.* **5**, 7 (1992).
- K. H. Johnson, *Phys. Rev. B* **42**, 4783 (1990).
- M. W. Johnson, D. H. Douglass, and M. F. Bocko, *Phys. Rev. B* **44**, 7726 (1991).
- R. D. Johnson, D. S. Bethune, and C. S. Yannoni, *Acc. Chem. Res.* **25**, 169 (1992).
- C. E. Johnson, H. W. Jiang, K. Holczer, R. B. Kaner, R. L. Whetten, and F. Diederich, *Phys. Rev. B* **46**, 5880 (1992).
- D. C. Johnston, H. Prakash, W. H. Zachariasen, and R. Viswanathan, *Mat. Res. Bull.* **8**, 777 (1973).
- D. C. Johnston and J. H. Cho, *Phys. Rev. B* **42**, 8710 (1990).
- Th. Jolicoeur and J. C. LeGuillou, *Phys. Rev. B* **44**, 2403 (1991).
- M. L. Jones, D. W. Shortt, and A. L. Schawlow, *Phys. Rev. B* **42**, 132 (1990).
- J. D. Jorgensen, M. A. Beno, D. G. Hinks, L. Soderholm, K. J. Volin, R. L. Hitterman, J. D. Grace, I. K. Schuller, C. U. Segre, K. Zhang, and M. S. Kleefisch, *Phys. Rev. B* **36**, 3608 (1987a); see also Schuller *et al.* (1987).
- J. D. Jorgensen, B. W. Veal, W. K. Kwok, G. W. Crabtree, A. Umezawa, L. J. Nowicki, and A. P. Paulikas, *Phys. Rev. B* **36**, 5731 (1987b).
- J. D. Jorgensen, B. W. Veal, A. P. Paulikas, L. J. Nowicki, G. W. Crabtree, H. Claus, and W. K. Kwok, *Phys. Rev. B* **41**, 1863 (1990).
- B. D. Josephson, *Phys. Lett.* **1**, 251 (1962).
- J. Jung, M. A.-K. Mohamed, S. C. Cheng, and J. P. Franck, *Phys. Rev. B* **42**, 6181 (1990).
- A. Junod, A. Bezing, and J. Muller, *Physica C* **152**, 50 (1988).
- A. Junod, in "Physical Properties of High Temperature Superconductors" (D. M. Ginsberg, Ed.), Vol. 2, Chap. 2, World Scientific, Singapore, 1990.
- A. Junod, D. Sanchez, J.-Y. Genoud, T. Graf, G. Triscone, and J. Muller, *Physica C* **185-189**, 1399 (1991).
- V. V. Kabanov and O. Yu. Mashtakov, *Phys. Rev. B* **47**, 6060 (1993).
- K. K. Kadish and R. S. Ruoff, (Eds.), "Recent Advances in the Chemistry and Physics of Fullerenes and Related Materials," Electrochemical Society, Pennington, N. J., 1994.
- K. Kadowaki, Y. Songliu, and K. Kitazawa, "Lorentz Force Independent Dissipation in HTSC," submitted for publication.
- A. Kadin, *Phys. Rev. B* **41**, 4072 (1990).
- A. Kahan, *Phys. Rev. B* **43**, 2678 (1991).
- A. B. Kaiser, *Phys. Rev. B* **35**, 4677 (1987).
- A. B. Kaiser and C. Uher, *Aust. J. Phys.* **41**, 597 (1988).
- A. B. Kaiser, *Phys. Rev. B* **37**, 5924 (1988).
- A. B. Kaiser and C. Uher, in "Studies in High Temperature Superconductors" (A. V. Narlikar, Ed.), Vol. 7, Nova Sci., New York, 1990.
- A. B. Kaiser and G. Mountjoy, *Phys. Rev. B* **43**, 6266 (1991).
- E. Kaldis, P. Fischer, A. W. Hewat, E. A. Hewat, J. Karpinski, and S. Rusiecki, *Physica C* **159**, 668 (1989).
- C. Kallin, A. J. Berlinsky, and W.-K. Wu, *Phys. Rev. B* **39**, 4267 (1989).
- V. Kalmeyer and R. B. Laughlin, *Phys. Rev. Lett.* **59**, 2095 (1987).
- A. Kampf and J. R. Schrieffer, *Phys. Rev. B* **41**, 6399 (1990).
- K. Kanoda, H. Mazaki, T. Mizutani, H. Hosoi, and T. Shinjo, *Phys. Rev. B* **40**, 4321 (1989).
- K. Kanoda, K. Akiba, K. Suzuki, T. Takahashi, and G. Saito, *Phys. Rev. Lett.* **65**, 1271 (1990).

- A. Kapitulnik and M. R. Beasley, C. Castellani, and D. DiCastro, *Phys. Rev. B* **37**, 537 (1988).
- S. G. Kaplan, T. W. Noh, A. J. Sievers, S.-W. Cheong and Z. Fisk, *Phys. Rev. B* **40**, 5190 (1989).
- V. R. Karasik, N. G. Vasil'ev, and V. G. Ershov, *Zh. Eksp. Teor. Fiz.* **59**, 790 (1970); *Sov Phys—JETP* **32**, 433 (1971).
- K. Karlsson, O. Gunnarsson, and O. Jepsen, *Phys. Rev. B* **45**, 7559 (1992).
- K. Karraï, E. J. Choi, F. Dunmore, S. Liu, H. D. Drew, Q. Li, D. B. Fenner, Y. D. Zhu, and F.-C. Zhang, *Phys. Rev. Lett.* **69**, 152 (1992).
- H. Kasatani, H. Terauchi, Y. Hamanaka, and S. Nakashima, *Phys. Rev. B* **47**, 4022 (1993).
- A. Kastalsky, A. W. Kleinsasser, L. H. Greene, R. Bhat, F. P. Milliken, and J. P. Harbison, *Phys. Rev. Lett.* **67**, 3026 (1991).
- R. Kato, Y. Enomoto, and S. Maekawa, *Phys. Rev. B* **44**, 6916 (1991).
- R. Kato, Y. Enomoto, and S. Maekawa, *Phys. Rev. B* **47**, 8016 (1993).
- K. Katti and S. H. Risbud, *Phys. Rev. B* **45**, 10155 (1992).
- R. L. Kautz and J. M. Martinis, *Phys. Rev. B* **42**, 9903 (1990).
- M. Kaveh and N. H. Mott, *Phys. Rev. Lett.* **68**, 1904 (1992).
- Z. A. Kazei and I. B. Krynetskii, "Landolt-Börnstein, Group III," *Solid State Physics*, Vol. 27, Subvol. f2, Springer, Heidelberg, 1992.
- A. Kebede, C. S. Jee, J. Schwegler, J. E. Crow, T. Mihalisin, G. H. Myer, R. E. Salomon, P. Schlottmann, M. V. Kuric, S. H. Bloom, and R. P. Guertin, *Phys. Rev. B* **40**, 4453 (1989).
- F. J. Kedves, S. Mészáros, K. Vad, G. Halász, B. Keszei, and L. Mihály, *Solid State Commun.* **63**, 991 (1987).
- O. Keller, *Phys. Rev. B* **43**, 10293 (1991).
- P. H. Kes, C. J. van der Beek, M. P. Maley, M. E. McHenry, D. A. Huse, M. J. V. Menken, and A. A. Menovsky, *Phys. Rev. Lett.* **67**, 2383 (1991).
- I. B. Khalfin and B. Ya. Shapiro, *Phys. Rev. B* **46**, 5593 (1992).
- A. F. Khoder, M. Couach, and J. L. Jorda, *Phys. Rev. B* **42**, 8714 (1990).
- A. F. Khoder and M. Couach, in "Magnetic Susceptibility of Superconductors and Other Spin Systems" (R. A. Hein, T. L. Francavilla, and D. H. Liebenberg, Eds.), Plenum, New York, 1992.
- A. Khurana, *Phys. Rev. B* **40**, 4316 (1989).
- R. F. Kiefl, J. W. Schneider, A. MacFarlane, K. Chow, T. L. Duty, T. L. Estle, B. Hitti, R. L. Lichti, E. J. Ansaldo, C. Schwab, P. W. Percival, G. Wei, S. Wlodek, K. Kojima, W. J. Ronamov, J. P. McCauley, Jr., N. Coustel, J. E. Fischer, and A. B. Smith III, *Phys. Rev. Lett.* **68**, 1347 (1992).
- Y. B. Kim, C. F. Hempstead, and A. R. Strnad, *Phys. Rev. Lett.* **9**, 306 (1962).
- Y. B. Kim, C. F. Hempstead, and A. R. Strand, *Phys. Rev.* **129**, 528 (1963).
- Y. B. Kim and M. J. Stephan, in "Superconductivity" (R. D. Parks, Ed.), Vol. 2, p. 1107, Dekker, New York, 1969.
- H. K. Kim and P. S. Riseborough, *Phys. Rev. B* **42**, 7975 (1990).
- D. H. Kim, K. E. Gray, R. T. Kampwirth, K. C. Woo, D. M. McKay, and J. Stein, *Phys. Rev. B* **41**, 11642 (1990).
- D. H. Kim, K. E. Gray, R. T. Kampwirth, and D. M. McKay, *Phys. Rev. B* **42**, 6249 (1990); **43**, 2910 (1991a).
- D. H. Kim, D. J. Miller, J. C. Smith, R. A. Holoboff, J. H. Kang, and J. Talvacchio, *Phys. Rev. B* **44**, 7607 (1991b).
- J.-J. Kim, H.-K. Lee, J. Chung, H. J. Shin, H. J. Lee, and J. K. Ku, *Phys. Rev. B* **43**, 2962 (1991).
- D. M. King, Z.-X. Shen, D. S. Dessau, B. O. Wells, W. E. Spicer, A. J. Arko, D. S. Marshall, J. DiCarlo, A. G. Loeser, C. H. Park, E. R. Ratner, J. L. Peng, Z. Y. Li, and R. L. Greene, *Phys. Rev. Lett.* **70**, 3159 (1993).
- K. Kinoshita, F. Izumi, T. Yamada, and H. Asano, *Phys. Rev. B* **45**, 5558 (1992).
- J. Kircher, M. K. Kelly, S. Rashkeev, M. Alouani, D. Fuchs, and M. Cardona, *Phys. Rev. B* **44**, 217 (1991).
- D. Kirillov, C. B. Eom, and T. H. Geballe, *Phys. Rev. B* **43**, 3752 (1991).
- W. P. Kirk, P. S. Kobiela, R. N. Tsumura, and R. K. Pandey, *Ferroelectrics* **92**, 151 (1989).
- T. R. Kirkpatrick and D. Belitz, *Phys. Rev. Lett.* **68**, 3232 (1992).
- J. R. Kirtley, R. T. Collins, Z. Schlesinger, W. J. Gallagher, R. L. Sandstrom, T. R. Dinger and D. A. Chance, *Phys. Rev. B* **35**, 8846 (1987).
- J. R. Kirtley, *Phys. Rev.* **41**, 7201 (1990a); *Int. J. Mod. Phys. B* **4**, 201 (1990b).
- L. B. Kiss and P. Svedlindh, *IEEE Trans. Electronic Devices*, **41**, 2112 (1994).
- T. J. Kistenmacher, *Phys. Rev. B* **39**, 12279 (1989).
- Y. Kitaoka, S. Hiramatsu, T. Kohara, K. Asayama, K. Oh-ishi, M. Kikuchi, and N. Kobayashi, *Jpn. J. Appl. Phys.* **26**, L397 (1987a).
- Y. Kitaoka, S. Hiramatsu, K. Ishida, T. Kohara, and K. Asayama, *J. Phys. Soc. Jpn.* **56**, 3024 (1987b).
- Y. Kitaoka, K. Fujiwara, K. Ishida, K. Asayama, Y. Shimakawa, T. Manako, and Y. Kubo, *Physica C* **179**, 107 (1991).
- K. Kitazawa and S. Tajima, in "Some Aspects of Superconductivity," (L. C. Gupta, Ed.), Nova Sci., New York, 1990.
- C. Kittel, "Introduction to Solid State Physics," Wiley, New York, 1976.
- S. Kivelson, *Phys. Rev. B* **39**, 259 (1989).
- Y. S. Kivshar and T. K. Soboleva, *Phys. Rev. B* **42**, 2655 (1990).
- Y. S. Kivshar, B. A. Malomed, Z. Fei, and L. Vázquez, *Phys. Rev. B* **43**, 1098 (1991).
- A. K. Klehe, A. K. Gangopadhyay, J. Diederichs, and J. S. Schilling, *Physica C* **213**, 266 (1992).

- A. K. Klehe, J. S. Schilling, J. L. Wagner, and D. G. Hinks, *Physica C* 223, 313 (1994).
- B. M. Klein, L. L. Boyer, D. A. Papaconstantopoulos, and L. F. Mattheiss, *Phys. Rev. B* 18, 6411 (1978).
- B. M. Klein, L. L. Boyer, and D. A. Papaconstantopoulos, *Phys. Rev. Lett.* 42, 530 (1979).
- U. Klein, *Phys. Rev. B* 40, 6601 (1989); 41, 4819 (1990).
- D. J. Klein, T. G. Schmalz, M. A. García-Bach, R. Valenti, and T. P. Zivkovic, *Phys. Rev. B* 43, 719 (1991).
- U. Klein and B. Pöttinger, *Phys. Rev. B* 44, 7704 (1991).
- L. Kleion and A. Aharony, *Phys. Rev. B* 45, 9926 (1992).
- R. Kleiner, F. Steinmeyer, G. Kunkel, and P. Müller, *Phys. Rev. Lett.* 68, 2394 (1992).
- A. Kleinhammes, C. L. Chang, W. G. Moulton, and L. R. Testardi, *Phys. Rev. B* 44, 2313 (1991).
- A. W. Kleinsasser and T. N. Jackson, *Phys. Rev. B* 42, 8716 (1990).
- R. A. Klemm and S. H. Liu, *Phys. Rev. B* 44, 7526 (1991).
- R. A. Klemm, *Phys. Rev. B* 47, 14630 (1993).
- R. A. Klemm, "Layered Superconductors," Oxford, NY, in press.
- P. Knoll, C. Thomsen, M. Cardona, and P. Murugaraj, *Phys. Rev. B* 42, 4842 (1990).
- F. Kober, H.-C. Ri, R. Gross, D. Koelle, R. P. Huebener, and A. Gupta, *Phys. Rev. B* 44, 11951 (1991).
- J. Kober, A. Gupta, P. Esquinazi, H. F. Braun, E. H. Brandt, *Phys. Rev. Lett.* 66, 2507 (1991).
- R. H. Koch, V. Foglietti, W. J. Gallagher, G. Koren, A. Gupta, and M. P. A. Fisher, *Phys. Rev. Lett.* 63, 1511 (1989).
- B. N. Kodess, Ph.D. thesis, Perm State University, Perm. Cited as Ref. 6.130 of Vonsovsky *et al.* (1982).
- V. G. Kogan, M. M. Fang, and S. Mitra, *Phys. Rev. B* 38, 11958 (1988).
- V. G. Kogan, *Phys. Rev. B* 38, 7049 (1988).
- V. G. Kogan and L. J. Campbell, *Phys. Rev. Lett.* 62, 1552 (1989).
- V. G. Kogan, N. Nakagawa, and S. L. Thiemann, *Phys. Rev. B* 42, 2631 (1990).
- S. Kohiki, T. Wada, S. Kawashima, H. Takagi, S. Uchida, and S. Tanaka, *Phys. Rev. B* 38, 7051, 8868 (1988).
- S. Kohiki, S.-I. Hatta, K. Setsune, K. Wasa, Y. Higashi, S. Fukushima, and Y. Gohshi, *Appl. Phys. Lett.* 56, 298 (1990).
- S. Koka and K. Shrivastava, *Physica B* 165-166, 1097 (1990).
- S. Kolesnik, T. Skoskiewicz, J. Igalson, and Z. Korczak, *Phys. Rev. B* 45, 10158 (1992).
- T. Komeda, G. D. Waddill, P. J. Benning, and J. H. Weaver, *Phys. Rev. B* 43, 8713 (1991).
- M. Konczykowski, F. Rullier-Albenque, E. R. Yacoby, A. Shaulov, Y. Yeshurun, and P. Lejay, *Phys. Rev. B* 44, 7167 (1991).
- J. Konior, *Phys. Rev. B* 47, 14425 (1993).
- J. Konior, "Some Properties of Narrow Band Systems Coupled to Phonons," submitted for publication.
- R. Konno and K. Ueda, *Phys. Rev. B* 40, 4329 (1989).
- P. Koorevaar, J. Aarts, P. Berghuis, and P. H. Kes, *Phys. Rev. B* 42, 1004 (1990).
- Y. Kopelevich, A. Gupta, P. Esquinazi, C.-P. Heidemann, and H. Müller, *Physica C* 183, 345 (1991).
- P. Kopietz, *Phys. Rev. Lett.* 70, 3123 (1993).
- A. E. Koshelev, G. Yu. Logvenov, V. A. Larkin, V. V. Ryazanov, and K. Ya. Soifer, *Physica C* 177, 129 (1991).
- A. A. Koshta, Yu. N. Shvachko, A. A. Romanyukha, and V. V. Ustinov, *Zh. Eksp. Teor. Fiz.* 103, 629 (1993); *Transl. Sov. Phys. JETP* 76, 314 (1993).
- I. Z. Kostadinov, V. G. Hadjiev, J. Tihov, M. Mateev, M. Mikhov, O. Petrov, V. Popov, E. Dinolova, Ts. Zheleva, G. Tyuliev, and V. Kojouharov, *Physica C* 156, 427 (1988).
- J. M. Kosterlitz and D. Thouless, *J. Phys. C* 5, L124 (1972); 6, 1181 (1973).
- N. Kosugi, Y. Tokura, H. Takagi and S. Uchida, *Phys. Rev. B* 41, 131 (1990).
- V. Kovachev, "Energy Dissipation in Superconducting Materials," Clarendon, Oxford (1991).
- Y. Koyama and M. Ishimaru, *Phys. Rev. B* 45, 9966 (1992).
- H. Krakauer, W. E. Pickett, D. A. Papaconstantopoulos, and L. L. Boyer, *Jpn. J. Appl. Phys.* 26, Suppl. 26-3, (1987).
- H. Krakauer, W. E. Pickett and R. E. Cohen, *J. Supercond.* 1, 111 (1988).
- H. Krakauer and W. E. Pickett, *Phys. Rev. Lett.* 60, 1665 (1988).
- V. M. Krasnov, V. A. Larkin, and V. V. Ryazanov, *Physica C* 174, 440 (1991).
- V. M. Krasnov, *Physica C* 190, 357 (1992).
- N. M. Kreines and V. I. Kudinov, *Mod. Phys. Lett. B* 6, 6 (1992).
- V. Z. Kresin and S. A. Wolf, in "Novel Superconductivity" (S. A. Wolf and V. Z. Kresin, Eds.), p. 287, Plenum, New York, 1987.
- V. Z. Kresin, and S. A. Wolf, "Fundamentals of Superconductivity," Plenum, New York, 1990.
- V. Z. Kresin and W. A. Little (Eds.), "Organic Superconductivity," Plenum, New York, 1990.
- V. Z. Kresin, H. Morawitz, and S. A. Wolf, "Mechanisms of Conventional and High T_c Superconductivity," Oxford Univ. Press, Oxford, 1993.
- A. Krimmel, P. Fischer, B. Roessli, H. Maletta, C. Geibel, C. Schank, A. Grauel, A. Loidl, and F. Steglich, *Z. Phys. B* 86, 161 (1992).
- G. Kriza, G. Quirion, O. Traetteberg, W. Kang, and D. Jérôme, *Phys. Rev. Lett.* 66, 1922 (1991).

RI
A.

H.

E. I
L. F
I
J
H. C
N
M
di
1.
R. Ki
R.
(1
M. L.
(19
J. Kul
Ma
A. D.
and
A. D. K
and
A. D. K
and
H. Kun
Phys
G. R. K
(1989
N. Kum.
5001
M. N. Ki
(1991
P. J. Kun
J. Y. C
Rev. I
S. Kuriha
E. Z. Kuri
S. Shu
E. Z. Kuri
Int. J. J
E. Z. Kur
Phys. B
E. Z. Kuri
Phys. 5,
H. Kuroda
Okawa,
G. Saito
A. Kussmau
P. M. Te
A. Kussmau
Gupta, P
A. L. Kuzem
Correlate

- A. Krol, Z. H. Ming, Y. H. Kao, N. Nücker, G. Roth, J. Fink, G. C. Smith, K. T. Park, J. Yu, A. J. Freeman, A. Erband, G. Müller-Vogt, J. Karpinski, E. Kaldis, and K. Schönmann, *Phys. Rev. B* **45**, 2581 (1992).
- H. W. Kroto and D. R. M. Walton, in "The Fullerenes: New Horizons for the Chemistry, Physics, and Astrophysics of Carbon," Cambridge Univ. Press, New York, 1993.
- E. Krüger, *Phys. Stat. Sol. B* **156**, 345 (1989).
- L. Krusin-Elbaum, A. P. Malozemoff, Y. Yeshurun, D. C. Cronmeyer and F. Holtzberg, *Phys. Rev. B* **39**, 2936 (1989).
- H. C. Ku, H. D. Yang, R. W. McCallum, M. A. Noack, P. Klavins, R. N. Shelton, and A. R. Moodenbaugh, in "High Temperature Superconductors" (U. Gubser and M. Schluter, Eds.), p. 177, *Mater. Res. Soc.*, Pittsburgh, 1987.
- R. Kuentzler, C. Hornick, Y. Dossmann, S. Wegner, R. El Farsi, and M. Drillon, *Physica C* **184**, 316 (1991).
- M. L. Kubic and R. Zeyher, *Phys. Rev. B* **49**, 4395 (1994).
- J. Kulik, Y. Y. Xue, Y. Y. Sun, and M. Bonvalot, *J. Mater. Res.* **5**, 1625 (1990).
- A. D. Kulkarni, J. Prade, F. W. de Wette, W. Kress, and U. Schröder, *Phys. Rev. B* **40**, 2642 (1989).
- A. D. Kulkarni, F. W. de Wette, J. Prade, U. Schröder, and W. Kress, *Phys. Rev. B* **41**, 6409 (1990).
- A. D. Kulkarni, F. W. de Wette, J. Prade, U. Schröder, and W. Kress, *Phys. Rev. B* **43**, 5451 (1991).
- H. Kumakura, M. Uehara, and K. Togano, *Appl. Phys. Lett.* **51**, 1557 (1987).
- G. R. Kumar and P. Chaddah, *Phys. Rev. B* **39**, 4704 (1989).
- N. Kumar and A. M. Jayannavar, *Phys. Rev. B* **45**, 5001 (1992).
- M. N. Kunchur and S. J. Poon, *Phys. Rev. B* **43**, 2916 (1991).
- P. J. Kung, M. P. Maley, M. E. McHenry, J. O. Willis, J. Y. Coulter, M. Murakami, and S. Tanaka, *Phys. Rev. B* **46**, 6427 (1992).
- S. Kurihara, *Phys. Rev. B* **39**, 6600 (1989).
- E. Z. Kurmaev, V. P. Belash, S. A. Nemnonov, and A. S. Shulakov, *Phys. Stat. Solid B* **61**, 365 (1974).
- E. Z. Kurmaev, V. I. Nefedov, and L. D. Finkelstein, *Int. J. Mod. Phys. B* **2**, 393 (1988).
- E. Z. Kurmaev and L. D. Finkelstein, *Int. J. Mod. Phys. B* **3**, 973 (1989).
- E. Z. Kurmaev and L. D. Finkelstein, *Int. J. Mod. Phys.* **5**, 1097 (1991).
- H. Kuroda, K. Yakushi, H. Tasima, A. Ugawa, Y. Okawa, A. Kobayashi, R. Kato, H. Kobayashi, and G. Saito, *Synth. Metals A* **27**, 491 (1988).
- A. Kussmaul, J. S. Moodera, G. M. Roesler, Jr., and P. M. Tedrow, *Phys. Rev. B* **41**, 842 (1990).
- A. Kussmaul, J. S. Moodera, P. M. Tedrow, and A. Gupta, *Physica C* **177**, 415 (1991).
- A. L. Kuzemsky, in *Int. Conf. Supercond. and Strongly Correlated Electron Systems*, Amalfi, Italy, 1993.
- E. Kuzmann, Z. Homonnay, A. Vértés, M. Gál, K. Torkos, B. Csákvári, G. K. Solymos, G. Horváth, J. Bánkuti, I. Kirschner, and L. Korecz, *Phys. Rev. B* **39**, 328 (1989).
- L. S. Kuzmin, P. Delsing, T. Claeson, and K. Likharev, *Phys. Rev. Lett.* **62**, 2539 (1989).
- L. S. Kuzmin, Yu. V. Nazarov, D. B. Haviland, P. Delsing, and T. Claeson, *Phys. Rev. Lett.* **67**, 1161 (1991).
- L. S. Kuzmin and D. Haviland, *Phys. Rev. Lett.* **67**, 2890 (1991).
- M. Kvale and S. E. Hebboul, *Phys. Rev. B* **43**, 3720 (1991).
- G. H. Kwei, J. A. Goldstone, A. C. Lawson, Jr., J. D. Thompson, and A. Williams, *Phys. Rev. B* **39**, 7378 (1989).
- G. H. Kwei, R. B. Von Dreele, S.-W. Cheong, Z. Fisk, and J. D. Thompson, *Phys. B* **41**, 1889 (1990).
- W. K. Kwok, U. Welp, G. W. Crabtree, K. G. Vandervoort, R. Hulscher, Y. Zheng, B. Dabroski, and D. G. Hinks, *Phys. Rev. B* **40**, 9400 (1989).
- W. K. Kwok, U. Welp, G. W. Crabtree, K. G. Vandervoort, R. Hulscher, and J. Z. Liu, *Phys. Rev. Lett.* **64**, 966 (1990a).
- W. K. Kwok, U. Welp, K. D. Carlson, G. W. Crabtree, K. G. Vandervoort, H. H. Wang, A. M. Kini, J. M. Williams, D. L. Stupka, L. K. Montgomery, and J. E. Thompson, *Phys. Rev. B* **42**, 8686 (1990b).
- H. S. Kwok, J. P. Zheng, and S. Y. Dong, *Phys. Rev. B* **43**, 6270 (1991).
- Y. K. Kwong, K. Lin, M. Park, M. S. Isaacson, and J. M. Parpia, *Phys. Rev. B* **45**, 9850 (1992).
- J. Labbé, *Phys. Rev.* **158**, 647, 655 (1967a).
- J. Labbé, S. Barisic, and J. Friedel, *Phys. Rev. Lett.* **19**, 1039 (1967b).
- B. M. Lairson, S. K. Streiffer, and J. C. Bravman, *Phys. Rev. B* **42**, 10067 (1990a).
- B. M. Lairson, J. Z. Sun, J. C. Bravman, and T. H. Geballe, *Phys. Rev. B* **42**, 1008 (1990b).
- B. M. Lairson, J. Z. Sun, T. H. Geballe, M. R. Beasley, and J. C. Bravman, *Phys. Rev. B* **43**, 10405 (1991).
- R. Lal and S. K. Joshi, *Phys. Rev. B* **45**, 361 (1992).
- Q. H. Lam, Y. Kim, and C. D. Jeffries, *Phys. Rev. B* **42**, 4846 (1990).
- M. D. Lan, J. Z. Liu, and R. N. Shelton, *Phys. Rev. B* **44**, 233 (1991).
- L. D. Landau, *Sov. Phys. JETP* **3**, 920 (1957a); **5**, 101 (1957b).
- C. T. Lane, "Superfluid Physics," Chap. 9, McGraw-Hill, New York, 1962.
- M. Lang, N. Toyota, T. Sasaki, and H. Sato, *Phys. Rev. Lett.* **69**, 1443 (1992a); *Phys. Rev. B* **46**, 5822 (1992b).
- J. Langen, M. Veit, M. Galfy, H. D. Jostarndt, A. Erle, S. Blumenröder, H. Schmidt, and E. Zirngiebl, *Solid State Commun.* **65**, 973 (1988).
- D. N. Langenberg, D. J. Scalapino, and B. N. Taylor, *Sci. Amer.* **214**, 30 (May 1966).

- W. Lanping, H. Jian, and W. Guowen, *Phys. Rev. B* **40**, 10954 (1989).
- D. C. Larbalestier, M. Daeumling, X. Cai, J. Suentjens, J. McKinnell, D. Hampshire, P. Lee, C. Meingast, T. Willis, H. Muller, R. D. Ray, R. G. Dillenburg, E. E. Hellstrom, and R. Joynt, *J. Appl. Phys.* **62**, 3308 (1987a).
- D. C. Larbalestier, M. Daeumling, P. J. Lee, T. F. Kelly, J. Seuntjens, C. Meingast, X. Cai, J. McKinnell, R. D. Ray, R. G. Dillenburg, and E. E. Hellstrom, *Cryogenics* **27**, 411 (1987b).
- A. I. Larkin and Yu. N. Ovchinnikov, *Sov. Phys. JETP* **38**, 854 (1974).
- A. Larsen, H. D. Jensen, and J. Mygind, *Phys. Rev. B* **43**, 10179 (1991).
- R. B. Laughlin, *Phys. Rev. Lett.* **60**, 2677 (1988a).
- R. B. Laughlin, *Science* **242**, 525 (1988b).
- W. E. Lawrence and S. Doniach, in "Proc. 12th Int. Conf. Low Temp. Phys. Kyoto, 1970" (E. Kanda, Ed.), p. 361. Keigaku, Tokyo, 1971.
- L. P. Le, G. M. Luke, B. J. Sternlieb, W. D. Wu, Y. J. Uemura, J. H. Brewer, T. M. Riseman, C. E. Stronach, G. Saito, H. Yamochi, H. H. Wang, A. M. Kini, K. D. Carlson, and J. M. Williams, *Phys. Rev. Lett.* **68**, 1923 (1992).
- M. A. R. LeBlanc, D. LeBlanc, A. Golebiowski, and G. Fillion, *Phys. Rev. Lett.* **66**, 3309 (1991).
- D. LeBlanc and M. A. R. LeBlanc, *Phys. Rev. B* **45**, 5443 (1992).
- K. Le Dang, J. P. Renard, P. Veillet, E. Vélú, J. P. Burger, J. N. Daou, and Y. Loreaux, *Phys. Rev. B* **40**, 11291 (1989).
- E. Lederman, L. Wu, M. L. denBoer, P. A. van Aken, W. F. Müller, and S. Horn, *Phys. Rev. B* **44**, 2320 (1991).
- T.-K. Lee, J. L. Birman, and S. J. Williamson, *Phys. Rev. Lett.* **39**, 839 (1977a); *Phys. Lett. A* **64**, 89 (1977b).
- T.-K. Lee and J. L. Birman, *Phys. Rev. B* **17**, 4931 (1978).
- M. Lee, M. Yudkowsky, W. P. Halperin, J. Thiel, S.-J. Hwu, and K. R. Poeppelmeier, *Phys. Rev. B* **36**, 2378 (1987).
- M. Lee, Y.-Q. Song, W. P. Halperin, L. M. Tonge, T. J. Marks, H. O. Marcy, and C. R. Kannewurf, *Phys. Rev. B* **40**, 817 (1989).
- S. J. Lee and J. B. Ketterson, *Phys. Rev. Lett.* **64**, 3078 (1990).
- S.-I. Lee, Y. H. Jeong, K. H. Han, Z. S. Lim, Y. S. Song, and Y. W. Park, *Phys. Rev. B* **41**, 2623 (1990).
- W. C. Lee and D. C. Johnston, *Phys. Rev. B* **41**, 1904 (1990).
- H. C. Lee, R. S. Newrock, D. B. Mast, S. E. Hebboul, J. C. Garland, and C. J. Lobb, *Phys. Rev.* **44**, 921 (1991).
- W. C. Lee and D. M. Ginsberg, *Phys. Rev. B* **44**, 2815 (1991).
- W. C. Lee, J. H. Cho, and D. C. Johnston, *Phys. Rev. B* **43**, 457 (1991).
- T. R. Lemberger, in "Physical Properties of High Temperature Superconductors" (D. M. Ginsberg, Ed.), Vol. 3, Chap. 6, World Scientific, Singapore, 1992.
- S. Lenck, S. Wermbter, and L. Tewordt, *J. Low Temp. Phys.* **80**, 269 (1990).
- S. Lenck and J. P. Carbotte, *Phys. Rev. B* **49**, 4176 (1994).
- H. Lengfellner, A. Schnellbögl, J. Betz, W. Prettl, and K. F. Renk, *Phys. Rev. B* **42**, 6264 (1990).
- H. Lengfellner, A. Schnellbögl, J. Betz, K. Renk, and W. Prettl, *Appl. Phys. Lett.* **60**, 1991 (1991a).
- H. Lengfellner and A. Schnellbögl, *Physica C* **174**, 373 (1991).
- H. Lengfellner, G. Kremb, A. Schnellbögl, J. Betz, K. F. Renk, and W. Prettl, *Appl. Phys. Lett.* **60**, 501 (1992).
- Y. Le Page, T. Siegrist, S. A. Sunshine, L. F. Schneemeyer, D. W. Murphy, S. M. Zahurak, J. V. Waszczak, W. R. McKinnon, J. M. Tarascon, G. W. Hull, and L. H. Greene, *Phys. Rev. B* **36**, 3617 (1987).
- F. Lera, R. Navarro, C. Rillo, L. A. Angurel, A. Badia, and J. Bartolome, *J. Magn. Mag. Mater.* **104-107**, 615 (1992).
- Ph. Lerch, Ch. Leemann, R. Theron, and P. Martinoli, *Phys. Rev. B* **41**, 11579 (1990).
- J. Lesueur, L. H. Greene, W. Feldmann, and A. Inam, *Physica C* **191**, 325 (1992).
- B. G. Levi, *Phys. Today* **19** (May 1988), p. 19.
- G. Levin, *Phys. Rev. B* **47**, 14634 (1993).
- L. Levitov, *Phys. Rev. Lett.* **66**, 224 (1991).
- J. A. Lewis, C. E. Platt, M. Wegmann, M. Teepe, J. L. Wagner, and D. G. Hinks, *Phys. Rev. B* **48**, 7739 (1993).
- J. Q. Li, C. Chen, D. Y. Yang, F. H. Li, Y. S. Yao, Z. Y. Ran, W. K. Wang, and Z. X. Zhao, *Z. Phys. B* **74**, 165 (1989).
- J. Q. Li, X. X. Xi, X. D. Wu, A. Inam, S. Vadlamannati, W. L. McLean, T. Venkatesan, R. Ramesh, D. M. Hwang, J. A. Martinez, and L. Nazar, *Phys. Rev. Lett.* **64**, 3086 (1990).
- Z.-Z. Li and Y. Qiu, *Phys. Rev. B* **43**, 12906 (1991).
- Y.-H. Li and S. Teitel, *Phys. Rev. Lett.* **66**, 3301 (1991).
- C. Li, M. Pompa, S. D. Longa, and A. Bianconi, *Physica C* **178**, 421 (1991).
- Y.-H. Li and S. Teitel, *Phys. Rev. B* **45**, 5718 (1992).
- Q. Li, M. Suenaga, T. Hikata, and K. Sato, *Phys. Rev. B* **46**, 5857 (1992).
- Q. Li, M. Suenaga, T. Kimura, and K. Kishio, *Phys. Rev.* **47**, 11384 (1993).
- R. L. Lichti, D. W. Cooke, and C. Boekema, *Phys. Rev. B* **43**, 1154 (1991).
- A. I. Liechtenstein, I. I. Mazin, C. O. Rodriguez, O. Jepsen, O. K. Andersen, and M. Methfessel, *Phys. Rev. B* **44**, 5388 (1991).
- K. K. Likharev, "Dynamics of Josephson Junctions and Circuits," Gordon & Breach, New York, 1986.

- L. Lilly, A. Muramatsu, and W. Hanke, *Phys. Rev. Lett.* **65**, 1379 (1990).
- Z. S. Lim, K. H. Han, S.-I. Lee, Y. H. Jeong, S. H. Salk, Y. S. Song, and Y. W. Park, *Phys. Rev. B* **40**, 7310 (1989).
- S.-Y. Lin, L. Lu, H.-M. Duan, B.-H. Ma, and D.-L. Zhang, *Int. J. Mod. Phys. B* **3**, 409 (1989).
- J. J. Lin, *Phys. Rev. B* **44**, 789 (1991).
- P. A. P. Lindberg, I. Lindau, and W. E. Spicer, *Phys. Rev. B* **40**, 6822 (1989).
- F. Lindemann, *Phys. Z.* **11**, 609 (1910).
- A. P. Litvinchuk, C. Thomsen, and M. Cardona, in "Physical Properties of High Temperature Superconductors," Vol. 4, Chap. 6, World Scientific, Singapore, 1994.
- W. A. Little and R. D. Parks, *Phys. Rev. Lett.* **9**, 9 (1962).
- Y. Liu, J. Y. Lee, M. J. Sumner, R. Sooryakumar, and T. R. Lemberger, *Phys. Rev. B* **42**, 10090 (1990).
- J.-X. Liu, J.-C. Wan, A. M. Goldman, Y. C. Chang, and P. Z. Jiang, *Phys. Rev. Lett.* **67**, 2195 (1991).
- J.-Z. Liu, Y. X. Jia, R. N. Shelton, and M. J. Fluss, *Phys. Rev. Lett.* **66**, 1354 (1991).
- J. Z. Liu, L. Zhang, M. D. Lan, R. N. Shelton, and M. J. Fluss, *Phys. Rev. B* **46**, 9123 (1992).
- L. Liu, J. S. Kouvel, and T. O. Brun, *Phys. Rev. B* **43**, 7859 (1991).
- R. Liu, B. W. Veal, A. P. Paulikas, J. W. Downey, H. Shi, C. G. Olson, C. Gu, A. J. Arko, and J. J. Joyce, *Phys. Rev. B* **45**, 5614 (1992).
- R. Liu, M. V. Klein, P. D. Han, and D. A. Payne, *Phys. Rev. B* **45**, 7392 (1992).
- L. Liu, J. S. Kouvel, and T. O. Brun, *Phys. Rev. B* **45**, 3054 (1992).
- C. J. Lobb, *Phys. Rev.* **36**, 3930 (1987).
- G. Yu. Logvenov, V. V. Ryazanov, A. V. Ustinov, and R. P. Huebener, *Physica C* **175**, 179 (1991).
- L. W. Lombardo, D. B. Mitzi, A. Kapitulnik, and A. Leone, *Phys. Rev. B* **46**, 5615 (1992).
- F. London and H. London, *Proc. Roy. Soc. (London)* **A 141**, 71 (1935).
- P. London, "Une Conception Nouvelle de la Superconductibilité," Hermann, Paris, 1937.
- F. London, "Superfluids," Wiley, New York, Vol. 1, 1950; Vol. 2, 1954, Dover, New York, 1961.
- J. M. Longo and P. M. Raccah, *J. Solid State Chem.* **6**, 526 (1973).
- C.-K. Loong, P. Vashishta, R. K. Kalia, M. H. Degani, D. L. Price, D. J. Jorgensen, D. G. Hinks, B. Dabrowski, A. W. Mitchell, D. R. Richards, and Y. Zheng, *Phys. Rev. Lett.* **62**, 2628 (1989).
- C.-K. Loong, D. G. Hinks, P. Vashishta, W. Jin, R. K. Kalia, M. H. Degani, D. L. Price, J. D. Jorgensen, B. Dabrowski, A. W. Mitchell, D. R. Richards, and Y. Zheng, *Phys. Rev. Lett.* **66**, 3217 (1991).
- C.-K. Loong, P. Vashishta, R. K. Kalia, W. Jin, M. H. Degani, D. G. Hinks, D. L. Price, J. D. Jorgensen, B. Dabrowski, A. W. Mitchell, D. R. Richards, and Y. Zheng, *Phys. Rev. B* **45**, 8052 (1992).
- Y. Lou, X. Lu, G. H. Dai, W. Y. Ching, Y.-N. Xu, M.-Z. Huang, P. K. Tseng, Y. C. Jean, R. L. Meng, P. H. Hor, and C. W. Chu, *Phys. Rev. B* **46**, 2644 (1992).
- A. J. Lowe, S. Regan, and M. A. Howson, *Phys. Rev. B* **44**, 9757 (1991).
- D. H. Lowndes, D. P. Norton, and J. D. Budai, *Phys. Rev. Lett.* **65**, 1160 (1990).
- J. P. Lu, K. Arya, and J. L. Birman, *Phys. Rev. B* **40**, 7372 (1989).
- J.-T. Lue and J. S. Sheng, *Phys. Rev. B* **47**, 5469 (1993).
- G. M. Luke, L. P. Le, B. J. Sternlieb, Y. J. Uemura, J. H. Brewer, R. Kadono, R. F. Kiefl, S. R. Kreitzman, T. M. Riseman, C. E. Stronach, M. R. Davis, S. Uchida, H. Takagi, Y. Tokura, Y. Hidaka, T. Murakami, J. Gopalakrishnan, A. W. Sleight, M. A. Subramanian, E. A. Early, J. T. Markert, M. B. Maple, and C. L. Seaman, *Phys. Rev. B* **42**, 7981 (1990).
- S. Lupi, P. Calvani, M. Capizzi, P. Maselli, W. Sadowski, and E. Walker, *Phys. Rev. B* **45**, 12470 (1992).
- J. Luzuriaga, M.-O. André, and W. Benoit, *Phys. Rev. B* **45**, 12492 (1992).
- J. W. Lynn, T. W. Clinton, W.-H. Li, R. W. Erwin, J. Z. Liu, K. Vandervoort, and R. N. Shelton, *Phys. Rev. Lett.* **63**, 2606 (1989).
- J. W. Lynn, (Ed.), "High Temperature Superconductivity," Springer-Verlag, Berlin, 1990a.
- J. W. Lynn, "High Temperature Superconductivity," Chap. 8, Springer-Verlag, Berlin, 1990b.
- J. W. Lynn, I. W. Sumarlin, S. Skanthakumar, W.-H. Li, R. N. Shelton, J. L. Peng, Z. Fisk, and S.-W. Cheong, *Phys. Rev. B* **41**, 2569 (1990).
- J. W. Lynn, *J. Alloys Compounds* **181**, 419 (1992).
- E. A. Lynton, "Superconductivity," Methuen, London, 1962.
- D. K. C. MacDonald, "Thermoelectricity, An Introduction To the Principles," Wiley, New York, 1962.
- H. Maeda, Y. Tanaka, M. Fukutomi, and T. Asano, *Jpn. J. Appl. Phys. Lett.* **27**, 209 (1988).
- A. Maeda, T. Shibauchi, N. Kondo, K. Uchinokura, and M. Kobayashi, *Phys. Rev. B* **46**, 14234 (1992).
- Y. Maeno, T. Tomita, M. Kyogoku, S. Awaji, Y. Aoki, K. Hoshino, A. Minami, and T. Fujita, *Nature* **328**, 512 (1987).
- G. D. Mahan, *Phys. Rev. B* **40**, 11317 (1989).
- G. D. Mahan, *Phys. Rev. B* **48**, 16557 (1993).
- F. Mahini, F. S. Razavi, and Z. Altounian, *Phys. Rev. B* **39**, 4677 (1989).
- R. Mailfert, R. W. Batterman, and J. J. Hanak, *Phys. Lett. A* **24**, 315 (1967).
- A. Majhofer, L. Mankiewicz, and J. Skalski, *Phys. Rev. B* **42**, 1022 (1990).
- K. Maki, *Prog. Theoret. Phys.* **39**, 897 (1968).
- K. Maki, *Phys. Rev. B* **43**, 1252 (1991); erratum, **43**, 13685 (1991).

- H. Maletta, A. P. Malozemoff, D. C. Cronmeyer, C. C. Tsuei, R. L. Greene, J. G. Bednorz, and K. A. Müller, *Solid State Commun.* **62**, 323 (1987).
- M. P. Maley, *J. Appl. Phys.* **70**, 6189 (1991).
- M. P. Maley, P. J. Kung, J. Y. Coulter, W. L. Carter, G. N. Riley, and M. E. McHenry, *Phys. Rev. B* **45**, 7566 (1992).
- M. Mali, D. Brinkmann, L. Pauli, J. Roos, H. Zimmermann, and J. Hulliger, *Phys. Lett. A* **124**, 112 (1987).
- S. K. Malik, C. V. Tomy, D. T. Adroja, R. Nagarajan, R. Prasad, and N. C. Soni, *Solid State Commun.* **66**(10), 1097 (1988).
- B. A. Malomed, *Phys. Rev.* **39**, 8018 (1989).
- B. A. Malomed, *Phys. Rev. B* **41**, 2616 (1990).
- B. A. Malomed and A. Weber, *Phys. Rev. B* **44**, 875 (1991).
- B. A. Malomed and A. A. Nepomnyashchy, *Phys. Rev. B* **45**, 12435 (1992).
- A. P. Malozemoff, in "Physical Properties of High Temperature Superconductors" (D. M. Ginsberg, Ed.), Vol. 1, Chap. 3, World Scientific, New York, 1989.
- P. Mandal, A. Poddar, A. N. Das, B. Ghosh and P. Choudhury, *Phys. Rev. B* **40**, 730 (1989).
- V. Manivannan, J. Gopalakrishnan, and C. N. R. Rao, *Phys. Rev. B* **43**, 8686 (1991).
- Y. Maniwa, H. Sato, K. Mizoguchi, and K. Kune, *Jpn. J. Appl. Phys.* **29**, 268 (1990).
- Y. Maniwa, T. Mituhashi, K. Mizoguchi, and K. Kume, *Physica C* **175**, 401 (1991a).
- Y. Maniwa, S. Sato, T. Mituhaski, K. Mizoguchi, and K. Kume, *Physica C* **185-189**, 1761 (1991b).
- M. B. Maple, J. W. Chen, S. E. Lambert, Z. Fisk, J. L. Smith, and H. R. Ott, cited in Stewart (1984).
- M. C. Marchetti and D. R. Nelson, *Phys. Rev. B* **41**, 1910 (1990).
- M. C. Marchetti, *Phys. Rev. B* **43**, 8012 (1991).
- R. Marcon, R. Fastampa, M. Giura, C. Maticotta, *Phys. Rev. B* **39**, 2796 (1989).
- R. Marcon, E. Silva, R. Fastampa, and M. Giura, *Phys. Rev. B* **46**, 3612 (1992).
- J. Marcus, C. Escribe-Filippini, C. Schlenker, R. Buder, J. Devenyi, and P. L. Reydet, *Solid State Commun.* **63**, 129 (1987).
- M. Marder, N. Papanicolaou, and G. C. Psaltakis, *Phys. Rev. B* **41**, 6920 (1990).
- L. Maritato, A. M. Cucolo, R. Vaglio, C. Noce, J. L. Makous, and C. M. Falco, *Phys. Rev. B* **38**, 12917 (1988).
- J. T. Markert, T. W. Noh, S. E. Russek, and R. M. Cotts, *Solid State Commun.* **63**, 847 (1987).
- J. T. Markert, Y. Dalichaouch, and M. B. Maple, in "Physical Properties of High Temperature Superconductors" (D. M. Ginsberg, Ed.), Vol. 1, Chap. 6, World Scientific, Singapore, 1989.
- R. S. Markiewicz, *Physica C* **177**, 171 (1991).
- R. S. Markiewicz, *Int. J. Mod. Phys. B* **5**, 2037 (1991).
- P. Marsh, R. M. Fleming, M. L. Mandich, A. M. DeSantolo, J. Kwo, M. Hong, and L. J. Martinez-Miranda, *Nature* **334**, 141 (1988).
- C. D. Marshall, I. M. Fishman, R. C. Dorfman, C. B. Eom, and M. D. Fayer, *Phys. Rev. B* **45**, 10009 (1992).
- F. Marsiglio and J. E. Hirsch, *Phys. Rev. B* **44**, 11960 (1991).
- F. Marsiglio, *Phys. Rev. B* **44**, 5373 (1991).
- F. Marsiglio, *Phys. Rev. B* **45**, 956 (1992).
- F. Marsiglio and J. E. Hirsch, *Phys. Rev. B* **49**, 1366 (1994).
- S. Martin, A. T. Fiory, R. M. Fleming, L. F. Schneemeyer, and J. V. Waszczak, *Phys. Rev. Lett.* **60**, 2194 (1988).
- S. Martin, A. T. Fiory, R. M. Fleming, G. P. Espinosa, and A. S. Copper, *Phys. Rev. Lett.* **62**, 677, (1989); see **63**, 582 (1989) for comment by P. C. E. Stamp and a reply by the authors.
- S. Martin, A. T. Fiory, R. M. Fleming, L. F. Schneemeyer, and J. V. Waszczak, *Phys. Rev. B* **41**, 846 (1990).
- S. Martin and A. F. Hebard, *Phys. Rev. B* **43**, 6253 (1991).
- M. Martin, C. Kendziora, L. Mihaly, and R. Lefferts, *Phys. Rev. B* **46**, 5760 (1992).
- M. C. Martin, D. Koller, and L. Mihaly, *Phys. Rev. B* **47**, 14607 (1993).
- T. P. Martin, U. Näher, H. Schaber, and U. Zimmermann, *Phys. Rev. Lett.* **70**, 3079 (1993).
- C. Martin, M. Hervieu, M. Huvé, C. Michel, A. Maignan, G. van Tendeloo, and B. Raveau, *Physica C* **222**, 19 (1994).
- J. A. Martindale, S. E. Barrett, C. A. Klug, K. E. O'Hara, S. M. DeSoto, C. P. Slichter, T. A. Friedmann, and D. M. Ginsberg, *Phys. Rev. Lett.* **68**, 702 (1992).
- J. L. Martins and N. Troullier, *Phys. Rev. B* **46**, 1766 (1992).
- A. Masaki, H. Sato, S.-I. Uchida, K. Kitazawa, S. Tanaka, and K. Inoue, *Jpn. J. Appl. Phys.* **26**, 405 (1987).
- H. Mathias, W. Moulton, H. K. Ng, S. J. Pan, K. K. Pan, L. H. Peirce, L. R. Testardi, and R. J. Kennedy, *Phys. Rev. B* **36**, 2411 (1987).
- P. Mathieu and Y. Simon, *Europhys. Lett.* **5**, 67 (1988).
- I. Matsubara, H. Tanigawa, T. Ogura, H. Yamashita, M. Kinoshita, and T. Kawai, *Phys. Rev. B* **45**, 7414 (1992).
- Y. Matsuda, N. P. Ong, Y. F. Yan, J. M. Harris, and J. B. Peterson, *Phys. Rev. B* **49**, 4380 (1994).
- Y. Matsuda, T. Hirai, S. Komiyama, T. Terashima, Y. Bando, K. Iijima, K. Yamamoto, and K. Hirata, *Phys. Rev. B* **40**, 5176 (1989).
- Y. Matsumoto, M. Katada, and T. Nishida, *Physica C* **185**, 1229 (1991).
- T. Matsuura and K. Miyake, *Jpn. J. Appl. Phys.* **26**, L407 (1987).

- H. Matsuyama, T. Takahashi, H. Katayama-Yoshida, Y. Okabe, H. Takagi, and S. Uchida, *Phys. Rev. B* **40**, 2658 (1989).
- L. F. Mattheiss, *Phys. Rev. B* **1**, 373 (1970).
- L. F. Mattheiss and D. R. Hamann, *Phys. Rev. B* **28**, 4227 (1983).
- L. F. Mattheiss, *Jpn. J. Appl. Phys.* **24**(2), 6 (1985).
- L. F. Mattheiss and D. R. Hamann, *Solid State Commun.* **63**, 395 (1987).
- L. F. Mattheiss, *Phys. Rev. Lett.* **58**, 1028 (1987).
- L. F. Mattheiss, E. M. Gyrogy, and D. W. Johnson, Jr., *Phys. Rev. B* **37**, 3745 (1988).
- L. F. Mattheiss and D. R. Hamann, *Phys. Rev. Lett.* **60**, 2681 (1988).
- L. F. Mattheiss and D. R. Hamann, *Phys. Rev. B* **39**, 4780 (1989).
- L. F. Mattheiss, *Phys. Rev. B* **42**, 359 (1990).
- B. Matthias, *Phys. Rev.* **92**, 874 (1953).
- B. Matthias, *Phys. Rev.* **97**, 74 (1955).
- D. C. Mattis and M. Molina, *Phys. Rev. B* **44**, 12565 (1991).
- E. Maxwell, *Phys. Rev.* **78**, 477 (1950).
- I. I. Mazin, O. Jepsen, O. K. Andersen, A. I. Liechtenstein, S. N. Rashkeev, and Y. A. Uspenskii, *Phys. Rev. B* **45**, 5103 (1992).
- K. F. McCarty, D. S. Ginley, D. R. Boehme, R. J. Baughman, and B. Morosin, *Solid State Commun.* **68**, 77 (1988).
- K. F. McCarty, B. Morosin, D. S. Ginley, and D. R. Boehme, *Physica C* **157**, 135 (1989).
- K. F. McCarty, J. Z. Liu, R. N. Shelton, and H. B. Radousky, *Phys. Rev. B* **41**, 8792 (1990a); **42**, 9973 (1990b).
- K. F. McCarty, H. B. Radousky, J. Z. Liu, and R. N. Shelton, *Phys. Rev. B* **43**, 13751 (1991).
- K. A. McGreer, J.-C. Wan, N. Anand, and A. M. Goldman, *Phys. Rev. B* **39**, 12260 (1989).
- M. E. McHenry, S. Simizu, H. Lessure, M. P. Maley, J. Y. Coulter, I. Tanaka, and H. Kojima, *Phys. Rev. B* **44**, 7614 (1991).
- W. R. McKinnon, J. R. Morton, K. F. Preston, and L. S. Selwyn, *Solid State Commun.* **65**, 855 (1988).
- W. L. McMillan, *Phys. Rev.* **167**, 331 (1968).
- T. McMullen, *Phys. Rev. B* **41**, 877 (1990).
- G. A. Medina and M. D. N. Regueiro, *Phys. Rev. B* **42**, 8073 (1990).
- N. I. Medvedeva, S. A. Turzhevsky, V. A. Gubanov, and A. J. Freeman, *Phys. Rev. B* **48**, 16061 (1993).
- D. Mehl, A. R. Köymen, K. O. Jensen, F. Gotwald, and A. Weiss, *Phys. Rev. B* **41**, 799 (1990).
- W. Meissner and R. Ochsenfeld, *Naturwissenschaft* **21**, 787 (1933).
- K. Mendelssohn, "Cryophysics," Chap. 6, Interscience, New York, 1960.
- R. L. Meng, Y. Y. Sun, J. Kulik, Z. J. Huang, F. Chen, Y. Y. Xue, and C. W. Chu, *Physica C* **214**, 307 (1993a).
- R. L. Meng, L. Beauvais, X. N. Zhang, Z. J. Huang, Y. Y. Sun, Y. Y. Zue, and C. W. Chu, *Physica C* **216**, 21 (1993b).
- M. Merkel, M. Knupfer, M. S. Golden, J. Fink, R. Seemann, and R. L. Johnson, *Phys. Rev. B* **47**, 11470 (1993).
- R. Meservey and B. B. Schwartz, in "Superconductivity" (R. D. Parks, Ed.), Vol. 1, Chap. 3, Dekker, New York, 1969.
- J. Metzger, T. Weber, W. H. Fietz, K. Grube, H. A. Ludwig, T. Wolf, and H. Wühl, *Physica C* **214**, 371 (1993).
- H. M. Meyer III, D. M. Hill, T. J. Wagener, Y. Gao, J. H. Weaver, D. W. Capone II, and K. C. Goretta, *Phys. Rev. B* **38**, 6500 (1988).
- H. M. Meyer III and J. H. Weaver, in "Physical Properties of High Temperature Superconductors" (D. M. Ginsberg, Ed.), Vol. 2, Chap. 6, World Scientific, Singapore, 1990.
- P. F. Miceli, J. M. Tarascon, L. H. Greene, P. Barboux, M. Giroud, D. A. Neumann, J. J. Rhyne, L. F. Schneemeyer, and J. V. Waszczak, *Phys. Rev. B* **38**, 9209 (1988).
- C. Michel and B. Raveau, *Rev. Chim. Miner.* **21**, 407 (1984).
- C. Michel, M. Hervieu, M. M. Borel, A. Grandin, F. Deslandes, J. Provost, and B. Raveau, *Z. Phys. B. Cond. Matt.* **68**, 421 (1987).
- R. Micnas, J. Ranninger, and S. Robaszkiewicz, *Phys. Rev. B* **36**, 4051 (1987).
- R. Micnas, J. Ranninger, and S. Robaszkiewicz, *Rev. Mod. Phys.* **62**, 113 (1990).
- A. R. Miedema, *J. Phys. (Paris)* **F3**, 1803 (1973).
- A. R. Miedema, *J. Phys. (Paris)* **F4**, 120 (1974).
- F. Mila, *Europhys. Lett.* **8**, 555 (1989).
- F. Mila and T. M. Rice, *Physica C* **157**, 561 (1989).
- S. L. Miller, K. R. Biagi, J. R. Clem, and D. K. Finnemore, *Phys. Rev. B* **31**, 2684 (1985).
- J. H. Miller, Jr., G. H. Gunaratne, J. Huang, and T. D. Golding, *Appl. Phys. Lett.* **59**, 3330 (1991).
- A. J. Millis, H. Monien, and D. Pines, *Phys. Rev. B* **42**, 167 (1990).
- A. J. Millis and S. N. Coppersmith, *Phys. Rev. B* **43**, 13770 (1991).
- A. J. Millis and H. Monien, *Phys. Rev. B* **45**, 3059 (1992).
- L. Mingzhu, T. Weihua, M. Xianren, L. Zhenjin, H. Wei, T. Qingyun, R. Yanru, and L. Zhenxing, *Phys. Rev. B* **41**, 2517 (1990).
- P. Minnhagen and P. Olsson, *Phys. Rev. Lett.* **67**, 1039 (1991).
- P. Minnhagen and P. Olsson, *Phys. Rev. B* **45**, 5722 (1992).
- N. Missert and M. R. Beasley, *Phys. Rev. Lett.* **63**, 672 (1989).
- M. G. Mitch, S. J. Chase, and J. S. Lannin, *Phys. Rev. Lett.* **68**, 883 (1992).
- L. Miu, A. Crisan, S. Popa, V. Sandu, and L. Nistor, *J. Supercond.* **3**, 391 (1990).
- L. Miu, *Phys. Rev. B* **45**, 8142 (1992).
- M. Miyazaki, J. Inoue, and S. Maekawa, *Phys. Rev. B* **40**, 6611 (1989).

- P. Mocaër, L. Tessler, M. Laguës, F. Laher-Lacour, C. Lacour, U. Dai, N. Hess, and G. Deutscher, *Physica C* **185-189**, 2505 (1991).
- M. A. K. Mohamed, J. Jung, and J. P. Franck, *Phys. Rev. B* **39**, 9614 (1989).
- M. A. K. Mohamed, J. Jung, and J. P. Franck, *Phys. Rev. B* **41**, 4286, 6466 (1990).
- M. A.-K. Mohamed and J. Jung, *Phys. Rev. B* **44**, 4512 (1991).
- R. Monaco, *Int. J. Infrared. Millimeter Waves* **II**, 533 (1990a); *J. Appl. Phys.* **68**, 679 (1990b).
- H. Monien and A. Zawadowski, *Phys. Rev. Lett.* **63**, 911 (1989).
- H. Monien and A. Zawadowski, *Phys. Rev. B* **41**, 8798 (1990).
- H. C. Montgomery, *J. Appl. Phys.* **42**, 2971 (1971).
- P. Monthoux and D. Pines, *Phys. Rev. B* **49**, 4261 (1994).
- J. S. Moodera, R. Meserve, J. E. Tkaczyk, C. X. Hao, G. A. Gibson, and P. M. Tedrow, *Phys. Rev. B* **37**, 619 (1988).
- H. A. Mook, D. McK. Paul, B. C. Sales, L. A. Boatner, and L. Cussen, *Phys. Rev. B* **38**, 12008 (1988).
- F. C. Moon, "Superconducting Levitation," Wiley, New York, 1994.
- J. Moreland, A. F. Clark, H. C. Ku, and R. N. Shelton, *Cryogenics* **27**, 227 (1987).
- J. Moreland, J. W. Ekin, L. F. Goodrich, T. E. Capobianco, A. F. Clark, J. Kwo, M. Hong, and S. H. Liou, *Phys. Rev. B* **35**, 8856 (1987).
- H. Mori, *Phys. Rev. B* **43**, 5474 (1991).
- D. E. Morris, J. H. Nickel, J. Y. T. Wei, N. G. Asmar, J. S. Scott, U. M. Scheven, C. T. Hultgren, A. G. Markelz, J. E. Post, P. J. Heaney, D. R. Veblen, and R. M. Hazen, *Phys. Rev. B* **39**, 7347 (1988).
- D. E. Morris, N. G. Asmar, J. Y. T. Wei, J. H. Nickel, R. L. Sid, J. S. Scott, and J. E. Post, *Phys. Rev. B* **40**, 11406 (1989).
- D. C. Morse and T. C. Lubensky, *Phys. Rev. B* **43**, 10436 (1991).
- A. Moser, H. J. Hug, O. Fritz, I. Parashikov, H.-J. Güntherodt, and Th. Wolf, *J. Vacuum Sci. and Technol.*, submitted for publication.
- A. Moser, H. J. Hug, I. Parashikov, B. Stiefel, O. Fritz, H. Thomas, A. Baratoff, H.-J. Güntherodt, and P. Chaudhari, *Phys. Rev. Lett.* **74**, 1847 (1995).
- M. Mostoller, J. Zhang, A. M. Rao, and P. C. Eklund, *Phys. Rev. B* **41**, 6488 (1990).
- M. Mück, *SPIE Symp. Adv. Electronic and Optoelectronic Matter*, Los Angeles, California, 1994, submitted for publication.
- H. Mukaida, K. Kawaguchi, M. Nakao, H. Kumakura, D. Dietderich, and K. Togano, *Phys. Rev. B* **42**, 2659 (1990).
- K. A. Müller, M. Takashige, and J. G. Bednorz, *Phys. Rev. Lett.* **58**, 1143 (1987).
- K.-H. Müller, *Physica C* **159**, 717 (1989).
- K.-H. Müller and A. J. Pauza, *Physica C* **161**, 319 (1989).
- K.-H. Müller, *IEE Trans. Magn. March* (1991).
- K.-H. Müller, M. Nikolo, and R. Driver, *Phys. Rev. B* **43**, 7976 (1991).
- H. Muller, M. Suenaga, and Y. Yokoyama, *J. Appl. Phys.* **70**, 4409 (1991).
- M. Murakami, H. Fujimoto, S. Gotoh, K. Yamaguchi, N. Koshizuka, and S. Tanaka, *Physica C* **185-189**, 321 (1991).
- M. Murakami, in "Studies of High Temperature Superconductors" (A. V. Narlikar, Ed.), Vol. 9, Nova Sci., New York, 1991.
- D. W. Murphy, S. Sunshine, R. B. van Dover, R. J. Cava, B. Batlogg, S. M. Zahurak, and L. F. Schneemeyer, *Phys. Rev. Lett.* **58**, 1888 (1987).
- P. Muzikar, D. Rainer, and J. A. Sauls, *Proc. NATO Adv. Study Inst. Vortices in Superfluids, Cargèse, Corsica* (N. Bontemps, Ed.), Kluwer, Dordrecht, 1994.
- J. A. Mydosh, *Phys. Scripta* **T19**, 260 (1987).
- T. Mzoughi, H. A. Farach, E. Quagliata, M. A. Mesa, C. P. Poole, Jr., and R. Creswick, *Phys. Rev. B* **46**, 1130 (1992).
- N. Nagaosa and P. Lee, *Phys. Rev. B* **43**, 1233 (1991).
- M. Nagoshi, Y. Fukuda, T. Suzuki, K. Ueki, A. Tokiwa, M. Kikuchi, Y. Syono, and M. Tachiki, *Physica C* **185**, 1051 (1991).
- M. Naito, A. Matsuda, K. Kitazawa, S. Kambe, I. Tanaka, and H. Kojima, *Phys. Rev. B* **41**, 4823 (1990).
- Y. Nakamura and S. Uchida, *Phys. Rev. B* **47**, 8369 (1993).
- K. Nakao, N. Miura, K. Tatsuhara, H. Takeya, and H. Takei, *Phys. Rev. Lett.* **63**, 97 (1993).
- A. V. Narlikar, Ed., "Studies of High Temperature Superconductors," Nova Sci., New York, 1989.
- K. Nasu, *Phys. Rev. B* **42**, 6076 (1990).
- B. Nathanson, O. Entin-Wohlman, and B. Mühlischlegel, *Phys. Rev. B* **45**, 3499 (1992).
- R. Navarro and L. J. Campbell, *Phys. Rev. B* **44**, 10146 (1991).
- D. R. Nelson, in "Fundamental Problems in Structural Mechanics V" (E. G. D. Cohen, Ed.), North-Holland, Amsterdam, 1980.
- D. L. Nelson, M. S. Whittingham, and T. F. George, Eds., "Chemistry of High-Temperature Superconductors," ACS Symposium Series No. 351, American Chemical Society, Washington, DC, 1987.
- D. R. Nelson and H. S. Seung, *Phys. Rev. B* **39**, 9153 (1989).
- D. R. Nelson and P. Le Doussal, *Phys. Rev. B* **42**, 10113 (1990).
- D. R. Nelson and V. M. Vinokur, *Phys. Rev. Lett.* **68**, 2398 (1992).
- E. Nembach, K. Tachikawa, and S. Takano, *Philos. Mag.* **21**, 869 (1970).
- R. Nemetschek, O. V. Misochko, B. Stadlober, and R. Hackl, *Phys. Rev. B* **47**, 3450 (1993).
- S. A. Nemnonov, E. Z. Kurmaev, and V. I. Minin, *IMF Akad. Nauk. USSR (Kiev)* **1**, 87 (1969).

- S. J. Nettel and R. K. MacCrone, *Phys. Rev. B* **47**, 11360 (1993).
- M. V. Nevitt, G. W. Crabtree, and T. E. Klippert, *Phys. Rev. B* **36**, 2398 (1987).
- V. L. Newhouse, in "Superconductivity" (R. D. Parks, Ed.), Vol. 2, p. 1283, Dekker, New York, 1969.
- E. J. Nicol and J. P. Carbotte, *Phys. Rev. B* **43**, 10210 (1991).
- E. J. Nicol and J. P. Carbotte, *Phys. Rev. B* **47**, 8205 (1993).
- Ch. Niedermayer, H. Glückler, A. Golnik, U. Binniger, M. Rauer, E. Recknagel, J. I. Budnick, and A. Weidinger, *Phys. Rev. B* **47**, 3427 (1993).
- L. Niel and J. E. Evetts, *Supercond. Sci. Technol.* **5**, S347 (1992).
- G. Nieva, E. N. Martinez, F. de la Cruz, D. A. Esparza, and C. A. D'Ovidio, *Phys. Rev. B* **36**, 8780 (1987).
- M. Nikolo and R. B. Goldfarb, *Phys. Rev. B* **39**, 6615 (1989).
- M. Nikolo, W. Kiehl, H. M. Duan, and A. M. Hermann, *Phys. Rev. B* **45**, 5641 (1992).
- H. Ning, H. Duan, P. D. Kirven, A. M. Hermann, and T. Datta, *J. Supercond.* **5**, 503 (1992).
- T. Nishida, M. Katada, and Y. Matsumoto, *Physica B* **165-167**, 1327 (1990a); *Jpn. J. Appl. Phys.* **29**, 259 (1990b).
- H. Nishihara, T. Ohtani, Y. Sano, and Y. Nakamura, *Physica C* **185-189**, 2733 (1991).
- T. Nitta, K. Nagase, S. Hayakawa, and Y. Iida, *J. Am. Ceram. Soc.* **48**, 642 (1965).
- R. K. Nkum and W. R. Datars, *Physica C* **192**, 215 (1992).
- C. Noce and L. Maritato, *Phys. Rev. B* **40**, 734 (1989).
- H. Noel, P. Gougeon, J. Padiou, J. C. Levet, M. Potel, O. Laborde, and P. Monceau, *Solid State Commun.* **63**, 915 (1987).
- T. Nojima and T. Fujita, *Physica C* **178**, 140 (1991).
- F. Nori, E. Abrahams, and G. T. Zimanyi, *Phys. Rev. B* **41**, 7277 (1990).
- M. R. Norman, *Phys. Rev. B* **42**, 6762 (1990).
- D. P. Norton, D. H. Lowndes, S. J. Pennycook, and J. D. Budai, *Phys. Rev. Lett.* **67**, 1358 (1991).
- D. L. Novikov, V. A. Gubanov, and A. J. Freeman, *Physica C* **191**, 399 (1992).
- P. Nozières and W. F. Vinen, *Philos. Mag.* **14**, 667 (1966).
- N. Nücker, J. Fink, J. C. Fuggle, P. J. Durham, and W. M. Temmerman, *Phys. Rev. B* **37**, 5158 (1988).
- N. Nücker, H. Romberg, X. X. Xi, J. Fink, B. Gegenheimer, and Z. X. Zhao, *Phys. Rev. B* **39**, 6619 (1989).
- N. Nücker, H. Romberg, M. Alexander, and J. Fink, in "Studies of High Temperature Superconductors" (A. V. Narlika, Ed.), Nova Sci., New York, 1992.
- B.-H. O and J. T. Markert, *Phys. Rev. B* **47**, 8373 (1993).
- S. D. Obertelli, J. R. Cooper, and J. L. Tallon, *Phys. Rev. B* **46**, 14928 (1992).
- B. Obst, *Phys. Status Solidi B* **45**, 467 (1971).
- S. P. Obukhov and M. Rubinstein, *Phys. Rev. Lett.* **65**, 1279 (1990).
- Y. Oda, H. Fujita, H. Toyoda, T. Kaneko, T. Kohara, I. Nakada, and K. Asayama, *Jpn. J. Appl. Phys.* **26**, L1660 (1987).
- T. Oguchi, *Jpn. J. Appl. Phys.* **26**, L417 (1987).
- A. Oguri and S. Maekawa, *Phys. Rev. B* **41**, 6977 (1990).
- I. Ohana, A. Kazeroonian, D. Heiman, M. Dresselhaus, and P. J. Picone, *Phys. Rev. B* **40**, 2255, 2562 (1989).
- K. Ohbayashi, N. Ogita, M. Udagawa, Y. Aoki, Y. Maeno, and T. Fujita, *Jpn. J. Appl. Phys.* **26**, L423 (1987).
- F. J. Ohkawa, *Phys. Rev. B* **42**, 4163 (1990).
- Y. Ohta and S. Maekawa, *Phys. Rev. B* **41**, 6524 (1990).
- T. Ohtani, *Mater. Res. Bull.* **24**, 343 (1989).
- N. Okazaki, T. Hasegawa, K. Kishio, K. Kitazawa, A. Kishi, Y. Ikeda, M. Takano, K. Oda, H. Kitaguchi, J. Takada, and Y. Miura, *Phys. Rev. B* **41**, 4296 (1990).
- E. Oldfield, C. Coretsopoulos, S. Yang, L. Reven, H. C. Lee, J. Shore, O. H. Han, E. Ramli, and D. Hicks, *Phys. Rev. B* **40**, 6832 (1989).
- O. H. Olsen and M. R. Samuelsen, *Phys. Rev. B* **43**, 10273 (1991).
- N. P. Ong, Z. Z. Wang, J. Clayhold, J. M. Tarascon, L. H. Greene, and W. R. McKinnon, *Phys. Rev. B* **35**, 8807 (1987).
- N. P. Ong, in "Physical Properties of High Temperature Superconductors" (D. M. Ginsberg, Ed.), Vol. 2, Chap. 7, World Scientific, Singapore, 1990.
- N. P. Ong, *Phys. Rev.* **43**, 193 (1991).
- H. Kamerlingh Onnes, *Leiden Commun.*, 120b, 122b, 124c (1911).
- M. Onoda, S. Shamoto, M. Sato, and S. Hosoya, *Jap. J. Appl. Phys.* **26**, L363 (1987).
- J. Orenstein, G. A. Thomas, A. J. Millis, S. L. Cooper, D. H. Rapkine, T. Timusk, L. F. Schneemeyer, and J. V. Waszczak, *Phys. Rev. B* **42**, 6342 (1990).
- T. P. Orlando and K. A. Delin, "Foundations of Applied Superconductivity," Addison-Wesley, Reading, MA, 1991.
- K. Osamura, Ed., "Composite Superconductors," Dekker, New York, 1993.
- J. A. Osborn, *Phys. Rev.* **67**, 351 (1945).
- S. B. Oseroff, D. C. Vier, J. F. Smyth, C. T. Salling, S. Schultz, Y. Dalichaouch, B. W. Lee, M. B. Maple, Z. Fisk, J. D. Thompson, J. L. Smith, and E. Zirngiebl, in "Novel Superconductivity" (S. A. Wolf and V. Z. Kresin, Eds.), p. 679, Plenum, New York, 1987.
- M. S. Osofsky, H. Rakoto, J. C. Ousset, J. P. Ulmet, J. Leotin, S. Askenazy, D. B. Crisey, J. S. Horwitz, E. F. Skelton, and S. A. Wolf, *Physica C* **182**, 257 (1991).

- J. G. Ossandon, J. R. Thompson, D. K. Christen, B. C. Sales, Y. Sun, and K. W. Lay, *Phys. Rev. B* **46**, 3050 (1992).
- J. G. Ossandon, J. R. Thompson, D. K. Christen, B. C. Sales, H. R. Kerchner, J. O. Thomson, Y. R. Sun, K. W. Lay, and J. E. Tkaczyk, *Phys. Rev. B* **45**, 12534 (1992).
- S. B. Ota, *Phys. Rev. B* **35**, 8730 (1987).
- S. B. Ota, V. S. Sastry, E. Gmelin, P. Murugaraj, and J. Maier, *Phys. Rev. B* **43**, 6147 (1991).
- C. E. Otis and R. W. Dreyfus, *Phys. Rev. Lett.* **67**, 2102 (1991).
- H. R. Ott, H. Rudigier, Z. Fisk, and J. L. Smith, *Phys. Rev. Lett.* **50**, 1595 (1983).
- H. R. Ott, in "Novel Superconductivity" (S. A. Wolf and V. Z. Kresin, Eds.), p. 187, Plenum, New York.
- H. R. Ott, "Ten Years of Superconductivity: 1980-1990," Kluwer, 1993.
- M. Oussena, S. Senoussi, G. Collin, J. M. Broto, H. Rakoto, S. Askenazy, and J. C. Ousset, *Phys. Rev. B* **36**, 4014 (1987).
- Yu. N. Ovchinnikov and B. I. Ivlev, *Phys. Rev. B* **43**, 8024 (1991).
- A. W. Overhauser, *Phys. Rev. Lett.* **4**, 462 (1960).
- A. W. Overhauser, *Phys. Rev.* **128**, 1437 (1962).
- A. W. Overhauser and L. L. Daemen, *Phys. Rev. Lett.* **62**, 1691 (1989).
- F. J. Owens, *Physica C* **178**, 456 (1991).
- F. J. Owens, *Physica C* **195**, 225 (1992).
- M.-A. Ozaki and K. Machida, *Phys. Rev. B* **39**, 4145 (1989).
- S. Pagano, B. Ruggiero, and E. Sarnelli, *Phys. Rev. B* **43**, 5364 (1991).
- E. J. Pakulis, *Phys. Rev. B* **42**, 10746 (1990).
- T. T. M. Palstra, A. A. Menovsky, and J. A. Mydosh; Coles (1987); *Phys. Rev. B* **33**, 6527 (1988).
- T. T. M. Palstra, B. Batlogg, L. F. Schneemeyer, and J. V. Waszczak, *Phys. Rev. Lett.* **61**, 1662 (1988).
- T. T. M. Palstra, B. Batlogg, R. B. Van Dover, L. F. Schneemeyer, and J. V. Waszczak, *Appl. Phys. Lett.* **54**, 763 (1989).
- T. T. M. Palstra, B. Batlogg, L. F. Schneemeyer, J. V. Waszczak, *Phys. Rev. Lett.* **64**, 3090 (1990).
- T. T. M. Palstra, R. C. Haddon, A. F. Hebard, and J. Zaanen, *Phys. Rev. Lett.* **68**, 1054 (1992).
- T. T. M. Palstra and R. C. Haddon, *Solid State Commun.*, **92**, 71 (1994).
- M. Palumbo, P. Muzikar, and J. A. Sauls, *Phys. Rev. B* **42**, 2681 (1990a).
- M. Palumbo, C. H. Choi, and P. Muzikar, *Physica B* **165-166**, 1095 (1990b).
- W. Pan and S. Doniach, *Phys. Rev. B* **49**, 1192 (1994).
- D. A. Papaconstantopoulos, A. Pasturel, J. P. Julien, and F. Cyrot-Lackmann, *Phys. Rev. B* **40**, 8844 (1989).
- M. Paranthaman, J. R. Thompson, Y. R. Sun, and J. Brynstad, *Physica C* **213**, 271 (1993).
- M. Paranthaman, *Physica C* **222**, 7 (1994).
- G. S. Park, C. E. Cunningham, B. Cabrera, and M. E. Huber, *Phys. Rev. Lett.* **68**, 1920 (1992).
- R. D. Parks and W. A. Little, *Phys. Rev.* **133**, A97 (1964).
- R. D. Parks, Ed. "Superconductivity," Vols. 1 and 2, Dekker, New York, 1969.
- Y. S. Parmar and J. K. Bhattacharjee, *Phys. Rev. B* **45**, 814 (1992).
- F. Parmigiani, Z. X. Shen, D. B. Mitzi, I. Lindau, W. E. Spicer, and A. Kapitulnik, *Phys. Rev. B* **43**, 3085 (1991).
- P. C. Pattnaik, C. L. Kane, D. M. Newns, and C. C. Tsuei, *Phys. Rev. B* **45**, 5714 (1992).
- D. McK. Paul, H. A. Mook, A. W. Hewat, B. C. Sales, L. A. Boatner, J. R. Thompson, and M. Mostoller, *Phys. Rev. B* **37**, 2341 (1988).
- D. McK. Paul, H. A. Mook, L. A. Boatner, B. C. Sales, J. O. Ramey, and L. Cussen, *Phys. Rev. B* **39**, 4291 (1989).
- L. Pauling and E. B. Wilson, "Introduction to Quantum Mechanics," McGraw-Hill, New York, 1935.
- L. M. Paulius, C. C. Almasan, and M. B. Maple, *Phys. Rev. B* **47**, 11627 (1993).
- S. D. Peacor and C. Uher, *Phys. Rev. B* **39**, 11559 (1989).
- S. D. Peacor, R. Richardson, J. Burm, C. Uher, and A. Kaiser, *Phys. Rev. B* **42**, 2684 (1990).
- S. D. Peacor, J. L. Cohn, and C. Uher, *Phys. Rev. B* **43**, 8721 (1991).
- S. D. Peacor, R. A. Richardson, F. Nori, and C. Uher, *Phys. Rev. B* **44**, 9508 (1991).
- W. B. Pearson, "Handbook of Lattice Spacings and Structures of Metals," p. 79, Pergamon, New York, 1958.
- M. J. Pechan and J. A. Horvath, *Am. J. Phys.* **58**, 642 (1990).
- N. F. Pedersen and A. Davidson, *Phys. Rev. B* **41**, 178 (1990).
- S. Pei, J. D. Jorgensen, B. Dabrowski, D. G. Hinks, D. R. Richards, A. W. Mitchell, J. M. Newsam, S. K. Sinha, D. Vaknin, and A. J. Jacobson, *Phys. Rev. B* **41**, 4126 (1990).
- K. E. Peiponen and E. Vartiainen, *Phys. Rev. B* **44**, 8301 (1991).
- M. Pekala, K. Pekala, and A. Pajaczowska, *Phys. Status Solidi B* **152**, K1 (1989).
- M. T. Pencarinha, C. P. Poole, Jr., H. A. Farach, and O. A. Lopez, *J. Phys. Chem. Solids* **56**, 301 (1995).
- D. R. Penn and M. L. Cohen, *Phys. Rev. B* **46**, 5466 (1992).
- T. Penney, S. von Molnár, D. Kaiser, F. Holtzberg, and A. W. Kleinsasser, *Phys. Rev. B* **38**, 2918 (1988).
- C. H. Pennington, D. J. Durand, D. B. Zax, C. P. Slichter, J. P. Rice, and D. M. Ginsberg, *Phys. Rev. B* **37**, 7944 (1988).
- C. H. Pennington, D. J. Durand, C. P. Slichter, J. P. Rice, E. D. Bukowski, and D. M. Ginsberg, *Phys. Rev. B* **39**, 274, 2902 (1989).

- C. H. Pennington and C. P. Slichter, in "Physical Properties of High Temperature Superconductors" (D. M. Ginsberg, Ed.), Chap. 5, World Scientific, Singapore, 1990.
- C. H. Pennington and C. P. Slichter, *Phys. Rev. Lett.* **66**, 381 (1991).
- S. J. Pennycook, M. F. Chisholm, D. E. Jesson, D. P. Norton, D. H. Lowndes, R. Feenstra, H. R. Kerkner, and J. O. Thomson, *Phys. Rev. Lett.* **67**, 765 (1991).
- F. Perez, X. Obradors, J. Fontcuberta, M. Vallet, and J. Gonzalez-Calbet, *Physica C* **185-189**, 1843 (1991).
- A. Pérez-González and J. P. Carbotte, *Phys. Rev. B* **45**, 9894 (1992).
- A. Pérez-González, E. J. Nicol, and J. P. Carbotte, *Phys. Rev. B* **45**, 5055 (1992).
- R. L. Peterson and J. W. Ekin, *Physica C* **157**, 325 (1989).
- R. L. Peterson and J. W. Ekin, *Phys. Rev. B* **42**, 8014 (1990).
- M. F. Petras and J. E. Nordman, *Phys. Rev. B* **39**, 6492 (1989).
- B. W. Pfalzgraf and H. Spreckels, *J. Phys. C* **27**, 4359 (1987).
- T. Pham, M. W. Lee, H. D. Drew, U. Welp, and Y. Fang, *Phys. Rev. B* **44**, 5377 (1991).
- J. C. Phillips, *Phys. Rev. B* **36**, 861 (1987).
- J. C. Phillips, "Physics of High- T_c Superconductors," Academic Press, New York, 1989a.
- J. C. Phillips, *Phys. Rev. B* **40**, 7348, 8774 (1989b).
- J. C. Phillips, *Mater. Lett.* **18**, 106 (1993).
- J. M. Phillips, in "High Temperature Superconducting Thin Films" (D. Shi, Ed.), Pergamon, New York, 1994.
- N. E. Phillips, *Phys. Rev.* **114**, 676 (1959).
- N. E. Phillips, R. A. Fisher, and J. E. Gordon, *Prog. Low Temp. Phys.* **19** (1991).
- T. Pichler, M. Matus, J. Kürti, and H. Kuzmany, *Phys. Rev. B* **45**, 13841 (1992).
- W. E. Pickett, H. Krakauer, D. A. Papaconstantopoulos, and L. L. Boyer, *Phys. Rev. B* **35**, 7252 (1987).
- W. E. Pickett, *Rev. Mod. Phys.* **61**, 433 (1989).
- W. E. Pickett, R. E. Cohen, and H. Krakauer, *Phys. Rev. B* **42**, 8764 (1990).
- W. E. Pickett, H. Krakauer, R. E. Cohen, and D. J. Singh, *Science* **255**, 46 (1992).
- M. W. Pieper, *Physica C* **190**, 261 (1992).
- S. W. Pierson and O. T. Valls, *Phys. Rev. B* **45**, 2458 (1992).
- C. G. S. Pillai, *Solid State Commun.* **80**, 277 (1991).
- W. Pint and E. Schachinger, *Phys. Rev. B* **43**, 7664 (1991).
- L. Pintschovius, J. M. Bassat, P. Odier, F. Gervais, G. Chevrier, W. Reichardt, and F. Gompf, *Phys. Rev. B* **40**, 2229 (1989).
- L. Pintschovius and W. Reichardt, in "Physical Properties of High Temperature Superconductors" (D. M. Ginsberg, Ed.), Vol. 4, Chap. 5, World Scientific, Singapore, 1994.
- A. B. Pippard, *Proc. R. Soc. London A* **216**, 547 (1953).
- M. Pissas, G. Kallias, A. Simopoulos, D. Niarchos, and A. Kostikas, *Phys. Rev. B* **46**, 14119 (1992).
- F. Pistolesi and G. C. Strinati, *Phys. Rev. B* **49**, 6356 (1994).
- B. Plaçais and Y. Simon, *Phys. Rev. B* **39**, 2151 (1989).
- B. Plapp and A. W. Hübler, *Phys. Rev. Lett.* **65**, 2302 (1990).
- I. Poberaj, D. Mihailovic, and S. Bernik, *Phys. Rev. B* **42**, 393 (1990).
- A. Poddar, P. Mandal, K. G. Ray, A. N. Das, B. Ghosh, P. Choudhury, and S. Lahiri, *Physica C* **159**, 226 (1989).
- D. Poilblanc and E. Dagotto, *Phys. Rev. B* **42**, 4861 (1990).
- D. M. Poirier and J. H. Weaver, *Phys. Rev. B* **47**, 10959 (1993).
- C. Politis, V. Buntar, W. Krauss, and A. Gurevich, *Europhys. Lett.* **17**, 175 (1992).
- E. Polturak, G. Koren, D. Cohen, E. Aharoni, and G. Deutscher, *Phys. Rev. Lett.* **67**, 3038 (1991).
- A. Pomar, A. Díaz, M. V. Ramallo, C. Torrón, J. A. Veira, and F. Vidal, *Physica C* **218**, 257 (1993).
- M. Pompa, C. Li, A. Bianconi, A. C. Castellano, S. Dalla Longa, A. M. Flank, P. Lagarde, and D. Udron, *Physica C* **184**, 51 (1991a).
- M. Pompa, P. Castrucci, C. Li, D. Udron, A. M. Flank, P. Lagarde, H. Katayamaa-Yoshida, S. Dalla Longa, and A. Bianconi, *Physica C* **184**, 102 (1991b).
- C. P. Poole, Jr., and H. A. Farach, "Relaxation in Magnetic Resonance," Academic Press, New York, 1971.
- C. P. Poole, Jr., "Electron Spin Resonance," 2nd ed., Wiley, New York, 1983.
- C. P. Poole, Jr., and H. A. Farach, "Theory of Magnetic Resonance," 2nd ed., Wiley, New York, 1987.
- C. P. Poole, Jr., T. Datta, and H. A. Farach, "Copper Oxide Superconductors," Wiley, New York, 1988.
- C. P. Poole, Jr. and H. A. Farach, *Magn. Reson. Relat. Phenom., Proc. 24th Ampere Congr., Poznan*, p. 601 (1988).
- C. P. Poole, Jr., T. Datta, and H. A. Farach, *J. Supercond.* **2**, 369 (1989).
- C. P. Poole, Jr., and H. A. Farach, Eds., "Handbook of Electron Spin Resonance," Amer. Inst. Phys., New York, 1994.
- A. Pöpl, L. Kevan, H. Kimura, and R. N. Schwartz, *Phys. Rev. B* **46**, 8559 (1992).
- A. M. Portis, K. W. Blazely, and F. Waldner, *Physica C* **153-155**, 308 (1988).
- A. M. Portis, "Electrodynamics of High Temperature Superconductors," World Scientific, Singapore, 1993.
- J. Prade, A. D. Kulkarni, and F. W. de Wette, U. Schröder, and W. Kress, *Phys. Rev. B* **39**, 2771 (1989).

- A. K. Pradhan, S. J. Hazell, J. W. Hodby, C. Chen, Y. Hu, and B. M. Wanklyn, *Phys. Rev. B* **47**, 11374 (1993).
- R. Prange and S. Girvin, Eds., "The Quantum Hall Effect," Springer-Verlag, Heidelberg, 1987.
- K. Prassides, J. Tomkinson, C. Christides, M. J. Rosseinsky, D. W. Murphy, and R. C. Haddon, *Nature* **354**, 462 (1991).
- K. Prassides, M. J. Rosseinsky, A. J. Dianoux, and P. Day, *J. Phys. Condens. Matter* **4**, 965 (1992).
- N. W. Preyer, M. A. Kastner, C. Y. Chen, R. J. Birgeneau, and Y. Hidaka, *Phys. Rev. B* **44**, 407 (1991).
- D. Prost, L. Fruchter, I. A. Campbell, N. Motohira, and M. Konczykowski, *Phys. Rev. B* **47**, 3457 (1993).
- T. Puig, L. M. Martinez, M. T. Aurell, A. Sanchez, D.-X. Chen, and J. S. Muñoz, in "Physics and Materials Science of High-Temperature Superconductivity" (R. Kossowsky, S. Methfessel, and D. Wohlleben, Eds.), p. 467, Kluwer Academic, Dordrecht, 1990.
- B. Pümpin, H. Keller, W. Kündig, W. Odermatt, B. D. Patterson, J. W. Schneider, H. Simmler, S. Connell, K. A. Müller, J. G. Bednorz, K. W. Blazey, I. Morgenstern, C. Rossel, and I. M. Savic, *Z. Phys. B* **72**, 175 (1988).
- B. Pümpin, H. Keller, W. Kündig, W. Odermatt, I. M. Savic, J. W. Schneider, H. Simmler, P. Zimmermann, E. Kaldis, S. Rusiecki, Y. Maeno, and C. Rossel, *Phys. Rev. B* **42**, 8019 (1990).
- P. Pureur and J. Schaf, *Solid State Commun.* **78**, 723 (1991).
- S. N. Putilin, I. Bryntse, and E. V. Antipov, *Mater. Res. Bull.* **26**, 1299 (1991).
- S. N. Putilin, E. V. Antipov, E. V. Chmaissem, and M. Marezio, *Nature* **362**, 266 (1993).
- D. S. Pyun and T. R. Lemberger, *Phys. Rev. B* **44**, 7555 (1991).
- K. F. Quader and E. Abrahams, *Phys. Rev. B* **38**, 11977 (1988).
- R. M. Quick, C. Esebbag, and M. de Llano, *Phys. Rev. B* **47**, 11512 (1993).
- M. Rabinowitz and T. McMullen, *Chem. Phys. Lett.* **218**, 437 (1994).
- H. B. Radousky, *J. Mater. Res.* **7**, 1917 (1992).
- R. J. Radtke, K. Levin, H.-B. Shüttler, and M. R. Norman, *Phys. Rev. B* **48**, 653 (1993).
- H. Raffy, S. Labdi, O. Laborde, and P. Monceau, *Phys. Rev. Lett.* **66**, 2515 (1991).
- D. Rainer and J. A. Sauls, in "Proc. 1992 Spring School on Cond. Mat. Phys., Trieste, Italy," World Scientific, Singapore, 1994, to be published.
- D. Rainer and J. A. Sauls, "Proc. 1992 Spring School on Cond. Matter Phys., Trieste, Italy," World Scientific, Singapore, 1994.
- A. K. Rajagopal and S. D. Mahanti, *Phys. Rev. B* **44**, 10210 (1991).
- P. F. Rajam, C. K. Subramaniam, S. Kasiviswanathan, and R. Srinivasan, *Solid State Commun.* **71**, 475 (1989).
- R. Rajput and D. Kumar, *Phys. Rev. B* **42**, 8634 (1990).
- B. Rakvin, M. Pozek, and A. Dulcic, *Solid State Commun.* **72**, 199 (1989).
- B. Rakvin, T. A. Mahl, A. S. Bhalla, Z. Z. Sheng, and N. S. Dalal, *Phys. Rev. B* **41**, 769 (1990).
- K. S. Ralls, D. C. Ralph, and R. A. Buhrman, *Phys. Rev. B* **40**, 11561 (1989).
- S. Ramakrishnan, R. Kumar, P. L. Paulose, A. K. Grover, and P. Chaddah, *Phys. Rev. B* **44**, 9514 (1991).
- R. Ramakumar, R. Kumar, K. P. Jain, and C. C. Chancey, *Phys. Rev. B* **48**, 6509 (1993).
- S. Ramasesha and C. N. R. Rao, *Phys. Rev. B* **44**, 7046 (1991).
- A. P. Ramirez, T. Siegrist, T. T. M. Palstra, J. D. Garrett, E. Bruck, A. A. Menovsky, and J. A. Mydosh, *Phys. Rev. B* **44**, 5392 (1991).
- A. P. Ramirez, A. R. Kortan, M. J. Rosseinsky, S. J. Duclos, A. M. Muzsca, R. C. Haddon, D. W. Murphy, A. V. Makhija, S. M. Zahurak, and K. B. Lyons, *Phys. Rev. Lett.* **68**, 1058 (1992a).
- A. P. Ramirez, M. J. Rosseinsky, D. W. Murphy, and R. C. Haddon, *Phys. Rev. Lett.* **69**, 1687 (1992b).
- J. Rammer, *Phys. Rev. B* **36**, 5665 (1987).
- J. Rammer, *Europhys. Lett.* **5**, 77 (1988).
- J. Rammer, *Phys. Rev. B* **43**, 2983 (1991).
- C. N. R. Rao, P. Ganguly, A. K. Raychaudhuri, R. A. Mohan Ram, and K. Sreedhar, *Nature* **326**, 856 (1987).
- K. V. Rao, D.-X. Chen, J. Nogues, C. Politis, C. Gallo, and J. A. Gerber, in "High Temperature Superconductors" (D. U. Gubser and M. Schluter, Eds.), p. 133, Mater. Res. Soc., Pittsburgh, 1987.
- C. N. R. Rao, *Philos. Trans. R. Soc. London Ser. A* **336**, 595 (1991).
- C. N. R. Rao, A. K. Santra, and D. D. Sarma, *Phys. Rev. B* **45**, 10814 (1992).
- U. Rauchschwalbe, F. Steglich, G. R. Stewart, A. L. Giorgi, P. Fulde, and K. Maki, *Europhys. Lett.* **3**, 751 (1987).
- J. Redinger, A. J. Freeman, J. Yu, and S. Massidda, *Phys. Lett. A* **124**, 469 (1987).
- M. Reedyk, T. Timusk, J. S. Xue, and J. Greedan, *Phys. Rev. B* **45**, 7406 (1992a).
- M. Reedyk, C. V. Stager, T. Timusk, J. S. Xue, and J. E. Greedan, *Phys. Rev. B* **45**, 10057 (1992b).
- M. E. Reeves, S. E. Stupp, T. Friedmann, F. Slakey, D. M. Ginsberg, and M. V. Klein, *Phys. Rev. B* **40**, 4573 (1989).
- J. D. Reger, T. A. Tokuyasu, A. P. Young, and M. P. A. Fisher, *Phys. Rev. B* **44**, 7147 (1991).
- M. N. Regueiro, B. Salce, R. Calemczuk, C. Marin, and J. Y. Henry, *Phys. Rev. B* **44**, 9727 (1991).
- W. Rehwald, M. Rayl, R. W. Cohen, and G. D. Cody, *Phys. Rev. B* **6**, 363 (1972).

- F. Reif, "Fundamentals of Statistical and Thermal Physics," McGraw-Hill, New York, 1965.
- Y. T. Ren, J. Clayhold, F. Chen, Z. J. Huang, X. D. Qiu, Y. Y. Sun, R. L. Meng, Y. Y. Xue, and C. W. Chu, *Physica C* **217**, 6 (1993).
- Y. T. Ren, H. Chang, Q. Xiong, Y. Y. Xue, and C. W. Chu, *Physica C*, **226**, 209 (1994).
- B. Renker, F. Gompf, E. Gering, D. Ewert, H. Riettschel, and A. Dianoux, *Z. Phys. B* **73**, 309 (1988).
- Ch. Renner, A. D. Kent, Ph. Niedermann, Ø. Fischer, and F. Lévy, *Phys. Rev. Lett.* **67**, 1650 (1991).
- L. Reven, J. Shore, S. Yang, T. Duncan, D. Schwartz, J. Chung, and E. Oldfield, *Phys. Rev. B* **43**, 10466 (1991).
- C. M. Rey and L. R. Testardi, *Phys. Rev. B* **44**, 765 (1991).
- A. P. Reyes, D. E. MacLaughlin, M. Takigawa, P. C. Hammel, R. H. Heffner, J. D. Thompson, J. E. Crow, A. Kebede, T. Mihalisin, and J. Schwegler, *Phys. Rev. B* **42**, 2688 (1990).
- A. P. Reyes, D. E. MacLaughlin, M. Takigawa, P. C. Hammel, R. H. Heffner, J. D. Thompson, and J. E. Crow, *Phys. Rev. B* **43**, 2989 (1991).
- C. A. Reynolds, B. Serin, W. H. Wright, and L. B. Nesbitt, *Phys. Rev.* **78**, 487 (1950).
- H.-C. Ri, F. Kober, R. Gross, R. P. Huebener, and A. Gupta, *Phys. Rev. B* **43**, 13739 (1991).
- H.-C. Ri, J. Kober, A. Beck, L. Alff, R. Gross, and R. P. Huebener, *Phys. Rev. B* **47**, 12312 (1993).
- J. K. Rice, S. W. McCauley, A. P. Baronavski, J. S. Horwitz, and D. B. Chrisey, *Phys. Rev. B* **47**, 6086 (1993).
- J. P. Rice, N. Rigakis, D. M. Ginsberg, and J. M. Mochel, *Phys. Rev. B* **46**, 11050 (1992).
- P. L. Richards and M. Tinkham, *Phys. Rev.* **119**, 575 (1960).
- R. A. Richardson, S. D. Peacor, F. Nori, and C. Uher, *Phys. Rev. Lett.* **67**, 3856 (1991).
- C. T. Riecke, Th. Wölkhausen, D. Fay, and L. Tewordt, *Phys. Rev. B* **39**, 278 (1989).
- E. Riedel, *Z. Naturforsch. A* **190**, 1634 (1964).
- E. K. Riedel, H.-F. Cheung, and Y. Gefen, *Phys. Scr.* **T 25**, 357 (1989).
- P. S. Riseborough, *Phys. Rev. B* **45**, 13984 (1992).
- B. Roas, L. Schultz, and G. Saemann-Ischenko, *Phys. Rev. Lett.* **64**, 479 (1990).
- B. W. Roberts, *J. Phys. Chem. Ref. Data* **5**, 581 (1976).
- G. I. Rochlin, *Am. J. Phys.* **43**, 335 (1975).
- C. O. Rodriguez, *Phys. Rev. B* **49**, 1200 (1994).
- E. Rodriguez, J. Luzuriaga, C. D'Ovidio, and D. A. Esparza, *Phys. Rev. B* **42**, 10796 (1990).
- J. P. Rodriguez, *Phys. Rev. B* **36**, 168 (1987).
- J. P. Rodriguez and B. Douçot, *Phys. Rev. B* **42**, 8724 (1990).
- J. P. Rodriguez and B. Douçot, *Phys. Rev. B* **45**, 971 (1992).
- C. T. Rogers, K. E. Myers, J. N. Eckstein, and I. Bozovic, *Phys. Rev. Lett.* **69**, 160 (1992).
- D. S. Rokhsar, *Phys. Rev. Lett.* **65**, 1506 (1990).
- D. B. Romero, G. L. Carr, D. B. Tanner, L. Forro, D. Mandrus, L. Mihaly, and G. P. Williams, *Phys. Rev. B* **44**, 2818 (1991).
- M. Rona, *Phys. Rev.* **42**, 4183 (1990).
- A. C. Rose-Innes and E. H. Rhoderick, "Introduction to Superconductivity," Pergamon, Oxford, 1994.
- P. A. Rosenthal, M. R. Beasley, K. Char, M. S. Colclough, and G. Zaharchuk, *Appl. Phys. Lett.* **59**, 3482 (1991).
- J. Rossat-Mignod, P. Burlet, M. J. G. M. Jurgens, J. Y. Henry, and C. Vettier, *Physica C* **152**, 19 (1988).
- M. J. Rosseinsky, A. P. Ramirez, S. H. Glarum, D. W. Murphy, R. C. Haddon, A. F. Hebard, T. T. M. Palstra, A. R. Kortan, S. M. Zahurak, and A. V. Makhija, *Phys. Rev. Lett.* **66**, 2830 (1991).
- C. Rossel, Y. Maeno, and I. Morgenstein, *Phys. Rev. Lett.* **62**, 681 (1989a); C. Rossel, Y. Maeno, and F. H. Holtzberg, *IBM J. Res. Dev.* **33**, 328 (1989b).
- C. Rossel, O. Peña, H. Schmitt, and M. Sergent, *Physica C* **181**, 363 (1991).
- S. J. Rothman, J. L. Routbort, U. Welp, and J. E. Baker, *Phys. Rev. B* **44**, 2326 (1991).
- L. D. Rotter, Z. Schlesinger, R. T. Collins, F. Holtzberg, C. Field, U. W. Welp, G. W. Crabtree, J. Z. Liu, Y. Fang, K. G. Vandervoort, and S. Fleshler, *Phys. Rev. Lett.* **67**, 2741 (1991).
- J. L. Routbort and S. J. Rothman, *Appl. Phys. Rev.*, submitted for publication.
- V. A. Rowe and R. P. Huebener, *Phys. Rev.* **185**, 666 (1969).
- J. M. Rowell and R. C. Dynes, in "Phonons" (M. A. Nusimovici, Ed.), Flammarion, Sciences, Paris, 1972.
- G. J. Rozing, P. E. Mijnders, A. A. Menovsky, and P. F. de Châtel, *Phys. Rev. B* **43**, 9523 (1991).
- A. E. Ruckenstein, P. J. Hirschfeld, and J. Appel, *Phys. Rev. B* **36**, 857 (1987); reprinted in "Theories of High Temperature Superconductivity" (J. W. Halley, Ed.), p. 137. Addison-Wesley, Reading, MA, 1988.
- S. Ryu, S. Doniach, G. Deutscher, and A. Kapitulnik, *Phys. Rev. Lett.* **68**, 710 (1992).
- M. S. Rzechowski, L. L. Sohn, and M. Tinkham, *Phys. Rev. B* **43**, 8682 (1991).
- S. Sachdev and Z. Wang, *Phys. Rev. B* **43**, 10229 (1991).
- S. Sachdev, *Phys. Rev. B* **45**, 389 (1992).
- E. Sacher and J. E. Klemberg-Sapieha, *Phys. Rev. B* **39**, 1461 (1989).
- C. A. R. Sá de Melo and S. Doniach, *Phys. Rev. B* **41**, 6633 (1990).
- C. A. R. Sá de Melo, Z. Wang, and S. Doniach, *Phys. Rev. Lett.* **68**, 2078 (1992).
- H. Safar, C. Durán, J. Guimpel, L. Civalé, J. Luzuriaga, E. Rodriguez, F. de la Cruz, C. Fainstein, L. F. Schneemeyer, and J. V. Waszczak, *Phys. Rev. B* **40**, 7380 (1989).

- H. Safar, H. Pastoriza, F. de la Cruz, D. J. Bishop, L. F. Schneemeyer, and J. Waszczak, *Phys. Rev. B* **43**, 13610 (1991).
- H. Safar, P. L. Gammel, D. J. Bishop, D. B. Mitzi, and A. Kapitulnik, *Phys. Rev. Lett.* **68**, 2672 (1992).
- H. Safer, P. L. Gammel, D. A. Huse, D. J. Bishop, W. C. Lee, J. Giapintzakis, and D. M. Ginsberg, *Phys. Rev. Lett.* **70**, 3800 (1993).
- L. Sagdahl, S. Gjølmesli, T. Laegreid, K. Fossheim, and W. Assmus, *Phys. Rev. B* **42**, 6797 (1990).
- L. Sagdahl, T. Laegreid, K. Fossheim, M. Murkami, H. Fujimoto, S. Gotoh, K. Yamaguchi, H. Yamauchi, N. Koshizuka, and S. Tanaka, *Physica C* **172**, 495 (1991).
- N. Sahoo, S. Markert, T. P. Das, and K. Nagamine, *Phys. Rev. B* **41**, 220 (1990).
- D. Saint-James and P. D. de Gennes, *Phys. Lett.* **7**, 306 (1963).
- D. Saint-James, E. J. Thomas, and G. Sarma, "Type II Superconductivity," Pergamon, Oxford, 1969.
- K. Saitoh and T. Nishino, *Phys. Rev. B* **44**, 7070 (1991).
- S. Saito and A. Oshiyama, *Phys. Rev. Lett.* **66**, 2637 (1991).
- K. Salama, Y. H. Zhang, M. Mironova, and D. F. Lee, "Proc. Sixth US-Japan Joint Workshop on High T_c Superconductivity," Houston, Texas, December 1993.
- M. B. Salamon and J. Bardeen, *Phys. Rev. Lett.* **59**, 2615 (1987).
- M. B. Salamon, in "Physical Properties of High Temperature Superconductors," (D. M. Ginsberg, Ed.), Vol. 1, Chap. 2, World Scientific, Singapore, 1989.
- S. Salem-Sugui, Jr., E. E. Alp, S. M. Mini, M. Ramanathan, J. C. Campuzano, G. Jennings, M. Faiz, S. Pei, B. Dabrowski, Y. Zheng, D. R. Richards, and D. G. Hinks, *Phys. Rev. B* **43**, 5511 (1991).
- A. V. Samoilov, A. A. Yurgens, and N. V. Zavaritsky, *Phys. Rev. B* **46**, 6643 (1992).
- B. A. Sanborn, P. B. Allen, and D. A. Papaconstantopoulos, *Phys. Rev. B* **40**, 6037 (1989).
- A. Sanchez and D.-X. Chen, in "Susceptibility of Superconductors and Other Spin Systems" (T. Francavilla, R. A. Hein, and D. Leiberger, Eds.), Plenum, New York, 1991.
- A. Sanchez, D.-X. Chen, J. Muñoz, and Y.-Z. Li, *Physica C* **175**, 33 (1991).
- P. Santhanam and C. C. Chi, *Phys. Rev. B* **38**, 11843 (1988).
- A. Santoro, in "High Temperature Superconductivity" (J. W. Lynn, Ed.), Chap. 4, Springer-Verlag, Berlin, 1990.
- J. Sapiel, J. Schneck, J. F. Scott, J. C. Tolédano, L. Pierre, J. Chavignon, C. Daguet, J. P. Chaminade, and H. Boyer, *Phys. Rev. B* **43**, 6259 (1991).
- E. Sardella, *Phys. Rev. B* **45**, 3141 (1992).
- D. D. Sarma, P. Sen, C. Carbone, R. Cimino, and W. Gudat, *Phys. Rev. B* **39**, 12387 (1989).
- W. M. Saslow, *Phys. Rev. B* **39**, 2710 (1989).
- J. S. Satchell, R. G. Humphreys, N. G. Chew, J. A. Edwards, and M. J. Kane, *Nature* **334**, 331 (1988).
- N. Sato, T. Sakon, N. Takeda, T. Komatsubara, C. Geibei, and F. Steglich, *J. Phys. Soc. Jpn.* **61**, 32 (1992).
- S. Satpathy and R. M. Martin, *Phys. Rev. B* **36**, 7269 (1987).
- C. B. Satterthwaite, *Phys. Rev.* **125**, 873 (1962).
- A. Saul and M. Weissmann, *Phys. Rev. B* **42**, 4196 (1990).
- J. A. Sauls, APS Fall Mtg. Symp. Kondo Lattices and Heavy Fermions, to be published.
- D. J. Scalapino, *Phys. Reports*, to be published.
- J. Schaf, P. Pureur, and J. V. Kunzler, *Phys. Rev. B* **40**, 6948 (1989).
- H. J. Scheel in "Adv. in Supercond.," Springer-Verlag, Berlin, New York, to be published.
- S. Scheidl and G. Hackenbroich, *Phys. Rev. B* **46**, 14010 (1992).
- A. Schenck, P. Birrer, F. N. Gygax, B. Hitti, E. Lippelt, M. Weber, P. Böni, P. Fischer, H. R. Ott, and Z. Fisk, *Phys. Rev. Lett.* **65**, 2454 (1990).
- A. Schenstrom, M.-F. Xu, Y. Hong, D. Bein, M. Levy, B. K. Sarma, S. Adenwalla, Z. Zhao, T. Tokuyasu, D. W. Hess, J. B. Ketterson, J. A. Sauls, and D. G. Hinks, *Phys. Rev. Lett.* **62**, 332 (1989).
- A. Schilling, M. Cantoni, J. D. Guo, and H. R. Ott, *Nature* **363**, 56 (1993).
- A. Schilling, M. Catoni, O. Jeandupeux, J. D. Guo, and H. R. Ott, in "Advances in Superconductivity" (T. Fujita and Y. Shiohara, Eds.), Vol. 6, Springer-Verlag, Berlin, 1994a.
- A. Schilling, O. Jeandupeux, S. Büchi, H. R. Ott, and C. Rossel, *Physica C* **235**, in press (1994b).
- J. E. Schirber, D. L. Overmyer, K. D. Carlsan, J. M. Williams, A. M. Kini, H. H. Wang, H. A. Charlier, B. J. Love, D. M. Watkins, and G. A. Yaconi, *Phys. Rev. B* **44**, 4666 (1991).
- Z. Schlesinger, R. L. Greene, J. G. Bednorz, and K. A. Müller, *Phys. Rev. B* **35**, 5334 (1987).
- Z. Schlesinger, R. T. Collins, J. A. Calise, D. G. Hinks, A. W. Mitchell, Y. Zheng, B. Dabrowski, N. E. Bickers, and D. J. Scalapino, *Phys. Rev. B* **40**, 6862 (1989).
- Z. Schlesinger, R. T. Collins, F. Holtzberg, C. Feild, G. Koren, and A. Gupta, *Phys. Rev. B* **41**, 11237 (1990a).
- Z. Schlesinger, R. T. Collins, F. Holtzberg, C. Feild, S. H. Blanton, U. Welp, G. W. Crabtree, Y. Fang, and J. Z. Liu, *Phys. Rev. Lett.* **65**, 801 (1990b).
- D. Schmeltzer, *Phys. Rev. B* **49**, 6944 (1994).
- A. Schmid, *Phys. Kondens. Mat.* **8**, 129 (1968).
- J. M. Schmidt, A. N. Cleland and J. Clarke, *Phys. Rev. B* **43**, 229 (1991).
- P. Schmitt, P. Kummeth, L. Schultz, and G. Saemann-Ischenko, *Phys. Rev. Lett.* **67**, 267 (1991).
- H. Schnack and R. Griessen, *Phys. Rev. Lett.* **68**, 2706 (1992).

- L. F. Schneemeyer, J. K. Thomas, T. Siegrist, B. Batlogg, L. W. Rupp, R. L. Opila, R. J. Cava, and D. W. Murphy, *Nature* **335**, 421 (1988).
- T. Schneider, *Z. Phys. B* **85**, 187 (1991).
- T. Schneider, Z. Gedik, and S. Ciraci, *Z. Phys. B* **83**, 313 (1991).
- T. Schneider, *Physica C* **195**, 82 (1992).
- T. Schneider and H. Keller, *Phys. Rev. Lett.* **69**, 3374 (1992).
- A. J. Schofield and Wheatley, *Phys. Rev. B* **47**, 11607 (1993).
- K. Schönhammer, *Phys. Rev. B* **42**, 2591 (1990).
- J. R. Schrieffer, "Theory of Superconductivity," Addison-Wesley, New York, 1964.
- J. R. Schrieffer, X.-G. Wen, and S.-C. Zhang, *Phys. Rev. Lett.* **60**, 944 (1988).
- E. A. Schuberth, B. Strickler, and K. Andres, *Phys. Rev. Lett.* **68**, 117 (1992).
- I. K. Schuller, D. G. Hinks, M. A. Beno, S. W. Capone II, L. Soderholm, J. P. Locquet, Y. Bruynseraede, C. U. Segre, and K. Zhang, *Solid State Commun.* **63**, 385 (1987).
- L. Schultz, E. Hellstern, and A. Thomä, *Europhys. Lett.* **3**, 921 (1987).
- H. J. Schulz, *Phys. Rev. Lett.* **64**, 2831 (1990).
- J. Schwartz, S. Nakamae, G. W. Raban, Jr., J. K. Heuer, S. Wu, J. L. Wagner, and D. G. Hinks, *Phys. Rev. B* **48**, 9932 (1994).
- H. Schwenk, F. Gross, C. P. Heidmann, K. Andres, D. Schweitzer, and H. Keller, *Mol. Cryst. Liq. Cryst.* **119**, 329 (1985); *Phys. Rev. B* **31**, 3138 (1985).
- P. Seidel, E. Heinz, M. Siegel, F. Schmidl, K. J. Zach, and H.-J. Köhler, in "Proc. 4th Int. Conf. on Superconducting and Quantum Effect Devices and Their Applications," Berlin, June 1991.
- G. T. Seidler, T. F. Rosenbaum, D. L. Heinz, J. W. Downey, A. P. Paulikas, and B. W. Veal, *Physica C* **183**, 333 (1991).
- G. T. Seidler, T. F. Rosenbaum, and B. W. Veal, *Phys. Rev. B* **45**, 10162 (1992).
- K. Semba, T. Ishii, and A. Matsuda, *Phys. Rev. Lett.* **67**, 769 (1991).
- S. Sengupta, C. Dasgupta, H. R. Krishnamurthy, G. I. Menon, and T. V. Ramakrishnan, *Phys. Rev. Lett.* **67**, 3444 (1991).
- S. Sengupta and D. Shi, in "High Temperature Superconducting Materials Science and Engineering," to be published.
- S. Senoussi, M. Oussena, and S. Hadjoudi, *J. Appl. Phys.* **63**, 4176 (1988).
- A. Sequeira, H. Rajagopal, P. V. P. S. S. Sastry, J. V. Yakhmi, R. M. Iyer, and B. A. Dasannacharya, *Physica B* **180-181**, 429 (1992).
- M. Sera, S. Shamoto, and M. Sato, *Solid State Commun.* **68**, 649 (1988).
- S. Sergeenkov and M. Ausloos, *Phys. Rev. B* **47**, 14476 (1993).
- R. D. Shannon and P. E. Bierstedt, *J. Am. Ceram. Soc.* **58**, 635 (1970).
- C. Shao-Chun, Z. Dong-Ming, Z. Dian-Lin, H. M. Duan, and A. M. Hermann, *Phys. Rev. B* **44**, 12571 (1991).
- B. Ya. Shapiro, *Phys. Rev. B* **48**, 16722 (1993).
- S. Shapiro, *Phys. Rev. Lett.* **11**, 80 (1963).
- R. P. Sharma, L. E. Rehn, and P. M. Baldo, *Phys. Rev. B* **43**, 13711 (1991).
- B. S. Shastri and B. I. Shraiman, *Int. J. Mod. Phys. A* **5**, 365 (1991).
- T. P. Sheahen, "Introduction to High T_c Superconductivity," Plenum, New York, 1994.
- V. Sh. Shekhtman, Ed., *The Real Structure of High- T_c Superconductors*, Springer-Verlag, Berlin, 1993.
- S.-Q. Shen and W. Lu, *Phys. Rev. B* **48**, 1105 (1993).
- Z.-X. Shen, P. A. P. Lindberg, B. O. Wells, D. S. Dessau, A. Borg, I. Lindau, W. E. Spicer, W. P. Ellis, G. H. Kwei, K. C. Ott, J.-S. Kang, and J. W. Allen, *Phys. Rev. B* **40**, 6912 (1989).
- Z.-X. Shen, R. S. List, D. S. Dessau, F. Parmigiani, A. J. Arko, R. Bartlett, B. O. Wells, I. Lindau, and W. E. Spicer, *Phys. Rev. B* **42**, 8081 (1990).
- Z.-X. Shen, W. E. Spicer, D. M. King, D. S. Dessau, and B. O. Wells, *Science* **267**, 343 (1995).
- Z.-Y. Shen, "High Temperature Superconducting Microwave Circuits," Artech House, Norwood, Massachusetts, 1994.
- Z. Z. Sheng, A. M. Hermann, A. El Ali, C. Almasan, J. Estrada, T. Datta, and R. J. Matson, *Phys. Rev. Lett.* **60**, 937 (1988).
- Z. Z. Sheng and A. M. Hermann, *Nature* **332**, 55 (1988).
- D.-N. Sheng, Z.-B. Su, and L. Yu, *Phys. Rev. B* **42**, 8732 (1990).
- D. Shi, M. S. Boley, U. Welp, J. G. Chen, and Y. Liao, *Phys. Rev. B* **40**, 5255 (1989).
- D. Shi, M. Xu, M. M. Fang, J. G. Chen, A. L. Cornelius, and S. G. Lanan, *Phys. Rev. B* **41**, 8833 (1990a).
- D. Shi, M. Xu, A. Umezawa, and R. F. Fox, *Phys. Rev. B* **42**, 2062 (1990b).
- D. Shi, X. S. Ling, M. Xu, M. M. Fang, S. Luo, J. I. Budnick, B. Dabrowski, D. G. Hinks, D. R. Richards, and Y. Zheng, *Phys. Rev. B* **43**, 3684 (1991).
- D. Shi and M. Xu, *Phys. Rev. B* **44**, 4548 (1991).
- D. Shi, Ed., "High Temperature Superconducting Materials Science and Engineering," Elsevier, Oxford, 1994.
- J. S. Shier and D. M. Ginsberg, *Phys. Rev.* **147**, 384 (1966).
- E. Shimizu and D. Ito, *Phys. Rev. B* **39**, 2921 (1989).
- E. Shimshoni, Y. Gefen, and S. Levit, *Phys. Rev.* **40**, 2147 (1989).
- E. Shimshoni and E. Ben-Jacob, *Phys. Rev. B* **43**, 2705 (1991).
- S. L. Shindé, J. Morrill, D. Goland, D. A. Chance, and T. McGuire, *Phys. Rev. B* **41**, 8838 (1990).
- T. Shinjo, T. Mizutani, N. Hosoito, T. Kusuda, T. Takabatake, K. Matsukuma, and H. Fujii, *Physica C* **159**, 869 (1989).

- T. Shinjo and S. Nasu, in "Mechanisms of High Temperature Superconductivity" (H. Kamimura and A. Oshiyama, Eds.), p. 166, Springer Series in Material Science, Springer-Verlag, Heidelberg, 1989.
- G. Shirane, R. J. Birgeneau, Y. Endoh, P. Gehring, M. A. Kastner, K. Kitazawa, H. Kojima, I. Tanaka, T. R. Thurston, and K. Yamada, *Phys. Rev. Lett.* **63**, 330 (1989).
- G. Shirane, J. Als-Nielsen, M. Nielsen, J. M. Tranquada, H. Chou, S. Shamoto, and M. Sato, *Phys. Rev. B* **41**, 6547 (1990).
- K. N. Shrivastava and K. P. Sinha, "Magnetic Superconductors: Model Theories and Experimental Properties of Rare-Earth Compounds," North-Holland, Amsterdam, 1984.
- K. N. Shrivastava, *Phys. Rev. B* **41**, 11168 (1990).
- J. D. Shore, M. Huang, A. T. Dorsey, and J. P. Sethna, *Phys. Rev. Lett.* **62**, 3089 (1989).
- L. Shu-yuan, L. Li, and Z. Dian-lin, H. M. Duan, W. Kiel, and A. M. Hermann, *Phys. Rev. B* **47**, 8324 (1993).
- Yu. N. Shvachko, A. A. Koshta, A. A. Romanyukha, V. V. Ustinov, and A. I. Akimov, *Physica C* **174**, 447 (1991).
- Q. Si and G. Kotliar, *Phys. Rev. Lett.* **70**, 3143 (1993).
- M. Siegel, F. Schmdl, K. Zach, E. Heinz, J. Borck, W. Michalke, and P. Seidel, *Physica C* **180**, 288 (1991).
- T. Siegrist, S. Sunshine, D. W. Murphy, R. J. Cava, and S. M. Zahurak, *Phys. Rev. B* **35**, 7137 (1987).
- T. Siegrist, S. M. Zahurak, D. W. Murphy, and R. S. Roth, *Nature* **334**, 231 (1988).
- M. Sigrist, T. M. Rice, and K. Ueda, *Phys. Rev. Lett.* **63**, 1727 (1989).
- P. Simon, J. M. Bassat, S. B. Oseroff, Z. Fisk, S.-W. Cheong, A. Wattiaux, and S. Schultz, *Phys. Rev. Lett.* **48**, 4216 (1993).
- R. R. P. Singh, P. A. Fleury, K. B. Lyons, and P. E. Sulewski, *Phys. Rev. Lett.* **62**, 2736 (1989).
- D. Singh, W. E. Pickett, E. C. von Stetten, and S. Berko, *Phys. Rev. B* **42**, 2696 (1990).
- D. J. Singh, *Physica C* **212**, 228 (1993a).
- D. J. Singh, *Phys. Rev. B* **48**, 3571 (1993b).
- D. J. Singh and W. E. Pickett, *Phys. Rev. Lett.*, **73**, 476 (1994).
- K. Sinha, *Ind. J. Phys.* **66A**, 1 (1992) in K. P. Sinha, "Magnetic Superconductors; Recent Developments," Nova, New York, 1989.
- S. Skanthakumar, H. Zhang, T. W. Clinton, W.-H. Li, J. W. Lynn, Z. Fisk, and S.-W. Cheong, *Physica C* **160**, 124 (1989).
- H. L. Shriver and I. Mertig, *Phys. Rev. B* **41**, 6553 (1990).
- V. Skumryev, R. Puzniak, N. Karpe, H. Zheng-he, M. Pout, H. Medelius, D.-X. Chen, and K. V. Rao, *Physica C* **152**, 315 (1988).
- V. Skumryev, M. R. Koblishka, and H. Kronmüller, *Physica C* **184**, 332 (1991).
- F. Slakey, S. L. Cooper, M. V. Klein, J. P. Rice, and D. M. Ginsburg, *Phys. Rev. B* **39**, 2781 (1989).
- F. Slakey, M. V. Klein, J. P. Rice, and D. M. Ginsburg, *Phys. Rev. B* **43**, 3764 (1991).
- A. W. Sleight, J. L. Gillson, and P. E. Bierstedt, *Solid State Commun.* **17**, 27 (1975).
- A. W. Sleight, *Am. Chem. Soc. Symp. Ser.* **351**, 2 (1987).
- L. C. Smedskjaer, A. Bansil, U. Welp, Y. Fang, and K. G. Bailey, *Phys. Rev. B* **46**, 5868 (1992).
- H. H. A. Smit, M. W. Dirken, R. C. Thiel, and L. J. de Jongh, *Solid State Commun.* **64**, 695 (1987).
- M. G. Smith, A. Manthiram, J. Zhou, J. B. Goodenough, and J. T. Markert, *Nature* **351**, 549 (1991).
- M. G. Smith, J. B. Goodenough, A. Manthiram, R. Taylor, W. Peng, C. Kimball, *J. Solid State Chem.* **98**, 181 (1992).
- R. Sobolewski, L. Shi, T. Gong, W. Xiong, X. Weng, Y. Kostoulas, and P. M. Fauchet, "Proc. High Temperature Supercond. Detectors," **2159**, to be published.
- J. O. Sofo, C. A. Balseiro, and H. E. Castillo, *Phys. Rev. B* **45**, 9860 (1992).
- L. L. Sohn, M. S. Rzchowski, J. U. Free, S. P. Benz, M. Tinkham, and C. J. Lobb, *Phys. Rev. B* **44**, 925 (1991).
- L. L. Sohn, M. S. Rzchowski, J. U. Free, M. Tinkham, and C. J. Lobb, *Phys. Rev.* **45**, 3003 (1992).
- P. R. Solomon and F. A. Otter, *Phys. Rev.* **164**, 608 (1967).
- S. N. Song, Q. Robinson, S.-J. Hwu, D. L. Johnson, K. R. Poepelmeier, and J. B. Ketterson, *Appl. Phys. Lett.* **51**, 1376 (1987).
- Y. S. Song, H. Park, Y. S. Choi, Y. W. Park, M. S. Jang, H. C. Lee, and S. I. Lee, *J. Korean Phys. Soc.* **23**, 492 (1990).
- Y. Song and J. R. Gaines, *J. Phys. Condens. Matter.* **3**, 7161 (1991).
- Y.-Q. Song, M. Lee, W. P. Halperin, L. M. Tonge, and T. J. Marks, *Phys. Rev. B* **44**, 914 (1991a).
- Y.-Q. Song, M. A. Kennard, M. Lee, K. R. Poepelmeier, and W. P. Halperin, *Phys. Rev. B* **44**, 7159 (1991b).
- Y. Song, A. Misra, P. P. Crooker, and J. R. Gaines, *Phys. Rev. B* **45**, 7574 (1992).
- Y.-Q. Song, W. P. Halperin, L. Tonge, T. J. Marks, M. Ledvij, V. G. Kogan, and L. N. Bulaevskii, *Phys. Rev. Lett.* **70**, 3127 (1993).
- J. Spalek and P. Gopalan, *J. Phys. France* **50**, 2869 (1989).
- J. Spalek and J. M. Honig, in "Studies in High Temperature Superconductors" (A. V. Narlikar, Ed.), Vol. 8, Chap. 1. Nova Sci., New York (1991).
- J. Spalek and W. Wojcik, *Phys. Rev. B* **45**, 3799 (1992).
- G. Sparn, J. D. Thompson, R. L. Whetten, S.-M. Huang, R. B. Kaner, F. Diederich, G. Grüner, and K. Holczer, *Phys. Rev. Lett.* **68**, 1228 (1992).
- P. N. Spathis, M. P. Soerensen, and N. Lazarides, *Phys. Rev. B* **45**, 7360 (1992).

- S. Spielman, J. S. Dodge, L. W. Lombardo, C. B. Eom, M. M. Fejer, T. H. Geballe, and A. Kapitulnik, *Phys. Rev.* **68**, 3472 (1992).
- Z. M. Stadnik, G. Stroink and R. A. Dunlap, *Phys. Rev. B* **39**, 9108 (1989).
- Z. M. Stadnik, G. Stroink, and T. Arakawa, *Phys. Rev. B* **44**, 12552 (1991).
- B. W. Statt and A. Griffin, *Phys. Rev. B* **48**, 619 (1993).
- T. Stauffer, R. Nemetschek, R. Hackl, P. Müller, and H. Veith, *Phys. Rev. Lett.* **68**, 1069 (1992).
- D. G. Steel and J. M. Graybeal, *Phys. Rev. B* **45**, 12643 (1992).
- F. Steglich, J. Aarts, C. D. Bredl, W. Lieke, D. Meschede, W. Franz, and H. Schäfer, *Phys. Rev. Lett.* **43**, 1892 (1979).
- P. Steiner, V. Kinsinger, I. Sander, B. Siegwart, S. Hüfner, and C. Politis, *Z. Phys. B Cond. Mat.* **67**, 19 (1987).
- C. H. Stephan and B. W. Maxfield, *J. Low Temp. Phys.* **10**, 185 (1973).
- W. Stephan and J. P. Carbotte, *Phys. Rev. B* **43**, 10236 (1991).
- G. R. Stewart, *Rev. Mod. Phys.* **56**, 755 (1984).
- G. R. Stewart, Z. Fisk, J. O. Willis, and T. J. Smith, *Phys. Rev. Lett.* **52**, 679 (1984).
- G. R. Stewart, J. O'Rourke, G. W. Crabtree, K. D. Carlson, H. H. Wang, J. M. Williams, F. Gross, and K. Andres, *Phys. Rev. B* **33**, 2046 (1986).
- S. T. Stoddart, H. I. Mutlu, A. K. Geim, and S. J. Bending, *Phys. Rev. B* **47**, 5146 (1993).
- E. C. Stoner, *Phil. Mag.* **36**, 803 (1945).
- H. T. C. Stoof, *Phys. Rev. B* **47**, 7979 (1993).
- J. A. Stratton, "Electromagnetic Theory," McGraw Hill, New York, 1941.
- S. K. Streiffer, B. M. Lairson, C. B. Eom, B. M. Clemens, J. C. Bravman, and T. H. Geballe, *Phys. Rev. B* **43**, 13007 (1991).
- A. R. Strnad, C. F. Hempstead, and Y. B. Kim, *Phys. Rev. Lett.* **13**, 794 (1964).
- S. E. Stupp, M. E. Reeves, D. M. Ginsberg, D. G. Hinks, B. Dabrowski, and K. G. Vandervoort, *Phys. Rev. B* **40**, 10878 (1989).
- S. E. Stupp, T. A. Friedmann, J. P. Rice, R. A. Schweinfurth, D. J. Van Harlingen, and D. M. Ginsberg, *Phys. Rev. B* **43**, 13073 (1991).
- C. K. Subramanian, M. Paranthaman, and A. B. Kaiser, *Physica C* **222**, 47 (1994).
- M. A. Subramanian, C. C. Torardi, J. C. Calabrese, J. Gopalakrishnan, K. J. Morrissey, T. R. Askew, R. B. Flippin, U. Chowdhry, and A. W. Sleight, *Science* **239**, 1015 (1988a).
- M. A. Subramanian, J. C. Calabrese, C. C. Torardi, J. Gopalakrishnan, T. R. Askew, R. B. Flippin, K. J. Morrissey, U. Chowdhry, and A. W. Sleight, *Nature* **332**, 420 (1988b).
- A. Sudbø and E. H. Brandt, *Phys. Rev. B* **43**, 10482 (1991a); *Phys. Rev. Lett.* **67**, 3176 (1991b).
- M. Suenaga, A. K. Ghosh, Y. Xu, and D. O. Welch, *Phys. Rev. Lett.* **66**, 1777 (1991).
- R. Sugano, T. Onogi, and Y. Murayama, *Phys. Rev. B* **45**, 10789 (1992).
- J. Sugiyama, S. Tokuono, S.-I. Koriyama, H. Yamauchi, and S. Tanaka, *Phys. Rev. B* **43**, 10489 (1991).
- J. Sugiyama, K. Matsuura, M. Kosuge, H. Yamauchi, and S. Tanaka, *Phys. Rev. B* **45**, 9951 (1992).
- S. B. Sulaiman, N. Sahoo, T. P. Das, O. Donzelli, E. Torikai, and K. Nagamine, *Phys. Rev. B* **44**, 7028 (1991).
- S. B. Sulaiman, N. Sahoo, T. P. Das and O. Donzelli, *Phys. Rev. B* **45**, 7383 (1992).
- P. E. Sulewski, A. J. Sievers, R. A. Buhrman, J. M. Tarascon, L. H. Greene, and W. A. Curtin, *Phys. Rev. B* **35**, 8829 (1987).
- P. E. Sulewski, P. A. Fleury, K. B. Lyons, S.-W. Cheong, and Z. Fisk, *Phys. Rev. B* **41**, 225 (1990).
- J. Z. Sun, D. J. Webb, M. Naito, K. Char, M. R. Hahn, J. W. P. Hsu, A. D. Kent, D. B. Mitzi, B. Oh, M. R. Beasley, T. H. Geballe, R. H. Hammond, and A. Kapitulnik, *Phys. Rev. Lett.* **58**, 1574 (1987).
- K. Sun, J. H. Cho, F. C. Chou, W. C. Lee, L. L. Miller, D. C. Johnston, Y. Hidaka and T. Murakami, *Phys. Rev. B* **43**, 239 (1991).
- C. S. Sundar, A. Bharathi, Y. C. Jean, P. H. Hor, R. L. Meng, Z. J. Huang, and C. W. Chu, *Phys. Rev. B* **42**, 426 (1990a).
- C. S. Sundar, A. Bharathi, W. Y. Ching, Y. C. Jean, P. H. Hor, R. L. Meng, Z. J. Huang and C. W. Chu, *Phys. Rev. B* **42**, 2193 (1990b).
- C. S. Sundar, A. Bharathi, W. Y. Ching, Y. C. Jean, P. H. Hor, R. L. Meng, Z. J. Huang, and C. W. Chu, *Phys. Rev. B* **43**, 13019 (1991).
- C. Sürgers, H. v. Löhneysen, and L. Schultz, *Phys. Rev. B* **40**, 8787 (1989).
- Y. Suwa, Y. Tanaka, and M. Tsukada, *Phys. Rev. B* **39**, 9113 (1989).
- M. Suzuki, Y. Enemoto, T. Murakami, and T. Inamura, "Proc. 3rd Meeting Ferroelectric Materials and Their Applications," Kyoto, 1981a.
- M. Suzuki, Y. Enemoto, T. Murakami, and T. Inamura, *Jpn. J. Appl. Phys.* **20**, Suppl. 20-24, 13 (1981b).
- M. Suzuki and M. Hikita, *Jpn. J. Appl. Phys.* **28**, L1368 (1989).
- M. Suzuki and M. Hikita, *Phys. Rev. B* **41**, 9566 (1990).
- M. Suzuki and M. Hikita, *Phys. Rev. B* **44**, 249 (1991).
- S. Suzuki, T. Takahashi, T. Kusunoki, T. Morikawa, S. Sato, H. Katayama-Yoshida, A. Yamanaka, F. Minami, and S. Takekawa, *Phys. Rev. B* **44**, 5381 (1991).
- H. Svensmark and L. M. Falicov, *Phys. Rev. B* **42**, 9957 (1990).
- A. Szasz, J. Hajdu, J. Kojnok, Z. Dankhazi, W. Krasser, T. Trager, and J. Bankuti, *J. Supercond.* **3**, 425 (1990).
- B. Szpunar and V. Smith, Jr., *Phys. Rev. B* **45**, 10616 (1992).

- M. Tachiki and S. Takahashi, *Solid State Commun.* **70**, 291 (1989).
- A. Tagliacozzo, F. Ventriglia, and P. Apell, *Phys. Rev. B* **40**, 10901 (1989).
- L. Taillefer, in "Hyperfine Interactions," to be published.
- S. Tajima, S. Uchida, A. Masaki, H. Takaki, K. Kitazawa, S. Tanaka, and A. Katsui, *Phys. Rev. B* **32**, 6302 (1985).
- S. Tajima, S. Uchida, H. Ishii, H. Takagi, S. Tanaka, U. Kawabe, H. Hasegawa, T. Aita, and T. Ishiba, *Mod. Phys. Lett. B* **1**, 353 (1988).
- Y. Tajima, M. Hikita, T. Ishii, H. Fuke, K. Sugiyama, M. Date, A. Yamagishi, A. Katsui, Y. Hidaka, T. Iwata, and S. Tsurumi, *Phys. Rev. B* **37**, 7956 (1988).
- S. Tajima and K. Kitazawa, in "Some Aspects of Superconductivity" (L. C. Gupta, Ed.) Nova Scientific Publ., New York, 1990.
- J. Takada, T. Terashima, Y. Bando, H. Mazaki, K. Iijima, K. Yamamoto, and K. Hirata, *Phys. Rev. B* **40**, 4478 (1989).
- Y. Takada, *Phys. Rev. B* **39**, 11575 (1989).
- H. Takagi, H. Eisaki, S. Uchida, A. Maeda, S. Tajima, K. Uchinokura, and S. Tanaka, *Nature* **332**, 236 (1988).
- T. Takahashi, H. Matsuyama, H. Katamaya-Yoshida, Y. Okabe, S. Hosoya, K. Seki, H. Fujimoto, M. Sato, and H. Inokuchi, *Phys. Rev. B* **39**, 6636 (1989).
- T. Takahashi, S. Sukuki, T. Morikawa, H. Katayama-Yoshida, S. Hasegawa, H. Inokuchi, K. Seki, K. Kikuchi, S. Suzuki, K. Ikemoto, and Y. Achiba, *Phys. Rev. Lett.* **68**, 1232 (1992).
- I. Takeuchi, J. S. Tsai, Y. Shimakawa, T. Manako, and Y. Kubo, *Physica C* **158**, 83 (1989).
- M. Takigawa, A. P. Reyes, P. C. Hammel, J. D. Thompson, R. H. Heffner, Z. Fisk, and K. C. Ott, *Phys. Rev. B* **43**, 247 (1991).
- M. Takigawa, J. L. Smith, and W. L. Hults, *Phys. Rev. B* **44**, 7764 (1991).
- J. L. Tallon, *Proc. 7th Intl. Workshop Critical Currents in "Superconductors, Tyrol, Austria,"* World Scientific, Singapore, 1994.
- K. Tamasaku, Y. Nakamura, and S. Uchida, *Phys. Rev. Lett.* **69**, 1455 (1992).
- T. Tamegai, K. Koga, K. Suzuki, M. Ichihara, F. Sadai, and Y. Iye, *Jpn. J. Appl. Phys. Lt.* **2**, 28, L112 (1989).
- Z. Tan, J. I. Budnick, W. Q. Chen, D. L. Brewster, S.-W. Cheong, A. S. Cooper, and L. W. Rupp, Jr., *Phys. Rev. B* **42**, 4808 (1990).
- Z. Tan, J. I. Budnick, S. Luo, W. Q. Chen, S.-W. Cheong, A. S. Cooper, P. C. Canfield, and Z. Fisk, *Phys. Rev. B* **44**, 7008 (1991).
- Y. Tanaka and M. Tsukada, *Phys. Rev. B* **40**, 4482 (1989a); *Solid State Commun.* **69**, 195, 491 (1989b).
- Y. Tanaka and M. Tsukada, *Phys. Rev. B* **42**, 2066 (1990).
- Y. Tanaka and M. Tsukada, *Phys. Rev. B* **44**, 7578 (1991).
- S. Tanda, M. Honma, and T. Nakayama, *Phys. Rev. B* **43**, 8725 (1991).
- C. Q. Tang, B. R. Li, and A. Chen, *Phys. Rev. B* **42**, 8078 (1990).
- X. X. Tang, D. E. Morris, and A. P. B. Sinha, *Phys. Rev. B* **43**, 7936 (1991).
- T. Tani, T. Itoh and S. Tanaka, *J. Phys. Soc. Jpn. Suppl. A* **49**, 309 (1980).
- S. Tanigawa, Y. Mizuhara, Y. Hidaka, M. Oda, M. Suzuki, and T. Murakami, *Mater. Res. Soc. Symp. Proc.* **99**, 57 (1988).
- D. B. Tanner and T. Timusk, in "Physical Properties of High Temperature Superconductors" (D. M. Ginsberg, Ed.), Vol. 3, Chap. 5, World Scientific, Singapore, 1992.
- H. J. Tao, A. Chang, F. Lu, and E. L. Wolf, *Phys. Rev. B* **45**, 10622 (1992).
- J. M. Tarascon, L. H. Greene, W. R. McKinnon, and G. W. Hull, *Phys. Rev. B* **35**, 7115 (1987a).
- J. M. Tarascon, W. R. McKinnon, L. H. Greene, G. W. Hull, and E. M. Vogel, *Phys. Rev. B* **36**, 226 (1987b).
- J. M. Tarascon, L. H. Greene, W. R. McKinnon, G. W. Hull, and T. H. Geballe, *Science* **235**, 1373 (1987c).
- J. M. Tarascon, P. Barboux, P. F. Miceli, L. H. Greene, D. W. Hull, M. Eibschutz, and S. A. Sunshine, *Phys. Rev. B* **37**, 7458 (1988a).
- J. M. Tarascon, Y. LePage, P. Barboux, B. G. Bagley, L. H. Greene, W. R. McKinnon, G. W. Hull, M. Giroud, and D. M. Hwang, *Phys. Rev.* **37**, 9382 (1988b).
- J. M. Tarascon, E. Wang, L. H. Greene, B. G. Bagley, G. W. Hull, S. M. D'Egidio, P. F. Miceli, Z. Z. Wang, T. W. Jing, J. Clayhold, D. Brawner, and N. P. Ong, *Phys. Rev. B* **40**, 4494 (1989a).
- J. M. Tarascon, Y. LePage, W. R. McKinnon, E. Tselepis, P. Barboux, B. G. Bagley, and R. Ramesh, in "Proc. Mater. Res. Soc. Symp.," San Diego, Apr. 23-28, 1989b.
- V. V. Tatarskii, M. Paranthaman, and A. M. Hermann, *Phys. Rev. B* **47**, 14489 (1993).
- Y. Taur, P. L. Richards, and T. Auracher, *Low Temp. Phys.* **3**, 276 (1974).
- W. M. Temmerman, G. M. Stocks, P. J. Durham, and P. A. Sterne, *J. Phys. F* **17**, L135 (1987).
- M. A. Teplov, O. N. Bakharev, A. V. Dooglav, A. V. Egorov, M. V. Eremin, M. S. Tagirov, A. G. Volodin, and R. Sh. Zhdanov, *Physica C* **185-189**, 1107 (1991).
- I. Terasaki, T. Nakahashi, S. Takebayashi, A. Maeda, and K. Uchinokura, *Physica C* **165**, 152 (1990a).
- I. Terasaki, S. Tajima, H. Eisaki, H. Takagi, K. Uchinokura, and S. Uchida, *Phys. Rev. B* **41**, 865 (1990b).
- T. Terashima, K. Shimura, Y. Bando, Y. Matsuda, A. Fujiyama, and S. Komiyama, *Phys. Rev. Lett.* **67**, 1362 (1991).

- B. M. Terzijska, R. Wawryk, D. A. Dimitrov, Cz. Marucha, V. T. Kovachev, and J. Rafalowicz, *Cryogenics* 32, 53 (1992).
- Z. Tesanovic and M. Rasolt, *Phys. Rev. B* 39, 2718 (1989).
- Z. Tesanovic, M. Rasolt, and L. Xing, *Phys. Rev. B* 43, 288 (1991).
- Z. Tesanovic, *Phys. Rev. B* 44, 12635 (1991).
- L. R. Tessler, J. Provost, and A. Maignan, *Appl. Phys. Lett.* 58, 528 (1991).
- L. Tewordt, S. Wermbter, and Th. Wölkhausen, *Phys. Rev. B* 40, 6878 (1989).
- L. Tewordt and Th. Wölkhausen, *Solid State Commun.* 70, 839 (1989).
- T. D. Thanh, A. Koma, and S. Tanaka, *Appl. Phys.* 22, 205 (1980).
- S. Theodorakis and Z. Tesanovic, *Phys. Rev. B* 40, 6659 (1989).
- S. L. Thiemann, Z. Radovic, and V. G. Kogan, *Phys. Rev. B* 39, 11406 (1989).
- T. Thio, T. R. Thurston, N. W. Preyer, P. J. Picone, M. A. Kastner, H. P. Jenssen, D. R. Gabbe, C. Y. Chen, R. J. Birgeneau, and A. Aharony, *Phys. Rev. B* 38, 905 (1988).
- G. Thomas, M. Capizzi, J. Orenstein, D. Rapkine, A. Millis, P. Gammel, L. Gammel, L. F. Schneemeyer, and J. Waszczak, in "Proceedings of the International Symposium on the Electronic Structure of High T_c Superconductors," p. 67, (A. Bianconi, Ed.) Pergamon Press, Oxford, 1988.
- R. S. Thompson, *Phys. Rev. B* 1, 327 (1970).
- J. R. Thompson, J. Brynstad, D. M. Kroeger, Y. C. Kim, S. T. Sekula, D. K. Christen, and E. Specht, *Phys. Rev. B* 39, 6652 (1989).
- J. R. Thompson, D. K. Christen, H. A. Deeds, Y. C. Kim, J. Brynstad, S. T. Sekula, and J. Budai, *Phys. Rev. B* 41, 7293 (1990).
- J. R. Thompson, J. G. Ossandon, D. K. Christen, B. C. Chakoumakos, Y. R. Sun, M. Paranthaman, and J. Brynstad, *Phys. Rev. B* 48, 14031 (1993).
- C. Thomsen and M. Cardona, in "Physical Properties of High Temperature Superconductors" (D. M. Ginsberg, Ed.), Vol. 1, Chap. 8, World Scientific, Singapore, 1989.
- R. J. Thorn, *ACS Symp. Ser.* 351, Chap. 3, (1987).
- C. Tien and I. M. Jiang, *Phys. Rev. B* 40, 229 (1989).
- T. S. Tighe, M. T. Tuominen, J. M. Hergenrother, and M. Tinkham, *Phys. Rev. B* 47, 1145 (1993).
- D. R. Tilley and J. Tilley, "Superfluidity and Superconductivity," Hilger, Boston (1986).
- T. Timusk and D. B. Tanner, in "Physical Properties of High Temperature Superconductors" (D. M. Ginsberg, Ed.), Vol. 1, Chap. 7, World Scientific, New York (1989).
- M. Tinkham, *Phys. Rev. Lett.* 13, 804 (1964).
- M. Tinkham and J. Clarke, *Phys. Rev. Lett.* 28, 1366 (1972).
- M. Tinkham, "Introduction to Superconductivity," Krieger, FL (1985).
- M. Tinkham and C. J. Lobb, *Solid State Phys.* 42, 91 (1989).
- J. E. Tkaczyk, R. H. Arendt, M. F. Garbauskas, H. R. Hart, K. W. Lay, and F. E. Luborsky, *Phys. Rev. B* 45, 12506 (1992).
- J. G. Tobin, C. G. Olson, C. Gu, J. Z. Liu, F. R. Solal, M. J. Fluss, R. H. Howell, J. C. O'Brien, H. B. Radousky, and P. A. Sterne, *Phys. Rev. B* 45, 5563 (1992).
- B. H. Toby, T. Egami, J. D. Jorgensen, and M. A. Subramanian, *Phys. Rev. Lett.* 64, 2414 (1990).
- K. Togano, H. Kumakura, K. Fukutomi, and K. Tachikawa, *Appl. Phys. Lett.* 51, 136 (1987).
- A. Tokiwa, M. Nagoshi, and Y. Syono, *Physica C* 170, 437 (1990).
- A. Tokiwa, Y. Syono, T. Oku, and M. Nagoshi, *Physica C* 185-189, 619 (1991).
- A. Tokiwa-Yamamoto, K. Isawa, M. Itoh, S. Adachi, and H. Yamauchi, *Physica C* 216, 250 (1993).
- A. Tokumitsu, K. Miyake, and K. Yamada, *Phys. Rev. B* 47, 11988 (1993).
- M. Tokumoto, H. Bando, H. Anzai, G. Saito, K. Murata, K. Kajimura, and T. Ishiguro, *J. Phys. Soc. Jpn.* 54, 869 (1985).
- T. A. Tokuyasu, D. W. Hess, and J. A. Sauls, *Phys. Rev. B* 41, 8891 (1990); T. A. Tokuyasu and J. A. Sauls, *Physica B* 165-166, 347 (1990).
- J. C. Tolédano, A. Litzler, J. Primot, J. Schneck, L. Pierre, D. Morin, and C. Daguet, *Phys. Rev. B* 42, 436 (1990).
- H. Tolentino, M. Medarde, A. Fontaine, F. Baudalet, E. Dartyge, D. Guay, and G. Tourillon, *Phys. Rev. B* 45, 8091 (1992).
- I. Tomeno, M. Yoshida, K. Ikeda, K. Tai, K. Takamuku, N. Koshizuka, S. Tanaka, K. Oka, and H. Unoki, *Phys. Rev. B* 43, 3009 (1991).
- J. Toner, *Phys. Rev. Lett.* 66, 2523 (1991a).
- J. Toner, *Phys. Rev. Lett.* 67, 2537 (1991b); see comment by T. Nattermann and I. Lyuksyutov, and reply 68, 3366 (1992).
- C. C. Torardi, M. A. Subramanian, J. C. Calabrese, J. Gopalakrishnan, K. J. Morrissey, T. R. Askew, R. B. Flippen, U. Chowdhry, and A. W. Sleight, *Science* 240, 631 (1988a).
- C. C. Torardi, M. A. Subramanian, J. C. Calabrese, J. Gopalakrishnan, E. M. McCarron, K. J. Morrissey, T. R. Askew, R. B. Flippen, U. Chowdhry, and A. W. Sleight, *Phys. Rev. B* 38, 225 (1988b).
- J. B. Torrance, *J. Solid State Chem.* 96, 59 (1992).
- J. B. Torrance, P. Lacorre, A. I. Nazzari, E. J. Ansaldo, and Ch. Niedermayer, *Phys. Rev. B* 45, 8209 (1992).
- H. Totsuji, *Phys. Rev. B* 43, 5287 (1991).
- M. Touminen, A. M. Goldman, Y. Z. Chang, and P. Z. Jiang, *Phys. Rev. B* 42, 412 (1990).
- S. W. Tozer, A. W. Kleinsasser, T. Penney, D. Kaiser, and F. Holtzberg, *Phys. Rev. Lett.* 59, 1768 (1987).
- J. M. Tranquada, G. Shirane, B. Keimer, S. Shamoto, and M. Sato, *Phys. Rev. B* 40, 4503 (1989).

- J. M. Tranquada, in "Early and Recent Aspects of Superconductivity" (J. G. Bednorz and K. A. Müller, Eds.), p. 422, Springer-Verlag, Berlin, 1990.
- J. M. Tranquada, P. M. Gehring, G. Shirane, S. Shamoto, and M. Sato, *Phys. Rev. B* **46**, 5561 (1992).
- A. Tressaud, K. Amine, J. P. Chaminade, J. Etourneau, T. M. Duc, and A. Sartre, *J. Appl. Phys.* **68**, 248 (1990).
- J.-M. Triscone, Ø. Fischer, O. Brunner, L. Antognazza, A. D. Kent, and M. G. Karkut, *Phys. Rev. Lett.* **64**, 804 (1990).
- V. N. Trofimov, A. V. Kuznetsov, P. V. Lepeschkin, K. A. Bolschinskoy, A. A. Ivanov, and A. A. Mikhailov, *Physica C* **183**, 135 (1991).
- A. Trokiner, R. Mellet, A.-M. Pougnet, D. Morin, Y. M. Gao, J. Primot, and J. Schneck, *Phys. Rev. B* **41**, 9570 (1990).
- A. Trokiner, L. LeNoc, J. Schneck, A. M. Pougnet, R. Mellet, J. Primot, H. Savary, Y. M. Gao, and S. Aubry, *Phys. Rev. B* **44**, 2426 (1991).
- N. Troullier and J. L. Martins, *Phys. Rev. B* **46**, 1754 (1992).
- S. A. Trugman, *Phys. Rev. Lett.* **65**, 500 (1990).
- J.-S. Tsai, A. K. Jain, and J. E. Lukens, *Phys. Rev. Lett.* **51**, 316 (1983).
- S.-F. Tsay, S.-Y. Wang, and T. J. W. Yang, *Phys. Rev. B* **43**, 13080 (1991).
- C. C. Tsuei, A. Gupta, and G. Koren, *Physica C* **161**, 415 (1989).
- M. Touminen, A. M. Goldman, Y. Z. Chang, and P. Z. Jiang, *Phys. Rev. B* **42**, 412 (1990).
- M. T. Tuominen, J. M. Hergenrother, T. S. Tighe, and M. Tinkham, *Phys. Rev. B* **47**, 11599 (1993).
- I. Tüttö, L. M. Kahn and J. Ruvalds, *Phys. Rev. B* **20**, 952 (1979).
- I. Tüttö and A. Zawadowski, *Phys. Rev. B* **45**, 4842 (1992).
- R. Tycko, G. Dabbagh, M. J. Rosseinsky, D. W. Murphy, R. M. Fleming, A. P. Ramirez, and J. C. Tully, *Science* **253**, 884 (1991).
- R. Tycko, G. Dabbagh, M. J. Rosseinsky, D. W. Murphy, A. P. Ramirez, and R. M. Fleming, *Phys. Rev. Lett.* **68**, 1912 (1992).
- S. Uchida, H. Takagi, K. Kitazawa and S. Tanaka, *Jpn. J. Appl. Phys.* **26**, L1 (1987).
- S. Uchida, T. Ido, H. Takagi, T. Arima, Y. Tokura and S. Tajima, *Phys. Rev. B* **43**, 7942 (1991).
- Y. J. Uemura, L. P. Le, G. M. Luke, B. J. Sternlieb, W. D. Wu, J. H. Brewer, T. M. Riseman, C. L. Seaman, M. B. Maple, M. Ishikawa, D. G. Hinks, J. D. Jorgensen, G. Saito and H. Yamochi, *Phys. Rev. Lett.* **66**, 2665 (1991).
- A. Ugawa, K. Iwasaki, A. Kawamoto, K. Yakushi, Y. Yamashita, and T. Suzuki, *Phys. Rev. B* **43**, 14718 (1991).
- C. Uher and W.-N. Huang, *Phys. Rev. B* **40**, 2694 (1989).
- C. Uher, *J. Supercond.* **3**, 337 (1990).
- C. Uher, in "Physical Properties of High Temperature Superconductors" (D. M. Ginsberg, Ed.), Vol. 3, Chap. 3, World Scientific, Singapore, 1992.
- S. Ullah, A. T. Dorsey, and L. J. Buchholtz, *Phys. Rev. B* **42**, 9950 (1990).
- S. Ullah and A. T. Dorsey, *Phys. Rev. Lett.* **65**, 2066 (1990).
- S. Ullah and A. T. Dorsey, *Phys. Rev. B* **44**, 262 (1991).
- J. S. Urbach, D. B. Mitzi, A. Kapitulnik, J. Y. T. Wei, and D. E. Morris, *Phys. Rev. B* **39**, 12391 (1989).
- A. V. Ustinov, T. Doderer, R. P. Huebener, N. F. Pederson, B. Mayer, and V. A. Oboznov, *Phys. Rev. Lett.* **69**, 1815 (1992).
- P. P. Vaishnava, C. A. Taylor, II, and C. L. Foiles, *Phys. Rev. B* **41**, 4195 (1990).
- J. M. Valles, Jr., R. C. Dynes, and J. P. Garno, *Phys. Rev. B* **40**, 6680 (1989).
- J. M. Valles, Jr., R. C. Dynes, A. M. Cucolo, M. Gurvitch, L. F. Schneemeyer, J. P. Garno, and J. V. Waszczak, *Phys. Rev. B* **44**, 11986 (1991).
- J. van den Berg, C. J. van der Beek, P. H. Kest, J. A. Mydosh, M. J. V. Menken, and A. A. Menovsky, *Supercond. Sci. Tech.* **1**, 249 (1989).
- J. van den Berg, C. J. van der Beek, P. H. Kes, J. A. Mydosh, G. J. Nieuwenhuys, and L. J. de Jongh, *Solid State Commun.* **64**, 699 (1987).
- A. M. van den Brink, G. Schön, and L. Geerligs, *Phys. Rev. Lett.* **67**, 3030 (1991).
- D. Van Der Marel, *Physica C* **165**, 35 (1990).
- H. P. van der Meulen, A. de Visser, J. J. M. Franse, T. T. J. M. Berendschot, J. A. A. J. Perenboom, H. van Kempen, A. Lacerda, P. Lejay, and J. Fouquet, *Phys. Rev. B* **44**, 814 (1991).
- H. S. J. van der Zant, F. C. Fritschy, T. P. Orlando, and J. E. Mooij, *Phys. Rev. Lett.* **66**, 2531 (1991).
- K. G. Vandervoort, U. Welp, J. E. Kessler, H. Claus, G. W. Crabtree, W. K. Kwok, A. Umezawa, B. W. Veal, J. W. Downey, A. P. Paulikas, and J. Z. Liu, *Phys. Rev. B* **43**, 13042 (1991).
- H. S. J. van der Zant, F. C. Fritschy, T. P. Orlando, and J. E. Mooij, *Phys. Rev. B* **47**, 295 (1993).
- R. B. VanDover, E. M. Gyorgy, A. E. White, L. F. Schneemeyer, R. J. Felder, and J. V. Waszczak, *Appl. Phys. Lett.* **56**, 2681 (1990).
- T. Van Duzer and C. W. Turner, "Principles of Superconductive Devices and Circuits," Elsevier, New York (1981).
- A. G. Van Vijfeijkenand and A. K. Niessen, *Philips Res. Rep.* **20**, 505 (1965a); *Phys. Lett.* **16**, 23 (1965b).
- B. J. van Wees, K.-M. H. Lenssen, and C. J. P. M. Harmans, *Phys. Rev. B* **44**, 470 (1991).
- C. M. Varma, S. Schmitt-Rink, and E. Abrahams, in "Theories of High Temperature Superconductivity" (J. W. Halley, Ed.), p. 211, Addison Wesley, Reading, MA, 1988.
- C. M. Varma, P. B. Littlewood, S. Schmitt-Rink, E. Abrahams, and A. E. Ruckenstein, *Phys. Rev. Lett.* **63**, 1996 (1989).

- B. V. Vasiliev, *J. Supercond.* **4**, 271 (1991).
- D. R. Veblen, P. J. Heaney, R. J. Angel, L. W. Finger, R. M. Hazen, C. T. Prewitt, N. L. Ross, C. W. Chu, P. H. Hor, and R. L. Meng, *Nature* **332**, 334 (1988).
- A. J. Vega, W. E. Farneth, E. M. McCarron, and R. K. Bordia, *Phys. Rev. B* **39**, 2322 (1989a).
- A. J. Vega, M. K. Crawford, E. M. McCarron, and W. E. Farneth, *Phys. Rev. B* **40**, 8878 (1989b).
- E. L. Venturini, D. S. Ginley, J. F. Kwak, R. J. Baughman, J. E. Schirber, and B. Morosin, in "High Temperature Superconductors" (D. U. Gubser and M. Schluter, Eds.), p. 97, Mater. Res. Soc., Pittsburgh, 1987.
- R. Vijayaraghavan, A. K. Ganguli, N. Y. Vasanthacharya, M. K. Rajumon, G. U. Kulkarni, G. Sankar, D. D. Sarma, A. K. Sood, N. Chandrabhas, and C. N. R. Rao, *Supercond. Sci. Technol.* **2**, 195 (1989).
- P. Villars and J. C. Phillips, *Phys. Rev. B* **37**, 2345 (1988).
- L. Ya. Vinnikov and I. V. Grigor'eva, *JETP Lett.* **47**, 106 (1988).
- V. M. Vinokur, M. V. Feigel'man, V. B. Geshkenbein, and A. I. Larkin, *Phys. Rev. Lett.* **65**, 259 (1990).
- V. M. Vinokur, M. V. Feigel'man, and V. B. Geshkenbein, *Phys. Rev. Lett.* **67**, 915 (1991).
- A. Virosztek and J. Ruvalds, *Phys. Rev. Lett.* **67**, 1657 (1991).
- V. M. Virosztek and J. Ruvalds, *Phys. Rev. B* **45**, 347 (1992).
- P. Visani, A. C. Mota, and A. Pollini, *Phys. Rev. Lett.* **65**, 1514 (1990).
- J. P. Vithayathil, D. E. MacLaughlin, E. Koster, D. L. Williams, and E. Bucher, *Phys. Rev. B* **44**, 4705 (1991).
- B. M. Vlack, M. C. Frischherz, S. Fleshler, U. Welp, J. Z. Liu, J. Downey, K. G. Vandervoort, G. W. Crabtree, M. A. Kirk, J. Giapintzakis, and J. Farmer, *Phys. Rev. Lett.* **46**, 6441 (1992).
- N. V. Volkenshteyn *et al.*, *Fiz. Met. Metalloved* **45**, 1187 (1978).
- A. R. von Hippel, "Dielectrics and Waves," p. 255, MIT Press, Cambridge, MA, 1954.
- S. von Molnár, A. Torresson, D. Kaiser, F. Holtzberg, and T. Penney, *Phys. Rev. B* **37**, 3762 (1988).
- F. von Oppen and E. K. Riedel, *Phys. Rev. Lett.* **66**, 84 (1991).
- S. V. Vonsovsky, Yu. A. Izyumov, and E. Z. Kurmaev, "Superconductivity in Transition Metals," Springer, New York (1982).
- A. Wadas, O. Fritz, H. J. Hug, and H.-J. Güntherodt, *Z. Phys. B* **88**, 317 (1992).
- S. F. Wahid and N. K. Jaggi, *Physica C* **184**, 88 (1991).
- D. R. Wake, F. Slakey, M. V. Klein, J. P. Rice, and D. M. Ginsberg, *Phys. Rev. Lett.* **67**, 3728 (1991).
- M. Wallin, *Phys. Rev. B* **41**, 6575 (1990).
- R. E. Walstedt and W. W. Warren, Jr., *Science* **248**, 1082 (1990).
- R. E. Walstedt, W. W. Warren, Jr., R. F. Bell, R. J. Cava, G. P. Espinosa, L. F. Schneemeyer, and J. V. Waszczak, *Phys. Rev. B* **41**, 9574 (1990).
- R. E. Walstedt, R. F. Bell, and D. B. Mitzi, *Phys. Rev. B* **44**, 7760 (1991).
- R. E. Walstedt, R. F. Bell, L. F. Schneemeyer, J. V. Waszczak, and G. P. Espinosa, *Phys. Rev. B* **45**, 8074 (1992).
- B. L. Walton, B. Rosenblum, and F. Bridges, *Phys. Rev. Lett.* **32**, 1047 (1974).
- Z. Wang, N. Zou, J. Pang, and C. Gong, *Solid State Commun.* **64**, 531 (1987).
- Z. Z. Wang, J. Clayhold, N. P. Ong, J. M. Tarascon, L. H. Greene, W. R. McKinnon, and G. W. Hull, *Phys. Rev.* **36**, 7222 (1987).
- S. J. Wang, S. V. Naidu, S. C. Sharma, D. K. De, D. Y. Jeong, T. D. Black, S. Krichene, J. R. Reynolds, and J. M. Owens, *Phys. Rev. B* **37**, 603 (1988).
- Y. R. Wang, *Phys. Rev. B* **40**, 2698 (1989).
- C.-P. S. Wang, in "High Temperature Superconductivity" (J. W. Lynn, Ed.), Chap. 5, Springer-Verlag, Berlin, 1990.
- Y.-Y. Wang, G. Feng, and A. L. Ritter, *Phys. Rev. B* **42**, 420 (1990).
- T. Wang, K. M. Beauchamp, D. D. Berkley, B. R. Johnson, J.-X. Liu, J. Zhang, and A. M. Goldman, *Phys. Rev. B*, **43**, 8623 (1991).
- Z. Wang, Y. Bang, and G. Kotliar, *Phys. Rev. Lett.* **67**, 2733 (1991).
- Y. Wang, A. M. Rao, J.-G. Zhang, X.-X. Bi, P. C. Eklund, M. S. Dresselhaus, P. P. Nguyen, J. S. Moodera, G. Dresselhaus, H. B. Radousky, R. S. Glass, M. J. Fluss, and J. Z. Liu, *Phys. Rev. B* **45**, 2523 (1992).
- K.-A. Wang, Y. Wang, P. Zhou, J. M. Holden, S.-L. Ren, G. T. Hager, H. F. Ni, P. C. Eklund, G. Dresselhaus, and M. S. Dresselhaus, *Phys. Rev. B* **45**, 1955 (1992).
- Z. D. Wang and C. S. Ting, *Phys. Rev. Lett.* **69**, 1435 (1992a).
- Z. D. Wang and C. S. Ting, *Phys. Rev.* **46**, 284 (1992b).
- Z. D. Wang and C.-R. Hu, *Phys. Rev. B* **44**, 11918 (1991).
- C. A. Wang, R. L. Wang, H. C. Li, H. R. Yi, C. G. Cui, S. L. Li, X. N. Jing, J. Li, P. Xu, and L. Li, *Physica C* **191**, 52 (1992).
- Z. H. Wang, A. W. P. Fung, G. Dresselhaus, M. S. Dresselhaus, K. A. Wang, P. Zhou, and P. C. Eklund, *Phys. Rev. B* **47**, 15354 (1993).
- N. L. Wang, Y. Chong, C. Y. Wang, D. J. Huang, Z. Q. Mao, L. Z. Cao, and Z. J. Chen, *Phys. Rev. B* **47**, 3347 (1993).
- Y. Watanabe, Z. Z. Wang, S. A. Lyon, D. C. Tsui, N. P. Ong, J. M. Tarascon, and P. Barbour, *Phys. Rev. B* **40**, 6884 (1989).
- Y. Watanabe, D. C. Tsui, J. T. Birmingham, N. P. Ong, and J. M. Tarascon, *Phys. Rev. B* **43**, 3026 (1991).

- K. Watanabe, S. Awaji, N. Kobayashi, H. Yamane, T. Hirai, and Y. Muto, *J. Appl. Phys.* **69**, 1543 (1991).
- J. H. P. Watson, *J. Appl. Phys.* **39**, 3406 (1968).
- H. L. Watson and R. P. Huebener, *Phys. Rev. B* **10**, 4577 (1974).
- C. H. Watson, D. A. Browne, J.-C. Xu, and R. G. Goodrich, *Phys. Rev. B* **40**, 8885 (1989).
- W. J. Wattamaniuk, J. P. Tidman, and R. F. Frindt, *Phys. Rev. Lett.* **35**, 62 (1975).
- B. D. Weaver, J. M. Pond, D. B. Chrisey, J. S. Horwitz, H. S. Newman, and G. P. Summers, *Appl. Phys. Lett.* **58**, 1563 (1991).
- W. Weber, *Phys. Rev. Lett.* **58**, 1371 (1987).
- W. Weber, *Z. Phys. B* **70**, 323 (1988).
- H. Weber and P. Minnhagen, *Phys. Rev. B* **38**, 8730 (1988).
- W. H. Weber, C. R. Peters, B. M. Wanklyn, C. Chen, and B. E. Watts, *Phys. Rev.* **38**, 917 (1988).
- W. H. Weber, C. R. Peters, and E. M. Logothetis, *J. Opt. Soc. Am. B* **6**, 455 (1989).
- W. H. Weber and G. W. Ford, *Phys. Rev. B* **40**, 6890 (1989).
- H. Weber and H. J. Jensen, *Phys. Rev. B* **44**, 454 (1991).
- M. Weger, *Rev. Mod. Phys.* **36**, 175 (1964).
- H. Weinstock, *IEEE Trans. Magn.* **27**, 3231 (1991).
- B. O. Wells, Z.-X. Shen, D. S. Dessau, W. E. Spicer, C. G. Olson, D. B. Mitzi, A. Kapitulnik, R. S. List, and A. Arko, *Phys. Rev. Lett.* **65**, 3056 (1990).
- U. Welp, W. K. Kwok, G. W. Crabtree, K. G. Vandervoort, and J. Z. Liu, *Phys. Rev. Lett.* **62**, 1908 (1989); *Phys. Rev. B* **40**, 5263 (1989).
- U. Welp, S. Fleshler, W. K. Kwok, J. Downey, Y. Fang, G. W. Crabtree, and J. Z. Liu, *Phys. Rev. B* **42**, 10189 (1990).
- Z. Y. Weng, C. S. Ting, and T. K. Lee, *Phys. Rev. B* **41**, 1990 (1990).
- F. Wenger and S. Östlund, *Phys. Rev. B* **47**, 5977 (1993).
- F. Werfel, G. Dräger, J. A. Leiro, and K. Fischer, *Phys. Rev. B* **45**, 4957 (1992).
- S. Wermbter and L. Tewordt, *Phys. Rev. B* **44**, 9524 (1991); *Physica C* **183**, 365 (1991).
- N. R. Werthamer, *Phys. Rev.* **132**, 2440 (1963).
- M.-H. Whangbo and C. C. Torardi, *Acct. Chem. Res.* **24**, 127 (1991).
- J. M. Wheatley, T. C. Hsu, and P. W. Anderson, *Phys. Rev. B* **37**, 5897 (1988).
- A. Widom, Y. N. Srivastava, C. Vittoria, H. How, R. Karim, and H. Jiang, *Phys. Rev. B* **46**, 1102 (1992).
- R. J. Wijngaarden, E. N. van Eenige, J. J. Scholtz, and R. Griessen, *High Pressure Res.* **3**, 105 (1990).
- F. Wilczek, *Phys. Rev. Lett.* **48**, 1144 (1982a).
- F. Wilczek, *Phys. Rev. Lett.* **49**, 957 (1982b).
- N. K. Wilkin and M. A. Moore, *Phys. Rev. B* **48**, 3464 (1993).
- G. P. Williams, R. C. Budhani, C. J. Hirschmugl, G. L. Carr, S. Perkowitz, B. Lou, and T. R. Yang, *Phys. Rev. B* **41**, 4752 (1990).
- P. J. Williams and J. P. Carbotte, *Phys. Rev. B* **43**, 7960 (1991).
- M. N. Wilson, "Superconducting Magnets," Clarendon Press, Oxford, 1983.
- A. Wittlin, L. Genzel, M. Cardona, M. Bauer, W. König, E. Garcia, M. Barahona, and M. V. Cabañas, *Phys. Rev. B* **37**, 652 (1988).
- T. Wittmann and J. Stolze, *Phys. Rev. B* **48**, 3479 (1993).
- S. A. Wolf and V. Z. Kresin, Eds., "Novel Superconductivity," Plenum, New York, 1987.
- Y. Wolfus, Y. Yeshurun, I. Felner, and H. Sompolinsky, *Phys. Rev. B* **40**, 2701; see *B* **39**, 11690 (1989).
- H. Won and K. Maki, *Phys. Rev. B* **49**, 1397 (1994).
- R. F. Wood and J. F. Cooke, *Phys. Rev. B* **45**, 5585 (1992).
- F. Wooten, "Optical Properties of Solids," p. 244, Academic Press, New York, 1972.
- R. Wördenweber, *Phys. Rev. B* **46**, 3076 (1992).
- A. H. Worsham, N. G. Ugras, D. Winkler, D. E. Prober, N. R. Erickson, and P. F. Goldsmith, *Phys. Rev. Lett.* **67**, 3034 (1991).
- T. K. Worthington, W. J. Gallagher, and T. R. Dinger, *Phys. Rev. Lett.* **59**, 1160 (1987).
- W. H. Wright, D. J. Holmgren, T. A. Friedmann, M. P. Maher, B. G. Pazol, and D. M. Ginsberg, *J. Low Temp. Phys.* **68**, 109 (1987).
- M. K. Wu, J. R. Ashburn, C. J. Torng, P. H. Hor, R. L. Meng, L. Gao, Z. J. Huang, Y. Q. Wang, and C. W. Chu, *Phys. Rev. Lett.* **58**, 908 (1987).
- J. Z. Wu, C. S. Ting, and D. Y. Xing, *Phys. Rev. B* **40**, 9296 (1989).
- D.-H. Wu and S. Sridhar, *Phys. Rev. Lett.* **65**, 2074 (1990).
- J. Z. Wu, C. S. Ting, W. K. Chu, and X. X. Yao, *Phys. Rev. B* **44**, 411 (1991a).
- J. Z. Wu, P. Y. Hsieh, A. V. McGuire, D. L. Schmidt, L. T. Wood, Y. Shen, and W. K. Chu, *Phys. Rev. B* **44**, 12643 (1991b).
- Z. Y. Wu, M. Benfatto, and C. R. Natoli, *Phys. Rev. B* **45**, 531 (1992).
- D. H. Wu, J. Mao, S. N. Mao, J. L. Peng, X. X. Xi, T. Venkatesan, R. L. Greene, and S. M. Anlage, *Phys. Rev., Lett.* **70**, 85 (1993).
- R. W. G. Wyckoff, "Crystal Structures," Vol. 1, Wiley, New York, 1963.
- R. W. G. Wyckoff, "Crystal Structures," Vol. 2, Wiley, New York, 1964.
- R. W. G. Wyckoff, "Crystal Structures," Vol. 3, Wiley, New York, 1965.
- R. W. G. Wyckoff, "Crystal Structures," Vol. 4, Wiley, New York, 1968.
- D. G. Xenikos and T. R. Lemberger, *Phys. Rev. B* **41**, 869 (1990).
- T.-K. Xia and D. Stroud, *Phys. Rev. B* **39**, 4792 (1989).
- W. Xia and P. L. Leath, *Phys. Rev. Lett.* **63**, 1428 (1989).
- G. Xiao, F. H. Streitz, A. Gavrin, Y. W. Du, and C. L. Chien, *Phys. Rev. B* **35**, 8782 (1987a).

- G. Xiao, F. H. Streitz, A. Gavrin, M. Z. Cieplak, J. Childress, M. Lu, A. Zwicker, and C. L. Chien, *Phys. Rev. B* **36**, 2382 (1987b).
- G. Xiao, M. Z. Cieplak, and C. L. Chien, *Phys. Rev. B* **40**, 4538 (1989).
- D. Y. Xing and M. Liu, *Phys. Rev. B* **43**, 3744 (1991).
- Q. Xiong, Y. Y. Xue, Y. Cao, F. Chen, Y. Y. Sun, J. Gibson, L. M. Liu, A. Jacobson, and C. W. Chu, *Phys. Rev. Lett.*, in press (1994).
- Y. Xu, M. Suenaga, A. R. Moodenbaugh, and D. O. Welch, *Phys. Rev. B* **40**, 10882 (1989).
- Y. Xu, M. Suenaga, Y. Gao, J. E. Crow, and N. D. Spencer, *Phys. Rev. B* **42**, 8756 (1990).
- M. Xu, D. Shi, and R. F. Fox, *Phys. Rev. B* **42**, 10773 (1990).
- Y. Xu and M. Suenaga, *Phys. Rev. B* **43**, 5516 (1991).
- Y.-N. Xu, M.-Z. Huang, and W. Y. Ching, *Phys. Rev. B* **44**, 13171 (1991).
- X.-Q. Xu, S. J. Hagen, W. Jiang, J. L. Peng, Z. Y. Li, and R. Greene, *Phys. Rev. B* **45**, 7356 (1992).
- J. V. Yakhmi and R. M. Iyer, in "High Temperature Superconductors" (S. K. Malik and S. S. Shah, Eds.), Nova Sci., New York, 1992.
- J. V. Yakhmi, "Chemistry and Physics of Fullerenes," in "Atomic and Molecular Physics," (S. A. Ahmad, Ed.) Narosa Publishing, New Delhi, India, 1994.
- K. Yamada, K. Kakurai, Y. Endoh, T. R. Thurston, M. A. Kaster, R. J. Birgeneau, G. Shirane, Y. Hidaka, and T. Murakami, *Phys. Rev. B* **40**, 4557 (1989).
- K. Yamamoto, H. Mazaki, H. Yasuoka, S. Kat-suyama, and K. Kosuge, *Phys. Rev.* **46**, 1122 (1992).
- K. Yamamoto, H. Mazaki, and H. Yasuoka, *Phys. Rev. B* **47**, 915 (1993).
- H. Yamasaki, K. Endo, S. Kosaka, M. Umeda, S. Yoshida, and K. Kajimura, *Phys. Rev. Lett.* **70**, 3331 (1993).
- Y. Yan and M. G. Blanchin, *Phys. Rev. B* **43**, 13717 (1991).
- K. N. Yang, J. M. Ferreira, B. W. Lee, M. B. Maple, W.-H. Li, J. W. Lynn, and R. W. Erwin, *Phys. Rev. B* **40**, 10963 (1989).
- C. Y. Yang, A. R. Moodenbaugh, Y. L. Wang, Y. Xu, S. M. Heald, D. O. Welch, D. A. Fischer, and J. E. Penner-Hahn, *Phys. Rev. B* **42**, 2231 (1990).
- I.-S. Yang, G. Burns, F. H. Dacol, and C. C. Tsuei, *Phys. Rev. B* **42**, 4240 (1990).
- S. Yarlagadda and S. Kurihara, *Phys. Rev. B* **48**, 10567 (1993).
- Z. Ye and S. Sachdev, *Phys. Rev. B* **44**, 10173 (1991).
- Z. Ye, H. Umezawa, and R. Teshima, *Phys. Rev. B* **44**, 351 (1991).
- W.-J. Yeh, L. Chen, F. Xu, B. Bi, and P. Yang, *Phys. Rev. B* **36**, 2414 (1987).
- N.-C. Yeh and C. C. Tsuei, *Phys. Rev. B* **39**, 9708 (1989); N.-C. Yeh, *Phys. Rev. B* **40**, 4566 (1989).
- J.-J. Yeh, L. Lindau, J.-Z. Sun, K. Char, M. Missert, A. Kapitulnik, T. H. Geballe, and M. R. Beasley, *Phys. Rev. B* **42**, 8044 (1990).
- N.-C. Yeh, *Phys. Rev. B* **42**, 4850 (1990).
- N.-C. Yeh, *Phys. Rev. B* **43**, 523 (1991).
- J.-J. Yeh, *Phys. Rev. B* **45**, 10816 (1992).
- N.-C. Yeh, W. Jiang, D. S. Reed, A. Gupta, F. Holtzberg, and A. Kussmaul, *Phys. Rev. B* **45**, 5710 (1992b).
- N.-C. Yeh, D. S. Reed, W. Jinag, U. Kriplani, F. Holtzberg, A. Gupta, B. D. Hunt, R. P. Vasquez, M. C. Foote, and L. Bajuk, *Phys. Rev. B* **45**, 5654 (1992a).
- Y. Yeshurun, A. P. Malozemoff, F. Holtzberg, and T. R. Dinger, *Phys. Rev. B* **38**, 11828 (1988).
- S.-K. Yip, O. F. DeA. Bonfim, and P. Kumar, *Phys. Rev. B* **41**, 11214 (1990).
- F. Yndurain and G. Martínez, *Phys. Rev. B* **43**, 3691 (1991).
- M. Yoshimoto, H. Koinuma, T. Hashimoto, J. Tanaka, S. Tanabe, and N. Soga, *Physica C* **181**, 284 (1991).
- M. Yoshimura, H. Shigekawa, H. Nejoh, G. Saito, Y. Saito, and A. Kawazu, *Phys. Rev. B* **43**, 13590 (1991).
- J. Yu, A. J. Freeman, and S. Massidda, in "Novel Superconductivity" (S. A. Wolf and V. Z. Kresin, Eds.), p. 367, Plenum, New York, 1987.
- R. C. Yu, M. J. Naughton, X. Yan, P. M. Chaikin, F. Holtzberg, R. L. Greene, J. Stuart, and P. Davies, *Phys. Rev. B* **37**, 7963 (1988).
- G. Yu, C. H. Lee, A. J. Heeger, N. Herron, and E. M. McCarron, *Phys. Rev. Lett.* **67**, 2581 (1990).
- J. Yu, A. J. Freeman, R. Podloucky, P. Herzig, and P. Weinberger, *Phys. Rev. B* **43**, 532 (1991).
- X.-J. Yu and M. Sayer, *Phys. Rev. B* **44**, 2348 (1991).
- R. C. Yu, J. M. Williams, H. H. Wang, J. E. Thompson, A. M. Kini, K. D. Carlson, J. Ren, M.-H. Whangbo, and P. M. Chaikin, *Phys. Rev. B* **44**, 6932 (1991).
- W. Yu, E. B. Harris, S. E. Hebboul, J. C. Garland, and D. Stroud, *Phys. Rev. B* **45**, 12624 (1992).
- B. D. Yu, H. Kim, and J. Ihm, *Phys. Rev. B* **45**, 8007 (1992).
- G. Yu, C. H. Lee, A. J. Heeger, N. Herron, E. M. McCarron, L. Cong, G. C. Spalding, C. A. Nordman, and A. M. Goldman, *Phys. Rev. B* **45**, 4964 (1992).
- R. C. Yu, M. B. Salamon, J. P. Lu, and W. C. Lee, *Phys. Rev. Lett.* **69**, 1431 (1992).
- J. Yuan, L. M. Brown, W. Y. Liang, R. S. Liu, and P. P. Edwards, *Phys. Rev. B* **43**, 8030 (1991).
- B. J. Yuan and J. P. Whitehead, *Phys. Rev. B* **44**, 6943 (1991).
- K. Yvon and M. François, *Z. Phys. B* **76**, 413 (1989).
- A. A. Zakhidov, A. Ugawa, K. Imaeda, K. Yakushi, H. Inokuchi, K. Kikuchi, I. Ikemoto, S. Suzuki, and Y. Achiba, *Solid State Commun.* **79**, 939 (1991).
- M. Zeh, H.-C. Ri, F. Kober, R. P. Huebener, J. Fischer, R. Gross, H. Müller, T. Sermet, A. V. Ustinov, and H.-G. Wener, *Physica C* **167**, 6 (1990).

- E. Zeldov, N. M. Amer, G. Koren, A. Gupta, R. J. Gambino, and M. W. McElfresh, *Phys. Rev. Lett.* **62**, 3093 (1989).
- H. R. Zeller and I. Giaever, *Phys. Rev.* **181**, 789 (1969).
- X. C. Zeng, D. Stroud, and J. S. Chung, *Phys. Rev. B* **43**, 3042 (1991).
- R. Zeyher, *Phys. Rev. B* **44**, 10404 (1991).
- F. C. Zhang and T. M. Rice, *Phys. Rev. B* **37**, 3759 (1988).
- L. Zhang, M. Ma, and F. C. Zhang, *Phys. Rev. B* **42**, 7894 (1990).
- J.-G. Zhang, X.-X. Bi, E. McRae, P. C. Eklund, B. C. Sales, and M. Mostoller, *Phys. Rev. B* **43**, 5389 (1991a).
- Z. Zhang, C.-C. Chen, and C. M. Lieber, *Science* **254**, 1619 (1991).
- H. Zhang, J. W. Lynn and D. E. Morris, *Phys. Rev. B* **45**, 10022 (1992).
- L. Zhang, J. Z. Liu, and R. N. Shelton, *Phys. Rev. B* **45**, 4978 (1992).
- L. Zhang, J. K. Jain, and V. J. Emery, *Phys. Rev. B* **47**, 3368 (1993).
- Z. Zhang and C. M. Lieber, *Phys. Rev. B* **47**, 3423 (1993).
- H. Zhang and H. Sato, *Phys. Rev. Lett.* **70**, 1697 (1993).
- Z. Zhao, L. Chen, Q. Yang, Y. Huang, G. Chen, R. Tang, G. Liu, C. Cui, L. Chen, L. Wang, S. Guo, S. Li, and J. Bi, in "Cooper Oxide Superconductors" (C. P. Poole, Jr., T. Datta, and H. A. Farach, Eds.), p. 274, Wiley, New York, 1987.
- Z. Zhao, F. Behrooz, S. Adenwalla, Y. Guan, J. B. Ketterson, B. K. Sarma, and D. G. Hinks, *Phys. Rev. B* **43**, 13720 (1991).
- B.-R. Zhao, S.-I. Kuroyamaru, Y. Horie, E. Yanada, T. Aomine, X.-G. Qiu, Y.-Z. Zhang, Y.-Y. Zhao, P. Xu, L. Li, H. Ohkubo, and S. Mase, *Physica C* **179**, 138 (1991).
- G. L. Zhao and J. Callaway, *Phys. Rev. B* **49**, 6424 (1994).
- C. Zhaojia, Z. Yong, Y. Hongshun, C. Zuyao, Z. Donquin, Q. Yitai, W. Baimei, and Z. Qirui, *Solid State Commun.* **64**, 685 (1987).
- H. Zheng, M. Avignon, and K. H. Bennemann, *Phys. Rev. B* **49**, 9763 (1994).
- X. Zhengping, J. Chunlin, and Z. Lian, *J. Supercond.* **3**, 421 (1990).
- H. Zhou, J. Rammer, P. Schleger, W. N. Hardy, and J. F. Carolan, *Phys. Rev. B* **43**, 7968 (1991).
- P. Zhou, K.-A. Wang, A. M. Rao, P. C. Eklund, G. Dresselhaus, and M. S. Dresselhaus, *Phys. Rev. B* **45**, 10838 (1992).
- J. Zhou and S. G. Chen, *Phys. Rev. B* **47**, 8301 (1993).
- D.-M. Zhu, A. C. Anderson, E. D. Bukowski, and D. M. Ginsberg, *Phys. Rev. B* **40**, 841 (1989).
- D.-M. Zhu, A. C. Anderson, T. A. Friedmann, and D. M. Ginsberg, *Phys. Rev. B* **41**, 6605 (1990).
- S. Zhu, D. K. Christen, C. E. Klabunde, J. R. Thompson, E. C. Jones, R. Feenstra, D. H. Lowndes, and D. P. Norton, *Phys. Rev. B* **46**, 5576 (1992).
- Y. Zhu in "High Temperature Superconducting Materials Science and Engineering," (D. Shi, Ed.), Pergamon, New York, 1994.
- G. T. Zimanyi and K. S. Bedell, *Phys. Rev. B* **48**, 6575 (1993).
- P. Zolliker, D. E. Cox, J. B. Parise, E. M. McCarron III, and W. E. Farneth, *Phys. Rev. B* **42**, 6332 (1990).
- X. Zotos, P. Prelovšek, and I. Sega, *Phys. Rev. B* **42**, 8445 (1990).
- Z. Zou and P. W. Anderson, *Phys. Rev. B* **37**, 627 (1988); (reprinted in Halley, 1988, p. 163).
- V. E. Zubkus, E. E. Tornau, S. Lapinskas, and P. J. Kundrotas, *Phys. Rev. B* **43**, 13112 (1991).
- F. Zuo, M. B. Salamon, T. Datta, K. Ghiron, H. Duan, and A. M. Hermann, *Physica C* **176**, 541 (1991).
- W. Zwerger, *Phys. Rev. B* **42**, 2566 (1990).

Hars
excel
of su
othe
sever
prese
table
Para
rame
ties,
Stanc
plots
lated
ature
shoul
ences
T
are ti
partic
penet
tracte
phase

**This Page is Inserted by IFW Indexing and Scanning
Operations and is not part of the Official Record**

BEST AVAILABLE IMAGES

Defective images within this document are accurate representations of the original documents submitted by the applicant.

Defects in the images include but are not limited to the items checked:

☒ **BLACK BORDERS**

☐ **IMAGE CUT OFF AT TOP, BOTTOM OR SIDES**

☒ **FADED TEXT OR DRAWING**

☐ **BLURRED OR ILLEGIBLE TEXT OR DRAWING**

☐ **SKEWED/SLANTED IMAGES**

☒ **COLOR OR BLACK AND WHITE PHOTOGRAPHS**

☐ **GRAY SCALE DOCUMENTS**

☒ **LINES OR MARKS ON ORIGINAL DOCUMENT**

☐ **REFERENCE(S) OR EXHIBIT(S) SUBMITTED ARE POOR QUALITY**

☐ **OTHER:** _____

IMAGES ARE BEST AVAILABLE COPY.

As rescanning these documents will not correct the image problems checked, please do not report these problems to the IFW Image Problem Mailbox.